AD-A205 363

EXTENDED ABSTRACTS

VOLUME 88-2

Battery
Corrosion
Dielectrics and Insulation
Electrodeposition
Electronics
Energy Technology
High Temperature Materials
Luminescence and Display Materials
Physical Electrochemistry
Sensors

DTIC
ELECTE
DEC 0 1 1988
S D

DISTRIBUTION STATEMENT A
Approved for public release
Distribution Unlimited

88 11 29 018



FALL MEETING

CHICAGO, ILLINOIS

DISCLAIMER NOTICE

THIS DOCUMENT IS BEST QUALITY PRACTICABLE. THE COPY FURNISHED TO DTIC CONTAINED A SIGNIFICANT NUMBER OF PAGES WHICH DO NOT REPRODUCE LEGIBLY.

BEST
AVAILABLE COPY

(1)

$40 00 P...

EXTENDED ABSTRACTS

VOLUME 88-2

N00014-88-J-1175

Battery
Corrosion
Dielectrics and Insulation
Electrodeposition
Electronics
Energy Technology
High Temperature Materials
Luminescence and Display Materials
Physical Electrochemistry
Sensors

DTIC
ELECTE
DEC 0 1 1988
S D
CD

DISTRIBUTION STATEMENT A
Approved for public release
Distribution Unlimited

88 11 29 013



FALL MEETING

CHICAGO, ILLINOIS

OCTOBER 9–14, 1988

Copyright 1988

by

The Electrochemical Society, Inc.

Presentation of a paper at a Technical Meeting of this Society does not guarantee publication in full by the Society. Extended Abstracts contained herein may not be reprinted and may not be digested by publications other than those of The Electrochemical Society in excess of 1/6 of the material presented.

* * * * * * * *

Not all illustrations to be presented during paper delivery are reproduced here. Production limitations to this volume caused illustration reduction to a point where a phenomenon described by the author may have, in some cases, been lost in reproduction. All magnifications are those existing before photographic reduction.

DTIC COPY INSPECTED 6

Accession For
NTIS GRA&I
DTIC TAB
Unannounced
Justification
By
Distribution/
Availability Codes
Dist | Avail and/or Special
A-1 21

Printed in the United States of America

Sold by:
The Electrochemical Society, Inc.
10 South Main Street
Pennington, NJ 08534-2896
Price: $40.00
First Class Shipping: $5.00

Abstract Number		Page Number
	BATTERY	
	Applications of Mathematical Models to the Development of Batteries	
1	Nucleation of Lead Sulfate in Porous Lead-Dioxide Electrodes D. M. Bernardi	1
2	A Mathematical Model for Discharge, Charge and Self-Discharge of a Lead Acid Cell N. R. Compangnone	3
3	Application of Transmission Line Analysis to Porous Battery Electrodes D. D. Macdonald, S. J. Lenhart, and B. G. Pound	4
4	The Effect of Sinter Rupture on Capacity Retention in the Nickel Oxide Electrode O. Lanzi and U. Landau	5
5	A Mathematical Model of a Zinc Bromine Flow Cell R. V. Shenov and J. M. Fenton	7
6	Mathematical Model of the Secondary Zn/NiOOH Cell K. G. Miller, F. R. McLarnon, and E. J. Cairns	8
7	Mathematical Model of the Secondary Current Distribution Mechanism for Zn Material Redistribution M. J. Isaacson, F. R. McLarnon, and E. J. Cairns	9
8	A Model of the Time-Dependent Response of Li/MnO_2 Batteries A. M. Creepir, D. R. Merritt, and P. M. Skarstad	11
9	A Mathematical *Model of a Lithium/Thionyl* Chloride Primary Cell T. I. Evans, T. V. Nguyen, and R. E. White	13
10	A Thermal Analysis of a Spirally Wound Battery Using a Simple Mathematical Model T. I. Evans and R. E. White	14
11	Modeling Studies of the Short Time/High Frequency Behavior of Pulse Batteries M. L. Daroux, B. D. Cahan, J. P. Discenza, and E. B. Yeager	15
12	Model for Leakage Current in a Bipolar Stack with Separate Electrolyte Loops H. Wu, M. Z. Yang, and J. R. Selman	17
13	Modeling of Chlorine Gas-Diffusion D. L. Thomas	19
14	Effect of Gas Bubbles on the Polarization Behavior of Porous Flow-Through Electrodes B. G. Ateya and B. E. El-Anadouli	20
15	Mathematical Modeling of High Power Density, Pulsed Discharge Lead Acid Batteries R. M. LaFollette and D. N. Bennion	21
	Materials and Processes for Lithium Batteries	
16	Inorganic Cells Utilizing Solvents Based on Combinations of SO_2 and Halogens S. Gilman and M. Binder	23
17	Electroreduction of $SOCl_2$: The Pt/LiCl - $AlCl_3$ - $SOCl_2$ System P. A. Mosier-Boss, S. Szpak, J. J. Smith, and R. J. Nowak	24
18	Investigation of High Rate Thionyl Chloride Cathode Collectors J. C. Bailey and G. E. Blomgren	26
19	The Voltage Delay in Li/$SOCl_2$ Cells G. Eichinger and W. Gabriel	27
20	Polymer Electrolyte-Based Lithium Batteries - A Review A. Hooper	29

Abstract Number		Page Number
21	Electrode and Electrolyte Materials for Polymer-Based Lithium Batteries B. Scrosati	30
22	Polymeric Solid Electrolytes: Microscopic Models and Motion Mechanisms M. A. Ratner and A. Nitzan	31
23	Polyphosphazene-Based Solid-State Secondary Lithium Batteries M. Alamgir, R. K. Reynolds, and K. M. Abraham	32
24	Effect of Gamma-Radiation on the Structure and Ionic Conductivity of 2-(2-Methoxy-Ethoxy-Ethoxy) Polyphosphazene + Lithium Salts G. Nazri and S. P. Meibuhr	34
25	Secondary Lithium Solid Polymer Electrolyte Cells K. A. Fix and A. F. Sammells	36
26	Implantable Power Sources--An Overview C. F. Holmes	37
27	Lithium Secondary Batteries: Role of Polymer Cathode Morphology K. Naoi, T. Osaka, and B. B. Owens	38
28	A Comparison of Lithium Ion-Conducting and Divalent Ion-Conducting Polymer Electrolytes in Secondary Solid-State Batteries A. Gilmour, M. Z. A. Munshi, B. B. Owens, and W. H. Smyrl	39
29	Li-Reactivity of Silicate Glasses: Influence of Glass Composition W. R. Cieslak, B. L. Maschhoff, and N. R. Armstrong	40
30	A Comparison of Lithium, Magnesium, and Calcium Anodes in Bromine Trifluoride K. H. Park, D. E. Stilwell, D. E. Bliss, R. A. Hollins, and M. H. Miles	42
31	An Ambient Temperature Solvated Electron Lithium Electrode for Secondary Batteries F. A. Uribe and A. F. Sammells	44
32	Reliability of Commercial Lithium Button Cells J.-P. Randin	45
33	Lithium Diffusion in Silver Vanadium Oxide E. S. Takeuchi and W. C. Thiebolt III	47
34	Impedance Studies of Alkali-Metal Electrodes in Nonaqueous Electrolytes T. R. Jow and L. W. Shacklette	49
35	Thin Film Positive Electrodes for Lithium-Iron Sulfide Batteries Produced by Atmospheric Pressure Chemical Vapor Deposition A. Petric, S. Crouch-Baker, R. M. Emerson, T. M. Gur, and R. A. Huggins	50
36	Discharge Behavior and Thermal Stability of Synthetic FeS_2 Cathode Material J. P. Pemsler, S. Dallek, B. F. Larrick, B. C. Beard, J. K. Litchfield, and R. K. F. Lam	51
37	Polymer Electrodes for Battery Applications L. W. Shacklette, T. R. Jow, M. Maxfield, and R. Hatami	53
38	Electrochemical and Stability Studies of the New Highly Conducting N-$(CH)_x$ R. Huq, G. C. Farrigton, J. Foreman, K. Wu, and N. Theorphilou	54
39	Intercalation Reactions of Monovalent and Divalent Cations in V_6O_{13} Single Crystals M. Z. A. Munshi, A. Gilmour, B. B. Owens, and W. H. Smyrl	55
40	The Influence of Additives on the Cycleability of the Li Anode L. A. Dominey, J. L. Goldman, and V. R. Koch	56
41	Investigation of Mixed Solvent Electrolytes for Ambient Temperature Secondary Lithium Cells D. H. Shen, S. Subbarao, F. Deligiannis, and G. Halpert	57

Abstract Number		Page Number
42	Electrochemical Oxidation of Lithium Bromide in $LiAsF_6$/Tetrahydrofuran Solutions W. K. Behl	59
43	Metal Halide Reducible Cathode Studies in Rechargeable Lithium Cells D. Reisner and M. Eisenberg	60
44	Rechargeable Lithium Battery Systems: An Overview F. B. Tudron	61
45	New Molybdenum Chalcogenides as Cathodes for Rechargeable Lithium Batteries D. M. Pasquariello, E. B. Willstaedt, and K. M. Abraham	63
46	Electrochemical Studies of TiS_2 and $NbSe_3$ Cathode Materials G. Nagasubramanian, B. V. Ratnakumar, S. Di Sefano, and C. P. Bankston	65
47	Development of Overcharge Tolerance in Li/FeS and Li/FeS_2 Cells T. D. Kaun, T. F. Holifield, M. Nigohosian, and P. A. Nelson	67
48	Chemical Overcharge/Overdischarge Protection for Li-Alloy/Transition-Metal Monosulfide Cells L. Redey	69
49	Lithium/Disulfide Cells Capable of Long Cycle Life T. D. Kaun, T. F. Holifield, and W. H. DeLuca	71
	Progress in High Power Density and Regenerative Fuel Cell Technology	
50	Fuel Cells as Energy Storage Devices for Multimegawatt Space Power Systems G. Hagey	73
51	Development of Monolithic Solid Oxide Fuel Cells for Aerospace Applications N. Q. Minh	75
52	Polarization Study of Fuel Cell with Four Reference Electrodes K. Mitsuda, H. Shiota, J. Aragane, and T. Murahashi	77
53	European Regenerative Fuel Cell (RFC) Technologies for Space Use R. Philippi, F. Baron, and W. Tillietz	79
54	Progress in High Power Density Fuel Cells S. Srinivasan and E. A. Ticianelli	80
55	Effects of Low Levels of CO on the Performance of PEM Fuel Cells S. Gottesfeld, M. T. Paffett, and J. Pafford	81
56	Modification of the Structure of Hydrogen Electrode Catalyst Particles Bonded to Solid Polymer Electrolytes S. D. Fritts and R. F. Savinell	82
57	Effect of Platinum Catalyst Distribution on the Performance of Solid Polymer Electrolyte Fuel Cells E. A. Ticianelli, J. G. Beery, and S. Srinivasan	84
58	Simulation of Oxygen Electrode Reactions in Molten Carbonate Fuel Cells P. K. Adamuvor, B. Dave, R. E. White, and A. J. Appleby	86
59	SNIFTIRS Study at Polycrystalline Pt and Au Surfaces in Aqueous Nafion Solutions M. Razaq, D. Chu, D. Gervasio, and E. B. Yeager	88
60	Ion Solvent Transport in Ion-Exchange Membranes I. A Macrohomogeneous Mathematical Model M. W. Verbrugge and R. F. Hill	90
61	Ion and Solvent Transport in Ion-Exchange Membranes II. A Radiotracer Study of the Sulfuric-Acid, Nafion-117 System M. W. Verrugge and R. F. Hill	92

Abstract Number		Page Number
62	A Dynamical Model of Porous Gas Diffusion Electrodes I. D. Raistrick and T. E. Springer	94
	General Session	
63	Bromine Transport in Zinc-Bromine Battery Separators J. McBreen	96
64	Zinc/Bromine Battery Electrolyte Investigations J. J. Bolstad and K. Yaccarino	97
65	Improved Chloride Tolerance at the H_2-Cl_2 Anode E. J. Taylor and E. Anderson	99
66	The Potentiodynamic Behavior of Lead in 5M Sulfuric Acid E. R. Gonzalez, G. Tremiliosi-Filho, L. A. Avaca, and C. V. D'Alkaine	101
67	Stibine Removal from Lead-Acid (Pb-Sb) Batteries N. Lindsey, A. H. Le, and C. M. Dacres	103
68	Automotive Battery Status Monitor T. Palanisamy and S. Mendelson	104
69	An Impedance Study of the Electrodis olution of Aluminum in 45 KOH at 25°C D. D. Macdonald, M. Urquidi-Ma donald, and S. Real	105
70	Morphological-Absorptive Characteristics of PAFC Anodes N. Giordano, E. Passalacqua, P. Staiti, H. Mirzaian, E. Recupero, E. Alderucci, Z. Poltarzewski, M. Vivaldi, E. J. Taylor, and G. Wilemski	106
71	Performance and Optimization of Phosphoric Acid Fuel Cell Gas-Diffusion Cathodes N. Giordano, E. Passalacqua, P. Staiti, H. Mirzaian, E. Recupero, E. Alderucci, R. Di Leonardo, M. Vivaldi, G. Wilemski, and E. J. Taylor	108
72	Development of Porous Gas Diffusion Electrodes for Oxygen Reduction in Alkaline Media E. J. Taylor, G. Moniz, M. Clawson, E. Anderson, and G. Wilemski	110
73	Methane Activation to C_2 Hydrocarbon Species in Solid Oxide Fuel Cell A. F. Sammells and N. U. Pujare	112
74	Organic Cathode Materials in Sodium Batteries B. V. Ratnakumar, S. Di Stefano, G. Nagasubramanian, R. M. Williams, and C. P. Bankston	113
75	Electrochemical Investigations of Organodisulfides M. Liu, S. J. Visco, and L. C. De Jonghe	115
76	Effect of R Groups on Na/RSSR Battery Characteristics S. J. Visco and L. C. De Jonghe	116
77	X-Ray Absorption Study of -Nickel Hydroxides P. L. Loyselle, B. C. Cornilsen, R. A. Condrate, and J. C. Phillips	117
78	In Situ Raman Spectra of the Nickel Electrode B. C. Cornilsen and P. L. Loyselle	118
79	Structural Influence of Cobalt Addition to the Nickel Electrode X. Shan, P. L. Loyselle, and B. C. Cornilsen	120
80	Effect of Cobalt on Fibrous Nickel Hydroxide Electrodes H. H. Law and J. Sapjeta	121
81	Impedances of Nickel Hydroxide Electrodes as Functions of Potential and Electrode Type M. A. Reid	122
82	AC-Impedence Studies on Nickel Oxide Electrode K. A. Murugesamoorthi, Y. J. Kim, S. Srinivasan, and A. J. Appleby	124

Abstract Number		Page Number
83	Effects of Hydrogen on the Self-Discharge of Nickel Oxide Electrodes Y. J. Kim, K. A. Murugesamoorthi, S. Srinivasen, and A. J. Appleby.....	125
84	On the Nature of Cadmium Electrode Capacity Fading D. H. Fritts and R. A. Flake.....	126
85	Study on Self-Discharge of a Metal Hydride Rechargeable Battery System Empolying $MmNi_{5-x}M_x$ Alloy M. Ikoma, Y. Ito, I. Matsumoto, and H. Ogawa.....	127
86	A New Thermally Stable AgO Cathode Material K. M. O'Neill, D. R. Glen, S. Dallek, B. F. Larrick, and A. N. Mansour.....	129
87	Structure and Stability of AgO A. N. Mansour, C. R. Anderson, M. K. Norr, S. Dallek, D. R. Glen, K. M. O'Neill, and B. F. Larrick.....	130
88	Chronopotentiometric and Ellipsometric Investigation of the Zinc Oxidation Behavior C. Y. Mak and H. Y. Cheh.....	131
89	Performance of Slurry Zn-Air Discharge and Recharge Cells with KOH-LiOH Electrolyte H. S. Alcazar, P. D. Nguyen, and A. A. Pinoli.....	133
90	In Situ FTIRRAS Studies of Glucose Oxidation on Platinum Electrode in the Presence and Abscence of Thallium Underpotential Deposition I. T. Bae, X. Xing, M. Daroux, E. B. Yeager, and C. C. Liu.....	135
	CORROSION	
	Dealloying	
91	Kinetic Models for Alloy Dissolution J. W. Halley.....	137
92	Mechanism of Selective Alloy Dissolution below and beyond the Breakthrough Potential H. Kaesche and H. Kaiser.....	138
93	The Percolation Model of Alloy Corrosion K. Sieradzki.....	139
94	TEM Investigation of Dealloyed Cu-Au Alloys J. D. Fritz and H. W. Pickering.....	140
95	Dealloying Kinetics of Silver-Gold Alloys A. J. Davenport and K. Sieradzki.....	141
96	Surface Instability under Conditions of Selective Dissolution in a Liquid Metal Environment P. F. Tortorelli.....	143
97	The Relationship Between Dealloying and Stress-Corrosion Cracking R. C. Newman, A. Mehta, T. Shahrabi, and K. Sieradzki.....	145
98	The Role of Dealloying in Transgranular Stress-Corrosion Cracking B. D. Lichter, W. F. Flanagan, J. B. Lee, and M. Zhu.....	146
99	Kinetics and Morphology of Aluminide Dealloying Reactions D. J. Young.....	147
100	Dealloying of Pt Alloy Fuel Cell Electrocatalysts M. T. Paffett and S. Gottesfeld.....	148
101	X-Ray Photoelectron Spectroscopy of Tarnished and Corroded Silver-Palladium Alloy H. J. Mueller.....	149

Abstract Number		Page Number
102	Exploitation of Dealloying in Corrosion Control of Aluminum Alloys K. Nisancioglu	150
103	Corrosion Improvement Through Mn Dealloying in Fe-Mn-Si-Al Alloys J. M. Oh, M. L. Glenn, and S. J. Bullard	151
104	Anodic Polarization Behavior of Tungsten Alloys in 3.5% NaCl Solution K. L. Vasanth, C. M. Dacres, R. Conrad and M. Fernandez	152
105	Transient Dezincification of Brasses in Aqueous Solution G. Gao and G. T. Burstein	154
	Tarnishing and Oxidation by Atmospheric Corrosion	
106	The Initial Stage of Atmospheric Corrosion J. H. Payer and S. K. Chawla	155
107	Corrosion Layer Constituents and Natural Minerals: Similarities, Differences, and Their Causes T. E. Graedel	157
108	Atmospheric Corrosion Behavior in Southern California F. Mansfeld and R. Vijayakumar	158
109	Vibrational Spectroscopy and XPS for Atmospheric Corrosion Studies on Copper D. Persson and C. Leygraf	160
110	*Darkening of Medieval Glass: A Special Type* of Atmospheric Corrosion of Glass S. Fitz	161
111	Atmospheric Tarnishing of Silver by H_2S Kinetic Studies Using a Flow Reactor L. Volpe and P. J. Peterson	162
112	The Effect of Condensation Mechanism on Atmospheric Corrosion of Metals P. A. Burda	163
113	Deposition Velocities of Airborne Ionic Pollutants: Distribution across Electronic Equipment Rooms J. D. Sinclair, L. A. Psota-Kelty, C. J. Weschler, and H. C. Shields	164
114	Indoor Corrosion of Copper and Silver Exposed in Japan and Asian Countries T. Fukushima, Y. Fukuda, A. Sulaiman, I. Musalam, C. L. Yap, L. Chotimongkol, S. Judabong, A. Potjanart, and O. Keowkangwal	165
115	Quartz Crystal Microbalance for Atmospheric Corrosion Studies on Metals S. Zakipour and C. Leygraf	167
116	Atmospheric Corrosion and Inhibition of Copper N. R. Sorensen and T. M. Christensen	168
117	Electrochemical Assessment of the Tarnish Resistance of Decorative Gold Alloys J.-P. Randin	169
118	The Formation of Sulfuric Acid on Gold in Humid Air Containing Sub-ppm Concentrations of SO_2 and NO_2 L.-G. Johansson and P. Ericsson	171
119	Elemental Surface Composition of Aged Copper R. Schubert and S. M. D'Egidio	172

Abstract Number		Page Number
	General Session	
120	Segregation of Alloying Elements into the Passive Films on Binary Nickel Alloys D. D. Macdonald, C. English, J. Pallix, and M. Ben-Haim	173
121	Role of Preexisting Oxide Films in the Passivation of Fe B. MacDougall	174
122	Composition and Structure of the Passive Oxide Film on Iron as Observed by Second Harmonic Generation M. W. Schauer, J. M. Frye, B. M. Biwer, M. J. Pellin, and D. M. Gruen	175
123	NEXAFS Studies of Passive Films on Iron and Iron-Chromium Alloys Z. Zhang, D. K. Tanaka, J. Kruger, and G. G. Long	177
124	A Variable Angle XPS Study of Active, Passive and Transpassive Ni Surfaces M. A. Helfand and C. R. Clayton	179
125	Investigation of the Growth of Porous Oxide Films on Different Pretreated Al Surfaces H. Terryn, J. Vereecken, J. Vanhellemont, and J. Van Landuyt	181
126	On the Influence of Surface Nitrides on Anodic Kinetics R. D. Willenbruch, M. Oversluizen, and C. R. Clayton	182
127	AC Impedance Measurements in Low Conductivity Media: Experiments and Model M. Keddam, S. Chechirlian, H. Mazille, P. Eichner, and H. Takenouti	183
128	Technique for Estimating Salt-Air Corrosion Rate Y. Miyata, R. Takekoshi, H. Takazawa, and K. Arita	185
129	A New Electrochemical Technique for Rapidly Evaluating Protective Coatings on Metals C. Lin and T. Nguyen	187
130	Corrosion Inhibition and Absorption Behavior of Some Thioamides on Mild Steel in H_2SO_4 B. G. Ateya, B. E. El-Anadouli, F. M. Eltaib Heakal, and F. M. El-Nizamy	188
131	Rapid Evaluation of Iron Corrosion Rate in Solution Containing Inhibitors by Using Coulostatic Method Y. Sato, T. Hamada, S. Sugiyama, T. Owa, and K. Kobayakawa	189
132	The Effect of Complexing Agents on the Anodic Dissolution of Iron M. F. Bell and R. Iyer	191
133	Stabilization of Metal-Metal Oxide Surfaces Using Conductive Polymer Films W. H. Smyrl, Z. Deng, and H. S. White	193
134	Temperature Dependence of the Low Frequency Impedance of Polymeric Coatings R. D. Granata, K. Kovaleski, and H. Leidheiser, Jr	195
135	Acoustic Microscopic Evaluation of Hydroxy-Terminated Polybutadiene on Steel M. Kendig, R. Addison, and S. Jeanjaquet	196

Abstract Number		Page Number
136	Corrosion of Inorganic Coatings in Molten Sodium Polysulfide F. Tanzella and M. McKubre	198
137	The Mechanism of Blister Formation and Rupture in the Pitting of Ion-Implanted Aluminum P. M. Natishan and E. McCafferty	199
138	Photoresponse of Stainless Steel Electrode Attached by Cl^- Ions in Acidic Medium S. Cai, S. Chen, Y. Dong, X. Chen, and H. Yang	20[illegible]
139	Effects of Halide Ions on the Corrosion Rate of Inconel 600 I.-H. Yeo, J.-w. Yean, and T.-y. Eom	202
140	Laboratory Study of Crevice Corrosion of Mild Steel H. Leidheiser, Jr., M. Ingle, and R. D. Granata	203
141	The Electrochemistry of Chromium and Chromium - Phosphorus Alloys T. P. Moffat, R. M. Latanision, and R. R. Ruf	204
142	The Nature and Composition of the Passive Film Formed on Ni-P-Cr Metallic Glasses M. A. Helfand, C. R. Clayton, N. R. Sorensen, and R. B. Diegle	205
143	Corrosion Behavior of Copper Alloys in Aqueous Solution by Surface Amalgamation J.-K. Wu and W.-L. Chen	206
144	Aqueous Corrosion and Stress Corrosion Behavior of Ductile Ni_3Al D. E. Hall, R. E. Ricker, and J. L. Fink	207
145	An XPS Study of the Anodic Behavior of Pure Mo and Mo in Stainless Steels Y. Lu and C. R. Clayton	208
146	Effects of Temperature on the Corrosion Resistance of N Bearing ALeX Stainless Steel K. G. Maitin, Y. C. Lu, and C. R. Clayton	21[illegible]
	CORROSION/ENERGY TECHNOLOGY	
	Corrosion of Nuclear Waste Containers	
147	Mineralogical Issues in Long-Term Corrosion of Iron and Iron-Nickel Alloys A. C. Van Orden and M. B. McNeil	211
148	Localized Corrosion and Stress Corrosion Cracking of Austenitic Candidate Materials for High-Level Radioactive Waste Disposal Containers: Analysis of Data W. G. Halsey, J. C. Farmer, R. D. McCright, R. A. Van Konynenburg, and D. B. Bullen	212
149	An Investigation of Low Temperature Sensitization (LTS) in AISI 316 Stainless Steel M. C. Juhas and B. E. Wilde	213
150	Nuclear Waste Package Container Corrosion in Simulated Salt Repository Environments H. J. Cleary	215
151	Phase Stability Effects on the Corrosion Behavior of the Metal Barrier Candidate Materials for the Nuclear Waste Management Program G. E. Gdowski, D. B. Bullen, R. D. McCright, and W. G. Halsey	216
152	A Data Base for Reviews and Evaluations of High-Level Waste Documents G. C. Interrante, C. Messina, and S. A. Harrison	218
153	The Effects of Hydrogen on the Metal Barrier Candidate Materials for the Nuclear Waste Management Program D. B. Bullen, G. E. Gdowski, R. D. McCright, and W. G. Halsey	219
154	Mathematical Model for Redox and Corrosion Potentials for High Level Nuclear Waste Container in Tuff Environments D. D. Macdonald and M. Urquidi-Macdonald	221

Abstract Number		Page Number
155	Pitting Kinetics of Carbon Steel and Low-Alloy Steel Exposed to a Groundwater/Packing Material Environment J. B. Lumsden and A. T. Allen	222
156	Corrosion Behavior of Low Carbon Steel in High pH Aqueous Media A. C. Fraker and J. S. Harris	223
157	Corrosion of Carbon Steel in Brine-Mg Effect B. E. Wilde, C. Manfredi, S. Kesavan, and T. A. Mozhi	224
158	Effect of Transport and Resistivity Characteristics of the Environment on the Corrosion of Steel E. Escalante and T. Oka	226
	CORROSION/EUROPEAN FEDERATION OF CORROSION	
	Transient Techniques in Corrosion Science and Engineering	
159	The Analysis of Electrode Processes by Alternating Current and Transient Techniques: Recognition of Mechanisms M. Sluyters-Rehbach and J. H. Sluyters	227
160	A Macroscopic Impedance Model for a Rotating Disk Electrode Analysis of the Dissolution of Copper in Chloride Solutions A. K. Hauser and J. Newman	228
161	A Shooting Method Treatment for Rotating Disk Electrode Impedance Data over the Entire Frequency Range W. H. Smyrl, R. Morris, and A. Kassimati	229
162	Impedance Spectroscopy for the Study of Anodic Copper Dissolution in Sulfuric Acid in Presence of Benzotriazole C. Clerc and R. C. Alkire	231
163	Surface Inhomogeneity Characterized by EIS W. J. Lorenz and K. Juttner	232
164	Measurement of Transient Processes from the Guillotined Electrode: A New Technique G. T. Burstein and R. J. Cinderey	233
165	In Situ Fracture Techniques for Studying Transient Reactions with Bare Steel Surfaces R. P. Wei and A. Alavi	234
166	The Influence of Surface Capacitance on the Measurement of Localized Corrosion Transient H. S. Isaacs and A. J. Davenport	235
167	Measurement of Passive Film Growth Kinetics on Bare Surface Niobium Band Microelectrodes A. J. Davenport and H. S. Isaacs	236
168	Fast Computer Supported Pulse Measurements of Ionic Processes in Oxide Films D. Ebling, M. M. Lohrengel, and J. W. Schultze	237
169	Electrochemical Transient Responses after a Controlled Depassivation R. Oltra, G. M. Indrianjafy, and M. Keddam	240
170	Study of Corrosion Processes by AC Quartz Electrogravimetry C. Gabrielli, S. Bourkane, and M. Keddam	241
171	Extension of AC Impedance Technique to Atmospheric Corrosion Studies--Application to a Scratched Galvanized Steel M. Keddam, P. Guillaume, and H. Takenouti	242
172	Application of Electrochemical Impedance for Studying Localized Corrosion M. Kendig and S. Jeanjaquet	243

Abstract Number		Page Number
173	Can the Kramers-Kronig (K-K) Transforms be Used for the Validation of Impedance Data? H. Shih and F. Mansfeld.	246
174	An Identification Procedure to Study the Dynamics of Metal Dissolution in Aqueous Media J. R. Vilche, R. H. Milocco, E. B. Castro, and S. G. Real	247
175	Transport Properties of Salt Films on Nickel in 0.5N HCl M. J. Danielson	248
176	Study of the Corrosion of Coated Metals with Impedance Measurements J. Vereecken and J. Hubrecht	249
177	Corrosion Inhibition in a CO_2-Saturated Chloride Solution by a Film-Forming Compound: Assessment by the Electrohydrodynamic Impedance Method D. Bernard, C. Deslouis, F. Olivier, T. E. Pou, and B. Tribollet	250
178	Inhibitor Effects of Phosphines on the Corrosion of Copper Studied by Electrohydrodynamical Impedance C. Fiaud, B. Tribollet, and I. Vastra	252
179	Impedance Study of Electronically Conducting Polymers W. H. Smyrl and C.-H.Paik	254
180	Impedance Anaylsis of Poly(Vinylferrocene) Films Spin Coated on Metal Substrates W. H. Smyrl and M. Lien	255
181	An Impedance and XPS Study of Passive Chromium T. P. Moffat and R. M. Latanision	256
182	Passive Layers and UHV-Grown Oxides on Ni(100): A Comparison by AC Impedance and Surface Spectroscopies F. T. Wagner and T. E. Moylan	257
183	Effect of Diffusion Layer Structure on the Determination of Corrosion Rates from DC Transient Measurements Z. Nagy, P. J. Hernes, M. Minkoff, G. K. Leaf, and R. H. Land	259
184	Corrosion Behavior of Chromium-Modified Copper-Nickel Alloy Compared to Other Alloys R. Beaudoin, P. R. Roberge, and E. Halliop	261
185	An Impedance Spectroscopy Investigation on the Passivability of Amorphous Fe-Cr-Metalloid Alloys S. Virtanen, B. Elsener, and H. Bohni	263
186	Impedance and Complex Collection Efficiency at a RRDE: Application to Active-Passive Transition of Fe and Fe-Cr Alloys N. Benzekri, R. Carranza, M. Keddam, and H. Takenouti	265
187	Pitting and Passivation of Al Alloys and Al-Based Metal Matrix Composites F. Mansfeld, S. Lin, Y. C. Chen, S. Kim, and H. Shih	266
188	Mechanism for the Intiation of Aluminum Etch Tunnels B. J. Wiersma and K. R. Hebert	268
189	The Role of Sulfide Inclusions on Initiation of Crevice Corrosion of 304 SS S. E. Lott and R. C. Alkire	270
190	A Microelectrochemical Probe with Segmented Electrodes (MEPSE) for Sensing Localized Corrosion and Scaling by Potable Waters H. B. Sierrra Alcazar, K. A. Kern, G. E. Mason, and P. D. Nguyen	271
191	The Influence of Deep-Level Electronic Defects on Characterization Methods Incorporating Mott-Schottky Theory D. B. Bonham and M. E. Orazem	273
192	Corrosion Inhibition of Steel by Phthalocyanine Coatings S. Hettiarachchi, R. B. Wilson, Jr., Y. W. Chan, and V. S. Agarwala	275

Abstract Number		Page Number
193	An Electrochemical Impedance Study of the Passive State on Nickel and Dilute Nickel Alloys D. D. Macdonald, S. J. Smedley, and M. Ben-Haim	277
194	Electropolishing of Iron in Phosphoric and Phosphoric-Sulfuric Acids M. Datta, L. F. Vega, L. T. Romankiw, and P. Duby	278
	DIELECTRICS AND INSULATION	
	Metallized Plastics: Fundamental and Applied Aspects	
195	Laser Stimulated Chemical Vapor Deposition of Metals on Polyimides S. J. Bezuk and C. Kryzak	280
196	Metallization of Nonconducting Substrates by Means of Composition Graded Interface Layered by Plasma Polymerization Technique H. K. Sun, D. L. Cho, and T. J. O'Keefe, and H. Yasuda	282
197	Metallization of Plastics with Resistance Heated Sources K. Anetsberger	283
198	Metallization of Composites and Thermoplastics via Electroless Metallized Conductive Coatings P. H. Kuzyk	284
199	High Rate Reactive Sputtering onto Flexible Polymer Sheet R. P. Howson	285
200	Method of Producing Activated Plastic (*Polystyrene*) Film and Metallizing it with Gold Using Electroless Techniques G. M. Ganu and S. Mahapatva	286
201	UV-Laser Induced Metallization on Polyimide from Electroplating Solution J. Zahavi, M. Rotel, D. Katz, and S. Levine	287
202	Simple, Metal-on-Plastics Patterning by Pulsed Electron Beam in Soft Vacuum J. Krishnaswamy, M. Eyolfson, T. Li, G. J. Collins, H. Hiraoka, and M. A. Caolo	289
203	Principles of Thermal Depositions of Metal Films on Plastics R. A. Myers	290
204	Optical Performance and Durability of Silvered Polymer Mirrors G. Jorgensen and P. Schissel	291
205	Deposition of Adherent, Thick, Copper Coatings on Glass W. C. Cowden, T. G. Beat, T. A. Wash, and J. W. Dini	292
206	A Novel Electroless Process of Deposition of Thin Ni-P Coatings on Polymethyl Methacrylate S. Mahapatra and L. G. Bhatgadde	293
207	Polymer Activation for Metallization: Theory and Application H. B. Petrov, E. D. Dobreva, and M. A. Encheva	295
208	Studies on Interaction of Polyimide with Copper in Curing Process K. Miyazaki, O. Miura, and S. Numata	296
209	Surface Spectroscopic Techniques Applied to Metallized Plastics N. J. DiNardo	298
210	Application of Mossbauer Spectroscopy to the Study of Metal/Polymer Interfaces--An Overview H. Leidheiser, Jr. and P. D. Deck	299
211	The Metal/Polymer Interface as Studied Nondestructively--An Overview P. D. Deck and H. Leidheiser, Jr	300
212	A Static SIMS Study of Metal-Polyimide Interfaces W. J. van Ooij, R. H. G. Brinkhuis, and J. M. Park	301

Abstract Number		Page Number
213	Electron Induced Vibrational Spectroscopy Study of the Incipient Interface Formation Between Evaporated Aluminum Layer and Polymer Films J. J. Pireaux, N. Degosserie, Y. Novis, M. Chtaib, and R. Caudano.....	302
214	XPS and HREELS Study of the Aluminum/poly(ethylene terephthalate) Interface and the Influence of Polymer Surface Pretreatment Y. Novis, M. Chtaib, J. Vohs, J. J. Pireaux, R. Caudano, P. Lutgen, and G. Feyder.....	303
215	Interfacial Chemistry of Metal Films on Polymers: Diffusion, Oxidation, Trace Components Studied by XPS, ISS, and SIMS G. R. Sparrow and L. Homstad.....	304
216	The Application of Rutherford Backscattering to the Characterization of Metallized Plastics M. D. Strathman.....	305
217	Metal Interlayers in Polymer Films: A Survey of Deposition Processes, Morphology, Electrical Properties, and Patterning Methods S. Mazur, L. E. Manring, M. Levy, G. T. Dee, and S. Reich.....	306
218	Surface Modification of Condensation Polyimides with Copper Complexes J. D. Rancourt, G. M. Porta, and L. T. Taylor.....	307
219	Various Stress Measurement Techniques for Thin Metal Films on Plastics N. L. Thomas.....	308
220	Dependence of Stress on Deposition Conditions for Sputtered Copper Films on Flexible Polyimide Substrates A. Entenberg, V. Lindberg, L. Fendrock, S-k. Hong, and R. S. Horwath.....	309
221	Adhesion of Chromium, Nickel, and Copper to Polymers Containing Basic Functional Groups S. R. Cain, L. J. Matienzo, and F. Emmi.....	310
222	Theoretical Study of the Chemistry at PMMA-Metal Interfaces A. K. Chakraborty, M. Tirrell, and H. T. Davis.....	311
223	Spectroscopic Study of the Chemistry at PMMA-Metal Interfaces R. Tannenbaum, B. Thakkar, and M. Tirrell.....	312
224	Plasma Surface Treatment of Plastics: An Overview P. W. Rose.....	314
225	Pretreatment of Polymers with Low Pressure Plasma G. Liebel.....	315
226	Characterization of Surface Modifications during Metallization of Polyetherimide M. C. Burrell, B. R. Karas, D. F. Foust, W. V. Dumas, E. J. Lamby, and J. J. Chera.....	317
227	Ion Bombardment of Polyimide Films: An XPS Study M. J. Vasile and B. J. Bachman.....	319
228	Radiation-Enhanced Adhesion of Metal Films on Polymers J. E. E. Baglin.....	320
229	Effect of the Plasma Pretreatment or the Ion-Plating on the Adhesivity of the Metallized Plastics K. Nakamae, S. Tanigawa, and T. Matsumoto.....	321
230	Thin Film Adhesion--A Review of the Mechanical Methods for Adhesion Assessment P. A. Steinmann and H. E. Hintermann.....	322
231	Adhesion and Deformation Behavior of Thin Metal Films on Polyimide Y. H. Jeng, F. Faupel, S. T. Chen, and P. S. Ho.....	323
232	Proposed Methods for Identification and Normalization of Strain Dynamic Effects in Adherence Testing of Metallized Plastics R. P. Riegert.....	324

Abstract Number		Page Number
233	Surface, Interface, and Adhesion Properties of Metallized Plastics P.-g. Cao	325
	DIELECTRICS AND INSULATION/ELECTRONICS	
	Isolation and Trench Technology	
234	Planarized Deep-Trench Process for Bipolar Device Isolations C. Hacherl, Y.-C. S. Yu, E. Patton, E. Lane, S. Dottarar, and T. Yamaguchi	326
235	CMOS Device Isolation Using Silicon Selective Epitaxial Growth C. H. Ting, A. Stivers, and J. O. Borland	328
236	Process and Device Simulation of Trench Isolation Corner Parasitic Device T. Furukawa and J. A. Mandelman	329
237	Si Crystallographic Defects on Trench-Isolated Bipolar IC Wafers Imaged with Nondestructive Thermal Wave Imaging S. Marks, W. L. Smith, and D. Willenborg	331
238	Deposition Processes for Borophosphosilicate Glass (BPSG) Films W. Kern and D. Freeman	333
239	Silicon Oxide Deposition from Cyclic Siloxane Precursors A. Lagendijk, A. K. Hochberg, and D. L. O'Meara	335
240	Planarized Borophosphosilicate Glass (BPSG) Deposited from Organometallic Sources D. W. Freeman, M. A. Logan, L. F. Wright, and J. R. Monkowski	337
241	Trench Oxidation for Minimization of Defects M. Kim, L. Tsou, S. Mukherjee, and D. McArthur	338
242	Process Parameters of the Trench RIE Deduced from the Laser Signal B. Leroy and F. Leverd	340
243	A Novel Process for High Speed Silicon Trench Etching J. M. McNamai and J. L. McNamara	341
244	A Low Ion Energy Trench Etch Process for Power MOS Applications C. J. Petti, J. P. McVittie, and J. D. Plummer	343
	Multilevel Metallization, Interconnection, and Contact Technologies	
245	Adhesion, Solderability, and Productivity: Next Generation PTH C. A. Deckert	345
246	Poly(vinylcinnamate) Photoresists for Fine Line Printed Circuitry S. Simoliunas, K. John and A. Tomson	346
247	Electrical Interconnection Through Silicon Wafer T. Dupeux, H. Sibuet, and P. Deroux Dauphin	348
248	Contact Resistance: A Review of Recent Developments in Measurement and Modeling S. E. Swirhun	350
249	Effects of Dry Etching on Shallow Titanium Silicide Contact M. F. Tseng, S. W. Chang, W. D. Su, and N. W. Wu	352
250	Inert Sputtered Titanium Nitride Films for ULSI Contact Technology T. Brat, J. Poole, C. S. Wei, and D. B. Fraser	354
251	Planarized Contact Process for Submicron VLSI Devices Using Resist Etch Back of CVD Tungsten S. Sivaram, D. Liao, L. Patterson, and K. Suh	356
252	Rapid Thermal Annealing of Ti and Ti-W Metallization on Si B. Mueller and T. S. Kalkur	358

Abstract Number		Page Number
253	Extremely Low Resistance and Reliable Al-TiW-$TiSi_2$ Contacts to n^+ and p^+ Si for Silicon VLSI and Smart Power Applications K. Shenai, P. A. Piacente, S. Al-Marayati, R. Saia, and B. J. Baliga	359
254	Planarization Processes for Multilevel Metallization G. C. Schwartz	361
255	Isoplanar Metallization Processes P.-L. Pai, and M. Paunovic, and C. H. Ting	362
256	Effect of Via Filling on the Via Resistance and Surface Topography P.-L. Pai and C. H. Ting	364
257	A Non-Etchback SOG Process for Multilevel Interconnection Technology C. H. Ting, H. Y. Lin, P. L. Pai, and T. Rucker	366
258	Chemical Vapor Depostion of Tungsten (CVD W) as Submicron Interconnection and Via-Stud P.-I. Lee, J. Cronin, and C. Kaanta	367
259	Application of Boron-Doped Plasma CVD TEOS for Intermetal Dielectric F. K. Moghadam and K. Suh	369
260	Etch Back of CVD Blanket Tungsten Films in a Hexode Reactor F. Y. Robb and K. W. Ginn	371
261	Two Step Tapered via Hole Etching Using Down Flow and Reactive Ion Etching T. Tsuchiya, J. Konno, S. Fujimura, T. Takada, and H. Yano	373
262	Characterization of an Oxygen Plasma Resistant Photoresist for Reactive Ion Etching of Organic Polymeric Materials F. Tranjan, S. Bobbio, T. DuBois, J. Poole, R. Frieser, and S. Jones	375
263	Rapid Thermal Annealing of Cobalt on Silicon A. R. Sitaram and S. P. Murarka	376
264	Titanium Silicide Formation and Arsenic Dopant Behavior under RTP in Vacuum R. Furlan and J. W. Swart	377
	DIELECTRICS AND INSULATION/ELECTRONICS/HIGH TEMPERATURE MATERIALS	
	Silicon Nitride and Silicon Dioxide Thin Insulating Films	
265	Thermal Response of Charge Decay in Silicon Oxynitride Films S. L. Miller and T. A. Dellin	379
266	Issues on Silicon Oxynitride Films H. J. Stein	380
267	$Si-SiO_2$ Interface Degradation Measurement Using the Floating Gate Technique A. K. Henning	382
268	Characterization of Electrical Properties of Oxygen/Hydrogen Rich Silicon Nitride Films for MNOS Devices D. Xu and V. J. Kapoor	384
269	The Effect of Growth Conditions on the Electrical Properties of Ultrathin Oxides V. Murali, A. T. Wu, D. B. Fraser, E. Kamieniecki, and J. Nulman	385
270	N-MOSFET Degradation and Aging due to Hot-Electon Trapping A. Samman, P. Roblin, and S. Bibyk	387
271	Comparison of DC and AC Stress for a NMOS Transistor H. Wang, R. Kaul, and S. B. Bibyk	389
272	Degradation of Polycide Gate MOS Capacitors A. Ohsaki, T. Okamoto, H. Kotani, S. Nagao, and N. Tsubouchi	391
273	Review of Silicon Nitride and Oxynitride Films for Nonvolatile Memory Device Technology V. J. Kapoor, D. Xu, and R. A. Turi	393

Abstract Number		Page Number
274	PECVD Silicon Nitride: Deposition and Postdeposition Modification for Application in Memory Devices W. D. Brown	394
275	A Review of Current Conduction in Stacked Silicon Dioxide-Silicon Nitride Layers on Silicon R. V. Giridhar	395
276	Influences of Processing Chemistry of Si_3N_4 Films on the Charge Trapping Behavior of ONO Capacitors B. Y. Nguyen, P. J. Tobin, K. M. Chang, K. W. Teng, and H. G. Tompkins	396
277	Nature of the Dominant Deep Trap in Amorphous Silicon Nitride D. T. Krick, P. M. Lenahan, and J. Kanicki	398
278	High Quality Nitrogen-Rich PECVD a-SiN_x:H Films for Application in Thin Film Transistors W. S. Lau, S. J. Fonash, and J. Kanicki	400
279	Silicon Dioxide and Silicon Nitride Films in Integrated Circuit Technology E. H. Nicollian	402
280	Oxide Thickness Dependence of Nitridation and Oxidation Reactions at a Si-SiO_2 Interface S. I. Raider	403
281	Thin Gate Oxides Grown in Argon-Diluted Oxygen with Steam and HCl Treatment F. Bryant and F.-T. Liou	404
282	The Role of Sacrifical Oxidation on the Integrity of Thin (20 nm) Gate Oxide I. Ahmed, H. Naguib, and C. Gomez	405
283	Vacancy Generation at the Si/SiO_2 Interface Caused by SiO Formation S. T. Ahn, H. W. Kennel, J. D. Plummer, and W. A. Tiller	407
284	Film Stress and Atomic Misfit Effect on Dopant Junction Profiles in Silicon C. K. Huang and R. J. Jaccodine	409
285	LPCVD Oxide Film Evaluation for Intermetal Dielectric S. Mittal, C. Chiang, R. Hsu, L. C. Yip, D. Fraser, and A. Haranahalli	411
286	Oxygen Transport in Vitreous Silica and Thermal Oxide Films J. D. Cawley	412
287	Infrared Dielectric Model for Silicon Dioxide Thin Insulating Films C. T. Kirk	413
288	Ellipsometric Study of the Structure of SIMOX B. J. Mrstik, P. J. McMarr, and V. M. Bermudez	414
289	Optical Modelling of Si-SiO_2 Interface A. Kalnitsky, S. P. Tay, J. P. Ellul, S. Chogsawangvirod, and E. A. Irene	416
290	A Laser Activated CVD Film for Interlayler Dielectric Application C. Chiang, N. Cox, D. Fraser, M. Lee, L. C. Yip, R. J. Kolenkow, R. Anderson, and G. Roche	418
291	Radiotracer Measurements of Sodium Penetration Through Thin Films of Phosphosilicate Glass S. V. Dunton, A. C. Ling, and W. G. M. van den Hoek	420
292	Mobile Ion Drift in High Quality PECVD SiO_2 Films G. Liu, W. S. Lau, S. Fonash, and J. Kanicki	422
293	Analog Nonvolatile Memory for Neural Network Implementations J. P. Sage and R. S. Withers	424
294	A Dual Polarity Nonvolatile Analog Memory for Use in Adaptive Artificial Neural Networks R. L. Shimabukuro, I. Lagnado, and P. Shoemaker	425

Abstract Number		Page Number
295	Utilization of Programmable Threshold Voltage Devices in Neural Network Integrated Circuits T. Borgstrom, R. Chau, K. Adkins, and S. B. Bibyk	426
296	Charge Trapping Kinetics and Dielectric Degradation in Silicon Nitride Films R. S. K. Chau and S. B. Bibyk	427
297	Hot Electron Effects in Semi-Insulating Polysilicon (SIPOS) and Polysilicon TFT's D. W. Greve and B.-C. Hseih	429
298	Hot Carrier Induced Excess Current in Polysilicon Emitter Bipolar Transistors D. W. Greve and T. Y. Chou	431
299	Dielectric Formation by Rapid Thermal Nitridation M. Kozicki, D. Henscheid, I. Zwiebel, R. Graham, G. Sheets, and E. G. Chang.	433
300	Process Induced Radiation Damage in IGFET Gate Insulators A. Reisman	435
301	Deposition Gas Ration and Post-Deposition RTA Improvements of LPCVD Silicon Dioxides in VLSI Processing J. K. Park, J. Clarke, and A. Reisman	436
302	The Characterization of Electron Cyclotron Resonance (ECR) Plasma Deposited Silicon Nitride and Silicon Oxide Films S. Van Nguyen and K. Albaugh	437
303	ECR Plasma Deposition under a Controlled Magnetic Field S. Nakamura and S. Nakayama	439
304	Plasma Induced Surface Modification of GaAs: An X-Ray Photoelectron Spectroscopy (XPS) Characterization N. C. Saha, G. Tam, and R. N. Legge	441
305	Physical and Chemical Properties of Magnetron Sputtered Silicon Nitride Films T. Carriere, I. Vickridge, B. Aguis, P. Alnot, J. Siejka, and R. Joubart	443
306	On the Constitutive Distributed Parameter Modeling for Phenomenal Control of the Multicomponent Plasma Processing. Part I. A Constitutive Distributed Parameter Mathematical Model of the Multicomponent Plasma Processing W. Niemiec	445
307	On the Constitutive Distributed Parameter Modeling for Phenomenal Control of the Multicomponent Plasma Processing. Part II. The Analytical Solution and Control Interpretation of the Constitutive Mathematical Model of the Multicomponent Plasma Processing W. Niemiec	446
	DIELECTRICS AND INSULATION/ELECTRONICS/ENERGY TECHNOLOGY	
	Reliability of Semiconductor Devices and Interconnection	
308	Electromigration in Submicron Interconnects and Multilevel Interconnection T. Kwok	447
309	Improved Electromigration Performance in Al/4%Cu Using a Range of Refractory Caps N. P. Armstrong	448
310	Stress-Induced Migration of Aluminum-Silicon Films: Influencing Factors and Countermeasures H. Katto and S. Shinji	450
311	A Study of Electromigration Performance in a Range of Al/Si/Ti Alloys N. P. Armstrong, R. J. Dulniak, and A. Turnbull	452
312	Humidity-Temperature-Voltage Acceleration Model for Corrosion of Thin Film Aluminum J. W. Osenbach and J. L. Zell	454

Abstract Number		Page Number
313	Corrosion Products and Surface Structure of PbSn Solder Pads H. L. Yeh and H. Dalal	455
314	A Practical Approach to HAST and Correlation with 85185 for Reliability Testing of IC's for Telecommunication Applications A. Hente, K. Allaert, and P. De Pauw	456
315	Hot Carrier Limited Operating Voltages for Submicron, non-LDD Shallow Junction MOSFET's P. K. Chaudhari, D. S. Wen, and C. M. Osburn	458
316	Anomalous Hot Electron Effects Induced by PECVD Passivation Processes S. U. Kim and F. Hinedi	460
317	Characteristics of Al-$TiSi_2$ Contacts to n^+ and p^+ Silicon K. Shenai, P. A. Piacente, S. Al-Marayati, and B. J. Baliga	461
318	Electrical Characteristics of Inter-Poly Si Oxide and Optimized Cell Structure for Reliable Flash EEPROM S. Tanaka, N. Tozawa, K. Kanebako, M. Hori, and M. Asano	463
319	Time-Dependent Degradation in MOS Devices C. Y. Yang, C. M. Wang, G. Lin, and J. J. Tzou	465
320	Reliability Issues for Ultrathin Insulators T. N. Nguyen, P. Olivo, and B. Ricod	467
321	Gate Oxide Leakage Reliability Failures in CMOS Circuits J. Vandenbroeck, P. De Pauw, M. Van Den Reeck, and L. Stevens	468
322	Reliability Study of PECVD Silicon Nitride for Composite Insulator D. Nguyen, H. Rathore, R. Edwards, V. DePalma, and G. Gati	470
323	Reliability of a 10 nm Stacked Insulator K. v. Sichart, L. Do Thanh, Th. Kleinert, S. Rohl, and H. Reisinger	471
	ELECTRODEPOSITION	
	Modeling of Electroplating Processes	
324	Determination of Fractal (Hausdorff) Dimension during the Electrodepositon of Zinc C.-P. Chen and J. Jorne	473
325	Stability Analysis of Metal Electrodeposition D. P. Barkey, R. H. Muller, and C. W. Tobias	475
326	Non-Steady-State Modeling of Transport Controlled Plating Additives D. Roha, and U. Landau	477
327	Copper and Additive Effects on Plating High Aspect Ratio Through Holes in Printed Circuit Boards W. Sonnenberg, R. Bernards, and G. L. Fisher	479
328	Secondary Current Distribution and Propagation of a Wavy Electrode: Two-Dimensional Model S.-L. Chiu and J. R. Selman	481
329	Effects of Nonuniform Current Distributions on the Interpretation of Kinetic Data A. C. West and J. Newman	483
330	Current Distribution in Pattern Plating of Nonuniformly Spaced and Isolated Lines R. T. Galasco, U. Landau, and J. Tang	484
331	Optimization of Electrodeposit Uniformity by the Use of Auxillary Electrodes J. Dukovic, S. Mehdizadeh, P. C. Andricacos, L. T. Romankiw, and H. Y. Cheh	486
332	A Novel Adaptation of the Finite Difference Method for Accurate Description of Non Orthogonal Boundaries W. M. Lynes and U. Landau	488

Abstract Number		Page Number
333	Effect of Agitation on the Electrodeposition of Nickel-Iron Alloys P. C. Andricacos, C. Arana, J. Tabib, J. Dukovic, and L. T. Romankiw.....	490
334	Microelectrode Assemblies for Electroplating Studies S. Fletcher and R. L. Deutscher.....	492
335	Hydrogen Uptake during Cadmium Electroplating M. M. Makhlouf, R. R. Biederman, and R. D. Sisson, Jr.....	494
	Properties and Structures of Electrodeposits	
336	Crystallography of Plated Film and Amorphous Plating T. Watanabe.....	495
337	The Effect of Hydrogen and Deposition Conditions on the Ductility of Electrodeposited Ni-P Amorphous Alloys R. L. Zeller III and U. Landau.....	496
338	Effects of Heat-Treatment on the Structure and Properties of Electrodeposited Amorphous Iron-Nickel-Phosphorus Alloys K. Sheppard and K. Sridharan.....	498
339	Structure and Electrical Resistivity of Electroless Nickel Thin Films M. Paunovic, M. Madden, C. H. Ting, P. L. Pai, and T. Ton.....	499
340	Correlation of Perpendicular Magnetic Anisotropy and Microstructure of Electroless Plated CoNiReP Thin Films T. Osaka and T. Homma.....	500
341	Electrodeposition of Ni-Co-Mn Alloys H.-S. Tong.....	502
342	Electrodeposition and Characterization of Multilayered Cu-Ni Ultrastructures S. Menezes and D. Anderson.....	503
343	Electrodeposition of Ni/SiC Composite Coating A. Lavanant and G. Maurin.....	504
344	Investigation of Dendritic Growth of Tellurium Electrodeposits by Electrohydrodynamic Impedance Analysis C. Deslouis, G. Maurin, and B. Tribollet.....	506
345	Mechanical Properties and Microstructure of Electroless Copper Deposits H. Akahoshi and K. Murakami.....	508
346	The Effect of Additives on the Morphology of Electroless Copper Deposits H. H. Wan and J.-Y. Gau.....	509
347	Properties of Electrodeposited Copper from Pattern Recognition Analysis of Cyclic Voltammetric Stripping Curves M. Kendig and D. Anderson.....	510
348	Mechanism of Carbide Formation by Electrochemical Deposition D. C. Topor and J. R. Selman.....	512
349	Current- and Potential-Pulse Plating of Uranium from Fused Chlorides S. L. Marshall and D. R. Vissers.....	513
350	Properties of Nickel Electrodeposited from Organic Solvent V. B. Singh and A. A. Sarabi.....	514
351	Corrosion of Electronic Materials and Devices R. P. Frankenthal.....	515
352	Metal Electrodeposition on Phosphated Steel Substrates H. Leidheiser, Jr. and W. Bilder.....	516
353	Under-Film Corrosion Mechanism of Zinc and Zinc Alloy Coated Steel Sheet for Automobiles K. Hayashi, Y. Ito, and Y. Miyoshi.....	517

Abstract Number		Page Number
354	Characterization of New Corrosion Resistant Nickel-Zinc-Phosphorus Alloys Obtained by Electrodeposition S. Swathirajan and Y. Mikhail	518
	General Session	
355	Steady-State Multiplicity Analysis of a Mechanistic Model for Zinc Electrodeposition M. Pritzker and T. Z. Fahidy	519
356	Electrodeposition of Transition Metal Oxide Phases: Thermodynamic Aspects S. Crouch-Baker and R. A. Huggins	520
357	The Use of Insoluble Films to Control the Rate of Electrodeposition of Metals T. C. Franklin, V. Totten, and A. Aktan	521
358	The Uses of Volumes of Activation to Determine the Mechanism of Action of Additives T. C. Franklin and S. A. Mathew	522
359	Electrocodeposition of Copper and Polystyrene Latex Particles on a Rotating Disc Electrode J. L. Valdes and H. Y. Cheh	523
360	Laser Interferometric Wet Etch and Deposition Rate Measurement In Situ at Solid-Liquid Interfaces O. Wolter, R. Vogel, and G. Makosch	524
361	Effect of Transport and Reaction on the Shape Evolution of Cavities Undergoing Etching D. Economou and C. B. Shin	526
	ELECTRODEPOSITION/ELECTRONICS/ENERGY TECHNOLOGY	
	Electrodeposition of Semiconductors	
362	Aqueous Electrochemistry of Tellurium at Glassy Carbon and Gold: A Combined Voltammetry-Oscillating Quartz Crystal Microgravimetry Study K. Rajeshwar, E. Mori, C. K. Baker, and J. R. Reynolds	528
363	Electrochemical Deposition and Characterization of $CdSe_xTe_{1-x}$ ($0 \leq x \leq 1$) Films K. Uosaki, M. Takahashi, N. Karube, and H. Kita	529
364	Cathodic Electrodeposition Characteristics of CdTe Films in a Nonaqueous Bath R. K. Pandey and R. R. Gore	530
365	A First-Order Numerical Analysis of the Effect of Internal Ohmic Voltage Drops on the Electrodeposition of Binary Compound Semiconductors R. D. Engelken and N. Sanders	532
366	Electrochemical Deposition of Single-Crystal CdTe Films from Organic Electrolytes A. C. Rastogi, K. S. Balakrishnan, and G. L. Malhotra	534
367	Electrodeposition of $Cd_{1-x}Zn_xS$ and $Cd_{1-x}Bi_xS$ Films C. D. Lokhande, V. S. Yermune, M. S. Jadhav, R. D. Madhale, and S. H. Pawar.	536
368	Electrodepositon of $CuInSe_2$ Thin Films from Aqueous Solution G. Maurin and D. Pottier	537
369	One-Step Electrodeposition of Polycrystalline $CuInSe_2$ Thin Films and Their Properties F. J. Pern and R. Noufi	539
370	Mechanism for the Electrodeposition of CdS from a Nonaqueous Solution M. Cocivera and S. Preusser	541

Abstract Number		Page Number
371	Development of a Novel "Generic" Triple Solvent Bath for Electrodeposition of Metal Chalcogenide and "Bright" Metal Films. I: Comparison/Contrast of Present Single/Double Solvent Baths R. D. Engelken, H. E. McCloud, D. Moss, E. Smith, H. Hormasji, and W. Wells.	542
372	Development of a Novel "Generic" Triple Solvent Bath for Electrodeposition of Metal Chalcogenide and "Bright" Metal Films. II: Description of the Triple Solvent Bath R. D. Engelken, H. E. McCloud, D. Moss, E. Smith H. Hormasji, and W. Wells..	543
373	Photoelectrochemistry and Surface Analyses of Electrodeposited SnS Thin Films K. Mishra.....	544
374	Electrodeposition of Semiconductors: A Panel/Audience Participation-Based Session to Survey and Define the State-of-the-Effort and Future of Electrodeposition of Compounds and/or Semiconductors R. D. Engelken, R. D. Rauh, and V. K. Kapur.....	545
375	Preparation of InX (X=P, As, Sb) Thin Films by Electrochemical Methods J. Ortega and J. Herrero.....	546
376	Electrodeposition of Indium Antimonide Semiconductor from Aqueous Electrolyte T. Okubo and U. Landau.....	547
377	Electrochemical Oxidation of a Ni-Based Amorphous Alloy V. I. Birss and K. Lian.....	549
378	Use of a Sulfur Powder Bath to Form Metal Sulfide Films from Flash Annealed Electrodeposited Metal Layers R. D. Engelken, H. E. McCloud, L. Mink, D. Moss, E. Smith, and W. Wells.....	550
379	Electrochemical Polymerization of Thiophene Containing an Ether Linkage at the 3-Position D. Mukherjee.....	551
380	Polyaniline/WO_3 Electrochromic Cell T. Yoshida, K. Okabayashi, T. Asaoka, and K. Abe.....	552
	ELECTRONICS	
	Beam Testing of Circuits and Devices	
381	Electro-Optic Sampling of Integrated Circuits and Devices Using InGaAsP Injection Lasers J. M. Wiesenfeld, and M. S. Heutmaker.....	554
382	Accuracy and Invasiveness of Direct Electro-Optic Probing of GaAs Integrated Circuits J. L. Freeman, D. M. Bloom, S. R. Jefferies, and B. A. Auld.....	556
383	Photoemission Probing of Fast Integrated Circuits and Devices R. Clauberg, A. Blacha, H. Seitz, and H. Beha.....	558
384	Internal Waveform Measurements in High Speed Silicon Circuits Using a Picosecond Photoelectron Scanning Electron Microscope J.-M. Halbout, P. May, Y. Pastol, and G.Chiu.....	559
385	Pulsed Nagative Electron Affinity Cathode for Time-Resolved Electron Microscopy and Electron Spectroscopy N. C. MacDonald and C. A. Sanford.....	561
386	Characterization of ps-Electronic Devices: A Challenge for E-Beam Testing M. Brunner, R. Schmitt, and D. Winkler.....	562
387	A Submicron Electron Beam Tester for VLSI Circuits J. Kolzer, F. Fox, and D. Sommer.....	564
	ELECTRONICS/DIELECTRICS AND INSULATION	
	Automated IC Manufacturing IV	
388	The Strategy and Study of Wafer FAB Automation in Sharp Corporation T. Kondoh, K. Kawamura, T. Nakato, J. Taketani, and H. Takeuchi.....	566

Abstract Number		Page Number
389	Control and Communications for Integration of Automated Materials Handling Systems in Wafer Fabrication Facilities J. C. Dilworth	565
390	An Intelligent Work-in-Process System M. Brain, A. Bonora, and M. Parikh	569
391	Implementation Considerations for Robotic Systems in a Wafer Fabrication Facility W. A. Livesley	571
392	A Rule-Based Diagnostic System for VLSI Process Flow K. Funakoshi, and K. Mizuno	572
393	Using Simulators to Minimize Transmitted Variability in IC Manufacturing S. Sharifzadeh, J. D. Shott, A. B. Owen, and J. R. Koehler	574
394	Computer Simulation of a Microelectronics Laboratory F. Miller	576
395	Equipment Models for Process Optimization and Control Using Smart Response Surfaces E. Sachs and G. Prueger	577
396	Out Gas-Free Corrosion-Resistant Surface Passivation of Stainless Steel for Advanced ULSI Processing Equipment T. Ohmi, T. Okumura, K. Sugiyama, F. Nakahara, and J. Murota	579
397	A Method of Low Contamination for Automated IC Manufacturing Utilizing the Wafer Carriers with Compact Cleaning Devices A. Machida, S. Tabuchi, S. Eifuku, A. Abiru, and T. Matsumoto	581
398	A Novel CVD System with Self-Cleaning Function for the Automation of LSI Manufacturing T. Ohmi, G. S. Jong, M. Morita, M. Kosugi, and H. Kumagai	582
399	Results from Comparing an Open Area SMIF Isolation Site (OASIS) with a Clean Room R. A. Hughes, G. B. Moslehi, D. Campbell, E. D. Castel, W. Lukaszek, K. Radigan, and L. Walsh	584
400	Application of Surface Photovoltage to Monitoring of Heavy Metal Contamination and Reproducibility of Internal Gettering during IC Processing L. Jastrzebski, R. Soydan, N. Armour, M. Blummenfeld, R. Kleppinger, E. Pelczar, C. Palmer, and B. Goldsmith	586
401	Development of On-Lined Method Gauging a Total Weight of Foreign Matters Semiconductor Pure Water S. Takahashi and Y. Koseki	588
402	A Distributed Architecture for Real-Time Heuristic Factory Control B. Martensen	589
403	Beyond the Spreadsheet: Wafer Production Planning with Start/Demand Rate Calculation Through Simulation Models R. A. Zuanich, D. F. Ruffcorn, and M. G. C. Resende	590
404	Dynamic Capacity Planning Using Simulation Models R. W. Atherton	591
405	Real-Time IC Process Control Automation Using Expert Systems C. F. Hiatt	592
406	Expert System Control of Dielectric Formation P. Rastogi, M. N. Kozicki, T. Patel, and G. Sheets	594
407	Ultra-High-Vacuum Compatible Wafer Transport and Holding System Using Electrostatic Chucks T. Ohmi, M. Onodera, G. Sato, T. Shibata, and M. Morita	596

Abstract Number		Page Number
408	Automatic Chemical Supply Unit and Systems M. Tamura, T. Saito, S. Oshima, and A. Yamashita.....	598
409	A SMIF-Vacuum Interface Chamber for 200 mm Wafer Cassette Loading and Unloading of a Multichamber Etching Apparatus I. Hussla, M. Walde, and P. Zeidler.....	599
410	Safety Mode Standardization for Semiconductor Manufacturing Equipment H. Unno and H. Harada.....	601
411	Integration of Automated Real-Time DI Water Monitoring with the IC Manufacturing Process J. Seaton, D. Grossman, and S. Becker.....	602
412	Image Processing for Wafer Identification M. Fukuda.....	604
413	In-Process Monitoring by Auto Focus Signal of Steppers N. Shimizu, H. Ikubo, and H. Kozawa.....	606
	Diagnostic Techniques for Semiconductor Materials and Devices	
414	Compositional Mapping with the Electron Microprobe and Secondary Ion Mass Spectrometry R. B. Marinenko, D. A. Newbury, D. S. Bright, and R. L. Myklebust.....	607
415	Neutron Activation Analysis in Electronic Technology R. M. *Lindstrom*.....	608
416	Backscattering Spectroscopy for Semiconductor Materials J. A. Keenan.....	610
417	Hydrogen in Thin Films W. A. Lanford.....	611
418	Accelerator Mass Spectrometry of Electronic Materials J. M. Anthony.....	612
419	Secondary Neutral Mass Spectrometry: The Application of Laser Post-Ionization to Trace Surface Analysis in Semiconductor Materials M. J. Pellin, C. E. Young, W. F. Calaway, J. W. Burnett, and D. M. Gruen.....	614
420	Quantitative Depth Profiling Analysis of Semiconductors and Superconductors by Secondary Neutral Mass Spectrometry N. Kelly, U. Kaiser, and H. Peters.....	616
421	Imaging Subsurface Interfaces by Ballistic-Electron-Emission Microscopy L. D. Bell and W. J. Kaiser.....	617
422	Sub-*ppm Monitoring of Transition Metal Contamination on Silicon Wafer Surfaces by* VPO-TXRF A. Huber, H. J. Rath, P. Eichinger, Th. Bauer, L. Kotz, and R. Staudigl.....	619
423	An Evaluation of Ultra-Surface (§3NM), Trace ($E11/CM^2$) Impurity Analysis of Silicon Using a New X-Ray Technique R. S. Hockett, S. Baumann, and E. Schemmel.....	621
424	X-Ray Topography and Precision Diffractometry of Semiconducting Materials B. K. Tanner.....	622
425	Characterization of Semiconductor Materials and Structures by Transmission Electron Microscopy R. J. Graham.....	623
426	Defect Characterization in Semiconductors by Positron Annihilation Spectroscopy A. Rohatgi, J. P. Schaffer, and A. B. DeWald.....	624
427	Cathodoluminescence Characterization of Semiconductor Materials R. J. Roedel, S. Hyhajlenko, J. L. Edwards, and K. Rowley.....	625
428	Subsurface Defect Structures in Ion Implanted, Annealed Si Wafers Imaged by Nondestructive Modulated Reflectance Imaging W. L. Smith, D. Willenborg, T. Miranda, G. A. Rozgonyi, and L. Larsen.....	626

Abstract Number		Page Number
429	Multiple Internal Reflection Spectroscopy: Applications to Electronic Materials J. E. Olsen, G. A. Rozgonyi, and F. Shimura	628
430	Minority Carrier Lifetime of Heterostructures, Surfaces, Interfaces, and Wafer Substrates E. Yablonovitch and T. J. Gmitter	629
431	Contactless Measurement of Silicon Generation Leakage and Crystal Defects by a Corona-Pulsed Deep-Depletion Potential Transient M.-S. Fung and R. L. Verkuil	631
432	Recombination Lifetime of p/p+ Epitaxial Silicon M. Aminzadeh and L. Forbes	633
433	Magneto-Electrical Characterization of Materials and Devices D. C. Look	635
434	Low Frequency Noise as a Process Development and Characterization Tool F. Scholz, G. N. Maracas, and D. K. Schroder	636
435	Defect Engineering and the Contact Resistance of Shallow and Deep Junctions in Silicon Discrete and Integrated Power Devices S. Al-Marayati, K. Shenai, N. Lewis, and B. J. Baliga	638
436	Spreading Resistance - Recent Developments in Implementation and Interpretation M. Pawlik	640
437	Recent Developments in the Interpretation of Spreading Resistance Profiles for VLSI-Technolgy W. Vandervosrt and T. Clarysse	641
438	Contactless Silicon Doping Measurements by Means of a Corona-Oxide-Semiconductor (COS) Technque R. L. Verkuil and M. S. Fung	643
439	Depletion Layer Solver for Nonuniform Impurity Profile using Analog Computation Techniques A. Shenay, H. C. Chien, H. C. Lin, and R. Ramaswami	645
	International Symposium on Focused Ion Beam Technology	
440	Mask Repair and Micromachining with Focused Ion Beams L. R. Harriot	647
441	Advances in Etching by FIB for Photomask Repair J. Glanville, Y. Nakagawa, T. Yamaoka, K. Aita, M. Sato and M. Yamamoto	648
442	Analytical Simulation of Focused Ion Beam Applications in X-Ray Mask Repair W. Burghause, U. Weigmann, and M. Weiss	649
443	Two-Dimensional Profile Simulation of Focused Ion Beam Milling of LSI F. Itoh, A. Shimase, and S. Haraichi	651
444	Focused Ion Beam SIMS for Micromachining Applications L. R. Harriott and M. J. Vasile	653
445	FIB Direct Write Lithography K. Gamo and S. Namba	654
446	Registration Accuracy in Focused-Ion-Beam Lithography for the Fabrication of GaAs FET with a Mushroom Gate T. Kato, K. Hosono, H. Morimoto, Y. Sasaki, and Y. Watakabe	655
447	Focused Ion Beam Lithography Using Novolak Based Resist S. Matsui, Y. Kojima, and J. Ochiai	656
448	FIB Direct Ion Implantation Technology and Its Applications for III-V Compound Semiconductors E. Miyauchi and H. Arimoto	658

Abstract Number		Page Number
449	Fabrication of 100 nm Si p-n Junction by Focused and Broad Beam Ion Implantation A. Steckl, C-M. Lin, and T. P. Chow	659
450	GaAs Quantum Wire Transistors Fabricated by Focused Ion Beam Implantation T. Odagiri, T. Hiramoto, K. Hirakawa, and T. Ikoma	660
451	Formation of Pd_2Si by Direct Implantation of a Focused Beam of Pd^+ Ions in Si S. Balakrishnan, J. C. Corelli, S. P. Murarka, E. Hall, and N. Lewis	661
452	Development of Focused Ion Beam Systems R. Aihara, H. Sawaragi, W. Thompson, and M. H. Shearer	662
453	Maximization of Current Densities in Focused Ion Beams by Automated Electrostatic Lens Design M. Szilagyi and J. Szep	663
454	Tomographic Approach to Two-Dimensional Focused Ion Beam Profile Measurement J. F. McDonald, H. T. Lin, and M. E. Haslam	664
455	Achromatic Lens and Mass Filter Design Using Crossed-Field Multipole Elements M. R. Smith and E. Munro	665
456	Ion Optical Performance of the MicroBeam NanoFab-150 Focused Ion Beam System E. Tsiang, W. P. Robinson, and J.C. Potosky	667
457	Development of Liquid-Metal-Ion Sources for Focused-Ion-Beam Applications T. Ishitani, K. Umemura, and Y. Kawanami	668
458	Emission Current Dependence in the *Fluctuation Power Spectra* of Gallium Liquid Metal Ion Sources D. L. Barr, D. J. Thomson, and W. L. Brown	669
459	Theory of Operation of Electrohydrodynamic Ion Sources: A Review P. H. Cutler, M. Chung, and N. M. Miskovsky	67[illegible]
460	Shape and Instability of Liquid Metal Ion Sources M. S. Chung, P. H. Cutler, C. Viskovsky, and N. M. Miskovsky	671
461	An Electrohydrodynamic Model for Ion and Droplet Formation in LMIS N. M. Miskovsky, P. H. Cutler, and M. Chung	672
	Joint General Session	
462	The Behavior of Metal Impurtities in Si Substrate K. Hiramoto, M. Sano, M. Horai, S. Sumita, N. Fujino, and T. Shiraiwa	673
463	An Advanced Crystal Growth Technique as Full Range Resistivity Controlled CZ (FCCZ) Technique Y. Yamashita, M. Kojima, and H. Hirano	675
464	TEM Observations of Crystallized LPCVD Silicon Films T. Aoyama, Y. Okajima, Y. Koike, T. Suzuki, N. Konishi, and K. Miyata	677
465	The Role of Film Stress on the Rate of Silicon Oxidation at Low Temperature P. Murray and G. F. Carey	679
466	Titanium Silicide Ohmic Contacts for High Temperature -SiC Devices S. M. Tang, W. B. Berry, R. Kwor, K. L. Jacobson, M. V. Zeller, N. S. Alvi, A. J. Nelson, and A. B. Swartzlander	680
467	The Influence of Process Atmosphere on Titanium Silicide Formation R. M. Vadjikar and R. P. Roberge	681
468	Modeling of the Influence of Oxide Geometry on Impurity Diffusion into Silicon S. A. Abbasi and A. A. Khan	683
469	The Effect of Fluorine on Dopant Diffusion in Silicon U. S. Kim, T. Kook, and R. J. Jaccodine	685

Abstract Number		Page Number
470	Source Drain Formation Using Spin-on Dopants and Subsequent Rapid Thermal Diffusion G. W. Sheets and M. N. Kozicki	687
471	The Depositon of N-type and P-type In Situ Doped Polysilicon by LPCVD J. P. McVittie, J. Gan, C. Chu, K. C. Saraswat, and R. M. Swanson	689
472	Temperature Gradient and Thermal Stress Distribution Study for Rapid Thermal Processing F. K. Yang, S. J. Pien, R. Kwor, and N. Alvi	691
473	Self-Gettering Effect of Ion Implanted N+ Layers M. Ogasawara, J. Sugiura, S. Shimizu, and H. Kozuka	692
474	Intrinsic Gettering for CMOS Process Using Low (Oi) Wafers M. Kitakata, F. Toyokawa, M. Mikami, and H. Tsuya	694
475	Thermal Analysis for the SiO_2-Si and SiO_2-GaAs Structures during Rapid Thermal Processing F. K. Yang, R. Kwor, and S. J. Pien	696
476	Diffusion of Zinc in Gallium Arsenide Through a Cubic Zirconia Passivation Layer J. E. Bisberg, F. P. Dabkowski, and A. K. Chin	697
477	A High-Precision Thinning Technique for GaAs Substrates T. Karaki-Doy, H. Nakada, and J. Watanabe	699
478	Submicron PMOS Transistors Formed by Implantation into $TiSi_2$ K J. Barlow	701
479	Electro-Optic Switches Based on Novel Conducting Polymer Technology: Enhancing Optical Switching Times P. Chandrasekhar	703
480	Fabrication and Characterization of Far Infrared Submicron Rectenna Devices A. B. Hoofring, V. J. Kapoor, and W. Krawczonek	704
481	A Wafer-Scale Thinning Process for High-Performance Silicon Devices C. M. Huang, B. B. Kosicki, B. E. Burke, and A. C. Anderson	705
482	Deposition and Characterization of Silicon Oxynitride by a less than 2% Silane PECVD Process L. C. Hsia and P. C. Li	706
483	An Etch Rate Study of Thermally Annealed TEOS-LPCVD SiO_2 Films C. Orfescu, C. Pavelescu, and M. Badila	708
484	An Analysis of the Chemical States of Phosphorus in CVD Phosphosilicate Glass Films C. Pavelescu and C. Cobianu	709

ELECTRONICS/ENERGY TECHNOLOGY

Heteroepitaxial Approaches in Semiconductors: Lattice Mismatch and Its Consequences

485	The Physical Foundations of Critical Thickness Calculations in Epitaxy J. H. van der Merwe and W. A. Jesser	710
486	The Elimination of Interface Defects in Mismatched Epilayers by a Reduction in Growth Area E. A. Fitzgerald, P. D. Kirchner, R. Proano, G. D. Pettit, J. M. Woodall, and D. G. Ast	711
487	The Partitioning of Elastic Energy during Misfit Dislocation Formation in Heteroepitaxial Layers Z. J. Radzimski, G. A. Rozgonyi, and S. M. Bedair	713
488	The Interaction of Surface Misfit and Steps at Crystal Surfaces J. H. van der Merwe and W. H. Kunert	715
489	Strain and Critical Thickness in GaSb/AlSb: An Ion Channeling Study H.-J. Gossmann, G. P. Schwartz, B. A. Davidson, and G. J. Gualtieri	716

Abstract Number		Page Number
490	Superlattice Characterization using Raman Scattering G. P. Schwartz, G. J. Gualtieri, and W. A. Sunder	717
491	Structural and Optical Properties of Highly Strained $InAs_xP_{1-x}/InP$ Heterostructures R. P. Schneider, Jr., D. X. Li, and B. W. Wessels	718
492	High-Resolution Transmission Electron Microscopy of $InAs_xP_{1-x}/InP$ Heterostructures D. X. Li, R. P. Schneider, Jr., B. W. Wessels, and W. A. Chiou	720
493	Core Level Photoemmission Measurements of Heterojunction Valence Band Offsets in Highly Strained Systems R. G. Nuzzo, G. P. Schwartz, G. J. Gualtieri, M. S. Hybertsen, J. Bevk, and J. P. Mannaerts	722
494	Optical Investigations of Strained InGaAs/GaAs Single Quantum Wells D. J. Arent, K. Deneffe, C. Van Hoof, J. De Boeck, and G. Borghs	723
495	Heterostructures of $GaAs_{1-x}Sb_x$ on GaAs Grown by Molecular Beam Epitaxy J. H. Zhao, J. C. Jeong, T. E. Schlesinger, and A. G. Milnes	725
496	Growth and Characterization of $ZnGeP_2/GaP$ Heterostructures by OMCVD G.-C. Xing, J. B. Posthill, K. J. Bachmann, G. Solomon, and M. Timmons	727
497	X-Ray Characterization of Heteroepitaxial GaAs on Si (001) H. Zabel, N. Lucas, and H. Morkoç	729
498	Controlled Formation of Misfit Dislocations for Heteroepitaxial Growth of GaAs on (100) Si by Migration-Enhanced Epitaxy W. Stolz, Y. Horikoshi, and M. Naganuma	731
499	X-Ray Characterization of $Cd_xHg_{1-x}Te$ Epitaxial Layers Grown onto GaAs Substrates by MOVPE G. T. Brown, J. Giess and S. J. C. Irvine	732
500	Effects of Misfit Dislocations and Thermally Induced Strain on the Film Properties of Heteroepitaxial GaAs on Si R. M. Lum, J. K. Klingert, R. B. Bylsma, A. M. Glass, A. T. Macrander, T. D. Harris, and M. G. Lamont	733
501	Epitaxial Layer Misorientation in Heteroepitaxial GaAs on Si R. J. Matyi, H. F. Schaake, D. G. Deppe, and N. Holonyak, Jr.	734
502	A Structural Investigation of Compositionally Graded $InAs_{1-x}Sb_x$ Buffer Layers R. M. Biefeld	736
503	Heteroepitaxy with Large Mismatch: *TiN and ZrN on Si(100)* C.-H. Choi, S. A. Barnett, L. Hultman, and J.-E. Sundgren	737
504	In Situ Characterization of Heteroepitaxy by Quasi-Elastic Ligh Scattering J. M. Olson	738
505	X-Ray Diffraction Study of $In_{0.17}Ga_{0.83}As/GaAs$ Strained-Layer Superlattices D. E. Grider, R. R. Horning, and T. Nohava	740
506	Relationship Between X-Ray Linewidth and Sign of the Mismatch of Highly Perfect InGaAs/InP Grown by Metal Organic Chemical Vapor Deposition A. T. Macrander, S. Lau, J. Long, and D. Mitcham	742
507	The Use of Lattice Mismatch Measurements on InGaAs Layers as a Means of Investigating VPE Growth Processes D. N. Buckley	743
508	Structural Characterization of Strained Layer Quantum Well Systems by Grazing Incidence X-Ray Scattering C. A. Lucas, D. F. McMorrow, and S. Bates	744
509	Lattice Mismatch of Simple and Complex Layer Structes by X-Ray Diffraction P. F. Fewster	746

Abstract Number		Page Number
510	Kinetics and Energetics Issues in Semiconductor Heteroepitaxy Using Molecular Beam Epitaxy J. Singh	747
511	II-VI/III-V Heterointerfaces: Epilayer on Epilayer Structures R. L. Gunshor, L. A. Kolodziejski, N. Otsuka, A. V. Nurmikko, and M. R. Melloch	748
512	Effects of Lattice Mismatch on the Photoluminescence Properties of Heteroepitaxial ZnSe on GaAs, InGaAs, and AlAs B. J. Skromme, M. C. Tamargo, J. L. de Miguel, R. E. Nahory, and W. A. Bonner	749
513	Synthesis of Epitaxial GaAs and (Al, Ga)As on (511) GaAs Surfaces by Molecular Beam Epitaxy E. Towe and C. G. Fonstad	750
514	Low-Temperature Growth of AlGaAs-GaAs Heterostructures by Migration-Enhanced Epitaxy Y. Horikoshi, M. Kawashima, and H. Yamaguchi	751
	ENERGY TECHNOLOGY	
	Environmental Effects of Energy Systems	
515	Electrochemical Flue Gas Desulfurization M. Franke, D. McHenry, and J. Winnick	753
516	Electrochemical Behavior of Graphite and Nickel-Chromium Electrodes in Sodium Polysulfide in the Absence and Presence of Hydrogen Sulfide Z. Mao, B. Dandapani, S. Srinivasan, R. E. White, and A. J. Appleby	754
517	Thermodynamic Aspects of H_2S Electrolysis in Aqueous NaOH and Molten Polysulfides A. A. Anani, Z. Mao, B. Dandapani, S. Srinivasan, and A. J. Appleby	756
518	$ZnCl_2$-HCl Plating Baths for Stripping and Recovery of Zinc from Galvanized Iron Scrap S. Zaromb, A. V. Fraioli, E. J. Daniels, G. V. Queen, and R. M. Bozen	757
519	Effect of HVDC Transmission Lines on the Charge Distribution of Aerosols G. B. Johnson and P. J. Carter	759
520	Electrochromism of Polyaniline: An In Situ FTIR Study M. A. Habib and S. P. Maheswari	760
521	Prediction of Electric Field and Ion Density of HVDC Transmission Lines G. B. Johnson and L. E. Zaffanella	762
522	Biological Effects of Spark-Decomposed SF_6 G. D. Griffin, M. G. Nolan, C. E. Easterly, and I. Sauers	763
523	The Electrical Environment of HVDC Transmission Lines G. B. Johnson	764
	HIGH TEMPERATURE MATERIALS/CORROSION	
	Fundamental Aspects of High Temperature Corrosion III	
524	Similarities and Differences Between Corrosion in High Temperature Gaseous Environments and Aqueous Environments T. A. Ramanarayanan and S. N. Smith	765
525	Deposition and Flow of Molten Salt Mixtures on Gas Turbine Blades: A Theroretical Treatment R. Nagarajan	767
526	Hot Corrosion of Austenitic Stainless Steels in Molten Carbonate Fuel Cell Environment C. Y. Yuh, A. Pigeaud, H. C. Maru, and G. H. Meier	768

Abstract Number		Page Number
527	Simultaneous Chromizing-Aluminizing of Nickel and Nickel-Base Alloys by Halide-Activated Pack Cementation V. A. Ravi and R. A. Rapp	770
528	Simulataneous Chromizing-Aluminizing Coating of Steels and Austenitic Steels by the Pack Cementation Method P. Choquet, E. Naylor, and R. A. Rapp	771
529	Reactions of Metals and Ceramics with Chlorine and Oxygen at Elevated Temperatures N. S. Jacobson, J. E. Marra, E. R. Kreidler, and M. J. McNallan	772
530	Effect of Chlorine Contamination on the Oxidation of Iron-Chromium Alloys under Conditions of Temperature Cycling J. C. Liu and M. J. McNallan	774
531	The Effect of Alloy Grain Size on Oxidation Kinetics of an Al_2O_3-Forming Alloy J. J. Goedjen and D. A. Shores	775
532	Effect of Ion-Implanted Cerium on the Growth Rate of Chromia Scales on Ni-Cr Alloys T. A. Ramanarayanan, N. Patibandla, and F. Cosandey	777
533	A Model Stress Relief in Oxide/Metal Systems during Cooling D. A. Shores, J. J. Barnes, and J. G. Goedjen	779
534	Role of Oxygen Supply in High Temperature Growing of Compact Oxide Scale D. Gozzi, M. Tomellini, G. Carnevale, P. L. Cignini, and L. Petrucci	781
	Chemical Interactions in High Temperature Composites	
535	Transition-Metal-Silicide/Refractory-Ceramic Interactions P. J. Meschter, R. J. Lederich, and J. E. O'Neal	782
536	Investigation of the Reactions Between Titanium Alloys and Ceramic Reinforcements at Elevated Temperatures B. London, P. J. Meschter, and S. M. L. Sastry	784
537	Compatibility of Several Reinforcement Materials with NiAl A. K. Misra	785
538	Chemical Interactions of SiC with Ti-Al and Nb-Al Alloys J.-M. Yang and K. T. Chiang	786
539	The Oxidation of Chemically Vapor Deposited Silicon Carbide J. W. Fergus and W. L. Worrell	787
539A	Electrical Properties of Novel Mixed-Conducting Oxides W. L. Worrell and S. S. Liou	788
	LUMINESCENCE AND DISPLAY MATERIALS	
	Luminescence Science and Technology	
540	Luminescent Materials Form Still a Challenge G. Blasse	789
541	Pair Luminescence as a Technique for Impurity Characterization G. F. Neumark	790
542	Magneto-Luminescence of $KZn_{1-x}Co_xF_3$ N. L. Rowell and D. J. Lockwood	791
543	Zero Phonon Lines, Photoburning of Spectral Holes, Optical Data Storage and Processing in Impurity-Doped Solids K. K. Rebane	793
544	Spectral Hole Burning in Amorphous Solids L. A. Rebane and A. A. Gorokhovskii	794

Abstract Number		Page Number
545	Femtosecond Lattice Relaxation Following Ultrafast Excitation of F_{2+} Center in LiF: A Coherent Phonon Description N. Terzi and G. Consolati	795
546	F.L.N. of the ^2E-$\rightarrow{}^4A_2$ Transition of GSGG:Cr^{3+} A. Monteil, C. Garapon, and G. Boulon	796
547	Exciton Relaxation and Thermal Equilibrium in PbI_2 T. Goto and J. Takeda	797
548	Perturbation Methods in Optical Spectroscopy W. A. Runciman	798
549	Investigation of ZnS:Tm^{3+} Powders by EXAFS and Site Selective Excitation of the Luminescence J. Dexpert-Ghys, Y. Charreire, P. Esteban-Puges, L. Albert, and H. Dexpert	800
550	X-Ray and EPR Studies of Compositional Defects in Y_2O_2S Red Phosphors M. Graciet, N. Ruelle, and J. Van Bardeleben	801
551	The Application of TL and TSC to the Study of Defect Formation in Alkali Halides by UV Radiation N. Kristianpoller and Z. Davidson	802
552	A New Contribution to Spin-Forbidden Rare Earth Optical Transition Intensities M. C. Downer, G. W. Burdick, and D. K. Sardar	804
553	Time Dependence of Decay of Delayed Luminescence A. K. Jonscher	806
554	Eu^{2+}--$\rightarrow$ Sm^{3+} Electron Transfer by Tunneling in MgS:Eu,Sm K. Chakrabarti, V. K. Mathur, L. A. Thomas, R. J. Abbundi, M. Hill, and J. J. Brown	808
555	Chemical Composition of and Eu^{2+} Luminescence in the Barium Hexa-Aluminates C. R. Ronda and B. M. J. Smets	809
556	Spectroscopy of Disordered $CdS_{1-x}Se_x$ Mixed Crystals F. A. Majumder, H. E. Swoboda, and C. Klingshirn	810
557	Industrial Application of Rare Earths Luminescence: Role of Starting Materials P. Maestro, P. Plaza, and R. Fitoussi	811
558	Spectroscopic Properties of Chromium (III) in Zirconium Barium Fluoride Glass (ZBLA) R. Balda, J. Fernandez, M. A. Illarramendi, and M. J. Elejalde	813
559	Charge Transfer Luminescence in Polysilanes J. R. G. Thorne, R. M. Hochstrasser, and J. M. Zeigler	815
560	Novel Technique in the Preparation of Eu^{2+} Doped Phosphors R. P. Rao and R. Jagannathan	816
561	Luminescence Properties of Thorium Phosphate Transparent Gels Doped with Rare Earths and Uranyl Ions E. Simoni, M. G. Iroulart, V. Brandel, and M. Genet	817
562	Novel Emission of Dy in Magnesium Fluoroborate X. Liu, Y. Zhang, Z. Wang, and S. Xu	818
563	Luminescence from Several Activators in $SrBeLa_2O_5$ G. Blasse and G. J. Dirksen	819
564	A Long-Persistent Blue Phosphor $SrSb_2O_6$:Mn^{2+} H. Yamada, H. Matsukiyo, T. Suzuki, H.Yamamoto, T. Okamura, T. Imai, and M. Morita	820
565	Enhancement of Cathodoluminescence in LaOBr:Tb by Codoping with Dy X. Xu, Y. Li, and X. Liu	821
566	Terbium-Activated Yttrium Silicate Lamp Phosphors T. E. Peters, R. B. Hunt, R. G. Pappalardo, and F. Taubner	822

Abstract Number		Page Number
567	Luminescene of Rare-Earth Cryptates G. Blasse and N. Sabbatini	824
568	Temperature Dependence of the Vibronic Spectrum and Lifetime of $LiGa_5O_8:Mn^{4+}$ T. Abritta and R. J. M. de Fonseca	825
569	Energy Transfer Process in Alkaline Earth Rare Earth Pentaborate Phosphors R. P. Rao, R. Jagannathan, and T. R. N. Kutty	826
570	Energy Transfer Between Pb^{2+} and Gd^{3+} Ions G. Blasse and H. S. Kiliaan	827
571	Luminescence and Energy Migration in $(Sr,Eu)B_4O_7$ A. Meijerink, J. Nuyten, and G. Blasse	828
572	Energy Transfer Effects in Beta"-Alumina L. A. Momoda, J. D. Barrie, B. Dunn, and O. M. Stafsudd	829
573	Studies of the Field Dependent Photoluminescence of n-GaAs Electrodes with and without Cobalt Films S. M. Ahmed, J. Leduc, and J. Trudel	830
574	A Comparative Study of Photoluminescence and Selective Pair Luminescence in GaAs Y. K. Yeo, J. R. Cavin, and R. L. Hengehold	832
575	Electroluminescence Spectra of CdSe/ZnTe Heterojunction S. Al-Dallah	833
576	Silent Discharge Luminescent Effect and Intrinsic Electroluminescence C-j. Wu, E-c. Wu, and S-m. Wen	834
577	Sun-Powered Enamel Electroluminescent Display C-j. Wu, S-m. Wen, and E-c. Wu	836
578	Random Alloy Effects for Fe in GaAsP P. Hong and Q. Huang	837
	Optical Imaging, Materials	
579	A Leddicon Target Sensitive in the 1000-2000 nm Waveband G. P. Hopkins and D. G. Swain	838
580	Avalanche Multiplication of the Photogenerated Carriers in Amorphous Semiconductor and Its Applicaiton to Imaging Devices S. Ishioka, Y. Takasaki, K. Tsuji T. Hirai, K. Tanioka, J. Yamazaki, K. Shidara, and K. Taketoshi	839
581	The Effect of Heavy Metal Contamination on Defects in CCD Imagers; Contamination Monitoring by Surface Photovoltage L. Jastrzebski, R. Soydan, H. Elab, W. Henry, and E. Savoye	841
582	Progress in Infrared Image Sensors with Schottky-Barrier Detectors W. F. Kosonocky	843
	Photonics	
583	Nonlinear Optics at Interfaces Y. R. Shen	844
584	Studies of Liquid Surfaces by Second Harmonic Generation K. B. Eisenthal	845
585	Measurements of the Structure and Dynamics of Thin Film Growth on Electrode Surfaces by SHG G. L. Richmond, V. L. Shannon, and D. A. Koos	846
586	SHG as A Probe of Surface Stability and Order in Solution D. A. Koos, V. L. Shannon, S. A. Kellar, and G. L. Richmond	847
587	Monolayer Vibrational Spectroscopy on Metal and Semiconductor Surfaces by Infrared-Visible Sum Generation A. L. Harris, C. E. D. Chidsey, N J. Levinos, and D. N. Loiacono	848

Abstract Number		Page Number
588	Population Relaxation of CO-Stretching Vibrations for Carbon Monoxide on Metal Clusters E. J. Heilweil, R. R. Cavanagh, and J. C. Stephenson	850
589	Can Chemical Reactions be Controlled with Picosecond Infrared Lasers? E. Mazur	851
590	Intramolecular Vibrational Relaxation Lifetimes by Picosecond Fluorescence Depletion Spectroscopy J. D. McDonald, J. Kauffman, M. Cote, and P. Smith	853
591	The Effect of Vibrational Motion on the Dynamics of Intramolecular Charge Transfer Reactions J. D. Simon and S.-G. Su	855
592	Femtosecond Raman Induced Quantum Beats in a Dye Molecule Observed by Polarization Sensitive Measurements J. Chesnoy and A. Mokhtari	856
593	Femtosecond Spectroscopy of Chemical Reactions in Condensed Phases K. A. Nelson, A. G. Joly, and L. R. Williams	857
594	Low Temperature Glass Relaxation and Interaction with Solutes Probed by Picosecond Photon Echo and Hole Burning Experiments M. Berg, C. A. Walsh, L. R. Narasimhan, K. A. Littau, and M. D. Fayer	859
595	Femtosecond Optical Kerr Dynamics in Molecular Liquids of Varying Structure W. T. Lotshaw, D. McMorrow, C. Kapouzos, and G. A. Kenney-Wallace	861
596	Cooperative Effects under Interaction of Coherent Radiation with Matter V. F. Cheltsov	862
597	Ultrafast Photonic Switching with Nonlinear Glass Guided-Wave Devices P. W. Smith	863
598	Ultrasmall Semiconductor Microresonators J. L. Jewell, S. L. McCall, Y. H. Lee, A. Scherer, A. C. Gossard, and J. H. English	864
599	Tunneling-Based Phenomena in Asymmetric Coupled Quantum Wells J. E. Golub, P. F. Liao, Y. Prior, D. J. Eilenberger, J. P. Harbison, and L. T. Florez	866
600	Quantum Wires and Quantum Dots: Physics and Applications K. Vahala	867
601	Quantum Mechanical Effects in Field-Effect Transistors with Nanostructured Geometries T. P. Orlando, P. F. Bagwell, H. I. Smith, and D. A. Antoniadis	868
602	Ultrafast Relaxation and Bandgap Renormalization in Semiconductors S. Das Sarma	869
603	The Role of Metastable Light-Induced Defects in the Picosecond Decay of Photoinduced Absorption in Intrinsic Hydrogenated Amorphous Silicon T. L. Gustafson, H. Scher, D. M. Roberts, and R. W. Collins	870
604	Nonequilibrium Optical Phonon Generation and Detection in Picosecond Photoexcited Germanium J. F. Young, A. Othonos, and H. M. van Driel	871
605	Ultrashort Wavelength Surface Acoustic Waves Induced on Silicon and Germanium by Picosecond Pulses H. M. van Driel, M. Ledgerwood, D. Jost, and J. E. Sipe	872
606	Laser Melting of Silicon: The First Few Picoseconds J.-K. Wang, P. Saeta, M. Buijs, and E. Mazur	873

Abstract Number		Page Number
607	Semiconductor Optical Damage in the Femtosecond Regime M. C. Downer, D. H. Reitze, and T. R. Zhang	874
608	Harmonic Cross-Phase Modulation in ZnSe P. P. Ho and R. R. Alfano	875
609	Coherent Transient Optical Effects in Semiconductors P. K. Sen and P. Sen	876
610	Ultrafast Dynamics of Ligand Rebinding to Heme at Low Temperature D. D. Dlott, J. C. Postlewaite, and J. B. Miers	877
611	Investigation of Optical Spectroscopy of Cancerous and Normal Human Tissues A. Pradhan, R. R. Alfano, G. C. Tang, and S. Wenling	878
612	Time-Resolved Fluorescence of Nucleic Acids T. M. Nordlund	879
613	Picosecond Time-Resolved Infrared Spectroscopy P. A. Hansen, J. N. Moore, and R. M. Hochstrasser	881
614	Ultrafast Electronic and Acoustic Effects in Conducting Polymers Z. V. Vardeny	882
615	Time-Resolved Absorption in Oriented Trans-Polyacetylene L. Rothberg, T. M. Jedju, P. Townsend, S. Etemadm, and G. L. Baker	883
616	Long Wavelength Determination of the Spectral Response of X^3 in Polyacetylene Using Infrared-Free-Electron Laser S. Etemad, W-S. Fann, S. Benson, J. Madey, G. L. Baker, and F. Kajzar	884
617	Picosecond Studies of PTS: Resolution of a New Metastable State G. L. Blanchard, J. P. Heritage, G. L. Baker, and S. Etemad	885
618	Ultrafast Imaging of Optical Damage and Laser-Induced Waves in PMMA H. Kim, J. C. Postlewaite, T. Zyung, and D. D. Dlott	887
619	$LiNbO_3$ for Integrated Optical Devices F. Leonberger, T. Findakly, P. Suchoski, and M. Abou el leil	888
620	Alternative Materials and Processes for Integrated Optics Y. Khawaja, M. N. Kozicki, J. L. Edwards, B. Qurashi, G. Bernstein, and A. E. Owen	890
621	Compound Semiconductor Electro-Optic Materials and Devices Y. J. Chen	892
622	Experimental Study of the Role of Color Centers on Silica Fiber Preparation for Second Harmonic Generation (SHG) J. R. Rotge and M. F. El-Hewie	893
623	Optical Pulse Propagation for a Nonlinear Dielectric Film S. V. Branis and J. L. Birman	894
624	Induced-Frequency Shift, Induced-Spectral Broadening, and Optical Amplification of Picoseond Pulses by Cross-Phase Modulation in a Single-Mode Optical Fiber P. L. Baldeck and R. R. Alfano	895
625	The Utilization of UV and IR Supercontinua in Gas-Phase Kinetic Spectroscopy J. H. Glownia, J. A. Misewich, and P. P. Sorokin	897
626	A New Class of Ultraviolet Femtosecond Sources M. C. Downer, G. Focht, and T. R. Zhang	898
627	Control of Solitons in a Femtosecond Dye Laser W. L. Nighan, Jr. and P. M. Fauchet	900
628	Effects of Detuning on Mode-Locked Pulse Trains of an Argon Ion Laser T. Kitahara	901
629	Temporal Reshaping of Ultrashort Laser Pulses Reflected by GaAs I. H. Campbell, S. K. Kirby, and P. M. Fauchet	903

Abstract Number		Page Number
630	Two Micron Focusing of Millijoule Femtosecond Pulses from a Conical Axicon Amplifier M. C. Downer, W. M. Wood, and G. Focht	904
	X-Ray Imaging	
631	Dual-Energy Chest Radiography: Physical Principles and Clinical Potential G. T. Barnes, R. G. Fraser, and P. C. Sanders	905
632	The Application of X-Ray Phosphors in Duel Energy Subtraction J.-T. Ho and R. A. Kruger	906
633	Ceramic Scintillators for X-Ray CT Use K. Yokota, N. Matsuda, and M. Tamatani	908
634	Ge(3+), Tb(3+), Gd(3+), Tb(3+) Activated Silicate X-Ray Luminescent Glasses for Real-Time Radiography C. Bueno and R. A. Buchanan	910
635	The Determination of X-Ray Phosphor Scintillation Spectra J. Beutel and D. J. Mickish	911
636	The Detective Quantum Efficiency of Screen-Film Systems P. C. Bunch	912
637	X-Ray Luminescence of Yttrium Strontium Tantalate Phosphors M. R. Royce, S. Nakamura, G. Shinoriya, S. Chikutei, and T. Kondo	913
638	X-Ray Excited Luminescence Spectroscopy of Activated and Unactivated Tantalates M. K. Crawford, L. H. Brixner, K. Somaiah, and G. Blasse	915
639	Luminescence and Radiographic Performance of Yttrium/Lanthanum Tantalates W. J. Zegarski and L. H. Brixner	917
640	High-Speed Stimulable Phosphor X-Ray Detector for Computed Radiography C. Umemoto, A. Kitada, K. Takahashi, and T. Matsuda	918
641	Properties of RbX:Tl(X=Br,I) Photostimulable Phosphors K. Amitani and S. Honda	919
642	Measurement Systems for the Characterization of Photostimulable Phosphors and Storage Phosphor Screens for X-Ray Imaging L. Struye	921
643	Some Synthetic Aspects of BaFBr:Eu Photostimulable Phosphor V. B. Reddy,	922
644	Principles of Photostimulated Charge Transfer in X-Ray Storage Phosphors H. von Seggern, T. Voigt, and K. Schwarzmichel	923
645	Study of the Photostimulable Luminescence Complex in the Storage Phosphor of BaFBr:Eu W. Knupfer, M. Mengel, K. Schwarzmichel, H. v. Seggern, and K. Huber	925
646	Effect of Grinding on Photostimuable Phosphors for X-Ray Screens R. P. Rao	927
	General Session	
647	Electrophoretic Deposition of High Resolution Phosphor Screens E. Sluzky and K. Hesse	929
648	TiO_2/SiO_2 Multilayered Insulating Films for ELD M. Hanazono, T. Nakayama, K. Onisawa, and M. Fuyama	930
649	Beam Penetration Phosphors for Adding Color Capability to HUD CRT's D. G. Etherington, J. D. Leyland, M. Naqvi, H. Tanner, and M. S. Waite	932
650	The Formation Process of $Y_2O_2S:Eu^{3+}$, a Red Phosphor C. H. Kim, C. I. Jeon, S. I. Mho and Q. W. Choi	934

Abstract Number		Page Number
651	Colloid Chemistry of Fluorescent Phosphors P. K. Whitman, M. E. Labib, and G. H. Thomas III	936
	LUMINESCENCE AND DISPLAY MATERIALS/ENERGY TECHNOLOGY	
	Optical Sensors	
652	Optical Taste Sensor with Fluorophore-Embedded Langmuir-Blodgett Film M. Aizawa, M. Matsuzawa, and H. Shinohara	937
653	Fiber Optic Pressure Sensors for Medical Applications T.-E. Hansen	938
654	Fiber Optic Fluoroimmunosensor: Determination of the Sensitivity and Dynamic Range D. E. Yoshida, D. A. Christensen, J. D. Andrade, and W. M. Reichert	940
655	Sensors for Determining the Composition of Falling Liquid Films L. N. Klatt, D. T. Bostick, and H. Perez Blanco	942
656	Optical Position Finding with CCD-Cameras P. P. L. Regtien and B. L. Verbraak	944
657	Programming of the Spectral Response of Silicon Photodiodes R. F. Wolffenbuttel	946
658	Silicon Color Sensors with a Digital Output R. F. Wolffenbuttel	948
659	Influence of Charge-Transfer States on Eu-Doped Phosphors for Temperature Sensor Appilcations S. W. Allison, M. R. Cates, G. J. Pogatshnik, and A. R. Bugos	950
660	Fiber Ring Resonators and Shock Excited Mechanical Oscillators M. A. Butler	952
661	Reflectrometric Study of CHemical Equilibria of Immobilized Indicators Used in Optical Sensors R. Narayanaswamy	953
662	Fiber Optic Surface Enhanced Raman Chemical Sensors M. M. Carrabba, R. B. Edmonds, P. J. Marren, and R. D. Rauh	954
663	Chemisorption-Induced Reflectivity Changes in Thin Metal Films A. J. Ricco and M. A. Butler	956
664	Optical Wavequide Sensors: Surface Fluorescence Excitation J. T. Ives, D. A. Christensen, and W. M. Reichert	958
665	An Investigation of Polymeric Film/Solute Vapor Solubility Parameters Using an Optical Waveguide Interfacial Probe Method J. F. Giuliani	960
666	Reversible SO_2 Detection Using a Multiple Reflecting Optical Waveguide Sensor R. L. Cook, R. C. MacDuff, and A. F. Sammells	961
667	Semiconductor Photoluminescence as a Sensor for Gaseous Acids and Bases G. C. Lisensky, A. B. Ellis, and G. J. Meyer	962
668	Electrochemical Modulation of Luminescence from a Conducting Polylmer Surface S. Basak, E. W. Tsai, L. Phan, and K. Rajeshwar	963
669	Electrochemistry of -Substituted (Soluble) Polythiophenes E. W. Tsai, S. Basak, J. Ruiz, J. R. Reynolds, and K. Rajeshwar	964
670	Highly Sensitive Optical Gas Detector of Squarylium Dye LB-Film Containing J-Aggregate M. Furuki, S. Kim, K. Ageishi, and L. S. Pu	966

Abstract Number | Page Number

PHYSICAL ELECTROCHEMISTRY

Magnetic Field Effects in Electrochemistry

671 Analysis of the Electron Transfer Processes of Electrochemical Reaction in the Magnetic Field by Means of Magnetohydrodynamic Electrode
R. Aogaki and K. Fueki 966

672 Preliminary Study of Saccharide Diffusion Through Inert Porous Membrane in an Externally Applied Magnetic Field
J. Lielmezs and H. Aleman 967

673 Magnetic Field on Mass Transport
O. Aaboubi, J. P. Chopart, J. Douglade, C. Gabrielli, A. Olivier, and B. Tribollet 969

674 Influence of Magnetic Field on the Corrosion of Iron in Sulfuric Medium
C. Gabrielli, J. P. Chopart, J. Douglade, A. Olivier, S. Sadki, and B. Tribollet 971

675 Magnetic Field Effect in the Electrochemical Reduction of Aquo Zn^{2+} in the Presence of a Paramagnetic Ion
K. S. V. Santhanam and R. N. O'Brien 973

676 Magnetic Field Effects in the Bulk of an Electrolytic Cell
D. Laforgue-Kantzer 974

677 Hall Effect in Dilute Electrolyte 1-1 Solutions
P. Gerard, R. Gerard, M. Meton, and E. J. Picard 975

678 The Enhancing Effect of Magnetic Fields on Convective Flow Patterns in an Electrolyte via Flow Visualization
A. Lau and T. Z. Fahidy 977

679 The Effect of Chloride Ion on Electrolytic Co[illegible] of Copper [illegible] Alumina in a Magnetic Field
J. Dash and F. Brace 978

680 Electrodeposition of Ni-Fe in Very High Magnetic Fields
J. Dash and L. T. Romankiw 979

681 Magnetic Field Effect on Electrodeposition of Metals
J. P. Chopart, J. Douglade, P. Fricoteaux, C. Gabrielli, A. Olivier, and B. Tribollet 980

682 Electromagnetic Microhydrodynamics of Aqueous Electrolytes
N. Ph. Bondarenko and E. Z. Gak 982

683 The Prospects of Using Magnetohydrodynamic Effects in Electrolytes to Control Charge and Mass Transfer Processes
E. Z. Gak and E. E. Rochinson 983

Tunneling Microscopy and Related Techniques

684 Molecular Imaging with the Tunneling and Force Microscopes - The Relation to Electrochemistry
C. F. Quate 984

685 STM Observation of Nanostructure of Electrode Surfaces
K. Hosaki and H. Kita 985

686 New Electrochemical Scanning Tunneling Microscope and Its Application
K. Itaya 986

687 In Situ Scanning Tunneling Microscopy (STM) of Semiconductor/Liquid Interface
E. Tomita and K. Itaya 987

688 Atomic Scale STM - Studies on an Electrode Surface under Potential Control
R. J. Behm, T. Twomey, D. M. Kolb, and J. Wiechers 988

Abstract Number		Abstract Number
689	Scanning Tunneling Microscopy in Combination with Scanning Electron Microscopy to Study Electrochemically Processed Surfaces L. Vazquez, A. Bartolome, A. M. Baro, C. Alonso, R. Salvarezza, and A. J. Arvia	990
690	Steps Toward Atomic-Resolution Studies of Metal Surfaces in Aqueous Solutions R. Sonnenfeld, O. Melroy, G. Singh, and J. Gordon II	991
691	Scanning Tunneling Microscopy of Vapor-Deposited and Electrodeposited Metals C. E. D. Chidsey	992
692	Surface Modification and Spectroscopy with the Scanning Tunneling Microscope A. De Lozanne	993
693	In Situ Scanning Tunneling Microscopy for Electrochemical Studies A. A. Gewirth, F.-R. F. Fan, and A. J. Bard	994
694	Scanning Electrochemical Microscope: High Resolution Deposition and Etching of Metals O. E. Husser, D. H. Craston, and A. J. Bard	995
695	STM Imaging of Organic Adsorbates J. E. Frommer and J. S. Foster	996
696	Scanning Tunneling Microscopy of Titanium in Air and Water L. D. McCormick, T. Thundat, L. Nagahara, and S. M. Lindsay	997
697	Molecular Rulers and the Use of Scanning Transmission Electron Microscopy L. L. Miller and F. R. Furuya	998
698	Characterization of Surfaces by Surface Forces, Scanning Tunneling, and Atomic Force Microscopy D. F. Evans, R. Yang, G. Lee, R. Matthews, and W. Hendrickson	999
699	Multilple-Beam Interferometry and the Study of Silver Films in a Surface Force Apparatus H. K. Christenson, M. T. Clarkson, and J. L. Parker	1000
700	Adhesion of Two Solid Surfaces in Water: Effect of Rotational Mismatch of Surface Lattices P. M. McGuiggan and J. N. Israelachvili	1001
701	Surface Forces and High Resolution In Situ Optical Imaging of the Electrode/Electrolyte Interface H. S. White, C. P. Smith, S. R. Snyder, and J. Norton	1002
	General Session	
702	Kinetic Isotope Effects of the Hydrogen-Evolution-Reaction (HER) at Gold and Platinum Electrodes D. Tegtmeyer and J. Heitbaum	1003
703	Electrocatalysis of Anodic Oxygen-Transfer Reactions: Modification of Electrode Surfaces by Formation of Thin PbO_2 and Bi(III)-Incorporated PbO_2 Ad-Layers via Electrochemical Reactions at Solid/Solid Interface H. Chang and D. C. Johnson	1004
704	Electrolytic Hydrogenation and Amorphization of Fcc-$Pd_{0.21}Zr_{0.79}$ J. Y. Huot, A. Van Neste, L. Brossard, and R. Schulz	1005
705	Electrocatalytic Properties of Metal Adatoms in a Potential Range Negative to Bulk Deposition X. Xing and D. Scherson	1007
706	Impedance of Sodium Beta" Alumina/Porous Electrode Interfaces in AMTEC Cells R. M. Williams, B. Jeffries-Nakamura, M. L. Underwood, C. P. Rankston, and J. T. Kummer	1009
707	The Hanging Meniscus Rotating Disk Electrode (HMRDE) H. M. Villullas and B. D. Cahan	1010

Abstract Number		Page Number
708	Trapezoidal Wave Cyclic Voltammetry in Study of Transfer of Ion Across the Interface Between Two Immiscible Electrolyte Solutions D. Qi and J. Li	1012
709	Novel Conducting Polymers as Optical Switches: Toward Microsecond Electrochromic Switching Times P. Chandrasekhar	1013
710	Electrochemical Studies of New Viologen Compounds M. H. Miles, R. A. Henry, and R. A. Hollins	1014
711	Electrochemical Studies on Electrodeposited Tungsten Trioxide Films D. E. Stilwell, K. H. Park, and M. H. Miles	1016
712	In Situ FTIRRAS Studies of Anion-Metal Oxide Interactions in Electrochemical Systems: Perchlorate and Nitrate Adsorption on Polycrystalline Pt and Au Surfaces D. Scherson, I. T. Bae, X. Xing, M. Razaq, and E. B. Yeager	1018
713	IRRAS Study of Dry Perfluorinated Sulfonic Acid Ionomer (PFSI) Films of Pt and Carbon Substrates D. Gervasio, D. Chu, M. Razaq, and E. B. Yeager	1020
714	Cyclic Voltammetric Study of the Reduction of Pu(III) to Plutonium Metal in Molten LiCl-NaCl-$CaCl_2$-$BaCl_2$-$PuCl_3$ D. S. Poa, Z. Tomczuk, and R. K. Steunenberg	1022
715	In Situ UV-Vis Difference Spectroscopy of Electrode/Electrolyte Interface with Integrating Sphere Assembly C. G. Chen, S. J. Tang, and Z. Q. Huang	1024
	PHYSICAL ELECTROCHEMISTRY/ENERGY TECHNOLOGY	
	Electrochemistry in Semiconductor Technology	
716	Laser-Induced Photodeposition of Metal on TiO_2 Films W. H. Smyrl, C. H. Paik, M. R. Kozlowski, and P. S. Tyler	1025
717	Photoelectrochemical Characterization of Defect Heterogeneities in Anodic TiO_2 Films M. R. Kozlowski, C.-H. Paik, P. S. Tyler, W. H. Smyrl, and R. T. Atanasoski	1026
718	Identification of Deep-Level Electronic Defects by Photoelectrochemical AC Impedance Spectroscopy D. B. Bonham and M. E. Orazem	1027
719	High Resistivity ZnO Films J. P. Srivastava, L. Agarwal, and A. B. Bhattacharyya	1029
720	Photoresponse of Stainless Steel Electrode Attacked by Cl^- Ions in Acidic Medium S. Cai, S. Chen, Y. Dong, X. Chen, and H. Yang	1031
721	Photoelectrochemical Etching of Blazed Eschelle Gratings in n-GaAs J. Li, M. M. Carrabba, J. P. Hachey, S. Mathew, and R. D. Rauh	1032
722	Thermodynamic and Phase Equilibria Studies of the Aluminum-Antimony System C. A. Coughanowr, J. J. Egan, and T. J. Anderson	1034
723	Electroreflectance Study of Metal Submonolayers on ZnHgTe Alloys C. Nguyen van Huong and P. Lemasson	1036
724	Electrocrystallization of Tellurium and Cadmiun Telluride at the Glassy Carbon Surface E. Mori and K. Rajeshwar	1038

Abstract Number		Page Number
725	Ohmic Contacts Prepared by Annealing of Indium:Gold Layers Deposited on (Photo)Electrochemically Arsenic-Enriched n-GaAs Surfaces P. Clechet, P. Person, J. R. Martin and J. P. Sandino	1039
726	Effects of Superficial Topography on Uniformity of Spun-On Resist Film M. Ikeno, H. Kawashima, O. Kaneda, and H. Saeki	1041
	PHYSICAL ELECTROCHEMISTRY/HIGH TEMPERATURE MATERIALS	
	Ionic Motion in Solid State Materials	
727	Mixed Ionic and Electronic Conducting Polymers L. J. Lyons, J. S. Tonge, and D. F. Shriver	1043
728	Solid Polymer Electrolytes: Zn(II) Mobility in Poly(ethylene Oxide) G. C. Farrington and H. Yang	1044
729	Mixed Polymer and Crystalline Ionic Conductors F. Croce and B. Scrosati	1045
730	Preparation and Electrochemical Properties of the SiS_2-P_2S_5-Li_2S Glass Coformer System J. H. Kennedy and Z. Zhang	1046
731	Diffusivity of Lithium Intercalated in Graphite from Molten LiCl-KCl Eutectic R. R. Agarwal	1048
732	Recovery of Oxygen from Carbon Dioxide in a High Temperature Electrochemical Reactor T. M. Gur, T. Nohmi, H. Wise, and R. A. Huggins	1050
733	Resistivity Measurements of High-Temperature Immobilized Electrolytes L. Redey and M. McParland	1051
734	Mixed-Conducting Membranes for Hydrogen Transporting S/L/S "Solid Electrolyte" Configurations M. Schreiber, J. Wolfenstine, and R. A. Huggins	1053
735	Solid-State Electrochromic Windows--An Overview R. D. Rauh	1054
736	Effect of Ionic Mobility on the Optical Properties of Cu^+ Doped Na^+-Beta"-Alumina J. D. Barrie, B. Dunn, O. M. Stafsudd, G. Hollingworth, and J. I. Zink	1056
737	Effect of Thermal History upon the Lanthanide β"-Aluminas R. B. Queenan and P. K. Davies	1057
738	Synthesis and Properties of Mixed Sodium-Cerium(III) Aluminogallate Compositions B. Dunn, J. Thery, G. Aka, D. Vivien, and C. T. Chu	1058
739	Comparison of Conductivity Measurements on Beta"-Alumina Isomorphs by Two- and Four-Probe Techniques M. W. Breiter, H. Durakpasa, G. Allitsch, and P. Linhardt	1059
	SENSORS	
	General Session	
740	Enzyme Embodied Electrode Device as a High Performance Detector for Flow Injection Analysis S. Yamauchi, Y. Ikariyama, M. Yaoita, T. Yukiashi, and H. Ushioda	1060
741	A Chemically Sensitive Bipolar Junction Transistor C. K. Y. Chun and J. W. Holm-Kennedy	1061
742	A Solid-State Oxygen Sensor Using Proton Conductor Operative at Room Temperature N. Miura, S. Kuwata, and N. Yamazoe	1063
743	Comparison Between the Sensitivities of Pt-Activated ZnO and SnO_2 Sensors in Hydrogen-Air Mixtures D. Narducci, N. Botta, and S. Pizzini	1064

Abstract Number		Page Number
744	The Use of Bulk Piezoelectric Crystal Sensors for Real-Time, In Situ Corrosion Analysis H. Hager, L. Sigalla, T. Nellikkattil, and N. Olson	1065
745	The Dependence of Bulk Piezoelectric Crystal Resonance Behavior on Fluid Properties: Implications to the Use of Piezoelectric Crystals for Fluid Analysis L. Sigalla, H. Hager, B. Kowalski, and R. Simpson	1067
746	Reference Electrodes/Sensors Using Low Resistivity Glass Membranes I. Bloom, J. J. Heiberger, M. A. Internoscia, K. Rea, and L. Redey	1068

Abstract No. 1

NUCLEATION OF LEAD SULFATE IN POROUS LEAD-DIOXIDE ELECTRODES

Dawn M. Bernardi
Physical Chemistry Department
General Motors Research Laboratories
Warren, Michigan 48090-9055

In the lead-acid battery, the nucleation and growth of $PbSO_4$ particles can influence the voltage characteristics and determine the available capacity by covering the active material. During constant-current discharge of fully charged PbO_2 electrodes, a minimum at the beginning of the voltage-time curve is observed. This phenomena is referred to as the "coup de fouet" and is believed to be caused by a supersaturated solution of lead ions occurring temporarily during discharge (1). The overall electrochemcial discharge reaction

$$PbO_2 + 4H^+ + 2e^- \longrightarrow Pb^{2+} + 2H_2O$$

produces lead ions, and the electrode voltage (relative to a reference electrode) falls in accordance with the degree of lead-ion supersaturation until the $PbSO_4$ nucleation and growth processes

$$Pb^{2+} + HSO_4^- \longrightarrow PbSO_4 + H^+ .$$

can overcome the electrochemical reaction process and thereby stabilize the potential by reducing Pb^{2+} supersaturation.

We present the results of a 1-dimensional mathematical model of a porous lead-dioxide electrode. Although similar to other models of these electrodes (2,3), the model presented includes $PbSO_4$ precipitate nucleation and growth kinetics. Classical, heterogeneous nucleation rate theory that is based on developments given by Moazed and Hirth (4) is applied in the model. The electrolyte, which consists of H^+, HSO_4^-, and Pb^{+2} ions in water, is treated with concentrated electrolyte theory much like the treatment given by Sunu and Bennion (5) for the electrolyte of the zinc-electrode. The model numerically solves eight finite difference equations: three material balance equations for electrolyte species and solid species, an electrochemical kinetic equation, Ohm's law in the electrolyte phase and the solid phase, an equation describing the electrolyte velocity, and a nucleation rate equation.

Figures 1a and 1b compare model and experimental results (1) of the electrode voltage, relative to a $PbO_2/PbSO_4$ reference electrode, for three discharge current densities. Figure 2 shows the calculated lead-sulfate number density during discharge, where number density is defined as particles per unit PbO_2 area within the electrode. (The variable x refers to the spatial dimension through the electrode thickness L. The position x=L corresponds to the face of the electrode in contact with a reservoir of electrolyte. The position x=0 is at the current collector within the electrode.) The slope of each curve in Fig. 2 is proportional to the nucleation rate. The nucleation rate at initial time and long times is near zero. We can distinguish an initial induction period where the nucleation rate is low, followed by a nucleation period in which the maximum nucleation rate occurs. During the growth period, relatively little nucleation occurs. Figure 3 shows the behavior of the lead ion concentration at various positions throughout the electrode cross section for the discharge rate of 9.6 mA/cm^2. The minimum in potential (Fig. 1) corresponds to a maximum in lead-ion concentration, and the maximum supersaturation ratio is approximately 2000. The shaded area of Fig. 4 indicates estimates of lead-sulfate number densities obtained from scanning electron micrographs of experimental electrode cross sections (6). The three large points indicate the number densities calculated during the growth period. Two unknown quantities in the nucleation rate expression ($PbSO_4$/electrolyte interfacial free energy (8×10^{-6} J/cm^2) and the fundamental lead-ion diffusion jump frequency (10^2 s^{-1})) were adjusted to allow the model results to fall within the range of experimentally expected values.

In conclusion, the proposed theoretical approach is satisfactory for describing lead-sulfate nucleation phenomena in porous lead-dioxide electrodes. Reasonable agreement between model and experimental results upholds postulates that the voltage dip is caused by temporary lead-ion supersaturation.

REFERENCES

1. D. Berndt and E. Voss, "The Voltage Characteristics of a Lead-Acid Cell During Charge and Discharge," Batteries 2, D. H. Collins, Editor, 2, pp. 17-27, Pergamon Press, Oxford (1965).

2. W. H. Tiedemann and J. Newman, "Mathematical Modeling of the Lead-Acid Cell," in Battery Design and Optimization, S. Gross, Editor, 79-1, pp. 23-38, The Electrochemical Society Softbound Proceedings Series, Princeton, NJ (1979).

3. H. Gu, T. V. Nguyen, and R. E. White, "A Mathematical Model of a Lead-Acid Cell: Discharge, Rest, and Charge," Journal of the Electrochemical Society, 134, 2953-2960 (December, 1987).

4. K. L. Moazed and J. P. Hirth, "On the Contact Angle in Heterogeneous Nucleation Upon a Substrate," Surface Science, 3, 49-61 (1964).

5. W. G. Sunu and D. N. Bennion, "Transient and Failure Analyses of the Porous Zinc Electrode," Journal of the Electrochemical Society, 127, 2007-2016 (September, 1980).

6. C. P. Wales and A. C. Simon, "Effects of Deep Cycling on Lead Positive Plates," Journal of the Electrochemical Society, 128, 2512-2517 (December, 1981).

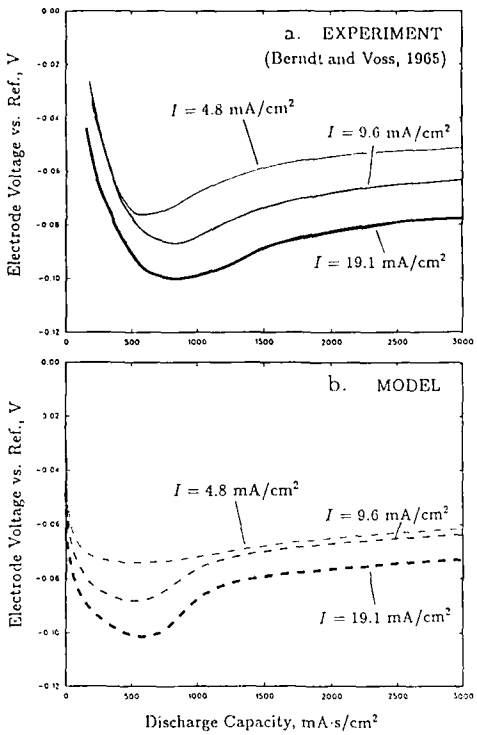


Figure 1. Initial voltage minima obtained for (a) experimental (1), and (b) model discharges of lead-dioxide electrodes at various discharge rates.

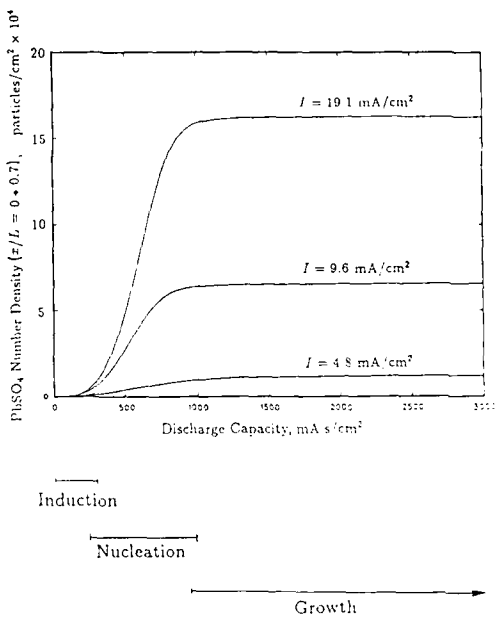


Figure 2. Calculated $PbSO_4$ number density (x=0) as a function of delivered discharge capacity for various discharge rates.

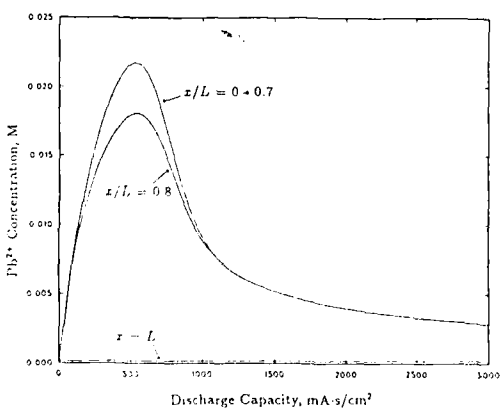


Figure 3. Calculated Pb^{2+} concentration at various positions within the electrode during discharge at a rate of 9.6 mA/cm².

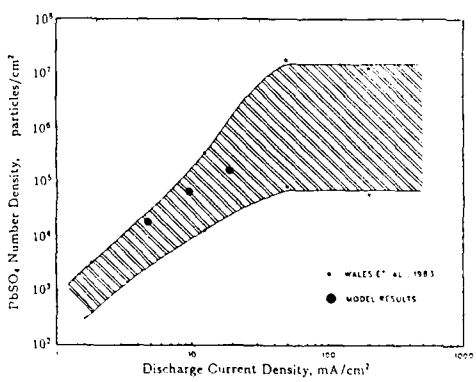


Figure 4. Calculated $PbSO_4$ number density and estimates of experimental number densities (6) as a function of discharge rate.

Abstract No. 2

A MATHEMATICAL MODEL FOR DISCHARGE, CHARGE AND SELF-DISCHARGE OF A LEAD ACID CELL

N.F.Compagnone

Industrie Magneti Marelli S.p.A.

24058 Romano di Lombardia, BG (Italy)

The lead acid cell is schematically thought as the site of two competing reactions: charge and discharge (primary reaction) and gas evolution (secondary reaction).

Each reaction is described by a Butler-Volmer type equation:

$$\begin{cases} I1 = H11(RD)^{\beta} e^{\alpha(V-VO-RI1)} \\ \qquad - H12(OX)^{\beta} e^{-\alpha(V-VO-RI1)} \end{cases} \qquad [1]$$

$$I2 = H2\,(e^{G(V-UO)} - e^{-G(V-UO)}) \qquad [2]$$

The two reactions are driven by the same voltage V. The sum of their rates I1 and I2 equals the externally impressed current I:

$$I1 + I2 = I \qquad [3]$$

I=0 is the self-discharge state while, conventionally, I>0 and I<0 are the charge and discharge conditions, respectively.

All the parameters of eq. [1] and [2] are constant except RD and OX which, for the step S at time t(S) of a step current discharge-charge cycle, are functions of the previous current-time history:

$$RD = \sum_{k=1}^{S} \frac{I1(k) - I1(k-1)}{ILrd(t(S)-t(k-1))} \qquad [4]$$

$$OX = 1 - \sum_{k=1}^{S} \frac{I1(k) - I1(k-1)}{ILox(t(S)-t(k-1))} \qquad [5]$$

Eq. [4] and [5] , which are similar to the analytical expression of the Hoxie-IEEE(1,2) method for sizing lead acid batteries, are the central algorithms of the model. They are derived from the superposition principle applied to a linear diffusion mechanism (3).

The limiting current functions ILrd(t) and ILox(t) are well described by the Liebenow equation (4):

$$IL(t) = \frac{-Cmax}{t + \gamma\sqrt{t}} \qquad [6]$$

where $\gamma=\gamma_1$ for ILrd(t) and $\gamma=\gamma_2$ for ILox(t).

The parameters are evaluated as follows:

H12 is a redundant parameter as it may be included in the exp(αVO) term. Thus, conveniently, H12 is set equal to 1.

At sufficiently high discharge rates, eq.[2] and the first term of the right-hand side member of eq. [1] can be neglected.

The experimental discharge curves V(t) of the initially fully charged cell, are plotted for different discharge rates I.

VO, α and R are obtained by best fitting the equation:

$$V(0) = VO-(1/\alpha)\ln(-I)+RI \qquad [7]$$

to the experimental initial voltage V(0) and discharge currents I.

Cmax and γ_2 are obtained by best fitting the linearized Liebenow equation:

$$(1/ItL) = (1/Cmax)+(\gamma_2/Cmax)(1/\sqrt{tL}) \qquad [8]$$

to the experimental transition times tL and discharge currents I.

β is derived from the slope β/α of the cell voltage with respect to lnOX according to the equation:

$$V= VO-(1/\alpha)\ln(-I)+(\beta/\alpha)\ln OX+RI \qquad [9]$$

A value of β/α constantly near 0.075 is observed.

At sufficiently high overcharge rates, eq.[1] and the second term of the right-hand side member of eq. [2] can be neglected.

The experimental steady state overcharge characteristic I(V) of the cell is plotted.

UO is the equilibrium voltage 1.23 V of the secondary reaction.

H2 and G are determined by best fitting the equation:

$$\ln I = \ln H2 + G(V-UO) \qquad [10]$$

to the experimental I(V) data. A value of G constantly near 10 V^{-1} is observed.

The remaining parameters H12 and γ_1 are evaluated tentatively by comparing calculated with experimental charge voltages during the charge phase of a simple discharge-charge cycle.

The system of the two eq. [1] and [2] with the condition [3] is solved numerically. As a surely convergent iteration algorithm, the bisection method (5) is suggested.

As response to a step current discharge and charge cycle which may include rest periods, the model yields the profiles of voltage, primary and secondary currents, gassing rates, apparent and real state of charge of the cell.

If a cycle includes constant power $\bar{W}$ or constant voltage $\bar{V}$ phases, these must be converted into a conveniently high number of short current steps, with the appropriate condition $I \times V = \bar{W}$ or $V = \bar{V}$ imposed at the end of each step, so that equations [4] and [5] can still be used.

REFERENCES

1. E.A.Hoxie,IEEE Trans.(Appl.Ind.),Vol. 73 p. 17, (1954)
2. IEEE Std 485, (1978)
3. J.Crank,"The Mathematics of Diffusion", pp. 11-12, Oxford University Press, London, (1957)
4. Liebenow,Zeitschrift für Elektrochemie, p. 58, (1897)
5. S.D.Conte,C.deBoor,"Elementary Numerical Analysis: An Algorithmic Approach", McGraw Hill Book Co., New York, (1981)

Abstract No. 3

APPLICATION OF TRANSMISSION LINE ANALYSIS TO POROUS BATTERY ELECTRODES

Digby D. Macdonald, Stephen J. Lenhart,
and Bruce G. Pound
SRI International, Menlo Park, CA 94025

AC impedance spectra of porous nickel battery electrodes were recorded periodically during charge/discharge cycling in concentrated KOH solution at various temperatures. A transmission line model (TLM) (Figures 1 and 2) was adopted to represent the impedance of the porous electrodes, and various model parameters were adjusted in a curve fitting routine to reproduce the experimental impedances. A typical example of this type of analysis is shown in Figures 3 and 4 in which calculated and measured impedance data are compared after cycling a rolled and bonded $Ni(OH)_2/NiOOH$ electrode twice to 100% DOD. Degradation processes were deduced from changes in model parameters with electrode cycling time. In developing the TLM, impedance spectra of planar (non-porous) electrodes were used to represent the pore wall and backing plate interfacial impedance. These data were measured over appropriate ranges of potentials and temperature, and an equivalent circuit model was adopted to represent the planar electrode data. Cyclic voltammetry was used to study the characteristics of the oxygen evolution reaction on planar nickel electrodes during charging, since oxygen evolution can affect battery electrode charge efficiency and ultimately electrode cycle life if the overpotential for oxygen evolution is sufficiently low.

Transmission line modeling results suggest that porous rolled and bonded nickel electrodes undergo restructuring during charge/discharge cycling prior to failure. The average pore length and the number of active pores decreases during cycling, while the average solid phase resistivity increases. The average solution phase resistivity remains relatively constant during cycling, and the total porous electrode impedance is relatively insensitive to the solution/backing plate interfacial impedance.

ACKNOWLEDGMENTS

The authors gratefully acknowledge the support of this work by the US Depart of Energy through Lawrence Berkeley Laboratory under Contract No. 712955.

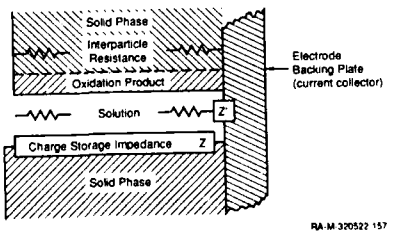


Figure 1 Right cylindrical model of ideal single pore

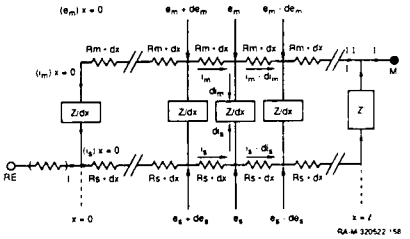


Figure 2 Discretized form of transmission line model for a porous battery electrode of finite thickness
e_m and e_s are potentials in the metal and solution phases respectively
i_m and i_s are currents in the metal and solution phases, respectively
I and I are the total current and the current flowing across the electrode backing plate/solution interface at the base of the pore, respectively
RE and M designate the reference electrode and current collector locations respectively

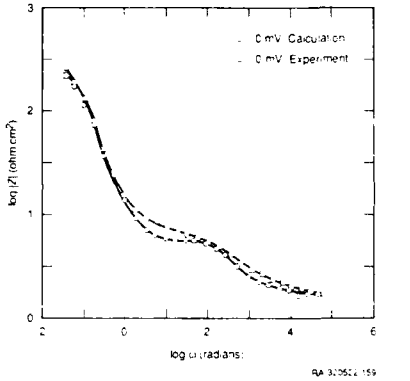


Figure 3 Experimental and calculated log |Z| versus log ω data at 0 mV and 23° C for a rolled and bonded porous electrode cycled twice (40 min CHG to capacity, and 20 min to 100% DOD). Determined from optimized TLM parameters described in text

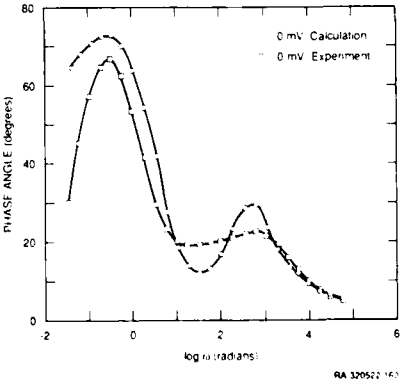


Figure 4 Phase angles corresponding to data shown in Figure 3

Abstract No. 4

THE EFFECT OF SINTER RUPTURE AND SOLID PHASE RESISTANCE ON CAPACITY RETENTION IN THE NICKEL OXIDE ELECTRODE

Oscar Lanzi and Uziel Landau
Dept. of Chemical Engineering
Case Western Reserve University
Cleveland, OH 44106

The nickel oxide electrode is used as the positive electrode in several different types of batteries (e. g., the nickel–cadmium, nickel–hydrogen, nickel–iron and nickel–zinc). It can be reversibly charged and discharged via the reaction formally written as

$$Ni(OH)_2 + OH^- \underset{\text{Charge}}{\overset{\text{Discharge}}{\rightleftharpoons}} NiOOH + H_2O + e- \qquad [1]$$

Typically, the electrode is fabricated by depositing the hydrated nickel oxide in a metallic nickel sinter matrix, intended to provide electronic conduction (Fig. 1). The electrolyte is usually concentrated KOH solution. It is generally observed that after many cycles this electrode delivers a decreased capacity on discharge, and this limits the cycle life of cells containing this electrode (1). This degradation has been attributed to the mechanical stresses exerted on the sinter by the above reaction, in which the reduced and oxidized species have different densities. These stresses eventually cause the sinter to crack in fatigue and thereby produce isolated regions (Fig. 2) where the hydrated nickel oxide must carry the electronic current. The oxide conducts poorly in the discharged state, and the resulting ohmic resistance leads to the formation of a thin insulating film which encapsulates material that would otherwise be available for discharge.

This effect can be modeled using conventional porous electrode theory and the one–dimensional model depicted in Fig. 3. The potential balances in the solid and liquid phases are as follows:

$$\frac{d\phi_S}{dz} = \frac{-i'_S f \tau_S}{\kappa_S} \qquad [2]$$

$$\frac{d\phi_L}{dz} = \frac{-i' \tau_L}{2t_- \kappa_L} \qquad [3]$$

in which ϕ is the potential, z is the coordinate indicated in Fig. 3, i' is the current density along the z–axis, τ is the tortuosity and κ is the conductivity. The factor $2t_-$, where t_- is the transference number of the anion, in the liquid phase balance arises from concentration gradients in the binary electrolyte. The variable f represents the fraction of the hydrated oxide which is not in contact with the sinter because of the breakage noted above. It is shown schematically in Fig. 4. As the electrode is cycled, the sinter breakage can be expected to increase, and this corresponds to an increase in f and hence to increased ohmic resistance in the solid phase.

The current balance and kinetics are given by

$$\frac{\epsilon_L}{dz}\frac{di'_L}{dz} = \frac{-\epsilon_S}{dz}\frac{di'_S}{dz} = ai \qquad [4]$$

$$i = -i_0 x \exp(-\beta\eta F/RT) \qquad [5]$$

in which ϵ represents the volume fraction, i represents the interfacial current density and x represents the state of charge. Using these equations it is possible to calculate the current and charge distributions in the electrode. Typically, these are nearly uniform for most of the discharge time, but as the oxide becomes discharged and less conductive, the interfacial current, hence the reaction, concentrates near the current collector and the oxide in this region discharges more rapidly than the bulk of the electrode. This leads to the formation of a discharged, insulating layer as shown in Fig. 5. The formation of this layer leads to a premature rise in the ohmic potential drop and hence to the observed loss in capacity (Fig. 6).

The important limitation on electrode performance is the voltage drop in the hydrated oxide phase. For a given current and charge distribution dimensional analysis shows that

$$\phi_S(0) - \phi_S(L) \propto |ai_{avg}|L^2 \qquad [6]$$

so that a reduction of the length L through which electronic current must penetrate the hydrated oxide significantly lowers the voltage drop and allows for greater capacity retention. This relation is independent of the assumed f value or the solid phase conductivity as a function of the state of charge, and it can be applied directly to experimental capacity–rate data to calculate the effect of reducing L. Using data from Ref. (1) it can be shown that the capacity retention for a cycled electrode can be increased by as much as 10% at typical discharge rates; this is a significant fraction of the 20–30% overall capacity reduction on cycling. A significant increase in cycle life may be realized by thus reducing the solid phase resistance. Fig. 7 depicts a possible method for reducing L by a factor of 2 without changing electrode dimensions or volume.

Acknowledgment

This work is being supported by a grant from NASA Lewis Research Center, Cleveland, OH. Useful discussions with Dr. Norman Hagedorn are also acknowledged.

Reference

(1) H. S. Lim, *Long Life Nickel Electrodes for Nickel–Hydrogen Cells*, NASA CR–174815, Dec. 1984

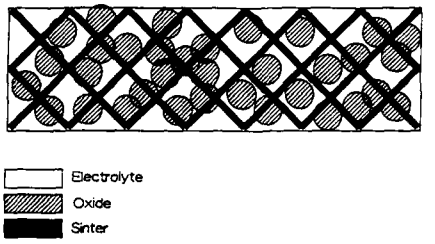


Fig. 1. Structure of the nickel oxide electrode containing concentrated KOH electrolyte, hydrated nickel oxide and metallic nickel sinter.

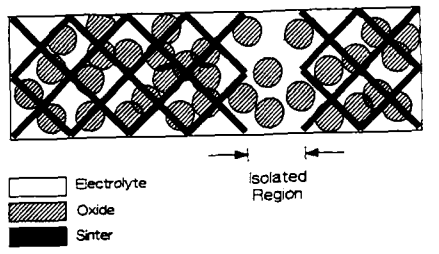


Fig.2. Structure of cycled electrode showing a crack or gap in the sinter. In the resulting isolated region electronic current must pass through the oxide.

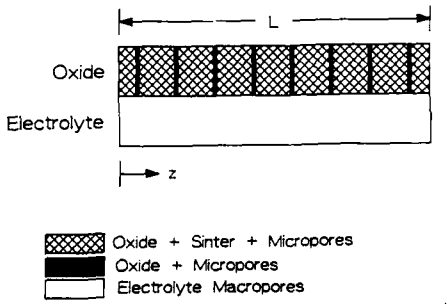


Fig. 3. Model of the nickel oxide electrode showing gaps in the sinter.

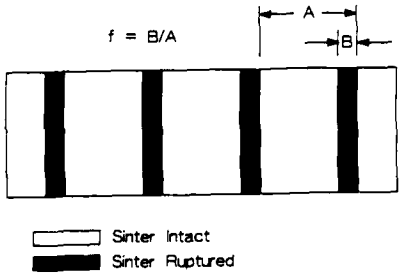


Fig. 4. Relation of f in solid phase potential balance to sinter rupture

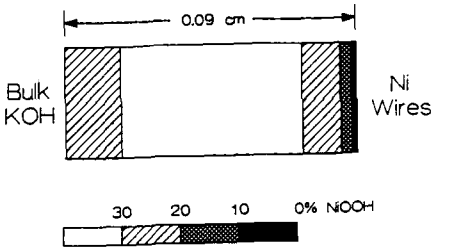


Fig. 5. Charge distribution (as % NiOOH) in a nickel oxide electrode with L = 0.09 cm, f = 0.06, rate = 1.37 C and 70% DOD, drawn to scale.

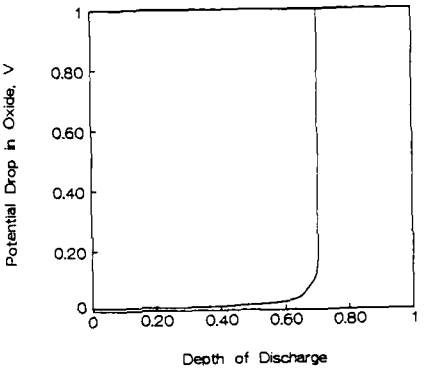


Fig. 6. Potential drop in hydrated oxide phase as a function of depth of discharge. L = 0.09 cm, f = 0.06.

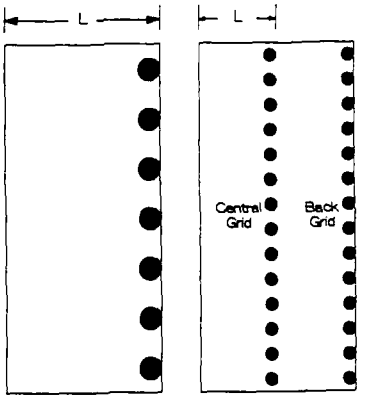


Fig. 7. Effect of introducing additional grid on electronic current penetration. With the central grid, the solid phase resistance is reduced by a factor of 4.

Abstract No. 5

A MATHEMATICAL MODEL OF A ZINC BROMINE FLOW CELL

Ravindra V. Shenoy and James M. Fenton

Department of Chemical Engineering.
University of Connecticut.
Storrs, CT 06268

The zinc bromine battery system has received considerable attention in recent years. Zinc bromine batteries are being considered for load-leveling applications in power plants and for automobile propulsion. Different designs are being pursued by various companies, including Energy Research Corporation (ERC), Exxon and Johnson Control. Mathematical models have been presented to study different designs and the various aspects of the zinc-bromine battery. Evans and White (1) reviewed mathematical models for different flow cell designs and flow stacks for the zinc bromine battery.

White et. al. (2, 3) formulated models for the Exxon design. The Exxon design is similar to the Gould/ERC design except that the porous electrode on the bromine side of the Gould/ERC design is replaced by a channel with a porous layer on the channel wall. Mader and White (2) presented a mathematical model of a parallel plate electrochemical cell based on the Zn/Br_2 redox couple with a separator and a homogeneous bulk reaction. They identified four independent variables for the system and predicted cell behavior during charge cycle. The porous layer on the channel wall on the bromine side was not included. Evans and White (3) further improvised this model to include the porous layer on the channel wall, predictions on discharge cycle and the round trip efficiency of the cell. The model by Evans and White (3) doesn't consider convective transport through the porous layer and hence applicability of the model is rather restricted to cases where the thickness of the porous layer is small as compared to the channel width.

In this work, a model will be presented for the Gould/Energy Research Corporation design and will be used to analyze the performance of the entire cell.

MODEL DEVELOPMENT

Figure 1 shows the Gould/ERC design of the flow cell. It consists of a flow-through porous electrode on the bromine side, a microporous separator and a planar electrode on the zinc side. An electrolyte comprising of bromine, sodium bromide and zinc bromide flows through the cell. During charging of the battery the energy is stored in the form of electrodeposited zinc which is subsequently dissolved. The current is in the direction perpendicular to the direction of the fluid flow. The concentration of the various species and the potential vary in both the axial and the normal direction. There is no significant variation in the third dimension.

Assumptions: The aqueous electrolyte is pumped to each side of the flow cell from separate tanks. The flow rates are adjusted so that there is no convective transfer through the separator. This is achieved by having the pressure drop per unit length on both sides of the separator equal. The electrolyte flows through the porous electrode at constant velocity (plug flow) and there is laminar flow in the zinc side channel. The aspect ratio is small enough to neglect axial diffusion and axial migration. The charge transfer reactions are characterized by Butler-Volmer kinetics. It is also assumed that the mobility of the ionic species follows the Nernst-Einstein equation. It is assumed that there is low conversion per pass so that the one-step model (2) can be used.

The model is presented for a charge cycle and the reactions that occur during the charge cycle are :

$$Br^- \rightarrow 1/2\, Br_2 + e^- \quad \text{(at anode)} \qquad (i)$$

$$Zn^{2+} + e^- \rightarrow 1/2\, Zn \quad \text{(at cathode)} \qquad (ii)$$

$$1/2\, Br_2 + e^- \rightarrow Br^- \quad \text{(at cathode)} \qquad (iii)$$

The tribromide complexation reaction occurs throughout the flow cell and the bromine, bromide and tribromide are in equilibrium through out the cell.

$$Br^- + Br_2 \rightleftharpoons Br_3^- \qquad (iv)$$

Model : The governing equations for the flow channel and the separator are the steady state species balances and the electroneutrality equation. The governing equation for the porous electrode are the steady state species balances the electroneutrality equation and the equilibrium relation for tribromide complexation. A pseudo-homogeneous production term is considered for the heterogeneous charge transfer reaction.

Method of Solution : The coupled ordinary differential equations are solved using Newman's technique (4). An accuracy of 0.01% is obtained within successive iterations.

REFERENCES

1. T. I. Evans and R. E. White, *J. Electrochem. Soc.*, 134, 2725 (1987).
2. M.J. Mader and R. E. White, *J. Electrochem. Soc.*, 133, 1297 (1986).
3. T.I. Evans and R. E. White, *J. Electrochem. Soc.*, 134, 866 (1987).
4. John Newman, "Electrochemical Systems," Prentice-Hall, Englewood Cliffs, N.J , (1973).

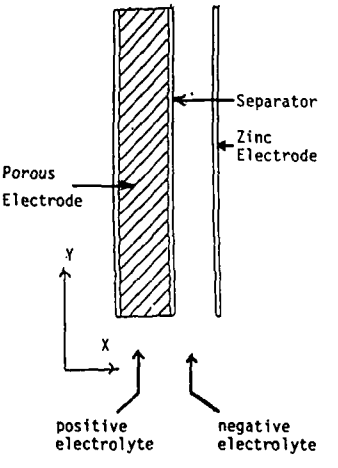


Figure 1. Gould/ERC design with a flow through porous electrode.

Abstract No. 6

MATHEMATICAL MODEL OF THE SECONDARY Zn/NiOOH CELL

K.G. Miller, F.R. McLarnon and E.J. Cairns
Applied Science Division
Lawrence Berkeley Laboratory
Berkeley, CA 94720

Introduction

The alkaline zinc electrode has long been considered for use in high-performance secondary batteries proposed for various portable-power applications. In practice, however, the electrode has been found to fail after 100-300 cycles due to significant capacity loss. This failure is attributed to the redistribution of active material over the surface of the Zn electrode (shape change), although in some cases dendrite shorting and passivation of the electrode may also be problems [1]. A major contributing factor to the rate of shape change is the high solubility of the discharge product, $Zn(OH)_4^{2-}$ (zincate) ion, in the alkaline electrolyte. Models have been proposed to explain shape change [2,3], but the forces driving this phenomenon remain uncertain.

Zinc Electrode Chemistry

The oxidation/reduction reaction at the zinc electrode proceeds by the following two steps:

$$Zn + 4OH^- = Zn(OH)_4^{2-} + 2e^- \quad (1)$$

$$Zn(OH)_4^{2-} = ZnO + 2OH^- + H_2O \quad (2)$$

The first reaction is the overall electrochemical reaction, which produces a soluble discharge product(zincate). Reaction 2 is a chemical precipitation (or dissolution) reaction that occurs when the KOH solution becomes supersaturated(or undersaturated) with zincate ion. Since the electrochemical reaction proceeds through the soluble zincate species, the rate of precipitation and dissolution of ZnO plays an important role in determining electrode performance.

The high solubility of zincate ion in the electrolyte is a major factor in the shape change phenomenon. If there are significant concentration gradients during a particular half cycle, or if reaction rates differ between charge and discharge, then the zincate species is free to migrate around the cell. Even if these are very small differences, over the course of a hundred cycles or more, there can be significant Zn material redistribution over the electrode.

Mathematical Model of the Zn/NiOOH Cell

A description of the model, the governing equations, and preliminary results have been presented previously [4]. Since that time, the equations have been modified resulting in the elimination of both the matrix and solution currents using Ohm's Law in both matrix and solution phases. In addition, the model was extended into the reservoir region so that its effect on processes at the top edge of the electrode could be determined.

The model equations were solved using various values of the physical parameters, such as diffusion coefficients, exchange current densities, conductivities, and the dissolution/precipitation rate constant for equation 2. The purpose was to determine which of these parameters are most important in promoting shape change in secondary zinc electrodes. In addition, the model equations were solved for various concentrations of KOH electrolytes (usually from 15-30 wt%), as well as for KOH electrolytes containing additives such as KF. The computations were carried out over many cycles to test the ability of the model to predict the different rates and extent of shape change which have been measured [5].

Results and Discussion

Figure 1 shows the calculated ionic concentrations of hydroxide and zincate species during one cycle for both the zinc and nickel oxide electrode compartments. These data represent a point midway between the top and bottom of of each of the electrodes. From the curves, it is evident that there is rapid electrolyte movement between the two electrode compartments (the concentration differences between them are very small), expected for a cell that employs a microporous separator. During discharge, it can be seen that the concentration of zincate ion builds to very high levels, until precipitation occurs. These concentrations also show good agreement with some concentration measurements using microreference electrodes in an operating Zn/NiOOH cell [6].

The model equations were also solved for different values of the precipitation/dissolution rate constant. It was found that a very narrow range of values of this parameter causes large changes in the zincate ion concentration. The hydroxide ion concentration was found to remain relatively constant over this same range of this parameter.

Conclusions

The model equations have shown the ability to predict concentrations over one cycle. The ability to predict the rate and extent of shape change in experimental cells for different of physical parameters is very important in determining the major driving forces that control shape change.

Acknowledgement

This work was supported by the Assistant Secretary for Conservation and Renewable Energy, Office of Energy Storage and Distribution of the U.S. Department of Energy under Contract No. DE-AC03-76SF00098.

References

(1) J. McBreen and E.J. Cairns, in *Advances in Electrochemistry and Electrochemical Engineering*, H. Gerischer and C.W. Tobias, eds., Vol. 11, p. 273 (1978).

(2) K.W. Choi, D.N. Bennion and J. Newman, *J. Electrochem. Soc.*, **123**, 1616 (1976).

(3) W.G. Sunu and D.N. Bennion, *ibid.*, **127**, 2007 (1980).

(4) K.G. Miller, F.R. McLarnon and E.J. Cairns, Abstract 149, The Electrochemical Society Extended Abstracts, Honolulu, Hawaii, Oct 18-23, 1987.

(5) J.T. Nichols, F.R. McLarnon and E.J. Cairns, *Chem. Eng. Commun.*, **37**, 355 (1985).

(6) M.J. Isaacson, F.R. McLarnon and E.J. Cairns, Abstract 147, The Electrochemical Society Extended Abstracts, Honolulu, Hawaii, Oct. 18-23, 1987.

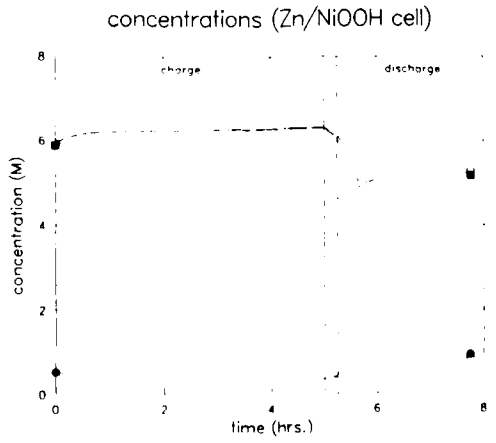


Figure 1. The concentrations of $K_2Zn(OH)_4$ and KOH during one cycle of operation. The curves are: ■ KOH, Zn electrode compartment; □ KOH, NiOOH electrode compartment; ● $K_2Zn(OH)_4$, Zn electrode compartment; ○ $K_2Zn(OH)_4$, NiOOH electrode compartment.

Abstract No. 7

MATHEMATICAL MODEL OF THE SECONDARY CURRENT DISTRIBUTION MECHANISM FOR Zn MATERIAL REDISTRIBUTION

M.J. Isaacson, F.R. McLarnon and E.J. Cairns
Applied Science Division
Lawrence Berkeley Laboratory
Berkeley, CA 94720

Introduction

Two mechanisms have been proposed for material redistribution in secondary Zn/ZnO cells: the electro-osmotic flow mechanism (1), and the secondary current distribution mechanism (2). Choi et.al.(1) developed a mathematical model of the electro-osmotic flow mechanism. However a quantitative treatment of the secondary current distribution mechanism has not appeared in the literature. The purpose of this work was to develop a two-dimensional model of the Zn/ZnO porous electrode and use it to mathematically investigate the secondary current distribution mechanism. It was not our purpose to show which of the mechanisms is dominant.

Reactions

Zn is oxidized during discharge, and $Zn(OH)_4^{-2}$ is reduced during charge:

$$Zn + 4OH^- = Zn(OH)_4^{2-} + 2e^- \qquad (1)$$

$Zn(OH)_4^{2-}$ precipitates as ZnO in supersaturated solutions, and ZnO dissolves in undersaturated solutions:

$$ZnO + 2OH^- + H_2O = Zn(OH)_4^{2-} \qquad (2)$$

The electrochemical and chemical reaction rate constants for reactions (1) and (2) are not accurately known. It is known that the precipitation of ZnO from supersaturated $Zn(OH)_4^{2-}$ proceeds very slowly until a critical concentration of about three times the equilibrium concentration is reached After the critical concentration is reached the reaction proceeds much faster.

Model Cell

The model cell is shown in Fig. 1. It consists of the porous Zn/ZnO electrode, an electrolyte reservoir, and the separator. The counter electrode was not included in the problem domain, and is therefore drawn with dashed lines. The Zn/ZnO electrode has 30% KOH electrolyte (before addition of ZnO) saturated with ZnO inside of the pores. The separator reduces the effective conductivity and ionic diffusivities but does not selectively influence the transport properties of individual ions.

Equations

The model cell was described mathematically with the equations shown in Appendix A. Material balances equations for KOH and $K_2Zn(OH)_4$ included diffusion, migration, and source terms for reactions (1) and (2), but neglected bulk fluid convection. Electrode kinetics were represented by the Butler-Volmer equations. Current flow in the electrolyte was described by Ohm's Law. Ohmic drops in the electrode matrix were assumed to be negligible.

Results and Discussion

Fig. 2 compares the calculated Zn/ZnO porous electrode potential with selected experimental data. The simulation accurately predicts the qualitative features of the charge/discharge curve. The potential decreases quickly during the first part of the charge and then reaches a steady-state value. During the first open-circuit period the potential increases to within a millivolt of the original open-circuit potential. During the discharge the potential initially increases, reaches a maximum and then decreases. The decrease in the potential results from the increase in the precipitation rate constant after the $Zn(OH)_4^{2-}$ stability limit is exceeded. After the end of the discharge the electrode potential decreases to a value close to that of the original open-circuit.

Fig. 3 shows calculated Zn distribution profiles at the end of one cycle. The active material has redistributed from the middle of the electrode toward the edge of the electrode, and from the back face of the electrode toward the front face of the electrode.

Conclusions

A mathematical model of the secondary current distribution mechanism of Zn material redistribution has been developed. Calculated electrode potentials are in good qualitative agreement with experimental data. The model shows redistribution of active material from the center of the electrode toward the edge of the electrode.

Acknowledgement

This work was supported by the Assistant Secretary for Conservation and Renewable Energy, Office of Energy Storage and Distribution of the U.S. Department of Energy under Contract No. DE-AC03-76SF00098.

References

(1) K.W. Choi, D.N. Bennion and J. Newman, *J. Electrochem. Soc.*, **123**, 1616 (1976).

(2) J. McBreen, *J. Electrochem. Soc.*, **119**, 1620 (1972)

(3) T.P. Dirkse, *J. Electrochem. Soc.*, **128**, 1412 (1981)

(4) A.G. Briggs, N.A. Hampson, and A. Marshall, *J. Chem. Soc Faraday Trans. 2*, **70**, 1978 (1974)

Appendix A

Mass Balances (KOH and $K_2Zn(OH)_4$):

$$\epsilon\frac{\partial c_i}{\partial t} = \nu\epsilon^{1+r}D_i\nabla^2 c_i - \left(\frac{s_{ir}}{nF} + \frac{t_i}{z_iF}\right)\nabla\cdot i_s + s_{ip}k_f(c_3 - c_{3e})$$

Ohm's Law in the Electrolyte:

$$i_s = -\kappa\epsilon^{1+r}\nabla\phi - \kappa\epsilon^{1+r}\left(\frac{s_{2r}}{\nu_{2A}} + \frac{nt_2}{z_2\nu_{2A}}\right)\nabla\left[\ln(c_1c_2)\right] - \kappa\epsilon^{1+r}\left(\frac{s_{3r}}{\nu_{3B}} + \frac{nt_3}{z_3\nu_{3B}}\right)\nabla\left[\ln(c_1^2c_3)\right]$$

Butler-Volmer Electrode-Kinetics:

$$\nabla\cdot i_s = aj = ai_0\left[e^{\frac{\alpha_a F}{RT}(\phi_m - \phi_s)} - e^{-\frac{\alpha_c F}{RT}(\phi_m - \phi_s)}\right]$$

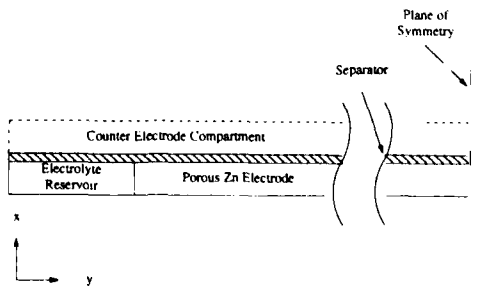


Fig. 1. Model Zn/ZnO Porous Electrode Cell

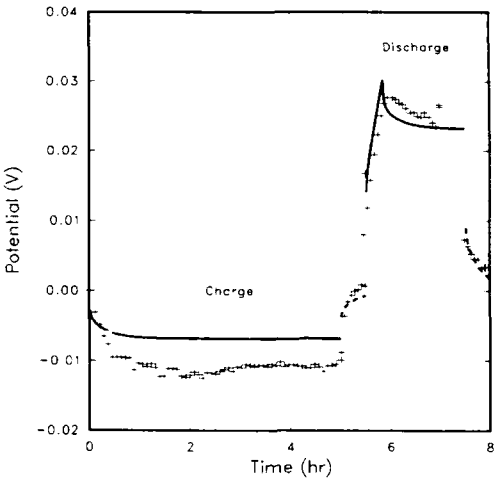


Fig. 2 Comparison of calculated and experimental Zn electrode potentials. — — , Calculated Potentials during charge and discharge; – – –, Calculated Potentials During open-circuits; +, Experimental Data.

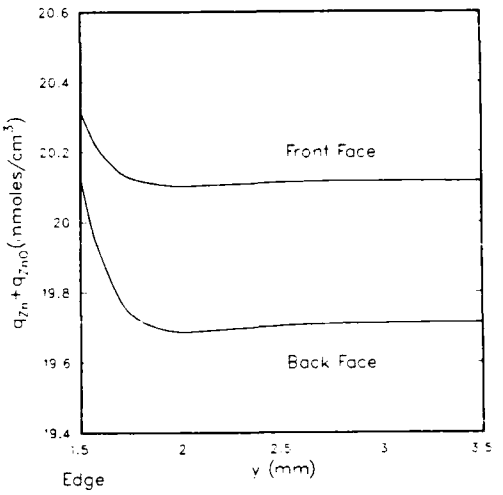


Fig. 3. Zn Material Distribution Pattern The edge of the electrode is located at y=1.5 mm.

Abstract No. 8

A MODEL OF THE TIME-DEPENDENT VOLTAGE RESPONSE OF Li/MnO_2 BATTERIES

Ann M. Crespi, Donald R. Merritt and Paul M. Skarstad

Medtronic, Inc.
6700 Shingle Creek Parkway
Brooklyn Center, MN 55430

INTRODUCTION

The application of Li/MnO_2 batteries in implantable medical devices includes high current pulses superimposed on a low background current. We have observed that the cell voltage may drop by several hundred millivolts during a pulse (in addition to iR drop), and the voltage recovery of Li/MnO_2 cells is known to be slow (1-3). In order to predict how a battery will perform during a high current pulse the polarization and relaxation characteristics must be well understood. The goal of this work is to model the time-dependent behavior of Li/MnO_2 batteries on open circuit and under load, and eventually to understand what processes give rise to the observed behavior.

EXPERIMENTAL

The cells used in this study consist of a central flat anode sandwiched between two cathode pellets in a case-positive design. The pellets are a composite of MnO_2 (heat-treated electrolytic), Shawinigan black carbon, and teflon. Nine such cells were discharged to various depths of discharge ranging from 6 to 67% at a constant current load of 0.17 mA/cm^2, then relaxed on open circuit for 2-3 months. The cells were then returned to the same load for two days, then again relaxed on open circuit. The voltage was monitored at a frequency of 10 Hz immediately after the current was switched and with decreasing frequency afterwards.

In the modeling, the parameters were refined by non-linear regression using the Marquardt (4) algorithm incorporated into Statgraphics (5).

RESULTS AND DISCUSSION

Even after 80 days on open circuit the cell voltages continued to increase. The data were found to fit the function shown in eq. 1, which yields an extrapolated open circuit voltage (OCV).

$$V(t) = OCV - \sum_{i=1}^{n} A_i \cdot e^{-\alpha_i t} \qquad (1)$$

A total of 15 parameters (OCV, A_i, α_i, i = 1-7) were required to fit the data. A plot of calculated open circuit voltage versus depth of discharge appears in Figure 1, and a typical fitted model appears in Figure 2. All models fit with R-squared > 0.999.

The voltage data on load were first corrected for the drop in open circuit voltage for the capacity range over which the cell was discharged (about 5% of stoichiometric capacity). The data were then fitted by the function shown in eq. 2.

$$V(t) = OCV - iR - \sum_{i=1}^{n} A_i \cdot \left(1 - e^{-\alpha_i t}\right) \qquad (2)$$

The OCV and i (current) were included as constants, and R, A_i and α_i were refined parameters. A typical plot of observed and calculated voltage versus time appears in Figure 3. The calculated values of R were consistently 2-6 Ω higher than those determined by complex impedance just before discharge began, indicating either a systematic difference in the two measurement methods or an additonal polarization that is too fast to be observed (see Figure 4).

The open circuit voltage declines throughout the range 6-67% of cell capacity at an average rate of -4.4 mV/%. The slope is not uniform but increases after about 40% depth of discharge. The magnitude of each pre-exponential term (A_i's) defines the amount of polarization that occurs in a given time regime, as determined by the corresponding time constant (α_i). The calculated values and physical interpretations of these parameters will be discussed.

CONCLUSIONS

The time-dependent voltage behavior of Li/MnO_2 cells on constant current load or open circuit can be modeled and excellent fits are achieved. The function consists of a sum of exponential terms subtracted from the open circuit voltage.

REFERENCES

1. J. C. Nardi, *J. Electrochem. Soc.*, **132**, 1787-1791 (1985).
2. M. Voinov, *Ibid.*, **128**, 1822-1823 (1981).
3. M. Voinov, *Electrochim. Acta*, **26**, 1373-1376 (1981).
4. D. W. Marquardt, *J. Soc. Ind. App. Math.*, **2**, 431-441 (1963).
5. Statgraphics, Version 2.6, Statistical Graphics Corp., 1987.

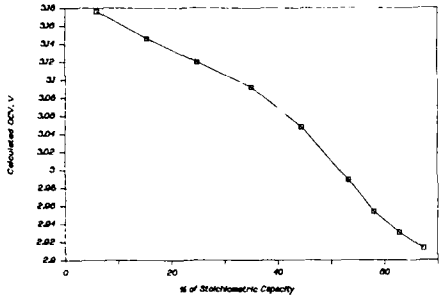


Figure 1. Plot of calculated OCV vs. % of total cell stoichiometric capacity.

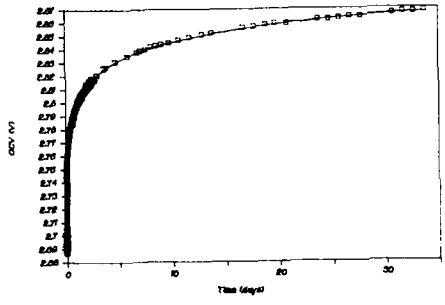


Figure 2. Plot of observed (squares) and calculated (solid line) OCV vs. time.

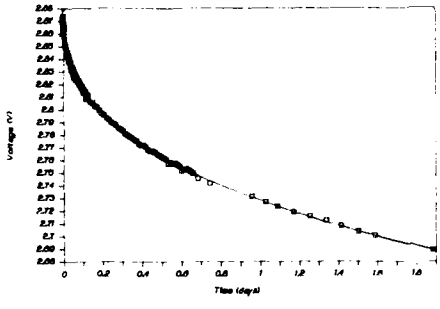


Figure 3. Plot of observed (squares) and calculated (solid line) load voltage vs. time.

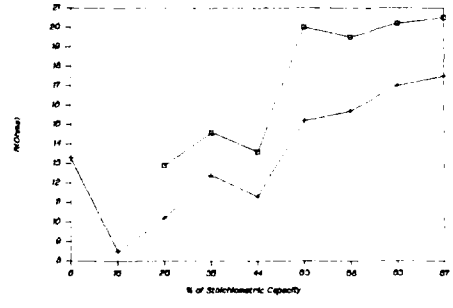


Figure 4. Comparison of calculated (squares) cell resistance and resistance measured by complex impedance (*).

Abstract No. 9

A MATHEMATICAL MODEL OF A LITHIUM/THIONYL CHLORIDE PRIMARY CELL

T. I. Evans, T. V. Nguyen, and R. E. White

Department of Chemical Engineering
Texas A&M University
College Station, Texas 77843

A one-dimensional mathematical model for the lithium/thionyl chloride primary cell has been developed to investigate methods of improving its performance and safety. The model includes many of the components of a typical lithium/thionyl chloride cell such as the porous lithium chloride film which forms on the lithium anode surface. The governing equations are formulated from fundamental conservation laws using porous electrode theory and concentrated solution theory. The model is used to predict one-dimensional, time dependent profiles of concentration, porosity, current, and potential as well as cell temperature and voltage. When a certain discharge rate is required, the model can be used to determine the design criteria and operating variables which yield high cell capacities.

Tsaur and Pollard (1, 2, 3) have presented a similar one-dimensional model of the $Li/SOCl_2$ cell. However, in their model development they assume that the reservoir is a well mixed solution of constant concentration, which may not be a valid assumption as shown by Gu *et al.* (4). For the reaction controlled conditions predicted here, this assumption seems to be a reasonable one. Also, they do not treat species transport in the LiCl film in their model.

The independent adjustable parameters, determined from the model development, are the porous electrode thickness, the initial porosity of the porous electrode, the thickness of the electrolyte reservoir, the thickness of the separator, the porosity of the separator, the LiCl film thickness, the LiCl film porosity, the initial electrolyte concentration, the heat transfer coefficient, the current density, and the temperature of the surroundings. For the discharge rates and design conditions studied, the model predictions show that cell performance is controlled primarily by the thionyl chloride reduction in the porous carbon cathode. Thus, the porous electrode thickness, initial porosity of the cathode, and the initial electrolyte concentration are the design criteria which most affect cell performance. Also, the LiCl film porosity can influence cell performance; porosities beyond 0.1 seem to have little effect on cell lifetime, voltage, or temperature, however, below a porosity of 0.1, cell voltage begins to decrease due to the greater hindrance of species transport in the film. These results show that it is advantageous to maintain low temperature storage (room temperature) so that the film does not become too compact.

REFERENCES

1. K. C. Tsaur and R. Pollard, *J. Electrochem. Soc.*, **133**, 2296 (1986).
2. K. C. Tsaur and R. Pollard, *J. Electrochem. Soc.*, **131**, 975 (1984)
3. K. C. Tsaur and R. Pollard, *J. Electrochem. Soc.*, **131**, 984 (1984).
4. H. Gu, T. V. Nguyen, and R. E. White, "A Mathematical Model for the Lead-Acid Cell: Discharge, Rest, and Charge," in press.

Abstract No. 10

A THERMAL ANALYSIS OF A SPIRALLY WOUND BATTERY USING A SIMPLE MATHEMATICAL MODEL

T. I. Evans and R. E. White

Department of Chemical Engineering
Texas A&M University
College Station, TX 77843

Many battery systems produce heat as they are discharged due to the exothermic nature of the electrochemical reactions occurring. This heat, if not conducted out of the cell, can increase temperatures to dangerous levels. In spirally constructed batteries, heat flow in the radial direction is inhibited due to regions of low thermal conductivity, such as the separator between electrodes. It has been questioned whether or not the heat transfer is improved in spiral designs by heat conduction out the spiral path along those regions of highest thermal conductivity. This path offers lower resistance to heat flow, however, a much greater distance must be traversed as opposed to the more direct radial path. A two-dimensional thermal model for spirally wound batteries has been developed to investigate this question. The model predictions show that conduction of heat out the spiral path in a spirally wound lithium/thionyl chloride ($Li/SOCl_2$) cell, during normal operation, reduces cell temperatures but does not substantially reduce the temperature drop in the cell. However, when hot spots are present in the cell conduction out the spiral is substantial and the temperature drop in the cell is reduced significantly.

Previous workers (1, 2) have presented thermal models for battery systems. Several models (3-7) have been presented which specifically address the thermal behavior of $Li/SOCl_2$ cells. All these models either assume uniform cell temperature, which changes only with time, or treat the cell interior as one pseudohomogeneous region having effective average thermal properties. These models cannot be used to investigate the effects of the arrangement of the cell components on the temperature distribution in the cell.

The governing equation of the model is the energy balance. Heat generated by polarization and heat generated due to the entropy change of the current producing reactions are included in the balance. To simulate thermal runaway, an additional term is included which represents additional heating caused by, perhaps, a cell defect and/or exothermic chemical reactions. This heat source is assumed to be localized causing a hot spot in the cell. This approach to simulating thermal runaway was used by Szpak *et al.* (4). Convective and insulated boundary conditions are used and the equations are solved using a finite element code called TOPAZ2D (8). The finite element mesh is generated using a preprocessor to TOPAZ2D called MAZE (9). The model is used to estimate two-dimensional temperature profiles within a spirally wound $Li/SOCl_2$ D-size cell. Simplified one-dimensional models have been used to predict best and worst temperature profiles.

The two-dimensional model and one-dimensional approximations have been used to understand better the thermal behavior of the spirally wound $Li/SOCl_2$ battery. Comparison of model predictions with experimental data support two contentions. The heat generation rate seems to be greatest at the center of the cell and diminishes towards the exterior of the cell. Also, thermal conductivities seem to decrease as the cell discharges. This could be due to the increasing volume occupied by cell gases as the discharge proceeds. Two thermal runaway situations were investigated using the model based on the theory that localized hot spots initiate thermal runaway. The effectiveness of the spiral design in conducting heat out of the cell is dependent upon where these hot spots are located in the cell. If hot spots are in contact with those regions of the cell having relatively high thermal conductivities then the spiral design serves to improve significantly heat dissipation.

REFERENCES

1. D. Bernardi, E. Pawlikowski, and J. Newman, *J. Electrochem. Soc.*, **132**, 5 (1985).
2. J. Lee, K. W. Choi, N. P. Yao, and C. C. Christianson, *J. Electrochem. Soc.*, **133**, 1286 (1986).
3. L. A. Parnell and S. Szpak, *Electrochimica Acta*, **30**, 913 (1985).
4. S. Szpak, C. J. Gabriel, and J. R. Driscoll, *Electrochimica Acta*, **32**, 239 (1987).
5. Y. I. Cho and G. Halpert, "Heat Dissipation of High Rate Li-$SOCl_2$ Primary Cells," *J. Power Sources* (1986).
6. Y. I. Cho and G. Halpert, "Thermal Analysis of Prismatic Li-$SOCl_2$ Primary Cells," presented at the 32nd International Power Series Symposium, Cherry Hill, NJ (May, 1986).
7. Y. I. Cho, *J. Electrochem. Soc.*, **134**, 771 (1987).
8. A. B. Shapiro, "TOPAZ2D - A Two-Dimensional Finite Element Code for Heat Transfer Analysis, Electrostatic, and Magnetostatic Problems," Lawrence Livermore National Laboratory, UCID-20824 (July 1986).
9. J. O. Hallquist, "MAZE - An Input Generator for DYNA2D and NIKE2D," Lawrence Livermore National Laboratory, UCID-19029, Rev. 2 (June 1983).

Abstract No. 11

MODELLING STUDIES OF THE SHORT TIME/HIGH FREQUENCY BEHAVIOR OF PULSE BATTERIES

M.L. Daroux, B.D. Cahan, J.P. Discenza and E.B. Yeager

The Chemistry Department and the Case Center
for Electrochemical Sciences,
Case Western Reserve University,
Cleveland, Ohio, 44106

Very high current discharge in physically large battery systems can be significantly limited by geometric and physical factors that are not usually taken into account in the design of conventional batteries. For example, Lander and Nelson [1] showed that even under short circuit conditions the discharge of large (7000 Ah capacity) Pb-acid cells was limited by a combination of internal and load impedance to rise times on the order of 10 to 100 milliseconds. The work described here is an attempt to combine electrochemical and transmission line concepts to provide a theoretical framework that can be used to identify the critical factors in the design of high power pulse batteries.

In a previous paper [2], we have shown for the example of semi-infinite parallel plate (stripline) geometry that, no matter how favorable the electrochemical properties of the interface, at sufficiently short times the impedance is limited by geometric and physical factors. We have now extended the modelling to predict the transient response to current or voltage pulses, and to take into account the finite length of practical cells. This permits these models to be applied on longer time scales where current can be drawn from the whole length of the battery.

Figure 1 shows an example of the impedance of a stripline cell calculated using the previously described [2] infinite model. Figure 2 shows the calculated impedance of the same cell but of finite length; that is of length shorter than the penetration length over at least part of the frequency range. For the values of the physical constants chosen, this cell behaves as if it were infinitely long at high frequencies and the calculated impedance is the same as that previously obtained using the infinite line model. At low frequencies, the behavior collapses to that of a simple capacitor. However, at intermediate frequencies, where the penetration length is comparable to the line length, reflection effects occur. The impedance oscillates with small changes in frequency as constructive or destructive interference between the pulse and its reflection from the end of the cell occurs.

Figures 3 and 4 show the transient voltage response of the same line to a constant current pulse of unit amplitude. Figure 3 shows the short time response, which is identical to that of an infinite line. At longer times however, as shown in Fig. 4, the voltage transient shows step-like increases resulting from reflection effects, as the signal (i.e. the withdrawal of charge) reaches the end of the cell. The effect is to increase the impedance or decrease the output of cell.

This extended model permits the output of the cell to be calculated together with the length for which the cell will appear to be infinitely long for any given pulse duration. It may be possible to use reflection effects to tailor the shape of the output and avoid some of the problems associated with switching large curents.

Further examples will be given, together with comparisons of predicted behavior with that found experimentally for test cells.

ACKNOWLEDGEMENTS: This research has been supported by ONR through a subcontract with Eveready Battery Co., Westlake, Ohio

REFERENCES

1. J.J. Lander, E.E. Nelson; JECS, 722, (1960)

2. B.D. Cahan, M.L. Daroux, E.B. Yeager ; 171st ECS Meeting Extended Abstracts, 87-1, Philadelphia, May 1987

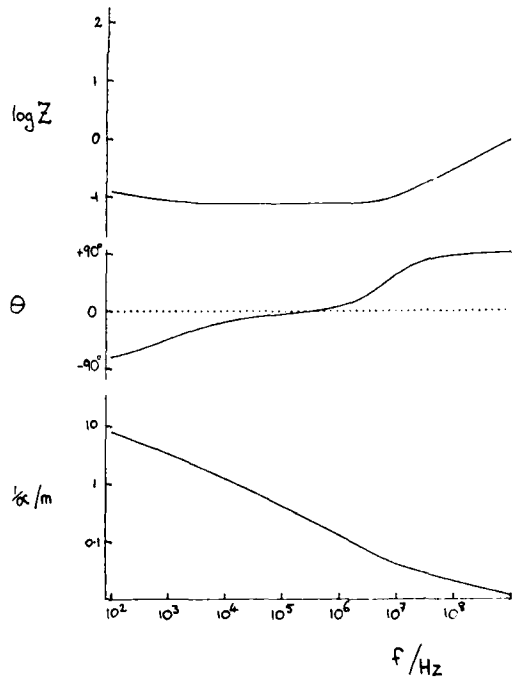


FIGURE 1 : Bode Plots showing, for an infinitely long stripline cell), a) log Z, b) Θ and c) $1/\alpha$ (Penetration Depth), as a Function of Frequency. Calculated for ρ_m (Electrode Resistivity) = 3.5×10^{-3} Ω-cm, ρ_E (Electrolyte Resistivity) = 10^{-2} Ω-cm, u (Electrode Spacing) = 0.1 cm, W (Cell Width) = 1.0 cm C_{dl} (Interfacial Capacitance) = 50 uF/cm^2, C_E (Cell Capacitance) = 7.17×10^{-5} uF/cm^2, L_s (Cell Inductance) = 1.255×10^{-9} H/m.

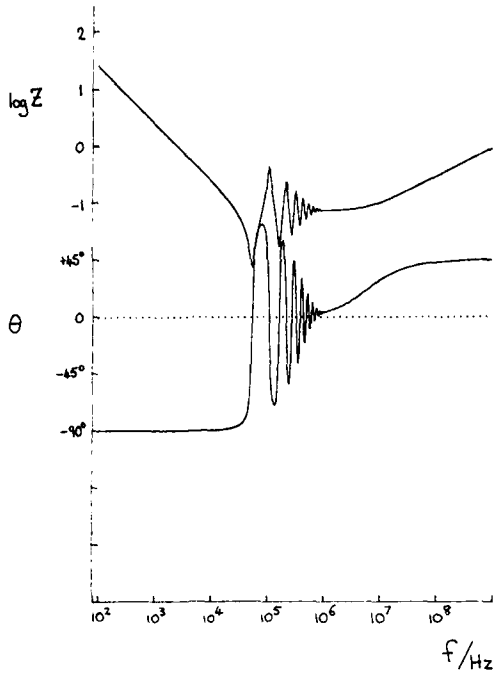


FIGURE 2 : Bode Plots for the same cell as in Fig. 1, but of length 0.25 m.

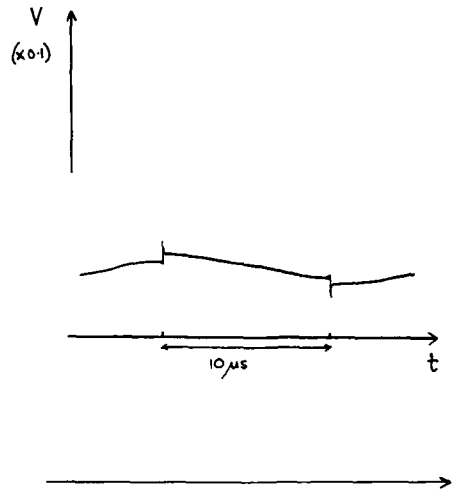


FIGURE 3 : Voltage Transient showing the response of the cell in Fig. 2 to a 10 microsecond current pulse of unit amplitude.

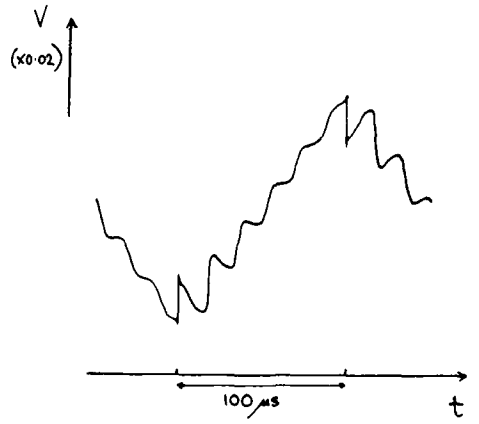


FIGURE 4 : Voltage Transient showing the response of the cell in Fig. 2 to a 100 microsecond current pulse of unit amplitude.

Abstract No. 12

MODEL FOR LEAKAGE CURRENT IN A BIPOLAR STACK WITH SEPARATE ELECTRODE LOOPS

M. Z. Yang, H. Wu and J. Robert Selman
Department of Chemical Engineering
Illinois Institute of Technology
Chicago, IL 60616

Introduction

Several models predicting leakage current in a bipolar battery stack has been presented in recent years[1]. The present work extends this by applying current balance and potential balance equations to a stack of cells with separators and with separate, possibly asymmetric, electrolyte circulation loops for positive and negative electrodes. It treats the separate electrolyte loops and manifolds, as well as membrane or separator as resistance elements in an electric circuit analog. This results in a set of linear difference equations with constant coefficients. Difference calculus is then applied to solve the coefficients. Leakage currents in stacks made up of different numbers of cells are predicted and the effect of each resistance component on stack performance is investigated.

Results and Discussion

A systematic study was made of the effect of varying each resistance component in the network. The effect of varying the number of cells was also investigated. In order to compare on a common basis, the leakage currents, manifold currents, and battery currents were calculated for a standard case (Table 1). The cell potential V_o, and the output load current, I_L, were kept constant. The total internal resistance R_t, defined as the sum of membrane resistance and electrolyte resistances, was constrained according to

$$R_t < V_o/I_L,$$

i.e., the current produced in each cell was always greater than the load current.

The power efficiency, defined as the ratio of power applied to the load between the positive and negative terminals of the battery stack to the total power generated by all the cells within, is calculated according to

$$\epsilon = (\Delta V \cdot I_L)/(V_o \cdot \sum i)$$

where i is the current flowing through the voltage source, and ΔV is the potential difference between battery terminals. The distribution profiles of the leakage current, battery current and the manifold current are similar in the calculations, therefore in the following discussion, we compare the changes in the maximum leakage current and in power efficiency.

(1) Number of cells

As shown in Fig 1, the leakage current increases as the number of cells N increases, but flattens out beyond 25 cells. The efficiency, on the other hand, decreases as N increases. Note that in these calculations the load current is kept constant. Thus, as N increases, the current generated in the cells has to leak to the manifold to maintain a constant current output. Consequently, although the battery voltage increases, the efficiency still decreases with increasing N.

(2) Total internal resistance

The effect of the total internal resistance on battery performance is shown in Fig 2. If the total resistance is kept constant, asymmetry of the electrolyte resistances does not have much effect on the current distribution even though the ratio of catholyte to anolyte resistance may vary from 1/3 to 4, and the separator resistance from zero to 80% of the total resistance. On the other hand, if the total resistance increases, the leakage current and the power efficiency both decrease, as shown in Fig 2. The decrease of leakage current is a result of Ohm's law: as the total resistance is increased, the current produced in each cell by a constant voltage source is less, consequently, less current is leaked to the manifolds, when a constant current output is maintained. The efficiency decreases because more power is consumed to overcome the internal resistance.

(3) Manifold resistances and lateral electrolyte resistance

As shown in Fig. 3, variation of manifold resistances affects only the compartment to which the manifold is connected, i.e. cathodic currents are affected only by the cathodic manifold resistance, but not by the anodic manifold resistance. The anodic leakage current, on the other hand, decreases sharply near the symmetry point (the intersection point of the two curves in Fig 3, where anodic and cathodic manifold resistances are equal), and tends toward a constant value.

The effect of lateral electrolyte resistance is very similar to that of manifold resistance: it affects only the current in the compartment whose manifold resistance is being varied, and the change of leakage current approaches a constant as the resistance value increases.

Conclusion

- Application of difference calculus leads to a method of calculating leakage currents in a bipolar battery stack that is very efficient compared to the matrix method, i.e., solving N by N simultaneous equations.
- The most sensitive component in the cell is the internal resistance in the direction of the battery current.
- Lateral electrolyte resistance and manifold resistance have some effect on the leakage current, but only on the current to their own compartments. This effect is much weaker than that of total internal resistance.

References

1. E. A. Kaminski and R. F. Savinell, *J. Electrochem. Soc.* **130**, 1103 (1983).

Acknowledgement

This work was supported by the US Department of Energy (Sandia National Laboratory), under a subcontract from Lockheed Missiles and Space Company, Sunnyvale. The interest of Mr. R. P. Hollandsworth and Dr. E. L. Littauer are gratefully acknowledged.

Table 1. Standard parameters used in the illustration.

$R_A = 1000\Omega$	$R_C = 1000\Omega$
$R_{e1} = R_{e2} = 0.5\Omega$	$R_s = 1\Omega$
$R_{MA} = 10\Omega$	$R_{MC} = 10\Omega$
$V_o = 1.5V$	$I_L = 0.5\ Amp$
$N = 20$	

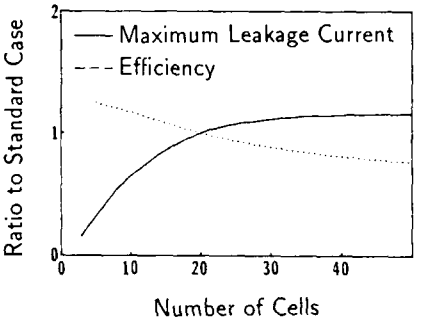


Figure 1: Effect of number of cells on the maximum leakage current and power efficiency in a bipolar stack, normalized with respect to the standard case.

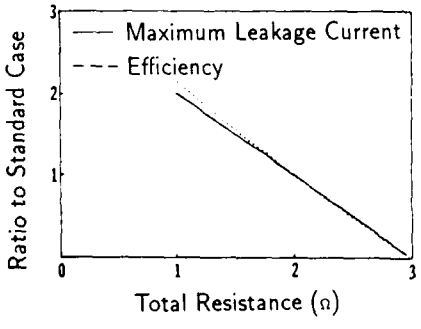


Figure 2: Effect of total resistance on maximum leakage current and power efficiency in a bipolar battery stack, normalized with respect to the standard case.

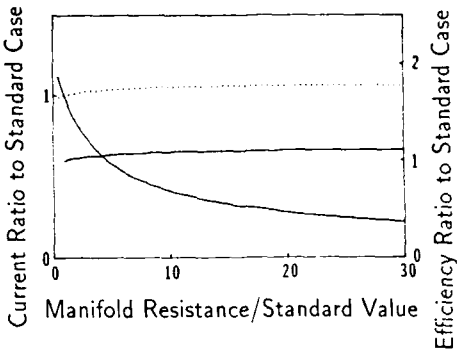


Figure 3: Effect of variation of anodic manifold resistance on the maximum leakage currents and efficiency in a bipolar battery stack, normalized with respect to the standard case. ···: Cathodic maximum leakage current, —: maximum of anodic leakage current and battery efficiency.

Abstract No. 13

Modeling of Chlorine Gas-Diffusion Electrodes

D. L. Thomas
Chemical Engineering Program
University of Alabama in Huntsville
Huntsville, AL 35899

Model

A mathematical model of a chlorine gas diffusion electrode has been formulated and solved. The model consists of charge balances in the electrolyte and solid phases of the electrode, an electrolyte mass balance, and a mass balance on gas phase chlorine:

$$\nabla \cdot i_1 + \nabla \cdot i_2 = 0$$

$$\nabla \cdot i_2 = -aj$$

$$\nabla \cdot N_{Cl^-} = \frac{aj}{F}$$

$$\nabla \cdot N_{Cl_2} = -\frac{aj}{2F}$$

Appropriate equations are used to express the mass and charge fluxes.

$$i_1 = -\kappa_{eff} \nabla \phi_1$$

$$i_2 = -\kappa_{eff} \nabla \phi_2 - \frac{\kappa_{eff}}{F}\left(\frac{a_v}{n\gamma_\pm} + \frac{t_+^0}{z_+\gamma_\pm} - \frac{a_v c}{nc_0}\right) \nabla \mu_e$$

$$N_{Cl^-} = -\frac{\gamma \alpha c_1}{\gamma RT} \frac{c_1}{c_0} c \nabla \mu_e + \frac{i_2 t_-^0}{z_- F} + c_1 v_0$$

$$N_{Cl_2} = -\frac{D_{Cl_2,g}}{RT} \nabla p_{Cl_2} + x_{Cl_2}(N_{Cl_2} + N_{inerts})$$

The notation used here is the same as that used by Newman (1, 2). Finally, an equation relating transfer current density to potential and solution phase concentrations is needed. A thin film transport model and Volmer-Heyrovsky kinetic model (3) were used. The equations were formulated and solved using the BAND technique (2).

The effect of fluctuating holdup (volume fraction of liquid within the gas-diffusion electrode of solution in the electrode) was also studied numerically. This phenomena can be caused by a fluctuating gas pressure, or by slowly sparging gas through the electrode. The liquid holdup decreases as the gas volume increases in the electrode. When a gas bubble escapes the pore liquid flows into the pore. This decreases concentration gradients and concentration polarization in the electrode.

An overall liquid phase mass balance in the porous electrode is

$$v = L \frac{d\epsilon_l}{dt}$$

where v is the electrolyte velocity, ϵ_l is the solution holdup in the electrode, and L is the electrode thickness. The electrolyte concentration and solution velocity can be divided into steady and transient parts

$$v = \bar{v} + v' \qquad c = \bar{c} + c'$$

If these definitions are used in the flux equation, and the flux equation is time-averaged, the following equation results

$$N_- = -\gamma_-\left(D\frac{dc}{dx} - \overline{c'v'}\right) + \frac{it_-^0}{z_- F}$$

The time average velocity is assumed to be zero. The correlation $\overline{c'v'}$ needs to be modeled in order to close the equations. This was done by assuming that the holdup and concentration were sinusoidal functions and were 90 degrees out of phase, which is equivalent to assuming that the velocity and concentration fluctuations were correlated.

$$\epsilon_l' = \epsilon_0' \sin(\omega t) \qquad c' = c_0' \cos(\omega t)$$

The equation for holdup can be differentiated to give the velocity, and the product of velocity and concentration integrated over the period $2\pi/\omega$ to give

$$\overline{c'v'} = \frac{\epsilon_0' c_0' \omega L}{2}$$

An expression for c′ is still needed. This was modeled by assuming that 1) c′ is proportional to the distance from the electrode/bulk solution interface, since c′ must be zero at that location, and that 2) c′ is proportional to the time averaged concentration gradient, since if there is no concentration gradient then there is no accumulation of electrolyte due to convection. The final expression for the flux is

$$N_- = -\gamma_-\left(D - \frac{\epsilon_0' \omega L}{2}(x - L)\right)\frac{d\bar{c}}{dx} + \frac{it_-^0}{z_- F}$$

This model describing how holdup fluctuations influence the concentration within a gas-diffusion electrode is similar in many ways to the mixing length model that is often used to describe turbulent flow.

1. J. S. Newman and C. W. Tobias, J. Electrochem Soc., 109, p 1183 (1962).

2. J. Newman, Electrochemical Systems, Prentice-Hall, Englewood Cliffs, NJ, 1973.

3. J.-T. Kim and J. Jorne, J. Electrochem. Soc., 124, p 1473 (1977).

Abstract No. 14

Effects of Gas Bubbles on the Polarization Behaviour of Porous Flow Through Electrodes. Formulation of the Problem.

Badr G. Ateya and Bahgat E. El-Anadouli
Chemistry Department, Faculty of Science,
Cairo University, Cairo, Egypt.

The evolution of gases at planar electrodes has significant effects on the rate and mechanism of mass transfer [1,2], on the electrolyte resistance and current distribution at the electrode surface [3-6] and on the hydrodynamic conditions near the electrode surface. Numerous experimental measurements and several empirical and mathematical treatments of these effects have been reported in the literature. The corresponding measurements and analyses at porous electrodes, although equally important, are clearly lacking. There are many systems where gas-electrolyte mixtures exist within porous electrodes the evolving gas may result from the main reaction or from a (parasitic) side reaction [7,8].

We have measured the current-potential relations for the hydrogen evolution reaction at (packed-bed) porous flow-through electrodes, and the pore electrolyte resistance under various conditions [9,10]. Measurements were obtained on packed beds of cu wool, cu turnigs and Ag wool.

In this paper we develop the equations of a mathematical model which simulates this process.

Model Equations:

Consider a porous flow-through electrode under the conditions illustrated in Fig. 1. In the experiment, the electrode is held vertically, and the electrolyte is fed from the bottom (entry) surface while the top (exit) surface is polarized. This arrangement facilitates the rising and removal of the generated gas bubbles. The porous matrix is assumed to be isotropic and highly conductive. The current increments di(x) generated in the space element dx is given by

$$di(x) = i_o \exp\left[-\alpha (E(x)-E_{rev})F/RT\right] S dx \qquad (1)$$

where i_o is the exchange current density and α is the transfer coefficient of the reaction, E(x) is the potential at distance x and S is the specific surface area of the porous medium in $cm^2 g^{-1}$, R, F and T have their usual meaning. The current is related to the potential gradient using Ohm's law

$$i(x) = \frac{1}{\rho(x)} \cdot \frac{dE(x)}{dx} \qquad (2)$$

where $\rho(x)$ is the pore electrolyte resistivity at x. The boundary conditions are

$$\begin{aligned} x = 0 \qquad & i(x) = 0 \quad \text{and} \quad E = E_o \\ & \text{i.e.} \quad dE(x)/dx = 0 \\ x = L \qquad & E = E_L \end{aligned} \qquad (3)$$

Note that the reaction rate is nonuniformly distributed throughout the pores and hence also the rate of gas evolution. Consequently, the gas void fraction and the pore electrolyte resistivity would vary with distance. For a porous electrode operating on liquid reactants and products in a supported electrolyte, the pore electrolyte resistance is independent of distance, and hence Equations 1 and 2 can be easily solved for this condition. In the present case the situation is quite different.

The current i(x) at a distance x produces a certain volume of gas per second. Upon establishing the proper balance, it can be shown that the gas void fraction $\epsilon(x)$ is given by

$$\epsilon(x) = ai(x)/v \qquad (4)$$

where a is a constant, a = 0.127 $cm^3 C^{-1}$ for hydrogen evolution at 25°C. In order to obtain the variation of $\rho(x)$ with distance, we use Equation 4 with either the Maxwell or the Bruggemann's equations (Equation 5 and 6, respectively)

$$\frac{\rho(x)}{\rho^o} = \frac{1 + 0.5\,\epsilon(x)}{1 - \epsilon(x)} \qquad (5)$$

$$\frac{\rho(x)}{\rho^o} = (1 - \epsilon(x))^{3/2} \qquad (6)$$

where ρ^o is the resistivity of the bubble-free electrolyte. The objective is to solve the system of simulataneous nonlinear Equation (1, 2, 4 and 5 (or 6)) using the boundary conditions (Equation 3) to obtain the dependence of current i(x), potential E(x) and pore electrolyte resistance $\epsilon(x)$ on the distance within the electrode.

References:

1. L.J.J. Janssen, Electrochim. Acta 23, 81 (1978).
2. N. Ibl, E. Adam, J. Venczel and E. Schalch, Chemie-Ingr-Tech. 43, 202 (1971).
3. Fumio Hine and Koichi Murakami, J. Electrochem. Soc. 127, 292 (1980); ibid 128, 64 (1981).
4. F. Hine, M. Yasuda, R. Nakamura and T. Noda, J. Electrochem. Soc. 122, 1185 (1978).
5. G. Kreysa and J. Kulps, J. Electrochem. Soc. 128, 979 (1981).
6. John Dukovic and Charles W. Tobias, J. Electrochem. Soc. 134, 331 (1987).
7. A.C.C. Tseung and P.R. Vassie, Electrochim. Acta 21, 315 (1976).
8. B. G. Ateya and E.S. Arafat, J. Electrochem. Soc. 130, 799 (1983).
9. B.G. Ateya, A.A. Ateya and M.E. Elshakre, J. Appl. Electrochem. 14, 357 (1984).
10. B.G. Ateya and M.E. Elshakre, J. Appl. Electrochem. 14, 367 (1984).

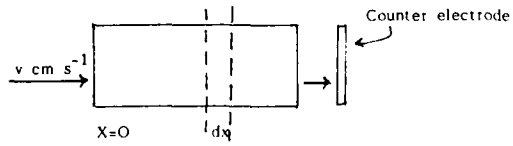


Fig. (1): Illustration of the system.

Abstract No. 15

MATHEMATICAL MODELLING OF HIGH POWER DENSITY, PULSED DISCHARGE LEAD ACID BATTERIES

Rodney M. LaFollette* and Douglas N. Bennion
Department of Chemical Engineering
Brigham Young University
Provo, UT 84602

Recent work has shown that secondary batteries may be designed to deliver high levels of pulsed power (1,2,3). Proper design of such batteries would require a bipolar configuration and the thinnest cell components possible. The lead acid system appears to be the leading candidate among well-developed secondary aqueous batteries for high power density application. Bipolar lead acid batteries of 100 - 800 kW/kg have been assembled and tested. Current densities of 20 A/cm^2 are typical for short times for bipolar lead acid stacks (2). Other studies have shown that at least 40 A/cm^2 can be obtained for longer times with high temperature molten salt systems (3).

Mathematical modelling must be used to study high power density battery design to aid interpretation of experimental results and to study aspects of battery performance which are difficult to examine experimentally. Mathematical modelling can provide insight into processes available in no other way.

The lead acid battery was modelled using the porous electrode modelling approach presented by Newman and Tiedemann (4). The basic model is similar to those of Tiedeman and Newman (5) and Sunu (6). The electrodes were treated on a macroscopic scale, ignoring the microscopic details of electrode structure. One key assumption was that the electrolyte composition within a pore was constant. Mass balances and concentrated solution theory flux expressions (7) were used to predict local acid concentrations in the cell. Ohm's law was used to describe the potential distribution in the solid electrode matrix. An analogous expression derived using concentrated solution theory was used to calculate the solution potential.

This model successfully predicts electrode behavior at current densities normally encountered in batteries. However, for high rate discharges, predicted current densities are almost invariant during a 1000 µsec discharge, while experimental results show a rapid drop in current density for 200 µsec, followed by a period of even steeper current density drop, before levelling off at a low value (see Figure 1). Model predictions are high because it fails to account for variations of electrolyte concentrations within electrode pores and because passivation by $PbSO_4$ is more pronounced than in other lead acid battery designs.

The porous electrode model was modified to both account for concentration variations at the solid/electrolyte interface within electrode pores and improve the prediction of $PbSO_4$ precipitation. The electrode pores were assumed to be of uniform diameter and axisymmetric. An equation describing both consumption of acid at the pore wall and mass transfer of species to the wall is

$$\partial C_{int}/\partial t = [3/(2Fa)^*di_2/dx + D_{H^+}/\delta_{mt}(C_b - C_{int})]/\delta_{pore} \qquad (1)$$

where C_{int} is the interfacial concentration of acid (mole/cm^3), F is Faraday's Constant, a is the electrode specific internal surface area (cm^{-1}), i_2 is the electrolyte current density (A/cm2), D_{H^+} is the diffusion coefficient of the hydrogen ion in sulfuric acid (cm^2/sec), δ_{mt} can be interpreted as a diffusion length for the hydrogen ion (cm), C_b is the acid concentration in the bulk of the pore (mole/cm^3), and δ_{pore} is the pore radius (cm). The first term on the right side of the equation represents the consumption of species due to chemical reaction. The second term on the right represents mass transfer between the bulk of the pore and the wall.

The precipitation model was derived in part from the work of Dunning et al. (8,9) and Tsaur and Pollard (10). The two-step discharge reaction at the PbO_2 electrode is

$$PbO_2 + 4H^+ + 2e^- = Pb^{2+} + 2H_2O \qquad (2)$$

$$Pb^{2+} + HSO_4^- = PbSO_4 + H^+ \qquad (3)$$

The second step, the precipitation of lead sulfate, occurs only after the product of Pb^{2+} and HSO_4^- have exceeded the solubility product. The rate of precipitation can be expressed as

$$r_p = (k_N + \varepsilon_p k_G)(C_{int}C_{Pb^{2+},int} - K_{sp}) \qquad (4)$$

where r_p is the rate of $PbSO_4$ precipitation (mole/cm^3/sec), k_N is a reaction rate constant for nucleation of $PbSO_4$ sites (cm^3/mole/sec), ε_p is the volume fraction of precipitate, k_G is the reaction rate constant for growth of $PbSO_4$ crystals (cm^3/mole/sec), $C_{Pb2+,int}$ is the interfacial concentration of $Pb^{2+}{}_{(aq)}$ (mole/cm^3), and K_{sp} is the solubility product of $PbSO_4$.

These equations were included in the model. Shown in Figure 1 is a prediction of current density using this model. Shown for comparison is the prediction of the original model and one with pore concentration variations but without precipitation. The model predicts cell behavior for the first 200 µsec. The initial drop in current density can be attributed to acid depletion at the electrode surfaces. Precipitation begins at around 100 - 200 µsec, which is close to what is observed experimentally. There is a decrease in current density after precipation begins, although it is not as great as is observed experimentally. The model predictions indicate that the steep decline in observed current density can be attributed to first concentration polarization and then precipitation.

1. LaFollette, R.M., Bennion, D.N., "Design Fundamentals of High Power Density, Pulsed Discharge Lead Acid Batteries," Extended Abstracts, Electrochem. Soc. Meeting, Philadelphia, PA, May 1986.
2. LaFollette, R.M., Bennion, D.N., "Experimental Studies of High Rate Lead Acid Batteries," Extended Abstracts, Electrochem. Soc. Meeting, Atlanta, GA, May 1987.
3. Gibbard, F., "Ultra-High-Power Batteries," Proc. of the Symposium on Electrochemical and Thermal Modeling of Battery, Fuel Cell, and Photoenergy Conversion Systems, (Selman, J. R., Maru, H. C., eds.), Proc. Vol. 86-12, Electrochemical Society, Pennington, NJ, 193 (1986).
4. Newman, J., Tiedemann, W., "Porous Electrode Theory with Battery Applications," AIChE Journal, **21**, (1975).
5. Tiedemann, W., Newman, J., "Mathematical Modelling of the Lead-Acid Cell," Battery Design and Optimization (Sid Gross, ed.), Electrochemical Society Proceedings Series, Princeton, N.J. (1979).
6. Sunu, W.G., "Mathematical Modelling for Design of Battery Electrodes: Lead-Acid Cell Modelling," White, R.E., Ed., Electrochemical Cell Design, Plenum: New York, 357 (1984).
7. Newman, J., Electrochemical Systems, Prentice-Hall, Princeton, NJ (1973).
8. Dunning, J.S., Bennion, D.N., Newman, J., "Analysis of Porous Electrodes with Sparingly Soluble Reactants," J. Elect. Soc., **118**, 1251 (1971).
9. Dunning, J.S., Bennion, D.N., Newman, J., "Analysis of Porous Electrodes with Sparingly Soluble Reactants II: Variable Solution Properties, Convection, and Complexing," J. Elect. Soc., **120**, 906 (1973).
10. Tsaur, K.C., Pollard, R., "Precipitation of Solids in Electrochemical Cells," J. Elect. Soc., **133**, 2296 (1986).

* Present address: International Fuel Cells, South Windsor, CT

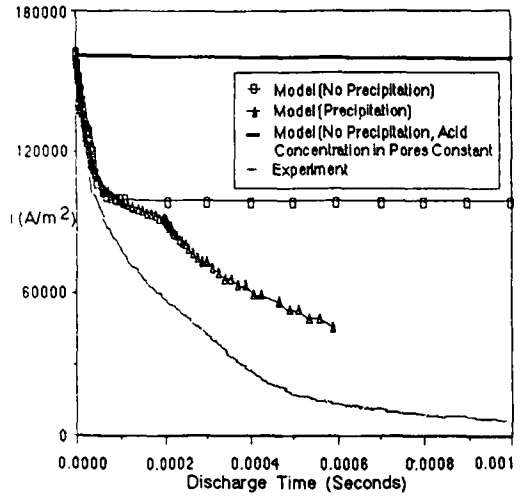


Figure 1. Predicted Current Density at 0.8 V Discharge - Comparison of Model Predictions with and without Precipitation

Abstract No. 16

Inorganic Cells Utilizing Solvents Based on Combinations of SO_2 and Halogens

Michael Binder and Sol Gilman

Power Sources Division
US Army Electronics Technology and
Devices Laboratory (LABCOM)
Fort Monmouth, NJ 07703-5000

INTRODUCTION

This review will be limted to scientific advances made in the areas of lithium based cells with carbon based cathodes where the totally inorganic electrolyte is either composed of combinations of sulfur dioxide and halogens or forms such mixtures during cell charge/discharge.

The systems we will discuss include Li/SO_2 rechargeable, Li/sulfuryl chloride primary and Li/sulfuryl chloride rechargeable technology. An excellent review article by Schlaikjer (1) has covered research up to 1983. Although it is practically impossible to cover all aspects of this growing field, we will attempt to gather the publicly available, published information on this subject appearing since 1983, and include some of our own in-house experiments in this area.

I. Li/SO_2 Rechargeable Cells

This technology, which has been actively studied by various research groups (2,3), uses a stable, highly conductive electrolyte formed when $LiAlCl_4$ reacts with either liquid or gasseous SO_2 to give a liquid complex/solvate of the form $LiAlCl_4 \cdot xSO_2$. Although the exact discharge products and mechanisms are unclear, it is believed that during the charge process, chlorine is formed. The formed chlorine can interact with SO_2 and either form sulfuryl chloride or other complexed species. Deliberate addition of halogens (4) or sulfuryl chloride (5) to the electrolyte has met with some success and has been shown to improve conductivity, raise load voltages and improve safety. Cell performance is also a strong function of the type of carbon black used to make the cathode (3). Because of the high chlorine concentration, chlorine resistant separators such as Tefzel have been used.

II. Li/SO_2Cl_2 Primary Cells

This technology has been actively investigated as a safe, low pressure alternative to the Li/thionyl chloride battery system since in discharge of sulfuryl chloride cells, no sulfur is formed. The lack of sulfur formed implies less of a chance for thermal runaways under abuse conditions. The preferred electrolyte salt is $LiAlCl_4$, although $LiB_{10}Cl_{10}$ and $LiGaCl_4$ (6) have shown desirable characteristics in terms of storage capabilities. Use of halogens or interhalogens (7) has been shown to improve cell performance, safety and storage capacity. The choice of carbon black for use in the cathode also strongly affects cell performance and storage capability (6).

III. Li/SO_2Cl_2 Rechargeable

This technology has very recently been considered as a limited cycle, high rate battery for applications where a single battery must function in primary as well as rechargeable operations (8). In this cell as well, the salt used is $LiAlCl_4$. Molecular chlorine formed during the charge cycle reacts with the discharge products to regenerate the starting materials. Cycling studies indicate that the lithium electrode cycles well in this electrolyte. Cell cycling losses are probably due to cathode failure and separator degradation. Use of separators that are resistant to chlorine is essential to the success of this system.

ACKNOWLEDGEMENTS

We wish to thank William L. Wade, Jr., Charles F. Walker, Jr. and Dr. Donald Foster of Power Sources Division, Fort Monmouth, NJ for many informative and valuable discussions.

REFERENCES

1. C. R. Schlaikjer, in "Lithium Batteries", edited by J. P. Gabano, Academic Press, NY, 1983.

2. A. N. Dey, H. C. Kuo, P. Keister and M. Kallianidis, Extended Abstracts of the Electrochem. Soc., Honolulu, Hawaii, October 18-23, 1987.

3. R. J. Mammone, S. Gilman and M. Binder, Proceedings of the 32nd Power Sources Symposium, Cherry Hill NJ, June 9-12, 1986.

4. R. J. Mammone, M. Binder, P. Keister and M. Kallianidis, J. Power Sources 21, 143 (1987).

5. R. J. Mammone and M. Binder, in "Practical Lithium Batteries", edited by C. R. Schlaikjer, 1988.

6. K. A. Klinedinst and R. A. Cary, J. Electrochem. Soc., 134, 1884 (1987).

7. P. W. Krehl and H. A. Hornung, IEEE Meeting, Halifax, Nova Scotia, September 28 - October 1, 1987.

8. P. H. Smith, A. A. Papanicolaou, M. H. Wilson, and S. D. James, Extended Abstracts of the Fall ECS Meeting, San Diego, CA, October 19-24, 1986.

Abstract No. 17

ELECTROREDUCTION OF $SOCl_2$: THE Pt/LiCl - $AlCl_3$ - $SOCl_2$ SYSTEM

P. Mosier Boss[1], S. Szpak[1]

J. J. Smith[2] and J. R. Nowak[3]

[1]Naval Ocean Systems Center, San Diego, CA 92152-5000

[2]Dept. of Energy, Washington, DC 20545

[3]Office of Naval Research, Arlington, VA 22217-5000

An optimization procedure, applied to the Li/$SOCl_2$ battery and based on sound models, falls short of expectations. The reason for this deficiency is attributed to a poor understanding of the elementary processes occurring within the porous structures of practical electrodes(1,2).

In the previous work(3,4), we examined the behavior and properties of a somewhat simpler system: Pt/$AlCl_3$ - $SOCl_2$ and concluded that the electroreduction of $SOCl_2$ in practical electrolytes follows a complex path of the cec-type. Moreover, the surface processes are modified by the selection of the electrode material. The introduction of an additional component, eg LiCl, is expected to complicate further the already complex reaction path. The increase in the complexity is demonstrated by using the ir-reflectance spectroscopy and linear scan voltammetry as the investigative tools.

IR-REFLECTANCE SPECTROSCOPY

The effect of LiCl addition on the composition of the Pt/$AlCl_3$ - $SOCl_2$ interphase both, at rest and cathodically polarized, was examined by the ir-reflectance spectroscopy. Representative results, shown in Figs. 1a and 1b, indicate an active participation of the Li^+ions in the electroreduction process. This participation involves establishment of new equilibria between the various species present at the elctrode surface as well as the corrective adjustment of elementary surface processes. A preliminary analysis suggests that, in acidic solutions, the $SOCl_2$ in the onium ion, $Cl_2Al[(<-OSCl_2)_2]^+$ is reduced first while in the $Li(<-OSCl_2)_2^+$ it occurs at $\eta > -1.2$ V. It is noteworthy that prior to its reduction, $Li(<-OSCl_2)_2^+$ accumulates in the interphase region. Furthermore, we note the formation of $Li(SO_2,SOCl_2)^+$ species at $\eta < -1.2$ V, ie, at potentials associated with the reduction of onium ions.

LINEAR SCAN VOLTAMMETRY

The tendency of $SOCl_2$ to solvate ions and form complexes, as well as the reactivity of the reaction product with other components of practical electrolytes, suggests coupling of the charge transfer to other participating processes. The shape of the lsv curve is governed by the mass balance equation, Eq.(1)

$$\frac{\partial c}{\partial t} = D\frac{\partial^2 c}{\partial x^2} - f(\chi,\lambda) \qquad (1)$$

where the source function $f(\chi,\lambda)$ depends on two parameters, viz. the thermodynamic parameter, $\chi = Kc^0$, and the kinetic parameter, $\lambda = \frac{RT}{F}\frac{k}{c^0 v}$. Here, c^0 is the concentration of electroactive species, k is the appropriate rate constant, K is the equilibrium constant, and v is the scan rate. The charge transfer cd, for N electroactive species and M adsorption processes, is given by an expression, Eq.(2)

$$j(0,t) = F\left[\sum_{i=1}^{N} n_i D_i \frac{\partial c(0,t)i}{\partial x} + \sum_{m=1}^{M} n\Gamma\frac{d\theta(t)}{dt}\right] \qquad (2)$$

where Γ denotes the maximum surface concentration and θ is the surface coverage.

As illustrated in Fig. 2, the addition of LiCl changes substantially the shape of the lsv curve for otherwise identical experimental conditions. The dominant effects are: (i) current densities are larger in the presence of LiCl, and (ii) the adsorption relationships are modified, especially at potentials less than - 100mV(4).

REFERENCES

1. R. J. Nowak, D. R. Rolison, J. J. Smith and S. Szpak, Electrochim. Acta, in press
2. K. C. Tsaur and R. Pollard, J. Electrochem Soc., 133,2296 (1986)
3. J. J. Smith, S. Pons, J. Li, W. West and S. Szpak, presentation SW-2, Third International Meeting on Li-Batteries, Kyoto (Japan), May 1986
4. P. Mosier-Boss, S. Szpak, J. J. Smith and J. R. Nowak, Ext. Abstr. Nr 487, Electrochem Soc. Spring Meeting, Atlanta GA, May 1988

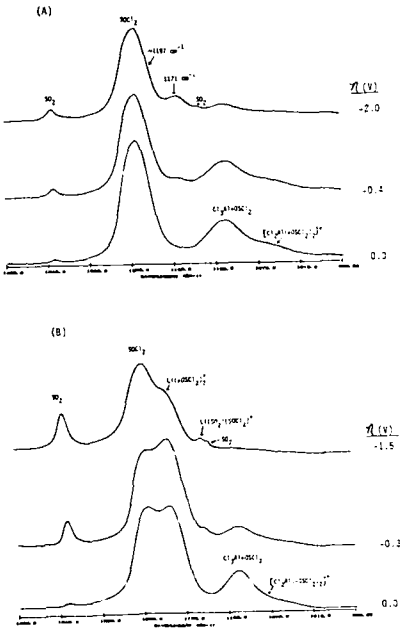


Fig. 1 The 940 - 1400 cm^{-1} spectral region of the metal/electrolyte interphase

A--Pt/4.0 M $AlCl_3$ - $SOCl_2$ interphase

B--Pt/1.0 MLiCl - 4.0 M $AlCl_3$ - $SOCl_2$ interphase

Overpotentials indicated

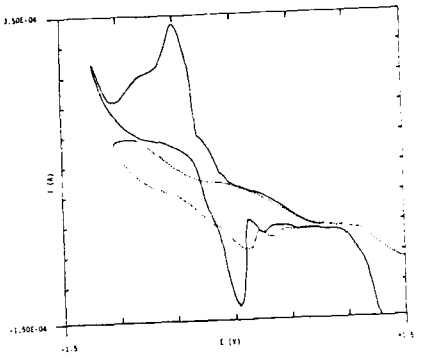


Fig. 2 Cyclic voltammograms

solid line: Pt/0.1 MLiCl-3.0 M $AlCl_3$ - $SOCl_2$ system

dashed line: Pt/3.0 M $AlCl_3$ - $SOCl_2$ system

electrode area: 0.3 cm^2

sweep rate: 30 mV s^{-1}

Abstract No. 18

Investigation of High Rate Thionyl Chloride Cathode Collectors

John C. Bailey and George E. Blomgren
Eveready Battery Company
P.O. Box 45035
Westlake, OH 44145

The capacity and high rate performance limitations of lithium thionyl chloride cells have been investigated by a number of authors. The cathode collector has been the electrode studied most often. Dey[1,2] investigated the performance of cells made using a variety of carbon blacks and graphite. These materials had a wide range of BET surface areas and particle sizes. He concluded that the cell capacity was not greatly affected by particle size or BET surface area although large particle size graphite gave poor performance. These conclusions were supported by the work by Christopulos and Gilman[3]. They found that the coulombic capacity was proportional to the pore volume of the collector rather than the BET surface area of the carbon used. However, more recent data by Gilman and Wade[4] found improved performance in Li-SO_2Cl_2 cells made with collectors containing high surface area carbons. These observations were supported by the work of Klinedinst[5,6], Ohsaki et al[7] and further work by Gilman and coworkers[9]. Electrodes made with the highest surface area carbons gave the highest discharge capacity. The discharge capacity has also been correlated with the DBP absorbtion number for most carbons[5]; however, since the electrode porosity was found to be proportional to the DBP absorption, the porosity rather than this carbon absorption property may be controlling the electrode capacity. The most surprising exception is Shawinigan acetylene black which has high DBP absorption, but comparatively low porosity and low capacity at high current density.[5] The use of additives and catalysts, chemical pretreatment and binders other than PTFE have also been reported to improve capacity.

In order to correlate and validate these approaches to rate improvement, we have evaluated examples of the types of electrodes mentioned above as well as some novel carbon materials. These studies have been carried out in a flooded test cell. The polarizations and capacities of cells made with these materials have been measured as a function of the current density. This data has been correlated with the details of the electrode pore structure.

A limited electrolyte cell which is intended to simulate the conditions found in a practical cell has been designed and built. This cell is equipped with a moveable reference electrode which can be accurately positioned to determine the potential drop as a function of position within the collector. These results should allow optimization of the high rate discharge capacity in practical sealed cells.

This work was supported in part by the Office of Naval Research.

References

(1) A.N Dey, J. Electrochem. Soc., 126, 2052 (1979)

(2) A.N. Dey, J. Power Sources 5, 57 (1980)

(3) J.A. Christopulos and S. Gilman, Record of the Tenth Intersociety Energy Corrosion Engineering Conference, The Institute of Electrical and Electronic Engineers, New York, 1975, p 437

(4) S. Gilman and W.L. Wade, J. Electrochem Soc., 127 1427 (1980)

(5) K.A. Klinedinst, J. Electrochem. Soc., 132, 2044 (1985)

(6) K.A. Klinedinst and R.A. Gary, First Quarterly Report, DELET-TR-83-0404-1 December 1983

(7) T. Ohsaki et al, Extended Abstracts, Vol 84-2, Fall Meeting of the Electrochemical Society, New Orleans, LA, October 7-12, 1984, Abstract No. 139, p. 207

(8) C.W. Walker, M. Binder, W.L. Wade an S. Gilman, J. Electrochem. Soc., 132, 1536 (1985)

Abstract No. 19

The Voltage Delay in $Li/SOCl_2$ Cells
Influence of Films at the Lithium Metal Surface

G. Eichinger and W. Gabriel
Sonnenschein Lithium GmbH, Industriestraße
D-6470 Büdingen, W-Germany

I. Introduction

Since lithium is thermodynamically not stable against all of the commonly used electrolyte solutions in lithium cells, a film formation occurs if lithium gets in contact with the electrolyte. This is due to a spontaneous reaction between the two components. The so formed film protects lithium from further reaction, but on the other hand causes a so called voltage delay which is especially pronounced in $Li/SOCl_2$ cells if no special treatments are used. The significance of the voltage delay is considerably influenced by the nature and morphology of the film. It is known that lithium exhibits very thin films of reaction products with the environmental gas atmosphere due to reactions with oxygen, carbon dioxide and moisture. Therefore, it will be an interesting task to find out correlations between the concentration of the original film on the lithium surface and the properties of the film which is formed later on in contact with the electrolyte.
By means of Fourier Transform Infrared Spectroscopy it was attempted to determine the chemical species that are present on the surface of a fresh lithium foil.

II. Experiental

FT-IR spectra were recorded with a Nicolet 5DXC-E instrument. The applied method is diffuse reflection which means that the laser beam is reflected at the lithium surface and that the reflected laser light is detected. To get spectra of reasonable good quality of the very thin films on the lithium surface, normally 500 scans were recorded. One scan takes one second. All spectra were recorded in a dry room, to prevent further excessive reaction of the lithium surface with the surrounding atmosphere. Humidity in the dry room was below 2 % by volume. Since the voltage delay was determined in technical bobbin type cells (size 1/2 AA or AA), the surface of the lithium was examined twice. First the surface of the foil was checked, then the foil was swaged to the inner wall of the can (which is typical for the test cells that were used) and the lithium surface was examined again, to take into account changes of the surface layers due to this mechanical process. The voltage delay of 1/2 AA cells was determined by discharging the cells through a resistor of 2.5 Ohm, 7 days after filling the cells. The storage was made at room temperature.

III. Results

FT-IR spectra are a good method to get information about the chemical nature of the protective films which are formed in lithium cells (1). The nature of those films are fairly well identified in the meantime (2). The IR method is, however, even more interesting to determine the nature of the chemical reaction layers which are formed on "pure" lithium foil during handling and storage.
Furthermore it is possible by that way to get some more information regarding the relative concentration of such surface contaminants in dependance of e.g. storage conditions. Such investigations may be used to establish this method as a regular quality acceptance test for incoming lithium which shall be used for lithium cells.
The impurities which can be identified as surface layers on a lithium foil are especially Li_2O, Li_2CO_3 and LiOH. It seems reasonable to assume that Li_2CO_3 and LiOH are follow products of Li_2O since it is well known that Li_2O easily picks up CO_2 and moisture, thus forming Li_2CO_3 and LiOH as secondary products. Obviously especially the concentration of Li_2CO_3 on the surface influences the LiCl film which is formed later on at the lithium surface in contact with $SOCl_2$ electrolyte. There are some indications that the TMV (transition minimum voltage) is lower if the concentration of Li_2CO_3 on the surface of the lithium foil is higher.
To get an easier comparison of the concentrations of the surface contaminants, the IR spectra were plotted in the Kubelka Munk mode and the heights of the typical and strongest absorption bands of the individual compounds were compared for different batches. Values for lithium which has been packed in different cans are presented in the table. Furthermore for control purposes the values of lithium that has been already swaged into a complete battery, including can to cover welding, have been determined. This battery was completed but without electrolyte and the filling hole in the cover was still open (diameter 1 mm), thus allowing penetration of the dry room atmosphere. After one week, the cell was cut and the lithium surface was inspected with IR. The results showed that even under these storage conditions the lithium surface has thicker surface layers than at the beginning.

References

1. K.M. Abraham and S. Chandhri, J. Electrochem. Soc., 133, 1367 (1986).

2. A. N. Dey, Thin Solid Films, 43, 131 (1977).

TABLE: Absorptions of lithium carbonate and lithium oxide on the lithium surface

	Kubelka Munk units				
Lithium batch number	Carbonate (lithium foil) absorptions at			Oxide (lithium foil) absorptions at	
	1500 cm^{-1}	880 cm^{-1}	530 cm^{-1}	680 - 630 cm^{-1}	380 cm^{-1}
C 467	0,0014	0,0028	0,0030	———	0,0024
C 497	0,0026	0,0042	0,0046	0,0028	0,0025
C 068	0,0022	0,0016	0,0061	0,0076	0,0010
C 028	0,0015	0,0027	0,0040	0,0011	0,0027
C 517	0,0006	0,0016	———	0,0009	0,0013

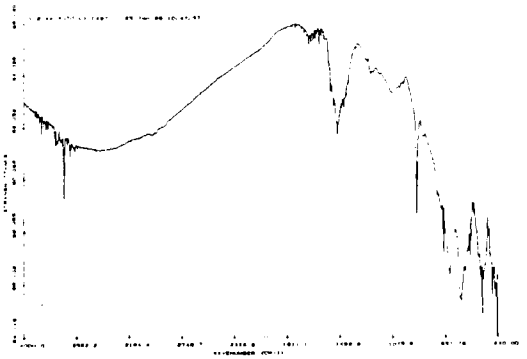


Fig. 1: FT-IR spectrum of a lithium metal surface with Li_2O, Li_2CO_3, LiOH

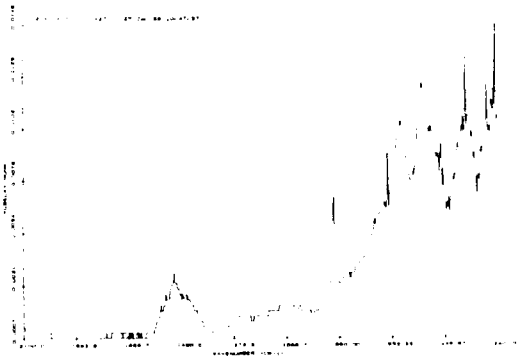


Fig. 2: Spectrum of fig. 1 in Kubelka Munk mode

Abstract No. 20

POLYMER ELECTROLYTE-BASED LITHIUM BATTERIES - A REVIEW

ALAN HOOPER

Applied Electrochemistry Centre,
The Harwell Laboratory,
Oxfordshire, OX11 ORA,
United Kingdom.

1. INTRODUCTION

Since the concept of all-solid-state, lithium-based, batteries employing ionically-conducting electrolytes was first discussed in 1978, their development has centred largely around rechargeable systems utilizing intercalation/insertion cathodes and poly(ethylene oxide), PEO, electrolytes. Early work was predominantly confined to operating temperatures in the range 80°C-140°C and was aimed at applications such as vehicle traction and load levelling. Lower temperature operation was also demonstrated, but at much reduced current densities.

Today, much more of the full potential of the technology is becoming exploitable. Improved performance at room temperature and below has opened up the possibility of new applications especially within the domestic consumer market. This has been brought about mainly via progress in polymer development.

2. POLYMERIC ELECTROLYTES

Over the last decade, there have been considerable efforts to develop alternative electrolyte materials with higher ionic conductivities at lower temperatures. A value of 10^{-4} ohm^{-1} cm^{-1} at room temperature is often seen as a useful goal. The results of such work, together with the concepts which underly it have been widely discussed and will not be considered in detail here. Attention will be drawn, however to, the validity of quoted ionic conductivities and to the many other conditions which need to be met in order to establish a material as a useful battery electrolyte. These include the use of non-hazardous materials; ease of thin-film fabrication; chemical, electrochemical and dimensional stability and low cost.

3. THE SOLID-STATE APPROACH

The concept of an all-solid-state cell employing a solid electrolyte offers the potential of a system which is easy to fabricate, rugged, leakproof and safe. This is made practically possible by the use of ionically conducting polymers which can be manufactured as, large area, thin films and which provide intimate contact with cell electrodes. When combined with the advantages of a lithium or lithium-based anode and a high performance primary or secondary cathode material, this provides a unique set of system properties.

The most thoroughly studied cell configuration comprises a lithium metal foil anode, a film of polymer electrolyte and a composite cathode incorporating a suitable active material together with an electronically conducting diluent, if required. Most attention has been given to secondary systems using intercalation (e.g. TiS_2) or insertion (e.g. V_6O_{13}) compounds as cathode materials.

The practical realization of the various cell components and the relative merits of available fabrication technologies will be discussed.

4. STATE-OF-THE-ART

Selected data will be used to illustrate general levels of achievement in cell performance.

With standard PEO-based electrolytes and a range of cathode materials, high initial material utilizations are found at 120°C at rates of up to a few hours. The substitution of more highly conducting electrolytes enables similar performance to be obtained at around room temperature.

A general phenomenon in the performance of intercalation/insertion cathode-based rechargeable cells is that of capacity decline with cycling. However, in many cases the rate of capacity decline is low, especially after the first few cycles and a number of systems have demonstrated the ability to maintain good utilizations to 100 deep discharge cycles or more.

A number of scaled-up experimental prototypes have been assembled since the latter part of 1985. At Harwell, individual cells with V_6O_{13}-based cathodes and capacities of up to 5Ah have been assembled and tested. The practical energy densities of these cells, including packaging is 85 Wh/kg and 200 Wh/litre. A 95°C, 10Wh cell and a room temperature, 1 Wh cell have been described by the IREQ Laboratory in Canada. Both cells were of a flat-plate design and constructed from double cathode/central anode, bi-cell, individual units. The characteristics of these various prototypes show no evidence of performance degradation when increasing scale by a factor of more than 1000 from earlier laboratory test cells.

At the other end of the dimensional scale, ultra-thin cells have also been fabricated and successfully operated.

Modelling studies have indicated practical operating energy densities in excess of 200 Wh/kg and 250 Wh/litre, for large battery modules.

Thermal management has also been addressed via both experimental and theoretical studies. Small temperature rises are generally predicted for batteries operating at most practical rates.

5. APPLICATIONS

The all-solid-state, polymer electrolyte-based, battery concept is capable of leading to a range of commercial products. The energy and power density requirements of applications such as electric vehicle traction can be achieved and, in the form of small and lightweight high energy density power sources operating at normal ambient temperatures, it is also capable of addressing the needs of a large and ever-growing domestic market in portable electronic devices. Electrochemical performance will be augmented by other device characteristics such as the ability to fabricate batteries into a variety of shapes and sizes, low self-discharge rates and the inherent safety characteristics of a rugged solid-state, leakproof, construction.

Since the solid-state concept is particularly suited to applications where a planar geometry is either desirable or necessary, this may also lead to the realization of integral, primary and rechargeable, solid-state power sources for electronic and microelectronic devices.

Although currently estimated costs do not rule out the technology for any of the applications considered above, the application of polymer electrolyte solid-state batteries is likely to begin in niche markets. Once established technically, wider application will ensue and, in some cases, superior performance characteristics will allow for a cost premium. In other situations economies of scale will reduce cost differences. In terms of battery size, small cells, perhaps of unconventional geometry, will emerge first with ongoing development and scale-up.

Abstract No. 21

ELECTRODE AND ELECTROLYTE MATERIALS FOR POLYMER-BASED LITHIUM BATTERIES

Bruno Scrosati
Dipartimento di Chimica, University of Rome, Italy.

The discovery of polymeric materials which are characterized by fast ionic transport(1) or by electrochemically induced doping processes(2) has opened a new area in lithium battery technology.

The availability of electrolytes which are plastic and can be easily prepared in the form of a thin film, is of extraordinary importance for the design of new types of batteries having unique construction properties, namely variable geometry, large active area, flexibility of operation and safety(3).

Accordingly, the possibility of electrochemically driving the oxidation-reduction processes of electronically conducting polymers, has favoured the use of these materials as new types of electrodes in rechargeable lithium batteries having important specific characteristics, such as high energy and safety.

The most common polymer electrolytes are complexes between poly(ethylene oxide),PEO, and lithium salts. These electrolytes are currently used in the development of rechargeable lithium batteries (5-8) based on 'conventional' electrode materials, i.e. a lithium metal anode and an intercalation compound cathode.

However, to date relatively few studies have been reported on the characteristics of the electrode/electrolyte interfaces, all this despite to the fact that the definition of the interfacial processes is most important for the effective evaluation of the battery performance.

Therefore, in this paper the kinetics of the lithium metal electrode and of selected intercalation electrodes in PEO-based electrolytes, will be discussed on the basis of cyclic voltammetry, polarization curves and a.c. impedance analysis.

PEO-based polymer electrolytes require a relatively high temperature of operation (typycally around 100 °C). This may not be a serious drawback if the polymer electrolytes are directed to the development of high-rate Li batteries. However, a temperature of operation above ambient may result critical for a successful application in power sources designed for the consumer electronic market. Since polymer-based Li batteries appear particularly suitable for this type of application, polymer electrolytes having improved low-temperature electrical properties would be mostly welcomed.

Along this line, we will report here the electrochemical characteristics of a modified polymer electrolyte having an enhanced room-temperature conductivity.

Among the various polymers which can be easily oxidized and reduced, those based on electrochemically synthesized heterocyclic compounds, such as polythiophene, polypyrrole and derivatives, appear to be as the most promising electrodes in lithium batteries(9-12).

The behavior of these polymer electrodes will be here considered in terms of rechargeability, energy content and charge retention.

Finally, polymer electrolytes and polymer electrodes can be combined to form polymer/polymer, thin-layer, lithium batteries. The characteristics and performance of this advanced type of solid-state power sources will be described and evaluated.

References.

(1)- C.A. Vincent, Progress in Solid State Chemistry, 17, 145 (1987).

(2)- B.Scrosati, Progress in Solid State Chemistry, 18 , 1 (1988).

(3)- B.Scrosati, in 'Polymer Electrolyte Reviews 1', C.A.Vincent and J.MacCallum Eds., Elsevier Appl. Science Pu.,London 1987, pag. 315.

(4)- A.G.MacDiarmid and R.B.Kaner, in 'Handbook of Conducting Polymers', T.A. Skotheim Ed., M.Dekker Pu.,New York 1986 pag.689.

(5)-A.Hooper and J.M.North, Solid State Ionics 9&10, 1161 (1983).

(6)- M.Gauthier et.al., J.Electrochem.Soc., 132, 1333 (1985).

(7)-M.Z.A.Munshi and B.B.Owens, Solid State Ionics, 26, 41 (1988).

(8)-F.Bonino,M.Ottaviani,B.Scrosati,G.Pistoia, J.Electrochem.Soc.,135, 12 (1988).

(9)-S.Panero,P.Prosperi,B.Klaptse,B.Scrosati, Electrochim.Acta, 31, 1597 (1986).

(10)-S.Panero,P.Prosperi,F.Bonino,B.Scrosati Electrochim.Acta,32, 1007 (1987).

(11)-S.Panero,P.Prosperi,B.Scrosati, Electrochim.Acta, 32, 1465 (1987).

(12)-B.Scrosati,S.Panero, P.Prosperi, J.Power Sources, 19, 27 (1987).

(13)-S.Panero,P.Prosperi,B.Scrosati, Electrochim.Acta, 32, 1461 (1987).

(14)-F.Croce,S.Panero,P.Prosperi,B.Scrosati Solid State Ionics, in press.

Abstract No. 22

Polymeric Solid Electrolytes: Microscopic Models and Motion Mechanisms

M. A. Ratner and A. Nitzan

Department of Chemistry
Northwestern University

Evanston, IL 60208

Although early treatments of the motion mechanism in polymer solid electrolytes were based upon the free-volume concept, it has become increasingly clear that the simple free-volume picture is inadequate. This inadequacy arises partly from the nature of the polymer motions that promote ion transport, and partly from the strong interactions both among the ions and between the ions and the solvating polymer. Early discussion in terms of a modified weak electrolyte model, in which the transport rate included a Boltzmann prefactor describing the concentration of free carriers, improves the picture somewhat. However, the high molar concentrations generally found in these materials imply the behavior to be roughly that of a solvated molten salt, in which the ionic coulomb interactions, while not determining the structure, are critical for understanding the transport.

Two important factors appear in the conductivity expression. The first of these is a one-particle factor, involving the mobility of the individual carriers. In this factor enter free-volume type terms, motion of the polymer host and size considerations. A second term involves interionic interaction; this may or may not be representable in terms of pair potentials, and is the major complication that extends beyond simple free-volume concepts.

Two models are discussed to deal with these complications attendant upon the conductivity in these materials. In the dynamic percolation picture, the ionic motion is discussed in terms of a site model, with the hopping probability from site to site determined by dynamical motions of the liquid (dependent upon the free volume). The percolation is, however, of interacting type; results are presented for interacting particles in a dynamic percolation context, and comments are made on transference numbers and mobilities. The second model is full-continuum Langevin dynamics, with interionic interactions included. The effective potential acting between the ions is described by a combination of macroscopic electrostatic concepts and microscopic interionic interactions.

Results for the conductivity, tracer diffusion, vibrational spectra, transference numbers and thermal dependence will be presented. Comparison with spectroscopic and transport measurements on polymer electrolyte systems will be presented.

Abstract No. 23

POLYPHOSPHAZENE-BASED SOLID-STATE SECONDARY LITHIUM BATTERIES

M. Alamgir, R. K. Reynolds and K. M. Abraham

EIC Laboratories, Inc.
Norwood, MA 02062

INTRODUCTION

Li-salt complexes of poly[bis-(methoxyethoxy-ethoxide)phosphazene], or MEEP, have Li^+ conductivities which are among the highest known for polymer electrolytes (1,2). Despite considerable interest in utilizing these electrolytes in solid-state Li batteries, reports of cell cycling performance with MEEP-based electrolytes have been rather limited. This is partly due to their dimensional instability that, unlike poly(ethylene oxide) (PEO)-based electrolytes, prevents them from being cast as free-standing, thin films. We have recently shown (3) that addition of high molecular weight PEO enhances the dimensional stability of MEEP-based electrolytes. Conductivity data and cycling results of Li/TiS_2 cells utilizing MEEP/PEO-$LiClO_4$ mixed electrolyte suggested significant performance improvements over cells containing PEO-based electrolytes. We report here our recent results for a series of MEEP/PEO-LiX mixed electrolytes in which LiX is $LiClO_4$, $LiBF_4$, $LiCF_3SO_3$ or $LiAsF_6$. In addition, we demonstrate the feasibility of utilizing pristine MEEP-LiX electrolyte in rechargeable Li/TiS_2 batteries by supporting it in a fiberglass separator matrix.

EXPERIMENTAL

MEEP was prepared according to the procedures described by Allcock et al. (4). MEEP-LiX electrolytes were prepared by dissolving MEEP and appropriate amounts of the Li-salts in acetonitrile. Mixed electrolytes were prepared by dissolving PEO (Polysciences, average MW = 5×10^6), MEEP and the Li salts in acetonitrile. Films were cast on Teflon dishes and were dried under vacuum at 50°C for 2 days.

Conductivities were measured by the AC impedance technique, between 100 kHz and 5 Hz, with stainless steel electrodes using an EG&G PAR Model 273 impedance system. Sample films were held between the electrodes by compression springs and the cell was housed inside an O-ring sealed glass tube having electrical leads. Conductivity versus temperature measurements were performed inside a constant temperature chamber. DSC measurements were carried out with a Perkin-Elmer model DSC7 calorimeter.

Li/TiS_2 cells were fabricated by sandwiching the MEEP.$(LiClO_4)_{0.25}$ or the fiberglass-supported MEEP.$(LiClO_4)_{0.25}$ electrolyte between a Li anode, pressed onto Ni screen, and a TiS_2 composite cathode. The electrode package was held tight between two steel plates by compression springs. The glutinous MEEP electrolyte was spread over one face of the Li anode and left overnight to form a uniform layer. In the other modification, a 2 mil thick fiberglass mat (porosity 90%) was laid over the electrolyte-coated Li anode and left overnight to wet. All the cells were prepared cathode-limited. Cells were discharged/charged galvanostatically between 3.0 and 1.6V.

RESULTS AND DISCUSSION

Figure 1 shows the discharge/charge performance of a Li/TiS_2 cell containing neat MEEP.$(LiClO_4)_{0.25}$ electrolyte at two different temperatures. The electrolyte showed a tendency to flow out of the cell on holding the cell in positions other than the horizontal. The cell shorted after a few cycles. It should be noted that several other attempts to fabricate neat MEEP.$(LiClO_4)_{0.25}$-based cells led to cell shorting in the first cycle. Figure 2 shows the performance of a Li/TiS_2 cell containing the fiberglass-supported MEEP-$(LiClO_4)_{0.25}$ electrolyte at room temperature. The cell had a cathode area of 2.0 cm^2 and a theoretical capacity of 2.3 mAh. At 0.2 mA, the discharge capacity obtained was 0.48 mAh, or 20% of the theoretical cathode capacity. The cell could be charged to recover ~50% of the discharge capacity at half the discharge rate. The reason for this poor charging efficiency is being investigated. While the fiberglass matrix supported-electrolyte allows the use of MEEP in practical cells, the high conductivity of the electrolyte is somewhat compromised by the porous glass matrix. We developed an alternate route to utilize the excellent conducting properties of the MEEP-electrolyte by blending MEEP with PEO (3).

During optimization studies of composition of the mixed polymer electrolytes, we found that it was not possible to cast a morphologically uniform film from an apparently homogeneous solution of pure MEEP and PEO in ratios containing 30 or more weight percent of MEEP. The films appeared nonuniform and isolated regimes of PEO and MEEP coexisted. There apparently occurs a separation of phases. Addition of a Li-salt to this solution allowed casting of smooth and homogeneous films. However, it appeared that above 70 w/o of MEEP, a mixture of MEEP/PEO/LiX does not form a homogeneous film. There is again separation of the MEEP and the PEO domains. The optimum composition with regard to conductivity and homogeneity of the film appeared to lie between 55 and 70 w/o of MEEP, or correspondingly between 45 and 30 w/o of PEO. Figure 3 shows the conductivity versus temperature data of 55 w/o MEEP:45 w/o PEO doped with different Li-salts. The Li^+ to oxygen ratios for PEO and MEEP were 1:8 and 1:4, respectively. The conductivity data in Figure 3 were obtained on a second heating cycle from room temperature. The highest temperature studied was 100°C. Below 60°C, the values in the first heating cycle were about an order of magnitude lower for $LiBF_4$ and $LiClO_4$. Above this temperature the conductivities on the first and the second heating cycle were essentially the same. $LiClO_4$ and $LiBF_4$ yielded the highest conductivities. The conductivities of the films containing $LiAsF_6$ were the lowest among the salts studied. DSC studies revealed that the melting of the $LiAsF_6$-complex occurred at a relatively high temperature of 112°C. However, the conductivity of the triflate film was puzzling. Its conductivity showed only monotonous increase over the temperature range of 25 to 100°C. A DSC trace of this film, however, showed a melting point peak of 67°C, which is virtually the same as the melting point of PEO alone. The DSC and x-ray diffraction studies suggest that the observed conductivity-temperature behavior of the various mixed electrolytes may be explained in terms of crystalline-amorphous phase transitions in these complexes. In the first heating, the crystalline phases melt around 65°C and a substantial amorphous phase is retained even after cooling to room temperature. Consequently, the near-ambient temperature conductivity is significantly higher following the first heating.

Acknowledgement: Financial support was provided by the Office of Naval Research, Contract N00014-87-C-0857.

REFERENCES

1. C. Vassort, M. Gauthier, P. E. Harvey, F. Brochu and M.B. Armand, "Primary and Secondary Ambient Temperature Lithium Batteries", J. P. Gabano, Z. Takehara and P. Bro, eds., The Electrochemical Society, PV88-6, 780 (1988).
2. P. M. Blonsky, D. F. Shriver, P. E. Austin and H. R. Allcock, J. Am. Chem. Soc., 106, 6854 (1984).
3. K. M. Abraham, M. Alamgir and S. J. Perrotti, J. Electrochem. Soc., 135, 535 (1988).
4. H. R. Allcock, P. E. Austin, J. T. Sisko, P. M. Blonsky and D. F. Shriver, Macromolecules, 19, 1508 (1986).

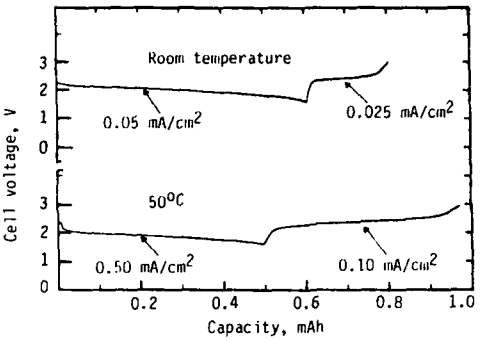


Fig. 1. A "neat" Li/MEEP.$(LiClO_4)_{0.25}/TiS_2$ cell. Theoretical capacity = 3.8 mAh, area = 2.0 cm^2.

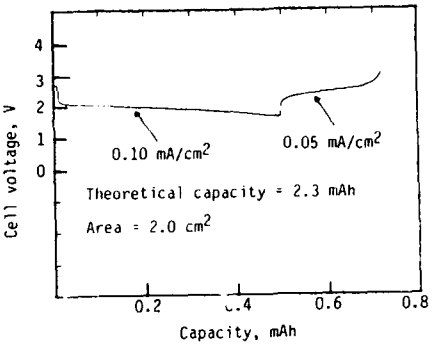


Fig. 2. Performance of a "supported" Li/MEEP·$(LiClO_4)_{0.25}/TiS_2$ cell at room temperature.

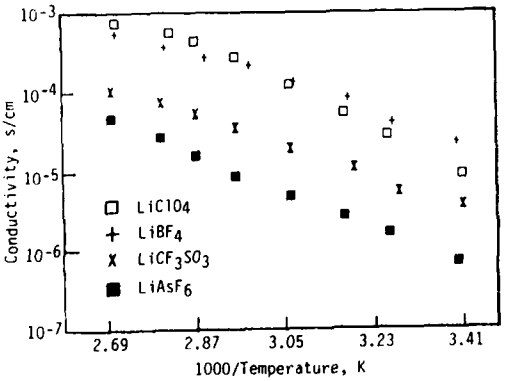


Fig. 3. Effect of salt-type on the conductivity of 55 w/o MEEP:45 w/o PEO mixed electrolyte.

Abstract No. 24

EFFECT OF γ-RADIATION ON THE STRUCTURE AND IONIC CONDUCTIVITY OF MEEP + LITHIUM SALTS.

Gh. Nazri and S.G. Meibuhr
Physical Chemistry Department
Gereral Motors Research Laboratories
Warren, MI 48090

Reports of high ionic conductivity in polyethylene oxide (PEO) + lithium salt systems at temperature >60 °C have stimulated interest in rechargeable lithium batteries, using polymer electrolytes. PEO polymers undergo a phase transition at 60-65°C to become amorphous. Different approaches to obtaining an amorphous polymer and thereby improving the ionic conduction at room temperature have included polymer modification by a) chemical modification to the polymer itself (1), b) physical modification to the polymer electrolyte by using addition agents (2), or c) the use of entirely new polymeric materials (3). A new polymer, 2-(2-methoxy-ethoxy-ethoxy) polyphosphazene (MEEP), was reported to have lithium ion conductivity greater than comparable polymers based on polyethylene oxide (4) at ambient temperature.

MEEP-salt complexes are elastomeric and readily undergo plastic flow. This report describes an examination of the structure of a MEEP-Li salt complex with infrared spectroscopy and measurements of the A.C. impedance. We also present results on the effect of γ-irradiation on the polymer as a means of decreasing its plastic flow through irradiation crosslinking.

Two types of experiments were performed on the MEEP containing lithium triflate. The A.C. impedance of the MEEP was measured between two electrodes at different temperatures and on samples before and after they were γ-irradiated. In the second series of experiments, the FT-IR spectra were collected from thin films of MEEP that had been deposited on gold. Spectra were also collected from these samples after they had been exposed to γ-irradiation.

The FT-IR spectrum of a thin film of MEEP containing lithium triflate is shown in Fig. 1. There is a large relative intensity change between the spectrum of these thin films and that of the bulk material. These relative intensity changes for different polarizations can be attributed to the preferred orientation of the molecule on the gold substrate.

Figure 2, which shows the spectra in the range 900 cm^{-1} to 1500 cm^{-1} for both non-irradiated and irradiated MEEP using only S-polarized light, (solid line corresponds to the non-irradiated sample) confirms that the PN backbone is still parallel to the substrate after irradiation; however, the CO and CC peaks show a contribution caused by a dipole moment normal to the substrate. This indicates an interaction of the sidechain of one polymer molecule with another polymer molecule. Due to this cross-linking, a polymer with higher viscosity is expected.

In Fig. 3 are shown the conductivity data vs 1000/T for MEEP samples that had been γ-irradiated to dosages of 2.8 and 10 MRads. Samples of MEEP that had been irradiated showed a significant reduction in fluid flow at room temperature. Since the IR study clearly showed evidence of crosslinking due to γ-irradiation, it appears that such crosslinking does not severely affect the conductivity of MEEP.

REFERENCES

1. D.W. Xia, D. Soltz, and J. Smid, Solid State Ionics, 14, 221 (1984).

2. G. T. Davis, National Bureau of Standards News Release in HIGH TECH Materials Alert, 2, March 1987.

3. R. Dupon, B. L. Papke, M. A. Ratner, and D. F. Shriver, J. Electrochem. Soc., 104, 586 (1984).

4. P. M. Blonsky, D. F. Shriver, P. Austin, and H. R. Allcock, J. Am. Chem. Soc., 106, 6854 (1984).

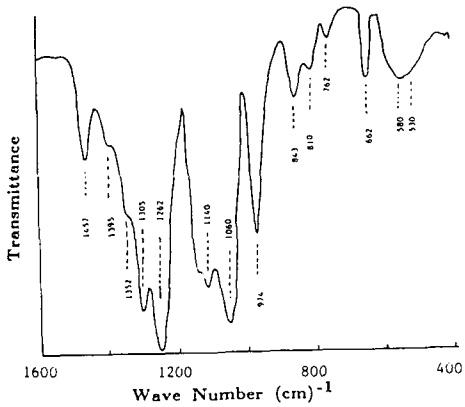


Fig. 1. Transmission infrared spectrum of a thin film of MEEP + $LiCF_3SO_3$ on a gold substrate.

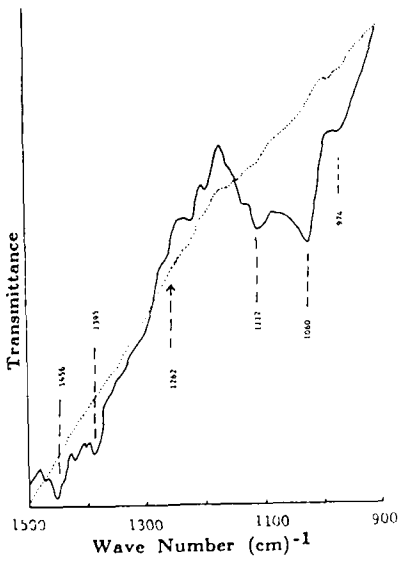


Fig. 2. FT-IR spectra of a γ-irradiated thin film of MEEP + $LiCF_3SO_3$, using S polarized line (solid line) and a non-irradiated sample (dotted line)

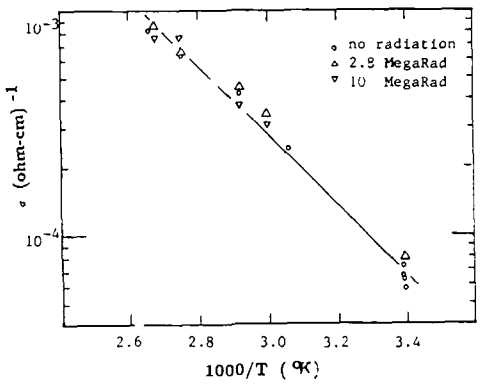


Fig. 3. Temperature dependence of ionic conductivity for γ-irradiated MEEP + $LiCF_3SO_3$.

Abstract No. 25

Secondary Lithium Solid Polymer Electrolyte Cells

Kathleen A. Fix and Anthony F. Sammells

Eltron Research, Inc.
4260 Westbrook Drive
Aurora, IL 60504

A strategy for developing morphologically invariant lithium/solid polymer electrolyte interface is being investigated via the use of lithium intercalated electrodes. Emphasis is being placed upon the rutile material Li_xWO_2 $0.1 < x < 1.0$. An absence of shape change at this interface is expected to result in both long cycle life electrochemical cells and the simultaneous maintenance of small interelectrode spacing so that low IR losses can be maintained.

During fabrication of cells investigated here both electrochemical and chemical lithium intercalation of WO_2 was pursued. In the case of larger WO_2 electrodes initially prepared for fully discharged state cells, electrochemical intercalation during cell charge was found to require significant time, and the reproducible achievement of complete uniform intercalation across the negative electrode became an issue. Emphasis was consequently placed upon cells fabricated using Li_xWO_2 electrodes initially chemically intercalated by lithium prior to cell assembly. Previous work[1-3] has demonstrated direct lithium intercalation of metal dichalcogenides using n-BuLi. Lithium activity in n-BuLi is, however, insufficient to achieve lithium intercalation of WO_2[4]. However, recent work has shown that WO_2 can be directly lithium intercalated upon immersion in lithium naphthalide[5,6]. Li_xWO_2 electrodes prepared in this work were intercalated using lithium naphthalide (0.8M) in 2MeTHF. Lithium intercalation was found to readily occur at room temperature, being initially rapid and slowing as bulk intercalation within the electrode proceeded. For electrodes intercalated in this manner, a relationship was identified between the degree of lithium intercalation and initial open-circuit potential in liquid non-aqueous electrolyte. Lithium ion conducting SPEs being investigated by us in this program include those based upon poly(ethylene oxide)[7,8], poly(ethylene oxide)/poly(ethylene glycol)[9], and the polyphosphazenes[10], thereby permitting cells of the general configuration

$$Li_xWO_2/Li^+SPE/TiS_2$$

to be prepared. Emphasis, however, has been placed upon the poly(ethylene oxide)/poly(ethylene glycol) SPEs (PEO/PEG), where the amorphous lithium ion conducting phase of PEO is stabilized by the PEG at temperatures close to ambient. Cells were prepared by contacting fully charged half-cells via a previously cured PEO/PEG film containing 1M $LiCF_3SO_4$, followed by a thermal excursion to 80°C under vacuum for 2 hrs. so as to achieve acceptable contact at each respective electrode/SPE interface. To delineate the respective electrochemical performance of each electrode, cells were also prepared containing a unit activity lithium reference electrode strategically placed coaxially in the counter electrode compartment.

Comparative electrochemical performance of half and full SPE cells as a function of fabrication technique and initial degree of lithium intercalation, will be addressed together with their potential utility as long cycle life galvanic devices.

ACKNOWLEDGEMENT

This work was supported by the National Science Foundation under the SBIR program.

REFERENCES

1. Whittingham, M. S. and Dines, M. B., J. Electrochem. Soc., 124, 1387 (1977).
2. Sinha, S. and Murphy, D. W., Solid State Ionics, 20, 81 (1986).
3. Whittingham, M. S. and Gamble, F. R., Mater. Res. Bull., 10, 365 (1975).
4. Murphy, D. W., DeSalvo, F. J., Carides, J. N. and Waszczak, J. V., Mater. Res. Bull., 13, 1395 (1978).
5. Dines, M. B., Mat. Res. Bull., 10, 287 (1975).
6. Abraham, K. M., Pasquariello, D. M., Willstaedt, E. B. and McAndrews, G. F., Paper #74 presented at The Electrochemical Society Mtg., Honolulu, Hawaii, 1987.
7. Wright, P. V., Br. Polymer J., 7, 319 (1975).
8. DuPon, R., Whitmore, D. H. and Shriver, D. F., J. Electrochem. Soc., 128, 715 (1981).
9. Kelly, I., Owen, J. R. and Steele, B. C. H., J. Electroanal. Chem., 168, 467 (1984).
10. Blonsky, P. M. and Shriver, D. F., J. Am. Chem. Soc., 106, 6854 (1984).

Abstract No. 26

IMPLANTABLE POWER SOURCES - AN OVERVIEW

Curtis F. Holmes

Wilson Greatbatch, Ltd.
10,000 Wehrle Dr.
Clarence, NY 14031

INTRODUCTION

Implantable biomedical power sources have been in use since the development of the implantable cardiac pacemaker in 1958 (1). For many years the pacemaker was the only implantable device requiring electrochemical power sources, and it remains the largest implantable application today. The past 9 or 10 years has seen the development and introduction of several more implantable devices; among them the neurostimulator, the drug delivery system, and the automatic defibrillator. These devices have presented significant challenges to battery developers because they require current-delivery capabilities far in access of those required by the pacemaker (2).

For the first fifteen or so years of the history of the pacemaker the system of choice was the zinc/mercuric oxide cell. Even though this cell demonstrated problems such as high self-discharge and gas evolution, it made pacemaking possible. In 1972 the first lithium-powered pacemaker was implanted. Over the next several years a variety of different lithium systems were used in pacemakers. Among the couples used in pacemakers were Li/$SOCl_2$, Li/Ag_2CrO_4, Li/CuS, Li/I_2-Polyvinylpyridine(PVP), and, in more limited use, Li/LiI(Al_2O_3)/ PbI_2, PbS, Pb. Of these, only the Li/I_2-PVP and Li/CuS systems remain in use in pacemakers today.

CURRENT IMPLANTABLE SYSTEMS

Over 85% of all cardiac pacemakers today employ the LI/ I_2-PVP system. This system contains a cathode/depolarizer which is a mixture of iodine and charge transfer complexes of iodine and PVP. The solid electrolyte LiI is formed *in situ* as the cell is discharged.

The Li/CuS system, also used in cardiac pacemakers today, is a solid cathode, liquid organic electrolyte cell with a two-step reaction which produces a lower voltage plateau near cell depletion, providing an indicator of approaching end of life.

Implantable drug delivery systems typically use soluble cathode technology because of the high voltage requirements and the milliampere-level pulse requirements. The Li/$SOCl_2$ system and the Li/ BCX system (BrCl in thionyl chloride) are in use.

The implantable automatic defibrillator requires a battery which can deliver pulses on the order of two amperes over a background current of about 25 microamperes. There can be no appreciable voltage delay. For this application, solid cathode/liquid organic electrolytes have proven to offer the best features. The Li/ V_2O_5 was the first system to be used in an implantable defibrillator. Lithium/ silver vanadium oxide ($Li/Ag_2V_4O_{11}$) cells have been developed and are being used in clinical evaluations.

There are currently under development several devices which will require secondary implantable batteries. Among these are the implantable gait assist device and the left ventricular assist device. It is likely that recent advances in the development of rechargeable lithium cells will lead to the availability of rechargeable lithium batteries to power these devices.

MATERIALS AND PROCESSES CONSIDERATIONS

The design and construction of implantable batteries presents a unique set of challenges. The obvious requirements of safety and reliability dictate that materials compatibility concerns be carefully considered and addressed. For example, the use of corrosion-resistant glasses in liquid organic electrolyte systems is required because of the longevity requirements of implantable devices. Redundancies need to be engineered into the cell designs.The production quantities of such batteries are rarely high enough to justify automation, so attention to the special problems associated with hand-type production methods is required. A comprehensive system of quality control and detailed documentation of construction and inspection steps is required. Finally, methods must be developed to predict and verify long-term performance on the basis of accelerated tests backed up by an extensive life-test program.

CONCLUSIONS

Power sources for implantable devices have been in use since the early 1960's. Lithium batteries have been used in implantable devices since 1972. The diverse nature of the requirements of present and future implantable devices has led to the development of several kinds of implantable lithium primary batteries. The next generation of implantable devices will likely require lithium secondary systems to meet their requirements. Methods have been developed for the design, manufacturing, and testing of medical batteries, which have generally demonstrated a high level of reliability.

REFERENCES

1. W. Greatbatch and C. F. Holmes, in *Proceedings of the Symposium on History of Battery Technology*, (A. J. Salkind, Ed.), 232, The Electrochemical Society, Pennington, N. J., 1987).

2. C. F. Holmes, in, *Proceedings of the Second Annual Battery Conference on Applications and Advances*, (R. Das, B. M. Eliash, H. A. Frank, and D. F. Pickett, eds.) The Electrochemical Society, Pennington, N. J. (1987), p. 25.

Abstract No. 27

Lithium Secondary Batteries: Role of Polymer Cathode Morphology

Katsuhiko Naoi*,**, Tetsuya Osaka** and Boone B Owens*

* Corrosion Research Center, Dept. of Chem. Eng., University of Minnesota, 112 Amundson Hall, 221 Church St SE, Minneapolis, MN 55455

** Dept. of Appl. Chem., Waseda Univ., 3 Okubo, Shinjuku, Tokyo 160, JAPAN

Promising cathode materials for rechargeable lithium electrochemical cells include solid intercalation compounds such as metal oxides or sulfides and electroactive, polymer cathode materials such as polyaniline or polypyrrole. The theoretical values for the specific energy of the electrode couples maybe calculated for these two classes of cathodes; the solid oxide type cathodes exhibit theoretical specific energies in the range of 300-1000 Wh/kg, compared to values of about 200-400 Wh/kg for the polymeric cathode materials. Lithium/polymer cathode cells have intrinsically lower values for specific energy because of the low doping level of the polymer films and the requirement of ionic doping associated with the faradaic reaction. Further, slow ion diffusion within the bulk of the polymer films results in limitations on the rate behavior of such cell systems.

An electrochemically-formed conducting polymer film of polypyrrole (PPy) has been grown on an electrode substrate; when the substrate is precoated with a film of nitrile butadiene rubber (NBR), a highly enhanced anion doping-undoping process results because of the oriented-growth structure. This is illustrated in Figure 1 which shows that the polypyrrole cathode materials are grown as continuous fibers or dendrites normal to the plane of the electrode (Ref 1). In order to prepare this high surface area electrode structure, the NBR film is solvent cast onto the surface of the electrode. When this insulated electrode is inserted in the electrolyte solution (for example, $LiClO_4$ in acetylnitrile) the NBR film is partially dissolved. As channels are opened up due to this dissolution, the electropolymerization of the pyrrole initiates at the electrode surface. The polypyrrole film then deposits in the direction perpendicular to the substrate, forming within the matrix of the NBR host-polymer. The guest PPy polymer grows through the fine channels etched by the penetration of the electrolyte into the NBR film during electropolymerization as shown in Figure 2. The host polymer of NBR film is subsequently removed in order to leave the backbone of the precipitated PPy film.

Potential step and AC impedance measurements for these electrodes demonstrate that the NBR/PPy electrode exhibits a faster anion doping process than an ordinary PPy electrode (Ref 1). Inspection of the surface of the film by Scanning Electron Microscopy revealed that the PPy film grown directly on platinum substrate exhibits a relatively compact structure of approximately 1 μm thickness. In contrast the PPy film formed by the NBR process exhibited a porous open structure with a thickness of about 2-3 μm when equivalent amounts of polymer were deposited (1 coulomb/cm^2).

The polypyrrole exhibits a doping level of about 33 percent and this cathode has been developed into a commercial battery design (Ref 2). More recently polyaniline (PAn) was reported to exhibit a doping level in excess of 80 percent (Ref 3); this results in an increase in the theoretical specific energy for a cell system utilizing such a cathode. The Li/PAn system has also been recently reported in a commercial battery development (Ref 4). With advances in the doping levels and also the ability to control the morphology in a manner that enhances the rate capability, there is renewed interest in lithium/polymer cathode cell systems. Although they do not appear to be capable of achieving the theoretical specific energies of the solid intercalation cathodes, under certain conditions they may exhibit superior values for the power density in energy storage devices.

References

1. Naoi, K. and Osaka, T., J. Electrochem. Soc., 134 2479 (1987).

2. "Electrically Conductive Polymers As Rechargeable Battery Electrodes," D. Naegele and R. Bittihu, Abstract No. A5-3, Extended Abstracts, p. 310, 6th International *Conference on Solid State Ionics*, Garmisch-Partenkirchen, September 6-11, 1987.

3. Ishihara et al., CRIEPI report T86055 (1987).

4. Ogawa et al., The 27th Battery Symposium; Japan, p. 197 (1986).

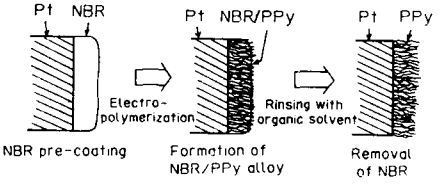


Fig.1 Preparation procedure of NBR/PPy film

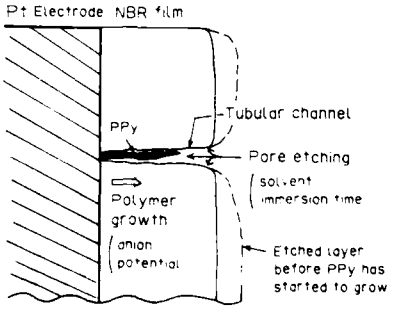


Fig.2 Schematic model for tubular channel formation into NBR film and polymer growth through it.

Acknowledgement

This investigation was supported in part by a Grant of Scientific Research from the Japanese Ministry of Education and in part by the Office of Naval Research.

Abstract No. 28

A COMPARISON OF LITHIUM ION CONDUCTING AND DIVALENT ION CONDUCTING POLYMER ELECTROLYTES IN SECONDARY SOLID STATE BATTERIES

A. Gilmour, M.Z.A. Munshi
B.B. Owens and W.H. Smyrl

Department of Chemical Engineering and Materials Science
Corrosion Research Center
University of Minnesota
221 Church St. SE
Minneapolis, MN 55455

Complexes of polyethylene oxide (PEO), and lithium salts have been shown to be promising materials as the solid state polymer electrolyte element in the development of high energy lithium batteries (1-5). The present study was focussed on divalent metal systems that might offer the possibility of increased specific capacity or energy density.

Magnesium is of particular interest because of its diagonal relationship in the periodic table with lithium. Recently, the solid magnesium perchlorate-PEO complex, (PEO_8:$Mg(ClO_4)_2$) has been shown to give conductivities between 10^{-5} and 10^{-6} S/cm at 80°C (6). This is comparable with that for lithium polymer electrolytes at similar temperatures.

The cells studied in this laboratory, M/MX in PEO/V_6O_{13}, have been based on a divalent metal anode, a polymer-divalent salt electrolyte and a V_6O_{13} composite cathode. The divalent metal systems being studied are based upon anodes of magnesium, calcium, zinc and copper. Cells of area 6.4 cm^2 have been cycled at constant current discharge and current limited constant voltage charge at various rates. Preliminary results indicate that the copper and zinc systems are reversible. Cycling data have been compared with those of the corresponding lithium systems.

The polymer electrolytes have been prepared by two methods

1) solvent casting,

2) hot-press technique (7).

The two preparative techniques were compared via a.c. conductivity measurements. The hot-press preparation permits synthesis without the complications of solvent addition and subsequent removal.

Acknowledgements

This work was carried out with the financial support from the Lawrence Berkeley Laboratory.

References

1) M. Armand, Solid State Ionics, 9/10, 745 (1983).

2) A. Hooper and B.C. Tofield, J. Power Sources, 11, 33 (1984).

3) M. Gauthier, D. Fauteux, G. Vassort, A. Belanger, M. Duval, P. Ricanx, J. Chabagno, D. Muller, P. Regaud, M. Armand and D. Deroo, J. Electrochem. Soc. 132 1333 (1985).

4) M. Gauthier, A. Belanger, D. Fateaus, M. Duval, B. Kapfer, M. Robitaille, R. Bellemore and T. Giguere, 3rd Int. Meeting on Lithium Batteries, Kyoto, Japan 1986, abst. N. ST-11.

5) M.Z.A. Munshi and B.B. Owens, Proc. of the Symp. on Primary and Secondary Ambient Temperature Lithium Batteries, Eds. J.P. Gabano, Z. Takehara and P. Bro, Proc. Vol. 88-6, The Electrochem. Soc., p. 737, (1987).

6) A. Patrick, M. Glasse, R. Latham and R. Linford, Solid State Ionics, 18/19, 1063 (1986).

7) F.M. Gray, J.R. MacCallum and C.A. Vincent, Solid State Ionics, 18/19, 282 (1986).

Abstract No. 29

Li - Reactivity of Silicate Glasses: Influence of Glass Composition

Wendy R. Cieslak
Exploratory Batteries Division
Sandia National Laboratories
Albuquerque, New Mexico 87185

Brian L. Maschhoff
Neal R. Armstrong
Department of Chemistry
University of Arizona
Tucson, Arizona 84721

Introduction

Although silica - based papers are commonly used as separators in Li/$SOCl_2$ cells, SiO_2 is thermodynamically unstable with respect to lithium. Many silicate glasses are highly reactive with lithium. For very long-life applications (i.e. 10 - 15 years) and for reserve lithium technologies, the reactivity of these silicate materials is expected to become a life-limiting factor. Nonetheless, a screening study[1] has indicated that some silica - based papers are much more resistant to lithium than others.

It is difficult to study corrosion processes involving lithium using most *ex situ* techniques because environmental reactions alter the surface of interest. However, it is possible to investigate surface interactions with lithium using *in vacuo* surface analytical techniques[2,3]. For example, X-ray photoelectron spectroscopy (XPS) has been used to monitor the reaction occurring when lithium is deposited on a freshly cleaved silica surface. Multiple states were found for silicon in the final product, rather than the complete reduction of SiO_2 to elemental Si. Furthermore, the resistance of sodium and potassium silicate glasses[4] to lithium degradation was found to be greater than that of pure SiO_2. This enhancement in durability was associated with the presence of non - bridging oxygens in the matrix. Investigations of lithium reactivity have been extended to a variety of glasses[2,5], including aluminosilicates, but have not yet included a wide range of both sodium and calcium additions to the aluminosilicate matrix.

Approach

Commercial glass separators vary substantially in composition, as shown for four silicate - based glass papers in Table I. The qualitative statements of reactivity in the Table are based on differential scanning calorimetry (DSC) tests of Li/separator samples conducted to 300°C. In general, Na_2O and K_2O appear to be associated with greater Li - reactivity, while CaO and Al_2O_3 are associated with lesser reactivity. However, the interactions between these different constituents are difficult to identify in commercial glasses that contain several other constituents. Therefore, we fabricated a series of experimental glasses, Table II, to study the reaction mechanism(s).

Summary

The variation in compositions of glass separators leads to different products having large differences in reactivity. Some commercial silicate - based glasses do not substantially react with Li in tests to 300°C. The present investigation has used experimental glasses of simplified compositions to differentiate the roles of Al_2O_3, CaO, and Na_2O in glass stability in the presence of Li. Reaction mechanisms will be proposed on the basis of XPS and quantitative DSC analyses.

Acknowledgements

This research was supported by the U. S. Department of Energy under contract no. DE-AC04-76DP00789, Sandia National Laboratories, and the Materials Characterization Program, State of Arizona. The authors are grateful to B. C. Bunker and R. D. Watkins, both of Sandia National Laboratories, for technical discussions and glass fabrication support.

References

1. W. R. Cieslak, Proceedings 33rd International Power Sources Symposium, Cherry Hill, NJ, 13-16 June 1988.

2. B. L. Maschhoff, K. R. Zavadil, K. W. Nebesny, and N. R. Armstrong, J. Vac. Sci. Technol., in press.

3. B. L. Maschhoff, K. R. Zavadil and N. R. Armstrong, Applied Surface Science 27 (1986) 285 - 298.

4. B. L. Maschhoff and N. R. Armstrong, Surf. Interface Anal., in press.

5. K. R. Zavadil, C. H. Peden, and N. R. Armstrong, to be published.

Table I: Analyzed Compositions of Commercial Glass Separators (mole %)

Constituent	#C001	#C002	#C003	#C004
SiO_2	65.9	65.7	57.8	58.4
Na_2O	14.1	10.6	0.9	0.7
K_2O	.8	1.5	0.5	0.4
CaO	6.8	3.0	25.4	24.0
Al_2O_3	3.2	4.2	9.0	9.5
B_2O_3	4.5	10.0	5.6	5.6
BaO	<.1	2.1	<.1	<.1
MgO	4.7	0.7	0.9	1.4
ZrO_2	<.1	2.2	<.1	<.1
Reactivity:	Severe	Severe	Very Little	Very Little

Table II: Target Compositions of Research Glasses (mole %)

Constituent	#S001	#S002	#S003	#S004	#S005
SiO_2	70	70	60	60	60
Al_2O_3	15	15	15	15	15
Na_2O	15	-	25	-	12.5
CaO	-	15	-	25	12.5

Abstract No. 30

A COMPARISON OF LITHIUM, MAGNESIUM, AND CALCIUM ANODES IN BROMINE TRIFLUORIDE

K. H. Park, D. E. Stilwell, D. E. Bliss,
R. A. Hollins, and M. H. Miles
Chemistry Division, Research Department
Naval Weapons Center, China Lake, CA 93555

INTRODUCTION

The use of bromine trifluoride with lithium, magnesium, and calcium anodes offers the possibility of new battery systems that have high cell voltages and energy densities (Table I). Bromine trifluoride is a very reactive substance that acts as a supplier of fluorine to the electrochemical cell. This interhalogen compound is a particularly suitable interhalogen solvent for battery applications because of its convenient liquid range (mp 8.8°C, bp 125.8°C) and relatively high specific conductance ($0.008\ ohm^{-1}\ cm^{-1}$) (1). The high conductivity of BrF_3 is attributed to its self-ionization reaction

$$2\ BrF_3 \rightleftharpoons BrF_2^+ + BrF_4^- \quad (K = 0.8) \qquad [1]$$

that yields equilibrium concentrations of nearly 0.9 M of the acidic (BrF_2^+) and basic (BrF_4^-) ions. A detailed review of the physical, chemical, and electrochemical properties of BrF_3, BrF_5, ClF_3, and ClF_5 was recently published (1).

The reduction of the BrF_3 solvent serves as the cathodic reaction in this battery system. Various electrochemical reactions have been proposed for the reduction of BrF_3 that involve the products of Br^-, Br_2, BrF, BrF_2 and even BrF_5 (1-3). We propose, for battery applications, that the reduction of BrF_3 can be represented by

$$BrF_3 + 3e^- \rightarrow 1/2\ Br_2 + 3\ F^- \qquad [2]$$

This is the cathodic process for the cell reactions proposed in Table I.

Most battery systems that use active metals in oxidizing solvents depend on passivating films on the anode consisting of chlorides or oxides. In BrF_3, the passivating films will consist of fluorides. This paper reports on the electrochemical behavior of lithium, magnesium, and calcium anodes in BrF_3 containing various supporting electrolytes. Also discussed will be the results of initial cell test for the Li/BrF_3/carbon system.

EXPERIMENTAL

The experimental set-up was constructed using Monel and Teflon parts, its description can be found elsewhere (4). This system provides both the chemical resistivity and safety required to run tests on BrF_3. The Teflon electrochemical cell was equipped with inlet and outlet ports for BrF_3 and three threaded feed-throughs for the electrodes. The PAR model 273 was used for both potential and current control. Experimental data was collected and analyzed on an IBM PC XT. The lithium electrode (A = 1 to 2 cm^2) was prepared from 0.16 cm sheet (ROC/RIC, 99.95% purity), and spot welded to a Pt wire. The calcium (ROC/RIC, 99.95% purity) and magnesium (Alfied Chemicals) electrodes were prepared from 0.02 inch sheet and spot welded to a Ni wire. The reference electrode was a Teflon coated Pt wire while a cylindrical Pt screen, having a diameter of about 3 cm served as the counter electrode.

A small prototype battery was constructed using a Teflon union tee. A Teflon filter membrane is sandwiched between a Li disc anode and a carbon disc. A [illegible] spot was used for an electrical contact.

The BrF_3 was obtained from Ozark-Mahoning and used without further purification. The fresh BrF_3 from the container was pale yellow indicating the presence of bromine. The set-up was evacuated and then filled with a nitrogen atmosphere prior to filling the cell with BrF_3. About 15 mL of BrF_3 was used for each experiment. Spent solvents were allowed to react with sand prior to disposal.

RESULTS AND DISCUSSION

The open-circuit potential of lithium in BrF_3 solution was stable at -5.12 ±0.03 V vs. Pt, whereas the equilibrium cell potential is calculated to be 5.26 V at 25°C, based on the cell reaction:

$$3\ Li + BrF_3 \rightarrow 3\ LiF + 1/2\ Br_2 \qquad [3]$$

The present of passivating films on active metal anodes can cause cell potentials to be significantly less than the theoretical expectations (5, 6). The discharge of the Li was performed at different current densities ranging from 5 to 50 mA/cm^2. The discharge curve becomes flatter as the current density is lowered. At low discharge current densities, a nearly flat discharge was possible for several hours. In Figure 1, the relationship between discharge current density and discharge capacity of the lithium anode is shown. The total discharge time increased significantly as the discharge current density was lowered. Similar results will be presented at lower current densities (below 5 mA/cm^2).

Figure 2 shows the results of constant current discharge (20 mA/cm^2) of a Li anode with and without 1 M NaF. Addition of 1 M NaF resulted in significant reduction in the discharge time. The NaF acts as a Lewis base and decreases the equilibrium concentration of acidic BrF_2^+ in BrF_3; this likely decreases the solubility of the LiF film and hinders the discharge of Li. Experiments were also performed in the presence of other supporting electrolytes to examine their effect on the discharge behavior of Li (e.g., LiF, AlF_3, $LiPF_6$).

The discharge behavior of lithium, magnesium, and calcium anodes during constant current discharge are shown in Figure 3. The passivation was so severe for calcium and magnesium in BrF_3 that they were polarized rapidly even at low current densities (<1 mA/cm^2) (4). This was explained by the fact that the passivating films of calcium and magnesium are essentially anion conductors. Hence, it is not possible for cations to pass through the passivating film during discharge. The passivation was less severe for a freshly prepared lithium anode in BrF_3 and discharge was possible at high current densities.

ACKNOWLEDGMENT

This research is sponsored by SDIO/IST and managed by ONR. Two authors (K. H. P. and D. E. S.) express their appreciation for ONT/ASEE postdoctoral fellowships.

REFERENCES

1. R. A. Rhein and M. H. Miles, Naval Weapons Center, China Lake, Calif., NWC Technical Publication 6822 (1988).
2. R. D'Achenko and R. H. Toeniskoetter, Union Carbide Research Institute, Tarrytown, NY, AD 442623 (1964).
3. N. Greenwood and A. Earnshaw, Chemistry of the Elements, Pergamon Press, pp. [illegible] (1984).
4. K. H. Park, M. H. Miles, D. E. Stilwell, D. E. Bliss, R. [illegible] Hollins, and R. E. Rhein, submitted to this Journal.
5. M. H. Miles, J. Appl. Electrochem., 11, [illegible] (1981).
6. M. H. Miles, G. E. McManis, and A. N. Fletcher, Electrochim. Acta, 29, 1003 (1984).

Table I. Thermodynamic Characteristics of Interhalogen Cells with Several Anode Materials at 25°C.

Interhalogen cell	Proposed Cell Reaction	E°, cell (V)	Energy Density	
			WHr/Kg	WHr/cm^3
Li/BrF_3	3 Li + BrF_3 → 3 LiF + 1/2 Br_2	5.26	2680	4.80
Ca/BrF_3	3 Ca + 2 BrF_3 → 3 CaF_2 + Br_2	5.22	2130	4.79
Mg/BrF_3	3 Mg + 2 BrF_3 → 3 MgF_2 + Br_2	4.72	2190	5.43

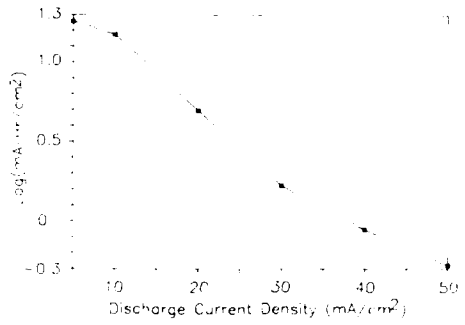


Fig. 1. Discharge rate vs. log discharge capacity of lithium in BrF_3 at 22°C.

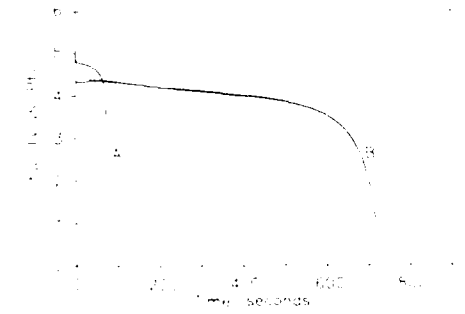


Fig. 2. Constant current (20 mA/cm^2) discharge curves of lithium anode in BrF_3 with (A) and without (B) 1 M NaF at 22°C.

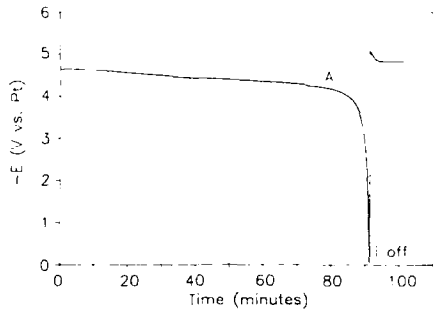


Fig. 3a. Constant current discharge curve for lithium (curve A) at 10 mA/cm^2 in BrF_3 at 22°C.

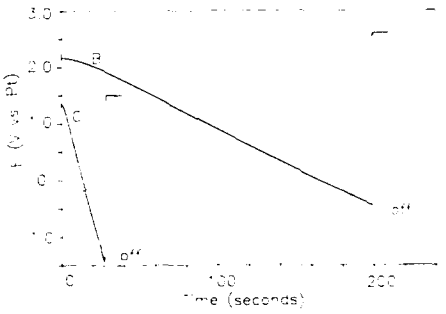


Fig. 3b. Constant current discharge curves for calcium (B, 0.5 mA/cm^2) and magnesium (C, 0.1 mA/cm^2) in BrF_3 at 22°C.

Abstract No. 31

An Ambient Temperature Solvated Electron Lithium Electrode for Secondary Batteries

Francisco A. Uribe and Anthony F. Sammells

Eltron Research, Inc.
4260 Westbrook Drive
Aurora, IL 60504

We wish to report recent work performed in our laboratory on a liquid lithium negative electrode consisting of lithium dissolved in liquid ammonia, giving a solvated electron lithium solution which has been operated at room temperature (120psi) in secondary cells. Lithium mediation from this lithium source to the liquid non-aqueous electrolyte in the positive electrode compartment was via use of the lithium intercalated electronically conducting ceramic membrane of general composition Li_xWO_2. To be discussed here are voltammetric measurements performance on respective electrodes in the cell

$$Li,NH_3/Li_xWO_2/LiAsF_6(1M),\text{non-aqueous solvent}/TiS_2$$

using the respective non-aqueous solvents 2-methyl-THF and liquid ammonia. The electrochemical cell used for containment of the liquid ammonia solution at ambient temperature is shown schematically in Figure 1. Argon introduced under pressure into the positive electrode compartment was used to compensate for vapor pressure differences present between the solvated electron ammonia solution and 2-methyl-THF, so as to avoid rupture of the WO_2 membrane.

Cells containing 2M Li in liquid ammonia possessed an open-circuit potential of 2.3V at 21°C. These voltages were reached typically within ~10 min. starting from a WO_2 membrane, suggesting that lithium intercalation to give Li_xWO_2 was quite rapid. Figure 2 shows a typical discharge-charge cycle for this cell at respective current densities of 0.5 and 0.25 mA/cm^2. Cell performance suggested reversible lithium transport across the Li_xWO_2 membrane.

The second cell

$$Li(2M),NH_3/Li_xWO_2/LiAsF_6(1M),NH_3/TiS_2$$

also operated at ambient temperature initially possessed an open-circuit potential of 2.0V and could be discharged at $1mA/cm^2$ and $0.3mA/cm^2$ upon charge. This cell possesses two distinct advantages: 1) there is no requirement for separate pressure equalization between electrode compartments, and 2) any unit activity lithium that might become deposited onto the Li_xWO_2/catholyte interface at higher charge current densities, would immediately become dissolved into the liquid ammonia and chemically react with the TiS_2 resulting only in a small loss in Faradaic efficiency.

The present status of this approach for achieving long cycle life and high energy density ambient temperature lithium batteries will be discussed.

ACKNOWLEDGEMENT

This work was funded by the National Science Foundation under the SBIR Program.

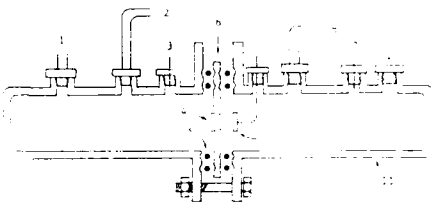


Figure 1. Pressure cell for working with liquid NH_3 at ambient temperature.
1) Liquid NH_3 inlet
2) To dome loaded pressure reducing regulator (TESCOM).
3) Electrical connection
4) WO_2 membrane
5) Ethylene propylene O-ring
6) Polyethylene disk to accommodate O-rings and WO_2 membrane.
7) Positive electrode (TiS_2)
8) To dome loaded pressure reducing regulator and Ar inlet.
9) Electrical connection
10) Solution inlet
11) Stainless steel case



Figure 2. Discharge and charge curve of the cell $Li^+,e_s^-(2M),NH_3/WO_2/LiAsF_6(1M),2\text{-MeTHF}/TiS_2$. T = 21°C. P = 120psi. i_{disch} = 0.5mA. i_{charg} = 0.25mA.

Abstract No. 32

RELIABILITY OF COMMERCIAL LITHIUM BUTTON CELLS

Jean-Paul Randin
ASULAB S.A., Research Laboratories of the SMH-Group
Passage Max-Meuron 6
2001 Neuchâtel (Switzerland)

1. Introduction

The presence of a protective surface film on lithium in organic electrolytes is generally recognized and has been the subject of numerous investigations (1). An increase of the activation resistance in commercial lithium/carbon monofluoride (CF) batteries was reported as a function of storage time at several states-of-discharge and attributed to a film formation on the lithium electrode (2).
The aim of the present study was to characterize the passivation resistance of commercial Li/MnO_2 and Li/CF button cells under several environments in an attempt to assess the reliability of such power sources under very low drain discharge. The lithium button cells presently used employ a plastic crimp seal and the main question is the long term reliability of such cells while driving devices to the maximum capacity of the power source. Under very low drain, the current is too low to break down the passivating layer on the lithium electrode. To further accelerate the passivation phenomenon, the cells used in the present study were measured after storage, i.e. without drawing any current.

2. Experimental

Fifty CR 2016 (20 mm diameter, 1.6 mm thickness) Li/MnO_2 cells, received fresh from Sanyo Electric Trading Co, Osaka, Japan in January 1985, and fifty BR 2016 Li/CF cells received fresh from Matsushita Battery Industrial Co, Osaka, Japan in November 1984, were used. The initial capacity was 92±2 and 78±2 mAh at a cut-off voltage of 2.0V when discharging into 30 kΩ at 20°C with a mean voltage of 2.9 and 2.8V, respectively.
Two cells of each type were stored under each of the following conditions defined in international standards: a) 20±2°C, 60±15% relative humidity (RH), b) 40±2°C, 93+2-3% RH and c) 55±2°C, using a constant temperature cabinet held in a 20°C/60% RH room.
The internal resistance of the cells was then measured at regular time intervals. After 720 days of storage, the resistive discharges were performed to determine the self-discharge.
The ac impedance was determined at the open circuit potential using a Frequency Response Analyzer, Solartron Type 1174 and an electrochemical interface Solartron Type 1186 controlled with a Hewlett Packard 9825 A calculator. The alternating voltage was 2.5 mV rms.
In addition to the impedance measurements, five undischarged cells of each type were stored at 40°C/93% RH and 55°C and regularly weighed.

3. Results

The impedance data are reported in Fig. 1 and 2 for the Li/MnO_2 and Li/CF cells, respectively. The as-received Li/CF cells showed a fairly well defined semi-circle at high frequencies (Fig. 2). As the storage time increased, the diameter of the high frequency semi-circle, R_{act}, increased and the center of the semi-circle moved below the real axis. The impedance locus for the Li/MnO_2 cells showed a depressed semi-circle (Fig. 1). The activation resistance has been taken as the intersect of the high-frequency semi-circle with the real axis, irrespective of the position of its center.

3.1 Li/MnO_2 cells : The variation of the activation resistance, R_{act}, as a function of the storage time under three environments is shown in Fig. 3. After storage at 20°C and 55°C, the activation resistance increased almost linearly with time up to about 540 days, then increased more rapidly. The activation resistance was about 10 Ω at the beginning of the storage and reached 40 and 90 Ω after 720 days at 20 and 55°C, respectively. At 40°C/93% RH, the activation resistance increased exponentially with storage time to reach 1 kΩ after less than 300 days. The increase in resistance was much larger at 40°C/93% RH than at 55°C.
The weight loss was 4 to 6 times larger at 55°C than at 40°C/93% RH (Fig. 4).
The resistive discharges performed after 720 days of storage indicated that the self-discharge increased with increasing temperature. The thickness of the cells after discharge were higher after storage in humid environment than at 20 and 55°C (Table 1).
3.2 Li/CF cells : The activation resistances were significantly higher than those of the Li/MnO_2 cells (Fig. 5). During storage at 20°C, R_{act} remained between 230 and 330 Ω with a maximum value after 30 days and a minimum after about 300 days. At 40°C/93% RH the activation resistance increased quite steeply at the beginning of the storage, then increased less rapidly and finally rose sharply after more than 300 days. At 55°C, a sharp increase was again recorded for short times followed by a decrease to reach a minimum value around 180 days and a sharp increase for longer storage times.
A weight loss was measured after storage at 55°C, while a slight weight increase was recorded at 40°C/93% RH (Fig. 4).
The resistive discharges performed after 720 days of storage indicated a total self-discharge twice as high at 40°C/93% RH as at 55°C. The thickness of the cells after discharge was higher after 720 days at 40°C/93% RH than at 55°C, and higher at 55°C than at 20°C (Table 1).

5. Conclusions

The results of the present study show that the permeations of the solvent from the electrolyte towards the outside and of water towards the inside of the cell simultaneously occur to different extents depending on the temperature and humidity of the environment and on the type of cell. The plastic crimp seal of the Li/MnO_2 cell exhibits a high permeation for the solvent and a low permeation for water whereas the opposite is observed for the Li/CF cell. The main contribution to the increase of the activation resistance is the water permeation.
The consequences of water permeation on the useful lifetime of lithium cells have also been investigated as a function of the state-of-discharge.
The expected lifetime of the Li/MnO_2 and Li/CF button cells has been estimated for the application in a wrist-watch. The approximate lifetime under humid environments is well below the expected value of 8 years claimed by the manufacturer (3).
For applications where the estimated lifetime is longer than 3-5 years, it would be advisable to use hermetically sealed cells, i.e. with glass-to-metal or ceramic-to-metal feedthroughs. Unfortunately such cells are not yet commercially available at the dimensions of interest for low power consumption devices.

6. Acknowledgments

The author is pleased to thank F. Züllig for his skillful assistance in the experimental work, R. Jeanmonod for discharge measurements and FTA Inc., Grenchen, member of the SMH Group, for interest and support.

REFERENCES
1. E. Peled, in "Lithium Batteries", J.P. Gabano, ed., Academic Press (1983), p. 43-72
2. J.R. Sandifer and M.R. Suchanski, J. Appl. Electrochem., 14 (1984) 329-340
3. M. Fukuda and T. Iijima, in "Lithium Batteries", J.P. Gabano ed., Academic Press (1983), p.211-239

Table I : Self-discharge, final thickness after the discharge following 720 days of storage in the undischarged state, as well as final activation resistance after 720 days of storage

	Storage	Self-discharge ($\%C_{nom}$)	Thickness (mm)	R_{act} (Ω)
Li/MnO_2	20°C	1	1.62	40
	40°C/93%RH	17	1.72	3000
	55°C	21	1.61	90
Li/CF	20°C	1	1.48	280
	40°C/93%RH	23	1.82	6000
	55°C	12	1.64	4500

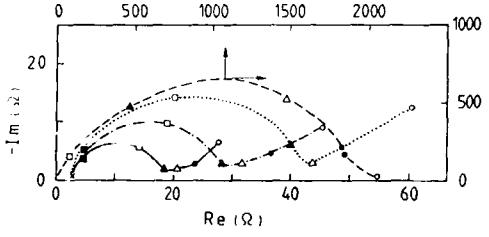


Fig. 1 : Complex plane impedance data for the undischarged Li/MnO_2 cell at the open circuit potential: freshly received from the manufacturer (—); after 360 days of storage at 20°C (-.-), 40°C/93%RH (---) and 55°C (...). The decades of frequency are shown as follows : 10^{-1} (○), 1 (●), 10 (△) 10^{2} (▲) 10^{3} (□), 10^{4} (■) and 10^{5} (x) Hz.

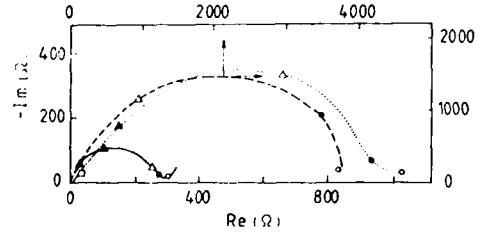


Fig. 2 : Same as Fig. 1 for the Li/CF cell. The response after 360 days of storage at 20°C is roughly the same as that in the fresh state

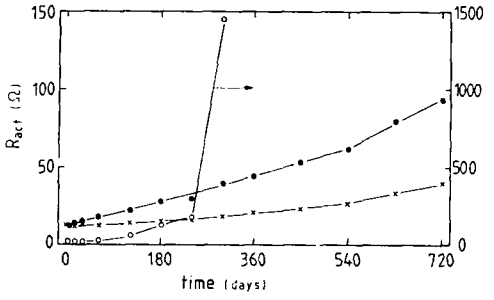


Fig. 3 : Dependence of R_{act} on storage time for the undischarged Li/MnO_2 cell stored at 20°C (x), 40°C/93%RH (○) and 55°C (●)

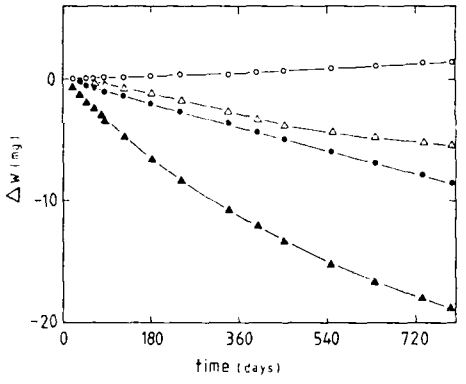


Fig. 4 : Change in weight as a function of storage time at 40°C/93% RH (open symbols) and 55°C (solid symbols) for the undischarged Li/MnO_2 (triangles) and Li/CF (circles) cells.

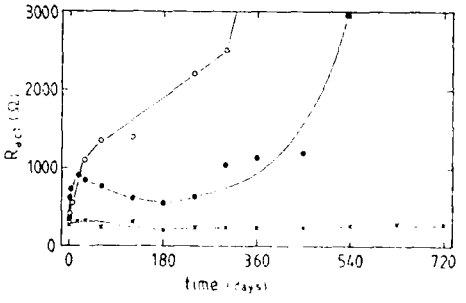


Fig. 5 : Same as Fig. 3 for the Li/CF cell

Abstract No. 33

LITHIUM DIFFUSION IN SILVER VANADIUM OXIDE

Esther S. Takeuchi and William C. Thiebolt III

Wilson Greatbatch, Ltd.
10,000 Wehrle Drive
Clarence, NY 14031, USA

INTRODUCTION

Lithium/silver vanadium oxide(SVO) batteries were developed in 1979 (1). Since that time they have been developed for use in implantable cardiac defibrillators and other medical devices (2-5). Several characteristics make the chemical system particularly useful for medical applications. The self-discharge of the system is less than 2% per year allowing for long shelf-life and long life under low drain rate (6). The Li/SVO system displays a voltage profile whose voltage decreases with depth of discharge, allowing the state of charge to be determined by interrogation of cell voltage.

The ability to determine a cell's state of charge and predict when replacement will become necessary is important in a medical device. In order to use the background voltage of a cell for this type of prediction, the voltage recovery after high current pulse discharge must be known. The voltage recovery in completed cells was characterized and this led to the more fundamental investigation of the rate of lithium diffusion in SVO which is reported here. Two techniques were used: the voltage recovery after single constant current pulses in test cells and voltammetry of thin layer SVO electrodes conducted at different scan rates.

EXPERIMENTAL

The completed cells used for the study had multiplate construction where alternating layers of SVO cathodes and Li anodes were assembled in prismatic configuration. The electrodes were separated by commercially available polypropylene membranes. The capacity of the cells was 5.5Ah.

Test cells for the single cathode pulse experiments consisted of parallel lithium and SVO plates held apart with a spacer. No separator material was used. Lithium was used as a reference electrode.

Electrodes for the voltammetry experiments were prepared by placing a thin layer of an aqueous suspension of graphite, SVO and polyacrylic acid on an inert metal disk. The water was evaporated to leave a very thin SVO electrode. The disk was mounted so that only the surface containing the SVO was exposed to the electrolyte. The voltammetry was conducted in 1M $LiAsF_6$ in a 50/50 by volume mixture of propylene carbonate/dimethoxy ethane using an EG&G PAR potentiostat in combination with an Apple IIe computer. Lithium was used for reference and auxiliary electrodes.

RESULTS AND DISCUSSION

A high rate pulse testing scheme used for discharge of the multiplate cells consisted of four 2.0A pulses every 30 minutes where each pulse lasted 10 seconds and was followed by 15 seconds of rest. A typical pulse discharge curve of a cell with a 5.5Ah capacity is shown in Figure 1, where the background, minimum first pulse and minimum fourth pulse voltages are shown. If a cell is partially discharged under pulse and the test is interrupted, the background voltage of the cell continues to recover for several days. Figure 2 shows a pulse test where the cell was pulsed every 30 minutes for 30 pulse trains and then allowed to stand at open circuit voltage until the voltage of the cell had stabilized. A stable voltage was defined as less than 5mV change per day. The voltage during this stabilization period was monitored and is shown versus time in Figure 3. After 667mAh of discharge (12% DOD) the cell required 11 days to stabilize and recovered a total of 0.790V. After 1.33Ah (24% DOD) of discharge the cell recovered 0.845V and needed 14 days to stabilize. After 2.0Ah (36% DOD) the cell took 6 days to stabilize and recovered 560 mV. What can be seen from this data is that the cells do not recover at the same rate or the same magnitude at all depths of discharge.

In order to explore the voltage recovery further, an investigation of the lithium diffusion rate in SVO was initiated. Test cells with single parallel plates were used for this portion of the experiment. Cells were discharged under constant loads for 16 hours under a variety of rates. After the load was removed, the cells were allowed to stabilize at open circuit voltage for 3 weeks. A single pulse was then applied and the voltage recovery was monitored. From this the rate of lithium diffusion was determined (7). The cells were discharged at rates that required from four to ten 16 hour discharge periods. Thus, lithium diffusion rates at multiple depths of discharge were obtained in SVO discharged at a variety of rates.

Voltammetry was, also, used to determine lithium diffusion rates. Voltammograms of thin SVO electrodes were conducted at scan rates ranging from 0.02 mV/s to 1 mV/s. A typical voltammogram is shown in Figure 4, where the scan rate was 0.08 mV/s. The multiple waves present in SVO discharge can be seen. The percent utilization of SVO at each scan rate was determined. These values were then used to determine lithium diffusion rates (8).

CONCLUSIONS

The rate and magnitude of voltage recovery of Li/SVO batteries after high rates of discharge is not constant at all depths of discharge. Thus, an investigation of the diffusion rates of lithium in SVO at multiple depths of discharge was conducted. Pulse methods were used to determine the diffusion rate at multiple depths of discharge of SVO discharged at different rates. In addition, voltammetry conducted at various rates was used as an alternate determination method of the lithium diffusion rates.

REFERENCES

1. C. C. Liang, M. E. Bolster and R. M. Murphy, U. S. Patents 4,391,729 and 4,310,609.
2. C. Holmes, P. Keister and E. S. Takeuchi, Progress in Batteries and Solar Cells, vol. 6 (1987) 64-66.
3. P. Keister, E. S. Takeuchi and C. F. Holmes, Cardiostim 86, Monte Carlo, Monaco, June 1986.
4. E. S. Takeuchi, B. C. Muffoletto, J. M. Greenwood and C. F. Holmes, VIIIth World Symp. on Cardiac Pacing and Electrophysiology, Jerusalem, Israel, June 1986.
5. E. S. Takeuchi, Proc. of the 3rd Annual Battery Conf. of Appl. and Advances, Jan. 1988, section VI 3.
6. G. M. Bergman, S. J. Ebel, E. S. Takeuchi, and P. Keister, *J. Power Sources*, 20, (1987) 179-185.
7. S. Basu and W. L. Worrell, Fast Ion Transport in Solids, P. Vashishta, J. N. Mundy and G. K. Shenoy, eds. Elsevier North Holland, New York, 1979, pgs. 149-152.
8. K. West, T. Jacobsen, B. Zachau-Christiansen and S. Atlung, *Electrochimica Acta*, 28 (1983) 97-107.

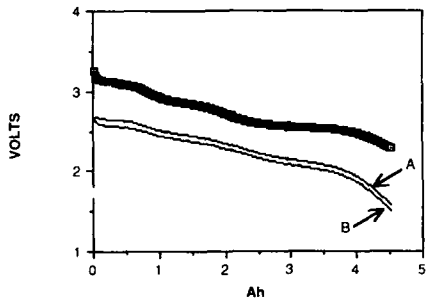


Fig. 1. Pulse discharge curve of multiplate cell showing OCV (heavy line), first pulse voltage minimum (A), and fourth pulse voltage minimum (B).

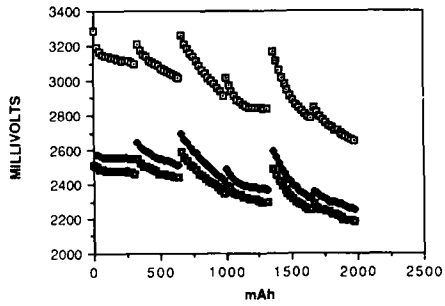


Fig. 2. Intermittent pulse discharge/rest of multiplate cell showing OCV, first pulse voltage minimum, and fourth pulse voltage minimum.

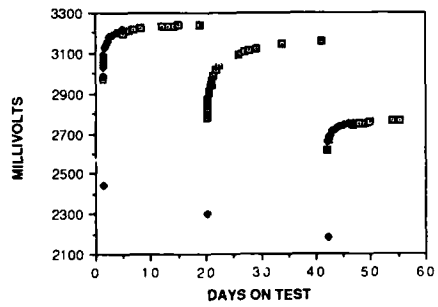


Fig. 3. Voltage recovery during rest period.

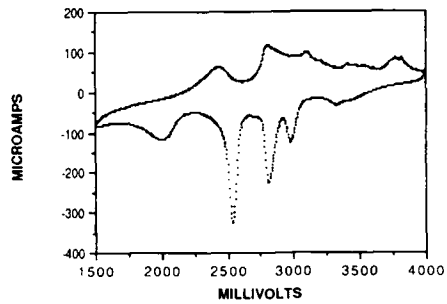


Fig. 4. Voltammogram of SVO vs. lithium at a scan rate of 0.08 mV/S.

Abstract No. 34

Impedance Studies of Alkali-Metal Electrodes in Non-aqueous Electrolytes

T.R. Jow and L.W. Shacklette

Allied-Signal, Inc
Corporate Technology
Morristown, N.J. 07960

The behavior of the lithium electrode in non-aqueous electrolyte is complicated. This is owing to the highly reactive nature of lithium metal in a non-aqueous electrolyte. It is generally agreed that a passivation layer is formed on the surface of the lithium electrode upon exposure to the electrolyte(1). This passivation layer is essential for the success of primary lithium batteries. However, this passivation layer plays a more complicated role in the development of rechargeable lithium batteries(2).

Studies directly related to the lithium electrode in non-aqueous electrolytes include lithium cycling efficiency experiments(2-5), impedance spectroscopy (IS) technique (6-10), static polarization (11-12), and potentiostatic and galvanostatic pulse techniques. [13] Electrode IS is more convenient than other methods for separating the different processes in electrode kinetics. The electrolyte system that has been studied most extensively using the IS technique is lithium perchlorate ($LiClO_4$) in propylene carbonate (PC)(9). The other systems studied are $LiClO_4$ in tetrahydrofuran (THF)(7), $LiClO_4$ in propylene carbonate/dimethoxyethane (DME), and lithium hexafluorophosphate ($LiPF_6$) in dimethyl sulfoxide (DMSO) (10), etc.

The cells that were used for the impedance measurement generally employed the half-cell configuration (6-10). Measurements were typically made at rest potential with respect to Li reference electrode. This means that the counter electrode is also lithium metal. The impedance diagram in the complex plan (Nyguist plot) of lithium in a non-aqueous electrolyte generally shows a semicircle which represents the combination of the charge transfer resistance R_{ct}, and the double-layer capacitance C_{dl}.

The R_{ct} value which corresponded to the length of the chord of the semicircle generally increased with storage time.(6-10) The R_{ct} value(9) was directly related to the film thickness. The impedance of Li in the electrolyte is a sensitive function of the solvent/solute combination and the initial condition of the Li surface. Therefore the rate of increase is also different for different electrolytes. In an electrolyte of lithium hexafluoroarsenate ($LiAsF_6$) in 2-methyltetrahydrofuran (2-MTHF), we found that the R_{ct} value measured in a half-cell configuration increased at a faster rate than the R_{ct} value measured at full cell configuration (V_6O_{13} was used as the counter electrode). This suggests that the Li surface is less reactive in the full-cell configuration.

This paper will present impedance data for alkali metals in various electrolytes both in half-cell and full-cell configurations. Their relationship to the cycling efficiency of the alkali-metal in full and half cells will also be discussed.

REFERENCES

1. A.N. Dey, Thin Solid Films, 43 131 (1977).
2. V.R. Koch and J.H. Young, J. Electrochem. Soc., 125 1371 (1978).
3. V.R. Koch and J.H. Young, Science, 204 499 (1979).
4. S.-I. Tobishima and A. Yamaji, Electrochimica Acta, 28 1067 (1983).
5. S.-I. Tobishima and T. Okata, Electrochimi Acta, 30 1715 (1985).
6. R.V. Mashtev and B. Puresheva, J. Electroanal. Chem., 180 609 (1984).
7. H. Yamin and E Peled, in "Lithium Batteries", A.N. Dey, Editor, P. 40. The Electrochemical Society Softbound Proceedings Series, PV 84-1, Pennington, N.J. (1984).
8. J.G. Thevenin, J. Power Sources, 14 45 (1985).
9. J.G. Thevenin and R.H. Muller, J. Electrochem. Soc., 134 273 (1987).
10. Y. Matsuda and M. Morita, in "Primary and Seconday Ambient Temperature Lithium Batteries", J.P. Gabano, Z. Takehara, and P. Bro, Editors, p. 602. The Electrochemical Society Softbound Proceedings Series, PV 88-6, Pennington, N.J. (1988).
11. S.G. Meibuhr, J. Electrochem. Soc., 132 2050 (1985).
12. R.F. Scarr, J. Electrochem. Soc., 117 295 (1970).
13. Y. Geronov, F. Schwager, and R.H. Muller, J. Electrochem Soc., 129 1422 (1982).

Abstract No. 35

Thin Film Positive Electrodes for Lithium-Iron Sulfide Batteries Produced by Atmospheric Pressure Chemical Vapor Deposition

A. Petric, S. Crouch-Baker, R.M. Emerson, T.M. Gur and R.A. Huggins

Department of Materials Science and Engineering
Stanford University
Stanford, California 94305

Thin films of FeS_x ($1 < x < 2$) have been produced by atmospheric pressure chemical vapor deposition (CVD). Their performance in a Li/FeS_x battery has been investigated at ambient temperature with a cell of the following configuration:

$$(-)\ Li \mid LiAsF_6 \text{ in PC} \mid FeS_x\ (+)$$

The CVD apparatus consisted of an open tunnel furnace and an injector head with three concentric ports. The two reactive gases, H_2S and $Fe(CO)_5$, and a nitrogen separator gas were directed onto Mo or Al foil substrates which passed under the injector head on a moving conveyor belt. The temperature was varied from ambient to 400 C. Nitrogen curtains were used to exclude air from the reaction zone. The composition of the films could be varied between FeS and FeS_2 by adjusting the flow ratio of the reactive gases. The deposition rate was found to vary linearly with both time and reactive gas flow rate.

Electrochemical tests were carried out at room temperature to determine both dynamic and open circuit voltages with respect to pure Li. Voltage plateaus (1.4 to 1.6 V) were found at current densities up to 0.1 mA/cm^2. Although previous work at room temperature has shown good recharge characteristics for bulk FeS_2 electrodes (1), we found high impedances after partially recharging our cells from the Li_2FeS_2 composition.

The thermodynamics of the cell reaction can be explained in terms of the ternary Li-Fe-S diagram. Some of the pertinent equilibrium potentials have been established at room temperature and are compared with previous work (2). The results of work with this thin film FeS_x cathode will be compared with those of other positive electrode materials.

Acknowledgements

This work was supported by the US Department of Energy under Subcontract LBL 4536310. The authors gratefully acknowledge the provision of CVD equipment and experimental assistance by Watkins-Johnson Company.

References

(1) R. Brec, A. Dugast and A. Le Mehaute, Mat. Res. Bull., **15**, 619-25, 1980.

(2) C. Iwakura, N. Isobe and H. Tamura, Electrochim. Acta, **28**, 277-83, 1983.

Abstract No. 36

DISCHARGE BEHAVIOR AND THERMAL STABILITY OF SYNTHETIC FeS_2 CATHODE MATERIAL

Steven Dallek and Benjamin F. Larrick
Electrochemistry Branch

Bruce C. Beard
Materials Evaluation Branch

Naval Surface Warfare Center
10901 New Hampshire Avenue
Silver Spring, MD 20903-5000

and

J. Paul Pemsler, John K. Litchfield
and Raymond K. F. Lam
Castle Technology Corporation
262 West Cummings Park
Woburn, MA 01801

INTRODUCTION

Thermal batteries based on the Li(alloy)/FeS_2 electrochemical system have been developed in recent years and successfully employed in numerous weapons systems. The FeS_2 cathode material is obtained as beneficiated ore from naturally occurring pyrite deposits or as a by-product flotation concentrate from processing base or noble metal ores.

It is highly unusual to find a naturally occurring substance used directly as a principal ingredient in a chemical system requiring components with extremely uniform properties. Nevertheless, this material has performed well in a wide variety of new lithium-alloy thermal batteries.

However, the availability and quality of pyrite have caused persistent problems for thermal battery manufacturers. In recent years, it has been very difficult to obtain the material from domestic sources. In addition, the quality of the pyrite has varied dramatically among sources and even between lots from the same source. It is axiomatic that the reproducibility of the cathode behavior would be improved by using pyrite of highly uniform physical and chemical properties.

A new thermal battery cathode material, synthetic FeS_2, has been developed as an alternative to naturally occurring pyrite material. Thus, a domestic source of FeS_2 cathode material is now available that is not subject to periodic interruption by national events such as strikes and mine closings. In addition, the availability of pure synthetic pyrite with highly uniform physical and chemical properties presents significant advantages in the reliability and cost of thermal batteries.

The composition, thermal stability, surface chemistry, and electrochemical discharge behavior of the new synthetic material were evaluated by thermogravimetry (TG), x-ray photoelectron spectroscopy (XPS), and single-cell and battery discharge studies. The TG analysis method for FeS_2 materials has great utility for monitoring the extent of sulfidation and the final product composition. Additionally, a multiple-heating-rate TG method (1) has been used to determine the decomposition rate of FeS_2 cathode materials at thermal battery operating temperatures (2). The effect of the particle size of synthetic FeS_2 material on its thermal stability and discharge performance was determined. XPS studies were conducted to analyze the surface oxidation products on synthetic and natural pyrite materials.

EXPERIMENTAL

Synthetic FeS_2 was prepared by a proprietary process (Castle Technology Corporation) by direct reaction between hydrogen-reduced electrolytic iron and a sulfidizing medium at elevated temperatures according to the reaction:

$$Fe + \frac{(1+x)}{2}S_2 \longrightarrow FeS_{1+x} \quad (1)$$

$$FeS_{1+x} + \frac{(1-x)}{2}S_2 \longrightarrow FeS_2 \quad (2)$$

After hydrogen treatment, the iron was kept under inert gas and transferred to an inert atmosphere glove box with a water vapor content of 10 ppm. The sulfidation reactor was loaded with the reactants in the glove box and was returned to the glove box for removal of the product. The product was packaged within the glove box so that the synthetic FeS_2 was not exposed to air before sampling for analysis or fabricating into cathodes.

The composition of the product was determined by TG using a DuPont 9900 or 1090 thermal analyzer interfaced to a 951 TGA module. Samples were run in platinum boats from 298 K to 1023 K in a helium atmosphere. The thermal stability of the material was determined by a multiple-heating-rate TG method previously reported (2) for FeS_2 decomposition kinetics studies. XPS surface chemistry studies were performed on the new synthetic FeS_2 and on naturally occurring FeS_2 materials with a Kratos ES-300 Photoelectron Spectrometer. Single-cell and battery discharge studies were performed, according to standard procedures, by the four U.S. thermal battery manufacturers, Catalyst Research Division of Mine Safety Appliances Company, Eagle-Picher Industries, Inc., Power Conversion Inc., and SAFT America, Inc.

RESULTS AND DISCUSSION

In general, cells with the synthetic FeS_2 had higher operating voltages, lower resistance, and were able to sustain higher current densities than cells with the natural pyrite material. This enhanced performance correlates directly with the fine particle size of the synthetic FeS_2 as compared with the much coarser natural material. Lower discharge capacity of the synthetic FeS_2 cells observed at low current densities is also consistent with the higher thermal decomposition rate expected for this finely divided material. The higher thermal decomposition rate predicted by TG kinetics measurements for the synthetic FeS_2 correlates well with the lower measured cell capacity. Larger particle size synthetic FeS_2 can be produced and should mitigate effects of rapid thermal decomposition.

TG curves and XPS spectra of synthetic FeS_2 that had been prepared and stored in an inert atmosphere showed, respectively, the material's high bulk purity and the absence of surface oxidation products. The SO_4^{-2} concentration on the surface of synthetic FeS_2 exposed to humid environments, as determined by XPS and TG, increased as a function of the exposure time. The high chemical reactivity of the synthetic FeS_2 also resulted in the formation of surface oxidation

products during fabrication of single cells and batteries under dry room conditions.

It was recently reported (3) that the use of fine particle size FeS_2 produced significant improvements in cell performance, i.e., reduction in impedance and increases in specific energy and power. Thus, synthetic FeS_2 may find great utility in increasing the performance capabilities of Li/FeS_2 thermal batteries while also providing a solution to many of the problems associated with the variable quality and availability of the presently used FeS_2 materials.

ACKNOWLEDGMENT

This work was supported by the Navy's Small Business Innovative Research (SBIR) Program under Contract No. N60921-87-C-0045.

REFERENCES

1. J.H. Flynn and L.A. Wall, Polymer Letters, 4, 323 (1966).
2. S. Dallek, Proc. 32nd International Power Sources Symposium, Cherry Hill, NJ, pp. 643-7, 9-12 June 1987.
3. L. Redev et al., Argonne National Laboratory Report ANL-87-6, April 1987.

Abstract No. 37

POLYMER ELECTRODES FOR BATTERY APPLICATIONS

L.W. Shacklette, T.R. Jow, M. Maxfield,
and R.S. Hatami

Allied-Signal, Inc.
Corporate Technology
Morristown, N.J. 07960

A variety of conducting polymers have been investigated with regard to their possible application in batteries. Among the most widely studied polymers are polyacetylene (PA) (1,2,3,), poly(p-phenylene) (PPP) (3,4), polypyrrole (PPy) (5,6), and polyaniline (PAn) (7,8). A conducting polymer can be either partially oxidized or reduced electrochemically to form either p-type or n-type conductors generally suited for use in cathodes or anodes respectively. The electrochemical oxidation or reduction process results in the formation of a highly conductive complex between the reduced or oxidized polymer and the appropriate counterion from the electrolyte. Most of the world wide effort toward developing a polymer battery has been directed toward the use of anion-inserted (p-type) polymers as the cathode (positive electrode). For example, Bridgestone and Seiko in Japan have recently announced the commercialization of a button cell based on a cathode composed of anion-inserted polyaniline and an anode composed of Li/Al alloy (9). This cathode-limited cell appears to have the virtue of very high cycle life (presumably aided by the use of an appreciable excess of Li/Al alloy). The cell, however, does not offer high energy density (values calculated from quoted data are 4.4 mWh/g and 1.5 mWh/cm^3). The cell is directed at markets which require long life and reliability over energy storage capacity. A comparison of fundamental properties of competing cathode materials is given in Table 1 which compares the observed capacity of several oxidized polymers inserted by BF_4^- anions with that of an inorganic lithium-cation inserting cathode material, Li_xMoS_2, which is employed in a cell being marketed by Moli Energy, Ltd. The mid-discharge voltages listed are the approximate open-circuit voltages at a point where half of the discharge capacity has been used. The capacities listed for the polymers include the weight of the inserted anion (BF_4^-), since this anion is a necessary constituent of the charged cell and must be considered in making comparisons with other materials. On a gravimetric basis the polymers compare very favorably with Li_xMoS_2, especially considering their higher operating voltage; however, on a volumetric basis, Li_xMoS_2 and other inorganic insertion compounds possess a distinct advantage. The major advantage of conducting polymers appears to lie with their polymer-like mechanical properties which provide the capability of high cycle life.

In order to take advantage of the fundamental properties of conducting polymers while still maintaining high cycle life we have developed composite negative electrodes (10,11) which utilize conductive polymers as a binder for alkali-metal alloys. These electrodes combine high volumetric capacity with high cycle life. Cells based on the couples Na/Pb vs. Na_xCoO_2 and Li/Pb vs $Li_xV_6O_{13}$ have been constructed. Such cells packaged in AF-size welded steel cans have to date demonstrated energy densities in the range 60 to 75 mWh/g and 150 to 175 mWh/cm^3 with values up to 100 mWh/g and 250 mWh/cm^3 possible in the near future.

Another opportunity for the use of conductive polymers lies with their catalytic properties. In work carried out at the U.S. Naval Research Lab., conducting polymers, for instance, show promise for use as a substrate for the reduction of thionyl chloride in lithium primary cells. More recently, work at the U.S. Army, LABCOM, at Ft. Monmouth, N.J. has shown that conductive polymers can catalyze the reduction of SO_2 and the reoxidation of the discharge products in secondary Li/SO_2 cells (12).

TABLE 1 - CAPACITIES OF POLYMERS THAT UNDERGO REVERSIBLE OXIDATION

	POLYACETYLENE $(CH)_x$	POLYPYRROLE $(C_4H_3N)_x$	POLYANILINE $(C_6H_5N)_x$	Li_xMoS_2
MAX. REPORTED NO. OF CHARGES PER REPEAT UNIT	0.09	0.33	0.5	0.8
MID-DISCHARGE VOLTAGE (vs. Li/Li$^+$)	3.5	3.3	3.4	1.9
GRAVIMETRIC CAPACITY[a] (Ah/g)	0.12	0.095	0.10	0.13
VOLUMETRIC CAPACITY[b] (Ah/cm^3)	0.14	0.12	0.13	0.6

(a) Including the weight of BF_4^- anions for the polymers

(b) Based on the limiting density

REFERENCES

1. K. Kaneto, M. Maxfield, D.P. Nairns, and A.G. MacDiarmid, J. Chem. Soc., Faraday Trans. 1, 78, 3417 (1982).
2. R.B. Kaner and A.G. MacDiarmid, J. Chem. Soc., Faraday Trans. 1, 80, 2019 (1984).
3. L.W. Shacklette, J.E. Toth, N.S. Murthy, and R.H. Baughman, J. Electrochem. Soc., 132, 1529 (1985).
4. L.W. Shacklette, R.L. Elsenbaumer, R.R. Chance, J.M. Sowa, D.M. Ivory, G.G. Miller, and R.H. Baughman, J. Chem. Soc., Chem. Commun., 361 (1982).
5. G.B. Street, "Polypyrrole: From Powders to Plastics", in "Handbook of Conducting Polymers Vol. 1" ed. by T.A. Skotheim (Marcel Dekker, New York and Basel, 1986).
6. K. Kaneto and K. Yoshino, Kino Zairyo (Japan) 4, 8 (1984).
7. E.M. Genies, A.A. Syed, C. Tsintavis, Mol. Cryst. Liq. Cryst. 121, 181 (1985).
8. A.G. MacDiarmid, S-L. Mu, N.L.D. Somasiri, and W. Wu, ibid., p. 187.
9. JEC Battery Newsletter No. 2, Mar.-April, 1988.
10. T.R. Jow, L.W. Shacklette, M. Maxfield, and D. Vernick, J. Electrochem. Soc. 134, 1730 (1987).
11. M. Maxfield, T.R. Jow, S. Gould, M.G. Sewchok, and L.W. Shacklette, J. Electrochem. Soc. 135, 299 (1988).
12. R.J. Mammone and M. Binder, J. Electrochem. Soc., in press.

Abstract No. 38

ELECTROCHEMICAL AND STABILITY STUDIES OF A NEW FORM OF POLYACETYLENE, [N-$(CH)_x$]

R. Huq*, G. C. Farrington*, J. Foreman*, K. Wu* and N. Theophilou+

*Department of Materials Science and Engineering
and
+Department of Chemistry
University of Pennsylvania
Philadelphia, PA 19104

Introduction

Several years ago, polyacetylene [$(CH)_x$] was widely investigated as a possible electrode material for non-aqueous batteries. The form of polyacetylene studied at that time was synthesized by the so-called, Shirakawa technique. Shirakawa polyacetylene [S-$(CH)_x$] stimulated considerable interest in this simplest of conjugated polymers [1]. Regrettably, its instability and modest energy density limited its potential applications.

Recently, new research by Naarmann and Theophilou [2,3] has produced an ultra-pure form of polyacetylene, so-called N-$(CH)_x$, which has a far lower concentration of chemical defects than S-$(CH)_x$. Another distinctive feature of N-$(CH)_x$ is its regular crystalline structure. Doped forms of N-$(CH)_x$ have exceptionally high electrical conductivities, on the order of 10^5 $(ohm\text{-}cm)^{-1}$ [4].

It is possible that the high purity and more regular structure of N-$(CH)_x$ may enhance its electrochemical and chemical stability and make it possible to achieve higher levels of oxidation and reduction than have been attained with S-$(CH)_x$. This paper presents one of the first studies of the the electrochemical oxidation and reduction reactions of N-$(CH)_x$ as well as insight into the general chemical and electrochemical stability of this new material. Particular attention is focused on the question of whether N-$(CH)_x$ may be more useful for battery applications than was S-$(CH)_x$.

References:

1. T. Ito, H. Shirakawa, S. Ikeda, J. Polym. Sci. Polym. Chem. Ed. 12 (1974) 12; and J. Polymer Sci. Polym. Chem. Ed. 13 (1975) 1942.
2. H. Naarmann and N. Theophilou, BASF-AG, German Patent DE-3717067.8, 21-5-87.
3. H. Naarmann and N. Theophilou, Synthetic Metals 22 (1987) 1-8.
4. N. Baseseu, Z-X. Liu, D. Moses, A. J. Heeger, H. Naarmann and N. Theophilou, Nature, 327 (1987) 403.

Abstract No. 39

Intercalation Reactions of Monovalent and Divalent Cations in V_6O_{13} Single Crystals

M.Z.A. Munshi
A. Gilmour
B.B. Owens
W.H. Smyrl

Department of Chemical Engineering and Materials Science
Corrosion Research Center
University of Minnesota
221 Church St. SE
Minneapolis, MN 55455

The use of V_6O_{13} as a cathode material in non-aqueous lithium secondary batteries was originally reported by Murphy, et al. in 1979 [1]. Subsequently, the Li/V_6O_{13} couple has been the subject of intense research by various groups [2-6]. From a secondary battery application, the key areas of interest for the cathode is defined by high electronic conductivity, high reversibility, high diffusivity (leading to high power densities), wide composition range (allowing high cell capacities) and minimal structural change with composition, and in this respect lithium satisfies most of the criteria. The theoretical energy density of the Li/V_6O_{13} couple is 890 Wh/kg, which is considerably greater when compared to some of the other intercalation cathodes such as TiS_2). This value together with the relative ease of manufacture of V_6O_{13} makes it a highly promising cathode material in rechargeable lithium batteries. However, the safety and cycle life of ambient temperature secondary lithium batteries, usually associated with the high reactivity of elemental lithium anode, poses a serious problem. This may be overcome, however, by finding alternative anodes which may be more stable and have reasonable energy densities.

So far there is no report in the open literature on intercalation studies pertaining to cations other than lithium. It would be highly desirable if V_6O_{13} was reversible to other cations from a battery technology viewpoint.

Previous emphasis has been placed on studying polycrystalline V_6O_{13}. In order to establish fundamental properties, single crystals need to be investigated.

In this laboratory, the process for growing large single crystals has now been well established. The first part of the investigation was to reproduce the work already performed for Li^+ insertion into the single crystal material. This was completed successfully by utilizing cells made of a lithium anode, a V_6O_{13} single crystal as cathode and $LiClO_4$ dissolved in propylene carbonate (PC) as the electrolyte. Thermodynamic EMF vs composition curves obtained by titrating lithium ions into the cathode were consistent with literature values.

The work has now been extended to include anodes such as Zn, Cu, Mg, Na and Ca. The initial results indicate that Zn and Cu may be inserted and removed reversibly from the V_6O_{13} cathode.

Acknowledgement

This work was supported in part by the Department of Energy and the Office of Naval Research.

References

1. D.W. Murphy, P.A. Christian, F.J. DiSalvo and J.N. Carides, J. Electrochem. Soc. 126, (1979), 497.

2. D.W. Murphy, P.A. Christian, F.J. DiSalvo J.N. Carides, and J.V. Waszcak, ibid. 128 (1981) 2053.

3. P.C. Spurdens, J. Drennen, J.R. Owen, B.C.H. Steel, J.M. Gonzales-Calbert and D.A. Jefferson, Solid State Ionics, 5 (1981) 335.

4. J.R. Owen, J. Drennen, G.E. Lagos, P.C. Spurdens and B.C.H. Steele, Solid State Ionics, 5 (1981), 343.

5. K. West, B. Zachau-Christiansen, T. Jacobsen and S. Atlung, J. Power Sources, 14 (1985) 235.

6. P.C. Spurdens and B.C.H. Steele, Solid State Ionics, 21 (1981) 151.

Abstract No. 40

The Influence of Additives on the Cycleability of the Li Anode

L. A. Dominey, J. L. Goldman and V. R. Koch

Covalent Associates, Inc.
52 Dragon Court
Woburn, MA 01801

The extreme reactivity of the Li anode with organic electrolytes has prompted a search in recent years for chemical additives which can be added in relatively low concentration to the bulk electrolyte. These additives are thought to enhance the cycleability of the Li electrode by a variety of mechanisms including:

- film formation on Li
- free radical scavenging
- neutralization of acidic cathode impurities
- depolarization of electrode processes
- adsorption of unreactive species between Li and electrolyte

While several patents are held on substances which are thought to act via each of these mechanisms, it is not clear in what electrolyte systems they may be most effectively employed or, in fact, if the proposed mechanisms are correct.

Many of these recently patented additives have been studied in non-ether electrolytes, which for the most part give Li cycleability inferior to that obtainable in ether electrolytes. We have, therefore, tested them in ether systems to expand our understanding of their applicability and to rank their relative effectiveness.

We used a common half cell test vehicle design which focuses on interactions with the Li anode. Since half cell cycling tests eliminate complexities arising from the cathode chemistry, they are only useful for addressing issues involving electrolyte and anode related cell failure modes. Extrapolation to full cell cycling is not appropriate except in the sense that a major positive effect in a half cell merits full cell evaluation. Certain selected additives were therefore also evaluated in Li/TiS_2 full cells containing THF or 2 MeTHF/$LiAsF_6$ electrolytes.

The half cells were all of identical design, containing 10 ml of 1.5M $LiAsF_6$/THF electrolyte with various additives. An initial plate of 6.2 coulombs cm^{-2} (C/cm^2) was plated from a 10 cm^2 strip of 10 mil Li onto stainless steel separated by Celgard 2400 and held under mild compression. Initial deposits at both 1.25 mA/cm^2 and 5 mA/cm^2 were studied. Subsequently, stripping and plating of 1.55 C/cm^2 at +0.3V was performed until polarization to 1.5V occurred during a stripping cycle. Full cell cycling was carried out in our standard 260 mAhr TiS_2 cell with Li/TiS_2 ratio of 3.8 to 1 and cycled at 40% DOD.

Abstract No. 41

INVESTIGATION OF MIXED SOLVENT ELECTROLYTES FOR AMBIENT TEMPERATURE SECONDARY LITHIUM CELLS

D.H. Shen, S. Subbarao, F. Deligiannis, and G. Halpert

Jet Propulsion Laboratory
California Institute of Technology
4800 Oak Grove Drive
Pasadena, California 91109

INTRODUCTION

The practical use of ambient temperature secondary lithium cells is presently limited because of their poor cycle life performance and rate capability (1). These limitations are understood to be mainly due to the poor conductivity and high reactivity of the electrolyte towards lithium (2). We are currently investigating a number of mixed solvent electrolytes consisting of 2-Methyltetrahydrofuran (2 MeTHF) and Tetrahydrofuran (THF) as base solvents to improve the performance capability of the rechargeable lithium cells. The co-solvents included in the present study are Ethylene Carbonate (EC), Propylene Carbonate (PC), and 3-Methylsulfolane (3 MeS). The paper describes the solvent purification methods, physical and electrochemical properties and cycle life performance of the various mixed solvent electrolytes investigated.

EXPERIMENTAL

The mixed solvent electrolytes investigated can be broadly divided into two groups. The base solvent of the first and second groups of electrolytes are 2 MeTHF and THF, respectively. EC, PC, and 3 MeS were used as the co-solvents/additives. Preparation of the electrolytes and all the experiments were carried out in a Argon atmosphere glove box at ambient temperature. The solvents THF and 2 MeTHF were dried over CaH_2 and distilled under Ar at reduced pressure. 3 MeS was purified according to the procedures reported previously (3). PC was purified according to the methods reported in the literature (4). EC was purified by drying over P_2O_5 and vacuum distillation (5). The $LiAsF_6$ was used as received from US Steel Agri chemicals and the electrolyte salt concentration was 1.5M.

The density, conductivity, and viscosity of the electrolytes were measured at room temperature. Cyclic voltammetry was used to determine the electrochemical window of each electrolyte. The stability of the electrolytes towards lithium was evaluated by the base line storage tests and microcalorimetry. Samples of electrolyte and freshly scratched Li foil were incubated in Teflon-line screw-cap culture tubes. Visual observations of lithium and electrolyte condition were noted periodically. Hermetically sealed lithium half cells were used in the microcalorimetry studies. The heat evolved from the half cell was measured periodically at ambient temperature. Electrochemical impedance spectroscopy was used to study the characteristics of the surface film formed on the lithium electrode.

Sealed experimental Li-TiS_2 cells were fabricated and cycled to 100% DOD to determine the cycle life performance and lithium cycling efficiency. Cells employed in this study had a theoretical capacity of about 200 mAh. These cells were cathode limited by design and the anode to cathode capacity ratio was 10:1. Each cell contained 4 ml of the electrolyte under study. Cathodes were fabricated by a brushing technique using TiS_2 prepared in house and EPDM binder(2). A porous polypropylene film (Celgard 2400) was used as the separator. Constant current method was used for discharging and charging the cells. The current densities were 2 and 1 mA/cm^2 for discharging and charging respectively. The cells were cycled between 1.7 and 2.7 V at room temperature.

RESULTS AND DISCUSSION

Density, conductivity, and viscosity of the various mixed solvent electrolytes studied are given in Table I. From the table it can be observed that addition of EC and PC to THF and 2 MeTHF base electrolytes results in increasing the conductivity and viscosity. Approximately 80% improvement in conductivity was observed due to the addition of 10% EC or PC to 1.5M $LiAsF_6$/2 MeTHF electrolyte. The higher conductivity of EC/2 MeTHF is mainly due to the combined effects of the high dielectric constant of EC and the low viscosity of 2 MeTHF (5). Addition of 3 MeS to 2 MeTHF did not result in improving the conductivity significantly. This may be due to the high viscosity of the 3 MeS / 2 MeTHF electrolyte. Marginal improvement in conductivity was only observed by adding EC or PC to 1.5M $LiAsF_6$/THF electrolyte. Similar beneficial results are observed by adding EC to 2 MeTHF/THF mixed electrolyte. Electrolytes containing EC or PC showed similar viscosity. 2-MeTHF + 3 MeS electrolyte has the highest viscosity among the electrolytes investigated. Density changes among the electrolytes are not significant.

Stability of the electrolytes towards lithium was investigated by microcalorimetry. Figure 1 gives the heat output as the function of time for three selected electrolytes. The highest heat output (13 microwatts after 50 hours) was shown by the cells containing 1.5M $LiAsF_6$/THF electrolyte. This is due to the high reactivity of THF with lithium. The 1.5M $LiAsF_6$/2 MeTHF showed lower heat output compared to the THF electrolyte. The heat output after 50 hours is approximately 5 microwatts. Addition of EC was found to improve the stability of the 2 MeTHF based electrolyte (3 microwatts after 50 hours). From the results it can be projected that EC/2 MeTHF electrolyte may have the highest cycle life compared to the other electrolytes.

Cycle life performance of the experimental Li-TiS_2 cells activated with different electrolytes is being evaluated. The electrolytes containing EC have shown better cycle life performance compared to the ones without EC. Among the EC containing electrolytes, the best cycle life performance was shown by 1.5 M $LiAsF_6$/10%EC+90%2 MeTHF. These cells have lost only about 15% of their capacity after completion of 120 cycles. These results are consistent with the predictions from the microcalorimetry data. Hence we feel microcalorimetry is a useful tool to screen the candidate electrolytes. The cycle life evaluation of these cells is still continuing.

We will describe the results of our investigation and the characterization of various mixed solvent electrolytes for ambient temperature secondary lithium cells. Attempts will be made to relate the cycle life data to the physical and chemical properties of the electrolytes.

ACKNOWLEDGEMENTS

This work represents on phase of research performed by the Jet Propulsion Laboratory, California Institute of Technology, sponsored by the National Aeronautics and Space Administration, contract NAS7 918. The authors would like to thank M. Pitts, L. Whitcanack, and E. Davies for their assistance in the laboratory work.

REFERENCE

1. B. Owens, EPRI final report, "Ambient Temperature Lithium Secondary Batteries Technology Assessment", August 18, 1986.

2. D.H. Shen, S. Subbarao, B.J. Nakamura, S.P.S. Yen, C.P. Bankston, and G. Halpert, The Electrochemical Society Fall Meeting, Hawaii, Oct. 1987. Extended Abstracts, Abstract 87-2.

3. S.P.S. Yen, D.H. Shen, R.P. Vasquez, B.J. Carter, and R.B. Somoano, Abstract 74, p. 119, The Electrochemical Society Extended Abstracts, Vol 83-2, Washington, DC, Oct. 9-14, 1983.

4. C. Nanjundiah, J. L. Goldman, L.A. Dominey and V.R. Koch, The Electrochemical Society Fall Meeting, Hawaii, Oct. 1987. Extended Abstracts, Abstract 87-2.

5. S. Tobishima, M. Arakawa, T. Hirai and J. Yamaki, Journal of Power Sources, 20(1987) 293-297.

TABLE I. PHYSICAL PROPERTIES OF ELECTROLYTES

ELECTROLYTE	DENSITY (g/ml)	VISCOSITY (cp)	CONDUCTIVITY 10^{-3} (ohm-cm)$^{-1}$
100%2MeTHF	1.07	3.96	3.40
10%EC+90%2MeTHF	1.12	4.95	6.17
30%EC +70%2MeTHF	1.19	4.96	8.21
10%PC+90%2MeTHF	1.12	2.32	6.08
25%3MeS+75%2MeTHF	1.11	10.38	3.60
100%THF	1.10	---	13.72
10%EC+ 90%THF	1.14	---	14.63
10%PC+ 90%THF	1.24	2.50	4.56
50%THF+50%2MeTHF	1.07	---	8.87
10%EC+45%THF+45%2MeTHF	1.10	---	10.47

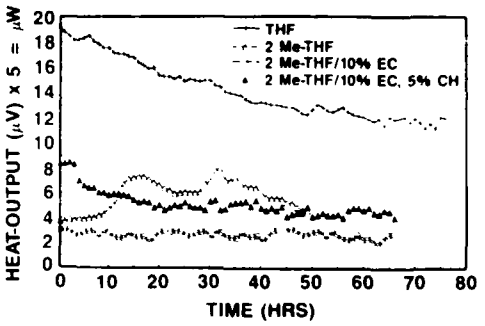


Figure 1. Microcalorimetry study of electrolytes

Abstract No. 42

Electrochemical Oxidation of Lithium Bromide in $LiAsF_6$/Tetrahydrofuran Solutions

Wishvender K. Behl

US Army Electronics Technology and Devices Laboratory, LABCOM
Power Sources Division
Fort Monmouth, New Jersey 07703-5000

INTRODUCTION

Recently, there has been considerable interest in providing an, in-situ, electrochemical mechanism that would prevent the oxidation of organic solvents during the overcharging operations of the rechargeable lithium batteries. In this connection, the use of electrolyte additives, such as lithium iodide, has been suggested (1). In order to determine the feasibility of using lithium halides as electrolyte additives to provide overcharge protection for rechargeable lithium batteries, we have studied the anodic oxidation of lithium iodide and lithium bromide in tetrahydrofuran (THF) solutions. The results on the kinetics of the iodide/triiodide/iodine redox reactions on platinum electrode were recently reported (2). In this paper, we report on the electrochemical oxidation of lithium bromide at glassy carbon and pyrolytic graphite electrodes in 1.5M $LiAsF_6$/THF solutions using the rotating disk and rotating ring-disk electrode techniques.

RESULTS AND DISCUSSIONS

The anodic oxidation of lithium bromide has been previously studied by Iwasita and Giordano (3) at rotating platinum disk electrodes in acetonitrile solutions. These workers found that the bromide ion was first oxidized to the tribromide ion which was then further oxidized to bromine:

$$3\ Br^- \longrightarrow Br_3^- + 2e \qquad (1)$$

$$2\ Br_3^- \longrightarrow 3\ Br_2 + 2e \qquad (2)$$

The steady-state polarization curves at glassy carbon and pyrolytic graphite rotating disk electrodes in 1.5M $LiAsF_6$/THF solutions containing lithium bromide also exhibited two limiting current waves corresponding to the stepwise oxidation of the bromide ion to the tribromide ion and bromine, respectively. The limiting currents for both current waves increased with increasing lithium bromide concentration as well as with increasing electrode rotation speeds. The diffusion co-efficienct of the bromide ion was calculated from the limiting currents and found to be 2.66×10^{-6} cm^2/s.

The tribromide ion was found to react with the tetrahydrofuran solvent at the electrode surface resulting in the deposition of a polymeric film, so that the first current wave in the polarization curves exhibited slight hysteresis when the potential was swept back to the initial value. The bromine formed in the second step, on the other hand, dissolved in the electrolyte and thus did not react with the solvent at the electrode surface. Therefore, the second current wave in the polarization curves did not exhibit any significant hysteresis on the reverse scan.

The ring-disk electrode experiments using either the glassy carbon ring-disk electrode or the platinum ring-pyrolytic graphite disk electrode showed that only the tribromide ion was detected at the ring electrode even in the potential range where bromine was formed at the disk electrode. Thus, in the presence of excess lithium bromide, bromine combines with the bromide ions in solution to form the tribromide ion which is then collected at the ring electrode and reduced to the bromide ion. This behavior is consistent with the high formation constant of the order of 10^7 reported for the tribromide ion in organic solvents (4).

The collection efficiencies at the ring electrodes were measured at various potentials and electrode rotation speeds from the ring current-disk potential and disk current-disk potential curves. Because of the reaction of the tribromide ion with the electrolyte at the disk electrode, the amount of the tribromide ion detected at the ring electrode, in the potential range of the first current wave, was smaller than predicted by the theory. On the other hand, the ring collection efficiencies at disk potentials in the region of the second current wave were close to the collection efficiency calculated (5) from the geometric dimensions of the ring-disk electrode and were also independent of the electrode rotation speeds. Therefore, it appears that the homogenous reaction of the tribromide ion with the tetrahydrofuran solvent is slow compared to the time scale of the rotating ring-disk electrode experiments. Nevertheless, solutions of bromine in tetrahydrofuran were not found to be stable even in the presence of excess lithium bromide. Thus, the reactivity of the tribromide ion as well as bromine towards tetrahydrofuran precludes the use of lithium bromide as an additive to provide overcharge protection for rechargeable lithium batteries which use electrolytes based on tetrahydrofuran as the solvent.

ACKNOWLEDGMENT

The author would like to thank Dr. D.-T. Chin for many helpful discussions.

REFERENCES

1. K. M. Abraham and S. B. Brummer in "Lithium Batteries", J. Gabano, Editor, Academic Press, New York (1983).

2. W. K. Behl and D.-T. Chin, J. Electrochem. Soc., 135, 16 (1988).

3. T. Iwasita and M. C. Giordano, Electrochim. Acta., 14, 1045 (1969).

4. I. V. Nelson and R. T. Iwamoto, J. Electroanal. Chem. and Interfacial Electrochem., 7, 218 (1964).

5. W. J. Albery and S. Bruckenstein, Trans. Faraday Soc., 62, 1920 (1966).

Abstract No. 43

METAL HALIDE REDUCIBLE CATHODE STUDIES IN RECHARGEABLE LITHIUM CELLS

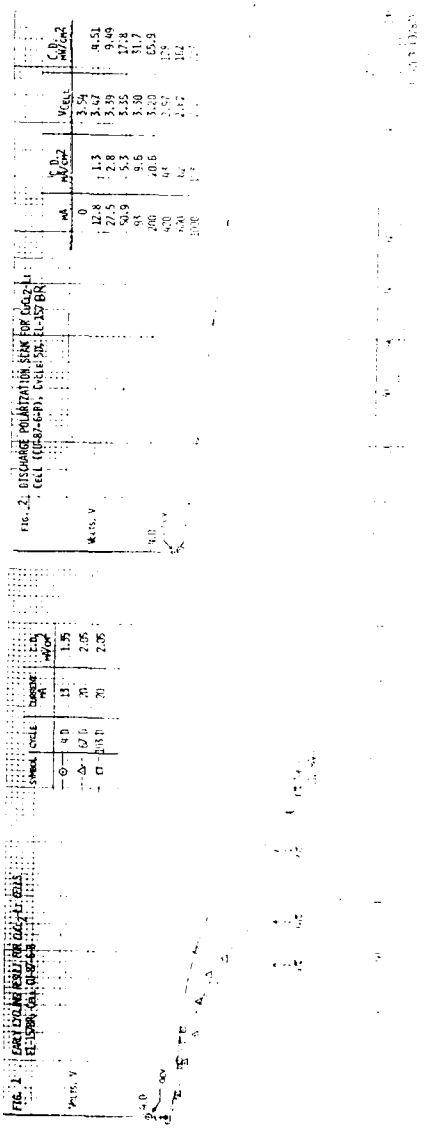
D. Reisner and M.Eisenberg

Electrochimica Corporation
20 Kelly Court
Menlo Park, CA 94025

Studies of metal halide, e.g., $CuCl_2$ cathodes in inorganic SO_2-based electrolytes were carried out in comparison to high surface carbon cathodes in rechargeable lithium cells. A $CuCl_2$ cathode can provide higher volumetric energy densities compared to high surface area carbon black (e.g., Ketjenblack) cathodes, e.g., 0.25-0.30 AH/cc of cathode volume.

Preliminary cycling tests on $CuCl_2$-Li were conducted to an 80-90% depth of discharge at a 3 hour rate to a 2.0 V cutoff. Fig. 1 illustrates Cycle #4 (at a discharge current density of 1.35 mA/cm^2) and Cycles #67 and #103 at a discharge current density of 2.05 mA/cm^2. On the basis of a 2-electron discharge and the weight of active cathode materials, (0.400 AH/g of $CuCl_2$) the cell had a theoretical capacity of 112 mAH. As can be seen, the initial cycle at a lower current density resulted in an 89% capacity utilization and the other two cycles yielded 64% and 50% respectively of the theoretical faradaic capacity, at the somewhat higher current density.

The cupric chloride-Li cells also showed a remarkable high current density capability as shown in Fig. 2. The cell has an open circuit voltage of 3.54 V and was scanned to 103 mA/cm^2 at which point the cell voltage dropped to 2.2 V. At this point, it yielded a remarkably high power density of 227 milli watts/cm^2. Even at 20 mA/cm^2 the cell voltage was still 3.2 V. It should be pointed out that this test was not carried out on a virgin cell but prior to the discharge in Cycle #5. Throughout the test range, the cell voltage-current density curve remains essentially linear.



Abstract No. 44

Rechargeable Lithium Battery Systems: an Overview

Frank B. Tudron

Eveready Battery Company
Westlake Technology Laboratory
Box 45035
Westlake, Ohio 44145

INTRODUCTION

The impetus for R&D programs on rechargeable lithium technology in industrial, government, contract research, and academic labs is easy to rationalize. Modern consumer and military electronics stress portability and miniaturization. The more sophisticated consumer is confronting the cost/convenience tradeoff embodied in the availability of both primary and rechargeable batteries. These and other factors provide the basis for optimistic projections of the future rechargeable battery market as a whole. Since lithium rechargeable systems have advantages in a number of areas (e.g., weight, energy density, charge retention), it is expected that they can participate in this growing market.

This paper deals with work on systems based on organic and inorganic liquid electrolytes as well as polymer electrolyte systems. Programs in industry, government, academic, and contract research labs is reviewed. A comparison of materials and systems under a consistent set of construction assumptions is presented. The problem of electrode inefficiency is discussed and impact on cycle life/energy density characteristics is treated.

DISCUSSION

A partial listing of participants in the research and development effort on rechargeable lithium batteries is presented as Table I.

Much in the way of excellent progress and innovation has resulted from these programs. Many detailed examples can be cited.

A theoretical comparison of a number of the more important electrochemical system can be made. calculations based on material properties provide theoretical primary and secondary energy densities. Based on the assumption that in a present state of the art high surface area spiral wound cylindrical cell construction, the active materials occupy about 25% of the total cell volume, practical calculated energy density values can be put forth. Table II is submitted as a comparison of a number of candidate systems.

Involved in the calculation of the theoretical secondary energy density is the negative-to-positive balance to which the cell is built. The literature is replete with references to problems associated with lithium replating inefficiency. Because of the loss of lithium capacity due to corrosion and/or isolation, additional negative capacity must be provided to ensure desired cycle life performance. A mathematical model of constant current time limited cycling permits elucidation of the relationship among electrode balance, depth of discharge, electrode cycling efficiency and cycle life.

$$N = \frac{R - D}{D(1-e^-) + D^2(1-e^+)}$$

where N is the number of cycles, R is the negative to positive ratio, D is the depth of discharge (based on positive electrode capacity), and e- and e+ are negative and positive cycling efficiencies respectively. Figure I shows the graphical relationship between cycle life and depth of discharge for a generic system with negative efficiency of 97.5% positive efficiency of 99.5% with negative to positive ratios ranging from 2:1 to 4:1. The importance of continued work in the area of electrolyte stability and electrode cycling efficiency is underscored by this exercise.

TABLE I

Organization	System
COMMERCIAL	
AT&T Bell Labs	Li/organic/$NbSe_3$
Eveready	Li/organic/TiS_2
Fuji	Li/organic/MoO_3
Hitachi Maxell	Li-Al/organic/TiS_2
Matsushita	Li-alloy/organic/ACF
Moli Energy Ltd.	Li/organic/MoS_2
NT&T	Li/organic/a-V_2O_5-P_2O_5
SAFT	Li/organic/V_2O_5,MoO_3
Sony Energytec	Li/organic/Li_xMnO_2
W.R. Grace	Li/organic/TiS_2
AMOCO	Li/SO_2/C
Ballard Research, Inc.	Li/SO_2/C
Combustion Engineering	Li/polymer/MX
CONTRACT/GOVERNMENT	
SOHIO	Li/polymer/Mx
Varta/BASF	Li/organic/polymer
Bridgestone/Seiko	Li-Al/organic/polyaniline
AERE et.al.	Li/polymer/V_6O_{13}
Altus (Duracell)	Li/$LiAlCl_4$:SO_2/$CuCl_2$
Covalent Associates	Li/organic/MX
EIC	Li/organic/TiS_2
Honeywell	Li/organic/V_2O_5
Hydro Quebec, et.al.	Li/polymer/TiS_2,MnO_2
JPL	Li/organic/TiS_2,$NbSe_3$
NSWC	Li/SO_2Cl_2/C

UNIVERSITY	
U. Penn.	Zn/aqueous/polyaniline Li/organic/polyacetylene
Northwestern U.	Li/polymer/TiS_2, V_2O_5
U. Rome	Li/polymer/MX
U. Munich	Li-Al/organic/MX
Imperial College	Li/polymer/$V6O_{13}$
Tech. U. Denmark	Li/polymer/$V6O_{13}$, TiS_2

TABLE II

RECHARGEABLE LITHIUM SYSTEMS COMPARISON

	----------Energy Density----------		
Material	Primary Theory	Secondary Theory	Secondary Practical
TiS_2	19.3	12.5	3.13
MoS_2	17.1	10.9	2.73
a-MoS_3	24.6	14.2	3.56
V_2O_5	18.4	13.3	3.31
V_4O_9	28.1	16.3	4.08
V_6O_{13}	20.4	13.4	3.35
V_6O_{13}	34.4	18.2	4.56
$V0.5Cr0.5S_2$	24.1	14.9	3.72
$V0.25Cr0.75S_2$	24.1	14.9	3.72
a-V_2S_5	28.2	15.4	3.84
CuS	20.7	12.0	3.01
λ-MnO_2	38.9	21.7	5.43
$LiMn_2O_4$	22.4	15.2	3.80
$NbSe_3$	26.2	14.1	3.52
Cr_3O_8	32.4	19.8	4.95
MoO_3	28.9	16.9	4.22

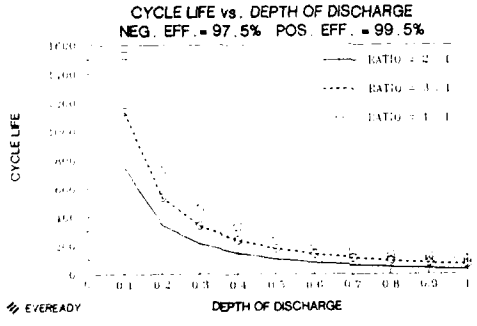


Fig. I: Dependence of cycle life on depth of discharge as a function of negative-to-positive ratio. Assumed negative efficiency = 97.5%; assumed positive efficiency = 99.5%.

(1410H)

Abstract No. 45

NEW MOLYBDENUM CHALCOGENIDES AS CATHODES FOR RECHARGEABLE Li BATTERIES

D. M. Pasquariello, E. B. Willstaedt and K. M. Abraham

EIC Laboratories, Inc.
111 Downey Street
Norwood, MA 02062

INTRODUCTION

A recent interest of our laboratory has been the investigation of novel molybdenum chalcogenides for use as secondary Li battery cathodes. This interest grew out of our earlier work with MoS_3 (1,2) in which we observed a high initial capacity (>2 Li/Mo), but rapid capacity loss as cycling proceeded. Alternate molybdenum chalcogenides with higher capacity and improved rechargeability have been sought. Some of the results of this research are presented herein.

EXPERIMENTAL

The molybdenum oxysulfides $MoOS_2$ and MoO_2S were prepared by the decomposition of $(NH_4)_2MoO_2S_2$ and $(NH_4)_2MoO_3S$, respectively, at ~300°C in an Argon atmosphere. $MoSe_3S$ was obtained as a precipitate when a 50:50 (v/o) mixture of H_2S and H_2Se was bubbled through a solution of ammonium molybdate in $NH_{3(aq)}$ (3,4). MoS_3 was prepared by thermal decomposition of $(NH_4)_2MoS_4$ (5).

X-ray diffraction was used to determine the amorphous nature of the solids, and their stoichiometries were established by elemental analysis. Chemical reactivity with Li was tested by using n-butyllithium (6). Electrochemical evaluation was performed using laboratory test cells of the type described elsewhere (3,4). A tetrahydrofuran (THF):2-methyl-tetrahydrofuran (2Me-THF)-$LiAsF_6$ mixed electrolyte was used (7). The cell configuration was Li/THF:2Me-THF-$LiAsF_6$ (1.5M)/molybdenum chalcogenide. In the case of the oxysulfides, the cathode composition was 60 w/o MoO_xS_{3-x}:30 w/o C:10 w/o Teflon. The data cited here for MoS_3 and $MoSe_3S$ were collected using cathodes containing 85 w/o of the chalcogenide:10 w/o C:5 w/o Teflon. Basically similar cycling behavior was observed for cathodes containing higher amounts of carbon. In all cases the cells were cathode-limited and electrolyte flooded. Cell cycling was performed galvanostatically at room temperature between the limits of 3.0V and 1.6V.

RESULTS AND DISCUSSION

All of the molybdenum chalcogenides we have investigated are amorphous. $MoOS_2$ and MoO_2S were prepared according to the reactions shown in equations [1] and [2].

$$(NH_4)_2MoO_2S_2 \xrightarrow{300°C} 2NH_3 + H_2O + MoOS_2 \qquad [1]$$

$$(NH_4)_2MoO_3S \xrightarrow{300°C} 2NH_3 + H_2O + MoO_2S \qquad [2]$$

Elemental analysis showed the compositions of these materials to be $MoO_{1.2}S_{1.7}$ and $MoO_{1.7}S_{0.95}$, respectively. Reaction of the oxysulfides with n-butyllithium indicated that the maximum Li insertion capability is 3.5 Li/Mo for $MoOS_2$ and 3.0 Li/Mo for MoO_2S. Typical cycling curves obtained for a Li/$MoOS_2$ cell are shown in Figure 1. The initial discharge capacity was 1.86 Li/Mo. Approximately 25% of this capacity was irrecoverable in the first charge so that a capacity of 1.39 Li/Mo was obtained in the second discharge. The recharge efficiency was 100% from the second cycle to the last. As shown in Figure 2, the capacity fade rate of the $MoOS_2$ cathode was very low from the second cycle onwards. The cycling behavior of MoO_2S resembled that of $MoOS_2$. As the data in Figure 2 show, a capacity of 1.59 Li/Mo was obtained for a Li/MoO_2S cell in the first discharge. This decreased to 0.95 Li/Mo in the second cycle; but, subsequently the capacity fade rate was very low. More than 150 deep discharge/charge cycles have been demonstrated.

In Table 1 we compare the first discharge capacities, mid-discharge potentials and quasi-theoretical specific energies of the molybdenum oxysulfide cells with those of two other molybdenum chalcogenide Li cells we have investigated, namely Li/MoS_3 (2) and Li/$MoSe_3S$ (3,4). The Li/MoS_3 cell has a very high initial specific energy of 720 Wh/kg. However, as the cycle life data in Figure 2 show, it exhibits the highest capacity fade rate of the four molybdenum chalcogenide cells. The Li/$MoSe_3S$ cell has an intermediate rate of loss of capacity per cycle. After about 100 cycles, its specific capacity was about the same as in the oxysulfides. The Li/ molybdenum oxysulfide cells differ substantially from both the Li/MoS_3 and Li/$MoSe_3S$ systems in that they maintain a steady level of cathode utilization following the first cycle. The molybdenum oxysulfides seem to have paved the way for a variety of hitherto unidentified transition metal oxysulfide cathodes for secondary lithium batteries.

ACKNOWLEDGEMENT

This work was supported by the U.S. Army, Contract No. DAAL01-87-C-0378, under the SBIR program.

REFERENCES

1. K. M. Abraham and S. B. Brummer, "Secondary Lithium Cells" in Lithium Batteries, J. P. Gabano ed., Academic Press, NY (1983).

2. G. L. Holleck, K. M. Abraham, P. B. Harris, J. L. Goldman, J. Avery, M. W. Rupich and S. B. Brummer, Proceedings of the 30th Power Sources Symposium, Atlantic City, NJ, 1982, p. 68.

3. K. M. Abraham, D. M. Pasquariello, and G. F. McAndrews, J. Electrochem. Soc., 134, 2661 (1987).

4. D. M. Pasquariello, and K. M. Abraham, Mat. Res. Bull., 22, 37 (1987).

5. A. J. Jacobsen, R. R. Chiannelli, S. M. Rich and M. S. Whittingham, Mat. Res. Bull., 14, 1437 (1979).

6. M. B. Dines, Mat. Res. Bull. 10 , 287 (1975).

7. K. M. Abraham, D. M. Pasquariello, and F. J. Martin, J. Electrochem. Soc., 133, 661 (1986).

TABLE 1

SPECIFIC ENERGIES OF SECONDARY Li BATTERY COUPLES

Cell	Material Utilization (Li/mole of cathode)	Mid-discharge Voltage (V)	Quasi-theoretical Specific Energy (Wh/kg)
Li/MoS_3	3.0	1.9	720
Li/$MoSe_3S$	4.0	1.75	477
Li/$MoOS_2$	1.9	1.92	515
Li/MoO_2S	1.6	1.92	466

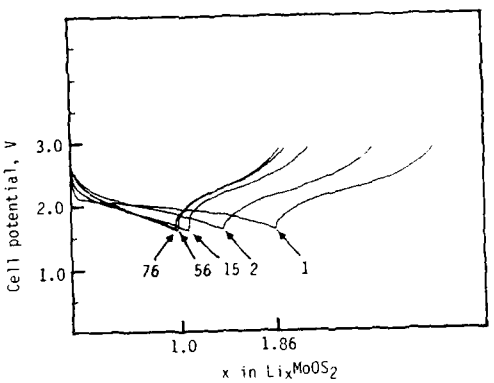


Fig. 1. Room temperature cycling curves for the $Li/MoOS_2$ cell. Current density was ± 0.5 mA/cm^2 for all cycles.

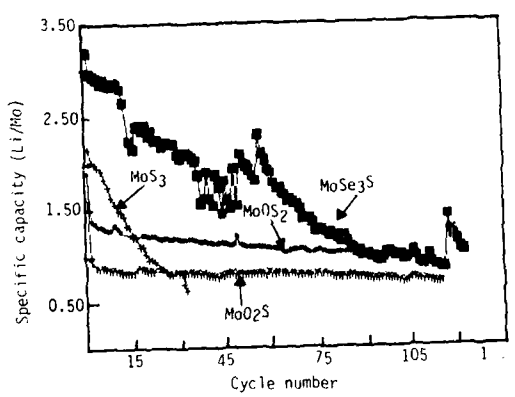


Fig. 2. Capacity vs. cycle number for molybdenum chalcogenides.

Abstract No. 46

ELECTROCHEMICAL STUDIES ON TiS_2 AND $NbSe_3$ CATHODE MATERIALS

B. V. Ratnakumar, G. Nagasubramanian,
S. Di Stefano and C. P. Bankston

Jet Propulsion Laboratory
4800 Oak Grove Drive
Pasadena, CA 91109

Niobium triselenide and titanium disulfide are two of the well developed positive electrodes for ambient temperature Li rechargeable cells. Both have ideal layered structure for reversible intercalation of large amounts (one equivalent in TiS_2 and three equivalents in $NbSe_3$) of Li at high positive potentials as well as for rapid transport of Li inside the lattice. Lithium-titanium disulfide and lithium-niobium triselenide cells thus offer high energy densities at fair to good power densities and long cycle life and hence are being evaluated at JPL for space applications. A detailed study on the mechanism and kinetics of $NbSe_3$ reduction was carried out earlier (1,2). Here we report the results of a comparative study on the kinetic parameters as well as the diffusion coefficient of Li in TiS_2 and $NbSe_3$.

$NbSe_3$ and TiS_2 were prepared by the reaction between chalcogenide vapor and valve metal. TiS_2 electrodes were made by applying the paste of TiS_2 powder and EPDM binder (dissolved in cyclohexane) onto an expanded Ni screen acting as current collector. $NbSe_3$ electrodes were made without any binder as described earlier (1,2). The electrodes were tested in glass prismatic cells with 1.5 M $LiAsF_6$/solution in 2Me-THF as the electrolyte and Celgard 3501 as separator. All the operations were carried out in an argon-filled dry box.

Both dc and ac electrochemical techniques such as linear polarization, linear sweep voltammetry and ac impedance were adopted to obtain the kinetic parameters including exchange current density, transfer coefficient, and diffusion coefficient. Diffusion coefficients of Li were also measured from chronoamperometry (3) and current-pulse, open-circuit potential relaxation techniques (4).

The ac impedance spectrum (Nyquist plot) of TiS_2 (Figure 1) contains a single relaxation loop corresponding to the intercalation of (one equivalent of) Li and a distinct mass transfer impedance characterized by a linearity, with slope close to unity, between real and imaginary components of the impedance. The ac impedance spectrum of $NbSe_3$ is rather complex with two relaxation loops corresponding to the two steps in the reduction of $NbSe_3$ and with mass transfer polarization also setting in in a partially discharged electrode (1,2). These data have been analyzed to obtain the values of exchange current density, cell internal resistance, and diffusion coefficient of Li.

Linear polarization curves yield the values of charge transfer resistance for both TiS_2 as well as $NbSe_3$. Linear sweep voltammetric curves of TiS_2 (Figure 2) and $NbSe_3$ (Figure 5 in Reference 2) exhibit limiting current at overpotentials $\geq$ 500 mV characteristic of diffusion governed processes. The kinetic parameters of TiS_2 have been directly calculated from the Tafel plot corrected for mass transfer polarization. Analysis of the linear sweep voltammetric curve is not straight forward in the case of $NbSe_3$ due to two overlapping charge transfer processes and was carried out as described earlier (2).

Finally, chronoamperometric curves were generated for $NbSe_3$ (virgin as well as partially discharged) and TiS_2 by applying a potential corresponding to diffusion limited regime. Also open-circuit potential relaxation after the interruption of galvanostatic pulse was monitored (Figure 3) to calculate the diffusion coefficients of Li inside the cathode. All the kinetic parameters thus obtained for TiS_2 and $NbSe_3$ are tabulated in Table 1.

ACKNOWLEDGEMENT

The work described here was carried out at the Jet Propulsion Laboratory, California Institute of Technology, under contract with the National Aeronautics and Space Administration. One of the authors (B. V. Ratnakumar) acknowledges the National Research Council for providing his Research Associateship during this work.

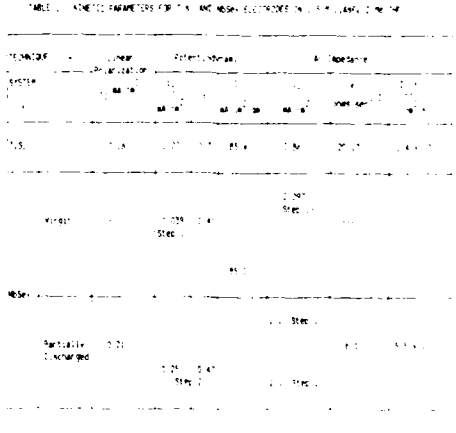
REFERENCES

1. B. V. Ratnakumar, C. L. Ni, S. Di Stefano, R. B. Somoano, and C. P. Bankston, Proc. Lithium Batteries, Electrochemical Society Fall Meeting, Honolulu, HI, October 19-23, 1987.

2. B. V. Ratnakumar, C. L. Ni, S. De Stefano, R. B. Somoano and C. P. Bankston, Submitted for publication.

3. Allen J. Bard and Larry R. Faulkner, "Electrochemical Methods, Fundamentals and Applications," John Wiley & Sons, Inc., New York, 1980, Ch. 5 and references therein.

4. S. Basu and W. L. Worrell, in J. N. Mundy, P. D. Vashita and G. K. Shenoy (Eds), Fast Ion Transport in Solids, North-Holland, Amsterdam, 1979, p. 149.



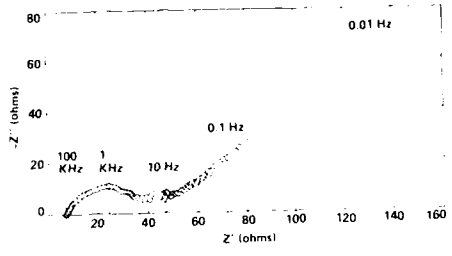


Fig. 1. Nyquist plot of 10 mAh prismatic TiS_2 electrode (area: 1 cm^2) in 1.5 M $LiAsF_6$ / 2 Me-THF.

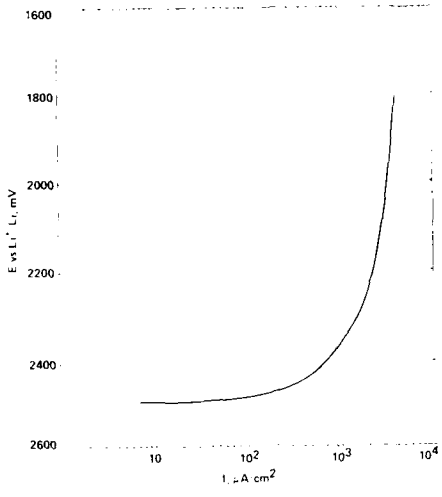


Fig. 2. Potentiodynamic curve of 10 mAh prismatic TiS_2 electrode (area: 1 cm^2) in 1.5 M $LiAsF_6$ /2 Me-THF at 0.5 mV/s.

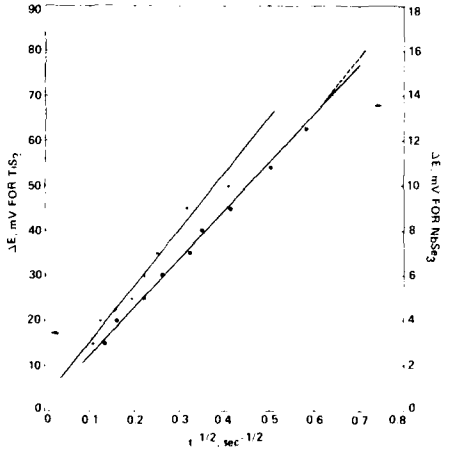


Fig. 3. Recovery of open-circuit potential of 10 mAh TiS_2 and 7 mAh $NbSe_3$ electrodes (area: 1 cm^2) in 1.5 M $LiAsF_6$ /2 Me-THF after interrupting a galvanostatic pulse of 3 mA/cm^2 for 15 s.

Abstract No. 47

DEVELOPMENT OF OVERCHARGE TOLERANCE IN Li/FeS and Li/FeS_2 CELLS

T. D. Kaun, T. F. Holifield,
M. Nigohosian*, and P. A. Nelson
Argonne National Laboratory
Chemical Technology Division
Argonne, IL 60439-4837

Li-alloy/FeS_x battery cells[1] with molten electrolyte currently require an electronic charge/equalizer to protect the cells from destructive overcharging. The development of Li/FeS_x cells which are overcharge tolerant would allow the elimination of electronic safeguards and aid battery development, especially for a bipolar design. An earlier innovation provided cells that could be overcharged at full battery charge current for a finite capacity.[2] The development to be reported on here is an additional unlimited trickle-charge tolerance. The mechanism behind the overcharge tolerance involves dependence upon a self-discharge rate controlled by the activity of the Li-alloy electrode. The proposed "lithium-shuttle" self-discharge mechanism involves (1) dissolution of Li^+ at the Li-alloy electrode surface, (2) diffusion to across the separator to the positive electrode, and (3) discharge of the Li^+ (possibly Li_2^+) to reduce the positive electrode capacity. We have investigated the controlling parameters of this mechanism, as well as operated compact prismatic cells to exhibit its effectiveness.

EXPERIMENTAL

Parametric investigations of the lithium-shuttle mechanism were conducted by a potentiometric method using a three-electrode cell within a He glovebox. A Li-alloy working electrode (e.g., Li-Al, LiAlSi, LiAlFe) of 0.25 cm^2 was positioned versus a counter electrode of Li-Al or FeS, 10 Ah, in about 100 g molten salt (e.g., LiF-LiBr-LiCl). Using a PAR 173 potentiostat, potentials of the working electrode were maintained in a range of 0 to -270 mV versus an α-Al+βLi-Al reference electrode to establish a self-discharge rate for a set of physical parameters (temperature, electrolyte composition, etc.). Steady-state self-discharge rates were established for >1/2 h by following a strip-chart recording.

Overcharge tolerance in Li/FeS_x cells was evaluated by galvanic and coulometric methods. The overcharge tolerant cells have Li-alloy electrodes which are modified to exhibit a bimodal stepwise change in Li-activity. Approximately 10% of the lithium capacity of the Li-Al electrode was replaced by Li-Al_5Fe_2.[3] These compact prismatic bicells (6-25 Ah capacity) have electrodes that are 8.7-cm high x 6.3-cm wide. The separator (100 cm^2) consists of MgO/electrolyte powders that have been cold-pressed into a plaque of 2.5-mm thickness. After assembly in an Ar glovebox, the cells are sealed with a BN-powder feedthrough. Cells were generally charged at 25 mA/cm^2 and discharged at 50 mA/cm^2. Overcharge tolerance was evaluated by establishing a trickle charge of 2 to 5 mA/cm^2 while the Li-alloy electrode exhibited electrode potentials (vs. Ni_3S_2 reference electrode) which are associated with the $Li_5Al_5Fe_2$ electrode (50 to 100 mV vs. Li^+). Under cycling to various charge voltage cutoffs, coulombic cell efficiency also indicated self-discharge rates for the normal capacity and overcharge states.

RESULTS AND CONCLUSIONS

The viability of developing Li/FeS_x cells with overcharge tolerance was indicated from the results of the potentiometric experiments. As shown in Fig. 1, significant rates of self-discharge (up to 20 mA/cm^2) were established by polarizing a Li-alloy electrode in molten LiF-LiCl-LiBr (22:31:47 mol%) at ~500°C. Appreciable self-discharge rates of 2-5 mA/cm^2 were attained at about -200 mV vs. the LiAl reference electrode. This potential is safely away from that for the deposition of Li^+ or formation of liquidus Li alloys. The Li-Al_5Fe_2 electrode is well suited for this potential range and maintains a stable electrode structure. Other alloys such as Li-Al, Li-Si, and Li-AlSi are less desirable due to variations in potential with composition. The effect of temperature on the lithium-shuttle mechanism is significant; a 50°C change can double the self-discharge rate. Other factor, such as electrolyte composition and separator thickness and porosity also affect the rate of self-discharge by the lithium shuttle mechanism. The dominance of the Li-electrode potential permits flexibility in establishing the remaining cell design factors.

The tests of modified cells for overcharge tolerance have verified the efficacy of the lithium-shuttle mechanism to provide sufficient levels of overcharge tolerance. The unique combination of overcharge capacity and unlimited tolerance of a trickle charge has been demonstrated. Modified cells have been operated for >200 cycles without the MgO separator shorting. A bimodal self-discharge rate is exhibited by the Li-Al + 10 mol% $Li_5Al_5Fe_2$/LiF-LiCl-LiBr(MgO)/FeS cell (6 Ah capacity) operated at 475°C. When charged to a 1.47 V cutoff, the cell exhibits 99+% coulombic efficiency and a self-discharge rate of 0.2-0.4 mA/cm^2. Due to a 150-200 mV step in Li-electrode potential by charging the overcharge capacity, the cell coulombic efficiency for a 1.57 V charge cutoff is noticeably reduced to about 93% (coulometric testing). As shown in Fig. 2, in the overcharge state, a trickle charge of 3 mA/cm^2 continues (for 4-8 h) without polarization of the sulfide electrode. (Excessive polarization of an FeS electrode results in deposition of iron in the separator to short the cell.) An additional 10-20% charge capacity (beyond the overcharge capacity) is tolerated under a condition of trickle charge balanced by self-discharge (galvanostatic testing). Similar overcharge tolerance (2-3 mA/cm^2) has been demonstrated for the LiAl + 10 mol% Li_5Al_5Fe/LiCl-LiBr-KBr(MgO)/upper plateau FeS_2 cell at 400°C. Overcharge tolerant Li/FeS_x cells would enable charge capacity equalization of battery cells without equalization electronics. The bimodal self-discharge rate allows a "weaker" cell to accept trickle-charge capacity at high efficiency, while cells in "overcharge" assume a static state-of-charge. The modified cells can lead to more reliable battery operation which, in turn, enhances durability and lowers cost.

ACKNOWLEDGMENT

This work was done under the auspices of the U.S. Department of Energy, Energy Systems Storage Branch, under contract W-31-109-Eng-38.

REFERENCES

1. T. D. Kaun, L. Redey, and P. A. Nelson, "Molten-Salt Battery Advances," Proc. of the 22nd IECEC, Philadelphia, PA, pp. 1085-1090 (1987).

2. T. D. Kaun and A. A. Chilenskas, U.S. Patent 4,324,846, issued April 13, 1982.

3. T. D. Kaun, U.S. Patent 4,158,720, issued June 19, 1979.

*Co-op Student, University of Illinois-Chicago.

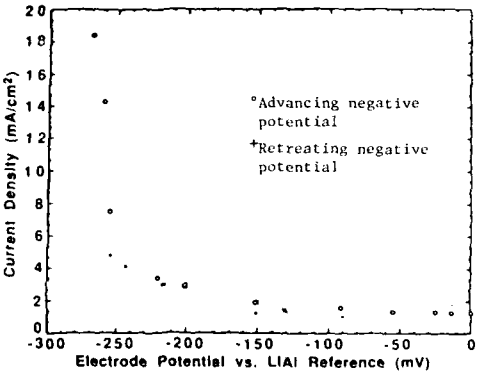


Fig. 1. Steady-state cell self-discharge rates for a Li-Al working electrode in LiF-LiCl-LiBr at 511°C.

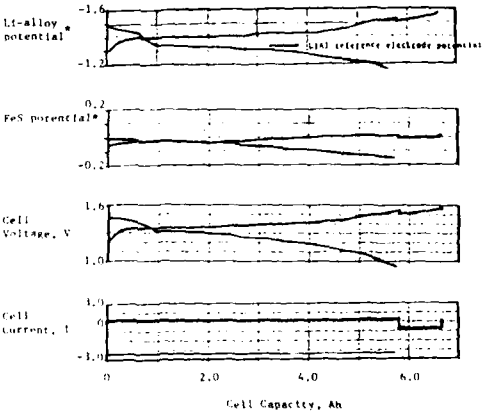


Fig. 2. Electrode potentials* (vs. Ni_3S_2 reference) of a Li/FeS cell during discharge (bottom) and successive charge with overcharge tolerance test (top). Test indicates 3 mA/cm² trickle-charge tolerance at 475°C.

Abstract No. 48

CHEMICAL OVERCHARGE/OVERDISCHARGE PROTECTION FOR Li-ALLOY/TRANSITION-METAL MONOSULFIDE CELLS

Laszlo Redey
Argonne National Laboratory
Chemical Technology Division
9700 S. Cass Ave., Argonne, IL 60439

BACKGROUND

The present lithium-alloy/metal sulfide cells require the careful monitoring of an experimentally established charge cutoff voltage limit to prevent overcharge of the cell.

Maintaining the charge voltage at or below the voltage limit and simultaneously reaching equal capacity in each serially connected cell of a lithium/metal sulfide battery over many cycles are difficult tasks. To overcome this difficulty, a special integrated charger/battery system has been developed [1]. Ideally, the cell/battery overcharge control, however, should rely on a built-in chemical mechanism that furnishes the cells with an inherent overcharge tolerance.

For lithium-alloy/disulfide cells, chemical overcharge protection by a polysulfide shuttle mechanism has been proposed [2]. This mechanism, however, is not available in monosulfide cells. For lithium-alloy/monosulfide cells, two phenomena suggest a possible method of chemical overcharge protection: dissolution of lithium from the negative electrode [3,4] and the associated self-discharge of the cell.

EXPERIMENTS AND RESULTS

To explore the possibility of chemical overcharge protection in monosulfide cells, several LiAlSi/FeS cells were built and tested. One of them, which is described here, was built according to the following parameters:

Negative electrode: $Li_{1.30}Al_{0.86}Si_{0.14}$, 1.54-mm thick, 115 mAh/cm^2 cycled capacity (=NCYC).
Separator: 9.6LiF-22.0LiCl-68.4LiBr + 25MgO (in wt%), 2.0-mm thick.
Positive electrode: $Li_{0.52}Fe_{1.10}S_{1.24}$, 1.92-mm thick, 194 mAh/cm^2 cycled and unused capacity.

The cell was cycled at 475°C in a glove box which contained He of about 1-ppm O_2/H_2O impurity level. The electrode material formulas represent electrode compositions that are normalized to 1 mole of the negative matrix material (Al and Si). Figure 1 shows typical charge/discharge cell voltage curves along with the potentials of the positive and negative electrode as measured with a reference electrode during charge. Three characteristic sections can be distinguished on the graph. These sections are associated with three different capacity ranges of the negative electrode and are identified by NUNC, NCYC, and NPRC symbols, which represent the unused-, cycled-, and protecting-capacity portions of the lithium alloy. As Fig. 1 shows, each section is associated with an important feature of the cell.

DISCUSSION

Out of the three sections in Fig. 1, overcharge protection is the most important for the present discussion. In this section, the charge curve reaches a constant cell voltage. This charge curve was obtained at a charge current less than the highest possible self-discharge rate under these conditions. The highest possible self-discharge rate is, in turn, related to the potential of the negative electrode and is controlled by mass-transport limitations. Figure 1 shows a charge half-cycle in which the current density was set back to 10 mA/cm^2 from 100 mA/cm^2 when the cell voltage reached 1.63 V. The cell is designed such that the ratios of the capacity sections for the positive and negative electrodes (Fig. 2) dictate a low self-discharge rate in the NCYC section and high rates toward the end of the charge in the NPRC section. Achieving the high self-discharge rate is facilitated by the rapid decrease of the negative electrode potential, as shown by the curve in Fig. 1. At the same time, the potential of the positive electrode increases only slightly and remains well below the critical value, which is about 1.60 V vs. Li-Al under the condition of the experiment.

The flat end section of the charge curve indicates a steady state in the cell. The steady-state condition is brought about by a lithium shuttle mechanism in which the lithium that dissolves from the negative electrode and diffuses to the positive electrode is then consumed at the positive electrode by a chemical reaction. The high rate of this reaction in the NPRC section, facilitated by proper cell design and charge conditions, counterbalances the anodic and cathodic formation of the electrode active materials and terminates the charge in the steady state before the onset of the detrimental anodic dissolution of the positive electrode components. The resulting zero percent coulombic efficiency of the charge current under this condition of the lithium shuttle mechanism results in overcharge tolerance and provides a means for cell capacity equalization in batteries.

At higher charge current densities, however, when the lithium shuttle can not keep up with the charge current and a sharp increase of the potential of the positive electrode occurs toward the end of charge. The broken line in Fig. 1 shows the increasing cell voltage due to the rising potential of the positive electrode when the charge current density was kept constant at 100 mA/cm^2.

The lithium-poor phases of the negative electrode in the NEGUN section, i.e., the α-Al and LiAlSi (1:1:1) phases, have poor charge/discharge kinetics; therefore, these are not normally utilized in cycling. The NUNC section, however, can be used for overdischarge protection when it is complemented by an available counterpart capacity in the positive electrode (PUNC).

ACKNOWLEDGMENT

This work was supported by the U.S. Department of Energy, Office of Energy Storage under contract No. W-31-109-ENG-38. The author is grateful to Dr. P. A. Nelson for his encouragement and support.

REFERENCES

1. W. H. DeLuca, A. A. Chilenskas, and F. Hornstra, Proc. of 14th IECEC, Boston, MA, 5-10, 1979, Vol. 1, p. 665 (1979).

2. L. Redey, Proc. of the Joint Internat'l. Symp. on Molten Salts, The Electrochemical Society, Pennington, NJ, Proc. Vol. 87-7, p. 631 (1987).

3. G. J. Reynolds, M. C. Y. Lee, and R. A. Huggins, Proc. of the 4th Internat'l. Symp. on Molten Salts, Proc. Vol. 84-2, The Electrochemical Society, Pennington, NJ, p. 519 (1984).

4. L. Redey, to be published.

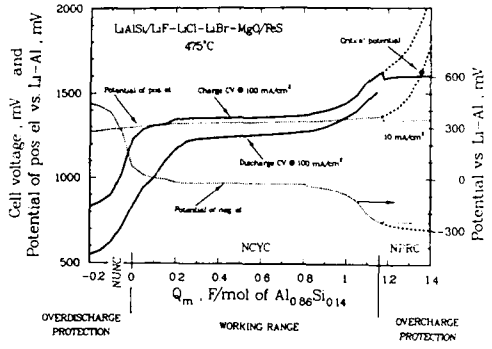


Fig. 1. Charge/discharge and electrode potential curves of an overcharge/overdischarge tolerant LiAlSi/FeS cell.

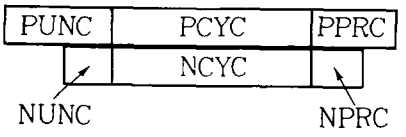


Fig. 2. Capacity ranges of the positive and negative electrodes and their relationships in the cell shown in Fig. 1. Capacities of the ranges are in proportion to the areas of the marked fields.

Abstract No. 49

LITHIUM/DISULFIDE CELLS CAPABLE OF LONG CYCLE LIFE

T. D. Kaun, T. F. Holifield and W. H. DeLuca
Chemical Technology Division
Argonne National Laboratory
Argonne, IL 60439-4837

A Li/upper plateau (U.P.) FeS_2 battery has intrinsic high-performance characteristics: high theoretical specific energy (~500 Wh/kg) and achieved high power (200-300 W/kg). Earlier advances in the Li/U.P. FeS_2 cell with LiCl-LiBr-KBr electrolyte resulted in high performance and capacity stability.[1] These advances enabled cells with 40% of theoretical specific energy to be realized through operation of high energy density electrodes.[2] Now, lithium/disulfide cell tests have demonstrated a 1000 cycle-life capability. Development of overcharge and overdischarge tolerant battery cells has reinforced their durability. Therefore, the performance and durability of the lithium/disulfide battery are highly suited to an electric van application. The results of a battery design study for the IDSEP Van[2] are reported.

EXPERIMENTAL

Prismatic bicells (12- and 24-Ah capacity) with BN-felt separator area of 100 cm^2 (Kenecott Corp.) were fabricated. Cold-pressed plaques of electrolyte/MgO powder (Culigan) were substituted for BN felt in some tests. The electrodes (8.7-cm high x 6.3-cm wide) were contained behind perforated-sheet current collectors--molybdenum for the central FeS_2 electrode and 1008 steel for the two Li-Al electrodes. The iron disulfide electrode contained FeS_2, typically with 15 mol% CoS_2 additive, for a total theoretical capacity of 12-24 Ah (on the upper voltage plateau). The slurry-formed Li-Al electrodes contained 53 at.% Li-Al alloy for 15-30 Ah capacity with 0.9-Ah/cm^3 loading density. Cells were assembled and operated in an Ar glovebox. The electrolyte (Anderson Physics Lab.) was added to the cells in the molten state. Cycle-life testing at a 8-h charge rate and 4-h discharge rate (50 or 100 mA/cm^2) was controlled between voltage cutoffs of 2.05 and 1.25 V (IR included), respectively. A Ni/Ni_3S_2 reference electrode indicated working-electrode potentials during the deep-discharge cycling. The improved FeS_2 cell has two major changes from earlier designs: a novel electrolyte, 25 mol% LiCl-37 mol% LiBr-38 mol% KBr (m.p. 310°C), rather than 58 mol% LiCl-42 mol% KCl (m.p. 352°C), and a higher loading density (2.4 vs 1.5 Ah/cm^3) for the FeS_2-15 mol% CoS_2 electrode, which is then operated only on its upper voltage plateau (U.P.) (1.75 V vs. Li-Al) rather than its two voltage plateaus (T.P.).

RESULTS AND DISCUSSION

A U.P. FeS_2 cell operated at 400°C has demonstrated a 100% increase in power density and a 50% improvement in energy density and capacity utilization as compared to those of the earlier T.P. FeS_2 cell at 427°C. In a group of five U.P. FeS_2 cells (Table 1), capacity utilization was 80-90%, depending upon discharge rate. The disulfide electrode remained at ≥90% of their initial values throughout the tests. (Coulombic efficiency was 96-99%.) The high utilization of the U.P. FeS_2 capacity provided quite good accounting of the sulfur capacity throughout the cycle-life tests. Excellent cycle-life stability has also been established with the 1000 cycle (7000 h) operation of cell KHP-4 (Fig. 1). No cell capacity loss was exhibited in the first 500 cycles, and thereafter, test facility equipment problems (e.g., glovebox failures) resulted in a 18% decline in capacity after 1000 cycles. A reference electrode indicated that cell capacity had become limited by the Li-alloy electrode. The high specific power capability of the cell was not degraded during the 1000 cycles of operation. Cell resistance vs. depth-of-discharge was unchanged, 0.65 to 0.75 Ω-cm^2 separator area. Coulombic efficiency was 96+%. Apparently, both time- and cycle-related capacity loss mechanisms of the earlier FeS_2 cells have been overcome.

Although cycle-life tests have been at 400°C, Li/U.P. FeS_2 cells have also been operated at 425-450°C for week-long durations without detectable impact on capacity stability. Cells are normally sealed, but cells have operated for months unsealed. There is apparently little, if any, capacity loss through vapor pressure. Open cell operation during periods of poor atmosphere (>1% N_2, O_2) led to cell capacity decline. Degradation of lithium-electrode capacity restricted discharge capacity. Currently, batteries will have to be operated in an inert atmosphere. This could change with development of a hermetic feedthrough.

Abuse tolerant battery cells are desirable for battery durability. Overcharge tolerance can be incorporated into the cell by a "lithium-shuttle" mechanism.[4] Overdischarge protection for the U.P. FeS_2 cell was achieved in a cell whose capacity was limited by the negative electrode (i.e., lithium-limited). With the high loading density of the FeS_2 electrode, the discharge must be restricted to the U.P. FeS_2 capacity to avoid excessive electrode expansion. Earlier, this had been achieved by limiting the discharge cutoff voltage to ≥1.25 V. For battery operation, this requirement is unacceptable. A lithium-limited U.P. FeS_2 cell has been operated with discharge cutoff voltages ranging from 1.0 to 1.3 V and has maintained 99% coulombic efficiency for over 900 cycles.

A design study intended to provide a comparison of advanced battery technologies for the IDSEP electric van[3] was completed for Sheladia Associates. According to design study specifications, the battery was to be sized to meet one of two limits, 700 kg or 600 L. These specifications allowed a Li-alloy/U.P. FeS_2 battery of 120 cells and 610 Ah capacity. Cells contribute about 80% of the battery weight. The battery capacity is 111 kWh at a 20.25 h discharge rate with 1.66 avg. V/cell. Peak specific power of 55 kW could be provided through 95% of discharge capacity. The slow discharge rate for the IDSEP Van application coupled with high-capacity utilization produces a 170 Wh/kg specific energy for a Li/U.P. FeS_2 battery. The IDSEP performance requirement could be met with a Li/FeS_2 battery about one-third the size limits. Such a down-sized battery could provide 400 kg of additional vehicle hauling capacity.

ACKNOWLEDGMENT

This work was done under the auspices of the U.S. Department of Energy, Energy Systems Storage Branch, under contract W-31-109-Eng-38.

REFERENCES

1. T. D. Kaun, Proc. of Joint Int'l. Symp. on Molten Salts, 172nd Electrochem. Soc. Mtg., Vol. 87-7 (1987).

2. T. D. Kaun, J. Electrochem. Soc., 132, 3063 (1985).

3. P. G. Patil and W. J. Walsh, "Battery Requirements for Urban Electric Vans," Proc. of the 21st IECEC, San Diego, CA, pp. 1034-1040 (1986).

4. T. D. Kaun, T. F. Holifield, M. Nigohosian, and P. A. Nelson to be published at this meeting.

Table 1. Cycle-Life Tests of Upper-Plateau Disulfide Electrode Cells*

Cell No., KHP-	Composition of Limiting Electrode	Performance: U.P. Util., %	Performance: Disch. Rate, h	Lifetime: Capacity Charge, %	Lifetime: Cycles
1	FeS_2:CoS_2 (85:15 mol%)	89	4	1	400
3	FeS_2CoS (85:15 mol%)	88	4	4	260
4	FeS_2:CoS_2 (85:15 mol%)	80	2	18	1020
5**	Li-Al, Carbon	55	1.3	10	900
6	FeS_2:NiS_2:Li_2S (50:50:5 mol%)	93	4	5	250

*Prismatic bicells use LiCl-LiBr-KBr (310°C m.p.) with BN-felt separator (100 cm^2) and 400°C operation.

**Furnace malfunction, 3 days at 565°C and remained U.P. FeS_2 cell.

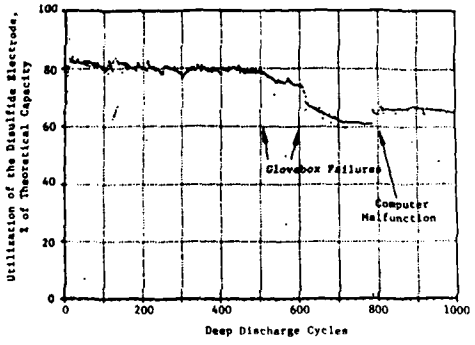


Fig. 1. Cycle life of cell KHP-4, U.P. FeS_2 electrode stability test. Cell capacity became limited by the Li-Al electrolyte after cycle 500.

Abstract No. 50

FUEL CELLS AS ENERGY STORAGE DEVICES FOR MULTIMEGAWATT SPACE POWER SYSTEMS

GRAHAM HAGEY

U.S. DEPARTMENT OF ENERGY
WASHINGTON, D.C. 20545

INTRODUCTION

Fuel cell power systems are a candidate technology for energy storage and multimegawatt burst power (up to 1,000 MW for up to 2,000 seconds) for Strategic Defense Initiative (SDI) applications. SDI fuel cell systems must have both high specific power and high specific energy. Preliminary SDI energy storage system performance goals target a specific power of 2.2 KW/kg and a specific energy of 444 W-hr/kg.[1] Specific power is the most important parameter and determines the high electrochemical performance required by candidate fuel cells.

Of the fuel cell technologies under development, advanced alkaline and solid oxide fuel cells (SOFC) appear capable of achieving the SDI energy storage system performance goals.

SDI ENERGY STORAGE SYSTEMS

SDI system concept studies indicate that power requirements may range from 100's of kilowatts to 1000's of megawatts over time periods from a few seconds to seven years. Power modes are generally described as base load, alert mode and burst mode. Table 1 indicates the typical power levels and power profiles for each mode. A typical SDI energy storage system utilizing a H_2/O_2 fuel cell is shown in Figure 1. A unique attribute which fuel cells have for SDI applications is their ability to recover all consumed reactants. This is accomplished by condensing the fuel cell water, which is a by-product of the power productive process, and subsequently converting the water back into fuel cell reactants. While other energy conversion devices may recover product water, unreacted fuel, such as H_2, is typically lost.

There are two methods for electrolyzing the water: one is to use a separate electrolyzer and fuel cell, as shown in Figure 1; the other is to combine the functions in a single, electrochemically reversible fuel cell. The approach selected is dependent on a number of factors: system weight, mission requirements, power systems simplicity and reliability, and the capacity of the fuel cell for electrolysis.

Weight is the principal operational constraint for SDI power systems. The limit for burst mode power is the weight of the energy storage system that must be lifted into orbit. At a power level of 100MW the weight of a typical fuel cell energy storage system capable of 1500 seconds of burst power is estimated to be about 100 metric tons. This weight equals the single launch payload capability of a heavy lift launch vehicle.

A discussion of advanced alkaline and advanced SOFC technologies follows.

ALKALINE FUEL CELL

The alkaline fuel cell has been the choice power system of past and present space applications. Alkaline fuel cells are well suited for space power application, offering efficiencies of up to 75 percent*, and potentially high specific power. They have demonstrated the ability to withstand the shock and vibration loads, other factors of launch as well as space power operation in low specific power. United Technologies Corporation (UTC) modified the Bacon alkaline fuel cell in the early 1960s which became the base for the Apollo spacecraft fuel cell power system. UTC alkaline cells were also used for the Space Shuttle Orbiter. The Orbiter power system consists of three power plants, each with 12 kW output. The fuel stack of this power plant has a specific power of 0.5 kW/kg.[2]

During the 1970s, UTC tested lightweight alkaline cell assemblies (12 cells plus cooler) with specific powers up to 4.2 kW/kg and 23 kW/m^2.[2] Current densities up to 9.1 A/cm^2 were achieved in single cells at voltages above 0.5 volt. A peak areal specific power of 30 kW/M^2 at 0.6 volt per cell was achieved at a cell pressure of 620 kPa (90 psia) and a temperature of 120°C.[2]

Under a current Air Force contract, UTC is developing advanced alkaline cells designed to provide specific power up to 27 kW/kg in megawatt-size stacks.[2] This high specific power would be achieved by a combination of cell weight reduction and increasing cell power output at a fixed level of efficiency. The objective for areal specific weight of this cell is 2.64 kg/m^2 (0.54 lb/ft^2). Reduced cell weight would result from the elimination of separate liquid coolers, and the use of lightweight materials and thinner cell components. The goal for total cell thickness is $57x10^{-3}$cm (22 mil). Improved cell performance is achievable from operation at a temperature of 150°C and a pressure of $1.37x10^3$ kPa (200 psia).

ALKALINE FUEL CELL DEVELOPMENT NEEDS - The reduction of stack specific weight is a primary factor in improved cell performance. Weight reduction would be accomplished by the use of lightweight cell components (e.g., electrodes and electrolyte matrix), and by the elimination of liquid coolers. The conventional cooling loop would be replaced by integrating evaporative cooling into the reactant flow passages. The key issue in the development of evaporative cooling is the uniform distribution of the coolant across the face of the cell, which would ensure uniform heat removal and cell temperature.

Improved cell performance is achievable by operation at elevated temperature and pressure. The temperature limits are constrained by cell corrosion and catalyst recrystallization. The pressure limits are constrained by the cross pressure capability of the cell stack and assembly seals, and by the design approach for stack pressure containment.

A reduction in cell internal resistance is expected from the use of a thinner electrolyte matrix (decreased to 0.005 cm). The limit of this reduction is determined by the cross pressure capability of the matrix.

* Lower Heating Value Using H_2 and O_2 Reactants

For missions requiring a rechargeable energy storage system where a reversible alkaline fuel cell system approach is selected, the issue of catalyst durability during reverse operation remains to be resolved.

Verification issues include SDI goals at the system level for specific power, operational life and the magnitude of burst power of multimegawatt stacks.

SOLID OXIDE FUEL CELL (SOFC)

The SOFC offers the potential for high specific power and approximately 70 percent* energy conversion efficiency. The SOFC is a high temperature (1000°C), reactant-gas cooled, solid state system with self-catalytic electrodes. The SOFC has been demonstrated to be reversible for regeneration of O_2 and H_2 from fuel cell produced H_2O.[3]

For SDI applications the only high specific power SOFC concept in design and preliminary research is the monolithic concept originated by Argonne National Laboratory.[4]

The monolithic design is a strong, lightweight honeycomb structure of small cells with thin walls. The small passages, similar to corrugated cardboard, are formed from 0.025 to 0.100 mm (1-4 mil) thick layers of active cell components connected through a bipolar connection plate. The fuel and oxidant flow through alternating passages. The monolithic cell is currently fabricated into an integrated array by simultaneously sintering cell components (anode, cathode, electrolyte matrix and interconnect).

SOFC DEVELOPMENT NEEDS - The SOFC technology development needs relate principally to cell materials compatibility and cell fabrication. Monolithic SOFC fabrication involves the simultaneous sintering of cell components made of different materials with different shrinkage rates and different coefficients of thermal expansion. Simultaneous sintering has caused cracks in the fuel cell electrolyte and interconnect layers, which must be gas tight. The thin walled ceramics, although strengthened by honeycomb type structures, are inherently brittle and potentially subject to thermal and mechanical shock failure. The cell failure mode experienced to date has been microcracking of cell components. Spalling of materials has not been experienced.[4]. The development and fabrication of cells and arrays free of mechanical stresses and gas leaks is necessary.

The design and testing of manifolds to improve the thermal expansion compatibility match of electrodes/electrolyte and to lower interfacial electrical resistances are required to achieve SOFC's theoretical performance potential. Also critical is the development of techniques for improved processing and fabrication of arrays and stacks with appropriate nondestructive qualification methods.[5]

* Lower Heating Value Using H_2 and O_2 Reactants

TABLE 1

Typical Power Requirements for SDI Applications
(Neutral Particle Beam, Free Electron Laser, Kinetic Energy Weapons)

Power Mode	Power Level	Operational Profile
Base Load	0.1-10 MW continuous	7 years
Alert	10-100 MW	On/off - 100 days to 1 year aggregate
Burst	100-1000 MW	200-2000 Sec

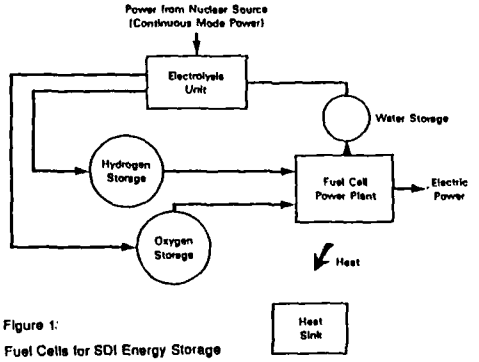


Figure 1:
Fuel Cells for SDI Energy Storage

References

1. Strategic Defense Initiative Multimegawatt Space Nuclear Power Program Summary. U.S. Department of Energy, Assistant Secretary for Nuclear Energy, Office of Defense Energy Projects and Special Applications, April 1986.

2. Private communication of data from United Technologies, January, 1987.

3. Private communications with D. Fee of Argonne National Laboratory, April and September, 1987.

4. "Multimegawatt Space Nuclear Power", D. C. Fee, et. al. ,Annual Report on Monolithic Fuel Cell Technology Development, Argonne National Laboratory, September 30, 1976.

5. Private communication of data and analyses from J. L. Bates, Battelle Pacific Northwest Laboratories, February 1987.

Abstract No. 51

DEVELOPMENT OF MONOLITHIC SOLID OXIDE FUEL CELLS FOR AEROSPACE APPLICATIONS

Nguyen Q. Minh
Allied-Signal Aerospace Company
AiResearch Los Angeles Division
2525, West 190 th Street
Torrance, CA 90504-6099

BACKGROUND

The monolithic solid oxide fuel cell (MSOFC), first proposed by Argonne National Laboratory in 1983, offers excellent prospects for aerospace and space applications owing to its high performance and high power density. In the coflow version, the MSOFC consists of a honeycomb-like array of adjacent fuel and oxidant channels that resemble corrugated paperboard (Fig. 1). Oxidant (air) channels are lined with a cathode, and fuel channels are lined with an anode. A gas-tight layer of electrolyte is located between the anode and cathode. A gas-tight layer of interconnection material connects the anode of one cell to the cathode of the next in electrical series. As seen from Fig. 1, the MSOFC is made of two types of laminated structures, each composed of three ceramics - anode/electrolyte/cathode and anode/interconnector/cathode). The laminated structure containing the electrolyte is appropriately corrugated. In the crossflow version, the gas flow channels form a separate layer for fuel and a separatelayer for oxidant (Fig. 2). The fuel and oxidant flow passages are at right angle to each other. The walls of the corrugations are formed from anode and cathode layers. The crossflow version offers a simpler means of ducting gases in and out of the monolithic fuel cell.

The size of individual cells in the MSOFC is very small. Typically, 1 to 2 mm is the repeat distance from cell to cell. Typical thickness of individual cell component layer is 50 to 100 microns. The small cell size increases the active surface area of the MSOFC and decreases its internal electrical resistance. As a result, the MSOFC has excellent performance and high efficiency. The MSOFC is a lightweight, low volume device. Owing to high surface area and low weight, the power density of the MSOFC is much higher than that of many conventional fuel cells and other electrical generating technologies. At present, the MSOFC employs Y_2O_3-stabilized ZrO_2 for electrolytes, Ni/ZrO_2 for anodes, Sr-doped $LaMnO_3$ for cathodes, and Mg-doped $LaCrO_3$ for interconnectors.

FABRICATION

The MSOFC places stringent requirements on materials and requires significant fabrication development. Fabrication of the MSOFC involves incorporation of four thin ceramic layers (anode, cathode, electrolyte, and interconnection) into a self-supporting monolithic structure. A fabrication scheme for the MSOFC must incorporate each material such that no thermal or chemical environment in any fabrication step destroys desired material characteristics of any of the individual layers. Two methodologies are currently being developed for the fabrication of the MSOFC: tape casting (Argonne) and hot roll milling/calendering (Allied-Signal Aerospace). In these methodologies, the MSOFC is fabricated by forming thin ceramic layers as green bodies, laminating them into trilayer composites, forming the monolithic structure from the trilayer composites, and sintering the structure at elevated temperature. In general, the fabrication of the MSOFC involves two important and critical aspects: (i) determination of processing/structure/property relationships for each cell component layer, and (ii) development of a methodology for cofiring all layers under the same conditions.

To date, Argonne has demonstrated the feasibility of fabricating the MSOFC by the tape casting technique. Stacks of the crossflow monolithic design (up to 3 W) have been fabricated and operated by Argonne. At Allied-Signal Aerospace, the hot roll milling technique is being developed and optimized for the MSOFC. Single cells (anode/electrolyte/cathode) and stacks have been fabricated. Figure 3 shows a micrograph of a polished single cell fabricated by hot roll milling.

AEROSPACE APPLICATIONS

If the MSOFC can grow from its present early stage to a full fledged power system, its first practical uses are likely to come in high technology, high cost applications such as aviation and space. Potential space and aerospace applications for the MSOFC include housekeeping power, burst power, energy storage (solar), airbreathing and non-airbreathing power, and propulsion/power intergration. A regenerative fuel cell system based on the MSOFC looks attractive for space applications. The system operates like a secondary battery and is applicable to darkside energy storage for solar photovoltaics. Regenerative capability of the MSOFC has been demonstrated.

ACKNOWLEDGMENTS

This work is supported in part by Gas Research Institute and Southern California Edison. The author would like to acknowledge the contributions of F. Liu, P. Staszak, T. Stillwagon, and J. Van Ackeren.

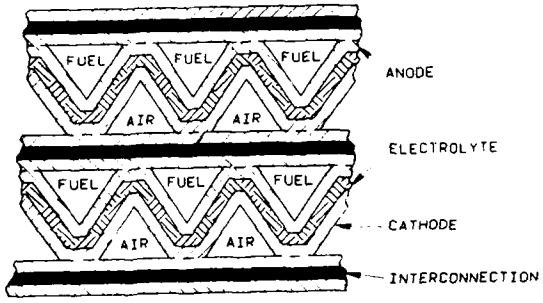


Fig. 1. Coflow Version of Monolithic Solid Oxide Fuel Cell Design



Fig. 3. Micrograph of Polished Cross-Section of a Single Cell Fabricated by Hot Roll Milling. From Top to Bottom: Cathode, Electrolyte, Anode.
Original Magnification: 200X.

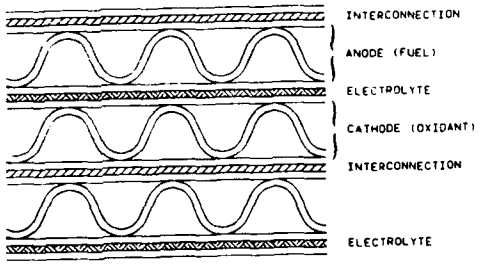


Fig. 2. Crossflow Version of Monolithic Solid Oxide Fuel Cell Design

Abstract No. 52

POLARIZATION STUDY OF FUEL CELL WITH FOUR REFERENCE ELECTRODES

K.Mitsuda, H.Shiota, J.Aragane and T.Murahashi

Central Research Laboratory,
Mitsubishi Electric Corporation
Tsukaguchi-honmachi 8-1-1, Amagasaki-shi,
Hyogo, Japan 661

Introduction:

Current distribution in the plane of a fuel cell has been studied using a mathematical modeling [1]. The polarizations of cathode and anode have been considered to be inhomogeneous in the plane according to the change of gas composition. We present here experimental results which show the inhomogeneous distribution of polarization in the plane of a cell.

We set four reference electrodes (RHE) imbeded in a matrix of a single cell of a phosphoric acid fuel cell at each corner of inlet or outlet of fuel and air. We investigated the change of cathode and anode potentials at each reference position changing gas composition or gas utilization.

Experimental:

The size of each electrode and matrix was 100 cm2 for a cathode,144 cm2 for an anode and 225 cm2 for a matrix and that of reference electrodes was 0.5 cm2. The arrangement of these cell components was shown in Fig.1.

Fig.2 shows a cross section view of a cell near the reference electrode. Four reference electrodes were numbered R1,R2,R3 and R4 as shown in Fig.1. The lead wires were inserted near the reference electrode which was contacted with the cathode or the anode. They were numbered C1,C2,C3 and C4 for the cathode, and A1,A2, A3 and A4 for the anode. The voltages between Cx-Rx,Ax-Rx,Cx-Ax and Rx-Ry (x,y =1,2,3,4) were measured. Ohmic losses were measured by current interruption method and the voltages were corrected to iR-free values.

H2,SRG (H2 80% + CO2 20%),RGC2 (H2 80% + CO2 18 % + CO 2%), RG10 (H2 10% + CO2 90%) or RG20 (H2 20% + CO2 80%) was used as a fuel. The single cell test was conducted at 190°C or 150°C under atmospheric pressure.

Results:

Fig.3 shows potential changes of cathode and anode at each position with H2 utilization of SRG. X-axis shows the position of reference electrodes, and RHE is the reference electrode potential at each position. R1 was indicated as I/I because it was located in the fuel inlet and air inlet corner of the cell. In the simillar way, R2, R3 and R4 were indicated as I/O, O/I and O/O, respectively.

In Fig.3, the potentials of cathode and anode at fuel outlet shifted toward cathodic, when H2 utilization of SRG was increased. At 95% utilization the potentials shifted up to about 500 mV. This means that,at fuel outlet, anode polarization increased and cathode polarization decreased.

It is well known that the corrosion current increases as cathode potential shifts toward cathodic [2]. The potential shift of cathode at fuel outlet is consistent to the observation that corrosion is found at the fuel outlet on a cathode.

The polarization of cathode at fuel inlet was increased when H2 utilization was increased as shown in Fig.3. It was caused by the change of current distribution in the plane of a cell. The current decreases in fuel outlet,and inversely the current in fuel inlet must increase. Then the polarization of cathode increases due to the rise of current density at fuel inlet.

The potential shift at fuel outlet was also increased by CO poisoning. Fig.4 shows the potential changes of cathode and anode by CO poisoning at 150°C, 100mA/cm2. The remarkable increase of an anode polarization at fuel outlet and increase of cathode polalization at fuel inlet were observed. The voltage loss due to poisoning by CO has been explained to be the increase of the polarization of the anode [3]. However, as observed in Fig.4, the voltage loss was also observed as the increase of the polarization of cathode. Because of the inactiveness of anode reaction in fuel outlet, increase of current density at fuel inlet was expected to occur. CO poisoning will have an accelerating effect on the carbon corrosion in the cathode, because the cathode potential shifts to cathodic at fuel outlet.

The potential shift at fuel outlet was not affected by dilution of H2 concentration. Fig.5 shows potential shifts of cathode and anode when several diluted hydrogen gases were used. The anode polarization was increased on the whole due to the decrease of hydrogen partial pressure. On the other hand, the increase of the potential shift at fuel outlet was not appreciable at all.

The results of Fig.3 and Fig.5 are interesting with respect to the fuel gas flow design. At the fuel outlet of return flow [4], where the partial pressure of H2 is lowered, the H2 utilization is reduced compared with that of the case of cross flow. This is important from the corrosive point of view, because cathode potential shifts to cathodic as fuel utilization increases.

Fig.6 (a) shows the potential variations of cathode and anode with redox potentials (H+/H2,H+, O2/H2O) against RHE (the reference electrode at each position). The reference potential at fuel outlet (R3,R4) shifted to anodic vs. R1 potential, and the shift value was equivalent to the potential shifts of cathode and anode in fuel outlet. Then, we can change the expression of Fig.6 (a) to Fig.6 (b), which was standardized by the potential of R1. Here the potential of cathode and anode vs. R1 are not changed at all, inversely the redox potential of H+/H2 or H+,O2/H2O vs. R1 is changed. The redox potentials are changeable by the PH change of the electrolyte (92 mV/PH at 190 C). The acidity of the electrolyte in fuel outlet should be changed to basic.

It is very interesting that the acidity of electrolyte in the plane of a cell could vary from location to location.

Acnowledgement:

This work was supported by Agency of Industrial Science and Technology, Ministry of International Trade and Industry, and New Energy Development Organization (NEDO) , Japan.

References

1.T.L.Wolf et al.J.Electrochem,Soc.,130,48 (1983).
2.A.J.Appleby, Corrosion'86,March 17-21,1986,No.80.
3.H.P.Dhar et al.J.Electrochem,Soc.,133,1574(1986).
4.H.R.Kunz et al.U.S.Patent 3,994,748.

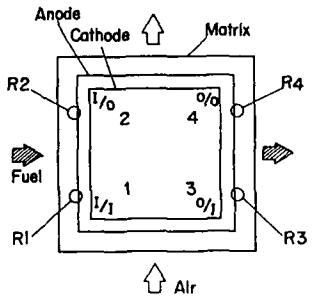


Fig.1 Schematic figure showing arrangement of single cell with four reference electrodes.

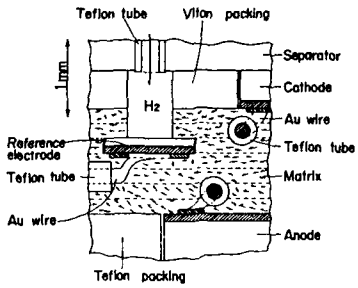


Fig.2 Cross-sectional view showing the position of cathode, anode and reference electrode near a reference electrode.

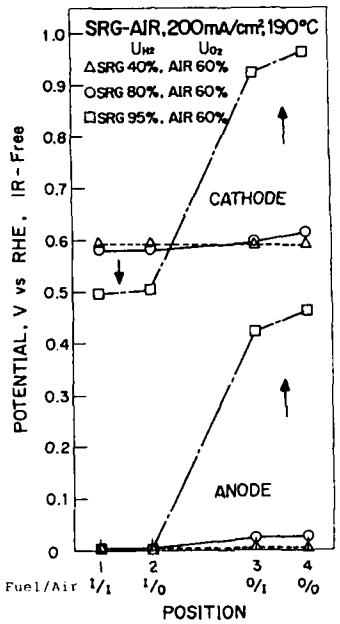


Fig.3 Potential changes of cathode and anode with H2 utilization of SRG.

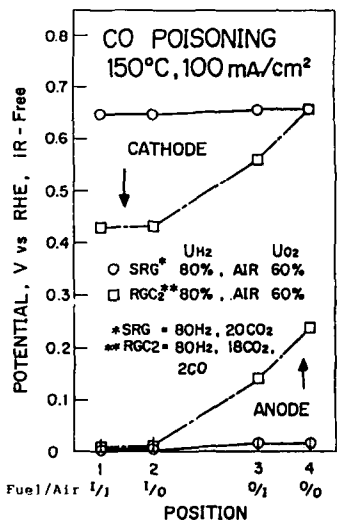


Fig.4 Potential changes of cathode and anode by CO poisoning at 150°C, 100mA/cm2.

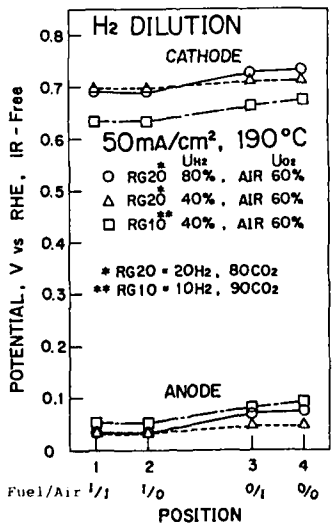


Fig.5 Potential changes of cathode and anode by diluted H2 gas.

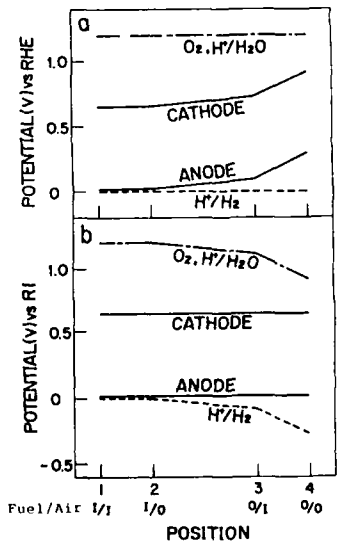


Fig.6 Representative potentials of cathode, anode and redox (H+/H2; O2,H+/H2O),(a) against RHE (the reference electrode at each position),(b) against R'.

EUROPEAN REGENERATIVE FUEL CELL (RFC) TECHNOLOGIES FOR SPACE USE

Francis Baron*, Ralf Philippi**,
Werner Tillmetz**

*) ESTEC, Postbus 299, 2200 Noordwijk, Netherlands
**) Dornier System, Postfach 1360, 7990 Friedrichshafen, W.-Germany

For energy storage and supply in space electrolyzers and fuel cells with very high efficiency and very mature development status are necessary. Within a study performed by Dornier System and funded by ESTEC, (title: Fuel Cell Component Development), European regenerative fuel cell (RFC) systems were investigated.

The technologies are

- mobile alkaline electrolyte systems
  - conventional
  - advanced (e.g. Eloflux technique of VARTA)
- immobile alkaline electrolyte systems
- ion exchange membrane (IEM) systems

For mobile alkaline electrolyte (KOH) electrolyzers as well as fuel cells a very wide know-how exists in Europe. Sophisticated systems can be found with various technical terrestrial applications. Variants on this technology, e.g. the Eloflux-technique, are already developed and have found technical application.

Immobile alkaline electrolyte systems, which are already used for space application in U.S., are of great interest for space application in Europe, too. Unfortunately only minor know-how on this techniques can be found in Europe.

In the field of IEM technologies, SPE (solid polymer electrolyte) electrolyzers are very well developed in contrast to SPE fuel cells and have a wide potential for terrestrial application.

Other technologies, e.g. phosphoric acid fuel cells, molten carbonate fuel cells and electrolyzers, high temperature solid oxide electrolyte electrolyzers, have a very promising development status but are not considered for space application yet.

Due to the space application general impacts on fuel cell and electrolyzers as well as on the peripheral components result. Special physical conditions such as μ-g environment, high acceleration forces and vibrations during launch and reentry as well as extreme requirements on safety, reliability (lifetime), volume and mass have to be considered. Some critical points are the gas/liquid and liquid/gas separation, the handling of hot concentrated potassium hydroxide, the water removal out of the electrolyte in mobile alkaline fuel cells and the reliable long-time operation of pumps as well as the aspects of thermal management. All components (inclusive peripherals) have to operate with the highest efficiency, which will have an influence on the system mass.

A short description and evaluation of the different RFC systems shall be given.

The characteristic of the mobile alkaline system is a KOH circuit with the advantage of a good water and heat management of the fuel cell and the electrolyzer. A disadvantage is the necessity of a gas/electrolyte separation for the electrolyzer and the water removal out of the electrolyte via an electrolyte regenerator for the fuel cells. The efficiency of this system (about 60 % fuel cell and about 90 % electrolyzer) needs further improvement. The main reason for the efficiency loss is the relatively wide gap between the electrodes which is required by the electrolyte flow.

The Eloflux technique of VARTA has the advantages of an electrolyte/gas separation inside the electrodes and of a very compact design. Disadvantages are high temperature- and concentration gradients within one electrode package.

Immobile alkaline electrolyte systems have the advantage of very small gaps between the electrodes which leads to high efficiencies (about 65 % for fuel cells and about 95 % for electrolyzers). No electrolyte circuits as well as electrolyte/gas separations are necessary. Disadvantages are the relatively sensible water management and the necessity of an extra cooling loop for the stack (cooling plates).

SPE techniques have the advantage, that an agressive electrolyte has not to be handled. Disadvantages are the necessity of cooling plates and the water/O_2 separation for the liquid water feed electrolyzer. For the SPE-fuel cell probably an O_2-humidifier is necessary to avoid a dry-out and ripping apart of the membrane. The efficiency of 55 % to 60 % for the fuel cell and 85 % to 90 % for the electrolyzer is relatively low. This is caused mainly by the membrane characteristics (conductivity, H_2-permeability). New membrane developments will bring improvements.

In principle one RFC system could be assembled of one SPE-electrolyzer and one alkaline fuel cell. Here the feasibility has to be investigated, e.g. the influence of KOH-contamination on SPE membranes.

One important point for the development is the weight of an RFCS. Here not only the electrolyzer, the fuel cell, the peripherals and the storage tanks have to be taken into account, but also the radiator and the solar panels. The efficiency of the fuel cell is responsible for the size (and weight) of the electrolyzer and the radiator. The efficiency of the electrolyzer determines the size of the solar panel.

KOH-circuits and gas/liquid separators of mobile electrolyte systems are problematic for safety and reliability considerations. On the other hand these sytems have a very simple temperature control.

A comparing summary of the most important evaluation and selection criteria will be shown as result of the first study phase. At the time being immobile alkaline systems seem to be the most promising for space application, followed by SPE and Eloflux techniques. The application of conventional mobile RFC systems for space use has to be considered as problematic.

The results of the first study phase are investigated more deeply at the time being within the second study phase on RFCS, which is funded by ESTEC and carried out by Dornier System.

Abstract No. 54

PROGRESS IN HIGH POWER DENSITY FUEL CELLS

Supramaniam Srinivasan and Edson A. Ticianelli

Center for Electrochemical Systems and Hydrogen Research, Texas A&M University Systems, College Station, TX 77843

Introduction

High power densities are essential to minimize the capital cost, weight, and volume of fuel cell power plants. High power densities should be achieved without sacrifice of efficiencies. Thus, if the efficiency of the electrochemical cell stack is to be greater than 40%, the cell potential under rated load should be greater than 0.6V. In addition, high power densities are necessary for several applications; one example is the transportation application in which a high power density is required during cruising of the vehicle, and two to three times the rated power is necessary for start-up and acceleration. Space and military applications also demand high power densities.

Examination of cell potential-current density behavior of fuel cells shows that to attain high power densities (i) the activation overpotentials needs to be very low ($\sim$300 mV at 1 A/cm^2); (ii) the slope of linear region of such plots should be smaller than 0.1 ohm cm^2; and (iii) mass transpot effects should be negligible up to very high current densities, say, 5 A/cm^2. In this context the phosphoric acid and the molten carbonate fuel cells have little chance to reach high power densities mainly because of the high overpotential of the oxygen reduction reaction ($\sim$0.45 V at 300 mA/cm^2) in the first, and the very high slope in the linear region (0.8 ohm cm^2), due to the relative poor conductivety of the electrolyte, in the second. Only the alkaline, the solid polymer electrolyte and the solid oxide fuel cell systems present the highest possibility of attaining high power densities. Thus, this paper focusses on the present and needed advances in these technologies.

Alkaline Fuel Cell System

The only fuel cell power plant in operation at high power density is the one with alkaline electrolyte and H_2 and O_2 as reactant, manufactured by United Technology Corporation (1) as an auxiliary power source for space vehicles. The electrodes are Teflon-bonded and contain unsupported platinum (anode) and gold/platinum (cathode) electrocatalysts. The electrochemical cell uses an extremelly thin (50μm) electrolyte matrix made with potassium titanate in which KOH 35% is immobilized. The cell potential vs current density plot shows that extremely high current densities are achieved in the predominantly activation-controlled region (about 1 A/cm^2 at 0.9 V), and the slope of the linear region is only 0.05 ohm cm^2. This low value of the slope and the negligible effect of mass transport are the main reasons for attaining high current densities (up to 10 A/cm^2) at a moderate cell potential (0.5 V).

SPE Fuel Cell Systems

A strong competitor for the alkaline fuel cell system is possibly the advanced solid polymer electrolyte fuel cell. Recent results from Siemens (Germany), Ballard Technologies Corporation (Canada), Dow Chemical (USA), Ergenic Power Systems, Inc. (USA), General Motors Corporation (USA) and Los Alamos National Laboratory (USA) strongly indicate the attainment of high power densities. Current densities of 4 A/cm^2 at a cell potential of 0.5 V, 80 °C, and 8 atm pressure have been reported by Ballard Technologies and by Dow Chemical in solid polymer electrolyte (Dow membrane) fuel cells with Teflon-bonded electrodes containing 4 mg/cm^2 unsupported platinum, and using pure H_2 and O_2 as reactants (2). The Los Alamos National Laboratory investigators are focusing on achieving high power densities in such fuel cells using low platinum loading electrodes (0.5 mg/cm^2 of Pt). Current densities of 2 A/cm^2 have been attained at a cell potential of 0.5 V using Nafion-impregnated electrodes prepared with supported platinum electrocatalysts (3). The slope of linear region in the cell potential-current density plots is 0.1 ohm cm^2 for the most advanced SPE fuel cell systems.

Solid Oxide Fuel Cell Systems

The rationale for developing solid oxide fuel cell as high power density systems is the high projected efficiency for electricity generation as compared with those of phosphoric acid and molten carbonate fuel cells (4,5). The total efficiency for the production of electrical energy from the chemical energy of coal or natural gas using the fuel cell system combined with a gas turbine operated with the waste heat is projected to exceed 60%.

Rapid advance in this technology have been made at Westinghouse Corparation (USA) and Argone National Laboratory (USA) during the past 5 years. Nickel is being used as the anode electrocatalyst and strontium-doped lanthanum manganite as the cathode one; yttria-stabilized zirconia is the electrolyte. The cell potential vs current density relation is linear, indicating that kinetic effects are not significant in the SOFC. Although the slope is relatively high, current densities up to 2.2 A/cm^2 has been observed (4). Further improvments are possible though reduction in the interfacial resistances within the cell.

Aknowledgements

E. A. Ticianelli is a Visiting Scientist at CESHR on leave of absence from Universidade de Sao Paulo at Sao Carlos (IFQSC), Brazil.

References

1. D.Watkins, D.Kircks, D.Fpp and A.Harkness, Proceedings of the 32nd Annual Power Sources Conference, The Electrochemical Society, Inc., Pennington, NJ, (1986), p.590. Also personal communication with D. Watkins (1987).

2. S.Srinivasan, J. Electrochem. Soc., Review submitted for publication (1988).

3. E.A.Ticianelli, C.R.Derouin and S.Srinivasan, J. Electroanal. Chem., in press.

4. D.C.Fee et al., Fuel Cell Seminar Abstracts, Courtesy Associates, Inc., Washington DC, (1986) p.40.

5. W.J.Dollard and J.T.Brown, Fuel Cell Seminar Abstracts, Courtesy Associates, Inc., Washington DC, (1986) p.28.

Abstract No. 53

EFFECTS OF LOW LEVELS OF CO ON THE PERFORMANCE OF PEM FUEL CELLS

M. T. Paffett, J. Pafford, and S. Gottesfeld

Los Alamos National Laboratory, MS D429
Los Alamos, NM 87545

CO severely poisons fuel cells operating at low temperatures. For proton exchange-membrane (PEM) fuel cells, which operate at temperatures of 100°C or below, the presence of low levels of CO in the anode feed could mean significant losses in cell performance. PEM fuel cells to be employed for potential terrestrial transportation applications and modes of extraterrestrial application are expected to use hydrogen that contains low levels of CO.

We describe first a detailed evaluation of the performance of PEM fuel cells employing gas-diffusion electrodes of low Pt loadings (0.4 mg/cm^2), in the presence of CO levels ranging from 10-1000 ppm. The performance of such cells on "clean" H_2/O_2, or on H_2/air, has recently been described in detail.[1] The effects of the following parameters have been investigated for each CO level in the anode feed: cell temperature, hydrogen and oxygen (or air) pressure, mode and degree of humidification, and the nature and thickness of the ionomeric membrane. Attention was paid to effects both at the anode and at the cathode. The latter is important because of possible penetration of CO through the membrane reaching the cathode catalyst sites. In another part of this discussion, we describe results of single cell testing obtained with binary alloys that have been considered in the past as anode catalysts with better "CO tolerance" than Pt.

The results of the PEM single cell testing are complemented by results of experiments with rotating Pt disk electrodes, performed at temperatures ranging between 25°C - 75°C in dilute sulfuric acid solutions. Such experiments have elucidated key factors in both the transient and steady-state response of a Pt catalyst surface that is operating in either a hydrogen oxidation mode or an oxygen reduction mode in the presence of low levels of CO. Data obtained at a Pt RDE for the oxygen reduction reaction (o.r.r.) in the presence of low levels of CO are shown in Figs. 1 and 2.

At low temperature (25°C), the decay rate of the o.r.r. due to CO poisoning becomes progressively slower as the anodic potential is gradually increased (Fig. 1). At V $\geq$ 0.65 V, CO is anodically removed from the Pt RDE surface, thereby allowing the o.r.r. current to be sustained.

A more complex and interesting behavior is observed for the o.r.r. at a Pt RDE at 75°C. As shown in Fig. 2, the decay rate of the o.r.r. due to CO poisoning is greatest between 0.35 V and 0.55 V. At potentials more positive than 0.55 V, CO is again anodically removed, as expected. However, CO less strongly blocks at V < 0.3 V, as evidenced by the slower decay of the o.r.r. current in the most cathodic potential regime and by the ability to sustain steady state o.r.r. currents (Fig. 2). These RDE results suggest that, within the Pt H region, less CO is strongly adsorbed at the Pt surface at T $\geq$ 75°C. With less CO at the Pt surface in the adsorbed hydrogen region, the oxygen molecule finds an effective route for reduction. Surface chemical mechanisms accounting for this complex interfacial behavior and the implications of this effect on the operation of PEM fuel cells at temperatures between 80°C - 100°C will be discussed.

REFERENCES

1. E. A. Ticianelli, C. R. Derouin, A. Redondo, and S. Srinivasan, Electrode Materials and Processes for Energy Conversion and Storage, 87-12, S. Srinivasan, S. Wagner, and H. Wroblowa, Eds., (The Electrochemical Society, Inc., Princeton, NJ, 1987) p. 166.

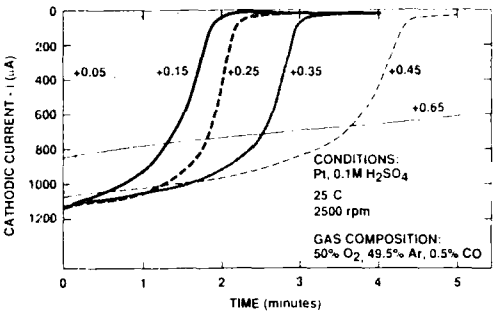


Fig. 1. Oxygen reduction reaction at 25°C as a function of time at constant potential for a Pt RDE. Experimental conditions were: rotation rate, 2500 rpm; gas flow, 400 sccm; gas composition, 0.50$_2$ + 0.495 Ar + 0.005 CO; and potentials reported versus a reversible hydrogen electrode. At t = 0, the Pt RDE was stepped from a potential of 1.2 V (complete removal of CO from the surface) to the potential of measurement.

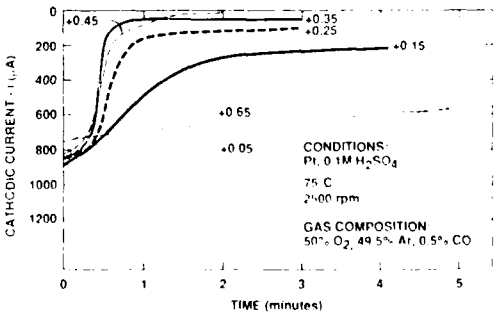


Fig. 2. Same parameters as Fig. 1, except T = 75°C.

Abstract No. 56

Modification of the Structure of Hydrogen Electrode Catalyst Particles Bonded to Solid Polymer Electrolytes

S. D. Fritts and R. F. Savinell
Case Western Reserve University
Department of Chemical Engineering
Cleveland, Ohio 44106

Catalyzed solid polymer electrolytes are used in hydrogen–halogen and PEM hydrogen–oxygen fuel cells. Only the hydrogen electrode is bonded to the cation exchange membrane in hydrogen–halogen fuel cells, while both the hydrogen and oxygen electrodes are bonded to the membrane in the PEM fuel cell. The purpose of this paper is to report studies of effects of modifications of the structure of the hydrogen electrode on cell performance. The specific system addressed here is the hydrogen–bromine fuel cell.

A schematic of a hydrogen–bromine fuel cell is given in Figure 1. An aqueous solution of hydrobromic acid and bromine flows by the carbon felt bromine electrode. In the other half–cell compartment, during discharge, hydrogen gas dissolves in the membrane and diffuses to the catalyst particles which are embedded in the membrane. There, the hydrogen electrochemically reacts to form protons. The protons transport through the membrane to the bromine half cell. Previous modelling work on a single hydrogen–bromine fuel cell indicated that the transport properties of the membrane are the most influential factors in controlling cell performance [1], so further efforts have been undertaken to study the membrane transport properties more closely [2].

The catalyst particles embedded in the membrane were modelled using macro–homogeneous porous electrode theory [3]. The dimensionless model equations are given in Table 1. The model takes into account the migration and diffusion of protons through the membrane, and the diffusion of dissolved hydrogen through the catalyst region.

For the modelling effort, the catalytic region is assumed to consist of spherical platinum particles that are dispersed in an ionomer membrane structure, (e.g. Nafion). The thickness of the catalyst zone is a few microns thick. The electrode structure has a significant effect on the performance of the membrane electrode assembly. When the catalyst particles are densely packed, the performance of the electrode is limited by mass transfer of the hydrogen gas to the catalyst sites. This is due to the restricted area for diffusion and limited hydrogen solubility. However, if the catalyst particles are loosely packed, the reaction becomes kinetically limited.

The model assumes that there is only platinum and ionomer in the catalyst zone, (i.e. no binder was present). Figure 2 shows the calculated membrane performance for several catalyst zone thicknesses and different platinum loadings. Here the electrode structure is constant throughout the catalyst zone. The optimum performance for each platinum loading occurs when the ionomer and platinum composition are about 50 volume percent.

One method of preparing the membrane electrode assembly is to hot press the platinum and ionomer mixture onto an ionomer film. This would cause the electrode structure to be non–uniform, with particles that are deeper in the membrane being less densely packed. Parametric studies on performance with constant and non–uniform catalyst distributions will be discussed. The effect of placing the catalyst such that the particles are less densely packed at the gas/membrane interface, then becoming more densely packed deeper in the membrane is treated as well as the opposite situation.

Further results of theoretical studies of electrode structure modifications will be presented, as well as some experimental work to support this modelling effort.

REFERENCES

1. Savinell, R. F., and S. D. Fritts, "Theoretical Performance of a Hydrogen–Bromine Rechargeable SPE Fuel Cell," Accepted by the Journal of Power Sources, July, 1987.

2. Fritts, S. D., and R. F. Savinell, Paper No. 162 Presented at The Electrochemical Society Meeting, Honolulu, Hawaii, Oct. 1987.

3. Newman, J., and W. Tiedemann, A.I.Ch.E. Journal, 21, (1975), p. 25.

ACKNOWLEDGMENTS

This research is supported by NSF Grant CBT–8696073, and the Energy Research Summer Fellowship of the Electrochemical Society.

Table 1. Dimensionless equations used to model the catalyst zone of the membrane electrode assembly.

Proton Mass Balance

$$PC(1-\epsilon)C_4 = -\left[\epsilon\frac{\partial C_1}{\partial X}\frac{\partial C_3}{\partial X} + C_1\frac{\partial \epsilon}{\partial X}\frac{\partial C_3}{\partial X} + C_1\epsilon\frac{\partial^2 C_3}{\partial X^2}\right] - \frac{1}{\alpha}\left[\frac{\partial \epsilon}{\partial x}\frac{\partial C_1}{\partial X} + \epsilon\frac{\partial^2 C_1}{\partial X^2}\right]$$

Hydrogen Mass Balance

$$PB\,(1-\epsilon)\,C_4 = \frac{\partial \epsilon}{\partial X}\frac{\partial C_4}{\partial X} + \epsilon\frac{\partial^2 C_2}{\partial X^2}$$

Charge Balance

$$-PA\,(1-\epsilon)\,C_4 = \frac{\partial \epsilon}{\partial X}\frac{\partial C_3}{\partial X} + \epsilon\frac{\partial^2 C_3}{\partial X^2}$$

Kinetic Expression

$$PD\,C_4 = C_2^{1/2}\exp(PE-C_3) - C_1\exp(C_3-PE)$$

Boundary Conditions

$$x = 0, \qquad \frac{\partial C_1}{\partial X} = 0, \quad C_2 = C_2^0, \quad \frac{\partial C_3}{\partial X} = 0$$

$$x = t_\delta, \qquad C_1 = C_1^0, \quad C_2 = Q\frac{\partial C_2}{\partial X}, \quad C_3 = C_3^0$$

Where

$$C_1 = \frac{C_{H+}}{1\ mol/l}, \quad C_2 = \frac{C_{H_2}}{1\ atm/R'T}, \quad C_3 = \frac{\alpha F \phi_2'}{RT},$$

$$C_4 = \frac{i'}{1\ A/cm^2}, \quad X = \frac{x}{t_\delta}$$

$$PA = \frac{3\alpha F(1\ A/cm^2)t_\delta^2}{\kappa RT r_p}, \qquad PB = \frac{3(1\ A/cm^2)t_\delta^2 R'T}{2r_p D_{H_2} F(0.001\ mol/cc)}$$

$$PC = \frac{3(1\ A/cm^2)t_\delta^2}{r_p D_{H+} F(0.001\ mol/cc)}, \qquad PD = \frac{1\ A/cm^2}{i_{0,ref}'}$$

$$PE = \frac{\alpha\phi_1'}{RT} \qquad Q = \epsilon\frac{t_\beta - t_\delta}{t_\delta}$$

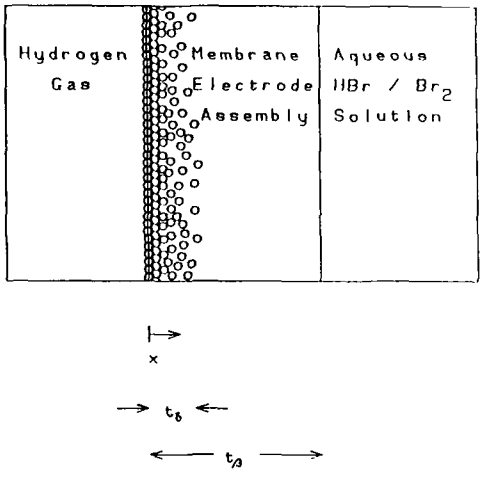


Figure 1. Schematic of hydrogen–bromine fuel cell.

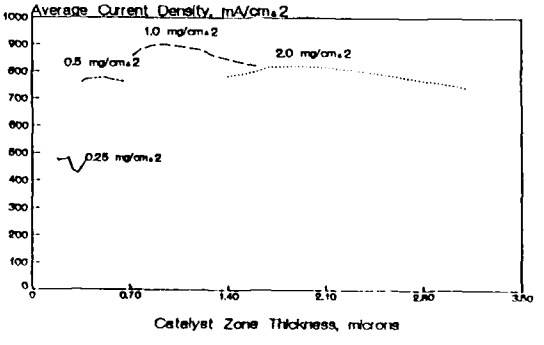


Figure 2. Calculated membrane performance for several catalyst zone thicknesses and different platinum loadings.

Abstract No. 57

EFFECT OF PLATINUM CATALYST DISTRIBUTION ON THE PERFORMANCE OF SOLID POLYMER ELECTROLYTE FUEL CELLS

E. A. Ticianelli*, J. G. Beery, and S. Srinivasan

Los Alamos National Laboratory, MS D429
Los Alamos, NM 87545

INTRODUCTION

One of the principal objectives of the Los Alamos fuel cell program is to develop high-power-density, solid-polymer-electrolyte fuel cell systems with electrodes containing a platinum loading of one tenth or less than that in state-of-the-art fuel cells. The essence of the approach used to attain this goal is to impregnate a proton conductor (Nafion)** into a porous electrode[1] containing only 0.4 mg/cm^2 of Pt and then to bond two of these electrodes to the proton conducting membrane. By using the standard 10-wt% Pt/C gas diffusion electrodes for preparing these membrane and electrode assemblies, a high power density (~0.3 W/cm^2)[2] is attained. However, to further increase the power densities, it was necessary to modify the electrode structure. This was achieved by using electrodes with a thinner electrocatalyst layer and by depositing a thin platinum film on the front surface.[3]

The morphologic characterization of these electrodes, using Scanning Electron Microscopy (SEM), Transmission Electron Microscopy (TEM), and Rutherford Backscattering Spectrometry (RBS), carried out during the development of these electrodes is presented in this paper. We also explain how the performance of SPE fuel cells with low-platinum-loading electrodes is dependent on their morphologic characteristics.

EXPERIMENTAL

Platinum-on-carbon electrocatalysts containing 10-, 20-, and 40-wt% Pt/C were custom-made by Prototech, Inc. Such powders were used by Prototech for preparation of low-catalyst-loading gas diffusion electrodes with thinner electrocatalyst layers. To concentrate the catalyst near the front surface, a thin layer of platinum (corresponding to a thickness of 500 Å on a smooth surface or to 0.05 mg/cm^2 on the electrode) was sputtered on the catalyst layer of the electrodes.

RESULTS AND DISCUSSION

SEM Analysis

Although some micrographs of the top of the catalyst layer of the electrodes were obtained, the SEM was also used to examine cross sections of the membrane and electrode assemblies. It was observed that such a small amount of sputtered Pt did not introduce any visible change to the micro-structure of the electrode at the resolution of the SEM. Within the sensitivity of the SEM analysis, the sputtered Pt seems to be completely dispersed over the high surface area of the carbon support.

TEM Analysis

Transmission electron microscopy was used to examine the supported platinum on carbon electrocatalysts and fragments of the catalyst layers from the electrodes. The TEM pictures of the Pt/C electrocatalysts were further analyzed to determine the distribution of the platinum particle sizes. An example of the results of the analysis for the 20-wt% Pt/C is presented in the bar charts in Fig. 1. The average sizes of the platinum crystallites were found to be 22 Å, 29 Å, and 37 Å for the 10-, 20-, and 40-wt% Pt/C catalysts, respectively. An analysis of the carbon particles with the sputtered platinum shows that the catalyst was deposited as fine particles with diameters ranging from 30 Å to a few hundred Å. There were some platinum particles that were either dispersed or agglomerated.

RBS Analysis

The porous gas diffusion electrodes were also submitted to RBS analysis. A typical result is presented in Fig. 2 for the 20-wt% Pt/C electrode in which the sputtered layer of Pt was applied. It is apparent from the figure that the sputtered Pt is localized within a thickness of ~500 Å on the front surface of the electrode.***

Correlation With the Electrochemical Results

Electrochemical experiments show that the sputtering technique for the standard electrode (10-wt% Pt/C) significantly enhances the power density (by 100-150% at 1A/cm^2). There was additional improvement in performance of the cells with 20- and 40-wt% Pt/C as compared with the 10-wt% Pt/C. The sputtering of Pt on the 20-wt% Pt/C gave rise to the highest power density in the fuel cell. These electrochemical results correlate well with the morphological data obtained in SEM, TEM, and RBS analysis.

ACKNOWLEDGMENTS

C. R. Derouin provided valuable assistance in obtaining the electrochemical results. C. Mombourquette sputtered the platinum films and S. Gottesfeld provided technical collaboration.

REFERENCES

1. I. D. Raistrick, Proceedings for the Symposium on Diaphragms, Separators, and Ion-Exchange Membranes, 86-13, J. W. Van Zee, R. E. White, K. Kinoshita, and H. S. Burney, Eds., (The Electrochemical Chemical Society, Inc., Princeton, NJ, 1986), p. 172.
2. E. A. Ticianelli, C. R. Derouin, A. Redondo, and S. Srinivasan, J. Electrochem. Soc., in press.
3. E. A. Ticianelli, C. R. Derouin, and S. Srinivasan, J. Anal. Soc., in press.

*Currently on leave from University of Sao Paulo, Sao Carlos, Brazil.

**Nafion is a registered trademark of the Dupont Company.

***For comparison, we have also included the RBS profile of a 20-wt% Pt/C with no sputtered layer.

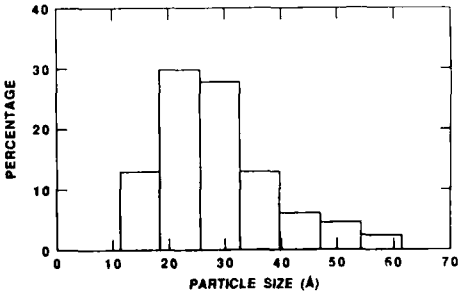


Fig. 1. Particle size distribution in the 20-wt% Pt/C catalyst powder. Particles were assumed to be spherical. The sizes correspond to the average diameters.

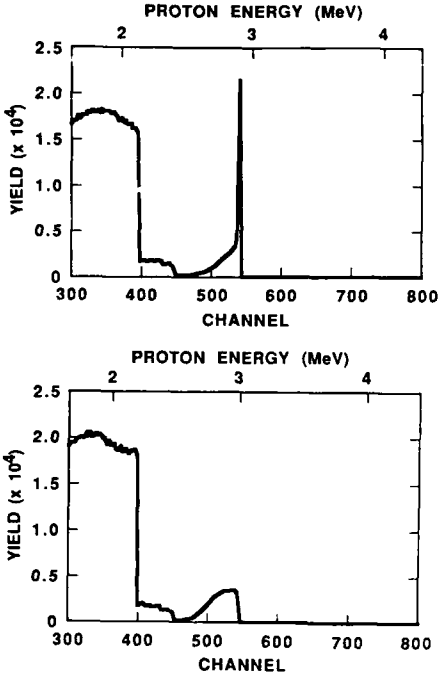


Fig. 2. Rutherford backscattering spectrum from fuel cell electrodes loaded with 20-wt% Pt/C. Top spectrum had 500 Å platinum layer sputtered on surface.

Abstract No. 58

SIMULATION OF OXYGEN ELECTRODE REACTIONS IN MOLTEN CARBONATE FUEL CELLS.

P.K. Adanuvor, B. Dave, R.E. White and A.J. Appleby

Center for Electrochemical Systems and Hydrogen Research
238 Wisenbaker Engineering Research Center
Texas A&M University
College Station, Texas 77843

INTRODUCTION

The kinetic reactions taking place in alkali carbonate melts depend on the acid-base properties of the melt (1). However, the uncertain nature of the melt chemistry makes it difficult to predict *a priori* the predominant species in the melt and, as a result, the dominant reaction pathway. Smith *et al.* (2) reported that the major reacting species in Li-K melt at 650 °C is the superoxide ion (O_2^-). On the basis of this, Vogel *et al.* (3) inferred that the electrode reaction occurs by the 3e⁻ superoxide pathway. On the other hand, Appleby and Nicholson (4) attributed the reduction process to the 2e⁻ peroxide pathway. The voltammetric results of Uchida (5) in K-rich melts supports the simultaneous reduction of both peroxide ($O_2^{=}$) and superoxide species. Therefore, the kinetic model proposed for this work combines the simultaneous reduction of O_2 and O_2^- species at the electrode (Eq. [3] and [4]) with the auto-catalytic reactions of these species in the bulk melt (Eq. [2] and [5]) and with the oxide neutralization reaction (Eq. [6]).

$$1/2[O_2 + 2CO_2 = 2O_2^- + 2CO_2] \quad [1]$$

$$1/6[O_2^- + 2O_2^- = 2O_2^{=}] \quad [2]$$

$$2/3[O_2 + 2e^- = 2O^-] \quad [3]$$

$$2/3[O_2^- + e^- = O_2^{=}] \quad [4]$$

$$1/6[O^- + 3/2O_2 = 2O_2^{=}] \quad [5]$$

$$7/6[O^- + CO_2 = CO_3^{=}] \quad [6]$$

$$1/2O_2 + CO_2 + 2e^- = CO_3^{=} \quad [7]$$

The objectives are to determine the effects of the auto-catalytic and the neutralization reactions on the electrode reactions, and to establish what influence the presence of physically dissolved O_2 in the melt has on the electrode kinetics.

RESULTS AND DISCUSSION

Figure 1 shows a significant increase in the reduction current with increase in the concentration of molecular (physically dissolved) O_2 in the melt. Two plateau regions are apparent. The plateau at the more positive potential (-0.3V) is not well-defined, and can be attributed mainly to reaction [4]. On the contrary, the second plateau at the more negative potential can be attributed predominantly to the reduction of O_2 species. Figures 2 and 3 show an enhancement of the current density, particularly in the Tafel region, at higher rates of the auto-catalytic reactions. An enhancement in the current density is again observed (but to a lesser degree) at high rates of the neutralization reaction (see Fig. 4.).

CONCLUSION

An enhancement in the polarization curves occurs in the presence of physically dissolved oxygen in the melt, and changes in the auto-catalytic reaction rates affect the polarization curves significantly, particularly in the Tafel region.

REFERENCES

1. B.K Andersen, Ph.D Dissertation, Technical Univ. of Denmark, Lyngby, Denmark, (1975).
2. S.W. Smith, W.M. Vogel and S. Kapelner, *J. Electrochem. Soc.*, **129**, 1668 (1982).
3. W.M Vogel, S.W. Smith and S. Bregoli, *ibid*, **130**, 574 (1983)
4. A.J. Appleby and S. Nicholson, *J. of Electroanal. Chem.*, **53**, 105 (1974).
5. N.I. Uchida, *Abstr. 50th Mtg. Jap. Electrochem. Soc. Meeting*, Tokyo, (March 1983).

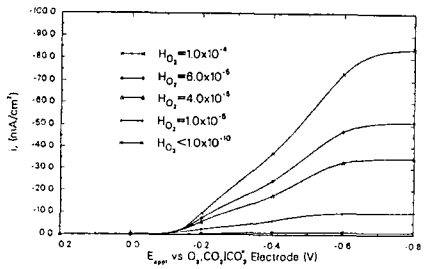


Fig. 1. Effect of physical solubility of oxygen on the steady state polarization curves in (68:32) Li/K carbonate melt

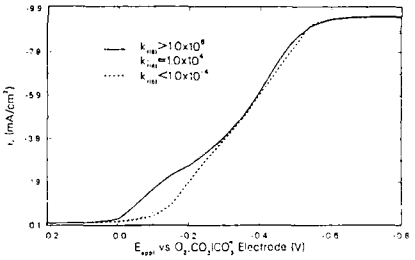


Fig. 3. Effect of auto-catalytic reaction rate constant in Eq. [5] on the steady state polarization curves in (68:32) Li/K carbonate melt (H_{O_2}=10^{-5} mol/atm/cm^3)

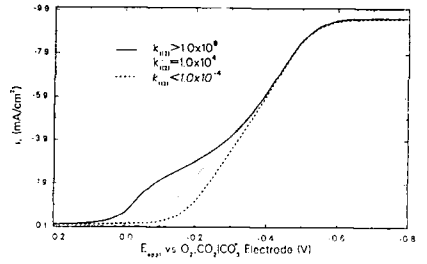


Fig. 2. Effect of auto-catalytic reaction rate constant in Eq. [2] on the steady state polarization curves in (68:32) Li/K carbonate melt (H_{O_2}=10^{-5} mol/atm/cm^3)

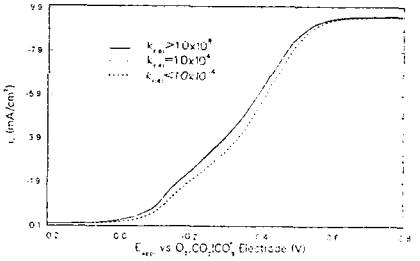


Fig. 4. Effect of oxide recombination reaction rate constant in Eq. [6] on the steady state polarization curves in (68:32) Li/K carbonate melt (H_{O_2}=10^{-5} mol/atm/cm^3)

Abstract No. 59

SNIFTIRS Study at Polycrystalline Pt and Au Surfaces in Aqueous Nafion Solution

M. Razaq, D. Chu, D. Gervasio and E. B. Yeager

Case Center for Electrochemical Sciences and the Chemistry Department, Case Western Reserve University, Cleveland, Ohio 44106

Introduction

Although there is continued interest in chemically modified electrodes with a surface film of a perfluorinated sulfonic acid ionomers (PFSI), like Nafion (DuPont) [1], little direct information is available concerning the orientation and interaction of such ionomers with electrode surfaces, particularly as a function of applied potential. The surface normalized interfacial Fourier transform infrared spectroscopic (SNIFTIRS) technique [2] has been used in the present research to study the interaction between a metal (Pt, Au) electrode surface at different potentials with Nafion in aqueous solution with and without the presence of a weakly adsorbing anion, perchlorate.

Experimental

Aqueous Nafion solution was prepared as described previously [3]. The spectroelectrochemical cell used for obtaining SNIFTIRS data was similar to that used by Bewick et al. [2]. Spectral measurements were made with an IBM Instruments IR-98AF Fourier transform infrared spectrometer with a liquid N_2 cooled mercury cadmium telluride detector. The spectral resolution was 2 cm^{-1}. The difference spectra were obtained by co-adding 1000 scans at a reference potential (0.05 V vs NHE) and subtracting these from 1000 scans co-added at a potential of interest. The potential of the electrode was switched between the reference potential and the potential of interest every 20 interferometer scans. The angle of incidence of both the p- or s-polarized radiation with the electrode surface was 65°. The spectroelectrochemical cell was fitted with a zinc selenide window.

Results and Discussion

Figure 1 shows the potential difference vibrational spectra using p-polarized radiation reflected from a Pt electrode in aqueous 3.6 wt% Nafion solution at a series of potentials. The reference potential in each case was 0.05 V vs NHE. The absorption spectrum characteristic of Nafion [4] appeared weakly at 0.5 V and became more intense as the potential was made more positive. This suggests that the concentration of the Nafion at and near the Pt surface was increasing with increasing positive potential. For potentials more positive than 0.9 V, however, there was no significant increase in the intensity of the spectral bands suggesting a constant coverage of the electrode by Nafion in this potential range. The order, in which the potentials of interest were applied, did not show any effect on the absorption spectra. The relative intensities and the positions of the absorption bands did not change with potential and are similar to those for the bulk transmission spectrum of Nafion. This suggests that there is no preferred orientation of the polar or nonpolar moieties of Nafion relative to the surface.

Figure 2 shows the SNIFTIRS spectra for p-polarized radiation reflected from a Au electrode at a series of potentials in the same Nafion solution used for the experiments with Pt as described above. A similar trend was found with Au as was found for Pt. For Au, however, the increase in intensity of the spectra levelled off when the potential was increased to 1.3 V vs NHE and greater. It is interesting to note that 1.3 V is roughly the potential for the onset of oxide formation on Au, whereas 0.9 V is just after the onset of oxide formation on Pt in acid media.

With p-polarized radiation reflected from the electrode, the observed changes in the intensity of absorption bands with changing potential indicate that the absorption bands predominately correspond to the species at the electrode/electrolyte interface. This was further supported by another evidence, namely that when the concentration of Nafion was lowered from 3.6 to 1.8 wt%, the intensity of Nafion absorption bands at a given potential reduced only by a factor of about 0.8. The non-linear response to bulk concentration is as expected for surface phenomena involving an adsorption isotherm. For a small optical absorption, a linear response to bulk concentration, on the other hand, would be expected for the absorption of radiation by species in the bulk solution. A strong interaction of anions (e.g., found with HSO_4^-) with metal surfaces leads to changes in the intensity as well as the position of the absorption bands [5]. No changes in the positions of the Nafion absorption bands were found implying Nafion is a relatively weakly adsorbing electrolyte, and/or only a small part of the polymer molecule is in contact with the surface with the remainder extending into solution.

It is possible that at more positive potentials the Nafion goes to the electrode simply to compensate charge resulting in the observed potential dependence of the intensity of the spectra. This is somewhat borne out by the surface spectra of the Pt and Au in aqueous 1.8 wt% Nafion solution containing ten-fold excess of perchloric acid (Baker Ultrex grade reagent) shown in Figure 3. With no added perchlorate, the spectra for the electrode surface in 1.8 wt% aqueous Nafion solution were found to be virtually the same as those for the electrode in the 3.6 wt% aqueous Nafion solution as shown in Figs. 1 and 2, except that the intensity of the absorption bands found with 1.8 wt% Nafion in solution were 0.8 times the intensity found with 3.6 wt% Nafion in solution, as mentioned above. Upon the addition of a ten-fold excess of perchloric acid to the 1.8 wt% Nafion solution, however, the intensity of the strong Nafion absorption bands between 1350 to 1100 cm^{-1} diminished over three-fold on Pt and Au, and a strong absorption band centered about 1100 cm^{-1}, which is characteristic of ClO_4^-, appeared. This apparently indicates that both electrolytes compete for the electrode surface.

Conclusion

The similarity between the relative peak intensities in the bulk transmission spectrum and the SNIFTIRS spectra with both Pt and Au surfaces suggests that there is a random orientation of Nafion at the electrode/electrolyte interface. Nafion apparently adsorbs on the metal electrode surfaces. The positions of the absorption bands do not change significantly, even at very positive applied potentials, indicating the infrared spectra do not give evidence for a strong interaction of the Nafion with the electrode surfaces.

Acknowledgement

The authors acknowledge support of this research by the Gas Research Institute, Office of Naval Research, the National Institute of Health and the State of Ohio Edison Center Program.

References

1. F. F. Fan and A. J. Bard, J. Electrochem. Soc., 133, 301 (1986).

2. A. Bewick and S. Pons, in "Advances in Infrared and Raman Spectrocopy", R. Hester and R. Clark, eds., Whily, Hayden (1985), Vol. 12, p 1.

3. D. Chu, D. Gervasio, M. Razaq and E. B. Yeager, Electrochemical Society Meeting, Atlanta, Extended Abstract 88-1, 24.

4. C. Heitner-Wirguin, Polymer, 20, 371 (1979).

5. M. Razaq, A. Bewick, J. W. Russell, Electrochemical Society Meeting, Atlanta, Extended Abstract 88-1, 332.

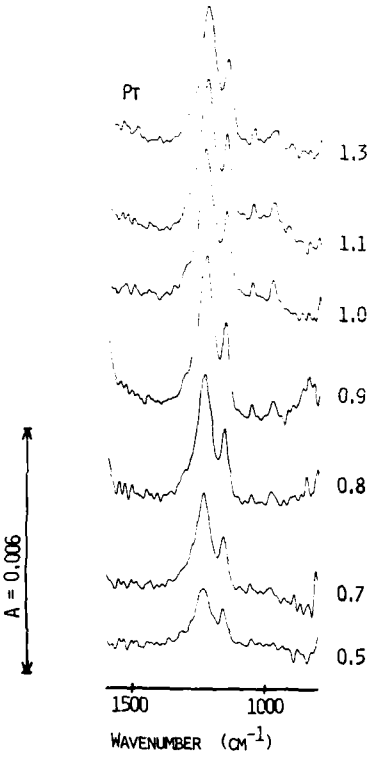


Fig. 1. SNIFTIRS spectra from the Pt/solution interface at various potentials. The aqueous solution contained 3.6 wt% Nafion. Reference potential was 0.05 V vs NHE.

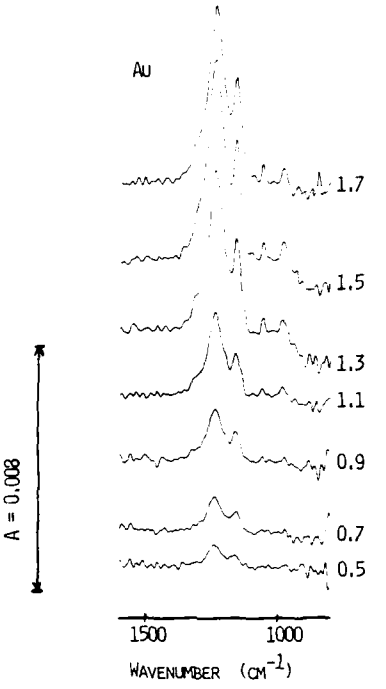


Fig. 2. SNIFTIRS spectra from the Au/solution interface at various potentials. The aqueous solution contained 3.6 wt% Nafion. Reference potential was 0.05 V vs NHE.

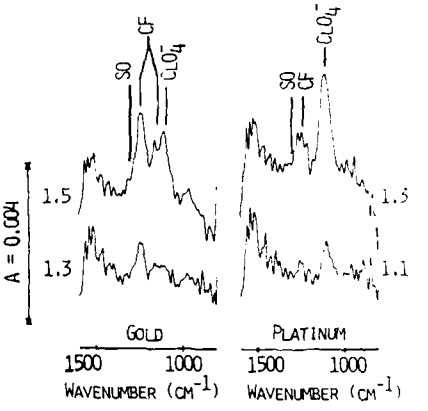


Fig. 3. SNIFTIRS spectra from the metal/solution interface at various potential. The aqueous solution contained 1.8 wt% Nafion plus $HClO_4$ (10-fold molar excess in terms of ionic constituents). Spectera with the Au electrode on the left; Pt electrode on the right. Refernece potential: 0.05 V vs NHE.

Abstract No. 60

ION AND SOLVENT TRANSPORT IN ION-EXCHANGE MEMBRANES I. A MACROHOMOGENEOUS MATHEMATICAL MODEL

Mark W. Verbrugge
Physical Chemistry Department

Robert F. Hill
Analytical Chemistry Department
General Motors Research Laboratories
Warren, Michigan 48090-9055

Although the fundamental principles underlying the behavior of ion-exchange membranes is not entirely understood, these materials have found use in many recent technologies. In this work, we provide a theoretical description of transport occuring in perfluorosulfonic-acid membranes—the model we develop, however, is general and could be used to explain transport in most all synthetic and biological membranes. Unlike other macrohomogeneous membrane models, no restrictive assumptions are employed in our solution to the equations describing ion and solvent transport, the adsorption of coions and counterions are treated, and all of the transport parameters are easily related to tabulated, physicochemical data. A schematic illustration of the membrane-pore system is shown in Fig. 1. Sulfonate groups constitute the fixed-charge sites ($-SO_3^-$); the counterion species are protons, and bisulfate ions are the coions.

For the characterization of ion transport in polymeric systems, we start with the Nernst-Planck equation with velocity

$$\mathbf{N}_i = -z_i \frac{F}{RT} D_i c_i \nabla\Phi \quad D_i \nabla c_i + c_i \mathbf{v} \tag{1}$$

(A bold font implies a vector quantity.) In writing the above equation, we have employed the Nernst-Einstein relationship for systems dilute in the transporting ion i. This allows for the elimination of the ion mobility u_i as an independent parameter (i.e., $u_i = D_i/(RT)$). In Eq. 1, the flux of an ion $\mathbf{N}_i$ is related to gradients in potential, concentration, and momentum, resulting in migration, diffusion, and convection, respectively. A *material-balance equation* and the Nernst-Planck equation can be combined to yield

$$\frac{\partial c_i}{\partial t} = z_i \frac{F}{RT} D_i (c_i \nabla\Phi + \nabla c_i \cdot \nabla\Phi) + D_i \nabla^2 c_i - \mathbf{v} \cdot \nabla c_i \tag{2}$$

Since the flow of charge is related to the current density $\mathbf{i}$ in solution, we can write for the electric potential

$$\nabla\Phi = -\frac{\mathbf{i}}{\kappa} - \frac{F}{\kappa}\left(\sum_i z_i D_i \nabla c_i\right) + \frac{F}{\kappa}\left(\sum_i z_i c_i\right)\mathbf{v} \tag{3}$$

The conductivity κ is position dependent as it is related to the concentration of charge carriers

$$\kappa = \frac{F^2}{RT} \sum_i z_i^2 D_i c_i \tag{4}$$

In many membrane systems, the counterions specifically adsorb to the fixed-charge sites. We represent such adsorption processes with a Langmuir expression

$$\beta_i c_i = \frac{c_{i,ads}}{c_m - c_{i,ads}} \tag{5}$$

where the subscript m refers to the membrane fixed-charge site. The concentrations of fixed-charge sites, coions, mobile counterions, and adsorbed counterions adjust so that any small volume element of membrane (corresponding to our differential element) is electrically neutral

$$z_m c_m + \sum_i z_i c_i + \sum_i z_i c_{i,ads} = 0 \tag{6}$$

In this electroneutrality expression, the fixed-charge sites are denoted with a subscript m.

Electric potential and pressure gradients generate convection within the pores of the ion-exchange membrane. We use a *modified version of* Schlögl's equation of motion[1,2] so that specific adsorption of coions and counterions can be treated.

$$\mathbf{v} = -\frac{k}{\mu}\left[\left(z_m c_m + \sum_i z_i c_{i,ads}\right) F \nabla\Phi - \nabla P\right] \tag{7}$$

The quantity P represents the combined effect of static pressure and gravitational forces.

The equation of mass continuity for incompressible fluid flow can be applied to Eq. 7, with the result

$$0 = \left(z_m c_m + \sum_i z_i c_{i,ads}\right) F \nabla^2\Phi - \nabla^2 P \tag{8}$$

Equations 2, 3, 4, 5, 7, and 8 represent $4 + 2i$ equations and are balanced by the $4 + 2i$ variables: c_i, Φ, κ, $c_{i,ads}$, $\mathbf{v}$, and P. Electroneutrality, Eq. 6, is used to remove one of the i material-balance equations. The variable x is used to represent the distance coordinate: x ranges from 0 at reservoir I to L at *reservoir II*, as is indicated in the following schematic.

$$\text{Reservoir } I \;\overset{x=0}{|}\; \text{Membrane} \;\overset{x=L}{|}\; \text{Reservoir } II$$

Initial and boundary conditions are

$$c_i(0,x) = c_i^o \tag{9}$$
$$c_i(t,0) = K_i c_i^I \tag{10}$$
$$c_i(t,L) = K_i c_i^{II} \tag{11}$$
$$\Phi(0) = 0 \tag{12}$$
$$P(0) = P^I \tag{13}$$
$$P(L) = P^{II} \tag{14}$$

The material balance for reservoir I, which is well mixed, is

$$\frac{dc^I}{dt} = -\frac{N}{\nu_3}\bigg|_{x=0} \frac{A}{V^I} + \frac{s^I I}{n^I F V^I} \tag{15}$$

where the concentration variable c and flux variable N without subscripts refer to binary electrolyte quantities (sulfuric acid in this work). Equation 15 would also be written for any *additional binary electrolytes present* in the system. The subscript 2 refers to coion quantities. The initial condition for Eq. 15 is

$$c^I(0) = c^{I,o} \tag{16}$$

A similar *material-balance equation* can be written for the acid concentration in reservoir II.

An example of the model results from a situation in which no current is passed between the two reservoirs; a 1.0M sulfuric acid solution exists on one side of the membrane, and a 0.1M solution on the other side. The dimensionless acid concentration within the membrane is shown in Fig. 2.

In summary, a macrohomogeneous mathematical model for the simulation of ion and solvent transport within an ion-exchange membrane is presented. Transport by diffusion, migration, and convection are treated. The physicochemical parameters used in this analysis are experimentally easy to obtain. In an accompanying paper, we present an experimental investigation utilizing this model for characterization purposes.

REFERENCES

1. R. Schlögl, *Z. physik. Chem. (Frankfurt)*, 3(1955)73.

2. R. Schlögl, *Ber. Bunsenges. Physik Chem.*, 70(1966)400.

LIST OF SYMBOLS

A	membrane superficial area, cm^2
c	concentration, mol/cm^3
D	diffusion coefficient, cm/s^2
F	Faraday's constant, 96487 C/equivalent
$\mathbf{i}$	current density, A/cm^2
I	current, A
k	permeability, cm^2
K	partition coefficient
L	membrane thickness, cm
n	number of electrons per reaction
$\mathbf{N}$	ion flux, $mol/cm^2 \cdot s$
P	pressure, N/m^2
R	gas constant, 8.314 $J/mol \cdot K$
s	stoichiometric coefficient for species in reaction
t	time, s
T	temperature, K
v	velocity, cm/s
V	volume, cm^3
z	charge number
β	Langmuir adsorption parameter (Eq. 5), cm^3/mol
μ	pore-fluid viscosity, $g/cm \cdot s$
ν	stoichiometric coefficient
Φ	electrical potential, V

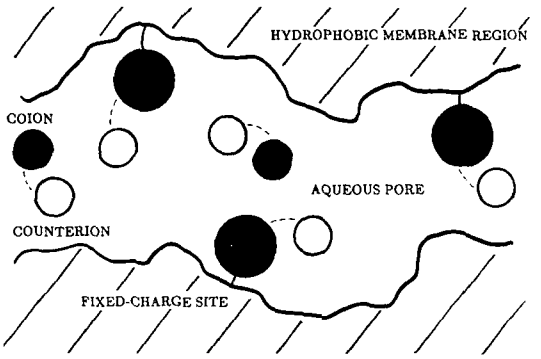


Figure 1. Schematic illustration of a pore within an ion-exchange membrane. ● refers to the fixed-charge sites (SO_3^-); • refers to the coions (HSO_4^-); and ○ refers to the counterions (H^+). The fixed charge sites, coions, and counterions are hydrated species.

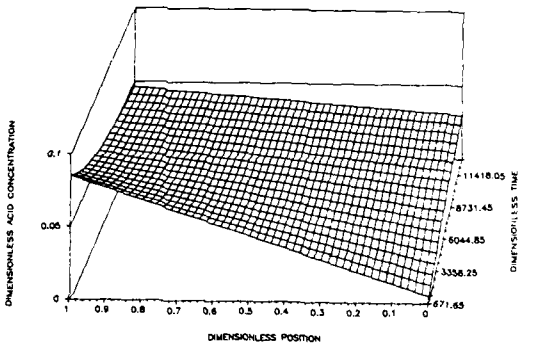


Figure 2. Membrane acid-concentration ($c/c^{II,o}$) profiles as a function of position (x/L) and time (tD/L^2).

Abstract No. 61

ION AND SOLVENT TRANSPORT IN ION-EXCHANGE MEMBRANES II. A RADIOTRACER STUDY OF THE SULFURIC-ACID, NAFION-117 SYSTEM

Mark W. Verbrugge
Physical Chemistry Department

Robert F. Hill
Analytical Chemistry Department
General Motors Research Laboratories
Warren, Michigan 48090-9055

In an accompanying Part I of this paper, the authors developed a mathematical model for the simulation of ion and solvent transport through ion-exchange membranes. In this paper, we describe radiotracer techniques that can be used in conjunction with the model to obtain the proton and bisulfate-ion diffusion coefficients within a Nafion 117[1] membrane separating two aqueous sulfuric acid reservoirs.

There has been a number of recent experimental studies of ion and solvent transport in perfluorosulfonic acid membranes. Most of these works have dealt with systems of interest to the chloro-alkali industry, since this is the largest industry in which perfluorosulfonic acid membranes can be utilized to present an immediate economic advantage as older production facilities are replaced. Radiotracer techniques are well suited for the study of transport within ion-conducting membranes because of the extreme accuracy and precision associated with them and the non-invasive (with regard to the membrane-electrolyte system) nature of the radioisotopes.

The most valuable contribution resulting from the acquisition of ion diffusion coefficients is an elucidation of membrane pore structures that could give rise to the determined values of the diffusion coefficients. A large amount of literature is devoted to structure studies of perfluorosulfonic acid membranes. A popular concept used to explain transport in these membranes, often termed the cluster-network model, is that narrow (≈10-Å) pores connect larger pores of ≈60 Å in diameter, and that the narrow pores dominate the ion and solvent transport characteristics. While 60-Å dimensions are easily seen with light-scattering techniques, as demonstrated in a number of structure studies, the purported concept of the narrow connecting pores has not been verified. The slow rate of coion transport, relative to counterion transport, within Nafion is attributed to the electrostatic-repulsion forces between the coions and the fixed-charge groups in the 10-Å-pore regions.

To determine the transport rates of bisulfate ions and protons through Nafion-117 membranes, radiotracer techniques were developed because of their high sensitivity and selectivity. A cell was designed and constructed that utilized two reservoirs of equal volume so that each reservoir could contain at least 50 mL of electrolyte (Fig. 1). This volume was selected to ensure that up to 0.1-mL aliquots of electrolyte could be removed from the reservoirs during the experiment for analysis without appreciably affecting the cell transport characteristics or the concentration of species in the reservoirs. Fifty-microliter aliquots of electrolyte were withdrawn from the cold reservoir (i.e., the reservoir not initially tagged with ^{35}S) at five intervals spaced over the duration of the experiment.

[1] *Registered trademark* of E. I. dupont de Nemours and Company

The first set of experiments about which we report concerns the acquisition of the bisulfate-ion diffusion coefficient. The reservoirs depicted in Fig. 1 were filled with identical concentrations of sulfuric acid. Then a small amount of $H_2{}^{35}SO_4$ was added to the hot reservoir at time zero. (The concentration of radiotracer species was always at least six orders of magnitude less than that of the reservoir concentrations of sulfuric acid.)

Data are shown in Fig. 2. The diffusion coefficients D_* are shown in Fig. 3. Note that when the partition coefficient (obtained in a separate experiment) is taken into account, the resulting diffusion coefficient of the $H^{35}SO_4^-$ ion is virtually constant even though the acid concentration varies from 0.003 to 1.0M.

It is apparent from the constant value of the diffusion coefficient below a 1.0M H_2SO_4 concentration that dilute-solution equations can be used to describe the coion transport within the pores of the membrane. Using a Bruggeman-type relationship, we can relate the membrane porosity θ (0.27 for this system) and the diffusion coefficient of the bisulfate ion in free solution at infinite dilution D_*°, which is 1.33×10^{-5} cm^2 s:

$$D_* = D_*^\circ \theta^B \qquad (1)$$

Using 1.43×10^{-6} cm^2 s for D_*, we obtain a value of 1.7 for B. This is very close to the 1.5 value obtained by Bruggeman for diffusion through close-packed spheres.

No special structure had to be introduced to explain the transport of the bisulfate ion over this broad range of concentrations.

Acquiring the proton diffusion coefficient is not as easily accomplished using radiotracer techniques as acquiring that of the bisulfate ion. Hydrogen atoms are present on bisulfate ions, protons, and water molecules - hence tritium atoms, for example, would partition themselves among these species as well.

Instead of using a hydrogen isotope to ascertain the rate of proton transport, we have made use of the diffusion potential that exists within an ion-exchange membrane if the coion and counterion diffusion coefficients are different and the reservoirs on either side of the membrane are of different concentration. The hot reservoir was filled initially with 1.0M sulfuric acid, and the cold reservoir's initial acid concentration was 0.1M. Since no current is passed during the experiment and the coion and counterion charges are of equal magnitude (−1 and +1, respectively), an electric-potential profile is formed so that the coions and counterions transport at the same rate. Diffusion and migration act in opposite directions for the counterion (proton) and in the same direction for the coion. Relative to the bisulfate-ion self diffusion case described in the last section, an $H^{35}SO_4$ radiotracer placed in the hot reservoir will transport across the membrane at a faster rate due to the additional migration component.

A plot of the acid concentration in the cold reservoir, obtained from the ^{35}S radiotracer data, is shown in Fig. 4. The model developed in Part I is used to obtain the solid line in Fig. 4.

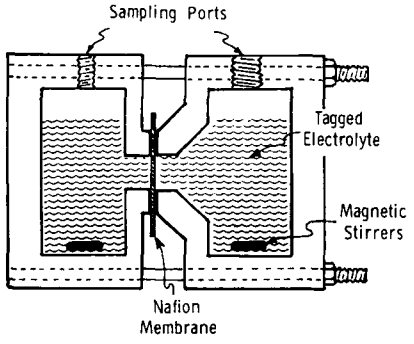


Figure 1. Schematic illustration of the radiotracer cell.

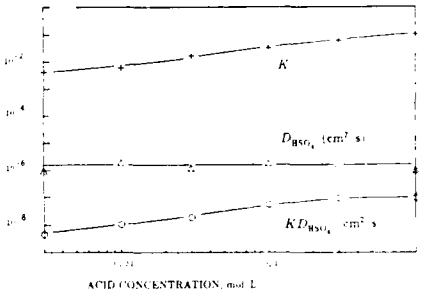


Figure 3. Acid partition coefficient K, coion diffusion coefficient $D_{HSO_4^-}$, and their product $KD_{HSO_4^-}$ versus the reservoir sulfuric acid concentration.

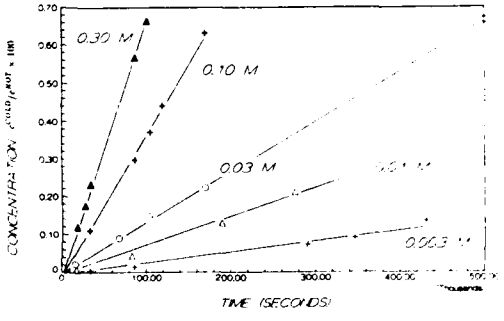


Figure 2. Radiotracer concentration in the cold reservoir, relative to that in the hot side, versus time. The sulfuric acid concentrations are listed for each curve. The symbols denote experimental data, and the solid lines represent simulations using bisulfate-ion diffusion coefficients yielding the best fit.

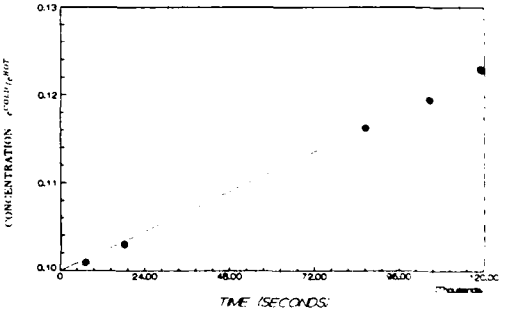


Figure 4. Results from the concentration-cell experiment. The cold reservoir acid concentration is plotted against time. The symbol • denotes experimental data, and the solid line results from the model with a proton diffusion coefficient of 3.5×10^{-6} cm^2/s.

Abstract No. 62

A DYNAMIC MODEL OF POROUS GAS DIFFUSION ELECTRODES

I. D. Raistrick and T. E. Springer

Los Alamos National Laboratory
Los Alamos, NM 87545

INTRODUCTION

Although significant attention has been given to steady-state modeling of porous gas diffusion electrodes for fuel cell applications, little development of dynamic models has taken place. This is partly due to the complex nature of the systems, in which the current distribution is a function of both DC potential and time (or frequency). The advantage of a dynamic model, however, is that the information content is very high, due to the out-of-phase or charge-storage components of the response. This allows the different contributions to the electrode polarization (ohmic, mass transport, and charge-transfer kinetics) to be separated by their characteristic time constants. In addition, a dynamic model allows the performance of the fuel cell to be evaluated under pulsed operating conditions. The general scheme adopted in this work may be outlined as follows:

1. An appropriate physical model of the electrode is defined.
2. The corresponding mathematical model is then developed.
3. The DC or steady-state behavior is calculated from the model.
4. A small-signal time-dependent perturbation analysis is carried out around a steady-state point.
5. The impedance may be compared with frequency- or time-domain measurements, and parameters may be adjusted by a nonlinear least-squared error fitting routine.

DESCRIPTION OF THE MODELS

The class of models examined so far may be described as generalized transmission line models. Early work in this area is reviewed by de Levie.[1] The double-layer charging and the Faradaic processes (including diffusion) are supposed to be distributed over a finite depth of reaction zone, and hence, over a finite pore resistance. This approach is appropriate if the electrode structure is uniform, i.e., the geometry of the processes is independent of the depth of current penetration. It is not appropriate if, for example, the electrode contains a continuous distribution of pore sizes, as is found in a fractal model. Some results have previously been reported for a thin-film model.[2] During that work, it was found that, although 'thin-film' mass transport limitations are present at high current densities, the model inadequately described the experimental potential dependence of the various contributions to the electrode impedance. The description of the electrode has therefore been extended to include a flooded agglomerate model,[3] as well as the thin film. A schematic representation of the model is shown in Fig. 1. Here the catalyst particles are supposed to be uniformly distributed in an agglomerate region, which is made up of both electronic (carbon) and ionic (electrolyte) components. The principal mode of gas transport is in large hydrophobic channels. The gas diffuses into the agglomerate through a thin film of electrolyte. Within the agglomerate, the concentration profile of the gas is determined by the Faradaic rate constant, diffusion coefficient, size of the agglomerate, and the overpotential. In contrast to the thin-film region, the concentration profiles are non-linear. Potential variations due to the electrolyte resistance in the agglomerate itself may be neglected, compared with those caused by the (electrolyte) resistance distributed through the thickness of the electrode.

RESULTS

The mathematical model corresponding to Fig. 1 is shown in Fig. 2. The small-signal impedance of a differential element of the pore wall has been calculated for the complete case of the thin film in series with the agglomerate using the LaPlace transformed time-dependent diffusion equations. Tafel kinetics were assumed to operate at the surface of the catalyst particles. Out-of-phase or dynamic response is caused by the delayed shift in the concentration profile following a shift in overpotential. An approximate equivalent circuit has been derived for this element, which consists of a finite-length diffusional component due to the thin film, coupled with a simple subcircuit of two resistances and a capacitance that represent the agglomerate. The dependence of the magnitudes of the circuit elements on the thin-film and agglomerate parameters, as well as on the independent variables of potential and concentration, has been derived. The complete electrode impedance is then calculated by distributing the film/agglomerate impedance along the length of the pore, in parallel with a distributed double-layer capacitance. In general, the model predicts three 'time constants' in the electrical response. The first of these is associated with distributed double-layer charging, the second with the agglomerate storage/dissipation processes, and the third with the thin-film finite-length diffusion processes.

The predictions of the model have been compared with the impedance of ionomer-impregnated supported-catalyst gas diffusion electrodes, used in solid polymer electrolyte fuel cells.[4,5] The data were fitted to the model for a variety of conditions (temperature, pressure, and electrode potential), and the quality of the models was assessed. Possible improvements to the models, such as introduction of a distribution of characteristic sizes, have been considered and will be discussed.

ACKNOWLEDGMENTS

This work was sponsored by the Department of Energy Office of Energy Storage and Distribution.

REFERENCES

1. R. de Levie in Advances in Electrochemistry and Electrochemical Engineering, P. Delahay and C. T. Tobias, Eds. (Interscience, New York 1967) 6, p. 329.
2. T. E. Springer and I. D. Raistrick, "Analysis and Interpretation of AC Impedance Data for Porous Electrodes," Proc. of Electrochemical Societ, Symposium on Electrode Materials and Processes for Energy Conversion, 87-12, 152-165 (1987).
3. J. Giner and C. Hunter, J. Electrochem. Soc. 116, 1124 (1969).
4. I. D. Raistrick, "Modified Gas Diffusion Electrode for Proton Exchange Membrane Fuel Cells," Proceedings of the Electrochemical Society Symposium on Diaphragms, Separators, and Ion Exchange Membranes, 86-13, 172-178 (1986).
5. S. Srinivasan, E. Ticianelli, C. Derouin, and A. Redondo, "Advances in Solid Polymer Electrolyte Fuel Cell Technology with Low Platinum Loading Electrodes," J. of Power Sources, in press.

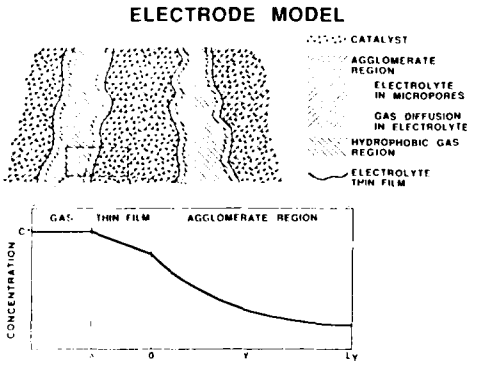


Fig. 1. Schematic representation of thin-film and agglomerate model of a single pore. The expanded region indicates one gas concentration profile through the flow and agglomerate regions.

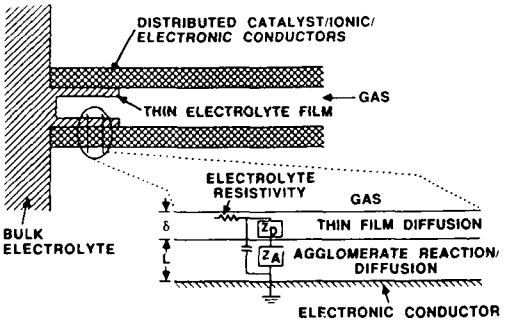


Fig. 2. Mathematical model of electrode assumes diffusion processes are orthogonal to the distributed ohmic resistance and to the current flow.

Abstract No. 63

BROMINE TRANSPORT IN ZINC BROMINE BATTERY SEPARATORS

James McBreen
De .rtment of Applied Science
Brookhaven National Laboratory
Upton, New York 11973

INTRODUCTION

The zinc-bromine battery is attractive for load leveling applications (1). Here overall AC/AC efficiency is very important. Combined power conditioning and battery pumping losses are in the vicinity of 10%. So a high electrochemical efficiency is desirable. Major reductions in cell resistance are unlikely. Therefore, further improvements have to be in coulombic efficiency. Coulombic efficiency is largely determined by the transport of bromine species through the separator during cell operation and standby. Other sources of losses are shunt currents. The modes of transport through the separator are diffusion, migration and convective flow. In modeling zinc-bromine batteries certain assumptions have to be made about the diffusivities of various bromine species (2). The presence of bromine complexing agents may also affect the ratio of the species present. The present paper is about a simple method for determination of the relative contributions of diffusion and migration of bromine species through separators.

EXPERIMENTAL

The cell used was a slightly modified version of a cell described previously (3). Provisions were made for passing current through the separator during the bromine permeation measurements. Most measurements were done on Daramic (W. R. Grace Co.) separators. Measurements were made in several electrolytes. Various combinations of bromine, zinc bromide and quaternary ammonium complexing agent were used to simulate cells at various stages of charge.

RESULTS AND DISCUSSION

As expected, the relative combinations of migration and diffusion depended on whether the cell was in charge or discharge mode. In 1M $ZnBr_2$, with 0.06M Br_2 on one side of the membrane, the permeation current was 0.95 mA/cm^2. A 40 mA/cm^2 charge decreases the current to a 0.55 mA/cm^2 and a 40 mA/cm^2 discharge increased the current to 1.42 mA/cm^2. The presence of the quaternary ammonium compound decreased both the diffusivity and the permeability.

REFERENCES

1. J. McBreen, Extended Abstracts, Vol. 87-2, The Electrochem. Soc., Pennington, NJ (1987) p. 163.

2. T. I. Evans and R. E. White, J. Electrochem. Soc. 134, 866 (1987).

3. R. S. Yeo and J. McBreen, ibid. 126, 1682 (1979).

Abstract No. 64

ZINC/BROMINE BATTERY ELECTROLYTE INVESTIGATIONS

J. Bolstad
K. Yaccarino

Johnson Controls, Inc.
Advanced Battery Business Unit
5757 North Green Bay Road
P.O. Box 591
Milwaukee, WI 53201

Introduction: Johnson Controls' circulating electrolyte zinc/bromine system is being developed for electric vehicle and load-levelling applications. The battery uses an all-plastic construction with bipolar electrodes. The electrolyte consists of an aqueous solution of zinc bromide, quaternary amines which complex bromine to reduce its activity and facilitate its storage outside the battery, and (optionally) monovalent chloride salts which increase the electrolyte conductivity.

The main source of inefficiency in the system is diffusion of aqueous bromine through the separator. For load-levelling applications, energy efficiency is the overriding concern; therefore the electrolyte composition must be optimized to achieve low aqueous bromine solubility in order to minimize diffusion of bromine across the separator.

For electric vehicle applications, the requirements are more difficult because many factors need to be considered. They include high power capability, high energy efficiency, minimum weight, and low freezing point.

Experimental: Electrolyte conductivity measurements were made with a Radiometer type CDM2e conductivity meter. Solution temperatures were held at 25 ± 1° C. Bromine solubility was measured by the iodometric titration method.

Cell testing was done with 90 cm^2 electrode cells with electrolyte gaps of .040". The separator was a polyethylene/silica type (Asahi SF-600). Cycling conditions were: 1.5-amp charge for 5 hours; 2.5-amp discharge to 1.0 volt. The cells were shorted after each cycle.

Results: The results are displayed in Figures 1 through 6. Figure 1 shows the resistivity of aqueous zinc bromide as a function of concentration. The solutions were adjusted to pH 3 ± 0.1 to avoid precipitation of zinc bromide when it was diluted (the zinc bromide had a molarity of approximately 9 as supplied). The results showed a resistivity minimum at about 2 molar, which is similiar to other published work.

Figure 2 shows the resistivity of aqueous solutions of one of the quaternary amines, N,N-methyl ethyl pyrrolidinium bromide (MEP).
The resistivity of MEP is quite high relative to zinc bromide; therefore its concentration in electrolyte needs to be kept as low as is feasible.

Figure 3 shows the resistivity and bromine solubility as a function of zinc bromide concentration for an actual electrolyte composition containing zinc bromide, potassium chloride, and quaternary amines. This plot shows the resistance penalty incurred if a high concentration of zinc bromide is used in order to minimize electrolyte weight for electric vehicle applications. The aqueous bromine solubility in this electrolyte reaches a plateau at a zinc bromide concentration of about 3 molar. This is a fortuitous occurrence. It suggests that there is no penalty other than increased resistivity, if the zinc bromide concentration is increased above 3 molar.

Figures 4 and 5 show the results of varying the amount of chloride salt additive in a given electrolyte composition. Figure 4 shows that potassium chloride and ammonium chloride are very similiar in their effects on electrolyte resisitivity. Figure 5 shows that while potassium chloride decreases the aqueous bromine solubility, ammonium chloride has the opposite effect.

However, in an actual battery, no performance difference between the ammonium and potassium chloride salts was seen. This is shown in Figure 6, in which cell efficiencies are plotted. Cycles 13-18 used electrolyte containing ammonium chloride, and cycles 19-31 used electrolyte containing the same concentration of potassium chloride. The reason for the lack of observable difference is not clear at this time.

Summary: In the zinc/bromine system the concentrations of zinc bromide, quaternary amines, and supporting electrolyte salts can be varied over a certain range in order to optimize certain parameters. We have presented results of some basic property measurements which illustrate how electrolyte compositions can be optimized for different applications.

References:

1. Bellows et al, "Development of a Circulating Zinc-Bromine Battery," Phase III, D. O. E. Contract #40-0483 Final Report, April 1982.

2. Bellows et al, "Development of a Circulating Zinc-Bromine Battery," Phase II, D. O. E. Contract #40-0483 Final Report, May 1987.

3. Will, F. G., Iacovangelo, C. D., Jackowski, J. S., and Secor, F. W., "Assessment of the Zinc-Bromine Battery for Utility Load Leveling," Final Report, D. O. E. Contract # EY-76-C-02-2950, March 1978.

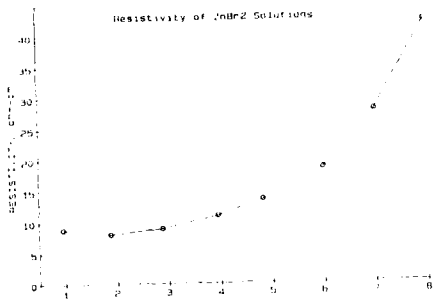


Figure 1

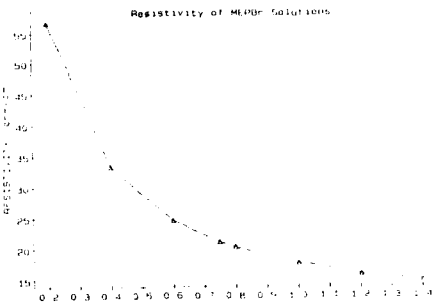


Figure 2

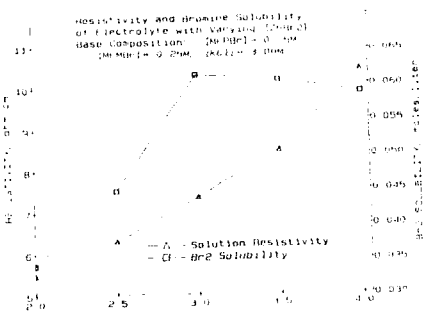


Figure 3

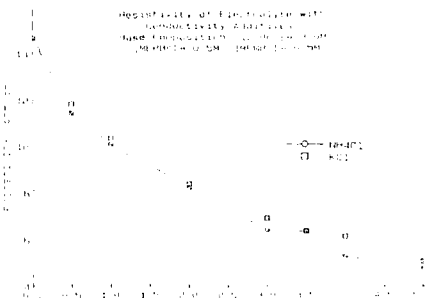


Figure 4

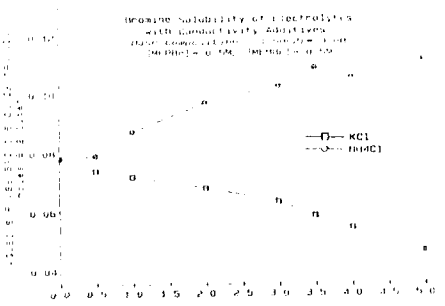


Figure 5

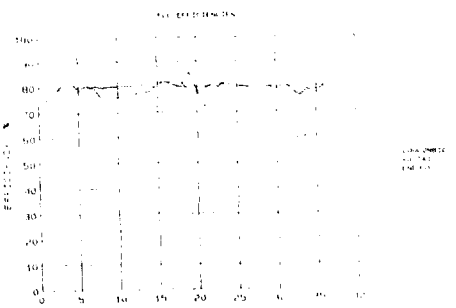


Figure 6

Abstract No. 65

IMPROVED CHLORIDE TOLERANCE AT THE H_2-Cl_2 ANODE

E.J. Taylor and E. Anderson
PSI Technology Company
P.O. Box 3100
Andover, MA 01810

INTRODUCTION

We are developing an electrochemical reactor for production of HCl.[1] In this reactor, a platinum catalyst is used at the anode for the oxidation of hydrogen. Since the anode is exposed to high concentrations of HCl, a major concern is the poisoning of the platinum by chloride ion. Halide ions, in general, and chloride in particular, have been shown to alter the adsorption isotherms of hydrogen on platinum.[2]

Regenerative hydrogen-halogen cells, developed for load leveling purposes, employ a cation exchange membrane to protect the platinum catalyst.[3] The membrane was pressed against a high loading (8 mg Pt/cm^2) platinum black anode. These cells have applications in space power where cost is not a major concern. To reduce the cost in our system, the electrocatalyst is a low loading (0.5 mg Pt/cm^2) carbon supported platinum analogous to that used in phosphoric acid fuel cell technology. Recent work by McBreen[4] indicates that pressing a membrane against this carbon supported electrocatalyst would not be effective in utilizing the platinum. Rather, the cation exchange material must be extended into the porous electrode to coat the individual platinum particles.

Other groups tried impregnation of porous electrodes with Nafion® cation exchange material to enhance oxygen reduction at the cathode in the phosphoric acid fuel cell.[5] We extended this concept to the enhancement of chloride tolerance for the H_2-Cl_2 anode.

EXPERIMENTAL

Electrochemically accessible platinum surface area was measured using cyclic voltammetry. Surface area measurements were conducted on Nafion coated and uncoated platinum in the absence and presence of chloride ion. The feasibility of the Nafion coating concept for the improved tolerance to chloride ion was first demonstrated on smooth platinum and then applied to carbon supported platinum in a porous gas diffusion anode. A novel coating technique was developed for gas diffusion anodes yielding Nafion loadings of 1-3 mg/cm^2. The coated and non-coated anodes were further characterized by scanning electron microscopy (SEM).

RESULTS AND DISCUSSION

The feasibility of the Nafion coating concept for improved chloride tolerance was demonstrated on smooth platinum. Figures 1 and 2 show cyclic voltammograms, in 1M HCl, of uncoated and Nafion coated platinum, respectively. In the presence of chloride ion the surface area of platinum decreased 46 percent for the uncoated electrode, but only a 16 percent reduction in available platinum surface area was observed for the coated platinum.

A presoaking/cycling pretreatment was developed to measure the platinum surface area in a gas diffusion anode using cyclic voltammetry. We demonstrated the effectiveness of this treatment by comparing the platinum surface area measured from a hydrophobic gas diffusion anode (high Teflon® content and sintering temperature) with an electrolyte flooded "CV" electrode structure (low Teflon content and sintering temperature). The measured platinum surface areas of an anode and a CV electrode were the same (Figure 5), indicating complete accessibility of the platinum in the gas diffusion anode.

Electrochemical accessibility of the platinum in the anode was maintained with Nafion coating as shown in Figures 3 and 4. The Nafion coated anode exhibited similar behavior to an uncoated anode during the cycling treatment (Figure 5). Improved chloride tolerance was observed for a Nafion coated anode versus an uncoated anode (Figure 6). As the chloride ion concentration increased to 1M, the available platinum surface area decreased less than 15 percent for the coated anode compared to a 75 percent decrease for the uncoated anode.

Examination of coated and uncoated anodes using SEM showed evidence of Nafion impregnation into the catalyst layer. Large regions of a "tree-like" structure of Nafion were apparent (Figures 7 and 8). There were also regions where we did not observe Nafion. However, based on the chloride tolerance results, we conclude that Nafion is coating most of the platinum particles. We are currently extending this concept to an operating anode under hydrogen consuming conditions.

This work is funded under DOE Contract No. DE-AC-02-86ER80366. The authors acknowledge the support and encouragement of Mr. W. Huber.

REFERENCES

1. Anderson, E., Taylor, E.J., and Gelb, A. (1988), "Fuel Cell Cogeneration of HCl for Brine Acidification in the Chlor-Alkali Industry," Quarterly Reports under DOE Contract No. DE-AC-02-86ER80366.

2. Brieter, M.W. (1963), "Voltammetric Study of Halide Ion Adsorption on Platinum in Perchloric Acid Solutions," Electrochem. Acta, 8, 925-35.

3. Yeo, R.S., McBreen, J., Tseung, A.C.C., Srinivasan, S., McElroy (1980), "An Electrochemically Regenerative Hydrogen-Chloride Energy Storage System: Electrode Kinetics and Cell Performance, J. Applied Electrochemistry, 10, 393-404.

4. McBreen, J. (1985), "Voltammetric Studies of Electrodes in Contact with Ionomeric Membranes," J. Electrochem. Soc., 132(5) 112.

5. Appleby, A.J. (1986), U.S. Patent 4,610,938.

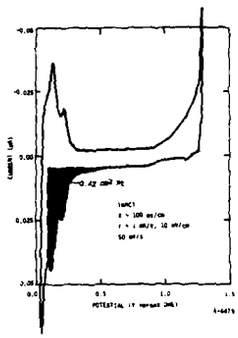


Figure 1. Cyclic Voltammogram of Smooth Platinum in 1M HCl

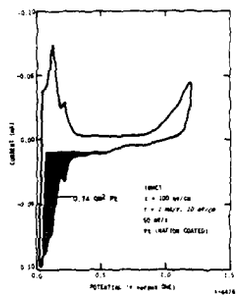


Figure 2. Cyclic Voltammogram of Nafion Coated Smooth Platinum in 1M HCl

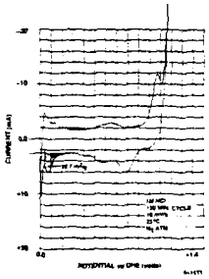


Figure 3. Cyclic Voltammogram of Uncoated Gas Diffusion Anode in 1M HCl

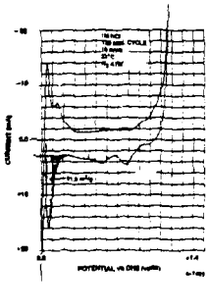


Figure 4. Cyclic Voltammogram of Nafion Coated Gas Diffusion Anode in 1M HCl

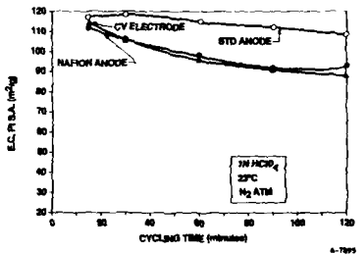


Figure 5. Results of Cycling Study of CV Electrode, Uncoated and Nafion Coated Standard Platinum Anodes

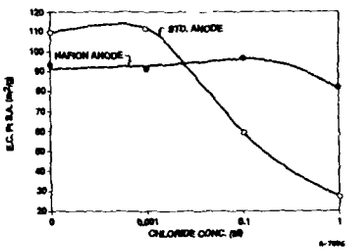
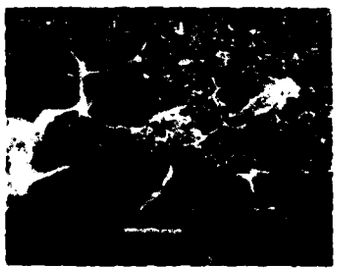


Figure 6. Results of Chloride Tolerance Study of Uncoated and Nafion Coated Standard Platinum Anodes



Figure 7. SEM Photomicrograph of Cross Section of Nafion Coated Anode (200 X)



V-232

Figure 8. SEM Photomicrograph of Cross Section of Nafion Coated Anode (2000 X)

Abstract No. 66

THE POTENTIODYNAMIC BEHAVIOR OF LEAD IN 5 M SULFURIC ACID

G. TREMILIOSI-FILHO, L.A. AVACA, E.R. GONZALEZ
Instituto de Física e Química de São Carlos
C.P. 369, 13560 São Carlos, SP, Brazil

AND

C.V.D'ALKAINE
Grupo de Eletroquímica - DQ UFSCar
C.P. 676, 13560 São Carlos, SP, Brazil

A detailed knowledge of the initial stages of formation/reduction of the different superficial films on lead in 5 M H_2SO_4 (the lead-acid battery electrolyte) is essential for the understanding of the processes that participate in the charge/discharge cycle of a lead-acid battery. Cyclic voltammetry is an adequate technique to study the system and numerous papers have been presented in the literature. However, most studies have been carried out over restricted potential ranges and without making use of all the advantages offered by the technique. In this work the potentiodynamic response of lead in 5 M H_2SO_4 is explored between the potentials corresponding to hydrogen and oxygen evolution reactions. Particular attention is given to the charges involved in each of the observed processes.

Experiments were carried out at room temperature using high purity lead rods (Aldrich 99.9995%, ϕ = 0.4 cm). The surface was polished with 600 grit emery paper, treated with a satured solution of CH_3COONH_4 and washed. The electrode was introduced into the electrolyte already polarized at - 1.2 V vs a $Hg/Hg_2SO_4/5$ M H_2SO_4 reference electrode.

GENERAL CHARACTERISTICS OF THE COMPLETE VOLTAMMOGRAM

As shown in Figure 1 the first oxidation process observed at - 0.9 V (A_1) is initially very fast but quickly inhibited and followed by plateau a_1. This plateau is detected only by increasing the sensitivity 10 times. If the potential is reversed at - 0.4 V only peaks A_2(anodic) and C_1(cathodic) are observed. Peak C_1 increases if the potential is held at - 0.4 V for varying times, indicating that A_1, a_1 and C_1 are associated to the formation/reduction of $PbSO_4$. As the switching potential moves into the region a_2, peaks C_2 and C_3 are observed. These peaks increase if the potential is held in the region a_2. In this region takes place the formation of an internal film of basic lead sulfates and lead oxide protected by the $PbSO_4$ film. Previously, peak C_2 was only observed at low temperatures and it was associated with the reduction of basic lead sulfate(1,2). In this work peak C_2 was observed either by increasing the sensitivity, by growing the film at the inversion potential or by extending the sweep anodically.

In the region a_3 is observed an activation of the surface related to both PbO_2 formation and O_2 evolution. The cathodic sweep shows complex processes in the region + 0.9 —— + 1.3 V which have been mentioned previously (1,3-6) but are not yet fully understood.

Figure 2 shows the ratio of the total anodic (q_t^a) and cathodic (q_t^c) charges as a function of the switching potential (E_λ). Region (a) corresponds to the formation of $PbSO_4$ which is only partially reduced. In region (b) the basic lead sulfate and lead oxide formed show better reduction characteristics. Region (c) shows an increase in q_t^a/q_t^c due to PbO_2 formation and O_2 evolution. Figure 2 defines potentiodynamically three distinct regions for the behavior of Pb in H_2SO_4.

REGION OF LEAD SULFATE (- 0.95/- 0.4 V)

An analysis of the charges involved in this region as a function of E_λ shows that the reversibility of the film (q_1^c/q_1^a) is low for values of E_λ before peak A_1 reaching more expressive values as E_λ increases. This leads to the conclusion that for surfaces incompletely covered, only a small fraction of the nuclei is reduced.

The fact that $q_1^c < q_1^a$ can be rationalized in terms of film - breaking due to internal tensions combined with a decrease in the electrostriction pressure during the cathodic sweep. The breaking of the film exposes small areas of fresh substrate resulting in peak A_2. This shows that, contrary to previous conclusions (1,2), it is not necessary to reach the region of PbO formation to observe the effects of film breaking. A study carried out as a function of the sweep rate shows that the charge corresponding to the broken film ($q_1^a - q_1^c$) is very small for slowly formed/reduced films increasing for highly defective films formed at fast sweep rates.

REGION OF THE BASIC LEAD SULFATE AND LEAD OXIDE (- 0.3/+ 1.3 V)

Figure 3 includes the voltammograms for switching potentials - 0.5 and + 0.9 V. The charges corresponding to the processes in the region a_2 were obtained as a difference from the two voltammograms. This shows that $q^a_{a_2} \simeq q^c_{a_2}$ indicating that the internal film is completely reduced. The charge corresponding to the formation of basic Pb(II) species in this region (q_2^a) corresponds to the area $\alpha + 2\beta$ and correlates well with that of peaks C_2 and C_3 (q_2^c). Also, the excess anodic charge (q_1^a), area $\gamma + 2\delta$, correlates with the increase in peak C_1 (q_1^c), so it can be attributed to the formation of $PbSO_4$ in region a_2.

REGION OF THE LEAD DIOXIDE (> 1.3 V)

Figure 4 shows some voltammograms recorded at different holding times (t_λ) at + 1.4 V. It seems reasonable to conclude that peak C_4 corresponds to the reduction of PbO_2 to $PbSO_4$. This process is superimposed with the reoxidation of the metallic substrate, due to film breaking, which produces peaks A_3 and A_4.

Figure 4 also shows that the cathodic peaks C_1, C_2 and C_3 increase when the potential is held at + 1.4 V, by an amount which is much larger than C_4. Thus, in this potential the formation of Pb(II) species also takes place.

REFERENCES

1 - T.G. Chang, M.M. Wright and E.M.L. Valeriote in "Power Sources 6", D.H. Collins (Ed.), Academic Press, London, 1977, p.69.

2 - R.G. Barradas and D.S. Nadezhdin, Can. J. Chem., **62** (1984)596.

3 - J.P. Carr, N.A. Hampson and R. Taylor, J. Electroanal. Chem., **33**(1971)109.

4 - H.S. Panesar in "Power Sources 3", D.H. Collins (Ed.), Oriel Press, Newcastle-upon-Tyne, 1971, p.79.

5 - J.G. Sunderland, J. Electroanal. Chem., **71**(1976)341.

6 - T.F. Sharp, J. Electrochem. Soc., a) **122**(1975)845; (b) **124**(1977)168.

ACKNOWLEDGMENTS

The authors thank the Fundação de Apoio a Pesquisa do Estado de São Paulo (**FAPESP**), Financiadora de Estudos e Projetos (**FINEP**) and Conselho Nacional de Desenvolvimento Científico e Tecnológico (**CNPq**), Brazil, for financial support.

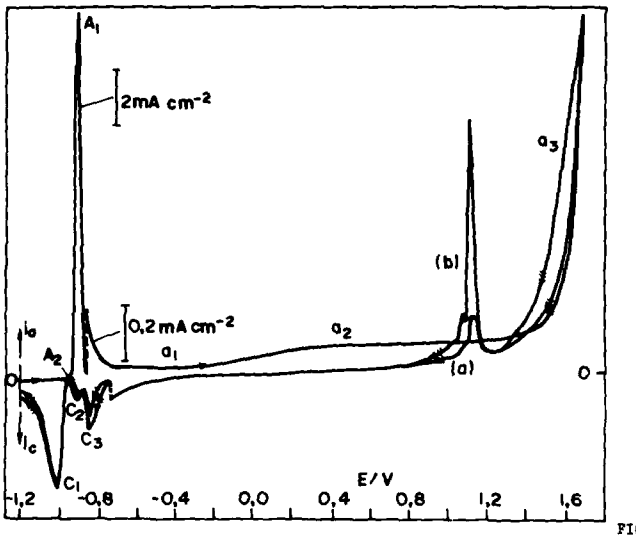


FIGURE 1 - Cyclic voltammograms of lead in 5 M H_2SO_4 : (a) Between - 1.2 V and + 1.6 V, (b) Between - 1.2 V and + 1.7 V. $v = 10$ mV s^{-1}.

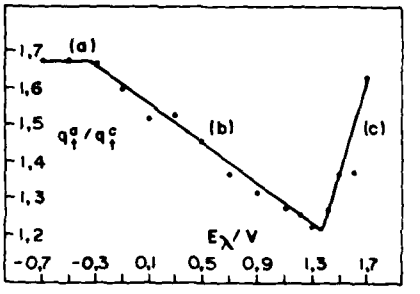


FIGURE 2 - Ratio of the total anodic and cathodic charges as a function of the switching potential. $v = 10$ mV s^{-1}.

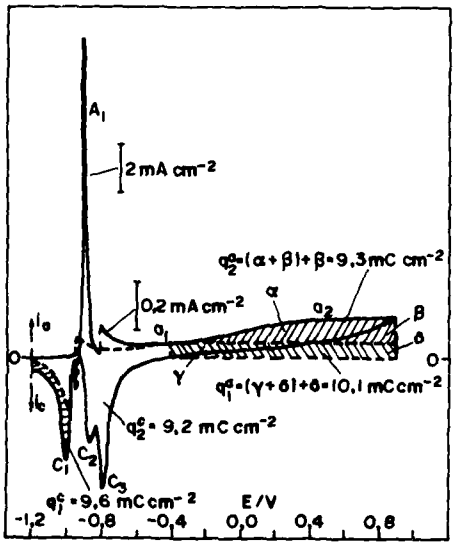


FIGURE 3 - Cyclic voltammograms of lead in 5 M H_2SO_4. (- - -) Between - 1.2 V and - 0.5 V, (——) Between - 1.2 V and + 0.9 V, showing the charges corresponding to the processes in the region a_2. $v = 10$ mV s^{-1}.

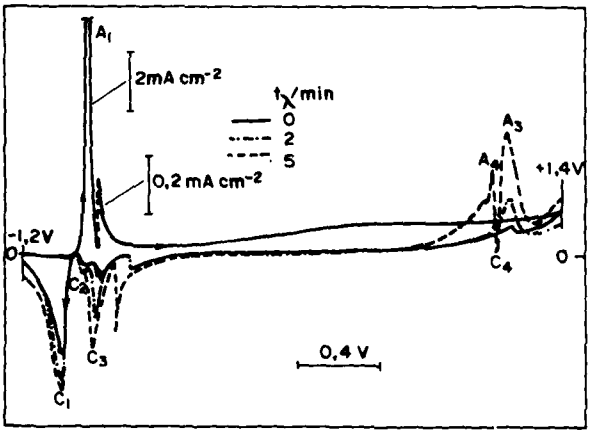


FIGURE 4 - Cyclic voltammograms of lead in 5 M H_2SO_4, between - 1.2 V and + 1.4 V for different holding times (t_λ) at + 1.4 V.

Abstract No. 67

STIBINE REMOVAL FROM LEAD-ACID (Pb-Sb) BATTERY

CORROSION TECHNOLOGY GROUP
ELECTROCHEMICAL BRANCH (R33)
NAVAL SURFACE WARFARE CENTER
WHITE OAK, SILVER SPRING, MARYLAND
20903-5000

A. H. LE
N. LINDSEY
C. M. DACRES

I. INTRODUCTION:

During charging, lead-acid batteries (Pb-Sb) will generate toxic stibine gas which may become a health hazard. The concentration of stibine in an isolated area where the lead-acid batteries are located could conceivably exceed the accepted levels for human safety. Therefore, stibine must be removed before it escapes from the lead-acid batteries. A stibine filter (1) was designed for this purpose and is located at the top of the flash arrestor. Initially this filter successfully controlled the stibine generation from the lead-acid batteries for the period of 8-hour charging at the voltage of 2.55 V by using charcoal as a adsorbent (2).

The objective of this research is to study the efficiency of activated charcoal and other materials for the removal of the toxic stibine gas from lead-acid batteries. By studying various adsorbents in different pore sizes, the optimum conditions can be obtained to ensure the safe use of lead-acid batteries in confined areas.

II. EXPERIMENTAL

Stibine is generated from a chemical mixture that contains potassium hydroxide, potassium antimony tartrate, sodium borohydride, tartaric acid, water and a sulfuric acid solution. Stibine gas is controlled by the addition of the sulfuric acid solution (3).

The amount of stibine adsorbed onto the adsorbent is determined by the change of the color at the end-point of a 0.1 N silver nitrate trapping solution. The stibine produced in the reaction vessel is flushed through the filter into the trapping solution by a carrier gas (either air or some inert gas) at a fixed flow rate.

Various adsorbents such as 6-14 and 50-80 mesh activated charcoal, 14-20 mesh silica gel and 4-8 and 8-12 mesh molecular sieve (zeolite) were used. To optimize the amount of the adsorbent, different weights varying from 5 grams up to 50 grams were tested.

III. RESULTS

The results revealed that activated charcoal is superior to the other adsorbents in trapping stibine. The differences of the adsorbed stibine sharply increased at the weight above 25 grams (see Figure 1).

The effectiveness of the adsorbent for stibine is increased from the order of silica gel, molecular sieve and activated charcoal. For each individual adsorbent, the smaller of the particle size the more stibine adsorbed. However, the 50-80 mesh activated charcoal caused some backup pressure which may incease the internal pressure of the lead-acid batteries.

The temperature study of activated charcoal revealed that adsorption of stibine on charcoal is an exothermic reaction. The maximum temperature was obtained at 105°C from the decomposition of stibine when 35 grams of 6-14 mesh activated charcoal used. Incidentally, this maximum temperature occurrs at the end-point where the charcoal is saturated with stibine.

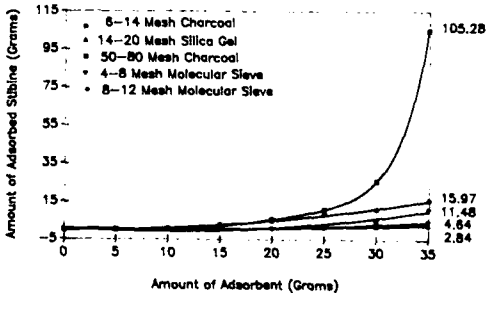
IV. REFERENCES

1. A. H. Le and C. M. Dacres, TR 84-328, Naval Surface Weapons Center, Silver Spring, MD, 1984.

2. A. H. Le, "Proceeding of the 32nd Power Sources Symposium" at Cherry Hill, NJ, June 1986, p. 351.

3. D. L. Haynes, S. S. Fratoni, L. Nanis and R. D. Weaver, Section I, p. 1-2, Special Report, May 1977, Electric Power Research Institute.

Figure 1: Stibine adsorption of Activated Charcoal – Silica Gel – Molecular Sieve



Abstract No. 68

AUTOMOTIVE BATTERY STATUS MONITOR

T. Palanisamy and S. Mendelson
Corporate Technology
Allied-Signal, Inc.
P.O. Box 1021R
Morristown, New Jersey 07960

Sensors for automotive components help preventive maintenance and also minimize maintenance costs. The automotive battery is one of those essential components which need such a sensor. In this work we have developed an automotive battery status monitor. The methodology, software and features of this monitoring system will be presented.

Historically, an ammeter and/or a voltmeter on the dashboard has served as a battery status monitor. However, they have provided only limited information, and that too only for "educated" drivers. In general, the car is taken to a garage where the battery is tested by discharging through a load by a skilled mechanic. From the battery characteristics during this test, the instruments display whether the battery is good or bad. Techniques using an a.c. signal without having to discharge the battery through a load have been described in the literature. However, they all need the battery disconnected from the electrical circuitry of the car. In this investigation we have developed a methodology and software for a microprocessor based device to test the status of the battery using the battery starting characteristics. This device also determines the low temperature limit below which the battery, under the existing conditions, may not be able to start the car. It also determines the defects, if any, in the battery as well as the charging system.

The battery status monitor determines the battery, characteristics from two sets of data; one collected during the normal usage of the SLI battery and the other during a special test profile typically in conditions like highway driving.

The test cycle involves imposing a linearly increasing current or voltage ramp onto the battery terminals and measuring the corresponding voltage or current response of the battery. Typically the current signal consists of an increasing ramp from 0 to 20 A in 60 seconds, holding constant at this level for 5 seconds, and a decreasing ramp from 20 to 0 A in 60 seconds. When voltage ramping is used, the signal consists of an increasing voltage ramp from open circuit voltage (OCV) to an end voltage corresponding to 0.5V higher than the OCV for each cell. In both cases if the voltage limit (2.6V/cell) is reached before the time limit (60 seconds), the increasing signal changes over to the holding portion. The presence of a maximum in dV/dI versus I_{ramp}, or a minimum in dI/dV versus V_{ramp} indicates the gas point. From the voltage at the gas point, the number of cells (NOC), is calculated using the formula: $NOC=V_{gas}/2.50$. In an automotive battery, this would normally be 6. Any other number may be indicative of a defective battery. We have found that the current at which the gas point occurs in the ramp-up direction, I_{gas-up}, is proportional to the battery capacity. The current at which the gas point occurs in the ramp-down direction, $I_{gas-down}$, reaches the lowest possible value, typically around 0.8 A, when the battery is fully charged. Thus, the battery capacity can be determined from the former, and the state of charge, from the latter parameter.

Batteries with mismatched cells give rise to two or more gas points in the ramp-up direction. Soft-shorted cells exhibit an inflection dV/dI at very early stages of the ramp. The presence of sulfated cells give rise to an inflection in the ramp-up, but no corresponding inflection in the ramp-down. Thus, several battery defects are detected in the test cycle.

A microprocessor with embedded software will control the functions of (1) alternator/regulator, (2) an optional clutch or field coil relay that engages and disengages the alternator with the drive system and (3) the battery. It measures the battery voltage, alternator/regulator output voltage and the current input and output from the battery. It can send an appropriate message to the indicator/display system on the dashboard.

The monitor provides the state of charge (SOC) of the battery at any time. When the battery is near its fully charged status, the monitor can cut out the alternator through the "clutch" - thus possibly enhancing the gas mileage. When either the state of charge is below a set limit, or the accessory drain current is above a preset limit, or the ambient temperature is below a preset limit, the power source is kept operational. When the car is off (car engine not running), and the drain current exceeds a present limit or the SOC is lower than a preset limit, the battery is isolated from the rest of the electrical system (or the accessories are cut off from the battery).

An important feature of this system is its capability to indicate the low temperature starting limit of the car with the battery's present conditions. The monitor arrives at a number for the low temperature limit by taking into account both the engine requirements and the battery's ability to meet them.

The battery status monitor can inform the driver whether the battery needs maintenance or replacement. The monitor can advise the driver when the battery terminals need cleaning. Likewise it does well in indicating the addition of water when the electrolyte level is too low. Conditions like the presence of one or more bad cells (low capacity, mismatched cells or soft-shorted cell(s)) indicate in advance the need to change the battery.

Abstract No. 69

AN IMPEDANCE STUDY OF THE ELECTRODISSOLUTION OF ALUMINUM IN 4M KOH AT 25°C

Digby D. Macdonald, Mirna Urquidi-Macdonald
and Silvia Real
SRI International
Menlo Park, CA 94025

An electrochemical impedance analysis of pure aluminum in 4M KOH at 25°C is reported. Impedance spectra have been obtained at 30-80 mV intervals extending from the hydrogen evolution region at -1.96 V (vs. Hg/HgO, 4M KOH) to the transpassive dissolution region at -1.35 V. The impedance spectra are found to consist of two intersecting capacitive semicircles with a loop at intermediate frequencies. The low frequency capacitive arc and the loop become increasingly dominant with respect to the high frequency relaxation as the potential is shifted in the positive direction (Table 1). The impedance spectra and the steady-state current/voltage characteristics (including the partial anodic and cathodic curves) are accounted for by a model involving the step wise addition of hydroxyl groups to surface aluminum atoms, culminating in the chemical dissolution of $Al(OH)_3$ to form $Al(OH)_4^-$ (Table 2). This anodic process is coupled to hydrogen evolution via competition for bare surface sites. Comparison of the experimental and predicted impedance spectra indicates that the total concentration of reactive sites on the surface varies with potential in a manner that parallels the anodic partial current. This variation is attributed to the existence of a porous corrosion product film on the surface. The impedance analysis also indicates small values (<0.1) for the transfer coefficients for elementary charge transfer reactions; these are attributed to the highly assymetric nature of the reaction coordinate for reactions involving reactive species ($Al + OH^-$) or to strong repulsive interaction between adsorbed species, as embodied in the Temkin adsorption isotherm. However, the impedance data do not provide strong evidence for autocatalysis and it appears that the simple step-wise mechanism (Mechanism I, Table 2) is the most appropriate for describing the electrodissolution of aluminum in 4M KOH at 25°C.

ACKNOWLEDGMENTS

The authors gratefully acknowledge support of this work by the U.S. Department of Energy through Lawrence Berkeley Laboratory under Contract No. LBL PO#4543710.

Table 1
NYQUIST DIAGRAMS CALCULATED WITH THE SET OF PARAMETERS SHOWN IN TABLE 9 COMPARED WITH EXPERIMENTAL VALUES FOR ALUMINUM 4 M KOH AT 25°C

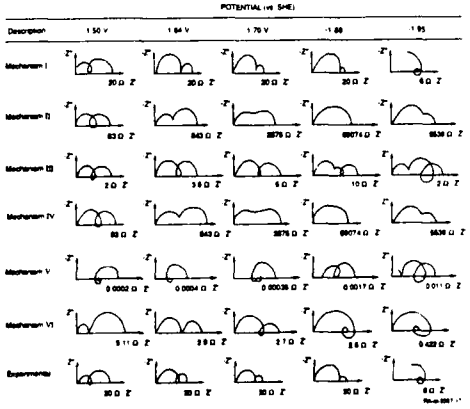


Table 2

THEORETICAL MODELS FOR THE CORROSION AND ELECTRODISSOLUTION OF ALUMINUM ALLOYS IN ALKALINE SOLUTIONS

	Mechanism	Reaction Scheme
I	*Irreversible coupled dissolution/hydrogen ion-atom evolution*	$Al(SS)^* + OH^- \xrightarrow{b_1} Al(OH)_{ads} + e^-$
		$Al(OH)_{ads} + OH^- \xrightarrow{b_2} Al(OH)_{2,\,ads} + e^-$
		$Al(OH)_{2,\,ads} + OH^- \xrightarrow{b_3} Al(OH)_{3,\,ads} + e^-$
		$Al(OH)_{3,\,ads} + OH^- \xrightarrow{b_4} Al(OH)_4^-$
		$SS + H_2O + e^- \xrightarrow{b_5} H + OH^-$
		$H + H_2O + e^- \xrightarrow{b_6} H_2 + OH^- + SS$
II	Coupled dissolution/ H-atom recombination	$Al(SS)^* + OH^- \xrightarrow{b_1} Al(OH) + e^-$
		$Al(OH) + OH^- \xrightarrow{b_2} Al(OH)_2 + e^-$
		$Al(OH)_2 + OH^- \xrightarrow{b_3} Al(OH)_3 + e^-$
		$Al(OH)_3 + OH^- \xrightarrow{b_4} Al(OH)_4^- + SS$
		$SS + H_2O + e^- \xrightarrow{b_5} H + OH^-$
		$H + H \xrightarrow{b_6} H_2 + 2\,SS$
III	Autocatalytic (I)/hydrogen ion-atom evolution	$Al(SS)^* + OH^- \xrightarrow{b_1} Al(OH) + e^-$
		$Al(OH) + OH^- \xrightarrow{b_2} Al(OH)_2 + e^-$
		$Al(OH)_2 + OH^- \xrightarrow{b_3} Al(OH)_3 + e^-$
		$Al(OH)_3 + OH^- \xrightarrow{b_4} Al(OH)_4^- + SS$
		$Al(OH)_4^- + Al \xrightarrow{b_5} Al(OH) + Al(OH)_3 + e^-$
		$SS + H_2O + e^- \xrightarrow{b_5} H + OH^-$
		$H + H_2O + e^- \xrightarrow{b_6} H_2 + OH^- + SS$
IV	*Autocatalytic (I)/H-atom recombination*	$Al(SS)^* + OH^- \xrightarrow{b_1} Al(OH) + e^-$
		$Al(OH) + OH^- \xrightarrow{b_2} Al(OH)_2 + e^-$
		$Al(OH)_2 + OH^- \xrightarrow{b_3} Al(OH)_3 + e^-$
		$Al(OH)_3 + OH^- \xrightarrow{b_4} Al(OH)_4^- + SS$
		$Al(OH)^- + Al \xrightarrow{b_5} Al(OH) + Al(OH)_3 + e^-$
		$SS + H_2O + e^- \xrightarrow{b_5} H + OH^-$
		$H + H \xrightarrow{b_6} H_2 + 2\,SS$
V	Autocatalytic (II)/ *H-atom recombination*	$Al(SS)^* + OH^- \xrightarrow{b_1} Al(OH) + e^-$
		$Al(OH) + OH^- \xrightarrow{b_2} Al(OH)_2 + e^-$
		$Al(OH)_2 + OH^- \xrightarrow{b_3} Al(OH)_3 + e^-$
		$Al(OH)_3 + OH^- \xrightarrow{b_4} Al(OH)_4^- + SS$
		$Al(OH)_4^- + Al \xrightarrow{b_5} Al(OH) + Al(OH)_3 + e^-$
		$SS + H_2O + e^- \xrightarrow{b_5} H + OH^-$
		$H + H \xrightarrow{b_6} H_2 + 2\,SS$
VI	Autocatalytic (II)/ hydrogen ion-atom evolution	$Al(SS)^* + OH^- \xrightarrow{b_1} Al(OH) + e^-$
		$Al(OH) + OH^- \xrightarrow{b_2} Al(OH)_2 + e^-$
		$Al(OH)_2 + OH^- \xrightarrow{b_3} Al(OH)_3 + e^-$
		$Al(OH)_3 + OH^- \xrightarrow{b_4} Al(OH)_4^- + SS$
		$Al(OH)_4^- + Al \xrightarrow{b_5} Al(OH) + Al(OH)_3 + e^-$
		$SS + H_2O + e^- \xrightarrow{b_5} H + OH^-$
		$H + H_2O + e^- \xrightarrow{b_6} H_2 + OH^- + SS$

SS represents a base surface site, i.e. Al(SS)

Abstract No. 70

MORPHOLOGICAL-ABSORPTIVE CHARACTERISTICS OF PAFC ANODES

N. Giordano, E. Passalacqua, P. Staiti, H. Mirzaian, E. Recupero, E. Alderucci, Z. Poltarzewski and M. Vivaldi
Institute CNR-TAE 98126 Pistunina-Messina (Italy)

E.J. Taylor and G. Wilemski
PSI Technology Co., Andover, MA 01810 (USA)

INTRODUCTION

Advancements in PAFC technology require a better knowledge of the morphological characteristics of the gas diffusion electrodes, both with regard to electrode fabrication procedures and to define correlations between morphology and electrochemical performance. We present correlations between hydrogen oxidation and morphological characteristics of PAFC's anodes.

EXPERIMENTAL

We prepared gas diffusion electrodes by a procedure described in a companion paper.[1] The preparation parameters varied were: a) % PTFE (30-70%) at constant sintering T (T_S = 350°C in air, 15 min); b) Pt loading, (W_{Pt}), from 0.2 to 0.5 mg Pt/cm^2 (constant T_S and % PTFE); c) T_S from 320°C to 360°C(15 min in N_2 or air) at constant % PTFE (50%); d) atmosphere (N_2 or air); e) final pressing of the electrode (from 15 to 45 kg/cm^2).

The as-prepared electrodes were characterized by porosimetric analysis (Carlo Erba Mod. 2000) and absorption of 98% w/w H_3PO_4 (P.A.) at 200°C for 24 hr. From the thickness of the electrode, Z_c (cm), total porosity, and P.A. absorption in the catalyst layer, we have derived the percent acid occupation.

RESULTS AND DISCUSSION

We have observed a strong correlation between anode performance and the percentage of acid occupation (PAO) by the catalyst layers.[1] PAO is defined as 100 (ϕ/θ_c) where ϕ is the fraction of catalyst layer volume occupied by electrolyte and θ_c is the porosity of the catalyst layer. PAO is determined from the experimentally measured values of (gH_3PO_4/g catalyst layer), the total pore volumes of the electrode (Ves), the catalyst layer (V_A), and the support (V). Plots of ϕ, Ves and V_A as a function of preparative variables (W_{Pt}, T_S, and % PTFE, respectively) show that PAO depends most strongly on ϕ, and Ves and V_A are relatively insensitive to the electrode preparative variables. Further, analysis of the results reveals that other morphological characteristics such as total gas porosity ($\theta_g = \theta_c - \phi$), porosity of the agglomerate region (θ, including all pores < 0.4 μ), residual porosity of the gas filled macropores in the agglomerate (θ_g^*, including all pores > 0.4μ) are correlated to the PAO (Figs. 1, 2 and 3). More particularly Fig. 2 shows that the total gas porosity of the gas filled pores, θ_g, decreases as PAO increases. Taking into account that $\theta_g = \theta_c - \phi$, the observed behavior confirms a variable degree of occupation, as preparative conditions are made to vary, of pore volumes occupied by the P.A. (ϕ) versus those left to the gas (θ_g). Further, we observed that θ and θ_g^* are relatively independent of PAO (cf. Fig. 2 and Fig. 3, respectively). We conclude that irrespective of the preparation variables (T_S, teflon, etc.) the morphological characteristics of the agglomerates (θ and θ_g^*) are strongly influenced by those of the original electrocatalysts. The preparation parameters affect the macroscopic structural characteristics of the electrodes, as evident from the descending trends of θ_g vs PAO (Fig. 1). This observation is more evident when "pore-filling" of the agglomerate is plotted vs PAO (Fig. 4). In fact, the ratio of the flooded to total pore volume of the agglomerate ϕ/θ (1-θ_g^*) generally increases with PAO. Since θ_g exhibits an opposite trend, we suggest that preparative variables affect the morphology of the electrode and its absorptive characteristics in opposed fashion (compare Figs. 1 and 4). Thus, while the gas phase porosity of the electrode changes in an obvious way with PAO (Figs. 1 and 4) there are no corresponding variations in the agglomerate's morphological-absorptive characteristics (Figs. 2-3).

REFERENCES

1. N. Giordano, E. Passalacqua, P. Staiti, H. Mirzaian, E. Recupero, E. Alderucci, R. Di Leonardo and M. Vivaldi, G. Wilemski and J. Taylor, "Performance and optimization of Phosphoric Acid Fuel Cells Gas-Diffusion Cathodes," Extended Abstracts, Electrochemical Society Meeting, Chicago, IL, October 1988.

ACKNOWLEDGEMENTS

The Authors wich to thank ENEA for permission to publish this work which was made under contract within the framework of "Progetto Volta".

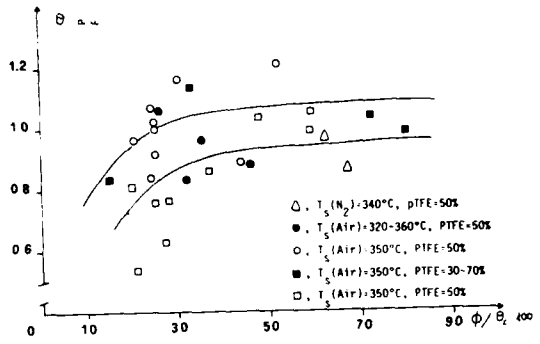


Fig. 1. Porosity of the agglomerate region vs. % acid occupation

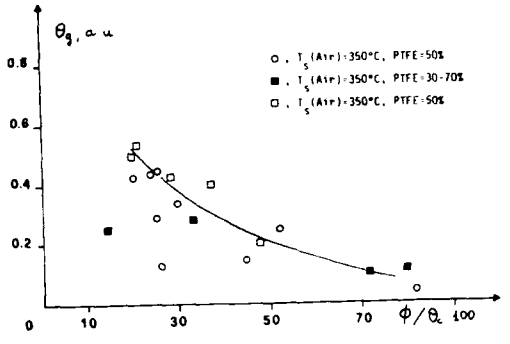


Fig. 2. Total gas porosity vs. % acid occupation

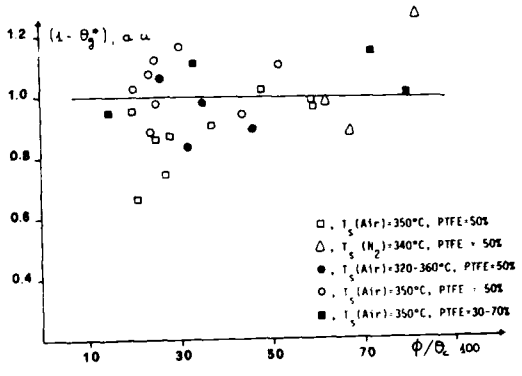


Fig. 3. Residual porosity of the gas-filled macropores in the agglomerate vs. % acid occupation

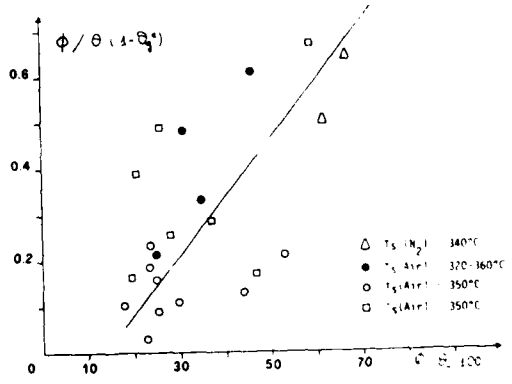


Fig. 4. Pore-filling of the agglomerate vs. % acid occupation

Abstract No. 71

PERFORMANCE AND OPTIMIZATION OF PHOSPHORIC ACID FUEL CELL GAS-DIFFUSION CATHODES

N. Giordano, E. Passalacqua, P. Staiti, H. Mirzaian, E. Recupero, E. Alderucci, R. Di Leonardo and M. Vivaldi
Institute CNR-TAE 98126 Pistunina-Messina (Italy)

G. Wilemski and E. J. Taylor
PSI Technology Co., Andover, MA 01810-7100 (USA)

INTRODUCTION

Although PAFC technology has greatly advanced up to the scale of large size units, there is a lack of published information as to the influence of the preparative conditions upon the electrochemical performance of electrodes. This paper faces the problem of establishing some correlations between preparative variables (such as Pt-loadings, sintering temperature (T_S) and %PTFE), and the electrode performance. The information is useful in assisting optimization of the preparative conditions and in modeling electrochemical behavior, as outlined in a previous paper.[1]

EXPERIMENTAL

Electrodes were prepared from carbon paper (Stackpole PC 206) which was wet-proofed with a solution of FEP, dried at 70°C and sintered at 340°C for 15 minutes. The catalyst ink was prepared by mixing and stirring (50-60°C, 15 min) 3 g of 10% Pt/C (MSA = 65 m^2/g Pt, S.A. of carbon = 61 m^2/g), 62 ml H_2O and 2.2 ml of Teflon solution (51% TFE). To the cold solution, 23 g of isopropyl alcohol were added and the flocculate was screen printed (Argon Modular 2) on the carbon paper. The electrode was dried in a controlled atmosphere (N_2 or air) at 120°C (1 hr), at 280°C (30 min) and then sintered, T_S (320°C to 360°C). Electrodes were made with varying PTFE constant (20 to 60%) and Pt loadings (0.3 to 0.7 mg Pt/cm^2). The cathodic reduction of O_2 or air was measured in a conventional halfcell made of Teflon, at 170°C in a 99% H_3PO_4 solution with an air flow-rate of 400 cc/min. The phosphoric acid (P.A.) absorption (g H_3PO_4/g electrode) was measured in an all-teflon apparatus at 200°C after equilibration (24 hr). The electrolyte filled porosity (ϕ) divided by the total porosity (θ_c) is the percentage acid occupation. This value was calculated from porosimetrically determined volumes of the catalyst layer electrode and the support.

RESULTS AND DISCUSSION

As predicted in a previous paper[1], the percentage of the P.A. occupation exerts a strong influence on the characteristics of the electrodes. Previous modeling analysis identified two main factors: the degree of wetting of the catalysts layer and the volume of pores left void for the passage of the gases. In Figs. 1 and 2 we present the percent acid occupation as a function of %PTFE and sintering temperature. As shown in Fig. 3, irrespective of the preparative conditions (i.e., Ts, %PTFE, Pt loading, etc.), the electrochemical activity on both air and O_2 exhibits a maximum at ca. 30-50% acid occupation. One notable characteristic is that the shape of these curves changes with the time of operation (cf. Figs. 3 vs. 4). Electrodes with greater than 50% acid occupation are more prone to structural modifications, as also confirmed by Mori[2].

The performance of the electrodes on air and O_2 was also screened in terms of O_2 gains. Plots of Oxygen gains exhibit a minimum as a function of T_S or % Teflon. More interestingly, plots combining different T_S and PTFE indicate that, irrespective of the imposed preparative conditions, oxygen gains are minimized at around 30-50% acid occupation (Fig. 5). This observation is relevant as it helps in identifying intervals of operating conditions, however obtained, which should assure better performance. The minimum oxygen gains at 100 and 700 mA/cm^2, as observed at about 30-40% acid occupation (Fig. 3), assures in fact that these characteristics mark, not only the points of highest activity, but also those with the greatest degree of utilization of the porous structure, i.e., less diffusion controlling conditions as well as of greatest electrochemical stability.

REFERENCES

1. N. Giordano, E. Passalaccua, V. Recupero, P. Staiti, V. Alderucci, D.G. Lister and G. Wilemski, "Analysis of Acid Occupation Effect on PAFC Cathode Performance," Int. Seminar on Fuel Cell Technology and Applications, Den Haag 26-29 October 1987, Extended Abstracts, pp. 301-308.

2. T. Mori, J. Imahashi, T. Kamo, K. Tamura and Y. Hishinuma, J.E.S. Vol. 133 n. 5 (May 1986) pp. 896-900.

ACKNOWLEDGEMENTS

The Authors wish to thank ENEA for permission to publish this work which was made under contract within the framework of "Progetto Volta".

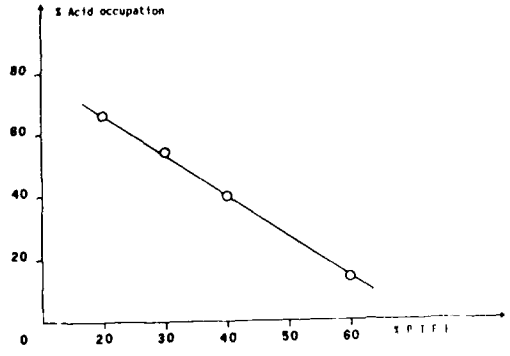


Fig. 1. % Acid occupation vs. % PTFE

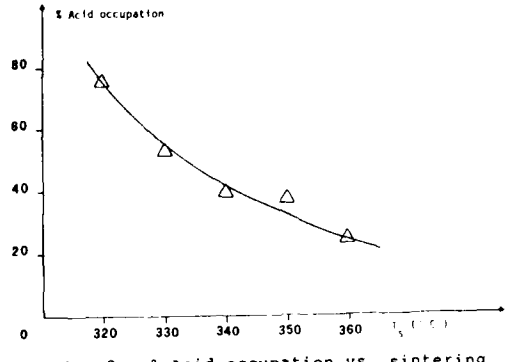


Fig. 2. % Acid occupation vs. sintering temperature

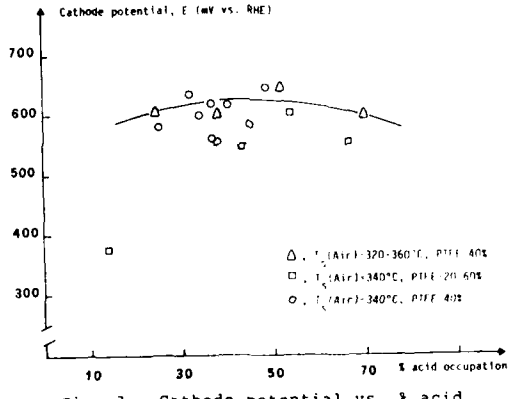


Fig. 3. Cathode potential vs. % acid occupation in air at t=0

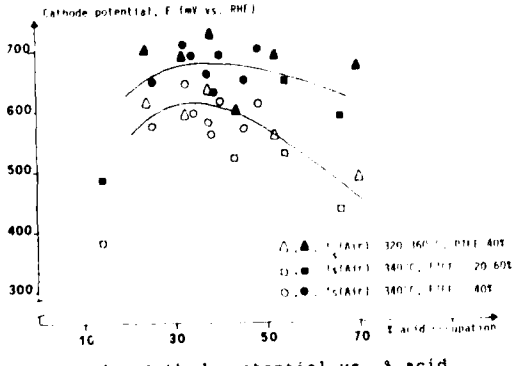


Fig. 4. Cathode potential vs. % acid occupation in air (Δ, ○) and in O_2 (▲,■,●) at t= 6 hrs

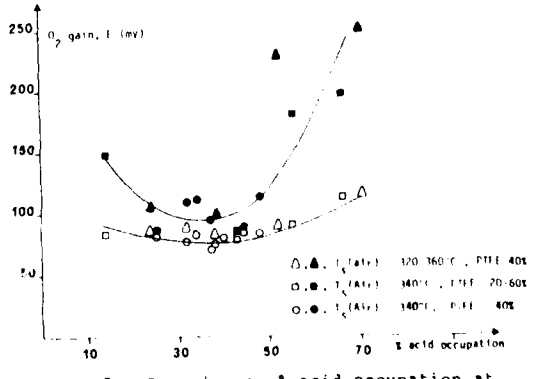


Fig. 5. O_2 gain vs. % acid occupation at 100 mA/cm^2 (Δ,□,○) and at 700 mA/cm^2 (▲,■,●)

Abstract No. 72

DEVELOPMENT OF POROUS GAS DIFFUSION ELECTRODES FOR OXYGEN REDUCTION IN ALKALINE MEDIA

E. J. Taylor, G. Moniz, M. Clawson,
E. Anderson and G. Wilemski
PSI Technology Company
P.O. Box 3100
Andover, MA 01810

INTRODUCTION

The performance of a porous gas diffusion electrode is determined by a number of highly interrelated factors. Pore structure, electrolyte content, surface area, transport phenomena and electrode kinetics are usually strongly coupled. This greatly complicates the interpretation of porous electrode performance and hinders the development of an optimally performing electrode.

To be effective, the porous electrode must be wetted by an appropriate amount of electrolyte. Low electrolyte content facilitates gas and liquid phase diffusion of reactants; however, it may result in high internal ohmic losses. Moreover, unwetted catalyst is inactive and not utilized. Conversely, high electrolyte content decreases internal ohmic losses; however, it increases diffusion losses due to flooding of catalytic sites. An electrode that is too thick suffers from excessive ohmic and gas diffusion losses, while an electrode that is too thin does not contain sufficient catalyst surface area to maximize performance.

For a given Pt + C electrocatalyst, there are optimum values for the electrolyte content and electrode thickness that will maximize electrode performance. These values depend on the electrode fabrication process which influences porosity, pore size distribution, and agglomerate size.

In sum, efficient porous gas diffusion electrodes must possess the proper balance between hydrophobic and hydrophilic character to allow the development of the proper three-dimensional distribution of solid catalyst, liquid electrolyte, and gaseous reactant. The main variables involved in gas diffusion electrode fabrication are 1) Teflon content, 2) Teflon sintering temperature, 3) electrode thickness, and 4) catalyst loading. We have investigated the effects of these electrode fabrication parameters on the performance of a carbon supported platinum electrocatalyst for oxygen reduction in alkaline media.

EXPERIMENTAL

We prepared carbon supported platinum electrocatalysts using a colloidal deposition technique. We determined the platinum particle sizes using transmission electron microscopy at the MIT Center for Materials Science. The platinum loadings were determined gravimetrically after burning the carbon in air at 900°C.

We fabricated gas diffusion electrodes on carbon paper (Stackpole PC 206), which was wet proofed with FEP (0.5 mg/cm^2, sintered at 275°C). A flocculate of carbon supported platinum electrocatalyst and Teflon was collected on a filter paper and was transferred to the carbon paper substrate. The electrode was dried at 100°C for one hour and at 200°C for one hour, and then sintered for fifteen minutes.

Electrodes with Pt catalyst and Pt + C electrocatalyst loadings of 0.45 mg/cm^2 and 5 mg/cm^2, respectively, were prepared with Teflon contents and sintering temperatures shown in Table 1. At a Teflon loading of 30% and sintering temperature of 300°C, we prepared electrodes with the Pt catalyst loadings shown in Table 2, and with the Pt + C electrocatalyst loadings shown in Table 3. We measured the electrocatalyst layer thickness using scaning electron microscopy. The oxygen reduction performance of our electrode preparations was measured in 30% NaOH at 75°C and corrected for iR loss.

RESULTS AND DISCUSSION

The measured platinum loadings and particle sizes of our electrocatalysts are given in Table 4. The specific surface areas were calculated assuming spherical particles. The average platinum particle sizes were 16 to 21Å.

We measured the polarization behavior of our electrodes on pure oxygen and synthetic air. The oxygen gain (difference between potentials on oxygen and air at a given current density) is a measure of the effectiveness of the electrode structure for reactant transport. In Figures 1 and 2, we present the oxygen gains as a function of Teflon content and sintering temperature. We observe the minimum oxygen gain (and hence most effective electrode structure) at 30% Teflon sintered at 300°C.

In Figure 3, we present the oxygen reduction data for various electrocatalyst layer thicknesses at a constant platinum loading of 0.5 mg/cm^2. As the electrocatalyst layer thickness is decreased from 260 to 80 μm, we observe an increase in the electrode performance. Since each electrode contains the same Pt catalyst loading, our catalyst utilization increases as our electrocatalyst layer thickness decreases.

In Figure 4, we present the oxygen reduction performance versus the percent Pt catalyst for a given electrocatalyst layer thickness. The performance increases as the platinum content increases.

We have summarized our results regarding the effects of various electrode fabrication parameters on oxygen gain and electrode performance. In addition, we will present the effects of these fabrication parameters on catalyst mass activity (mA/mg Pt) and specific activity (μA/cm^2 Pt). These data will be correlated with the electrode morphology (i.e., porosity and pore size) and wettability (i.e., electrolyte filled porosity and gas filled porosity).

This work is funded under cooperative agreement with the DOE, No.DE-FC07-84ID12495. The authors acknowledge the support and encouragement of Dr. S. Priebe and Mr. W. Sonnett.

Table 1. Teflon Contents and Sintering Temperatures for Electrode Fabrication

Percent PTFE	Sintering Temperature (°C)				
	275	300	325	345	375
20				X	
30	X	X	X	X	X
40				X	
50				X	
60				X	
70				X	

Table 2. Electrocatalyst Loadings, Weight Percentages of Platinum and Catalyst Loadings for Loading Study

Electrocatalyst (Pt & C) Loading (mg/cm^2)	% Pt on Ketjen	Catalyst (Pt) Loading (mg/cm^2)
5.00	5	0.25
5.00	9	0.45
5.00	10	0.50
5.00	15	0.75
5.00	20	1.00

Table 3. Electrocatalyst Loadings, Weight Percentages and Catalyst Loadings for Thickness Study

Electrocatalyst (Pt & C) Loading (mg/cm^2)	% Pt on Ketjen	Catalyst (Pt) Loading (mg/cm^2)
2.50	20	0.50
3.33	15	0.50
5.00	10	0.50
10.00	5	0.50

Table 4. Platinum Catalyst Loadings, Particle Sizes and Surface Areas

Target Pt Loading (%)	Actual Pt Loading (%)	Mean Particle Size (Å)	Calculated Pt Surface Area (m^2/g)
5	4.9	15.9	176
10	9.5	18.6	150
15	14.4	16.7	168
20	19.3	21.0	133

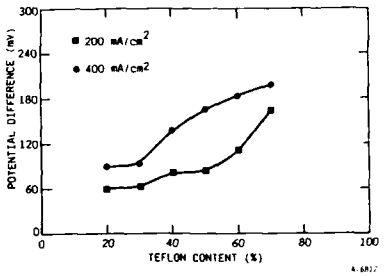


Figure 1. Oxygen gains at 200 and 400 mA/cm^2 as a function of Teflon content

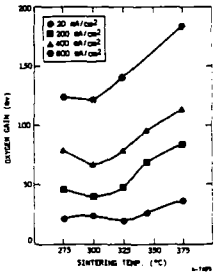


Figure 2. *Oxygen gains at 20, 200, 400 and* 800 mA/cm^2 as a function of sintering temperature

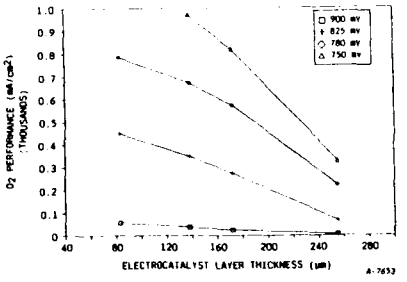


Figure 3. Oxygen reduction performance versus electrocatalyst layer thickness

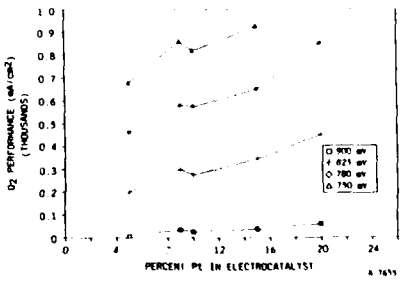


Figure 4. Oxygen reduction performance versus platinum catalyst weight percentage

Abstract No. 73

Methane Activation to C_2 Hydrocarbon Species in Solid Oxide Fuel Cell

Nirupama U. Pujare and Anthony F. Sammells

Eltron Research, Inc.
4260 Westbrook Drive
Aurora, IL 60504

The solid oxide fuel cell:

$$CH_4,Pt/Sm_2O_3/La_{0.89}Sr_{.10}MnO_3/YSZ/La_{0.89}Sr_{.10}MnO_3/Pt,O_2(air)$$

was fabricated using a closed-one-end yttria stabilized zirconia (YSZ) solid electrolyte tube. Anode fuel gas typically comprised 10% CH_4 in argon. At 760°C the cell possessed an open-circuit potential (OCP) of 1.25V. The cathode oxygen source was air. Analysis of anode reaction products was performed using a GOW-MAC Model 69-750 FID gas chromatograph using a 6'x1/8" stainless steel column packed with 80/100 mesh Carbosphere (Alltech Associates, Inc.). No C_2 species were evident from either the methane or argon sources used in this work.

Initial measurements were performed under OCP conditions with O_2 being intentionally introduced into CH_4/Ar mixture at the anode. C_2H_6 was found to be the major product. Upon passing current through this fuel cell, where oxygen was only available via its Faradaic transport from the air cathode to the anode, C_2 species were formed. The dependency of total C_2 species upon cell current is summarized in Figure 1. C_2H_4, C_2H_6 and C_2H_2 were identified as Faradaic methane oxidative dimerization products whose distribution was 58% C_2H_4, 37% C_2H_6 and 4% C_2H_2. At 760°C 11% of the Faradaically transported oxygen participated in promoting methane oxidative dimerization. Anode electrode potentials were always negative of the oxygen electrode potential, hence the Faradaic oxidative dimerization reaction did not rely upon unit activity oxygen being produced in the anode compartment. Anode half-cell reactions leading to C_2 hydrocarbon species can be represented by:

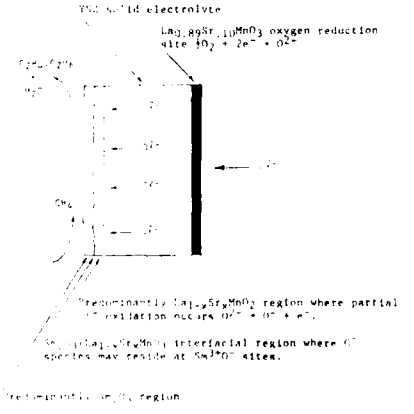
$$O^{2-} + 2CH_4 \rightarrow C_2H_6 + H_2O + 2e^-$$

$$2O^{2-} + 2CH_4 \rightarrow C_2H_4 + 2H_2O + 4e^-$$

and

$$3O^{2-} + 2CH_4 \rightarrow C_2H_2 + 3H_2O + 6e^-$$

If one assumes that the goal of this anode electrocatalysis strategy is to maximize the local population of O^- species for promoting methane oxidative dimerization, then one might represent electrocatalytic processes occurring at the $Sm_2O_3/La_{1-x}Sr_xMnO_3$ interface in this SOFC, as follows:



Ethane may then subsequently react at O^- sites via the reaction sequence[1,2]:

$$C_2H_6 + O^- \rightarrow C_2H_5^{\cdot} + OH^-$$

$$C_2H_5 + O^{2-} \rightarrow OC_2H_5^- + e^-$$

$$OC_2H_5^- \rightarrow C_2H_4 + OH^-$$

to give ethylene. Acetylene formation may occur via an analogous oxidative path involving ethylene.

ACKNOWLEDGEMENT

This work was supported by the Gas Research Institute.

REFERENCES

1. Keller, G. E. and Bhasin, M. M., J. Catal., 73, 9 (1982).
2. Ito, T., Wang, J., Lin, C. and Lunsford, J. H., J. Am. Chem. Soc., 107, 5062 (1985).

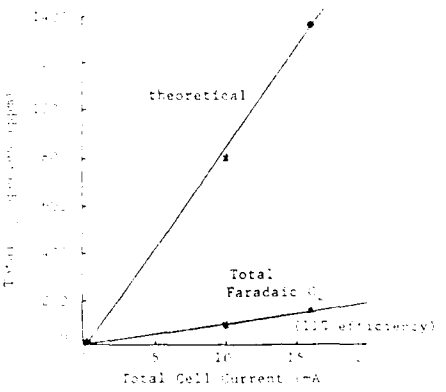


Figure 1. Total C_2 species (C_2H_6, C_2H_4 and C_2H_2) vs. cell current for the cell

$CH_4,Pt/Sm_2O_3/La_{0.89}Sr_{.10}MnO_3/Pt/YSZ/La_{0.89}Sr_{.10}MnO_3/Pt,O_2(air)$.

Initial OCP 1.27V. Anode gas comp. 10% CH_4, 90% Ar. Flow rate 50ml/min. Temp. 760°C.

Abstract No. 74

ORGANIC CATHODE MATERIALS IN SODIUM BATTERIES

B. V. Ratnakumar, S. Di Stefano,
G. Nagasubramanian, R. M. Williams,
and C. P. Bankston

Jet Propulsion Laboratory
4800 Oak Grove Drive
Pasadena, CA 91109

Several rechargeable systems based on sodium/β"-alumina have been proposed for various applications. The sodium-sulfur battery has the highest energy density and is the most developed of these. [1] Other systems, however, also offer considerable promise. In particular, solid inorganic cathodes, e.g., $FeCl_2$ and $NiCl_2$ together with $NaAlCl_4$ molten electrolyte have high energy densities (~900 Wh/kg) and operate at high power densities. Other advantages of this family of compounds are their low cost and ease of operation. [2-4]

In this paper we report the use of an organic cathode material in combination with Na-β" alumina half cell. The cell consists of liquid tetracyanoethylene (TCNE) or tetracyanoquinone (TCNQ) in molten electrolyte $NaAlCl_4$ and a platinum (or carbon) current collector in the cathode compartment and liquid sodium in the anode compartment, both being separated by β"-alumina solid (Na^+ ion conducting) electrolyte. The advantages associated with these organic depolarizers are a) a high energy density in excess of 600 Wh/kg, and b) an absence of corrosion at positive current collector or any undesirable reaction with β" alumina electrolyte.

The test cell (Figure 1) assumes a cylindrical configuration with the cathode mix containing TCNE and $NaAlCl_4$ inside the β" alumina tube and liquid sodium outside. The cell operates at temperatures above 200°C (m.p. of TCNE: 199°C).

The cyclic voltammetric curve of TCNE (Figure 2) shows a single reduction peak around 3.0 V and an oxidation peak around 3.7 V. The electrolyte $NaAlCl_4$ is stable up to 4.5 V vs. Na^+/Na on the positive side. On the negative side at 1.6 V aluminum deposition occurs. The cell thus operates between 4.0-2.0 V. At lower scan rates, the voltammograms exhibit current plateaus which may be attributed to the slow approach of TCNE (oxidized and reduced) species to the electrode.

A linear sweep voltammetric curve of TCNE (Figure 3) exhibits the mass transfer limited current. By optimization of the cell design, i.e., electrode/β tube distance, ratio of TCNE/$NaAlCl_4$, etc., it is possible to achieve much higher limiting current densities and thus higher power densities in the battery. The kinetic parameters exchange current density and transfer coefficient for the reduction of TCNE calculated from the Tafel plots corrected for mass transfer polarization are 3.6×10^{-4} A/cm² and 0.1, respectively.

The mass transfer polarization is also evident from the ac impedance Nyquist plot of TCNE (Figure 4) which shows a single relaxation loop and a linearity between real and imaginary components of impedance. The exchange current density and diffusion coefficient of TCNE in $NaAlCl_4$ obtained therefrom are 1.05 mA/cm² and 2.3×10^{-11} cm²/s.

Figure 5 gives the voltage vs. time curves of TCNE during discharge and charge at 1 mA/cm² in the fifth and sixth cycles. The electrode is fairly reversible with no loss in capacity over a few cycles tested. The coulombic efficiency is close to 65% and may be improved by optimizing the cell design.

To summarize, these organic materials show promise as high energy density cathode depolarizers in secondary batteries. Further developmental studies on TCNE and TCNQ are currently underway.

ACKNOWLEDGEMENTS

The work described here was carried out at the Jet Propulsion Laboratory, California Institute of Technology, under contract with the National Aeronautics and Space Administration. One of the authors (B. V. Ratnakumar) acknowledges the National Research Council for providing his Research Associateship during this work.

REFERENCES

1. J. L. Sudworth and A. R. Tilley, "The Sodium Sulphur Battery," Chapman and Hall, London, 1985.

2. J. Coetzer, J. Power Sources, 18, 377 (1986).

3. R. C. Galloway, J. Electrochem. Soc., 134, 256 (1987).

4. R. J. Bones, J. Coetzer, R. C. Galloway and D. A. Teagle, J. Electrochem. Soc., 134, 2379 (1987).

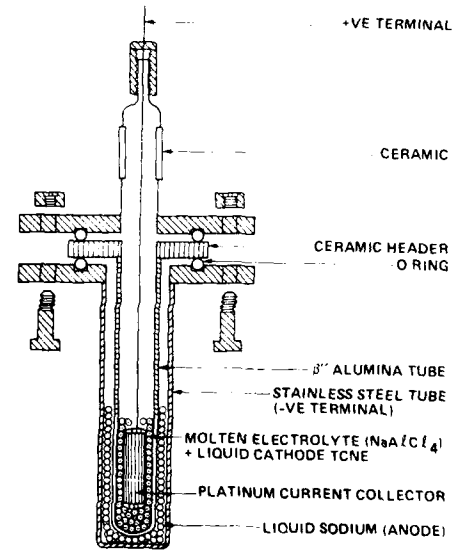


Fig. 1. Schematic representation of Na/β"-alumina/TCNE (Pt) in $NaAlCl_4$ molten electrolyte test cell.

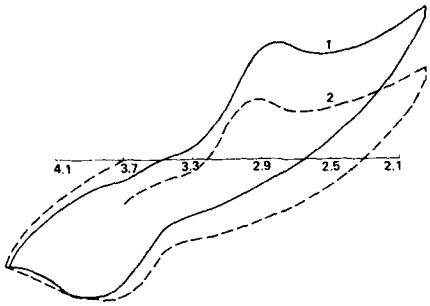


Fig. 2. Cyclic voltammogram of (10%) TCNE in $NaAlCl_4$ on platinum electrode at 230°C at scan rate of 1) 5mV/s, and 2) 2 mV/s. The scale on Y axis: 20 mA/cm.

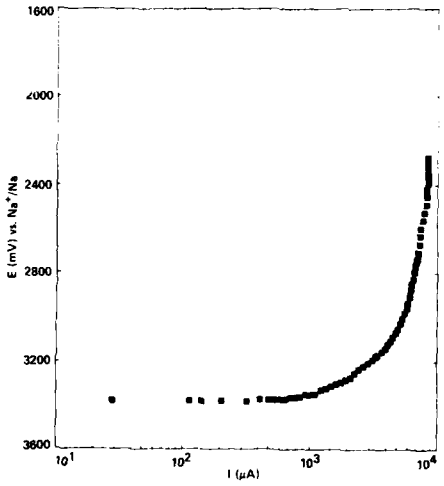


Fig. 3. Linear sweep voltammetric curve of (10%) TCNE in $NaAlCl_4$ on platinum electrode (area: 6 cm^2) at 230°C at 0.5 mV/s.

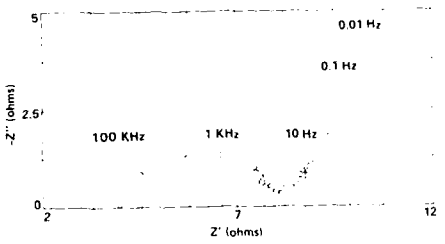


Fig. 4. Nyquist plot of (10%) TCNE in $NaAlCl_4$ on platinum electrode (area: 6 cm^2) at 230°C.

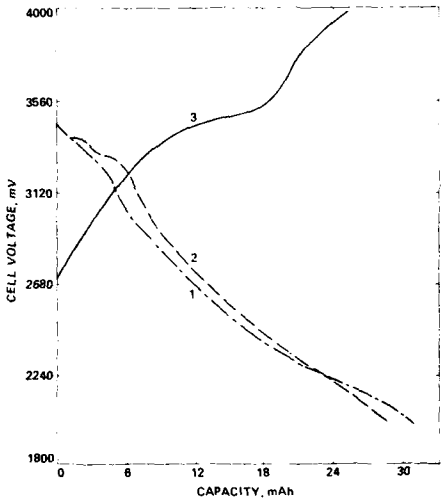


Fig. 5. Typical voltage vs. capacity curves of 45 mAh Na/β"-alumina/TCNE (Pt) in $NaAlCl_4$ during discharge in 1) 3rd cycle, 2) 4th cycle, and 3) charging at 1 mA/cm^2 at 230°C.

Abstract No. 75

Electrochemical Investigations of Organodisulfides

Meilin Liu, S. J. Visco, and L. C. De Jonghe

Materials and Chemical Sciences Division
Lawrence Berkeley Laboratory
and
Department of Materials Science and Mineral Engineering
University of California
Berkeley, CA 94720

A group of organic disulfides have been recently introduced as positive electrodes for high-energy-density battery applications[1]. The advantages of these compounds includes low operating temperature, high energy density, low cost, passive behavior to many materials, and low toxicity. Furthermore, their properties can easily be modified by appropriate choice of the organic groups. To date, however, the fundamental physical, chemical, and electrochemical properties of these materials have not been established. The purpose of this study is to investigate the redox behavior, chemical stability and reversibility, kinetic reversibility, and adsorption phenomena of organodisulfides at electrode surfaces.

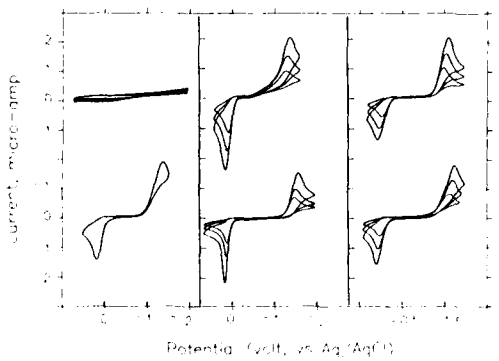
EXPERIMENTAL

Organic disulfides used in the experiment were obtained from Aldrich and purified in our laboratory, as described by Visco et al [2]. Sodium thiolate salts were either obtained from Aldrich or synthesized in our laboratory. Tetraethyl ammonium perchlorate (TEAP) and tetramethyl ammonium chlorate (TMAC) were obtained from Southwestern Analytical Chemicals. All solid compounds were recrystallized from appropriate solvents, and kept under vaccum in a dessicator. Dimethylsulfoxide (DMSO), acetonitrile (AN), and propylene carbonate (PC) were obtained from Aldrich and stored over molecular sieves in an argon atmosphere dry box.

Three-electrode electroanalytical cells, with platinum counter electrodes and Ag/AgCl reference electrodes, were used throughout the experiment. Platinum metal, graphite or glassy carbon electrodes were used as the working electrode.

In linear sweep voltammetry (LSV) or cyclic voltammetry (CV), a linear or triangular potential function, generated using a Potentiostat (Model 173, EG&E) in conjunction with a Universal programmer (Model 175, EG&E), was applied to a stationary electrode immersed in a quiet solution. The corresponding currents were measured as a function of potential or time and recorded with a Bascom-Turner recorder. The sweep rates used in the study ranges from 10mv/sec to 1000mv/sec.

In potential-step techniques, an excitation signal of one or more potential steps (with pulse width of 10-500 msec), was generated from a IBM-PC/AT equipped with a data aquisition board (Data Translation 2801-A) and Scientific ASYST/ASYSTANT Software and interfaced to a PAR 173 potentiostat/Galvanostat. The computer controlled output signals were applied to a stationary electrode immersed in a quiet solution and the corresponding current or charge response were measured as a function of time and acquired to the computer.



An Electrode Rotator and Speed Controller (Model ASR, PINE instrument Co.) were used to modulate the rotation speeds of a disk or ring-disk electrode. The limiting currents for reduction of the organic disulfides and for oxidation of the thiolate anions were measured as a function of rotation speed. In conjunction with single-step potential chrono-amperometry or chronocoulometry, the RDE has been successfully used to determine n, the number of electrons participating in the overall electrochemical reaction.

RESULTS AND DISCUSSIONS

Cyclic voltammograms for different organic disulfides are shown in Fig.1. These voltammograms give direct insight into the kinetic and/or thermodynamic reversibility of the redox couple. Linear sweep voltammograms and the corresponding differential voltammograms were used to determine the peak currents and potentials at diferent sweep rates. The fairly large peak separations and the linear relationship between E_p and ln v indicate that the kinetics are sluggish and the redox couples are kinetically or thermodynamically irreversible. In addition, the transfer coefficents for charge transfer processes were estimated from the dependence of peak potentials on sweep rates.

Double-potential step chronocoulometric measurements indicated that the specific adsorption of these materials on platinum electrodes is negligible. Voltammograms obtained at RDE indicated that chemisorption of alkali metal cations on platinum and graphite electrodes is present.

The characteristic ratio of diffusion-controlled charge, $Q_d(2\tau)/Q_d(\tau) = 0.414$, indicated that the systems studied are chemically stable and reversible under the experimental conditions. This microscopic reversibility is a fundamental criterion for a secondary system in energy storage or conversion.

The number of electrons transferred, n, and diffusion coefficients, D, were determined through the measurement of the convective diffusion limited currents at a RDE in combination with the measurement of the diffusion limited current or the corresponding charge at a stationary electrode. The diffusion coefficients of neutral disulfides and thiolate anions in different solvents were calculated from the slopes of linear chronoamperometric (i_d vs $1/t^{1/2}$) and linear chronocoulometric (Q_d vs. $t^{1/2}$) plots, and from Levich plots. The total number of electrons participating in the electrode reaction was estimated to be 2, and therefore, the overall reaction takes the form of

$$RSSR + 2\,e^- = 2\,(RS^-)$$

where R represents a organic moiety.

CONCLUSIONS

These RSSR/RS^- couples are chemically reversible, yet, kinetically slow. The overall electrochemical redox reaction for this couple is $RSSR + 2\,e^- = 2\,(RS^-)$. The microscopic reversibility of these compounds makes it possible to construct rechargeable batteries based on the organodisulfides. The sluggish kinetics indicate that the introduction of suitable electrocatalysts to assist charge transfer will probably prove useful in this system. Since the adsorption of organic disulfides on platinum electrode is negligible, the electrode kinetics can be described using simple electrodic equations and studied without consideration of surface coverage.

REFERENCES

1. S. J. Visco, C. C. Mailhe, L. C. De Jonghe, and M. B. Armand, J. Electrochem. Soc., submitted 1987.
2. S. J. Visco, this meeting.

Abstract No. 76

EFFECT OF R GROUPS ON Na/RSSR BATTERY CHARACTERISTICS

S. J. Visco and L. C. De Jonghe

Lawrence Berkeley Laboratory
Materials and Chemical Sciences Division
1 Cyclotron Road, Berkeley, CA 94720

Advanced secondary batteries operating at intermediate temperatures, i.e. 100 to 200°C, have attracted considerable research interest due to their inherent advantages over higher temperature systems such as the Na/S or Li/FeS_2 batteries. Current work in this laboratory has involved research on a novel class of intermediate temperature batteries based on a concept similar to the sodium/beta"-alumina/sulfur battery, but operating within the range of 100 to 150°C, and having an organosulfur positive electrode (1). The organosulfur electrodes are based on the reversible electrochemical 2 electron reduction of the organo-disulfide to the corresponding thio anion,

$$RSSR + 2\,e^- \rightleftharpoons 2\,RS^-,$$

where R is an organic moiety. The oxidation of thiols to disulfides has been long established, but has not been considered previously in the context of energy conversion. The attraction of such a generic organic redox couple for battery research is the ability to tailor the physical, chemical, and to a lesser extent electrochemical properties of the molecule through choice of the organic moiety. The viscosity, liquidus range, dielectric constant, equivalent weight, and redox potential, of the organosulfur electrodes can in fact by varied in a predictable manner.

EXPERIMENTAL

Methyl disulfide, Gold Label (Aldrich), was used without further purification. Phenyl disulfide (Aldrich), was recrystallized from ethanol prior to use. *Difluorophenyl disulfide was made from* the oxidation of 4-fluorothiophenol (Aldrich) by iodine in water, and subsequently extracted with petroleum ether, and finally distilled under reduced pressure. Dipentafluorophenyl disulfide was similarly made from pentafluorothiophenol (Aldrich), which was purified by recrystallization from ethanol. Ethoxyethyl disulfide and Methoxyethyl disulfide were made by the reaction of 2-chloroethyl ethyl ether and 2-chloroethyl methyl ether with potassium hydrogen sulfide in methanol under pressure to yield the corresponding mercaptan; the β-ethoxy-alkyl mercaptans were fractionally distilled and the purified mercaptans oxidized to the disulfides which were distilled under reduced pressure prior to use. Transition metal phthalocyanines (Pfaltz and Bauer) were used as is. All solvents were obtained from Aldrich and stored over molecular sieves in an argon atmosphere dry box prior to use.

Beta"-alumina tubes (10 cm x 1 cm, .8 mm wall) were filled with highly purified sodium metal (2), sealed with high temperature epoxy to an aluminum cap through which a stainless wire contacted the sodium metal electrode. The beta"-alumina tube/sodium electrode was tightly wrapped in graphite felt and inserted into a stainless steel cell yielding approximately 20 cm^2 of electrolyte surface area. The cell was sealed with silicone o-rings, and fitted with a transducer to monitor the internal pressure of the positive electrode. All cells were subsequently cycled galvanostatically under computer control using a IBM PC/AT with a Data Translation 2801-A data aquisition card, interfaced to a PAR 373 Potentiostat/Galvanostat, and an Omega PX600 pressure transducer.

RESULTS

The theoretical energy density of a Na/CH_3SSCH_3 cell is 770 Whrs/Kg if the organosulfur electrode is used without solvents. Solubility studies indicated that an approximate weight ratio of DMSO to dimethyl disulfide (DMDS) of 3 to 1 was sufficient to completely dissolve the sodium thiomethoxide generated on cell discharge at the cell temperature of 110°C. Accordingly, positive electrodes were assembled using a range of 30% to 80% solvent to facilitate cell discharge. Open circuit voltage of the Na/DMDS cells ranged from 2.0 to 1.8 volts; discharge rates were 10 mA/cm^2 at 1.2 volts to 100% of available capacity, and recharged at 10 mA/cm^2 at an average of 2.4 volts to 95% of capacity. The addition of an electrocatalyst, cobalt phthalocyanine (CoPc), boosted the charge/discharge rates by a factor of five. Na/DMDS cells having 1 wt% CoPc were able to discharge at 50 mA/cm^2 for over 50% of available capacity (fig. 1) corresponding to a power density of 225 W/Kg, and charge rates of approximately 20 mA/cm^2. The cells could be cycled up to three times before excessive internal pressure led to cells leaks. The pressure increase was attributed to slow chemical reduction of DMSO by thiomethoxide to yield CH_3SCH_3 as well as electrochemical reduction of the solvent. The use of solvents less susceptible to reduction, such as dimethyl sulfone, alleviated this problem.

Positive electrodes were constructed using a series of aromatic disulfides, with 50 % solvent to ensure dissolution of cell products. Sodium/ phenyl disulfide cells exhibited open ciruit voltages of 2.0 volts, and were able to discharge at rates of 7.5 mA/cm^2 at 1.6 volts to 50 % of available capacity. The effect of fluorine substitution on cell performance was dramatic. Sodium/difluorophenyl disulfide cells exhibited open circuit voltages of 2.4 volts and discharged at rates of 10 mA/cm^2 to 90 % of available capacity. Sodium/dipentafluorophenyl disulfide cells exhibited open circuit voltages of 3.0 volts, and were capable of similar discharge rates.

Sodium/alkoxyalkyl disulfide cells were assembled and cycled. The effect of incorporation of the ether linkage in the disulfide appeared to be to increase the solubility of the sodium salts as well as to increase chemical stability of the electrode. The tested cells were able to cycle at 10 to 15 mA/cm^2 to full capacity without pressure increase or evidence of degradation of the solvent.

CONCLUSIONS

Sodium/organosulfur batteries operating at intermediate temperatures (100 to 150°) can be cycled at high rates, 50 mA/cm^2, for a fraction of available capacity, and at lower rates, 5 to 10 mA/cm^2 for all of the available capacity. The open circuit voltage of these cells as well as other properties can be manipulated in a predictable manner by choice of the R group in RSSR.

REFERENCES

1. S. J. Visco, C. C. Mailhe, L. C. De Jonghe, and M. B. Armand, *J. Electrochem. Soc.*, submitted 1987.

2. C. Mailhe, S. Visco, and L. C. De Jonghe, *J. Electrochem. Soc.*, 134, 1121 (1987).

This work was supported by the United States Department of Energy under Contract no. DE-AC03-76F00098.

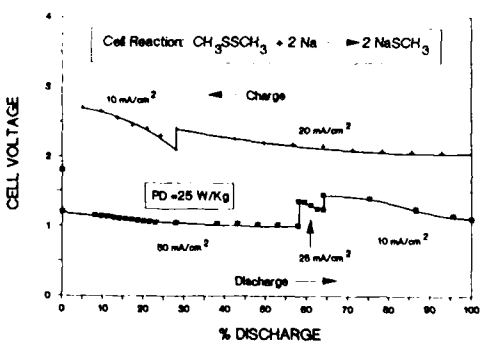


Fig. 1. Charge/discharge behavior of a Na/CH_3SSCH_3 cell at an operating temperature of 110°C.

Abstract No. 77

X-ray Absorption Study of β-Nickel Hydroxides

Patricia L. Loyselle and Bahne C. Cornilsen
Dept. of Chemistry and Chemical Engineering
Michigan Technological University
Houghton, MI 49931

Robert A. Condrate
New York State College of Ceramics
Alfred University
Alfred, NY 14802

James C. Phillips
State University of New York X3 Beam Line, NSLS
Brookhaven National Laboratory
Upton, NY 11973

The EXAFS spectrum for ordered β-$Ni(OH)_2$ is interpreted in terms of the known crystal structure for this material and compared with the EXAFS spectra of disordered β-type hydroxides. The experimental pattern has been fitted using crystallographic bond distances and coordination numbers for the first four shells (Figure 1). These parameters are summarized in Table I. Additional shells, at higher radii, contribute to the spectrum but do not correspond to crystallographic distances. These may involve multiple scattering events.

A comparison of absorption edges (E_0) for the ordered material with those for disordered β-$Ni(OH)_2$ materials shows a dramatic shift to higher energy for the latter. Shifts in E_0 are known to be dependent upon oxidation state, coordination number and type of bonding (1). These materials contain no active oxygen but do exhibit unique Raman spectra which indicate coordination number changes (2).

These results indicate that care must be taken when interpreting nickel edge shifts for nickel electrode materials in terms of oxidation state changes alone. A shift in E_0 may result from a change in coordination number as well as oxidation state. Coordination number changes are significant in beta-nickel hydroxides and are expected to be significant in active mass as well.

This work is part of a study of nickel electrode "model compounds." The EXAFS spectra were collected on the SUNY beamline, X21, at the National Synchrotron Light Source at Brookhaven National Laboratory. The Dept. of Energy supported part of this research.

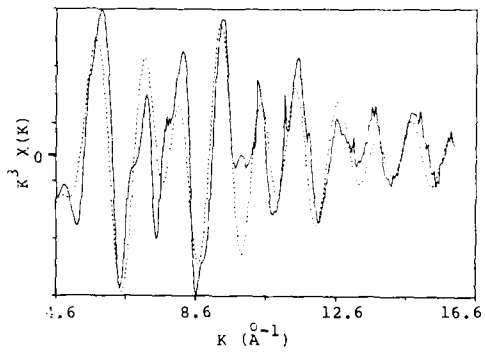


Figure 1. Calculated (dotted line) and experimental (solid line) EXAFS spectra of recrystallized β-$Ni(OH)_2$.

Table I

Shell	Coordination Number	Radius	Debye-Waller Factor
Ni-O	6	2.116	0.067
Ni-Ni	6	3.126	0.069
Ni-O	6	3.775	0.072
Ni-O	6	3.938	0.077

References

1. J. C. J. Bart, Advances in Catalysis, Vol. 34, edited by D. D. Eley, H. Pines, and Paul B. Weisz, Academic Press, Inc., New York, 1986, p.203

2. B. C. Cornilsen, P. J. Karjala, and P. L. Loyselle, J. Power Sources, 22 (1988) 351.

Abstract No. 78

In Situ Raman Spectra of the Nickel Electrode

Bahne C. Cornilsen and Patricia L. Loyselle
Dept. of Chemistry and Chemical Engineering
Michigan Technological University
Houghton, MI 49931

Extreme care must be taken to define the starting material used in any electrochemical study of a nickel electrode because of the diversity of structures which can be produced within the normal ranges of the experimental variables. The electrochemistry is strongly influenced by the precursor structure. Diverse structural phases can be differentiated using laser Raman spectroscopy, phases which cannot be distinguished using other methods (1,2). Furthermore, unique solid state structural information can be extracted from the spectra.

In situ Raman spectra of plaque electrodes have been studied, under controlled potential. Thin film electrodes are compared with formed and cycled plaque electrodes. The structural influence of cobalt addition can be observed. These structures will be contrasted with the cathodic alpha-phase precursor structure. We have also shown that *in situ* spectra can be collected during cyclic voltammetry scans . (Fig. 1).

The *in situ* results confirm conclusions drawn from *ex situ* Raman spectra (1,2). Spectra in Fig. 2 demonstrate the structural similarity. 1) The spectra of active mass differ from those observed for the traditional model compounds. 2) Discharged active mass is not isostructural with α-$Ni(OH)_2$ nor with β-$Ni(OH)_2$. 3) The structure of discharged active mass is more closely related to that of charged active mass. 4) Charged active mass has a nonstoichiometric, non-close packed layered structure in the NiOOH space group. These results demonstrate the potential of *in situ* Raman spectroscopy for the study of electrode structures and their influence on the electrochemistry.

This work has been supported by NASA-Lewis Research Center.

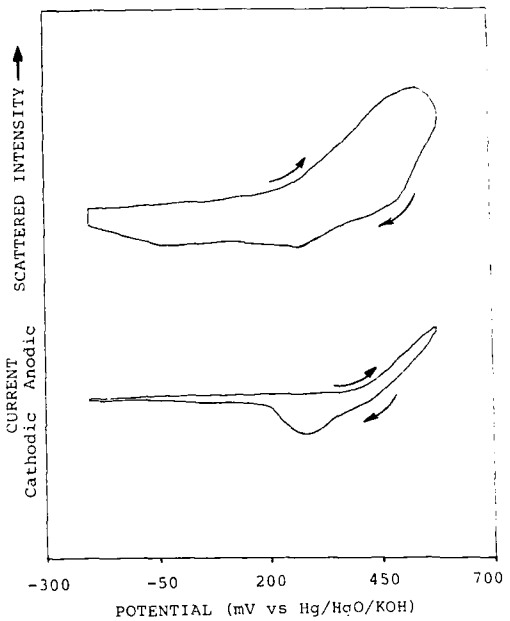


Figure 1. Simultaneous *in situ* Raman intensity at 550 cm^{-1} (a) and cyclic voltammogram (b).

References

1. P. L. Loyselle, P. J. Karjala, and B. C. Cornilsen, Proc. Symp. on Electrochemical and Thermal Modeling of Battery, Fuel Cell, and Photoenergy Conversion Systems, edited by J. R. Selman and H. C. Maru, Electrochemical Society, Pennington, NJ, 1986, p. 114.

2. B. C. Cornilsen, P. J. Karjala, and P. L. Loyselle, J. Power Sources, 22 (1988) 351.

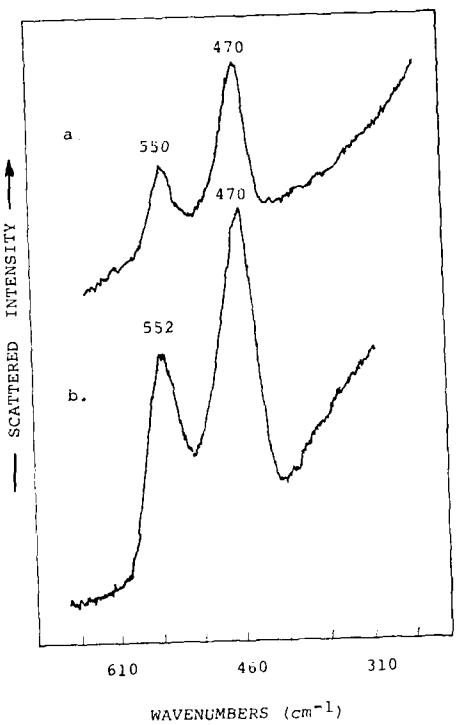


Figure 2. Comparison of *ex situ* (a) and *in situ* (b) Raman spectra of a plaque electrode. *Ex situ* removed after equilibrium at +0.48 V (vs Hg/HgO/KOH). *In situ* electrode held at +0.475 V.

Abstract No. 79

Structural Influence of Cobalt Addition to the Nickel Electrode

Xiaoyin Shan, Patricia L. Loyselle, and Bahne C. Cornilsen

Department of Chemistry and Chemical Engineering

Michigan Technological University
Houghton, MI 49931

Cobalt is added to nickel electrodes to improve electrochemical properties such as capacity, conductivity, and cycle life (1,2). The objective of the research discussed today is to develop an understanding of how the cobalt improves the electrode, from a structural point of view. To do this we have studied the structures of electrode precursors (cathodic alpha phases) before and after cycling in KOH. The influence of cobalt has been measured by varying the cobalt concentration and comparing doped to undoped materials. Structure changes have been monitored using cyclic voltammetry and vibrational spectra, Raman and FT-IR spectroscopy.

Without cobalt, as deposited materials and cycled materials have different structures (3,4). However, the addition of cobalt enhances this difference. The structure of the cobalt containing cathodic deposit is drastically different from that deposited without cobalt (see Fig.1). Variation of the cobalt concentration also influences the structure of the precursor. After charging and cycling, spectra indicate that the active mass incorporates the cobalt by substitution on nickel sites in the nonstoichiometric NiOOH-type oxyhydroxide. We propose that the cobalt stabilizes a unique and optimum, nonstoichiometric NiOOH structure. Our earlier spectroscopic results showed that active mass contains significant nonstoichiometry which enhances proton and electronic conductivities in the solid state (3,4).

These results suggest that cobalt controls the structure of the active mass by way of controlling the precursor structure. Design of an optimum precursor structure (including the optimum nonstoichiometry) will allow control and improvement of electrochemical properties.

References

1. A. H. Zimmerman and P. K. Effa, J. Electrochem. Soc., 131 (1984) 709.
2. David H. Fritts, J.T. Maloy, J. Electrochem. Soc., 125 (1978) 1026.
3. P. L. Loyselle, P. J. Karjala, and B. C. Cornilsen, Proc. Symp. on Electrochemical and Thermal Modeling of Battery, Fuel Cell, and Photoenergy Conversion Systems, edited by J. R. Selman and H. C. Maru, Electrochemical Society, Pennington, NJ, 1986, p. 114.
4. B. C. Cornilsen, P. J. Karjala, and P. L. Loyselle, J. Power Sources, 22 (1988) 351.

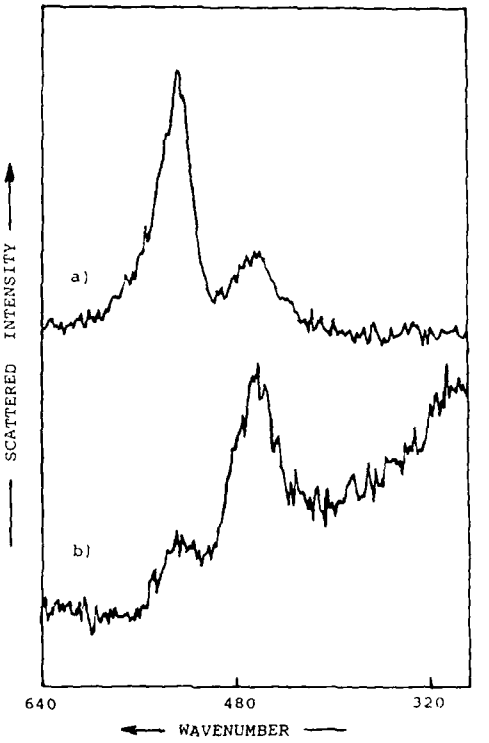


Figure 1. Raman spectrum of cathodic α-$Ni(OH)_2$ in the lattice mode region;
a) containing 10 % cobalt, and
b) without cobalt.

Abstract No. 80

Effect of Cobalt on Fibrous Nickel Hydroxide Electrodes

H. H. Law
J. Sapjeta

AT&T Bell Laboratories
Murray Hill, New Jersey 07974

The nickel-cadmium battery, known for its long cycle life and high energy density, is likely to remain the rechargeable battery of choice for some time to come. It is therefore desirable to increase its energy density. Our recent work [1] explored the possibility of improving the specific energy by employing a fibrous nickel mesh, Fibrex*, as the electrode substrate. The Fibrex electrodes that were initially prepared had about the same energy density by weight as the sintered nickel electrodes in common use today, though about 20-30% less energy per volume. Initial results showed that cobalt improved the electrode performance.

In the present study, an effort was made to characterize the influence of co-precipitation of cobalt hydroxide on Fibrex electrodes. Fritts [2] has attributed the beneficial effect of cobalt addition to improved mechanical properties of the sintered nickel hydroxide electrode, based on his observation that the rigidity of the active material is reduced in the presence of cobalt. Fibrex electrodes, having much more active material per unit surface area than sintered electrodes, would be more sensitive to effects caused by physical changes in the active material. The fibrous substrate is also a good medium for detecting such changes because it is somewhat flexible and thus does not hold the thickness of the electrode constant.

As a result of this non-rigid structure, the degree of swelling of Fibrex electrodes upon discharge is significant, as much as 17%. Since swelling of this magnitude is unacceptable in actual battery operation, electrodes were pressed to try and reduce it. A pressure of 1000 psi was chosen as the desired applied pressure because it contained swelling to within 5%.

The reduction of swelling caused by pressing is inversely proportional to the cobalt content of the electrode. This result indicates that cobalt increases the elasticity of the active material, and makes the electrode performance less sensitive to both the internal stress incurred during charge/discharge cycling (as evidenced by reduced swelling) and to an external stress such as pressing.

When cycled after pressing, electrodes with low cobalt content often showed a dramatic capacity loss, probably as the result of the separation of the active material from the current collector during pressing due to the brittleness of the active material. Electrodes with higher cobalt content were unlikely to suffer this capacity loss, and electrodes containing 15% cobalt frequently had capacity gains of up to 25% after pressing.

The capacity change due to pressing clearly depends on the cobalt content of the active material. This dependence demonstrates directly that when the active material contains at least 5% cobalt, it is much less brittle and less sensitive to stress, leading to a longer cycle life. It also confirms what was previously deduced by Fritts [2], that the addition of cobalt to nickel hydroxide electrodes results in strongly modified elastic properties of the active material.

References

[1] H. H. Law and J. Sapjeta, *Proc. of the 22nd Intersociety Energy Conversion Engineering Conference*, Philadelphia, PA, Aug. 10-14, 1987.

[2] D. H. Fritts, *J. Electrochem. Soc.*, 129, 118 (1982).

* Trademark of National-Standard Company, Niles, Michigan.

Abstract No. 81

IMPEDANCES OF NICKEL HYDROXIDE ELECTRODES AS FUNCTIONS OF POTENTIAL AND ELECTRODE TYPE

Margaret A. Reid
Electrochemical Technology Branch
NASA Lewis Research Center
Cleveland, OH 44135

Introduction:

A number of studies have been made of the impedance spectra of nickel hydroxide electrodes and Ni/Cd batteries using a variety of techniques (1-6). Zimmerman (1) has measured the impedances of nickel electrodes during discharge by following the voltage changes after a step in the discharge current. He and others have found that impedance increases dramatically at low states of charge.

Our studies have shown that the impedance varies not only with voltage but with the manufacturing method, and that impedance parameters even vary considerably for electrodes from manufacturing lot to lot and within the same lot. We are studying the possibility of using the impedance method as a tool for predicting the life and performance of Ni electrodes and complete Ni/H_2 cells. Investigators at Rockwell and Jet Propulsion Laboratory (3) have attempted this for a number of Ni/Cd cells and have seen some possible correlations. Their measurements were taken only for the fully discharged state after being short-circuited for a day. Impedance curves for Ni/H_2 cells are similar to those of the Ni/Cd cells. We are making measurements at other states of charge and are also making half-cell measurements on several types of electrodes in order to find the conditions that provide the best correlation with life and performance.

Experimental:

Since impedance is sensitive to the voltage and the time that the electrode has been held at that voltage, spectra were measured after the electrodes had been equilibrated at the desired voltage. Electrodes prepared by chemical impregnation and by aqueous and alcoholic impregnation were studied.

All electrodes had a sintered Ni substrate and were impregnated to about 1.6 g/cc void. The electrolyte was 31% KOH, and the reference electrode was Hg/HgO. Measurements of the electrochemically impregnated electrodes were taken after 10 formation cycles, the first five at C/10 charge for 16 hours and C/4 discharge to a voltage of 1.0 V vs an amalgamated Zn electrode (~0.42 V vs a Hg/HgO electrode), the last five cycles at a C/2 charge rate with 10% overcharge followed by a C/4 discharge.

Impedance measurements were made with the PAR 378 potentiostat and M378 software. This uses a synthesized wave form with an FFT to deconvolute the results. Experiments were carried out from 5-10 Hz down to 0.0007 Hz. Above 10-20 Hz the inductance predominates.

Results:

The impedance spectra of a typical electrochemically impregnated electrode at about 1-2% SOC is shown in Fig. 1. The electrode had been held at 0.200 V vs the Hg/HgO electrode for 1 hour after the formation cycles. The circuit for the cell at a few percent SOC (0.200 - 0.250 V vs Hg/HgO) can be expressed to a first approximation as a typical series-parallel circuit with a Warburg impedance term (Fig. 2). The semicircle is slightly depressed. At higher voltages, above about 10 % SOC (Fig. 3), the only measurable quantity is the Warburg coefficient, while at lower voltages (Fig. 4) usually only the IR drop and the left-hand portion of the semicircle can be measured accurately.

The parallel resistance associated with the semicircle has been attributed to charge transfer resistance and/or boundary layer conduction (1). Since the magnitude appears to change with voltage in the same manner as the Warburg coefficient, we feel that it is probably associated with the boundary layer conduction process.

The changes of the Warburg coefficient with equilibrium voltage for a typical chemically impregnated electrode are depicted in Fig. 5. Measurements were started in the charged state after the electrode had been cycled three times at the C rate. After each measurement the voltage was lowered and the electrode held at the new potential for at least one hour. After reaching 0.2 V the potential was increased again. In agreement with others, we attribute the hysteresis to the formation of a resistive layer of lower valent hydroxide adjacent to the sinter which is only slowly oxidized.

Table 1 shows the Warburg coefficient of a number of electrochemically impregnated electrodes from the same manufacturer. Measurements were made after equilibration for an hour at 0.200 V after the formation cycles. Substantial variations are evident.

Conclusions:

The impedance of a nickel electrode increases slightly during discharge until it is over 95% discharged at which point it increases by about two orders of magnitude. There is considerable hysteresis. The impedance of electrodes prepared by different impregnation procedures varies considerably, and even with the same process there is variation from lot to lot and within lots. We hope to correlate these differences with life and performance.

References:

1. A. Zimmerman, M. R. Martinelli, M. C. Janecki, and C. C. Badcock, J. Electrochem. Soc. 129, 289 (1982).
2. A. H. Zimmerman, J. Power Sources 12, 233 (1984).
3. R. Haak, C. Ogden, D. Tench and S. Di Stefano, J. Power Sources 12, 289 (1984)
4. R. T. Barton, R. Leek, S. A. G. R. Karunathilaka and N. A. Hampson, J. Appl. Electrochem. 15, 399 (1985).
5. P. Delorme, J. M. Harismendy, and M. Comsat, ESA report, Contract 4999/82.
6. S. J. Lenhart, D. D. MacDonald and B. G. Pound, 19th IECEC Meeting, 875 (1984).

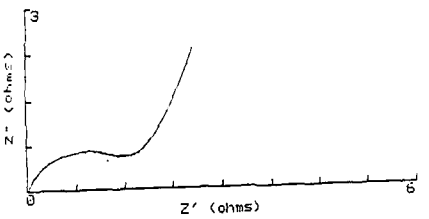


Fig. 1. Impedance of typical electrochemically impregnated electrode at 0.200 V vs Hg/HgO.

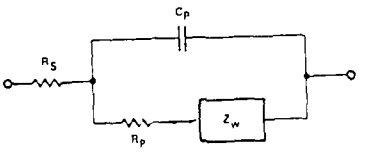


Fig. 2. Circuit diagram for nickel hydroxide electrode.

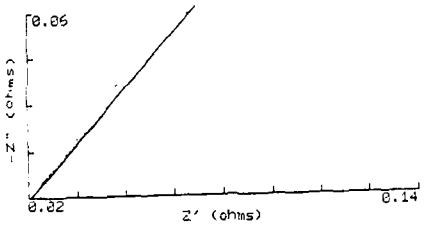


Fig. 3. Impedance of typical electrochemically impregnated electrode at 0.050 V vs Hg/HgO.

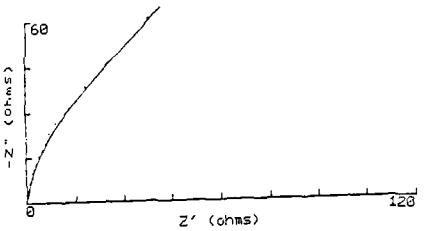


Fig. 4. Impedance of typical electrochemically impregnated electrode at 0.400 V vs Hg/HgO.

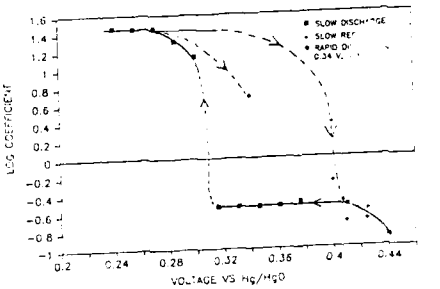


Fig. 5. Warburg coefficient of chemically impregnated electrode as function of voltage.

Table 1

VARIATIONS IN WARBURG COEFFICIENT OF AN ELECTROCHEMICALLY IMPREGNATED ELECTRODE WITHIN LOTS AND BETWEEN LOTS

Electrode and Lot	Warburg Coefficient (Ohm cm^2 $sec^{-1/2}$)
1A	4.02
2A	2.15
3A	1.29
4A	2.19
5A	2.35
6A	2.57
1B	1.90
2B	5.11
3B	4.14

Abstract No. 82

AC IMPEDANCE STUDIES ON NICKEL OXIDE ELECTRODE

K.A.Murugesamoorthi, Y.J. Kim, S. Srinivasan and A.J. Appleby

Center for Electrochemical Systems and Hydrogen Research
238 Weisenbaker ERC
Texas A & M University
College Station, TX 77843

INTRODUCTION:

Ni-H_2 batteries are widely used in space applications due to their advantages like long cycle life, higher operating current denisty, overcharge/overdischarge protection, pressure indication of state of charge etc. However, the self discharge rate of the Ni-H_2 battery (about 10% per day) is much higher. Usually hydrogen is stored under high pressure in these cells (about 30 to 40 atmospheres). Hence it is strongly suspected that the high self discharge rate is caused by hydrogen. Hydrogen may cross over to the nickel oxide electrode either through the electrolyte or externally. An attempt was made to find the effect of hydrogen on the self discharge of nickel oxide electrodes by AC impedance measurement. The impedance technique has been used to find the state of charge of the various cells [1-3].

EXPERIMENTAL:

Nickel hydroxide film was deposited on clean nickel foil (1.2 x 2.75 cm) by electrochemical deposition from 2M nickel nitrate solution at 75°C by applying a cathodic current of 80 mA/cm^2.

The film composition was confirmed by X-ray diffraction. Platinum spiral and zinc wire were used as counter and reference electrodes respectively. The reference electrode was kept in a separate compartment. The electrolyte was 30 % KOH. AC impedance measurements were carried out from 0.01 Hz to 80 KHz at 25°C by using EG&G Model 273 Potentiostat/Galvanostat and Model 5301A Lock-In-Amplifier with Model 5315 Preamplifier. Provision was made to bubble argon or hydrogen into the electrolyte. The nickel oxide electrode was charged at the rate of C/10 and discharged at C/5 rate. After several charge /discharge cycles, the AC impedance measurements were made at a potential of 1.95 V on a fully charged electrode. A 5 mV AC signal was used for the impedance measurements.

RESULTS AND DISCUSSION:

Fig.1 shows the plot of log frequency versus log |Z| for the specimen exposed to argon and hydrogen for one hour. The impedance of the electrode was increased when it is exposed to hydrogen. This increase in impedance suggests a decrease in the state of charge. This may be due to the partial transformation of more conducting NiOOH to less conducting $Ni(OH)_2$.

Fig.2 shows the plots of log |Z| versus log frequency of nickel oxide electrodes at different exposure time to hydrogen. It is evident that the impedance of the nickel oxide electrode increases with time when it is exposed to hydrogen. When the specimen was exposed to argon, no significant change in the impedance was obnserved.

The above results are in good agreement with data of cyclic voltametry [4].

ACKNOWLEDGEMENT:

The authors thank Dr.J. McBreen, Brookhaven National Laboratory, for useful discussions.

REFERENCES:

1. T. Osaka and Y. Yatusuda,Electrochim. Acta, 29(5), p 677 (1984).
2. S.J. Lenhant, D.D. Macdonald and B.G. Pound, NASA Conference Publication 2484, p 257 (1987).
3. M.J. Madou and M.C.M. Mckubre, J. Electrochem.Soc., 130(5), 1056 (1983).
4. Y.J. Kim, K.A. Murugesamoorthi, S. Srinivasan and A.J. Appleby, Also to be presented in this ECS meeting.

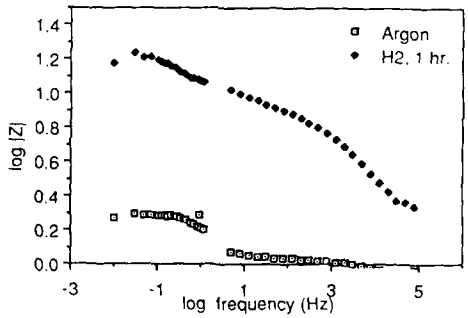


Fig.1 log frequency vs. log|Z| of the fully charged nickel oxide electrode under argon and hydrogen.

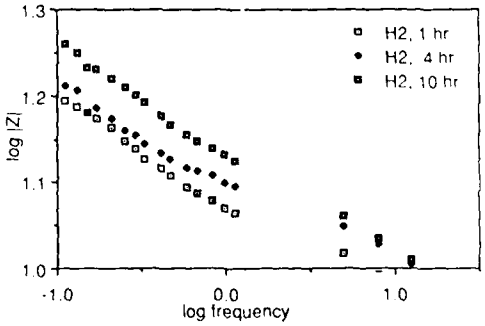


Fig.2 Effect of hydrogen exposure on impedance of nickel oxide electrode.

Abstract No. 83

EFFECTS OF HYDROGEN ON THE SELF DISCHARGE OF NICKEL OXIDE ELECTRODES

Y.J. Kim, K.A. Murugesamoorthi, S. Srinivasan, and A.J. Appleby

Center for Electrochemical Systems & Hydrogen Research
The Texas A&M University
238 Wisenbaker ERC
College Station, TX 77843-3577

Introduction

The electrochemical behavior of the nickel hydroxide electrode has been investigated for several decades due to its battery applications as the positive plate in Ni-Cd, Ni-Fe, and Ni-H_2 batteries (1). Among the alkaline electrolyte storage batteries, the nickel-hydrogen battery, with high energy density, long cycle life, direct pressure indication of state of charge or discharge, and tolerance to overcharge or overdischarge, is being used in tele-communication satellites (2). Several researchers have studied the electrochemical characteristics of Ni-H_2 battery (3,4,5). It was found that hydrogen pressure rises from about 0.5 MPa in the fully discharged state to 3-10 MPa when charged and can be used to monitor the state of charge or discharge. However, the self-discharge rate is about 10% per day at 30°C, even though the reaction between hydrogen and nickel oxide is expected to be relatively slow.

The purpose of the present study is to investigate hydrogen oxidation on nickel oxide electrode in 30% KOH at 25°C in order to understand its contribution to the self-discharge mechanism of Ni-H_2 battery.

Experimental

Nickel hydroxide films were prepared by electrochemical deposition from 2M nickel nitrate solution on nickel foil substrate (99.99% Ni from Alfa Products). Prior to use, the foils were cleaned electrochemically in 1M HNO_3 with an anodic current of 10 mA/cm^2 for 1 minute and rinsed with acetone and deionized water. After cleaning, the electrochemical deposition process was conducted at 75°C with a nickel foil counter electrode in a Pyrex cell by applying a cathodic current of 80 mA/cm^2. Nickel hydroxide films were examined by SEM and confirmed by X-ray diffraction.

The electrolyte was 30% KOH and purged with argon or hydrogen at 25°C. The electrochemical cell consisted of a nickel oxide working electrode, a Pt counter electrode, and a Zn wire reference electrode. The reference electrode was isolated from the test solution by means of Luggin capillary.

Results and Discussion

Figure 1 shows typical charge/discharge characteristics of the nickel oxide electrode; this electrode was first charged at C/10 for 9 hours and followed by discharge at C/5 to 1.0V. There are two voltage plateaus during discharge. It was explained that the upper voltage plateau is controlled by the proton diffusion within the active material and the lower plateau controlled by the resistance of poorly conductive material formed on the interface between the nickel substrate and the active material (6).

Figure 2 shows cathodic voltamograms on charged nickel oxide electrodes in 30% KOH at 25°C after exposure to argon or hydrogen for various times. The amount of cathodic charge, represented by the whole area of the peak, decreases with increase of exposure time to hydrogen. This suggests that the conductive NiOOH film is transformed to the less conductive $Ni(OH)_2$ by the hydrogen oxidation on nickel oxide and/or the nickel foil substitute such as

$$H_2 \longrightarrow 2\,H_{ads}$$

$$H + OH^- \longrightarrow H_2O + e^-$$

$$NiOOH + H_2O + e^- \longrightarrow Ni(OH)_2 + OH^-$$

References

1. S.U. Falk and A.J. Salkind, "Alkaline Storage Batteries", John Wiley & Sons, Inc., New York (1969).
2. J.D. Dunlop, "Handbook of Batteries & Fuel Cells", edited by D. Linden, McGraw-Hill Book Company, New York (1984).
3. J. Giner and J.D. Dunlop, J. Electrochem. Soc., 122, 4(1975).
4. J. McBreen, "Comprehensive Treatise of Electrochemistry, V-", edited by J. O'M. Bockris, B.E. Conway, E. Yeager, and R.E. White, Plenum Press, New York (1981).
5. C.A. Vincent, "Modern Batteries", Edward Arnold Ltd., London (1984).
6. A.H. Zimmerman, J. Power Sources, 12, 233 (1984).

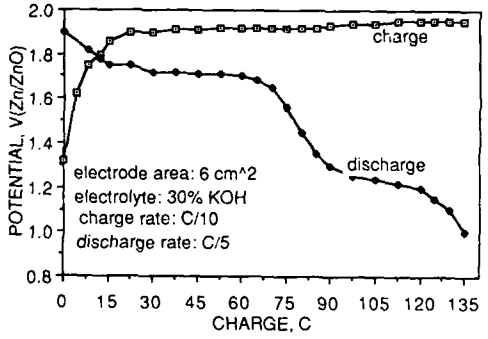


Figure-1: Charge/discharge behavior of nickel oxide electrode electrochemically deposited on nickel foil.

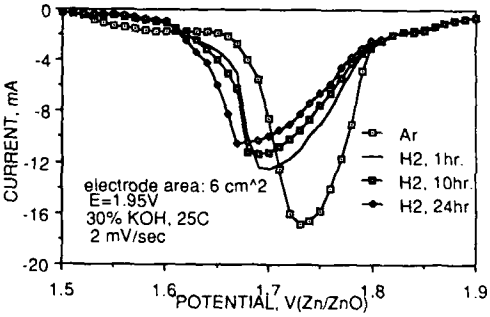


Figure-2: Cathodic voltamograms on charged nickel oxide electrodes in 30% KOH at 25°C after exposure to argon or hydrogen for various time.

Acknowledgement

The authors express their gratitude to Dr. J. McBreen of Brookhaven National Laboratory for helpful discussions.

Abstract No. 84

On the Nature of Cadmium Electrode Capacity Fading

D. H. Fritts and R. A. Flake

Aero Propulsion Laboratory
AFWAL/POOS-2
Wright-Patterson AFB, OH 45433

The fading of capacity in cadmium electrodes under cycling conditions, for example in nickel-cadmium batteries, is a well known phenomena. To compensate for this gradual loss of capacity, the stoichiometry of nickel-cadmium cells is generally heavily in favor of the cadmium electrode; typically 1.5 to 1. The cause of capacity fading has been generally attributed to the inability to fully recover the discharge product, $Cd(OH)_2$ upon recharging the cell. $Cd(OH)_2$ crystals have been shown to become electrically isolated or presumed to be such (1,2) by many investigators.

In this work precise measurements of the resistance change that occurs when a cadmium electrode is cycled was used to quantify the degree of capacity fading. In Figure 1 an equivalent circuit of a cadmium electrode is shown. It is simply two resistors in parallel with one being the active material and the other being a fixed resistance due to the nickel sinter substrate. The resistance change is apparent from the half cell reaction.

$$Cd + 2(OH)^- + 2e \rightleftharpoons Cd(OH)_2$$

where cadmium is an electronic conductor and $Cd(OH)_2$ is not. Thus when charged the resistance of a cadmium electrode is less than when it is discharged.

To obtain the data a three electrode test cell was fabricated where the cadmium electrode was placed between two nickel hydroxide electrodes. The electrolyte was 31% KOH. The stoichiometry was in favor of the nickel-hydroxide electrodes. It is thus assumed the cadmium electrode was limiting the capacity.

The resistance was measured by continuously passing a one amp test current through the cadmium electrode in a circuit independent of the charge-discharge circuit. During an actual resistance measurement the charge-discharge circuit was opened and the voltage drop due to the test current measured. A characteristic value of resistance was 35 $m\Omega$ with a resolution of less than 10$\mu\Omega$.

In Figure 2, the resistance, cell internal temperature, and cell amp-hour status are plotted. Note that the resistance gets less with decreasing cell capacity.

Based on the previous discussion, it would seem that as the cadmium electrode's capacity fades the resistance would rise as less and less material is available for recharging. What is observed is just the opposite, i.e., the resistance declines with capacity fading. This implies that capacity fading is due to the isolation of metallic cadmium during discharge. This would be consistent with the results of Fritts and Dueber (3), if the cadmium deposition was thicker than 3.5×10^{-3} cm, which was found to be a characteristic physical depth of discharge for cadmium passivation.

At present all the data has been collected at the above temperature as the capacity fading is very apparent at this point. Additional testing is being done at other temperatures to determine if the behavior reported herein is a valid observation for cadmium electrode fading in general, or if the observed mechanism is characteristic of high temperature cycling.

Acknowledgements

The authors thank Messrs. J. Leonard, G. Loeber and C. Riepenhoff for their technical support, without which this work could not have been accomplished.

References

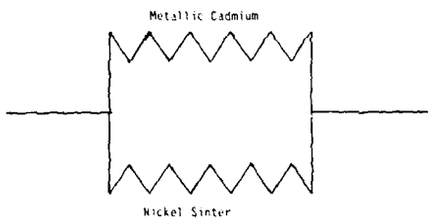
1. K. L. Dick, T. Dickinson, R. J. Doran, SEA Pomroy, and J. Thompson, in "Power Sources 7," J. Thompson, Editor, p. 195, Academic Press, London (1979).

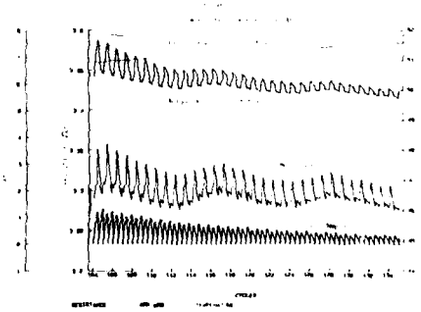
2. S. W. Mayer, Journal of the Electrochemical Society, 123, 159 (1976).

3. D. H. Fritts, and R. E. Dueber, Journal of the Electrochemical Society, 132, 2039 (1985).

Figure 1

Cadmium Electrode Equivalent Circuit for Electronic Conduction





Abstract No. 85

STUDY ON SELF-DISCHARGE OF A METAL HYDRIDE RECHARGEABLE BATTERY SYSTEM EMPLOYING $MmNi_{5-x}M_x$ ALLOY

M.Ikoma, Y.Ito, I.Matsumoto and H.Ogawa

Technology Laboratory
Matsushita Battery Industrial Co., Ltd.
1, Matsushita-cho, Moriguchi
Osaka 570, Japan

1.INTRODUCTION

Recently, researches to develop Ni-H(MH) battery employing hydrogen storage alloy of multicomponent $LaNi_5$[1], $MmNi_5$[2], and Ti-Ni[3] have been done extensively. But this battery has a disadvantage, that is, its self-discharge is extremely larger than Ni-Cd battery.

So, various factors accelerating the self-discharge in the sealed-type Ni-H(MH) battery (AA size) and its mechanism were studied. The impurities from electrodes and especially from the separator were decreased, and the performance of self-discharge was improved as same as that of Ni-Cd battery.

2.EXPERIMENTAL

The negative electrode used an alloy powder with formula $MmNi_{5-x}M_x$(Mm: Misch metal, M: Mn, Al, and Co). As the positive electrode foamed nickel positive plate[4] was used. As the separator non-woven fabric made of polyamide (PA) and polypropylene (PP, included surfactant) and non-woven fabric whose main material was a chemically stable polypropylene with hydrophilic property (h-PP) were used.

3.RESULTS AND DISCUSSION

Self-discharge of Ni-H(MH) battery using $MmNi_{3.55}Mn_{0.4}Al_{0.3}Co_{0.75}$ and h-PP is shown in Fig. 1. As the reference, characteristics of Ni-H(MH) battery using PA and Ni-Cd battery are also shown on the same figure. When PA is used, capacity retention became almost 0% after 14 days storage at 45°C. In contrast of this, when h-PP is used, capacity retention became 50 to 55% after 30 days storage, that is, the self-discharge is extremely decreased and th characteristic of this battery could be improved to the level of Ni-Cd battery.

Here, the following 5 items are taken as the factors which have effects on the self-discharge and the effect of each item was discussed.

(a)Self-decomposition rate of positive plate
(b)Nitrate ion in positive electrode
(c)Oxygen and hydrogen gases
(d)Organic impurities from the separator
(e)Metal ions from the hydrogen storage alloy

(a) The self-decomposition rate of positive plate was studied by experiments with a half-cell and the results are shown in Fig. 3. It was recognized that the positive electrode occurs self-decomposition of 20 to 22% after 30 days storage at 45°C.

(b) In this experiment, the nitrate ion free positive plate is used, so it is impossible that nitrate anion relates the redox reaction of the electrodes.

(c)Then, the influence of oxygen and hydrogen gases on the self-discharge were studied with a half cell. As the result, influence of oxygen is hardly recognized in the range of the partial pressure, 0 to 20%(Fig.2). Also, it became clear that hydrogen of partial pressure, 1 atm or less, scarcely affects reduction reaction of the positive electrode.

(d)Next, the effect of separator on the self-discharge was studied with the Ni-Cd battery whose negative plate was considered to give no metal ion, except Cd ion, and the result is shown in Fig. 3. When PA is used, the capacity retention is 45 to 50% after 30 days storage at 45°C. When PP and h-PP are used, the capacity retentions are 55 to 60% and 75% respectively. These results exhibit almost the same tendency to the Ni-H(MH) battery (Fig.1) and it became clear that the stabler separator against electrolyte is used, the more the self-discharge is decreased.

From these results, it is considered that organic impurities which is dissolved from the separator, accelerate the self-discharge. Then, the decomposed products from PA were studies by IR spectroscopy and absorptions which are assigned to carboxylate and amine were found. Ammonium ion is found with ion-chromatograph. From these facts, it is considered that PA is hydrolyzed to form hexamethylenediamine, ammonia, and adipate ion. Then these impurities are added into electrolyte and effect of them on the self-discharge was studied with chemically stable h-PP. The results are shown in Fig. 4. As for amine and ammonia as well as NO_3^-, it became clear that the self-discharge is accelerated with increase in concentration of them. Consequently, when PA is used as the separator of Ni-H(MH) battery, amine and ammonia take part in the redox reaction as well as NO_3^-[5] in Ni-Cd battery, and the self-discharge is accelerated (Fig.5).

(e) But Ni-H(MH) battery has large self-discharge than Ni-Cd battery even when impurities are checked by using h-PP. Then metal ions are considered to accelerate the self-discharge. Alloy powder represented by the formula $MnNi_{3.95-x}Mn_xAl_{0.3}Co_{0.75}$ was used as the negative electrode, and the self-discharge was studied. The results are shown in Fig. 6. When number of substituted atoms increases from 0.2 to 0.4, capacity retention increases from 24% to 54%. Though the cause of this phenomenon is being discussed now, it seems that the suitable substitution of Mn decreases the elusion of cobalt from the alloy.

4.CONCLUSION

To decrease self-discharge, it is important to use chemically stable separator even at high temperature. The self-discharge of Ni-H(MH) battery in which comparatively stable hydrogen storage alloy is used, it also improved to the level where it can be used practically without any problem.

5.REFERENCES

1) J.J.G.Willems; Phillips J.Res., 39, No.1 (1984)
2) M.Ikoma, et al.; The 27th Battery Symposium in Japan, 89 (1986)
3) K.Sapru, et al.; U.S.Patent, No.4, 551,400 (1985)
4) I.Matsumoto, et al.; Presented at the 16th Power Source Symposium (1988)
5) S.U.Falk, et al.; Alkaline Storage Batteries, 631 (1969)

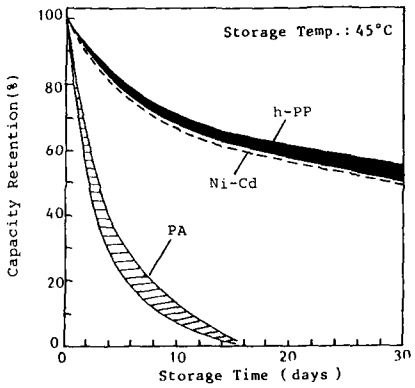


Fig.1 Effect of h-PP separator of Ni-H(MH) batteries empolying $MmNi_{3.55}Mn_{0.4}Al_{0.3}Co_{0.75}$ negative plates on self-discharge comparing with that of Ni-H(MH) battery using PA separator and conventional Ni-Cd battery.

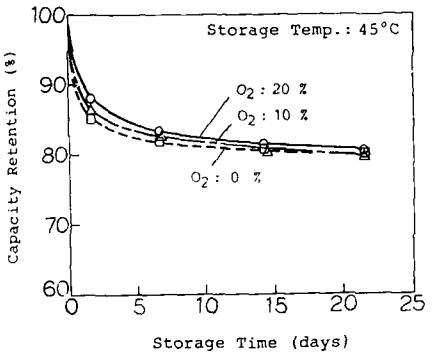


Fig.2 Influence of oxygen gas on the decomposition rate of NiOOH with starved electrolyte in half cell using nickel screen as counter electrode.

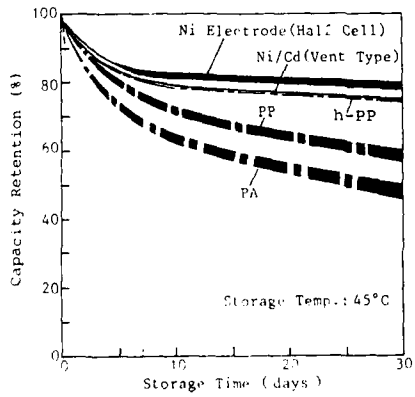


Fig.3 Influence of various separators on self-discharge of sealed-type Ni-Cd batteries and the decomposition rate of NiOOH.

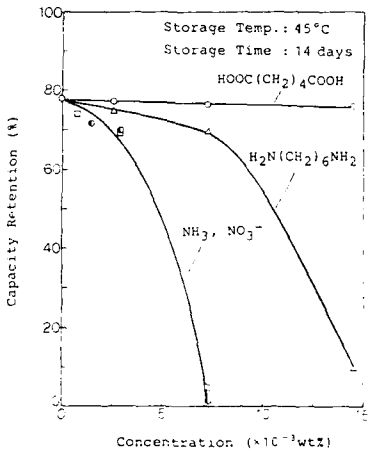


Fig.4 Effect of various ions added into the electrolyte on the self-discharge of Ni-Cd battery with chemically stable h-PP separator.

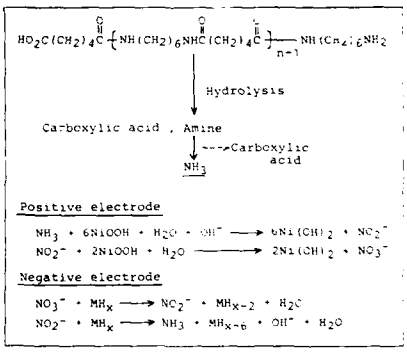


Fig.5 Self-discharge mechanism of Ni/H(MH) battery when polyamide is used as the separator.

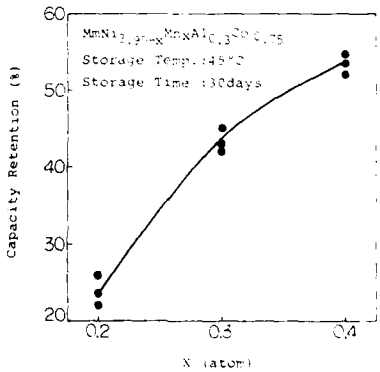


Fig.6 Influence of manganese contents in alloy on self-discharge of Ni-H(MH) batteries with chemically stable h-PP separator.

Abstract No. 86

A NEW THERMALLY STABLE AgO CATHODE MATERIAL

K. M. O'Neill, D. R. Glen,
S. Dallek, and B. F. Larrick
Electrochemistry Branch

A. N. Mansour
Materials Evaluation Branch

Naval Surface Warfare Center
Silver Spring, MD 20903-5000

INTRODUCTION

Silver oxide/zinc (AgO/Zn) batteries are widely used as power sources in various commercial, military and aerospace applications. AgO cathodes prepared electrochemically by anodization of sintered silver plates in aqueous KOH electrolyte (1) are used in high-rate batteries. AgO material prepared chemically by persulfate oxidation of aqueous alkaline solutions of $AgNO_3$ (2) or by ozonization (3) is used for low-rate applications.

The anomalously high thermal decomposition rate of numerous electrochemically prepared (EP) AgO cathode materials used in primary reserve AgO/Zn batteries has been a persistent problem for battery manufacturers. Capacity losses, pressure build-ups, activation time delays, and voltage regulation problems have all been attributed to the thermal decomposition of the AgO cathode during storage of the battery (4).

We have recently reported on the decomposition kinetics of AgO cathode materials by thermogravimetry (TG) (5-7). These studies showed a tremendous range of thermal stability among a wide variety of CP and EP AgO cathode materials. In general, however, the CP samples had much higher thermal stability than the EP samples.

In this paper, we report on the preparation procedure and decomposition kinetics of a new EP AgO cathode material that has extremely high thermal stability. The thermal stability of the new material was determined by thermogravimetry (TG). An accelerated-aging study of the new material and other AgO cathode materials was conducted, based on a typical military specification temperature/time test regime. The amount of AgO decomposition was then compared with the decomposition rate predicted from the kinetic parameters determined by TG.

EXPERIMENTAL

EP AgO cathodes were formed by galvanostatic charging of sintered silver plates at current densities of 2-4 mA/cm^2 over a range of temperatures from 298 K to 383 K in 31 % KOH electrolyte. Numerous additional EP and CP samples were obtained from commercial sources. TG studies were performed with a DuPont 9900 thermal analysis system interfaced to a 951 TGA module. The composition of the cathode was determined by a combined thermogravimetry-gas chromatography (TG-GC) method reported earlier (8). The decomposition kinetics of AgO was determined by a multiple-heating-rate TG method (9) applied previously to AgO stability studies (5). TG samples were run in platinum boats at heating rates of 1.0-20.0 K/min over a temperature range of 298-773 K in a flowing atmosphere (50 cm^3/min) of dry helium. A Shimadzu GC-9A gas chromatograph was used for the GC measurements. Accelerated-aging studies were conducted at 333 K for 21 days in a vacuum oven.

RESULTS AND DISCUSSION

The determination of the Arrhenius activation energy, E_a, pre-exponential factor, Z, and specific rate constant, k, by TG for the AgO decomposition reaction was discussed earlier (5). Transition metal impurities, particularly copper, that may become incorporated into the cathode during the electrochemical formation procedure were shown to be a major cause of AgO destabilization (6). Pure EP AgO cathodes containing very low concentrations of transition metals (e.g., Ni, Co, Cu 10 ppm) were shown to have much higher thermal stability.

As part of a comprehensive stability improvement program, we modified the standard charging procedure of sintered silver plates by performing the charging at elevated temperatures (343-383 K). It was postulated that AgO material formed at high temperature should possess superior thermal stability. The formation of less stable modifications of the material would be impeded during the preparation procedure. (It should be noted also that thermally stable CP material is synthesized at elevated temperature (2)). The new material was found to have extremely high thermal stability with an E_a of 146 kJ mol^{-1}. The E_a values of other EP AgO materials reported earlier (5) ranged from 100 to 133 kJ mol^{-1}. The excellent thermal stability of the new material was confirmed by an accelerated-aging study. No measurable AgO decomposition was found after 21 days storage at 333 K, whereas up to 15 % decomposition was measured for other AgO samples, in excellent agreement with the calculated TG kinetics parameters.

Combined TG, x-ray diffraction (XRD), extended x-ray absorption fine structure (EXAFS) studies have shown that the lattice structure of EP AgO can be highly oxygen-deficient (10). The correlation between thermal stability and structure of AgO cathode materials is discussed in another paper (11).

REFERENCES

1. S.U. Falk and A. Fleischer, in "Zinc-Silver Oxide Batteries," A. Fleischer and J.J. Lander, Editors, pp. 199-207, John Wiley and Sons, New York (1971).
2. R. Hammer and J. Kleinberg, in "Inorganic Syntheses," Vol. II, J.C. Bailar, Jr., Editor, pp.12-14, McGraw Hill Book Company, New York (1953).
3. A.S. McKie and D. Clark, in "Batteries," D.H. Collins, Editor, pp. 285-295, The Macmillan Company, New York (1963).
4. "Zinc-Silver Oxide Batteries," A. Fleischer and J.J. Lander, Editors, John Wiley and Sons, New York (1971).
5. S. Dallek, W.A. West, and B.F. Larrick, J. Electrochem. Soc., 133, 2451 (1986).
6. S. Dallek, D.R. Glen, K.M. O'Neill, and B.F. Larrick, Proc. 16th North American Thermal Analysis Society Conf., Washington, DC, 27-30 September 1987.
7. S. Dallek, D.R. Glen, K.M. O'Neill, B.F. Larrick, Extended Abstract No. 153, The 172nd Electrochem. Soc. Meeting, Honolulu, HI, 18-23 October 1987.
8. W.A. Parkhurst, S. Dallek, and B.F. Larrick, J. Electrochem. Soc., 131, 1739 (1984).
9. J.H. Flynn and L.A. Wall, Polymer Letters, 4, 323 (1966).
10. A.N. Mansour, S. Dallek, K.M. O'Neill, C.R. Anderson, D.R. Glen, and B.F. Larrick, Extended Abstract No. 152, The 172nd Electrochem. Soc. Meeting, Honolulu, HI, 18-23 October 1987.
11. A.N. Mansour, C.R. Anderson, M.K. Norr, S. Dallek, K.M. O'Neill, D.R. Glen, and B.F. Larrick, This Meeting, Chicago, IL, 9-14 October 1988.

Abstract No. 87

STRUCTURE AND STABILITY OF AgO

A. N. Mansour, C. R. Anderson, and M. K. Norr
Materials Evaluation Branch
And
S. Dallek, D. R. Glen,
K. M. O'Neill, and B. F. Larrick
Electrochemistry Branch

Naval Surface Warfare Center
10901 New Hampshire Avenue
Silver Spring,MD 20903-5000

INTRODUCTION

Silver oxide/zinc alkaline batteries have found numerous commercial and military applications as primary power sources due to their high energy and power densities. The *electrochemically* and chemically prepared AgO (EP and CP-AgO) cathodes are used for high and low rate applications, respectively. EP-AgO is thermally less stable than CP-AgO and its decomposition rate is excessively high for many applications, leading to performance degradation problems. Tremendous variations in the thermal stability of dry EP-AgO occur and have been found to depend on preparation procedures.[1,2] Electrochemically induced structural and physical variations could play an important role in controlling the decomposition rate. Therefore, an improved knowledge of the structure and physical properties of EP-AgO as a function of preparation procedures could prove invaluable to the solution of thermal instability. In this paper, a combination of techniques including extended x-ray absorption fine structure (EXAFS), x-ray diffraction (XRD), x-ray photoelectron spectroscopy (XPS), scanning electron microscopy (SEM), thermogravimetry (TG), and gas chromatography (GC) have been used to determine the structure, composition, morphology, and stability of AgO cathodes. From the results, we developed a model for the stability of AgO materials.

EXPERIMENTAL

EP-AgO cathodes were produced by means of constant current anodization of sintered silver plates.[3] Plates were charged in 31 or 40 wt % KOH in distilled water at various apparent surface current densities. The effects of charge-discharge cycling as well as the temperature of the electrolyte were investigated. A Norelco XRD unit with copper x-rays and a nickel filter was used for bulk compositional analyses. A Kratos ES300 XPS with a dual Al/Mg x-ray anodes was used for oxidation state and surface compositional analyses. An Amray 1000A SEM was used for investigating the particle size and shape of the AgO crystallites. An electron beam at a voltage of 20 KeV, current of 0.01 na, and a diameter of the order of 100 Å was used in the SEM. TG-GC experiments were described elsewhere.[1,4] EXAFS experiments were performed on x-ray beam line 11-A at the National Synchrotron Light Source (NSLS) in December of 1986.[5] Spectra of the silver K-edge were measured in the transmission mode at room temperature (298 K) and near the temperature of liquid nitrogen (77 K).

RESULTS AND DISCUSSION

Because of EXAFS sensitivity to the local rather than the long range structure in materials, it is uniquely suited for detecting electrochemically induced small structural variations. EXAFS provides information regarding the interaction of oxygen with silver which is essential to understand the decomposition mechanism. Analyses of EXAFS data proved that the dominant product produced by the anodization of sintered silver plates is an oxygen-deficient form of AgO.[6] That is, $AgO_{1-\delta}$ is formed rather than a mixture of separate phases of stoichiometric AgO and Ag_2O as previously thought. The degree of oxygen deficiency, δ, depends on preparation procedures and can take on values between 0.00 and 0.25. A few of the EP-AgO cathodes contained almost entirely Ag_4O_3 (i.e, $AgO_{1-\delta}$ *with* δ=0.25). The atomic structure of this phase is derived from that of AgO[7] by creating one oxygen vacancy adjacent to each of the Ag^{+3} ions without altering the structure near the Ag^{+1} ions. Thus, Ag^{+3} in the AgO lattice is converted to Ag^{+2} in Ag_4O_3 in agreement with our XPS results and with earlier results which indicated the presence of paramagnetic centers in CP-AgO.

XRD patterns of EP-AgO consist mainly of Bragg diffraction lines whose positions are characteristic of CP-AgO but whose full width at half maximum are significantly broader. The degree of broadening was found to vary with preparation procedures and to increase with an increase in δ. XRD compositional analyses showed that for most, but not all, cathodes at least one of the phases Ag, Ag_2O, or Ag_2CO_3 was present in small quantities.

With structural insights from the EXAFS results, a new approach based on TG and XRD which takes into account the existence of oxygen-deficient AgO has been developed for the quantitative analysis of AgO cathodes. This model provides an alternative approach to EXAFS for the determination of δ. This allows the ready correlation of δ with the stability of the material. TG analyses indicated that the stability of AgO cathodes is a strong function of oxygen-deficiency and particle size.

REFERENCES

1. S. Dallek, W.A. West, and B.F. Larrick, J. Electrochem. Soc., **133**, 2451 (1986).
2. K.M. O'Neill, D.R. Glen, S. Dallek, B.F. Larrick, and A.N. Mansour, Extended Abstract, The Electrochemical Society Meeting, Chicago, IL, 9-14 October 1988.
3. S.U. Falk and A. Fleischer, in "Zinc-Silver Oxide Batteries," A. Fleischer and J.J. Lander, Editors, pp. 199-207, John Wiley and Sons, New York (1971).
4. W. Parkhurst, S. Dallek, and B.F. Larrick, J. Electrochem. Soc., **131**, 1739 (1984).
5. D.E. Sayers, S.M. Heald, M.A. Pick, J.I. Budnick, E.A. Stern, and J. Wong, Nucl. Instr. and Meth., **208**, 631 (1983).
6. A.N. Mansour, S. Dallek, K.M. O'Neill, C.R. Anderson, D.R. Glen, and B. F. Larrick, Extended Abstract 152, The Electrochemical Society Meeting, Honolulu, HI, 18-23 October 1987.
7. V. Scatturin, P. Belon, and A.J. Salkind, J. Electrochem. Soc., **108**, 819 (1961).

Abstract No. 88

CHRONOPOTENTIOMETRIC AND ELLIPSOMETRIC INVESTIGATION OF THE ZINC OXIDATION BEHAVIOR

Cecilia Y. Mak[1] and Huk Y. Cheh

Columbia University
Department of Chemical Engineering
and Applied Chemistry, New York, New York

During the oxidation of zinc in an alkaline solution, a porous covering film of precipitation products is frequently found to deposit on the electrode surface prior to passivation. The initial presence of this film, however, does not seem to affect the continual passage of current. Under galvanostatic discharge conditions, the electrode potential has remained relatively constant until passivation occurs.

Since the film is highly porous during the early stages of its growth, it is conceivable that despite the low conductivity of the zinc oxide precipitate, the electrical resistance imposed by the initial film is not pronounced enough to cause a distinct shift in the electrode potential. Therefore, although chronopotentiometry is viable for detecting the occurrence of passivation, the method is not sensitive enough to signal the onset of film formation.

In view of this difficulty in studying the film formation behavior during zinc oxidation via electrical methods, Yamashita and coworkers [1] applied the technique of chronoellipsometry [2] to monitor additionally the optical changes at the electrode surface. They recorded two break points in the phase shift transient signal. The first break point was suggested to be due to the precipitation of a Type I zinc oxide film [3] from a supersaturated zincate solution. The occurrence of the second break point was reported to coincide with the chronopotentiometric transition and indicated passivation of the zinc electrode.

Following the approach of Yamashita and coworkers, ellipsometry is conducted in this work to complement chronopotentiometric measurments to gain additional insights into the surface processes during zinc oxidation. A data acquisition system has been interfaced to the experimental equipment to synchronize the recording of the electrochemical and the ellipsometrical signals. Figure 1 shows the typical transient behavior of the electrode potential and the ellipsometric parameters, Δ and ψ, observed during galvanostatic oxidation in a 2 N KOH solution at 100 mA/cm^2. The ellipsometric signals are presented as deviation from their initial values, $\tilde{\Delta}$ and $\tilde{\psi}$.

As the current is first switched on, the electrode potential increases immediately because of ohmic potential drop in the solution. Thereafter, it remains relatively constant until passivation occurs. At passivation, the electrode potential increases abruptly. A black film is seen to be covering the electrode surface. Oxygen gas is also seen to be evolving at the zinc anode.

While the electrode potential remains relatively constant during the oxidation period, some characteristic features are observed on the ellipsometric signals. Upon initial dissolution, both Δ and ψ decrease continuously. After some time later, these parameters reverse in direction and begin to increase. The increase in ψ usually leads the increase in Δ, which gives the loop behavior on the Δ/ψ plot. Towards the end of the experiment, Δ undergoes a sharp decrease while ψ increases simultaneously. Our digitally acquired data reveal that the final decrease in Δ and increase in ψ occur after the potential transition (see the expanded scale in Figure 2). This result indicates that the cause of zinc passivation cannot be attributed to the formation of the black film. Rather, its formation is likely to be a consequence of the passivation event.

The optical signal is interpreted as the following. The initial decrease in both Δ and ψ is due to roughening of the electrode surface as a result of metal dissolution. The subsequent increase of these two parameters indicates the growth of a thick porous precipitation film. The final decrease in Δ and increase in ψ is due to the formation of the black film. In order to test the validity of this interpretation of the optical signal, a series of supplemental experiments have been conducted. These experiments comprise examining the system behavior during linear sweep voltammetry, potential step, potential step reversal, and the modification in the galvanostatic behavior upon zinc oxide pre-saturation, stirring, deaeration, and current interruption.

Our results are consistent with a dissolution-precipitation film formation mechanism. The ψ transient indicates that a fourfold zincate supersaturation is required to initiate phase transformation at the electrode surface.

References

1. M. Yamashita, T. Yoshimura, Y. Imanaka, and H. Futura, Doshisha Daigaku Rikogaku Kenkyu Hokoku, 18, 58 (1977).

2. A. K. Reddy, M. A. Devanathan, and J. O'M Bockris, J. Electroanal. Chem., 6, 61 (1963).

3. R. W. Powers and M. W. Breiter, J. Electrochem. Soc., 116, 719 (1969).

---

[1]*Present Address:* IBM Corporation, T. J. Watson Research Center, Yorktown Heights, New York.

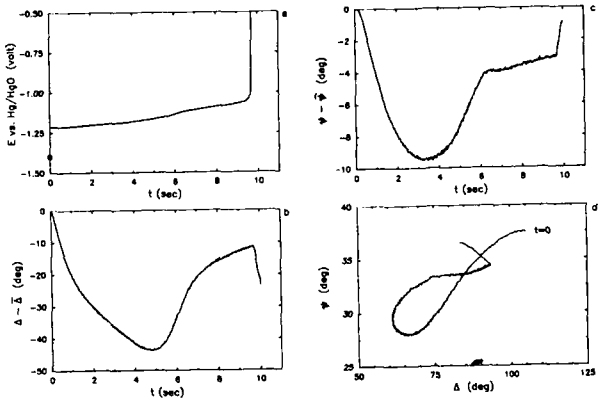


Figure 1. Galvanostatic Oxidation of zinc in a 2N KOH solution at 100 mA.cm^{-2}

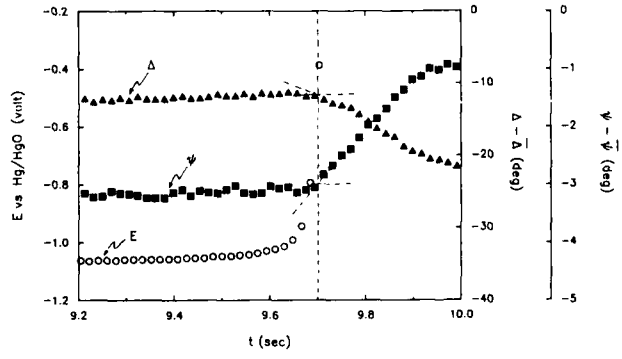


Figure 2 *Electrochemical and ellipsometric behavior just prior to zinc passivation*

Abstract No. 89

PERFOHMANCE OF SLURRY Zn-AIR RECHARGE AND DISCHARGE CELLS WITH KOH-LiOH ELECTROLYTE

H. B. Sierra Alcázar, Phu D. Nguyen, A. A. Pinoli
Pinnacle Research Institute, Inc.
10432 N. Tantau Avenue
Cupertino, CA 95014

Interest in the slurry Zn-Air battery system with separate discharge and recharge stacks derives from its projected high energy density to power electrical vehicles (1). Recharge can be either hydraulic or electric or both. Electrical recharge is done by deposition of dendritic Zn on a suitable substrate, such as Mg or glassy carbon plate (2), from which it can be mechanically scraped and returned to the discharge cell as a slurry. Electrical recharge can be performed on-board or at strategically located central stations. Anodic hydrogen depolarization can reduce the cost of recharge considerably (1) in central recharge stations.

The most important factor that determines the energy density of Zn-air batteries is the ability of the electrolyte (12 M KOH) to carry oxidized zinc (either as $Zn(OH)_4^{++}$ ions or as micelles and/or polymers with ZnO). The nature of the electrochemically generated zincate stabilized with LiOH is not understood and requires study. The choice of LiOH is definitely Edisionian: T.A. Edison first chose it. More recently Flerov (3) reported that Li^+ ion retarded the precipitation of ZnO from electrochemically generated oversaturated solutions of zincate in KOH.

This work reports on improvements to the state of the art discharge capacity of the slurry Zn-air battery obtained with LiOH additive. There was a concern that the improved stability of zincate or ZnO in solution obtained with LiOH and other capacity extension additives would make the recharge process more difficult. This work, however, concludes that production of dendritic Zn from oversaturated zincate solutions stabilized with LiOH is feasible and can proceed with low energy requirements. The benefits are not necessarily extended to other systems with static or flowing electrolyte because of the unique characteristics of the slurry system that involve a fluctuating discharge potential coupled with brisk hydrodynamic conditions on discharge and dendritic rather than smooth Zn deposition on recharge.

The specific capacity of pure 12 M KOH determined with a 200 cm^2 bi-cell (4) was 106 Ah/l (87 g Zn^{++}/l). The capacity can be increased by adding a type A additive (25 g/l silicate) to aid in the formation of micelles around minute ZnO particles. A further increase in specific discharge capacity to 203 Ah/l (248 g Zn^{++}/l) can be obtained by combining with a Type B additive (25 g/l silicate + 15 g/l sorbitol) that helps stabilize polymeric chains involving ZnO molecules (4). The highest discharge specific capacity was 228.8 Ah/l (279 g Zn/l) obtained with 25 g/l LiOH in 12 M KOH (5). All the above capacities were determined at 200 mA/cm^2 constant current density discharge. Lower current densities and higher slurry flow rates are expected to improve these capacities. However, the capacity obtained by discharging with an air cathode with static catholyte is not the maximum that could be obtained, since the porous air cathode passivates before the circulating anode (Zn particles). The most likely mechanism of passivation is ZnO precipitation inside the air cathode pores due to a decreased concentration of water in the electrolyte (water is depleted by reacting with O_2 to form OH^-).

A useful method to evaluate the inherent capacity extension provided by additives, independent of the behavior of the air electrode, is based in the determination of passivation time, t_p, measured after galvanodynamic steps are applied to a Zn rotating disk electrode in the test electrolyte. The results shown in Fig. 1 followed the Sand equation; they were used to determine a critical current density, i_c, as a function of zincate concentration and additive concentration. The concentration of zincate at which the critical current density becomes zero defines the inherent capacity extension of the additive for the particular temperature and hydrodynamic conditions of the experiment. The maximum inherent discharge capacity was extrapolated from the concentration vs critical current density curve shown in Fig. 2. The inherent discharge capacity of 25 g/l LiOH in 12 M KOH thus calculated is 302 Ah/l (368.5 g Zn/l), it represents an improvement of 32% over the air cathode limited discharge capacity. This improvement can be reasonably expected to became a reality by preventing the build up of zincate concentration in the air cathode.

The cell voltages and specific peak powers (with respect to exposed area of the air cathode) obtained during discharge are a function of current density and DoD, as seen in Fig. 3 and 4 respectively. It is expected that the voltage vs current density curve and peak power corresponding to discharge initiation would remain the same through all the discharge cycle on solving the air cathode passivation problem. The measured coulombic efficiency for discharge was better than 96%. To make adequate contact to the current collector, a minimum of 60 g of Zn powder per liter of slurry are required. Zn utilization can, nevertheless, be higher than 99% by running a battery with batches of slurry prepared from separately stored solid and liquid components.

The recharge of zincate oversaturated electrolyte was studied at room temperature with a cell where evolved hydrogen was measured. The cathode substrate used was a Mg plate where dendritic Zn was deposited and scraped at periodic intervals with a polymeric blade. The anode was a nickel mesh. Temperature was found to decrease the time averaged cathode potential at all depths of charge. Figure 5 shows this effect on electrolyte containing 51 g of dissolved Zn. However, at low current densities higher temperature promotes smooth Zn deposits. In Figure 5, an arrow indicates the only acceptable dendritic deposit on the 101 mA/cm^2 curve. Dendritic Zn was deposited at all higher current densities.

The average half-cell energy density (cathode overpotential times current density) is plotted against current density in Figure 6 for constant current deposition at various depths of charge (DoC), expressed as grams of dissolved Zn per liter. The arrows indicate the lowest current density at which an acceptable dendritic Zn was deposited. It can be seen that the charge energy required has a minimum at DoC of about 100 g Zn/l. This is so because higher voltages are required at low DoC in order to insure high currents for dendritic deposition (under diffusion control), and high DoC concentration polarization requires again higher voltages even at low current densities. It might be possible that the higher zincate concentrations obtained with LiOH additive cause a reduction of overall charge energy. More measurements are required to prove this point but at least it can be concluded that specific half-cell energies of less than 0.3 Wh per gram of dendritic Zn deposited at 300 c/cm^2 (or more specific charge) are feasible in the presence of LiOH additive

Acknowledgement

This work was supported by Lawrence Berkeley Laboratory, Technology Base Research program, on behalf of DOE.

REFERENCES

1. H.B. Sierra Alcázar, P.D. Nguyen, A.A. Pinoli "The Secondary Slurry Zn-Air Battery for EV Propulsion". 33rd International Power Sources Symposium. 13-16 June 1988. Cherry Hill, New Jersey. Proceedings published by the Electrochemical Society.
2. H.B. Sierra Alcázar, P.D. Nguyen "Technology Base Research on the Slurry Zn-Air Battery ". Extended Abstract. 172nd Electrochemical Soc. Meeting. 20 Oct 1987, Honolulu, Hawaii.
3. V.N. Flerov, Zh. Fiz. Khim., **31**, 49 (1957).
4. H.B. Sierra Alcázar, P.D. Nguyen "Additives to increase the Discharge Capacity of the Moving Bed Zn-Air Battery". Paper 879397. 22nd Intersociety Energy Conversion Engineering Conference. August 10-14, 1987. Philadelphia, Pennsylvania.
5. H.B. Sierra Alcázar, P.D. Nguyen, A.A. Pinoli. "Slurry Zn-Air Battery R & D". 8th Battery and Electrochemical Contractors Conference. Organized by DOE. Vienna, Virginia, November 19, 1987.

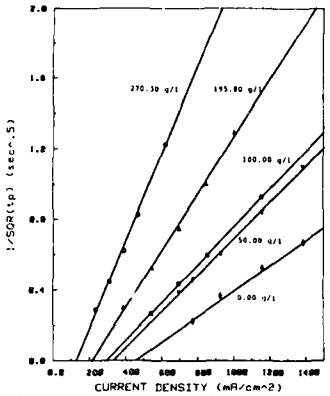


Fig. 1. Inverse square root of passivation time vs. current density. Performed in a rotating disc apparatus with an electrode area of .1307 cm^2 and rotating speed of 1000 rpm. Electrolyte was 25 g/l LiOH and various concentrations of Zn^{++} in 12 M KOH.

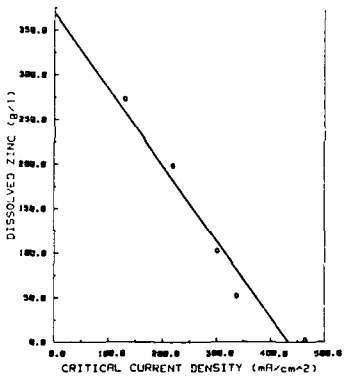


Fig. 2. Dissolved Zn vs. critical current density (Inherent capacity for 25 g/l LiOH).

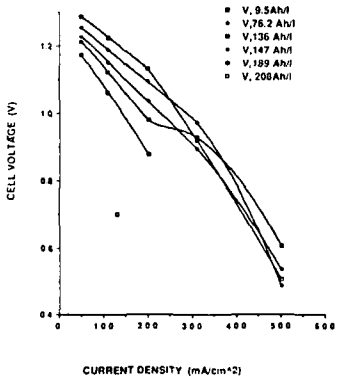


Fig. 3. Cell potential vs. current density with respect to DoD. Polarization was performed at 55°C with 12 M KOH, 350 g/l fresh Zn and compressed air as the cathode depolarizer.

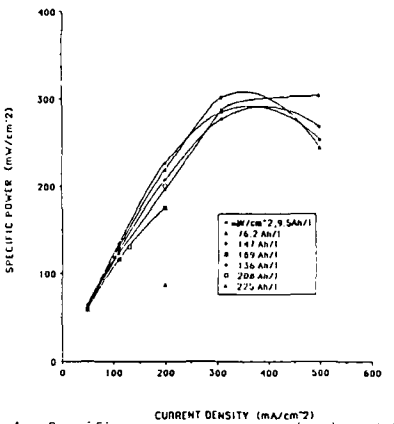


Fig. 4. Specific power vs. current density with respect to DoD. Polarization was performed at 55°C with 12 M KOH, 350 g/l fresh Zn and compressed air as the cathode depolarizer.

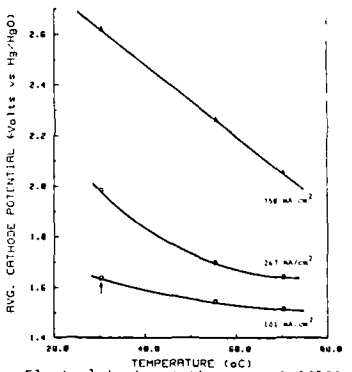


Fig. 5. Electrolyte temperature vs. average cathode potential. Recharge was performed on a planar Mg disc with Zn^{++} concentration of 51 g Zn/l and total specific charge of 300 c/cm^2.

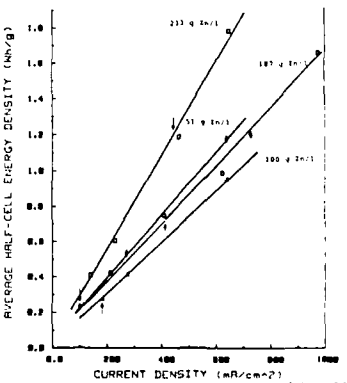


Fig. 6. Current density vs. average half-cell energy density. Recharge was performed at room temperature on a planar Mg disc with a total specific charge of 300 c/cm^2.

Abstract No. 90

In situ FTIRRAS Studies of Glucose Oxidation on Platinum Electrode in the Presence and Absence of Thallium Underpotential Deposition

In Tae Bae, Xuekun Xing, M. Daroux and E. Yeager

Case Center for Electrochemical Sciences
and the Department of Chemistry

C. C. Liu

Chemical Engineering Department
Case Western Reserve University
Cleveland, Ohio 44106

Anodic oxidation of glucose on noble metal electrodes has been studied for the last twenty years because of the possibility of utilizing this electrochemical reaction for fuel cells and glucose sensors [1]. Although the electrochemical oxidation of glucose is strongly dependent on experimental conditions such as electrode material, solution pH, the presence of foreign ions in solution, etc, it has been suggested [2] that the reaction proceeds by a mechanism similar to those recently studied for elementary organic substances as formic acid, formaldehyde and methanol. However, some aspects of the mechanism of glucose oxidation, including the identity of solution products, reaction intermediates, and adsorbed species on the electrode, are still controversial [3]. We present here the results of **in situ** Fourier transform infrared reflection absorption spectroscopic (FTIRRAS) studies of β-D(+)-glucose oxidation on a platinum electrode in acid in the presence and absence of underpotentially deposited (UPD) thallium which has been found [4] to promote this reaction.

The measurements were performed for solutions of 0.11 M β-D(+)-glucose in 0.1 M $HClO_4$ with and without additions of 6×10^{-4} M $TlClO_4$ over a potential range of 0.0 to 0.5 V vs. SCE. A prototype glass spectroelectrochemical cell [5] was used, in which a mirror-finished platinum disk(0.79 cm^2) was pushed against a CaF_2 window. The cell was mounted to a specially constructed reflection accessory consisting of three mirrors equipped with a gold wire grid polarizer in the FTIR bench (IR/98, IBM Instruments INC.) (see Fig. 1). The electrode potential was alternately switched between the sample(E_S) and the reference potential(E_R) by synchronizing the potentiostat to the spectrometer in such a way as to collect 20 interferometer scans at each potential. The spectra shown are the average of a total of 400 scans at each potential. The potential difference spectra were obtained by taking the ratio of sample spectra to reference spectra and calculating $-\Delta R/R$.

In the voltammogram for glucose oxidation on bare platinum, there are two anodic peaks at 0.2 V and 0.6 V vs. SCE(labeled as I and II respectively in Fig. 2) at potentials negative to the platinum oxide region. Fig. 3 shows the spectra obtained for the platinum electrode in 0.1 M $HClO_4$ containing glucose over this potential range. The characteristic feature in the region 2030 - 2080 cm^{-1} indicates that the major surface species during the first step of glucose oxidation (peak I) is the linearly adsorbed CO [6]. The CO peak gradually increases in intensity and frequency with positive polarization, reaching a maximum at 0.2 V vs. SCE where a current maximum also occurs(Fig. 2). On further polarization, both the frequency and the intensity of this peak decrease again as the CO is oxidized from the surface (peak II). CO oxidation at this potential has been well established in the literature [6].

In the presence of thallium UPD the glucose oxidation current is greatly increased [6], but the CO peak was greatly reduced in intensity and shifted ca. 6 cm^{-1} to low frequencies (Fig. 4). This suggests that the thallium UPD layer enhances the oxidation process by preventing the adsorption of CO on platinum, at least at potentials up to 0.6 V(SCE). In the presence of thallium the reaction occurs in the normal double layer, giving a single oxidation peak without surface-poisoning by CO species [7]. It is not clear whether the low frequency shift is due to lowered coupling at low CO coverages, diminished adsorption on the thallium modified surface, or interaction between neighboring thallium atoms and CO on platinum.

Acknowledgement

This research was supported by the US Office of Naval Research, the Department of Energy, NIH and the State of Ohio Edison Program.

References

1. H. Warner and B. W. Robinson, A Glucose Fuel Cell, Digest of 7th Intern. Conf. on Medical and Biol. Engin., Stockholm, 1967, p.530; J. Giner and P. Malachesky, Proc. Artif. Heart Program Conf. U. S. Dept. Health, Education and Welfare, 1969, p.839.

2. Yu. B. Vassilyev, O. A. Khazova and N. N. Nikolaeva, J. Electroanal. Chem., 196 (1985) 127.

3. A. E. Bolzan, T. Iwasita and W. Vielstich, J. Electrochem. Soc., 134 (1987) 3052; S. Ernst, J. Heitbaum and C. H. Hamann, J. Electroanal Chem., 100 (1979) 173.

4. M. Shao, X. Xing and C. C. Liu, Bioelectrochem. Bioenerg., 17 (1987) 59.

5. A. Bewick and S. Pons in "Advances in Infrared and Raman Spectroscopy", Ed. R. Hester and R. Clark, (Hayden, London, 1985)

6. D. S. Corrigan and M. J. Weaver, J. Electroanal. Chem., 241 (1988) 143, K. Kunimatsu and H. Kita, J Electroanal. Chem., 218 (1987) 155; F. Feddrix, I. T. Bae, P. W. Faguy and E. Yeager, to be published

7. P. Stonehart and G. Kohlmayr, Electrochim Acta, 17 (1972) 369.

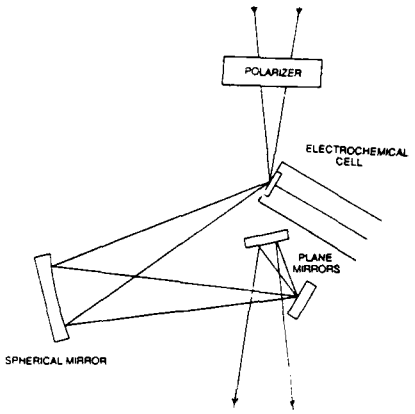


Fig 1 Optical configuration for in situ measurements in IBM-IR/98; incident angle, 60°, CaF_2 window, p-polarization.

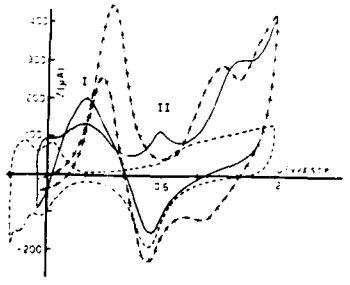


Fig. 2 Comparison of the cyclic voltammograms for the oxidation of glucose in the presence and absence of underpotential-deposited thallium (---) 1 M $HClO_4$, (——) 1 M $HClO_4$ + 0.5 M glucose, (···) 1 M $HClO_4$ + 0.5 M glucose + $5\cdot10^{-4}$ M $TlClO_4$. Scan rate = 50 mV/s, A = 2.2 cm^2. (taken from ref 5)

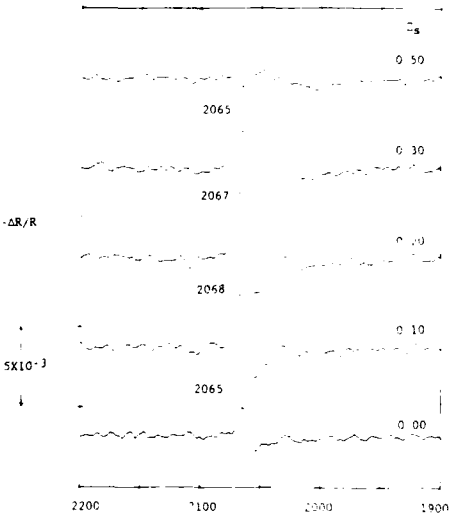


Fig. 3 in situ FTIRRA spectra of adsorbed CO on Pc surface at various E_s in 0.1 M $HClO_4$ containing 0.11 M β-D(+)-glucose; 400 scans, p-polarization, 2 cm^{-1} resolution, E_r= -0.1 V vs. SCE.

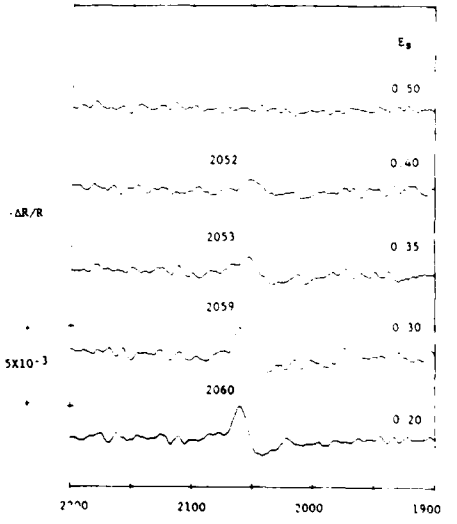


Fig 4 in situ FTIRRA spectra of adsorbed CO on Pc surface at various E_s in 0.1 M $HClO_4$ containing 0.11 M β-D(+)-glucose and $6\cdot10^{-4}$ M $TlClO_4$, the other conditions are the same as in Fig. 2

Abstract No. 91

KINETIC MODELS OF ALLOY DISSOLUTION

J.W. Halley
School of Physics and Astronomy
University of Minnesota
Minneapolis, MN 55455

We show that, in the limit of low concentration of dissolving species selective dissolution of binary alloys should lead to stable interfaces if the process is controlled by diffusion of the dissolved species away from the electrode but to unstable surfaces if the limiting step is diffusion of the dissolving species inside the alloy. The argument is based on an application of the physical reasoning which accounts for the instability of planar interfaces in solidification processes as orginally discovered by Mullins and Sekerka[1].

At higher concentrations of the dissolving species, the form of the interface is expected to depend on whether the concentration p of the dissolving species is less than, equal to or greater than the the percolation concentration p_c. If $p < p_c$, then we argue that, at long enough times and on long enough length scales, the arguments mentioned in the preceding paragraph apply. In that case and when the limiting step is diffusion inside the sample, then we show that the kinetics are essentially those of the diffusion limited aggregation model[2] (DLA) and the interface will have the fractal character associated with that model. When $p = p_c$, then the interface results from the "eating out" of the rapidly dissolving species in the large percolation cluster and the geometrical shape of the interface is accordingly the shape of the surface of the large percolating cluster and will be fractal with a different dimension than that found in the case $p < p_c$. In the case $p > p_c$, we argue that at sufficiently long times and large distances, the problem is geometrically the same as the problem at $p = 1$ where it is evident that the dissolution process will lead to the type of interface associated with the Eden model for growth. This model does not lead to a fractal interface, but the width of the interface grows with time as a fractional power of the time.

These results are quite general but depend on the assumption that the rate of dissolution from the surface is more rapid than the rate of diffusion of dissolving species inside the metal. We suggest that the experimental variation of the potential on the electrode which is dealloying changes the ratio of these two rates. We will discuss the possibility that the thresholds which are observed in dealloying processes as a function of this electrode potential may arise as a consequence of the change from control by the dissolution step at the interface to control by diffusion inside the metal (in the case $p < p_c$) or by diffusion in electrolyte (in the case $p > p_c$).

The model on which these results are based does not take explicit account of diffusion rates at the surface which are different than diffusion rates in the bulk. We will discuss the effects of more rapid diffusion at the surface. The main conclusions are not effected at large enough distances and times.

The effects of special adsorption sites on the surface will affect the short range structure of the interface but will not change the fundamental conclusions.

We will present numerical calculations on a two dimensional model which confirm the main conclusions. This work has been supported in part by the Department of Energy through the Corrosion Research Center and in part by IBM corporation.

1. W. W. Mullins and J. Sekerka, J. Appl. Phys. 34, 323 (1963), J. Appl. Phys. 35, 444 (1964).
2. T. Witten and L. Sander, Phys. Rev. Lett. 47, 1400 (1981), Phys. Rev. B 27, 5686 (1983).

Abstract No. 92

Mechanism of Selective Alloy Dissolution Below and Beyond the Breakthrough Potential

H. Kaiser and H. Kaesche

Institut fuer Werkstoffwissenschaften, Universitaet Erlangen-Nuernberg, Federal Republic of Germany

Beginning with a description of early parting limit concepts [1,2] and a brief discussion of recent percolation models [3,], the theory of selective alloy dissolution is summarized under special consideration of the ("critical") breakthrough potential, above which the current density of less noble components increases abruptly. The transport of such components to the electrode surface by (rate-limiting) volume diffusion, as one possible mechanism [4], was examined by an investigation of the anodic dissolution of In and Cu from low-melting (high diffusivity) InSn and higher-melting (low diffusivity) CuPd alloys, respectively. In the former case, the volume diffusion mechanism was confirmed by both electrochemical techniques and direct electron microprobe detection of In-depletion within the interdiffusion zone (Fig. 1). Phase transformations initiated by the selective removal of In from the intermetallic β- and γ- phases were also analyzed [5], and the new phases developing from the surface were shown to grow either in accordance with the principles of diffusion-controlled transformations [6], i.e. with a planar interface due to the establishment of interfacial equilibrium (see Fig. 2), or in a morphologically unstable (porous) form, probably as a consequence of kinetic control. With CuPd alloys, on the other hand, a decrease of the Cu concentration, even after prolonged polarization below the breakthrough potential was only observed (Fig. 3) by combined Auger electron spectroscopy and ion sputtering within a distance of about 2 nm from the electrode surface (close to this method's depth resolution) [7]. At the same time a dense coverage of vicinal faces with epitaxially grown Pd crystallites with a diameter of similar magnitude is observed by transmission electron microscopy, most probably illustrating the blocking of kink sites and steps by the more noble component. From these results it can be concluded that an interdiffusion zone resulting from the volume diffusion mechanism is absent in higher-melting alloys. This view is corroborated by the additional observation of dissolution nuclei that are formed at a rate that increases at lattice defects and shows a sharp rise above the breakthrough potential. The lateral growth of these nuclei appears to be limited by the decoration of their peripheral edges with Pd crystallites via surface diffusion, the final growth morphology being a 3-dimensional network of microtunnels that propagate in low-indexed crystallographic directions [7,8].

References:

1. G. Tammann, "Lehrbuch der Metallkunde", pp. 439 - 450, L. Voss, Leipzig, 1932.
2. U. Dehlinger and R. Glocker, Ann. Physik, 16, 100 (1933).
3. K. Sieradzki et al., sub. to Phil. Mag.
4. H.W. Pickering and C. Wagner, J. Electrochem. Soc., 114, 698 (1967).
5. H. Kaiser, publication in preparation.
6. C. Wagner, cited in G.H. Geiger and D.R. Poirier,"Transport Phenomena in Metallurgy", pp. 451-496, Addison-Wesley, Reading (1973).
7. B. Kabius, thesis, University Erlangen-Nuernberg, 1987.
8. B. Kabius et al., Proc. Int. Symp. Honor. N. Hackerman: Surfaces, Inhibition and Passivation. (E. McCafferty and R.J. Brodd edts.), The Electrochemical Society, San Diego, 1986.

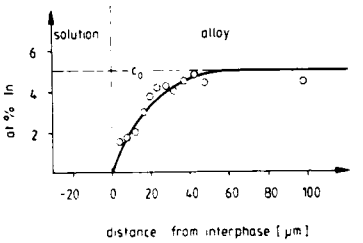


Fig. 1. Concentration profile of In in a Sn 5 a/o In alloy after 105 hrs. anodic polarization in 3 N NaCl/0.01 N HCl solution at 25 °C and E_s = - 0.47 V. Open circles from electron microprobe measurements, solid line calculated for $D = 5 \cdot 10^{-12}$ cm²/s and zero concentration at the interphase.

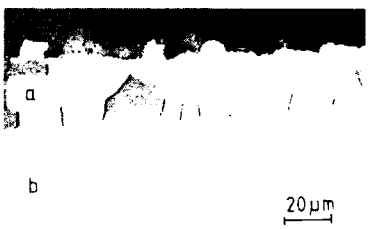


Fig. 2. Interfacial stability during diffusion-controlled growth of a β-Sn transformed layer (a) by the selective dissolution of In from a γ-SnIn alloy (b). 513 hrs. anodic polarization in 3 N NaCl/0,01 N HCl at E_s = - 0.47 V.

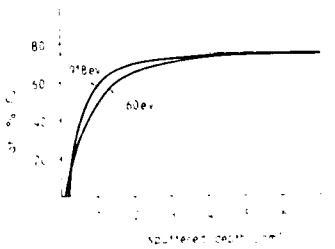


Fig. 3. Concentration-depth profiles of Cu in a Cu 25 a/o Pd alloy after 24 hrs. anodic polarization in acidified 1 N Na_2SO_4 solution below the breakthrough potential (E_s = - 0.53 V) [8]. Data from Auger electron sputtering profiles, corrected for the escape depth influence.

Abstract No. 93

The Percolation Model of Alloy Corrosion

K. Sieradzki

Department of Materials Science and Engineering
The Johns Hopkins University
Baltimore, Maryland 21218

De-alloying is an important aspect of corrosion in alloy systems. The theoretical framework for the high temperature corrosion or oxidation of alloys was developed by C. Wagner 35 years ago [1,2] and this seminal work included detailed discussions of selective oxidation processes. In Wagner's description of high temperature oxidation the interplay of volume diffusion processes in the metallic and oxide phases determined the roughness of the metal-oxide interface as well as the overall rate of oxidation.

A similar theoretical treatment was developed by Pickering and Wagner (P&W) [3] 15 years later in order to account for the electrolytic dissolution of binary noble metal alloys. The proposed transport process allowing dissolution to proceed at ambient temperatures was a solid state di-vacancy diffusion mechanism. Various difficulties exist regarding the general utility and appropriateness of the P&W analysis and we will discuss some of these issues.

One example of such a difficulty relates to results of recent experiments [4] examining selective dissolution as a function of alloy composition in Al-Cu and Zn-Cu alloys as illustrated in Figure 1. This result demonstrates that sharp *critical* compositions or de-alloying thresholds exist below which de-alloying does not occur. This critical behavior is not consistent with the notion that a bulk diffusion mechanism is responsible for transport of the less noble metal constituent to the metal-electrolyte interface.

We will present a new theoretical framework for alloy corrosion based upon concepts derived from percolation theory [5]. According to the theory an A_pB_{1-p} alloy immersed in an electrochemically aggresive environment can undergo selective removal of A only if continuous connected clusters of A exist throughout the solid. The probability of the existence of such an infinite cluster of A atoms is the subject of percolation theory which describes a critical composition referred to as the percolation threshold below which this probability is zero and above which this probability is one. The percolating cluster of atoms provides a continuous active path for the electrolyte to follow into the bulk solid, allowing the corrosion process to continue. The dissolved structure consists of a continuous nano-porous layer enriched in B. Owing to the atomistic dimensions of these ligaments an extremely rapid form of Ostwald ripening occurs which leads to a coarsening of the initial structure. This coarsening allows for the further penetration of the electrolyte and also diminishes the effects of various other transport limiting processes.

We will discuss how electrochemical effects modify the simple concepts presented above. Various unresolved issues related to de-alloying will be discussed in terms of the theory including the so-called critical potential, anodic dissolution kinetics above and below the de-alloying threshold, and the magnitude of de-alloying thresholds or parting limits for various metal-electrolyte systems.

References

1. C. Wagner, *J. electrochem. Soc.*, **99**, 369 (1952)
2. C. Wagner, *J. electrochem. Soc.*, **103**, 571 (1956)
3. H.W. Pickering and C. Wagner, *J. electrochem. Soc.*, **114**, 698 (1967)
4. K. Sieradzki, J.S. Kim, A.T. Cole, and R.C. Newman, *J. electrochem. Soc.*, **134**, 1635 (1987)
5. K. Sieradzki, R.R. Corderman, K. Shukla, and R. C. Newman, *Phil. Mag.*, in press

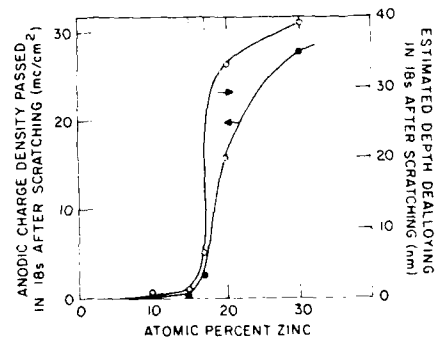


Figure 1. Dependence of the de-alloying charge density and estimated de-alloyed layer thickness on alloy composition for Zn-Cu.

Abstract No. 94

TEM INVESTIGATION OF DEALLOYED Cu-Au ALLOYS

J. D. Fritz[+] and H. W. Pickering

Department of Materials Science and Engineering
The Pennsylvania State University
University Park, PA 16802

[+]Currently at Savannah River Laboratory
Hydrogen Technology Division
Aiken, SC 29801

Foil samples of Cu-13%Au and Cu-18%Au (atomic %) were prepared by ion beam milling. The thinned foils were spot welded to a Pt wire and dealloyed by anodic polarization in an electrolyte of 1N Na_2SO_4 - 0.01N H_2SO_4. The dealloyed morphologies were examined using either a Philips 300 or 420 TEM. Samples dealloyed at potentials less noble than the breakaway or critical potential (E_c) showed some isolated pitting with pit diameters of 50 - 100A, as shown in Figure 1. Samples dealloyed at $E > E_c$ showed regions of complete pit coverage near foil edges, and isolated pits and pit clusters on regions removed from the foil edge. The pit diameters at $E > E_c$ ranged from 100 - 500 A with the larger pits occurring near foil edges. Samples showed Moire fringe patterns that resulted from the overlapping of the Au-rich dealloyed material and the substrate alloy, as shown in Figures 2 and 3. The spacing between fringes corresponds to a dealloyed composition of 93% Au. These patterns indicate the formation of small Au-rich nuclei (Figure 2) and the accumulation of Au on pit walls and region around pits (Figure 3) as the dealloying reaction proceeds. Surface migration may account for the Au accumulation.



Figure 1. Sample of Cu-18%Au after anodic treatment at E=542mV (SHE) showing a region of isolated pitting near a tear in the foil.

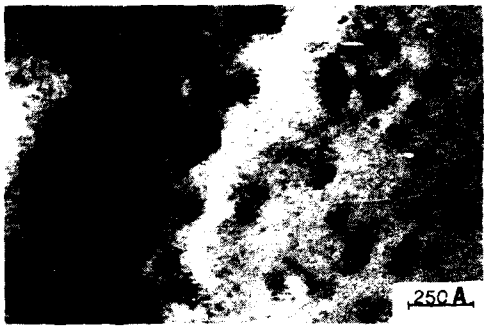


Figure 2. Sample of Cu-18%Au dealloyed at E=642 mV (SHE) showing the formation of small round Moire fringe patterns.



Figure 3. Sample of Cu-18%Au dealloyed at E=742mV (SHE) showing Moire fringes on pit walls and on regions around pits.

Abstract No. 95

Dealloying Kinetics of Silver-Gold Alloys

A. J. Davenport and K. Sieradzki*
Department of Applied Science
Brookhaven National Laboratory
Upton, NY 11973

Selective dissolution (dealloying) is often the dominant process in the aqueous corrosion of metal alloys. In this phenomenon, an A_pB_{1-p} alloy immersed in an aggressive environment undergoes a process in which the less noble component (A) is selectively removed from the alloy. Metal-environment systems display sharp compositional dealloying thresholds or parting limits below which only superficial dealloying occurs and above which bulk dealloying is observed. The principle morphological change associated with selective dissolution is the development of a nano-or micro-porous dealloyed layer. The conventional theories of dealloying in a (binary) alloy rely on the following mechanisms: (1) selective dissolution of the less noble metal atoms and aggregation of the more noble metal atoms by surface diffusion [1]; (2) selective dissolution of the less noble metal as transport occurs by divacancy volume diffusion [2]; and (3) dissolution of atoms of both elements followed by redeposition of the more noble metal atoms. None of these theories can explain the existence of sharp dealloying thresholds.

The origin of the dealloying thresholds and other aspects of the selective dissolution process are clarified in a new theory of dealloying [3] which is based upon percolation theory. According to this theory, in order for the A atoms to be selectively dissolved from more than just the surface of the alloy, a continuous connected cluster of these atoms must exist. This percolating cluster provides an active path for the dissolution process to occur and also provides a path for the electrolyte to penetrate into the bulk solid. The remaining structure is enriched in B and consists of a porous network of ligaments which are of atomistic dimensions. Owing to the extraordinarily high surface to volume ratio of these ligaments coarsening quickly occurs at ambient temperatures. This coarsening occurs immediately behind the dissolution front and allows for easy penetration of the electrolyte. If the elements are sufficiently different in reactivity, then the dealloying threshold will be close to the 3-dimensional site percolation threshold for the lattice. If the elements in the alloy do not differ greatly in reactivity then dealloying proceeds by a layer-by-layer process and the threshold will be close to the relevant 2-dimensional site percolation threshold. The variation in the dealloying threshold from one system to another relates to the differing tendency of the atoms of the more reactive element to dissolve from (and the atoms of the more noble element to diffuse from) surface sites of varying coordination number.

The Pickering and Wagner analysis [2] based on the volume diffusion mechanism predicts that the dissolution of the more reactive element results in a dealloying current proportional to $t^{-1/2}$. We believe that the surface diffusion mechanism also yields $i \propto t^{-1/2}$ and the predictions of a dissolution-redeposition mechanism are not clear. The percolation theory of dealloying predicts different functionalities for the current decays below and above the dealloying threshold, p*.

Specifically:

(a) Below p* the dealloying rate is determined by the A atom cluster structure. The current should have the following form:

$$i(t) \propto \int_t^\infty t^{-\alpha} \exp(-ct^\delta)\, dt$$

where $0 \leq \alpha \leq 1$ and $1 < \delta \leq 2$ for dissolution via a layer-by-layer process.

(b) Above p* the dealloying rate should initially be controlled by the coarsening rate. For a mixed surface-volume controlled coarsening process the average pore size increases as t^β so that

$$i \propto t^{\beta-1}$$

where, $1/4 \leq \beta \leq 1/3$. As the porous structure develops the current will become limited either by mass transport in the electrolyte or IR effects.

Figures 1 and 2 show current transients obtained on scratching a $Ag_{0.6}Au_{0.4}$ and a $Ag_{0.7}Au_{0.3}$ alloy at an applied potential of 1.0 V (SCE). Previous work at Brookhaven [4] and that of Tischer and Gerischer [5] indicate that the 60% Ag alloy is just below p* for this system. This alloy (Fig. 1) shows a rapid current decay which returns almost to the base current level within 200 ms. The 70% Ag alloy (Fig. 2) shows a much slower current decay consistant with substantial dealloying from the bulk alloy. The scratched electrode technique provides a method of testing the new dealloying model through analysis of dissolution current transients.

Acknowledgments

This work was performed under the auspices of the U.S. Department of Energy, Division of Materials Sciences, Office of Basic Energy Science under Contract No. DE-AC02-76CH00016.

References

1. A. T. Forty and G. Rowlands, Philos. Mag. A 43, 171 (1981).

2. H.W. Pickering and C. Wagner, J. Electrochem. Soc. 114, 698 (1967).

3. K. Sieradzki, R.R. Corderman, K. Shukla, and R.C. Newman, Philos. Mag. A, in press.

4. Rong Li and K. Sieradzki, in preparation.

5. R.P. Tischer and H. Gerischer, Z. Electrochem. 62, 50 (1962).

*Department of Materials Science and Engineering, The Johns Hopkins University, Baltimore, MD 21218.

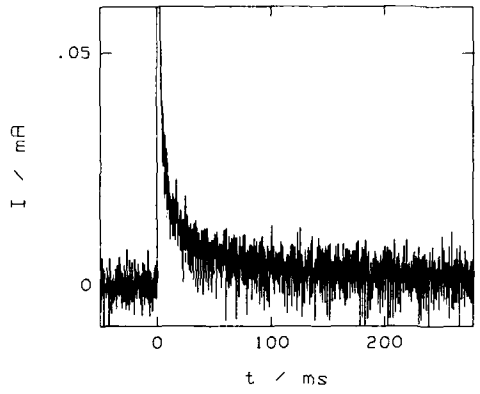


Fig. 1. Decay of a current transient resulting from scratching $Ag_{0.6}Au_{0.4}$ at 1.0 V(SCE) in 1M $HClO_4$. The scratch dimensions are 2000 μm x 50 μm.

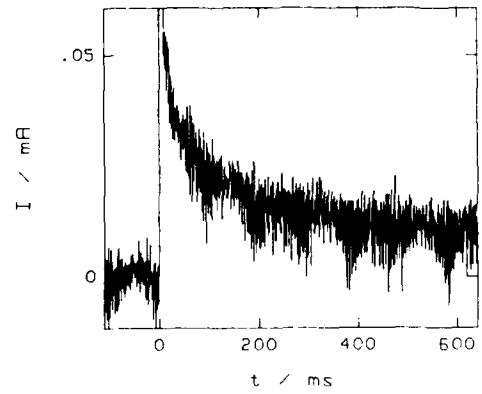


Fig. 2. Decay of a current transient resulting from scratching $Ag_{0.7}Au_{0.3}$ at 1.0 V(SCE) in 1M $HClO_4$. The scratch dimensions are 2000 μm x 50 μm.

Abstract No. 96

Surface Instability Under Conditions of Selective Dissolution in a Liquid Metal Environment*

P. F. Tortorelli
Oak Ridge National Laboratory
P.O. Box 2008
Oak Ridge, TN 38731

Introduction

Selective dissolution of one or more components from an alloy (also referred to as "dealloying") has been observed in aqueous, liquid metal, molten salt, and gaseous environments. In many of these cases, selective dissolution leads to the formation of a "porous" or highly irregular surface zone on the exposed solid. It is shown that, for the specific case of austenitic stainless steel exposed to molten lead-lithium, a surface destabilization model best describes the observed corrosion morphology and the effect of cold work on this type of attack.

Results and Discussion

It has been previously reported that molten lead-lithium is quite aggressive towards ferrous alloys, particularly in the presence of a thermal gradient.[1-3] With austenitic (Fe-Cr-Ni) steels, exposure to Pb-17 at. % Li under an imposed temperature gradient causes deep irregular attack as a result of penetration by the liquid metal (Fig. 1). Under similar exposure conditions, Fe-Cr-Mo steels corrode uniformly (Fig. 2). Analysis of the corrosion layers, such as shown in Fig. 1, revealed lead-filled channels penetrating deeply into the steel. The solid in this corrosion zone is depleted in nickel and chromium relative to the starting composition of the type 316 stainless steel [65Fe, 17Cr, 12Ni, 2Mo, 2Mn, 2Si, 0.08C, (wt %)]. The average postexposure composition in this region is 86Fe-8Cr-4Ni-2Mo (wt %), which was fairly independent of exposure time. In addition, it was found that the extent and directionality of the penetration was strongly influenced by the rolling direction of the steel. Penetrations were deeper and tended to be parallel to the rolling direction (see Fig. 3). The cold work effectively "biased" the penetration process. In contrast, the Fe-Cr-Mo steel-liquid metal interface remains planar during dissolution (Fig. 2) and no tendency for preferential depletion has been detected.

While it may seem as though the type 316 stainless steel has suffered preferential dissolution of both nickel and chromium, the depletion of these elements arise due to different causes. Nickel is directly dissolved, while the loss of chromium is most probably related to the formation of a lithium-chromium-nitrogen corrosion product,[4] which is removed during exposure or during specimen cleaning. Chromium and iron are both "noble" with respect to nickel; their solubilities in lead-lithium are similar, but much lower than that of nickel. Preferential dissolution of chromium with respect to iron is therefore not expected and has not been observed for Fe-Cr steels (see above).

In attempting to explain the observed corrosive attack of the Fe-Ni-Cr steel, the most simple mechanism would be that of localized penetration along highly reactive paths. Recent work[5] has treated selective dissolution (dealloying) of Cu-Zn and Cu-Al alloys in aqueous environments in terms of a percolation model, in which alloy components of significantly differing reactivity can lead to selected dissolution and porosity if extended, connected paths of the more reactive species exist in the lattice. The probability of existence of a significant number of such paths is a direct function of the concentration of the reactive element and can be derived within the formalism of percolation theory.[6] Although this mechanism is intuitively attractive, simple calculations showed an insufficient concentration of reactive (nickel) atoms to produce the connective path needed to get the observed penetrations.

Several other models of environmentally induced "porosity" or irregular corrosion (including redeposition and vacancy agglomeration) were considered. It was found that the surface destabilization approach of Harrison and Wagner[7] fits the experimental observations quite well. In such a process, initial surface perturbations grow into a series of deep penetrations under conditions where one element is selectively depleted. While Harrison and Wagner[7] treated this process for liquid metal attack, similar surface instability considerations have been demonstrated for other environments. Examples include oxide scale formation on alloys containing elements of significantly differing nobility[8] or volatilization of an element from an alloy.[9] In the absence of preferential dissolution, the destabilization model predicts that a planar liquid-solid interface would be the equilibrium state. This prediction agrees exactly with the observations of the contrasting corrosion of Fe-Cr-Ni and Fe-Cr described above. Furthermore, the growth kinetics predicted by this model are in fairly good agreement with measured values of the penetration depth as a function of time. Finally, such a mechanism can also explain the effect of cold work on the corrosion morphology. A cold-worked surface supplies perturbations that can trigger the destabilization and subsequent growth of an irregular interface. Grain boundaries or slip lines can serve as such perturbations sites.[7] It therefore appears that the attack of Fe-Ni-Cr steel by liquid lead-lithium can be described in terms of surface instability due to selective dissolution and the associated penetration kinetics.

References

1. P. F. Tortorelli and J. H. Devan, J. Nucl. Mater. 141-143, 592-98 (1986).

2. O. K. Chopra and D. L. Smith, J. Nucl. Mater. 141-143, 566-70 (1986).

3. H. U. Borgstedt et al., "Corrosion Testing of Steel X 18 CrMoVNb 12 (1.4914) in a Pb-17 Li Pumped Loop," J. Nucl. Mater. 154-156, to be published.

4. M.G. Barker et al., J. Nucl. Mater. 114, 143-49 (1983).

5. K. Sieradzki et al., J. Electrochem. Soc. 134, 1635-9 (1987).

6. D. Stauffer, Introduction to Percolation Theory, Taylor and Francis, London, 1985.

7. J. D. Harrison and C. Wagner, Acta Metall. 7, 722-35 (1959).

8. C. Wagner, J. Electrochem. Soc. 103, 571-80 (1956).

9. H. W. Pickering and Y. S. Kim, pp. 455-[illegible] in Proc. Symp. on Chemical Metallurgy - A Tribute to Carl Wagner, TMS-AIME, 1981.

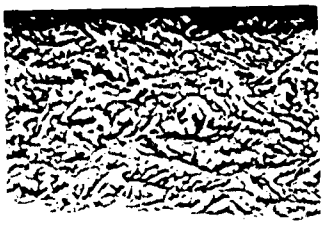
*Research sponsored by the Office of Fusion Energy, U.S. Department of Energy under contract DE-AC05-84OR21400 with Martin Marietta Energy Systems, Inc.



Fig. 1. Scanning electron micrograph of polished cross section of type 316 stainless steel exposed to thermally convective lead-lithium for 2472 h at 500°C.



Fig. 2. Scanning electron micrograph of polished cross section of Fe-12Cr-1Mo steel exposed to thermally convective lead-lithium for 7027 h at 500°C.



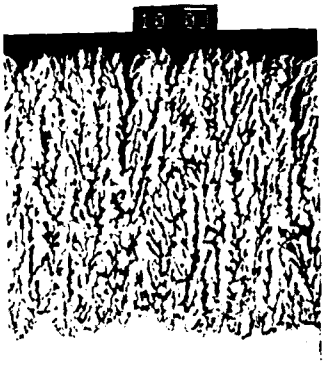


Fig. 3. Scanning electron micrographs of polished cross section of type 316 stainless steel exposed to thermally convective lead-lithium for 3886 h at 500°C. (a) Rolling direction parallel to liquid-steel interface. (b) Rolling direction perpendicular to liquid-steel interface.

Abstract No. 97

THE RELATIONSHIP BETWEEN DEALLOYING AND STRESS-CORROSION CRACKING

R.C. Newman, A. Mehta and T. Shahrabi
Corrosion and Protection Centre
UMIST
P.O. Box 88, Manchester, M60 1QD, U.K.

K. Sieradzki
Department of Materials Science and Engineering
Johns Hopkins University
Baltimore, MD 21218, USA.

Dealloying has often been cited as a contributory factor in stress-corrosion cracking (SCC), beginning with L. Graf's work in the 1940s. Recently there has been renewed interest associated with the film-induced cleavage model of SCC, in which nanoporous dealloyed layers are believed to be very important and the compositional dependence of dealloying has been correlated with that of transgranular SCC [K. Sieradzki and R.C. Newman, J. Phys. Chem. Sol. 48, 1101 (1987)]. Our recent work has focussed on Cu-Zn, Fe-(Cr)-Ni and Au-Ag alloys, with several objectives:

1. To understand further the compositional dependence of dealloying.

2. To analyze thin dealloyed layers, especially on Fe-Cr-Ni alloys.

3. To understand the development of nanoporosity in the layers by a combination of computer simulation, mechanical property measurement and AC impedance spectroscopy.

4. To examine the ability of dealloyed layers, formed on unstressed smooth specimens, to nucleate single cleavage events.

The computer simulations are described in another paper in this symposium.

In austenitic stainless steels we find that dealloying in hot, acidified LiCl solution produces a nickel-enriched but by no means pure nickel layer; our best estimate of its typical composition is Fe-30%Ni. The occurrence of dealloying has been correlated with SCC to a limited extent, e.g. at 90°C dealloying and SCC occur on 304 and 316 steels but not on 310 steel, while at 136°C or at 90°C with added thiourea, all three steels show dealloying and SCC. In order to understand the roles of chloride and nickel enrichment, we have carried out DC and AC electrochemical studies on binary Fe-Ni alloys (3% and 10% Ni) in chloride and sulphate solutions at pH 1 and 80°C; the results show evidence for dealloying in chloride solution (tarnishing, irreversible polarization curves, impedance spectra characteristic of porous conducting layers), but not in sulphate solution. We conclude that chloride causes dealloying by affecting the partial anodic kinetics and/or surface diffusivity of the alloy components. Impurities such as N or P may enhance SCC by 'pinning' the dealloyed layer in its nanoporous, brittle state, hindering excessive coarsening by surface diffusion.

Studies of 12 μm α-brass foils have shown that unstable brittle fracture occurs in the presence of a dealloyed layer less than 100 nm in thickness, thus validating the film-induced cleavage concept. The fracture surfaces show cleavage facets of up to 10 μm in length, together with some brittle intergranular fracture. The embrittlement is most easily seen when the foils are stressed in the cuprous ammonia test solution, but is also evident after rapid freezing in liquid nitrogen. Washing and/or drying reverses the embrittlement, probably due to coarsening of the nanoporous layer when the environment is removed. Ammonia (or cuprous ammonium ions) may play a role in pinning the surface diffusion process responsible for the coarsening.

Similar studies of Au-Ag alloys, using anodic polarization in perchloric acid, gave less convincing evidence for transgranular film-induced cleavage. Instead, brittle intergranular events of remarkable extent (50 μm) were observed, and again the embrittlement was reversible. One conclusion of this work is that intergranular SCC, in systems where transgranular SCC is possible, occurs by the same brittle mechanism.

Abstract No. 98

THE ROLE OF DEALLOYING IN TRANSGRANULAR STRESS-CORROSION CRACKING

B. D. Lichter, W. F. Flanagan, J. B. Lee, and M. Zhu

Department of Mechanical and Materials Science
Vanderbilt University
Nashville, TN 37235

(Work supported by the National Science Foundation Grant No. NSF DMR 8420965)

Analyses of stress-corrosion cracking are frequently based on the slip dissolution model or other models for which crack advance is presumed to occur primarily by Faradaic charge transfer due to bare-surface dissolution and/or film growth at a crack tip.[1,2,3] Although such an approach may adequately describe intergranular stress-corrosion (I-SCC)[4], it fails to account for several established features of transgranular stress-corrosion (T-SCC) for which crack advance appears to occur primarily by a process of mechanical cleavage.[5-10] The evidence includes (a) the distinctive "facet-step" morphology of the fracture surface, (b) the crystallographic uniqueness of steps and facets, (c) the exact matching of opposing fracture surfaces, (d) the appearance on the fracture surface of naturally occuring crack-arrest markings, and (e) the correlation between acoustic emission and crack arrests or current transients.

Recently we have shown that copper-gold alloys containing 15, 25, and 50 atomic percent gold, when tested in aqueous NaCl, $FeCl_3$, or acid-sulfate media, display many of the features which support the mechanical cleavage hypothesis of T-SCC.[10-14] Copper-gold alloys in these media have been selected for study because they present an attractive model system with which to isolate possible candidate mechanisms of T-SCC. For example, our studies of T-SCC have been carried out under conditions for which selective dissolution of copper, or dealloying, occurs; whereas, hydrogen discharge is excluded on thermodynamic grounds.[15] Thus, we are now attempting to discover how near-surface dealloying may produce conditions allowing propagation of a cleavage crack into the uncorroded alloy matrix.

In the present work, both steady-state and transient dealloying were studied for single crystals of disordered Cu-25 Au in aqueous NaCl and $FeCl_3$. Using slow strain-rate conditions, the effect of dynamic elastic and plastic straining as well as of prior plastic deformation on the steady-state selective electrodissolution of copper was measured. Transient dealloying was measured using scratching techniques and was also observed in the form of current pulses during crack propagation under slow strain-rate deformation. In both cases the transient currents decayed relatively rapidly (~1 second) and showed a similar time-dependence during the decay. The average crack propagation rate was determined by correlating the time intervals between pulses with crack arrest markings observed on the fracture surface or by direct observation of the propagating crack using a cathetometer. An attempt is made to interpret the rate of crack growth from the measured rates of dealloying.

REFERENCES

1. F.A. Champion: Symposium on Internal Stresses in Metals and Alloys, Institute of Metals, London, 1948, pp. 468-69; H.L. Logan: J. Res. Nat. Bur. Stds., 1952, vol. 48, pp. 99-105.

REFERENCES CONT.

2. D.A. Vermilyea: J. Electrochem. Soc., 1972, vol. 119, pp. 405-07.

3. J.C. Scully: Corrosion Science, 1975, vol. 15, pp. 207-23.

4. P. Ford: Embrittlement by the Localized Crack Environment, R.P. Gangloff, ed., TMS-AIME, 1984, pp. 117-47.

5. A.J. Bursle and E.N. Pugh: Environment-Sensitive Fracture of Engineering Materials, Z. Foroulis, ed., TMS-AIME, 1979, pp. 18-47.

6. E.N. Pugh: Atomistics of Fracture, R.M. Latanision and J.R. Pickens, eds., NATO Conference Series VI, Plenum Press, 1983, vol. 5, pp. 997-1010.

7. E.N. Pugh: Corrosion, vol. 41, pp. 517-26.

8. K. Sieradzki and R.C. Newman: Philos. Mag., 1985, vol. 51, pp. 95-132.

9. E.I. Meletis and R.F. Hochman: Corrosion Sci., 1986, vol. 26, pp. 63-90.

10. B.D. Lichter, T.B. Cassagne, W.F. Flanagan, and E.N. Pugh: Microstructural Science, 1985, vol. 13, pp. 361-78.

11. T.B. Cassagne, W.F. Flanagan, and B.D. Lichter: Metall. Trans. A, 1986, vol. 17A, pp. 703-10.

12. T.B. Cassagne, W.F. Flanagan, and B.D. Lichter: Chemistry and Physics of Fracture, R.M. Latanision and R.H. Jones, eds., NATA Advance Science Institues Series E, Martinus Nijhoff, 1987, No. 130, pp. 659-69.

13. T.B. Cassagne, W.F. Flanagan, and B.D. Lichter, Metall. Trans. A, 1988, vol. 19A, pp. 281-92.

14. D. Massinon: M.S. Thesis, 1987, Vanderbilt University.

15. U. Bertocci: Paper presented at the 10th International Congress on Metallic Corrosion, 7-11 Nov. 1987, Madras, India, (to be published in Bulletin of Electrochem.).

Abstract No. 99

KINETICS AND MORPHOLOGY OF ALUMINIDE DEALLOYING REACTIONS

D. J. Young
School of Chemical Engineering & Industrial Chemistry
The University of New South Wales
P.O. Box 1, Kensington, N.S.W. Australia, 2033

The dissolution in alkali of aluminium from $CuAl_2$, $NiAl_3$ and Ni_2Al_3 has been studied at temperatures of from 274 to 380 K. In all cases the aluminium was eventually dissolved to leave a residue of porous, but essentially pure, noble metal. In the cases of $CuAl_2$ and Ni_2Al_3, this residue remained as a rim around a core of as-yet unreacted alloy, and the external dimensions of the sample remained unchanged during reaction. The residue of $NiAl_3$ dealloying was initially coherent but began to disintegrate after a thickness of about 200 μm was reached, and was lost from the sample.

The interface between dealloyed rim and unreacted alloy core was in all cases sharply defined. As reaction progressed and this interface moved inwards, it remained parallel to the external surface of the rim. The microstructure of the parent alloy was accurately reproduced in the dealloying product: grain or dendrite size, shape and orientation were preserved. These observations are interpreted as evidence that the reaction mechanism is one of selective dissolution.

Dealloying kinetics were observed by measuring metallographically the thickness of the leached rim as a function of time. The $CuAl_2$ and Ni_2Al_3 reactions proceeded according to parabolic kinetics[3] whereas the $NiAl_3$ reaction continued at a constant, rapid rate. The parabolic kinetics are shown to be consistent with rate control by diffusion within the liquid-filled pores of the dealloyed rim. Reaction rates for Ni_2Al_3 dealloying were much slower than for $CuAl_2$, and were not measurable at temperatures below about 340 K. One factor contributing to this difference in rates is the difference in aluminium activities between the phases. The linear kinetics found for $NiAl_3$ dealloying are consistent with the fact that no coherent product accumulates, and the liquid-phase diffusion path is of more-or-less constant length. The failure of the $NiAl_3$ residue to form a coherent structure is attributed to its high pore volume fraction of 0.81 compared to values of 0.74 and 0.60 for $CuAl_2$ and Ni_2Al_3 respectively.

Detailed morphologies of the dealloying reaction products were examined using gas adsorption to measure surface areas and pore volumes, mercury intrusion porosimetry to determine pore size distributions, x-ray diffraction line broadening to estimate crystallite sizes, electron probe microanalysis to measure concentration profiles within the reacted rims, and, in the case of $CuAl_2$ residues, direct transmission electron microscopy to view the copper structure.

The most complete set of information is available for the $CuAl_2$ residue, which was found to consist of very thin, single crystal, copper fibres aligned with their average direction parallel to the direction of the leaching reaction. At any given depth within the product rim, the cylindrical fibres were remarkably uniform in diameter, an observation borne out by the narrow pore size distributions. The average fibre spacing was found to increase with depth of leaching at the same temperature, and, for a given depth of leaching, to decrease as temperature increased. The process whereby the parent $CuAl_2$ phase is transformed into an ordered two-phase product (copper plus liquid solution of aluminium) is considered to be a cellular phase transformation reaction. The relationship between fibre spacing and reaction rate predicted by this model was verified for $CuAl_2$ dealloying. Fibre spacings are rather small, ranging from about 40 nm in a residue produced at 274 K up to about 110 nm after reaction at 366 K. Lateral segregation of alloy constitutents towards the advancing copper and pore-liquid phases must occur at or near the reaction front, over distances of the order of the structure's spacing. The mechanism of segregation was found to be interfacial diffusion.

The copper residues have high surface areas which are inherently unstable in alkali, because the solubility of copper, although low, is not zero. In fact, a coarsening of the structure is observed to occur at a rate which increases with temperature and pH. This process occurs independently of the dealloying reaction, and involves slow dissolution and reprecipi-tation of the copper. A model based on Ostwald ripening has been developed and found to describe the kinetics of this process. It is concluded that $CuAl_2$ dealloying occurs in the first instance by selective dissolution, but that the residue's final structure is modified by dissolution-reprecipitation.

Morphological development during Ni_2Al_3 dealloying is a more complex process, and occurs in at least two stages. Throughout most of the course of the reaction, the residue consists of an inner layer containing about 22 wt.% Al, and an outer layer containing Al levels varying from 12 to 24 wt.%. This inner layer was found to consist of two phases, Ni and Ni_2Al_3; the outer layer was more fully dealloyed, but contained considerable amounts of reprecipitated $Al_2O_3.xH_2O$. As the central alloy core was exhausted, the aluminium content of the inner layer was reduced to near zero and nickel was the only phase remaining. The outer layer converted to a mixture of nickel and amorphous hydrated alumina. It is not known why some of the parent Ni_2Al_3 is apparently more readily leachable than the remainder. The pore structure of the residue is obscured by the reprecipitated alumina. However, nickel crystallite sizes were very small, of approximate order 10 nm, and the residue morphology could be very fine.

References

1. J.B. Friedrich, D.J. Young and M.S. Wainwright, J. Electrochem. Soc., 128, 1840, 1845 (1981).
2. A.D. Tomsett, D.J. Young and M.S. Wainwright, J. Electrochem. Soc., 131, 2476 (1984).
3. J. Szot, D.J. Young, A. Bourdillon and K.E. Easterling, Phil. Mag. Lett., 55, 104 (1987).

Abstract No. 100

DEALLOYING OF Pt ALLOY FUEL CELL ELECTROCATALYSTS

M. T. Paffett and S. Gottesfeld

Los Alamos National Laboratory, MS D429
Los Alamos, NM 87545

Numerous binary and ternary Pt alloys have been investigated as potential anode and cathode electrocatalysts for use in fuel cell devices. Various theories have been suggested to explain the apparent enhancement in specific electrocatalytic reactions occurring at fuel cell electrodes employing these alloy catalysts as compared with Pt-only electrodes with the same specific precious metal loading. These explanations have evoked alterations in electronic character,[1,2] lattice spacing changes,[3] and specific surface chemical interactions brought about by the presence of the secondary alloy component.[4] Investigations of several of these alloys (e.g., PtCr, PtCo) have demonstrated that a major reason for the apparent enhancement of the electrocatalytic activity towards the oxygen reduction reaction (o.r.r.) is a process of dealloying that can generate a porous metal network of high surface area.[5] With regard to the hydrogen oxidation reaction, we have also investigated a bulk alloy (i.e., PtRu) that is reported to possess superior performance, as compared to bulk Pt, in the presence of moderate amounts of CO. In this case, an optimal surface dealloying of the bulk electrode material can produce a surface with both components still present but not with the bulk stoichiometry. At such a surface, significant variation and improvement in the electrocatalytic activity is seen. We review in this presentation results of in situ and ex situ analysis of bulk alloy samples undergoing dealloying under potential electrochemical conditions encountered in a fuel cell application. We will describe the net effect that this dealloying can have on the intended electrocatalytic reaction.

The in situ techniques employed include electrochemical and ellipsometric methods.[6] We will specifically describe how the dielectric spectrum of a metal-deficient surface layer can be evaluated ellipsometrically to yield information on the thickness of the dealloyed layer, the volume fraction of the "metal skeleton" in the dealloyed surface, and the degree of interconnectedness between the residual metal domains. Analysis of the optical results, in terms of effective medium theory, distinguishes between aggregate random structures and well interconnected ("swiss-cheese") porous structures.

The ex situ analysis techniques have included x-ray photoelectron spectroscopy, sputter profiling, low-energy ion surface scattering, and Rutherford backscattering spectroscopy. This particular combination of techniques has allowed us to explicitly characterize the surface and near-surface region of these alloys for the distribution of the chemical constituents. The results of such an analysis, coupled with conventional electrochemical techniques, have allowed us to define potential domains in which dealloying occurs.

The impact of dealloying on the apparent electrocatalytic activity will be demonstrated for the cases mentioned above. For the Pt alloys used for the o.r.r., it will be shown that the enhancement in activity is largely due to an increase in effective Pt surface area following the process of dealloying, thereby yielding larger catalytic currents per unit geometric area. The beneficial effects of superficial dealloying of the outermost surface layer of the PtRu electrode will be described in terms of the complex interfacial chemistry occurring when the hydrogen oxidation reaction is run in the presence of moderate amounts of CO (1%).

REFERENCES

1. P. N. Ross, Jr., EPRI Report EM-1553, 1980.
2. B. C. Beard and P. N. Ross, Jr., LBL Report 21184, 1986.
3. V. Valan and E. J. Taylor, J. Electrochemical Soc., 130 (1983) 2299.
4. M. T. Paffett, K. A. Daube, S. Gottesfeld, and C. T. Campbell, J. Electroanal. Chem., 220, (1987) 269.
5. M. T. Paffett, J. Beery, and S. Gottesfeld, J. Electrochem. Soc., in press, 1988.
6. S. Gottesfeld, "Ellipsometry: Principles and Recent Applications in Electrochemistry," in Electroanalytical Chemistry, Vol. 15, A. J. Bard, ed., Marcel Dekker, New York, 1988.

Abstract No. 101

X-RAY PHOTOELECTRON SPECTROSCOPY OF TARNISHED AND CORRODED SILVER-PALLADIUM ALLOY

H.J. Mueller

Council on Dental Materials,
Instruments and Equipment
American Dental Association

211 E. Chicago Ave
Chicago, IL

Alloys from the silver-palladium system find applications as dental materials. Due to oral environmental exposures, surface layers of the alloy become dealloyed via tarnishing and corrosion reactions. The purpose of this project was to obtain the compositions of the top-most surface layers of a Ag-Pd alloy in a number of surface conditions which simulated tarnish and corrosion lilely occurring intra-orally. Changes in composition with film thickness were also of interest.

Experimental

An alloy (Albacast) containing by weight 70% Ag, 25% Pd, and 5% In, Cu, and Zn was used. The 12 x 18 mm x 2 mm thick samples were polished on one face to a 1 µm alumina finish, ultrasonically soaked in detergent, in deionized water, and finally in acetone. Several as-polished samples were treated in a Harrick glow discharge unit with argon. Other as-polished samples were tarnished for 24 hrs with a rotating wheel apparatus, by exposing the samples to artificial saliva for 15 sec and to air for 45 sec per revolution (1 rpm). Other samples were corroded in artificial saliva by potentiostatically holding at 0.17 V (SCE) until cathodic currents ensued. This required the passage of 47 mc of anodic charge (fig. 2). The artificial saliva was composed (wt %) of 0.04 NaCl, 0.04 KCl, 0.05 $CaCl_2$, 0.002 Na_2S, 0.07 $NaH_2PO_4.H_2O$, and 0.1 urea. The near surfaces (≈ top 100 Å) in all four conditions were analyzed for ejected photoelectrons by ESCA techniques. Survey scans were first obtained followed by high resolution scans at particular binding energies. Some of these included the C(1s), O(1s), Cl(2p), Pd(3d), P(2p), S(2P), Cu(2p), Zn(2p), and Si(2p). Compositions were estimated from the survey data by dividing the integrated peak areas (IPA) by the atomic sensitivity factors (ASF) and normalized with the summated IPA/ASF from all elements present. The high resolution spectra were curve-fitted to resolve the presence of multiple energy states. Depth profiling was performed on the corroded sample by obtaining high resolution data for C(1s), O(1s), Cl(2p), Pd(3d), S(2p), Cu(2p), Ag(3d), and In(3d5) with sputtering time.

Results and Discussion

Figure 1 shows the cyclic voltammetry of Ag-Pd alloy. A passive region with a current density (I/A) of about 1uA/cm² occurred from corrosion potential (≈ -0.3 V) to +0.17 V, where I/A increased to about 8 x 10^{-6} uA/cm² Beyond +0.32 V further increases in I/A occurred by about 1 order in magnitude. The reversal cycle shows one large reduction peak at 0 V. Figure 2 shows a charge vs time plot for the alloy held at +0.17 V. Corrosion ceased at 17 hrs (dc/dt = 0).

Table 1 presents the compositions within the top 100 Å of alloy in all four states.

TABLE 1 (atomic %)

Sample	C	N	O	F	Na	Si	P	S	Cl
as-pol	50	1.3	26	-	0.4	4.8	-	-	1.3
AGD	26	3.0	42	-	-	3.5	-	1.8	1.6
tarn	47	1.4	30	1.6	-	-	3.7	4.7	-
corr	38	-	16	-	-	-	-	19	-

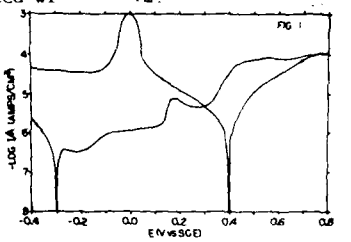
TABLE 1(con't)

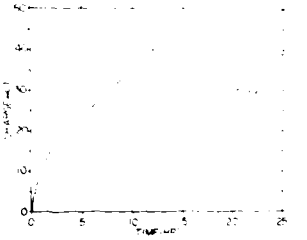
Sample	Cu	Zn	Pd	Ag	In	I
as-pol	-	-	3.5	12	0.6	-
AGD	-	3.8	3.9	13	0.7	-
tarn	1.5	-	1.0	8.2	-	0.2
corr	-	-	2.2	25	-	-

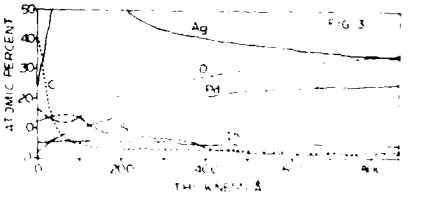
The AGD reduced the C level by about 1/2 from that on as-pol surface, increased N and O, and had little effect upon Si, Cl, Pd, Ag, & In. Zinc was detected on only the AGD surface, while Na was detected on only the as-pol surface. The tarnished and corroded surface treatments generated moderate to high levels of S, 4.7, and 19 at %, respectively, and reduced levels of Pd. Only the corroded treatment generated higher levels of Ag and reduced levels of C and O. On the tarnished treated surface F, P, Cu, & I were detected.

The high resolution peak assignments were C_1 as C-R (R=C, H), C_2 as C-OR, C_3 as O=C-OR, O_1 as C=O, MeOH, O_2 as C-O-R, Cl as Cl^-, Pd_1 as elemental Pd (for as-pol and AGD), Pd_2 as Pd oxide (for tarn and corr), P as P oxide, S_1 as elemental S, S^- (for tarn and corr), S_2 as SO_x(x=3, 4)(for AGD), Cu as elemental Cu, Cu oxide, Zn as Zn oxide, and Si as silicone, silicates. Figure 3 shows the composition of corroded alloy with thickness.

The film formed on the corroded surface contained a near surface layer enriched in Ag S, and C. Palladium and O levels increased with film thickness. Low levels of In occurred throughout film. No Cl, or Cu were detected with[illegible] film.







Abstract No. 102

EXPLOITATION OF DEALLOYING IN CORROSION CONTROL OF ALUMINUM ALLOYS

Kemal Nisancioglu

Department of Chemistry
Laboratories of Industrial Electrochemistry
Norwegian Institute of Technology
N-7034 Trondheim Norway

The electrochemical and corrosion behavior of aluminum alloys in aqueous media are often controlled by dealloying processes which alter the passivating properties of the surface oxide. Dealloying can occur readily by selective dissolution of the more active aluminum and enrichment of significantly more noble alloying elements at the surface. The paper gives a few case examples, in which the dealloying of Al-base solid solution alloys and intermetallic compounds is an important factor in attaining either corrosion resistant or active surfaces depending on the application.

Etching

Caustic etching of aluminum alloys is a frequently employed surface cleaning technique prior to corrosion testing and various surface treatment processes. Caustic etching often deteriorates the corrosion resistance of the alloy (1). It is shown that this is caused by the dealloying of iron containing intermetallic compounds and formation of a highly porous and iron rich layer which catalyzes the cathodic reaction rate. Etching, however, improves the corrosion resistance of AlMn alloys, in which manganese is present both in solid solution with the matrix and in the intermetallic compounds. As a result of exposure to a caustic solution, Mn is enriched at the surface of both phases. When the treated alloy is subsequently exposed to a neutral chloride environment, the surface exhibits a more passive behavior with improved pitting resistance and reduced cathodic reaction rate. Alloying aluminum with manganese is known to improve the corrosion resistance in general (2) because similar dealloying phenomena occur at varying rates also in neutral and acid environments.

Cathodic Protection

Dealloying of iron containing particles is paradoxically an indirect cause of low current demand for the cathodic protection of aluminum alloys in general. Potentiostatic tests carried out in natural sea water and various salt solutions with selected alloys indicate that low current demand results from the destruction of cathodic sites at an early stage after the onset of cathodic protection. This occurs by crevice corrosion of the matrix adjacent to the particles and detachment of these from the surface without exposing new ones from underneath (3). The removal rate is proportional to the dealloying rate of particles, which in turn is controlled by the applied potential. The current rate of hydrogen evolution on the enriched particles stabilizes an alkaline layer of electrolyte adjacent to the surface of the particles, thereby making possible highly localized etching of the matrix alloy around them.

Active Anodes

The properties sought in developing aluminum anodes for the alkaline Al/air battery include high current output, high current efficiency and a negative potential. Unalloyed aluminum is too passive, and the presence of iron at concentrations as low as a few ppm is effective in reducing the current efficiency. Super-pure (> 99.99 %) aluminum alloyed with, **e.g.**, tin satisfies the stated requirements (4). Dissolution of the anode occurs by the continuous formation and destruction of numerous dealloyed sites, where the presence of metallic tin activates the surface locally. At the same time the hydrogen evolution reaction is kept at a low rate, resulting in high current efficiencies, because tin has a high hydrogen over-potential. These effects are obtained only if tin is in solid solution. However, the solid-solution solubility of tin in aluminum is limited to 0.1 %, which is too low to give the desired properties to impure aluminum containing a few hundred ppm of iron. Manganese, with solid solution solubility in aluminum exceeding 1 %, is shown to be a possible alternative for the less pure alloys.

The mechanism of aluminum transport through the activated site is yet to be clarified. The fact that a high melting-point metal like manganese can activate aluminum rules out the hypothesis that the transport occurs through a surface alloy which is maintained at the liquid state by heat generation at the interface (4,5). A surface diffusion enhanced mechanism appears to be more likely for the present case.

References

1. O. Lunder and K. Nisancioglu, **Corrosion**, in press.

2. M. Zamin, **ibid.**, 37, 627 (1981).

3. K. Nisancioglu, O. Lunder and H. Holtan, **ibid.**, 41, 248 (1985).

4. K. Nisancioglu, L. Odden and A. F. Grande, **Proc. 2nd Symp. on Electrode Materials and Processes for Energy Conversion and Storage**, p. 499, The Electrochemical Society, Pennington, N. J. (1987).

5. N. F. Fitzpatrick and G. M. Scamans, **New Scientist**, 111(1517), 34 (1986).

Abstract No. 103

CORROSION IMPROVEMENT THROUGH SURFACE Mn DEALLOYING IN Fe-Mn-Si-Al ALLOYS

by J. M. Oh, M. L. Glenn, and S. J. Bullard

Albany Research Center
Bureau of Mines
U.S. Department of the Interior

1450 Queen Avenue, SW.
Albany, OR 97321

One of the Bureau of Mines research goals is to minimize the requirement for domestically scarce minerals through substitution. Concern for critical elements, such as chromium, has generated renewed interest in Fe-Mn-Al-Si alloys as substitutes for stainless steels.

In this research on the corrosion behavior, phase transformation and dealloying of Fe-30Mn-Si-Al alloys were investigated. Experimental alloys were prepared by arc-melting high-purity materials into 100 g buttons or 2.5 kg ingots. These buttons and ingots were homogenized for 20 hours at 1,200° C and then hot rolled. Nominal alloy compositions are presented in table 1.

TABLE 1. - Nominal alloy compositions (Fe based).

	Mn	Al	Si
A	30	6	-
B	30	3	3
C	29	2	4
D	30	-	6
E	30	-	10
F	20	-	4.5

Figure 1 shows the oxidation kinetics of alloys at 700° C with thermal cyclings. The oxidation rates increased with higher Mn and Si content in the alloys. Alloy A had oxide spalling after the second thermal cycle. Alloys B and C had similar weight gains. Alloys D, E, and F formed a transformed metallic layer on the base metal surface during oxidation. The formation of this transformed layer was due to the removal of Mn in the alloy by the selective oxidation of Mn during the oxidation reaction.

Figure 2 shows the Mn and Si concentration profiles of alloy D when cross-sectioned after 8 hours of oxidation at 800° C. The depletion of Mn near the surface promoted a local increase of Si content more than 50 pct from the base composition. This phenomena was applied to increase the surface layer concentration of Si in the Fe-30Mn-10Si alloy so that this formable alloy can be used in some applications. Conventionally, alloys which have high Si content can only be made by casting.

Figure 3 shows an anodic polarization curve for the Fe-30Mn-10Si alloy 1N H_2SO_4 after hot rolling and an oxidation treatment of 2 hours at 900° C in solution. The plot for AISI 430 SS is also included for comparison.

The polarization plot for the Fe-30Mn-10Si alloy is similar to that reported for the binary Fe-15Si alloy under the same conditions. These results indicate that the transformed layer formed in Fe-30Mn-10Si alloy has a corrosion resistance similar to those of the Fe-15Si binary alloy and the conventional stainless steels.

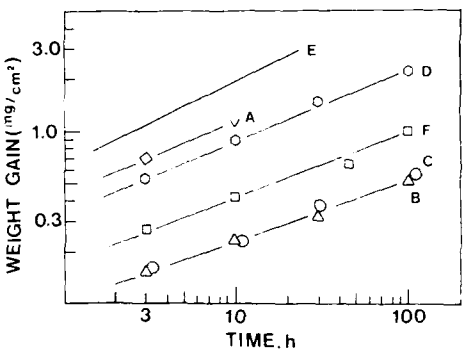


Figure 1. - Oxidation kinetics of alloys at 700° C.

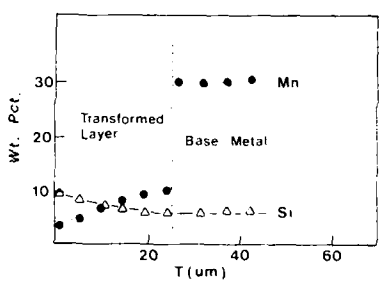


Figure 2. - Mn and Si concentration profiles of alloy D after 8 h of oxidation at 800° C.

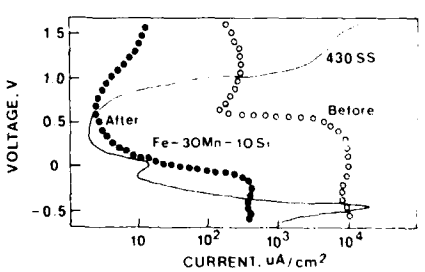


Figure 3. - Anodic polarization curves for alloy E tested before and after oxidation treated for 2 h at 900° C.

Abstract No. 104

ANODIC POLARIZATION BEHAVIOR OF TUNGSTEN ALLOYS IN 3.5% NaCl SOLUTION

K. L. Vasanth, C. M. Dacres, R. Conrad and M. Fernandez
Naval Surface Warfare Center
10901 New Hampshire Avenue
Silver Spring, MD-20903-5000

High density tungsten alloys are in great demand for various applications. Andrew, et al (1) reported that a 90 W-7.5 Ni-2.5 Co alloy readily corrodes when exposed to air saturated with water vapor. Koger (2) observed that the corrosion rate for tungsten-3.5 Ni-1.5 iron alloy increased as a function of pH. Vasanth and Dacres (3,4) reported the polarization resistance behavior in 3.5% NaCl and Scanning Electron Micrographs (SEM) of corroded tungsten alloys, and showed that Ni-Fe-W matrix alloy precipitated between tungsten particles corroded. The present paper reports the anodic polarization behavior in 3.5% NaCl and the field performance of 5 tungsten alloys exposed to natural sea water and marine atmosphere.

Results and Discussion

Anodic Polarization

The compositions of sintered tungsten alloys considered here, were determined by Energy Dispersive X-ray Analysis (EDAX) and are given in Table 1. Typical microstructure of these alloys consisted of rounded tungsten particles surrounded by a matrix alloy of Fe-Ni-W.

1.2 cm diameter discs mounted in epoxy were wet polished with 320 A, 400 A and 600 A silicon carbide, rinsed with distilled water, air dried and immediately put into corrosion cell containing 3.5% NaCl. The NaCl solution was kept aerated.

Anodic polarization scans for each tungsten alloy were run after allowing the system to equilibrate for an hour by which time the open circuit potential was almost constant. The potential was varied from the open circuit potential to +2.5V versus standard calomel electrode (SCE) and the change in current monitored. A scan rate of 0.5 mv/sec was used. The anodic polarization curves obtained for three tungsten alloys are given in Figure 1. Alloys showed active-passive transitions indicating some degree of corrosion. Four distinct knees were observed on each polarization curve. Koger (2) reported the presence of three distinct knees for W-3.5 Ni-1.5 Fe alloy when studied in 0.1M NaCl at pH 4. It has been observed that tungsten remains passive above +2.5V versus SCE. Examination of samples after anodic polarization scans indicated that S2 and K1 had very few shallow pits while S1 and T1 showed a high density of similar pits.

Field Tests

Tungsten alloys were subjected to three types of field tests - a) continuous immersion in natural sea water, b) alternate immersion in natural sea water and c) marine atmospheric exposure. These tests are still on-going after 14 months, at the NSWC Corrosion test site, Ft. Lauderdale, Florida. Weight-loss data from continuous immersion test were used to calculate corrosion rate in mils per year (MPY). A plot of corrosion rate in MPY versus time of immersion in months is given in Figure 2. At the end of 12 months, T2 had a corrosion rate of 1.5 MPY (highest) while S1 or S2 had about 0.6 MPY (lowest).

Samples exposed to alternate sea water immersion and marine atmospheric exposure field tests did not show any noticeable degradation and weight-loss.

A visual observation of alloy samples from continuous sea water immersion test showed that alloys S1 and S2 exhibited preferential corrosion and the rest corroded uniformly over their surface.

Summary

1. Corrosion rates of tungsten alloys tested were under 2 MPY.

2. Sea water immersion studies indicated that alloy T2 had the highest corrosion rate (1.5 MPY) and S1 and S2 the least (0.6 MPY).

3. Visual and SEM examination indicated that alloys S1 and S2 showed localized corrosion.

4. After anodic polarization only few shallow pits were seen in S2 and K1, and a high density of such pits in S1 and T1.

References

1. J. F. Andrew, M. T. Baker and H. T. Heron., "Corrosion and Protection of Sintered Alloy Ammunition Components," Proc. 2nd Charlottesville Conf. on high Density KE Penetrator Materials (1980).

2. J. W. Koger., " Corrosion of Tungsten -3.5 Nickel-1.5 Iron and its constituent Phases in Aqueous Chloride Solutions," Preprint Y-DA-6063, Union Carbide Oak Ridge Y-12 Plant, Oak Ridge, Tennesse, Nov. 1974.

3. K. L. Vasanth and C. M. Dacres., "Corrosion behavior of Tungsten Alloys," Abstract No.274, 172nd Meeting of the ECS, Honolulu, Howaii, Oct 18-23, 1987.

4. K. L. Vasanth and C. M. Dacres., "Corrosion of Tungsten Alloys in Marine Environments," Proc. 1987 Tri-Service Conference on Corrosion, AFWAL-TR-87-4139, Vol II, 165-186, 1987.

Table 1
Composition of Tungsten Alloys by EDAX

Alloy	Weight % Tungsten	Iron	Nickel
K1	98.5	0.6	0.9
S2	98.3	0.6	1.1
S1	94.8	1.9	3.4
T1	94.5	1.8	3.8
T2	93.5	1.9	4.6

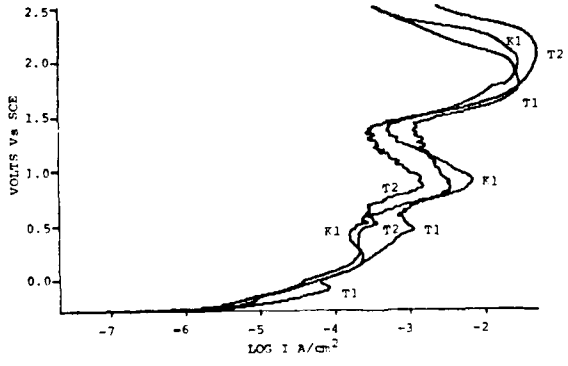


Figure 1. Anodic Polarization curves for 3 Tungsten Alloys.

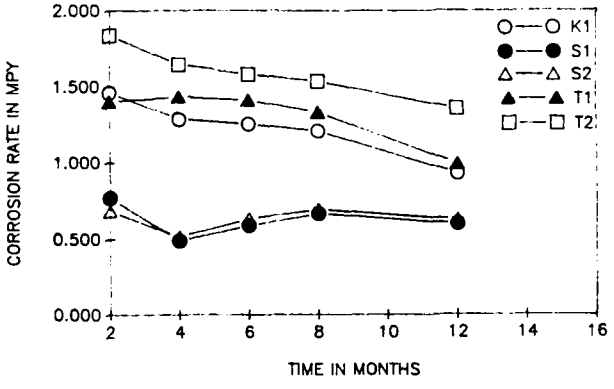


Figure 2. Corrosion Rate of Tungsten Alloys in Natural Sea Water.

Abstract No. 105

Transient Dezincification of Brasses in Aqueous Solution

G. Gao and G.T. Burstein

Department of Materials Science
and Metallurgy
University of Cambridge
Pembroke Street
Cambridge CB2 3QZ
United Kingdom

The electrochemical behaviour of freshly generated brass surfaces in aqueous solutions reveals a range of complex phenomena associated with oxidation of both copper and zinc components. These phenomena are difficult to resolve into individual reactions of the individual components. By examination of the potential range defined between the limits of equilibration of zinc with the solution and that of copper equilibration with the solution however, the behaviour of zinc in the brass matrix can be explored. The processes described in this paper relate to this regime.

Copper and brass electrodes were separately examined in solution using the potentiostatically controlled scratched rotating disc electrode; in this technique a small scratch is generated in the disc surface in situ in ~0.7ms and the consequent current transient is recorded. Current transients measured for freshly generated copper and 70/30 α-brass surfaces in 1.0M KOH at the same electrode potential are shown in Fig. 1. Two features are to be observed. First, the potential of -0.505V(she) is below the potential at which copper equilibrates with its bulk oxide (Cu_2O) at pH 14 (E_o = -0.356V(she); despite this, the new copper surface gives rise to an anodic current transient which decays. Second, the freshly generated brass surface also produces an anodic current transient which is larger in magnitude than that on copper, and takes longer to decay. Similar measurements have been made over a range of potential in a number of electrolytes; all show that copper is anodically active at an underpotential with respect to equilibration with the bulk oxide and that brass, also anodically active, produces a significantly larger current density, decaying over a significantly longer period.

Kinetic analysis of such transients produced on copper demonstrate that the currents emanating from the scratch arise from formation of a single monolayer of oxide; integration of such transients produces a charge density of ~0.2mC cm^{-2}, estimated to be the charge associated with a single monolayer of CuOH (or Cu_2O), independent of potential and pH. No further reaction of copper at these low potentials has been detected.

The excess current detected for brass surfaces must arise from anodic oxidation of zinc which lies at an anodic overpotential. Integration of the excess current with respect to time reveals substantially larger charge densities, up to ~2mC cm^{-2} after 1s of reaction dependent upon pH. Such excess charge cannot arise from oxidation of zinc from the metal surface alone; rather, the zinc emerges from depths of many atom layers within the electrode. The process is modelled by allowing the rate of decay of the current transient to be controlled by the accelerated non-steady state diffusion of zinc to the free metal surface at which it reacts. The origins of such modelling lie in the potential independence of the rate of reactions of zinc from the brass matrix, both in alkaline and in acidic solutions. The data presented reveal a diffusion coefficient some ten orders of magnitude higher than the coefficient for zinc in bulk brass. Such enormous acceleration arises from the vacancies generated in the metal lattice by the dezincification process itself. Quantitative computer modelling is presented showing agreement with experimental data.

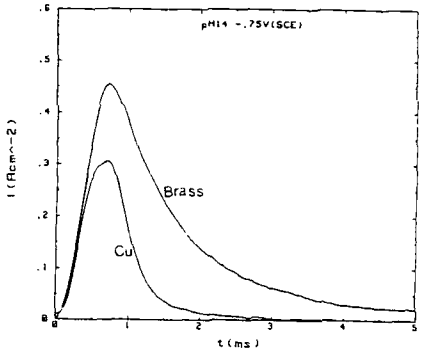


Fig. 1 Current transients on freshly generated copper and 70/30 α-brass surfaces measured under identical conditions below the Cu/Cu_2O equilibrium potential.
Electrolyte = 1.0M KOH.
E = -0.505V(she)

Abstract No. 106

THE INITIAL STAGE OF ATMOSPHERIC CORROSION

Joe H. Payer and Sandeep K. Chawla

Department of Materials Science
and Engineering
Case Western Reserve University
Cleveland, Ohio 44106

INTRODUCTION

Electrochemical corrosion processes in thin films of electrolyte and condensed moisture layers are not well understood. While the science and technology of outdoor atmospheric corrosion are fairly well established on a macroscale, the understanding of indoor atmospheric corrosion requires a knowledge of processes on the microscale.

The objective of this research is to understand the initial stage of atmospheric corrosion. Eelectrochemical science can be extended to the unique microcell corrosion geometries during the initial corrosion stage. The role of tiny clusters of water (50 nm radius) on the corrosion process has not been widely recognized and is a principal component of this study. Payer and Chawla relate the presence of water clusters to the severe corrosion observed in the early stages of condensation (1). It is believed that this extension to traditional views will more satisfactorily describe observed behavior. This has strong implications regarding the understanding of strategies to control microcell corrosion and methods to monitor atmospheric corrosion both indoors and outdoors.

EXPERIMENTAL

The early stage of atmospheric corrosion is studied by the determination of surface chemical compositon and surface structure before and after exposure to corrosive environments. Copper and silver were selected for the initial experiments because of the wealth of data available on their atmospheric corrosion behavior. The metal specimens are exposed to atmospheric conditions with controlled relative humidity and mixed gas composition. Subsequent to exposure the distribution, morphology and chemistry of the corrosion process are determined by TEM, XPS, AES and SEM/EDAX.

RESULTS AND DISCUSSION

An important aspect of this study is the characterization of the morphology of corrosive damage. This is critical for any attempt to corroborate model predictions of corrosion rates, because the morphology of attack is related to the amount of damage at any instant. This forms a phenomenological basis for the model and a data base to test the model's predictions.

Preliminary results from our laboratory show the morphology of corrosion of copper exposed to a 70% relative humidity with sulfur dioxide. Figure 1 is a TEM micrograph of microcell corrosion sites on a copper foil. The size, shape and distribution of microcell corrosion sites are evident from the corrosion damage. The initial sites of microcell corrosion are documented as well as their growth with respect to shape and size as a function of exposure time and the environment.

Clustering of water molecules at sub monolayer coverage leads to the accumulation of significant local surface volumes of water where the properties of adsorbed water approach that of bulk water. This inhomogeneous adsorption of water from the atmosphere presents the condition for initiation of microcell corrosion. This has not been widely recognized in the existing models of atmospheric corrosion.

The concept of a critical relative humidity is well established (2). Furthermore, it is clear that this value is a function of gas composition (3), particles on the metal surface (4) and surface irregularities (5). The distribution and form of water on the surface is also critical.

Water does not adsorb as a uniform film on the surface but rather as water clusters (6)(7). Our view of the stages of adsorption of water are shown schematically in Figure 2. The first water forms an oxyhydroxide layer of the metal. Higher relative humidity results in the formation of water clusters, and still higher relative humidities result in a continuous moisture film.

Rice et. al. (8,9) related the morphology of corrosion observed on thin foils of metal to the presence of water clusters on the surface. Their calculations determined a circular cap configuration for the clusters with a radius of 50 nm and a cap height of 17.5 nm.

Water clusters can effectively scavenge atmospheric pollutants thereby attaining high ionic concentrations and exhibiting increased conductivity. Under such conditions, local microcorrosion cells can be set up on the metal surface. The condensate cluster provides an ionic conduction path between anodic and cathodic regions within the microcorrosion cell. The chemistry of the electrolyte in these condensate clusters and its relationship with the nature and concentration of atmospheric gases is critically important.

A theoretical development of condensate cluster chemistry has been attempted by several researchers (10)(11). All such models implicitly use thermodynamic equilibrium criteria of equating the chemical potentials of gaseous species in the vapor phase and in the aqueous phase. The changes in ionic concentration as a result of corrosion reactions and desorption are not accounted for by such models, and the effects of these latter phenomena can be significant. The goal of this research is to combine experimental observations with the development of a model of microcell corrosion to better understand the initial stage of atmospheric corrosion.

PEFERENCES

1 J.H. Payer and S.K. Chawla, 2nd SAMPE Metals and Metals Processing Conference, Dayton, Ohio, August 1988.

2 W.H.J Vernon, Trans. Faraday Soc., No. 27, pp255-277, 1931.

3 F.Mansfeld, J.V.Kenkel, Corros. Sci., Vol.16, pp111-122, 1976.

4 F.Mansfeld, J.V. Kenkel, Corrosion, Vol.33, No.I, pp13-16, 1977.

5 N.D.Tomashov "Theory of Corrosion and Protection of Metals" pp367-398, The Macmillan Co., 1966.

6 K.Kiier, J.H.Shen, A.C.Zettlemoyer, J. Phy. Chem.,Vol.77, No.11, pp1458-1465, 1973.

7 B.D.Yan, S.L.Meilink, G.W.Warren, F Wynblatt, Proc. 36 Conf. on Electronic Components, pp95-99, IEEE, 1986.

8 D.W.Rice, P.B.P.Phipps, R.Tremoureux, J. Electrochem. Soc., Vol.126, No.9, pp1459-1466, 1979.

9 D.W.Rice, P.B.P.Phipps, R.Tremoureux, J. Electrochem. Soc., Vol.127, No.3, pp563-568, 1980.

10 S.C.Byrne, A.C.Miller "Atmospheric Corrosion of Metals" ASTM STP 767, eds. S.W.Dean, E.C.Rhea, pp359-373, American Soc. for Testing and Materials, 1982.

11 T.E.Graedel, Corros. Sci., Vol.27, No.?, pp721-740, 1987.

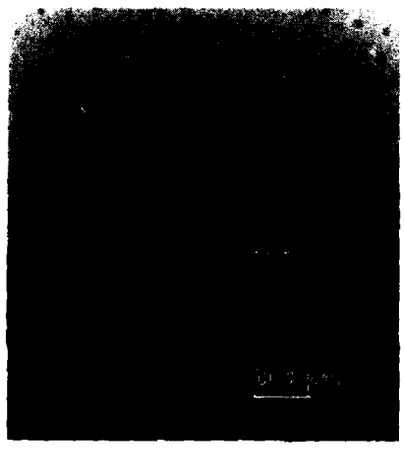


FIGURE 1 : TEM micrograph of microcell corrosion sites on a vacuum-deposited copper foil exposed to 70% RH with sulfur dioxide.

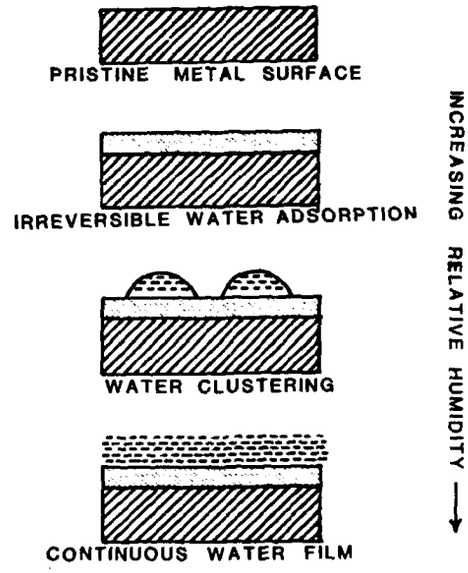


FIGURE 2 : Schematic of stages in water adsorption on metal surfaces.

Abstract No. 107

CORROSION LAYER CONSTITUENTS AND NATURAL MINERALS: SIMILARITIES, DIFFERENCES, AND THEIR CAUSES

T.E. Graedel
AT&T Bell Laboratories
Murray Hill, NJ 07974

Many natural minerals are formed under conditions of moderate temperature, moisture, and normal atmospheric pressure. Similar conditions are present during the formation of corrosion layers on metals exposed to the atmosphere. To explore similarities and differences in the occurrence of chemical constituents in these two systems, seven common industrial metals and their corrosion products are surveyed and compared with the inventory of natural minerals.

If concentrations of dissolved anions were the only consideration in atmospheric corrosion, information on the chemistry of atmospheric gases and precipitation would lead to the prediction of high concentrations of nitrates in surface corrosion layers, with somewhat lesser and roughly similar amounts of sulfates, chlorides, and carbonates. Such a prediction is not borne out by analyses of the relative abundances of corrosion layer constituents for the seven metals and comparison with the simplest stable related mineral which incorporates both the metal cation and the appropriate counterion. The data all refer to outdoor exposures, for which by far the greatest amount of information is available.

Several chemical characteristics of the corrosion layers, some trivial, some less so, are immediately revealed:

- If no naturally-occurring mineral is known that incorporates the metal cation and the counterion, no corrosion product incorporating those constituents is found. This result implies that natural mineral forming processes at atmospheric temperature and pressure (called "supergene" processes by mineralogists) are similar or identical to the chemical processes involved in the formation of corrosion layers.
- Except for silver, which does not naturally form an oxide at atmospheric temperature and pressure, oxides of the metals occur naturally and are major constituents of the corrosion layers. The stoichiometry is in each case that of the simplest possible oxide. The oxides are quite insoluble, so they are retained in the corrosion layer once they are formed.
- If a stable hydroxide or oxyhydroxide mineral for a given metal is known to occur in nature, it is present as well in corrosion layers. Copper has no stable hydroxide mineral, and its dihydroxide appears in corrosion layers only as a thin covering atop the oxide. Tin(II) dihydroxide has not been reported, but is probably present on the surface of exposed tin and might be found if sought. In the case of lead, the equilibrium favors the oxide rather than the hydroxide. The hydroxides are generally rather insoluble, but their solubility products vary widely.
- Sulfate minerals are common in the environment and sulfate corrosion products are common on the surfaces of metals exposed outdoors. In the cases of iron, zinc, and lead these products are the simple sulfates, sometimes with waters of hydration included. In the case of copper, the most stable sulfate-containing species is the relatively complex hydroxysulfate mineral brochantite [$Cu_4(SO_4)(OH)_6$]. The simplest stable aluminum sulfate mineral is about as complex as brochantite, but has not been found; rather, an amorphous hydroxysulfate occurs on aluminum in substantial abundance. This metastable species is known to be very insoluble, a property which probably accounts for its presence in aluminum corrosion layers. No stable silver sulfate mineral is known, but silver sulfide minerals are sometimes seen in nature and in corrosion layers. Sulfates are generally soluble, but silver sulfide and the hydroxysulfates are not.
- Stoichiometrically simple chlorides are rarely found either in nature or on corrosion layers. The principal reason for this fact is that the simple chlorides are highly soluble, except for those of silver and lead. Iron, copper, and zinc form hydroxychlorides or oxychlorides, some of which are seen in atmospheric corrosion layers. The zinc hydroxychloride is quite complex; it may have been misidentified in lieu of one of the simpler possible forms. Structurally simple aluminum and lead hydroxychlorides occur naturally but have not been found in corrosion layers; this may be another instance of overlooked constituents. In addition to the relatively common FeOCl, iron inevitably forms a constituent referred to as "green rust"; this quasi-amorphous transitory corrosion product has been tentatively identified as $2Fe(OH)_2{\cdot}FeOHCl{\cdot}FeCl(OH)_2$. Little information is available on the solubility of the hydroxychlorides, but they are thought to be less soluble than the simple chlorides.
- The situation with carbonate salts of the metals resists easy characterization. Zinc carbonate is extremely abundant in atmospheric corrosion layers. Lead carbonate is apparently common as well. Except for the possible occurrence of small amounts of a copper hydroxycarbonate, no other carbonate corrosion products are known for any of the other metals despite the natural occurrence of carbonates, the presence of relatively high concentrations of bicarbonate in the aqueous surface films, and the fact that carbonates are generally insoluble.
- The only nitrate species known to occur in corrosion layers is an hydroxynitrate compound of copper, and it is not abundant. Natural metal nitrate minerals are also quite uncommon.

Thus, most of the corrosion products found on metal surfaces following exposure to the atmosphere are identical with minerals that are formed in or on the earth by natural processes. In both cases, stable products are formed in an environment characterized by abundant water, dissolved oxygen, and competition among anions. Over long periods of time, those products that are thermodynamically favored in such environments will be produced. Kinetic processes and transitions through metastable intermediates may be important on shorter time scales. Solubility considerations are obviously involved, since the rarity of nitrates and simple chlorides in the corrosion layers is consistent with the high aqueous solubility of those minerals, just as the ubiquitous presence of oxides, hydroxides, and mixed hydroxy salts reflects their low solubility. Mineralogists have been no more successful than corrosion scientists at reducing all of these processes to a tidy formalism, but it is clear that the chemical and physical steps involved in the formation of natural minerals and those involved in the formation of corrosion layers on metals exposed to the atmosphere are similar or identical, despite the vastly different time scales involved for mineral formation in the two regimes.

Abstract No. 108

ATMOSPHERIC CORROSION BEHAVIOR IN SOUTHERN CALIFORNIA

F. MANSFELD
Materials Science Department
University of Southern California
University Park, Los Angeles, CA 90089-0241

and

R. VIJAYAKUMAR
Environmental Monitoring and Services, Inc.
Camarillo, CA 93010

RESULTS AND DISCUSSION

The effects of acid deposition on materials are being investigated at present at three sites in Southern California and a site in Northern California which serves as a background site. Laboratory studies are being performed in support of these field tests. Samples of galvanized steel (non-passivated), nickel 200, flat latex paint (with and without carbonate expander) and concrete have been exposed starting in March 1986 (1).

The test sites in Burbank, Long Beach and Upland, located in the Greater Los Angeles area, were selected based on their characteristic SO_2 and NO_2 levels. The test samples (10.2 x 15.2 cm^2) were exposed at a 30^o angle to the south on racks according to ASTM G50-76. Five sets of samples were exposed between March 1986 and July 1987. Duplicate samples were removed after periods of 100 to 500 days. Atmospheric corrosion rate monitors (ACRM) (2) were mounted on galvanized steel and nickel plates, respectively, with one sensor of each material facing the sky and one facing the ground. The ACRM data are collected on magnetic tape using a data logger.

Figure 1 shows the weight loss data for galvanized steel at the four test sites. Several interesting observations can be made by inspection of Fig. 1. It can be seen that there is not much difference in weight loss at the four sites. At Upland the weight loss after one year was somewhat less than that at the "clean" site at Salinas. Corrosion rates are very low amounting to less than 0.5 μm/year which is typical for a rural site (3). For Burbank and Upland the differential corrosion rate is very low for the time between October 1986 and January 1987. This can be seen in more detail in Fig. 2 for Burbank, where the weight loss data are plotted for samples which were first exposed at different times in 1986 and 1987. By comparing the slope of the weight loss-time curves for the first three months it becomes obvious that corrosion rates are similar for samples which were first exposed in February and June 1986, but much lower for first exposure in October 1986 and January 1987. The fifth set which was exposed in July 1987 shows the highest corrosion rate. The very low weight loss data in the winter months have been observed at all four test sites.

Corrosion rates are also very low for nickel and decrease for the winter months. Corrosion damage is the lowest at the site in Salinas and the highest at Burbank and Long Beach.

The pronounced seasonal effects on the corrosion rates of galvanized steel (Figs. 1 and 2) and nickel are reflected also in the ACRM data which have a much finer time resolution. Fig. 3 shows plots of the cumulative corrosion damage INT for the four sensors exposed at Burbank between April 1986 and September 1987. The value of INT is determined by integration of the $1/R_p$-time curves for 12 h intervals, where R_p is the polarization resistance (2). In all cases corrosion rates start to decrease between August and November 1986 and increase again in May 1987. It will be noted that this time dependence of the corrosion rates does not follow the linear time dependence of the cumulative time-of-wetness, t_{80}, which is the time (in h per month) for which the relative humidity RH exceeded 80%. Fig. 3 also shows that for both zinc and nickel the sensor facing the sky has higher corrosion rates than the sensor facing the ground. These results demonstrate convincingly the detailed information which can be obtained with continuous monitoring of atmospheric corrosion phenomena using electrochemical techniques.

The weight loss data from the laboratory test have shown that only SO_2 has an accelerating effect on the corrosion rates of galvanized steel and nickel under the conditions used in these tests (RH = 80%, 1.5 h cooling cycle 6h (1)). NO_2 and O_3 might have a slightly inhibiting effect; however, a detailed statistical analysis of the data has not been carried out so far. At present the effects of HNO_3 aerosols are being investigated.

SUMMARY AND CONCLUSIONS

A preliminary analysis of the results obtained so far in this on-going study has produced some very interesting and to a certain extent unexpected results. Zinc or galvanized steel have been used in most studies of atmospheric corrosion carried out so far. The corrosion rate can be used to characterize the corrosivity of a given test site. Previous results obtained for zinc in a thorough exposure program in Scandinavia and Czechoslovakia have been summarized by Kucera (4) who pointed out the dominating effect of SO_2 in inland sites. For an exposure period of one year the weight loss K (g/m^2) was a linear function of the SO_2 deposition rate c_{SO2} ($mg/m^2.d$):

$$K = 7.21 + 0.13\ c_{SO2};\ r = 0.81. \qquad (1)$$

Inclusion of the time-of-wetness did not improve the correlation r significantly (4). The weight loss data shown in Fig. 1 for one year correspond to an average value of K of about 2.3 g/m^2, which is lower than the weight loss according to Eq. 1 for c_{SO2} = 0. An explanation of this result could be given by assuming that the time-of-wetness at the present exposure sites is sufficiently less then that in the study cited by Kucera (4) and that all other pollutants either do not have an accelerating effect on corrosion or act as inhibitors. Based on the data obtained for t_{80}, the time-of-wetness would be between 2000 and 3000 h/y which is typical for sites in the temperate climatic zone (3).

The weight loss data for galvanized steel characterize the corrosivity of the atmosphere in the Greater Los Angeles area as one typical for rural areas with SO_2 deposition rates of less than 10 mg $SO_2/m^2.d$ and corrosion rates of zinc between 0.2 and 2 μm/y (3). The observed corrosion rates were about 0.3 m/y (Fig. 1). This is indeed a surprising result considering the heavy pollution in the test area and the reported low pH values for acid dew and fog. However, pollution in this area is different from most others insofar as SO_2 levels are very low.

The seasonal effects observed for galvanized steel (Fig. 1 and 2) are also very interesting considering the fact that rain occurs in Los Angeles only during the winter months which is the time during which corrosion rates dropped to very low values. Apparently, tne rain has mainly a cleaning effect. It will be noted that usually corrosion rates are the highest during the winter months when SO_2 concentrations reach their maximum. Again, the present study has revealed trends which are entirely different.

A thorough analysis of the results obtained in the projects discussed here will result in dose-response or damage functions for the Greater Los Angeles area. While in principle a universal damage function should be applicable to any type of atmosphere, it seems that the damage functions which have been developed so far (3) do not apply to the present situation which is quite unique.

Acknowledgement

The work described here has been funded by the California Air Resources Board under Contracts No. A4-110-32 and A5-137-32. The authors acknowledge many helpful discussions with the Project Officer M. Ahuja. S.L. Jeanjaquet (Rockwell International Science Center) and G. Chen (USC) carried out the laboratory studies, R. Hillstead (EMSI) conducted the field tests.

References

1. F. Mansfeld and R. Vijayakumar, "Corrosion Damage Due to Acid Deposition in Southern California" APCA '88, June 20-24, 1988, Paper No. 1514.

2. F. Mansfeld, S.L. Jeanjaquet, M.W. Kendig and D.K. Roe, Atmosph. Env. 20, 1179 (1986).

3. V. Kucera and E. Mattson, "Atmospheric Corrosion," in "Corrosion Mechanisms," F. Mansfeld, editor, M. Dekker, 1986.

4. V. Kucera in "Materials Degradation Caused by Acid Rain," ACS Symp. Series 318, p. 104 (1986).

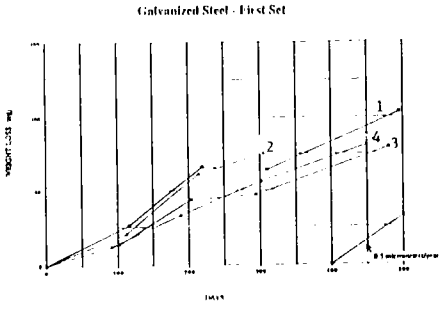


Fig. 1. Weight loss data for galvanized steel (first set) at Burbank (1), Long Beach (2), Upland (3) and Salinas (4).

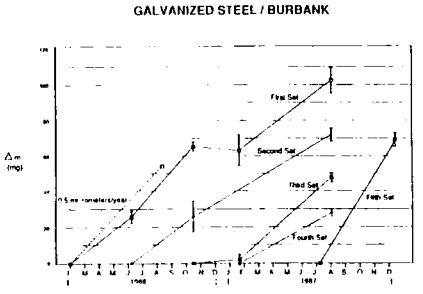


Fig. 2. Weight loss data for five sets of galvanized steel at Burbank.

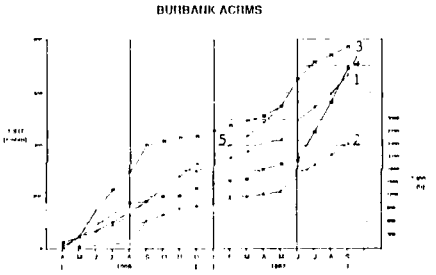


Fig. 3. Cummulative values of INT and t_{80} for the four sensors at Burbank. 1, Zn up; 2, Zn down; 3, Ni up; 4, Ni down; 5, t_{80}.

Abstract No. 109

VIBRATIONAL SPECTROSCOPY AND XPS FOR ATMOSPHERIC CORROSION STUDIES ON COPPER

D. Persson and C. Leygraf

Royal Institute of Technology
Division of Corrosion Science,
S-100 44 Stockholm, Sweden

Surface analytical techniques are important tools in mechanistic corrosion studies, since they can provide structural and chemical information on a corroding surface. Because of inherent possibilities and limitations it is often necessary to use more than one technique when solving problems in surface science. This requires the knowledge of a wide range of methods in order to select a suitable combination giving the proper complementary information. Methods using electrons and ions as probing particles have been more frequently applied to studies related to atmospheric corrosion (1-3). Optical techniques such as infrared and Raman spectroscopy on the other hand, have despite their possibility to obtain in-situ information so far found only very limited use in the field of atmospheric corrosion.

In the present work Fourier transform infrared reflection absorbtion spectroscopy (FT-IRRAS), Raman spectroscopy and X-ray photoelectron spectroscopy (XPS) have been used to study thin corrosion products formed on copper exposed to humid air with minor additions of SO_2 and NO_2. The results presented were obtained under "ex-situ" conditions but the optical techniques FT-IRRAS and Raman spectroscopy may well yield in-situ information when modified with a convenient experimental set-up.

Copper samples were diamond polished, washed with distilled water and ethanol and exposed to flowing air at a relative humidity of 75% to which 0.25 ppm of both SO_2 and NO_2 were added. The time of exposure was 2, 7, 20 and 170 hours respectively. Some unexposed samples were left as reference samples and stored in an atmosphere free of humidity and corrosive gases. The FT-IRRAS measurements were made with a Bruker FT-IR spectrometer, IFS 113 V (located at Bruker Analytische Messtechnik, GmbH in Karlsruhe) with p-polarised light incident at an angle of 80^0. The Raman measurements were made with an argon laser at an excitation wavelength of 488 nm. The XPS and Raman spectrometers have been described elsewhere (3, 4).

Estimates of the thickness of corrosion products at various exposure time were obtained by means of catnodic reduction which shows a thickness of 5 nm after 2 hours of exposure whereas the thickness after 7, 20 and 170 hours were 8, 17 and 36 nm respectively.

The infrared spectra are rather complex. The samples exposed 2, 7 and 20 hours exhibit spectra with peaks that were assigned to hydrous copper sulfate or hydrous copper sulfite. The XPS result support the latter alternative as judged from the binding energy of the S2p-peak. On the sample exposed for 20 hours a peak assigned to hydrous copper nitrate has begun to grow and in the spectrum of the 170 hours sample it is the strongest peak present. The assignment of the peak to hydrous copper nitrate is supported by the XPS-data which show a nitrogen, N1s-peak with a binding energy corresponding to nitrate.

In order to gain some insight into the possible in-depth distribution of S and N a separate XPS study of the 170 hours sample was performed, were the surface sensitivity was varied by changing the take-off angle of the detected photoelectrons with respect to the entrance slit of the photoelectron analyser. The variation of the ratio N/(N+S) when going from higher surface sensitivity (tilting the sample with respect to the analyser) to lower surface sensitivity (90^0 between sample surface and analyser) shows that the ratio increases with higher surface sensitivity. This together with the FT-IRRAS results described earlier suggests that the nitrate layer has grown on top of the hydrous sulfite layer.

The Raman measurements gave spectra with bands that were assigned to Cu_2O. When going from thinner to thicker corrosion films the Cu_2O bands increase, suggesting that the amount of Cu_2O is higher in the thicker than in the thinner films. No peaks due to nitrate or sulfate/sulfite phases could be detected. This can be explained by considering the Raman scattering mechanism. Cu_2O is known to show resonance Raman scattering, giving an considerable enhanced Raman signal. The other corrosion products are probably not resonance Raman scatterers and are probably too thin to be detected when normal Raman scattering mechanisms are operating.

To summarize, the present study illustrates how different complementary surface sensitive techniques can be used to obtain chemical or structural information on the initial growth of thin layers caused by atmospheric corrosion of metals. Hence when Cu interacts with flowing air at 75% relative humidity and with addition of SO_2 and NO_2 at 0.25 ppm the compounds listed below could unambiguously be identified by the following techniques used:

- Copper oxide Cu_2O (Raman spectroscopy) growing most likely next to the metal substrate.
- Hydrous copper sulfite (IRRAS and XPS).
- Hydrous copper nitrate (IRRAS and XPS) growing on top of the hydrous copper sulfite layer.

References:

1. Graedel, T.E., Franey, J.P., Gualtieri, G.J., Kammlott, G.W. and Malm, D.L., Corrosion Science, 25, 1163(1985)

2. Sharma, S.P., J. Electrochem. Soc., 127, 21(1980)

3. Zakipour, S. and Leygraf, C., J. Electrochem. Soc., 133, 21(1986).

4. Thierry, D. and Leygraf, C., Surf. Sci., 149, 592(1985)

Abstract No. 110

Darkening of medieval glass. A special type of atmospheric corrosion of glass.

Stephan Fitz
Umweltbundesamt
Bismarckplatz 1, D-1000 Berlin 33, Germany

The weathering of medieval stained glass windows which is accelerated by air pollutants leads to surface degradation and pitting of the glass together with the formation of weathering crust (1,2,3). Beside this extensively studied and until now fairly understood mechanism of deterioration of this unique works of art a number of glasses shows loss of transparency, shift of their color toward brownish tones or even darkening up to total opacity. Beside the discoloration there could not be found any other changes of these glasses by visual inspection : no corrosion products were deposited and the original gloss of the glass surface seemed to be without changes.

First hints for the real nature of the observed effect gave microscopic examination of the darkened glass. The surface shows a net of fine fissures along which a deep brown discoloration can be observed, obviously due to the deposition of some brown compounds. Because of the extremely small amount of the compounds an analysis of the observed products could not be carried out in our laboratory. The fact that the darkening has been observed only at glass with high content of iron and manganese has led to the assumption that the observed dark parts in the crizzled surface layer of the glass are unsoluble oxides or oxide-hydrates of $Fe3^+$, $Mn3^+$ and $Mn4^+$.

The mechanism leading to this type of changes of the glass is initiated by an acidic attack on the glass surface. In an ion-exchange reaction the protones which were deposited at the surface for example by acid rain are exchanged by the most mobile cations of the glass matrix - at typical composed medieval glasses mainly pottasium or calcium ions. When the voluminous potassium and calcium cations are removed from the glass matrix the remaining compounds of the original glass - mainly silicon dioxide - form a gel at the surface. Normal climatic changes as variation in temperature or relative humidity in the surrounding lead to a destabilization of the gel by loss of water and cause the formation of a crizzled surface. At the surface oxygen has free access to $Fe2^+$ and $Mn2^+$-ions which initially have been bond within the glass matrix. The color of the newly formed oxidation products turns from the initial pale green, resp. pink color to dark brown of $Fe3^+$- and $Mn3^+$- resp. $Mn4^+$-ions. As the solubility of the new products (oxides and oxidhydrates of iron an manganese) is very low, they remain at the outer surface of the silicagel, especially within the microscopic fissures. Restoration of these darkened glasses is not possible with suitable methods without undesirable loss of substance: the usually applied mechanical cleaning methods which are more or less successful when weathering crusts are removed, fail because the dark layers are only extremely thin coatings at very sensitive surfaces. Etching or abrasion of the discolored surface layer, as it was carried out in the early sixties at medieval stained glass windows of St.Brigida at Legden/Westfalen is contradictory to a modern understanding of conservation.

For restoring original color perception of the glass there had to be found a chemical treatment by which the undesirable oxidation of the iron- and manganese compounds could be reversed, all other components of the already corroded glass should be left unaltered however. The only reducing agent which in experiment yielded the desired effect, was found a 24% aqueous solution of hydrazine. All other tested reducing agents failed, since they caused serious damaged the original glass matrix. The positive effect of hydrazine was very surprising, since this solution with a pH of 11.5 would be expected to attack glass. Leaching experiments of medieval glass by several different alkaline agents as sodium hydroxide or ammonium hydroxide showed strong attack on the glass. Medieval glass from Altenberg cathedral, which was available in greater amounts and is dated 1380 was used for the experiments. After a 90hours treatment with hydrazine the weight loss is even much lower then that of a reference sample treated with deionized water with a pH of 6.

A final explanation of this passivation effect of hydrazine against alkaline attack on glass cannot be given. The described method gives a very useful tool for the conservator of historic stained glass windows. The treatment of darkened glass by the hydrazine method nevertheless has to be followed by additional precautionary measures in order to prevent a reoxidation of $Fe2^+$ and $Mn2^+$, which has been left in the gel layer after reduction treatment. A slight reoxidation of a treated stained glass window, as it was observed at Marienstern/DDR, made additional steps necessary. A removal of the $Fe2^+$ and $Mn2^+$ ions by a weak acid, as proposed by Müller (4) can cause additional damage due to further acidic attack. Probably more successful might be a protective coating by special organic modified silicates by the method of Tünker et.al. (5), which applied after the hydrazine treatment, could protect the sensitive glass surface from further oxidation. This method is tested in a field test at original stained glass windows in Sweden for a period of 4 years now. No changes has been observed until now.

References:

(1) Frenzel, G.: The Restoration of Medieval Stained Glass, Scientific American, May 1985, p. 126-135.
(2) Fitz, S.: Do air pollutants damage historic stained glass windows? Proc.Electrochem. Soc. 1986, p. 227-236
(3) Newton, R.G.:The Deterioration and conservation of painted glass/ A critical bibliography. London:Oxford University Press 1982
(4) Müller, W., et.al.:Extreme Dunkelung von Glasmalereien. Glastech. Ber. 54 (1981), p. 96-102
(5) Tünker, G., et.al.: Neue Wege zur Erhaltung historischer Glasfenster. Glastech. Ber. 59 (1986), p. 272-278

Abstract No. 111

ATMOSPHERIC TARNISHING OF SILVER BY H_2S: KINETIC STUDIES USING A FLOW REACTOR

Leo Volpe and Phillip J. Peterson

International Business Machines Corporation
General Products Division
San Jose, California 95193, U.S.A.

Gaseous air pollutants are known to play a key role in atmospheric corrosion of metals. The mechanism and kinetics of corrosion depend on the type and level of corrodents at the surface. When the metal corrodes, the rate of corrodent delivery from surrounding air is trying to keep up with the rate of consumption by the sample. As a result, the surface concentration of a reactive gas generally falls below the observable bulk-air concentration, and the corrosion rate is reduced accordingly. The extent of this decrease depends not only on the metal's chemical reactivity but also on the conditions of mass transfer of gaseous pollutants. Experimentally, the effect of mass transport on the rate is manifested in the influence of air velocity and flow pattern near the sample, which is well recognized in the corrosion literature.

As an example of a process affected by mass transfer, we examined the tarnishing of Ag in corrosive mixtures contaminated with sub-ppm levels of H_2S. The sulfidation, important as the major cause of silver corrosion, has been extensively studied. Our samples were metal foils in the form of circular tubes (Figure 1). Inside them, air with H_2S or H_2S-containing mixtures was passed. As we varied the mixture composition, flow rate, tube length, and duration of exposure, we monitored gas concentrations at the tube inlet and outlet. This gave the instantaneous rate of corrodent incorporation into the foil. After exposing the sample to a gas mixture for a period of time, we determined the type and amount of solid corrosion product as a function of distance from the tube's entrance.

The tubular reactor has well-defined and controlled flow conditions allowing us to separate the intrinsic kinetics of surface reactions from the details of corrodent delivery. From data on reactor conversion and rate of Ag_2S film growth, we derived the pollutant deposition velocity at the surface and the corresponding reaction probability (γ), i.e., the probability that an H_2S molecule colliding with the sample will form sulfide.

In dry air at 293 K, H_2S transformed Ag into Ag_2S with γ between $1 \cdot 10^{-6}$ and $5 \cdot 10^{-6}$. The rate was constant with time. Addition of H_2 to the gas mixture did not inhibit the rate. This shows that the reaction does not produce H_2 and is likely to involve O_2 as a reactant.

With H_2S-NO_2 mixtures in dry air, γ was $1.5 \cdot 10^{-5}$ to $3.5 \cdot 10^{-5}$ when the concentrations of the two corrodents were similar. The deposition velocity rose sharply with increasing NO_2 level. In the process, NO_2 was consumed twice as fast as H_2S, quantitatively converting to HNO_2 gas. Thus, a reaction not reported in the literature, $2Ag + H_2S + 2NO_2 = Ag_2S + 2HNO_2$, is responsible for the accelerated sulfidation.

In a humid air mixture having 0.5, 0.3, 0.04, and 0.003 ppm of NO_2, SO_2, H_2S, and HCl, respectively, surface sulfidation prevailed over chloridation. The rate held steady even after the build-up of hundreds of Ag_2S monolayers. This is consistent with high mobility of Ag^+ in the sulfide film. At 298 K, the reaction probability with H_2S lay between 10^{-1} and 1, as shown in Figure 2. These high values are believed to stem mainly from the excess of NO_2. The rate is controlled by the delivery of pollutant to the Ag foil. Under most environmental conditions, mass transfer of corrodent gas to the surface is expected to limit the rate of sulfidation.

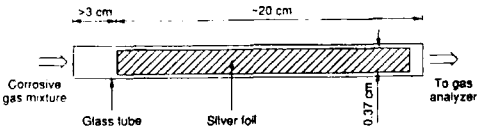


Figure 1. Tubular corrosion reactor. The metal foil lines the tube's inside diameter.

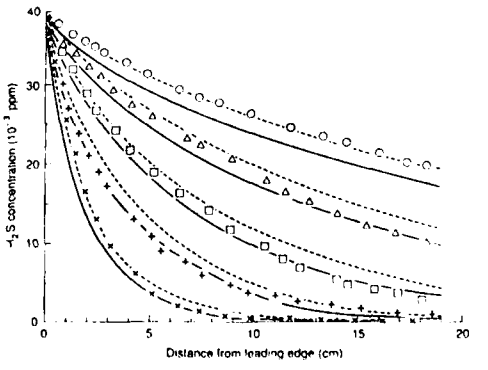


Figure 2. Depletion of H_2S from corrosive air (0.5, 0.3, 0.04, and 0.003 ppm of NO_2, SO_2, H_2S, and HCl, respectively, at 298 K, 70% relative humidity) flowing in Ag tubes. Experimental results for flow rates (cm^3 [STP] s^{-1}): ○ – 51.8, △ – 27.3, □ – 14.3, + – 7.67, × – 3.83. Theoretical prediction for reaction probabilities of 10^{-1}: dashed curves; 1: solid curves.

Abstract No. 112

"THE EFFECT OF CONDENSATION MECHANISM ON ATMOSPHERIC CORROSION OF METALS."

PAUL A. BURDA

Pacific Gas & Electric Company
Department of Technical and Ecological Services
3400 Crow Canyon Road
San Ramon, CA 94583

The influence of intensity condensation on the atmospheric corrosion of metals was investigated in this study with intention to explain the relationship of important factors for efficient design of permanent and/or temporary methods of the metals protection.

The quantitative relationships were obtained between "inside factors" (associated with the mass, heat capacity, heat conductivity, and specific heat of metals) and the "outside factors" (associated with temperature and humidity of the unpolluted environment) with regard to intensity of condensation on the steel, aluminum, copper, and lead surfaces.

The model of the laboratory microclimatic setup, used in this study, allowed that:

a) the temperature of the air was constant and differed from the temperature of the metal surface. The metal could follow the temperature of an environment,

b) the starting temperatures of the metals and the air were the same, the temperature of the environment changed and the metal followed these changes.

The influence of mass of metals on intensity of condensation had been determined under the changing temperature of environment. Very low corrosion rate of steel found in the air with 100% relative humidity at the constant temperature of metal and environment, progressively increased with an increasing amount of condensations. It was demonstrated that the kinetics of atmospheric corrosion and the intensity of condensation depend on heat capacity, while heat conductivity was not found to be a dominant factor. A linear relationship between specific heat and intensity of condensation was found in the range of specific heat from 0 to 2×10^{-2} cal/°Cg. It was also determined that the mass of metals increased intensity of condensation by letting down the metal temperature below the temperature of the air.

The conclusions of laboratory experiments were compared with the results of atmospheric outdoor tests of steel mass samples (up to 20 pounds) and aluminum (up to several hundred pounds). These results agreed with the laboratory findings that heat capacity has a dominant affect on intensity of condensation and on existence of the electrolyte on the surface of metals and therefore, it is an important factor of long time of atmospheric corrosion. The larger mass of aluminum exhibited a higher corrosion rate. It was found that the highest atmospheric corrosion rate, caused by higher mass of steel, occurred mostly during the spring time of the year.

Based on the results found, the following can be concluded:

a) the parameters of the atmosphere are influencing the effect of mass and heat capacity on kinetics of atmospheric corrosion. The highest corrosion rate was found under intensive condensation conditions caused by different temperatures of metals and the environment.

b) the temperature changes of the metal surface, effecting the condensation mechanism, depend on heat capacity of the metal.

c) the corrosion rate increase depends also on the mass of the metals.

References

1. Burda, P.A., Atmospheric Corrosion of Aluminum Ingots, Corrosion 87, San Francisco, CA, NACE, Paper No. 419.

Abstract No. 113

Deposition Velocities of Airborne Ionic Pollutants: Distribution Across Electronic Equipment Rooms

J. D. Sinclair and L. A. Psota-Kelty

AT&T Bell Laboratories
Murray Hill, New Jersey 07974

C. J. Weschler and H. C. Shields

Bell Communications Research
Red Bank, New Jersey 07701

In earlier studies, we reported on measurements of airborne concentrations and surface accumulations of ionic substances at electronic equipment installations at Wichita, Kansas and Lubbock, Texas[1,2]. Dichotomous samplers were used to collect samples of airborne substances at a convenient central location in the equipment room and outdoors on the roof of the equipment building. Practical considerations (cost and air flow requirements of the sampler compared to total room air flow) dictated that only one dichotomous sampler could be used indoors in the Wichita and Lubbock studies. Samples of fine and coarse particulates (0.1 - 2.5 and 2.5 - 15 μm aerodynamic diameter, respectively) were collected on Teflon filters at weekly or twice weekly intervals for several months. The separation of particulates into fine and coarse fractions is particularly useful in understanding the accumulation behavior of ionic substances on horizontal and vertical surfaces, as discussed in the earlier work[1-3]. Sampling of ionic substances that accumulated on surfaces was accomplished using filter paper extraction[4] of structural zinc and aluminum surfaces associated with the equipment. Sixty surface extractions, sampling both horizontal and vertical surfaces, were taken at both Wichita and Lubbock. In these initial studies, the sampling and analytical methods were optimized, but the duration of the airborne sampling (2-4 months) and the extent of surface sampling were not sufficient to achieve a quantitative measure of the deposition process for all the major ions in fine and coarse particles. More extended studies were recently completed at equipment locations in Newark, New Jersey[1,5] and Neenah, Wisconsin[6]. In each of these studies, detailed surface sampling was spread across the entire equipment room (500 sampling points on 25 equipment frames), and samplings of indoor and outdoor airborne concentrations were obtained for a one year cycle, using dichotomous samplers. From these and the previous studies it became evident that: (1) reliable indoor/outdoor concentration ratios could be estimated from readily available air handling system parameters; and (2) deposition velocities, calculated as the ratio of the average surface accumulation rates to the airborne concentrations, are reasonably consistent for each of the dominant ions commonly present in fine or coarse particles, irregardless of location. The consistency of the deposition velocities can be attributed to the narrow range in the average air flow velocities at these locations, which is typically 3-6 m/min. From items (1) and (2) a methodology was developed for predicting average indoor surface accumulation rates from outdoor concentrations, which are well known in many parts of the world. While the methodology provides reliable estimates of average surface accumulations, it was also clear from the measurements at these locations that there is a substantial variation in the surface accumulation rate across equipment rooms. From the original data, however, it could not be determined if these variations were a result of variations in airborne concentrations or variations in the deposition process.

In this paper further measurements at Newark and Neenah are reported in which compact personal air sampling pumps have been used in conjunction with Teflon filters mounted in cassettes. These pumps collect total suspended particulates (TSP), which is a disadvantage compared to the size fractionated data obtainable using dichotomous samplers, but the small size and low flow rates of these pumps allow a large number of them to be used without appreciably altering the airborne concentration and they can be placed in close proximity to the surface sampling locations. Comparisons between accumulation of ionic substances on horizontal or vertical surfaces and their concentrations in the fine and coarse particulate fractions cannot be made directly from the data, but can be calculated using the percentages of fine and coarse particles in the TSP, as determined using the dichotomous sampler. It was anticipated that comparison of the surface accumulation rates on horizontal and vertical surfaces with the corresponding concentrations of ions in the fine and coarse particle fractions would: (1) establish the degree to which the surface accumulation variations can be attributed to variation in the local airborne concentrations; and (2) determine if the data obtained using the dichotomous samplers are representative of concentrations across the entire equipment room for each sampling interval.

The airborne concentrations of ionic substances measured across the equipment room floors at both Newark and Neenah have been found to be remarkably similar. For example, the ranges in airborne sulfate associated with fine particles at Newark and Neenah were $0.83 - 1.08$ and $0.73 - 0.81$ $\mu g/m^3$, respectively. In comparison, the range in surface accumulation rates for sulfate on vertical surfaces were $0.07 - 0.29$ and $0.04 - 0.10$ $\mu g/cm^2 yr$, respectively. The ranges of the calculated deposition velocities obtained from the surface and airborne concentrations are $0.002 - 0.010$ and $0.0002 - 0.004$ cm/sec respectively.

These results demonstrate that: (1) the variation in surface accumulations is not attributable to the airborne concentrations and thus should be attributed to other factors probably related to air currents; and (2) airborne indoor concentrations of ionic substances are sufficiently constant across the equipment room floor for a typical sampling interval that the results obtained previously[1] using a single dichotomous sampler reasonably approximate the concentrations across the entire equipment room.

REFERENCES

[1] J. D. Sinclair, L. A. Psota-Kelty, "Proceedings of the International Congress on Metallic Corrosion", Volume 2, Toronto, Canada, June 3-7, p. 296, 1984.

[2] J. D. Sinclair, L. A. Psota-Kelty, C. J. Weschler, *Atmos Environ., Vol. 19*, p. 315 (1985).

[3] J. D. Sinclair, L. A. Psota-Kelty, C. J. Weschler, S. P. Kelty, Proceedings of the Conference on Indoor Air Quality, Ottawa, Canada, April 29 - May 1, 1985, to be published.

[4] J. D. Sinclair, *Anal. Chem., Vol. 54*, p. 1529 (1982).

[5] J. D. Sinclair, L. A. Psota-Kelty, C. J. Weschler, *Atmos. Environ.*, 22, 461 (1988).

[6] J. D. Sinclair, L. A. Psota-Kelty, C. J. Weschler, H. C Shields, submitted for publication.

Abstract No. 114

Indoor corrosion of copper and silver exposed in Japan and ASEAN countries

T.Fukushima*, Y.Fukuda*, A.Sulaiman**, I.Musalam**, C.L.Yap***, L.Chotimongkol***, S.Judabong****, A.Potjanart****, O.Keowkangwal
*National Research Institute for Metals
**Research and Development Centre for Metallurgy - LIPI
***Singapore Institute of Standards and Industrial Research
****Thailand Institute of Scientific and Technological Research
*2-3-12, Nakameguro, Meguro-ku, Tokyo, Japan
**Jalan Cisitu - Bandung, Indonesia
***1 Science Park Drive, Singapore 0511
****196 Phahonyothin Road, Bangkok 10900, Thailand

Introudction

Copper and silver are extensively used in the electronic equipment, and in this study, these metals were subjected to indoor exposure tests carried out at various sites in ASEAN countries and Japan. The effects of atmospheric pollutants on their corrosion were also investigated.

Experimental

Test specimens (30 x 30 x 0.3 mm) are of 99.9 % Cu and 99.9% Ag. They were mounted with an adhesive on acrylic resin panels (100 x 100 x 3 mm). Each specimen was polished with gauze and alumina paste, then rinsed in distilled water, followed by alcohol immersion, and finally dried. A total of 23 sites for indoor exposure were selected in Bandung, Singapore, Bangkok and Tokyo. At each of these sites, the panel with copper and silver specimens and a set of sampling devices for atmospheric pollutants (SO_2, solid Cl^-, gaseous Cl^-, NO_2, S^{2-}) were hung vertically for 1 to 6 months.

Results

(1) Microscopic examination and EPMA

Thick corrosion products were sporadically resulted on copper surfaces, and C, S, Cl and O accumulated there, but Na was not detected (Fig.1). Silver surfaces were uniformly covered with corrosion product films.

(2) XPS

The probable states of the elements detected are as follows:
Copper - Cu(I, II), O^{2-}, OH^-, SO_4^{2-}, S^{2-}, Cl^-, C (graphite, organic substance),
Silver - Ag(I), O^{2-}, OH^-, SO_3^{2-}, SO_4^{2-}, S^{2-} Cl^-, C (graphite, organic substance).

(3) AES

On every copper surface (Fig.2), O and C were detected and in some cases, Cl, N and/or S were also detected. C was found in abundance inside the film, but Cl, N and S were in small quantities. On silver surfaces, S and C were present in comparatively large amounts. In most cases, C was detected only in the outermost layer, but S penetrated into the depth of the film. Cl, N and/or were also found in some cases.

(4) IRS (KBr disk method)

On copper surfaces, H_2O, OH^-, SO_4^{2-}, NO_3^- and carboxylate were found, and on silver surfaces, H_2O, OH^-, and SO_4^{2-} were detected.

(5) Electrolytic reduction

On copper surfaces, corrosion products could not be indentified by the reduction potential. The amount of electricity required to reduce the corrosion products was not correlated to the deposition rate of any pollutant. On the other hand, corrosion products of silver were identified as Ag_2S from the reduction potential (-0.75V SCE). The AG_2S thickness increased with increasing deposition rate of H_2S or SO_3 (Figs.3 and 4).

Discussion

Carbon, detected on copper surfaces, is considered not to originate from CO_3^{2-}, but from organic substance. Carboxylate was found in certain cases by the IRS technique. Cl accumulated at the center (at the anode) of the pit, but Na was not detected around the pit (at the cathode). This suggests that Cl in this case comes from HCl in air. In addition, SO_2, H_2S, NO_2 and organic acids in the atmosphere also reacted with copper, leading to the formation of basic salts in mixture. The cathodic reaction seems to be in the oxygen consumption process.

Oxide films of silver formed during the preparation of specimens were changed to Ag_2S, Ag_2SO_4, AgCl and $AgNO_3$ by reacting with the pollutants dissolved in the adsorbed water. Oxygen was detected on the surface in mild indoor environments, but it was not detected on the surface exposed to the atmosphere which was heavily polluted by H_2S.

Conclusions

No significant variations in the amount of air pollution have been among the countries: the amount of air pollution depends on the locality of the exposure site.

Copper undergoes complex influences of organic acid, Cl^-, SO_2, H_2S and NO_2 which are different in concentration and reactivity, and is apt to be corroded sporadically. The corrosion products on copper consist of basic salts in mixture. The product amount is not correlated to the deposition rate of any pollutant.

Silver is affected mainly by S^{2-} and SO_2, and the general corrosion occurs uniformly. The main corrosion products of silver were identified as Ag_2S, the thickness increasing with increasing H_2S or SO_2 deposition rate.

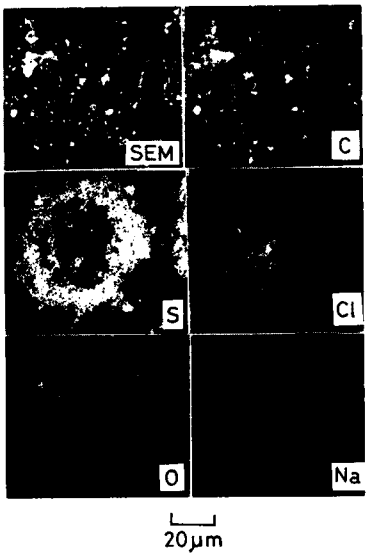


Fig.1 Secondary-electron and corresponding characteristic X-ray images of a copper pit (Bangkok, Work shop, 3 months)

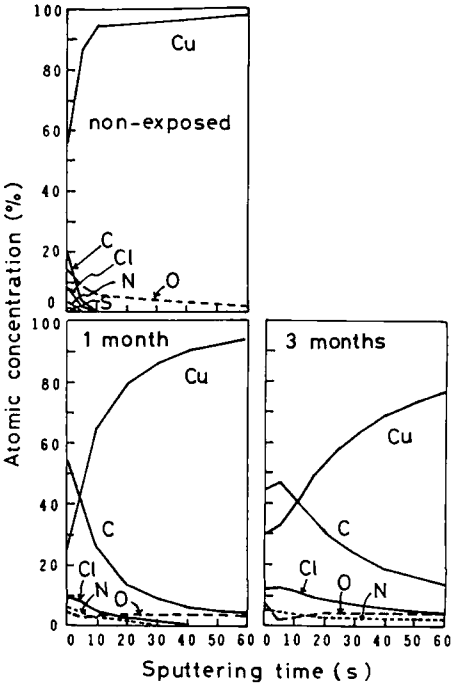


Fig.2 AES in-depth profile for copper. (Tokyo, Office, 1 & 3 months)

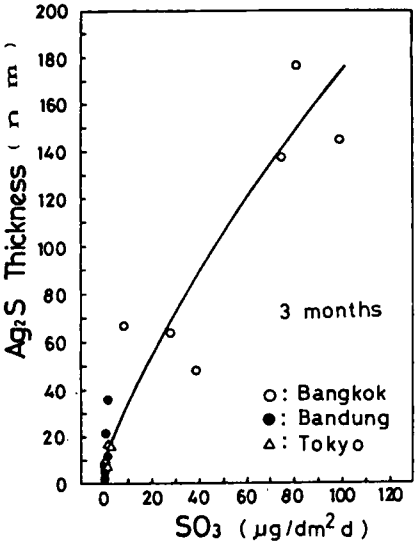


Fig.4 Ag_2S thickness vs. SO_3 deposition rate at each exposure site.

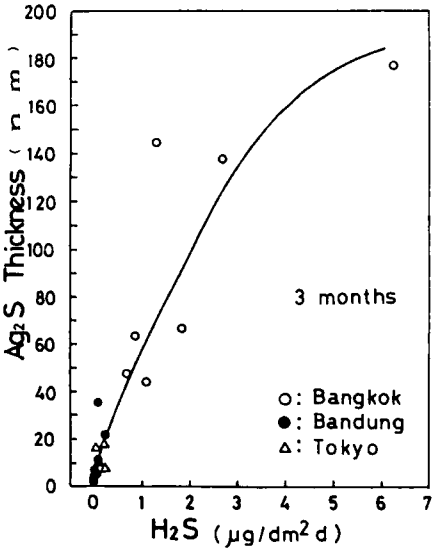


Fig.3 Ag_2S thickness vs. H_2S deposition rate at each exposure site.

Abstract No. 115

QUARTZ CRYSTAL MICROBALANCE FOR ATMOSPHERIC CORROSION STUDIES ON METALS

S. Zakipour
Swedish Corrosion Institute
Roslagsvägen 101, Hus 25
S-104 05 Stockholm, Sweden

and

C. Leygraf
Royal Institute of Technology
Division of Corrosion Science
S-100 44 Stockholm, Sweden

The Quarts Crystal Microbalance (QCM) method has the unique capability of detecting very small mass changes of metals under real atmospheric corrosion conditions. In a recent study it was found that a mass sensitivity of less than 10^{-8} g/cm^2 could be obtained when the corrosion kinetics of various metals was studied under in-situ laboratory exposure conditions (1). As such, the method is a most valuable complementary technique to other surface sensitive techniques which can provide information on structure or chemical composition of thin layers of corrosion products, such as Auger electron spectroscopy, X-ray photoelectron spectroscopy or Fourier transformation infrared reflection absorption spectroscopy. The main aim of the present work is to further explore the possible use of QCM not only under laboratory exposure conditions but also under field exposure conditions.

The QCM method consists of a piezoelectric quartz single crystal which oscillates at its resonance frequency. By deposition of very thin layers of the metal to be investigated on both sides of the quartz crystal it is possible to monitor small mass changes of the oscillating unit by measuring the change in resonance frequency which is a function of the total mass of the oscillating quartz and metal unit. The mass change can be monitored during exposure in an atmospheric corrosion testing apparatus. The QCM technique and the apparatus for atmospheric exposure tests have been described in more detail elsewhere (1, 2).

As an example of results that can be obtained under laboratory conditions FIG. 1 illustrates mass changes of nickel - which was electroplated on a thin evaporated gold layer on quartz - during exposure at 75% relative humidity for 96 hours (curve I). After 96 hours the supply of humid air was terminated which resulted in a significant decrease in mass caused by the loss of physisorbed water. Curves II and III represent two independent studies in which 0.25 ppm of both SO_2 and NO_2 were introduced simultaneously after 24 hours of exposure. The close agreement between curves II and III indicates that the reproducibility in exposure and measuring conditions are acceptable. From curves I, II and III is concluded that the introduction of both SO_2 and NO_2 under present conditions results in a marked increase in corrosion rate. This rate is an order of magnitude higher than if SO_2 or NO_2 is introduced alone (1). Similar result have been obtained for electroplated tin and evaporated copper.

Curve IV, finally, represents the same exposure conditions as in curves II and III with the exception that minor amounts of a vapor phase inhibitor, dicyclohexyl ammonium nitrite (Dichan) were present during the whole sequence of exposure conditions. As inferred from curve IV, the presence of Dichan seems to suppress not only the corrosion processes caused by SO_2 and NO_2 (curves II and III) but also the interaction of humid air with the nickel surface (curve I).

Field exposures were performed in two storing areas at the Nordiska Muséet, Stockholm. Both museum environments are characterized by very mild corrosion conditions as shown by separate investigations. The mass change of evaporated silver was monitored during exposure in both storing areas. It is concluded that a mass increase of 0.2 µg/cm², corresponding to only one day of exposure can be detected. After 30 days of exposure the mass increase is large enough to be estimated also with cathodic reduction. When taking into account the accuracy of both methods the results as obtained from QCM and from cathodic reduction are in agreement with each other.

To summarize, the QCM method can provide valuable information on atmospheric corrosion kinetics obtained under laboratory as well as under field exposure conditions.

References:

1. Zakipour, S., Leygraf, C. & Portnoff, G., J. Electrochem. Soc., 133, 873(1986).

2. Zakipour, S. & Leygraf, C., J. Electrochem. Soc., 133, 21(1986).

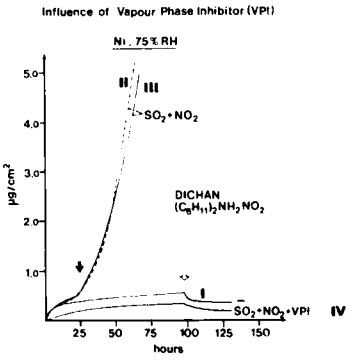


FIG. 1. Mass changes of electroplated Ni in flowing air at 25°C and 75% relative humidity. The filled arrow indicates introduction of SO_2 and/or NO_2, and the open arrow indicates termination of the supply of gaseous pollutants and of high humidity in the flowing air.

Abstract No. 116

Atmospheric Corrosion and Inhibition of Copper

N. R. Sorensen
T. M. Christensen

Sandia National Laboratories
Albuquerque, New Mexico
87185

Copper, used extensively in the microelectronics industry, is subject to atmospheric corrosion and tarnishing. Such corrosion can lead to increased contact resistance, open circuits, problems in soldering processes, and additional cleaning cycles during processing. Inhibitors are used routinely to maintain a metallic, untarnished appearance on the copper. A number of organic compounds have been used as corrosion inhibitors for copper in aqueous and atmospheric exposures with varying degrees of success[1]. Two that appear to be particularly effective for copper are benzotriazole (BTA) and tolyltriazole (TTA), which significantly decrease the copper dissolution rate in aqueous environments[2]. We are investigating the mechanism by which these organic inhibitors limit oxidation, the effect of atmospheric pollutants (NO_2, H_2S, SO_2, and H_2O) on the inhibition efficiency, and the effect of the inhibitors on manufacturing processes such as soldering. Atmospheric exposures are being run in our Facility for Atmospheric Corrosion Testing (FACT) which allows control of the contaminant gasses to concentrations ranging from several ppb to several ppm.

Work on Cu inhibition by organic inhibitors (benzotriazole, BTA) has led to the development of a model that describes both the inhibition results and the solderability data following the application of the inhibitor. To inhibit the corrosion reaction, the inhibitor reacts with the Cu surface, to form a thin (<100 A) layer of a Cu-BTA complex. The BTA molecule is bound to two Cu atoms through the nitrogen lone pair with the plane of the molecule approximately perpendicular to the Cu surface[3]. In this configuration the surface Cu atoms can be tied up in the Cu-BTA complex leaving no free surface Cu atoms to act as corrosion sites. Both inhibitors reduced the oxidation rate of copper at elevated temperature and humidity, with application from an aqueous solution providing better inhibition than from the methanol solution. When exposed to 70 C, 80% RH air, the corrosion film on the inhibited samples approached a limiting thickness after ~100 days while that on the as-cleaned samples continued to grow. At 127 days the BTA_{water} and $BTA_{methanol}$ inhibited samples exhibited weight changes that were 43% and 34%, respectively, of that for the uninhibited samples.

Auger Electron Microprobe (AEM) depth profiles indicate that several differences exist between the cleaned and inhibited surfaces. The surface oxygen and copper concentrations are considerably lower for the inhibited surfaces, while the surface carbon concentration (C is present in the organic inhibitor) is higher. In addition, the copper oxide film is much thicker on the cleaned sample. These data suggest that, even in laboratory air at room temperature, BTA is effective as an inhibitor to oxidation. They are also consistent with the accepted theory that BTA reacts with Cu_2O on the surface to form a Cu-BTA complex which provides the inhibiting action.

In the soldering process, low values of surface tension and contact angle, high wetting rates, and a short time to 90 degree turn-around (T_{90}) indicate good solderability. When the inhibitor is applied to the surface, the surface tension, contact angle, and wetting rate decrease, while T_{90} increases. Contact angle and surface tension indicate equilibrium conditions, and T_{90} and wetting rate relate to kinetics. These data suggest that the inhibitors improve the intrinsic solderability of the copper by replacing or altering the surface oxide, but adversely affect the kinetics of the soldering process because the inhibitor must be thermally oxidized, rendering it ineffective before wetting can occur. During the soldering operation, the temperature exceeds 200 C. At these elevated temperatures, the BTA is unstable, it is oxidized in the air and leaves the surface. As it is removed, the resulting surface is essentially bare Cu, which is solderable. We have also found that BTA is not an effective inhibitor in sulfur containing environments. We are pursuing these observations in order to determine the mechanism by which sulfur destroys the inhibiting effect of BTA on Cu.

References

1. H.G. Tompkins and S.P. Sharma, Surface and Interface Analysis, Vol 4, No. 6, pp. 261, (1992).

2. P.G. Fox, G. Lewis, and P.J. Boden, Corrosion Science, Vol. 19, pp. 457, (1979).

3. B.S. Fang, C.G. Olson, and D.W. Lynch, Surface Science, Vol. 176, pp. 476, (1986)

Abstract No. 117

ELECTROCHEMICAL ASSESSMENT OF THE TARNISH RESISTANCE OF DECORATIVE GOLD ALLOYS

Jean-Paul Randin
ASULAB S.A., Research Laboratories of the SMH-Group
Passage Max-Meuron 6
2001 Neuchâtel (Switzerland)

1. Introduction

The presence of non-noble metals in gold alloys has a strong influence on its corrosion resistance, especially its tarnishing. The latter process is attributed to the formation of a metal sulfide which darkens the surface of the metal rendering it aesthetically unacceptable. The tarnish resistance of silver, copper and gold alloys has most often been tested by exposing samples to sulfide containing gaseous environment (1). The development of rapidly performed electrocnemical tests in predicting the tarnishing behavior of gold alloys would be of great interest. Polarization measurements have been used recently in sulfide-containing electrolytes in attempts to assess the tarnishing of dental alloys (2-4). A correlation was found between the current density at a given potential in sulfide-containing artificial saliva and the non-noble metal content in the alloy (3). The test was proposed as a quantitative method of characterizing the tarnish resistance. While several investigations have appeared on the tarnish resistance of gold alloys used in electronics and dentistry (1), none is available on the jewellery alloys.

2. Experimental details

Three commercially available, 10 µm thick alloys, roll-clad on 0.5 mm thick AISI 430 ferritic stainless steel were studied. Their typical chemical compositions are shown in Table I. Comparative measurements were also performed on three electroplated gold coatings deposited on AISI 304 austenitic stainless steel. The thickness and compositions are given in Table II.

The as-received roll-clad samples were very lightly mechanically polished with 1 µm diamond paste. All samples were ultrasonically washed in an alkaline cleaner followed by rinsing in water, then in a 1:1 acetone-isopropanol mixture and dried in hot air. The apparent surface area of the electrodes were between 0.5 and 4 cm^2. It was defined with an epoxy resin and an acrylonitrile-styrene varnish covering the back of the samples and the holder. All data are given with respect to the apparent surface area of the electrode.

Quasi steady-state current potential curves were automatically recorded using a 10 mV potential step per minute. Cyclic constant-current chronopotentiometric measurements were usually performed with identical anodic and cathodic current densities.

3. Results and discussion

Potentiostatic measurements: The anodic polarization of the various alloys investigated in 1N NaOH sulfide-free solution have shown that the background current density on gold alloys in the sulfidation and sulfide oxidation potential range, i.e. at E< 0.2 V, was negligibly small.

The cathodic polarization for alloys 18, 14 and 14 Zn in O_2-saturated 1N NaOH solution have shown that the oxygen reduction reaction occurred at potentials lower than 0.18 V. It follows that any anodic reaction which takes place at potentials lower than 0.18 V will be thermodynamically possible in the presence of oxygen.

The influence of the sulfide concentration in N_2-saturated 1N NaOH electrolytes is shown in Fig. 1. The presence of sulfide shifted the equilibrium potential and the first rise in the anodic current density in the cathodic direction by about 0.4, 0.5 and 0.6 V for the gold alloys tested in 10^{-5}, 10^{-3} and 10^{-1} M Na_2S concentrations, respectively.

The influence of the gold alloy composition on the anodic current density at a given potential is shown in Fig. 2. Although the scatter from one alloy to the other was quite significant, a linear log i vs non-metal content plot denoting an exponential relationship may be observed in 1N NaOH-containing electrolytes. In 0.26 M Na_2S there was also a correlation between the current density and the non-noble metal content but the linear log i vs non-metal content relationship was not verified. The large scatter arose at least partly from the variety of non-noble metals present in the alloys investigated. It may be seen that, for a given gold content, the current density between -0.4 and -0.1 V was lower for the 18 ct AuCuCd than for AuAgCu and for alloy 14 Zn than for alloy 14.

Chronopotentiometric measurements : Potential-time plots corresponding to one oxidation-reduction cycle for an oxidation time of 2 min in 1N NaOH + 10^{-3} M Na_2S are shown in Fig. 3. For pure silver and copper, the cathodic charge (Qc) was equal to the anodic charge (Qa) up to Qa >10 mC/cm^2. It followed that the product of the anodic reaction remained at the electrode surface. Such a behavior is consistent with the sulfidation-desulfidation of the non-noble metals. On the contrary, for gold the cathodic charge was constant and did not depend on the anodic charge up to Qa >10 mC/cm^2. The charge imbalance arose either because the product of the anodic reaction did not remain at the gold surface or oxidation proceeded to oxo anions of sulfur in addition to the formation of sulfur or polysulfides and these species were not reduced on the return scan.

The behavior of electrodeposited gold alloys was similar to that of pure gold (Fig. 3). For roll-clad gold alloys the ratio Qc/Qa was still very small, indicating that a significant part of the anodic charge was used for the sulfidation of the non-noble metals. By contrast, the cathodic charge of roll-clad gold alloys slightly increased with increasing anodic charge. The higher the value of Qc at a given Qa, the higher the increase of Qc with increasing Qa. The cathodic charge at a given anodic charge increased from one alloys to the other in the following increasing order (see Table I for the abbreviation of the alloys) : Au < 18 < 14 Zn < 14.

4. Conclusions

The electrochemical results have shown that the sulfidation of the non-noble metals of the gold alloys occurred in parallel with the oxidation of sulfide ions. Only the first reactions contributed to tarnish by producing insoluble, adherent and colored sulfide films, while the oxidation of sulfide led to mainly colorless and non-adherent species. Thus the anodic charge reflects only to a minor extent the tarnish level.

The occurrence of two parallel reactions implies that the reaction rate of the former cannot be increased by holding the potential at a higher value without increasing also the rate of the second reaction. This is the reason why the time needed to reach a visible tarnishing by electrochemical means is roughly similar to that obtained by using a "chemical potentiostat", i.e. by oxygenating the solution. For both experimental conditions, hours are needed to get a color change well visible with the naked eye. However with electrochemical tests there is no need to reach such a strong tarnish level since more sensitive means are available to assess

the tarnishing rate.

In sulfide-containing electrolytes, the current density measured at a properly chosen potential of the potentiostatic scan correlates with the non-noble metal content of the alloy (Fig. 2).

The tarnish resistance of the alloys investigated was found to decrease in the following order :

23F > 22E > 18E > 18 > 14 Zn > 14

The ranking is mainly determined by the gold content and somewhat modulated by the silver and copper concentrations. The higher the silver content, the higher the tarnish susceptibility.

Acknowledgments

The author is pleased to thank R. Rocchi for technical assistance and Rado Watch Co., a member of the SMH Group, for interest and support. This presentation is based on a paper published in Surface and Coatings Technology, 34 (1988), 253-275.

References

1. A.T. Kuhn and G.H. Kelsall, Br. Corros. J., 18, (1983) 168; A.T. Kuhn, M.S. Chana and G.H. Kelsall, Br. Corros. J., 18, (1983) 174

2. W. Popp, H. Kaiser, H. Kaesche, W. Brämer and F. Sperner, Proc. 8th Int. Congress Metallic Corrosion, Mainz, Sept 1981, in "Metallic Corrosion", Vol. 1, Dechema, Frankfurt am Main, 1981, p. 76

3. E. Angelini and F. Zucchi, Surf. Tecnol., 21 (1984) 179

4. M. Marek, in "Corrosion and Degradation of Implant Materials:Second Symposium", ASTM STP 859, A.C. Fraker and D.C. Griffin, Eds, American Society for Testing and Materials, Philadelphia, 1985, p. 168

Table I : Composition of roll-clad gold alloys

Alloy	Composition (weight percent)				
	Au	Ag	Cu	Zn	Ni
18	75.0	16.0	9.0	-	-
14	58.5	29.2	11.5	0.3	0.5
14Zn	58.5	7.5	24.0	10.0	-

Table II : Thickness and composition of electroplated gold coatings

Abbreviation	Coatings	Thickness (µm)	Composition
18E	underlayers	0.5	Au
	main layer	7.0	AuCuCd, 18 ct
22E	underlayers	0.5	Au
	1st layer	3.5	AuCuCd, 18 ct
	topcoat	3.0	AuNi 22 ct (hard gold)
23F	underlayers	0.5	Au
	1st layer	3.5	AuCuCd, 18 ct
	topcoat	3.0	AuNi, 22 ct (hard gold)
	flash coloring	0.5	AuNiIn, 23 ct

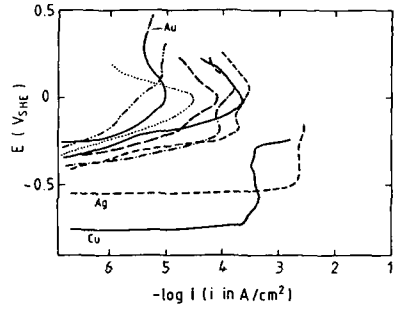


Fig. 1 : Anodic polarization curves for gold alloys in N_2-saturated 1N NaOH + 10^{-3} M Na_2S, 18 (——), 14 (– –), 14 Zn (-.-), 18E (— —), 22E (...) and 23F (-..-). The polarization curves for pure Au, Ag and Cu are also shown.

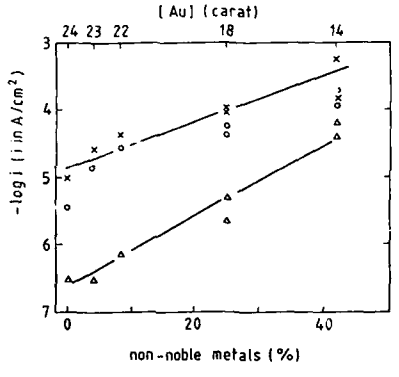


Fig. 2 : Plots of log i versus non-noble metal content of the gold alloys in anodic polarization measurements performed in N_2-saturated 1N NaOH + 10^{-3} M Na_2S at E = -0.25 V (Δ), 1N NaOH + 0.1 M Na_2S at E = -0.35 V (x) and in 0.26 M Na_2S at E = -0.35 V (o)

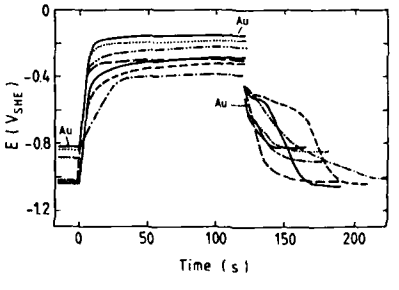


Fig. 3 : Reverse-current chronopotentiograms at gold alloys electrodes in N_2-saturated 1N NaOH + 10^{-3} M Na_2S at constant current densities between 15 and 20 µA/cm². Same symbols as in Fig. 1

Abstract No. 118

The Formation of Sulfuric Acid on Gold in Humid Air Containing sub-ppm Concentrations of SO_2 and NO_2.

P. Ericsson and L.-G. Johansson
Department of Inorganic Chemistry, Chalmers University of Technology and the University of Göteborg,
S-41296 Göteborg, Sweden.

Introduction

Synergistic effects on corrosion involving SO_2, NO_2 and water vapour have been studied at this laboratory during the last few years. Svedung et al (1) reported on the formation of sulfuric acid on gold-plated brass in humid air containing SO_2 and NO_2. It was assumed that the stoichiometry of the reaction was that of the so-called lead chamber process:

$$SO_2 + NO_2 + H_2O \longrightarrow H_2SO_4(aq) + NO(g)$$

Later the corrosion effects of combinations of SO_2 and NO_2 towards different metals e.g. copper and steel and on calcareous building stones have been investigated (2,3)
In order to learn more about the nature of the SO_2 - NO_2 - H_2O interaction on surfaces this investigation was started which focusses on the reactions occuring on pure gold.

Experiment

The experiments were performed using a piece of gold foil with a surface area of 20 cm^2. The foil was suspended on a gold wire in a vertically oriented glass cell with a diameter of 30 mm. The cell was immersed in a water tank thermostated to 22.00 +- 0.03 ^oC. Through the cell flowed a gas mixture made up from dried and purified air, water vapour, SO_2 and NO_2.
Part of the air steam was saturated with water vapour at the temperature of the exposure cell. Relative humidity was controlled by mixing measured amounts of dry and humidified air.
The trace gases were added from permeation tubes using the dry air as a carrier.

In order to minimize apparatus/pollutant interactions the apparatus was made from glass and teflon only.
The rate of gas flow was 1.00 $dm^3\ min^{-1}$ resulting in a net wind speed of 2.4 cm s^{-1} in the cell. SO_2 and NO_2 concentrations were 0.50 and 0.65 ppm respectively.
The gas emanating from the glass cell was analysed simultaneously for SO_2, NO and NO_x throughout all experiments. SO_2 was measured using a fluorescence instrument while NO and NO_x were analysed by an instrument based on chemiluminescence. Both instruments had a sensitivity of 1 ppb and a time constant of one minute. The two instruments were coupled in parallel so that half the total flow was directed through each analyser.
In this way SO_2 deposition and NO evolution on the gold foil was measured quantitatively.
Before exposure the gold foil was cleaned, the last step consisting of a heat-up to 400 ^oC in air. The foil was transferred directly to the cell after heating.
The experiments were started by introducing the gold foil into the cell.
The maximum decrease in SO_2 concentration due to reaction on gold amounted to less than 15% of the total amount present.

Results and discussion

The reaction is strongly dependent on humidity. At 0% r.h. no sulfuric acid forms.The rate of formation increases with humidity and reaches a maximum at 90% r.h. with ca $0.9 \cdot 10^{-6}\ gcm^{-2}h^{-1}$. At higher humidity there was a slight decrease in the rate of sulfuric acid production. The rate of formation was fairly constant on the time scale of these experiments (36 hours).
Without NO_2 present in the gas H_2SO_4 did not form on the gold surface except at 99% r.h. where minute amounts were deposited.
The stoichiometry of the NO_2/SO_2 reaction varies with humidity. The H_2SO_4/NO ratio is close to unity between 60 and 85% r.h. At higher and also at lower humidity NO evolution is less than it would be according to the formula given above, the ratio approaching two in some cases.
The non-stoichiometry of the reaction may be explained if the reduced N-O species formed in the reaction with SO_2 is reoxidized by oxygen before it is given off as NO.
Nonstoichiometry at high humidity may also be connected to the slight oxidation of SO_2 by oxygen on gold detected at 99% humidity.

The effect of the pretreatment of the foil was also investigated. The activity of the gold surface decreases rapidly with the time elapsed between the heat treatment (400^oC in air) and the start of the experiment. The amount of sulfuric acid formed after 36 hours exposure at 70% r.h. was reduced to ca 25% of the original by aging the gold foil in a desiccator for 50 minutes after the heat treatment. The great importance of the pretreatment for the formation of sulfuric acid on gold indicates that the reaction is catalysed by the gold surface itself.

References

(1) Corrosion of Gold-Coated Contact Materials Exposed to Humid Atmospheres Containing Low Concentations of SO_2 and NO_2
O.Svedung, L.-G.Johansson & N.-G.Vannerberg
IEEE Transactions on Comp., Hybrids and Manuf.Tech. (1983) 6, 349-355

(2) The Role of NO_2 in the Atmospheric Corrosion of Different Metals
P.Ericsson & L.-G.Johansson
10th Scand. Corr.Congr.,Stockholm(1986) Proceedings,43-48

(3) Corrosion of Calcareous Stones in Humid Air Containing SO_2 and NO_2
L.-G.Johansson, O.Lindqvist &R.Mangio
Accepted for publication in Durability of Building Materials.

Abstract No. 119

ELEMENTAL SURFACE COMPOSITION OF AGED COPPER

Rudolf Schubert and Susan M. D'Egidio

Bell Communications Research, Inc.
Red Bank, NJ 07701-7020

It is of interest to the electrical and electronics industries to understand how fast and by what mechanisms copper tarnishes at ambient temperature and in various environmental conditions. A range of oxidation rate values exists for copper in air at 300°K.[1] This slow rate is confused by trace atmospheric impurities[2] and the simultaneous formation/deposition of other compounds.

Electrolytic grade copper busbars with exposures ranging from 2 to as long as 49 years in the same telephone central switching office site have been collected. The site is Jamaica, NY, a heavily populated area on suburban Long Island, NY and is within 3 miles of bodies of salt water to both the north and south. The five story building was air-conditioned in 1958; prior to that time building windows were opened routinely. Busbar samples were removed from the top vertical edge of electronic equipment frames 2.7 m from the floor and in general were not handled after the initial installation.

Samples 0.5 cm wide were sheared, not sawn, from the center of 0.5 X 2.5 cm cross-section bars of various lengths. Areas with obvious human contact, such as fingerprints and grease spots were avoided. After shearing, samples were ultrasonically washed first in dichloromethane and then isopropyl alcohol. After washing they were blown dry and stored covered in laboratory air.

Before and after washing, the sample surface color ranged from bright copper for the newer samples to dirty brown copper for the oldest sample. On any given sample minor shades of color variation did exist. NO typical green copper patina was seen on any of the samples as is typical of samples exposed out of doors.[3]

Samples have been examined by Auger electron spectroscopy and argon ion sputter depth profiling for elemental surface analysis to a depth of 9000 Å or less, depending on the thickness of the nonmetallic surface film. A 10 keV, 20 namp primary electron beam was used for analysis in the stationary mode on a spot of ≈0.3 μm diameter. Multiple spots with lighter coloring, and which were laterally separated by millimeters or more were arbitrarily chosen for analysis from each sample. Two samples, separated by tens of cm, were chosen from busbars of different vintage for analysis.

Surface film composition was similar for all the samples examined, differing only in film thickness and the ratio of C/Cu. The films on the Cu substrates consist primarily of carbon with smaller amounts of oxygen, chlorine, sulfur, and nitrogen. As expected, Cu increases monotonically from the surface to the bulk metal. Nitrogen is only located in the top few monolayers of the surface and is at maximum concentration at the surface. Cl and S are dispersed surprisingly uniformly through the entire surface film and decrease linearly with depth. Oxygen concentration reaches a maximum slightly below where the film switches concentration from primarily C to primarily Cu. A typical depth profile, atomic concentration[4] versus sputter time, for the 49 year old sample is shown in Figure 1.

Arbitrarily defining the surface film to penetrate to where the Cu concentration reaches 70%, we can calculate the relative percentages of the elemental composition in the film.

TABLE I. Average thickness and percent atomic concentration.

AGE	THICKNESS	C	Cu	O	Cl
3	415 Å	35	53	8	4
31	850 Å	49	41	8	3
49	7900 Å	53	35	8	4

Note that as the films become thicker with age the concentration of C in the film also increases.

Our results differ markedly from Opila's similar analyses on outdoor exposed samples from a similar geographic region.[5] All of Opila's samples (1-100 years old) had oxygen(≈ 60 at.%) as the major elemental component on the surface and negligible amounts of carbon. The Cl and S concentrations are comparable, but the film thicknesses are from 5 to 60 times thicker for the outdoor exposure.

Insufficient oxygen concentration is present in our films to postulate the formation of S containing minerals such as brochantite, antlerite, or posnjakite; furthermore, no patina was observed. If one assumes that the oxygen signal is due to the formation of primarily Cu_2O, then the calculated cuprite thickness is approximately 960 Å for the 49 year old sample. This is substantially higher than what one would predict for simple oxidation in clean air, which is approximately 62 Å. However, it is known that the presence of trace amounts of pollutants, specifically reactive chlorine, will accelerate the oxide formation on Cu.[2],[6]

Although the indoor exposed samples reported on in this paper have similar concentrations of S and Cl as outdoor samples from similar geographic locations[5], the total film thicknesses are substantially less. This demonstrates the effect of building shrouding and lack of surface wetness effects. The C content of the indoor surface films is substantially greater. This demonstrates the effect of indoor air composition and implies that an indoor source of carbon compounds is present in the building.

REFERENCES

1. A. Ronnquist and H Fischmeister, "The Oxidation of Copper", J. Inst. Metals, **89**, 65(1960).

2. To be published by R. Schubert

3. The entire issue of *Corrosion Science*, **27**,7 in 1957 is a special issue dealing with copper patina formation.

4. L. E. Davis, N. C. MacDavis, P. W. Palmberg, G. E. Riach, and R. E. Weber, *Handbook of Auger Electron spectroscopy*, second ed., Perkin-Elmer Corp, Eden Prairie, MN, c1976.

5. R. L. Opila, "Copper Patinas: An Investigation by Auger Electron Spectroscopy", Corr. Sci., **27**, 685(1987).

6. W. H. Abbott, "The Development and Performance Characteristics of Mixed Flowing Gas Test Environments", 33rd IEEE-Holm Conference on Electrical Contacts, Chicago, 63(1987).

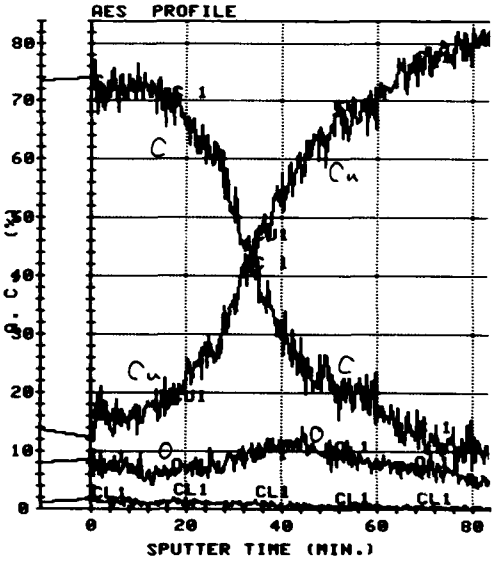


FIGURE 1. AES depth profile of a washed Cu sample had been installed in a Jamaica, NY telephone office in 1939. For the conditions used the calibrated sputtering rate was 113Å/min on SiO_2. This was the thinnest film found on 49 year old busbar samples; the thickest film was 1.6 times as thick. Only the Cl signal is shown but S is also present with similar intensity. Trace surface N is also omitted. Analysis of the raw data counts shows that the O intensity reaches a maximum well below the initial surface, as is indicated in the figure.

Abstract No. 120

SEGREGATION OF ALLOYING ELEMENTS INTO THE PASSIVE FILMS ON BINARY NICKEL ALLOYS

Digby D. Macdonald, Catherine English,
Joan Pallix and Mordehai Ben-Haim
SRI International
Menlo Park, CA 94025

Introduction

The role(s) of alloying elements in modifying the resistance of structural metals to general and local corrosion is not fully understood, to the extent that corrosion resistant alloys cannot be designed from first principles. The development of this capability must await more detailed knowledge of the structural and electronic properties of the thin passive films that grow on corrosion-resistant metals and alloys.

In this study, we investigated the segregation of Al^{3+}, Ti^{4+}, and Mo^{6+} into the passive films that form on the dilute binary alloys Ni-X(X=Al, Ti, Mo) under potentiostatic conditions.

Experimental

Passive films were grown on various Ni-Al, Ni-Ti, and Ni-Mo alloys under potentiostatic conditions (mV vs. SCE) in 0.5m H_3BO_3 + 0.25 m KOH at 25°C (pH = 9.2). The elemental compositions of the films and the base alloys were then determined on two spots (~1 mm x 1 mm diameter) on the surface using SALI (Surface Analysis by Laser Ionization). This technique provides quantitative elemental analyses by mass spectrometry of completely (laser) ionized ablated material just above the surface.

Results and Discussion

Plots of the enrichment factor (X_{film}/X_{alloy}) versus alloy composition (X, % relative to nickel) for the binary alloys is shown in Figure 1. While considerable scatter exists in the data for Ni-Mo alloys, possibly reflecting an inhomogeneous surface composition, the enrichment factors are in the order: Mo>Ti>Al. Assuming that the oxidation states for Mo, Ti, and Al are +6, +4, and +3 it is clear that the most strongly segregated alloying element is that with the highest charge.

The above data can be interpreted in terms of a model which assumes that segregation results from competition between the host metal (M_A) and the alloying element (X_A) in the alloy for cation vacancies as the metal/film interface passes through the metal phase. This competition can be described by the following reactions

$$M_A + V_M^{\chi'} \rightleftharpoons M_M + \chi e' \qquad (1)$$

$$X_A + V_M^{\chi'} \rightleftharpoons X_M^{(\delta-\chi)+} + \delta e' \qquad (2)$$

where $X_M^{(\delta-\chi)+}$ is an alloying element ion substituted into a cation vacancy in the film and χ and δ are the oxidation states of the host cation (e.g., Ni^{2+}) and solute (e.g., Mo^{6+}), respectively. Assuming quasi-equilibrium at the metal/film interface we derive the segregation factor as

$$SF = \frac{N_v \theta \exp[(\delta-\chi)[(0.5-\alpha)V + \epsilon F_v]F/RT]}{N_v + [V_f \theta \exp[(\delta-\chi)[(0.5-\alpha)V+\epsilon F_v]F/RT] - V_a][X_A]} \qquad (3)$$

where N_v is Avogadro's number, α is the dependence of the potential difference across the film/solution interface on the applied voltage, V_a and V_f are the molal volumes per cation of the alloy and the film, respectively, ϵ is the electric field strength, F_v is a constant, and X_A is concentration (No./cm^3) of the solute element in the alloy. The parameter θ is a function of the dielectric constant of the film, amongst other quantities. Provided that $\alpha < 0.5$ (1), and since $\delta > \chi$, equation (3) predicts that the more highly-charged solutes are the most strongly segregated into the film, as observed. Segregation is also facilitated by a high film dielectric constant, as indicated by an analysis of θ.

ACKNOWLEDGMENTS

The authors gratefully acknowledge the support of the US Dept. of Energy, Basic Energy Sciences, under Contract No. DE-FG03-84ER45164. We also thank Ms. Joan Pallix, Chemical Physics Dept., SRI International, for performing the SALI experiments.

REFERENCES

1. K. S. Lei, D. D. Macdonald, B. G. Pound, and B. E. Wilde, "Breakdown of the Passive Film on Polycrystal and Single Crystal (100) Nickel by Chloride," J. Electrochem. Soc., in press (1988).

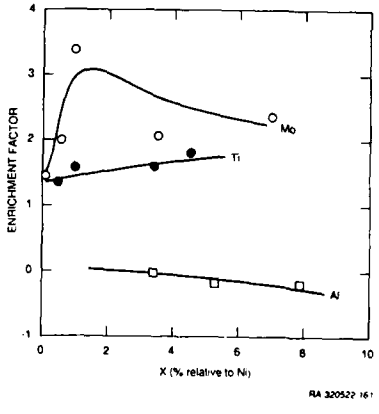


Figure 1 Segregation of alloying elements into Ni - X (X = Al, Ti, Mo) alloys as a function of alloy composition

Abstract No. 121

Role of Pre-Existing Oxide Films in the Passivation of Fe

B. MacDougall

National Research Council of Canada
Division of Chemistry
Ottawa, Ontario, Canada K1A 0R9

Previous work on the anodic behavior of Fe in acid and neutral sulfate and perchlorate solutions has shown that a prior surface oxide film is required for efficient passivation (1-4). After complete cathodic reduction of the prior film, very large anodic charges are passed before passivation occurs. In this case, the passivation process relies on the formation of a salt film at the electrode surface. As less and less of the prior film is cathodically removed before the anodic potential step, the efficiency of passivation increases from <<1% to values approaching 100%. Although it has been suggested that the remainder of the original oxide film might somehow interact with the developing salt film and/or act as nuclei for passive film formation in sulfate (2,4), there was no direct evidence that this was the case. In the present work, SIMS analysis in conjunction with ^{18}O labelling of the oxide film is used to establish directly whether any of a non-reduced oxide film remains on the surface after a potential step passivation in sulfate.

Experimentally, a passive film 2.65 nm thick containing 10% ^{18}O was prepared by stepping the *potential* of an oxide-free, cathodically reduced Fe electrode to 0.42 V (SCE) for 5 min. The *solution* used to prepare this standard prior film was pH 8.4 borate buffer enriched in ^{18}O to 10% (5,6). The sample was then transferred to a pH 8.4 (0.15N) Na_2SO_4 solution and cathodically reduced to various extents at 20 $\mu A\ cm^{-2}$, after which the electrode was either removed from solution, or the potential stepped to 0.42 V (SCE) and the anodic current-time response recorded. All samples were analyzed for ^{18}O by SIMS. The unreduced sample had a thickness of 2.65 nm and a constant ^{18}O enrichment level, representative of the solution enrichment, and was therefore used as a standard (6). The amount of oxide remaining on the surface after treatment in Na_2SO_4 was calculated from the decrease in ^{18}O as described previously (6). Passivation in the sulfate solution without any cathodic reduction of the prior film does not result in any loss of this prior film, consistent with the fact that only a very small amount of anodic charge flows. On the other hand, complete reduction of the prior film results in a decrease of the ^{18}O enrichment level to the natural abundance of 0.2%, indicating that all of the prior film has been removed. Between these two extremes, there is a range of extents of removal of the prior passive film. Importantly, there is no change in the equivalent thickness of the prior film remaining on the surface before and after the potential step in Na_2SO_4. This is true even when very large anodic charges flow, and, correspondingly, the initial anodic currents are very high. Clearly, significant amounts of oxygen from the prior film can remain on the surface even during a very inefficient passivation in sulfate, and do control the efficiency of passivation (4). The importance of this result is that it is a direct observation of surface oxide persisting during the high rate dissolution of Fe in neutral sulfate. The fact that the remaining oxide can control the efficiency of passivation has considerable relevance for the corrosion and passivation of Fe.

The passivation of iron has also been studied in acetate, borate and phthalate solutions using cyclic voltammetry and potential-step anodization techniques. Special attention is given to the existence of a pre-passive film on the surface, corresponding to ~ 2 nm of a γFe_2O_3 oxide film. While large anodic dissolution currents can be sustained even in its presence, this film does appear to be an important precursor for highly efficient potential-step passivation. The persistence of this film during rapid anodic dissolution is studied and the results are compared with those obtained upon passivation in sulfate solutions with prior films remaining on the surface. The requirements for efficient passivation of iron in different environments is discussed in light of the electrochemical and surface-analytical results.

REFERENCES

1) D.B. Gibbs and M. Cohen, J. Electrochem. Soc., 119, 416 (1972).
2) S. Szkarska-Smialowski and G. Mrowczynski, Br. Corr. J., 10, 1987 (1975).
3) B. MacDougall, J.A. Bardwell and M.J. Graham, Proc. Intern. Symposium on Surfaces, Inhibition and Passivation, Published by Electrochem. Soc. (Vol. 86-07), 1986, p.254.
4) B. MacDougall and J.A. Bardwell, J. Electrochem. Soc. (in press).
5) R. Goetz, D.F. Mitchell, B. MacDougall and M.J. Graham, ibid., 134, 535 (1987).
6) J.A. Bardwell, B. MacDougall and M.J. Graham, ibid., 135, 413 (1988).

Abstract No. 122

COMPOSITION AND STRUCTURE OF THE PASSIVE OXIDE FILM ON IRON AS OBSERVED BY SECOND HARMONIC GENERATION*

M. W. Schauer, J. M. Frye, B. M. Biwer,
M. J. Pellin, and D. M. Gruen

Argonne National Laboratory
9700 South Cass Avenue
Argonne, IL 60439

The technique of Second Harmonic Generation (SHG) as a surface analytical tool has progressed to the point where scientific information, not easily observed by other means, can be obtained for systems such as metal surfaces undergoing electrochemical reactions.[1] Despite extensive study, the compositional and structural details of the passive oxide layer on iron are not well understood. SHG is extremely sensitive to compositional changes as an iron electrode is cycled. Resonance enhancement of the SHG signal can be correlated with the expected electronic spectroscopy of the various iron oxide species believed to be present. In addition, by using an incident frequency for which no resonance enhancement is observed, changes in the SHG signal can be interpreted as due to charging. This provides further information about the electrical properties of the film. By comparing the SHG results for the iron electrochemical system with previous models of the iron passive layer, new understanding about the composition of this system has been realized.

SHG intensity as a function of potential is plotted in Fig. 1 for cycling an Fe electrode. The top curve represents the current and shows the well-known waves associated with oxidation and reduction of iron. The second curve shows the SHG intensity using 1.06 μ (detecting 532 nm) light as the fundamental. We believe that surface charging contributes significantly to the SHG intensity in the 1.06 μ SHG experiment. On the other hand, resonance enhancement is largely responsible for the intensity in the 532 nm SHG experiment. The lower curve displays the SHG intensity using 532 nm light as the fundamental (detecting 266 nm).

These data are largely consistent with the "chemiconductor" model proposed by Cahan et al.[2] The results lend support to and will be discussed in terms of this model.

The use of Fe single crystals takes advantage of the tensor nature of the SHG experiment to provide structural information about the passive oxide layer on iron. The SHG intensity can be monitored as the sample is rotated about the surface normal, and the resulting pattern reveals the symmetry of the interface being observed. In the absence of resonance interactions the SHG pattern for the Fe(110) surface reveals its bilateral symmetry (Fig. 2). By coupling to an electronic resonance of a surface species the three-fold symmetry of the air-formed oxide is revealed. This represents the first measurements of the structure of thin oxide layers on iron outside ultrahigh vacuum. Studies are in progress to extend this work to UHV and electrochemical environments.

*Work supported by the U.S. Department of Energy, BES-Materials Sciences, under Contract W-31-109-ENG-38.

References

1. (a) B. M. Biwer, M. J. Pellin, M. W. Schauer, and D. M Gruen, Langmuir 4, 121 (1988); (b) B. M. Biwer, M. J. Pellin, M. W. Schauer, and D. M. Gruen, Surf. Sci. 176, 377 (1986); (c) V. L. Shannon, P. A. Koos, and G. L. Richmond Applied Optics 26 3579 (1987).

2. B. D. Cahan, Chin-Tien Chen, J. Electrochem. Soc. 129 921 (1982)

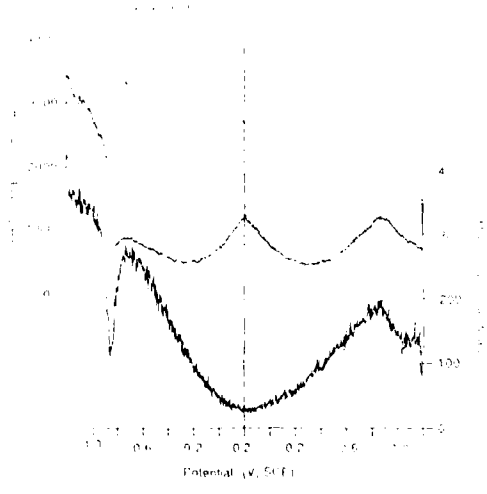


Fig. 1.

Current and SHG intensity as a function of potential for an iron electrode cycling at 2 mV/s in 0.1 M NaOH. The top line is the current. The middle scan is SHG signal using 1.06 μ laser light as the fundamental (intensity scale is on the left). The bottom scan is SHG intensity using 532 nm laser light (scale is on the right).

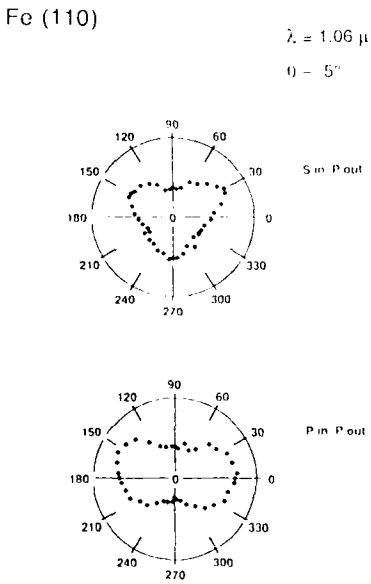


Fig. 2.

SHG intensity (plotted radially) as a function of the angle of rotation about the surface normal for an Fe(110) surface in air. The top spectrum reveals the 3-fold symmetry of the surface oxide observed when the detected polarization is perpendicular to the incident polarization. The lower spectrum shows the bilateral symmetry of the Fe(110) surface observed when the detected polarization is parallel to the incident polarization.

Abstract No. 123

NEXAFS Studies of Passive Films on Iron and Iron-Chromium Alloys

Z. Zhang, D.K. Tanaka, and J.Kruger
The Johns Hopkins University
Baltimore, MD 21218
and
G.G. Long
National Bureau of Standards
Gaithersburg, MD 20899

A method for studying passive layers using x-ray absorption spectroscopy that has a particular sensitivity to surface layers is the measurement of reflectivity as a function of incident photon energy and grazing angle. The data analysis in this case is complicated by the fact that the absorption coefficient is less simply related to the reflectivity than it is to the fluorescence (x-ray or Auger electron) signal. The advantages of this technique called ReflEXAFS (1) are that the surface sensitivity is very good and the signal-to-noise is excellent. We have developed theoretical and experimental approaches enabling the study of passive films and applied them to the study of the passive films that form on iron and iron-chromium alloys in a borate buffer solution.

Under the "total" reflection conditions used in ReflEXAFS, there is no wave propagating in the medium. Instead there are waves of varying amplitude (evanescent waves) present which decrease with increasing penetration. These waves enter the medium and then emerge again from the same surface. The 1/e penetration depth can be calculated and we have calculated that for angles smaller than the critical angle the penetration depth in the chemical system we are investigating for photon energies up to 800 eV would be less than 3 nm. Films thicker than this will appear to be semi-infinite insofar as refl-EXAFS measurements are concerned and problems with thin film-bulk surface interference effects are avoided.

Compositional Effects of Cr in Passive Film on Fe and Fe-Cr Alloys

Near edge x-ray absorption fine structure (NEXAFS) was applied to the study of the compositional effects of chromium additions to the passive film via chromate passivation to examine the valance state of the chromium that is present in oxide layers on iron or iron-chromium alloys.

Results found for the 3 nm passive film on iron formed in a chromate passivating solution by exploiting the surface sensitivity of a newly developed photocathode grazing incidence detector. Although a rather small amount of Cr was present in this thin film, there were some indications, which have to be evaluated by further measurements, that Cr(VI) was present in the surface layers. The quality of the data obtained during a single 30 min scan on a sample with an approximate monolayer of Cr attests to the sensitivity of the new technique.

Electronic properties of passive films on Fe and Fe-Cr alloys

ReflEXAFS measurements at the oxygen K-edge have been carried out on thin films formed on pure iron. Since the oxygen K-edge and the Fe $L_{II,III}$ edges are only about 170 eV apart, these data are generally not optimal for EXAFS analysis, but they can be very useful for the study of near edge (NEXAFS) fine structure which provides information about electronic transitions.

The oxygen near edge structure of thin films formed in nitrite and chromate and in borate borate buffer by anodic polarization have been measured. Although a more detailed analysis is currently in progress, it is immediately evident that the films formed in borate buffer and nitrite solutions are electronically closely related because of the appearance of a similar excitonic feature on the absorption edge (Fig. 1). For the film formed in chromate, three features are evident on the oxygen-K absorption edge in Fig. 1. We have shown earlier that chromium is present in the passive film on Fe formed in chromate passivation solution (2). Since there is oxygen-bonding between O-Fe and O-Cr, it is natural to assume that the additional features are due to the O-Cr bonds. Further, the O-Fe feature is shifted to slightly higher energy.

The oxygen K-edge spectrum measured for the air formed film on Fe looked very similar to the spectrum from the nitrite-formed film, with the excitonic peak less-pronounced than in the borate case. Only when the films were produced under potentiostatic control in borate-buffer solutions were we able to reduce the air-formed film. (Of course, the time in air was kept to minimum for the passivating solution preparations.)

Since chromium ions were present in the chromate-formed film on pure iron, it was natural to compare these results with films formed on Fe-Cr alloy. The data on films formed in borate on Fe-14% Cr and Fe-24% Cr showed differences with films formed in chromate on iron. The edge structure of the film on Fe-14% Cr was more similar to that of a film on Fe formed in borate than for a film formed in chromate (Fig. 2). The film on Fe-24% Cr showed even less edge structure. Because the air-formed film could not be reduced from the alloy, we were concerned that these effects might be due to that, but the edge structures for the Fe-Cr alloys are less pronounced than for an air-formed film on iron.

Effect of chloride during breakdown induction period

When chloride ions are added to the solution, the edge structures change further (Fig. 2). Even though we have not analyzed these data in detail for Fe-14% and Fe-24% Cr as yet, we find the fact that the edge structure changes can be detected to be very encouraging because the structural effects in the early part of breakdown are subtle (see arrows in Fig 2). Therefore it appears that the electronic effects occurring during breakdown are clearly visible for the passive layer on the alloy Fe-14% Cr (Fig 2). Virtually no effects due to Cl^- was found for the Fe-24% Cr alloy. This is not too surprising since optical studies by McBee and Kruger (2) found that breakdown effects are much less pronounced and take much longer times to become evident as the Cr content increases.

We are grateful to the National Science Foundation for their partial support of this work.

REFERENCES

1. G. Martens and P. Rahe, Phys. Stat. Sol., A58, 415 (1980).

2. C.L. McBee and J. Kruger, in "Passivity and its Breakdown on Iron and Iron Base Alloys" Staehle and Okada, Eds., Nat. Assoc. of Corros. Engrs., 1976, p. 131.

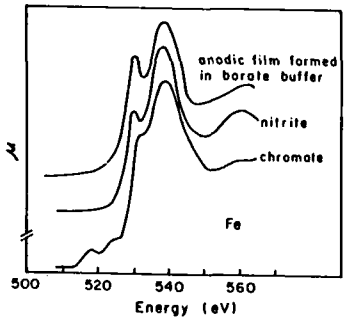


Fig. 1 The oxygen near edge structure of passive films formed on Fe in nitrite and chromate solutions and in borate buffer by anodic polarization.

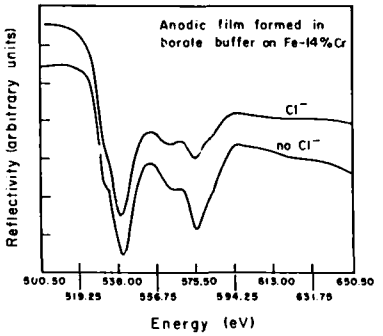


Fig. 2 The effect on the near edge structure by the addition of chloride ions on the anodic film formed on Fe-14%Cr in borate buffer.

Abstract No. 124

A VARIABLE ANGLE XPS STUDY OF ACTIVE, PASSIVE AND TRANSPASSIVE Ni SURFACES

Martin A. Helfand and Clive R. Clayton

Department of Materials Science
and Engineering
State University of New York at Stony Brook
Stony Brook, New York 11794-2275

Nickel is an element of tremendous technological importance because of its mechanical and catalytic properties, in addition to its ability to resist degradation. Nickel's resistance to dissolution is attributable to the formation of a passivating film. Therefore the nature and composition of the film is of considerable interest, and has been examined by numerous investigators and techniques. Unfortunately, there is considerable controversy in the literature regarding both the passivation potentials and the species responsible.

In this study the surfaces of pure (99.999%) polycrystalline Ni (Materials Research Corp.) were examined with X-ray photoelectron spectroscopy (XPS) at six photoelectron take-off angles; 10^{o}, 20^{o}, 30^{o}, 40^{o}, 50^{o} and 60^{o}, measured with respect to the plane of the sample surface. Decreasing the angle of take-off enhances the signals obtained from the outermost regions of the surface (1). Separate freshly prepared Ni electrodes were analyzed following various surface treatments which are as follows; mechanical polishing, cathodic polarization, and anodic polarization at active, passive and transpassive polarization. The primary electrolyte utilized was deaerated 0.1M H_2SO_4. All specimens were transferred to the vacuum system anaerobically to prevent further modification of the electrochemically formed species.

The primary motivation behind this study was to determine how consistently well variable angle XPS can describe the physical state of the surface following passivation and dissolution. The data yielded information regarding the morphology of the film including the distribution of S within it. In addition, following the work of Fadley (2), the variable angle data also provided surface roughness information. A surface roughness index was assigned to each of the cases examined. A knowledge of the physical state of the surface is essential in developing a model to accurately predict the dissolution process.

The results obtained here indicate that passive and transpassive Ni surfaces are composed of a bilayer film, consisting of an NiO inner layer and $Ni(OH)_2$ outer layer. The prepassive or active Ni surface was observed to consist solely of $Ni(OH)_2$. While these finding are consistent with some (3), they are contradictory with others (4).

Acknowledgements

This work was supported by the National Science Foundation under contract DMR 8418873 administered by Dr. Bruce MacDonald. The V.G.S. electron spectrometer and V.G.S. 1000 data system were acquired from N.S.F. equipment awards DMR 7718319 and DMR 8117321.

References

1. Castle, J.E., Clayton, C.R., Corr. Sci., 16(7) (1977).

2. Fadley, C.S. Prog. in Solid State Chem., 11, 265 (1976).

3. Dickinson, T., Povey, A.F., Sherwood, P.M.A., J. Chem. Soc. Faraday Trans. I, 73, 327 (1977).

4. Melendres, C.A., Paden, W., Tani, B., Walczak, W., J. Electrochem. Soc., 134, 762 (1987).

Abstract No. 125

Investigation of the Growth of Porous Oxide Films on Different Pretreated Al Surfaces.

Terryn, H., Vereecken, J.
Dept. of Metallurgy, Electrochemistry and Materials Science
Vrije Universiteit Brussel
Pleinlaan 2, B-1050 Brussels, Belgium

Vanhellemont, J., Van Landuyt, J.
Centre for High Voltage Electron Microscopy
Universiteit Antwerpen, RUCA
Groenenborgerlaan 171, 2020 Antwerpen, Belgium

TEM studies, performed by Thompson and Wood, on the growth of porous layers in sulphuric and phosphoric acid permitted a detailed description of the initial barrier layer formation and pore initiation processes [1]. The films were basically formed upon electropolished aluminium surfaces to obtain reproducible flat surfaces. Such studies pointed out that the dimensions of the porous structure are dependent on the anodizing conditions. More specifically it was found that pore and cell diameter and barrier layer thickness are in proportion to the anodizing voltage.

Additionally, the composition and roughness of the aluminium substrate may have an influence on the anodic oxide film formation. Although a significant part of the literature deals with the growth of the porous layer, little information is available about the role of the substrate roughness. Roughness is of practical importance in many industrial applications such as in preparing lithographic printing plates and electrolytic aluminium capacitors.

This part of the study was focused on the growth of the porous layers on relatively rougher surfaces, prepared by two different industrial pretreatment processes: rolling and AC electrochemical etching. During AC electrograining, the aluminum is polarized under alternating current conditions in an electrolyte such as hydrochloric acid, which assists in the controlled production of a relatively high population density of pits in the presence of chloride anions which are aggressive to the aluminium metal [2,3,4]. Such treatments tend to introduce topographical and compositional heterogeneities on the Al surface.

The different Al_2O_3 interfaces were examined by means of high voltage electron microscopy at an accelerating voltage of 1000 keV. Cross-sectional specimens of the anodized samples were obtained with a completely different sample preparation technique, based on sawing and subsequent ion thinning of the sample, in contrast to the commonly used ultramicrotome [2]. The discussion of the results allows comparison of the two techniques.

The transient potential-time curves, obtained during the growth of the porous layers allow differentiation between different pretreated aluminium surfaces. This is illustrated in figure 1 for the growth of a porous film in phosphoric acid on respectively rolled and AC etched aluminium, with and without cleaning of the etch products. The corresponding HVEM observations are represented in figure 2 a and b. Examination of the different morphologies proved that the steady-state anodic film morphology, consisting in hexagonal cells with a central pore is valid on all treated aluminum substrates. The initial non-steady-state situation, during which the incipient pores are formed, is found at the outer surface of the oxide film. The initiation of these incipient pores is related with the aluminium substrate morphology, induced by the pretreatment process. Figure 3 shows for example the morphology of the incipient pores on a rolled aluminium substrate. Extensive and quicker pore initiation occur above these lines present on the rolled aluminium surface. If the aluminium surface is smut with etch products, inhibition of the initial anodic film formation is noted. The remnant of the etch products are found at the outer surface of the oxide film (figure 4).

Acknowledgement

Authors greatfully acknowledge Agfa Geveart for financial support.

References

1. Thompson, G.E. and Wood, G.C., "Anodic Films on Aluminium", Chap.5 "Treatise on Material Science and Technology", ed Scully, J.C., Academic Press, London, Vol. 23 (1983) p. 205.
2. Terryn, H. , Vanhellemont, J. , Vereecken J., Van Landuyt J.,"Aluminium Surface Treatments Technology", eds. Alwitt, R.S. and Thompson, G.E., Electrochem.Soc. ,Pennington (1986) p.291.
3. Terryn, H., Vereecken, J. and Thompson, G.E., to be published

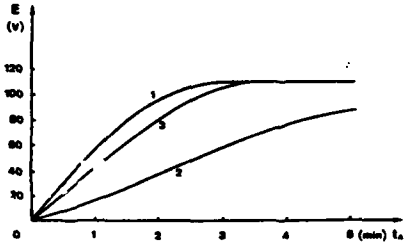


Figure 1 Voltage-time transient curves, obtained on different pretreated aluminum surfaces (anodizing conditions; 0,4 M H_3PO_4, temperature 22 °C, current density 100 A/m^2) 1-rolled, 2- AC grained, 3- AC grained+cleaned

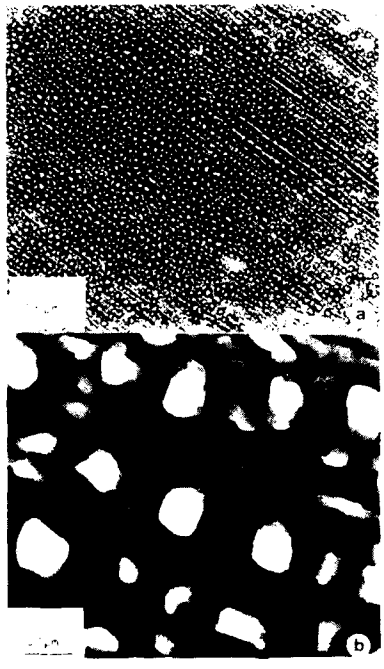


Figure 3 HVEM plan views of a stripped porous film formed on rolled Al.
a-low magnification
b-high magnification



Figure 2 a Cross-sectional HVEM micrograph of a porous film formed on rolled Al.



Figure 2 b Cross-sectional HVEM micrograph of a porous film formed on AC grained Al.



Figure 4 Cross-sectional HVEM view of a porous film, covered with the remnants of etch products.

Abstract No. 126

On the Influence of Surface Nitrides on Anodic Kinetics

R.D. Willenbruch, M. Oversluizen and C.R. Clayton*

Department of Materials Science and Engineering
State University of New York at Stony Brook
Stony Brook, New York 11794

Surface nitrides have been generated on the surface of high purity samples of Fe, Cr, Ni and Mo and on the surface of types 304, 317LX, 904L and AL6X stainless steel. The technique employed cathodic reduction of the pre-existing surface oxide films in 0.1M HCl followed by continued cathodic polarization following addition of 0.5M $NaNO_3$. The reduction of NO_3^- to N^{3-} results in surface nitride formation. Anodic polarization was then performed in deaerated 0.1M HCl to determine the influence of the surface nitride on the anodic kinetics. XPS analysis of the nitride surfaces following cathodic treatment and anodic scanning to 0mV (SCE) was performed in order to determine the nature and degree of retention of the surface nitride. The mechanism by which surface nitrides modify the anodic kinetics of pure metals and stainless steel is discussed.

Acknowledgements

This work was supported by a grant (N0001485K0437) from the U.S.O.N.T. (Dr. A.J. Sedriks, Contract Officer).

Abstract No. 127

A.C. IMPEDANCE MEASUREMENTS IN LOW CONDUCTIVITY MEDIA : EXPERIMENTS AND MODEL

S. CHECHIRLIAN, H. MAZILLE
Laboratoire de Physico Chimie Industrielle, INSA, 69621 VILLEURBANNE Cédex, FRANCE.

P. EICHNER
Rhône-Poulenc Industrialisation, Centre de Recherches de Décines, BP 166, 69151 DECINES Cédex, FRANCE.

M. KEDDAM, H. TAKENOUTI, LP 15 du CNRS "Physique des Liquides et Electrochimie, UPMC, tour 22, 4 place Jussieu, 75252 PARIS Cédex 05, FRANCE.

It is commonly experienced that cell impedance in the high frequency (H.F.) range (f > 10 kHz) exhibits beyond the series electrolyte resistance Re one or several loops irrelevant to the electrode process (1, 2, 3, 4). In low conductivity media encountered in spreading corrosion studies (natural waters, organic, ...) these relaxations overlap the faradaic range thus making interpretation of data extremely questionable (3). This problem was dealt with here in the framework of the corrosion study of austenitic stainless steel (304 L and 316 L) in concentrated acetic acid (ACOH).

EXPERIMENTAL

Cell : Cylindrical with axial R.D.E. (W.E.) 1.13 cm in diameter embedded in a Teflon sheath (2 cm in diameter). Counter-electrode (C.E.) is a platinum mesh covering the cell walls (lateral + bottom). Reference electrode (R.E.) was either a Ag/Ag Cl in (ACOH + 0.1 M $LiClO_4$) + Luggin capillary or the tip of a Pt wire (0.05 cm in diameter).

Electrolytes : 100 % ACOH (ρ = 12 MΩ.cm) or 80 % ACOH (ρ = 0.2 kΩ.cm) with no chemicals addition.

Measurements set-up : Solartron equipment (1286 interface + 1250 FFA).

RESULTS

R.E. arrangement, electrolyte resistivity and distance x from R.E. tip and S.S. surface were investigated.

Ag/AgCl + Luggin capillary as R.E.

80 % ACOH : Fig. 1 gives a set of diagrams as a function of x. All plots display a H.F. capacitive arc with constant size and frequency spacing followed by a M.F. loop which changes from capacitive to inductive shape as x is decreased. The L.F. branch represents the true interface capacitance. Re estimated by the Newman's formula is given by the intercept of this L.F. branch on the real axis at frequency close to 100 Hz.

100 % ACOH : Similar results are shown in Fig. 2. Frequencies are shift towards lower values whilst the inductive behaviour dominates the range usually covered by faradaic impedance.

Pt wire as R.E.: Fig. 3 shows the results corresponding to Fig. 1. The side effect is wellknown in fairly conductive electrolytes (capacitive loop at large x) or cell with very small impedance of W.E. (inductive loop at small x).

MODELLING

The behaviour shown in Fig. 1 represents the whole range of possible features. It has been modelled by the network shown in Fig. 4. Similar approach was proposed in (1) but C_2 was neglected. The impedance actually measured is calculated as $Z_{exp} = E_{RE}/I$. As point out in (1) the inductive behaviour is due to C_1.

As proved by Fig. 5 and 6 the model restitutes with an excellent precision the experimental data when the distance x and electrolyte resistivity are simulated by varying the resistancesvalues. The H.F. capacitive arc ($(R'e + Re)C_1/(C_1 + C_2)$) in diameter arises from the frequency dependence on the dividing bridge $C_1/(C_1 + C_2)$ applied to the entry voltage across ($R'e + Re + C_{dl}//R_p$). Increasing x is simulated by the ratio Re/R'e at constant (Re + R'e).

REFERENCES

1. H. GÖHR, M. MIRNIK and C.A. SCHILLER
J. Electroanal. Chem., 180, 279 (1984).

2. B.B. SAVOVA-STOYNOV and Z.B. STOYNOV
J. Appl. Electrochem., 17, 1150 (1987).

3. J.P. DE SOUZA, O.R. MATTOS, L. SAHTLER and H. TAKENOUTI
Corros. Sci., 27, 1351 (1987).

4. C. FIAUD, M. KEDDAM, M. KADRI and H. TAKENOUTI
Electrochim. Acta, 32, 445 (1987).

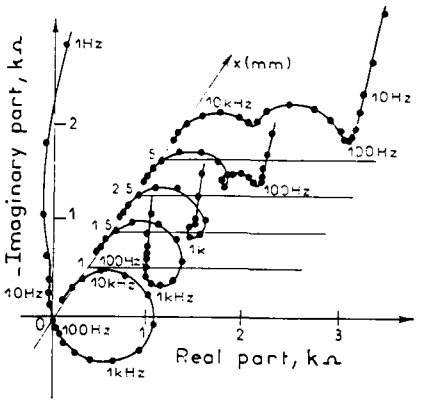


Figure 1 : Impedance diagrams as a function of the distance x between the tip of the capillary and the electrode surface. Reference electrode : Ag/AgCl/0.1M $LiClO_4$. Acetic acid 80 %, ρ = 10.2 kΩ.cm.

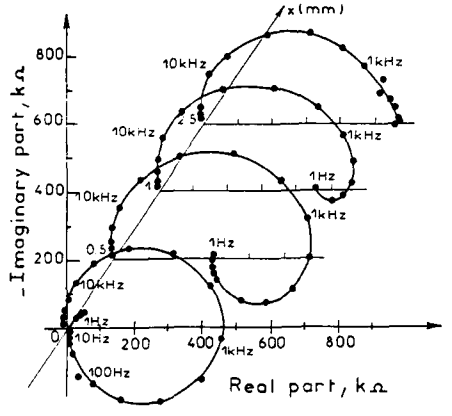


Fig. 2 : Conditions identical to Fig. 1. Acetic acid 100 % ; ρ = 12 MΩ.cm.

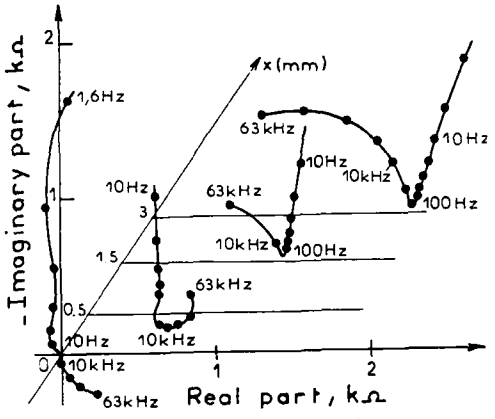


Fig. 3 : Conditions identical to Fig. 1. Reference electrode : Pt wire.

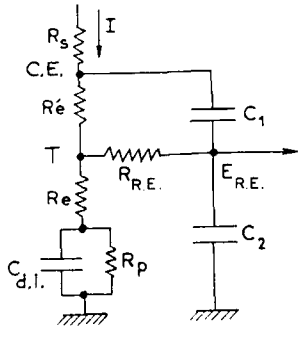


Fig. 4 :

Electrical network simulating the H.F. impedance of the cell.

Re, R'e : electrolyte resistances.

T : tip of R.E.

C_1 and C_2 : stray capacitances between R.E. and C.E. (C_1), and W.E. (C_2).

R_{RE} : resistance of R.E.

C_{dl}/R_p : faradaic impedance of W.E.

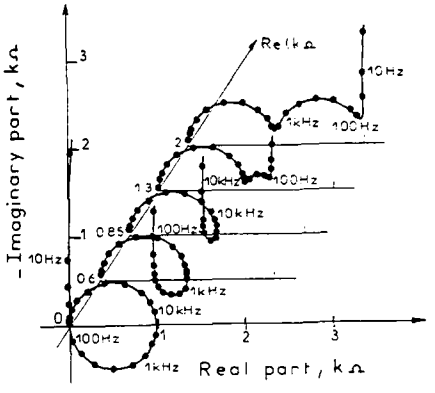


Fig. 5 : Simulated diagrams corresponding to Fig. 1.

C_1 = 1 nF ; C_2 = 3 nF ;

Re + R'e = 4 kΩ ; R_{RE} = 100 kΩ.

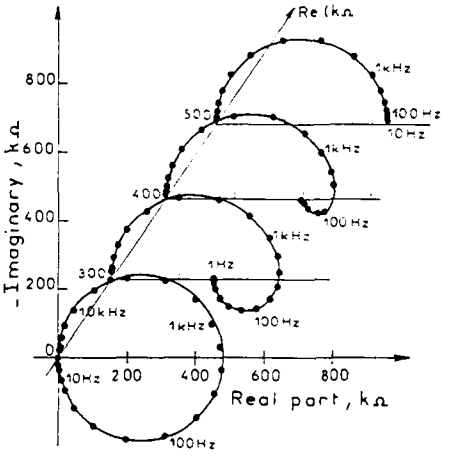


Fig. 6 : Simulated diagrams corresponding to Fig. 2.

C_1 = C_2 = 0.1 nF

Re + R'e = 1 MΩ

R_{RE} = 1 MΩ

Abstract No. 128

Technique for Estimating Salt-Air Corrosion Rate

Y. Miyata, R. Takekoshi, H. Takazawa and K. Arita
NTT Technical Assistance and Support Center
9-11 Midori-Cho 3-Chome, Musashino-Shi, Tokyo 180 Japan

1. Introduction

Salt damage[1] is a serious problem for metallic materials used in outdoor facilities in island countries such as Japan. Sea salt mainly determins corrosion rate. This rate varies with distance from the sea[2], and ranges from severely damaging in coastal areas to mildly damaging in inland areas. It also varies with the climate at individual places. Therefore, few studies have estimated corrosion rate by investigating the synthesis of the effects of each corrosion element. This paper discusses a method for estimating metal corrosion rate based on the results of our nationwide exposure test.

2. Estimating the Corrosion Rate

2-1 Basic Data

Exposure corrosion tests were conducted to collect basic data on metal corrosion in 21 areas throughout Japan as shown in Fig. 1(a). Plates of Hot-dipped galvanized steel, a widely used anticorrosion material, were used. The plate dimensions were 50 mm×100 mm×3 mm. The results of 1 and 2-year exposure tests were used to estimate the corrosion rate. The estimation functions were also used to estimate the distribution of sea-salt particle levels at 30 areas in Choshi City, Chiba Prefecture as shown in Fig. 1(b).

2-2 Corrosion Elements

The main factors which affect corrosion rate are sea-salt particle levels, temperature, moisture, and precipitation. Except for sea-salt particle levels, this data can be obtained from standard meteorological data. Sea-salt particle levels can be evaluated using wind direction and velocity, which are also meteorological data, and the distance to the coast, which can be obtained from a topographical map. Monthly averages of meteorological data were used to simplify the estimates and to reflect seasonal weather variations.

2-3 Estimation of Sea-Salt Particle Levels

Sea-salt particles are transferred by wind. Their direction and speed change constantly. We assume that the wind can be resolved into two vectors: an invariable component with average direction and speed (wind-1), and a second component with a constantly varying velocity (wind-2). Then the steady-state distribution of sea-salt particles can be formulated using the followwing partial differential equation.

$$D\left(\frac{\partial^2 C}{\partial X^2}+\frac{\partial^2 C}{\partial Y^2}\right)+V_x\frac{\partial C}{\partial X}+V_y\frac{\partial C}{\partial Y}-KC=0 \quad (1)$$

where C = the amount of floating sea-salt particles, D = diffusion constant due to wind-2, Vx and Vy represent the components of wind-1, and K = the ratio of particles falling to the ground within a unit time.

Based on this equation, the elliptical distribution is given as shown in Fig. 2. The function to estimate sea-salt particle distribution is formulated to add up all elements from the sea in 16 directions. The observed particle levels shown in Fig. 1 were used in a multivariate analysis to determine optimum coefficients for these functions. The correlation coefficient between estimated and observed values is 0.89 as shown in Fig. 3.

2-4 Estimation of the Metallic Corrosion Rate

Atmospheric corrosion, including salt damage, can be classified as wet corrosion. Wet corrosion progresses with water film on the surface acting as a medium which helps the flow of corrosion current due to local-action cells. The water film thickness is closely related to the atmospheric moisture level. Therefore corrosion does not progress at a constant rate, but changes with the moisture level. Changes in corrosion rate during the day as monitored with chemical impedance measurements[3],[4] are shown in Fig. 4. They indicate that dew formation and rainfall are the most important factors in the average corrosion rate. Therefore the approximation shown in Fig. 5 serves as a model for the progression of atmospheric corrosion. Total corrosion is described as

$$F = A\,f_1(m)\,f_2(T)\,f_3(C) + B\,f_4(r)\,f_2(T)\,f_5(C) \quad (2)$$

where m = moisture, T = temperature, C = sea-salt particle level, r = the number of rainy days, and A and B are the proportional constants. Each element's effect on corrosion rate is represented by one of the independent functions, f_1, ---, f_5.

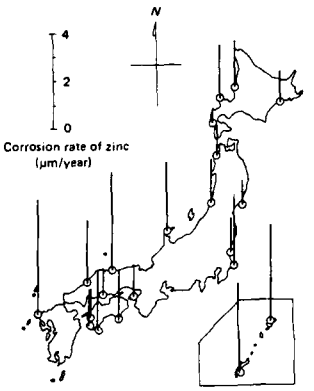
Each coefficient described in Eq. (2) is set to maximize the correlation coefficient between the logarithm of the estimated corrosion degree and the test data. The relationship between two corrosion levels is shown in Fig. 6. 80% of the test data values corresponds to the estimated values with an accuracy of ±30% accuracy.

3. Conclusion

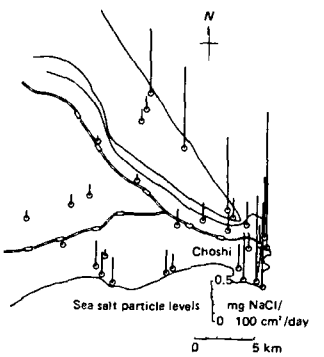
Functions to estimate corrosion rate have been formulated. These functions use variables that are easily obtained from meterological data, and distances to the coast obtained from topographic maps. These functions estimate the salt-damage-related corrosion rate for metallic materials to within ±30% accuracy.

REFERENCES

(1) Yu. M. Panchenko and L. A. Shuvakhina: Zashch. Met., 20, 5, p.748, 1984.
(2) S. Yasukawa, K. Kato, M. Yamada and H. Imaizumi: Boshoku Gijutsu (in Japanese), 29, 6, p.337, 1980.
(3) S. Haruyama, T. Tsuru and M. Anan: Boshoku Gijutsu (in Japanese), 27, 9, p.449, 1978.
(4) K. Hladky and L. M. Callow: Brit. Corros. J., 15, 1, p.20, 1980.
(5) P. R. Vassie and M. Mackenzie: Corros. Sci., 25, p.1, 1985.



(a) Exposure corrosion test results



(b) Sea-salt particle level observation results

Fig. 1 Basic data used to develop corrosion-rate estimation

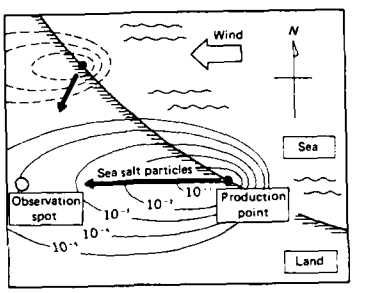


Fig. 2 Simulation results and estimation model of sea-salt particle distribution

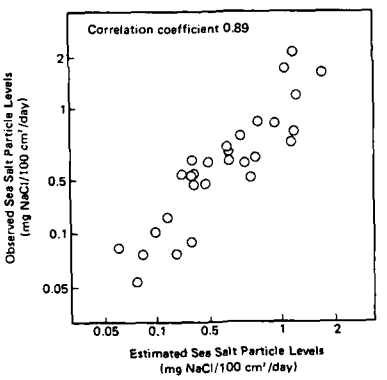


Fig. 3 Accuracy of sea-salt particle estimation function (1-year average)

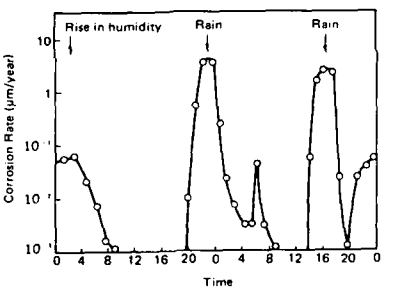


Fig. 4 An example of changes in atmospheric corrosion rate during the day (monitored by measuring the chemical impedance of the corroding surfaces)

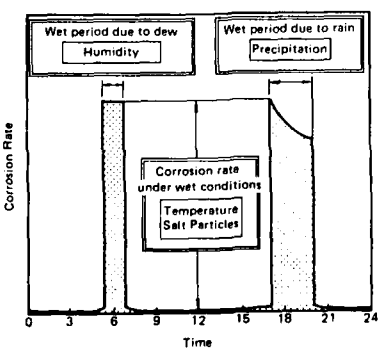


Fig. 5 Progression model for atmospheric corrosion (shadowed area indicates amount of corrosion)

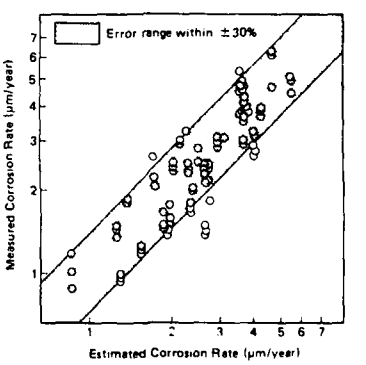


Fig. 6 Effect and accuracy of corrosion-rate estimation for zinc

Abstract No. 129

A NEW ELECTROCHEMICAL TECHNIQUE FOR RAPIDLY EVALUATING PROTECTIVE COATINGS ON METALS

Changjian Lin* and Tinh Nguyen

National Bureau of Standards
Gaithersburg, MD 20899

*Guest Worker from Xiamen University, Xiamen, China

Despite widespread applications of organic coatings for corrosion protection of metallic substrates, no universally acceptable method exists for evaluating their corrosion protective performance. One of the main reasons for this void is that the performance of an organic protective coating system is dependent upon many factors, including properties of the metal substrate, the coating, the metal/coating interactions, and the environments to which it is exposed.

Techniques used for evaluating the effectiveness of corrosion protection of coated metals can be divided into two main groups: non-electrochemical and electrochemical. Since many failures of a coating system, such as blistering, cathodic delamination, and corrosion are controlled by the conducting (or resistant) properties of the coating and the electrochemical processes occurring at the metal/coating interface, evaluation techniques based on the electrochemical principles may provide useful means to assess the protective ability of a coating against corrosion of a metal. Indeed, work at Lehigh University has shown that there is a direct relationship between the conductivity of the coating and the rate of corrosion.

Since corrosion of coated metal is a complicated phenomena, single technique may not be adequate to evaluate the corrosion protection of a particular system. It is necessary to combine various techniques, including non-electrochemical techniques, to more effectively evaluate the corrosion protection performance of coating systems for metals. In this study, a new electrochemical technique, the multicyclic potentiodynamic polarization (MCPDP) technique, was used to evaluate the corrosion protection ability of coatings on metal.

In the multicyclic potentiodynamic polarization technique, the applied potential scans forward, starting at the corrosion potential, and continues in the positive (anodic) direction. When it reaches a preprogrammed positive potential value, it reverses and begins in a negative (cathodic) direction, past the corrosion potential. When it reaches a preprogrammed negative potential, it reverses and scans in the positive direction again. This cycle may be repeated many times until the polarization current (anodic or cathodic) occurred. The scanning times and the polarization currents are recorded. The current and scanning times are compared for a set of samples. The lower the polarization current at any particular scanning time, or the longer the scanning time at the same polarization current, the better the corrosion resistance of the coating. The parameters of measurement can be changed depending upon the requirements of the samples. The scanning rate is typically between 1mV/sec. and 100mV/sec. In this study, positive potentials between 0.8 and 1.8V and negative potentials between - 0.8 and - 1.8V were selected.

This paper presents the results of preliminary studies to develop the method and apply it to assessments of several key factors which contribute to the performance of coating systems; these include coating type, coating thickness, curing conditions, substrate surface contamination, and defects in the coating.

Abstract No. 130

Corrosion Inhibition and Adsorption Behaviour of Some Thioamides on Mild Steel in H_2SO_4

B.E. El-Anadouli, F.M. Eltaib Heakal, F.M. El-Nizami and B. G. Ateya
Chemistry Department, Faculty of Science,
Cairo University, Cairo, Egypt.

Introduction and Objectives:

The use of organic sulfur compounds as metallic corrosion inhibitors has been widely investigated [1-4]. Particular attention was often paid to compounds containing thioamide functional groups e.g. thiourea and its derivatives. We have been interested in studying the effects of a series of such compounds on the corrosion kinetics of mild steel in H_2SO_4. These compounds are: thioacetamide (TA), $CH_3.C : S.NH_2$, thiourea (TU), $H_2N.C : S.NH_2$ and thiosemicarbazide $H_2N.NH.C : S.NH_2$. We measured the effects of these compounds on the polarization curves, corrosion current and potential, activation energy and polarization resistance at various concentrations and temperatures. The adsorption behaviour of thiourea and its effects on the corrosion kinetics were reported elsewhere [5,6]. The purpose of the present work is to evaluate the effects of thioacetamide and thiosemicarbazide on the corrosion kinetics of mild steel. Furthermore, their adsorption behaviour was analysed in order to choose the appropriate adsorption isotherm and hence determine the free energy of adsorption. Subsequently the results are to be compared with those obtained on thiourea. The similarities and difference, are discussed in view of the differences in the molecular structure of the compounds.

Adsorption isotherms:

A knowledge of the adsorption behaviour of these inhibitors is necessary to understand their inhibitive action. The surfaces of metals in aqueous solutions are alwasys hydrated with adsorbed water dipoles. Consequently, the adsorption of an organic inhibitor on the metal surface requires the displacement of a number of water molecules. It is regarded as a substitutional adsorption process i.e.

$$Org_{(sol.)} + x\, H_2O_{(ads)} \rightleftharpoons Org._{(ads)} + x\, H_2O_{(sol.)} \quad (1)$$

where x is called the size ratio which is the number of water molecules displaced by one molecule of the organic adsorbate. It is also viewed as the ratio between the corss-sectional area of the organic molecule to that of water when adsorbed on the metal surface. There are many isotherms which can be used to describe the above equilibrium e.g. the Frumkin [7], the Flory-Huggins [8], the Bockris-Swinkels [9] and the Parsons [10] isotherms, or modifications of them, equations 2-5, respectively.

$$\frac{\theta}{1-\theta} \exp(-2a\theta) = KC \quad (2)$$

$$\frac{\theta}{e^{x-1}(1-\theta)^x} = KC \quad (3)$$

$$\frac{\theta}{(1-\theta)^x} \cdot \frac{[\theta + x(1-\theta)]^{x-1}}{x^x} = KC \quad (4)$$

$$\frac{\theta}{1-\theta} \exp\left[\frac{2-\theta}{(1-\theta)^2} - 2a\theta\right] = KC \quad (5)$$

where θ is the degree of coverage of the metal surface with inhibitor and a is the coefficient of lateral interaction. The adsorbability K is related to the standard free energy of adsorption, G^o_{ads} by:

$$K = (1/55.5) \exp(-\Delta G^o_{ads}/RT) \quad (6)$$

Inspection of the above isotherms reveals that the free energy of adsorption, ΔG^o_{ads} depends on both X and θ. Improper choice of X and/or a results in erroneous values of ΔG^o_{ads}. A reasonable estimate of X may be obtained from consideration of the structure of the compound e.g. bond lengths and bond angles.

Test of isotherms:

The configurational factors of the various isotherms (l.h.s. on equations 2-5) are essentially functions of coverage θ and size ratio X, i.e. $f(\theta, X)$. The above isotherms may be converted into the general equation

$$\ln\left[\frac{f(\theta, X)}{C}\right] = -\frac{\Delta G^o_{ads}}{RT} + 2a\theta \quad (7)$$

where a is the coefficient of lateral interaction. The most suitable isotherm was chosen by fitting the experimental data (coverage-concentration-temperature) to Equation 7. The function $f(\theta, X)$ is evaluated at various values of X, and the l.h.s. of equation 7 plotted versus coverage θ. A straight line was obtained invariably indicating the validity of the isotherms. The lateral interaction coefficient a is given by the slope of the straight line. At 20°C, the best fit was obtained with X=2 for the three inhibitors with significant lateral (repulsion) interaction; the computed a values are about equal for thioura and thioacetamide while a considerably greater value was obtained for thiosemicarbazide. The value of X=2 means that two water molecules are displaced for each inhibitor molecule. Since the cross-sectional area of a water molecule is about 12.5 A^{02}, it follows that at 20°C the inhibitor molecule occupies an area of about 25 A^{02}. Comparison of this area to those predicted by molecular models indicates that the inhibitors are adsorbed vertically i.e. the thio-carbonyl group >C=S is held perpendicular to the metal surface. On the other hand, at temperatures of 30-50°C the best fit was obtained with X=4 and $a \simeq 0$ i.e. no lateral interaction. Under these conditions, the area occupied by each inhibitor molecule is about 50 A^{02} which is compatible with planar adsorption. With this orientation the molecular dipoles are parallel to the metal surface, hence they do not excercise lateral interaction with each other. Further details, analyses and interpretations are to the presented.

References

1. G.G. Eldredge and J.C. Warner, in Corrosion Handbook, H.H. Uhlig, Editor, p. 905, Wiley, New York (1948).
2. J.N. Putilova, S.A. Balezin and V.P. Brannik, Metallic Corrosion INhibitors, Pergamon Press, Oxford (1960).
3. G. Trabanalli and V. Carassiti, Advances in Corrosion Science and Technology, M.G. Fontana and R. Staehle Editors, p. 147, Plenum Press, New York (1970).
4. I.L. Rozenfeld, Corrosion Inhibitors, McGraw-Hill, New York (1981).
5. B.G. Ateya, B.E. El-Anadouli and F.M. El-Nizamy, Corros. Sci. 24, 497 (1984).
6. Ibid 24, 509 (1984).
7. A. Frumkin, Z. Physik. 35, 792 (1926).
8. H.P. Dhar, B.E. Conway and K.M. Joshi, Electrochim. Acta 18, 789 (1973).
9. J. O'M. Bockris and D.A.J. Swinkels, J. Electro. Chem. Soc. 111, 736 (1964).
10. R. Parsons, J. Electroanal. Chem. 7, 136 (1964); ibid 8, 93 (1964).

Abstract No. 131

Rapid Evaluation of Iron Corrosion Rate in Solution Containing Inhibitors by Using Coulostatic Method

Yuichi Sato, Tomoyoshi Hamada, Shoichi Sugiyama, Takehiro Owa and Koichi Kobayakawa

Department of Applied Chemistry, Faculty of Engineering, Kanagawa University

Rokkakubashi, Kanagawa-ku, Yokohama 221 Japan

Introduction

The polarization resistance method of obtaining metal corrosion rates in solution is a familiar electrochemical technique. However, it involves several problems, such as an ohmic drop correction and the length of time involved in the case of a low corrosion rate(1). To overcome these defects, the coulostatic method was successfully applied to corrosion rate measurement(2).

The applicable range of the method is not so clear. To expand its applicability to a wide range of corrosion systems, we tested the method by measuring the corrosion rates of steel in water containig various types of corrosion inhibitors and confirmed that the results gave good agreement with those obtained by the weight loss method.

Experimental

When a small charge pulse is supplied to the electric double layer of a corroding metal, the potential jumps from the corrosion potential to another potential. The overvoltage immediately after charging is a function of the double layer capacity of the metal and is given as follows:

$$\eta_0 = \Delta q / Cd \qquad [\ 1\ ]$$

where η_0 is the initial overvoltage, Δq is the supplied charge and Cd is the double layer capacity of the test piece. The charge increment is then consumed progressively by the corrosion reaction, which causes the potential to drift back to the corrosion potential, Ecorr. This potential decay, η_t, proceeds exponentially with time,t, according to the next equation,

$$\eta_t = \eta_0 \exp\{-t/(CdRp)\} \qquad [\ 2\ ]$$

where Rp is the polarization resistance. By using equation [1] and [2], Cd and Rp can be obtained. For the calculation of the corrosion current density, icorr, anodic and cathodic Tafel slopes are necessary, which can also be determined by the coulostatic method(3).

In the Tafel slope measurement, the amount of charge is chosen to yield a 50 mV or larger overvoltage in order to eliminate the effect of the opposite reaction. The final formula for calculating the Tafel slope is given in Eq.3.

$$\beta = \Delta\eta / \log\{(t_3-t_2)/(t_2-t_1)\} \qquad [\ 3\ ]$$

where $\Delta\eta$ is an arbitary interval of overvoltage which divides the decay curve, t_1, t_2 and t_3 are read three succeeding time from these cuceeding points, as shown in Fig.1 The value of $\Delta\eta$ is usually from 5 to 10 mv. To obtained the anodic Tafel slope, βa, a test piece is polarized in the anodic direction and in the reverse direction for the cathodic Tafel slope, βc. Both βa and βc can be calculated in the same manner, using Eq.3. Thus, a corrosion current density can be obtained by following the Stern-Geary formula.

$$icorr = \frac{\beta a \cdot \beta c}{2.3(\beta a+\beta c)} Rp^{-1} \qquad [\ 4\ ]$$

The overvoltage decay curves necessary for calculating the polarization resistance and Tafel slopes were measured by using a corrosion meter(Hokuto Denko HK-201) which could apply a given amount of electric charge to a test piece in solution, a transient time converter(Riken Denshi TCC-1000-11) and a Y-t recorder. Commercially available steel coupons(JIS SS41) were used as test pieces, which were also used as a counter electrode. Two steel coupons immersed in the solution were measured alternately as a test electrode. A saturated calomel electrode was used as a reference electrode. The solution used in experiments(see Table 1) were made from reagent grade chemicals with distilled water. All measurements were carried out at a room temperature(26±2°C) under atmospheric pressure without expelling dissolved oxygen in the solution.

Results and Discussion

A typical overvoltage-time curve to obtain Rp value is reproduced in Fig.2, which is measured in 0.1% NaCl solution containig 100 ppm $K_2Cr_2O_7$. Qualitatively, the potential decays fast to initial value(Ecorr), if the corrosion rate is high. The log η_t-t plot obtained from Fig.2 indicates a good linearity in agreement with logarithmic equation of Eq.2(Fig.3). By extrapolating log η_t plot to t = 0, the value of η_0 was found to be 3.7 mV, from which differential capacity Cd was calculated as 1.36 F/m². Polarization resistance, Rp, was deduced as 0.93 Ωm² from the slope of log η_t plot, shown in Fig.3 with the aid of Cd value. Then the Tafel slopes were obtained. In Fig.4, anodic and cathodic overvoltage-time curves for steel in 0.1% NaCl solution containing 100 ppm $K_2Cr_2O_7$ are shown, by which the Tafel slopes are calculated, showing βa is equal to 30.1 mV and βc is equal to 23.9 mV respectively with the aid of Eq.3. From Eq.4, icorr computed is 7×10^{-4} A/m². Fig.5 shows time dependence of icorr for steel in 0.1% NaCl solution containing 100 ppm $K_2Cr_2O_7$. This system is in inhibited condition and the corrosion rate is almost constant with time. The corrosion rate for each system was calculated and averaged for the total immersion period. At the same time, the corrosion rate by the weight loss method for the same test pieces were measured. These are tabulated in Table 1. The corrosion rates obtained by the coulostatic method coincided with those obtained by the weight loss method.

References

1. D. A. Jones and N. D. Green, Corrosion, 22, 198(1966).
2. K. Kanno, M. Suzuki and Y. Sato J.Electrochem.Soc., 125, 1389(1978).
3. K. Kanno, M. Suzuki and Y. Sato Corrosion Sci., 20, 1059(1980)

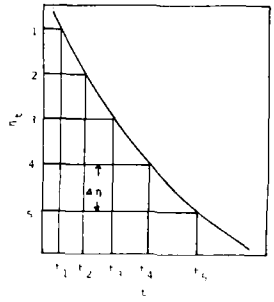


Fig. 1 Scheme of overvoltage decay curve for Tafel slope determination.

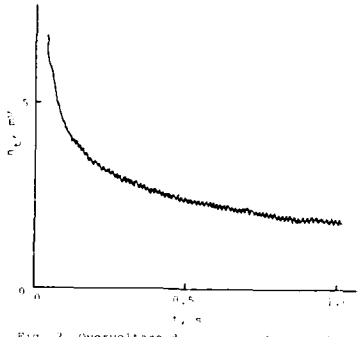


Fig. 2 Overvoltage decay curve for steel (SS 41) in 0.1 % NaCl solution containing 100 ppm $K_2Cr_2O_7$ after immersion for 506 hours.

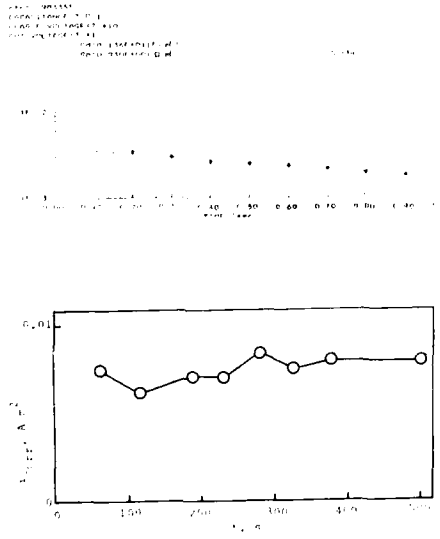


Fig. 3 Change in corrosion rate of steel (SS41) in 0.1% NaCl solution containing 100 ppm $K_2Cr_2O_7$.

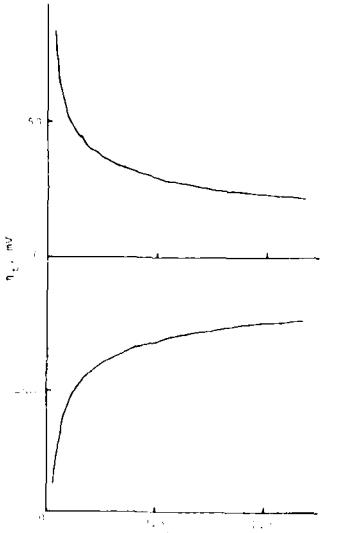


Fig. 4 Overvoltage decay curves for Tafel slope determination for steel (...) in 0.1% NaCl solution containing ... ppm $K_2Cr_2O_7$.

Table 1 Corrosion rate of steel (SS 41) in 0.1% NaCl solution containing various types of inhibitors

Inhibitor	Immersion Time (hrs)	Corrosion Rate (mdd)	
		Coulostatic Method	Weight Loss Method
no inhibitor	505	43.5	52.7
100ppm $K_2Cr_2O_7$	506	1.7	2.9
200ppm $K_2Cr_2O_7$	506	2.3	3.2
300ppm $K_2Cr_2O_7$	506	1.7	1.8
100ppm $H_6P_4O_{13}$	506	25	36
100ppm $H_6P_4O_{13}$ + 100ppm Ca^{2+}	496	8.5	11.3
200ppm $NaNO_2$	499	1.1	0.8

Abstract No. 132

The Effect of Complexing Agents on the Anodic Dissolution of Iron.

M.F. Bell and R. Iyer.

Laboratories for Inorganic Materials,
Dept. of Chemistry,
Concordia University,
1455 DeMaisonneuve Blvd. West,
Montreal, Quebec H3G 1M8.

INTRODUCTION

In the alkaline pH ranges, it is well known that dissolved iron exists as amorphous $Fe(OH)_3$ species [1]. Interestingly, however, various studies [2,3] have indicated that complexing agents such as organic soil matter (in the form of fulvic acid) can form complexes with the Fe^{3+} species and may thus aid corrosion by either stabilising the Fe^{3+} ion or the colloidal $Fe(OH)_3$ species by adsorption. In this paper, we describe our initial attempts to study these phenomena at a iron rotating disc electrode.

EXPERIMENTAL

Initially, sulfosalicylates, citrates and tannic acids were chosen as role models for the investigation of the more important species such as *fulvic acid*. The oxidation experiments were carried out by potentiostatic control on a rotating disc electrode in deaerated boric acid - NaOH buffer solutions in the pH range 7.5-9.

RESULTS AND DISCUSSION

The addition of citrate and sulfosalicylates (SSA) at a single pH shifts the rest potential in the cathodic direction (Figure 1); citrate ions having the greatest effect. This behaviour is consistently observed in the range of pH 7.5-9 but at pH>9, the concentration of OH^- ions is high enough to instantaneously passivate the electrode negating the effect of the complexing agent. This confirms the theory [2] that the citrate and SSA ions form solvating sheaths with Fe^{2+} ions making it more stable than the equivalent aquo ion. This corresponds to a schematic energy diagram [4] shown in Figure 2. The stabilisation of the Fe^{2+} ion corresponds to a decrease in the Gibbs *Free Energy* of the final state. This also decreases the height of the activation barrier causing an increase in the exchange current density, i_o. As the dissolution reaction is balanced by hydrogen evolution, this causes a cathodic shift in the rest potential and an increased rate of metal dissolution. However no change is observed in the anodic Tafel slope suggesting that the dissolution mechanism is not changed. These results indicate that the primary effect is the stabilisation of the Fe^{2+} ion.

In all cases, we observe that the peak potential is rotation speed dependent suggesting that passivation occurs by a dissolution precipitation mechanism as discussed by Armstrong [5]. In this pH range, it is observed that the overpotential for the onset of passivation is greater for citrate than for SSA. In both cases, this is again related to stabilisation of the free Fe^{2+} ion as a complex so that the solubility product criteria to initiate precipitation of $Fe(OH)_3$ is not met until higher potential. This, in turn, increases the peak current. We also conclude that the citrate-Fe^{2+} complex is more stable than the Fe^{2+}-SSA complex which is consistent with the exchange current density values.

With tannic acid, we see an interesting change in the shape of the current-voltage curve (Figure 3). A plateau region appears anodic to the peak potential. At present, no firm explanation of this phenomenon can be given but we suspect that the Fe^{2+}/Fe^{3+} couple is interacting with the tannic acid in an ECE mechanism involving the oxidation of the organic molecule. Further experiments are required to test this hypothesis.

We conclude from these measurements that the stabilisation of ionic species through complexation are an important factor in the corrosion of iron in alkaline soils and its transport in natural waters.

REFERENCES

1. W. Stumm and J.J. Morgan, Aquatic Chemistry, 2nd. Ed., Wiley Interscience.
2. C.H. Langford, R. Kay, G.W. Quance and T.R. Khan, Analytical Lett., 10(14) 1249-1260 (1977).
3. *R.K. Skogerbe and S.A. Wilson*, Anal. Chem., 53 228-232 (1981).
4. J.M. West, Electrodeposition and Corrosion Processes, 2nd. Ed., Van Nostrand Reinhold (LONDON) 1970.
5. R.D. Armstrong, Corrosion Science, 11, 693-697 (1971).

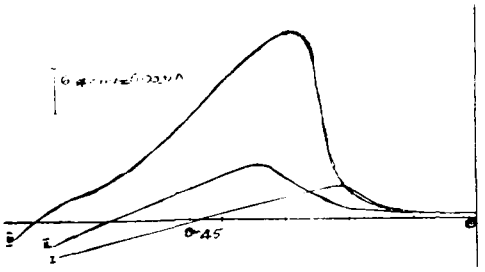


Figure 1 Current-Voltage curve with and without complexing agents at pH=8.1
I. Blank buffer.
II. With Sulfosalicylate (10^{-2}M).
III. With Citrate (10^{-2}M).
(scan rate = 10 mV.s^{-1}).

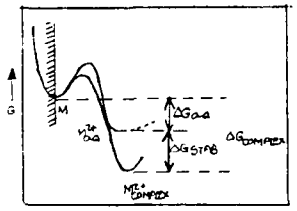


Figure 2. Schematic Energy Diagram for a Complexed Metal Ion.

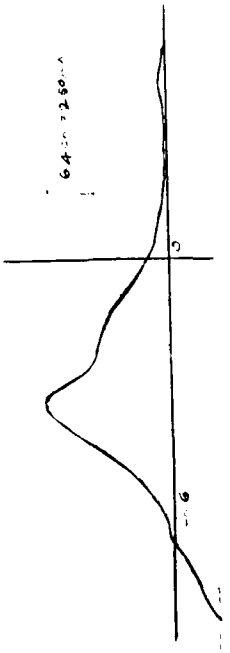


Figure 3. Current-Voltage curve for Iron in the presence of Tannic Acid.
(scan rate = 10 mV.s^{-1}).

Abstract No. 133

Stabilization of Metal-Metal Oxide Surfaces Using Conductive Polymer Films

Zhi Deng, Henry S. White and William H. Smyrl

Corrosion Research Center
Dept. of Chemical Engineering and Materials Science
University of Minnesota
421 Washington Ave. SE
Minneapolis, MN 55455

The passivation of many metals, such as Fe and Ti, can stabilize them against attack in aggressive environments(1). This is because the rate of metal dissolution is suppressed by thin oxide films formed on the surface of the metals. The result is the life of the protected metal is extended, in some cases, by orders of magnitude. Then the stability of oxide films is important in the protection of the substrates. Because the rate of metal dissolution is generally very low on passivated metals, the potential of free standing specimens is generally unpoised and prone to shifts induced by the presence of redox species. In reducing environment, the potential is shifted towards negative potentials where the metal is in active region, and in oxidizing environment it is shifted towards positive potentials where the metal is transpassive. In both cases, the rate of metal dissolution will increase dramatically.

In this paper, we describe a general strategy using redox polymer coatings to stabilize the potential of a metal/metal oxide system well within its passive region. The role of the polymer is to poise the potential of the oxide covered metal at an intermediate value between the active and the transpassive potential regions. Thin films of conductive polymers such as poly(3-methylthiophene) can be partially and reversibly oxidized, establishing a well defined potential that remains constant in the absence of redox reactions that may change the charge capacity of the polymer film. The potential of a partially oxidized P(3-MT) film, for instance, will drift towards more negative values as the film is chemically reduced. Coating an oxidized film of P(3-MT) on Ti/TiO_2 has been shown to control the potential of the metal in its passive range. The small but finite anodic current to the passive surface at steady state, however, leads to a slow discharge of the polymer film according to the process given by:

$$(1/4)Ti + (1/m)P(3\text{-}MT)^{+m} = (1/n)Ti^{+4} + (1/m)P(3\text{-}MT)^{0}$$

One then is led to the conclusion that the polymer film alone will not stabilize the passive surface at steady state, and a second reaction must be used to compensate the anodic dissolution current.

We chose the second reaction to be the reduction of dissolved O_2. Dispersed Pt particles within the polymer film act as catalyst for the O_2 reduction. The polymer film not only poises the potential of the substrate surface, but also serves as the site for a reduction reaction. In this context, it is useful to think of O_2 reduction on the polymer as a low-power, in situ, current generator that biases the metal into the passive region. Conceptually, this suggests that the polymer film need not uniformly coat the entire substrate.

Our objective was to experimentally demonstrate the use of P(3-MT) supported Pt catalyst as a source to bias the potential of Ti into its passive region. Similar application of poly(aniline) and prussian blue films have been recently reported(2). However, these papers have not described the principles by which the systems behave. Our experiments have focused on these two points: First, although the electrochemistry of P(3-MT) films have been extensively investigated by several laboratories(3), questions regarding the stability of P(3-MT) films in aqueous solution still remain unresolved. It has been studied in the present investigation in relation to the ability of the film to maintain a constant open-circuit potential. Second, investigations have been directed to show that the potential of Ti/TiO_2 can be poised by an oxidized P(3-MT) film. And only in the presence of Pt particles, which catalyze the O_2 reduction, can the Ti/TiO_2 be poised at a constant potential within the passive region for indefinite periods.

In order to separate out the effect of polymer films acting as inert barriers, P(3-MT) films were actually deposited onto an inert substrate such as glassy carbon. Then it was galvanically coupled to an oxide-covered Ti electrode. This, in addition, gave us control over the area ratio of exposed Ti surface to polymer film covered surface.

Ideally, the open-circuit potential of an oxidized (or reduced) conducting polymer film should not change with time in the absence of any redox reactions. However, the open-circuit potential of an oxidized P(3-MT) film slowly shifts toward more negative with time in aqueous solution. This potential decay is shown to be due to the charged species underwent an irreversible chemical degradation in the solution.

Figure 1 shows the E_{oc} time dependence for a P(3-MT) film coupled to oxide-covered Ti in the absence of O_2 reduction. As a comparison, E_{oc} of a Ti electrode was also monitored. The experimental results indicates that the potential of the coupled system was poised by the potential of P(3-MT) film and the potential continuously shifted toward more negative potentials in the absence of O_2 reduction. However, after Pt was dispersed in P(3-MT) film to catalyze the O_2 reduction, the coupled system reached a constant open-circuit potential in a short time (Figure 2).

References

(1) (a) H.H. Uhlig and R.W. Rivie, Corrosion and Corrosion Control, 3rd Edition, John Wiley & Sons, Inc., N.Y. (1985).
(b) M.G. Fontana and N.D. Greene, Corrosion Engineering, 2nd Edition, McGrao-Hill Book Co., N.Y. (1978).
(c) H. Kaescne, Metallic Corrosion, NACE, Houston (1985).
(2) (a) D.W. DeBerry, J. of Electrochem. Soc., 132, 1022 (1985).
(b) D.W. DeBerry and A. Viehbeck, Proc. of Electrochem. Soc.,(Fundamental Aspects of Corrosion Protection by Surface Modification) v.84-3 (1984).
(c) N. Ahmad and A.G. MacDiarmid, APS abstract, (1987).
(3) (a) J.W. Thackeray, H.S. White and M.S. Wrighton, J Phys. Chem., 89, 5133 (1985).
(b) R.J. Waltman, J.Bargon, and A.F. Diaz, J. Phys. Chem., 87, 1459 (1983).
(c) G. Tourillon and F. Garnier, J. Electroanal. Chem., 161, 407 (1984).

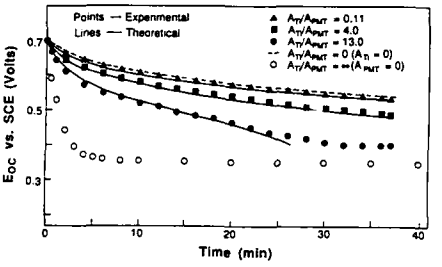


Figure 1

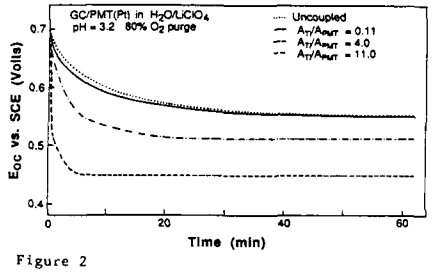


Figure 2

Abstract No. 134

TEMPERATURE DEPENDENCE OF THE LOW FREQUENCY IMPEDANCE OF POLYMERIC COATINGS

Richard D. Granata, Kevin Kovaleski and Henry Leidheiser, Jr.

Department of Chemistry and
Zettlemoyer Center for Surface Studies
Lehigh University, Bethlehem, PA 18015

The electrical properties of polymeric organic coatings on metal substrates have been studied by many investigators but little attention has been paid to the temperature dependence of the electrical properties. Polymer coatings are expected to provide corrosion protection, to retain adherence and appearance, and to maintain other physical properties for long periods of time. This paper describes the electrochemical impedance properties as a function of temperature for an epoxy air-dried coating, a baked polyester enamel coating and a baked polybutadiene coating.

Epoxy samples were prepared from 10 x 20 x 0.05 cm coated 1010 SAE steel panels. The panels were wet ground with 240 grit SiC paper and rinsed with ethanol. Epoxy primer MIL-P-24441/1 was applied by draw bar at a thickness of 0.015 cm wet. The panels were allowed to air cure overnight. Two coats of epoxy topcoat MIL-P-24441/5 were applied at 0.018 cm wet thickness by draw bar. The first topcoat was allowed to air cure overnight. The final coat was allowed to air cure one week. The panels were cut into 5 cm squares. Final dry thicknesses ranged from 0.017 to 0.024 cm.

Substrates for polybutadiene coatings were prepared in the same manner, but were cut into 5 cm squares before applying the coating. The polybutadiene was applied by spin-coating, followed by a 30 min cure at 195°C. Dry film thicknesses ranged from 0.002 to 0.003 cm.

Polyester samples were prepared in the same manner as polybutadiene samples with a 20 min cure at 190°C. Dry film thickness was 0.006 cm.

Impedance data were obtained from a system consisting of an EG&G Princeton Applied Research Corp. Model 173/276 potentiostat with computer-controlled Solartron Model 1250 frequency response analyzer. The impedance spectra were determined from 65.5 kHz to 1 mHz. The amplitude was 15 mV above 100 mHz and 50 mV below 100 mHz.

The electrochemical cell was a glass cylinder clamped and O-ring sealed to the sample surface. The seal exposed 8.8 cm^2 of sample surface to the distilled water test medium. The reference electrode was Ag/AgCl and a carbon rod served as the counter electrode.

Studies were conducted on three sets of samples, each at a different elevated temperatures (40, 60 and 80°C). The impedance spectrum was taken at room temperature, the sample was incubated at the test temperature for 1.5 h and the impedance spectrum was taken at the elevated temperature. The sample was equilibrated at room temperature for 1.5 h and a spectrum was recorded. Epoxy samples were equilibrated at ambient laboratory conditions (22°C and 50% RH) for approximately 2 weeks and a final spectrum recorded.

Table 1 shows the results of impedance measurements on the epoxy, polybutadiene and polyester coatings. Polybutadiene and polyester exhibited a lesser temperature dependence versus epoxy, only differing by approximately an order of magnitude at 1 mHz between room temperature and 80°C. However, the epoxy exhibited a substantial temperature dependence. At 80°C, the impedance of the epoxy decreased by a factor of more than 10^4 relative to the room temperature value at 1 mHz.

TABLE 1

Summary of Impedance Data

Sample	Temperature	Log |Z|, $\Omega \cdot cm^2$ (1 mHz)	Log |Z|, $\Omega \cdot cm^2$ (1 kHz)
Epoxy	1st RT	10.9	6.6
	40°C	9.2	6.3
	60°C	6.7	6.2
	80°C	6.1	5.7
	2nd RT	9.0	6.4
	Final RT	10.8	6.6
Polybuta-diene	1st RT	10.4	6.0
	40°C	10.3	5.9
	60°C	9.9	6.0
	80°C	9.6	5.8
	2nd RT	10.2	6.0
Polyester Enamel	1st RT	10.8	6.2
	60°C	9.2	6.0
	2nd RT	10.4	6.1

The behavior of all three coatings was reversible. The second room temperature spectra of the polybutadiene and polyester were within 0.4 order of magnitude of the first spectrum run at room temperature. This reversibility was not observed immediately with the epoxy. However, after two weeks of exposure to the atmosphere, the epoxy samples yielded spectra identical to those obtained initially at room temperature.

The phenomena described above have important consequences in understanding charge transport through polymeric coatings.

Abstract No. 135

Acoustic Microscopic Evaluation of Hydroxy-Terminated Polybutadiene on Steel

M. Kendig, R. Addison and S. Jeanjaquet
Rockwell International Science Center
Thousand Oaks, CA 91360

Introduction

Corrosion of organic polymer-coated steel involves the initiation of anodic dissolution of the metal at virtual pores or defects in the coating.[1,2] The anodic defect drives the adjacent region cathodic where oxygen reduction occurs, thereby maintaining the corrosion reaction. The reduction of oxygen produces a locally alkaline environment at the coating/metal interface which causes disbonding and therefore allows the corrosive degradation of the coated steel to propagate.

Until now, no rapid nondestructive, in situ technique was available for characterizing the disbonding morphology while instantaneously measuring the disbond rate. Although optical microscopy might be considered for in situ monitoring cathodic disbonding of polymer coatings, the sensitivity of acoustic microscopy to a disbond or weak bond as compared to optical microscopy makes it a superior method for detection of features at the disbond front, such as zones of polymer swelling, weak fluid boundaries and microblistering. Contrast in optical micrographs depends on the degree of refractive index mismatch between the fluid of the disbond and the polymer which is not great, whereas acoustic microscopy depends on the acoustical impedance mismatch between interfaces with and without weak bonds or disbonds. The contrast observed with scanning acoustic microscopy (SAM) is governed by the interaction of surface waves with the interface (as shown schematically in Fig. 1), and is therefore sensitive to the mechanical properties of solid/solid interfaces. Furthermore, differences in the velocity of sound in the coating polymer, as governed by water uptake and extent of crosslinking, may be expected under certain conditions to provide acoustic contrast. An example of this last point is our observation that alkaline degradation of hydroxy-terminated polybutadiene which shows no optical contrast gives a pronounced acoustic microscopic contrast.

We have recently applied acoustic microscopy to the study of cathodic disbonding of polymer-coated steel.[3,4]

Experimental

A filtered (0.2 μm) solution of four parts of hydroxy-terminated polybutadiene (PBOH) (R45HT from the Sartomer Co.) in three parts mineral spirits containing Modiflow™ (0.1% by weight of active ingredients) were spin-coated on polished 600 grit and degreased 0.055 cm thick steel coupons. Some additional surface preparations were also used. The samples were air dried and degreased at room temperature for 12 h followed by a cure in an air oven reaching 205°C for 9 min.

The resulting coupons were scribed (2.5 cm perpendicular marks using a SiC tool) and placed with the scribe mark to the electrolyte in the acoustic microscope cell shown in Fig. 2. In this manner, the specimens could be polarized to different cathodic potentials and monitored in situ as a function of time with the acoustic microscope. The region monitored was always chosen to be adjacent to the scribe mark parallel to the 600 grit polishing scratches.

Results

Figure 3 shows a typical time development of the disbond in the region adjacent to the scribe (scribe is on the left). As the cathodic potential is applied, a zone containing what appear to be spherical "microblisters" grows away from the scribe with time. The distance, d, that this region extends away from the scribe varies with the square root of time, and can be described by the equation

$$d = K_d(t-t_o)^{1/2} \quad \text{for } t > t_o \qquad (1)$$

which is plotted for several experiments in Fig. 4. The slope K_d shows a general increase with decreasing potential and the initiation time, t_o, appears to decrease with increasing cathodic polarization. The fringes around the "microblisters" result from changes in the velocity of leaky surface waves that produce alternating constructive and destructive interference as the acoustic path changes by a half wavelength with blister growth above the coating metal interface. Given the 1 GHz wavelength of the acoustic waves, a rise of 1-2 μm is estimated for the "blister" growth. However, combined acoustic and optical microscopy leads to the conclusion that the "microblisters" exist entirely within the polymer and do not result from local swelling that lifts the polymer. This suggests that the features are not actually "blisters" as such, but result from the transformation of regions of the polymer by reaction with sodium hydroxide formed at the interface. In a simple test, we found that a 1M sodium hydroxide droplet applied to the polymer irreversibly altered the acoustic behavior of the film.

In general, the "microblisters" correlate with the disbonding. However, acoustic micrographs on highly polished surfaces required for optimum resolution suggest that preliminary disbonding occurs slightly before the formation of the "microblister" front.

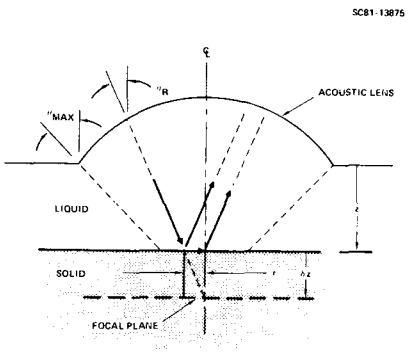
The ability to follow the kinetics of disbonding using acoustic microscopy has allowed a precise determination of the dependence of cathodic disbonding on the applied potential and has allowed us to rapidly distinguish between the effectiveness of various surface treatments for improving adhesion in the presence of a corrosive environment.

References

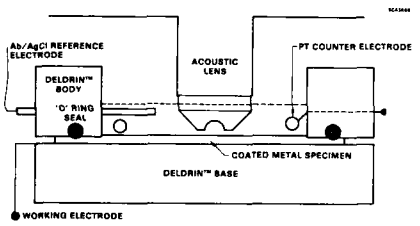
1. M. Kendig and L. Leidheiser, J. Electrochem. Soc. 123(7), 982 (1976.
2. F. Mansfeld and M. Kendig, "Electrochemical Impedance Tests for Protective Coatings," ASTM Special Testing Publications, No. 866 (1985).
3. M. Kendig, R. Addison and J. Jeanjaquet, "Environmental Integrity of Coating/Metal Interface," Annual Progress Report No. 1 for the period February 1, 1987 through January 31, 1988, Contract N00014-87-C-0075, 1988.
4. R. Addison and M. Kendig, "In Situ Measurement of Cathodic Disbonding of Polybutadiene Coatings on Steel," 17th International Symposium on Acoustical Imaging, Sendai, Japan, June 1988.

Acknowledgment

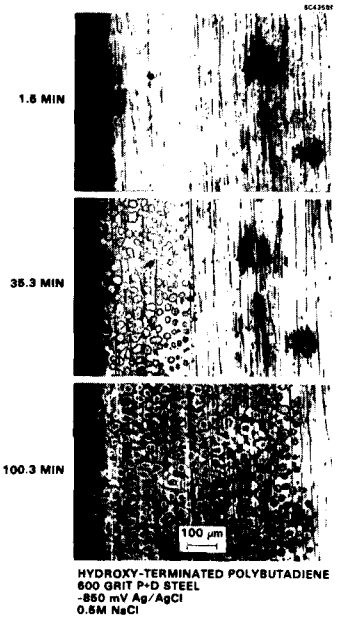
The authors gratefully acknowledge the support of the Office of Naval Research under Contract N00014-87-C-0075.



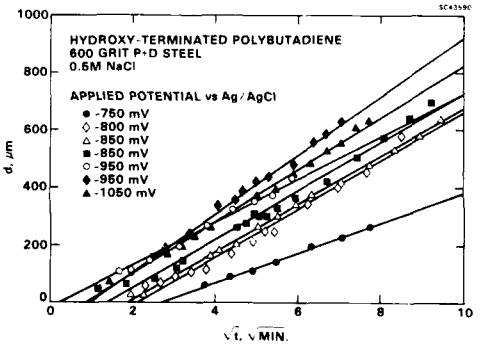
1. Schematic of the acoustic lens illustrating the generation of a surface acoustic wave (SAW) by rays incident on the surface at the appropriate angle (θ_R). The SAW propagates along the surface as it reradiates energy back into the water. Some of this energy enters the lens at the correct distance from the lens axis to be refracted parallel to the lens axis and returns to the transducer.



2. Schematic of the in situ cell.



3. Acoustic micrograph for a hydroxy-terminated polybutadiene coated steel specimen for 1.5, 35.3 and 100.3 min exposure at -850 mV vs Ag/AgCl.



4. The distance of the disbond from the scribe mark, d, as a function of the square root of time in minutes for scribed specimens polarized at the indicated potentials vs Ag/AgCl.

Abstract No. 136

CORROSION OF INORGANIC COATINGS IN MOLTEN SODIUM POLYSULFIDE

F. Tanzella
M. McKubre

SRI International
Menlo Park, California 94025

An important failure mode for Na/S cells is believed to be corrosive attack of the current collector or container by the sodium polysulfide. We have manufactured and tested several coatings which are expected to be electron-conductive, and resistant to corrosion by sodium polysulfide. Also coatings which are expected to form on electron-conductive corrosion product layers were tested. AC impedance spectroscopy was used to evaluate the corrosion of the coatings while exposed to sodium polysulfide.

Inorganic coatings were prepared via three methods. First, alloy coatings of NiZr, NiTi and NiCe were prepared by dipping cylindrical steel substrates into the appropriate eutectic composition at ~100°C above their respective melting points. This high processing temperature precluded the use of aluminum substrate. Coatings of NiTi were reacted with low partial pressures of oxygen and nitrogen at elevated temperatures to selectively form TiO_2 and TiN_x layers respectively. A NiCe alloy was chosen in hopes that a conductive CeS_x coating would form in-situ and passivate against further corrosion.

A Si_3N_4 coating was prepared by polymerization of a $[Si(CH_3)_2\ NCH_3]_x$ oligomer. The ceramic silicon nitride formed is electron-conductive and resistant to oxidation at 350°C. The polymerization of the silizane was carried out at 400°C and was used to coat aluminum substrates. Arc plasma spray methods were used to coat aluminum substrates with NiTi and NiZr coating. The small particles cool quickly and don't heat the substrate to more than 200°C. The NiTi surface was nitrided by passing nitrogen with the powder into the plasma. CeS which melts at over 2500°C was applied directly to an Al substrate using this technique.

In different experiments, five samples and a carbon rod were exposed to molten sodium polysulfide (Na_2S_7 or $Na_2S_{4.3}$) at 350°C in a graphite crucible in a pressure vessel. A pseudo-galvanostatic AC perturbation was applied via a potentionstat while the real and imaginary components of the voltage and current across the sample were measured. Generally, the impedance responses could be attributed to a Randles type equivalent circuit and discreet diffusion-controlled and kinetic controlled processes were identified. The diffusion of $S_x^=$ to the substrate was predicted to be the rate-determining step in the corrosion process.

The nitrided NiTi alloy survived exposure with the least amount of damage. The Si_3N_4 and CeS coatings showed the most promising results of the other samples suggesting that further work is warranted. Pure Ce and NiCe alloy both dissolved through formation of a CeS_x non-passivating corrosion product. The remaining coatings tested showed unacceptable levels of corrosion when exposed to molten polysulfide.

Abstract No. 137

THE MECHANISM OF BLISTER FORMATION AND RUPTURE IN THE PITTING OF ION-IMPLANTED ALUMINUM

P. M. Natishan and E. McCafferty
Naval Research Laboratory
Washington, DC 20375-5000

Scanning electron and optical microscopy of ion-implanted aluminum after anodic polarization in deaerated, 0.1M NaCl has shown that corrosion pits are associated with the formation and rupture of blisters caused by gas evolution at the oxide/metal interface. See Figure 1 for an example of a ruptured blister. The physical appearance of these blisters and calculations of hydrogen pressure support a modified version of the mechanisms proposed by Bargeron and Givens (1,2) for blister formation and rupture on aluminum and anodized aluminum.

The observations in this investigation differ from those of Bargeron and Givens in that cracks of various size were seen to radiate from the centers of the blisters and were present before total rupture. These cracks, which are referred to here as secondary cracks, appear to initiate at and propagate from a primary crack or from a pore leading from the solution to the oxide/metal interface. These secondary cracks are apparently the result of stresses caused by hydrogen production at the oxide/metal interface. The secondary cracks propagate perpendicular to the initial imperfection; and when the hydrogen pressure is great enough, the oxide film ruptures.

Griffith-type calculations show that the internal hydrogen pressure required to rupture a typical blister is of the order of 10^3 atmospheres, whereas thermodynamic data indicate that the internal hydrogen pressure generated within localized corrosion cells on aluminum is about 10^4 atmospheres. Thus the internal hydrogen pressure is sufficiently large to cause rupture of blisters on aluminum.

References

1. C. B. Bargeron and R. B. Givens, J. Electrochem. Soc., 124, 1845 (1977).

2. C. B. Bargeron and R. B. Givens, Corrosion, 36, 618 (1980).

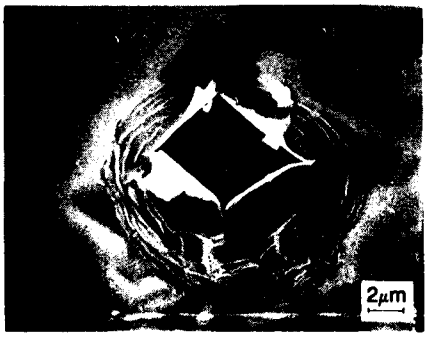


Figure 1. Ruptured blister on aluminum implanted with 4 atomic percent molybdenum.

Abstract No. 138

Photoresponse of Stainless Steel Electrode Attacked by Cl^- Ions in acidic medium

Shengmin Cai[+], Shenhao Chen[++], Yaohua Dong[+], Xiao Chen[++], Huaquan Yang[+]
+ Department of Chemistry, Peking University, Beijing, China
++Department of Chemistry, Shandong University, Jinan, China

Introduction

The photoresponse of the stainless steel in neutral medium was identified in previous reports. Photoresponse measured in acidic medium has not been reported. In this work we obtained the photoresponse in acidic medium when Cl^- ions were added into 0.5M H_2SO_4 solution. The photocurrent increased gradually when the total current increased rapidly. To the best of authors' knowledge, no work has been found on this topic.

Experimental Methods

All experiments were performed on 1Cr18Ni9Ti type stainless steel electrode with diameter of 0.5 cm. The electrode was sealed with epoxy resin (DEVCON), and only the working area was exposed. Before using in each experiment, it was polished with emery papers to mirror-like brightness, then rinsed with alcohol and distilled water separately(1). All solutions were deaerated with purified nitrogen. The reference electrode was Hg/Hg_2Cl_2 in the same solution and all potentials reported here were referred to the normal hydrogen electrode (NHE). The light source was 40 watt halogen-tungsten lamp with light intensity of 81 mw/cm^2. The photocurrents measured with chopper frequency 11.1 Hz were interfaced to IBM-PC/XT computer after it had been amplified by lock-in amplifier (PAR M5206, time constant of low pass filter is 3 seconds). The computer had the functions of data discrimination and data averageing. All measurements were conducted at room temperature of 21±2°C with circuit improved on the basis of (2,3) (see Fig.1)

Results and Discussion

Fig.2 shows the variation of the photocurrent I_{ph} and total current I_t with time. The electrode was passivated in 0.5M H_2SO_4 at 0.70 V for 10 minutes, no photoresponse had been detected in this period. Concentrated KCl was added at zero second to 0.4M, three currents were measured chronometrically (photocurrent I_{ph}, the readout of the same I_{ph} when light was chopped off manually and the total current passing the electrode I_t). From Fig.2, it reveals that I_{ph} can be stabilized at zero for some time. This relates to the induction time of pitting. Afterwards I_{ph} start increasing at about 360th second and relevent total current also increased gradually. It obviously meant that pitting started. From the fact that I_{ph} still decreased to zero as light was chopped off, we confirmed that I_{ph} measured was real photocurrent. No other reason such as instrumental characteristics, electric noise etc. may be account for this I_{ph}.

Fig.3 shows the typical results in the case that the electrode was derectly inserted in 0.5M H_2SO_4 +0.35M KCl solution at 0.70 V and all currents were measured at once. The induction time of pitting was shorter than that of Fig.2. The photocurrent was increased gradually still the same as the total current increased rapidly. The light was chopped on and off manually at periods of 60 seconds for each case. Apparently we still obtained 'true' I_{ph} because this I_{ph} decreased to almost zero when light was off.

Fig.4 shows the results when the electrode surface was illuminated continuously. All other experimental conditions remained similar to Fig.3. The increasing rate of I_{ph} and I_t are larger than that of Fig.3. A possible partial exploration is photocorrosion.

Fig.5 shows the influence of concentration of Cl^- ions where it was changed to 0.30M. In this case the competation of the two processes (forming of pitting and repairing of film on the electrode surface) resulted in the fluctuation of I_t. I_{ph} also fluctuated correspondingly and became noisy. We found 0.30M of Cl^- of the above phenomenon is critical concentration.

In Fig.6, the solution was not deaerated with purified nitrogen. The increasing rate of I_t was slower than that of Fig.5. It resulted from elimination of fluid movement due to nitrogen bubbling.

The I_{ph} measured were always position. this was due to the n-type semiconductive property of the electrode(4). We believe the increase of I_{ph} when Cl^- existed in solution was mainly the result of oxygen ions of the passive film partly replaced by chloride ions (5). Changes of related energy levels, band gap, surface states as well as concentration of charge carriers may be also responsible for this effect. No conclusion should be made at this moment but the present method can probally be used to detect the induction period of pitting and study the changes of composition and structure of the electrode surface when Cl^- ions were added.

Acknowledgement

Projects supported by the Chinese National Science Fund.

References

1. D.M.Drazic and S.Chen, Electrochim.Acta, 27,1409 (1982).
2. C.Liu, S.Cai, S.M.Wilhelm, S.D.Kapusta, A.Viehbeck and N.Hackerman, Scientia Sinica (series B), 27,225 (1984).
3. S.Cai, J.Zang, B.Shao, Y.Wu and J.Wang, Acta Energiae Solaris Sinica, No.4,353 (1986).
4. S.M.Wilhelm and N.Hackerman, J.Electrochem. Soc., 128,1668 (1981).
5. T.E.Pou, O.J.Murphy, V.Young and J.O'M Bockris, J.Electrochem.Soc., 131,1243 (1984).

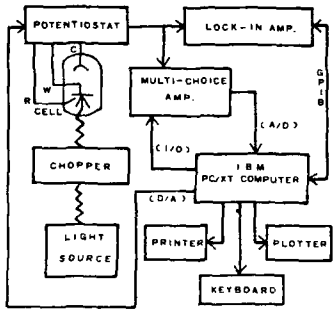


Fig.1 Schematic diagram of determining photocurrent and total current.

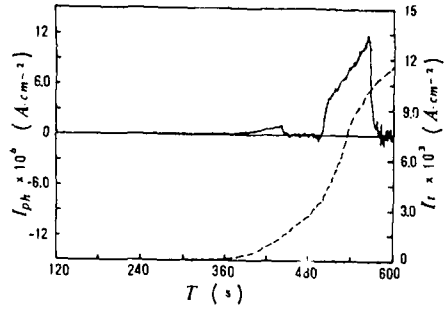


Fig.2. Variations of photocurrent I_{ph} and total current I_t with time t/sec./. Prior experiment, electrode was passivated in 0.5M H_2SO_4 solution for 10 minutes. 0.4M KCl added at the beginning of measuring. Electrode potential E=0.70V.

—— I_{ph} : -------- I_t

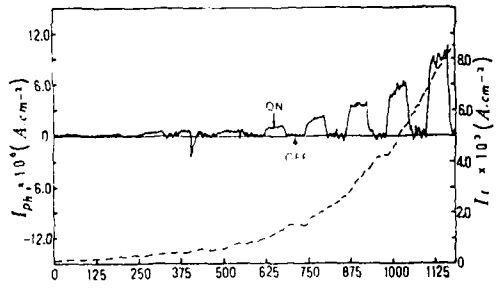


Fig.3. Variations of I_{ph} and I_t with time. Electrode was derectly inserted in 0.5M H_2SO_4 +0.35M KCl solution and experiment started at once. Electrode potential E=0.70V.

—— I_{ph} : -------- I_t

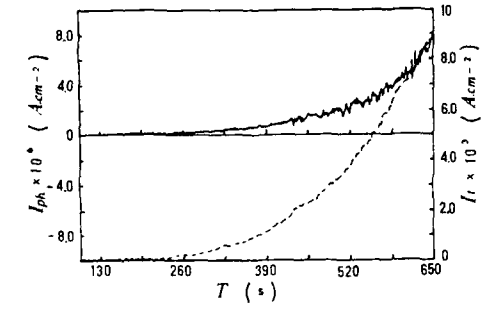


Fig.4. Variations of I_{ph} and I_t when the electrode surface was illuminated continuously. Other conditions were same as Fig.3.

—— I_{ph} : -------- I_t

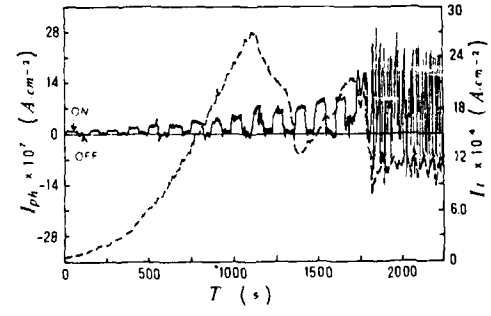


Fig.5. Variations of I_{ph} and I_t as concentration of Cl ions was equal to 0.30M. Other experimental conditions were same as Fig.3.

—— I_{ph} : -------- I_t

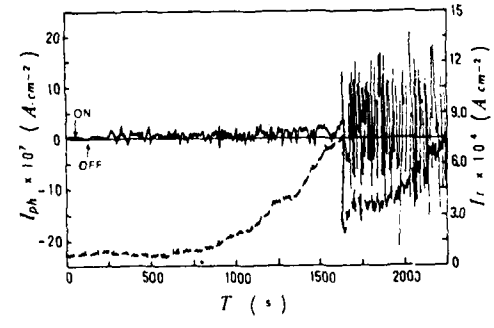


Fig.6. Variations of I_{ph} and I_t as the solution was not deaerated with purified nitrogen. Other conditions were same as Fig.5.

—— I_{ph} : -------- I_t

Abstract No. 139

Effects of Halide Ions on the Corrosion Rate of Inconel 600

In-Hyeong Yeo, Jae-won Yean, and Tae-yoon Eom

Department of Electrochemistry, Korea Advanced Energy Research Institute, P.O.Box 7, Daedukdanji, Choong-Nam. 301-353, Korea

Electrochemical measurements with a computerized potentiostat were performed to study the corrosion behavior of Inconel 600, high-Nickel alloy, in 1M H_2SO_4 at room temperature. Cathodic and anodic polarization curves of Inconel 600 were measured under non-steady state potentiostatic conditions by applying large overpotential with respect to corrosion potential, Ecorr.

Corrosion current, corrosion rate and Tafel constant were calculated from the polarization curves obtained in the absence and presence of halide ions, Cl^-, Br^- and I^-. The corrosion currents were determined by extrapolation of the anodic and cathodic branch of the polarization curves. Corrosion rate, then, was estimated using the following equation,

$$\text{Corrosion rate(MPY)} = \frac{(0.13)\ (i_{corr})\ (E.W)}{d}$$

where i_{corr} is corrosion current, E.W is the equivalent weight in grams, d is the density of Inconel 600 in grams per cm^3 and 0.13 is conversion factor to represent corrosion rate with miliinch per year.

From the analysis of cathodic polarization curve, it is observed that the reduction of hydronium ion, probably main reaction at cathodic process in acidic solution in the N_2 atmosphere, is interferred by the adsorption of the halides. In the presence of iodide, reduction of iodine produced in low pH solution seems to occur simultaneously with the reduction of hydronium ion. It is also observed that iodide ion inhibit both charge transfer controlled corrosion reactions, i.e., cathodic hydrogen evolution and anodic metal ion dissolution.

The dissolution of each components of Inconel 600 at the anodic process is also affected by the presence of halides. It is noticeable that the value of anodic Tafel constant is decreased as the concentration of chlorides increases. This indicates that rate of dissolution of Inconel 600 becomes faster in the presence of chloride. In the case of iodide, strong adsorption of iodide may retard the dissolution of the alloy or the formation of porous layers of oxidic corrosion products. Therefore, the corrosion rate of the alloy seems to be decreased.

The surface morphology of the alloy electrode was observed with a scanning electron microscope and oxidic corrosion products formed on the surface of the electrode were analyzed by X-ray fluorescence. The mixed oxide containing NiOx was formed on the surface of the electrode eventhough Ni(II) ion is the most stable species in low pH solution, which is expected from Pourbaix diagram. Analysis of X-ray fluorescence spectrum indicates that composition of the mixed oxide is slightly different from that of Inconel 600 without oxide and the amount of chromium in the mixed oxide is relatively more abundant than the bare Inconel 600. From the comparison of the standard reduction potential of Ni, Cr, Fe, main components of Inconel 600, it is expected that chromium is more likely to be oxidized than the other components, i.e., Ni and Fe.

Among the tested halide ions, the effect of bromide on the corrosion rate is negligible and chloride is more corrosive than the others. It is concluded that reduction of iodine is a main cathodic reaction at low pH solution.

References

1. W.J. Lorenz and F. Mansfeld, Corrosion Sci., 21, 647 (1981)
2. S.J. Lennon and F.P.A. Robinson, ibid, 26, 995 (1986)
3. Manuals for corrosion measurement software, Princeton Applied Research Corp. (1986)

Abstract No. 140

LABORATORY STUDY OF CREVICE CORROSION OF MILD STEEL

Mark Ingle, Richard D. Granata, and
Henry Leidheiser, Jr.

Departments of Chemistry and Materials Science
& Engineering, and the
Zettlemoyer Center for Surface Studies
Lehigh University, Bethlehem, PA 18015

Crevice corrosion of structural steels is a serious problem affecting exposed structures such as bridges and utility towers. This work was undertaken to obtain information about the principles governing this phenomenon.

The crevices were formed between a 1018 steel cylinder, a concentric steel pipe, and a transparent cover of ACRYCAL plastic. All samples were 25 or 50 mm in diameter. Experimental data obtained included: change in dimension caused by corrosion product buildup, current flow between interior and exterior surfaces of the crevice, potential within the crevice, pH within the crevice and the electrochemical impedance. Three different electrolytes were utilized: distilled water, 3% NaCl and pH 4.5 H_2SO_4. The crevice specimens were immersed in electrolyte and removed from the electrolyte on a regular cycle. The interior of the crevice remained wet even after the specimen was removed from the electrolyte.

The corrosion in the crevice was most severe when the specimen was removed from the electrolyte and atmospheric oxygen diffused into the solution trapped in the crevice. Specimens exposed to 3% NaCl electrolyte yielded a solution with the lowest pH in the crevice, 4.2. This low pH may be explained by the oxygen access to the solubilized ions in the crevice. When the crevice solution was exposed to atmospheric O_2, the ferrous ions in the crevice solution oxidized to ferric ions. Subsequent hydrolysis of the ferric ions significantly lowered the pH within the crevice. Immersion of the specimen in fresh electrolyte after exposure to atmospheric oxygen resulted in the pH returning to near neutral values.

Impedance measurements were performed periodically on freely corroding crevice specimens in order to characterize the initial corrosion rate in the crevice. The buildup of corrosion products in the crevice caused the solution resistance to increase and the corrosion rate to decrease.

The dimensional changes of the crevice corrosion specimens were measured over a 5000-hour period. The dimensional changes were caused by corrosion products filling the initial gap, exerting pressure on the assembly, and eventually deforming the crevice corrosion specimens. Table I shows measurements of these dimensional changes in specimens exposed to repeated cycles of immersion in 3% NaCl for 1 day followed by exposure to a 98% humidity atmosphere for 7 days.

These laboratory measurements of crevice expansion induced by corrosion product buildup correlate with field observations of deformation in structural connections due to mild steel crevice corrosion. The significance of the wet/dry cycle on the crevice corrosion of mild steel is also apparent from these studies.

Table I

25 mm Diameter 1018 Steel Crevice Dimensional Changes

Original Crevice Gap (mm)	Net Dimensional Change in mm 500 h (mm)	1000 h (mm)	5000 h (mm)
0.025	0.00	0.038	0.063
0.13	0.013	0.10	0.14
0.18	0.051	0.19	0.29
0.30	0.11	0.30	0.47
0.41	0.10	0.14	0.17
0.46	0.20	0.25	0.36
0.56	0.025	0.076	0.19

Abstract No. 141

THE ELECTROCHEMISTRY OF CHROMIUM AND CHROMIUM-PHOSPHORUS ALLOYS

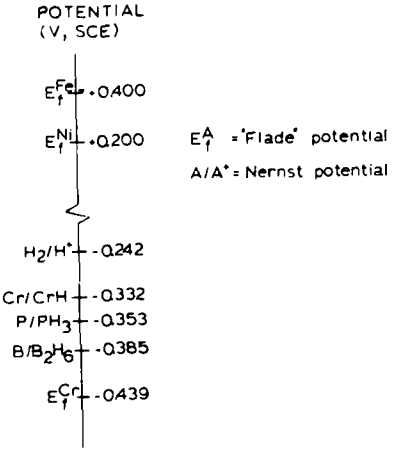
T.P. Moffat, R.M. Latanision,
MIT, Dept. of Mat. Sci. and Eng., 8-202,
Cambridge, MA 02139

and

R.R. Ruf, IBM Thomas J. Watson Research Center,
Yorktown Heights, NY

It is fairly well established that chromium-metalloid interactions represent the key to understanding the remarkable corrosion behavior of Fe-Cr-metalloid metallic glasses. Consequently, the electrochemistry of a series of rapidly quenched Cr-P alloys are being examined. These materials exhibit very high corrosion resistance in highly acidic Cl^- media (i.e. 12M HCl). Examination of these materials by a variety of electrochemical techniques as well as XPS yields the following conclusions. The corrosion resistance can be attributed to two effects a) the passive films formed on these materials contain oxidized phosphorus species which inhibit the adsorption of the aggresive Cl^- species and more importantly b) if film breakdown occurs, spontaneous passivation immediately follows due to significant depolarization of the hydrogen reaction on these materials. This is thought to be associated with phosphorus hydride redox chemistry.

It is proposed that a more general understanding of the electrochemical behavior of transition metal-metalloid glasses may be obtained by comparing the passivation potential of the base transition element with the redox potential of the elemental metalloid hydrides as shown in the figure below.



Abstract No. 142

THE NATURE AND COMPOSITION OF THE PASSIVE FILM FORMED ON Ni-P-Cr METALLIC GLASSES

M.A. Helfand[1], C.R. Clayton[1], N.R. Sorensen[2], and R.B. Diegle[2]

1Department of Materials Science and Engineering
State University of New York at Stony Brook
Stony Brook, New York 11794-2275

2Sandia National Laboratories
Albuquerque, New Mexico 87185

The presence of both Cr and P in transistion-metal metalloid glasses has been observed to promote the development of very stable, protective passive films (1). In order to investigate the interaction of Cr and P in the formation of passive films four alloy systems where chosen for study; Ni-20P, Ni-20P-3Cr, Ni-20P-6Cr and Ni-20P-10Cr (at.%). All the alloys were prepared by melt spinning and the glassy structure was confirmed by X-ray and electron diffraction, and by transmission electron microscopy.

We have examined the anodic behavior and the composition of the passive film formed on these alloys in 0.2N HCl (pH=0.7) and 0.2N H_2SO_4 (pH=1.2) using electrochemical techniques and surface analysis (XPS and AES) (2,3). A very interesting property of the glassy alloys containing either P or P and Cr together is their insensitivity to Cl ion attack. We have speculated that this may be due to a cation selective effect which is induced by phosphate anions in the outermost portion of the passive film. Increasing Cr additions enhances this effect. The alloys exhibit wider passive potential regions and lower passive current densities as the Cr content is increased. A second interesting property of the Ni-P-Cr alloys is the composition and chemical make-up of the passive film. XPS results obtained from the surfaces of the polish-formed films and passive films on the glassy alloys show the polish-formed films to contain Cr_2O_3, which is considered by many to be the main passivating species of stainless steels (4), however the passive films on the glassy alloys were observed to contain no Cr_2O_3. We have also employed the same techniques to examine the passive films formed on comparable crystalline counterparts, i.e. Ni and Ni 10Cr. In general, we observe the passive films on the crystalline counterparts to be composed of an oxide inner layer and hydroxide outer layer. The passive films formed on the glassy alloys are composed of a chromium phosphate inner layer and chromium hydroxide outer layer in the lower passive potential regime (approximately -300 to +200 mV(SCE)), and appear to polymerize into a single phase chromium hydrogen phosphate film at higher potentials.

A second portion of the study is concentrated on examining the passive film formed on the Ni-20P-10Cr alloy in both neutral and basic pH ranges. For this purpose we chose 0.3M NaCl (pH=5.4) as the primary electrolyte, and titrated this solution with NaOH to examine the anodic behavior at higher pH's. In addition we have also added 0.16M $NaMoO_4$ to the base 0.3M NaCl to determine if MoO_4 anions interact with the passive Ni-P-Cr surface. Specifically we are interested in determining why solution borne anions do not appear to interact with these surfaces and if there is a point of pH iso-selectivity (5) in these very unique passive films.

Acknowledgements

Portions of this work were performed at Sandia National Laboratories supported by the U.S. Department of Energy under contract no. DE-AC04-76DP00789. CRC gratefully acknowledges N.S.F. equipment awards DMR 7718319 and DMR 8117321 for the V.G.S. electron spectrometer and data system.

References

1. Kawashima, A., Asami, K., Hashimoto, K., J.Non-cryst. Solids, 70, 69 (1985).

2. Diegle, R.B., Clayton, C.R., Helfand, M.A., Sorensen, N.R., Accepted for publication J.Electrochem.Soc.

3. Clayton, C.R., Helfand, M.A., Diegle, R.B., Sorensen, N.R., in "Corrosion, Electrochemistry and Catalysis of Metallic Glasses", Eds, R.B. Diegle and K. Hashimoto, Electrochemical Soc., Pennington, N.J. p.134 (1988).

4. Sedricks, A.J., "Corrosion of Stainless Steels", John Wiley & Sons, Inc., New York, 1979.

5. Sato, N., Corr. Sci., 27, 421 (1987).

Abstract No. 143

CORROSION BEHAVIOUR OF COPPER ALLOYS IN AQUEOUS SOLUTION BY SURFACE AMALGAMATION

Wen-Lian Chen , and Jiann-Kuo Wu

DEPARTMENT OF MATERIALS ENGINEERING
TATUNG INSTITUTE OF TECHNOLOGY
TAIPEI,TAIWAN,10451,R.O.C.

In a study of surface amalgamation on the corrosion protection of galvanized steel in acid media, it was recently found that corrosion rate never exceeds 80 mdd.The problem of corrosion of copper alloys in sea water has become a topic of considerable interest with the dealloyed surface layers. Thus, for the corrosion resistance enhancement of copper alloys,we also studied the corrosion protection of surface amalgamation by contact between three commercial copper alloys and a solution containing a soluble mercury salt($HgCl_2$).

The materials used in this study were brass (Cu 65.0,Zn 35.0 W/0),bronze (Cu 93.2,Sn 6.3 W/0),Cupronickel (Cu 64.0,Ni 18.0,Zn 17.2 W/0) and electrolytic tough-pitch copper. Test solutions (3% NaCl add 0-1% $CuCl_2$ by weight) were prepared from reagent grade chemical and deionized water. Sample were amalgamated by immersion in a saturated mercuric chloride solution for 1 day and 2 days respectively. The average corrosion rates of these uncoupled specimens and simple galvanic cell (Brass-Cu, Bronze-Cu and Cupronickel-Cu) after 168 hr in aerated 3%NaCl, 3%NaCl+0.1%$CuCl_2$ and 3%NaCl+1.0%$CuCl_2$ determined. The galvanic current densities for coupled alloys in various solutions also recorded.

The corrosion rates of most uncoupled surface amalgamated copper alloys immersed in various test solutions is not improved. But the corrosion resistance of coupled surface amalgamated brass and cupronickel show excellent improvement. This is consistant with the surface of metal amalgamates with brass and cupronickel, making them more noble . The partial resaults are listed in Table 1 and 2. Changes in morphology of surface amalgamated alloysd and corrosion products were examinated by scanning electron microscopy and X-ray diffraction.

Table I. Weight loss (mdd) of coupled brass-Cu in various solutions

Test solution	Brass-Cu		Brass*-Cu	
3%NaCl	7.62	(4.67)	-41.0**	(1.91)
3%NaCl+ 0.1%$CuCl_2$	823	(100)	547	(503)
3%NaCl+ 1.0%$CuCl_2$	3037	(1617)	675	(1986)

* :surface amalgamated for 2 days
**:wt gained
():corrosion rate of copper

Table II. Weight loss (mdd) of coupled Cupronickel-Cu in various solutions

Test Solution	Cupronickel-Cu		Cupronickel*-Cu	
3%NaCl	10.5	(12.4)	651	(48)
3%Nacl+ 0.1%$CuCl_2$	336	(787)	841	(481)
3%NaCl+ 1.0%$CuCl_2$	2098	(2406)	-113**	(4236)

* :surface amalgamated for 2 days
**:wt gained
():corrosion rate of copper

REFERENCES

[1] F. A. Calvo, E. Otero and A. Pardo, Br.corros. J., Vol.22 No.3, pp185-189 (1987).

Abstract No. 144

AQUEOUS AND STRESS CORROSION BEHAVIOR OF DUCTILE Ni_3Al

D. E. Hall, R. E. Ricker and J. L. Fink
Corrosion Group
Institute for Materials Science and Engineering
National Bureau of Standards
Gaithersburg, MD 20899

INTRODUCTION

Nickel aluminide, Ni_3Al, is a promising structural material because of its high strength. However, polycrystalline Ni_3Al is intrinsically brittle, especially at low temperatures. Recently, the ductility of polycrystalline Ni_3Al has been improved by controlled microalloying with boron. This important development has increased interest in Ni_3Al and derivative alloys for high temperature applications such as gas and steam turbines, and casting molds for Al and glass, as well as low temperature applications such as forging dies and oil and gas well fittings. Ni_3Al is also being studied as both a matrix and reinforcing material in metal matrix composites.

Published information on the corrosion of Ni_3Al and derivative alloys is limited (1,2). As a result, this investigation on the aqueous and stress corrosion behavior of Ni_3Al was conducted.

EXPERIMENTAL

Aqueous and stress corrosion studies were carried out in 0.5 M solutions of NaOH, NaCl, Na_2SO_4, and H_2SO_4. These electrolytes represent conditions of high nickel and low aluminum corrosion resistance (NaOH), pitting of both parent metals (NaCl), passivation of both parent metals (Na_2SO_4), and possible hydrogen embrittlement with low Ni and Al corrosion resistance (H_2SO_4).

Nickel aluminide specimens were IC-50 alloy, containing 86.8 w/o Ni, 11.5 w/o Al, 1.4 w/o Hf, and .018 w/o B, received from Oak Ridge National Laboratory. The alloy was studied in both the cold worked and annealed (1100°C, vacuum) conditions.

Aqueous Corrosion Studies

Electrodes for aqueous corrosion studies were made by embedding 1.25 cm x 0.076 cm alloy specimens in epoxy resin. For comparison studies, high purity Ni and Al electrodes were made similarly. All electrodes were polished to a 0.05 μm finish, then washed in ethanol and double distilled water immediately before use.

Each electrode was inserted into a cell containing a Pt counter electrode, and an SCE reference electrode in a capillary with a porous glass tip. The open circuit potential was recorded vs. time until a steady state value or a drift rate of no more than a few mV per hour was reached. Cyclic voltammetric sweeps were then made at 5, 20, and 50 mV/sec over the potential range between the anodic and cathodic limiting processes. Steady state voltammograms were recorded.

The microstructures of the cold worked and annealed Ni_3Al, and the surface morphologies produced by exposure to the test electrolytes, were studied using standard metallographic techniques.

Stress Corrosion Studies

The stress corrosion cracking (SCC) resistance of cold worked and annealed Ni_3Al was evaluated by conducting slow strain rate (SSR) tests at a crosshead speed of 2.54×10^{-8} m/sec. The Ni_3Al specimens used in these experiments were 0.076 cm thick with a gauge section 2.54 cm long and 0.3 cm wide. The electrolytes were contained in a polyethylene vessel sealed at the bottom with a silicone sealant and open to air at the top. Only the specimen, the container and the sealant contacted the electrolyte. The load and stroke were monitored and recorded by computer and the fracture surfaces were examined in a scanning electron microscope (SEM).

RESULTS

Aqueous Corrosion

In all electrolytes, the open circuit potentials (E_{oc}) of both cold worked and annealed Ni_3Al were between those of Ni and Al, as shown in Figure 1. In each case, the alloy E_{oc} values were close to the Ni values, indicating that the alloy behavior at open circuit was dominated by Ni surface species. In 0.5 M Na_2SO_4, where both parent metals are passive, the influence of nickel on the alloy open circuit potentials was relatively less than in the other electrolytes.

Voltammetric behavior of the alloys was also very similar to that of Ni. In 0.5 M NaOH, for example, the peaks characteristic of Ni valence transitions were also clearly observed on Ni_3Al (Figure 2.) In 0.5 M NaCl, the current rise indicating breakdown of the passive film began at essentially the same potential on Ni and Ni_3Al (Figure 3). No current was observed on Ni_3Al corresponding to the film breakdown on Al at about -0.7 V_{SCE}.

Despite nearly identical E_{oc} and current-voltage characteristics, the cold worked and annealed Ni_3Al electrodes experienced different modes of attack. In 0.5 M NaCl, for example, large, separate circular pits developed on the cold worked alloy. The annealed alloy, however, developed a high etched surface characteristic of grain boundary attack.

Stress Corrosion Cracking

The results of the slow strain rate tests are given in Table 1. The data indicate that the strain to failure in all of the aqueous electrolytes is lower than that observed in air. The decrease in strain to failure, however, is not very significant except in 0.5 M H_2SO_4. In that electrolyte, both the strain to failure and the maximum tensile stress are greatly reduced, and the magnitude of this reduction as a percentage of the air values is much greater for the annealed material.

Examination of the fracture surfaces generated during the slow strain rate tests in air showed a dimple fracture morphology indicative of ductile fracture processes, with a few small regions of intergranular separation. The fracture morphology was essentially the same in the aqueous electrolytes, with the exception of sulfuric acid. In 0.5 M H_2SO_4, the fracture surface was almost entirely intergranular with numerous secondary cracks

ACKNOWLEDGEMENT

The authors thank Dr. Vinod Sikka of Oak Ridge National Laboratory for supplying Ni_3Al specimens and for helpful discussions. This work was funded by an initiative award from Dr. Lyle Schwartz, Director of the Institute for Materials Science and Engineering.

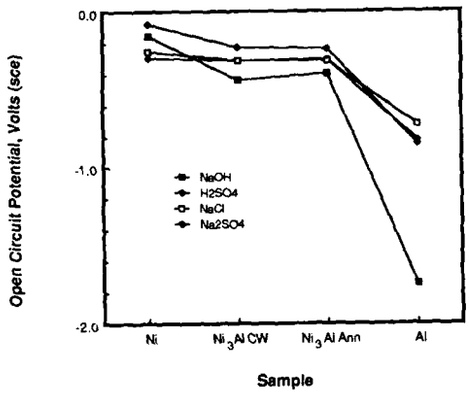


Figure 1 Open circuit potentials of Ni, Al and both cold worked and annealed Ni_3Al in the four test electrolytes.

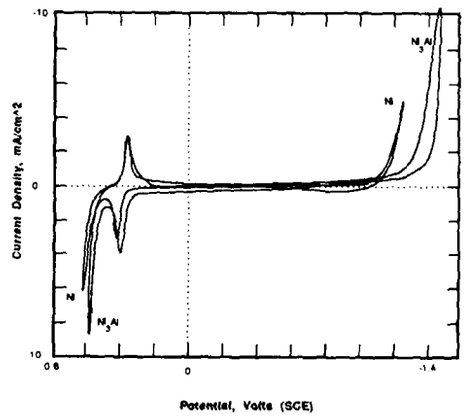


Figure 2 Cyclic voltammograms of Ni and annealed Ni_3Al in 0.5 M NaOH at a sweep rate of 5 mV/s.

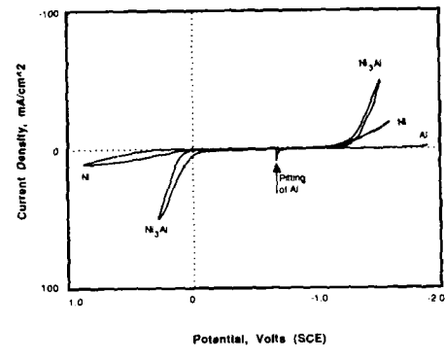


Figure 3 Cyclic voltammograms of Ni, Al and annealed Ni_3Al in 0.5 M NaCl at a sweep rate of 5 mV/s.

Table I: Results of the slow strain rate tests on cold worked (A) and annealed (B) Ni_3Al in air and 0.5 M solutions.

A. Cold Worked Ni_3Al

Environment	t_f (hrs.)	t_f/t_f (%)	σ_{uts} (MPa)	Ratio (%)
Air	24.21	100.0	1283	100.0
H_2SO_4	11.95	49.4	307	23.9
NaCl	18.77	77.5	1300	101.4
Na_2SO_4	19.63	81.1	1307	101.9
NaOH	18.84	77.8	1283	100.0

B. Annealed Ni_3Al

Environment	t_f (hrs.)	t_f/t_f (%)	σ_{uts} (MPa)	Ratio (%)
Air	135.08	100.0	1851	100.0
H_2SO_4	9.34	6.9	1256	68.6
NaCl	107.16	79.3	1821	98.4
Na_2SO_4	92.65	68.6	1845	99.7
NaOH	94.71	70.1	1828	98.7

REFERENCES

1. R. A. Buchanan and J. G. Kim, "Aqueous Corrosion Characteristics of Nickel Aluminides," Six Months Progress Report to The Nickel Development Institute, University of Tennessee, Knoxville, TN, (1987).

2. A. K. Kuruvilla and N. S. Stoloff, *Scripta Met.*, **19**, 83, (1985).

Abstract No. 145

AN XPS STUDY OF THE ANODIC BEHAVIOR OF PURE Mo AND Mo IN STAINLESS STEELS

Y. C. Lu and C. R. Clayton

Dept of Materials Science and Engineering
State University of New York at Stony Brook
Stony Brook N Y 11794

Variable angle XPS was employed to detect the nature of passive and transpassive films formed at specified potentials on Mo in deaerated 0.1 M HCl. Molybdenum is passive between -396 mV and 125 mV(SCE). The passive films were found to be comprised of MoO_2 and $Mo(OH)_2$. The transpassive product of molybdenum is a mixture of MoO_2, $MoO(OH)_2$, Mo_2O_5 and MoO_3. $HMoO_4^-$ was observed as a dissolution product.(1) Molybdenum appears to be present as hydrated MoO_2,$Mo(OH)_2$, and MoO_4^{2-} in the passive films formed on the molybdenum bearing alloys in the same solution. Even in the potential region corresponding to the transpassive region of pure Mo, no transpassive products of molybdenum were observed. It was proposed that in the molybdenum bearing alloy, MoO_4^{2-} anions are formed in the solid state along with CrO_4^{2-}, which together are responsible for producing, in 0.1 M HCl , a bipolar film consisting of a cation selective outer layer containing CrO_4^{2-} and MoO_4^{2-} and an intrinsically anion selective inner layer. The ion selective property of this duplex film is considered to be largely responsible for the development of an interfacial chromium oxide barrier and resisting Cl^- and OH^- ingress. Both of these properties provide greater resistance to breakdown of passivity in Cl^- ion media.(2)

On comparing the difference of the anodic behavior between pure Mo and the alloying Mo in stainless steels, the following questions have to be answered.

(1) Why are MoO_4^{2-} oxyanions only detected in the passive films formed on stainless steels and not in those formed on pure molybdenum ?

(2) What causes Mo to stop forming transpassive products in the stainless steels at potentials corresponding to the transpassive region for pure Mo?

(3) How does MoO_4^{2-} form ?

(4) Is MoO_4^{2-} transference and redeposition possible ?

To study the mechanism of MoO_4^- formation, XPS was used to examine the surface species formed on pure Mo following anodic polarization in 0.1 M HCl solution at -180 mV(SCE) for 1 hour under the influence of Fe or Ni cations(3). The source of the metal cations was an independently anodically polarized electrode of pure Fe or Ni brought into close proximity to a high purity Mo electrode. It was found that in the presence of Fe and Ni cations , Mo was observed by XPS to produce a similar passive film, but in addition, MoO_4^{2-} was detected on the exterior surface. However, when Cr was polarized in the vicinity of Mo, no MoO_4^{2-} was observed to form on the film of Mo. This was expected due to the low Cr cation flux generated by the passive Cr. However, the surface of the Cr passive film was observed by XPS to contain MoO_4^{2-} and $MoO(OH)_2$ species. It was experimentally determined that soluble molybdenum chlorides were not responsible for the transference of Mo to Cr.

When Mo was mounted with iron and polarized at 250 mV, Mo was seen to passivate apparently as a result of ferrous molybdate precipitation. It would appear that the precipitated layer of $FeMoO_4$ created a barrier between the underlying Mo^{4+} species and water which stifled the transpassive reactions. In similar way, Mo in a stainless steel is prevented from forming transpassive products at 250 mV, because of the formation of an Fe rich film which prevents water from reacting further with the Mo species. The resulting formation and stablization of a molybdate species in the outer regions of the passive film formed on stainless steel is then able influence ion transfer through the passive film by way of its cation selective characteristics.

In summary, when Mo is polarized in 0.1 M HCl at -180 mVit will react with water through a three step reaction to form MoO_4^{2-} which subsequently dissolves into the solution. In the presence of Fe, Cr or Ni metal cations , an insoluble molybdate precipitate will be formed. This molybdate precipitate layer may hinder the transpassive reaction of molybdenum by preventing water from reacting further with the underlying Mo^{4+} species to generate transpassive products.

In an acidic solution containing chloride, molybdenum may dissolve as molybdate and transfer through the solution to the adjacent chromium surface, where it is adsorbed at the chromium surface. Soluble molybdenum chlorides, $MoCl_5$ and $MoCl_4$, are not responsible for the transference of molybdenum through the solution.

Acknowledgement

This work was supported by the National Science Foundation under Grant No. 8418873 (administered by Dr. Bruce MacDonald) The VGS Electron Spectrometer and VGS 1000 Data System were acquired from NSF equipment awards DMR 7718319 and DMR 8117321.

The authors would like to thank Dr Hugh Isaacs of BNL for valuable discussions and for providing us with the Stonehart Model BC1200 potentiostats used in some of the experiments.

Reference

1. Y. C. Lu and C. R. Clayton, Corros. Sci.,(Submitted).

2. C. R. Clayton and Y. C. Lu, J. Electrochemical Soc.,133, 2465, (1986)

3. C. R. Clayton and Y. C. Lu, Corros. Sci.,(Submitted).

Abstract No. 146

Effects of Temperature on the Corrrosion Resistance of N Bearing AL6X Stainless Steel

K.G. Martin, Y.C. Lu and C.R. Clayton*

Department of Materials Science
and Engineering
State University of New York at
Stony Brook
Stony Brook, New York 11794

ABSTRACT

XPS and electrochemical analysis have been used to determine the nature of the influence of N addition to AL6X stainless steel as the solution temperature is raised. In our studies on the pitting behavior of AL6X (0.042 wt% N) and AL6XN (0.19 wt% N) in deaerated 2M NaCl + 0.1M HCl between 22° and 45°C, it was observed that the higher N steel exhibited higher breakdown potentials than the low N steel as the temperature was raised. XPS analysis of the passive films formed after 10s at 0mV, at 22° and 45°C was performed and from this data it can be seen that some compositional differences occurred. At 22°C, the high N alloy produces a passive film with approximately 50% more Cr and Mo compared to the low N alloy. At 45°C, the higher N steel generated a passive film which had approximatley 12% more Cr and 25% more Mo. The underlying substrate composition showed little variation in Cr and Mo with increase in N content and temperature of the electrolyte. However, in each case it is apparent that Cr and Mo is enriched by approximatley 50% relative to Ni and Fe, compared to the bulk composition. Ni was generally found to be depleted in the substrate by at least 50%. It was also apparent that 0.042 wt% N is not an insignificant alloy addition, since it is clearly anodically segregated and is present as a nitride, and as NH_3 and NH_4^+ in the passive films at 22° and 45°C.

Acknowledgements

This work was supported by a grant (N0001485K0437) from the U.S.O.N.R. (Dr. A.J. Sedriks, Contract Officer).

We gratefully acknowledge receiving alloy specimens from Dr. J. Kearns of Allegheny Ludlum Steel Corporation.

Abstract No. 147

Mineralogical Issues in Long-Term Corrosion of Iron and Iron-Nickel Alloys

A.C. Van Orden
National Bureau of Standards
Gaithersburg, MD 20899

and

M. B. McNeil
Naval Coastal Systems Center
Panama City, FL 32407

Demonstration that a metallic container will remain intact over a period of 300-1000 years, as required by the NRC regulation 10 CFR 60, requires that schemes be developed for convincingly extrapolating short term test results over very long periods of time for any alloys being considered for high level nuclear waste overpacks. Validation of extrapolation schemes for geological phenomena for such time periods is often done through the study of existing "natural analogues;" i.e., systems which have reacted under fairly well known conditions for appropriately long times, and it appears necessary to extend this technology to corrosion extrapolation.

Prediction of very long term corrosion behavior of buried objects in general requires taking into account that the corrosion processes themselves alter the local conditions. Recent work by Sharland and the other members of the Harwell group (1) has analyzed corrosion processes in terms of trajectories on Pourbaix diagrams and appears to offer the prospect for using short-term corrosion tests to project corrosion behavior over very long periods.

A corrosion analysis or model can be validated only by comparison of its predictions to experimental observations, (in the case of 300 to 1000 year corrosion, natural or archaeological analogues), and the purpose of this paper is to present the present state of knowledge in two areas where there are data on natural/archaeological analogues which appear relevant to high level nuclear waste containers and to comment on the use of this technique as a check on Sharland-type analyses.

Two different classes of materials are considered here: essentially pure iron, which is an analogue to the carbon steel design overpacks for the salt and basalt sites (on which work has been suspended at present), and iron-nickel alloys, which are the best analogues available for some of the alloys being considered on the tuff site. There are a number of sources of data on corrosion of iron over archaeological times; the data used in this paper (2) are from the recent National Bureau of Standards work on Roman iron nails for Inchtuthill in Scotland, which can be dated fairly precisely to about 70 A.D. and whose method of production is understood. The only available source of natural-analogue data on Fe-Ni alloys is the corrosion of meteorites. The data used in this paper are those collected by Buchwald and Clarke on antarctic meteorites (3).

The corrosion rates of both the nails and the meteorites show great variability (due to local variability of environment) and so are not considered specifically. What is examined is the question of the mineralogy of the corrosion products, since the use of Pourbaix diagrams makes it possible to make fairly clear statements about what phases ought or ought not be present.

The observations on the nails indicate the presence of wüstite, which has also been observed in the buried portion of the iron pillar of Delhi(4).

The observations on the meteorites contain two interesting points. First, the corrosion products contain a very large amount of akageneite, a very rare mineral corresponding to β -FeOOH, and the corrosion products are enriched in Cl^- over normal antarctic ice by a factor of about 100. These observations are discussed and their implications for nuclear waste conjectured.

It is shown how the presence of wustite can be rationalized in terms of its metastability and how, although the presence of akageneite is much less well understood because of lack of thermodynamic data and the fact that the mechanisms of the reactions which produce and consume it are conjectural, the observations on meteorites can be rationalized on the basis of reasonable assumptions concerning the thermochemistry of the $Fe/O_2/H_2O$ system and the mechanisms of various alteration reactions. The implications of the work for the projection of long-term behavior of nuclear waste containers is discussed in terms of trajectories on Pourbaix diagrams modified by the inclusion of metastable phases.

REFERENCES

1. Sharland, S.M. et al., "Chemical Perturbations in the Disturbed Zone of a Nuclear Waste Repository," Materials Research Society Annual Meeting, Boston, 1987.
2. Van Orden, A.C. and McNeil, M.B., "The Archaeological Data Base Relevant to the Long-Term Corrosion of A-216 Mild Steel," Materials Research Society Annual Meeting, Boston, 1987.
3. Buchwald, V.F. and Clark, R.S., "Chlorine-Containing Akageneite and the Corrosion of Iron Meteorites in Antarctic Environments," to appear in American Mineralogist.
4. Wranglen, G. Corrosion Science 10, 761-770 (1970).

Abstract No. 148

LOCALIZED CORROSION AND STRESS CORROSION CRACKING OF AUSTENITIC CANDIDATE MATERIALS FOR HIGH-LEVEL RADIOACTIVE WASTE DISPOSAL CONTAINERS: ANALYSIS OF DATA

W. G. Halsey, J. C. Farmer, R. D. McCright, R. A. Van Konynenburg, and D. B. Bullen,
University of California
Lawrence Livermore National Laboratory
Livermore, California 94550

Three austenitic alloys, 304L, 316L and 825, are being considered as candidate materials for fabrication of high-level radioactive waste containers. Waste will include fuel assemblies from reactors, as well as borosilicate glass forms, and will be sent to the Yucca Mountain site in Nevada for disposal. The containers must maintain mechanical integrity for 50 years and substantially complete containment for 300-1000 years. Radioactive decay of the radionucleides will result in substantial heat generation and fluences of gamma radiation. Materials may undergo any of several modes of degradation in this environment, including atmospheric oxidation, uniform aqueous phase corrosion, pitting, crevice corrosion, sensitization and intergranular stress corrosion cracking (IGSCC), and transgranular stress corrosion cracking (TGSCC). This paper is an analysis of relevent pitting, crevice corrosion, and stress corrosion cracking (SCC) data.

RESULTS OF SURVEY

For example, Asphahani has found that all austenitic candidates undergo pitting and crevice corrosion in chloride containing environments (1). However, 825 has the greatest resistance to these forms of localized attack (2,3). Hodgkiess and Rigass have measured the corrosion and pitting potentials in aerated sea water and have found that the resistance to pitting of 825 is greater than that of 316L (2). Resistance to pitting is quantified as the difference between the pitting and corrosion potentials, Ec-Ecorr (Fig. 1). Scarberry et al. has found that 825 is more resistant to pitting than either 300 series stainless steels such as 304 and 316 (3). Asphahani et al. also found that both 304L and 316L are susceptible to SCC in acidic chloride media. In contrast, they found that 825 does not undergo SCC under comparable conditions (1). Furthermore, gamma irradiation has been found to enhance SCC of 304 and 304L stainless steels, but has no detectable effect on the resistance of 825 to SCC (4). The effect of gamma irradiation of sensitized 304 is illustrated in Figure 2. Microbial induced corrosion effects have been observed for 300 series stainless steels. Fortunately, nickel-based alloys such as 825 seem to be immune to such problems. This analysis indicates that the candidates should be ranked according to their resistances to localized corrosion and SCC as follows: 825 (best) > 316L > 304L (worst).

REFERENCES

1. Asphahani, Matls. Perform. 19 (Nov. 1980) 9.

2. Hodgkiess, Rigas, Desalination 44 (1988) 283.

3. Scarberry et al., Corrosion/79, Paper 245.

4. Furuya et el., R-D Kobe Seikosho Gijutsu Hokoku 33 (Jan. 1985) 43.

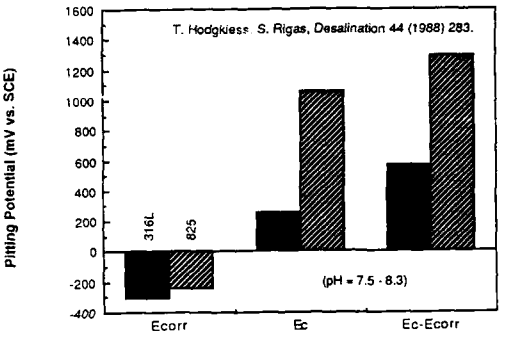


Fig. 1. Comparison of the resistances to pitting of 316L and 825.

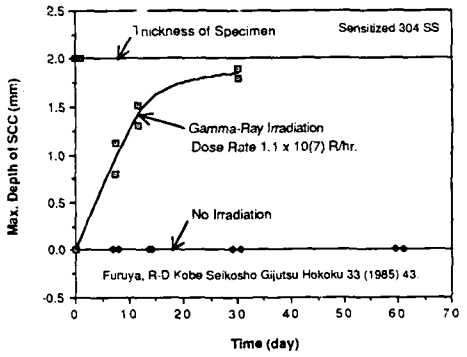


Fig. 2. Effect of gamma irradiation on SCC of sensitized 304 stainless steel.

ACKNOWLEDGEMENTS

Dennis Fleming is thanked for preparation of the text and figures. This work was performed under the auspices of the United States Department of Energy by Lawrence Livermore National Laboratory under Contract Number W-7405-ENG-48.

Abstract No. 149

"An Investigation of Low Temperature Sensitization (LTS) in AISI 316 Stainless Steel"

Mary C. Juhas and Bryan E. Wilde
The Ohio State University
Fontana Corrosion Center
116 W. 19th Avenue
Columbus, Ohio 43210

Type 316L stainless steel (SS) is among several alloys which are being extensively characterized as possible containment materials for high-level nuclear waste. The current reference design for the container is a seamless cylinder to which a lid is welded forming a permanent seal. Because post weld hea treatment is impractical in this situation, the heat affected zone (HAZ) may be susceptible to intergranular corrosion and possibly intergranular stress cracking in the event of intrusion by an oxidizing medium.

The combination of the weld thermal cycle an prolonged exposure (more than 100 years) in the 200°C temperature regime renders the HAZ potentially susceptible to Low Temperature Sensitization (LTS). Figure 1 shows a schematic representation of the 2-step thermal treatment which produces LTS; the nucleation stage, ahead of the nose of the typical time-temperature-sensitization (TTS) curve (550 - 800°C), followed by the long-term isothermal hold below this temperature range. Stable $M_{23}C_6$ carbides have been shown to grow as a result of this combine heat treatment [1,2]. The classical TTS curves are often reported based on electrochemical tests or thermodynamic models. In both cases, the material is considered to be "sensitized" when the grain boundary carbide has grown to the extent of substantial Cr depletion in the adjacent area (<0.13 mole fraction Cr). At this point, the carbides are usually visible using conventional electron microscopy techniques and the material is susceptible to intergranular corrosion in typical laboratory screening tests [3].

In contrast, LTS arises from a seemingly innocuous situation. The short, high temperature excursion provides ample time for stable nucleation in alloys of relatively high carbon content. The present investigation involves the study of the effect of systematic variations of carbon and nitrogen on the LTS behavior of AISI 316 SS. A thermodynamic model has been developed to determine the time-to-sensitization in 4 alloys at temperatures similar to those expected in the repository [4]. Two electrochemical tests are used to corroborate the model predictions; the electrochemical potentiokinetic reactivation (EPR) test [5] and the boiling ferric sulphate (ASTM A-262-B) weight loss test.

The thermodynamic model is based on previous theoretical models for 304 SS in the 500 - 850°C range [6-11]. The time to sensitization is calculated using the Stawtrom and Hillert equation [6]:

$$t = m^2 \left(X^o_{Cr} - \tfrac{1}{2}X_{Cr}\right)^3 / 4D \left(0.13 - \tfrac{1}{2}X_{Cr}\right)^3 \qquad (1)$$

where m is the distance perpendicular to the austenite grain boundary where the mole fraction of Cr falls below 0.13. The derivation of each component of equation (1) as well as the extension of the model to the low temperature regime have been published elsewhere [4]. The assumptions of the model are based on growth of a stable carbide which nucleated in the normal sensitization temperature range. The growth stage of carbides at low temperatures is modeled by the appropriate selection of the apparent diffusivity of Cr in the matrix and along high diffusivity paths [12,13].

The value of m in equation (1) is typically 20 nm. The nose of the TTS curve moves to the left as the value of m decreases, as shown in Figure 2. Figure 3 shows TTS curves generated for the 4 experimental alloys of compositions shown in Table 1. The cooling curve to the left of the TTS curves represents the nucleation thermal cycle used to simulate the weld (HAZ) 0.5 cm from the fusion line. While the model sucessfully predicts that decreasing the %C or increasing the %N retards sensitization, it is important to recognize that the TTS curves derived from the model represent isothermal heat treatments. If stable carbides are able to nucleate in the short term exposure of a weld thermal cycle, it is apparent that the model must be adjusted to account for very small m values.

In this study, specimens have been exposed to a HAZ simulation using the Gleeble. A peak temperature of 900°C was maintained for 5 seconds, followed by a cooling rate of 7 °C/s to 690 °C, 5 °C/second from 690 °C to 490°C, and finally free cooling to room temperature. After the nucleation stage, specimens were heat treated at either 300 °, 350 °, or 400 °C for 50, 500, 1,000, and 2,000 hours. The popular "LTS" heat treatment of 24 hours at 500°C was also used.

Carbide growth was detected by the 2 electrochemical tests mentioned above. The results of these tests, in relation to the model predictions will be discussed.

References

[1] M.J. Povich, Corrosion, 34, 1978, p. 60.
[2] M.J. Povich and R. Rao, ibid, p. 269.
[3] ASTM A-262 Practices A-E.
[4] T.A. Mozhi, M.C. Juhas, B.E. Wilde, Scripta Met., 21, 1987, p. 1547.
[5] A.P. Majidi and M.A. Streicher, Corrosion, 40, 1984, p. 584.
[6] C. Stawstrom and M. Hillert, J. Iron Steel Inst., 207, 1969, p. 77.
[7] C.S. Tedmon, Jr., D.A. Vermilyea, and T.H. Rosolowski, J. Electrochem. Soc., 118, 1971, 192
[8] R.L. Fullman, Acta Met., 30, 1982, p. 1407.
[9] E.L. Hall and C.L. Briant, Met. Trans., 15A, 1984, p. 793.
[10] T.A. Mozhi, W.A.T. Clark, K. Nishimoto, W.B. Johnson, and D.D. McDonald, Corrosion, 41, 1985.
[11] T.A. Mozhi, H.S. Betrabet, V. Jagannathan, B.E. Wilde, and W.A.T. Clark, Scripta Met., 20, 1986.
[12] R.L. Fullman, 'Proc. Seminar on Counter Measures for Pipe Cracking in BWR's', 1, Paper #26, WS -79-174, EPRI, 1980.
[13] D. Turnbull and R.E. Hoffman, Acta Met., 2,1954.

Figure 1
Schematic representation of LTS

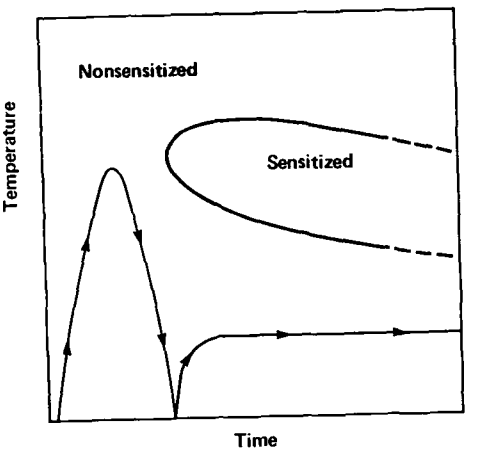


Figure 2
TTS CURVES FOR C3N1 W/ VARIABLE [illegible]

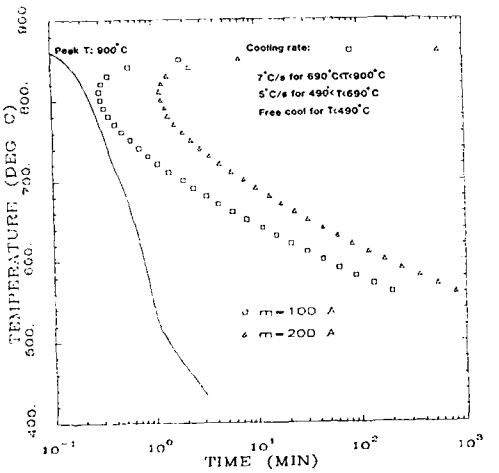


Figure 3 TTS Curves for Experimental Alloys Generated by Model & HAZ Thermal Simulation.

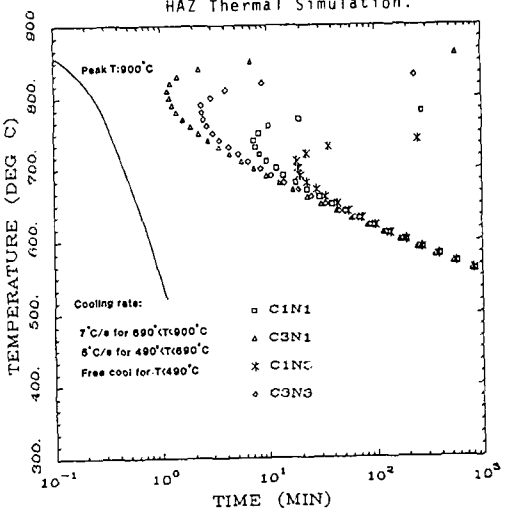


Table 1
Composition of Experimental Alloys

	Alloy Code			
	C1N1	C1N3	C3N1	C3N3
C	0.029	0.021	0.082	0.081
N	0.049	0.171	0.045	0.176
Mn	1.60	1.55	1.60	1.57
Si	0.40	0.43	0.41	0.44
Cr	16.0	16.1	16.7	16.1
Ni	12.8	12.5	12.4	12.3
Mo	2.49	2.46	2.48	2.50
P	0.002	0.002	0.002	0.002
S	0.005	0.003	0.005	0.004
Al	0.022	0.022	0.026	0.036

Abstract No. 150

Nuclear Waste Package Container Corrosion in Simulated Salt Repository Environments

Harold J. Cleary

Columbia General, Inc.

110 N. 25 Mile Avenue
Hereford, Texas 79045

This paper presents an overview of the program conducted by the DOE Salt Repository Project to develop a waste package for long-term containment of high level commercial and defense nuclear wastes in a geological bedded-salt deposit in Deaf Smith County, Texas. Although this location has recently been dropped from further consideration as a possible site for the first national repository, a discussion of the work on corrosion in hot brine environments should be of general interest.

A brief review of the geochemistry of the environment, including the stratigraphy and composition of the rock/salt strata, will be described because of their importance to corrosion processes. The initial waste package conceptual design incorporated low-carbon steel (ASTM A216, Grade WCA), which served as the reference material for corrosion studies. Computer-derived temperature profiles for the steel container surface/salt interface were employed to reflect the decay of waste package radiation levels with time. A scenario of expected corrosion behavior was developed to facilitate planning of corrosion experiments and to qualitatively anticipate effects of temperature, radiation, pressure (due to salt creep), and geochemical conditions on the container surface/environment interactions.

The basic requirement that must be met by the waste package container has been established by the U.S. Nuclear Regulatory Commission: radionuclides of the nuclear waste must be contained within the waste packages for 300 to 1000 years after closure of the repository. Low carbon steel was selected early in the program because of its good mechanical properties, ease of fabrication (including weldability), low cost, and anticipated low susceptibility to localized corrosion in brine environments. When employed as a thick-walled container, steel would also provide some shielding of the radiation emanating from the waste form. Specific dimensions of the reference container designs varied with the different types of nuclear waste form (defense waste versus assemblies of commercial spent fuel from pressurized-water or boiling-water reactors). The largest container, designed to contain boiling-water reactor fuel assemblies, measured 15.8 feet in length by 33.3 inch outer diameter, and a cylinder wall thickness of 3.9 inches. The wall thickness required to resist lithostatic pressure is 3 inches, leaving an allowance for corrosion losses of 0.9 inch. A total of about 36,000 packages is estimated to be ultimately needed for the first repository using these waste packages designs.

Degradation modes that are believed possible for low carbon steel in the rock salt environment are: uniform (general) corrosion, pitting, crevice corrosion, stress corrosion cracking, microbial corrosion, hydrogen-related failures, galvanic/thermogalvanic corrosion, intergranular corrosion, aging reactions and mechanical failures.

An extensive materials testing program undertaken at the Battelle Pacific Northwest Laboratories for the Salt Repository Project included immersion testing in the presence and absence of appropriate radiation levels, testing in solid salt/liquid brine mixtures, several types of stress corrosion cracking tests, localized (pitting, crevice) corrosion tests, hydrogen-effects studies, and electrochemical investigations. During the course of this testing program, geochemical work conducted by the Salt Repository Office established the existence of high Mg-content water inclusions in the rock, and it was also demonstrated that transport of this water to the hot container surface can occur due to thermal migration effects. These findings were of considerable importance because steel corrosion rates are greatly accelerated when high concentrations of Mg ions are present in the brine.

A workshop review of all available corrosion data from the program was conducted by an independent panel of corrosion experts in September, 1986, [Reference 1]. This workshop produced several conclusions and recommendations for testing and design. The main findings of the panel were the following: (1) because of the very high (general) corrosion rates measured for low-carbon steel in high Mg brine, further testing would be required before steel could be recommended as the container material, (2) testing of alternatives materials, including wrought Ni-Cr-Mo alloys (C-276, C-22, and 625), as well as Cu-30 Ni alloy, should be initiated, and (3) new testing techniques and waste package designs described in the panel's report should be considered. A discussion of these findings and the extent of their implementation in the Salt Repository Program will be presented.

Reference 1: Container Materials for Isolation of Radioactive Waste in Salt. Proceedings of a Workshop, held in Columbus, Ohio, September 25-26, 1986. ANL/EES-TM-339.

Abstract No. 151

PHASE STABILITY EFFECTS ON THE CORROSION BEHAVIOR OF THE METAL BARRIER CANDIDATE MATERIALS FOR THE NUCLEAR WASTE MANAGEMENT PROGRAM

G. E. Gdowski[1], D. B. Bullen[1], R. D. McCright[2], and W. G. Halsey[2].

[1]Science & Engineering Associates, Inc., 5820 Stoneridge Mall Rd., Suite 100, Pleasanton, CA 94566.
[2]University of California, Lawrence Livermore National Laboratory, P. O. Box 808 L-369, Livermore, CA 94550.

Six candidate materials are currently under consideration by the Nuclear Waste Management Program (NWMP) at Lawrence Livermore National Laboratory as potential metal barrier materials for high-level nuclear waste storage. The waste package, which must meet the Nuclear Regulatory Commission licensing requirements for the Nevada Nuclear Waste Storage Investigations Project (NNWSI), will contain spent fuel from civilian nuclear power plants (PWR and BWR fuel assemblies), commercial high level waste (CHLW) in the form of borosilicate glass containing commercial spent fuel reprocessing wastes and defense high level waste (DHLW) contained in borosilicate glass. The waste package is being designed for emplacement in the unsaturated zone above the water table at the Yucca Mountain site in Nevada. This location should result in a slightly oxidizing repository environment.

The Metal Barrier Selection and Testing Task is responsible for the selection of the materials to be employed in the waste package container. The candidate materials include three iron to nickel-based austenitic materials and three copper-based alloy materials. The austenitic materials are AISI 304L stainless steel, AISI 316L stainless steel and alloy 825. The copper-based alloy materials are CDA 102 (OFHC copper), CDA 613 (Cu-7Al) and CDA 715 (Cu-30Ni). The selection of the final metal barrier material is dependent upon the expected behavior of these materials in the repository environment.

The design criteria for the metal barrier require that the waste container maintains mechanical integrity for a period of approximately 50 years after emplacement to permit retrieval of the nuclear waste (if desired) during the preclosure phase of repository operation. The engineered barrier system is required to provide substantially complete containment of the waste for a period of up to 1000 years. The metal barrier is part of the engineered barrier system. During the containment period, the metal barrier will be exposed to a varying environment. A few years after emplacement the surface of a representative spent fuel waste package container will reach a maximum temperature of about 250°C due to decay heat from the high-level waste. This temperature will drop to about 150°C within approximately 100 years following emplacement. This time period will also include the highest gamma radiation field from the decay of the high-level waste. The expected temperatures and gamma radiation fields around CHLW and DHLW packages are less than for spent fuel waste packages.

The phase stability of the metal barrier material during the containment period will impact the mechanical and corrosion properties of the container. Changes in the microstructure can result in considerable reduction in the fracture strength of the container material. Precipitate formation, such as carbides at grain boundaries in the austenitic materials or intermetallics in the copper-based alloys, can modify the local alloy composition resulting in conditions favorable to intergranular corrosion and stress corrosion cracking.

SUMMARY OF RESULTS

An analysis of the data in the technical literature with respect to phase stability of the austenitic materials noted significant data dealing with phase stability in the stainless steel alloys. The 304L and 316L, which are located near the $\alpha+\gamma$, $\alpha+\gamma+\sigma$, and $\gamma+\sigma$ phase fields of the Fe-Ni-Cr ternary phase diagram in Figure 1 [1], were identified as metastable materials at repository relevant conditions. Metastability was defined as nonequilibrium phase formation due to kinetic limitations [2,3]. In the 304L and 316L stainless steels, the diffusion processes that permit precipitation are severely limited at low temperatures (T < 600°C) [4].

Carbide precipitation was identified in all of the austenitic candidate alloys. The precipitation of $M_{23}C_6$ carbides was predominant in the 304L alloy. Similar precipitation behavior was noted for 316L with somewhat shorter time periods for the onset of grain boundary $M_{23}C_6$ precipitation. Intermetallic phase formation was noted in 316L at relatively long times. These intermetallic phases include sigma, chi and Laves phases [5]. Sigma phase formation was shown to significantly reduce the impact strength of austenitic alloys due to its hard brittle microstructure. No intermetallic phase formation was documented in alloy 825.

Very little phase stability data was identified for alloy 825. The limited data that was found dealt primarily with $M_{23}C_6$ carbide precipitation. The $M_{23}C_6$ carbides that precipitated in the 825 alloy had varying composition [6]. The chromium and titanium contents of these precipitates were a function of precipitation time and temperature. Increased Ti content in these precipitates limited the depletion of Cr near the precipitate and preserved the corrosion resistance of the alloy. Speculation about the possibility of "submicroscopic" sigma phase precipitation in alloy 825 was noted [7]. However, no data was identified to substantiate this claim.

Considering the effect of phase stability only, the following ranking of the austenitic candidate materials is proposed: Alloy 825 (best) > 316L > 304L (worst). This order is based on the fact that alloy 825 is a stable austenite at all temperatures. The only documented precipitation noted for alloy 825 was the formation of $M_{23}C_6$ carbides. These carbides, which had varying Cr content, did not appear to significantly affect to corrosion resistance of the alloy.

The 316L stainless steel is susceptible intermetallic phase formation including the formation of the sigma phase. Sigma phase formation can result in significant degradation in the mechanical properties of the alloy. The 316L alloy was also affected by $M_{23}C_6$ carbide precipitation which could deplete Cr near the precipitates and promote grain boundary attack.

The 304L stainless steel also exhibited significant $M_{23}C_6$ carbide precipitation which could result in grain boundary attack. This alloy is also more prone to martensite formation than 316L stainless steel.

An analysis of the data in the literature with respect to the phase stability of the copper-base candidate materials (CDA 102, CDA 613, and CDA 715) notes that all the candidate materials are single-phase to at least 300°C. There is a proposed two phase region for CDA 715 at temperatures less than 200°C as shown in Figure 2 [8], but constituent diffusion rates [9] are so slow at the expected repository temperatures that a phase transformation does not appear likely.

Iron migration in both CDA 613 and CDA 715 may be a potential source of mechanical degradation of these materials. The mechanical properties rely on small iron particles being uniformly dispersed throughout the bulk [10]. Calculations indicate that the iron diffusion length should be small under the expected repository conditions [11-14], but it is not known what the potential degradation of the mechanical properties would be even for relatively small perturbation of the iron particle distribution.

Considering only the phase stability of the three copper-based alloys, the following ranking is proposed: CDA 102 (best) > CDA 613 = CDA 715. CDA 102 is ranked first because it is essentially pure copper and is single phase. CDA 613 and CDA 715 are also known to be single phase at high temperature, but they are ranked lower than CDA 102 for two reasons. 1) There may be an unknown phase transition that occurs at the expected repository temperatures after extended time periods. 2) Iron migration may occur in the bulk and cause mechanical degradation. Preliminary calculations indicate that these effects may not be critical, but more extensive modeling is suggested.

Analysis of the data available in the literature with respect to phase stability of the candidate materials at repository relevant conditions has identified alloy 825 as the superior austenitic alloy and CDA 102 as the superior copper-based alloy. Both alloys are single phase materials over the entire temperature range from solidus to room temperature. Other factors besides phase stability will also influence which material is eventually selected for fabricating nuclear waste containers.

ACKNOWLEDGEMENT

This work was performed under the auspices of the U. S. Department of Energy by Lawrence Livermore National Laboratory under Contract W-7405-Eng-48.

REFERENCES

1. W. Betteridge, Nickel and Its Alloys, (John Wiley &Sons, New York, 1984).
2. E.C. Bain and R.H. Aborn, in Metals Handbook, (American Society for Metals, Metals Park, Ohio, 1948), p. 1261.
3. G.R. Speich, in Metals Handbook, Vol. 8, (American Society for Metals, Metals Park, Ohio, 1973) p. 425.
4. B. Weiss and R. Stickler, Metall. Trans., 3 (1972) 851.
5. C.J. Bechtoldt and H.C. Vacher, J. Res., Nat. Bur. Stand., 58 (1953) 7.
6. E.L. Raymond, Corrosion, 24 (1968) 180.
7. H.R. Copson, B.E. Hopkinson and F.S. Lang., Proc. ASTM, 61 (1961) 879.
8. Metals Handbook, 8th Edition, ASM Handbook, ASM, Metal Park, Ohio.
9. E.A. Feest and R.D. Doherty, J. Inst. Metals 99 (1971) 102.
10. E.G. West, Copper and Its Alloys, John Wiley, 1982.
11. S.K. Sen, M.B. Dutt and A.K. Barua, Phys. Stat. Sol. 45 (1978) 657.
12. J.G. Mullen, Phys. Rev. 121 (1961) 1649.
13. G. Salje and M. Feller-Kniepmeier, J. Appl. Phys. 49 (1978) 229.
14. J. Bernardini and J. Cabane, Acta Metall. 21 (1973) 1561.

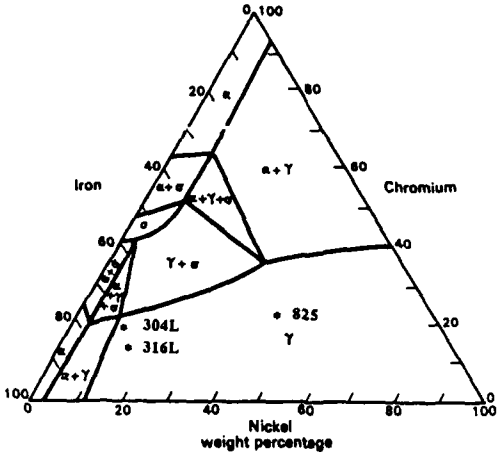


Figure 1. Iron-Chromium-Nickel equilibrium phase diagram at 650°C [1]. Not the location to the alloys 304L, 316L and 825.

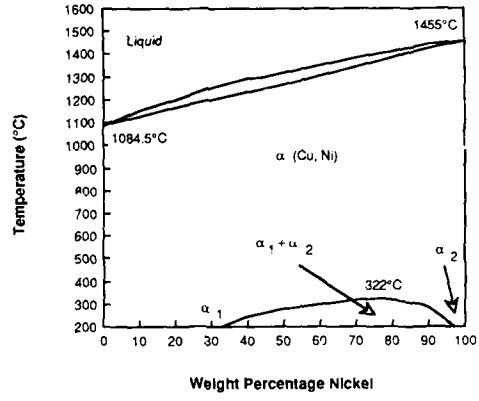


Figure 2. Equilibrium phase diagram for the Cu-Ni system [8]. The miscibility gap is proposed [9] but has not been experimentally observed.

Abstract No. 152

A Database for Reviews and Evaluations of High-Level Waste Documents

C. G. Interrante, C. Messina, and S. A. Harrison
National Bureau of Standards, Gaithersburg, MD 20899

An automated storage and retrieval system that uses a commercially available database management system (DBMS) has been developed to serve as a data index for high-level waste (HLW) reports and as a database containing NBS evaluations of HLW reports. The evaluations are critical reviews of reports, generated mainly by the Department of Energy (DOE), on topics related to processes involved in the degradation of the engineered barrier system designed to contain and control the release of radionuclides contained in waste packages to be placed in a repository for HLW. The intention is to use this system within the framework of the capabilities of a personal computer. The data can be accessed with a DBMS that operates on no more than 512K of memory.

All aspects of the PC system are fully functional in respect to the usage of scientific notations, Greek letters and super- and sub-scripts. Thus, on-screen displays, print outs and search strings may contain chemical formulas or proper scientific names. The following example, taken from an NBS review [1] of a paper by McCright, R. D., 1985 [2] is used to illustrate these aspects of the system:

"The authors, rightly, emphasize the fact that the major source of uncertainty in the corrosion behavior of Cu-base alloys in the Nevada repository is the lack of information concerning the effect of γ-radiation. Some of the experimental results indicate that one of the major consequences of radiation is H_2O_2 production, so that the addition of H_2O_2 mimics reasonably well the radiation effects.."

Many DBMSs limit the sizes of both the records and fields used in the database. Each review of a document is one record in this database. Each sub-category within the review is a field. The capabilities of a number of DBMSs were examined during the period in which the requirements of a computer assisted database for reviews and evaluations on HLW data were being analyzed [3]. At present, the system contains almost 100 reviews of 13 fields per review while the largest review has over 21,000 ASCII characters, others may be only a fifth or a tenth of this size. All of these reviews can be searched in the full text mode. This requirement for search of large text fields was only one of sixteen requirements taken into consideration in the selection of a suitable DBMS for this application. The number of reviews that can be contained in this system is limited by the size of the mass storage units used with the PC. The theoretical limit to the number of reviews is 64,000 in one file, but multiple files can be used if needed.

The principal barriers proposed for use in the waste package are metal alloys and borosilicate glass. The technical problems of primary interest in the waste package involve leaching of the glass, corrosion of the alloys, transport processes within the waste package, and modelling efforts aimed at permitting prediction of long-term behaviors. The reviews focus attention on the availability of data that are applicable to the resolution of technical issues that must be considered in the process of obtaining a license to build a repository.

The automated system is designed to store and quickly retrieve pertinent reports on relevant topics using a set of keywords that are structured into the four major categories of the technical reviews: Technical Description of the Report, Environmental Factors of the Test, Materials Tested (metallic, non-metallic, radioactive, environmental), and Properties and Failure Modes Studies. The major categories are divided into 25 sub-categories that facilitate the storage and retrieval processes, which presently involve the use of about 300 keywords.

In addition to the normal searches of bibliographic information, the search capability is extended to any other aspect or all other aspects of the technical review, such as the "uncertainties in the data" or the "general comments of the reviewer." These alternative searches are intended to be used after an initial cut of the existing database is made using the keywords to focus attention on a few documents of interest. A keyword search, may be followed by a text search of a specific sub-category before the much slower search of the full text of the most pertinent reviews is contemplated. In this way, short total search times on a personal computer are achieved. This storage and retrieval system for reviews of HLW documents is expected to be complementary to a separate system, under development elsewhere, for storage and retrieval of the full text of all HLW documents.

References

[1] C. Interrante, E. Escalante, A. Fraker, M. Kaufman, W. Liggett, and R. Shull, "Evaluation and Compilation of DOE Waste Package Test Data: Biannual Report December 1985 - July 1986," NUREG/CR-4735, Vol. 1, March 1987.

[2] R. D. McCright, "FY 1985 Status REport on Feasibility Assessment of Copper-Base Waste Package Container Materials in a Tuff Repository", UCID 20509, September 30, 1985.

[3] C. Interrante, C. Messina, S. Harrison, R. Shull, M. Kaufamn, U. Bertocci, and E. Escalante, "An Analysis of the Requirements for a Computer Assisted Database for Reviews and Evaluations on High Level Waste Data," NBSIR 86-3363 (NRC) (R), June 1986.

Abstract No. 153

THE EFFECTS OF HYDROGEN ON THE METAL BARRIER CANDIDATE MATERIALS FOR THE NUCLEAR WASTE MANAGEMENT PROGRAM

D. B. Bullen[1], G. E. Gdowski[1], R. D. McCright[2], and W. G. Halsey[2].

[1]Science & Engineering Associates, Inc., 5820 Stoneridge Mall Rd., Suite 100, Pleasanton, CA 94566.
[2]University of California, Lawrence Livermore National Laboratory, P. O. Box 808 L-369, Livermore, CA 94550.

The Nuclear Waste Management Program (NWMP) at Lawrence Livermore National Laboratory is responsible for the development of the waste package design to meet the Nuclear Regulatory Commission licensing requirements for the Nevada Nuclear Waste Storage Investigations Project (NNWSI). This waste will include spent fuel from civilian nuclear power plants (PWR and BWR fuel assemblies), commercial high level waste (CHLW) in the form of borosilicate glass containing commercial spent fuel reprocessing wastes and defense high level waste (DHLW) contained in borosilicate glass. The waste package is being designed for emplacement in the unsaturated zone above the water table at the Yucca Mountain site in Nevada. This location should result in a slightly oxidizing repository environment.

The Metal Barrier Selection and Testing Task is responsible for the selection of the materials to be employed in the waste package container. Six candidate materials are currently under consideration. These materials include three iron to nickel-based austenitic materials and three copper-based alloy materials. The austenitic materials are AISI 304L stainless steel, AISI 316L stainless steel and alloy 825. The copper-based alloy materials are CDA 102 (OFHC copper), CDA 613 (Cu-7Al) and CDA 715 (Cu-30Ni). The selection of the final metal barrier material is dependent upon the expected behavior of these materials in the repository environment.

The design criteria for the metal barrier require that the waste container maintain mechanical integrity for a period of approximately 50 years after emplacement to permit retrieval (if desired) of the nuclear waste during the preclosure phase of repository operation. The engineered barrier system is required to provide substantially complete containment of the waste for a period of up to 1000 years. The metal barrier is part of the engineered barrier system. During the containment period, the metal barrier will be exposed to a varying environment. A few years after emplacement the surface of a representative spent-fuel waste package container will reach a maximum temperature of about 250°C due to the decay heat of the high-level waste. This temperature will drop to about 150°C within approximately 100 years following emplacement. This time period will also include the highest gamma radiation field from the decay of the high level waste. This radiation will promote radiolytic decomposition of water vapor near the container surfaces. The hydrogen evolved by this radiolysis process has the potential to significantly alter the metallurgical behavior of the container material. Another source for hydrogen is from the slow electrochemical decomposition of water on a corroding metal surface. The expected temperatures and gamma radiation fields around CHLW and DHLW packages are less than for spent fuel waste packages.

SUMMARY OF RESULTS

An analysis of the available data with respect to the effects of hydrogen on the austenitic candidate materials 304L, 316L, and alloy 825 has been completed. There is significant documentation to show that 316L is less susceptible than 304L to hydrogen embrittlement at room temperature [1]. Both alloys are less susceptible to hydrogen when they have finer grain sizes and are not sensitized, although 316L appears to be less sensitive to sensitization for finer grain sizes.

There is a definite lack of literature on hydrogen effects in alloy 825. The only published data indicates that 825 may be slightly more susceptible to hydrogen than 316 [2]. In this study, hydrogen was introduced by cathodic charging in 5% sulfuric acid saturated with CS_2 for periods of 2 to 32 days. The results from this study have shown that hydrogen concentrations on the order of tens of parts per million were sufficient to cause degradation of the mechanical properties of all three alloys.

Some hydrogen embrittlement studies in 304 showed that the alloy was less susceptible to degradation at elevated temperatures. In one study [3] no slow crack growth in hydrogen was reported at 170°C. In another study [4], no ductility losses due to hydrogen were reported at 107°C. There were no reported elevated temperature studies for either 316 or alloy 825.

Modeling the possible deleterious effects of hydrogen will require a knowledge of hydrogen solubilities and diffusivities in the container material. These properties for 304 and Ni are shown in Figures 1 and 2 [5-7]. At room temperature solubilities are of the order of parts per million and diffusivities are of the order of 10^{-10} to 10^{-12} cm^2/sec in both materials. There is no data for 316, but hydrogen solubility and diffusivity in the stainless steel austenites are reported to be similar. There is no data for hydrogen in 825, so pure nickel data is presented as a first approximation.

The effects of hydrogen on the candidate materials CDA 102, CDA 613 and CDA 715 have also been analyzed. There is a significant body of data documenting the effect called "hydrogen sickness", which is the reduction of Cu_2O impurities located on the grain boundaries [8,9]. This reduction results in the formation of a water molecule and a void space which is stabilized by the water vapor. The interconnection of these cavities results in significant degradation of the mechanical properties of the metal and the subsequent brittle failure mode, which is observed experimentally. This can occur with as little as 22 atomic parts per million (appm) oxygen and, in the worst case, with enough hydrogen to titrate the oxygen, that is, 44 appm [10]. Although this is a significant hydrogen concentration, the long term containment requirements of the repository may result in oxide reduction by radiolytic hydrogen or corrosion by-product hydrogen that slowly diffuses into the grain boundaries of the container material.

The solubility of hydrogen in copper was documented and the data were plotted in Figure 3 over the temperature range of interest for repository applications [11-13]. The diffusivity and permeability of hydrogen in copper were also documented over the same temperature range. Theoretical models and experimental evidence of the trapping of hydrogen in copper and copper-aluminum were noted. The detrapping temperatures varied slightly for pure copper (50°C) [14] and the copper-aluminum alloy (110°C) [15]. Direct application of these models and data to repository conditions is not suggested since the hydrogen charging and trapping methods employed in these studies were very extreme.

There was very little available data on hydrogen effects in the copper-nickel alloy system. The results that were available indicate that the solubility of hydrogen increases with increasing nickel concentration as shown in Figure 4 [16]. This result, coupled with the lack of data in the literature, suggest that there is probably little observable hydrogen effect in the copper-nickel system.

Analysis of the available hydrogen effects data suggests that alloy 825 and 316L stainless steel may be superior to 304L in resisting degradation in a hydrogen environment. CDA 715 appears to be more resistant to hydrogen degradation than CDA 613 and CDA 102. Direct comparisons between the austenitic alloys and the copper-based alloys were not attempted. Other factors besides resistance to hydrogen effects will also influence which material is eventually selected for fabricating nuclear waste containers.

ACKNOWLEDGEMENT

This work was performed under the auspices of the U. S. Department of Energy by Lawrence Livermore National Laboratory under Contract W-7405-Eng-48.

REFERENCES

1. E. Minkovitz and D. Eliezer, J. Mater. Sci., 17 (1982) 3165.
2. D.L. Graver, Corrosion of Nickel-Base Alloys, American Society for Metals, (1984) 79.
3. D. Eliezer, D.G. Chakrapani, C.J. Altstetter and E.N. Pugh, Met. Trans. 10A (1979) 935.
4. G.R. Caskey, Scripta Metall. 11 (1977) 1077.
5. T. Perng and C.J. Altstetter, Acta Metall. 34 (1986) 1771.
6. J. Cernak and A. Kufudakis, J. Less-Common Metals 49 (1976) 309.

7. E. Fromm and E. Gebhardt, eds., Gase und Kohlenstoff in Metallen, Springer Verlag, (1976).
8. E. Mattsson and F. Schuckher, J. Inst. Metals 87 (1959) 241.
9. C.E. Ransley, J. Inst. Metals 65 (1939) 147.
10. E. Albert, R. Kirchheim and E. Fromm, Gase in Metallen, Deutsche Gesellschaft fur Metallkunde, Darmstadt (1979) 45-49.
11. T. Ishikawa and R.B. McLellan, J. Phys. Chem. Solids 46 (1985) 445.
12. L. Katz, G. Guinan and R.J. Borg, Phys. Rev. B, 4 (1971) 330.
13. Y. Sakamoto and K. Takao, J. Jap. Inst. Metals, 46 (1982) 285.
14. W.R. Wampler, T. Schoeber and B. Lengeler, Hydrogen in Metals, Proceedings of the Second International Congress on Hydrogen in Metals, Paris, (1977) 1B11.
15. J.J. Kim and J.G. Byrne, Mat. Sci. Engr., 74 (1985) 201.
16. W. Himmler, Z. Physik. Chem. 195 (1950) 244.

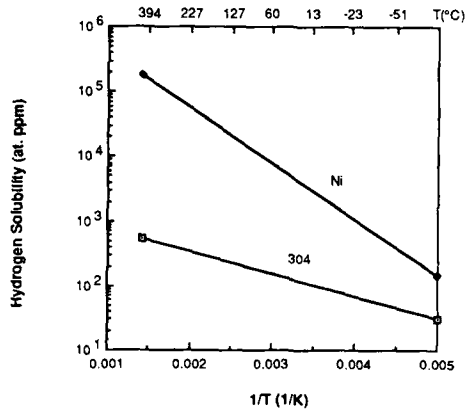


Figure 1. Plots of the best fit equations to experimental data for hydrogen solubility (at a pressure of 1 atmosphere) in 304 [5] and Ni [7]. The experimental data is in the temperature range 200°C < T < 350°C.

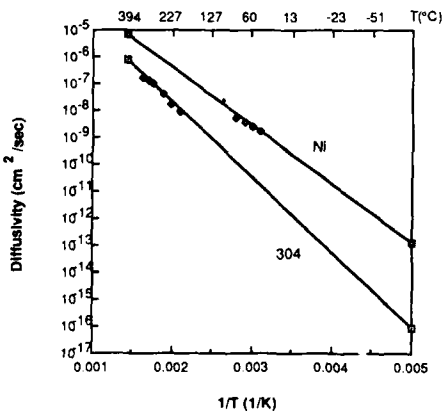


Figure 2. Hydrogen diffusivity for 304 [5] and Ni [6] with best fit equation to experimental data.

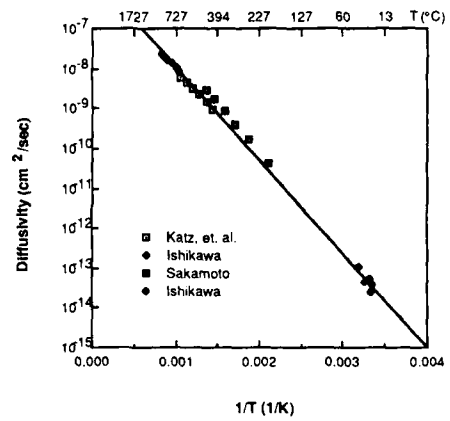


Figure 3. Hydrogen diffusivity in copper as a function of temperature [11-13].

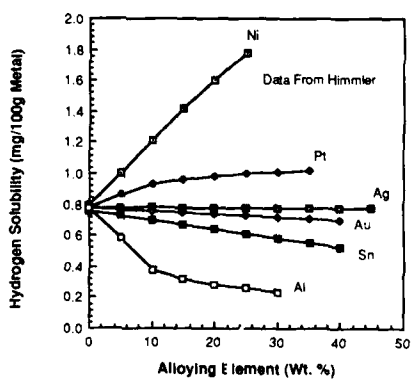


Figure 4. Hydrogen solubility in copper alloys as a function of alloying element (wt. %) at 1225°C. Note the increase in hydrogen solubility with increasing nickel content [16].

Abstract No. 154

MATHEMATICAL MODELS FOR REDOX AND CORROSION POTENTIALS FOR HIGH LEVEL NUCLEAR WASTE CONTAINERS IN TUFF ENVIRONMENTS

Mirna Urquidi-Macdonald and Digby D. Macdonald
SRI International
Menlo Park, CA 94025

Recently, the Yucca Mountain tuff site was selected as the repository for high level nuclear waste (HLNW) for the United States. Characteristic features of this repository include that it is a "dry" environment, in that the containers are not expected to be in contact with liquid water but instead will be exposed to moist air, and that the pressure exerted by the environment on the canisters will be approximately *atmospheric*. The paramount consideration in selecting a container material is that it must be sufficiently corrosion resistant to provide "substantially complete" containment for a period of no less than 300 years and up to 1000 years after closure of the geological repository. In order that this question can be addressed rationally, it is necessary to predict how the environment will evolve over a period of time that is an order of magnitude longer than our experience in quantitative corrosion science.

As part of the Nevada Nuclear Waste Storage Investigation Project, we have developed mixed potential models for predicting the environment redox potential and corrosion potentials for HLNW containers in tuff repositories. The models assume that the container is in contact with a thin aqueous layer on the surface, possibly present as a capillary condensate in the pores of a corrosion product *film* (Figure 1). This water layer is subject to n and γ radiolysis to produce electroactive species, such as H_2, O_2, H_2O_2, OH, O_2^-, HO_2^-, HO_2, H, e_{aq}^-, H^+, and OH^- via a mechanism that involves 33 homogeneous reactions. Additionally, these nonequilibrium species are assumed to undergo charge transfer reactions at the metal surface in addition to the oxidation of the container material itself. These reactions take place such that the total current is zero; the mixed potential at which this occurs is termed the "redox potential" if the container is not corroded but is the "corrosion potential" when container oxidation is taken into account. The eleven coupled, nonlinear, second order partial differential equations that describe the transport, generation, and reaction of the radiolysis products within the film are solved *numerically*, with the additional constraints that the film must be electrically neutral at all points and that the temperature and n and γ intensities decay exponentially with time.

Using estimates for the various kinetic parameters for reactions at the container surface (exchange current densities, transfer coefficients, etc.) we have calculated corrosion potentials as a function of time for carbon steel, AISI 304L SS, AISI 316 SS, Alloy 825, copper, and copper alloys CDA-102, CDA-163 and CDA-715. Typical calculations of the change in corrosion potential for AISI 304L with time are shown in Figure 2 and estimated concentrations of the various radiolysis products are displayed in Figure 3. Generaly, we predict that the corrosion potential shifts sharply in the positive direction at short times followed by a slow drift to more positive values as time goes on. This is attributed to the competing effects of decreasing temperature and (γ, n) intensity; the former tends to shift the corrosion potential in the noble direction while the latter results in a shift in the active direction. Apparently, for the parameter values selected in this study, the effect of decreasing temperature dominates.

ACKNOWLEDGMENTS

The authors gratefully acknowledge the keen interest shown in this work by Drs. R. D. McCright, R. Van Konynenberg, R. Glass, and C. Acton of the Lawrence Livermore National Laboratory. The work was supported through Contract No. W-7405-ENG-48.

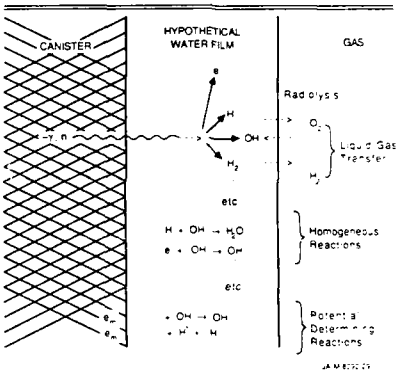


Figure 1. Schematic of the layer reaction model

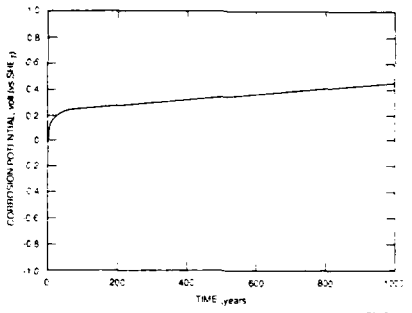


Figure 2. Calculated corrosion potential for 304L stainless steel versus time

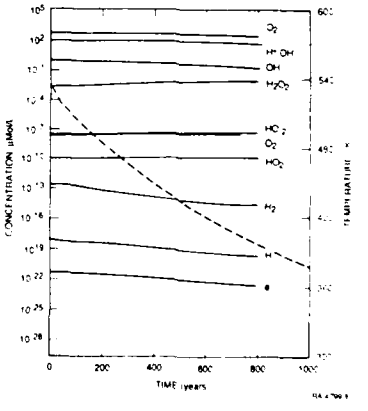


Figure 3. Calculated evolution of different radiolytic species, as a function of concentration over film thickness, with time

Abstract No. 155

Pitting Kinetics of Carbon Steel and Low-Alloy Steel Exposed to a Groundwater/Packing Material Environment

J.B. Lumsden and A.T. Allen

Rockell International Science Center

1049 Camino Dos Rios
Thousand Oaks, CA 91360

R.L. Fish

Westinghouse Hanford Co.
P.O. Box 1970
Richland, WA 99352

Laboratory investigations were conducted on carbon steel and low-alloy steel to assess their potential corrosion performance in the hydrothermal conditions that were anticipated at the Hanford repository basalt site. The work reported focused on obtaining kinetic relationships of pitting processes. The test environment used was a synthetic groundwater-packing material mixture, which consisted of 75% crushed basalt and 25% bentonite. Measurements were carried out with specimens in pressure vessels at 50, 100, 150 and 200°C. Before the pressure vessels were sealed, the oxygen content of the synthetic groundwater was lowered to less than 50 ppb by sparging with argon gas.

To establish conditions required to initiate pitting, anodic and cathodic potentiodynamic polarization curves were generated, using an interrupter technique to correct for ohmic potential drops. Polarization curves were taken after 1, 24 and 168 h exposures at open circuit conditions to evaluate aging effects. Passivation and pitting were observed at all conditions investigated for low-alloy steel. Carbon steel did not passivate at 50°C. However, passivation and pitting were observed in carbon steel at 100, 150 and 200°C. The extent of the passive range of potentials increased with exposure time, indicating that the protective properties of the passive film increased with aging time.

To establish pit growth rates, a device was designed and constructed which could be used to measure the penetration time of pits propagating through thin-walled specimens mounted in autoclaves. Using this apparatus, pitting kinetics were determined from penetration times through specimens with varying wall thicknesses. The specimens were polarized at potentials, ΔE_p, 50 and 25 mV above the pitting potential. Table 1 shows the expressions obtained for the time dependence of pit depth. These relationships have the form $d_p = at^b$. Under all conditions, the power of the time dependence is less than one. Thus, the rate of pit growth decreases with time, indicating that pit-growth will effectively cease in materials sufficiently thick.

The protection potential, E_{pr}, the potential below which pits will not propagate if initiated, was determined for carbon steel. Pits were initiated by pulsing the potential above the pitting potential, after which it was stepped down to values below E_p. These values were the following:

$E_{pr}(100°C) = -315\ mV_{SHE}$

$E_{pr}(150°C) = -290\ mV_{SHE}$

$E_{pr}(200°C) = -120\ mV_{SHE}$.

Table 1
Expressions for the Time Dependence of the Pit Depth (inches) in Carbon Steel and Low-Alloy Steel Polarized Above the Pitting Potential, ΔE_p, and at Various Temperatures

	Carbon Steel		Fe-9Cr-1Mo	
$T/\Delta E_p$	50 mV	25 mV	50 mV	25 mV
200°C	$2.0 \times 10^{-3} t^{0.24}$	$2.6 \times 10^{-3} t^{0.45}$	$4.7 \times 10^{-3} t^{0.28}$	$2.0 \times 10^{-3} t^{0.62}$
150°C	$2.0 \times 10^{-3} t^{0.53}$	$1.8 \times 10^{-3} t^{0.58}$	$2.7 \times 10^{-3} t^{0.58}$	$2.0 \times 10^{-3} t^{0.61}$
100°C	$1.2 \times 10^{-3} t^{0.41}$	$7.9 \times 10^{-4} t^{0.41}$	$7.0 \times 10^{-4} t^{0.76}$	$1.\ldots \times 10^{-3} t^{0.64}$
50°C	--	--	$1.4 \times 10^{-3} t^{0.49}$	$1.4 \times 10^{-3} t^{0.54}$

Abstract No. 156

Corrosion Behavior of Low Carbon Steel in High pH Aqueous Media

Anna C. Fraker and Jonice S. Harris
National Bureau of Standards, Gaithersburg, MD 20899

The purpose of this work was to study the corrosion behavior and localized corrosion susceptibility of low carbon steel in simulated ground water at a pH of 9.75 and a temperature of 95 C. These studies were conducted as part of a program to evaluate materials for long term nuclear waste storage. The test conditions used in the present study typify those of a basalt repository in the state of Washington, but selected aspects of the results are applicable to low carbon steels in other environments of similar composition.

Previous studies of low carbon steel in this environment indicated that pits were occasionally found after testing but stated that pitting would not develop in repository conditions[1]. In general, pitting would not be expected in low carbon steel in aqueous media due to the absence of surface passivation[2,3,4]. Other reports on corrosion of low carbon steel in aqueous media indicated uneven attack over the specimen surface but did not indicate pitting attack[5].

Modeling studies[6] of pit propagation in low carbon steel showed that pit depth propagation increased with the presence of inert or nonreactive pit walls. It has not been determined that sufficient pit depth and corrosion product accumulation would develop to produce this protective effect assumed in the model.

The present investigation applied conventional electrochemical techniques to study pitting susceptibility of low carbon steel, and procedures and results are discussed. Testing involved making cyclic anodic polarization measurements of the A 27 low carbon steel specimens in Grande Ronde No. 4 water at a temperature of 95 C. The pH was approximately 9.75. Some tests were made in Grande Ronde No. 4 water containing a mixture of 75 percent basalt and 25 percent bentonite. The basalt and bentonite mixture were to fill one half of the testing flask, but the bentonite expanded upon becoming wet and the mixture filled approximately two thirds of the volume of the flask. The solution and mixture were held at temperature for one hour prior to inserting the specimen and beginning the test.

The specimen was placed in the 95 C solution and left at open circuit potential for fifteen minutes prior to making the polarization measurements. The potentiostatic polarization measurements were made by applying a potential to the specimen at the rate of 0.01 V/ 15 sec. All voltages are in reference to a saturated calomel electrode (S.C.E.).

Electrochemical measurements indicated that pitting would not be occurring. Microscopic examination of corroded specimens indicated overall general uneven surface corrosion with some shallow local attack in the ferritic phase. Since the specimen never passivated, the localized attack was related to preferential surface sites, and not to the usual electrode potential difference and current densities for producing pits of unknown depth and damage. These results indicate that pitting, as classically defined, does not occur in this low carbon steel. The overall general corrosion, thick surface films, and nonpassivating conditions resulted in limited and shallow localized attack. Observations of surfaces after the thick film was removed revealed preferential attack in the pearlitic regions.

References

1. Lumsden, J. B., Pitting Behavior of Low Carbon Steel, BWI-TS-014, August, 1985.

2. Kruger, J., Fundamental Aspects of the Corrosion of Metallic Implants, American Soc. for Testing and Materials Special Tec. Pub. 684, 107-127, 1979.

3. Syrett, B. C., PPR Curves - A New Method of Assessing Pitting Corrosion Resistance, Corrosion, Vol. 33, 6, 221, 1977.

4. Szklarska-Smialowska, Z., Pitting Corrosion of Metals, Nat. Assoc. of Cossosion Engineers, Houston, TX 77084, 1986.

5. Westerman, R. E., Haberman, J. H., Pitman, S. G., Pulsipher, B. A. and Sigalla, L. A., Corrosion and Environmental-Mechanical Characterization of Iron/Base Nuclear Waste Package Structural Barrier Materials, PNL-5426, UC 70, 1986.

6. Beavers, John. A. and Markworth, Alan J., Pit Propagation of Carbon Steel in Groundwater, NRC contract, B-0708, 1987.

Abstract No. 157

CORROSION OF CARBON STEEL IN BRINE: Mg^{++} EFFECT

C. Manfredi, S. Kesavan, T.A. Mozhi and B.E. Wilde

Fontana Corrosion Center,
Department of Metallurgical Engineering,
The Ohio State University,
Columbus, Ohio 43210.

INTRODUCTION

Carbon steel has potential as a candidate material for containment of high level nuclear waste in permanent repositories in rock salt. In addition to large amounts of NaCl, rock salt contains significant amounts of other chlorides, especially Magnesium chloride. The increase in corrosion rate of carbon steel in brines containing Mg^{2+} ions has been reported previously(1,2). The objective of the present investigation was to identify the mechanism which leads to the observed high corrosion rates of carbon steel in Mg^{2+} containing brines.

EXPERIMENTAL PROCEDURE

The material used in this investigation was A 216 grade WCA carbon steel. Anodic and Cathodic polarization experiments, controlled anodic potential current/time and linear polarization experiments were carried out at 150, 125, 100, 75 and 50°C in saturated NaCl with appropriate Magnesium Chloride additions. The experiments at temperatures above 100°C were conducted in static Hastelloy autoclaves. A conventional Pyrex glass cell with an electrical heating mantle was used for tests conducted at temperatures below 100°C. High temperature pH measurements were made using a Yttria stabilized Zirconia tube as the pH sensor.

RESULTS AND DISCUSSION

Figure 1 shows anodic and cathodic polarization curves at 100°C for A216 carbon steel in saturated NaCl solution with varying Mg^{2+} additions. Anodic polarization curves exhibit a well defined Tafel behaviour before the appearance of an anodic limiting current plateau. It is clear from the anodic polarization curves that there is no significant change in the anodic behaviour of carbon steel due to Mg^{2+} additions to saturated brine. The observed increase in the corrosion rate with Mg^{2+} additions is due to a change in the cathodic Tafel slope. This change in the cathodic Tafel slope also leads to a positive shift in the corrosion potential.

High Temperature pH measurements (Table 1) in Mg^{2+} containing brines show a sharp decrease in pH proportional to Mg^{2+} additions. This result strongly suggests hydrolysis of $MgCl_2$ leading to a build up of HCl. The probable equation is:

$$MgCl_2 + H_2O \rightarrow Mg(OH)Cl + HCl$$

Linear polarization experiments were conducted to monitor corrosion rate continuously over a period of time. Figure 2 shows a typical plot of corrosion rate versus time obtained using linear polarization technique. Steady state corrosion rate is reached after approximately 60 hours and it is about an order of magnitude lower than the corrosion rate at the start of the experiment. Table 2 shows the steady state corrosion rates obtained at 150°C.

CONCLUSIONS

The very high corrosion rates found in brines containing Mg^{2+} ions is due to hydrolysis of $MgCl_2$ at high temperatures.

REFERENCES

1) J.W. Braithwaite and N.J. Magnani, Scientific Basis for Nuclear Waste Management, G.J. McCarthy ed., Plenum Press, New York, Vol. 1, p.283,1979.

2)R. Westerman, S.H. Haberman, S.G. Pitman and L.A. Sigalla, Annual report FY 1984: "Corrosion environmental-mechanical characterization of Iron base Nuclear Waste package structural barrier materials", Pacific Northwest Laboratories,1984.

Figure 1: Anodic and Cathodic polarization curves at 100°C for A 216 WCA grade carbon steel in saturated NaCl with Mg^{2+} additions.

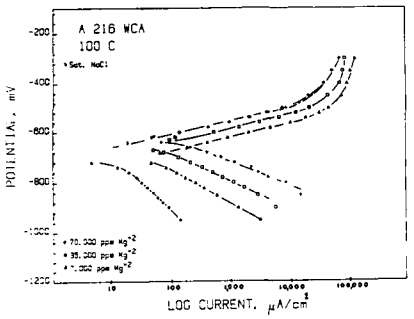


Figure 2: Corrosion rate/time plot at 150°C (obtained by linear polarization technique) for A216 WCA grade steel in saturated NaCl with 70K and 35K ppm Mg^{2+} additions.

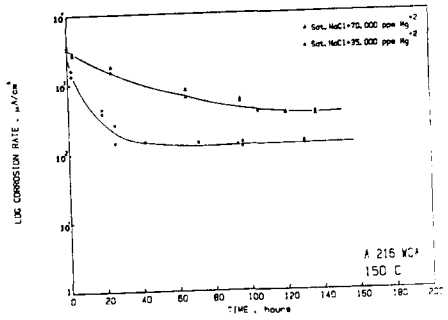


Table 1: Results of pH measurements at 150°C in saturated brines ccntaining varying concentrations of Mg^{2+} ions.

SYSTEM	E_T $mV_{Ag/AgCl}$	pH @150°C	pH @ R.T
Saturated NaCl	490	4.05	5.7 (5.7)
NaCl+7K ppm Mg^{2+}	680	1.80	5.8 (6.2)
NaCl+35K ppm Mg^{2+}	690	1.68	4.2 (5.8)
NaCl+70K ppm Mg^{2+}	780	0.60	3.4 (4)*

* The pH values in brackets correspond to the pH of the respective system measured after autoclaving and at room temperature.

Table 2: Steady state corrosion rates for A216 WCA grade steel in Saturated NaCl with varying Mg^{2+} ion concentrations (@150°C).

SYSTEM	i_{corr} (at steady state) $\mu A/cm^2$
Saturated NaCl	1.5
NaCl+35K ppm Mg^{2+}	130.0
NaCl+70K ppm Mg^{2+}	400.0

Abstract No. 158

EFFECT OF TRANSPORT AND RESISTIVITY CHARACTERISTICS OF THE ENVIRONMENT ON THE CORROSION OF STEEL

E. Escalante and T. Oka*
National Bureau of Standards
Gaithersburg, MD 20899

Most studies on corrosion of High Level Waste container materials are carried out in aqueous solutions in which the transport processes of diffusion and convection are high. However, it is important to consider the effect of low transport and high resistivity properties, as expected in the tuff environment of Yucca Mountain, on the corrosion of metals. Conditions of low transport and high resistivity can cause localized corrosion, as observed in other environmetal systems, resulting in higher penetration rates than would develop under conditions of uniform corrosion. In this study, transport and resistivity are controlled over several orders of magnitude, and their effect on the rate and form of corrosion are observed.

Small steel coupons are immersed in a matrix of environmental conditions in which transport and resistivity are controlled, and the corrosion rate of each coupon is measured periodically. Measurements of corrosion rate are carried out using polarization resistance and a. c. impedence techniques. The technique of polarization resistance allows a rapid determination of corrosion rate, however, correction for iR error in the potential measurements, in high resistivity media, must be performed. During the corrosion measurement, specimens are polarized from -10 to 10 mV, versus open circuit potential, and the current applied to obtain this change is measured. Corrosion rates are calculated from the data that results. More information is obtained using a. c. impedance, but the measurement requires more sophisticated evalution compared to the polarization resistance technique. In addition to corrosion rate data, without the problem of iR compensation, a. c. impedance provides information on the mechanism of corrosion and resistivity of the media-oxide. Gravimetric weight loss measurements are made for verification on total weight loss. The extent of pitting and uniform corrosion are also evaluated at the end of the exposure period.

Transport properties of the environment are controlled by using liquid, sand, and agar in the electrolyte media. The transport of oxygen through these media is affected by several factors including the reduced cross-section of the electrolyte, the increased diffusion path of the diffusing species, and possible ionic interactions between the electrolyte and the agar or sand. Using spherical and cylindrical gold electrodes, the cathodic reduction of oxygen is carried out using polarographic techniques. The rate of oxygen reduction at the gold surface is related to the concentration and rate of transport of oxygen through the media as defined by the general equation:

$$i = (nFAD_TC/r)(t^{-1/2}) + k$$

where i = Transient current
n = electron exchange
F = Faraday number
A = Surface area of the gold electrode
D_T = Transport constant for the media
C = Initial concentration of oxygen
r = radius of the gold electrode
t = Transient time
k = geometric constant

It is interesting to note that the thickness of the diffusion layer influences the rate of transport. As the thickness of this layer, controlled by the transient time, decreases to a small fraction of the media particle size, the transport constant approaches the diffusion constant in the liquid environment. Conversely, as the diffusion layer thickness approaches the radius of the media particle size, the transport constant increases.

Resistivity of the different media is controlled by the concentration of the electrolyte. During the initial study, sodium chloride solutions were used as the electrolyte. Measurements of a. c. impedance on the cylindrical gold electrodes in the media provide a measure of resistivity. Transport and resistivity, along with corrosion rate of the steel coupons, are measured each week.

The results of the first stage of this study indicate that transport properties in the various media differ by approximately an order of magnitude, with the liquid environment having the largest transport constant ($D_T \approx 1.5 \times 10^{-5}$ cm^{2}s), sand the lowest ($D_T \approx 5 \times 10^{-7}$ cm^{2}s), and agar in between ($D_T \approx 3 \times 10^{-6}$ cm^{2}s). Resistivities of the media ranged from 40 Ω cm for the 3.5 % sodium chloride solutions to 6500 Ω cm in 0.0035 % sodium chloride solutions. The greatest degree of pitting and the highest corrosion rates were observed in the sand media followed by the liquid environment, and the lowest corrosion rates and most uniform corrosion were observed in the agar media.

Abstract No. 159

THE ANALYSIS OF ELECTRODE PROCESSES BY ALTERNATING CURRENT AND TRANSIENT TECHNIQUES: RECOGNITION OF MECHANISMS.

M. SLUYTERS-REHBACH and J.H. SLUYTERS
Van 't Hoff Laboratory, University of Utrecht
Padualaan 8, P.O.BOX 80 051, 3508 TB Utrecht
The Netherlands.

Stimulated by the enormous progress in the development of electronics during the last three decades, the ac and transient techniques for the study of electrode processes have evolved to an outstanding level as regards precision and potentialities. The initial aim being the determination of the kinetic parameters k_s (standard rate constant) and α (transfer coefficient) of the Butler-Volmer formalism [1], it was soon recognized that these techniques are eminently suited to be applied with the aim of understanding the partial processes contributing to the overall electrochemical process, provided that the appropriate methodology was derived [2-4].

The overwhelming number of different techniques may be classified as follows:

(i) large amplitude techniques; e.g. chronopotentiometry, chronoamperometry, chronocoulometry
(ii) small amplitude techniques; e.g. potentiostatic or galvanostatic pulse perturbations
(iii) first order ac techniques; second harmonics, rectification or demodulation measurements.

Each of these has specific potentialities as well as specific limitations. In our laboratory considerable experience was collected on this matter, leading to the conclusion that combined application of three principally different types of methods is most beneficial, namely [5-7]

- dc voltammetry, chronoamperometry or chronocoulometry
- impedance voltammetry, i.e. impedance measurements as a function of a dc bias potential
- demodulation voltammetry, i.e. measurements of the demodulation voltage response to a modulated ac current perturbation, also as a function of a dc bias potential.

The information obtained with these methods is partly identical and thus mutually confirmative, but partly also complementary. In view of the large amount of data, computerized equipment has been built for automatic or semiautomatic performance. In the first instance the data are manipulated to separate the contributions of ohmic resistance and of double-layer charging. Next they can be used diagnostically to identify the processes controlling the electrode reaction(s). Finally, by quantitative analysis the detailed mechanism of these processes can be investigated. Besides mass transfer that inevitably always has to be accounted for properly (both in the ac and the dc sence) the following cases should be distinguished.

1. Charge transfer. From manifold studies during the last fifteen years it became evident that even "simple" model reactions, like metal ion reductions, proceed via multi-step mechanisms, containing not only single electron transfer steps, but also heterogeneous chemical reaction steps. Of the latter sometimes the nature is obvious, e.g. protonation or dissociation, but sometimes their nature is still unidentified. The intermediates in these mechanisms are supposed to be relatively unstable.
2. Successive charge transfer. In this case two or more charge transfer processes occur successively, but with stable or relatively stable intermediates. This means that the intermediate can undergo mass transfer, or can adsorb at the interface.
3. Reactant adsorption. If an electroactive species is also adsorbed, the response of the three techniques is extremely sensitive to the extent of this adsorption, and detailed information can be obtained about isotherm parameters as a function of the dc potential.
4. Coupled homogeneous reactions. Due to the large time scale covered by the various techniques, the occurrence of preceding, intermediate and following reactions in the solution phase can well be detected and their kinetics determined.
5. Electrochemical phase formation. When a new phase is deposited on the electrode, its kinetics have to be described in terms of nucleation and growth. In a way these processes are to be related with the foregoing items.

Several examples of the mentioned items have been studied successfully, and the effects of solution composition, inhibitors and catalysts have been interpreted on the basis of the formalisms developed. Mostly these studies concern model systems, i.e. relatively "simple" electrode reactions occurring at mercury, gold or vitreous carbon electrodes. In the case of the solid electrodes, special attention has been paid to the anomalous behaviour of the interfacial impedance, known since long as the phenomenon of the Constant Phase Element. The very recently proposed description of this behaviour based on the concept of fractal roughness, appears to provide a satisfactory explanation [8,9].

References

1. P. Delahay, New Instrumentals Methods in Electrochemistry, Interscience, New York, London, 1954.
2. D.E. Smith in A.J. Bard (Ed.), Electroanalytical Chemistry, Vol.1, Marcel Dekker, New York, 1966.
3. D.E. Smith, Crit. Rev. Anal. Chem. 2 (1971) 247.
4. M. Sluyters-Rehbach and J.H. Sluyters in A.J. Bard (Ed), Electroanalytical Chemistry, Vol.4, Marcel Dekker, New York, 1970.
5. A.J. Bard and L.P. Faulkner, Electrochemical methods. Fundamentals and Applications, Wiley, New York, 1980.
6. M. Sluyters-Rehbach and J.H. Sluyters in E. Yeager et al. (Eds.), Comprehensive Treatise of Electrochemistry, Vol.9, Plenum Press, New York, London, 1984.
7. M. Sluyters-Rehbach and J.H. Sluyters in C.H. Bamford and R.G. Compton (Eds.), Comprehensive Chemical Kinetics, Vol.26, Elsevier, Amsterdam, New York, Oxford, Tokio, 1986.
8. L. Nyikos and T. Pajkossy, Electrochim. Acta, 30 (1985) 1533
9. W.H. Mulder and J.H. Sluyters, Electrochim. Acta, 33 (1988) 303.

Abstract No. 160

A Macroscopic-Impedance Model for a Rotating Disk Electrode. Analysis of the Dissolution of Copper in Chloride Solutions: Data Reduction and Prediction

Alan K. Hauser and John Newman

Materials and Chemical Sciences Division,
Lawrence Berkeley Laboratory, and
Department of Chemical Engineering,
University of California, Berkeley, CA 94720

Ac impedance is recognized as a most useful method for studying the electrochemical nature of many systems. An advantage of this spectroscopic technique is that the impedance, as a function of frequency, often displays the constituting characteristics of the system separately. Therefore, the electrode frequency response is helpful for elucidating the rate-determining processes of an electrochemical system. However, due to intricate coupling of charge-transfer reactions at the surface and mass transfer in the presence of a nonuniform electric field in the solution, the quantitative interpretation of experimental data is not always easy. Equivalent circuits labeled as "theoretical models" still are frequently used, even though Grahame[1] pointed out the shortcomings of that approach over thirty years ago: "The objection to this procedure is that one has no way of knowing whether or not a given equivalent circuit is, in fact, equivalent to the interface under consideration except by carrying out an independent analysis of the problem which is the objective of those who use this method to avoid." Consequently, the inability to understand frequency-response data quantitatively is probably the biggest problem with using the ac-impedance technique. Controversy in the interpretation of impedance measurements is common and will continue until better methods for data reduction and analysis are available.

Methodology

The objective of this work is to attempt to bridge the gap between experimental and theoretical impedance analysis. Combining the two is unavoidable if our goal of understanding the phenomena that give rise to a particular frequency response for a given electrochemical system is to be achieved. Quantitative agreement between experimental impedance data and theoretical calculations, based on fundamental governing equations, should yield insight and understanding of the electrochemical system being investigated.

The specific objectives of this paper are as follows. First, a generalized theoretical framework for the calculation of the total impedance is to be presented as a function of thermodynamic and kinetic parameters, as well as multicomponent mass-transport properties. Second, a generalized procedure that has been developed for obtaining the fundamental and necessary input parameters from experimental frequency-response data will be discussed. Third, the parameters obtained from this procedure will be used in the macroscopic model to calculate the total electrochemical impedance as a function of frequency for various conditions. Comparisons will then be made with the experimental results[2] for the dissolution of a copper rotating disk in chloride solutions.

Model Description

A mathematical model has been developed that calculates the frequency response of a rotating disk accounting for multicomponent diffusion, migration, and homogeneous and heterogeneous reactions. The working algorithm uses concentrated-solution theory, incorporating the Stefan-Maxwell transport equations, and accounts for a finite Schmidt number and interfacial velocity. The governing equations within the disk boundary layer along with the electrode boundary conditions are solved using a finite-difference procedure, first for the steady-state problem, and then as a function of frequency.

Additionally, the electrochemical impedance of the disk electrode is analyzed theoretically, including a detailed breakdown of the total potential. Examining the impedance due to each contribution of the cell potential and total current gives rise to impedance terms typically neglected in other ac-impedance treatments. This approach makes it possible to see where certain assumptions have been made in the electrochemical impedance literature, although they are not always clearly stated.

Data Reduction

The data reduction scheme that has been developed is based on analytic solutions for the faradaic impedance. The simplifying expressions are derived from dilute-solution theory with no migrational effects, as opposed to the more general Stefan-Maxwell multicomponent transport equations. The resulting analytic forms of the faradaic impedance are helpful for verifying ones intuition and for testing the more general, complex model, which requires a numerical solution. These equations are most useful for analyzing impedance results and for yielding new ways of plotting the experimental data for determining important kinetic and transport parameters of an electrochemical system. For example, a plot of the real part of the impedance *versus* $\omega^{-1/2}$ provides a method for determining the kinetic and thermodynamic parameters for a particular system. The characteristic time constants of the mass-transfer and kinetic impedance loops also are given.

Model Predictions

The total electrochemical impedance of a copper rotating disk in chloride solutions is calculated as a function of frequency by the Stefan-Maxwell macroscopic model. The model results are used to meet the following objectives. First, the validity of the generalized program was checked by comparing the concentrated-solution model in the limit of dilute solutions, excess of supporting electrolyte, and infinite Schmidt number to known analytic solutions. Excellent agreement was obtained. Second, the copper-chloride results are plotted in various forms enabling additional information about the given system to be obtained. For example, the effect of finite rates of the homogeneous complexation reaction and the effects of the Schmidt number and different rotation speeds on the frequency-response of the faradaic impedance were examined. Finally, a new way of plotting the dimensionless convective-diffusion impedance is proposed that reduces the Schmidt number dependence of the frequency response nearly to one curve by stretching the abscissa using $(\omega/\Omega)Sc^{1/3}$.

References

[1] David C. Grahame, "Mathematical Theory of the Faradaic Admittance (Pseudocapacity and Polarization Resistance)," *Journal of the Electrochemical Society*, *99*, 370C-385C (1952).

[2] William H. Smyrl, "Digital Impedance for Faradaic Analysis. II. Electrodissolution of Cu in HCl," *Journal of the Electrochemical Society*, *132*, 1555-1562 (1984).

Abstract No. 161

A SHOOTING METHOD TREATMENT FOR ROTATING DISK ELECTRODE IMPEDANCE DATA OVER THE ENTIRE FREQUENCY RANGE

Rael Morris, Anna Kassimati and William Smyrl

Department of Chemical Engineering
and Materials Science
University of Minnesota
Minneapolis, MN 55455

INTRODUCTION

Transient techniques are often used in electrochemical systems for the study of electrode kinetics and mass transfer. Disturbing the reaction from the steady state, by applying a perturbation to the system, allows the elementary processes occurring to relax. As these various processes respond to the perturbation at different rates, the time response of the system can be analyzed to characterize them. The results of such techniques are referred to as impedance data.

In order to meaningfully analyze the impedance data, they have to be compared with an analytic expression for the measured quantity (1). The value of the parameters in such an analytic expression which are found to best fit the measured data, are then ascribed physical or chemical significance. In this way important physical and chemical constants (such as diffusion coefficients or rate constants) may be obtained for the system.

It is highly desirable for the calculation procedure to be fast and accurate, so that parameters can be estimated in a routine fashion while the data is being measured. In this contribution, we describe a method for solving the differential equations associated with the convective mass transfer to a rotating disk electrode, appropriate for *online* laboratory analysis.

ANALYTIC MODEL

A successful model of a simple electrochemical system invariably has to include terms to account for ohmic resistance, double layer capacitance, kinetic factors, and a convection-diffusion term (2). Of these it is the latter which gives mathematical complexity to the characterization of these systems.

If a small sinusoidal perturbation is imposed on a rotating disk electrode system at steady state, then a linear response can be expected in perturbations of electrode concentrations. This results in a separated variable solution to the convective diffusion equation, yielding an ordinary differential equation in the spatial component of the concentration perturbation (Θ) given by (3):

$$\frac{d^2\Theta}{d\xi^2}+\left[3\xi^2-\left(\frac{3}{a^4}\right)^{1/3}\frac{\xi^3}{Sc^{1/3}}+\frac{b}{6}\left(\frac{3}{a}\right)^{5/3}\frac{\xi^4}{Sc^{2/3}}+\cdots\right]\frac{d\Theta}{d\xi}-iK\Theta=0 \qquad [1]$$

where ξ is dimensionless axial coordinate, K is a dimensionless frequency of the perturbation signal, Sc is the Schmidt number, and a and b are constants. The following boundary conditions are imposed on equation [1]:

$$\Theta = 1 \text{ at } \xi = 0, \quad \Theta \to 0 \text{ as } \xi \to \infty \qquad [2]$$

requiring that the concentration perturbation be zero far from the disc, while at the interface the amplitude of the perturbation remain at a specified constant value.

Equation [1] with boundary conditions [2] can be solved by splitting the solution into real and imaginary parts, and solving a coupled system of equations. The coupled equations can be solved most economically, by using a shooting method approach (4), and solving two related initial value problems. Any time stepping procedure may be used to calculate the solutions to these resulting initial value problems, and hence the solution to [1].

A rigorous mathematical description of the experimental system has thus been developed, and can be used in a generalized minimization or non-linear least squares routine, in order to choose the 'best' values of the physical and chemical constants that characterize the system (5,6).

RESULTS AND DISCUSSION

The 2^{nd} order Runge-Kutta (R-K) method, applied to the initial value problems, allows [1] to be solved with significantly less work than the traditional finite element and finite difference formulation or Chebychev collocation methods (5,6).

The resulting coupled system of equations has been solved numerically by applying a 16 point Chebychev collocation method to the original system, and 8 and 16 point 2^{nd} order R-K methods applied to the shooting method initial value problems; the results have been compared. The ξ domain extends out to infinity from the electrode surface; however numerical experimentation has shown that $\xi_{max} = 2.7$, and $\xi_{max} = 1.7$ for the Chebychev and R-K techniques respectively are sufficient. The relative execution times of the three methods were recorded: the 8 point R-K was found to be 16 times faster than the Chebychev method: and the 16 point R-K method ran 8 times faster than the Chebychev method.

Values of $\{ -1 / \Theta'(0) \}$ were calculated using these three methods, and compared with an exact solution for infinite values of Sc. The maximum relative error in either the real or imaginary parts of the convective Warburg impedance is within 0.1% for both the Chebychev and 16 point R-K methods, and within 0.6% for the 8-point R-K method. Application of the 2^{nd} order R-K method to the decoupled system gives results with an acceptable precision in a faster and more simple manner than conventional methods for handling coupled boundary value problems.

In Figure 1 is presented the calculated values of real and imaginary parts of the dimensionless convective Warburg impedance $\{ -1 / \Theta'(0) \}$ as a function of Sc. The curve for infinite Sc deviates significantly from the curve for low Sc, thus necessitating a similar treatment to the one presented here in order to successfully analyze impedance data for these systems.

The solution of boundary value problems for the purpose of parameter estimation, is generally a method that can only be tackled successfully by large scale mainframe computers. Numerical solutions of these types of problems invariably require the manipulation of large systems of linear equations, a memory intensive and time consuming procedure. Further, the solution to the differential equations are usually required many times in the course of the iterative parameter estimation process.

Thus we have reduced a seemingly intractable problem into one that can be very easily handled by a laboratory scale computer, quickly, effectively, and in real time. This method may be applied to other types of linear systems of differential equations, but certainly for the calculation of Warburg impedances it shows marked improvement over the conventional numerical schemes.

REFERENCES

1. J. Ross Macdonald and J.A Garber, *J. Electrochem. Soc* , **124**, 1022 (1977)
2. C.Ho, I.D.Raistrick, and R.A Huggins, *J. Electrochem. Soc* , **127**, 343 (1980).
3. B. Tribollet, J. Newman, and W.H. Smyrl, To be published
4. H. B. Keller, "Numerical Methods for Two-Point Boundary-Value Problems", Blaisdell Publishing Company, pg 43, (1968)
5. R. Morris and W. H. Smyrl, "DIGITAL IMPEDANCE FOR FARADAIC ANALYSIS - IV Rigorous treatment of Rotating Disk Electrode Impedance Data Over the Entire Frequency Range ", paper submitted to *J. Electrochem. Soc.*
6. B.T. Bell, M.S. Thesis, University of Minnesota (1986)

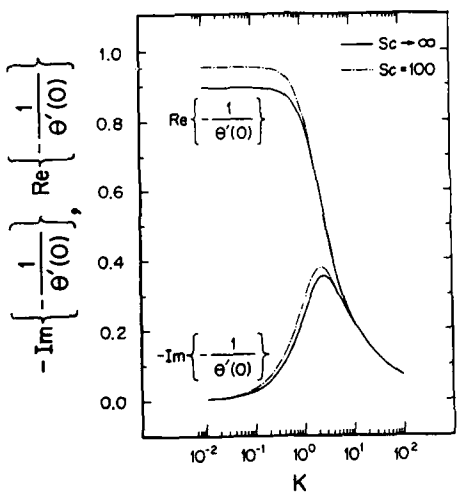


Figure 1

Comparison of $\{-1/\Theta'(0)\}$ at finite and infinite Schmidt number, calculated using the shooting method with a 16 point 2^{nd} order Runge-Kutta scheme.

Abstract No. 162

IMPEDANCE SPECTROSCOPY FOR THE STUDY OF ANODIC COPPER DISSOLUTION IN SULFURIC ACID IN PRESENCE OF BENZOTRIAZOLE

Claude Clerc and Richard C. Alkire

Department of Chemical Engineering
and
Materials Research Laboratory
University of Illinois

Urbana, Illinois 61801

The presence of an anodic surface film dramatically affects the electrochemical behavior of dissolving electrode in processes like corrosion inhibition, passivity, electropolishing or pitting. The present study was initiated to learn more about the physical properties of the surface films present at the surface of a copper electrode during anodic dissolution in 0.5 M sulfuric acid and 40 mM benzotriazole (BTA) at 25 °C. This study is of practical importance because this organic compound is widely used for corrosion inhibition and as etching additive.

The impedance spectra measured after 10 min of polarization (with a SOLARTRON 1250 Frequency Response Analyser and a SOLARTRON 1286 Electrochemical Interface) were analyzed by comparison with a physical model of the electrochemical interface in which the passive electrode is covered with a barrier layer. The main assumptions are that this barrier layer is a good electronic insulator of stoichiometric composition and that charge transfer reactions and double layer charging occur at both metal-barrier layer and barrier layer-electrolyte interphases. This model also considers the change in the barrier layer thickness under the influence of the applied potential.

Least squares fitting of measured impedance spectra yield physical parameters of reasonable order of magnitude to support the proposed model. As predicted by Cangellari (1), it was found that the barrier layer is itself covered by an outer porous film of corrosion products and that the metallic ions transfer through the barrier layer under high field conduction. By comparing the crystallographic lattice parameters and the dielectric constants of different copper compounds, the jump distance was determined to be about 5.5 Å, indicating that the barrier layer is likely to be an hydrated copper sulfate ($CuSO_4 \cdot 5H_2O$). The values of the electric field across the barrier layer ($\mathcal{E} \simeq 1.1 \cdot 10^6$ V/cm), its thickness for the range of experimental conditions involved (30 Å < l < 500 Å) and the pre-exponential factor for high field conduction ($i_0 \simeq 9.5$ mA/cm^2) were also determined and are in agreement with those reported in the literature (2,3).

An other set of experiments carried out in absence of BTA indicates that on the current plateau, as for nickel dissolution in concentrated chloride solution (4), the metal electrode is covered with a dual surface film and that the dissolution rate is controlled by the diffusion of the corrosion products from the surface of the electrode into the bulk of the solution. The analysis of the high frequency part of the impedance spectra shows that the barrier layer is also a good electronic insulator of stoichiometric composition through which metallic ions transfer under high field conduction. The lower value of the jump distance (a ≃ 3.5 Å) and the higher value of the pre-exponential factor ($i_0 \simeq 50$ mA/cm^2) indicate that the barrier layer has a chemical composition different from that prevailing in presence of BTA and is likely to be a less hydrated form of copper sulfate.

Acknowledgments

This work was funded by grants from the Fonds National Suisse de la Recherche Scientifique, and U.S. Department of Energy via the Materials Research Laboratory (DE-AC02-76ERO1198(51)). The authors are grateful for this support.

References

1.- A.Cangellari, "The Effect of Corrosion Inhibitors on the Anodic Dissolution of Fe and Cu in Presence of Fluid Flow," Ph.D. Thesis, University of Illinois, Urbana (1985)

2.- T.R.Beck, *Chem.Eng.Commun.*, **38**, 393 (1985)

3.- K.J.Vetter, "Electrochemical Kinetics," Academic Press, New York (1967)

4.- C.Clerc and D.Landolt, to be published in *Electrochim. Acta*

Abstract No. 163

Surface Inhomogeneity characterized by EIS

K.Jüttner *), W.J. Lorenz *)

*) Institute of Physical Chemistry and Electrochemistry, University of Karlsruhe, Kaiserstr. 12 D-7500 Karlsruhe, Germany

Solid electrode surfaces are principally inhomogeneous due to their crystallographic and morphological surface structure including different kinds of crystal imperfections which may act as active sites for electrochemical phase boundary reactions. Additionally, sorption effects and the formation of surface layers leads to partial blockage effects.

Consequently, corrosion processes are also strongly influenced by surface inhomogeneities of different dimensions. EIS was found to be a powerful in-situ method in order to characterize the influences of surface inhomogeneities on various electron and ion charge transfer processes. The paper is dealing with the influences of 2-D and 3-D surface inhomgeneities on different metal corrosion processes and interface and interphase corrosion inhibition.

References

W.J.Lorenz and F.Mansfeld,
Dynamic System Analysis in Corrosion Testing.
DECHEMA-Monographs Vol. 101, p. 185,
VCH Verlagsgemeinschaft, Weinheim 1986.

E.Schmidt, J.Hitzig, J.Titz, K.Jüttner, and W.J.Lorenz,
Electrochim.Acta 31, 1041 (1986).

G.Schöne, W.Wiesbeck, M.Stoll, and W.J.Lorenz,
Ber.Bunsenges. Phys.Chem., 91, 469 (1987).

G.Schöne, W.Wiesbeck, and W.J.Lorenz,
J.Electroanal.Chem., 229, 407 (1987).

K.Jüttner, W.J.Lorenz, M.W.Kendig, and F.Mansfeld,
J.Electrochem.Soc., 135, 335 (1988).

F.Mansfeld and W.J.Lorenz,
Impedance Spectroscopy of Corrosion Phenomena.
in "Techniques for Characterization of Electrodes and Electrochemical Processes" ed. by R.Varna and J.R.Selman, Electrochem. Society Monograph Serie, John Wiley and Sons, in preparation.

K.Jüttner, W.J.Lorenz, and W.Paatsch,
The Role of Surface Inhomogeneities on Corrosion Processes - Electrochemical Impedance Spectroscopy (EIS) on Different Aluminium Oxide Films.
Corrosion Sci., submitted.

Abstract No. 164

Measurement of Transient Processes from the Guillotined Electrode: A New Technique

G.T. Burstein and R.J. Cinderey

Department of Materials Science
and Metallurgy
University of Cambridge
Pembroke Street
Cambridge CB2 3QZ, United Kingdom

A new technique for examination of the electrochemical behaviour of freshly generated metal surfaces in aqueous electrolyte solutions is presented. The technique employs a microelectrode mounted on insulating polymer such that only the end-surface of the electrode is exposed to the electrolyte. A specially designed chisel is then used to shear the entire electrode surface. The chisel is constructed as a steel shank with a cutting blade made of boron nitride. Above the boron nitride blade, a hole machined into the steel shank is positioned such that when the blade comes to rest at the end of its travel the hole lies directly over the new metal surface, allowing the Luggin probe to "see" it. The chisel itself is spring-loaded and is driven with a cutting speed of ca. 1m s^{-1}, allowing a 1mm dia specimen to be cut in ca. 1ms. Data are collected digitally in a fast transient recorder which is triggered by passage of the chisel unit, before transference to computer for processing.

The technique is complementary to the scratched rotating disc electrode from which it is distinguished by two important features. First, the electrode is stationary, convection being introduced only in the early stages by passage of the chisel. Second, the electrode surface is renewed in its entirety, permitting accurate measure of potential transients either in open circuit or under galvanostatically applied current.

Data are presented describing the electrochemical behaviour of freshly generated aluminium surfaces in aqueous solutions. Potential transients were measured at open circuit and under galvanostatically applied current, both anodic and cathodic. In neutral solution the corrosion potential of the new metal surface is initially very negative. The potential then rises linearly in log t, a phenomenon describing growth of the oxide film driven by the local cathodic reduction of water and dissolved oxygen. The reaction is approximately independent of the neutral solution composition although in tap-water an increase in the rate of repassivation at longer times is ascribed to the effects of small concentrations of bicarbonate.

Under externally applied anodic current a linear rise of E with log t similar to that seen in open circuit is observed in the initial stages of oxide film growth. At a particular value of E, however, the rate of rise of E with t is accelerated, the parameters controlling this acceleration being dependent on the applied anodic current. These data are used to establish the local self-corrosion current density as a function of potential and time during repassivation.

In neutral chloride solutions under anodic polarisation the nucleation of stable pitting is marked by a sudden arrest in the rising potential, the characteristics of which depend on the chloride concentration and the applied current density. Following this event, the potential does not rise further, save for the superimposed noise. Similar experiments performed in an anodising bath (ammonium borate) show that a similar event occurs after a period of passive film growth. The event is succeeded however, by a further steady rise in potential, but at a far slower rate. These observations are attributed to nucleation and growth of the classical porous overlayer on top of the passive oxide film. The data demonstrate that the nucleation of pits in chloride solution, and the nucleation of pores in anodising solution are events of similar origin.

Some data describing the cathodic behaviour of freshly generated aluminium surfaces are also presented. They show that even under fairly high cathodic current densities nucleation and growth of the oxide film dominates the process initially. The potential then falls as the increasing electronic resistance of the growing oxide film imparts higher overpotential to the cathodic process.

Abstract No. 165

IN SITU FRACTURE TECHNIQUES FOR STUDYING TRANSIENT REACTIONS WITH BARE STEEL SURFACES*

R. P. Wei
Lehigh University,
Bethlehem, PA 18015
and
A. Alavi
Sherwin-Williams Company
Chicago, IL 60628

To assist in the understanding of environmentally assisted crack growth in aqueous environments, in situ fracture techniques have been developed to study the transient reactions of bare steel surfaces with the electrolyte. In this paper, the measurement techniques and test results will be described and discussed in relation to crack growth response in steels.

The techniques utilized a specially designed electrochemical (corrosion) cell, Fig. 1, and the bare surfaces were produced by in situ fracture of a notched round (5mm notch diameter) tensile specimen [1]. The specimen was coated with lacquer and was further isolated with shrink tubing so that only the fracture (bare) surfaces (with a total nominal area of 0.4 cm^2 for the two halves) would be exposed to the electrolyte during measurement. Each of the measurement techniques utilized a variant of the cell shown in Fig. 1 to represent the conventional 3-electrode cell, and a 3-electrode and a 4-electrode analogue of the local electrochemical cell at a crack tip. The measurements provided information on the reaction kinetics, and furnished insight on the crack tip conditions and crack growth response.

The conventional cell configuration was used for basic studies (e.g., the influences of potential and pH) on bare surface reactions under potentiostatic control. In this variant, the four round rods (Fig. 1) were replaced by a cylindrical platinum counter electrode, and a saturated calomel electrode (SCE) was used as the reference electrode, with the tip of the connecting Luggin probe placed near the specimen notch. The current transient following specimen fracture was recorded digitally by a high speed data acquisition system.

The cell (Fig. 1) was originally conceived as an analogue for the crack tip, and was designed for measuring the equilibration galvanic current (or charge transfer) between the bare crack tip surfaces and the "oxidized" or filmed crack flank under free corrosion [1]. The crack-tip surfaces were simulated by in situ fracture of the notched tensile specimen, and the crack flank by the "oxidized" rods of the same material. The Luggin probe was included to monitor the mixed (cell) potential. The amount of charge transferred during the reactions with the fracture surfaces was obtained by numerical integration of the current transients, and was used to demonstrate electrochemical reaction control of corrosion fatigue crack growth in high strength steels [1,2].

For crack growth under external potentiostatic control, however, it was recognized that the bare surfaces at the occluded crack tip and the "oxidized" crack flank must be viewed as a composite and isolated electrode system. This composite electrode is polarized with respect to reference and counter electrodes that are located outside of the crack. The actual crack-tip potential and current flow, however, would reflect potential (IR) drop along the crack. A more appropriate test, then, therefore, would be a 4-electrode cell, consisting of a bare surface and an "oxidized" or filmed surface in one cell, and counter and reference electrodes in a separate cell, which are linked by a salt bridge [see Fig. 2]. The current, under free corrosion, would be zero. This arrangement, using two specimen halves cut as in Fig. 1, represents the real crack in the actual size of

Fig. 2. A zero-resistance ammeter (ZRA) was used in each branch to measure the current flow, and an auxiliary reference electrode was included to measure the mixed potential within the corrosion cell.

Measurements have been made on low alloy and austenitic stainless steels, and have been correlated with corrosion fatigue crack growth data. This correlation demonstrated electrochemical reaction control of corrosion fatigue crack growth, and suggested that the temperature and frequency dependence for fatigue crack growth rate could be predicted directly from the electrochemical reaction data for bare steel surfaces. A similar correlation has been established for stress corrosion crack growth. The reactions of interest are localized at the crack tip, and are those that bring the newly created surfaces into equilibration with the "oxidized" crack flanks. Because of IR drop along the crack, the mixed potential in the "local" cell tended to remain close to the free corrosion potential. Specific results will be used for illustration, and the implications of these techniques and findings on future research in stress corrosion and corrosion fatigue will be discussed.

(*Work supported in part by the Office of Basic Energy Sciences, Department of Energy, under Grant No. DE-FG02-84ER45138).

1. A. Alavi, C. D. Miller and R. P. Wei, Corrosion, Vol. 43, No. 4, pp. 204-207 (1987).
2. R. P. Wei and A. Alavi, "A 4-electrode analogue for measuring electrochemical reactions with bare metal surfaces at the crack tip", Scripta Metallurgica, submitted for publication (1987).

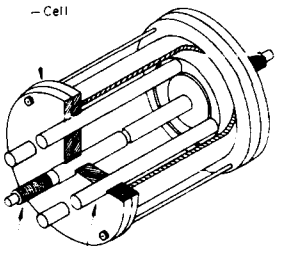


Fig. 1. Schematic illustration of the special electrochemical (corrosion) cell.

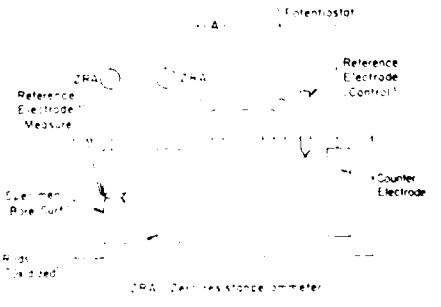


Fig. 2. Schematic diagram of the cell for the corrosion fatigue crack

Abstract No. 166

The Influence of Surface Capacitance on the Measurements of Localized Corrosion Transients

H. S. Isaacs and A. J. Davenport
Department of Applied Science
Brookhaven National Laboratory
Upton, NY 11973

The difficulty of measuring the early stages of localized corrosion transients during pit growth, the repeated step growth in stress corrosion cracking or scratching, arises from the charging of the capacitance of the passive surface surrounding the actively corroding area. The charging of the surface delays the transmission of the potential during open circuit measurements or the current response of the potentiostat when under potential control.

The effect of surface capacitance on the flow of current has been presented by Newman [1]. At high frequencies (or short times) the low effective interfacial impedance makes electrodes behave as equipotential surfaces with very high current densities at the edges. Oltra and Keddam [2] have discussed the measurement of impedance of capacitative surfaces with active pitting, and the distribution of current to surfaces with localized corrosion taking place [3]. The capacitance of the surface was also found to dominate potential transients when pits grew for a few seconds [4].

The measurement of the kinetics of the early stages of pitting corrosion is an important aspect of the understanding of the processes controlling the development of pits. Two approaches have been used to separate the contributions of the surface impedance to the observed transients. The first was the measurement of signal transmission along metal surfaces. The second was a computer simulation of the processes.

The measurement of signal transmission was made with wire electrodes under potentiostatic control. An Alloy 600 wire was supported in a tubular cell with the tip of one reference electrode positioned at various distances along the wire. A second reference electrode and an exposed wire tip auxiliary electrode were placed at a fixed position close together near one end of the wire. These electrodes were used to produce a local single rectangular potential transient on the wire and the second reference electrode was used to monitor the propagating pulse along the wire.

The rate of propagation can be simply approximated by the product of the solution resistance and capacity of the metal surface. The reciprocal of this product is equivalent to a diffusion coefficient of the order of magnitude of 10^3 cm^2/s. The results have indicated that it should be possible to determine the position of pit initiation sites from time of arrival of transients at reference electrodes positioned at known locations over metal surfaces.

Simulation of cell geometries under potentiostatic control and metal surfaces with defined interfacial processes have been carried out to analyze the charging transients. The simulations have shown the importance of the positioning of both the reference and counter electrodes on the observed transients occurring over a short time period.

Acknowledgments

This work was performed under the auspices of the U.S. Department of Energy, Division of Materials Sciences, Office of Basic Energy Science under Contract No. DE-AC02-76CH00016.

References

1. J. Newman, J. Electrochem. Soc. 117, 198 (1970).
2. R. Oltra and M. Keddam, Corrosion Sci. 28, 1 (1988).
3. R. Oltra and M. Keddam, Intern. Conf. on Localized Corrosion, NACE, 1987.
4. H. S. Isaacs and Y. Ishikawa, J. Electrochem. Soc. 132 1288 (1985).

Abstract No. 167

Measurement of Passive Film Growth Kinetics on Bare Surface Niobium Band Microelectrodes

A. J. Davenport and H. S. Isaacs
Department of Applied Science
Brookhaven National Laboratory
Upton, NY 11973

Microelectrodes have a number of advantages over electrodes of conventional size. These include a reduction in ohmic (IR) drop in the solution and an increase in mass transport rates to and from the electrode surface [1]. As a result, microelectrodes have been increasingly used in areas such as high speed cyclic voltammetry [2] and in corrosion studies [3,4].

Measurement of the growth kinetics of passive oxide films is often carried out by potentiostatic pulsing of cathodically reduced surfaces. In such experiments it is not certain that the entire oxide film is reduced and, particularly with base metals, there is the attendant risk of charging the surface with hydrogen. Such effects may be avoided by mechanical creation of a bare metal surface by scratching or breaking the electrode. However, it has been shown that the repassivation kinetics recorded using either method are significantly affected by the IR drop in the solution [5]. Furthermore, a current transient flowing from a scratch in an otherwise passive electrode may be affected by the capacitance of the surrounding oxide film [6]. All these problems may be overcome by the in situ creation of a bare metal surface by fracture of a microelectrode.

The formation of band microelectrodes by exposing the edge of a thin metal film sputter-deposited onto an insulating substrate has been described by Wehmeyer et al. [7]. In this study, a film of niobium ~4000 Å thick was sputtered onto a glass cover slide and a second glass cover slide was stuck to the surface of the film with an epoxy adhesive leaving one end of the film exposed to allow electrical connection. In order to prepare the composite for fracture, both the top and bottom glass slides were scored directly opposite each other, with a diamond stylus. The scored part of the electrode was immersed in the solution and placed under potentiostatic control. The composite was then fractured along the scored lines by impact, exposing a bare metal band microelectrode ~2 cm in length and a width equal to the thickness of the sputtered film (~4000 Å). The bare surface oxidizes rapidly: the resulting current transient was captured on a high speed transient digitizer. Fig. 1 shows the decay of a typical current transient plotted on logarithmic scales. The lower part of the decay shows a very shallow curve with an approximate gradient of -0.8, consistent with film growth by Cabrera-Mott high field kinetics [5]. At higher current densities, greater curvature is found which is affected by the IR drop in the electrolyte [5].

The solution resistance to such an electrode may be calculated using the equation of Pearson et al. [8]

$$R = \frac{1}{2\pi\sigma b} \ln\left(\frac{2b}{a}\right)$$

where σ is the solution conductivity and a and b are the half width and half length of the electrode. Using values of a=2000 Å and b=1 cm and σ=0.328 Ω^{-1} cm^{-1} (1M H_2SO_4), the resistance is found to be ~5 Ω. At the highest current recorded, ~10^{-4} Å, the IR drop is thus 0.5 mV. Below I=10^{-5} A with the corresponding IR drop of 50 μV, the effect of ohmic resistance is negligible. Neglecting any surface roughness, the electrode area is ~10^{-4} cm^2 so a current density of 10^{-5} A corresponds to a current density of 100 mA cm^{-2}.

Thus, the microelectrode technique offers a method of studying the electrochemical reactions occurring at bare metal surfaces at much shorter times and higher current densities with lower IR drop than those attainable with other techniques.

Acknowledgments

This work was performed under the auspices of the U.S. Department of Energy, Division of Materials Sciences, Office of Basic Energy Science under Contract No. DE-AC02-76CH00016.

References

1. S. Pons and M. Fleishmann, Ultramicroelectrodes, M. Fleischmann, S. Pons, D. R. Rolison, and P. P. Schmidt, Editors, p. 1, Datatech Systems, Inc., 1987.
2. R. M. Wightman and D. O. Wipf, Abstract No. 451, Electrochemical Society Spring Meeting, Atlanta, Georgia (1988).
3. R. T. Atanasoski, H. S. White, and W. H. Smyrl, J. Electrochem. Soc. 133, 2435 (1986).
4. J. Osteryoung and K. Wikiel, Abstract No. 455, Electrochemical Society Spring Meeting, Atlanta, Georgia (1988).
5. A. J. Davenport and G. T. Burstein, Abstract No. 27, Electrochemical Society Spring Meeting, Atlanta, Georgia (1988).
6. H. S. Isaacs and A. J. Davenport, This symposium.
7. K. R. Wehmeyer, M. R. Deakin, and R. M. Wightman, Anal. Chem. 57, 1918 (1985).
8. H. J. Pearson, G. T. Burstein, and R. C. Newman, J. Electrochem. Soc. 128, 2297 (1981).

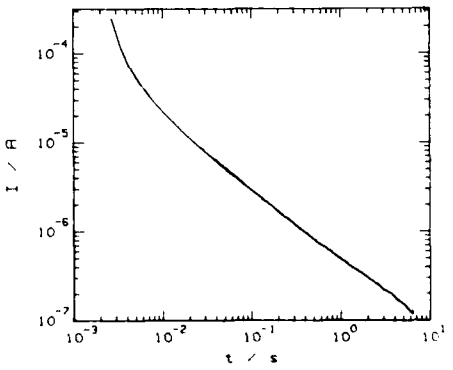


Fig. 1. Decay of a current transient measured on a bare niobium microelectrode in 1M H_2SO_4 at 1.0V(SCE) plotted on logarithmic scales.

Abstract No. 168

FAST COMPUTER SUPPORTED PULSE MEASUREMENTS OF IONIC PROCESSES IN OXIDE FILMS

D. Ebling, M.M. Lohrengel and J.W. Schultze

Institut für Physikalische Chemie und Elektrochemie der Universität Düsseldorf

Universitätsstraße 1, D-4000 Düsseldorf, Germany

In order to analyse the problems of the passive layer formation detailed knowledge of charge transfer and charge distribution is necessary. Methods were developed to measure the transients of layer formation far from the state of equilibrium and to study the semiconducting properties, charge distribution and kinetics of ionic movement./1-4/

Computer supported potentiostatic equipment realizes the synthesis of fast complex pulses and the records of current and charge transients up to 10^{4} seconds with a resolution of 0.2 μs. Currents are registered from 0.1 $\mu A/cm^2$ to 10 A/cm^2 by an autoranging amplifier with a response time of 1 μs.

Two types of transient measurements were carried out where the formation of the oxide film on aluminum was investigated as an example.

Fig. 1 shows the pulse programme and the change in thickness for the i(t) type. The appropriate current response is shown in Fig. 2. Common models of high field mechanism of oxide growth are confirmed for longer times (>1s) and different thicknesses of the oxide at a constant field strength. For shorter times an inductive period for oxide growth could be seen which depends on the thickness of the film. This correlates with an injection of ions into the oxide layer which is free of charge carriers at the beginning.

Fig. 3 shows the investigations we carried out with the use of short staircase pulses on the potential dependence of layer formation of instationary oxide films with negligible distortion of the layer. Every stair complex represents an lg i / E measurement under almost constant layer properties (change in thickness <<1%). Each step of the staircase pulses must not be longer than 800 μs to avoid too much oxide growth. On the other hand a step has to be long enough to obtain the Faraday current after reloading the double layer capacity.

The accuracy of the described method is confirmed by the obtained Tafel diagrams which show a linear lg i / E relationship and the expected decreasing slope with increasing thickness.

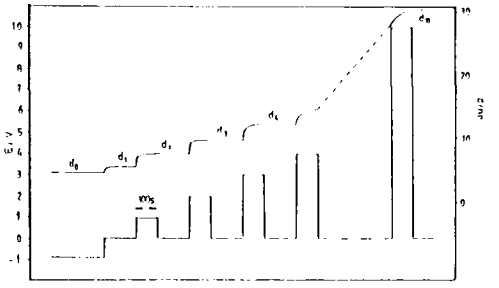


Fig. 1: Potential - time - diagram and corresponding thicknesses of the oxide film for anodic current transients

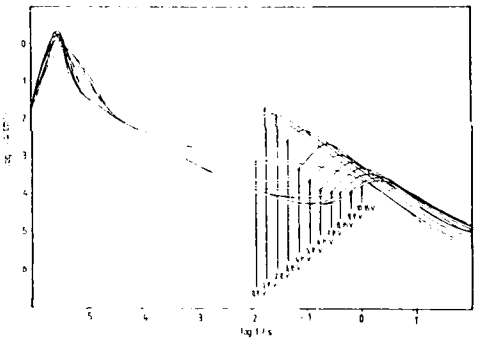


Fig. 2: Anodic current transients measured on aluminum in acetate buffer pH 5.9

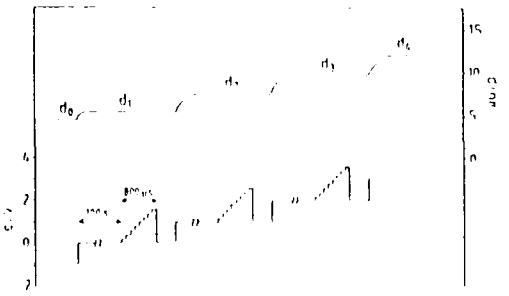


Fig. 3: [illegible]

References

1 D. König and M.M. Lohrengel, Dechema Monographien 103, 99 (1985)

2 M.M. Lohrengel, J.W. Schultze, H.D. Speckmann and H.H. Strehblow, Electrochim. Acta 32, 733 (1987)

3 D. König, M.M. Lohrengel and J.W. Schultze, Ber. Bunsenges. Phys. Chem. 91, 426 (1987)

4 D. König and J.W. Schultze, J. Electroanal. Chem. [illegible] (1988)

Abstract No. 169

ELECTROCHEMICAL TRANSIENT RESPONSES AFTER A CONTROLLED DEPASSIVATION

R.OLTRA, G.M. INDRIANJAFY, M.KEDDAM*
UA 23 CNRS, Université de Bourgogne, 21004 DIJON FRANCE
*LP 15 CNRS, Université PARIS VI, 75232 PARIS FRANCE

Purpose :
The aim of this paper is to discuss the application of the transient electrochemical measurement for assessing the repassivation kinetics. From previous studies it was concluded that the measured current during the repassivation of a reduced area of fresh metal, is under the control of electrical parameters depending on the geometry of the electrochemical cell, Fig.1 (1).
An equivalent electrical circuit has been proposed to describe the electrical response during a local depassivation under potentiostatic regime (1).
From the following experiments the role of the surrounding surface has been more precisely explained and the actual steps of the repassivation process have been tentatively defined.

Experimental :
Experimental transient measurements have been performed on the "disk-ring" electrode in order to look for the interaction which could also exist between the depassivated disk and the passive ring. Using the Laser depassivation technique it is possible to depassivate a passive disk, embedded or not, in a passive ring of the same metal. Measurement of the current transients for the disk and the ring is achieved by means of zero-impedance current voltage converters as shown in Fig.2 allowing to separate the coupling transient currents from the current flowing through the potentiostat loop.

Results :
i)The electrical coupling model described in (1) has been improved by the simultaneous measurement of all the currents involved in the dual electrode, as shown in Fig.3
ii)Assuming an electrical equivalent circuit, the calculated transient responses due to the fast connection of the impedance of the depassivated area to the impedance of the passive surface one, allows one to explain the electrical coupling shown in Fig.3. Nevertheless the controlling parameter which remains unclear is the imposed potential which must be ascribed to a zero-potential.
The role of the surrounding passive surface can be compared to a low-pass filter one. Indeed the charge involved in the repassivation of the disk can be compared to the charge measured with the the current transient in the potentiostatic loop (table 1).
iii)The initial peak of current transient measured on the disk alone remains to be dependent on the size of the electrode even if a general depassivation can be assumed (Fig.4). This latter has been related to the ohmic drop, so then a kind of polarisation curve can be plotted after the correction of the ohmic drop assuming the Newman's formula for the electrolyte resistance associated to the disk. As shown in Fig.4 the initial peak current density is linear with potential. The existence of the resistance Ri, i.e. the slope of the line, at the time of the peak current density remains unexplained. On the other hand the zero current intercept potential, Vc, cannot be reached for iron in the test solution owing to the activation of the surface. Work is in progress to compare the behavior of passive iron to stainless steels [1]. Nevertheless it can be noticed that such results have been found by BECK for repassivation of titanium [2].

Conclusions :
The main feature of the coupling of a small depassivated surface in a large surrounding passive surface is an electrical coupling which depends on the value of the potential of the passive surface related to the zero-intercept potential, Vc.
At very short times, the presence of the resistance Ri, allows to assume the first step of the repassivation process related to adsorption phenomena. Whereas at longer time the independence of the charge as function of the coupling effect seems to demonstrate that a second step is related to faradaic processes. For iron in $HClO_4$ pH=1, the charge density for repassivation corresponds to approximately a *monolayer of ferrous species* (3). Unfortunately it seems very difficult to define the time constant related to this second electrochemical step from transient measurement.

References :
(1)R.OLTRA, C.GABRIELLI, F.HUET, M.KEDDAM, Electrochemica Acta, 31, 1501, 1986
(2)T.R.BECK, "Passivity of Metals", Ed.R.P. FRANKENTHAL and J.KRUGER, p.1035, 1979
(3)M.BADDI, C.GABRIELLI, M.KEDDAM, H.TAKENOUTI, "Passivity of Metals", Ed.R.P. FRANKENTHAL and J.KRUGER, p.625, 1979

E (mV/ESS)	q ($\mu C/cm^2$)
+500	130
+200	116
0	108

Table 1- Electrical charge involved in the repassivation of iron in $HClO_4$ pH=1

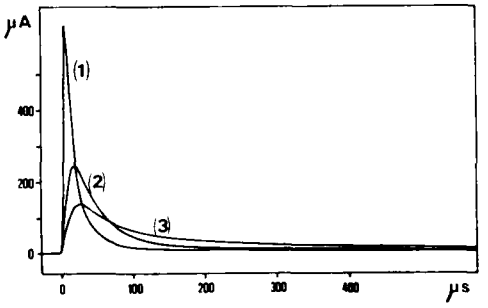


Fig.4- Dependence of the electrochemical current transient as function of the size of the passive electrode for a constant depassivated area corresponding to the surface of the wire (curve (1)= wire diam. .4mm
curve (2)= diam. .mm ; curve (3) diam. .8mm
E= +500mV vs SCE; $HClO_4$ pH 1

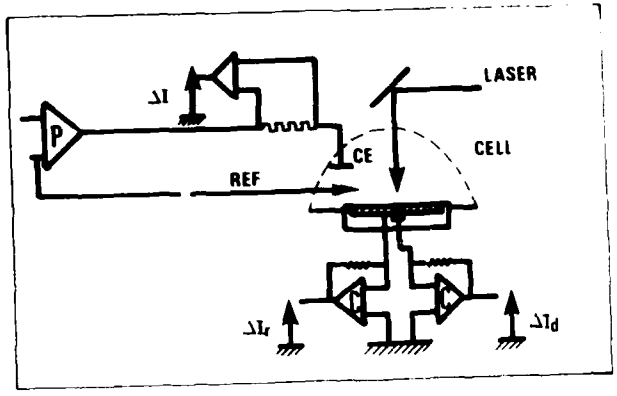


Fig.2- Experimental set-up for depassivation experiment on the dual electrode

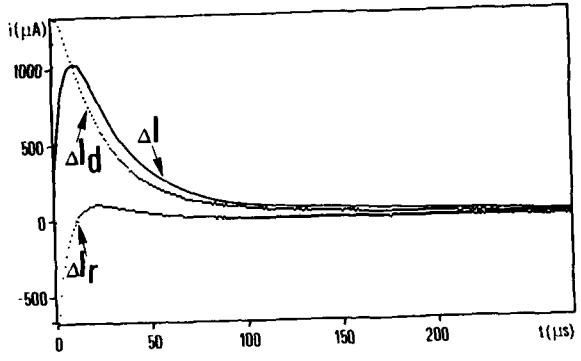


Fig.3- Comparison of the coupling currents (ΔI_r and ΔI_d) to the current in the potentiostatic loop (ΔI)

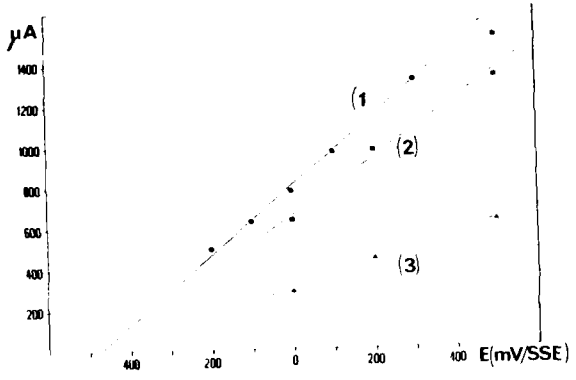
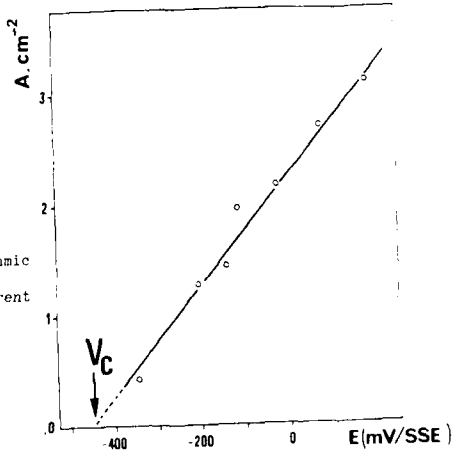


Fig.4- Peak current versus imposed potential as function of the size of the depassivated area; passive iron wires in $HClO_4$ pH=1
curves (1) and (2): diam. 0.25mm
curve (3): diam. 0.16mm

Fig.5- Initial peak current density as a function of the potential corrected of the ohmic drop; the value of Vc is extrapolated at the zero current intercept.



Abstract No. 170

STUDY OF CORROSION PROCESSES BY A-C QUARTZ ELECTROGRAVIMETRY

S. BOURKANE, C. GABRIELLI and M. KEDDAM

LP 15 du CNRS "Physique des Liquides et Electrochimie"
Université P. & M. Curie, tour 22, 4 place Jussieu,
75252 PARIS Cédex 05, FRANCE.

The use of a quartz crystal for measuring small mass changes (of the order of 10^{-9} g) is relatively ancient in vacuum or at atmopsheric pressure. The principle of this quartz microbalance is based on the property of the resonance frequency of a quartz crystal to vary in a proportional way for small changes of the mass of a foreig· substance deposited on one of its sides. Hence by measuring the change of the frequency of an oscillator, where the quartz is inserted, the change of the mass can be detected and evaluated (1-2). It seems that the first application of this technique to an electrolytic medium have been done by T. NOMURA (3) in 1981 for analytical purposes. A few years later and practically at the same time S. BRUCKENSTEIN (4) and K.K. KANAZAWA (5) have used this technique for electrochemical kinetics studies. Since, some applications have been proposed in the field of corrosion science (6).

So far all the results have been obtained by quasi steady-state techniques : the variation of the quartz resonance frequency, i.e. the mass variation has been recorded under experimental condition changes. In this paper it will be shown how the same principle can be used in order to obtain dynamic informations about the mass changes. A sinusoidal perturbation of the electrolysis current which flows through the electrode allows the classical impedance and a new mass-voltage transfer function to be simultaneously measured (7).

First of all copper is electrochemically deposited in sulfate medium ($CuSO_4$ 0.5 M + H_2SO_4 0.5 M) on one of the electrode of a quartz crystal resonator which is called the working crystal. The latter is inserted in an oscillator which has to be tuned in order that it oscillates even when the crystal resonator is strongly damped by the electrolytic solution. The processing of the oscillating signal during the dissolution of copper in the same solution gives the change of the resonance frequency of the working crystal and hence the decrease of the mass of copper deposited on the quartz electrode. The modulation of the resonance frequency Δf related to the sinusoidal perturbation of the current ΔI about the steady-state polarization current I_0 is analyzed by means of a transfer function analyzer (Solartron-Schlumberger 1254) in order to obtain the mass-voltage transfer function by means of $\Delta f/\Delta E$. This arrangement allows the classical impedance ($\Delta E/\Delta I$) to be obtained at the same time (Fig. 1).

In Fig. 2 and 3 are given the impedance and the mass-voltage transfer function at I_0 = 200 µA during copper dissolution at ambient temperature.

In Fig. 4 the theoretical mass-voltage transfer function is given for a metal dissolution in two steps :

$$Me \cdot Me^{+}_{ads} + e$$

$$Me^{+}_{ads} \cdot Me^{++} + e$$

There is a good agreement with the experimental results concerning the general trends of the mass voltage transfer function.

References

(1) C. LU and A.W. CZANDERNA
Ed. of Applications of piezoelectric quartz crystal microbalances. Methods and phenomena Vol. 7. Elsevier, Amsterdam 1984.

(2) G. SAVERBREY
Z. Phys., 155, p. 206 (1955).

(3) T. NOMURA and M. IIJIMA
Anal. Chim. Acta, 131, p. 97 (1981).

(4) S. BRUCKENSTEIN and M. SHAY
J. Electroanal. Chem., 188, p. 131 (1985).

(5) J.H. KAUFMAN, K.K. KANAZAWA and G.B. STREET
Phys. Rev. Letters, 53, p. 2461 (1984).

(6) H.E. HAGER, R.D. RUEDISUELI and M.E. BUEHLER
Corrosion, 42, p. 345 (1986).

(7) S. BOURKANE
Thèse, Paris (to be submitted).

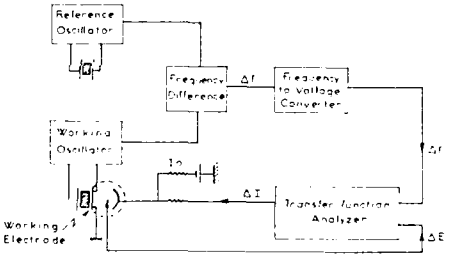


Fig. 1 : Experiment arrangement used for the measurement of the mass voltage transfer function $\left(\frac{dm}{dE}\right)_I = k \frac{\Delta f}{\Delta E}$.

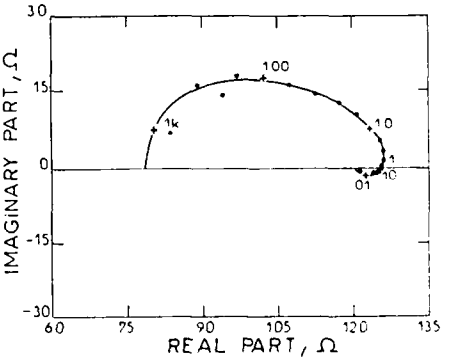


Fig. 2 : Electrochemical impedance measured during the dissolution of copper in H_2SO_4 0.5M + $CuSO_4$ 0.5M medium at 200 µA.

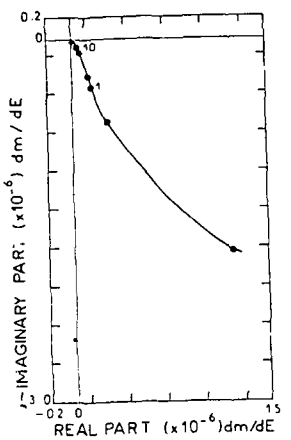


Fig. 3 : Mass-voltage transfer function measured in the same conditions as for Fig. 2.

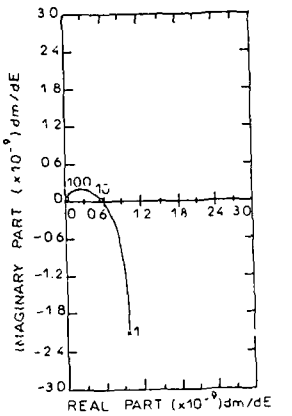


Fig. 4 : Theoretical mass-voltage transfer function.

Abstract No. 171

EXTENSION OF A.C. IMPEDANCE TECHNIQUE TO ATMOSPHERIC CORROSION STUDIES : APPLICATION TO A SCRATCHED GALVANIZED STEEL

R. GUILLAUME, M. KEDDAM and H. TAKENOUTI

LP 15 du CNRS "Physique des Liquides et Electrochimie"
Université P. & M. Curie, tour 22, 4 place Jussieu
75252 PARIS Cédex 05, FRANCE.

INTRODUCTION

The rate of atmospheric corrosion can be monitored by electrochemical cells in which to identical or different materials are coupled in a flush edge-by-edge arrangement. The electrolytic medium is constituted by a thin layer of condensed water in which atmospheric pollutants and corrosion products are dissolved. Corrosion rate is estimated from the short-circuit current supplied by the cell, it depends strongly upon the ambient hygrometry. However mechanistic informations can only be gained from more elaborated experiments : d.c. and preferably a.c. polarisation measurements. The goal of the present work was to investigate the applicability of a.c. impedance to an atmospheric corrosion cell simulating a scratch on a coated + galvanized steel during a climatic test. Previous attempt to associate a.c. techniques to atmospheric corrosion was limited to resistance measurements (1).

EXPERIMENTAL

- Principle : Fig. 1 depicts the principle of the in-situ electrochemical sample. The zinc coating is electrically insulated from the steel substrate by making a sandwich structure. Two types of sample were prepared by :

  - gluing two thin foils of Zn (Good-Fellow Ltd.) on the steel back ground (e = 50 µm, d = 30 µm),

  - thin layer technology : R.F. sputtering of 1 µm Al_2O_3 + 3 µm SiO_2 + 1 µm Cermet (SiO_2 + 90% Fe) (d = 5 µm). Then e = 10 µm of Zn is electrodeposited.

Both types of sample are finally coated with h = 13 µm of cataphoretic paint. Thin layer samples are grooved by laser beam machining to simulate the scratch. The former type of sample allows to probe the potential of the scratch bottom by introducing thin platinum wires across the steel sheet.

- Polarization and measuring set-up :

d.c. : Short circuit conditionsprevailing at real life operation are reproduced by closing the cell loop on a current follower (zero impedance current to voltage converter). Open circuit potential is measured with voltage follower.

a.c. : Figure 2 shows the equipment used for impedance measurements under short-circuit (potentiostated E = 0 between cell terminals). A 2-electrode or 3-electrode configuration was used according to the sample investigated. The 3-electrode set-up allowed to separate the contribution of Zn and Steel half-cells in the overall response.

RESULTS

A large set of data have been accumulated as a function of environmental parameters. Impedance data are significative of the corrosion processes even in the dry conditions where the impedance cell is very high. The only spurious contribution arises in the H.F. domain from the small capacity of the insulating layer in parallel with the cell impedance. Fig. 3 displays a time recording of the short-circuit current $I_{s.c.}$ during an experiment going through the whole test. A good correlation is found between the d.c. electrochemical and environmental parameters. A salient feature is the decay of $I_{s.c.}$ from cycle to cycle attesting the progressive loss of protection by the sacrificial Zn layer (2).

Figure 4 shows a set of 3 complex impedance plots. It is verified as a self-consistency criterium that W is the sum of individual impedance Zn and St. The Pt probe is a satisfactory a.c. reference down to 0.1 Hz. The informationsmade available are :

- In the HF range : The ohmic resistance of the corrosion products in the scratch which plays the role of electrolyte by bridging Zn to Steel.

- In the MF and LF ranges : Electrochemical polarisation apparently due to mass transfer effects are prevailing. Both contributions to the cell impedance depend dramatically on temperature T and relative humidity RH. But at all T and RH values ohmic contribution to the cell behaviour remains small.

The influence of potential distribution within the cell has been investigated with the 3-electrode set-up. Figure 5 shows the impedance of the Steel electrode under various T and RH conditions. The phase rotation in excess of 90° has been recently proved to appear when in a pore or transmission line model the potential reference is located at the extremity opposite to the current entry (3). The higher the resistance of the corrosion products (low T, low RH), the larger this distribution effect. This allowed to ascribe the frequency dependence at lower frequency essentially to transport phenomena.

It is concluded that the impedance of the Zn half-cell is controlling the corrosion behaviour of the scratched area.

CONCLUSIONS

- a.c. impedance techniques proves to be applied successfully to investigate the mechanism of atmospheric corrosion.

- Separation of the various factors in the electrochemical kinetics can be performed owing to the use of a probe acting as a microreference electrode.

One of us, R.G., is grateful to ANRT and CRD Usinor Montataire for a financial support. M. SELLA and MARTIN (CNRS Meudon) and LEBRAS (Micro control) are acknowledged for their help in samples preparation.

REFERENCES

(1) B. HARRIS and P.B.P. PHIPPS
156th Meeting Electrochemical Society, Los Angeles, (USA), October 1979. Extended Abstracts n° 242, p. 626.

(2) R. GUILLAUME and M. KEDDAM
Eurocorr 87, Karlsruhe (GFR), April 1987. Preprints p. 739.

(3) C. FIAUD, M. KEDDAM, M. KADRI and H. TAKENOUTI
Electrochim. Acta, 32, 445 (1987).

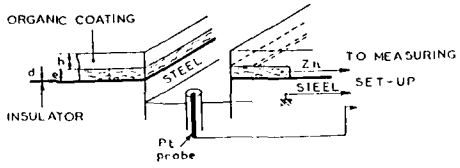


Fig. 1 : View of the sandwich sample simulating a scratch on a galvanized steel protected by an organic coating. "d", "e" and "h" : thickness of respectively the insulator, the zinc and the coating layers.

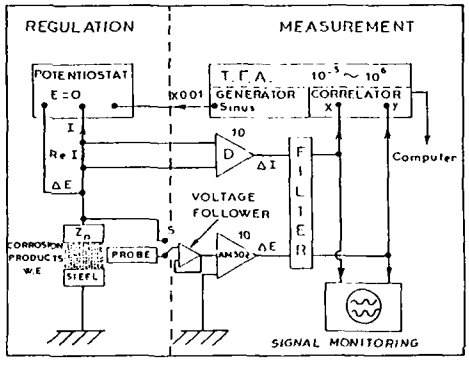


Fig. 2 : Set-up for impedance measurement of the atmospheric corrosion cell in a 2 or 3 - electrode arrangement (Shown in 3-electrode configuration).

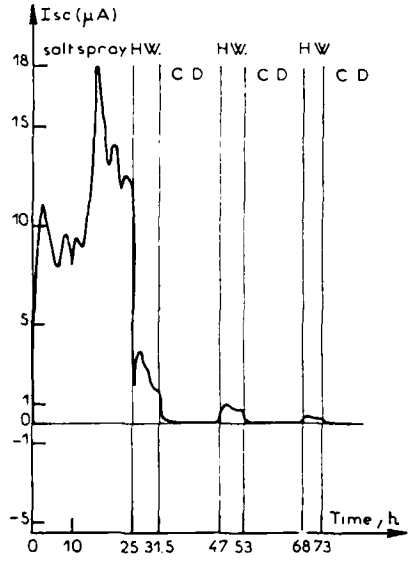


Fig. 3 : Short circuit current I_{sc} vs time profile under salt spray and during the first three days of climatic cycling.
H.W. : hot (T = 40 °C) / wet (R.H. 95 %).
C.D. : Cold (T = 25 °C) / dry (R.H. 73 %).

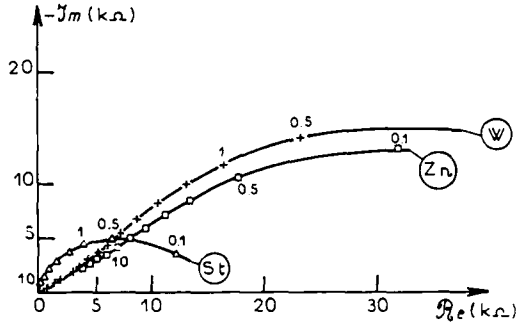


Fig. 4 : Complex impedance plots of the steel electrode (St), the Zinc electrode (Zn) and the whole cell (W). Cold and dry environment .

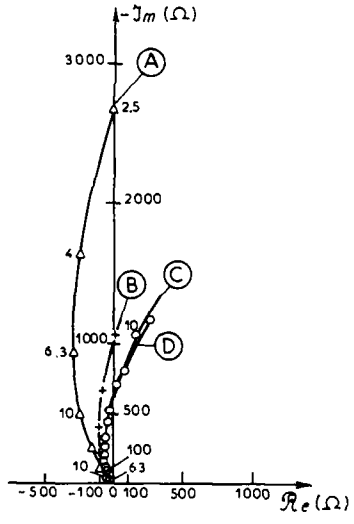


Fig. 5 : Magnified high frequency range displaying the characteristic transmission line effect when the a.c. potential is measured on the Pt probe.
A : T = 20 °C - R.H. = 70 %
B : T = 20 °C - R.H. = 95 %
C : T = 30 °C - R.H. = 95 %
D : T = 40 °C - R.H. = 95 %

Abstract No. 172

Application of Electrochemical Impedance for Studying Localized Corrosion

M. Kendig and S. Jeanjaquet

Rockell International Science Center

1049 Camino Dos Rios
Thousand Oaks, CA 91360

BACKGROUND

With few exceptions, electrochemical reactions and, hence, corrosion, vary spatially in rate and mechanism on metal surfaces due to inherent surface inhomogeneity. A continuing problem for rapid, in-situ corrosion monitoring has been the lack of methods for evaluating localized corrosion. Electrochemical impedance methods have typically been applied to the study of general corrosion although recent advances take into consideration the heterogeneous nature of electrode surfaces (1,2). Scanning ac probe methods (3) and methods for evaluating corrosion fatigue (4) represent some unique applications of electrochemical impedance methods for evaluating localized corrosion processes. There has been evidence that localized corrosion in the form of pits can give rise to structure in the impedance spectra (5). A model pit made by drilling through a Ni coating on carbon steel gave rise to two time constant impedance spectra from which the ohmic resistance in the pit was evaluated (6,7). A more detailed analysis of the impedance spectrum of localized regions using a frequency-dependent current distribution model has been described (8). To gain a better understanding of how and why localized variations in electrochemical reactions influence the impedance spectra, a model heterogeneous rotating cylinder electrode (RCE) containing an active Sn alloy in an inactive Cu matrix was constructed. This system was motivated by the previous work of Isaacs (9) who used this system to test his scanning reference probe. Our objective has been to see whether the impedance of the heterogeneous surface could be related to the specific impedances of the respective homogeneous surfaces.

EXPERIMENTAL

Heterogeneous electrodes were formed by placing drops of 95% Sn 5% Sb solder into holes drilled in a Cu rotating cylinder electrode. Impedance measurements were made of both this heterogeneous electrode, and rotating cylinder electrodes of the pure materials polarized to nearly the same potential as the heterogeneous surface in aerated 0.09 M Na_2SO_4 / 0.01 M H_2SO_4. A concentric Pt screen counter electrode and a saturated calomel reference electrode in a luggin capillary were used. A gold wire pseudoreference coupled with an 0.1 μF capacitor to the reference was incorporated into the system. The impedance measurement was performed as described elsewhere (10).

THEORETICAL

The impedance for a heterogeneous surface can be described as a series of i parallel elements having specific Z_i. The total impedance is then:

$$Z = 1/\Sigma_i(P_i/Z_i), \qquad (1)$$

where P_i is the area fraction of the region having Z_i specific impedance (in units of Ω cm²). For simple cases, each region Z_i can be modeled as

$$Z_i = R_s + R_{pi}/(1 + (j\omega C_i R_{pi})^{\alpha i}), \qquad (2)$$

where R_{pi} is a polarization resistance, C_i is a capacitance for each region and α_i is a unitless constant.

Figures 1 and 2 show plots of log Z vs log ω (ω is the angular frequency) simulations of impedance spectra for variations in the area fraction and series resistances, R_{si}, respectively. As the area fraction of the active site increases from low to high values (0.01 to 0.1 Ω), an additional time constant appears (Fig. 1), and as the ohmic resistance decreases an additional time constant also appears (Fig. 2).

RESULTS

Figure 3 shows the frequency dependence at open circuit (-171 mV vs SCE) for the impedance modulus and phase angle for the heterogeneous surface (area fraction A_f of the Sn/Sb equal to 0.025). The broken lines are the experimental results and the solid lines are computerized simulation using parameters obtained from a nonlinear least squares fitting procedure. The broken lines in Fig. 4 show the respective impedance spectra for homogeneous electrode of the individual metals and the solid lines are computerized simulation obtained using parameters from a nonlinear least squares fitting procedure. Table 1 shows the results for the computerized fit of the data in Figs. 3 and 4. Note that the specific values for R_p as determined from the heterogeneous surface exceed those obtained from the homogeneous surfaces polarized to roughly the same potential (-151 mV) as the open circuit potential of the heterogeneous surface (-171 mV). The Sn exhibits a high pseudocapacitance in excess of 1000 μF/cm² which is greater for the homogeneous surface, as compared to the heterogeneous sample. The solution resistance for the Cu surface was observed to be 34 Ω cm². This anomalously high value may reflect a geometric variation in the placement of the reference electrode in the rather resistive 0.1 N electrolyte.

The anomalously high R_p values for the heterogeneous case might reflect either passivation of the Sn when coupled directly to the Cu or the variation might be explained by field distribution effects which have not specifically been considered in this simple model, but have been considered by Oltra and Keddam (8). A more detailed model considering a frequency distribution of alternating current is now under consideration.

REFERENCES

1. W.J. Lorenze and F. Mansfeld, Electrochem. Acta 31, 467 (1986).

2. K. Juettner, W.J. Lorenz, M.W. Kendig and F. Mansfeld, J. Electrochem. Soc. 135(2), 332 (1987).

3. H. Isaacs and M.W. Kendig, Corrosion 36, 269 (1980).

4. M. Kendig and F. Mansfeld, "Application of Electrochemical and Mechanical Impedance Techniques for Evaluation of SCC and CF," Corrosion '86, NACE, Houston, TX (1986).

5. F. Mansfeld, S. Lin, S. Kim and H. Shih, "Corrosion Protection of Al Alloys and Al-Based Metal Matrix Composites by Chemical Passivation," Corrosion '88, No. 380, NACD, Houston, TX (1988).

6. M. Kendig, E. Meyer, G. Lindberg, F. Mansfeld, Corrosion Sci. 23(9), 1007 (1983).

7. M. Kendig and F. Mansfeld, Proc. Fall Meeting Electrochem. Soc. 82-2, 105 (1982).

8. R. Oltra and M. Keddam, Corrosion Sci. 28(1), 1 (1988).

9. H. Isaacs and G. Kissel, J. Electrochem. Soc. 119, 129 (1972).

10. M. Kendig, A. Allen and F. Mansfeld, J. Electrochem. Soc. 131, 935 (1984).

Table 1
Impedance Parameters Determined from Computerized Fit of Spectra

	0.025 A_f Sn in Cu		Homogeneous Materials	
	Sn Alloy	Cu	Sn Alloy	Cu
R_{pi}, Ω cm^2	180	10^4	86	$3.5\ 10^3$
C_i, μF/cm^2	$1.7\ 10^3$	33	$9.6\ 10^3$	10.5
α_i	0.7	0.8	0.8	0.9
R_s	12	12	11	34
E, mV (SCE)	-171		-151	

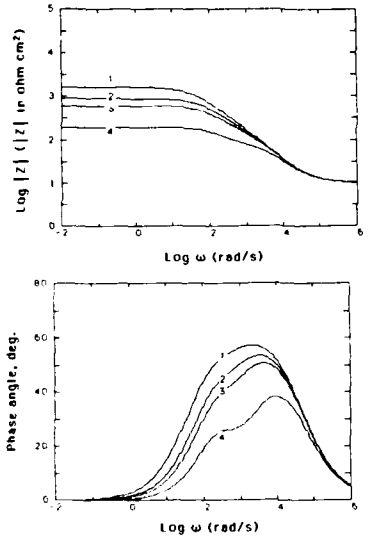


Fig. 1 Frequency dependence for the impedance modulus (a) and phase angle (b) of simulated impedance spectra for area fractions: (1) 0.01, (2) 0.02, (3) 0.03 and (4) 0.1 of an active site.

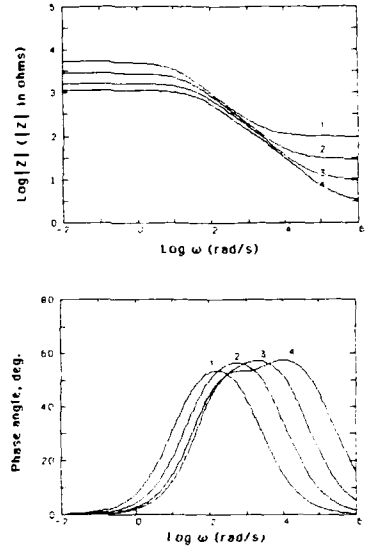


Fig. 2 Frequency dependence for the impedance modulus (a) and phase angle (b) of simulated impedance spectra for R_{si}: (1) 100 Ω (2) 30 Ω, (3) 10 Ω, and (4) 1 Ω.

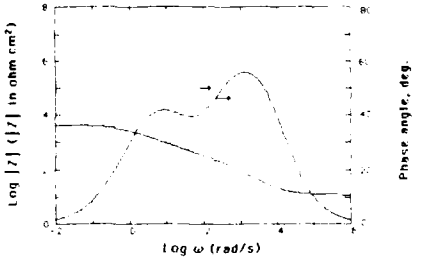


Fig. 3 Frequency dependence for the impedance modulus and phase for a Cu RCE containing an Sn alloy region of area fraction 0.025. Sample exposed for 4 h in 0.09 N Na_2SO_4/0.01 N H_2SO_4.

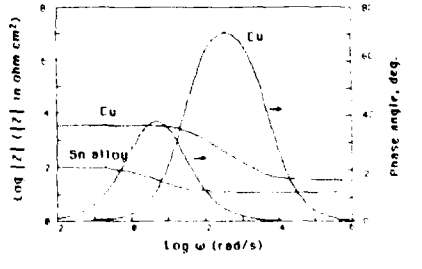


Fig. 4 Frequency dependence for the impedance modulus and phase for a Cu RCE, and Sn alloy RCE after exposure for 4 h in 0.09 N Na_2SO_4/0.01 N H_2SO_4.

Abstract No. 173

Can the Kramers-Kronig Transforms be Used for the Validation of Experimental Impedance Data?

Hong Shih and Florian Mansfeld
Dept. of Materials Science
University of Southern California
Los Angeles, CA 90089-0241

Macdonald et al. (1,2) have recently suggested the use of the Kramers-Kronig (K-K) transforms (3) as diagnostic tools for determining the validity of experimental impedance data. It was shown for several examples, with often complicated frequency dependence of the impedance spectra, that in certain cases the experimental data and the K-K transforms matched very well, while in others they did not. It was concluded that in the latter case the experimental data were not true impedance data and had to be discarded.

The application of the K-K transforms to a number of corrosion phenomena which are being studied in this laboratory has shown that severe problems exist with their use in the validation of impedance data. These problems become obvious in the simplest case of an impedance which is a resistance R_s in series with a parallel combination of a resistance R_p and a capacitance Cd. Fig. 1 shows the theoretical data for such a case with R_s = 10 ohm, $R_p = 10^5$ ohm and Cd = 100 μF. Also shown are the K-K transforms. In Fig. 1a the lowest frequency used is 10^{-2} Hz, in Fig. 1b it is 10^{-3} Hz and in Fig. 1c it is 10^{-4} Hz. It can be seen that good agreement between the two curves occurs only when the K-K transform is carried out to sufficiently low frequencies. This, of course, also means that experimental data have to be available for these frequencies.

The results in Fig. 1 suggest that great care has to be taken in the use of the K-K transforms. The fact that agreement with theoretical data is not obtained if the frequency range for the calculation is not sufficient serves as a warning that valid data might be considered to be invalid. The reason for this problem seems to be that the K-K transforms produce valid data only if the real and the imaginary part of the impedance have reached their dc limit in the frequency range used for the calculation. These problems were not noticed by Macdonald et al. (1,2), apparently, because in their systems the impedance values were very low.

The findings reported here demonstrate that the K-K transforms cannot be used for many of the most important corrosion systems. Very corrosion resistant systems which can be studied with electrochemical impedance spectroscopy (EIS) include inhibited solutions, polymer coated metals and anodized surfaces. In most of these cases the impedance data do not reach a *dc limit* in the frequency range which is experimentally accessible. In fact, the challenge in EIS studies for these systems is the extraction of meaningful corrosion parameters from such data. Even for the simple case of a metal corroding in aerated, neutral media it can be very difficult to determine the parameters from which corrosion rates are calculated (4). As shown elsewhere for systems involving a diffusion impedance or a transmission line, the impedance data do not reach a dc limit at the lowest frequencies which can be measured and the K-K transforms fail (5).

Acknowledgement

This work has been performed under Contract No. DAAL-03-86-K-0156 with the U.S. Army Research Office.

References

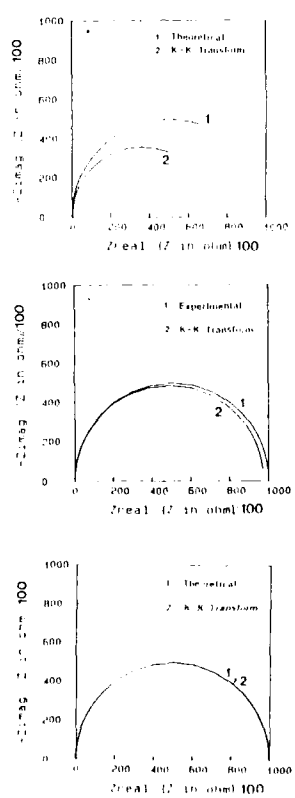
1. D.D. Macdonald and M. Urquidi, J. Electrochem. Soc. 132, 2316 (1985).

2. M. Urquidi-Macdonald, S. Real and D.D. Macdonald, ibid. 133, 2018 (1986).

3. R.L. van Meirhaeghe, E.C. Dutoit, F. Cardon and W.P. Gomes, Electrochim. Acta 21, 39 (1976).

4. K. Juettner, W.J. Lorenz, M.W. Kendig and F. Mansfeld, J. Electrochem. Soc. 135, 332 (1988).

5. H. Shih and F. Mansfeld, "Concerning the Use of the Kramers-Kronig Transforms for the Validation of Impedance Data," submitted to Corr. Sci.



1. Nyquist plots for theoretical and K-K transform data; lower frequency limit: a) 10 mHz, b) 1 mHz, c) 0.1 mHz; R_s = 10 ohm, R_p = 10^5 ohm, Cd = 100 μF.

Abstract No. 174

AN IDENTIFICATION PROCEDURE TO STUDY THE DYNAMICS OF METAL DISSOLUTION IN AQUEOUS MEDIA

R.M. Milocco
Laboratorio de Electrónica Industrial Control e Instrumentación (LEICI), Facultad de Ingeniería, Universidad Nacional de La Plata, 1900 La Plata, Argentina

and

E.B. Castro, S.G. Real and J.R. Vilche
Instituto de Investigaciones Fisicoquímicas Teóricas y Aplicadas (INIFTA), Facultad de Ciencias Exactas, Universidad Nacional de La Plata, Sucursal 4 - C.C. 16, 1900 La Plata, Argentina

The estimation of the transfer function impedance can be derived from the experimental data set. The complex impedance diagram provides the experimental information which requires to be transformed in a quantitative mathematical expression to study the dynamics of corrosion processes.

The aim of this paper is to analyze an identification procedure developed to obtain the coefficients of the electrochemical impedance based on an algorithm which minimizes the mean square error related to the difference between the experimental and the model data.

The complex impedance diagrams were calculated through two techniques. In the first one, the spectral density functions were estimated either by means of the discrete finite Fourier transform of correlation functions or in terms of direct Fourier transforms of the original data records, employing a pseudo-random binary sequence as perturbation signal. The power spectrum of the signal had an envelope of the form $S = t_m[\sin(\pi f t_m)/(\pi f t_m)]^2$, where $f = \omega/2\pi$ and t_m is the clock pulse period of the binary sequence, which was generated either by software from a digital computer (PDP 11) or by a low-cost binary-signal generator built-up in the laboratory. In the second case, deterministic perturbations in the form of typical sinusoidal excitation at discrete frequencies were applied (Solartron, 1250 frequency response analyzer and 1186 electrochemical interface).

Data quality and degree of causality between excitation and response signals were characterized by both the squared coherency spectrum and Kramers-Kronig transforms.

The experimental impedance data, $Z(\omega) = Z'(\omega) + jZ''(\omega)$, were compared with a model expressed by the quotient of two polynomial terms, according to

$$\frac{P(\omega)}{Q(\omega)} = Z(\omega) + \varepsilon(\omega) \qquad (1)$$

where the error $\varepsilon(\omega) = \varepsilon_E(\omega) + \varepsilon_M(\omega)$ involves both the experimental one, ε_E, and the difference between data obtained and mathematical model, ε_M, for a fixed number of frequencies ($\omega_0, 2\omega_0, \ldots, m\omega_0$). Under these conditions, the equations

$$P(\omega) = p_0 + p_1(j\omega) + \ldots + p_{np}(j\omega)^{np} \qquad (2a)$$

and

$$Q(\omega) = 1 + q_1(j\omega) + \ldots + q_{nq}(j\omega)^{nq} \qquad (2b)$$

provide the coefficients p_i and q_i to be determined in order to minimize the following function:

$$J = \sum_{n=1}^{m} |\varepsilon(n\omega_0)|^2 \qquad (3)$$

Let us now describe eq. (1) in the form

$$P(\omega) - Q(\omega)Z(\omega) = \varepsilon(\omega)Q(\omega) \qquad (4)$$

and after defining a new polynomial term, $\hat{Q}(\omega)$, which takes into account the numerical values of $Q(\omega)$ estimated at $\omega = n\omega_0$, for $n = 1,2,\ldots,m$, in place of eq. (4) one obtains

$$\frac{P(\omega)}{\hat{Q}(\omega)} - \frac{Q(\omega)}{\hat{Q}(\omega)} Z(\omega) = \varepsilon(\omega)\frac{Q(\omega)}{\hat{Q}(\omega)} = \hat{\varepsilon}(\omega) \qquad (5a)$$

Using matrix notation, eq. (5a) can be given by

$$\begin{bmatrix} \mathrm{Re}\,\hat{\varepsilon}(\omega) \\ \mathrm{Im}\,\hat{\varepsilon}(\omega) \end{bmatrix} [\theta] = [\Phi][\theta] = \begin{bmatrix} Z'(\omega) \\ Z''(\omega) \end{bmatrix} + \begin{bmatrix} \mathrm{Re}\,\hat{\varepsilon}(\omega) \\ \mathrm{Im}\,\hat{\varepsilon}(\omega) \end{bmatrix} \qquad (5b)$$

where Φ includes $\hat{Q}$ at the different frequencies and θ the p_i and q_i coefficients. To minimize the J function, it was considered that

$$\theta = (\Phi^T\Phi)^{-1}\Phi^T Z \qquad (6)$$

where Φ^T is the transpose of Φ. However, as $Q(\omega)$ is unknown, its value for the k-th iteration step was approached using that corresponding to the (k-1)-th step. Finally, after the proper convergence, $Q_k(\omega) = Q_{k-1}(\omega)$ and $\hat{Q}(\omega) = Q(\omega)$ in order to minimize J in eq. (3).

The developed identification procedure for data obtained from the two described experimental techniques was applied to the study of iron dissolution in different aqueous electrolytes.

Abstract No. 175

Transport Properties of Salt Films on Nickel in 0.5 N HCl

Mike J. Danielson

Pacific Northwest Laboratory
Box 999; Mail stop P8-44
Richland, WA 99352

The transport of corrosion products across salt films is of major importance in studying pitting, crevice corrosion, and electrochemically-assisted stress cracking processes. The major difficulty that has hindered the study of transport across salt films is the determination of their thickness. In this study, a nickel chloride salt film is precipitated on nickel using an artificial pit configuration in 0.5 N HCl. It is necessary that the pit be corroding under steady state conditions.

The technique is based on the observation that once a salt film is precipitated, the steady state corrosion rate is independent of the external potential. If the potential is abruptly stepped to less anodic potentials, the current decreases while the film thins and then returns to the same original current again. If one integrates this deviation in current from the steady state value over time, a measure of the amount of salt film that was lost with film thinning can be obtained. This charge can be measured using a Princeton Applied Research Model 179 coulometer in the null mode. Simultaneously, the AC impedance is measured at a high enough frequency that only the purely resistive component is apparent. This change in charge to the change in resistance (R) in coulombs/ohm contains within it the salt film thickness and electric field strength. The potential is stepped in 50 mV increments until the salt film dissolves. The resistance at the point of unsaturation is necessary in order to calculate the absolute resistance of the salt film. By assuming the salt film to be nickel chloride hexahydrate and using the value for its' molar volume, and determining dV/dR, the electric field strength across the salt film was calculated to be -388 V/cm. This value indicates a low field (ohmic) transport process is operative across the salt film. The thickness of the salt film is directly proportional to the external potential once the film is precipitated at a constant crevice depth. For instance, the thickness is about 12 microns for a .1 cm crevice depth when the potential is 700 mV more anodic than the initial potential for precipitation. The salt film thickness is also directly proportional to the depth of the crevice. Assuming that the salt film is crystalline but porous, the porosity was calculated to be 1. E-3. The pH at the metal/salt interface should be more basic than the bulk electrolyte (unless the metal contains a component like chromium) and it can be shown that the local increase in pH should be directly proportional to the voltage drop across the salt film. This may be important to explaining why spontaneous passivation is sometimes observed under salt films.

Abstract No. 176

STUDY OF THE CORROSION OF COATED METALS WITH IMPEDANCE MEASUREMENTS

J. HUBRECHT **J. VEREECKEN**

VRIJE UNIVERSITEIT BRUSSEL
Dept. Metallurgy, Electrochemistry and Materials Science
Pleinlaan 2, 1050 BRUSSELS, Belgium

Introduction

The AC impedance technique has proved to be a very useful electrochemical technique [1-6] to study the mechanism of the corrosion of coated metals. An important advantage of this technique is that it is possible to characterize the coating and the behavior of the metal.

Experimental

ARMCO iron coated with ERCUSON AS250 (a styrene-acrylic polymer) pigmented with red ironoxide and strontium chromate has been tested in an aerated sodium chloride solution. Coating thickness, NaCl concentration and oxygen content have been the investigated parameter. The coated samples are mounted in a special cell described elsewhere [2].

In an attempt to subdivide the whole corrosion reaction into its partial processes a special corrosion cell of two identical electrodes has been build [3]. The coated metal of both cells is connected electrically and the solutions electrolytically. The only difference is the oxygen content in the solutions. As a consequence one of the cells behaves as an anode the other as a cathode. Measurements of mixed potential, corrosion current between both cells and AC impedance on the separate cells are then easy to perform.

The AC impedance have been measured with a 1250 Frequency Response Analyser and an 1186 Electrochemical Interface both of SOLARTRON SCHLUMBERGER. The frequency of the applied voltage sine wave ranges between 60 KHz and 10 mHz. The amplitude is 20 mV. The impedance results are plotted in the complex plane.

Results and Discussion

A typical AC impedance result for sample 1 (190 µ) and 2 (220 µ) after 26 days immersion is shown in figure 1. Through the solution of cell 1 N_2-gas is continuously bubbled, through the solution of cell 2 O_2-gas.

It is explained elsewere [3] that the impedance of submersed coated iron sheet contains three distinct sections according to the frequency domain. The flattened semi circle which is found at high frequencies reflects the physical behaviour of the coating. At intermediate frequencies the double layer and the charge transfer can be characterized and at low frequencies the mass transport.

The simulation of the corrosion process of coated iron with the aid of a differential aeration cell led to the conclusion that the cathodic kinetics seems to be controlled by diffusion and the anodic kinetics by charge transfer. The pore resistance decreases more rapidly in the coating of the cathodic sample than in the one of the anodic sample.

Scanning electron microscopy and X-Ray micro-analysis show that the anodic metal/coating interface oxidation products are formed, block the coating pores and cause blistering.

In the case of thinner coating layers the influence of the diffusion of electroactive species is less important.

References

[1] EPELBOIN I., KEDDAM M., TAKENOUTI H.
J. Appl. Electrochem., 2, 71, (1972).

[2] HUBRECHT J., VEREECKEN J., PIENS M.
J. Electrochem. Soc., 131, 2010, (1984).

[3] HUBRECHT J., VEREECKEN J.
J. Electrochem. Soc., 132, 2886, (1985).

[4] WALTER G.W.
Cor. Sc., 26, 681, (1986).

[5] MANSFELD F., JEANGAQUET S.L., KENDIG M.W.
Cor. Sc., 26, 735, (1986).

[6] LEIDHEISER H., GRANATA R.D.
Corrosion, 43, 296, (1987).

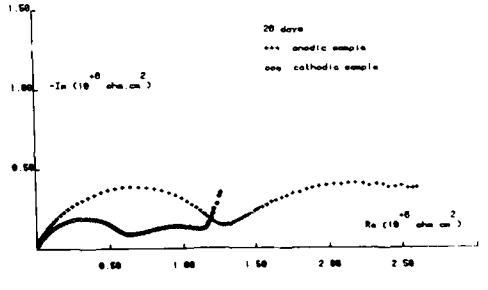


Figure 1

Abstract No. 177

CORROSION INHIBITION IN A CO_2 SATURATED CHLORIDE SOLUTION BY A FILM FORMING COMPOUND : ASSESSMENT BY THE ELECTROHYDRODYNAMIC IMPEDANCE METHOD

D. BERNARD[1], C. DESLOUIS[2], F. OLIVIER[1], T.E. POU[1], B. TRIBOLLET[2]

1 CECA SA (Groupe Elf Aquitaine), 95 rue Danton, 92303 Levallois Perret - FRANCE

2 LP15 CNRS - Physique des Liquides et Electrochimie 4 place Jussieu, 75252 Paris Cedex 05 - FRANCE

INTRODUCTION

CO_2 corrosivity in oil wells constructed with usual carbon steel equipment involves complex cathodic partial reactions where proton reduction is effected either directly or via the different carbonic species. The anodic partial reaction is also complicated by carbonate precipitation and occurence of galvanic couples inducing localized corrosion.

Since mass transport has been identified as partly controlling the corrosion rate, a way to reduce the corrosion rate can be to slow down the rate of mass transport of reactants or products and, therefore, a film forming inhibitor can be anticipated as an appropriate solution. Partial mass transport control was another reason for testing the EHD impedance technique which has been already justified as well suited for corrosion studies (1).

EXPERIMENTS

Steady state and EHD impedance measurements were performed by means of an electrochemical interface Solartron 1286 and coupled with a frequency analyzer Solartron 1250.

The experiment was carried out in 3% of NaCl solution saturated with CO_2.

The N80 carbon steel rotating disc is used as working electrode.

The detail of EHD impedance measurement technique is given elsewhere (2).

RESULTS

Steady state measurements :

The cathodic current potential-curves obtained display an inflection point corresponding to a limitation by mass transport (curves A and B for a rotating speed Ω = 1000 and 300 rpm in fig.1).

The addition of a film forming inhibitor containing a mixture of fatty amines and known as film forming*, leads to a substantial decrease of the cathodic current (curves C and D in fig.1) for a concentration as low as 20 ppm.

In the absence of inhibitor, the current in the region of the inflection point is increasing with Ω but does not obey the Levich relation. Close to E_{corr} a similar relative variation of the current is followed. Hence, a significant non diffusional component is hidden in the overall current and so the data are plotted in fig.2 as I vs Ω. The current reduction increases with the inhibitor amount (10 and 30 ppm, curves C and D in fig.2) and beyond 30 ppm no further improvement is observed.

EHD impedance measurements :

In the absence of inhibitor, the Bode plots diagrams in fig.3 and 4 vs the dimensionless frequency $p=\omega/\Omega$ (ω is the modulated frequency of the disk speed) show no qualitative difference between the "diffusion plateau" domain (-.8V/SCE) and E_{corr}. This confirms the previous steady state result about the similar relative variations of the current with Ω at the same potentials.

However, different diagrams are obtained for increasing Ω, at variance with the theory predicting a single diagram vs p (3). Therefore, mass transport toward a uniformly reactive electrode is not the only rate determining step and the influence of Ω on the diagrams suggests two possible explanations, one involving a partial blocking of the interface (4) and the other a coupling of the electrochemical reaction with a chemical reaction (5).

For a 10 ppm inhibitor concentration (fig.7) the impedance behavior shows more clearly at high frequency a blocking effect and a better reducibility with p in the mid region.

For a 50 ppm inhibitor concentration the observed behavior is now characteristic of mass transport partly proceeding by molecular diffusion through a solid layer (6).

DISCUSSION

The observed results for CO_2 corrosivity present some relevance with the proposed models so far :

The cathodic reaction model of Schmidt and Rothman (7) considers, in fact, the direct proton reduction, its wall concentration being also controlled by the dissociation reactions of H_2CO_3.

In the anodic range, the earlier stages of metal dissolution are ruled by the Bockris mechanism (8) and are followed by the precipitation of $FeCO_3$ (9).

Therefore, both the anodic and cathodic reactions can produce a partial blocking of the interface. However, a frequency analysis of the EHD impedance in the LF domain yields a Schmidt number value around 1000 -i.e. a diffusion coefficient of $10^{-5}cm^2.s^{-1}$ which seems too low for H^+- and should rather indicate a control of the cathodic current by H_2CO_3 diffusion.

So presumably, both effects (i.e. partial blocking and chemical coupled reaction) can be invoked.

EHD impedance visualized at low inhibitor concentration a partial coverage of the metal by the inhibitor, whereas at 50 ppm the inhibitor seems to cover uniformly the metal and over a certain thickness.

The technique used is thus able to predict accurately the minimum inhibitor concentration enabling a good protection without localized corrosion. A comprehensive study of corrosivity in the absence of inhibitor needs, however to be done in view of those preliminary data.

CONCLUSION

The EHD impedance measurement, applied to a film forming corrosion inhibitor, is proved to be a powerful technique to study the corrosion inhibition.

REFERENCES

(1) C. Deslouis and B. Tribollet "Electrochemical methods in corrosion research" Material Science Forum, 8 (1986) 1-11.
(2) C. Deslouis, C. Gabrielli and B. Tribollet 166th ECS Meeting, New Orleans, Oct. 1984.
(3) K. Tokuda, S. Bruckenstein and B. Miller J.E.C.S., Vol 22, n° 10 (1975) 1316-1322.
(4) A. Caprani, C. Deslouis, S. Robin and B. Tribollet J. Electroanal. Chem., 238 (1987) 67-91.
(5) C. Deslouis and B. Tribollet Journées d'Electrochimie, Dijon, Juin 1987.
(6) C. Deslouis, B. Tribollet, M. Duprat and F. Moran J.E.C.S., 134 (1987) 2496.
(7) G. Schmidt and B. Rothman Werkst.n.Korr., 29 (1978) 237-245.
(8) J.O'M. Bockris, D. Drazic and A.R. Despic Electrochim. Acta, 4 (1961) 326.
(9) G.I. Ogundele and W.E. White N.A.C.E., Vol 42, n° 2 (1986) 71-78.

* A product by CECA Company under the trade-name NORUST PA23D

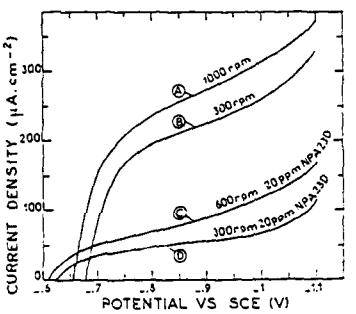


Figure 1 : Current-potential curves. NaCl 3% solution saturated with bubbling CO_2. A , B blank. C and D with 20ppm NPA23D inhibitor.

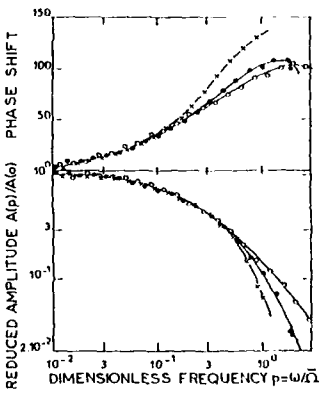


Figure 2 : EHD impedance diagrams in Bode coordinates, E = -.8V/SCE. Ω = 150 (o), 300 (•) and 600 (x) rpm. Blank solution.

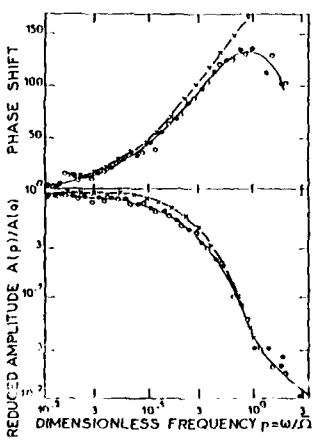


Figure 3 : Same conditions and symbols as in Fig.2 with 10ppm NPA23D.

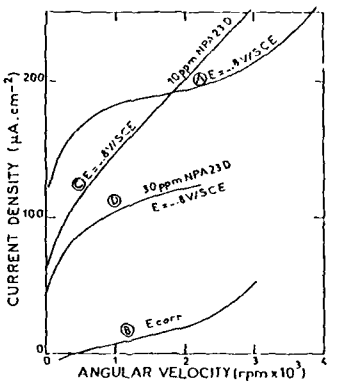


Figure 4 : I-Ω (rpm) curves at -.8V/SCE (A , C , D) and E_{corr} (B).

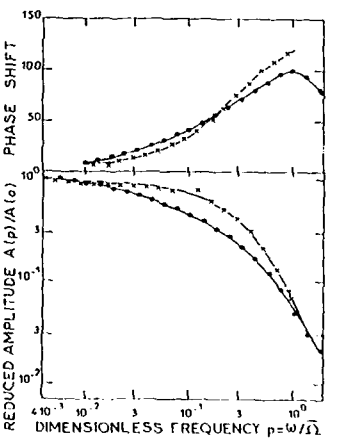


Figure 5 : Same symbols as in Fig.3 ; E = E_{corr}.

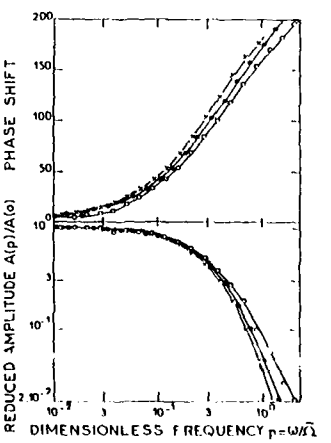


Figure 6 : Same conditions and symbols as in Fig.5 with 30ppm NPA23D.

Abstract No. 178

INHIBITOR EFFECTS OF PHOSPHINES ON THE CORROSION OF COPPER STUDIED BY ELECTROHYDRODYNAMICAL IMPEDANCE

C. FIAUD*, B. TRIBOLLET**, I. VASTRA*

* UA CNRS 216, Electrochimie Analytique et Appliquée, Groupe Corrosion, 11 rue P. & M. Curie, 75231 Paris Cédex 05, FRANCE.

** LP 15 CNRS, Physique des Liquides et Electrochimie, tour 22, Université P. & M. Curie, 4 place Jussieu, 75252 Paris Cédex 05, FRANCE.

Phosphines of the phenylphosphine type are efficient molecules for inhibiting the uniform corrosion of metals such as zinc, iron or copper in deaerated acidic solutions. It was previously established that the $P\emptyset_3$ ($\emptyset = C_6H_5$) molecule acts through its co-adsorption with hydrogen atoms at the metal surface (1,2). However, the distribution of the inhibitor species at the surface was not investigated, nor was the effect of oxygen on the efficiency of the phosphines.

The oxygen reduction on copper interface is mass transfer limited, so the blocking effect of the phosphine can be studied by DC measurements of the current versus the rotation speed of the disk electrode and by electrohydrodynamical (EHD) impedance. This last technique consists on the frequency response analysis of the system to a sinusoidal speed modulation at a rotating disk electrode (3,4). In particular when the reactivity of the interface is non-uniform, the EHD impedance shows some characteristic features (5). In the low frequency range, the response behaviour corresponds to that of a uniform accessible disk electrode and in the high frequency range, its response is similar to the response of an isolated active site. The frequency lag between the two regimes is related to the dimension of the active site and to its radial coordinate.

Acidic solution

In 0.1 N H_2SO_4 solutions, the mass transfer of oxygen towards the cathode controls the reaction :

$$O_2 + 4\,H^+ + 4\,e^- \rightarrow 2\,H_2O$$

and the limiting current i_D of oxygen reduction obeys the Levich relationship, whereas, in the presence of $P\emptyset_3$, i_D is decreased, indicating an inhibiting effect of the molecule. The $i_D^{-1} = f(\Omega^{-1/2})$ curve plotted in the absence of $P\emptyset_3$ (curve a, Fig. 1) goes through the origin, indicating the uniform accessibility of the interface. The same curve plotted in the presence of the phosphine molecule (curve b, Fig. 1) shows two linear parts. At low rotation rate, the curve is parallel to the curve "a" obtained in absence of $P\emptyset_3$ and intercepts the ordinate axis at point A'. This behaviour may correspond to a blocking effect of the $P\emptyset_3$ molecule. At high rotation rate, the curve becomes a straight line crossing the origin. An interpretation of these data can be obtained after analysing the EHD impedance.

The diagrams obtained in absence of $P\emptyset_3$, at different rotation rate, in the conditions of figure 1a, are reduced by using the dimensionless frequency $p = \omega/\Omega$ in agreement with the theory for a uniform accessible interface (Fig. 2). In presence of $P\emptyset_3$ the different diagrams are not reducible in the whole frequency range. The low frequency part of the diagrams is the same for solutions containing phosphine or not. This eliminates any layer effect of the inhibitor according to previous work (6). At dimensionless frequencies $p > 1$, a steep decrease of the phase shift θ is observed in presence of phosphine, followed by a rise of θ. This behaviour is characteristic of a partially blocked electrode (5). The phase lag given by the ratio p_c^*/p_d^* is related to the diameter d of the active site :

$$\frac{p_c^*}{p_d^*} = \left(\frac{0.8\,R}{0.51\,d}\right)^{2/3}$$

where R is the radius of the rotating disk electrode.

Table 1 shows that the dimension of the active site d increases when Ω increases. This variation of the blockage with the rotation speed is in agreement with the DC measurements obtained for a rotation speed high enough.

Neutral solution

The same type of experiments was conducted in neutral conditions (aerated 0.1 N Na_2SO_4). The corresponding reduction reaction for oxygen is :

$$O_2 + 2\,H_2O + 4\,e^- \rightarrow 4\,OH^-$$

In absence of $P\emptyset_3$, the $i_D^{-1} = f(\Omega^{-1/2})$ curve (Fig. 3a) is a straight line parallel to the corresponding curve obtained in acid media and crossing the origin. This behaviour may correspond to different interpretations: a mixed control of the cathodic reaction, a porous layer, a partial blocking of the surface ... In the presence of phosphine, the inhibition of the cathodic reaction is more effective at higher rotation speeds (Fig. 3, curve b).

In the absence of inhibitor, the EHD impedance plots (Fig. 4) answer some of the previous questions : the behaviour is characteristic of a blocking effect due probably to some intermediate reaction products adsorbed on the electrode. In the presence of $P\emptyset_3$, the curves (Fig. 5) show the same trends as in acidic solutions, i.e. a blocking effect of the inhibitor. Although no p_c^* can be obtained and so no quantitative d value can be given, we may conclude that the dimensions of the active sites in neutral solution are smaller than those in acidic conditions.

References :

(1) C. FIAUD, I. DEMESY, S. BENSARSA, M.T. ZINMANN, Br. Corr. J., 22, 109 (1987).

(2) C. FIAUD, I. VASTRA, I. DEMESY, 6th European Symposium on Corrosion Inhibitors, Ferrara, 1985.

(3) C. DESLOUIS, C. GABRIELLI, Ph. SAINTE ROSE FANCHINE, B. TRIBOLLET J.E.C.S., 129, 107 (1982).

(4) B. TRIBOLLET, J. NEWMAN J.E.C.S., 130, 2016 (1983).

(5) A. CAPRANI, C. DESLOUIS, S. ROBIN and B. TRIBOLLET J. Electroanal. Chem., 238, 67 (1987).

(6) C. DESLOUIS, B. TRIBOLLET, M. DUPRAT and F. MORAN J.E.C.S., 134, 2496 (1987).

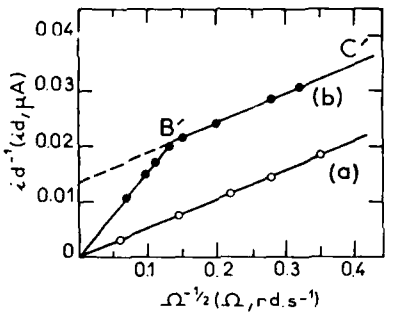


Figure 1 : Stationary conditions. Copper in 0.1 N H_2SO_4 (a) ; + $P\emptyset_3$ (b).

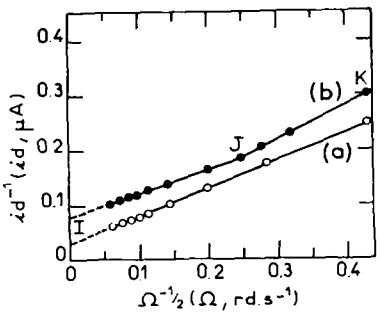


Figure 3 : Stationary conditions. Copper in aerated 0.1 N Na_2SO_4 (a) ; + $P\emptyset_3$ (b).

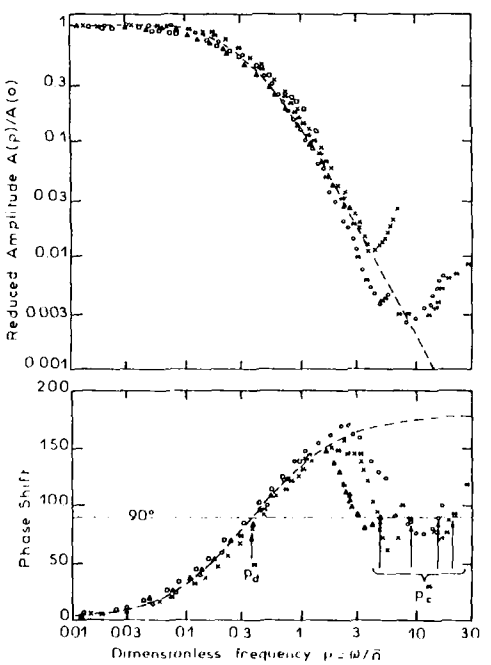


Figure 2 : EHD impedance on copper in 0.1 N H_2SO_4 (E = - 0.6 V/ECS) : without inhibitor (-) + $P\emptyset_3$: 80 rpm (*), 120 rpm (o), 400 rpm (x), 800 rpm (▲), 2000 rpm (o).

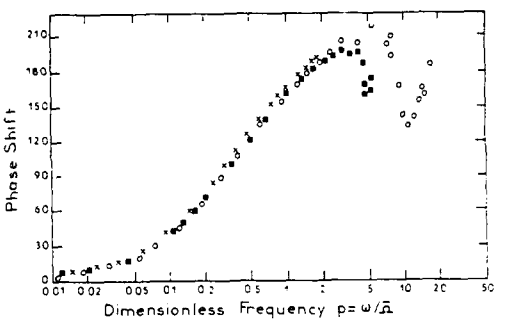


Figure 4 : Phase shift of the EHD impedance on copper in 0.1 N Na_2SO_4 (E = - 0.75 V/ECS), 120 rpm (o), 400 rpm (■), 1200 rpm (x).

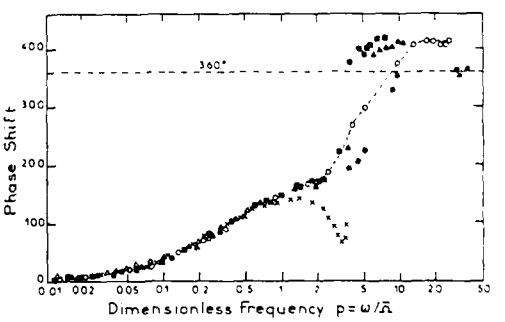


Figure 5 : Phase shift of the EHD impedance on copper in 0.1 N Na_2SO_4 + $P\emptyset_3$ (E = - 0.75 V/ECS), 80 rpm (*), 120 rpm (o), 240 rpm (▲), 400 rpm (■), 800 rpm (x).

Abstract No. 179

IMPEDANCE STUDY OF ELECTRONICALLY CONDUCTING POLYMERS

Chi-Hum Paik, and W.H. Smyrl
Corrosion Research Center
Department of Chemical Engineering and Materials Science
University of Minnesota
Minneapolis, MN 55455

Recently, much attention has been focussed on the electrochemical studies of conductive polymers. Since these polymers exhibit large variations in both structure and conductivity, there are many possible applications in electronic and chemical systems, such as light-weight batteries, corrosion protection, sensors, and microelectronic and photovoltaic devices.

These materials can be catagorized by their differences in structure and redox mechanisms, but for the purposes of this paper electroactive polymers will be divided into two broad classes. One can be classified as a "redox polymer", where conduction is by electron hopping between redox centers attached to the polymer chain. The other class of polymers, which we focus on here, were prepared from monomers of heterocyclic aromatic compounds. Electrons delocalized along the polymer backbone give them their conductive properties. The materials studied here were poly(thiophene), poly(3-methylthiophene), and poly(pyrrole). All three polymers were found to have similar impedance characteristics, related to the processes of (1) charge injection (2) diffusion in the polymer, and (3) redox capacitance.

A technique called Digital Impedance for Faradaic Analysis (DIFA) (Smyrl, 1985 abc) was used to study the kinetics of redox behavior of the polymers. In the studies, the polymers, present as a thin film on the electrode, was charged to a specific state and maintained at equilibrium. A modulating input perturbation signal was then applied to observe the response of the polymer, and the measurements were repeated at several different charge states of the polymer. The perturbation was a multiple frequency voltage signal, and both the response and the perturbation was transformed by a Fast Fourier Transform (FFT) so that the impedance could be obtained at all the input frequencies simultaneously. A PDP11/44 computer controller was at the heart of the experimental system, and an Analogic Array Processor performed the FFT in real time.

Oxidation of the polymer films occurred by hole injection into the polymer backbone, with simultaneous injection of anions from the electrolyte to maintain electroneutrality. At high frequencies, this is the rate controlling process, and leads to a charge transfer semicircle in the complex domain. The charge transfer resistance decreased with the concentration of charge (holes plus anions) in the films. From the analysis, one is able to obtain an exchange current density and a double layer capacitance for the polymer/electrolyte interface.

At lower frequencies transport of the charged species in the film was rate determining, and gave a Warburg impedance whereby both the real and the imaginary parts of the impedance had an inverse square root dependence on the frequency of the perturbation. Analysis of the date led to a diffusion coefficient that was a function of charge concentration, and changed by orders of magnitude as the charge concentration was varied. At higher charge concentration, the diffusion coefficients were of the order of 10^{-7} cm^2/sec for all three polymers.

When compared to the earlier results of the impedance behavior of poly(vinylferrocene) (Hunter et.al, 1987), the same relaxation processes are seen in all cases. However, in the case of the redox polymer, the diffusion coefficient was only a modest function of charge concentration, and changed by a factor of two over the entire range of charge concentration.

REFERENCES

W.H. Smyrl, (a) J.Electrochem.Soc. 132, 1555(1985), (b) ibid. 132, 1563(1985), (c) ibid. 132, 1569(1985).

T.B. Hunter, P.S. Tyler, W. H. Smyrl, and H.S. White, J.Electrochem.Soc 134, 2198(1987).

Abstract No. 180

IMPEDANCE ANALYSIS OF POLY(VINYLFERROCENE) FILMS SPIN COATED ON METAL SUBSTRATES

Mary Lien and W.H. Smyrl
Corrosion Research Center
Department of Chemical Engineering and Materials Science
University of Minnesota
Minneapolis, MN 55455

Subtle variations in polymer composition, structure, and means of casting can have profound effects on permeability. The most important parameter affecting this is the amount of "free volume" within the polymer. Electrochemical behavior of redox polymer films is a strong function of the density of packing of the polymer chains.

Solvents and even non-solvents penetrate glassy polymers and induce backbone motions. In the presence of any low molecular weight liquid, the polymer is swollen, and the free volume increases. The free volume may also change as the result of electrochemical cycling between the neutral and oxidized form of PVF (1), the polymer used in this study.

PVF films on Pt have been studied recently by impedance techniques and were found to have three regions of behavior, characterized by different relaxation times. At high frequencies, the simultaneous injection of holes (oxidation of the ferrocene pendant groups) and anions (to maintain charge neutrality) is the rate controlling process. At lower frequencies, diffusion in the film is rate limiting, and for solution cast films it was found that the diffusion coefficient was of the order of 10^{-9} cm^2/sec (2). At the lowest frequencies, the finite thickness of the films cause the impedance to become purely capacitive. The latter region has been termed the redox capacity region of impedance.

Spin coating films on ultra flat substrates is important for a number of technological applications, and our interest is in developing thin film polymer batteries. Thus PVF films were spun onto Pt or Au thin films on single crystal Si wafers. Electrical contact was made to the metal film and the electrode was immersed in an electrolytic solution in acetonitrile (0.1M tetra(n-butylammonium) perchlorate). Cyclic voltammograms of the films were stable for many hours after the initial break-in.

Impedance measurements were made as a function of oxidation state of the polymer film. A multiple frequency voltage signal was imposed on the film and the current response was measured. Both voltage and current signals were transformed with a Fast Fourier Transform, and the impedance was calculated at all the input frequencies simultaneously. The measurements (Digital Impedance for Faradaic Analysis) are performed with an array processor-enhanced PDP11/44 (2). The diffusion coefficients measured on the spin coated films are more than two orders of magnitude larger than the films studied earlier, i.e. D_{CT} was found to be 10^{-7} for the spin coated films. In addition, the films give evidence of increased porosity as determined by impedance. Both characteristics are indicitive of greater free volume for the spin coated films. Other results will also be described.

REFERENCES
1. A.H. Schroeder and F. Kaufman, J. Electroanal. Chem. 113, 209(1980).

2. T.B. Hunter, P.S. Tyler, W.H. Smyrl, and H.S. White, J. Electrochem. Soc. 134, 2198(1987).

Abstract No. 181

AN IMPEDANCE AND XPS STUDY OF PASSIVE CHROMIUM

T.P. Moffat and R.M. Latanision,
MIT, Dept. of Mat. Sci. and Eng., 8-202,
Cambridge, MA 02139

The electrochemistry of chromium has been examined in acid sulfate media. The impedance was measured as a function of potential. Mesurements were done between 65 kHz and 0.1 mHz. In 1M H_2SO_4, one inhomogeneous relaxation is apparent in the passive domain. The dispersion of the response is constant between -0.1 and 0.6 V SCE and then increases as the transpassive domain is approached. The calculated high frequency capacitance, i.e. at 10.3 kHz, yields a simple dielectric type (potential/film thickness) behavior between -0.1 and 0.6 V SCE. This capacitance reaches a minimum at 0.6 to 0.7 V and then increases as the transpassive domain is approached. These results are being correlated with angle-resolved XPS data which yields depth-sensitive information on the distribution of oxidized species within the passive film. Additional work is in progress.

Abstract No. 182

PASSIVE LAYERS AND UHV-GROWN OXIDES ON Ni(100): A COMPARISON BY AC IMPEDANCE AND SURFACE SPECTROSCOPIES

Frederick T. Wagner and Thomas E. Moylan
Physical Chemistry Department
General Motors Research Laboratories
Warren, MI 48090-9055

The clean coupling of an ultrahigh vacuum sample preparation/analysis system to an aqueous impedance cell gives promise of direct spectroscopic testing of the adsorption and structural effects inferred from impedance data. We have used such a system to compare lectrochemical passive films grown on Ni(100) in 10 mM $HClO_4$ with saturation oxide layers grown in UHV by dosing with gaseous O_2 at room temperature. The two films share a common component of 2-4 layers of NiO and share simple impedance behavior at 1.05 V vs. RHE characterized by 20 $\mu F/cm^2$ capacitances and low frequency resistive or quasi-resistive impedances exceeding 10^5 Ωcm^2. They differ subtly in chemical composition and structure. The clean and UHV-oxidized surfaces differ dramatically in the amount of anodic charge required to achieve steady-state passivation upon contact with electrolyte.

Experimental. The main UHV preparation/analysis chamber was equipped for X-ray photoemission spectroscopy (XPS), high resolution electron energy loss spectroscopy (HREELS), low energy electron diffraction (LEED), temperature programmed desorption (TPD), and Auger electron spectroscopy (AES). The Ni(100) sample wafer was Ar^+-sputtered and then annealed before each experiment to produce a clean, well-ordered surface. In some experiments the sample was exposed at room temperature to a saturation dose of 500 s of O_2 at 10^{-6} Torr. The sample was then pulled into a second chamber which was backfilled with purified Ar. A ~300 μl drop of 10 mM $HClO_4$ was placed on a horizontal Pt disk counterelectrode with a central Pd-H reference. The front face of the Ni(100) sample was contacted with this drop under potentiostatic control at 1.05 V vs. RHE. A digital coulometer recorded the charge passed upon contact. AC impedance measurements were made via a fast fourier transform technique with a PAR 173/276 potentiostat and a HP 5420A digital signal analyzer interfaced to a microcomputer. The coherence function was calculated to check the self-consistency of the impedance data. After all liquid was drained from the cell, the chamber was evacuated and the sample returned to the main chamber for analysis.

Results and Discussion. Fig. 1 compares O(1s) XPS data for the a) UHV-grown oxide and the b) water-rinsed and c) unrinsed passive layers formed at 1.05 V RHE. The gas-phase oxide yields a single O(1s) component at 529.5 eV corresponding to NiO. Nuclear reaction studies have established the thickness of this UHV-saturated oxide as 2-3 layers [1]. LEED shows the presence of small ordered domains with NiO(100)||Ni(100). The rinsed and unrinsed passive layers show the same size NiO-type O(1s) component as the UHV film. The rinsed layer gives an additional small O(1s) component at 531.5 eV which disappears upon heating to 700 K. Kim and Winograd [2] have shown that both nickel hydroxide and Ni_2O_3 give O(1s) signals at this energy. Heating the rinsed passive layer to 700 K removes the O-H stretching mode seen in HREELS at 3720 cm^{-1} and evolves gaseous O_2 seen in TPD, suggesting that both hydroxyls and a higher nickel oxide are present as minority components in the passive layer. The unrinsed passive layer gives third O(1s) component at 532.1 eV due to nonvolatile $Ni(ClO_4)$ corrosion products left behind upon evaporation of the electrolyte.

The LEED pattern of the rinsed passive layer gives strong diffuse intensity plus very weak, broad spots ascribable to (111) NiO [3]. The passive layer is thus largely amorphous, but contains minor elements of an epitaxy different from that which we observed for the gas-phase oxide. The UHV-oxidized surface, after contact with electrolyte at 1.05 V, yields the same XPS and HREELS spectra as the passivated clean surface. However, LEED still shows the same, albeit weakened, NiO(100) symmetry which was seen before electrolyte contact. Thus, electrochemical passivation causes chemical, but not complete structural, modification of the UHV-grown oxide.

Contact of the clean surface with electrolyte at 1.05 V gives anodic charge transients corresponding to the oxidation of 7 layers of Ni(0) to Ni(II) within 30 s and 12 layers within 10 min (steady-state passive current subtracted). Since these values far exceed the amount of oxygen shown by XPS, the current efficiency for passivation is low. In contrast, the UHV-oxidized surface gives transients of only 0.7 layers (30 s) and 1.5 layers (10 min). Thus, little charge is needed to convert the UHV-grown NiO into a complete passive layer.

Figures 2 and 3 show Bode plots of experimental impedance data (dots) at 1.05 V and calculated fits (z's and a's) of models for clean and UHV-oxidized Ni(100), respectively. The similarity of the impedance data and the ~3 $\mu A/cm^2$ DC passive currents measured for both surfaces demonstrate the near-equivalence of the electrochemical properties of the films, despite the different elements of epitaxial order attested to by LEED. The double layer capacities, C, of 18 and 20.8 $\mu F/cm^2$ are identical within experimental reproducibility. An $R_s+(R_p||C)$ analysis (R_s and R_p are the solution and charge transfer resistances) of the UHV-oxidized surface data yields an R_p of $1.1x10^5$ Ωcm^2. The clean surface data yields $R_p \geq 2.5x10^5$ Ωcm^2; loss of data coherence at low frequencies prevents determination of anything more than a lower limit for R_p. The data show a suppression of the phase angle maximum relative to that for the calculated models, despite the use of a single crystal sample which should minimize the roughness elements and inhomogeneities often invoked to explain such effects. A possible explanation for the low phase angles lies in an alternate model: $R_s+(W_f||C)$, where W_f is a finite-diffusion Warburg impedence. The σ (Warburg) and K (thin-layer) parameters [4] for this model (assuming only one important diffusing species) listed in the figure captions give z's and a's on the same curves as the R_sR_pC models shown. For aqueous diffusion (diffusion constant $D\sim10^{-5}$ cm^2/s) these parameters yield unphysically low values of the diffusion layer thickness δ and the AC component of the surface concentration c_s. However, if one takes as δ the ~10 Å passive layer thickness indicated by the vacuum spectroscopies, then the K and σ values imply $D=10^{-14}$ cm^2/s (plausible for a largely amorphous film) and $c_s=10^{18}/cm^3$. The mathematically more complex inclusion of a second diffusing species with a slightly different D might account for the observed suppression of the phase angle maximum [4]. Whatever the physical interpretation of the low-frequency data, the very high impedance magnitudes, compared to the 3-4 $\mu A/cm^2$ passive currents, show that there cannot be a simple relationship between the impedance data and the kinetics of the passive dissolution process (which would appear to be almost completely independent of small potential changes around 1.05 V RHE). Work at other potentials should give better access to kinetic parameters.

References:
1. P.F.A. Alkemade, S. Deckers, P.H.P.M. Habraken and W.P. Van der Weg, Surface Sci. 189 (1987) 161.
2. K.S. Kim and N. Winograd, Surf. Sci. 43 (1974) 625.
3. D.F. Mitchell, P.B. Sewell and M. Cohen, Surface Sci. 61 (1976) 355.
4. J.L. Dawson and D.G. John, J. Electroanal. Chem. 110 (1980) 37.

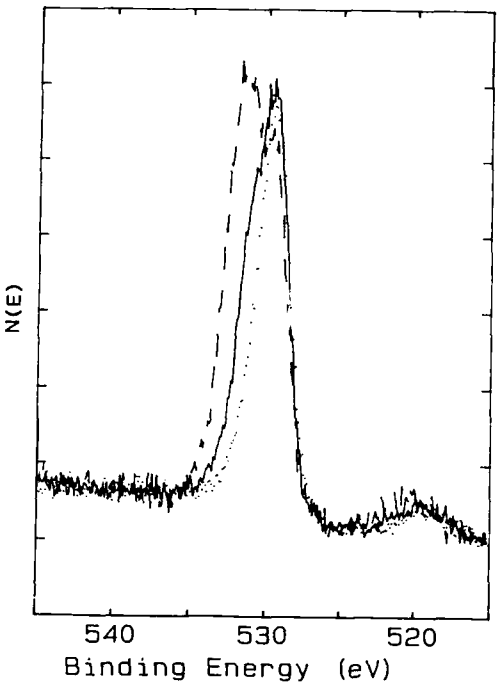


Fig. 1. Oxygen (1s) XPS data for a) UHV-grown oxide on Ni(100) (dots), b) water-rinsed passive layer formed at 1.05 V RHE in 10 mM $HClO_4$ (solid line), and c) unrinsed passive layer (broken line). Al Kα radiation, 50 eV pass energy. Peak at 520 eV is satellite due to $K\alpha_3$ X-rays.

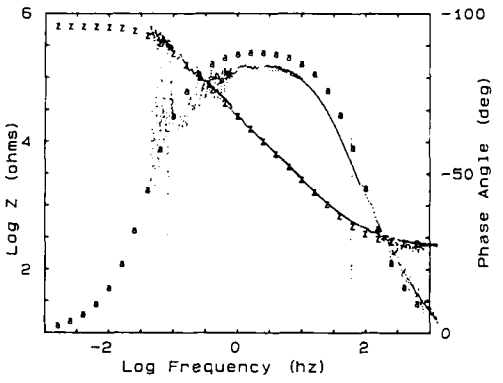


Fig. 2. Bode plot of impedance data for clean Ni(100) passivated and analyzed at 1.05 V RHE in 10 mM $HClO_4$, contact area 0.35 cm^2 (plotted as individual points which overlap to form continuous curves in some regions); and model-calculated values of impedance magnitude (s's) and phase angle (a's). Model parameters: (1) R_s=250 Ω, C=18 μF/cm^2, R_p=2.2x10^5 Ωcm^2; or (2) R_s=250 Ω, C=18 μF/cm^2, σ=8x10^5 Ωcm^2$s^{1/2}$, K=0.8 $s^{1/2}$.

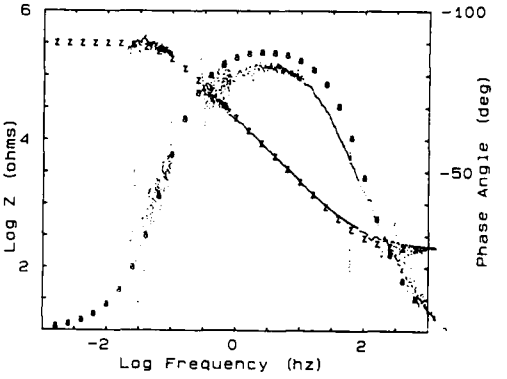


Fig. 3. Bode plot of impedance data for UHV-oxidised Ni(100) analysed at 1.05 V RHE in 10 mM $HClO_4$, contact area 0.35 cm^2. Model parameters: (1) R_s=195 Ω, C=20.8 μF/cm^2, R_p=1.1x10^5 Ωcm^2; or (2) R_s=195 Ω, C=20.8 μF/cm^2, σ=4x10^5 Ωcm^2$s^{1/2}$, K=0.8 $s^{1/2}$.

Abstract No. 183

EFFECT OF DIFFUSION LAYER STRUCTURE ON THE DETERMINATION OF CORROSION RATES FROM DC TRANSIENT MEASUREMENTS

Z. Nagy, P. J. Hernes*, M. Minkoff,
G. K. Leaf, and R. H. Land

Argonne National Laboratory
Divisions of Materials Science, Chemical Technology,
and Mathematics and Computer Science
Argonne, Illinois 60439-4837

In the theory of electrochemical transient measurements, the equation describing the relaxation of the system after the application of the measuring pulse is invariably obtained by solving a set of partial differential equations of the type:

$$\frac{\partial C_j^s(x,t)}{\partial t} = D_j \frac{\partial^2 C_j^s(x,t)}{\partial x^2} \tag{1}$$

with the following initial and boundary conditions:

$$C_j^s(x,t) = C_j, \text{ for } x \geq 0,\ t = 0 \tag{2}$$

$$C_j^s(x,t) \rightarrow C_j, \text{ for } x \rightarrow \delta,\ t > 0 \tag{3}$$

$$\frac{\partial C_j^s(x,t)}{\partial x} = \pm \frac{i_f(t)}{nFD_j}, \text{ for } x = 0,\ t \geq 0 \tag{4}$$

where C_j^s stands for the concentration of the species taking part in the surface reaction; this concentration is a function of the distance from the electrode surface (x) and of time (t). D_j stands for the diffusion coefficient, n is the number of electrons transferred in the reaction, F is the Faraday constant, and i_f is the Faradaic current density.

The initial condition states that, before the application of the measuring pulse, the concentration of all species at the electrode surface is the same as their bulk concentration (C_j). The first boundary condition states that at a certain distance from the electrode surface (δ) the concentration of all species remains equal to the bulk concentration at all times. This distance is usually considered to be so large that for all practical considerations it is infinity. The second boundary condition expresses the equivalence of the rate of the surface reactions (expressed as the Faradaic current density) and the diffusion fluxes.

These conditions are correct for a typical redox reaction of $O + ne = R$. In the investigation of this reaction, the measurement starts from equilibrium, where the oxidation of R and the reduction of O occur at the same rate: therefore, no net current is flowing and no net chemical change is taking place before the application of the measuring pulse. Furthermore, the measurement is being carried out in such a short time scale that convection does not interfere with the diffusional mass transport, and δ can, indeed, be set to infinity.

The situation is completely different for a corroding electrode because a corroding metal is not in equilibrium, only in a steady state. Two distinctly different partial reactions, the dissolution of the metal ($M \rightarrow M^{n+} + ne$) and the reduction of a component of the environment (e.g., $2H^+ + 2e \rightarrow H_2$), occur at the same rate. (It is usually assumed that the rates of the reverse reactions are negligible.) Under these conditions, while there is no net current flowing through the system, there is a net chemical change taking place: the corrosion of the metal. Therefore, there must be a continuous flux of reactants to, and a flux of products away from the surface. Consequently, even in steady state, there are concentration gradients which are proportional to the corrosion rate, as expressed by Eq. 4. Then, however, the initial condition expressed by Eq. 2 is not fulfilled.

Furthermore, the corrosion is a steady state process occurring over a long period of time, and it can not be assumed that convection does not play a role in the mass transport. The simplest, but often correct, model to describe the system is the Nernstian diffusion layer. Nernst assumed that the mass transport occurs solely by diffusion in a thin, hydrodynamically stagnant, solution layer on the electrode surface, while outside of this layer, convection occurs and it is the predominant mode of mass transport. Then, under steady state conditions, there must be a linear concentration gradient of all reacting species within this layer (called the diffusion layer), while a uniform bulk concentration exists in the convection areas. A schematic representation is shown in Fig. 1. Such a situation can exist even in seemingly stagnant solutions because there is always some convection generated by unavoidable vibrations as well as concentration and density fluctuations. The only effect of mechanical agitation or solution flow is to make the diffusion layer thinner. Then, the initial and boundary conditions should be written as:

$$C_j^s(x,t) = C_j^s(0,0) + \frac{C_j - C_j^s(0,0)}{\delta} x, \text{ for } 0 \leq x < \delta,\ t = 0 \tag{5}$$

$$C_j^s(x,t) = C_j, \text{ for } x \geq \delta,\ t \geq 0 \tag{6}$$

$$\frac{\partial C_j^s(x,t)}{\partial x} = -\frac{i_c(t)}{nFD_j}, \text{ for } x = 0,\ t \geq 0 \tag{7}$$

where i_c is the cathodic partial current density. For a corroding metal, only the differential equation relating to the reducible species must be solved since the metal dissolution is not affected by mass transport.

Under these conditions, the differential equation can be solved only by numerical methods. A series of calculations was carried out, for both galvanostatic and potentiostatic pulses, to compare the relaxation curves calculated using Eq. 2-4 with those calculated using Eq. 5-7. The main variables affecting the results were found to be the ratio of the corrosion current density to the limiting diffusion current density, the polarization, and the cathodic Tafel slope. Some examples of the deviation between these calculated relaxation curves as a function of these variables are shown in Fig. 2-3 for potentiostatic transients. The consequences of this effect for the determination of corrosion rates from electrochemical transient measurements will be presented and discussed.

ACKNOWLEDGMENT

This work was supported in part by the Division of Materials Sciences, Office of Basic Energy Sciences, U. S. Department of Energy, and in part by the Applied Mathematical Sciences subprogram of the Office of Energy Research, U. S. Department of Energy, under Contract No. W-31-109-Eng-38.

*Research Participant from Luther College, Decorah, Iowa 52101

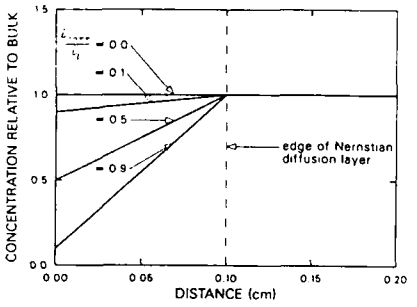


Fig. 1. Schematic representation of the concentration distribution in the diffusion layer for different ratios of i_{corr}/i_l.

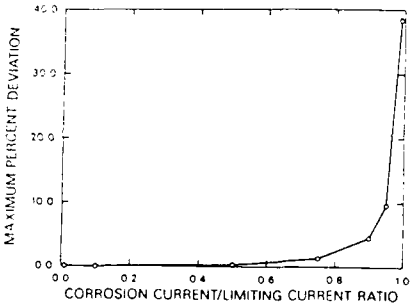


Fig. 2. Absolute value of the deviations between the calculated relaxation curves as a function of i_{corr}/i_l at a polarization of −100 mV, b_a = 0.06 V, and b_c = 0.60 V.

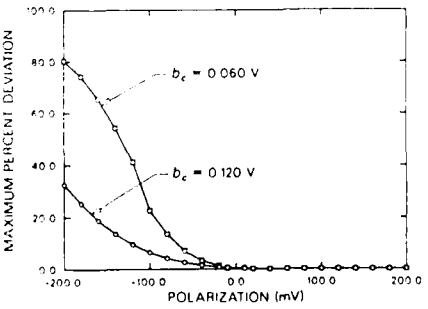


Fig. 3. Absolute value of the deviations between the calculated relaxation curves as a function of polarization at i_{corr}/i_l = 0.99 and b_a = 0.06 V.

Abstract No. 184

Corrosion behavior of a chromium modified copper-nickel alloy compared to other alloys.

R. Beaudoin, P. R. Roberge and E. Halliop.
Department of Chemistry and Chemical Engineering
Royal Military College of Canada
Kingston, Ontario K7K 5LO

1. Introduction:

To overcome the difficulty of brazing technique, it is being proposed that the firemains on the new ships be of all welded construction. Since copper-nickel alloys for marine usage are superior to other alloys, two cast alloys were chosen for intensive evaluation: a standard cast 70/30 copper-nickel alloy, modified with niobium (UNS C96400) (1), and a nonstandard chromium modified cast 70/30 copper-nickel alloy (IN 768) (2). A study of the foundry characteristics, weldability and mechanical properties of these alloys showed that both alloys are satisfactory to specifications (3).

Electrochemical impedance technique is adequate to study corrosion of these passivated alloys. It can be best achieved by avoiding potentiostatic or galvanostatic control, thus leaving the metallic surface under study free to find its natural equilibrium with the environment. When the corrosion processes are happening uniformly on the surface and when this surface is passivated, a valid correlation can be obtained between the charge transfer resistance and the resistance of the alloy to corrosion.

However, fast analysis of impedance curves is still a problem. Complex curve fit (4) and graphical methods (5,6) are not simple, fast or easy to use. A geometric extrapolation technique (7) combined with permutation of the data point has been developed. This technique makes use of each point of the diagram. Rejection criteria can be used to eliminate points outside of the RC semicircle.

2. Discussion:

The method of analysis consists of finding the centre of an arc formed by three data points on the complex impedance diagram (7). This analytical technique was first designed to follow the corrosion current (via Rp) of a prepassivated alloy under hydrodynamic conditions especially during fast changes of the impedance (8).

Refinement of the technique has been achieved first to obtain an error evaluation on the extrapolated centre (9) and also to make the best use of the full impedance diagrams. A permutation technique that compares each point with its first, second, etc..., neighbor generates a large number of centers' values from which a standard deviation is obtained. A simple rejection technique has been used to eliminate the data that are not part of the semicircle created by the impedance diagram.

Figure 1 and 2 shows the impedance diagram obtained with the 70-30 Cu-Ni alloy containing niobium and the alloy containing chromium respectively, in the same conditions. If a histogram is made with the values of Rp obtained with the permutation technique previously described, a clear difference between the two alloys can be made as shown in figure 3 and 4. A much larger distribution of the data is systematically observed in the case of the chromium alloy. Another parameter which differentiates the two alloys is the depression of the semicircle. Typical values for Rp and for the depression of the semicircle are shown in Table 1 for the two alloys. It can be noticed that the depression is always more important for the chromium alloy than for the niobium alloy even though Rp is in the same order of magnitude.

This depression of the semicircle has often been attributed to surface heterogeneity caused by a distribution of the reaction rate with the location on the electrode surface (10). Figure 5 shows a SEM (scanning electron microscope) micrograph of the electrode surface after 10 days in 3% NaCl solution. Intergranular corrosion appears to be an important cause of corrosion for this alloy whereas uniform corrosion is likely to happen with usual Cu-Ni alloys in those conditions. However, there is concern with respect to crevice and preferential corrosion related to the casting procedure for chromium modified Cu-Ni alloys. The general corrosion rate for this type of alloy is usually less than 0.05 mm/y as it is measured in this study.

3. Conclusion:

It can be shown that, by using an appropriate analysis technique, localized corrosion can be suspected if not detected with A.C. impedance, 1) from the depression of the semicircle and 2) from the dispersion of the extrapolated centre.

Table 1. Comparison of the data obtained for the two alloys.

70-30 Cu-Ni	Rp ($Ohms.cm^2$)	s %	angle (Deg.)	s %
(Nb) rest	47400	15	22	13
(Nb) rotation	18900	5	21	12
(Nb) rest	55100	12	22	11
(Cr) rest	41900	45	32	10
(Cr) rotation	10100	14	28	10
(Cr) rest	39200	22	31	7

4. References:

1. "ASTM Book of Standards. Part 6: Copper and Copper Alloys", B369-72 (1978).

2. "Copper-Nickel-Chromium-Silicon Casting Alloy IN 768", Preliminary Data Sheet, INCO, New York (September 1970).

3. C.M. Hanham, M. Sahoo and R.S. Hollingshead, 1983 ASM Metals Congress, Philadelphia, Pennsylvania (October 1983).

4. M.W. Kendig, E.M. Meyer, C. Lindberg and F. Mansfeld. Corros. Sci., 23, 1007-15 (1983).

5. K. Hladky, L.M.Callow and J.L. Dawson. Brit. Corr., 15, 20 (1980).

6. L. Lemaitre, M. Moors and A.P. Van Peteghem. J. Appl. Electrochem. 13, 803 (1983).

7. P.R. Roberge and R. Beaudoin. J. Appl. Electrochem. 18, 38-42 (1988).

8. P.R. Roberge and R. Beaudoin. J. Appl. Electrochem. 18, (1988).

9. P.R. Roberge, R. Beaudoin and E. Halliop. Extended Abstract, Atlanta, FCS, 1988.

10. A. Bonnel, F. Dabosi, C. Delouis, M. Duprat, M. Keddam and B. Tribollet. J. Electrochem. Soc., 130, 753 (1983).

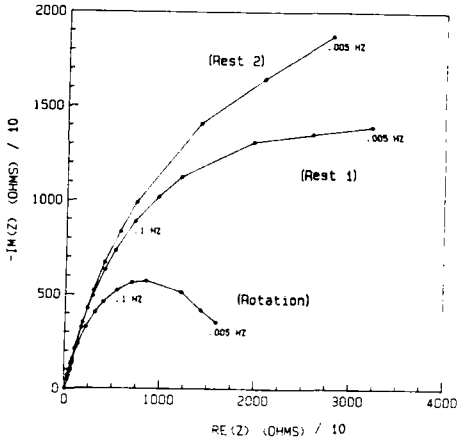


Fig. 1. Impedance diagrams made on a 10-day passivated 70-30 Cu-Ni containing niobium: 1, at rest, after 8 hours of rotation at 5000 rpm and 2, at rest 16 hours after the rotation period.

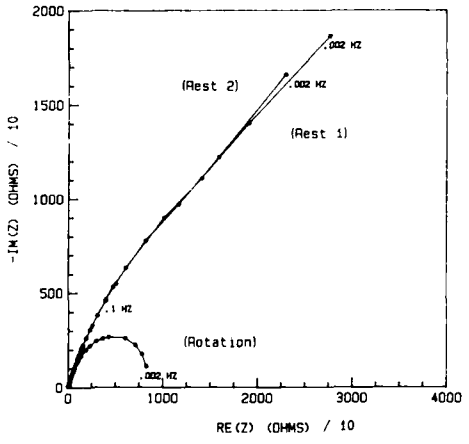


Fig. 2. Impedance diagrams made on a 10-day passivated 70-30 Cu-Ni containing chromium: 1, at rest, after 8 hours of rotation at 5000 rpm and 2, at rest 16 hours after the rotation period.

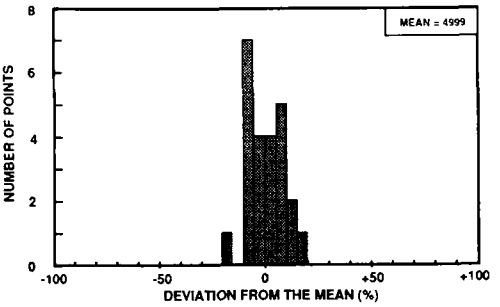


Fig. 3. Typical histogram representing the distribution of Rp values obtained from analysis of the impedance diagram of the 70-30 Cu-Ni containing niobium.

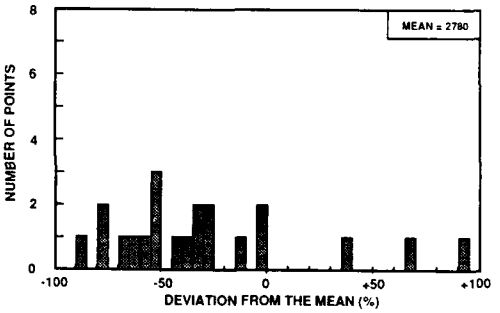


Fig. 4. Typical histogram representing the distribution of Rp values obtained from analysis of the impedance diagram of the 70-30 Cu-Ni containing chromium.

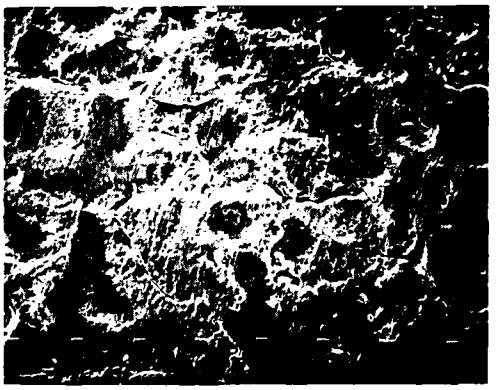


Fig. 5. Microscopic (SEM) representation (150 x) of the surface of the 70-30 Cu-Ni containing chromium 10 days after immersion in 3% NaCl solution.

Abstract No. 185

An impedance spectroscopy investigation on the passivability of amorphous Fe-Cr-metalloid alloys

S. Virtanen , B. Elsener , H. Böhni
Institute for Materials Chemistry and Corrosion
Swiss Federal Institute of Technology
ETH- Hönggerberg, CH- 8093 Zurich, Switzerland

Introduction

The excellent corrosion resistance of amorphous iron-chromium alloys containing phosphorus as a major metalloid is well known /1,2/. According to Hashimoto et al. the role of phosphorus is to accelerate the dissolution rate in the active range of the alloys thus leading to a rapid enrichment of the passivating species in the alloy/solution-interface /3,4/. The detailed mechanism of the active/passive-transition of the P-containing alloys has not yet been cleared, though.

The impedance spectroscopy can reveal further information about the passivation process. Our first results of an impedance spectroscopy study on amorphous Fe-Cr-metalloid alloys show that phosphorus modifies the mechanism of the active/passive-transition /5,6/. The passivation of the amorphous phosphorus-free boron-containing alloys takes place through a mechanism similar to that found for the crystalline steels.

Experimental

The investigated amorphous alloys were Fe-10Cr-13B-7C , -13B-7P, -13P-7B and -13P-7C, respectively. The alloys were prepared by melt-spinning and were in form of ribbons. As a reference material a commercial 17 % Cr steel was used. The alloys were electrochemically characterized by polarization measurements and impedance spectra in 1 N H_2SO_4 and 1 N HCl. For experimental details see /5,7/.

Results and Discussion

The dissolution rate in the active range of the alloys is very strongly accelerated through addition of phosphorus (Table 1.). Alloying with boron, on the other hand, decreases the dissolution rate. This behaviour is due to differences in the kinetics of the cathodic reaction. Phosphorus, on the contrary to boron which retards the hydrogen evolution reaction rate, very strongly accelerates this reaction. The dissolution rate of the P-containing alloys increases with time. This is combined with a formation of a black surface film, which further on very strongly accelerates the cathodic reaction. The formation of the black film leads to high capacitance values suggesting a high porosity of the film (Fig. 1). The surface of the P-containing alloys is covered by the black film till about E = +200 mV SCE. The XPS measurements suggest an iron-phosphate film.

The impedance measurements show that the passivation of the P-containing alloys takes place in two stages. The first current decrease is due to blocking of the surface through the iron-phosphate pre-passive layer. The final passivation takes place in the pores of this pre-passive layer. The gradual passivation of the metal in the pores leads to increasing values of the normalized charge-transfer resistance and to decreasing capacitance values (Fig. 2). The formation of the passivating chromium oxide layer is facilitated through an enrichment of chromium ions in the pore electrolyte.

The dissolution rate in the passive range strongly decreases with increasing phosphorus content and with decreasing boron content of the alloys (Table 2.). Further on, only the alloys with 13 % phosphorus can be passivated in 1 N HCl. The XPS measurement showed that both oxidized boron and phosphorus get incorporated in the passive film.The oxidized boron species possess a low stability in the passive range of the alloys and thus lower the resistance of the passive film. The incorporated phosphorus as phosphates can lower the mobility of the anions in the film and thus make it more resistant against Cl^--attack.

References :
1. K.Hashimoto, T. Masumoto : Mat. Sci. and Eng. 23 (1976) 285-288
2. K. Hashimoto, K. Osada, T. Masumoto, S. Shimodaira : Corr. Sci. 16 (1976) 71-76
3. K. Asami, K. Hashimoto, T. Masumoto, S. Shimodaira : Corr. Sci. 16 (1976) 909-914
4. M. Naka, K. Hashimoto, T. Masumoto : J. Non.Cryst. Solids 28 (1978) 404-413
5. B. Elsener, S. Virtanen, H. Böhni : Electrochim. Acta 32 (1987) 927-934
6. S. Virtanen, B. Elsener, H. Böhni : Proc. Eurocorr 87, Karlsruhe 1987, 763-765
7. B. Elsener, H. Böhni : Werkstoffe und Korrosion 35 (1984) 501-51

Table 1. Polarization resistances at the corrosion potential

Material	R_p (ohm·cm^2)	
	1 N H_2SO_4	1 N HCl
Fe-17Cr, cryst.	17 11	$75_{1)}$ $38_{2)}$
Fe-10Cr-13B-7C	57 82	580 970
Fe-10Cr-13B-7P	24 17	17 6
Fe-10Cr-13P-7B	68 23	8 6
Fe-10Cr-13P-7C	1000 466	51 18

1) 1. Measurement

2) 2. Measurement

Table 2. Polarization resistances in the passive range

Material	R_p (kohm·cm^2)	
	1 N H_2SO_4	1 N HCl
Fe-17Cr, cryst.	80	*
Fe-10Cr-13B-7C	20	*
Fe-10Cr-13B-7P	65	*
Fe-10Cr-13P-7B	80	15
Fe-10Cr-13P-7C	130	57

* cannot be passivated in 1 N HCl

Figure 1. Impedance spectra of the alloy Fe-10Cr-13P-7C at the corrosion potential in 1 N HCl

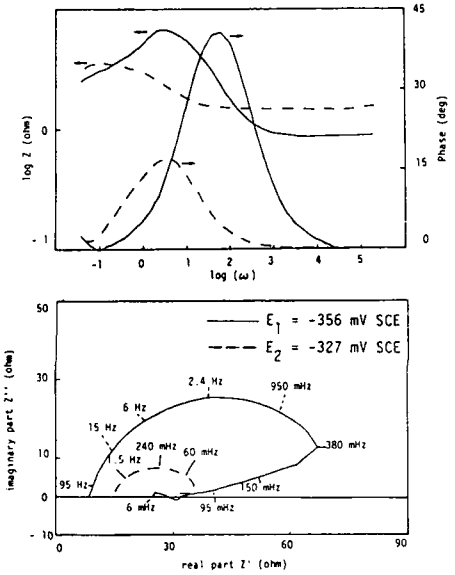
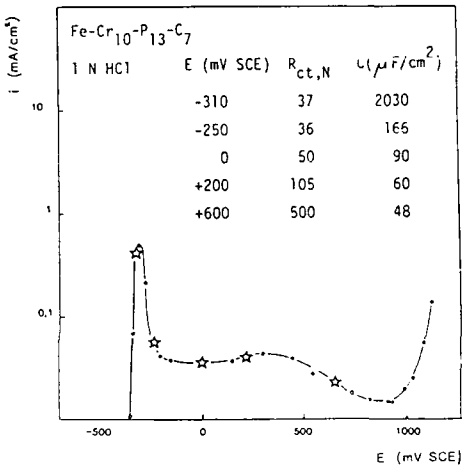


Figure 2. The normalized charge transfer resistance and the capacitance values at various points of the polarization curve of the alloy Fe-10Cr-13P-7C



E (mV SCE)	$R_{ct,N}$	C ($\mu F/cm^2$)
-310	37	2030
-250	36	166
0	50	90
+200	105	60
+600	500	48

Abstract No. 186

IMPEDANCE AND COMPLEX COLLECTION EFFICIENCY AT A RRDE : APPLICATION TO ACTIVE-PASSIVE TRANSITION OF Fe AND Fe-Cr ALLOYS

N. BENZEKRI, R. CARRANZA, M. KEDDAM and H. TAKENOUTI

LP 15 du CNRS "Physique des Liquides et Electrochimie, Université P. & M. Curie, tour 22, 4 place Jussieu, 75252 PARIS Cédex 05, FRANCE.

Non-steady-state regime at a Rotating Ring Disk Electrode is able to supply valuable data on the time dependent balance of charges trapped on the disk surface by adsorption or film growth (1). In the frequency domain the information is drawn from the simultaneous measurement of the frequency dependent complex collection efficiency $N(\omega) = \Delta I_R(\omega)/\Delta I_D(\omega)$ and of the faradaic impedance of the disk $Z_{F,D}$. This is one of the fields of application of multi-channel transfer function analyzers to corrosion. Experimental details were published previously (2). This paper reports recent data on the active-passive transition of Fe, Fe-7Cr and Fe-22Cr alloys.

GENERAL BACKGROUND

According to a generally accepted model passivation involves the anodic formation of a surface film. Due to simultaneous dissolution and passivation $Z_{F,D}$ does not provide a straightforward information on the film forming process. Charge balance on the disk surface can be generally expressed as :

$$I_D = n_D F \Phi_D(E,Q) + \frac{dQ}{dt} \qquad [1]$$

I_D : disk current, Φ_D : flux of species generated at the disk, n_D the number of electrons exchanged and Q the charge stored at the surface.

Linear form of [1] under a.c. polarisation of the disk gives :

$$n_D F \frac{\Delta\Phi_D}{\Delta I_D} = n_D F N_D(\omega) = 1 - j\omega \frac{\Delta Q}{\Delta I_D}(\omega) \qquad [2]$$

$N_D(\omega) = \Delta\Phi_D/\Delta I_D$ = kinetic component of the collection efficiency is obtained by correcting $N(\omega)$ for the transport contribution (2). Charge conservation in the low frequency limit ($\omega \to 0$) leads to $n_D F N_D(0) = 1$.

By introducing the faradaic impedance of the disk [2] becomes :

$$n_D F N_D(\omega) = 1 - j\omega \frac{\Delta Q}{\Delta E} \frac{1}{Z_{F,D}} \qquad [3]$$

From [3] the frequency dependence of $\frac{\Delta Q}{\Delta E}(\omega)$ can be gained at any potential providing an accurate view of the kinetics of film formation.

RESULTS

Fig. 1 to 3 display the complex plot of $2FN_D(\omega)$ ($n_D = 2$) for Fe, Fe-7Cr and Fe-22Cr alloys in the vicinity of the Flade potential ($\Delta I_D/\Delta E_D < 0$). In agreement with theoretical predictions (2), for a passivation process $\mathcal{I}m.N_D(\omega) > 0$.

$2FN_D(\omega)$ is close to 1 for iron as expected while it decreases as I_D is increased for Fe-Cr alloys showing a higher contribution of Cr to dissolution. At the same time the diagrams are shifted upwards under the influence of dissolution. Fe-7Cr exhibits clearly a second loop at HF located above the real axis. This establishes the existence of two distinct charge storing coverages, one involved in passivation ($\mathcal{I}m.N_D(\omega) > 0$), the other one in the dissolution mechanism ($\mathcal{I}m.N_D(\omega) < 0$).

Fig. 4 shows an example of data processed according to Eq[3] for Fe. The complex plot of $(\Delta Q/\Delta E).(\omega)$ is a semi-circle according to :

$$\frac{\Delta Q}{\Delta E_D}(\omega) = \frac{\Delta Q/\Delta E_D(0)}{1 + j\omega/\omega_0} \qquad [4]$$

This result directly supports the basic assumption of the kinetic model used in the impedance derivation. Values of $(\Delta Q/\Delta E_D)$ (0) when compared to the faradaic capacitances deduced from $Z_{F,D}$ allow to estimate the relative weight of dissolution and passivation. Integration of $(\Delta Q/\Delta E_D)$ (0) over a given range of E_D yields the total increment of charge consumed in the film growth.

REFERENCES

1. W.J. ALBERY, A.H. DAVIS and A.J. MASON Faraday Discussion 56, "Intermediates in Electrochemical Reactions", The Chemical Society (1971).

2. N. BENZEKRI, M. KEDDAM and H. TAKENOUTI "Surfaces, inhibition and passivation", Proceedings Volume 86-7, The Electrochemical Society Ed. E. Mc. Cafferty and R.J. Brodd, p. 524.

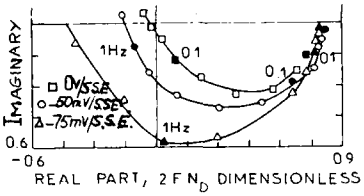


Fig. 1 : Dimensionless kinetic collection efficiency relative to the disk-Iron.

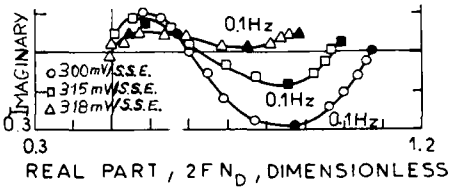


Fig. 2 : Identical to Fig. 1. Fe-7Cr alloy.

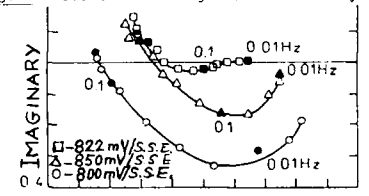


Fig. 3 : Identical to Fig. 1. Fe-22 Cr alloy.

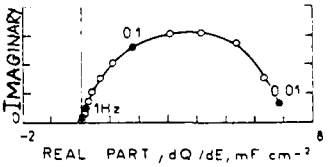


Fig. 4 : $(\Delta Q/\Delta E_D)$ for iron calculated from Eq[3].

Abstract No. 187

Pitting and Passivation of Al and Al-Based Metal Matrix Composites

F. Mansfeld, S. Lin, S. Kim, Y.C. Cheng and H. Shih
Materials Science Department
University of Southern California
Los Angeles, CA 90089-0241

Introduction

It has been shown previously (1,2) that immersion of Al 6061/SiC in 1000 ppm $CeCl_3$ produces changes in the protective oxide film which make the surface much more resistant to pitting. Electrochemical impedance spectroscopy (EIS) was used to monitor the passivation and the corrosion processes. A model has been developed which describes the observed impedance behavior as pitting initiates and pits propagate (1-4). Further work has shown that passivation can also be achieved for other Al alloys and Al-based metal matrix composites. In additional experiments immersion in $NiCl_2$ has been evaluated as passivation process. Surface analysis with scanning Auger microscopy (SAM) has been used to determine the composition of the films formed by chemical passivation.

Experimental Approach and Results

Passivation in $CeCl_3$ has been carried out for Al 7075 in the T6 and the T73 condition, Al 6061, Al 6061/SiC (25 v/o of 10 μm particulates) and Al 6061/graphite (55 v/o of P 100 graphite fibers, cladded with a 50 μm face sheet). Immersion at the open-circuit potential was carried out for one week in most cases. During this time EIS-data were collected on a daily basis. The corrosion tests were carried out in 0.5 N NaCl, open to air, until pitting occurred as indicated by significant changes in the impedance spectra and by visual observation. It was noted that the surface preparation was an important factor in the passivation process. Tests were therefore conducted for samples which were degreased only and samples which were degreased followed by alkaline cleaning and deoxidizing.

Fig. 1 shows Bode-plots for untreated and passivated Al 6061 as a function of exposure time to NaCl. For the untreated sample impedance spectra which are characteristic of the pitting process were observed already after only one day. These spectra show a decrease of the impedance in the capacitive region as pits grow and a transmission line type frequency behavior at the lowest frequencies. The spectra in Fig. 1 can be fitted to the model discussed previously (1-4) as shown in Fig. 2, where R_s is the solution resistance, R_p^s the polarization resistance of the passive film, C_t the total measured capacitance, $R_{pit}(eff) = R_{pit}/F$ the polarization resistance of the pit, n the slope of the impedance curve at the lowest measured frequencies and FK a parameter of the transmission line impedance. F is the fraction of the surface for which pitting has occurred. So far it has not been possible to obtain the values of R_{pit} and F separately from the fit. Excellent agreement between the experimental and the fitted data is observed. For the passivated sample (Fig. 1), the impedance spectra did not change for one month which indicates that the surface was very stable and did not suffer from localized attack. For this sample pitting did not occur for 90 days immersion in NaCl as shown in Table 1 which gives a summary of the tests with passivation in $CeCl_3$.

A comparison of the times at which pitting was first indicated by pronounced changes in the impedance (Table 1) shows that the passivation process is very effective for Al 7075-T6, but not for the T73 treatment. Similar problems have been observed for conversion coatings in salt spray tests and have been explained by the presence of Cu precipitates as a result of the T73 heat treatment. For Al 6061 it was found that the removal of the natural oxide film makes the passivation process in $CeCl_3$ less effective. A sample which was degreased only before passivation did not pit in NaCl for 90 days, while the sample which was deoxidized before the passivation process pitted in less than 3 days. However, for this sample it was found that immersion in $CeCl_3$ for 1 month improved the corrosion resistance of the passive film significantly. For Al/SiC pitting did not occur for 90 days; however, crevice corrosion was observed under the O-ring used in the test cell. Similar problems had been found earlier with anodized samples (5). Since crevice corrosion never occurred for any of the other samples tested, it can be assumed that it is due to the SiC particulates at the surface. For Al/graphite pitting did not occur for 40 days which is a result of the improved corrosion resistance of the Al 6061 face sheet.

Preliminary results of the SAM study have shown that the films formed in $CeCl_3$ consist mainly of mixed cerium oxides and Al oxides. Aging in air (especially at elevated temperatures) converts the film into CeO_2 which has a yellow color. The corrosion resistance of this film is being determined at present.

The next step in this on-going study will be an evaluation of the passivation process in other rare earth chlorides. As a comparison to the results in $CeCl_3$, passivation in 1000 ppm $NiCl_2$ has been used for Al 6061. In Fig. 3 pitting occurs after one day immersion in $NiCl_2$ as indicated by the low-frequency behavior of the impedance and the corresponding second maximum of the phase angle. Apparently, pitting attack stops during further immersion in $NiCl_2$ as can be seen from the changes of the impedance between the first and seventh day of exposure. However, when this sample was immersed in 0.5 N NaCl, pitting occurred in less than 3 days.

Conclusions

Immersion of Al alloys and Al-based metal matrix composites in $CeCl_3$ greatly improves their corrosion resistance. The degree of improvement depends on the alloy chemistry, presence of particles such as SiC, surface pretreatment and time of passivation. For Al 7075-T6 passivation in $CeCl_3$ produced a surface with a corrosion resistance which was similar to that of a surface treated with a commercial chromate conversion coating.

EIS is a very powerful tool for the monitoring of the passivation as well as the corrosion processes. The type of corrosion occurring can be determined from the impedance spectra using the pitting model (1-4). Further development of this model should allow determination of pit growth rates from the values of R_{pit} and the fraction F of the area which is pitted.

Acknowledgment

This work has been funded by the U.S. Army Research Office under Contract No. DAAL 03-85-K-0156 and the Office of Naval Research under Contract No. N00014-88-K-0034.

References

1. F. Mansfeld, S. Lin, S. Kim and H. Shih, Corr. Sci. 27, 997 (1987).

2. F. Mansfeld, S. Lin, S. Kim and H. Shih, 172nd meeting of The Electrochem. Soc., Ext. Abstr., Vol. 87-2, paper No. 277.

3. F. Mansfeld, S. Lin, S. Kim and H. Shih, Corrosion/88, NACE, paper No. 380.

4. F. Mansfeld and H. Shih, J. Electrochem. Soc. 135, 1171 (1988).

5. F. Mansfeld and S.L. Jeanjaquet, Corr. Sci. 26, 727 (1986).

Table 1. Times for Initiation of Pits (t_p) and Crevices (t_c)

Material	Pretreatment	t(day)
Al 7075-T6	deoxidized	$t_p > 24$
Al 7075-T73	deoxidized	$t_p < 1$
Al 7075-T73	degreased	$t_p < 1$
Al 6061	deoxidized	$t_p < 3$
Al 6061*	deoxidized	$t_p > 29$
Al 6061	degreased	$t_p > 90$
Al 6061/SiC	deoxidized	$t_p > 90$ $t_c < 8$
Al 6061/Graphite	deoxidized	$t_p > 40$

*1 month $CeCl_3$ treatment.

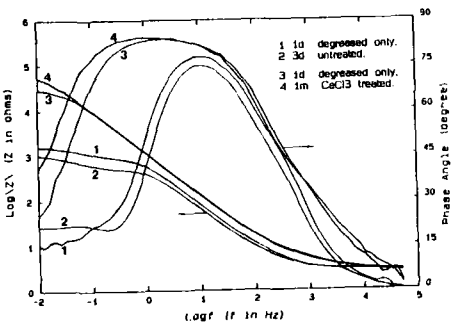


Fig. 1. Bode-plots for untreated and passivated Al-6061 as a function of exposure time to 0.5 N NaCl.

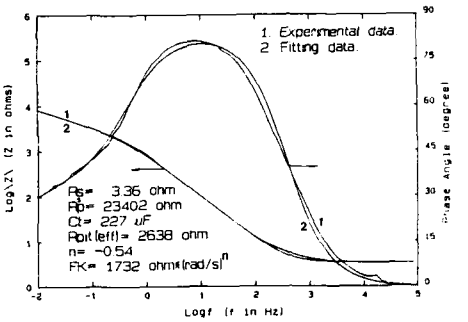


Fig. 2. Experimental impedance data and fit to model for passivated Al 6061 after one week in 0.5 N NaCl.

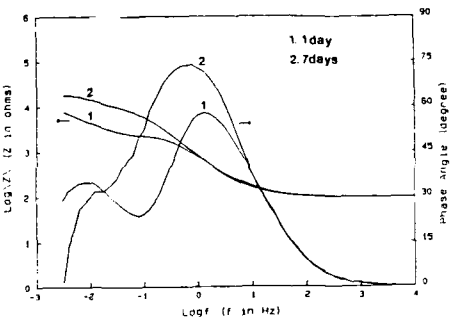


Fig. 3. Bode-plots for Al 6061 during exposure in 1000 ppm $NiCl_2$.

Abstract No. 188

MECHANISM FOR THE INITIATION OF ALUMINUM ETCH TUNNELS

B. J. Wiersma and K. R. Hebert

Department of Chemical Engineering
Iowa State University
Ames, IA 50011

Galvanostatic etching of aluminum in a hot aqueous chloride solution produces two regularly shaped and reproducible corrosion structures. Cubic etch pits, which occur due to dissolution on the (100) crystal planes, initiate at sizes between 0.1-1 μm. An etch tunnel forms as the sidewalls of an etch pit passivate and the active area becomes localized at the bottom face (1). As the tunnel penetrates the metal, the sidewalls are continuously passivated so that the tunnel width remains nearly constant. Since the transition from cubic to linear growth is accomplished by passivation, an investigation of the process by which etch pits transform into tunnels may lead to an understanding of the repassivation mechanism in corrosion pits on aluminum in chloride solutions.

The etching experiments were performed with 99.99 % aluminum foil in 1 N HCl at 65 °C. A constant anodic current of 10 mA/cm^2 was applied and potential transients were measured with respect to a Ag/AgCl reference electrode positioned far away from the aluminum surface. Scanning electron microscopy was used to determine pit and tunnel morphology.

An example of the potential transient for the first 100 ms of an etching experiment is shown in Fig. 1. Etching phenomena within this time period have been studied previously, using a current balance model and pit size distributions measured with SEM (2). During the first 28 ms, etch pits nucleate rapidly on the metal surface, and no passivation takes place. The applied current is supplied by capacitive charging and by metal dissolution. At 28 ms, the slope of the potential transient changes from -150 V/s to 0 V/s within a time of about 1 ms. Since the capacitance is 9.6 μF/cm^2, the metal dissolution current is reduced at this time by 1.5 mA/cm^2, or 10 %, in order to maintain the constant applied current. The potential at 28 ms is near the critical repassivation potential of aluminum. The dissolution current reduction occurs by passivation of active area in the pits.

At about 30 ms, a 10-40 mV dip in potential in a time of about 1 ms is observed in transients. It is hypothesized that this negative deviation from the critical repassivation potential provides the driving force for sudden passivation of much of the active pit area. Because of the small pit size and time interval, changes in potential with time due to concentration or potential gradients associated with individual pits are small and may be neglected (3), so that any change in the experimentally measured potential is associated with the surface potential. The current balance is

$$I_a = C\, d\eta_s/dt + i_d \rho A(t)/\varepsilon \qquad [1]$$

in which I_a is the applied current density, C capacitance, η_s surface overpotential referred to the repassivation potential, i_d metal dissolution current density, ρ the surface pit density, A(t) the average pit area at time t, and ε current efficiency for metal dissolution. According to the hypothesis, when $\eta_s < 0$, the time dependence of A(t) is determined by the passivation rate, which is assumed, for simplicity to depend linearly on the surface overpotential.

Results of experiments, in which the applied current was interrupted for 0.1-1 ms at 20 ms intervals during tunnel etching (4), were used to evaluate k. An interruption time longer than 0.1-1 ms was necessary to passivate tunnels. The current balance model was used to derive a relationship between the passivation time and the rate constant for passivation. The solution to the differential equation obtained when Eq. [1] is differentiated with respect to time and the kinetic expression for passivation substituted is

$$\eta_s = (d\eta_s/dt)_0 \sin(mt)/m \qquad [2]$$

where $(d\eta_s/dt)_0$ is the slope of the transient just prior to 30 ms, and m is a parameter $m^2 = \rho i_d k/\varepsilon C$, where k in the rate constant for passivation. With appropriate experimental values for the constants, the model predicts that the potential dips to a minimum 50 mV below the critical repassivation potential and returns to this potential in 1 ms. This prediced behavior agrees with the experimental transient in Fig. 1, and therefore supports the proposed passivation mechanism.

After the short passivation transient at 30 ms, the original etch pits are either partially or completely passivated, and, since the potential remains constant with time thereafter, then, according to Eq. [1], the total active area in the pits is controlled at a constant value. This control can be accomplished through the potential dependence of the passivation reaction, since the surface is at the repassivation potential. It is proposed further that the active area within individual pits is constant, and that this requirement causes the cubic pits to transform into the tunnel geometry. Fig. 2 shows a cubic pit of depth r_o in which, during the initial passivation, the oxide film has advanced a distance x_o down the sidewalls. If the remaining active surface continues to corrode in the <100> direction, then at some later time at which the pit has reached a width 2r, the oxide film will have advanced to a position x, given by

$$8(r-x)r + 4r^2 = 8(r_o - x_o)r_o + 4r_o^2 \qquad [3]$$

since the original active area has been preserved. Eventually, since Eq. [3] indicates that the oxide film advances faster than the pit growth velocity, the film reaches the corners of the pit, after which the requirement of constant active area dictates that lateral expansion of the pit stops, so that further growth would proceed as a tunnel.

Eq. [3] indicates that tunnel growth should be preceded by a short region of length no more than $1.7r_o$ in which the width expands by a factor between 1 and 1.7. SEM micrographs of tunnels show that this width expansion is frequently observed near the mouths of tunnels; a contraction in width is never observed. Further measurements of tunnel shape profiles will be made to test quantitative agreement with Eq. [3].

References

1. R. S. Alwitt, H. Uchi, T. R. Beck, and R. C. Alkire, J. Electrochem. Soc., 131, 13 (1984).
2. B. J. Wiersma and K. R. Hebert, Electrochemical Society Extended Abstracts, Spring Meeting, May 15-20 (1988).
3. J. Newman, D. N. Hanson, and K. Vetter, Electrochim. Acta, 22, 829 (1977).
4. R. S. Alwitt, private communication (1987).

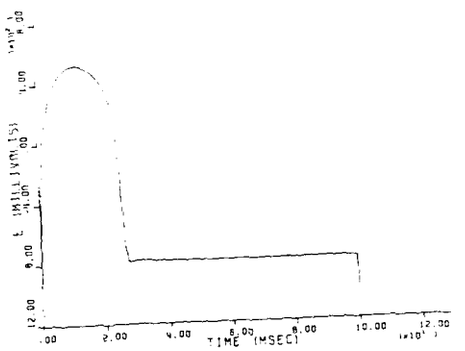


Figure 1. Potential transient in etching experiment. Applied current density 10 mA/cm^2, etchant 1 N HCl, 65 °C. Potential relative to SCE.

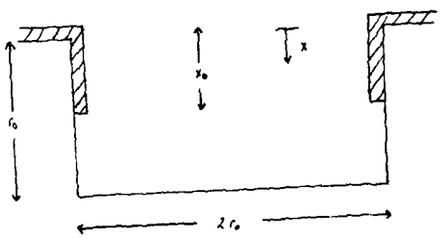
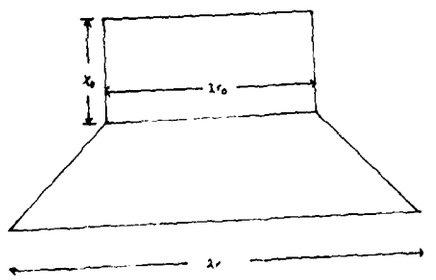


Figure 2. Cross-sectional views of an etch pit. (a) Pit after initial passivation, at 28 ms in Fig. 1.



(b) Pit after further growth, during which active area has been kept constant. Transition to tunnel occurs when x = r.

Abstract No. 189

THE ROLE OF SULFIDE INCLUSIONS ON INITIATION OF CREVICE CORROSION OF 304 SS

Stephen E. Lott and Richard C. Alkire

Department of Chemical Engineering
and Materials Research Laboratory
University of Illinois, Urbana, 61801

The initiation of pitting and crevice corrosion on 304 stainless steel is generally recognized to occur at sulfide inclusions. In this study, the onset of crevice corrosion was investigated both experimentally and theoretically by: (a) determining the mechanism of depassivation in the presence of MnS inclusions, (b) modeling reaction and transport processes in crevice regions, and (c) comparing model predictions with data obtained in an instrumented artificial crevice cell.

The following work is based on previously reported experimental findings (1) that chromium dissolution and acidification is a consequence, not a cause, of corrosion initiation. In the present work, the hypothesis is further suggested that initiation occurs first in the vicinity of sulfide inclusions, the dissolution of which alters the local solution composition and leads to passivity breakdown.

A series of controlled dissolution experiments were carried out with MnS electrodes in deaerated 0.1 N NaCl. By qualitative analysis, it was found that the products of the MnS oxidation were elemental sulfur and thiosulfate. By quantitative analysis with use of a UV spectrophotometer, it was found that 8 coulombs passed per mole of thiosulfate produced. In addition, it was found that elemental sulfur was produced on the surface, and the pH did not decrease during MnS dissolution. Based on these data, it is suggested that the dissolution occurs as

$$2MnS + 3H_2O = S_2O_3^{=} + 2Mn^{+2} + 6H^{+} + 8e^{-}$$

$$2H^{+} + MnS = Mn^{+2} + S + H_2$$

A series of galvanostatic experiments were carried out with 304 SS electrodes in solutions of various combinations of thiosulfate and chloride ions. Figure 1 summarizes the results; each point represents an experiment in which the electrode either became active or remained passive. For conditions above the solution line, the stainless steel became depassivated. These results suggest that entrapment of thiosulfate within a crevice, along with ingress of chloride ions by migration, may cause local depassivation in the vicinity of sulfide inclusions.

An artificial crevice cell was fabricated by placing an optically flat glass disk against an optically flat metal disk (2.54 cm dia) that was polished to various roughnesses, the value of which served to determine the crevice gap. Crevice gaps between 2.7 and 9.2 ± 0.2 μm were investigated. The crevice was formed at "time zero" by bringing the two surfaces together with use of a modified microscope stage. The time at which corrosion initiated, determined by direct electrochemical measurement of current, was found for various gap settings, applied potential, and inclusion density. In general, initiation was slower in the presence of large gaps, negative applied potential, and low inclusion density. For sufficiently extreme values of these parameters, it was found that initiation of crevice corrosion would not occur.

A mathematical model was developed to simulate transient transport and reaction phenomena which occur upon formation of the crevice. The model included consideration of diffusion and migration of ions, potential-dependent dissolution of MnS inclusions, and a critical breakdown condition based on the local concentration of chloride and thiosulfate ions. Numerical calculations were carried out to predict the time at which initiation of crevice corrosion would occur. It was found that predicted behavior was in agreement with experimental data

The model was used to construct diagrams for predicting conditions under which initiation of crevice corrosion on 304 SS could be avoided. Figure 2 illustrates results for a range of crevice geometry, applied potential and inclusions density (N). The region below the lines corresponds to operating conditions under which initiation will not occur. Above the line, the thiosulfate/chloride ion buildup is sufficient to trigger breakdown.

The consistent agreement found from a variety of experimental and numerical routes serve to support the proposed "thiosulfate entrapment" mechanism.

ACKNOWLEDGEMENTS

Financial support was provided by the Department of Energy (Grant 1198 via the Materials Research Lab.). SEL received fellowship support from the Exxon Education Foundation, IBM Corporation, and Union Carbide.

REFERENCES

1. S. E. Lott and R. C. Alkire, "Variation of Solution Composition During Initiation of Crevice Corrosion on Stainless Steel," Corrosion Science, in press.

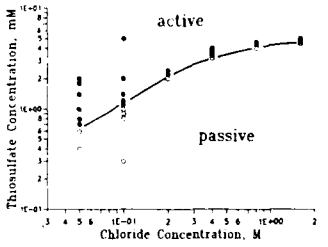


Figure 1: Experimental measurements of conditions under which 304 SS becomes active or remains passive during dissolution at 25 μm/cm² in deaerated NaCl/$Na_2S_2O_3$ solutions.

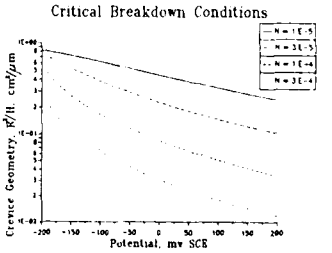


Figure 2: Theoretical calculations of operating conditions (geometry, applied potential, inclusion density) under which a crevice in 304 SS is predicted to become active (above the line) or remain passive (below the line).

Abstract No. 190

A MICROELECTROCHEMICAL PROBE WITH SEGMENTED ELECTRODES (MEPSE) FOR SENSING LOCALIZED CORROSION AND SCALING BY POTABLE WATERS

H.B. Sierra Alcázar, K. Kern, G. Mason, P.D. Nguyen
Pinnacle Research Institute, Inc.
10432 N. Tantau Avenue
Cupertino, CA 95014

Potable water can corrode or scale the distribution system and appurtenances in which it flows or resides, causing enormous economic problems, nuisance, and even contamination by corrosion products that might threaten public health. Excessive scaling can reduce pipe carrying capacity or completely clog pipes.

The water chemistry and the nature of the internal pipe surfaces change with time and location in the distribution system. It is necessary to monitor the corrosion damage or scale build up at representative and critical sites, so that preventive action can be taken locally or at the central plant. The sensor needed for this task should be able to monitor the general and localized corrosion rates, as well as the scale build-up rates in real time. The economic importance of a network of corrosion/scaling sensors is proportional to the annual cost of corrosion of water distribution systems and associated customer installations (residential, industrial and commercial plumbing systems). This cost has been estimated to be as high as 12 billion dollars in the United States by Miller Morgan et al (1). This paper demonstrates the feasibility of concepts that can lead to the development of a sensor to make scaling and corrosion control measurement more effective.

Localized corrosion can be detected in situ and in real time by identifying anodic and cathodic sites. The anodic reaction involves the release of electrons that travel electronically to the cathodic reaction sites, and can be, in principle, measured with a zero impedance ammeter in a segmented electrode. The circuit is completed by the movement of ionic species in the electrolyte. Positive ions are created in anodic sites, and a positive ion current is established towards cathodic sites. Small potential changes between anodic and cathodic sites are developed in the electrolyte, and can be used to map localized corrosion. There is a reciprocal effect between scaling and corrosion. Near anodic sites a lower pH will develop, contributing to the destabilization of the water. Scaling can result from deposition of salts (carbonates, silicates...) from an oversaturated electrolyte in the vicinity of the metal electrode (pipe). Scaling can also be the result of corrosion products depositing at or near the anodes. Cuprous oxide or iron oxide products can form flow reducing tubercles in steel or copper pipes. If scaling is a barrier for electron transfer general corrosion will decrease; if it is porous or discontinuous, however, localized corrosion is increased.

Generally, film quality increases with increasing alkalinity, calcium hardness, and velocity of flow in the system. Higher temperature, or presence of chlorides and sulfates,decrease the protective action of the calcium carbonate film . Since these parameters vary with location in the distribution system, it is important to have a distributed network of corrosion/scaling sensors that will enable plant managers to determine in real time the chemical doses necessary for stabilization.

Isaac et al. (2) have recorded the potential gradients in the solution near a corroding metal and Sierra Alcazar et al. (3) have recorded the potential of micro-areas in a metal tube. The approach involves closely scanning the metal surface (typically at 0.1 mm) with a very fine microelectrode and recording the potential difference with respect to another electrode in the electrolyte bulk. In this case the potential signals indicate the direction of ionic currents flowing in the electrolyte. Calibration is necessary because the amplitude of the potential depends critically on the distance of the microelectrode from the metal surface, furthermore a significant part of the ionic currents flows undetected between the microelectrode and corroding metal.

In order to simplify the scanning of the ID surface of a tube, the MEPSE sensor uses a number of pairs of 0.005 in.diameter wires (Ni-Cr alloy) in the function of microprobes and running parallel to the ID of tube segments (at approximately 0.0007 in. distance from the surface), as shown in Fig 1. Each wire-segment combinatio addresses a site inside the segmented tube. Potentials were scanned electronically by means of a multiplexer to produce Type 1 profiles.

The electronic currents between segments were measured with a PAR coulometer. All of the above measurements were performed with segments coupled or uncoupled to each other or coupled to Al anodes. The latter being for the purpose of determining the throwing power alterations produced by scale. The Type 2 profile (throwing power) is formed with the ionic currents to each segment; it was calculated from the measured electronic currents to the segments.

The response of the MEPSE sensor was measured while flowing four types of water through the MEPSE: deionized water, deaereated deionized water (DDI), corrosive water with a nominal Langelier-Ryznar (L.R) index of -1.0 and scaling water with a L.R index of 1.0. The last two types were prepared from a common stock of Champaign- Urbana tap water (U-C) with a Langelier index of 0.2. The chemical characteristics of this water were further altered by dissolving 1.000 g of $CaCO_3$ and 3.125 g NaCl per 5 gal of C-U water to increase their scaling and corrosive potential. The L.R indexes of the corrosive and scaling waters were obtained from altered C-U water by bubbling CO_2 or N_2 respectively.

The potential profiles (Type 1) for DDI, corrosive and scaling water are shown in Fig. 2. The DDI water shows very small localized variations in potential compared with the corrosive and scaling waters. The scaling water measurements were initiated on the surface already corroded by previous exposition to corrosive water during three weeks. This might explain the similar localized variation in potential in both potential profiles. The DC levels were lower for the scaling water though. Other potential profiles not shown revealed large potential variations in sites that had been previously utilized to determine polarization curves (60 mV excursion from rest potential) or impedance spectroscopy. Preferential scaling and corrosion was physically observed in such sites. This activity was also observed as large potential (from Type 1 profiles) and current peaks (from Type 2 profiles) measured after the disturbing AC and DC measurements were concluded. The throwing power of Al anodes located a few inches downstream from the MEPSE was higher under scaling conditions than under corrosive conditions as shown in the ionic current (cathodic protection currents) of Figure 3. Leveling of current distribution with time occurred in all cases but distinct differences remained between corrosive and scaling waters.

To perform electrochemical measurements (such as polarization curves, impedance spectroscopy, etc.) a wire w_2 was connected as auxiliary electrode, the companion wire, w_1, functions as a pseudoreference electrode. The effective micro area will depend on factors such as electrolyte conductivity, distance between tube and microprobe, reaction kinetics, and time or frequency. Typical impedance spectra for corrosive and scaling conditions are shown in Fig. 4. The flat semicircle is explained by an increasing effective micro-area with decreasing frequency; it indicates corrosion under activation control. Under scaling conditions a Warburg impedance is apparent, indicating partial diffusion control by the scale (no effect with flow rate changes). Specific capacitance, charge transfer resistance and uncompensated resistance can be extracted from the high frequency arc from both impedance spectra. Tafel slopes were determined from DC measurements with the three point method (4). DC and AC determined corrosion rates were comparable. Higher capacitances (3 $\mu F/cm^2$) and lower corrosion rates (0.3 $\mu A/cm^2$) were found for scaling conditions, localized corrosion rates were comparable to those found under corrosion conditions, but general corrosion was an order of magnitude higher in corrosive water.

Acknowledgement for support of this work is here given to the Department of the Army Construction and Engineering Research Laboratory. SBIR program.

References

1. J. Miller Morgan, T. M. Walski, M. W. Corey, Technical Report EL-84-6, (1984), DTIC No. AD-A144 670.
2. H.S. Isaacs, Y. Ishikawa, J. Electrochem Soc. **132-6**, (1985).
3. H. B. Sierra Alcazar, M. C. H. McKubre, "Development of a Scanning Micro-Electrochemical Probe to Study Pitting in Steam Generators", Final report, (SRI project 6253), for EPRI (1984).
4. S. Barnartt, Electrochimica Acta, **15**, 1213 (1970).

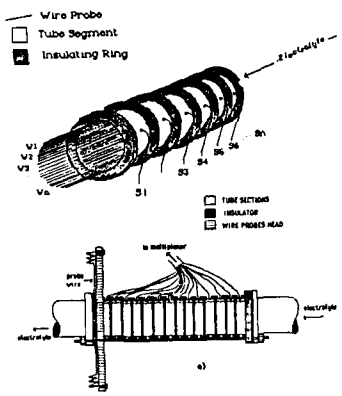


Figure 1. Diagrams of layout and assembly of MEPSE sensor.

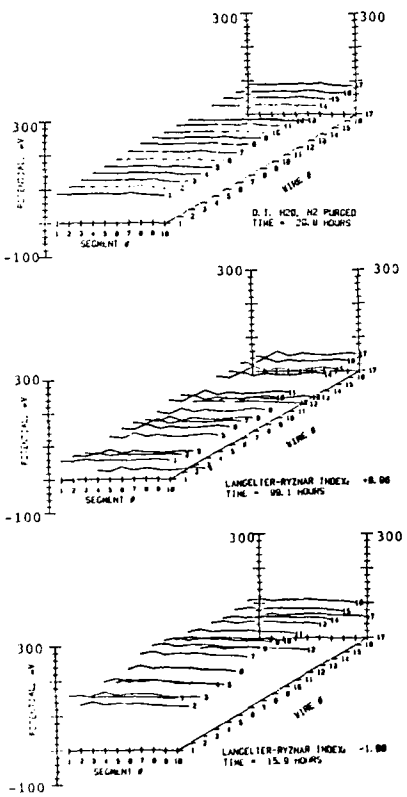


Figure 2. Segment-wire potential profiles in de-aerated de-ionized water, "scaling" water, and "corrosive" water.

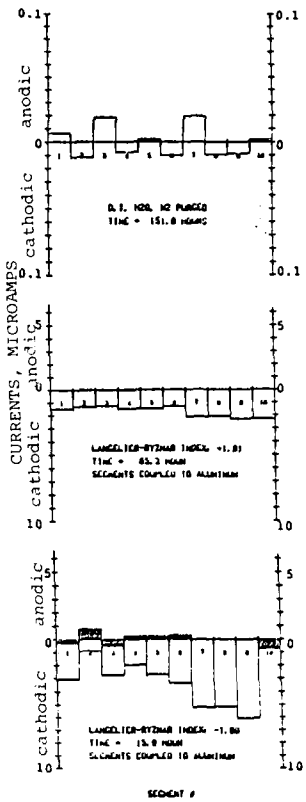


Figure 3. Comparison of Currents observed in de-aerated de-ionized water, "scaling" water, and "corrosive" water. Shaded areas describe measurements of currents without contact to aluminum. Scale for D.I. H_2O measurements is expanded 100x.

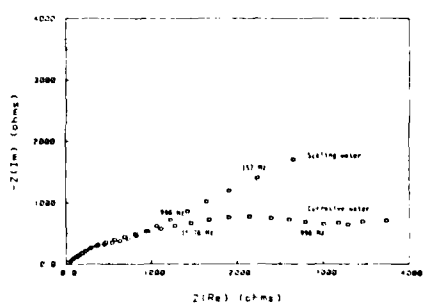


Figure 4. Impedance diagram for copper in scaling and corrosive water with Langelier-Ryznar Index +1, and -1, respectively.

Abstract No. 191

The Influence of Deep-Level Electronic Defects on Characterization Methods Incorporating Mott-Schottky Theory

D. Bivings Bonham and Mark E. Orazem
Department of Chemical Engineering
University of Virginia
Charlottesville, Virginia 22901

A mathematical model, developed to account for the transport and recombination reactions involving electrons, holes, and electronic defects located within the bandgap, was used to evaluate the use of Mott Schottky theory in the presence of deep level defects.

Mott-Schottky Theory

Under the assumptions that the semiconductor electrode is ideally polarized, that electron and hole concentrations follow a Boltzmann distribution, and that the majority and minority carrier are negligible when compared to the doping concentration (the depletion layer approximation) the space charge capacity C is related to the dopant concentration by the Mott Schottky expression,[1] i.e.,

$$\frac{1}{C^2} = -\frac{2(V + RT/F)}{\epsilon F (N_d - N_a)}, \qquad (1)$$

where V is the applied potential, referenced to the flatband potential, R is the gas constant, T is absolute temperature, F is Faraday's constant, ϵ is the permittivity, and $N_d - N_a$ is the effective ionized donor concentration. In using this equation, the semiconductor is usually assumed to be modeled by a series combination of the space charge capacity and a bulk resistance. Mott Schottky theory is generally used to determine the dopant concentration and the flatband potential. Any contribution to the ionized donor concentration by deep level defects will, in principle, be reflected in the space charge capacity, measured as a function of potential.

Mathematical Model

A transport based mathematical model[2] was developed to calculate the impedance response of an ideally polarized semiconductor electrode to a sinusoidal current perturbation. The model accounts explicitly for electron and hole transport as well as for generation and recombination through band to band mechanisms and through bulk inter band electronic states of specified energy. Material balances were applied to all electronic species, and Poisson's equation was used to relate the local potential to the charge density in the semiconductor. The contributions of electrons, holes, ionized doping species, and ionized electronic defects were included in the local charge density. The equations which govern the semiconductor under steady state conditions were linearized, written in finite difference form, and solved using the BAND algorithm[3] coupled with Newton Raphson iteration. This method for solution of the governing equations required no linearization approximations and avoided assumptions involving depletion or neutral regions. The time dependent equations were solved for the response to a superimposed sinusoidal current by assuming a sinusoidal form for the dependent variables to eliminate explicit time dependence and linearizing about the steady state solution. The resulting set of linear ordinary differential equations was also solved with the BAND algorithm and an iterative technique was used to minimize round off errors.

Results and Discussion

The parameters used for the mathematical model correspond to an n type GaAs electrode. The Mott Schottky plot for a uniform dopant concentration of 10^{16} cm^{-3} and uniform inter band donor concentrations of 10^{14} cm^{-3} (curve (a)) and 10^{16} cm^{-3} (curve (b)) are presented in Figure 1. The inter band donor energy was assumed to be 1.1 eV, referenced to the valence band energy. The capacity is insensitive to inter band states at concentrations much lower than the doping concentration (curve (a)). When the concentration of inter band states is of the same order as the dopant concentration, the slope of the Mott Schottky curve changes with increasing potential. This reflects the increased concentration of ionized inter band donors with increased band-bending. The slope of this line at large potentials might be expected to yield a total donor concentration of 2×10^{16} cm^{-3}, corresponding to the sum of the ionized inter band donor and dopant concentration. The total donor concentrations calculated from equation (1), however, was significantly smaller (from 1×10^{16} at lower potentials to 1.38×10^{16} cm^{-3} at higher potentials).

This behavior can be explored by examining plots of the calculated total donor concentration as a function of semiconductor depth, given in Figure 2. The minimum total donor concentration (made dimensionless with respect to doping level) is 1.0 due to the doping species, which are always completely ionized. The presence of inter band defects is not seen until a potential is applied. Increased potential results in an increase in the dimensionless total donor concentration to a maximum of 2.0 near the surface. In cases where sufficient potential is applied, a transition region or "ionization wave" is seen to extend to greater depths with an increase in potential. The value of the donor concentration, obtained through application of equation (1), is averaged over a region encompassing the "ionization" wave.

When inter band donors are localized at the semiconductor surface, the Mott Schottky plots obtained have a characteristic shape like that given in Figure 3 for an n type semiconductor with a uniform doping level of 10^{16} cm^{-3}. For low concentrations of deep level states (curve (a)) typical Mott Schottky behavior is observed. In Curve (b), obtained for a near surface distribution of defects, the influence of deep level states is reflected in a decrease in the Mott Schottky slope in the potential range of 0.2 to 0.4 V. At higher potentials, however, the curve returns to the slope associated with only dopant species (*e.g.*, curve (a)). The potential at which these changes in slope occur reflect the energy level of the inter band defects. Mott Schottky curves of this type have been attributed to the presence of surface states.[4] This work supports that interpretation.

Conclusions

Transport based models of A.C. impedance provide a useful tool in the interpretation of experimental impedance results. The capacitive component, used in standard Mott Schottky theory, was found to be insensitive to bulk electronic states within the band gap if the concentration of these states is significantly less than the doping level. In contrast, the resistive component is much more sensitive to deep level defects.[2] For high concentration of defects, changes in the slope of the Mott Schottky curve can be interpreted in terms of partial

ionization of deep level defects. It should be noted that these effects could be attributed either to a nonuniform dopant distribution or to ionization of inter-band states with applied potential. Sub band gap photo excitation of electronic states or observation of a frequency-dependent capacity could be used to facilitate distinguishing between the possible causes of this behavior.

References

1. J. Joffe, *Electrical Communication* **22** (1945), 217-225.
2. D. B. Bonham and M. E. Orazem, *AIChE Journal* **34** (1988), 465-473.
3. J. Newman, *Ind. Eng. Chem. Fund.* **7** (1968), 514-517.
4. P. Allongue and H. Cachet, *Solid-State Communications* **55** (1985), 49-53.

Acknowledgement

This material is based upon work supported by the National Science Foundation under Grant No. EET-8617057.

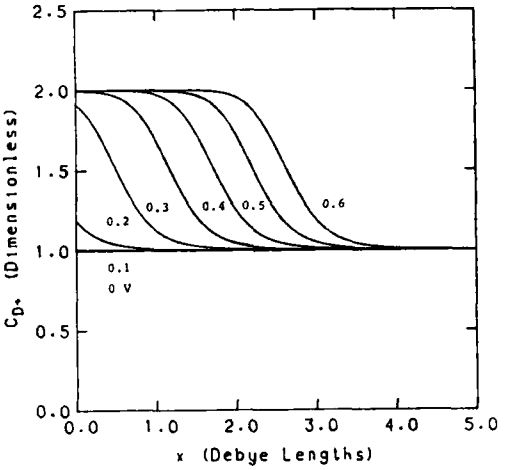


Figure 2. Total donor concentration (including inter-band and dopant species) as a function of depth for curve (b) of Figure 1 with applied potential as a parameter.

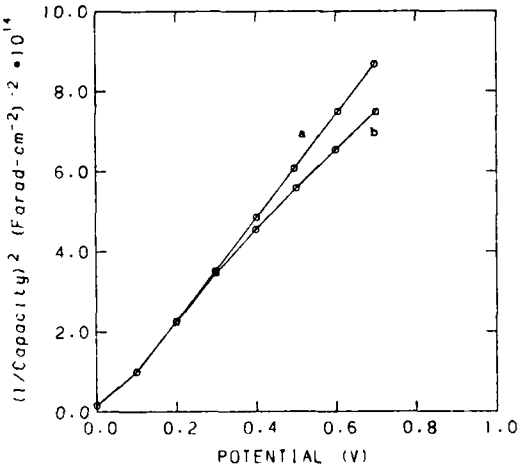


Figure 1. Mott Schottky plots for an n-type semiconductor with a doping level of 10^{16} cm^{-3} and an even distribution of inter-band donors with an energy of 1.1 eV referenced to the valence band. Curve (a), the state concentration is 10^{14} cm^{-3}; curve (b), the state concentration is 10^{16} cm^{-3}.

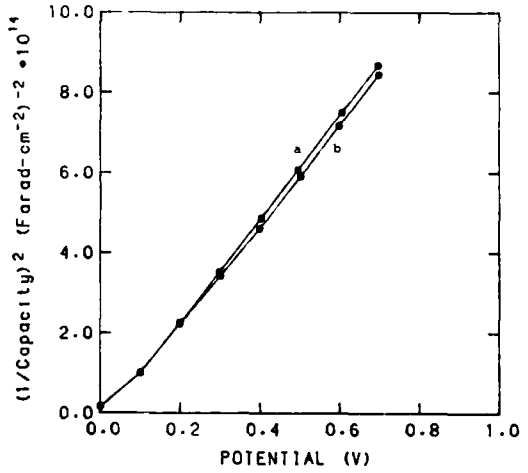


Figure 3. Mott-Schottky plots for an n-type semiconductor at equilibrium with varying distributions of inter-band donors. The doping level is 10^{16} cm^{-3} and the inter-band energy is 1.1 eV referenced to the valence band for both curves. In curve (a), the inter band concentration is 10^{14} cm^{-3} throughout the semiconductor; in curve (b), inter-band concentration is 10^{16} cm^{-3} at the surface, decaying to 1% of this value at 500Å.

Abstract No. 192

Corrosion Inhibition of Steel By Phthalocyanine Coatings

S. Hettiarachchi, R.B. Wilson Jr., Y.W. Chan
SRI International, Menlo Park, CA 94025
and
V.S. Agarwala
NADC, Warminster, PA 18974

Among the macrocyclic corrosion inhibitors studied, phthalocyanines appear to be the most effective class of corrosion inhibitors because of their multi-functionality. As a result, the interest in phthalocyanines as corrosion inhibiting coatings has been rapidly growing in the recent years[1-3]. Phthalocyanines have several attractive features in that they have a large area per molecule, show strong adsorption on metal surfaces, exhibit good lubricating properties[4-6] and have good electronic conductivity when appropriately doped. Thus, while inhibiting corrosion, phthalocyanines are capable of retaining the surface conductivity of a metal.

The electrochemical experiments were conducted with steel in 1% NaCl of pH = 2. AC impedance spectroscopy was primarily used in the corrosion inhibition studies.

Phthalocyanines studied included metallo-phthalocyanines and metallo-polyphthalo-cyanines [TCPC] containing various metal ionic centers such as Co(II), Fe(III), VO(IV), Cr(III), Si(IV) and Zn(II). Among these phthalocyanines the highest inhibition efficiency was obtained with the Fe(III) TCPC coating that showed an inhibition efficiency of 82%. It is interesting to note that although the addition of chromium and silicon to steel improve its corrosion resistance, the degree of inhibition provided by Cr(III) TCPC and Si(IV) TCPC were 52 and 64%, much lower than the degree of inhibition (82%) provided by Fe(III) TCPC. This result clearly shows that the corrosion inhibition is not totally due to a coverage effect, but that electronic factors are playing a significant role in the interfacial corrosion inhibition process. This effect was also observed with unpolymerized phthalocyanine coatings containing five and ten carbon alkyl chains indicating the presence of an electronic effect in the inhibition process.

Recent studies conducted by us show that unpolymerized phthalocyanines containing four aliphatic chains (five carbon and ten carbon) with Fe(III) metal ionic center [Fe(III)TCACPC](Figure 1) and[Fe(III)TCAUPC] (Figure 2) respectively, gave higher corrosion inhibition than the corresponding polyphthalocyanine [Fe(III)TCPC]. The corrosion inhibition efficiency obtained with Fe(III)TCAUPC is 86% with a single dip coating having a thickness of approximately 1μm. A significant advantage in using long alkyl chain containing phthalocyanines is that they require only a low temperature heat treatment of approximately 100°C as compared to polyphthalocyanines that require a heat treatment as high as 450°C.

We believe that further improvements to corrosion inhibition effectiveness can be achieved by understanding the nature of the electronic effect operating at the metal/coating interface. It is possible that Fe(III) centered phthalocyanines provide an electronic barrier[7] for the charge transfer process by increasing the band gap across the metal/semiconductor type interface. This interpretation is under further investigation at the present time. Once this effect is completely understood, it will be possible to choose the appropriate metal ion that will result in the highest band gap.

Another attempt we made to improve the degree of corrosion inhibition of polyphthalocyanines by filling the void between the phthalocyanine molecules in the polymer network with additional surface anchoring groups was not successful. However, we believe that this approach has potential to improve inhibition efficiencies and should be pursued further.

References

1. S. Hettiarachchi, Y.W. Chan, R.B. Wilson Jr., and V.S. Agarwala, Paper No. 223, CORROSION'87, March 9-13, San Francisco, California (1987).
2. S. Hettiarachchi, Y.W. Chan and R.B. Wilson Jr., Final Report to Naval Air Development Center, Contract No. N62269-85-R-0290 (1988).
3. S. Hettiarachchi, Y.W. Chan, R.B. Wilson Jr., and V.S. Agarwala, CORROSION Journal (1988), in print.
4. L.C. Lipp and E.N. Klemgard, Lubrication Eng., 22, 187 (1966).
5. G.Salomon, A.Begelinger and A.W. DeGee, Wear, 10, 383 (1967).
6. NASA NTIS Technical Note, NTN86-1116, October (1986).
7. F.C. Jain, J.J. Nosato and K.S. Kalonia, Paper presented at the Materials Research Society Symposium, April 5-9, Reno, Nevada (1988).

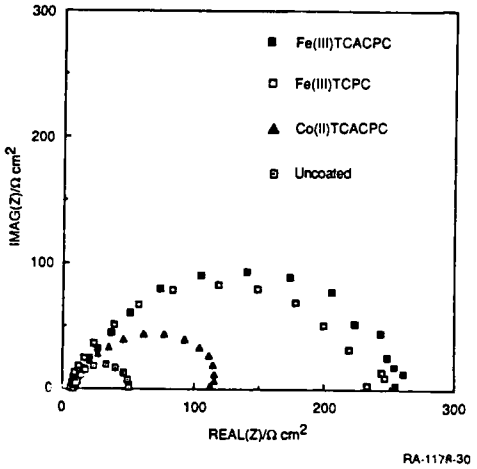


Figure 1 Comparison of the Nyquist plots of Fe(III) TCPC coated and five carbon alkyl chain containing phthalocyanine coated steel.
Mild steel: 1% NaCl; pH = 2; T = 298 K; 255 rpm.

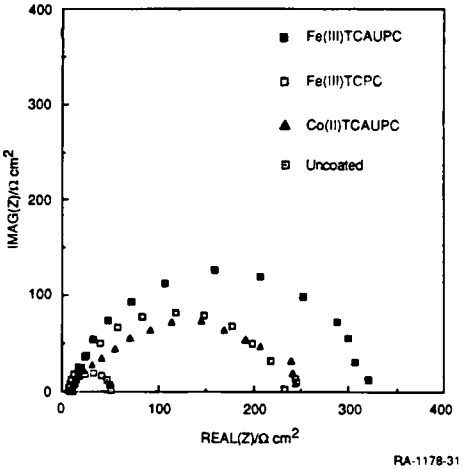


Figure 2 Comparison of the Nyquist plots of Fe(III) TCPC coated and ten carbon alkyl chain containing phthalocyanine coated steel.
Mild steel: 1% NaCl; pH = 2; T = 298 K; 255 rpm.

Abstract No. 193

AN ELECTROCHEMICAL IMPEDANCE STUDY OF THE PASSIVE STATE ON NICKEL AND DILUTE NICKEL ALLOYS

Stuart J. Smedley, Mordehai Ben-Haim,
and Digby D. Macdonald
SRI International
Menlo Park, CA 94025

Introduction

The growth of passive films on reactive metals and alloys is a subject of continuing interest because they are responsible for the kinetic stability of these materials in aqueous environments. Over the past eight years, we have employed electrochemical impedance spectroscopy to investigate the passive state on polycrystalline (1) and single crystal [100] (2) nickel in borate and phosphate buffer solutions at 25°C. To date, the low frequency impedance data have been interpreted in terms of a point defect model[PDM] (1), in which reactions involving cation and anion vacancies at the metal/film and film/solution interfaces are assumed to be in equilibrium. The present study relaxes this constraint to account for slow interfacial relaxations and extends our previous work on pure nickel to dilute nickel alloys containing Al, Ti, and Zr as alloying elements.

Experimental

Electrochemical impedance data were obtained using a computer-controlled SOLARTRON Model 1250 Frequency Response Analyzer. The control and data acquisition systems were periodically checked against a resistive/capacitive electrical "dummy" cell having properties similar to those of the systems under study.

Results and Discussion

Typical impedance spectra for nickel single crystal (100) in phosphate buffer solutions at pH = 11 and as a function of potential is shown in Figure 1. The impedance spectra display a low frequency Warburg response and a partially resolved semicircle at high frequencies. The low frequency Warburg behavior was previously detected and discussed for this system (1) and has been predicted theoretically by the PDM. However, this previous theoretical treatment was not capable of accounting for the high frequency relaxation.

The PDM has been modified by introducing a kinetic description of the interfacial processes:

$$M + V_M^{x'} \underset{k_{-1}}{\overset{k_1}{\rightleftharpoons}} x e' \qquad (1)$$

$$M \underset{k_{-2}}{\overset{k_2}{\rightleftharpoons}} M_M + \tfrac{x}{2} V_O + x e' \qquad (2)$$

Metal/film interface

and

$$M_M \underset{k_{-3}}{\overset{k_3}{\rightleftharpoons}} M^{x'} \qquad (3)$$

$$V_O + H_2O \underset{k_{-3}}{\overset{k_3}{\rightleftharpoons}} O_O + 2H^+ \qquad (4)$$

Film/solution interface

Assuming Tafel kinetics and by solving the Nernst-Planck equations for the movement of cation and anion vacancies across the film with a single set of k_i^o and α_i values, where

$$k_{ti} = k_{ti}^o \exp(\pm\alpha_i F\phi_i/RT) \qquad (5)$$

ϕ_i is the potential drop across the metal/film (i = 1,2) or film/solution (i = 3,4) interfaces, and α_i is the appropriate transfer coefficient, we are able to account for the impedance spectra over the entire frequency range and at the three potentials investigated.

These studies are currently being extended to dilute nickel alloys containing substitutionally present in the film ($Al_{Ni}^{\bullet}$, $Ti_{Ni}^{\bullet}$, $Mo_{Ni}^{\bullet}$) and mobile cation vacancies.

ACKNOWLEDGMENTS

The authors gratefully acknowledge the support of this work by the U.S. Department of Energy, Basic Energy Sciences, under Contract No. DE-FG03-84ER 45164, Dr. J. Darby, Technical Monitor.

REFERENCES

1. C-Y. Chao, L. F. Lin, and D. D. Macdonald, J. Electrochem. Soc., 129, 1874 (1982).

2. D. D. Macdonald, R-Y. Liang and B. G. Pound, J. Electrochem. Soc., 134, 2981 (1987).

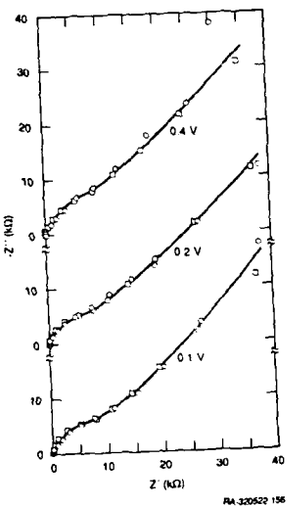


Figure 1 Impedance spectra for Ni(111) single crystal in 0.1 NH_3PO_4/NaOH, pH = 11, as a function of applied voltage
○ : experimental, □ : simulated. Data are from Ref. (2)

Abstract No. 196

Electropolishing of Iron in Phosphoric and Phosphoric-Sulfuric Acids.

L. F. Vega, M. Datta, L. T. Romankiw, P. Duby*
IBM Corporation, T. J. Watson Research Center,
Yorktown Heights, NY 10598
* Metallurgical Engineering Department,
Columbia University, New York, NY 10027

Electropolishing is widely employed in industry for microfinishing of different metallic components (1,2). A large number of electrolytic baths with different operating conditions and electrolyte compositions are reported in literature (1-4) but there is little information available on the mechanisms involved in electropolishing. In recent years, some of the fundamental aspects of electropolishing have been investigated (5-8). Much work, however, remains to be done for a better understanding of the processes that lead to electropolishing of different materials. Electropolishing of steel and stainless steel is generally carried out in phosphoric-sulfuric acid electrolytes (1-4, 8). In the present study, we have investigated the anodic dissolution of iron in phosphoric and phosphoric-sulfuric acids as a first step towards understanding the mechanisms involved in electropolishing of iron based alloys.

Rotating disk iron electrodes, 5 mm in diameter, insulated with a teflon sleeve and an alumina tubing, were used in the present study. A platinum electrode was used as a cathode which was separated from the anodic compartment of the cell by a glass frit. The luggin capillary was placed 10 mm below the disk surface. Electrolytes were prepared from pure acids (85% phosphoric acid and 96% sulfuric acid). The electrolyte temperature was maintained constant by circulating thermostated water through an enclosed outer compartment of the cell. Potentiodynamic and potentiostatic experiments were performed using a PAR 273 potentiostat and the measured data were recorded in a Nicolet Oscilloscope equipped with a magnetic disk storage.

The anodic polarization curves for iron in a 14M H_3PO_4 solution at two different temperatures are shown in Figure 1. After an initial region of active dissolution, marked current fluctuations are observed at all the temperatures employed in the present study. We believe that the current fluctuations are related to the formation and breakdown of anodic surface films. At 25°C, the current fluctuations are followed by a sharp decrease in current in the passive range. A renewed increase in current in the transpassive potential region is mainly due to oxygen evolution. Electropolishing is not observed under these conditions up to a potential as high as 2.5 volts. At 90°C, the plateau current beyond fluctuations is relatively high indicating that metal dissolution at high rates occur through surface films that are of different nature than those present at low temperatures in the same potential range. Dissolution of iron at or beyond the current plateau leads to electropolishing. The value of the current plateau increased with increasing rotation speed.

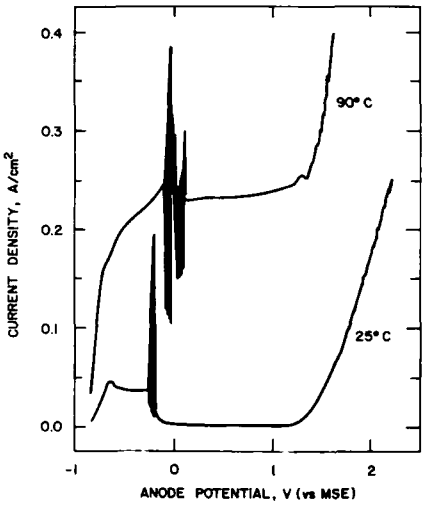


Figure 1. Potentiodynamic anodic polarization curves for Iron in 14 M Phosphoric Acid at two different temperatures. The scanning rate is 5 mV/s and the rotation speed of the disk electrode is 1000 rpm.

Figure 2 shows anodic polarization curves for iron in phosphoric-sulfuric acid mixture (9.8M H_3PO_4 + 6M H_2SO_4 + 6.3M H_2O) at 90°C. A complete polarization curve from the open circuit potential up to 2 volts is shown at a rotation speed of 1000 rpm. The data indicate that the active dissolution mode is absent in this electrolyte but transpassive metal dissolution sets in before the oxygen potential. Electropolishing is observed when the metal dissolution takes place at or beyond the limiting current. The value of the limiting current increases with increasing rotation speed following a Levich type behavior. This is demonstrated in Figure 3 which

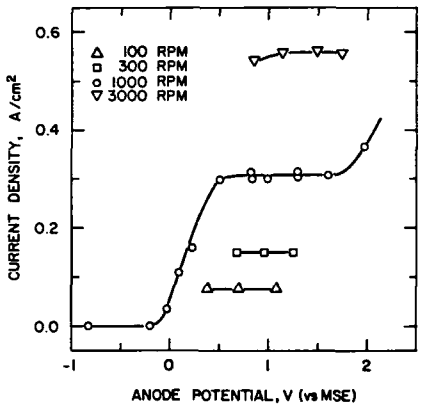


Figure 2. Potentiostatic anodic polarization curves for Iron in $9.8MH_3PO_4 + 6MH_2SO_4 + 6.3MH_2O$ at 90°C. A complete polarization curve is measured at 1000 rpm. At other rotation speeds, polarization measurements were taken in a restricted potential region to determine the limiting currents.

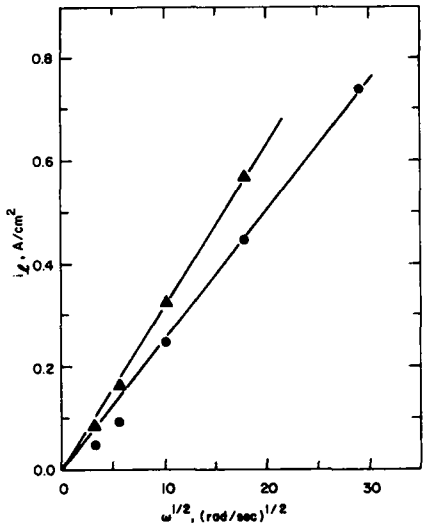


Figure 3. Limiting current density as a function of the square root of the rotation speed in (●) 14M H_3PO_4 and (▲) $9.8MH_3PO_4 + 6MH_2SO_4 + 6.3MH_2O$. The electrolyte temperature is 90°C

shows the measured limiting current density as a function of the square root of the rotation speed for both the electrolytes.

The above results indicate that the electropolishing of iron in phosphoric and phosphoric-sulfuric acids is a mass transport controlled process. In order to identify the rate limiting species, we have further investigated the influence of acid concentration, water content, and bulk metal ion concentration on the measured limiting current. For a semiquantitative evaluation of the obtained data, we have taken into consideration the influence of physical properties of the electrolytes on the ionic transport. For this purpose, we have experimentally determined the viscosity of these solutions and estimated its influence on the diffusion coefficient. The results indicate that a salt film precipitation involving rate limiting transport of Fe^{3+} is a most probable mechanism that leads to electropolishing of iron in these electrolytes.

References:

1. I. Rajagopalan, Finishing Industries, September 1978, p 27.
2. W. Schwartz, Plating and Surface Finishing, 68(6), 42 (1981).
3. W. J. McTegart, The Electrolytic and Chemical Polishing of Metals, Pergamon Press, London (1956).
4. P. V. Shigolev, Electrolytic and Chemical Polishing of Metals, 2nd Edition, Freund Publ., Tel-Aviv, (1974).
5. D. Landolt, Electrochim. Acta, 32, 1 (1987).
6. D. R. Gabe, Corrosion Science, 13, 175 (1973).
7. S. H. Glarum, J. H. Marshall, JECS, 132, 2872 (1985).
8. L. Ponto, M. Datta, D. Landolt, Surface and Coatings Technology, 30, 265 (1987).

Abstract No. 195

LASER STIMULATED CHEMICAL VAPOR DEPOSITION OF METALS ON POLYIMIDES

S.J. Bezuk, C. Kryzak, UNISYS Corp., San Diego, CA 92127

Polyimides are of great interest as insulators for microelectronic fabrication due to their low dielectric constant and planarizing properties. We report on the laser CVD of nickel on polyimide and the effects of this deposition on the electrical and mechanical surface properties of polyimides as well as a review of the microelectronic applications of this technology.

Experimental

The polyimides used in this experiment were Toray SP-710, Hitachi PIQ-13, and Ciba-Geigy 284. Films of each sample were spun onto 4 inch p-type silicon substrates and cured at 420°C. Plasma deposited SiO_2 films were compared to polyimide films. The thickness of all films tested was 1.2μm. Figure 1 shows the apparatus used for these studies. A 514.5nm Ar-ion laser beam was folded into the optical path of a microscope and focused through a suprasil window onto the substrate surface to a spot size of 12μm. The substrate was moved under the laser beam using translation stages. Nickel was deposited from $Ni(CO)_4$ (Strem Chemical) at reduced pressure and room temperature in a static chamber.

Results and Discussion

The deposited nickel lines were characterized by a smooth surface without periodic structure and without physical damage to the underlying polyimide. Auger spectroscopic measurements detected less than 5% carbon and oxygen in the nickel deposits. Measurements of the deposit resistivity were approximately 2 times the bulk resistivity of nickel without post deposition processing. These results are similar to previously reported results [1,2,3] for depositions of nickel on inorganic materials.

Figure 2 shows a comparison of the deposition of nickel as a function of the scan rate for polyimide and SiO2. An enhancement of the deposition rate by a factor of 3 to 10 was found on polyimide as compared to SiO_2. The temperature rise at the surface at the laser spot is determined the thermal properties of SiO_2 and polyimide[1]. The thermal conductivity of SiO_2 (3.9E-3 cal/cm-sec°K) is a factor of 8.5 greater than polyimide (3.9E-4 cal/cm-sec°K). This translates to a higher temperature and therefore deposition rate on polyimide for the same incident power.

Figure 3 shows results for line shapes obtained for nickel deposits as a function of scan speed. At low scan speeds, line shapes tended toward rounded peaks, flattening intermediate speeds and at the highest speeds studied became double-humped. The results can be explained by an increase in temperature at the depositing edge of the line[1,2].

Figure 4 shows the observed position of the focused incident laser beam with respect to the leading edge of the depositing nickel line. At low scan speed, the laser beam is on the top of the nickel deposit which allows incident power to be dissipated by the nickel conductor resulting in a low temperature at the deposits leading edge. At higher scan speeds the laser reflection moves to the leading edge of the deposit and more power is dissipated at the thinner leading edge of the deposit and substrate resulting in a higher temperature at the deposition point. This is confirmed by the observation that for a given input power the decomposition of polyimide films is a direct function of the scan speed. As the scan speed is increased, the amount of decomposition in the polyimide also increases.

I-V measurements were made on an interdigitated capacitor which was deposited over a region of the polyimide exposed to laser-induced nickel deposition. The capacitor was biased from 0 to 100 volts and temperature stressed from 25°C to 125°C. A film resistivity of approximately 9.0E15 ohm cm was found. The surface resistivity on polyimide not covered with nickel was 2.0E15 ohm cm. These values are typical of the bulk resistivities of polyimide indicating the CVD reaction did not affect the surface.

Applications

Applications of this technology within the areas of IC circuit and packaging manufacturing and repair are emerging. This technology is being applied to GaAs circuit processing[4], and photolithographic mask processing[5] and other metals have also been demonstrated, i.e., Tungsten[4,5] and Gold[6].

References

1. Dieter Bauerle, Laser Processing and Diagnostics, (Springer-Verlag, New York, 1984), p. 166.

2. W. Krauter, D. Bauerle, and F. Fimberger, Appl. Phys. A31, 13 (1983).

3. Irving P. Herman, Roderick A. Hyde, Bruce M. McWilliams, Andrew H. Weisberg and Lowell L. Wood, Materials Research Society Symposia Proceedings, Vol. 17, (Elsevier Science, Inc., 1983), p. 9.

4. J.G. Black, S.P. Doran, M. Rothschild, and D.J. Ehrlich, Appl. Phys. Lett. 50, 1016 (1987)

5. W.M. Grossman and M. Karnezos, JVST B5, 843 (1987).

6. T.H. Baum, J. Electrochem. Soc., 134, 2616 (1987).

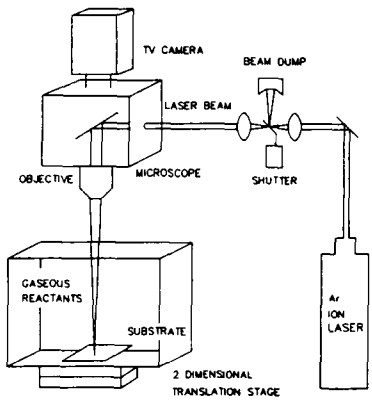


Fig. 1. Schematic of laser CVD system.

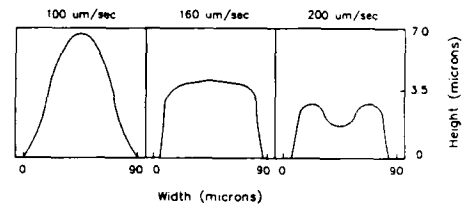


Fig. 3. Cross section of nickel lines as a function of scan speed for laser power of 0.65 W and Ni(CO)4 pressure of 1 torr.

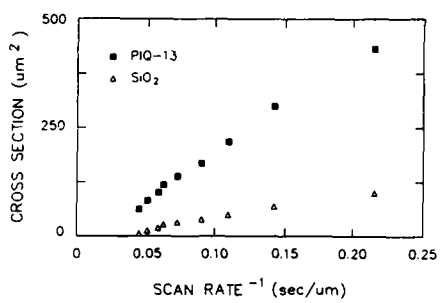


Fig. 2. Cross section of nickel lines as a function of 1/scan rate, for a laser power of 0.94 W and Ni(CO)4 pressure of 1 torr.

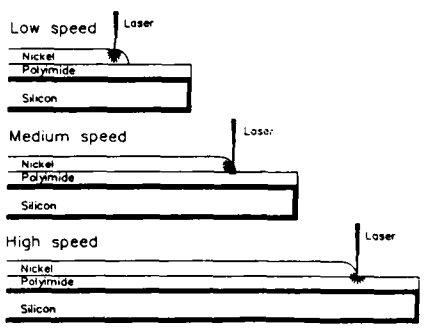


Fig. 4. Position of laser focus as a function of scan speed.

Abstract No. 196

METALLIZATION OF NONCONDUCTING SUBSTRATES BY MEANS OF COMPOSITION GRADED INTERFACE LAYERED BY PLASMA POLYMERIZATION TECHNIQUE

Byung K. Sun, Dong L. Cho, Thomas J. O'Keefe, and H. Yasuda
Department of Metallurgical Engineering,
Department of Chemical Engineering, and
Graduate Center for Materials Research
University of Missouri-Rolla
Rolla, MO 65401

Structural incompatibility between nonconducting substrates and conducting coatings, in terms of both chemical bonding and properties, makes it technically difficult to metallize insulators. Adhesion between polymers and metals is known to be poor due to the absence of any primary chemical bonding. In addition to that, the high stress developed at the interface due to sudden changes in structure across the interface, has been blamed for a major portion of failures of metallized parts under operating conditions. Therefore, mechanical interlocking or formation of chemical bonds through surface modification have been tried in an attempt to improve metal-polymer adhesion. Also, many of the present wet chemical processes for metallizing nonconductors require costly rigorous chemical and process control and consist of numerous steps, each requiring precise handling and conditioning of the materials involved.

The research described here deals with the application of a composition graded interface for use as a preplate for metallizing nonconducting materials. Such gradients are beneficial in minimizing many of the problems cited previously. The composition of the graded films, which changes from 100% organic to nearly 100% metallic over the thickness of the films, eliminates sudden changes in material structure and chemical composition between two dissimilar materials and assists in establishing a stronger, more durable interface. Strong adhesion between the polymer substrate and metallizing material can be obtained through chemical bonding between the polymer substrate surface and the plasma polymer film at the bottom of the composition graded interface and metallic bonding between the nearly pure metallic layer at the top of the interface and subsequent metallizing material. In this case, the process scheme consists of 1) layering a composition graded interface by sputter deposition of a suitable electrode material with simultaneous plasma polymerization, followed by 2) deposition of the desired metallizing material by electroless- or electro-plating. This process also seems to have fewer limitations with respect to the polymeric substrates which can be metallized. Emphasis in this study was on FRP (fiber reinforced plastic) substrates with copper metal coatings.

Abstract No. 197

METALLIZATION OF PLASTICS WITH RESISTANCE HEATED SOURCES

Kevin Anetsberger

MIDWEST TUNGSTEN SERVICE, INC.
7948 S. Madison Street
Burr Ridge, Illinois 60521

Since the advent of the use of resistance heated sources for the metallization of plastic substrates in the 1940's, both the sources and the process have undergone many changes.

Evaporative sources have evolved from single strand to multiple strand wires, then to coil and basket forms. Resistance heated crucibles and boats came into use for more difficult evaporative materials. The development of intermetallic boats opened the door to the coating of plastic film.

Although today there are more options available for coating plastics, resistance heated sources still play an important role in both decorative and functional coatings. The versatility and cost effectiveness of using this method of vacuum deposition still makes it an alternative worth considering almost 50 years since it became commercially available.

This paper will give a brief description of resistance heated evaporation and will discuss how present day methods such as ion-assisted plating evolved.

Metallization of plastics can be accomplished several ways. Several factors need to be considered when selecting a process. Metallization via resistance heated sources will be compared and contrasted to electron beam deposition and sputtering. Special attention will be given to capital equipment costs, deposition rate and overall output, and applicability of each process to specific materials.

This paper will also give an overview of the most popular areas for metallization of plastics today. It will target decorative, optical, shielding, and packaging uses for metallized products.

Abstract No. 198

METALLIZATION OF COMPOSITES AND THERMOPLASTICS VIA ELECTROLESS METALLIZED CONDUCTIVE COATINGS

Peter H. Kuzyk

Enthone Inc.
350 Frontage Rd.
West Haven, CT 06516

There exists a trend in today's aerospace, electronic and automotive industries toward increased applications for composite materials. The transition from metals to composites and thermoplastics for strength and weight considerations also presents new problems in the area of electromagnetic/radio frequency interference. To compensate for these inherent problems, metallization of the composite material is required. Many methods of metallization have been used in an attempt to meet these requirements. Typical materials considered for this purpose to date include: screen mesh and metal foils, flame spray, metal filled conductive paints, vacuum metallization and metallized fibers/fillers. While effective in counteracting many of the problems, no one material has demonstrated the ability to effectively meet all the performance parameters required of a metallized coating.

In this paper Enshield CMT, a new emerging technology incorporating electroless plating will be highlighted. This system incorporates a duplex metal layer: a highly conductive copper layer and a protective corrosion/wear resistant electroless nickel top coat. This technology provides a wide range of performance benefits required of a metallized coating including the ability to provide high levels of attenuation for EMI/RFI shielding, EMP and ESD applications, as well as providing protection to composites in lightning strike applications. In addition, the system offers major processing advancements in its ability to be field repaired using a simple , economical brush plating procedure. This procedure, along with the general characteristics of the coating and its method of application , are discussed in this paper.

Abstract No. 199

HIGH RATE REACTIVE SPUTTERING ONTO FLEXIBLE POLYMER SHEET

R.P. Howson

The Department of Physics,
The University of Technology,
Loughborough, Leicestershire,
LE11 3TU, England, UK

The production of complex materials in thin film form onto polymer foils is complicated by the inability of these materials to tolerate high temperatures. Energy is required by the depositing film in order to produce the desired compound or structure, which cannot be given from substrate temperature. In order to produce stoichiometric compounds or precise alloys the deposition process must be accurately controllable, and energy supplied simultaneously to activate reactions for molecular or structural arrangement. High rates are required for economic production, which can generate a loss of heat.

This paper considers the use of a d.c. planar magnetron, used with optical emission control of the reactive gas, and a controlled magnetron field to allow plasma to be directed onto the growing film. It is demonstrated that these techniques lead to stable processes allowing the high rate production of compound films, with precisely controlled stoichiometry and structure, onto flexible and rigid polymer substrates. ( )

Detailed examples are given for the production of indium oxide and titanium oxide films by the reactive sputtering of the metal in an argon/oxygen atmosphere. Film resistivities of around 4×10^{-4} ohm.cm were achieved with indium and indium/tin oxides during high rate production onto both flexible P.E.T. and rigid acrylic, with high visible transparancies.

Refractive indices of up to 2.55, measured at 633nm, could be obtained with T_iO_x film made with self biasing above -20Volts.

References

(1) A.G. Spencer, R.P. Howson and R.W. Lewin, "Pressure Stability in Reactive Magnetron Sputtering", Thin Solid Films, 158 (1988) 141-149

(2) K. Oka and R.P. Howson, "The Control of the Plasma in a D.C. Planar Magnetron", Proc. IPAT, 87 158-163 CEP Consultants, Edinburgh

(3) R.W. Lewin and R.P. Howson, "The Reactive Sputtering of Alloy Metal Oxide Thin Films of the Indium-Tin System", ibid 464-469

Abstract No. 200

Method of Producing Activated Plastic(Polystyrene) Film and Metallizing it with Gold using Electroless Techniques.

S.K. Dany and S. Mahapatra
Advanced Centre for Research in Electronics,
Indian Institute of Technology, Bombay 400076.
INDIA.

Electroplating of plastics requires that the substrate surface be made sufficiently conducting to allow electrochemical deposition of metals and the surface should be prepared to allow for good adhesion of the metal to the substrate(1). Plating on plastics (POP) involves five basic steps(2). They are (i) Preconditioning (ii) Sensitizing (iii) Activating (iv) Electroless deposition and (v) Electrolytic plating. A new approach to POP, now a days, consists of coating the non conducting substrate with elastomeric binder, containing selected metal oxides. These metal oxides are then reduced to the metal through electrochemical reduction and the coating is made electrically conducting so that it can be electroplated directly or can be plated from electroless solutions(3).

This paper describes a successful method of producing an activated plastic (polystyrene) film directly during its casting. Thus 4-5 g of finely powdered polystyrene is slowely dessolved in about 100 ml of xylene. During dissolution a few drops of an aryl alcohol are added while stirring with a glass rod. To 20-25 ml of this viscous fluid are added 5-6 mg each of gold potassium cyanide $KAu(CN)_2$, and potassium hydroxide KOH. The mixture is rapidly mixed by vigorous stirring with glass rod. This is allowed to stand for about five minutes. The mixture is again stirred vigorously as before and again allowed to stand. This is repeated several times till the colour of the solution turns to clear canary yellow from colourless. The yellow colour of the solution is an indication that gold potassium cyanide has reduced to gold metal. Pour the solution (about 2-3 ml) on a cleaned and dried glass slide. Allow to settle. On drying the film, pour more solution on it and again dry. Repeat this till a film of sufficient thickness (0.1 mm) is cast. Remove the film and preserve it in desiccator. After curing, coat the film with gold using electroless technique as follows: Immerse the film in a solution mixture containing a gold complex solution (1.5 g/l $KAu(CN)_2$, .5 g/l KCN, 10 g/l KOH) and potassium borohydrate (0.01 %) as the reducing agent at room temperature. The two films, one before electroless gold and other with electroless gold deposit, are then examined by SEM and ESCA techniques. SEM studies revealed that the film which was cast showed uniform distribution of gold particles in the form of glittering particles against dark polystyrene matrix. Film with electroless gold showed a network of fine gold threads. ESCA studies of both these films confirmed the presence of metallic gold. Although the colour of liquid was clear yellow the films formed from it were not yellow but pale violet or grey black in colour. This might be due to atomised gold reduced. Photomicrographs showed well distinguished areas of polymer and gold. The film formed was rather brittle in nature.

The procedure of producing of activated film, outlined in this paper, offers a new approach to metal-finishing of plastics having following advantages: The activated film is produced from a non aqueous media containing an organic solvent and a reducing agent. The method does not involve the steps such as preconditioning, sensitizing and activating the substrate normally adopted in the conventional methods of POP. As the activation and subsequent metallization takes place from within the substrate film, adhesion of the metal deposited and the plastic matrix is excellent due to mechanical bonding. This method has potential to be applicable to a great variety of plastic such as polymethyl methacrylate, cellulose acetate, PVC, nylon and many types of styrene. The selection of proper solvent for the plastics, the metal complex and a suitable organic reducing agent are the main criteria of the method. Other non conducting substrates can be made conducting by spraying polymer plastic solution with an organic reducing agent and an non aqueous media containing the metal ions having proper pH, simultaneously. In such cases the adhesion is poor due to discontinuity in the coefficient of thermal expansion between the original non conducting substrate and the sprayed activated film.

The finely distributed metal particles in the plastics obtained by this method provide for a gradual transition from high coefficient of thermal expansion of the plastic to the low value of the coefficient for the metal. Moreover, the plastic matrix may assist in averaging the forces between the substrate and the metal finish during expansion or shrinkage.

Experimental evidence indicated that the rate of reduction of gold potassium cyanide to gold metal decreased at higher concentration of KCN and low rate of stirring while activating the plastic solution.

(1) J.V. Lupinski and J.J. Grunson, Plating, 61, 439(1974) (2) T.S. Wrulis, J.Electrochem.Soc.,121(1974).

(3) J.V. Lupinski, J.Appl.Polymer.Sci. 17, 1139(1973).

Abstract No. 201

UV LASER INDUCED METALLIZATION ON POLYIMIDE FROM ELECTROPLATING SOLUTION

J. Zahavi*, M. Rotel*, D. Katz** and S. Levine***

*Israel Institute of Metals
Technion, Haifa, Israel
**Department of Material Engineering
Technion, Haifa, Israel
***I.B.M. Corporation D/879, P.O.Box 1500
Bromont, Quebec JOE 1LO, Canada

Recently direct laser metallization of semiconductor substrates immersed in electroplating solution without use of external current or lithography procedures have been reported by several investigators (1-4). No major efforts, however, have been devoted to laser induced direct metal deposition on polymeric substrate immersed in electroplating solutions (4). Use of pulse UV laser irradiation for direct metal deposition without any surface treatment such as sensitization, or activation and without external power and masking procedures makes the research work a new one as compared to previous studies (4,5).

Experimental

A polyimide "Kapton H" (produced by Du Pont, U.S.A.) was immersed up to 1mm depth in $HAuCl_4$ (20 gr/l in ethanol) and irradiated perpendicularly by a U.V. laser beam at 193nm using a Lambda Physics excimer laser model 201MSC. Two levels of laser energy, one at 160-200mg/pulse and the other at less than 100 mj/pulse were used. Laser repetition rates of 2Hz to 30Hz and numbers of pulses from 5 to 2000 were used for each energy level in this work. Specimen observations and detections of presence of elemental gold were carried out by SEM + EDS, ESCA and Auger techniques.

Results and Discussion

Gold deposit produced via UV laser irradiation on polyimide substrate is shown in Fig. 1. The effect of increasing the number of pulses at constant high energy level (160 mj/pulse) at a repetition rate of 10Hz is characterized by bubble formation (Fig. 1). At number of pulses higher than one hundred, bubbles were formed and grew (Fig. 1B) while at lower numbers of pulses no bubbles were observed (Fig. 1A). White zones shown in Fig. 1A indicated local concentrations of gold deposit. The same phenomenon was observed at other repitition rates. Irradiation of polyimide under the same conditions without gold solution resulting in bubble formation suggested damage events in the polyimide substrate.

The data indicated that the bubble diameter as well as the surface coverage by bubbles changed significantly with the number of pulses. A typical relationship between surface coverage and number of pulses is of S type. A linear relationship was established between bubble diameter and number of pulses. From the data presented (Fig. not shown), nucleation rate was calculated to be $4 \cdot 2 \cdot 10^4$ $cm^{-2}sec^{-1}$.

Auger depth profile analysis of bubbles that were produced in gold solution revealed that the presence of elemental gold was associated with that of carbon.

However, at a laser energy level of 95 mj/pulse no bubbles were detected at the irradiated zones. Under these conditions gold deposits without bubbles were formed at 5Hz and 7Hz, while the number of pulses ranged up to 2000 to give gold deposit thickness up to 1.0μm (Fig. 2). The gold deposit produced by this technique was carbon free as revealed by Auger spectroscopy through film thickness of more than 5000A°. Gold sheet resistance measured by four probe points was found to be 1.45 Ω/□ and 2.45 Ω/□ for 1000 and 2000 laser pulses at low laser energy respectively. Measurement done on the polyimide and on the gold deposit produced by high level laser energy (bubble covered area) did not show current transfer with our instrument for sheet resistance measurements.

Laser induced metallization on polyimide substrate appeared to be a complicated phenomenon. Thermal and photochemical processes were apparently involved. The temperature increase in the substrate under irradiation was large (300°C and more at the surface (6)) even at a number of pulses as low as 50 and less at laser energy density around $5 \cdot 10^8$ watt/cm². This directly due to the absorption coefficient ($B = 10^5 cm^{-1}$ at 193nm) which confined the depth of penetration to around 10^3A°. This local heating, with subsequent pyrolysis, modified the polyimide into semiconductor-type material (7-9). The higher laser energy irradiation resulted in local heating and the temperature rise caused formation of bubbles containing probably gases such as CO_2, CO, N_2, HCN, a fact reported by several investigators (7,8). This behavior will contribute to photoelectron generation at the polyimide surface which will penetrate the substrate-electrolyte interface to give an atomic metal deposit (10,11,12). The deposit was found to consist of pure elemental gold under all irradiation conditions. Further discussion will follow in the paper.

References

1) R.F. Karlicek & V.M. Donnely, J. Apply. Phys. 58(2), 1084-1090. (1982).
2) Y.C. Kiang, J.R. Moulic and J. Zahavi, IBM Technical Disclosure Bulletin, Vol. 26, No. 1, p. 327 (June 1983).
3) J. Zahavi, S. Tamir and M. Halliwell, Mat. Research Soc. Symp. Proceeding, Vol. 7, pp. 387-393 (1986).
4) J. Zahavi, S. Tamir and M. Halliwell, Plating and Surface Finishing, pp. 47-64, 1986.
5) J. Zahavi, S. Tamir and M. Halliwell, "Laser Gold Deposition on Polyimide", Proceedings Interfinish 1984, 11th World Congress on Metal Finishing, Jerusalem, Israel, p. 497, (October 21-26, 1984). Published by International Ltd., 10 Rothschild Blvd. 65121, Tel Aviv, Israel.
6) V.S. Srinivasen, M.A. Smithe and S.V. Babut, J. Appl. Phys. 59 11, pp. 3861-3867 (1986).
7) H.B. Brown, Y. Avirom, A. Broers and B. Summers, Solid State Communications, Vol. 35, 135-139 (1980).
8) A. Burger, E. Fitzer, M. Heym and B. Terwiesch, Carbon, Vol. 13, No. 3, pp. 149-157 (1973).
9) D. Bruck, Polymer (London), 6 319, 1965).
10) A. Felske, W.J. Plieth, J. Optical Soc. of Am. 3(5), 815 (1986).
11) D.V. Podlesnik, H.H. Gilgen, A.E. Willner, R.M. Osgood, J. Optical Soc. of Am 3(5) 775 1986.
12) Yu, Ya Gurevich, Y. V. Pleskov, Z.A. Rotenberg, "Photoelectro-Chemistry" Consultants Bureau, N.Y. (1980).

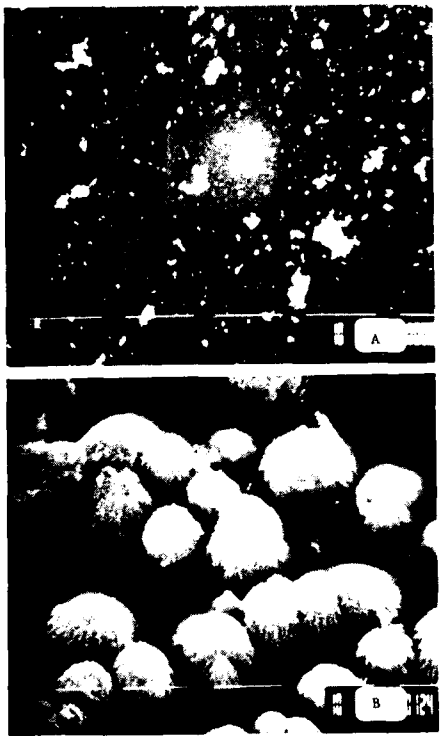


Fig. 1. SEM observations of gold deposit obtained on polyimide substrate immersed in gold-ethanol solution (1 gr $HAuCl_4$/50ml). Laser repetition rate 10Hz, laser energy at 193nm 160mj/pulse. A. Number of pulses 34; bright areas indicate presence of gold. B. Number of pulses 600, bubbles present in the area.

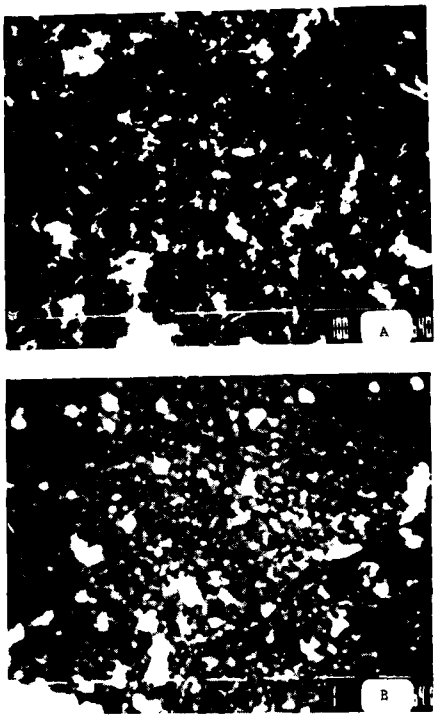


Fig. 2. SEM observations of gold deposit obtained on polyimide substrate immersed in gold-ethanol solution (1 gr $HAuCl_4$/50ml). Laser energy at 193nm 95 mj/pulse, laser repetition rate 5Hz. A. General view, × 350. B. Enlargement of A, × 10,000.

Abstract No. 202

Simple Metal-on-Plastics Patterning by Pulsed Electron Beam in Soft Vacuum

J. Krishnaswamy, M. Eyolfson, L. Li, G. J. Collins
Department of Electrical Engineering
Colorado State University, Fort Collins, CO 80523

H. Hiraoka
IBM Almaden Research Center, San Jose, CA 95120

M. A. Caolo
Hewlett-Packard Inc., Fort Collins, CO 80525

Metal incorporation into polymers is of great interest in many technical areas. Metal interaction with polyimide has been extensively studied with the idea of improving mechanical [1] and adhesive properties properties [2]. Enhanced surface reflectivities have also been reported for polyimides doped with copper [3] and silver salts [4]. In the case of palladium salt incorporation into polyimide, it has resulted in a ten-fold increase in surface conductivity [5]. These reports mainly discuss the chemical state of the elements present in the film, their relative concentration, and the effect of subsequent thermal curing on metal migration. The successful metalization may suggest useful applications like a direct imaged seed-layer fabrication with good adhesion to polyimide film and others. We like to report here our study of direct patterning of polyimide images with a buit-on-metal layer on the images, by combining our direct imaging method of polyimide films by pulsed electron beam exposures in soft vacuum and metal-salts incorpoation in polyamic acid films. We have already reported our direct patterning of polyamic acid using pulsed electron beams in solft vacuum [6,7].

$AgNO_3$ doped polyamic acid patterning

Two grams of silver nitrate was dissolved in 5 ml of N-methyl-pyrollidinone (NMP) and homogeneously mixed with about 20 ml of polyamic acid, PI2555. The $AgNO_3$-doped polyamic acid film with a 0.6 μm thickness spin-coated on a silicon wafer was soft-baked at 50°C for 30 min. The film was then exposed in a proximity mode to 50-100 pulses of 28 KeV electrons produced in 30 mTorr air, with a total dose of 5 x 10^{-4} to 1 x 10^{-3} C/cm^2 The images was completely developed in NMP for about 1 min. The pattern was heated to 300°C for 1 hr. The exposed surface turns shiny and a foggy metallic luster. The bright region of Fig. 1 was obtained in this way. The darker region of Fig. 1 has an additional process of electron beam hardening prior to 300°C heating. Clearly the darker area has more metalization than the bright area.

The distributions of each element in the film as a function of Ar sputter time, and so of depth from the surface before heating, after 300°C curing, and after electron beam hardening and 300°C curing are shown in Fig. 2a, 2b and 2c, respectively. The result clearly demonstrates silver migration to the surface, particularly after the electron beam hardening. The electron beam exposure may assist silver reduction from cationic state to neutral state.

Patterning of gold and copper doped polyamic acid

Patterning and metalization of gold and copper doped polyamic acid were carried out with Engelhard's gold compound (6854) and cupric chloride, respectively, using pulsed electron beams as described for silver doped polyimide film. In gold-doped polyamic acid there is a tendency for phase separation to gold-rich and gold-poor regions. With copper-doped polyamic acid the curing had to be done in vacuum in order to avoid oxidation.

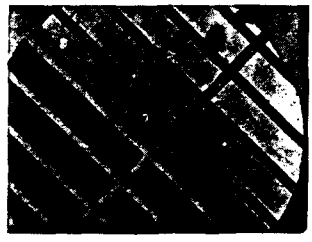


Fig. 1 Patterning of $AgNO_3$ doped polyamic acid and effect of electron beam hardening: imagewise exposure at 28 KeV, 50 pulses, electron beam hardening with 150 pulses only in dark region, curing at 300°C.

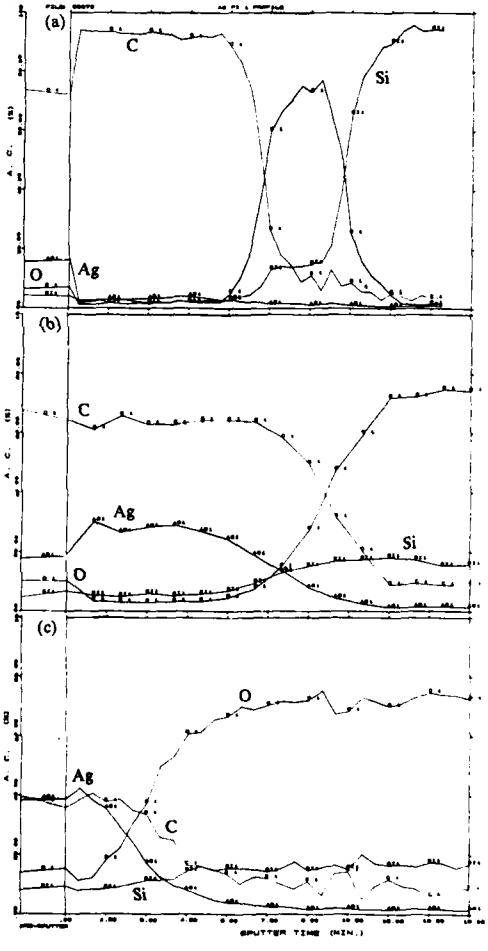


Fig. 2 Elemental distributions as a function of depth from the surface. (a) before curing, sputter time from 0 to 40 min with sputter rate of 73.2 nm/min (b) after curing at 300°C, sputter time from 0 to 15 min with 23.0 nm/min rate (c) after e-beam hardening and curing, sputter time from 0 to 15 min with 23.0 nm/min rate.

Abstract No. 203

PRINCIPLES OF THERMAL DEPOSITIONS OF METAL FILMS ON PLASTICS

R. Allen Myers

Deep Coat Metallizing, Inc.
Lemont, IL 60439

When evaluating functional vacuum metallizing two types of questions arise. There are the what questions and the how questions. The what questions are what can be plated, what coating will be most effective, and what will it cost. The how questions are how it is done, how thick are the coatings, how much production can be achieved, and how can the process be controlled.

There are many metals and combinations of metals which can be deposited on a wide variety of platics. Thermal and thermal-set plastics are routinely metallized for electrical purposes. Proper handling and surface preparation will maximize bonding strength in regards to the vertical pull test. In some instances, the choice of metal will significantly affect bonding.

To evaluate which coating will be most adequate for any application a number of factors must be considered. Environment can adversely affect some metal depositions, abrasion can be a factor, and the end use might require either a high or a low surface resistivity. Coating options can be either monolayer or laminated depositions and may even have some nonmetallic components.

Because this is a batch process, the question of what it will cost and how much production can be achieved are closely related. Most shielding is discriminate so different masking requirements can mean more labor to load or unload parts. There will always be some amount of fixturing which must be fabricat d to hold the parts in the vacuum chamber. In every case, there is one constant factor, and that is the more parts which you can get into the vacuum chamber and still affectively coat the lower your cost will be and the greater will be your production.

Several factors determine the thickness of the coatings. The level of vacuum determines the mean free path. Rate and duration of evaporation and the mass of the charge determine how much metal vapor can be produced and with what force it can be thrown from the filaments. Finally, the geometry of the shot is very important because thermal deposition is essentially a line of sight process.

When multi cavity fixed tooling has been fabricated, masking on each part should be typical from one part to another. Surface resistivity does vary, but it can be held within acceptable limits so it is useful as a SPC measurement. Advancements in equipment design augur well for improved monitoring and shot to shot consistency.

Vacuum metallizing has been around a long time. Functional coating, and by that I refer to EMI/RFI and ESD shielding, is a new aspect to an old art. As a process metallizing is deceptively simple and easy to understand. It's versatility is impressive and it is environmentally friendly. This paper won't make you a metallizer, but you will be able to talk to one effectively regarding your own application.

Abstract No. 204

Optical Performance and Durability of Silvered Polymer Mirrors

Gary Jorgensen and Paul Schissel

Solar Energy Research Institute

1617 Cole Blvd., Golden, CO

Use of solar energy to generate electric power and process heat frequently requires large mirrors to provide high levels of concentrated sunlight. Hundreds of millions of square meters per year of collection area could ultimately be needed to substantially displace conventional fuel usage. The weight and fragility of glass-metal mirrors impose considerable structural support constraints that, coupled with the material costs, are economically infeasible. Metallized polymeric reflector materials offer significant system weight reduction and price savings, while affording greater flexibility in terms of system design. Such materials must maintain high optical performance over extended service lifetimes.

On the basis of optical performance, silver is the reflector material of choice. The hemispherical reflectance of a freshly deposited silver film weighted over the solar spectrum (0.3-3.0 micrometers) is greater than 97%. A transparant front surface protective layer is required to shield the silver from abrasion, soiling, and corrosion. Typically, an acrylic polymer with UV absorbers (to inhibit ultraviolet-photon-activated degradation) is used. The solar-weighted hemispherical reflectance of such an unweathered silvered acrylic material exceeds 92%.

To attain high system energy conversion efficiencies, concentrated sunlight must be used. This means that hemispherical reflectance is not an adequate measure of optical performance; candidate mirror materials must exhibit very good specular reflectance as well. Depending upon the solar technology application, the system requirement is 90% reflectance into a full cone angle of 4-8 mrad. Such performance has been demonstrated for unweathered materials; the present thrust is to maintain this level over a minimum 5-year lifetime.

The durability of candidate metallized polymer reflector materials is a critical issue. Resistance to optical degradation caused by ultraviolet radiation, atmospheric pollutants, abrasion, and soil retention must be demonstrated. Adhesion at the silver/polymer interface is another potential problem exacerbated by moisture absorption. Several approaches were undertaken to mitigate these effects. Hard coats were synthesized and shown to impede abrasion. Such hard coats could possibly serve as barriers to water vapor and external pollutants as well. Typically, hard coats are thermally cured. Substantial savings in manufacturing costs can potentially be realized by a UV curing process, but the weatherability of UV-cured hard coats may be a problem.

Another approach to preventing degradation is to deposit a passivation layer at the silver-polymer interface. Such a layer may take the form of a very thin metallic coating or an organic coating. By creating a barrier at the interface, protection against both external and internally generated (i.e., within the polymer film) reactants can be provided. At the same time, such a coating could also promote adhesion.

Durability studies of candidate silver polymer mirrors were carried out as a function of real-time outdoor weathering and accelerated exposure. Major progress was made toward achieving a long-term goal of demonstrating a specular reflectance of 90% that is maintained for at least 5 years.

Abstract No. 205

Deposition of Thick, Adherent Copper Coatings on Glass

W. C. Cowden, T. G. Beat, T. A. Wash and J. W. Dini

University of California
Lawrence Livermore National Laboratory
P. O. Box 808
Livermore, California 94550

Thick (1 mm), adherent copper was needed on low coefficient of expansion glass to serve as a heat sink for a laser calorimeter. Also, adherent, diamond-turnable coatings on glass approximately 75 μm thick were sought for possible improvements in the optics of systems currently fabricated from metal.

To meet these requirements, vacuum deposition and electroplating were combined. An initial adherent, thin layer was deposited by magnetron sputtering and then thick copper was built-up by electroplating. This combined usage of these two different coating processes is but one example of applications wherein these technologies can complement one another (1,2).

The conventional technology used by platers for metallizing non-conductors via stannous chloride/palladium chloride activation followed by electroless deposition prior to final electroplating is not acceptable for glass when thick coatings are required. With this process, deposits thicker than around 12.5 μm (0.5 mil) easily separate from the glass substrate.

The generally accepted criterion for adhesion between a metal film and an oxide substrate such as glass is that the metal must be oxygen active to react chemically with the oxide surface, forming an interfacial reaction zone (3). The more negative the heat of formation, the higher the affinity for oxygen. Metals which have worked well as binding (or glue) layers for glass include chromium, titanium and vanadium.

For this work, a low stress titanium binder layer 1000 Å thick was first applied and without breaking the vacuum in between the coating steps, this binder layer was overcoated with 60,000 Å of copper by magnetron sputtering. The samples were then electroplated to final thickness (1 mm) in a proprietary acid copper solution (4).

An extremely important part of this work was the deposition of coatings with as close to zero stress as possible. Data were generated on the influence of pressure on stress during magnetron sputtering and the influence of current density on stress during copper electroplating. During magnetron sputtering, it was shown that as the pressure increased, the tensile stress in the deposit decreased, reaching zero at a pressure of 20 microns. During electroplating, zero deposit stress was obtained when plating was done at a current density of 1.6 A/dm^2 (15 A/ft^2).

References

1. J. W. Dini, Plating and Surface Finishing, 72, 48 (July 1985)

2. J. W. Dini, "Synergism of Electroplating and Vacuum Processes", Proceedings, 1st International SAMPE Metals Conference, August 1987.

3. D. M. Mattox, Thin Solid Films, 18, 173 (1973).

4. UBAC No. 1, OMI International Corp., Warren, MI.

Abstract No. 206

A Novel Electroless Process of Deposition of Thin Ni-P Coatings on Polymethyl Methacrylate

L.G. Bhatgadde and S. Mahapatra

Advanced Centre for Research in Electronics, Indian Institute of Technology, Powai, Bombay-400 076, INDIA

Electroless nickel plated polymethyl methacrylate is employed in automative parts, reflectors, waveguides, aircraft windshields, EMI shieldings etc. Present studies pertain to development of a novel and cost-effective electroless technique for depositing thin Ni-P coatings on this thermoplastic material.

In the experimental, 5 cm x 5 cm, 3 mm thick substrates cut from a sheet were plated in the sequence given in Table 1. As polymethyl methacrylate has a polar side chain, it is attacked by polar solvents such as methanol, which cleans and etches its surface. Further treatment in hot NaOH increased the wettability and produced anchors, which helped to adsorb $SnCl_2$ on sensitization. Upon activation, Pd grains were formed on the surface.

Next, the activated substrate was electroless plated in the bath heated to 88-93°C. The ratio of volume of substrate to volume of solution was 1:2. The bath composition and other operating conditions are presented in Table 2. Further electroplating nickel/copper was possible after this metallization.

The coating thickness, sheet resistance and adhesivity were measured by the conventional techniques. The as-deposited adhesivity was very low. The plated substrates were annealed at different temperatures in the range of 40-150°C for different periods. The annealing cycle finally optimized is given in Fig. 2. The values of sheet resistance and adhesivity before and after annealing were 36 and 21.1 Ω/□ and 6.5 and 65 kg/cm^2 respectively.

The as-deposited coating on the substrate had a honey-comb structure [Fig. 1(a)]. A cross section of the plated plastic revealed, that initial adhesion occurs by a mechanical keying effect [Fig.1(c)]. However, after annealing the internal stresses present both in the substrate as well as in the coating are relieved. The entrapped gases are also expelled [Fig. 1(b)]. Hence, the bond strength increased. The bond strength became maximum near/above the softening point of the plastic, which suggested the possibility of a cohesive bonding between the metal and plastic.

References

1. W. Goldie, Metallic Coating of Plastics, Vol. 2, Electrochemical Publications, England, 1969, Ch. 18.

2. W.L. Fields et.al., Metals Handbook, Vol. 5, American Society for Metals, Ohio, 1982, pp. 219-243.

3. K. Parker, Plat. and Surf. Fin., 74, 60 (Feb. 1987).

4. T. Kita and K. Sato, Ibid, 74, 58 (July 1987).

Table 1

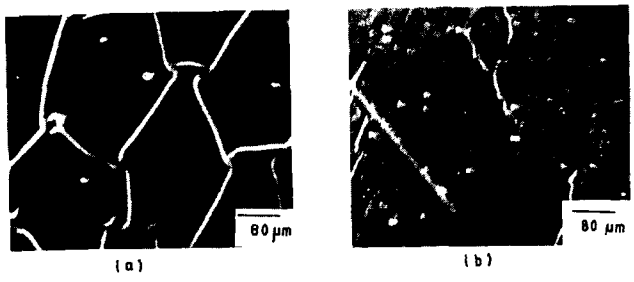
Polymethyl Methacrylate Plating Process

Step	Solution	Temp. (°C)	Time (min)
Degreasing	Alkaline cleaner	60-70	5
Rinsing	DI. water	Room	5
Etching	Methanol	Room	3
Alkaline treatment	NaOH(20%)	60-70	5
Rinsing	DI. water	Room	5
Sensitizing	$SnCl_2$(1 g/L) + HCl (1 ml)	Room	2
Rinsing	DI. water	Room	5
Activating	$PdCl_2$(1 g/L) + HCl(1 ml)	Room	2
Rinsing	DI. water	Room	5
Electroless plating	Electroless nickel	90	20

Table 2

Bath Composition and Conditions

$NiCl_2.6H_2O$	0.2 g/L
$NaH_2PO_2.H_2O$	1.2 g/L
pH	6.1
Temperature	90°C
Plating time	20 min
Coating thickness	1000 A°



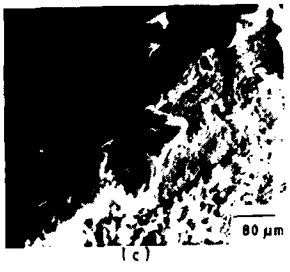


Fig. 1 : SEM micrographs of
(a) as-deposited Ni-P
(b) annealed and
(c) cross section

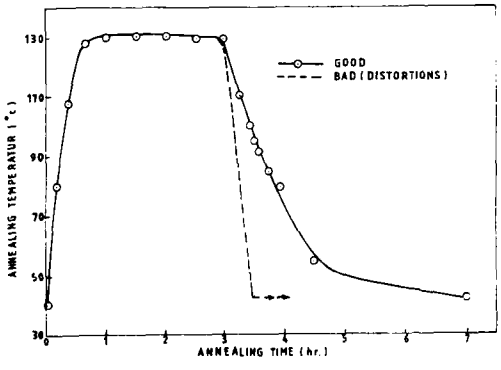


Fig. 2 Annealing cycle for plated polymethyl methacrylate

Abstract No. 207

Polymer Activation for Metallization: Theory and Application

Hristo B. Petrov, Ekaterina D. Dobreva, Milka A. Encheva

Department of Chemistry, Higher Institute of Mechanical and Electrical Engineering, 1156 Sofia - Durvenitsa, Bulgaria

After introduction of industrial electroless metal deposition on plastic, glass, ceramic and other dielectric surfaces, three theories have been put forward - silicate, hydrolysis, and ion-exchange - which seek explanation for the mode of retention on these polymers of the tin(II), silver(I) and palladium (II) ions upon activation in the first generation of electrolytes.

At the end of the 'sixties the authors were the first to apply the radiochemical method and, as a result of extensive studies, they established that the sensitization and activation of plastic surfaces is the result of adsorption-diffusion processes. Determinant is the ionic adsorption of the complex tin(II) chloride ions, the palladium(II) chloride ions respectively. It depends on the real surface of the plastic, on the concentration of the metal ions, and on the pH of the electrolyte, as well as on the temperature and duration of the treatment.

The sorption of the tin(II) chloride ions is of primary significance in the sensitization. The colloid particles consisting of a core of hydrated SnO_2 and of an outer adsorption layer rich in $[SnCl_n]^{2-n}$ or $[Sn_x^{2+}(OH^-)_y Cl_z^-]^{n-}$, which are present in a small amount in the sensitized electrolyte or are additionally introduced, raise insignificantly the concentration of the tin sorbed by the plastic (colloid adsorption). At the subsequent activation, both from the plastic surface and from the hydrolysis products of the tin are sorbed $[PdCl_4]^{2-}$ which react with $[SnCl_n]^{2-n}$ to the respective complex Pd-Sn-Cl ions:

$$[PdCl_4]^{2-} + [SnCl_n]^{2-n} + [Sn_x^{2+}(OH^-)_y Cl_z^-]^{n-} \longrightarrow [Pd_x^{2+} Sn_y^{2+} Cl_z^-]^{n-}$$

The second stage is redox reaction to Pd and Sn^{4+}:

$$[Pd_x^{2+} Sn_y^{2+} Cl_z^-]^{n-} \longrightarrow xPd + p[SnCl_6]^{2-} + q[SnCl_n]^{2-n}$$

It is possible that the palladium nuclei formed are a Pd-Sn alloy.

Using SEM, nucleation was observed at the consecutive sensitization, ionic activation, and electroless copper deposition on various plastic surfaces.

On the basis of these adsorption-diffusion concepts the authors developed and optimized the second generation of electrolytes of the direct ionic activation and the fourth generation - that of colloid activation. They demonstrated theoretically the inexpediency of the third generation of electrolytes of etch-activation.

The processes involved in obtaining colloidal activating palladium solution were systematically investigated. The first stage is also connected with reaction of the tin(II) and palladium(II) chloride ions to several complex Pd-Sn-Cl ions. The large excess of tin(II) chloride in the solution ($3 < Sn/Pd < 80$) accounts for the high speed of the complexing reaction.

The second stage is characterized by gradual transition of Pd-Sn-Cl ions into palladium, accordingly into a Pd-Sn alloy core stabilized with $[SnCl_3]^-$:

$$[Pd_x^{2+} Sn_y^{2+} Cl_z^-]^{n-} \longrightarrow k(Pd\text{-}Sn)[SnCl_3]_m^- + p[SnCl_6]^{2-} + q[SnCl_n]^{2-n}$$

At a ratio of $Sn/Pd < 3$ in the solution, the Pd-Sn particle obtained is insufficiently stabilized and agglomeration appears:

$$x(Pd\text{-}Sn)[SnCl_3]_m^- \longrightarrow \{(Pd\text{-}Sn)[SnCl_3]_m^-\}_x$$

The colloid nature of the activating solution was proved by means of the radiochemical method, SEM, light scattering and ultracentrifugation.

The authors have established that the colloidal activation of graft ABS, polypropylene, polystyrene, synthetic tissue (PETF) etc. is likewise the result of adsorption-diffusion processes. These processes underlie also the activation with alkaline electrolytes on the basis of complex palladium ions with organic ligands.

Abstract No. 208

STUDIES ON INTERACTION OF POLYIMIDE WITH COPPER IN CURING PROCESS

K. Miyazaki, O. Miura and S. Numata

Hitachi Research Laboratory
4026 Kuji-cho, Hitachi, Ibaraki
319-12 Japan

Introduction

Polyimides(PI) have been regarded as an excellent insulating material in wiring systems of mounting substrates[1] for LSI, because of its low dielectric constant and the high temperature stability. It is very important to study in detail the interfacial phenomena of the PI and the wiring metals for insuring the quality of the devices.

The interaction at the PI-Copper(Cu) interface has been reported previously[2)-5)], but most work was on the interaction of fully cured PI with Cu deposited on it.

The purpose of this study is to investigate the interaction of the PI with Cu in the curing process of the precursor-solution. The characteristics of the PI films cured on Cu and the dissolving behavior of Cu into the PI have been studied.

Experimental

The precursor-solution used in this study was prepared by dissolving polyamic acid(Fig.1-a) into DMAC-NMP solvent. A 15% precursor-solution was spin coated onto Cu vapor-deposited on Si wafers, and thermally cured at 100～350℃ for 30min in N_2 atmosphere. (Polyamic acid can be fully imidized at 350℃ for 30min and the imidized structure is shown in Fig.1-b)

The PI films cured at each temperature were peeled off from the Si wafers, and measured the thermal decomposition temperature and mechanical properties of the films.

The structual change of the PI films cured on Cu was investigated by FT-IR spectra, and the Cu content in PI was measured by atomic absorption analysis and visible spectrophotometer.

Results and Discussion

Table 1 shows the characteristics of PI-films cured at 350℃ for 30min on Cu and other materials(Al, Cr, SiO_2). The PI films cured on Cu are inferior to other films in thermal stability (thermal decomposition temperature) and mechanical properties.

Fig.2 shows the results of FT-IR analysis of the PI films cured on Cu at 330～350℃.

A remarkable decrease can be seen in the absorbed signals due to the imide bonds with the curing temperature. And this is considered to be due to the decomposition of the imide bonds at such a lower temperature.

Fig.3 is Cu content in the PI films cured on Cu at 100～350℃, showing that a considerable amount of Cu is contained in PI at a fairly low temperature. And as shown in Fig.4, the dissolving Cu comes into precipitation in the form of Cu_2O by curing above 300℃. It can be considered that the decrease in the thermal decomposition temperature and mechanical properties are related to the Cu dissolved in PI films.

In order to investigate the reason of the dissolution of Cu in the precursor-solution, the solubility of Cu to DMAC, NMP and the precursor-solution were measured.
The results of Fig.5 indicates that the dissolution of Cu into the precursor-solution is significantly enhanced by the polyamic acid.

Further experiments have been done to know which functional group in the polyamic acid caused the dissolution of Cu by employing carboxylic acid and benzanilide-solution, carring only carboxyl and amide respectively. As shown in Fig.6, it became clear that carboxyl in polyamic acid is the main reason of the Cu dissolution into PI films.

Reference

(1) T. A. Lane, F.J.Belcourt and R. J. Jenson; IEEE Trans. Components, Hybrids, Manuf. Technol., vol. CHMT-12, 577 (1987)
(2) P. S. Ho, P. O. Hahn, J. W. Bartha, G. W. Rubloff, F. K. LeGoues and B. D. Silverman; J. Vac. Sci. Technol. A, vol.3, 739 (1985)
(3) R. C. White, R. Haight, B. D. Silverman and P. S. Ho ; Appl. Phys. Lett., vol.51, 483 (1987)
(4) F. S. Ohuchi and S. C. Freilich ; J. Vac. Sci. Technol. A4, 1039 (1986)
(5) S. P. Kovalczyk, Y. H. Kim, G. F. Walker and J. Kim ; Appl. phys. Lett., vol.52, 375 (1988)

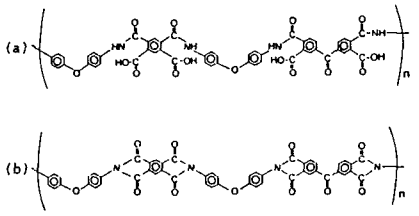


Fig.1 Molecular structure of polyamic acid and polyimide
(a) Polyamic acid (b) Polyimide (PI)

Table 1 The characteristics of PI-films cured on Cu and other materials

Materials of basis films	Decomposition Temp.(°C)	Tensile Strength(MPa)	Elongation (%)
Cu	380	107.8	8.0
SiO_2	450	132.3	17.0
Cr	450	131.3	16.8
Al	450	132.3	16.7

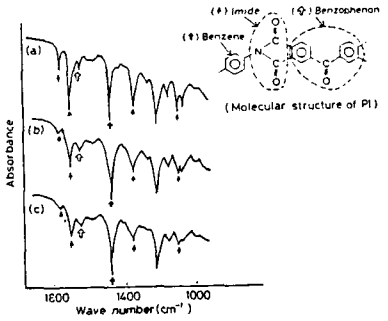


Fig.2 FT-IR spectra of PI films cured on copper
(a) at 330°C (b) at 340°C (c) at 350°C

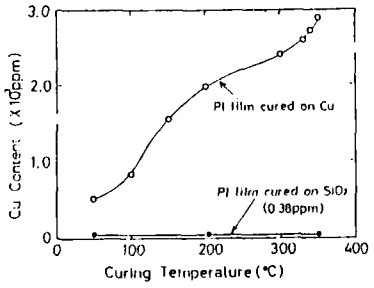


Fig.3 Cu content in polyimide films in curing process

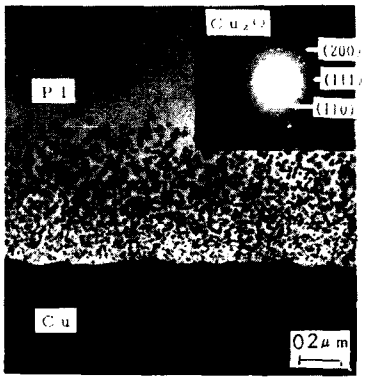


Fig.4 TEM image and electron diffraction pattern of precipitates in PI film cured at 350°C

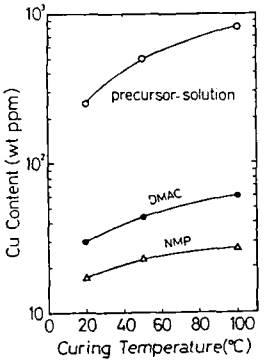


Fig.5 The solubility of copper to precursor solution and solvents

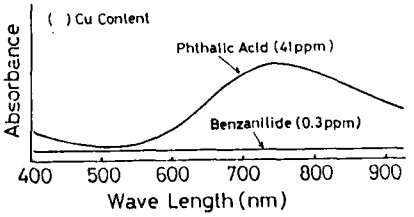


Fig.6 Visible spectra of benzanilide and phthalic acid

Abstract No. 209

Surface Spectroscopic Techniques Applied to Metallized Plastics

N. J. DiNardo

Drexel University
Department of Physics and Atmospheric Science
Philadelphia, PA 19104

The local chemical bonding of metal atoms to functional polymer groups provides a microscopic basis for macroscopic interfacial adhesion in metallized plastics. Applications for metallized plastic interfaces constrain materials properties beyond the desired adhesion characteristics. For example, in microelectronics device technology, insulation of a metal film from the substrate by a polymer layer is a novel direction for advanced processing. Sharp, homogeneous interfaces are desired; stability must be maintained during processing and throughout operation; and the dielectric properties must be compatible with the application.

We discuss several surface spectroscopic and structural techniques as applied to metallized plastics. Spectroscopic measurements of metal-polymer interfaces can provide a means to determine the nature of local bonding interactions. Surface science techniques have undergone significant development over recent years. Optical techniques are being used more extensively, but particle beams (electrons, ions, and atoms) operating in vacuum are the most widely-applied probes. The relatively short mean free paths of particle beams allow surface sensitivity to be maximized. A scientific goal is to extend techniques that are applied to the study of solid surfaces and interfaces to such problems. Equivalence must still be established between standard metallization techniques such as electrochemical deposition and *in-vacuo* processing. Here, we briefly introduce electron spectroscopic techniques and consider their application to study chemical trends in the metallization of a thin polyimide film by example.

Consider the bonding of an organic adsorbate on a clean, well-characterized metal surface and relevant electron spectroscopic techniques to characterize the adsorption process. Core and valence electronic structure can be studied with x-ray (XPS) and ultraviolet photoemission (UPS) spectroscopies, respectively. Core level spectra at an interface can provide information on the elements present, their concentrations, and the bonding interactions by observing energy shifts in particular levels due to electrostatic or chemical effects. Valence photoelectron spectra probe states which may be involved directly in chemical bonding. However their interpretation is often rather complex since energy levels related to substrate, intra-adsorbate, and adsorbate-substrate bonds proliferate throughout this region. Vibration spectra obtained with Electron Energy Loss Spectroscopy (EELS) give discrete features related to local adsorbate vibrational modes, adsorbate-substrate vibrations, and substrate phonons. For an analysis of the surface bonding, clean surface and isolated molecular bands are first considered as well as possible bands of analog gas phase complexes which might exist as reacted species. As in infrared spectroscopy, general comparison of these reference bands with experimental data for the adsorbed species indicates which structural features of the molecule which are retained. A possible interpretation of missing bands is the occurrence of bond scission upon adsorption. Vibrational bands shifted from gas phase values can be related to the bonding interaction and are the most interesting. Selection rules related to the interaction mechanism can be used to understand.

Application of electron spectroscopy techniques to insulating organic films and metallized surfaces present numerous difficulties but also are producing fascinating results. First, electron spectroscopic measurements are performed in high vacuum environments. Assuming sample stability *in-vacuo* and realizing that much of the sample preparation, e.g. spinning on a substrate and curing, is performed outside the vacuum system, a sample transfer stage is required to introduce samples into the spectroscopy chamber. Since samples are irreversibly altered after metal deposition, several samples generally need to be transferred during a spectroscopic study of metal coverage dependence or preparation. The sample holder should contain provisions to mildly heat the samples for further *in-vacuo* curing. The insulating nature of many polymer samples dictate that very thin layers be used to avoid charging; otherwise sample stabilization might be obtained by an electron flood-gun with the disadvantage of possible sample deterioration.

As an example, experiments have been performed to characterize clean and metallized polyimide surfaces and these have produced very encouraging results. Hahn, et al. compared Nickel and Chromium films on polyimide with UPS and XPS [1]; DiNardo, et al. [2] used EELS to compare Palladium and Cr bonding on the polyimide surface. These studies concluded that Ni and Pd are weakly bound while Cr forms a strong bond in the vicinity of the carbonyl group. Information concerning adhesion is derived from the experimental determination of spectroscopic changes between the clean and metallized surface. In addition, theoretical calculations of metal-organic bonding can be compared to experiment.

UPS [1] indicates the formation of metal-metal bonds during film growth as broad metal d-state emission. Polymer valence emission at about 4 eV bonding energy is reduced for Cr films suggesting strong reactivity of Cr with the substrate. However, due to the overlap of many valence features of the polymer chains, the bonding location is not readily deduced. XPS spectra of the C(1s) core levels [1] which can be identified as a function of local environment clearly shows that the carbonyl site is most affected by reaction with a metal and that Cr substantially affects this site. EELS vibrational spectra of clean polyimide films [3,4] have been analyzed by comparison to infrared absorption data, and discrete vibrational bands have been assigned. Deposition of a metal film eventually gives a spectroscopic indication of the formation of a conducting layer [2]. Most significant, however, is the observation that Cr immediately shifts the carbonyl stretching vibration to lower energy [2]. This result indicates retention of the carbon-oxygen bond at low coverage and charge transfer from Cr to antibonding states which reduces the carbonyl stretching frequency. These techniques in combination have provided a rather compete spectroscopic picture of the microscopic bonding interactions of a metal on a polymer surface.

Further studies relevant to adhesion science which has been obtained using both surface spectroscopic and structural techniques will be reviewed, including applications of STM, infrared spectroscopy, RBS, and TEM. Technical issues such as interfacial homogeneity, the use of surface optical techniques and interface microscopy, and obtaining a further understanding the sampling depth are important aspects are currently being addressed. Surface science techniques will continue to increase our understanding of the basic chemical mechanisms for metallization at polymer surfaces as the techniques and experimental analyses are refined for application to such complex interfaces.

I gratefully acknowledge IBM Research, particularly J.E. Demuth and T.C. Clarke, for support of my work on metal-polymer interfaces.

1. P.O. Hahn, G.W. Rubloff, J.W. Bartha, F. Legoues, R. Tromp, and P.S. Ho, in: Electronic Packaging Materials Science, E.A. Geiss, K.-N. Tu, D.R. Uhlmann (Ed.), vol. 40, pp. 251-253. Materials Research Society, Pittsburgh (1985).

2. N.J. DiNardo, J.E. Demuth, and T.C. Clarke, J. Chem. Phys. 85(11), 6739-6749 (1986).

3. N.J. DiNardo, J.E. Demuth, and T.C. Clarke, Chem. Phys. Lett. 121(3), 239-244 (1986).

4. J.J. Pireaux, C. Gregoire, P.A. Thiry, R. Caudano, and T.C. Clarke, J. Vac. Sci. Technol. A 5(4), 598-602 (1986).

Abstract No. 210

APPLICATION OF MÖSSBAUER SPECTROSCOPY TO THE STUDY OF METAL/POLYMER INTERFACES— AN OVERVIEW

Henry Leidheiser, Jr., and Philip D. Deck
Department of Chemistry
and
Zettlemoyer Center for Surface Studies
Lehigh University, Bethlehem, PA 18015

Mössbauer spectroscopy can be utilized to study the interface between a metal and a polymer by the use of emission techniques. The active isotope is concentrated at the surface of the metal, the polymer is applied and the gamma ray emission spectrum is determined. Alternatively, the metal may be formed on the polymer. The gamma ray emission spectrum, since it originates exclusively from the metal/polymer interfacial region, generates chemical information about the interfacial region. The magnitude of the chemical shift gives information about the valence state of the metal atom at the interface; the chemical shift and the quadrupole splitting give information about the nature of the chemical bond between the metal and the polymer. Differences in the spectra obtained at room temperature and at liquid nitrogen temperature allow one to speculate about the nature of metal species that diffuse into the polymer.

Two metals are convenient for studies involving emission Mössbauer spectroscopy, cobalt and tin. Work to be reported will be limited to cobalt. Information will be presented for the following polymeric materials: polybutadiene, polyimide, poly(acrylic acid), polyacrylamide, a thermoplastic acrylic, an aliphatic amine-hardened epoxy, a vinyl ester and a silicon-modified alkyd. Polymers undergoing oxidative cure, such as polybutadiene and the alkyd, caused reduction of Co(III) species at the interface. Polymers with pendant acid functionalities, such as poly(amic acid) and poly(acrylic acid), yielded Co(II) carboxylate species at the interface.

Information will also be presented on the nature of chemical changes that occur as a function of time of exposure to the atmosphere or to an aqueous medium.

Suggestions will be made concerning the application of the technique to studies of metallized polymers.

Abstract No. 211

THE METAL/POLYMER INTERFACE AS STUDIED NONDESTRUCTIVELY -- AN OVERVIEW

Philip D. Deck and Henry Leidheiser, Jr.
Department of Chemistry
and
Zettlemoyer Center for Surface Studies
Lehigh University, Bethlehem, PA 18015

Interfacial chemistry existing between an organic polymer coating and a metal substrate was investigated using internal reflectance Fourier transform infrared spectroscopy (IR-FTIR) and emission Mössbauer spectroscopy. Special sample preparation for both techniques allowed for interfacial probing without interface disruption. The advantages and limitation of each technique will be outlined.

Two coatings, with different curing mechanisms, were investigated through IR-FTIR for their interaction with several metal substrates. The degree of interfacial polymer oxidation of polybutadiene was dependent on the substrate metal. Polyimide, which is the cyclodehydration product of poly(amic acid), gave evidence for the presence of ionized acid groups within the polymer in the interphase region with some metal substrates.

The above two coatings, along with poly(acrylic acid), polyacrylamide, a thermoplastic polyimide, a thermoplastic acrylic, an aliphatic amine-hardened epoxy, a vinyl ester polymer, and a silicone-modified alkyd were studied on cobalt substrates using emission Mössbauer spectroscopy. Coatings undergoing oxidative cure, such as polybutadiene and the alkyd, caused reduction of Co(III) species at the interface. Polymers with pendant acid functionalities, such as poly(amic acid) and poly(acrylic acid), yielded Co(II) carboxylate species at the interface.

Abstract No. 212

A STATIC SIMS STUDY OF METAL-POLYIMIDE INTERFACES

W.J. van Ooij,* R.H.G. Brinkhuis* and J.M. Park**,
*Department of Chemistry and Geochemistry, Colorado School of Mines, Golden, CO 80401
**IBM, Endicott, NY 13687

The interface between evaporated films of Cu or other metals and polyimides have traditionally been studied by XPS [1]. Such studies have demonstrated an attack of the carbonyl oxygen by a reactive metal such as Cr, Al or Ti, and a lack of interaction in the case of copper. Despite such studies, the metal-polyimide adhesion is still not completely understood.

We have applied static SIMS to the study of the interfaces between copper or chromium films and polyimide (PI) of the PMDA-ODA type. In recent publications we have demonstrated that SIMS is a very powerful technique for the characterization of polymer surfaces and of surface modifications [2].

The copper films were of 50 μm thickness, the chromium films were applied as 50 nm interlayers between copper films and polyimide layers spun-coated and cured on silicon wafers. The metal films were peeled off in ambient conditions and immediately analyzed. The Cu-PI interface was also analyzed following heating in vacuum for 2 hours at 300°C. This treatment increased the peel strength of the films markedly.

SIMS analyses were carried out with quadrupole instruments employing either a Ga^+ primary source of 5 keV and 0.5 nA in a 2x2 mm^2 area or a 4.5 keV Xe^+ source of 7 nA/cm^2 current density. Ion beam damage or sputtering effects can be excluded under these strictly static SIMS conditions [2]. For all samples, positive and negative spetra were recorded.

Some of the observations and conclusions from these analyses are the following. These results are summarized in Table I, in which some important peak intensity ratios are plotted.

* the failure is in an organic layer for both metals but the film remaining on the metal side is very thin;

* the PI side of the Cu-PI interface is more PI-like than the PI side of the Cr-PI interface;

* the PI sides of both interfaces form higher yields of aromatic fragments (e.g. 50+51, Table I) than the PI control;

* the organic material remaining on the metal sides of both samples is different from the original PI: it forms a higher yield of CNO^- ions, is less aromatic and less unsaturated;

* the metal sides of the two samples seem to contain metal complexes which are different for the two metals;

* the yields of CNO^- and CN^- ions from the Cr-PI interface are higher than from the Cu-PI interface, suggesting cleavage of the C-C bond between a CNO group and an aromatic ring;

* after annealing the Cu-PI interface spectra have become identical to those of the Cr-PI interface;

* the PI-sides of the interface with both metals contain some Cu or Cr; during annealing more copper diffuses into the polymer.

These qualitative results suggest a chemical modification of the PI by the metals. Cr is more reactive than Cu which requires a post-deposition heating step for the same modification. This modification seems to be directly related to the adhesion of the metal films. The metal seems to react with the imide functionality and rupture of the planar imide structure could result in the formation of more mobile polar groups which then form complexes with the metal. These remain on the metal side of the interface. The spectra of that side, especially in the case of chromium, are consistent with a complex of the type:

$$-O-Cr-OCN-C_6H_4-O-C_6H_4-$$

More detailed studies, e.g. with model systems, are in progress.

1. H. Lefakis and P.S. Ho, Bull. Am. Phys. Soc., 32, 731 (1987).
2. W.J.van Ooij and R.H.G. Brinkhuis, Surf. Interface Anal., in press.

Table I

SIMS intensity ratios in PI, Cu-PI and Cr-PI

ratio:	$\frac{CN^-}{CH^-}$	$\frac{CNO^-}{CH^-}$	$\frac{O^-}{CH^-}$	$\frac{CNO^-}{CN^-}$	$\frac{50+51}{55}$	$\frac{27}{29}$
PI	6.0	0.9	2.5	0.16	1.2	1.15
PI (Cu)	5.1	0.8	2.8	0.16	2.1	1.38
PI (Cr)	14.5	3.2	2.8	0.22	2.8	1.71
PI*(Cu)	13.6	3.1	2.8	0.23	2.7	1.69
Cu	6.0	2.4	2.0	0.40	0.3	0.74
Cr	10.8	4.9	2.4	0.45	0.5	0.94
Cu*	10.4	4.8	2.5	0.41	0.5	0.91

*annealed 2hrs at 300°C

Abstract No. 213

ELECTRON INDUCED VIBRATIONAL SPECTROSCOPY STUDY OF THE INCIPIENT INTERFACE FORMATION BETWEEN EVAPORATED ALUMINUM LAYER AND POLYMER FILMS

J.J. Pireaux, N. Degosserie, Y. Novis, M. Chtaïb and R. Caudano

Facultés Universitaires Notre-Dame de la Paix, Laboratoire Interdisciplinaire de Spectroscopie Electronique, Rue de Bruxelles 61, B-5000 NAMUR (Belgium)

Should a scientist work on the increase of adhesion properties between metal and polymer films, then should he be highly interested in the understanding of the fundamental processes bonding the two layers. These mechanisms are known, for example as an electrostatic interaction, or a true chemical bonding between the layers ; thus they involve a (partial) charge transfer between the metal and one (or more) polymer atom(s). Amongst the experimental techniques used to characterize the interface formation during the polymer metallization, X-ray induced photoelectron spectroscopy (XPS or ESCA) has certainly contributed to the major achievements in this field ; e.g. if the polymer contains oxygen atoms, the metallic atoms do generally interact with the substrate oxygen to form metal-oxygen-polymer complexes (1). However, the analysis of the binding energy shifts of the XPS peaks, especially of the "hydrocarbon type" C1s one around 285 eV, is in some case not straightforward ; hydrogen cannot be detected ; the exact geometrical configuration of the metal-polymer entity cannot be deduced.

Optical (Infrared or Raman) spectroscopies should be capable of answering these questions ; however, they need very special improvements to be sensitive enough to probe an interface that is a few tens of angström thin. Recently, the adaptation of another vibrational technique, namely High Resolution Electron Energy Loss Spectroscopy (or HREELS), has been extremely successful in characterizing polyimide / evaporated chromium, palladium (2) and aluminum (3) interfaces.

HREELS is a UHV spectroscopy using as a probe a low energy electron beam (0 to 10 eV impact energy) that is highly monochromatized (usual resolution on a polymer sample = 10 meV or 80 cm^{-1}). The beam backscattered from the sample surface is analyzed in energy, and presents an ensemble of loss peaks, attributed to the electron excitation of vibrational modes of chemical groups at the extreme polymer surface. The study of the incipient interface formation between aluminum and polyimide at room temperature is particularly rich in information : when the metal is evaporated at very low rate (about 1 Å/min) from a Knudsen effusion cell, its equivalent coverage on the polymer surface can be precisely measured, and different successive "chemical reactions" are distinguished : first, the Al atoms do react with half of the C=O carboxyl in the polymer, to form a C-O-metal complex ; then, other Al atoms do diffuse into the polymer, breaking bonds, leaving new CH and OH species on the surface; finally, the formation of a metal oxide (or carbide) developped on the surface. During the formation of the polymer-metal complex at the very interface, a very large electronic delocalization is evidenced, with a concomitant modification of the geometry of the polymer monomeric unit, after bonding with the aluminum atoms (3).

Polyimide is a very important technological material ; it presents a particularly complex monomeric unit, with many different chemical groups. In order to unravel the relative reactivities of specific chemical functions, it was mandatory to study the aluminization of simpler polymers.

Poly(acrylic acid) or PAA contains both C=O and C-OH functionalities. The HREELS spectrum of a clean PAA film reveals however the OH groups are not available, as they are all involved in hydrogen bondings between different polymeric chains. Therefore, evaporated aluminum atoms are first seen to react close to the carboxyl unit, whose vibrational intensity around 1 700 cm^{-1} rapidly and completely disappears ; surprisingly no band characteristic of either a metal-O-polymer complex or aluminum oxide is detected. At larger Al coverages, a highly structured and broad band appears around 800 cm^{-1}, where the Al-O or Al-C stretches should be seen.

Poly(vinyl alcohol) or PVOH presents on its surface -OH groups to the evaporated Al atoms. Indeed, the ν(OH) band intensity completely disappears as soon as Al atoms are deposited ; at the same time, the ν(C-H) band intensity increases, and a new structure appears around 600 cm^{-1}. After further Al evaporations, a broad feature developped between 600 and 800 cm^{-1}.

Polystyrene is another interesting polymer as it does not contain any heteroatom, but saturated and unsaturated bonds. The aluminization of PS is not detected by any HREELS feature - except a broadening of the elastic peak - before about ten Å layer has been deposited ; then, the aromatic CH stretch bands decreases, with the growing up of a broad band around 800 cm^{-1}. This last feature is still growing after subsequent Al evaporation.

Those observations will be commented in more detail and a model explaining the interaction of aluminum atoms with the different chemical functionalities will be proposed.

References

(1) W.J. VAN OOIJ, in Physicochemical Aspects of Polymer Surfaces, edited by K.L. Mittal (Plenum, New York, 1983) Vol. 2, p. 1035.

(2) N.J. DINARDO, J.E. DEMUTH, T.C. CLARKE, Chem. Phys. Lett. 121, 239 (1985) ; J. Vac. Sci. Technol. A4, 1050 (1986).

(3) J.J. PIREAUX, M. VERMEERSCH, Ch. GREGOIRE, P.A. THIRY, R. CAUDANO, T.C. CLARKE, J. Chem. Phys. 88, 3353 (1988).

Abstract No. 214

XPS AND HREELS STUDY OF THE ALUMINUM / POLY (ETHYLENE TEREPHTHALATE) INTERFACE AND THE INFLUENCE OF POLYMER SURFACE PRETREATMENT.

Y. Novis , M. Chtaïb , J. Vohs , J.J. Pireaux , and R. Caudano,

Facultés Universitaires Notre Dame de la Paix, Laboratoire Interdisciplinaire de Spectroscopie Electronique, rue de Bruxelles , 61, B-5000 NAMUR (BELGIUM).

P. Lutgen , G. Feyder,

Research Department, Du Pont de Nemours (Lux.)s,a. L-2984 CONTERN (Grand-Duchy of LUXEMBOURG).

Interface properties between evaporated metal and polyester films are important technological issues in various fields. Polymer supported magnetic media, metallized plastics for flexible food packaging or capacitors are often faced with the need for adhesion improvement between the deposited layer and its substrate.

The presence of polar functionnalities at the polymer surface and its structure (crystallinity, cross-linking,...) are known to be key parameters which can affect drastically the metal adhesion to polymer.(see e.g. ref. 1 & 2.)

Poly (ethylene terephthalate) - PET - Mylar^{R} films have been superficially modified in different ways in order to change their surface structure and chemical composition.

Creation and/or modification of surface functionalities have been analysed by X-ray Photoelectron Spectroscopy (XPS) from the shape , area and binding energies of C 1s, O 1s and N 1s core level spectra of PET before and after various treatment like Corona, low pressure plasma,U.V. laser and U.V. lamp irradiation in various atmospheres (O_2 , N_2 , air, NH_3.)

These analysis have been correlated with the evolution of the adhesion strength in peel test.

Corona treatment in air , N_2 and NH_3 produces a strong increase in adhesion that can be attributed to both crosslinking of the surface and introduction of polar (C≡N , C=O , C-O...) functionalities. Presence of O_2 in the discharge tends to be a negative factor for adhesion improvement. This is probably due to the appearence of some chain scission effect with O_2, while N_2 and NH_3 produce crosslinking (ref 3.) This is indirectly confirmed by XPS data on these samples after thermal annealing in vacuo. The high temperature stability (up to 200 °C) of Nitrogen functionalities compared to oxygenated groups (around 120 °C) can be interpreted as a sign of a network created by Nitrogen atoms, preventing surface reorganization far above the glass transition temperature of the polymer , while Oxygen produces low molecular weight fragments via chain scission.

Low pressure plasma, U.V. lamp and U.V. laser treatment have been studied in a similar way. They all produce new chemical functions at the polymer surface. However, the superficial structure created in the polymer differs strongly from one treatment to another, giving dramatic changes in metal adherability. An empirical conclusion is that ,if incorporation of polar function can be of interest for improving adhesion of Aluminum to PET, this is surpassed - by far - by the effect of the structural changes (photolytic chain scission, crosslinking, amorphisation...) in the polymer surface.

High Resolution Electron Energy Loss Spectroscopy (HREELS) has recently been implemented (ref 4) to elucidate interaction mechanisms between evaporated metal and PET. Preliminary results with this vibrationnal spectroscopy will be presented. It shows that, on the unmodified PET samples, Aluminum reacts preferentially with Carboxyl groups in the submonolayer coverage regime when evaporated by a Ultra High Vacuum Knudsen cell. Further studies are planned in order to approach the interface formation in the case of modified polymer surfaces.

Acknowledgment: This work is supported by EEC grant N° RI 1B-0178.

References:

1. D.L. Allara, F.M. Fowkes, J. Noolandi, G.W. Rubloff, M.V. Tirell; Mat. Sci. and Eng., 83, 213 (1980).

2. S.L. Vogel and H. Schonborn; Journ. of Polym. Sci.,23, 495 (1979).

3. J. Amouroux, M. Goldman, F. Revoil ; Journ. of Polym. Sci.,Pol. chem. ed., 19 1373 (1982).

4. J.J. Pireaux, N. Degosserie, Y. Novis, M. Chtaïb and R. Caudano; this Symposium.

Abstract No. 215

Interfacial Chemistry of Metal Films on Polymers: Diffusion, Oxidation, Trace Components Studied by XPS, ISS, and SIMS.

Gene R. Sparrow
Larry Homstad

Advanced R & D, Inc.
American Thin Films, Inc.

245 E. 6th St.
St. Paul, MN, 55101

The ultimate appearance and performance of metallized polymers is greatly affected by the thickness and chemistry of the particular thin film. Even subtle changes in deposition conditions can greatly affect this chemistry. Three obvious features of these films include the nature of the outer 5 to 10 Angstroms, the nature of the bulk or major film itself, and especially the chemistry of the interface. Although the chemistry of these three layers can be controlled to some extent by processing, it is nearly impossible to prevent some aspects which are inherent in this chemistry and processing.

One of these is the occurrence of at least some diffusion of metal and polymer at the interface. This not only depends on the original chemistry of the polymer surface, but also on the specific conditions used to prepare the polymer for deposition and the initial deposition conditions. Another natural occurring problems is that of oxidation of the metal at the outer surface and its subsequent contamination by foreign materials.

A third and very difficult problem involves the level of contaminants incorporated into the bulk of the thin metal. For active metals such as Al and Ti this can be very extensive oxidation which is very dependent on the rate of deposition and the nature of the vacuum in sputter or vapor deposition systems. In electrochemical depositions, it can be very dependent on the specific conditions and the amount of water, -OH, and trace components incorporated during depositions.

We have utilized the three extremely sensitive techniques of XPS (X-ray Photoelectron Spectroscopy or ESCA), ISS (Ion Scattering Spectroscopy), and SIMS (Secondary Ion Mass Spectroscopy), to investigate the detailed chemistry of several systems including Al, Ti, and Cu films. ISS has been extremely useful in monitoring the detailed changes ocurring in the outer few Angstroms of the surface as well as at the interface, and ESCA or XPS has been key at monitoring actual changes in bonding chemistry of individual elements, especially C and O throughout the thin film. SIMS has been unique in monitoring the nature of trace contaminants and their changes throughout the entire films as well as providing unusual information concerning variations indicative of changes in the nature of bonding within the bulk metal film itself.

Most of the work presented was accomplished using sputter-coated metals on either polyethylene or polypropylene webs 10 to 20 incheds in width. The majority of this work involved deposition of Al, Ti, or Cu metals. The analysis was conducted using a KRATOS X-SAM 800 combined Scanning Auger Microprobe (SAM) / ESCA (XPS) system. Concentration depth profiles of the various elements detected were obtained by slowly sputtering the surface using a low energy of Ar ions across an area about 20 square mm. The distribution of oxygen and carbon in different forms was also monitored quantitatively using software deconvolution of these peaks obtained using high energy scanning to acquire the data. The distribution of oxygen at the interface was of primary interest. SIMS data were obtained using a KRATOS Model 535 BX combined ISS / SIMS instrument. Trace levels of Na, K, Cl, and other inpurities were monitored by SIMS.

Although most systems were found to be susceptible to heating, which broadened the interface, very thin films of Al were found to be the most severely affected. This was evident by extensive incorporation of oxygen into the entire thickness of the film. Cu was least affected, however, it exhibited the greatest complexity as far as contaminants.

Illustrations obtained from these three analytical techniques will be presented and will include profiles showing the variation of Oxygen from the surface to the interface, the effects of heating and other processing variations on the nature of the interfacial boundary, and where various trace contaminants tend to segrate due to processing.

Abstract No. 216

The Application of Rutherford Backscattering to the Characterization of Metallized Plastics

Michael D. Strathman
Charles Evans & Associates
301 Chesapeake Dr.
Redwood City, CA 94063

Rutherford Backscattering Spectrometry (RBS) is one of several MeV-Ion techniques currently being used for the characterization of thin film systems. This paper will discuss the application of this rapid analytical technique to the analysis of thin metal film systems which have been deposited on plastic substrates. Several important techniques which can be used to minimize ion beam modification of the materials system during the analytical procedure will also be presented. Some of the systems which will be examined include quantitative determination of the stoichiometry of optical films, investigation of adhesion problems of metallic thin films on plastic, and the determination of the hydrogen content of these metallic layers.

Abstract No. 217

METAL INTERLAYERS IN POLYMER FILMS: A SURVEY OF DEPOSITION PROCESSES, MORPHOLOGY, ELECTRICAL PROPERTIES, AND PATTERNING METHODS

S. Mazur, L. E. Manring, M. Levy,
G. T. Dee, and S. Reich

Central Research and Development Department
E. I. du Pont de Nemours & Company, Inc.
Experimental Station
Wilmington, Delaware 19898

Metal interlayer deposition comprises a family of processes(1-3) for growing a thin, electrically conductive metal film within the bulk of a preformed polymer film. The metal is formed by in situ reduction of a metal salt which is allowed to diffuse into the polymer film from one surface while the reducing agent simultaneously diffuses from the opposing surface.

Three different variants of this process have been explored. In an electroless version(1), the polymer film is employed as a free-standing membrane separating two reagent solutions. The electrochemical versions employ a film supported on the surface of an inert cathode immersed in an electrolyte solution containing the metal ions. Electrons from the cathode are transported to the reaction zone either by redox-exchange reactions of the polymer itself (polymer mediated electrodeposition(2)), or else by means of an independent organic redox reagent dissolved in the electrolyte (electron carrier mediated electrodeposition(3)). In all cases, it is neccessary that the polymer be swollen by the solution in order that a significant flux of reagents is maintained.

Depositions have been carried out in both amorphous and semicrystalline polymers including cellulose, aromatic polyimides, PVC, PVF and PVF_2. Metals have included Ag, Au, Cu, Hg, and Pb. In all cases the metal precipitates in the form of microparticles with diameters generally less than 100 nm (often in the range of 15 nm). The local volume fraction of metal achieveable can vary considerably with the process conditions, and can be as high as 0.72. The location(1-3) and distribution(4) of particles within the interlayer is governed by the reagent transport parameters, reaction rate constants, and experimentally regulated parameters (film thickness, concentrations, and applied potential). A theoretical model was developed(4) which successfully accounts for virtually all morphological detail on length scales greater than 100 nm.

Electrical properties were studied for Au and Ag interlayers in the polyimide derived from pyromellitic dianhydride (PMDA) and 4,4'-oxydianiline (ODA). The as-deposited interlayers have bulk conductivities approximately 500 times lower than that of the equivalent bulk metal. However, it was discovered(5) that annealing at temperatures between 200 and 350 °C results in a dramatic increase in conductivity (close to bulk metal) without detectable decomposition of the polymer. The evidence indicates that this behavior results from a partial sintering of the microparticles.

Patterned and contoured interlayers may be created by a number of different strategies. Patternwise regulation of reagent concentrations at the film surfaces can be achieved using patterned cathodes(2,4) or photo-conductive cathodes(6). These approaches result in systematic curvature at the edges of the metallized pattern. Alternatively, the bulk permeability of the film itself can be controlled(7) to create two-dimensional patterns, for example, by the use of a photopolymerized network. This approach avoids curvature and is capable of creating high aspect ratio conductive traces 10 microns in width (ca. 2 microns thick in 25 micron thick film).

References

1. L.E. Manring, Polym. Commun., 1987, 28, 68.
2. S. Mazur and S. Reich, J. Phys. Chem., 1986, 90, 1365.
3. M. Levy, L.E. Manring, & S. Mazur, J. Electrochem. Soc., in press.
4. G.T. Dee, L.E. Manring, S. Mazur, J. Phys. Chem., 1987, 91, 6699.
5. S. Reich, S. Mazur, P. Avakian, & F.C. Wilson, J. Appl. Phys., 1987, 62, 287.
6. H.C. Hadley & S. Mazur, U.S. Patent #4,457,833.
7. L.E. Manring, unpublished results.

Abstract No. 218

SURFACE MODIFICATION OF CONDENSATION POLYIMIDES WITH COPPER COMPLEXES

G. M. Porta, J. D. Rancourt and L. T. Taylor

Virginia Polytechnic Institute and State University

Department of Chemistry
Blacksburg, VA 24061-0212

Aromatic condensation polyimides are useful for aerospace, electronic and specialty consumer markets because of their excellent chemical and thermal stability and favorable mechanical properties [1]. Although in some applications the extremely high electrical resistivity is a beneficial attribute ($\sim 1 \times 10^{18}$ ohm cm at 0% R. H. and 25°C), in other applications this high resistivity is a detriment because it allows substantial levels of static charge to accumulate. And, of course, there is great utility in rendering selective portions of insulative materials conductive or semiconductive as is done in the fabrication of circuit boards and electronic devices.

In an effort to reduce the surface electrical resistivity of polyimides while maintaining the other useful engineering properties, polyimides have been modified with a variety of metal salts and metal complexes. During thermal imidization of the poly(amide acid) the dopant migrates to the surface of the film and is converted to either metal or metal oxide. This methodology has been shown, in previous work, to be capable of producing oxides of cobalt, copper and lithium and, palladium, silver, copper and gold metal surface layers, for example.

Recently, the physical structure and electrical properties of the surface region of these films were modeled [2]. This model allows one to predict the surface conductivity that will be attained for a given type, thickness and position of a conductive layer. It had been shown that the process thermal conditions required to convert the poly(amide acid) to the polyimide, in conjunction with controlled cure atmospheres, result in a wide range of surface electrical properties for a particular dopant in a given film. For example, the surface resistivity of polyimide films modified with cobalt chloride was varied over three orders of magnitude simply by altering the cure atmosphere. It was considered likely that other process variables may similarly influence the final properties of the films. An experimental strategy that allows economical screening of a variety of variables was adopted and implemented.

Polyimide films were obtained by reacting equimolar amounts of 1,3-bis(3-aminophenoxy)benzene (APB, National Starch and Chemical Co., Bridgewater, NJ) with 3,4,3',4'-benzophenonetetracarboxylicdianhydride (BTDA, Allco Chemical Corp., Dallas, TX) in N,N-dimethylacetamide (DMAc, HPLC Grade, Aldrich Chemical Co. Milwaukee, WI). Solutions were prepared at 15-20 wt% solids concentration at room temperature under a dynamic nitrogen atmosphere. The solutions were modified with bis(trifluoroacetylacetonato)copper(II), $Cu(TFA)_2$ and, after the solution was homogenous, were cast on soda-lime glass plates or onto fully cured polyimide films with a doctor blade to a thickness of 0.019". The films were subsequently cured to 80°, 100°, 200° and 300°C. The actual process variables used to produce films are listed below.

VARIABLE	LOW VALUE	HIGH VALUE
Dopant Level	6 mole %	20 mole %
Curing Atmosphere	Dry Air	Moist Air
Casting Substrate	Polyimide	Glass
Time at 80°C	20 min.	120 min.
Max. Cure Temp.	200°C	300°C
Time at T_{max}	20 min	120 min.

The fractional factorial strategy employed allows the effect of each of the variables to be assessed within 12 experimental runs. The variable settings for each run were determined using a 12-run Plackett-Burman design. The techniques used to characterize these films have been described elsewhere [2].

In general, good quality films were produced regardless of the combination of process conditions employed. There were, however, vast differences in the amount of material that was deposited on the air-side of the film. Within the sampling depth of X-ray photoelectron spectroscopy from 1.0 to 29.0 atomic percent copper was detected. The higher levels of copper were attained when the higher conversion temperature and/or the higher dopant level were used. The surface atomic composition of the films, determined by XPS, indicates the presence of fluorine, which is a measure of the amount of copper that is not present as either copper metal or copper oxide. The most fluorine was retained when the dopant level was high, the time at T_{max} was short, the B-stage was long (i.e. time at 80°C), and the film was cured in dry air.

The fluorine that is present on the surface of the films appears in two chemical states. One form is copper fluoride while the other is residual dopant, $Cu(TFA)_2$. The films are being evaluated by other techniques to more completely characterize this polymer/dopant system. Details pertaining to the evaluation and understanding of these materials will be presented.

Acknowledgements

The authors gratefully acknowledge the financial support from the National Aeronautics and Space Administration, Langley Research Center. The microscopy evaluations performed by M. L. Porta are also appreciated.

References

1. K. L. Mittal, ed., Polyimides: Synthesis, Characterization and Applications, Vol. 2, Plenum Press, NY (1984).

2. J. D. Rancourt, R. K. Boggess, L. S. Horning and L. T. Taylor, J. Electrochem. Soc., 134, 85 (1987).

Abstract No. 219

Various Stress Measurement Techniques for Thin Metal Films on Plastics*

Norman L. Thomas

Lawrence Livermore National Laboratory

P.O. Box 808, Livermore, California 94550

Thin film stress can play an important part in the fabrication of thin metal films on plastic substrates, and can cause unwanted deformations and failure. The stress parameter has been shown to be adjustable by varying the deposition parameters during thermal evaporation or sputtering. For example, ion assisted reactive evaporation is a deposition technique which has been shown to be useful in controlling stress, in addition to other thin film parameters. The successful application of these techniques requires that the stress be monitored, in situ, during a coating run, or, by means of a piggy-backed stress monitor disk whose curvature is measured after the coating run.

Several stress measurement techniques will be described, including:

1. X-ray diffraction
2. Raman shift
3. Resonance membrane
4. Cantilever beam
5. Laser scanning
6. Geometrical optical
7. Moire fringes
8. Optical interference

Thin film stress is caused by lattice strain caused by the manner in which the film condenses, and by differential thermal contraction of the film and substrate during cooling. These stress contributions are known as the intrinsic and thermal parts.

The x-ray diffraction and Raman techniques are used to determine the lattice, strain, directly. The other techniques measure the bending of a disk or rectangular beam by optical methods.

Some data will be presented on thin film stress versus deposition parameters in order to illustrate how one can control thin film stress by adjusting those parameters.

*Work performed under the auspices of the U.S. Department of Energy by Lawrence Livermore National Laboratory under contract #W-7405-Eng-48.

Abstract No. 220

DEPENDENCE OF STRESS ON DEPOSITION CONDITIONS FOR SPUTTERED COPPER FILMS ON FLEXIBLE POLYIMIDE SUBSTRATES

A. Entenberg, V. Lindberg, L. Fendrock, Sang-ki Hong; Department of Physics and Center for Materials Science and Engineering, Rochester Institute of Technology, Rochester, New York, 14623;

R. S. Horwath Systems Technology Division, IBM Corporation, Endicott, New York 13760.

We have investigated the dependence of internal stress on argon pressure[1] and deposition rate for 0.25 μm copper films sputtered onto a 1-mil (25 μm) - thick polyimide substrate, A dc planar magnetron was used to deposit the copper onto a flexible substrate (Kapton) which was held flat by top and bottom edges. We observed two types of stress: tension, in which the film is trying to contract on the substrate and compression, in which the film is trying to expand on the substrate. The stress is primarily of an "intrinsic" nature, relating to the interfacial mismatch between the natural atomic structures of the growing film and the substrate surface. Using a formula due to Stoney, stress was estimated directly from the resulting radius of curvature of the relaxed film and substrate. At a fixed deposition rate of 2.0 A/s, there is a stress transition from compression to tension at a pressure of about 2.5 mTorr. At a fixed pressure of 5.0 mTorr, there is a stress transition from tension to compression at a deposition rate of about 4.8 A/s. Scanning electron micrographs (SEM) show columnar grains with a void network for films under tension and smooth, tightly packed surfaces for films under compression. The origin of the tensile morphology is a "shadowing" mechanism operative at higher argon pressures; at lower pressures, an "atomic peening" mechanism is responsible for the compressive morphology.[2] The morphology data are consistent with the Movchan-Demchishin zone model diagram as extended by Thornton for the growth of sputtered films.[3] Film resistivity and reflectivity were closest to their bulk values for compressive films deposited at low argon pressure and high deposition rate. At a deposition rate of 2 A/s, the critical pressures at which resistivity starts to rise and reflectance begins to decrease are very close to the aforementioned stress transition pressure.[1] In general, the data are consistent with the dependencies of physical properties on pressure and deposition rate observed for other metals. We are currently examining the effects of film thickness and residual gas pressure on stress. The ultimate goal of this research is to correlate stress with the adhesion between film and substrate.

1. A. Entenberg, V. Lindberg, K. Fletcher, A. Gatesman, R. S. Horwath, J. Vac. Sci. Technol. A 5, 3373 (1987).

2. D. W. Hoffman and J. A. Thornton, Thin Solid Films 40, 355 (1977).

3. J. A. Thornton, in Deposition Technologies for Films and Coatings, edited by R. F. Bunshah (Noyes, Park Ridge, NJ, 1982), pp. 211-219.

Abstract No. 221

ADHESION OF CHROMIUM, NICKEL, AND COPPER TO POLYMERS CONTAINING BASIC FUNCTIONAL GROUPS

Stephen R. Cain
Luis J. Matienzo
Francis Emmi

IBM Systems Technology Division
1701 North Street
Endicott, NY 13760

Adhesion of metals to polymers depends on the chemical, mechanical, and electrostatic nature of the interface, as well as diffusion phenomena [1]. In this paper, attention has been focused on the chemical component of adhesion, which is governed to a large extent by acid-base interactions.

Surface acidity of a variety of metal oxides have been characterized by their isoelectric points [2], but this approach has been limited to aqueous media, where the Bronsted-Lowry concept of acids is applicable. In devising a theory which is applicable to non-aqueous systems, e.g. vacuum deposition, the more general Lewis definitions should be used. Interactions of electron pairs (Lewis acid-base chemistry) is readily addressed by molecular orbital calculations.

From a quantum chemical perspective, acidity is determined by two factors: 1) the number of empty orbitals which can interact with a base, and 2) the energy of the empty orbitals. The first factor is somewhat intuitive: the larger the number of empty orbitals available to accept electron lone pairs, the greater the probability of bonding to a base. The second factor is derived from application of perturbation theory to acid-base systems. Species (atomic or molecular) are acidic if their empty orbitals are low in energy. These criteria are readily determined for a large surface by performing band calculations. From such calculations, the Fermi level (energy of the highest occupied molecular orbital) and the Density of States (number of orbitals in the energy range E to E+dE) can be obtained. For a solid to be strongly acidic, the Fermi level, ε, must occur at low energy (criterion 2), and the Density of States, DOS, immediately above ε must be large (criterion 1).

Surface acidity of chromium, nickel, and copper and their oxides was investigated by performing extended Huckel type band calculations on these materials. Special attention was given to the position of ε, as well as the DOS immediately above ε. Interactions with basic functional groups encountered in polymers were investigated explicitly by studying the adsorption chemistry of ammonia, a model base, on these metal (metal oxide) surfaces. Substrate-ammonia bonding was analyzed in terms of the adsorption energy and the metal-ammonia overlap population. (Overlap populations are a measure of the degree of bond formation between two atoms. Essentially, overlap populations are refined bond orders.)

As an example of the analyses employed, consider the DOS plots shown in Figure 1, along with the position of ε. For chromium and nickel, ε occurs in the prominent 3D band, where the DOS is high. Thus, there are many empty orbitals with which a base can interact. On the other hand, the DOS for copper is small in the immediate vicinity of ε. Further, ε of copper is at higher energy than ε of either chromium or nickel. Acidity of the metals should follow the trend,

$$Cr > Ni > Cu$$

A similar trend holds for the metal oxides.

In addition, the calculations indicated that nickel and chromium oxides are much more acidic (in the Lewis sense) than the clean metals, owing to the decrease in metal orbital energy with increased oxidation state. On the other hand, a clean surface of copper was found to be about as acidic as the oxide, a result of balance between increased oxidation state and decreased DOS of unoccupied bands. Acidity for all the systems studied follows the trend,

$$Cr_2O_3 > NiO > Cr > Ni > Cu_2O \approx Cu$$

The chemical component of adhesion is expected to follow the same trend, where the polymer of interest contains basic functionalities (e.g. amino groups).

REFEPENCES

1. K.L. Mittal; Polymer Eng. Sci.; 17 (1977); p. 467.

2. J.C. Bolger; in "Adhesion Aspects of Polymer Coatings"; vol. 1, K.L. Mittal, ed., Plenum Press, New York (1983); p. 3.

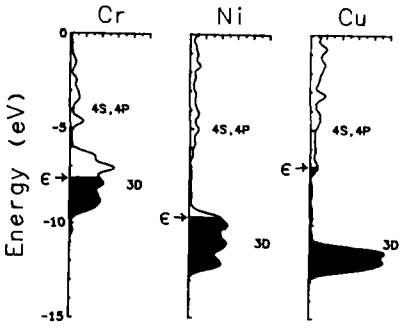


Figure 1: DOS of Cr, Ni, and Cu. Shaded areas indicate filled bands. Fermi levels are indicated on the energy axes.

Abstract No. 222

THEORETICAL STUDY OF THE CHEMISTRY AT PMMA - METAL INTERFACES

Arup K. Chakraborty, Mathew Tirrell, H. Ted Davis
Department of Chemical Engineering and Materials Science
University of Minnesota
Minneapolis, MN 55455.

Polymer - metal interfaces are an integral part of several processes and devices that are important to the microelectronics, aerospace, and other industries. The adhesion of macromolecules to metallic surfaces and the metallization of plastics are just two examples of specific applications wherein an understanding of metal - polymer interfaces is required. Due to the technological import of such interfaces, they have been the subject of a fair amount of research in recent years [e.g. 1, 2, 3, 4]. However, a fundamental understanding of the role of molecular forces in determining the strength of the interfacial bonds formed has not yet evolved. In this work we examine how polymeric molecules bearing reactive functional groups interact with metal atoms and surfaces. The problem has been approached from a theoretical viewpoint. In particular, quantum mechanical theoretical tools such as molecular orbital theory (MOT) and density functional theory (DFT) have been applied towards studying how the electronic properties of the polymer and the metal affect the strength of the interfacial bonds and the morphology of the interface.

The specific polymer that has been chosen for study is polymethyl methacrylate (PMMA); however, the results are easily extended to other non - aromatic polymers bearing carbonyl (C=O) functional groups. The interactions of PMMA with two metals, Al and Cr, have been studied. The studies of PMMA - Al interactions are more extensive in scope.

A polymer - metal interface may be constructed in two different ways. On one hand, the interface may be prepared by spin coating a polymer on to a metal surface that has been suitably protected from contamination. On the other hand, the interface could also be prepared by evaporating or sputtering the metal on to a polymer surface. It is important to note that the evolution of the interface, and the interactions that occur in the two cases are different even in principle. In the case wherein the polymer is spin coated on to a metal surface, the polymer molecules interact with the delocalized electronic state inherent to a metal surface. In contrast, when the metal atoms are evaporated on to a polymer surface the reactive functional groups of the polymer molecules initially interact with individual metal atoms or clusters of atoms. Thus, they interact with the localized electronic states (or orbitals) characteristic of the metal atoms. In this work both these related but dissimilar scenarios are examined. The interactions of metal atoms and clusters with model compounds of PMMA have been studied via both semi - empirical molecular orbital calculations (using the MNDO Hamiltonian) and *ab initio* molecular orbital calculations using gaussian basis sets. The results of these calculations have also been interpreted within the framework of perturbation molecular orbital theory. The interactions of model compounds for PMMA with metallic surfaces have been studied within the framework of DFT wherein the delocalized metallic surface is represented as a jellium.

The model compound for PMMA that we have chosen to study is $C_5H_{10}O_2$. This molecule incorporates carbonyl and methoxy groups which are the potentially reactive functional groups in the PMMA monomer unit. Molecular orbital calculations for the interactions of Al with this model compound show that metal atoms interact primarily with the carbonyl group. The methoxy group does not interact with the metal in any significant manner. This result has been rationalized based on the molecular orbital manifold, and frontier molecular orbital theory. Our results also show that at least two Al atoms are required to interact with the carbonyl functional group. This is consistent with the fact that Al being a Group III metal prefers to form multinuclear organometallic complexes. The formation of an "Al - carbide - oxide" species is predicted by the molecular orbital calculations. This is consistent with the experimental XPS studies of DeKoven and Hagans [5] who have studied the interactions of sputter deposited Al with polyacrylic acid, PAA (a non-aromatic polymer bearing carbonyl groups). The changes in spectral features observed by these workers upon the interaction of Al with PAA can also be rationalized based on our molecular orbital calculations. The multinuclear nature of the interaction has important implications for the reactions of a polymer molecule with Al atoms. Multinuclear interactions necessitate that the carbonyl group orient itself in specific configurations with respect to at least two Al atoms. Interesting future experiments exploring this aspect of the interaction are suggested. Theoretically, this issue has been briefly explored by examining the interactions of dimers of the model compound with Al atoms. The multinuclear nature of the interactions of Al with carbonyl bearing polymers also serves to rationalize the experimentally observed clustering of reacted metal atoms observed by Weaver et al. [6] and Bartha et al. [7] for the reactions of Al with polyimides.

The interactions of the model compound for PMMA with a metal surface have been studied in this work by representing the surface as a jellium. A jelium model considers the surface to consist of a uniform background of positive charge that just neutralizes the electronic charge. A linear response analysis within the framework of DFT that owes its origins to the work of Smith et al. [8] is presented. The results of these calculations when compared to the molecular orbital calculations clearly show the role of the continuum of eigenstates embodied by a metal surface in determining the strength of the adhesive bond.

In addition to the results of investigations of Al - PMMA interactions outlined above, our preliminary theoretical results studying the reactions of a transition metal (Cr) with the PMMA model compound are also presented. Important differences that have been observed compared to Al are discussed and related to ongoing XPS investigations in this laboratory [9].

1) N.J. Chou, D.W. Dong, J. Kim, A.C. Liu, J. Electrochem. Soc. 131, 2335 (1984).
2) F.S. Ohuchi, S.C. Freilich, J. Vac. Sci. Tech., A 4 (3), 1039 (1986).
3) P.N. Sanda, J.W. Bartha, J.G. Clabes, J.L. Jordan, C. Feger, B.D. Silberman, P.S. Ho, J. Vac. Sci. Tech., A4 (3), 1035 (1986).
4) A.R. Rossi, P.N. Sanda, B.D. Silberman, P.S. Ho, Organometallics, 6, 580 (1987).
5) B.M. DeKoven, P.L. Hagans, App. Surf. Sci., 27, 199 (1986).
6) Lj. Atanasoka, S.G. Anderson, H.M. Meyer III, Z. Lin, J.H. Weaver, J. Vac. Sci. Tech., A5 (6), 3325 (1987).
7) J.W. Bartha, P.O. Hahn, F. LeGoues, P.S. Ho, J. Vac. Sci. Tech., A3 (3), 1390 (1985).
8) J.R. Smith, S.C. Ying, W. Kohn, Phys. Rev. B, 11, 1483 (1975).
9) B. Thakkar, R. Tannenbaum, M. Tirrell, to be submitted, Langmuir (1988).

Abstract No. 223

SPECTROSCOPIC STUDY OF THE CHEMISTRY AT THE PMMA-METAL INTERFACE

Rina Tannenbaum, Bimal Thakkar and Matthew Tirrell

Department of Chemical Engineering and Materials Science
421 Washington Ave. S.E.
University of Minnesota,
Minneapolis, Minnesota 55455

The adhesive interface between insulating polymers and metals is useful in a wide variety of areas such as microelectronic devices, flexible connects and solar cells. A comprehensive understanding of the relationship between chemical bonding and the adhesion phenomenon at metal-polymer interfaces is of fundamental interest in surface science. The details of the physical interactions and solid state chemical reactions between polymer surface atoms and metal surface or near surface atoms may be correlated to the macroscopic properties of the system.

A variety of interesting studies of metal-polymer surface interactions and adhesion have been reported in the past few years. Most of the work is concerned with the surface interactions of polyimide (PI) with a variety of metals in a high vacuum environment. In all these cases, the surface atoms of the molecule encounter highly pure metal atoms, and hence the interactions depicted in these systems may be attributed uniquely to the metal-polymer interface.

Unfortunately, high vacuum techniques can only rarely mimic "real" interfaces, and the fundamental information gained from such systems may not be relevant to metal-polymer interfaces found in various devices which operate at ambient conditions. In this paper, we concern ourselves with metal-polymer interactions in systems where the metal surfaces have been exposed to the environmental atmosphere and hence these surfaces are not "clean", but contain a mixture of the metal, metal oxide and metal hydroxides. As a result, the polymer surface comes in contact with a variety of metal compounds and the subsequent reactions may be quite different than those found in the high vacuum-generated interfaces.

The polymer chosen for this study was PMMA, because its C=O and C-O groups would be the primary site of interaction with the metal surface, and moreover, PMMA generates much interest in electronics due to its photoresist properties. Therefore, understanding its chemistry on a metal surface would be important from both fundamental and practical points of view. The metals used in this first study were the first row (3d) transition metals Cr and Ni.

The metal surfaces were obtained by electron beam evaporation on a substrate, and subsequently analyzed by electron diffraction to determine the presence of the various oxide species formed on the surface. The PMMA layer was deposited by spin-coating over the metal surface and the film thickness was determined by ellipsometry. Finally, the resulting interfaces were examined by means of XPS (X-ray photoelectron spectroscopy). Based on these measurements, possible reactions at the PMMA-metal interface may be identified.

The detailed analysis of the metal films reveals the presence of three main species on the Cr surface: Cr^0, $Cr_2^{III}O_3$ and $Cr^{III}O(OH)$. Similar compounds are formed on the Ni surface as well.

Since the systems studied here are very complex, very rigid rules had to be set for the interpretation of the XPS data. As a first step, the XPS spectra of a 230Å PMMA film (considered for this study as bulk PMMA) deposited on a Si substrate are shown in *Figure 1(a,b)*. The C (1s) core level photoemission spectrum of PMMA (*Figure 1a*) was fitted into 3 main peaks and the O (1s) core level photoemission spectra of the same PMMA film (*Figure 1b*) was fitted into two main peaks. Special attention should be focused on some of the peak parameters, i.e. the binding energy, the % gaussian and the full width at half of the peak's maximum (FWHM). Since the spectra of the bulk PMMA will be used as a reference in the consequent analysis of the PMMA-metal interfaces, it is critical to fix the position of the peaks, the % gaussian and the FWHM within very narrow limits. The second step in the proceedure is applying the restrictions described above also for the O (1s) core level photoemission spectra of the metal/metal oxide film which were already analyzed. The third step in the analysis of the PMMA-metal interfaces is the use of the C (1s) and O (1s) core level spectra, obtained from the metal oxide surfaces and bulk PMMA, as baseline. Therefore, the carbon region spectra of the PMMA-metal interface should be fitted with at least three peaks (all originating from the polymer), while the oxygen region spectra of the interface should be fitted with at least five peaks (three from the metal surface and two from the polymer). At this point it becomes clear why this type of analysis cannot work without such rigid requirements. A small shift in the peak position, % gaussian or FWHM in only one of the peaks may cause the superposition of two adjacent peaks, thus resulting in critical loss of information and a distortion of the experimental data.

Figure 2(a,b) shows the C (1s) core level photoemission spectra of a 40Å PMMA film deposited on a Cr/Cr oxide surface *(2a)* and on a Ni/Ni oxide surface *(2b)*. The assignment of the peaks has been performed after taking into account the correction due to surface charging. After fixing the three peaks originating from the polymer, a new peak had to be added in order to deconvolute the spectrum to a reasonable degree of satisfaction. This new peak, in both systems, is positioned at a higher binding energy than that of a the carbon-oxygen single bond. In addition, the relative decrease in the intensity of the C-O bond compared to the C=O bond, effect which is seen in both the chromium and the nickel systems, suggests that the reaction between the metal oxide and the polymer takes place primarily at the H_3C-O bond.

In order to understand the breakage of the H_3C-O bond it is important to examine the changes that occur on the metal oxide surfaces upon addition of the polymer. The ratio between the oxide and oxyhydroxide species increases upon deposition of PMMA on the metal oxide surface. This change indicates that the oxyhydroxide compound may have reacted with the carbon-oxygen single bond in a manner which resulted in the breakage of that bond. Theoretically, since the thickness of the polymer layer (40Å) is smaller than its radius of gyration (~100 Å), every H_3C-O bond along the polymer chain may come in contact with the metal surface and undergo this type of reduction of the carbon-oxygen bond.

The intent of the work presented in this paper in not merely to state experimental results which pertain to interactions in a metal-polymer system, but also to introduce the notion of "real life" interfaces and the high degree of complexity associated with such systems. Moreover, we have attempted to show that it is possible to study interfaces of this type, if one has the ability to characterize both the bare surfaces and the resulting interfaces by adhering to a very restrictive set of self-imposed rules, whose purpose is to minimize the analytical error margin. The results which we have obtained show that a limited reaction takes place between the Cr/Cr oxide and the Ni/Ni oxide surfaces and the PMMA at the interface, and as a result a complex is formed together with other changes in the metal and polymer films. Additional support for these results shall be obtained via UPS and FTIR experiments.

References

1. P. S. Ho, P. O. Hahn, J. W. Bartha G. W. Rubloff, F. K LeGoues and B. D. Silverman, *J. Vac. Sci. Technol.* **A 3(3)**, 739-745 (1985).
2. J. L. Jordan, C. A. Kovac, J. F. Morar and R. A. Pollak, *Phys. Rev. B, Condensed Matter*, **36**, 1369-1377 (1987).
3. Lj. Atanasoska, S. G. Anderson, H. M. Meyer III, Zhangda Lin and J. H. Weaver, *J.Vac. Sci. Technol.* **A5(6)**, 3325-3333 (1987).
4. B. M. DeKoven and P. L. Hagans, *J. Appl. Surface Sci.* **27**, 199 (1986).
5. J. M. Burkstrand, *J. Appl. Phys.* **52(7)**, 4795 (1981).

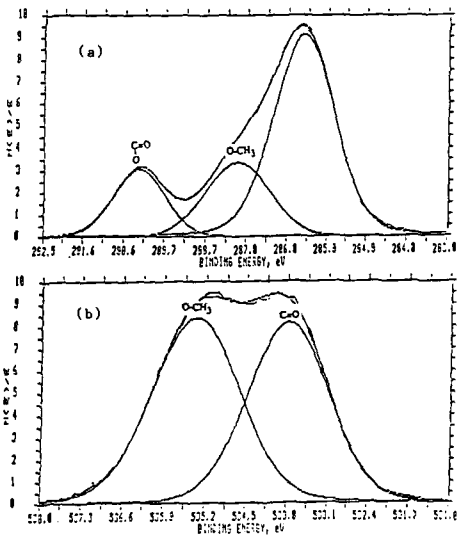


Figure 1 The photoemission spectra of a 230Å PMMA film. (a)C(1s) core level electrons and (b) O(1s) core level electrons.

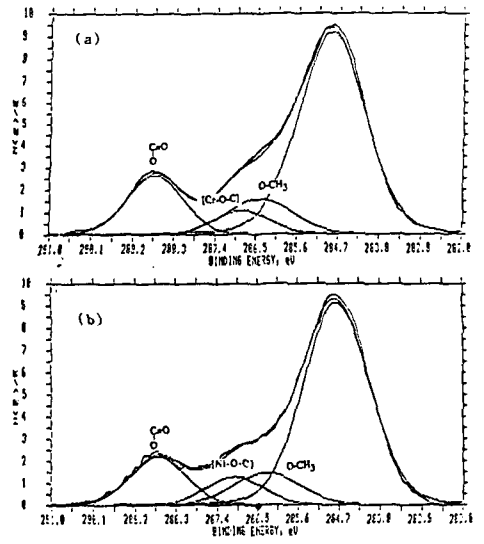


Figure 2 The C(1s) core level photoemission spectra of a 40Å PMMA film. (a) on a Cr/Cr oxide surface and (b) on a Ni/Ni oxide surface.

Abstract No. 224

Plasma Surface Treatment of Plastics: An Overview

Peter W. Rose
Plasma Science, Inc
272 Harbor Blvd,
Belmont, CA 94002

Adhesion of coatings on plastics is a re-occurring and difficult problem to solve satisfactory. Materials originally selected for chemical resistance or low cost are being used in applications where metallization, decorative coating, structural adhesive bonding, encapsulation, environmental potting, or permanent marking is essential. Historically, incompatibilities have been overcome by the use of chemical etchants, solvents, mechanical abrasion, and in some cases with corona treatment. All of these approaches have inherent disadvantages in the costs of storing, handling, and disposal. Traditional treatment techniques are often lacking in the level and reproducibility of the results.

A proven, yet relatively unknown technology is quickly becoming recognized as a efficient, economic, versatile, and effective solution to adhesion problems- cold gas plasma surface treatment which capitalizes on the unique and reactive properties of ionized gases at low pressures. Plasma is effective over a wide range of materials, from olefins, to elastomers; engineering thermoplastics to fluorocarbons. Typically, the adhesion is increased many fold, often resulting in cohesive bond failures.

In metallization processes, plasma is used first for removing contamination and mold releases; then to roughen the surface on a microscopic scale, providing a favorable topography for mechanical adhesion; and finally for altering the surface chemistry thus promoting wetting and enhancing chemical interaction between substrate and coating. The excellent adhesion characteristics that plasma affords sometimes allows the elimination of primers and tie-layer coating steps. Plasma is beneficial for evaporative, sputtered, arc-sprayed and electrodeless deposited coatings.

A common analogy considers plasma to be a fourth state of matter. As in the transition of matter from solid to liquid, and liquid to gas, additional energy into the gas will ionize it, creating a plasma. In commercial plasma systems energy is supplied by rf (radio frequency) power. As in any phase transformation, a pressure/temperature relationship exists for the formation of a plasma. At high pressures a great deal of energy is required to strike a plasma and so the thermal characteristics are very hot. High pressure plasmas are used for fission experimentation for this reason. At atmospheric pressures the plasma contains properties of hot plasmas and of cold plasmas, which occur at vacuum pressures. Examples of atmospheric "mixed plasmas" are lightning, corona, and plasma-arc spray coating processes- processes characterized by an arc discharge where regions of high ionization act at low resistance current paths.

At reduced pressures a uniform glow discharge is created as excited species in the ionized gas cloud combine and return to ground state. The spectrum (color) of the glow discharge is characteristic of the gas chemistry. Environmentally, a plasma is uniquely active. Ionized gases form a multitude of species which are chemically active and kinetically energetic enough to break bonds on the surface of plastics. The low pressure assures that the bulk temperatures of the plasma remains at or near room temperature, thus thermally delicate materials can be safely treated.

Cold plasmas contain positive and negative ions, electrons, free radicals, metastables and high energy UV radiation. Any organic material exposed to this environment will have a significant density of free radicals formed on their surface. These sites are then available for reaction with the gas resulting in a chemical modification of the surface. The types of groups added to the surface are well controlled by the gas chemistry selected and by the processing conditions. From example, an oxygen plasma will put hydroxyls, carbonyls, esters, ethers etc. on the surface, producing a very hydrophilic surface much greater than 73 dynes/cm with extremely low contact angles. Conversely, tetrafluoromethane (Freon 14) plasmas will provide highly fluorinated surfaces with surface energies less than 26 dynes/cm and contact angles in excess of 110°. Other gas chemistries commonly used include ammonia, nitrous oxide, air, nitrogen, argon, helium, and other non-reactive gases.

In addition to surface modification, plasma have other concurrent and competing effects on the surface of materials. Plasmas are extremely efficient at cleaning organics such as environmental contaminants, mold releases and other additives from the surface. Thus plasma is also often used for the super cleaning of inorganic substrates such as metals, ceramics and glasses. More aggressive cleaning ablates or etches the top molecular layers of organic substrates. Useful for example if a weak boundary layer exists or if micro-roughening is desirable.

Plasma induced grafting is where free radicals are generated on the substrate with a noble gas (argon, helium, etc...) plasma which cannot react. If the power is turned off and the system is back flushed with an unsaturated monomer gas, a graft polymerization chain reaction can be initiated. Proper selection of the monomer can lead to very interesting chemistries on the surface. One example is the use of acrylic acid to graft acrylic side chains.

Rf power when organic gases are present, produces the potential for plasma polymerization. The gas is split into polymerizable groups by the plasma and then react in the gas phase or combine on surfaces to form unique, highly crosslinked, pinhole free, polyhydrocarbon materials. Methane will form a coating on objects placed within the plasma.

Cold plasma surface treatment technology offers significant technological and economic advantages over other treatment techniques. The capability of modifying sensitive, chemically resistant materials in a safe and reproducible manner, makes plasma an ideal technology for solving today's manufacturing problems, while allowing the product designer an opportunity to develop unique and better quality products for the future.

Abstract No. 225

Pretreatment of Polymers with Low Pressure Plasma

G. Liebel
Technics Plasma GmbH
Dieselstrabe 22
D8011 Kirchheim
Germany

1. Principal of the plasma process
One of the salient features of the plasma process is the use of gases instead of liquid chemicals as the reaction partners, making it a dry process. Under a pressure of about 0,5 to 2,0 mbar a gas or a mixture or gases is introduced into a vacuum chamber serving as process chamber. By application of a high-frequency alternating voltage a gas discharge (plasma) is ignited whereby the gas in the chamber is brought to an ionized state. The chemical radicals resulting during this discharge react with the surface, depending on the type of gas, and form volatile compounds which are sucked off by the vacuum pump. The plasma contains electrical uncharged particles (molecules), charged particles(ions and electrons) and ultra-violet radiation is developed. The reaction is essentially due to the radicals and the ultra-violet radiations.
This so-called low-pressure plasma is characterized by reactions taking plasma at temperatures between about 60 and 100°C; under atmospheric pressure such reactions are only possible at temperatures of several hundred °C. This fact permits the treatment of organic materials like plastics which must not be exposed to high thermal loads.
The process gases most widely used in the treatment of plastics comprise oxygen, air, inert gases, nitrogen and tetrafluoromethane(CF_4) as well as hydrogen in isolated cases. Typical process parameters are given in Table 1.

2. Plasma systems
The systems offered on the market are supplied in various frequency ranges (kHz, MHz, GHz), the efficiency of the reaction increasing with rising frequency.
Current barrel systems are available both as laboratory scale designs with chamber capacities from 10 to 20 litres and as commercial scale designs (from several hundred litres up to several cubic metres). The process times are in the range of several minutes with variations between the individual materials.

3. Improved adhesion in cementing, printing and metallizing
Whereas on the inorganic materials the plasma is in most cases used for cleaning purposes, a change of the surface with the effect of a drastic increase in wettability can be produced on many plastics. At the Institute for Welding and Joining Technology of the Berlin Technical University studies were conducted on a number of thermoplastics with the aim at representing the effect of plasma treatment in improving adhesion. The results are given in Fig. 1 to 3. The adhesion levels obtained essentially are a function of the type of gas used and the time of treatment. Of the various gases tried, oxygen has proved to be the most suitable one for most plastics. It was found that treatment times even of less than 1 min yielded improvements of adhesion which only increased negligible even over prolonged periods of time.
For several thermoplastics, the influence of the holding time was also determined; this is understood to be the period of time between plasma treatment and cement application. For PE and PP the result was such that no adverse effect has occurred even after several hundred hours.

4. Case histories
Many industries would like to make wider use of plastics, if the inadequate adhesion properties were not prohibitive. Here the plasma process opens up new perspective. The few case histories presented below demonstrate how the advantages of the plasma process have so far been industrially utilized.
   - Automotive industry: Parts from PP and PE, such as bumpers [e.g.9], instrument panels, reflectors and fascias, are treated in the plasma prior to painting or metallizing. This allows the use of less expensive plastics.
   - Electrical industry: By the plasma treatment of PP cups for capacitors the adhesion in the ensuing potting operation using epoxy resin is considerably increased. Very good results are also obtained in the treatment of silicone rubber parts (e.g. for plugs) prior to screen printing or cementing.
   - Manufacture of printed circuit boards: Here plasma treatment yields improved adhesion of copper layers on Teflon.
   - Chemical, pharmaceutical, biological, med equipment: In these application areas, advantage is taken of an increased wettability of treated plastics surfaces, e.g. with mouldings from PE, such as bottles, pipes and containers. Other applications are known from the sector of film fabrication and the textile industry.

5. Integration in production lines
Plasma processes are suited to replace wet chemical methods as well as other conditioning processes in production. For integration into a production line care should be taken that the system selected involves an intermittent vacuum process. Typically cycle times of between 5 and 15 min can be indicated. Process chambers with capacities of several cubic metres are now commercially available.

6. Cost of plasma treatment
The cost of a plasma treatment facility is often compensated by the fact that equipment for wet chemical treatment and ensuing rinsing processes can be dispensed with. Space and personnel requirements are low. The operating costs can be indicated as very low, because of minimum chemical requirement (e.g. 0.5l/min oxygen). Another advantage becomes obvious in this respect, which is the easy disposal of the chemicals. When using oxygen or inert gases, the exhaust gas of the pump can be fed directly to a suitable exhaust ventilation system.
In addition, a plasma system ensures a very high safety level in the working area as the system is hermetically sealed during the process.
As environmental regulations are becoming more stringent, the plasma technology gains increasing importance.

References:
1. Rasche, M.: Modifizierung von Kunststoffoberflachen durch Niederdruckplasmabehandlung zur Verbesserung der Adhasionseigenschaften. Adhasion 25 (1986) 3, p. 25/28.
2. Liebel, G.; Kegel, E.: Anlagenentwicklung beim Plasma-und Ionenstrahlatzen. VDE-Plasma Kolloquium, Hagen, November 1986.
3. Dorn, L.; Bischoff, R.; Rasche, M.: Klebeflachenvorbehandlung im Niederdruckplasma. Kunstsoffberater 29 (1984) 7/8, p. 22/26.
4. Lowe, O.: Untersuchungen der Veranderungen von im Sauerstoffniederdruckplasma behandelten Polypropylenoberflachen. Studienarbeit, TU Berlin, April 1986.
5. Friedrich, J.; Kuhn, G.; Gahde, J.: Untersuchungen zur Plasmaatzung von Polymeren. Acta Polymerica 30 (1979) 8, p. 470/477.
6. Schnabel, W.: Polymer Degradation. Hanser Verlag, Munchen, 1981:
7. Feichtmayr, F.; Schlag, J.; Wurstlin, F.: Abbau von Polyathylen und Polyvinylchlorid in elektrischen Teilentladungen. Kunststoff, 64 (1974) p. 405/409.
8. Dorn, L.; Bischoff, R.: Prufverfahren zur Haftfestigkeitsbewertung von Kunststoff-Metall-Verbindungen. Symposium der DGM "Haftung von Verbandwerkstoffen und Stoffverbunden," Konstanz, 1986.
9. Takahasi, Y.; Fukuta, K.; Kaneko, T.: Plasma Treatment for Painting of Polypropylene Bumper (Toyota Motor Corp.), Intern. Congress, Detroit, Marz 1985.

Table 1. Typical process parameters for low-pressure plasma treatment

Process pressure	0.6 to 1.5 mbar (60 to 150 Pa)
High-frequency power	several 100 W (up to several kW)
Process gas	oxygen
Gas flow rate	50 to 500 ml/min
Process time	1 to 15 min
Temperature	60 to 100 °C (max. 150 to 200 °C)

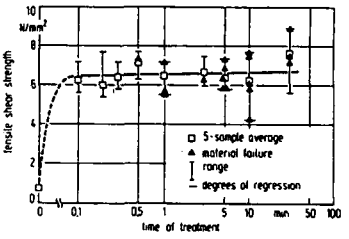


Fig. 1. Tensile shear strength of PP as a function of the time of treatment in the oxygen plasma

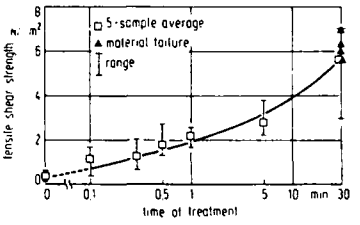


Fig. 2. Tensile shear strength of an epoxy cemented POM/steel joint as a function of the time of oxygen plasma treatment

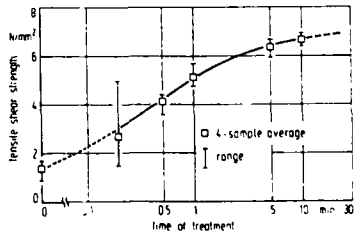


Fig. 3. Tensile shear strength of PE as a function of the time of argon plasma treatment

Abstract No. 226

Characterization of Surface Modifications During Metallization of Polyetherimide

Michael C. Burrell, Bradley R. Karas, Donald F. Foust, William V. Dumas, Edward J. Lamby, and John J. Chera

GE Corporate Research and Development
Schenectady, New York 12301

The chemical and compositional modifications of a polyetherimide surface during metallization processes have been monitored using x-ray photoelectron spectroscopy (XPS). Figure 1 shows a simplified outline of a typical process scheme for the production of metallized Ultem® (polyetherimide) circuit boards. Characterization of the Ultem surface at several stages of the metallization sequence (those marked with asterisks in Figure 1) has aided in the identification of several process problems, and has provided some fundamental understanding of the chemistry of the polymer surface and adsorbed metallization catalysts.

The detection of surface contamination is the simplest application of XPS to these systems. For example, residual silicone mold release agents on the initial surface was found for a series of parts exhibiting poor metal/plastic adhesion. Surface concentrations of 2-4 atomic % Si are sufficient to cause de-bonding. The effectiveness of various surface cleaning agents for removing the contaminants was determined.

Chemical modification of the polymer structure has also been addressed. The primary reaction relevant to Ultem involves hydrolysis of the imide functionality, according to the reaction sequence illustrated in Figure 2. Since the surface may be exposed to aqueous and/or alkaline environments during different process steps, the ability of XPS to detect the occurrence of this reaction was investigated. Model reactions of the surface with alcoholic KOH was used to produce a hydrolyzed surface layer. For hydrolyzed surfaces rinsed only with alcohol, the XPS spectra showed that imide groups had been converted into the potassium salt of the carboxylic acid plus an amide link. Subsequent rinsing with water or dilute acid converts the potassium carboxylate into the carboxylic acid. The characteristic changes in the C 1s, O 1s, and N 1s photoemission lines which accompany these modifications will be discussed.

As shown in Figure 1, the conditioned Ultem surface is initially metallized in an electroless process. Determination of the amount and chemical nature of adsorbed metallization catalysts has been conducted. The systems discussed here are based on palladium compounds or Sn/Pd colloids (1). The chemical shift in the Pd 3d photoemission lines is used to distinguish ionic forms (Pd (+2)) from the active Pd(0), as illustrated in Figure 3. The XPS line intensities can be used for semi-quantitative comparisons of the total catalyst coverage, but due to the limited sampling depth of XPS (ca. 50 angstroms), some of the catalyst may not be detected. Therefore, quantification of the absolute catalyst coverage is accomplished by Rutherford backscattering spectrometry (RBS). This provides a calibration between XPS atomic % and the absolute coverage determined by RBS (atoms/cm^2). The calibration constant, however, is specific for a given catalyst system, due to differences in the catalyst distribution in the surface layer produced by different catalyst treatments. For example, the combined XPS and RBS results for Ultem surfaces treated with an organometallic compound and those treated with colloidal Sn/Pd are compared in Figure 4.

These methods have been used to measure changes in the catalyst composition during sequential sensitization and acceleration steps for surfaces treated with a commercial Sn/Pd colloidal catalyst (2). After the sensitization step, the surface contains a large excess of Sn hydroxides, although metallic Pd is observable. After the acceleration step most of the Sn is removed, and metallic Pd and Sn are present in about a 7-to-1 ratio. These results are compared to previously reported XPS results (3) for the same catalyst on other surfaces.

Production problems related to the metallization catalyst have also been identified. Incomplete electroless plating of Ultem circuit boards was attributed to an unacceptably low amount of catalyst present on the surface. Quantification of surface Pd as a function of catalyst solution concentration and temperature and as a function of surface conditioning aided in the selection of an appropriate commercial surface conditioner. In another example, electrical leakage between metal runs on a patterned circuit board was due to the presence of metallization catalyst which remained on the plastic surface after the copper had been selectively etched away. Commonly used copper etches were not effective at removing the residual Pd. Small spot XPS analysis between the metallized runs was used to verify that the additional processing steps developed removed the residual Pd and left the polymer surface composition and the other metallization unaltered.

*Ultem is a registered trademark of the GE Company

References

1. For example, see R. L. Cohen and R. L. Meek, J. *Colloid Interface Sci.*, 55, 156 (1976); N. Feldstein, M. Schlesinger, N. E. Hedgecock, and S. L. Chow, J. Electrochem. Soc. 121, 738 (1974); C. R. Shipley Jr. U. S. Pat. 3,011,920; or reference 3 below.

2. M. C. Burrell, G. A. Smith, and J. J. Chera. Surface and Interface Analysis, 11, 160 (1988).

3. T. Osaka, H. Takematsu, and K. Nihei. J. Electrochem. Soc., 127, 1021 (1980).

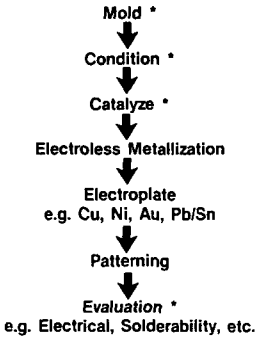


Figure 1. Schematic of Typical Process Sequence in the Production of Metallized Plastic Circuit Boards

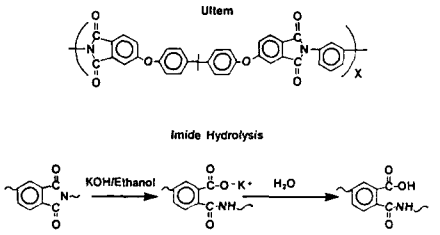


Figure 2. Ultem Structure, and Hydrolysis Reaction of Imide Moeity

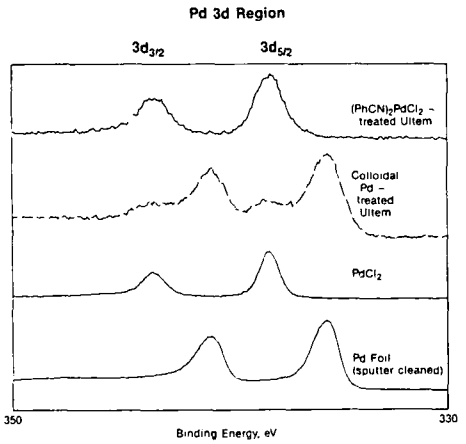


Figure 3. Pd 3d Photoemission Signal For Pd(0) and Pd(+3) Species

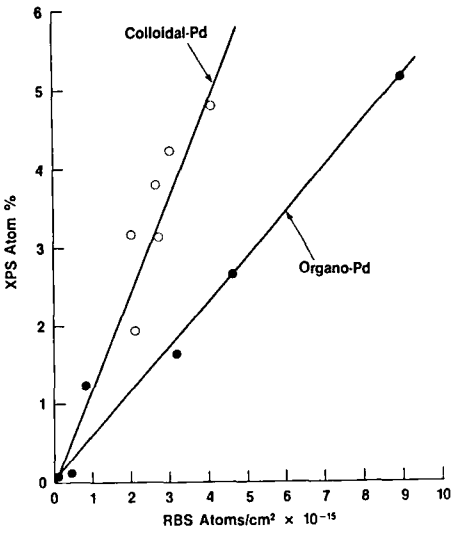


Figure 4. Observed XPS Surface Pd Content Versus Total Amount Determined by RBS

Abstract No. 227

Focused Ion Beam SIMS for Micromachining Applications

L. R. Harriott

M. J. Vasile

AT&T Bell Laboratories

Murray Hill, New Jersey 07974

Liquid metal ion sources which provide very highly focused (5,000 to 500Å dia.) high current density (1.0 to 0.5 A/cm^2) ion beams have offered the prospect of extending the technique of secondary ion mass spectrometry well into the sub-micron lateral resolution range. This tantalizing prospect has been cited numerous times, but only a few successful instruments have been reported. Levi-Setti and coworkers have published a detailed and thorough review of their recent work which describes their focused ion beam (liquid metal) SIMS, in which the emphasis is on the general utility of high resolution scanning ion microscropy.[1] Kingham, et al have shown some examples of ion images obtained with a liquid metal ion source SIMS, but give only a cursory account of the instrument and operating techniques.[2]

Our intention is to use SIMS as an adjunct, in-situ diagnostic tool for micromachining applications which utilize a liquid Ga ion source. The primary applications are for end-point detection when sputtering through thin films with micron sized rastered areas, and for element mapping by mass selected ion images taken on raster fields from one millimeter to 10μm.

The approach we have taken is quite pragmatic: The detection of secondary ions must be done without compromising any of the functions or operating parameters of the focused ion beam processes. Signals must be adequate to record mass spectra or mass-selected ion images within a matter of one or two minutes. Ion extraction to the SIMS for mass spectral analysis must not interfere with the normal total secondary ion imaging, and a minimum number of variables (one or two) for SIMS signal optimization is essential for convenient operation.

End-point detecton of Cr micromachining on photomasks was done with raster sizes ranging from 10μm x 10μm to 3μm x 3μm. The chromium oxide enhanced $^{52}Cr^+$ signal at the Cr/glass interface was used as the end-point indicator. Verification of this effect was obtained by XPS profiling through the Cr film. SIMS end-points, total ion images, and transmitted light measurements show that the ion-milling can be controlled to stop prior to, or after, the Cr/glass interface. Measurements on a common sample show that the absolute sensitivity of the FIB/SIMS is equivalent to that of a commercially-made SIMS which uses 3 KeV O_2^+ primary ions (3 x 10^4 cps $^{52}Cr^+$/nA primary ion, 100μm raster). Mass selected secondary ion images have been obtained for high yield ions such as $^{52}Cr^+$ and $^{27}Al^+$ on raster fields of 25μm in time intervals ranging from 20 to 100 sec. Al^+ SIMS images of 1μm lines and spaces from a VLSI test pattern have been obtained.

References

1. R. Levi-Setti, Y. L. Wang and G. Crow, Appl. Surf. Sci., 26 (1986) 249.

2. D. R. Kingham, P. Vohralik, D. Fathers, A. R. Waugh and A. R. Bayley, "Applied Materials Characterization", Mater. Res. Soc. Symp. Proc., Vol. 48 (1985), W. Katz and P. Williams Eds., p. 319.

Abstract No. 228

RADIATION ENHANCED ADHESION OF METAL FILMS ON POLYMERS

J. E. E. Baglin

IBM Research Division

Almaden Research Center
650 Harry Road
San Jose, CA 95120

It has been shown that ion beam techniques can be used to create strong interfacial adhesion between polymer substrates and vapor deposited metal films. One example is that of copper on Teflon, where Chang et al [1] have obtained stable bonding with peel strength 80 gm/mm by means of pre-sputtering the Teflon surface with 500 eV argon ions in situ prior to deposition of copper, followed by thermal annealing. In that situation, it was found by XPS that the deposited copper was chemically bonded; in addition, the polymer surface was roughened, creating a mechanically tougher interface region. It is expected that both the substrate roughening and the production of surface dangling bonds are responsible for the adhesion of deposited metal, the interface atom configurations no doubt being stabilized by the heat treatment.

A similar large improvement in Cu-Teflon bonding was produced by irradiation of a pre-formed Cu-Teflon system with a penetrating (250 keV) beam of neon ions. Presumably the formation of new interface structures was, in this case, the result of ion mixing displacements of interface atoms, possibly dispersing interface contaminants at the same time.

The application of such techniques to other systems of technological importance invites further exploration. In this paper, we shall examine systems that have been studied, with particular emphasis on the possibilities of interface structure tailoring offered by the process of pre-sputtering of the polymer substrate.

1. C-A. Chang, J.E.E. Baglin, A.G. Schrott and K. C. Lin. Appl. Phys. Lett. 51 , 103 (1987).

Abstract No. 229

EFFECT OF THE PLASMA TREATMENT OR THE ION-PLATING ON THE ADHESIVITY OF THE METALLIZED PLASTICS

Katsuhiko Nakamae, Satoshi Tanigawa
and Tsunetaka Matsumoto
Department of Industrial Chemistry, Faculty of Engineering, Kobe University
Rokkodai, Nada, Kobe 657 Japan

INTRODUCTION

Plastic metalizing is widely used, e.g. for the flexible print circuit, the transparent conductive film and the high density recording medium etc.. The various properties for such materials are required. In particular, the adhesion of the metel thin films on polymers is an one of the most important factor in the field of all[1]. However such adhesion strength of the materials prepared by the vacuum deposition is not enough. It was proved for us that the pretreatment of the surface of polymer films or the using by the metal vapor with high energy, for example ion-plating or sputtering, were improved with the adhesion strength of the deposited thin films on polymers[2].

In this study, polyimide films have a thermal high resistance and an essential mechanical properties were pre-treated by O_2 plasma in order to improve the adhesion strength of the deposited metal thin films on polyimide.

EXPERIMENTAL

Polyimide film is poly[N-(oxy-1,4phenylene)-N'-(1,4phenylene)pyromellitimide] (Kapton) produced by Du pont Co.LTD., its thickness is 70μ m. Vacuum deposition is possible to carry out in-situ followed O_2 plasma treatment. Plasma treatment was applied R.F. electric field of 13.56MHz, and vacuum deposition was carried out by the electric gun. The adhesion strength was measured by the 90° peeling test. The characteristics of polyimide surface was evaluated by the contact angle and the ESCA spectra etc..

RESULT AND DISCUSSION

The adhesivity of deposited metal thin film on polyimide was improved upon the increasing in the time and R.F. power of plasma treatment on the polyimide surface. The functional groups on polyimide surface were analyzed quantitatively by ESCA spectra, so as to evaluate the chemical nature of surface by treatment of O_2 plasma. Figure shows the relationship between the C/O ratio of atomic concentration calculated by ESCA spectra and the peel strength at metal/polyimide interface. Consequently, it was proved that the adhesion strength of the deposited metal thin films on polyimide was greatly dependent upon the amount of the functional groups on polyimide surface. Furthermore the accerating voltage and the R.F. power at ion-plating significantly affected the adhesion strength similarly to the case of the surface pretreatment.

REFERENCES

1. K.L.Mittal, J. Vac. Sci. Technol., 13, 19 (1979).
2. K.Sumiya, T.Taii, K.Nakamae, T.Matsumoto, J. Adhesion Soc. Japan, 18, 345 (1982); K.Nakamae, K.Yamaguchi, K.Sumiya, T.Matsumoto, ibid, 22, 347 (1986).

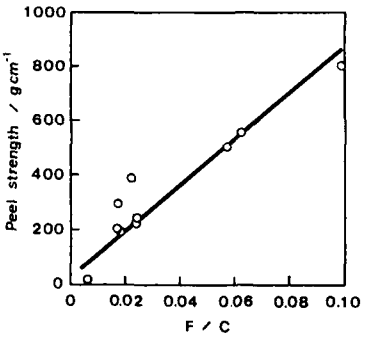


Fig. Relationship between the peel strength and the ratios of atomic concentration after derivatization.

Abstract No. 230

THIN FILM ADHESION - A REVIEW OF THE MECHANICAL METHODS FOR ADHESION ASSESSMENT

P.A. Steinmann* and H.E. Hintermann

Swiss Center for Electronics and Microtechnology, Inc.

P.O. Box 41, CH-2007 Neuchatel, Switzerland

As already has been stated by Mittal[1], no engineering test is able to measure the basic adhesion, i.e. the interfacial bond strength. However, a rather large number of tests have been proposed to characterize the practical adhesion of thin films.
The objective of this paper is to discuss the mechanical methods enabling to give quantitative data for adhesion[1-4] with a special emphasis on the scratch testing technique[5].
There are essentially two types of tests which are distinguished by the kind of stresses generated in the interfacial region, namely, tensile and shear tests. Direct tensile, electromagnetic tensile, acceleration and shock wave tests belong to the tensile test group, whereas adhesive tape, direct shear, peel and scratch tests belong to the shear test group.
The choice of the test for measuring practical adhesion should be based upon the type of stresses the test specimen is going to encounter in practice[1]. Nevertheless, it has been shown[3] that most of these methods are limited either to poor adherent films, namely the adhesion is lower than the bulk resistance of the bonding agent (glue or solder in the pull-off test for instance), or to thick coatings, since the maximum tensile stress generated in the interfacial region is proportional to the mass of the coating. Furthermore, methods requiring large accelerations or shock waves are generally difficult to perform and are costly.
Among all these tests, the only practical one capable to assess the adhesion of thin and well-adherent films is the scratch test.
In this particular test, proposed by Heavens[6] and then extensively used by Weaver and coworkers[7,8], a stepwise[9] or continuously loaded[10] spherical scratching point is drawn across the coated sample. The scratching point produces an increasing elasto-plastic deformation of the film-substrate system until a damage occurs in the surface region which can be adhesive or cohesive in nature. The minimum load at which an adhesive failure occurs is called the critical load (L_c) and is representative of the coating adhesion.
Besides adhesion the critical load depends on several parameters whose each individual dependence has to be known in order to determine the adhesion.
In a recent study[5], the instrument related intrinsic parameters as well as the tested sample related extrinsic parameters have been considered in order to improve the interpretation of the critical load as it relates to adhesion. This experimental work has been very recently supported by a new model developed by Burnett and Rickerby[11], which describes the behavior of hard coatings. This model is based on an energy balance approach where the energy required to create two new surfaces by debonding (L_c) is equal to the stored elastic energy in the film. This later energy is described as the sum of three energy contributions, namely, indentation, internal stress and friction.

The applicability of the scratch test to metallized plastics is not very well established although some authors[12,13] have demonstrated that it is a valuable tool for quantitatively comparing the adhesion of metal films on polymeric substrates.
Lately, using a tensile test, Van de Leest[14] has shown that acoustic emission is generated in the interface of metallized plastics prior to debonding, and has used this technique to compare qualitatively the adhesion strengths of thin metal films on polymers. This is of particular interest since the commercially available scratch-testers are equipped with an acoustic emission sensor.

*present address: Lewis Research Center, National Aeronautics and Space Administration, Cleveland, Ohio 44135, U.S.A.

(1) K.L. Mittal, in K.L. Mittal (ed.), Adhesion Measurement of Thin Films, Thick Films and Bulk Coatings, ASTM Spec. Tech. Publ. 640, 1978, p.134 (ASTM, Philadelphia, PA).
(2) A.J. Perry, P. Laeng and H.E. Hintermann, Proc. 8th Int. Conf. on Chemical Vapor Deposition, Electrochem. Soc., Pennington, NJ, 1981, p.475.
(3) P. Laeng, P.A. Steinmann and H.E. Hintermann, Oberflaeche-Surface, 23(4),(1982)108.
(4) J. Valli, J.Vac.Sci.Technol., A4(6),(1986)3007.
(5) P.A. Steinmann, Y. Tardy and H.E. Hintermann, Thin Solid Films, 154,(1987)333.
(6) O.S. Heavens, J.Phys.Radium, 11,(1950)355.
(7) C. Weaver and R.M. Hill, Philos.Mag., 3(1958)1402.
(8) P. Benjamin and C. Weaver, Proc.Roy.Soc., 254A, (1960)163.
(9) P. Laeng and P.A. Steinmann, Proc. 8th Int.Conf. on Chemical Vapor Deposition, Electrochem. Soc., Pennington, NJ, 1981, p.723.
(10) P.A. Steinmann, P. Laeng and H.E. Hintermann, Mater. Tech., 13(1),(1985)85.
(11) P.J. Burnett and D.S. Rickerby, Thin Solid Films, to be published.
(12) C. Weaver, Faraday Special Disc., n°2,(1972)18.
(13) L.F. Goldstein and T.J. Bertone, J.Vac.Sci. Technol., 12,(1975)1423.
(14) R.E. Van de Leest, Thin Solid Films, 124,(1985)335.

Abstract No. 231

Adhesion and Deformation Behavior of Thin Metal Films on Polyimide

F. Faupel, Y. H. Jeng, S. T. Chen and P. S. Ho

IBM Research Division, T. J. Watson Research Center
P. O. Box 218
Yorktown Heights, NY 10598

Metalized polyimide structures are widely used in microelectronic packaging and on the chip level because of the unique properties of polyimide such as low dielectric constant, high thermal stability, low processing temperature, and planarized capability. Adhesion is one of the major concerns since residual stresses generated due to thermal expansion mismatch during fabrication can introduce large deformations, which can lead to delamination failure at the metal/polyimide interface.

Several experimental methods have been developed to measure the adhesion energy of these films on ductile substrates which is defined as the minimum energy per unit area required to separate two surfaces. The standard tests such as the peel and blister tests, are designed for measuring adhesion strength, but yield results strongly dependent on the deformation behavior of the film and the substrate. To predict the actual performance of a film/substrate structure, it is important to know not only the adhesion energy, but also the fracture mode and the deformation characteristics of the film/substrate structure. A stretch-deformation method has been developed by us to investigate such deformation behaviors in addition to measure the adhesion energy of metal/polymer structures. This method is based on measuring the stress vs. strain dependence in combination with in-situ optical microscopy as well as SEM and TEM observations.

In this paper, results from the stretch-deformation method will be reported on metal/polyimide bilayer and trilayer structures containing Cu and Cu/Cr. Upon straining, we exhibit an extended plastic range beyond the yield point, where twinning and slip were observed. At a critical elongation which depends on the film thickness, crack formation starts. Defects in the polyimide, such as small bubbles originating from the curing process seem to play an important role in the initiation of the cracks in the metal. Due to the much higher modulus of the coating, substantial stress concentration occurs at the cracks. As a consequence, delamination always starts at cracks and, depending on the thickness ratio of metal and polyimide, preferential straining of the latter can be observed.

In these tests, after the complete delamination of the metal films, the difference in the load vs. elongation curves of the multilayer and the pure polyimide can be used to determine directly the adhesion energy. The basis of this analysis will be discussed. Finite element analysis taking into account plastic deformation reveals the stress distribution in the sample. Especially a strong increase in the shear stress at cracks is found elucidating the experimental findings. An interfacial layer of a well adhering brittle material like Cr substantially influences the build-up of stress and the starting point of crack formation and delamination. In a trilayer structure, cracks typically start in the brittle interface layer and propagate through the whole coating due to stress concentration. The influence of the interfacial layer thickness is discussed.

Abstract No. 232

Proposed Methods for Identification and Normalization of Strain-Dynamic Effects in Adherence Testing of Metallized Plastics

Richard P. Riegert
Quad Group

133 Palm Avenue
Santa Barbara CA 93101

Adhesion testing of metallized non-plastic surfaces has evolved to yield at least relative or near-quantitative data for virtually any coating or substrate using simple test methods.

In the case of metallized plastics, especially those of thermo-plastic character and for thin sheet plastics, there are factors which lead to a sense of uncertainty, even when measured values are within narrow limits of each other.

As an example, various measurement methods show extreme sensitivity to rate of load application, high susceptibility to residual coating stress and even minute variations in direction of load application. The intrinsic characteristics of certain specific plastics such as short-term creep, effects of surface anomalies and anisotropic strain require special attention.

Yielding of any segment of the test bond interface results in asymmetrical load distribution manifesting unit load intensification wherever yielding is minimal. Models are proposed for flow induced strain-dynamics and consequential stress redistribution effects in adherence testing by z-axis tensile, shear, tipple-tear, lap-shear, sheet substrate stretch and two forms of ninety degree peel tests.

Finally, a strategy for cross-correlation between two or more tests may offer promise of enhanced reliability of adherence testing in at least some of the myriad forms of metallized plastics.

Abstract No. 233

Surface, Interface and Adhesion Properties of Metallized Plastics

Cao Pu-guang

Central Laboratory
Pejing Electron Tube Factory
Pejing, China

The paper explains the properties of metallized plastics film adhesion, and used surface analysis ED/SEM, AES/SEM, ESCA and SIMS during studies.

Experiment result shows that for metal evaporation film, the adsorption mechanism is dominant, but sometimes mechanical and diffusion mechanism will also be important; for hollow cathode ion plated film, the diffusion is sometimes the dominant, but sometimes the other two will also be important.

A comparison of the interface width produced in ion-plated and evaporated thin film, has shown that the interface width in a metal film-substrate system is independent on the method of deposition.

These results are used to explain the adhesion properties of ion-plated and evaporation film. A graded interface produced between metal and substrate is due to atomic mixing and diffusion, ion implantation and ion induced diffusion. Conclusion is that metal film adhesion is mainly determind by substrate surface and interface properties, which is dependent on surface pretreatment.

In microelectronic areas the failures are due to electrochemical corrosion. The corrosion rate dependent on ion concentration, electron state, high temperature, bias and applied bias voltage.

Abstract No. 234

Planarized Deep-Trench Process for Bipolar Device Isolation

Y.-C.S. Yu, C. Hacherl, E. Patton,
E. Lane, S. Dottarar and T. Yamaguchi

Tektronix, Inc., MS 59-234,
Beaverton, Oregon 97077

A planarized device isolation process has been developed by using a deep-trench isolation technology combined with a local oxidation of silicon (LOCOS) process for self-aligned double-polysilicon bipolar integrated circuits. To obtain a desirable trench etch profile and a uniform polysilicon etchback process, the reactive ion etch processes have been optimized in terms of gas ratio, pressure, and power density. As a result of a deep-trench isolation, the collector-substrate capacitance was minimized at 9.0 fF, while maintaining a transistor-to-transistor isolation voltage of 25 volts. A cut-off frequency of 15.5 GHz and a 4-bit A/D converter with a sampling rate of 1.5 GS/s were demonstrated.

An isolation structure, as shown in Fig. 1(a), combining silicon deep-trench technology and LOCOS was used for device isolation in an advanced double-polysilicon bipolar process. Trenches were etched into a p-type silicon substrate through an n-type epitaxial and an n^+ buried layer using an oxide film as an etch mask. Following this deep-trench etch, boron ions were implanted into the trenches using the same oxide film as a mask. A p-type layer was formed at the bottom of the deep-trench by this implant. The masking oxide was then stripped, and the trench surface was thermally oxidized. The trenches were refilled by a polysilicon film. The polysilicon film was etched back using an RIE process. A surface oxide film was left after this polysilicon etchback process. This oxide film was stripped and a stress relief oxide film was grown. Device islands were then defined in a silicon nitride film deposited on top of the oxide film. A thick thermal oxide was then grown on top of the trenches as well as on the rest of the field areas.

In this process, any overetch during the polysilicon etchback removed the polysilicon film inside the refilled trenches. This exposed the vertical walls along the upper edges of the trenches after the surface oxide was stripped. During the subsequent device island patterning, an anisotropic nitride etch left residual nitride along these walls. This nitride residue prevented lateral oxidation of the trench sidewall and resulted in a narrow depression in the field oxide on top of the trenches. This depression was filled with a conducting polysilicon film during the subsequent steps of the self-aligned double-polysilicon bipolar process. This conducting polysilicon film was continuous along the trench, and therefore shorted the emitter and collector of bipolar transistors which had emitter and collector electrodes overlaying the trenches.

A new process, as shown in Fig.1(b), eliminated this problem by incorporating the LOCOS mask, i.e. a thin thermal oxide and a nitride film, as part of the mask during the trench etch. The thermal oxide film was grown and the nitride film was deposited immediately before depositing an LPCVD oxide film used as a trench etch mask. Trenches were etched, refilled and etched back as previously described, now using the nitride film as an etch stop during the polysilicon etchback process. An oxidation for the trench polysilicon was then performed immediately following the etchback process. This oxidation smoothed the seam along the center of the trench, and raised the trench surface to be even with or above the wafer surface. After this oxidation, device islands were defined and a field oxide was thermally grown as previously described. Since the trench surface was even with or above the wafer surface, the device island patterning left no vertical sidewalls. The field oxide grown on top of the trench, therefore, was smooth. The field oxide depression and the resultant collector-emitter shorts were completely eliminated.

Optimization of the reactive ion etching parameters was necessary to achieve this structure. Fig. 2 showed the deep-trench profile. The silicon deep-trench was etched in a parallel plate batch reactor, using $SiCl_4$, Cl_2 and He in a 1 : 1 : 2 ratio. Process pressure was 0.1 Torr and power density was 0.6 W/cm^2. Electrodes were covered with a polymeric material to prevent metal sputtering and contamination during the etch, and also to provide sidewall passivation and prevent undercutting when etching through an n^+ buried layer. Silicon etch rate was 200 nm/min with a selectivity of 7 : 1 to the LPCVD oxide. The polysilicon etchback process was optimized for uniformity and smoothness of the etched polysilicon film. Two different chemistries were investigated. Chlorine chemistry consistently resulted in severe texturing of the trench polysilicon and the LOCOS nitride layer. This texturing could be reduced by increasing pressure and by reducing power, but was never eliminated entirely. However, a combination of CF_3Br and SF_6 was found to produce an extremely smooth surface. The optimized process, i.e. CF_3Br and SF_6 in a 2 : 1 ratio, 65 mTorr and a power density of 6.0 W/cm^2, resulted in a very uniform etch and an extremely smooth surface, as shown in Fig. 3, so that almost no overetch was needed.

This planarized process has been applied to fabrication of self-aligned-double polysilicon bipolar transistors. Transistor-to-transistor isolation voltages were characterized at various implant doses. At a dose of 1.4 x 10^{13} cm^{-2}, the isolation voltages of 25 volts and 30 volts were achieved using one trench and two trenches, respectively. These trenches are 4 microns deep and 1.5 microns wide. The collector-substrate capacitance was minimized at 9.0 fF for a bipolar transistor with an area of 7 x 11 μm^2 while maintaining the transistor-to-transistor isolation voltage of 25 volts. A transistor cut-off frequency of 15.5 GHz and a 4-bit A/D converter with a sampling rate of 1.5 GS/s have been demonstrated.

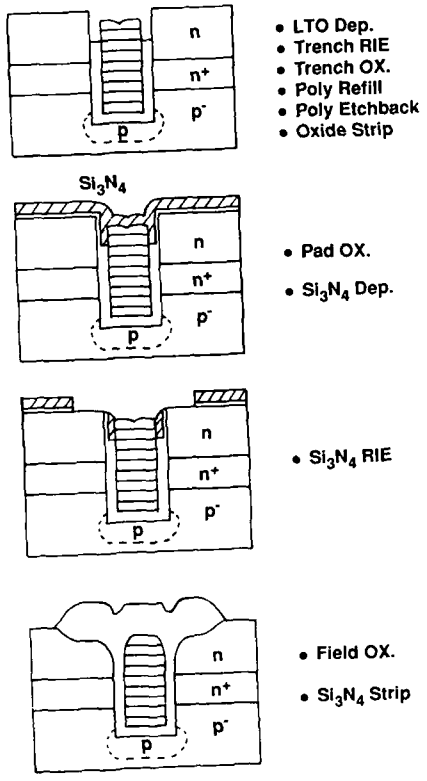


Fig. 1(a) Original deep-trench process

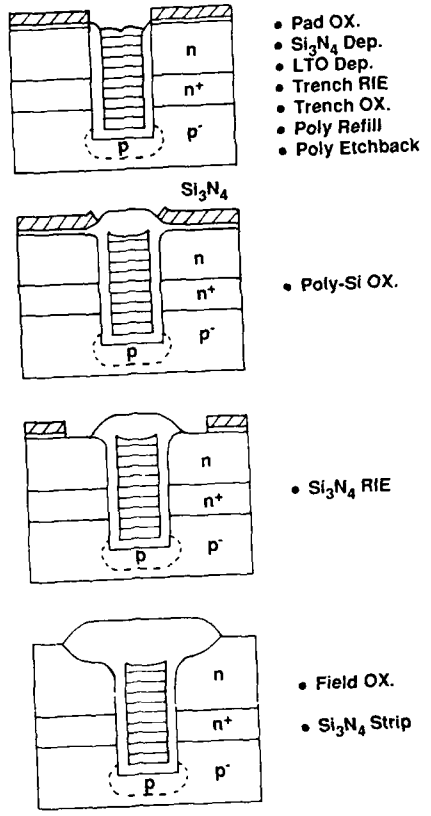


Fig. 1(b) New planarized deep-trench process

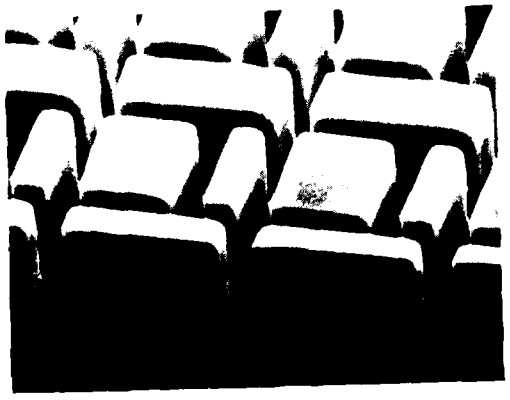


Fig. 2 Silicon deep-trench profile

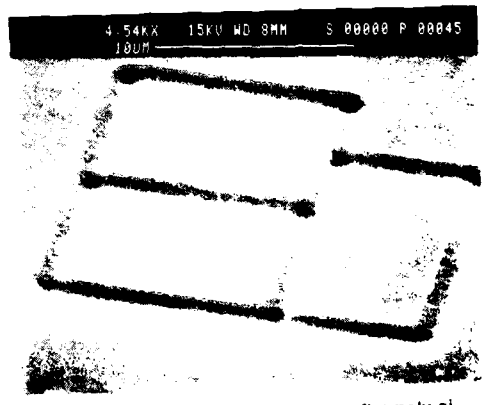


Fig. 3 Silicon deep-trench surface after poly-si etchback

Abstract No. 235

CMOS Device Isolation Using Silicon Selective Epitaxial Growth

C. H. Ting and A. Stivers
Intel Corporation
Components Research, SC9-45
P.O. Box 58125
Santa Clara, CA 95052-8125

J. O. Borland
Applied Materials, Inc.
3050 Bowers Ave.
Santa Clara, CA 95051

Introduction:

The continuation of device dimension scaling and higher levels of integration require close examination of all aspects of device structures. One of the serious limiting factors for improved device density is the isolation structure. Conventional isolation technology using local oxidation of silicon, or LOCOS, wastes approximately 1 um space for the thin-to-thick oxide transition region known as bird's-beak encroachment. This is not acceptable for submicron devices. Therefore, new isolation technology has been an active research area for VLSI fabrication technology.

A variety of proceses have been proposed to reduce the bird's-beak encroachment of LOCOS isolation, such as recessed LOCOS, SILO and SWAMI, etc. The improved LOCOS process, however, only compacts the bird's beak, but does not eliminate it. Furthermore, in LOCOS-isolated CMOS technologies, lateral isolation of n and p wells depends as much on junction isolation as on the LOCOS structure. Bird's-beak free isolation can best be achieved by isolation structures that are not modifications of LOCOS, such as trench isolation and selective epitaxial growth (SEG). Trench isloation has been intensively studied. Its use is, however, very limited due to its process complexity. In comparison to trench isolation the SEG isolation process is considerably simpler. It can be used to laterally isolate n and p wells as well as single devices. Since the SEG process is completely bird's beak free, the minimum isolation for the CMOS process will be limited only by lithographic capabilities.

In the present study active the device pattern is first etched in the thick oxide layer by RIE. This anisotropic etch can readily define isolation structures of submicron dimension and with verticle sidewalls. The oxide removed in this step is replaced with device-quality silicon by selective epitaxial growth. The SEG thickness is chosen to achieve a planar surface. The SEG growth was carried out using SiH_2Cl_2, HCl, and H_2 in a commercially available reduced pressure epitaxial reactor. The growth parameters are investigated in terms of temperature, pressure and flow rates.

Facet formation was found to be dependent on pattern geometry as well as the deposition temperature and pressure. At lower deposition temperatures (875 C) facet depth can be 80% of the SEG thickness at certain corners of <100> oriented patterns. These facets form on <111> crystallographic planes. At higher deposition temperatures (950 C) shallower and less steep facets on <311> crystallographic planes are formed. The overall surface topography of the SEG grown at 950 C is therefore better than that grown at 875 C. The material quality of the SEG is studied by defect decoration and junction diode leakage current. Higher quality material is obtained at lower growth temperatures. This is opposite to the deposition condition for minimizing facet formation.

Polysilicon gate CMOS devices are successfully fabricated in SEG material using an ion-implanted retrograde-well process. The device characteristics and latch-up susceptibility have been determined and compared to devices fabricated with the standard LOCOS process. The SEG devices have the same mobility as the bulk LOCOS devices, but with better isolation characteristics and latch-up immunity. The subthreshold characteristics and reverse leakage current of the SEG devices are not as good as the LOCOS devices. These differences will be explained. The advantages of planarizing the SEG surface for device fabrication will also be discussed.

Abstract No. 236

PROCESS AND DEVICE SIMULATION OF TRENCH ISOLATION CORNER PARASITIC DEVICE

T. Furukawa
J. A. Mandelman

IBM General Technology Division
Essex Junction, Vermont 05452

INTRODUCTION

By eliminating the bird's-beak seen with local oxidation of silicon (LOCOS) isolation, oxide filled trench isolation offers scalability leverage of high density, high performance VLSI into the submicron regime. However, there are fundamental concerns which must be addressed with trench technology. One concern is the existence of a parasitic device at the trench edges of an active n-channel device. This parasitic device has been seen to turn on at voltages lower than the main channel due to electric field enhancement at the trench/active device corner, resulting in a "hump" in the channel current vs gate voltage curves. Thus, the parasitic device increases the subthreshold leakage current of the active device. Several studies of this parasitic effect (Ref. 1-3) have been reported, but most investigate only long channel device behavior with emphasis on suppression of the parasitic device or "hump" by doping the trench side walls. Thinning of the gate oxide at the trench edge is another concern. Thinned gate oxide not only degrades gate oxide reliability but also worsens the parasitic device problem.

In this study, two-dimensional process simulation and a three-dimensional device simulation have been used to investigate in depth the nature of the parasitic device, particularly its short channel characteristics. Subthreshold leakage current of an active device has been analyzed as a function of device lengths. Simulation results have been compared with experimental data.

PROCESS SIMULATION

Two-dimensional geometry and doping distributions were simulated with the finite element diffusion simulation system (FEDSS) (Ref. 4). The result of a representative simulation is shown in Fig. 1. Trench side wall doping was not used in this case. It is noteworthy that gate tailor boron is depleted into the trench and gate oxides during gate oxidation. This boron depletion at the trench corner lowers the threshold voltage of the parasitic device. Gate oxide thinning and sharpened corner geometry at the trench edge are also seen in Fig. 1. Both thinned gate oxide and sharp corner geometry increase the electric field strength at the trench corner, also lowering the threshold voltage of the parasitic device.

DEVICE SIMULATION

Electrical characteristics of devices bounded by isolation trenches have been simulated in three dimensions by the finite element device analysis program (FIELDAY) (Ref. 5), using FEDSS simulated doping profiles which include boron segregation effects. A 90 degree corner angle has been assumed. In Fig. 2, normalized device current per cm width is plotted against gate voltage for various device widths at 1 micron channel length. For very large width (infinitely wide in the models), no humps exist. However, a hump appears at narrower width, growing more prominent with decreasing width. For devices narrower than approximately 1 micron, the characteristic is completely dominated by the corner parasitic. Figure 3 shows electron concentration contours at slightly below device threshold. The maximum concentration is seen as clearly occurring at the corner.

The hump becomes more prominent with increasing source to substrate voltage because the parasitic device has a lower substrate sensitivity than the mid-portion of the device. This is a consequence of field lines fringing into the trench oxide.

The sensitivity of the hump to drain to source voltage and to channel length is demonstrated with the modeled characteristics of Figs. 4 and 5, respectively. Modeling shows that the short channel effects (both threshold sensitivity to drain to source voltage, and to channel length) of the parasitic device are smaller than those of the main device. Figure 6 and Fig. 7, confirm these results experimentally. It has also been demonstrated that the current distribution associated with the corner parasitic is independent of overall device width, down to the narrowest width studied (0.48 um). From this property it has been shown that the leakage current per unit width at zero gate to source voltage is proportional to the reciprocal of the device width. In Fig. 8, simulated subthreshold leakage current of an active device is plotted as a function of device width for different device lengths. From the slope of the curve, leakage current due to the parasitic device can be calculated.

SUMMARY AND CONCLUSIONS

2-D process and 3-D device modeling have been used for studying the electrical characteristics of n-channel oxide filled trench isolated devices. The modeling has focused on the influence that the corner parasitic device has on the transfer characteristic of the total device. Earlier work based on 2-D modeling (assumed infinite channel length) led to a conclusion that extra boron doping is required at the corner to suppress the parasitic current. However, the 3-D modeling work discussed in this paper shows that the short channel roll-off of the parasitic device is less severe than for the main part of the device. This result has also been confirmed experimentally. Therefore, at short channels the threshold voltage difference between the parasitic device and the main device is reduced, relaxing the requirement for extra boron doping for leakage current control.

ACKNOWLEDGEMENT

Samples were prepared at IBM Essex Junction Laboratory by C. Koburger, D. Horak, M. Kerbaugh, D. Martin and others. Authors wish to thank for their important contributions to this work. We also thank B. Davari from IBM Yorktown for the discussion.

REFERENCES:

1. K. Kurosawa, T. Shibata, H. Iizuka, "A NEW BIRD'S-BEAK FREE FIELD ISOLATION TECHNOLOGY FOR VLSI DEVICES," IEDM 1981, pp.384-387.

2. T. Iizuka, K.Y. Chiu, J.L. Moll, "DOUBLE THRESHOLD MOSFETS IN BIRD'S-BEAK FREE STRUCTURES," IEDM 1981, pp. 380-383.

3. G. Fuse, M. Fukumoto, A. Shinohara, S. Odanaka, M. Sasago, T. Ohzone, "A NEW ISOLATION METHOD WITH BORON-IMPLANTED SIDEWALLS FOR CONTROLLING NARROW-WIDTH EFFECT," IEEE Trans. Elect. Dev. Vol ED-34, 1987, pp. 356-359.

4. L. Berucki, H. H. Hansen, K. Varahramyan, "FEDSS-A 2D SEMICONDUCTOR FABRICATION PROCESS SIMULATOR," IBM J. Res. Develop. 29, 1985, pp. 264-276.

5. E. Buturla, P. Cottrell, B. Grossman, K. Salsburg, "FINITE-ELEMENT ANALYSIS OF SEMICONDUCTOR DEVICES: THE FIELDAY PROGRAM," IBM J. Res. Develop. 25, 1981, pp. 218-231.

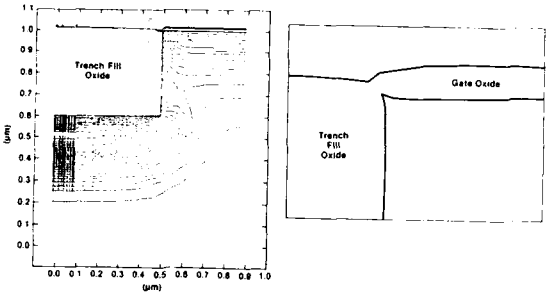


Figure 1. Process model of boron doping and gate oxide growth.

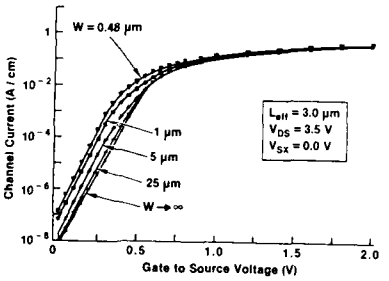


Figure 2. Turn-on sensitivity to channel width

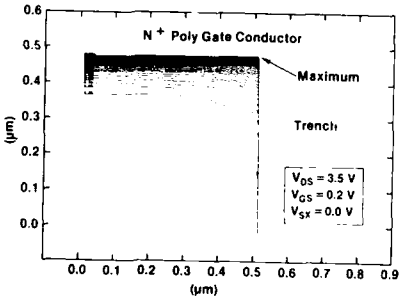


Figure 3. Log of electron density contours transverse to channel.

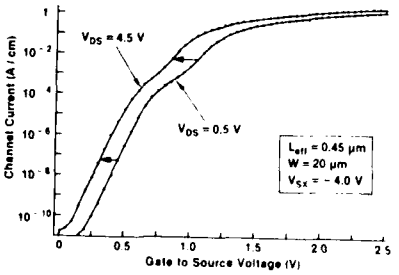


Figure 4. Sensitivity of hump to drain to source voltage (model)

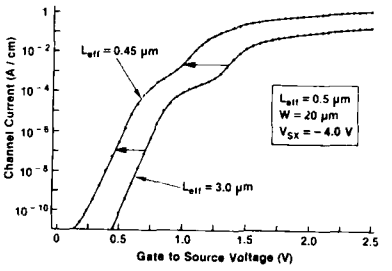


Figure 5. Sensitivity of hump to channel length (model)

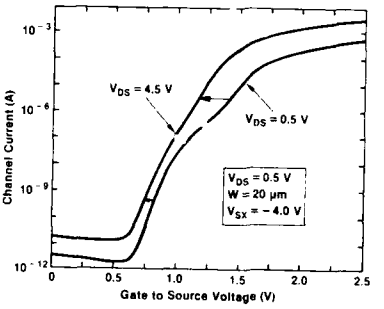


Figure 6. Sensitivity of hump to drain to source voltage (experimental)

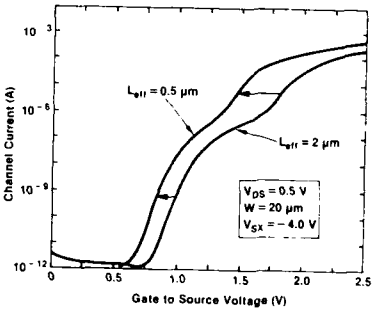


Figure 7. Sensitivity of hump to channel length (experimental)

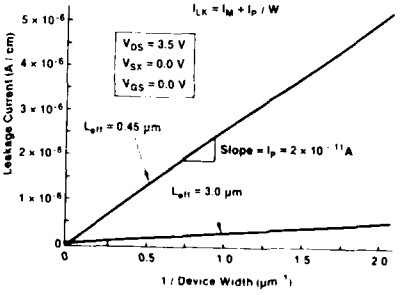


Figure 8. Leakage sensitivity to device width

Abstract No. 242

PROCESS PARAMETERS OF THE TRENCH RIE DEDUCED FROM THE LASER SIGNAL

Bernard LEROY and François LEVERD

IBM FRANCE, Dept 1736/23D,
BP 58, 91102, CORBEIL ESSONNES, FRANCE

A trench is etched by a plasma through a hole in a multilayered structure (SiO_2 and Si_3N_4) covered by a d_o thick SiO_2 film (fig.1). The depth of the silicon etched is monitored by a laser signal (λ=632.8nm); E is the amplitude of the electric field, J the intensity proportionnal to E^2, and ϕ the phase. In the reflected beam, three beams interfer: the beam reflected on SiO_2 (E_o,ϕ_o) the beam reflected on the multilayer film (E_f,ϕ_f) and the beam reflected on the bottom of the trench, at a depth d_T (E_T,ϕ_T). Let S_o be the part of the surface covered by the oxide, $(1-S_o)$ the part where the trench is opened and S_T the flat area of the bottom of the trench ($S_T < 1-S_o$). The signal is:

$$J = |E|^2 = \left|\vec{E_T}S_T + \left[\vec{E_o}+\vec{E_f}\right]S_o\right|^2$$

During the etch, d_o is reduced and d_T increases. The signal can be calculated with respect to S_o and S_T, either by a computer simulation, or by measurements on an abacus.

The signal is studied in three types of patterns:

1- In the first area, there is no oxide (S_o=0) When the bottom of the trench is flat, S_T=1 and the signal is constant. When the bottom is rough, a part of the signal is not reflected in the right direction, and the intensity is reduced. The observation of this reduction is the best way to quantifie this roughness (black silicon) and the moment of the plasma cycle when it begins.

2- In the second area there is no trench (S_o=1); the signal is the interference between $\vec{E_o}$ and $\vec{E_f}$. In our case where $\Delta\phi_{films}$ is 1.52 rad (fig 1), the maximum of J is for $d_o=d_{om}$= 104.5 + m*217.2 (nm) (m: integer). This signal monitors the etch rate of SiO_2.

3- On a partially opened area (S_o=0.8), the signal fluctuates periodically (figure 2), due to the interferences between E_i and E_i+E_o. -If r is the etch rate ratio between Si and SiO_2, the period is $\lambda/(1+r)/2n$ = 1,1 d_{om}. It means the silicon etch rate, is the oxide etch rate is measured on the 2nd area.

-The maximum of the envelops of the curves corresponds to a value of d_{om} and gives the knowledge of the absolute value of d_o and d_T. The information is available at the beginning of the plasma cycle (t=0), giving a measurement of the initial conditions

-The distance between the envelops is proportionnal to S_T, and measures the reduction of S_T during the cycle, either in the case of roughness of the bottom (correlated with the reduction of J in the first area), or when facets exist at the bottom of the trench (no correlation with J reduction in the first area).

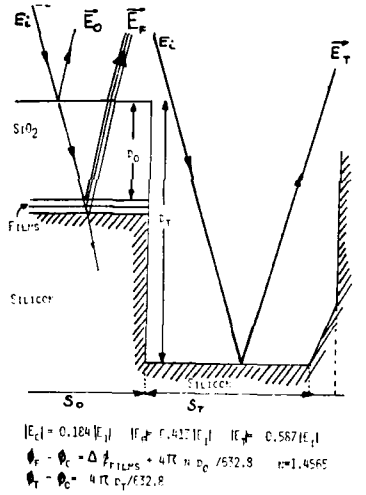


Figure 1: section of the trench, reflected beams electric field, amplitudes and phases

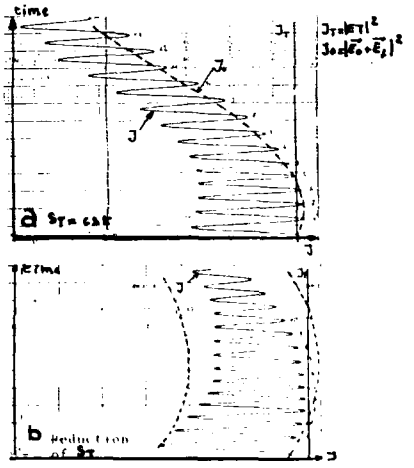


Figure 2: Laser signal intensity vs time

static C-V technique. The result of these additional experiments will be presented.

ACKNOWLEDGMENTS

The authors would like to thank S. Ueland and his staff for the processing of the test structures used in the experiments.

REFERENCES

1) Y. Tomaki, S. Isomae, K. Sagara and T. Kure, J. Electrochem. Soc., Vol. 135, 726 (1988).

2) S. Isomae, J. Appl. Phys., Vol. 52, No. 4, 2782 (1982).

3) S. Mukherjee, M. Kim, L. Tsou, and M. Simpson, To be published.

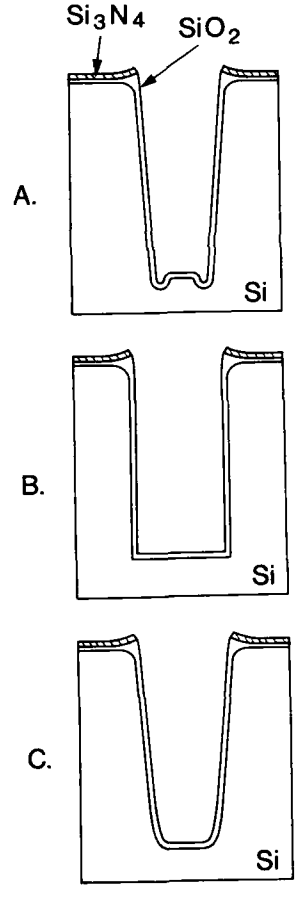


Fig. 1. Schematic cross-section diagrams for three different types of trenches: A) corner deepening, B) right angle corner, and C) rounded corner.

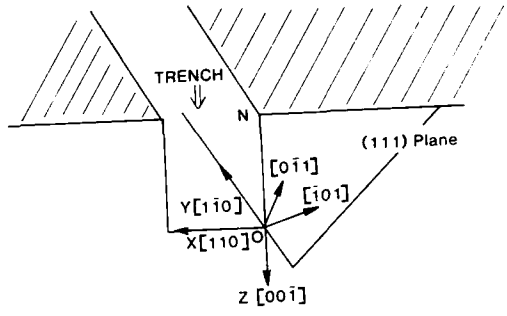


Fig. 2. Schematic diagram of dislocation generations at the trench corner and the gliding plane.

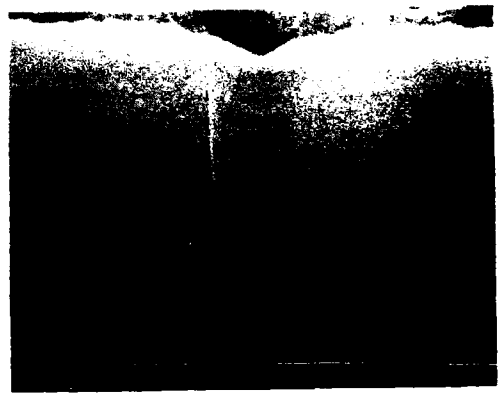


Fig. 3. SEM photomicrograph of an ideal trench with rounded corner: in-situ poly is filled in after a thin trench oxidation.

Abstract No. 241

TRENCH OXIDATION FOR MINIMIZATION OF DEFECTS

M. J. Kim, L. Tsou, S. Mukherjee, and D. C. McArthur

Philips Laboratories
North American Philips Corp.
Briarcliff Manor, N.Y. 10510

I. INTRODUCTION

Trench technology is getting more attention for VLSI as well as power IC development. Trenches can be used to make various kinds of silicon device structures including those for isolation, storage capacitor of DRAM, vertical DMOS (doubly diffused MOS-FET), and other three dimensional devices. Since the trench is etched into silicon substrate to be filled with an other material, it can generate potential problems unless a special process is used to overcome them. There have been many studies on trench formation and the follow-up processes in conjunction with the applications to device fabrication. In almost all cases, a thermal oxidation is needed to maintain the interface integrity. The stress distribution and the defect generation scheme however are unique for the trench oxidation since it is taking place in a confined space. Defect generation associated with the trench oxidation was recently evaluated for thick oxide (1).

The purpose of this study is to investigate trench oxidation to minimize defect generation. In order to reduce defect generation during trench oxidation, it is necessary to improve the entire trench process. The trench corner must be rounded to avoid stress concentration. A corner deepening is particularly detrimental. Thin oxide induces less stress and can make a good isolation with a refill poly, as long as the thickness is optimized to sustain the required breakdown voltage. The oxidation temperature must be above viscous flow temperature so that the stress from oxide volume expansion is relieved within the oxide instead of transmitting to the silicon. The formation mechanism of the oxidation induced dislocation will be discussed.

Effect of cleaning on surface states density is also studied. The fast and slow states are measured using high frequency and quasi-static C-V measurements. The trench surface defects can further be removed by a sacrificing oxidation. The method of poly refill is also reviewed for fabrication of a active device. Using the trench DMOS, the interface characteristics such as mobility, leakage current, threshold voltage, etc are also evaluated.

II. EXPERIMENTAL METHODS

Silicon wafers used in this study were n-type silicon of (100) orientation with a resistivity range of 0.5 and 1.2 ohm-cm. A pad oxidation of 500A was thermally grown followed by a 1400A nitride deposition using LPCVD. A trench resist pattern was made with Kodak 820 and reactively etched to a depth range of 2.5 and 7.0 microns. In some cases, one micron LTO has been used instead of the resist mask. Various methods of RIE techniques have been tried to control the trench shape. Three different methods were used to clean the trench surface: standard wet cleaning, dry cleaning in a gas phase etch and wet chemical etch. In the two latter cases, a few hundreds Angstroms of silicon were removed to reduce any residue or damage caused by the trench RIE. One thousand Angstroms of sacrifice oxide was grown and wet etched for a further reduction of the surface damage.

The final trench oxide was grown to 1000A in a temperature range from 750C to 1100C. A wet oxidation was tried at the lower temperature range, 750C-1000C, whereas dry TCA oxidation was done in the higher temperature range, 950C-1100C. The trench was filled with in-situ poly doped with phosphorus. A trench of 1.2 micron wide could easily be filled with 1.0 micron thick poly without creating any voids. The characteristics of the narrow trench can represent sidewall quality. For the bottom surface study, a wide trench in square form was formed to make poly-to-substrate capacitors. High frequency and quasi-static C-V measurements were done to find the slow and fast states densities.

When trench DMOS was made the p-body was diffused first before the trench etching. The refilled poly was planarized, followed by n+ source implantation. The trench DMOS allowed us to measure the surface mobility, leakage current, etc, which are also useful criteria to define the trench quality. Cross section analysis was done with SEM and chemical etching. Secco etch was applied to a cleaved surface to characterize dislocation density change with respect to oxidation temperature and surface treatment before oxidation.

III. RESULTS AND DISCUSSION

The shape of trench is very important to make a good quality oxide and reduce defects in the silicon. There are essentially three types of trench shapes as shown in Fig. 1. When a trench is anisotropically etched, a corner deepening similar to Fig. 1A is likely to be obtained. This type of pointed corner generates the worst quality oxide with formation of a large number of defects due to a wedge stress effect caused by volume expansion of oxide. A better control of reactive gas composition can improve it nearly to a right angle of the type B in Fig. 1. This of cause is better than type A but can also create a large number of defects. A large volume expansion of the thermal oxide induces compression in the oxide and tension in the silicon. The stress is concentrated at the end of a dielectric pattern (2) in a planar structure.

Figure 2 shows a schematic presentation of dislocation generation during the oxidation. The stress is concentrated at the corner due to the physical limitation of the trench sidewall. This will generate a large amount of shear stress in X direction. Since trench is made in parallel with wafer flat, the stress will be in the [110] direction. The dislocation gliding plane (111) passing through the corner O is schematically presented in Fig. 2. When stress surpasses the yield point, dislocations will be generated on the (111) plane with $[\bar{1}01]$ and $[0\bar{1}1]$ Burgers vectors. As oxide thickness increases, more stress will be generated to form additional dislocations to be glided along (111) plane. A similar stress center will also be created at the top edge N where both dielectrics meet at a right angle. In this case the dislocations are gliding downward on another {111} plane generating dislocation tangles in the middle of the silicon steps. Many dislocation pits were observed along the {111} planes after a thick trench oxidation (1). The dielectric breakdown measurements shows as low as 30 V for the 1000A oxide. This indicates that the sharper corners also create weak spots within the oxide. Therefore, corner rounding is very important for the trench etching.

Figure 3 shows an ideal trench shape with rounded corner. Reproduction of the rounded corner is not a easy task. It requires aprecise control of the gas composition and etching rate in several stages. A thinner oxide is preferred because of less stress generation. Since the large stress caused by the oxide volume expansion can only be relieved either by defect generation or viscous flow, a high temperature oxidation, above the viscous flow temperature 1050C, is desired to reduce defect generation. The rounded corner is helpful because a relatively uniform viscous flow is expected. The structure is Fig. 3 has 1000A thin oxide with filled-in poly. This structure is expected to be relatively free from defects and can be used for isolation or 3D device fabrications.

Trench DMOS was made using the structure in Fig. 3. Ultra low on-resistance (3) could be achieved with the high density DMOS of 1.2 micron trench. It was found that off-state leakage was much lower with the high temperature gate oxide, which could be linked to the reduction of defects. The rounded corner device showed higher dielectric breakdown voltage. A more systematic study of the oxide integrity is under way to establish a more precise inter-relationship of the oxide quality with the device performance parameters. The measurement of the states densities at the trench oxide interface are also progressing, using quasi-

Abstract No. 240

PLANARIZED BOROPHOSPHOSILICATE GLASS (BPSG) DEPOSITED FROM ORGANOMETALLIC SOURCES

Dean W. Freeman, Mark A. Logan, Lloyd F. Wright, and Joseph R. Monkowski
Monkowski-Rhine Incorporated, San Diego, CA

INTRODUCTION

As device technology drives towards double and triple level metal with shrinking pitch sizes, planarization prior to metallization is becoming increasingly important. As a result, the requirements for the borophosphosilicate glass used as the interlevel dielectric are becoming more stringent. These glasses need to deposit conformally, and then reflow in such a manner to efficiently refill or planarize the device surface prior to metallization. More importantly, the thermal budget of the deposition and reflow must be kept to a minimum in order to be compatible with the shallow junction depths needed for advanced devices.

State of the art BPSG deposition techniques employ hydride chemistries of silane, oxygen (or nitrous oxide for plasma), diborane, and phosphine to deposit BPSG. These films are typically deposited at ~400°C, then reflowed at higher temperatures. The resulting film topology is a mounded surface with roughly 30° angles over the 90° steps into the contacts.[1]

As device geometries shrink, however, the hydride chemistries do not provide sufficient step coverage into the contacts. As a result, organometallic sources, which are also safer, have been substituted for these hydrides.[2,3] Becker, et al., introduced TEOS, trimethylborate (TMB), and phosphine into a horizontal LPCVD furnace and were able to deposit uniform BPSG films. When they attempted to use trimethylphosphate (TMPate) in place of PH3, Becker et al. observed low wt % P resulting from the low vapor pressure and reactivity of TMPate. When they attempted to use trimethylphosphite (TMPite), they observed nonuniformities and depletion due to the reactivity of the TMPite. More recently, Becker has demonstrated the ability of the TEOS, TMB, and PH3 BPSG films to achieve complete refill and planarization of high aspect ratio trenches. The reflow was accomplished with a post deposition anneal.

Recent work by Levy, et al., has demonstrated that an organometallic-based BPSG process can produce conformal films for small wafer loads.[4] Although conformal deposition was achieved, a subsequent anneal was required to reflow the films.

In this paper the authors demonstrate that organometallic sources can be used to deposit a TEOS BPSG film. In addition to depositing a conformal BPSG film we will demonstrate that these films can be reflowed in-situ at temperatures lower than those currently used for BPSG reflow, thus reducing cycle time and thermal budget.

EXPERIMENTAL

A novel LPCVD reactor was used to deposit BPSG on 4-6 inch wafers. TEOS, TEB, and t-butylphosphine, supplied by American Cyanimide, were used as the sources for the deposition of the glass. Temperature, pressure, and vapor flow rates were varied in order to achieve optimum trench fill and planarization characteristics. Thickness was determined using a Nanometrics Nanoline/AFT and a Rudolph AutoEl ellipsometer. Dopant concentrations were determined with a Digilab Biorad FTIR and wet chemical techniques.

RESULTS AND DISCUSSION

BPSG films of up to three microns thickness were deposited for trench refill and planarization. The films are compressive; thus no cracking of the films was observed. Dopant concentrations were varied from 0 wt% to 10 wt% for phosphorus and from 0 wt% to 5 wt% for boron. The conformality of these films is nearly 100%, which allows for complete trench or contact refill without the formation of voids.

If reflow of the film is desired the reflow may be performed insitu at temperatures as low 800 degrees C. This allows for a very planar surface. The ability to perform the reflow of the glass in-situ at such a low temperature not only reduces the total thermal budget, but eliminates a process step, reducing the overall cycle time of the BPSG deposition and reflow sequence.

CONCLUSION

The authors have demonstrated that conformal BPSG films can be deposited from organometallic sources. These glasses can be reflowed in-situ to yield a planar surface for subsequent metallization.

REFERENCES

1. J.S. Mercier, Solid State Technology, Vol. 30, No. 7, p. 85 (1987).

2. F.S. Becker, D. Pawlik, H. Schafer, Journal of Vacuum Science Technology B. Vol. 4, No. 3, p. 732 (1986).

3. F.S. Becker, Journal of Electrochemical Society, Vol. 134, p. 2923 (1987).

4. R.A. Levy, P.K. Gallagher, F. Schrey, Journal of Electrochemical Society, Vol. 134, p. 430 (1987).

Table I

TMCTS - Oxygen Film Properties

Process Conditions	
Temperature	600°C
Oxygen: TMCTS	> 4:1
Pressure	400 mTorr
Properties	
Refractive Index (632.8 nm)	1.450 ± .005
P-Etch Rate (25°C)	< 1 nm/sec
Breakdown Voltage	4-6 x 10^6 volts/cm
Film Stress	
< 300 nm	< 2 x 10^9 dynes/cm^2 compressive
500-1500 nm	< 3 x 10^9 dynes/cm^2 tensile
Stoichiometry	1.0 Si : 2.0 (RBS)
Carbon Content	< 0.01 % (SIMS)
Film Uniformity	± 2% (Quartzware dependent)

Abstract No. 239

Silicon Oxide Deposition from Cyclic Siloxane Precursors

A.K. Hochberg, A. Lagendijk, and D.L. O'Meara

J.C. Schumacher Company
1969 Palomar Oaks Way
Carlsbad, Ca. 92009

The requirement for lower temperature processing in VLSI device fabrication and the need for the elimination of hazardous gas sources from the workplace have spurred extensive investigations into new chemical vapor deposition source materials.

Tetraethoxysilane, TEOS, has been used as a silicon oxide source for many years in the temperature range of 650 to 750°C, and the resulting conformal coatings have been applied for trench filling. Lower temperature oxide depositions will be needed however in the presence of VLSI silicide layers.

Plasma- assisted TEOS processing has been attempted in the temperature range of 300 to 425°C (1), but trench filling and doping still require further investigation. Low temperature silane oxides thermally deposited at (400±50)°C have poor conformality (2). In addition, silane is quite hazardous.

Mono-alkyl cyclic siloxanes have been found to be suitable sources for silicon oxide deposition at temperatures below those for TEOS. For instance, 2,4,6,8-Tetramethyl-cyclotetrasiloxane, TMCTS, can produce silicon oxide films with deposition rates and conformality equal to those from TEOS, but at temperatures 100°C lower.

The decomposition of TMCTS is dependent on the oxygen to TMCTS ratio, with negligible deposition occurring in the absence of oxygen, as indicated in Figure 1. The volatile reactive species, possibly Si-O, appears to have surface migration characteristics comparable with those of TEOS decomposition products as evident by the trench filling shown in Figures 2a and 2b. The TMCTS film properties are indicated in Table 1.

Alternate alkyl cyclosiloxanes have also been investigated. As expected, the introduction of other alkyl groups results in a different deposition temperature range. The tetraethyl homologue of TMCTS, TECTS, appears to be a lower temperature source, with practical silicon oxide deposition rates at a temperature of 440°C.

The kinetic data presented in Figure 3 shows, clearly, the usable temperature range for TEOS, TMCTS and TECTS. While the sources can be used at higher temperatures, the increased reactivities may lead to nonuniform depositions in conventional 'stacked wafer' LPCVD reactors. In general, however, the cyclic siloxanes are very promising candidates for neat and doped silicon oxide depositions.

1. B.L.Chin and E.P.van de Ven, Solid State Technology 31(4), 119 (1988).

2. R.M.Levin and K.Evans-Lutterodt, J. Vac. Sci. Techn. B1(1), 54 (1983).

Fig.1

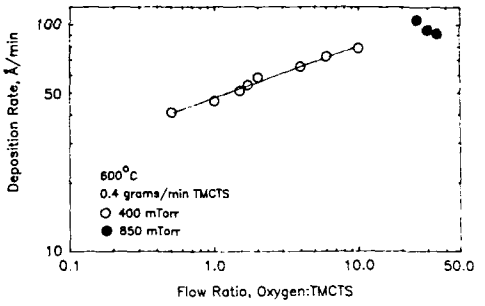
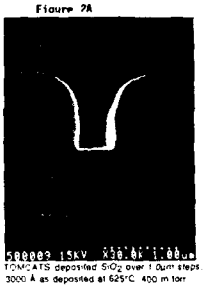


Figure 2A



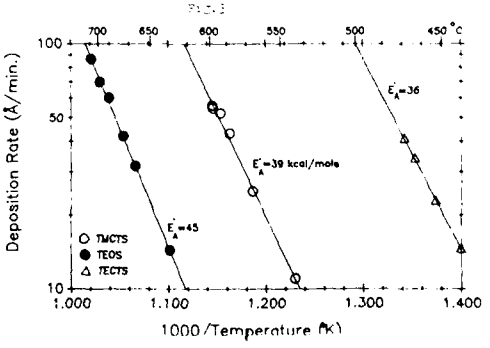
TOMCATS deposited SiO_2 over 1.0μm steps
3000 Å as deposited at 625°C 400 m torr

Figure 2B



Trench filled with TOMCATS deposited SiO_2
8800 Å as deposited at 600°C 400 m torr

Fig.3



10. I. Avigal, "Inter-Metal Dielectric and Passivation-Related Properties of Plasma BPSG," Solid State Technology, vol. 26 (10), pp. 217-224 (1983); see also Errata, vol. 27 (2), pp. 139 (1984).

11. J. E. Tong, K. Schertenleib, R. A. Carpio, "Process and Film Characterization of PECVD Borophosphosilicate Films for VLSI Applications," Solid State Technology, vol. 27 (1), pp. 161-170 (Jan 1984).

12. S. Shanfield, S. Bay, "Process Characterization of PSG and BPSG Plasma Deposition," J. Electrochem. Soc., vol. 131, pp. 2202-2X203 (1984).

13. J. Houskova, K. K. N. Ho, M. K. Balazs, "Characterization of Components in Plasma Phosphorus Doped Oxides," Semiconductor International, VOL. 8 (5), PP 236-241 (1985).

14. F. S. Becker, D. Pawlik, H. Schafer, G. Staudigl, "Process and Film Characterization of Low Pressure Tetraethylorthosilicate - Borophosphosilicate Films," J. Vacuum Science Technology, vol. B4 (3), pp. 732-744 (1986).

15. D. S. Williams, E. A. Dein, "LPCVD of Borophosphosilicate Glass From Organic Reactants," J. Electrochem. Soc., vol. 134, pp. 657-664 (1987).

16. R. A. Levy, P. K. Gallagher, F. Schrey, "A New LPCVD Technique of Producing Borophosphosilicate Glass Films by Injection of Miscible Liquid Precursors," J. Electrochem. Soc., vol. 134, pp. 430-437 (1987).

17. R. A. Levy, P. K. Gallagher, F. Schrey, "LPCVD of BPSG Films Produced by Injection of Miscible DADBS-TMB-TMP Liquid Sources," J. Electrochem. Soc., vol. 134, pp. 1744-1749 (1987).

18. R. A. Levy, K. Nassau, "Reflow Mechanisms of Contact Vias in VLSI Processing," J. Electrochem. Soc., vol. 133, pp. 1417-1423 (1986).

19. R. A. Levy, K. Nassau, "Viscous Behavior of Phosphosilicate and Borophosphosilicate Glasses in VLSI Processing," Solid State Technology, vol. 29 (10), pp. 123-130 (1986).

20. P. B. Johnson, P. Sethna, "Using BPSG as an Interlayer Dielectric," Solid State Technology, vol. 11 (10), pp. 80-84 (1987).

21. J. S. Mercier, "Rapid Flow of Doped Glasses for VLSIC Fabrication," Solid State Technology, vol. 30 (7) pp. 85-91 (1987).

Table 1

DEPOSITION PROCESSES AND CONDITIONS FOR BPSG FILM FORMATION

CVD Type	Reactor Type	Reactant Types	Reactants	Diluent	O_2/Hydride mol ratio	Temp., °C	Pressure Torr	Dep. Rate nm/min
AP	planar rotary, conveyorized dispersion, or injector	hydride	SiH_4, B_2H_6 PH_3, O_2	N_2	40-60	340-375	760+	120
					40-60 12-150	340-375 300-450		120 100-300
LP	vertical isothermal	hydride	SiH_4, B_2H_6, PH_3, O_2	none	1.5	400	0.19	20-25
LP	tubular horizontal	hydride -chloride	SiH_4, BCl_3, PH_3, O_2	none	1.5	425	0.18-0.40	15-20
LP	modified tubular horizontal	organic	TEOS, $(CH_3O)_3$ B, $(CH_3O)_3$ P or PH_3, O_2	"2, Ar		620-680	0.5	5-10
PF	tubular horizontal, (planar radial)	hydride	SiH_4, B_2H_6, PH_3, O_2, N_2O	none	(N_2O+O_2)/Hy 35-40	380	0.83	200-500

Abstract No. 238

DEPOSITION PROCESSES FOR BOROPHOSPHOSILICATE GLASS FILMS

Werner Kern, Dean Freeman
Monkowski-Rhine, Incorporated
San Diego, CA 92126

Films of borophosphosilicate glasses (BPSG) have been successfully used for the planarization and interconductor insulation of VLSI silicon circuits because of their excellent properties and viscous flowability at relatively low temperatures. Several CVD processes have been developed for synthesizing films of BPSG. This paper reviews the various options that are now available to the process engineer. Details are summarized in Table 1.

The original process[1,2] was based on the CVD reaction at atmospheric pressure from the N_2-diluted hydrides SiH_4, B_2H_6, and PH_3 with O_2 at 430°C using conventional rotary and conveyorized reactors. Lowering the temperature to 340-375°C and increasing the O_2/hydride ratio from 20:1 to 40:1-60:1 and beyond increases the rate of film formation by reducing the particle generation.[3-5] An advanced conveyorized APCVD reactor, currently available, features a slotted gas injection system that leads to improved uniformity of film thickness, with lowered particle densities.[6]

Hydride based low-pressure CVD in tubular horizontal reactors prevents the introduction of sufficient B_2H_6 because of decomposition in the hot gas distribution tube inside the reactor. The thermally more stable BCl_3 can be substituted[7] but leads to 0.5% Cl in the BPSG films.[8] One approach to preventing depletion effects has been the use of a vertical-flow LPCVD batch reactor. This reactor uses hydride chemistry and eliminates gas depletion, but requires rather high concentrations of hydrides.[9]

Plasma-enhanced CVD has been used for forming BPSG films from the hydrides.[10-12] The application of a plasma seems redundant since temperatures similar to APCVD or LPCVD are used and some undesirable side effects occur.[13]

The synthesis of BPSG can also be based on tetraethylorthosilicate (TEOS) with trialkyl borates and phosphates or phosphites, as well as PH_3.[14,15] The high surface mobility of TEOS leads to excellent conformal coverage, a key requisite for void free planarization. The lowered toxicity of these organic reactants compared to the hydrides is an additional advantage. The reactants can be introduced in the reactor by conventional methods or by liquid injection.[16,17]

The fusion flow of BPSG,[18,19] which typically contains 3-5 wt% B and P each, is usually done in a tube furnace for 20-30 min. in N_2, O_2, or steam at 800-950°C. Reflow after etching the vias must be done in a dry ambient, usually O_2, to grow a thin protective oxide layer, followed by N_2.[1-3,5,20] Rapid thermal heating allows flow in seconds instead of minutes, but at 100-175°C higher temperatures.[3,21] However, rapid thermal heating is not always advantageous in preventing dopant diffusion into the substrate.[8]

REFERENCES

1. W. Kern, G. L. Schnable, "Chemically Vapor-Deposited Borophosphosilicate Glasses for Silicon Device Applications," RCA Review, vol. 43, pp. 423-457 (1982).

2. C. Ramiller, L. Yau, "Borophosphosilicate Glass for Low Temperature Reflow," Paper presented at SEMICON/WEST '82, May 25, 1982, San Mateo, CA; Technical Program Proceedings, pp. 29-37.

3. W. Kern, "Optimized Atmospheric-Pressure CVD of Borophosphosilicate Glass Films," RCA Review, vol. 46, pp. 117-152 (1985).

4. C. Dornfest, "The Effect of Reducing Deposition Temperature in an Atmospheric Pressure BPSG Process," Electrochem. Soc. Ext. Abst., vol. 85-1, pp. 347 (May 1985).

5. W. Kern, R.K. Smeltzer, "Borophosphosilicate Glass for Integrated Circuits," Solid State Technology, vol. 28 (6), pp. 171-179 (1985).

6. H. H. Hurley, L. D. Bartholomew, D. T. Bordonaro, "BPSG Films Deposited by APCVD," Semiconductor International, vol. 11 (10), pp. 91-95 (1987).

7. T. Foster, G. Hoeye, J. Goldman, "A Low Pressure BPSG Deposition Process," J. Electrochem. Soc., vol. 132 (2), pp. 505-507 (1985).

8. W. Kern, unpublished results.

9. A. J. Learn, W. Baerg, "Growth of Borosilicate and Borophosphosilicate Films at Low Pressure and Temperature," vol. 130, pp. 103-111 (1985); see also: "Full Spectrum CVD System," Solid State Technology, vol. 26 (12), pp. 61-62 (1983).



(a) (b)

Fig. 1. (a) Modulated reflectance image of a stacking fault on a patterned Si wafer. The two bright dots which taper toward one another are the ends of the bounding dislocation. The actual distance between the two dots is approximately 40 microns. This image is measured through a SiO2 film (348 Angstroms) [2].
(b) Conventional optical photomicrograph (at slightly larger magnification) of the same region as in (a) after oxide strip and Wright decoration etch [2].

Abstract No. 237

Si CRYSTALLOGRAPHIC DEFECTS ON TRENCH-ISOLATED BIPOLAR IC WAFERS IMAGED WITH NONDESTRUCTIVE THERMAL WAVE IMAGING

S. Marks
Advanced Micro Devices
8611 Military Drive West
San Antonio TX 78245

W. Lee Smith and D. Willenborg
Therma-Wave, Inc.
47734 Westinghouse Dr.
Fremont CA 94539

Trench isolation is a technology to which the IC industry worldwide is becoming heavily committed as a means of achieving further increases in packing density [1]. Issues of reliability and yield of trench structures are basic to this effort.

In this article, we describe the application of a newly emerging subsurface Si defect imaging technique [2] to problems of process control of trench-isolated bipolar VLSI circuits. We focus on issues of process control, defect generation and detection that arise uniquely with trench structures. The pragmatic goal of this study was to develop a real-time subsurface Si defect inspection method, usable in a nondestructive manner on in-process product wafers, for minimization of process-induced subsurface defects such as dislocations originating from furnace contamination or oxidation-induced stress.

The laser-based, thermal wave modulated reflectance images are generated in a noncontact, nondestructive manner with image acquisition time of 1 minute for a 100 micron by 100 micron image. The spatial resolution is 1 micron; however defects much smaller than that size are detectable. An unusual aspect of this technique is that each image shows a projection of all defects contained within the sampled volume, which typically extends from the surface to a depth of 3 - 5 microns into the Si. The method operates in room ambient conditions (no vacuum), requires no special sample preparation, and is able to image through transparent overlayers such as silicon dioxide. As such, it is able to operate on in-process wafers at various production steps, such as after trench etching or field oxidation, prior to metallization for detection of process-induced defects.

The first images generated with this method [2] were those of stacking faults and dislocations induced in silicon wafers by a damaging gettering technique followed by oxidation. An example is included here as Fig. 1. The comparison of the post-oxidation thermal wave (TW) images with standard optical microscope images made after oxide stripping and Wright etch showed a spatially definitive correspondence between the two methods.

In the present study we examined VLSI bipolar wafers for subsurface defects by using conventional, destructive decoration etching methods and the new method of thermal wave modulated reflectance imaging. Comparisons were made in a spatially located manner so that the exact same silicon area could be first thermal wave imaged and then decoration etched and microphotographed. Wafers were examined after the processing steps of field oxidation, base diffusion and emitter implant anneal.

Thermal wave images show the presence of defects extending predominantly from the trenches into the active interior region of the transistor cells. Adjacent cells may show significantly different defect behaviour. Crystallographic slip, apparently associated with the trench oxidation process, was also imaged on some wafers.

In addition to the comparative examples of this defect imaging method, we will describe the current status and expectations of this method as a production monitor for yield enhancement of trench bipolar VLSI circuits.

References:

1. V. Rice, "Cell Structures of Next-Generation VLSIs", J. Electronics Engineer., Nov. 1987, p. 38.

2. B. Witowski, W. Lee Smith and D. Willenborg, "Nondestructive Technique for the Detection of Dislocations and Stacking Faults on Si Wafers", Appl. Phys. Lett. 52, 640 (1988).

Abstract No. 243

A Novel Process for High Speed Silicon Trench Etching

Jeanne M. McNamara, James L. McNamara

Harris Semiconductor
Melbourne, Florida 32906

Introduction

Traditional silicon trench etch processes have faced difficulty in simultaneously optimizing the etch rate, selectivity, profile, and uniformity. A high speed silicon trench etch has been developed using a high pressure, low power SF_6/O_2 process. This process has been developed in a Drytek 102 Plasma Etcher. The process is capable of producing trenches as deep as 12 microns in 2 minutes. It produces near vertical sidewalls with good replication of the masking pattern. Both photoresist and photoresist on oxide masks have been studied during the optimization of this process.

Experimental Procedures

Feasibility tests were run to determine the process physical limits and to gather basic information on the probable settings for the optimum process. The trench etch pilot wafers were <100> n-type, 3-5 ohm-cm 100 mm diameter, CMOS starting material. The trench mask was a single width trench isolation mask with nominal 5 micron lines. The wafers were coated with 1.2 microns of Shipley 1400-27 resist. The trench pattern was transferred to the wafers by exposure on a Perkin-Elmer 200 series projection aligner and the photoresist hardbaked in a 130 degree convection oven. Based on the preliminary results, response surface methods were used to design a three factor matrix, studying the effects of chamber pressure, applied power, and process gas ratio on the responses of etch rate and trench profile. The etch time was fixed at two minutes, the electrode spacing was chosen to be 5/16 of inch. The other available variables in the process were also fixed, since they did not appear to be critical factors. Each matrix was run in ramdom order. This design also looked at etch uniformity and repeatability, and took into account any interactive effects of the basic factors. Each matrix consisted of 17 runs sampling 5 levels of each factor as shown in Table 1.

Table 1 Levels of Process Settings

Level	Parameters		
	Pressure (mtorr)	Power (watts)	SF_6/O_2 Ratio
1	475	125	3.33
2	550	200	2.50
3	650	300	2.00
4	750	400	1.67
5	825	475	1.43

Flow ratios were determined with SF_6 flow fixed at 50 sccm. Power settings were for the single wafer etcher; settings for the stacked system were higher to account for the higher wafer area.

The full matrix was repeated for both oxide masked patterns and for photoresist masked patterns. This process has been run in both a single wafer Drytek 102 and the standard 5-wafer stacked electrode Drytek 102.

Results and Discussion

Results were measured by SEM cross sections of the trenches produced. These results show the ability to produce trenches of different depths and shapes by selective choice of process parameters. The optimum response for both masking types came at a pressure of 550 mtorr, power of 200 watts, and a flow ratio of 2.50. At these settings, the oxide mask produced trenches 11 microns deep, 7 microns wide (from a 5 micron mask) and an 80 degree sidewall angle (Fig. 1). The photoresist mask produced trenches 6.3 microns deep, 6.7 microns wide (from the same 5 micron mask) and a 90 degree sidewall angle (Fig. 2). The difference in width/undercut is explained by the probable inhibition of the passivating sidewall oxide formation by the oxide mask. The increased depth is most likely caused by a focusing effect when the plasma passes through the oxide surface mask. The ultimate depth limitation of the process is not known at this time. Minimum masking geometry has also not been studied. Profiles from vertical to sloped are achievable and repeatable. Oxide masked trenches showed some evidence of undercut which can be overcome by mask sizing. Photoresist masking is as effective as oxide masking. As opposed to the oxide mask undercut, there was some edge erosion with the photoresist. However, no special methods were employed to harden the resist. The bottom corners of the trenches are rounded and the bottom is smooth and nearly flat, since this is an oxide passivated directional etch process instead of a true anisotropic etch. This provides an optimum profile for oxide refill of the trenches. Selectivity to both oxide and photoresist is excellent with photo-resist selectivity equal to 20:1 and oxide selectivity equal to 70:1.

Conclusion

The basic issue of sacrificing etch rate (and therefore process efficiency) to achieve acceptable etch profiles and the issue of needing multilevel masking materials have been effectively resolved by the development of the described process. The 4 to 6 microns per minute etch rate, the near 90 degree sidewall, and the flexibility in available masking materials all combine to make this the process of choice for many silicon trench operations. Of particular promise is the corner shape at the base of the trenches, in light of the reported difficulties with oxide refill. Studies to improve this process will continue. At present, estimated throughput in a production environment would be 60 wafers/hour in the stacked electrode Drytek 102.

Acknowledgement

The authors would like to thank Mike Shlepr, Richard Belcher, and Jack Linn of the Harris Semiconductor Analytical Lab for their support in taking the many SEM micrographs needed to complete this project.

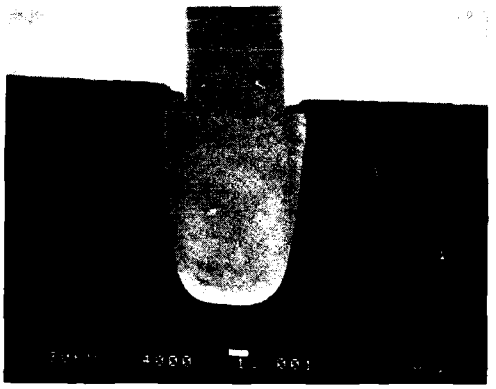


Fig. 1: SEM photograph of photoresist/oxide masked silicon trench.

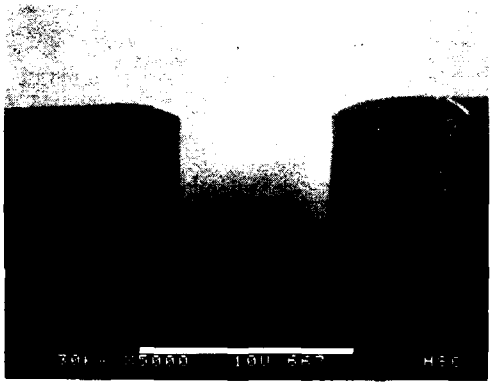


Fig. 2: SEM photograph of photoresist masked silicon trench.

Abstract No. 244

A LOW ION ENERGY TRENCH ETCH PROCESS FOR POWER MOS APPLICATIONS

C. J. Petti, J. P. McVittie, and J. D. Plummer

Center for Integrated Systems, Stanford University, Stanford, CA 94305

When considering MOS devices for high power applications, a prime criterion is the current carrying capability per unit chip area. This current density can be greatly increased by incorporating the channel area of the device onto the sidewall of a trench [1,2]. Also, some power device designs require deep MOS-structure trenches to divert current flow and bring the device out of a regenerative state [3], or to access layers deep within the device [4]. All of these applications require MOS structures that can withstand high voltages without breaking down. Therefore, the smoothness of the trench profile is of paramount importance.

The dry etch process presented here features a low ion energy to insure a damage free etched surface [5]. This process uses SF_6 and C_2ClF_5 in a symmetric, equal electrode area RF reactor with the sample sitting on the grounded electrode. The energy flux density on the sample was $\sim 0.36 W/cm^2$. The anisotropy of the etch was caused by the deposition of a thin (< 50 Å) polymer etch inhibitor layer on the sidewalls [6]. This deposition requires the presence of a photoresist layer on the sample. This photoresist layer was etched away at a rate 1/7 times that of the underlying silicon. The silicon etched vertically at a rate of 3700 Å/min, typically, and the lateral undercut for this process was on the order of 200 Å/min, or roughly 1 μm laterally, per side, for every 18 μm vertically.

A typical trench cross section is shown in figure 1. In this figure, the bottom corners of the 14 μm deep trench are rounded. This effect, caused by slightly different etch rates for the (111) and (100) crystallographic planes [7], is desirable, since it reduces the amount of oxide thinning [8] and electric field line crowding at the corners.

Trenches like the one in figure 1 whose sidewalls are (110) planes, as well as trenches whose sidewalls are (100) planes, were etched and subsequently oxidized under either wet or dry conditions, so that an oxide of either $\sim$ 500 Å or $\sim$ 1000 Å was grown (no special post-etch treatment was given to these trenches). After polysilicon deposition and patterning, the trench capacitors were tested for destructive gate oxide breakdown voltage. The resulting breakdown fields for simultaneously fabricated trench and surface capacitors are plotted versus oxide thickness in figure 2. The oxide thicknesses were measured with capacitance techniques or scanning electron microscopy.

The breakdown fields shown in figure 2 are generally higher than for trenches etched with a higher power density in a chlorine based chemistry [9]. This is because those trenches have sharp, sometimes acute, bottom corner angles. In fact, visual inspection of our trench capacitors after breakdown has shown that most of the oxide ruptures were occuring at a top corner of the trench, where the polysilicon comes out of the trench to be contacted, rather than inside the trench itself. This corner breakdown phenomenon explains the fact that our trench capacitors still break down at lower voltages than surface capacitors.

In conclusion, a dry trench etching process using a low energy ion bombardment and a flourine-based chemistry is presented. This process produces trenches with rounded bottom corners, which prevents high electric fields from developing inside capacitors built on these trenches. The result is a trench suitable to incorporate into high voltage, low on-resistance MOS devices.

REFERENCES

[1] D. Ueda, H. Takagi, and G. Kano, "An Ultra Low On-Resistance Power MOSFET Fabricated by Using a Fully Self-Aligned Process," *IEEE Trans. Electron Devices*, vol. ED-34, no. 4, pp. 926-930, 1987.

[2] H. R. Chang, B. J. Baliga, J. W. Kretchmer, and P. A. Piacente, "Insulated Gate Bipolar Transistor (IGBT) with a Trench Gate Structure," *IEDM Tech. Dig.*, 1987, paper 29.5, pp. 674-677.

[3] C. J. Petti and J. D. Plummer, "The Field-Assisted Turn-Off Thyristor: A Regenerative Device With Voltage Controlled Turn-Off," *IEDM Tech. Dig.*, 1987, paper 29.2, pp. 662-665.

[4] D. K. Y. Liu and J. D. Plummer, "A Novel Trench-Injector Power Device With Low On-Resistance and High Switching Speed," *IEEE Elect. Dev. Lett.* **EDL-9**, no. 7, 1988.

[5] C. Gonzales and J. P. McVittie, "A Study of Trenched Capacitor Structures," *IEEE Elect. Dev. Lett.* **EDL-6**, no. 5, pp. 215-218, 1985.

[6] J. P. McVittie, T. A. Lin, and A. J. Bariya, "A New Method for Analyzing Thin Sidewall Inhibitor Layers", *Mat. Res. Soc. Symp. Proc.*, **84**, pp. 200-210, 1987.

[7] J. I. Ulacia F., C. J. Petti, and J. P. McVittie, "Crystal Orientation Dependent Etch Rates and a Trench Model For Dry Etching," *J. Electrochem. Soc.*, **135**, no. 7, 1988.

[8] D. B. Kao, K. C. Saraswat, J. P. McVittie, and W. D. Nix, "Two Dimensional Silicon Oxidation Experiments and Theory," *IEDM Tech. Dig.*, Paper 14.6, 1985, pp. 388-391.

[9] C. Kobburger, F. R. White, L. Neslit, and S. D. Emmanuel, "Process Dependent Properties of Three Dimensional Capacitors," *IEEE Trans. Elec. Dev.* **ED-33**, no. 6, pp. 766-771, 1986.

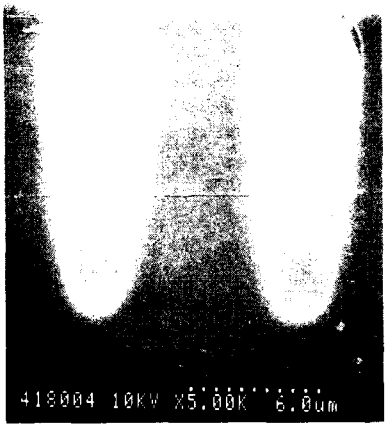


Figure 1: Trenches etched with low ion energy process. Etch time was 40 minutes; trench depth is 14 μm .

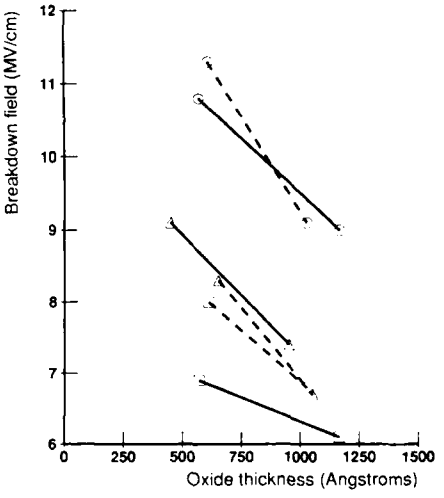


Figure 2: Gate oxide breakdown field vs. gate oxide thickness for (100) sidewall trench capacitors (squares), (110) sidewall trench capacitors (triangles), and surface capacitors (circles). Dashed lines represent wet oxidation; solid lines represent dry oxidation.

Abstract No. 245

ADHESION, SOLDERABILITY, AND PRODUCTIVITY: NEXT GENERATION PTH

Cheryl A. Deckert
Shipley Company, Inc.
2300 Washington Street
Newton, Massachusetts 02162

Over the 30 years, more or less, since the first large scale manufacture of printed circuit boards, many changes in the way of materials, processes, designs, test methods, and end product requirements have taken place. One very technically complex sequence of steps whose basic function has endured over the years is the plated-through-hole process, which creates the base conductive layer on the board's hole wall surfaces that permits build-up of subsequent electrolytic metallization.

Though the general function of the PTH process has remained the same, gradual and continual evolution of the technology has occurred, generally directed toward either quality or productivity improvements. In recent years, since the productivity improvement afforded by introduction of "heavy-build" (2-2.5 µm) electroless coppers about ten years ago, these process changes have been strongly quality-driven, with the trend to more complex boards, especially multilayers, being a major factor.

The term "quality", as related to PTH processing, is defined by numerous parameters[1]. Traditionally, electroless copper coverage and adhesion on all board surfaces have been the main determinants of quality. In more recent years, the benefits of a dense, fine-grained electroless deposit, in comparison with the coarser deposits of the past, have become evident, as interconnect integrity and thermal test requirements have become increasingly more stringent. Finally, the demonstration of a high level of consistency and wide operating window in the overall process has come to be expected.

Achievement of the best process results has been found to be strongly linked with ensurance of a well prepared hole wall substrate surface, and this surface has been best achieved through use of alkaline permanganate hole wall treatment. Permanganate treatment, normally used as a desmear procedure for multilayer boards, has been shown recently to solve a variety of technical problems[2-7]; hence its use has spread widely, not only for MLBs, but in certain areas for double-sided board treatment as well. Dramatic improvements in hole wall adhesion and end board solderability have resulted.

However, needless to say, in today's highly competitive electronics environment, it is most desirable that all quality advances utilized be accompanied by good results in process productivity as well.

Because of the lengthy process line involved when permanganate treatment is employed for all boards, recent efforts have sought to create a new PTH process which would include the permanganate desmear treatment, yet which would fit into the tank space of existing PTH equipment, thus greatly improving productivity. The end result of this work is a novel and already widely production-proven new PTH process[8].

This new process successfully combines various desmear/PTH functions so as to yield a significantly shortened overall process sequence, which actually improves on the quality advances of recent years. This paper will discuss the development and chemistries involved in the new system, as well as production experience gained since the system introduction.

References

1. C.A. Deckert, G.M. Wilkinson, R.J. Covington, and J.J. Doubrava, Proceedings 4th Printed Circuit World Convention, Tokyo, June, 1987, Paper WCIV-51.

2. C.A. Deckert, E.C. Couble, and W.F. Bonetti, InterNepcon U.K., Brighton, U.K., October, 1983; Proceedings 3rd Printed Circuit World Convention, Washington, D.C., May, 1984, Paper WCIII-37; U.S. Patent 4,515,829 (issued May 7, 1985).

3. F.J. Nuzzi, Printed Circuit Fabrication 7 (4), 50 (April, 1984).

4. M.J. Barmuta, Printed Circuit Fabrication 7 (4), 50 (April, 1984).

5. J. Tate, Printed Circuit Fabrication 8 (3), 26 (March, 1985).

6. J. Wynschenk and A Delgobbo, Circuit World 13 (1), 78 (October, 1986).

7. C.A. Deckert, Circuit World 13 (3), (April, 1987).

8. C.A. Deckert, Printed Circuit Fabrication, to be published.

Abstract No. 246

POLY(VINYLCINNAMATE) PHOTORESISTS FOR FINE LINE PRINTED CIRCUITRY

Koshy John, Saulius Simoliunas, and Arthur Tomson
Kimplate Incorporated, 665 W. Warren
Detroit, MI 48201 USA

From 1967 until present the technical and patent literature reveals around 400 entries in the use of poly(vinylcinnamate), [24968-99-8] liquid negative working resist system in the photofabrication of electronic devices.

In fifties and sixties poly(vinylcinnamate) was the photoresist of choice in producing fine line circuitry(1). Then the meaning of fine line was 10 mils separated by 10 mils space.

However, this liquid photoresist was replaced by dry film technology, which was automated.

In the late seventies and now in the eighties poly(vinylcinnamate) liquid photoresist is returning for the new definition of high density (1 mil line and space) printed circuitry(2).

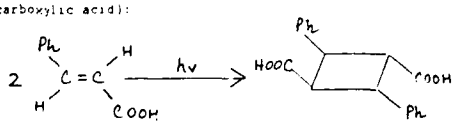
As dry film industry expert R. H. Wopschall has pointed out:

"Dry film photoresist technology is now used to fabricate most of the high-density printed circuit boards for computers, telecommunications and aerospace applications. A 15 to 100 micrometers thick photopolymer layer, protected between transparent films before use, is applied and then exposed to ultraviolet light through a photographic transparency representing the desired circuit pattern. Most circuit line conductors are 100 micrometers wide or wider. Dimensions of 25 micrometers are achieved with advanced processing techniques and even smaller dimensions are expected in the future."(3).

This assessment is in agreement with today's practical production limits, which currently stand around 4 mil lines and spaces (IPC - TR -578).

Liquid film applied to about 1 mil thickness dries out to 0.1 mil solid layer on the plate and inside the plated through hole. By contrast, dry film photoresists are thinned down to 0.25 mil for the tenting and etching mode of operation to achieve finer lines and spaces. The significant limitations of dry film photoresists occurs in tenting and etching, where, in case of rupture of the tent, the copper in the plated through hole is etched away.

Poly(vinylcinnamate) crosslinks by the mechanism for the dimerization of cinnamic acid to form truxillic acid (trans, trans - 2, 4 - diphenyl - 1, 3 - cyclobutanedicarboxylic acid):



The number of crosslinks per unit of light or exposure time is increased by sensitizers, such as Michler's ketone, anthraquinone, and p - nitroaniline (triplet sensitizers). The crosslinking may be effected by other sensitizers through electron transfer mechanism.

Cinnamate moieties have been attached to various polymer backbones by every type of known organic structural link. Despite the appearance of many exotic structures, the polymer of choice for most commercial applications remains poly(vinylcinnamate).

10% poly(vinylcinnamate) in a suitable solvent is applied on panel plated copper surfaces with an average thickness of 1 mil. The coating is dried leaving a film of average thickness of 0.1 mil. The exposure to ultraviolet through phototools yields good resolution to 1 mil patterns. The image is developed in solvent vapors. The unwanted copper is etched away. The photoresist is stripped in common strippers, leaving copper patterns and copper plated through holes. Hot air solder leveling or tin immersion followed by tab plating ensue to complete the process. This process is superior to dry film technology in that again it is the only process capable of such fine resolution of detail. Hence, the use of liquid photo - resists has returned to printed circuitry. An important variation of this process is the use of pattern plating, then stripping of photoresist and depositing new photoresist for protection of conductors and plated through holes. This requires superior registration and good cleaning cycle for pattern plating.

Here is the procedure in detail with pertinent comments.

1. Drilling of the copper clad laminate by manual or NC methods. If NC methods are unavailable, ½ to ½ oz. copper cladding is preferred. Vapor degrease in chlorinated solvents. Flow coat with photoresist, dry in a convection oven at 250°F for 1 hour. After removing the board, cool it to room temperature, place it on the printing machine and expose to UV, develop in the solvent vapors, dye in Gentian violet in toluene, rinse off the unexposed resist with water spray, then rinse in isopropyl alcohol, spray with water, 5% HCl rinse, air dry.

This provides good contrast reliable pattern, which can be used in hand drilling operation. The resist pattern is only 0.1 mil thick, it is quite pliable nd does not chip as dry film photoresist, which is quite brittle and a magnitude thicker. A good driller can thus provide prototype cards by manually drilling 3 or 4 card stacks.

2. Electroless copper deposition cyle. The photoresist pattern has to be stripped in common strippers, such as 50% by volume water, some ammonium hydroxide, and surfactant. Rinse in water spray. Dry in an oven at 212°F to drive out water. Degrease in chlorinated solvent, etch in ammonium persulfate (10% by wt) aqueous solution. Rinse, 10% by vol. H_2SO_4 dip, rinse. Stannous chloride, rinse palladium chloride, rinse cycle can be used. This cycle is preferred, because there are no complexing agents deposited on the board from stabilized palladium-stannous chloride catalysts, which are commercially available. As for electroless copper itself, the electroless copper deposit produced from dilute aqueous solution of copper EDTA complex, nickel chloride, sodium hydroxide and formaldehyde only approaches, but never becomes identical to plain copper sulfate electrolyte copper foil in mechanical properties. But this deposit is better than that from the commercial electroless copper solutions, which are loaded with stabilizers and produce porous films, although the solutions last longer. From the engineering viewpoint, bath stability at the expense of mechanical properties of the deposit does not make any sense. The porosity has a saving grace that it provides subsequent keying of electroplate to original foil The recommendation is to sand off the electroless copper deposit altogether. Then the control of electroless copper thickness becomes unnecessary.

3. Copper panel electroplating should be done from plain copper sulfate electrolyte to simulate and surpass the commercial foil in higher tensile strength and bending ductility. Already twenty five years ago a new plating philosophy, which may be called antibrightener

and antileveler approach, was demonstrated in electroplating baths without additives.

4. Photoresist application. Light sanding of copper electroplated panels. Photoresist can be sprayed or one can dip boards in it, let dry at 250°F for ! hour in air circulated oven. Adhesion is excellent. Air drying is a must, since oxygen inhibits polymerization - crosslinking. The photoresist has viscosity of 12 centistokes, solids about 10% by wt, specific gravity about 1.01.

5. Etching, stripping of photoresist, hot air solder leveling finish the cycle. Hot air solder leveling provides pure entectic solder, which cannot be produced by electroplating.

For flow charts of processes one may consult a former communication(4).

Bibliography

1. U. S. Pats. 2,670,285; 2,670,286; 2,670,287 (Feb.23, 1954), L. M. Minsk and coworkers.

2. K. John, G. G. Perrin, Jr., and S. Simoliunas, "Liquid Photoresists for Higher Resolution in Printed Circuitry," IPC - TP - 577, April, 1986, Boston, MA

3. R. H. Wopschall, "Dry Film Photoresists," Solid State Technol. 29, 153 (1986).

4. A. Price, G. G. Perrin, Jr., and S. Simoliunas, "Liquid Photoresist Process for Subtractive and Semiadditive Printed Circuitry," American Electroplaters' Society 67th Annual Technical Conference Proceedings, June, 1980, Milwaukee, WI

Abstract No. 247

ELECTRICAL INTERCONNECTION THROUGH SILICON WAFER

T. Dupeux*, H. Sibuet**, P. Deroux Dauphin**

THOMSON/LCC
CEA/IRDI/D.LETI

* THOMSON/LCC BP 13 92403 COURBEVOIE

**CENG 85 X 38041 GRENOBLE CEDEX
France

Introduction

Electrical connections through a wafer are becoming a new way to solve interconnection problems in integrated circuit designs. T.H.C. so called "Through Hole Connections" or intraconnections have already been proposed in many applications and technological devices such as :

- AsGa FET's designed for low impedance contacts (1)
- Low resistance connection to ground in hybrid microwave thin film circuits (2)
- CMOS/SOS technology (3)

However, T.H.C can also be applied in silicon technology . In a double-sided technological approach, it could provide for instance, the interconnection levels requested by designers in Wafer Scale Integration (Fig 1). It is even a way to realize stacked 3-D structures through chip or wafer assembly technology (Fig 2). In the same approach, it can be used to couple integrated circuits with magnetic or optoelectronic devices(4).

In focusing our research on direct use of the process we used the following requirements :

- Realization of through silicon wafer connections
- Compatibility of our process with microelectronic technology and equipment
- Good yield and reproductibility of each step of the process

In this paper, we will describe the whole T.H.C fabrication process, namely : laser-drilling parameters, insulator growth, metallization of holes , filling and encapsulation. Electrical testing results and yield measurements will also be presented.

Experimental and Results

In previous studies several ways to realize the hole have been analyzed : chemical anisotropic etching, dry etching, ultrasonic drilling and laser drilling. Among all of these techniques laser drilling was chosen to permit :

- Good precision on hole positionning that allows double-sided alignement
- High aspect ratio diameter versus depth hole
- High drilling speed (about 10 hole/s).

A new laser-drilling machine has been specially designed by Microcontrole (located in Evry, France) to achieve the above requirements. This machine is also compatible with the standardized microelectronic equipment.

The laser we have used to drill wafers is a commercially available Nd-YAG Q-swithed laser delivering 10 watt output in a continuous wave mode. The wavelength of 1.063 micrometer is particularly suitable for absorbtion by electronic transition through the silicon gap. A good choice of laser parameters, such as pulse repetition rate, pumping current and number of pulses minimizes the random walk effect described by T.R Anthony (5). Figure 3 shows a plot of average error on the positionning versus peak power of pulses. Figure 4 shows diameter hole vs peak power of pulses. An analysis of these diagrams indicates that choosing a good positionning commands the hole dimension. As it has been reported previously (6), the potential drilling speed of such a kind of laser reaches 100 to 1000 holes per second, considering approximately 10 milliseconds to drill one hole. Many perfectly positionned holes are needed. This commands the use of x-y table to displace the wafer under the laser beam with high speeds (200 mm/s) and high acceleration ($1m/s^2$). Consequently the throughput is determined by a holes network and at the same time is limited by time displacement.

Principal sources of damage to a wafer undergoing laser drilling are :

- External ; condensed silicon drops around holes (7).
- Internal ; SiO_xN_y debris on the inner surfaces of holes.

External and internal damages are easily removed in a silicon etchant by enlarging the diameter hole. This treatment improves the flatness and smoothness which of the inner surface permitting proper growth of thermal SiO_2 insulator and constant metal layer thickness on inner surface holes (Fig 5).

In fact , holes are not perfectly cylindrical. In a cone-shaped hole approximation (Fig 6), theoretical resistance can be calculated with the following formula :

$$R = \frac{\rho}{\pi e} \cdot \frac{L}{D_2 - D_1} \ln \frac{D_2}{D_1}$$

Figure (7) shows a plot of 1200 T.H.C resistance measurements. In our investigations, we focused on resistance value of 1 ohm. However according to the above formula, resistance value of 0.1 Ohm can be obtained with the same process. Assuming a perfect filling of holes with a conductor, it can further be lowered some mOhm.

Conclusions

A through hole metallization process using laser drilling has been developped. An important part of the process is the control of laser parameters. Electrical testing indicates a process yield of 96%. This excellent yield can still be improved.
In addition to our current research we are further analyzing the THC process in respect to complete devices in our laboratory.

References

1. C.B. Cooper III and al. J.E.S. vol 134 n10
2. R.T Thomson, B.W. Whitacker 32nd Electric Components Conf. San Diego Proc. 82
3. T.R Anthony J. Appl. Phys.52 (8) August 1981
4. Y. Akasaka and al. Solid State Techn. February 1988
5. T.R. Anthony J. Appl. Phys. 51 (2) February 1982
6. T.R. Anthony IEEE Trans On CMHT Vol. CMHT-5 no 1 March 1982
7. D. Gevrey an al Journal de Physique. Colloque C7. Suppl. au no 12. Tome 48 December 1987.

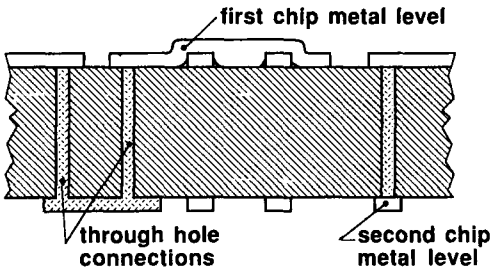


Fig 1 : T.H.C. in double sided technological approach

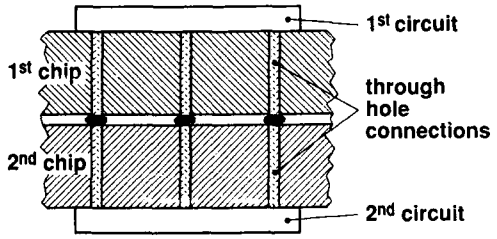


Fig 2 : Stacked 3-D structure including T.H.C.

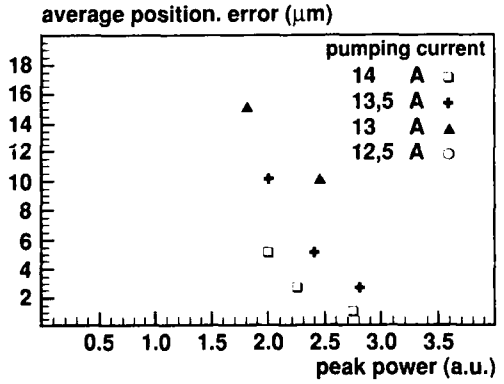


Fig 3 : Average positionning error (um) VS peak power (arbitrary unit)

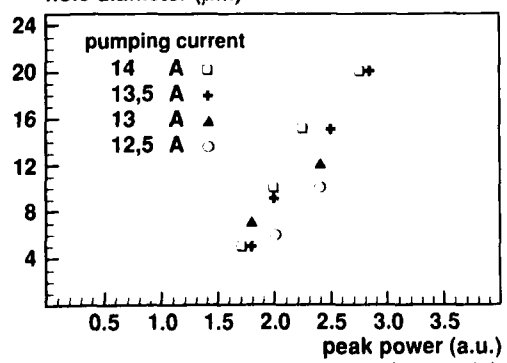


Fig 4 : Hole diameter (um) VS peak power (arbit.unit)

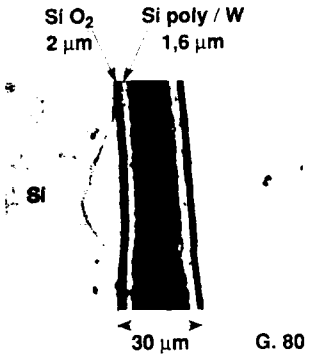


Fig 5 : Cross-section of a Through Hole Connection

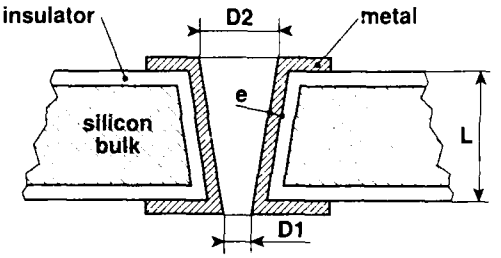


Fig 6 : Through Hole Connection in the cone shaped approximation.

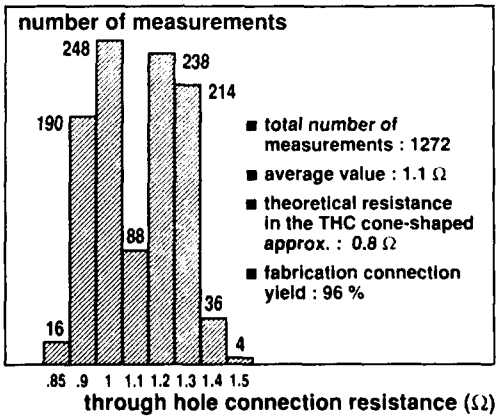


Fig 7 : Through Hole Connection resistance measured on a whole wafer.

Abstract No. 248

Contact Resistance: A Review of Recent Developments in Measurement and Modeling

Stan Swirhun, Honeywell SSPL, 10701 Lyndale Avenue S., Bloomington, MN 55420

Introduction:

As semiconductor device dimensions shrink both vertically and laterally, device currents and current densities increase. If metal to semiconductor contact area is also scaled, contact resistance also increases, and with it the deleterious effects of contact potential drops. As a result, the proper and accurate measurement of contact resistance and the physical parameter specific contact resistivity ρ_c, and the characterization of the dependence of contact resistivity on doping density, metal type temperature is essential. Recently, there has been a great deal of interest[1, 2, 3] in proper techniques for extraction of specific contact resistivity ρ_c, from contact resistance measurements of planar test structures. Here, this recent work on modeling and extracting specific contact resistivity will be reviewed, the key experimental and theoretical results concerning modeling ρ_c will be discussed and areas of where further investigation is required will be highlighted. The discussion will focus primarily on ohmic contacts to Si.

Proper Extraction of ρ_c

ρ_c is defined as the incremental resistance of an infinitely small area of the metal to semiconductor interface passing a small, uniform current density. Contact resistance, on the other hand is a measured macrscopic quantity that depends on ρ_c, but also on the contact size, semiconductor sheet resistance, and the contact geometry. ρ_c is the single measurement independent parameter that describes the quality of the interface and for this reason it is the proper focus of study and optimization. Devices and test structures have a contact resistance component that is dependent on the exact current flow. Consequently, extracting ρ_c from a measured contact resistance is not straighforward because the complications of non-uniform current flow in the semiconductor must be modeled[1]. Parasitic resistance contributions due to spreading resistance, current crowding at the contact edges and test structure collars must be removed in order to accurately extract low ρ_c values from measured contact resistances. Both bulk[3, 4] and planar[1] test structures commonly are used to extract ρ_c. The three most common test structures - the cross-bridge Kelvin resistor (CBKR) the contact end resistor (CER) and the tranmission line tap resistor (TLTR) are discussed in [1]. For each, current is passed between one semiconductor and one metal arm and the voltage is measured between the other two arms. The measured contact resistance is V/I. Differences arise because each structure measures the voltage at a different position of the contact and R_{cbkr}, R_e and R_{ltm} are in general different - even for identically sized, identically fabricated contacts. Fig. 1[1] illustrates this graphically. The normalized end resistance R_e measured on a series of adjacent test structures with identical 5 micron square contact sizes varies by 2 orders of magnitude depending on the width W of the n+ Si bar it contacts. Exact two-dimensional simulations of the test structure accurately models this strong dependence with a single low ρ_c value. Fig. 1 illustrates two other important points on which a consensus has been reached: i) the severity of the parasitic resistance effect increases with increasing semiconductor sheet resistance and contact overlap. ii) ignoring the parasitic effect will always cause overestimation of the contact resistance.

The recently very active discussion in the published literature concerning the proper extraction of ρ_c was initially sparked by claims[6] of accurate extraction of ρ_c using simple test structures and one-dimensional analytical expressions. Subsequent experimental and 2-D simulation work[1, 2] clearly showed that this technique was unreliable for low ρ_c values. By using numerical simulations it was shown unambiguously that by employing data from an array of test structures with systematically varied contact or overlap dimensions, accurate ρc values could be extracted although the parasitic resistance effects may dominate. A set of generalized curves unique to the test structures to be used has been presented[1] to assist in this extraction. Fig. 2 illustrates such a family of curves to allow extraction of ρc using measured resistances Rk from CBKR test structures. Recently, approximate analytical solutions for the most common CBKR test structures now exist.

Theory and modeling of ρ_c

The ohmic metal-semiconductor contact is usually modeled as a highly doped Schottky diode. In this model, the specific contact resistivity is due to the effects of a potential barrier of height φ_b (considered independent of doping) limiting the current transport. Complete theories of contact resistivity based on the Schottky model date[5] from 1969. Carrier transport is modeled as a combination of thermionic emmission over the barrier - favored in lightly doped semiconductors, low barriers and at high temperatures - and tunneling through the barrier - favored in heavily doped semiconductors. A wide assortment of other assumption garnishes the basic theory including image force barrier lowering, effective mass changes with doping and temperature and quantum interface dipoles[9]. Other well established physical effects such as band-gap narrowing have never been considered, however. Little solid experimental data of ρ_c(Nd,Na,T) has been presented to validate any model, and much of the data that has been presented is suspect because accurate methods may not have been used to extract ρc. The most quoted data of Chang et al[10] fits available theory for ρ_c as low as 10^{-6} ohm-cm^2 but these ρ_c values are just barely ohmic. Modern devices require $\rho_c<10^{-5}$ and this is the range in which ρ_c(Nd,Na,T) must be tested. This is a difficult task since the state of the semiconductor surface at the time of metal deposition is critical in determining the quality of the contact, and technology to control the quality of the interface is much more advanced now.

Fig. 3 plots the experimentally determined ρc dependence on donor concentration for PtSi and W contact to n+ Si. Also plotted are predictions of the dependence of contact resistance on doping density made using the most common theory. The theoretical predictions grossly understimate ρ_c unless image force barrier lowering is excluded from the model; in this case the fit is adequate for both W and PtSi contact. This approach also allows better fitting of the best of the other available ρ_c(Nd) data[11, 4] altough it is difficult to justify theoretically. More experimental and theoretical work is required.

Fig. 4 plots predictions of the temperature dependence[12] of ρ_c contact to n-type <100> Si with barrier height and doping as parameters. Experimental data[13] (normalized to its value at 305K) in Fig. 5 poorly replicates the strong theoretically predicted temperature dependence. The T dependence of measured ρ_c is much weaker than predicted. The lack of agreement with theoretical predictions points out that there is a great deal of room for improvement in our understanding ohmic contacts.

References:

(1) W. M. Loh, et al., IEEE TED, Vol. ED-34, no. 3, pp. 512-524, Mar. 1987.

(2) A. Scorzoni, et al., IEEE TED, Vol. ED-34, no. 3, pp. 525-532, Mar. 1987.

(3) S. J. Proctor, et al., IEEE TED, Vol. ED-30, no. 11, pp 1535-1542, Nov. 1983.
(4) G. P. Carver, et al., IEEE, Vol. 35, No. 4, April 1988.
(5) R. H. Cox, et al., Solid-State Electron., Vol. 10, pp. 1213-1218, 1967.
(6) S. J. Proctor, et al., IEEE Electron Device Lett., Vol. EDL-3 no. 10, pp. 294-296, Oct. 1982.
(7) J. Chern, et al., IEEE Electron Device Lett., Vol. EDL-5, pp. 178-180,May 1984.
(8) B. Schwartz, Ohmic Contacts to Semiconductors, Ed. New York: Electrochem. Soc., 1969
(9) D. K. Schroder, et al., IEEE TED, Vol. ED-31 no. 5, pp. 637-647, May 1984.
(10) C. Y. Chang, et al., Solid-State Electron, Vol. 14, pp. 541-550, July 1971.
(11) D. Pramanik, et al., Solid-State Technol., Vol. 26, pp. 127-133, Jan. 1983 and Solid-State Technol. Vol. 26, pp. 131-138, Mar. 1983.
(12) S. Swirhun, R. M. Swanson, unpublished.
(13) S. E. Swirhun, et al., IEEE Electron Device Letters, EDL-6 (12):639-641, 1985.

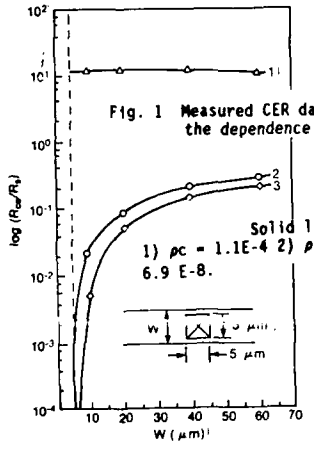


Fig. 1 Measured CER data points and the dependence on width W.

Solid line is predicted 1) ρc = 1.1E-4 2) ρ_c = 5.0 E-8 3) ρ_c = 6.9 E-8.

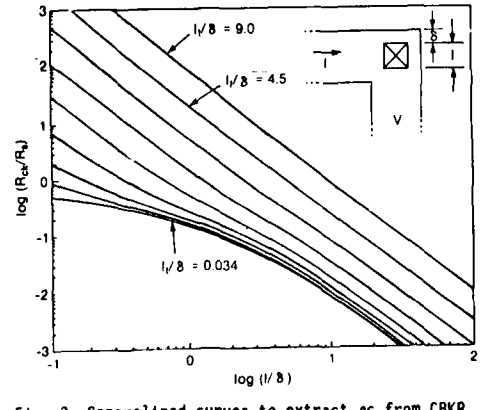


Fig. 2 Generalized curves to extract ρc from CBKR structures. R_k and R_s are measured and the optimum l_t is extracted. $l_t \stackrel{\Delta}{=} \sqrt{(\rho c/R_s)}$.

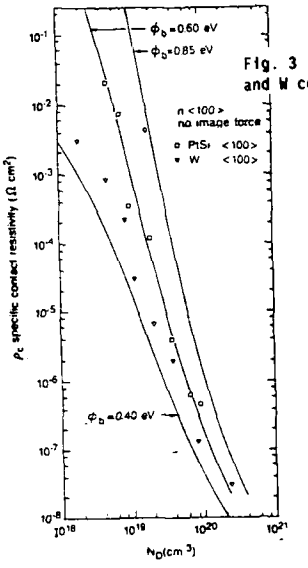


Fig. 3 ρ_c data for PtSi and W contact to n-type Si

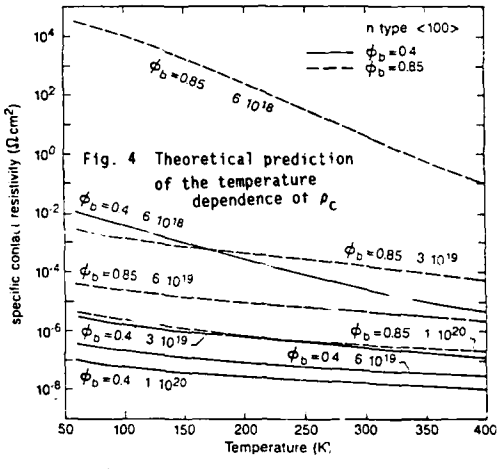


Fig. 4 Theoretical prediction of the temperature dependence of ρ_c

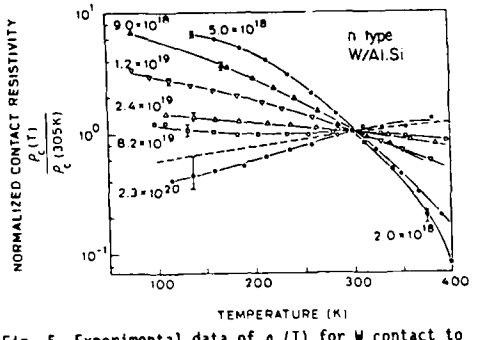


Fig. 5 Experimental data of $\rho_c(T)$ for W contact to n-type Si.

Abstract No. 249

EFFECTS OF DRY ETCHING ON SHALLOW TITANIUM SILICIDE CONTACT

M.F. Tseng, S.W. Chang, W.D. Su and N.W. Wu

Semiconductor Process Development Department
Electronics Research and Service Organization
ITRI, Hsin-Chu, Taiwan, R.O.C.

The shrinkage of lateral dimensions of VLSI circuits towards the submicron range requires shallow source and drain junctions in order to minimize short-channel effects in devices. Titanium silicide has attracted much attention as ohmic contacts, because of its ability to reduce interfacial oxides and its high conductivity [1], to reduce the inherently high resistance of shallow junction depth and small contact area.

Reactive ion etching (RIE) provides the highly anisotropic etching capabilities and has been widely used in contact opening of VLSI circuits. However, dry etching can produce residue polymer layer on the surface of contact area [2] and has to be removed by additional Ar ion bombardment step in RIE process. Except for inducing a lattice damage layer [3], the polymer removal step can etch silicon at contact area. This phenomenon not only decreases the junction depth of source/drain region but also lowers the impurity concentration, and therefore affects the performance of shallow junction devices. It has been discussed elsewhere that the metal-silicon reaction consumes silicon at the junction region to form titanium silicide which could be associated with both contact resistivity and junction leakage problems [4]. In order to achieve low contact resistivity and prevent junction leakage problem, it is important to pay attention to control the processing time of RIE for contact opening.

In this paper, a contact metallurgy employing a titanium silicide layer in contact regions and a Ti-W alloy of composition $Ti_{0.3}W_{0.7}$ as a barrier material has been evaluated for use with shallow junctions and Al-Si metallization. n+ and p+ junctions are formed by implanting As and BF_2 into silicon substrate. Determined by SUPREM III simulation and SRP technique, the junction depth about 0.15 um for n+ and 0.25 um for p+ are achieved. Titanium films are sputter deposited and then reacted with the implanted silicon region by two-step annealing and a self-registered process to form the low resistivity $TiSi_2$ phase. After Ti-silicidation, the remaining junction depths, about 0.1 um for both n+ and p+ region, are estimated by SRP data. The Auger depth profile indicates that the composition of Ti-silicide layer on p+ region is more uniform in thickness than that on n+ region. The semi-quantitative atomic ratio is Ti:Si:N = 17:68:10 for Ti-silicide film formed on either p+ region or bare silicon substrates.

Fig.1 and Fig.2 show the effect of different contact etching time on leakage yield. The reverse leakage current of finger shape diodes of area 74100 um^2 and perimeter 10920 um was measured at the reverse bias of 7.5 volts. Diodes with leakage currents greater than 100 pA were defined as failures. It is obviously that, for both n+ and p+ junction contacts, the yield of well-controlled etching condition (SJC etch) is better than that of longer-time etching condition (VC etch). In case of the contact resistance measurement, both SJC etch and VC etch condition assure the same order of low contact resistance: <20 ohm/contact for n+ and <50 ohm/contact for p+. (1.2*1.2 um^2 contact area).

NMOS device structures such as the lightly doped drain (LDD) and the double diffused drain (DDD) have been proposed for the reduction of hot-carrier degradation and acceptable short-channel characteristics in VLSI technology. Fig.1 and Fig.2 also illustrate the LDD (phosphorus, 30 keV, 3E+13) and DDD (phosphorus, 50 keV, 5E+13) structures combined with shallow n+ junctions. After total thermal cycle, the n+ junction depths were about 0.22 um and 0.24 um for LDD and DDD structures respectively. Apparently, the yields are improved to approximately 100 percent for wafers included LDD or DDD structure which is much better than that of traditional shallow junction structure, even using VC etch condition. Fig.3 and Fig.4 show the leakage current as a function of reverse bias. For all experimental conditions, the breakdown voltages are above 17 V and 20 V for n+ and p+ junctions respectively.

The effect of Ti thickness on junction leakage are also shown in Fig.1 and Fig.2. The unacceptable leakage yields were obtained for 650 A Ti, eapecial for p+ junction, even with well-controlled SJC etch condition. For n+ junction, due to the fact that the thickness of titanium silicide formed on n+ diodes was less than that on p+ diodes, this limit to usable Ti thickness is not so clear as p+ junction and can be relaxed by accompanied LDD or DDD structure. Note that for thinner initial Ti thickness, 400 A, well-controlled contact etching is still needed to preserve low leakage current and high junction yield.

REFERENCES

1. C.Y. Ting and M. Wittmer, Thin Solid Films, 6, 327 (1982)
2. J.H. Thomas III, X.C. Mu and S.J. Fonash, Extended Abstracts of the 171st Meeting of the Electrochemical Society, Abstract no. 252 (1987)
3. X.C. Mu and S.J. Fonash, IEEE Electron Device Lett., 6, 410 (1985)
4. T. Brat, C.M. Osburn, D. Sharma, W-K. Chu, N. Parikh, D. Griffis and S. Liu, Extended Abstracts of the 171st Meeting of the Electrochemical Society, Abstract no. 185 (1987)

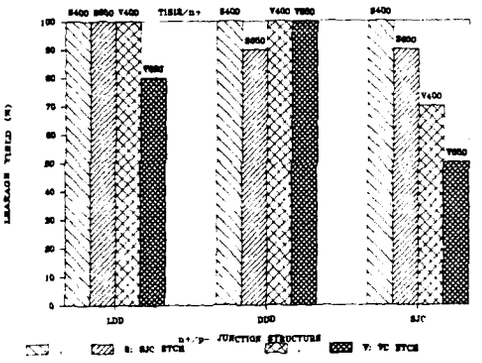


Fig.1 Yield of n+/p diodes versus process conditions including different junction structure (shallow junction -SJC, with LDD, with DDD), contact etching (well controlled -SJC etch, longer etching time -VC etch) and initial Ti thickness (400 A, 650 A)

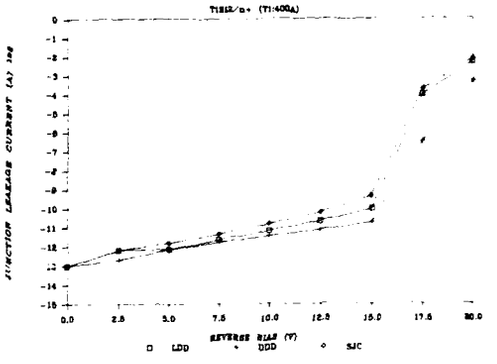


Fig.3 n+/p junction leakage current as a function of reverse bias for LDD, DDD and traditional shallow junction contact structures.

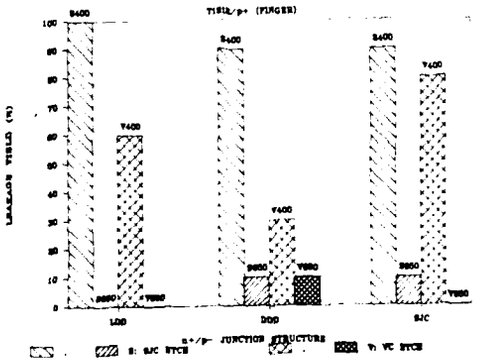


Fig.2 Yield of p+/n diodes versus process conditions for the same wafers as described in Fig.1

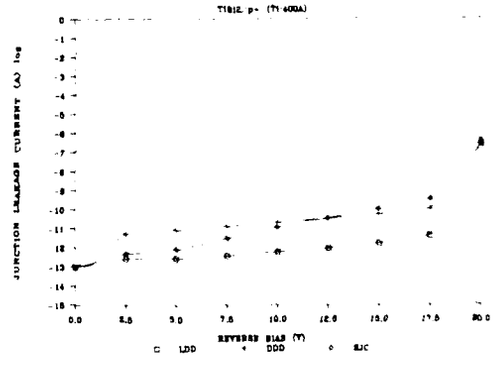


Fig.4 p+/n junction leakage current as a function of reverse bias for the same wafers as described in Fig.3

Abstract No. 250

INERT SPUTTERED TITANIUM NITRIDE FILMS FOR ULSI CONTACT TECHNOLOGY

T. Brat[+], C.S. Wei[++], D.B. Fraser[++], and J. Poole[+]

+ Varian Specialty Metals Division
3515 Grove City Road, Grove City, OH 43123
++ Components Research, Intel Corporation, Santa Clara, Ca 95052

High yield, low resistance contacts are essential for future ULSI technology. These contacts must also provide a diffusion barrier film to prevent metal reaction and penetration of the underlying junctions [1]. It is important for the contacts to withstand the extended thermal cycles introduced by the multilevel metallization process.

Titanium nitride (TiN) is one of the most promising diffusion barrier materials for semiconductor contact metallizations because of its thermodynamic stability [2], low diffusivity, and high conductivity. Three main techniques are currently used to produce TiN films: reactive evaporation [3], reactive sputtering a Ti film in a nitrogen rich ambient [4-6], and furnace annealing [7] or rapid thermal nitridation of a Ti film in a N_2 or NH_3 ambient [8]. The properties of the TiN films strongly depend on the actual growth conditions, and consequently on the processing parameters.

This work reports the physical properties, diffusion barrier characteristics, and electrical behavior of TiN films sputter deposited from novel TiN targets, 99.5% and 99.99% nominal purity, in a Varian 3280^{TM} cassette-to-cassette sputtering machine. 50-200 nm thickness films were deposited in a dc-magnetron mode with a base pressure of 2×10^{-7} Torr and a backfill pressure of high purity argon gas of 7×10^{-3} Torr. Some film depositions were performed on substrates with temperatures ranging from room temperature to 410°C.

Figure 1 shows the variation of deposition rate and resistivity of TiN films deposited on Si(100) as a function of the sputtering power and substrate deposition temperature. The deposition rate for an input power of 3 KW is 2.7 nm/sec, the films reaching a resistivity value of about 55 μΩ-cm. High rates of deposition on hot Si(100) substrates produce films with a resistivity as low as 40 μΩ-cm.

Rutherford backscattering spectrometry (RBS) performed on films deposited on amorphous carbon substrates indicates the presence of Ti, N, and O as principal components of the films, as shown in Figure 2, while Ar is not detected. X-ray photoelectron spectroscopy (XPS) depth profiles of the deposited films indicate that Ti and N are present in compound form throughout the thickness of the films [9].

The stress measured on $TiN/SiO_2/Si(100)$ structures is compressive, ranging between $1-5 \times 10^{10}$ dynes/cm^2, depending strongly on the TiN film sputtering conditions [10]. The performance of TiN films as a diffusion barrier was studied with Auger electron spectrometry. Processed CMOS device wafers with contact chains and diode structures were used to evaluate junction integrity and specific contact resistivity of the metallizations $Al/TiN/Si(100)$ and $Al/TiN/TiSi_2/Si(100)$ on N^+ and P^+ junction regions. The structures were annealed at 460°C for 30 min., in H_2 atmosphere. The specific contact resistivity results are shown in Table I. They indicate that the presence of a $TiSi_2$ layer between the TiN film and the Si(100) substrate lowers one order of magnitude the specific contact resistivity of the P+ contact structure, without affecting the results on the N+ contact.

ACKNOWLEDGEMENT

The authors would like to thank John Muller and the technical staff of Varian SMD for their collaboration in the target fabrication. Our thanks to K. Palmer for help in the film deposition, and Dr. C.E. Wickersham for project support.

REFERENCES

[1] C.M. Osburn and A. Reisman, J. of Electronic Materials, 16, 223 (1987).
[2] M.A. Nicolet, Thin Solid Films, 52, 415 (1978).
[3] C.Y. Ting, J. Vac. Sci. Technol., 21, 14 (1982).
[4] M. Wittmer, J. Vac. Sci. Technol., A3, 1797 (1985).
[5] S. Kanamori, Thin Solid Films, 136, 195 (1986).
[6] J. Stimmell, J. Vac. Sci. Technol., B4, 1377 (1986).
[7] H. Kaneko, M. Koyanagi, S. Shimizu, Y. Kubota, and S. Kishino, IEEE Trans. Electron Dev., 33, 1702 (1986).
[8] T. Okamoto, K. Tsukamoto, M. Shimizu, Y. Mashiko, and T. Matsukawa, in Symposium on VLSI Technology, 1986, p. 51.
[9] T. Brat, N. Parikh, N.S. Tsai, A.K. Sinha, J. Poole and C.E. Wickersham, J. Vac. Sci. Technol., B5 (6), 1741 (1987).
[10] T. Brat, N.S. Tsai, N. Parikh, C.E. Wickersham, and A.K. Sinha, 172th Electrochemical Society Meeting, Ext. Abstract No 689, Vol. 87-2, 976 (1987).

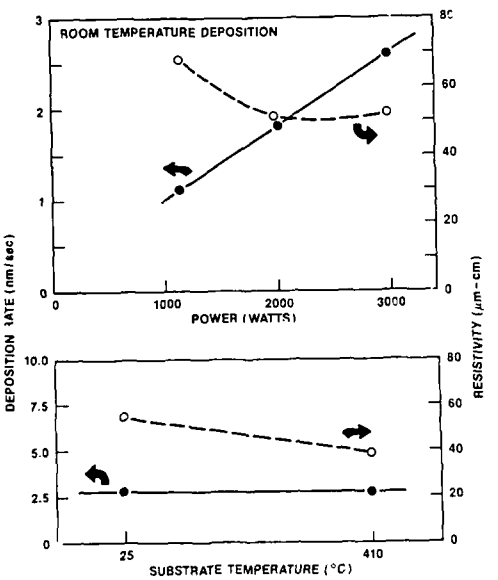


Figure 1: Variation of deposition rate and resistivity of TiN/Si(100) films as a function of the sputtering power (top) and substrate temperature (bottom).

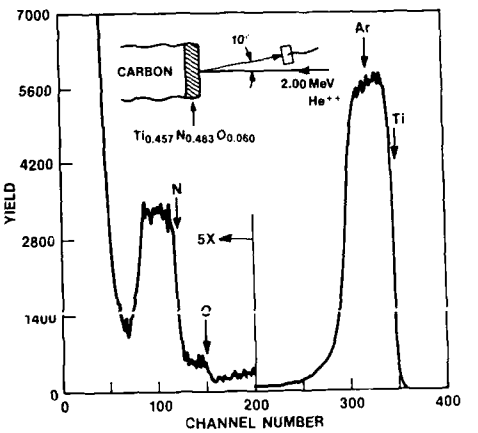


Figure 2: 2.00 MeV He^{++} Rutherford backscattering spectra from a 80 nm TiN film deposited on amorphous carbon. Note that the signal has been enlarged x5 in the y axis for channels smaller than 200.

Table I

SPECIFIC CONTACT RESISTIVITY [Ω-cm^2]

	4E15 cm^{-2} As^+ 60 KeV	4E15 cm^{-2} BF_2^+ 80 KeV
Al/TiN/Si(100)	1.4×10^{-7}	1.2×10^{-5}
Al/TiN/$TiSi_2$/Si(100)	2×10^{-7}	2.4×10^{-6}

Abstract No. 251

PLANARIZED CONTACT PROCESS FOR SUBMICRON VLSI DEVICES USING RESIST ETCH BACK OF CVD TUNGSTEN

D. LIAO, L. PATTERSON, S. SIVARAM AND K. SUH

SUBMICRON TECHNOLOGY DEVELOPMENT, INTEL CORPORATION
SANTA CLARA, CA. 95052-8121

INTRODUCTION

Lack of planarity in VLSI circuits results in poor step coverage of metallic interconnects. Severity in topography can also cause electromigration problems, metal stringers during etching, depth of focus problems in lithography and incompatibility with multilayer metallization. In this paper we demonstrate a planarization scheme using LPCVD tungsten to fill submicron contacts. CVD tungsten exhibits good step coverage in high aspect ratio pores and the use of a sacrificial resist layer during etchback prevents punch-through of the centers of the contacts. Such a contact metallurgy also results in excellent device characteristics.

EXPERIMENTAL

Wafers for tungsten filling were fabricated on p-type Si substrates using conventional isolation and gate formation. Submicron lithography was used in defining the layer patterns. Splits were introduced after contact etch, with control wafers proceeding without the tungsten planarization and all other wafers going through CVD tungsten deposition and etch back, described in the following sections. All wafers then received aluminum-silicon metallization, patterning and metal etch.

Tungsten deposition was carried out in a commercially available cold wall CVD system (Genus 8402). The tungsten deposition conditions were as follows: temperature: 450°C, pressure: 200 mTorr, H_2: 2500 sccm, SiH_4: 180 sccm and WF_6: 500 sccm. The deposition rate was approximately 1600A/min and the film uniformity on a 100 mm wafer was better than 5%, 3 sigma. As stress level in these tungsten films was extremely high, spontaneous delamination was observed when the film was deposited directly on either Si or oxide. In order to promote adhesion, 'glue' layers had to be deposited on the patterned substrates prior to tungsten deposition. Two types of adhesion layers were studied: a. *in situ* deposited layer of WSi_x and b. sputtered layer of Ti. In both cases the underlayer was 1000A thick.

Blanket CVD tungsten etchback was performed in a single wafer etcher with the top electrode powered. A sacrificial resist layer approximately 5500A thick was spun on the wafers prior to etch back. An SF_6 and O_2 chemistry (33% O_2 in SF_6) was used in the first step of the etch back process to etch the photoresist and the tungsten films with a one to one selectivity. The resultant film etch rate was approximately 5000A/min with a etch uniformity of ±6%. The end point trace was monitored by the optical emission line of fluorine (704 nm) and triggered at the interface between tungsten and the glue layer. Chlorine was added in the second step along with SF_6 and O_2 to prevent undercutting at the contact edges during the over etch cycle. The final step in the etchback process was etch-residue removal from the glass surface using a 50:1 HF dip for 60 seconds.

RESULTS AND DISCUSSION

a. Etch related undercutting:

When contacts were etched with the photoresist etch back process, it was found that the edges of the contacts were etching faster compared to the center, which was protected by the photoresist. This accelerated etching of the contact edge has been termed 'undercutting'. Films on WSi_x showed a more severe undercutting problem compared to films on Ti. The proposed hypothesis links the extreme stress concentration in the portion of the film closer to the substrate to stress enhanced etching (1). At the vertical wall of the contact edge, a cross section of the film is exposed to etching. Stress enhanced etching results in different etch rates across this cross section, with the edge etching faster than the center. The result of this differential etching is notching of the contact edge.

It was found that adding an anisotropic component to the etch, which is less sensitive to substrate mechanical characteristics, alleviated undercutting. Hence chlorine was added to the overetch cycle along with SF_6 and O_2. Figure 1 shows a planarized tungsten filled contact after etchback, using this two step scheme.

b. Electrical characteristics of contacts after etchback with the two step process:

We compared the electrical characteristics of the tungsten filled wafers, with the control split with no tungsten in the contact metallurgy (Ti/Al-Si on Si). N^+ contact resistance was measured on single contact Kelvin test structures where the contact size was 1.0x1.0 um. Tungsten wafers on the titanium underlayer and the non-tungsten wafers typically exhibited similar contact resistances of 1.2 - $2x10^{-7}$ ohms/cm^2. Tungsten wafers on WSi_x showed one to two orders of magnitude higher contact resistance. This result can be explained by the inability of WSi_x to reduce the more stable native oxide of Si in the contacts. Even though the wafers were dipped in buffered HF immediately prior to CVD deposition, there is still a sufficiently thick native oxide in the contact, especially before the start of the deposition, when the wafer is at 450°C, in a relatively poor vacuum. Because of the poor contact resistance characteristics of the WSi_x, further discussion of electrical results is confined to the titanium underlayer.

A reverse bias n^+ junction I-V plot for tungsten filled contacts is shown in figure 2 . The plot exhibits no low level leakage and shows a breakdown voltage of 10 volts. The cumulative probability plot of junction breakdown shown in figure 3 illustrates the tight distribution of failures. Tungsten wafers with titanium underlayer show a slightly better breakdown characteristic compared to the silicide underlayer. It is thus seen that the planarized tungsten fill process gives acceptable process and device characteristics when it is deposited on a titanium underlayer.

CONCLUSIONS:

We have shown the feasibility of developing a completely planarized contact metallurgy, using the resist etch back of CVD blanket tungsten. We have demonstrated the ability of the resist in protecting weak spots created by the deposition process in the centers of contacts. We have tested this planarized process electrically and have shown that tungsten filled contacts compare favorably with conventional contact metallurgy, while making the overall structure less sensitive to topography related issues.

REFERENCE:

1. S. Sivaram, D. Liao, S. Chen, R. Shukla and D. Fraser, in 'Tungsten and other refractory metals for VLSI applications III', Ed. V. Wells, MRS Pittsburgh, 1988, p407.

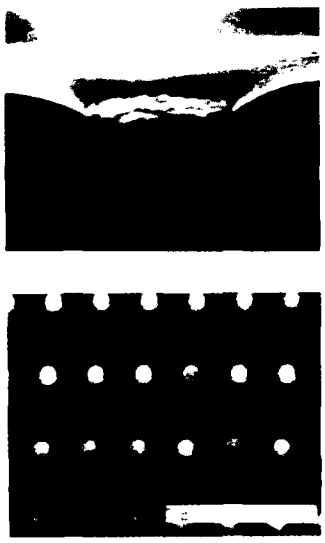


Fig. 1 A planarized tungsten filled contacts after etch back.

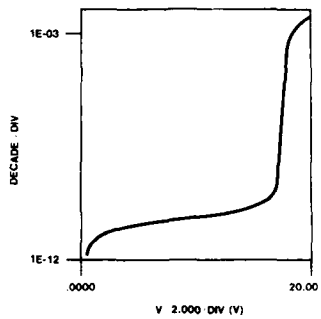


Fig. 2 Reverse bias n^+ junction I-V plot.

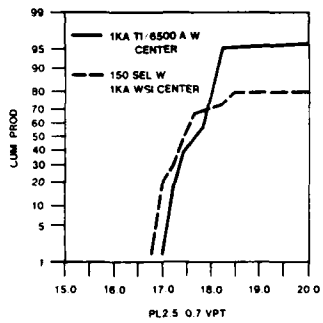


Fig. 3 *Cumulative probability plot of junction breakdown.*

Abstract No. 252

Rapid thermal Annealing of Ti and Ti-W metallisation on Si

T. S Kalkur and Brian Mueller*

Microelectronics Research Laboratories,
Department of Electrical Engineering,
University Of Colorado at Colorado Springs, CO 80933
* Honeywell Inc., Solid State Electronics Center,
Colorado Springs, CO 80933

Rapid Thermal annealing is becoming increasingly important in the formation of refractive metal silicides on silicon[1-4]. Among the various refractory metals, Tungsten and Titanium has attracted the attention of many investigators. More recently, double layer or intermixed, refractory metal layers were investigated for use as contacts, interconnects or barrier layers. In this paper, we are reporting the results of direct silicidation of Titanium and co-deposited Titanium-Tungsten layers by rapid thermal annealing.

The samples used for the investigation were n and p-type wafers. The p type layer was formed on n type wafers by implanting BF_2^+ ions at a dose of $3x10^{15}/cm^2$ at energy 40 KeV and n type layer was formed on p type layers by implanting with ions at the dose of $9.5\ x10^{15}/cm^2$ at energy 40 KeV. The ion implantation damage was removed by annealing the wafers in a furnace. For some wafers, Titanium layers of thickness 1000 A were deposited by electron beam evaporation. For the rest of the wafers, $Ti_{80}W_{20}$ layer of thickness 1200 A were deposited by magnetron sputtering. Test patterns for the measurement of contact resistivity and sheet resistivity were formed on these wafers by standard photolithography and etching techniques. The wafers were rapid thermally annealed in nitrogen and argon ambients in A.G.Associates *Heatpulse-410 system* for temperature ranges between 400 C to 90 C and for various annealing times. For Ti-Silic system, the sheet resistivity of the metallisation layers started decreasing with increase in the annealing temperature from 400 to 900 C for a processing time of 10 seconds (as shown in Fig.1). For a steady state temperature of 600 C, the sheet resistivity was found to be increasing with increase in processing time. The contact resistivity as measured by circular Transmission line method was was also found to be decreasing with increase in annealing temperature. The surface morphology of the RTA annealed contacts were found to be smooth even upto an annealing temperature of 900 C. In the case of $Ti_{80}W_{20}$ metallisation system, the sheet resistivity of the metallisation layer was found to be increasing with increase in annealing temperature above 600 C (shown in Fig.1). This might be due to the presence of traces of oxygen in the RTA chamber. The extent of increase in sheet resistance was reduced by using long purge times after loading the wafer. The current-voltage characteristics of $Ti_{80}W_{20}$ contacts with silicon were ohmic at RTA processing temperature in the range 400-900 C. The contact resistivity was also found to deteriorate slightly when the annealing temperature exceeded 800 C. The surface morphology was found to be smooth at annealing tempertures in the range 400-900 C. The contact characteristics of RTA annealed samples were compared with furnace and vacuum annealed samples. The contact metallisation structure was investigated with automatic X-ray diffractometer and an attempt was made to correlate structural properties with electrical characteristics of the contacts.

Acknowledgement

The authors wish to thank Director of Microelectronics Laboratory for supporting this project.

References

[1] S. P. Murarka, Silicides for VLSI Applications, Academic Press, New York, (1983)

[2] C. D. Capio, D. S. Williams and S. P. Murarka, J. Appl. Phys.,Vol. 62, 1257 (1987)

[3] C. S. Wei, J. Van Der Spiegel, M. Setton, J. Santiago, M. Tanielian and S. Blackstone, MRS symp. Proc., vol. 52, 297, (1986)

[4] Y. H. Ku, S. K. Lee, E. Lous, D. K. Shih and D.L Kwong,MRS symp. Proc., vol.92, 155, (1987)

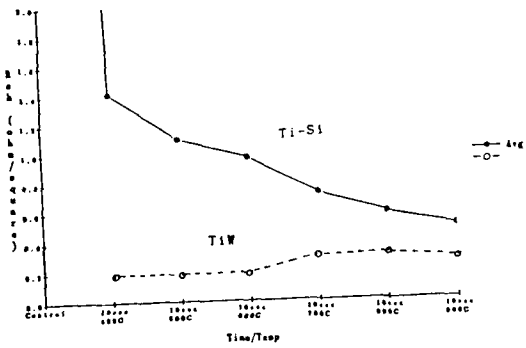


Fig.1 Sheet resistance of Ti and TiW on Si vs rapid thermal anneal temperature.

Abstract No. 253

Extremely low resistance and reliable Al-TiW-$TiSi_2$ contacts to n^+ and p^+-Si for silicon VLSI and smart power applications

K. Shenai, P. A. Piacente, S. Al-Marayati
R. Saia, and B. J. Baliga

General Electric Company
Corporate Research and Development Center
Schenectady, New York 12301

I. Introduction

For smart power applications, logic circuitry at the VLSI complexity need to be interfaced with the high voltage integrated circuit technology [1-3]. Smart power systems require low resistance and reliable contact and interconnect metallurgy to reduce the on-resistance of the intrinsic device and to reduce the power dissipation and propagation delay of interconnect lines. The contact and interconnect metallurgy must be also compatible with the multilayer metallization technology for efficient integration and communication among various components on the silicon chip.

It is generally well known that aluminum based alloys are prone to hillock formation and electromigration related problems [4,5]. This problem becomes particularly severe for contacts with small features [6,7]. When switching large voltages and currents at high frequencies, electromigration, interelectrode sparking, adhesion, and aluminum spiking can cause severe reliability problems.

Refractory metals and their silicides have been shown to provide low sheet resistances when deposited on both polysilicon and single crystal silicon [8,9]. In addition to providing low contact resistances to gate, drain and source electrodes, significant improvements in the gate propagation delay [10], gate power consumption [11], and device reliability can result by using highly conductive refractory silicides. For low loss, high speed interconnects between devices and external environments, efficient multilayered metallizations are required with silicide technology [12,13]. Recently, low resistance contacts to n^+-Si have been reported based on improved Al-TiW-$TiSi_2$ contact metallurgy [14]. Simultaneous low resistance contacts to both *n*- and *p*-type silicon are required in bipolar mode power devices [15-17], power MOSFET's [18,19], and CMOS and bipolar devices for silicon VLSI applications [20].

In this investigation, we report on the fabrication, characterization, and modeling of extremely low resistance and reliable $TiSi_2$ contacts to both n^+ and p^+-Si for silicon VLSI, smart power, and multilevel metallization applications. These low resistance contacts resulted from careful optimization of silicon and $TiSi_2$ sheet resistances, and *in situ* sputter etching of the silicide surface prior to TiW deposition to reduce the interfacial contact resistance. The specific contact resistivity (ρ_c) obtained for n^+ silicon is nearly an order of magnitude smaller than that of Al (i.e., $\rho_c < 5\times10^{-8}$ Ω-cm^2), and that of $TiSi_2$ to p^+ silicon is comparable to Al (i.e., $\rho_c < 1\times10^{-7}$ Ω-cm^2). These results represent the best ever reported specific contact resistivities to either *n*- or *p*-type silicon with $TiSi_2$ contact and interconnect metallurgy [21,22].

II. Experimental Results

The experimental device structures consisted of a variety of As, B, and P diffused regions formed on <100> oriented silicon substrates. Contact patterns were defined by RIE etching 8 kA of densified LPCVD SiO_2. About 2000A of $TiSi_2$ was formed by *rf* sputtering 1000A Ti and then siliciding using two-step furnace anneal (FA) or rapid thermal anneal (RTA) to obtain a range of $TiSi_2$ sheet resistances [23,24]. About 1000A of TiW was then sputter deposited on $TiSi_2$. In some samples, the $TiSi_2$ surface was *in situ* sputter etched prior to TiW deposition without breaking the vacuum. The metal patterning was defined by wet etching 3 μm of *rf* sputtered Al + 1% Si or ...

Contact test structures to study Al-TiW and TiW-$TiSi_2$ interfacial resistances as well as Al-TiW-$TiSi_2$-nSi contact resistances were fabricated. Extensive measurements of cross-bridge Kelvin resistors were made to study the contact resistance, contact linearity, and contact yield across 4 inch diameter silicon wafers. Negligible changes in the contact resistance and interface morphology were seen after sintering aluminum at 465 °C in forming gas. Contacts with sputter etched $TiSi_2$ had more than a factor of 2 lower Kelvin resistance, ^2R_K compared to Alusil contacts on *n*-type silicon as shown in Table 1 where x_j corresponds to the dopant junction depth obtained from spreading resistance analysis, and R_{SH} is the silicon sheet resistance measured using the four point probes, both prior to silicidation. Detailed SEM, TEM, RBS, and Auger analyses showed a layer of titanium oxide at the interface between TiW and $TiSi_2$ for samples with no sputter etching of the silicide surface prior to TiW deposition. RTA silicide yielded slightly better contact resistance due to lower silicide sheet resistance, less dopant redistribution, and uniform silicide film with smoother silicide surface. Sputter etched $TiSi_2$ contacts to *p*-type silicon had comparable Kelvin contact resistance to that of Alusil contacts.

References

[1] B. J. Baliga, IEEE Trans. ED-33, p. 1936, 1986.
[2] M. F. Chang, et al, IEEE Trans. ED-33, p. 1992, 1986.
[3] G. Thomas, et al, IEEE Trans. ED-33, p. 2016, 1986.
[4] P. B. Ghate, in Proc. Int. Reliability Physics, p. 292, 1982.
[5] R. N. Hall, et al, in Proc. Workshop on Tungsten and Other Refractory Metals for VLSI Applications, Material Research Society, Pittsburgh, PA, p. 231, 1987.
[6] M. H. Woods, in Int. Reliability Physics Symp. Tutorials, p. 6, 1984.
[7] D. S. Gardner, et al, IEEE Trans. ED-34, p. 633, 1987.
[8] D. M. Brown, et al, Solid State Electron. 11, p. 1105, 1968.
[9] S. P. Murarka, Silicides for VLSI Applications, Academic Press, 1983.
[10] H. C. Lin, et al, IEEE Trans. ED-22, p. 255, 1975.
[11] G. M. Dolny, et al, in Proc. High Frequency Power Conversion, p. 149, 1986.
[12] W. E. Engeler, and D. M. Brown, IEEE Trans. ED-19, p. 54, 1972.
[13] A. K. Sinha, in Proc. First Int. Symp. VLSI Sci. Technol., p. 173, 1982.
[14] K. Shenai, et al, presented at the First Int. Symp. on Advanced Materials for ULSI, 1988 Spring Mtg. of ECS, Atlanta, GA, May 15-20, 1988, Abstract No. 200, Extended Abstracts Volume, p. 310, 1988.
[15] B. J. Baliga, et al, in IEEE IEDM Tech. Digest, p. 264, 1982.
[16] J. P. Russel, et al, IEEE Electron Dev. Lett. EDL-4, p. 63, 1983.
[17] B. J. Baliga, et al, IEEE Electron Dev. Lett. EDL-5, p. 323, 1984.
[18] K. Shenai, et al, General Electric TIS Rep. 87CRD207, 1987.

[19] K. Shenai, et al, presented at the Workshop on Metals, Dielectrics, and Interfaces for VLSI, San Juan Bautista, CA, May 9-12, 1988. Also to appear in J. Vac. Sci. Tech. B, 1988.
[20] S. M. Sze, *Physics of Semiconductor Devices*, 2nd Ed., Wiley:New York, 1981.
[21] C. Y. Ting, in IEDM Tech. Digest, p. 110, 1984.
[22] J. Hui, et al, IEEE EDL-6, p. 479, 1985.
[23] K. Shenai, et al, presented at the Workshop on Metals, Dielectrics, and Interfaces for VLSI, San Juan Bautista, CA, May 9-12, 1988. Also to appear in J. Vac. Sci. Tech. B, 1988.
[24] K. Shenai, et al, presented at the Symp. on Rapid Thermal Processing of Electronic Materials and Devices, 1988 Spring Mtg. of ECS, Atlanta, GA, May 15-20, 1988, Abstract No. 90, Extended Abstracts Volume, 1988.

Table 1. Contact data at 300K for 5 micron dry etched square contacts.

DOPANT	CONTACT METALLURGY	x_j (μm)	R_{SH} ($\Omega/\square$)	R_K (Ω)
P	Alusil	0.9	12.5	6.0
As	Alusil	0.3	41	12
B	Alusil	5.8	4.6	2.2
P	Al-TiW-$TiSi_2$	0.9	12.5	2.8
As	Al-TiW-$TiSi_2$	0.3	41	4.9
B	Al-TiW-$TiSi_2$	5.8	4.6	3.0

Abstract No. 254

PLANARIZATION PROCESSES FOR MULTILEVEL METALLIZATION

Geraldine Cogin Schwartz
IBM East Fishkill, Route 52
Hopewell Junction, NY 12533

The efficiency of wiring densely packed chips is improved significantly by the use of multiple wiring planes.

As each successive layer of a multilevel metal/insulator structure is built, the topography, introduced at the contact hole level, worsens. Severe topography causes problems in lithography and in step coverage by the deposited films. A planar structure is desirable, but difficult to realize. Several approaches have been used; some mitigate the effects of severe topography, others attempt to achieve complete planarization.

Processes have been developed to smooth an inorganic insulator so that it is easier to cover adequately by the next metal layer. These include: flowage of P- or P/B-doped oxides at high temperatures; "spacer technology"; bias PECVD deposition; deposition/etch cycles; and blanket dry etching a deposited insulator.

Polyimides have been used as the interlevel dielectric, replacing inorganic insulators, to planarize the structure partially and to smooth underlaying steep steps.

Among the early planarization processes was the fabrication of embedded structures; this approach is still pursued.

Deposition processes, which result in a planarized dielectric layer, include: bias sputtering; bias electron cyclotron resonance plasma deposition; and a sequence of deposition/etch cycles.

There is also a vast variety of "etch-back" procedures for planarizing a deposited insulator; they use several kinds of sacrificial layers or masking schemes.

More recently, planarization of metal films has been accomplished. In some of the techniques, the via holes in the interlevel insulator can be filled, without voids, while providing a planarized blanket metal film for subsequent patterning. Examples include: bias sputtering; enhanced surface diffusion during sputtering by the use of heat and bias; "flowage bias sputtering"; and sequential evaporation/sputter etch cycles. Via filling by partially ionized beam deposition, followed by deposition at a higher temperature, was used to form a planar aluminum layer. Another technique is deposition of a metal film over the via holes by standard methods and filling the holes by melting the metal briefly by exposure to laser pulses.

Other schemes depend on "hole filling"; these include selective CVD tungsten and electroless nickel deposition only in the holes. When the holes are of different depths, some will be over-filled and the excess metal must be removed. A layer of metal is then deposited on the planar surface and the next conductor level formed.

This paper presents and discusses the details of these processes. They are often complex and, therefore, time-consuming and expensive. Effort is being expended to simplify the processes; therefore greater use of multilevel metallization can be expected.

Abstract No. 255

Isoplanar Metallization Processes

P.L. Pai, M. Paunovic, C.H. Ting

Components Research
Intel Corporation
2250 Mission College Blvd.
Santa Clara, California

The advances in VLSI technologies have increased significantly the device counts per chip. As a result, single layer of conductor is no longer adequate and multilevel interconnection is widely practiced today. One of the major limiting factors in the further advancement of interconnection technology is the topography generated by each process step. The high resolution lithography demands a more planar surface, and the step coverage of deposited thin film also suffers from topography. As the number of conductor layers increases, these problems become more severe and have a detrimental effects on the improvement of VLSI technology. A truly planar metallization process is therefore needed.

For each conductor layer, there are two main components: the conductive films to form signal lines and the dielectric films to isolate these signal or power lines. If the metal film is deposited and patterned before the dielectric film, as in conventional metallization processes, an additional planarization process is needed to smooth the topography[1]. For the planarization techniques available today, there is no global planarization process except by mechanically lapping. Most planarization processes leave a smooth surface but can not reduce the step height over large patterns. A promising process to achieve truly planar surface is "buried metal process", in which the metal film is deposited after the embedding dielectric is deposited and atterned.

The buried metal process must fulfill two requirements: self-aligned metal patterning and good electrical properties. No alignment method can align metal patterns to the dielectric patterns exactly, and a self-aligned method is needed. Examples of self-aligned patterning rocess include lift-off[2] and selective deposition[3-5]. n this paper, we used electroless deposition process to selectively deposit metal film into dielectric trenches. The schematic of a self-aligned process is shown in Fig.1. The embedding dielectric film is deposited and patterned first(Fig.1(a)). Then an etching process transfers the pattern into the dielectric(Fig.1(b)). The desired metal film is selectively deposited only into the trenches(Fig.1(c)). As can be seen from this process flow, the bottom of the trench is also dielectric film; otherwise, the signals on one metal line will disturb the signals on the other. Depositing metal film selectively into the trenches requires some modification of the dielectric surface at the bottom of the etched trench.

A self-aligned lift-off process(LOPED)[6] can deposit a thin catalytic film into the trench, then the desired metal film can be deposited selectively on this film. Ti has been used in one example as the catalytic film, and the result is a planar surface with conductor buried in dielectric(Fig.2). Other approaches to deposit a catalytic film on the dielectric surface at the bottom of trenches will also be addressed. After the catalytic material is deposited, an electroless deposition process can deposit the desired conductive film.

The conductor system must also have good electrical properties. The metal patterns in VLSI circuits are typically long and narrow. As a result, the resistivity of the conductive film should be low and the electromigration resistance should be high. The two most promising candidates are Cu and Au due to their good conductivity. The resistivity of Cu is 1.6μohm-cm and that of Au is 2.35μohm-cm. Both Cu and Au are believed to have high electromigration resistance.

Reference

[1] A.N. Saxena, D. Pramanik, *Solid State Technology*, p.95, 1986.

[2] A.L. Wu, *Abstract #355*, ECS Fall Meeting, San Diego, CA, Oct. 1986.

[3] D.C. Thomas, S.S. Wong, *IEEE IEDM*, Los Angels, CA, Dec. 1986.

[4] C.H. Ting, *Abstract #512*, ECS Fall Meeting, Honolulu, HI, Oct. 1987.

[5] P.L. Pai, W.G. Oldham, M. Paunovic, C.H. Ting, *Abstract #481*, ECS Fall Meeting, Honolulu, HI, Oct. 1987.

[6] P.L. Pai, W.G. Oldham, *IEEE Trans. on Semiconductor Manufacturing*, vol.1, No.1, p.3, Feb. 1988.

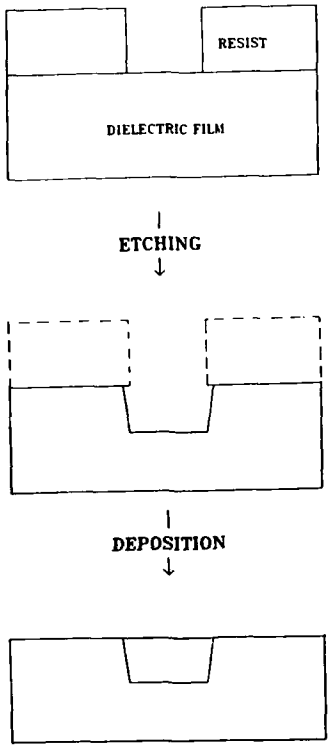


Fig.1 The schematic of buried metal process. (a) The embedding dielectric is deposited and patterned first. (b) An etching process transfers the pattern into dielectric. (c) The desired metal film is deposited into the dielectric patterns only.

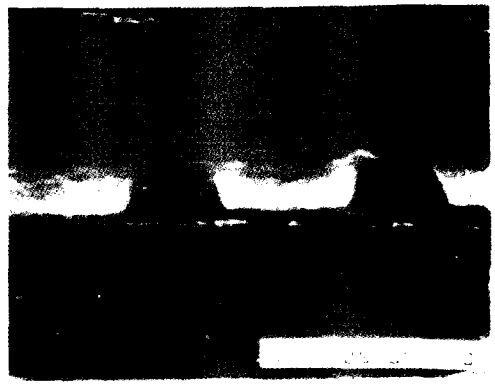


Fig.2 An example of buried metal film. A 0.8μm Cu film is deposited by electroless deposition process into low-temperature CVD oxide film. The surface is smoothed by coating a thin layer of spin-on glass. The planarity of this process is far better than most other processes.

Abstract No. 256

Effect of Via Filling on the Via Resistance and Surface Topography

Pei-Lin Pai and Chiu H. Ting
Components Research
Intel Corporation
2250 Mission College Blvd.
Santa Clara, California

Several processes have been proposed to fill high-aspect-ratio vias in VLSI technologies, including selective CVD tungsten[1-3], blanket deposited tungsten with etch-back[4], via pillars or studs[5,6], and selective electroless deposition[7,8]. In this paper, the advantages of via-filling to improve electrical properties and topography are studied by using SAMPLE simulation[9] program and experiments.

Any via filling scheme should have low via resistance and high electromigration resistance. Via resistance is affected by both the via filling material and the properties of the interface. The contribution from the via material will be studied in this paper. The interface properties will not be discussed. The electromigration performance will be addressed only in terms of topography.

The shadowing effect from sputtering process creates at the bottom of vias a thinner film than that of open areas. This may contribute significantly to via resistance if substantial thinning occurs. For a 1μm by 1μm via of 1μm deep, the resistance contributed from the via material is

$$R_{via} = \rho \times \frac{\text{length}}{\text{area}} = \rho(\text{in } \mu\Omega\text{–cm}) \times 10^{-2}$$

This is usually a small portion for small vias (25% for a via filling process resulting in $2\times10^{-9}\Omega$–cm specific resistance if a 5μΩ–cm material is used.) If the thinning in the vias increases this part significantly, the total via resistance will be affected. SAMPLE simulation program was used to study the effect of partially filled vias on the step coverage in small vias. The vias are assumed to be square in dimension for simplicity in calculation, the width is varied from 0.8μm to 1.5μm, and the depth between 1.0μm and 0.6μm. The results from this calculation can give an estimate of the improvement we can expect from filling the vias. The calculated via resistance is normalized to a 100% filled vias in Fig.1, thus the materials with different resistivity used in via filling will not change the results.

As clearly can be seen from Fig.1, the improvement in via resistance from filling the via is at best a factor of two for the smallest vias (0.8μm by 0.8μm, and 1.0μm deep.) For the 1.0μm cube vias, the contribution from the bulk via increases from 50 mΩ to 90 mΩ. However a word of caution is needed here, the simulation program often results in a better step coverage than what we can actually get from experiment. Therefore, the improvement may be better than a factor of 2 in reality. Another factor which is not taken into consideration is that significant contribution for high via resistance may be due to poor interface, whose properties are not directly related to the via filling material.

SAMPLE simulation program shows that the top portion of the deposition profiles remains the same as the vias are filled (Fig.2). The 1μm deep via generates the worst deposition profile, with significant thinning at sidewalls and at the bottom of the vias. As the vias are filled, the via depth becomes shallower, but the topography for upper deposition profiles remains essentially unchanged from that of unfilled via. From the deposition profiles shown in Fig.2, we know the thinnest part of metal film is always near the bottom of vias. Therefore, for partially filled vias the metal deposition profiles are completed before reaching the thinnest areas, then the step coverage should improve. The step coverage, defined as the ratio of the thinnest film thickness to the thickness on a flat surface, is plotted against the filling (Fig.3). The step coverage does improve as the via are filled, with the steepest increase around 60% filling. The electromigration performance in vias is expected to improve with better step coverage, since less current crowding is expected.

Another advantage of via-filling is that the aspect ratios of surface topography in the top metal will decrease. A high aspect ratio on the surface makes subsequent processing more difficult, and also excludes the possibility of stacking one via over the other, a scheme that can save significant amount of chip areas. SAMPLE simulation program is again used to study the improvement of aspect ratios (Fig.4). Since the deposition profiles do not change as the vias become shallower, the minimum opening of the top metal does not decrease. As a result, the aspect ratio decreases slowly as the depth of the via decreases. Once the via filling reach 80%, the aspect ratio decreases to about 1. Further filling of vias can really help to smooth the remaining topography.

From these results it is concluded that the filling of via helps most at around 80% filling. A shallower deposition, e.g. 50%, will help the electrical properties, but the advantages in topography is not significant.

Reference

[1] I. Beinglass, " Selective CVD Tungsten Deposition - A New Technology for VLSI and Beyond," *1985 Silicide Workshop*, Material Research Soc., p.13 (1985).

[2] R.W. Stoll, R.H. Wilson, "Highly Selective, High Rate Tungsten Deposition for Via Filling Using a Hot Plate Heater," Proc. of the Sym. on Multilevel Metallization, Interconnection, and Contact Technology, Electrochemical Soc., Vol. 87-4, p.232(1987).

[3] S.L. Lanny Ng, P. Merchant, "Electrical Characteristics of Via Structures Containing Selective CVD Tungsten Plugs," *IEEE VLSI Multilevel Interconnection Conf.*, p. 186(1987).

[4] K. Shiozaki, K. Mitsuhashi, K. Ohtake, M. Koba, "Low Resistive, High Aspect Ratio Via-Hole Filling System Completely Planarized by Selective W Deposition and Subsequent Etch-Back," *the 19th Conf. on Solid State Devices and Materials*, Tokyo, p. 435(1987).

[5] E.R. Sirkin, I.A. Blech, " A Method of Forming Contacts Between Two Conducting Layers Separated by a Dielectric," *J. Electrochem. Soc.*, 131(1), 123(1984).

[6] M.T. Welch, C. Garcia, " Pillar Interconnections for VLSI technology," *VLSI Multilevel Interconnection Conf.*, 450, (1986).

[7] Y. Harada, K. Fushimi, S. Madokoro, H. Sawai, S. Ushio, " The Characterization of Via-Filling Technology with Electroless Plating Method," *J. Electrochem. Soc.*, 133(11), 2428 (1986).

[8] C.H. Ting, M. Paunovic, G. Chiu, "Selective Electroless Metal Deposition for Via Hole Filling in VLSI Multilevel Interconnection Structure," ECS Fall Meeting, *Abstract # 514*, Oct. 18-23, 1987; and in "Electroless Deposition of Metals and Alloys," edited by M. Paunovic and I. Ohno, the Electrochemical Society, p.252(1988).

[9] SAMPLE simulation program has been developed at the University of California at Berkeley on process modelling with Professor A.R. Neureuther and W.G. Oldham.

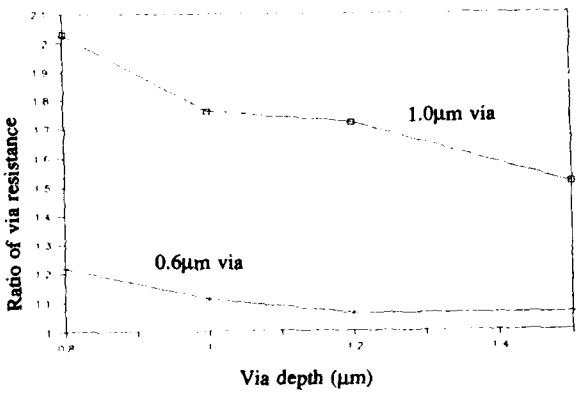


Fig.1 The ratio of the via resistance of an un-filled via to that of a completely filled via with two depth, 1.0μm and 0.6μm.

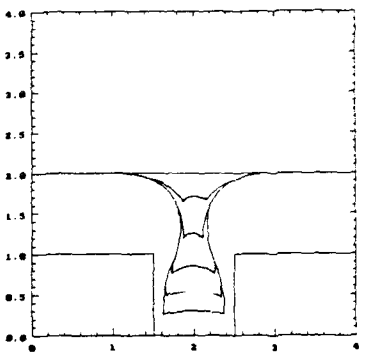


Fig.2 Deposition profiles from SAMPLE simulation program for partially filled and un-filled vias. The top metal thickness is 1.0μm and the via depth is 1.0μm. The profiles from top represent the metal film deposited into a 100% filled, 80% filled, 60% filled, 40% filled, 20% filled, and unfilled via.

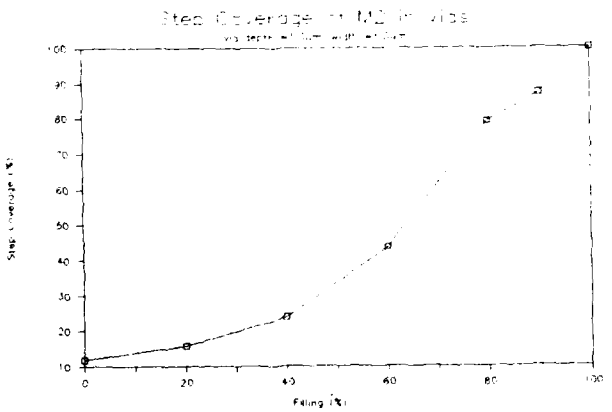


Fig.3 The step coverage of a 1.0μm metal film deposited into a partially filled via.

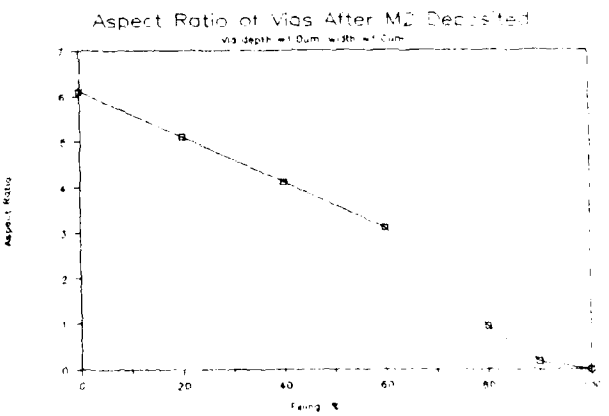


Fig.4 The aspect ratio of a 1.0μm metal film deposited into a partially filled via.

Abstract No. 257

A Non-Etchback SOG Process For Multilevel Interconnect Technology

C.H. Ting, H.Y. Lin, P.L. Pai and T. Rucker
Components Research
Intel Corporation
2250 Mission College Blvd.
Santa Clara, CA 95052-8125
(408) 765-9977

A planarized interlevel dielectric layer is needed for multilevel interconnection used in VLSI circuits. Many different methods have been developed to planarize the interlevel dielectric layer for subsequent processing. Recently, interlevel dielectric planarizing process based on Spin-On-Glass(SOG) has been under intense study because of its simplicity. Due to limitations in material properties, a partial SOG etchback process is usually used[1,2]. However, the etchback process not only increases process complexity, it also limits the further scaling to smaller geometries[3]. A non-etchback SOG process is therefore highly desirable.

For a non-etchback SOG process, the SOG material must have good mechanical properties (i.e. non-cracking) as well as good dielectric properties. Such a material is available commercially. The material properties were determined by stress measurements and FTIR measurements[4]. Furthermore, the outgassing properties of SOG was determined in an UHV chamber (10^{-9} Torr). The cured SOG was found to have negligible outgassing up to 550°C. This is illustrated in Fig.1. However, when this SOG material was used in conjunction with an LTO dielectric layer in our standard device fabrication process, signs of severe outgassing were observed. This results in poor and non-uniform metal step coverage over the via hole. Under optical microscope, the vias appear as dark circles.

The cause of this SOG outgassing problem was traced to process-material interactions rather than poor properties of as cured SOG material. FTIR analysis after plasma processing for via etching and resist stripping indicates dramatically increased hydroxyl content, illustrated in Fig.2. By making some changes in wafer processing conditions, such as adding a high temperature annealing step after via hole etching and an in-situ sputter clean cycle before metal deposition, the outgassing problem can be eliminated. Smooth metal step coverage over via holes and good via resistance have been obtained using this non-etchback SOG process. Details of material analysis, processing conditions, and measured results will be presented.

Reference

[1] V.J. Multani, J. Chu, S. Mittel and J. Orton, *Proc. IEEE VLSI-Multilevel Interconnection Conf.*, p.474(1986).

[2] S.K. Gupta, S.W. Kirtley and I.B. Vines, *ibid.* p.506(1986).

[3] R.M. Brewer and R.A. Gasser, *ibid.* p.376(1987).

[4] P.L. Pai, A. Chetty, R. Roat, N. Cox and C.H. Ting, *J. Electrochem. Soc.*, 134 p.2829(1987).

[5] C.H. Ting, H.Y. Lin, P.L. Pai, W.G. Oldham, *Proc. IEEE VLSI-Multilevel Interconnection Conf.*, p.61(1987).

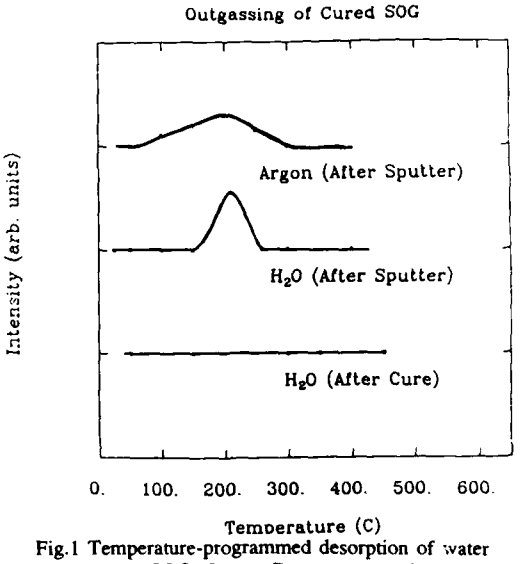


Fig.1 Temperature-programmed desorption of water from cured SOG films. Bottom trace shows no water desorption after curing. The mid-trace shows small amount of water desorption after one-hour sputtering. For comparison, top trace shows the amount of argon desorption after sputtering.

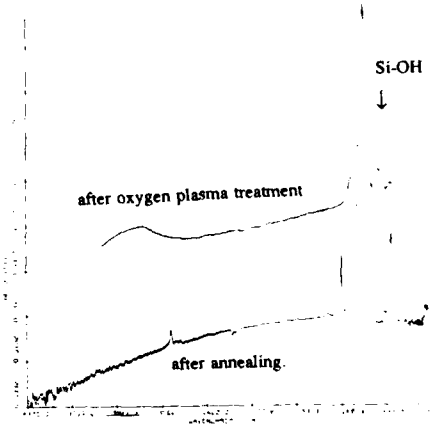


Fig.2 FTIR spectra after annealing and after O_2 plasma resist stripping process. The areas corresponding to hydroxyl groups at 940 cm^{-1} increase dramatically after the oxygen plasma treatment.

Abstract No. 258

Chemical Vapor Deposition of Tungsten (CVD W) as Submicron Interconnection and via-stud

Pei-Ing Lee, John Cronin, Carter Kaanta
IBM General Technology Division
Essex Junction, Vermont 05452

EXTENDED ABSTRACT

As circuit density increases in VLSI technology, the limitations of conventional metallization techniques become more apparent. In general, polysilicon based interconnects are limited by their high RC (resistance x capacitance) delay. While sputtered and evaporated aluminum (Al) based metallurgies do not present RC delay difficulties, they have other limitations. The limitations include the difficulty of achieving a conformal deposition, and their relatively poor thermal and mechanical stability and electromigration resistance properties. Chemical vapor deposition of tungsten (CVD W) has been used as a multilevel interconnect in an IBM DRAM technology. This is because CVD W does not have the aforementioned limitations of Al systems. Figure 1 shows CVD W applied as contact, wiring, and interlevel via-stud (1).

CVD W was deposited in a cold wall reactor by silane and/or hydrogen reduction of tungsten hexafluoride. No detectable difference in film resistivity and film composition can be found between silane and hydrogen reduced tungsten films. It was found that silane reduced tungsten deposition readily becomes mass transfer limited, and insufficient hole fill may result. This is due to the higher deposition rate of the process Process optimization did not efficiently improve hole fill. On the other hand, excellent hole fill can be obtained by hydrogen reduced tungsten deposition. The deposition rate is however three times slower at the same temperature, and throughput is dramatically decreased. Therefore, silane and hydrogen reduction processes were combined to optimize both hole fill and throughput. Figure 2 shows a comparison between the original hole fill and the improved tungsten hole fill achieved by the new process.

The adhesion of CVD W on such insulators as borophosphero-silicon-glass (BPSG), thermal oxide (TOX) and plasma enhanced CVD oxide or nitride were extremely poor. An adhesion layer was required between tungsten and the various substrate interfaces. This adhesion layer strongly influences the etchability of CVD W metallurgy as well as the contact resistance. It has been found that adhesion layers such as tungsten silicide, molybdenum, titanium, titanium/tungsten alloy, and sputter tungsten, have either caused undercut etching (isotropic) in the tungsten reactive ion etch (RIE) patterning, or resulted in high contact resistance between the CVD W and underlying conductive structures. TiN as an adhesion layer has been found to resolve all the concerns of etchability, adhesion, and contact resistance. Table I compares the adhesion of CVD W on non-nitridized Ti and on TiN. It is important to note that while various preclean techniques did not improve adhesion, nitridation of titanium by annealing improves adhesion significantly. It has also been found that reactive sputter titanium nitride also improves adhesion.

Table II shows a comparison of CVD W contact resistance when Ti or TiN is used as an adhesion layer. Two orders of magnitude improvement in contact resistance were achieved when TiN was used. Neither Ti annealing in argon or post annealing after tungsten deposition provides any improvement in contact resistance, indicating that nitridation is essential for contact resistance improvement. The TiN can be formed by either nitrogen or forming gas annealing of titanium. The lower contact resistance can be obtained by higher annealing temperatures. Figure 3 shows the relative nitrogen to titanium ratio determined by Rutherford backscatter spectroscopy (RBS). The ratio at various temperatures is normalized to the ratio at 850°C annealing temperature. The nitrogen to titanium ratio increases as the annealing temperature is increased.

Solid phase interdiffusion thru contact barrier materials has long been a concern for contact metallurgies(2). However, this is probably not a concern for the CVD W system. In the current case, diffusion into the underlying conductive structure by the reactive by-product in the CVD W reactor may be a concern. It is interesting to note that the TiN may be acting as an effective diffusion barrier in situ in the CVD W reactor to prevent by-product diffusion. Depth profile by secondary ion mass spectroscopy (SIMS) has revealed a significant concentration of fluorinated species in the non-nitridized Ti layer (Figure 4). There was a significant reduction in fluorine concentration found for CVD W on the TiN samples. The relative amount of fluorine is plotted as a function of nitridation temperature in Figure 5. This result seems to be consistent with the contact resistance data shown in Table II, suggesting that the fluorine in the underlying conductive layer effects contact resistance.

The etchability of TiN/CVD W stack was shown in Figure 6. Here an anisotropic etch can be easily achieved by using TiN. On the other hand, adhesion layers such as tungsten silicide, titanium/tungsten alloy, and sputter tungsten show an isotropic attack on the adhesion layers. The tungsten films can be patterned by RIE in a chlorinated or fluorinated chemistry (3). It is also important to note that for TiN-CVD W metallurgy used for via-studs, no selective attack of the adhesion layer (on the sidewall of the via-stud) was found.

In summary, CVD tungsten technology has been proven to be applicable for submicron multilevel interconnect technology. TiN has been shown to play a key role for CVD tungsten adhesion, submicron patternability, and contact resistance. Superior hole fill can be obtained by CVD W for via-stud application using a two step W reduction process. Excellent results have been obtained from process characterization, electrical characterization, and reliablity stress (1).

REFERENCE

1. C. Kaanta, W. Cote, J. Cronin, K. Holland, P. Lee, T. Wright, p 209, IEDM December 1987
2. J.M. Poate, K.N. Tu, J.W. Mayer, "Thin Films-interdiffusion and reactions" Wiley-Interscience publication, 1978
3. K. Holland, T. Wright, W. Cote, p 692 ECS Extended Abstract, Fall Meeting 1987

ACKNOWLEDGEMENT

The authors are greatly in debt to George Slusser, Edward Adams, Laird MacDowell, and Robert Frenette for SIMS and RBS support, to Mike Leach, Thom Hartswick, William Cote, Terry Wright, and Karey Holland for technical support and valuable discussion. Appreciation is also extended to Dick Dreves, Chris Culter, Faith Ichishita, Gary Viens, and Pete Rath for process piloting.

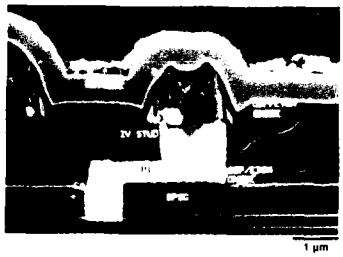


Figure 1. CVD tungsten as a key feature of submicron interconnection.

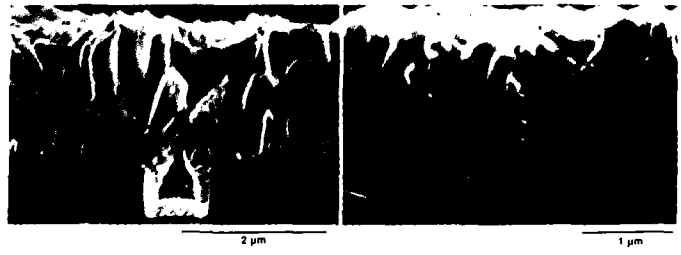


Figure 2. A comparison of worst case CVD tungsten hole fill vs improved tungsten hole fill.

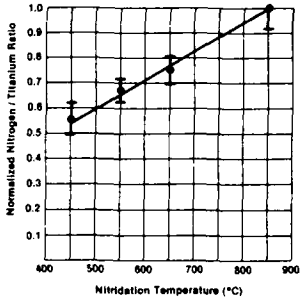


Figure 3. Normalized N / Ti ratio in the adhesion layer as a function of nitridation temperature. The ratio is determined by RBS.

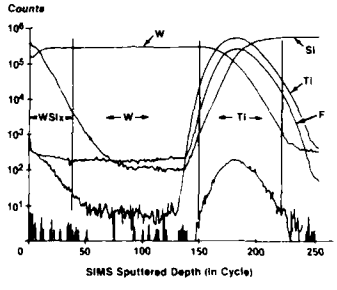


Figure 4. The SIMS depth profile of CVD tungsten film using non-nitridized Ti as an adhesion layer. Note that the fluorine concentration is extremely high in the adhesion layer.

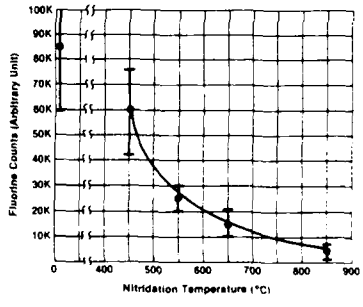
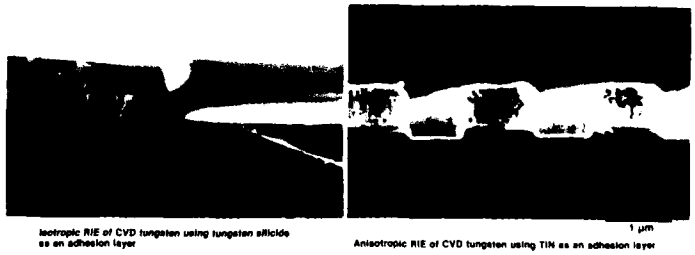


Figure 5. Fluorine concentration within the Ti adhesion layer by SIMS analysis. Note that the F concentration decreased significantly as the nitridation temperature increased.



Isotropic RIE of CVD tungsten using tungsten silicide as an adhesion layer

Anisotropic RIE of CVD tungsten using TiN as an adhesion layer

Figure 6. A comparison of isotropic and anisotropic RIE of CVD tungsten.

Table I. Adhesion of CVD W using titanium as an adhesion layer.

Process Description: Three substrates (TiSix, BPSG, TOX) were precleaned with different solutions, and deposited with a layer of sputtered titanium. The substrate with titanium is either formed TiN by thermal nitridation or without nitridation, then deposited with CVD W. The whole stacks were then subjected to adhesion test.

Note: The TiN provides better adhesion between CVD W and substrates.

Substrate	Precleon	Ti Nitridation	Scotch Tape Pull Test	Instron Pull Test
TiSix	No	No	Pealed	5800lb / in²
	+ BHF	No	Pealed	6500lb / in²
	* C / P	No	Pealed	5100lb / in²
	# BDE	No	Pealed	5900lb / in²
TOX	No	No	Pealed	5400lb / in²
BPSG	No	No	Pealed	6000lb / in²
TiSix	No	Yes	Adhered	> 9600lb / in²
	+ BHF	Yes	Adhered	> 9600lb / in²
	* C / P	Yes	Adhered	> 9600lb / in²
	# BDE	Yes	Adhered	> 9600lb / in²
TOX	No	Yes	Adhered	> 9600lb / in²
BPSG	No	Yes	Adhered	> 9600lb / in²

TOX: Thermal oxide, BPSG: Boro-Phosphore-silicon glass, # BDE: ammonium phosphate, + BHF: 100 : 1 buffered HF, * C / P: 95 / 50 chromic phosphoric acid

Table II. Contact resistance of CVD W using titanium as an adhesion layer

Process Description: The CVD W was made contact to N+ P+ diffusions and polysilicon using either non-nitridated or nitridated titanium as adhesion layer. The thickness of titanium temperature was varied from 450°C to 850°C. The result from the submicron contacts were summarized.

Note: The TiN as an adhesion layer provides superior contact resistance for CVD metallurgy.

Contact Substrate	Contact Size	Nitridation Temperature	Contact Resistance (Ohm)
N+ Diffusion	0.8	No Anneal	> 1,300
P+ Diffusion	0.8	No Anneal	> 1,300
Polysilicon	0.8	No Anneal	> 1,300
N+ Diffusion	0.8	450°C	0.5 to 8.0
P+ Diffusion	0.8	450°C	0.6 to 8.5
Polysilicon	0.8	450°C	0.5 to 8.0
N+ Diffusion	0.8	650°C	0.4 to 1.0
P+ Diffusion	0.8	650°C	0.4 to 1.2
Polysilicon	0.8	650°C	0.4 to 1.3
N+ Diffusion	1.0	850°C	0.4 to 0.8
P+ Diffusion	1.0	850°C	0.4 to 0.8
Polysilicon	1.0	850°C	0.6 to 1.0

Note: The contact resistance is measured on a four-point probe structure.

Abstract No. 259

APPLICATION OF BORON-DOPED PLASMA CVD TEOS FOR INTERMETAL DIELECTRIC

Farhad K. Moghadam, Kwang Suh
Intel Corporation
Submicron Technology Development

The plasma deposition of boron doped TEOS-based oxide (BSG) is studied in a single wafer parallel plate CVD reactor. The evaluation of different process parameters on the film properties indicates that RF power, TEOS:O2 ratio, elctrode spacing have a pronounced effect on the resulting film properties (stress, density, moisture absorption). The SIMS analysis of BSG showed very low carbon content (less than 1 atomic %) and presence of no other impurities was detected in the film, regardless of process conditions.

The application of moisture evolution analysis (MEA) technique to different films showed significant quantity of moisture pickup (0.55% by weight) for the films deposited at lower RF powers (200 Watts) as compared with higher RF power (300 Watts). The moisture outgassing was very well correlated to OH peak observed in FTIR spectrum.

The process parameters were adjusted in order to obtain a low compressive stress value (<100 MPa). The effect of temperature ramp-up and cool-down on the stress revealed the presence of hysteresis loop. The size of stress hysteresis loop is found to be correlated to the moisture content of the film. The higher the moisture content, the larger the loop. As it is shown in Fig.1 a and b, the film deposited at the lower RF power showed the larger stress hysteresis loop, consistent with FTIR and MEA observations. The stress was observed to change depending on the time duration between deposition and measurement, film becomes more compressive as it absorbs moisture. A change of 200 and 28 MPa were recorded for 200 and 300 Watts film after one week of post-deposition storage at room temperature, respectively.

The wet etch rate in a buffered HF (BHF) solutuon is measured to be a strong function of RF power which actually affects the film density. Higher RF power yields to a denser oxide due to more bombardments, which in turn leads to lower etch rate in BHF. In 6:1 HF acid, the measured etch rates for high temperature steam grown oxide, 300 and 200 Watts BSG are. 900,1200,1900 A/min, respectively.

The breakdown voltages (BVG) of thin BSG films (800-1000A) showed the values of 2-3 MeV/cm, which indicates low defect density (i.e. pinhole-free) films.

The C-V evaluation of different BSG films demonstrates a large positive faltband voltage shift (in excess of 5V) for all cases upon high temperature stress (250C, 10V for 15 mins). This observation eludes to the presence of negative oxide trapped charges (Qot). A large concentration of fast surface states (Qss), ~5E11/cm2, is also mens red by C-V analysis.

The BSG film with optimum properties (stress, density) was applied to a double metal CMOS process as an intermetal dielectic layer. The process was optimized to provide void-free and good planarity of dielectric over topology. Via holes were opened by wet etch in BHF followed by RIE. To complete the double metal process, second layer of metal was deposited and patterned. Fig.2 shows the via chain resistance on topography for 1.1X1.1um vias. It is found that 200 Watts BSG has a higher resistance and larger scatter than 300 Watts BSG. This is due to metal quality degradation by outgassing of dielectric film during metal deposition. The metal quality degradation was also noticed through line resistance measurements as shown in Fig.3. The metal line bridging test results on topography are shown in Fig.4, low leakage current between the 1um space metal lines is the indication of good planarity for both dielectrics (200 and 300 Watts BSG).

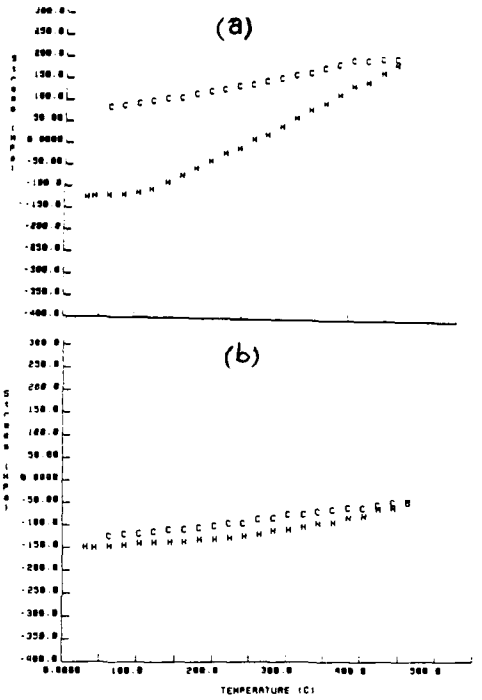


Fig.1. Stress Hysteresis Loop of a) 200 Watts, b) 300 Watts BSG Films. Large loop is seen at lower RF power.

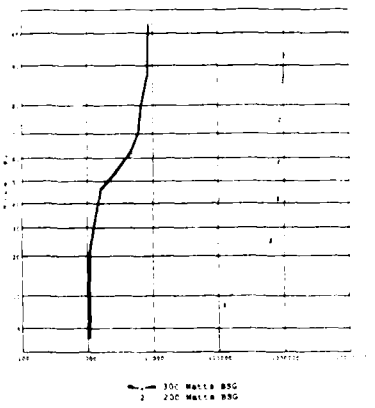


Fig.2. Via Chain Resistance Distribution Plot for 1.1X1.1um Via Size in 200 and 300 Watts BSG Films. Higher resistance, by two orders of magnitude, is seen in 200 Watts BSG, compared with 300 Watts BSG.

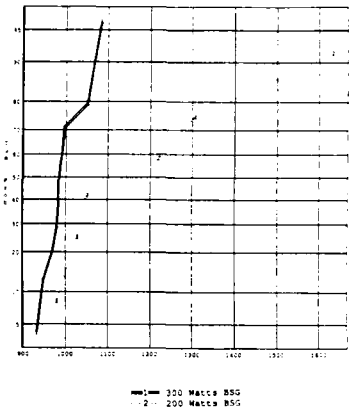


Fig.3: Second Level Metal Line (1.7um wide) Resistance over Topography. Larger spread for 200 Watts BSG is evident.

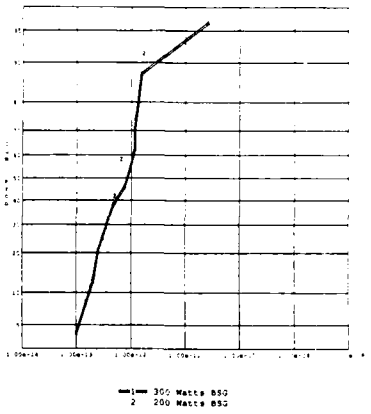


Fig.4: Second Level Metal Line Bridging (1um space) Results over Topography. No bridging in either case is seen.

Abstract No. 260

Etchback of CVD Blanket Tungsten Films in a Hexode Reactor

Francine Y. Robb and Kathleen W. Ginn

Motorola, Inc.
2200 W. Broadway Road
Mesa, Arizona, 85202

The conformal step coverage of CVD tungsten (W) allows the filling of high aspect ratio contacts and vias for VLSI circuit applications. The relatively high resistivity of tungsten alone, limits its use as an interconnect and leads to contact plugging. Since numerous problems have been encountered with selective deposition of tungsten, non-selective CVD tungsten deposition and subsequent etchback is studied as an alternate way to contact plugging.

The primary goal of this study was to develop an etchback plug process for CVD blanket W films in a AME 8130 hexode system. The process, as initially envisioned, utilized a planarizing resist layer to smooth rough grains and allow the use of large underfilled vias. A $CF_4/Cl_2/O_2$ chemistry was chosen because of both the published success (1) of the similar CCl_2F_2/O_2 chemistry and the availability of these three gases in a standardly configured AME 8130.

RESULTS AND DISCUSSION

Etchback With Resist Screening experiments using the $CF_4/Cl_2/O_2$ chemistries helped to define which variables controlled the W-to-resist selectivity, as a 1:1 selectivity is essential for successful tungsten etchback in the presence of a planarizing resist layer. The major results from these experiments included slow (<280 A/Min) tungsten etch rates, poor tungsten etch rate reproducibility, <1:1 W:resist selectivities, and a "proximity" effect whereby blanket resist films etched significantly faster than resist films adjacent to etching tungsten (See Figure 1).

The W etch rate reproducibility was affected by numerous variables. Thicker films, longer etch times, a BCl_3 "breakthrough" step, increased hexode temperature (60°C vs 45°C) and the use of resist dummies (instead of silicon) improved the reproducibility to <10% (2σ).

Table I summarizes the results of a full factorial characterizing the variables (%O_2, %Cl_2, and pressure) identified as most important in the screening studies. Both tungsten and resist rates were increased by 10% additions of either Cl_2 or O_2. A comparison with screening data, which showed that 15-30% O_2 caused the W etch rate to decrease, suggests that a maximum W rate evidently exists at ≈10% O_2. In addition, the use of Cl_2 produced the earlier observed resist "proximity" effect. The W to-resist selectivity was less than 1:1 in all cells, ranging from 0.41 to 0.91.

The W to resist selectivity was closest to 1:1 in the cells with 10% O_2 in CF_4. Routine use of this CF_4/O_2 etchback was not attempted, however, as residue is typically encountered when pure fluorine chemistries are used in the presence of non-etchable aluminum-containing reactor materials.

Direct Etchback (No Resist) The elimination of resist from the etchback, although limiting the contact/via size to those which can be completely filled with tungsten, greatly simplifies etch considerations, with a greater than 3:1 W-to-oxide selectivity the primary concern.

Initial direct etchback studies utilized a standard tungsten etch, designed for anisotropic etching of W and TiW films underlying aluminum in a stacked metallization. The process, which uses a 20 sccm CF_4/20 sccm Cl_2 mixture, 15 mTorr pressure and 300 Vdc bias, produces a tungsten etch rate of ≈180 A/min and a less than desired 1.1-1.5 W-to-PSG selectivity. Etch back of blanket tungsten in such a poor selectivity process produces rough PSG surfaces, with high PSG loss.

Oxygen addition to Cl_2 was found to improve the W-to-PSG selectivity to greater than the 3:1 goal. Figure 2 shows that the W etch rate peaks at around 10% O_2 in Cl_2, while the W-to-PSG selectivity continually increases with increasing O_2 (due mainly to decreasing oxide rates). Severe across-the-wafer non-uniformities, observed at ≈50% O_2, limited the maximum usable O_2. In addition, Figure 2 shows that the PSG selectivity in 30% O_2/Cl_2 increased from 6:1 to 12:1 as the etch time increased from 7 to 17 minutes, probably due to the diminishing effect of residual BCl_3 used in the breakthrough step.

Several loading effects were apparent during the scale-up of a 30% O_2/Cl_2 process. Figure 3 shows that the PSG rate increases (and the W-to-PSG selectivity decreases) as the load size is increased from 1/2 to 5 tungsten wafers. Thus tungsten chloride products evidently enhance the oxide etching ability of a chlorine plasma, similar to CCl_4 and $SiCl_4$. In addition, Figure 4 shows that the W rate is accelerated during overetch to two times the bulk W rate. This causes the W plug to recess into the contact/via more rapidly than expected.

CONCLUSIONS

The etchback of CVD tungsten films for contact plug applications using a standard AME 8130 is reported. A chlorine-induced resist "proximity" effect and generally very low W-to resist selectivity prohibited the development of a $CF_4/Cl_2/O_2$ etchback in the presence of a planarizing resist. A direct etchback (no resist) of totally filled contacts was developed utilizing a 30% O_2/Cl_2 chemistry and is currently being tested on device vehicles. Concerns include an accelerated W rate during overetch and a batch-size dependent tungsten-to-PSG selectivity.

REFERENCES

(1) R.J. Saia, B. Gorowitz, D. Woodruff, and D.M. Brown, Proc. 6th Symp. Plasma Processing, 87-6, 173 (The Electrochem. Soc., 1987).

Table I. Trends from the 2^3 full factorial characterizing O_2/Cl_2 addition to a CF_4 plasma and pressure effects are summarized below. ANOVA techniques were used to analyze data, with a confidence (α) level of less than 0.10 selected for significance. A 45 sccm total gas flow, 350 Vdc bias, 60°C and all resist dummy wafers were used.

DEPENDENT VARIABLE	INDEPENDENT VARIABLES					COMMENTS
	%Cl	%O2	PRESSURE	INTERACTIONS	DATA MAX / MIN	
W ETCH RATE	↑ 2 α = 0.078	↑ 1 α = 0.023		NONE DEFINED	799:65 (A/MIN)	HIGHEST RATES WITH Cl_2 AND O2 ADDED AT 90 mTorr
PATTERNED RESIST RATE	↑ 2 α = 0.013	↑ 1 α = 0.006	↑ 3 α = 0.017	Cl_2*O2*PRES α > 0.054	422:207 (A/MIN)	
BLANKET RESIST RATE	↑ 2 α = 0.06	↑ 1 α = 0.04		NONE DEFINED	515:206 (A/MIN)	
PSG RATE		↓ 2 α = 0.03	↑ 1 α = 0.007	MANY SIGNIFICANT INTERACTIONS	326:231 (A/MIN)	
SURFACE ROUGHNESS	NOTHING SIGNIFICANT				710:535 (A)	ALL SURFACES ROUGH
W/PATT RESIST		↑ 1 α = 0.02		O2*PRES α = 0.05 Cl_2*PRES α = 0.06	0.91:0.41	
BLANKET/PATT	↑ 1 α = 0.04			NONE DEFINED	1.46:0.99	
W/PSG	↑ 2 α = 0.03	↑ 1 α = 0.007		O2*PRES α = 0.07	1.18:0.33	
LEVELS STUDIED	(-) = 0% (+) = 10%	(-) = 0% (+) = 10%	(-) = 35 (+) = 90 mTorr			

Figure 1. The resist etch rates obtained in the screening experiments are plotted as a function of the tungsten etch rate measured in the same run.

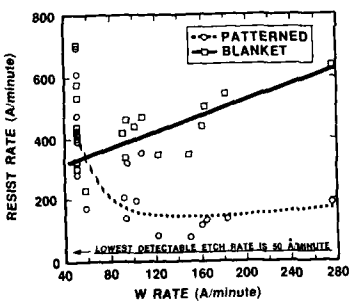


Figure 2. The tungsten and PSG rates are plotted as a function of O_2 addition to pure Cl_2.

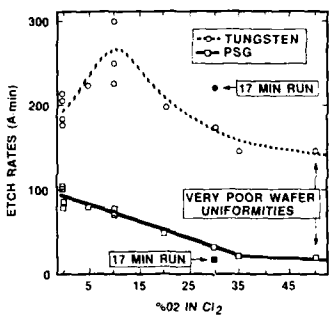


Figure 3. The PSG etch rate and tungsten-to-PSG selectivity are plotted as a function of the number of tungsten wafers in the etch system.

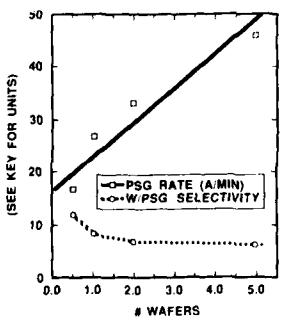
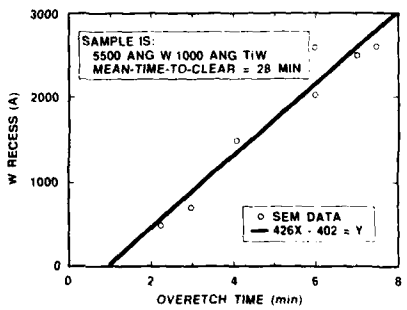


Figure 4. The amount the tungsten plug has recessed into the contact opening (as measured by SEM) is plotted as a function of the overetch time in the 30% O_2/Cl_2 process.



Abstract No. 261

Two step tapered via hole etching using down flow and reactive ion etching

T. Tsuchiya, J. Konno, T. Takada
Bipolar Process Division

S. Fujimura, H. Yano
Process Development Division

FUJITSU LIMITED

1015, Kamikodanaka, Nakahara-ku, Kawasaki, 211, Japan

Introduction

In multilevel interconnections, a tapered via hole profile is necessary for good metal coverage. Also via hole size control is important for recent fine pattern devices.

A tapered profile in SiO_2 can be obtained by reactive ion etching using a resist mask[1]-[3]. This technique makes use of the controlled simultanious etching of the resist mask and the SiO_2. However, this technique is not repeatable. Because slope of via hole depends critically on the resist profile and the etch rates of resist and SiO_2.

In this work we studied two step etch of via hole. At the first step, about a half of thickness of insulator is etched isotropically. Thus slope of via hole is made in this step. At the second step, remained insulator is etched off anisotropically. The bottom size of the via hole is determined in this step. Since to prevent flow of resist mask, the isotropic etching have to be done at low temperature. The conventional plasma etcher demands high temperature to etch SiO_2 fast. Thus, this type of etcher is difficult to use in this process. We find that the down flow etcher is suitable for this process. Through the two step via hole process using down flow etcher, good step coverage and low contact resistance were realized.

System description

The isotropic etching was done with the single wafer down flow etcher which consist of plasma chamber and adjoining the etching chamber. A reactive gas plasma is generated in the plasma chamber by 2.45GHz microwave. In addition, the etching chamber is shielded by the aluminum shower head from the plasma. Thus neutral active species lead to the etching chamber. A wafer is positioned on the aluminum stage in the etching chamber. The wafer can be heated using a resistance coil setted in the stage. Stage temperature is monitored by the thermocouple attached to the stage. SiO_2 isotropic etching is accomplished using CF_4+O_2 for the process gases.

The anisotropic etching was done using a typical single wafer parallel plate etcher. CF_4+CHF_3 were used for process gases.

Isotropic etching characteristic

Thermal SiO_2 or P-doped (8% by weight) PECVD SiO_2 films were deposited on 4 inches diameter Si wafers. These wafers were then coated with positive photoresist(NPR-820;Kodak), exposed, developed, and baked at 120℃.

The standard operating conditions are:

CF_4 flow rate	400 sccm
Pressure	1.0 Torr
microwave power	1.0 Kw.

O_2 percentage in CF_4+O_2 gases mixture was varied from 0 to 34%. The stage temperature was varied from 70 to 175℃.

Figure 1 shows the effect of O_2 concentration on the etch rates of P-doped SiO_2 and photoresist (at the stage temp.=70℃). In agreement with a data of another down flow etcher[4], the etch rate of the doped SiO_2 is improved by addition of O_2 to CF_4. And this improvement is saturated at over 20% O_2. The etch rate of the photoresist increase gradually with increase of the amount of O_2 in process gases. Considering SiO_2 etch rate and selectivity to the resist, we fixed the O_2 percentage to 17.

Etch rates of SiO_2 (thermal and P-doped PECVD) and photoresist, as related to stage temperature, are shown in Figure 2. There is a linear relationship between the etch rates and the stage temperature. Resist flow was observed in the wafers etched at over 120℃ stage temperature. Thus we fixed the stage temperature to 110℃.

The etch rate of doped SiO_2 is about 4000Å/min. and the selectivity of doped SiO_2 to photoresist is more than 20.
Uniformity of SiO_2 etch rate across the wafer is within ±5%.

Figure 3 shows the isotropic etch profile.

Two step etch process

P-doped SiO_2 with 1um thick was used for interlevel insulator. Contact test structure used for electrical measurement consist of 1.4um□ and 2.0um□ "via string". The "via string" has 11120 or 50000 vias which conected in series.

The isotropic etching depth was varied from 0 to 0.8 um. Figure 4 shows the "via string" resistance as related to the isotropic etching depth. The "via string" resistance is improved by increase of the isotropic etching depth.

Figure 5 shows the via profile which formed by two step etching.

With this process, we obtained good metal coverage and low contact resistance. The bottom size of via hole do not increase from the size of resist mask. This process has good repeatability and producivility.

Acknowledgement

The authers wish to thank M. Nakamura and T. Kurahashi for their helpful discussion.

Reference

(1) J.A. Bondur and R.G. Frieser, in Proc. of Symposium on Plasma Etching and Deposition, R.G. Frieser and C.J. Mogab Eds., The Electrochemical Society Vol 81-1, 180 (1981).
(2) E. Crabble and E.R. Sirkin, ECS Extended Abstract Vol.1, 261 (1983).
(3) J.S. Pflug and P.M. Mccarthy, ECS Extended Abstract Vol.2, 593 (1984).
(4) Y. Horiike and M. Shibagaki, "Semiconductor Silicon" H.R. Huff and E. Sirtle Eds. (Electrochemical Society Softbound Symp. Series) 1071 (1977)

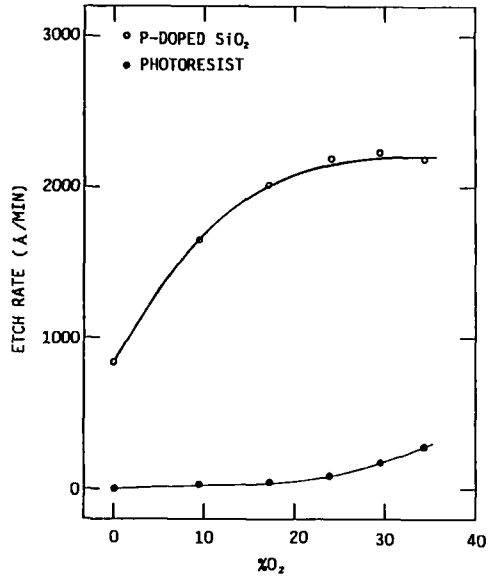


Figure 1 Etch rates of P-doped PECVD SiO_2 and photoresist versus O_2 percentage in CF_4 + O_2 mixtures.

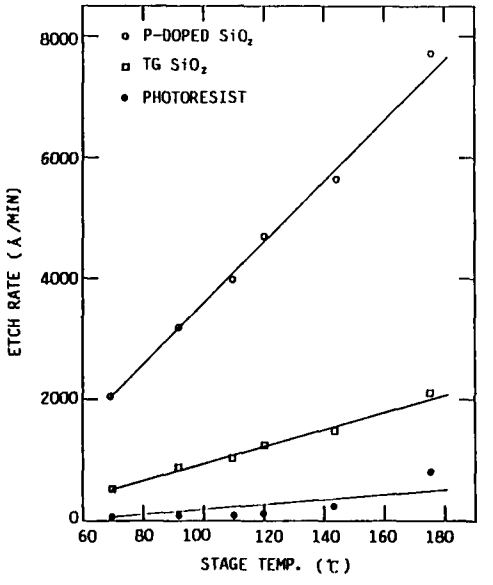


Figure 2 *Etch rates of P-doped PECVD SiO_2, TG SiO_2 and photoresist versus stage temperature.*

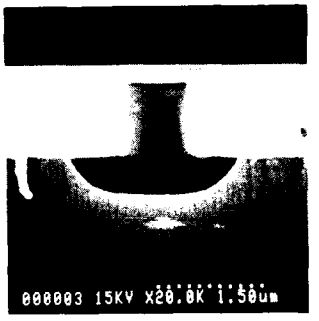


Figure 3 SEM cross section showing isotropic etch profile.

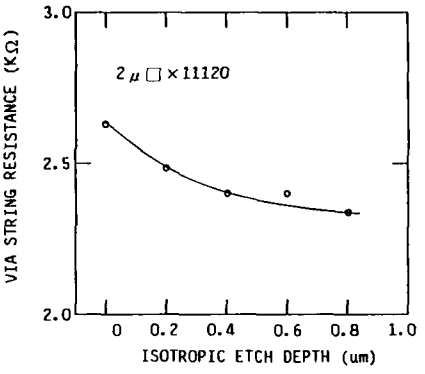


Figure 4 "Via string" resistance versus isotropic etching depth.

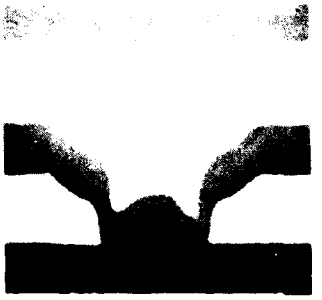


Figure 5 SEM cross section showing aluminum step coverage. The aluminum has been etched away leaving a clear image of the step coverage encapsurated in the passivation layer.

Abstract No. 262

CHARACTERIZATION OF AN OXYGEN PLASMA RESISTANT PHOTORESIST FOR REACTIVE ION ETCHING OF ORGANIC POLYMERIC MATERIALS

P. Tranjan[1], S. Bobbio[1,2], T. DuBois[3],
J. Poole[1], R. Frieser[3], S. Jones[2]

[1]Department of Electrical Engineering
University of North Carolina at Charlotte
Charlotte, North Carolina 28223

[2]Microelectronics Center of North Carolina
Post Office Box 12889
Research Triangle Park, North Carolina 27709

[3]Department of Chemistry
University of North Carolina at Charlotte
Charlotte, North Carolina 28223

Introduction

Anisotropic Reactive Ion Etching (RIE) of organic polymeric materials is becoming increasingly important in both VLSI and advanced packaging applications for via formation in dielectric layers. Film thicknesses may range from 1μm to more than 10μm.

A number of different masking techniques have been used to pattern the films. Trilayer structures typically involve a plasma enhanced vapor phase deposition (300°C) of an inorganic material (silicon oxide or nitride) above the organic film. The inorganic layer is patterned with a conventional resist and RIE is used to transfer the pattern through both the inorganic and organic layers[1]. Considerable simplification of the process results if the resist material itself is resistant to oxygen plasma. In this case the resist should contain an inorganic component which oxidizes during the course of the organic layer subetch so as to form a stable mask. Other investigators have shown how the addition of silicon to the resist increases the RIE stability to a point where it becomes useful for patterning relatively thin organic films[2,3,4].

Experimental Results and Discussion

In this work we have added a non silicon inorganic species to a conventional positive photoresist[5] and used the material to pattern polyimide films which are as thick as 8μm. The inorganic source compound is simply added, in the appropriate amount, to the resist to form astable mixture having an indefinite shelf life. It may be spin applied, exposed, and developed in the conventional way.

Figure 1 shows the etch characteristics of the modified resist. The etch tool used to transfer the pattern was a high rate magnetron system designed and developed at the Microelectronics Center of North Carolina[6]. A flow of 50 sccm N_2 and 10 sccm O_2 at 1200 watts gives an etch rate on polyimide of approximately 7kA/min.

In the Figure, the film thickness which remains after etching is shown by the data points and full curve. For reference, the result for unmodified resist is shown by the dashed line. The data in Figure 1 was obtained using a resist material which contained 10% by weight of the inorganic material.

Figure 2 is an SEM micrograph which shows the modified resist layer intact above a 4μm polyimide layer[7] which has been overetched 100% using the same etch process as Figure 1. The resist layer in Figure 2 shows no sign of cracking and remains soluble after etching in commercially available stripping solutions[8].

In contrast to the results shown in Figures 1 and 2, if an insufficient amount of inorganic is retained, the modified resist etches much more quickly and eventually breaks up even under relatively mild RIE conditions.

Although the main focus of this presentation will be the oxygen RIE characteristics of the modified resist, a brief discussion of the chemical and photolithographic properties of the material will also be given.

Acknowledgement

The authors wish to thank Dr. A. Reisman, Dr. C.M. Osburn and the Semiconductor Research Corporation for their support of this work. Additionally, they thank Dr. Giora Dishon (the AVX Corporation) for supplying the polyimide samples and suggesting the application to advanced packaging interconnects.

References

1. J. M. Moran and D. Maydan, J. Vac. Sci. Technol., 16, 1620 (1979).
2. W. C. Cunningham and C. E. Park, Proc. SPIE, 32 (1987).
3. W. C. McColgin, J. Jech Jr., R. C. Daly, and T. B. Brust, Symp. on VLSI Technol., Karuizawa, Japan (1987).
4. F. Coopmans and R. Roland, Poc. SPIE, 262 (1986).
5. Shipley 1431 series photoresist; Shipley, 2300 Washington St., Newton, MA 02161.
6. S. M. Bobbio and Y. S. Ho, Proc. 6th Symp on Plasma Etching, Electrochem. Soc., 47 (1987).
7. Dupont 2525 polyimide; E. I. Dupont, Pyralin Division, Barley Mill Plaza, Wilmington, DE. 19898.
8. Accustrip photo resist stripping solution; General Chemical Corporation, Morristown, NJ 07960.

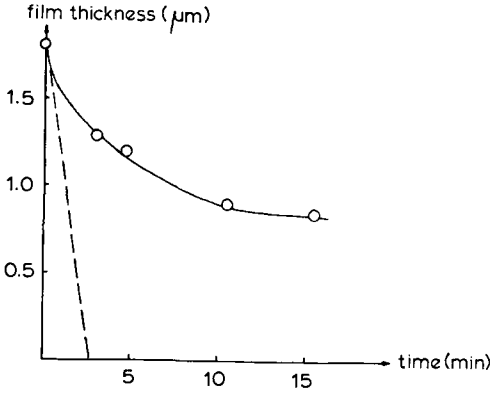


Figure 1: Etch performance of the modified resist. The full curve and data points represent the film thickness remaining after etching for the times shown on the abcissa. The dashed line shows the same result for unmodified resist.

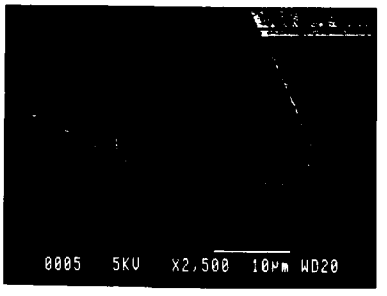


Figure 2 The modified resist and resulting polyimide pattern after a 100% overetch of the polyimide.

Abstract No. 263

Rapid Thermal Annealing of Cobalt on Silicon

A.R. Sitaram and S.P. Murarka

Dept. of Materials Engineering/
Center for Integrated Electronics

RPI, Troy, NY 12180

The continued downscaling of device dimensions and the use of shallow junctions has resulted in lowering of the processing temperatures to below 950°C. This has permitted the use of Group VIII metal silicides for gate level, and interconnection and also as contact metallization. Of these silicides, $CoSi_2$ offers the greatest advantages with its low resistivity (~15 $\mu\Omega$-cm in a polycrystalline thin film) and its ease of adaption into existing processes. In addition it can be formed in a self aligned manner [1]. Simultaneously, rapid thermal annealing (RTA) has emerged as a technology tailored for submicron dimensions and shallow junctions. RTA, with its high heating rates and short annealing times, restricts dopant redistribution, and so has applications in metallization, contact alloying, thin gate dielectrics, planarization and in implant activation and anneal. In view of the applicability of $CoSi_2$ and of the RTA process, a study of the kinetics of formation of $CoSi_2$ by RTA was undertaken. In this paper the results of this study are presented and with those obtained after annealing in a conventional furnace.

Boron doped (100) Si wafers, with a typical resistivity of ~20 Ω cm were subjected to RCA clean. These were then backsputter cleaned, in situ, to remove approximately 100Å from the surface. Approximately 1000Å cobalt was then sputter deposited. Specimens from these wafers were then annealed in the AG210T Heatpulse unit at temperatures ranging from 400°C to 650°C, for times ranging from 10 to 60 sec. The annealing ambient was ultrapure Argon. Phase changes and growth were monitored using x-ray diffraction and sheet resistance measurements. At the early stages of annealing, our x-ray diffraction results indicate the growth of CoSi from Co_2Si, with the latter still in contact with the unreacted Co. Thus CoSi, Co_2Si, and Co were coexisting together contrary to the findings of both furnace annealing [2] and RTA [3]. Also, $CoSi_2$ was observed to form at temperatures as low as 450°C, almost 100°C lower than the temperature of formation of $CoSi_2$ in furnace anneals. Figures 1 and 2 show the $CoSi_2$ growth rate data. A $t^{1/2}$ dependence of the growth is observed (Fig. 1). Figure 2, a Arrhenius type plot, gives an activation energy of 0.83 ev compared to the value 2.6ev reported in Ref. 2. Similar results were obtained using the sheet resistance measurements.

A $t^{1/2}$ dependence of the silicide growth indicates a diffusion controlled mechanism during RTA, similar to that reported for furnace annealing. The early formation of the disilicide can be attributed to the observed decrease in the activation energy. The mechanisms that would cause such a lowering of the activation process will be discussed.

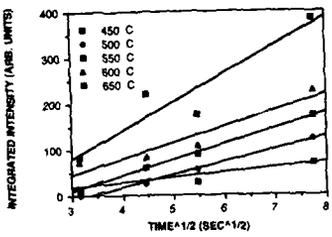


Figure 1: Growth of Cobalt disilicide

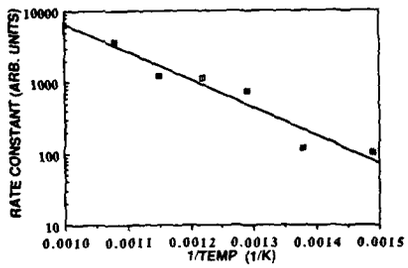


Figure 2: Arrhenius plot

References

1. S.P. Murarka, D.B. Fraser, A.K. Sinha, H.J. Levinstein, E.J. Lloyd, R. Liu, D.S. Williams, and S.J. Hillenius, IEEE Trans. Electron. Dev., ED-34, 2108 (1987).

2. S.S. Lau, J.W. Mayer, and K.N. Tu, J. Appl. Phys., 49, 4005 (1978).

3. B.S. Lim, E. Ma, M.-A. Nicolet, and M. Natan, J. Appl. Phys., 61(11), 5027 (1987).

Abstract No. 264

TITANIUM SILICIDE FORMATION AND ARSENIC DOPANT BEHAVIOR UNDER RTP IN VACUUM

R. FURLAN and J.W. SWART
LSI - Escola Politécnica
Universidade de São Paulo,
Caixa Postal 8174
01051 São Paulo, S.P., Brasil

Introduction

The titanium silicide formation can be affected depending on the type of dopant and implanting conditions[1,2]. Additionally, the formation process induces a dopant loss and the redistribution mechanism is related with the dopant type[3,4]. Besides the influence of the dopants itself on the silicide formation, the influence of impurities like oxigen and carbon has been adressed[5-7]. Oxigen present in the annealing ambient can oxidize the titanium surface. This problem can however be minimized by means of the use of rapid thermal processing[8-10].

Within the large amount of publications, however, contradicting results are reported, related to phases formed and to the influence and behavior of dopants.

In this paper titanium silicide formation on lightly doped and heavily arsenic surface doped silicon wafers is studied considering temperature and time of rapid thermal processing. Also the arsenic behavior during silicide formation is studied.

Experimental Procedure

The substrates used in this study were p-type silicon wafers with (100) orientation and resistivity of 5-25Ωcm. The wafers were gathered in four series, as shown in Table I, according to the arsenic ion implantation and annealing conditions.

After these initial sample preparation steps the wafers were dipped in diluted HF and loaded in a RF sputtering equipment. Titanium films were deposited with film thickness between 40 and 48nm. All RTP steps (ion implantation annealing and silicidation) were done in a home made graphite heater with vacuum of about 5.10^{-6} Torr[11]. The RTP times mentioned in this work include the temperature rise time.

The processed samples were characterized by four point probe, XRD, RBS and AES.

Results and Discussion

Figure 1 shows the final sheet resistance of samples of series A and B processed at 550°C, 600°C and 700°C. The sheet resistance of samples processed at 800°C are depicted in figure 2, including samples of series A,B,C and D.

Initially, for short times, the sheet resistance increases, oxigen and carbon are incorporated in the film, as observed by AES, and a non-well defined phase is formed with XRD peaks possibly corresponding to Ti_5Si_3, Ti_5Si_4, TiSi or Ti phases.

For longer treatments at 550°C, 600°C and 700°C the sheet resistance has an intermediate value and a three layer film is observed. Figure 3 shows the Auger depth profile of the sample of series B processed at 550°C-240s. The films are composed of layers of $TiSi_2$ with C49 structure, $TiSi_x$ with x close to 1 and TiO_x on the outer surface. The thickness of the $TiSi_x$ layer decreases with increasing temperature while the thickness of the $TiSi_2$ increases with a concomitant repulsion of oxygen and carbon. The $TiSi_2$ - C49 phase was identified by means of XRD while the Si/Ti ratio of ~2 was confirmed by AES and RBS analysis. From RBS analysis of samples of series A and B with sheet resistance in the intermediate value it was observed that thinner $TiSi_2$ - C49 layers are formed when an arsenic n^+ junction is present. This result is in accordance with earlier publications[1-3,10,12,13].

At 700°C treatments, the $TiSi_2$ phase transforms its structure from C49 to C54 after a time between 60s and 90s (Fig.1), when a lower sheet resistance is obtained. This transformation occurred earlier for silicides formed on n^+ arsenic junctions indicating that arsenic eases this phenomenum.

For silicidation treatments at 800°C (Fig.2), the $TiSi_2$ - C54 phase is promptly obtained after the initial stage. In this case the influence of the arsenic layer on the silicide formation was less evident.

For silicidation treatments at 550°C and 600°C no snowplow effects was observed and a small loss of dopant occurred. This led to a decrease of up to 20% of the maximum concentration. However for silicidation treatments at 800 °C a snowplow effect was observed for very short times (~ 5s) at which no $TiSi_2$ phase was formed. For longer times, when the $TiSi_2$ - C54 phase is formed, an increasing arsenic loss is observed. This led to a decrease of the maximum concentration of 70% for the 32s treatment. The dopant behavior at 800°C is depicted in figure 4 for the samples of series C after the titanium silicide stripping.

Conclusion

A correlation between the film phase composition and the RTP treatments in vacuum was shown. Arsenic dopant loss was observed for different RTP conditions. Arsenic snowplow effect was noticed for short treatments at higher RTP temperatures.

Acknowledgements

The authors wish to acknowledge Dr. J. Van der Spiegel for helpfull discussion, N.I. Morimoto for XRD analysis, Dr. J.P. Souza, Dr. C.M. Hasenack and A.A.M. Laganá for their contribution in RBS analysis and the Instituto de Pesquisas Tecnológicas for the AES facilities. This work has been supported by FIPEC, FINEP and FAPESP.

References

1. H.K. Park, J. Sachitano, M. McPherson, T. Yamaguchi and G. Lehman, *J. Vac. Sci. Technol.*, A2(2), 264, (1984).
2. H. Matsui, H. Ohtuki, M. Ino, and S. Uchio, *Mat. Res. Soc. Symp. Proc.*, 54, 769 (1986).
3. P. Révész, J. Gymesi, and E. Zsoldos, *J. Appl. Phys.*, 54(4), 1860 (1983).
4. T.P. Chow, W. Katz, R. Goehner, and G. Smith, *J. Electroh. Soc.*, 132, p. 1914 (1985).
5. G. Bomchil, G. Goeltz, and J. Torres, *Thin Solid Films*, 140, 59 (1986).
6. R. Beyers and R. Sinclair, *J. Appl. Phys.*, 57(2), 5240 (1985).
7. M. Natan, *Semicon Fast*, p. 32 (1986).
8. T. Okamoto, K. Tsukamoto, M. Shimizu, and T. Matsukawa, *J. Appl. Phys.*, 57(12), 5251 (1985).
9. F.M. d'Heurle, R.T. Hodgson, and C.Y. Ting, *VLSI Science and Technology, Electrochem. Soc.*, p.261 (1985).
10. T. Okamoto, M. Shimizu, K. Tsukamoto, and T. Matsukawa, MRS Fall Meeting, Boston (1984).
11. M. Kawano, C.M. Hasenack, N.I. Morimoto, A.A.M. Laganá, J.W. Swart, J.P. Souza, and R. Furlan, presented at VIII Congresso Brasileiro de Aplicações de Vácuo na Indústria e na Ciência, Brazil, July (1987).

12. T. Brat, C.M. Osburn, T. Finstad, J. Liu, and B. Ellington, *J. Electrochem. Soc.*, 133, p.1451, (1986).
13. C.M. Osburn, T. Brat, D. Sharma, N. Parikh, W.-K. Chu, D. Griffis, S. Corcoran, and S. Lin, *Microelectronics Center of North Carolina*, Technical Report TR 87-13, June (1987).

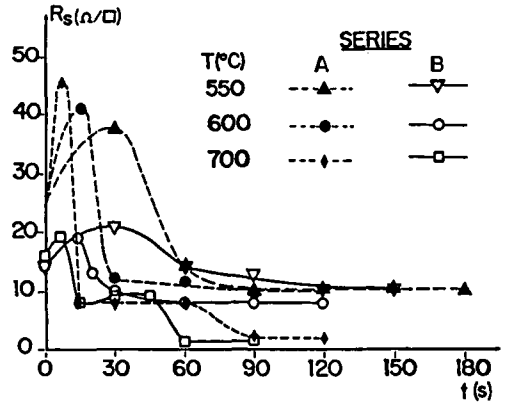


FIG. 1 - Final sheet resistance as a function of silicidation annealing time at 550°C, 600°C and 700°C of samples of series A and B.

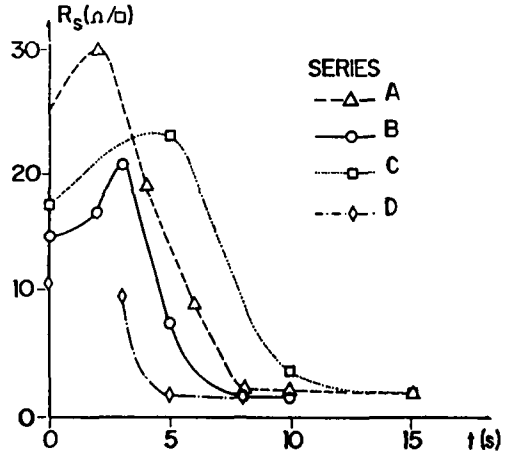


FIG. 2 - Final sheet resistance as a function of silicidation annealing time at 800°C of samples of series A,B,C and D.

Table I - Conditions of sample preparation.

Series	$^{75}As^{+}$ Ion implantation at 110 KeV (cm^{-2})	SiO_2 deposition by CVD (nm)	Annealing time by RTP at 1100°C	SiO_2 stripping in BHF	Sheet Resistance of n^{+} junction (Ω/□)
A	–	–	–	–	–
B	7.0×10^{15}	100	20	YES	30±1
C	7.0×10^{15}	–	10	–	36±2
D	1.5×10^{16}	100	20	YES	19.8±0.5

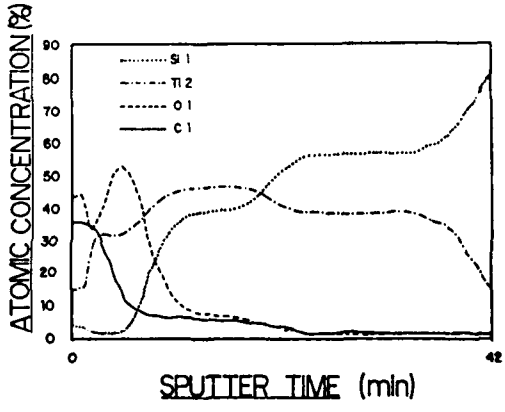


FIG. 3 - Auger depth profile of a sample of series B after silicidation anneal at 550°C for 240s.

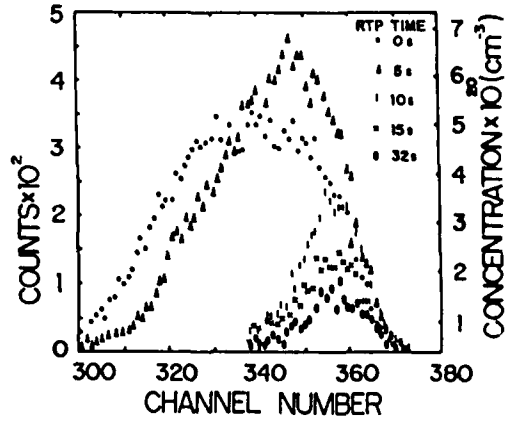


FIG.4 - RBS spectra of arsenic concentration of samples of series C as a function of silicidation annealing time.

Abstract No. 265

THERMAL RESPONSE OF CHARGE DECAY IN SILICON OXYNITRIDE FILMS

Samuel L. Miller and Theodore A. Dellin
Sandia National Laboratories
Albuquerque, NM 87185

Silicon Nitride Oxide Silicon (SNOS) nonvolatile memories are experiencing an increased use in commercial and weapon/space applications. Improving data retention in SNOS transistors is important in both of these application areas. For commercial applications, improving retention will make it easier to scale down the transistor dimensions to those required in higher density EEPROMs. For weapon/space applications, improving retention will allow EEPROMs to operate in radiation and extended thermal environments.

The data retention of SNOS transistors is determined by the charge trapping and transport properties of the insulating films. The data retention can be improved by optimizing the composition and/or geometry of the memory stack dielectrics. The purpose of the present paper is to describe the improvement in the data retention that results from substituting silicon oxynitride for silicon nitride in SNOS transistors.

The nitride and oxynitride transistors were processed in Sandia's CMOS nonvolatile memory process. The N-channel SNOS transistors were fabricated in a p-well with a surface doping concentration of $3E16/cm^3$. A 16A tunnel oxide was then grown by a 15 minute, 600°C dry oxidation. This is followed by a 750°C LPCVD process that deposits either 250A of silicon nitride (9:1 NH_3:DCS) or 250A of silicon oxynitride (7:3:4 NH_3:DCS:N_2O). Next, a top capping oxide was grown with a 3 hour, 900°C steam oxidation. Then, a polysilicon gate was deposited, degenerately doped and patterned to a gate length of ~4 microns. Later in the process when the contacts are opened, the transistors are annealed for 1 hour at 900°C in 100% H_2.

The writing/erasing and data retention properties of the SNOS test transistors were measured on an automated, multiplexed test system. In EEPROMs, no bias is applied to the SNOS gate during storage or reading. Therefore, to simulate conditions in the EEPROMs, the transistors were stored with the gate and substrate grounded.

The oxynitride transistors are slower in writing and erasing than the corresponding nitride transistors for short pulse widths. This is presumably due to a difference in the charge tunneling barrier height.

The substitution of oxynitride for nitride has been shown to primarily affect two aspects of charge decay, both of which result in significantly improved retention properties. Of greatest impact is the significantly reduced decay rate and thermal activation of excess trapped holes (negative threshold state). This combination of properties significantly improves data retention for the excess hole logic state in practical applications requiring long retention in environments spanning a wide temperature range. Retention experiments spanning the temperature range of -55°C to +150°C have been performed.

The second aspect of the charge decay properties which differs significantly between silicon nitride and silicon oxynitride is the degradation resulting from endurance cycling. The primary effect of cycling for both dielectrics is associated with the excess hole state; the decay rate increases with increasing number of write/erase cycles, resulting in premature loss of data. Though the decay rate of holes trapped in silicon oxynitride does increase with increased cycling, the magnitude of the degradation is considerably less than that of silicon nitride for the range of endurance cycling investigated (up to 10000 cycles).

While the oxynitride improves the performance of the excess hole memory state, it has no significant effect on the excess electron memory state. The decay rate, thermal activation, and cycling response of the excess electron state is nominally the same for both the nitride and oxynitride samples. This reinforces our previous observation that the excess electron and excess hole states are not symmetrical, but involve different physical processes.

A single oxynitride composition was evaluated in the present study. It may be possible to produce further improvements in the data retention by optimizing the chemistry and/or deposition conditions of the oxynitride films.

Abstract No. 266

ISSUES ON SILICON OXYNITRIDE FILMS

H. J. Stein
Sandia National Laboratories
Albuquerque, New Mexico 87185

There is an increasing interest in thin amorphous oxynitride films for dielectrics in microelectronics [1]. Compositions for these films can be varied continuously from Si_3N_4 to SiO_2 including Si_2N_2O [2] of crystalline oxynitride. New methods of film growth and processing have been introduced in response to the expanded interests [1]. For example, ion implantation of combinations of O and N has been explored as a method for producing a buried dielectric layer in Si. Nitrided thin oxide films and oxidized thin nitride films on Si are new thrusts toward engineering of thin dielectric layers for specific applications. Chemical vapor deposition (CVD) and plasma (or photo) enhanced CVD continue to be improved and remain the primary methods for oxynitride film growth.

There are several interrelated issues on oxynitride films: 1) growth processes, 2) composition and structure, 3) stability and reconstruction, 4) impurity diffusion, 5) charge trapping and transport, 6) band structure, and 7) electronic levels. The most extensive studies have been made on composition and structure where information from element analysis and chemical bonding have been combined to infer film structure. Rand and Roberts [3] concluded in early studies that reacting silane, nitrous oxide and ammonia on a Si surface produced a thin insulating Si, O, N polymer, rather than a mixture or codeposit of SiO_2 and Si_3N_4. Further studies [1,4,5] of deposition characteristics, Si fraction, chemical bonding of H, and film properties have supported the general conclusion, and have indicated polymeric transitions with changes in atomic composition. Illustrated in Fig. 1 are ratios of (O + N)/Si and of percent H versus percent O for oxynitride films formed by plasma enhanced CVD (PECVD) [6], atmospheric pressure CVD (APCVD)[4], and low pressure CVD (LPCVD) [7]. Measurement techniques utilized in such studies include: ion beam analysis, Auger Electron Spectroscopy (AES) and infrared spectroscopy (ir). These, and other studies, have shown that the H concentration goes through a maximum on the N-rich side. The (O + N)/Si ratio increases markedly in all materials between 0 and 30 atomic percent of O. Substitution of N-H for O to switch from a nitride-like to an oxide-like structure below 30 atomic percent O was suggested to explain the increase in (O + N)/Si ratio for APCVD N-rich oxynitride. The N-H concentration is too small, however, to satisfy the substitution for O concentrations > 10 atomic percent, except in PECVD films where N-H decreases in direct proportion to the increase in O above 25 atomic percent. The PECVD films exhibited electron spin resonance signals attributed to Si clusters [8], which, together with the high concentration of H, can explain the low value for (O + N)/Si ratios in the PECVD films. The ratio trend toward 2.0 is apparent in LPCVD oxynitride even though N-H concentrations are lower than those in APCVD films. Thus, there may be a significant difference between the structure of PECVD films, where N-H replacement of O can be satisfied, and LPCVD oxynitride films.

Remmerie and coworkers [9] used combinations of the three infrared absorption spectra sketched in the lower half of Fig. 2 to fit observed spectra through the stretch frequencies for Si-N and Si-O bonds in oxynitride films. Their observed spectra for N = 0 and for O/(N + O) equal to 0.03 and 0.55 are sketched in the top half of Fig. 2 where the three general features of the fitting spectra are apparent. The authors labeled the intermediate frequency spectrum as SiO but emphasized that this absorption feature is not necessarily an indication of a separate phase since different structural and electronic environments can shift absorption frequencies. While only three components were used, it is a minimum requirement for fitting and there may be other contributions. For example, absorption between 900 and 1000 cm^{-1} in crystalline Si_2N_2O has been assigned [2] to Si-N vibrations in Si-N rings connected by O. In addition, the three component fitting does not explain (N + O)/Si ratios in N-rich oxynitride. Studies of N in crystalline Si [10] indicated the predominant mode for N bonding into Si is N-N pairs, and that O will bond in sites adjacent to the pairs. Thus, pairing of N bonded to Si is a possible explanation for large (O + N)/Si ratios in N-rich oxynitrides.

Another aspect of the question of structure is reconstruction under annealing. Plasma hydrogenation of APCVD silicon nitride after annealing produced a reintroduction of H [11], and the results were interpreted as an indication of nonreconstruction. Partial rehydrogenation of nitride films in molecular H has also been observed [12]. One the other hand, films densify upon annealing which is an indication of reconstruction. Reconstruction and hydrogenation in oxynitride films are not well understood, and they are important in Si device processing [13].

Relating electrical characteristics to film composition and structure is especially challenging [14,15]. Trapped charge density and decay rates for electrons and holes versus O/(O + N) ratio from the work of Maes et al. [15] for polysilicon/LPCVD-oxynitride/tunneling-oxide/Si structures are illustrated in Fig. 3. The trapped charge density injected with equal oxide fields decreased with increasing O content, particularly for ratios greater than 0.2. This was interpreted [15] as a decrease in trap concentration with increasing O concentration. Decay rates for small trapped charge concentrations after 10^6 write/erase cycles (Fig. 3) show marked changes for ratios above 0.35, and the authors suggested deeper active charge traps to explain the effects. A factor of two decrease in the decay rate for holes with increasing ratio between 0 and 0.35 was shown for larger injected charge concentrations, while the decay rate for electrons remained relatively constant. Measurements of the memory window center indicated an increase in net negative fixed charge with an increase in O content.

Theoretical calculations [16] on band structure and band gap levels for silicon nitride and oxynitride provide a general guide for discussing relationships between composition and electrical properties. Silicon dangling bonds and Si-Si bonds are candidates for active centers since conductance increases with excess Si, and theory indicates levels within the gap for these defects[16]. Hydrogen affects the net trapped charge either by passivating existing centers or by introducing additional centers through interactions with Si or N. A discrepancy exists, however, between trap concentrations on the order of $10^{18} cm^{-3}$ exercised electrically and impurity concentrations (eg, H and Cl) which tend to be two or three orders of magnitude higher. Hughes [17] suggested actual trap concentrations can be orders of magnitude larger than electrically-alterable concentrations, and that electrical measurements only detect a net difference in trapped charge. Large trap concentrations can explain small mobility-lifetime ($\mu\tau$) products, and small differences in mobility for electrons and holes can explain net trapped charge at equilibrium [17].

In summary, there is a large quantity of data available in the literature on oxynitride films. Understanding, however, of the composition and structure for films prepared by different methods, and of relationships between structure and electrical properties is still in an early stage.

This work performed at Sandia National Laboratories, supported by the U. S. Department of Energy under Contract #DE-AC04-76DP00789.

REFERENCES:

1) See relevant papers in ECS Proceeding Vol. 87-10, "Silicon Nitride and Silicon Dioxide Thin Insulating Films", edited by V. J. Kapoor and K. T. Hankins, The Electrochem. Soc. Inc., Pennington, NJ, 1987.
2) M. I. Baraton, J. C. Labbe and P. Quintard, J. of Molecular Structure, 79, 333 (1982).
3) M. J. Rand and J. F. Roberts, J. Electrochem. Soc., 120, 446 (1973).
4) V. A. Wells and M. V. Hanson, in ECS Proceeding Vol. 79-3, "Chemical Vapor Deposition", Edited by T. O. Sedgwick and H. Lydtin, The Electrochem. Soc. Inc., Pennington, NJ. 1979, p.190; P. S. Peercy, H. J. Stein, B. L. Doyle and V. A. Wells, ibid.,p. 198.
5) C. M. M. Denisse, J. F. M. Janssen, F. H. P. M. Habraken and W. F. van der Weg, Appl. Phys. Lett. 52, 1308 (1308).
6) C. M. M. Denisse, K. Z. Tropost, J. B. Oude Elferink, F. H. P. M. Habraken, and W. F. van der Weg, J. Appl. Phys. 60, 2536 (1986).
7) Dan Xu and V. J. Kapoor, in ECS Proceedings Vol. 87-10," Silicon Nitride and Silicon Dioxide Thin Insulating Films", edited by V. J. Kapoor and K. T. Hankins, The Electrochem. Soc. Inc., Pennington, NJ, 1987, p. 168.
8) C. M. M. Denisse, J. F. M. Janssen, F. H.P. M. Habraken, and W. F. Van der Weg, J. Appl. Phys. 62, 832 (1987).
9) J. Remmerie and H. E. Maes, in ECS Proceedings Vol. 87-10, "Silicon Nitride and Silicon Dioxide Thin Insulating Films", Edited by V. J. Kapoor and K. T. Hankins, The Electrochem. Soc., Pennington, NJ, 1987,p.189.
10) H. J. Stein, in MRS Proceedings Vol. 59, "Oxygen, Carbon, Hydrogen and Nitrogen in Crystalline Silicon", edited by J. C. Mikkelsen, Jr., S. J. Pearton, J. W. Corbett, and S. J. Pennycook, Materials Research Society, Pittsburgh, PA, 1986, p. 523.
11) H. J. Stein, P. S. Peercy and D. S. Ginley, in "The Physics of MOS Insulators", Edited by G. Lucovsky, S. T. Pantelides, and F. L. Galeener, Pergamon Press, New York, NY, 1980, p. 147.
12) H. J. Stein, P. S. Peercy and R. J. Sokel, Thin Solid Films 101, 291 (1983).
13) G. Schols and H. E. Maes, in ECS Proceeding Vol. 83-8, "Silicon Nitride Thin Insulating Films", Edited by V. J. Kapoor and H. J. Stein, The Electrochem. Soc. Inc., Pennington, NJ, 1983, p. 94.
14) H. J. Stein and V. A. Wells, ECS Proceedings Vol. 79-3, "Chemical Vapor Deposition" Edited by T. O. Sedgwick and H. Lydtin, The Electrochem. Soc. Inc., 1979, p. 198.
15) H. E. Maes and E. Vandekerckhove, in ECS Proceedings Vol. 87-10, " Silicon Nitride and Silicon Dioxide Thin Insulating Films", Edited by J. J. Kapoor and K. T. Hankins, The Electrochem. Soc. Inc., 1987, p. 28.
16) See for example: J. Robertson and M. J. Powell, Appl. Phys. Lett. 44, 415 (1984); L. Martin-Moreno, E. Martinez, J. A. Verges, and F. Yndurain, Phys. Rev. B. 35, 9683 (1987).
17) R. C. Hughes, J. Appl. Phys. 56, 1044 (1984).

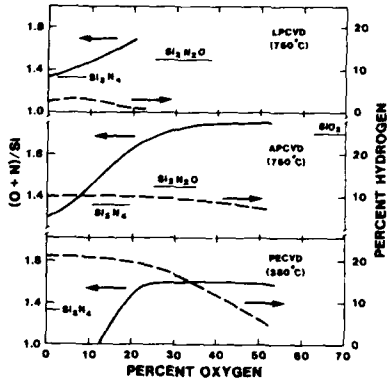


FIGURE 1. Ratios for (O + N)/Si and percent H versus percent O in oxynitride films deposited by different Chemical Vapor Deposition Methods.

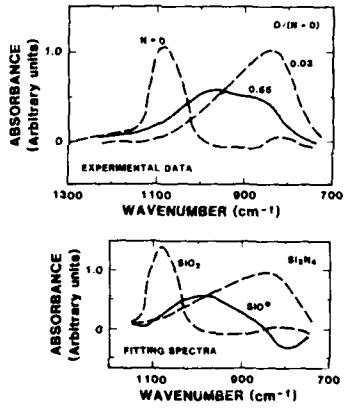


FIGURE 2. Infrared absorption spectra for different atomic compositions of LPCVD oxynitride films, and three component fitting spectra from Ref. 9.

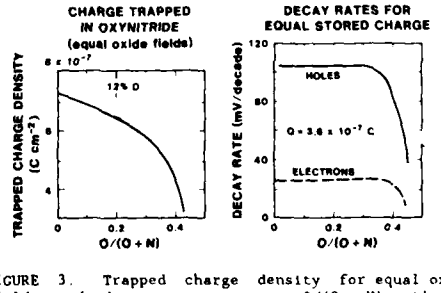


FIGURE 3. Trapped charge density for equal oxide fields and decay rates versus O/(O + N) ratios in polysilicon/LPCVD-oxynitride/tunnel oxide nonovolatile memory structures. Decay rates are for a small trapped charge density after cycling.

Abstract No. 267

Si-SiO_2 INTERFACE DEGRADATION MEASUREMENT USING THE FLOATING GATE TECHNIQUE

Albert K. Henning

Thayer School of Engineering
Dartmouth College
Hanover, NH 03755

INTRODUCTION

The ultimate goal in Si MOSFET technology development is to simulate, with physical accuracy, all important device aspects, from fabrication through operation to reliability. Achievement of this goal results in faster overall process development, combined with reduced exposure to the high costs of actual manufacture. To achieve physical accuracy, simulations must be done with 2-D or 3-D simulator tools, on the microscopic level. In terms of MOSFET device design for hot carrier resistance, such simulators seek to predict processing effects on substrate current [1,2], gate current [3,4], and eventually interface degradation [5,6].

No simulator can stand on its own, however; it must rest on accurate measurement. Previous work has explored gate current measurements [7-10] and interface degradation [11-13] as separate phenomena. This work investigates the interconnection of the two measurements, and its effect on gate current and interface degradation simulation.

CHARACTERIZATION

The floating gate technique [8,9] was used to measure gate current in NMOS FET's at 300K and 80K [7]. Figure 1 shows a sample of the data. Figure 2 shows a raw data curve of I_{DS} vs. time, from which one of the data points in Figure 1 was extracted. The extraction procedure involves the equation:

$$I_G(V_G) = C_G(V_G)\frac{dV_G}{dI_{DS}}\frac{dI_{DS}}{dt}$$

The raw data curve can be broken down into four parts. First is the $t<0$ region, where the gate has not been set floating, and changes in I_{DS} are due to heating (assuming no threshold or mobility changes are occuring). Second, just as the gate probe is lifted to set the gate afloat, a current transient occurs due to the removal of the probe capacitance from the floating gate circuit. Third, the active device begins to charge or discharge the floating gate, depending upon the sign of the gate current flowing from device channel to floating gate. Finally, the slope dI_{DS}/dt decreases from its value at $t=0$.

At high current levels [9], this change in slope results merely from the expected change in I_G with changing V_G. However, at low current levels, I_G decreases far more rapidly than would be expected from the I_G vs. V_G characteristic. This may be seen in Figure 3. Here, the starting floating gate voltage is approximately 6.5V. However, the logarithmic slope of V_G vs. I_G is 80mV/decade; while the expectation from the full gate current curve is nearly 1000mV/decade.

The full set of data from which the V_D=2.5V curve is extracted is shown in Figure 4. The data of Figure 1 is also plotted for comparison. Figure 5 shows gate current derived using the continuous method of Saks, *et al.* [9]. In particular, it shows the transition from the high gate current regime, unaffected by growing interface charges, and the low gate current regime, very much affected by the interface character.

DISCUSSION

The steep slopes seen in the low gate current regime (Figure 4) require understanding, since this is the I_G range experienced by devices under actual operating conditions - not the accelerated field or temperature conditions most frequently used because of their ease and speed of measurement. Several factors might account for the observation. First, the channel mobility may be changing due to gate-current-induced changes in the Si-SiO_2 interface. This is ruled out, since monitor of the low-field transconductance and threshold voltage before and after the floating gate current measurement shows no perceptible change in either g_m or V_T. Second, surface leakage from the floating gate might cause departures from the expected gate current curve. However, such leakage must be greater than the true, channel-induced gate current in order to be noticed; yet, the observed characteristic is less than the expectation. Also, monitor of the charge leakage off of the floating gate placed an upper bound on surface leakage of 10^{-18}A. The remaining alternative is that thermionic gate current from the device channel alters the interface as it passes. In particular, the thermionic barrier height must be increasing at least linearly with time to cause the observed gate current characteristic.

This effect is shown schematically in Figure 6. Gate current from the channel, if energetic enough, crosses the barrier and is collected at the gate electrode. However, in passing through the insulator, the interface is altered. Either interface states are created, which are then charged due to the position of the Fermi level; or, bulk traps are filled.

It is assumed, and may be verified qualitatively by examining the potential contours in a 2-D simulation of the device being measured, that the gate potential changes expose a fresh portion of the interface to the channel field-induced gate current density. Thus, the passage of gate current at the low current densities experienced during actual device operation causes localized changes in the Si-SiO_2 interface.

Refering to Figure 5, these changes are not noted in the higher current regime. The increases in the interface barrier height are more than compensated by image force barrier lowering [14] due to the (relatively) high current density. Based on this Figure, the transition current from a regime dominated by image force barrier lowering, to one dominated by barrier height increases, is about 1fA. However, strictly speaking this should be put in terms of a current density, which requires a 2-D gate current simulator on a microscopic level.

The low-level hole gate current in an NMOS device [7] also exhibits increased barrier height as holes are transported across the interface (see Figure 4). This occurs, effectively, in the accumulation regime of the local MOS capacitance, while the electron gate current occurs in the depletion or inversion regime. The increased barrier height to holes means positive charge is growing at the interface, which may be due to deep, ionized donor states in the band gap. Conversely, the increase of interface charge in the inversion regime indicates the presence of deep acceptor states at the interface.

Data such as that in Figure 2 leads to the characterization of the gate current by the equation:

$$I_G \sim \exp\left(\frac{-q\Delta\phi_B}{kT_e}\right)$$

Thus, estimates of the relative change in barrier height (and so the relative change in interface charge), and the carrier temperature T_e characterizing the free carrier distribution as it approaches the interface, may be made.

If the barrier height is increased too much, the net charge transported across the interface may change sign. This occurs since frequently, both holes and electrons are being transported across the interface on a global level; if the dominant charge carrier is suppressed locally, the other may take its place, resulting in a sign change in I_G.

It must be noted that these measurements do not preclude creation or charging of interface states caused by hot carriers with energy insufficient to surmount the thermionic barrier. However based on other experimental work [15], it appears likely that only the gate current emitted thermionically contributes to the change in the interface.

CONCLUSIONS

Gate current measurements at realistic biases in MOSFET's lead to perceptible changes in the Si-SiO_2 interface. These changes are attributed to charged interface states, charged and/or created during the passage of gate current emitted thermionically across the interface. The changes are a direct result of the gate current transported across the interface; thus, simulation of the gate current must either subtract out the interface changes, or account for them strictly. Experimental verification of the simulation results must take care to account for the interface changes as well. In particular, because of the build-up of interfacial charge, the sign of the apparent gate current may be reversed.

References

[1] A.K. Henning, *et al.*, *Elec. Dev.* **ED-34**, p. 64 (1987)
[2] W. Hänsch and S. Selberherr, *Elec. Dev.* **ED-34**, p. 1074 (1987)
[3] A. Phillips, Jr., *et al.*, *IEEE IEDM, Dig. Tech. Papers*, p. 39 (1975)
[4] B. Ricco, *et al.*, *IEEE IEDM, Dig. Tech. Papers*, p. 559 (1986)
[5] S. Baba, *et al.*, *IEEE IEDM, Dig. Tech. Papers*, p. 734 (1986)
[6] S. Bibyk, *et al.*, *Proc. Symp. Low Temp. Electronics and High Temp. Superconductors* (S.I. Raider, *et al.*, eds.), Electrochemical Soc. Proc. Vol. **88-9**, p. 161 (1988)
[7] A.K. Henning and J.D. Plummer, *Proc. Symp. Low Temp. Electronics and High Temp. Superconductors* (S.I. Raider, *et al.* eds.), Electrochemical Soc. Proc. Vol. **88-9**, p. 130 (1988)

[8] F.H. Gaensslen and J.M. Aiken, *Elec. Dev. Lett.* **EDL-1**, p. 231 (1980)
[9] N. Saks, *et al., Elec. Dev.* **ED-33**, p. 1529 (1986)
[10] Y. Nissan-Cohen, *Elec. Dev. Lett.* **EDL-7**, p. 561 (1986)
[11] E. Takeda and N. Suzuki, *Elec. Dev. Lett.* **EDL-4**, p. 111 (1983)
[12] F.-C. Hsu, *Elec. Dev. Lett.* **EDL-5**, p. 50 (1984)
[13] P.E. Cottrell, *et al.*, *J. Solid State Circuits* **SC-14**, p. 442 (1979)
[14] C.N. Berglund and R.J. Powell, *J. Appl. Phys.* **42**, p. 573 (1971)
[15] S.J. Wang, *et al., IEEE IEDM, Dig. Tech. Papers*, p. 46 (1987)

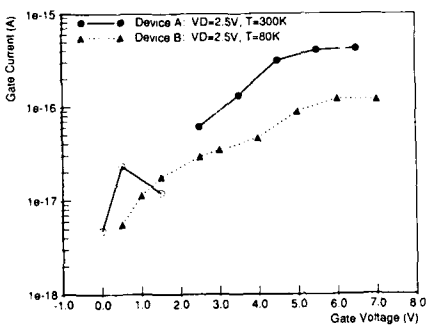


Figure 1: I_G for V_D = 2.5V, L_e = 0.8 μm. T = 80K and 300K. Holes, open symbols; electrons, closed symbols.

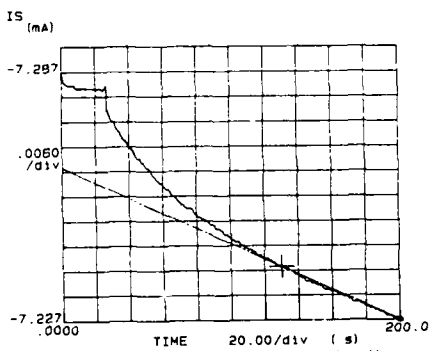


Figure 2: Typical I_D vs. time characteristic. V_D = 2.5V, V_G = 5.5V

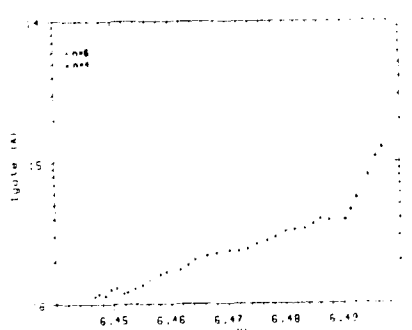


Figure 3: Extraction of gate voltage and current from I_D vs. time. The capacitive discharge is seen in the steep, initial slope. V_D = 2.5V, V_G = 6.5V

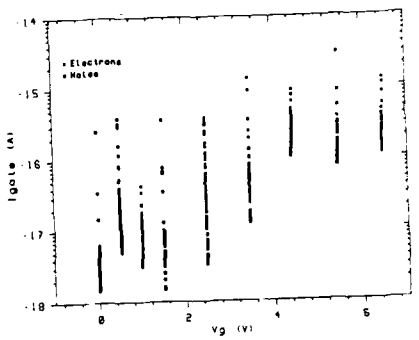


Figure 4: Dependence of gate current on interface degradation.

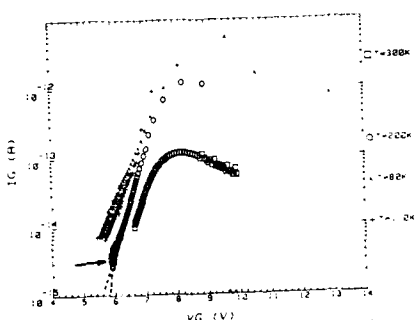


Figure 5: CHE gate current vs. temperature. Arrow indicates change from high-current to low-current regimes. See Discussion.

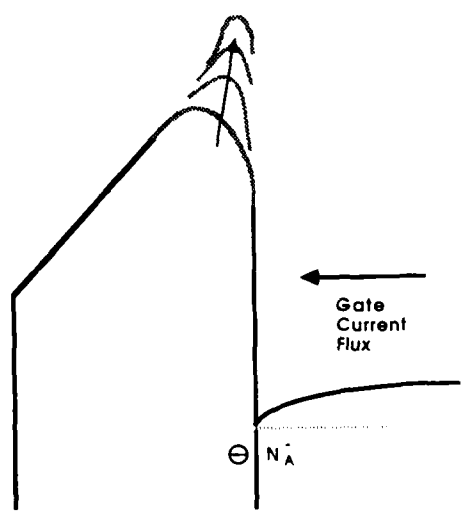


Figure 6: Time evolution of electrostatic barrier height. I_G flux causes increases in $\Delta\phi_B$ over time, reducing I_G exponentially.

Abstract No. 268

CHARACTERIZATION OF ELECTRICAL PROPERTIES OF OXYGEN/HYDROGEN RICH SILICON NITRIDE FILMS FOR MNOS DEVICES

Dan Xu and Vik J. Kapoor

Electronic Devices and Materials Research Laboratory

Department of Electrical and Computer Engineering

University of Cincinnati

Cincinnati, Ohio 45221-0030

Thin silicon nitride films is one of the second most widely used insulating films in microelectronics after silicon dioxide. Thin silicon nitride films have been attracting growing attention in recent years because of its fundamental importance in VLSI electronic devices with possible applications as a passivation layer, encapsulent, diffusion mask, gate dielectric, optical device coating and semiconductor non-volatile memory devices' carrier storage layer.

The thin silicon nitride films used in this work were deposited using low pressure chemical vapor deposition (LPCVS) method which provided good uniformity across the wafer and good stoichoimetry. Our LPCVD processing by microelectronics facility at NCR involved decomposing ammonia (NH_3) and dichlorosilane ($SiCl_2H_2$) at the temperature ranging from 650 C to 850 C with 50 C intervals. Oxygen impurity was introduced into the silicon nitride films by adding nitrous oxide (N_2O) gas into the LPCVD deposition chamber. The semiconductor non-volatile memory devices were subsequently fabricated in a metal-nitride-oxide-silicon configuration. In order to fully characterize the material property of silicon nitride films for memory devices, Auger electron spectroscopy (AES), X-ray photoelectron spectroscopy (XPS) and multiple-internal-reflection (MIR) infrared spectroscopy have been employed to characterize the stoichoimetry of deposited film. Ellipsometry were also used to measure the thickness and refractive index of the film. The internal photo-electric effect technique was used for non-destructive quantitative measurements of defect-related electron/hole traps in these insulating films. The electrical properties of MNOS devices were investigated using high-frequency C-V, quasi-static C-V, conductance method, retention and endurance test.

The results of AES showed that the depth profiles of nitrogen, silicon and oxygen were uniform across the bulk of LPCVD deposited silicon nitride films.

Trapped electron density as a function of deposition conditions was determined via photocurrent-voltage technique in combination with high frequency method. This technique does not require an assumption of any particular distribution form of the trapped charge. Results showed that the trapped charge density decreased from 2.9 to 2.6×10^{16} cm^{-3} for 0 to 17 atomic % of oxygen concentration. By changing the gate electrode from aluminum to gold, the trapped hole concentration was also determined in a similar fashion.

The flatband voltage monitored photodepopulation technique in combination with photoinjection was used to investigate the first order kinetics of trap emptying in the LPCVD thin silicon nitride films [1]. The photoionization cross section was determined from 18.9 to 4.9×10^{-19} cm^{-2} over the photon energy range of 2.06 - 3.1 eV for the film containing 7 to 17 atomic % of oxygen.

The interface state density for virgin samples at mid-gap were about 10^{11} cm^{-2} eV^{-1}. Those samples with 0 sccm N_2O gas flow rate were subsequently annealed at 900 C in an N_2/H_2 ambient so as to detect the influence of N-H and Si-H bond to the trapping property. The results showed a general trend that the trapped electron density was increased after annealing.

It is speculated that one or various combinations of silicon dangling bonds, Si-O bond may be responsible for the trapped charge in the film. Besides normal silicon nitride bonding, silicon or nitrogen dangling bonds may exist due to imperfections in crystal structure. It was likely that oxygen/hydrogen atoms compensated these dangling bonds, therefore subsequent reduction of trapped charge density was observed.

[1] Dan Xu and Vik J. Kapoor, Proc. of Electrochem. Soc., New Jersey, 1987, 87-10, p. 168

Abstract No. 269

The Effect of Growth Conditions on The Electrical Properties of Ultra-Thin Oxides

V. Murali, A.T. Wu, and D.B. Fraser
Intel Corp., 3601 Juliette Lane, Santa Clara, CA 95051.

E. Kamieniecki
Optical Diagnostic Systems, 46 Manning Road, Billerica, MA 01821.

J. Nulman
AG Associates, 1325 Borregas Ave., Sunnyvale, CA 94089.

INTRODUCTION: Growth and characterization of high quality ultra-thin silicon oxides is of major importance in VLSI technology. The study of growth kinetics and electrical properties of ultra-thin oxides is incomplete due to a number of complicating factors: the growth rate of such thin oxides is very rapid (Ref 1) and hence controlled growth in conventional furnaces is difficult. Further, oxide charge (Q_f) and interface state density (D_{it}) are generally measured by fabricating MOS capacitors which requires the deposition and the definition of a gate electrode. The possible interaction of the electrode material with the oxides, the effect of the electrode deposition/definition conditions on oxide properties, and the uncertainity regarding the metal-silicon work function difference may obscure the intrinsic oxide properties. In this work, Rapid Thermal Oxidation (RTO) techniques were used to grow ultra-thin oxides ($40A-200A$) and a novel surface-photovoltage technique (Ref 2) was used to evaluate Q_f and D_{it}. The surface photo-voltage technique eliminates the need for gate electrode deposition/definition. The combination of these techniques allows the accurate determination of the effect of process parameters on growth kinetics and on Q_f and D_{it}. In this paper we report the effects of processing conditions on Q_f.

EXPERIMENT: 100mm dia, P-type, 50 Ω–cm, (100) Si wafers were used in this study. The wafers were subjected to an RCA clean prior to oxidation in an AG 2146 RTP system (Ref 3).The wafer temperature measurements were made using an optical pyrometer and the temperature, as read by the pyrometer, was within $\pm 1^{\circ}C$ of the desired temperature. The oxidations were performed either in a pure O_2 ambient or in an oxygen ambient containing 4% HCl. Oxidation temperatures ranged from $1000^{\circ}C$ to $1200^{\circ}C$. Oxidation times typically ranged from 5secs to 300secs during which oxides $40A$ to $200A$ thick were grown. Some wafers then received an in-situ $1050^{\circ}C$, 30secs anneal in Ar (containing 2% O_2) and/or a $400^{\circ}C$, 45min anneal in forming gas. Oxide thickness was ellipsometrically measured at nine points on the wafer using an automated ellipsometer. A refractive index of 1.46 was assumed for all cases. The thickness uniformity was better than ±3% across each wafer. Subsequently, Q_f and D_{it} measurements were made using the photon-microscope (Ref 2) which measures the capacitance of the space charge region created by shining monochromatic light on the wafer. One batch of wafers were subjected to polysilicon deposition and after subsequent $POCl_3$ doping, electrodes were patterned to form MOS capacitors which were then used for conventional high frequency and quasi-static C-V measurements.

RESULTS AND DISCUSSION: Figure 1 is a plot of Q_f as a function of oxide thickness. These oxides were grown at $1100^{\circ}C$ in pure oxygen and received no Post Oxidation Anneal (POA). It is clear that Q_f is a function of oxide thickness and that thinner oxides have higher Q_f. Similar results have been reported previously (Ref 4,5). Fig.2 is a plot of oxide growth rate as a function of oxide thickness for the same growth conditions. The oxide growth rate is obtained by assuming linear growth between adjacent points on the oxide thickness vs oxidation time curve and the local slope is calculated. These values are then plotted against the calculated mean of the oxide thicknesses. The striking similarity between Fig.1 and Fig.2 suggests a close relationship between the oxide growth mechanism and the origin of fixed charge. Similar results are observed for oxides grown in O_2 ambients containing 4% HCl. As seen in Fig.3, the Q_f is higher for thinner oxides but the overall magnitude of the Q_f is about half those reported for oxides grown in pure O_2 (Fig.1). The magnitude of the growth rate for these oxides is, however, about twice those reported in Fig.2. These results imply that while Q_f is definitely a function of growth rate, it is not a function of the absolute magnitude of the growth rate or else oxides grown in HCl containing ambients would have a higher Q_f. Fig.3 also shows the effect of a $1050^{\circ}C$, 30sec POA in Ar (2% O_2). The O_2 was added to suppress the $Si + SiO_2 = 2SiO$ reaction which may occur during such anneals in pure Ar. During these anneals typically a $10A$ increase in oxide thickness was observed. It is seen from Fig.3 that the Q_f is reduced by this anneal and the oxide thickness dependence of Q_f is eliminated. Subsequent annealing of these wafers in forming gas has an insignificant effect on Q_f. Fig.4 is a plot of Q_f vs oxidation temperature, for $150A$ oxides grown in pure O_2 ambients. For as-grown wafers, it is seen that the Q_f is higher for oxides grown at higher temperatures which is contrary to the results obtained for thicker ($>1000A$) oxides (Ref 5). A $1050^{\circ}C$, 30sec POA in Ar is seen (Fig.4) to reduce the Q_f of these wafers by a factor of two in all cases. On the other hand, the flatband voltage vs oxide thickness data (Fig.5) obtained from MOS C-V measurements give a good linear fit indicating that the Q_f is independent of oxide thickness irrespective of whether or not the wafers received a POA. However, it is to be noted that these wafers have experienced a high temperature cycle ($920^{\circ}C$) during the $POCl_3$ doping of the polysilicon gate and hence it is expected that these wafers behave similar to wafers that have received extended POA. In fact, these data are in good agreement with those seen in Fig.2. The D_{it} shows a complex dependence on the processing conditions and these results will also be presented.

CONCLUSIONS: Growth kinetics and electrical data for ultra-thin oxides have been obtained. The effect of various parameters such as oxide thickness, growth ambient, POA and growth temperature on Q_f and D_{it} have been investigated. The use of RTO and the surface-photovoltage measurement technique have allowed the evaluation of these parameters accurately without any influence of post-oxidation steps involved in MOS capacitor fabrication. The data also suggests a close relationship between the growth mechanism of these thin oxides and their electrical properties and sheds some light on the oxide growth mechanism.

REFERENCES

1) B.E. Deal and A.S. Grove, J. Appl. Phys., 36, 3770(1965).
2) Optical Diagnostic Systems, 46 Manning Road, Billerica, MA 01821, patent pending.
3) AG Associates, 1325 Borregas Ave., Sunnyvale, CA 94089.
4) V. Murali and S.P. Murarka, Electrochem. Meeting, Extended Abstract#164, May, 1987.
5) H.Z. Massoud, Ph.D Thesis, Stanford, 1983.

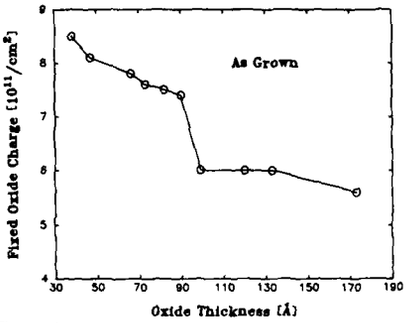


Fig.1 Fixed oxide charge as a function of oxide thickness for wafers oxidized in pure O_2 ambients at 1100°C.

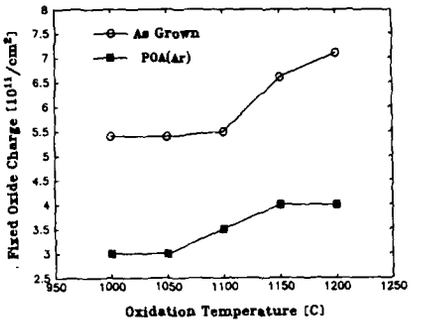


Fig.4 Fixed oxide charge as a function of oxidation temperature for 150Å oxides grown in pure O_2. The solid line is for as grown wafers and the dashed line indicates wafers that have received an in-situ POA in Ar(2% O_2).

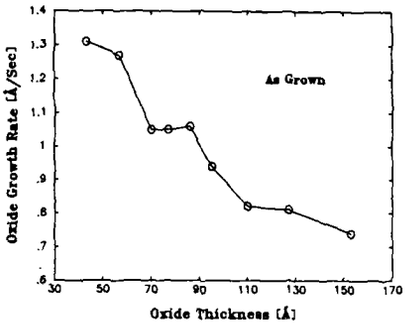


Fig.2 Oxide growth rate as a function of oxide thickness for wafers oxidized in pure O_2 ambients at 1100°C.

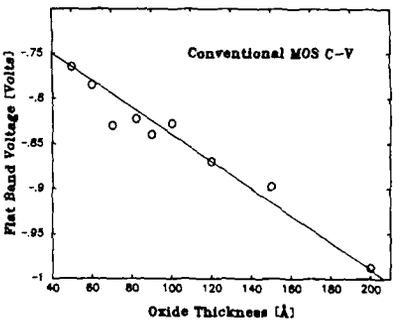


Fig.5 Flat band voltage as a function of oxide thickness. The measurements were made on poly gate capacitors using conventional MOS C-V techniques.

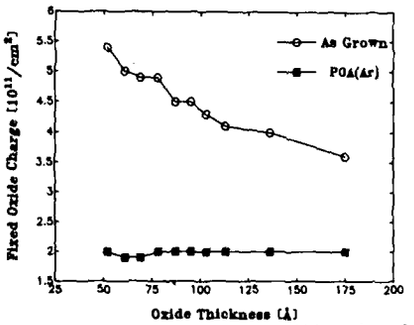


Fig.3 Fixed oxide charge as a function of oxide thickness for wafers oxidized in (O_2 + 4%HCl) ambients at 1100°C. Solid line is for as grown wafers and dashed line indicates wafers that have received an in-situ POA in Ar(2% O_2).

Abstract No. 270

N-MOSFET Degradation and Aging due to Hot-Electron Trapping

Amer Samman, Patrick Roblin, and Steven Bibyk
Solid State Microelectronics Laboratory
Department of Electrical Engineering
The Ohio State University, Columbus, Ohio 43210

1 Introduction

Hot-carrier induced n and p channel MOSFET degradation mechanisms have been experimentally shown to be similar, with the degradation region located near the drain and stretching toward the source with increasing stressing time. MOSFET current degradation is mainly due to carrier trapping in the oxide near the interface, and the generation of interface states by hot-electrons. This work is concerned with the analysis of the performance degradation of a one-micron gate-length n-MOSFET, resulting from hot-electron trapping in the oxide, and with the modeling and simulation of the hot-electron trapping dynamics.

In our approach we have used a physical model of hot-electron trapping and applied it to derive a new equation simulating the trapping rate. This physical trapping model was then used together with a two-dimensional device simulator (PISCES) to determine both the location and density of trapped electrons. The aging process was simulated dynamically by solving the trapping equation consistently with the PISCES simulation of the MOSFET throughout the aging process.

2 Discussion

First, a degraded MOSFET was simulated by introducing a sheet of fixed negative charge at the Si-SiO_2 interface near the drain. As a result, the degraded device was found no longer symmetric. The localized negative charge has greater effects on the performance of the MOSFET when operated in the low V_D (linear or ohmic) region. The IV characteristics of the degraded device showed an increase in the threshold voltage (Figure 1), an increase in the maximum channel transconductance for $V_D = 0.1V$, and an upward curvature (diode-like) in the I_D-V_D curve (forward mode)for $V_G = 1V$ that disappears for $V_G \geq 2V$ (Figure 2).

The introduced fixed negative charge causes a channel potential drop near the drain that pinches off the channel and increases the effective channel resistance of the stressed MOSFET in the linear region. This potential drop is overcome by either increasing V_G or V_D, the drain acting like a second narrow gate (short channel effect). The effect of the drain and gate voltages on the channel potential drop explains the diode-like turn-on characteristic of the degraded MOSFET in the low V_D region of the IV characteristic curves (Figure 2).

In the saturation mode, the stressed device shows practically no sign of degradation in performance (Figure 2). The channel potential drop is absorbed in the two dimensional drain region of the channel, and the drain current is restored to its maximum value (unstressed I_D) by the unaffected Gradual Channel Approximation (GCA) region.

The rate of hot-electron trapping per unit area of the interface, is proportional to the electron density in the channel, the hot-electron generation rate, and segregation probabilities. Hot-carriers in the channel need to acquire enough kinetic energy to overcome the interface potential barrier with their momentum redirected toward the interface to be successfully trapped in the SiO_2 by already existing traps (no trap generation). Neglecting detrapping, the rate of hot-electron trapping in the oxide near the interface can be approximated by [3]

$$\frac{dN_{trap}(t)}{dt} \cong \left(K_s \frac{q}{m^*} \frac{E}{v_{d\,sat}}\right) \times \left(\frac{1}{4} \frac{E\lambda}{\phi_b} e^{-\phi_b/E\lambda}\right) \times \left(\int_0^\infty n(y) e^{-y/\lambda} dy\right) \times (N_{max} - N_{trap}(t))\,\sigma_{trap} \qquad (1)$$

The first product represents the rate of hot-electron scattering events expressed in terms of the high electric field chordal mobility [3], where m^* is the electron's effective mass, E is the lateral channel electric field, $v_{d\,sat}$ is the saturation velocity of the electrons, and $K_s < 1$ is a constant weighting the rate of ballistic electron launching. The second product gives the probability of an electron travelling a distance d without loosing its energy through collisions, becoming *hot*, then being redirected (due to scattering) toward the interface [1], [3]. E is the channel lateral electric field assumed constant over the distance d. λ is the mean free path of hot-electron between collisions (assumed constant) , and ϕ_b is the effective potential barrier height at the interface [1]. The third product gives the maximum number of hot-electron per unit area of the interface that can be trapped at any time. It is a function of the channel carrier concentration $n(y)$ and the probability ($e^{-y/\lambda}$) of the scattered electron traveling to the interface without further redirection. The last product represents the probability of an electron injected in the SiO_2 to be captured by an empty trap, where $N_{trap}(t)$ is the density of traps filled per unit gate area ($N_{trap}(t = 0) = 0$), N_{max} is the initial density of empty traps per unit gate area, and σ_{trap} is the trapping cross section of SiO_2 at the interface (technology dependent) [3] [4]. Even though there is no reported value for K_s yet, comparative as well as qualitative study of aging in different device structures can still be performed.

This model of hot-electron trapping was used to simulate the degradation of a $1\mu m$ nMOSFET in time. Aging was conducted by solving the trapping equation simultaneously with the PISCES simulation of the MOSFET. The applied stressing voltages ($V_{sub} = V_S = 0$, $V_G = 3V$, and $V_D = 5V$) remained the same during the entire aging process. The trapped electron distribution obtained at different aging steps is given in Figure 3 which reveals that hot-electron trapping starts with a rate that peaks at location $\sim 1.57\mu m$, some 300Å from the drain junction, and moves toward the drain before spreading toward the source, progressing at an exponentially decreasing rate [3] [4]. The peak degradation rate depends on the applied stressing voltage. The aging times associated with some of the intermediate aging steps are shown in a table in Figure 3 normalized with respect to the first step.

The channel electric field is found to increase in the high field region next to the drain junction, and to decrease in the adjacent GCA region closer to the source (Figure 4). This explains why the degradation proceeds first toward the drain, then slows down as it propagates toward the source.

One notices that the threshold voltage has slightly increased through the first 17 aging steps. A slight reduction in the transconduction is also observed. After 17 aging steps the degradation starts moving toward the source, and a strong increase in the threshold voltage results (Figure 1). The trap-

ping of electrons in the high field drain region weakly affects the MOSFET IV characteristics, whereas the trapping in the GCA region results in a strong variation in the threshold voltage. One can therefore use the I_D-V_G characteristics to monitor the progress of the degradation in the channel [4].

The aging simulation results are in qualitative agreement with reported experimental results. Cham *et al* [2] recently pointed out that the projection of the device's lifetime by accelerated stress can lead to large errors. Indeed, they experimentally demonstrated that the degradation rate was slowing down with increasing stress bias and time. The simulation of MOSFET degradation in time can provide an alternative method of predicting the MOSFET lifetime under normal operation .

REFERENCES

[1] S. Tam, P.-K. Ko, and C. Hu, "Lucky-Electron Model of Channel Hot-Electron Injection in MOSFET's," *IEEE Trans. on Electron Devices*, ED-31, September 1984.

[2] K. M. Cham, J. Hui, P. V. Voorde, and H. S. Fu, "Self-Limiting Behaviour of Hot Carrier Degradation and its Implication on the Validity of Lifetime Extraction by Accelerated Stress," *IRPS* (1987).

[3] Amer Samman, Master Thesis, *The Ohio State University*, Columbus, Ohio, 1988.

[4] P. Roblin, A. Samman, and S. Bibyk, "Simulation of Hot Electron Trapping and Aging of nMOSFET's," to be published.

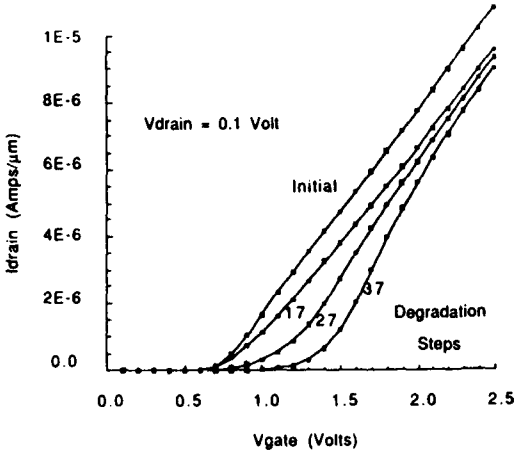


Figure 1: I_D versus V_G characteristics of the original device and after 37 degradation steps. $V_D = 0.1$ Volt.

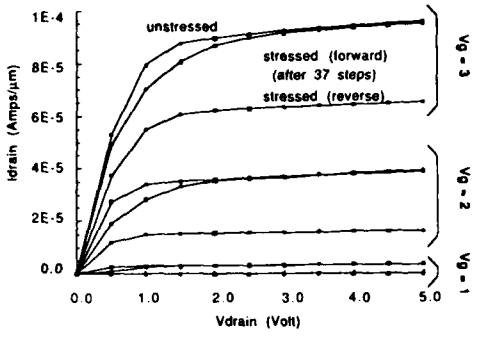


Figure 2: I_D vs. V_D characteristic curves of the original device and after 37 aging steps in the forward and reverse mode. V_G = 1, 2, and 3 Volts.

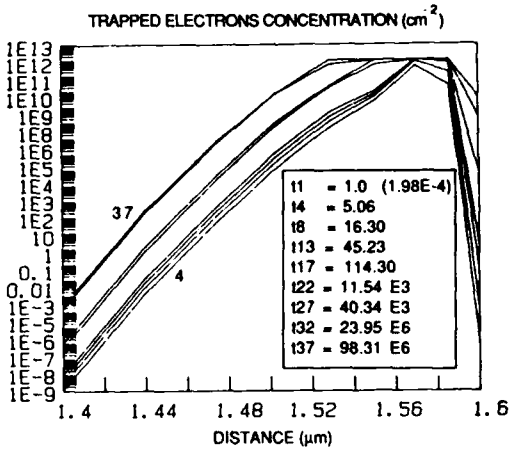


Figure 3: Trapped electron distribution after different aging steps

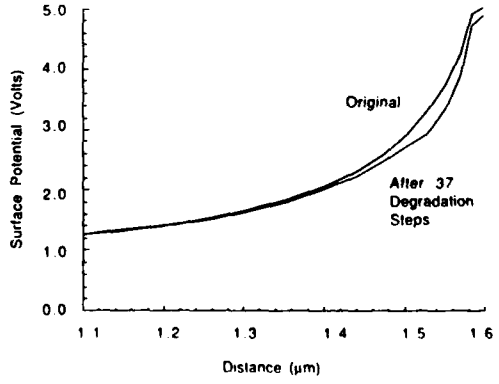


Figure 4: Surface potential of the original normal device and after 37 simulated degradation steps.

Abstract No. 271

COMPARISON OF DC AND AC STRESS FOR AN NMOS TRANSISTOR

Hai Wang, Rich Kaul, Steven Bibyk

Solid State Microelectronics
Department of Electrical Engineering
The Ohio State University

2015 Neil Ave.
Columbus, OH 43210

There is growing interest in device degradation under an AC stress condition[1]. Our experimental data show that device degradation under an AC stress is dependent on the frequency, phase characteristic of the stress signal, operation temperature, and less dependent on the load capacitance.

Initial device degradation under an AC stress condition has been found to be dominated by a transconductance decrease. The threshold voltage increased as stress continued. The time for threshold voltage to increase depended on the stress condition and transistor size. For a DC stress, the boundary between these two degradation mechanisms was not very obvious. It is shown in Fig. 1 that threshold voltage for a 1.8μm NMOS transistor at 77 K did not change during first 40 minutes AC stress period, while at time 200 minutes the threshold voltage shift dominated the device degradation. The initial transconductance degradation was contributed by the generation of fast interface state near the drain. These interface state are generated by the hot-carrier during the AC voltage transient time. The threshold voltage shift is caused by the negative charge trapping inside the gate oxide.

Both transistor parameter shifts were found to be saturated as stress time increased[2]. A hypothesis of carrier path change due to the charge accumulation near the drain is presented to explain this saturation phenomenon. For an AC stress, this saturation phenomenon is not as obvious as a DC stress, because the injection current for an AC stress consists not only of the channel hot-carrier, but also the transient current component, which is not sensitive to the additional electrical field formed by the charge trapping inside the gate oxide.

Device degradation under an AC stress condition has a strong temperature dependency[3]. Fig.2 shows the comparison of the stress results for two different temperatures, 300K and 77K. The threshold voltage shift at 77K is larger than the those at 300K for the same device size. Longer carrier-mean free path and higher trapping efficiency are believed to be responsible for the enhancement of device degradation. For an AC stress, the transient current component is also changed by the temperature due to the change in the gate capacitance and charge distribution inside the gate oxide. Because this transient current component plays a very important role in device degradation, the degradation was expected to be different than that for DC stress.

The comparison of DC stress and AC stress results are shown in Fig.3. The AC stress showed less degradation than DC stress. We conclude that the transient current during the stress can actually ease the device degradation by introducing the positive charges into the gate oxide to compensate the negative charges which were trapped there during the DC stress period.

Acknowledgement

The authors wish to thank A. Samman, D.C. Kau, S. Chou, C. Michael and Prof. P. Roblin for their assistance. The encouragement and support of this research by H. Hilbrink, D. Lauffer, and T. Tonnu of the NCR Corp. is much appreciated.

References

1. Fu-Chieh Hsu, Kuang Yi Chiu, "Hot-Electron Substrate-Current Generation During Switching transients", IEEE Tran. on Elec. Devices, vol. ED-32, NO.2, Feb. 1985

2. H. Wang, C. Michael, R. Kaul, S. Bibyk, "MOS Device Life Time Criteria for Circuit Performance", to be published

3. S. Bibyk, H. Wang, P. Borton, "Analyzing Hot Carrier Effects On Cold CMOS Devices IEEE Trans. Elec. Dev. ED-34, 83-88 (1987)

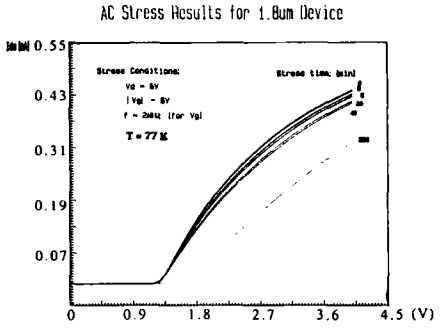


Fig. 17 Pre- and post-stress I-Vg curves for 1.8um device at 77K

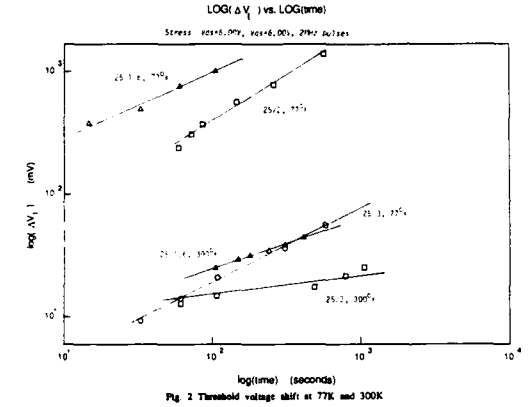


Fig. 2 Threshold voltage shift at 77K and 300K

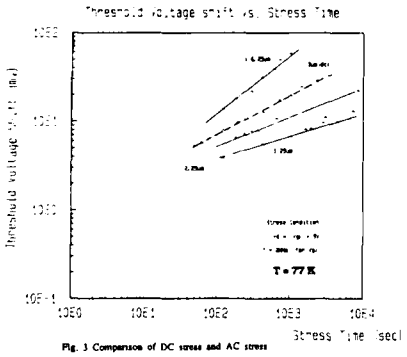


Fig. 3 Comparison of DC stress and AC stress

Abstract No. 272

DEGRADATION OF POLYCIDE GATE MOS CAPACITORS

A.Ohsaki, T.Okamoto, H.Kotani,
S.Nagao and N.Tsubouchi

LSI R&D Lab., Mitsubishi Electric Corp.
4-1 Mizuhara, Itami Hyogo 664, Japan

1. INTRODUCTION

Polycide gates are widely used in recent MOS LSI's. However, internal stress of silicides is 10^9 ~10^{10} dyne/cm^2 , which is one order of magnitude greater than that of poly-Si. In a previous paper, it was reported that positive charge trap centers at gate electrodes/SiO2 interfaces are generated due to the large stress, and the influence of the stress can be reduced by increasing the thickness of poly-Si.(1) We have found, however, that the degradation of MOS capacitors occurs even if thicker poly-Si is used. The purpose of this study is to investigate the degradation mechanisms of the polycide gate MOS capacitors in more details.

2. EXPERIMENTAL PROCEDURES

W-polycide gate MOS capacitors with two different gate patterns 'striped' and 'planar' were fabricated on p-type silicon substrates, as shown in Fig.1. The thicknesses of gate oxides, poly-Si and WSi2 layers were 25nm, 100-300nm and 230nm, respectively. After the fabrication of polycide gates, BPSG/SiO2 overlayers were deposited by CVD methods. Subsequently, annealing was carried out at 900°C for 20 min in O2 or H2/O2 ambient. Ramp I-V characteristics of the MOS capacitors were measured with a negative gate polarity.

3. RESULTS and DISCUSSION

Figure 2 shows the dependence of breakdown voltage of MOS capacitors with 'striped' polycide gates on poly-Si thickness. When the thickness of poly-Si layers becomes thinner than 150nm, the breakdown voltage decreases irrespective of annealing ambient. The degradation is also observed in the capacitors with 'planar' polycide gates. All of the degraded samples show hysteresis (2) in their ramp I-V characteristics, as shown in Fig.3. This hysteresis is caused by positive trap centers at electrodes/SiO2 interfaces induced by the tensile stress of the WSi2 layer.(1) Because both gate structures show the same degradation, it can be concluded that the trap centers are generated whole over the gate electrodes/SiO2 interface. It is seen that the stress can be reduced by increasing the thickness of poly-Si in the case of O2 annealing, as shown in Fig.2.

However, when the thickness of poly-Si layers becomes thicker , the degradation of breakdown strength and the hysteresis in I-V characteristics are observed only in the 'striped' gate capacitors annealed in H2/O2 ambient [see Fig.2 and 4]. The dependence on gate structure strongly indicates that the degradation of gate oxides occurs at the edges of gate electrodes. Moreover, the annealing ambients are related to this degradation mechanisms. H2/O2 annealing produces 'bird's beaks' which extend into gate regions, while O2 annealing dose not. Then, the compressive stress which are generated in the 'gate bird's beaks' during H2/O2 annealing, induces the positive trap centers at the gate electrodes/SiO2 interface.

At the optimum poly-Si thickness (150-200nm), the compressive stress due to the 'gate bird's beaks' would be relaxed by the tensile stress of the WSi2 layer. In this case, the number of trap centers is minimized, and dielectric breakdown strength is almost the same as the value estimated from inherent strength of SiO2.

4. CONCLUSIONS

Characteristics of the polycide gate MOS capacitors have been studied. The gate oxides are degraded due to two different mechanisms: When the thickness of poly-Si layer is thin, the positive charge trap centers induced by the tensile stress of the WSi2 layer affect the gate oxide, irrespective of the gate patterns and the annealing ambients (O2 or H2/O2). At the thicker side, the degradations caused by the 'gate bird's beaks' occur only in the 'striped' gate annealed with H2/O2 ambient. At the optimum thickness (150-200nm), no degradation is observed, because the stress due to the 'gate bird's beaks' may be relaxed by the WSi2 layer.

ACKNOWLEDGMENT

The authors would like to express their thanks to Dr.K.Shibayama for their encouragement.

REFERENCES

(1) N.Yamamoto, in Proceedings of the 19th Conference on Solid State Devices and Materials, Tokyo, 1987, p.415.
(2) P.Solomon, J.Appl.Phys., 48, 3843, (1977).

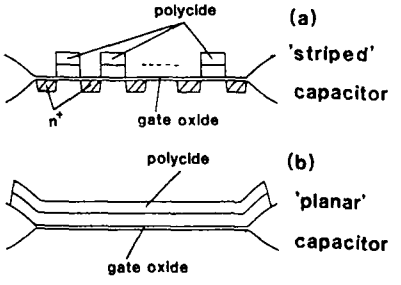


Fig.1 Schematic structures showing MOS capacitors; (a) 'striped' and (b) 'planar'.

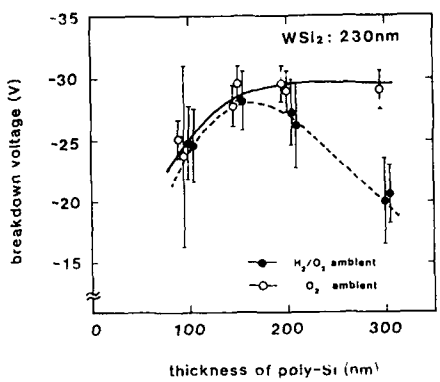


Fig.2 Breakdown voltage of 'striped' polycide gate capacitors vs poly-Si thickness. Breakdown voltage was measured under the constant current limit of 2.5mA/cm².

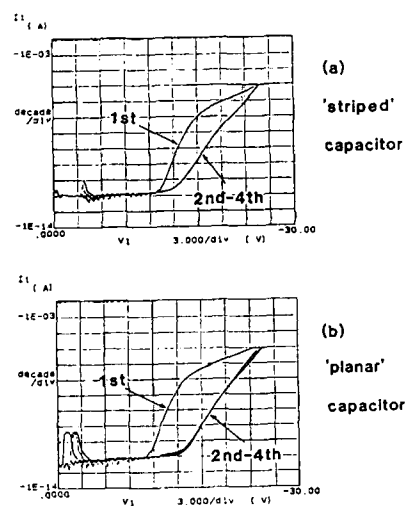


Fig.3 Typical ramp I-V characteristics of MOS capacitors with WSi2(230nm)/Poly-Si(100nm) gates annealed in O2 ambient; (a) 'striped' and (b) 'planar'.

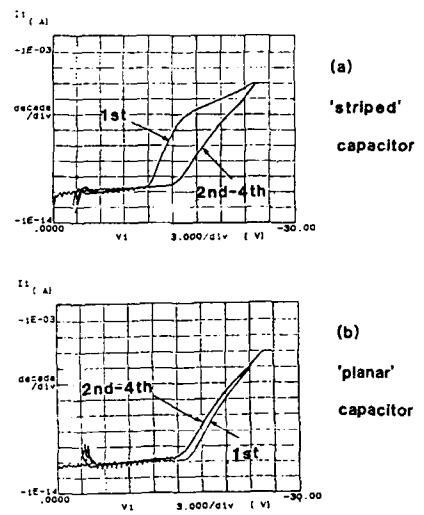


Fig.4 Typical ramp I-V characteristics of MOS capacitors with WSi2(230nm)/Poly-Si(300nm) gates annealed in H2/O2 ambient;(a) 'striped' and (b) 'planar'.

Abstract No. 273

REVIEW OF SILICON NITRIDE AND OXYNITRIDE FILMS FOR NONVOLATILE MEMORY DEVICE TECHNOLOGY

V. J. Kapoor and D. Xu

Electronic Devices and Material Research Lab
Department of Electrical and Computer Engineering
University of Cincinnati
Cincinnati, Ohio 45221-0030

R. A. Turi

NCR Microelectronics Division
Colorado Springs, Colorado 80916

The Al-Si_3N_4-SiO_2-Si (MNOS) capacitor structures and polysilicon - Si_3N_4-SiO_2-Si (SNOS) transistors were fabricated on p-type <100> - oriented silicon substrates with resistivities of 1-9Ωcm. After standard etching and cleaning procedures, the substrates were thermally oxidized and annealed so as to eliminate electron trapping centers in the oxide film. The oxide thickness was measured to be 50 Å, which was thick enough to block electron and hole injection from the substrate during photoinjection from the gate. For SNOS transistors the thickness of the silicon dioxide was approximately 15-20 Å. The silicon nitride (Si_3N_4) films were deposited onto the oxidized wafers by low pressure chemical vapor deposition (LPCVD) from a gaseous NH_3-SiH_2Cl_2 mixture. A controlled amount of oxygen was introduced into the film using N_2O gas during deposition. The Si_3N_4 films were deposited in three separate groups. In the first group, the Si_3N_4 films were deposited at 750C and the NH_3 to SiH_2Cl_2 gas ratio was varied from 3.5:1 to 30:1. The second group of Si_3N_4 films were deposited at temperatures which were varied from 650C to 850C with the NH_3 to SiH_2Cl_2 gas ratio 3.5:1. The third group of Si_3N_4 films were deposited at 750C with NH_3-SiH_2Cl_2 gas ratio of 3.5:1, but with varying N_2O gas flow from 20 sccm to 80 sccm. The thickness of all Si_3N_4 films used in our investigation was 400 A, as determined by ellipsometry.

The transparent gate electrode was used for internal photoelectric-effect technique. Semi-transparent aluminum electrodes, of 100 Å thickness were deposited onto the Si_3N_4 films. A 500 Å thick aluminum back contact was used to ensure a noise free contact to the external circuitry.

Auger electron spectroscopy (AES) has been utilized in conjunction with argon-ion sputtering in order to measure the variation in the stoichiometry and distribution of oxygen impurity in the silicon nitride film of the MNOS devices. In addition, X-ray photoelectron spectroscopy (XPS) was used to determine the chemical nature and bonding of the film. The silicon, nitrogen, oxygen and hydrogen atomic concentrations in the bulk of the Si_3N_4 film were found to vary as a function of NH_3 to SiH_2Cl_2 gas ratio, deposition temperature and N_2O gas flow. The results of the measurements indicated that oxygen was incorporated into the film by replacing the nitrogen atoms during the LPCVD process. The refractive index of the Si_3N_4 film was also found to be sensitive to the stoichiometry of the film.

The internal photoelectric-effect technique was employed in combination with capacitance-voltage (C-V) measurements for detail characterization of defect and impurities-related electronic charge trapping states in the nitride film of MNOS structure. The internal photoelectric-effect technique essentially consists of a photoinjection and photodepopulation sequence.

In the photoinjection process (defined as charging process or "write" operation), the charges are injected by internal photoemission from the metal electrode into the Si_3N_4 insulator of a MNOS structure by means of a UV light. Some fraction of these charges are captured by Si_3N_4 traps with a certain capture probability. The effect of photo-injection under bias is the introduction of negative charge in the Si_3N_4 films of a MNOS structure by the capture of charges into impurity/defect related traps. During this process, a partial discharge of the filled traps can also occur. For the given applied voltage bias, the traps will fill to some steady-state level determined by the ratio of the time constants of photoinjection and the partial discharge process. The storage of negative charge due to trapping process in the Si_3N_4 film causes a shift in the flatband voltage as determined from 1 MHz capacitance voltage characteristics and gives a measure of the centroid-weighted nitride trapped charge density.

The photo I-V technique allowed us to measure the trapped charge density and normalized centroid without the assumption of a particular charge distribution. This technique employed measurement of the flatband voltage and the photocurrent at the gate electrode to detect the field at the electrode-nitride interface. While the MNOS structure is under negative bias, the photocurrent was measured at the gate of a sample with no charge in the nitride. After electrons have been trapped in the silicon nitride the photocurrent was measured again. The internal electric fields in the nitride caused by the trapped charge oppose the applied bias, therefore a higher negative applied bias is required to measure the same photocurrent at the gate as before charges existed in the insulator. This increase in applied bias necessary to measure the same photo-current was measured from the shift in the photo-current voltage curve before and after injection, and reflected the amount of charge trapped in the film.

The SNOS transistors were fabricated and then tested to evaluate the retention characteristics of the memory devices. These devices incorporated the same LPCVD silicon oxynitride films as discussed above. The results show that varying the NH_3 to SiH_2Cl_2 ratio with no N_2O flow has little effect on the normalized decay rates for both written and erased states. However, normalized decay rate significantly improved as the N_2O flow and the resulting oxygen content is increased. This occurs for both the written and erased states. The decrease in the decay rates is indicative of a decrease in the trapped electron density. Therefore, it is the oxygen content and not the NH_3-SiH_2Cl_2 ratio that affect the device retention characteristics.

The normalized decay rates versus deposition temperatures with and without N_2O showed a clear trend for the nitride samples of smaller decay rates for lower deposition temperatures. However, for the oxynitride samples with N_2O=40 sccm, the retention of the device is significantly improved.

It is speculated the danglingsilicon bonds in silicon nitride are likely candidates for shallow (2eV) electron trapping centers. The Si-Si dangling bonds may be responsible for the deep traps.

Abstract No. 274

PECVD SILICON NITRIDE: DEPOSITION AND POST-DEPOSITION MODIFICATION FOR APPLICATION IN MEMORY DEVICES*

W. D. Brown
Department of Electrical Engineering
University of Arkansas
Fayetteville, Arkansas 72701

INTRODUCTION

Historically, silicon nitride used in the Metal-Nitride-Oxide-Semiconductor (MNOS) nonvolatile memory transistor has been deposited using APCVD or LPCVD [1]. Both of these methods require deposition temperatures in excess of 700°C and present difficulties in the processing of peripheral MOS circuits for operation in a radiation environment [2]. Recently, however, renewed research interest in silicon nitride deposited by plasma-enhanced chemical vapor deposition (PECVD), a low temperature process (<400°C), has provided evidence that PECVD silicon nitride may be used successfully in the MNOS structure [3,4]. Studies have shown a strong dependence of some electrical properties of these films on deposition parameters [4], and have concluded that properties of PECVD nitride, important for nonvolatile memory device operation, are comparable to those of high temperature CVD nitride [5].

This paper discusses the results of a research effort directed at defining "optimum" deposition parameters and post-deposition processing of PECVD nitride for application in MNOS devices. Post-deposition processing involved annealing and implant/annealing to enhance memory characteristics or these devices. Electrical and physical properties of the films were studied as a function of deposition conditions and subsequent processing with the goal of understanding their relationship to charge transfer, trapping and loss.

SAMPLE PREPARATION

Silicon nitride films (350Å to 800Å thick) were deposited in a 13.56 MHz, capacitively-coupled, parallel-plate reactor. MNOS capacitors were fabricated on n-type <111> silicon substrates with aluminum electrodes and a gold back contact. Samples used for Fourier Transform IR and UV spectroscopic analysis were deposited on optically polished, high resistivity silicon and high quality quartz plates (T20 Superasil 2), respectively.

RESULTS AND DISCUSSION

The electrical and physical properties of silicon nitride thin films are known to be sensitive functions of deposition conditions [6]. It follows then, that the memory performance of nonvolatile memory devices which utilize silicon nitride as the charge trapping medium is influenced by the deposition and post-deposition processing of the nitride [7].

"AS-DEPOSITED" PECVD SILICON NITRIDE

Since the primary objective of this work was to deposit PECVD silicon nitride of sufficient quality for an MNOS structure, optimization of the deposition process was based on the memory window size of an MNOS capacitor for given write/erase conditions. Deposition parameters examined were RF power, substrate temperature and gas composition. Both nitrogen and argon were used as carrier gases.

"Optimization" of the deposition parameters yielded a substrate temperature of 300°C, an RF power density of 34 mW/cm^2 and NH_3/SiH_4 = 0.8. Memory window size varied as a function of the flow of nitrogen carrier, but was independent of argon flow. Window sizes varied from 2 to 12 volts for a writing field of 5×10^6 V/cm and pulse widths between 1 microsecond and 10 milliseconds. The memory performance correlates closely with the Si-H bond concentration. Retention and endurance performance compared favorably with LPCVD and APCVD silicon nitride devices.

ANNEALING

Post-deposition annealing in argon and nitrogen produced increases in memory window size of up to 25 percent for an anneal temperature and time of 475°C and 30 minutes, respectively. This treatment minimizes the Si/N ratio, increases the Si-H bond concentration and reduces the insulator fixed charge. Higher temperatures and longer times evolve hydrogen from the film and severely degrade memory performance. Some results suggest that nitrogen can be supplied to or lost from the film during annealing.

IMPLANTATION/ANNEAL

Implantation of argon and nitrogen was used to modify the memory properties of the nitride films. Improvement in memory window size of up to 70 percent was obtained for implant energies in the range of 25 to 45 KeV, implant fluences in the range of 10^{12} to 10^{14} ions/cm^2 and beam currents of 1 to 5 microamperes. The implants were followed by a 475°C anneal in nitrogen for 30 minutes. Higher energies and fluences produced damage that could not be recovered using the annealing procedure. Higher beam current levels caused the insulator to charge up and shifted the threshold voltage of the MNOS capacitors to values less than -20 volts. Penetration of the Si/Si_3N_4 interface by the implant also destroyed the memory properties of the device. Changes in memory window size correlated with changes in Si-H bond concentration. Increases in Si-H bond concentration caused by implantation occurs by transfer of hydrogen from nitrogen to silicon. The modification of the silicon nitride using this procedure did not adversely affect the retention and endurance performance of MNOS capacitors.

CONCLUSIONS

Careful control of deposition parameters will permit the deposition of memory quality PECVD silicon nitride. Post-deposition annealing and implantation/annealing can be used to enhance the memory performance of MNOS devices. Memory window size correlates with Si-H bond concentration.

REFERENCES

1. H. J. Stein, J. Appl. Phys. 57(6) 2040, 1985.
2. P. J. McWhorter, S. L. Miller and T. A. Dellin, IEEE Trans. Nucl. Sci., NS-33 (6) 1414, 1986.
3. T. E. Nagy, C. D. Fung and W. H. Ko, Proc. Sym. on Silicon Nitride Thin Insulating Films, Electrochem. Soc., 83-8, 167, 1983.
4. M. A. Khaliq, O. A. Shams, W. D. Brown and H. A. Naseem, Proc. Sym. on Silicon Nitride Thin Insulating Films, Electrochem. Soc., 87-10, 201, 1987.
5. D. Jousse, J. Kanicki and F. Mehran, "Electron Spin Resonance Study of Defects in PECVD Silicon Nitride", presented at the 172nd ECS Meeting, Honolulu, Hawaii, Oct. 18-23, 1987.
6. A. M. DeAlmeida and S. S. Li, Solid State Electronics, 30(9) 889, 1987.
7. B. Y. Nguyen, P. J. Tobin, K. W. Teng, H. G. Tompkins and K. M. Chang, J. Electrochem. Soc., 135(3) 776, March 1988.

*This work was supported by a grant from the National Science Foundation.

Abstract No. 275

A Review of Current Conduction in Stacked Silicon Dioxide-Silicon Nitride Layers on Silicon

R.V.Giridhar
Intel Corp, Santa Clara, CA 95051

Stacked silicon nitride-silicon dioxide layers are of interest in such applications as storage dielectrics for DRAMs [1] and interpoly dielectric in floating gate non-volatile memories [2]. An understanding of the current transport mechanisms in such layers is vital for the successful scaling of these stacks for use in future technologies.

Thermal oxide layers on silicon have been extensively studied because of their importance to all of silicon MOS technology. It is generally accepted that the current conduction in silicon dioxide layers on silicon is dominated by electrons and the current-field characterestics can be modeled by the well known Fowler Nordheim tunneling equation [3].

Early studies of current conduction in silicon nitride by Sze [4] led to the conclusion that at high electric fields, the conduction is bulk-limited and can be described by the Poole-Frenkel characteristics. This mechanism depends on the field enhanced thermal ionization of trapped carriers. In general, the current density (J)- electric field (E) characterestics for several different mechanisms are exponential (ignoring the field dependence of the pre-exponential factor) and of the form:

$$J \sim \exp(aE^n)$$

with n=-1 for Fowler Nordheim (tunneling) characterestics and n=1/2 for Poole-Frenkel conduction and Schottky emission and 'a' is a field-independent factor which is also temperature independent for tunneling [5].

Because of this, it is difficult to distinguish between these mechanisms on the basis of current field characterestics alone especially over small ranges of electric field. Sze [4] used the self consistency between the static dielectric constant of silicon nitride and the dielectric constant calculated from the Poole-Frenkel plots to infer that silicon nitride exhibited Poole-Frenkel conduction. In addition, the current-field characterestics were found to be essentially independent of substrate material, film thickness and bias polarity, supporting a bulk-limited process.

Sze [4] assumed that electrons were the carriers transporting charge although no specific evidence for that was seen. The subject of the dominant current carrier in silicon nitride layers has been revisited several times. Three basic techniques (all of which employ a p-n junction in some form) have been used for separating the hole current from the electron current. Weinberg [6] used a shallow junction to separate the carriers and suggested that holes dominate the current conduction in silicon nitride for both bias polarities. Schroder and White [7] used complementary emitter bipolar transistors for carrier separation and concluded that holes are the dominant carriers in silicon nitride. Ginovker et. al. [8] used an MIS transistor for carrier separation and suggested a polarity dependence for the dominant carrier in silicon nitride. Arnett and Weinberg [8] have reviewed the evidence for hole conduction in silicon nitride.

More recently, Yau [9] studied MIS transistors with oxide-nitride stacks and proposed that electrons are the dominant carriers in silicon nitride irrespective of the thickness of interfacial oxides while Liou and Chen [10] have argued that hole conduction dominates irrespective of the thickness of interfacial oxide layers.

Our work on the current-field characteristics and behavior of trapped charge in thick oxide SNOS structures [11,12], suggests that both electrons and holes can participate in the conduction in thick oxide SNOS structures. But under conditions where hole injection is not impeded (as with a blocking oxide, holes will dominate conduction in silicon nitride films.

In view of the controversy surrounding the conduction in silicon nitride, the understanding of current conduction in stacked dielectrics is still in its infancy. Although the primary current carrier in silicon nitride has been the focus of several studies, an understanding of the current component due to the secondary carrier is very important in understanding and modeling the current in stacked dielectrics. Also, in several applications, a good understanding of the low-field current conduction in such layers is needed.

Current conduction and charge trapping in silicon nitride will be reviewed. Thickness regimes where electron or hole transport is expected to dominate conduction in silicon nitride in stacked oxide-nitride dielectrics will be identified. Implications of the dominance of hole conduction in silicon nitride, for the design of low-leakage stacked dielectrics will be examined.

References:

1) T.Watanabe, A.Menjo, M.Ishikawa and J.Kumagai, IEDM Technical Digest, p173, 1984.
2) S.Mori, N.Matsukawa, Y.Kaneko, N.Arai, T.Shinagawa, Y.Suizu, N.Hosokawa and K.Yoshikawa, IEDM Technical Digest, p257, 1987.
3) D.A.Weinberg, J.Applied Physics, v53-7), p5052, 1982.
4) S.M.Sze, J. Applied Physics,38, 2951, 1967.
5) S.M.Sze, Physics of Semiconductor Devices, 2nd Edition, Wiley Interscience, p402 (1981).
6) D.A.Weinberg, Appl. Physics Lett., v29, No.8, p477, 1976.
7) D.K Schroder and M.H.White, IEEE Trans. on Electron Devices, ED-26 No. 6, p899, 1979.
8) A.S.Ginovker et. al. Phys. Status Solidi, v26a, p489, 1974.
9) L.D.Yau, IEEE Electron Dev. Lett. v EDL-5 No.8, p316, 1984.
10) F.T.Liou and S.Chen, IEEE Trans. on Electron Devices, vED-31, no. 12, p1796, 1984.
11) S.Nozaki and R.V.Giridhar, Electron Dev. Lett.,EDL-7, No.8, p466, 1986.
12) M.Aminzadeh, S.Nozaki and R.V.Giridhar, IEEE Trans. Electron Devices, p459, 1988.

Abstract No. 276

INFLUENCES OF PROCESSING CHEMISTRY OF SILICON NITRIDE FILMS ON THE CHARGE TRAPPING BEHAVIOR OF OXIDE/CVD-NITRIDE/OXIDE CAPACITORS

B-Y Nguyen, P.J. Tobin, K.M. Chang, K.W. Teng and H.G. Tompkins*
Advanced Products Research and Development Laboratory
Motorola Inc., Austin, Texas 78721
* Bipolar I/C Group, Motorola Inc., Mesa, Arizona 85008

INTRODUCTION

In recent years silicon nitride films have begun to play an important role in thin dielectric applications for advanced memory technology; the oxide/nitride/oxide (ONO) stacked film has become one of the most promising candidates for an ultra-thin gate dielectric (1-4). The well-known advantages of ONO films over thin oxide films include low defect densities, high breakdown fields and good barrier properties for impurity diffusion and radiation damage. However, certain properties such as charge trapping and instability of ONO films still need clarification and improvement. In this study, we examined the effect of the processing conditions of silicon nitride films on the chemical nature and charge trapping behavior of ONO films.

DEVICE FABRICATION

The Polysilicon-ONO-Silicon (SONOS) capacitors were fabricated on P-type (100) silicon substrates with resistivities of 14-22 ohm-cm. After LOCOS processing, a 35A bottom oxide was thermally grown in diluted O2 in Ar with 1% HCL at 900C. The wafers were then split into three groups which received NH3:SiH2CL2 gas ratios of 5:1, 10:1 and 20:1 during deposition of the nitride films. For all wafers, the deposition temperature was 720C, and the nitride thickness was 80+/-5A as determined by an ellipsometer on an accompanying test wafer. The groups were combined and subjected to steam ambient at 830C for 3 hours to grow approximately 20A of oxide on top of the nitride. Next, in-situ phosphorus-doped polysilicon gates were fabricated to form SONOS capacitors with areas of 6.5 x 10-4 cm2. The capacitance-voltage technique was employed to investigate the charge trapping behavior of the ONO films. The SONOS capacitors were subjected to constant voltage stresses under both positive and negative gate polarities. A microscope light was used for positive gate bias to provide inversion layer charge. The flat-band voltage shifts (VFB) were monitored as a function of time until they were saturated.

PHYSICAL AND ELECTRICAL CHARACTERISTICS

The oxygen, nitrogen and silicon atomic concentrations of three ONO films, which had the same oxide equivalent thickness of 90+/-5A but different nitride deposition gas ratios, are shown in Figure 1. These Auger depth profiles show that the nitride films fabricated with the 20:1 gas ratio have better resistance to the steam oxidation than those fabricated with the 5:1 gas ratio. This can be seen from the relative height of the oxygen signal compared to the nitrogen signal in the nitride (now oxynitride) layer. Additionally, it should be noted that ONO films fabricated with the highest gas ratio show a thinner bottom oxide and a stronger nitrogen signal in the bottom oxide. At this point, it is not clear whether the stronger nitrogen signal is real or is a depth profiling measurement artifact. ESCA results on the other ONO films show that no nitrogen could be detected in the bottom oxide layer after removal of the top oxide and nitride in wet selective chemical etch solution (5). However, our work using Auger electron spectroscopy and quasi-static CV techniques suggests that during the short period of silicon nitride deposition, nitrogen appears to penetrate the 35A bottom oxide layer (6). The interface trap densities of the 20:1 gas ratio ONO dielectric films were also observed to be higher compared to those of oxide films thus providing further evidence of nitrogen penetration.

Figure 2 illustrates the linear relationship between intrinsic flat-band voltage and NH3:SiH2CL2 gas ratios. The flat-band voltage decreases slightly as the gas ratio increases.

The influences of NH3:SiH2CL2 gas ratios on the saturated flat-band voltage shift as a function of time and E-field under positive gate voltage (Vg) are shown in the Figures 3 and 4. These Figures demonstrate that negative charge trapping dominated for all three types of ONO film as indicated by a positive VFB shift. The VFB shift of ONO films increases as the gas ratio increases. It is also noted that the VFB shift increases and rapidly saturates as a function of stressing time and stressing E-field.

Under negative Vg stressing, Figures 5 and 6 show that both negative and positive charge trapping are present in the ONO films fabricated with NH3:SiH2CL2 gas ratios of 10:1 or higher. At the 5:1 gas ratio, only negative charge trapping occurs as indicated by positive VFB shift regardless of stressing conditions. It also appears that the ONO films fabricated with a low NH3:SiH2CL2 gas ratio reach VFB shift saturation in a shorter stressing time and at a lower stressing E-field: on other hand, the ONO films fabricated with high NH3:SiH2CL2 gas ratio have more charge trapping and an unstable VFB shift as shown in Figure 6. The VFB shifting behavior of these ONO films could be explained by the final film thickness and composition of each constituent layer(7). And these results are consistent with the data presented in Figure 1.

CONCLUSION

Our results show that nitride processing chemistry can play an important role in charge trapping, carrier transport and chemical nature of thin ONO dielectric films. In particular, as the NH3:SiH2CL2 gas ratio decreases, the resistance of the nitride films to steam oxidation decreases, thereby enhancing the thickening of the bottom oxide. If the nitridation of the thin bottom oxide suggested by Figure 1 is confirmed, it is apparently more pronounced at higher gas ratios.

ACKNOWLEDGEMENTS

The authors wish to thank A. Tasch, E. Reed and L. Parrillo for their support of this project and special thanks to Peter Gill for his assistance.

REFERENCES

1. T. Watanabe, A. Menjoh, T. Mochizuki, S. Shinozaki, and O Ozawa, in Int. Reliability Physics Symp., p. 18 (1985).

2. E. Suzuki and Y. Hayashi, IEEE Trans Electron Devices, ED-33, 214(1986).

3. S. Nozaki and R. V. Giridhar, IEEE Electron Device Lett., EDL-7, 486(1986).

4. K. Rajkanan and J. S. Multani, This Journal, 130, 1152(1983).

5. Naresh C. Saha, Motorola Inc., Private communication

6. J. S. Johannessen, C. R. Helms, W. E. Spicer, and Y. E. Strausser, IEEE Trans Electron Devices, ED-24, 547(1977).

7. M. M. Moslehi and K. C. Saraswat, IEEE J. Solid-State Circuit., SC-20, 26(1985).

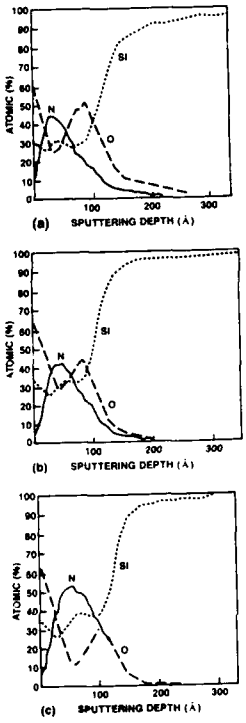


Fig. 1. THE AUGER DEPTH PROFILE OF THIN ONO NITRIDE FILMS WITH THE MIDDLE LAYERS DEPOSITED AT VARIOUS NH_3:SiH_2Cl_2 GAS RATIOS: (a) NH_3:SiH_2Cl_2 = 5:1; (b) NH_3:SiH_2Cl_2 = 10:1; (c) NH_3:SiH_2Cl_2 = 20:1

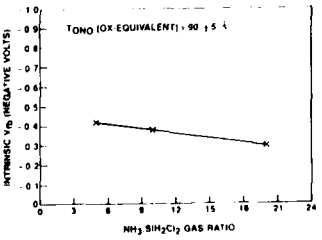


FIG. 2 THE INTRINSIC FLAT-BAND VOLTAGE OF SONOS CAPACITORS AS A FUNCTION OF NH_3:SiH_2Cl_2 GAS RATIO

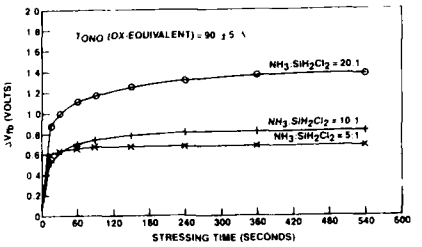


FIG. 3. THE EFFECTS OF NH_3:SiH_2Cl_2 GAS RATIO ON THE FLAT-BAND VOLTAGE SHIFT OF SONOS CAPACITORS UNDER 7 MV/cm E-FIELD STRESS AS A FUNCTION OF TIME

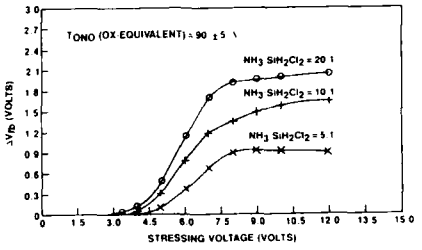


FIG. 4. THE EFFECTS OF NH_3:SiH_2Cl_2 GAS RATIO ON THE FLAT-BAND *VOLTAGE SHIFT OF SONOS CAPACITORS STRESSED AT DIFFERENT* POSITIVE GATE VOLTAGES FOR 120 SECONDS

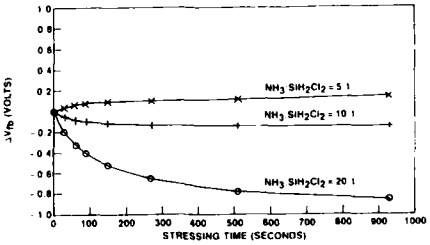


FIG. 5. THE EFFECTS OF NH_3:SiH_2Cl_2 GAS RATIO ON THE FLAT-BAND VOLTAGE SHIFT OF SONOS CAPACITORS UNDER – 7 MV/cm E-FIELD STRESS AS A FUNCTION OF TIME

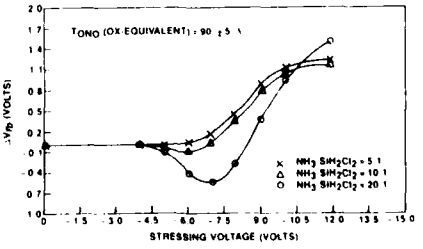


FIG. 6 THE EFFECTS OF NH_3:SiH_2Cl_2 GAS RATIO ON THE FLAT-BAND VOLTAGE SHIFT OF SONOS CAPACITORS STRESSED AT DIFFERENT NEGATIVE GATE VOLTAGES FOR 120 SECONDS

Abstract No. 277

NATURE OF THE DOMINANT DEEP TRAP IN AMORPHOUS SILICON NITRIDE

D.T. Krick and P.M. Lenahan
The Pennsylvania State University
227 Hammond
University Park, PA 16802

J. Kanicki
IBM Thomas J. Watson Research Center
P.O. Box 218
Yorktown Heights, NY 10598

The importance of silicon nitride in the microelectronics industry is well established. It has traditionally been used as a passivating layer in silicon dioxide device technology, as well as in nonvolatile memory devices. More recently, however, it has been proposed as the primary dielectric in amorphous hydrogenated silicon thin film transistors (TFT's). It is well established that the electronic properties of silicon nitride are dominated by the presence of deep trapping centers[1,2]; these centers may seriously limit the usefulness of silicon nitride in TFT's[3]. Although intense effort has gone into identifying these trapping centers[4-8], no direct experimental evidence exists until now directly linking a specific structural defect with the trapping behavior in amorphous silicon nitride.

We report results of a study in which we inject positive and negative space charge via corona discharge into amorphous silicon nitride films. We use electron spin resonance to monitor the density of silicon dangling bond centers, and electrical (capacitance versus voltage, or CV) measurements to calculate the density of trapped charge. We find that the capture of either positive or negative charge by the trapping centers is consistently accompanied by an approximately equal decrease in the density of paramagnetic silicon dangling bond centers. We also find that ultraviolet (UV) illumination of charged nitrides eliminates space charge and that this disappearance of trapped charge is accompanied by an approximately equal increase in the density of silicon dangling bond centers. Our results provide the first direct evidence that the dominant deep trap in silicon nitride films is an amphoteric silicon dangling bond.

The silicon nitride samples used in this study were deposited via low pressure chemical vapor deposition (LPCVD) to a thickness of 5500Å. Substrates were crystalline <111> silicon on which a 250Å oxide had been previously grown. This thin oxide layer eliminated charge injection in our nitride films at moderate fields, and made our CV measurements reliable. At high fields, however, this layer was thin enough to permit the tunnelling of carriers through the oxide.

Initially, virgin LPCVD silicon nitride films were illuminated for 20 minutes using a 100W mercury lamp and a 4.9eV mercury line interference filter; the light intensity from this lamp/filter combination was estimated at 1μW-cm^{-2}. This UV illumination not only creates a substantial increase in paramagnetic defect density[9] (3.6×10^{13} spins-cm^{-2}), but also annihilates any space charge previously trapped in the nitride (Fig. 1a,c,e). UV illumination thus allows us a reference point in our experiment. In other words, we can cycle the samples through a series of charging conditions, always returning to our starting conditions (i.e. a large paramagnetic defect density and no trapped charge) with the aid of UV illumination.

After UV illumination, the samples were subjected to a positive bias (with respect to the substrate) via (positive) corona discharge for ten minutes. During biasing, the current density in the samples was monitored and found to be 0.7μA-cm^{-2}. Under positive corona bias, electrons tunnel from the silicon substrate through the oxide and into the nitride, where they can be trapped. After biasing, ESR measurements indicate a decrease in paramagnetic spin density of 1.1×10^{13} spins-cm^{-2} to a value of 2.5×10^{13} spins-cm^{-2}, and CV measurements show the midgap voltage (V_{mg}) has shifted +85 volts (Fig. 1b). This shift corresponds to roughly 8×10^{12} trapped electrons-cm^{-2} in the silicon nitride. This increase in the number of negatively charged trapping centers is (within experimental error) equal to the decrease in paramagnetic defects in the silicon nitride (Fig. 2). Electron trapping renders these formerly paramagnetic and neutral centers both diamagnetic and negatively charged.

Next, the samples were subjected to UV illumination for 20 minutes; the number of paramagnetic defects increased to 3.6×10^{13} spins-cm^{-2}, and V_{mg} shifted -85 volts back to the origin (Fig 1c). This could be explained several ways; one possible explanation is that the UV light photodepopulates the electrons previously trapped during biasing, which in turn eliminates any trapped charge in the nitride. In any case, UV illumination annihilates any charge in the nitride. The negatively charged centers' return to a paramagnetic state is accompanied by their loss of an electron. The silicon dangling bond center in amorphous silicon nitride is again neutral in its paramagnetic state.

The samples were at this point subjected to a negative bias (with respect to the silicon substrate) using (negative) corona ions for ten minutes; current through the samples was the same as in the case of positive bias. Under negative corona bias, hole injection from the silicon substrate takes place via tunnelling, and holes are trapped in the nitride. This biasing resulted in a decrease in paramagnetic center density of 8×10^{12} spins-cm^{-2} to a value of 2.8×10^{13} spins-cm^{-2}. CV measurements indicate V_{mg} shifted -35 volts, indicating roughly 3×10^{12} trapped holes-cm^{-2} in the nitride (Fig. 1d). The decrease in paramagnetic centers is again (within experimental error) approximately equal to the number of charged centers in the nitride (Fig. 2). Holes trapped at the neutral paramagnetic centers render these centers both positively charged and diamagnetic.

Finally, the samples were illuminated with UV light for 20 minutes; the spin density increased by 8×10^{12} spins-cm^{-2} to its original value of 3.6×10^{13} spins-cm^{-2} and V_{mg} shifted +30V to a value of -5V (Fig. 1e). This is again consistent with the disappearance of holes at silicon dangling bond centers, rendering the centers both paramagnetic and neutral.

In conclusion, we present for the first time conclusive evidence that paramagnetic neutral silicon dangling bond defects in silicon nitride may capture either electrons or holes. The capture of either an electron or a hole renders the neutral defect diamagnetic and charged. These dangling bonds are on silicon atoms bonded to three nitrogen atoms[10]. Charged defects can be returned to their neutral paramagnetic state with the aid of 4.9eV illumination. Our results suggest that this is the dominant defect responsible for the trapping behavior observed in silicon nitride films. Furthermore, our ability to cycle the defect between its paramagnetic neutral state and both its charged diamagnetic states suggests that the optical generation of dangling bonds in amorphous silicon nitride involves no complex structural rearrangement, but simply changes in the charge and spin states of the defect.

1. P.C. Arnett and B.H. Yun, Appl. Phys. Lett. 26, 94 (1975)
2. H. Maes and R.J. Van Overstraeten, Appl. Phys. Lett. 27, 282 (1975)
3. A.R Hepburn *et al.*, Phys. Rev. Lett 56, 2215 (1986)
4. K.L. Ngai and Y. Hsia, Appl. Phys. Lett. 41, 159 (1982)
5. D. Frohman-Benctchowsky, Proc. IEEE 58, 1207 (1970)
6. J. Robertson and M.J. Powell, J. Appl. Phys. 44, 415 (1984)
7. C.T. Kirk, Jr., J. Appl. Phys. 50, 4190 (1979)
8. V.J. Kapoor, R.S. Bailey, and H.J. Stein, J. Vac. Sci. Technol. A1, 600 (1983)
9. D.T. Krick, P.M. Lenahan, and J. Kanicki, Appl. Phys. Lett. 51, 608 (1987)
10. T. Makino and M. Maeda, Jpn. J. Appl. Phys. 25, 1300 (1986)

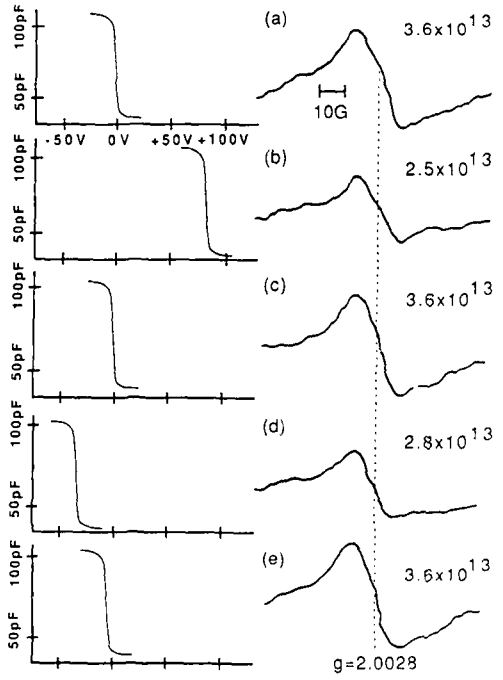


Figure 1. ESR and CV data; (a) following 20 minutes of UV illumination, (b) following 10 minutes positive corona bias, (c) following a second 20 minute exposure to UV illumination, (d) following 10 minutes of negative corona bias, (e) following a third 20 exposure to UV illumination.

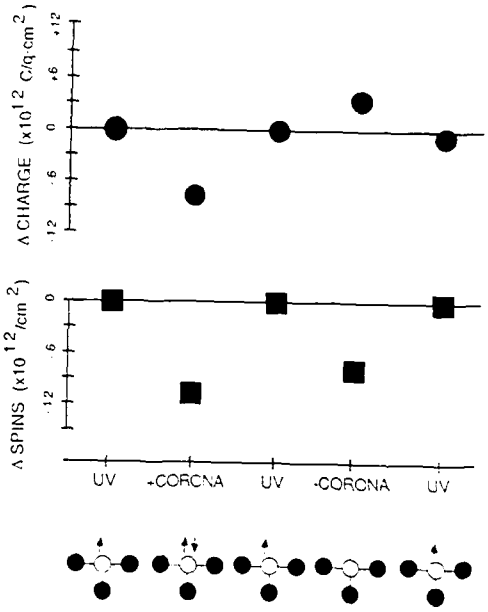


Figure 2. CV (Δ charge) and ESR (Δ spins) data plotted to show the relative changes in paramagnetic and electrically active defect densities following biasing and illumination operations performed throughout the study. The charge and spin states of the defect at each point throughout the study are also shown.

Abstract No. 278

HIGH QUALITY NITROGEN-RICH PECVD a-SiN_x:H FILMS FOR APPLICATION IN THIN FILM TRANSISTORS

W.S. Lau and S. J. Fonash
Center for Electronic Materials and Devices,
and Enginnering Science Program,
The Pennsylvania State University,
University Park, PA 16802

J. Kanicki
IBM Research Division
Thomas J. Watson Research Center,
P. O. Box 218, Yorktown Heights, NY 10598

Introduction

In general, silicon nitride films deposited at low temperatures (below 500°C) by plasma enhanced chemical vapor deposition (PECVD) tend to be silicon-rich. Carrier trapping in such silicon-rich films ($x<1.33$) has been found to be a problem.[1] Hence, these films may be useful for passivation in IC technology but they are normally not suitable for applications as gate dielectrics in MIS devices. Nevertheless, silicon-rich PECVD nitride films have been used in thin film transistors (TFT) with modest stability by limiting the maximum operating electric field to about or below $3x10^5$ Vcm^{-1}.[2,3] Recently, it was found that under some experimental conditions, nitrogen-rich films ($x>1.33$) can be deposited by PECVD technique. It has also been shown that nitrogen-rich films have less carrier trapping problems than silicon-rich films.[1,4] We report here on the investigation of the electrical stability of these films as gate dielectrics in metal-nitride-semiconductor (MNS) devices with Al-a-SiN_x:H-n-Si capacitor structures and explore the possibility of enhancing film properties by rapid thermal annealing (RTA).

Experimental

The silicon nitride films of this study were deposited by PECVD technique from undiluted silane and ammonia gas mixtures on n-type silicon wafers chemically cleaned by the RCA method. The deposition conditions such as deposition temperature T_s, RF power density P_{rf}, the ammonia to silane flow ratio and the pressure P together with the resulting chemical composition in terms of Si/N ratio and hydrogen concentration C_H are summarized in Table I. After film deposition, aluminum dots were deposited by magnetron sputtering onto the top surface of the nitride films. Each sample was subsequently cut into three or more pieces: one for control, one for 400°C and the other for 600°C RTA, respectively. RTA was usually performed for five minutes with an AG 210 heat pulse system. It was found that after 600°C RTA for five minutes in Ar, either before or after Al gate deposition, most of the samples became very leaky. However, most of the investigated samples remained highly insulating after 400°C RTA for five minutes. Consequently, only the results before and after 400°C RTA are discussed. The flatband voltage (V_{FB}), the hysteresis in flatband voltage (ΔV_H), the density of fixed charge (N_f) and the mid-gap interface states density (N_{mg}) were deduced from low frequency (10Hz) and high frequency (1MHz) capacitance-voltage (C-V) measurements at room temperature for 0 to -20V sweeps. Electrical stability was evaluated by performing bias temperature stress (BTS) experiments.

Results and Discussions

Table II compares the electrical properties observed for a number of samples deposited at various deposition conditions. The data also show the the effect of rapid thermal processing on film properties; that is, results are given for samples before and after a 400°C RTA for 5 minutes. By comparing a silicon-rich sample, sample SFMNS#1, and a nitrogen-rich sample, sample SFMNS#2, deposited at the same temperature, 250°C, it can be seen that the hysteresis is smaller for a nitrogen-rich sample. By comparing samples SFMNS#2, SFMNS#4 and SFMNS#5, which are nitrogen-rich films deposited at different temperatures, it can be seen that the hysteresis is smallest at around 400°C. In general, both the fixed charge density N_f and the mid-gap density of states N_{mg} are decreased after RTA.

The thickness of films in the SFMNS series is about 800Å. This is very thin when compared with the thickness of nitride films used in TFTs in the literature, which is about 3000-5000Å.[2,3] Hence to get a fair assessment of the electrical stability for the same stress voltage as that used in the literature[2,3], a thicker film has to be considered. Bias temperature stress (+15V, 80°C) results for sample SF#2, a 2150Å thick nitrogen-rich film deposited at 350°C, before and after 400°C RTA, are shown in Fig. 1. V_{FB} of sample SF#2A (SF#2 as deposited) continued to shift in the positive direction during BTS. However, V_{FB} of sample SF#2B (SF#2 after RTA) remained constant for more than 10 hours during BTS. This is true over a wide temperature range from 25°C to 80°C. The advantage of the 400°C RTA is therefore very significant. This is excellent when compared with +12V BTS results on 3000-5000Å thick silicon-rich nitride films in the literature.[2,3]

References

1. B. L. Jones, J. Non-Cryst. Solids, 77/78, 957 (1985).
2. M. J. Powell, in "Comparison of thin film transistor and SOI technologies", eds. H. W. Lam and M. J. Thompson, Materials Research Society Symp. Proc., 33, 259 (1984).
3. K. Hiranaka, T. Yoshimura and T. Yamaguchi, J. Appl. Phys., 62, 2129 (1987).
4. J. Kanicki and P. Wagner, Proc. Symp. on Silicon Nitride and Silicon Dioxide Thin Insulating Films, eds. V. J. Kapoor and K. T. Hankins, Electrochemical Society, 87-10, 261 (1987).

TABLE I

The deposition parameters and the resulting chemical composition of PECVD a-SiN_x:H films

Sample	T_s (°C)	P_{rf} (Wcm^{-2})	NH_3/ SiH_4	Pressure (Torr)	Si/N	C_H (at. %)
SFMNS#1	250	0.047	3	0.43	1	
SFMNS#2	250	0.047	12	0.43	0.62	37.4
SFMNS#4	400	0.047	12	0.43	0.62	31.5
SFMNS#5	500	0.047	12	0.43	0.62	23.8
SF#2	350	0.21	15	0.43	0.61	

TABLE II

Some electrical properties of PECVD a-SiN_x:H films before and after 400°C 5 min. RTA

Sample	Thickenss (Å)	RTA (400°C 5 min)	V_{FB} (V)	ΔV_H (V)	N_f (cm^{-2})	N_{mg} ($cm^{-2}eV^{-1}$)
SFMNS#1A	950	No	-4	5.5	$1.7x10^{12}$	$\sim10^{12}$
SFMNS#1B	950	Yes	-3.5	10.5	$1.6x10^{12}$	$\sim10^{11}$
SFMNS#2A	800	No	-7	3.8	$3.5x10^{12}$	$\sim10^{12}$
SFMNS#2B	800	Yes	-1.3	3.5	$7x10^{11}$	$\sim10^{11}$
SFMNS#4A	800	No	-10.2	1.5	$5.9x10^{12}$	$\sim10^{12}$
SFMNS#4B	800	Yes	-3	2	$1.5x10^{12}$	$\sim10^{11}$
SFMNS#5A	900	No	-5	3.5	$2.6x10^{12}$	$\sim10^{11}$
SFMNS#5B	900	Yes	-7	5.3	$2x10^{12}$	$\sim10^{11}$
SF#2A	2150	No	-10	1.8	$1.4x10^{12}$	$\sim10^{12}$
SF#2B	2150	Yes	-5.5	0.5	$7x10^{11}$	$\sim10^{11}$

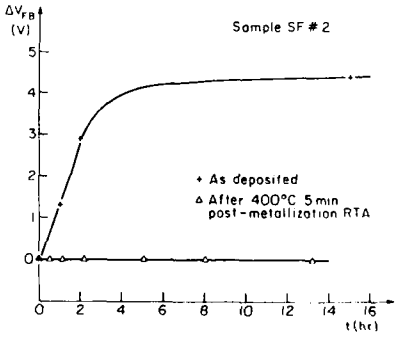


Figure 1. The flatband voltage shift ΔV_{FB} under +15V 80°C BTS of a MNS capacitor with a nitrogen-rich PECVD silicon nitride film before and after 400°C 5 min. RTA.

Abstract No. 279

Silicon Dioxide and Silicon Nitride Films in Integrated Circuit Technology

Edward H. Nicollian
University of North Carolina at Charlotte, Charlotte, N.C. and Microelectronics Center of North Carolina, Research Triangle Park, N.C.

1.0 Introduction

Emphasis in this talk will be on silicon dioxide and silicon nitride films because these two dielectrics are the most widely used in modern integrated circuit technology. Their uses and the chemical and electrical properties that result in their widespread use, and the methods of preparation that produce the properties desired are the major topics of this talk.

2.0 Silicon Dioxide

The thermal oxidation of silicon is one of the key processes of modern integrated circuit technology. No known insulator - semiconductor system can be fabricated with electrical properties that maximize transistor and diode performance, yield, and stability to the same extent as the thermally grown silicon dioxide - silicon system. Thermally grown silicon dioxide is used: (1) to passivate or render the silicon surface electrically neutral and inert in planar bipolar transistors and p-n junction diodes, (2) for gate dielectric in unipolar transistors, (3) to isolate one device from another, (4) to isolate multiple levels of device interconnection from one another and from the substrate, and (5) as a mask against dopant impurities during integrated circuit processing.

Thermal oxides are usually grown in a resistance heated furance held at a temperature around 1000 ^{o} C by a temperature controller, a cylindrical fused quartz tube in which the silicon wafers are placed, and a source of either pure dry oxygen or pure water vapor. It has been experimentally demonstrated that an oxidizing species moves through a previously grown oxide film and reacts with the silicon at the silicon-silicon dioxide interface. Therefore, the valence bonds of the silicon surface atoms are satisfied by the silicon atoms below the surface and by oxygen atoms above the surface. However, a small density, typically one atom in a thousand silicon surface atoms, of electrically active defects is observed. Such defects are likely to be formed because the oxide occupies a volume about 2.2 times the volume of the silicon from which it forms. Defects are formed to accommodate this volume expansion. Because of the extreme sensitivity of the silicon surface to small amounts of charge, even such a small density of electrically active defects is undesirable. The defects are minimized by annealing, described in the talk, to acceptable levels of about one defect in about 100,000 silicon atoms. The defect densities can be maintained at such low levels by encapsulation with a thin film of silicon nitride.

3.0 Silicon Nitride

Because silicon nitride is a much denser material than silicon dioxide, it is used as an oxygen barrier or mask in integrated circuit fabrication, and a sodium barrier to maintain integrated circuit stability against environmental contamination during operation. Used as an oxidation mask, it is possible to have oxide isolation rather than junction isolation resulting in reduced device size. The oxidation masking feature also allows self-alighment and simplified masking that translate into higher yields and lowered costs. The most commonly used method to deposit thin films of silicon nitride is chemical vapor deposition from a gaseous mixture of either silane or silicon tetrachloride diluted to 1-3% in hydrogen and ammonia. The volatile silicon compound, silane or silicon tetrachloride, reacts with the ammonia at temperatures above 850 ^{o} C to form silicon nitride which then deposits on the substrate to form a continuous film.

Abstract No. 280

Oxide Thickness Dependence of Nitridation and Oxidation Reactions at a Si-SiO_2 Interface

S. I. Raider
IBM T. J. Watson Research Center
Yorktown Heights, N.Y. 10598

Deal and Grove (1) proposed that oxide growth rates are separable into two oxide thickness regimes. In their model, growth of thick oxides is limited by oxygen diffusion to the interface whereas growth of thin oxides is limited by the rate of the interfacial reaction and is independent of oxide thickness. However, during thin oxide growth in dry O_2, the oxidation rates deviate from this model (1). An anomalously high growth rate is observed which decreases with increasing film thickness. Many models were proposed to account for the thin oxide growth rate dependence on oxide thickness but no single model is generally accepted. This remains a key unanswered question in Si oxidation kinetics.

The effect of SiO_2 film thickness on alternate reactions at a Si-SiO_2 probes those factors that affect thin SiO_2 growth. The reaction between Si and SiO_2, in which the reactants are at the interface, is dependent on thermal oxide film thickness (2). Similarly, the nitridation reaction at a Si-SiO_2 interface with N_2 is thickness dependent (3). Reactant transport to the interface is not rate-limiting for either reaction. The observed thickness dependencies are separable into two oxide thickness regimes that are comparable to the regimes in the Deal and Grove model. A mechanism, which is applicable to thin oxide growth in O_2, is proposed for the thickness dependencies of the interfacial oxidation and nitridation reactions.

References

1. B.E. Deal and A.S. Grove, J. Appl. Phys., *36*, 3770 (1965).
2. S.I. Raider, unpublished results.
3. S.I. Raider, R.A. Gdula and J.R. Petrak, Appl. Phys. Lett., *27*, 150 (1975).

Abstract No. 281

THIN GATE OXIDES GROWN IN ARGON DILUTED OXYGEN WITH STEAM AND HCL TREATMENT

Frank Bryant and Fu-Tai Liou
SGS-Thomson Microelectronics
1310 Electronics Drive, MS2200
Carrollton, Texas 75006
214/466-6000

Introduction

The effects of shrunk process technologies at constant gate operation voltages on the quality requirements of gate oxides has provided an enormous challenge to state of the art technology in semiconductor manufacture. This paper presents the results of an effort to improve gate oxide quality through process modification with the goal to provide a manufacturable growth technique for thin gate oxides around 175A with the use of dilute steam treatment during the oxidation, followed by an anneal in dry oxygen.

Experimental Methods

The method of time-zero dielectric reliability determination by ramp voltage to breakdown (1,2) was extensively used for first order growth technique comparison. Also used were a forced current method while monitoring the voltage across the oxide in time, before and after stress I-V comparisons, and Vfb shifts after constant current stressing. Finally, transistors were built and performance comparisons were made between standard gate oxidation process techniques and experimental techniques.

A range of capacitor sizes from 6.35E-2 cm2 to 6.35E-4 cm2 was constructed on silicon wafers to examine as grown oxide quality. The capacitor edges terminated on thick oxide to prevent influence from high fields at the top capacitor plate edge. A two photomask sequence and standard process technique was used in fabrication. The samples were processed together except at the oxidation step, but the same equipment was used to grow the various oxides. Once an as grown oxide quality improvement was seen on the capacitors, transistors were built using a 0.8um CMOS technology to examine the oxide's sensitivity to full process. Also examined was the influence of the oxidation technique on the operation parameters of the transistor.

Results and Discussions

Field breakdown distributions from large capacitors were used to generate TDDB plots based upon the assumption that the time required for dielectric breakdown of an oxide depends exponentially on the applied electric field, i.e. log t(F)=logt (R)+γ[Eb-Ea]; where: t(R) = 1/(ln10) (γ) (ramp rate), γ = the field acceleration factor (3), Eb = the breakdown field and Ea = the desired operating field. By this method, a 5V oxide pinhole density and latent defect densities from TDDB plots, for the as grown oxides could be determined. The steam/anneal treated oxides have a two-fold improvement in the pinhole density (ln Y = exp [-AD], Y = yield, A = area, D = defect density) using a total test area of over 10 cm2 per sample wafer. A 70 times improvement is seen in the 3000 hour defect density, about 35 FITs calculated from the TDDB plots. Field breakdown distributions from small capacitors gave us comparisons of the intrinsic breakdown of the oxides. Small capacitors on the as grown test vehicle as well as the capacitors built with fully processed devices have higher field breakdown values when the oxides are grown with the steam/ anneal techniques rather than in dry oxygen.

I-V curve comparisons of dry and steam/ anneal treated oxides show little difference in Fowler-Nordheim electron tunneling at voltage ramp rates of 0.7 volts/second.

CV measurements were taken before and after several current density stresses (2E-4 amps/cm2 range) were applied to capacitors. Vfb shifts and voltage drift to maintain a constant leakage current through the oxide show that the steam/anneal oxides have lower electron trap densities than the dry oxides (4,5). Constant leakage current tests also showed longer times to fail for a given current density for the steam/anneal oxides. Transistors built to 0.8 um CMOS technology with the experimental technique show little difference in the Vt, Gm or BVDII from standard process. The breakdown fields of n+ and p+ finger structure capacitors on the completed devices also are similar between the dry and steam/anneal growth techniques.

Summary

A thin gate oxide process has been developed and illustrated, which improves 0.8 um CMOS device yield and reliability. The growth technique used to improve the gate oxide quality involves a diluted oxygen in argon step at the beginning of the growth cycle, followed by the addition of hydrogen and chlorine. The third step of oxidation involves an anneal in dry oxygen before the ramp down in argon. The stability of the DC parameters of the CMOS transistors is believed to be due to the fact that the interfaces are of oxides grown from dry oxygen.

References

(1) A. Berman, 19th Annual Proc. Rel. Phys. Symp., pp. 204-209, 1981.
(2) F. Bryant, F.T. Liou, Y.P. Han, J.J. Barnes, "Thin Dielectric Quality/Yield Study Using a Constant Voltage Ramp Method," submitted for publication.
(3) J.W. McPherson, D.A. Baglee, Proc. 23rd Annual IEEE/IRPS, 1985.
(4) D.J. DiMaria, Proc. International Topical Conf. Phys. SiO2 and Its Interfaces, pp. 160-178, 1978.
(5) W.K. Meyer, D.L. Crook, Proc. 21 Annual IEEE/IRPS, 1983.

Abstract No. 282

THE ROLE OF SACRIFICIAL OXIDATION ON THE INTEGRITY OF THIN (20nm) GATE OXIDE.

Iftikhar Ahmed, Hussein Naguib, and Carlos Gomez
Xerox Microelectronics Center, 701 South Aviation Blvd, El Segundo, CA 90245

INTRODUCTION

The oxidation process recipe is an important factor in determining the integrity of thin gate oxides (1). A sacrificial oxidation step before the gate oxidation of MOS devices is also known to improve the oxide integrity(2, 3, 4). However, the relative improvement in gate oxide integrity from different gate oxide processes in conjunction with different sacrificial oxidation processes is not known. To this end, experimental splits with two different sacrificial and gate oxidation processes were performed. The splits included wafers which were slightly damaged by reactive ion etching during nitride etching process after field oxidation step (4,5).

It is shown that the gate oxide integrity is a function of sacrificial oxidation process as well as of the final gate oxidation recipe. Improvements in gate oxide breakdown was observed for slight etching(20nm) of silicon in agreement with results reported in reference (3, 5).

EXPERIMENTAL METHODOLOGY

A specially designed test structure containing large number of MOS capacitors with areas ranging from 0.01 mm^2 to 10 mm^2 was used in this work. The devices were fabricated by growing first an initial pad oxide of 250 Å thickness on p-type <100> 20 Ω-cm resistivity wafers. A CVD nitride film of 1200 Å thickness was deposited and patterned to define field oxidation windows on silicon prior to gate oxidation process. To simulate a CMOS fabrication cycle, an n-well ion implant was carried out with doubly ionized phosphorous ions at beam energy of 300 KeV. Also, a phosphorous n-well field implant was performed at 40 KeV. The ion implantation was followed by a dry oxidation cycle at 900 °C for 150 minutes and a well drive cycle in N_2 at 1150 °C for 140 minutes. Boron field implant was then performed at 65 KeV, followed by field oxidation cycle at 1000 °C for approximately five hours.

After field oxidation, the wafers were divided into three groups and processed according to the schematics shown in Fig. 1. Tables 1 and 2 show the sacrificial and gate oxidation recipes used for this split. At the end of the gate oxidation, the wafers were combined together and processed as a single lot. After polycide (CVD WSi/poly) and cap oxide depositions, contact windows were opened to polycide gate for electrical measurements. A forming gas anneal was done at 450 °C for 20 minutes before measurements.

The oxide breakdown (V_{ox}) measurements were performed on Kiethly system 300 parametric tester. The voltage was increased in 1 volt steps until a current of .1um was reached. This was taken as the breakdown criterion for 20nm thick oxide. A mean breakdown voltage of 18 volts was obtained for good devices. However, for statistical analysis of breakdown data, a V_{ox} of 15 volts was taken as 80 % yield value for the 20 nm thick gate oxide.

RESULTS AND DISCUSSION

A total of 28,000 devices were probed and analyzed for this experiment. The defect densities were calculated by plotting yields vs device area for different recipes as shown in Fig. 2. Poisson distribution function was used to calculate the defect densities.

A graph of calculated defect density for each of the different area test structures against the edge/area ratio is shown in Fig. 3 for some of the results shown in Fig. 2. It appears from Fig. 3 that the edge to area ratio is the controlling factor for increased defect density for small area devices. It may also be concluded that the edge defects are the dominant defects removed after sacrificial oxidation process. This extreme edge/area dependence of small area devices accounts for the data point deviation from graph lines of Fig. 2 for oxides without sacrificial oxidation process compared to the oxides with sacrificial oxidation process. Straight line behavior of data points in Fig. 2 further shows that simple Poisson distribution function is adequate to evaluate the gate oxide defect densities from results of thin gate oxide ($T_{ox} \leq$ 200 Å) experiments.

Table 3 summarizes the results of average defect densities obtained for each split performed. The relative improvement in dry oxide defect density after sacrificial oxidation process is significant compared to wet oxide. Unlike dry gate oxide results, the defects from wet oxide do not seem to have been removed significantly after sacrificial oxidation process. These results indicate that the defect removal after the sacrificial oxidation process is a strong function of final gate oxidation recipe. In these splits two different sacrificial oxidation recipes were used as shown in Table 1 and Table 2. One of these had no anneal and had short wet oxidation process compared to the other recipe. Despite these differences, no advantage of one of these recipe over the other in removing defects from gate oxide was observed, indicating that the final gate oxide recipe is relatively more important in removing the defects from these devices.

Another important split for this lot has been the silicon etching at the nitride etching step after field oxidation. The results for this split are shown in Table 3. Apparently a marked improvement in oxide breakdown is observed after silicon etching. These results are in agreement with results reported by Itsumi et al and D. Jullie (3, 5). A cautious conclusion is that the slight silicon surface etching can help improve the thin gate oxide integrity.

CONCLUSION

The greatest impact of sacrificial oxidation process is observed on gate oxide grown with dry process compared to wet process as most of the non random defects are completely eliminated from oxide after sacrificial oxidation process. No significant difference in oxide integrity is observed if sacrificial oxidation recipe is changed from wet to dry/wet oxidation recipe with or without anneal. It is also shown that gate oxide integrity is improved if there is slight etching of silicon prior to gate oxidation process. However, no further improvement in gate oxide integrity is observed with sacrificial oxidation process once the reactive ion etching of silicon has taken place. Finally, it has been shown that simple Poisson distribution is quite adequate for defect analysis of thin gate oxide.

ACKNOWLEDGMENT

The authors are greatly indebted to N. Matz for her assistance in oxide breakdown measurements.

REFERENCES

1 R. G. Cosway; J. Electrochem. Soc., 132, 3052, (1985).
2 H. S. Lee; Solid State Electron., 29, 25, (1986).
3 M. Itsumi and F. Kiyosumi; J. Electrochem. Soc., 129, 800, (1982).
4 N. Liftshitz; J.Electrochem.Soc., 130, 1550, (1983).
5 D. Jullie; J. Electrochem. Soc., Ext. Abs., 681, 962, (1987).

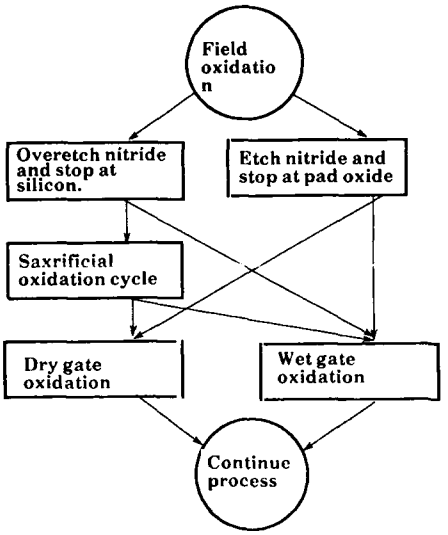


Fig. 1 Schematicss of the splits used to study sacrificial oxidation effects on gate oxide quality.

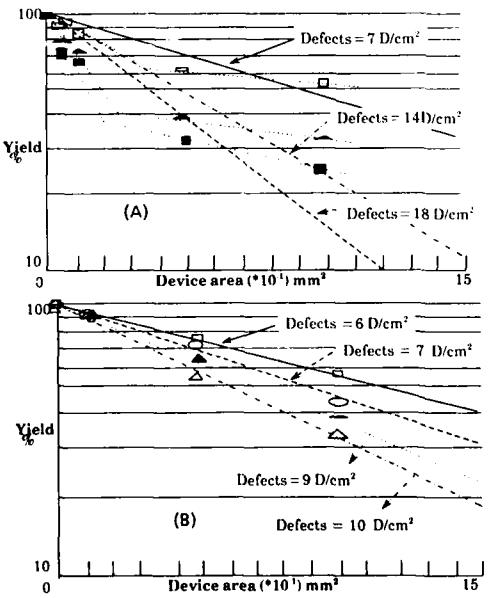


Fig. 2. Typical plots of yield vs device area of different wafers from the same lot. Each straight line represents data from a single wafer. A): Dry gate oxide without sacrificial oxide. Dotted lines show two slope behavior of plotted data. B): Dry gate oxide with sacrificial oxide. Note the reduction in defect density and collinearity of data points for group (B) compared to group (A) wafers.

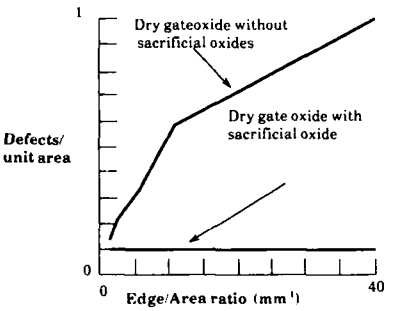


Fig. 3 Change in defect density with respect to change in the edge to area ratio of MOS devices.

Table 1. Sacrificial oxidation recipes

Dry/wet recipe	Dry oxidation in O_2 at 900 oC for 5 min Wet oxidation in O_2 + H_2 + HCl for 5 min. Anneal in N_2 at 9000 °C for 15 min
Wet recipe	Wet oxidation in O_2 + H_2 + HCl for 11.5 min at 800 °C No anneal

Table 2. Gate oxidation recipes

Dry gate oxide recipe	Dry oxidation in O_2 + HCl at 950 °C for 22 min Anneal in N_2 at 950 °C for 15 min.
Wet gate oxide recipe	Wet oxidation in O_2 + H_2 + HCl for 11.5at 850 °C Anneal in N_2 at 1000 °C for 20 min

Table 3. Defect densities tabulated against the splits performed in this experiment.

Split type	Defect density
Wet oxide with sacrificial oxide	1.0
Wet oxide without sacrificial oxide	1.0
Dry oxide without sacrificial oxide	1.0
Dry oxide with sacrificial oxide	0.7
Etched silicon with sacrificial oxde	0.4
Etched silicon without sacrificial oxide	0.4

Abstract No. 283

Vacancy Generation at the Si/SiO_2 Interface Caused by SiO Formation

S. T. Ahn, H. W. Kennel, J. D. Plummer† and W. A. Tiller

Department of Materials Science and Engineering
† Integrated Circuits Laboratory
Stanford University, Stanford, CA 94305

At high temperatures and low oxygen partial pressures, the decomposition of SiO_2 can occur by reacting with Si supplied from the substrate to form volatile SiO, $Si + SiO_2 \rightarrow 2\,SiO$[1]-[3]. As Si atoms cross the Si/SiO_2 interface to form SiO, excess vacant lattice sites will be left. Thus, the Si/SiO_2 interface could act as a vacancy source when annealed in an inert atmosphere at high temperature. A vacancy supersaturation in Si would lead to retarded diffusion of P and enhanced diffusion of Sb, since P and Sb are known to diffuse predominantly by interactions with self-interstitials and vacancies[4], respectively. It would also lead to an accelerated shrinkage of extrinsic stacking faults[5]. It is the purpose of this work to identify if there is vacancy generation during SiO formation by observing P and Sb diffusion and stacking fault shrinkage.

For the dopant diffusion studies, a dose of either $10^{14}/cm^2$ P or Sb were separately implanted into p-type float zone (FZ) silicon wafers. After growing an oxide of about 40 nm thickness, LPCVD Si_3N_4 films were deposited and patterned. The resulting test structures had P or Sb uniformly implanted and alternating stripes of SiO_2 and Si_3N_4/SiO_2, as shown in Fig. 1. The annealing was done in Ar at 1100°C for 8 h. Junction profiles were subsequently observed by the angle-lapping and staining technique. For the stacking fault experiment, large stacking faults were obtained by Si^+ implantation with a dose of $5 \times 10^{13}/cm^2$ followed by thermal oxidation at 1100°C for 12 h. Stacking fault shrinkage under thin SiO_2 and Si_3N_4/SiO_2 was observed as the samples were further annealed at 1100°C in Ar.

Figure 2 shows a junction profile with P. P diffusion under the thin SiO_2 film is retarded compared to that under Si_3N_4/SiO_2 , while Sb shows the opposite behavior. It diffuses faster under SiO_2 than under Si_3N_4/SiO_2, as shown in Fig. 3. The change in the average stacking fault size with annealing time under SiO_2 and Si_3N_4/SiO_2 is shown in Fig. 4. Stacking faults under thin SiO_2 shrink much faster than those under Si_3N_4/SiO_2.

The dopant diffusion and stacking fault results obtained here strongly suggest that there is a vacancy supersaturation in Si under the SiO_2 film annealed in Ar at high temperature and that it is the result of vacancy generation at the Si/SiO_2 interface by SiO formation. The presence of Si_3N_4 on SiO_2 is expected to suppress SiO formation by blocking outdiffusion of SiO.

This work was supported by the Defense Advanced Research Projects Agency (DARPA) and the DOD VHSIC Program under Contract No. DAAL 01-86-K-0101 and by the Semiconductor Research Corporation under Contract No. SRC 87-SJ-101.

References

[1] C. Gelain, A. Cassuto, and P. LeGoff, *Oxid. Met.*, **3**, 139 (1971).

[2] R. Tromp, G.W. Rubloff, P. Balk, F.K. LeGoues, and E.J. van Loenen, *Phys. Rev. Lett.*, **55**, 2332 (1985).

[3] K. Hofmann, G.W. Rubloff, and R.A. McCorkle, *Appl. Phys. Lett.*, **49**, 1525 (1986).

[4] T.Y. Tan and U. Gösele, *Appl. Phys.*, **A 37**, 1, (1985).

[5] Y. Hayafuji, K. Kajiwara, and S. Usui, J. Appl. Phys. **53**, 8639 (1982).

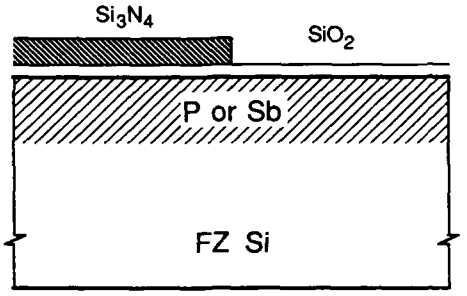


Figure 1: Test structure for dopant diffusion.

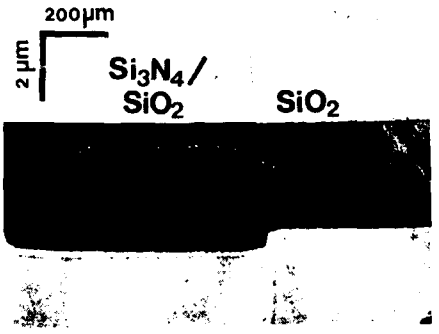


Figure 2: Phosphorus junction profile after annealing for 8 h at 1100°C in Ar.

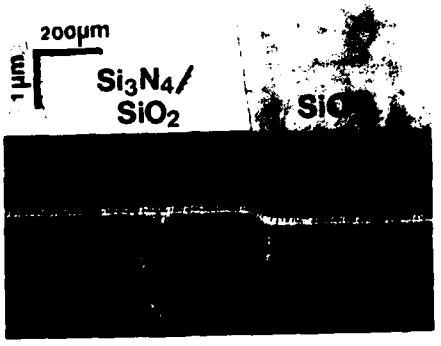


Figure 3: Antimony junction profile after annealing for 8 h at 1100°C in Ar.

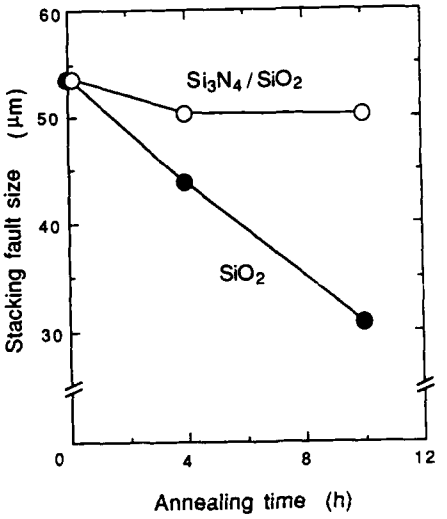


Figure 4: The change of the size of stacking faults in Si under SiO_2 and Si_3N_4/SiO_2 with annealing time at 1100°C in Ar.

Abstract No. 284

Film Stress and Atomic Misfit Effect on Dopant Junction Profiles in Silicon

C.K. Huang and R.J. Jaccodine
Sherman Fairchild Center for Solid State Study
Lehigh University, PA 18015

In VLSI processing, thermally grown SiO_2 is extensively used as a dielectric film and LPCVD nitride (Si_3N_4) is used as a passivation or isolation layer. However, LPCVD nitride is known to be in a state of high intrinsic film stress which can not be relaxed even at 1000°C. Hence, direct deposition of nitride on bare silicon is shown to generate dislocations [1,2] or even crack the wafer [3] if film thickness is not properly controlled. Therefore, a pad oxide is used to reduce or compensate the stress resulting from LPCVD nitride. Even though a pad oxide can effectively reduce the stress from LPCVD nitride, the discontinuous film edge has been shown by x-ray topography [4-7] or x-ray diffraction theory on Pendellösing fringes [8-10] to introduce stress in the substrate which can not be eliminated at high temperature. Another common stress source in VLSI processing is atomic misfit which results from the tetrahedral radius difference between an impurity species and the Si matrix. Misfit dislocations are generated [11,12] with increasing impurity concentration. This study is designed to reveal the combined effect of film edge and atomic misfit on dopant diffusion.

In order to reveal film edge effects, a mask with different window widths ranging from 200μm to 1μm is used. The film is composed of LPCVD nitride/pad oxide layer with thickness ratios varying from 1.1 to 7.0. Dopant species (boron, arsenic, and antimony) are implanted uniformly into the substrate before the windows are open. The annealing is always carried out in N_2 atmosphere in a double wall furnace system. This sequence allows us to compare directly thediffusion at window edges with a control area under the dual insulators.

Figure 1 shows a typical angle lapped and stained boron junction profile with an implantation dose of $3 \times 10^{15}/cm^2$ on (100) wafer. Thickness ratio of LPCVD nitride and pad oxide is 6.5 and window width is 200μm. Retardation or "cusp" junction profiles are observed at the vicinity of film edge. The interaction of adjacent film edges on junction profiles was observed [13] with decreasing window width. This retardation or cusp junction profile is mainly observed at an implantation dose above 3×10^{14} and for nitride/oxide ratios larger than 4.4.

Figure 2 shows similar test structure of antimony junction profiles with an implantation dose of $2.5 \times 10^{15}/cm^2$ on (111) wafers. The LPCVD nitride/pad oxide ration is 3.3 and window width is again 200μm. Enhancements or "down cusp" junction profiles were observed. This effect is opposite to boron. With thinner nitrides, no such enhancement was observed.

For arsenic with an implantation dose of $1 \times 10^{16}/cm^2$ on (100) wafers, no junction profile abnormality can be found even at LPCVD nitride/pad oxide ratios which yield effects with boron and antimony. Typical arsenic out diffusion can be observed only after a long annealing time.

The results obtained here show clear evidence of dopant species and concentration dependence of junction profiles in window regions. It is plausible that the observed junction profiles for boron and antimony are related to the film edge induced elastic stress field on the substrate. However, it is observed that the combination of atomic misfit and film edge induced stress can exceed the critical shear stress of silicon and hence generate dislocations. The observed abnormal " cusp " for boron and " down cusp " for antimony are accompanied by a very dense array of dislocations along the film edge. It is proposed that the observed effects are related to the influence of combined misfit and window edge stresses as well as the generation and movement of dislocations.

REFERENCES

1. S. Isomae, Y. Tamaki, A. Yajima, M. Nanba and M. Maki, J. Electrochem Soc.,126, 1014 (1979).
2. I. Magdo and A. Bohg, J. Electrochem. Soc.,125, 932 (1978).
3. S. Wolf and R.N. Tauber, SILICON PROCESSING FOR THE VLSI ERA, Vol.1 : Process Technology, Lattice Press, Unset Beach,CA,1986, P.109.
4. I.A. Blech and E.S. Meieran, J. Appl. Phys.,39, 2913 (1967).
5. G.W. Schwuttke and J.K. Howard, J. Appl. Phys.,39, 1581 (1968).
6. J.R. Patel and N.Kato, Appl. Phys. Lett.,13, 40 (1968).
7. E.J. Saccocio, Appl. Phys. Lett.,17, 149 (1970).
8. N. Kato and J.R. Patel, J.Appl. Phys.,44, 965 (1973).
9. J.R. Patel, and N.Kato, J. Appl. Phys.,44, 971 (1973).
10. Y. Ando, J.R. Patel and N. Kato, J. Appl. Phys.,44, 4405 (1973).
11. S. Prussin, J. Appl. Phys., 32, 1876 (1961).
12. H.J. Queisser, J. Appl. Phys., 32, 1776 (1961).
13. C.K. Huang and R.J. Jaccodine, Appl. Phys. Lett., to be published (1988).

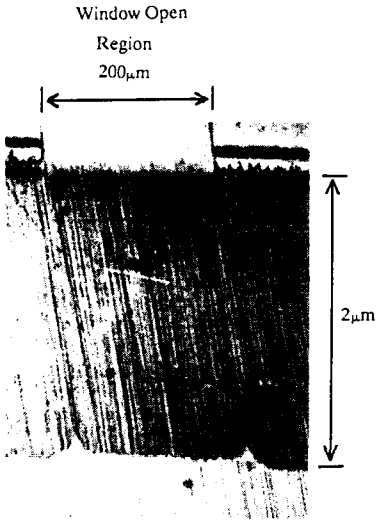


Figure 1. The window edge effect on boron junction profiles. Thickness ratio of LPCVD nitride and pad oxide is 6.6 (3172Å/484Å). Window width is 200μm. Retardation or "cusp" can be observed at the vicinity of film edge. Lapping angle : 0.33°. Magnification : 200X .

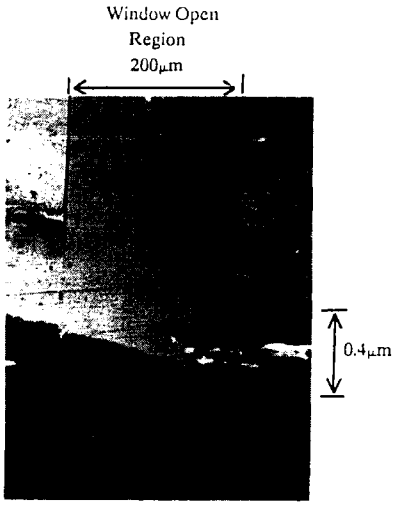


Figure 2. The window edge effect on antimony junction profiles. Thickness ratio of LPCVD nitride and pad oxide is 3.3 (3025Å/922Å). Window width is 200μm. Enhancements or "down cusp" junction profiles exist at the vicinity of film edge. Lapping angle : 0.20°. Magnification : 200X .

Abstract No. 285

LPCVD OXIDE FILM EVALUATION FOR INTERMETAL DIELECTRIC

S. Mittal, C. Chiang, R. Hsu, L.C. Yip*, D. Fraser, and A. Haranahalli

Intel Corporation
Santa Clara, California 95052

*currently at U.C. Berkeley, California.

INTRODUCTION

In this work, LPCVD oxide films have been evaluated for use as an intermetal dielectric film. For use as an intermetal dielectric, the LPCVD film must meet requirements of good integrity and not affect susbsequent metal quality. This work was initiated because LPCVD film substrates were found to degrade the quality of metal deposited on the glass. Degradation of metal quality by LPCVD oxide substrates has been previously observed (1). The degraded metal film quality was reflected in poor electromigration performance of the metal lines.

EXPERIMENT

Low temperature LPCVD oxide films of varying phosphorus concentrations (0%, 2%, 4%, and 8%) were deposited on bare Si wafers with an vertical LPCVD reactor. Stress and FTIR spectrum of the LPCVD oxide films was monitored as a function of time from deposition. Al-1%Si was sputtered on another set of oxide wafers which had been allowed to "age" in air for different periods in time. After Al-1%Si deposition, the reflectance and residual resistance ratio (R^2) of the metal was measured. R^2 is the ratio of metal sheet resistance at room temperature to that at liquid nitrogen temperature.

RESULTS

Metal film quality turned out to be the most sensitive monitor of LPCVD oxide substrate integrity. The variation in Al-Si R^2 with phosphorus concentration in the oxide substrate is shown in Figure 1. The 8% P oxide did not appear to degrade metal film quality at all, while the 4% P oxide substrate resulted in the worst metal film quality. Stress measurements showed no change in oxide film stress (20 MPa to -20 MPa) for any of the films over a period of three weeks. Also, the stress temperature ramp for the 0% P glass showed no hysteresis as a function of temperature (room temperature to 600C) as shown in Figure 2. FTIR spectrum showed the presence of -OH in all the LPCVD oxide films except for the 8% P glass. Even after 3 weeks of exposure to air, the FTIR spectrum of the 8% P oxide film showed no -OH peaks.

The model to explain this behavior is that the moisture concentration is significant only near the surface of these LPCVD oxide films and this moisture appears to be loosely bonded to the glass. During subsequent metal sputter deposition, the moisture outgasses and results in poor metal film quality. Since the moisture exists predominantly close to the glass surface, it does not significantly affect the oxide film stress and make it more compressive, as would be expected from absorption of moisture into the bulk of the glass. Finally, LPCVD oxide films dipped in a buffered HF solution immediately prior to metal deposition (to remove ~1000A of the glass surface) resulted in improved R^2 of the Al-Si by approximately 0.5, again, indicating high surface concentration of moisture. To better understand the mechanism by which phosphorus concentration in the glass substrate affects metal quality we are undertaking moisture emission analysis and further FTIR measurements of these films.

CONCLUSIONS

Phosphorus concentration of LPCVD oxide film substrates was found to have a strong effect on subsequent metal film quality. According to the proposed model, the absorption and subsequent outgassing of moisture at the surface was found to degrade metal quality on low phosporus LPCVD oxide substrates.

ACKNOWLEDGEMENTS

Thanks to M. Rebugio for doing the R^2 and reflectance measurements on the metal. Also, thanks to J. Pr[illegible] for helping with the LPCVD depositions a[illegible] FTIR measurements, and to N. Cox for moistu[illegible] emission analysis.

REFERENCE

1. Y.S. Lin, Private communication, 1987.

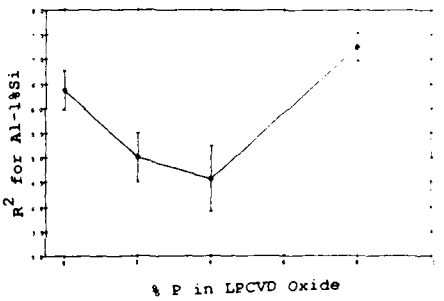


Fig. 1: R^2 of Al-1%Si as Function of Phosphorus Concentration in LPCVD Oxide.

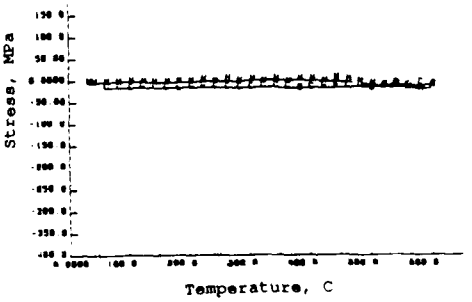


Fig. 2: Stress Temperature Ramp for 0% P LPCVD Oxide.

Abstract No. 286

Oxygen Diffusion in Vitreous Silica and Thermal Oxide Films

James D. Cawley
Department of Ceramic Engineering
The Ohio State University
2041 College Road
Columbus OH 43210-1178

Introduction

Despite the fact that oxygen diffusion in vitreous silica has been widely studied over the past thirty years, contradictions continue to surface in the literature. Reported activation energies range from 82 to 454 kJ/mol and the range in the absolute magnitude of reported diffusion coefficients covers several orders of magnitude at any particular temperature. In addition, it has been argued that the oxygen transport mechanism in thermally grown silica films is qualitatively different than in bulk vitreous silica. As a result of oxygen-18 tracer studies in bulk vitreous silica, double oxidation experiments on single crystal silicon, and determination of electric potentials generated during thermal oxidation of molybdenum disilicide, we have concluded that oxygen is mobile by two independent mechanisms, one involving step wise motion within the network oxygen and the other involving the motion of dissolved interstitial oxygen. The fractional concentration of oxygen-18 is not, in general, at equilibrium between the two types of oxygen.

Double Oxidation

Two sets of double oxidation experiments have been carried out. In these experiments a sample of single crystal silicon is oxidized in an atmosphere of natural oxygen to grow a thermal oxide film roughly one half micron, the atmosphere is then switched to one enriched in oxygen-18 and oxidation is allowed to continue. The distribution of the oxygen-18 within the final oxide film is determined using either SIMS or NRA.

A SIMS profile (showing the absolute counting rates for mass-16 and mass-18 as a function of distance) on a specimen oxidized for 3.4 hr in natural oxygen followed by oxidation for 15 hr in an oxygen-18 enriched atmosphere at 1000°C is shown in figure 1. Two regions of oxygen-18 enrichment are observed: one near the free surface of the thermal oxide and the other at the interface between the silicon and the oxide. The enrichment near the free surface is ascribed to gas exchange and diffusion via the network oxygen. The enrichment near the silicon is ascribed to permeation of the thermal oxide by interstitial oxygen which does not undergo a tracer exchange reaction with the network. This indicates that oxygen is mobile by two distinct mechanisms in the glass structure. As such it is appropriate to model the development of the concentration profile as the sum of two independent solutions to the diffusion equation.

More recent work has shown that at temperatures in excess of 1100°C substantial network-interstitial isotope exchange occurs, as can be seen in figure 2. The consequence of network-interstitial exchange is to add an additional term in the governing partial differential equation:

$$\frac{\partial C}{\partial t} = D\frac{\partial^2 C}{\partial^2 x} + \beta(C\text{-}1)$$

A solution to this equation, involving three constants: a surface exchange coefficient; a network oxygen diffusion coefficient, D, and a network-interstitial exchange coefficient, ß, was developed, analyzed, and applied to the observed concentration profiles.

Self-Diffusion in Vitreous Silica

Gas exchange experiments were carried out with high purity bulk vitreous silica samples over the temperature range of 800-1200°C. The resultant oxygen-18 profiles are qualitatively consistent with the results obtained from double oxidation. Samples exchanged at low temperatures have concentration profiles which are well fit by a complementary error function while those exchanged at high temperture (see figure 3) display a deeply penetrating low level "tail" as expected with network-interstitial exchange.

It is concluded that the same processes are operative in both bulk vitreous silica and thermal oxide films although the relative rates of the process differ somewhat in magnitude.

Electric Potential Development Across Growing Thermal Oxide

Tracer results suggest that oxidation is solely the result of oxygen motion via an interstitial mechanism, i.e. that oxygen moving through the network does not contribute. It hypothesized that this is observed because the network transport requires the motion of charged defects while the interstitial transport is by neutral molecules. If the transference number of the oxide is sufficiently close to one a space charge will rapidly develop which opposes the oxygen chemical potential gradient and the driving force for network diffusion is restricted to the tracer concentration gradient. Experimental measurements found that significant voltages are developed across a thermal oxide scale on a rod of $MoSi_2$ at temperatures on the order of 1000°C indicating that this is a reasonable interpretation.

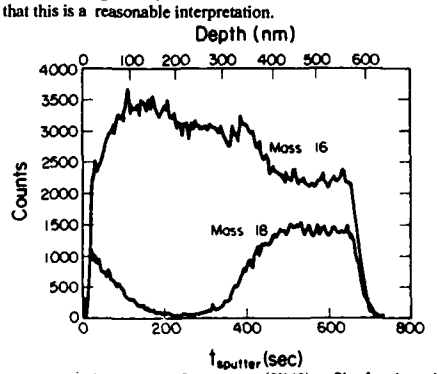


Figure 1. Secondary Ion Mass Spectrometry (SIMS) profile of an thermal oxide film grown under natural oxygen for 3.4 hours and an oxygen-18 atmosphere for 15 hours at 1000°C.

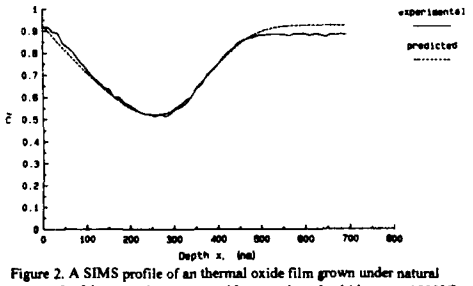


Figure 2. A SIMS profile of an thermal oxide film grown under natural oxygen for 3 hours and an oxygen-18 atmosphere for 14 hours at 1200°C. The dashed line represents the best fit to the profile using a solution to the diffusion equation which accounts for network-interstitial exchange.

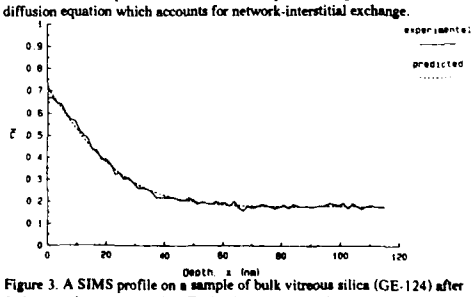


Figure 3. A SIMS profile on a sample of bulk vitreous silica (GE-124) after 24 hour exchange at 1100°C. The "tail" is well described using a solution which includes network interstitial exchange.

Abstract No. 287

Infrared Dielectric Model for Silicon Dioxide Thin Insulating Films

C. T. Kirk

M.I.T. Lincoln Laboratory
Lexington, MA 02173

INTRODUCTION

This paper is concerned with the quantitative interpretation of the infrared dielectric function of thin amorphous silicon dioxide (a-SiO_2) films.

With the discovery[1] of the longitudinal optic (LO)-transverse optic (TO) frequency splitting of the vibrational modes in tetrahedral glasses and a-SiO_2 in particular, certain problems have arisen concerning some of the infrared vibrational modes of a-SiO_2. These problems pertain to the frequency assignment of it's highest frequency LO mode[1,2] and to the origin and nature of the optical mode that corresponds to highest frequency peak in it's vibrational density of states (VDOS) spectrum.[3,4] Added to these problems, as will be shown, is the problem of making a correct determination of the strength of the TO mode associated with the highest frequency LO mode of a-SiO_2.

This paper shows how a reinterpretation of the a-SiO_2 infrared dielectric behavior to include the LO-TO frequency splitting of an additional vibrational mode can remove these disagreements in frequency and mode assignments and allow the correct determination of the TO mode strength.

DISCUSSION

The infrared dielectric behavior of a-SiO_2 is analyzed in terms of it's optically active LO-TO vibrational modes. It is found that the usual, three optical mode, independent oscillator model fails to model the infrared dielectric function of a-SiO_2 correctly. In particular, it is found that the three mode dielectric function for a-SiO_2 fails to yield a consistent value of mode strength for the optically active oxygen asymmetric stretch (AS_1) TO mode at 1075 cm^{-1} (in-phase motion of adjacent oxygen atoms) when different but equivalent methods of measurement and analysis are used.

This inconsistency is resolved by introducing "disorder-induced" mechanical coupling between the AS_1 mode and the relatively optically inactive oxygen asymmetric stretch (AS_2) mode (out-of-phase motion of adjacent oxygen atoms) into the oscillator model for the dielectric function. As a result, this coupling gives rise to a fourth optically active mode in a-SiO_2 with an inverted LO-TO frequency pair spectrum.

Coupled AS_1 and AS_2 mode LO-TO frequency pairs are experimentally observed as peaks at approximately 1256 - 1076 cm^{-1} and 1160 - 1200 cm^{-1}, respectively, in oblique-incident p-polarized absorption spectra of thin a-SiO_2 films grown thermally on c-Si wafers. Additionally, two other LO-TO mode pairs are observed in these spectra as absorption peaks at approximately 820 - 810 cm^{-1} and 507 - 457 cm^{-1}.

Analysis shows that the simplest form of the coupled-mode model consistent with experimental results is one in which LO-TO frequency splitting of the AS_1 vibrational mode is due to the relatively large transverse effective charge that is associated with this mode whereas the splitting of the AS_2 mode is due to the mechanical coupling between these two modes and not to the transverse effective charge that is associated with the AS_2 mode which is negligibly small. The nature of the vibrational modes at approximately 1200 and 1256 cm^{-1} is resolved and shown to be the AS_2 TO and the AS_1 LO modes, respectively, consistent with experimental results and analytic requirements that LO and TO modes be interspersed and that as a result of lying between the LO-TO frequencies of the AS_1 mode the LO-TO frequency splitting of the AS_2 mode be inverted.

Comparison of these experimental LO-TO mode pair frequencies with the VDOS spectrum of a-SiO_2 shows that the VDOS spectral peaks correspond quite well with the AS_1 and AS_2 TO absorption peaks and that no salient VDOS spectral features correspond with the AS_1 and AS_2 LO absorption peaks. The results of this comparison are consistent with a recently published numerical simulation study of LO-TO frequency splitting of vibrational modes in AX_2 type glasses.[4] In that study, it is shown that TO modes produce peaks in the VDOS spectrum but because of the strongly negative dispersion of the LO modes there are no LO peaks in the VDOS spectrum.

CONCLUSION

An optically active fourth vibrational mode with an inverted LO-TO frequency spectrum is found in a-SiO_2 and shown to be due to "disorder-induced" mechanical coupling of the two AS modes. This fourth optical mode is able to resolve the problem of the frequency assignment of the highest frequency LO mode of a-SiO_2, putting it at 1256 cm^{-1}. It is able to allow the making of a correct determination of the strength of the 1076 cm^{-1} TO mode associated with the highest frequency LO mode of a-SiO_2. Finally, this fourth optical mode is able to explain the origin and TO nature of the optical mode that corresponds to the highest frequency peak in the VDOS spectrum of a-SiO_2 at $\approx$1200 cm^{-1}.

ACKNOWLEDGEMENT

This work was sponsored by the Department of the Air Force. The views expressed are those of the author and do not reflect the official policy or position of the U.S. Government.

REFERENCES

[1] F. L. Galeener and G. Lucovsky, Phys. Rev. Lett. 37, 1474 (1985).

[2] V. N. Denisov, B. N. Mavrin, V. B. Podobedov, and Kh. E. Sterin, Sov. Phys. Solid State 20, 2016 (1978).

[3] F. L. Galeener, A. J. Leadbetter, and M. W. Stringfellow, Phys. Rev. B 27, 1052 (1983).

[4] S. W. de Leeuw and M. F. Thorpe, Phys. Rev. Lett. 55, 2879 (1985).

Abstract No. 288

ELLIPSOMETRIC STUDY OF THE STRUCTURE OF SIMOX

B. J. Mrstik, P. J. McMarr,* and V. M. Bermudez
Naval Research Laboratory
Washington, D.C. 20375

I. Introduction

The usefulness of SIMOX (Separation by IMplanted OXygen) material as substrates for radiation hard devices depends upon the quality of the top Si layer, the buried oxide, and the interfaces. There have been several previous studies of the structural properties of SIMOX, including the use of XTEM (cross-section transmission electron microscopy) to determine the thickness and crystallinity of the layers, and SIMS and RBS to determine the stoichiometry of the oxide (1). Although these techniques are useful for characterizing reasonably homogeneous materials, they have limited utility for studies on materials which may contain mixtures of, for example, SiO_2 and crystalline Si.

We report here the results of a study of the structure of SIMOX using spectroscopic ellipsometry. It has been demonstrated that such measurements can be used to determine the thickness and stoichiometry of each layer of a multilayer structure as well as provide quantitative information on the extent of mixing of crystalline and amorphous material (2). In addition, the technique is nondestructive and does not require perturbative sample preparation (as does XTEM) which may affect sample quality.

II. Experimental

The samples consisted of single crystal (100) Si, implanted at near normal incidence with 2.3×10^{18} O atoms/cm^2 at 180 keV. Sample temperatures during implant- ation were maintained at 500 °C. Following preparation one sample was further annealed at 1275 °C for 2 hours. The samples were then briefly etched in dilute HF to remove the surface oxide which might have formed during implantation and annealing.

The wavelength-scanning polarization-modulated ellipsometer used for the measurements has been described elsewhere (3). Measurements of the ellipsometric angles Δ and Ψ were performed over the photon energy range from ~ 1.5 - 4.5 eV. The angle of incidence was 61.42 degrees.

III. Results

Comparisons of Δ and Ψ for the unannealed and annealed samples are shown in Fig. 1. The sensitivity of the measurements to changes caused by implantation and annealing is clearly evident.

Analysis of these measurements uses the same procedure described elsewhere (2). Briefly, this procedure uses n-laver models, the Bruggeman effective medium approximation for physical mixtures (4), the model of Zuther for chemical mixtures (5), and regression analysis for characterization of a particular material system.

For the unannealed sample the simplest model consists of a crystalline Si overlayer, a stoichiometric oxide (assumed to have the dielectric function of fused silica (6)) and a crystalline substrate. The differences ($\delta\Delta$ and $\delta\Psi$) between the experimental measurements and the best fit values using this simple model are plotted in Fig. 2 (Model (a)).

Previous studies have shown that samples prepared under similar conditions may lack sharp interfaces (1), and some IR studies have suggested that the buried oxide may be non-stoichiometric (7). Therefore, additional model calculations were performed which included these possibilities.

The structure which results in the best agreement with the data is shown in Fig. 3, and the $\delta\Delta$ and $\delta\Psi$ values are shown in Fig. 2 (Model (b)). The best fit structure for the unannealed sample is fairly complicated, with oxide precipitates in the crystalline Si overlayer and additional transition layers at the crystalline Si overlayer/ noncrystalline SiO_2 and noncrystalline SiO_2/Si substrate interfaces.

The same analysis procedures were used for the annealed sample. Values of $\delta\Delta$ and $\delta\Psi$ are shown in Fig. 4 (Model (a)) for a structure assumed to consist of a crystalline Si overlayer, a noncrystalline SiO_2 layer and a Si substrate. The best fit structure for the annealed sample is diagrammed in Fig. 5, and the $\delta\Delta$ and $\delta\Psi$ values are shown in Fig. 4 (Model (b)). The unusual feature is the inclusion of crystalline Si regions (with a volume fraction of 9 ± 0.5 %) in the noncrystalline SiO_2 layer.

IV. Discussion and Conclusions

For the unannealed sample the best fit model (Fig. 3) indicates that the oxide is stoichiometric SiO_2. This is in apparent contradiction to infrared measurements (7) but in agreement with the results of SIMS and RBS (8,9). However, the value of 0.031 for the unbiased estimator (defined in (2)) indicates that the model may be inaccurate, since values less than 0.02 can typically be attained (2). The large value of the unbiased estimator might be due to two assumptions used in the model calculations: (1) that the formed oxide is fused silica, and (2) that the dielectric functions of nonstoichiometric oxides are adequately represented by the model of Zuther. Hensel et al. (9) have suggested that radiation damage (rather than non- stoichiometry) may be responsible for the IR shift in unannealed SIMOX. In this case the buried oxide which forms prior to annealing may have a structure (and therefore optical properties) different from either fused silica or the nonstoichiometric oxides examined by Zuther. Further experiments are in progress to investigate these possibilities.

For the sample annealed at 1275 °C our measurements indicate that the oxide is stoichiometric, but contains about 9 % crystalline Si. The existence of these regions was confirmed by removing the Si overlayer with a hydrazine etch (which does not attack noncrystalline SiO_2) and observing that the remaining oxide layer was pitted. Profilometer measurements showed that many of these pits extended through the oxide. Since this was the only sample studied which had been annealed at 1275 °C, it is unclear whether such Si inclusions are common in high temperature annealed SIMOX. Some XTEM stidies (10) have also indicated the presence of Si islands in the oxide after annealing at 1300 °C. The annealed sample also has a transition layer between the oxide and the substrate which consists of a mixture of crystalline Si and 7% noncrystalline SiO_2. This transition layer has been observed in several previous studies (1).

In conclusion, we have used ellipsometry to determine the structure of SIMOX. For the annealed sample we have found that the oxide contains crystalline Si, and for the unannealed sample we have found that the oxide may not be fused silica, as has commonly been assumed

*NRL-ONT Postdoctoral Research Associate

REFERENCES

1. For example, see references in *Semiconductor-on-Insulator and Thin Film Transistor Technology*, Materials Research Society Symposium Proceedings Vol. 53, edited by A. Chiang, M.W. Geis and L. Pfeiffer (Materials Research Society, Pittsburgh, PA, 1986).
2. P. J. McMarr, K. Vedam and J. Narayan, J. Appl. Phys. **59**, 694 (1986). K. Vedam, P. J. McMarr and J. Narayan, Appl. Phys. Lett. **47**, 339 (1985).
3. V. M. Bermudez and V. H. Ritz, Appl. Opt. **17**, 542 (1978).
4. D. A. G. Bruggeman, Ann. Phys. (Leipzig) **24**, 636 (1935).
5. G. Zuther, Phys. Status Solidi A **59**, K109 (1980).
6. *American Institute of Physics Handbook*, Third Edition, edited by D. E. Gray (McGraw-Hill, New York, 1972), p. 6-29.
7. R. E. Stahlbush, W. E. Carlos and S. M. Prokes, IEEE Trans. Nucl. Sci. **NS-34**, 1680 (1987).
8. P. L. F. Hemment, E. Maydell-Ondrusz, K. J. Stevens, J. A. Kilner, and J. Butcher, Vacuum **34**, 203 (1984).
9. E. Hensel, K. Wollschlager, D. Schulze, U. Kreissig, W. Skorupa and J. Finster, Surf. and Interfac. Anal. **7**, 207 (1985).
10. J. Stoemenos and J. Margail, Thin Solid Films **135**, 115 (1986).

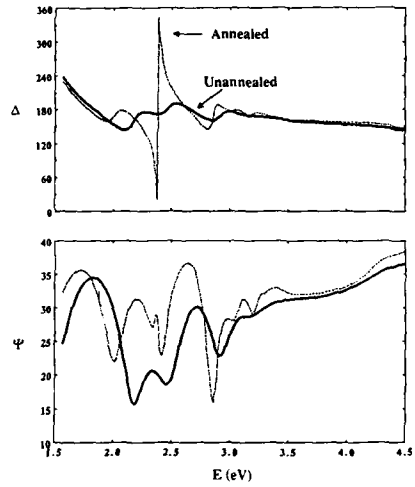


Figure 1. Δ (top panel) and Ψ (lower panel) versus photon energy (E (eV)) for the unannealed sample (solid curve) and the annealed sample (dashed curve).

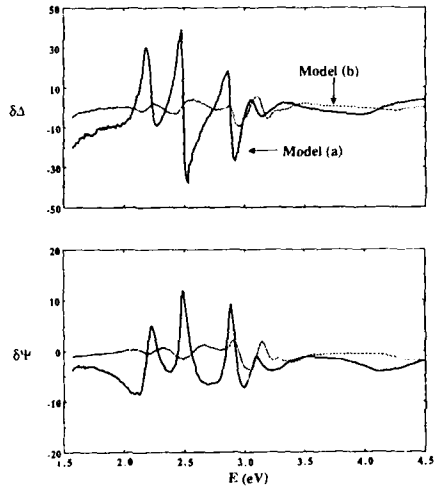


Figure 2. Differences between the measured and calculated values of Δ (δΔ , top panel) and Ψ (δΨ, bottom panel) for two models. Model (a) (solid curve) consists of a Si surface layer and a noncrystalline SiO_2 layer on a Si substrate. Model (b) (dashed curve) is the best fit model.

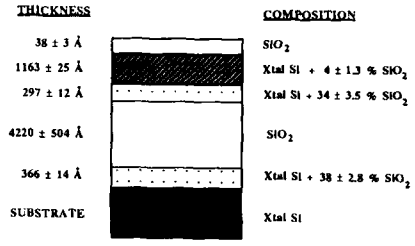


Figure 3. Structure for the unannealed sample.

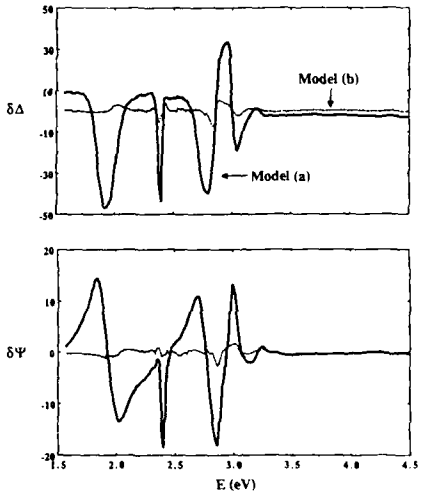


Figure 4. Differences between the measured and calculated values of Δ (δΔ, top panel) and Ψ (δΨ, bottom panel) for two models. Model (a) (solid curve) consists of a Si surface layer and noncrystalline SiO_2 layer on a Si substrate. Model (b) (dashed curve) is the best fit model.

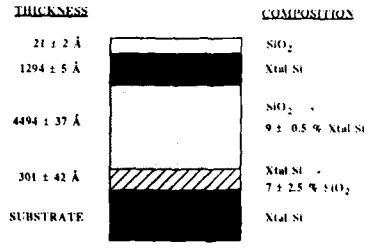


Figure 5. Structure for the annealed sample.

Abstract No. 289

OPTICAL MODELLING OF Si-SiO_2 INTERFACE

A. Kalnitsky, S.P. Tay, J.P. Ellul
Northern Telecom Electronics Ltd.,
P.O. Box 3511, Station C,
Ottawa, Ontario, Canada K1Y 4H7

S. Chongsawangvirod and E.A. Irene
Department of Chemistry,
University of North Carolina,
Chapel Hill, N.C. 27514

INTRODUCTION

Fixed wavelength ellipsometric analysis of thin SiO_2 films on silicon usually yields refractive index values much higher than the customary value of n = 1.46 for the bulk material. This effect is often attributed to deficiencies in the data reduction software, hence the index value information is discarded as erroneous.

Systematic study of the apparent increase in SiO_2 refractive index with decreasing oxide thickness is the objective of the present work.

EXPERIMENTAL RESULTS

Samples for this study were prepared by dry oxidation of Si(100) in the 700°C to 1050°C temperature range. High- and atmospheric-pressure reactors were used. One set of examined samples was prepared by LPCVD technique. Fixed wavelength (632.8 nm), 70° angle of incidence ellipsometric measurements were interpreted in terms of film thickness and effective refractive index with the aid of the algorithm reported in [1]. In this work the substrate complex refractive index was assigned the value of 3.858 - 0.018i.

Some of the results are summarized in Figure 1 as a plot of extracted refractive index vs extracted oxide thickness. The most interesting feature of the present data set is lower sensitivity of effective refractive index to apparent oxide thickness for higher temperature oxides. Deposited SiO_2 exhibits the weakest dependence of refractive index on thickness.

DISCUSSION

For the purpose of optical modelling and subsequent discussion of experimental results we shall adopt the Si-SiO_2 interface model developed in [2]. According to this model, high density interfacial oxide undergoes a transition to bulk density dynamically, in the process of film growth. The distance over which density relaxation takes place must be related to oxide viscosity at the growth temperature [2]. Since viscosity undergoes a transition at viscous flow point at approximately 950°C [3,4,5], the thickness of the high density transition region should be minimized at higher temperatures and longer oxidation times. Our optical model of the interfacial region is based on a process temperature-dependent transition region width of approximately 3 nm, as suggested in [2]. It also takes into account the suggestion by Aspnes and Theeten that a realistic interface model should be based on a continuously graded structure [6]. We assume that oxide refractive index at any point is adequately approximated by the simple relationship:

$$n = 2.44 \exp[-0.5 * (X/S)^2] + 1.46 \qquad (1)$$

where X is distance measured from Si-SiO_2 interface, and S is the parameter describing the transition region width. Numerical values of 2.44 and 1.46 in expression (1) are selected to accomodate the range of refractive index values from bulk (1.46) to the space-averaged 3.2 $\pm$ 0.4 reported for the interface [6,7]. Film stratification is illustrated in Figure 2. The structure is composed by successively adding 0.2 nm wide regions to the film, starting with bare Si substrate. Each added layer is assigned a constant value of refractive index, as shown in Figure 2. The topmost layer of the structure is assigned n = 1.46 when expression (1) yields $n \leq 1.460001$. The thickness of the topmost layer is then incremented for modelling of films thicker than the transition region width. Simulated 'iso-index' curves for n = 1.46 and transition region width of 1.5 nm (S = 5), 3.5 nm (S = 10) and 5.5 nm (S = 15) are plotted in Figure 3. A characteristic feature of the simulated iso-index plots, for structures with assumed transition region width, is movement of Ψ to the left of the origin for very thin films. We now take the simulated values of Δ and Ψ and use them to extract the effective refractive index and corresponding film thickness. The data set generated with S = 5 (1.5 nm wide interface) and S = 10 (3.5 nm wide interface) were used to compute refractive index values. Results are summarized in Tables I and 2. Simulated data for wider transition region widths (S = 10) give much stronger refractive index vs thickness dependence than narrow (S = 5) transition region results. Film thickness values extracted in this exercise are somewhat lower than the thickness values used to generate iso-index data.

The optical model of the interface presented in this paper qualitatively explains the results of Figure 1 as follows: the narrowest transition region is expected for deposited SiO_2 films, where transition region is expected to be equal to the native oxide thickness regrown on Si in the short time period between surface preparation and film deposition. Oxides grown at 950°C are expected to have thinner transition region than 900°C and 700°C material [4,5], hence the observed refractive index vs thickness dependence.

SUMMARY AND CONCLUSIONS

An optical model of the Si-SiO_2 interface is presented. This model is consistent with the physical model of high density transition region present in the oxide at Si surface. This model qualitatively explains the experimentally observed dependence of refractive index on oxide thickness for deposited and thermally grown SiO_2. Effective values of extracted refractive index for thin oxides is believed to carry information on the properties of the interfacial transition region.

REFERENCES

[1] A. Kalnitsky, S.P. Tay, I.D. Calder, Journal of Electrochem. Soc., 135, 5 (1988) 1271.

[2] F.J. Grunthaner, P.J. Grunthaner, "Chemical and Electronic Structure of the Si/SiO_2 Interface", Material Science Report, Volume 1, No. 2,3, December 1986.

[3] E.P. EerNisse, G.F. Derbenwick, IEEE Trans. Nucl. Sci. NS-23 (1976) 1534.

[4] E.A. Irene, Z. Tieney, J. Angilello, Journal of Electrochem. Soc., 129, (1982) 2594.

[5] E.A. Irene, J. Appl. Phys., 54 (1983) 5416.

[6] D.E. Aspnes, J.B. Theeten, Journal of Electrochem. Soc., 127 (1980) 1359.

[7] E. Taft, L. Cordes, Journal of Electrochem. Soc., 126 (1979) 131.

Table 1. Refractive index extraction from Δ, ψ data simulated for narrow (S = 5) 1.5 nm transition region.

SIMULATED VALUES			Extracted	Extracted
Tox(nm)	Δ	ψ	N	Tox(nm)
0.0	179.252	10.3962		
4.0	168.139	10.5407	1.733	3.30
8.0	157.169	10.9705	1.509	7.50
12.0	147.142	11.6419	1.489	11.50
16.0	138.224	12.5071	1.478	15.60
20.0	130.410	13.5178	1.474	19.60
24.0	123.596	14.6320	1.471	23.60
28.0	117.649	15.8157	1.469	27.60
32.0	112.437	17.0430	1.469	31.60
36.0	107.841	18.2949	1.467	35.60

Table 2. Refractive index extraction from Δ, ψ data simulated for wide (S = 10) 3.5 nm transition region.

SIMULATED VALUES			Extracted	Extracted
Tox(nm)	Δ	ψ	N	Tox(nm)
0.0	179.252	10.3962		
4.0	168.830	10.5096	1.912	2.995
8.0	157.797	10.9207	1.819	6.350
12.0	147.689	11.5767	1.639	10.200
16.0	138.687	12.4299	1.502	15.000
20.0	130.794	13.4318	1.493	19.020
24.0	123.912	14.5397	1.485	23.060
28.0	117.908	15.7190	1.481	27.060
32.0	112.645	16.9433	1.478	31.100
36.0	108.008	18.1931	1.476	35.100

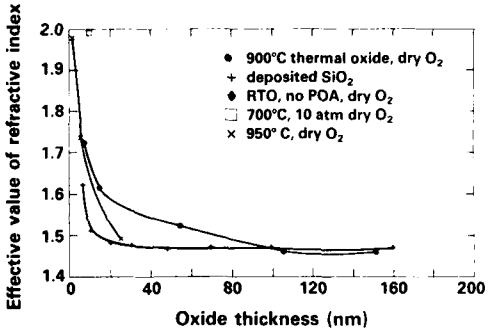


Figure 1. Experimental dependence of extracted refractive index vs oxide thickness for material grown at different temperatures.

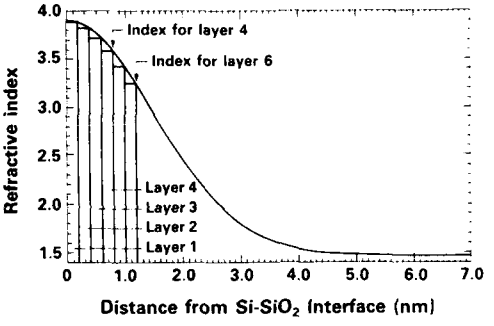


Figure 2. Stratification of the SiO_2 film, 2 nm wide layers are successively added to the structure until bulk value of refractive index is attained.

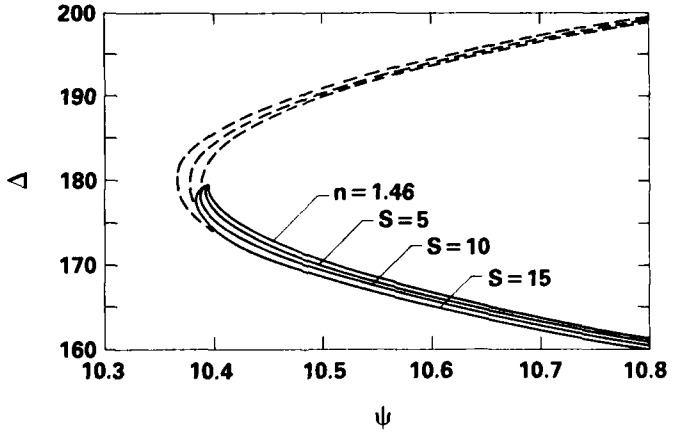


Figure 3. Computed 'iso-index' curves for bulk oxide n = 1.46, and for oxide with transition layer incorporated in the structure.

Abstract No. 290

A LASER ACTIVATED CVD FILM FOR INTERLAYER DIELECTRIC APPLICATION

C. Chiang, N. Cox, D. Fraser, M. Lee
and L.C. Yip*
Intel Corp., Components Research
2250 Mission College Blvd.
Santa Clara, CA 95052

R.J. Kolenkow, R. Anderson and G. Roche
Photolytics, General Signal Thin Film Co.
2972 Stender Way
Santa Clara, CA 95054

Silicon dioxide films deposited by an LACVD (laser activated CVD) technique has been evaluated for ILD (interlayer dielectric) application. Using silane and N_2O as reaction gases and excimer laser as energy source, we have deposited silicon dioxide at various conditions in a research reactor. As seen in the FTIR spectra (see Figure 1) the $-N$ and $-H$ content decreased as the N_2O/SiH_4 ratio increased, indicating more complete oxidation. Consistent with the FTIR data, the corresponding refractive indices decreased from 1.54 to 1.46. The $-H$ and $-N$ content did not seem to be affected by the deposition temperature as shown in Table 1.

The film hygroscopicity is determined mainly by the deposition temperature. The stress of films deposited at low temperature ($<350°C$) drifted toward compressive region with time indicating the film was absorbing moisture. The film deposited at 400°C has shown stable stress over time. Table 2 summarizes the evolution of film stress with time. Figure 2 is a stress-temperature curve of a sample deposited at 250°C. The hysteresis indicated materials are evolving from the film. The stress-temperature curve of a 400°C sample shows no significant difference between the heating and cooling curves (see Figure 3).

Film step coverage is better than conventional LTO and is equivalent to PECVD oxynitride. The film integrity is largely dependent upon the deposition temperature. The oxide deposited at 250°C (see Figure 4) showed preferential etch at the corners after dipped into dilute HF. No such defects were seen for 400°C film (see Figure 5).

Under all conditions, the film thickness uniformity is within $\pm 4\%$ range within a run. By choosing the optimum chemistry and temperature, we can obtain good oxide for ILD application using the LACVD technique.

Table 1. Comparison of −N and −H Content in Various Films

	SiH (10E21 B/CC)	N−H (10E21 B/CC)
LECVD (Low N_2O/SiH_4)		
400°C	4.6 ± 3%	1.8 ± 7%
250°C	5.0	3.0
LECVD (High N_2O/SiH_4)		
400°C	1.64	0
300°C	1.36	0
125°C	1.70	0

Table 2. Evolution of Film Stresses with Time

Date	Stress (MPa)				
	Low N_2O/SiH_4		High N_2O/SiH_4		
	250°C	400°C	125°C	300°C	400°C
As Deposit	N/A	N/A	−28	15	−39
After Heating	N/A	N/A	140	140	−20
One Month	−54	20	21	34	−47
Two Months	−75	15	N/A	N/A	N/A
After Heating	+80	30	N/A	N/A	N/A
Three Months	−40	13	N/A	N/A	N/A

ACKNOWLEDGEMENTS

We would like to thank R. Villasol, A. Podelski and V. Ochoa at Intel and P. Oakley and R. Orr at Photolytics for their support.

*Current address: Department of Material Science, UC Berkeley, Berkeley, CA 94720

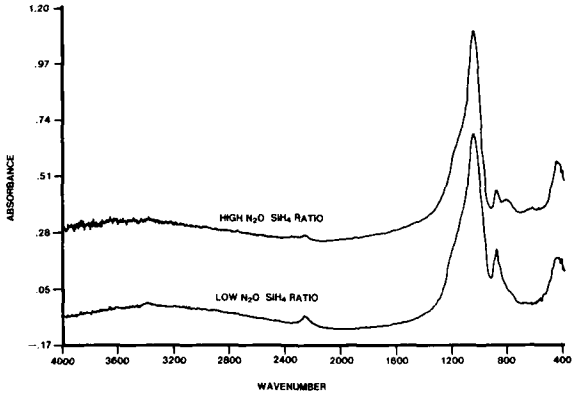


Figure 1. FTIR Spectra of Samples with Different N_2O/SiH_4 Ratio

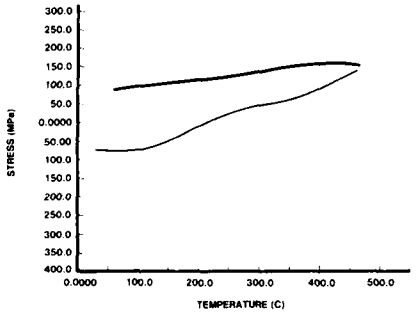


Figure 2. Stress-Temperature Curve of a 250°C Sample

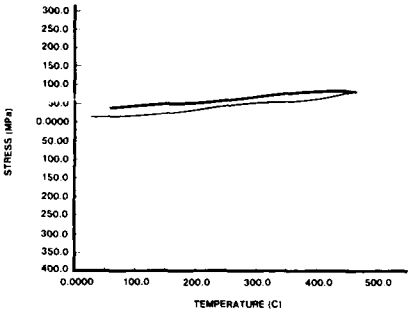


Figure 3. Stress-Temperature Curve of a 400°C Sample



Figure 4. SEM Micrograph of a 250°C Sample Decorated by HF

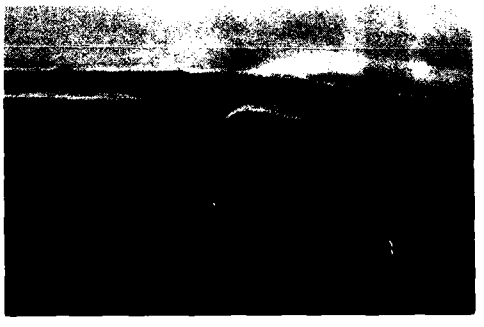


Figure 5. SEM Micrograph of a 400°C Sample Decorated by HF

Abstract No. 291

Radiotracer Measurements of Sodium Penetration Through Thin Films of Phosphosilicate Glass

S. Vance Dunton and Alan Campbell Ling
Department of Chemistry
San Jose State University
One Washington Square
San Jose, CA 95192

Wilbert G. M. van den Hoek
Philips Research Laboratories Sunnyvale
c/o Signetics Corporation
Sunnyvale, CA 94088-3409

Abstract

Sodium ion penetration through thin films of APCVD and PECVD phosphosilicate glasses has been evaluted by $^{22}NaCl$ radiotracer measurements of thermal Na^+ penetration at 400°C. Surprisingly, it was found that the ability of Na^+ to penetrate PECVD and APCVD PSG films increased with increasing weight percent P_2O_5.

Introduction

Phosphosilicate glass (PSG) thin films deposited by chemical vapor deposition (CVD) are used as contact, intermetal dielectric and passivation overcoat layers in integrated circuits. One critical property of PSG layers is their ability to retard migration (getter) of alkali ions (1). Field-assisted migration of Na^+ in thermally grown SiO_2 doped with phosphorus by evaporation of P_2O_5 in an ambient of N_2-$POCl_3$-O_2 has been evaluated by C-V and Q-t measurements (2). Thermally induced Na^+ migration in APCVD PSG films has been evaluated by Na-22 radiotracer measurement (3). In this paper we report the effects of phosphorus content and film densification on thermal penetration of Na^+ through PSG films deposited by atmospheric pressure CVD (APCVD) and plasma enhanced CVD (PECVD).

Experimental

The APCVD films were deposited from silane (SiH_4), oxygen (O_2) and phosphine (PH_3) in a Tempress reactor at 400 °C. PECVD films were deposited from SiH_4, PH_3 and nitrous oxide (N_2O) at 300 °C and 380 kHz in an ElectroTech model ND 6200 batch reactor and in a Novellus single wafer reactor at 400 °C and 13.56 MHz. The PSG films were densified under flowing nitrogen for 30 minutes at 1000°C. Total phosphorus was measured by x-ray fluorescence (XRF) and energy dispersive x-ray (EDX) spectrometry. Weight percent P_2O_5 was measured by ion chromatography (IC) of etching fractions.

Thermal penetration by Na^+ through the films was determined by depositing a carrier free solution of Na-22 chloride on the film surfaces and annealing at 400°C for 24 hrs. Na-22 decays by positron emission, and is detected by measuring the intenstiy of the 0.511 MeV Na-22 annihilation photopeak. Na^+ penetration depth profiles were evaluated by progressively etching the film surface in a buffered oxide etch (BOE) solution and counting the radioactivity remaining in the unetched layer. Film thickness measurements were made with a Tencor Alpha-Step depth profilometer. A sodium iodide scintillation detector and multichannel analyzer were used for detection of the annihilation photopeak. Sensitivity was 4×10^8 atoms per count per second.

Effects of Densification

Figure 1 shows the effect of the densification step on the PSG films. The PECVD PSG films deposited at 300°C showed a significant (approximately 20%) decrease in thickness on annealing. Figure 2 shows the effect of densification on the phosphorus in the films. Increases in the amount of P_2O_5 on annealing can be understood as further oxidation from the trivalent (P_2O_3) to pentavalent (P_2O_5) oxidation states. The differences between total phosphorus and oxidized (P_2O_3 and P_2O_5) phosphorus in the films must be accounted for as some other form of phosphorus such as trapped PH_3 gas.

Sodium Depth Profiles

Sodium-22 concentration distribution profiles in the as-deposited APCVD PSG films are shown in Figure 3. On densification, the Na^+ distribution profile of the PSG film changed, with an enhancement of the ability of the upper layers of the film to trap Na^+ ions and a uniform concentration distribution in the underlying bulk. The same effect was observed in the films deposited in the ET system (Figure 4). Densified and as-deposited films from the Novellus reactor had essentially equivalent Na^+ distribution profiles before and after annealing (figure 5).

Conclusions

The ability of Na^+ to penetrate PECVD and APCVD PSG films increased with increasing weight percent P_2O_5. There was no such correlation between Na^+ penetration and total phosphorus content.

References

1. W. Kern, *Semiconductor Int.* **8**(7), 121-129 (1985).
2. J. M. Elderidge and D. R. Kerr, *J. Electrochem. Soc* **118**, 986 (1971).
3. W. Kern and G. L. Schnable, *RCA Rev.* **43**, 423 (1982).

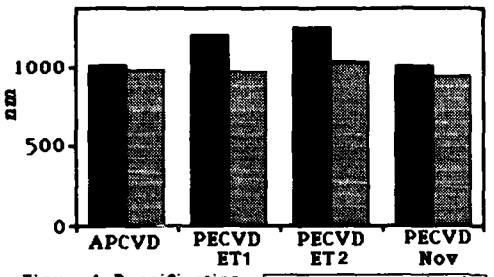


Figure 1: Densification of PSG films (ET: films deposited in ElectroTech reactor. Nov: film deposited in Novellus reactor).

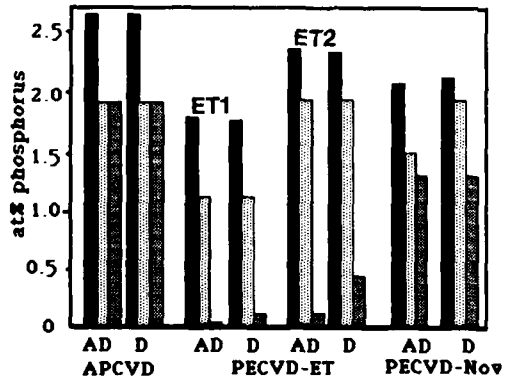
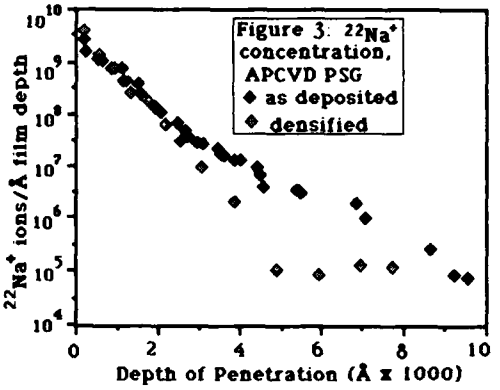
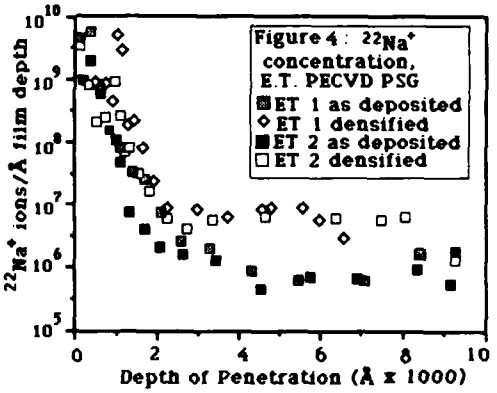
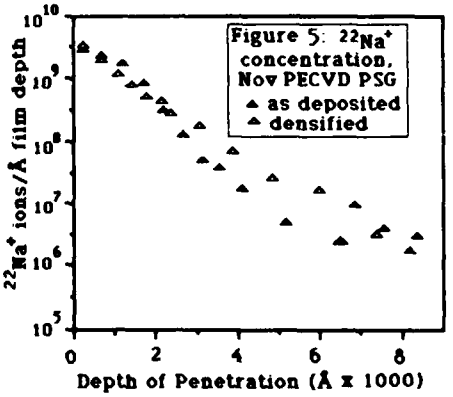


Figure 2: At% total phosphorus and at% phosphorus as P_2O_5 before and after densification.







Abstract No. 292

MOBILE ION DRIFT IN HIGH QUALITY PECVD SiO_2 FILMS

G. Liu , W. S. Lau and S. Fonash
Center For Electronic Materials and Devices
The Pennsylvania State University
University Park , PA. 16802

J. Kanicki
IBM Research Division
Thomas J. Watson Research Center
P. O. Box 218 , Yorktown Heights, NY. 10598

INTRODUCTION

Extensive studies have been done over the years on insulating films such as thermally grown silicon dioxide, deposited amorphous silicon dioxide (SiO_2) and silicon nitride (Si_3N_4) for applications in MIS and MNOS structures. From these studies it is well known that thermally grown SiO_2 shows the best stability among these insulators but obviously requires high temperature processing. It is also generally accepted that deposited Si_3N_4 has higher carrier trapping than SiO_2 layer. However, deposited SiO_2 films generally do not exhibit the excellent diffusion barrier provided by deposited Si_3N_4. In this report our studies are focused assessing the ability of plasma enhanced chemical vapor deposition (PECVD) SiO_2 layers to serve as mobile ion barriers. Specifically, we report here on the transient behavior of mobile ions in MOS structures which have been fabricated using PECVD silicon dioxide films. These MOS structures were fabricated using a variety of annealing conditions and gate materials. The annealing procedures included furnace annealing and rapid thermal annealing. The goal of this study is to examine the mobile ion drift mechanism intrinsically present in these films and to explore approaches for improving film stability.

EXPERIMENTAL

Silicon dioxide films were deposited by the PECVD technique at a substrate temperature of 275°C on n-type 1 Ω cm single crystal silicon substrates. The approximately 130 nm thick amorphous films used in this study were deposited in an RF glow discharge from 2% helium-diluted silane, helium, and nitrous oxide (N_2O) gas mixture. Total pressure, RF power density, and flow rate of 2% helium-diluted silane, helium, and nitrous oxide were, respectively, 1 Torr, 35 mW/cm^2, 40 sccm, 2000 sccm, and 100 sccm. The silicon to oxygen atomic ratio and hydrogen content in this film was around 0.5 and below 2 atom percent, respectively. The growth rate was 4.5 nm/sec and room temperature etching rate in buffered oxide etch solution was around 2 nm/min . To form the metal oxide semiconductor (MOS) structures used in this study Al and Ti metal gates were evaporated on the silicon dioxide films before or, in some cases, after annealing to study the effects of metal gate / SiO_2 interaction. The post-metallization rapid thermal annealing (400°C for 2min in Ar ambient) used for some samples was performed by a AG 210 Heatpulse System; furance annealing(400°C for 30min in forming gas ambient) was employed for other samples.

EXPERIMENTAL RESULTS AND DISCUSSION

To characterize metal gate / SiO_2 structures, interface state densities, fixed charge, and mobile ion drift were measured on as-deposited samples, pre-metallization RTA and furnace annealed samples, post-metallization RTA and furnace annealed samples as well as on samples with different gate metals. The time dependence of flat band voltage shift (ΔV_{FB}) was measured using the bias temperature stress (BTS) technique[2]. It was found that at elevated temperatures (80°C- 120°C) the mobile ions tended to relax during the measurement of flat band voltage, particularly during the period when negative voltage is applied to the gate. Therefore, samples were cooled down below 30°C before the C-V measurements were taken in order to "freeze-in" the mobile ions present in the films.

In general, fixed charge and interface state densities decreased after either of the annealing processes used in this study as may be seen in Table 1. For example, after 400°C 30min furnace annealing, the fixed charge and interface state density (mid-gap values) dropped from 10^{12} cm^{-2} and 10^{13} cm^{-2} eV^{-1} to 10^{11} cm^{-2} and 10^{10} cm^{-2} eV^{-1}, respectively. However, the effects of annealing on mobile ions in these films was observed to be more complicated than in thermally grown SiO_2 films.

The mobile ion drift mechnism in PECVD silicon dioxide was found to be different from that in thermally grown silicon dioxide. In thermally grown silicon dioxide it is well established that the flat band voltage shift is principally due to Na^+ drift. Further, in thermally grown SiO_2 this mobile ion drift is limited by trapping at boundaries and the flat band voltage shift is found to follow one of the following rules[1]:

$$\Delta V_{FB} \propto 1 - \exp(-t/\tau) \qquad (1)$$

or

$$\Delta V_{FB} \propto \sqrt{t} \qquad (2)$$

where, (1) is valid for the trapping centers having a single energy level and (2) is valid for the trapping centers having a spread energy distribution. However we found that the ΔV_{FB} vs. time curve for PECVD silicon dioxide did not fit either of these models implying that the controling mechanism in mobile ion drift in PECVD silicon dioxide is not the same as that in thermally grown silicon dioxide. To simplify the assessment of this complex ion drift process in PECVD SiO_2 we define both the initial and recovery time constant as the time required for the normalized ΔV_{FB} to reach 0.5. The data for these measured time constants for the various classes of samples used in this study are listed in Table 2. The corresponding data for a thermally grown silicon dioxide , obtained from the literature[1], are also shown for comparison. Based on our results, the initial drift (from metal to silicon) time constant of the as-deposited SiO_2 is shorter than that for one would extrapolate at 80°C for thermally grown silicon dioxide as seen in Table 2. Pre-metallization 400°C 30min furnace annealing increased this initial drift time constant by a factor of three. However, post-metallization 400°C 30min furnace annealing or RTA decreased this time constant by one or two orders of magnitude as also noted in Table 2. At the same time, all annealing processes used in this study increased the mobile ion density roughly by a factor of three. Hence our results show that the drift mechanism in PECVD SiO_2 is quite different than that in thermally grown SiO_2. Our resultes also show that this drift is sensitive to gate deposition and annealing history.

References

1. S. R. Hofstein, IEEE Trans. Electron Devices, ED-13, 222 (1966).
2. B. Yurash and B. E. Deal, J. Electrochem. Soc. , 115, 1191 (1968).

TABLE 1
FIXED CHARGE AND INTERFACE STATE DENSITY OF PECVD SiO_2 FILMS

SAMPLE	MID-GAP INTERFACE STATE DENSITY (cm^{-2} eV^{-1})	FIXED CHARGE (cm^{-2})
AS-DEPOSITED	$2x10^{13}$	$3x10^{12}$
FURNACE ANNEALING 400°C 30min	10^{10}	$6x10^{11}$
RTA 400°C 2min	$7x10^{11}$	$5x10^{11}$

TABLE 2
SUMMARY OF ION DRIFT PROPERTIES OF VARIOUS SiO_2 FILMS

SAMPLE	BTS Bias/Temp. (V)/(°C)	INITIAL DRIFT TIME CONST. (sec) *	RECOVERY TIME CONST (sec) *	MAX. DRIFT (V)	MOBILE ION DENSITY cm^{-2}
THERMALLY GROWN SiO_2 (thickness 1000Å)	+20/200	10^4	0.1	---	---
AS-DEPOSITED (thickness 1300Å)	+10/80	$3x10^4$	$2x10^2$	10	$3x10^{12}$
POST-METALLIZATION FURNACE ANNEALING 400°C 30min (thickness 1300Å)	+10/80	$2x10^3$	10^2	30	10^{13}
PRE-METALLIZATION FURNACE ANNEALING 400°C 30min (thickness 1300Å)	+10/80	10^5	10^2	36	10^{13}
POST-METALLIZATION RAPID THERMAL ANNEALING 400°C 2min (thickness 1300Å)	+10/80	10^2	40	34	10^{13}

* Defined as the time required for normalized flat band voltage to reach 0.5

Abstract No. 293

Analog Nonvolatile Memory for Neural Network Implementations *

Jay P. Sage and Richard S. Withers

Lincoln Laboratory
Massachusetts Institute of Technology
Lexington, MA 02173-0073

Neural networks, modeled to a degree after biological brains, offer an alternative approach to artificial intelligence computations. In contrast to deductive, rule-based AI methods, neural network paradigms are based on inductive response to training data (experience). In contrast to conventional computers with their small number of complex, powerful central processing units, neural network implementations use very large numbers of very simple processing elements. The required processing operations are often so simple that symbolic computation using arithmetic and logic units (ALUs) can be replaced by physical methods of computation, allowing very high computation rates to be achieved with very small structures.

By analogy with biological nervous systems, artificial neural networks contain synapses and neurons. The synapses are simple memory/processing elements that connect two neurons. They store a single value called a weight, receive an input signal from one neuron, and deliver an output signal to another neuron. The operation performed by the synapse on the input signal is usually a simple one, such as multiplication or subtraction. Each neuron typically receives signals from many synapses, combines those signals (generally by simple addition), and then performs a nonlinear operation on the result. The output from the neuron is typically sent to many synapses.

As an example of how physical computation can speed operation and simplify hardware, consider the neuron's task of adding the signals from hundreds of synapses. To compute the result numerically (symbolically) in a single step, a very complex ALU with hundreds of multibit inputs and hundreds of thousands of gates would be required. Simpler hardware in a pipeline architecture can be used but at a significant sacrifice in computing speed. Alternatively, physical computation can be used. By representing the signals from the synapses in the form of charge packets and transferring those packets onto a simple wire serving as a capacitor, the physical law of conservation of charge carries out the summation virtually instantaneously.

In conventional computers performing conventional tasks, physical computation cannot be used because accuracy is limited. The tasks performed by neural network computers, however, are quite different. Although some neural networks, especially those used to preprocess optical or acoustic sensory data, have fixed weights, most neural networks embody learning rules that provide for modification (adaptation) of the synaptic weights in response to training (experience). This adaptation, or experience- controlled feedback, is expected to make it possible for neural networks to provide accurate system performance despite limited accuracy components.

Because of this expected ability to tolerate lower accuracy devices, neural networks offer a new opportunity for technologies that could not meet the requirements of digital computation and signal processing. One of these technologies is *analog* nonvolatile memory based on floating gate or metal-nitride-oxide-semiconductor (MNOS) devices. We will illustrate the application of analog MNOS technology to neural networks by describing an exploratory network we designed, fabricated, and tested. This network was the first to include *on the chip* mechanisms for adapting the weights stored in the synapses.

In digital applications of floating-gate and MNOS devices, there is no need to control the exact amount of charge on the floating gate or in the nitride traps. Satisfactory (probably optimum) operation can be achieved with saturated levels of positive and negative charge representing the two binary states.

The distinguishing feature of our technology is the use of charge-controlled mechanisms. Charge-coupled device (CCD) techniques are used in the neural network synapses to meter out charge packets of specific size. During a learning operation, these charge packets are formed in such a way that they represent the amount by which the weight stored in the synapse should be modified. The charge packets are transferred to the channel of the MNOS device, and application of a large bias voltage to the control gate of the MNOS device causes the charge in the packets to tunnel into the nitride traps.

During readout operations of the network, the MNOS device in the synapse is used as part of another CCD charge metering circuit. In this case, the MNOS gates are maintained at a low bias voltage so that no writing occurs. The charge packets are formed with sizes that depend in the desired way on the input signal to the synapse and on the synaptic weight represented by the trapped charge in the nitride layer of the MNOS device. These charge packets are then transferred to the neuron, where they are summed.

In the talk we will describe the structure and operation of the MNOS/CCD neural network in greater detail. We will also discuss some alternative ways under development in other laboratories to use floating-gate and MNOS analog nonvolatile memory devices to implement neural network circuits.

*This work sponsored by the Department of the Air Force

Abstract No. 294

A DUAL POLARITY NONVOLATILE ANALOG MEMORY FOR USE IN ADAPTIVE ARTIFICIAL NEURAL NETWORKS

R. L. SHIMABUKURO, I. LAGNADO AND P. A. SHOEMAKER

NAVAL OCEAN SYSTEMS CENTER
SAN DIEGO, CA 92152-5000, USA

Artificial neural networks are currently of great interest for applications in a wide variety of fields. Computer simulations of these parallel distributed processing systems have shown potential applications for associative memories, motor-control, visual and speech recognition, and a variety of other problems for which conventional computing systems are not well suited [1]. The results of these simulations are stimulating a great deal of effort in implementing neural-type networks in VLSI circuitry.

A typical processing element in a neural network operates on a weighted sum of inputs from other elements or external sources. Therefore, the weighting matrix which represents the relative interconnection strengths is a crucial component of the neural network. Most useful applications require on the order of several thousand to several million weights. In many networks these weights can be either excitatory (positive) or inhibitory (negative). In a learning network the weights must also be modifiable. Therefore, an analog circuit element which performs the weighting function should have a long storage lifetime, be continuously adjustable, compact in size, and be able to represent a positive or negative weight. Also, since many learning rules compute a change in weighting values, one would like to be able to update the weights incrementally in either the positive or negative direction.

The Naval Ocean Systems Center, under the aegis of the Office of Naval Technology, is working on the implementation of neural networks in analog integrated circuitry using CMOS technology. We have designed and fabricated a four-transistor MOS analog memory (MAM) cell based on standard silicon processing technology, which we believe is an excellent candidate for a neural circuit memory element.

We employ the mechanism of avalanche or hot-carrier injection to move charge onto a floating-gate structure. This mechanism was first used in the mid-1970's for digital memory applications in the FAMOS (floating gate avalanche injection MOS) device, which consisted of a p-channel MOSFET with an isolated gate [2]. At an appropriate biasing voltage, hot electrons are generated in avalanche breakdown, which have sufficient energy to conduct across the gate oxide and charge the gate. In an n-channel device, a complementary process takes place, with holes rather than electrons injected onto the floating gate. The potential due to the charge influences the state of the transistor under the gate just as would an externally applied voltage.

The memory cell [3] which we have fabricated consists of two complementary pairs of transistors sharing a common floating gate. This configuration allows us to store an analog weight value, which may be increased with holes injected by an n-channel writing device, and decreased with electrons from a p-channel device (charges are mobile and free to recombine because the gate is a conductor). It is possible to increment or decrement the value by very small amounts by pulsing the writing voltages. The floating gate is surrounded by insulating silicon dioxide. This provides a very large energy barrier preventing charge leakage. From data reported in previous studies, we predict that values may be stored on the order of years at room temperature [4].

Although in digital memories the same transistor which injects charge also senses its presence on the gate, in our circuits the gate is common to a second complementary pair of transistors, which perform the weighting function. These are depletion-mode devices (i.e., conducting at zero gate-to-source bias). The circuit in which they are used performs an approximate, four-quadrant multiplication, supplying an output current into virtual ground (as at the input node of a summing amplifier) which is roughly proportional to the product of the gate potential relative to ground, and an input signal [5].

We present and discuss experimental results obtained from test multiplier and MAM circuits fabricated at NOSC. We also describe alternative configurations intended to improve device performance.

[1] A Review of Artificial Neural Systems I & II, CRC Critical Reviews in Artificial Intelligence, P. K. Simpson, to be published.

[2] FAMOS - A New Semiconductor Charge Storage Device, D. Frohman-Bentchkowsky, Solid-State Electron., vol. 17, p. 517, 1974.

[3] Patent Pending. Navy case No. 71105

[4] DIFMOS - A Floating-Gate Electrically Erasable Nonvolatile Semiconductor Memory Technology, W. M. Gosney, IEEE Trans. Electron Devices, vol. ED-24, no. 5, p. 594, 1977.

[5] Patent Pending. Navy case No. 70748

Abstract No. 295

Utilization of Programmable Threshold Voltage Devices in Neural Network Integrated Circuits

Tom Borgstrom, Robert Chau, Ken Adkins, and Steve Bibyk

Solid State Microelectronics Laboratory
Department of Electrical Engineering
Ohio State University, Columbus 43210

INTRODUCTION

Recently, there has been a resurgence in the development of neural network circuitry, both from a VLSI development capability and in new concepts [1]. Neural networks often utilize threshold logic gates with many inputs, and each gate output is connected to the inputs of all the other gates. The processing that is performed by this circuitry is done by changing the output function of each gate. This can be done by weighting the strength of each input and and allowing the value of the weight to be modified based on the values of the gate outputs. This can be considered a learning or adaptation process [2]. The weighting functions can be implemented in digital circuit form but the resultant number of components required for fine weight resolution becomes unreasonable for development of practical adaptive systems. What is necessary for the weighted input connection is to have a conductance which can be varied continuously over a wide range and takes up little space. An attractive method is to develop a variable threshold voltage transistor.

The write/erase models used for nonvolatile memory development need to be evaluated for their use in neural networks. In order to program a particular synapse, circuitry must be developed to alter the threshold voltages. The traditional write/erase cycling models do not apply for this type of device operation, since the device thresholds are changed in an incremental manner. Also, the speed of the charge storage can now be much faster than for full digital programming. A second serious consideration is that the retention ability of the MNOS device. The voltage decay must be carefully analyzed since the devices are written for incremental changes. Therefore, the retention of the device is now much more critical than the endurance capability.

SIMULATION AND TESTING

Previous models of MNOS device operation [3,4] are being analyzed for their use in neural networks. Experiments are being done on MNOS devices to program them in an incremental mode and investigate over what range of threshold voltages the devices operate best for neural circuits. Both MNOS devices and floating gate devices are considered. The best point of operation is given by minimizing the effects of drift. The retention problem is being evaluated by using two MNOS devices in parallel and taking the difference of their threshold voltages. Various pulse amplitude pulse width combinations are used to determine how the devices should be written as the threshold voltage varies over a significant range since the shift will not be linear.

After many changes of the threshold voltage, the programming pulse to achieve the same increment of threshold shift has changed. Since the system is adaptive, it may take longer to learn after the device has been stressed.

DISCUSSION

Some method of write inhibition must be developed when a programming voltage is applied to a row of synapses. Circuitry is needed which will allow the MNOS device to be either programmed or simply accessed for a computation. In an array of connection weights, layout of the row and column selects will affect the write inhibition requirements.

The memory gate can be designed so that a voltage is not applied to it except during the programming mode. The conductance of the device is then varied by the programming voltage only.

ACKNOWLEDGEMENTS

The authors wish to thank L. Pham for his assistance. The encouragement and support of Profs. H.C. Ko and M. White is much appreciated.

REFERENCES

[1] J. Sage, K. Thompson, and R. Withers, "An Artificial Neural Network Integrated Circuit Based on MNOS/CCD Principles," in *AIP Conference Proc. 151*, ed. J. Denker, Neural Networks for Computing, Snowbird, Utah (1986) 381-385.

[2] Marvin White et al., "CCD Adaptive Discrete Analog Signal Processing," *IEEE J. Sol. State Cir.*, SC-14 (1979) 132-144.

[3] R.A. Williams and M.E. Beguwala, "The Effect of Electron Conduction on Si3N4 on the Discharge of MNOS Memory Transistors," in *IEEE Trans. Elec. Dev.*, ED-25, 1019-1027 (1978).

[4] M.E. Beguwala and T.L. Gunckel, "An Improved Model for the Charging Characteristics of a Dual Dielectric (MNOS) Nonvolatile Memory Device," *IEEE Trans. Elec. Dev.*, ED-25, 1023-1030 (1978).

Abstract No. 296

CHARGE TRAPPING KINETICS AND DIELECTRIC DEGRADATION IN SILICON NITRIDE FILMS

Robert S.K. Chau and Steven B. Bibyk

Solid State Microelectronics Laboratory
Department of Electrical Engineering
The Ohio State University, Columbus, Ohio 43210

INTRODUCTION

Thin silicon nitride films have been embodied in various semiconductor devices such as dynamic random-access-memories and nonvolatile memories. Among properties of the silicon nitride layer, charge conduction and trapping are two of the most important issues in understanding the operation and degradation of these devices. Recently it has been shown that under high field conditions, a two-carrier conduction and trapped charge distribution develops in the nitride film [1]. Such distribution gives rise to a peak electric field in the bulk dielectric which is speculated to cause conductivity changes and the onset of short circuit breakdown and damage in the device structures [2]. The exact correlation between charge trapping and dielectric degradation and breakdown processes is not completely known at the present time. However, some of the most important physical mechanisms of these processes can be revealed with the aid of a general high field transport model. We report here a computer-based multiple-trap model of charge trapping kinetics in silicon nitride films subjected to high field stressing. This model takes into account the combined effect of charge injection, trapping, emission and recombination of holes and electrons in the dielectric. It is used in conjunction with various experimental techniques and novel device structures to yield a detailed description of electric field and current distributions in the dielectric, as well as trapped hole and electron spatial distributions at different trap levels in the forbidden band gap. These computer simulations are useful for analyzing charge transport measurement and material measurement results for various experiments using MNOS devices.

THEORETICAL AND EXPERIMENTAL

In formulating the charge transport model, it is assumed that the trapping sites in the amorphous nitride layer give rise to a distribution of trapping levels in the forbidden band gap. The trapping levels above the midgap are considered as acceptor-type traps and those below it are considered as donor-type traps. The transport is assumed to be described adequately by the continuity equation for both holes and electrons, Poisson's equation which serves to couple the transport of holes and electrons and which causes the problem to be nonlinear, and the Shockley-Read equation for possible trapping, detrapping and recombination of holes and electrons for each trapping level. It is believed that direct recombination between holes and electrons are unlikely. In the formulation, three considerations will be used for the steady state and transient situations. First, the electric field is large enough so that the free-carrier velocity is saturated. Second, the trapped space charge dominates the free-carrier space charge which is low at high fields. Third, the trapped charge density dominates the diffusion of the free-carrier space charge density which is negligible at high fields. The set of partial differential equations used in the model are given below:

$$\frac{dp}{dt} = -\frac{1}{q}\frac{dJ_p}{dx} - \sum_i \frac{\sigma_p(i)J_p[N_{pt}(i) - P_i(i)]}{q} + \sum_i [e_p]_i P_i(i) - \sum_j \frac{\sigma_{rh}(j)J_p n_r(j)}{q}$$

$$\frac{dn}{dt} = -\frac{1}{q}\frac{d\,|J_n|}{dx} - \sum_j \frac{\sigma_n(j)\,|J_n|\,[N_{nt}(j) - n_r(j)]}{q} + \sum_j [e_n]_j n_r(j) - \sum_i \frac{\sigma_{re}(i)\,|J_n|\,P_i(i)}{q}$$

$$\sum_i \frac{dP_i(i)}{dt} = \sum_i \frac{\sigma_p(i)J_p[N_{pt}(i) - P_i(i)]}{q} - \sum_i [e_p]_i P_i(i) - \sum_i \frac{\sigma_{re}(i)\,|J_n|\,P_i(i)}{q}$$

$$\sum_j \frac{dn_r(j)}{dt} = \sum_j \frac{\sigma_n(j)\,|J_n|\,[N_{nt}(j) - n_r(j)]}{q} - \sum_j [e_n]_j n_r(j) - \sum_j \frac{\sigma_{rh}(j)J_p n_r(j)}{q}$$

$$\frac{dE}{dx} = \frac{q}{\epsilon_{ox}}\left[\sum_i P_i(i) - \sum_j n_r(j)\right]$$

$$[e_p]_i = N_v v_{th}\sigma_p(i)\exp\left[-\frac{q}{KT}\left[\theta_{pt}(i) - B(E)^{\frac{1}{2}}\right]\right]$$

$$[e_n]_j = N_c v_{th}\sigma_n(j)\exp\left[-\frac{q}{KT}\left[\theta_{nt}(j) - B(E)^{\frac{1}{2}}\right]\right]$$

In steady state, the variables do not vary with time and the above equations can be simplified. The boundary values can either be calculated or determined from experiments. For example, the values of the contact hole current $J_p(0)$ and the contact electron current $J_n(0)$ at the oxide-nitride interface can be inferred from charge seperation measurement on a MNOS transistor structure and the results are shown in Figure 1. The contact field E(0) at the oxide-nitride interface can be inferred from threshold voltage measurement and charge pumping measurement on the transistor. With the boundary values known, the general approach taken to solve the problem is to apply the finite difference method to the spatial variables. In order to obtain an accurate solution , a fine spatial mesh in the vicinity of the oxide-nitride interface and the gate electrode is required. This is because the boundary conditions may lead to steep gradients in the hole and electron density near the injection boundaries and cause the problem stiff.

SIMULATION RESULTS

Computer simulation results of a four-trap silicon nitride system are shown in Figure 2. Plotted are the overall charge density, the trapped carrier densities and the electric field in the dielectric. The interesting result is that a shallower hole trap can be more populated than a deeper hole trap even when the dielectric is subjected to high field stressing. This can occur if recombination is a significant mechanism in which case a trap level closer to the midgap will be more efficient and hence less occupied. This result has been well established in studies of charge trapping in semiconductors, but has been ignored in models of two-carrier charge transport in silicon nitride , leading to the possibly inaccurate approximation that a shallower trap level is always less occupied than a deeper trap level. Note also that the trapped charge distribution causes a peak electric field to develop in the bulk of the nitride layer. This peak field can gradually wear out the insulator and enhance its conductivity, and eventually causes dielectric breakdown

ACKNOWLEDGEMENTS

The authors acknowledge the encouragement of this research by Dr. D. Silversmith of the National Science Foundation, Dr. K.M. Chang of the Motorola Corp., and Dr. Y.H. Lee of the Intel Corp.. This research was supported by the National Science Foundation.

REFERENCES

1. K.M. Chang and S.B. Bibyk, the Electrochemical Society Extended Abstract, 85-2, 304 (1985).
2. S.B. Bibyk, Proc. Silicon Nitride and Silicon Dioxide Thin Insulating Films, ed. V.J. Kapoor and K.T. Hankins, the Electrochemical Society, Pennington, NJ, 87-10, 10 (1987).

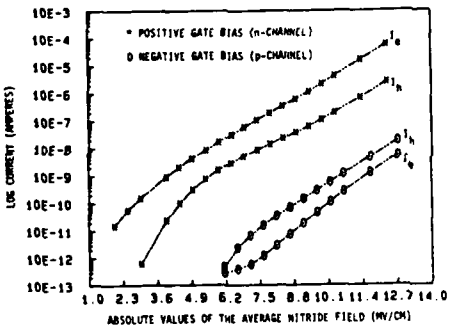


Figure 1: Contact Electron Current and Contact Hole Current Components at the Oxide/Nitride Interface Under High Fields.

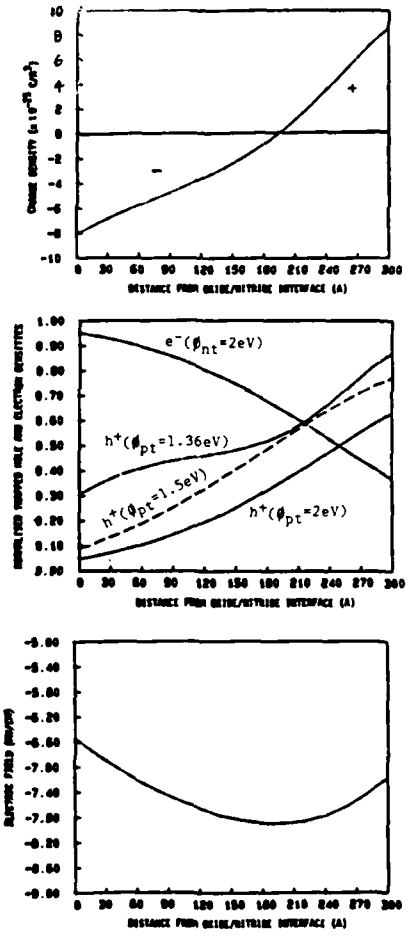


Figure 2: Computer Simulation of a Four-Trap Silicon Nitride System Subjected to High Field Stressing.

Abstract No. 297

Hot Electron Effects in Semi-Insulating Polysilicon(SIPOS) and Polysilicon TFTs

Biay-Cheng Hseih and David W. Greve
Department of Electrical and Computer Engineering
Carnegie Mellon University
Pittsburgh, PA 15213

I. Introduction

Large flat panel displays for portable computers and other applications require active matrix addressing in order to obtain adequate contrast. Process design for fabrication of thin film switching transistors in flat panel displays involves a number of difficult compromises. Low temperature thin film transistors processes are preferred so that low cost glass substrates can be used with minimal warpage during processing. We have reported that polycrystalline silicon thin film transistors (TFTs) have been fabricated with the use of semi-insulating polysilicon (SIPOS) deposited at 600°C as gate insulator[1]. As a result of prolonged exposure to wet oxygen at 600°C, this material is converted into silicon dioxide with low leakage current and drift. By combining the SIPOS gate insulator with a technique for producing large grain crystallized silicon films previously reported [2], we have fabricated TFTs with excellent characteristics, even though no process temperature exceeds 600°C. In our approach, a completely oxidized gate insulator of about 130nm thickness can be obtained in 24 hr in contrast to thermal oxidation [3] which requires 96 hr to produce a film only 80nm in thickness.

It is the object of this study to investigate the susceptibility of our polysilicon TFTs to hot electron stress. Hot-electron effects have been observed in our polysilicon TFTs and further studied in MOS capacitors with an oxidized SIPOS insulator. We have characterized the oxide traps in the SIPOS films by examining the change of TFT I-V characteristics and the trapping phenomena due to the hot electron injection into the SIPOS films during avalanche breakdown.

II. Experiment

Polysilicon TFTs were fabricated on 3~5 Ω-cm (100) n-type silicon wafers. After the growth of 1 μm oxide by wet oxidation, amorphous silicon films of 108 ± 5nm were deposited in an LPCVD system at 545 °C. Crystallization of amorphous films was performed at 560 °C for 72 hr. After polysilicon islands were defined, the source and drain were doped by arsenic implantation at 40 KeV to a dose of 2 x 10^{15} cm^{-2}. No dopants was introduced into the channel. A 101 ± 5nm SIPOS film was deposited at 600 °C with the flow rate ratio of (N_2O/SiH_4) = 1.67 in the same LPCVD reactor used for deposition of amorphous silicon. Following wet oxidation at 600 °C for 24 hr, the SIPOS films are converted to SiO_2 with a final thickness of 134 ± 5nm. Then, aluminum was evaporated to form the gate as well as the contacts to source and drain. Finally, hydrogen plasma passivation was performed in a Technics PE-IIA reactor at a power level of 250 W for 3 hr with a pressure of 0.7 torr and substrate temperature of 300 °C. The final device structure is shown in Fig. 1.

TFT characteristics were measured in two different modes before and after hot electron stress. First, we designated source and drain contacts and measured the transistor characteristics (subsequently referred to as forward mode). Then, we remeasured by switching source and drain contacts (reverse mode). All forward and reverse mode measurements were at V_{DS} = 1 V, and V_{GS} was swept from -20 V to 20 V in 30sec. Stress was applied by biasing the transistor at $V_{DS} = V_{GS}$ = 7.5 V for various stress times at room temperature.

MIS capacitors with oxidized SIPOS films as gate insulator for hot electron studies were fabricated on 0.1~0.5 Ω-cm (100) p-type silicon wafers. The SIPOS films are identical to the gate insulator of TFTs described previously except they did not receive hydrogen plasma passivation. Aluminum was deposited on top of the oxidized SIPOS films, followed by definition of dots of 7.85 x 10^{-3} cm^2 and deposition of aluminum back contact. Avalanche injection of hot electrons into the MOS capacitor insulator was used to study electron trapping in the SIPOS films. Hot electrons were injected by applying a high frequency a-c signal of sufficient amplitude across the capacitor [4].

III. Result and Discussion

The I-V characteristics of TFTs before and after hot electron stress are shown in Fig. 2. For all devices tested, the forward mode and reverse mode characteristics were identical before hot electron stress. After application of the stress, the reverse mode characteristic remained unchanged while the forward mode characteristic showed only a change in its leakage current behavior ($V_{GS} < 0$ V) but no change in its ON-state behavior ($V_{GS} > 0$ V). The fact that the reverse mode characteristic is unchanged after stress is consistent with hot carrier generation of interface states near the drain (in forward mode operation).

For $V_{GS} < 0$, there is a component of drain current due to interface state generation. This is responsible for the observed increase in leakage current. When V_{GS} becomes more negative, a monotonic increase in leakage current is observed. This is due to the high electric field near the drain which results in field-enhanced leakage current.

After we observed hot electron effects in the TFT I-V characteristics, we examined the details of electron trapping in oxidized SIPOS films by hot electron injection in SIPOS MOS capacitors. Fig. 3 shows trapping efficiency due to avalanche injection of hot electrons into oxidized SIPOS of an MIS capacitor. The trapping efficiency is defined as

$$\eta_{eff} \equiv \frac{dN_{eff}}{dN_{collected}}$$

where N_{eff} is the number of electron charges trapped per unit area and $N_{collected}$ is the number of hot electrons per unit area collected by the gate electrode. A plot of the logarithm of η_{eff} vs. N_{inj} does not show any straight line portions. As a result, we cannot characterize the trapping by a small number of different trap cross sections.

Also shown in Fig. 3 is the result of similar measurements on MOS capacitors with wet thermal SiO_2. The curve for SIPOS insulator approaches that of wet thermal SiO_2 grown at 800 °C at an injection level of 10^{16} e/cm^2. However, the oxidized SIPOS films cannot be stressed beyond this level or breakdown will occur. We conclude that SIPOS contains a significant number of traps with larger capture cross sections than thermal SiO_2. The electron capture cross section of wet thermal SiO_2 was calculated as 3 x 10^{-19} cm^2 which can be attributed to the moisture-related centers reported by Nicollian et al. [4].

In summary, interface state generation due to hot electron stress on TFTs has been observed. Trapping of electrons in oxidized SIPOS films has also been studied. The results show that the SIPOS films have a higher trapping efficiency than thermal SiO_2 and probably a distribution of trap cross sections.

References

1. B.-C. Hseih et al., submitted to *IEEE Transactions on Electron Device.*

2. M. K. Hatalis and D. W. Greve, *J. Appl. Phys.*, vol.63, p2260, (1988).

3. A. C. Ipri and G. Kaganowicz, *IEEE Transactions on Electron Device.* vol.35, p.708, (1988).

4. E. H. Nicollian and C. N. Berglund, *J. Appl. Phys.*, vol.41, P3052, (1970).

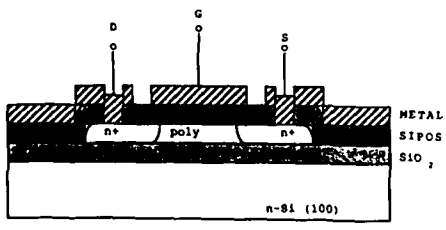


Fig. 1 Cross section of polysilicon thin-film transistor.

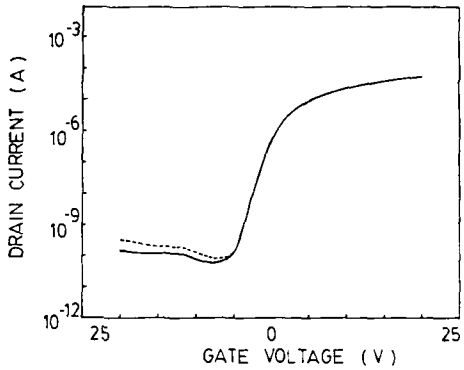


Fig. 2 I-V characteristic of TFT with channel length of 25 μm and channel width of 75 μm *before* (——) and *after* (- - -) a 30 min stress at $V_{GS} = V_{DS} = 7.5$V.

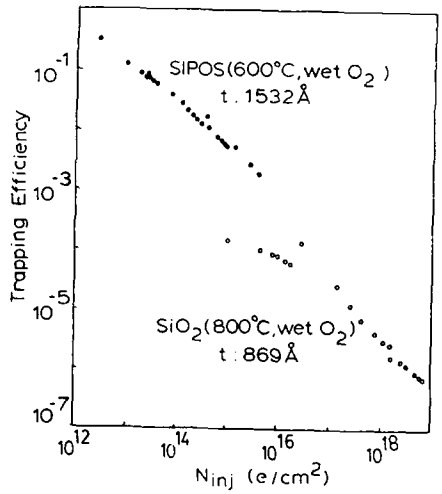


Fig. 3 Trapping efficiency vs injection charge density of oxidized SIPOS and thermal grown wet SiO_2 over a wide range of injected charge.

Acknowledgement

The authors would like to thank Dr. M. K. Hatalis for helpful discussions. This project was supported by IBM Thin Film Sciences Program at Carnegie Mellon University.

Abstract No. 298

Hot- Carrier Induced Excess Current in Polysilicon Emitter Bipolar Transistors

D.W. Greve and T.Y. Chou
Department of Electrical and Computer Engineering
Carnegie- Mellon University
Pittsburgh, PA 15213

Introduction

It has long been recognized that hot carriers can cause degradation in the current gain of bipolar transistors [1]. This can be a consequence of either generation of interface states or trapped charge in the oxide which influences the surface potential [2]. In either case, hot carrier- induced degradation becomes more important as the junction electric field increases. As a result, there have been two recent investigations of degradation in advanced polysilicon emitter transistors [3,4]. In this paper, we report measurements of hot carrier- induced degradation in polysilicon emitter transistors with and without hydrogen passivation treatments and we show that the dependence of excess base current on injected charge and bias can be understood based on a published model [5] for hot carrier degradation in MOSFETs.

Experiment

The devices used in this study were polysilicon emitter transistors fabricated on 1- 5 Ω-cm (111) silicon wafers. The base was formed by implanting boron at 100 keV to a dose of 2.5 x 10^{13} cm^{-2}. Polysilicon was deposited at 625 °C followed by a 100 keV arsenic implant to a dose of 3 x 10^{15} cm^{-2} or 10^{16} cm^{-2}. The emitter drive- in was either 30 minutes at 950 °C or 15 minutes at 950 °C followed by 15 minutes at 1000 °C. Some wafers were passivated by implantation of 10^{15} cm^{-2} hydrogen at 40 keV. All wafers received a post-metallization anneal at approximately 385 °C in forming gas. The emitter size of the transistors investigated was 10 µm x 10 µm.

The hot carrier stress was performed by biasing the emitter- base junction to a voltage $V_{BE} < 0$ and injecting electrons into the depletion region by forward biasing the collector- base junction. This method was initially used by bosselaar [6] and has the advantage that both the voltage across the emitter- base junction and the injecting current can be independently varied. At intervals, the bias was removed and $I_B(V_{BE})$ was recorded with $V_{CB} = 0$ together with the total charge injected across the emitter- base junction Q_{inj}. Typical results are shown in Fig. 1 for both passivated and unpassivated transistors. As expected, an excess base current is observed at low currents which has been attributed to pair generation through interface states [3,4]. The measurements were repeated on different transistors in order to examine the effect of V_{BE} and the passivation treatment. We observed the following trends:

1) The degradation for a particular stress charge was more rapid for hydrogen passivated transistors.
2) The excess base current increases more rapidly with stress charge at more negative values of V_{BE}.
3) The excess base current has a voltage dependence of approximately 120 mV/ decade for unpassivated transistors but has a smaller value (≈ 105 mV/ decade) for passivated transistors.

Analysis

In order to understand these results we refer to the model of Hu et al. [5]. A kinetic model yields for the interface state density N_{it} [cm^{-2}]

$$N_{it} = C\left[\frac{Q_{inj}}{P} e^{-\varphi_{it}/q\lambda E_m}\right]^n$$

where P is the perimeter of the transistor, φ_{it} is the electron energy required to surmount the oxide barrier and generate an interface state, λ is the electron mean free path, E_m is the maximum junction electric field during injection, and the exponent n is between .5 and 1. The interface states will produce an excess base current due to pair generation given by

$$\Delta I_B = \frac{q}{2} P N_{it} \sigma v_{th} n_i W_F e^{qV_{BE}/mkT}$$

where W_F is the part of the emitter- base depletion width active in recombination, σ the capture cross section, and v_{th} the thermal velocity. The ideality factor m is usually equal to 2 but may have other values when field enhanced emission [7] and/ or a nonuniform distribution of interface states [8] is present. At a particular value of V_{BE}, we therefore expect

$$\Delta I_B \sim (Q_{inj} e^{-\varphi_{it}/q\lambda E_m})^n .$$

In Fig. 2, we present the excess base current $\Delta I_B(V_{BE} = .48\ V)$ as a function of injected charge Q_{inj} on a log- log plot. The data for all transistors is fit reasonably well by a straight line with slope corresponding to n ≈ 0.5. Also visible is the strong dependence on electric field E_m. We can determine the ratio φ_{it}/λ, since we expect for constant injected charge $\log(\Delta I_B^2) \sim -\varphi_{it}/q\lambda E_m$. This analysis is illustrated in Fig. 3 for the unpassivated transistor, where the maximum electric field has been determined from capacitance measurements. Assuming $\varphi_{it} = 3.7$ eV, we obtain λ = 33 Å, which is in fair agreement with previous reports [5]. For passivated devices, a higher value is obtained for λ. We regard the results for passivated devices as less reliable because the higher values of N_{it} may cause the electric field at the surface to be different from the rest of the junction.

In conclusion, we note that the rate of interface state generation is greater in passivated devices, even for similar doping profiles. This is consistent with models for interface state generation which involve hydrogen [5,9]. As a result, hydrogen passivation to increase the current gain [10] may adversely influence the stability of polysilicon emitter transistors.

Acknowledgements

This work was supported by the Semiconductor Research Corporation. The authors also wish to thank D.L. Chen for providing the samples.

References

1. D.R. Collins, *IEEE Trans. Electron Devices* **ED-16**, 403 (1969).
2. J.F. Verwey, *Microelectronics and Reliability* **9**, 425 (1970).
3. S.A. Peterson and G.P. Li, *IEDM Tech. Digest* p. 22 (1985).
4. S.P. Joshi et al., *IEDM Tech. Digest* p. 182 (1987).
5. C. Hu et al., IEEE *Trans. Electron Devices* **ED-32**, 375 (1985).
6. C.A. Bosselaar, *Solid-State Electronics* **16**, 648 (1973).
7. D.W. Greve et al., *Solid-State Electronics* **28**, 1255 (1985).
8. J.C.S. Woo et al., *IEEE Trans. Electron Devices* **ED-34**, 130 (1987).
9. F.J. Feigl et al., *J. Appl. Phys.* **52**, 5665 (1981).
10. G.L. Patton et al., *IEEE Trans. Electron Devices* **ED-33**, 1754 (1986).

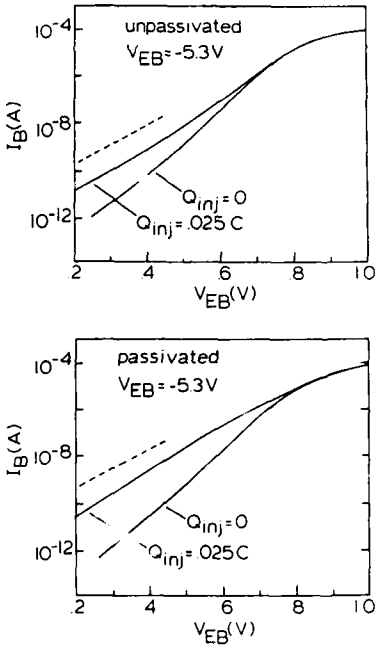


Fig. 1. $I_B(V_{BE})$ with V_{CB} = 0 before and after stress. The top curve is for an unpassivated transistor and the bottom curve for a passivated transistor. The dotted line indicates a slope of 120 mV/ decade.

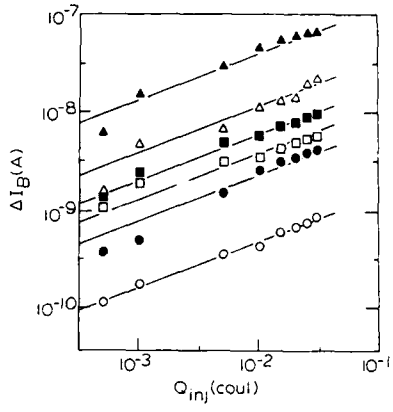


Fig. 2. Plot of $\log(\Delta I_B)$ as a function of $\log Q_{inj}$ for three transistors: (●,○) unpassivated with 30 min drive-in at 950 °C and 10^{16} cm^{-2} arsenic dose; (▲,△) same transistor with hydrogen passivation; and (■ , □) passivated with 3 x 10^{15} cm^{-2} arsenic diffused 15 min at 950 °C followed by 15 min at 1000 °C. The solid points correspond to V_{BE} = -5.3 V and the open points V_{BE} = -4.5 V.

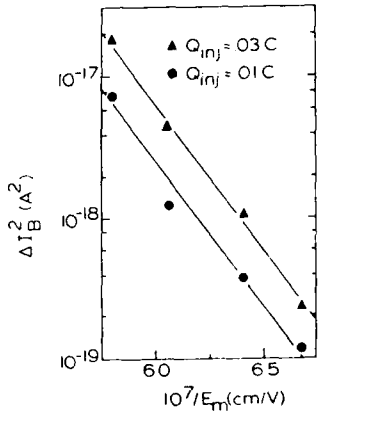


Fig. 3. Plot of $\log(\Delta I_B^2)$ as a function of $1/E_m$ for an unpassivated transistor. The emitter drive- in time was 30 min at 950 °C. The lines correspond to λ = 33 Å.

Abstract No. 299

DIELECTRIC FORMATION BY RAPID THERMAL NITRIDATION

D. Henscheid, M. Kozicki, I. Zwiebel, R. Graham*,
G. Sheets, and E.G. Chang**
Center for Solid State Electronics Research
Arizona State University
Tempe, AZ 85287

Advances in VLSI technology have made the reduction of gate insulator thickness necessary for high density integrated components. As the dielectric film thickness approaches the 10 nm regime, the use of SiO_2 is no longer appropriate due to problems such as hot electron effects, high-field instabilities, radiation damage, poor impurity masking and slow trapping in this material [1]. One of the most promising alternatives to thin SiO_2 is nitrided SiO_2. Thermal processing in an ammonia ambient results in the nitridation of the SiO_2 and an oxynitride is thus formed. Conventional thermal furnace methods are traditionally used to achieve nitridation. However, long exposure at high temperature, (typically >1100°C for several hours), results in the degradation of the electrical characteristics of MOS devices [2]. On the other hand, high processing temperatures can provide good electrical characteristics if decreased processing times are used [3].

Rapid Thermal Nitridation (RTN) is proving to be a viable alternative to conventional thermal methods. Processing is performed at very high temperatures for short times (<120 sec.). In order to achieve an optimal gate dielectric, a greater understanding of the RTN process with respect to structural and electrical properties must be obtained. Unfortunately, data on short-time nitridation of SiO_2 is limited. This paper reports on the results of a study of the electrical and structural properties of thin dielectric films produced by the RTN process. Dependence of film properties on RTN time and RTN temperature are stressed.

Experimental Procedure

SiO_2 films 10 nm thick were grown on 100 mm, <100>, 7.5-12.5 ohm-cm, n-type (P) silicon substrates. After a one hour HCl tube clean, oxidation was performed for 15 minutes at 900°C in dry O_2. Nitridations were performed in a Tamarack 180M Rapid Thermal Processor using a pure ammonia ambient at atmospheric pressure. The wafers were nitrided at four different temperatures, 900°C, 1000°C, 1100°C, and 1200°C for four diffcrent nitridation times, 3 sec, 15 sec, 60 sec and 90 sec. The temperature was ramped up to within 25°C of the designated processing temperature within 3 seconds, and after nitridation was ramped down to below 600°C within three seconds.

Structural characteristics were analyzed using Auger Electron Spectroscopy (AES), X-ray Photoelectron Spectroscopy (XPS) and Secondary Ion Mass Spectroscopy (SIMS). Layer morphology was examined using High Resolution Transmission Electron Microscopy (HRTEM). Electrical characterization was performed using capacitance-voltage (C-V) techniques.

Results and Discussion

The results, in general, confirm the work of previous researchers but also provide new data on the RTN technique. Selected AES results are shown in Fig. 1. For low temperature, short time nitridation (900°C, 3 sec), AES shows minimal surface nitrogen with no observable nitrogen in the bulk or at the interface. As RTN time increases with the RTN temperature remaining low (900°C, 60 sec), or as the RTN temperature increases with the RTN time remaining short (1100°C, 3 sec), the interfacial nitrogen concentration increases without an appreciable increase in surface nitrogen. At long RTN times and high RTN temperatures (1100°C, 60 sec), the concentration of nitrogen throughout the entire SiO_2 film is significantly increased.

Data from XPS demonstrates that at low RTN time (1100°C, 3 sec), the surface nitrogen fraction, [N]/([N]+[O]), measures .038 and the interfacial nitrogen fraction measures .016. Increasing RTN times increase the surface N fraction to approximately .092 and the interfacial N fraction to .091. At very high RTN times and temperatures (1200°C, 60 sec), the surface N fraction measures over .15 and the interfacial N fraction measures .07. This maximum surface concentration differs by more than an order of 2 from the 0.35 fraction measured by Chang et al. [2]. SIMS analysis shows a very sharp hydrogen concentration peak near the surface, decreasing significantly within several angstroms and then slowly decreasing through the bulk of the wafer, dropping off towards zero at the interface. No interfacial hydrogen peak was observed.

A possible model for this nitridation reaction can be derived from the above results. The nitrogen profiles observed are probably the combination of the profiles of two separate nitrogen species; nitrogen reacted with silicon, and nitridant (NH_x, x=0,1,2,3). As nitrogen diffuses through the SiO_2 some of it reacts with the first several monolayers of the surface. In addition, because of the high density of states, the SiO_2/Si interface acts as a nitrogen sink, causing the nitrogen to react, thus creating a favorable driving force for nitrogen to diffuse. As observed in Fig. 1, in the interface region the nitrogen accumulates confirming that the interface must be a very strong sink. As the concentration of nitrogen increases with time, nitridation of the surface proceeds and further diffusion of the nitrogen into the SiO_2 layer becomes slow. This gives rise to a larger concentration of nitrogen at the surface, even larger than at the interface.

The presence and relative quantities of both nitrogen and hydrogen have a profound effect on the electrical characteristics of the processed films. There is a marked shift in flatband voltage with an increasing negative swing for 900°C and 1100°C up to 60 sec processing time. Longer processing times at these temperatures result in a less negative swing. The worst case shift of approximately -1.0 V occurs for 1100°C at 60 sec. At 1200°C, the trend is repeated but over a much shorter time scale, with the peak shift (-0.6 V) occurring around 3 sec. The shift in flatband voltage is created by the change in the amount of fixed charge within the films, which rises and subsequently falls with increasing processing time. The rise correlates with rising interfacial nitrogen, whereas the decrease corresponds to a subsequent increasing hydrogen concentration near the interface.

With regard to morphology of the layers, short processing times, as shown by HRTEM analysis, have little effect on the silicon/dielectric interface. Fig. 3 shows a smooth interface similar to the transmission electron micrographs of layers not subjected to nitridation. A dramatic difference is observed at 1100°C for 60 sec. [Fig. 4]. Here the interface is by no means smooth and there appears to be other amorphous regions penetrating randomly into the silicon surface. Due to the large quantity of nitrogen (and a small amount of hydrogen) at the interface for these processing conditions, it is likely that we are witnessing the formation of silicon-rich oxynitride or perhaps even silicon nitride amorphous regions.

Acknowledgements

We would like to acknowledge the efforts of Dr. Derwin Flowers and Dr. Mike Kottke, Motorola Semiconductor Inc., Phoenix, AZ, for their AES data contribution, and Dr. Peter Williams, Arizona State University, for his SIMS data contribution.

References

1. Ito, T., T. Nakamura, H. Ishikawa, J. Electrochem. Soc., **129**, Jan. 1982.
2. Chang, C. C., A. Kamgar, D. Kahng, IEEE Electron. Device Lett., EDL-6, Sept. 1985.
3. Moslehi, M. M., S. Shatas, K. Saraswat, Proc. Electrochem. Soc., **86-4**, 1986.

* Center for Solid State Science, ASU
** Visiting Professor, Chung-Ang University, Korea

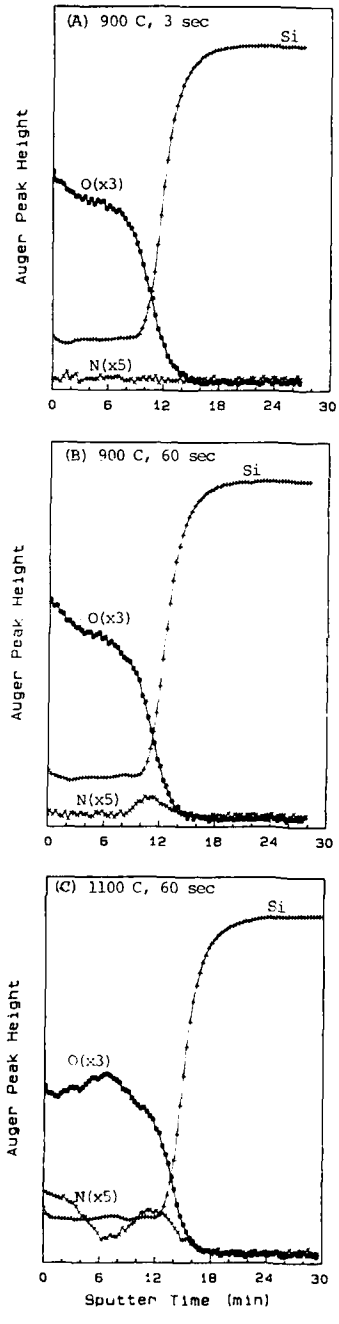


Fig. 1. Comparison of the Auger profiles of SiO_2 layers nitrided at various RTN conditions. (A) 900°C, 3 sec., (B) 900°C, 60 sec., (C) 1100°C, 60 sec.

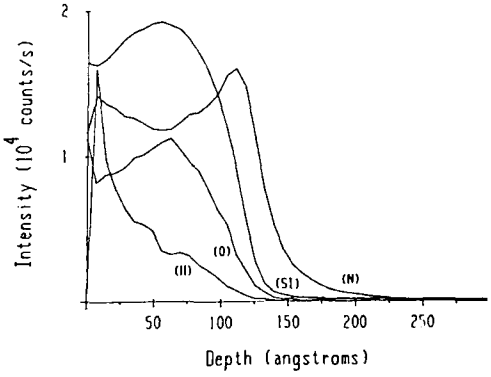


Fig. 2. SIMS analysis of a SiO_2 layer nitrided by RTN at 1100°C, 60 sec.



Fig. 3. TEM micrograph of a 10 nm SiO_2 layer nitrided at 900°C, 60 sec. by RTN methods.



Fig. 4. TEM micrograph of a 10 nm SiO_2 layer nitrided at 1100°C, 60 sec. by RTN methods.

Abstract No. 300

Process Induced Radiation Damage in IGFET Gate Insulators

Arnold Reisman[1,2]

[1]Microelectronics Center of North Carolina, P. O. Box 12889,
Research Triangle Park, North Carolina 27709

[2]Department of Electrical Engineering, North Carolina State University,
Raleigh, North Carolina 27695-7911

In terms of initial device yield, and long term reliability, process induced radiation damage represents an area of considerable concern.[1-6] The processes that need to be examined include Ion Implantation, X-Ray, E-Beam and Ion Beam lithography, Electron Beam metal evaporation, Sputtering, Reactive Ion Etching, and even SEM examination.

The talk will discuss the effects of synchrotron X-radiation in the energy range 300-100 eV, as well as Al Kα exposures which simulate X-ray lithographic procedures. It will describe such effects in the context of preliminary studies dealing with varying rad exposure level at constant gate insulator thickness, as well as the behavior at several, rad exposue levels as a function of gate insulator thickness.

Data will be presented indicating that despite prevailing beliefs, damage in the synchrotron range follows a linear relationship over the thickness range from less thatn 10nm to 50nm, indicating strongly that damage resides near the interface and is constant with increasing insulator thickness. It will be shown that such behavior is consistent with a simple model. Even if such damage can be annealed completely using normal techniques, which is questionable, there are wide-ranging implications concerning the rad hardness of scaled devices.

Preliminary studies of silicon implantation effects in gate insulators will also be discussed, as will questions relating to defect annealing behavior in insulators subjected to different forms of radiation. The silicon implantation studies are intended to simulate inadvertent implantation damage in the gate insulator of an IGFET. The focus will be on the electrical effects of such implantation, and the annealing behavior, or lack thereof, and radiation tolerance observed with such devices. In addition, based on existing trapping model equations, data was generated for trap cross sections and densities, of both coulombic and neutral centers ranging in X-section from $10^{-13}cm^2$ to $10^{-17}cm^2$.

References

1. A. Reisman and C. J. Merz, J. Electrochem Soc., 130, 1384 (1983)
2. A. Reisman, C. J. Merz, J. R. Maldonado and W. W. Molzen, Jr., J. Electrochem. Soc., 131, 1404, (1984)
3. A. Reisman, Proc. IEEE, 71, 550 (1983)
4. J. R. Maldonado, A. Reisman, H. Lezec, C. K. Williams and S. S. Iyer, J. Electrochem Soc., 133, 628 (1986), J. Vac. Science and Tech.B, 5, 248 (1987)
5. A. Reisman, C. K. Williams and J. R. Maldonado, J. Appl. Phys., 62, 868 (1987)
6. C. K. Williams, A. Reisman, P. K. Bhattacharya and W. Ng, J. Appl. Phys. 63, 0000, (1988) In Press

Abstract No. 301

Deposition gas ratio and Post-deposition RTA improvement of LPCVD silicon dioxides in VLSI processing

[1]J.K. Park, [1]J. Clarke, and [1,2]A. Reisman

[1]Microelectronics Center of North Carolina
Research Triangle Park, North Carolina 27709,

[2]Department of Electrical Engineering, North Carolina State University,
Raleigh, North Carolina 27695-7911.

Introduction

Chemical deposition of silicon dioxide films are widely in use in VLSI processing[1,2,3]. However, the characteristics of as deposited CVD films are different from those of thermal silicon dioxides. The present study investigates improvements in the mechanical and physical characteristics of LPCVD silicon dioxide films subjected to rapid thermal annealing in an oxygen ambient atmopsphere. The oxygen to silane gas ratio, O_2/SiH_4, and the reactant partial pressure were used to control deposition rate and uniformity of the deposited oxides.

The changes in dielectric constant, etch rate, electric field breakdown strength, bias-temperature stress instability, refractive index, and I.R. absorption and transmission were examined on a series of samples to estimate the level of improvements associated with annealing[4].

The changes in mechanical and physical properties indicate that oxidation of "silicon rich" films and densification of the lower density LPCVD oxides occurs during rapid thermal annealing.

Experimental

For these experiments, 4 inch, P-type, (100) orientation gettered device quality silicon wafers were used. After standard cleaning in $NH_4OH:H_2O_2:H_2O$, $HCl:H_2O_2:H_2O$ and buffered HF etch/rinse cycles, the wafers were coated with LPCVD oxides.

These films were deposited on closely packed vertical wafers in a hot wall resistance heated furnace using SiH_4 and O_2 mixtures. The O_2/SiH_4 gas ratio was varied from 2 to 9. The deposition pressure was approximately 250 mTorr for all runs and the wafer temperature during the depositions was 400°C ± 0.5°C.

Following deposition, rapid thermal annealing in an oxygen ambient atmosphere was conducted for varying lengths of time and temperatures. Times up to 100 seconds and temperatures up to 1050°C were employed.

An automated ellipsometer was used to measure the oxide thickness, uniformity, and refractive index. Etch rate studies were conducted to provide additional information. An automated capacitance-voltage plotter was used to measure the bias-temperature stress instability and dielectric constants of annealed and un-annealed films. A special set-up using a digital electrometer was employed to measure electric field breakdown strength of oxides with and without rapid thermal annealing.

At temperature above 1000°C, rapid thermal oxygen annealing reduced the as deposited dielectric constant from values as high as 4.41 for films presumed to be silicon rich to approximately 3.80, essentially independent of the value of the as deposited dielectric constant. For 1050°C annealing, the dielectric constant approached 3.84, characteristic of thermally grown oxides on silicon.

Post-deposition annealing produced a shift in the I.R. absorption and transmission peak frequency toward that of thermal oxides. The amount of the shift generally increased with the annealing temperature.

The refractive index of the deposited oxides was as high as 1.47. However, after being fully annealed they all approached a value of approximately 1.46.

Dielectric breakdown voltages have been measured for samples approximately 1200Å thick. For as deposited samples the peak in the histograms of breakdown voltage corresponds to breakdown field strengths of 4.9-5.5 MV/cm. Annealed samples showed a modest improvement in the breakdown voltage.

Results

The initial results have shown that the gas ratio (SiH_4/O_2) has a marked influence on both the dielectric constant and breakdown field strength of as deposited oxides.

The gas ratio study confirmed some of the information available in the literature[1]. However, the post-deposition annealing study in oxygen ambient atmosphere in a RTA furnace provided significant improvement of as deposited LPCVD oxides whereby their properties approached the characteristics of the thermal oxide.

References

1. Richard S. Rosler, *Solid State Technology*, p.63-70, April, 1977.

2. A.C. Adams et al, *Solid State Science and Technology*, and *J. Electrochem. Soc.* Vol. 128, No. 7, 1981.

3. T.I. Kamins et al, *Solid State Technology*, p.51-57, July, 1979

4. Yasuo Uoochi et al, *Solid State Science and Technology*, *J. Electrochem. Soc.*, Vol. 134, No. 8, 1987.

Abstract No. 302

THE CHARACTERIZATION OF ELECTRON CYCLOTRON RESONANCE PLASMA DEPOSITED SILICON NITRIDE and SILICON OXIDE FILMS

Son Van Nguyen and Kevin Albaugh

IBM General Technology Division
Essex Junction, VT 05452

INTRODUCTION

Low temperature plasma deposited silicon nitride and oxide films are excellent materials that can be used for final passivation layers and interlevel dielectric films for very large scale integrated circuit fabrication[1] Generally, the deposition substrate temperature must be 350°C or higher to obtain good quality films. For ultra large scale intergrated circuits (ULSI) fabrication, better interlevel dielectric films with lower hydrogen concertration are needed. In recent reports[2,4] silicon nitride and oxide films deposited by electron cyclotron resonance (ECR) plasma processing were found to have lower hydrogen concentrations and other promising physical properties. In this paper, we present a systematic study of the physical and chemical properties of ECR plasma silicon nitride and oxide films deposited at room temperature and compared these properties with those of thermal and plasma chemical vapor deposited (CVD) films.

EXPERIMENTAL

ECR plasma silicon nitride and oxide films were deposited in an ECR deposition system similar to the system described in[2]. Silane and nitrogen and silane and oxygen were used as reactant gases for silicon nitride and oxide films respectively. Both films were deposited at room temperature using 2.45 GHz microwave excitation with a magnetic field of 875 Gauss at 1 to 2 mTorr pressure. The film's physical and bonding properties were analyzed using ellipsometry, Auger, Fourier transform infrared, X-ray photoelectron spectroscopy, transmission electron microscopy, buffered HF etching and nuclear reaction analysis for hydrogen analysis techniques. Plasma and thermal CVD films deposited at much higher temperature (350° and 800°C) were also analyzed and compared with ECR plasma films. Both ECR plasma silicon nitride and oxide films were also deposited over silicon trench topography and their step coverage was analyzed under various process conditions.

RESULTS and DISCUSSIONS

Ellipsometric measurement of as deposited silicon nitride and oxide films have refractive indices of 2.15 and 1.47 respectively. Auger depth profiles analysis showed the nitride film has poor depth profile uniformity and higher silicon concentration than the stoichiometric composition of Si_3N_4. This result is consistent with the higher film refrative index. For silicon oxide films, the Auger depth profiles is much more uniform, with the composition of $SiO_{1.9}$ (nearly stoichiometric SiO_2)

FTIR spectra show the presence of Si-N (≈ 880 cm^{-1}) bonds and smaller amount of N-H (≈ 3340 cm^{-1}) and Si-H (≈ 2000 cm^{-1}) bonds in the silicon nitride film.

The principal Si-O bonds (≈ 1065 and 830 cm^{-1}) and much smaller amounts of Si-H bonds were observed in silicon oxide films. Table I showed that halfpeak width comparison between ECR, thermal and plasma deposited nitride and oxide films. The halfpeak width of plasma films are normally broader while those of ECR and thermal films are about the same. This suggested that the ECR films quality are similar to thermal films.

Nuclear reaction analysis for hydrogen showed the hydrogen concentration in ECR films deposited at room temperature are about half of the hydrogen concentration in plasma films deposited at 300°C. The hydrogen depth profiles of the ECR oxide films are also more uniform than observed with nitride films. However, the hydrogen concentrations in ECR films are still much higher than those of thermal films (Table II). It should be noted that the amount of hydrogen observed in our films is near the upper limit of the hydrogen concentration range detected in ECR films reported by T. Hirao[2,4]. Buffered HF etching of ECR, thermal and plasma deposited films showed that the ECR films etch much slower than plasma films; however, the etch rates are still significantly faster than thermal films.

X-ray photoelectron spectroscopy analysis showed some carbon contamination (8-13% a/o) on both ECR nitride and oxide surface. The surface compositions are $SiO_{1.7}$ for silicon oxide and Si_4N_3 silicon nitride films. No significant differences in surface composition were observed between ECR, plasma and thermal nitride and oxide films of similar bulk compositions.

Both nitride and oxide films have very nonconformal step coverage. Films deposited without RF bias have very poor (< 0.4) sidewall coverage. Under many conditions, high aspect ratio grooves cannot be filled by ECR silicon oxide and nitride films.

Transmission electron micrographs show that sidewall film coatings may have voids, are more porous and etch much faster in buffered HF solution compared to films deposited on planar surfaces (Figs. 1-2). This is due to the enhanced vertical ion bombardment characteristic of ECR processing[5], which densifies films deposited on planar surfaces. With RF bias, oxide films showed good planarization characteristic as has been observed by Machida[6]. The film in Fig. 1 was deposited without RF bias during the initial stage of film growth, then with bias for the remainder of the film. The voids occur in the portion of the film deposited without bias, and the fissure occurs during deposition with bias.

CONCLUSION

The physical and bonding characteristic of ECR plasma deposited silicon nitride and oxide films were analyzed using various analytical techniques. ECR films deposited at room temperature showed better qualities than those of plasma deposited films at higher temperature (350°C). The oxide film qualities are almost comparable to thermal CVD films; however, the nitride film qualities are slightly poorer. For both films, the step coverage is very nonconformal and sidewall films are much more porous under most deposition conditions. This is due to the anisotropic ion bombardment properties of ECR processing. RF biasing can reduce this effect.

ACKNOWLEDGEMENT

The authors wish to acknowledge the contributions of D. CiCicco, K. Furland, S. Fridmann, D. Harmon R Gleason, L. Nesbit, and J. Rembetski.

REFERENCES

1. Son Van Nguyen; J. Vac. Sci. Technol. B4(5), pp. 1159-1167 (1986)
2. T. Kikkawa, S. Chikaki, Y. Matsumoto, T. Ueno and H. Wanatabe; Proceed. of the Symp. on Reduced Temperature Processing for VLSI, V. 86-5, pp. 235-246 (1986), The Electrochemical Society Publication.
3. T. Hirao, K. Setsune, M. Kitagawa, T. Kamada, K. Wasa, T. Izumi; Jap. J. of Appl. Phys., V. 26, pp. 2015-2021, December 1987.
4. T. Hirao, K. Setsune, M. Kitagawa, T. Kamada, K. Wasa, T. Izumi; Jap. J. of Appl. Phys., V. 27, pp. 30-34, January 1988.
5. T. Hirao, K. Setsune, M. Kitagawa, Y. Manabe, K. Wasa, S. Kohiki; Jap. J. of Appl. Phys., V. 26, pp. L544-546, May, 1987.
6. K. Machida, H. Oikawa, J. Vac Sci. Technol. B, V. 4, pp. 818-821 (1986).

Table I. FTIR bonding analysis of ECR, thermal and plasma films

Film Type	SiN / SiO Band Position (cm^{-1})	Peak Width (cm^{-1})	Film Refractive Index (N)	Deposition Temperature (°C)
ECR SiO_2	1065	110	1.476	25°
PECVD SiO_2	1050	230	1.47	300
LPCVD SiO_2	1090	110	1.46	800°
ECR Si_3N_4	865	210	2.15	25°
LPCVD Si_3N_4	870	215	2.00	800°
Plasma ASM Si_3N_4	900	240	2.00	350°
Plasma ASM Si_3N_4	895	250	1.97	300°

Table II. Hydrogen content in ECR film vs 7 : 4 : 1 buffer HF etching

	Film	H_2Atomic %	Etch Rate (Å / min)
ASM PECVD (300°)	Nitride	20-24%	200 Å
	Oxide	9-12%	100Å
CVD (800°C)	Nitride	1.5-2.5%	10 Å
	Oxide	1-2%	50-200 Å
ECR (25°C) 300W	Nitride	13-15%	80 Å
	Oxide	4-6%	270 Å

Subject: TEM Analysis of ECR SiO_2

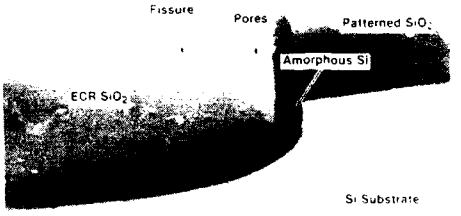


Figure 1. Lower corner of an ECR SiO_2 filled trench. Note the pores in the oxide along the vertical surface, and the fissure in the oxide where the oxides grown from the bottom and sidewall of the trench meet.



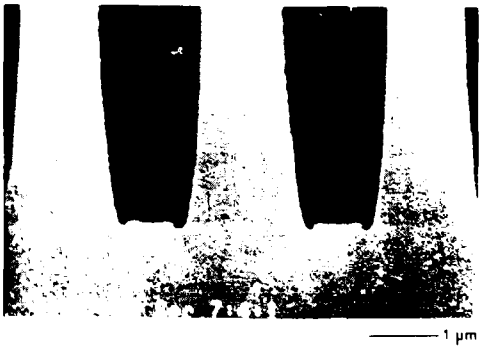


Figure 2. ECR SiO_2 in trench - relief etched in 7:4:1 SI etch. Note oxide layer at trench bottom

Abstract No. 303

ECR PLASMA DEPOSITION UNDER A CONTROLLED MAGNETIC FIELD

S. Nakamura and S.Nakayama

Technical Research Laboratries,
Sumitomo Metal Industries Ltd.,
1-3,Nishinagasu Hondori,Amagasaki,660,JAPAN

An electron-cyclotron-resonance (ECR) plasma CVD process[1] is potentially effective for semiconductor fabrication. It can deposit a high quality insulator film(SiO2, Si3N4 etc.) on a semiconductor substrate without heating. The ECR plasma CVD process, however, has shortcomings to be overcome; (1) the deposited film thickness is not uniform especially on a large substrate, e.g. 6 inches wafer, and (2) it is unsymmetrical in the periphery of the substrate when the film is deposited on a pattern. This paper describes an improved ECR plasma CVD process, in which the shortcomings of a conventional ECR plasma CVD process are solved by controlling a magnetic field.

A conventional ECR plasma CVD apparatus is shown in Fig.1. Plasma is generated in a plasma chamber by microwaves with the frequency of 2.45GHz, and extracted toward a substrate efficiently by a divergent magnetic field. The shortcomings of the conventional ECR plasma CVD process are due to the divergent magnetic field. The electron mobility in a magnetoplasma is given by

$$M_\perp / M_\parallel = D_\perp / D_\parallel = 1 / (1+(\omega_c / \nu)2), \quad (1)$$

where M is the electron mobility, D the diffusion coefficient, ω_c the electron cyclotron frequency (=eB/m, B the magnetic field, m the mass of electron), ν the collision frequency, and the suffices, $\perp$ and $\parallel$, indicate perpendicular and parallel component to B respectively. Thus, the following condition is valid for the conventional ECR plasma process.

$$M_\perp / M_\parallel = D_\perp / D_\parallel << 1 , \quad (2)$$

because of $\omega_c >> \nu$. The equation(2) implies that electrons(also ions in consequense of ambipolar electric field induced by electron motion[2]) move along the magnetic force line and scarcely diffuse across the magnetic force lines. Therefore the plasma density just above the substrate, i.e. deposition rate, becomes nonuniform even if the generated plasma is uniform in the plasma chamber. Furthermore the slant incidence of ions onto the substrate is unavoidable and yields unsymmetrical deposition on a pattern.

Uniform deposition in ECR plasma CVD process is achieved by a dual magnetic coil (DMC) as shown in Fig.2. The DMC consists of inner and outer coils with cylindrical yorks located co-axially below the stage. With the combination of the divergent field by ECR coil, the inner coil generates a cusp magnetic field and the outer one generates a mirror field. The distribution of B measured above the stage is shown in Fig.2. There is a low magnetic field region just above the substrate surrounded by a relatively high magnetic field region. In the low magnetic field region, the following condition of

$$M_\perp / M_\parallel = D_\perp / D_\parallel \simeq 0 \quad (3)$$

is realized; therefore the plasma can diffuse isotropically in this region, and ions incident normally onto the substrate due to the sheath electric field. The plasma density averaged on the substrate, i.e. the deposition rate, is approximately the same as that in a conventional ECR process, because the plasma cannot diffuse out across the high magnetic field region.

Using the ECR apparatus with the DMC, SiO2 film is deposited on a 6 inches wafer with O2 gas introduced into the plasma chamber and SiH4 gas into the reaction chamber. The uniformity of the film thickness is <±5% against ±18% in the conventional data (Fig.3). The film properties, refractive index and buffered hydroflouric acid etching rate, within the wafer are also uniform.

Furthermore, the ions' incident angle at the edge of the wafer is simultaneously improved. Fig.4 shows the SiO2 step-coverage at edge of the wafer. With the conventional divergent magnetic field, the SiO2 film is deposited unsymmetrically on the pattern, but using the DMC, deposited symmetrically.

In summery, both the uniformity of SiO2 film in ECR plasma CVD and the ions' incident angle at the edge of the wafer is drastically improved by controlling the magnetic field with keeping a high deposition rate.

REFFERENCES

[1] S.Matsuo, M.Kiuchi and T.Ono : Proc. 10th Sympo. on ISIAT"86, Tokyo (1986)471
[2] R.Geller, N.Hopfgarten, B.Jacquot and C.Jacquot : J. Plasma Physics, vol.12, part3 (1974)467

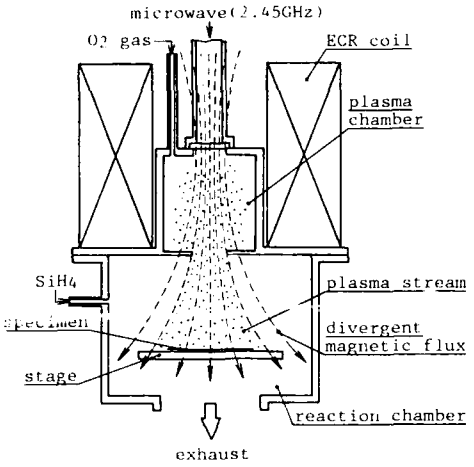


Fig.1 ECR plasma CVD apparatus

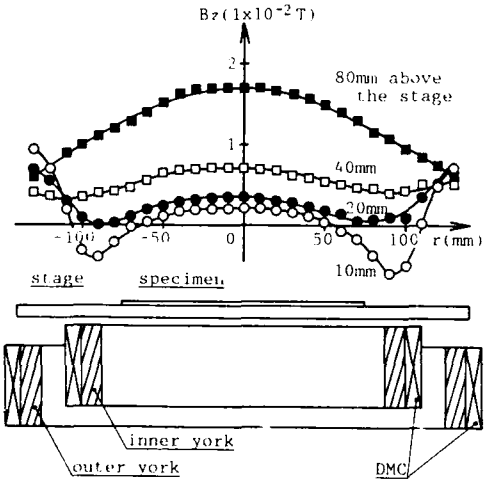


Fig.2 The cross-sectional view of DMC and the distribution of Bz above the stage in outer coil current of 1.2A and inner of -2.8A
r:the distance from the stage center
Bz:the perpendicular component of B to the stage

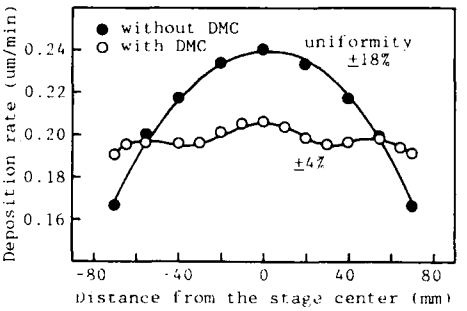
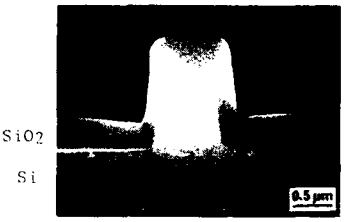
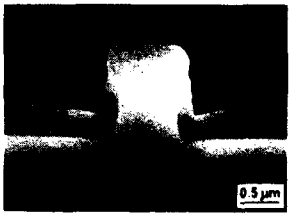


Fig.3 The distribution of SiO2 deposition rate within a 6"ϕ wafer



(a) Using divergent magnetic field



(b) Using magnetic field controlled by DMC

Fig.4 SiO2 step-coverage at the edge of a 6"ϕ Si wafer

Abstract No. 304

Plasma Induced Surface Modification of GaAs : An X-ray Photoelectron Spectroscopy (XPS) Characterization.

Naresh C. Saha
Bipolar Technology Laboratory

Gordon Tam and Ronald N. Legge
phoenix Corporate Research & Development

Motorola Inc., 5005 E. Mc Dowell Road
Phoenix, AZ 85008

PECVD dielectric films have been used extensively for passivating GaAs devices. However, drift in high frequency performance, degradation in DC parameters and high leakage current are still of major concern. Many of the device failures can be attributed to the instability and/or chemistry of the passivating film/GaAs interface (1). The efforts to passivate this interface by hydrogenation, nitridation or by chemical treatments have shown encouraging results (2–3). In this paper, we examined, using x-ray photoelectron spectroscopy (XPS), the nature of chemical modifications of the GaAs surfaces upon exposure to different plasma environments relevant to PECVD Si_3N_4 and SiO_xN_y deposition conditions.

GaAs (100) wafers were exposed to NH_3/N_2, N_2, N_2O/N_2, SiH_4/Ar and Ar plasmas separately 7.0 minutes at 250°C before the plasma treatment. Except for SiH_4/Ar, all plasma treatments were done for 5.0 minutes at a substrate temperature of 250°C using a power density of 0.03 W/cm^2 . SiH_4 plasma was exposed for 40 seconds only.

All samples were transported into the XPS spectrometer chamber within 5.0 minutes of plasma treatments. GaAs samples after fresh NH_4OH etch and 250°C bake were also analyzed for comparison. All XPS analyses were carried out in a Perkin Elmer 5300 spectrometer with variable angle measurement capability.

The high resolution XPS data of As 3d, Ga 3d, O 1s, N 1s, Si 2p and Si KLL regions were collected at different take-off angles (5°-75°) to delineate the chemistry and to obtain the nondestructive chemical depth profiles of the atoms in the modified layers and their interfaces with GaAs. In all cases, the photoelectron signal due to GaAs substrate was detectable at higher take-off angles and hence both surface and the modified layer/GaAs interface chemistry could be examined. From the relative intensity of the high resolution peaks, O/(Ga+As), As/Ga and N/(Ga+As) ratios were determined as a function of take-off angle of measurements (Table-I).

All surfaces were extensively modified by plasmas. The nature and extent of modifications were found to be characteristic of the individual plasma to which the samples were exposed. As/Ga ratios in the top 5Å of the surface layer ranged from 1.90 to 0.05. As 3d and Ga 3d spectra were complex in many cases due to presence of more than one components, especially when nitrogen was found incorporated in the sample. Fig.1 illustrates the modifying effect of nitrogen containing plasmas on the As chemistry. These spectra were curve-fitted to individual component peaks to determine the chemistry of different species. The main peak at around 41.4 eV was due to As in GaAs. While only one additional peak was detected in the As 3d spectrum after NH_3/N_2 treated sample, the spectra from the N_2 and N_2O/N_2 plasma treated samples showed additional peaks.

Four types of surface modifications were identified, e.g., (i) the incorporation of nitrogen, (ii) oxidation of GaAs, (iii) removal of native oxide layer and (iv) formation of an amorphous Si layer.

Nitrogen was incorporated only during N_2 and NH_3/N_2 plasma exposure. Although, the extent of nitrogen incorporation was comparable in the two cases, the chemistry of the surface layers was different. In the N_2 only plasma treated sample, three As peaks with chemical shifts of 4.6, 3.5 and 2.2 eV from the substrate As peak were detected (Fig.2). The first two peaks were identified as due to As_2O_5 and As_2O_3. The amplitude of the third peak increased with increasing depth of analysis. This was interpreted as evidence of formation of As-N bonding (e.g., AsN, AsO_xN_y or $GaAsO_xN_y$) near the interface. The Ga 3d and N 1s spectral features also indicated formation of GaN, Ga_2O_3, GaO_xN_y or $GaAsO_xN_y$ types of bonding.

The exposure of GaAs to the NH_3/N_2 plasma caused severe depletion of As from the surface. The thickness of this arsenic depleted region extended well beyond the analysis depth (>60Å) of this study. GaO_xN_y and $Ga(OH)_3$ were found to be the major constituents of the surface layer. Arsenic, detected at the interface, was present predominantly as GaAs with only a small amount of As_2O_3 .

The exposure to N_2O/N_2 plasma resulted in the oxidation of GaAs. The presence of As_2O_3, Ga_2O_3 and $GaAsO_4$ at the oxide/GaAs interface were evidenced.

The NH_4OH treatment prior to loading the sample in the plasma chamber produced a thin native oxide layer containing As_2O_3 and Ga_2O_3 . Heating the sample at 250°C in the plasma chamber in vacuo only increased the thickness of the native oxide layer. The oxidized surface layers inthese cases were found to be As_2O_3 rich.

Both SiH_4/Ar and Ar plasma exposure virtually eliminated the native oxide layer. An amorphous silicon surface layer was formed during SiH_4/Ar treatment.

The XPS data characterized the chemical nature of different plasma induced surface modifications of GaAs surfaces. These results will be used for treatment of GaAs surfaces prior to depositing different PECVD dielectric passivation films to further understanding the effects of interface modifications on device performance.

References:

1. J. G. Tenedorio and P. A. Terzian, IEEE Electron Device Lett., 5(6), 199 (1984)
2. F. Capasso and G. F. Williams, J. Electrochem. Soc., 129, 821 (1982)
3. E. Yablonovitch, C. J. Sandroff, R. Bhat and T. Gmitter, Appl. Phys. Lett., 51, 439 (1987)

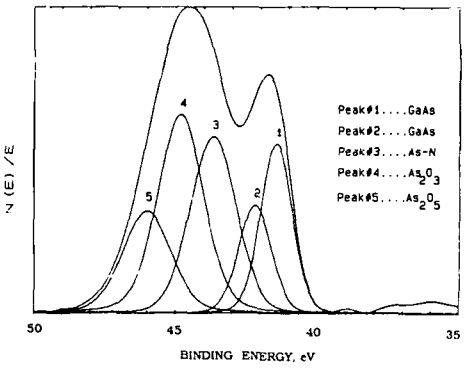


Fig.2: Curve-fitted As 3d XPS spectrum after N_2 plasma exposure showing presence of different oxidized species.

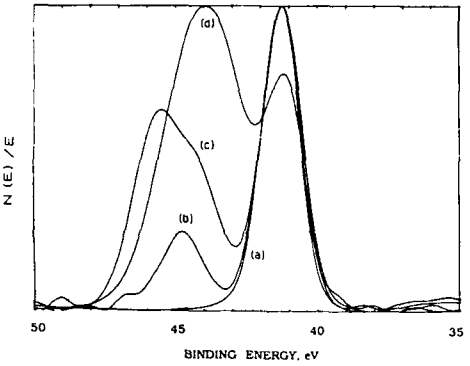


Fig.1: As 3d XPS spectra from GaAs surface after exposure to : (a) Ar^+ sputter, (b) NH_3/N_2 plasma, (c) N_2O/N_2 plasma and (d) N_2 plasma.

Table-I: **Elemental compositions (at%) of GaAs surfaces after various plasma and chemical treatment.**

Treatment	θ	As/Ga	O/(As/Ga)	N/(Ga+As)
NH4OH(1:10)	5°	1.95	1.02	
	45°	1.52	0.31	
	75°	1.08	0.20	
NH_4OH(1:10), 250°C bake	5°	1.35	1.05	
	45°	1.24	0.46	
	75°	1.44	0.39	
Ar plasma	5°	0.84	1.31	
	45°	0.90	0.39	
SiH_4/Ar plasma	45°	1.29	0.46	
N_2O/N_2 plasma	5°	1.06	2.27	
	45°	1.06	1.18	
	75°	1.12	0.97	
N_2 plasma	5°	0.92	1.22	0.39
	45°	0.95	0.71	0.32
	75°	1.34	0.71	0.23
NH_3/N_2 plasma	5°	0.05	1.62	0.41
	45°	0.24	0.85	0.27
	75°	0.32	0.71	0.27

Abstract No. 305

PHYSICAL AND CHEMICAL PROPERTIES OF MAGNETRON SPUTTERED SILICON NITRIDE FILMS

T. CARRIERE - I.VICKRIDGE** - B. AGIUS* - P. ALNOT*** - J. SIEJKA** and R. JOUBART***

*I.U.T. UNIVERSITE PARIS SUD
B.P.23 - 91406 ORSAY
CEDEX FRANCE

**GROUPE DE PHYSIQUE DES SOLIDES
de l'E.N.S. TOUR 23
11 Quai St Bernard
75005 PARIS FRANCE

***THOMSON-CSF
DOMAINE DE CORBEVILLE
91401 ORSAY CEDEX FRANCE

EXTENDED ABSTRACT

INTRODUCTION

The development of appropriate passivation and/or encapsulation schemes for III-V compound semiconductors is of considerable interest for application to integrated circuit, electro-optic, and high speed high power devices. III-V semiconductors require low temperature processing, and for this reason plasma deposited silicon nitride films have been used extensively in industry. Unfortunately, plasma-enhanced chemical vapour deposition and ultra violet chemical vapour (PECVD and UVCVD respectively) result in films contaminated by hydrogen, which can degrade device performance by diffusion into the substrate.

An alternative approach is cathodic sputtering, which can produce hydrogen-free silicon nitride at low temperatures. In addition, if magnetron system confinement is used rather than a diode system configuration, then lower deposition pressures can be used. A further advantage of magnetron confinement is a much reduced cathode plasma potential, leading to a much reduced flux of energetic neutrals scattered from the cathode. The ability to use lower power density and absence of energetic neutrals reduce the generation of defects at the film/substrate interface.

Magnetron sputtering is thus a potentially attractive method for production of silicon nitride thin films.

The objective of the present report is to describe the preparation and properties of silicon nitride films deposited on GaAs substrates by reactive sputtering in an R.F. plasma magnetron apparatus. We show that under appropriate conditions the deposited film is suitable as an annealing encapsulation.

EXPERIMENTAL

Silicon nitride films were deposited at room temperature on GaAs semi-insulating (001) substrates in a 13.56 MHz magnetron ALCATEL SCM 440 device. For low plasma power densities (1.27 and 2.56 W cm^{-2}), magnetron mode with pressures between 2.10^{-3} and 2.10^{-2} mbar were used with equal mass flows of N_2 and Ar.

Nuclear reaction analysis (NRA) was used to measure the atomic composition of the films. The new method used to directly measure the relative atomic ratio N/Si with a precision of between 1 and 2% will be described in detail elsewhere (1). Oxygen was measured by $^{16}O(d,p_1)$ method at $\theta_{lab}=90°$. In addition to NRA, x-ray photoelectron spectroscopy (XPS) and ellipsometry were used, and film stress and HF dissolution rates were measured.

RESULTS

The results given in table 1 show a clear correlation between the plasma power density and film deposition rate. Film composition determined by NRA (colums 6 and 7) and the XPS measurements (figure 1), suggest that the lower indices measured by ellipsometry are closely tied to higher oxygen contamination in the films. The stress decreases rapidly with oxygen contamination (figure 2). These results show that a compromise should be found between oxygen contamination and stress ; they also suggest that the intermediate deposition pressure ($\sim 7\ 10^{-3}$ mbar in our experimental conditions) must be choosen to elaborate ideal films for GaAs encapsulation.

(1).I.VICKRIDGE, to be submitted to NIM.

Power density W/cm²	Deposition pressure mbar	N_N 10^{16} at/cm².nm	N_{Si} 10^{16} at/cm².nm	N_{16_O} 10^{16} at/cm².nm	$\frac{N}{Si}$	$\frac{O}{N+Si}$ (at%)	Ellipsometric index	Deposition rate nm/mn
2,5	$2\ 10^{-3}$	7,4	5,3	1,95	1,40	0,15	2.07	13
2,5	$5\ 10^{-3}$	7,2	5,2	7	1,38	0,6	1.99	12,6
2,5	10^{-2}	6,3	4,7	22	1,32	2	1.95	12
2,5	$2\ 10^{-2}$	5,5	4,3	39	1,28	4	1.88	12,1
1,2	$2\ 10^{-3}$	2,5	1,8	1,3	1,45	0,3	2.05	4,4
1,2	$5\ 10^{-3}$	2,3	1,6	2,6	1,39	0,7	2.01	4,1
1,2	10^{-2}	2	1,5	11,2	1,33	3,2	1.95	3,9
1,2	$2\ 10^{-2}$	1,8	1,4	16,8	1,27	5,2	1.9	3,8

Table 1 : Silicon nitride characterization

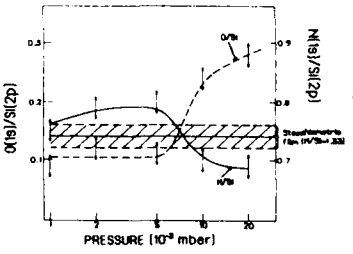


Figure 1 : O(1s)/Si(2p) and N(1s)/Si(2p) ratios as a function of total reactor pressure.

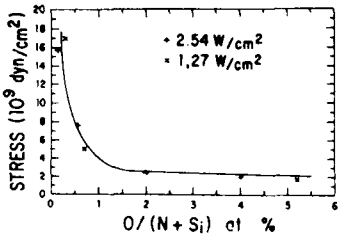


Figure 2 : Stress vs oxygen contamination of the film

Abstract No. 306

ON THE CONSTITUTIVE DISTRIBUTED PARAMETER MODELLING FOR PHENOMENAL CONTROL OF THE MULTICOMPONENT PLASMA PROCESSING.

PART I. A CONSTITUTIVE DISTRIBUTED PARAMETER MATHEMATICAL MODEL OF THE MULTICOMPONENT PLASMA PROCESSING.

Wacław NIEMIEC
Mathematical Modelling and Control for Distributed Parameter Systems, Silesian Technical University, Ul. Barska 33, PL-33-300 Nowy Sącz, Poland.

ABSTRACT.

The problem of this paper is to construct an original system of the partial differential constitutive state equations of the mathematical model of the distributed parameters of the multicomponent plasma processing.

INTRODUCTION.

The world literature containing the plasma questions does not have to solved the problems of both kinetics and phenomenal distributed parameter modelling of the plasma processing specially connected with the multicomponent gas phase [1-5]. On the basis of the reciprocal constant image for the isotropic and anisotropic nonhomogeneous media with the space and time memories of the source [6], the definition of the following derivative and the partial differential equation of the continuity for every state variable of the multicomponent plasma processing [7], an original system of the partial differential constitutive state equations has been deduced. This approach is connected to the INPUT-SOURCE-PLASMA PROCESSING-OUTPUT interpretation of the appearance and the existence of the multicomponent plasma [8].

THE LOCALLY DISTRIBUTED PARAMETERS OF THE MULTICOMPONENT PLASMA PROCESSING.

We need to introduce the definition

DEFINITION 1. For every processing point $P(x,y,z,t)$ of the multicomponent plasma exists the locally selected volume-time element $\Omega^{\delta}(x,y,z)t$, having cuboidal shape for which is fulfilled relation

$$P(x,y,z,t) \in \Omega^{\delta}(x,y,z)t \in \Omega_{Rt} \quad (1.1),$$

where: the point $P(x,y,z,t)$ is the geometric centre of $\Omega^{\delta}(x,y,z)t$, Ω_{Rt} - the working space volume-time of the plasma apparatus.

As a consequence of the introduce of this point of view we have:

DEFINITION 2. For the constant coordinates point $P(x,y,z,t)$ exists in Ω_{Rt}, the variable coordinates point $Q^{R}(\xi,\eta,\zeta,\tau)$ assuring the reciprocal relation of the physical phenomenon and its source.

Making use of all known physical phenomena of the multicomponent plasma processing in the way of above definitions is deduced the mathematical model of the distributed parameters of the multicomponent plasma processing, of the electrons and ions aspects.

THE PARTIAL DIFFERENTIAL CONSTITUTIVE STATE EQUATIONS DESCRIBING THE MULTICOMPONENT PLASMA PROCESSING.

From the kinetics and phenomenal analysis of the multicomponent plasma processing we have its description:

$$\frac{DC_{(e,i)}}{Dt} = -D_{(e,i)}\nabla^2 C_{(e,i)} \pm C_{(e,i)}\,\mathrm{div}v_{(e,i)} + \sum_{r=1}^{R'} \beta_{(e,i)r}\nabla^2 T_{(e,i)r} - \sum_{r=1}^{R'} D_{T(e,i)r}\nabla^2 T_{(e,i)r} \pm \sum_{r=1}^{R'}\sum_{l=1}^{L} A_{rl}(t) \quad (1)$$

$$C_{(e,i)}\rho_{p(e,i)}\frac{DT_{(e,i)}}{Dt} - C_{(e,i)}T_{(e,i)}\left(\frac{\partial \Omega_R}{\partial T_{(e,i)}}\right)_{P_{(e,i)}}\frac{DP_{(e,i)}}{Dt} =$$

$$= -\lambda_{(e,i)}\nabla^2 T_{(e,i)} \pm C_{(e,i)}T_{(e,i)}\,\mathrm{div}v_{(e,i)} - \sum_{r=1}^{R'}\lambda_{D(e,i)r}\nabla^2 C_{(e,i)r} - \sum_{r=1}^{R'}\beta_{(e,i)r}\nabla^2 U_r \pm \sum_{r=1}^{R'}\sum_{l=1}^{L} G_{rl}(t) \quad (2)$$

$$\frac{Dj_{(e,i)}}{Dt} = -\sum_{r=1}^{R'}\alpha_{(e,i)r}\nabla^2 U_r - \sum_{r=1}^{R'}\phi_{(e,i)r}\nabla^2 T_{(e,i)r} \pm j_{(e,i)}\,\mathrm{div}v_{(e,i)} - \sum_{r=1}^{R'}\phi_{(e,i)r}\nabla^2 C_{(e,i)r} \pm \sum_{r=1}^{R'}\sum_{l=1}^{L} S_{rl}(t)$$

$$j_{(e,i)}\frac{DU}{Dt} = U_{\alpha(e,i)}\alpha_{(e,i)}\nabla^2 U - \sum_{r=1}^{R'} U_{T(e,i)r}\phi_{(e,i)r}\nabla^2 T_{(e,i)r} \pm j_{(e,i)}U\,\mathrm{div}v_{(e,i)} - \sum_{r=1}^{R'} U_{C(e,i)r}\phi_{(e,i)r}\nabla^2 C_{(e,i)r} \pm \sum_{r=1}^{R'}\sum_{l=1}^{L} S_{rl}(t) \quad (3)$$

$$C_{(e,i)}\frac{Dv_{(e,i)}}{Dt} = \eta_{w(e,i)}\nabla^2 v_{(e,i)} \pm C_{(e,i)}v_{(e,i)}\,\mathrm{div}v_{(e,i)} + \frac{\eta_{w(e,i)}}{3}\mathrm{grad}\,\mathrm{div}v_{(e,i)} - \mathrm{grad}P_{(e,i)} \pm \sum_{r=1}^{R'}\sum_{l=1}^{L} M_{rl}(t) \quad (4)$$

(5)

where:

$\frac{D}{Dt}\frac{\partial}{\partial t} = v_{(e,i)}\mathrm{grad}$ (sum if adequate gradient operations) [7] be proved from the condition $\frac{D}{Dt}=0$ [7], by the constant and variable coefficients [9].

CONCLUSIONS.

The deduced mathematical model contains the very wide class of the problems of the identification and control of the multicomponent plasma.

NOTATION.

For: r-components, l-partial processings, (e,i)-(electrons/ions), $C_{(e,i)r}$-concentration kg/m^3, $v_{(e,i)}$-velocity m/s, U_r-voltage V, $T_{(e,i)r}$-temperature ^oK, $P_{(e,i)}$-pressure N/m^2, $j_{(e,i)}$-current density A/m^2, sources: kg/m^3s, $G_{rl}(t)$ W/m^3, $R_{rl}(t)$ A/m^3s, $S_{rl}(t)$ W/m^3, $M_{rl}(t)$ N/m^3, coefficients: $D_{(e,i)r}$-diffusion m^2/s, $\alpha_{(e,i)r}$-conductivity kg/mVs, $D_{T(e,i)r}$-thermic diffusion kg/m^3Ks, $c_{(e,i)r}$-specific heat J/kg^oK, Ω_R-active volume m^3/kg, $\lambda_{(e,i)r}$-heat transfer W/m^oK, $\lambda_{D(e,i)r}$-diffusion heat transfer Wm^2/kg, $\beta_{(e,i)r}$-electric current heat transfer W/mV, $\sigma_{(e,i)r}$-voltage electric current density A/Vs, $\phi_{(e,i)r}$-electric current by temperature gradient $A/^oKs$, $\zeta_{(e,i)r}$-elastric current by concentration gradient Am^2/kgs, own voltages: $U_{\alpha(e,i)}$-electric current V, $U_{T(e,i)r}$-of temperature V, $U_{C(e,i)r}$-of concentration V, $\eta_{w(e,i)}$-coefficient of dynamic viscosity Ns/m^2, t-time s.

REFERENCES.

[1] Celiński, Z., Plazma, Warszawa, PWN 1980.
[2] Czernietski, A.W., Wstęp do fizyki plazmy, Warszawa, PWN 1971.
[3] Norwood, J., Fizyka współczesna. Warszawa, PWN 1982.
[4] Krall, N.A., Trivalpiece, A.W., Fizyka plazmy. Warszawa, PWN 1979.
[5] Pai, S., Magnetogasdynamics and plasma dynamics. Wien, Springer Verlag 1962.
[6] Nowacki, W., Dynamiczne zagadnienia termosprężystości. Warszawa, PWN 1966.
[7] Średniawa, B., Hydrodynamika i teoria sprężystości. Warszawa, PWN 1977.
[8] Węgrzyn, S., Podstawy automatyki. Warszawa, PWN 1974.
[9] Morgan, A.J.A., On the construction of constitutive equations for continuous media. Archiwum Mechaniki Stosowanej, Vol. 17, No. 1, pp. 145-174, (1965).

REMARK.

The locally selected volume-time element $\Omega^{\delta}(x,y,z)t$ is phenomenally closed, so that the influences of every phenomenon on the state vector in the point $P(x,y,z,t)$ can be treated in the separate way [7].

Abstract No. 307

ON THE CONSTITUTIVE DISTRIBUTED PARAMETER MODELLING FOR PHENOMENAL CONTROL OF THE MULTICOMPONENT PLASMA PROCESSING.

PART II. THE ANALYTICAL SOLUTION AND CONTROL INTERPRETATION OF THE CONSTITUTIVE MATHEMATICAL MODEL OF THE MULTICOMPONENT PLASMA PROCESSING.

Wacław NIEMIEC
Mathematical Modelling and Control for Distributed Parameter Systems, Silesian Technical University, Ul. Barska 33, PL-33-300 Nowy Sącz, Poland.

ABSTRACT

The article is devoted to the analytical solution of system (I) being deduced in the PART I of the paper and its interpretation from the point of view of the distributed parameter control theory. Two cases of this solution have been considered:
A^δ–the existence of the initial conditions,
B^δ–the existence of the initial and boundary conditions,
for the composite phenomenal solutions.

INTRODUCTION.

In the aim of this part we need to solve the deduced in the Part I[1], the system of the partial differentiel constitutive state equations (I). The solution can contain two cases: A^δ–the existence of the initial conditions, B^δ–the existence of the initial and boundary conditions. The procedure of the solution of the system (I) has the operations:

1°. The modification to the source system of the time ordinary differential equations, in every point P(x,y,z,t).
2°. The disposition of the homogeneous part of the system (I) for the systems of [2]:
   a/the partial differential equations of the potential fields,
   b/the partial differential equations of the rotational field /velocity vector/.
3°. The separation of the single phenomena from the system (2^δ.a).
4°. The analytical solutions of the phenomenal partial differential equations from the systems (2^δ.a) and (2^δ.b) for the cases A^δ and B^δ.
5°. The summation of the effects of the phenomenal partial differential equations (2^δ.a)+(2^δ.b)+(1^δ), pertinent to the state variables [2],[3].

The discussion of the obtained results of the solution of the system (I) for the phenomenal control has been suggested [4].

THE SOLUTION OF THE SYSTEM (I).

The point 1°. In every point P(x,y,z,t) the system (I) gets its new time form:

$$\left.\begin{aligned}
&\frac{dC_{(e,i)}}{dt} = \pm\sum_{r=1}^{R'}\sum_{l=1}^{L} A_{rl}(t) \int_0^t (1)\, C^z_{(e,i)}(t),\\
&C_{(e,i)}c_{p(e,i)}\frac{dT_{(e,i)}}{dt} = \pm\sum_{r=1}^{R'}\sum_{l=1}^{L} G_{rl}(t) \quad (2)\, p^z_{(e,i)}(t),\\
&\frac{dR_{(e,i)}}{dt} = 0 \qquad\qquad (3)\, j^z_{(e,i)}(t),\\
&\frac{dj_{(e,i)}}{dt} = \pm\sum_{r=1}^{R'}\sum_{l=1}^{L} R_{rl}(t) \quad (4)\, U^z(t),\\
&j_{(e,i)}\frac{dU}{dt} = \pm\sum_{r=1}^{R'}\sum_{l=1}^{L} S_{rl}(t) \quad (5)\, v^z_{(e,i)}(t).\\
&C_{(e,i)}\frac{dv_{(e,i)}}{dt} = \pm\sum_{r=1}^{R'}\sum_{l=1}^{L} M_{rl}(t)
\end{aligned}\right\} \quad (II)$$

The initial conditions: (6)

$C_{(e,i)/o}, T_{(e,i)/o}, R_{(e,i)/o}, j_{(e,i)/o}, U_o, v_{(e,i)/o}$

modulus of eq.(4) to eq.(5) – the possibility of the inverse processing.

The point 2°. Exists $B_{(e,i)}$, so that $v_{(e,i)} = \mathrm{rot}B_{(e,i)}$ and $\mathrm{divrot}B_{(e,i)} \equiv 0$ [2]. From this point of view we have:

The point 2°,a. The variable point of the potential fields $Q^R(\xi,\eta,\zeta;\tau) \equiv Q(\xi,\eta,\zeta,\tau)$ and we have from the system (I)

$$\frac{\partial C_{(e,i)}}{\partial t} = -D_{(e,i)}\nabla^2 C_{(e,i)} + \sum_{r=1}^{R'}\alpha_{(e,i)r}\nabla^2 U_r - \sum_{r=1}^{R'} D_{T(e,i)r}\nabla^2 T_{(e,i)r} \quad (1)$$

$$C_{(e,i)}c_{p(e,i)}\frac{\partial T_{(e,i)}}{\partial t} = -\lambda_{(e,i)}\nabla^2 T_{(e,i)} - \sum_{r=1}^{R'}\lambda_{D(e,i)r}\nabla^2 C_{(e,i)r} - \sum_{r=1}^{R'}\mu_{(e,i)r}\nabla^2 U_r \quad (2)$$

$$\frac{\partial p_{(e,i)}}{\partial t} = 0 \cdot \left[C_{(e,i)}T_{(e,i)}\left(\frac{\partial c_R}{\partial T_{(e,i)}}\right)_{p_{(e,i)}}\right] \quad (3)$$

$$\frac{\partial j_{(e,i)}}{\partial t} = \sum_{r=1}^{R'}\alpha_{(e,i)r}\nabla^2 U_r - \sum_{r=1}^{R'}\mu_{(e,i)r}\nabla^2 T_{(e,i)r} - \sum_{r=1}^{R'}\alpha_{(e,i)r}\nabla^2 C_{(e,i)r} \quad (4)$$

$$j_{(e,i)}\frac{\partial U}{\partial t} = U_{\alpha(e,i)}\alpha_{(e,i)}\nabla^2 U - \sum_{r=1}^{R'} U_{T(e,i)r}\mu_{(e,i)r}\cdot\nabla^2 T_{(e,i)r} - \sum_{r=1}^{R'} U_{\alpha(e,i)r}\alpha_{(e,i)r}\nabla^2 C_{(e,i)r} \quad (5)$$

$$C_{(e,i)}\frac{\partial v_{(e,i)}}{\partial t} = -\mathrm{grad}p_{(e,i)} \quad (6)$$

The point 2°,b. The variable point for the rotational field $Q^R(\xi,\eta,\zeta,\tau) \equiv Q(\xi,\eta,\zeta,\tau)$ and from the system (I) is:

$$\frac{DC_{(e,i)}}{Dt} = \pm C_{(e,i)}\mathrm{div}v_{(e,i)} \quad (1)$$

$$C_{(e,i)}c_{p(e,i)}\frac{DT_{(e,i)}}{Dt} = \pm C_{(e,i)}c_{p(e,i)}T_{(e,i)}\mathrm{div}v_{(e,i)} \quad (2)$$

$$\frac{Dp_{(e,i)}}{Dt} = 0 \cdot \left[C_{(e,i)}T_{(e,i)}\left(\frac{\partial c_R}{\partial T_{(e,i)}}\right)_{p_{(e,i)}}\right] \quad (3)$$

(IV)

$$\frac{Dj_{(e,i)}}{Dt} = \pm j_{(e,i)}\mathrm{div}v_{(e,i)} \quad (4)$$

$$j_{(e,i)}\frac{DU}{Dt} = \pm j_{(e,i)}U\mathrm{div}v_{(e,i)} \quad (5)$$

$$C_{(e,i)}\frac{Dv_{(e,i)}}{Dt} = \rho_{w(e,i)}\nabla^2 v_{(e,i)} \pm C_{(e,i)}v_{(e,i)}\mathrm{div}v_{(e,i)} + \frac{\rho_{w(e,i)}}{3}\mathrm{graddiv}v_{(e,i)} \quad (6)$$

where: $\frac{D}{Dt} = \frac{\partial}{\partial t} + v_{(e,i)}\mathrm{grad}$ [3].

The point 3°. The separation of the single phenomena is connected to the ideal media, so that consequently only one coefficient is assumed as different than zero, but others are equal to zero [3].

The point 4°. For every state variable and every physical phenomenon with its source function, the following relation is fulfilled

$$W(P,t) = \int_0^t \int_R G(P,t;Q^R,\tau) m_s(Q^R,\tau) dQ^R d\tau \quad (4^\delta.1)$$

where: W(P,t)–the resultant state variable, G(P,t;Q^R,τ)–the phenomenal Green function, $m_s(Q^R,\tau)$–the phenomenal source function. For the cases A^δ and B^δ important role play the phenomenal Green functions and their properties [2–3].

The point 5°. For every state variable "W" is assured the summation of: $(5^\delta.1)$

$W_c = W_s + W_{pot.} + W_{rot.}$ by: W_c–the complete solution, W_s–the source, $W_{pot.}$–the point 2°.a, $W_{rot.}$–the point 2°.b.

CONCLUSIONS.

The above analysis allows to consider for "W" INPUT–SOURCE–PLASMA PROCESSING–OUTPUT (W) PHENOMENAL DISTRIBUTED PARAMETER CONTROLLER for the distributed parameter control theory [4]

NOTATION. See Part. I. [1].

REFERENCES. [1] Niemiec, W., Part I. [2] Trajdos, T., Matematyka dla inżynierów. Warszawa, PWN 1974. [3] Średniawa, B., see [7] in Part I. [4] Wągrzyn, S., see [8] in Part I.

Abstract No. 308

Electromigration in Submicron Interconnects and Multilevel Interconnection

Thomas Kwok

IBM Research Division
Thomas J. Watson Research Center
Yorktown Heights, N.Y. 10598

Multilevel interconnection usually consists of metal lines of different lengths, widths and thicknesses, and contains geometrical structures such as bends, studs and vias. It is necessary to study the effects of metal line length, width and thickness, and these geometrical structures on electromigration resistance in order to determine the maximum current densities allowable in interconnects. Moreover, the linewidth of interconnects is shrinking into the submicron range to improve circuitry density and speed performance. With the projected high current density in submicron metal lines and current crowding in these geometrical structures, there is increasing reliability concerns of electromigraton-induced failures in VLSI multilevel interconnection. A number of studies on linelength [1-3] and linewidth [1,4-8] dependence of electromigration lifetime in metal lines wider than 1.0 μm have been reported. This paper summarizes our results on the dependence of electromigration lifetime on linelength, linewidth, film thickness and number of bends in submicron metal lines. The effects of current crowding and local heating in studs and vias on electromigration resistance in multilevel interconnection are also discussed.

Several metal line testsites of different line lengths and widths, and with or without bends were designed for electromigration lifetime measurements. Testsite patterns were generated by electron-beam lithography and samples were fabricated using lift-off technique. Different thicknesses of Al or Al-4wt.%Cu films were deposited on the substrate by evaporation from RF induction of Al or Al-Cu alloy sources, respectively. Patterned wafers were passivated with 6.5 μm sputtered quartz. Data on voltage and current measurements of each test stripe was taken every 15 or 30 minutes until the test stripe failed either by void-open or extrusion-short. Microstructure studies on these metal lines were carried out by transmission electron microscopy (TEM).

The electromigration lifetime of Al-Cu submicron lines, 10 to 500 μm in length, have been measured under a current stressing of 2.5 MA/cm^2 at 227°C.[9] The lifetime was found to decrease with increasing linelength from 10 to 50 μm and then level off between 50 to 500 μm. The insensitivity of lifetime to linelength for length greater than 50 μm can be understood by assuming that electromigration-induced failure in these metal lines is caused by intrinsic defects. The electromigration lifetime of Al and Al-Cu lines, 0.5 to 2.0 μm in width, have also been measured under a current stressing of 1 MA/cm^2 at 182°C.[10] The lifetime was found to decrease with decreasing linewidth and then increase beneath a critical width. The critical width was found to lie between 0.625 and 2.0 μm for film thickness ranging from 0.35 to 0.9 μm. The grain structure was found to approach a bamboo structure in those submicron metal lines with linewidth comparable to or smaller than film thickness.[11] These submicron metal lines were also found to have longer lifetime than other metal lines.[12] The effects of linewidth and film thickness on lifetime can thus be correlated with grain size and grain morphology in these metal lines.

Electromigration lifetime measurements on Al-Cu submicron bend lines were carried out under a current stressing of 2.0 MA/cm^2 at 162°C.[9] Each Al-Cu submicron line contains 12 to 96 horizontal bends with separation between adjacent bends ranging from 80 to 10 μm. The lifetime was found to decrease linearly with increasing number of bends at a rate of 0.4% per bend. No dramatic changes in grain structure from the straight line portion to the bend structure in these submicron lines were observed. Current density distributions in studs and vias have been calculated by finite element method.[13] Our results revealed the presence of two current density peaks in a vertical bend structure (stud). Their magnitudes were found to be two times the average current density. The high current density peak and the associated flux divergence in the bend structure can account for the observed decrease in electromigration resistance in metal lines with bend structures. Our data also indicated that current density peak in studs increases with decreasing stud width and increasing aspect ratio or metal line thickness. The rate of increase is faster for submicron lines than for wider lines. Current density peak in the via step region was also found to increase with increasing step angle.

In conclusion, the stud width and its ratio to metal line thickness are dominant factors in controlling the extent of current crowding and electromigration resistance. As multilevel interconnection consists of metal lines of different geometry and with different numbers of bends, when one defines the maximum current density allowable in interconnects, one should consider the weakest metal line geometry with the largest number of bends.

References

1. B.N. Agarwala, M.J. Attaro and A.P. Ingraham, *J. Appl. Phys.* 41 (10), 3945 (1970).
2. A.J. Learn and W.H. Shephard, in *Proc. of 9th Int'l Relia. Phys. Symp.*, IEEE, eds., (1971), p.129.
3. H.A. Schafft, T.C. Station, J. Mandel and J.D. Shott, *IEEE Trans.* ED-34 (3), 673 (1987).
4. G.A. Scoggan, B.N. Agarwala, P.P. Peressini and A. Brouillard, in *Proc. of 13th Int'l Relia. Phys. Symp.*, IEEE, eds., (1975), p.151.
5. S. Vaidya, T.T. Sheng and A.K. Sinha, *Appl. Phys. Lett.* 36 (6), 464 (1980).
6. E. Kinsbron, *Appl. Phys. Lett.* 36 (12), 968 (1980).
7. S.S. Iyer and C.Y. Ting, *IEEE Trans.* ED-31 (10), 1468 (1984).
8. K. Eden, W. Roth and H. Beneking, *Microelectronic Engineering*, 1, 263 (1983).
9. T. Kwok, J. Finnegan and D. Johnson, *Proc. of 5th Int'l VLSI Multilevel Interconnection Conf.*, IEEE, ed., (1985), in press.
10. T. Kwok, in *Proc. of 1st Int'l ULSI Sci. and Tech. Symp.*, ECS, ed., (1987), p.593.
11. T. Kwok, C.Y. Ting and J.U. Han, in *Proc. of 2nd Int'l VLSI Multilevel Interconnection Conf.*, IEEE, ed., (1985), p.83.
12. T. Kwok, in *Proc. of 4th Int'l VLSI Multilevel Interconnection Conf.*, IEEE, ed., (1987), p.456.
13. T. Kwok, T. Nguyen, P. Ho and S. Yip, in *Proc. of 25th Int'l Relia. Phys. Symp.*, IEEE, ed., (1987), p.130.

Abstract No. 309

IMPROVED ELECTROMIGRATION PERFORMANCE IN AL/4%CU USING A RANGE OF REFRACTORY CAPS

N P Armstrong

Plessey Research Caswell Ltd
Caswell, Towcester, Northants, England

INTRODUCTION

Al/Cu alloys are not universally used in metallisation, due largely to difficulties in dry pattern definition. However, they have been widely used in applications where high current density and/or high operating temperature give Al and Al/Si an inadequate life to electromigration failure. Although Median Time to Failure (MTF) data suggest Al/4%Cu to be adequate for these applications, the very large number of current-carrying tracks in ULSI demands that the very early part of the failure distribution be taken into account, making the slope as important as the mean. The track microstucture, which may be constrained by process or equipment considerations, has a very large effect on both MTF and slope [1,2]. In narrow lines (1-2μm), several researchers [2,3,4] have observed increased MTF, but recent lifetest data at various linewidths [5] has shown a corresponding increase in spread, with overall adverse effect upon time to early failures. Hence it is desirable not so much that MTF be increased as that the failure distribution be tight, corresponding to a very low initial failure rate, rapidly increasing near the MTF.

Recently a number of researchers [6,7] have reported dramatic improvements in MTF compared to Al/Cu alloys, using multi-layered films. However, some such structures [6] may be unnecessarily complex - and hence difficult or time-consuming to produce in a production environment, particularly using pipelined single wafer sputterers. The present need is for a tighter failure distribution with the minimum additional complexity.

EXPERIMENT

The use of a silicon free alloy demands a barrier material between it and the Si substrate at contacts - a sputtered refractory underlayer such as TiW has been widely used. A capping layer may be useful to suppress thermal hillocks and to reduce reflection during photolithography. Thus with three layers the process complexity is not increased purely for the sake of electromigration resistance, particularly if TiW is the cap, so that only one extra material is required. However, also within the three-layer maximum are films similar to those reported by Shen [7], using a thin Ti cap. Adding Al/Cu and TiW + AlCu controls, the range of films selected for the current evaluation is shown in table 1. The film cross-section is shown in figure 1.

All depositions were performed using a Varian 3180 sputterer, without vacuum break or RF etch between layers. The test vehicle used for lifetest was close to that recommended by Shaft [8], being 3.5μm wide by 1750μm long, with voltage taps at each end. Films were on 0.5μm thermal SiO_2 and were unpassivated. Track temperature was measured using both temperature coefficient of resistance and thermocouples in contact with the base of the package.

The lifetest was run at 189degC, $10^6 A/cm^2$, and films with AlCu alone failed with MTF = 980 hours. After 3000 hours, none of the films on TiW had failed, so current density was increased fourfold, with resultant temperature increase by Joule heating to 216degC. All samples failed within a few hundred hours at the higher stress, except the thin Ti-capped films which mostly lasted beyond the 2000 hour duration of the higher stress test.

Failure times are summarised in table 1, showing MTF and times to 2% failures (T2F). The Al/Cu figures in brackets have been converted to the higher stress for comparison, as has the 3000 hours at the lower stress which all other films received, using E_a=0.7eV and n=2 in the empirical Black model [9]. The 12-fold increase in MTF of the combination films over Al/Cu is evident, but of greater interest is the effect on spread - evident in the ratio MTF/T2F. The provision of an underlayer and the provision and thickening of a cap progressively reduce the spread, through the protection of damaged sections or sections having particularly adverse local grain boundary configurations. See figure 2.

The reason for the very long life of the Ti-capped films is not clear, though a change in failure mode is evident from the form of the damage in figure 3 (cf. figure 2 - TiW cap). AES profiles suggest that the Ti caps are mainly oxidised.

Some whisker growth (figure 2) was seen on all combination films after lifetest, but SEM examination of a further lifetest at the higher stress, terminated after only 286 hours, suggests that these mainly grew after the time to 20% resistance increase, as current continued to flow considerably longer. The thin Ti cap delayed whisker growth, as no whiskers were seen on Ti-capped films after 286 hours.

CONCLUSIONS

1. In narrow tracks with grain size a significant proportion of trackwidth, early failures due to adverse local configuration may limit operation of Al/Cu metallisation in VLSI to commercial temperatures unless it is shunted and/or capped by a refractory layer.
2. A 0.2μm TiW layer under 0.5μm Al/Cu increases MTF by 7x, and time to 2% failures (T2F) by 40x. Addition and thickening of a TiW cap progressively tightens the failure distribution, causing improved MTF without effecting MTF.
3. The growth of long regular whiskers determine usable life of Al/Cu films shunted with TiW, though life remains far in excess of Al/Cu alone.
4. A thin partly oxidised Ti cap greatly enhances life to open circuit failure, inhibits resistance increase and delays onset of whisker growth.
5. The statistical significance of large numbers of tracks within a VLSI ASIC demands a very tight failure distribution. In the absence of quantitative data on Ti-capped films, the film tested which best meets this requirement is TiW+AlCu+TiW(.15μm).

ACKNOWLEDGEMENTS

This work was partly funded by the EEC under ESPRIT project 14: "Advanced Interconnect for VLSI". Thanks are due especially to N.P.Francis who performed the lifetests.

REFERENCES

1. P.Merchant & T.Cass, Proc. 22nd IEEE IRPS, pp259-263 (1984)
2. S Vaidya & A K Sinha, Thin Solid Films, 75, pp253-259 (1981)
3. S Vaidya, Sheng & A K Sinha, App Phys Lett, 36 (6), pp464-466 (1980)
4. T Kwok, Proc 4th IEEE VMIC, pp456-462 (1987)
5. R.J.Dulniak, to be published
6. D.S.Gardner, T.L.Michalka, P.A.Flinn, T.W.Barbee Jr, K.C.Saraswat & J.D.Meindl, Proc. 2nd IEEE VMIC, pp102-113 (1985)
7. B.W.Shen, T.Bonifield & R.Blumenthal, Proc. 3rd IEEE VMIC, pp191-197 (1986)
8. H.A.Shaft, IEEE Trans. ED-34, pp673-681 (1987)
9. J R Black, IEEE Trans ED-16, pp338-347 (1969)

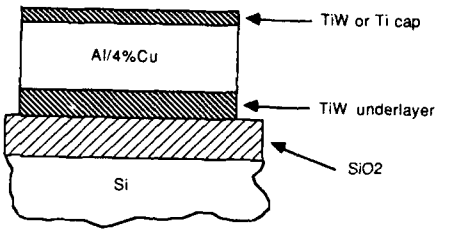


Figure 1: Structure evaluated

TiW + AlCu + TiW			T2F	MTF	Ratio
	0.5		(1.4	23)	16.9
0.2	0.5		48	300	6.25
0.2	0.5	0.05	67	300	4.48
0.2	0.5	0.10	82	280	3.41
0.2	0.5	0.15	130	242	1.86
0.2	0.5	.02 Ti		>2185	
0.2	0.5	.03 Ti		>2065	

Table 1: Failure times (hours) for Al/4%Cu with refractory underlayer and caps. 216degC, 4E6 A/cm2

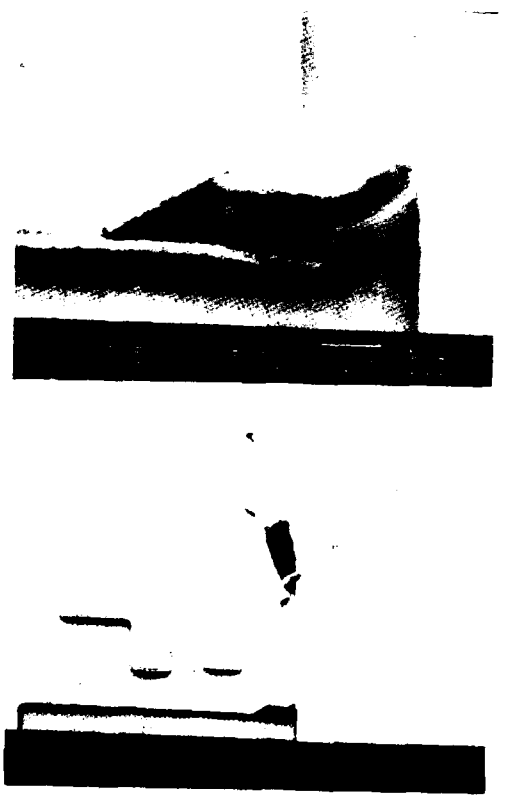


Figure 2: TiW + AlCu + TiW (.15µm) after 3000 hours (216degC, $4x10^6 A/cm^2$)

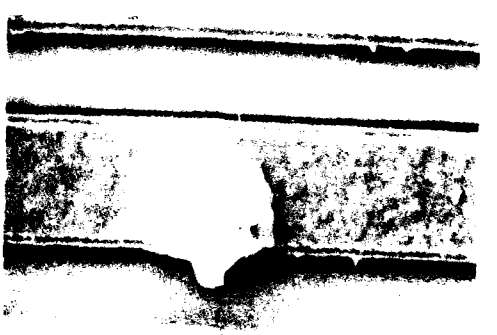


Figure 3: TiW + AlCu + Ti after 3000 hours (216degC, $4x10^6 A/cm^2$)

Abstract No. 310

STRESS INDUCED MIGRATION OF ALUMINUM-SILICON FILMS: INFLUENCING FACTORS AND COUNTERMEASURES

H. Katto and S. Shimizu*
Musashi Works, Hitachi, Ltd.
1450 Josuihon-cho, Kodaira, Tokyo, 187 JAPAN
*Device Development Center, Hitachi, Ltd.
2326 Imai, Ome, Tokyo, 198

INTRODUCTION Sputtered aluminum-silicon (Al-Si) conductor lines fail at high temperatures under the mechanical stress of the overlaid intermetal insulator and/or passivation film without current stress [1]. Especially in multi-layer technologies, the lower metal lines see a greater stress from the overlaid insulators including the intermetal SiO_2 film.

While electro-migration failures can be often avoided by proper layout, stress induced migration limits allowable widths of metal lines. It affects chip size, and gives an essential, physical limit to multi-layer metal systems.

We have developed a technique to evaluate stress induced migration by using a test site, and successfully applied it to study the process parameters affecting conductor life, and to advise techniques to improve metal reliability.

SAMPLE & MEASUREMENT Metal is sputtered onto substrates with thermal-SiO_2 (or PSG) on silicon, and photo-etched. Metal length is typically 1.0-1.4m. A passivation layer of Sp-SiO_2/p-SiN, p-SiO/SOG/p-SiO, or p-SiN/PSG is deposited on top of the metal (Sp= Sputtered, p= Plasma). H_2 or N_2 anneal is made before the storage test. Standard anneal condition is 450-475℃/30min + normal cooling rate.

Poly-Si + isolation steps with PSG overcoat are used as substrates when step enhanced failures are to be tested.

In the storage test, metal resistance is first measured at the room temperature of all test chips in a wafer. Wafers are then stored in an oven at 125-300℃. No current stress is applied. Metal resistance is monitored at the room temperature at intervals. Metal open is defined by 10MΩ.

INFLUENCING FACTORS Stress induced migration of aluminum depends essentially on (1) metal quality, (2) metal dimensions, (3) overlaid insulator, (4) annealing conditions, and (5) storage temperature. Also, steps in the substrate affect the metal life.

N_2 inclusion during the metal deposition [2] makes aluminum so hard and brittle, and failures are greatly accelerated (Fig. 1). Failures at steps are found dependent on silicon content [3] in Al-Si (Table I). The following experiments are made by using N_2-free aluminum with moderately low Si content of 1.0-1.5%.

The key factor of the stress induced migration is the overlaid insulator. The use of Sp-SiO_2 or p-SiO is found to affect the metal reliability greatly (compare Figs. 1 and 2). Our experiments are made mainly by using Sp-SiO_2 or p-SiO as overcoat. Using our standard p-SiN passivation results in much fewer failures.

Temperature and cooling rate of anneal after passivation are important factors affecting reliability. Especially, very slow cooling from T≧450℃ makes many wedge-shaped voids like those reported for high stress p-SiN [4] and degrades metal reliability. Under normal annealing/cooling conditions, higher the annealing temperature, normally larger the S.I.M. failure rate.

The use of Sp-SiO_2 or p-SiO increases wedge-shaped voids along the metal side edge after a long period of storage test, and there is no doubt that the reliability is affected, with stress apparently playing an essential role. From the comparison of the three materials, Sp-SiO_2, p-SiO, and p-SiN, however, no clear correlation is found between failure rate and film stress as monitored by wafer bend. Detailed study of microscopic insulator properties seems to be needed.

Steep steps in the substrate enhance stress and increase failures (Table I). However, the use of planarization techniques such as glass flow, BPSG and SOG effectively reduces step accelerated failures.

COUNTERMEASURES The conductor life is improved by adding copper (Cu) to Al-Si (Fig. 2) [1, 4]. Cu is already known to improve metal life against electro-migration. This suggests that grain boundaries are a place to fail. The difference is that the "bamboo" structure may be good against electro-migration, but not necessarily against S.I.M. Addition of palladium (Pd) to Al-Si shows a similar (normal cool) or much better (slow cool) improvement (rig. 3). On the contrary, addition of titanium (Ti) resulted in very poor reliability.

The layered structures of AlCuSi and $MoSi_2$ show much longer conductor life (Fig. 3). However, many wedge-shaped voids, though not fatal, are observed along the AlCuSi lines after a long period of stress. This probably suggests a sophisticated mechanism: the aluminum life may not be improved essentially by the use of $MoSi_2$, but $MoSi_2$ probably forms an electrically conducting bridge where aluminum fails.

To reduce S.I.M. failures, controlling the film properties of overlaid insulators must be an important solution to be pursued. We have not yet found good means to do so, however, because the oxide deposition conditions are determined by taking many other requirements for intermetal insulators into consideration.

TOLERABLE METAL WIDTH The metal life without steps is dependent on metal dimensions (width W, thickness T) and the temperature T by

$$\tau \propto W^{n_1} \cdot T^{n_2} \cdot \exp(Ea/kT)$$

where, parameters are experimentally given by

$n_1 = 3.2$, $n_2 = 2.8$, and $Ea = 0.6$ eV ($T \leqq 200$℃)

for AlCu(0.5%)Si with Sp-SiO_2 passivation (Figs. 4, 5, and 6). These values are different from those obtained by Al-Si with p-SiN passivation [4] suggesting different failure mechanisms dependent on insulators.

By extraporation from the test data, the minimum allowable line width of Al-Si to assure 100 fit at 70℃ in 10 years is 3.2μm (T= 800nm) for the metal length of L= 5mm using p-SiO or Sp-SiO_2 passivation (Fig. 7). Narrower metal lines can be used only if p-SiN is used as the overlaid layer, or in case the metal length is much smaller.

In case of Al-Cu(0.5%)-Si, the minimum allowable line width is 1.3-1.6μm (T= 500nm, L= 5-10m) by the same criterion.

This indicates that sub-micron LSIs need new metal systems where multi-layer technologies using p-SiO are a norm in many categories of products. Layered structures are important candidates for this purpose. The metal life of the layered structures using $MoSi_2$ is found well below 1μm, although not clearly identified yet due to insufficience of test time.

DISCUSSION ON LAYERED STRUCTURES To make the local resistance of the bridging $MoSi_2$ low enough where aluminum is open, it is desirable to make it thick enough. Replacing it with such low resistivity materials as TiW or TiN will also help. The power density in aluminum with resistivity ρ(Al) under the current density J is given by

$$P_o = \rho(Al) * J^2.$$

After the aluminum opens leaving a $MoSi_2$ (or any other material with resistivity ρ(M)) bridge, the power density at the bridge is given by

$$P = \rho(M) * [T(Al)/T(M)]^4 * J^2$$

and so the ratio is given by

$$R = P/P_o = [\rho(M)/\rho(Al)] * [T(Al)/T(M)]^2.$$

It is important to make R small. Otherwise, the bridge is heated locally so as to melt near-by aluminum to accelerate degradation of the metal system [5].

REFERENCES:
[1] N. Owada et al, Proc. VMIC, p. 173 (1985).
[2] J. Klema et al., Proc. IRPS, p. 1 (1984).
[3] S.J. O'Donnell et al., Proc. IRPS, p. 9 (1984).
[4] S. Mayumi et al., Proc. IRPS, p. 15 (1987).
[5] J.A. Maiz and B. Sabi, Proc. IRPS, p. 145 (1987).

Table I Si content dependence of step enhanced S.I.M. failures in Al-Si (125℃, 384H, p-SiN/PSG.)

Si content	Al-Si line width		
	2.6μm	3.0μm	3.4μm
0.7%	0/80	0/80	0/60
1.2%	5/94=5.3%	0/60	0/50
3.8%	4/43=9.3%	1/60=1.7%	0/50

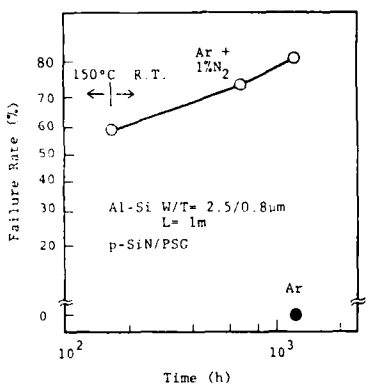


Fig. 1 Stress induced migration enhanced by N_2 contamination

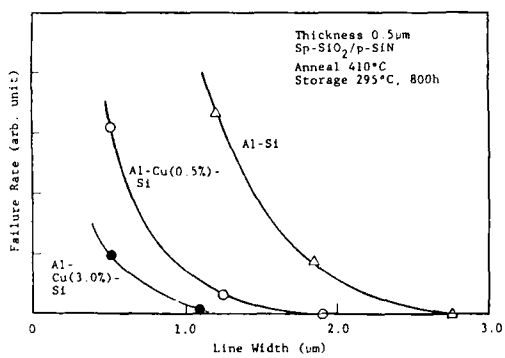


Fig. 2 Stress induced migration of AlCuSi

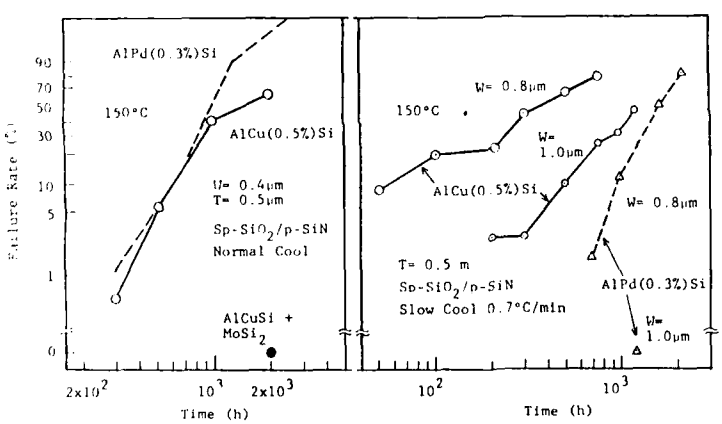


Fig. 3 Comparison of AlCuSi, AlPdSi, and layered structures of AlCuSi and $MoSi_2$

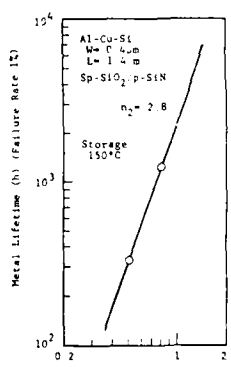


Fig. 4 Thickness dependence

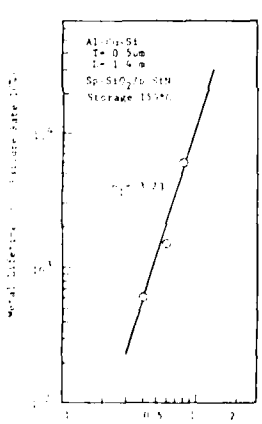


Fig. 5 Line width dependence

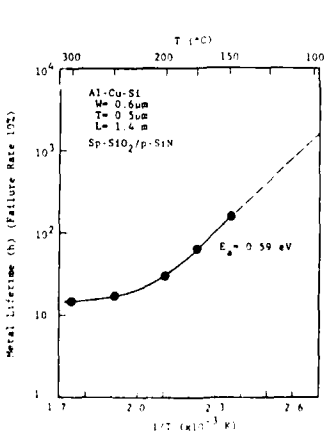


Fig. 6 Temperature dependence

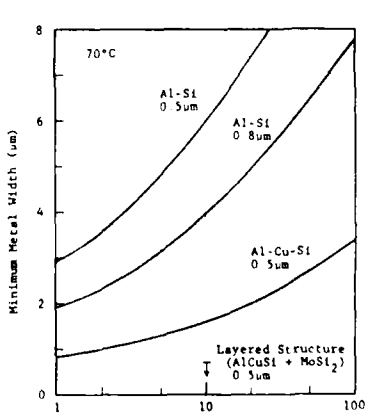


Fig. 7 Minimum allowable metal widths

Abstract No. 311

A STUDY OF ELECTROMIGRATION PERFORMANCE IN A RANGE OF AL/SI/TI ALLOYS

N P Armstrong
Plessey Research Caswell Ltd
Caswell, Towcester, Northants, England

R J Dulniak and *A Turnbull
GEC Hirst Research Centre, Wembley, England

INTRODUCTION

In the last four years, there has been interest [1,2,3] in the use of Al/Si/Ti alloys as an alternative to Al/Si and Al/Cu/Si alloys. However, this has generally been from the stand-point of requiring improved life over Al/Si, without incurring the complications associated with addition of Cu. Fischer [1,2] compares Al/Si and Al/Si/Ti, showing 15x increase in Median Time to Failure (MTF) for the latter under stress test. But this remains far short of the Al/Cu performance. Furthermore, the alloys reported have all included about 1% Si as they have their origin before the wide acceptance of barrier metallisation schemes. This level of Si is no longer desirable as it leads to precipitation incompatible with 1μm sized contacts. Can the Si content be reduced or even omitted? Several observations have been reported [3,4] implying interactions between Ti and Si, which might suggest film instability if Si were omitted.

EXPERIMENT

In the current work, an array of eight Al/Ti and Al/Si/Ti alloys (4x2) were deposited by co-sputtering: Si 0, 0.2, 0.5, 1%; Ti 0.2, 1.0%. These were compared to Al/Cu and Al/Cu/Si from composite targets. All films were deposited on 0.5μm thermal SiO_2.

Before lifetesting, films were assessed for dry etchability, Si precipitate formation and thermal hillock formation. Using an AME 8131 batch etcher and BCl_3/Cl_2 mixture, the etch rate of Al/Si/Ti was lower than for Al/Cu/Si, but uniformity was improved, requiring less overetch. No post-etch corrosion was seen on any Al/Si/Ti wafers, whereas both Cu-containing controls showed corrosion on some wafers. Si precipitates were counted using dark field illumination: table 1 shows data normalised per 25K vias. SEM examination of thermal hillocks after cycling between room temperature and 450degC revealed evidence of a bi-modal distribution in hillock size, particularly for Al/4%Cu; hillocks were either >4μm or <1μm wide (and generally as high). Table 1 shows density per bond pad (.02mm^2) for both large and small hillocks.

Independent lifetests were performed at two sites for corroboration. Acceleration conditions were 200degC, $2x10^6$A/cm^2. The structure chosen for the lifetest was close to that recommended by Schafft [4], being 1mm long, without corners, and 4μm wide. Voltage probe points were provided at each end.

Failure times (Log-Normal model) are shown in tables 2 (site A) and 3 (site B). The tables show open-circuit MTF and, where applicable, MTF for 20% increase in resistance (dR). The factor of about 2 between the lifetimes at the two sites is explained in part by different processed linewidths and linewidth measurement techniques. Most Ti-containing alloys have much shorter MTF than Al/Cu or Al/Cu/Si. Addition of Si progressively degrades MTF, giving Al/1%Si/0.2%Ti a MTF less than a tenth that of Al/4%Cu. The 1%Ti alloys generally had longer open-circuit MTF than the 0.2%Ti alloys, but all suffered large resistance increases (figure 1), resulting in times to 20% dR similar to their 0.2%Ti counterparts. The nominal Al/0.2%Ti alloy (omitted from site B data) was later found to have approx. 0.8%Ti - hence the 20% dR MTF in table 2.

Observation by SEM of failed samples revealed long whiskers (figure 2) on samples with high Ti content (including the Al/0.2%(0.8%)Ti), but not on any other alloys (figure 3). Thus there appears to be a connection between whisker growth and large resistance increases. In a follow-up test, samples were removed at regular intervals. In the zero-Si alloys, having the best MTF performance in the matrix, whiskers were seen after only 5% of the open circuit MTF - 12% of the resistance increase MTF.

DISCUSSION

The tendency toward whisker growth associated with high Ti content is unfortunate in view of the reported [3] increased activation energy with Ti content greater than 0.6-0.8%. Towner [3] has observed that the required microstructural changes for increased activation energy only occur in the ternary case - with 1% Si also. Unfortunately, the evidence in table 1 suggests 0.2% Si to be the critical level with regard to Si precipitation. Above this level, the number of precipitates increases very rapidly with Si content, and even the level seen with 0.2%Si could constitute a yield hazard.

The clear tendency seen in table 1 for Al/Cu and Al/Cu/Si films to produce a lower overall thermal hillock density but a larger number of very large hillocks may give cause for concern. Depending on dielectric material and thickness, this may cause a greater short circuit yield loss than any of the Ti-containing alloys, particularly if a dielectric planarisation process is used.

The observed trends in electromigration data suggest the untested Al/0.2%Ti as a possible compromise, having MTF approaching that of Al/Cu, but without early onset of whisker growth. Towner's observations [3] suggest that the activation energy for Al/0.2%Ti would be as for pure Al - about 0.55eV - implying significant disadvantage compared to Al/Cu (about 0.7eV) at normal operating temperatures.

CONCLUSION

In summary, results show very early failure with high Ti content through growth of long whiskers, and progressive degradation of performance with increasing Si content. The trends observed suggest that a true Al/0.2%Ti alloy might be the optimum combination, with performance approaching that of Al/4%Cu. MTF is likely to be somewhat inferior to that of Al/4%Cu, but without etch difficulties or corrosion, as neither was encountered on any of the Al/Ti alloys.

ACKNOWLEDGEMENTS

This work was partly funded by the EEC under ESPRIT project 14: "Advanced Interconnect for VLSI". Thanks are due especially to A J McGeown of Electrotech for deposition of Al/Si/Ti alloys, to N P Francis who performed lifetests at Caswell, and to W G Freeman, V J Phelan and A J Vale of GEC Hirst Research Centre who carried out analysis of films

REFERENCES

1. F.Fischer, Siemens Forshungs- und Entwicklungs Berichte, 13 (1), pp21-27 (1984)
2. F Fischer & F Neppl, Proc 22nd IEEE IRPS, pp190-192 (1984)
3. J M Towner, A G Dirks & T Tien, Proc 24th IEEE IRPS, pp190-192 (1984)
4. D S Gardner, T L Michalka, K C Saraswat, T W Barbee Jr, J P McVittie & J D Meindl, IEEE Trans ED-32, pp172-183 (1985)
5. H.A.Schafft, IEEE Trans. ED-34, pp673-681 (1987)

*present address: British Aerospace, Stevenage, England

Si %	Ti %		Cu %
	0.2	1	4
0	0 1/760	0 1/920	0 9/480
0.2	9 1/1360	1 1/840	KEY:
0.5	108K 1/1360	21K 3/2120	•Si Precipitates per 50K vias •Hillocks lge/small
1	406K 5/1600	256K 0/1520	360K 6/640

Table 1: Si precipitates and thermal hillocks

Si %	Ti %				Cu %	
	0.2		1		4	
0	*[162 76] [.30 .58]		173 61 .30 .32		155 .77	MTF Sigma
.2	25 1.46		89 28 1.23 .42			MTF Sigma
.5	48 .92		49 19 .51 .32			MTF Sigma
1	10 .83		29 24 .50 .26		118 .60	MTF Sigma
	O/C	20%dR	O/C	20%dR	O/C	

Table 2: MTF (hours) at site A. 202degC 2E6A/cm2
*0.8% Ti by analysis (see text)

Si %	Ti %				Cu %	
	0.2		1		4	
0			512 183 .71 .13		364 .26	MTF Sigma
.2	86 .61		276 54 .75 .13			MTF Sigma
.5	65 .49		101 34 .60 .09			MTF Sigma
1	32 .39		47 30 .98 .48		278 .49	MTF Sigma
	O/C	20%dR	O/C	20%dR	O/C	

Table 3: MTF (hours) at site B. 200degC 2E6A/cm2

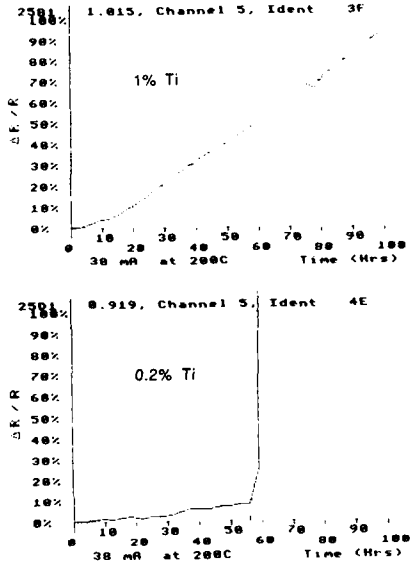


Figure 1: Track resistance during lifetest



Figure 2: Whiskers on Al/1%Ti after lifetest

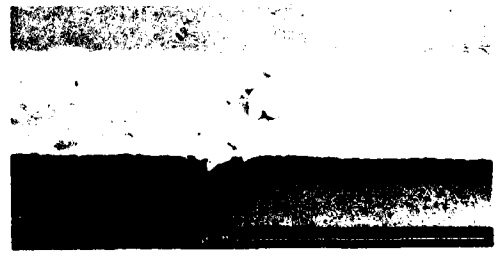


Figure 3: Typical damage on 0.2%Ti alloys (Al/1%Si/0.2%Ti)

Abstract No. 312

HUMIDITY-TEMPERATURE-VOLTAGE ACCELERATION MODEL FOR CORROSION OF THIN FILM ALUMINUM

J. W. Osenbach and J. L. Zell

AT&T Bell Laboratories
P.O. Box 13566
Reading, PA 19612-3566

We have studied how temperature-humidity- and voltage effect corrosion of thin film aluminum. This was done by aging RTV-coated unpassivated aluminum triple-track test structures at temperatures between 85°C and 150°C, at relative humidities between 50% and 85%, and at electric fields between two 2 x 10^3 V/cm to 2 x 10^5 V/cm. Using these results, we develop temperature-humidity-bias acceleration models which are based on sound chemical and physical principles.

We found that for the defect (contamination) controlled failure population that an acceleration model of the form

$$\text{time-to-failure } \alpha [RH]^{-n} \exp(E_a/kT)$$

fit the data. For those humidity ranges where water was able to absorb onto the device surface, $2.3 \le n \le 3.2$ and was independent of voltage. For those humidity regions where water could not absorb, the humidity exponent was much larger $n>6$. For all humidity regions, the activation energy E_a was between 0.75 and 1.2 eV and was independent of voltage. The voltage acceleration factor was not well defined in this region of the failure population.

We have developed a theory based on electrochemistry, which suggests that the humidity exponent is directly related to the type of contaminant on the surface which leads to corrosion. For those positive ions such as Na^+ or K^+, we calculate an exponent of 3. For the negative ions such as Cl^-, the humidity exponent is also 3. Based on these results, we conclude that for those devices which are packaged in "dirty" materials, or which have contaminated surfaces prior to encapsulation, the acceleration model given by Peck should be used for data analysis. However, for those devices packaged in "clean" materials the acceleration model given below should be used.

The part of the population which failed due to wearout can be modeled by an equation of the form

$$\text{median-time-to-failure } \alpha \exp\left[(-V_A(E_{app})\right] \cdot \exp(-A \cdot \%RH) \exp(-E_A)$$

where $-V_A$ is the voltage acceleration factor which is a function of encapsulant and surface passivation. It also depends upon the voltage which is applied. This is because the surface mobility reaches a maximum at some voltage which depends on the surface conditions. The humidity acceleration factor A is 0.1±0.05(hr/%RH) and the activation energy E_A is 0.98±0.13 eV. Both A and E_a are independent of voltage.

We have developed a theory again based on electrochemistry, which suggests that the activation energy (E_a) and humidity acceleration factor (A) for devices which fail due to wearout is due to conduction of OH^- and H^- ions over the device surface between the anode and cathode. Therefore, corrosion which occurs due to wearout is controlled by the water absorption isotherm and the surface mobility of the OH^- and H^+ ions of that system of interest.

Abstract No. 313

Corrosion Products and Surface Structure of PbSn Solder Pads

Helen L. Yeh* and Homi Dalal**

IBM

*Research Division, T. J. Watson Research Center, P. O. Box 218, Yorktown, N. Y., 10598

**General Technology Division, East Fishkill, Route 52, Hopewell Junction, N. Y., 12533-0999

Lead/Tin alloys have been used in microelectronics industry for past 25 years. In this paper we study the effect of tin content (from 0-10 wt%) on the corrosion of high Pb alloy. We identify the corrosion products, their morphology, the formation methods and correlate the corrosion with the bulk and surface tin content in solder balls.

Because corrosion resistance of solder pads is a surface related topics, in order to understand the surface structure of solder pads and important parameters controlling the corrosion of solder pads, various solder pads were studied by SAM (scanning Auger microscope) and the results were correlated with corrosion tests.

We found disk-shaped and crust forms of corrosion products on the C4 solder balls examined. Detailed X-ray diffraction patterns showed Mendipite ($2PbO \cdot PbCl_2$) and plumbonacrite ($6PbCO_3 \cdot 3Pb(OH)_2 \cdot PbO$) were found on all of the corroded chips besides Al, Al_2Cu, and Pb.

We found plumbonacrite ($6PbCO_3 \cdot 3Pb(OH)_2 \cdot PbO$) on the Temperature/Humidity (T/H ,75°C and 85% humidity) corroded pure lead blanket wafers after either H_2/flux or double H_2 reflow.

Among the three different kinds of reflowed solder pads, flux, hydrogen containing forming gas and ion beam (Ref. 1), SAM surface studies showed that flux reflowed pads had the lowest and forming gas reflowed pads had the highest amount of tin on the surface. It confirms the report that flux removes tin preferentially, Ref. 2. In all of the reflowed pads examined by SAM, tin was present more on the top of the pads than on the side areas because of the single source deposition method. The presence of more tin, i.e. less lead, on top areas of solder pads was consistent with the findings that some of the corroded pads showed more corrosion products on the side than on the top.

The lack of enough tin compound to protect the surface of flux reflowed C4 pad seemed to be the main reason that the flux reflowed pads were vulnerable to corrosion. When surface tin content was not high, lead showed up on the surface and was corroded by two methods to form lead carbonate related compound. One method was with the presence of chlorine ions which might play a role in accelerating the corrosion. The chlorine ions reacted with lead oxide to form lead, oxygen, and chlorine related compounds and then transformed to more stable lead carbonate compound in the presence of water and CO_2. The detection of mendipite and plumbonacrite confirmed this formation method. The other formation method only needed high humidity and high temperature and no chlorine. The presence of plumbonacrite but no lead oxide chloride on corroded pure lead blanket wafer after T/H tests proves this method.

The high tin on the surface of hydrogen reflowed pads protects the C4 pads from the attack of chlorine and humidity and generally have less corrosion problem.

References

1. "Ion Beam Joining Technique", J. M. E. Harper, H. L. Yeh and K. R. Grebe, J. Vac. Sci. Technol., Vol. 20, No. 3, p. 359 (1982).
2. "A DSC Technique to Measure the Amount of Indium or Tin Leached from Lead Based Solders by Rosin Fluxes", S. Teed and V. C. Marcotte, Proceedings of the Eleventh North American Thermal Analysis Society Conference, New Orleans, Louisiana, Vol. 11, Oct. 1981.

Abstract No. 314

A Practical Approach to HAST and Correlation with 85/85 for Reliability Testing of Plastic Encapsulated IC's for Telecommunication Applications

A. Hente K. Allaert P. De Pauw

Reliability and Qualification Department

Alcatel Bell Telephone N.V.
Francis Wellesplein 1
B-2018 Antwerpen, Belgium

Plastic packages have become a common fact for consumer applications and their reliability is since being improved contineously [1]. However for many high reliability applications, 25 years must be guaranteed under tough climatological conditions [2]. Therefore 3,000 hrs of THB test are needed for simulation. The THB 85/85 test is commonly used as a standard stress test for corrosion on plastic encapsulated semiconductor devices. This test however puts strong constraints on the on-line quality control and it extends the design-to-market time with several months.

The answer to this problem may be HAST (Highly Accelerated Stress Test) as it has a much higher acceleration factor than the 85/85 test. Unfortunately up to now the implementation of HAST is not well understood and many problems have been reported about the correlation between HAST and 85/85 [1]. Both suppliers and customers are therefore rather sceptical with respect to HAST.

Because of the urgent need to reduce turnaround times we put a lot of effort in experiments that should give us a better understanding of HAST. Therefore both tests have been run simultaneously for several qualifications for more than one year.

Tests in HAST have been done at 115, 125 and 135°C, all at a constant relative humidity of 85 %. Earlier tests on TTL standard devices showed us that at temperatures above 135°C different failure mechanisms can be initialised.

We have found a satisfactory correlation between HAST at temperatures below 135°C and 85/85. The failure mechanism was found to be identical in both tests and the data could well be fitted to the Arrhenius model with a *maximum likelihood estimation* (Fig. 1).

The observed acceleration factors and activation energies correspond to previously published data. Activation energies found are between 0.7 eV and 0.8 eV. This is a value that is generally accepted for estimating acceleration factors. Acceleration factors between 85/85 and HAST are in the range of 6 (115/85) and 23 (135/85).

The DUT's are 3 μm CMOS custom VLSI's with a double passivation layer of silicon oxide and silicon nitride on top in plastic DIL packages of 16, 24 and 28 pins. Some components had a silicone die coat, others not. The test where continued until more than 50 % failures occured. The main failure mechanism was found to be corrosion of the Al interconnections caused by imperfections such as cracks and pinholes in the passivation layer (Photo 1, 2). These failures could also be observed on both the samples, with and without die coating. They could therefore not be caused by the filler grains in the moulding compound, neither by thermally induced shear stresses at the interface between die and plastic [3, 4].

We may conclude that, based on the great number of tests being performed, HAST at 125°C/85 % RH is a high reliable alternative to the more extended 85°C/85 % RH tests for telecommunication devices.

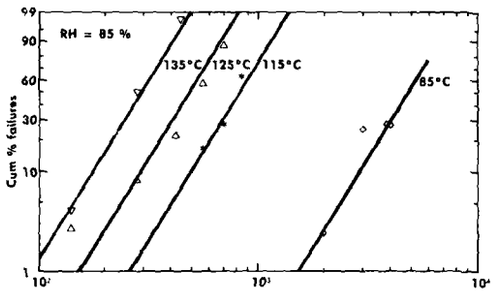
References

[1] L. Gallace and M. Rosenfield
«Reliability of Plastic Encapsulated Integrated Circuits in Moisture Environments», RCA Review, Vol. 45, 1984

[2] N. Sinnadurai
«The Reliable Operation of Plastic Encapsulated Micro-electronics Components in Severe Climatological Conditions», 3rd Int. Conf. «Quality in Electronic Components», 1987

[3] Swee Yong Khim, Ting Tziat Tze
«Filler Induced Failures in Plastic Encapsulated DRAMS», IPFA proceedings, 1987

[4] S. Sazaki, K. Serizawa, A. Kaneda, K. Nishi, S. Hashizume
«The Development of a High Reliable Heat-Proof Plastic IC Package», Int. Conf. on Reliability and Maintainability, proceedings, 1986



Cumulative number of functional failures

Time (hrs)	135/85 N = 24	125/85 N = 36	115/85 N = 36	Time (hrs)	85/85 N = 40
140	1	1	0	500	0
280	12	3	0	1,000	0
420	24	8	0	2,000	1
560	—	21	6	3,000	10
700	—	32	10	3,880	11
840	—	—	23	4,000	11
980	—	—	31		

Fig. 1 Weibull plot and table with functional failures of 2.4 μm CMOS custom VLSI in 24 pin PDIL package



Photo 1 Failure in 85/85 after 3,880 hrs of test Sample with die coating



Photo 2 Failure in HAST after 280 hrs in 135/85 Sample with die coating

Abstract No. 315

Hot Carrier Limited Operating Voltages for Submicron non-LDD Shallow Junction MOSFET's

P.K. Chaudhari[1], D.S. Wen[2], and C.M. Osburn[1,2]

[1]Microelectronics Center of North Carolina, P.O. Box 12889, Research Triangle Park, North Carolina 27709,

[2]Department of Electrical Engineering, North Carolina State University, Raleigh, North Carolina 27695-7911.

Introduction

Device degradation due to hot carrier simulated stress has been widely explained as being due to trapping of the hot carriers in the gate dielectric and/or interface trap generation. With the continuous scaling of VLSI devices, high-field-induced degradation from channel or avalanche hot-electron injection, and its subsequent impact on the device parameters namely subthreshold slope change, threshold voltage shift, and the degradation in transconductance, become a major reliability concern in circuits employing these submicron MOSFET's. When a transistor is subjected to such an operation for longer periods of time, these parameters can change and exceed the limits of specification permanently. Therefore, to evaluate accurately the device reliability to realize submicron VLSI's, it is very important to have some kind of guide lines to predict the device operational life time.

Avalanche hot carrier injection near the drain provides the greatest source of concern[1]. Accordingly the device degradation has a strong correlation with the impact-ionization-induced substrate current, i.e. the gate bias condition which causes the most severe degradation as shown in Fig. 1.

In this study, using accelerated stress-aging under such worst case biasing conditions, device degradation is modelled to predict the device life time as a function of its operating parameters like drain bias, channel length and gate bias for the non-LDD, 0.18μm shallow junction NMOSFET process studied here.

Experimental results and discussion

Discrete NMOSFET's with effective channel lengths from 0.65 to 1.65μm and a width of 20μm used here were fabricated using a retrograde n-well CMOS technology with shallow junctions formed by Ge-preamorphization followed by As^+ implantation and two step annealing: 30 min @ 550°C in Argon followed by 1050°C, 10 seconds rapid thermal annealing (RTA)[2]. Gate oxide thickness, substrate doping, and junction depth were 22.5 nm, $1x10^{16}$ cm^{-3}, and 180 nm respectively. Accelerated stress-aging was carried out for various drain and gate biases with $V_{sub} = 0$ at room temperature. The device characteristics before and after stress were measured in the reverse mode, i.e. with source and drain interchanged. The threshold voltage was defined such that at $V_s = 0.1V$, $I_s = 1.0x(W_{eff}/L_{eff})$ μa. The transconductance G_m, is the maximum in slope of I_s-V_s curve at $V = 0.1V$.

Fig.2 summarizes typical V_T shift versus aging time, as a function of stress bias for a device with $L_{eff} = 0.65\mu m$. A positive threshold voltage shift, as seen in Fig.2, was observed in all cases of $V_G < V_D$. The threshold voltage shift, ΔV_T, increases with time as

$$\Delta V_T = At^n$$

where $n = 0.65$[3,4]. The pre-exponential factor, A, is an exponential function of $1/V_D$[3]. Since the substrate current is an exponential function also of $1/V_D$ and $1/L_{eff}$, the life time of the submicron devices, defined by a specified threshold voltage shift, depends exponentially on drain bias and channel length as shown in Figs. 3 and 4 respectively. Therefore, using the data of Fig.3, the maximum allowable operating voltage for defined life time can be predicted. The device lifetime τ can be expressed as $\tau \propto \exp(b/V_D - L_o/L_{eff})$ where b and L_o are constants. Using the slopes of figs. 3 and 4, values for b and L_o were determined to be 144V and 4.7μm respectively.

As can be seen from Figs. 1 and 3, the most rapid degradation occurs when $V_G \approx \frac{1}{2} V_D$. For the low temperature technology used here, 100,000 hour lifetime at 100% duty cycle could be achieved without the need of a lightly doped drain process. A more realistic 3% duty cycle permits use of 4.6V

In summary, device degradation in non-LDD, shallow junction, submicron MOSFET's due to avalanche hot carrier has been studied. Device operating life time, τ, varies exponentially with drain bias and the effective channel length. From this drain bias -lifetime relationship the maximum allowable operating drain voltage can be predicted.

Acknowledgement - The authors wish to express their gratitude to Dr. Reisman for his continued encouragement and the silicon processing personnel of the Microelectronics Center of North Carolina Central labs for wafer fabrication. Portions of this work were supported by the Semiconductor Research Corporation. One of the authors, P.K. Chaudhari, participated under the IBM Academic Leave Program.

References

1. E. Takeda et.al., *IEEE Electron Devices*, ED-30, 652(1983)

2. D. Sharma et.al, Proc. First Inter. Symp. on ULSI, The Electrochem. Soc., 87-11, 49-63 (1987)

3. E. Takeda and N. Suzuki, *IEEE Trans. Electron. Dev. Lett.* EDL-4, 111 (1983).

4. C. Hu et.al, *IEEE Electron Devices*, ED-32, 375 (1985).

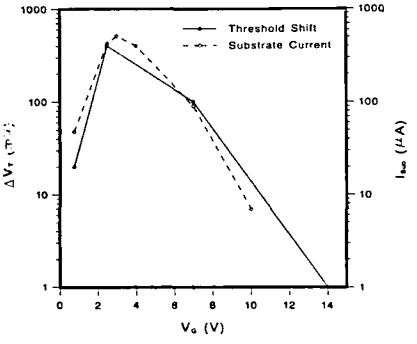


Figure 1 Threshold voltage shift and substrate current as a function of gate voltage of a 0.65μm device. Devices were stressed for 10 minutes at V_D=7.0V.

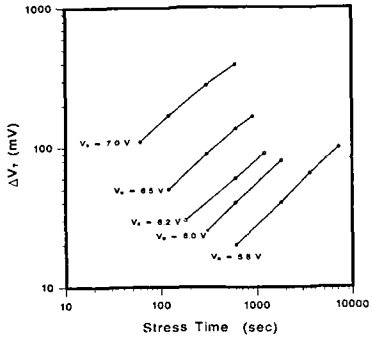


Figure 2 Threshold voltage, V_t, degradation of 0.65μm devices as a function of stress time with V_D as a parameter at V_G=2.5V.

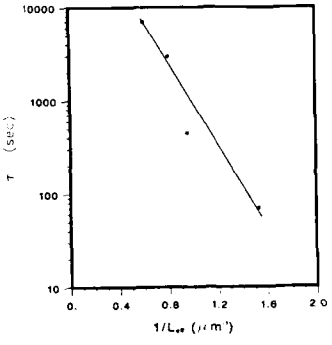


Figure 4 Dependence of life time, τ, on L_{eff}. Devices were stressed at V_D=7.5V and V_G=3.0V.

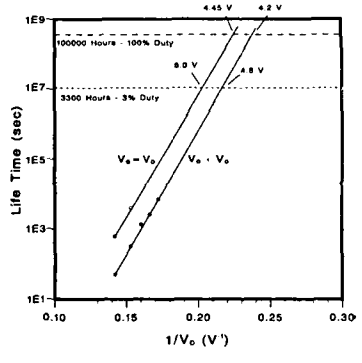


Figure 3 Dependence of life time, τ, on V_D for 0.65μm NMOSFET's.

Abstract No. 316

Anomalous Hot Electron Effects Induced By PECVD Passivation Processes

Sang U. Kim and Fahd Hinedi

INTEL CORP.
5000 W. Chandler Blvd.
Chandler, AZ 85226

PECVD (Plasma Enhanced Chemical Vapor Deposition) Silicon Nitride and Oxynitride are widely used in today's VLSI as the passivation layer. Therefore, impact of such films on device instability, particularly hot electron effects must be clearly understood. It has been generally believed in the IC world until most recently that the passivation process including PECVD has no impact on hot electron performance. However, this view is changing. Recently, the problems related to hot electron instability induced by PECVD passivation processes appears increasingly in literatures. New degradation mechanisms have been reported, involving hole injection and interface state generation through a still unknown electro- chemical reaction with hydrogen present in the plasma nitride caps [1]. The conventional hot electron methodology no longer can be applied in this case. It must be revised to include the new degradation mechanisms. This study was undertaken to develop a better understanding of the new degradation mechanisms associated with PECVD passivation processes and to establish a new hot electron stress methodology by which hot electron lifetime can be predicted.

In order to determine the impact of PECVD passivation processes on hot electron effects, devices with and without passivation were used. For passivated devices, the PECVD silicon nitride and oxynitride passivations used most widely today were chosen. Also, devices with and without Ldd structures were used to determine the impact of such structures. Several gate voltages were used in stress to determine a maximum hot electron degradation condition at a given drain voltage Vd. Threshold Vt, transconductance Gm, drain saturation current Idsat and impact ionization current Isub were measured before and after each stress.

Two gate voltages were used to determine a Vg dependence on hot electron degradation: Vg = 3.2V at which a maximum Isub occurs, and Vg = 1.5V, a maximum hole injection condition. Vd = 7V was used for all cases. Vg = 3.2V is a condition commonly used in the conventional hot electron stress. At this voltage the maximum Isub takes place. Device degradation occurred mostly in Gm. Vt shift was negligible. This was particularly so with PECVD passivation.

For unpassivated units the maximum Gm degradation occurred with a maximum Isub, Vg = 3.2V as expected. No degradation was observed with Vg = 1.5V for a 1,500 minutes stress. These results are consistent with the conventional hot electron stress data. That is, the maximum degradation occurs approximately at Vg = 1/2 Vd or Vg = 3.2V with Vd = 7V in this case.

For passivated units an entirely new phenomena was observed. The maximum degradation no longer occurred at a maximum Isub. Instead, a significantly higher Gm degradation was observed at Vg = 1.5V. Experimenting with different gate voltages, Vg = 1.5V was found to be a voltage at which a maximum Gm degradation occurred, and from this, a universal relationship for a maximum degradation condition was derived:

Vg = 1/2 Vg (at Isub maximum)....(1)

For example, if the maximum Isub occurs at Vg = 4V in an Isub versus Vg curve with Vd as a parameter, Vg = 1/2(4V) = 2V at which a maximum Gm degradation will occur. The new relationship can be applicable to both PECVD nitride and oxynitride passivation. It was also observed that the relationship (1) corresponded to a condition most favorable to net hole injection. This new Vg dependence criteria must be used in order to obtain a maximum Gm degradation with PECVD passivation.

We also observed a strong impact of PECVD passivation processes on Gm degradation, an enhanced degradation compared with no passivation. These results suggest a new degradation mechanism associated with the PECVD passivation process. The new degradation mechanism must account for enhanced Gm degradation, hole injection, the presence of hydrogen and their interaction which were observed in this study. The PECVD nitride or oxynitride films are known to have excess hydrogens which may diffuse toward the SiO_2 - Si interface during the PECVD passivation process, and may participate in generating interface states. Based on those results, a phenomological model for Gm degradation was developed, and will be presented along with other experimental findings.

References:

[1] R.B. Fair and R.C. Sun, IEEE Trans. Electron Devices Vol. ED-28, P83, 1981.

Abstract No. 317

Characteristics of Al-$TiSi_2$ contacts to n^+ and p^+ silicon

K. Shenai, P. A. Piacente, S. Al-Marayati, and B. J. Baliga

General Electric Company
Corporate Research and Development Center
Schenectady, New York 12301

I. Introduction

Refractory metals and their alloys are known to provide highly conductive films when deposited on silicon or polysilicon [1,2]. Among all the available silicides on silicon or polysilicon, $TiSi_2$ offers the lowest sheet resistance, R_{SH} [3]. In many applications, the silicide must be able to withstand post processing temperatures in excess of 800°C [4,5]. At these processing temperatures, film uniformity, stress, adhesion, oxidation, and subsequent etching all become extremely important. The silicide must also be able to preserve the integrity of the gate oxide when deposited on polysilicon in MOS gated devices [6]. It has been shown that between conventional furnace annealed (FA) and rapid thermally annealed (RTA) $TiSi_2$, RTA silicide has better film uniformity, lower sheet resistance, smoother film surface, and causes minimal perturbation in doping profiles [7-9].

Conventional high voltage discrete and integrated devices are fabricated with heavily doped polysilicon as the gate material which also serves as a self-aligned mask for subsequent dopant diffusions [10,11]. Phosphorous diffusion in polysilicon and its contamination at the gate oxide at process temperatures in excess of 1100°C are the key yield limiting factors in this technology [12]. For fast switching devices, a low gate sheet resistance [13] and simultaneous low contact resistances to gate, source and drain diffusions are required [14].

In this work, we report on low resistance Al-$TiSi_2$ contacts to As, B and P diffused junctions for silicon VLSI and smart power applications. The $TiSi_2$ was formed by RTA annealing sputtered Ti using a two-step anneal in nitrogen [7]. The optimal silicide conductivity was obtained by carefully selecting the dopant implant/diffusion parameters, Ti thickness and RTA activation parameters to reduce the silicon surface damage, to obtain minimal silicon sheet resistance, and to form uniform silicide films with negligible porosity. Contacts to $TiSi_2$ were formed by RIE etching about 8 kA of densified LPCVD SiO_2 and *rf* sputtering 1 micron Al at room temperature. Cross-bridge Kelvin resistors [15] and transmission line contact (TLC) structures [16] were fabricated by wet etching Al. Extensive contact resistance measurements were made using an automated measurement set up. The contact resistances obtained in this work are among the lowest reported in the literature for Al-$TiSi_2$ metallization to both *n*- and *p*-type silicon [17,18].

II. Experimental Results

The experimental device structures were fabricated on As, B, and P diffused regions formed on <100> oriented silicon substrates to obtain a range of junction depths ($0.3\mu m \leq x_j \leq 6.0\mu m$) and silicon sheet resistances ($8\ \Omega/\Box \leq R_{SH} \leq 50\ \Omega/\Box$). Contact patterns on silicon were defined by RIE etching 8 kA of densified LPCVD SiO_2 in CHF_3/CO_2 plasma. The oxide was deposited at 450°C and densified in nitrogen at 800°C for 60 min. A second low ion-bombardment plasma etch was used to remove the silicon surface damage created by ion-bombardment in the CHF_3/CO_2 plasma [19] which resulted in the degradation of silicon sheet resistance due to loss of surface dopant charge [20,21]. $TiSi_2$ with varying thicknesses and sheet resistances were formed by *rf* sputtering 600 A-1400 A Ti and siliciding using a two-step RTA anneal in nitrogen in the temperature range of 550°C-850°C. Contacts to $TiSi_2$ were formed by *rf* sputtering 1 micron Al at room temperature. Some samples were *in situ* sputter etched prior to Al deposition without breaking the vacuum to clean the $TiSi_2$ surface.

Table 1 lists the measured interfacial Kelvin resistance R_K between Al and $TiSi_2$ for as-deposited, and samples successively sintered at 400°C for 60 min. in H_2. The first row for sintered data corresponds to wafers not pre-tested (R_{K1} not measured) whereas the second row corresponds to those that were characterized for R_{K1}. Pre-testing prior to Al sintering and Al sintering had profound effects on the interfacial Kelvin resistances due to Al-$TiSi_2$ interfacial oxide rupturing and Al spiking. RTA silicide yielded lower interfacial resistance compared to furnace annealed (FA) silicide due to lower silicide sheet resistance and smoother silicide surface. Table 2 lists the contact resistances of sintered Al-$TiSi_2$-nSi on As and P doped silicon without any sputter etching of the $TiSi_2$ surface. It can be seen that RTA silicide consistently yielded lower Kelvin resistance compared to FA silicide and P diffused junctions had lower R_K than As diffused junctions due to enhanced current crowding in shallower junctions [20]. Extensive contact resistance measurements of sputter etched samples coupled with detailed material analyses using SIMS, RBS, Auger, and TEM will be reported at the conference.

References

[1] D. M. Brown, et al, Solid State Electron. 11, p. 1105, 1968.
[2] S. P. Murarka, Silicides for VLSI Applications, Academic Press, 1983.
[3] S. P. Murarka, et al, IEEE JSSC, SC-15, p. 474, 1980.
[4] C. Y. Ting, et al, J. ECS. 133, p. 2621, 1986.
[5] K. Shenai, et al, in Proc. Symposium G: Polysilicon Films and its Interfaces, 1987 Fall Mtg. of the Material Research Soc., Boston, MA, 1987.
[6] K. Shenai, et al, in Proc. Symposium F: SiO_2 and its Interfaces, 1987 Fall Mtg. of the Material Research Soc., Boston, MA, 1987.
[7] K. Shenai, et al, in Proc. Workshop on Tungsten and Other Refractory Metals for VLSI Applications III, Material Research Society, Pittsburgh, PA, p. 333, 1987.
[8] K. Shenai, et al, presented at the Symp. on Rapid Thermal Processing of Electronic Materials and Devices, 1988 Spring Mtg. of ECS, Atlanta, GA, May 15-20, 1988, Abstract No. 90, p. 129 of Extended Abstracts Volume, 1988.
[9] K. Shenai, et al, presented at the Workshop on Metals, Dielectrics, and Interfaces for VLSI, San Juan Bautista, CA, May 9 - 13, 1988. Also to appear in J. Vac. Sci. and Tech. B, 1988.
[10] B. J. Baliga, and D. Y. Chen, Power Transistors, New York:IEEE Press, 1984.
[11] M. F. Chang, et al, IEEE Trans. ED-33, p. 1992, 1986.
[12] K. Shenai, et al, General Electric TIS Rep. 87CRD207, 1987.
[13] H. C. Lin, et al, IEEE Trans. ED-22, p. 255, 1975.
[14] K. Shenai, and B. J. Baliga, Extended Abstracts of the 172nd Electrochemical Soc. Meeting, Honolulu, Hawaii, Abstract No. 705, p. 1005, 1987.
[15] S. J. Proctor, and L . W. Linholm, IEEE EDL-3, p. 294, 1982.
[16] H. H. Berger, Solid State Electron. 15, p. 145, 1972.
[17] C. Y. Ting, in IEDM Tech. Digest, p. 110, 1984.
[18] J. Hui, et al, IEEE EDL-6, p. 479, 1985.
[19] M. J. Kim, et al, IEDM Tech. Digest, p. 134, 1984.
[20] K. Shenai, et al, in Proc. Workshop on Tungsten and Other Refractory Metals for VLSI Applications, Material Research Society, Pittsburgh, PA, p. 219, 1987.

[21] K. Shenai, et al, presented at the Seventh Symp. on Plasma Processing, 1988 Spring Mtg. of ECS, Atlanta, GA, May 15-20, 1988, Abstract No. 114, p. 169 of the Extended Abstracts Volume, 1988.

Table 1. Kelvin resistances (R_K) of 1.8 micron diameter circular contacts of Al on $TiSi_2$.

SILICIDE TYPE	SPUTTER ETCH	R_{K1} (as-dep) (Ω)	R_{K2} (400°C, 60') (Ω)	R_{K3} (400°C, 120') (Ω)
FA	NO	206 ± 28	158 ± 42 93 ± 89	18 ± 23 4 ± 9
FA	YES	19 ± 2.8	20 ± 4 0.26 ± 0.12	0.22 ± 0.10 0.16 ± 0.08
RTA	NO	230 ± 53	214 ± 25 113 ± 61	
RTA	YES	11.3 ± 1.8	0.15 ± 0.08	

Table 2. Contact data at 300K for 5 micron dry etched square contacts.

DOPANT	SILICIDE TYPE	x_j (μm)	R_{SH} (Ω/□)	R_K (Ω)
P	FA	0.9	12.5	10.0
P	RTA	0.9	12.5	7.5
As	FA	0.28	41.2	17
As	RTA	0.28	41.2	13

Abstract No. 318

Electrical Characteristics of Inter-Poly Si Oxide and Optimized Cell Structure for Reliable Flash EEPROM

Shinichi Tanaka, Noriyoshi Tozawa
Kazunori Kanebako, Masayuki Hori
Masamichi Asano

Toshiba Corporation, Micro Electronics Center
Integrated Circuit Division

KOMUKAI 1, SAIWAI-KU, KAWASAKI-CITY
KANAGAWA 210, JAPAN

Introduction

The flash EEPROM featured by electrical erasing for entire cell array simultaneously has been expected to emerge as the low cost, high density most excellent non-volatile memory, not only making it possible to replace UV EPROM markets but having new further market potential. Main requirements for flash EEPROM performances are (1) high density, (2) fast writing speed-same as UV EPROM-, (3) fast erasing speed and (4) reliability on write-erase cycles. In order to meet these requirements, a new compact flash EEPROM cell with one transistor has been developed using sophisticated triple level Poly Si technology[1] and new circuits.[2] This paper deals with electrical characteristics of inter-poly Si oxide for the reliable flash EEPROM.

Experiment and Discussion

In the flash EEPROM, write operation is similar to the UV EPROM, i.e. hot electrons are injected into the floating gate during a write cycle and are emitted into the positive biased erase gate, through the thin poly Si oxide during an erase cycle. (All cells are erased at the same time.) The poly Si oxide also must act as an injected barrier between the erase and the floating gates for non-selected cells to prevent an unfavorable programming during a write cycle since the erase gate is designed to be negative against the floating gate in this cycle. Therefore, it is one of the key technologies how to optimize the large injection from the floating gate to the erase gate for a quick erasing, while suppressing electron injection from the erase gate into the floating gate to prevent an unfavorable programming. To meet these demands, we have investigated the electrical characteristics of poly Si oxide on the memory cell varying the structure and phosphorus concentration in the 1st poly Si. Two types of the flash EEPROM cells, which are shown in Fig. 1 were fabricated using triple poly Si technology.

Fig. 2 shows F-N leak current plots of inter-poly Si oxide for three phosphorus concentrations in the 1st poly Si and bias conditions. Positively biased 2nd poly Si significantly leads to higher electron injection than reversely biased case as phosphorus concentration in the 1st poly Si goes higher. Fig. 3 shows SEM photographs of the 1st poly Si surface under the three phosphorus concentration conditions corresponding to above F-N leak current plots. In the condition of phosphorus concentration as low as 2×10^{20} cm^{-3}, poly Si surface asperity appears to be rather roughened than the other high doped ones. In the case of lower phosphorus concentration, poly Si grain growth is suppressed during oxidation or annealing after phosphorus deposition, so poly Si surface appears to be roughened figure. If the 2nd poly Si is positively biased, the leak current through the poly Si oxide increases due to enhanced electrical field concentration at the sharp asperities. On the other hand, in the case of the 1st P Si positive, the electrical field concentration isn't occured even for the low phosphorus concentration because the bottom surface of the 2nd poly Si is comparatively smooth. As a result, it is preferable to use the 1st poly Si for the floating gate and 2nd poly Si for the erase gate as the Type-II cell from a view point of quick erasing and preventing unfavorable programming.

Fig. 4-a shows the typical erase time of the flash EEPROM type-II cells. It is measured to be about 500 msec at the phosphorus concentration of 2×10^{20} cm^{-3} which is about one-hundredths to the case of 6×10^{20} cm^{-3} (oxide thickness is 350 Å). It coincides with the simulation result where the equation $d\phi/dt = F\text{-}N$ current is numerically solved. The slow erasing is observed for the type-I flash EEPROM cells due to small injection (Fig. 4-b). Fig. 5 demonstrates the threshold voltage shift as a function of stress time for three gate stress voltages. The type-II cell provides large endurance for the gate stress, where the floating gate is positively biased. This is good agreement with the simulation results. For the type-I, however, the large Vth shift can be expected by the simulation.

Time dependent breakdown characteristics of poly Si oxide under constant 1 A current stress is measured using poly-poly capacitor with 1st poly Si edge under 2nd poly Si positively biased. The charge to breakdown improves under the lower phosphorus condition shown as cumulative failure rate while plots in Fig.6. This result is attributed to the roughness of the 1st poly Si asperity. Since leak current flows at the limited area near sharp asperities where enhanced electrical field concentration is formed, injected electrons seldom encounter to weak spots in the poly Si oxide. In the operation of write-erase cycles in the flash EEPROM cells, main failure segment is poly Si oxide breakdown between the floating gate and the erase gate due to defects, corresponding to above time dependent breakdown characteristics measured by poly-poly capacitor. The 256K flash EEPROM cells with roughened 1st poly Si asperity (low phosphorus concentration 2×10^{20} cm^{-3}) also have good endurance for write-erase cycles. As is shown in Fig. 7 we have accomplished about 1000 write-erase cycles, which is a target in flash EEPROM, with sufficient reliability under the low phosphorus condition and using optimized cell structure. The type-II cell with roughened 1st poly Si asperity, that is, the preferable structure for the flash EEPROM.

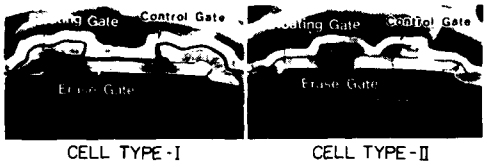
Summary

The electrical characteristics of inter-poly Si oxide for the reliable flash EEPROM cells has been described. Controlling poly Si oxide leakage current and developing reliable oxide with good endurance for time dependent breakdown are main key technologies. We have successfully accomplished these purposes by optimizing cell structure and poly Si oxide thickness.

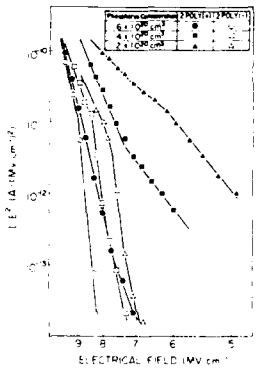
References

(1) Masuoka F. et al., A New Flash EEPROM Cell Using Triple Polysilicon Technology, IEDM Digest of Tech., papers P464; Dec., 1984.

(2) Masuoka F. et al., A 256k-bit Flash EEPROM Using Triple-Polysilicon Technology, SOLID-STATE CIRCUIT, Volume SC-22, Number 4, P548; August 1987



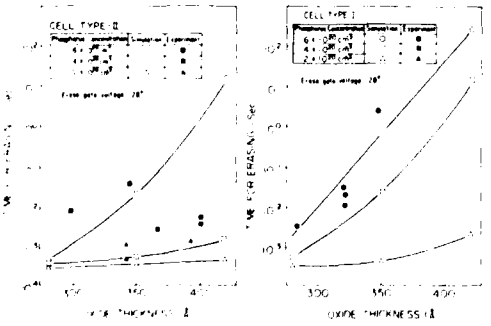
[Fig.1] SEM photographs of the cross sectional view of the two types of the flash EEPROM memory cells (type-I up, type-II bottom)



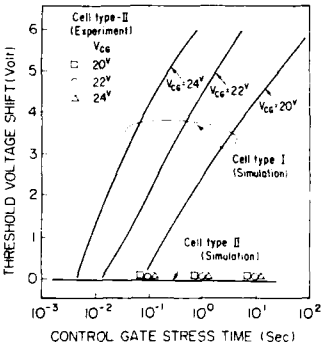
[Fig.2] F-N leak current plots of inter-poly Si oxide for phosphorus concentrations in poly Si and bias conditions.



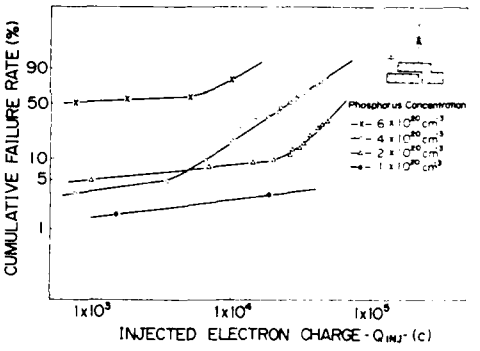
[Fig.3] SEM photographs of 1st poly Si surface asperity fabricated under the three phosphorus concentration conditions. (a) 6×10^{20} cm^{-3} (b) 4×10^{20} cm^{-3} (c) 2×10^{20} cm^{-3}



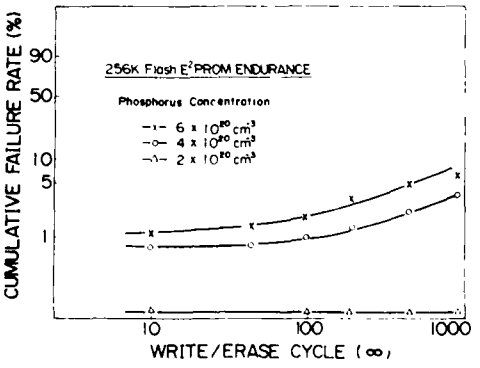
[Fig.4] Oxide thickness vs. erase time for the two types of the flash EEPROM memory cells as a parameter of phosphorus concentration in poly Si.



[Fig.5] The threshold voltage shift of the memory cell of 2×10^{20} cm^{-3} as a function of gate stress time for three stress voltages applied to the floating gate.



[Fig.6] Cumulative failure rate vs. injected electron charge as a function of phosphorus concentration in poly Si.



[Fig.7] Cumulative failure rate in write-erase cycles for 256K flash EEPROM as a parameter of phosphorus concentration.

Abstract No. 319

TIME-DEPENDENT DEGRADATION IN MOS DEVICES

C.Y. Yang, C.M. Wang, G. Lin, and J.J Tzou

Microelectronics Laboratory
Santa Clara University
Santa Clara, California 95053

Unidirectional and bidirectional channel stress measurements are performed to examine hot-carrier-induced degradation in NMOSFET. Unidirectional channel stress (UCS) refers to both stress and current-voltage measurements being in the usual "forward" direction (1-4). "Reverse" stress and I-V measurements are made with source and drain interchanged. The term bidirectional channel stress (BCS) is used to indicate measurements of forward/reverse I-V characteristics under both stress conditions.

Results of fractional transconductance shifts due to from UCS DC stress are shown in Figure 1. The gate oxide thickness used is 200Å. Lightly-doped-drain (LDD) structure is employed in each UCS device. Maximum substrate current occurs near the stress condition: V_{ds}=7V, V_{gs}=3V. This condition corresponds to maximum degradation as shown in Figure 1. AC stress is conducted by applying a 50% duty-ratio pulse train to the gate at several frequencies. The drain voltage is fixed at 7V, but the gate pulse height is allowed to vary. Comparison of transconductance shifts due to AC stress for different gate pulse heights is shown in Figure 2. Degradation increases with gate pulse height, which seems contrary to the results for DC stress shown in Figure 1. Dependence on pulse frequency is shown in Figure 3 for pulse height equal to 5V.

Comparison of DC and AC stresses with the maximum substrate current (V_{ds}=7V, V_{gs}=3V) is shown in Figure 4. Under this condition, the DC stress registers about twice as much degradation as AC. This is consistent with the quasi-static model for device lifetime: $t_{ac}=t_{dc}$ (peak I_{sub})/duty-ratio (5). Under a different stress condition (V_{ds}=7V, V_{gs}=7V), shown in Figure 5, the degradation due to AC stress is about an order of magnitude larger than DC. Further, this degradation, which corresponds to less than the maximum substrate current, is even more severe than that caused by DC stress at V_{ds}=7V, V_{gs}=3V, which yields maximum substrate current. Thus for AC stress generating less than maximum substrate current during the duty-cycle, the lifetime-I_{sub} relation proposed for DC stress (3) no longer applies. This result is consistent with recent findings (6-7).

Typical BCS data obtained for NMOS devices are shown in Figure 6. The device is stressed with V_{gs}=3V and V_{ds}=7.5V. The results show that whenever the stress direction is opposite to that of the measurement, the degradation rate is significantly larger. A simple electrostatics model based on trapped carriers near both source and drain is proposed to elucidate the effect of BCS on the channel electric field and the difference in hot-carrier-induced degradation rates. This model is also used to explain the UCS results for AC stress.

1. T.H. Ning, P.W. Cook, R.H. Dennard, C.M. Osburn, S.E. Schuster, and H.N. Yu, IEEE Trans. ED-26, pp. 346-353, 1979.
2. E. Takeda, H. Kume, T. Toyabe, and S. Asai, IEEE Trans. ED-29, pp. 611-618, 1982.
3. C. Hu, S.C. Tam, F.C. Hsu, P.K. Ko, T.Y. Chen, and K.W. Terill, IEEE Trans. ED-32, pp. 375-385, 1985.
4. C. Yao, J. Tzou, R. Cheung, H. Chan, and C.Y. Yang, Proc. IRPS, pp. 195-200, 1987.
5. T. Horiuchi, H. Mikoshiba, K. Nakamura, and K. Hamano, IEEE EDL-7, pp. 337-339, 1986.
6. J.Y. Choi, P.K. Ko, and C. Hu, Tech. Dig. Symp. on VLSI Tech., pp. 45-46, 1987.
7. K.M. Cham, H.S. Fu, and Y. Nishi, Proc. IRPS, pp. 30-33, 1988.

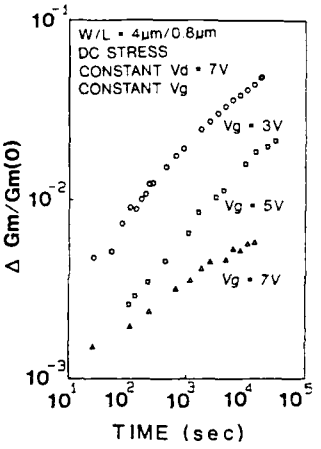


Figure 1 Fractional transconductance reduction in NMOSFET under DC stress at various gate biases.

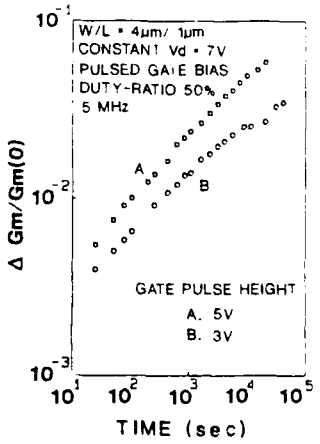


Figure 2 Fractional transconductance reduction in NMOSFET under AC stress for different gate pulse heights.

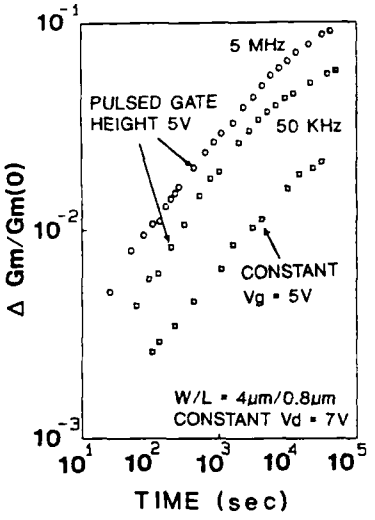


Figure 3 Fractional transconductance reduction in NMOSFET at different frequencies.

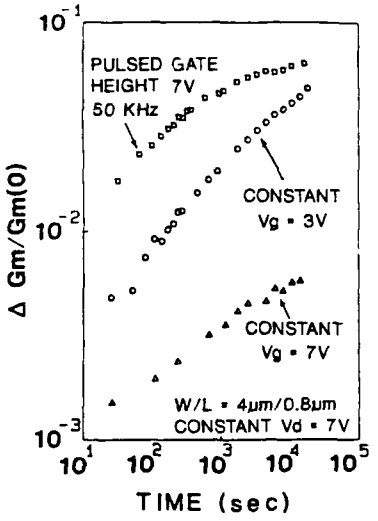


Figure 5 Comparison of transconductance degradation under AC and DC stresses.

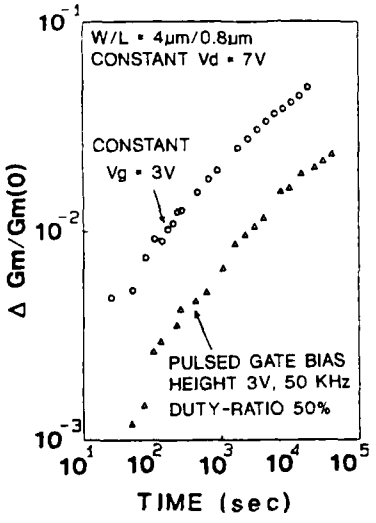


Figure 4 Fractional transconductance reduction in NMOSFET under DC and AC stresses.

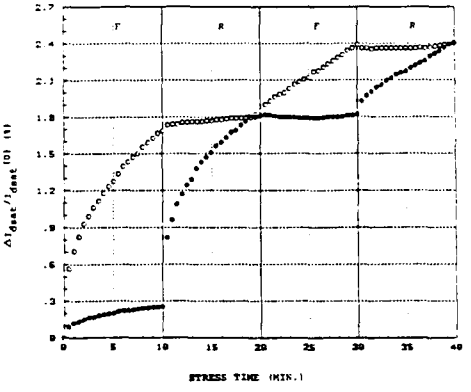


Figure 6 Bidirectional channel stress for NMOS. Forward measurement data are indicated by solid circles, reverse by open circles. F/R indicate forward/reverse stress cycles.

Abstract No. 320

RELIABILITY ISSUES FOR ULTRA-THIN INSULATORS

Thao N. Nguyen
IBM Research Division, Thomas J. Watson Research Center
P.O. Box 218, Yorktown Heights, New York 10598

P. Olivo and B. Ricco'
DEIS, Universita' di Bologna
Viale Risorgimento 2, 40136 Bologna, Italy

Long-term reliability of thin dielectric films has been an important issue for MOS VLSI technology and has received considerable attention [1-5]. In future ULSI circuits where the insulator thickness is expected to reduce to 50 - 100 Å, the issue will become even more critical. For these ultra-thin films, measurement and characterization can be a challenge because simple models used for thick films may become invalid [6] and the films may exhibit very different behavior [7]. This paper addresses two issues related to reliability testing and projection of ultra-thin SiO_2: failure detection and field accelerated testing.

Ultra-thin thermal oxides exhibit a new failure mode which occurs long before destructive breakdown. The failure is induced by high field stress and appears in the form of excessive leakage current at low fields. The onset of the leakage current depends on, among other things, the stress intensity and time but is independent of substrate type, gate material, electrode area and oxidation conditions. Once the leakage current occurs, it increases at a decreasing rate with stress time, eventually stops growing, and finally jumps to a high level when the oxide breaks catastrophically. The stress-induced oxide leakage is regarded as an oxide failure because many circuit applications cannot tolerate much leakage current. In conventional tests, oxide breakdown is typically detected by monitoring a large and sudden current increase at high fields. These tests fail to detect the leakage current at low fields and tend to result in overestimation of yield and reliability data. The detection of the new failure mode requires a different test procedure in which the high-field stress bias is periodically pulsed to a low-field monitor bias to determine the onset of a critical oxide leakage.

The origin of the oxide leakage is investigated using ramp I-V, constant V stress and C-V techniques in addition to computer simulations. The dependence on stress polarity and calculations show that the leakage current is not due to the generation and accumulation of positive charge. It is proposed that the leakage originates from localized, defect-related weak spots where the oxide has experienced significant deterioration from electrical stress. The deterioration seems to be a physical and/or chemical change rather than of electrical nature because the oxide leakage is permanent and thermally stable. This change leads to a reduced tunneling barrier and causes a local enhancement of the injection current, which appears as the stress-induced oxide leakage at low fields. The I-V measurements at different temperatures and theoretical calculations suggest that the conduction mechanism of the leakage is thermally-assisted tunneling through a reduced barrier of about 1 eV.

The prediction of thin insulator reliability is often obtained by extrapolating time-to-failure data from high-field stress tests to device operating fields. This approach implicitly assumes that mechanisms/physics at high fields also operate at low fields and no additional failure mechanisms exist at low fields. Recent experimental data [8] indicate that these assumptions may not be valid. The spread in the time-to-failure distributions depends on the stress field. Under high fields, the distributions are very tight and similar to intrinsic breakdown of uniform oxides. Under lower fields, the distributions for the same oxide broaden due to an increasing domination of premature failures. The result suggests that either defects require some amount of time to develop and evolve to a destructive stage or different breakdown mechanisms take place at lower fields. The high-field accelerated tests appear to be incapable of revealing localized defects causing premature oxide breakdown and therefore tend to produce optimistic projection of reliability at low operating fields.

The authors are very grateful to Drs. G.W. Rubloff and N.O. Lipari for their support of this work.

REFERENCES

[1] S.P. Li and J. Maserjian, "Effective Defect Density for MOS Breakdown: Dependence on oxide thickness", IEEE Trans. Electron Devices, 23, 525 (1976).

[2] Y.-P. Han, J. Mize, I. Mozdzen, T. O'Keepe, J. Pinto and R. Worley, "Ultra-thin Gate-Oxide Characteristics and MOS/VLSI Scaling Implications", IEDM Technical Digest, 98 (1982).

[3] I. C. Chen, S. Holland, K. K. Young, C. Chang, and C. Hu, "Substrate Hole Current and Oxide Breakdown", Appl. Phys. Lett., 49, 669 (1986).

[4] I.C. Chen, S. Holland, and C. Hu; "Hole Trapping and Breakdown in Thin SiO_2", IEEE Electron Device Letters, EDL-7, 164 (1986).

[5] M.-S. Liang and J. Y. Choi, "Thickness Dependence of Oxide Breakdown under High Field and Current Stress", Appl. Phys. Lett., 50, 104 (1987).

[6] B. Ricco', P. Olivo, T.N. Nguyen, T.S. Kuan, G. Ferriani, "Oxide Thickness Determination in Thin Insulator MOS Structures", IEEE Trans. Electron Devices, 35, 432 (1988).

[7] T. N. Nguyen, P. Olivo and B. Ricco', "A New Failure Mode of Very Thin Thermal SiO_2 Films", Proc. Int. Reliability Phys. Symp., 66 (1987).

[8] P. Olivo, T. N. Nguyen and B. Ricco', "Field Dependence of Time-to-Breakdown Distribution of Thin Oxides", presented at Symp. Phys. and Tech. of Armophous SiO_2, Les Arcs, France, Jun. 29 - Jul. 3, 1987.

Abstract No. 321

GATE OXIDE LEAKAGE RELIABILITY FAILURES IN CMOS CIRCUITS

J. Vandenbroeck*, P. De Pauw,
M. Van den Reeck, L. Stevens

Alcatel-Bell Telephone
Francis Wellesplein 1
B-2018 Antwerpen
Belgium

Introduction

Digital signal processing chips used in telecommunications environment have very stringent reliability requirements. Although several reliability concerns may be present on such circuits processed using CMOS technologies, control of gate oxide leakage remains a major problem. Usually gate oxide quality is monitored by performing breakdown measurements on simple test capacitors. During this study we found that, although gate oxide quality is excellent on simple capacitor structures, still failures due to gate oxide leakage occur in large circuits.

Experimental

Lifetest conditions & failure percentage :
Our DSP-circuit (ref 1) was initially processed using 3 um CMOS double poly,single metal technology. Because of circuit packing density requirements (lower cost) some poly lines were used for large interconnections. The circuit uses a power supply voltage of 10 V and is operating at 4 MHz. An overview of the most important process parameters is shown in table 1. The IC's were tested during 3000 hour at normal operating voltage and at 125 C. In a second test a total amount of 120.000 devices were tested during several periods of 1 week. Failure percentage was 0.15 %.

Failure analysis

Two important types of failures were observed after lifetest and field test of the DSP-circuits.
A first problem occurred at the end of a long poly line of several mm driving an invertor. Due to leakage observed in the pMOS (30 uA at 4.5 V) the resistive voltage drop across the poly lines becomes excessively large, resulting in the inability of turning on the nMOS transistor (Vt = 1 V). A second problem was found in a debouncer operating at 8 KHz. This circuit part is merely a switch consisting of an nMOS and a pMOS transistor driven in parallel. The information was found to leak away and the problem became worse at lower frequencies. Again the pMOS transistor was found to show leakage between S/D and gate. At room temperature the leakage current was 50 nA at 5 V.

Discussion

From the failure analysis it becomes clear that the major reliability concern can be found in leakage of a pMOS transistor driven by a long poly line. Breakdown plots performed on simple geometry capacitors of 15 x 30 um2 (fig. 1a) are shown in fig. 2a both for n-well and p-substrate type. As can be seen, quality of the gate oxides is very good, showing no low or medium field breakdowns. If, however the same measurement is performed on capacitor structures as shown in fig. 1b, 8 % failures are found between 0 and 5 V for a poly length on field oxide of 3 x 2000 um2 for the capacitors on n-well (fig. 2b). The capacitors on p-substrate show less low field breakdowns (3 %). The primary cause for the appearance of the low field breakdowns on these structures is charge build up of the poly lines during implantation of source and drain. This problem has been reported before (ref. 2), but usually neutralization of the charge with an electron shower during ion implantation strongly reduces the problem (ref. 3). Using test capacitors having varying lengths of poly lines "driving" the top plate over gate oxide, it is shown that, even under optimal beam neutralization, the capacitors with a long poly interconnect are still sensitive to this problem and show leakage currents of several nA at 5 V. This is shown in table 2 which shows the relative amount of low field breakdowns for capacitors with different poly lengths on field oxides. A pragmatic approach to solve the problem lies in the reduction of the poly interconnect length (through bypassing with metal 1; at the expense of area on chip). A maximum value of 1 mm is used now. The reason why the leakage is always found on the n well capacitors (i.e. the pMOS transistor) can be explained by the mask structure used. The p+ implant mask only allows the B to penetrate in the p-active regions, whereas the n+ As is implanted in the "non-p+"-regions. Therefore the total amount of charge on top of both poly lines is almost the same. The only difference between the nMOS and pMOS transistors can be found in a parasitic doping of the gate oxide during S/D implant. As is known to be an effective electron trap as compared to Boron. In (4) it is shown that gate oxides having a large amount of electron traps show less low field breakdowns because of the neutralization of the injected charge by the presence of local fields due to the already trapped electrons.

Conclusions

A new reliability problem was observed in CMOS circuits having long poly lines driving pMOS transistors. The problem is correlated with the charging of the poly during ion implantation of the source/drain. Longer poly lines are more susceptible than shorter ones, due to more accumulated charge, leading either to premature breakdown of the gate oxides, either to damage that will induce increased leakage at elevated temperature, and will pose a TDDB problem. Technology solutions consist in optimization of the procedure for neutralization of the charge. Design solutions consist in imposing a design rule for the maximum length of the poly interconnect.

References

1. P. Defraeye, D. Rabaey, M. Roggeman, J. Ide and L. Kiss, "A 3 um CMOS digital CODEC with programmable echo cancellation and gain setting", IEEE J. Solid State Circ., SC-20, Nr 3, June 1985.
2. C. M. Osburn, A. Cramer, A.M. Schweighart, M.R. Wardeman, "Edge breakdown in poly-si gates over thin oxides during ion implantation" VLSI Science and Technology, 1982.
3. C. P. Wu, F. Kolondra, and R. Hesser, "Electron Flood techniques to neutralize beam charging during ion implantation" RCA Review, March 1983.
4. D.J. DiMaria, D. Young and D. W. Ormond, App. Phys Letters-31,N-7,680,1977.

P-sub doping concentration : 2E15/cm3

n-well doping concentration : 1E16/cm3

gate oxide thickness : 40 nm

field oxide thickness : 1 um

poly Si thickness : 600 nm

p+ S/D I/I : dose 4E15/cm2; 50 KeV, B

n+ S/D I/I : dose 5E15/cm2; 140 KeV, As

poly Si doping : POCL3

Table 1 : Most important processing parameters of the 3 um n-well double poly, single metal CMOS process.

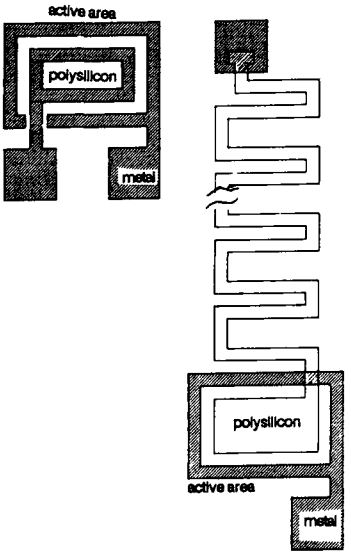


fig1a – b: test capacitors used for evaluation of the breakdown strength of the gate oxides.
The test structure of fig1a is merely a rectangular polysilicon gate structure of 15 x 30 um.
The test capacitor of fig1a consists of the same rectangular poly gate over gate oxide, in series with a long serpentine structure. The dimensions of the poly over field oxide ranged from 3x200 um2 to 3x3000um2.

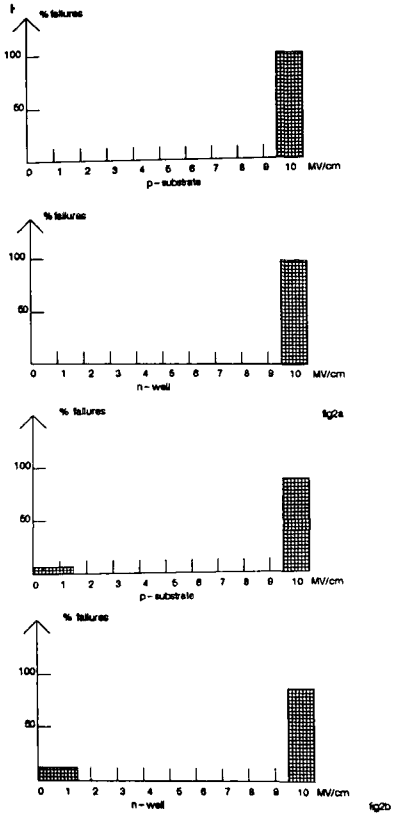


Fig 2a – b: breakdown histograms obtained on the structures of figs 1a – b
Breakdown detection current was set at 1 uA.
For structure b the dimensions of the poly gate on field oxide were 3x2000 um2.

POLY GATE DIMENSIONS ON FIELD OXIDE	% LOW FIELD BREAKDOWNS N-WELL	P-SUB
3 x 200 um2	0.5	0.4
3 x 500 um2	1.5	1.2
3 x 1000 um2	4.0	2.0
3 x 2000 um2	8.0	3.0
3 x 3000 um2	12.0	5.0

Table 2 : % low field breakdowns as a function of the poly length on field oxide, both for capacitors on n-well and p-sub.

Abstract No. 322

Reliability Study of PECVD Silicon Nitride For Composite Insulation

D. Nguyen, H. Rathore, R. Edwards, G. Gati, V. DePalma
IBM General Technology Division East Fishkill
Rte. 52 Hopewell Junction, New York 12533

Interlevel short (ILS) is one of the major time-dependent failure mechanisms in multilevel interconnection structure. The ILS problem become more critical as the circuitry get more complex and more than two levels of metal and used in fabrication of VLSI product. Gati and al. (1) reported that the use of composite insulator (sputtered SiO2/PECVD Silicon Nitride) resulted in significant ILS improvement and yield enhancement.

In this work, defects (holes) were formed in the sputtered SiO2 by the use of special mask and processing. A thin film of PECVD nitride was deposited over the sputtered SiO2. Therefore, the insulator at the defect site is only a thin layer of PECVD nitride for the time-dependent failures and to project field reliability. Two tests were used in this study: one is a voltage ramp and the other is a constant voltage life test. The voltage ramp tests were conducted at three different ramp rates, each at two temperatures. The life test was done at three voltages and two temperatures. The data were used to derive electric field acceleration factor and the temperature dependence of the life time of the PECVD nitride in this configuration.

(1) G.S. Gati, Application of Surface Science 22/23 (1985) 997-1003 North-Holland, Amsterdam

Abstract No. 323

Reliability of 10 nm ONO stacked insulator

K. v. Sichart, L. Do Thanh, Th. Kleinert, S. Röhl and H. Reisinger
Siemens AG, Microelectronics Technology Center
Otto-Hahn-Ring 6, D 8000 München 83, Germany

Introduction

The quality of the dielectric in storage capacitors plays an important role in the reliability of dynamic RAM's. The development of new DRAM generations with capacity beyond 4 Mbits requires thin insulators with thicknesses of about 10 nm or thinner even in three dimensional structures, e.g. the widely used stacked and trench capacitors. It is known that the use fo very thin thermally grown SiO_2 films in such structures leads to many problems in the reliability /1/. Recently oxide-nitride-oxide (ONO) stacked films are used as a possible alternative to SiO_2 /2/. However, to our knowledge, informations about the long term stability of very thin ONO films are hardly found in the literature.
In this paper, we present a study on the reliability of very thin (d≤10 nm) stacked insulators using different characterization techniques.

Experimental

Planar MIS capacitors with poly-Si gate and p-Si substrate were used as test samples in our study. The gate insulator is an oxide-nitride-oxide triple layer with 10 nm effective thickness. The bottom and top oxide layers were grown by thermal oxidation of the Si substrate and the nitride respectively. For comparison some samples with nitride-bottom oxide (ON) double insulator of 7.8 nm effective thickness or 10.8 nm thermally grown SiO_2 were also prepared. The defect density of the films was evaluated from time zero dielectric breakdown measurements. Both constant voltage and constant current stress at different temperatures were used to study the long term reliability of the films. The density of injected charge to breakdown Q_{bd} was evaluated from both constant current and constant voltage stress experiments.

Results and discussion

Very low defect density (<0.1 cm^{-2}) and high breakdown field strength (E_{BD} > 12MV/cm) were found for ONO and also for ON stacked films.
Fig. 1 shows the time dependent dielectric breakdown (TDDB) characteristics of 10 nm ONO film obtained by constant voltage stressing at 150° C and different field strengths. The shape of the Weibull plots indicates that the intrinsic breakdown is the dominating mechanism which controls the reliability of the investigated ONO films. the mean time to breakdown of ONO films is larger than that of 10.8 nm SiO_2 layers. Similar results are also obtained for 7.8 nm ON double layer dielectrics, however the mean time to breakdown of ON films is about three orders of magnitude shorter. In some samples the Weibull plot deviates clearly from a straight line. We found that this deviation correlates with the film thickness inhomogeneity of the wafer.
Fig. 2 shows acceleration plots of time to reach 20% and 63% failures. These log t vs. 1/E plots fit well to a model proposed in /3/ to explain the breakdown properties of thin SiO_2 films. This may indicate that a similar mechanism as described in /3/ can also occur in ONO structures. The electric field acceleration factor is extracted to be about 0.55. Extrapolation to 2.5 MV/cm which is typically the field across the stroage dielectric of 4M DRAMs yields a life time of about 150 years at 150°C. The slope of the Weibull plots remains unchanged by stressing the ONO samples at different temperatures ranging from 30° C to 150° C
In fig. 3 the gate area dependence of the TDDB characteristies is illustrated. The decrease in the time to breakdown with increasing gate area can not be well described by a random distribution of defects as found for SiO_2 films /4/. The insert in fig. 3 shows the topological inhomogeneity of the results for 4 mm^2 structures as an example. This inhomogeneity is due to deviations in film thickness. The size of the squares is proportional to log (time), a cross marks capacitors with time to breakdown over 10 sec.
The density of injected charge leading to breakdown is widely used as the crucial parameter for intrinsic breakdown /4/. Usually Q_{bd} is calculated from the time to breakdown by constant current injection. In our study Q_{bd} was evaluated from both constant voltage and constant current stress experiments. For ONO samples, no substantial difference was found in Q_{bd} values extracted from the two stressing techiques. However we found that higher Q_{bd} values found by constant current stress does not necessarily indicate a longer life time as extracted from constant voltage stressing. Fig. 4 compares the Q_{bd} values of ON, ONO and SiO_2 films obtained by constant current stressing. Although the SiO_2 film shows larger Q_{bd} values, acceleration test yields a much shorter life time than that of ONO film (fig. 2). While there is only a small difference in the Q_{bd} values of ONO and ON films (about factor 2-3), the time to breakdown by stressing with the same field strength is many orders of magnitude larger for ONO structure. Since in each device operation cycle, the storage capacitor is stressed by a constant voltage rather than by a constant current, the constant voltage stress appears to be more suitable to predict the long term reliability of the films.

Summary

The reliability of ONO and ON stacked insulating films with thicknesses of 10 nm and below was investigated using constant voltage and constant current stress experiments. Although the density of injected charge to breakdown of ONO films is much lower compared to SiO_2, the time dependent dielectric breakdown investigation showed that ONO stacked films are more reliable than SiO_2 when used as dielectrics in storage capacitors of future DRAM's.

References:

/1/ D.A. Baglee, J. Vac. Sci.Technol. A, 4, 1002 (1986)
/2/ T. Watanabe et. al., Proc. of Intern. Rel. Phys. Symp. 1987, p. 50
/3/ I.C. Chen et. al., IEEE J. of Sol. St. Circuits, SC-20, 333 (1985)
/4/ D.R. Wolters et.al., J. Vac. Sci. Technol. A, 5, 1563 (1987)

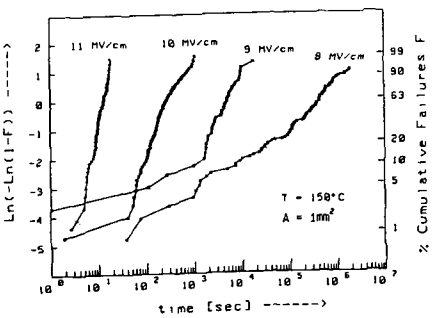


Fig. 1: Field dependence of time to breakdown by constant voltage stressing of ONO stacked layer at 150° C. Field is related to 10 nm effective thickness.

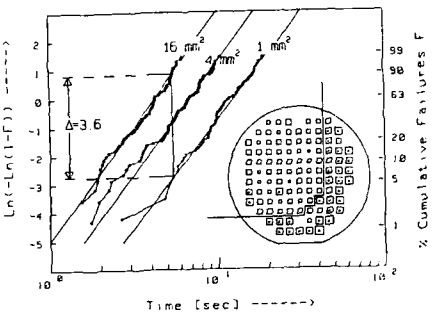


Fig. 3: Gate area dependence of TDDB characteristics of 10 nm ONO dielectric at 11 MV/cm constant field and 150° C. In the Weibull plots only results from the upper left part of the wafer are taken. For a random distribution of defects Δ should be 2.7, i.e. ln (A_2/A_1), rather than 3.6

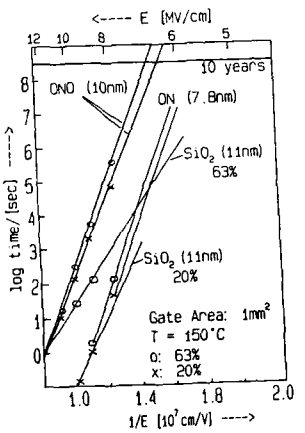


Fig. 2: Acceleration plots of 10 nm ONO, 7.8 nm ON and 10.8 nnm SiO_2 films. Measurements carried out at 150° C.

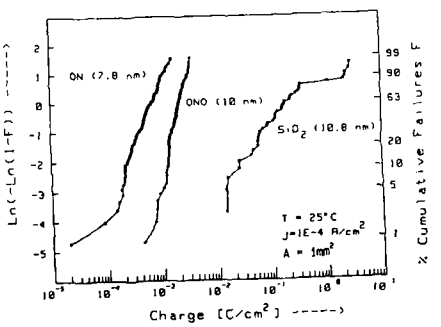


Fig. 4: Charge to breakdown from constant current stressing at 25° C.

Abstract No. 324

DETERMINATION OF FRACTAL (HAUSDORFF) DIMENSION DURING THE ELECTRODEPOSITION OF ZINC

Chao-Peng Chen and Jacob Jorné
Department of Chemical Engineering
University of Rochester
Rochester, NY 14627

A simple method is proposed to measure the fractal (Hausdorff) dimension of the electrodeposition of zinc by current integration. Under our experimental conditions (C=0.01 M $ZnSO_4$ and V=2-12 volt or I=0.1-1.0 mA), scale invariance is observed. The fractal dimension of the two dimensional zinc deposit increases with the applied potential, or the applied current, while the microstructure changes from the highly branched random aggregate to the radial dense structure. These phenomena seem to suggest that ionic migration, in addition to diffusion, plays an important role in the morphology of the deposition.

Electrodeposition of zinc has been demonstrated as one of the real physical systems which exhibits a structure similar to the theoretical diffusion-limited aggregation (DLA) model.[1,2] The fractal (Hausdorff) dimension of this system is usually determined by digitizing photographs and taking the best-fit slope of Ln[N(r)] vs. Ln(r), where N(r) is the number of pixels contained within a radius r.[3-5] In the present communication we present a simpler method which may be used to determine the fractal dimension in a more direct way.

Our electrodeposition cell consisted of a zinc ring anode with a diameter of 8.4 cm which was set into a petri dish. Aqueous 0.01 M $ZnSO_4$ solution was confined in a uniform 0.2 mm film covered by a thin glass. Thin 0.5 mm diameter copper wire, or graphite core, was centrally located as the cathode. It is to be noted that a copper ring is not suitable as the anode because co-deposition of copper and zinc was observed. A constant, potential, ranging from 2 to 12 volt, was applied between the anode and the cathode by using a power supply with a voltage regulator, designed to compensate the ohmic drop of the shunt. The precision of the current measurement was 0.01 mA. In some experiments, constant currents, ranging from 0.1 to 1.0 mA, were applied, while changes in potential were recorded.

The Hausdorff dimension is given by the equation:

$$M(r) \sim r^{D_f} \qquad (1)$$

where the mass of the aggregate M(r) within the radius r may be obtained by the integration of the current over the deposition time. This method is valid only when the current efficiency is 100%. No competitive reaction such as hydrogen evolution was observed during the zinc electrodeposition and the current efficiency approached 100%. Current efficiencies were calculated by titration of the zinc deposits with dilute sulfuric acid and comparing to current-time data. Figure 1 shows a typical zinc deposit obtained from 0.01 M $ZnSO_4$ solution under an applied potential of 6V.

Figures 2 and 3 show typcial current and growth curves, respectively, during zinc electrodeposition experiments. Figure 2 can be integrated to give the mass vs. time curve by using Faraday's law. Then by logarithmically plotting the mass of the deposit vs. its radius, the Hausdorff dimension can be obtained from the slope of the line as shown, for example, in Figure 4. The results show that the scale-invariance characteristics always exist under the present experimental conditions. Similar results have been obtained by Brady and Ball[6] for copper electrodeposition in a three demensional system, D_f=2.43. In this region, the microstructure of the aggregates has been considered as the DLA-type. Figure 5 shows the dependence of the fractal dimension on the applied potential. The fractal dimension increases with the applied voltage, as the morphology of the deposition changes from the highly branched random aggregate to the radial dense structure. Similar behavior was obtained under galvanostatic operation in which various constant currents, rather than potentials, were applied between the growing aggregates and the ring anode. Figure 6 shows that the fractal dimension incrases with the applied current. This trend, which is very similar to previous results obtained by computer simulation[7], indicates that electrical migration of the ions, in addition to diffusion, plays an important role in the transport of zinc ions. From the microscopic observations we also found that under higher voltage, the growth of the deposition was radially oriented, as previously reported.[4,5,8,9] In electrolytic solutions, the diffusion length, $\lambda = \sqrt{2Dt}$, is very small, on the order of 0.1 cm, thus if the process is diffusion-limited than the deposition should be limited to the electrolyte in the immediate surrounding of the aggregate. However, according to our analysis, the mass deposited is much larger than the original mass of the zinc ions within the aggregate. Consequently, the electrical migration of the ions dominates the process, and the dimension of the aggregates is larger than that of the DLA, especially under higher applied potentials.

Financial support, provided by the National Science Foundation under Grant No. CBT-8518479, is gratefully appreciated.

1. T.A Witten and L.M. Sander, Phys. Rev. Lett. 47, 1400 (1981), and Phys. Rev. B29, 5686 (1983).
2. P. Meakin, Phys. Rev. A27, 604, 1495 (1983).
3. M. Matsushita, M. Sano, Y. Hayakawa, H. Hopjo, and Y. Sawada, Phys. Rev. Lett. 53, 286 (1984).
4. Yasuji-Sawada, A. Dougherty, and J.P. Gollub, Phys. Rev. Lett. 56, 1260 (1986).
5. D. Grier, E. Ben-Jacob, Roy Clarke, and L.M. Sander, Phys. Rev. Lett. 56, 1264 (1986).
6. R.M. Brady and R.C. Ball, Nature, 309, 225 (1984).
7. D. Bensimon, E. Domany and Aharony, Phys. Rev. Lett. 51, 1394 (1983).
8. E. Ben-Jacob, G. Buetcher, P. Garik, Nigel D. Goldenfeld and Y. Lareah, Phys. Rev. Lett. 57, 1903 (1986).
9. D.G. Grier, D.A. Kessler and L.M. Sander, Phys. Rev. Lett. 59, 2315 (1987).



Figure 1: Dense aggregate of zinc electrodeposition 0.01 M $ZnSO_4$, 6V, 15 minutes.

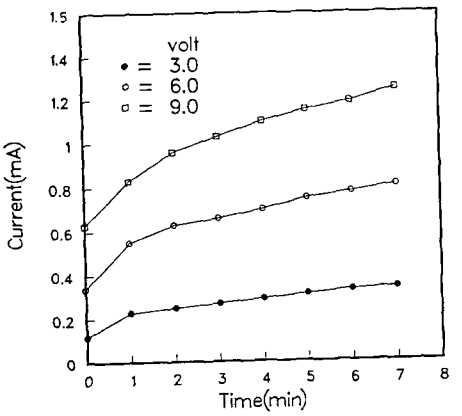


Figure 2: Current vs. time for zinc electrodeposition under various applied potentials.

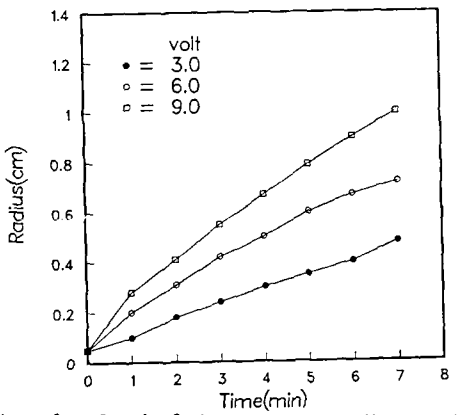


Figure 3: Growth of zinc aggregate: radius vs. time under various applied potentials.

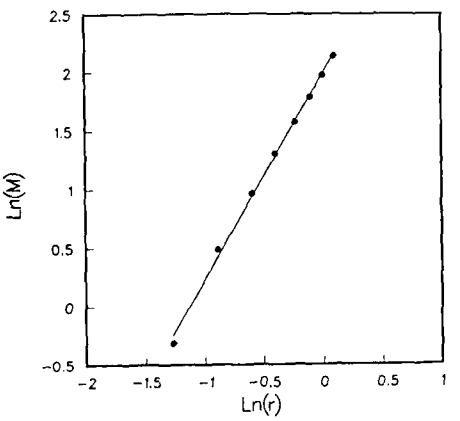


Figure 4: Logarithmic plot of aggregate mass vs. its radius under applied potential of 9 volt. D_f = 1.75.

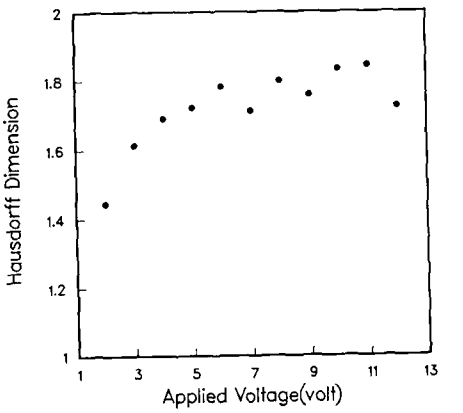


Figure 5: Fractal (Hausdorff) dimension vs. applied potential for zinc electrodeposition from 0.01 M $ZnSO_4$ solution.

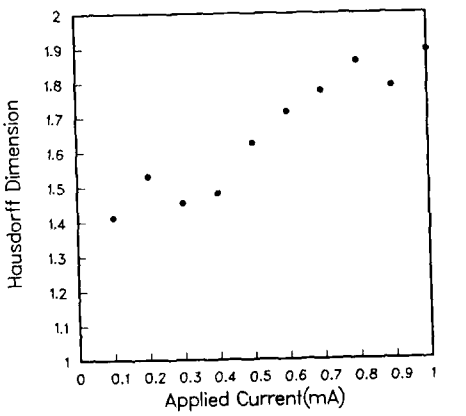


Figure 6: Fractal (Hausdorff) dimension vs. applied current for zinc electrodeposition from 0.01 M $ZnSO_4$ solution.

Abstract No. 325

STABILITY ANALYSIS OF METAL ELECTRODEPOSITION

Dale P. Barkey*, Rolf H. Muller, C.W. Tobias

Department of Chemical Engineering
University of California, Berkeley

and

Lawrence Berkeley Laboratory
Berkeley, California

A stability analysis of metal electrodeposition on a smooth surface has been formulated and applied to copper deposition on a rotating cylinder. The analysis is an extension of Landau's treatment to include the electric field explicitly (1). Current distribution on a sinusoidal profile was found by a first order perturbation technique accounting for ohmic, kinetic and concentration overpotentials, and the derived current distribution was used to evaluate the rate of growth or decay of the perturbation.

In agreement with Landau's result, deposition was found to be unstable for all practical conditions. The only stabilizing influence, the surface free energy, is insignificant for features larger than one micrometer. The rate of surface amplification is, however, sensitive to electrolysis parameters that can be controlled, and the analysis therefore provides useful information on conditions favorable to the production of coherent deposits and on expected protrusion spacing.

The first order perturbation solution for the rate of amplitude growth of a sinusoidal profile is,

$$\frac{\partial \ln A}{\partial t} = \frac{\nu}{nF}\kappa\omega\sqrt{2}\,\frac{\dfrac{RT\,i}{n^2F^2 c_b\left(1-\dfrac{i}{i_L}\right)D} - \dfrac{2\nu\gamma\omega^2}{nF}}{1 + \dfrac{RT\kappa\omega}{nF\,i_L\left(1-\dfrac{i}{i_L}\right)} + \dfrac{RT\kappa\omega}{i\,nF\,\alpha}}$$

where ω is the spatial frequency of the profile, υ the molar volume of metal, k the solution conductivity, δ the surface free energy, c_b the bulk ion concentration and i_l the limiting current density. If ω is taken as the characteristic dimension, the last two terms in the denominator become the Wagner number, Wa, and a concentration Wagner number, Wc, respectively (2).

$$\frac{\partial \ln A}{\partial t} = \frac{\nu}{nF}\kappa\omega\sqrt{2}\,\frac{\dfrac{RT\,i}{n^2F^2 c_b\left(1-\dfrac{i}{i_L}\right)D} - \dfrac{2\nu\gamma\omega^2}{nF}}{1 + Wc + Wa}$$

Large magnitudes of these two groups indicate low rates of amplitude growth or decay.

A negative amplitude growth rate, or decay of the perturbation, occurs only if the surface energy term in the numerator exceeds the concentration term. With the definition of a surface overpotential number,

$$Ws = \frac{2\nu\gamma\omega^2}{\delta RT}$$

the stability criterion becomes,

$$\frac{\dfrac{i}{i_L}}{1-\dfrac{i}{i_L}} < Ws$$

Experimental studies of copper deposition were carried out under controlled mass transfer conditions, and Fourier transforms of deposit surfaces were compared with predictions of the stability analysis (3). For low amplitude roughness, the analysis applies to individual terms in the Fourier representation of an arbitrary surface profile, and the predicted and observed protrusion spacing may be calculated by finding a weighted mean of the transform.

Decrease in spatial period with increasing current density and increase in spatial period with increase in fraction of limiting current are correctly predicted. The predicted magnitudes, however, are about half those observed. Increase in amplitude growth rate is correctly predicted for approach to limiting current. However, the amplitude of protrusions was observed to decrease with increasing current density, rather than to increase, as predicted by the analysis. Deposits became more compact and finely textured as current density was increased at constant fraction of limiting current. This result is evidently a consequence of factors not considered in the stability analysis, such as the influence of nucleation density and variation in boundary layer thickness over the roughened surfaces.

References

(1) U. Landau in "Zinc Electrodeposition and Dendritic growth from Zinc Halide Electrolytes", EPRI Report EM-2393, Electric Power Research Institute, Research Reports Center, Box 50490, Palo Alto, CA 94303, (1982)

(2) G.A. Prentice, C.W. Tobias, J. Electrochem. Soc., 129, 316 (1982)

(3) D.P. Barkey, R.H. Muller, C.W. Tobias "Studies on High Speed Electroforming", submitted for publication in J. Electrochem. Soc.

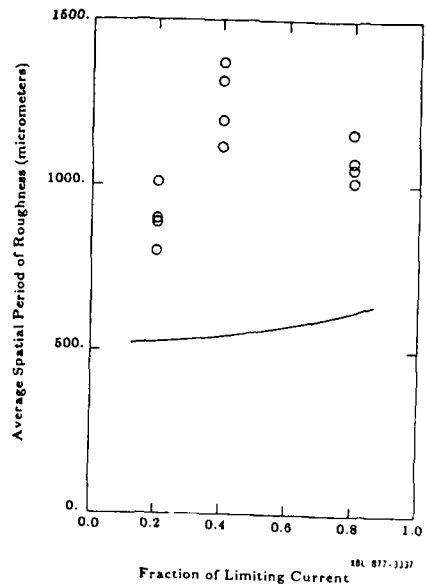


Figure 1. Average spatial period of roughness predicted by stability theory versus fraction of limiting current for deposition from a 1.0M $CuSO_4$ 1.0M H_2SO_4 electrolyte at 50°C at 0.8 A/cm^2. Also shown are the measured values.

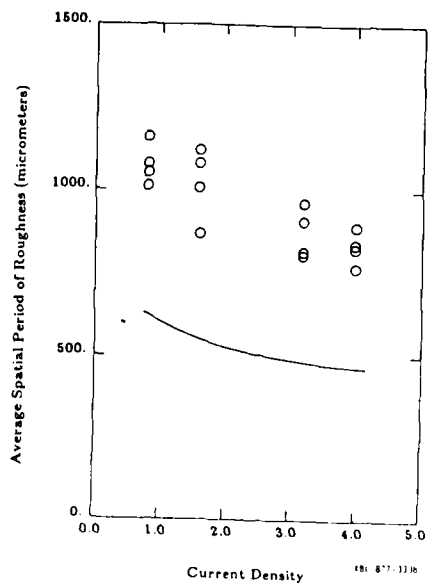


Figure 2. Average spatial period of roughness predicted by stability theory versus current density for copper deposition from a 1.0M $CuSO_4$ 1.0M H_2SO_4 electrolyte at 50°C at 80% of limiting current. Also shown are the measured values.

Abstract No. 326

NON STEADY STATE MODELING OF TRANSPORT CONTROLLED PLATING ADDITIVES

David Roha and Uziel Landau

Case Western Reserve University
Chemical Engineering Department
Cleveland, Ohio 44106

In a previous paper (1) we have presented a steady–state transport based model of leveling additives in plating. Among other things, the model can be used to plot plating maps which identify those regimes of additive concentration, current density and effective boundary layer thickness which lead to smooth deposition and those which do not. This model also predicts the shape of the polarization curves with additive present, as shown in Fig. 1. Until now, however, this model has been strictly theoretical and evaluated with arbitrarily selected physical parameters. In order to make predictions on the behavior of real plating systems, the basic physical parameters of the model, (i.e. the inclusion constant, k_i, the adsorption and desorption constants, k_a and k_{-a}, and the additive diffusivity, D_a) must be determined experimentally

One obvious approach is to obtain the parameters from regression of the experimental polarization curves with additive present. To demonstrate this approach, we have generated polarization curves for the systems of sodium lignin sulfonate and coumarin in the fluoborate lead plating bath, by linearly sweeping the current. The shapes of the curves obtained (e.g. Fig. 2) are somewhat different than those of the steady state model and very dependent on the sweep rate, indicating that steady state has not been attained. Although in theory one can always approximate steady state by sweeping slowly enough, this is not always practical. For polarization sweeps lasting over several hours, the electrodeposit may grow significantly, reducing the IR potential drop, and may also become rough, thereby increasing its effective surface area. Such growth related factors are difficult to separate from the additive–kinetic related factors we wish to study. Therefore a means to extract the basic parameters from the non–steady state polarization behavior of additive systems is needed.

As is illustrated in Fig. 3, the processes of additive diffusion, adsorption and inclusion are coupled in series. Additive adsorption has been found to be the rate determining process. Accordingly, we construct a quasi–steady state model with the rate of additive diffusion set equal to the net rate of additive adsorption. The change in concentration of aqueous phase additive is slow enough to allow the mass transport of additive, N_d, to be treated as a steady–state process:

$$N_d = \frac{D_a(C_{a0}-C_{ab})}{\delta}$$

Here, C_{a0} and C_{ab} are the interfacial and bulk concentrations of additive, respectively, and δ is the equivalent mass transport boundary layer thickness which is treated as being constant with time. A mass balance on the adsorbed additive yields

$$\Gamma_1\frac{d\theta}{dt} = \left[\frac{k_{-a}\theta + D_aC_{ab}/\delta}{(1-\theta)+(D_a/\delta k_a)}\right](1-\theta) - (k_{-a}+k_i i)\theta$$

where Γ_1 is the surface concentration of one monolayer of adsorbed additive, θ is the surface coverage of additive and i is the current density which is assumed to vary with time. Given an initial surface coverage, one can compute the coverage at any later point in time through numerical integration of the above mass balance.

We choose to use fourth order Runge–Kutta integration. To save computation time the program remembers values of θ from previous integrations with the same set of parameters. The current density value used at any given point in time is that experimentally recorded during the polarization sweep. When the time step is too large, the algorithm becomes unstable and we must subdivide the experimental time interval using linear interpolation With θ computed, the overpotential can be found from the additive blocking equation:

$$i = (1-\epsilon\theta)i_b(\eta)$$

where ϵ is the blocking efficiency of the additive and $i_b(\eta)$ is the current density of a bare additive free surface under the same overpotential, η. Once $i_b(\eta)$ is found, η can be solved for (explicitly for linear and Tafel kinetics, implicitly for Butler–Volmer kinetics).

A typical galvanostatic polarization curve with coumarin is shown in Fig. 2, along with the best fit curve of the non–steady state model. It should be noted that although there is a peak in overpotential on the sweep up, there is none on the sweep down. This is at odds with the behavior predicted by the steady–state model shown in Fig. 1, where since the curve is identical for both sweep directions, the same peak should manifest during the down sweep as well. This may reflect the fact that although additive can be readily removed from the surface through inclusion, readsorption of additive is an inherently slow process. Indeed although the down–sweep peak has not been observed experimentally, the model predicts its appearance at extremely slow sweep rates.

The non–steady state model also explains the observed shifting of the sweep–up peak to higher current densities and its broadening as the sweep rate is increased. Also reproduced by the model is the shortening of the inclusion peak with extremely slow sweep rates. Although this model predicts the occurence and size of certain peaks in overpotential, it still does not quite reproduce the exact shape of certain peaks. We believe that the actual inhibition mechanism of the additive may therefore be more complicated than simple blocking of the surface.

We should also point out that not all parameters can be deduced from polarization curves. It is also necessary to obtain the adsorption isotherm of the additive on the metal surface. From the isotherm monolayer surface concentration, Γ_1, can be obtained. Although the desorption constant, k_{-a}, can in theory be obtained from the regression of the polarization curves, its actual influence on the experimental data is so insignificant that its uncertainty is several orders of magnitude greater than its own value. However analysis of the isotherm also yields the ratio k_a/k_{-a} from which the desorption constant may be obtained.

REFERENCES

1) D. Roha and U. Landau, A Transport Based Theory for Leveling Additives, Extended Abstract # 571, Fall meeting of The Electrochem. Soc., Honolulu, Hawaii, Oct. 1987

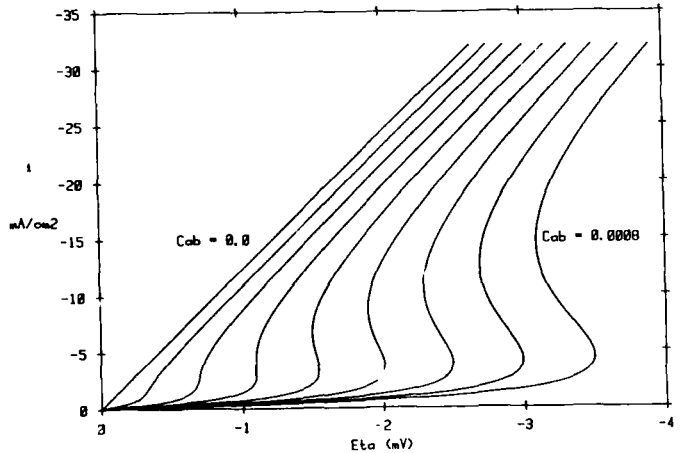


Fig. 1 Polarization curves with additive present according to steady state model

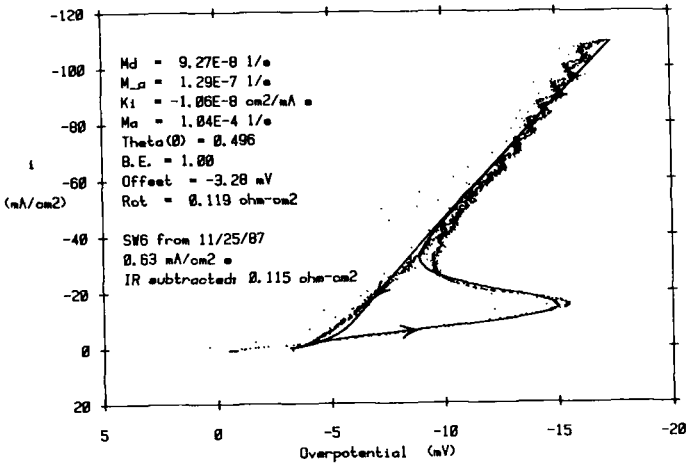


Fig. 2 Polarization curve with coumarin present and non-steady state model fit

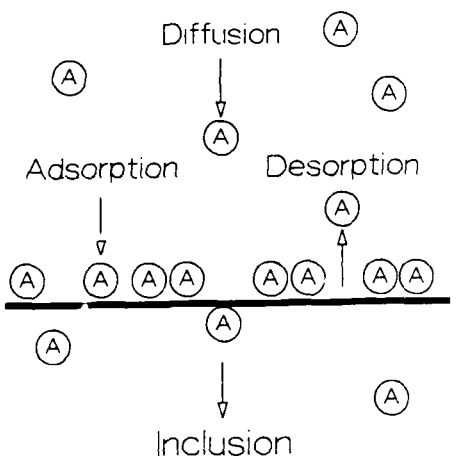


Fig. 3 Scheme of additive material balance

Abstract No. 327

Copper and Additive Effects on Plating High Aspect Ratio Through Holes in Printed Circuit Boards

W. Sonnenberg, R. Bernards, and G.L. Fisher

Shipley Company, Newton, MA

Introduction

The advent of surface mount technology is having a major impact on multilayer circuit board construction. Circuit boards with 30-40 layers and greatly increased circuit density will not be uncommon in the future. In order to gain the maximum board real estate, through hole diameters will be limited only by drilling technology. It is generally accepted that the hole center to surface thickness ratio in thick, high aspect ratio PC boards must exceed 0.67:1(1). Thus electroplating of high aspect ratio holes in thick PC boards poses a difficult challenge to electrochemists.

This investigation was initiated to clarify the role of plating additives in the electrodeposition of copper in high aspect ratio through holes, which is still unclear (1,2).

Experimental

It is well known that throwing power measurements are strongly dependent upon cell geometry. Therefore a device to roughly simulate plating conditions within a through hole was constructed as follows. Two parallel stainless steel plates, approximately 7 cm x 10 cm and 1 cm apart were suspended in a small plating tank. An exaggerated hole was then formed by the solution /air interface and a polymer block attached to the lower edge of the plates. Each plate had three stainless steel strips 1 cm wide embedded in it; one at each end and the other at the center. These were electrically isolated from the remainder of the electrode. Electrically isolated electrodes, 5 cm x 7 cm, were placed at the ends of each plate and perpendicular to it to represent the surface of a circuit board. Paddle agitation of the channel electrode was by a motor and cam device to give a 4 cm stroke every 2 seconds. Bar anodes were placed at each end of the tank 25 cm from the channel cell.

Throwing power measurements were made by applying a voltage to produce a total cell current of 6 amps (approx. 20 mA/cm^2) and measuring the current flowing at each of the isolated electrodes.

These predictions were tested by plating high aspect ratio holes drilled in FR-4 multilayer circuit boards. The boards were 6.0 mm or 7.9 mm thick with holes 0.33 mm in diameter. The holes were prepared for electroplating using a standard permanganate desmear process followed by an electroless copper deposit 1-2 microns thick. Small coupons, 2 cm x 4 cm, taken from each board were mounted in the central opening of a 10 cm x 20 cm copper clad laminate. These were plated in a 65 liter tank using paddle and air agitation. After plating, samples were prepared for metallographic examination to determine throwing power and deposit quality.

Electrochemical studies of the plating overpotential of the various plating solutions was conducted using a PAR 273 potentiostat/ galvanostat, a Pine Instruments MSR speed control and rotator, and a 4 mm diameter Pt disc rotating electrode.

Results

The throwing power of various acid copper plating baths determined using the channel cell is given in Figure 1. A maximum in throwing power occurred at a specific copper metal:sulfuric acid ratio for each level of copper studied.

This behavior was not due solely to changes in solution conductivity since, above 200 g/L of sulfuric acid, conductivity varied only very slightly. Studies of the cathodic polarization behavior of these solutions indicated a strong relationship between throwing power and the magnitude of the plating overpotential.

Predictions of throwing power from the channel cell when various carriers were added to a plating bath containing 30 g/L $CuSO_4$ 5 H_2O, 300 g/L H_2SO_4, and 50 mg/L HCl are shown in Figure 2. The maximum throwing power is dependent upon the carrier type and current density. These and other carriers were added individually to the above bath to plate high aspect ratio holes in the PC boards. The surface current density was maintained at 12 mA/cm^2. As shown in Figure 3, the current density at the center of the hole varies widely depending upon carrier type.

Two component additives containing a brightener and a carrier were also investigated. Depending upon the brightener employed, the throwing power either remained the same as that obtained with the carrier alone or became worse. Again, a strong correlation was observed between an increase in throwing power and the magnitude of the shift in plating overpotential caused by the additive.

References

1. E. K. Yung, L. T. Romankiw, & R. C. Alkire, Proced. Electrodeposition Technology Symp., pgs. 107-102, ECS, 1987.

2. T. Kessler & R. Alkire, Plat. Surf. Fin., 63, (9) 22 (1976)

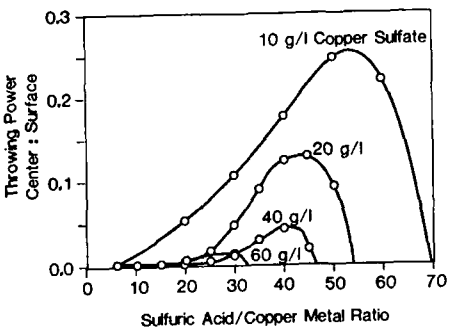


Figure 1. Channel Cell Prediction of Throwing Power of Various Acid Copper Plating Baths.

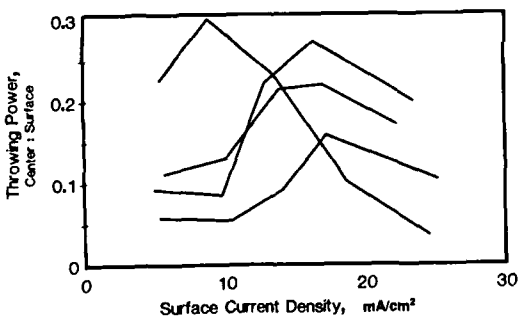


Figure 2. Effect of Various Carriers on Throwing Power of an Acid Copper Plating Bath.

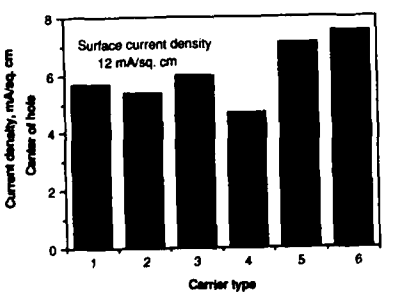


Figure 3. Current Density at the Hole Center as a Function of Carrier type. Hole aspect ratio=18:1

Abstract No. 328

Secondary Current Distribution and Propagation of A Wavy Electrode: Two-Dimensional Model

Shih-Liang Chiu and J. Robert Selman
Department of Chemical Engineering
Illinois Institute of Technology
Chicago, IL 60616

The surface of most electrodes used in electrochemical deposition is usually not smooth, either on a macroscopic or on a microscopic scale. The surface roughness may be caused by: (1) surface pretreatment, e.g., mechanical polishing or electropolishing; (2) preferential nucleation and growth sites (dendrite formation) or preferential dissolution sites (corrosion pitting); (3) hydrodynamic effects (e.g., spiral formation at a rotating disk electrode). Usually, the surface roughness or profile has a certain periodicity. The current distribution at such "wavy" surfaces is of interest since their propagation is very inportant in applications such as surface finishing, electrowinning and battery charging.

Because its relevance for zinc/bromine batteries[1], the parallel-plate flow electrode is studied in this paper. The secondary current distribution and the propagation of a two-dimensional surface with small amplitude to wave length ratio is analyzed. Different shapes of electrode profile are also studied. The effect of the corrosion reaction on the amplification or leveling of the profile is of special interest.

In the following analysis, a 2-D wavy working electrode (WE) of profile $y_w = f(x)$, wave length λ, and a flat counter electrode (CE) of infinite length (see Figure 1) is used. The CE is assumed to be nonpolarizable. The potential between the WE and the CE (Φ_o) is kept constant (potentiostatic control). Applying conservation of current to the bulk electrolyte, the secondary current distribution problem can be described by the Laplace equation with the appropriate boundary conditions. Once the current distribution is known, the propagation of the WE can be calculated. The detailed numerical analysis is given in Reference [2].

Figure 2 shows the primary current distribution at the peak (i_p) and the valley (i_v) of a sinusoidal surface as a function of its amplitude-to-wave-length ratio (k/λ). The CE is assumed to be located infinitely far away. For comparison, the perturbation solution obtained by Fedkiw[3] is also plotted. As the surface amplitude is increased, i_v becomes smaller and approaches zero as expected. In other words, the "potential shadowing" effect is important even when k/λ is relatively small (≈ 0.2).

Using results obtained by Thorsness and Hanratty[4], the limiting corrosion current distribution along a sinusoidal surface with flow in the transverse direction may be calculated. Figure 3 shows the surface propagation velocity ($i_p - i_v$) as a function of α^* for different k's. α^* is the dimensionless wave length, $\lambda/(\nu/u^*)$, where ν is the kinematic viscosity and u^* is the friction velocity. The coulombic efficiency in the present study is fixed at about 80%. It should be noted that when u^* (i.e., the Reynolds number) increases, the corresponding α^* decreases. As is clear from Figure 3, the presence of the corrosion reaction will retard the growth of the profile only above a certain α^* value. At high convection rates (small α^*), the profile will grow faster in the presence of corrosion than without corrosion.

The propagation history of a sinusoidal surface with initial amplitude (divided by wave length) 0.001, is shown in Figure 4. The apparent tip radius of the profile (at x=0) increases with time (broadening at the peak compared to original sine wave). This is largely due to the lateral deposition around the peak. The current distribution of a profile with original amplitude $k \cos 2\pi x e^{(-1+\cos 2\pi x)}$ (see Figure 5), is shown in Figure 6 for $k = 0.05$ and 0.1. This profile is characterized by a sharper peak (at x=0) and an extended smooth valley (at x=0.5). Because of the increase in current when x is greater than 0.25, prolonged deposition results in the appearence of a secondary peak at x=0.5 (see Figure 7). This behavior clearly demonstrates that the "potential shadowing" effect has a limited range, in this case, limited to the protruding part of the surface. The region out of the range of this effect will grow faster than the region within the range.

Acknowledgement: This project is supported by Department of Energy through Lawrence Berkeley Laboratory.

References

[1] Exxon Research and Engineering Company, Linden, NY. "Development of a Circulating Zinc-Bromine Battery". Phase II Final Report. (1982)
[2] Shih-Liang Chiu, "Corrosion and Electrodeposition of Zinc from Flowing Acidic Zinc Bromide Solutions". Ph.D. Thesis. Illinois Institute of Technology, Chicago, IL. (1988)
[3] P. Fedkiw. J. Electrochem. Soc. 127 (1980)1304
[4] C.B. Thorsness and T.J. Hanratty. AIChE J. 25 (1979)677

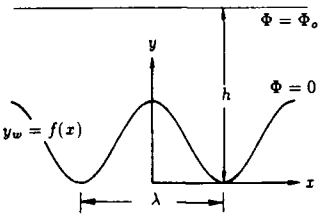


Figure 1. Parallel-plate electrodes with 2-D wavy working electrode.

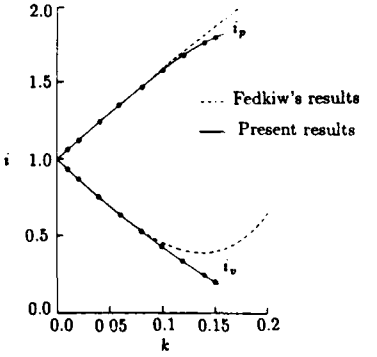


Figure 2. Primary current distribution at a sinusoidal surface.

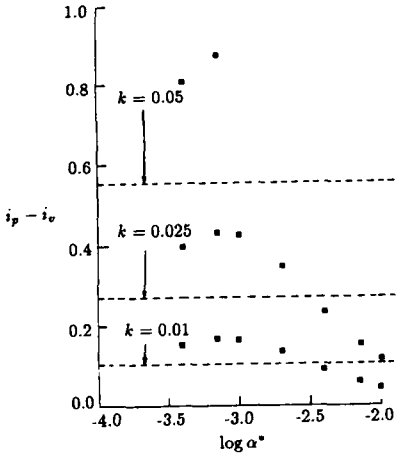


Figure 3. Propagation velocity of a sinusoidal surface in the presence of corrosion. The dashed lines indicate propagation when corrosion is absent.

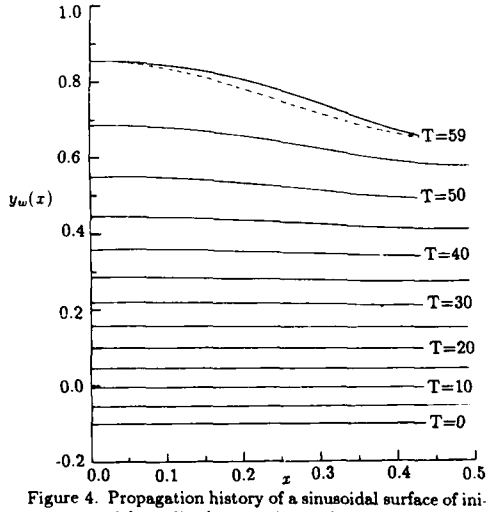


Figure 4. Propagation history of a sinusoidal surface of initial amplitude 0.001 (normalized to λ).

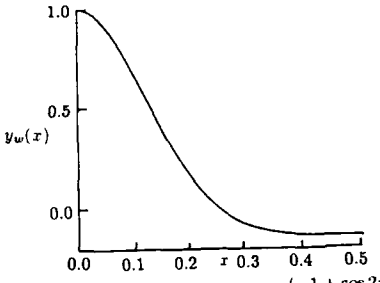


Figure 5. Profile of amplitude $\cos 2\pi x e^{(-1+\cos 2\pi x)}$.

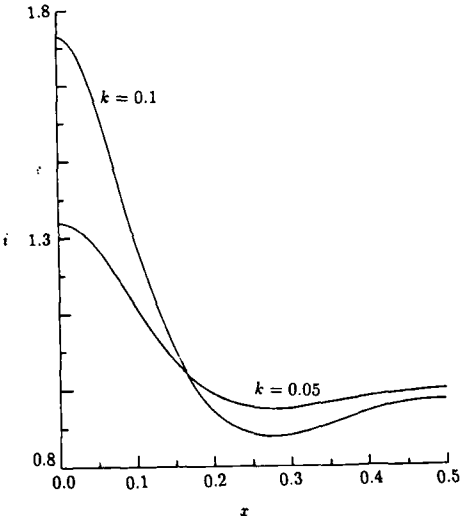


Figure 6. Secondary current distribution for the profile shown in Fig. 5.

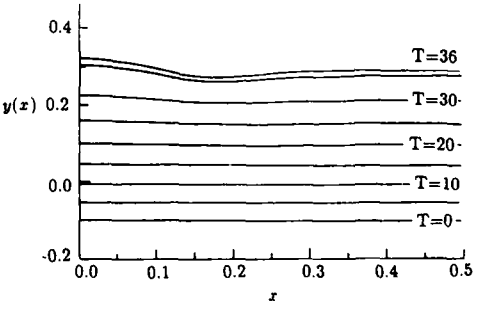


Figure 7. Propagation history of the profile shown in Fig. 5.

Abstract No. 329

Effects of Nonuniform Current Distributions on the Interpretation of Kinetic Data

Alan C. West and John Newman

Materials and Chemical Sciences Division
Lawrence Berkeley Laboratory
and
Department of Chemical Engineering
University of California
Berkeley, California 94720

It has long been recognized that a geometry with a nonuniform primary current distribution is less than ideal for measuring the kinetic rate constants of an electrochemical reaction [1]. Nevertheless, there may be practical reasons for using such geometries. This talk shows quantitatively the effects that nonuniform distributions can have on interpretating kinetic data, assuming that ohmic correction is made by the interruption of current.

The difficulty in interpretation is caused by an uncertainty due to the current interrupter method and the inability to measure a local current density. Elaboration on these phenomena can be found in Newman [2] and in Tiedemann *et al.* [3]. This shows how the exchange current density and the charge transfer coefficient can be obtained from the average current density and an apparent surface overpotential.

Results are given for Tafel kinetic measurements taken on a rotating disk electrode for three reference electrode placements. Additionally, results are shown for measurements taken in the linear and Tafel kinetic regions in a channel geometry.

Corrections to determine an exchange current density from an apparent exchange current density obtained with a disk electrode are shown in figure 1, assuming that the transfer coefficient is equal to the apparent transfer coefficient. Figure 2 gives an indication of when this assumption holds. δ_{app} is a dimensionless average current density, defined in Newman [4], except that the apparent transfer coefficient, obtained from experimental data, is used. Determining the true kinetic parameters from data is discussed by West and Newman [5].

In summary, this analysis confirms suggestions that the reference electrode should be placed far from the working electrode when possible. Methods are given to determine the true kinetic parameters from the apparent parameters obtained from measurements without corrections. Additionally, it is shown when these corrections are negligible.

[1] John Newman, "Current Distribution on a Rotating Disk below the Limiting Current," *J. Electrochem. Soc.*, 113, 1235 (1966).

[2] John Newman, "Ohmic Potential Measured by Interruptor Techniques," *J. Electrochem. Soc.*, 117, 507 (1970)

[3] William H. Tiedemann, John Newman, and Douglas N. Bennion, "The Error in Measurements of Electrode Kinetics Caused by Nonuniform Ohmic-Potential Drop to a Disk Electrode," *J. Electrochem. Soc.*, 120, 256 (1973).

[4] John Newman, *Electrochemical Systems*, p. 348, Prentice-Hall, Englewood Cliffs, N. J. (1973).

[5] Alan C. West and John Newman, "Correction to Kinetic Measurements Taken on a Disk Electrode," submitted to *J. Electrochem. Soc.*

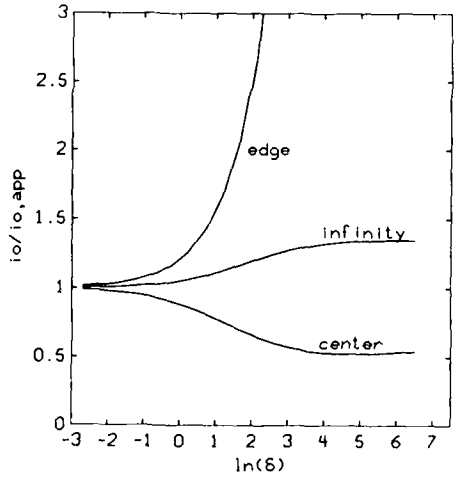


Figure 1. Correction to the exchange current density for three reference electrode placements, assuming $\alpha_a = \alpha_{a,app}$.

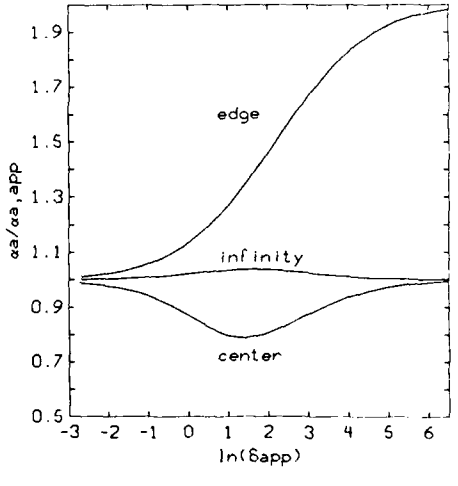


Figure 2. Correction to the transfer coefficient for three reference electrode placements as a function of δ_{app}.

Abstract No. 330

CURRENT DISTRIBUTION IN PATTERN PLATING OF NONUNIFORMLY SPACED AND ISOLATED LINES

Uziel Landau
Department of Chemical Engineering
Case Western Reserve University
Cleveland, OH 44106

and

Raymond T. Galasco and John Tang
Development Laboratory
IBM Corp.
Endicott, NY 13760

Increased complexity of electronic devices often requires the design of printed circuits with highly non-uniform conductor line spacings and widths. Uniform plating of such patterns is known to be difficult; thin isolated lines typically plate considerably faster than closely spaced lines. When the deposit on isolated lines exceeds the photoresist level it often evolves into undesirable mushroom-like shape with rough texture. Presented here is a model that explains the phenomena and provides design guidelines.

The underlying reason for the enhanced deposition on isolated lines is that they resemble line sinks offering lower resistance and access to two-dimensional transport. By contrast, dense line clusters resemble a planar electrode accessible only to one dimensional transport (Fig. 1). We analyze here primary, secondary and tertiary current distributions and present approximate analytical expressions and some numerically computed results.

PRIMARY DISTRIBUTION

In the absence of kinetics and transport limitations, we find by conducting approximate voltage balances on an isolated line and on the line cluster region:

$$\frac{i_s}{i_c} \approx \frac{d_c - \frac{W_c}{\pi}\,\ell n f + \frac{NW_c}{2}\frac{K\,(1/\cosh^2 \delta)}{K(\tanh^2 \delta)}}{d_s + \frac{W_s}{\pi}\,\ell n\,\frac{S}{W_s} + \frac{W_s}{2}} \qquad [1]$$

The geometric parameters are defined in Fig. 1. The subscripts s and c designate the isolated line and the line cluster region, respectively. N is the number of lines within the dense cluster and f is the area fraction covered by lines within this densely patterned region: $f = W_c/(W_c + S_c)$; K(m) is the complete elliptic integral of the first kind and $\delta = \pi N (W_c + S_c)/4S$. When typical values are assigned to the parameters: $d_s = d_c = W_s = W_c = S_c = 2$ mil, S = 40 mil and N = 10, Eq. [1] indicates that the current density on the isolated line is 2.67 times higher than on lines within the dense cluster. This is in excellent agreement with numerical computations (1) indicating an average (primary) current density ratio of 2.66 (Figs. 2 and 3).

SECONDARY DISTRIBUTION

When both kinetics and ohmic limitations are important, assuming Tafel polarization, the current densities can be expressed implicitly:

$$i_c\left(d_c - \frac{W_c}{\pi}\,\ell nf + \frac{NW_c}{2}\frac{K\,(1/\cosh^2 \delta)}{K\,(\tanh^2 \delta)}\right) - i_s\left(d_s + \frac{W_s}{\pi}\,\ell n\left(\frac{S}{W_s}\right) + \frac{W_s}{2}\right) = \frac{\kappa RT}{\beta F}\,\ell n\,\frac{i_s}{i_c} \qquad [2]$$

Here, κ is the electrolyte conductivity and β the cathodic transfer coefficient. When values typical to copper plating are introduced ($\kappa = 0.55$ S/cm, $\beta = 0.5$ and $i_c = 30$ mA/cm^2) we find that the kinetic resistance is completely dominant and consequently only marginal difference ($\approx 4\%$) is anticipated between current densities on isolated lines and dense regions. Numerical secondary distribution computations substantiate this analytical prediction; yet, experimental observations are in complete *disagreement* with this result.

TERTIARY DISTRIBUTION

The disparity between secondary distribution predictions and experiments indicate that mass transport effects are important and tertiary distribution must be considered. Analysis indicates, however, that the mass transport resistance is small in comparison to kinetics. The key to the seemingly contradictory evidence is that although mass transport resistance is not dominant by itself, it does bring about variations in the surface concentrations, which have, in turn, a pronounced effect on the kinetics. Since the latter control the deposition rate, this leads to significant differences in the current densities. A voltage balance, accounting for kinetics and mass transport but neglecting the comperatively minor ohmic component yields:

$$\frac{i_s}{i_c} = \left(\frac{C_s}{C_c}\right)^{(\beta/n)+\gamma} \qquad [3]$$

Here, C_s and C_c are the reactant concentrations near the isolated and clustered line electrodes, respectively. In deriving Eq. [3] we made use of the relation $i_o \propto C^{\gamma}$. When we assign a numerical value of 0.5 to γ (2) we find:

$$(i_s/i_c) = (C_s/C_c)^{0.75} \qquad [3']$$

The surface concentrations can be determined by solving the flow pattern within the cell in conjunction with the convective – diffusion–migration equations (3). Instead, we estimate the surface concentration ratio by a relaxation model (4) to obtain:

$$\frac{C_s}{C_c} = \frac{\tan^{-1}\left[\left(\frac{S}{W_c}\right)^{1/2}\right]}{\tan^{-1}\left[\left(\frac{1}{f} - 1\right)^{1/2}\right]} \qquad [4]$$

Introducing the former parameter values ($S/W_c = 20$, $f = 0.5$), Eq. [4] predicts that the surface concentration on the isolated line is 1.72 times higher than on the closely clustered lines. Eq. [3] then indicates a current density on the isolated line which is about 1.5 times higher than within the cluster. Fig. 4 shows the current density ratio between isolated and closely spaced lines as indicated by our model. It is noted that the current density ratio is strongly influenced by the separation distance at low to moderate separations, however, when the separation distance exceeds about 50 times the gap between the close lines ($S/S_c \cong 50$) further changes in the current density become small.

Sparse line clusters can accommodate larger separations to an isolated line than dense clusters while maintaining the same current density ratio.

ACKNOWLEDGEMENT

Key suggestions by Oscar Lanzi III are gratefully acknowledged. Also acknowledged is help from W. Michael Lynes.

REFERENCES

1. CELL-DESIGN^R, Software for computer aided design of electrochemical cells, L-Chem, Inc., 13909 Larchmere Blvd. Shaker Heights, OH 44120.

2. J. D. Reid and A. P. David, J. Electrochem. Soc., 134 (6) 1389–1394 (1987).

3. M. Menon and U. Landau, Current Distribution Modeling in Cells with Forced Convection, Abstract #224, The Electrochem. Soc. 168th Meeting, Las Vegas, Nevada, Oct. 1985.

4. O. Lanzi III, private communication.

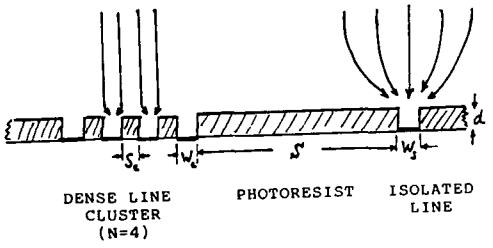


Fig. 1: Schematic section through a patterned circuit board indicating a dense line cluster (left) and an isolated line (right).

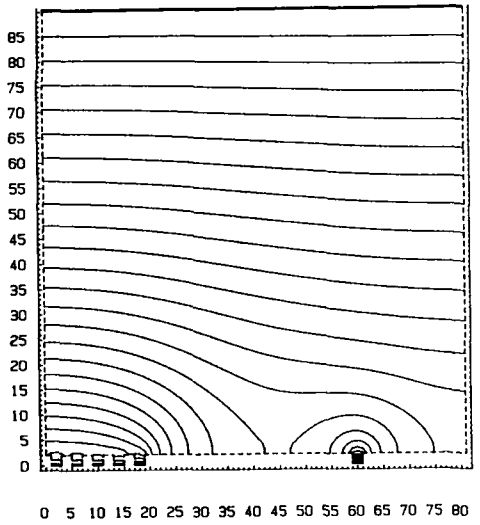


Fig. 2: Equipotential lines primary distribution in pattern plating of line cluster (left) and an isolated line (right). Each grid spacing corresponds 1 mil. *Potential lines are spaced 0.16 mV apart.* Numerical computations (1).

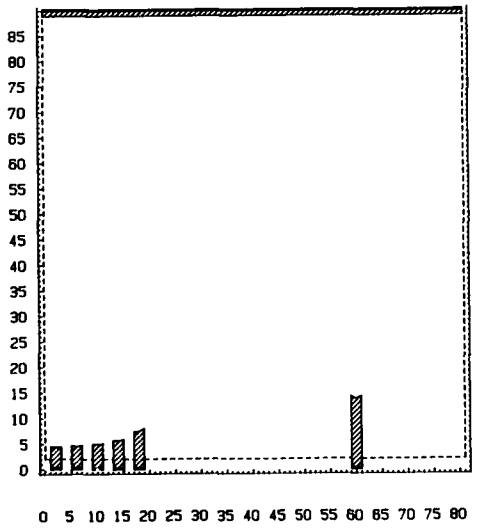


Fig. 3: Primary current density distribution in pattern plating of 2 mil lines in the configuration shown in Figs. 1 and 2. Height of dashed regions is proportional to the current density. Average current density within the clustered lines (left) is 30 mA/cm^2. Numerical computations (1).

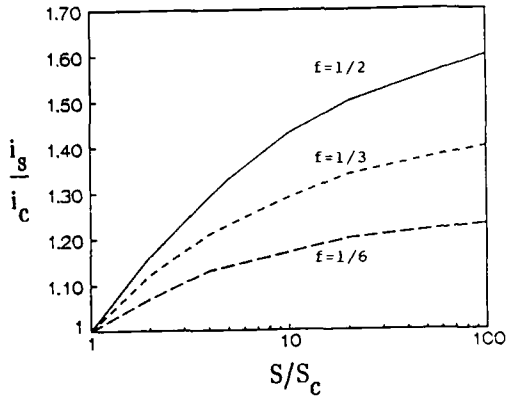


Fig. 4: Current density ratio between an isolated line (i_s) and dense line cluster (i_c) as function of a *dimensionless separation distance* S/S_c. (S is the separation distance between the isolated line and the dense cluster, S_c is the gap between lines within the dense cluster). The parameter f is the fraction of patterned area within the dense line region ($f = W_c/W_c + S_c$).

Abstract No. 331

Optimization of Electrodeposit Uniformity by the Use of Auxiliary Electrodes

S. Mehdizadeh, J. Dukovic, P.C. Andricacos, L.T. Romankiw
IBM Research Division, T.J. Watson Research Center, P.O. Box 218, Yorktown Heights, NY 10598

H.Y. Cheh
Department of Chemical Engineering and Applied Chemistry, Columbia University, New York, NY 10027

Auxiliary cathodes, or "thieves" are frequently used in industrial electrodeposition to obtain uniform thickness distribution (1-4). The particular case of an auxiliary electrode frame surrounding a planar substrate has found application in the electronics industry (5). Such planar substrates are patterned by photolithography to create metallized regions with strictly controlled thickness and properties that strongly depend on local current density (6-11). In some cases, a highly uniform current distribution (maximum deviation of a few percent from the mean) may be required to obtain an acceptable product.

In this study, numerical techniques are employed to predict the effectiveness of a coplanar auxiliary electrode in achieving optimum current distribution on a planar working substrate, hereafter referred to simply as the cathode.

Figure 1 shows a schematic cross section of an axisymmetric cell with a coplanar, concentric current thief surrounding the cathode. A gap of nonconducting material separates the cathode from the auxiliary electrode so that each can be independently controlled by a galvanostat. In the base case chosen for this study, the outer radius of the auxiliary electrode, r_{AUX}, is taken as twice that of the cathode, r_C, with a gap size $g = 0.02\, r_C$. The anode and the side wall are sufficiently remote that their position does not affect the current distribution on the cathode.

Concentration overpotential is assumed to be negligible in the potential-theory model. The Butler-Volmer equation for overpotential is assumed at both the cathode and the auxiliary electrode surfaces. A boundary-element code described elsewhere (12), modified to treat the three-electrode problem, is employed to solve the boundary-value problem.

Figure 2 shows the change in current distribution on an axisymmetric section of the cell, as the average current density on the auxiliary electrode, $\bar{i}_{AUX}$, is allowed to vary; in all cases, the average current density on the cathode, $\bar{i}_C$, is fixed. The current distribution in the case of no auxiliary electrode is solely dependent on the Wagner number, W, which characterizes the electrodeposition process. In the Tafel region, which applies to virtually all industrial electrodeposition processes, W can be expressed as:

$$W = \frac{RT\kappa}{F\alpha_C \bar{i}_C r_C} .$$

A base value of $W = 0.25$, typical of acid-copper deposition at 10 mA/cm² on a 125-mm diameter substrate, has been used in Figure 2.

As a quantitative measure of current distribution uniformity on the cathode, the normalized root-mean-square deviation of the current density, i_C, from its average, $\bar{i}_C$, is used:

$$\sigma^2 = \frac{1}{\pi r_C^2} \int_{r=0}^{r_C} \int_{\theta=0}^{2\pi} \left(\frac{i_C}{\bar{i}_C} - 1 \right)^2 r\, d\theta\, dr .$$

An algorithm has been developed to calculate $\bar{i}_{AUX}$ that produces the minimum value of σ on the cathode for a prescribed value of $\bar{i}_C$. An optimum current distribution on the cathode is thus obtained, and the effect of various parameters of the model on this optimum has been investigated.

Under the conditions of the base case, the value of $\bar{i}_{AUX}$ that achieved the best uniformity possible (in this case, $\sigma = 0.008$) was 2.13 times $\bar{i}_C$. This optimum value, however, depends on the Wagner number, W, and on several geometric values such as gap size, auxiliary-electrode size, wall position, and anode position. For instance, smaller values of σ can be achieved as the size of the auxiliary electrode is increased. Figure 3 shows the dependence of σ on the ratio of average current densities, $\bar{i}_{AUX}/\bar{i}_C$, for various sizes of the auxiliary electrode. In the limit of very large r_{AUX}, the nonuniformity in the optimized current distribution on the cathode is largely confined to the edge and can only be reduced further by reducing the gap size (Figure 4). However, at large values of r_{AUX}, σ becomes more sensitive to $\bar{i}_{AUX}$, as shown in Figure 3.

The optimum arrangement of an auxiliary cathode for a particular application in electrodeposition depends on all the variables mentioned above, and a detailed numerical analysis provides useful results for the design of such processes.

REFERENCES

1. S. Dalby, J. Nickelsen and L. Alting, *Electroplating and Metal Finishing*, **28**, 18-23 (Nov 1979).

2. S.Y.S. Parn, M. McCormick, D. Howe and J.A. Naismith, *Trans. Inst. Metal Finishing*, **59**, 61-67 (1981).

3. M. McCormick, D. Howe and S.Y.S. Parn, *Trans. Inst. Metal Finishing*, **63**, 129-134 (1985).

4. L.T. Romankiw, and T.A. Palumbo, in "Electodeposition Technology, Theory and Practice," L.T. Romankiw and D.R. Turner, Editors, p.25-26, The Electrochemical Society Softbound Proceedings Series, Pennington, NJ (1987).

5. L. Berger, R. Boeckl, R. Kronemann and D. Meyer, *IBM Tech. Disclosure Bull.*, **23**, 201 (1980).

6. L.T. Romankiw, S. Krongelb, E.E. Castellani, J. Powers, A. Pfeiffer, and B.J. Stoeber, *Proceedings of the International Conference on Magnetism, ICM-73*, **VI**, 104 (1973).

7. L.T. Romankiw, S. Krongelb, E.E. Castellani, A. Pfeiffer, B.J. Stoeber, and J.D. Olsen, *IEEE Trans. Mag.*, **MAG-10** (3), 828 (1974)

8. L.T. Romankiw, *Electrochem. Soc. Extended Abstract No. 462*, **79-2**, 1165 (1979).

9. L.T. Romankiw, S. Krongelb, D.A. Thompson, R. Anderson, E.E. Castellani, P.M. McCaffrey, A. Pfeiffer, and B.J. Stoeber, *Electrochem. Soc. Extended Abstract No. 465*, **79-2**, 1170 (1979).

10. R. Alkire, and T.J. Chen, *Electrochem. Soc. Extended Abstract No. 466*, **79-2**, 1173 (1979).

11. L.T. Romankiw, S. Krongelb, M.C. Blakeslee, A. Pfeiffer, and B.J. Stoeber, *Electrochem. Soc. Extended Abstract No. 474*, **79-2**, 1190 (1979).

12. J. Dukovic and C.W. Tobias, *J. Electrochem. Soc.*, **134**, 331 (1987).

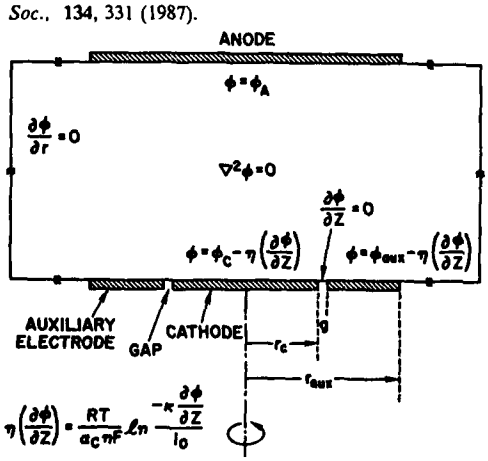


Fig. 1. Schematic cross section of a cell with concentric auxiliary electrode: computational domain and boundary conditions

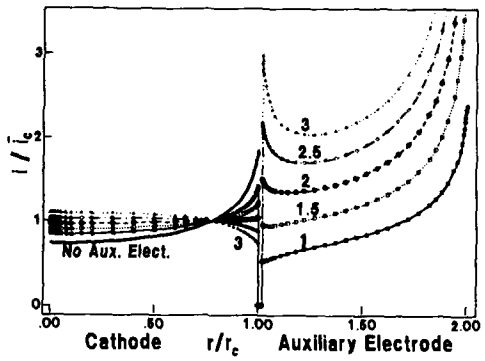


Fig. 2. Secondary current distributions with Tafel polarization on the cathodes for various ratios of average current densities $\bar{i}_{AUX}/\bar{i}_C$

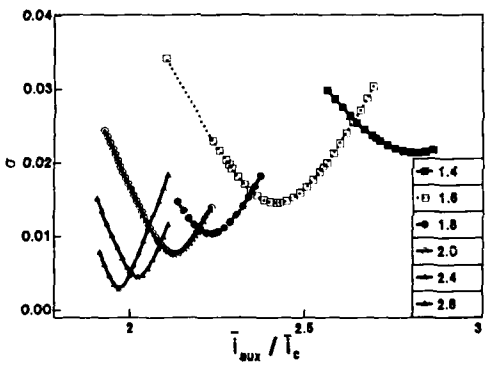


Fig. 3. The effect of varying the ratio of average current densities $\bar{i}_{AUX}/\bar{i}_C$ on the uniformity over the cathode with size ratio r_{AUX}/r_C as a parameter

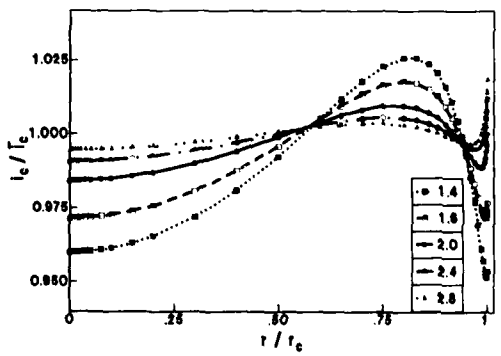


Fig. 4. Optimized current distributions on the cathode for various size ratios r_{AUX}/r_C

Abstract No. 332

A Novel Adaptation of the Finite Difference Method for Accurate Description of Non–Orthogonal Boundaries

W. Michael Lynes and Uziel Landau

Department of Chemical Engineering
Case Western Reserve University
Cleveland, Ohio 44106

Modeling of current and potential distribution in electrochemical cells requires solving Laplace's equation for the potentials. This can be achieved in a general geometry cell by a number of numerical techniques including finite difference, finite element, boundary integral, and orthogonal collocation. The finite difference method is particularly attractive because of its speed, simplicity, and robustness (1). Its main difficulty, however, lies in accurately describing non–orthogonal boundaries (i.e. corners that are not right angles). Described here is a novel extension of the finite difference technique which enables accurate description of such boundaries. The method has been applied to modeling current and potential distributions in general geometry (2–D) electrochemical cells and implemented on various personal computers (2). Comparison with other numerical techniques has been quite favorable.

The basic concept embodied in the finite difference method is a current balance solved at each point in the grid. For a point in the interior of the electrolyte, the control volume for this current balance is a square (unit depth) as seen in Figure 1. Ohm's law in this setting takes the form:

$$i = -\kappa \nabla \phi \qquad [1]$$

where i is the current density, κ is the conductivity, and $\nabla\phi$ is the potential gradient. Current densities through each side of the control volume can be calculated in terms of the grid point potentials following equation [1]. Multiplying the current densities by the respective areas provides the current which enters any one of the faces. An iterative scheme is used to adjust the potentials at each grid point until the current exiting each control volume is zero.

Angular boundaries are typically handled in the finite difference approach by the 'staircase' approximation shown in Figure 2. This approximation has the following problems:(1) it distorts the shape of the boundary, and (2) it changes the surface area of the boundary.

These problems are substantial when the boundary is an electrode. The shape distortion introduces much 'noise' into the current densities at each grid point on the boundary. The surface area distortion causes errors in calculating the kinetic and mass–transfer effects at the electrode surface.

These problems, however, can be completely avoided by applying the approach described herein. The key is to modify the control volumes adjacent to the boundary rather than the boundary itself. Figure 3 shows a typical example of these modified control volumes.

The new technique is based on conducting current balances on these non–rectangular elements. A potential gradient is assigned to each face of the non–rectangular elements. The current contributions associated with each of these are carefully added and interfaced with the boundary conditions. The potential assigned to a sloping electrode element is determined by extrapolation of the grid point potentials. The procedure is then incorporated within an efficient ADI (3) iteration algorithm.

Comparison to Other Techniques

The method described above was implemented on an IBM PC. Speed and accuracy were compared to both a standard finite difference technique and an adaptive finite element technique. The geometry for this comparison was a wedge–shaped cell (Figure 4). The primary distribution has been solved analytically (4) providing a standard for comparison. Table 1 shows the results. It can be seen that (1) the new technique is identical in speed to the standard finite difference approach, and (2) the new technique is an order of magnitude faster than the finite element program at reaching a desired accuracy.

Primary and tertiary distributions of a Hull cell are shown in Figures 5–7. These calculations take about 100 seconds on an IBM PC using the method described herein. The finite element technique requires this much time to execute on a main frame computer (5).

Figures 8–10 show a cell which is sensitive to surface area distortion. Table 2 compares the results of the new approach to those of the 'staircase' approximation. The new angular technique accurately approaches the maximum current limit where the staircase method fails.

Acknowledgement

Development of the technique was supported by DOE contract No. DE–AC01–83ER80064 to Helipump Corporation. Portions of the software are based on earlier work by W. J. Cook.

References

1. W. J. Cook and U. Landau, "Numerical Modeling of Current and Potential Distributions – Personal Computer Implementation," in *Engineering of Industrial Electrolytic Processes*, U. Landau, R.E. White, and R.J. Varjian Eds., The Electrochem. Soc. Softbound Proceedings Series, Pennington, N.J. (1986).

2. CELL–DESIGN ® Software for Computer Aided Design of Electrochemical Cells, L–Chem, Inc. 13909 Larchmere Blvd. Shaker Heights, Ohio 44120

3. Donald W. Peaceman, *Fundamentals of Numerical Reservoir Simulation*, Elsevier Scientific, New York, New York (1977).

4. F. Bowman, *Introduction to Elliptic Functions with Applications*, Dover, (1961).

5. M. Matlosz, et al. *J. Electrochem. Soc.* 134 (12) pp. 3015 – 3021 (1987).

Table 1 Speed and Accuracy Comparison for Wedge–shaped Cell
Analytical solution: Dimensionless Conductance = 1.279

"staircase" Approximation

Mesh intervals	Dimensionless Conductance	Calculation time (seconds)*
12 X 24	1.248	27
24 X 48	1.2625	111
48 X 96	1.2704	652

Angular version

Mesh intervals	Dimensionless Conductance	Calculation time (seconds)*
12 X 24	1.2856	33
24 X 48	1.2817	101
48 X 96	1.2802	372

Adaptive finite element system

Refinement Termination Threshold	Dimensionless Conductance	Nodes	Calculation Time (seconds)*
25%	1.307	33	12
15%	1.287	329	140
10%	1.2857	451	232

*Calculations for finite difference were performed on an IBM PC(4.77 Mhz). Finite element calculations were performed on an IBM AT (6–8 Mhz).

Table 2 Surface Area Distortion Comparison

Staircase Total Current	Angular Method Total Current	Maximum Possible (Lim X Surface Area)
0.9555	0.8991	0.9425

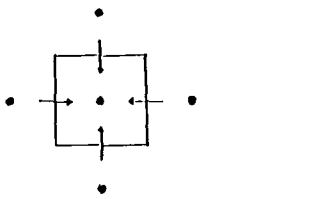


Figure 1
Current balance control volume

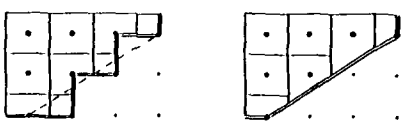


Figure 2
stairstep approximation

Figure 3
non-rectangular control volumes

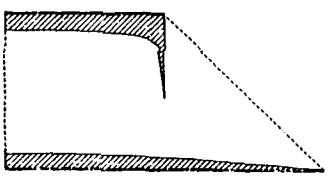


Fig. 4. Wedge-shaped geometry for speed and accuracy comparison (primary current distribution)
Dashed area is proportional to the current density.

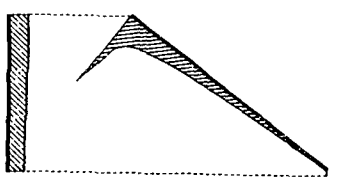


Fig. 5. Hull Cell – primary current distribution

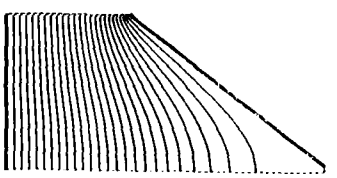


Fig. 6. Hull Cell – primary potential contours

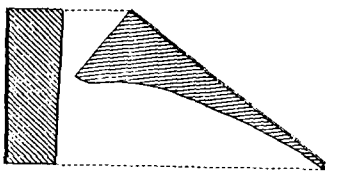


Fig. 7. Hull Cell – tertiary current distribution with:
$i_0 = 1.3\ mA/cm^2$; $\alpha/\beta = 0.391$; n = 2 ;
$i_{Lim} = 50\ mA/cm^2$; $\kappa = 0.26$ mho/cm ; voltage = .1V

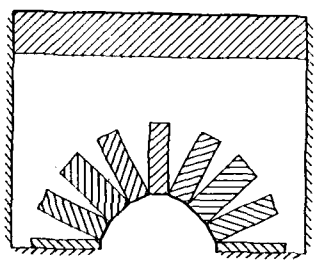


Fig. 8. Angular approximation of circular geometry for surface area distortion comparison – tertiary current distribution with: 30 X 25 grid ; 1cm grid spacing
voltage = 1V ; κ = 1 mho/cm; $i_0 = 1\ mA/cm^2$
$\alpha/\beta = 0.333$; $i_{Lim} = 50\ mA/cm^2$; n = 2
cathode surface area = $6\pi\ cm^2$
All dashed boundaries are insulating.

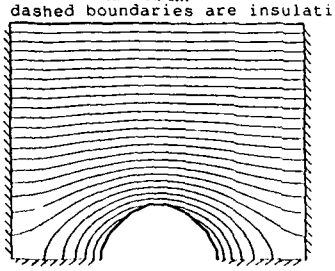


Fig. 9. Potential contour map for above conditions

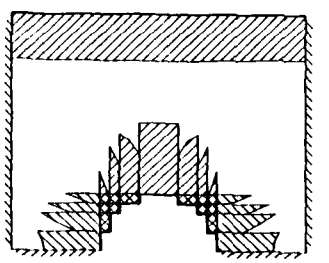


Fig. 10. Staircase approximation of circular geometry for surface area distortion comparison – tertiary current distribution with same conditions as Fig. 8.

Abstract No. 333

Effect of Agitation on the Electrodeposition of NiFe Alloys

P.C. Andricacos, C. Arana,[1] J. Tabib,[2] J. Dukovic, and L.T. Romankiw

IBM Research Division
T.J. Watson Research Center
P.O. Box 218, Yorktown Heights, N.Y. 10598

Although agitation plays a significant role in alloy electrodeposition, very few experimental data are available in the literature describing its effects on alloy composition, bath current efficiency, electrode potential, and partial current densities. In this paper, we provide such data for the particular case of NiFe alloy plating; this system is interesting both because of its mechanism (1) and because of and its relevence to computer storage technology (2, 3).

Studies of alloy plating usually require a large number of experiments to be performed including analysis of the thickness and composition of the plated alloy-films. We have recently demonstrated (4) that a Rotating Ring-Disk Electrode (RRDE) can be conveniently used for this purpose, in place of instruments such as Electron Microprobes or Atomic Absorption / Inductively Coupled Plasma Spectrometers. The use of a RRDE allows plating to be done on the disk under well characterized hydrodynamic conditions, while the alloy composition and bath current efficiency can be determined by exploiting the collection property of the ring (4).

In this study NiFe alloys were plated from a chloride-based solution described in References 2 and 3. It contained 0.5 M NaCl, 0.4 M H_3BO_3, 0.2 M $NiCl_2$, and 0.005 M $FeCl_2$ acidified to a pH of 3 with HCl. All plating runs were done galvanostatically at 25 °C.

Figures 1 and 2 show the effect of rotation speed and total plating current density on the composition of the plated film and the current efficiency of the solution, respectively. It is seen that both parameters play a significant role; any alloy composition between roughly 5 and 40 wt. percent Fe can be obtained from this plating solution by selecting the current density and agitation conditions; similarly, the current efficiency varies roughly between 20 and 100 percent.

The polarization behavior of each reaction involved in the NiFe plating system is seen in Figures 3, 4, and 5 for Ni deposition, Fe deposition, and H_2 evolution, respectively. In Figure 3, the kinetics of Ni deposition when it co-deposits with Fe are compared with the kinetics of the same reaction when it occurs from a solution identical to the one described above without the Fe salt. It is seen that Ni deposition is inhibited by Fe co-deposition and this effect manifests itself as a shift of the Tafel line in the cathodic direction. The shift depends on agitation but only in the region where the Fe deposition reaction is influenced by mass transport.

The kinetics of the Fe deposition reaction is shown in Figure 4. Due to the preferential deposition of Fe and to the low concentration of Fe^{2+} in the plating solution, the Fe deposition reaction becomes mass transfer limited at sufficiently cathodic potentials as witnessed by its dependence on agitation and relative insensitivity to the potential. Examination of the oxidation of Fe^{2+} ion in the same solution reveals that the diffusivity of the ion is the same in both reactions and equal to 4.6×10^{-6} cm²/s.

Tafel plots for H_2 evolution during NiFe deposition are shown in Figure 5. It is seen that agitation has a significant effect on the reaction rate, while the dependence on the potential is weak. Experiments conducted in a solution similar to the one described above but without the metal ions revealed that both H^+ and H_2O contribute to the net rate of H_2 evolution. Hydrogen ion reduction on NiFe becomes mass transport limited over the same potential range at which NiFe deposits, thereby explaining both the strong effect of agitation and the weak dependence on the potential. Hydrogen evolution rates on Ni and NiFe substrates were found to be similar to those obtained during Ni and NiFe deposition.

References

1. H. Dahms and I.M. Croll, J. Electrochem. Soc., **112**, 771(1965)

2. E.E. Castellani, J.V. Powers, and L.T. Romankiw, U.S. Patent 4,102,756 (July 25, 1978)

3. N.C. Anderson and C.R. Grover, U.S. Patent 4,279,707 (July 21, 1981)

4. P.C. Andricacos, J. Tabib, and L.T. Romankiw, J. Electrochem. Soc., 135, 1172(1988)

---

[1] Present Address: Department of Chemistry, Baker Laboratory, Cornell University, Ithaca, N.Y. 14753

[2] Present Address: IBM San Jose, 5600 Cottle Road, San Jose, Ca. 95193

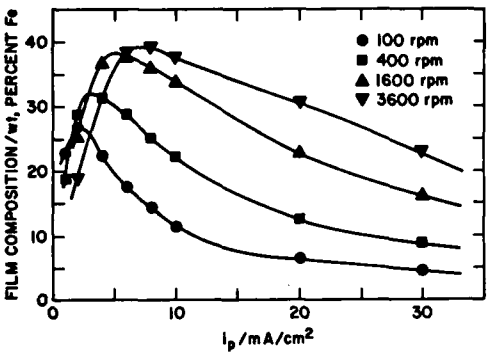


Figure 1: Composition of the plated NiFe film as a function of total plating current density for several rotation speeds

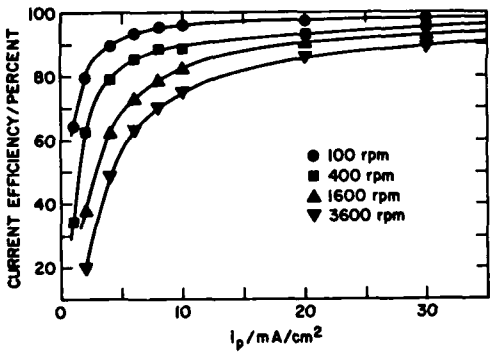


Figure 2: Current efficiency of the NiFe plating solution as a function of total plating current density for several rotation speeds

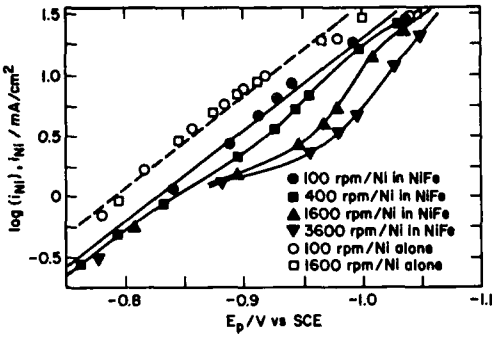


Figure 3: Tafel plot for Ni partial current

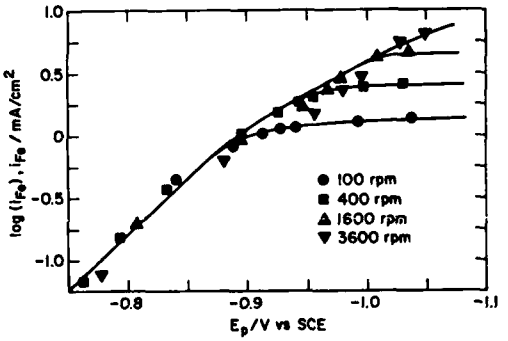


Figure 4: Tafel plot for Fe partial current

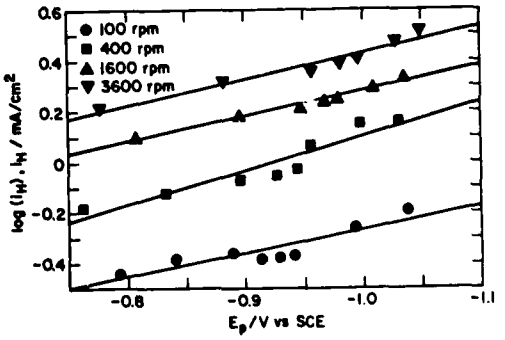


Figure 5: Tafel plot for H_2 partial current

Abstract No. 334

MICROELECTRODE ASSEMBLIES FOR ELECTROPLATING STUDIES

Rex Louis Deutscher and Stephen Fletcher

CSIRO
Institute of Minerals, Energy, and Construction
Division of Mineral Products
P.O. Box 124
Port Melbourne, Victoria 3207, Australia

ABSTRACT

The development and use of microelectrode assemblies for nucleation studies is described. It is shown how this new technology can be used to deconvolute nucleation and crystal growth rates, thereby revealing unexpected properties of metal plating processes. Recent advances achieved by the electrometallurgical processing group at CSIRO include the discovery of nucleation rate dispersion and the first observations of nucleation after-effects.

INTRODUCTION

Over the past thirty years, a major problem in studies of nucleation in electrochemical systems has been the lack of a suitable method of counting the time-varying numbers of crystals N(t) formed during the course of a reaction. This is an annoying problem because many related parameters can be measured with high accuracy, such as the total reaction rate (the electrical current) and the driving force for nucleation (the electrode potential). Yet in the best crystal-counting method reported so far - the "double potential step" method - crystals are counted one at a time under a microscope, with the result that it is very difficult to produce accurate or even statistically representative data [1-7]. Moreover, even when sufficient data are accumulated for them to be considered representative, there remains the problem that they may not be directly compared with the predictions of classical theories of heterogeneous nucleation because nucleation sites (active sites) are occluded by the diffusion zones of growing crystals. As a result, the correct functional form of the experimental time-dependence of the number of crystals has never been accurately determined.

In the present paper we report a new development in this field of research; namely, an on-line computer method of deconvoluting N(t) curves from potentiostatic current-time i(t) transients, using an apparatus which avoids the need for microscopy, and which guarantees that nucleation sites are not occluded by the diffusion zones of growing crystals. The basic idea is to deposit crystals on an assembly of microelectrodes which are so far apart that the crystals cannot interact in any way. Besides removing the problem of the occlusion of nucleation sites, this circumvents three serious difficulties that plagued the older method. Firstly, it is a "single shot" method and so does not require a series of separate measurements of different durations to re-construct the N(t) curve point-by-point; secondly, it removes the tedium of counting crystals one-at-a-time under a microscope; and thirdly it provides access to a much wider range of N(t) values than was possible before.

EXPERIMENTAL

Two microelectrode assemblies were constructed; one consisting of 2500 carbon fibre microdisks (each of ~8 μm diameter) and the other of 40,000 carbon fibre microdisks (each of ~5 μm diameter). Both were potted in a matrix of non-conducting epoxy resin. A micrograph of part of the first one is shown in Fig. 1.

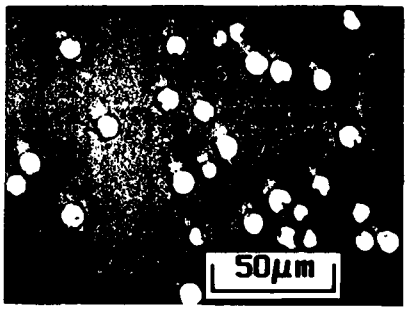


Fig. 1. Micrograph of a microelectrode assembly. Each microelectrode consists of the disk-shaped end face of a carbon fibre; the matrix is a non-conducting epoxy resin.

RESULTS

Some typical data obtained using the microelectrode assembly technique are shown in Figs. 2-4. The results have profound implications for the modeling of electroplating phenomena; the non-steady state of nucleation must be considered, and a spread of activities of active sites on electrode surfaces must also be taken into account.

REFERENCES

1. R.L. Deutscher and S. Fletcher, J. Electroanal. Chem. 239 (1988) 17-54.

2. R.L. Deutscher and S. Fletcher, in "Electrochemistry: Current and Potential Applications", proceedings of the 7th Australian Electrochemistry Conference (7AEC), Sydney, 15-19 Feb. 1988 (RACI, Melbourne, 1988) pp. 308-311.

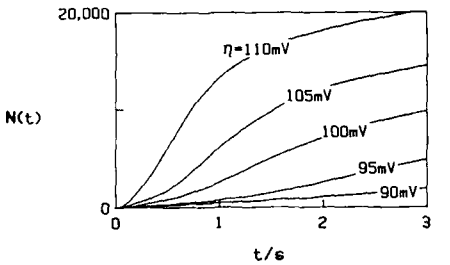


Fig. 2. The number of crystals as a function of time, for lead crystals deposited on carbon from an aqueous solution of 2 x 10^{-3}M $Pb(Ac)_2$ in a mixture of 0.1M NaAc and 0.1M HAc. Note that the results do not obey the Bewick-Fleischmann-Thirsk 'progressive' nucleation law.

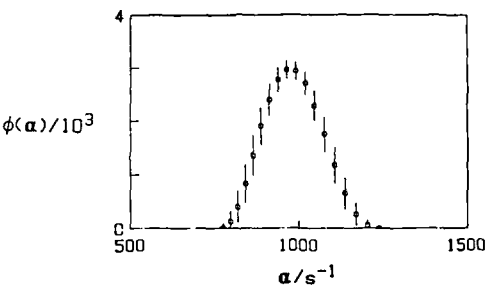


Fig. 3. The discovery of nucleation rate dispersion. This plot shows the spread of nucleation rates (α) on one electrode, for similar deposition conditions to those shown in Fig. 2, except the concentration of $Pb(Ac)_2$ was 10^{-2}M. Empirically it is found that the size of the spread depends on the nature of the electrode preparation procedure.

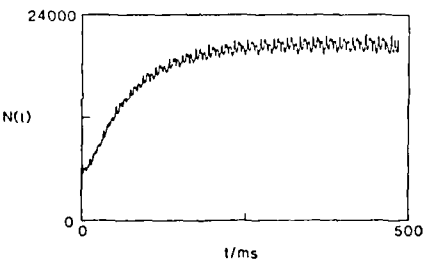


Fig. 4. Experimental observation of a "nucleation after-effect" caused by the continuation of nucleation after the completion of a brief pulse of potential. Nucleation continues after a pulse is switched off because of the relaxation of the cluster-size distribution of sub-critical clusters: direct evidence for the validity of Volmer's concept of unstable clusters acting as "seeds" for the nucleation process. System: as in Fig. 2. Pulse: -150 mV for 5 ms. Growth potential: -40 mV.

Abstract No. 335

HYDROGEN UPTAKE DURING CADMIUM ELECTROPLATING

M. M. Makhlouf, R. R. Biederman and R. D.Sisson, Jr.

Worcester Polytechnic Institute
Mechanical Engineering
100 Institute Road
Worcester, MA 01609

It is a common practice to electrodeposit cadmium on high strength low alloy steels as a protective measure against corosive environments [1]. Unfortunately, most of the commercially available cadmium electroplating baths codeposit a significant amount of hydrogen during the plating process [2]. This hydrogen diffuses to areas of high triaxial stress, enbrittles the steel and eventually leads to catastrophic failure of parts during service [3].

The surface finish and temper condition of the steel, as well as the bath composition and electroplating process parameters are important factors in determining the amount of hydrogen uptaken by the steel. These factors are examined both experimentally and analytically and their effect on the flux of hydrogen is explained.

A Devanathan cell [4] was used to measure the flux of hydrogen uptaken by 4340 steel during electroplating from cadmium baths. The steel samples were quenched and tempered to three different hardness levels and their surfaces were modified by silicon carbide polishing paper to produce two different surface finishes. The electroplating process parameters were varied and their effect on the hydrogen flux was measured and explained in terms of the deposit microstructure and the well known barrier mechanism [5].

A computer program based on the Caskey and Pillinger solution [6] of the McNabb and Foster equations [7] was developed and used to explain the experimental data in terms of hydrogen entry, trapping and permeation into the steel. The original model by McNabb and Foster was modified to account for limited mass transfer between the steel's surface and the electroplating bath [8]. Comparison of the experimental data with computer predictions was found to be very difficult due mainly to the large number of trapping coefficients involved.

REFERENCES:

1. F. A. Lowenheim: ASTM STP785, American Society for Testing and Materials, Phila., PA, 1982.
2. J. B. Boodey and V. S. Agarwala: Corrosion 87, Paper No. 224.
3. J. P. Hirth: Trans. AIME, 1980, vol. 11A, pp. 861.
4. M. Devanathan and Z. Stachurski: Proc. Roy. Soc., 1962, vol. A270, pp. 90.
5. M. Zamanzadeh, et. al.: J. Electrochem. Soc.: Electrochemical Science and Technology 1982, vol. 129, NO. 2, pp. 284.
6. G. R. Caskey and W. L. Pillinger: Met. Trans. A, 1975, vol. 65, pp. 467.
7. A. McNabb and P. K. Foster: Trans. TMS-AIME, 1963, vol. 227, pp. 618.
8. M. M. Makhlouf and R. D. Sisson, Jr.: Proc. of the Third International Conference on Environmental Degradation of Engineering Materials, 1987, pp. 665.

Abstract No. 336

CRYSTALLOGRAPHY OF PLATING FILM AND AMORPHOUS PLATING

Tohru Watanabe

Department of Industrial Chemistry
Faculty of Technology
Tokyo Metropolitan University

2-1-1 Fukazawa, Setagaya-ku, Tokyo, Japan 158

1. Introduction

Plating technology is said to have been bipolarized recently. The one is a surface finishing technology aiming anticorrosion, anti-abrasion and glazed-finish etc., and the other is to manufacture a functional material using the plating technology. The latter has been a positive manufacturing technology of functional material recently, rather than a plating technology, due to the rapid development of the delicate and highly efficient functionarization, which could have been said as one of high technologies. From such view point, the plating technology seems to have been in a revolutionary stage. Under such circumstance, the plating technology should take a step toward the positive manufacturing technology of functional material, apart from the traditional/old concept of passive image. As the first step toward a positive way, although it seems a daring way of thinking, it is recommended to aim an image-up of the technology by taking a new naming (such as a "fine plating"), independently to the traditional ward of "plating technology". The other view is to take a method of study to control the crystalline structure so that the aimed physical properties can be obtained by observing in detail the plating film metallographically and crystallographically.

2. Crystallographical study of plating technologies

"The physical property of the plating film is directly resulted from its crystalline structure". The plating film should never be of a simple thin-coating, but has a significant thickness micrographically, among which we can observe an extremely interesting fine structure. This structure changes sensitively by even minor change of the plating conditions. Such sensitivity shall be kept strictly in mind. If the structure changes, it is quite natural that the physical properties change. As an example, in the Photograph 1, for the case of a crystalline plating film growth, the structures of the surface and the fracture section can be seen. At the view of the fracture section, a growth of column state crystalline is observed, but neighbouring to the substrate, the crystalline has been in a fine particle state, which is shown simulately in Fig. 1. For the case that a plating film takes an amorphous structure, the conditions of the surface and the fracture section can be seen in Photograph 2. The structure differs so much from Photograph 1. Such differences of the structure result naturally in those of the physical properties. The study of plating technologies shall be proceeded considering what kind of structures are necessary for good plating films and what kind of conditions are necessary for platings to hold such favourable structures.

3. Amorphous plating

Generally it is said that the amorphous alloys have various peculiar properties which are called "Dream Materials" materiallographically. Such amorphous alloys can be easily obtained, too, by plating methods. As chemical agents of glazing, stress-relieving and anti-cracking for the plating work, P,S,B and As etc. are often added into the plating films. These metalloid contribute to make finer the crystalline at all. More the quantity of these agents, the plating film structures result ultimately in the amorphous state. The reason why the most popular Ni-P plating has the favourable properties as well as the high corrosion-resistance is that this plating film has become an amorphous structure. As mentioned above, amorphous alloys have various interesting physical properties. The biggest structural features of this amorphous state are to have been uniform in chemical compositions and structure as shown in Photograph 2. These features have been the origin of various interesting properties. Even by the plating method, as indicated on Table 1, various amorphous alloys are obtained and by the study of this author, it has been cleared up so far that each amorphous alloy has respectively different/peculiar physical properties. The amorphous alloy manufacturing method by this plating technology has more merits than the other methods. I think that the studies of amorphous alloy manufacturing methods and of the applications are essential and have to be further developed toward the future realization.

1)T.Watanabe:"Crystallographic Relationship between Plating Film and Substrate", J. Metal Finishing Soc. of Japan, 37 (1986)440.
2)T.Watanabe & Y.Tanabe:"Formation of Amorphous by Plating Techniques", J. Metal Finishing Soc. of Japan, 32 (1981)600.
3)T.Watanabe:"Amorphous Plating", J. Metal Finishing Soc. of Japan, 37 (1987)210.
4)T.Watanabe:"High Corrosion Resistant Amorphous Plating", J. Institute of Iron and Steel of Japan, 73 (1987)2180.
5)T.Watanabe & N.Usuzaka:"Amorphous Plating —Preparations of Co-Gd Amorphous Alloy Film by the Electroplating Method—", Proc. American Electroplaters and Surface Finishing Soc., Inc. 73erd, Annual Technical Conference-Chicago, General Interest II,(1987)F5.

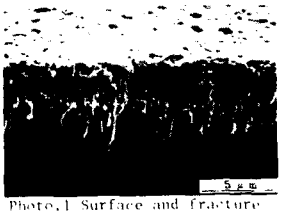


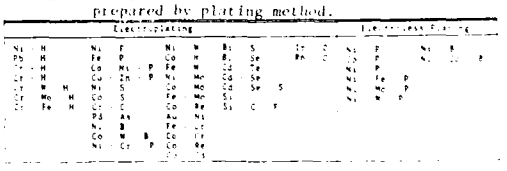
Photo.1 Surface and fracture section of crystalline Ni electroplating film.

Fig.1 Schematic diagram of Photo.1.



Photo.2 Surface and fracture section of Co-Mo amorphous alloy film prepared by electroplating method.

Fig. 1 Amorphous alloys and amorphous-like alloys prepared by plating method.



Abstract No. 337

THE EFFECT OF HYDROGEN AND DEPOSITION CONDITIONS ON THE DUCTILITY OF ELECTRODEPOSITED Ni–P AMORPHOUS ALLOYS

Robert L. Zeller III and Uziel Landau
Department of Chemical Engineering
Case Western Reserve University
Cleveland, Ohio 44106

Amorphous alloys are characterized by unique and highly attractive mechanical, chemical, and magnetic properties. Electrodeposition potentially offers an easy one-step technique to form monolithic parts out of amorphous alloys with appreciable thickness and controlled shape. Electrodeposited amorphous alloys are extremely brittle, as compared to the analogous material prepared by melt-quenching, which results in severe restrictions on their practical application. Suzuki et al. (1) found that the atomic and electronic structure of electrodeposited and melt-quenched Ni–P amorphous alloys were essentially the same, yet the electrodeposited alloy was significantly less ductile than the melt-quenched alloy. They hypothesized that hydrogen may have embrittled the electrodeposited alloy. Other researchers have found hydrogen embrittlement in iron-based amorphous alloys (e.g., 2, 3). The purpose of this work is to elucidate the causes for brittleness in electrodeposited Ni–P amorphous alloys, determine the effect of diffusible hydrogen, and explore the effects of deposition conditions on the ductility of Ni–P amorphous alloys.

Low temperature vacuum anneal (LTVA) experiments at 102 °C were conducted following the technique of Okinaka and Straschil (4). The hydrogen content was analyzed using a LECO RH-2 Hydrogen Determinator. Differential Scanning Calorimetry (DSC) curves exhibited identical transition temperatures and energies throughout the annealing process, indicating that no microstructural changes were occurring. The alloys were deposited using the bath composition and operating conditions presented in Table 1. The electrodeposition technique is detailed elsewhere (5). The ductility was measured in two ways. The first was quantitative, using a mechanical bulge tester, following Nakahara, et al. (6), where results are expressed in percentage elongation at fracture. The second was semi-quantitative, in which the sample was bent over a very small radius and the angle at fracture was measured.

The results of the LTVA experiment are presented in Figure 1. As shown, the hydrogen content decreases with increased annealing time and approaches zero at long times, indicating that all the hydrogen is diffusible. This data can be fit to a model for estimating the hydrogen diffusion coefficient, D, through the electrodeposit. The system can be described as a solid bounded by two parallel planes, in which the following transport equation holds:

$$\frac{\partial C}{\partial t} = D\frac{\partial^2 C}{\partial x^2} \qquad [1]$$

with the boundary conditions:

1. At $x = \pm\ell$, $C = 0$
2. At $t = 0$, $C = C_i$
3. At $x = 0$, $\frac{\partial C}{\partial x} = 0$

Solving equation [1] subject to the boundary conditions, and integrating from $-\ell$ to ℓ, we find:

$$\frac{\bar{C}}{2\ell C_i} = \frac{8}{\pi^2}\sum_{n=0}^{\infty}\frac{1}{(2n+1)^2}\exp\left[-\frac{D(2n+1)^2\pi^2 t}{4\ell^2}\right] \qquad [2]$$

where $\bar{C}$ is the total hydrogen content in the electrodeposit.

The best fit diffusion coefficient for the data presented in Figure 1 is 4.6 (±1.3) x 10^{-10} cm²/s. This compares well with values presented in the literature for hydrogen diffusion through P– ion implanted nickel, ($D \simeq 2 \times 10^{-10}$ to 8×10^{-10} cm²/s, (7)), but is one order of magnitude larger than the diffusion coefficient reported for Allied Metglas MBF-60 melt-quenched $Ni_{81}P_{19}$ amorphous alloy, ($D = 2.2 \times 10^{-11}$ cm²/s, (2)).

The ductility of the electrodeposits, measured by two different techniques, as a function of annealing time is presented in Figure 2. As shown, the effect of annealing time (or hydrogen content) has very little effect on the ductility. The results are compared to the ductility of the MBF-60, which exhibits a much greater ductility. These results indicate that diffusible hydrogen has a negligible effect on the ductility of Ni–P amorphous alloys.

To further support this observation, ductility and tensile tests were performed on hydrogen charged and as received MBF-60 samples. The results of the ductility and tensile tests are shown in Table 2 and are in agreement with those reported by Chen, et al.[8] for melt-quenched $Ni_{80}P_{20}$, ($E = 0.103 \times 10^6$ MPa). These results also indicate that diffusible hydrogen has little effect on the ductility of Ni–P amorphous alloys, although a 25 percent reduction in the ultimate tensile strength was observed.

The effect of deposit thickness on its ductility was investigated using the bath composition and operating conditions presented in Table 1, except that the pH was 1.09. The ductility versus deposit thickness is shown in Figure 3. The data illustrates that ductility slightly decreases with increasing thickness, opposite to the trend reported by Okinaka and Straschil [4] for electroless copper. This may indicate that defects in the deposit microstructure, or the microstructure itself, may cause the brittleness observed in electrodeposited Ni–P amorphous alloys.

A comprehensive study was conducted to explore the effects of the plating process parameters on the ductility of the electrodeposited Ni–P amorphous alloys. The microstructure of these alloys were quantified using SEM/EDS, DSC, x-ray diffraction, and Transmission Electron Microscopy. Results indicate that the microstructure plays the dominate role in determining the ductility of electrodeposited Ni–P amorphous alloys.

Acknowledgement

This work was conducted with the support of the Aluminum Company of America (Alcoa). Helpful discussions with Alfred F. LaCamera are acknowledged.

References

(1) Suzuki, K., F. Itoh, T. Fukunaga, and T. Honda, *Rapidly Quenched Metals, Proc. Int. Conf., 3rd*, 2, 410 (1978).

(2) Latanision, R.M., C.R. Compeau, and M. Kurkela, *Hydrogen Embrittlement and Stress Corrosion Cracking*, R. Gibala and R.F. Heheman, Eds., ASM, Metals Park, Ohio, 297 (1984).

(3) Kawashima, A., K. Hashimoto, and T. Masumoto, *Corros. Sci.*, 16, 935 (1976).

(4) Okinaka, Y. and H.K. Straschil, *J. Electrochem. Soc.*, 133, 2608 (1986).

(5) Zeller III, R.L. and U. Landau, *Corrosion, Electrochemistry, and Catalysis of Metallic Glasses*, R.B. Diegle and K. Hashimoto, Eds., The Electrochemical Society, 88-1, 322 (1988).

(6) Nakahara, S., Y. Okinaka, and D.R. Turner, *J. Test. Eval.*, 5, 178 (1977).

(7) Nishimura, R., R.M. Latanision, and G.K. Hubler, *Corrosion, Electrochemistry, and Catalysis of Metallic Glasses*, R.B. Diegle and K. Hashimoto, Eds., The Electrochemical Society, 88-1, 277 (1988)

(8) Chen, H.S., J.T. Krause, and E. Coleman, *J. Non-Crystalline Solids*, 18, 157 (1975).

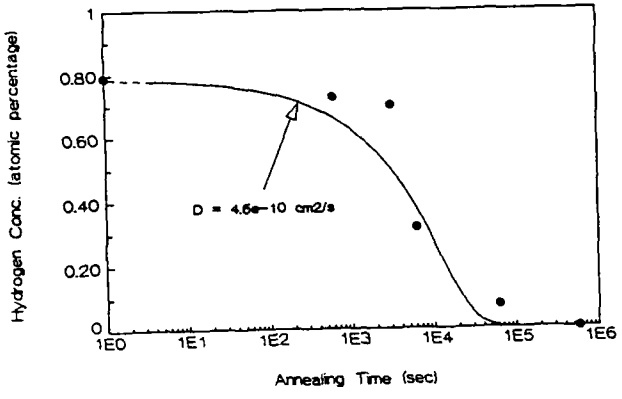


Figure 1: Atomic percentage of hydrogen versus annealing time for electrodeposited Ni–P amorphous alloy with best fit theoretical curve.

Table 1: Ni–P Bath Composition, Operating Conditions and Results.

Bath Composition

$NiSO_4 \cdot 6H_2O$	150.0 g/l
$NiCl_2 \cdot 6H_2O$	45.0 g/l
H_3PO_3	40.0 g/l
H_3PO_4	40.0 ml/l
pH adjusted to	1.16

Operating Conditions

Temperature	85°C
Current Density	0.250 mA/cm²
Time of Plating	45 minutes
RDE rotation rate	2000 rpm

Results (Based on 7 experiments)

Overpotential	-0.683 ± 0.003 V vs SCE
Deposit Composition	24.0 ± 0.3 atomic percent P
Thickness	72 ± 3 μm

Table 2: Ductility and Tensile Test Results For Allied Metglas MBF–60.

	As Received	Hydrogen Charged
Hydrogen content (atomic percentage)	0.085%	1.93%
Ductility Tester (percentage elongation)	1.0%	1.0%
Bend Test	180°	180°
Ultimate Tensile Strength UTS, (MPa)	1221	899
Modulus Of Elasticity E, (MPa x 10^{-6})	0.132	0.115
Tensile Tester (percentage elongation)	1.00%	0.80%

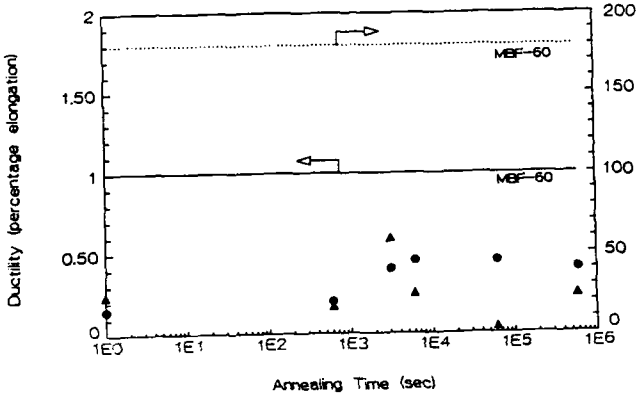


Figure 2: Ductility and bend test versus annealing time for electrodeposited Ni–P amorphous alloy, compared with melt–quenched Allied Metglas MBF–60.
▲ Ductility; ● Bend Test.

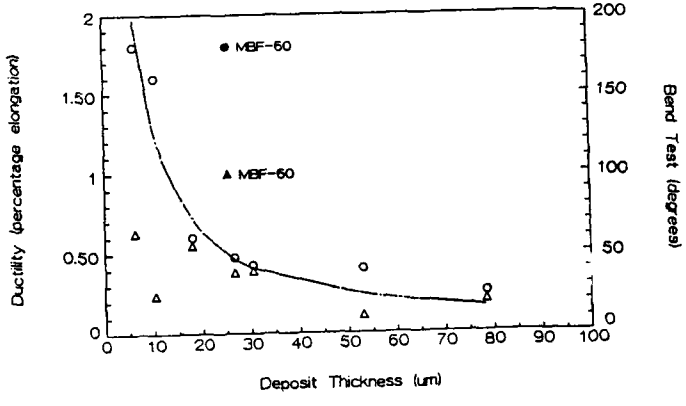


Figure 3: Ductilty and bend test versus thickness for electrodeposited Ni–P amorphous alloy, compared with melt–quenched Allied Metglas MBF–60.
▲ Ductility, MBF–60; ● Bend Test, MBF–60; △ Ductility, electrodeposit; ○ Bend Test, electrodeposit; —·— Best Fit line for Bend Test data.

Abstract No. 338

EFFECTS OF HEAT TREATMENT ON THE STRUCTURE AND PROPERTIES OF ELECTRODEPOSITED AMORPHOUS IRON-NICKEL-PHOSPHORUS ALLOYS

K. Sridharan and K. Sheppard
Department of Materials and Metallurgical Engineering
Stevens Institute of Technology
Hoboken, NJ 07030

In recent years there has been considerable research interest in metallic glasses, i.e., metallic alloys exhibiting a metastable short-range atomic ordering, but not possessing the long-range crystalline ordering normally associated with metals. Metallic glasses have proven to have unusual or superior properties compared to their crystalline counterparts. Most of the research focus has been on metallic glasses produced by rapid solidification. However, electrodeposition offers the possibility of a low cost, low temperature route to producing amorphous metallic alloy coatings or electroformed complex shapes not achievable by rapid solidification.

Autocatalytically deposited nickel-phosphorus (electroless nickel) was in fact the first metallic glass discovered and its structure and properties have been extensively studied [1]. This material can also be produced by electrodeposition with similar properties [2]. Recently the electrodeposition of iron-nickel-phosphorus alloys was reported that were amorphous over a wider range of composition [3]. In this paper we report on the crystallization behavior on heating of these metastable alloys.

The Fe-Ni-P alloys were electrodeposited from a sulfate bath containing sodium hypophosphite as the source of phosphorus. Deposition was onto anodized titanium to allow easy stripping for characterization. The effect of heating on the crystallization behavior was studied for various amorphous alloy compositions by differential scanning calorimetry. By using different heating rates it was possible to obtain an activation energy for crystallization that suggested that nickel-rich alloy crystallization was dominated by nickel self-diffusion. For the iron-rich alloys no simple diffusion process matched the activation energy data. Isothermal heat treatments were also conducted at various temperatures and times and the crystallization kinetics evaluated from X-ray and transmission electron microscopy data. Properties, in particular microhardness, were measured for the amorphous and crystallized materials. Crystallization to the thermodynamically stable phase $(NiFe)_3P$ resulted in microhardness increases from about 700 VHN to 1050 VHN. These values both before and after annealing are in the same range as rapidly solidified metallic glass of similar composition.

References

[1] "The Properties of Electrodeposited Metals and Alloys," W.H. Safranek, Ed., American Electroplaters and Surface Finishers Society, Orlando, Florida 1986, pp. 497-529.

[2] D.S. Lashmore and J.F. Weinroth, Plating and Surface Finishing, 69, 72 (1982).

[3] K. Sridharan and K. Sheppard, Extended Abstract 502, Vol. 86-2 (1986), The Electrochemical Society.

Abstract No. 339

STRUCTURE AND ELECTRICAL RESISTIVITY OF ELECTROLESS NICKEL THIN FILMS

M.Paunovic,M.Madden,C.H.Ting, P.L.Pai,and T.Ton
Components Research
Intel Corporation, SC3-06
2250 Mission College Blvd.
Santa Clara, CA 95052-8125

One new area of application of selective electroless metal deposition is deposition for fabrication of microelectronic circuits (1-3). In the very large-scale integration (VLSI) of microelectronic circuits elements of the conductive pattern are in micrometer dimensions. These dimensions require that the deposited metal has fine structute and very smooth surface topography. Dimensions of the growth features, in the plane parallel and in the plane normal to the substrate, must be in the sub-micrometer range. This is the first criterion for applicability of electroless metal deposition in integrated circuit (IC) fabrication. The second criterion is electrical resistivity. It is known that films of one and the same metal, when prepared by different techniques, may have resistivities varying by several hundred percent (4).

There is a very limited number of published studies on structure of electroless nickel (6-8). According to the published studies Ni deposits have lamellar structure, or lamellar structure superimposed upon a columnar structure. Average thickness is of the lamellae is between 1 and 2 μm (5).Lamellae are composed of fine crystallites with crystallite diamter about 20 Å (6). There is no extensive study on relationship between structure, solution composition, kinetic parameters, and electrical properties of electroless nickel. The purpose of this study is to determine this relationship.

Both, structure and electrical properties of the electroles deposit, depend on composition of the electroless solution. In order to understand the above mentioned relationship two types of solutions were used. In the first type the reducing agent was sodium hypophosphite and in the second dimethylamine borane (DMAB). Solutions without and with additives were used. The effect of following additives was studied: $(NH_4)_2SO_4$, $K_3[Co(CN)_6]$,MBT (sodium 2-mercaptobenzothiazole), and Triton X-100. Three classes of substrates were used: (i) Al (1 μm thick) sputtered on SiO_2 grown on Si wafer, (ii) Ti (1μm thick) on Si wafer, and (iii) glass (microscope slide). The sequence of events which occur as the Ni film thickness is increased up to 2 μm was followed.

Structure of electroless Ni parallel and perpendicular to the substrate was examined by transmission electron microscopy (TEM). Samples parallel to the substrate were thinned by ion milling. Samples embedded in an epoxy resin were thin-sectionned perpendicular to the substrate with a diamond knife using ultramicrotome. Surface morphology (microtopography) was examined by scanning electron microscopy (SEM), TEM replica technique, and stylus measurement system. The electrical resistivity of thin films was measured using either a two-point resistivity probe or a four-point resistivity probe (4).

REFERENCES

1. C.H.Ting,M.Paunovic,and G.Chiu, Abstract 239, The Electrochemical Society Extended Abstracts, Philadelphia, PA,May 1987.
2. C.H.Ting,in "Electroless Deposition of Metals and Alloys", M.Paunovic and I.Ohno, Editors,p.223,The Electrochemical Society Softbound Proceedings Series,Pennington,NJ (1988).
3. Y.Harada,K.Fushimi,S.Madokoro,H.Sawai, and S.Ushio,J.Electrochem.Soc.,133,2428(1986).
4. A.Gangulee,A.M.Tuxford,L.T.Romankiw,and *A.F.Mayadas,in "Properties of* Electrodeposits,Their Measurements and Significance",R.Sard,H.Leidheiser,Jr.,and F.Ogburn,Editors,p.374,The Electrochemical Society Softbound Proceedings Series,Princeton,NJ (1975).
5. A.Brenner,Metal Finish.,52,68(1954).
6. G.O.Mallory,Trans.Inst.Metal Finish.,56,81(1978).
7. P.Cavallotti and G.Salvago,Abstract 435,p.656,The Electrochemical Society Extended Abstracts,Fall Meeting,San Diego,California,Oct.19-24,1986.
8. T.Osaka,H.Nagata,E.Nakajima,and I.Koiwa,J.Electrochem.Soc. 133,2345(1986).

Abstract No. 340

CORRELATION OF PERPENDICULAR MAGNETIC ANISOTROPY AND MICROSTRUCTURE OF ELECTROLESS PLATED CoNiReP THIN FILMS

Tetsuya Osaka and Takayuki Homma

Department of Applied Chemistry
Waseda University
Okubo, Shinjuku-ku, Tokyo 160, Japan

Perpendicular magnetic recording method is suitable for a high density data storage. The authors have attempted to prepare perpendicular magnetic recording media by an electroless plating method and have developed electroless CoNiReP films with excellent characteristics.[1-4] The magnetic properties of these films are able to be controlled by the plating bath factors,[2] underlayers,[3] catalyzing process[4] and so on. In those papers, relationships between the magnetic properties and the microstructure were studied. However, the origin of the anisotropy has not been discussed yet. Thus magnetic and structural properties of the electroless CoNiReP films with various compositions were investigated to clarify the origin of the perpendicular magnetic anisotropy.

The CoNiReP films were electroless-plated on Cu substrate. The plating bath composition is shown in Table 1. The film composition was varied by changing the $CoSO_4$ concentration in the bath and was determined by an inductively coupled argon plasma emission spectrophotometer (ICP). Magnetic properties were measured with a vibrating sample magnetometer (VSM) and a torque magnetometer (TM). Structural properties were investigated with a scanning electron microscopy (SEM) and an X-ray diffractometer (XRD) with Fe target.

Figure 1 shows the effect of $CoSO_4$ concentration on the film composition. The cobalt content in deposits increases with an increase in $CoSO_4$ concentration in the bath. On the contrary, the contents of nickel and phosphorus decrease with an increase in $CoSO_4$ concentration. The rhenium content slightly decreases with an increase in $CoSO_4$ concentration. From these results, it is clear that film composition of the electroless CoNiReP films is able to be varied widely by changing the $CoSO_4$ concentration in the bath.

Figure 2 shows the effect of Co content in deposits on the values of saturation magnetization, Ms, and uniaxial anisotropy energy, Ku. In Fig. 2 a, Ms value increases with an increase in Co content in deposits. On the other hand, Ku value, shown in Fig. 2 b, increases upon rising in Co content and shows the maximum value at ca. 30 at.% of Co content, while the value decreases sharply over ca. 30 at.%. Perpendicular coercivity, Hc(⊥), and perpendicular anisotropy field, Hk values showed similar behavior as that of Ku value.

Figure 3 shows the MH-loops, a, cross-sectional views, b and XRD patterns, c for the typical four samples, A, B, C and D, with various compositions. Their compositions are shown in Fig. 1. As shown in Fig. 3 b, the cross-sectional views of the films change from fine grainy condition to clear columnar structure with a rise in Co content in deposits. The cross-sectional view of sample B, which shows the highest Ku value, does not show a clear columnar structure. From the results of XRD analysis, the crystallinity of hcp Co raised upon increasing in Co content up to ca. 40 at.%. However, the Ku value decreased abruptly over ca. 40 at.%. From the results shown in Figs. 3 b and c, it is clear that there are no relationships between the columnar structure in the cross-sectional morphorogy and the crystallographic properties, such as c-axis orientation and/or crystallinity of hcp Co.

Among these four samples, the highest crystallinity is observed for sample C. However, the Ku value for sample C becomes negative (see Fig. 2 b). On the contrary, sample B with lower crystallinity shows the highest positive Ku value. The high Ms value of the former film (see Fig. 2 a) is considered to enhance the demagnetizing field, and thus the overall anisotropy becomes directed to in-plane direction.

It is concluded that the perpendicular magnetic anisotropy of electroless plated CoNiReP films is mainly caused by the magnetocrystalline anisotropy of Co hcp crystal and that the smaller demagnetization due to the smaller Ms value enhances the anisotropy, leading the anisotropy to perpendicular direction.

References:

1) I.Koiwa, H.Matsubara, T.Osaka, Y.Yamazaki and T.Namikawa, J. Electrochem. Soc., 133, 685 (1986).
2) T.Osaka, I.Koiwa, M.Toda, T.Sakuma, Y.Yamazaki, T.Namikawa and F.Goto, IEEE Trans. Magn., MAG-22, 1149 (1986).
3) H.Matsubara, M.Toda, T.Sakuma, T.Homma, T.Osaka, Y.Yamazaki and T.Namikawa, Proc. of 172nd Meeting of the Electrochem. Soc. (1988) in press.
4) T.Osaka, H.Matsubara, T.Sakuma, T.Homma, S.Yokoyama, Y.Yamazaki and T.Namikawa, J. Mag. Soc. Jpn. (1988) in press.

Table 1 Basic bath composition for CoNiReP thin films.

Chemicals	Concentration
$NaH_2PO_2 \cdot H_2O$	0.20 mol dm^{-3}
$(NH_4)_2SO_4$	0.50
$CH_3(COONa) \cdot H_2O$	0.75
$C_3H_5(OH)_2(COONa) \cdot 2H_2O$	0.20
$CH(OH)(COOH)_2$	0.05
$CoSO_4 \cdot 7H_2O$	0.00 ~ 0.20
$NiSO_4 \cdot 6H_2O$	0.08
NH_4ReO_4	0.003
Bath temperature	80°C
pH adjusted by NH_4OH	8.7

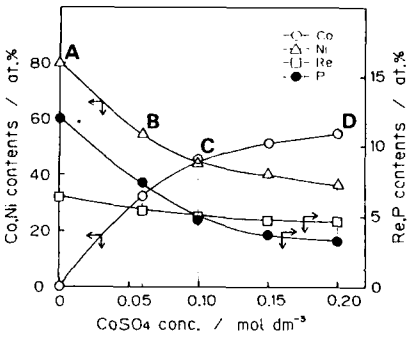


Fig. 1 Effect of $CoSO_4$ concentration on the film composition.

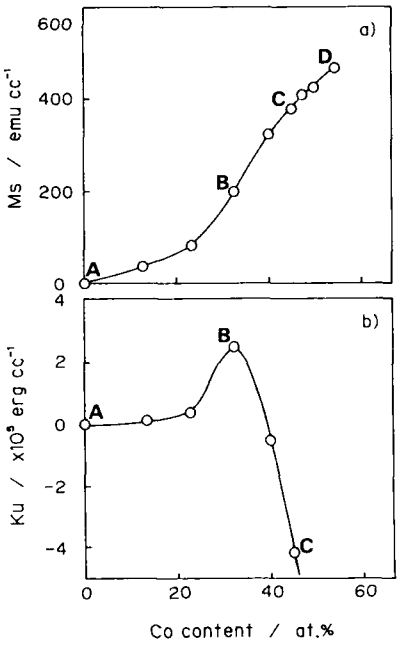


Fig. 2 Effect of the cobalt content on Ms, a and Ku, b values of the films.

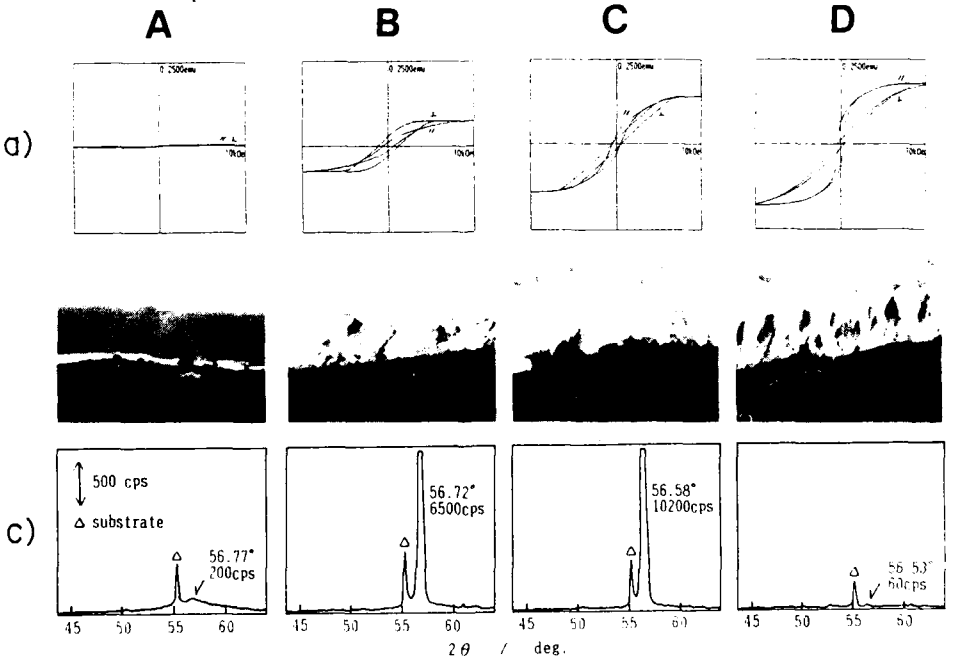


Fig. 3 MH-loops a, Cross-sectional views b, and XRD patterns c for the 2μm thick CoNiReP films.

Abstract No. 341

ELECTRODEPOSITION OF NI-CO ALLOYS

HUA-SOU TONG

ZENITH ELECTRONICS CORPORATION

MELROSE PARK, IL 60160

Electrodeposition technique has been widely used in consumer electronics industries becuase its relatively easy processing and cost effectiveness. In this presentation, electrodeposition of Ni-Co and Ni-Co-Mn alloys was investigated. In an effort to develop a new "stamper" for Videodisc (trade name of RCA) disc pressing, electrodeposition of Ni-Co alloys from a sulfamate bath was explored to develop a stamp with superior scratch resistance. The effect of the solution Ni/Co ratios and the current densities applied on the composition, hardness, and microstructure of the deposits was studied. Results indicated that, while increasing the Co content increases the hardness of the Ni-Co deposit in general, a drastic increase in hardness is evident with the deposit containing higher than 5% of Co. Changes in microstructure from a columar to a laminar structure was also observed correspondingly.

The presence of internal stress in the deposits during the Ni-Co electrodeposition process was detected. An organic type stress reliever was added to minimize this effect. However, the deposit exhibited thermal embrittlement behavior after being aged at 500°C for 1/2 hr.. This behavior was found to be attributed to the much faster diffusion rate of sulfur in the deposits at an elevated temperature, and subsequent formation of Ni_3S_2 at the grain boundaries of Ni-Co deposits.

To overcome this embrittlement behavior, a third element, Mn, was introduced to the Ni-Co deposits. With approximately 15 g/l Mn added in the electrolyte, Ni-Co-Mn deposits showed a completely ductile fracture characteristics after being aging at 500°C for 1/2 hr.

Abstract No. 342

ELECTRODEPOSITION AND CHARACTERIZATION OF MULTILAYERED Cu-Ni ULTRASTRUCTURES

S. Menezes and D. Anderson

Rockwell International Science Center
Thousand Oaks, CA 91360

Unusual and enhanced material properties can be obtained by artificially tailoring materials at atomic or molecular levels with periodic one-dimensional composition modulation (1,2). Composition modulated materials or multilayered ultrastructures (MU) have been artificially fabricated by vapor, sputter and electrodeposition methods. Tensile strength enhancements have been observed for vapor or electrodeposited bimetallic MU, as the layer thickness was decreased to ~ 0.1 μm (3,4). Anomalous effects, which include a maximum at a wavelength of ~ 20Å for several mechanical properties of vapor deposited MU, were seen (1,2,5). Since electrodeposition allows fabrication of relatively thick foils with discrete, epitaxial layers, a previously reported method of MU deposition from a single electrolyte (4) has been modified and extended to fabricate MU with layers of the order of a few angstroms. For electrodeposition of two or more metals from different, incompatible baths a new method, based on a thin-layer flow cell, has been developed.

Cu-Ni MU foils, with total thicknesses between 25-50 μm and a configuration of 10% Cu-90% Ni, were electrodeposited from a single electrolyte, containing 72-80 g/l Ni, 37-40 g/l boric acid, 0.15 g/l SNAP (sodium dodecyl sulfate) and 4-13 mM Cu. The method involves alternate deposition of Cu and Ni by synchronous modulation of solution mass transport rate and the deposition current (or potential), at an Inconel rotating cylinder cathode from a common electrolyte. The electrode rotation rate, current density, periodicity and atomic percent of the two metals were varied with computer control. The catholyte was separated from the anolyte by a fritted, concentric inner compartment. A saturated calomel electrode was used as a reference. The plating bath was maintained at 50°C.

Mechanical properties of MU are extremely structure sensitive, particularly when the layer thickness is reduced to the order of a few angstroms. In order to obtain smooth deposits with uniform, ultrathin layers and reduced lattice defects and dislocations, the effects of plating parameters on structural and mechanical properties were investigated. The deposit properties were considerably improved by eliminating Cu from the basal layer, limiting the Cu concentration to 7-8 mM during MU deposition and introducing a delay time between deposition pulses.

Tensile properties were measured with a specially designed sample holder attached to an Instron machine. The specimens were pulled to failure. The data are plotted in Fig. 1 along with that obtained for pure Cu and Ni foils plated without pulsing under the same conditions. The tensile strength exhibits a maximum at a nominal Cu layer thickness of 20Å (180Å-thick Ni layer). The maximum strength is 3 and 4.5 times greater than that for homogeneous Ni and Cu foils, respectively, deposited continuously without pulsing. This curve is in excellent agreement with previous results on electrodeposited 10% Cu-90% Ni foils with thicker layers (> 0.1 μm Cu, > 0.9 μm Ni) (4), thus extending the results into the angstrom regime.

The MU foils were characterized with SEM, TEM and x-ray diffraction. Cu and Ni layer formation was discernible with SEM and TEM for relatively thick layered foils (> 100Å). These methods do not allow satisfactory resolution of few angstrom thick layers. X-ray diffraction was used to examine ultrathin-layered foils. The diffraction peaks evidence a strong (100) texture and coherence along a direction normal to the deposition front. Satellite peaks flanking the (200) x-ray diffraction peaks were seen for a 9Å Cu-80Å Ni multilayered foil. The satellite peaks provide direct evidence for the presence of a superlattice within the layered material. The multilayers were also found to develop increased texture as they are deposited. The outer half of the electrodeposited region was totally textured with [100] direction normal to the foil plane. The texture was much weaker for the 1 μm-thick-Ni basal layer deposited on a polycrystalline Inconel substrate.

Criteria for deposition of bimetallic MU from a single electrolyte include a mutually soluble electrolyte and a significant difference in the deposition and dissolution potentials. A method is thus limited to a few bimetallic pairs. The thin layer cell was designed to circumvent these limitations. The cell permits electrodeposition of two or more metals from different electrolyte baths. It provides an ultrathin (< 100 μm) liquid layer for deposition and a pumping/switching system for delivery of solution to the cell. This cell is specifically tailored to the fabrication of discrete ultrathin layered structures since: (1) it allows precise control over the number of atoms deposited; (2) it eliminates complicated mass transport effects by providing immediate access to the electrode surface; (3) it assures layer purity and uniform nucleation (current distribution); and (4) it may be used with imcompatible bimetallic pairs. Preliminary results obtained with this cell indicate formation of ultrasmooth and coherent deposits. Enhanced tensile strengths have been observed even for pure Ni, when deposited in a layered configuration, as compared to a continuously deposited homogeneous Ni foil.

References

1. Modulated Structures, AIP Conference Proceedings, Ed., J.M. Cowley, J.B. Cohen, M.B. Salamon and B.J. Wuensch, American Institute of Physics, N.Y.,(1979).

2. Modulated Structure Materials, NATO ASI Series 83, Ed., T. Tsakalakos, Martinus Nijhoff, Dordrecht, Netherlands (1985).

3. R.F. Bunshah, R. Nimmagadda and H. J. Doerr, Thin Solid Films 72, 261 (1980).

4. D. Tench and J. White, Metallurgical Transactions A 15A, 2039 (1984).

5. D. Baral, J.B. Ketterson and J.E. Hilliard, J. Appl. Phys. 57, 1076 (1985).

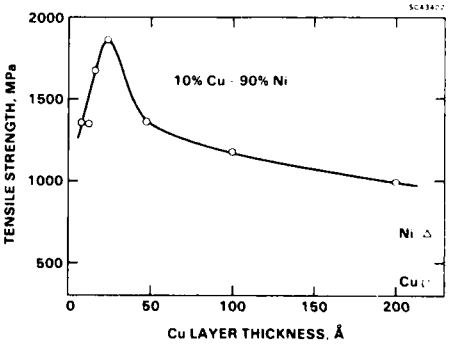


Fig. 1 Plot of ultimate tensile strength vs Cu layer thickness for 10% Cu-90% Ni MU and for homogeneous Cu and Ni foils, electrodeposited under similar conditions.

Abstract No. 343

ELECTRODEPOSITION OF Ni/SiC COMPOSITE COATING

A. LAVANANT, G. MAURIN

LP15 du CNRS "Physique des Liquides et Electrochimie"
Tour 22 - 4 place Jussieu
75252 Paris Cedex 05 - FRANCE

Composite Ni-non conducting particles electrodeposits are known for several years (1,2,3). In particular, Ni-SiC layers present a good resistance against wear and are, still now, used in the car industry to coat the internal surface of cylinders of aluminium engine blocks. However, the mechanism of the simultaneous deposition of metallic ions and ceramic particles is not well understood. It is generally admitted that particles are positively charged by adsorbed Ni^{++} cations, and, according to Gugliemi (4), they undergo a double step adsorption at the cathode surface. It is experimentally known that a vigorous stirring of the electrolyte is necessary to ensure the incorporation of particles in the metallic matrix.

The aim of this study is to identify and interpret some specific effects of various parameters onto the rate of incorporation of particles in the deposit. A special attention was paid to hydrodynamical conditions. The cathode is a rotating disc. The electrolyte circulates vertically in a cylindrical cell under the effect of an external pump. The velocity of the fluid is set to be just sufficient to maintain the particles in suspension and to minimize the turbulences, in such a way that the convection phenomena bringing the particles at the cathodic interface are mainly due to the rotation of the disc electrode. The electrolyte is a conventional sulfamate bath (pH=4.5 ; θ = 50°C) containing 10 to 100 g/l of SiC particles (mean diameter ≈ 2µm).

On Fig.1 are presented the variations of the mean concentration α of SiC in the deposit versus Ω. Two regimes are clearly visible.
- At low rotation rates α increases with Ω ; that is to say, with the normal velocity v_z of the fluid near the surface. According to the theory of the rotating disc electrode, in first approximation $v_z \approx \Omega^{3/2}$ (5). At $\Omega = 0$, $v_z = 0$ and α is very small. This result *illustrates the fact that migration and adsorption* effects are weak in front of convection effects. According to electrochemical impedance measurements, the double layer capacitance of the cathodic interface is not significantly affected by the presence of the particles, whatever the rotation rate and the current density are. Fiber textures of nickel electrodeposits are also known to be sensitive to adsorption phenomena (6). However, addition of SiC have a little effect on the axis of preferred orientation (<110> at low CD, <100>at high CD).
- At high rotation rates, α decreases with Ω. This can be attributed to the fact that the mean residence time t_r of particle in the vicinity of the electrode varies as Ω^{-1}. The centrifugal ejection of particles by the Stockes'forces varies as $r\Omega$ contribute also to decrease α. Effectively, the local concentration, measured along a radius by X rays energy dispersive analysis, diminishes versus r when Ω increases (Fig.2). For the same reason, only small particles are embedded far from the center. For example, on the T.E.M. micrograph (Fig.3) it can be observed, as a black area, a small particle included inside a nickel grain characteristic of the <100> texture.

On Fig.4 are plotted experimental curves α *vs* the current density for various rotation speeds. The incorporation rate of the particles is clearly potential dependent according the previous hypothesis. The discharge of cations adsorbed on the particles surface is an important step in the embedding process. However, the shape of α/I curves depends also of the hydrodynamic conditions. At high Ω, α decreases with I, indicating that the discharge of adsorbed cations is slower than the discharge of solvated cations Ni^{++}. Gugliemi (4) found a positive slope of the α/I curve but the conditions of agitation of the bath were certainly different. At low rotation speeds, α is very small at low current densities and increases progressively.

All these results put on evidence that the surface concentration of particles before the incorporation process is governed more by the antagonist hydrodynamical effects than by a loose Langmuir's adsorption.

References

(1) D.K. Ramanauskene, E.S. Mikailene and Y.Y. Matulis
Proceedings of 10th Lithuanian Conference of Electrochemists, Vilnius 1968, English translation p.34.
(2) E.C. Kedward and B. Kiernan
Metal Finishing 1967, p.116.
(3) S. Rashkov and N. Atanassov
J. Appl. Electrochem. 1980, p.535.
(4) N. Gugliemi
J. Electrochem. Soc., 119, 1972, p.1009.
(5) V.G. Levich
"Physicochemical Hydrodynamics"
Prentice Hall, N.J., 1962.
(6) M. Froment and G. Maurin
J. Microsc. Spectrosc. Electron. 1987, p.379.

Acknowledgments

This study was partially supported by the P.S.A. company (Peugeot-Citroën Automobiles).

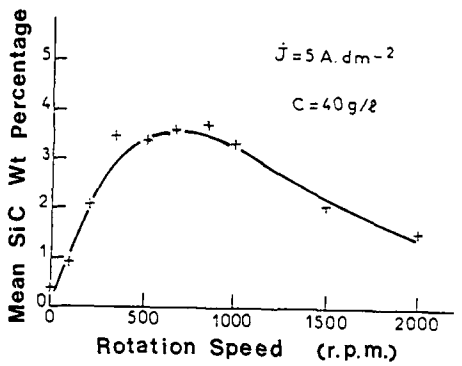


Figure 1 : Mean SiC weight percentage of composite deposits versus the rotation speed of the disc electrode.

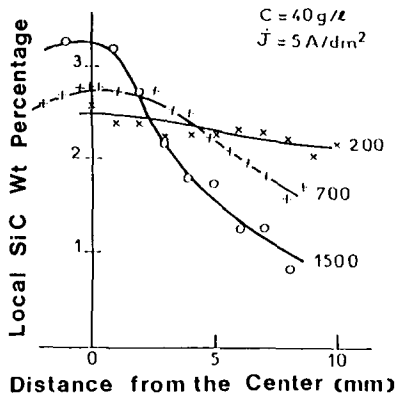


Figure 2 : Local SiC weight percentage measured along a radius for various rotation rates.

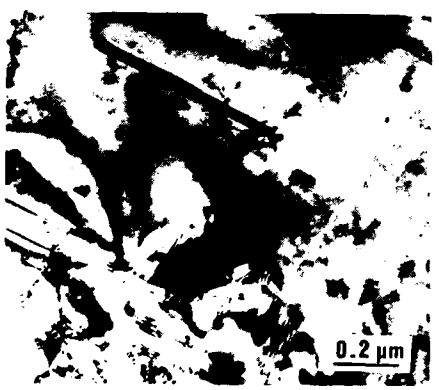


Figure 3 : TEM micrograph of a Ni/SiC composite deposit ($\dot{J}$ = 10A/dm^2, ω = 500rpm). SiC preferred orientation.

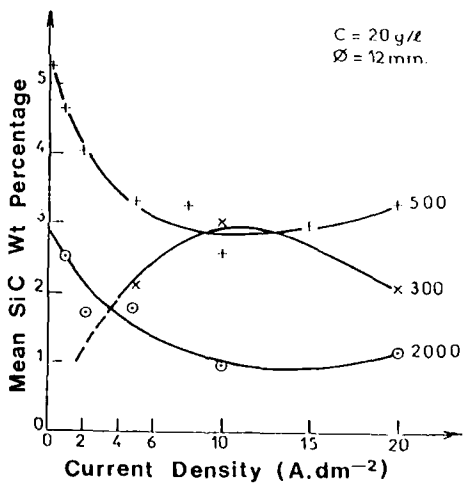


Figure 4 : Mean SiC weight percentage versus current density for various rotating rates.

Abstract No. 344

INVESTIGATION OF DENDRITIC GROWTH OF TELLURIUM ELECTRODEPOSITS BY ELECTROHYDRODYNAMICAL IMPEDANCE ANALYSIS

C. DESLOUIS, G. MAURIN, B. TRIBOLLET

LP 15 du CNRS "Physique des Liquides et Electrochimie", Université P. & M. Curie, tour 22, 4 place Jussieu, 75252 PARIS Cédex 05, FRANCE.

Dendritic electrodeposits are generally obtained in the case of a fast interfacial kinetics and a limitation of the growth rate by convective diffusion in the electrolyte. The radial current distribution around the tips of crystals tends to promote their growth in the vertical direction (1,2). The aim of this work is to attempt a correlation between morphological feature of tellurium electrodeposits, as observed by SEM, and kinetic informations provided by EHD impedance measurements.

This technique consists in the frequency analysis of the current response ΔI to a sinusoidal modulation $\Delta\Omega$ of the rotation speed of the disc electrode (3). According to recent theoretical calculations, EHD impedances are sensitive to the non uniform character of the reactivity of an electrode. At low frequencies, the EHD response is identical to that of a uniform surface whereas at high frequencies, it is similar to the response of an isolated site. The frequency lag between the two regimes is linked to the average dimensions of the active sites (4).

Tellurium was potentiostatically deposited on a (Ti or Ni) rotating disc electrode from an aqueous solution of 0.2 M K_2SO_4 saturated with TeO_2 ($c < 10^{-3}$ M/l) and maintained at 85°C. These conditions are similar to that one used for CdTe electrodeposition (5). The mechanical and electronic set up were described in detail in (6). Steady state I/V curves exhibit a plateau current between about - 0.7 and - 1 V/SSC corresponding to the limitation by diffusion, followed by a fast current rise related with hydrogen evolution and the development of large fern-like dendrites.

The effects of various parameters -potential, mean rotation rate $\bar{\Omega}$, pH, hold time t- on both morphology and EHD responses were investigated (7). For example, Fig. 1 and 2 illustrate the effect of $\bar{\Omega}$ for fixed values of potential (- 0.7 V/SSC) and hold time (2E'). At high $\bar{\Omega}$ ($\bar{\Omega}$ = 600, 900, 1200 rpm) all the data plotted in Bode coordinates (phase ϕ and normalized modulus versus the dimensionless frequency $p = \omega/\bar{\Omega}$) fall on a single curve (corresponding to the theoretical response (dashed line) of a uniform surface for a fitted Schmidt number of 125. In this velocity range, there is a mixed control of the overall kinetics, and the deposit is made of a dense packing of tiny crystals (Fig. 2a). For low rotation rate ($\bar{\Omega}$ = 60, 120 rpm) the current is totally limited by mass transport. The surface is covered by microdendrites gathered in bushes (Fig. 2b). The EHD impedances exhibit a marked transition between the LF and the HF regimes, typical of a partially blocked surface, as predicted above. From the measured frequencies p_d and p_c characteristic of the two regimes the site dimension d is given by :

$$d = 2.1^{3/2} R \left(p_d / p_c \right)^{+3/2} \qquad <1>$$

where R is the radius of the disc electrode.

The value obtained (≈ 40 µm) corresponds to the size of the bushes and not to that one of the individual microdendrites. The transition between the mixed control and the purely diffusional control, and its consequence on morphology and EHD responses was also obtained, at a constant $\bar{\Omega}$, by changing the potential.

On the diffusion plateau, the duration of deposition is another important parameter : for EHD impedances, whereas LF regime remains always identical, the HF regime changes slowly from a uniformly accessible response (t < 15 mn) to a partially blocked surface response (t > 20 mn) (Fig. 3). According to Eq. 1, the dimensions of active zones are 15 µm (25 mn), 170 µm (40 mn), 500 µm (2h 30 mn). That corresponds to the evolution of the morphology from small bushes to large cauliflower-structures separated by deep valleys (Fig. 4).

This study illustrates the interest of EHD impedance technique to perform a in-situ detection of the outgrowth during electrodeposition and to provide an average characteristic dimension of the space distribution. The results presented here thoroughly differ from that one obtained previously with CdTe electrodeposition. In this last case, a strong surface inhibition hinders dendritic formation and the EHD impedances are therefore characteristic of a uniformly accessible surface (8).

References :

(1) N. IBL
Oberfläsche Surface 16, n° 2, p. 23 (1975).

(2) A.R. DESPIC, K.I. POPOV
in "Modern Aspects of Electrochemistry", Ed. Plenum Press, n° 7, p. 199 (1972).

(3) B. TRIBOLLET, J. NEWMANN
J. of Electrochem. Soc., 130, 2016 (1983).

(4) A. CAPRANI, C. DESLOUIS, S. ROBIN, B. TRIBOLLET
J. Electroanal. Chem. (to be published).

(5) M. FROMENT, G. MAURIN
Invited lecture, 31st IUPAC Meeting, Sofia (1987). Proceedings p. 76.

(6) C. DESLOUIS, C. GABRIELLI, B. TRIBOLLET
168th Electrochem. Soc. Meeting, New Orleans, Oct. 1984.

(7) C. DESLOUIS, G. MAURIN, N. PEBERE, B. TRIBOLLET
J. Applied Electrochem. (to be published).

(8) C. DESLOUIS, G. MAURIN, D. POTTIER, B. TRIBOLLET
38th ISE Meeting, Maastricht, Sept. 1987.

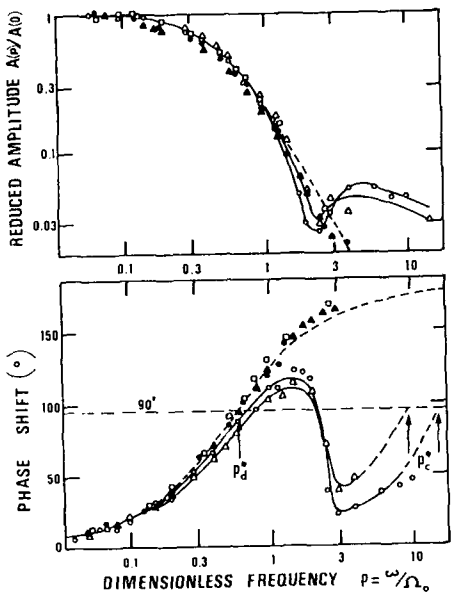


Fig. 1 : EHD diagrams in Bodes coordinates at E = - 0.7 V/SSE and at (0) 60 rpm ; (Δ) 120 rpm ; (Δ) 600 rpm ; (□) 900 rpm ; (0) 1200 rpm.

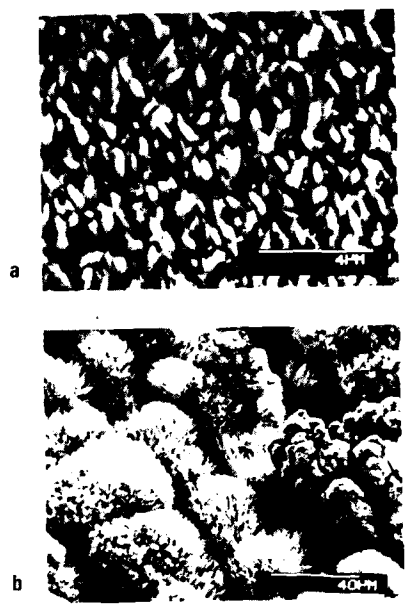


Fig. 2 : SEM micrographs of Te at - 0.7 V/SSE.
a) = 1200 rpm
b) = 64 rpm

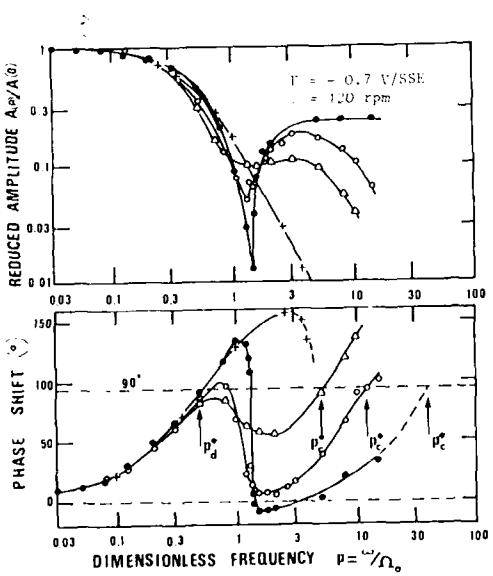


Fig. 3 : EHD diagrams for different times : (+) 15 mn ; (0) 25 mn ; (0) 40 mn ; (Δ) 2h 30.

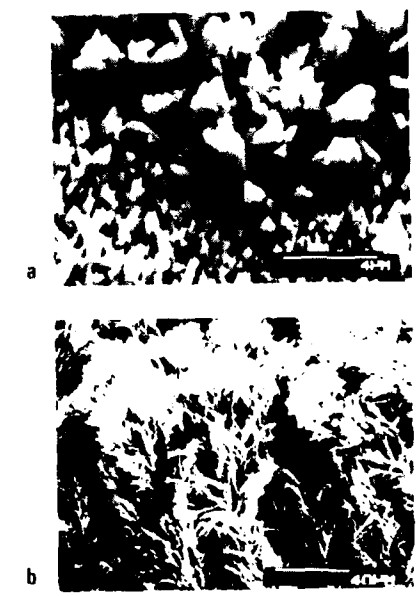


Fig. 4 : Evolution of dendrites distribution.
a) t = 15 mn
b) t = 2h 30.

Abstract No. 345

MECHANICAL PROPERTIES AND MICRO STRUCTURES OF ELECTROLES COPPER DEPOSITS

Haruo Akahoshi and Kanji Murakami
Hitachi Research Laboratory, Hitachi, Ltd.
4026 Kuji-cho, Hitachi-shi
Ibaraki-ken, 319-12 Japan

INTRODUCTION

Through hole plating technology is an important step in manufacturing of multilayer printed wiring boards. Attaining uniformity and good quality of the deposits is critical. Recent trends in high density packaging require increased numbers of circuit layers and reduced through hole diameters for multilayer boards. Thus, the aspect ratio of the through hole is very high and it is difficult to obtain a uniform thickness in such a narrow hole by conventional electrolytic plating methods. An electroless copper plating technique has an advantage of uniform thickness of the deposits. However, in order to ensure high reliability of continuity, even in such a high aspect ratio through hole, the plated copper has to withstand fatigue damage from thermal stress cycles. For simplicity, it has been considered that ductility, or tensile strength of the copper deposit is of primary importance in determining reliability of the plated through hole. The purpose of this study was to investigate the relationship between the through hole reliability and properties of electroless copper deposits in more detail.

EXPERIMENTS

A high temperature type EDTA bath containing 2,2'-bipyridyl was employed for through hole metalization. Plating conditions (temperature, pH and concentration of the major components) were varied under a fixed basic composition. A 5.2mm thick glass-epoxy copper clad laminate, with drilled holes, was used as substrate. Average thickness of the plated through hole was 40 um. The reliability of the plated through hole continuity was evaluated as the number of the breakdown cycle in thermal shock cycle tests, according to MIL-STD-202,M107,condition B. Breakdown of the plated through hole was detected by observation of cracks on the cross-section of the through hole copper, after the thermal shock cycle tests. The through hole reliability was ranged from 40 to over 200 cycles, under the examined conditions. Physical properties of the electroless copper deposit were examined using copper foils deposited on stainless steel substrates with through hole plating done under the various conditions.

RESULTS

MECHANICAL PROPERTIES---Ductility and tensile strength were measured by strip tensile tests under various temperatures (-38°C to 180°C). Ductility of the deposits ranged from 10 to 30% at 20°C. A rough correlation was observed between ductility and reliability of the plated through hole. However the breakdown occurred from 40 to over 100 cycles at the same ductility level. This indicated that there were other factors affecting through hole reliability. Tensile strength showed no correlation with reliability.

Fatigue flex tests were also carried out at room temperature with 135° bending, but no significant difference was detected between samples having different reliability level.

IMPURITY ANALYSIS --- Inclusion of hydrogen, nitrogen, oxygen, and carbon in the plated copper were quantitatively analyzed.[3,6] Hydrogen content ranged from 5 to 50 ppm. Oxygen content was several times larger than hydrogen, while nitrogen and carbon contents were at almost the same level as hydrogen. These impurity contents were about ten times larger than those found in pyrophosphate electroplated copper. But no clear relationship between impurity contents and reliability was observed.

MICROSTRUCTURE,MORPHOLOGY and TEXTURE --- Microstructures of the electroless copper crystal were examined by X-ray diffraction. Orientation of the 220 lattice was observed [1,2]. Crystallite size, calculated from full width of half maximum intensity of the diffraction line was in the range of 800 to 1200A. But no significant relationship with reliability of the through hole was detected from X-ray diffraction data. Pyramidal surface morphlogies were observed by scanning electron microscope(SEM) on every sample.

Cross-sectional texture of the deposits was also observed by SEM. No voids or defects were observed for normal etching conditions in any sample. However, after rapid deep etching to about a 2um depth, etch-pits were detected on the cross-section of plated through hole with low reliability. The number of etch-pits in same sized cross-sectional area showed an inverse relationship with the through hole reliability. Results of this study, etch-pits indicated the existence of micro-defects which related fatigue breakdown of the plated copper through hole. Residual lattice strain, defects or uneven distribution of the impurity at the crystal grain boundary were expected to promote the local etching rate and cause etch-pits on a cross-section.

Small hydrogen bubble voids[4-6] are considered to reduce the ductility of the electroless deposits. However, in this case, there was no relationship between the etch-pit formation and hydrogen content of the copper deposits. The existence of micro defects, which was detected by deep etching of the cross-section, did not affect physical properties examined in this study, but had a large influence on resistance to fatigue damage of plated through holes caused by thermal stress cycles.

REFERENCES

[1] H.Akahoshi, K.Murakami and M.Wajima Extended Abstract No.446, 166th ECS meeting, (1984)
[2] H.Akahoshi, K.Murakami, M.Wajima and S.Kawakubo, IEEE Trans. Components, Hybrids, and Manufacturing Technology, *CHMT-9*, No.2,181 (1986)
[3] K.Murakami, H.Akahoshi, M.Wajima and M.Kawamoto, Proceedings of 68th Tech. Meet. of the Metal Finishing Society of Japan, B-12 (1983)
[4] Y.Okinaka and S.Nakahara, J.Electrochem. Soc.,*123*,475 (1976)
[5] S.Nakahara and Y.Okinaka, Acta Metall., *31*,713 (1983)
[6] Y.Okinaka and H.K.Straschil, J.Electrochem.Soc.,*133*,2608 (1986)

Abstract No. 346

THE EFFECT OF ADDITIVES ON THE MORPHOLOGY OF ELECTROLESS COPPER DEPOSITS

Haewei H. Wan and Jhy-Yeong Gau

Materials Research Laboratories
Industrial Technology Research Institute
Chutung, Hsinchu, Taiwan 31015, R.O.C.

Electroless copper plating is a crucial step of plated-through-hole (PTH) process in the manufacturing of printed circuit boards (PCBs). In the late 1950s conventional electroless copper systems for subtractive PCBs were developed. By 1970s an important advance came with the development of high speed electroless copper. This process eliminated an electrolytic flash. In the early 1980s the demand of surface-mounted devices has been increased significantly. As a result, the trend of printed circuit manufacturing is toward progressively finer lines, smaller holes as well as higher speed. The fully additive process undoubtedly provides an excellent alternative to overcome the limitation of conventional boards. The circuit pattern is then produced by a full build of electroless rather than electroplating bath. In the past two decades, a lot of efforts were devoted to the enhancement of plating rate of electroless copper (1-4). A number of studies have been focused on the mechanical properties of electroless copper (5-7). However, as far as the stability, plating rate and quality of deposits are concerned, the existing processes are far from perfect. More intensive research should, therefore, be conducted in the future.

In this investigation, a systematic approach is performed to elucidate the effect of additives on the morphology of electroless copper deposits. The plating bath contained copper sulfate, sodium hydroxide, formaldehyde and a stabilizer. Different kinds of additives such as tartrate, EDTP, CDTA, pyridine, glycine and coumarin were chosen to investigate rate enhancement effect. The morphology of copper deposits were studied by a scanning electron microscope (SEM). Typical examples are illustrated in Figs. 1 and 2. The surface composition of the electroless copper were analyzed by scanning Auger micrograph (SAM). The spectra is shown in Fig. 3.

Mechanical properties measurements are carrying out to further clarify the relationship among deposit quality, morphology as well as quantity of additives.

References:

(1) M. Paunovic, J. Electrochem. Soc., 124, 349 (1977)

(2) F. J. Nuzzi, Plat. Sur. Fin., 1, 51 (1983)

(3) M. Paunovic and R. Arndt, J. Electrochem. Soc., 130, 794 (1983)

(4) D. Vitkavage and M. Paunovic, Plat. Sur. Fin., 4, 48 (1983)

(5) M. Paunovic and R. Zeblisky, ibid., 2, 52 (1985)

(6) K. F. Blurton, ibid., 1, 52 (1986)

(7) S. Mizumoto, H. Nawafune, M. Kawasaki, A. Kinoshita and K. Araki, ibid., 12, 48 (1986)



Fig. 1 SEM photo of electroless copper deposit from bath with 100 mg glycine



Fig. 2 SEM photo of electroless copper deposit from bath with 3 mg pyridine

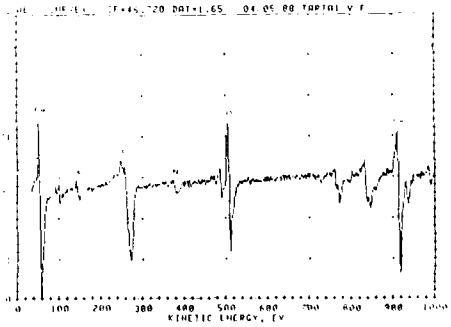


Fig. 3 scanning Auger micrograph (SAM) of electroless copper deposit from bath with 4.5 mg tartrate

Abstract No. 347

Properties of Electrodeposited Copper from Pattern Recognition Analysis of Cyclic Voltammetric Stripping Curves

M. Kendig and D. Anderson
Rockwell International Science Center
Thousand Oaks, CA 91360

Background

Often a direct measurement of the properties of a complex mixture or performance of a complex process is impossible or impractical. This is the case for monitoring in real time the strength of electrodeposited copper from production baths. It is impossible to measure the tensile strength and the % elongation for a bath continuously since these values can be obtained only from time-consuming mechanical testing. However, previous research at the Science Center[1] demonstrated that the rapid electroanalytical procedure of cyclic voltammetric stripping (CVS), which directly measures electrokinetic properties of the plating bath, relates indirectly to the mechanical properties of the electrodeposited product. Features in the CVS curves correlate with bath impurities which degrade deposit properties.[2]

The goal of pattern recognition is to classify an object on the basis of indirect measurements.[3] The general approach has been applied recently to electrochemical problems.[4,5] In the case of plating bath monitoring and analysis, the objective is to classify the bath performance, as defined by mechanical properties of the electrodeposit, from electrochemical kinetic parameters obtained from the CVS waveform. Given a sufficiently large number of data sets (CVS parameters), pattern recognition can be used to develop a discriminant in terms of the CVS parameters which categorizes the bath as being either acceptable or unacceptable with regard to predicted electrodeposit properties. Clustering methods of pattern recognition can determine the natural grouping of objects (a set of CVS parameters), thereby enabling a clearer understanding of how the indirectly measured set of parameters relate to the desired mechanical properties. The general approach of pattern recognition is, therefore, well suited for developing control criteria or discriminants for plating baths based on the electrochemical measurements.

Relationship of CVS to Deposit Properties Using Pattern Recognition

Figure 1 shows CVS waveforms for a Cu bath before and after different treatments. The total charge producing the large positive current peak between -0.25 to 0 V represents the anodic stripping of the copper. The R-ratio, the ratio of the stripping charge under electrode rotation to that under static conditions, relates to the concentration of a necessary bath additive, dimercaptothiadiazole. The current shoulder of magnitude I_{oxs} or I_{oxr}, for static and rotating conditions respectively, observed near 1.0 V results from the oxidation of an impurity that builds up in the plating bath. It was found that the species giving rise to I_{ox} may only be removed by inert anode dummying, but not by carbon and peroxide treating (Fig. 1).

To demonstrate the applicability of pattern recognition methodology to plating bath control, the features from CVS waveforms were recorded along with tensile strength (KPSI) and % elongation (%E) determined from foils generated on a rotating cylinder electrode (RCE). Two production baths (A and B) and a laboratory-generated bath (S) were analyzed. A classification algorithm uses the nondestructive, in-process bath parameters of (1) R-ratio, (2) I_{oxr}, and (3) I_{oxs} to predict the resulting strength of the electrodeposit.

Each plating bath analysis is considered as an event described by the two labeling features (KPSI and %E) and the three in-process features (R-ratio, I_{oxr}, I_{oxs}). Each plating bath analysis is labeled as being a member of one of two classes based on post-plating destructive measurements of the tensile strength (KPSI) and % elongation (%E) of the specimen. Class 1 defines poor properties of %E < 12.5 and KPSI < 40 and Class 2 defines the passing properties of %E > 12.5 and KPSI > 40. Note that the performance is defined as demonstrated here in terms of both KPSI and %E. Description of bath behavior usually focuses on either %E or KPSI, but not both. This does not need to be the case when one uses pattern recognition algorithms.

Using labeled data, i.e., sets of in-process features (R-ratio, I_{oxr}, I_{oxs}), with known KPSI and %E responses, and a definition of the ranges of KPSI and %E for each class, is the means μ_{ij} and standard deviations, σ_{ij} for each i^{th} in-process feature distinguishes behavior between the different classes and can be assessed from a two-dimensional projection of the hyper-volume of the feature space defined by the range of standard deviations about the mean. From the "training set" of labeled data, a new set of unlabeled data comprising the in-process features defining coordinates for a point p in feature space can be classified by first determining the normalized distances, d, of the point, p, in feature space from each class j:

$$d^2_j = \Sigma(\mu_{ij} - p)^2/\sigma^2_{ij}$$

where p is the coordinates of the new data set in feature space. Clearly, the new data, p, is placed in the class j which minimizes d_j. Given sufficient labeled data to cover all possible classes of interest, this approach can classify any new, unlabeled in-process data obtained directly from a bath and, therefore, defines a discriminant function. This method has been used previously at the Science Center for performing pattern recognition on acoustic emission signals.[6]

Results

Table 1 shows the data (labeling features and in-process features) collected for a number of Cu pyrophosphate plating baths. Figure 2 shows the separation of the two classes, using two-dimensional plots defining one standard deviation of R-ratio and I_{oxr} (Fig. 2a) or R-ratio and I_{oxs} (Fig. 2b) for the two classes. As can be seen, a low R-ratio (R < 1) and high I_{ox} above 250 μA places the bath in Class 1, the unacceptable class, while a low I_{ox} and R ratio between 1 and 1.2 centers the behavior within the acceptable class, Class 2.

Clustering has also been performed on the plating bath data to determine the natural groupings that the plating bath analyses fall into. To do this, the density of events in the space of in-process features is determined from normalized distances between each point. In other words, the number of runs which are similar to many others are determined. While the statistical significance of this information increases with the number of data sets obtained, we performed clustering analysis for the 24 sets of features listed in Table 1. Using a cluster volume of radius 0.75 normalized units in the parameter space, three clusters as defined by the parameters in Table 2 were obtained.

The natural clusters which are observed provide a great deal of information about the underlying processes. For example, a high quantity of contaminant as measured by high I_{oxr} and I_{oxs} appears in Cluster 2, which exhibits a relatively low value of R (Table 2). This suggests that the high I_{oxr} and I_{oxs} are associated with depletion of the additive and could therefore be a breakdown product. As stated previously, three types of baths in this study included two production baths, A and B, and a standard bath, S, made up in the laboratory to contain controlled quantities of additives. The distribution of the resulting analyses for these three baths appear in Table 3. As can be seen, none of the laboratory-produced baths fell into Cluster 2 corresponding to a low R ratio and high I_{oxr} and I_{oxs} since a certain amount of aging in actual production must occur to produce the high I_{ox}. Of the three analyses from production bath B, two could not be classified and a third was classified with the high I_{ox} low R ratio (Cluster 2, Table 2).

Summary

This work demonstrates a method for rapidly developing criteria, from an indirect but easily made measurement on a complicated mixture such as an electroplating bath, for controlling the performance of the process. A discriminant based on features from the indirect measurement can provide criteria for controlling the bath. For example, Figs. 2a-b show the limits needed on observed voltammetric parameters to assure electrodeposits of sufficient strength. In addition, cluster analysis classifies data into naturally occurring categories that lead to further insights into the interrelationship of process parameters and bath performance.

References

1. D. Tench, C. Ogden, J. Electrochem. Soc., 125, 194 (1978).
2. B. Lowry, C. Ogden, D. Tench and R. Young, Plating and Surf. Finishing, 70(9), 70 (1983).
3. P.C. Jurs, Science, 232, 1219 (1986).
4. B.R. Kowalski, C.F. Bender, J. Amer. Chem. Soc., 94, 5632 (1972).
5. A. Byers, B. Fessler and S. Perone, Analy. Chem. 55, 620 (1983).
6. L.J. Graham and R.K. Elsley. J. Acoustic Emission, 2, 47 (1983).

Acknowledgment

This work was supported by Rockwell International Independent Research and Development. The authors acknowledge useful discussions with Dr. R. Elsley relating to pattern recognition analysis.

Table 1

Results of Plating Bath Analyses

%E	KPSI	R	I_{oxs}* μA	I_{oxr}* μA
11.2	41.5	0.8	405	263
1.0	65.2	0.8	68	68
11.3	35.8	0.9	545	290
6.9	57.7	0.8	115	98
6.4	47.6	0.8	85	80
11.6	40.9	0.8	104	87
1.6	56.7	0.9	85	77
16.7	44.1	1.0	425	222
7.4	54.6	1.0	104	93
7.1	42.6	1.0	120	90
6.1	38.7	1.0	455	270
6.1	44.1	1.0	140	110
7.0	53.3	1.0	475	270
16.4	38.2	1.0	92	86
8.1	41.5	1.1	150	96
16.4	38.2	1.2	100	87
4.9	75.6	1.2	535	297
25.4	46.8	1.2	134	96
3.4	66.3	1.3	210	110
6.3	41.7	1.3	132	92
5.9	88.5	1.4	147	93
9.4	61.8	1.1	635	353
11.3	63.5	0.9	640	540
17.5	32.1	0.8	845	390

*Electrode area = 0.45 cm^2.

Table 2

Cluster Analysis

Cluster No.	Number in Cluster	R	I_{oxs}* μA	I_{oxr}* μA
1	12	1.02 ± 0.14	140 ± 41	110 ± 25
2	6	0.89 ± 0.12	545 ± 104	290 ± 45
3	3	1.25 ± 0.10	210 ± 71	110 ± 18

*Electrode area = 0.45 cm^2.

Table 3

Distribution of Bath Properties

Bath	Number in No Cluster	Number in Cluster #1	Number in Cluster #2	Number in Cluster #3
S	1	6	0	3
A	1	5	5	0
B	2	0	1	0

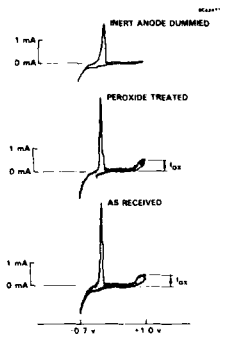


Fig. 1 Cyclic voltammograms for a copper pyrophosphate bath, as-received and after different treatments. Electrode area = 0.46 cm^2.

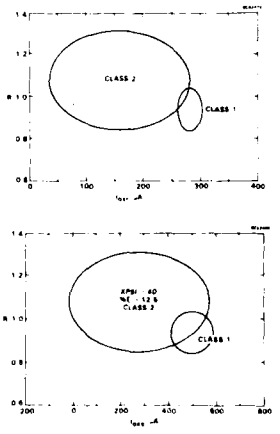


Fig. 2 Set of parameter values (a) R and I_{oxr} and (b) R and I_{oxs} within one standard deviation about the mean for class 1 (KPSI < 40, %E < 12.5) and class 2 (KPSI > 40, %E > 12.5). Electrode area = 0.45 cm^2.

Abstract No. 348

MECHANISM OF CARBIDE FORMATION BY ELECTROCHEMICAL DEPOSITION

D.C. Topor and J.R. Selman
Illinois Institute of Technology
Department of Chemical Engineering
Chicago, Illinois 60616

An electrolytic method to produce materials for use in corrosive environment at high temperature is illustrated by the deposition of molybdenum and molybdenum carbide coatings on steel substrates.

Electroplating bath based upon molten alkali fluorides as solvent have been employed successfully with refractory metals and compounds. High temperature and highly pure reactants are, however, required for deposition of coherent coatings. Optimization of the plating procedure is thus necessary for future application and commercialization.

The electrodeposition of molybdenum from a FLINAK electrolyte with additions of alkali molybdates was investigated using cyclic voltammetric, chronopotentiometric and potential step methods.

A typical voltammogram (Fig. 1) indicated a rather large peak separation specific to an irreversible deposition of the metal. The low valence molybdenum intermediate appears to be reduced at relatively high overpotentials.

The chronopotentiogram with current reversal in Fig. 2, recorded at 71.4 mA/cm^2, is well defined and shows two reduction and two oxidation waves. The first cathodic wave appears at -0.58 V and the second at -0.93 V vs. a platinum quasi-reference electrode. The second wave is smaller than the first and is not clearly outlined, which makes the determination of its transition time difficult. If one assumes two consecutive charge transfer reactions (diffusion controlled) at sufficiently different potentials, the number of electrons involved in each step may be estimated. A preliminary result indicated in this case $n_1 = n_2 = 2$.

Potential step data were obtained at relatively high polarization vs. platinum quasi-reference electrode and for a small range of potentials around -1.0 V. In the Fig. 3 the current response at a platinum electrode clearly indicates the presence of a nucleation process.

Similar data will be presented for molybdenum and molybdenum carbide deposition on various substrates, including the effect of temperature and other experimental parameters.

Finally, a possible mechanism will be suggested for the formation and growth of both coatings.

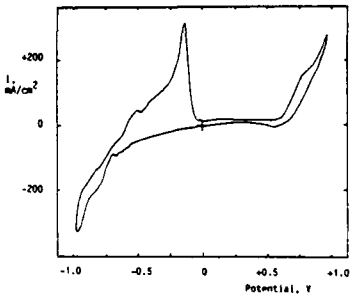


Fig. 1 Cyclic voltammetry of Na_2MoO_4 (2.8×10^{-5} mol cm^{-3}) at Pt in molten FLINAK at 630°C. 20 mV/s vs Pt QRE.

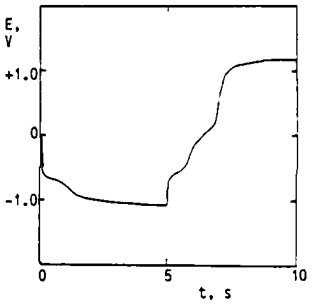


Fig. 2 Chronopotentiogram for the reduction of Na_2MoO_4 in molten FLINAK at 630°C. Current density 71.4 mA cm^{-2}.

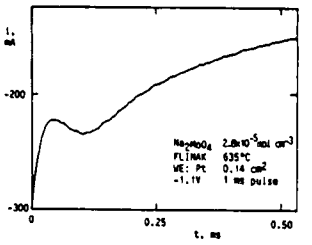


Fig. 3 Nucleation current for Mo electrocrystallization on Pt in molten FLINAK at 635°C.

Abstract No. 349

Current- and Potential-Pulse Plating of Uranium From Fused Chlorides

S.L. Marshall and D.R. Vissers

Chemical Technology Division
Argonne National Laboratory
9700 South Cass Avenue
Argonne, IL 60439-4387

Introduction

Existing work on the electrodeposition of U metal from fused chlorides [1-3] has noted a strong tendency toward dendrite formation. Recently [4], we showed that dendrite formation may be avoided by application of short potential pulses (cathodic to the U reference electrode) separated by rest periods at zero potential.

This paper describes the application of this technique to the plating of U onto metal coupons of area A = approximately 6 cm^2, and some additional results that we have obtained using bipolar current-pulse plating [5].

Experimental

The two electrolyte systems that were used in this work were as follows: 1) a 20 w/o solution of UCl_3 in LiCl/KCl eutectic, prepared as described in Ref. 4; 2) a ternary eutectic mixture of composition UCl_3 12.0 m/o (=42.4 w/o); KCl 58.5 m/o (=44.8 w/o); LiCl 29.5 m/o (=12.8 w/o), prepared by reaction of U metal with $FeCl_2$ dissolved in a molten LiCl-KCl mixture of the appropriate composition. Experiments were carried out at 445°C with electrolyte 1) and at 510°C with electrolyte 2). The cathodes consisted of cylindrical coupons of Ni and Cu which, prior to use, were polished to a 1 µm finish.

The pulse-plating signal was applied using a potentiostat, and a DC power supply was used for anodization and nucleation pulses. Potentials are expressed relative to a U reference electrode in the same solution. Other experimental details are as described in Ref. 4.

Results and Discussion

A. Controlled-Potential Pulse-Plating

These experiments were conducted in electrolyte 1), and involved application of a plating potential of -75 mV for 0.1 ms followed by a relaxation period of 1.0 ms at 0 mV.

On Ni coupons, the deposits were in all cases dendrite-free and well-bonded to the substrate. The uniformity of the deposit increased markedly when a large nucleation pulse (-706 $mAcm^{-2}$ for 2s) was applied before commencement of the potential signal. The deposits on Cu were also dendrite-free, but tended to become less uniform when a nucleation pulse was applied.

Anodization of the Ni coupons prior to the nucleation pulse resulted in a slight improvement of the quality of the deposit. In contrast, for Cu coupons the quality of the deposit was significantly poorer with preanodization.

B. Controlled-Current Pulse-Plating

This technique involves alternate application of cathodic current I_c for time t_c and anodic current I_a for time t_a, resulting in the removal of a fraction of the material deposited during the cathodic pulse. The reciprocal of this fraction is

$$q = I_c t_c / I_a t_a$$

In terms of the ratio of pulse lengths $R = t_c/t_a$ and the time-averaged current <I>, the values of I_a and I_c are given by

$$I_a = \langle I \rangle . (1+R)/(1+q)$$

$$I_c = \langle I \rangle . q(1+R)/R(1+q)$$

in which all currents are supposed to retain their signs (negative = cathodic, positive = anodic). The remaining variable required for the specification of the experimental conditions is the cathodic pulse length t_c or, equivalently, the amount of material to be deposited during each cathodic pulse. All experiments were carried out on Ni coupons in electrolyte 2).

As in the controlled-potential experiments, the deposits were obviously polycrystalline, but the crystals were of approximately uniform size, and coverage of the immersed section of the coupons was complete. Our results using this technique suggest that uniformity of coverage is favored by use of q values close to -1. The beneficial effect of such q values can, however, be canceled out by dendrite formation if the cathodic pulse current density $i_c = I_c/A$ becomes too large, and if t_c is not shortened to compensate for the larger currents required. The optimal range for i_c appears to be -20 to -40 $mAcm^{-2}$ and that for i_a 30 to 40 $mAcm^{-2}$, which for R = 2 correspond to values of q between -1.3 and -1.5.

Acknowledgement

This work was supported by the U.S. Department of Energy under contract Nos. W-31-109-Eng-38 and DE-AC05-840R21400.

References

1. M. Kolodney, J. Electrochem. Soc., 129: 2438 (1982)

2. G. Boisde, G. Chauvin, H. Coriou and J. Hure, Electrochim. Acta, 4: 54 (1961)

3. M. Broc, "Etude de Revetements Metalliques Prepares par Electrolyse Ignee", Prench Atomic Energy Commission Report CEA-R4291 (1978)

4. S.L. Marshall and D.R. Vissers, Electrochemical Society 173rd Meeting, Atlanta GA May 15-20 1988, Extended Abstract No. 280

5. U. Cohen, J. Electrochem. Soc., 128: 731 (1981)

Abstract No. 350

PROPERTIES OF NICKEL ELECTRODEPOSITED FROM ORGANIC SOLVENT

V.B.Singh and A.A.Sarabi
Department of Chemistry
Banaras Hindu University
Varanasi - 221 005.
India.

Nickel has been electrodeposited from organic solvents (ethylene glycol, Diethylene glycol and Triethylene glycol) using nickel chloride and nickel sulphate separately. The highest cathode current efficiency has been obtained in case of ethylene glycol. The effect of current density, bath temperature and annealing temperature, on the structure and physical properties has been studied. In general, deposits with improved physical properties have been obtained. The microhardness of the deposits decreased with an increase in bath temperature and annealing temperature as well. The decrease in hardness due to annealing has been explained in terms of recrystallization of grains. The microstructure examination of the deposits by SEM and TEM showed some interesting results with respect to dislocation and texture. Our results are not in agreement to the observations reported by earlier workers[2-4]. The observations have been discussed in light of the consequences due to hydrogen evolution/inclusion in the deposits. The adverse effect of hydrogen inclusion in the nickel deposits has been found to be almost nominal.

Reference

1. "Nickel and its alloys" S.J.Rosenberg, NBS monograph (1968) p.52.

2. S.Nakahara, J. Electrochem. Soc., 129, 1049 (1978).

3. S.Nakahara and E.C.Felder, J.Electrochem. Soc., 129, 45 (1982).

4. S.Kaja, H.W.Pickering and W.R.Bitler, Plat. and Surf. Fin., Jan., 58 (1986).

Abstract No. 351

Corrosion of Electronic Materials and Devices

R. P. Frankenthal
AT&T Bell Laboratories
Murray Hill, NJ 07974

The corrosion phenomena encountered in electronic materials and devices are basically the same as those found with other metals and alloys, whether they are electroplated, rolled, drawn, etc. However, the small dimensions and, in certain situations, the applied voltages encountered in microelectronic devices may cause complete failure with only a minute amount of corrosion, as, e.g., in the electrolytic corrosion of conductor stripes. Similarly, small amounts of atmospheric corrosion at pores in electroplated contacts or connectors may lead to unacceptably high noise levels in high-reliability communications systems. Also dissimilar metals in physical contact, such as aluminum and gold at a bonding pad on an integrated circuit or copper and gold at the edge of contact fingers, may undergo galvanic corrosion through the formation of local electrochemical cells.

Numerous factors affect the corrosion of electronic materials and devices. Here, we concentrate on the environmental factors and on directions for future research that may lead to a better understanding of these factors. We first outline some problems associated with the oxidation of electronic materials, then those arising from the effect of moisture, and finally those due to the synergistic effect of moisture and contaminants. Where possible, we emphasize applications to electroplated materials. A more detailed discussion is given in references 1 and 2.

Air oxidation is one cause of corrosion of conductors, contacts, and connectors in devices and interconnec' systems and of elements in various thin film systems. For example, the magneto-optic properties of rare-earth/transition-metal alloy thin films, e.g., terbium-iron, are a strong function of alloy composition. Degradation of these properties is due to changes in composition caused by oxidation (3,4). Because of the high reactivity of the rare earth metals, protecting these alloys from oxidation and corrosion is a nontrivial task.

The influence of moisture on the corrosion of most metals and alloys is well known but not fully understood. For example, moisture usually accelerates the oxidation of metals at moderate temperatures, e.g., nickel (5). However, it retards the oxidation of copper (6). Although both observations have been explained, the basic mechanisms are not well understood. This is also true for corrosion of electronic devices. But here, the concern is not only for the adsorption of moisture on metals and their native oxides but also on the dielectric that separates and insulates adjacent conductor stripes. Only a few careful studies have been reported for the adsorption of water on well-characterized dielectrics. Yan et al. (7) looked at the adsorption of moisture on clean α-Al_2O_3 and at the effect of the adsorbed water on the surface conductivity of the substrate. Further studies on different well-characterized substrates as a function of relative humidity, temperature and controlled amounts of well-characterized impurities need to be undertaken.

A few monolayers of adsorbed water may increase by several orders of magnitude the surface conductivity of the dielectric separating two conductor stripes. Then, if the voltage difference between conductors is sufficiently large and the spacing between them is sufficiently small, corrosion can occur, as has been demonstrated for gold conductors on integrated circuits (8). As conductor width and separations on integrated circuits decrease, this problem becomes more severe. At the present time, these dimensions are 0.8-1 μm for commercial devices, and prototype devices with 0.5μm dimensions have been built.

Many electrical contacts and connectors are electroplated with a noble metal, such as gold, to prevent tarnishing and unacceptably high contact resistances. However, if the substrate is exposed at the base of pores or at the edge of the contact or connector, corrosion of the base metal may cause failure if the corrosion product migrates onto the contact surface.

In the presence of any ionizable impurity and water, an electrolyte solution will form and may cause corrosion. Most electronic circuits are encapsulated in plastics, all of which are permeable to water vapor. Ionic contaminants may be deposited on the device surface during manufacturing or may come from impurities in the plastic. Among the many contaminant ions that may be found on a device surface, chloride is, perhaps, the most dangerous. The presence of chloride can lead to corrosion of b.th positively-biased and negatively-biased aluminum by destroying the protective native oxide (9-11). Chloride also gives rise to corrosion of positively-biased gold conductors (8).

The chemistry and physics of particulate contamination is beyond the scope of this talk. However, it should be mentioned here that, although large contaminant particles can readily be filtered from the environment, small sub-micron particles are significantly more difficult to remove. As conductor dimensions and separations on devices continue to decrease, the size of a particle that is large, relative to the dimensions of the device, shrinks. The industry is rapidly approaching the point at which it will be necessary to avoid the presence of just about any particulate matter on the surface of devices. This will undoubtedly pose many new challenges in device design and manufacturing processes.

Acknowledgements

I wish to thank Messrs. R. B. Comizzoli, P. C. Milner and J. D. Sinclair for many thought-provoking discussions.

References

1. R. B. Comizzoli, R. P. Frankenthal, P. C. Milner, and J. D. Sinclair, *Science*, **234**, 340 (1986).
2. R. P. Frankenthal, in "Properties of Electrodeposits: Their Measurement and Significance," R. Sard, H. Leidheiser, Jr., and F. Ogburn, Eds., The Electrochemical Society, Inc., Pennington, NJ, 1975, p. 142.
3. R. B. van Dover, E. M. Gyorgy, R. P. Frankenthal, M. Hong, and D. J. Siconolfi, *J. Appl. Phys.*, **59**, 1291 (1986).
4. R. P. Frankenthal, D. J. Siconolfi, R B. van Dover, and S. Nakahara, *J. Electrochem. Soc.*, **134**, 235 (1987).
5. S. H. Kulpa and R. P. Frankenthal, *J. Electrochem. Soc.*, **124**, 1588 (1977).
6. W. E. Campbell and U. B. Thomas, *Trans. Electrochem. Soc.*, **91**, 623 (1947).
7. B. D. Yan, S. L. Meilink, G. W. Warren, and P. Wynblatt, *Proc. Electron Compon. Conf.*, **36**, 95 (1986).
8. R. P. Frankenthal and W. H. Becker, *J. Electrochem. Soc.*, **126**, 1718 (1979).
9. S. C. Kolesar, *Annu. Proc. Reliab. Phys.*, **12**, 155 (1974).
10. W. M. Paulson and R. W. Kirk, *Annu. Proc. Reliab. Phys.*, **12**, 172 (1974).
11. R. B. Comizzoli, *RCA Rev.*, **37**, 483 (1976).

Abstract No. 352

METAL ELECTRODEPOSITION ON PHOSPHATED STEEL SUBSTRATES

Henry Leidheiser, Jr., and Wayne Bilder

Department of Chemistry
and
Zettlemoyer Center for Surface Studies
Lehigh University, Bethlehem, PA 18015

Painted steel that is expected to withstand severe atmospheric corrosion conditions is conventionally phosphated prior to the application of the paint. Phosphated steels are generally used in automotive applications, are often used as substrates for coating appliances and are often used in coil coated products. The phosphating process requires that some bare steel be available as an anode for driving the deposition of the phosphate. Much proprietary research has been done to optimize the coverage of the steel by the phosphate and to control the nucleation and grain size and shape of the phosphate crystals. The fact that bare steel is exposed after phosphating is shown by the fact that electron exchange processes will proceed on the phosphated surface.

The purpose of the studies reported herein was twofold: (1) to develop a method for determining the area of steel not covered by phosphate and (2) to seek principles that might be utilized in developing a superior, corrosion protective system for painted steel.

A non-proprietary zinc phosphating solution was utilized in order that the composition of the solution could be reported. Such solutions yield lower coverages and larger crystals than proprietary solutions.

Tin was electroplated on phosphated steel from the alkaline bath. Typical conditions were a cell voltage of 5.5 V and a plating time of 6 s. The phosphate was stripped in a chromic acid bath and the area of the substrate covered by tin was determined. Tin was observed on 30-50% of the steel. Steel that was phosphated and tinned showed improved performance in a scribe test and in a typical automotive cyclic test after painting.

Experiments using phosphated surfaces electroplated with zinc, nickel and cobalt are incomplete at the time of writing this abstract and will be reported at the meeting.

Abstract No. 353

Under-film corrosion mechanism of zinc and zinc alloy coated steel sheet for automobiles

K.Hayashi,Y.Ito and Y.Miyoshi

R&D Laboratories I,
NIPPON STEEL CORPORATION

5-10-1,Fuchinobe,Sagamihara,
229 Kanagawa,Japan

INTRODUCTION

Experiments were conducted for various zinc alloy coated steel sheets to investigate (I)the mechanism of under-film corrosion, with much attention to its initial stage; and (II)reproducibility of the cyclic corrosion test to the atmospheric exposure test.

EXPERIMENT

①Specimen preparation:the specimens have the following surface structures:
cold rolled steel sheet/Zn,Zn-Fe alloy,Zn-Ni alloy coating layer/chromate,zinc phosphate /paints
These were cross-scribed before the corrosion test.
②Corrosion test:(a)accelerated atmospheric exposure test,(b)cyclic corrosion test(CCT test condition is shown in Table 1).
③Analysis: The specimens tested were sectioned perpendicularly to the scribe, polished and observed by EPMA.

RESULT AND DISCUSSION

Figure 1 shows the EPMA analysis results of Zn-Ni alloy coated steel sheet subjected to the atmospheric exposure test. The observed area is located at the vicinity of the tip of the corrosion and the scribe is located at the left-hand side of the area. X-ray images indicate that Cl is selectively distributed on the coating layer and that neither the coating layer nor the steel sheet is oxidized. The SE image indicates that the Cl-covered coating layer becomes friable. These suggest that Zn in the coating layer changed to chloride at the initial stage of the corrosion. At a later stage, ZnO was observed in the corrosion layer. The above observations indicate that Zn is transformed once into chloride and subsequently the chloride is transformed maybe through hydroxide into ZnO. The same result was obtained also in Zn and Zn-Fe alloy coated steel sheets.

Figure 2 shows the results of Zn-Ni alloy coated sheet subjected to the CCT. The figure indicates that the corrosion behavior in the CCT agrees with that in the atmospheric exposure test, which suggests that the corrosion mechanisms in both tests are identical.

REFERENCE

1.W.Funke,in"Corrosion Control by Coatings," H.Leidheiser,Editor,p.35,Science Press, Princeton(1979).
2.N.Masuko,BOSHOKU GIJUTSU,30,699(1981).

Table 1 Cyclic Corrosion Test

SST	4 hrs
Drying (70℃, RH60%)	2 hrs
Humidifying (49℃, RH95%)	2 hrs
Freezing (-20℃)	1 hrs

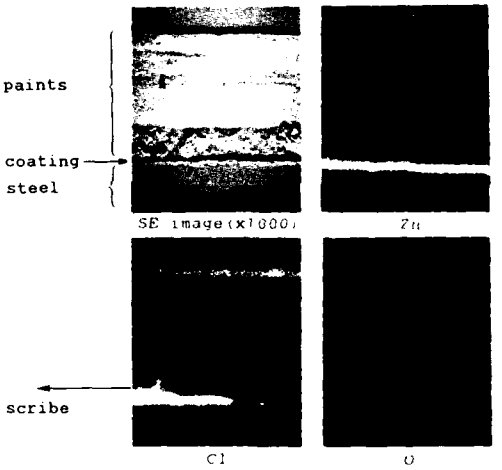


Fig.1 EPMA analysis of painted Zn-Ni alloy coated steel sheet exposed to atmospheric test

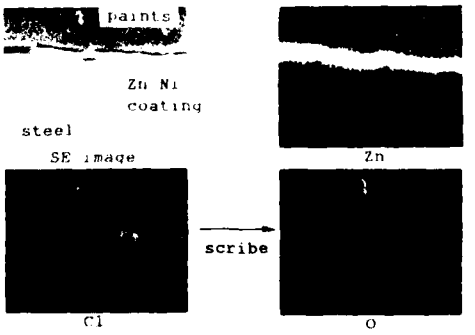


Fig.2 EPMA analysis of painted Zn-Ni alloy coated steel sheet subjected to the CCT

Abstract No. 354

CHARACTERIZATION OF NEW CORROSION RESISTANT NICKEL-ZINC-PHOSPHORUS ALLOYS OBTAINED BY ELECTRODEPOSITION

S. Swathirajan and Y. M. Mikhail
Physical Chemistry Department
General Motors Research Laboratories
Warren, MI 48090-9058

The electrodeposition of a family of NiZnP alloy coatings was carried out at a rotating cylinder electrode at various deposition current densities and temperatures. The codeposition of phosphorus with the various phases of NiZn was investigated in our efforts to enhance the corrosion resistance and paintability of the alloy coatings.

Alloy Composition and Current Efficiency

The electrodeposition current density was varied between 28 and 950 mA/cm^2 in the temperature range 45-80°C. The deposition was carried out from a chloride electrolyte at an electrode rotation speed of 2000 rpm and a pH of 4.7. Ammonium chloride and sodium citrate were used to complex the metal ions in the electrolyte. Sodium hypophosphite was used as the source of phosphorus.

At least five types of NiZnP coatings were identified using energy dispersive X-ray (EDX) analysis of the deposited samples and their compositions are shown in Table I. The variation of alloy composition and current efficiency with applied current density is shown in Fig. 1. An interesting feature of the deposition process is that at very high current densities (> 0.6 A/cm^2) the coating composition is independent of the current density and temperature (≥ 45°C) and yields only the type B coating which has a supersaturated amount of zinc dissolved in nickel. The partial deposition current densities of the alloy components and the mass transfer coefficient at the rotating cylinder electrode showed that the deposition of zinc was mass transfer controlled at high current densities at all temperatures. The apparent current efficiency, which was not corrected for the parallel electroless deposition of nickel, varied in the range 60-92 % for the various coatings.

SEM and Auger Depth Profile Studies

The SEM examination of the alloy coatings revealed four morphology types. The deposit microstructure depended more on the deposition current density than the temperature or the deposit composition. The coating type B did not show any grain structure even at very high magnifications, but showed microcracks probably caused by lattice distortion due to the presence of a supersaturated amount of zinc in nickel. The Auger analysis of the coatings B,C and D showed a depletion of zinc and the enrichment of nickel and phosphorus near the surface. The zinc-rich coating D showed an enrichment of nickel to a thickness of about 7 nm and the depletion of zinc over a depth of about 20 nm, demonstrating the formation of a passive film of probably nickel oxide reinforced with P.

Corrosion Behavior

The corrosion behavior of the coatings was studied using the polarization resistance technique. This method was used to compare the abilities of the coatings to passivate after external polarization. The corrosion rates of the various coatings after polarization to 100 mV positive to their corrosion potentials are shown in Table I.The corrosion rate of the supersaturated Ni-rich alloy B was lower than that of A probably due to the deposit morphology. Of the two zinc-rich phases, E was superior to D probably due to the profound surface enrichment of Ni and P in E, as revealed by the Auger depth profile analysis.

TABLE I

OPEN-CIRCUIT CORROSION RATES

COATING TYPE	COMPOSITION	APPROXIMATE CORROSION RATE (μA/cm^2)
A	80.8Ni-13.3Zn-5.9P	7.0
B	62.2Ni-34.8Zn-3.0P	5.9
C	49.7Ni-49.1Zn-1.2P	14.8
D	33.4Ni-66.0Zn-0.6P	35.0
E	20.0Ni-79.4Zn-0.5P	21.9

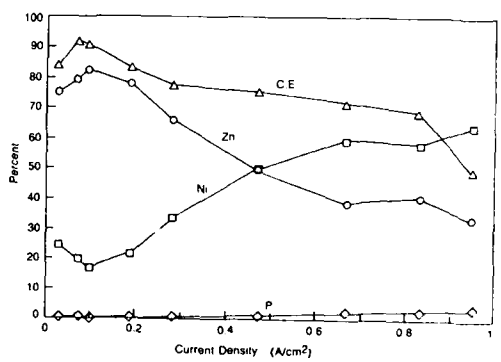


Fig.1 The dependence of alloy composition and current efficiency of NiZnP alloy on the applied current density at a copper rotating cylinder at 2000 rpm and 45°C

Abstract No. 355

Steady-State Multiplicity Analysis of a Mechanistic Model for Zinc Electrodeposition

Mark D. Pritzker and Thomas Z. Fahidy
Department of Chemical Engineering
University of Waterloo
Waterloo, Ontario, Canada N2L 3G1

Electrodeposition processes often exhibit behaviour characteristic of non-linear systems, such as the onset of oscillations, fluctuations, chaos and multiple steady-states, something which has generated some interest in using techniques of non-linear dynamics for their analysis. Recent developments in singularity theory now permit the steady-state multiplicity features of systems to be determined in a systematic way without an exhaustive parametric study (1-3). The primary objectives of this work are to introduce some of these techniques to electrochemists and to apply them to a mechanistic model of the electrodeposition of zinc proposed several years ago by Epelboin et al (4).

Model

Zinc electrodeposition is particularly attractive for this analysis since it has been observed to exhibit multiple steady-states (4,5). In the model proposed by Epelboin et al (4), Zn deposition, H_2 evolution, and the anodic adsorption of an anion A^- compete for available sites on the electrode surface according to the following scheme:

$$H^+ + e^- \xrightarrow{k_1} H_{ads} \qquad [1]$$

$$H^+ + H_{ads} + e^- \xrightarrow{k_2} H_2 \qquad [2]$$

$$Zn^{2+} + Zn^+_{ads} + e^- \underset{k'_3}{\overset{k_3}{\rightleftharpoons}} 2\,Zn^+_{ads} \qquad [3]$$

$$Zn^+_{ads} + H_{ads} \xrightarrow{k_4} Zn^\circ + H^+ \qquad [4]$$

$$Zn^+_{ads} + e^- \xrightarrow{k_5} Zn^\circ \qquad [5]$$

$$Zn^{2+} + H_{ads} + e^- \xrightarrow{k_6} Zn^+_{ads} + H_{ads} \qquad [6]$$

$$Zn^\circ + A^- \underset{k_7}{\overset{k'_7}{\rightleftharpoons}} ZnA_{ads} + e^- \qquad [7]$$

The kinetics of the process is expressed in terms of three state variables: the coverages of adsorbed intermediates H_{ads} (denoted as θ_1), Zn^+_{ads} (θ_2) and ZnA_{ads} (θ_3). Under steady-state conditions, the system can be described by the cubic equation

$$F(\theta_2, E, pH, [Zn^{2+}], [A^-]) = \theta_2^3 + B\theta_2^2 + C\theta_2 + D = 0 \qquad [8]$$

where B, C and D are each functions of potential E, pH, $[Zn^{2+}]$ and $[A^-]$.

Steady-State Multiplicity Analysis

A method which was developed recently can be used to map the regions in E-pH and $[Zn^{2+}]$ - pH space having particular numbers of feasible steady-states (1,2). For a function of the form of eqn [8], the boundaries of the parameter regions with different numbers of solution are determined by constructing the loci of fold points which satisfy the condition

$$F = \frac{dF}{d\theta_2} = 0 \qquad [9]$$

In addition, solutions to eqn [8] which fall outside the physically possible range of $0 \le \theta_2 \le 1$ must be rejected. This is done by constructing the loci of points for which F intersects the boundaries at $\theta_2 = 0$ and $\theta_2 = 1$, then superimposing them on the fold points.

A plot showing the number of solutions in E-pH space at $[Zn^{2+}] = 1$ M and $[A^-] = 1$ M (Figure 1) reveals some interesting features. Multiple steady-states exist in two separate regions of parameter space. The boundary set for $\theta_2 = 1$ intersects both of the regions having three solutions thereby reducing the number of allowable steady-states from three to two in the small regions bounded by the boundary sets and the loci of fold points. Equally interesting is the appearance of the large area at intermediate potentials where eqn [8] admits no feasible solutions.

Aside from knowing where multiple steady-states occur, the shapes of the curves describing the dependence of θ_2 (and current) on E are also of interest. Recently, a method has been developed to divide the parameter space into regions having specific types of bifurcation curves without having to solve the state equation directly and do an extensive parametric study (2,3). Details of this technique, the type of associated bifurcation curves and implications of the results for the model of zinc electrodeposition are discussed in the oral presentation.

References

1. Th. Bröcker and L. Lander, Differential germs and Catastrophes. Cambridge University Press (1975).
2. V. Balakotaiah and D. Luss, Chem. Eng. Sci., 39, 865 (1984).
3. M. Golubitsky and D.G. Schaeffer, Singularity and Groups in Bifurcation Theory, Vol. 1, Springer-Verlag, New York (1985).
4. I. Epelboin, M. Ksouri and R. Wiart, J. Electrochem. Soc., 122, 1206 (1975).
5. I. Epelboin, E. Lejay and R. Wiart, Compt. Rend. Acad. Sci. Paris, 274C, 178 (1972).

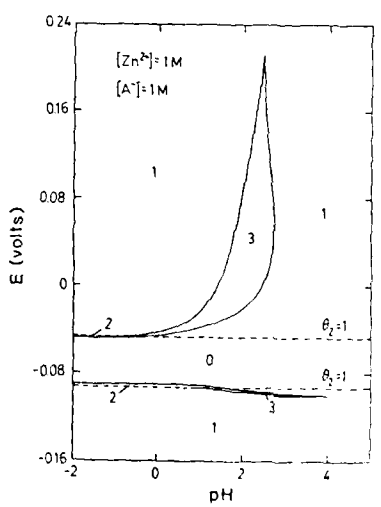


Figure 1. Regions in E-pH space having particular numbers of feasible steady-states for $[Zn^{2+}] = 1$ M and $[A^-] = 1$ M.

Abstract No. 356

Electrodeposition of Transition Metal Oxide Phases: Thermodynamic Aspects

Steven Crouch-Baker and Robert A. Huggins

Department of Materials Science and Engineering,
Stanford University, Stanford CA 94305, USA

Electrodeposition, typically from molten salt solvent systems at elevated temperatures, has been employed previously in a number of cases for the preparation of multicomponent transition metal oxide - based phases (1). However, it is apparent that only minimal attention has been given previously to the consideration of such electrodeposition processes in terms of the thermodynamic phase behaviour present in the solute - solvent system. Here, it will be demonstrated how the appropriate isothermal phase diagrams may be employed to rationalise and / or predict the various electrochemical reactions which may occur at both positive and negative electrodes during electrodeposition.

In order to successfully electrodeposit materials from molten salt solvent systems, it is essential that the solvent be electrochemically inert at both the working positive and negative electrode potentials. In this work it is shown how isothermal phase diagrams relevant to the solvent systems may be employed in order to calculate their voltage stability ranges.

Acknowledgement

This work was supported in part by ONR / DARPA under subcontract N00014 - 87K - 0800.

References

1. A. Wold and D. Bellavance, in Preparative Methods in Solid State Chemistry, ed. P. Hagenmuller (Academic Press, 1972) p. 279 and references therein.

Abstract No. 357

The Use of Insoluble Films to Control the Rate of Electrodeposition of Metals

Thomas C. Franklin, Venita Totten and Ali Aktan

Chemistry Department, Baylor University
Waco, Texas 76798

A study was made of the effect of additives on the rate of deposition of metals that form insoluble compounds involving the depositing metal. This film should, in certain cases produce a situation in which the metal is reduced from the insoluble film while the film inhibits the reduction of other metals. This technique is similar to the process that occurs in anomalous codeposition of metals (1,2,3).

Experimental

Voltammetric, current efficiency and alloy composition measurements were used to demonstrate the effects of the additives. Voltammetric measurements used standard potentiostatic techniques with platinum working and counter electrodes and a saturated calomel reference electrode.

Current efficiency determinations were made using platinum or copper foil cathodes. Deposition was made at 2.8 ma/cm^2 for two hours from 0.1 M solution of the metal ion. The efficiency was calculated from the weight of the deposit. Alloy deposition was done under similar conditions. The alloys were analyzed by x-ray fluorescence using a Princeton Gamma Tech, Energy Dispersive X-Ray Fluorescence Apparatus.

Results and Discussion of Results

The Use of Insoluble Films of Intermediate Valences.

One system studied was the formation of insoluble film from a reaction with intermediates in the reduction process. Thus, in the Cu(II) reduction,

$$Cu^{+2} \xrightarrow{+e} Cu^{+1} \xrightarrow{+e} Cu$$

Cu (I) will react with bromide to precipitate CuBr on the electrode. Voltammetric studies of this system indicated that addition of bromide ion inhibited hydrogen evolution but did not appreciably affect reduction of Cu(II). By comparison, deposition of cadmium, which does not form insoluble bromides, is not appreciably affected by bromide in the absence of copper deposition. This effect is also shown in current efficiencies and alloy composition studies. Tables 1 and 2.

[illegible]

Table 1

The Effect of Sodium Bromide on the Current Efficiency

Metal	Concn.(M)	Current Efficiency (%)
Cu	0	45
Cu	10^{-5}	45
Cu	10^{-1}	64
Cu	1	74
Cd	0	27
Cd	10^{-5}	26
Cd	10^{-1}	16

Table 2

The Effect of Bromide and Chloride on the Composition of Electrodeposited Alloys

Additive	Concn.(M)	Ratio of Cu/Cd
None	----	2.41
NaBr	10^{-5}	3.16
NaBr	1	3.73
NaCl	10^{-5}	3.92

electrolysis at hydrogen evolution in a sandwich type cell allows one to isolate the film and show by x-ray analysis that its formula is $Pb_6O_5(NO_3)_2$. One can show by voltammetry that tetrabutylammonium perchlorate (TBAP) protects this film from dissolution in the alkaline solution. Because of this protection addition of TBAP has a pronounced effect on the plating of lead. Table III shows the effect of TBAP on current efficiency and composition of electrodeposited alloys.

Table 3

The Effect of TBAP on Current Efficiency and Alloy Composition in Lead Deposition

Current Efficiency in lead deposition	Without TBAP 40%	with TBAP [illegible]%
Alloy Composition		
Ratio Pb/Tl	3.45	[illegible]
Ratio Pb/Cu	0.85	[illegible]
Ratio Pb/Ni	3.54	[illegible]

[illegible]

Acknowledgment

[illegible]

References

[illegible]

Abstract No. 358

The Use of Volumes of Activation to Determine The Mechanism of Action of Additives

Thomas C. Franklin and Shaj A. Mathew
Chemistry Department, Baylor University
Waco, Texas 76798

This study was a follow up of a previous study (1,2) demonstrating the possibility of utilizing volumes of activation (ΔV^*) changes to obtain information about mechanisms by which additives affect rates of deposition. In the previous study it was shown that in a $NiSO_4$, K_2SO_4, dilute KCl solution ΔV^* for nickel deposition was 13.4cm^3/mol, corresponding to the loss of two waters prior to electron transfer. At higher chloride concentrations or in the presence of borate ΔV^* dropped to 6.8 cm^3/mol, corresponding to loss of one H_2O prior to electron transfer indicating that chloride and borate form inner sphere electron transfer bridges. Thiocyanate caused ΔV^* to drop to 0.0 indicating that it served as an outer sphere bridge. In this paper the study was extended to include (a) The azide ion, (b) Some sulfonates and (c) Cobalt deposition.

Experimental

The high pressure vessel, which goes to 1750 atm(1), contained a Teflon electrochemical cell immersed in mineral oil. The pressure was adjusted with a hydraulic jack. The cell contained a small cathode of the metal and a Hg/Hg_2SO_4 counter electrode. The volume of activation was calculated from the equation

$$\Delta V^* = -RT\left(\frac{\partial \ln i_o}{\partial P}\right)_{n,T}$$

where the quantity in parenthesis was obtained from the slope of graphs of ln (i_o) vs pressure.

Results

Table I shows nickel results. Addition of azide, with its π clouds, causes ΔV^* to eventually drop to 0.0, indicating that the azide forms an electron bridge around the water.

Table I

Volumes of Activation (ΔV^*) for Nickel Deposition From Solutions Containing 0.5M $NiSO_4$, 0.1M K_2SO_4 and x "ME".

Additive	ΔV^* (cm^3/mole)
None	13.4
0.01M NaN_3	13.4
0.05M NaN_3	13.4
0.1M NaN_3	13.4
0.1M [illegible]	13.4
0.1M [illegible]	13.4
0.1M [illegible]	13.4
0.1M [illegible]	13.4
0.1M [illegible]	13.4
0.1M [illegible]	13.4
0.1M [illegible]	13.4

The sulfonates were strongly adsorbed. Propane sulfonic acid caused no change in the number of water molecules displaced, indicating that it acts as a blocking agent. However, when the unsaturated analog was introduced ΔV^* dropped to a low value indicating that it was an outer sphere electron bridge. In the presence of the naphthalene sulfonic acid ΔV^* dropped to 5.2 cm^3/mole indicating that the adsorbed naphthalene sulfonate served as a bridge for electron transfer. However, different from anionic additives, ΔV^* is slightly lower than ΔV^* for the loss of a water molecule in homogeneous water exchange.

Table II shows cobalt results. It can be seen that they are similar to nickel results

Table II

ΔV^* for Cobalt Deposition from Solutions Containing 0.5M $CoSO_4$ and 0.1M K_2SO_4

	Additive	ΔV^* ($cm^3 mole^{-1}$)
1.	0.01M KCl	12.4±0.3
2.	0.1M KCl	6.0±0.2
3.	1M KCl	5.9±0.2
4.	2M KCl	6.0±0.4
5.	3.5M KCl	6.0±0.3
6.	0.01M $NaClO_4$	12.3±0.2
7.	0.01M KCl,0.00001M KSCN	12.0±0.2
8.	0.01M KCl,0.01M KSCN	0.0±0.2

The ΔV^* for homogenous exchange of one water molecule on the cobalt ion is 6.1 cm^3/mole(3). The observed ΔV^*'s correspond to two waters lost without additive, one water lost with chloride (Inner sphere bridging) and zero waters lost with thiocyanate (Outer sphere bridging).

Acknowledgement

We express our appreciation to the Robert A. Welch Foundation of Houston, Texas for the financial assistance they have given to this work.

References

1. T.C. Franklin and S.A. Mathew, J. Electrochem. Soc., 134, No. 2 (1987).

2. T.C. Franklin and S.A. Mathew, "The Measurement of Volumes of Activation as a Tool for Understanding the Mechanism of Action of Additives in Electrodeposition," Paper presented at the Fall, [illegible] Meeting of The Electrochemical Society, [illegible] submitted to J. Electrochem. Soc.

3. [illegible]

Abstract No. 359

Electrocodeposition of Copper and Polystyrene Latex Particles on a Rotating Disc Electrode

Jorge L. Valdes* and Huk Y. Cheh

Department of Chemical Engineering and Applied Chemistry
Columbia University
New York, New York 10027

Electrocodeposition of metal and colloidal particles can yield composite structures with unique physicochemical properties. In order to advance a more fundamental understanding of this process an experimental study was conducted on the electrocodeposition of monodisperse colloidal polystyrene latex particles from an acidic copper sulfate electrolyte on a rotating disc electrode (RDE). This work focuses on elucidating two important mechanistic aspects of this process: 1) the influence of the rate of metal electrodeposition and 2) the prevailing transport conditions on the rate of particle deposition. Both of these factors are known to have an appreciable influence on the number density of particles incorporated in an electrodeposited composite film (EDC).

A monodisperse system of amide-modified polystyrene colloidal particles (Seragen Diagnostics) was used in the electrocodeposition experiments. The particles have an average diameter of 0.345μm with a standard deviation of 0.0035μm as determined by electron microscopy. Amide-modified polystyrene particles with active surface bound hydrophilic groups were found to have a high degree of particle stability in electrolytic solutions used in this study ($0.5MH_2SO_4$ and $0.05MCuSO_4$). A stable non-flocculating dispersion is essential to achieving uniform deposition and homogeneous composite films. In acidic solutions, the particles will have a positive surface charge density since the amide groups are expected to be protonated. A particle number concentration of $8.86x10^8/cm^3$ was kept constant throughout and conforms to dilute solution conditions. The electrolytic dispersion was prepared just prior to each experiment by measuring an accurate volume of the original 10% by weight suspension and introducing it into Milli-Q reagent grade water. In order to insure uniform dispersion of the particles, the solution was put into a mild ultrasonic bath for about 30 min.

Particle electrocodeposition experiments were performed on freshly electroplated copper surfaces. In order to minimize the influence of surface morphology and particle blocking effects we considered initial rates of particle electrocodeposition. The thickness of each composite film formed was kept constant and commensurate with the particle diameter. Electron microscopy was used to analyze the surfaces of EDC films and obtain an estimate on the intrinsic rate of particle deposition.

In Figure 1 are shown experimental results obtained for this electrocodeposition system. The particle Sherwood number is shown as a function of the applied current density and for various rotation speeds. The Sherwood number is a dimensionless way of expressing the flux or rate of particle deposition. We find that the intrinsic rate of particle deposition is not a function of the rate of the metal electrodeposition reaction. These results necessarily dictate that the volume fraction of particles in a composite film will decrease with increasing current density. In dimensionless terms, the volume fraction of particles in a composite film, f_v, can be expressed as,

$$f_v = \frac{Sh}{Sh + \beta\theta} \qquad [1]$$

where Sh is the particle Sherwood number, θ is the ratio of the applied current density to the limiting current density, and β is a dimensionless system parameter that accounts for the volume differential between the electrodeposited metal and particles.

In Figure 2 are shown experimental results obtained for the Sherwood number as a function of the particle Peclet number. The Peclet number is a dimensionless quantity which expresses the relative importance of hydrodynamic convection to Brownian diffusion. A larger Peclet number indicates a higher rotation speed. As a means of comparison, we have also plotted on this graph the expected curve for the deposition of particles under "perfect sink" or purely mass transport controlled conditions. For low Peclet numbers, the experimental data approaches "prefect sink" deposition. For larger Peclet numbers the kinetics of the interfacial particle deposition step becomes more rate determining. Assuming first-order kinetics in the deposition step, the experimental data can be described by the following rate expression,

$$Sh = \frac{0.616\,k\,Pe^{1/3}}{0.616\,Pe^{1/3} + k} \qquad [2]$$

A non-linear regression analysis of the experimental data yields a dimensionless rate constant k=0.238 for this system. The theoretical line corresponding to this value of the kinetic rate constant is also shown in Figure 2. The volume fraction of particles in the composite film can now be predicted by combining eqns.[1-2]. For the particle electrocodeposition system under investigation we find that the volume fraction of particles in the composite decreases precipitously with increasing current density. In general, the highest volume fractions are obtained at the lowest current densities. This kind of kinetic information is essential in designing process parameters to attain composite films with the desired particle number density.

REFERENCES

1. J.L. Valdes, *Deposition of Colloidal Particles in Electrochemical Systems*, Doctoral Dissertation, Columbia University (1987).

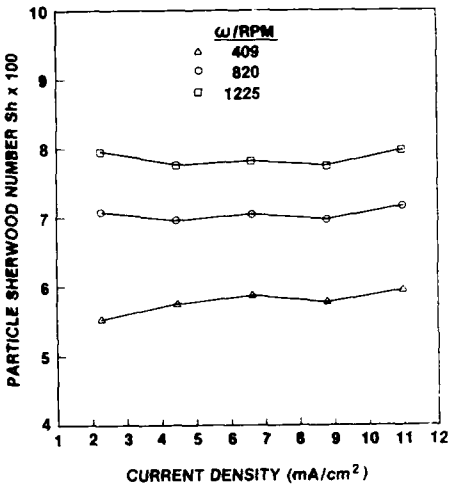


Fig. 1 The effect of current density and particle hydrodynamic transport on the intrinsic rate (Sherwood number) of polystyrene deposition.

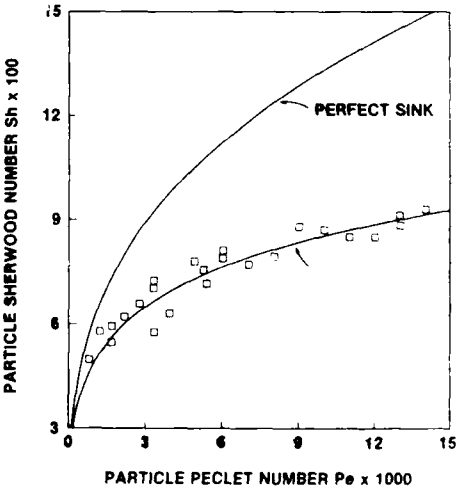


Fig. 2 Dependence of particle Sherwood number on Peclet number. "perfect sink" curve corresponds to particle mass transport controlled deposition

* AT&T Bell Laboratories, 600 Mountain Ave, Murray Hill, New Jersey 07974

Abstract No. 360

Laser Interferometric Wet Etch and Deposition Rate Measurement In-Situ at Solid/Liquid Interfaces (LESLI)

R. Vogel, O. Wolter, G. Makosch

German Manufacturing Technology Center,
IBM Germany, P.O. Box 266
7032 Sindelfingen, Germany

INTRODUCTION

Wet processes for deposition, dissolution or etching, play an important role in microelectronic manufacturing technology.

Among these we can distinguish between galvanic processes where the applied electrical current is a direct measure of the deposited or dissolved material, and so-called electroless processes. These latter ones are characterized by one or more additional electrochemical or chemical reactions occurring simultaneously at the electrode thus resulting in a zero net current.

Hence there is no electrical signal for the reaction rate with wet electroless processes.

METHOD

We could solve this problem by measuring in-situ the change in surface topography of a planar electrode during the electroless reaction. This is performed by directing the probe beam of a common path dual-beam interferometer towards the surface of the sample within a region where the reaction takes place (Fig. 1). The reference beam is focussed on a masked part of the electrode where the reaction is prevented.

The height or depth h of the unmasked region increases with progressing reaction and is linearly related to the measured phase difference Φ between the two reflected laser beams according to

$$h = \frac{\lambda}{4\pi \cdot n} \cdot \Phi$$

with λ being the vacuum wavelength of the laser beam and n the refractive index of the electrolyte.

This technique is based on using a Laser Spot Scanning Interferometer /1,2/ in combination with an electrochemical cell.

SILICON ETCH RATE MEASUREMENT

The anisotropic etching of silicon in aqueous KOH solutions is one of the key processes in Silicon Micro Machining. Therefore the electrochemical cell has been designed for etch rate measurement of Si in alcaline solutions enabling a precise positioning of the etch test pattern of the Si-wafer with respect to the window for the laser beams. Furthermore, we provided for the supply of electrolyte, heating, temperature measurement as well as monitoring and controlling the electrical potential of the Si-electrode referred to the reversible hydrogen electrode.

Fig. 2b shows the variation of the phase difference while silicon is etched in a concentrated KOH solution at a considerably high temperature of 59°C. At this temperature a strong formation of gas is observed which is supposed to disturb the phase evaluation. But data points are computed within 4 ms that means under quasi steady state conditions.

Therefore, only a few data points are randomly distributed as can be seen from Fig. 2b. These points contain no depth information. They are easily identified by simultaneously measuring the intensity of the reflected laser light (Fig. 2a) and eliminated. Fig. 2c shows the resulting etch depth versus time revealing a constant etch rate of 4.9 nm/s which corresponds to a current density of 15.7 mA/cm^2 with galvanic (anodic) dissolution of Si.

CONCLUSIONS

This example demonstrates the good sensitivity of this method the measured etch rate being far beyond the limit of detection. For practical purposes this limit can be estimated to 0.003 nm/s corresponding to 10 μA/cm^2 in the case of Silicon. To summarize we can state that LESLI is a true in-situ method for wet processes allowing the time saving measurement of etch or deposition rates.

REFERENCES

/1/ G. Makosch, B. Solf, SPIE 316(1981)
/2/ G. Makosch, B. Drollinger, Applied Optics 23, 4544 (1984)

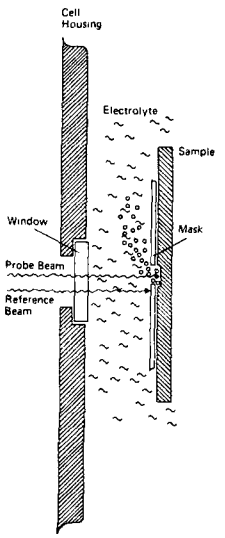


Figure 1: Principle of the etch or deposition rate measurement.

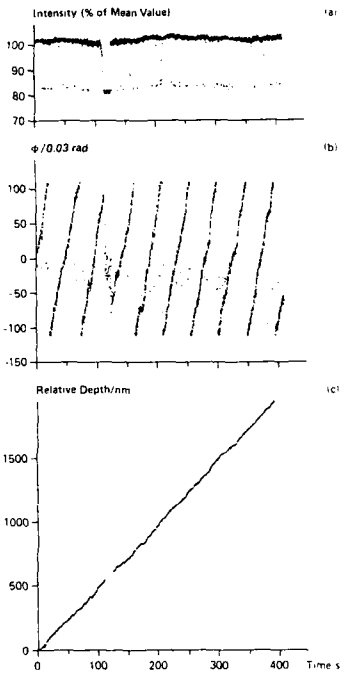


Figure 2: Total light intensity (a) reflected from the wafer as well as measured phase difference (b) between probe and reference beam versus time during the etching of <100> oriented silicon in 35 wt % KOH solution at 59 °C. (c) Etch depth versus time after data analysis.

Abstract No. 361

EFFECT OF TRANSPORT AND REACTION ON THE SHAPE EVOLUTION OF CAVITIES UNDERGOING ETCHING

Chee Burm Shin and Demetre Economou
Department of Chemical Engineering
University of Houston
Houston, TX 77004

INTRODUCTION

Etching and deposition in cavities is of great importance in the modern electronics industry. Examples include etching of GaAs for high speed devices and lasers, and copper deposition for printed circuit board fabrication. During wet etching of a thin film partially protected by a masking layer, the shape of the resulting cavity depends in a complex manner on the fluid flow distribution in the cavity region, on the mass transfer to and from the solid surface, and on the reactivity of the surface. Shape evolution studies in stagnant solutions (pure diffusive transport)(1), or convective transport in cavities of invariant shape(2) have been reported in the literature. However, the authors are not aware of any studies on the shape evolution of two-dimensional cavities under the influence of fluid flow.

The effect of fluid flow, transport, and reaction on the shape evolution of two-dimensional etching cavities was studied. The Streamline Upwind/Petrov-Galerkin (SUPG) finite element method(3) was employed since it is better suited for convection dominated flows (high Peclet numbers). A moving boundary scheme allowed for the shape evolution to be followed.

THEORETICAL

The computational domain and the finite element grid used are shown in Fig.1. The time dependent position of surface S influences the fluid flow distribution which in turn affects the further evolution of surface S. The fluid velocity profile in the near cavity region was obtained by solving

$$\frac{\partial \mathbf{u}}{\partial T} = -\nabla p + \frac{1}{Re}\nabla^2 \mathbf{u}$$

along with the continuity equation

$$\nabla \cdot \mathbf{u} = 0$$

Here the Reynolds number $Re = u_0 L/\nu$, where u_0 is the fluid velocity at the center of the mouth of the cavity, and L is the halfwidth of the cavity mouth. Also, $T = tu_0/L$. Boundary conditions included $u_y = 0$ on all boundaries, $u_x = 0$ on the lower boundary, u_x = constant on the upper boundary, and $\partial u_x/\partial x = 0$ on the left- and right-hand boundaries. The initial condition was $\mathbf{u} = \mathbf{u}_0$ at $T = 0$. The concentration distribution was found by solving

$$\frac{\partial C}{\partial T} + \mathbf{u}\cdot\nabla C = \frac{1}{Pe}\nabla^2 C$$

Here the Peclet number $Pe = u_0 L/D$. Boundary conditions included $\nabla_n C = -Sh\, C$ along the etching cavity surface, $C = 1$ along the left boundary where fluid enters, and $\nabla_n C = 0$ on all other boundaries. Here $Sh = Lk/D$, with k the surface reaction rate constant. The initial condition at $T = 0$ was $C = 0$ everywhere in the computational domain except that $C = 1$ at the left-hand boundary. In addition, the movement of the boundary was described by

$$\nabla_n C = -B v_n$$

where $B = u_0 L/\sigma c_0$, with σ a material property, c_0 the bulk reactant concentration, and v_n the velocity of the moving boundary. In the case of pure diffusion (no fluid flow) the diffusion equation solved was

$$\frac{\partial C}{\partial T^*} = \nabla^2 C$$

where $T^* = tD/L^2$. Boundary conditions included $\nabla_n C = -Sh\, C$ along the etching cavity surface, $\nabla_n C = 0$ along the mask surface, and $C = 1$ far from the etching surface. The initial condition was $C = 1$ everywhere at $T^* = 0$. The movement of the interface was described by $\nabla_n C = -B^* v_n$, where $B^* = D/\sigma c_0$. One notes that $B = Pe\, B^*$ and $T = Pe\, T^*$.

RESULTS AND DISCUSSION

Figure 2 shows a comparison of shape evolution profiles obtained using our numerical FEM solution with an asymptotic (perturbation) solution obtained for pure diffusion, and infinitely fast reaction(4). Good agreement is observed at early times for which the perturbation solution is valid. The agreement deteriorates with time since the perturbation solution is not valid for longer times. The etched profiles show a characteristic bulging near the mask edge. This is because of higher etch rate there due to reactant diffusion from areas above the inert mask. Figure 3 shows the shape evolution of a cavity etched under conditions identical to Fig. 2 except that the mask thickness was 25% of the cavity mouth width (instead of the infinitely thin mask of Fig.2). The bulging effect is much less pronounced due to the larger diffusion path of the reactant from the area above the inert mask to the etching surface. Etch anisotropy(ratio of cavity depth at x=0 to mask undercut) is also enhanced using a finite thickness mask.

The effect of fluid flow on the shape evolution of a cavity is shown in Fig.4. Conditions were otherwise the same as in Fig.3. The time scale on this figure has been rendered directly comparable with that of Fig. 3. One observes much faster etching as compared to the case of pure diffusion (about 5 times faster under the present conditions). The etched profiles are now asymmetric owing to fluid flow. At early times ($T^* < 20$) the cavity aspect ratio-(depth/width) is small and the external flow field invades the bottom of the cavity bringing fresh reagent in the cavity. The etch rate is then higher around the area where the fluid first encounters the bottom of the cavity (to the left of the centerline). The situation changes drastically at later times at which the cavity aspect ratio increases and a large recirculating fluid eddy occupies most of the cavity (see also Fig. 5). Under such conditions, fresh reactant first encounters the area around the right mask and the etch rate becomes faster there. For the same reason the undercut of the right mask is larger than of the left mask. Nevertheless, anisotropy is improved as compared to the pure diffusion case.

Figure 5 shows a velocity vector plot for the cavity corresponding to $T^* = 34.7$ in Fig.4. In addition to a large eddy filling most of the cavity volume, weak recirculation patterns are observed in the undercut regions. If etching is transport limited, the weak convection in the undercut regions reduces mass transfer resulting in enhanced etching anisotropy. Fig. 6 is a concentration contour plot for the same cavity as in Fig. 5. Larger concentartion gradients are observed in the undercut area of the right mask as compared to the left mask. This is the the reason for higher rate of undercuting of the right mask.

In conclusion, a mathematical procedure has been developed to analyze the shape evolution of two-dimensional etching cavities under fluid flow conditions. The model provided insight into the complex interaction of transport, reaction and cavity shape, and may be used to identify process operating conditions that lead to high rate anisotropic etching.

REFERENCES

1. C. Vuik and C. Cuvelier, J. Comput. Phys., 59, 247(1985)
2. R. C. Alkire, D. Reiser, and R. Sani, J. Electrochem. Soc., 131(12), 2795(1984)
3. A. N. Brooks and T. J. R. Hughes, Comp. Methods in Appl. Mech. Eng., 32, 199(1982)
4. H. K. Kuiken, Proc. R. Soc. London A 396, 95 (1984)

Acknowledgements

We are grateful to Drs. N. Aguilera and R. Glowinski for helpful advice and to Dr. H. Deans for use of his microVax computer.

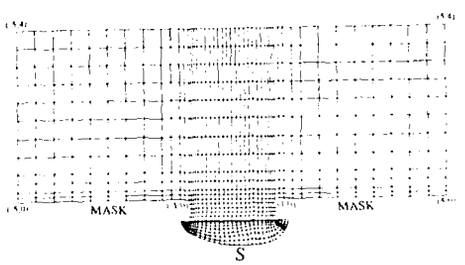


Fig. 1. Computational Domain and Finite Element Grid. The Final Cavity Shape Corresponds to Dimensionless Time of 34.7 under the Conditions of Fig. 4.

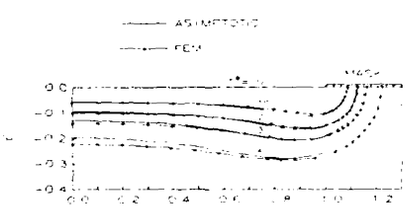


Fig. 2. Comparison of the Numerical Solution with an Asymptotic Solution Presented in Ref. 4. Stagnant solution (no fluid flow), and infinitely thin mask. $B^*=100$ and $Sh=\infty$.

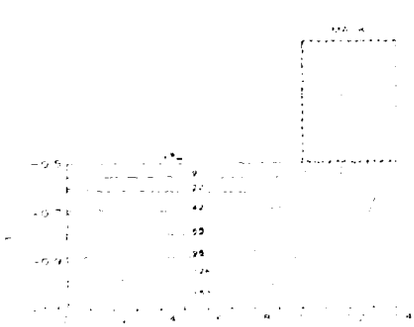


Fig. 3. Shape Evolution of a Cavity in a Stagnant Solution and with a Mask Thickness 25% of the Cavity Mouthwidth B^* 100 and $Sh=\infty$

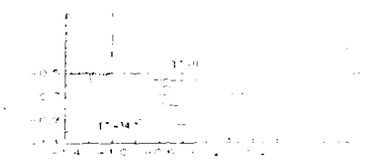


Fig. 4. Shape Evolution of a Cavity Under Fluid Flow Conditions. $Pe=100$, $Re=0.1$, $B^*=100$, and $Sh=\infty$. Cavity Wall Profiles are for Dimensionless Times T^* of 0, 1.88, 4.04, 7.31, 12.3, 18.9, 26.9, and 34.7 Respectively.



Fig. 5. Velocity Vector Plot in the Cavity Corresponding to $T^*=34.7$ of Fig. 4. Velocities are Normalized with Respect to the Velocity at the Center of the Cavity Mouth.



Fig. 6. Concentration Contour Plot in the Cavity Corresponding to $T^*=34.7$ in Fig. 4. Contour Named A Corresponds to Dimensionless Concentration $C=0.99$ Contour B (Wall of Cavity) Corresponds to $C=0$. Linear Interpolation Applies for the Contours in Between.

Abstract No. 362

AQUEOUS ELECTROCHEMISTRY OF TELLURIUM AT GLASSY CARBON AND GOLD: A COMBINED VOLTAMMETRY-OSCILLATING QUARTZ CRYSTAL MICROGRAVIMETRY STUDY

Eric Mori, C. K. Baker, J. R. Reynolds*
and K. Rajeshwar*
Department of Chemistry
The University of Texas at Arlington
Arlington, Texas 76019-0065

The electrochemistry of tellurium has been extensively studied in recent years because of its biological significance. Tellurium is also a component in binary and ternary HgCdTe. The cathodic electrochemistry of Te^{4+} is complicated by adsorption and homogeneous chemical reactions. In the course of our research on CdTe electrodeposition mechanisms (1), we observed a remarkable sensitivity of the voltammetry profile of tellurium to the nature of the electrode substrate. This aspect is addressed in this paper via comparative studies on glassy carbon and gold electrodes.

A sub-theme of this paper is the enhanced interpretative capability offered by the combined use of voltammetry and microgravimetry in studies on complex systems such as tellurium. Microgravimetry was performed using the oscillating quartz crystal balance. The data in this paper constitute what we believe to be the first examples of the use of this powerful *in situ* weighing technique in studies of semiconductor electrodepositions.

The representative voltammetry profiles in Figures 1 and 2 for glassy carbon and gold electrodes will be discussed with the aid of appropriate reaction schemes. The correctness of these reaction schemes was verified by concurrent data collected from coulometry and microgravimetry. The strong adsorption of Te^{4+} at the gold surface leads to a direct six-electron reduction of $HTeO_2^+$ to H_2Te. This process is not observed at the glassy carbon surface. Additionally, the adsorption of H_2Te at the gold surface leads to a catalytic pre-wave leading to the deposition of Te^0.

The above data are discussed within the context of related work done by previous authors on the electrodeposition mechanism of CdTe at the Pt surface (2).

ACKNOWLEDGMENTS

This research was supported in part by grants from the National Science Foundation (Grant MSM-8617850), the Defense Advanced Research Projects Agency (grant monitored by the Office of Naval Research), and the Research Corporation. The oscillator/potentiostat circuit for microgravimetry was donated by IBM Research Division, San Jose, CA.

REFERENCES

1. R. N. Bhattacharya, K. Rajeshwar and R. N. Noufi, J. Electrochem. Soc. 131, 939 (1984). R. N. Bhattacharya and K. Rajeshwar, J. Electrochem. Soc. 131, 2032 (1984). R. N. Bhattacharya, K. Rajeshwar and R. N. Noufi, J. Electrochem. Soc. 132, 732 (1985). E. Mori and K. Rajeshwar, to be published.

2. W. J. Danaher and L. E. Lyons, Aust. J. Chem. 37, 689 (1984).

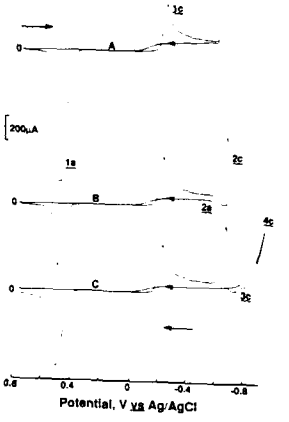


Figure 1. Cyclic voltammograms for Te electrochemistry at a glassy carbon electrode. Scans A through C had increasingly negative switching potentials: A -0.60 V; B: -0.70 V; C: -0.95 V.

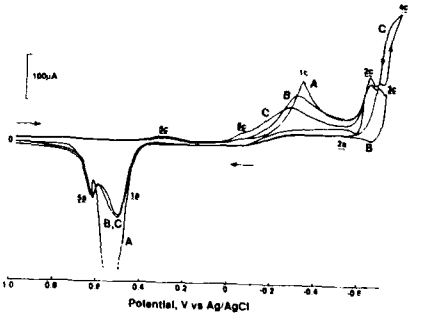


Figure 2. Cyclic voltammograms for Te electrochemistry at a Au electrode. Switching potentials for scans A through C were: A -0.55 V; B -0.65 V; C -0.70 V.

Abstract No. 363

ELECTROCHEMICAL DEPOSITION AND CHARACTERIZATION OF $CdSe_x Te_{1-x}$ ($0 \leqq x \leqq 1$) FILMS

Kohei Uosaki, Makoto Takahashi*, Noboru Karube and Hideaki Kita

Department of Chemistry, Faculty of Science, Hokkaido University, Sapporo 060, Japan

*Present address: High-Technology Research Laboratories, Kawasaki Steel Corporation, Chiba 260, Japan

II-VI compound semiconductors such as CdS, CdSe and CdTe are considered to be promising materials for low cost thin film photovoltaic and photoelectrochemical cells. Although a variety of methods have been employed to deposit semiconductor thin films, electrochemical deposition has many advantages including easy control of thickness, composition and properties of deposited films. In this paper, in order to establish a deposition method of a semiconductor films of desired energy gap, the electrochemical deposition of $CdSe_xTe_{1-x}$ ($0 \leqq x \leqq 1$) was attempted. Furthermore, effects of heat treatment on crystalline diameter and electronic properties of electrochemically deposited CdTe films were also studied.

The $CdSe_xTe_{1-x}$ films were deposited from aqueous solution of pH 1.4 containing $CdSO_4$ and TeO_2+SeO_2, the total concentration of which was 1 mM, on Ti sheets which were degreased by chloroform and ethanol vapor, etched in 10% HF and washed in purified water before use. The reageant-grade chemicals were used without further purification. Water was purified by Milli Q water purification system (Millipore Corp.). The usual three electrode cells were used and a platinum sheet and a Ag/AgCl electrode were used as a counter and a reference electrode, respectively. The heat treatment of the films was carried out in a quartz tube under a He gas flow. X-ray diffraction measurements were carried out by using Philips PW-1352 x-ray diffractometer.

Fig. 1 shows current-potential relations of Ti electrode in sulfuric acid solutions (pH=1.4) containing 1M $CdSO_4$ and various concentration of TeO_2 and SeO_2 (total concentration was 1 mM). In all cases, when the electrode potential became negtive, the cathodic current increased first but reached limiting value at more negative potentials. The higher the SeO_2 ratio was, the more negative the onset potential for the cathodic current was. The limiting current was considered to be controlled by the diffusion of TeO_2 and SeO_2 and did not depend on the SeO_2/TeO_2 ratio. When the potential became more negative than -0.65V, very large cathodic current due to Cd deposition flowed. Since current, i.e., reaction rate, is controlled by the diffusion of SeO_2 and TeO_2 in the limiting current region, it is expected that Se and Te are included in the deposited film depending on the SeO_2/TeO_2 ratio in the solution. In fact, $CdSe_xTe_{1-x}$ film where x depended on the solution composition was obtained by the potentiostatic deposition in the potential region where the limiting current was observed. Although the stable structure of CdSe is wrutzite, all the deposited films had zinc blend structure. The lattice constant varied depending on the SeO_2/TeO_2 ratio in solution as shown in Fig. 2.

Effects of heat treatment on crystalline diameter and electronic properties of electrochemically deposited CdTe films will be also reported.

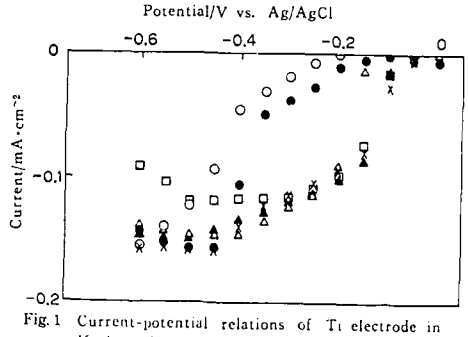


Fig. 1 Current-potential relations of Ti electrode in sulfuric acid solution (pH=1.4) containing 1 mol·dm⁻³ $CdSO_4$ and SeO_2+TeO_2

○ : SeO_2 1 mmol·dm⁻³
● : SeO_2 0.8 mmol·dm⁻³+TeO_2 0.2 mmol·dm⁻³
△ : SeO_2 0.6 mmol·dm⁻³+TeO_2 0.4 mmol·dm⁻³
▲ : SeO_2 0.4 mmol·dm⁻³+TeO_2 0.6 mmol·dm⁻³
× : SeO_2 0.2 mmol·dm⁻³+TeO_2 0.8 mmol·dm⁻³
□ : TeO_2 1 mmol·dm⁻³

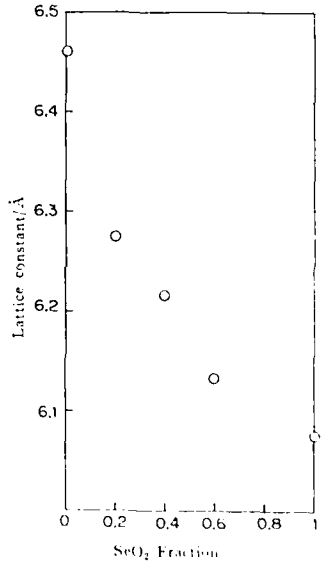


Fig. 2 Lattice constant of the electrochemically deposited films as a function of SeO_2 fraction in solution

Abstract No. 364

CATHODIC ELECTRODEPOSITION CHARACTERISTICS OF CdTe FILMS IN A NON AQUEOUS BATH.

R.K.Pandey, R.B.Gore
Department of Physics, Bhopal University,
Bhopal - 462 026, INDIA.

The renewed interest in electrodeposition of CdTe stems mainly because of its application in photovoltaic solar cells. Panicker et al. [1] reported the electrodeposition of CdTe from aqueous solutions. However, the grain sizes of the deposit are small (500-1000A^{o}) and the control of stoichiometry is difficult [2]. It is necessary to work at higher temperatures to obtain larger grain sizes and to use alternative source of tellurium to control the stoichiometry. In a recent report by the authors [2] it has been shown that large grained and stoichiometric CdTe layers for photovoltaic applications can be grown using a non aqueous bath of ethylene glycol (EG) containing $CdCl_2$, $TeCl_4$ and KI at 160^{o}C. In this paper, we report the cathodic deposition characteristics of Cd^{2+} and Te^{4+} in EG and the conditions to obtain nearly stoichiometric deposits.

The cathodic deposition characteristics of CdTe were investigated on polished nickel cathodes with respect to a platinum reference electrode. The increasingly negative potential sweeps were applied between the cathode and another platinum anode immersed in EG at 160^{o}C.

Fig.1 exhibits the cathodic polarisation curves for three cases viz. EG only (curve 1), EG+ M/3.3 KI (curve 2) and EG+M/3.3 KI+1M $CdCl_2$ (curve 3). The absence of any structure in curve 1 indicates that EG can be used safely for the electrodeposition purposes over a wide range of potentials. In curve 2, the cathodic current rises abruptly for potentials 1V (vs.Pt). This rise in current can be attributed to the onset of potassium deposition. The presence of Cd^{2+} in the bath however, prevents the onset of this process as is obvious from curve 3. The J_{Cd} onset point occurs at approximately 0.3V.

Fig.2 exhibits the cathodic polarisation characteristics in a bath containing EG+ M/3.3 KI and different concentrations of $TeCl_4$ at 160^{o}C. The commencement of J_{Te} onset can be seen to depend strongly on the $TeCl_4$ concentration. The J_{Te} onset shifts towards more negative values as the $TeCl_4$ concentration is increased. This negative shift is large initially and slows down for higher $TeCl_4$ concentrations.

The cathodic polarisation characteristics in presence of M/3.3 KI, 1M $CdCl_2$ and different molar concentrations of $TeCl_4$ are shown in Fig.3. Three distinct regions can be seen in this figure. The plateau region corresponds to CdTe formation. The region to the left of the plateau favours Te deposition while that towards right favoured Cd deposition. The deposition current can be seen to increase on both sides of the plateau region as the potential is swept in the negative direction. This behaviour is characteristic of a compound electrodeposition process where the deposition of one of the species is limited by diffusion [3,4]. The plateau current can be seen to increase in fig. 3 as higher concentrations of $TeCl_4$ were used.

The J_{Te} and J_{Cd} onset can also be seen to shift towards more negative values with increasing $TeCl_4$ concentration. The reasons for the observed negative shifts in the onset potentials are not very clear at this stage. One may associate the observed shift in the J_{Cd} onset potential to two possible reasons (i) An extra potential term due to the IR drop caused by the increased thickness of the CdTe film. (ii) The existence of an over potential term for the deposition of cadmium on CdTe.

One of the possible explanation for the shift in J_{Te} onset with the use of higher $TeCl_4$ concentration could be the adsorption of Te^{4+} ions on the cathode surface. A thin greyish overcoat was indeed observed on unbiased cathodes dipped in the electrodeposition bath. The compositional analysis of this overcoating was carried out with the help of an ESCALAB Mark II X-ray photoelectron spectrograph (V G Scientific, England) under ultrahigh vacuum conditions using MgK$_{\alpha}$ source and sputtering with Ar ion gun (for details see ref.5). The depth profile of this film is shown in Fig.4. Although signals corresponding to cadmium were also detected in the Survey scan, however, the narrow scan XPS peaks corresponding to Cd were very broad and their binding energies were not well defined. It thus, follows that, cadmium is present in traces only. A major part of the film was found to consist of tellurium whose concentration increased with increasing sputtering time. Our findings, therefore, give clear evidence of Te^{4+} adsorption on nickel cathodes. A possibility emerging from the above studies is that the non aqueous electrodeposition of CdTe consists of atleast two steps viz.(i) the adsorption of Te^{4+} on the cathode surface and (ii) its subsequent conversion into CdTe by the discharging Cd^{2+} ions.

According to the theory of compound electrodeposition [3,4], fairly stoichiometric films can be plated at a potential lying in the plateau region close to the J_{Cd} onset. It has been found by us that the potentiostatic deposition at 800mV in a bath containing 1M $CdCl_2$ and M/100 $TeCl_4$ yields fairly stoichiometric deposits. The depth profile of a typical as grown film under these conditions is shown in fig.5. The Cd:Te ratio in the bulk is 1:0.96 which is fairly close to the stoichiometric composition of CdTe. The presence of impurities of C and O can be due to their incorporation during handling of the samples and/or from the electrolyte. Carbon can be easily removed by subjecting the films to a post deposition annealing treatment.

The surface topography of the above films using SEM [2] revealed a fairly uniform surface with grain sizes $\gtrsim$1 μm. No sign of cracking could be observed in samples aged for seven days. Electrochemical photovoltaic cells with V_{oc} = 530 mV, J_{sc} = 5.6mA/cm^2, fill factor = 0.4 and efficiency = 2.4% have been fabricated from the as deposited films which proves their potential for photovoltaic applications.

References

1. M.P.R.Panicker, M.Knaster and F.A.Kroger, J. Electrochem. Soc. 125, 566 (1980).

2. R.B.Gore and R.K.Pandey, Thin Solid Films, (In press) (1988).

3. F.A.Kroger, J. Electrochem. Soc. 125, 2028 (1978).

4. R.D.Engelken and T.P.Van Doren, 132, 2904 (1985)

5. R.B.Gore, R.K.Pandey and S.K.Kulkarni, to be published.

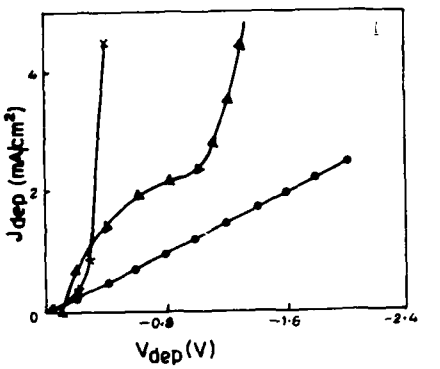
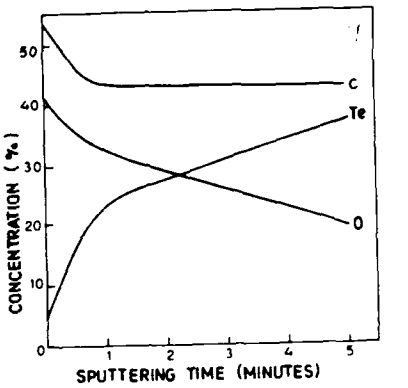


Fig.1 Cathodic deposition characteristics of [illegible] only; o—o : [illegible] Δ—Δ : [illegible] $CdCl_2$ x—x .



[illegible]

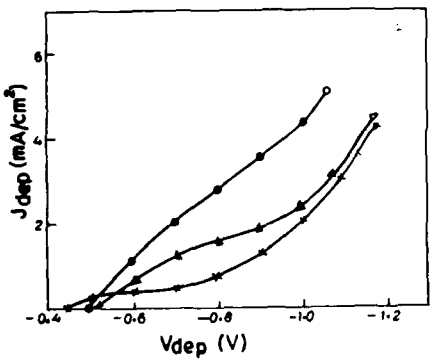
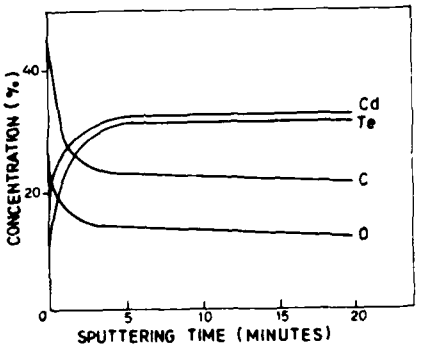
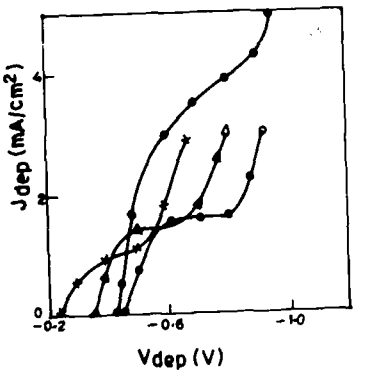


Fig.2 Cathodic deposition characteristics in presence of [illegible] /50 o—o : [illegible] /100 Δ—Δ : [illegible] /200 x—x $TeCl_4$ only.



[illegible]



[illegible]

Abstract No. 365

A FIRST-ORDER NUMERICAL ANALYSIS OF THE EFFECT OF INTERNAL OHMIC VOLTAGE DROPS ON THE ELECTRODEPOSITION OF BINARY COMPOUND SEMICONDUCTORS

Robert D. Engelken and Neal Sanders,
Department of Engineering, P.O. Box 1080,
Arkansas State University,
State University (Jonesboro), Arkansas 72467

It has been speculated[1] that ohmic voltage drops within the bulk of electrodeposited semiconductor films can have appreciable effects on the deposition mechanism and resultant film stoichiometry, especially with potentiostatic control. However, no detailed treatment of the problem, either theoretical or experimental, exists in the literature and such possible shifts in film surface deposition potential (E_S) are usually neglected experimentally without a real "feel" for whether this is justified. When superimposed onto additional voltage drops in space-charge regions at the deposit-substrate and deposit-electrolyte interfaces, these ohmic drops could conceivably cause dramatic effects.

We report preliminary theoretical analysis of the effect of bulk, ohmic voltage drops on the conventional underpotential deposition[1b] of II-VI compounds such as CdTe. The analysis and accompanying computer simulation indicates that (1) These voltage drops rarely have significant effects upon standard voltammograms with common sweep rates > 1 mV/s and (2) Deposition of intrinsic material at the potential of perfect stoichiometry (PPS) is extremely sensitive to these voltage drops with any deposition outside of the narrow, high resistivity[2] potential range near the PPS leads to sufficiently large native doping concentrations and low resistivities that deposition is relatively unaffected.

The analysis was conducted in terms of R.D.E.'s previous model for CdTe deposition[1b,c] by changing the "E-E°" terms in the exponential arguments of the Butler-Volmer Equations 4° and 4' in Reference 2a to "E-E° + $\beta_{total} \sum_{i=1}^{n} \rho_i j_{i-1}$", where E is the substrate-to-reference voltage, E° is standard reduction potential, "E-E°" is the standard overpotential, β_{total} is the total cathodic current density, and ρ_i is the resistivity of the differential thickness t_i plated during iteration i. Thus, $\beta_{total} \sum_{i=1}^{n} \rho_i j_{i-1}$ is simply the present current density (to be determined) multiplied by the total series resistance of the film as obtained by adding the individual resistances of each thickness element (on a per cm^2 basis).

Equations 4° and 4' become a two equation-two unknown set: $j_{Te} = f_{Te}(E, j_{Cd}, j_{Te})$ and $j_{Cd} = f_{Cd}(E, j_{Cd}, j_{Te})$ since E is specified at each t_i of the iteration.

This equation set was solved on a personal computer by an iterative procedure using the Turbo PASCAL Numerical Methods Toolbox™ programs: SECANT. INC (Borland International, Inc., Scotts Valley, CA, 1986). Normally, potentiostatic deposition was assumed with E(t) specified and j_{Te}, j_{Cd}, and hence, the stoichiometry determining variable $M = j_{Cd}/j_{Te} = 1/\chi$ subsequently determined. In other cases, β_{total} and M were specified and E(t) calculated.

The real gist of the problem is the change in resistivity, ρ, with stoichiometry and time. The prediction of intrinsic resistivity from native excesses or deficiencies in an extremely difficult problem[3] involving coupled equilibria between multiply-ionized vacancies and interstitial atoms and self-compensation effects. No completely satisfactory model exists in the literature. To initially avoid the order of magnitude increase in problem complexity associated with the defect thermodynamics, we used a first- order estimate of the native resistivity (related) Equation 11 and Fig. 4--Reference [3]:

$$\rho = \frac{1}{q(\mu_n n + \mu_p p)} \quad \text{where} \quad n = \frac{1}{2}\left[(N_D - N_A) + \sqrt{(N_D - N_A)^2 + 4n_i^2}\right], \quad p = n_i^2/n$$

N_D and N_A are MAX $\chi_{Cd} - \chi_{Te}$, 0 and MAX $\chi_{Te} - \chi_{Cd}$, 0 respectively, where χ_{Cd} and χ_{Te} are the gross Cd and Te, respectively, mole fractions in the deposit layer (t_{i-1}) under consideration, and n_i is the intrinsic carrier density. This assumes monovalent defects and complete ionization but gives a "ballpark" estimate of the change in ρ with ρ^{-1} due to stoichiometry changes about the PPS. ρ_{min} was taken as n_i^2/ρ_{maj}. Although somewhat simplistic, this model was convenient to utilize and provides first order ideas of how the bulk film voltage drops affect deposition.

Figure 1 exhibits a plot of the total cathode substrate-to reference (SHE) voltage required to force perfect stoichiometry in a 1cm² CdTe deposit. Since, j_{Te} is assumed to equal a constant diffusion-limited value of 103.90 μA/cm² near perfect stoichiometry, this is equivalent to the voltage required to force $j_{Cd} = 0.5 \, j_{Te} = 51.95$ μA/cm² so that $M = j_{Cd}/j_{Te} = 1/2$. Experimentally Fig. 1 would represent a plot of the compliance voltage versus time for a galvanostat set to 154.3[6] μA/cm². The intrinsic carrier density was estimated to be 7×10^{5}/cm³ which yielded, with mobility values $\mu_n = 1000$ cm²/V-s and $\mu_p = 50$ cm²/V-s, an intrinsic resistivity of 2×10^{9} ohm-cm. The iteration steps were set at 1[6] seconds of deposition per finite thickness element which corresponded to roughly 5.1 nm per second of deposition.

Figure 2 exhibits a corresponding plot of resistance vs. time showing the rapid buildup of film resistance with the intrinsic material. It has a slope of approximately [illegible] ohms/s which, with a current density of 154.3[6] μA/cm² over 1 cm², produces a slope of 0.012 V/s, a major drift. This indicates that if one can experimentally determine the true PPS for potentiostatic control, the rapidly increasing internal voltage drop would shift the actual deposit-surface-to-reference voltage positive, out of the narrow high-ρ region, and into a lower region heavily rich in Te interstitials and Cd vacancies. At this point, deposition will proceed with little subsequent change in surface voltage, stoichiometry, and resistivity.

This same effect might be anticipated with potentiostatic voltammetric analysis as E drifts negatively across the PPS. However, the simulations show that for "reasonable" sweep rates (< 1 mV/s , the time that the voltage is in the high-ρ region is short (< 1's) so the resistance buildup and ohmic voltage drop [illegible] ring with "reasonable" current densities (< 1 mA/cm²) are insufficient to perceptively alter voltammetric structure. However, space-charge regions and [illegible] effects, not considered in this analysis, might still cause visible structures.

Further work will focus on refinement of the model for resistivity as a function of stoichiometry and inclusion of solubility and phase segregation effects.

ACKNOWLEDGEMENTS: This work was supported, in part, by National Science Foundation Grant MSM-8[illegible]. We thank Dr. Krishnan Rajeshwar at the University of Texas-Arlington for his assistance.

REFERENCES:

1.(a) M.P.F. Paeleken, M. Enselen, and P.A. Kroon, J. Electrochem. Soc., 134, [illegible]; (b) R.D. Engelken and T.P. Van Doren, ibid., [illegible],
..(a) R.D. Engelken and T.P. Van Doren, ibid., [illegible], (1984); (b) R.D. Engelken, ibid., [illegible], (1987); (c) R.D. Engelken, ibid, [illegible].
3. K. Zanio, Cadmium Telluride-Semiconductors and Semimetals Volume 13, Academic Press, New York, [illegible] and references therein.

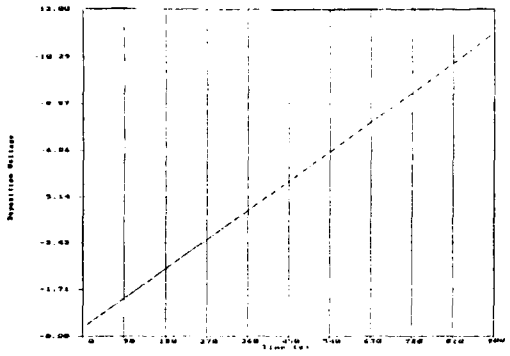


Fig. 1: Graph of total cathode substrate to reference electrode voltage required to maintain perfect (intrinsic) CdTe surface stoichiometry versus time for j_{total} = 154.35 μA/cm^2. Note the pronounced voltage drift (dV/dt = 12 mV/s).

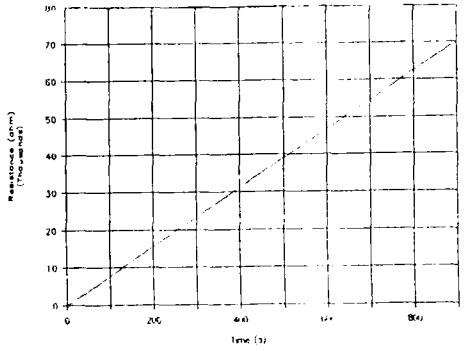


Fig. 2: Graph of CdTe film resistance versus time corresponding to Fig. 1; dR/dt = 77 ohms/s.

Abstract No. 366

Electrochemical Deposition of Single Crystal CdTe Films from Organic Electrolytes

A.C.Rastogi, K.S.Balakrishnan & G.L.Malhotra

National Physical Laboratory
Dr. K.S.Krishnan Road, New Delhi 110012 INDIA

Cadmium Telluride in thin film form is emerging as potential material for several optoelectronic devices including solar cells. A key requirement for such applications is that CdTe films should comprise of large size oriented crystallites. Electroplated CdTe films generally show nonstoichiometry, macroscopic cracks and poor crystallinity [1,2]. We describe here an electrochemical technique and growth conditions which yield essentially true single crystal CdTe films. Here, an organic electrolyte DMSO in place of an aqueous medium is employed. This enables deposition at higher temperatures ~140-150°C instead of the usual 80°C for aqueous medium. Thus the ions have sufficient kinetic energy on the substrate during deposition. Further, Te ionic species are made available in the electrolyte by dissolving Te in the elemental rather than reducible compound form. This overcomes the problem of wide variations in the overpotentials for Cd and Te ionic formation and deposition and hence that of film stoichiometry.

The electrodeposition of CdTe was carried out over precleaned SnO_2 coated conducting glass substrates. Other details are given elsewhere [3,4]. The electrolyte was 1M $CdCl_2$ & .1M Te dissolved in DMSO at 120°C. Films were deposited in the galvanostatic mode with nominal deposition current densities in the range 0.12 to 1.0mA/cm^2. Energy dispersive X-ray analysis show the film composition is near stoichiometric (Cd44%; Te56%) and remained invariant with the deposition current densities in the range studied. Thus the CdTe film formation is first by deposition of Te followed by a sufficiently rapid Cd-Te reaction with the tellurium ions. A well crystallised phase was present in the majority of CdTe films. The surface morphology as well as the crystallite size of CdTe films varied with the bulk concentration of ionic species. At low supersaturations [3], corresponding to current density <.25mA/cm^2, essentially the single crystal film or with its dimensions ~ .1 - 1. μm in ~ 10-20 thick film. The X-ray diffraction pattern was hexagonal crystallite structure with (111) planes parallel to the substrate (Fig.1). At higher supersaturations, the deposits are all polycrystalline with a preferred orientation. The crystallite size increases from the nominal to mixed cubic phase as deposition current density is increased from 0.05mA/cm^2 to 1mA/cm^2. Morphologically films are coherent, smooth and generally cracks free. The average crystallite size for a ~0.03μm thick film is ~7.5μm considerably larger than 0.1μm obtained by aqueous deposition [1]. During deposition cathodic overpotentials are observed to build up over few hundred ms to a steady state value. Ions at the substrate are thus unable to adjust to the new steady state condition and probably tend to diffuse on surface. This is evident from linear plots in Fig.2, which show time dependent deviation from steady state overpotentials ($\eta_t - \eta_\infty$) for different deposition currents in accordance with surface diffusion analysis [5] given by equations.

$$\ln(\eta_t - \eta_\infty) = -\ln(RT F^2 \cdot F k^2 o) - kT$$

and $\eta_\infty = RT F \cdot i / i_o + RT F^2 \cdot i k^2_o$

Relevent parameters from this analysis are shown in Table 1. Calculated equilibrium current density i_o, assuming a surface diffusion controlled growth, is in reasonable agreement with i_o determined from Butler-Volmer equation at high overpotentials only when the current density is below 0.25mA cm^{-2}. It differs by orders of magnitude at higher currents. This shows that growth of single crystal CdTe film is due to cooperative processes in which ions in the double layer first adsorb at planar sites on substrate, transfer charges and then diffuse across the surface to be eventually at either another nuclei, growth step or defect as shown in Fig.4. Surface diffusion tendency increases as deposition current densities increase and finally it ceases to be the deposition rate controlling process. Polycrystalline growth is then expected as is indeed observed. The critical nucleus size for a sustained growth is also very small under these conditions. Fig.4 enables every cluster of ions to form a nucleus. Below .25 mA cm^{-2} the growth nuclei are orders of magnitude richer, hence colonal nuclei with well defined crystallographic planes tend to grow. Thus the single crystal CdTe film growth in the present case is attributed to the preferred formation of initial nuclei with special orientation which finally determines the crystallite form of crystallites.

References:

1. M.P.R Panicker, M.Knaster and F.A.Kroger, J.Electrochem.Soc., 125,566 (1978)
2. L.P.Bicelli, G.C.Morisco, J.M.Bockris & E.C. Reys, J. Electrochem.Soc.,131, 2101 (1984)
3. A.C.Rastogi and K.S.Balakrishnan Int.J. Electron.,56,1,89 (1984)
4. A.C.Rastogi and K.S.Balakrishnan Electrochim.Acta, 31, 335 (1986)
5. W.Mehl and J. M.Bockris Can. J. Chem., 37, 189 (1959)

Table 1

SURFACE DIFFUSION GROWTH PARAMETERS

Current Density mA/cm²	k	Co (moles/cm³)	Equilibrium current density i: (A/cm²) io*	io+
.132	.640	1.04E-5	6.4E-8	4.0E-7
.18	.947	8.0E-6	7.3E-8	1.2E-7
.246	1.34	9.0E-6	1.2?E-7	1.85E-7
.69	2.07	1.2E-5	2.?0E-7	3.1E-10
.??	2.35	1.??E-5	2.49E-7	3.?E-11

* is by surface diffusion analysis

\+ is by Butler-Volmer steady state equation at high potentials

k : Coefficient of ion diffusion flux $J_{sD}=k(C_s-C_o)$

Co: Equilibrium adion concentration



Fig.1 Electron micrograph of ~600Å thick film deposited at current densities ~2.5mA·cm⁻² showing single crystal platelets ~1μm. Inset electron diffraction bar indicates .25μm



Fig.2 Electron micrograph of a ~600Å thick polycrystalline CoSe film deposited at current density ~1mA·cm⁻². Inset shows electron diffraction. Bar = .1μm

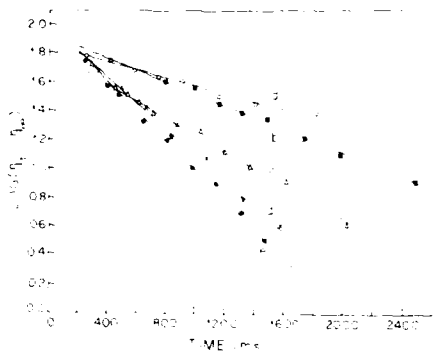


Fig.3 [illegible] transient time [illegible] for deposition reaction controlled by ionic surface diffusion as the rate determining process.

A,B,C,D,E,F = proposed curve shapes [illegible] ~1mA·cm⁻², room temperature.





Fig.4 Critical nuclei size calculated from measured steady state current-potential [illegible] for [illegible] ion concentration [illegible] ~1mA·cm⁻²

Abstract No. 367

ELECTRODEPOSITION OF $Cd_{1-x}Zn_xS$ and $Cd_{1-x}Bi_xS$ FILMS

C.D. Lokhande, V.S. Yermune, M.S. Jadhav,
R.D. Madhale and S.H. Pawar

Energy Studies Laboratory, Department of Physics,
Shivaji University, Kolhapur -
416 004 (India).

The preparation of thin film semiconductors with electrodeposition technique has some advantages over other physical and chemical deposition techniques. It is easy and economical as semiconductors with no or small waste of materials could be prepared. A flexibility in the electrodeposition technique is attractive. A variety of electrodeposition techniques, either singly or in combination with others have been reported to produce better quality semiconductors. This technique has been employed for the deposition of elemental, binary and ternary semiconductor thin films onto different substrates[1-3]. The ternary semiconductors include $CuInSe_2$, $CuInS_2$, $CuInTe_2$, $AgInSe_2$, HgCdTe etc.

In this paper, we report on the electrodeposition of $Cd_{1-x}Zn_xS$, and $Cd_{1-x}Bi_xS$ thin films ($0<x<1$). The films were prepared from aqueous acidic and alkaline solution baths. Sodium selenosulfate was used as a sulphur source and EDTA was used as a complexing agent. The films were deposited on ITO, Ti and stainless steel substrates. All depositions were carried out at room temperature without stirring the bath.

As deposited $Cd_{1-x}Zn_xS$ films were well adhesive to the substrates and the film thickness was 2-3 um for the deposition period of 30 min. The films are polycrystalline in nature. The polarization curves showed that the electrodeposition potentials for alkaline baths were higher than in the acidic baths and films were of better quality with alkaline baths. The bandgaps of CdS and ZnS were estimated as 2.4 and 3.55 eV, respectively. The nonlinear dependence of bandgap on Zn content was observed.

The $Cd_{1-x}Bi_xS$ films from acidic baths were rough and amorphous or consisted of fine grains. The alkaline bath films were smooth. The electrodeposition potentials varied between - 200 to - 100 mV(SCE) as Bi content increased in the films. The optical absorption studies showed that the Bi_2S_3 has indirect (1.4 eV) and direct (1.8 eV) bandgaps. The dependence of Eg on Bi content in $Cd_{1-x}Bi_xS$ films is nonlinear.

The (photo) electrochemical studies of $Cd_{1-x}Zn_xS$ and $Cd_{1-x}Bi_xS$ films showed that the films are photoactive and n type in nature.

1. D. Elwell, J. Cryst. Growth 52 (1981) 741.

2. B. Fatus, P. Herrasti and F. Arjona. E.G. Camarero. Abst. 327. 169th Electrochem. Soc. Meeting, Boston, May 4-9 (1986) Vol. 86-1.

3. C.D. Lokhande, J. Electrochem. Soc. 134 (1987) 1727.

Abstract No. 368

ELECTRODEPOSITION OF $CuInSe_2$ THIN FILMS FROM AQUEOUS SOLUTION

G. MAURIN, D. POTTIER

LP15 du CNRS "Physique des Liquides et Electrochimie"
Tour 22 - 4 place Jussieu
75252 Paris Cedex 05 - FRANCE

$CuInSe_2$ is a semiconducting material specially attractive to make absorbing electrodes in photoelectrochemical devices. It was demonstrated that a single crystal electrode in contact with a I/I^- redox solution is protected against photocorrosion by a solid heterojunction and, so, presents a good solar conversion efficiency during very long times (1,2). Several attempts were performed in order to prepare thin polycrystalline $CuInSe_2$ films by various techniques and more particularly by using electrocrystallization. A first approach consists in preparing a Cu-In film, by alloy deposition or by alternating deposition of Cu and In layers, followed by a chemical treatment of selenization (3,4). The simultaneous codeposition of the three elements was also successfully achieved, however the deposits were generally quite amorphous and required a heat treatment to improve their crystallinity (5,6).

The aim of this study is to analyse the electrocrystallization kinetics involved in the simultaneous deposition of the three elements, in order to determine the conditions leading to the formation of the definite compound with a good chalcopyrite structure (7). Considering the disparate values of the equilibrium potentials (E_{Se} = -0.05V ; E_{Cu} = -0.38V and E_{In} = -1.06V/SSE, for $c = 10^{-2}$M/l and pH = 2) the addition of a complexing agent appears to be necessary. On the base of the works of Chassaing and al (8) on copper electrodeposition, a sulfate solution containing citrate ions was chosen. Compound layers were deposited at room temperature on a Ti or Ni rotating disc electrode (Ω = 500 rpm) and investigated by various techniques as X-Ray diffraction, SEM and energy dispersive X-Ray analysis. The bandgap was evaluated by spectrophotometry of reflected light. The electrolyte solution is an acidic aqueous solution ($1.5 < pH < 4.5$) of $CuSO_4$ (5 to 10mM/l), $In_2(SO_4)_3$ (10 to 20mM/l), SeO_2 (10mM/l) and K_2SO_4 (60 to 80mM/l) containing 20 to 80mM/l of sodium citrate.

In a preliminary step the electrodeposition of the CuIn, Cu-Se and In-Se binary alloys was explored. For example Fig.1 deals with the Cu-In system. Without any complexing agent (polarization Curve 1) pure copper is formed at first. The current tends to be limited by Cu^{++} diffusion. Beyond E_{In} = -1.06V/SSE, In^{3+} ions are also reduced. The deposit is then a black, poorly crystallized Cu + Cu_4In + Cu_9In_4 mixture. Its pulverulent structure induces an irreversible rise of the current. Addition of citrate (Curve 2) shifts E_{Cu} towards negative values, lowers the plateau current corresponding to the diffusion of free Cu^{++} ions, and a new plateau appears beyond ≈ -1.45V/SSE which corresponds to the formation of smooth and well crystallized layers of Cu_9In_4. The formation of this definite compound appears to be correlated with the slowing down of the interfacial reaction by the citrate ions.

Polarization curves corresponding to the deposition of the ternary compound are presented on Fig.2. Without citrate (Curve 1) the current is not stationary because of the formation of a powdery deposit of a Cu_3Se_2 + Cu mixture. Traces of In are detected by microanalysis. After addition of complexing agent (Curve 2) appears two plateaus. On the first one, more or less marked depending on $\langle Cu^{++} \rangle$, are obtained heterogeneous layers of $Cu_{2-x}Se$ belonging to the Berzelianite structure. The second plateau is relevant to the formation of smooth and dense layers of Cu-In-Se alloys (Fig.3). Like in the case of the CdTe electrodeposition (7), the variations of this plateau current versus the rotation rate (in a I^{-1} vs $\Omega^{-1/2}$ plot) do not follow the Levich's law indicating that the overall deposition rate is limited by mass transport and by a slow surface process. On the plateau, the composition of the deposit varies with the potential, in particular, the Cu/Se ratio decreases then the potential becomes more negative. Finally the best deposits are obtained at -0.95V/SSE. The X-Ray diffraction diagram (Fig.4) is characteristic of the tetragonal chalcopyrite structure, with a strong (204,220) preferred orientation.

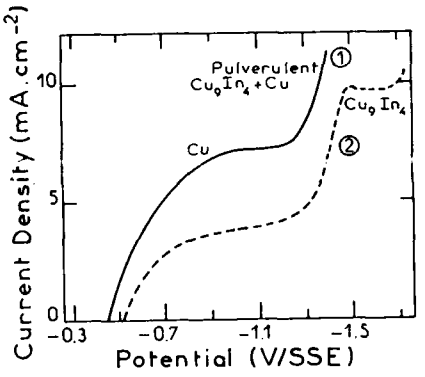
As CdTe, $CuInSe_2$ is obtained at a potential less negative than the equilibrium potential of the less noble metal. According to the Kröger's theory (9), this shift of potential would be due to the gain of Gibbs free energy provided by the crystallization of the definite compound.

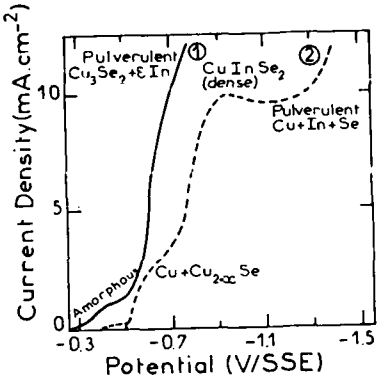
The Fig.5 presents the total light reflectance versus the wavelength for deposits prepared at two different potentials. The bandgaps (0.95eV and 1.16eV) evaluated from the characteristic wavelengths are close to the theoretical value (1.08eV).

The responses of these layers used as active electrode in a photoelectrochemical cell are presently investigated.

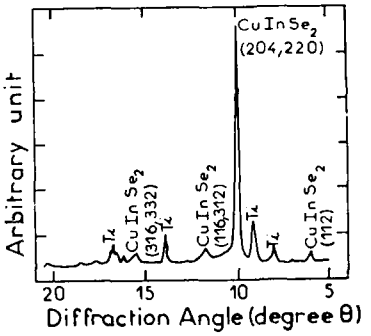
References

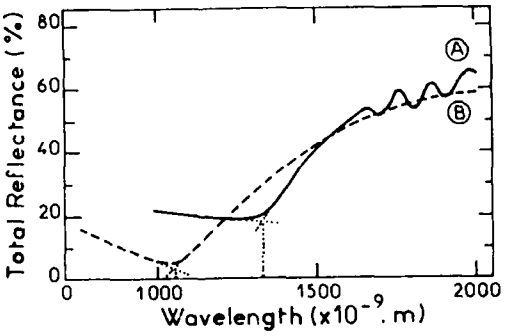
(1) S. Menezes
Appl. Phys. Letters, 45, 148 (1984).
(2) J. Szot, D. Haneman
J. Appl. Phys., 59, 2249 (1986).
(3) G. Hodes, D. Canen
Solar Cells, 16, 245 (1986).
(4) V.K. Kapur, B.M. Basol, E.S. Tseng
Comm. Meeting of Electrochem. Soc., Boston (1986), Abstract n° 312.
(5) R.P. Singh, S.L. Singh, S. Chandra
J. Phys., D. Appl. Phys., 19, 1299 (1986).
(6) R.N. Batthacharya
J. of Electrochem. Soc., 130, 130 (1983).
(7) M. Froment, G. Maurin
31st IUPAC Meeting, Sofia, July 1987.
(8) E. Chassaing, K. Vu Quang, R. Wiart
J. of Appl. Electrochem., 16, 591 (1986).
(9) F.A. Kröger
J. of Electrochem. Soc., 125, 2028 (1978).


Current Density (mA.cm^{-2})
Potential (V/SSE)
Pulverulent
Cu_9In_4+Cu
Cu_9In_4
Cu
①
②


Current Density(mA.cm^{-2})
Potential (V/SSE)
Pulverulent
Cu_2Se_2+2In
①
CuInSe$_2$
(dense)
②
Pulverulent
Cu+In+Se
Amorphous
Cu+Cu_{2-x}Se




Arbitrary unit
Diffraction Angle (degree θ)
CuInSe$_2$
(204,220)
CuInSe$_2$
(316,332)
CuInSe$_2$
(116,312)
CuInSe$_2$
(112)
In
In
In


Total Reflectance (%)
Wavelength (x10^{-9}. m)
Ⓐ
Ⓑ

Abstract No. 369

One-Step Electrodeposition of Polycrystalline $CuInSe_2$ Thin Films and Their Properties

F. J. Pern and R. Noufi

Solid State Research Branch
Solar Energy Research Institute
1617 Cole Blvd.
Golden, CO 80401

Introduction

Polycrystalline $CuInSe_2$ thin films have shown promise as a stable semiconductor material for producing high efficiency solar cells (1,2). For achieving low-cost, large area production of $CuInSe_2$ thin films, electrodeposition is an attractive process with high efficiency in material use and scalability. There has been significant efforts devoted in electrodepositing $CuInSe_2$ thin films with varied degree of success (3,4). In this paper, we discuss our efforts in the development of the one-step electrodeposition process. Effects of post-annealing conditions and chemical treatments will also be described.

Experimental

The thin films were deposited potentiostatically from a unstirred, deareated aqueous solution onto Molybdenum (Mo)-coated substrates. The solution formulation and the concentrations of the key ingredients (Cu(II), In(III), and H_2SeO_3) were adjusted empirically. The deposition process was controlled by a computer-based instrumentation with a program developed to deposit either single layer or bi-layer films with desired thickness (5). Post-annealing was carried out in flowing argon in a tube furnace. Potentials are reported vs. SSCE.

Results and Discussion

One-Step Electrodeposition Process

Since In cannot be directly deposited on Mo due to poor surface affinity, the one-step electrodeposition method required modification of the Mo surface. This was accomplished by depositing a layer of Cu and Se mixture that would provide the reaction (deposition) sites needed for In ions from Cu^{2+} and H_2SeO_3, whose reduction potentials on Mo electrode surface are 0.18 V and 0.0 V, respectively. Formation of a smooth layer of Cu and Se mixture on Mo promoted the underpotential deposition of In at potential as low as -0.2 V when compared to the reduction peak potential of -0.80 V (no In film formation) of In^{3+} on Mo.

Solution Formulation vs. Film Quality

The solution formulation is critical for a successful one-step electrodeposition to produce high quality $CuInSe_2$ thin films with desired composition, uniformity, smooth morphology, high density and good adhesion. To achieve smooth morphology, deposition rates of Cu and Se had to be controlled by using relatively low solution concentrations of $CuSO_4$ and H_2SeO_3, which also promoted higher film density. Leveling agents were also used to further improve the film morphology (6). The electrodeposited films have also shown good adhesion.

Deposition Conditions

The films were deposited potentiostatically from unstirred solution to establish the steady state mass transfer-limited reaction condition in 30 seconds. This helped produce good compositional and thickness uniformity. Fig. 1 shows the film composition as a function of deposition potential in the range from -0.75 V to -0.55 V. The as-deposited films are normally rich in Se (> 50 at%), which is reduced to ~ 50 at% upon annealing in Ar while the Cu/In ratio remains virtually unchanged. For making bi-layer $CuInSe_2$ films, a two- or three-potential method was employed. The potential change was computer-controlled.

Thin Film Structure

The as-deposited thin films normally have small grains, whose size is increased upon annealing. Chalcopyrite structure is observed for Cu-rich or near-stoichiometric thin films. Figure 2 shows the x-ray diffraction patterns of (a) as-deposited and (b) annealed film, compared to (c) a vacuum-evaporated $CuInSe_2$ thin film. As the film composition becomes In-rich, sphalerite structure is observed.

Chemical Treatments

The effects of etchants on removing the impurities from grain boundaries and on the film composition, structure and electrical propetties are interesting. Data will be presented which will show how Cu-rich films are converted into In-rich films upon treatment in cynide-based solutions.

Photovoltaic Devices

Devices made of the annealed $CuInSe_2$ thin films were all photovoltaically active. Their spectral responses and performance will be presented.

References

1. R. A. Mickelsen and Wen S. Chen, Proc. 16th IEEE Photovoltaic Specialists Conf., San Diego, CA, Sept. 27-30, 1982, IEEE, New York, 1982, pp. 781-785.
2. R. A. Mickelsen and W. S. Chen, Proc. 7th Int. Conf. on Ternary and Multinary Compounds, Snowmass, CO, Sept. 10-12, 1986, pp. 39-47, MRS, Pittsburgh, PA.
3. R. N. Bhattacharya and K. Rajeshwar, Solar Cells, 16 (1986) 237.
4. I. Shih and C. X. Qiu, Proc. 19th IEEE Photovoltaic Specialists Conf., New Orleans, LA, May 4-8, 1987, IEEE, New York, 1987, pp. 1291-1294.
5. F. J. Pern, J. Goral, R. J. Matson, T. A. Gessert and R. Noufi, to be published in Solar Cells.
6. F. J. Pern, R. Noufi, A. Mason, and A. Swartzlander, Proc. 19th IEEE Photovoltaic Specialists Conf., New Orleans, LA, May 4-8, 1987, IEEE, New York, 1987, pp. 1295-1298.

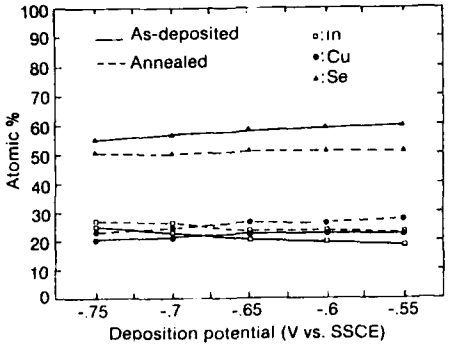


Fig. 1. Composition of as-deposited (———) and annealed (----) single layer thin films deposited at various potentials.

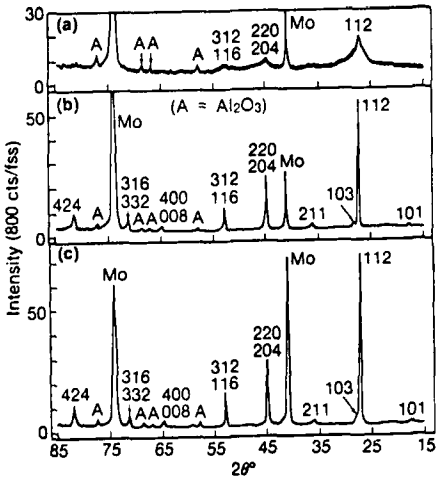


Fig. 2. X-ray diffraction patterns of (a) a as-deposited film, (b) annealed film, and (c) a vaccum-evaporated $CuInSe_2$ showing the chalcopyrite structure.

Abstract No. 370

MECHANISM FOR THE ELECTRODEPOSITION OF CdS FROM A NONAQUEOUS SOLUTION

Steffen PREUSSER* and Michael COCIVERA

The Guelph-Waterloo Centre for Graduate Work in Chemistry
University of Guelph, Guelph, Ontario N1G 2W1 (Canada)

Stoichiometric cadmium sulfide thin films have been successfully prepared from nonaqueous solutions (propylene carbonate) using triphenylstibine sulfide (TSS), cadmium perchlorate and lithium perchlorate as a supporting electrolyte[1]. Using room temperature deposition baths, CdS coatings were fabricated that had good, reproducible solar conversion properties. The advantage of utilizing ambient temperatures is that the electroplating solutions are stable almost indefinitely (some have been kept for over two months). Galvanostatic deposition conditions were used because of the high resistivity of the as-deposited films (~10^6 Ω·cm). Unfortunately the reported current densities needed to procure uniform and stoichiometric films were quite low (~100 μAmp/cm²), necessitating long deposition times (1-2 hours). For this reason, the electrodeposition mechanism was studied to determine conditions that permit increased current densities without the risk of incorporating cadmium metal impurities and the results are reported in the present paper. After the first few monolayers, the electrochemical process occurs at the CdS/solution interface. As a result, almost all of the film growth is determined by the electrochemistry at this interface. Consequently the electrodeposition mechanism was studied at this interface.

To determine if the mechanism changed with temperature, the process was studied at various temperatures up to 100°C. The kinetic order at 100°C was the same as that at 22°C. For the elevated temperature experiments, triflate salts were used, due to the instability of perchlorates at these temperatures.

Because films of CdS containing cadmium metal deposits are not photoactive, limiting deposition currents were determined. The minimum current density at which cadmium deposition begins depends on the [TSS]:[Cd^{2+}] ratio in solution and on the temperature. The electrodeposition of CdS from TSS solution was also found to occur electrolessly at 100°C at a very slow rate.

Reference

1. S. Preusser and M. Cocivera, Solar Energy Materials, 15, 175-188 (1987).

Abstract No. 371

DEVELOPMENT OF A NOVEL "GENERIC" TRIPLE SOLVENT BATH FOR ELECTRODEPOSITION OF METAL CHALCOGENIDE AND "BRIGHT" METAL FILMS

PART I: COMPARISON/CONTRAST OF PRESENT SINGLE/DOUBLE SOLVENT BATHS

Robert D. Engelken, Hal McCloud
David Moss, Emmett Smith
Hoshang Hormasji, and Wendell Wells
Arkansas State University, P.O. Box 1080
State University (Jonesboro), Arkansas 72467

The Molecularly Dissolved Chalcogen (MDC) method for electrodepositing metal sulfides and selenides, as pioneered by Baranski and Fawcett[1] and investigated by us[2], utilizes organic solvents (e.g. ethylene glycol) in which metal salts are ionically soluble and sulfur and/or selenium are soluble in the elemental, molecular, zero-valence states; e.g. S_X molecules, X = 1-8. The compound film is formed by (1) The plating of the metal followed by rapid chemical reaction with the double layer chalcogen and/or (2) Reduction of chalcogen molecules to anions (e.g. $S^=$) which precipitate with "free" metal ions at nucleation sites on the cathode surface. The method is versatile and valuable for depositing a wide range of metal chalcogenides.

However, strong coordination complexes formed between the solvent and metal ions limit the concentration of "free" metal ions as well as reduce the effective rate constants/transfer coefficients. Thus, metal deposition is often "sluggish" in pure organic solvents, especially near room temperature (T). Current densities (j) may be as low as 10-100 $\mu A/cm^2$ at voltages sufficiently low in magnitude to avoid rapid solvent electrolysis (and bath "poisoning") at anode and cathode. The increased viscosity of many organic solvents over that of H_2O also reduces ionic mobility and bath conductivity, and increases voltage drops across the bath.

Another problem with pure organic baths is that many of the anions of soluble metal salts are troublesome. For example, chlorides tend to form dendritic, powdery deposits, especially with pure metal plates. Nitrates drastically decrease cathode current efficiency and perchlorates are hazardous and themselves cathodically reduced. Organic anions are subject to electrochemical modification and often chelete the metal ions and inhibit deposition. The "perfect" anion, sulfate, is rarely useable since most metal sulfates are relatively insoluble in pure organics.

Molecular chalcogen is itself only moderately soluble in most organics near room T. For example, the solubility of sulfur in ethylene glycol is of order 10^{-2} M at room T.

At the other extreme, molecular, unionized chalcogen is not soluble in pure aqueous solutions so the MDC method is not readily applicable. Furthermore, aqueous solutions tend, in the absence of chelating or brightening agents (e.g. CN^-), to yield large-grained, mat-like metal deposits rather than mirror-smooth plates with microscopic uniformity, as often desired in semiconductor applications. Industrial sulfate-based plating baths often require brightening agents to be effective.

For example, one area where absolutely uniform metal plates are needed is the formation of metal chalcogenides such as $CuInSe_2$ by sequential electroplating of precision thicknesses of some or all of the elements followed by annealing, often in an atmosphere of H_2X.[3] Furthermore, j's $\geq$ 100's $\mu A/cm^2$ and high current efficiencies (η) are desirable. EDTA can shift $E_{M^{+Z}_M/M}$ sufficiently negative that η is reduced due to H_2O electrolysis and metal hydroxides are formed in aqueous baths. In general, there exists a reciprocal relationship between "brightness"/uniformity and η and optimum practical baths often require additives specific to that metal (e.g. sulfamate for indium, β-napthol for tin, nitrosohalides for ruthenium). Simple, safe, convenient, and "generic" baths superior to the cyanide bath would be valuable.

Our previous works[4] describe development of a novel, patented[4c] mixed organic acid (e.g. propionic acid)/H_2O bath in which [S] --> 1 M and the free H^+ introduced by the H_2O dissociation of the acid greatly increase the concentration of "free" uncomplexed metal ions and enhances metal plating. Furthermore, the low pH (0-2) shifts the standard reduction potential of the

$$2\ H^+_{(liq)} + S_{X(liq)} \quad 2e = H_2S_{(liq)} + S_{X-1(liq)}$$

to + 0.142 V (SHE) and allows for copious H_2S formation.

The disadvantages of this bath are the tendencies toward (1) Dendritic pure metal plates due to the low pH and (2) Powdery metal sulfide deposits, in the presence of sulfur, because of (1) and the H_2S precipitating with free, unplated metal ions in the double layer.

Thus, as discussed in Part II, a strong need exists for alternate baths for convenient, fast, and economical deposition of adherent metal sulfides or mixed sulfides/tellurides or selenides.

REFERENCES

1. (a) A.S. Baranski and W.R. Fawcett, J. Eletrochem. Soc., 127,766 (1980); (b) A.S. Baranski and W.R. Fawcett, ibid., 131,2508 (1984).
2. (a) R.D. Engelken and H.E. McCloud, ibid., 132, 567 (1985); (b) R.D. Engelken, T.P. Van Doren, J.L. Boone, A.K. Berry, and A. Shahnazary, ibid., 133,581 (1986); (c) R.D. Engelken, H.E. McCloud, M. Slayton, and E. Smith, Extended Abstracts Volume 87-1, The Electrochem. Soc. Inc., 715 (1987).
3. See, for example, (a) V.K. Kapur, B.M. Basol, and E.S. Tseng, "High Efficiency, Copper Ternary Thin Film Solar Cells" Contract Number DE-ACO-2-83CH10093, Solar Energy Research Institute, Golden, CO, 1987; (b) G. Hodes and D. Cahen, Solar Cells, 16, 245 (1986); (c) R.D. Engelken, "Formation of Large Grain, Photovoltaic-Grade $CuInSe_2$ Thin Films Via Electrodeposition of Separate Elemental Layers and Subsequent Annealing", Final Report-1987 NASA Lewis Research Center Summer Faculty Fellowship; (d) R.D. Engelken, H.E. McCloud, E. Smith, D. Moss, and H. Hormasji, "Formation of Metal Chalcogenides Such as $CuInS_2$ by Resistive Flash Annealing of Electroplated Metal Layers in Electrochemically In-Situ Generated Nonmetal Hydrides Such as H_2S", Extended Abstracts Vol. 88-1, The Electrochemical Soc. Inc., 1988; (e) R.D. Engelken, H.E. McCloud, E. Smith, D. Moss, N. Sanders, and H. Hormasji, "Formation of Semiconductor Metal Sulfides Via In-Situ Electrogeneration of H_2S and Subsequent Reaction with Resistively Heated Metal Films/Foils," Abstracts Volume of the 1988 Spring Meeting of the Texas Section of the American Physical Society, March, 1988.
4. (a) R.D. Engelken and H.E. McCloud, Bull. Am. Phys. Soc., 29, 1501 (1984); (b) R.D. Engelken, T. Martin, T. Harbi, J. Hayenga, H.E. McCloud, T. Oshiro, and A. Copelin, Extended Abstracts Vol. 85-1, The Electrochem. Soc. Inc., 723 (1985); (c) R.D. Engelken and H.E. McCloud, U.S. Patent 4,681,777, 1987; (d) R.D. Engelken, H.E. McCloud, C. Lee, M. Slayton, and H. Ghoreishi, J. Electrochem. Soc., 134,6962 (1987).
5. R.D. Engelken and T.P. Van Doren, J. Electrochem. Soc., 132, 2904 (1985).

Abstract No. 372

DEVELOPMENT OF A NOVEL "GENERIC" TRIPLE SOLVENT BATH FOR ELECTRODEPOSITION OF METAL CHALCOGENIDE AND "BRIGHT" METAL FILMS

PART II:

DESCRIPTION OF TRIPLE SOLVENT BATH

Robert D. Engelken, Hal McCloud
David Moss, Emmett Smith,
Hoshang Hormasji, and Wendell Wells

Arkansas State University
P.O. Box 1080
State University (Jonesboro), Arkansas 72467

Part I discussed various advantages and disadvantages associated with baths presently used to electrodeposit metals and/or metal chalcogenides.

In light of the factors discussed in Part I, we report development of "generic" mixed ethylene or propylene glycol, H_2O, organic acid bath which exhibits potential for electroplating very smooth, uniform, small-grained/bright metal or metal chalcogenide films, depending on whether molecular and/or ionic chalcogen is introduced to the bath, from metal sulfate or EDTA salts.

The nominal solvent composition is, by volume, 40:10:3 glycol: H_2O: acid. Each liquid plays an important role.

The water allows dissolution of the metal sulfates which have a very low solubility in pure glycols. The bath is saturated with sulfate salts and the excess lies at the cell bottom. Stirring produces a turbid bath due to the suspension of undissolved salts but this has no detrimental effect on the electrodeposition.

The water/acid combination allows acid ionization and lowered pH's; without the H_2O, the acetic, propionic, or butyric acids do not ionize to any appreciable extent. The H^+ minimizes the coordination/complexing of the metal ions by the solvent, thus, producing much less sluggish deposition and j's > 1 mA/cm^2 in most cases. Also, bath conductivity salts are not needed. The H_2O also provides for O_2 evolution at inert anodes and circumvents serious solvent breakdown.

The glycol serves as a brightening agent since it is the majority solvent. Simple H_2O/organic acid baths tend to yield powdery, dendritic plates with sulfate baths, but mirror-bright metal plates are produced in the triple solvent baths.

The glycol, through the dilution effect, also serves as a pH moderator; i.e. relatively large organic acid additions can be accommodated without a tremendous decrease in pH. Thus, the glycol serves as a physical, rather than chemical, buffer. There is no indication that glycol-acid (analogous to alcohol-acid) reactions occur near room T and the baths are very stable.

Another key advantage of the propylene glycol/H_2O/propionic acid solvent is its extremely low toxicity; both propylene glycol and propionic acid are common food/cosmetic additives.

EDTA as a complexing agent produces an additional brightening effect for metals such as copper. The acid shifts the complex dissociation equilibria more toward the free ion, thus, increasing j while still preserving bright deposits not containing oxide or hydroxide contaminants, as form in neutral aqueous solutions at high j. Since many metal-EDTA complexes are soluble in pure organics (e.g. [$CuNa_2EDTA$] ~ 0.1 M in ethylene glycol), the EDTA also tends to increase metal ion concentrations over that with sulfate salts.

Chalcogen remains molecularly soluble in the dominantly organic bath and metal chalcogenides are conveniently plated with j's usually greater than with pure organics. However, one key disadvantage of the MDC method is accented: the tendency to form metal-rich films. That is, since higher currents flow at room T where the M-X reaction rate is relatively low, it is easy to form metal-rich films unless j's are controlled via a galvanostat. Another interesting but troublesome effect with multi-valence state compound families is the tendency of the film to "catastrophically" convert from one phase to the other. For example, green CuS films are easily deposited at room T from 40:10:3 ethylene glycol/H_2O/propionic acid baths of $CuNa_2EDTA$ and S (saturated)[1]. However, commonly there will[2] suddenly appear brown/gray "splotches" on the same substrate yielding a "mosaic" or "camouflage" pattern. It appears that random protrusions or localized j maxima/irregularities cause enhanced electric fields that propagate the protrusions and associated localized j increases even more, causing a "run-away" copper current that shifts the film toward thick, brown/gray Cu_2S in these regions and leaves the green CuS background relatively unchanged. This effect is not observed with Cu_xS deposition from pure glycol solutions (Ref. 2a-Part I).

Without H_2O to ionize the acid, the bath acts very similar to the pure glycol baths and yields smooth/uniform metal sulfide films. However, the large S solubility in propionic acid (~ 1 M) changes to gross solubility to ~ 0.1 M, depending on the solvent ratios. Oddly, > 50% of pure acid tends to impede deposition and plating is difficult out of pure anhydrous acids. Near the 50%/50% mix, very stoichiometric metal sulfides are deposited due to the acid S "loading".

Probably the greatest utility of the triple solvent bath is its ability to yield mirror-bright plates of a wide range of pure metals by use of readily available and trouble-free sulfate and/or EDTA salts. Outstandingly uniform copper plates are produced from 0.1 M $CuNa_2EDTA$ baths of 40:10:3 ethylene glycol/H_2O/propionic acid baths. 80:20:3 mixtures containing $(In)_2(SO_4)_3$ have just recently been developed to yield indium plates superior (in terms of brightness) to even those of sulfamate baths, albeit at lower current efficiencies. Preliminary work with $SnSO_4$ in the 40:10:3 bath indicates bright deposits but[4] there is a tendency toward dendrites near the substrate corners and use of tin anodes rapidly changes the deposits to a powdery form, presumably due to different tin ion forms, perhaps Sn^{+4}. Other metals are under investigation with encouraging results.

Thus, this bath type is useful for fabrication of uniform/homogeneous semiconductor films via sequential plating of the pure elements followed by annealing. It should also prove useful for conventional electroplating of uniform/bright metal alloys and conventional underpotential deposition of semiconductor compounds (Ref. 5-Part I). The bath is especially attractive for deposition of mixed sulfide/telluride (e.g. $CdS_{1-x}Te_x$) films from baths of TeO_2 and molecular sulfur.

ACKNOWLEDGMENTS

This work was supported, in part, by the NASA Lewis Research Center, the ASU Economic Development Committee/Funds, and National Science Foundation Grant MSM 8617850. We especially thank Dr. Dennis Flood and Dr. Shelia Bailey for their support.

Abstract No. 373

PHOTOELECTROCHEMISTRY AND SURFACE ANALYSES OF ELECTRODEPOSITED SnS THIN FILMS

K. Mishra and K. Rajeshwar*
Department of Chemistry
The University of Texas at Arlington
Arlington, Texas 76019-0065

Among the metal chalcogenides, the II-VI compounds (e.g., CdTe) and layered materials (e.g., MoS_2) have received the most attention from a photoelectrochemical (PEC) perspective. In the search for new semiconductor candidates, both for energy conversion and for other (e.g., photoelectrosynthesis) applications, we describe in this paper the characterization of a relatively new compound semiconductor, namely SnS. This compound is a member of the IV-VI family (1), which has been less extensively examined.

Compound semiconductors have been electrodeposited either by an anodic technique, involving the (reactive) metal anode and chalcogenide anions, or by the cathodic co-reduction of the metal ions and the oxidized chalcogenide species. A variant of the latter method involves the use of molecular chalcogen in an organic bath. This discharges then only by chemical reaction/precipitation with the plated metal. The SnS thin films in this work were prepared at Arkansas State University by this new technique (2). The advantage with this method is better stoichiometric control in that excess metal may be dissolved away by appropriate control of the cathode potential.

Photoelectrochemical measurements are described using chopped-light band-gap illumination of the SnS thin-film electrodes, which were supported on transparent indium tin oxide. The shape of the photocurrent spikes is discussed within the context of the p-type conductivity of the SnS thin films. Experiments with several redox couples including $Fe(CN)_6^{3-}$, $S_2O_8^{2-}$, Eu^{3+} and Cu^{2+} are described. Using these data, the surface energy levels of SnS are mapped. Photoaction spectra are presented and the derived information compared with optical measurements.

Pourbaix diagrams have been developed for the SnS-H_2O system at 25°C. Using these and the PEC data, the photocorrosion behavior of SnS is discussed. The presence of significant levels of O in the SnS as detected by surface analyses is attributed to incipient corrosion of the thin film. Auger and X-ray photoelectron spectra are presented for the SnS thin films, as well as semi-quantitative estimates of the Sn:S ratio in the as-deposited thin films, as probed by surface analyses.

ACKNOWLEDGMENTS

This research was supported in part by the National Science Foundation (Grant MSM-8617850) and by the Organized Research Fund of The University of Texas at Arlington. The authors thank Prof. R. D. Engelken for donation of the SnS thin films as well as for several discussions, Prof. Alex Weiss for assistance with surface analyses, and LTV for access to surface analysis instrumentation.

REFERENCES

1. N. Kh. Abrikosov, V. P. Bankina, L. V. Paretskaya, L. E. Shelimova and E. V. Skudnova, "Semiconducting II-VI, IV-VI and V VI Compounds" (A. Tybulewicz, Engl. Translation, Editor), Chap. II, p. 65, Plenum, New York (1969).

2. K. Mishra, K. Rajeshwar, A. Weiss, M. Murley and R. D. Engelken, to be published.

Abstract No. 374

Electrodeposition of Semiconductors: A Panel/Audience-Participation-Based Session to Survey and Define the State-of-the-Effort and Future of Electrodeposition of Compounds and/or Semiconductors.

R.D. Engelken
Arkansas State University, P.O. Box 1080
State University (Jonesboro), AR 72467

V.K. Kapur, International Photovoltaic Systems
9540 Donna Ave., Northridge, CA 91324

R.D. Rauh, EIC Laboratories, Inc.,
111 Downey St., Norwood, MA 02062

This hour-long session will be moderated by the organizing and session chairman of the symposium "Electrodeposition of Semiconductors" and involve active audience participation in a "rap/brainstorming" session to survey and define the state-of-the-effort, key problems/opportunities, and future of electrodeposition as a means to produce compounds and/or semiconductors. Another objective of the session is the acquaintance of experts in this broad, interdisciplinary field to increase future cooperation/collaboration in compound electrodeposition and related fields.

The topics discussed will include, but not necessarily be limited to, those outlined in the Call for Papers: 1. Techniques for in situ characterization and control of deposition kinetics and the deposit (stoichiometry, morphology, carrier type, etc.): 2. Theoretical analysis, modeling and simulation of compound electrodeposition processes: 3. Parameter modulated processes including voltage and current pulsing and illumination, temperature, mass transport, and magnetic field variations: 4 Novel or hybrid techniques, such as sequential element deposition/annealing or anodic deposition, especially "forgiving" or feedback-based techniques: 5. Novel electrolytes, such as organics and fused salts, and practical advantages: 6. Crystallization kinetics and methods to improve crystallization, morphology, and adhesion: 7. Pre-and post-treatment of substrate and deposits: 8. New materials, especially III-V, ternary, and phosphide compounds, and new applications such as optical filters, superconductors, electrochromic devices, corrosion inhibitors, catalysts, lubricants, and battery materials: 9. Doping of electrodeposited semiconductors: 10. Economic, safety, and commercialization considerations.

Abstract No. 375

PREPARATION OF InX (X=P, As, Sb) THIN FILMS BY ELECTROCHEMICAL METHODS

J. Ortega and J. Herrero
Instituto Energías Renovables. CIEMAT
Avda. Complutense, 28040 MADRID, SPAIN

At present time it becomes desirable to apply to III-V compounds some of the electrochemical preparation and characterization techniques, which have proven useful for II-VI semiconductor compounds (1,2). While the photoelectrochemical techniques has been used for characterization of the III-V semiconductor compounds, their electrochemical preparation has not been very well investigated. GaP, InP and GaAs have been electrodeposited from fused salts (3).

In-Sb alloys haven been electrodeposited from a variety of electrolytes (4), but the electrodeposition of In-As compounds heretofore have not been carried out satisfactorily.

We have electrodeposited thin films of InSb onto titanium substrate by potentiostatic technique from a citric bath. The films were very adherent and polycrystalline, face-centered cubic InSb.

Nevertheless, the InAs electrodeposited from a citric bath, by potentiostatic technique was amorphous and showed photoelectrochemical activity during the electrodeposition process. The amorphous InAs films annealed at 400°C for 30 min. passed to crystalline form, face-centered cubic InAs.

InP thin films can be prepared by phosphorization of electoplated indium films. Indium thin films, 1-5 μm, were obtained galvanostatiquement from a citric bath onto titanium subtrate.

The titanium electrode with its indium film was put in a test tube which contained 50-100mg of red phosphorus. The tube was sealed under moderate vacuum with Bunsen flame. The sealed tube was annealed at 400°C for 3h in order to obtain InP. The film obtained was polycrystalline InP face centered cubic, and the diffractogram showed very sharp lines, indicating a good crystallinity.

Routine characterization of the InP obtained, I-V curves, carried out in a PEC, 0.5M HCL, has served for determing that the conductivity of the samples was n-type and the onset of the anodic photocurrent occurs about -0.5 V vs. SCE.

Mott-Shottky measurements were carried out in 0.5 M HCl solution under potentiostatic conditions in order to determine the flatband potential, energy of the Fermi level. The Mott-Shottky plots showed a linear behaviour in the frecuency range of 0.5-5 KHz and the flat band potential obtained was -0.42 ± 0.09 V vs. SCE.

The photoelectrochemical spectra response of the InP samples gave a value of 1.29 eV for the bandgap and showed to be a direct one.

The determination of the samples stoichiometry was performed by dissolution in concentrated HNO_3 and susequent atomic absorption analysis.

The possibility of a suitable doping during the In electrodeposition step and the simplicity of the phosphorization process make interesant this preparation of InP.

REFERENCE.

(1) J.Herrero and J.Ortega, Sol. Energy Mater., 16 (1987) 477.

(2) To be published in Sol. Energy Mater.

(3) J.J.Cuomo and R.J.Gambino, J. Electrochem. Soc., 133 (1986) 755.

(4) Y.N.Sodana and J.P.Sigh, Plating and Surf. Finishing, 12 (1985) 64.

Abstract No. 370

ELECTRODEPOSITION OF INDIUM ANTIMONIDE SEMICONDUCTOR FROM AQUEOUS ELECTROLYTE

Toshikazu Okubo
Electronic and Specialty Metals Group
Nippon Mining Co., Ltd.
Tokyo, Japan

and

Uziel Landau
Department of Chemical Engineering
Case Western Reserve University
Cleveland, Ohio 44106

Indium antimonide belongs to the class of III–V compound semiconductors which are technologically significant. InSb is traditionally obtained by vapor–phase deposition or by growth from a liquid phase. This paper presents the development of a new process for direct electrodeposition of semiconducting InSb from an aqueous solution. Potential advantages of this process include lower initial capital and operating costs, and possibly better control of the semiconductor composition.

EXPERIMENTAL PROCEDURE

Electrodepositon was mainly performed under potentiostatic control in a beaker using magnetic stirrer. To quantitatively characterize mass transfer effects, rotating disk electrode (RDE) experiments were also performed. *Pt plate was* used as the counter electrode.Copper was used as the substrate for plating.

The electrolyte is made of $InCl_3$,$SbCl_3$,citric acid ($H_3C_6H_5O_7$)and sodium citrate ($Na_3C_6H_5O_7$). The relative concentration of the components was varied to investigate the effects of pH and composition of In and Sb ions, but the sum of $InCl_3$ and $SbCl_3$ concentration, and citric acid and sodium citrate concentration was always set at 0.344 mol/L and 1.427 mol/L, respectively.

The composition of deposits was analysed using energy dispersion spectroscopic techniques.

RESULTS

A. Effects of the deposition parameters on the deposit composition

Fig.1 shows the relationship between the potential and the deposit composition plated from solutions in which the ratio of In/Sb and pH were varied.

Fig.2 and 3 were obtained using RDE in a solution where In/Sb ratio was 1/1 and the pH was 2.2. The effects of mass transfer on the cathodic current and the composition of the deposits are noted. Following is a brief discussion of the effect of various parameters.

(1) Effects of potential

The deposit composition was not affected much by the potential in the region more negative than –0.8V (vs.Ag/AgCl),although the cathodic current increased with increasing negative polarization. Hydrogen evolution took place at –1.0 ~ –1.2 V(vs. Ag/AgCl),but the current efficiency of deposition of In and Sb was still high; 85% at –1.2V(vs.Ag/AgCl) in the solution of In/Sb=1/1 and pH 2.1.

(2) Effects of pH

pH changes were effective in controlling the composition of the deposits. The higher the pH was, within the pH range of 2–5,the smaller the amount of In the deposit contained.

(3) Effects of solution composition

The composition of the solution also affected the composition of the deposits. The higher the In content of the solution, the more In the deposit contained.

(4) Effects of agitation

Mass transfer effects were minor. Increasing the rotation rate increased the cathodic current density and decreased the content of In in the deposits, but the extent of the change was small, except for no agitation at all.

B. Morphology of the deposits

The deposits containing less than 55–60% of In had smooth shinny and silver appearance, but they became brittle as their thickness increased, especially in cases where the In content was close to 50%.The deposits containing more than 55–60% of In,however,had black rough and mat appearance.

C. Characterization of In/Sb deposits with 1:1 composition ratio

(1) Preparation of In/Sb=1/1 deposits

An Indium antimonide deposit with 1:1 atomic ratio could be obtained by controlling the solution composition at an almost constant pH value of 2.1~ 2.2.

Typical conditions are as follows:
In/Sb= 0.54/0.46 (mol.ratio) in the electrolyte
citric acid + sodium citrate = 1.427 mol/L
pH ≈ 2.2
ambient temperature ≈ 25°C
–0.8 V(vs.Ag/AgCl)
Magnetic stirrer agitation

The current density was 25 mA/cm² and the current efficiency for deposition was 97%.

(2) Structure of the deposit

X–ray diffraction of the deposit as plated on stainless steel substrate under the condition described above indicated that the deposit was amorphous. After annealing at 350°C,1h in N_2 atmosphere, a crystalline film was obtained indicating peaks corresponding to InSb on the diffraction pattern.

(3)Thermal dependence of electrical resistivity

The resistivity of the electrodeposited InSb film (5μm thick)was measured at various temperatures after removal of the Cu substrate. Fig.4 indicates that the film resistivity decreases with increase of temperature indicating semiconductor behavior. The resistivity values measured were somewhat larger than specific values of InSb,
probably because the film had some cracks due to brittleness.

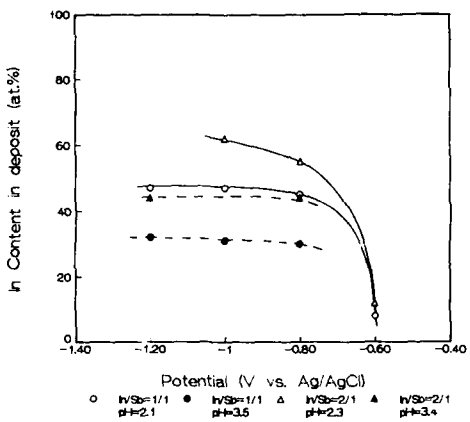


Fig.1 The relationship between potential and content of In in deposits electroplated from solutions with various composition and pH.

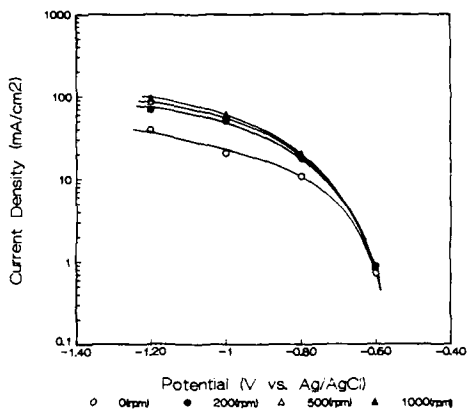


Fig.2 Current-potential curves for In and Sb deposition measured at various electrode rotation rates in the solution with In/Sb=1/1 and pH 2.2

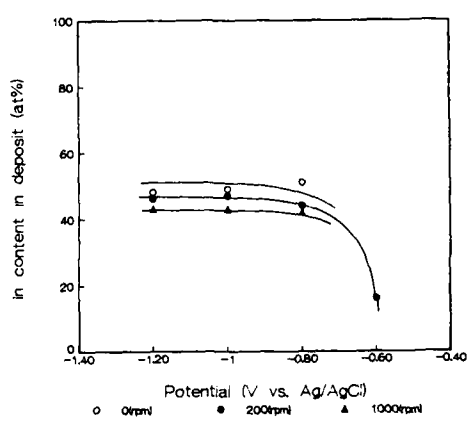


Fig.3 The effect of rotation rate on In content in deposits plated from the solution with In/Sb=1/1 and pH 2.2.

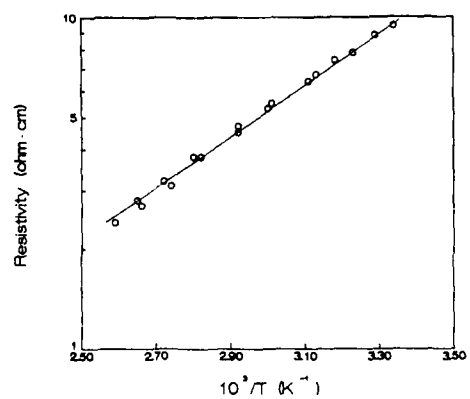


Fig.4 Thermal dependence of the resistivity of the InSb film obtained by electrodeposition.

Abstract No. 377

ELECTROCHEMICAL OXIDATION OF A Ni-BASED AMORPHOUS ALLOY

V.I. Birss and K. Lian
Department of Chemistry, University of Calgary
Calgary, Alberta, Canada T2N 1N4

INTRODUCTION

The electrochemical formation of microporous, hydrous oxide films at metals such as Ir, Rh and Co has been studied in some detail by a number of previous workers (1-3). These oxides possess electrochromic properties and also appear to have applications as battery electrodes and in electrocatalysis. The oxidation/reduction of these oxides occurs by a change in the oxidation state of the metal sites within the oxide film. Charge transfer is believed to occur by a metal site-to-site electron hopping mechanism, with charge neutrality being maintained within the oxide film by the injection/expulsion of appropriate counter ions. These processes are relatively rapid, and hence hydrous oxide electrochemistry is generally kinetically reversible.

We have previously reported that a hydrous oxide film can be formed at amorphous Ni-Co alloy electrodes (4). The electrochemical behavior of these alloy electrodes displays characteristics which are a mixture of those observed at crystalline Ni and Co electrodes. In this paper, the mechanism of hydrous oxide deposition and build-up is discussed. Also, the electrochemical properties of these oxide films will be shown to be very similar to those of redox polymer electrodes, i.e. involving the swelling and de-swelling of the oxide film as ions and associated solvent are injected into, and expelled from the oxide film, respectively, during its oxidation and reduction.

EXPERIMENTAL

Cyclic voltammetry and chronoamperometry were carried out using a glassy alloy ribbon, having the composition of $Ni_{51}Co_{23}Cr_{10}Mo_7Fe_{5.5}B_{3.5}$, as the working electrode. The reference electrode was either a reversible hydrogen electrode (RHE) or the SCE. Most experiments were carried out in 1 M NaOH, and solutions were deaerated with argon before and during the course of the experiments. All experiments were conducted at room temperature.

RESULTS

Hydrous oxide films can be deposited at Ni-based glassy alloy electrodes by either potential cycling or pulsing between particular limits of potential. The rate of growth of the oxide increases as these limits are extended, and a maximum amount of oxide, equivalent to ca. 0.12 ± 0.02 mC/cm^2, can be deposited per cycle of potential.

Analogous to the case of the growth of Ir oxide films at crystalline Ir electrodes (1), this result indicates that a maximum of one complete monolayer of hydrous oxide film can be deposited per cycle of potential. The fact that the maximum growth rate per cycle is one monolayer, and that critical potential limits must be reached for this growth to occur, is an important clue to the mechanism of hydrous oxide growth. It is considered that a critical positive potential limit is required in order to oxidize the surface (one monolayer) of the underlying metal surface to a sufficiently high oxidation state. A critical lower potential limit is required in order to release this monolayer of oxide from the metal surface to the growing hydrous oxide film.

As the hydrous oxide film thickness increases at these amorphous alloy electrodes, a significant hysteresis develops between the anodic peak (or current transient) and the cathodic peak (or i/t response). In the cyclic voltammogram, the anodic peak becomes very sharp and narrow, while the cathodic peak remains broad. In the chronoamperometric response, the anodic transient frequently displays a peak, while the cathodic i/t response is typical of a diffusion controlled reaction. These effects are influenced dramatically by the potentials utilized, and the time spent at these potentials. These observations have been interpreted in terms of the injection of ions (and solvent) during the oxidation step, and hence film swelling, and de-swelling of the oxide during oxide reduction. These results are very similar to those observed at particular redox polymer covered electrodes (5,6).

Another unique aspect of the electrochemical behavior of these hydrous oxides is that the cathodic charge passed during chronocoulometric measurements is significantly less than the oxidation charge. These results will be discussed in terms of disproportionation reactions occurring within the oxide during film reduction, brought about by differences in pH in various regions of the oxide. These non-steady-state effects support the notion that these hydrous oxides are flexible and gel-like in nature and could be described as inorganic polymeric materials.

REFERENCES

1. P.G. Pickup and V.I. Birss, J. Electroanal. Chem., 220 (1987) 83.
2. D.N. Buckley and L.D. Burke, J. Chem. Soc. Far. Trans. (I), 71 (1975) 1447.
3. L.D. Burke and E.J.M. O'Sullivan, ibid, 93 (1978) 11.
4. K. Lian and V.I. Birss, Proc. of the Fall Meeting, Electrochem. Soc. Inc., Honolulu, Hawaii, October 1987.
5. P. Daum and R.W. Murray, J. Electroanal. Chem., 103 (1979) 289.
6. A.H. Schroeder, F.B. Kaufman, V. Patel and E.M. Engler, ibid, 113 (1980) 193.

Abstract No. 378

USE OF A SULFUR POWDER BATH TO FORM METAL SULFIDE FILMS FROM FLASH ANNEALED ELECTRODEPOSITED METAL LAYERS

Robert D. Engelken, Hal McCloud,
Lawrence Mink, David Moss,
Emmett Smith, and Wendell Wells
P. O. Box 1080
Arkansas State University
State University, Arkansas 72467

Recent works[1,2a] have indicated that large-grain metal chalcogenide films can be produced by sequential electrodeposition of some or all of the elements of the compound followed by annealing, often in an atmosphere of H_2X. In the case of Se and Te, the "nonmetal" can itself be plated along with the metal(s) and subsequent annealing homogenizes/reacts the elements to form the compounds. Our previous work[2b] demonstrated the utility of (1) In-situ electrochemical formation of the H_2X from a novel mixed organic/H_2O electrolyte and (2) High speed resistive flash annealing of high m.p., relativity inert, and thin (<0.1 mm) substrate "ribbons" such as Mo, Ta, and graphite.

We now report investigation of a deceptively "simple"/obvious variation of the sequential electroplating/chalcogenization/annealing method to form semiconductor compounds.

The method involves the following steps.

(1) The metal(s) (cations) of the desired compound are sequentially electroplated onto ribbon (e.g. 1 cm x 6 cm) in precision thicknesses controlled via I-t product and chronogalvanostatic/potentiostatic determination of current efficiency. For example, a stoichiometry-matched Cu/In/Cu structure can be sequentially plated from novel mixed solvent baths described in another paper[3] of this symposium.

(2) The entire ribbon is mounted/connected to heavy binding posts but droops between the posts in a "U" configuration.

(3) Fine-meshed sulfur powder is poured over and around the "valley" of the "U" (i.e. the lower center of the ribbon) and agitated to remove voids.

(4) After covering the foil with sulfur, the annealing vessel is tightly closed and purged with argon for several minutes to completely displace O_2 from the sulfur powder.

(5) The argon is shut-off and large currents (e.g. 10-35 A) are applied to the ribbon and rapidly (seconds to minutes depending on /I/and /dI/dt/) heat it to 100's of °C.

(6) The sulfur adjacent to the submerged foil rapidly melts and vaporizes. The molten and vaporized sulfur reacts quickly with the hot plated layers to form the compound with a stoichiometry depending upon (1) The relative metal molar ratio (in the case of ternary or higher-order compounds), (2) The existent phases possible, and (3) The rate and extent of metal-S reaction through the temperature, total plated layer thickness, cell volume, S depth, etc. In almost all cases, thin films (< 1 micron) are completely chalcogenized within minutes. Copper, with its huge reaction rate with sulfur, forms gray $Cu_{2-x}S$ within seconds.

(7) The closed cell prevents S vapor from leaving, so even though solid and molten sulfur "migrate" radially away from the substrate, this void is filled with S vapor. If the cell is not sealed, especially with a continuing argon purge, S vapor leaves the void growing around the ribbon, leaving it surrounded by an argon atmosphere and halting chalcogenization. Another key factor is the thermal insulation provided by the sulfur powder and subsequent resolidified cylindrical sulfur "doughnut" around the foil. This allows, with the same current values, higher temperatures to be obtained.

(8) To prevent elemental sulfur condensation on the foil as it is cooled, the cell is finally repurged with argon to displace all sulfur vapor from the growing void. Since m.p.$_S$ = 110°C and b.p.$_S$ = 445°C, the only way the sulfur can discharge on the film at high temperature is through reaction with the plated metals. Thus, S-richness is precluded.

(9) In nearly all cases, notably with Cu/In, large-grain polycrystalline compound films ($CuInS_2$) are produced. Some problems with multiple phases (e.g. Cu_2S, CuS, InS, In_2S, In_2S_3) might be anticipated but careful control of all experimental conditions precludes this.

(10) The remaining sulfur (most still in powder form) can be recrushed with mortar and pestle and used again. Thus, in addition to being convenient and fast, the technique is material-conserving. Also the much lower toxicity of S vapor over H_2S and easy scale-up to large lengths and areas make the method attractive.

Although, at the time of this writing, we have not conducted the analogous experiment with selenium, its low m.p. (217°C) and b.p. (685°C) indicate that the method should work equally well, although there is much more hazard associated with selenium powder than with sulfur. Thus, this "obvious" method should have practical utility for economically and conveniently forming polycrystalline metal chalcogenide films, as it presently has for doping preexistent semiconductor films with Group VI elements.

REFERENCES

1. See, for example, (a) V. K. Kapur, B. M. Basol, and E. S. Tseng, "High Efficiency, Copper Ternary Thin Film Solar Cells", Contract DE ACO 2-83CH10093, Solar Energy Research Institute, Golden, CO, 1987; (b) G. Hodes and D. Cohen, Solar Cells, 16, 245 (1986).
2. (a) R. D. Engelken, "Formation of Large-Grain Photovoltaic-Grade $CuInSe_2$ Thin Films via Electrodeposition of Separate Elemental Layers and Subsequent Annealing", 1987 NASA Lewis Research Center Summer Faculty Fellowship Final Report; (b) R. D. Engelken, H. E. McCloud, E. Smith, D. Moss, H. Hormasji, and N. Sanders, "Formation of Metal Chalcongenides Such as $CuInS_2$ By Resistive Flash Annealing of Electroplated Metal Layers in Electrochemically In-Situ Generated Nonmetal Hydrides Such as H_2S", Abstract 80, The Electrochemical Society Extended Abstracts Series 88-1, 1988.
3. R. D. Engelken, H. E. McCloud, D. Moss, E. Smith, H. Hormasji, and W. Wells, "Development of a Novel 'Generic' Triple Solvent Bath for Electrodeposition of Metal Chalcogenide and 'Bright' Metal Films", This Volume: Electrochemical Society Extended Abstracts 88-2, 1988.

Abstract No. 379

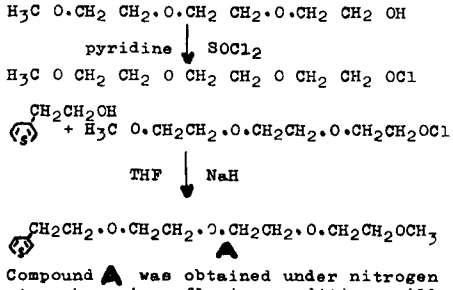
Electrochemical polymerization of thiophene containing an ether linkage at the 3-position

D Mukherjee
Department of Chemistry
IIT Kharagpur 721 302
India

Recent years have seen a literal explosion of interest in the area of conducting polymers (1,2) and increasing interest has been paid to those derived from heterocyclic monomers (1,3-5). Although most of the studies have been devoted to polypyrroles, extensive work on polythiophenes (6) has also been described. The potential applications for most of these new polymers in the field of conductors, organic batteries (7,8) and display devices (5) are, however greatly impeded by their high reactivity towards oxygen and moisture which requires constraining experimental conditions such as argon controlled atmosphere and a highly purified medium. The development of a stable polymer which could be reversibly doped and undoped under very rough conditions would represent a very attractive goal, given the large area of applications.

Our aim was to synthesize a novel polymer which would have as its backbone an electron conducting conjugated carbon chain, as in polyacetylene or polypyrrole, but the pendant moieties would have the polar characteristics required for ion solvation and conduction. The polar groups would also increase the solubility of the polymer in polar organic solvents, thus giving the polymer an important processability advantage over most polyconjugates yet reported.

The present report describes the polymerization of a 3-substituted thiophene derivative,  , where R contains suitably disposed wther oxygens which could provide solvation for the cation. The original thiophene monomer was prepared as shown in the following reaction scheme :



Compound **A** was obtained under nitrogen atmosphere in refluxing condition. All monomers gave satisfactory analytical and spectroscopic data. Polymerization was carried out at 10°C under nitrogen atmosphere in a three-electrode two-compartment cell using a platinum anode. Details of electrochemical polymerization of the monomer **A** are given in the following table. All electrolyte (tetraethylammoniumtetrafluoroborate) and solvents were dried and distilled prior to electrolysis. The optimum current density for electropolymerization was 2.8 mA cm^{-2}. Dc conductivity measurement of the oxidized polymer was obtained on a free-standing film that had been peeled off the anode using a four-probe technique. High conductivity (10^{-3} S cm^{-1}) was obtained reproducibly for the present polymer. The polymer was found to be insoluble in common organic solvents and stable up to 160°C.

Solvent	Concn. of monomer (molar)	Concn. of electrolyte (molar)	Conductivity (S cm^{-1})
$PhNO_2$	0.1	3×10^{-2}	6×10^{-3}
CH_2Cl_2	0.1	3×10^{-2}	8×10^{-3}
CH_3CN	0.1	3×10^{-2}	4.5×10^{-3}

References :

1 "Handbook of Conducting Polymers", T A Skotheim, Editor, Marcel Dekker, (1986)

2 J E Frommer and R R Chance, in "Encyclopedia of Polymer Science and Engineering", M Grayson and J Kroschwitz, Editors, Wiley, (1987)

3 A F Diaz, Chem. Scrip., 17, 145(1981)

4 W D Gill, T C Clarke, and G B Street, Appl. Phys. Comm., 2, 211(1982)

5 G Tourillon, and F Garnier, J. Electroanal. Chem., 135, 173(1982)

6 F Garnier and G Tourillon, J. Electroanal. Chem., 148, 299(1983)

7 P J Nigrey, D McInnes, P D Nairns, A G MacDiarmid, and A J Heeger, J. Electrochem. Soc., 128, 1651(1981)

8 S Chao, and M S Wrighton, J. Am. Chem. Soc., 109, 2197(1987).

Abstract No. 380

POLYANILINE / WO_3 ELECTROCHROMIC CELL

Takashi Yoshida, Katsuaki Okabayashi
Takahiko Asaoka and Katsushi Abe

Toyota Central Res. & Dev. Labs. Inc.
Nagakute-cho, Aichi, Japan

Introduction

The application of conducting polymers to electrochemical devices has been sought in many research field since the electrochemical doping and undoping of polyacetylene was discovered in 1978. One of the promising application seems to be as a battery electrode. We have carried out our research on conducting polymers with the intention of clarifying the possibility of using the material as the positive electrode in a lithium secondary battery and found that polyaniline has superior performance compared with other conducting polymers, such as polyacetylene, polythiophene or polypyrrole [1]. In brief, polyaniline shows a higher stability in deep charge / discharge repetitions and less self-discharge than other polymers in nonaqueous electrolytes.

On the other hand, it is well known that conducting polymers generally show electrochromic properties. As for polyaniline, electrochromism in an acidic aqueous electrolyte was first reported by Diaz and Logan [2]. Kobayashi et al. later reported [3] the detailed electrochromic properties of polyaniline in aqueous electrolyte and identified the color changes as transparent yellow $\rightleftharpoons$ green $\rightleftharpoons$ dark blue $\rightleftharpoons$ black. However, the electrochromism of polyaniline in nonaqueous electrolytes has not been revealed yet.

We found that a thin film of polyaniline formed on ITO glass also shows a stable electrochromic reaction in the nonaqueous electrolyte of $LiClO_4$ / propylene carbonate (PC) or $LiBF_4$ / PC system as in aqueous electrolyte. The result has led to the development of a duplicated new electrochromic device consisting of polyaniline / WO_3, which is summarized in this abstract.

Cell construction

A 6000 Å thickness polyaniline film was electropolymerized onto ITO glass from an aqueous solution of 0.2M $HClO_4$ containing 0.1M aniline monomer. A WO_3 film was formed on the ITO glass by an ordinary sputtering method. The two electrodes with the glass were assembled as shown in Fig.1. 1M $LiClO_4$ / PC solution was used as the electrolyte.

Results

Visible spectrum : The color of polyaniline reversibly changes from transparent light yellow in the reduced state to blue in the oxidized state. On the other hand, WO_3 changes its color reversibly from transparency in the oxidized state to light blue in the reduced state. Hence, the combined color change in total is transparent light yellow to dark blue, which is observed in a visible spectrum as shown in Fig.2.

Optical density : The change in optical density (ΔOD) accompanied by the color change is defined as $-\log I/I_0$, where I_0 is the transmissivity in the bleached state and I is that in the colorized state. OD changes linearly with the injected charge as shown in Fig. 3. The coefficient of the slope, the colorizing efficiency, is 0.06 cm^2/mC in the duplicated cell, which is nearly twice the value obtained at each independent electrode.

Response : When 1.5 V is applied to the 5 × 5 cm^2 cell in the bleached state, the transmissivity changes from 80 % to 30 % ($\Delta OD = 0.4$) in a second and from 80 % to 4 % ($\Delta OD = 1.3$) in 1 minute as shown in Fig.4.

Cycle life : Repetitive bleaching and colorizing were carried out by applying 1.5 V and -1.5 V to the cell and alternatively holding the cell at each potential for 1 second. The change in ΔOD during the test was compared with the initial value, ΔOD = 0.4. The cyclability of the cell reached nearly 10^6 times as shown in Fig. 5. If an aqueous $HClO_4$ solution was used as the electrolyte instead of $LiClO_4$ / PC, the cycle life decreased to 10^3 times, because dissolution of ITO film and deterioration of the polyaniline film occurred in the acidic electrolyte.

Memory characteristic : The bleached (80 % transmissivity) and colorized (30 % transmissivity) cells were left at room temperature for two days and the variation in transmissivity was measured. Both transmissivities scarcely changed during that period as can be seen in Fig. 6.

These results may suggest practical applications of the polyaniline / WO_3 electrochromic device for non-glare mirrors or light controlling glasses.

References

[1] F. Goto, K. Abe, K. Okabayashi, T. Yoshida and H. Morimoto, J. Power Sources 20, 243 (1987)
[2] A. F. Diaz and J. A. Logan, J. Electroanal. Chem., 111, 111 (1980)
[3] T. Kobayashi, H. Yoneyama and H. Tamura, J. Electroanal. Chem., 161, 419 (1984)

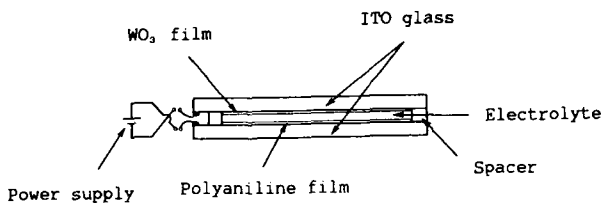


Fig. 1 Construction of the cell

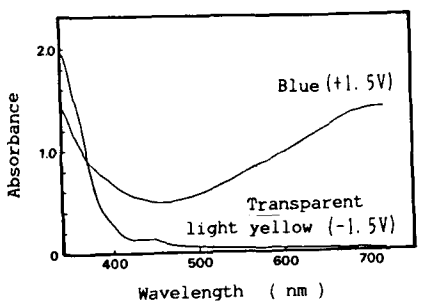


Fig. 2 Visible spectrum of the duplicated cell

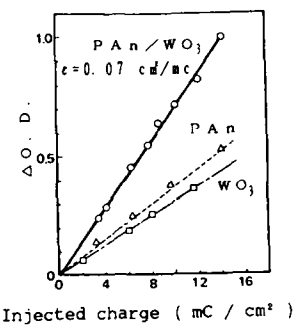


Fig. 3 ΔOD and injected charge

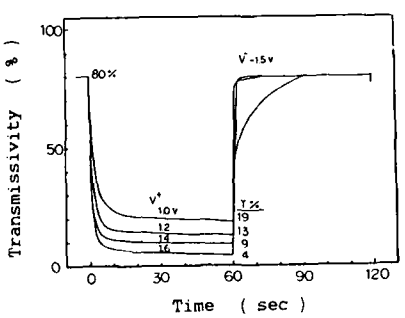


Fig. 4 Response of the cell

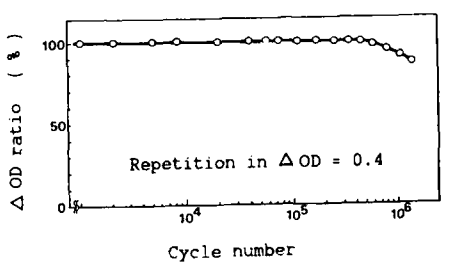


Fig. 5 Cycle life

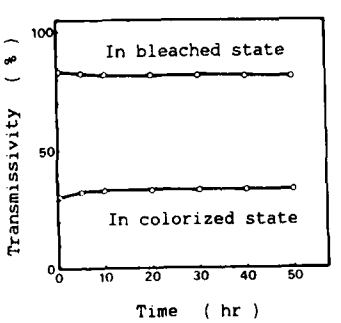


Fig. 6 Memory characteristic

Abstract No. 381

Electro-Optic Sampling of Integrated Circuits and Devices Using InGaAsP Injection Lasers

J. M. Wiesenfeld
AT&T Bell Laboratories
Crawford Hill Lab
Holmdel, N. J. 07733

M. S. Heutmaker
AT&T Engineering Research Center
Princeton, N. J. 08540

The electro-optic sampling technique has been used to great advantage to measure electrical signals with ultrashort time resolution [1] and to non-invasively measure waveforms internal to GaAs [2] or InP integrated circuits (ICs). To maximize temporal resolution and voltage sensitivity, it is necessary to use an optical probe beam with pulse durations as short as possible, and with average power as large as possible, respectively. Accordingly, using large, sophisticated laser systems, subpicosecond temporal resolution [1] and voltage sensitivity better than 1 $mV/\sqrt{Hz}$ [2] have been achieved. In our work, we have developed a compact and simple electro-optic sampling system that uses pulsed semiconductor injection lasers. [3,4] The system is capable of measurements over a large range of bandwidth and sensitivity, and has been able to achieve temporal resolution of ~10 ps, and voltage sensitivity of 2 $mV/\sqrt{Hz}$ [3,4]. In this talk, we report the operation of this system and discuss the advantages and limitations of using injection lasers for electro-optic sampling. We also compare back-side and front-side sampling geometries for probing planar ICs. For illustration, we present results obtained by sampling a high-speed GaAs decision circuit, that is mounted in its production package. [5,6]

A schematic of the basic experimental arrangement is shown in Fig. 1. Two frequency synthesizers, phase-locked to a common oscillator, are used: one drives a gain-switched InGaAsP laser, the other drives the IC under study. Pulses from the laser (1.3 μm wavelength, 18 - 20 ps duration, 100 μW average power) are made circularly polarized, and impinge on the IC at the position of the internal node to be interrogated. The voltage present at the node causes a small change in the polarization state of the probe beam by the electro-optic effect in the substrate of the IC, which is converted to an amplitude change upon detection of the reflected probe beam after passage through a polarization analyzer. The optimum geometry for probing a planar IC is the "back-side" geometry, in which the probe beam enters the IC from the back (inactive) side. [7] This geometry maximizes voltage sensitivity and spatial resolution, but cannot be used with a packaged IC, in which the back surface is inaccessible. For such a packaged IC, the probe beam must enter from the front (active) surface. In spite of reduced sensitivity and spatial resolution compared to the back-side probing geometry, front-side probing is effective for electro-optic sampling of planar ICs. [5]

Recent electro-optic sampling experiments performed on a packaged GaAs decision circuit (AT&T 494A) [5,6] illustrate the utility of the front-side probing geometry, as well as some of its disadvantages compared to back-side probing. The decision circuit, which amplifies and synchronizes an input data stream at ~2 GHz, consists of an input amplifier, a type D flip-flop, and output buffers. Figure 2 shows several waveforms from the circuit, measured by electro-optic sampling. The circuit is driven by a 2 GHz clock signal (CK, 2(a)) and 1 GHz sinusoidal data (DN, 2(b)). After the input amplifier, the data is inverted and saturated (D, 2(c)), and the output of the circuit is a square wave synchronized to the clock (Z, 2(d)).

The front-side probing geometry is susceptible to problems from apparent crosstalk, since the probe beam must be positioned between contact lines on the IC, and the electro-optic effect in the substrate will be due to the sum of fields from both contact lines. This problem is illustrated in Fig. 3. Figure 3(a) shows the layout of two active lines (QB and CK) and two inactive lines (GND and V_{DD}) at a particular location in the circuit, and also shows the positions of the probe beam for the data of Fig. 3(b)-(e). The signals measured between QB and GND (3(b)) and CK and V_{DD} (3(c)) are free from apparent crosstalk. When the beam is between the active lines (3(d) and (e)), we observed superpositions of the signals from the two active lines. The magnitude of the apparent crosstalk can be explained quantitatively by considering the transverse spatial variation of the electric fields produced by the time-varying voltages on the active lines. This can be seen from the data in Fig. 4. For this data, only the CK line is active. Fig. 4(c) shows the spatial variation of the detected fractional intensity modulation of the probe beam, $\Delta I/I$, which is proportional to the electro-optic signal. The large magnitude of $\Delta I/I$ on both sides of the CK line is due to the field produced by the voltage signal on CK. (There is no signal when the probe beam is positioned on the CK line because, in the front-side probing geometry, the probe beam is reflected from the contact and does not enter the electro-optic substrate.) Thus, even near the QB line, there is a strong signal from the CK line, as seen, and this is the origin of the crosstalk in Fig. 3(d). The signal from CK does not extend to the far side of QB, however. Thus, for accurate results, the probe beam should be positioned between an active and an inactive line (Figs. 3(b) and (c)). Factors relating to determination of the amplitude of the signal measured by electro-optic sampling are more complex [5] and will be discussed.

By a modification of the experimental arrangement of Fig. 1, which consists of replacing the oscilloscope which follows the receiver with an electronic spectrum analyzer, it is possible to directly measure the response of the IC in the frequency domain. [6] The amplitude transfer function thus measured for a single FET amplifier in the input stage of the decision circuit, normalized to its value at 1 GHz, is shown in Fig. 5. The 3-dB point is between 4 and 4.5 GHz.

In summary, we describe a compact electro-optic sampling system based on semiconductor injection lasers, and discuss its performance and limitations. With this system, waveforms internal to several ICs have been analyzed non-invasively, using both front-side and back-side probing geometries. The system has also been used to exploit the high-speed potential of the electro-optic effect to measure the 67 GHz bandwidth of high-speed InGaAs photodiodes. [8]

1. J. A. Valdmanis, G. A. Mourou, and C. W. Gabel, IEEE J. Quant. Electron., **QE-19**, 664 (1983).
2. B. H. Kolner and D. M. Bloom, IEEE J. Quant. Electron., **QE-22**, 79 (1986).
3. A. J. Taylor, J. M. Wiesenfeld, G. Eisenstein, R. S. Tucker, J. R. Talman, and U. Koren, Electron. Lett., **22**, 61 (1986).
4. A. J. Taylor, R. S. Tucker, J. M. Wiesenfeld, C. A. Burrus, G. Eisenstein, J. R. Talman, and S. S. Pei, Electron. Lett., **22**, 1068 (1986).
5. M. S. Heutmaker, T. B. Cook, B. Bossachi, J. M. Wiesenfeld, and R. S. Tucker, IEEE J. Quant. Electron., **QE-24**, 226 (1988).
6. J. M. Wiesenfeld and M. S. Heutmaker, Electron. Lett., **24**, 106 (1988).
7. J. L. Freeman, S. K. Diamond, H. Fong, and D. M. Bloom, Appl. Phys. Lett., **47**, 1083 (1985).
8. R. S. Tucker, A. J. Taylor, C. A. Burrus, G. Eisenstein, and J. M. Wiesenfeld, Electron. Lett., **22**, 917 (1986).

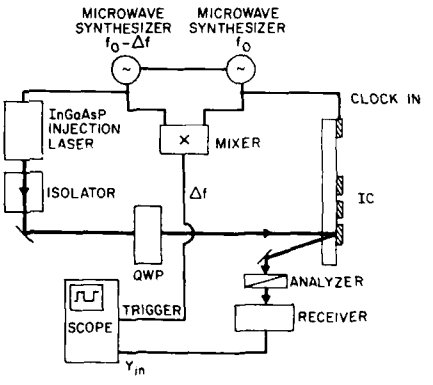


Figure 1: Experimental schematic. QWP is a quarter-wave plate.

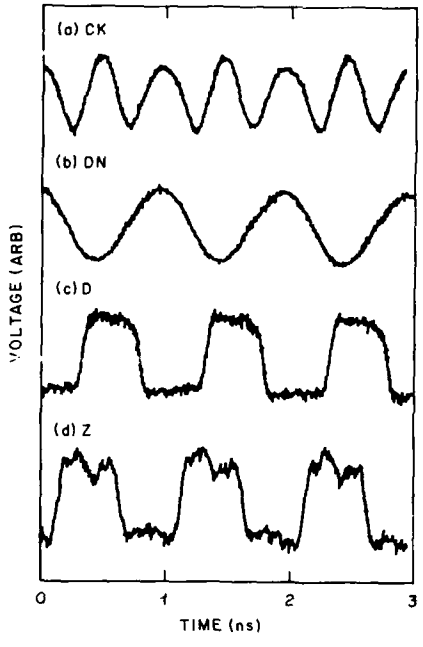


Figure 2: Measured electro-optic signals at various points in the decision circuit.

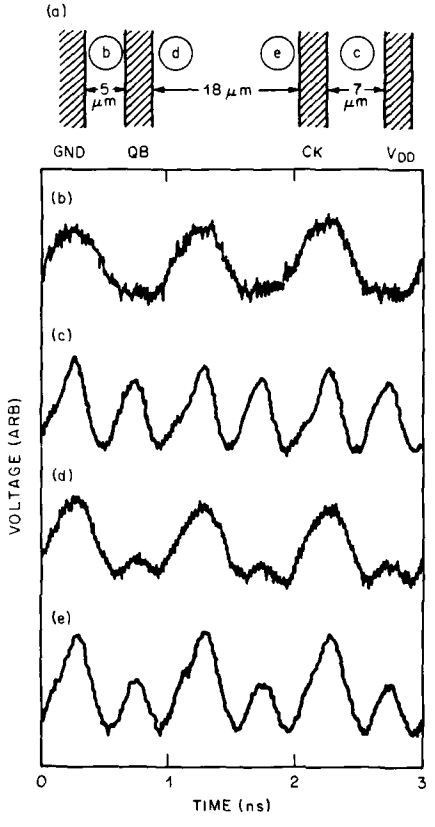


Figure 3: Crosstalk when the probe is positioned between active lines.

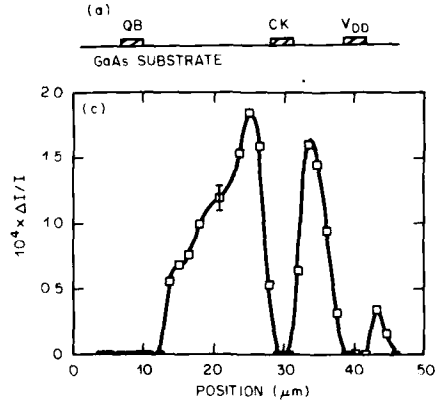


Figure 4: (a) Layout of circuit lines. (c) Fractional electro-optic modulation vs probe beam position.

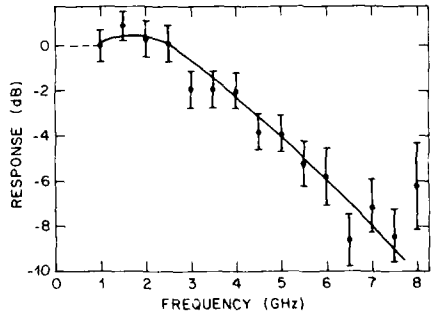


Figure 5: Amplitude transfer function of a FET amplifier within the input stage.

Abstract No. 382

Accuracy and Invasiveness of Direct Electrooptic Probing of GaAs Integrated Circuits

J.L. Freeman, D.M. Bloom, S.R. Jefferies, and B.A. Auld
Edward L. Ginzton Laboratory, Stanford University, Stanford, CA 94305-4085

Direct electrooptic probing uses a mode-locked 1.06 μm Nd:YAG laser with 1.25 ps pulses to probe internal nodes of GaAs circuits [1]. Its timing resolution is set both by the pulse duration, whose power spectrum currently has a -3 dB bandwidth of over 200 GHz, and the laser timing jitter, which is actively stabilized to less than 0.3 ps. Fall-times as fast as 3.5 ps have been measured in a monolithic nonlinear transmission line [2], and dispersion properties of coplanar waveguide (CPW) transmission lines have been studied up to 100 GHz [3]. The continued popularity of the technique in probing such circuits depends on its accuracy in characterizing frontside voltages and the magnitude of its invasiveness.

Accuracy errors in the electrooptic probe divide into calibration and crosstalk. If a measurement of a signal depends on the configuration of the conductors, a calibration error exists. If the electrooptic measurement includes signal components from other signal lines, and those components *do not exist on the line being probed*, electrooptic crosstalk exists. Both electrooptic calibration and crosstalk errors arise from spot-size averaging of the frontside potential and from nonzero potentials at the substrate backside. To evaluate these errors, we have made extensive electrooptic measurements on test structures and confirmed these results with numerical simulations.

Since CPWs have only one main signal line, no crosstalk errors exist. If the wafer backside is ungrounded, though, significant backside potentials occur, leading to electrooptic calibration errors. The backside potential appears as a negative electrooptic signal beneath the ground plane and a nearly equal reduction in the center conductor signal. Figure 1 plots measurements of this backside signal for 50 Ω CPWs of varying center-conductor width on 20 mil semi-insulating GaAs. The points are experimental data and the curve is from finite-difference calculations. CPWs of a size typically used in microwave circuits exhibit backside potential calibration errors 20 dB the applied center conductor signal. Note that CPWs with large backside potentials not only exhibit larger electrooptic errors but are also more susceptible to multi-moding [4] and are undesirable microwave transmission structures.

Electrooptic accuracy in probing digital circuits is more complex. Spot-size and backside potential effects create both electrooptic crosstalk and calibration errors. One model of a complex digital circuit is an array of parallel lines of equal width at a fixed pitch. To find the electrooptic crosstalk from an individual line, use superposition: apply a signal to one line and ground the rest. The electrooptic measurement beneath the grounded lines is then the crosstalk. Figure 2 plots this electrooptic crosstalk as a function of line number for arrays of long 5 μm lines at 4 different pitches. Note that the backside potential is nearly constant over several hundred microns from the signal. In measurements of the closest lines, where the frontside potential in the gaps is greatest, the positive spot-size crosstalk partially cancels the negative backside contribution, reducing total electrooptic crosstalk. In these structures, crosstalk is smaller than -30 dB; a two-layer array of perpendicular lines – an even closer approximation to a real digital circuit – will have significantly less electrooptic crosstalk.

Electrooptic probing at 1.06 μm generates charge in the GaAs through deep-level absorption (EL2) [5] and through two-photon absorption (TPA). To determine the relative contributions of the two processes at the power levels used in electrooptic probing (typically 30 mW), the short-circuit current of a well-characterized MBE Schottky diode [2] was examined as a function of optical power (see Figure 3). TPA dominates above a few mW, in agreement with calculations of this current from the diode parameters, published TPA coefficients [6,7], and EL2 optical cross sections [8]. Typical currents in this diode are tens of microamps. Similar charge creation within a MESFET increases the drain current, probably through trap excitation at the substrate-channel interface [9]. Although this increase can be significant when the beam is within the device or is scattered from surface irregularities to the device, most electrooptic probing examines interconnect metallization not devices.

References

[1] See K.J. Weingarten, M.J. Rodwell, and D.M. Bloom, IEEE J. of Quant. Electr. **QF 24**, 198 (1988) and references therein.

[2] C.J. Madden, M.J.W. Rodwell, R.A. Marsland, D.M. Bloom, and Y.C. Pao, Electr. Dev. Lett., **9** (6) to be published.

[3] R. Majidi-Ahy, K.J. Weingarten, M. Riaziat, B.A. Auld, and D.M. Bloom, presented at the 1988 IEEE MTT-S International Microwave Symposium.

[4] M. Riaziat, I.J. Feng, R. Majidi-Ahy, and B.A. Auld, Electr. Lett. **23**, 1281 (1987)

[5] G.M. Martin, A. Mitonneau, and A. Mircea, Electr. Lett. **13**, 191 (1977).

[6] A. Saissy, A.Azema, J. Botineau, and F.Gires, Appl. Phys. Lett. **15**, 99 (1978).

[7] E.W. Van Stryland, H. Vanherzeele, M.A. Woodall, M.J. Soileau, A.L. Smirl, S. Guha, and T.F. Boggess, *Optical Engr.* **24**, 613 (1985).

[8] P. Dobrilla and J.S. Blakemore, J. Appl. Phys. **58**, 208 (1985).

[9] C. Kocot and C.A. Stolte, *IEEE Transactions on Electr. Dev.* **29**, 1059 (1982).

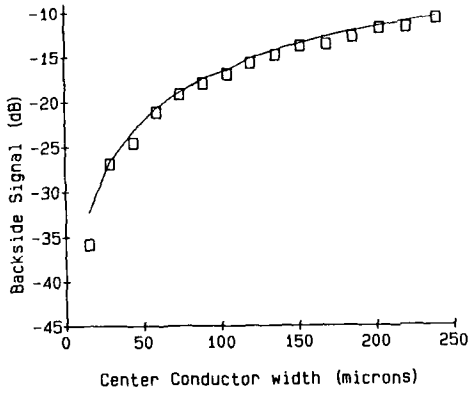


Figure 1: Calibration errors in electrooptic probing of CPWs. □ - experimental; —— - finite-difference calculations.

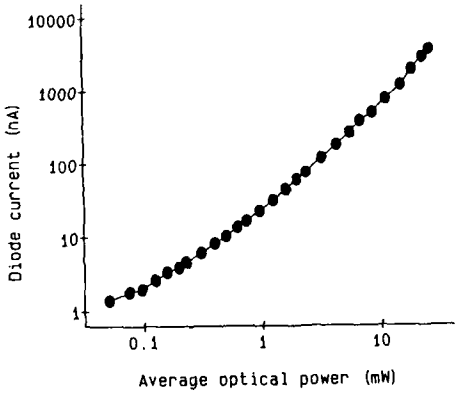


Figure 3: Dependence of induced short-circuit diode current on optical intensity. The slope reveals that two-photon absorption dominates above a few milliwatts.

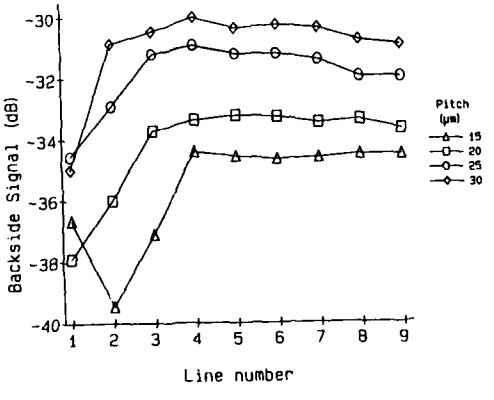


Figure 2: Electrooptic crosstalk in probing arrays of 5 μm lines. The backside signal is partially canceled by spot-size averaging for lines near the driven one.

Abstract No. 383

Photoemission Probing of Fast Integrated Circuits and Devices

Rolf Clauberg, A. Blacha, H. Seitz, H. Beha

IBM Research Division, Zurich Research Laboratory
8803 Rüschlikon, Switzerland

In the last two years photoemission probing has evolved as a new tool for the characterization of ultrafast devices and integrated circuits.[1-5] The main motivation for starting this new approach is twofold. First, it was the lack of a method allowing the determination of ultrafast signals in the lower picosecond range on Si-based devices. Second, it was the chance to do such measurements much faster than with the existing electron-beam method, thereby enabling new applications prohibited before in the picosecond range.

In this work we will estimate the capability and the limits of photoemission probing in its sampling, i.e., time-resolved mode, as well as in its voltage-contrast mode. The ultimate limits and special effects of photoemission probing coincide partly with those of electron-beam probing, but partly also differ very much from them. One main difference is the lower kinetic energy of the photoemitted electrons. In present photoemission probing systems, the kinetic energies of the emitted electrons range from zero energy to about 1 eV in the one-photon excitation[1,2] and up to 2 eV in the three-photon excitation.[3-5] In comparison, the secondary electron peaks in electron-beam probing are around 2-3 eV for atomically clean surfaces and around 9 eV for air-exposed samples. The low energies in photoemission probing require the application of extraction fields, depending on the geometry and the voltages on the chip close to the point where the measurement is done. However, due to the transit-time effect,[6,7] extraction fields are also required in electron-beam sampling if a time resolution in the picosecond range is desired.

On the other hand, the small width of the photoelectron energy distribution leads to a very high voltage sensitivity which, together with the high number of electrons per pulse in photoemission, in principle enables the measurement of series of waveforms on an integrated circuit in a rather short time. Effects, limiting the acceptable number of electrons per pulse are, e.g., the space charge build up by the emitted electrons and the Coulomb repulsion between these electrons. While the space charge limits the number of electrons which can be emitted per pulse, the Coulomb repulsion leads to a pulse spreading in energy as well as in space and time. In photoemission probing this energy broadening results in a voltage sensitivity worse than that predicted by the shot-noise limit, but does not affect the time resolution. In electron-beam probing this effect in the primary beam limits the time resolution.

For voltage contrast measurements the interesting question is how far materials contrast effects will interfere with voltage contrast and what limits these effects set to the detectable voltage contrast.

In this work we will present voltage contrast measurements and their interference with materials contrast effects, rise time and device delay measurements on integrated circuits, and an investigation of the Coulomb spread as a function of incident laser intensity.

References:

1. R. Clauberg, H.K. Seitz, A. Blacha, J.A. Kash, H. Beha, in "High Speed Electronics, Springer Series in Electronics and Photonics", edited by B. Källbäck and H. Beneking (Springer, Berlin, 1986) Vol. 22, p. 200.
2. A. Blacha, R. Clauberg, H.K. Seitz, J. Appl. Phys. **62**, 713 (1987).
3. J. Bokor, A.M. Johnson, R.H. Storz, W.M. Simpson, Appl. Phys. Lett. **49**, 226 (1986).
4. R.B. Marcus, A.M. Weiner, J.H. Abeles, and P.S.D. Lin, Appl. Phys. Lett. **49**, 357 (1986).
5. A.M. Weiner, P.S.D. Lin, R.B. Marcus, Appl. Phys. Lett. **51**, 358 (1987).
6. R. Clauberg, J. Appl. Phys. **62**, 1553 (1987).
7. R. Clauberg, J. Appl. Phys. **62**, 4017 (1987).

Abstract No. 384

Internal Waveform Measurements in High Speed Silicon Circuits Using a Picosecond Photoelectron Scanning Electron Microscope

J.-M. Halbout, P. May, Y. Pastol, and G. Chiu
IBM Research Division
T.J. Watson Research Center
P.O. Box 218, Yorktown Heights, NY 10598

The advances in process technology and the better understanding of design and scaling principles have led recently to the realization of very high speed LSI and VLSI circuits. These circuits have gate delays as short as 13 ps (in the case of 0.1 μm NMOS) [1] and characteristic feature and wiring interconnect sizes smaller than one micron. Circuits built today are already beyond the testing capabilities of conventional equipment, both in terms of the access to internal nodes and in terms of their temporal resolution. Electron beam voltage contrast testing systems provide an attractive solution to the noncontact probing of internal nodes, particularly as the nonintrusive probe of these systems is electrically nonloading and can be positioned very accurately on the circuit. However, such systems have traditionally lacked the time resolution that is now needed. In order to answer this problem, we have recently developed a picosecond laser pulsed electron microscope, designed for the noncontact measurement of internal waveforms on high speed VLSI circuits. We first describe the instrument itself and then present unique measurements we have performed on high speed silicon bipolar ECL circuits and on a 0.5 μm CMOS SRAM test vehicle. It is the first time that such high speed waveforms have been measured directly in situ on advanced silicon circuits.

The Picosecond Photoelectron Scanning Electron Microscope (PPSEM) is shown schematically in figure 1. This novel instrument provides a temporal resolution of less than 5 ps for risetime measurements and 1 ps for delay measurements, a spatial resolution of 0.1 μm for both the probe size and for its positioning accuracy, and a voltage resolution of $3mV/\sqrt{(Hz)}$ [2]. The measurements can be performed at any point on circuit interconnect lines that are accessible from the top surface. The signals are sampled by stroboscopic voltage contrast where the waveform on the circuit is progressively shifted in time with respect to the electron probe pulse. The pulsed electron probe beam impinging on the metal lines of the circuit results in the emission of secondary electrons whose energy distribution is shifted by the instantaneous voltage at the particular node of the circuit. Because of the superior capability of the laser driven electron source, the system operates at low beam energy (below 2 keV) where charging problems can be avoided and no damage to the devices is expected. It takes only about twenty seconds to recover a waveform at the 100 MHz repetition rate determined by the mode-locked laser. Although it is constantly operating in a pulsed mode, the system provides full viewing of the chip under test on a TV screen obtained by raster scanning of the electron beam. The beam can then be accurately positioned on this image at the desired measurement point and, switching to a spot mode, the waveform is then acquired. Typically one thousand points are acquired per waveform with a time span which can extend to several nanoseconds. The waveforms are stored in an IBM PC-XT and can be averaged or signal processed at will.

As a first example of application of this instrument, we present here the detailed characterization of sub-100 ps silicon bipolar ECL ring oscillators [3]. These circuits are fabricated with an emitter size on the wafer of 0.8x2.0 μm^2. The circuit is made up of ten stages connected in in series and a feed back loop. The basic ECL gate is shown in figure 2(a) with the measurement points of interest. For these measurements the self oscillation of the circuit is disabled at the first stage and an enable input on the second stage is used as a trigger input for synchronization. We measure the waveforms at the different points within the ECL gates as the switching pulse progresses down the chain. Figure 2(b) shows the waveforms measured at the collector node of the switching transistor and the emitter-follower output node for a typical unloaded internal gate. Most of the measured total gate delay of 90 ps arises in the current switch which exhibits a 78 ps delay while the output emitter follower contributes only 12 ps. The simulated waveforms at these nodes using ASTAP models are shown in figure 2(c) for comparison. The excellent agreement is evident and show how the models can be tuned to match as built circuits. Such measurements can also provide information on process variation at the scale of the circuits, from the differences in the measured delays. We have studied the in situ operation of these ECL gates under various conditions of bias, voltage swing and loading thereby providing detailed information about their internal workings which was not accessible up to now.

The second example of application of this instrument involves the measurement of the access time for a 0.5 μm CMOS SRAM and the study of the breakdown of this access time among the different circuits in this complex, fully functional chip [4]. The circuit on this chip are fast enough that the conventional e-beam testing systems cannot resolve the waveforms. The chip is a 596 bit SRAM experimental test vehicle fabricated with a selectively scaled 0.5 μm CMOS process [5]. In order to make measurements on both metal interconnect levels, the insulator separating the two layers was removed where it was not covered by the second level metal. The polyimide was chemically wet etched and the underlying nitride removed by RIE. The chips were checked to be fully functional after this procedure with no measurable difference in their performance. Figure 3(a) shows the measurements taken on the path from the clock input to the selected memory cell. They show the delays encountered through the different logic stages as outlined in figure 3(b). Wiring delays which also contribute to the access time can also be measured. As the chip get faster and larger, these wiring delays will have to be taken into account in the design of future chips. We measured a total access time to the data output of 3.5 ns when a "0" is read. The read a "1" access time is 10% longer. Let us also point out that for these measurements the chip was clocked at 100 MHz, which emphasizes the high performance of this emerging technology.

In summary, the technique we have presented here allows one to measure and fully characterize the internal waveforms within a circuit, as well as to resolve the risetimes and the contributions to the delay of the different components with picosecond resolution. The measurements we have presented here on high performance silicon circuits are unique and unprecedented, and have hardly stretched the capabilities of the instrument. Moreover, the loading effects usually encountered in electrical measurements are avoided in this noncontact technique, thus making it a unique tool for the characterization of high speed VLSI circuits. Further improvements of the system include a cold chuck capable of cooling the chip down to 77 K and an image processing system to improve viewing and navigation in very complex circuits.

References:

1. G. Sai-Halasz, et al., subm. to IEEE Elect. Dev. Letters.

2. P. May, et al., Appl. Phys. Lett., 51, pp. 145-147, (1987).

3. P. May, et al., IEDM Technical Digest, 1987, pp. 92-95.

4. J.-M. Halbout, et al., ISSCC Technical Digest, 1988, pp. 82-83.

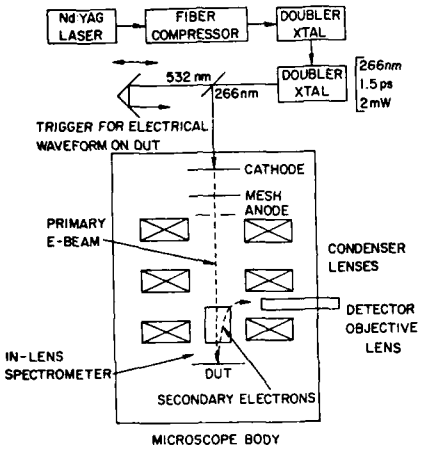


Figure 1. Schematic of the experimental setup for the photoelectron scanning electron microscope. (DUT is the device under test).

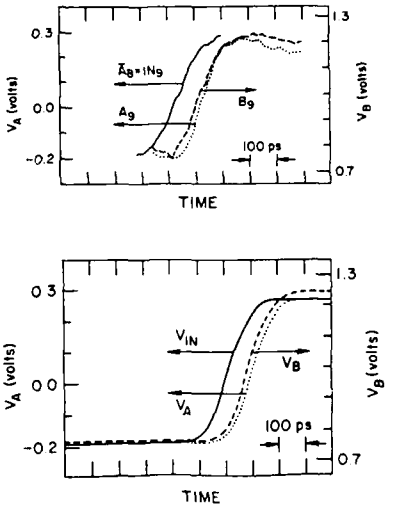


Figure 2. b) Measured waveforms at designated internal nodes c) Simulated waveforms at these nodes

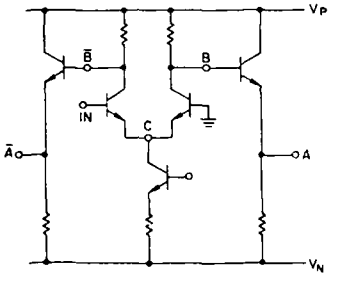


Figure 2. a) Schematic of the basic ECL gate

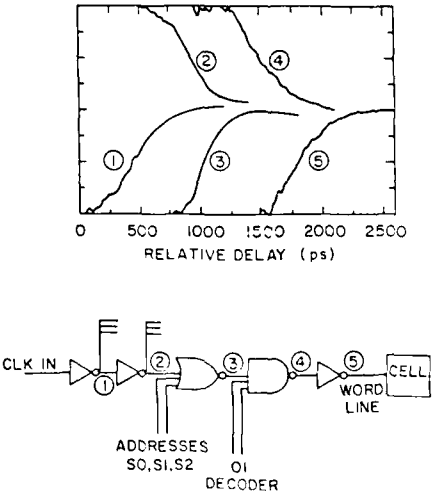


Figure 3 a) Measured waveforms from the first inverter to the memory cell. (Note that the dc level have been arbitrarily shifted for easy timing comparison) b) Schematic of the corresponding logic path

Abstract No. 385

PULSED NEGATIVE ELECTRON AFFINITY CATHODE FOR TIME-RESOLVED ELECTRON MICROSCOPY AND ELECTRON SPECTROSCOPY

N.C. MACDONALD AND COLIN A. SANFORD

Department of Electrical Engineering
and the National Nanofabrication Facility
Cornell University, Ithaca, New York 14853

Since the late 1960's the scanning electron microscope (SEM) has been used to study spatially resolved, time varying phenomena (1,2) with a beam pulse width of 200 ps (2). Time-resolved SEM measurements at a GHz bandwidth were achieved in the 1970's (3-5) with a beam pulse width of 2 ps (5). However, these time-resolved SEM's and numerous subsequent SEM systems have been severely limited by the effectiveness of the high speed, beam blanking systems to produce short electron pulses without reducing the effective brightness of the electron optical system. Furthermore, to achieve a sufficient number of electrons in the picosecond duration pulses, designers were forced to increase the source brightness by the use of field emission sources; these field emitters required a UHV environment and produced additional noise above the shot noise limit.

Recently, May, Halbout and Chiu (6,7) devised a method to eliminate the SEM blanking optics and increase the source brightness. They replaced the conventional SEM electron cathode (e.g. Lanthanum Hexaboride, tungsten, etc.) with a high brightness (A cm^{-2} str^{-1}) laser-pulsed electron cathode, and achieved a substantially improved time resolution of 5 ps for the measurement of a voltage waveform on an integrated circuit. The authors used a new photocathode made of a thin film of gold deposited on quartz and excited by a pulsed UV (266 nm) laser in transmission mode. For an average optical power of 2 mW; a conversion efficiency of 2 x 10^{-4}; an emission current of 10 nA; a beam energy of 1.8 keV; an average beam current of 50 pA; and a spot size of 100 nm, they achieved 3-5 electrons/pulse for a pulse duration of 1.5 ps (7). The gold film UV cathode was operated in a typical SEM environment at pressure of 10^{-5} torr.

The voltage contrast application for laser-pulsed cathode of May, et.al. illustrates one exciting application for a laser pulsed electron cathode.

In this paper we discuss the operation of a GaAs negative electron affinity (NEA) laser pulsed cathode mounted in a UHV scanning Auger microprobe (SAM). The GaAs NEA electron cathode can be excited by either a CW or a pulsed laser source for a nominal wavelength range of 600 to 750 nm. Since high average power semiconductor (.1W) or gaseous (5 watts) lasers are quite common for these wavelengths, many laser-cathode electron gun configurations are possible. The ability to operate the NEA cathode in the CW mode using a semiconductor laser offers the possibility for replacing the conventional Lanthanum Haxaboride source with a higher brightness, compact NEA cathode that can also operate in the pulsed mode for beam blanking.

Enhanced electron emission from GaAs under photon excitation is achieved through special in-situ preparation of the GaAs surface. The effective negative electron affinity condition may be obtained on the surfaces of heavily doped p-type GaAs (8) upon which monolayer quantities of cesium-oxide are grown. The effective negative electron affinity photocathodes have an inherently narrow energy distribution due to their room temperature operation and an electron refraction property which causes emitted electrons to be refracted toward the normal of the emitting surfaces. Typically such cathodes use lasers to photoexcite electron-hole pairs, and because lasers can easily produce optical pulses less than 100 ps at high repetition rates (>100 MHz), these cathodes are well suited for electron beam sampling techniques. Furthermore, because of the high conversion efficiency of incident photons to emitted electrons, high brightness electron sources are possible.

For CW operation of the GaAs NEA cathode, we have achieved a source brightness measured at the sample of 2 x 10^5 (A cm^{-2} sr^{-1}) for a beam energy of 3 keV and an incident laser power of 30 mW at λ = 647 nm. Only a fraction of the laser power was available to excite electrons in the present electron gun design, because the large spot size (500 μm diameter) of the laser source also illuminates non-emitting surfaces adjacent to the cathode. Straightforward improvements in the electron gun design-particularly the laser coupling optics to the GaAs substrate-should improve the source brightness by at least two orders of magnitude.

We demonstrate the use of the system to perform high spatial resolution (75nm), time-resolved (100 ps) voltage waveform measurements on integrated circuits and Auger electron spectroscopy for the study of time varying surface phenomena.

REFERENCES

1. G.S. Plows and W.E. Nixon, J. Sci. Instrum. (ser. 2) **1**, 595 (1968).

2. N.C. MacDonald, G.Y. Robinson and R.M. White, J. Appl. Phys. **40**, 4516 (1969).

3. G.Y. Robinson, Rev. Sci. Instrum. **42**, 251 (1971).

4. A. Gopinath and M.S. Hill, IEEE Trans. Electron Devices **ED-20**, 610 (1973).

5. T. Hosokawa, H. Fujioka, and K. Ura, Appl. Phys. Lett. **31**, 340 (1977).

6. P.G. May, J. Halbout and G. L.-T. Chiu, Appl. Phys. Lett., Vol. **51**, 145 (1987).

7. P.G. May, J. Halbout and G. L.-T. Chiu, IEEE J. Quantum Electron., **24**, 234 (1988).

8. J.J. Scheer and J. Van Laar, Surf. Sci. **18**, 130 (1969).

Abstract No. 386

CHARACTERIZATION OF ps-ELECTRONIC DEVICES: A CHALLENGE FOR E-BEAM TESTING

M. Brunner, R. Schmitt, D. Winkler
Siemens Research Laboratories,
Otto-Hahn-Ring 6, D-8000 Munich, Germany

Microwave and digital ICs, based on GaAs as well as silicon bipolar technologies, have reached operating speeds above 10 GHz and gate delays below 10 ps [1,2]. Progress towards even higher speeds continues and is accompanied by growing complexity and further miniaturization of the structures. The testing and probing techniques required for technology and circuit development have to keep pace with this development. Both functional tests as well as internal waveform measurements are necessary to characterize timing, signal levels, transient response and coupling effects. Furthermore, internal waveform measurements are needed to verify simulations. Mechanical probing introduces a capacitive load and influences the circuit's function. The small sizes of the structures to be probed additionally limit the applicability of mechanical probes.

Several new methods using laser or electron-beam sampling are therefore under development [3-14]. Lasers utilizing electrooptic effects allow a unique time resolution in the fs range. However, the device must be triggered by an electrooptic switch and the laser governs device operation. On the other hand, a probing technique which allows the characterization of all the specifications listed above has to be flexible in driving the device under test. That is, the device under test has to be operated at different input frequencies, input voltages, with different output loads, power voltages, etc. A digital circuit needs digital addressing and the sampling mechanism has to be synchronized with the digital signals.

The e-beam technique [11-14] is superior to other techniques with respect to the requirements of flexibility. The device under test can be driven with signals of continuously variable levels and frequencies between dc and several GHz. The e-beam is moreover not limited to electrooptic materials like some laser methods. It is also a proven technique since a version with nanosecond time resolution has been in practical use for more than ten years on large and very large scale integrated circuits [15-19]. It is known not to interfere with the device function and is nonloading because the primary e-beam current and the current of secondary electrons compensate each other.

The e-beam test technique focusses short e-beam pulses to a spot size of typically 0.5 µm on an IC-internal test point. Smaller spot sizes down to 0.1 µm are possible [20]. Secondary electrons are analyzed with respect to their energy which reveals the voltage of the probed point. The voltage sensitivity is limited by the shot noise of the beam and thus depends on the pulse repetition rate. It is 20 mV/$\sqrt{\text{Hz}}$ at a repetition rate of 10 MHz, which reduces to 2 mV/$\sqrt{\text{Hz}}$ at 1 GHz. IC input or output signals are used to trigger the electron-pulse generation. In order to record a complete waveform, the phase relation between the IC signals and the sampling electron pulse is shifted. High-speed applications require the e-beam pulses to be short and need a very stable synchronization between the signal to be recorded and the e-beam pulse. An effective pulse duration of 15 ps has been achieved including the influence of jitter in the synchronizing electronics [14]. Improving the trigger stability should improve the effective pulse duration to below 10 ps. The time resolution is then ultimately limited by the transit time effect of secondary electrons [21,22] to a value between 5 and 10 ps. Further improvement needs mathematical methods to correct the signal for the influence of this effect. Different methods of synchronization between the device under test and the e-beam are possible depending on the application:

- The device under test and the e-beam can both be triggered by an external clock or input signal.
- The device can be free-running (e.g. an oscillator) and an output signal can be used for synchronizing the e-beam.
- The device can be driven by an external signal but the e-beam can be triggered by an output signal from the device,

and so on.

Some results of practical applications will now be reported to demonstrate that the e-beam technique can satisfy present and near-future needs of high-speed circuit characterization. Fig. 1 shows a measurement on a coplanar strip line which was driven by a step recovery diode. The nominal rise time of 35 ps is clearly resolved but the measurement shows an increase to 38 ps by convolution with the 15 ps pulse. For precise rise time measurements this can be corrected mathematically because the pulse duration is known. The signal propagation delay between the two probed points is measured to be 3.5 ps corresponding to a velocity of $114 \cdot 10^6$ m/s. This velocity agrees very well with the theoretical value based on the propagation on a coplanar line with an electrostatic constant of $\varepsilon_r = 9$ of the substrate. This example demonstrates that both rise time measurements and timing measurements in the ps range are possible with the e-beam.

The flexibility of the e-beam pulse synchronization allows measurements on frequency dividers [23] operating the device under different conditions (Fig. 2). In this application the e-beam is triggered by the device output yielding a repetition rate of almost 1 GHz. In this way the synchronization and the repetition rate automatically match all internal signals. The measured waveforms show overshooting of the first divider stage which increases with input frequency. Internal differential input stages avoid sensitivity to these overshots and allow operation up to 7.67 GHz of this particular device under test. The device failed above this frequency. Among others, these measurements demonstrate that e-beam probing of internal voltages below 200 mV is possible with good results.

The combination of the e-beam tester with a wafer prober stage allows measurements directly on the wafer. The prober stage [24] is specially designed for use in the e-beam tester. Its height is only 1 mm in the region above the chip to allow for a short working distance of the secondary electron spectrometer. Signals up to 12 GHz can be applied to the chip via the prober with the possibility of verifying the input signal in situ. (Fig. 3) shows measurements on a GaAs ring oscillator [25] using the prober stage. The oscillator output is contacted via the prober to synchronize the e-beam. The measurement allows gate delays t_d of individual stages to be determined while the values calculated from the oscillator frequency are mean values. The delay of a single transistor can also be determined. The result further shows that the voltage levels of the different stages differ. The measurement also reveals the internal signal rise time t_r which is not otherwise known.

It can be concluded that e-beam testing is able to characterize present and near-future high-speed devices allowing a high degree of flexibility for device operation. It is in the range of one ps and below that electrooptic techniques become superior.

References:

[1] Kellner, W.: Mikroelektronik Bd. 1, Berlin Offenbach vde-Verlag, 1987; 64-67.
[2] Wieder, A. W.: 18th Int. Conf. on Solid State Dev. and Mat., Tokyo 1986; 261-265.
[3] Zhang, X.-C.; Jain, R. K.: Electronics lett. 22 (1986), 264-265.
[4] Heutmaker, M. S.; Cook, T. B.; Bosacchi, B.; Wiesenfeld, J. M.; Tucker, R. S.; IEEE J. Quantum Electr. 24 (1988) 226-233.
[5] Valdmanis, J. A.; Mourou, G.: IEEE J. Quantum Electr. QE-22 (1986) 69-78.
[6] Kolner, B. H.; Bloom, D. M.: IEEE J. Quantum Electr. QE-22 (1986) 79-93.
[7] Beha, H.; Seitz, H.; Blacha, A.; Clauberg, R.: Microelectronic Egineering 7, Amsterdam Tokyo, North-Holland Elsevier Scl. Publ., 1987; 351-359.
[8] Weiner, A. M.; Lin, P. S. D.; Marcus, R. B.: Appl. Phys. Lett. 51 (1987) 358-360.
[9] Bokor, J.; Johnson, A. M.; Storz, R. H.; Simpson, W. M.: Appl. Phys. Lett. 49 (1986) 226-228.
[10] May, P.; Halbout, J. M.; Chiu, G.: Appl. Phys. Lett. 51 (1987) 145-147.
[11] Schmitt, R.; Winkler, D.; Lischke, B.: Microelectronic Engineering 5, Amsterdam Tokyo, North-Holland Elsevier Scl. Publ., 1986; 523-530
[12] Lischke, B.; Winkler, D; Schmitt, R.: Microelectronic Engineering 7, Amsterdam Tokyo, North-Holland Elsevier Scl. Publ., 1987; 21-39
[13] Schmitt, R.; Winkler, D.; Brunner, M.; Lischke, B.: Electronics Lett. 24 (1988) 235-236.
[14] Brunner, M.; Winkler, D., Schmitt, R.; Lischke, B.: Scanning 9 (1987) 201-204.
[15] Wolfgang, E.: Microelectronic Engineering 4, Amsterdam Tokyo, North-Holland Elsevier Scl. Publ., 1986; 77-106
[16] Ura, K.: 11th Int. Cong. on Electron Microscopy Vol 1, Kyoto, (1986) 173-176.

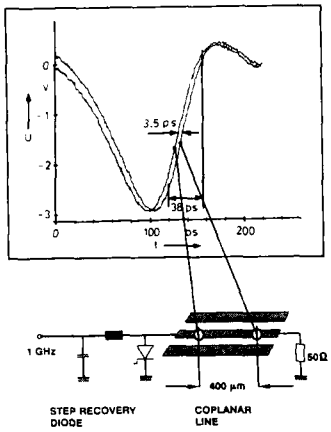


Fig. 1: Signal of a step recovery diode sampled by e-beam on a coplanar line. A propagation delay of 3.5 ps between two probed points is resolved and agrees with the theoretical value.

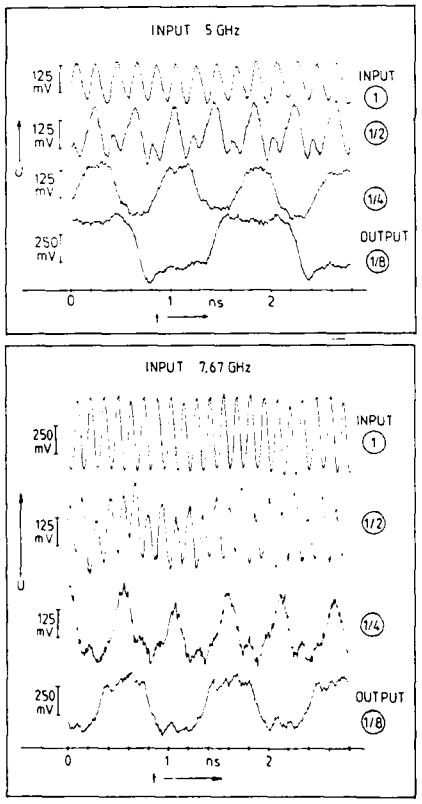


Fig. 2: E-beam probed internal signals of a silicon bipolar static 8:1 frequency divider. Overshooting causes device malfunction at frequencies above 7.67 GHz.

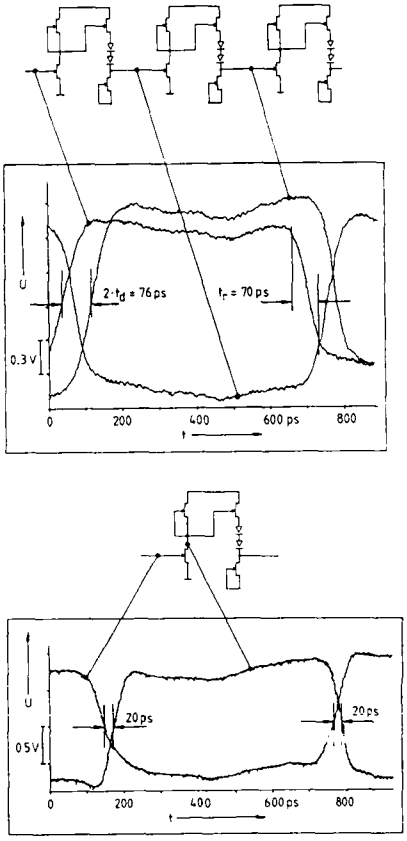


Fig. 3: Internal signals of a GaAs ring oscillator measured directly on the wafer by the e-beam using a prober stage. Signal rise times t_r, variations of gate delays t_d, voltage levels and switching speeds of individual transistors can be determined.

[17] Rehme, H.: Elektronenstrahl-Potentialmeßtechnik. Meß- und Prüftechnik. M. Zerbst (ed.), München: Springer Verlag, 1986.
[18] Menzel, E.; Kubalek, E.: Scanning 5 (1983) 103-122.
[19] Feuerbaum, H. P.: Scanning 5 (1983) 14-24.
[20] Frosien, J.;Plies, E.:Microelectronic Engineering 7, Amsterdam Tokyo, North-Holland Elsevier Sci. Publ., 1987;163-172.
[21] Fujioka, H.; Nakamae, K.; Ura, K.: J. Phys. D: Appl. Phys 18 (1985) 1019-1027.
[22] Clauberg, R.: J. Appl. Phys. 62 (1987) 1553-1559.
[23] Weger, P.; Rein, H.-M.: ESSDERC (1987) 1051-1054.
[24] Schmitt, R.; Winkler, D.; Brunner, M.; Lischke, B.: to be published.
[25] Grave, T.; Anger, K.; Hoepfner, J.; Schmitt, R.; Winkler, D.; Siwerls, H.-J.; Müller, J.-E.; Kellner, W.: Europ. Workshop on Compound Sem. Dev. and Integr. Circuits 1988, in press.

The authors thank P. Weger and L. Treltinger for making the 8:1 divider available. This work has been supported by the EEC's Esprit Programme, Project 843.

Abstract No. 387

A submicron electron beam tester for VLSI circuits

Jochen Kölzer, Fred Fox and Diether Sommer#
Siemens AG
Corporate Research and Technology
Components Group
Otto-Hahn-Ring 6, D-8000 München 83
Federal Republic of Germany

In recent years, the underlying principles of electron beam testing (EBT) have been thoroughly investigated [1,2], and this has become a well established method [3,4] of chip verification and failure analysis of VLSI circuits. The advantages of this contactless and nonloading method for chip-internal measurements compared with the mechanical probe are undisputed, as can be seen from the range of commercial available EBT systems [5,6,7]. However, none of these systems can resolve all the problems currently arising in the testing of integrated circuits. Important performance criteria are the attainable spatial, temporal and voltage resolution as well as the availability of specific measuring modes and operating conditions. The performance of the ICT 9010 e-beam tester* used for the present investigation will be measured on the basis of the specifications defined by the Siemens 4 Mbit dynamic random access memory (4M DRAM) development [8].

In the first place this means that measurements at low primary electron (PE) energies (typically $E_{PE} = 1$ keV) and high probe currents ($I_{PE} \geq 1$ nA) must be performed on *submicron interconnection lines*, i.e. with extremely good spatial resolution. Consequently, the diameter d of the PE probe must be smaller than 0.2 μm to satisfy the condition $d \leq 1/5\ w$ (w: interconnection width). Since conventional scanning electron microscopes (SEMs) do not satisfy this requirement, a new electron-optical column (EOC) was developed [5,10]. A schematic representation of the main components of this EOC can be seen in Figure 1. In combination with the immersion condenser and the spectrometer objective lens, the low-voltage triode electron gun (LaB_6 cathode, $\beta = 3.2 \cdot 10^4$ A/cm^2 sr at $U_{PE} = 1$ kV, heated to about 1550°C [5]) takes into consideration the strong dependence of the spot diameter on the chromatic aberration coefficient and on electron-electron interactions at low PE energies. The EOC was consequently optimized and a PE probe diameter of $d \leq 0.12$ μm ($I_{PE} = 2.5$ nA, $U_{PE} = 1$ kV, final aperture $\alpha = 0.02$ rad, working distance 2 mm) could be realized. This is fully sufficient for measurements on submicron lines up to the 16M DRAM generation.

The *temporal resolution* required for analyzing 4M DRAMs is less exacting. The switching times of the CMOS device have values of about ≤ 1 ns at a cycle time of about 150 ns (typical access time: 70 ns). The temporal resolution derived from this has to be better than 200 ps, since the PE pulse width τ_P should correspond to 1/5 of the rise/fall time $\tau : \tau_P \leq 1/5\ \tau$ [9]. The pulse repetition rate depends on the specifications of the beam-blanking generator (5 MHz). The ICT 9010 beam blanking system which operates independently of the PE voltage alterations is integrated into the anode. A temporal resolution of about 150 ps could be demonstrated by measuring a nominal 500 ps 0V/5V edge, which is sufficient for the diagnosis of 4M DRAMs.

The most serious problem arising in the 4M DRAM design verification are the *voltage resolution and accuracy* when measuring the interior of the chip in the submicron range. Detectability of a 20 mV voltage swing (4M DRAM sense signal $\Delta\Phi$ is about 150 mV) and an overall accuracy of 3% should be ensured. However, high-precision voltage measurements are usually impaired by local fields, caused by switching of adjacent lines [11]. Such influences have to be minimized as far as possible, calling for an optimized secondary electron (SE) spectrometer design which analyses the penetrating SEs independently of their emission angle. This could be realized by an in-lens spectrometer objective [12] and by arranging the crossover of the SE trajectories to be in the center of the two hemispherical grids. After passing the retarding field built up by the spherical grids, the SEs are detected by a double Everhard-Thornley assembly. The behavior of the SEs inside the spectrometer objective lens has been described extensively in [13]. Figure 2 allows an experimental quantification to be made of the theoretically predicted performance characteristics with respect to suppression of the local field effect. The experimental arrangement is illustrated by the *timing diagram* (Figure 2a) which is a measuring method giving the designer a very fast overview of the chip's internal logic in combination with the *logic state mapping* micrograph (Figure 2b) which represents the chip's logic behavior in a more sophisticated manner. Four adjacent lines of the 4M DRAM address bus each with a pitch of 2.3 μm (line width 1.1 μm) were supplied by the indicated test program (lines 1, 2, 4: 0V/5V, line 3: 0V/3V). Figure 2c shows the result of corresponding *waveform measurements* and Figure 2d lines 1, 2 and 3 on an enlarged voltage and time scale. Whereas Figure 2c roughly indicates that voltage coupling is small and comparable to the noise level (250...300 mV). Figure 2d allows a quantitative estimation of less than 2% to be made of the coupling (200...250 mV for a 5 V supply). On the other hand, the voltage accuracy due to the signal level is excellent, showing the same order of magnitude (see Figure 2 again). The required voltage resolution of 20 mV could also be confirmed by an appropriate test procedure. Nevertheless it should be mentioned that such good results can only be obtained by carefully adjusting the whole system. On the other hand the beam has to be positioned precisely and the surface at the measuring location has to be absolutely clean. Besides this, it should be kept in mind that EBT is in principle unable to perform DC measurements. The ICT 9010 gets around this by normalizing the actual lowest voltage swing to zero.

Finally, an example of 4M DRAM analysis requiring utilization of all system features - high spatial, temporal and voltage resolution - is shown in Figure 3. A design weakness, indicated by the signal oscillations in front of the "ATDN" spike was subsequently identified by *logic state mapping* (Figure 3b) and *waveform analysis* (Figure 3c). This example illustrates that the newly developed EOC satisfies all the requirements for internal measurements on submicron structures.

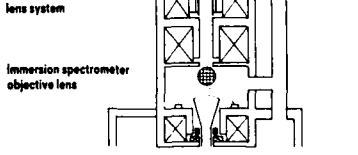


Figure 1. Schematic representation of the ICT 9010 electron-optical column.

We would like to thank F. Bonner, Dr. J. Harter, M. Killian, J. Otto, Dr. E. Plies and Dr. W. Pribyl for fruitful discussions as well as R. Michell from the Siemens Language Services Department for translating this paper. The support of M. Schweiser for using the D. E. Knuth's typesetting system TEX is gratefully acknowledged. Special thanks go to Dr. K. Horninger, Dr. E. Wolfgang and Prof. Dr. H.-J. Pfleiderer for their general support. This report is based on a project which has been supported by the Minister of Research and Technology of the Federal Republic of Germany under the support-nr. NT 2698. For the contents the authors alone are responsible.

* Integrated Circuit Testing GmbH, D-8011 Heimstetten/München

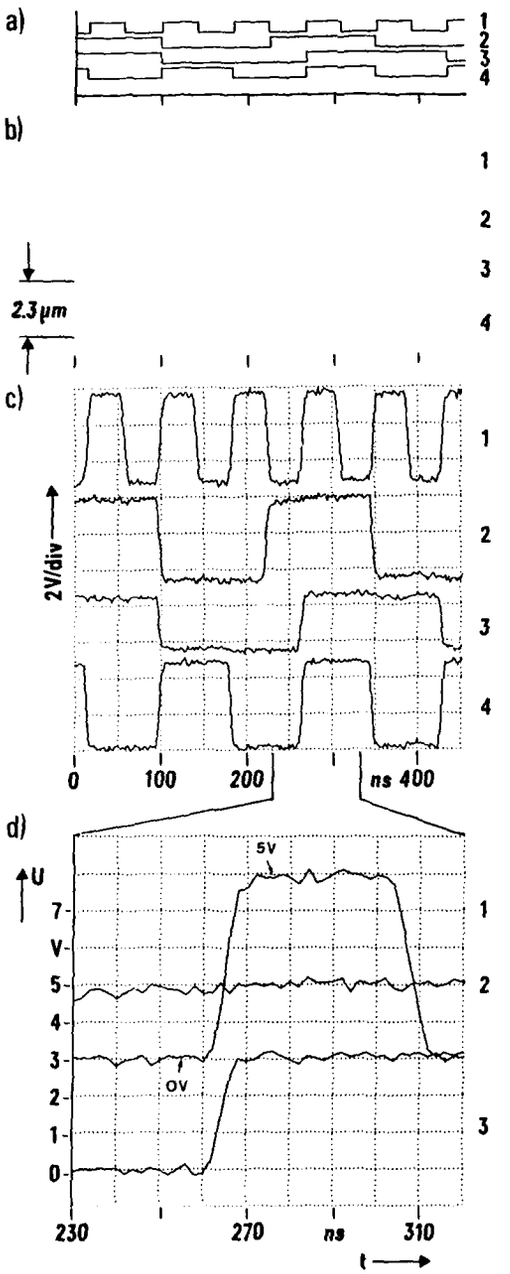


Figure 2. Internal measurements on the 4M DRAM bus structure (pitch: 2.3 μm, linewidth: 1.1 μm). (a) Timing diagram and (b) logic state mapping indicating the supplied test sequence (lines 1, 2 and 4: 0V/5V, line 3: 0V/3V). (c) Corresponding waveforms and (d) expanded part of waveforms 1, 2 and 3 (e-beam pulse width: 1 ns).

References:

1. H.-P. Feuerbaum, Scanning 5(1983), pp. 14–24
2. E. Menzel, E. Kubalek, Scanning 5(1983), pp. 103–122
3. E. Wolfgang, Microelectronic Engineering 4(1986), pp. 77–106
4. K. Ura, Proc. XIth Int. Congr. on Electron Microscopy, Aug. 31–Sep. 7, 1986, Kyoto, pp. 173–176
5. J. Frosien, E. Kehrberg, M. Sturm, H.-P. Feuerbaum, Journal of the Electrochemical Society, in print
6. E. Menzel, R. Buchanan, Proc. SEMICON/West, May 19–21, 1987, San Mateo, pp. 30–41
7. S. Concina, N. Richardson, Proc. 1987 International Test Conference, Washington, pp. 554–560
8. W. Pribyl, J. Harter, W. Müller, Siemens Forsch.-u. Entwickl.-Ber. 16(1987), pp. 253–260
9. E. Plies, J. Otto, Scanning Electron Microscopy IV(1985), pp. 1491–1500
10. J. Frosien, E. Plies, Microelectronic Engineering 7(1987), pp. 163–172
11. K. Ura, H. Fujioka, N. Nakamae, Scanning Electron Microscopy III(1984), pp. 1075–1080
12. E. Plies, J. Kölser, Proc. XIth Int. Congr. on Electron Microscopy, Aug. 31–Sep. 7, 1986, Kyoto, pp. 625–626
13. E. Plies, M. Schweiser, Siemens Forsch.-u.Entwickl.-Ber. 16(1987), pp. 30–36

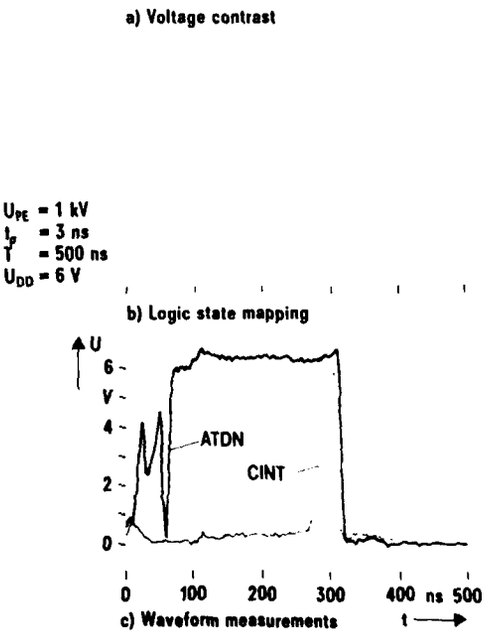


Figure 3. Detection of 4M DRAM design weakness. (a) Voltage contrast micrograph. (b) Logic state mapping performed across the marked line in (a). (c) Corresponding waveform measurements.

Abstract No. 388

THE STRATEGY AND STUDY OF FAB AUTOMATION IN SHARP CORPORATION

TERUHIKO KONDOH, KOHICHI KAWAMURA, TATSUO NAKATO*1
JIN TAKETANI, HIROMITSU TAKEUCHI

INTEGRATED CIRCUIT GROUP
SHARP CORPORATION
2613-1, Ichinomoto-cho, Tenri, Nara, 632 Japan

*1 SHARP MICROELECTRONICS TECHNOLOGY,INC
3l2 SE Stonemill Dr., Vancouver, WA 98684 U.S.A

In 1984 we constructed one of the most advanced semiconductor factories in the world. Now again we are taking on an aggressive probgram to construct the most evolutionary, fully automated wafer fab possible.

In the past four years we have learned quite a few lessons from operating our production lines, obtaining numerous successful results. Highly important is the ability to establish particle-free processes, with the result of increasing yield and device quality, although a luck of computing maturity has prevented the implementation of full automation. This ability to maintain high yields allows the manufacture of such advanced devices as the 1MB DRAM, 256K SRAM, and 400K pixel CCD.

However, there are many problems to be solved at the present time, such as decreasing turnaround time, instituting dynamic schedule changes,etc. Our next fab, which we have just begun to construct, will become one in which dynamic factors can be optimized by the computer system, meaning the approach of complete automation.

The followings are the strategies and studies of each phase:

Phase 1 (1984)

1. Strategy

We wished to achieve complete automation, but key items, such as computer hardware, software, and communication technology were insufficient to realize our goal. We then focused on establishing particle free processes by using Computer Aided Manufacturing (CAM) technology at the local island level. Also the system was built around our production pattern, making it inflexible to change.

2. Concept

a) Manufacturing fine pattern devices based on particle free technology
   Super-clean room (class 10)
   Eliminate operators from the point ofprocessing
   Particle-free wafer handling systems
   Pure materials (i.e., gas, water, chemicals, etc.)
b) Creating a high performance structure of equipment system

3. System outline

a) Clean room structure
   Two levels separated by grating gave us a reliable laminar flow, which facilities and "dirty" equipment placed on the lower level. Wafer processing equipments was placed on the upper level. The upper level is divided into processing and maintenance areas. Operators are kept away from the processing area.
b) Transferring system between islands
   Each island has its own storage (stocker). A "linear motor" transfer system handles nearly 50% of the transfers between these stockers.
c) Transferring system within islands
   Each equipment has its own stocker which can supply wafer cassettes automatically. (Typical are shown in Figures 1 & 2)
d) Improvement of equipment
   Wafer (or cassette) handling mechanisms can never be placed above wafer surfaces. All equipment is bulkhead mounted and load/unload points are located under laminar flow.
e) Pure materials supply system
   D.I. water : Dead-end free and continuously circulated architecture guarantees the purity at use points.
   Gas : Row-particle materials for piping are chosen and particulate is intensively monitored.

4. Results and future topics

We have achieved results satisfactory enough to manufacture 1.0 um design rule devices at high yields based on this total system including another particle reduction methods such as the study of non-static materials, reactant cleaning procedures, etc. Also total throughput is increasing with CAM improvements.

The topics that we have to consider for the next fab are how to increase manufacturing flexibility, how to manage schedule changes, and how to reduce inefficiencies.

Phase 2 (1987)

1. Strategy

In order to obtain higher yield, greater throughput, shorter turnaround time, and higher quality, we will have to establish Computer Integrated Manufacturing(CIM) system. this will include simulation and Artificial Intelligence (AI) technology, which can tightly control many different dynamic factors related to the realization of complete automation.

2. CIM system outline (Shown in Figure 3)

a) Networking
   Hierarchical and distributed architecture based on Local Area Networking (LAN)
b) Database configuration
   Integrate process and product data in a relational database
c) Total control software
   Production and process control including dynamic scheduling
d) Equipment interface
   Real-time equipment monitoring and data gathering using cell controllers and based on SECS communication protocol

3. Automated transferring system outline

Supply wafers directly to each equipment with sufficient throughput and cleanliness, organized into three sections: intelligent stockers, robotics and highways.

Fig. 1 Photo Zone System

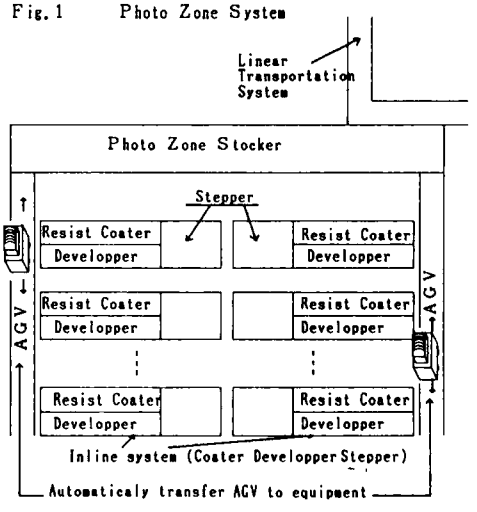


Fig. 2 Ionimplant Zone System

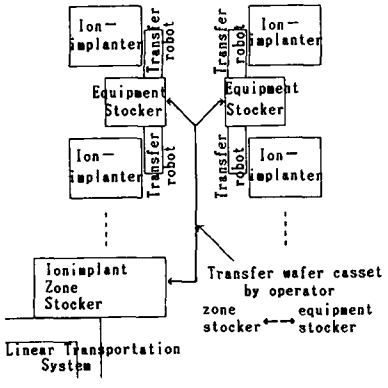
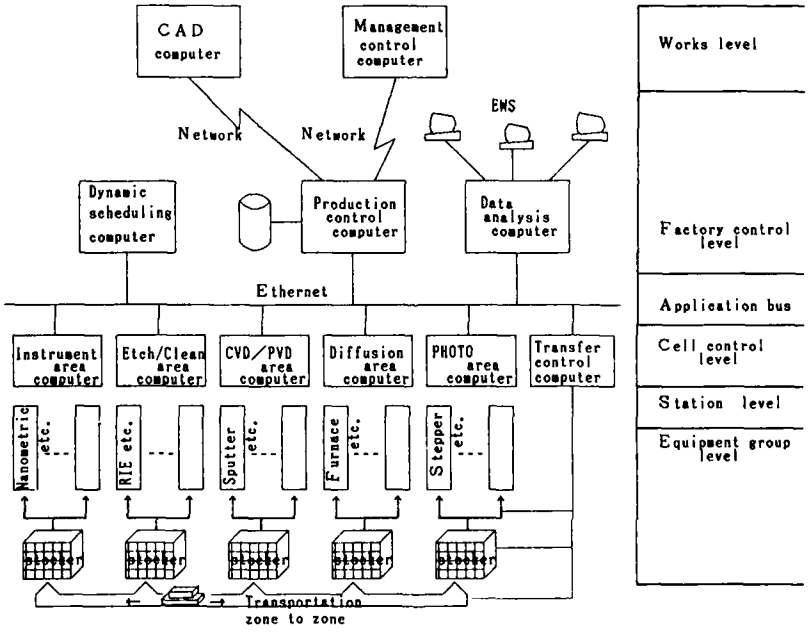


Fig. 3 Concept of computer network



Abstract No. 389

Control and Communications for Integration of Automated Materials Handling Systems in Wafer Fabrication Facilities

John C. Dilworth
Cranfield Robotics and Automation Group
College of Manufacturing
Cranfield Institute of Technology
Cranfield, Bedford MK43 OAL
England

In-line Wafer Handling

In some process areas wafers may be transferred one at a time from one process machine to another in a fixed route. A transfer device could be a conveyor or a robotic arm, for example. This type of transfer is characterized by its simplicity: in most cases the transfer device repeats the same cycle for each wafer being transferred. Whatever the complexity of the controller needed to operate the transfer device, it is possible to activate it by very simple signals.

Most process equipment intended for in-line operation can be supplied with digital I/O signalling capability to control the wafer transfer operation, which could be achieved using only four TTL optically isolated signal lines between the pieces of process equipment(1). Unfortunately this has not been standardized, and each equipment manufacturer uses its own signalling protocol. Interfacing two machines with a transfer device often requires a custom microprocessor solution. This can be expensive and time consuming and may also result in loss of productive time while debugging during commissioning.

Cassette Transfer in Flexible Routing Systems

Cassettes can be transferred between machines in-line as above, in which case similar communications and control strategies could be applied. However, most cassette transfer systems provide flexible routing between machines, work-in-progress (WIP) stations, or process areas. Examples of such systems are mobile robots, automated guided vehicles (AGVs), magnetically levitated 'space vehicles', and clean tunnel vehicles. The control architecture of these systems is generally hierarchical. In the lowest tier are the controllers of the individual vehicles or motors in the tracks, and the load/unload station controllers. These are often connected via a network to a transport host in a higher tier. The transport host can connect to a superior area or factory host. This is usually done via a SECS RS232C link.

SECS for Materials Transfer

For automatic remote operation using SECS, each item of process equipment would normally be connected via an RS232C serial port to a host computer. The SECS II standard, stream 4, defines a handshake which could be implemented between the sending and receiving process equipment in order to effect material transfer(2). As the pieces of equipment are not directly connected, these messages must be passed unchanged through the host.

SECS transactions (SECS messages plus associated replies) can be grouped together into a 'scenario' in which a series of transactions to perform a particular task is defined. Standardized scenarios are being developed for the control of automated materials handling equipment Associated with these it is being found necessary to overhaul and expand the SECS II Stream 4 message definitions relating to material movement. The proposals include more precise definitions of the material being delivered and the transport locations. In many of the proposed scenarios, transactions are defined between the transport host and process equipment. Again, these must be routed unchanged through the factory or area host.

Alternatively, each piece of process equipment could be fitted with extra RS232C ports to handle the materials transfer messages directly. A proposal for all process machines to be fitted with parallel I/O lines for this purpose has also been made(3).

Network Issues

Some of the difficulties with SECS for factory control with automated materials handling relate to the network structure dictated by those standards. SECS I specifies point to point connections. The network configuration this implies in a two layer hierarchical system is a star with a host device at the hub. In a multi-layer hierarchy the configuration becomes a tree structure. Peer to peer communication as required for both in-line and flexible routing automated materials transfer can only take place through a superior host node, with the host acting as a passive transparent device. This is not very satisfactory as it will needlessly absorb some of the processing capacity of the host, and it will require different routings for nodes located at different points in the tree, requiring complex bespoke routing software.

This places a severe disadvantage on the use of SECS as currently formulated. Some of the problems could be eliminated by the use of a more suitable network for communications between host and area controllers, process machines and transport devices.

In one materials handling system, process equipment can be linked via SECS I & II to the nearest WIP station and then via the transport system's LAN and transport host to the factory host(4). Other transport system manufacturers claim to be able to supply proprietary networks to handle all communications, although the degree of adherence to standards can vary.

Work has been carried out to send SECS II messages via Ethernet using DARPA TCP/IP protocols(5). Another development program has been undertaken to send SECS II messages on a Manufacturing Automation Protocol (MAP) network(6). This is an Open Systems Interconnect (OSI) network with features especially suitable for manufacturing. Unlike Ethernet, it has the advantage of a nominal guaranteed maximum response time. A SECS Message Service (SMS) for semiconductor manufacturing is being developed to run alongside MAP's own MMS (Manufacturing Message Service) which has more general application in other industries. The eventual aim of the program is to develop SMS to a point where it can be integrated into the MAP specifications and SEMI standards.

These efforts in sending SECS II messages on industry standard networks will enable complex routings to be made with a minimum of wiring and demands on process equipment capabilities. They are therefore especially relevant to the communications and control requirements of wafer fabs with automated materials handling in which connections need to be made between nodes on the same hierarchical level, with each node needing multiple connection capability. They will also enable logical configuration without regard to the physical topology of the network. Such a network could handle all factory communications with SECS II. The use of such a network will probably force a change in the structure of the SECS II protocols and scenarios to cope with multiple open communications connections between devices.

The author has had practical experience in implementing MAP networks and is researching the use of networks with standardized protocols for the future communications needs of automated wafer fabs.

Acknowledgements

The author thanks the Science and Engineering Research Council for its financial support.

References

(1) R.C. Heim; Solid State Technology, 29-1 p65 (1985).
(2) SEMI Standards, vol 2, Equipt. Automation (1987).
(3) H. Kuroda & H. Harada; 172nd Electrochem Soc. Meeting, 87-2 p 940 (1987).
(4) J.G. Harper, G.B. Burkhardt & R.R. Nelson; Solid State Technology, 28-2 p 119 (1985).
(5) E.J. Wood, H. Schenck, J. Wijaya; 172nd Electrochem Soc. Meeting, 87-2 p 922 (1987).
(6) L.C. McAfee, R. Atallah & J. Moyne; Tech. Proc. Semicon East p 204 (1987).

Abstract No. 390

An Intelligent Work-In-Process System

M. Brain, A. Bonora, M. Parikh
Asyst Technologies, Inc.
1745 McCandless Drive
Milpitas, California 95035

An automated storage system for managing and controlling work-in-process wafer cassettes and reticles can have tremendous impact on integrated circuit manufacturing efficiency. A system is proposed which automatically keeps track of material in storage and provides real-time access to this information.

The architecture of the system (shown in figure 1) is based on a small electronic device attached to each container of material[1]. This "tag" consists of a microprocessor, an LCD display, and a 9600 BAUD infrared communications system. One of these tags is attached to containers of work-in-process wafers or substrates, and also to containers of masks or reticles. An infrared communications probe is placed in each bin of the material storage racks, allowing a local personal computer to directly read and write the tag on each box. The tag is programmed by these same probes with information about the material inside the box, and is continually updated to reflect current material status.

An operator places a material container in any empty bin of a storage area. A personal computer automatically logs the material into storage and reads the tag on the box for up-to-date information about the material. This information is instantly available to operators and supervisors using a light pen menu at the PC.

Any removal of material from storage is automatically recorded as a legal or illegal removal. Operators may request permission to remove material from storage using the light pen at the PC. Permission to remove material is granted based on user-established "approval algorithms". When permission is given, the operator is guided to the material by a graphical display on the PC and a flashing LED at the storage bin itself. The LCD on the tag offers final verification that the correct material has been located.

Management summary reports may be printed at regular intervals or made available to PC's outside the cleanroom in real-time via a local area network. Central CAM (computer aided manufacturing) systems may directly access a storage area PC through a SECS I/II or LAN connection. This central host may obtain information about the current status of material in storage for more accurate reports. If desired, the storage system can automatically update the host system as to the processing history of material based on information found in the tags on arriving material. This can reduce or eliminate the need for operator interaction with expensive, space consuming terminals.

Automated transportation systems (AGV's, tracks, etc.) may also access these storage area PC's to determine the location of material. Once the material has been located, the tag attached to the container may be interrogated by the transport system to verify identity and/or destination.

An LCD display on each tag provides operator information. This LCD shows the name of the lot(s) or reticle(s) inside the container and the next destination for this container. The LCD can also give information about the next process step to be performed.

Use of the tag may be extended throughout the facility with a tag reader at each process station (figure 2). Each reader has read/write access to the tag when material arrives at the equipment for processing. If the material does not belong at this process step, the operator is warned by a flashing red light. If parallel or serial (SECS) communication is supported by the process tool, processing of material may be locked out by the local tag reader unless the correct destination is in the tag. When the correct material arrives, the process recipe or process parameters may also be downloaded from the tag to the process tool. This method of coding processing information into the material carrier allows material to be drawn through a "self-selected" process by the needs of the end-user[2].

Accurate, real-time status of inventory allows operators to reduce the time spent searching for material and logging material in and out of storage (figure 3). This time is immediatly transformed into improved operator and equipment utilization. Semiconductor manufacturers are justifiably concerned with quick turnaround and accurate yield prediction to allow management to make realistic commitments to customers[3]. Real-time visibility of wafer and reticle inventories is essential to this goal.

The system described above satisfies these requirements and allows for maximum flexibility. All of the elements of production are integrated into the system, including people, process tools, wafers, and reticles. In addition, the distributed nature of the system provides for maximum system reliability and availability.

REFERENCES

[1] M. Brain, "A Particle and Material Control Automation System", Electronic Manufacturing Technology and Automation Symposium (EMTAS), Society of Manufacturing Engineers (SME), March 20, 1986.

[2] Keith M. Gardiner, "Manufacturing For The Future", Strategic Manufacturing Research Initiative Workshop, National Science Foundation, March, 1987.

[3] Warren F. Hastings, "The Relationship between Corporate Strategy and Automation Planning as it Applies to VLSI/ASIC Production", Technical Proceedings SEMICON Southwest, 1987.

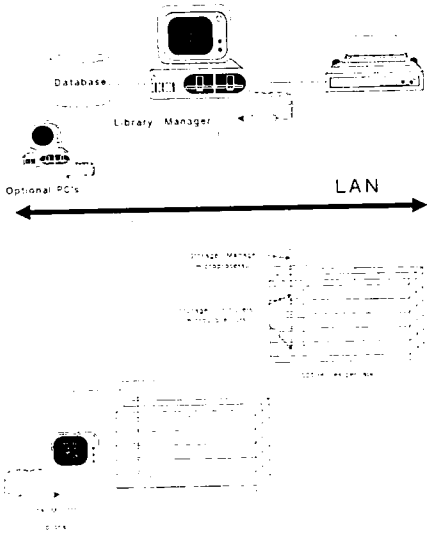


FIGURE 1: SYSTEM ARCHITECTURE

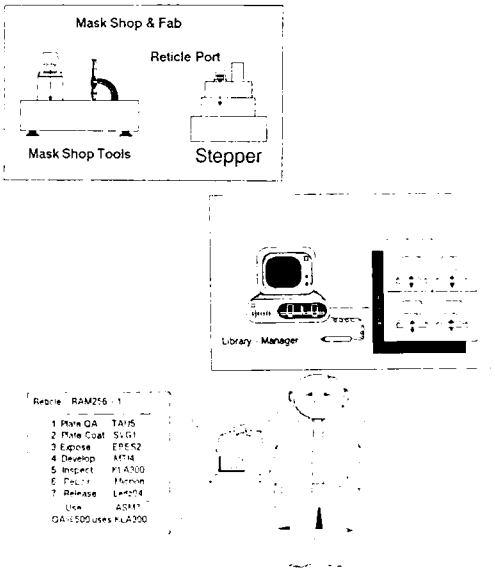


FIGURE 2: RETICLE CONTROL EXAMPLE SYSTEM

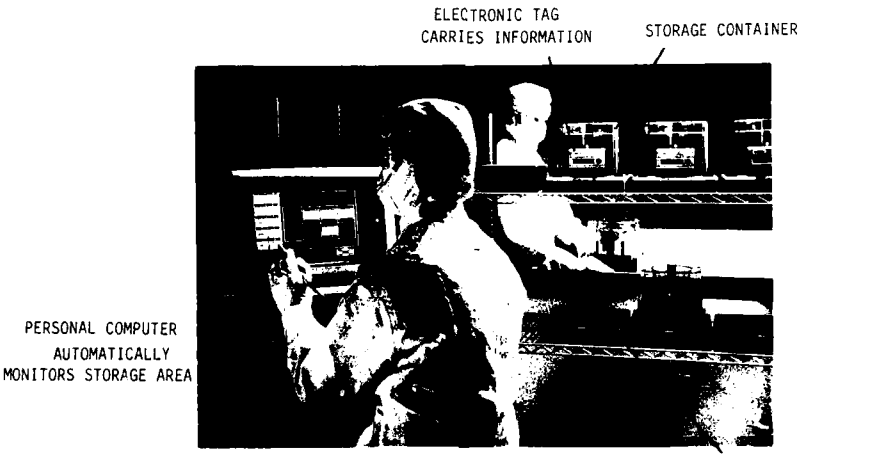


FIGURE 3: AUTOMATED STORAGE AREA FOR WAFERS AND RETICLES

Abstract No. 391

Implementation Considerations for Robotic Systems in a Wafer Fabrication Facility

W. A. Livesley MSc
Research Assistant
Cranfield Robotics and Automation Group

College of Manufacturing
Cranfield Institute of Technology
Cranfield
Bedford, MK43 OAL, England

Introduction

The worldwide Semiconductor Industry is currently considering the third stage of materials handling automation - integrated inter-machine automation. The reasons for using third stage automation are well understood:-

- Reduction in Particulate Contamination Leading to Increased Yield
- Consistent Product Quality
- Reduction in Order to Delivery Time
- Minimisation of Clean Volume
- Reduction in Work-in-Progress

However, the criterion for choosing a particular strategy, and the problems inherent in implementing it are less clear.

This paper seeks to examine the use of a particular tool, the robot, in cell integration. This is achieved in three stages:-

- Review of Available Products
- Examination of Considerations in Specification and Design of Robot Systems
- Examination of Some Implemented Systems

Having established some of the problems enccuntered when implementing robot systems, the implications that these problems have on automation strategy can be examined.

Specification and Design of Robot Systems

In general, the Semiconductor Industry envisages robots as entirely flexible devices, able to perform a range of different tasks with no additional equipment required. However, in practice, the very flexibility of a robot means that it may require considerable configuration for each task. When designing a robot system, therefore, there are a number of factors to be considered:-

- Robot Selection: The choice is unlikely to be simple, particularly as no product will be completely suitable for the application. The robot needs to be evaluated for load capacity, reach, programming capabilities, cleanliness, kinematics, and interfacing capabilities. This is particularly true in a Wafer Fabrication Facility (WFF) as the robot must not only perform its required tasks, but is also required to use a particular path, to avoid on-wafer contamination, whilst minimising its occupied volume.
- Gripper Design: Currently, two gripper types are used, zero-force programmable edge grippers, and vacuum back-side, or front-side, grippers. As only the gripper directly touches the wafer, the robot performance (in terms of cleanliness, repeatability, and wafer handling) cannot be better than the performance of the gripper.
- Operator and Services Safety: Robots are intrinsically hazardous and a WFF, whilst very clean, contains noxious substances fed to a small area with a high density of expensive process equipment; the clean room. However, of primary importance is operator safety. In such an environment, it is easy for an operator, particularly when in full protective clothing, to forget the presence of a robot.
- Programming: Whilst basic programming of a robot is straightforward, the designer should also be aware of the possibility of system failure. From the range of error scenarios, suitable alternative procedures, supported by the necessary instrumentation should be developed. It must also be recognised that the robot positions will need to be manually taught, in-situ. In future enclosed cells, direct programming may not be suitable and alternatives must be considered.

It is likely that a range of solutions will be produced to any problem. Choosing the best system will not be easy. However, by considering some general systems design rules, the problems of implementation and operation can be reduced.

Review of Implemented Systems

Information is currently available on a number of systems in the USA and Japan (1) (2) (3). This will be supplemented by presenting some of the experience gained during the course of several current projects, including the integration of a photo-lithography area and the retrofitting of a robot to a chemical wet processing bench.

Conclusions - Strategic Implications of Robot Systems

By examining design and implementation problems, particularly when related to real systems, it should be possible to evolve design rules for robot systems. With this information, it should be possible to determine some of the techniques used in integrated handling automation, and provide some idea of the problems and considerations when using these techniques.

Acknowledgements

The author wishes to thank the Science and Engineering Research Council for its financial support.

References

(1) Albrecht, P.D., Golland, D.I., Krusell, W.C., Puerto, F.A.; The Clean Module: A Fully Integrated Approach to the Final Cleaning, Inspection and Packaging of Silicon Wafers; Integrated Circuit Manufacturers Conference, Coventry, England (1988).

(2) Hume, E.C., Mueller, R.P., Schick, H., Conway, J.; Automated Cells for Submicrometer Lithography; 172nd Electrochemical Society Meeting (1987) - in press.

(3) Komiya, H.; Totally Automated IC Manufacturing; 172nd Electrochemical Society Meeting (1987) - in press.

Abstract No. 392

A Rule-Based Diagnostic System for VLSI Process Flow

Kiyohiko Funakoshi
Hitachi Central Research Laboratory
Kokubunji, Tokyo 185, Japan

Kazushi Mizuno
Hitachi VLSI Engineering
Kokubunji, Tokyo 185, Japan

1. Introduction

As the VLSI integration scale increases, it becomes increasingly difficult for process engineers to design VLSI manufacturing process flow (recipe). There are two reasons for this. (1) VLSI process flow has become so complex that it contains several hundred steps. (2) There is a great amount of knowledge in VLSI process technology because VLSIs are intrinsically very sensitive to contamination, and because very many parameters affect processing results. This problem is especially serious in research lines and ASIC lines where various types of VLSIs are processed.

To solve this problem, we have developed a new process CAD system, a rule-based diagnostic system for VLSI process flow. This system assists process flow design by pointing out incorrect or questionable conditions in the designed process flow. We implemented this system in our VLSI research facility, and confirmed that it increases the efficiency and quality of process flow design.

2. VLSI Process knowledge

VLSIs are intrinsically very sensitive to contamination, and very many process parameters affect VLSI structure and characteristics. Thus there is a great amount of knowledge about cleaning, resist removal, and optimum conditions. Some examples of process knowledge are listed in Table 1. If Si wafers are processed under conditions conflicting with process knowledge, not only dose the targeted VLSI become impossible to manufacture, but the process equipment is contaminated.

Therefore, until now, process engineers have made great effort to carefully design and check process flow in detail.

3. Diagnostic Algorithm

We have devised a diagnostic algorithm for VLSI process flow in order to correctly diagnose various types of process flow (Fig. 1). In this algorithm, process flow is diagnosed by applying diagnostic rules to process conditions, and to the Si wafer state which is simulated from process conditions by rule-based simulation.

Each diagnostic rule corresponds to a piece of process knowledge, e.g. that no contamination should be brought into furnaces.

Wafer state means what materials and what kind of contamination exist on the Si wafer, and their physical and chemical properties. Wafer state is expressed in LISP association lists.

To diagnose the i-th step, the diagnostic rules are first applied to the conditions of the i-th step, the Si wafer state at that step, and the conditions of preceding and following steps if necessary. If an erroneous or questionable situation is found, the system outputs an appropriate warning message and eliminates the error factor. Then the change in wafer state by the i-th step is simulated by applying simulation rules. All process conditions are diagnosed by repeating this process from the first step to the last step. A diagnosis example is shown in Fig. 2.

This algorithm diagnoses various types of process flow such as CMOS DRAM and SRAM, bipolar, EEPROM, and experimental flows highly accurately.

4. Implementation

We implemented this system as part of the laboratory automation system for our VLSI research facility as shown in Fig. 3(a). This diagnostic system's structure is shown in Fig. 3(b). The system uses LISP on a HITAC M-680 computer. The system has about 160 diagnostic rules and about 50 simulation rules. It takes only 40 s CPU time to diagnose typical CMOS DRAM process flow.

5. Results

We implemented this system in our research facility and confirmed that it increased the efficiency and quality of process flow design.

This system makes process flow design very easy by pointing out erroneous conditions such as (1) out-of-limit or unallowed conditions, (2) erroneous process sequence, (3) conditions causing such situations as loading of contaminated wafers into clean process equipment, and (4) nonoptimum conditions for wafer state, etc. (see Table 1).

Process experts have checked such errors until now. Since this system eliminates trivial errors, experts can now check process flow from a higher perspective. That is, they can evaluate whether the onditions of the designed process flow are optimumm to fabricate the intended VLSI. In our research facility, process experts' comments regarding trivial errors at the final check have decreased by 75%. Comments regarding optimum conditions increased, although these conditions had been overlooked before. Thus this system optimizes process flow for fabricating the intended VLSI.

This system is also very effective for informing process engineers of process knowledge.

6. Summary

We have developed a new process CAD system, a rule-based diagnostic system for VLSI process flow. This system effectively increases the efficiency and quality of process flow design.

7. Acknowledgement

The authors wish to thank Drs. Seiki Harada and Tetsuya Hayashida for their encouragement. They also wish to thank Drs. Susumu Seki, Michiaki Yasumura, and Masatoshi Matsuda, and Messrs. Shigeru Takahashi and Tatsuo Sasagawa, for their helpful discussion.

Table 1 Some examples of process knowledge

	Knowledge about	Comment and examples
1	Alloved conditions	Upper and lower limits of furnace temperature Available etching gases
2	Process sequence	Pre- and post-cleaning Alloved process sequence
3	Contamination and impurity	No contamination should be brought into clean *etchant* Heavy metal should not be brought into clean furnace
4	Optimum conditions	
i	for other conditions	Recomended combination of process conditions
ii	for wafer state	Relation between resist state (thickness, hardened, baked etc.) and removal method Optimum annealing temperature for wafer with Al
iii	for intended structure	Optimum photolithography method for intended minimum feature size
iv	for intended characteristics	

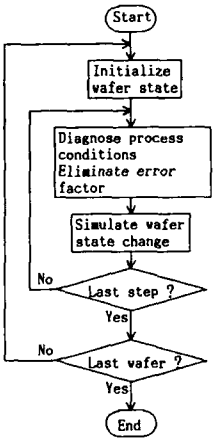


Fig. 1 New diagnostic algorithm for VLSI process flow

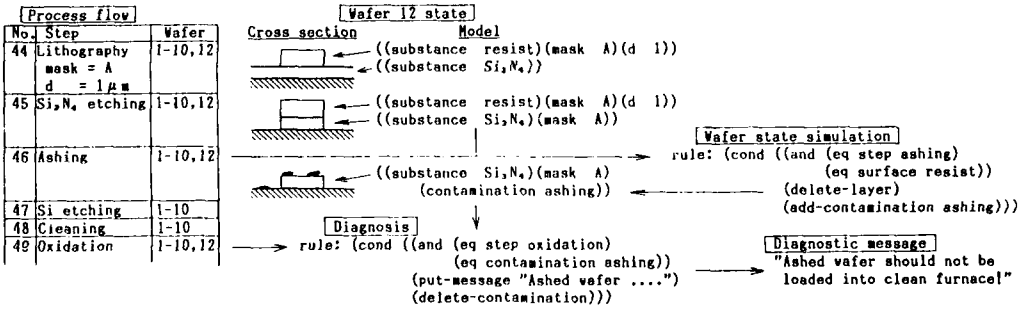


Fig. 2 An example of process flow diagnosis

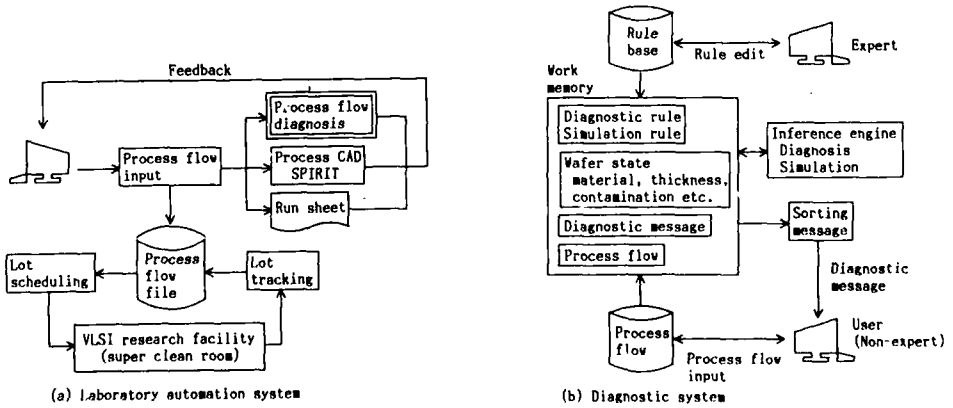


Fig. 3 System structure

Abstract No. 393

Using Simulators to Minimize Transmitted Variability in IC Manufacturing*

Shahin Sharifzadeh, John D. Shott, Art B. Owen, and James R. Koehler
Center for Integrated Systems
Stanford University
Stanford, CA 94305
(415) 725-1682

The yield of VLSI circuits and hence their economic viability often depend on the variability of certain device characteristics. Though some variability is unavoidable, much of it is transmitted to the device characteristics from variability in the process input settings about their design values. The process designer can reduce this transmitted variability by carefully choosing the design values for the input settings. An experimental approach to finding such input values is usually too expensive to be feasible and too slow given the competitive environment in which ICs are manufactured. We therefore turn to physically based simulators, in this case PISCES and SUPREM, to model the steps in IC fabrication and to compute the device characteristics as a function of the inputs.

Even for small problems, these numerical simulators are too slow for an exhaustive search to be made. Therefore we adopt the approach taken by Alvarez et al. [1] and Aoki et al. [2]. This approach is to run the simulator at the points of a statistical experimental design, and to fit a response surface model for the device characteristics. Letting X represent a vector of input settings, the device characteristics are a vector $f(X)$. The simulators compute a function $g(X)$ based on physical models. Running the simulator we find $g(X_i)$ where $X_1, \ldots, X_n$ are the points of the experimental design. We then fit a response surface model $h(X)$ to these values. The simulators are designed so that $\|f - g\|$ is small over the range of interesting X and we choose our model so that $\|h - g\|$ is also small.

The model g helps to find input settings at which the device characteristics are near their targets. We can also use g to estimate the transmitted variability. As X varies from the design values X_0, the device characteristics deviate from their nominal values $f(X_0)$. The transmitted variability is approximately $\nabla f^T var(X) \nabla f$. Therefore to ensure that our model of transmitted variability is good we should have $\|\nabla h - \nabla g\|$ small. But the response surface models h are usually low order polynomials and it is possible for $\|h - g\|$ to be quite small while $\|\nabla h - \nabla g\|$ is large. Therefore using the gradient of the model h as the model for the gradient can be misleading. This also applies when the gradient is used implicitly by simulating the distribution of X and finding the distribution of $h(X)$.

Our major point of departure from [1] and [2] is to make direct measurements of ∇g. These direct measurements allow us to improve our models for transmitted variability. Perhaps more importantly it becomes possible to assess how accurate our model gradients are. We can estimate that derivative with one extra simulation at each design point. If $var(X) = diag(\sigma_1^2, \ldots, \sigma_p^2)$ then the variance transmitted to $f_j(X)$ by variability in X is approximately

$$(f_j(X_0 + \delta\sigma) - f_j(X_0))^2 / \delta^2$$

where $\delta > 0$ is small, σ is a vector of input standard deviations and X_0 is the design value for the inputs.

Once models relating the input parameters to the device characteristics and their variabilities are available it is possible to explore the relationships and tradeoff between the characteristics. The approach is illustrated on Stanford's 2μ CMOS process. The five process parameters used were: boron concentration in the wafer, well implant dose, threshold adjust implant dose, gate oxidation temperature and drawn channel length. The device characteristics considered were threshold voltage, linear transconductance, and saturation current.

The experimental design used was a variation on the central composite design (Box, Hunter and Hunter [3]). The design takes 43 points. The projection of the design onto any two variables is given by the square points plotted in Figure 1. The points used to obtain the directional derivative information appear in Figure 1 as asterixes. The total simulation effort is 86 simulations, including the 43 simulations used to obtain information on the gradients. SUPREM, a 1-D numerical process simulator and PISCES, a 2-D device simulator are the simulators used. For each set of input conditions, 15,000 to 20,000 MicroVax II CPU seconds are needed to complete the simulation of the three desired device characteristics.

One of the device characteristics measured was V_{tn}, the threshold voltage of a NMOS transistor. A quadratic model fit to the V_{tn} values by least squares explained $R^2 = .996$ of the observed variability. How well can we expect the model to fit at points other than the ones observed? One way to assess this is by cross-validation. We drop one point and fit the model to the other 42. Using that model we predict the V_{tn} at the dropped point and compare it to the value measured. Then we put the point back into the data and repeat the above for each observation in turn. When the sum of squared errors in R^2 is replaced by a cross-validated sum of squared errors the result is $R^2_{CV} = .971$. This is still very good. If V_{tn} is really quadratic, we should find that the directional derivative of V_{tn} in any direction is a linear function of the inputs. For a linear regression fit to ∇V_{tn} we found $R^2 = .67$ and $R^2_{CV} = .57$. Therefore the best we can expect from the directional derivative of a quadratic model h for V_{tn} is that it would explain about 57% of the variability of the directional derivative of g, the simulator value for V_{tn}. This still gives some idea of transmitted variability, but not as much as one might have expected given the excellent fit of the simulator V_{tn}'s to the quadratic model. It may be that some power transformation of V_{tn} is nearly quadratic in the inputs. We found that $\sigma^T \nabla (V_{tn})^{.6}$ fit a linear model with $R^2_{CV} = .77$, a worthwhile improvement on .57. The quadratic model for $V_{tn}^{.6}$ fit well too, with $R^2_{CV} = .962$.

The lesson that emerges is that it can be much more difficult to model the transmitted variation than to model the response value itself. Even an extremely high value for R^2 does not guarantee that the model will be useful for modelling transmitted variation. This applies whether one simulates the distribution of the X's or uses the derivative approximation above. The results for models fitted to other output characteristics are given in Table 1.

To explore the results of this model, we convert the directional derivative models to variance models and re express the variances as coefficients of variation (standard deviation divided by mean). We now have 6 response functions and 6 coefficient of variation (cv) functions defined on 5 input variables. To explore the relationships among these 17 quantities, we evaluated the 12 functions at 5000 different values of the input vector X. The points were chosen using a number theoretic scheme due to Korobov (see Stroud [4]). These schemes fill out the gaps in the input space better than do points of a regular grid.

Figure 2 shows the cv of I_{satp} versus I_{satn} for the 5000 points. It is clear that variability in one of these quantities can be minimized only by increasing variability in the other. By way of contrast the cv's of g_{mn} and g_{mp} plotted in Figure 3 increase or decrease together. We isolated those points with small values for both g_{mn} and g_{mp}. Figure 4 is a plot of the threshold adjust implant dose versus the channel length for those points for which the cv of both g_{mn} and g_{mp} was below 6%. The implication is that variability in the g_m's is reduced by raising one or both of these quantities from the values used in the center point of the design.

* This work has been supported by SRC and DARPA

References

[1] A.R. Alvarez et al. "Application of Statistical Design & Response Methods to Computer Aided VLSI Device Design" *IEEE Transactions on Computer Aided Design*, 7(2):271-288, February 1988.

[2] Y. Aoki et al. "A New Design Centering Methodology for VLSI Device Development" *IEEE Transactions ... Computer Aided Design*, CAD 6(3):452-461, May 1987

[3] G.E.P. Box, W.G. Hunter, J.S. Hunter "*Statistics for Ex*

parameters: An Introduction to Design, Data Analysis, and Model Building". Wiley, New York, 1978.

[4] A.H. Stroud. *"Approximate Calculation of Multiple Integrals"*. Prentice-Hall Inc, New Jersey, 1971.

Characteristic	R^2_{CV} (Dic. Det.)	R^2_{CV} (Function)
V_{tn}	0.11	0.962
V_{tp}	0.24	0.944
g_{mn}	0.81	0.980
g_{mp}	0.69	0.915
I_{satn}	0.72	0.969
I_{satp}	0.87	0.989

Table 1: The R^2_{CV} for the fitted models.

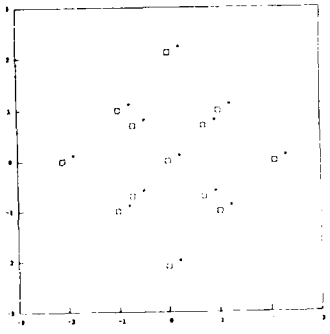


Figure 1: Projection of the design on two variables.

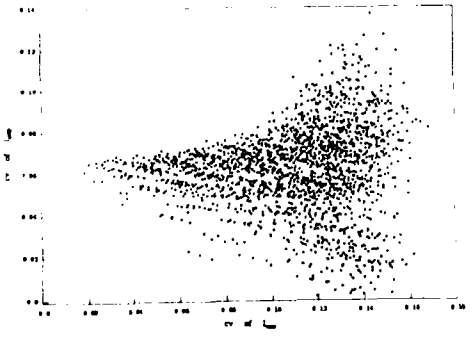


Figure 2: *cv* of I_{satp} vs *cv* of I_{satn}.

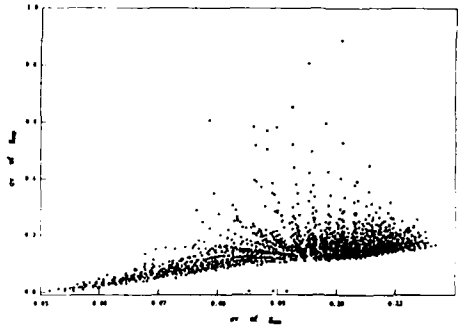


Figure 3: *cv* of g_{mn} vs *cv* of g_{mp}.

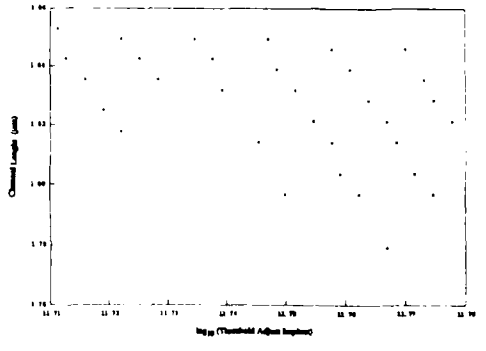


Figure 4: $L_{Effective}$ vs Threshold Adjust Implant for points with stable g_m

Abstract No. 394

Computer Simulation of a Microelectronics Laboratory

Floyd Miller

Lehigh University

Sherman Fairchild Center #161
Bethlehem, PA 18015

Use of the computer graphics capability combined with simple mathematical modeling allows this program to simulate an integrated circuit processing laboratory. Available operations include oxidation, diffusion, CVD, lithography, metallization, mask design, etc. The user operates the simulated equipment in much the same manner as would be required in the real laboratory. For example, when doing an oxidation a furnace is displayed and the operator must set the proper temperature, ambient and time of the oxidation. As an added aid the operator can select to watch a cross section of the wafer as the oxide grows. An individual can experiment with process variables without the time and expense of a laboratory setting.

Figure 1 shows an example of the graphics used to run an oxidation using the computer simulation. F1, F2 and F3 represent computer function keys and are used to operate the laboratory. For example, different ambiants can be selected by pressing F1. Selecting F3 loads the wafers into the furnace at the beginning of a run. When the run is finished F3 is again selected and the wafers are removed from the furnace. F2 changes the temperature of the furnace. The time display will indicate the length of time that the wafers have been in the furnace.

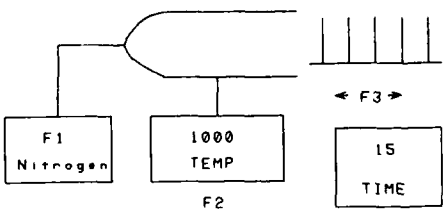


Figure 1

Abstract No. 395

EQUIPMENT MODELS FOR PROCESS OPTIMIZATION AND CONTROL USING SMART RESPONSE SURFACES

Emanuel Sachs
George Prueger
Massachusetts Institute of Technology
77 Massachusetts Avenue
Cambridge, Massachusetts 02139

Introduction

An equipment model is a tool that can be used to predict outputs of interest from a manufacturing process and related processing equipment given information about the inputs. As shown schematically in Figure 1, there are two classes of inputs. Process parameters are those inputs over which direct control is exercised, such as temperature, pressure and flowrate. Disturbances are those inputs that are subject to unintended and undesired variations, such as variations in the properties of incoming raw material or variations in the process parameters themselves. Outputs of interest would typically include rates and uniformities.

There are two fundamentally different approaches to equipment modeling; mechanistically based models and empirically based models. Mechanistic models seek to make predictions based on fundamental physical understanding. Empirical models are most effectively constructed using the methods of statistical design of experiments. Two suitable methods are Taguchi orthogonal array [1, 2] and factorial design and response surface analysis [3, 4]. The common element in these two methods is that many or all of the parameters are varied simultaneously in contrast to the more conventional single variable experimental methods. The result is an efficient exploration of experimental space. The weakness of the empirical approaches is that little or no advantage is gained from the physical understanding of the process. For example, a response surface is a least squares fit of a general polynomial (usually a quadratic) to the data.

The purpose of this work is to fuse basic process physics with the methods of experimental design and thereby construct response surfaces which take their general shape from the physics and are calibrated using data derived by design of experiments, resulting in a "smart response surface".

This work presents the construction of an equipment model for the LPCVD of polysilicon in a horizontal tube furnace with three sites of silane injection. The model accepts as inputs the temperature at three thermocouple positions, tube pressure, wafer number, size and location, flowrates through three injectors, and position of the injectors. The predicted output concerns uniformity of deposition rate down the length of the wafer load. As indicated schematically in Figure 2, two separate paths are followed through this work. The first path involves the execution of a series of designed experiments and the optimization of the process from that experimental design. The parallel path involves the construction of a mechanistically based model and the calibration of a smart response surface based on that model using the results of the designed experiments. The model is then used to optimize the process and that optimum is compared with the experimentally determined optimum.

Experimental Optimization

A nine experiment orthogonal array was designed to investigate the effect of four parameters, each at three levels. As shown in Figure 3, the four parameters of interest are the tube pressure, two of the three injector flowrates, and the position of the source end injector. Total flowrate into the system was maintained into the system at 150 sccm for all experiments, and the temperature was fixed at 625° C to maintain the proper grain size.

Figures 4 and 5 show profiles of growth rate down a load of 150 six-inch wafers for the parameters of experiments one and nine. These figures show both the data measured and the model predictions (to be discussed below). The error bars are calculated from the results of five replicate runs. As can be seen, the two experiments span a wide range of performance of the system.

Experimental results were used to predict a combination of process parameters for optimized performance by first calculating a "signal to noise ratio" for each of the nine experiments. The signal to noise ratio is basically a measure of the ratio of the mean to the standard deviation for each curve [1]. The average signal to noise ratio is then calculated for each level of each parameter and the parameter level which gives the highest signal to noise ratio is selected, resulting in a set of optimized parameters [1]. Figure 6 shows the experimental results from running the set of optimized parameters. The experimental results in Figure 6 are well within the specifications of the equipment vendor.

Model Construction and Calibration

The mechanistically based model was constructed by using order of magnitude analysis to identify the important features of the physics. This process resulted in a one-dimensional finite difference approximation with disk and annular elements stacked down the tube length. The model incorporates convective and diffusive mass transport in the annular space between the wafers and the tube walls, and models the chemical reaction as being surface rate limited and dependant on local concentrations and temperature.

The model incorporates five adjustable coefficients which stem from uncertainty about the reaction kinetics and the nature of the mixing of the injector flow into the annular volume.

The five adjustable coefficients were calibrated by least squares fit to the nine experimental runs resulting in the model predictions depicted as solid lines in Figures 4 and 5. As may be seen, the model does a good job of capturing both the qualitative and quantitative nature of the experimental results.

Optimization from the Model

The calibrated model was then run with a nonlinear optimization program in order to predict an optimum set of operating conditions from the model. This procedure incorporated the addition of disturbances (variations) to thirteen of the model parameters, thus simulating disturbances that would take place during normal operation. The parameters found by optimization of the model are very close to those found by the experimental optimization procedure described above.

Figure 6 shows the model prediction for the set of parameters selected by the optimization scheme as a solid line. The dotted line is the model prediction for the parameters found by the Taguchi parameter optimization.

Conclusions

An equipment model of the LPCVD of polysilicon has been constructed by calibrating a mechanistically based model using statistically designed experiments. The resulting smart response surface equipment model has been used to optimize the operation of the process. The optimum operating parameters predicted by the model are very close to those found by an experimental process parameter optimization. The model can be used for both process optimization and control. Minor extensions of the model can be used to examine the impact of equipment design.

Acknowledgements

The authors gratefully acknowledge the support of the Defense Advanced Research Projects Agency under contract N0014-85-0213 as well as the support of the Microelectronics and Computer Technology Corporation. BTU Engineering Corp. is acknowledged for providing access to experimental facilities.

References

1. Taguchi, G., *Introduction to Quality Engineering*, Krauss International Publications, White Plains, New York 1986.
2. Taguchi, G. *System of Experimental Design: Engineering Methods to Optimize and Minimize Costs*, Vol. 1 and Vol. 2, Kraus International Publications, White Plains, N.Y.
3. Box, G., Hunter, W., Hunter, J., *Statistics for Experimenters, and Introduction to Design Data Analysis and Model Building*, Wiley, 1978.
4. Box, G., Draper, N., *Empirical Model-Building and Response Surfaces*, Wiley, 1987.

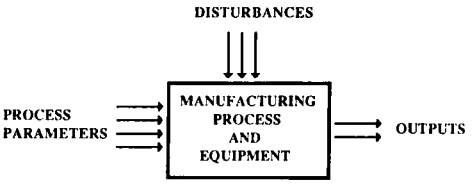


Figure 1. Generic Form of an Equipment Model

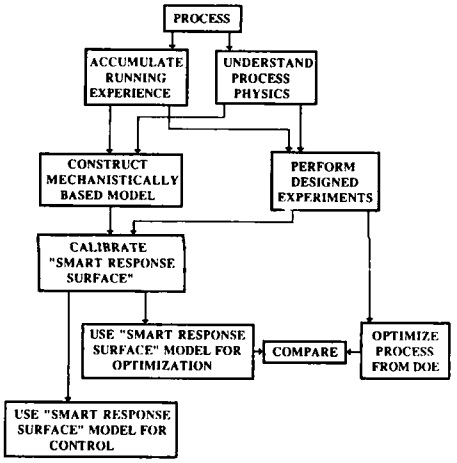


Figure 2. Flow diagram of two paths to optimization discussed in this paper.

Experiment Number	Pressure (mtorr)	Q_{load} (% of total)	Q_{center} (% of total)	X_{source} (% of tube length from center)
1	200	20	26.7	9
2	200	30	36.7	12
3	200	40	46.7	15
4	250	20	36.7	15
5	250	30	46.7	9
6	250	40	26.7	12
7	350	20	46.7	12
8	350	30	26.7	15
9	350	40	36.7	9

Figure 3. The nine experiment orthogonal array used to optimize the LPCVD process and calibrate the model.

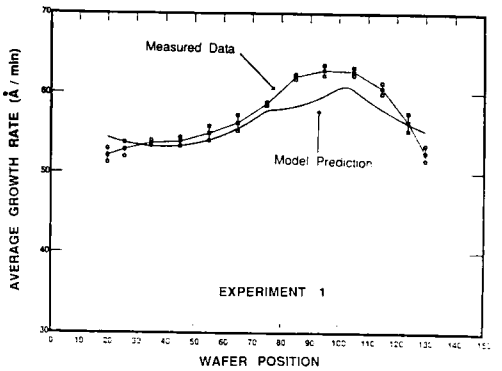


Figure 4. The experimental results and model predictions for the first experiment of the array.

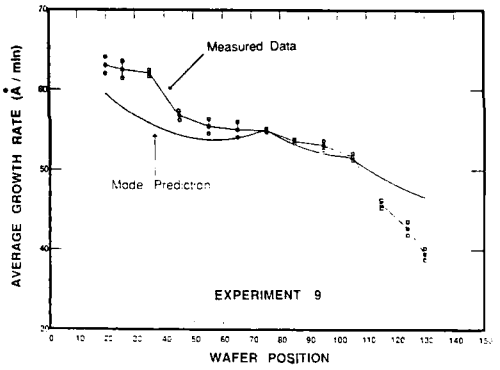


Figure 5. The experimental results and the model prediction for the ninth experiment of the array.

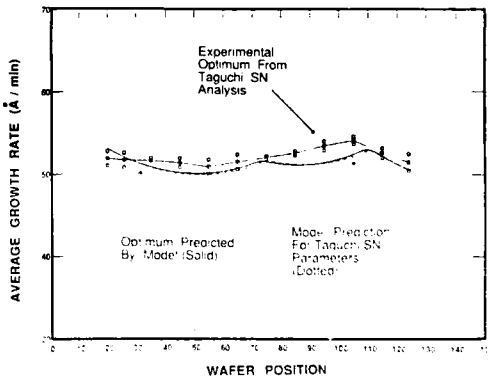


Figure 6. The experimental and predicted results for the experimentally determined optimum parameters and the predicted optimum performance.

Abstract No. 396

Outgas-Free Corrosion-Resistant Surface Passivation of Stainless Steel for Advanced ULSI Processing Equipment

T. Ohmi, T. Okumura, K. Sugiyama, F. Nakahara, and J. Murota*

Department of Electronics, Faculty of Engineering Tohoku University, Sendai 980, Japan.

*Research Institute of Electrical Communication, Tohoku University, Sendai 980, Japan.

The net working rate of processing equipment in LSI manufacturing lines is, in general, quite low due to the large amount of time required for maintenance operations. The cleaning of processing chambers to remove the deposited materials on their inner surfaces constitutes the main part of the cleaning operation. Since such cleaning operations are carried out manually by technicians by opening the vacuum chambers each time, it takes a lot of time. In addition, adsorption of air molecules, especially that of H_2O molecules to the chamber inner surface severely degrades the quality of processing to be done with the equipment(1). Therefore it is essentially important to develop maintenance-free equipment to establish high-performance processing needed for ULSI manufacturing as well as for automated IC manufacturing. We have developed a novel surface passivation technology for stailess steel(2) that forms highly corrosion resistant films on its surface. Since the passivation film shows excellent anti-corrosion characteristics against violent gases like Cl_2, HCl, and so forth, the deposited materials on the passivated stainless steel chamber surfaces are able to be removed by dry etching using there gases. Thus the automated cleaning operation has become possible instead of manual cleaning. Furthermore,the passivated surface exibits minimized gas molecule adsorption as well as outgas-free characteristics. As a result, the new passivation technology has shown large impacts not only on processing chambers but also on a number of components made of steinless steel such as gas pipes, gas components, vacuum components and so forth in order to realize high performance processes.

In this paper, we describe the formation of passivation films on stainless steel by completely moisture-free thermal oxidation and the characteristics of these films. Anti-corrosion characteristics as well as outgas characteristics are also presented in this paper.

0.5mm thick stainless steel(SUS316L) plates of 35mm in diameter was used for oxidation experiments, which were mirror-polished on one sides by electro-chemical buffing. Oxidation was carried out in qualtz tube furnace at 400-600°C using dry oxygen gas, the moisture level of which is less than 10ppb. Prio to the oxidation, stainless steel plates were cleaned in NH_4OH/H_2O_2 and rinsed in DI water. After HF etching of native oxide, DI water rinsing, and IPA(Isopropyl Alcohol) vapour drying, the plates were put into the furnace in an argon gas ambient, and then oxidized. The film characteristics were analyzed by ellipsometry and ESCA and the outgas characteristics were evaluated using APIMS(Atmospheric Pressure Ionization Mass Spectrometry)(3).

Table 1 shows the measured thickness and refraction index of a passivation film for various oxidation temperature and time. The table shows the thickness of the passivation film does not depend on the oxidation time below 500°C. It is considered that formation of the passivation film at this temperature range is controlled predominantly by the field assisted oxidation mechanism(4). Above 550°C, the passivation film thickness increases with oxidation time. In this case, the diffusion of oxygen across the oxide film to the film growth in addition to the field assisted mechanism. The results of ESCA analysis for the passivation films formed at 400°C and 550°C, are shown in Figs 1(a) and (b), respectively. It was found that the predominant compound existing on the surface of the passivation film formed below 500°C is Fe_2O_3, while that formed at 550°C or above is Cr_2O_3. Table 2 summarizes the results of corrosing experiment of oxidized samples when dipped in the 35% hydrochloric acid solution. It took longer time for the sample passivated at 550°C to begin to evolve hydrogen gas. The golden color of the film by interference did not disappear untill the evolution occured. Non oxidized samples and the samles oxidized without mirror-polishing both generated hydrogen gas immediately after dipped. The passivation films as thin as 165A which were formed by oxidation at 550°C for 9 hours are very dense films having no pinhole difects. Figure 2 shows the outgas characteristics from the inside surface of stainless steel tubes which were passivated by various methods. They are the changes with time of the water content in Ar carrier gas during 120 minutes of flow. The sample passivated by the technology (shown by solid circles) shows the decrease of water content to 2.5 ppb, the background level, in 10 minutes after the beginning of measurement. The results indicate that removal of water adsorbed on the surface is greatly enhanced by the passivation film formation. Table 3 shows the measured water content in Ar carrier gas when passed through various kind of tubes which were kept at 120°C, 200°C, and 300°C for one hour(5). It is obvious from the table that the total amount of water released from the sample (d) passivated using the new technology is smallest of all. It is conclused that the complete removal of moisture from the oxidizing ambient is essential to minimize the outgassing from the passivation film.

The best quality of passivation film on stainless steel surface is formed by oxidizing the surface using completely moisture free oxgen, at temperature above 550°C for more than 9 hours, with mirror polishing of the stainless steel surface. The film is consisted of a dense layer of Cr_2O_3, existing at the surface, and exibit excellent corrosion-resistance as well as degassing-free characteristics. These passivation films have a wide range of application not only to high performance processing equipments but also to a number of other ultra clean grade components such as, process chamber, clean cylinder, gas delivery system and the like. The realization of

maintenance free equipment by this passivation technology is especially impartant for automated IC manufacturing.

We express heartily thanks to Kobe Steel, Ltd., Motoyama Eng. Works. Ltd., Ultra Finish Technology Co., Ltd. as well as to peoples in Ohmi's laboratory, the Faculty of Engineering, Tohoku University. This study was done in the Super Clean Room in Laboratory for Microelectronics, Research Institute of Electrical Communication, Tohoku University.

REFERENCES

1) T. Ohmi and K. Sugiyama, "Water removal as the greatest problem of gas derivery systems", Nikkei Micro Devices, pp.100-108, No.28, October 1987.
2) K. Sugiyama, F. Nakahara, T. Okumura, T. Ohmi and J. Murota, "Superficial Treating Technology For Outgas-Free Corrosion-Proof Stainless Steel", T. Ohmi and T. Nitta, Ed., "ULSI Ultra Clean Technology Symposium No.6 High Performance Process III", Semiconductor Basic Technology Series, Realize Inc., pp.247-268, January 1988.
3) Y. Mitsui, "Ultra high Purity Gas Analyzer", T. Ohmi and T. Nitta, Ed., "Ultra High Purity Gas Supplying System", Semiconductor Basic Technology Series, Realize Inc., pp.401-429, September 1986.
4) N. Cabrera and N. F. Mott, "Theory of the Oxidation of Metals",Rep. Progr. Phy., 12, 163 (1948).
5) T. Ohmi, E. Morikawa and T. Hatayama, "Baking Gas Supply System by Electric Heating System ", T. Ohmi and T. Nitta, Ed., "Ultra High Purity Gas Supplying System", Semiconductor Basic Technology Series, Realize Inc., pp.430-447, September 1986.

Table 1 Thickness and refraction index of the passivation film for various oxidation conditions.

OXIDATION TEMPERATURE (°C)	OXIDATION TIME (Hr)	OXIDE FILM THICKNESS (Å)	REFRACTIVE INDEX
400	1	114	2.71
	4	110	2.87
500	1	125	2.93
	2	126	2.91
	4	126	2.96
	9	124	2.90
550	1	130	3.02
	4	141	3.13
	9	164	2.98
600	1	156	3.03
	4	180	3.36

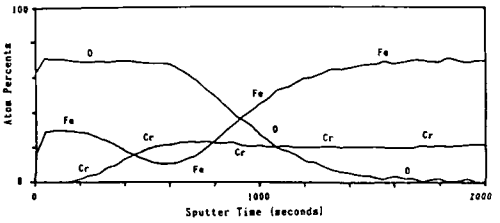
Table 2 Corrosion resistance of passivation film in 35% HCl solution.

Sample	Film Thickness (Å)	Result
non-oxidized	7	Gas evolution occured immediately after dipping
400°C. 4hr	110	Interference color (gold) disappered immediately after immersion; gas evolution after about 20 minutes
500°C. 4hr	126	The same as above
550°C. 4hr	140	The same as above
550°C. 9hr	164	Gas evolution after about 45 minutes
600°C. 4hr	180	Gas evolution after about 30 minutes

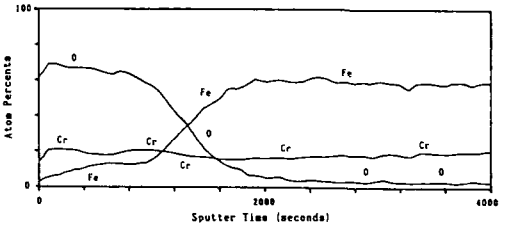
Table 3 Impurity concentration in argon gas passed through various kind of tubes.

(ppb)

	SAMPLE \ TEMP. (°C)	R.T.~120	120~200	200~300
(a)	EP	420	600	860
(b)	EP+HNO_3	750	630	990
(c)	EP+O_2	260	230	2150
(d)	EP+O_2 (S.C.R.)	25	70	100



(a) SUS316L-ECB-400℃-4Hr



(b) SUS316L-ECB-550℃-9Hr

Fig. 1 Chemical composition of passivation film in various oxidation conditions.

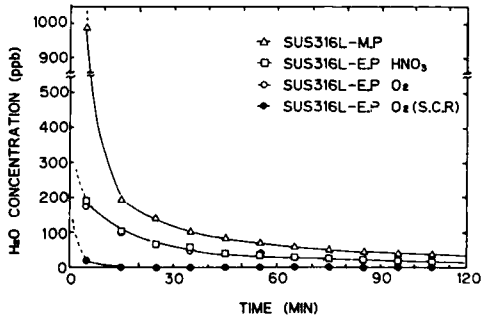


Fig. 2 Time dependence of water concentration in argon gas passed through passivated tube at 25°C.

Abstract No. 397

A METHOD OF LOW CONTAMINATION FOR AUTOMATED IC MANUFACTURING UTILIZING THE WAFER CARRIERS WITH COMPACT CLEANING DEVICES

A.Machida, S.Tabuchi, S.Eifuku, A.Abiru and T.Matsumoto

Process System Div.
FUJITSU LIMITED
1015 Kamikodanaka, Nakahara, Kawasaki Japan

In IC manufacturing, it is most efficient to make local area surrounding wafers clean. Then we need the technique to clean small area using compact cleaning devices.

In 1984, we made a concept to clean only inner area of a wafer carrier by continuous air flow using a compact cleaning device. In 1986, we made first prototype that structure was a wafer carrier which had a small cleaning device, including a secondary battery as a power source, a motor fan, and an air filter (ULPA filter), and a storing chamber directly connected to the air cleaning device for storing the wafers. Total size and weight were under 1.5 times of a standard plastic carrier.

In an environment of over class 1,000,000, the wafer carrier was placed and the motor fan was operated. After 30 seconds operation, the resulted cleanness inside the wafer carrier was below 3 (0.1micron class). This means that the number of particles larger than 0.1 micron contained in the wafer carrier was below 1. (The volume of the 6 inches wafer carrier is approximately 0.1 cubic feet)

25 silicon wafers (6 inches diameter) were stored in that wafer carrier and the same number of the wafers in a standard plastic carrier at the same time, for 72 hours, in a clean room of class 1,000 where operators were working. The number of the particles with sizes larger than 0.2 micron, attached to surface of the wafers, were measured. The inclease in the number of the particles after 72 hours, was 16 per wafer in average for the new wafer caarier, and 1600 for the standard wafer carrier.

The wafer carrier with compact cleaning device could not be loaded onto almost all the station of process equipments without reconstruction of interface mechanism, because the standard interface of process equipments were made for only the motion of standard wafer carriers. To break the problem, we designed a mechanism which had a same efficiency of cleanliness as the original wafer carrier with a compact cleaning device and could be loaded onto the station of process equipments without any reconstruction.

In 1987, we made a first prototype of this concept. That was a compact air shower box (AS-BOX), which holded a standard wafer carrier while transporting and freed the wafer carrier when it was on the station of process equipment. The size and weight of AS-BOX were almost same as them of the original wafer carrier with a compact cleaning device.

By the concept of AS-BOX, we will be able to manufacture high quality ICs in a low level clean room or absolutely not in the clean room. We estimated the possibility and utility of this concept by use of the prototype of AS-BOX in our laboratory.

Abstract No. 398

A NOVEL CVD SYSTEM WITH SELF-CLEANING FUNCTION FOR THE AUTOMATION OF LSI MANUFACTURING

T. Ohmi, G. S. Jong, M. Morita, M. Kosugi, and H. Kumagai*

Department of Electronics, Tohoku University
Sendai 980, Japan

*Tokyo Electron Limited
1 Higashikata-machi, Midori-ku, Yokohama 226, Japan

A novel Chemical Vapor Deposition (CVD) system with self-cleaning function which is characterized by no deposition of the reaction by-products on the chamber inner surface has been developed for the automation of LSI manufacturing in the future. In this system, the film formation is performed by the surface reaction without the vapor phase reaction, which is realized by using a free-jet molecular-flow gas supply into the ultra-high vacuum chamber, resulting in expelling the manual cleaning of by-products deposited on the chamber inner surface. The high-rate (0.8 μm/min) film formation of epitaxial Si has been also achieved at temperatures as low as 700°C.

In order to control the CVD process in the LSI manufacturing automatically, it is indispensable to maintain the cleanliness of the reaction environment in the chamber. In the conventional CVD system which is widely employed for the formation of various films, the source gas flows the whole reaction chamber at a viscous flow. The viscous-flow gas supply essentially accompanies the vapor phase reactions of source gas molecules(1). The vapor phase reaction results in the creation of microparticles and the deposition of a large amount of the chemical by-products on the chamber inner surface. The by-products deposited on the chamber surface act as contamination sources in the film formation process while fabricating LSI devices. The ceaceless manual cleaning to eliminate the by-products from the chamber inner surface has been really carried out in the LSI production line. This cleaning procedure causes the frequent suspending of the machine operation and the degradation of the environment cleaniness in the chamber. Because the chamber inner surface is contaminated by air; particularly moisture molecules whenever the cleaning procedure is carried out. Thus, it is very difficult in these conventional CVD system to control the chemical reaction automatically, because the film formation mechanism inevitably includes the process contaminating the reaction environment. In this paper, we discribe a novel CVD system using a free-jet molecular flow, which has the cleaning-free function to keep the cleanliness in the reaction chamber at all times.

The schematic diagram of the newly developed film formation system(2) is illustrated in Fig.1. The inner surface of the stainless steel chamber is coated with an anticorrosive TiN layer. In order to eliminate the impurities in the reaction chamber, the chamber is always pumped down with a turbo molecular pump (2000 l/s) to the pressures of less than 5×10^{-8} Torr even during the heating of the substrate. An ultra pure source gas (Si_2H_6) filled in an ultra-clean cylinder was supplied into the chamber through the ultra-clean gas delivering system(3). The source gas was directry introduced only onto the substrate surface with high velocity through the gas nozzle having a diameter of 50 um, for suppressing the thermal convection even when the substrate temperature is raised up. The pressures near the chamber inner surface was approximately 10^{-3} Torr during the film formation. The Si substrate was preferentially heated by the irradiation with the collimated light of a xenon lamp. The chemically-cleaned and dried Si substrate having a diameter of 50 mm was set flat on the susceptor in the reaction chamber by the loadlock system with electrostatic wafer chuck(4), which was utilized so as to prevent the contamination of the reaction chamber by the impurities in air during the transportation of the wafer.

Figures 2 and 3 show the flow rate dependence of the film growth rate of epitaxial Si on p-(100) Si and polycrystaline Si on SiO_2(100nm)/p-(100)Si for the substrate temperatures as a parameter. High-rate film formation (0.8 um/min or higher) of the epitaxial Si on the Si substrate has been achieved at temperatures as low as 700°C for Si_2H_6 flow rate of 100 sccm. The reflective electron diffraction pattern indicates that the epitaxial Si layer posseses a high crystalographic perfection (see Fig.4). The film formation was concentrated on the substrate surface and on the heating susceptor surface.

It is concluded from these results that the film formation in this system is dominated by the surface reaction without accompanying the vapor phase reaction, which is realized by supplying the source gas only onto the heating substrate into ultra high vacuums at a free-jet molecular flow. And the ultra-high vacuum system enable to eliminate by-products from the substrate surface immediately, resulting in the high-rate and high-quality film formation. The single wafer processing machine which forms the film with a good uniform thickness on the wafer having a large diameter can be realized by applications of these technologies. This system has gotten the features that the cleaning procedure opening the reaction chamber is not necessary and that the reaction environment is ridded of the contamination, resulting from that the by-products deposition on the chamber inner surface is prevented due to suppressing the vapor phase reaction of the source gas extremely. The periodical self-cleaning function equipped both by using the chamber and the tubing system of which the inner surfaces are passivated by the ultra clean oxidation(5) and by using etching gases such as Cl_2 and HCl, will complete the performances for the automatic LSI manufacturing.

This study was performed in the Super Clean Room in Laboratory of Microelectronics, Research Institute of Electrical Communication, Tohoku University.

(1) F. C. Everstern, P. J. W. Severin, C. H. J. V. D. Brenkel, and H. L. Peek, J. Electrochem. Soc. 117, 925 (1970).
(2) T. Ohmi, M. Nikoshiba, and K. Tsubouchi, Proceedings of the First International Symposium on Ultra Large Scale Integration Science and Technology, Pennsylvania 1987 (to be published).
(3) T. Ohmi, J. Murota, Y. Kanno, Y. Mitsui, K. Sugiyama, K. Kawasaki, and H. Kawano, ibid (to be published).
(4) T. Ohmi, M. Onodera, G. Sato, T. Shibata, and M. Morita (to be submmited to the abstracts of this symposium).
(5) T. Ohmi, T. Okumura, K. Sugiyama, F. Nakahara, and J. Murota (to be submmited to the abstracts of this symposium).

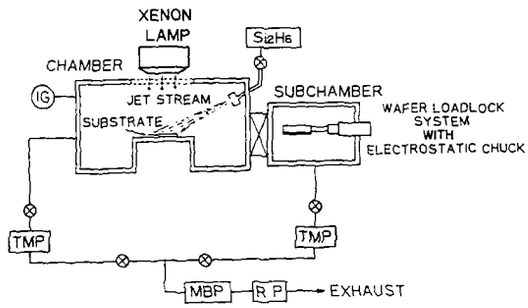


Fig.1 Film formation system.

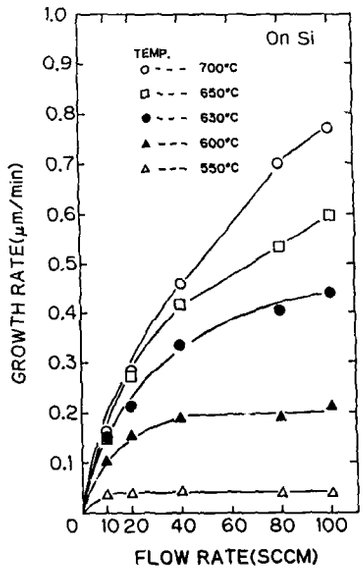


Fig.2 Flow rate dependence of film growth rate of epitaxitial Si on p-(100) Si for the substrate temperatures as a parameter.

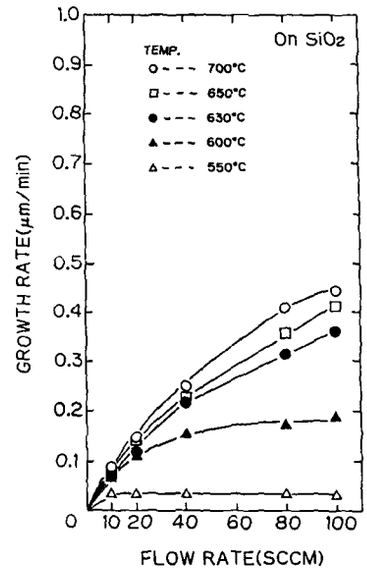


Fig.3 Flow rate dependence of film growth rate of polycrystaline Si on SiO_2/p-(100)Si for the substrate temperatures as a prameter.

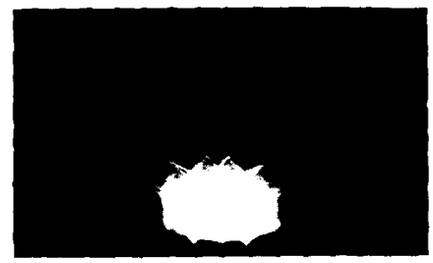


Fig.4 Reflective electron diffraction pattern of epitaxial Si layer formed at 700°C.

Abstract No. 399

Results from Comparing an Open Area SMIF Isolation Site (OASIS) with a Cleanroom

R.A. Hughes, G.B. Moslehi, D. M. Campbell,
E.D. Castel, K. Radigan, L. Walsh,
National Semiconductor Corp., 4001 Miranda Avenue,
Palo Alto, CA 94304, and W. Lukaszek,
Stanford University (CIS) Stanford, CA. 94305

INTRODUCTION: One potential means of increasing productivity and creativity, as well as cutting the basic costs of producing semiconductor devices, is to eliminate the need for cleanrooms. This paper describes the results obtained in a project established to demonstrate the feasibility of processing wafers in an open area (i.e., a typical office environment) while maintaining a defect density equivalent to that obtained in a cleanroom. Results are presented that were generated using Standard Mechanical Interface (SMIF) and isolation technology with a standard photolithography equipment module.

BACKGROUND: Since Hewlett-Packard first published their SMIF ideas many companies have investigated this concept as a means to improve the conventional cleanroom environment. The Open Area SMIF Isolation Site (OASIS) project[1,2] was initiated at National Semiconductor Research to investigate the advantages and problems associated with eliminating the need for using a cleanroom. While References 1 and 2 describe the motivation, goals/objectives, and experiences obtained in establishing the OASIS facility, the resulting experimental data and conclusions will be presented in this paper.

Photolithography Equipment Module: The separate pieces of process equipment used in the OASIS room for this comparison study consisted of a vacuum prime oven, coat bake/develop bake track and a 10X stepper. Other major pieces of SMIFed equipment are for inspection/CD measurement and surface particle counting. With the exception of the inspection/CD measurement equipment, all the equipment was re-engineered, cleaned and modified to improve airflow patterns inside the enclosures before canopies were added.

Evaluation Techniques: Four techniques were used to evaluate the quality of the photolithographic operations conducted on the OASIS line: airflow visualization tests, airborne particle counts inside equipment canopies, measurement of the number of particles added to the wafers during processing, and electrical measurement of a series of passive test structures.

1. Airflow Visualization Tests. Before the equipment canopies were designed and major changes made in the equipment airflow, visualization studies were conducted to understand the existing flow patterns. Tests were repeated after the equipment changes to check the results.
2. Airborne Particulates. Airborne particle measurements were conducted with optical particle counters. Additionally, the particulate levels in each piece of SMIFed equipment were continuously monitored and displayed using an automated central sampling system.
3. Particles Added. Measurements of the particles added to the wafer during each processing step or PWP (particles per wafer) were performed on bare silicon using a laser surface particle counter.
4. Electrical Measurement. An Electrical test structure was used which contains sets of patterns and line widths designed to maximize the ability of the structure to capture defects over a range of defect densities. The test chip, shown in Figure 1, was also designed to minimize testing errors.

Experimental Phases: The experiments involved several basic phases. In the first phase, the mechanical functionality of each piece of equipment was checked and detailed operating procedures were developed.

The second phase involved qualification of the photolithographic equipment and processes. This was a particularly sensitive and difficult task because the equipment was old (first generation) and the process was current technology.

Visualization tests, airborne particle counts and PWP measurements formed the third phase of experiments.

In the fourth phase, a comparative study between cleanrooms and the OASIS line was made. The experiments consisted of processing parallel lots of wafers in the cleanrooms and in the OASIS facility. Figure 2 shows the processing steps used for fabrication of the defect-sensitive electrical test structure, which requires one masking level. The process sequence involves oxidation and metallization, followed by lithography (prime, spin, expose, develop, inspect), and ends with metal etch, strip, and electrical test. Comparisons were made only for the lithography portion of the process flow.

Data Analysis Techniques: Several Methods were used to analyze and screen the electrical data. First, wafer maps showing test structure defects were generated. These wafer maps were used to eliminate systematic defects (using algorithms, optical and SEM microscopy, etc.). The remaining defects were verified for randomness using statistical techniques. Test structure yields for the known areas were then used to calculate defect densities using standard yield models.

RESULTS: Prior to processing the lots of 25 wafers for comparison of the electrical data, PWP data were generated. Results were obtained prior to any clean-up and at subsequent intervals after that time. As expected, dramatic order of magnitude improvements were made as a result of being able to monitor and control each enclosure.

Other results that were obtained during the preparation period show the times required to clean-up the equipment after a significant repair has been made and the enclosure has been exposed to the open OASIS environment.

Electrical test results were generated from the wafers that were processed on the OASIS line and in the other fabs. Results will be presented which show comparisons from an initial phase where preliminary OASIS results (yield and defect densities) were compared to two working fabs and for the final phase experiment where OASIS was cleaned and fully characterized prior to similar comparisons.

SUMMARY

One of the prime reasons for conducting the OASIS investigation was to challenge whether or not cleanrooms and their associated costs and hostile working environment are really necessary. While one OASIS lithography module cannot be extrapolated to make conclusions about a complete manufacturing line, the results obtained to date indicate that no difficult technology is required whick would preclude such an event.

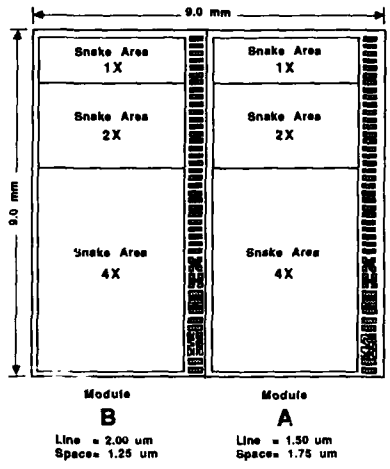


Figure 1. OASIS Test Chip

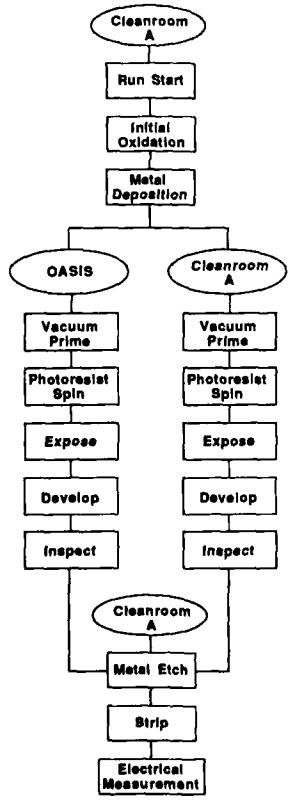


Figure 2. OASIS Experiments

1. R. Hughes, B. Moslehi and E. Castel, "Experiences with an Open Area SMIF Isolation Site (OASIS)," Proceedings of the Microcontamination Conference, October 1987.

2. R. Hughes, B. Moslehi and E. Castel, "Eliminating the cleanroom: Experiences with an Open Area SMIF Isolation Site (OASIS)", Microcontamination, April 1988.

3. R. Ulmer and H.K. Chung, "Microcontamination Reduction Studies in Equipment Used for GaAs LSI/VLSI Fabrication", Proceedings of the U.S. Conference on GaAs Manufacturing Technology, October 1987.

4. S. Titus and P. Kelly, "Defect Density Reduction in a Class 100 Fab Utilizing Standard Mechanical Interface", Solid State Technology, November 1987.

5. U. Kaempf, "Statistical Significance of Defect Density Estimates", Proceedings of the 1988 IEEE International Conference on Microelectronic Test Structures, February 1988.

6. W. Lukaszek, et al., "CMOS Test Chip Design for Process Problem Debugging and Yield Prediction Experiments", Solid State Technology, Vol. 2. March 1986.

7. W. Maly, M.E. Thomas, J.D. Chinn and D.M. Campbell, "Double-Bridge Test Structure for the Evaluation of Type, Size, and Density of Spot Defects", Joint technical report, Fairchild Semiconductor and Carnegie Mellon University, 1987.

8. J. Burnett, "World Class Contamination Control Practices", Semiconductor International, April 1988.

Abstract No. 400

APPLICATION OF SURFACE PHOTOVOLTAGE TO MONITORING OF HEAVY METAL CONTAMINATION AND REPRODUCIBILITY OF INTERNAL GETTERING DURING IC PROCESSING

L. Jastrzebski, R. Soydan,
David Sarnoff Research Center
Princeton N.J. 08540

N. Armour,* M. Blumenfeld,** R. Kleppinger***
E. Pelczar,**** C. Palmer,***** B. Goldsmith******

INTRODUCTION

The application of Surface Photo Voltage (SPV) to monitor the presence of heavy metal contamination in oxidation furnaces has been investigated. SPV has also been used to monitor the reproducibility of denuded zone formation in internally gettered wafers during CMOS and bipolar processing. Until now, the denuded zone depth has been typically monitored by etching of cleaved or angle lapped silicon wafers. The SPV method is non-destructive, does not require any additional sample preparation (test structures), and provides information very quickly. Therefore this approach is attractive for QC monitoring of the denuded zone and heavy metal contamination during IC processing.

EXPERIMENTAL

Heavy metal contamination in oxidation furnaces was monitored using 100 mm in dia. float-zone n- or p- type, 10-20 Ω-cm silicon wafers. For CMOS and bipolar devices standard CZ wafers were purchased from three different manufacturers (100mm Dia. 1-5 Ω-cm) with 15-17 PPM of interstitial oxygen. The oxygen precipitation kinetics of internally gettered wafers was optimized to give the most efficient internal gettering during CMOS processing (1). The diffusion length and the interstitial oxygen concentration of the control wafers were measured after various processing steps by SPV and Fourier spectroscopy, respectively, in the control wafers. These wafers did not go through photo steps and did not receive any implantation or diffusion. Otherwise they were processed identically to product wafers. A number of samples were removed after each processing step. They were cleaved and etched to reveal the precipitates and the denuded zone.

EXPERIMENTAL RESULTS

Figure 1 shows the relationship between normalized yield of C^2L circuits and heavy metal contamination level in the field oxide furnace. A significant reduction in normalized yield took place two weeks after a large reduction in the diffusion length values was observed. Wright etching of silicon wafers with low diffusion lengths (<20μm) revealed a large number of stacking faults. These defects, which were associated with leakage and yield decrease, were not observed in wafers with higher values of diffusion length (>60μm). Heavy metals from a contaminated field oxide furnace caused stacking fault nucleation and decoration in these wafers. A similar relationship was also observed during the bipolar process. A substantial reduction of yield caused by an increase in leakage was related to heavy metals introduced during epitaxial growth (Fig. 2). The heavy metal contamination during epi growth was not high enough to cause haze in the epi, but the SPV measurements were able to reveal the presence of these contaminations.

Diffusion length measurements for internally gettered and float zone wafers using the constant signal photovoltage method are shown in Figs. 3a and 3b. A linear dependence between the light intensity and the reciprocal of absorption coefficient is observed for float-zone wafers. Two separate regions are visible for short and long wavelengths in the internally gettered wafers. For the short wavelengths most of the minority carriers are generated in the denuded zone and reach to the surface. Bulk recombination in the denuded zone is much slower than interfacial recombination at the oxygen precipitates, and therefore the diffusion length of the minority carriers generated in the denuded zone is controlled by the denuded zone depth for these wavelengths. The intersection of this line with the "x" axis corresponds to the depth of the denuded zone. The dependence for the longer wavelengths is not yet clear, but it is believed to be influenced by the bulk precipitate density. At low bulk precipitate densities the long wavelength dependence is sublinear, whereas it is superlinear with the high oxygen precipitate density (Fig. 3b). The denuded zone depth, and the bulk precipitate densities (as revealed by etching of cleaved wafers) are listed along with the diffusion length measured by SPV (Table 1). It seems that the wafers with the highest oxygen precipitate densities have a conversion factor close to two, whereas in wafers with the lower precipitate density this factor is one. The conversion factor is defined as a ratio between the denuded zone depth and the diffusion length. This is consistent with theoretical predictions (2). SPV was able to reveal the initial stages of the oxygen precipitation which could not be detected by IR absorption. Therefore, during annealing, SPV measurements were more sensitive to the formation of oxygen precipitates than IR absorption. When the diffusion length reaches a value which does not change any further with subsequent heat treatment, its value corresponds to the depth of the denuded zone formed.

CONCLUSION

Good correlation was established between yield degradation and an increase in the heavy metal contamination level, as monitored by SPV during CMOS and bipolar processing. Since the measurements are carried out without any additional preparation, they can provide recovery lifetime information more rapidly than any other technique. Since a relationship exists between the values of diffusion length and the denuded zone depth in the wafer with the well developed denuded

zones, SPV can also be used to non-destructively monitor the uniformity and reproducibility of the denuded zone depth across a wafer and from wafer to wafer.

References

(1) L. Jastrzebski, R. Soydan, J. McGinn, R. Kleppinger, M. Blumenfeld, G. Gillespie, N. Armour, B. Goldsmith, W. Henry, S. Vecrumba, J. Electrochem, Soc. 134, 1018, (1987).

(2) T. I. Chappel, P. W. Chye, M. A. Tavel, Solid State Electronics 26 (1), 33, (1983).

Present Addresses

* AMD San Antonio, TX 78245
** Sprague Electric Co., Willow Grove, PA 19090
*** RCA/GE SSD, Somerville, N.J.
**** Martin Marietta Electronic System Division, Orlando, Fl 32862-8007
***** Harris Semiconductor Div., Melbourne, Fl 32901
******RCA/GE SSD, Findlay, Oh 45840

TABLE I

SUPPLIER	L (μm) Front of wafer	L (μm) Back of wafer	DENUDED ZONE (μm)	DENSITY OF BULK PRECIPT	CONVERSION FACTOR (dsart)
C	6	4	12	1.0 E12	2.00
X	7		12	1.0 E12	1.70
Y	8		12	1.0 E12	1.50
C	7	9	15	1.0 E12	2.10
Y	12		15	7.0 E08	1.25
X	10		18	7.0 E09	1.60
Y	7		19	8.0 E11	2.70
X	20	25	19	6.0 E08	0.95
C	10		21	8.0 E11	2.10
Y	15		21	1.0 E09	1.40
X	15	20	25	7.0 E09	1.70
Y	20	18	25	1.0 E09	1.30
X	30		29	5.0 E09	1.00
C	14		32	7.0 E11	2.10
C	22		32	5.0 E10	1.50
Y	34		32	8.0 E07	1.00
C	18		39	8.0 E11	2.00
Y	40	30	40	8.0 E07	1.00
X	50		42	1.0 E08	0.80
Y	47		46	7.0 E07	1.00
Y	58		50	7.0 E07	0.90

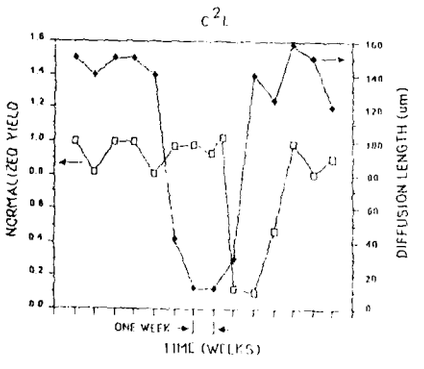


Figure 1.

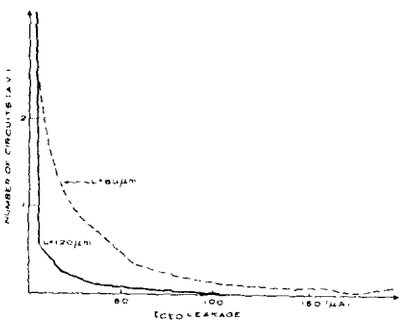


Figure 2.

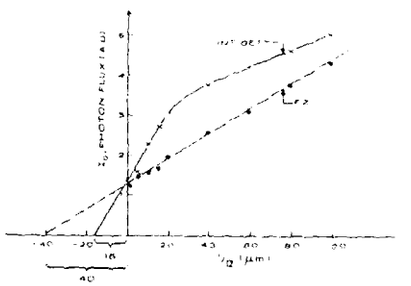


Figure 3a.

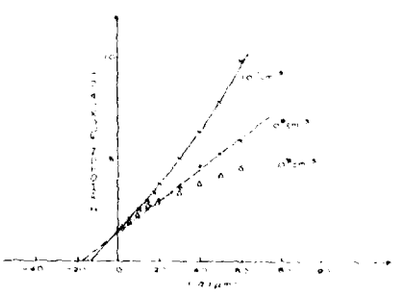


Figure 3b.

Abstract No. 401

Development of On-lined method gauging a total weight of foreign matters in IC pure water

Sankichi Takahashi, Yasuo Koseki
Hitachi Res. Lab., Hitachi Ltd.
4026, Kuji-cho, Hitachi city, Japan.

1.Introduction

Foreign matters in IC pure [illegible] refered to make a great influence to a quality of SiO_2 film formed on a wafer. So that, It is important to get correct datas on a quality of water on real time. the water quality is generally evaluated with five items of specific conductivity, TOC and so on.

Others than specific conductivity are gauged in off-line. Moreover, The value for each item required for IC manufacture has almost been beyond the limit in gauging. Then, we planned to develop a new on-lined method which could more directly evaluate an influence given by foreign matters to the quality of film.

2.Priciple and apparatus of a new method.

Figure 1 shows a schematic diagram of apparatus.

After gauging a air flow rate, Filtrating gets clean air out of dust of 0.1um over in size. The water is atomized into fine droplets with a nozzle driven with the clean air heated to 70 ℃. Each droplet immediately and completely vapourize itself and makes into a fine particle suspeding in the air flow.

It is made from the foreigners dried up. A total volume of particles is calculated on the next equation from the number and diameter of them gauged by a laser particle counter which can be measured to 0.1um in diameter.

$$v = 0.5236 \cdot \frac{C}{\gamma} \cdot a \times 10^{-18} \int_{D_{min}}^{\infty} D^3 \cdot F_{ref}(D) \cdot b(D) dD$$

Their shape and size is observed by SEM too. The water is feeded by a feed system which is paid the greatest attention to it never to give any contamination to the water.

3. Experimental results

Their shape is sphere of 0.08 to 1 um in diameter.

As the concentration of foreigners gets lower, The diameter gets smaller. Fig.2 shows the relation between a concentration and a total volume. The limit of a laser counter in gauging makes it wider the difference between a calculated line and experimental results in range of 1000 ppm below.

So that, The development is made on basis of the line experimentally got. Some experiments for IC pure water are made to certify the relation between results gauged with the new method and those with conventional ones. Fig.3 shows it's result. The concentration of inorganics is calculated from the value of specific conductivity. The limit of each conventional method in gauging makes each line for them deviate from it's results gained in range of higher concentration. The result of the new method makes a good coincidence with the result added each result of inorganics, organics and SiO_2.

4. Field test result

The method is made a test in a real water system.

It can clearly sence the change of water quality given by each water treatment.

5. Conclusion

1) Development of the new on-lined method makes it possible to gauge the water quality of IC pure water
2) It can evaluate the total quantity of foreigners in water
3) The value gauged has a good coincidence with result added inorganics, organics and SiO_2 which is measured by each present methods

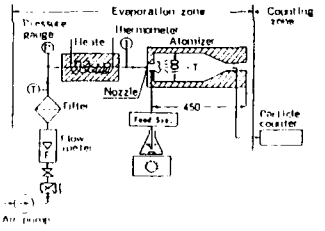


Fig. 1. Schematic diagram of experimental apparatus

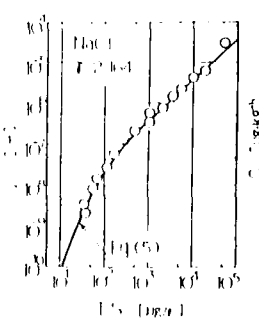


Fig. 2. Relations between concentration of foreigner (NaCl) and volume of particles

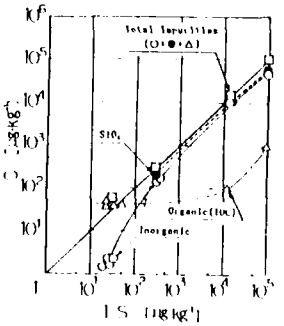


Fig. 3. Relationships between the new method and conventional methods
□:Total foreigners(O+●+△)
●:SiO_2, O:Inorganic matter
△:Organic matter(TOC)

Abstract No. 402

A DISTRIBUTED ARCHITECTURE FOR REAL-TIME HEURISTIC FACTORY CONTROL

BARBARA MARTENSEN

MOTOROLA, INC.

5005 E. MCDOWELL ROAD, M.D. E110
PHOENIX, ARIZONA 85008

Fundamental to the pursuit of Computer Integrated Semiconductor Manufacturing is the realization of a "To Be" enterprise model or architecture, a vision that continuously evolves but is always aligned to the fundamental design criteria of a distributed-networked virtural system. Implementation of this architecture provides a persistent distinct competitive advantage through the utilization of the most accurate and competent manufacturing resource: The knowledge base of the factory floor.

The strategic objective the enterprise model achieves is the on-time delivery of perfect quality product. The enterprise model is comprised of two general models supporting capacity driven logistics and process characterization/control. These two general models are tightly coupled enabling the enterprise architecture to control the execution of processing, in addition to providing an optimum plan and schedule. These models are driven by knowledge data bases which custom tune the models to the relative uniqueness of each processing area. These subordinate entities of the enterprise architecture work in concert to first predict and configure, then to execute to the optimum model. This configuration resolves the historical difficulty in supplying generic solutions that maximize software development but are not specific enough to ensure precise execution to the goals. Both the logical and functional descriptions of this architecture are presented.

Functionally, higher level systems present to the model, the prioritized customer or forecasted demands that the enterprise model couples with the current process description and relative specifications. This is also the criterion to which the customer will measure the quality and usefulness of the deliverable. The model interpretets, from the knowledge domains, the networks of possible processing flows and resource consumption formulae required to plan the process activities of each demand, in order to facilitate the model representation of the factory.

The arbitration of committments for resources to process material is resolved by an objective function that reflects the current strategic business needs of the company. A primary output of this simulation is the micro specification "when and where" necessary to process each demand. The exact sequence of processing events expressed in time intervals of seconds, coupled with exact resource committments, are passed both to the factory floor in order to direct material movements and also to the generic process control modules that interface directly to the process equipment. Using the specific knowledge of the product and machine states, coupled with the accumulated knowledge of previous experience and adaptive techniques, the process control modules predict the optimum process plan.

Accordingly, compiled programs and recipes are generated and modified to accommodate the exact characteristics of a specific machine, then downloaded to the target machine in time for the product arrival.

Compliance to the planned model is ensured through the implementation of an execution control subsystem referred to as process control managers. The execution control subsystem receives the processing plans and directs the the execution of processing activities relative to the plan. The execution control subsystem is able to recognize real time exceptions to the processing plan, and analyze recovery alternatives ensuring minimum impact on current and future plans. Finally, the knowledge resulting from the analysis of these deviations and successes is stored in the knowledge domain for future use in predicting optimum process configurations.

In order to most efficiently manage and utilize massive quantities of data elements and associated information, frames are used to represent facts and relationships, such as resources and their respective attributes. Data structures are organized so that objects can be easily associated with a collection of features both descriptive and procedural. These are depicted as slots with their associated contents. Frames are presented as two-part nodes: The fixed node represents the permanent attributes of an object, and the variable node houses the changing attributes and current associated values. This organization allows predictions to be made without complete knowledge of all variables.

A logically distributed architecture is selected in order to provide a platform for company-wide modular expandability, flexibility, and redundancy. Logically, modules have two personalities: generic and specific. Procedures, relationships and functions that are common to all manufacturing areas are expressed as standard alogrithms in the generic modules. These generic or fractal sets integrate to a specific set of shells which become personalized as "scripts" are selected to comprise a frame, filling in the variable slots in the knowledge domain. Specific software modules take on the role of "actors", as frames are invoked.

Network concepts are explored in depth. The distributed networked architecture is implemented, using a communication control application layer that manages message passing and their respective routing between processes on either a local or remote node. Message destinations can each be identified logically or physically, as required by the application. This network manager, refered to as the network object, enjures a high speed communication link between generic and specific process sets for the duration of each conversation. Network flexibility and tuning are implemented on a functional application basis, since it is at this level that the rules for connection/disconnection are defined. The network manager provides a low overhead distribution of information, allowing logical referencing so that generic and specific integration of processes can occur.

Abstract No. 403

Beyond the Spreadsheet: Wafer Production Planning with Start/Demand Rate Calculation through Simulation Models.

Richard A. Zuanich,
Donald F. Ruffcorn,
Maurico G. C. Resende*

National Semiconductor Corporation
2900 Semiconductor Drive
Santa Clara, California 95052

***consultant, AT&T Bell Laboratories**

FabSim II simulation and calculation tools, generally found on a mainframe, now run real-time on an IBM PC/AT (with a 8-MIP OPUS 32532 cpu card) that is integrated with the CIM computer network. Production forecasters simulate a manufacturing model (equipment, operators, dispatch algorithm, work-in-progress,...) to calculate model statistics (wafers out, inventory, cycle-times,...). An inventory projection algorithm then transforms the wafer demand schedule into a new (and better) wafer start schedule from these statistics. Other **FabSim II** user services are for CIM data loading, user interfaces, and model building conventions.

The application and use of **FabSim II** is described in terms of the manufacturing work areas modeled, the gathering and network loading of CIM data to **FabSim II**, simulation runs and comparison to actual fab behavior, 'what-if' manufacturing capacity use and results, the critical elements for long and short term predictive behavior, and the hardware support environment.

FabSim II has been specifically designed to provide an on-line tool that can be used for two main manufacturing planning functions; **production planning** and **capacity analysis.**

Production Planning - FabSim II can be used to determine a product start schedule from input demand, taking into account current work-in-progress and the expected manufacturing environment. Iterative runs of the simulation using updated cycle times can provide a more accurate start schedule than currently used non-simulation techniques.

Capacity Analysis - FabSim II can be used to assess the impact of factory design and operating policies on product throughput, cycle times and work in process. Parameters which can be studied include; facility personnel (number of), processing equipment (number of, productivity, reliability, setup and loading), preventive maintenance, product mix, lot size, rework and yield rates, dispatch rules and lot start policies.

Manufacturing Model - A manufacturing facility is modeled as a network of queues serving production work stations. Product lots move into the queues and are routed to a piece of equipment in the work station by dispatch algorithms. **FabSim II** operates by maintaining a dynamic list of scheduled events, such as: processing completions, equipment failures and repairs, and lot starts. As events occur, the state of the modeled system changes, statistics are collected, and new events scheduled. The frequency of these events is controlled by user-defined parameters that include lot start rates, equipment failure rates, and process specifications. User-friendly interfaces allow the factory and work flow to be defined in detail.

Performance - FabSim II is written in '**C**' running under Unix System V. Performance of **FabSim II** (on the 8-MIP 32532 cpu) allows simulation of 10 products processed through 60 steps at 38 work stations (containing 60 pieces of equipment) for 50 production days in 11 seconds (cpu time). This corresponds to approximately 122,000 simulated events per minute.

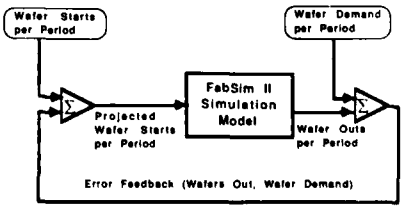
References

[1] J. E. Dayhoff and R. W. Atherton, "Simulation of VLSI manufacturing areas," *VLSI Design*, Dec. 1984.

[2] M. G. C. Resende, "Shop floor scheduling of semiconductor wafer manufacturing," Ph.D. dissertation, Dept. Industrial Engineering Operations Research, Univ. California, Berkeley, CA, 1987.

[3] C. Rodger Glassey and Maurico G. C. Resende, "Closed-Loop Job Release Control for VLSI Circuit Manufacturing", *IEEE Transactions on Semiconductor Manufacturing*, VOL. 1, NO. 1, pp. 36-46, Feb. 1988.

FabSim II
Production Planning Feedback



Abstract No. 404

Dynamic Capacity Planning Using Simulation Models

Robert W. Atherton
In-Motion Technology
444 Castro St., Suite 434
Mountain View, Calif. 94041

The factory is a physical system, and thus, it has a physical limit or capacity (1,2). Accurate determination of the capacity of real factories under dynamic conditions is difficult. This difficulty has lead to the use of standard, but approximate, capacities (3) in production planning and factory design. Errors in these capacity estimates naturally propagate into errors in planning and design. Simulation-models, however, provide more accurate values for dynamic capacity, and thus, a more firm basis for production planning.

Dynamic capacity is the capacity of the factory under dynamic operating conditions and with dynamic loading. This capacity is usually substantially less than the theoretical or "spreadsheet" capacity calculated from load sizes, processing times, and number of machines. Such calculations neglect several phenomena which result in capacity losses in real factories. These phenomena, treated in the simulation-model, include congestion and delay (queueing), product competition, equipment availability, set-up effects, batching effects, and rework.

Electronics factories like wafer fabs contain several different types of manufacturing equipment. The factory may be organized into work centers or work stations; each work station contains a set of like equipment. A process flow or manufacturing routing determines the path and set of work stations necessary to complete fabrication. For the process flow each workstation will have a dynamic capacity, and there will be a minimum capacity among the set of workstations. The minimum capacity determines the limiting or bottleneck work stations. Thus, the dynamic capacity of the factory for the process flow is the capacity of the bottleneck workstation.

Different process flows can impose different demands on the factory, and thus, experience different dynamic capacities. In the standard operating mode for wafer fabs, products from several processes must be fabricated simultaneously. Calculating the dynamic capacity for a mixture of process flows is especially difficult.

The simulation-model generates a variety of output variables describing factory performance. These system performance variables include queue lengths and waiting times, throughput reports by process step and by work station, and equipment utilization reports. Analysis of these performance variables allows the determination of bottlenecks and dynamic capacities under the conditions simulated.

Bottleneck analysis can be complex. However, the interpretation of the simulation results has been reduced to a set of cases. Each case is characterized by a set of rules. These rules have been incorporated into software, and this software can be viewed as a rule-based expert system.

References:

1. R.W. Atherton, "Factory Scheduling Using Simulation Models," Proceedings of the Third Symposium on Automated Integrated Circuit Manufacturing, Electrochemical Society, Princeton, New Jersey, pp.333-345, 1988.

2. R.W. Atherton and J. E. Dayhoff, "Signature Analysis: Simulation of Inventory, Cycle Time, and Throughput Trade-Offs in Wafer Fabrication," IEEE Trans. Components, Hybrids, Manufacturing Technology, vol. CHMT-9, 498-507, 1986.

3. T. E. Vollman, W.L. Berry, D.C. Whybark, Manufacturing Planning and Control Systems, Dow-Jones Irwin, Homewood, Illinois, 1984.

Abstract No. 405

Real-Time IC Process Control Automation Using Expert Systems

C. Fred Hiatt

Prosys Technologies, Inc.
Computer Aided Processing Group
Minneapolis, MN 55431

Introduction

Computer-Aided Manufacturing (CAM) and Computer-Integrated Manufacturing (CIM) systems being developed by universities and industry are responding to concern about the United States microelectronics industry's ability to compete in worldwide markets. Software now available or being developed for the semiconductor industry tracks wafer progress through the process line, assists in scheduling, collects process-related data and then presents this data in a variety of report formats for interpretation. However, due to the complexity of modern processes it is not possible, using current systems, to analyze or act upon the data in a timely manner. The result is process deviation and product failure.

One solution is to develop Computer-Aided Processing (CAP) using expert system technology to capture the knowledge of one or more human experts, analyze the available data in real-time and provide automated closed loop control of the manufacturing process.

Expert Systems

Evolving from computer science technology's research into artificial intelligence, the expert system concept is a useful tool to address integrated circuit processing with its multiple variables, uncertainties and subjective measurements. By combining the expert system concept with traditional software techniques, an innovative way to deal with qualitative as well as quantitative processing data and variables is created.

An expert system consists of two main components: 1) a knowledge base containing the domain knowledge of the expert as well as the real-time (variable) observations and 2) an inference engine which contains the rules and general problem solving knowledge by which the reasoning process is guided. Thus a knowledge based system can manipulate knowledge by algorithms and heuristics (rules of thumb) to reach a conclusion. Figure 1. is a simplified diagram of an expert system.

Computer-Aided Processing

The CAP system is designed to provide real-time process control using a microcomputer-based expert system. The system monitors, controls the process and advises the process engineer of unusual process conditions requiring immediate human intervention. The system 'learns' from the process engineering expert (domain expert) and, over time, becomes a 'smart system' thus making the expert's knowledge available regardless of the work shift or other reasons for the expert's absence. In addition, the CAP system adds discipline to manufacturing operations and allows the expert to concentrate on more challenging manufacturing tasks.

The CAP system utilizes a modular approach to control each manufacturing process work cell (see Figure 2.). A work cell is defined as a machine or group of machines which perform(s) a major process function (photo, etch, deposition, etc.). The advantages to this approach are:

a. Modular systems are easier to implement on a work cell by work cell basis and can be interconnected via a network as the installed system base grows.

b. Work cells can expand to interface with VAX or MICRO-VAX systems as integration of the factory system into CIM becomes more practical.

c. Software modules can be developed generically (by operation type, i.e. photo, etch, deposition). These modules are then 'customized' for specific machines and process parameters. The system is capable of interacting with the domain expert(s) thereby 'learning' from their experience and capturing the best of the expert's knowledge.

d. Microcomputers at the work cell level make knowledge base and rule storage easier to manage. Faster access is possible than a mainframe multi-user computer since the knowledge, data and rules for each module are stored locally. In addition, the knowledge base and module rules may be easily updated to include process changes and new technology.

e. Data processing between work cells via a network provides backward and forward communications during problem or status analysis. This analysis capability is crucial for real-time process control.

f. Statistical Experimental Design (SED) and Statistical Process Control (SPC) methods can be used to assist in development and transfer of new processes.

The CAP system accepts input from the domain expert(s) for manual data entry as well as data query. The system collects real-time data from the physical environment (clean room) as well as from the production equipment, both of which directly affect process performance. Machine failures or process settings outside of designated limits are recognized and reported to the user along with the corrective actions to be taken. System overrides allow the process engineer to run experiments without system interference. System data can be queried by run/lot number, date of process, process machine ID or other process parameters. The result is an ability to analyze faults or failures by process step, machine used for the process, date the process was performed, or a combination thereof.

Applications for the CAP system being developed are not limited to integrated circuit manufacturing. This concept can be used for any automated manufacturing process control application which contains many interrelated variables.

Conclusion

In reviewing the current status of factory automation, the work cell modular approach to process control as described above has real merit. Integrating the expert system concept into a process control strategy increases the capabilities far beyond traditional approaches. A computer-aided processing expert system provides the foundation needed to achieve a CIM system. Integrated circuit manufacturing technologies are complex. The dependence on computer systems to process data and make decisions based on experience and intelligent reasoning is an absolute necessity. Efficient and highly productive manufacturing systems are essential to the economic welfare of this industry.

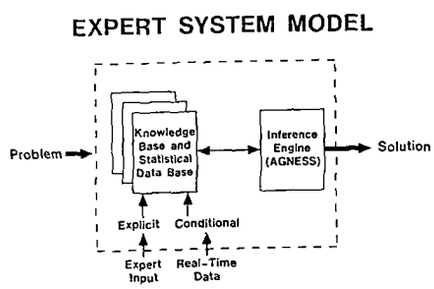


Figure 1.

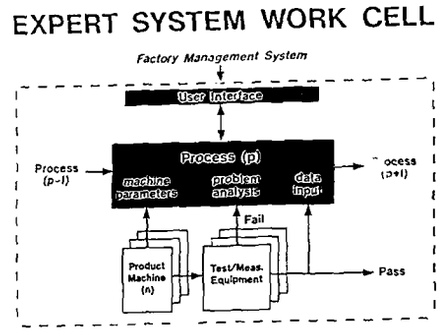


Figure 2.

Abstract No. 406

EXPERT SYSTEM CONTROL OF DIELECTRIC FORMATION

M.N. Kozicki, T. Patel, P. Rastogi and G.W. Sheets
Center for Solid State Electronics Research
Arizona State University
Tempe, AZ 85287-6206

Introduction

As the processes used in the fabrication of advanced silicon integrated circuits become more complex, there is an ever increasing need for a higher degree of process control. This is becoming evident at the individual process level, process cell level, and ultimately at the production line level. With decreasing lateral and vertical dimensions within the devices and circuits, small absolute deviations in parameters such as layer thickness, resistivity, etc., will naturally mean large relative errors. These errors, if they occur at a critical process step, will ultimately lead to device characteristics which are out of specification. Therefore, tight process control is particularly important in critical process steps.

Optimal process control is traditionally achieved in many processes within the semiconductor industry by strict adherence to the long standing "non-alteration" creed, where individual pieces of equipment are dedicated to "set" processes which require identical "set" process parameters. Unfortunately, this approach is slowly becoming impractical as flexible manufacturing concepts are beginning to be applied in the semiconductor industry. The possibility of "application specific processes" is highly desirable and will ultimately lead to a high degree of product optimization. Unfortunately, we are therefore faced with something of a dichotomy as tight process control by traditional means and flexible manufacturing are largely orthogonal concepts. This dichotomy may be broken by utilizing a control system which is sufficiently adaptable to cope with process conditions which not only change during the process (e.g. real time temperature control) but also may be deliberately altered from run to run.

This paper reports the design of such a control system based on an expert system core. Our test application is the formation of dielectric layers for MOS devices by rapid thermal processing.

Process and Control Equipment

The equipment used in this study is a Tamarack 180M rapid thermal processor which has been modified to perform dry oxidation and ammonia nitridation at atmospheric pressure. The dedicated system controller is an IBM-PC which runs a customized software PID temperature controller which is fed with wafer temperature readings from an infra-red pyrometer (Fig. 1). Note that this system will act to maintain temperature for a preprogrammed time and in no way can determine whether the correct process result (e.g. oxide thickness) has been obtained. The PC would normally also be used for user interface functions, but in our application it is merely required to continually monitor and control the wafer temperature and to communicate with an external control system. (Note that essentially any equipment controller with an appropriate communications interface could be used in this control concept, e.g. a DPC/DTC unit on a diffusion furnace).

The external control system resides on an AT compatible (80286) machine (Fig. 2). The size and speed of this machine limits functionality but it is nevertheless adequate for concept demonstration. The controller system wheel is shown in Fig. 3. The core is an expert system written in a high level "OPS" (5 or 83) language. This is supported by 3 rule bases: (1) an "equipment" rule base which has information on equipment capabilities, (2) a "process" rule base which defines the effects of process parameters on the product, (3) an "adaptable" rule base which contains the rules for updating the other rule bases when new information on the effect of processing becomes available from subsequent process or measurement steps. Maintenance information may also be used to update the equipment rule base through the rules in the adaptable base. Since we cannot measure the growth of the oxide or the nitridation of that oxide in-situ, an accurate simulation of the process is included and this acts as a "dynamic rule" which may be used in one of two ways: (1) it can help with decisions regarding set-up parameters, e.g. choosing an appropriate temperature and time to grow a particular thickness of oxide, (2) it may be used real time, being fed with measurable parameters from the system at regular intervals, to simulate the dielectric formation as it occurs so that the control system can make decisions on what action should be taken in order to stay "on target". The final area in the system contains the I/O functions, and these include equipment controller and user (or cell control computer) interfacing. A serial data link joins the two computers.

System Operation

We have operated and evaluated the system in a number of modes: (1) selection of set-up parameters for a particular process by the expert system/simulation combination, (2) real time process control by simulation only, (3) real time process control by the expert system/simulation combination, (4) post-hoc process control using parameters measured ex-situ. The "set-up mode" relies on rules which govern equipment limitations (e.g. highest possible temperature, minimum processing time, etc.) and process rules, i.e. which temperature ranges will produce the appropriate type of dielectric in the most ergonomic fashion. Once temperature and time ranges have been selected, the simulation is used to determine exact set-up parameters which are then fed to the process system controller. Process control by "simulation only" relies on the real time simulator to "monitor" the dielectric formation and cease processing when it calculates that the desired effect (e.g. thickness) has been achieved [1]. When combined with the expert system, decisions as to which parameters to alter may be made during the process so that the effects of fluctuations which arise during processing may be nulled out. This brings us closer to the "perfect part every time" concept. Finally, the "post-hoc" control experimentation was designed to test the system's ability to adapt to conditions the expert system failed to predict during processing and could only be determined by subsequent ex-situ measurement, e.g. constant or regularly changing offsets which arise due to problems with equipment calibration.

Our system performed adequately during simple functionality testing. However, it should be noted that in a real process control situation, all the above functions would be combined and be performed by a more powerful control computer so that more complex real time functions could be realized.

1. E. Cameron, J. Robertson and R. Holwill, "Control of oxide growth by real-time simulation", in Simulation of Semiconductor Devices and Processes, Vol. 2, K. Board and D.R.J. Owen, Eds., Pineridge Press, Swansea, U.K., 1986.

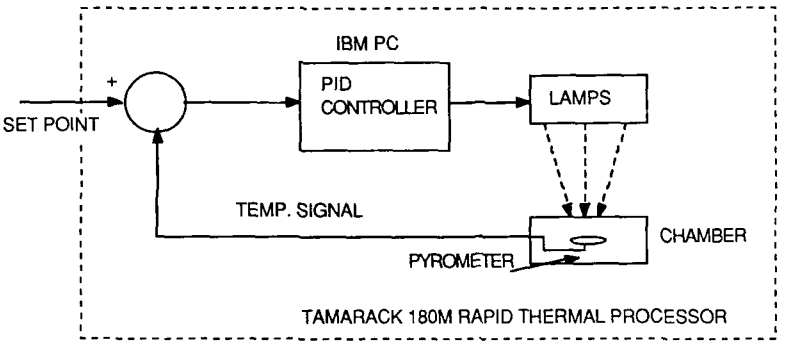
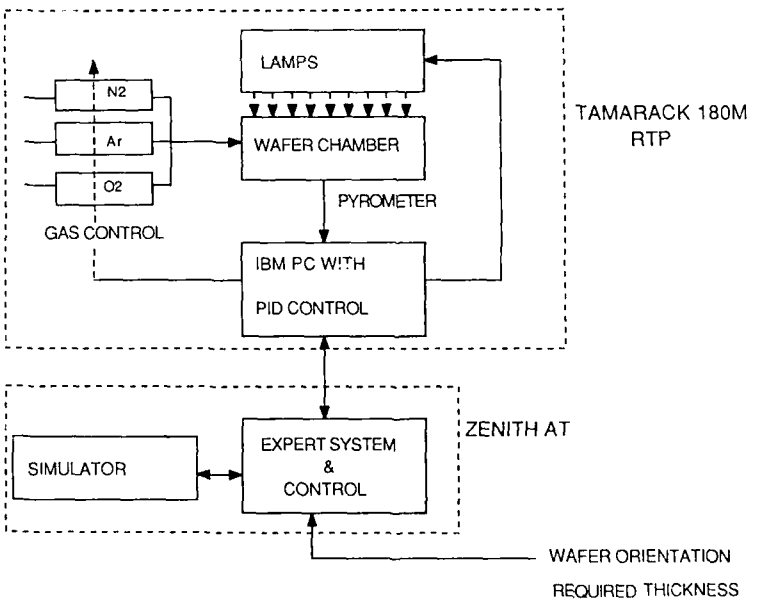


FIGURE 1. SCHEMATIC DIAGRAM OF RAPID THERMAL PROCESSOR SYSTEM.

FIGURE 2. SCHEMATIC DIAGRAM OF ALTERNATIVE CONTROL SYSTEM.



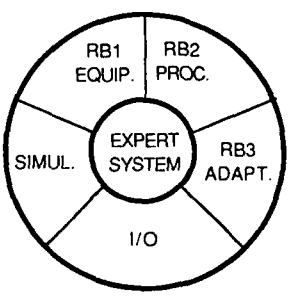


FIGURE 3. SYSTEM WHEEL FOR EXPERT SYSTEM CONTROLLER.

Abstract No. 407

Ultra-High-Vacuum Compatible Wafer Transport and Holding System Using Electro-Static Chucks

T. Ohmi, M. Onodera, G. Sato, T. Shibata, and M. Morita

Department of Electronics,
Faculty of Engineering, Tohoku University,
Sendai, 980, Japan

Phenomenal growth in the integrated circuit technology has been observed during the last decade, and the manufacturing of ULSI chips with submicron to lower-submicron design rules will come about in very near future. In order for such LSI manufacturing in ultimately small dimensions to be successful, the accuracy of process control must be much higher than that we have today. Such high-accuracy of process control will be realized only by eliminating all possible contamination sources from the processing environment that cause uncontrollable fluctuations or ambiguities in the process (1)(2). This is why ultra high vacuum compatible chambers are needed for future ULSI fabrication process equipment. The most important issues of ultra high-vacuum system are how to transport wafers quickly and reliably in a high vacuum and also how to hold wafers firmly on wafer stages in order to get a good thermal contact as well as an electrical contacts.

We have developed wafer transport and holding systems using electro-static chucks that meet the all requirements mentioned above. Since wafers are not hold mechanically but by an electro-static force, the system is essentially particle-free. The purpose of this paper is to describe the basic characteristics of electro-static chucks and the method of fabrication. Application of the system to various advanced processing equipment, such as ultra-high vacuum ion implanter(3), surface-reaction CVD system, reactive-ion etching system etc. are also presented in this paper.

The structure and the principle of operation of electro-static chucks are shown in Fig. 1. The holding chuck that is used to hold wafers during processing is illustrated in Fig. 1(a).The wafer is stuck to the holder by a Coulomb attractive force between the charges induced in the wafer and the holder electrodes which are separated by an insulative layer formed on the electrode. The force of attraction is calculated as,

$$F=\frac{\epsilon^2 S V^2}{2\epsilon_0 d^2}$$

where, ϵ_0 is the permittivity of free space, ϵ the dielectric constant of the insulator, d the insulator thickness, S the electrode area, and V the voltage applied across the insulator determined by the voltage source V_1 in Fig. 1(a). The results of calculation is shown in Fig.2 along with the experimental data where polyimide was used as an insulator. Large difference observed between the calculation and the experimental data is due to the surface roughness of the insulator. The surface roughness, creates a gap between the wafer surface and the insulator surface, which reduces the effective dielectric constant of the insulator. Since the gap spacing relative to the total insulator thickness is reduced by using thicker polyimide layer, a large attractive force (about 40% of the calculated value) was obtained for 35μm thick polyimide sample. In order to enhance the attractive force, it is essential to make a chuck surace as smooth as possible. The metal electrode typically made of SUS 316L was mirror-polished to create a smooth surface which is both microscopically and macroscopically flat. Then polyimide was coated onto the electrode surface. After being cured, the polyimide surface was also mirror polished to get excellent planarity. A thin over-coating layer of polyimide of about 2-3μm was spin-coated on the surface for blocking contaminations introduced during polishing. The thickness of total polyimide layer is typically in the range of 30-60μm, and attractive forces over 50% of the calculated value are typically obtained. Large attractive forces obtained is quite important to realize a precise temperature control of wafers during processing. With the configuration shown in Fig. 1(a), it is also possible to control the wafer DC bias voltage by the DC power supply V_2, which is important for controlling ion energies in plasma processes such as in the RF-DC coupled mode bias sputtering(6).

The electro-static chuck used for wafer transport is illustrated in Fig.1(b), which holds a wafer at the periphery from the front surface by two electrodes. The charges induced in the two electrodes by an externally applied voltage are distributed among the wafer and the two electrodes as shown in the figure. As a result, the wafer sticks to the chuck without applying any biases to the wafer.

The electro-static chuck wafer transport and holding system designed for ultra high vacuum ion-implanter is schematically shown in Fig. 3. Wafers are loaded on the holding chucks in the 1st chamber and transferred to the transport chuck mounted at the tip of the flog-leg, which conveys the wafers from the 1st chamber to the implant chamber. Excellent thermal contact of the wafer to the wafer holder prevents the temperature rise during the implantation that is quite important to suppress the damage formation in the ion-implanted layer.

Figs. 4 and 5 show the electro-static chucks for wafer transport specially designed for the reactive-ion etching (RIE) system and the surface-reaction CVD system(4)(5), respectively. Four wafers are simultaneously held by four wafer chucks and transported to the etching chamber by a frog-leg mechanism in the RIE system.

Electro-static chucks have been developed to construct a new wafer-transport and holding system. The system has established a particle-free wafer transportation in ultra high vacuum environment in combination with a flog-leg mechanism. Exellent thermal contact of the wafer to the wafer stage as well as the electric potential control of the wafer during processing has been also realized by the electro-static chucking technique. Such systems will play important roles in future ULSI automated manufacturing that require high precision control of all processing steps.

This work was done in the Superclean Room of Laboratory for Microelectronics, Research Institute of Electrical Communication, Tohoku University.

(1)T. Ohmi, N. Mikoshiba, and K. Tsubouchi, ECS spring Meeting, Ext. Abst. No.212, Philadelphia, May, 1987.
(2)T. Ohmi, J. Murota, Y.Mitsui, K. Sugiyama, and, H. Kawano, ibid., Ext. Abst. No.216.
(3)T. Ohmi, K. Masuda, T. Shibata, M. Kato, and Y. Ishihara, Ext. Abst. 19th Conf. Solid State Devices and Materials, 299, Tokyo1987.
(4)T. Ohmi,M. Morita,T. Kochi,M. Kosugi, H.Kumagai, and M.Itoh, (to be published in Appl. Phys. Lett.)
(5)T. Ohmi, G. S. Jong, M. Morita, M. Kosugi and H. Kumagai, this Symposium.

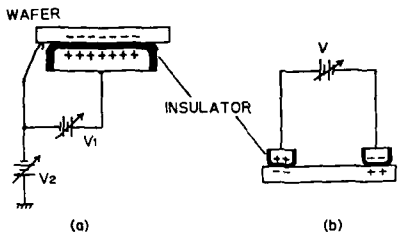


Fig.1 Schematic of a electro-static chuck used as a wafer stage during processing (a) or that used for wafer transport (b).

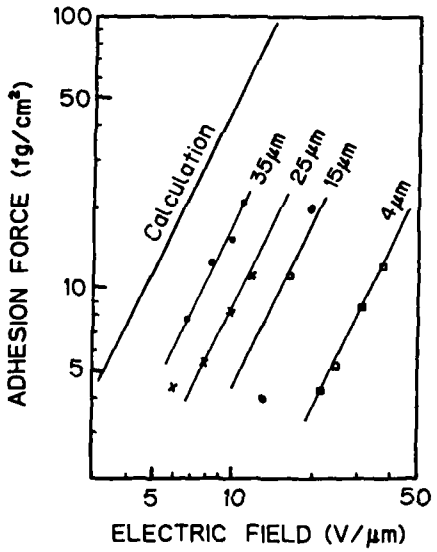


Fig.2 Force of adhesion as a function of electric field for varying polyimide thicknesses.

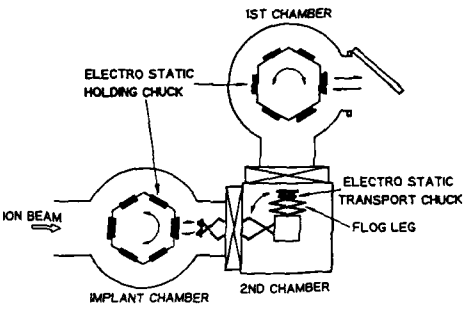


Fig.3 Electro-static wafer transport and holding system used in UHV ion-implanter.

Fig. 4 Four electro-static chucks mounted at the tips of a flog-leg for transporting wafersfrom the loading chamber to the etching chamber of an advanced RIE system.

Fig.5 Transport wafer chuck utilized in a surface-reaction CVD system.

Abstract No. 408

Automatic Chemical Supply Unit and System

Mitsuro Tamura, Tsugio Saito, Suehiro Oshima and Asaaki Yamasita
KANTO CHEMICAL CO., INC.
Chuo-ku, TOKYO, Japan

1. Introduction

The chemicals used in the semiconductor industry are mainly used for washing and etching process. Since these chemicals contact with silicon wafer, it is essential that these chemicals be of consistently high quality. In particular, chemicals so prepared as to minimize metal impurities and particles, which adversely affect the characteristics and the yield of semiconductor device, are in great demand.

Current semiconductor manufacturers request the extreme high purity chemicals which present ppb level or less of the metal impurities (specified on SEMI Standard) and 10pcs./ml or less(0.5μm) of particles.

Automatic chemical supply unit and system were developed to distribute such high purity chemicals to the semiconductor processing equipment and these unit and system have been actively adopted by the Japanese semiconductor manufacturers during the recent years.

Advantages of automatic chemical supply unit are as follows.

1) Automatic supply prevents chemicals from contamination with particles usually encountered when manually opening and closing of cap of small container from which chemicals are poured into the tank of processing equipment.
2) It is possible to distribute the low particle content chemicals which were filtered just before using by the microfilters incorporated into the supply unit and system.
3) It eliminates handling operation of chemicals in clean room. Therefore, it elilminates generation of particle from operator and chemical container, serves saving of labor and serves safety operation.
4) Distribution from large chemical container allows easy quality control of chemicals.

However, automatic chemical supply system have some problems as summarized bellow.

(1) If quality problem develops, it will affect the entire system.
(2) If chemicals leak from piping, it is highly dangerous.
(3) If unit and system are in trouble, chemical supply stops.

Measures against above problems are listed bellow.

(1) Either implement receiving check or purchase chemicals from chemical manufacturers with tight quality control.
(2) Protection of chemical piping and valves by double layer piping and protective box.
(3) Adoption of reliable supply unit and system.

Automatic chemical supply unit and system will produce many advantages but also create problems as described above. It is, therefore, essential to maximize the advantages and minimize the problems.

2. Outline and Current Status of Automatic Supply Unit and System

2.1 Supply Method

There are two different types of automatic chemical supply method available at present, one is N_2 gas pressurizing supply method and other is pumping supply method. Most of the Japanese semiconductor manufacturer adopt the N_2 gas pressurizing supply method from the viewpoint of easy maintenance and maintaining the quality of chemicals.

2.2 Main Materials of Unit

Automatic chemical supply unit and system have two types classified by kind of chemicals, one is for corrosive (Acid and Alkali) and other is for solvent. Main materials of the unit are fluorocarbon polymer for corrosive use and stainless steel for solvent use.

2.3 Type of Unit

Various kinds of chemicals are used in the semiconductor manufacturing factory and the chemical consumption depends on the kind of chemical.

Types of unit are selected by considering the chemical consumption, area and location to be installed, required flow rate of chemicals and type of chemicals.

Representative types of automatic chemical supply unit are:

(1) Small-scale supply unit: Cica S～vagon
(2 nos. of 15～20ℓ Containers→Filter→Point of use)
(2) Medium-scale supply unit: Cica LS-100
(2 nos. of 100ℓ Containers→Filter→Point of use)
(3) Small-scale fixed type supply unit
(100ℓ container→2 nos. of Supply Tank→Filter→Point of use)
(4) Large-scale fixed type supply unit
(1000ℓ Container→Pre-filter→Storage Tank→2 nos. of Supply Tanks→Supply Filter→Point of use)

Chemicals are distributed under N_2 gas pressure from container to each processing equipment directly via microfilters for small-scale and medium scale supply unit. With regard to fixed type, chemicals are received to storage and /or supply tanks and then distribute to each point of use via microfilter by N_2 gas pressure.

2.4 Safety Measure

Many of the semiconductor chemicals are highly hazardous and great care shall be taken when handling these chemicals. Following consideration have been taken into the automatic chemical supply unit as safety measure.

(1) Protection against the leakage of chemicals and chemical gas.
(2) Selection of proper materials which have the corrosion resistance against the treating chemicals.
(3) Function of checking if the connecting parts such as connector of chemical container are securely connected.
(4) Safety device for protection of operators such as door switch of chemical container booth. (N_2 gas pressure in the container is released when door is opened.)
(5) Protection of electrical equipment and parts against the corrosion caused by chemical gas.

2.5 Piping

Materials of chemical piping are stainless steel for solvent and fluorocarbon polymer for corrosive.

There are two different method for corrosive piping, one is fluorocarbon polymer lining stainless pipe and another is double layer piping (inside: PFA tube, outside: PVC protective tube). Double layer piping is adopted in most of the Japanese semiconductor manufacturer because of the following advantages.

(1) Seamless piping of PFA tube is practical and it is superior in leakage trouble compare with flange connection.
(2) Easy piping work.
(3) Easy quality control (If there is a pinhole in the lining part of fluorocarbon polymer lining pipe, metal (Fe, Ni, Cr) will dissolved into the chemical and it is difficult to find the part of pinhol).

3. Future Innovation

The automatic chemical supply unit and system have been improved regarding to safety, simple operation and high performance, but still have some points remaining to be improved, modified and developed such as pumps, valves, fittings, materials, filters, etc.

Now, coming into the era of the megabit, we have to pursue more reliable supply unit and system to challenge the supply of ultrapure chemicals.

Abstract No. 409

A SMIF-Vacuum Interface Chamber for 200 mm Wafer Cassette Loading and Unloading of a Multichamber Etching Apparatus

I. Hussla, M. Walde, and P. Zeidler
Leybold AG, Coating Technology
Electronics and Optics
Siemens Strasse 100, 8755 Alzenau/FRG

In order to approach a higher level of computer aided semiconductor manufacturing (CAM), the Standard Mechanical Interface (SMIF), a Hewlett Packard product (Ref. 1), is already used and tested by major semiconductor manufacturers. The future manufacturing concept will be a modular local cleanroom one with micro climate zones and standardized interfaces to Class 10,000 environment (Ref. 2). An improved dynamical SMIF box being a small local clean room with fan and HEPA filter will be employed (Ref. 3). For the etching equipment vacuum elevators for individual wafer handling are used. Therefore, there is a need to develop a SMIF vacuum interface chamber.

Main operation of the designed SMIF vacuum interface chamber is to bring a cassette for 200 mm wafer processing from any environment via SMIF box into the vacuum cassette elevator of the etching equipment.

The interface chamber is built as a separate unit at the cleanroom front of the etcher and consists of a SMIF box interface (ports), a horizontal cassette transport system, a two-stage vertical cassette elevator, a mechanical interface to the individual wafer handling cassette elevator (load lock to vacuum cassette elevator), and a laminar flow system, class 1.

In Fig. 1 the adaptation of the designed SMIF vacuum interface chamber onto a multichamber production etching equipment Leybold MPE 3000 is shown. Two independently working interfaces (SMIF box ports) are actually needed for loading and unloading of wafer cassettes from the SMIF box into the vacuum individual wafer cassette handling chamber. The device is a Leybold patent and the design concept is based on the following criteria and additional demands as given by the semi-conductor industry:

(i) Lowest particulate generation due to installation of cassette drives underneath individual waferhandling.
(ii) Minimum of moving parts.
(iii) installation of interface under laminar flow, class 1, or better.
(iv) Smallest cleanroom footprint possible.
(v) SMIF box interface height 1000 mm (SEMI standard).
(vi) Coupling of SMIF box following general SEMI standards.
(vii) Compatibility to other systems.
(viii) Wafer sizes up to 200 mm.

In Fig. 2 a description of the mechanics of the newly developed device is given. Preliminary results regarding particulate generation and cleanliness of the main components were obtained exploying measurements of the air borne particles. These measurements are backed up by particle measurements on-the-wafer by means of laser surface scanning methods.

ACKNOWLEDGEMENTS

We would like to acknowledge that this work was funded by CEC in part via ESPRIT 1563 contract, a joint venture between Bertin & Cie (France), European Silicon Structure (France), Mietec (Belgium), Plasma Technology (UK), and Leybold AG (W-Germany). The project is concerned with automatic control of an ASIC fabrication sequence as demonstrated in the plasma etch area.

References:
1. "Robotic Automation for IC Manufacturing" Howard R. Huff, Rose F. Hole, Microelectronic Manufacturing and Testing, April 1986
2. "Computer Automated Ic Manufacturing Demands for VLSI Wafers", Solid State Technology, September 1985
3. Asyst Technologies in cooperation with Meissner & Wurst, Stuttgart, and Fraunhofer Institut für Produktionstechnik und Automatisierung (IPA), Stuttgart.

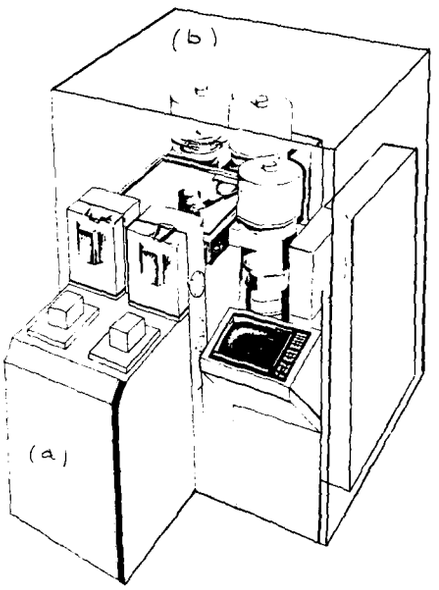


FIGURE 1

Adaptation of a SMIF vacuum interface chamber (a) to MPE 3003, a three-chamber etching system with vacuum wafer-transport-chamber for individual wafer handling (b).

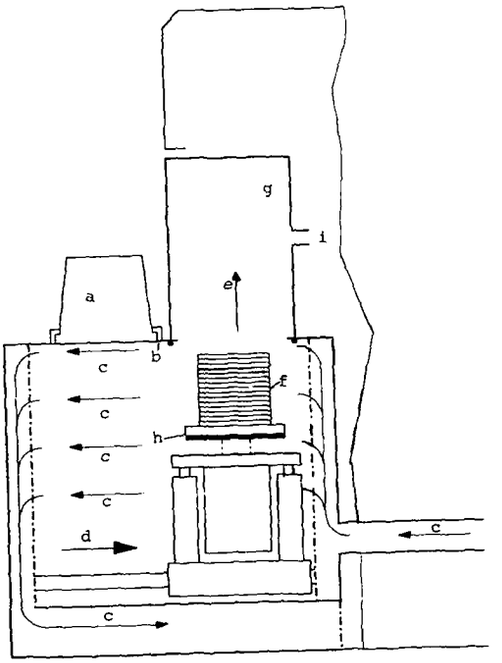


FIGURE 2

Mechanics of a SMIF vacuum interface chamber:

a) SMIF box
b) SMIF box interface
c) Laminar flow
d) Horizontal movement
e) Vertical movem.
f) Wafer cass. elevator
g) Vacuum cassette elevator
h) vacuum interface
i) lock for indiv. wafer handling MPE 3003

Abstract No. 410

Safety Mode Standardization for Semiconductor Manufacturing Equipment

Hideyuki Unno and Hiroyuki Harada

NTT LSI Laboratories

3-1, Morinosato Wakamiya, Atsugi-shi, Kanagawa Pref., 243-01 Japan

1. Introduction

Semiconductor manufacturing equipment uses dangerous gases, chemicals and high voltage in the clean room, which is a closed space and has been further complicated recently. It is difficult for workers to stop the equipment safely and quickly when an accident occurs. Manufacturing equipment now more than ever needs emergency safety features. Present safety features for manufacturing equipment are independently provided by each equipment maker and are not standardized. Furthermore, due to automated IC manufacturing, the number of workers employed in an IC manufacturing line has decreased. Therefore, safety mode standardization for automated IC manufacturing is desired in order to ensure that manufacturing equipment can be stopped safely, despite the fewer number of workers present.

In order to ensure safe automated IC manufacturing lines it is necessary that the safety mode for not only equipment but also facilities connected to the equipment et al. are standardized. This paper proposes a safety mode standard for manufacturing equipment which is a basis for standardization. The proposed standardization feature is "power-off safety mode" where the power-off state actuates the safety mode for manufacturing equipment. When an equipment accident occurs, by depressing the power-off switch or an alarm circuit linked to a detector the power is shut off and the equipment is stopped safely. Simultaneously the supply dangerous gases such as hydrogen, oxygen and toxic gases used in the equipment can be shut off automatically. Inert gas such as nitrogen or argon automatically purges the gas lines that supply the dangerous gases.

2. Details of Standardization

2.1 Power-off Switch

1)The power switch should be the self-hold type to prevent an automatic power supply after the recovery from an interruption of electric service and must have a shut-off terminal that connects with an alarm signal. The shut-off signal is sent to the shut-off terminal through an electromagnetic relay. The shut-off signal from detector, such as a bimetal sensor, that does not have a power supply may be directly sent to the shut-off terminal.

2)The emergency switch shuts off the equipment power and should be placed where it can be seen most clearly, such as on the front operational panel. The height of the emergency switch should be 150cm±10cm above the floor.

3)When the equipment is composed of multiple units, emergency switches are accordingly placed at each unit. The function of each emergency switch is the same, and the power to all the units is shut off when any one of the emergency switches is depressed.

4)When the equipment is placed between the clean-space and the power-space in the clean room, an emergency switch is provided on both the clean-space side and the power-space side.

2.2 Gas Shut-off Valve

1)The valve used for toxic gases, oxygen, and combustible gases should be the normally closed (NC) type, and should be be closed by the power shut-off switch in emergencies. The valve to allow inert gases to purge toxic gases, oxygen and combustible gases should be the normally open (NO) valve which is opened by shutting off the power supply.

2)When the shut-off valve consists of an electromagnetic valve and an air-operated valve, each valve must be used as follows: A combination of the NC electromagnetic valve and the NC air-operated valve should be used for toxic gases, oxygen and combustible gases, and a combination of the NO electromagnetic valve and the NC air-operated valve should be used for the purging gas.

3)The power of the equipment attachment, such as a toxic gas cylinder cabinet, should be taken from the main equipment power source. The valve in the equipment attachment should be closed by shutting off the equipment power and thereby stopping the toxic gas.

2.3 Alarm and Status Signal Interface

2.3.1 Alarm Signals

1)An alarm signal should be either a voltage signal or open/close circuit signal using two terminals.

2)Under normal conditions the voltage signal sent from the alarm is 0V. When an abnormal condition is detected, it changes from 0V to 100V(or commercial voltage of each country).

3)The open/close circuit is normally closed, and is opened when an abnormal condition detected.

2.3.2 Equipment Status Signals

The equipment should have an open/close circuit to indicate the equipment state. This circuit is closed under normal conditions and is open under an abnormal one.

2.4 Alarm Level to turn to the Power-off Safety Mode

Alarm levels from various detectors which actuate the power-off safety mode are different because of the detector's reliability and their installed position. Although, alarm levels can not be decided uniquely the following should be generally considered.

1)Toxic Gas

Gas concentration in a working environment should be less than threshold limit value (TLV) of each toxic gas. However, alarm level of detector installed in the closed equipment which does not leak gas outside should not be fixed at TLV. This is because the detector fixed at TLV occasionally gives a false alarm signal. Alarm level to adequately detect a toxic gas leak must be discussed.

2)Combustible Gas

Alarm level to stop an equipment should be less than a quarter of the lower explosive limit of each combustible gas.

3) Earthquake Acceleration Level

In case of shutting off the power with a seismograph, the acceleration level for power-off is 150 gal.

4)Others

Alarm levels for a fire and a water leak etc. is fixed by the circumstances of each manufacturing line.

3. Summary

We have proposed a safety mode standard that shuts off the power by depressing the emergency switch or, by receiving alarm signals sent by various detectors. By shutting off the power the dangerous gases are shut off and the gas lines are automatically purged by inert gas.

By standardizing the safety mode of manufacturing equipment the total safety of manufacturing lines which include facilities connected with equipment can be assured.

Abstract No. 411

INTEGRATION OF AUTOMATED REAL-TIME DI WATER MONITORING WITH THE IC MANUFACTURING PROCESS

J. Seaton, D. Grossman, and S. Becker

Honeywell Solid State Electronics Division
Research and Development Center
12001 Highway 55
Plymouth, Minnesota 55441

To achieve a controlled IC manufacturing process, all important variable inputs must be either controlled themselves, accounted for by the adjustment of other variables, or continually monitored so that processing may be halted should they exceed specified limits. The importance of ultra-pure DI water as a variable in IC manufacturing is well established. Of equal importance is the integration of the information collected from the DI water monitoring system with the IC manufacturing process.

Implementation of an integrated DI monitoring/IC manufacturing system should proceed through the following stages:

- Determination of significant variable inputs
- Establishment of real-time monitoring capabilities for each variable
- Assurance that monitors are run under statistical control with adequate precision
- Establishment of real-time display and analysis
- Implementation of data archiving

Significant DI water variables for IC processing might include resistivity as well as silica, total oxidizable carbon (TOC), and particle levels. Automated real-time monitoring is essential since the lag time associated with grab samples and laboratory analysis precludes the immediate use of the data for ongoing processing decisions and grab sampling frequencies can not follow the faster variable fluctuations. Interfacing of the monitoring equipment to computers permits the implementation of automated statistical control as well as data collection, display, analysis and archiving.

Not only contaminant level data but also data representing the performance of the monitoring equipment (i.e. the results of automated calibration/ standard checks) must be collected and analyzed in real-time. Continual analysis of this performance data by statistical process control techniques can insure the reliability of analytical results. Control charts for individual calibration measurements or calibration subgroup ranges have proven useful for this purpose. Control charts and other statistical tools can also be used to insure that the measurement pecision meets the important criterion of being significantly less than the variability of the measured input. Figure 1 shows such a chart for the periodic calibration check of an automated DI water silica analyzer. The 3-sigma statistical control limits are shown on either side of the process average. Only when the calibration checks fall within these limits can the analytical results be reliably used for processing readiness decisions. Correlation of processing problems to contaminant levels, specification setting, and control of the water purification process. In this example, data collected between periodic checks 300 and 325 could be used for processing decisions only with caution since the measurement process was out of control at that time, as evidenced by the points lying beyond and repeatedly near the 3-sigma limits. Equipment adjustments at periodic check 170 led to improved measurement precision as indicated by the tightening of the 3-sigma limits.

The configuration of DI monitors, PC and facility computer used at Honeywell to integrate the automated DI water monitoring process into the manufacturing process are illustrated in Figure 2. Analytical results are collected from the monitoring equipment and organized in real-time by the PC. A continuously updated display on the PC screen and pre-set alarm levels are used to control IC processing by immediately notifying the operators when levels are approaching or have exceeded the levels at which processing must be halted. Trends are easily observed by using a graphical display of current and previous variable levels (see Figure 3). Statistical control charts for the monitoring equipment can be automatically updated and displayed to insure the integrity of the measurement process.

Data are also transferred to the facility computer for further analysis, historical data file compilation and distribution to system users. These historical files and the statistical capabilities of the larger computer have proven useful for correlating DI water contaminant levels to processing problems. Such correlations form the basis for rational DI water contaminant specifications. New specifications are fed back to the IC processing area in the form of revised alarm and warning levels. Through this process, the IC manufacturing technology dependence of processing DI water specifications is elucidated and reliance on third party specifications is avoided. Figure 4 illustrates some historical DI water TOC levels collected at Honeywell with the high frequency sampling capabilities of the automated monitoring and data collection system. This data led to a correlation between TOC levels and wafer hazing during wet chemical processing. Revisions of processing DI water specifications could then be made to eliminate the problem.

Automation and integration of the DI water monitoring process into the IC manufacturing process resulted in a more fully controlled IC process and nearly $100,000 in annual system monitoring cost savings due to a reduction in labor and off-site analytical fees.

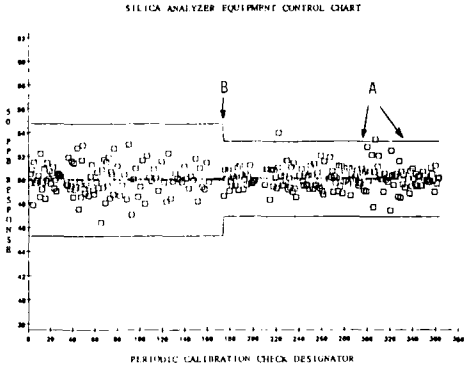


Figure 1 Statistical equipment control chart used to monitor the variation in the performance of an on-line DI water silica analyzer. Data collected in period A is suspect since calibration checks fall outside and repeatedly near the 3-sigma lines. Adjustment of the monitoring equipment at B resulted in improved measurement precision as evidenced by the tighter control limits.

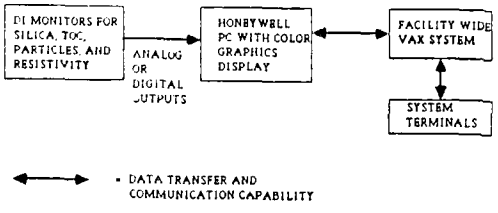


Figure 2. Schematic illustration of the linkage between monitoring equipment, PC, VAX and terminals.

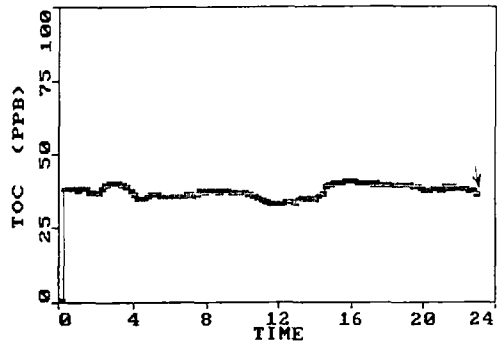


Figure 3. PC display screen illustrating the real-time display capabilities achieved by interfacing the PC to the process monitors. The final point of the line (see arrow) represents the current level of TOC in the processing DI line.

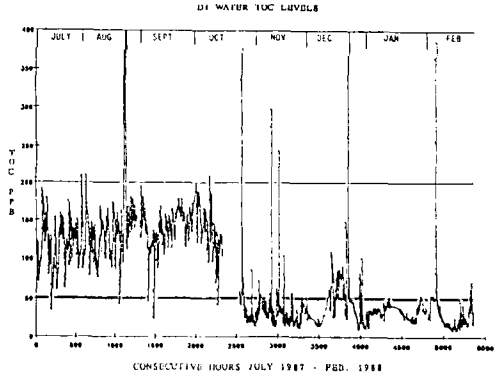


Figure 4. DI water TOC levels over several months. This graph was constructed from data collected by automated DI water analysis equipment and archived on the facility VAX computer. As noted, higher levels corresponded to periods of observed wafer hazing during wet chemical processing.

Abstract No. 412

Image Processing for Wafer Identification

Makoto Fukuda

NTT, LSI Laboratories

3-1 Wakamiya, Morinosato, Atsugi-shi, 243-01,Kanagawa-pref., Japan

1 Introduction

The recent ASIC manufacturing requires the individual level wafer control in order to correspond to product variability increase. Automatic wafer identification is a key technology for individual wafer control in automatic ASIC manufacturing.

The conventional wafer identification technology has been incapable of obtaining sufficient mark contrast on inscribed surfaces after such wafer processing steps as deposition and etching. This is because mark surface topography changes significantly after the processing steps. Therefore, in-process wafer identification requires more basic approach to provide sufficient contrast. In this paper, an image processing system with a diffraction grating mark and circular illuminating light is proposed. The system achieves sufficient contrast for in-process wafer identification.

2 Mark Contrast

There are two ways to obtain scribed mark contrast: one is using a diffused reflection from irregularly scribed surfaces, as with a laser scribing mark; the other is using a diffracted reflection from periodical grating marks(Fig.1). It is difficult to obtain sufficient contrast for the diffused reflection method because the reflected surface direction changes with thin film deposition in LSI process. On the other hand, the diffracted reflection method may enable the mark contrast to be controlled because the reflected direction doesn't change even after etching or deposition in LSI process. The reflected direction from the grating mark depends on only the grating pitch which doesn't change with the etching and deposition. Thus the diffraction grating mark is useful for in-process wafer identification.

It is difficult to obtain mark contrast accurately from optical characteristics of marks(reflection, absorptive properties), light sources(wavelength, illuminating power, illuminating time) and detectors(sensitivity etc.). In this paper, a camera signal is used as mark brightness, the brightness at a point is defined by the average of 4 points on neighboring image pixels. Mark contrast signal(MCS) is thus defined as follows; MCS=(Imax - I)/Imax (%), where Imax is the maximum brightness in a considered mark area, I is the considered point brightness. MCS represents an index of the contrast on an image taken by a camera and it changes with factors such as illuminating power and time.

3 Image Processing

Image processing consists of image input, orientation-flat detection, mark reading, and result output(Fig.2).

Figure 3 illustrates the image input system. This consists of a CCD camera and a circular illuminating light. Infrared LEDs are used in the circular light to avoid resist exposure. The combination of a diffraction grating mark and circular illumination relieves the mark direction constraint. The position of the orientation-flat on a wafer-circumference is detected by a circular mask search method. In this method, a wafer-circumference curvature is detected by a circular mask on an input image(Fig.4). Orientation flat position and its direction are obtained from the curvature information. In the mark reading process, a floating threshold level resolves the brightness change problem caused by different wafer surface conditions. The host machine typically receives the wafer identified data through an RS232C interface.

4 Experiment

A mark contrast change with wafer rotation was measured using the system and the contrast change was confirmed to be within 10% in a complete rotation, which leads to the advantage of identification without mechanical orientation alignment.

Figure 5 shows the relationship between MCS and LED current and it is found that MCS increases LED current.

The mark contrasts was measured in various samples on which a diffraction grating mark was etched in bare Si surface and SiO_2 film or Al film were deposited. The results indicate that the mark contrast is not greatly influenced by a thin film deposition (Fig.6). Furthermore, it was ascertained that the identification rate was obtained more than 99% even for bare Si with about 45% MCS. The diffraction grating mark provides sufficient contrast for mark reading in thin film deposited wafers. Total identification time, from wafer arrival to reporting the identificated data, is less than 2 seconds.

5 Conclusion

In-process wafer identification has become very important in custom or ASIC semiconductor manufacturing. MCS which is an index of a contrast is useful to evaluate an identification system. The combination of a diffraction grating mark and circular illumination provides a sufficient mark contrast for wafers undergoing etching and deposition processes. The developed wafer identification system makes it possible to effectively read identification marks without mechanical positioning and alignment.

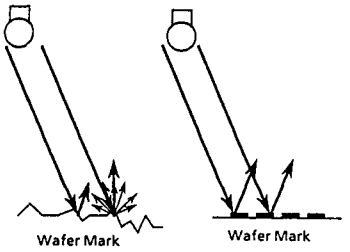


Fig.1 Mark Contrast

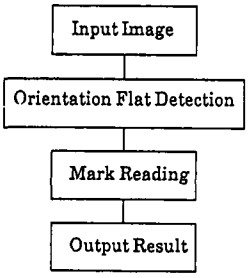


Fig.2 Wafer Identification Process

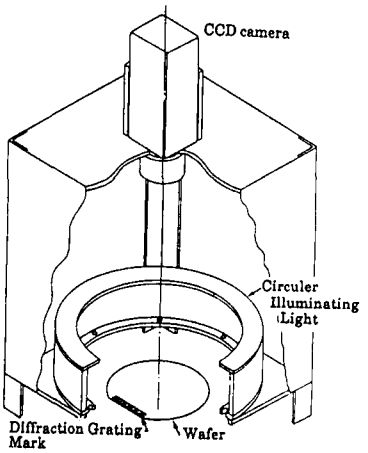


Fig.3 Circular Illumination and Image Input System

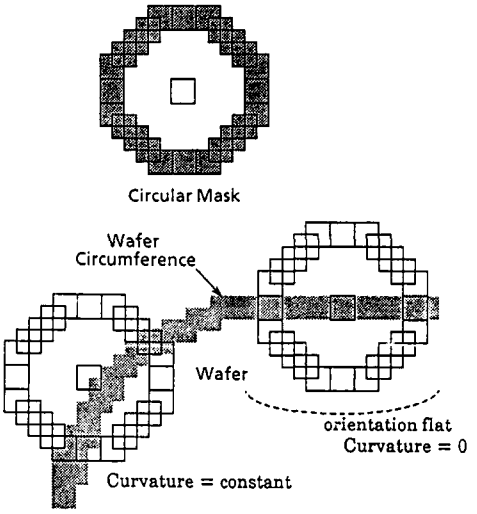


Fig.4 Orientation Flat Detection

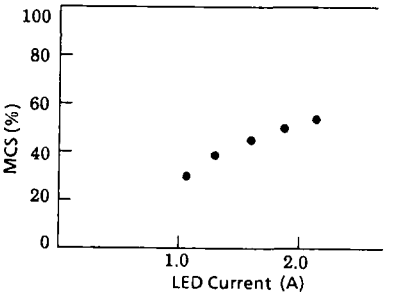


Fig.5 MCS change by LED power change (bare wafer)

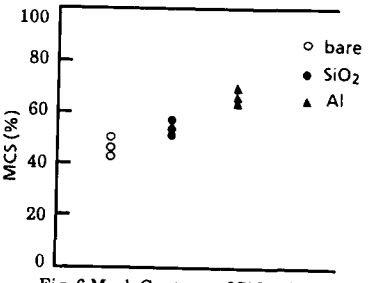


Fig. 6 Mark Contrast of SiO_2, Al Film (LED current = 2.0A)

Abstract No. 413

IN-PROCESS MONITORING BY AUTO FOCUS SIGNAL OF STEPPERS

N.Shimizu, H.Ikubo and H.Kozawa
Process Development Div.
Fujitsu Limited
Kawasaki Japan

This is reported on the process of development of a stepper-aligner system which can monitor wafer flatness during exposure and its effect. As developing from 1M to 4M and 16M, finer pattern are required, the numerical aperture(NA) becomes lager and depth of focus(DOF) of steppers becomes shallower. DOF is more than 4 micron meters for 1M-DRAM at present, but it is required to be less than 2 micron meters for 4M-DRAM. The origin of wafer flatness during exposure are resist and wafer thickness variation over topography surface, mechanical setting and flatness of vacuum chuck, and contamination of wafer back side. This warp causes focus error and should be as small as possible. This system we developed can monitor the warp such as stated above in realtime and will effectively help to cut down the focus trouble in production line.

[INTRODUCTION] Recently, as the integration of devices increase finer patterns are required more and more. In order to achieve higher integration the precision controll becomes more important in each process. Also in photo-lithography, NA of lens becomes lager, the DOF becomes severely shallower. Thus precision controll is required not only for optical system but also for chuking condition. Deposited films especially such as silicide make wafer warp by inner stress and nowadays even chuck structure(or method) have to be considered. We have evaluated the ability of our system by having investigated the influences of the warp of chucks and deposited films by means of measurment of flatness.

[SYSTEM] The developed system consists of stepper-aligner and personal computer. The stepper is positioned with X-Y stage and ajust the focus by using signal from auto-focus system, then wafer is exposed by opening the shutter. This stepper is partly reformed in order to take out the Z-axis stage signal and the shutter signal. The Z-axis stage signal means position signal of Z-axis which follows to wafer warp by auto-focus system. Thus wafer setting condition can be measured by sampling the stage signal. When shutter is opening, the personal computer picks up this position signal of Z-axis and converts these signal from analogue to digital. We can get necessary information by various processing of data.

[EXPERIMENT]
1 CHUCK EVALUATION We have applied this system to characteristic evaluation of some chucks. Stored data are not inspected one by one, but fitted by least square method and indicate the contour map in order to obtain the profile of wafer surface. The relation between wafer warp level and chucking condition is easily obtained by this method. This method provides the information of, not only chuck efficiency but setting conditions. Figure 1 shows tipical example.

2 DEFOCUS We have investigated the influence of defocus caused by wafer warp. Figure 2 shows maximum difference of depth of eight neighbor shots. Maximum difference of depth of them is smaller than depth variation in the shot. Therefore, if this value is smaller than the value of DOF determined by optical system, a focus error would not occur. If otherwise, there would be possibilities of some errors.

3 PRODUCTION CONTROLL We have analyzed statistically by considering the data of fifty wafers. The horizontal axis in figure 3 is the wafer number and the vertical axis is maximum value shown in experiment 2. If the dash-doted line in this figure shows maximum tolerance level and where is beyond this level, the warning signal could be generated. Checking this trend chart, We can grasp the tendency of change of slope, warp, and setting conditions. It will help to find the origin of errors, we can prevent a trouble from occurring previously.

[CONCLUSION] The follwing conclusion can be drawn.
1 This system provides the data of flatness of wafer under chucking and can be used to evaluate not only wafer flatness but also the configuration of vacuum chack stage.
2 Setting condition are easily tested and the ajustment will be done in short time.
3 For DOF of optical system which will be shallower in future, this system can be used to detect the defocus effectively during exposure.
4 It is a recent tendency that the production controll is based on statistical analisys, and thus this system can be used as a gathering tool of the wafer flatness data for such statistical controll system.

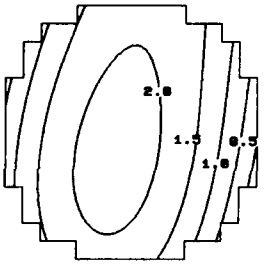
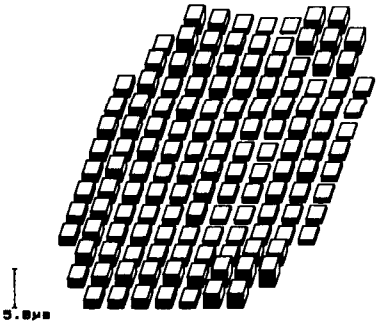
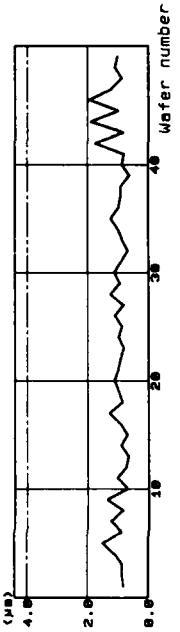


Fig.1 Chucked wafer profile (um)



		1.8	1.3	0.6	0.2	0.2	1.6	1.6	
	0.8	1.9	1.3	1.1	0.8	0.4	1.6	1.6	1.6
	1.5	1.3	1.4	1.1	1.1	0.9	0.6	1.4	1.4
0.9	1.6	0.8	0.9	0.9	0.9	0.9	0.8	0.4	0.6	0.6
0.9	1.4	0.9	1.1	0.6	0.7	0.7	0.9	0.9	0.8	0.6
1.2	1.3	1.1	0.6	0.7	0.7	0.9	0.7	1.0	0.7	0.2
1.0	1.1	1.2	0.8	0.7	0.6	0.6	0.4	0.9	0.8	0.7
1.0	1.6	0.9	0.6	0.7	1.1	0.7	0.5	0.9	1.1	0.7
0.9	1.3	0.9	0.8	0.7	1.1	0.8	0.7	0.9	0.7	0.5
1.0	1.6	0.7	0.6	0.6	1.0	0.6	0.5	0.7	0.6	0.5
1.0	1.6	1.0	1.0	0.7	0.6	0.5	0.5	0.8	0.6	0.6
	1.6	1.3	0.8	1.0	1.0	0.8	0.9	1.6	1.6	
	1.0	1.3	1.5	1.5	1.6	1.3	2.1	2.1	2.1	
		1.1	1.1	1.2	1.0	0.8	1.8	1.8	

Fig.2 Maximum defference of depth of eight neighbor shots (um)



Maximum defference of depth of eight neighbor shots

Fig.3 Change of the wafer setting conditions

Abstract No. 414

Compositional Mapping with the Electron Microprobe and Secondary Ion Mass Spectrometry

Dale E. Newbury, Ryna B. Marinenko, David S. Bright, and Robert L. Myklebust

Center for Analytical Chemistry
National Bureau of Standards
Gaithersburg, MD 20899

Microbeam analysis techniques such as electron probe microanalysis (EPMA) and secondary ion mass spectrometry (SIMS) are traditionally used for quantitative elemental analysis at single beam locations ("point analysis") or along vectors of points [1]. These point analyses are often augmented by images of the specimen which give some indication of the spatial distribution of the elemental constituents. Images can be prepared from non-characteristic signals, such as backscattered electrons in the EPMA and ion-induced secondary electrons in the ion microprobe, or from signals which are characteristic of specific elements, such as x-rays in the EPMA or secondary ions in the SIMS instruments. For scanning beam instruments, the technique of "dot mapping" is widely used to produce images with characteristic signals. Because of the relative paucity of signal, the dot written on a cathode ray tube (CRT) scanned in synchronism with the specimen is intensity-modulated to full brightness whenever a characteristic event is detected. This display is then photographed onto film to produce the final image. While powerful, dot mapping suffers from several severe drawbacks: (1) The intensity range is one bit ("off-on"), and no continuous gray scale information is available. (2) The count rate at each beam location, which is the basic information needed for quantification, is lost in the recording process, and therefore the images are qualitative in nature. (3) Dot mapping has limited sensitivity, about 1 weight percent of a constituent in the best case for the EPMA, and has very poor contrast sensitivity. Although the sensitivity of SIMS is much better, often in the parts per million or parts per billion range, the dot maps are still subject to limitations on the contrast. (4) The image in the form of a photograph is not amenable for subsequent processing. In the direct imaging ion microscope, the secondary ion signal is converted at an imaging detector into a display which may be photographed or viewed by means of a television camera. These direct ion images are again qualitative in nature, because the fundamental information on the count rate is lost in the recording process.

The technique of compositional mapping overcomes most of the limitations of qualitative imaging by dot mapping or direct ion imaging. In compositional mapping a complete quantitative analysis is performed at each location in an image. The final image is constructed in a digital image processor with a gray or color scale which is determined by the actual concentration of a constituent and not merely the raw signal from the spectrometer. The strategy for making these image arrays of quantitative analyses differs according to whether EPMA or SIMS is used [2,3].

In EPMA, the x-ray count rates for each element of interest are recorded in a computer memory from the wavelength-dispersive and/or energy dispersive spectrometers as the beam is digitally scanned in a matrix pattern. All of the steps necessary for conventional quantitative analysis are performed: deadtime correction, background correction, standardization relative to pure element or compound standards, and matrix correction for atomic number, absorption, and fluorescence effects. In addition, special procedures must be applied to correct for instrumental artifacts such as spectrometer defocussing [2]. The procedure for background correction must also account for the special conditions imposed by the act of scanning the beam [4]. After all corrections have been applied, the matrices of raw count rates are converted into matrices of elemental concentration values. For maps with a digital density of 128x128, the data recording time is approximately 1 hour for major constituents (> 10 weight percent) and 10 hours or more for trace constituents (500 parts per million). Computer calculations to quantify the data require less than 5 minutes.

The quantitation procedure in SIMS uses the method of relative sensitivity factors. The relative sensitivity factor is a ratio of measured instrument response on one element compared to a reference element, where both elements co-exist in a known multielement standard. By means of this factor, the ratio of measured intensities for the same two species in an unknown can be converted into a ratio of concentrations. This procedure is carried out on a pixel-by-pixel basis in the digitized ion images to yield the compositional maps. Different procedures for digitization of the ion images are used in the ion microprobe and ion microscope. In the ion microprobe, the ion count rate at each beam position can be digitized directly from the pulse-counting multiplier detector. In the direct imaging ion microscope, a true mass-filtered secondary ion image is produced. The analytical strategy requires first that the ion intensity measured at the image detector be converted into the equivalent ion count as detected at the pulse counting electron multiplier [3]. The individual ions which comprise the image may be counted with a positionally sensitive direct-to-digital detector such as the resistive anode encoder [5], or the ion signal may be converted to light at a phosphor screeen and viewed with a TV camera. For the TV camera images, conversion to ion counts is accomplished by means of a calibration curve determined on a homogeneous target. Experiments have shown that the imaging detector response curve depends strongly on the specific ion species, so that an appropriate response curve must be determined [3]. The light intensity measured by the TV camera is digitized by computer and converted into equivalent ion counts with the response curve.

Once the compositional maps have been determined by EPMA or SIMS, the concentration data can be converted into images by assigning a gray or color scale to the numerical values and displaying the result on a digital image processor. In this digital form, computer-aided imaging techniques can be used to enhance the contrast of the chemical microstructure to render it more easily visible to an observer. A wide variety of image processing functions is available for this task, including several developed specifically for microstructural analysis [6]. The great power of compositional mapping derives from this combination of the image information, where spatial inter-relationships can be readily recognized, and numerical concentration data (with the statistics of measurement) available at every pixel for subsequent interrogation.

The EPMA and SIMS compositional mapping techniques are mutually complementary, with the weaknesses of one being offset by the strengths of the other. EPMA offers highly accurate quantitation (+- 2% relative) with simple elemental standards and a wide variety of associated morphological and structural imaging techniques. However, it has poor sensitivty for elements below atomic number 11, and is inherently a slow process. Trace level images at sensitivities of a few hundred ppm require 10 hours or more. SIMS provides extraordinary sensitivity in the ppm or ppb range for many elements, with especially good sensitivity for the light elements. Trace level images can often be obtained in 10 seconds. Quantitation of SIMS images is subject to far greater uncertainties than EPMA. By applying a combination of EPMA and SIMS compositional mapping, many problems in materials science can be solved.

References:

1. J.I. Goldstein, D.E. Newbury, P. Echlin, C.E. Fiori, and E. Lifshin, "Scanning Electron Microscope and X-ray Microanalysis" (Plenum, New York, 1981).
2. R.B. Marinenko, R.L. Myklebust, D.S. Bright, and D.E. Newbury, J. Microscopy, v 145 (1987) 207.
3. D.E. Newbury and D.S. Bright, Secondary Ion Mass Spectrometry VI (in press).
4. R.L. Myklebust, D.E. Newbury, R.B. Marinenko, and D.S. Bright, Microbeam Analysis-1987 (San Francisco Press) 25.
5. R.W. Odom, B.K. Furman, C.A. Evans, C.F. Bryson, W.A. Petersen, M.A. Kelly, and D.H. Wayne, Anal. Chem. v 55 (1983) 574.
6. D.S. Bright, J. Microscopy, v 148 (1987) 51.

Abstract No. 415

Neutron Activation Analysis in Electronic Technology

Richard M. Lindstrom
Center for Analytical Chemistry
National Bureau of Standards
Gaithersburg, Maryland 20899

Neutron activation analysis (NAA) is one of a number of methods of elemental analysis that have been applied to the characterization of silicon and other materials important in the electronics industry. With the ready availability of high-purity silicon, little characterization of substrate material needs to be done, by NAA or other methods, for the fabrication of present-day microcircuit devices. As the density of devices increases, however, higher material purity will become necessary for good yield, so that there will continue to be a need for increasingly sensitive analytical techniques to solve research and production problems. It is the purpose of this paper to point out some recent nontraditional applications of NAA, as well as to discuss its use in general.

Neutron activation and other nuclear methods of analysis offer a number of differences from methods based on chemical reactions or other atomic phenomena. Some of these differences are advantageous in solving research and development problems:

1.
The combination of simple physics and highly penetrating probe and indicator radiations make NAA substantially free from systematic errors related to the chemical nature of the sample. Interfering nuclear reactions can be enumerated by inspection of a table of nuclides. Interferences can be detected and corrections made whenever, as is often the case, multiple activation products or multiple gamma lines are available. Qualitative identification of nuclides from gamma ray energies gives assurance that the nuclide measured is indeed the one intended.

2.
Nuclear methods are complementary to atomic methods in that the physical phenomena and experimental procedures employed are so different that common sources of systematic errors are improbable. For example, if NAA and atomic absorption spectroscopy agree, it is probable that both are correct.

3.
NAA is free from reagent blank and other problems related to sample dissolution. Many major elements used in electronics -- H, C, N, O, and Si -- produce little or no radioactivity on neutron irradiation so that matrix interferences are small. Even when post-irradiation radiochemical separations are performed to free the nuclide of interest from a radioactive matrix, contamination by stable isotopes of the sought-for element is unimportant.

4.
Since radioactive decay and detection are digital processes, an estimate of the analytical precision is obtained from the Poisson statistics of counting. A simple t test between duplicates shows whether there are additional random errors in the measurement process.

5.
As many as twenty elements can be determined in a single sample. A gamma ray spectrum contains lines from all gamma emitters present, ensuring that no components are overlooked because they were not searched for.

6.
Finally, neutron activation analysis is one of the few methods available with sufficient sensitivity for determinaing picogram quantities of many elements.

The broad elemental coverage, nondestructive nature, and high sensitivity of NAA have made it useful for bulk analysis, and also for some specialized problems. The most common application of neutron activation to electronics materials has been the measurement of trace (μg/g) and ultratrace (ng/g) concentrations of impurity elements in bulk silicon and other materials. Applications have been made to the determination of minor (percent) and major components as well, and to the analysis of thin films.

Abstract No. 416

BACKSCATTERING SPECTROSCOPY FOR SEMICONDUCTOR MATERIALS

Joseph A. Keenan
Materials Science Laboratory
Texas Instruments, Inc.
P.O. Box 655936, M/S 147
Dallas, Texas, 75265

Physical and chemical diagnostic techniques seek to explain the electrical properties of semiconductor material from an atomic perspective. Such direct measurements are often less sensitive to defect structure than actual device parameters due to their finite spacial resolution and sensitivity. Therefore synergistic use of physical, chemical and electrical diagnostics is normally required for an understanding of the role of materials in device performance. The cross correlation of physical, chemical and electrical data to explain device performance requires an understanding of the strengths and limitations of the various diagnostic techniques. The purpose of this paper is to provide the required perspective for synergistic use of data from backscattering spectroscopy.

Backscattering spectroscopy measures the masses of impurities, the depth distribution of impurities and the stoichiometry of compound layers [1]. For helium backscattering quantitative results are derived from fundamental physical principals and well known parameters such that five percent accuracy is attainable without standards. Channeling experiments probe the depth distribution of disorder and the lattice position of impurities. Extremely accurate and sensitive surface analysis is also possible using backscattering spectroscopy. Finite mass resolution and poor sensitivity for light elements in a more massive matrix are the primary weaknesses for backscattering spectroscopy.

Since the depth scale for depth profiles is based upon a knowledge of stopping powers rather than ion sputtering rates, buried interfaces are less likely to be distorted using backscattering depth profiles. Moreover, the backscattering cross sections do not exhibit matrix dependence. Therefore multilayer depth profiles can be done without complex calibration for each type of layer. An example of the depth profile for a multilayered molybdenum-copper metalization scheme is shown in Fig. 1.

The extraction of diagnostic information from backscattering spectroscopy requires expert interpretation of the data and clear presentation of that interpretation [2]. There is a need for communication between experts in device performance and the expert in backscattering spectroscopy which can be satisfied in part through computer programs. Interpretation of a backscattering spectrum faces a critical ambiguity because the energy axis is a convolution of the distribution of masses and depth distributions of masses. Therefore, there is not a unique explanation for any one backscattering spectrum. Since backscattering spectroscopy is a diagnostic technique with a firm basis in physical principals and well known parameters, model spectra can be readily computed [3,4]. The accuracy of model specira is clear when they are used to predict results and design experiments. Because of the mass/depth distribution ambiguity a high quality of fit between a model spectrum and an experimental spectrum is a necessary condition for the validation of sample analysis but it is not a sufficient condition [5].

[1] W.K. Chu, J.W. Mayer and M.A. Nicolet, Backscattering Spectroscopy (Academic Press, New York 1978).

[2] P.A. Saunders and J.F. Ziegler, Nucl. Instr. Meth. 218 (1983) 67.

[3] L.R. Doolittle, Nucl. Instr. Meth. B9 (1985) 344.

[4] E. Norbeck, L.W. Li, H.H. Lin, and M.E. Anderson, Nucl. Instr. and Meth. B9 (1985) 197.

[5] E. Rauhala, J. Appl. Phys. 62 (5) (1987) 2140.

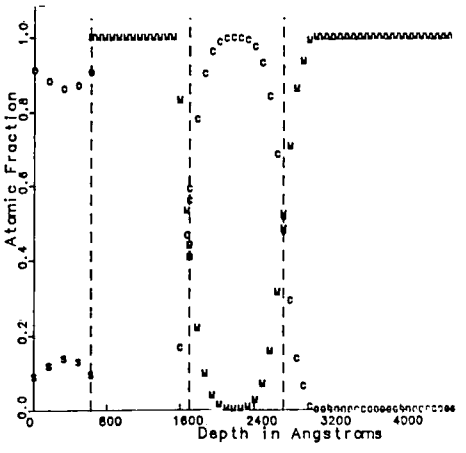


Fig. 1 A depth profile derived from a backscattering spectrum. The layers are silicon dioxide(2.32 g/cc), molybdenum(10.2 g/cc), copper(8.96 g/cc), and molybdenum. Layer thicknesses were selected to allow the mass resolution needed to study interdiffusion.

Abstract No. 417

HYDROGEN IN THIN FILMS

W. A. Lanford
Physics Department
SUNY Albany
Albany, New York 12222

The role of hydrogen in thin films is discussed and illustrated. The fact that hydrogen is commonly present, very mobile, and chemically active, results in hydrogen having many interesting effects on the properties of thin film materials, including changes on the electrical, chemical, physical, and mechanical properties of some films. Nuclear reaction analysis for hydrogen is described and examples of the various effects hydrogen can have are briefly illustrated.

Until recently, analysis for hydrogen in materials, especially thin film materials, has been notoriously difficult; most traditional methods of analysis are *blind to hydrogen. Because of this, the* possible presence and effects of hydrogen in materials had been largely ignored. However, with the development and utilization of nuclear reaction analysis (NRA) and improved methods of secondary ion mass spectrometry (SIMS), hydrogen has *become the focus of a wide range of studies* in a variety of materials. From these studies, it has become apparent that hydrogen plays a number of unique and *interesting roles deserving increased* attention.

In retrospect, the features that make hydrogen unique and interesting are not very surprising.

First, experience of the last decade indicates that hydrogen is a very common contaminant, perhaps the most common elemental contaminant. This is especially true when *considering* thin film materials which are made by vacuum deposition (where most of the residual gases in the deposition contain hydrogen), or chemical vapor deposition (where hydrogen containing carrier gases are universally used) or by electrodeposition (where solutions of hydrogen containing liquids are used). Even films that are grown without hydrogen often become "contaminated" upon brief exposure to air (or poor vacuum, during transfer to another chamber.

Second, in most solids, hydrogen is by far the most mobile element by many orders of magnitude. For example, the room temperature diffusion coefficient for hydrogen in many metals is on the order of 10^{-5} cm^2/sec, which is typically 10 to 20 orders of magnitude larger than the diffusion coefficients for other common contaminants such as C, N and O. This large diffusion coefficient means that if hydrogen is available at the surface of a material, it is often available throughout the bulk in very short times. Hence, in some situations, one should consider hydrogen as one of the components of the material, not simply as a possible contaminant.

Third, the hydrogen atom is chemically very versatile. If it either takes up one electron or gives up one electron, its atomic electrons form a completely full or a completely empty major shell. Hence, it is happy to react with elements on either side of the periodic table of the elements. In electronic sense, that means hydrogen can be either a donor or acceptor; in a more general materials sense, that means that hydrogen will readily react with most any dangling bond.

Because of the above, hydrogen has effects on a remarkable range of material *characteristics including:* effects on the electrical properties of semiconductors (e.g. passivating electrically active dopants in crystalline semiconductors), effects on the mechanical properties of metals (e.g. hydrogen embrittlement), effects on the chemical properties of plasma deposited materials (e.g. the relationship between etch rate and hydrogen content of plasma deposited silicon nitride), effects on transport properties of atoms in solids (e.g. the dramatic decrease of electromigration and interdiffusion of metals in hydrogen gas), and the ability of hydrogen to "terminate" surfaces or interfaces. The above is but a partial list; others in the field would likely suggest a different group of generic effects as well as different specific examples.

Nuclear reaction analysis for hydrogen will be briefly described along with some of the examples listed above.

Abstract No. 418

ACCELERATOR MASS SPECTROMETRY OF ELECTRONIC MATERIALS

J. M. Anthony
Materials Science Laboratory
Texas Instruments, Inc.
Dallas, Tx. 75265

Accelerator Mass Spectrometry (AMS) has become the method of choice for measurements of isotopic ratios in solid samples at abundance sensitivities below 1 ppb. Originally proposed as a possible alternative to conventional beta decay counting for carbon dating of small samples (1,2), AMS has evolved significantly in the last decade, and now includes applications in a variety of disciplines including archeology, hydrology, oceanography, etc.(3) The method utilizes high energy particle acceleration techniques to remove common sources of interference and background present in conventional mass spectrometers and involves several stages, including ionization, acceleration, analysis and detection steps.

To date the technique of AMS has been applied almost exclusively to the study of radioisotopes, primarily due to an interest in using isotopic ratios as chronological markers in a variety of fields. The results of these works have been quite impressive, with removal of all typical sources of mass spectrometric interference (molecular ions, multiply charged particles, scattered ions, etc.) as well as demonstrations of ratios as low as $5x10^{-16}$ in some cases(4). The method in principle is applicable to the study of stable elements as well as radioisotopes, but these applications have not been extensively explored yet. A method of impurity detection in solid samples with detection limits in the parts per trillion (ppt) range and no sources of spectral interference would have immediate application in a variety of fields, including electronic materials.

A schematic for a typical AMS system is shown in Fig. 1, which is a diagram for the NSF Regional Facility for Radioisotope Dating at the Univ. of Arizona. Most AMS instruments consist of 5 sections, including 1) a method for producing negative ions from the sample of interest, 2) a pre-injection analysis (typically through momentum analysis by a magnet) to remove unwanted beams generated during the initial ionization process, 3) acceleration and charge exchange during passage through the tandem accelerator, 4) post-acceleration analysis of the resultant positive ions, and 5) detection of the surviving ions. Optimization of each stage is important for effective stable element analysis.

During the acceleration stage injected negative ions are accelerated by the high voltage at the center of the tandem at which point they pass through either a thin C foil or a region of moderate gas pressure. Several electrons are stripped from the negative ions through collisions in the stripper region and the resultant positive ions are accelerated away from the high positive potential, gaining an energy QeV after stripping, where Q is the particle charge state, e is the electronic charge, and V is the terminal voltage. This step removes the most common sources of interference in conventional mass spectrometers. For instance, molecular ions with charge states >2 (and = 2 in some cases(5)) are unstable due to Coulomb repulsion, and post-analysis of ions with Q>2 guarantees the absence of molecular peaks in the spectra. Analysis of the molecular fragments is possible but their kinematic properties will now be different (in almost all cases) from the elemental ion of interest.

Table I lists the results of several studies of stable element impurities in materials using AMS. The terminal voltage used for these measurements was <3 MV in all cases. At present the detection limits are defined by impurities deposited on the sample during the sputtering process, and a redesign of some ion source components is necessary to achieve ppt level detection.

In principle this technique is also capable of depth profiling, similarly to SIMS, by monitoring the detected count rate as a function of time as the sputtering beam erodes the sample. This capability has been investigated at the University of Arizona facility by analyzing a 5 um thick Ge doped Si layer on a Si substrate(6). Fig. 2 shows the results of both SIMS (as measured on a Cameca IMS-3f system) and AMS profiles of the mass 72 signal. The AMS data show the expected Ge level ($\sim 2.8x10^{17}$) in the layer, while the SIMS signal is dominated by the presence of an $^{28}Si_2O$ molecular interference. The slight signal due to the Ge doping can be seen in the top 5 um. The slow fall of the AMS Ge signal is due to interface smearing produced by the static Cs beam (the Arizona system does not have rastering capability for the incident Cs beam).

An instrument devoted to AMS would appear to be increasingly competitive with SIMS instrumentation for analysis of stable elements in electronic materials. Detection limits < 1 ppb have been demonstrated, and ppt level capability is possible through careful attention to contamination sources. System efficiencies for AMS are comparable to SIMS in most cases, and will be substantially better than SIMS in the measurement of elements with significant mass interferences. Depth profiles of shallow and deep structures are possible without the complicated high mass resolution apparatus required on SIMS systems.

REFERENCES

1. R.A. Muller, Science 196, 489 (1977).

2. K.H. Purser et al, Rev. Phy. Appl. 12, 1487 (1977).

3. H.E. Gove et al, Ed., "Accelerator Mass Spectrometry", Nucl. Instr. and Meth. in Phy. Res., B29 (1987).

4. M. Suter et al, Nucl. Instr. and Meth. in Phy. Res. B10/11, 877 (1985).

5. G.E. Aardsma, Nucl. Instr. and Meth. in Phy. Res. A238, 170 (1985).

6. J.M. Anthony and D.J. Donahue, Nucl. Instr. and Meth. in Phy. Res. B29, 77 (1987).

7. R.J. Blattner et al, Secondary Ion Mass Spectrometry, Springer-Verlag, Berlin, 192 (1986).

Table 1. AMS detection limits
(contamination limited)

Element	Matrix	Concentration	
As	Si	$3x10^{14}$	(6)
Ge	Si	$5x10^{13}$	"
P	Si	$1x10^{14}$	"
Te	GaAs	$2x10^{15}$	"
B	Si	$3x10^{13}$	"
B	GaAs	$3x10^{13}$	"
Cr	GaAs	$2x10^{15}$	"
Au	HgCdTe	$3x10^{12}$	"
Sb	Si	$2x10^{14}$	(7)

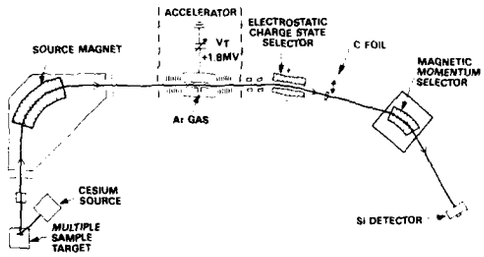


Fig. 1 - Schematic diagram of the experimental AMS apparatus at the Univ. of Arizona.

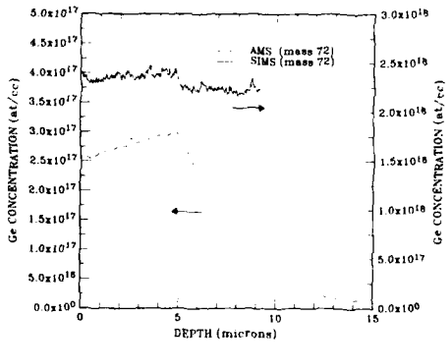


Fig. 2 - SIMS and AMS depth profiles of the mass 72 signal from a 5 um thick Ge doped Si epitaxial layer on an undoped Si substrate.

Abstract No. 419

Secondary Neutral Mass Spectrometry: The Application of Laser Post Ionization to Trace Surface Analysis in Semiconductor Materials *

M. J. Pellin, C. E. Young, W. F. Calaway,
J. W. Burnett, and D. M. Gruen

Argonne National Laboratory
Materials Science and Chemistry Divisions
Argonne, IL 60439-4831

I. **Introduction**. Contamination control in all aspects of semiconductor fabrication, beginning with the substrate materials themselves, continuing through various processing steps, and extending to the study of thin-film depositions, is crucial to the successful fabrication of ultra-large scale integrated (ULSI) circuits. As device sizes shrink both laterally and in depth, increasing strain is being placed on analytical techniques. The ability to analyze for trace impurities in small sample volumes (e.g., single monolayers with 10μ x 10μ lateral dimensions or 10^9 atoms total) is critically dependent upon two parameters - discrimination and useful yield. Discrimination allows the identification of part per billion (ppb) trace impurities against the large bulk signal. Useful yield is defined here as a total instrument transmission number - atoms detected per atom removed. High useful yields are required in order that analyses can be accomplished at trace levels of impurity atoms with minimal sample consumption.

Recently, significant research activity has been directed at the technique of Secondary Neutral Mass Spectrometry (SNMS).[1,2] This technique utilizes the secondary neutral sputtered fraction for analysis. SNMS under certain conditions can provide dramatic increases in both useful yield and quantitative analysis.[1-5] These increases are the direct result of the proclivity of the sputtering process to produce ground state neutral atoms rather than ions.[6] The detection of the major sputtering products allows for substantially higher useful yields.[3] This paper will center on the use of lasers to ionize and then detect the sputtered neutral particles.

Laser ionization of the neutral fraction of sputtered particles can be extremely efficient.[3-5] Moreover, in laser postionization SNMS the matrix dependence of the ionization process is removed allowing calibration in many cases to be much easier.[3] Basically, laser ionization SNMS can be grouped into two rather artificial divisions - resonant[3-8] and nonresonant[9] ionization. The terms, resonant and nonresonant, refer to the atomic absorption spectroscopy of the sputtered atoms. When at least one of the laser colors is carefully chosen to match an absorption frequency of the atom of interest, the measurement is referred to as "resonant." In this situation, much lower laser intensities are required and efficient ionization can be accomplished over relatively large laser volumes. Resonant laser ionization can be extremely discriminative with a single component of the sputtered flux alone being ionized. Nonresonant ionization is generally accomplished with an intense fixed-frequency laser. This process generally is less efficient and laser volumes need to be smaller in order to increase input intensities. With these caveats, even nonresonant ionization can for many elements achieve saturation.[10] Nonresonant ionization generally does not substantially add to the discrimination of the laser ionization SNMS mass spectrometer but rather ionizes to some extent all the constituents of the sputtered flux.

This paper emphasizes resonant laser ionization since trace surface analysis requires the enhanced discrimination and useful yield which this technique provides. Indeed, the removal of isobaric overlaps at the 500 ppt level has already demonstrated the inherent discrimination which resonance ionization spectroscopy laser ionization SNMS provides.[3,5,7] Furthermore, demonstrated sensitivity at the ≅100 ppt level with a noise equivalent level of >30 ppt indicates the power of these measurements.[8] This is not to imply that this method is the optimal choice for all analysis. Each technique has a particular set of advantages and disadvantages meaning that the technique of choice must be matched to the problem of interest. The SARISA technique is suited for analysis of this important class of analytical problems. The high useful yield and discrimination of SARISA has allowed Fe analysis of Si substrates at the 500 ppt level in a single monolayer.[3] The ability of SARISA to detect neutral atoms significantly reduces the artifactual effects of oxygen, and the use of resonance ionization eliminates problems with isobaric overlaps.

Depth profile studies of the concentration of ^{56}Fe in several different Si samples are displayed in Figs. 1 and 2. Before describing the samples themselves, it is useful to contrast the depth profiling method used in SARISA measurements as opposed to the method normally used in a SIMS experiment. Because SARISA measurement of the concentration of trace constituents is made with removal of only a small fraction of a monolayer, it is necessary to combine the pulsed ion beam techniques of SARISA measurement and a continuous but rastered ion beam for sample removal. Thus, the symbols displayed in Figs. 1 and 2 are individual concentration measurements made with a lateral area of 0.0225 mm^2 and with a removal of 0.1 ML at most. Between measurements a rastered ion beam (4 mm^2) was used to profile into the substrate, thus establishing the depth scale of the two graphs.

Figure 1 depicts the Fe concentration of an oxygen implanted Si sample. The implant dose was 2 x 10^{18} atoms/cm^2 at 170 keV. The sample was subsequently annealed at 900°C for 10 hrs. The Fe profile in this sample is quite interesting. First and foremost, the concentration of Fe in this sample is extremely high, peaking at 20 ppm. The shape of the impurity profile is also unusual. The dip in the concentration at 7 x 10^{-3} μ is near the native SiO_2/Si interface in this sample. Moreover, the Fe profile in the 10^{-2} to 10^{0} μ depth range closely follows the expected O_2^+ implant concentration.

If the Fe in the sample arrived during the high dose implant, one can determine that the efficiency of Fe atom arrival *per O* atom is about 10^{-5}. This is not an unreasonable amount to arrive from apertures in the implanter itself. Other processes might also be involved. The Fe impurity profile immediately following Fe introduction would be a high concentration located very near to the sample surface since low energy Fe atoms would not penetrate the sample surface. Subsequent annealing of the sample, however, may allow Fe atoms to freely diffuse in the Si substrate. The depth profile presented in Fig. 1 gives strong evidence that the Fe tends to migrate to O-rich regions.

The mobility of Fe in Si is demonstrated in Fig. 2. This sample was treated under identical conditions to one shown in Fig. 1 except for an additional step. This step was the growth of a 0.38 μ epitaxial Si layer. A shallow depth profile of this epitaxial region clearly shows the presence of a substantial Fe impurity content. This may be the result of the relatively low solubility of Fe in Si.

V. Conclusions. The usefulness of laser ionization sputtered neutral mass spectrometry has at present been clearly demonstrated in several laboratories. While a complex analysis tool, laser ionization SNMS provides at once a high useful yield and highly discriminative analysis technique which can provide unique analysis for many systems. The laser ionization SNMS tool represents a 2-3 order of magnitude increase in sensitivity for samples of limited size such as monolayer films. In the near future, we expect laser ionization SNMS to take its place among the specialized tools available to the analyst.

References

1. W. Reuter, in: Secondary Ion Mass Spectrometry (SIMS V), Eds. A. Benninghoven et al. (Springer, Berlin,1986).
2. U. Kaiser and J.C. Huneke, MRS Bulletin 48, August (1987).
3. M.J. Pellin, C.E. Young, W.F. Calaway, J.W. Burnett, B. Jorgensen, E.L. Schweitzer, and D.M. Gruen, Nucl. Instr. and Meth. Phys. Res. B18, 446 (1987).
4. J.E. Parks, H.W. Schmidt, G.S. Hurst, and W.M. Fairbanks Jr., Thin Solid Films 8, 69 (1983).
5. C.E. Young, M.J Pellin, W.F. Calaway, J.W. Burnett, B. Jorgensen, E.L. Schweitzer, and D.M. Gruen, Inst. Phys. Conf. Ser. No. 84,163 (1986).
6. D.M. Gruen, M.J. Pellin, C.E. Young, and W.F. Calaway, J. Vac. Sci. Technol. A4, 1779 (1986).
7. C.E. Young, M.J. Pellin, W.F. Calaway, J.W. Burnett, and D.M. Gruen, 4th International Symposium on Resonance Ionization Spectroscopy and Its Applications, Gaithersburg, MD, April 10-15,1988.
8. D. Hrabuchek, N. Winograd,4th International Symposium on Resonance Ionization Spectroscopy and Its Applications, Gaithersburg, MD, April 10-15,1988.
9. C.H. Becker and K.T. Gillen, Anal. Chem. 56, 1671 (1984).
10. C.H. Becker and K.T. Gillen in Secondary Ion Mass Spectrometry (SIMS V), Eds. A. Benninghoven et al. (Springer, Berlin, 1986), p. 85.

*Work supported by the U. S. Department of Energy, BES Materials Sciences, under Contract W-31-109-ENG-38.

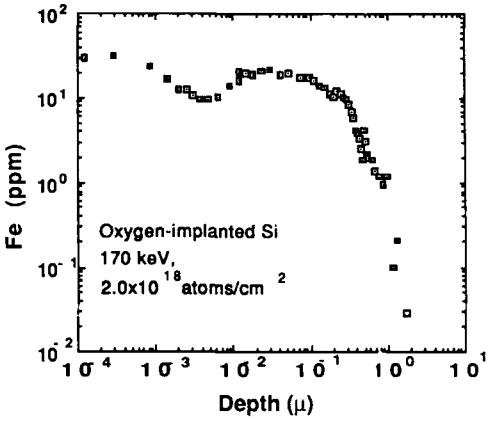


Fig. 1. A depth profile of the Fe concentration in a Si substrate. The substrate was prepared by an oxygen implantation at 170 keV of 2 x 10^{18} atoms per cm^2. Subsequently the sample was annealed at 900°C for 10 hrs. The surface silicon oxide layer was ≅78 x10^{-3}μ.

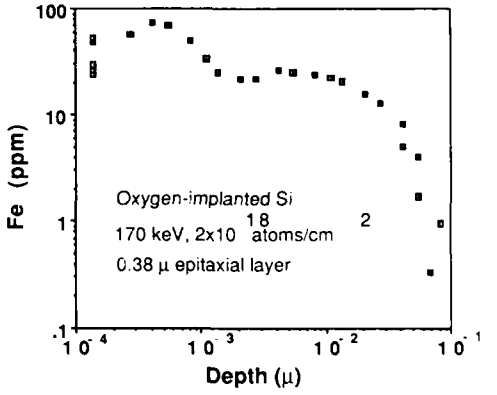


Fig. 2. A depth profile of the Fe concentration in a Si substrate. The substrate was prepared by an oxygen implantation at 170 keV of 2 x 10^{18} atoms per cm^2. Subsequently, the sample was annealed at 900°C for 10 hrs. Following annealing, a 0.38 μ thick epitaxial layer of Si was grown on the surface

Abstract No. 420

Quantitative Depth Profiling Analysis of Semiconductors and Superconductors by Secondary Neutral Mass Spectrometry (SNMS)

N. Kelly, U. Kaiser, and H. Peters

Leybold Inc.

1860 Hartog Drive
San Jose, CA 95131

In recent years, the need for a quantitative surface and thin film analytical technique has prompted progress in the field of Secondary Neutral Mass Spectrometry (SNMS). This technique involves the sputtering of the surface by ion bombardment, followed by post-ionization of the ejected neutrals. Since the sputtering and ionization processes are decoupled, matrix effects which are known to hinder quantitation in SIMS, are avoided. A high density plasma is used for sputtering in one mode of operation, providing a high sample current density. As a result, high sputtering rates may be achieved, even at very low sputtering potentials, thus minimizing problems such as ion-induced mixing and "knock-on" effects.

SNMS is ideally suited to the quantitative compositional analysis as a function of depth of $Al_xGa_{1-x}As$ material systems. Relative ion yields are found to be independent of the Al concentration, x. This technique is also very useful for the analysis of thin film and bulk superconductor materials. Recent results in these areas of application are discussed.

Abstract [illegible]

IMAGING SUBSURFACE INTERFACES BY BALLISTIC-ELECTRON-EMISSION MICROSCOPY

L. D. Bell and W. J. Kaiser
Jet Propulsion Laboratory
California Institute of Technology
Pasadena, California 91109

Semiconductor interfaces are of central importance in solid state physics and device technology. However, the experimental investigation of semiconductor interface electronic structure is complicated by the necessity to probe subsurface properties. Further, conventional interface diagnostic methods measure only a spatial-average of interface properties. A new technique, Ballistic-Electron-Emission Microscopy (BEEM), for spatially-resolved spectroscopic investigation of subsurface interface properties has recently been developed. BEEM enables, for the first time, nanometer-resolution imaging of electronic structure at subsurface interfaces. BEEM has been demonstrated by direct investigation of important metal-semiconductor Schottky barrier interfaces.

The BEEM method combines Scanning Tunneling Microscopy (STM) [1] techniques with unique ballistic electron spectroscopy capabilities to enable probing of subsurface properties. Elastic tunneling of electrons between the STM tunnel tip and the structure under study results in the injection of ballistic electrons into the structure. The injected ballistic electrons propagate through the structure and probe subsurface properties. BEEM may probe subsurface structure at depths greater than 100 - 300Å since typical ballistic electron attenuation lengths in metals and semiconductors are greater than 100 Å. Figure 1 shows energy band diagrams for application of the BEEM method to a metal-semiconductor Schottky barrier heterostructure. In this three-terminal configuration, electrodes are attached to the STM tunnel tip, the metal film (base), and to the semiconductor collector. For base-tip bias, V, less than the Schottky barrier height, V_b, there will be no collector current, since the ballistic electron distribution has insufficient energy to surmount the energy barrier. However, if V exceeds V_b as shown in Figure 1c, a fraction of the ballistic electrons may propagate through the interface and into the collector where the current is detected. The collected current depends on the detailed base-collector interface properties, including the fundamental Schottky barrier height and defect structure at the interface. Spectroscopic analysis of the collector current directly yields information on each of these critical interface properties. Figure 2 shows BEEM spectra obtained for Au-Si and Au-GaAs heterostructures. The spectra display the expected abrupt threshold in collector current at the Schottky barrier voltage.

BEEM imaging is accomplished while scanning the STM tunnel tip over the heterostructure top surface. The collector current is measured and while scanning the tip so as to produce simultaneous images of the top surface topography and subsurface electronic structure. BEEM spectroscopy and imaging techniques have been employed to extensively characterize Au-Si and Au-GaAs Schottky barrier heterostructures. BEEM images show nanometer-scale features at interfaces buried 100Å below the surface. These results, for the first time, directly reveal the homogeneity of the Au-Si SB interface, and the contrasting heterogeneity of the Au-GaAs SB properties.

* Research supported by ONR and SDIO/IST.

1. G. Binnig, H. Rohrer, Ch. Gerber, and E. Weibel, Phys. Rev. Lett. 49, 57 (1982);

2. W. J. Kaiser and L. D. Bell, Phys. Rev. Lett. 60, 1406 (1988).

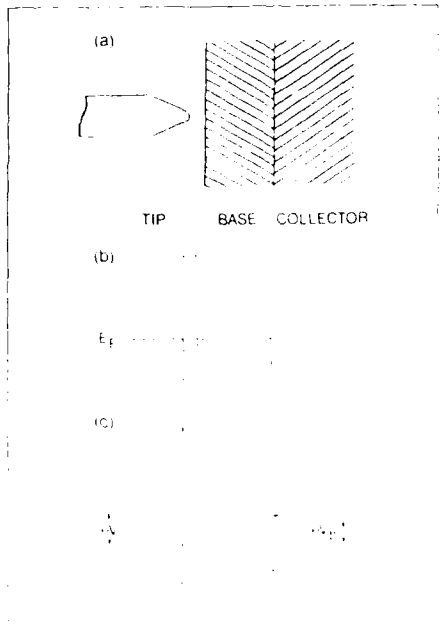


Figure 1. (a) The three-terminal BEEM method for investigation of a metal-semiconductor Schottky barrier. The tunnel tip is separated by a vacuum barrier from the metal base electrode. Three terminals are applied to the tunnel tip, metal base, and semiconductor collector. The collector current, I_c, is measured between base and collector. (b) The energy band diagram for zero tunnel bias, $V = 0$. (c) The energy band diagram for tunnel bias greater than the Schottky barrier voltage, $eV > eV_b$.

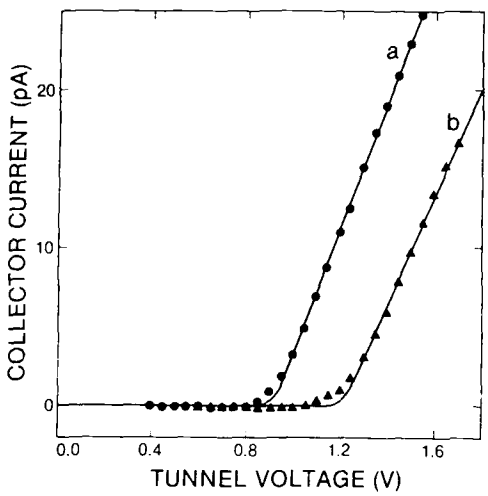


Figure 2. BEEM spectroscopy results for Au-Si and Au-GaAs heterojunctions. (a) BEEM spectrum of collector current, I_c, versus tunnel voltage, V, for a Au-Si SB structure. The spectrum (dots) was measured at a constant tunnel current, I_t, of 0.87 nA. The calculated spectrum (solid line) corresponds to a barrier height value, eV_b, of 0.92 eV. (b) BEEM I_c - V spectrum (triangles) for the Au-GaAs SB heterojunction obtained at I_t = 1.0 nA. The calculated spectrum (solid line) corresponds to an eV_b value of 1.2 eV.

Abstract No. 422

SUB-PPM MONITORING OF TRANSITION METAL CONTAMINATION ON SILICON WAFER SURFACES BY VPD-TXRF

A. Huber, H.J. Rath, and P. Eichinger
GeMeTec Gesellschaft für Meßtechnik und Technologie mbH, Paul-Gerhardt-Allee 50, D-8000 München 60, Germany

Th. Bauer, L. Kotz, and R. Staudigl
Wacker-Chemitronic GmbH, Postfach 1140, D-8263 Burghausen, Germany

Total reflection X-ray fluorescence analysis (TXRF) has recently been demonstrated to be a valuable tool for monitoring surface contamination on silicon wafers [1]. Using a molybdenum tube as X-ray source, the sensitivity of this non-destructive multielement analysis technique is in the order of 10^{10}-10^{11} atoms per cm^2 for the technologically important transition metals, corresponding to 10-100 ppma of a monoatomic layer on a silicon surface. Still better sensitivities (0.1-10 ppma) have been reported for atomic absorption spectrometry (AAS) combined with a chemical preconcentration technique known as vapor phase decomposition (VPD,[2]). With this technique the wafer surface is exposed to HF vapor which dissolves the surface oxide (native or thermal). The resulting liquid condensate is either collected in the reaction vessel with a vertical multiwafer configuration, or concentrated into a droplet in the center of the wafer with a horizontal single-wafer configuration [3] due to the hydrophobic surface character and the kinetics of the reaction, which starts from the wafer edge. The latter preparation technique is ideally suited for TXRF if the VPD droplet is allowed to dry on the wafer surface and is analyzed in situ. This eliminates chemical treatment and handling of the VPD liquid as is necessary for AAS. The sensitivity enhancement of VPD-TXRF as compared to pure instrumental TXRF can be estimated from the ratio of the total wafer area to the analysis area of instrumental TXRF (0.5 cm^2).

Figure 1 shows the schematic arrangement for TXRF with the VPD residue in the analyzed area. Figure 2 and 3 demonstrate the dramatic increase in sensitivity as a result of VPD concentration. Wafers with impurities below the detection limit of instrumental TXRF show a distinct contamination pattern when subjected to VPD. Actually measured transition metal concentrations are given in table 1 together with detection limits estimated for VPD-TXRF under the assumption that all impurities are collected in the residue.

Summarizing, VPD-TXRF is able to detect transition metal contaminations with a sub ppb sensitivity and is, therefore, considered to be at present the most sensitive multielement analysis technique for evaluating wafer surface purity at various processing steps like cleaning, dry processing etc. Further to, the technique is relatively fast and simple with little danger of introducing artefacts.

References :

[1] P. Eichinger, H.J. Rath and H.Schwenke
Semiconductor Fabrication: Technology and Metrology, ASTM STP 990, 1988

[2] A. Shimazaki, H. Hiratsuka, Y. Matsushita and S. Yoshii
Extended Abstracts of 16th Conference on Solid State Devices and Materials, Kobe, 1984, p. 281

[3] T. Shiraiwa, N. Fujino, S. Sumita and Y. Tanizoe
Semiconductor Fabrication: Technology and Metrology, ASTM STP 990, 1988

table 1 : results of VPD-TXRF measurement of contaminations on a 100 mm silicon wafer

element	concentration [10^9 at/cm^2]	estimated detection limit [10^9 at/cm^2]
Ca	191	5.0
Cr	21	1.8
Fe	80	1.1
Ni	10	0.7
Cu	6	0.6
Zn	69	0.5
Ba	50	10.0
Pb	3	0.7

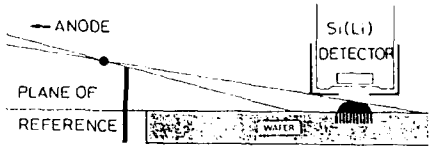


figure 1 : schematic arrangement of TXRF

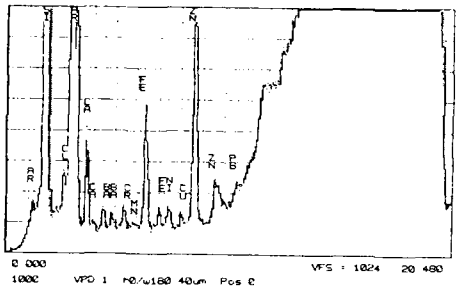


figure 2 : TXRF-spectrum of VPD droplet

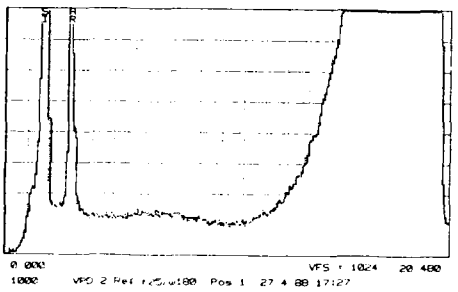


figure 3 : TXRF-spectrum of wafer prior to VPD treatment

Abstract No. 423

AN EVALUATION OF ULTRA-SURFACE (<3NM), TRACE (E11/CM^2) IMPURITY ANALYIS OF SILICON USING A NEW X-RAY TECHNIQUE

R. S. Hockett*, S. M. Baumann*, and E. Schemmel+

*Charles Evans & Associates, 301 Chesapeake Drive, Redwood City, California 94063; +ATOMIKA Technische Physik GmbH, Postfach 450135, D-8000 Munchen 45, FRG

INTRODUCTION

Unwanted impurities can be a problem for semiconductor devices when the impurities are eventually located in the electrically active region after device processing. Problems include leakage, lifetime reduction, premature gate oxide breakdown, and inversion layers. Elimination of these impurities often requires both the identification of the origin of the impurities and also their measurement.

The choice of quantitative measurement technique for these impurities is influenced by their location with respect to the substrate or device. For the purposes of this discussion we limit ourselves to the ultra-surface region (1-3 nm) of the substrate, where unwanted impurities may be found from a variety of sources.

The quantitative measurement techniques for trace (<0.1% atomic of a monolayer, or < E13 atoms/cm^2 for silicon) impurities in the silicon substrate ultra-surface region can be divided into two categories. (A) IMPURITY REMOVAL AND ANALYSIS, or those techniques which attempt to remove the impurities from the substrate ultra-surface region, e.g. in an etched solution, and then analyze the solution for the impurities. Examples include neutron activation analysis, atomic absorption analysis, and flameless atomic absorption analysis of etchant-removed silicon or silicon dioxide. These techniques must assume all the surface impurities of interest are removed by and remain in the etchant. (B) ANALYSIS ON SUBSTRATE, or those techniques which make the measurement with the impurities remaining in the ultra-surface region of the substrate. Examples include polyencapsulation/-SIMS and total reflection X-ray fluorescence analysis (TXRF).

An evaluation of TXRF was undertaken for this study using the ATOMIKA XSA-8000 instrument. In this method [1], which was originally designed for liquids analysis, an X-ray beam from a conventional X-ray tube, typically a molybdenum anode, strikes the substrate surface at glancing incidence so that (i) the condition for total reflection of the X-rays is met and (ii) the analysis depth is limited to about the top 3 nm of the surface. The fluorescence radiation from the surface is collected by a Si(Li) X-ray detector and quantitation is completed using substrate surfaces intentionally contaminated with a known number of atoms in the analysis area to provide reference samples. Detection limits on silicon are reported to be E10/cm^2 to E11/cm^2 for the transition metals, and the improved detection limits over conventional thin film X-ray fluorescence (XRF) mainly stem from the major reduction in the background signal of the substrate.

EXPERIMENTAL

Four silicon samples were separately contaminated with Ni, Cu, Au and Pb using Inductively Coupled Plasma Analysis standard solutions with 100 ppmw of the metal contaminant in solution. Three other silicon samples were commercial wafers from three different silicon vendors, and another three silicon samples were taken from three different cleaning processes.

The TXRF analyses were performed on an XSA-8000 at ATOMIKA using a Mo X-ray anode, an 8 mm diameter aperture, and either a 40 or 80 micron thick metal X-ray filter between the source and sample. The TXRF results were correlated against the following other measurement techniques: Rutherford backscattering spectrometry (RBS), Auger electron spectrometry (AES), and quadrupole-based secondary ion mass spectrometry (SIMS).

RESULTS AND DISCUSSION

The comparison between the XSA-8000 and RBS analyses on intentionally contaminated samples shows good agreement considering the inhomogeneity in the surface contamination as indicated by the RBS analyses in different areas of the samples. The sample preparation is assumed to be the cause of differences.

The TXRF results for the three cleaning samples and the three vendor samples are shown in Table 1. Measurements on the cleaning samples used an 80 micron filter, while those on the silicon vendor samples used a 40 micron filter. The data indicate there are heavy metals, particularly Fe, Cu and Zn, on these cleaning samples at E11 to E13/cm^2 levels, and on vendor wafers at E11 to E12/cm^2 levels. These data are consistent with prior reports using other analytical techniques. There also appears to be differences among the silicon vendor samples.

SUMMARY

In summary an evaluation of total internal X-ray fluorescence analysis (TXRF) using the ATOMIKA XSA-8000 has shown the technique promises to be an invaluable tool in the quantitative surface analysis of silicon wafers. The technique's primary attributes over other approaches are: (1) it's simplicity of operation, (2) it's survey capability of the heavy metals, and (3) it's detection limits at the E11/cm^2 level. The measurement should be useful to those developing or controlling: (a) wafer cleaning processes, (b) impurity levels in cleaning chemicals, (c) dry etching processes, (d) ion implantation contamination, and (e) semiconductor-related gases and ambients.

REFERENCE

1. "Application of Total Reflection X-Ray Fluorescence Analysis for Metallic Trace Impurities on Silicon Wafer Surfaces," P. Eichinger, H. J. Rath, and H. Schwenke, Semiconductor Fabrication: Technology and Metrology, ASTM STP 990, Dinesh C. Gupta, editor, American Society for Testing and Materials, 1988.

TABLE 1. XSA-8000 RESULTS ON CLEANING AND VENDOR WAFERS
(Cleaning samples measured once, Vendor samples measured four times and averaged; units of E12/CM^2)

SAMPLE	Ca	Cr	Fe	Cu	Zn	Sr	Ta	W
Clean 1	2.9			19.9	16.8			
Clean 2	2.6		0.8	0.4	2.5			
Clean 3		0.9		0.2	0.9			
Vendor 1	1.5		<0.1	0.4	1.6	<0.2	0.1	0.2
Vendor 2	<1.4		0.2	0.3	0.6	0.6	0.2	0.5
Vendor 3	<1.4		0.4	0.3	0.6	0.6	0.1	0.5

Abstract No. 424

X-RAY TOPOGRAPHY AND PRECISION DIFFRACTOMETRY OF SEMICONDUCTING MATERIALS

B K Tanner

Department of Physics, University of Durham, South Road, Durham, DH1 3LE, U.K.

The application of double axis X-ray diffractometry and topography to the non-destructive characterization of semiconducting materials is reviewed. Double axis X-ray diffractometry has now become widespread for assessment of epitaxial layer structures, particularly of electro-optic materials. The double crystal rocking curve provides directly the following data;
[1] lattice mismatch and hence composition,
[2] layer thickness,
[3] layer and substrate perfection,
[4] wafer curvature,
[5] mismatch and layer thickness variation across the wafer.

Attention is paid to the sensitivity and reliability of the data, particularly in the standard experimental geometry suitable for all commercial diffractometers. The recent observation of interference fringes from ABA sequence structures such as used for lasers is discussed and the use of the period for direct thickness determination highlighted.

Matching of simulated and experimental rocking curves provides a powerful method for non-destructive determination of the layer composition as a function of depth. The application is discussed for graded layers and for multiquantum well structures. In the case of very thin layers, use of grazing incidence geometry permits the study of layers only a few tens of nanometres thick and determination of layer thickness and interface roughness to Ångstrom precision.

Triple axis techniques enable diffuse scattering to be examined, as well as providing enhanced signal to noise. These instruments can also be used to measure the specular reflectivity. Analysis of the interference fringes observed from thin layer structures permits the determination of electron density, layer thickness and interface roughness at the Ångstrom level for single crystal, polycrystalline and amorphous films.

X-ray topography provides information on the spatial distribution of the diffracted X-ray beam. It is the X-ray analogue of transmission electron microscopy. Although it is a mature technique, unlike double crystal rocking curve analysis, it has seen little industrial application and has not yet developed to a stage where it is appropriate for an on-line quality control technique. It is pointed out that little attempt has been made to match detector resolution and speed to the information required. As an example, it is shown that X-ray section topography is a powerful method for assessing the extent of the denuded zone in silicon formed by intrinsic oxygen gettering. For a quality control application, micron resolution is unnecessary and use of fast X-ray or dental film quite appropriate.

Projection topography, unlike section topography, gives a full survey of the defects in the wafer and detection of slip is a particularly important screening technique. Again, for routine surveying, fast film and a rotating anode permits 6 inch wafers to be examined non-destructively in a time comparable to that required for defect-specific etching.

Double crystal topography can be performed on a double axis diffractometer with minor modification to collimator geometry. The technique is particularly useful for strain contour mapping and detection of long range strains. It has higher defect contrast in the Bragg (surface reflection) geometry than single crystal methods and the strain sensitivty can be tuned by suitable choice of reference crystal.

Abstract No. 425

CHARACTERIZATION OF SEMICONDUCTOR MATERIALS AND STRUCTURES BY TRANSMISSION ELECTRON MICROSCOPY

R.J. Graham
Center for Solid State Science, Arizona State University,
Tempe, AZ 85287-1704

Transmission electron microscopy (TEM) is now a well established diagnostic technique in the field of semiconductor materials and devices. The appeal and success of this technique is due to its ability in providing images and information on the microstructure of a wide range of materials and fabricated structures with submicron or atomic resolution. The goal of TEM applied in this way is to characterize materials subject to various processing procedures to understand how the microstructure will affect device behaviour and to provide feedback to the fabrication or growth process. TEM is particularly useful when coupled with other analytical or diagnostic techniques, for example, other spectroscopies or electrical methods, which may afford greater sensitivity without the spatial resolution or provide different information all together. This is also applicable to the various techniques encompassed within TEM itself since usually several techniques are employed for a complete characterization. It is the purpose of this paper to review and demonstrate, with examples, how this can be achieved, the limitations of such investigations and the range of materials and problems to which TEM is being applied.

TEM can basically be divided into two types, high resolution electron microscopy (HREM) and analytical electron microscopy (AEM). With HREM we are usually interested in imaging materials at the highest possible resolution so that at selected orientations of the specimen, lattice images are produced. AEM is concerned with imaging and characterizing materials with usually lower spatial resolution than HREM and the techniques which will be described here include convergent beam electron diffraction, X-ray microanalysis, electron energy loss spectroscopy and cathodoluminescence.

High Resolution Electron Microscopy (HREM)

One of the most useful applications of HREM has been in the imaging of semiconductor interfaces since the structure or quality of these has been identified as being important in device viability and function. The examples considered here include those found in superlattice (SL) or multiple quantum well (MQW) structures and methods for imaging and assessing the interfacial quality. Heteroepitaxial layers of II-VI semiconductors grown on III-V substrates and other heteroepitaxial systems such as GaAs on Si, metal/semiconductor contacts and amorphous-on-crystalline systems such as SiO_2 on Si are also considered. Cases where the interfacial structure has been correlated with other techniques, for example electrical and photoluminescence, will also be described.

Analytical Electron Microscopy (AEM)

In many cases one or more AEM techniques will be required to complement or confirm HREM analysis.

Convergent Beam Electron Diffraction (CBED)

By using a convergent beam of electrons, diffraction from small volumes of specimen may be used to analyse small particles or regions in semiconductor structures. CBED patterns may be used in the identification of known phases or in the symmetry and structure determination of new ones which may be important in device characterization. Other recent applications are also considered including the determination of compositional variations in III-V and II-VI alloys, the identification of antiphase boundaries in GaAs on Si and the measurement of local strain in strained-layer superlattices.

X-ray Microanalysis (EDX)

Elemental composition in the TEM may be determined by X-ray microanalysis. The analysis of particles found in semiconductor materials such as precipitates or phases in an alloyed metal-semiconductor contact provides useful elemental information complementary to structural information available through HREM or diffraction. Other applications relate to the assessment of compositional variations in single crystal material. The limitations of this are examined using the determination of compositional variations in GaAlAs/GaAs SL and InGaAs/InP MQW structures as examples. The determination of dopant or impurity distributions at a submicron level by the ALCHEMI technique (Atom Location by Channelling Enhanced Microanalysis) is discussed.

Electron Energy Loss Spectroscopy (EELS)

In addition to providing a means of elemental analysis as does EDX, EELS affords the ability to detect low Z elements and superior spatial resolution. Chemical shifts and fine structure in the ionization edges and the form of the low loss region in the EELS spectrum can additionally provide analysis on the chemistry, structure and electronic nature of the material. Examples of this are considered including the analysis of interfacial oxides and the probing of the electronic structure of a misfit dislocation at the GaAs/GaInAs interface. A new application involving the coincidence between EELS and cathodoluminscence (CL) events to map carrier lifetime at high spatial resolution will be described.

Cathodoluminescence (CL)

Although the characterization of semiconductor materials by CL is usually performed in the scanning electron microscope (SEM), this technique is finding application in the TEM. It is the most sensitive analytical technique, for suitable materials, available on the TEM capable of detecting the presence of impurities in the parts per million level. The technique offers the advantage and chance to investigate the relationship between electronic and atomic structure of defects since it is possible to simultaneously image the specimen and characterize defects at the submicron level while acquiring CL data. Applications to materials of optoelectronic importance are considered including the effects of dislocations on the luminescence of ZnSe on GaAs, InP, Si and GaAs on Si. The technique may also be used to assess changes in materials as a result of processing. With the development of new materials for use in infrared imaging technology and the desire to investigate deep levels in, for example, III-V materials, the spectral range in CL detection will have to be extended to several microns. This can be achieved by use of a Fourier Transform spectrometer which has been recently successfully used, as well as a conventional dispersive grating type, to detect infrared CL from GaInAs in the TEM.

Abstract No. 426

DEFECT CHARACTERIZATION IN SEMICONDUCTORS BY POSITRON ANNIHILATION SPECTROSCOPY

A. Rohatgi, J.P. Schaffer, and A.B. DeWald
Georgia Institute of Technology
Atlanta, Georgia 30332

The potential of positron annihilation spectroscopy (PAS) for defect characterization in semiconductors is demonstrated using examples from both the literature and our own current work. The materials discussed include Si, GaAs, ZnO, SiO_2/Si interfaces and AlGaAs/GaAs heterostructures. The types of defects studied include: i) vacancy complexes, ionized dopants, and antisite defects, ii) irradiation damage and subsequent recovery via defect annealing, iii) the influence of cooling rates on spatial non-uniformities in defects over the whole wafer, and iv) characterization of buried interfaces. In several instances, the results of the PAS investigations are correlated with data from other established semiconductor characterization techniques.

For example, PAS was used to investigate the influence of oxygen on the minority carrier lifetime in Si. Magnetic Czochralski (MCZ) growth was used to vary the oxygen concentration in the range of 1-5 ppm. Figure 1 shows the correlation between the Doppler S-parameter and the interstitial oxygen concentration measured by FTIR. For all three sets of samples the Doppler PAS S-parameter increases as the oxygen interstitial concentration increases. Figure 1 also shows the inverse relationship between the PAS S-parameter and the minority carrier lifetime in MCZ silicon, measured by photoconductive decay (PCD), as a function of oxygen concentration. In these MCZ samples, an increase in the S value is accompanied by a decrease in the carrier lifetime.

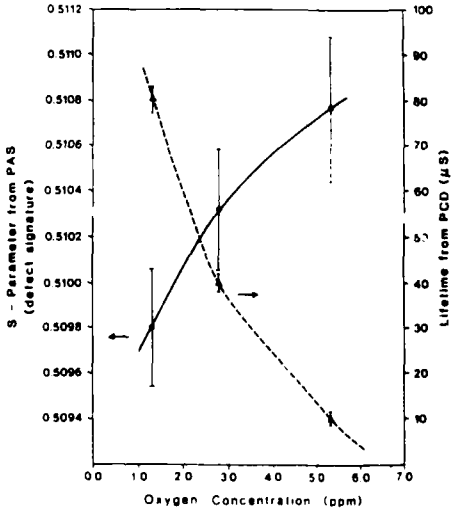


Figure 1. Correlation of the Doppler PAS S-parameter and the minority carrier lifetime, measured by PCD, as a function of oxygen concentration, in MCZ silicon.

ZnO is a popular material for making lightening arresters and varistors. However, its performance and stability depend on the bulk and grain boundary defects. In a recent study (1) PAS and several other techniques were used to characterize the changes in the defect structure in a ZnO varistor as a result of annealing. DLTS was used to delineate the electrically active traps (N_t) while C-V measurements were performed to obtain the doping density (N_d) at the edge of the depletion region. The doping density within the grains was determined by FTIR. These results were correlated with those of a previous study of device stability (2).

As shown in Figure 2, PAS indicates a minimum at 800°C which coincides with the minimum in N_d. A minimum in N_t was observed at 600°C which coincides with the optimum annealing conditions for most stable devices. This suggests that the E_c-0.26 eV trap is related to instability in ZnO varistors and that PAS probably measures a total defect concentration of (N_d + N_t + other defects) which in this case is roughly equal to N_d since the doping density is fairly high (~10^{17} cm^{-3}). If so, the local minimum in S or N_d around 600-800°C could be attributed to the competition between: i) the diffusion and subsequent loss of Zn_i to grain boundaries and ii) the thermal generation of Zn_i (Frenkel defects). PAS also indicated that the post-anneal cooling rate is important in tailoring the defect state in ZnO varistors.

References

(1) M.S. Ramanachalam, J.P. Schaffer, A. Rohatgi, T.K. Gupta, and W.D. Straub, in preparation.

(2) T.K. Gupta and W.G. Carlson, J. Appl. Phys. 53, 7401, 1982.

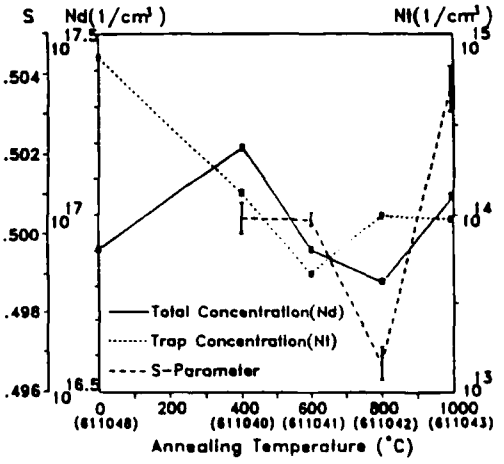


Figure 2. Correlation of the PAS S-parameter with the density of the E_c-2.6 eV trap (DLTS) and the doping density (C-V) in a ZnO varistor, as a function of annealing temperature.

Abstract No. 427

Cathodoluminescence Characterization of Semiconductor Materials

R.J.Roedel, S.Myhajlenko, J.L.Edwards, and K.Rowley

Center for Solid State Electronics
Arizona State University
Tempe, AZ, 85287-6206

Cathodoluminescence (CL) techniques are extensively used for the characterization of direct bandgap semiconductors, such as GaAs, InP, and CdTe. CL is normally carried out in a scanning electron microscope (SEM), and the incident electron beam can create a vast number of electron hole pairs near the surface of the semiconductor sample under test. In direct bandgap semiconductors a significant portion of the electron hole pairs may recombine radiatively. The resulting luminescence emerging from the top of the sample may be detected, converted to an electrical signal, and displayed on the SEM's CRT in sychronization with the rastered electron beam. This CL image, or luminescence map, of the sample often shows significant contrast; the contrast in turn is generally due to spatially varying radiative recombination efficiency in the sample. The radiative efficiency may depend upon the dopant and the doping concentration, the presence of internal electric fields, and material defects, such as dislocations, stacking faults, or inclusions. Hence, CL has often been employed as an imaging technique to find, respectively, doping striations, the location of pn junctions, or the number of electrically active dislocations.

Conventional CL characterization is carried out at room temperature and in a panchromatic mode (that is, all wavelengths collected). This embodiment of the technique is routine and typically quite easy to employ. However, the extension of the CL technique beyond this approach can be rather advantageous. In fact current trends in CL characterization include progress in four areas: cryogenic CL, spectrally resolved CL, admixture of CL with other e-beam produced signals, and extension to infrared materials. For example, there are several advantages in pursuing CL at cryogenic (near liquid helium) temperature. There are large increases in photon emission rates, there is significantly reduced beam damage to the sample, and optical spectra are sharper and more significant than room temperature results. This is demonstrated in part in figures (1) and (2). In these figures, both secondary electron (SE) and panchromatic CL images from a CdTe sample held at 15 K are displayed. The sample consisted of a CdTe substrate upon which a five micron thick CdTe epitaxial layer was grown by liquid phase epitaxy. A portion of the epitaxial layer was chemically removed, so that the left side of each figure shows the epitaxial layer, the right side the substrate. The entire sample was etched in a defect revealing etchant that produced the prominent rectangular etch figures. CdTe is a semiconductor that is particularly difficult to image with CL because of its inherent relatively low emission efficiency (compared to GaAs, for example). Consequently, one must generally use high beam currents to produce adequate excitation, but this often leads to enormous surface damage, including surface dissociation or even melting.

The CL image shown in figure (2) was produced with a beam voltage of 25kV, and a beam current of one nanoampere. This is possible because of the low temperature of the sample: the photon generation rate is now enormous compared to that at room temperature. In addition, there was no noticeable beam damage produced during this examination. With identical beam conditions at room temperature, there was no CL image whatsoever.

The CL contrast shown in figure (2) has two sources. The rectangular dark patches obviously correspond to the etch figures, but the darkness does not indicate that locally the emission efficiency is lower; this is predominantly a geometrical shadowing effect. On the other hand, the network of small dark spots, quite prevalent on the substrate side, but still noticeable on the epitaxial side, are most certainly due to some radiation killing defect in the material. Whether these defects are a network of dislocations or some type of point defect has not yet been determined.

This is just one example of the efficacy of the cryogenic CL technique. In the remainder of the paper, additional cases will be presented. It will be shown that (a) spectrally and spatially resolved cryogenic CL can be used to determine both the types of defects present and their location in the material as well, (b) comparison of CL with transmission cathodoluminescence and electron beam induced current signals can be used to differentiate optically and electrically active defects, and (c) defects in infrared materials, such as (In,Ga)As and (Hg,Cd)Te can also be imaged with cryogenic CL with the use of appropriate detectors and custom amplifiers.

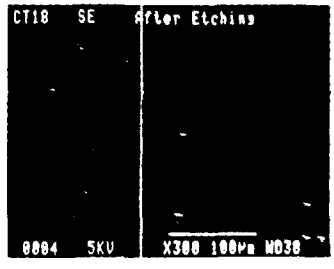


Fig.(1) SE image of CdTe sample at 15K

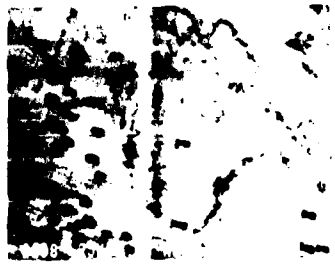


Fig.(2) CL image of same CdTe sample at 15K

Abstract No. 428

SUBSURFACE DEFECT STRUCTURES IN ION IMPLANTED, ANNEALED Si WAFERS IMAGED BY NONDESTRUCTIVE MODULATED REFLECTANCE IMAGING

W. Lee Smith and D. Willenborg
Therma-Wave, Inc., 47734 Westinghouse Dr.
Fremont CA 94539

G. A. Rozgonyi
Materials Engineering Department
North Carolina State University, Raleigh NC 27695

T. Miranda*
Fairchild Camera and Instrument Corporation
Gate Array Div., 1801 McCarthy Blvd., Milpitas CA 95035

L. Larsen
National Semiconductor, 2900 Semiconductor Dr.
Santa Clara CA 95051

A new method of imaging physical/crystallographic defects in silicon is presently emerging. This laser-based method [1] uses thermal wave modulated reflectance to generate defect images in a noncontact and nondestructive manner with image acquisition time of typically 1 minute for a 100 um x 100 um image. The spatial resolution is 1 micron; however, defects much smaller than that size are detectable. An unusual aspect of this technique is that each image shows a projection of all defects contained within the sampled volume, which typically extends from the surface to a depth of 3 to 5 microns in Si. The method operates in room ambient conditions (no vacuum), requires no special sample preparation, and is able to image through transparent overlayers such as silicon dioxide. As such, it is able to operate on in-process product IC wafers for detection of process-induced defects [2].

The first images generated with this automated method were those of stacking faults and dislocations induced in silicon wafers by a damaging gettering technique followed by oxidation [1]. The comparison of the post-oxidation thermal wave (TW) images with standard optical microscope images made after oxide stripping and Wright etch showed a spatially definitive correspondence between the two methods. An example is included here as Fig. 1.

In the research reported here, a study was made of thermal wave images and magnitudes on Si wafers that were ion implanted with B^+, P^+ and As^+ and annealed in ambient or oxidizing conditions. The implant dose range was 1E12 to 1E16 ions/cm2. The objectives were to measure the changes in the total amount of implant damage and in the degree of development of discrete defects during the transition from as-implanted to "fully annealed" state. The parameters measured are (a) the magnitude of the TW signal after implant and after each of four 30-min. anneals, and (b) the TW images of the residual defects remaining in the "fully annealed" wafers.

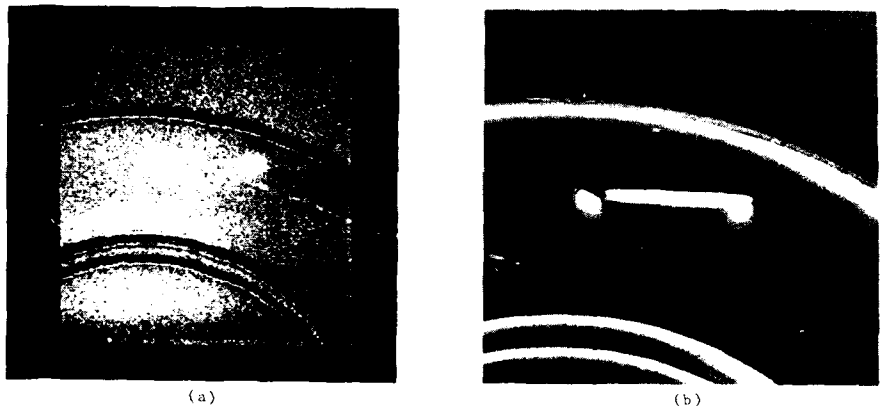
As examples, we show in Fig. 1 selected TW images of "fully annealed" samples:
(a) 3E14 ions/cm2 P^+ dose, oxidizing anneal,
(b) 3E14 B^+ dose, N2 anneal,
(c) 1E16 B^+ dose, N2 anneal,
(d) 1E16 B^+ dose, oxidizing anneal,
(e) 3E14 As^+, N2 anneal,
(f) 1E16 As^+, N2 anneal.

We will discuss the various features in these and other TW images and, by comparing them with TEM and decoration-etched micrographs, examine this new, rapid, noncontact defect imaging method.

*presently with Seeq Technology, Inc., San Jose CA.

References:

1. B. Witowski, W. Lee Smith and D. Willenborg, "Nondestructive Technique for the Detection of Dislocations and Stacking Faults on Silicon Wafers", Appl. Phys. Lett. **52**, 640 (1988).
2. S. Marks, W. Lee Smith and D. Willenborg, "Si Crystallographic Defects in Trench-Isolated Bipolar IC Wafers Detected with Noncontact Thermal Wave Imaging", submitted to Electrochem. Soc. Meeting, Oct. 1988, Chicago, IL.

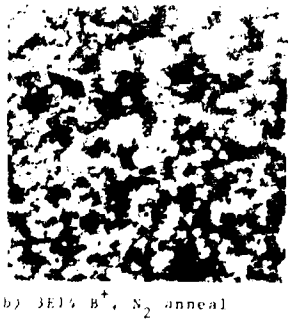


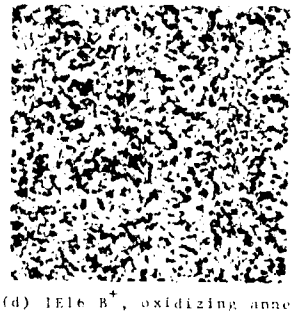
(a) (b)

Fig. 1. (a) Modulated reflectance image of a stacking fault on a patterned Si wafer. The two bright dots which taper toward one another are the ends of the bounding dislocation. The actual distance between the two dots is approximately 40 microns. This image is measured through a SiO2 film (348 Angstroms) [1].
(b) Conventional optical photomicrograph (at slightly higher magnification) of the same region as in (a) after oxide strip and Wright decoration etch [2].



(a) 3E14 P^+, oxidizing anneal (c) 1E16 B^+, N_2 anneal (e) 3E14 As^+, N_2 anneal





(b) 3E14 B^+, N_2 anneal (d) 1E16 B^+, oxidizing anneal (f) 1E16 As^+, N_2 anneal

Fig. 2. Thermal wave modulated reflectance images of approximately 60 microns x 60 microns for various implant and anneal conditions.

Abstract No. 429

MULTIPLE INTERNAL REFLECTION SPECTROSCOPY: APPLICATIONS TO ELECTRONIC MATERIALS

J.E. Olsen, G.A. Rozgonyi and F. Shimura
Department of Materials Science and Engineering
North Carolina State University
Raleigh, NC 27695-7916

In recent years, transmission infrared spectroscopy has become a popular tool for studies of defects in bulk silicon (1-3). The surface regions that contain the circuits, however, are likely to have different defects and impurities than the bulk. In principle, conventional external reflectivity could be used to study these surfaces. But for reasonably accurate results, substantial absorptivity is required (α>1000 cm^{-1}). Defects in electronic grade silicon have absorptivities many orders of magnitude lower than this, making some sort of spectral amplification necessary. Electronic amplification increases the noise in the spectrum. Multiple internal reflection, on the other hand, easily provides a sensitivity of less than 1 cm^{-1} without adding noise.

To briefly summarize the principle(4-6): light passing through the interface of two transparent materials is refracted according to Snell's Law ($n_1 \sin \emptyset_1 = n_2 \sin \emptyset_2$). For light passing from the higher refractive index material to the lower index material, there is a critical incident angle such that the refracted angle is equal to 90°. At this angle, there is no loss in reflection. But if there is an imaginary component of the refractive index (absorption) in the lower index material, the total reflection is attenuated proportional to the magnitude of this imaginary component. An attenuated internal reflection spectrum may thus resemble an absorption spectrum except that it samples a very shallow region of the surface (about 5 microns, but it varies with wavelength).

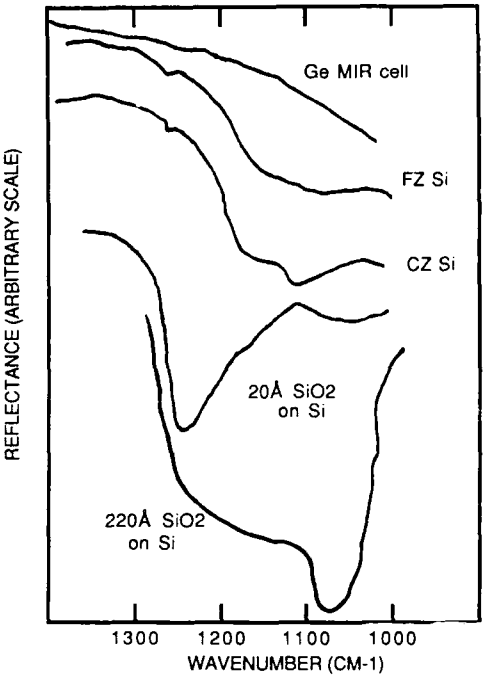
The relative effective thickness d_e expresses the sensitivity of an internal reflectance spectrum relative to a transmission spectrum. The relative thickness is calculated from the penetration depth of the evanescent wave, the electric field strength at the interface, the sampling area, and the strength of coupling. Harrick and du Pre have developed equations for estimating the effective thicknesses of bulk materials and thin films (6).

For bulk materials:

$$\frac{d_{e\perp}}{\lambda_1} = \frac{n_{21}\cos\emptyset}{\pi(1-n_{21}^2)(\sin^2\emptyset - n_{21}^2)^{\frac{1}{2}}}$$

$$d_{e\parallel} = \frac{(2\sin^2\emptyset - n_{21}^2)}{(1-n_{21}^2)\sin^2\emptyset - n_{21}^2} d_{e\perp}$$

The experimental setup is simple, comprised of a 60° germanium MIR plate (52x20x2mm.) in a Foxboro Model 9 MIR attachment. The effective thickness in silicon is about 130 microns. A Perkin-Elmer 1420 Infrared Spectrophotometer was used to obtain the spectra. The samples were clamped to both sides of the MIR plate. In this abstract, we show internal reflection spectra taken from float zone (FZ) silicon, Czochralski (CZ) silicon, a 20Å native oxide, and a 220Å thermal oxide. The CZ silicon clearly shows the 1106 cm^{-1} peak of dissolved interstitial oxygen. The peak height corresponds reasonably well to that predicted from the calculated effective thickness and transmission measurements on the same wafer. As expected, the FZ silicon shows no oxygen peak.



The 20Å native oxide and 220Å thermal oxide yield very different spectra. The most obvious conclusion is that the oxide structures are also very different, the native oxide being much denser than the thermal oxide as a result of incomplete oxidation or stress from volume expansion. The bonds in a denser film would likely be more rigid and have higher vibrational frequencies (7-9). Because of "anomalous" dispersion, internal reflection spectra of oxides present difficulties in interpretation (as do transmission spectra of oxides). Interpretation of these spectra require further experimentation and a more exact solution of the thin film internal reflection equations than those given by Harrick and du Pre (6).

ACKNOWLEDGEMENTS

The authors would like to thank R.A. Craven and P.A. Tierney from Monsanto Electronic Materials Company for their encouragement and support.

REFERENCES

1. F. Shimura, H. Tsuya, and T. Kawamura, Appl. Phys. Lett. **37**, 483 (1980).
2. P. Gaworzewski, E. Hild, F.G. Kirscht, and L. Vecsernyes, Phys. Stat. Sol. **A85**, 133 (1984).
3. F. Shimura, J.P. Baiardo, and P. Fraundorf, Appl. Phys. Lett. **46**, 941 (1985).
4. J. Fahrenfort and W.M. Visser , Spectrochimica Acta. **18**, 1103 (1962).
5. N.J. Harrick, *Internal Reflection Spectroscopy*, (Wiley, New York, 1967).
6. N.J. Harrick and F.K. du Pre, Appl. Opt. **5**, 1739 (1966).
7. E.R. Lippincott, A. Van Vakenburg, C.A. Weir, and E.N. Bunting, J. Res. Natl. Bur. Stand. **61**, 61 (1958).
7. R.J. Hemley, H.K. Mao, P.M. Bell, and B.O. Mysen, Phys. Rev. Lett. **57**, 747 (1986).
8. M. Nakamura, R. Kanzawa, and K. Sakai, J. Electrochem Soc. **133**, 1167 (1986).

Abstract No. 430

MINORITY CARRIER LIFETIME OF HETEROSTRUCTURES, SURFACES, INTERFACES AND BULK WAFERS

E. Yablonovitch and T. J. Gmitter
Bell Communications Research
Navesink Research Center
Red Bank, N.J. 07701-7020

We have developed a contactless laser-pumped minority carrier lifetime probe which is of general utility in semiconductor electronics.

This inductively coupled radio frequency apparatus, which is illustrated in Figure (1), monitors the absolute sheet conductivity of the semiconductor as a function of time. A brief flash of pulsed incoherent light, in this case from a Q-switched doubled Nd-Yag laser scattering off a white surface, injects electrons and holes into an epilayer or into the bulk substrate wafer itself. The recombination of electrons with holes is monitored by the decay of the conductivity associated with the optically injected carriers In a numerical algorithm, conductivity is divided by the carrier density dependent mobility to convert it to a density decay curve. If the epilayer thickness L is sufficiently small, the decay of excess carrier density n is simply the sum of a bulk and a surface term[1]:

$$dn/dt = -[\tau_b^{-1} + 2S/L]\, n$$

where τ_b is the bulk recombination lifetime, S is the surface recombination velocity, and the factor 2 accounts for the front and back surfaces. The reciprocal of the quantity in brackets was called by Shockley[1] the "*filament lifetime*" τ, which in general may depend on n. Irrespective of the absorption depth of the light source, the injected carrier density n will become spatially uniform and eq (1) will be valid provided that $L \ll \sqrt{D\tau}$ where D is the ambipolar diffusion constant and $\sqrt{D\tau}$ is the diffusion length. If the front and back surfaces of the epilayer are inequivalent then $(S_f + S_b)$ should be substituted for 2S.

In this paper we will review the operation of the minority carrier lifetime bridge and show how it can be a real workhorse in the laboratory environment. The main advantage of this equipment is that it can give immediate answers about the semiconducting quality of unprocessed or partially processed materials. We will examine the utility of this type of apparatus by reviewing some of the applications where it was found useful.

The first application will be to compare[2] the quality of III-V double heterostructures which are grown by the three most common growth methods: organo-metallic chemical vapour deposition (OMCVD), liquid phase epitaxy (LPE) and molecular beam epitaxy (MBE). In making these comparisons, it is significant that the epitaxial layers are not subjected to any processing after growth. Because there are no contacts required, we see the material quality directly as grown. The best and most consistent minority carrier properties came from OMCVD, but the other growth methods were almost as good.

The second application we will discuss is the exploration for surface chemical treatments[3] which produce a surface recombination velocity (SRV) which begins to compete with the excellent AlGaAs/GaAs interface. The minority carrier lifetime bridge is a superb exploratory tool since different chemical preparations can be tried one after the other with no special device fabrication in between. A "cut and try" approach makes sense if we can try many different chemical reagents in a brief time. Then we can quickly converge on a good chemical process by trying many different variations on any approach that seems to work well. The best chemical treatments so far: For[3] GaAs, a polycrystalline film of $Na_2S{\cdot}9H_2O$; For[4] $In_{0.53}Ga_{0.47}As$, a polycrystalline film of NaOH; For[5] Silicon, treatment in HF acid. The chemical treatments for GaAs have increased the gain[6] of heterojunction bipolar transistors sixty-fold.

A by-product of the capability to create a nearly ideal semiconductor surface chemically, is that it allows us to eliminate the surface as a problem in order focus in on bulk quality. In this case we have looked at the bulk minority carrier lifetime of substrate wafers whose surfaces had been chemically treated to effectively eliminate surface recombination. The conclusion is that III-V wafer material never seems to have a lifetime longer than 10 or 20 nsec, while epitaxial material grown on those wafers can be as much as 100 times better. Similarly we surveyed bulk Silicon wafers and found that commercial float-zone Silicon is sometimes as good as 40 msec but that Czochralski material is generally 1000 times worse.

I should emphasize that these measurements are taken on essentially unprocessed wafer material. The results could be worse as a result of thermal processing. This suggests the use of the lifetime bridge as a process monitor. Since it requires no special wafer processing itself it is excellent for before/after tests. We have used it to make seemingly minor, but critical adjustments in Silicon oxidation conditions to sustain minority carrier lifetime in oxidized float-zone material. Likewise, we have used it to perfect the process conditions for minimizing the forward leakage current of SIPOS heterojunction contacts[7] on Silicon.

Let us mention two physics applications of the contactless minority carrier lifetime probe. The chemical surface preparations leave a sufficiently good surface quality to allow the formation of "naked" quantum[4] wells. These are single sided quantum wells with one face exposed for chemical modification. A second application is the study of bulk radiative recombination in the direct gap such as GaAs. There is a resurgence of interest in the physics of spontaneous emission of light in high refractive index materials.

REFERENCES

1. W. Shockley, "Electrons and Holes in Semiconductors", (van Nostrand, New York 1950) see p. 318
2. "Survey of Defect Mediated Recombination Lifetimes in GaAs Epilayers Grown by Different Methods", E. Yablonovitch, R. Bhat, J. P. Harbison and R. A. Logan, Appl. Phys. Lett. 50, 1197 (1987).
3. "Nearly Ideal Electronic Properties of Sulfide Coated GaAs Surfaces", E. Yablonovitch, C. J. Sandroff, R. Bhat, and T. Gmitter, Appl. Phys. Lett. 51, 439 (1987).
4. "Nearly Ideal Electronic Surfaces on Naked $In_{0.53}Ga_{0.47}As$ Quantum Wells", E. Yablonovitch, H. M. Cox and T. J. Gmitter, App. Phys. Lett. 52, 1002 (1988)
5. "Unusually Low Surface Recombination Velocity on Silicon and Germanium Surfaces", E. Yablonovitch, D. L. Allara, C. C. Chang, T. Gmitter and T. B. Bright, Phys. Rev. Lett. 57, 249 (1986).
6. "Dramatic Enhancement in the Gain of a GaAs/AlGaAs Heterostructure Bipolar Transistor by Surface Chemical Passivation", C. J. Sandroff, R. N. Nottenburg, J.-C. Bischoff and R. Bhat, App. Phys. Lett. 51, 33 (1987).
7. E. Yablonovitch and T. Gmitter, IEEE Elec. Device Lett. EDL-6, 597 (1985).

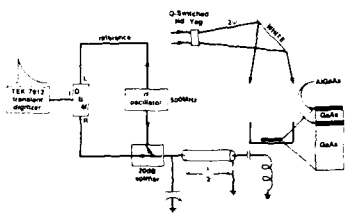


FIG. 1 Doubled Nd:YAG laser scatters off a white surface and injects carriers into a GaAs double heterostructure epilayer. The transient conductivity is probed by rf induction at 500 MHz. The series resonant circuit, adapted from NMR technology, includes a $\lambda/2$ section of coax for convenient access to the tuning element. A 20-dB splitter separates the incoming from the reflected signal. The imbalance in the circuit caused by the carriers is phase detected by a wide dynamic range double-balanced mixer (DBM) and then digitized. The AlGaAs layer is then removed and the experiment repeated with a wide variety of possible surface treatments.

Abstract No. 431

Contactless Measurement of Silicon Generation Leakage and Crystal Defects by a Corona-Pulsed Deep-Depletion Potential Transient

Min-Su Fung and R. L. Verkuil

IBM Corp., East Fishkill
Hopewell Junction, NY 12533

Silicon minority carrier generation leakage and crystal defects have been studied with Metal-Oxide-Silicon pulsed transient capacitance measurement by many authors [1-6]. This paper introduces a contactless measurement technique to detect similar silicon properties. We use a corona discharging to pulse a silicon surface into deep depletion and observe the resultant open-circuit surface potential transient. The measurement does not require a metal-gate or ohmic contact, thus a few undesired MOS process-related problems can be prevented, such as accidential contamination and incorrect metal anneal, which often disturb the measurement sensitivity and alter the test sample's property of interest.

Measurement Principle

The Corona-Pulsed Deep-Depletion technique uses Corona-Oxide-Semiconductor (COS) apparatus similar to prior work [7,8] and is described by another paper in this conference [9]. A field-induced junction, required for a repeatable measurement, is created on an oxidized silicon surface with uniform selective corona (Fig. 1). The junction is (corona) biased in silicon inversion to minimize surface leakage from interface states. Perimeter leakage is reduced with a corona-induced silicon accumulation ring around the junction edge

Silicon deep-depletion is induced by pulsing from inversion with a single burst of constant corona current. The corresponding deep-depletion recovery is monitored with a Kelvin system which detects the surface potential of the oxidized silicon with respect to bulk silicon without making a direct contact (Fig. 2).

At any time t, the surface potential (Vs) is divided between the oxide and the silicon depletion:

$$\begin{aligned}\Delta Vs(t) &\equiv Vs(t) - V_{inv} \\ &= \Delta Vox + \Delta[\psi s(t) - \psi_{inv}] \\ &= \Delta Qc/Cox + \Delta\psi s(t) \end{aligned} \quad (1)$$

where V_{inv} is the junction initial inversion bias potential, Vox the potential across the oxide, Cox the oxide capacitance, ψ_{inv} the inversion band bending, and Qc the corona charge. Given a constant total corona-pulse charge ΔQc and assuming negligible oxide leakage, Eq.(1) leads to

$$dVs/dt = d\psi s/dt \quad (2)$$

Eq. (2) says the rate of change of Vs transient is a direct measure of the rate of change of silicon deep-depletion band-bending ψs. Equating the silicon image charge, Qsi, to Qc for conservation of charge, charge neutrality requires

$$\begin{aligned}\Delta Qc = \Delta Qsi &= \Delta Q_{inv}(t) + qN_B \Delta X(t) \\ &= Cox\ [\Delta Vs(t) - \Delta\psi s(t)] \end{aligned} \quad (3)$$

Eq. (3) assumes no charge loss to the surface and perimeter; where N_B is the silicon doping, assumed uniform, $\Delta X(t)$ $(= X - X_{inv})$ the instantaneous depletion depth increment from the equilibrium value X_{inv}, and Q_{inv} is the inversion minority carrier charge.

If the deep-depletion silicon capacitance, $Csi(t) = \epsilon si/X(t)$, is contributed solely by the doping charge, we have $d\psi s/dX = qN_B X/\epsilon si$, and the generation leakage can be obtained from Eqs. (2), (3), assuming negligible diffusion component at room temperature:

$$\begin{aligned}Ig = dQ_{inv}/dt &= -\ qN_B\ dX/dt \\ &= -\ [\epsilon si/X]\ d\psi s/dt \\ &= -\ Csi(X)\ d\psi s(t)/dt \end{aligned} \quad (4)$$

Note that Eq.(4) has a simpler expression for Ig than the MOS theory under similar assumptions, as per Zerbst relation [10]. This is a consequence of holding the pulse charge constant instead the gate-voltage constant. Unlike MOS, COS does not need the extra gate charge, Cox dψs/dt, to maintain a fixed gate voltage. Thus it will result in a lower final oxide field for the same pulsed depletion depth. This is an advantage for working with thin oxide.

Considering centers with equal steady-state generation and recombination rates, uniformly distributed in X, the generation lifetime τg of the minority carriers can be evaluated by

$$\begin{aligned}Ig &= qn_i[X(t) - X_{inv}]\ /\tau g \\ &= [\epsilon si/X]\ dVs/dt \end{aligned} \quad (5)$$

Eq (5) shows a linear relation between dVs/dt and $X(X-X_{inv})$, which can be used to examine the measurement model.

Results

Samples of 1E15 p-silicon, with or without thermal pre-treat, and 1E16 n-epitaxial with an n+ buried layer on a p-substrate are studied. MOS results and chemically etched defects are compared.

I. Generation Leakage

Fig. 3 shows the plots of dVs/dt versus $X(X-X_{inv})$ for several samples. The linear regime of the plots shows where the corona-pulsed potential measurement for generation lifetime is valid. The life times, as calculated from the linear slope $[(qn_i)/(\epsilon si\ \tau g]$, are consistent with the MOS lifetimes.

The deviation of the curves in Fig. 3 from an ideal linear relation is caused by high-field effects in the strong deep-depletion and a non-uniform surface doping in the weak deep-depletion.

II. Random Single Crystal Defects

Similar to the method of MOS, random single silicon crystal defects at low density (< 1 defect/cm²) will result in very short duration COS potential transient. Such detection normally is difficult to achieve with preferential etch. In the presence of a single crystal defect, an extroadinarily rapid generation-recombination rate occurs at a very localized site, thus the concept of uniform generation-recombination is no longer valid. Instead, the silicon deep-depletion behavoir is dominated by the property of the *local defect-center*. We shall show this sensitivity on an epitaxial silicon sample.

Fig. 4 shows a population of transient potential traces collected from an epitaxial sample. Four electrically defective sites manifest themselves by much more rapid recovery transient, mostly accompanied with smaller maximum $\Delta\psi_s$. MOS results from these sites show consistent excessive leakages, 2 - 4 orders of magnitude higher than the average population. With preferential etch, a single bulk epitaxial etch pit(s) is exclusively found within the area of electrically defective sites. Band bending pinning at the physical defect is believed to limit the full extent of the deep-depletion depth. This effect allows us to estimate the approximate depth of a bulk defect from the maximum $\Delta\psi$ measurement of a defective site. The calculated defect depths can be compared with defect unlayering in repeated etching steps.

References

1. A. Eder, C. Werner, Lifetime Factors in silicon, ASTM STP 712, ASTM Symp. 1979.

2. W.M. Gosney, Lifetime Factors in Silicon, ASTM STP 712, 1979.

3. D.K. Shroder, et.al., VLSI Sci. and Tech./1985, ECS PV85-5, 1985.

4. P.L.Fejes, F.Secco d'Aragona, J.W.Rose, VLSI Sci.Tech./1985, ECS PV85-5, 1985.

5. E.M. Murray, M.P. Scott, S. Hahn, Ext. Abs. 276, Ecs Spring Meeting, 1983.

6. A. Morgro-Campero, R.P. Love, Ext. Abs. 319, V. 83-1, ECS Spring Meeting, 1983.

7. H.W. Curtis, M.S. Fung, R.L. Verkuil, four joint and individual IBM Invertion Disclosures on using corona discharge for contactless characterization of dielectrics and silicon, 1983 - 1987.

8. M.S. Fung, R.L/Verkuil, Ext. Abs. 284, V. 85-1, ECS Spring Meeting, 1985.

9. R.L. Verkuil, M.S. Fung, "Contactles Silicon Doping Measurement by Means of a Corona-Oxide-Semiconductor (COS) Technique," ECS Fall Meeting, 1988.

10. M. Zerbst, Z. Angew, Physik, 22, 1966.

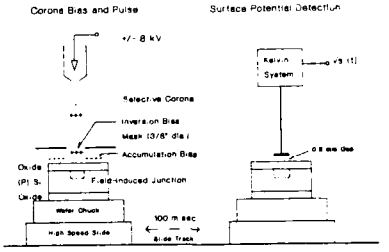


Figure 1 Corona-Pulsed Deep-Depletion Potential Technique

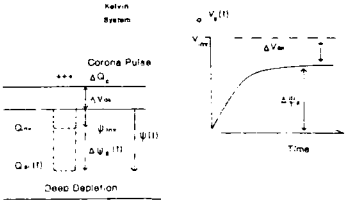


Figure 2 Corona-pulsed deep-depletion potential transient

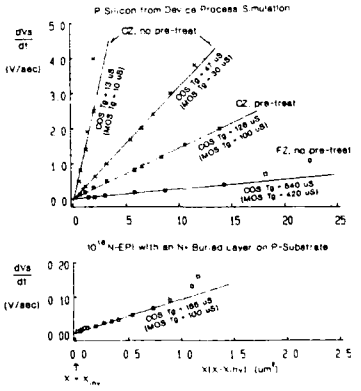


Figure 3 The Corona-Pulsed Deep-Depletion mode for silicon generation lifetime calculation

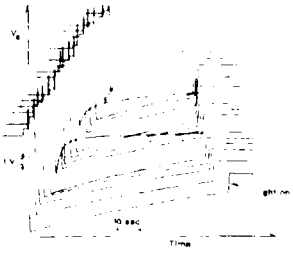


Figure 4 Corona-pulsed vs transient traces from an epitaxial sample. Randomly distributed defective sites are marked by faster recovery.

Abstract No. 432

Recombination lifetime of P/P$^+$ epitaxial silicon*

M. Aminzadeh & L. Forbes

Oregon State University, Dept. of Electrical Engr.
Corvallis, OR 97331

The pulsed MOS capacitor technique at elevated temperatures [1] was employed for characterization of recombination lifetimes, τ_r on p-type epitaxial layers. This technique relies on the dominance of the quasi-neutral bulk generation (diffusion current) over the generation within the space charge region and surface generation at elevated temperatures. The lateral contribution of the diffusion current was taken into consideration [2] for the MOS capacitors fabricated on thin p-type epitaxial layers. Previously [2], it was assumed that the contribution of minority carriers at the epi-layer - p$^+$ substrate interface is negligible; however, a significant number of minority carriers seem to generate from this interface which result in low apparent lifetimes of the p-type epitaxial material. Therefore, the recombination lifetimes calculated based on the assumption of zero generation of minority carriers at the epi-layer - p$^+$ interface are apparent values rather than the actual τ_r values. Investigation of various epitaxial layer thicknesses reveals that a significant number of minority carriers are generated at the epi-layer - p$^+$ substrate interface causing an order of magnitude reduction in measured or apparent recombination lifetimes.

Extremely high generation lifetimes of the order of 20-30 msec were observed on p-type epi-layers of doping concentrations of 4×10^{14} cm^{-3} which was supported by DLTS measurements where no significant deep levels with concentrations higher than 3×10^{11} cm^{-3} were present. The density of interface states at the Si-SiO$_2$ interface was lower than 10^{10} cm^{-2} eV^{-1}. These measurements indicate that the active region of the epitaxial material is free from defects or impurities.

The return to equilibrium in the pulsed MOS capacitor is sum of four processes which may be written in terms of current density [2]. It consists of diffusion of minority carriers within the epitaxial layer, generation of carriers at the epi-layer - p$^+$ substrate interface (J_{pp+}), generation within the depletion region (J_{gen}), and surface generation (J_s).

$$J_{total} = q\frac{n_i^2}{N_a}\frac{D_n}{L_n^2}W_B\left(1+\frac{4L_n}{D}\right) + J_{pp+} + J_{gen} + J_s \qquad (1)$$

where N_a is the doping concentration of the p-type epi-layer, L_n the diffusion length, W_B the epi-layer thickness, and D the diameter of the MOS capacitor. At elevated temperatures generation within the space charge region and surface generation (last two terms) are negligible. Therefore, J_{total} is linearly proportional to the epitaxial thickness for short base width devices ($L_n > W_B$). The total current density contributing to the return to equilibrium after application of the voltage pulse can be obtained from the time derivative calculation of the C-t response [3] as follows:

$$J_{total} = \frac{N_a}{2}\frac{\epsilon_{si}}{\epsilon_{ox}}\frac{d}{dt}\left(\frac{C_{ox}}{C(t)}\right)^2 \qquad (2)$$

where T_{ox} is the oxide thickness and C_{ox} is the oxide capacitance.

The main motivation for C-t measurements at elevated temperatures using different epitaxial thicknesses is to clarify whether the epi-layer - p$^+$ interface has a significant impact on the recombination lifetime of the epitaxial layers. Therefore, a set of epitaxial wafers with identical substrate and epitaxial growth conditions except different epi-layer thicknesses were prepared for this study.

The apparent recombination lifetimes based on zero J_{pp+} assumption are plotted versus the epitaxial thickness in Fig. 1. As the epitaxial thickness is increased the apparent recombination lifetimes increases. Since the samples had identical growth conditions, the actual recombination lifetimes of the epi-layers are expected to be the same regardless of epi-layer thickness. A plot of J_{total} obtained from the C-t transient response at 70°C using Eqn. (2) versus the epitaxial thickness is shown in Fig. 2. Each data point in this figure represents an average of 30 measured values. The actual recombination lifetime of the p-type epitaxial material is 19 μsec which is calculated from the slope of Fig. 2 using Eqn. 1. This is equivalent to an actual diffusion length of 245 μm. This is an order of magnitude larger than the apparent values for thin (13 μm) epi-layers shown in Fig. 1. Since the combined contribution of the generation within the space charge region and the surface generation is only about 4 nA/cm^2 at 70°C, the interface of epi-layer - p$^+$ substrate (J_{pp+}) is responsible for the remaining current seen from the intercept of Fig. 2. This suggests that the interface of the epi-layer - p$^+$ substrate constitutes 70% of the total current for thin (13 μm) epitaxial layers. As the diffusion current increases with respect to J_{pp+} by increasing the epitaxial thickness, the apparent recombination lifetimes approach the actual τ_r values of the epi-layer in Fig. 1. Therefore, the main limitation in the recombination lifetimes in p/p$^+$ epitaxial wafers is due to a localized degradation of lifetime at the interface of the epi-layer - substrate rather than the epitaxial layer itself.

REFERENCES

[1] D.K. Schroder, J.D. Whitfield, C.J. Varker, "Recombination lifetime using the pulsed MOS capacitor," IEEE Trans. Elec. Dev., Vol. ED-31, No. 4, pp. 462, 1984

[2] M. Aminzadeh, L. Forbes, "Recombination lifetime of short base width devices using the pulsed MOS capacitor technique," IEEE Trans. Elec. Dev., Vol. ED-35, No. 4, pp. 518, 1988

[3] M. Zerbst, Z. angew. Phys., Vol. 22, pp. 30, 1966

* This work was supported by SEH America, Inc.

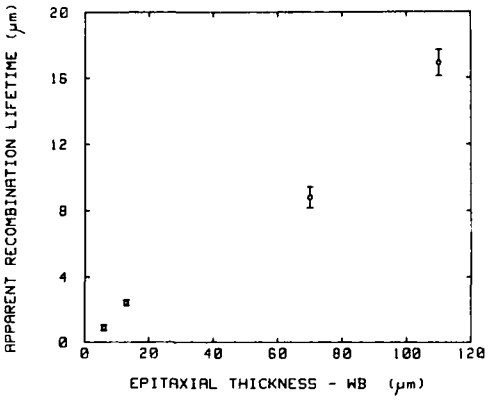


Figure 1) Apparent recombination lifetimes versus the epitaxial thickness.

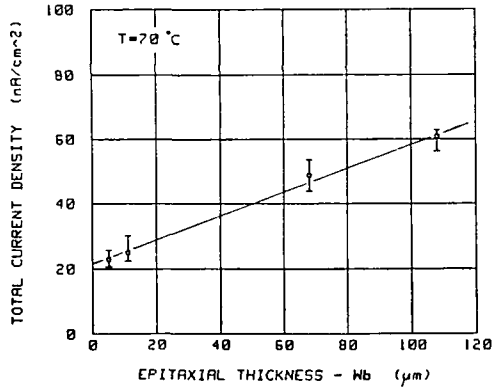


Figure 2) Current density as a function of epitaxial thickness at T=70°C.

Abstract No. 433

MAGNETO-ELECTRICAL CHARACTERIZATION OF MATERIALS AND DEVICES

David C. Look

University Research Center

Wright State University

Dayton, OH 45435

The use of magnetic fields in the electrical characterization of semiconductor materials is familiar to everyone, in the form of Hall-effect measurements. However, there is another magnetic-field-based phenomenon, magnetoresistance (MR), which is highly useful but not nearly so familiar to the majority of workers. One of the unique features of MR measurements is their applicability to common device structures, in particular, field-effect transistors (FET's) and contact-resistance patterns. We will show how channel mobility information can be extracted from the MR data in metal-semiconductor FET's (MESFET's) and modulation-doped heterostructure FET's (MODFET's), and also how the material under ohmic contacts can be compared with the unprocessed material to see if appreciable contact-element diffusion has occurred. Finally, we will consider some common problems which are often overlooked in performing simple Hall-effect measurements on thin structures. Some useful formulas and plots are presented.

Abstract No. 434

LOW FREQUENCY NOISE AS A PROCESS DEVELOPMENT AND CHARACTERIZATION TOOL

F. Scholz
Northern Telecom Electronics Ltd.
San Diego, CA 92127

G.N. Maracas and D.K. Schroder
Center for Solid State Electronics Research
Arizona State University
Tempe, AZ 85287

Introduction:

Low frequency noise measurements are used as a powerful process development and characterization tool for field-effect transistors (FETs). By measuring the spot frequency gate-referred noise power as a continuous function of temperature at different spot frequencies as well as measuring the gate and drain bias dependence of the noise for different wafer process variations, very useful process development and characterization information can be obtained.

Theory:

The sources of low frequency noise in MOSFETs are flicker noise, generation-recombination (G.R.) noise and thermal noise. These types of noise will be present in other types of FETs to varying degrees.

The temperature dependence of the spot frequency noise curves for flicker noise is determined by the energy dependence of the oxide trap density. In general, flicker noise has a gradual change with temperature. Theoretically it is possible to obtain a spot *frequency noise* peak when the sample temperature is scanned which would not shift to higher temperatures with increasing spot frequency.

Generation-recombination noise, on the other hand, has strong peaks at specific temperatures depending on the spot measurement frequency. As the spot frequency increases, the peaks reduce in magnitude and shift to higher temperatures. The G.R. trapping parameters can be extracted in a manner analogous to Deep Level Transient Spectroscopy (DLTS). This is accomplished by an Arrhenius analysis of spot frequency noise versus temperature of the noise peaks.

Thermal noise can dominate in long narrow channel devices operated at low drain voltage and higher frequencies where flicker noise is low. It usually decreases gradually with temperature in MOSFETs.

Experimental results:

Room temperature noise measurements performed at a spot frequency of 1kHz for four different process variations, and as a function of drain voltage are shown in Figure 1.

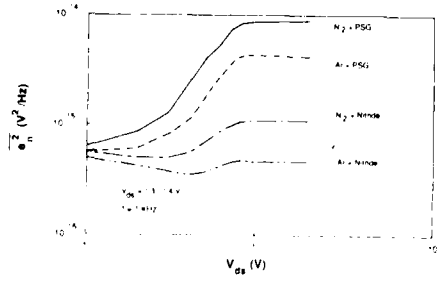


Figure 1. Gate referred mean squared noise voltage versus drain voltage at a spot frequency of 1 kHz for four different Si MOSFET passivation processes. V_{gs} = 1.35 to 1.4 V so that $I_d$sat= 40μA.

The process with an Argon gate oxidation push and anneal and with PECVD silicon nitride final passivation gives the lowest noise and is also independent of drain voltage. This is believed to be due to the prevention of nitridation during the oxidation process and even more important, the high hydrogen content of the PECVD silicon nitride process. Hydrogen becomes encapsulated by the silicon nitride and reduces interface states.

Figure 2 shows values of the density of interface traps as determined from noise measurements and compared with values from charge pumping experiments. Noise measurements show the greater sensitivity especially for the lower noise level processes.

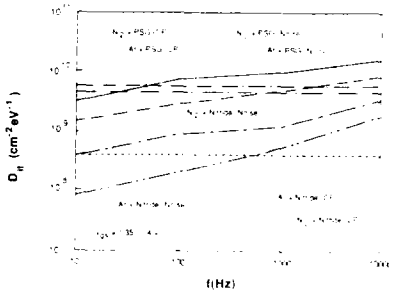


Figure 2. A comparison D_{it} calculated from low frequency noise *and charge pumping* experiments vs. spot frequency. The devices are Si MOSFETs passivated by four different processes. Phosphorus silicate glass (PSG) and silicon nitride under N_2 and Ar atmospheres. V_{gs} = 1.35 to 1.4 V so that $I_d$sat= 40μA.

Strong GR noise can be identified by the peaks in the family of spot frequency noise versus temperature curves of Figure 3, where the peaks shift to higher temperatures as the spot frequencies are increased.

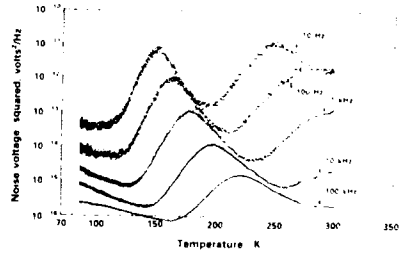


Figure 3. Measured spot frequency gate-referred noise power as a function of temperature for 3N158, p-channel MOSFET.

The GR trapping parameters are then extracted from these peaks in a manner analogous to DLTS measurements using a spot frequency noise Arrhenius plot. There is good agreement between these results and DLTS measurements on the same devices. Various combinations of flicker noise and GR noise may exist. When PECVD silicon nitride passivation is used in place of PSG passivation, the flicker noise is reduced while the GR noise peak amplitudes remain unchanged (see Figures 4a and 4b).

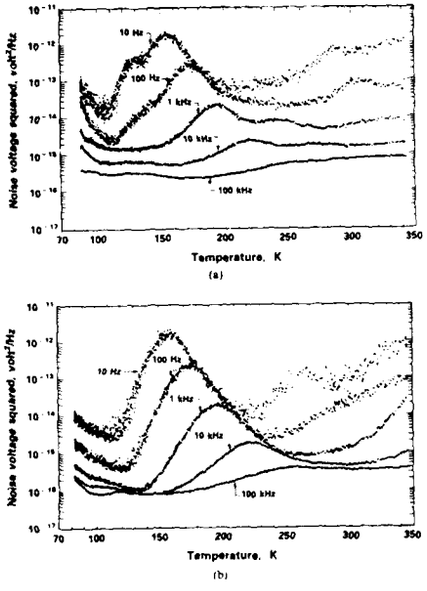


Figure 4. Spot frequency gate-referred noise power as a function of temperature for CMOS device, p-channel W/L = 23/5, V_{gs} = -1.9 V; passivated with (a) pyrox and (b) PECVD silicon nitride.

This is because traps in the depletion region are not reduced by the hydrogen as are the surface traps.

Noise measurements can also be performed on other FET devices. Spot frequency noise versus temperature measurements for AlGaAs/GaAs modulation doped FET devices indicate GR traps which are most easily observed at low drain voltages (Figure 5a).

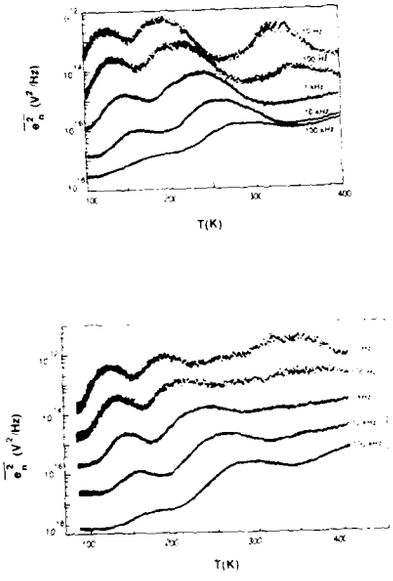


Figure 5. Spot frequency noise versus temperature for an AlGaAs/GaAs MODFET with W/L = 300/100. (a) V_{gs} = 0, V_{ds} = 0.5V and (b) V_{gs} = 0, V_{ds} = 0.5V.
As the drain voltage is increased into saturation, GR noise tends to be obscured by flicker noise (Figure 5b).

Details of these results will be presented.

Abstract No. 435

Defect engineering and the contact resistance of shallow and deep junctions in silicon discrete and integrated power devices

S. Al-Marayati, K. Shenai, N. Lewis, and B. J. Baliga

General Electric Company
Corporate Research and Development Center
Schenectady, New York 12301

I. Introduction

Low contact resistances to both shallow and deep junctions are required in discrete and integrated high voltage devices to minimize the power dissipation, to increase the switching efficiency, and to improve the frequency response characteristics [1-4]. For smart power applications, low voltage logic circuitry at the VLSI complexity need to be monolithically integrated with high voltage switching devices [5]. This function requires simultaneous low resistance contacts to both *n*- and *p*-type silicon and to both shallow and deep junctions. It is generally well known that contacts of aluminum based alloys to *p*-type silicon have low resistances because of relatively smaller Schottky barrier height [6,7].

In bipolar mode power devices such as the Insulated Gate Transistor (IGT) [8-10], reliable contact metallurgy with low contact resistance is needed to both *n*- and *p*-type silicon to reduce the latch-up susceptibility, to reduce the forward drop, and to improve the device safe operating area (SOA). In power MOSFET's, low contact resistances to source, drain, and channel diffusion result in reduced power dissipation, enhanced frequency response, and improved device ruggedness to high surge currents typically observed when delivering power to inductive loads [11,12]. High quality shallow and deep junctions with low defect density are required to reduce carrier recombination and generation effects and to improve the high frequency switching characteristics. Defect engineering to fabricate a variety of silicon junctions with low contact resistances and defect densities is therefore a necessity.

In this investigation, we report on a detailed study conducted to understand the contact characteristics of a variety of shallow and deep As, B, and P diffused junctions typically used in discrete and integrated power semiconductor technologies. A number of implantation/diffusion and predeposition/diffusion cycles were used to obtain a range of sheet resistances, doping profiles, junction depths, and surface defect morphologies. High resolution TEM, SEM, and silicon surface etch delineation techniques were used to understand the structural transformations and dopant precipitation mechanisms; spreading resistance profiling (SRP), SIMS, and the four-point probe measurements were used to measure electrically and chemically active dopant concentrations, silicon sheet resistance and junction depths. Both the transmission-line contact (TLC) test structures [13] and cross-bridge Kelvin resistors [14] were fabricated and detailed contact resistance measurements were performed. Correlation between the material and electrical contact characteristic is made based on these results and an optimum contact processing sequence with Al and Al + 1%Si contact metallurgy is derived.

I. Contact Fabrication Procedure

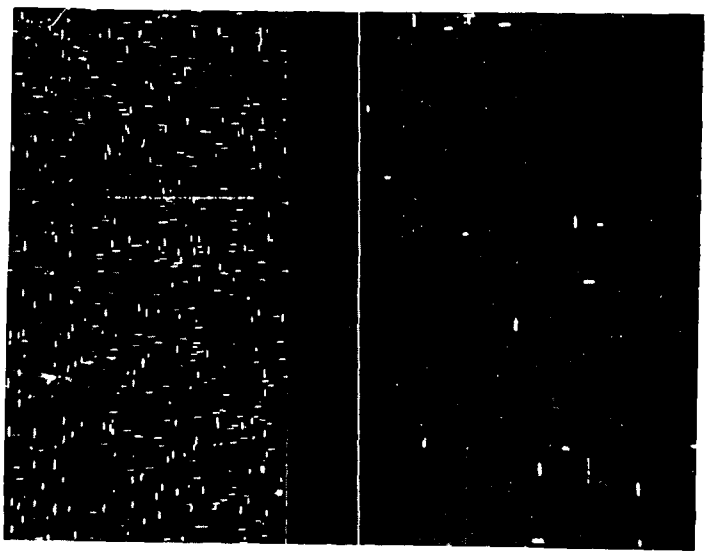
The experimental device structures consisted of As, B, and P diffused regions fabricated on <100> oriented silicon substrates. Shallow As and deep P doped junctions were formed by implanting As-75 and P-31 species and the implantation and diffusion parameters were varied to obtain a range of doping profiles. Shallow B doped junctions were fabricated by implanting B-11 species whereas deep junctions were formed by the predeposition and diffusion of boron from a boron nitride source. The boron predeposition was carried out at two different temperatures to minimize the silicon surface damage. Typical micrographs of boron doped silicon surface delineated using Wright etch are shown in Fig. 1 for predeposition carried out at two different temperatures. Significant reduction in the silicon lattice defect density can be seen for specimens where the predeposition was performed at 800°C. Contact test structures were fabricated by wet or dry etching [15] a layer of densified oxide and sintering *rf* sputtered Al or Alusil metal layers in hydrogen or forming gas at 465°C.

III. Contact Characterization

Detailed contact resistance measurements were performed using cross-bridge Kelvin resistors and TLC test structures to understand the contact resistance uniformity, contact linearity with current density, and contact string yield across 4 inch. diameter silicon wafers. These measurements were also performed at a number of different temperatures in the range of 0°C - 225°C to understand the contact reliability. Specific contact resistivity was determined from measured contact resistance, contact dimensions and distributed two-dimensional contact modeling. Detailed correlation between the electrical and material characteristic will be made based on extensive contact resistance measurements and material analysis performed using SIMS, SRP, SEM, TEM, four-point probe measurements, and silicon surface defect density measurements made from surface delineation techniques.

References

[1] C. Hu, et al, IEEE Trans. ED-31, pp. 1693, 1984.
[2] B.J. Baliga, in IEDM Tech. Digest, pp. 102, 1986.
[3] K. Shenai, and B. J. Baliga, Extended Abstracts of the 172nd Electrochemical Soc. Meeting, Honolulu, Hawaii, Abstract No. 705, p. 1005, 1987.
[4] K. Shenai, et al, in Proc. Workshop on Tungsten and Other Refractory Metals for VLSI Applications, Material Research Society, Pittsburgh, PA, p. 219, 1987.
[5] B. J. Baliga, IEEE Trans. ED-33, p. 1936, 1986.
[6] C. Y. Chang, et al, Solid State Electron. 14, p. 541, 1971
[7] S. M. Sze, *Physics of Semiconductor Devices*, 2nd Ed., Wiley:New York, 1981.
[8] B. J. Baliga, et al, in IEEE IEDM Tech. Digest, p. 264, 1982.
[9] J. P. Russel, et al, IEEE Electron Dev. Lett. EDL-4, p. 63, 1983.
[10] B. J. Baliga, et al, IEEE Electron Dev. Lett. EDL-5, p. 323, 1984.
[11] K. Shenai, et al, General Electric TIS Rep. 87CRD207, 1987.
[12] K. Shenai, et al, presented at The Workshop on Metals, Dielectrics, and Interfaces for VLSI, San Juan Bautista, CA, May 9 - 12, 1988. Also to appear in J. Vac. Sci. Tech. B, 1988.
[13] H. H. Berger, Solid-State Electron. 15, p. 145, 1972.
[14] S. J. Proctor, and L. W. Linholm, IEEE Electron Dev. Lett. EDL-3, p. 294, 1982.
[15] K. Shenai, et al, presented at the Seventh Symp on Plasma Processing, 1988 Spring Mtg. of ECS, Atlanta, GA, May 15-20, 1988, Abstract No. 114 of the Extended Abstracts Volume, p. 169, 1988.



(a) (b)

Fig. 1 Surface micrographs of boron deposited silicon surfaces delineated using the Wright etch for 2 min. (a) Boron deposition performed from a boron nitride source at 850°C (17,000 defects/cm^2), and (b) Boron deposition performed from a boron nitride source at 800°C with significantly reduced defect density.

Abstract No. 436

SPREADING RESISTANCE - RECENT DEVELOPMENTS IN IMPLEMENTATION AND INTERPRETATION

M Pawlik

GEC Hirst Research Centre
East Lane, Wembley
Middlesex, HA9 7PP, UK

During the last few years considerable progress has been made in the implementation of the spreading resistance technique and in the interpretation of results obtained by using the technique. There have been developments in experimental procedures, in data reduction techniques and in the understanding of the results, particularly in resolving differences between carrier and dopant profiles. This paper will consider each of these in turn and will discuss results of analyses performed on conventional IC type structures as well as more demanding structures grown by Molecular Beam Epitaxy.

The preparation of the bevelled sample and the conditioning of the probes remain the two most important parts of the experimental process. There is now general agreement that diamond bevelled surfaces give electrically stable surfaces. The preparation of probe tips is still based on empirical data but a procedure has been developed [1] which gives good electrical characteristics and is reproducible. This procedure involves unique methods of probe conditioning as well as a rigorous process of probe qualification. One important result of this process is that a calibration curve is always generated which has a slope which is greater than unity. This gives considerable advantages in the subsequent use if correction factor algorithms as there are no problems with apparent negative barrier resistances.

The need for efficient algorithms for the conversion of raw spreading resistance data into carrier concentrations has long been recognised [2] as has the need for good data smoothing prior to the application of such algorithms [3]. A new form of data smoothing has recently been proposed which is based on the concept of constrained cubic splines [4]. This has been extensively tested and has been found to offer signifcant advantages in its ability to follow general data trends and to simultaneosuly reduce noise to an acceptable level. This algorithm requires little operator input and allows complex multilayer type structures to be smoothed. Furthermore it can be implemented on a desk top computer and does not require excessive computation time. Examples of the applications of this algorithm will be presented.

The calculation of the sampling volume correction factor has always proved difficult but there is now a choice of algorithms which can be used as circumstances demand. The Berkowitz-Lux method has been extended to include barrier resistance and as a consequence gives greater accuracy in situations where a conducting lower boundary exists. e.g. n -n^+ or p-p^+ epitaxial layers. This method is however only directly applicable if the effective barrier resistance is positive. In most facilities this condition is violated for p type material but the probe conditioning procedures we employ overcome this problem. Different formulations of the algorithms using a variable radius formulation are also now available and the value of these will be assessed.

By combining our experimental technique with the best choice of smoothing and the appropriate formulation of the correction factors, we obtain carrier concentration profiles which are the best that can currently be achieved. Despite this, there are numerous examples where there is a large discrepancy between carrier concentration profiles as determined by spreading resistance and atomic or dopant profiles as determined by SIMS or Neutron Activation Analysis e.g. low dose implants [5] and high to low rapid resistivity transitions which can be achieved by Molecular Beam Epitaxy. In an attempt to try and resolve these discrepancies experimental studies have been undertaken by profiling samples in the normal and in the "upside-down" configuration [6]. These studies have been complemented by modelling the system by solving the one dimensional Poisson equation with particular boundary conditions to give an "or bevel" carrier distribution. A coherent picture has emerged from these studies which shows that one dimensional carrier spilling is responsible for most of the observed discrepancies. Examples will be shown of cases when carrier spilling must be taken into account to be able to infer vertical carrier distributions and ultimately dopant distributions.

Acknowledgements

The author would like to thank the European Economic Community for their partial support of this work under Esprit Project 519. He would also like to thank his partners in this project W. Vandervorst and T. Clarysse of IMEC and A. Casel of AEG for permission to use some of their data.

References

1 Ogden E.J., Esprit Project 519 - Special Report, September 1987

2 Pawlik M., In ASTM STP 960, Eds. D.C. Gupta and P.H. Langer, 1988

3 Pawlik M., Proc 1st Int. Symp. on Molecular Beam Epitaxy, Vol 85-7, The Electrochemical Society, 1985

4 Clarysse T. and Vandervorst, W., Solid State Electronics, Vol 31, p. 53, 1988

5 Godfrey D.J., Groves R.D., Dowsett M.G. and Willoughby A.F.W., Physica 129B, 1986

6 Casel A. and Jorke H., Appl. Phys. Lett., Vol 50, p. 989, 1987

Abstract No. 447

Recent developments in the interpretation of spreading resistance profiles for VLSI-technology

W.Vandervorst and T.Clarysse

IMEC vzw

Kapeldreef 75, B-3030 Leuven, Belgium

The accurate determination of the electrical carrier and dopant profile is an important issue in the control of VLSI-processes dealing with submicron devices. The use of submicron devices has highlighted the problems associated with the standard interpretation of spreading resistance profiles. In particular the difference between the *electrical carrier* and the *atomic dopant* distribution has not been accounted for on a routine basis in commercially available correction routines.

In the present work we report on the implementation of a *one dimensional* model which relates the carrier and the dopant profiles through the solution of the Poisson equation. In this model the on-bevel carrier concentration is computed by simulating the influence of the bevel angle by sequentially removing incremental layers from the atomic doping profile [1]. The use of this carrier spilling model allows to explain the anomalies observed when profiling *low dose implants* into same and opposite type substrates. In the latter case a profile much shallower and apparently much lighter doped is observed than in the former case. This can however be explained based on the carrier spilling effects (Fig 1). Also in the case of *abrupt junctions* (n+ on p, p+ on n) the model explains why no "junction peak" can be observed. Extensive comparisons with the carrier spilling effects calculated with two-dimensional simulators indicate that the two-dimensional effect is extremely small for most practical applications. In fact the one-dimensional calculation can also predict the maximum two-dimensional effect such that always the accuracy of the model can be evaluated.

The correct interpretation of spreading resistance measurements is further complicated by the fact that presently available schemes rely on the Schmann and Gardner multilayer theory which evaluates the resistance based on the carrier levels on the bevel [2]. However for submicron ranges one should definitely use the "*underlying vertical carrier profile*" and not the on bevel carrier profile since it is the first one which determines the actual current distribution and hence the correction factor to be applied. Therefore a simple reverse Poisson solution after calculating the on-bevel carrier profile will not lead to the correct results. Finally on should realize that current schemes use a mobility value for converting resistivity to concentration, based on the carrier concentration whereas in extreme cases of carrier spilling the dopant concentration, which can be quite different, is the determining factor. A new correction scheme is proposed which takes into account the correct calculation of the correction factor using instantaneous vertical carrier profiles as well as the correct mobility value through the calculation of the on bevel as well as vertical carrier and dopant distribution.

Experimentally the analysis of devices can also be influenced by the current restriction in these *small structures*. In this case the measured spreading resistance will not correspond to the value measured on a homogeneous substrate. Using specially designed structures we have measured the effect of close-by boundaries on the spreading resistance of identical profiles. It was found that the resistance increases significantly (factor 2-5, Fig. 2) as the boundaries come closer than the probe spacing. Theoretical calculations using a 3D-solution to the Poisson equation confirm that the effect can solely be ascribed to the restriction of the current flow in these analysis. In addition it was found that this increase in spreading resistance in these small structures leads to an incorrect evaluation of the integrated dose of the profile. No effect on the measured junction depth was found.

References:

[1] A. Casel, Appl. Phys. Lett. 50, 989 (1987)

[2] P.A. Schumann and E.E. Gardner, Solid State Electronics 19, 561 (1976)

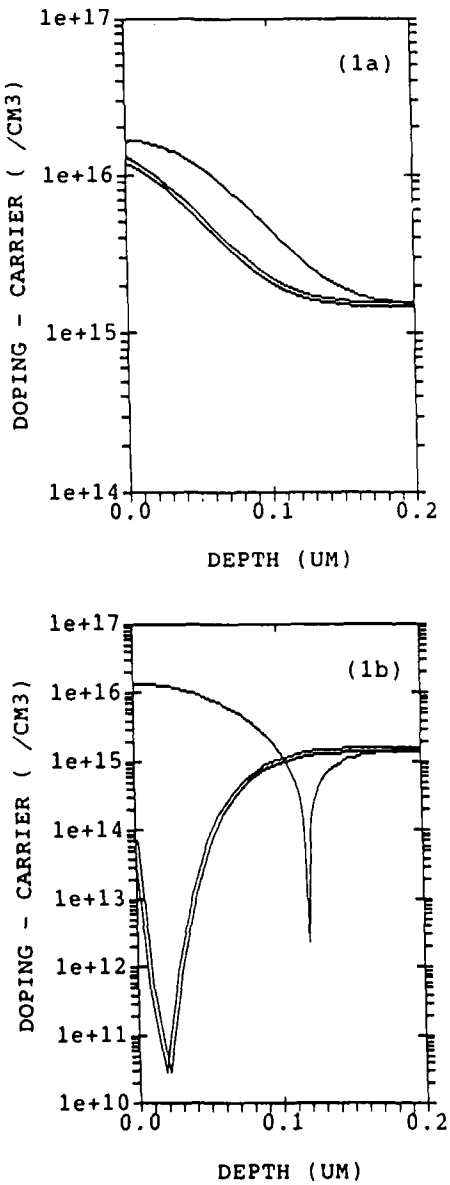


Figure 1: *Apparent carrier profile for low dose implant into p-type (a) and n-type (b) substrate. The solid lines correspond to the dopant profiles, the double lines to the carrier profiles calculated using the one dimensional carrier spilling model.*

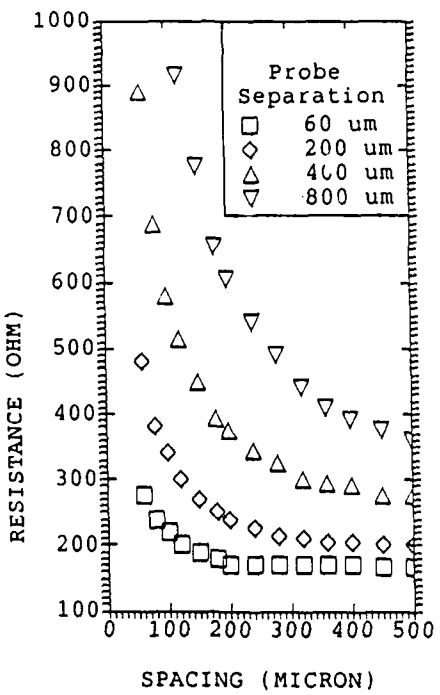


Figure 2: *Variation of the spreading resistance measured at the surface of a B-implant into n-type substrate ($10^{14}cm^{-3}$, 50 keV), with the distance between two insulating boundaries parallel with the probe points.*

Abstract No. 438

CONTACTLESS SILICON DOPING MEASUREMENTS BY MEANS OF A CORONA-OXIDE-SEMICONDUCTOR (COS) TECHNIQUE

R.L. Verkuil and M.S. Fung

IBM Corp., E. Fishkill
Hopewell Junction, NY 12533

INTRODUCTION - A contactless, Corona-Oxide-Semiconductor, COS, technique for P or N type silicon doping measurements is presented as a convenient alternative to conventional Metal-Oxide-Semiconductor, MOS, methods [1,2]. As in MOS, we use silicon depletion theory [3]. Unlike MOS, we use a corona discharge to replace the metal MOS electrode, similar to [4,5] and our later work [6,7,8]. Furthermore, unlike earlier corona applications in the semiconductor industry, this paper and another paper [9] at this meeting feature pulsed silicon deep depletion measurements with a corona discharge [6].

COS TEST APPARATUS - Fig. 1 shows, for example, an oxidized N type wafer on a vacuum chuck riding on an X-Y stepper. The stepper moves selected wafer testing locations between two corona discharge guns and a customized, automatic Kelvin Probe System for contactless surface potential measurements. Each corona gun consists of a needle, connected to a +/- 6-8Kv source, and associated electrodes for creating and directing a well defined beam of ionized room air down to the wafer surface. Beam diameters of the large and small guns are controlled by metal masks, similar to [6,7,8,10]. The Kelvin Probe System is actually a combination of two automatic Kelvin Systems that eliminate the need for a backside wafer contact by measuring changes in wafer surface potential, V_s, relative to wafer bulk. Measurement response time is about 100 ms. The top Kelvin System senses a selected wafer testing location via capacitive coupling across a small air gap. The bottom Kelvin system similarly senses the back of the wafer. All of the above apparatus is housed in a dark enclosure.

COS DOPING MEASUREMENT PROCEDURE - Consider an N type silicon example. First, a 2 cm diameter region on the wafer surface is accumulated by positive charging from the large corona gun, as shown in Fig. 2a. Then, as shown in Fig. 2a, a 1 cm diameter area within the accumulated region is inverted by negative charging from the small corona gun. This results in a field induced P-N junction, with a perimeter surrounded by an accumulated silicon guard ring to minimize surface effects. Next, a 100 ms negative corona burst from the small gun pulses the junction into deep depletion. The junction is then rapidly centered under the pick-up plate of the top Kelvin System to capture the resultant V_s transient shown in Fig. 3. From Fig. 3, the changes in silicon surface potential, dV_{si}, and oxide potential, dVox, are combined with the known oxide thickness, T_{ox}, to calculate silicon doping concentration, N_d, using [3].

COS DOPING MEASUREMENT PRINCIPLES - Fig. 4 shows a field induced P-N junction immediately after the deep depletion negative corona burst, dQ_{ox}. For example, consider the case of uniform doping, N_d: W_{inv} and PSI_{inv} are the silicon depletion depth and surface potential, respectively, corresponding to strong inversion. From [3]: $W_{inv} = \{2(E_{si})PSI_{inv}/(q(N_d))\}^{1/2}$, where: $PSI_{inv} = (KT/q)(Ln(N_d/ni) + 2.08)$, as per Lindner [3]. dW is the additional depletion depth resulting from instantaneous silicon charge imaging of dQ_{ox}. From conservation of charge: $dQ_{ox} = (E_{ox}/T_{ox})(dV_{ox}) = dQ_{si} = qN_d(dW)$. From [3], for deep depletion: $W_{inv} + dW = \{2(E_{si})(PSI_{inv} + dV_{si})/(q(N_d))\}^{1/2}$. Combining the above relationships leads to an implicit expression for N_d, which can be solved by iteration. For non-uniform doping, we are extending the same apparatus to do profiling with a pulsed Q-V method similar to MOS pulsed C-V [2]. Incrementally increasing corona pulses are used to obtain silicon capacitance, $C_{si} = dQ_{si}/dV_{si}$.

RESULTS, COS VS MOS - Eleven experimental, N type, epitaxial silicon wafers were processed to produce a range of N_d from 7e15 - 1e17 at/cc. Aluminum MOS dots (20 mil diam.) were evaporated on a portion of each wafer, with blank space reserved for COS testing. N_d was measured at 3 sites/wafer by *COS and the MOS* Cmax-Cmin method [1]. Fig. 5 shows the good agreement obtained.

DISCUSSION/CONCLUSIONS - The COS technique is primarily limited by corona discharge beam characteristics and control: Uniformity affects accuracy, sharpness of edge definition affects fast surface states related errors and repeatability is critical for attempting doping profiles. In the absence of silicon defects, the deep depletion transients we obtained were so slow (tens to hundreds of seconds) that the several hundred ms required for charging, moving and sensing during COS testing was not a limitation. The major COS advantage is no need for evaporated metal dots or contaminating liquid contacts.

REFERENCES

[1] E.H. Nicollian and J.R. Brews, MOS (Metal Oxide Semiconductor) Physics and Technology, John Wiley and Sons, NY, (1982) pp 407-408
[2] Ibid, pp 383-385
[3] Ibid, pp 58-63
[4] M.H. Woods and R. Williams, J. Appl. Phys., Vol. 44, No. 12 Dec., (1973).
[5] R.B. Comizzoli, J. Electro. Chem. Soc., Vol. 134, No. 2, pp. 424-429 (1987)
[6] H.W. Curtis, M.S. Fung and R.L. Verkuil, internal pat. pubs., '83 -'87.
[7] M.S. Fung, J.A. Bruce and R.L. Verkuil, Electro. Chem. Soc. Ext. Abs. 284, May, '85 Mtg.
[8] R.L. Verkuil and M.S. Fung, Electro. Chem. Soc. Ext. Abs. 169, May '88 Mtg.
[9] M.S. Fung and R.L. Verkuil, Electro. Chem. Soc. Ext. Abs. ___, Oct. '88 Mtg.
[10] Z.A. Weinberg., et.al., Appl. Phys. Lett., Vol. 25, No. 1, p. 42, (1974).

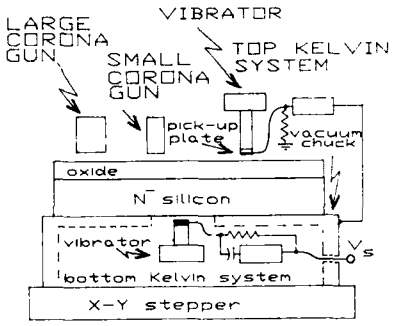


FIG. 1 - CDS APPARATUS

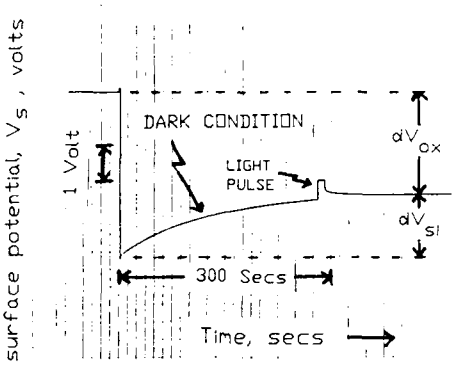


FIG. 3 - ACTUAL MEASURED DEEP DEPLETION SURFACE POTENTIAL, V_S, TRANSIENT.

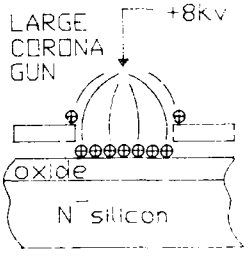


Fig. 2a - N⁻ silicon ACCUMULATED BY POSITIVE CORONA

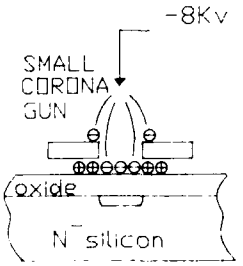


FIG. 2B - N⁻ SILICON INVERTED BY NEGATIVE CORONA

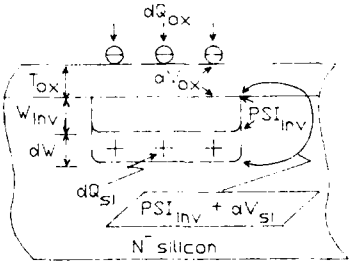


FIG. 4 - VERTICAL CROSS SECTION SHOWING INSTANTANEOUS DEEP DEPLETION AFTER NEGATIVE CORONA BURST, DQ_{ox}.

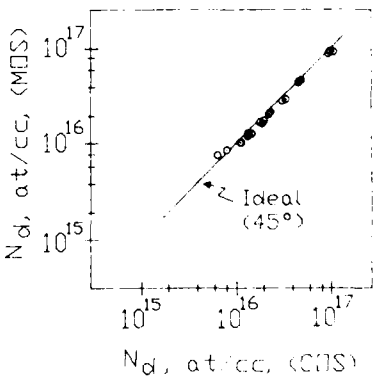


FIG. 5 - N_d, MOS METHOD VS N_d, CDS METHOD

Abstract No. 439

Depletion Layer Solver for Nonuniform Impurity Profile using Analog Computation Techniques

A.Shenoy, H.C.Chien*, H.C.Lin, R.Ramaswami*

Dept. of Electrical Engineering
University of Maryland
College Park, MD 20742

This technique is a fast and straight forward approach to determine the junction parameters like the electric field and depletion width of a semiconductor device doped with a nonuniform impurity profile.

The common impurity profiles like the Gaussian and complementary error functions are not normally available from a standard function generator. The object of this work is to generate these waveforms for a single sided junction and to use the simulated analog waveform to represent the impurity profile input to a Poisson equation solver. The waveforms are generated using a personal computer along with an interface board consisting of D/A converters and this makes the waveform generation technique very flexible enabling us to generate waveforms of any specification and frequency. The Poisson equation solver is an analog circuit that solves the junction parameters and is unique since it is capable of generating the constants of integration when the Poisson equation is integrated. Assuming that the depletion approximation holds good we represent the Poisson equation by

$$\frac{d^2V}{dx^2} = \frac{q}{\epsilon}(N_A - N_D) \tag{1}$$

where $N_A - N_D$ is the net dopant concentration. The electric field is the first integral given by

$$-E(x) = \frac{dV}{dx} = \int_0^x \frac{-qN(x)}{\epsilon}dx + C1 \tag{2}$$

C1 denotes the constant of integration which is

$$C1 = \int_0^w \frac{qN(x)}{\epsilon}dx \tag{3}$$

The analog circuit used is as shown in Figure 1. By using the set control signals correctly it is possible to control a set of switches which make the circuit operation feasible. The impurity profile $\bar{V}$ is the input to the solver. The time of integration is varied such that V_1 at the output of the first integrator represents the first constant of integration. The constants of integration are important since they are obtained by varying the signal frequency and the frequency of the signal is a direct indication of the depletion width. The second integral of the Poisson's equation yields the potential distribution

$$V(x) = \int_0^x \left(\int_0^x \frac{-qN(x)}{\epsilon}dx + \int_0^w \frac{qN(x)}{\epsilon}dx\right)dx \tag{4}$$

Figure 2 shows the control signals used. The control signals are also generated with the aid of the personal computer such that the input signal $\bar{V}$ is perfectly synchronized with the control signal S_1. Signal S_2 has half the frequency of S_1 and is used mainly to control the switch of the sample and hold circuit which is the component of the solver that stores the constant of integration C1. Hence the frequency of the input signal is varied until the equation (4) is satisfied and equals the applied reverse bias V_a at $x = w$ where w denotes the depletion width. The calculated versus predicted depletion widths are indicated in Table 3 which are off by an average of about 4 percent which could be attributed to the leaky capacitors and also human error in voltage measurements.

The photographs indicate the waveforms obtained at various points in the solver during the course of the experiment. The approach is quite attractive since it is possible to evaluate the depletion width and electric field for any specification of the impurity doping profile and is much faster than digital computation techniques.

References

[1] Lin H. C., "*Calculations of a Double-Diffused Junction*," Electron Devices, vol. ED-27, No 9, September 1980 pp. 1839.

[2] Shenai K., Lin H. C., "*CAD Modeling Of Diffused p-n Junctions*," COMPEL- The International Journal for Computation and Mathematics in Electrical and Electronic Engineering, vol. 1, No 2, 11-127 (1982).

[3] Handbook of Mathematical Functions (National Bureau of Standard, Washington, D.C.).

* Now with Intel Corp, Folsom, CA 956430

⋆ Now with Allied Bendix, Columbia, MD 21045-1998

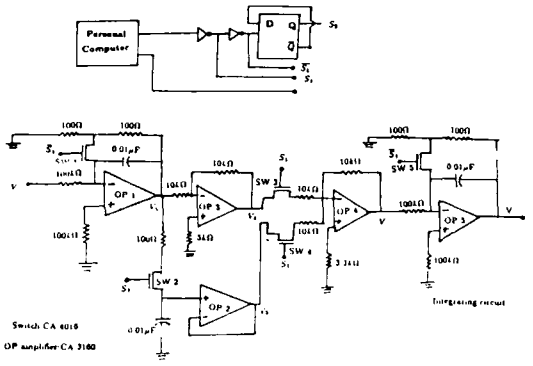


Figure 1

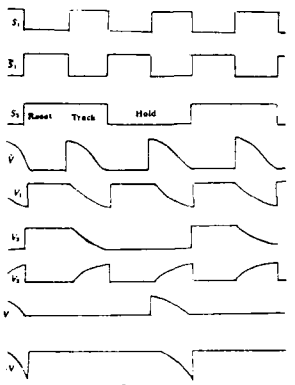


Figure 2

Solution for a Gaussian distribution

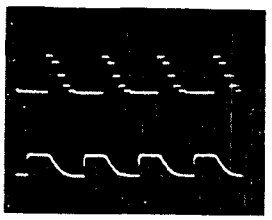


Plate A3 V_1

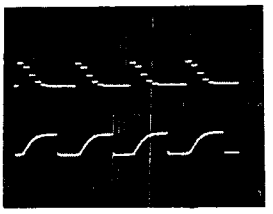


Plate A5 V_3

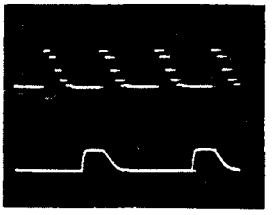


Plate A4 V_2

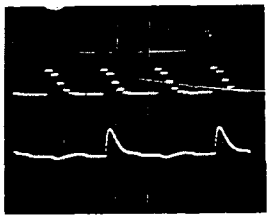


Plate A6 V

Voltage V	$P_s = 10^{14}/cm^3$			$P_s = 10^{15}/cm^3$			$P_s = 10^{16}/cm^3$		
V_a	W_m	W_p	% error	W_m	W_p	% error	W_m	W_p	% error
1V	5.03	4.93	1.99	2.40	2.31	3.75	1.89	1.86	1.59
2V	7.01	6.73	3.99	2.89	2.73	5.54	1.92	1.91	0.31
3V	8.25	8.14	1.30	3.30	3.09	6.36	[illegible]	1.97	1.50
4V	9.50	9.16	3.48	3.50	3.41	2.37	2.15	2.02	6.05
5V	11.4	10.4	8.77	3.80	3.71	10.0	2.20	2.10	4.55

P_s = Surface Concentration in /cm³
V_a = Applied reverse bias in volts
W_m = Measured depletion width in μm
W_p = Predicted depletion width μm
Approximate formula used to measure the depletion width is
$[\frac{V_a}{V_{bi}} + 1] = W^3[\sqrt{B} - \frac{B}{3}]$
where
$A = P_s$
and $B = \frac{A_{eq}(\frac{q}{\epsilon_{Si}})}{(V_{bi})^2}$

Table 3

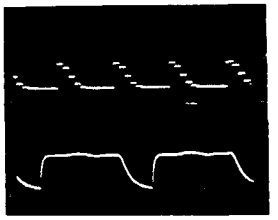


Plate A7 Potential Distribution

Abstract No. 440

MASK REPAIR AND MICROMACHINING WITH FOCUSED ION BEAMS

L.R. Harriott

AT&T Bell Laboratories
600 Mountain Avenue
Murray Hill, New Jersey 07974

Defect repair for lithographic masks is currently the largest commercial application for focused ion beams.[1-6] Defects in the form of excess mask material are removed by physical sputtering and those in the form of missing mask material are repaired by gas-phase ion-induced material deposition. As circuit and mask features have become smaller with advancing VLSI technology, it has become evident that laser ablation was no longer adequate for photomask defect repair. Despite the advantage of focused ion beam photomask repair in resolution, there are difficulties and limitatations. The major limitation for the performance of focused ion beams in mask repair is mask charging. Mask structures are typically a patterned chrome absorber on a quartz or glass substrate. As the substrates are insulating, the beam tends to charge the substrate and electrically isolated Cr features to a positive potential. If not compensated, the substrate will charge up and deflect the incomming ions, causing beam placement errors. Electron flood beams are generally used to alleviate this problem. Because of the large ion current density, this process does not always work entirely. For most situations, the beam placement performance is about +/- 0.1 micron, however. Focused ion beam repair has been applied successfully to photomasks and will become more widely needed and accepted over the comming years.

Focused ion beam micromachining has also been applied to integrated circuits.[7-9] The primary purpose for this is as part of the diagnostic process. It has been applied to debugging new circuit designs by correcting errors and isolating sections of circuits for testing. The alternative to this type of design fault diagnosis is often guesswork followed by weeks of delay for processing of new wafers. In addition to cutting circuits by milling, focused ion beam induced metal deposition can be used to complete circuit connections allowing arbitrary circuit editing. In the comming years, this application is expected to be the dominant one for focused ion beams in terms of numbers of machines.

Three dimensional structures produced by focused ion beam micromachining have found application in optoelectronic devices.[10-12] In semiconductor laser devices, the mirror facets necessary to form optical resonators are generally formed by mechanical cleaving making integration of devices difficult. Focused ion beam milling has been shown to be capable of producing optical quality mirror facets indicating that integrated devices were possible with this technique.

A review of focused ion beam micromachining systems and applications will be presented. The machines have been developed for applications including X-ray and optical mask repair, integrated circuit modification and fabrication of integrated optical structures. These systems include provisions for secondary electron and ion imaging, charge neutralization, material removal by physical or chemically assisted sputtering, gas phase material deposition,and secondary ion mass spectroscopy (SIMS).

1. A.Wagner, D.L.Barr, D.K.Atwood, and J.H.Bruning, 1983 Intl. Symp. on Electron,Ion, and Photon Beams, Los Angeles.

2. D.K.Atwood, G.J.Fisanick, W.A.Johnson, A.Wagner, Proc. SPIE,vol.471,(1984), p.127.

3. W.P.Economou, D.C.Shaver, B.Ward, Proc. SPIE, vol. 773,(1987), p.201.

4. T.D.Cambria, Proc. SPIE, vol. 773, (1987), p.201.

5. M.Yamamamoto, M.Sato, H.Kyogoku, K.Aita, Y.Nakagawa, A.Yasaka, R.Tahasawa, and O.Hattori, Proc. SPIE vol. 632, (1986), p.97.

6. H.C.Kaufman, W.B.Thompson, and G.J.Dunn, Proc. SPIE vol. 632, (1986), p. 60.

7. L.R.Harriott, A.Wagner, and F.Fritz, J. Vac. Sci. Technol. B4(1) 1986, p. 181.

8. J.Melngailis, C.R.Musil, E.H.Stevens, M.Utlaut, E.M.Kellogg, R.T.Post, M.W.Geis, and R.W.Mountain, J. Vac. Sci. Technol. B4(1), 1986, p.176.

9. D.C.Shaver and B.W.Ward, J. Vac. Sci. Technol. B4(1), 1985, p.185.

10. L.R.Harriott, R.E.Scotti, K.D.Cummings, and A.F.Ambrose, Appl. Phys. Lett. 48(25), 1986, p.1704.

11. L.R.Harriott, R.E.Scotti, K.D.Cummings, and A.F.Ambrose, J. Vac. Sci. Technol. B5(1), 1987, p.204.

12. J.Puretz, R.K.DeFreez, R.A.Elliott, and J.Orloff, Electronics Letters 22(13), 1986, p.700.

Abstract No. 441

Advances in etching by FIB for photomask repair

Y. Nakagawa, T. Yamaoka, K. Aita, M. Sato,
M. Yamamoto

Seiko Instruments Inc.
Oyama, Shizuoka, JAPAN

J. Glanville

Seiko Instruments U.S.A.
San Jose, Calitornia

Focused ion beam (FIB) technology for photomask repair has become widely accepted as a practical tool for photomask repair, primarily because it makes submicron repair capability a reality. FIB induced deposition of carbon films is regarded as an acceptable method of repairing clear defects.[1] The repair of opaque defects, however, still presents problems which must be overcome. For example, residual chrome may be present due to incomplete etching. Excessive etching may damage the substrate and gallium is implanted in the etching process. All of these factors will contribute to a loss in transmissivity of repaired areas. In an effort to improve transmissivity, it has been suggested that post-repair processing using CF_4 plasma etching, or CHF_3+O_2 reactive ion etching, can reduce the gallium present in the repaired areas.[2,3] These processes subject the entire photomask surface to the etching action of the plasma, which changes surface reflectivity by reducing the thickness of the chrome-oxide antireflective layer. This added processing can take up to 20 minutes per mask, and there is a possibility that new defects will be created. The resulting reduction in overall repair throughput makes such post-repair processing undesirable.

We have developed a method of secondary ion mass analysis coupled with chemically assisted FIB sputter etching of opaque defects, which results in 98% transmissivity, without any additional post-repair processing.

The apparatus used is the SIR-1000 FIB photomask repair system with assist gas attachments, manufactured by Seiko Instruments Inc.[4,5] As the primary Ga^+ beam strikes the mask surface, secondary Cr and Si ions are emitted, collected, and mass separated by a sector magnet, then detected by individual channeltrons. This detection method provides a very high signal-to-noise ratio and allows for precise monitoring of secondary Cr and Si ion intensities during the etching process to determine end-point, and ensure the complete removal of the Cr layer, without overetching. Our current etching technique, as it is referred to later in this work, utilizes only the real-time end-point monitoring described previously. Our chemically assisted technique simply introduces a reactive gas locally into the opaque defect region during etching. The introduction of the gas coupled with the real-time end-point monitor software, reduces the gallium concentration level by 48%, as confirmed by Auger electron spectroscopy.

Transmissivity was compared between the current opaque defect repair technique and our chemically assisted technique and the data are shown in Table 1. The SL and QZ listed in the table represent soda lime and quartz substrates, respectively. CR and BC represent Cr and CrO_x films, respectively. Mask blanks from four manufacturers, one U.S. and three Japanese, were etched using both techniques and transmissivity of the repaired areas was measured using a Konica PDM-5 microdensitometer. The data shown are from 10X20um etched areas. This comparison shows an average increase in transmissivity of 15% using the chemically assisted technique, resulting in almost the same transmissivity as virgin glass. Table 1 also shows that the substrate material and the chrome type have little or no effect on transmissivity.

A lithography test was also performed to compare the current technique and our chemically assisted technique. A Perkin-Elmer M340HT projection aligner was used to expose wafers with 1.3-um-thick HPR204 photoresist after a 110°C 90-s prebake. We compared etching results at exposure threshold (ETH) and underexposure levels. Figures 1(a) and 1(b) show two optical microscope photos of resist patterns exposed at ETH and at 30% below ETH, respectively. Circle area 1 was etched using the current technique and circle area 2 was etched using the chemically assisted technique. Although area 1 in Fig. 1(a) shows an unacceptable residual resist image, area 2 in Fig. 1(b) shows a degree of resist exposure equal to virgin glass.

Acknowledgments: The authors wish to thank Hiu Ip and Susan Chiang of Micrel and Mitch Lashman and Andrew Cosio of Nikon Precision Inc. for their assistance in conducting the lithography testing. The assistance of Dr. Arthur Turner of Perkin-Elmer PHI Laboratories is gratefully acknowledged.

References:

[1]S. Noguchi, STEP/SEMI Technical Education Programs, 1987.
[2]T. Cambria, STEP/SEMI Technical Education Programs, 1987.
[3]H. Oneda, in Extended Abstracts of the 48th Autumn Meeting of the Japan Society of Applied Physics, 1987, p. 424.
[4]M. Yamamoto, SPIE 632,97 (1986).
[5]M. Yamamoto, in the 17th Symposium on Ion Implantation and Submicron Fabrication, 1986, pp. 181-18..

Table 1

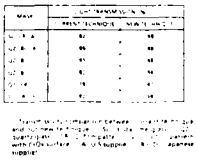


Fig. 1(a)



Fig. 1(b)



Abstract No. 442

ANALYTICAL SIMULATION OF FOCUSED ION BEAM APPLICATIONS IN X-RAY MASK REPAIR

H. Burghause, U. Weigmann, M. Weiß

Fraunhofer-Institut für Mikrostrukturtechnik (IMT)
Dillenburger Str. 53, 1000 Berlin 33, Germany

In microlithography one application of focused ion beam milling is the repair of opaque defects on masks for optical as well as for X-ray lithography. Several specific problems arise in X-ray mask repair, which are of no importance in the repair of photomasks because the absorber structures of X-ray masks are ten times higher (ca. 1 µm) than of optical masks. The ion milling result is influenced by trenching effects, ion beam energy, beam profile (current density), and the applied milling strategy. However, the most important problem in X-ray mask repair is the generation of new defects at absorber edges by the redeposition of sputtered defect material. To understand the consequences of these interdependent occuring sputter effects, a computer simulation of the milling process is necessary to evaluate the limiting factors of the attainable resolution in X-ray mask repair and to develop appropriate milling strategies. The ultimate aim of the simulation is an online software support for the X-ray mask repair process.

In a first attempt a two dimensional focused ion beam milling simulation program based on the string algorithm /1/ was developed, which takes care of most of the mentioned sputter effects /2/. Since the numerical method used suffers from an unacceptable long computing time for a complete process simulation making the program unsuitable for in situ applications, a new 2D-simulation program concentrating on redeposition effects was conceived. This program is based on the analytical formation of Smith et al. /3/. It assumes the removal of a free-standing defect close to an absorber edge and calculates the time dependent evolution of the absorber edge shape according to the occuring redeposition. The needed computing time is in the range of seconds and, therefore, of interest for an online application.

The width of the defect to be removed, the defect height, the milling depth per ion beam scan, the ion energy, and the beam diameter can be varied. Fig. 1 shows a simulated redeposition profile at an absorber edge. The absorber height of 2 µm was chosen to illustrate the shape of the redeposition profile. The width of the ion beam with an assumed square-wave intensity distribution was 100 nm, the beam was scanned once from left to right over the defect area so that the 0.5 mm wide defect was removed in five steps. In the graphics every removed defect "column" corresponds to one redeposition profile at the absorber edge.

An alternative defect repair strategy can be simulated where the ion beam is scanned five times faster over the defect area (see Fig. 2). Then five milling steps in the z-direction are necessary to remove the defect completely. The profile of the redeposited defect material differs from the redeposition profile of Fig. 1 due to the different milling strategy (all other parameters are kept constant). The antinode of the redeposition club in Fig. 2 has shifted in the +z-direction. The real situation where the absorber height is only 1 µm, is closer to a redeposition profile indicated by dashed line in Fig. 2. Therefore, milling strategies where defects are removed in layers reduce redeposition.

The angular distribution of the sputtered material depends on the energy of the incoming ions /4/. For high energies as used in X-ray mask repair this distribution is strongly backward oriented referred to the incoming ions and yields, therefore, smaller redeposition as can be seen in Fig. 3.

A comparison with the experiment allows Fig. 4. A 1 µm thick gold defect on an X-ray mask was removed. The 100 keV ion beam was scanned once from left to right over the defect. Sputtered gold redeposited at the nearby absorber edge. The redeposition club confirms the theoretical model (see Fig. 1).

/1/ J. Lorenz, J. Pelka, H. Ryssel, A. Sachs, S. Seidl, M. Svoboda,
IEEE Trans. Computer Aided Design, Vol. CAD-4, No. 4, Oct. 1985

/2/ K.P. Müller, U. Weigmann, H. Burghause,
Microelectronic Engineering 5 (1986), 481-489

/3/ R. Smith, S.S. Makh, J.M. Walls,
Philosophical Magazine A, 1983, Vol. 47, No.4, 453-481

/4/ J.L. Vossen, 1979, J. Phys. E, 12 159

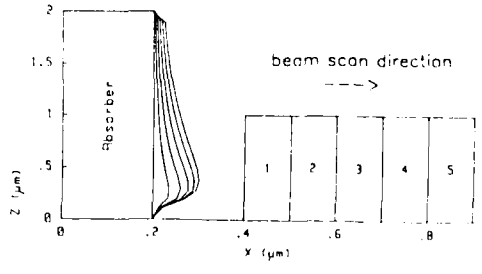


Fig. 1. Simulated redeposition profile, the ion beam was scanned once over the defect area

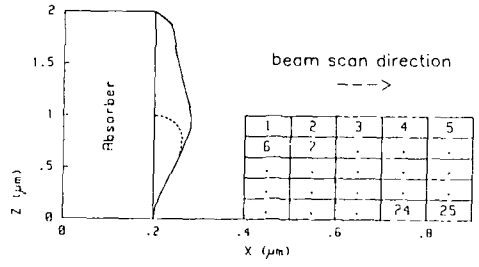


Fig. 2: Simulation of an alternative repair strategy, the defect is *milled in* layers

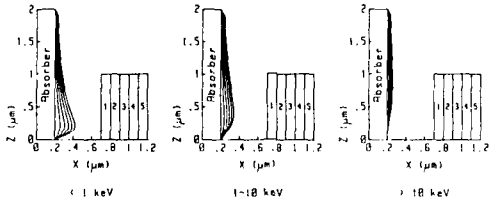


Fig. 3: Redeposition profiles for different ion energies



Fig. 4: SEM-micrograph of redeposited gold at an absorber edge on an X-ray mask

Abstract No. 443

2-Dimensional Profile Simulation of Focused Ion Beam Milling of LSI

Fumikazu Itoh, Akira Shimase, Satoshi Haraichi

Production Engineering Research Laboratory, Hitachi, Ltd., Yokohama 244, Japan

The focused ion beam is a very effectual tool for modifying and debugging of microcircuits(1-3). Milling depth control is one of the most important techniques when cutting conductors covered with several layers of insulation. The milling depth is well known to be proportional to the injected dose per unit area. However, this is not true when the milling area is close to the beam diameter. This may be because of a beam profile and redeposition of the sputtered material. In order to analyze this, we have developed a milling profile simulator, in consideration of both sputtering and redeposition. The simulation scheme is based on ESPRIT(4).

Simulation procedure

Coordinate systems.--Figure 1 shows a coordinate O-xyz for describing the milling profile of a specimen, and another coordinate O_B $x_B y_B z_B$ for an ion beam profile. The 2-dimensional milling profile is given by sereal points, Pi(xi,zi). The beam profile is assumed to be a Gaussian distribution. The beam is scanned in the y-direction with velocity v. Then the scanning center is shifted scan to scan by a given pitch.

Sputter etching model.--Sputtered volume dVs of an element PiPi+1 is proportional to the dose dQ injected into the element.

$$dVs = Sr(\theta) \cdot dQ \ [m^3] \quad (1)$$

were Sr(θ) is the sputtered volume ratio as a function of the incident angle θ, as shown in Figure 2. Displacement of each element dhs is assumed to be normal to the surface.

$$dhs = dVs/(dl \cdot 1) \ [m] \quad (2)$$

where dl is a length of the element PiPi+1, and the thickness of the element in the y-direction is assumed to be unity.

Redeposition model.--We have assumed that the direction of sputtered particles has a cosine distribution. Figure 3 shows that a redeposited volume dVr onto an element PjPj+1 from the element PiPi+1 is a hatched portion of the sputtered volume dVs from the element PiPi+1.

$$dVr = (F(\beta) - F(\alpha)) \cdot dVs \ [m^3] \quad (3)$$

where F(α) is a volume of a portion of the sputtered direction distribution sphere which is between the x-axis and a plane of angle α. Displacement of each element dhr is assumed to be normal to the surface.

$$dhr = (dVr)/(dl \cdot 1) \ [m] \quad (4)$$

Total displacement dh of each element is:

$$dh = dhs - dhr \ [m] \quad (5)$$

Simulation flow.--The displacement dh of all the elements is calculated in each beam scanning. This is performed until the necessary frames are completed.

Milling condition.--Figure 4 shows the milling parameters. Their values were as follows:

beam diameter(FWHM)	0.5, 2um
beam current	1.5nA for 0.5um beam 8.0nA for 2um beam
scanning velocity	625um/s
scanning pitch	0.019um
scanning width	0.5 - 8 um

Dose per unit scan area was a constant value of 23.1nC/um² in any case, which is an appropriate dose for milling SiO2 to 6um depth.

Results and discussion

Figure 5 shows the simulation results of the milling depth of various scanning widths, using a 0.5um beam. The results are in agreement with our experiments. When the beam scanning width is less than 2um, the milling depth becomes shallower.

Redeposition effect.--In order to analyze the above mentioned effect, we performed a simulation without redeposition. Figure 6 illustrates the results with and without redeposition. On the side walls, we can see a significant redeposition effect. However, on the bottom, there is less redeposition, especially in the case of the 2um beam.

Scanning width effect.--Figure 7 shows milling profiles without redeposition. In the 0.5um beam case, the milling depth gets shallower when the scanning width is less than 1um. On the other hand, in the 2um beam case, the scanning width less than 4um provides a shallower milling depth. This is because of the spread beam tail which strikes outside the scan area. In the Gaussian beam case, when the scanning width is less than 4σ, the maximum value of the integrated dose becomes small as shown in Figure 8. Therefore, a major reason for the decrease in depth is the beam profile. And the redeposition is a major factor for the bottom area decrement.

Conclusion

A milling profile simulator which takes into consideration redeposition has been developed. The results of the simulation are in agreement with our experiments. It has been demonstrated that when the beam scanning width is less than 4σ of the Gaussian beam profile, the depth becomes shallower, primarily due to the dose deficiency. Redeposition is not a major factor of the milling depth, but it has a notable effect on bottom area decrement.

Acknowledgment

The authors wish to thank Dr. T. Ishitani for his discussion on FIB milling, and Mr. S. Yamamoto for his contribution on the simulation scheme herein presented.

REFERENCES

1. L.R.Harriott et al., J.Vac.Sci.Technol,B4(1),181(1986).
2. J.Melngailis et al., ibid., B4(1), 176(1986).
3. D.C.Shaver et al., ibid.,B4(1),185(1986).
4. S.Yamamoto et al., IEEE Trans., CAD-6(3), 417(1987).

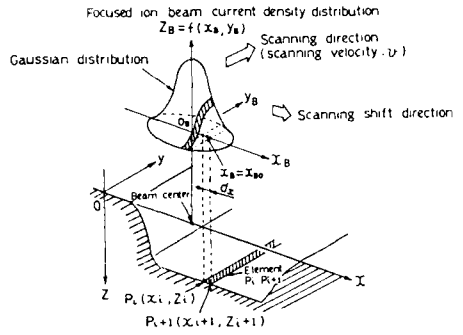


Figure 1 Coordinate systems

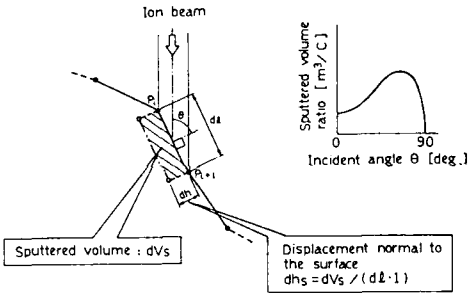


Figure 2 Sputter model

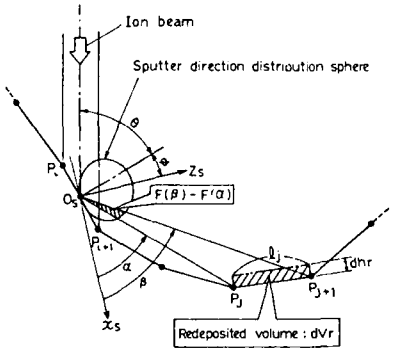


Figure 3 Redeposition model

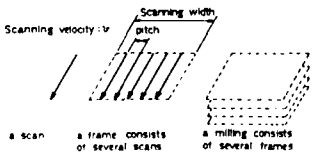


Figure 4 Scan and frame

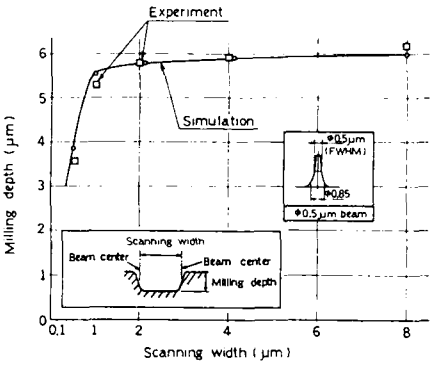


Figure 5 Relation between scanning width and milling depth

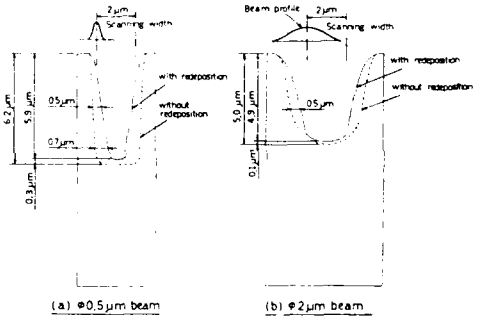


Figure 6 Milling hole profile by simulation

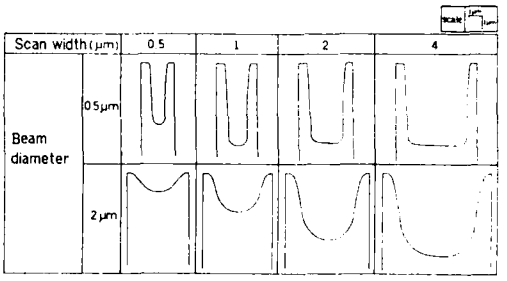


Figure 7 Results of simulation (without redeposition)

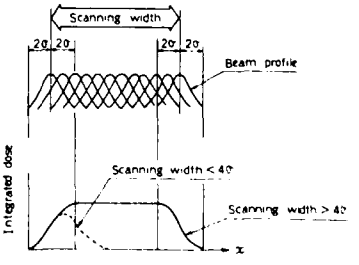


Figure 8 Scanning width and integrated dose

Abstract No. 444

Focused Ion Beam SIMS for Micromachining Applications

L. R. Harriott

M. J. Vasile

AT&T Bell Laboratories

Murray Hill, New Jersey 07974

Liquid metal ion sources which provide very highly focused (5,000 to 500Å dia.) high current density (1.0 to 0.5 A/cm^2) ion beams have offered the prospect of extending the technique of secondary ion mass spectrometry well into the sub-micron lateral resolution range. This tantalizing prospect has been cited numerous times, but only a few successful instruments have been reported. Levi-Setti and coworkers have published a detailed and thorough review of their recent work which describes their focused ion beam (liquid metal) SIMS, in which the emphasis is on the general utility of high resolution scanning ion microscropy.[1] Kingham, et al have shown some examples of ion images obtained with a liquid metal ion source SIMS, but give only a cursory account of the instrument and operating techniques.[2]

Our intention is to use SIMS as an adjunct, in-situ diagnostic tool for micromachining applications which utilize a liquid Ga ion source. The primary applications are for end-point detection when sputtering through thin films with micron sized rastered areas, and for element mapping by mass selected ion images taken on raster fields from one millimeter to 10μm.

The approach we have taken is quite pragmatic: The detection of secondary ions must be done without compromising any of the functions or operating parameters of the focused ion beam processes. Signals must be adequate to record mass spectra or mass-selected ion images within a matter of one or two minutes. Ion extraction to the SIMS for mass spectral analysis must not interfere with the normal total secondary ion imaging, and a minimum number of variables (one or two) for SIMS signal optimization is essential for convenient operation.

End-point detecton of Cr micromachining on photomasks was done with raster sizes ranging from 10μm x 10μm to 3μm x 3μm. The chromium oxide enhanced $^{52}Cr^+$ signal at the Cr/glass interface was used as the end-point indicator. Verification of this effect was obtained by XPS profiling through the Cr film. SIMS end-points, total ion images, and transmitted light measurements show that the ion-milling can be controlled to stop prior to, or after, the Cr/glass interface. Measurements on a common sample show that the absolute sensitivity of the FIB/SIMS is equivalent to that of a commercially-made SIMS which uses 3 KeV O_2^+ primary ions (3 x 10^4 cps $^{52}Cr^+$/nA primary ion, 100μm raster). Mass selected secondary ion images have been obtained for high yield ions such as $^{52}Cr^+$ and $^{27}Al^+$ on raster fields of 25μm in time intervals ranging from 20 to 100 sec. Al^+ SIMS images of 1μm lines and spaces from a VLSI test pattern have been obtained.

References

1. R. Levi-Setti, Y. L. Wang and G. Crow, Appl. Surf. Sci., 26 (1986) 249.

2. D. R. Kingham, P. Vohralik, D. Fathers, A. R. Waugh and A. R. Bayley, "Applied Materials Characterization", Mater. Res. Soc. Symp. Proc., Vol. 48 (1985), W. Katz and P. Williams Eds., p. 319.

Abstract No. 445

FIB Direct Write Lithography

Kenji Gamo and Susumu Namba

Faculty of Engineering Science
Osaka University
Toyonaka, Osaka 560, Japan

1. Introduction

Focused ion beam is attractive for various direct maskless processing including resist exposure and direct etching. Several techniques to delineate resist patterns by FIB have been investigated. These are conventional ion beam exposure and wet development[1], in-situ development by FIB bombardment[2] in vacuum or in reactive gas ambient, and doping or modification technique by Ga implantations[3]. In the present paper, the current-state-of-art of FIB direct write lithography will be presented.

2. Ion Beam Lithopgraphy

Ion beam lithography(IBL) is new potential means to delineate patterns with deep submicron or smaller dimensions. Currently ion beam lithography is being studied for applications to high resolution lithography. The high resolution of IBL can be inferred from the small forward- and back-scattering of the incident ions and the small range of secondary electrons. Theoretically, this has been shown clearly by a Monte Carlo simulation[4]. The negligible proximity effect enables one to eliminate data processing step for proximity effect correction. Nanometer pattern delineation and negligible proximity effect was demonstrated by using Be FIB exposure[1,5].

IBL provides a very high speed exposure technique. This is due to a large energy deposition rate of ion beams to resist materials. The doses required to expose resist is 10^{11} to 10^{13} ions/cm^2, a value of which depends on impinging ion mass and is 2 to 3 orders of magnitude smaller than a value required to electron beam exposure. The resist exposure mechanism may be similar to electron beam exposure. For PMMA, it was reported that the g-value (the number of chemical events occured per 100eV of deposited energy) for electronic collision is the same between ion and electron beam exposures[6] and for nuclear collision, the g-value is almost half of electronic collision.

A dose of 1×10^{13}/cm^2, for example, corresponds to only 10 ions on average impinging in a pixel with an area of say, 10x10 nm^2. At this small number, statistical fluctuations in the number of impinging ions becomes significant, and there is significant probability of under- or over-exposure in the pixel. A simple calculation indicates that for a resist with a sensitivity of 1×10^{-6}C/cm^2 (=6.3×10^{12}ions/cm^2), eg, PMMA, there is already a significant probability of receiving 60% of fluctuation in 10 nm square pixel, and for high sensitive resist with 3×10^{-7}c/cm^2, it seems rather impossible to delineate 10 nm sized pattern. Therefore, both statistical fluctuation and ion scattering limit the ultimate resolution.

3. Self-Development and Ion Beam Assisted Process

Self development of resist has been investigated by electron, ion and laser exposure. This is attractive to eliminate wet development step from lithography process and thus, to reduces a possibility of contamination and realize process simplification. Moreover, this enables one to develop resist thicker than the ion range. Therefore, we may use very low energy focused ion beams and reduce damage in the substrate. This is very attractive because damages induced in the underlying substrate are very severe problems to make use of extremely high resolution of ion beam lithography.

It was observed that nitrocellulose and PMMA shows a relatively high self-development rate for FIB exposure[2,7]. A 400-500nm thick resist layer can be removed at a dose of and 1×10^{14} and 3×10^{15}/cm^2, for nitrocellulose and PMMA, respectively. The sensitivity depends on the ion mass and is higher for light ion which has a dominant electronic stopping power over nuclear stopping power. This may be because for electronic collision, side-chain scission and evaporation of volatile fragment is dominant process, while for nuclear collision, carbonization is dominant. Because of this carbonization at the surface, heavy ion bombardment shows low self-development rate. For PMMA, it was observed that the surface becomes carbonized by heavy ion bombardment at a dose higher than 1×10^{15}/cm^2 and self-development rate decreases to 1/7 of that for fresh PMMA.

Carbonized layer is removed by bombarding FIB in reactive gas ambient like XeF_2[7]. The chemical reaction between the resist and PMMA is enhanced by both nuclear and electronic collision, and consequently, heavy ions which have larger total energy deposition rate shows higher removal rate. This ion beam assisted etching has been applied to direct paterning of various materials including Si and GaAs.

4. Defects

For silicon, it is reported that proton irradiation to MOS devices at a beam energy of 45 to 150 keV and at a dose of 1x to 10×10^{13}/cm^2 induces no difference in V_T and g_m between irradiated and unirradiated samples after annealing at 450°C. For GaAs and InP, ion irradiations induce deep $_2$ compensating center at a dose between 10^{12} and 10^{14}/cm^2 but these centers are eliminated by thermal annealing. Irradiation and annealing effects on device characteristics should be investigated in more details. However, it can be expected that damage effect may be small because the dose required for exposure is low compared to a dose required for ion implantation. It is also possible to avoid penetration of ions into the substrate by selecting proper beam energy.

References

1) Y. Ochiai et al: J. Vac. Sci. Technol.(to be published).
2) Y. Yasuoka et al: Microelectronic Eng. 5(1986) 335.
3) H. Kuwano et al: Jpn. J. Appl. Phys. **19** (1980) L615.
4) L. Karapiperis et al: J. Vac. Sci. Technol. **19** (1981) 1259.
5) T. Shiokawa et al: Jpn. J. Appl. Phys. **23** (1984) L232.
6) M. Komuro et al: J. Electrochem. Soc. **126** (1979) 483.
7) H. Hamauzu et al: J. Vac. Sci. Technol. (to be published).

Abstract No. 446

REGISTRATION ACCURACY IN FOCUSED-ION-BEAM LITHOGRAPHY FOR THE FABRICATION OF GaAs FET WITH A MUSHROOM GATE

T. Kato, K. Hosono, H. Morimoto, Y. Sasaki, and Y. Watakabe

LSI R&D Laboratory, Mitsubishi Electric Corporation
4-1 Mizuhara, Itami, 664 Japan

1. Introduction

Utilizing advantages of focused ion beam (FIB) technology, high resolution and a capability of obtaining T-shaped resist structure,[1] a mushroom gate with narrow gate length and low gate resistance for GaAs microwave HEMT has been fabricated. Hybrid lithography of different ion species, Si and Be emitted from Au-Si-Be liquid-metal ion source, is used to determine the T-shaped resist structure. This device shows excellent noise characteristics, minimum noise figure of 0.68dB and 0.83dB at 12GHz and 18GHz, respectively.[2] In this paper, the registration technology including the mark structure and the mark detection, which influences the overlay accuracy in the device fabrication, will be presented. In this hybrid process, registration accuracy of both Si and Be beams should be taken into consideration.

2. Experiments

The focused-ion-beam equipment is JIBL-200S, a computer-controlled system with a laser interferometric stage.[3] The registration mark is Au-Ge pattern with a cross-shape window on GaAs substrate, which is simultaneously formed at the fabrication of source and drain electrodes. The resist on the mark is removed prior to the FIB exposure. The length and width of the mark are 50μm and 6μm, respectively. 260keV Si^{++} and 192keV Be^{++} with a beam current of 10pA and approximate beam diameter of 0.1μm for both beams are evaluated. In registration, a scan step is 0.02μm and a scan clock is 100 kHz. The registration signal is an output of annular type microchannelplate, which detects secondary electrons from the mark irradiated by Si or Be ion beams.

3. Results and discussions

Figure 1 shows a detection probability, which is defined as a frequency rate of successful detections for a square of mark detection tolerance (Δp^2) in 100 detection scans. The mark detection tolerance is defined as an allowance of scattering in measured edge locations, and the detected data beyond this allowance is omitted by software. This parameter is set to the detection system prior to the registration. According to the figure, the plot of Si^{++} is shifted to right in comparison with that of Be^{++} by 3 ~ 4 times, that is, about 2 times in the mark detection tolerance. This corresponds to the fact that the S/N of the registration signal of Si^{++} is about 2 times higher than that of Be^{++}. It is found that the mark locations are all detected successfully at the $\Delta p \sim 0.03\mu m$ ($\Delta p^2 \sim 0.001$) for Si^{++} and the $\Delta p \sim 0.05\mu m$ ($\Delta p^2 \sim 0.0025$) for Be^{++}.

Figure 2 shows the measured overlay accuracy for 100 measurements. The value of x represents a deviation from the center position between source and drain electrodes. The number of scan for one scan position was set up to 2 in order to minimize the irradiation damage of the marks. The 10-times averaging with a raster step of 0.1μm was performed.

As for the positioning error (x), 0.04μm for Be^{++} and 0.01μm for Si^{++} were obtained. Considering the positioning error of 0.1μm or less in beam calibration, it is proper conclude that the present limit of calibration accuracy is reflected in these results. Besides, the overlay repeatabilities (3σ) for Be^{++} and Si^{++} were almost the same values, that is, 0.11μm and 0.13μm respectively.

The distribution of the overlay accuracy for Si^{++}, however, seems a little spread rather than that for Be^{++}. It is considered to be attributed to the fact that the developed resist patterns becomes obscure because of the irradiation of the isotopes for Si^{++}. Si is made up of ^{28}Si,^{29}Si,^{30}Si with an atomic content of about 92%,5% and 3%, respectively. The isotopes cannot be completely separated by E × B mass filter, because the mass resolution of the filters is 1/20. Although this FIB system is designed to adjust all the unseparated isotopes at the target, there remains some residual displacement of the beams due to the beam misalignment and so on.

4. Conclusion

The registration and overlay accuracy in FIB lithography for GaAs devices has been investigated. A window mark formed by lift-off of Au-Ge is used for registration. In the registration, if the mark edge is in good condition, the positioning error (x) is less than 0.04μm, and the repeatabilities are 0.11μm for Be^{++} and 0.13μm for Si^{++}.

REFERENCES

[1] H.Morimoto, H.Onoda, T.Kato, Y.Sasaki, K.Saitoh and T.Kato, J. Vac. Sci. Technol. B4, 205 (1986).
[2] K. Nagahama, M. Nakanishi, Y. Sasaki, K. Hosono, H. Morimoto, T. Katoh, R. Hirano, T. Murotani, A. Kawagishi, Electr. Lett. 24(4), 242 (1988).
[3] R.Aihara, H.Sawaragi H.Morimoto, K.Hosono, Y.Sasaki, T.Kato and M.H.Shearer, J. Vac. Sci. Technol. B6(1), 245 (1988).

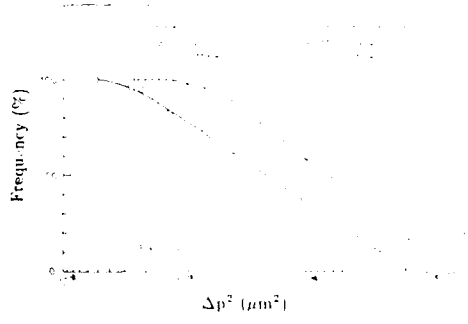


Fig.1 Detection probability for Be^{++} and Si^{++} ion beams

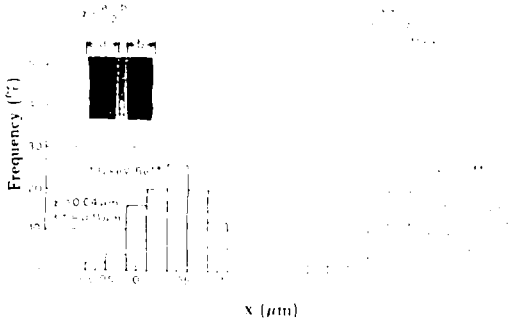


Fig.2 Measured overlay accuracy

Abstract No. 447

FOCUSED ION BEAM LITHOGRAPHY USING NOVOLAK BASED RESIST

Shinji Matsui, Yoshikatsu Kojima, and Yukinori Ochiai

Fundamental Research Laboratories, NEC Corporation, Miyazaki, Kawasaki 213, Japan

INTRODUCTION

Recently, there has been increasing interest in focused ion beam (FIB) use for microcircuit fabrication. This can be utilized for maskless ion implantation[1], maskless ion etching[2], and high resolution lithographic processes[3-5]. Ion beam lithography is a new potential means for producing electronic devices with submicron dimensions. Electron beam lithography is commonly applied for the delineation of patterns with submicron dimensions. However, it involves several problems, such as low resist sensitivity, backscattering and proximity effects, for submicron lithography. On the other hand, ion beam lithography is a new technique which overcomes the above-mentioned problems. First, as a general rule, resists are more sensitive to ions than to electrons. Depending on the mass of the exposing ions, resist exposure sensitivity for ion beam lithography is two or more orders of magnitude higher than that for electron beam lithography. Second, ion beam lithography has an advantage in submicron device microfabrication, because of negligible ion scattering in the resist and low backscattering from the substrate. In contrast to electrons, ions produce only low-energy secondary electrons, and produce no high-energy backscattered electrons. Therefore, the structures are defined by the primary ion beam, and are limited only by ion straggling, which extends laterally to a much smaller distance than the range of scattered electrons in electron beam lithography. This results in the possibility of exposing structures with submicron dimensions without backscattering and proximity effects. Up to now, the high resolution and high sensitivity of FIB lithography have been demonstrated. PMMA resist has been applied as a positive resist for those experiments. PMMA has high resolution, less than 10nm, but low resistance for dry etching processes. On the other hand, novolak based resist has very high resistance to dry etching and serves as a good etch mask for such processes as plasma etching and reactive ion beam etching. Novolak based resist is applied as a representative positive resist for optical and electron beam lithography in device processes. FIB lithography using novolak based resist has not been reported. In this paper, FIB exposure characteristics using novolak based resist are described.

EXPERIMENTAL

All FIB exposures were carried out with JIBL-150 FIB system. The accelerating voltage used was 130kV. In this experiment, MP2400 resist (Shipley Far East LTD.) was used as novolak based resist. A 0.5μm MP2400 resist was spin-coated on Si substrate. Prebaking was carried out in a nitrogen atmosphere at 100°C for 30 minutes. After ion-beam exposure, the MP2400 resist coated wafers were developed by dipping in MP2400 developer and H_2O in a 1:3.5 ratio. Then, they were rinsed in H_2O. The etched depth and residual thickness after development were measured by α-step.

RESULTS AND DISCUSSION

The MP2400 resist sensitivity for 130kV FIB exposure was measured. Figure 1 shows MP2400 resist sensitivity curves for 260keV Si^{++} and Be^{++} ions. The MP2400 resist sensitivity depends on the ion species. The sensitivity for Si ions is higher than that for Be ions. This can readily be understood in terms of energy deposited per unit volume. Moreover, the sensitivity curves indicate that a dose region for a positive resist is narrow, compared with other resists, such as PMMA. The positive region for Be ions is from a 2.3×10^{12} to a 4.0×10^{12} ions/cm^2 dose and changes to a negative region at over a 4×10^{12} ions/cm^2 dose. On the other hand, the positive region for Si ions is from a 1.4×10^{12} to a 2.3×10^{12} ions/cm^2 dose and changes to negative region at over a 2.3×10^{12} ions/cm^2 dose. The γ values were calculated from the sensitivity curves, as shown in Fig. 1. The γ values for Si and Be ions as a positive resist are 1.12 and 0.98, respectively. On the other hand, the γ values for Si and Be ions as a negative resist are 2.64 and 2.84, respectively. The γ values as a negative resist for both Si and Be ions are about twice those for a positive resist. This result indicates that MP2400 resist is useful as a negative resist in FIB lithography.

Figure 2 shows development characteristics (normalized thickness vs. development time) for MP2400 resist after 260keV Be^{++} FIB exposure. The positive and negative patterns can be fabricated at 3×10^{12} and 2×10^{13} ions/cm2 doses, respectively, as shown in Fig. 1. The MP2400 resist is etched without ion exposure, merely by soaking in the developer. Development characteristics were measured for unexposed, 3×10^{12} and 2×10^{13} ions/cm^2 doses, as shown in Fig. 2. A positive resist pattern with 65% residual thickness can be fabricated at 120 second development time. The residual thicknesses for unexposed and 2×10^{13} ions/cm^2 doses at 300 second development time are 0 and 100%, respectively. Therefore, a negative resist pattern with 100% residual thickness can be fabricated at more than 300 second development time. These results indicate that both positive and negative resist patterns can be obtained by choosing appropriate ion doses.

Figure 3 shows a cross section view for the MP2400 positive resist pattern, which was fabricated by 260keV Be^{++} FIB at 4.0×10^{12} ions/cm^2 dose. The linewidth and resist thickness are 0.4 and 0.35μm, respectively. The pattern has slanting sidewalls. It is considered that the sidewall inclination angles can be improved by choosing other development conditions.

Figure 4 shows a cross section view of MP2400 negative resist pattern, which was fabricated by 260keV Be^{++} FIB at 3.0×10^{13} ions/cm^2 dose. The pattern was achieved by soaking for 300 second in developer after ion beam exposure. The linewidth and resist thickness are 0.3 and 0.5μm, respectively. The pattern has vertical sidewalls. The negative resist pattern demonstrates that the image reversal method developed here is very useful for device processes, such as a submicron gate pattern formation.

CONCLUSION

FIB lithography using novolak based resist has been investigated. The resist sensitivity and development characteristics were measured. As a result, it became clear that both positive and negative resist patterns can be achieved by choosing appropriate ion doses. The positive resist pattern with 0.4 μm linewidth could be fabricated by 260 keV Be^{++} FIB at 4.0×10^{12} ions/cm^2 dose. Moreover, the negative resist pattern with 0.3 μm linewidth could be achieved by 260 keV Be^{++} FIB at 3.0×10^{13} ions/cm^2 dose. The negative resist patterns with vertical sidewalls demonstrated that the image reversal method, developed here, is very useful for device processes, such as a submicron gate formation.

REFERENCES

1. R.R. Hart, C.L. Anderson, H.L. Dunlop, R.L. Seliger, and V. Wang, Appl. Phys. Lett. 35, 865 (1979).
2. R.L. Seliger, R.L. Kubena, R.D. Olney, J.W. Ward, and V. Wang, J. Vac. Sci. Technol. 16, 1610 (1979).
3. R.L. Seliger, R.L. Kubena, R.D. Olney, J.W. Ward, and V. Wang, J. Vac. Sci. Technol. 16, 1610 (1979).
4. S. Matsui, K. Mori, K. Saigo, T. Shiokawa, K. Toyoda, and S. Namba, J. Vac. Sci. Technol. B4, 846 (1986).
5. S. Matsui, K. Mori, T. Shiokawa, K. Toyoda, and S. Namba, J. Vac. Sci. Technol., 5, 853 (1987).

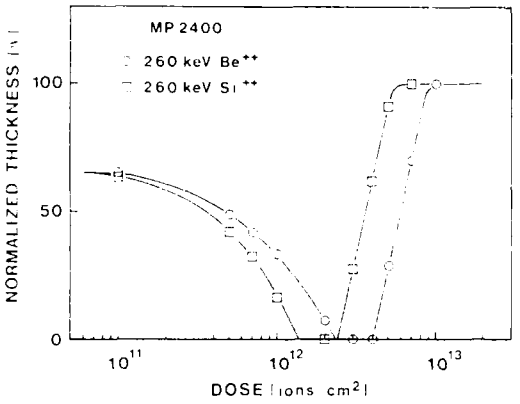


Fig. 1 MP2400 resist sensitivity measurement for 260 keV Si^{++} and Be^{++} FIB.

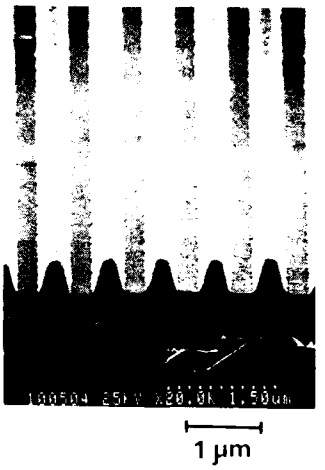


Fig. 3 MP2400 positive resist patterns on Si substrate, exposed by 260 keV Be^{++} FIB at 4.0×10^{13} ions cm^{-2} dose.

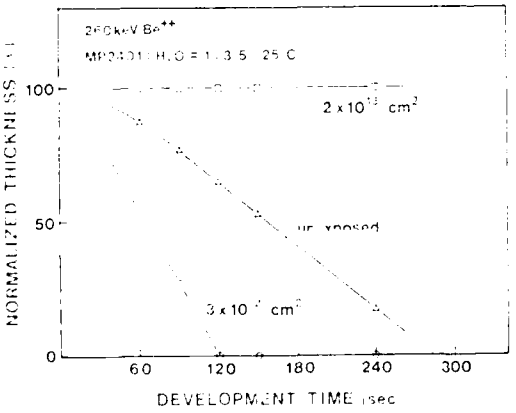


Fig. 2 MP2400 resist development characteristics for 260 keV Be^{++} FIB at unexposed, 3×10^{12} and 2×10^{13} ions cm^{-2} doses.

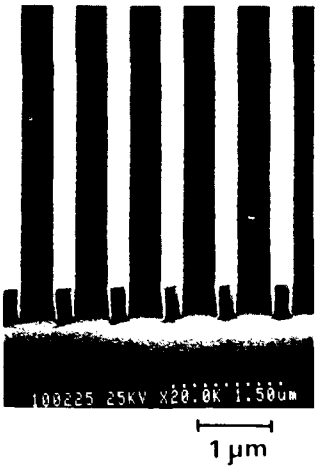


Fig. 4 MP2400 negative resist patterns on Si substrate, exposed by 260 keV Be^{++} FIB at 3.0×10^{12} ions cm^{-2} dose.

Abstract No. 448

FIB Direct Ion Implantation Technology and Its Applications for III-V Compound Semiconductors.

Eizo Miyauchi and Hiroshi Arimoto

Fujitsu Laboratories Ltd.
10-1 Morinosato-Wakamiya, Atsugi, Kanagawa

We review the recent developements in FIB (Focused Ion Beam) direct implantation technology. In a typical FIB implanter, dopant ion species are emitted from a field-ionization-type liquid metal (sometimes ailoyed) ion sources, and are mass-separated and focused down to the semiconductor substrate. The submicron diameter FIBs formed on the semiconductor are implanted by scanning over the assigned area through computer commands. This new technology has several important advantages as follows.

(1) Formation of submicron-size doping structures without using masks (only through computer software).
(2) An alloyed liquid metal ion source offers ion species for p, n and isolation type dopants which can be switched rapidly by computor control during device processing.
(3) Doping profiles can be easily controlled both in lateral and depth directions.
(4) The maskless process is compatible with UHV, which leads to in-situ all vacuum processing.

With these advantages, this technology can grow up to ideal CAD/CAM processes to open a new world for IC fabrication technology. These advantages are considered to be more useful for III-V compound semiconductors rather than for Si. The former provides not only electrical and optical devices but also new quantum-effect devices. These variety of devices can be integrated monolithically on the same substrate by the FIB-based maskless process, and the new type of ICs will contribute to future sophisticated information processing systems. More than that, the clean process accompanied by the maskless process is indispensable to the III-V compounds. Ion sources suitable for the III-V compounds are found to be quite stable and reliable. It is also found that the electrical and optical properties of the FIB implanted crystals are almost the same as those with conventional broad ion beam implantation. Until recently, these advantages have been proved to some extent, although still in the preliminary experiment stage. Some of the recent developments on this technology are shown as follows.

1. FIB Direct Implanter

Presently, the general purpose FIB equipment is commercially available with an accelerating voltage of up to 200kV and with stable LM ion sources. The minimum beam size is 0.1 μm.

To make the most of the potential advantages of the FIB implantation, a 100kV FIB implanter with a sophisticated computor-control system has been developed. In this system, such important implantation parameters as dopant species (Si,Be and B), FIB energies (40-200keV) and beam diameters (0.1-1.0μm) are rapidly and precisely controlled so that p, n and isolation type ion species with given energies can be arbitrarily switched just during device processing as if it was a single beam implantation. This FIB implanter is operated in UHV, too.

2. Characteristics of the FIB Implanted GaAs

Doping profiles with FIB implantation have been experimentally estimated and found predictable by simple calculation assuming that FIBs have Gaussian intensity distributions and that implanted profiles both in lateral and depth directions are also Gaussians.

FIBs usually have a current density of up to 1A/cm^2. This corresponds to 10^4 to 10^6 times as much as those of conventional broad ion beams. Despite such high current density implantation, measured electron mobilities and PL intensities of focused Be and Si implanted and annealed GaAs are almost the same as those of conventional ion implantation.

3. Application to Device Structures

Due to the maskless process capability, it can be applied to various novel structures for future devices. Since this is compatible with UHV crystal growth systems such as MBE, combination processings are expected to become powerful tools for maskless planer-structure fabrication.

Among typical applications demonstrated so far are:
(1) Basic structures fabrication of three-dimensional impurity doping such as lateral and depth dimension controls, multilayer doping structures, self-aligned polycrystal growth layer and MQW gratings.
(2) Optical and electrical devices having unique structures which can not be fabricated other than by using the FIB technology such as planer structured MQW lasers, photo-diodes, and quantum wires.

4. Concluding Remarks

FIB direct implantation technology is promissing for the device fabrication processes where very fine (nano-meter) structures or planer/three-dimensional structures are required. Versatility and cleaness of this technology will develop to a one hundred percent CAD/CAM process (only-through-software processing) in corporation with other compatible dry processes such as MBE, ion beam etching, and maskless metallization.

However, the fine-beam process inevitably faces low throughput problem. The present FIB implanter technology has to be improved in terms of ion source, optical lens and deflection columns for large beam current and variable beam shapes.

Abstract No. 449

Fabrication of 100 nm Si p-n junction by focused and broad beam ion implantation

A.J. Steckl and C-M. Lin
Center for Integrated Electronics and Department of Electrical, Computer and System Engineering
Rensselaer Polytechnic Institute
Troy, N.Y. 12180

T.P. Chow
General Electric Co.
Corporate Research and Development Center
Schenectady, N.Y. 12301

VLSI sub micron technology requires very shallow p-n junctions with low sheet resistance and leakage current[1,2]. In this paper, we report on the fabrication of 100-nanometer-range p-n junctions using focused and broad beam ion implantation. Rapid thermal annealing was used to activate the implanted ions while minimizing diffusion.

To obtain such shallow junctions we have investigated the use of heavy ions such as Ga and In, for p-n junction formation by either conventional (broad beam) ion implantation or focused (sub micron) ion beam implantation. Ga and In ions, because of their large mass, have a penetration range in Si which is more than 6 times smaller than B. FIB technology can perform the direct doping of selected regions thus implementing a maskless and resistless process. The use of Si self-implantation as a pre-amorphization procedure in conjunction with subsequent Ga or In doping was also investigated.

Unlike boron which requires high temperature to obtain a high activation percentage, Ga requires only a 550-600^{0}C anneal for 15 seconds. A junction depth of 100 nm with a sheet resistance of 150 ohm/square was achieved in the case of 75 keV Ga broad beam implantation with a Si preimplant. The Ga FIB implantation resulted in a significantly higher proportion of activated Ga in the tail of the distribution leading to a deeper junction but with a lower sheet resistance. The Si preimplant was found to significantly reduce the junction depth. Unfortunately, the end of range damage region in the Si preimplant is not fully annealed leading to a greater leakage current in the p-n junction. In the absence of the Si self implant, 50 keV Ga implanted p-n junctions annealed at 600^{0}C exhibited a leakage current density of 1 nA/cm^{2} at 5 Volt reverse bias.

References:
[1] M.R. Wordeman, A.M. Schweighart, R.H. Dennard, G.A. Sai Halasz, and W.W. Molzen, IEEE Trans. Electron Devices, vol. ED-32, p. 2216, 1985.
[2] G.A. Sai Halasz, H.B. Harrison, IEEE Electron Device Lett., vol. EDL-7, p.536, 1986.

Abstract No. 450

GaAs Quantum Wire Transistors Fabricated by Focused Ion Beam Implantation

Takahide Odagiri, Toshiro Hiramoto, Kazuhiko Hirakawa, and Toshiaki Ikoma

Institute of Industrial Science, University of Tokyo,
7-22-1 Roppongi, Minato-ku, Tokyo 106, Japan

PURPOSE

In very narrow semiconductor wires with width comparable to the electron de Broglie length, electron transport properties are affected by quantum size effects and quantum interference effects. In an ideal-1D wire enhanced quantum effects are expected to appear as compared with in 3D or 2D structures. In this study both p and n type GaAs quantum wire transistors were fabricated by focused ion beam (FIB) implantation in order to investigate carrier transport properties in the 1-D wires and to explore a possibility to realize complementary devices.

SAMPLE PREPARATION

Figure 1 shows schematic views of the n-type quantum wire structure fabricated in this study. First, focused Be^+ ions were implanted into semi-insulating GaAs at 100keV with a dose of $6\times10^{12}cm^{-2}$. Then the focused Si^+ ion beam with 0.1 μm diameter was line-implanted across the Be-implanted area at 80keV with a line-dose of $9\times10^{8}cm^{-1}$. Rapid thermal annealing (RTA) was performed to activate implanted ions at 1000°C for 1 s. Consequently, an n-GaAs wire was formed in the p-GaAs region. This process is the same as the one applied to fabricate the pn-junction quantum wire.[1] P-type wire structures were also fabricated by similar procedure but, the wafers were n-GaAs ($n=3\times10^{15}cm^{-3}$) and a focused Be^{2+} beam was line-implanted at 200keV with dose varying from $2\times10^{8}cm^{-1}$ to $8\times10^{9}cm^{-1}$. Some of the wire structures were cleaved for observation of the implanted ion profiles. The calculated profiles are compared with the observed ones. The measured conductance of the wire decreased with increasing the reverse-bias voltage across the pn-junction, indicating that this structure acts as a junction FET.

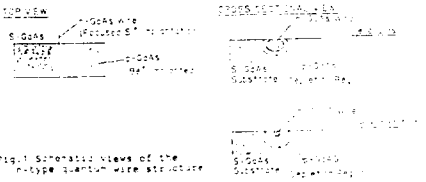


Fig.1 Schematic views of the n-type quantum wire structure

RESULTS

Figure 2 shows a scanning electron micrograph of the cleaved surface which was etched with an HF solution. The white curved lines under the surface corresponds to the pn boundaries. Figure 3 shows a calculated ion profile of the p-GaAs wire. Gaussian distribution of ions in a focused beam, the LSS theory and a simple diffusion equation are assumed to calculate this profile. In this case the calculations fairly agree with the experiments. The implanted Be ion was spread in a larger volume as shown theoretically and experimentally, although the beam diameter was about 0.1μm.

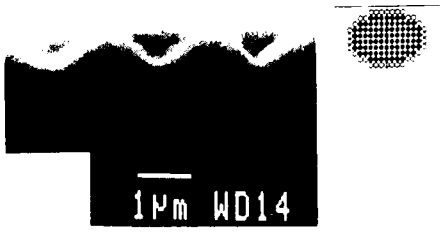


Fig.2 SEM image of the cleaved surface
Be line dose 2E9cm⁻¹

Fig.3 Calculated ion profile
● p-type more than 3E17cm⁻³
○ p-type less than 1E15cm⁻³
other region is n-type
the same scale as Fig.2

Figure 4 shows the calculated Si profile implanted in p-type GaAs under the present experimental condition. From this simulation it was found that the cross-sectional area of the n-type wire is only 0.3μm×0.4μm even at zero bias and the peak concentration is more than $10^{18}cm^{-3}$. Since Si ion is much heavier and has a smaller diffusion coefficient than Be, an n-type wire can be much narrower than a p-type wire.

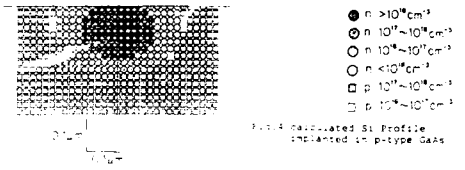


Fig.4 Calculated Si Profile implanted in p-type GaAs

Figure 5 shows the I-V characteristics of the n-type GaAs-wire transistor. The transconductance (g_m) was about 2.1×10^{-5}S. In this GaAs wire FET, the depletion layer expands cylindrically i.e. in two dimensions, and hence improvement in g_m is expected as compared with a planar FET in which the depletion layer expands in one direction.

It is interesting to compare transconductance of a wire FET with that of the planar FET. An equivalent g_m of the wire FET having a 1mm channel width is 26mS/mm. Considering that the channel length of the present FET is 13μm, this value of g_m is equivalently the same as that of a conventional FET. Theoretically transconductance of a wire-FET should be about 2π times higher than that of a planer FET. With the more optimized design, transconductance will be improved.

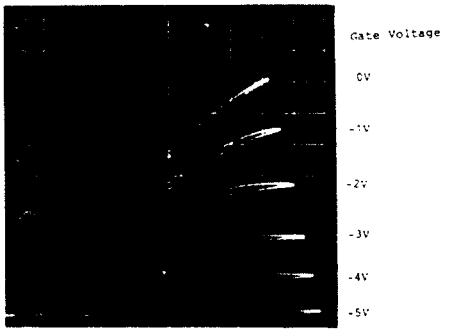


Fig.5 The I-V characteristics of the n-type GaAs-wire transistor

CONCLUSION

We have successfully fabricated n- and p-type GaAs quantum wire transistors by focused ion beam implantation. It is found both theoretically and experimentally that an n-type GaAs wire can be much narrower than a p-type one because of heavy mass and a small diffusion coefficient of Si ion. Improvement of transconductance is expected in such n-type GaAs wire transistors as compared with normal GaAs MESFETs.

Reference
1)T.Hiramoto, K.Hirakawa, and T.Ikoma, in Japan - USA Seminar on Focused Ion Beam Technology and Application, Osaka and Mie, November, 1987, J. of Vac. Sci. Technol. B5, (in press)

Abstract No. 451

"Formation of Pd_2Si by Direct Implantation of a Focused Beam of Pd^+ Ions in Si"

S. Balakrishnan, J.C. Corelli, and S.P. Murarka

Center for Integrated Electronics
Rensselaer Polytechnic Institute
Troy, New York 12180

and

E. Hall and N. Lewis

General Electric Corporate Research and Development Center
Schenectady, New York 12301

The increase complexity of silicon based devices used in very large scale integrated (VLSI) circuits in recent years has given rise to new methods to produce electrical contacts. Specifically, the use of a variety of metals e.g., W, Co, Pt, Ti, and Pd; to form silicides have found new applications in gate metallization and interconnects. The silicides must have good electrical conductivity, resist oxidation and be stable at temperatures in the 400 - 600°C range. In addition, it is important and advantageous to be able to fabricate the silicides at low temperature and by direct maskless patterning.

In this paper we present the first results on the use of a focused beam of palladium ions to directly implant a pattern of palladium into a silicon wafer. Our experiment was designed to achieve the objective of fabricating samples of implanted areas of silicon which were directly implanted by Pd^+ ions without the use of masks.

A PdB liquid metal ion source was used in a focused ion beam (FIB) implantation system. The FIB system was operated so as to accelerate Pd^+ ions to 75 keV and was equipped with an EXB mass separator to filter out unwanted boron ions from the beam. The Pd^+ ion beam was scanned electrostatically to obtain a series of implanted areas $0.4x0.4(mm)^2$. The silicon wafers used in our study were Sb doped with (100) orientation. The implanted dose was $1.7x10^{16}$ Pd/cm^2, and the sample temperature during implantation was 70°C. The analytical methods used to determine the presence of palladium and formation of palladium silicide in the implanted regions included electron beam microprobe, x-ray diffraction. Rutherford backscattering (RBS), and transmission electron microscopy (TEM). The x-ray diffraction studies were done using the Cornell High Energy Synchrotron Source (CHESS). Annealing experiments on the implanted samples were performed in a nitrogen ambient at temperatures in the 250°C to 500°C range to observe temperatures at which palladium silicides were formed.

After implantation electron microprobe analysis confirmed the presence of Pd in the sample areas exposed to the ion beam. The x-ray diffraction studies indicated the presence of a broad peak in the diffraction spectrum corresponding to interplanar spacings of 0.227 nm to 0.236 nm. From the x-ray spectrum one could not distinguish between the silicides Pd_2Si, Pd_3Si and Pd_4Si as well as Pd metal since they all have strong diffraction maximum and interplanar spacings in the 0.227 to 0.236 nm range. We carried out a micro-Rutherford backscattering (RBS) study on the unannealed sample, using 3 MeV He^+ with a beam diameter of 5 μm. The sample was subjected to consecutive anneals of 175°C, 250°, and 300°C, with the sample held at each of these temperatures for a period of 30 mins. Although confirming the presence of Pd in the sample the RBS measurements did not have sufficient sensitivity to give definitive proof for the presence of Pd_2Si in the implanted region.

The definitive study to characterize the presence of Pd_2Si was done using transmission electron microscopy (TEM). A sample of the implanted region was prepared by mechanical grinding and ion milling to perforation suitable for TEM analysis. The implanted sample exhibited a tri-layer structure, amorphous below the surface exposed to beam, followed by a region of amorphous Si containing small crystalline precipitates then crystalline Si. The microstructure of the crystallites (5 nm in size) observed by TEM yielded an interplanar spacing of 0.23 nm. After annealing at 3.50 °C for 30 min. The crystallites grew in size to 10 nm while maintaining the same 0.23 nm interplanar spacing. Microdiffraction on a single crystallite yielded a diffraction pattern that was indexed as being due to $(\bar{1}100)$ Pd_2Si. Annealing to 500°C caused the crystallite precipitates to grow to 100 nm size and the interplanar spacings of 0.23 nm were again observed. This spacing is consistent with a Pd_2Si structure. The 0.23 nm interplanar spacing corresponds to the (1121) and (1211) planes in the Pd_2Si structure and are identified with the most intense lines observed in the x-ray diffraction pattern. The growth in crystallite size with anneal temperature results were analyzed and yielded an activation energy of 0.4 to 0.5 eV. This energy is about a factor 3 lower than the 1.5 eV activation energy obtained by others for thermally formed Pd_2Si in which a deposited Pd film is annealed (300-500°C) to form the silicide.

We conclude that the presence of Pd in the directly implanted region by RBS and electron microbeam analysis together with the transmission electron microscopy studies which showed the presence of microcrystals of Pd_2Si with the well known interplanar (1121) and (1211) spacing of 0.23 nm, indicated conclusively the formation of Pd_2Si by FIB. The formation of the silicide microcrystals was observed to occur at 300°C. We explain the low temperature of formation and low activation energy 0.4 - 0.5 eV as arising from the presence of large numbers of vacancies produced by Pd ions in which their energy is utilized to make the reaction occur between Pd and silicon atoms. It is interesting to note that none or very little dislocation defect content was observed by TEM.

Abstract No. 452

DEVELOPMENT OF FOCUSED ION BEAM SYSTEMS

R.Aihara, H.Sawaragi, *B.Thompson and M.H.Shearer
JEOL LTD. Musashino 3 1 2, Akishima, Tokyo 196
*JEOL USA INC. Peabody, Massachusetts 0196

1. INTRODUCTION

Recently, FIB technology has been drawing wide attention because of its ability to fabricate sub micron structure in semiconductor devices. The final goal for FIB technology may be for a complete in line processing. A number of FIB systems have been developed for fundamental experiments into the potential applications of FIB technology. For the next stage of the investigation and uses, advanced FIB systems have been developed, because some applications are now coming into practical use.

2 FOCUSED ION BEAM LITHOGRAPHY SYSTEM (FIBL)

2.1 Ion optical system

The JIBL 150 [1] and 200S [2] which are developed for precise pattern writing on the substrate,consist of a liquid metal ion source , a double stage focusing system , beam blanking units , an ExB mass filter, a post lens deflector, stigmators , and three sets of beam alignment units . A schematic illustration of the column is shown in figure 1. The deflector scans ion beams over a 1mmx1mm area for all accelerating voltages . Beam blaking plates are installed before and after the ExB mass filter to perform a beam blanking at the virtual crossover point . In order to measure an ion beam diameter , line and space patterns were exposed on an Si wafer coated with PMMA resist of 0.5um thickness with 260keV, Be++, 1.5x10**8 ions/cm.As a result,0.08um line width patterns with a high aspect ratio were obtained.

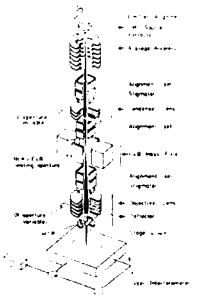


FIG.1 Ion optical system of FIBL

2.2 Control system

FIBL has two computer system for pattern writing and system control. A slave computer, HP9920, controls the ion optical system, an alignment mark detection unit and a stage controller and other system controllers. A VAX11/730, host computer, takes charge of pattern handling management of schedule files and other system files, and control of the slave computer connected with a GP IB line. The beam scanning is performed by using 16 bit D/A converters and high speed deflection amplifiers. The maximum scanning speed, minimum scanning steps and registration steps are 0.5usec/step, 0.02um and 0.02um, respectively. The pattern writing is performed by a combination of beam vector scanning and an interferometric stage movement. With this computer control, the FIBL has the ability to write patterns with high accuracy under various beam conditions, including CPU controlled changes of the ion energy, ion species and ion dosage for each rectangle or trapezoid pattern.

2.3 Writing accuracy

The over lay and stitching accuracies were evaluated by measuring vernier patterns. The first and second level vernier patterns were exposed on an Si wafer coated with PMMA resist of 0.6um thickness with 300keV, Si++ ions. The measured stitching and overlay errors were 0.12um and 0.22um, respectively. At present, the major contributions to the stitching and overlay errors are considered to be due to ion beam drift, yawing motion of the stage movement and a mark detection accuracy.

3 LOW ENERGY FIB SYSTEM

With low accelerating voltage, a fine beam, or high current density cannot be obtained with a conventional FIB column because the energy spread dV to the beam energy Va ratio dV/Va increase, and the chromatic aberration dominatesthe beam size.

Figure 2 shows the schematic illustration of the experimental system,so called a retarding mode FIB system, for a low energy (<5kV) region [3] . A target of this system is kept at high positive potential with respect to ground. Ions emitted from an ion source are accelerated to an initial energy Vo and decelerated to a landing energy Ve between the objective lens and the target surface . Figure 3 shows the relationship between rp and Ip as a function of the beam acceptance angle. Figure 4 a) shows the secondary ion image with Ve of 5keV in the retarding mode with Vo 30kV and b) shows a secondary electron image with Vo 5keV in the normal mode . In these photographs, the image resolution are approximately a)0.3um and d)1.2um, respectively.

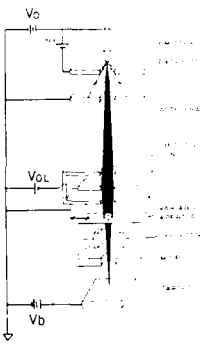


FIG.2 Retarding system

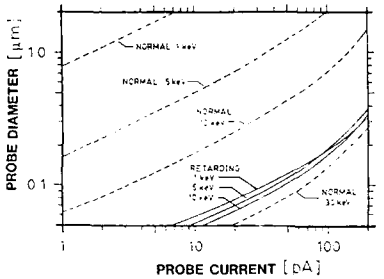


FIG.3 Calculated focusing properties



—— 5um —— 10um
(a) Retarding mode (b) Normal mode

FIG.4 Obtained SI and SE images

4. CONCLUSION

Computer controlled focused ion beam lithography systems (JIBL 150 and JIBL 200S) have been developed. Both the systems can perform the pattern writing with high registration accuracy by a combination of beam vector scanning and step and repeat stage movement. These systems have been confirmed for fabrication of microstructure devices or ASIC chips with short turn around time. For the low energy application,retarding mode FIB system has been developed and submicron ion probe were observed with 5keV, Ga beam. An FIB system with this retarding technique will be useful for shallow doping and other low energy uses.

REFERENCES

1. H.Sawaragi et al ,Microcircuit Eng 6(1987)361-366
2. R.Aihara et al ,J.Vac.Sci.Technol B6(1)245,1988
3. H.Kasahara et al ,J.Vac.Sci.Technol B,May-Jun to be published (1988)

Abstract No. 453

MAXIMIZATION OF CURRENT DENSITIES IN FOCUSED ION BEAMS BY AUTOMATED ELECTROSTATIC LENS DESIGN

M. Szilagyi and J. Szép*

Department of Electrical and Computer Engr., University of Arizona, Tucson, Arizona 85721

The design of electrostatic lenses with minimum aberrations is one of the cornerstones of the focused ion beam technology. We have abandoned the usual approach of trial and error and developed a program package for automatic design of axially symmetric electrostatic lenses with minimized spot size (maximized current density) at the target. The lens synthesis is based on rigorous mathematical procedures (constrained nonlinear optimization techniques). The source parameters (angular brightness, acceptance angle, energy spread, virtual source size, source extraction voltage), the final beam energy, the object- and image-side working distances, the maximum possible electrode potentials and the maximum allowed electrostatic fields are the given constraints that the lens design must satisfy. The program package is based on our previous work [1-3] but it contains a significant improvement. Our optimized lenses consist of several electrodes of nonconventional form (spline lenses [4]) or have the form of multielectrode lenses with very simple electrodes.

In the improved version of optimization we have changed the way of handling the constraints. Previously we used the SUMT method [5] which sequentially tightens the constraints during the procedure. Now this method is used with the simultaneous swapping of the optimization itself between two proven methods (the Davidon-Fletcher-Powell algorithm and the Hooke-Jeeves method [5]). Thus, the constraints are tightened and loosened periodically. This is a longer procedure than the previous one, but it has two important advantages. First, the result of the optimization depends much less on the initial values of the variables. This is important because to find good initial values had always been a problem previously. The second major advantage is that the optimization does not terminate in shallow local minima. Consequently, the final result is definitely better.

Our results are presented in the form of comparisons with some well-known designs [6]. Keeping the given constraint parameters constant one can achieve very essential increases of the target current densities by replacing the original lenses with our designs.

For <u>liquid metal</u> ion sources the main term in the target spot diameter is the chromatic aberration disk. The value of the chromatic aberration coefficient, however, is just slightly sensitive for changes in the axial potential distribution. Nevertheless, our improved procedure made it possible to increase the target current densities by 47% - 488% compared with previous designs.

We applied the optimization program to two different final beam energies: V_f = 5 kV and V_f = 25 kV. The source extraction voltage was 7.5 kV in both cases. The working distances were 10 mm and 50 mm on the object and image sides, respectively. Two values of the acceptance half-angle were examined: α = 5 mrad, and α = 1 mrad. The best results were achieved for the V_f = 5 kV, α = 5 mrad case, where the target current density of our 12-electrode lens is larger by 488% than that produced by the Orloff-Swanson lens which was the best in performance comparison of [6]. For the case of V_f = 5 kV and α = 1 mrad the improvement is 145% with the 12-electrode lens. Generally, for larger values of V_f and smaller values of α we could achieve smaller improvements. If V_f = 25 kV and α = 5 mrad, the improvement is 124% with a twenty-electrode lens. In the worst case, for V_f = 25 kV, and α = 1 mrad our twenty-electrode multielectrode lens produces a current density only 47% larger than that of the Kurihara lens which was the best for the same conditions in [6]. (The current density could have been increased by 67%, but the axial potential distribution in this case is so complicated that the lens would require about thirty electrodes which does not seem too practical.) Usually, for the case of V_f = 25 kV the optimized axial potential distributions are very complicated. That is the reason why in this case we have to use twenty-electrode multielectrode lenses to obtain significantly improved results. The specific numerical value of the optimized target spot size is sensitive to the constraints, especially to the value of the image-side working distance.

For <u>field ionization</u> sources we could achieve much more substantial improvements. In this case the main term in the target spot diameter is that of the spherical aberration disk. The spherical aberration coefficient is very sensitive even to small changes in the axial potential distribution; therefore, the optimization procedure could drastically reduce the target spot sizes. As a result, for α = 5 mrad the current density can be increased by 2820% and 3240% for V_f = 5 kV and V_f = 25 kV, respectively. In the first case the twelve-electrode lens is used, the second result is achieved with a five-electrode spline lens.

Acknowledgement: This work is supported by the National Science Foundation under Grant ECS 8700849.

References:

[1] M. Szilagyi, Proc. IEEE <u>73</u>, 412 (1985).
[2] J. Szép and M. Szilagyi, IEEE Trans. Electron Devices <u>ED-35</u> (1988).
[3] M. Szilagyi and J. Szép, J. Vac. Sci. Technology (in press) (1988).
[4] M. Szilagyi, J. Vac. Sci. Technol. <u>A5</u>, 273 (1987).
[5] G. R. Walsh, <u>Methods of Optimization</u>, Wiley, New York (1979).
[6] R. A. Burghard, L. Swanson and J. Orloff, J. Vac. Sci. Technol. <u>A5</u>, 364 (1987).

* Permanent Address: Department of Solid State Physics, Eötvös University, Budapest, Hungary.

Abstract No. 454

TOMOGRAPHIC APPROACH TO TWO DIMENSIONAL FOCUSED ION BEAM PROFILE MEASUREMENT

J. F. McDonald , H. T. Lin, and M. E. Haslam

Center for Integrated Electronics
Rensselaer Polytechnic Institute
Troy, New York 12181

The focused Ion Beam (FIB) is an extremely useful tool for a variety of applications in VLSI and in ULSI. Figure 1 shows a cross section view of the VG IBL 100S FIB used in these experiments.

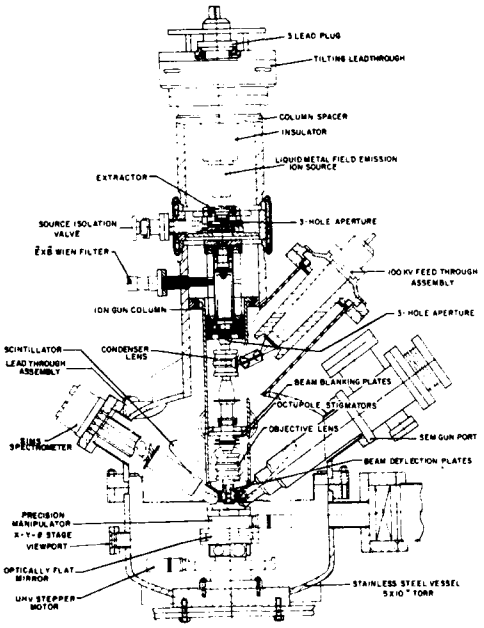


Figure 1. Cross section of VG IBL 100S FIB showing particularly the SIMS attachment.

Of particular interest to users of the FIB technology is the spot size and beam profile for the beam. The focusing of the machine is largely manual and a means for quantifying the degree of focus is desired. One approach involves scanning an abrupt GaAs/AlGaAs heterojunction with the beam with an orientation perpendicular to the junction. By monitoring the Al content in the sputtered material using the SIMS attachment of the FIB the integral of the beam current covering the Al region can be obtained. By stepping the beam center towards the junction, more and more of the beam covers the Al region producing a projection of an integrated profile of the beam current distribution. The projection is taken in the direction perpendicular to the junction. A sample integrated projection is shown in Figure 2.

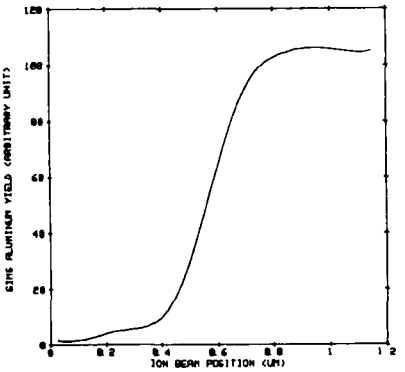


Figure 2. Typical projection integrated profile for GaAs/AlGaAs Heterojunction sweep.

This may be differentiated to obtain one of the projections, as shown in Figure 3. To obtain the two dimensional current distribution a projection sequence must be collected by rotating the table and sweeping the beam perpendicularly across the junction for each angle. A typical differentiated projection is shown in Figure 3.

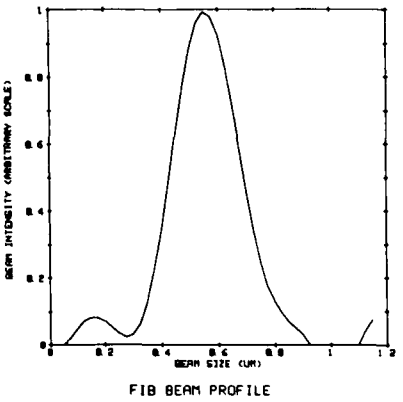


Figure 3. Spatial derivative of Figure 2 giving the projection for the beam distribution at one angular orientation of the heterojunction.

Reconstruction of the two dimensional beam current distriribution I(x,y) is by the Fourier Backprojection method in Tomography. Depending on the sensitivity of the SIMS attachment the technique can give information not only about the two dimensional distrubution of the current but also information about the low tails of the distribution far removed from the aiming point of the beam. Large numbers of projections are needed to do this, however.

Abstract No. 455

ACHROMATIC LENS AND MASS FILTER DESIGN USING CROSSED-FIELD MULTIPOLE ELEMENTS

M.R. Smith and E. Munro

Optics Section, Blackett Laboratory, Imperial College, Prince Consort Road, London SW7 2BZ, England

Two of the main factors currently limiting the performance of focused ion beam columns are chromatic aberrations of the focusing system (caused by the large energy spread in the source) and aberrations of the mass filter used for selecting an individual ion species. This paper aims to show how both these types of aberrations could be reduced by using multipole elements with crossed electric and magnetic fields. The results are based on numerical modelling of the three dimensional fields and ion trajectories.

The 3D electrostatic and magnetic scalar potential distributions in the multipole lenses were computed by the charge density method [1]. The computed potential values near the axis were used to obtain the multipole field functions, which were then used in computing the optical properties with a unified aberration theory [2]. The programs were tested with analytic models to ensure that the field functions and aberration coefficients would be accurate to within about 2%. Full details of the theory and computational techniques are given in [3].

Achromatic Lens Design

Fig. 1 shows the cross-section of a typical crossed-field achromatic quadrupole lens. Three such lenses are required to obtain stigmatic focusing with equal magnifications in x and y, and an achromatic triplet suitable for focusing a 50 keV proton beam was reported previously [4]. Here a modified design is presented for focusing heavier ions, such as Si_{28}^{++} or B_{11}^{+}, at 50 keV. Each lens has the cross-section of Fig. 1, and a length of 70 mm, which enables them to focus the heavier ions without magnetic saturation. The axial arrangement of the system (Fig. 2) provides unity magnification. There are two distinct focusing modes: (i) Without an intermediate crossover in either the x or y ray, or (ii) With a crossover in one of the rays. The crossover mode is shown in Fig. 3. This is the preferred mode of operation, because although the system can be made achromatic in either mode, it is only in the crossover mode that the primary aperture aberrations can be eliminated using three electrostatic octopoles, as proved in [3].

Table 1 shows the lens settings for achromatic focusing in the crossover mode, and Table 2 shows the corresponding axial chromatic aberration coefficients. The chromatic aberration $(\delta x_c, \delta y_c)$ at the image plane z_i is

$$\delta x_c = C_{x1} x_i' (\Delta\Phi/\Phi) + C_{x12} x_i' (\Delta\Phi/\Phi)^2$$

$$\delta y_c = C_{y1} y_i' (\Delta\Phi/\Phi) + C_{y12} y_i' (\Delta\Phi/\Phi)^2$$

where (x_i', y_i') are the ray slope components at z_i, $\Delta\Phi$ is the energy spread and Φ is the beam energy. The primary chromatic coefficients (C_{x1}, C_{y1}) are effectively zero (see Table 2).

The primary aperture aberration coefficients (A_1, A_2, B_1, B_2) are defined such that the geometrical aberration $(\delta x_g, \delta y_g)$ at z_i is

$$\delta x_g = A_1 x_i'^3 + A_2 x_i' y_i'^2, \qquad \delta y_g = B_1 y_i'^3 + B_2 y_i' x_i'^2$$

The required octopole potentials for effectively eliminating A_1, A_2, B_1, B_2 are listed in Table 3. Since the octopole potentials have no effect on the primary chromatic aberrations, the lenses can be adjusted to make the system simultaneously free of primary axial chromatic and primary aperture aberrations.

The programs have also been used to design demagnifying triplets and quadruplet systems.

Wien Filter Design

In this section, the properties of a single and a double Wien filter placed between two electrostatic round lenses are investigated. The purpose of such a filter is to select ions of a certain charge/mass ratio from a beam containing several species. The case analysed was a 50 keV beam of Si_{28}^{+}, Si_{28}^{+}, Au_{127}^{++} and Au_{127}^{+} ions, with Si_{28}^{++} as the species to be selected. The cross-section of the Wien filters is shown in Fig. 4. The axial arrangement of the single Wien filter system is shown in Fig. 5. The round lenses were adjusted to give an intermediate crossover at the mid-plane of the Wien filter. The ratio of electric and magnetic fields was adjusted to allow the Si_{28}^{++} ions to pass through undeviated. The paraxial rays for the other species are shown in Fig. 6; the aperture A in Fig. 5 removes these deflected species from the beam. The primary astigmatism of the filter was corrected by applying a small electrostatic quadrupole potential to the filter electrodes. The primary and secondary geometrical aberrations of the entire system were then computed. It was found that the dominant aberrations were the primary spherical and chromatic aberration of the round lenses (C_s and C_c), and that the aberrations of the Wien filter were negligible in comparison. (Physically, this is because the primary geometrical aberrations of the filter are cancelled out when the filter field is symmetric and the focusing ray is antisymmetric about the mid-plane, and the chromatic aberration of the selected species is compensated because the image plane is conjugate with the filter plane.)

A different focusing mode was then analysed, with a parallel beam between the two lenses, and no intermediate crossover. This reduced C_s and C_c for the focusing system by more than a factor of 2. However, the Wien filter aberrations then became significant, because the system symmetries and conjugate image plane mentioned above no longer held. To restore the favourable properties in the parallel beam case, the single Wien filter was replaced by two Wien filters excited in opposition (Fig. 7). This creates an antisymmetric filter field, which combines with the symmetric focusing ray to again cancel the filter's primary geometrical aberration. The dispersed rays now emerge parallel from the filter (Fig. 8), and thus those ions which pass through the aperture are all refocused at the image plane, hence minimising the chromatic blurring. Thus the parallel beam arrangement with a double Wien filter minimises the overall aberrations of the system. Detailed values of the aberration coefficients are given in [3].

Acknowledgements

The authors gratefully acknowledge financial support of this work from FEI, Micrion, Tektronix and VG Semicon.

References

[1] A.B. Birtles, B.J. Mayo and A.W. Bennett, Proc. IEE **120**, 213 (1973).
[2] M.R. Smith and E. Munro, Optik **74**, 7 (1986).
[3] M.R. Smith, PhD Thesis, University of London (1988).
[4] M.R. Smith and E. Munro, J. Vac. Sci. Technol. B. **5**, 161 (1987).

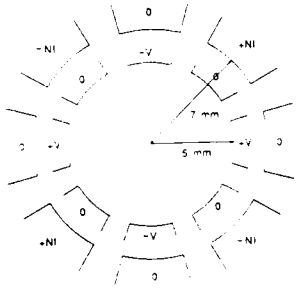


Fig. 1 Cross-section of a crossed-field achromatic quadrupole

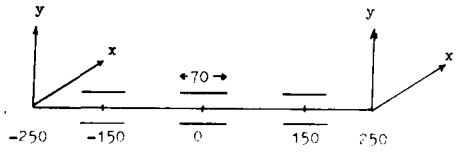


Fig. 2 Axial arrangement of the crossed electrostatic and magnetic quadrupole triplet lens (dimensions in mm)

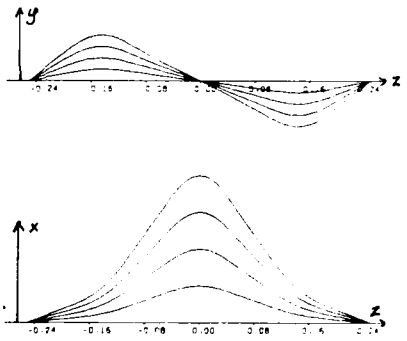


Fig. 3 Paraxial rays through the triplet in the crossover mode

Species	V_1	V_2	V_3	NI_1	NI_2	NI_3
Si_{28}^{++}	−410	264	−412	1530	−983	1530
B_{11}^{+}	−410	264	−411	1350	−871	1350

Table 1 Computed excitations on each lens for achromatic focusing (V_i in volts and NI_i in ampere-turns)

	Coefficients (mm)			
Species	C_{x1}	C_{y1}	C_{x12}	C_{y12}
Si_{28}^{++}	0.017	0.021	−7.85	−67.43
B_{11}^{+}	−0.096	−0.008	−7.85	−67.40

Table 2 Computed axial chromatic aberration coefficients for the quadrupole triplet

Species	O_1	O_2	O_3	A_1	B_1	$A_2=B_2$
Si_{28}^{++}	275	0.261	−251	$<10^{-10}$	$<10^{-10}$	$<10^{-10}$
B_{11}^{+}	270	0.261	−275	-5.4×10^{-5}	-7.5×10^{-6}	4.4×10^{-5}

Table 3 Computed octopole excitations (in volts), and residual primary aperture aberration coefficients

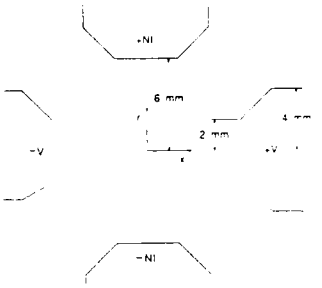


Fig. 4 Wien filter cross-section

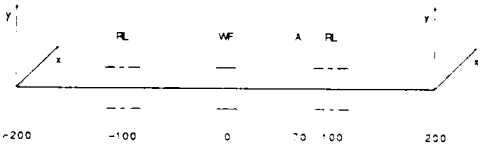


Fig. 5 Axial arrangement of the single Wien filter system (dimensions in mm)

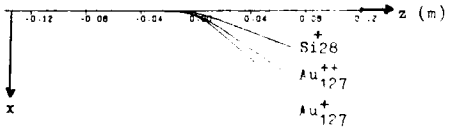


Fig. 6 Dispersed rays for the single Wien filter system



Fig. 7 Axial arrangement of the double Wien filter system (dimensions in mm)

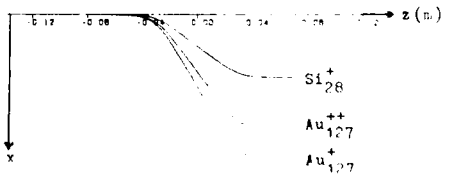


Fig. 8 Dispersed rays for the double Wien filter system

Abstract No. 456

Ion Optical Performance of the MicroBeam NanoFab-150 Focused Ion Beam System

Eugene Tsiang
William P. Robinson
John C. Potosky

MicroBeam, Inc.

1125 Business Center Drive
Newbury Park, CA 91320

MicroBeam has developed the NanoFab-150 focused ion beam system for fabricating submicron devices and structures. The system is fully automated for ease-of-use and repetitive operations.

Three target beam spot diameters between 50 and 500 nanometers may be selected, depending on the aperture chosen. The beam voltage may be set between 4kV and 150kV, at current densities of up to 5 amperes per square centimeter. A primary beam mass filter is used to select the desired ion species. An automated loadlock provides rapid sample throughput. An x-y stage, whose position may be monitored by a laser interferometer, accomodates 7-inch substrates. High speed cryopumping is used for evacuating both the optical column (housing the ion source, lenses and mass filter) and the target chamber (housing the x-y stage, position sensors and secondary particle detectors). The target and optical chambers are differentially pumped, allowing for pressure differences of several orders of magnitude. This feature permits the injection of gas into the target chamber for gas-modified ion beam processes, without compromising liquid metal ion source performance and lifetime.

During device fabrication, the NanoFab-150 may be used for patterned implantation of dopants into semiconductors, or for resist exposure. During imaging, the system collects secondary electrons or ions. Integral high efficiency SIMS optics may be supplied for use in process endpoint detection and for species-specific high resolution images.

In this paper, the NanoFab-150 system configuration, optical design, performance test results and ultimate design goals are discussed.

Abstract No. 457

Development of Liquid-Metal-Ion Sources for Focused-Ion-Beam Applications

T.Ishitani, K.Umemura, and Y.Kawanami

Central Research Laboratory, Hitachi, Ltd., Kokubunji, Tokyo 185, Japan

Prototype liquid-metal-ion sources (LMISs) have been developed for focused-ion-beam (FIB) application. The investigation has included commonly used ions such as Ga and In and others such as B, P, and As. Ion emission of the latter elements, which are dopants in Si semiconductor, are difficult because of several problems associated with strong corrosive effect of B at high temperature on the metal electrode, and with high vapor pressure of P and As. By adding new results, the present paper reviews LMIS structure, suitable source materials, LMIS characteristics, and FIB profile connected with LMIS characteristics.

1. Movable needle type LMIS

A movable needle type LMIS[1] has been developed. The needle is supported to allow precise movement along its axis, and is mechanically and/or electrically controlled from the outside of the vacuum chamber, even during LMIS operation. Needle movement plays three important roles: (1) complete wetting of the virgin needle with molten metal by sticking the tip into the molten metal, (2) recovering the metal film on the needle apex after undesirable disruption, (3) stabilization of ion emission for any LMIS by optimizing the distance from the heater to the needle apex.

Combinations of source-alloy/needle for B, P, and As LMISs are Ni-B-Si/SiC, Pt-P-Sb/W, and Ni-As/Re, respectively. The source lifetime is over 250 h for B and 200 h for P. The As LMIS has been tested up to 30 h and no obvious deterioration has been observed.

2. Suitable base-element of source alloy

When M^{2+} ion flux is large enough for FIB application, M^{2+} ions are more suitable than M^{+} ions with respect to FIB fineness. This is due to a semi-empirical rule that M^{2+} ions have a narrower energy spread per charge[2]:

$$(\Delta E(M^{2+})/2 < \Delta E(M^{+}) < \Delta E(M^{2+})).$$

Another point is that M^{+} ions have a low-energy tail but also a high energy tail on their energy distribution curve when M^{+} + M^{2+}. Here, the chromatic aberration is assumed to be dominant in determining FIB size.

The base elements of the source alloy affect the charge distributions of emitted ions. For example, the intensity ratio of P^{2+} to P^{+} ions are about 0.2 for Cu-P alloy and about 2 for Pt-P alloy. To enhance the intensity ratio of M^{2+}/M^{+} from an M-X alloy, a base element X with higher surface tension γ must be chosen.[3] This is based on the consideration that a molten alloy with a higher γ requires a higher electrostatic field, which leads to a higher probability of post-ionization of the field evaporated M^{+} ions. Typical favorable base elements, which have high γ (> 1500 dyn/cm) and form rather low melting point alloys (< 1000 C), are Ni, Pt, and Pd.

3. FIB current density distribution

Detailed experiments have shown that the profile deviates from the Gaussian at 1 to 3 orders of magnitude below the peak and has wider skirts. Analytical expression is obtained for the normalized FIB current-density distribution, J_n, which consists of three components[3]; (1) a normalized Gaussian distribution, $j_{n,g}$, which holds good near the FIB center, (2) a profile connected with lens chromatic aberration, $j_{n,c}$, and (3) a profile caused by FIB collisions with residual gas, $j_{n,c}$.

It is worthy of note that the $j_{n,c}$ profile is affected by the ion energy distribution. On the other hand, $j_{n,c}$ is affected only by collision characteristics such as residual gas pressure. It is generally suggested that to form an FIB with a smaller spot and narrower skirt, M^{2+} ions are more suitable than M^{+} ions when M^{2+} > M^{+}.

REFERENCES

1) T.Ishitani, K.Umemura, and T.Aida, J. Vac. Sci. Technol. A5, 2907 (1987).
2) T.Ishitani, K.Umemura, and Y.Kawanami, J. Appl. Phys. 61, 748 (1987).
3) T.Ishitani, K.Umemura, and Y.Kawanami, J. Vac. Sci. Technol. B (in press)

Abstract No. 458

Emission Current Dependence in the Fluctuation Power Spectra of Gallium Liquid Metal Ion Sources

Barr, D. L.
Thomson, D. J.
Brown, W. L.

AT&T Bell Laboratories
600 Mountain Avenue
Murray Hill, NJ 07974

Liquid metal ion sources have been observed to produce material beams of widely differing constitution and charge state. This includes everything from uncharged neutral particles[1] to singly and multiply charged ionic species, singly and multiply charged clusters[2] , and finally charged droplets as large as a fraction of a micron[3]. Results of experiments deriving the total mass transport from a LMIS as a function of current[4] indicate that only a fraction of the total mass is emitted as the ionic species at currents above a few microamperes. Any theory that attempts to describe the ion current-voltage behavior of the LMIS must also describe emission of these other species, since they must have a perturbative influence on ion emission. Although the emission of atomic ions is generally accepted as being due to field evaporation, the origin of clusters and droplets is still quite uncertain. It seems likely that they are a reflection of some nonrandom fluctuation in the liquid tip.

A model has been proposed by Kingham and Swanson[5] to describe the ionization mechanism of the LMIS, taking into account neutral, cluster, and droplet creation. They arrive at this model by assuming the emission site to be a cusp. Ions are generated through field ionization or field evaporation from the end of the cusp, while clusters are formed through the coalescence of thermally evaporated neutrals from the shank of the cusp, which are drawn to the tip by polarization forces, where they are field ionized. Bahasadri[6] adopts a different point of view, namely that the liquid metal cusp behaves as a fluid jet, and therefore has a set of electrohydrodynamic oscillation modes which give rise to droplet (and perhaps cluster) emission. The experiment described here is an attempt to observe characteristic modes at high frequency and as a function of total emission current.

The current results are extensions of an earlier report[7]. The apparatus used is shown in figure one. A gallium LMIS and extractor (fig 1a and 1b) generate a broad beam of ions. A rectangular slit (fig 1c) defines a fan of the beam 140 mrad in width by 1 mrad in height. The ion fan is swept across a gated chevron multichannel plate (fig 1f) using a voltage ramp that is adjustable from 4 μsec to 100 nsec. A video camera records the image produced on the phosphor screen, and the video image is then transferred to a computer where the digitized images are fourier analyzed and two dimensional power spectra are calculated.

The previously reported results of time and angle correlations in ion emission have been extended to measure the power spectrum as a function of total source current. The time and angular behavior of the emission was studied at emission currents of 5, 10, 25, 50, amd 75 μA. Figure 2 shows one such power spectrum, calculated from images taken at an emission current of 75 μA. The axes are $\log_{10}$power versus $\log_{10}$frequency and $\log_{10}$angular wave number. Power rolloffs are evident in both angular wave number and frequency. The rolloff in angular wave number is present at all source currents and has approximately the same slope of 13 db/octave, independent of source current. This is attributed to coulomb repulsion between ions which are emitted the order of 200 Å apart. There is also a distinct rolloff in fluctuation power with increasing frequency. The slope of this rolloff increases with increasing source current, with the power falling 4.7 db per octave at 5 μA and falling 6.2 db/octave at 75 μA at frequencies above 160 Mhz. Preliminary results also indicate that the total power in the statistical fluctuations is roughly proportional to the axial current density for the source (not the total source current). There is no indication in the 10-500 Mhz range reported here of any resonant behavior in the emission correlations, such as have been reported by Bahasadri et al at much lower frequencies.

[1] S. P. Thompson, Vacuum **34**, 223 (1984).

[2] D. L. Barr, J. Vac. Sci. Technol. B **5**, 184 (1987).

[3] C. D'Cruz, K. Pourrezaei, and A. Wagner, J. Appl. Phys. **58**, 2724 (1985).

[4] G. L. R. Mair and A. Von Engel, J. Phys D **14**, 1721 (1981).

[5] L. W. Swanson and D. R. Kingham, Appl. Phys. A **41**, 223-232 (1986).

[6] A. Bahasadri, Ph.D. Thesis, Drexel Univ. (1987).

[7] D. L. Barr, D. J. Thomson, and W. L. Brown, J. Vac. Sci. Technol. B **6**(1), 482 (1988).

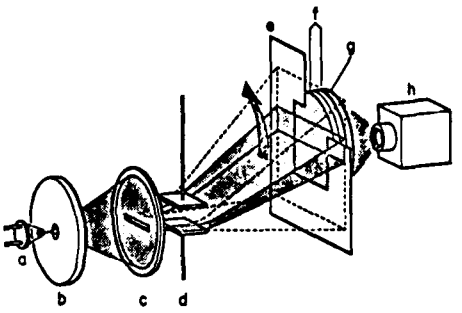


Figure 1

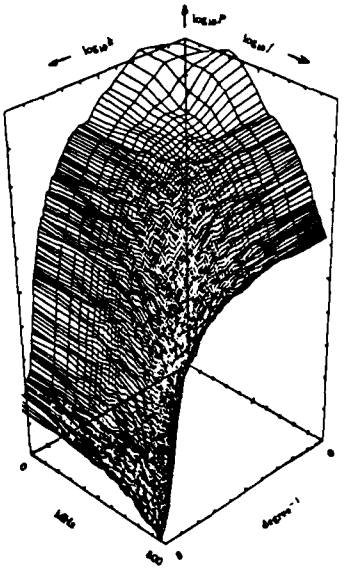


Figure 2

Abstract No. 459

THEORY OF OPERATION OF ELECTROHYDRODYNAMIC FOCUSED ION BEAM SOURCES: A REVIEW†

P. H. Cutler and N. M. Miskovsky
Department of Physics
The Pennsylvania State University
104 Davey Laboratory
University Park, PA, 16802 U.S.A.

and

M. Chung
Department of Physics
Ulsan University
Muga, Ulsan, Kyungnam, Korea

Electrohydrodynamic (EHD) ion sources have attracted much interest since the late 1960's. These devices provide a high brightness (~10^6 Acm^{-2}/sr^1), high-resolution quasi-point surface of ions at low currents (~1 - 10 μA). For currents greater than ~10 - 50 μA, droplet emission of variable mass and charge begins to dominate[1-3]. Even though the detailed mechanism of operation is not completely understood, EHD source applications have facilitated the growth of important fields of contemporary technology and science[4]. Some applications of focused ion beams (FIB) include ion implantation, microfabrication and high resolution surface analysis[4]. In addition, there is interest in their use for electrical propulsion of space craft[5] and as a light ion beam driver for inertial confinement fusion[6]. In recent years, there has been renewed effort in studying possible application of droplet emission to metallic film deposition[2,7], and mask repair[4,8].

By applying a strong electric field (~few V/A) to a liquid metal or alloy (e.g., Ga, Al, Au, Cs, etc.) at the opening of a narrow capillary tube or deposited on a metallic whisker tip, one obtains elongated liquid profiles with diameters of $\gtrsim$ 100A as a quasi-static equilibrium shape. At a certain critical voltage, the liquid microprotrusions[8] begin to oscillate and finally emit a narrow beam of singly and multiply charged ions, as well as neutral and charged clusters, and microdroplets[1-3,9].

Some of the basic physical problems which must be addressed in order to understand the operation of these devices are:

1. The spatial and temporal evolution of the microprotrusions ($\gtrsim$500A) on the liquid surface, which are thought to be the source of the ions and droplets.

2. The mechanism(s) predicting where and how surface instabilities arise and result in fragmentation and subsequent emission.

3. The specific quantum-mechanical mechanism for ion and charged cluster or droplet formation.

The most important physical parameter necessary to describe the ion and droplet formation mechanism is the electric field on the surface of the fluid near or at the apex of the source. This, in turn, requires a knowledge of the static and dynamic shape of the stressed fluid surface. Therefore, a fundamental problem in the theory of operation of EHD sources is the prediction of the static and dynamic configuration of the liquid emitter subject to strong electric fields.

An exact mathematical treatment of the problem of an electrostatically stressed fluid, from zero field to the onset of instability gives rise to non-linear electrohydrodynamic equations. To make the problem tractable, one considers two limiting regimes, the electrohydrostatic (EHS) and the electrohydrodynamic (EHD) regimes. In the EHS case, the fields and velocities are assumed to be so small that quasi-static equilibrium exists and the fluid surface is essentially at rest. In the EHD limit, pressure and field-gradients give rise to fluid flow. Hence, the pressure in the Laplace-Young stress balance condition is a time-dependent quantity. Fluid flow is now included in the description of the deformation of the fluid surface in response to the field.

In the paper, we first present some of the relevant experimental results for EHD sources. Earlier treatments of stability in the EHS model are critically reviewed. Some recent theoretical results in the EHS limit are then presented. These suggest the essential features necessary for a correct description of the fluid in the dynamical limit. We then examine new EHD theories and calculations of the dynamical shape and stability. Finally, recent theoretical attempts to explain ion and droplet formation will be discussed.

†This work was supported in part by NSF Grant No. INT-8714799.

References:

1. C. D. Cruz, K. Pourrezael and A. Wagner, J. Appl. Phys. 58, 2724 (1985).
2. M. Francois, K. Pourrezael, A. Bahasadri and D. Nayak, J. Vac. Sci. Technol. B5, 178 (1987).
3. D. Nayak, K. Pourrezael, M. Francois and A. Bahasadri, Rev. Sci. Instrum. (1987).
4. J. Melngailis, "Focused Ion Beam Technology and Applications: A Critical Review," J. Vac. Sci. Technol. B5, 468 (1987).
5. J. Mitterauer, J. de Physique Colloque C6, 48, C6-171 (1987).
6. A. R. Preganzer, J. Appl. Phys. 58, 4509 (1985).
7. P. D. Prewett, L. Gowlano, K. L. Aitkin and C. M. O. Mahoney, Thin Solid Films 80, 1.7 (1981).
8. G. Benassayag, P. Sudraud and L. W. Swanson, Surf. Sci. 181, 3627 (1987).
9. G. Benassayag, P. Sudraud and B. Jouffrey, Ultramicroscopy 16, 1 (1985).
10. A. Wagner, T. Venkatesan, P. M. Petroff and D. Barr, J. Vac. Sci. Technol. 19, 1186 (1981).

Abstract No. 480

SHAPE AND INSTABILITY OF LIQUID METAL ION SOURCES

M.S.Chung, P.H.Cutler* and N.M.Miskovsky**

Department of Physics, University of Ulsan
Ulsan, Kyungnam, Korea

* Department of Physics, The Pennsylvania State University, University Park, PA 16802, USA

** Department of Physics, The Altoona Campus, The Pennsylvania State University, PA 16601,

A fundamental problem in the study of Liquid Metal Ion Sources(LMIS) is to describe the ion formation phenomenon occurred at the onset voltage. It is the macroscopic problem of instability of the electrically stressed fluid and is the microscopic problem of field evaporation of ions from a liquid surface.

For the macroscopic description of the phenomenon, electrohydrodynamic(EHD) equations are applied to a conical model of the conducting fluid.[1] Since the Taylor[2] cone is given at overall equilibrium across the entire cone surface, it is used as the zeroth-order shape. The model surface is chosen to be a deformed cone which is described by the first-order term of deformation. By taking out the first-order contribution terms of electric and mechanical stresses and pressure difference, we have the first-order EHD equations. The obtained first-order Laplace-Young stress condition yields the shape deformarion and critical voltage at the onset of instability. This approach is similar to the analysis of the linear surface wave occurred at the horizontal overall equilibrium surface. However, even though instability is a universal Phenomenon, the two first-order stability analyses are different in that for the conical model, there already exists a geometrical singularity in the zeroth-order surface. The current attempt leads to a success to obtain the evolved shape and critical voltage for breakdown of a three-dimensional fluid surface in much better agreement with experiment. It is also worth while to mention that the instability obtained here is localized at the cone apex, which cannot be explained in the Taylor analysis. To avoid mathematical difficulties in the EHD theory, we first treat the fluid quasi-hydrostatically. By quasi-hydrostatically we mean that no flow is allowed even though a small deformation is considered. This implies that deformation is independent of time. The criterion for instability is assumed to be zero pressure difference, $\Delta p = 0$ as in the hydrostatis case. The obtained shape is a concave cone and the associated cirtical voltage is approximetely equal to two thirds of that obtained in the Taylor argument. Secondly, we make several assumptions and approximations to have some EHD results. In this case, fluid flow is allowed and then deformation depends upon time. Mathematically, the first-order Laplace-Young condition can yield the dispersion relation for ω, the frequency associated with a perturbed surface wave. For the condition $\omega = 0$, the critical voltage for the onset of instability is obtained. The corresponding shape is also calculated. However, the shape form and critical voltage are not uniquely determined.

For the microscopic description of the ion formation mechanism, the spherical model of fluid is chosen. In addition to the role of the planar model[3] which has been mostly used, it yields the size and field penetration effects with ease. This model is also directly related to the macroscopic drop whose instability has been studies for more than a century. The field ionization and the space charge effect in this model are briefly discussed.

References

1. M.Chung, P.H.Cutler, T.E.Feuchtwang, E.Kazes and N.M.Miskovsky, J. de Phys, 47, C-7, 351 (1986).

2. G.I.Taylor, Proc.Roy.Soc. (London) 280 A 383 (1964).

3. R.Gomer, Appl. Phys, 19, 365 (1979).

Abstract No. 461

AN ELECTROHYDRODYNAMIC FORMALISM FOR DROPLET FORMATION IN ELECTRICALLY STRESSED CONDUCTING FLUIDS.

N. M. Miskovsky, M. Chung, P. H. Cutler

Department of Physics
Pennsylvania State University
University Park, PA 16802

Some of the basic physical problems which must be addressed in order to understand the operation of EHD sources are:

1. The spatial and temporal evolution of the microprotrusions (<50nm) on the liquid surface, which are thought to be the source of the ions and droplets.
2. The mechanism(s) predicting when and how surface instabilities arise and result in fragmentation and subsequent emission.
3. The delineation of the specific ion and charged droplet formation mechanisms. These are fundamentally microscopic and quantum mechanical in nature and will not be treated in this paper.

Solution of these problems should provide information on the following predictive features and parameters which can be compared with experimental observations:

a. The droplet size distribution and charge to mass ratio (1,2).
b. The critical field necessary for breakdown of the surface.
c. The characteristic time associated with the growth and decay of instabilities on the surface of the stressed fluid (3,4,5,6).
d. The size (wavelength), amplitude, and the position of the instabilities on the stressed fluid (3,4,7).

An exact macroscopic dynamical theory to treat problems 1 and 2 involves the simultaneous solution of the Navier-Stokes equation, Maxwell's equations, and the time-dependent Laplace-Young stress condition. These equations are non-linear in the velocity and not amenable to closed form solution.

Chung, et. al. (8) have recently developed an electrohydrodynamic theory for an ideal conducting fluid, and applied this analysis to a fully three dimensional model of a liquid metal ion source whose initial unperturbed state was that of a ideal Taylor cone model. Equations to be solved simultaneously are the Laplace equation for the electric potential, Φ and the velocity potential Ω, Bernoulli's equation for an incompressible and irrotational fluid, the boundary conditions on the potentials, and the time-dependent Laplace-Young stress condition.

This exact set of coupled EHD equations and boundary conditions is intrinsically non-linear in the velocity term u^2. To make the problem tractable, the EHD equations were linearized and solved to first order in the potentials and the surface deformation. It is important to note, however, that the Chung, et. al. (8), analysis only treats the very-long wavelength surface modes and does not allow for any azimuthally dependent capillary wave modes. Thus, processes such as "necking" or fragmentation, which can provide a mechanism for droplet emission, cannot occur. Also, the results obtained by Chung, et. al., are restricted to be commensurate in size with the macroscopic dimensions of the fluid sample (i.e., those used by Taylor (9)). This is a consequence of restricting the calculations to the long wavelength limit. It is apparent that for the more general case of excitation of a spectrum of capillary wave modes, instabilities of submicron size can develop.

In this paper we describe an electrohydrodynamic theory and present numerical results for localized ion and cluster emission that includes dissipative effects (i.e., viscosity). This analysis is based on the formalism developed by Grossmann and Müller (10), but is no longer restricted to radial fields in cylindrical geometry. The formalism outlined here relaxes this restriction, and is applied to a model with both radial and longitudinal electric fields which are present in most EHD sources.

Assume $u_1(r,t)$ and $p_1(r,t)$ represent the deviations of the velocity and the pressure fields from their equilibrium values, u_0 and p_0. Then the Navier-Stokes equation in linearized form for these deviations becomes (10),

$$\rho \frac{\partial u_1}{\partial t} = -\nabla p_1 - \nu\rho\nabla \times (\nabla \times u_1) \text{ with } \nabla \cdot u_1 = 0 \ldots$$

where ρ is the density and ν is the viscosity. The dynamical quantities can be completely determined if one applies the boundary conditions at the free surface of the fluid. The first of these is the compatability condition between the shape of the fluid surface and the velocity inside to the fluid. The other boundary conditions on the potentials, and the Laplace-Young condition must also be satisfied.

The above formalism when applied yields solutions for u_1 and p_1 which satisfy the boundary conditions. This allows for the determination of the eigenmodes and eigenfrequencies of the system as well as the limits of the stability regimes of the stressed fluid. The general form of the eigenmodes u as a function of r, θ, ϕ are now determined as a function of frequency. Similarly, the frequencies of the eigenmodes are calculated by substituting the solutions for u_1 and p_1 into the time-dependent Laplace-Young stress condition. This gives the relationship between the restoring stresses provided by the surface tension, the outward stress due to the electric field and the inertia of the fluid from which one determines the possible eigenfrequencies. In the present analysis, the real part of the eigenfrequency is related to the decay rate of the excited eigenmode, and the imaginary part is related to the energy associated with that mode. It is important to note that the solutions for the velocity field involve Bessel functions which contain the parameter k. The significance of this is that these are essentially the characteristic wavelengths associated with the perturbed eigenmodes or surface disturbances on the fluid. The functional form of the mode ampitudes, which contain terms such as $\sin(\tau \ln r)$, is consistent with what is expected on physical grounds. This is seen from the following argument. The parameter τ contains the *wavelegnth dependence of the modes*. The spacing betwen nodes is not equidistant but increases with distance from the apex. Physically, this implies greater stability of the perturbed surface as one moves away from the apex region, that is, this gives a local dependence of the stability of the excited eigenmodes with the instability most likely to occur at or near the apex where the fields are highest. Since the excited eigenmodes constitute a spectrum of wavelengths, then, in the short wavelength limit, they can account for the microprotrusions observed experimentally.

Numerical calculations of the eigenfrequency spectrum are presented. From this data, the stability regimes are delineated as well as the breakdown voltage for the stressed fluid. From the real part of the calculated eigenfrequencies the localized growth and decay rates are examined. In addition, the calculated local amplitude variation provides information on the droplet size distribution which is compared to experiment.

This work was supported in part by NSF grant INT-8714799.

1. C. D'cruz, K. Pourrezaei and A. Wagner, J. Appl. Phys. 58, 2724 (1985)
2. M. Francois, K. Pourrezaei, A. Bahasadri and D. Nayak, J. Vac. Sci. Technol. B5, 178 (1987).
3. A. R. Preganzer, J. Appl. Phys. 58, 4509 (1985).
4. M. D. Gabovich, Sov. Phys. Usp. 26(5), 447 (1983).
5. a) V. G. Dudnikov and A. L. Shabalin, Sov. Phys. Tech. Phys. 30, 462 (1985).
   b) V. G. Dudnikov and A. L. Shabalin, Sov. Phys. Tech. Phys. 32, 112 (1987).
6. P. H. Cutler, M. Chung and N. Miskovsky, "Theory and Application of Electrodydrodynamic Ion Sources," 11th International Seminar on Surface Physics, Piechowice, Poland (May 1987).
7. G. Benasayag, P. Sudraud and B. Jouffrey, Ultramicroscopy 16, 1 (1985).
8. M. Chung, P. H. Cutler, N. Miskovsky, T. E. Feuchtwang and E. Kazes, J. Vac. Sci. Technol. B5, 1628 (1987).
9. G. I. Taylor, Proc. Roy. Sci. (London) A280, 383 (1964).
10. S. Grossmann and A. Müller, Z. Phys. B57, 161 (1984).

Abstract No. 462

The behaviours of metal impurities in Si substrate

K.Hiramoto, M.Sano, M.Horai, S.Sumita,
N.Fujino and T.Shiraiwa

Kyushu Electric Metal Co.,Ltd.
Osaka Titanium Co., Ltd,

Kamioda, Kohokucho, Kishimagun, Saga, Japan
Amagasaki, Hyogo, Japan

1. Introduction

There are many chances to contaminate silicon wafers with metal impurities such as Fe, Ni and Cu even in the automated LSI manufacturing processes. Heavy metal contaminations on silicon wafers are one of the most serious causes which degrade the device performance[1-4]. As the feature size of silicon LSI is reduced, the study and control of metal impurities become more important. Although many works[5-8] about metal impurities have been reported, the quantitative study for the metal precipitations and the influence to electrical characteristics have been scarcely reported.

In this presentation the behaviours of metal impurities at the surface are discussed after quantitative metal contamination[9]. And their dependence on sorts of impurities, amounts of impurities and heat processes are shown by observation of etch pits, transmission electron microscopy (TEM), and electrical characteristics such as gate oxide integrity (GOI) and carrier lifetime. From these results quantitative monitering methods have been developed[10]. Then gettering techniques to remove such metal impurities and their efficiency during heat treatment are discussed.

2. Experiment

For the experiments n- and p-type, Czochralski-grown (CZ), 4"Φ and (100)-oriented wafers were used. Sample wafers were contaminated quantitatively by spin coating of metal salt solution on their front surface. In order to measure the concentration of metal, a native oxide film on the front surface was decomposed in HF vapour and dissloved solution was analyzed by a flameless type of Atomic Absorption Spectrometer[9].

After sample wafers were contaminated with 10^{12}-10^{13} atoms/cm^2 of Ni, Cu and Fe, they were put into a furnace at 1000° C and heated up to 1150°C with ramping rate of 5°C/min. Then they were annealed at 1150°C for 1 hour in N_2 and cooled to room temperature through two types of processes. In one case (HT1), they were cooled down to 1000°C with the rate of 3° C/min and pulled out of the furnace. In another case (HT2), they were cooled down to 650°C with the rate of 1°C/min and pulled out of the furnace. After HT1 or HT2, sample wafers were also annealed at 1000°C for 4 hours in dry O_2 (HT3). Then the surface defects were observed by an optical microscope after preferential etching and TEM.

In order to investigate the influence on GOI and carrier lifetime, oxide films were removed after HT1 or HT2 and MOS capacitors were fabricated. MOS capacitors for GOI evaluation had 25 nm oxide films and 3mm X 3mm polysilicon electrodes. MOS capacitors for lifetime evaluation had 75 nm oxide films and 1mm X 1mm Al electrodes with guard electrodes. Gettering efficiencies during heat treatment were evaluated concerning intrinsic gettering (IG), backside damage by shot blast (BD) and polysilicon back coating (PG), they were investigated by electrical characteristics after quantitative contaminations.

3. Results and Discussion

Figure 1 shows the correlations between surface metal concentration and shallow pit density by an optical microscope after HT1. Precipitations of Cu and Ni were observed as shallow pits after preferential etching, and they grew into stacking faults and dislocations after HT1. However no defects were observed by Fe contaminations. We could not also find any defects on all contaminated wafers after HT2 or HT2 + HT3. Figure 2 shows a cross-sectional TEM image after HT1 (a) and a plane-view TEM image after HT1 + HT3 (b) for a Cu contaminated wafers. Precipitations grown along (110) plane were observed in (a) and they induced stacking faults after subsequent annealing in (b). These precipitations were found to be Cu silicides by EDX analysis. The similar results were obtained for Ni contaminated wafers. Therefore the behaviours of Cu, Ni and Fe in silicon strongly depend on surface concentration of metal and the condition of subsequent heat treatments after contamination. Cu and Ni impurities tend to precipitate at the surface and Fe dissolves into bulk.

The correlations between the surface metal concentration and GOI are shown in Figure 3. Breakdown strength was reduced in the samples, whose precipitations were observed after HT1. However it was also reduced in the samples, Cu contaminated with 10^{12} atoms/cm^2 after HT2 and Ni contamination after all heat treatments, in which we could not find any precipitations. These results indicate that GOI is more sensitive for metal contaminations than the observation of shallow pits. Fe impurities did not degrade GOI, but they decreased generation lifetime. It is considered that Fe dissolves into bulk during heat treatment and form carrier generation centers.

The gettering efficiencies were studied after heat treatments simulating a C-MOS process. These results show that IG is more effective than BD and PG stably.

4. Conclusion

The behaviours of heavy metal impurities in silicon were studied by the observation of defects and the measurement of MOS capacitors characteristics after quantitative contamination by spin coating.

(1) Ni and Cu precipitate metal silicides at the surface and grow into stacking faults or dislocations after heat treatment. Their behaviours strongly depend on the condition of heat treatment. Gate oxide integrity is reduced by precipitations of Ni and Cu.

(2) Fe diffuses and dissolves into bulk and decreases carrier lifetime.

(3) The methods to investigate the gettering eficiency are developed and it is found that IG is more effective than BD and PG.

References

1) L.Jastrzebski, R.Soydan, B.Goldsmith, and J.T.McGinn : J.Electrochem.Soc. 131 (1984), 2944.
2) B.M.Lacquet and P.L.Swart : Nucl. Instrum. & Methods in Physics Research. B6 (1985), 372.
3) K.Honda, A.Ohsawa, and N.Toyokura : Appl. Phys. Lett. 45 (1984), 270.
4) K.Honda, A.Ohsawa, and N.Toyokura : ibid. 46 (1985), 582.
5) K.Graff and H.Pieper : Semiconductor Silicon 1981 edited by H.R.Huff, R.J.Kriegler, and Y.Takeishi, Pennington, NJ, (1981), 331
6) E.R.Weber : Appl. Phys. A30 (1983), 1.
7) A.Ohsawa, K.Honda, and N.Toyokura : J. Electrochem. Soc. 131, (1984), 2964.
8) M.Yosnida and K.Furusho : Jpn. J. Appl.phys. 3 (1964), 521.
9) T.Shiraiwa, N.Fujino, S.Sumita, and Y.Tanizoe : Proc. 5th International Symposium on Semiconductor Processing, Santa Clara Feb., 1988 (to be published)
10) cotributed to Proc. Semicon Osaka 1988

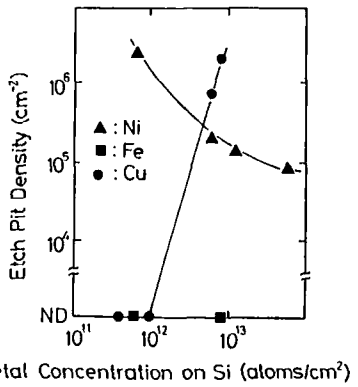


Fig.1 Dependence of etch pit density on surface metal concentration on silicon (The size of etch pits is different with the concentration of Ni)

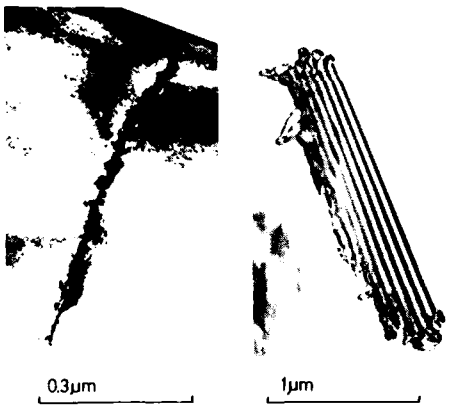


Fig.2 TEM images of samples contaminated with 7.6 X 10^{12} atoms/cm^2 of Cu. (a) is cross-sectional TEM image after HT1 and (b) is plane-view TEM after HT1 + HT3

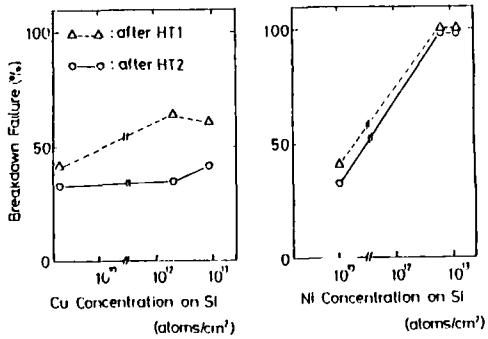


Fig.3 Dependence of gate oxide integrity on surface metal concentration on silicon (a) contaminated by Cu and (b) by Ni

Abstract No. 463

AN ADVANCED CRYSTAL GROWTH TECHNIQUE AS FULL RANGE RESISTIVITY CONTROLLED CZ (FCCZ)TECHNIQUE

Y.Yamashita,M.Kojima and H.Hirano

Semiconductor Materials Engineering Dept.
Toshiba Corporation

72,Horikawa-cho,Saiwai-ku,Kawasaki,210,
Japan

When a semiconductor single crystal is grown from a melt in a crucible,by the conventional CZ technique,impurity concentration distribution C in the longitudinal direction of the grown single crystal varies according to the following eqation,

$$C = kC_0(1-G)^{k-1} \quad \text{---------- (1)}$$

where k is the segregation coefficient, C_0 is the initial impurity concentration of the melt, and G is the solidification rate.

Therefore, significantly decreasing the formation yield for a single crystal having an impurity concentration within a predetermined range when segregation coefficient k is small.

Conventionally, a pulling technique, known as the floating crucible technique,has been proposed,to solve the above problem[1),2)] However there are few reports in the Si crystal growth[3),4)]

Recently,we have developed a new double-crucible CZ technique for obtaining uniformly doped Si single crystals from top to tail on the basis of the idea by A.V.Valcic[5)]. This is called the FCCZ(Full Range Resistivity Controlled CZ)technique. This uniformity is accomplished in the followsing manner.
(A) A special double-structure quartz crucible is used. The inner crucible, containing a melt doped with an impurity,is arranged concentrically and integrally with the outer crucible to contain an undoped melt. The inner-crucible diameter is $\sqrt{k}$ times that of the outer crucible, when the impurity segregation coefficient is k.
(B) These inner and outer crucibles connect through a quartz pipe like passege,which prevents diffusion of an impurity from the inner-crucible melt to the outer-crucible melt, and prevents exchange of melts between inner and outer crucibles, before and during crystal pulling.

The principle for obtaining uniformly doped single crystals is as follows. First, it is assumed that the outer crucible radius is R, the inner crucible radius is r, the segregation coefficient for an impurity is k, the impurty concentration in the inner-crucible melt is C_i .The following relationship is satisfied at the liquid surface height of the melt from which the crystal is to be pulled (see Fig.1);

$$r = \sqrt{k} \times R \quad \text{---------- (2).}$$

When the melt surface height in the crucibles is decreased by ΔH as the single crystale is pulled,the total grown crystal volume is $\pi R^2 \Delta H$,so the total impurity amount taken into the single crystal is as follows;

$$\pi R^2 \Delta H \times kC_i$$

In addition, an impurity amount originally present in the melt in the inner crucible having height ΔH is represented by

$$\begin{aligned} &\pi r^2 \Delta H \times C_i \\ &= \pi R^2 \Delta H (r^2/R^2) C_i \quad \text{(due to eq.(2))} \\ &= \pi R^2 \Delta H \times kC_i \quad \text{---------- (3),} \end{aligned}$$

and thereby corresponds to the total impurity amount taken into the single crystal. That is, the impurity present in the melt in the inner crucible with height ΔH is completely taken into the grown crysyal. Therefore, the impurity concentration in the melt in the inner crucible is always maintained at constant value C_i , so that in the pulled crystal is always maintained at constant value $k \times C_i$.

We have succeeded in obtaining phosphorus doped 5″ø diameter <111> or <100> dislocation free Si single crystals with nearly uniform resistivity in the longitudinal direction, by using the proposed double crucibles, as r/R is 11″ø/16″ø(see Fig.2 and Fig.3).

Power devices were manufactured,for which the sub-wafer is demanded to have a strictly narrow resistivity range, for trial in using Magnetic Field applied FCCZ wafers and recognized that the formation yield for the devices is eqivalent to that in using R'nely used NTD Wafers.

There are other merits in using the FCCZ technique during the Si crystal growth beside the longitudinal resistivity uniformity, such as;
(A) The resistivity uniformity of the grown crystal in the radial direction is improved by using the "small" inner crucible as the breeding vessel.
(B) By pulling the crystal in a strong magnetic field, it is easy to obtain a single crystal whose resistivity is comparatively uniform, not only in the longitudinal direction but also in the radial direction.
(C) It is easy to obtain comparatively high [O_i] Si crystals, although crystal pulling is implemented in a magnetic field through use of the "small" inner crucibles.
(D) This new pulling technique can be utilized merely by exchnanging a conventional single crucible for the double crucible presently developed. Therefore it is possible to use a conventinal Si CZ pulling machine without changing the format.

We think that FCCZ technique is the closest cut to the continious pulling technique,which is a dream many year's standing, for Si crystal industry.

References

1.W.F.LEVERTON, J.Appl.Phys.29, 1241(1958).
2.J.GOORISEN, Phillips Tech.Rev.21, 185(1960).
3.W.Lin and C.W.Pearce, J.Appl.Phys. 51(1980) 5540.
4.W.Lin and D.W.Hill, in:Silicon Processing, Ed.D.C.Gupta(ASTM,Philadelphia,PA,1983)p.24.
5.A.V.VALCIC,Solid-State Electron.5,131(1962).

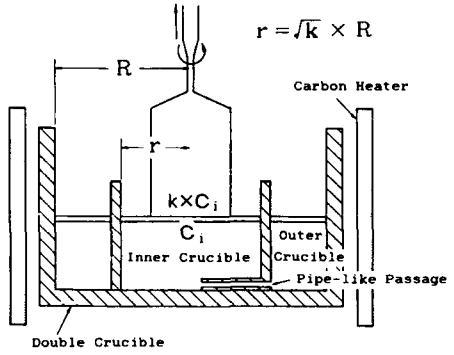


Fig.1 The schematic drawing of presently developed double crucible

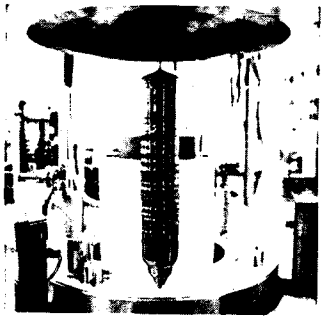


Fig.3 The pulled 5″ø Si single crystal by using FCCZ technique

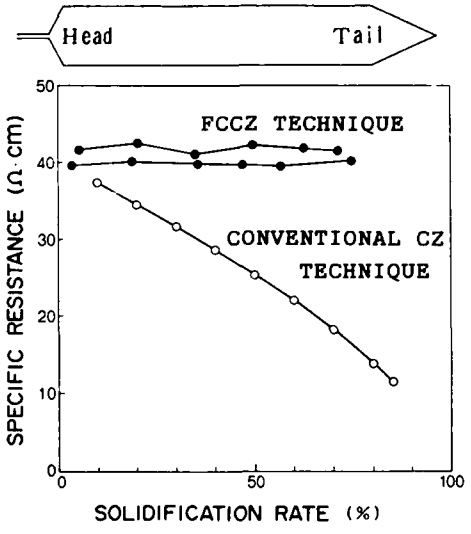


Fig.2 The comparison of the FCCZ technique with the conventional CZ technique

Abstract No. 464

TEM OBSERVATIONS OF CRYSTALLIZED LPCVD SILICON FILMS

T. Aoyama, Y. Okajima, Y. Koike
T. Suzuki, N. Konishi, and K. Miyata

Hitachi, Ltd., Hitachi Research Raboratory
Hitachi, Ibaraki 319-12 Japan

1. Introduction

Active matrix thin film transistors (TFT's) have attracted attention for their applications to liquid crystal (LC) TV's and displays. With the requirement of monolithic drivers' integration around display panels (1), polycrystalline silicon instead of amorphous silicon is becoming important due to its high carrier mobility. With either materials, however, the process temperature should be lower than about 600°C to allow use of glass substrates (2).

In order to increase carrier mobility of polysilicon films, the grain size should be increased and the crystallinity (total crystalline volume) should be as high as possible (3).

In this paper, we investigated the structure of crystallized LPCVD silicon films which were deposited at an optimum deposition temperature of 550°C (4). A number of twinning structures and stacking faults were observed inside grains.

2. Experimental

LPCVD silicon films were deposited on glass substrates (100 mm × 100 mm) using 20 % SiH_4 diluted by He. Deposition temperature and pressure were between 500 and 620°C, and between 0.3 and 1.5 Torr, respectively. Film thickness was typically 150 nm, as measured by elipsometry.

The LPCVD films were annealed in N_2 ambient at 600°C in an oxidation reactor.

The crystallinity of the films were measured by x-ray diffraction; the incident beam was fixed by 2° from the sample surface. Electron spin density was measured by ESR in x-band at room temperature. The TEM observations were performed at the accelation voltage of 200 kV. The LPCVD films were thined by a solution of $HF:HNO_3:CH_3COOH$ = 1:40:1.

3. Results and Discussion

Fig. 1 shows the effect of deposition temperature on the volume of (111) crystalline component before and after annealing. For as-deposited films, crystalline phase appeared above about 580°C. After annealing, however, the crystalline volume had a maximum for the films deposited at about 550°C. Almost no increase was observed for the films deposited above 580°C.

Fig. 2 shows the effect of deposition temperature on electron spin density for the films. A maximum spin density was observed for the as-deposited films at 550°C. As electron spin density increased for as-deposited films, the crystallinity was increased for annealed films. Dangling bonds rather than distorted bonds between silicon atoms in amorphous phase seem to fascilitate solid phase crystallization.

Fig. 3 shows TEM top views of annealed films deposited at the optimum temperature. Grain structures about 600 to 2000Å were observed in Fig. 3 (a). Fig. 3(b) shows a lattice image of the film; inside of irregular grain boundaries, twin structures along (111) were observed on (110) planes. Another periodic structures, probably stacking faits, were seen with an interval of about 10Å.

4. Acknowledgements

We would like to thank Y. Kawamoto, R. Nashimoto, H. Suzuki, and K. Suzuki for their helpful discussions and encouragement.

References

(1) J. Ohwada, M. Takabatake, H. Kawakami, Y. Ono. A. Mimura, K. Ono, K. Konishi, T. Suzuki, and K. Miyata, Ext. Abst. 19th Conf. Solid State Dev. and Mat., Tokyo, 1987, pp55
(2) A. Mimura, N. Konishi, K. Ono, J. Ohwada, Y. Hosokawa, Y. A. Ono, T. Suzuki, K. Miyata, and H. Kawakami, IEDM Tech. Dig. 436 (1987)
(3) M. H. Hatalis and D. W. Greve, IEEE Elect. Dev. Lett., EDL-8, 361 (1987)
(4) T. Aoyama, N. Konishi, T. Suzuki, and K. Miyata, to be published in Proc. of the 1987 MRS Meeting

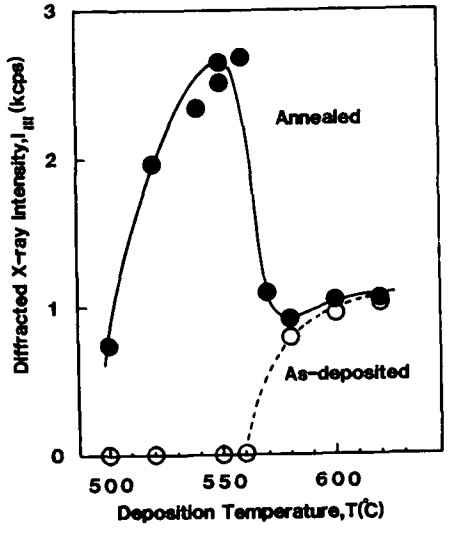


Fig. 1 Diffracted x-ray intensity as a function of deposition temperaturefor as-deposited (○) and annealed (●) films; deposition pressure: 0.6 Torr, annealing: 600°C, 24 h.

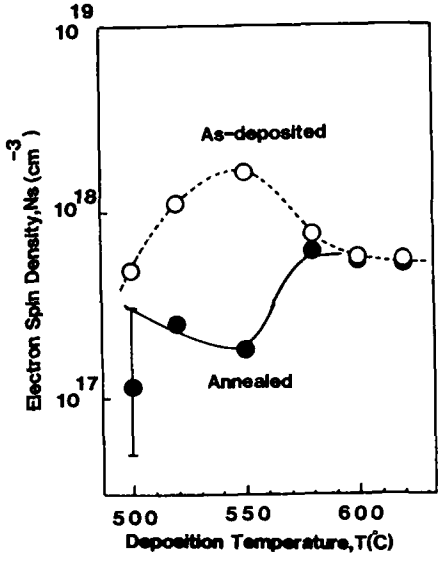


Fig. 2 Electron spin density as a function of deposition temperature for as-deposited (○) and annealed (●) films; deposition pressure: 0.6 Torr.

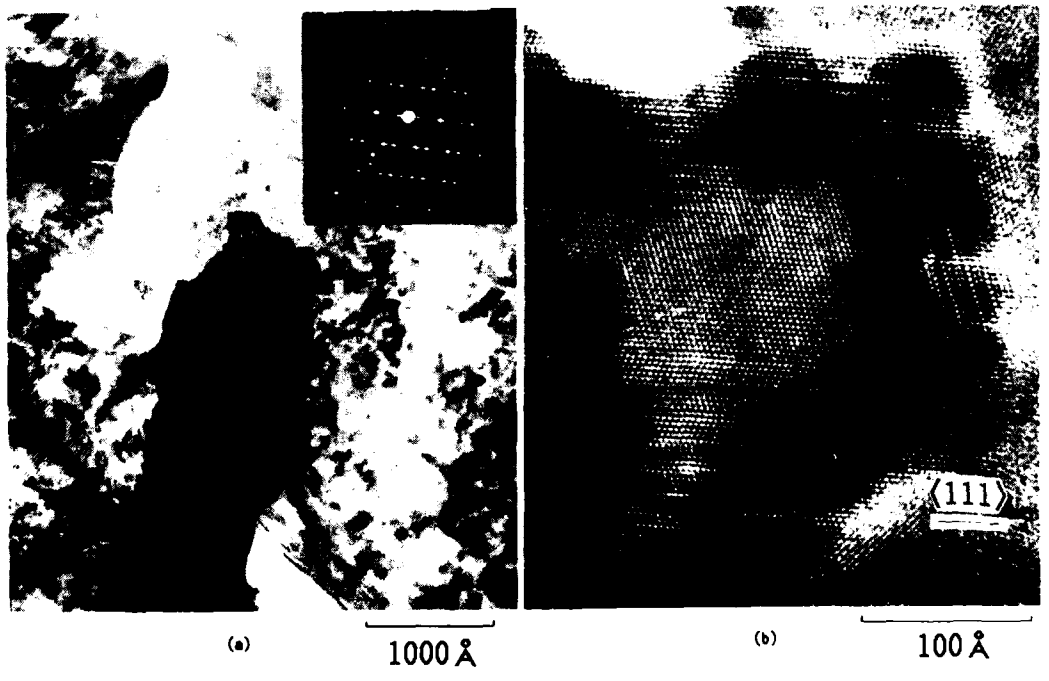


Fig. 3 TEM micrographs for crystallized films deposited at 550°C, (a)grain structures (b)lattice images.

Abstract No. 465

The Role of Film Stress on the Rate of Silicon Oxidation at Low Temperature

Paul Murray and G.F. Carey
Aerospace Engineering & Engineering Mechanics
The University of Texas at Austin
Austin, Texas 78712

During growth of oxide films on silicon, compressive stresses which develop in the film relax at a time scale proportional to the viscosity of oxide. As the temperature decreases, the viscosity dramatically increases and compressive stresses become more significant. It has been conjectured that a high film stress at low processing temperature decreases the diffusivity of oxidizing gas through the oxide film. The growth of oxide at the oxide-silicon interface is determined by the quantity of gas reaching the silicon surface. A decreased diffusion rate of gas through the oxide film (due to the high compressive stress) results in a reduction of the overall growth rate. Therefore, it is essential to understand mechanical stress in oxide films and its influence on the transport process to be able to accurately model silicon oxidation.

We present a theoretical model for silicon oxidation that includes the effect of stress on the growth rate of thin oxide films. Our model is based on the treatment of oxide as a compressible, Newtonian fluid and the assumption that the diffusiviiy of oxidizing gas through the oxide is decreased by film pressure. Expressions for interfacial pressure and bulk oxide pressure are developed and applied to study the effect of film stress on the growth rate. Moreover, use of a general expression for oxide stress enables calculation of film thickness for both planar and cylindrical silicon surfaces. This, in turn, leads to an explanation of thinning in oxide films on curved surfaces.

During oxidation the oxidizing gas diffuses through the film to react at the silicon surface. There is a net flux of oxide away from the moving silicon surface to accomodate for the difference in molar volume between silicon and oxide. Film stress exists because oxide is compressed as it is produced during the reaction of silicon with the oxidizing gas. A slightly compressed oxide at the oxide-silicon interface results in a velocity gradient through the film which causes a compressive stress in directions parallel to the interface. Our model confirms that high oxide viscosity at low temperature (below 1000° C) inhibits stress relaxation so that pressure remains high throughout the film. Conversely, at high temperature lower viscosity enables rapid relaxation of stress, thus confining high pressure to the interfacial region near the silicon surface. Therefore, stress effects are especially important for low temperature oxidation.

We apply the model to three important issues of current interest: (1) the initially rapid oxidation rate at low temperature; (2) the crossover in rates observed for reactions at the (110) and (111) silicon surfaces; and (3) the occurrence of thinner oxide films on cylindrical surfaces. These phenomena are not yet fully understood and previous theoretical models employ overly restrictive assumptions on the oxide stress. We show that the new model predicts the above three phenomena and confirms that they are related to the high stress in the oxide film during oxidation. Moreover, use of dimensionless variables and a general expression for oxide stress enables us to perform calculations designed to determine the important physical parameters governing the oxidation process.

Abstract No. 466

TITANIUM SILICIDE OHMIC CONTACTS FOR HIGH TEMPERATURE β-SiC DEVICES

S. M. Tang, W. B. Berry, R. Kwor, K. L. Jacobson, Univ. of Notre Dame, Notre Dame, IN 46556; M. V. Zeller, L. G. Matus, NASA LeRC, Cleveland, OH 44135; N. S. Alvi, Delco Electronics, Kokomo, IN 46902; A. J. Nelson, A. B. Swartzlander, SERI, Golden, CO 80401.

In recent years, efforts have been made to develop high temperature β-SiC devices. One major area of research is on the investigation of ohmic contact materials which are stable and retain electrical quality at high temperatures. Common contact materials such as Al, Ni, W, Ti, Ta and Cr have been studied [1,2]. However, many of these metals tend to diffuse into the SiC during high temperature annealing. Au/metal layered contact structures have been examined using oxygen sensitive metals [3,4]. Unless a H_2 atmosphere is used during annealing the metals migrate through the Au coating to the surface resulting in delamination of the contact. Refractory metal silicides, known for their high temperature stability and low resistivity, may be more suitable as ohmic contacts for β-SiC. Tantalum disilicide ($TaSi_2$) ohmic contacts have been successful at 400°C for eight hours in air (5). In this study, titanium silicide ($TiSi_x$) is chosen as the contact material because it has the lowest resistivity amoung common refractory silicides (6). Of special interest is the aging effect of $TiSi_x$ on β-SiC at high temperatures. The goal is to determine the maximum temperature for which this material retains good electrical quality.

The n-type SiC samples were heteroepitaxially grown on off-axis (100) silicon substrates by chemical vapor deposition (7). Immediately before metallization, the samples were etched with HF to remove any surface oxide. A 1000Å thick $TiSi_x$ layer was deposited on the SiC surface using RF sputtering to co-sputtered Si and Ti. A stainless steel shadow mask was used to define the contact patterns. After deposition, the samples were rapid thermal annealed (RTA) at 950°C for 15 seconds for silicide formation. Post-deposition heat treatments were performed in a quartz tube furnace under a H_2 atmosphere. The heat treatments ranged from 450°C to 750°C for up to 9.5 hours in logarithmic time-period increments. Current-voltage characteristics and specific contact resistances (SCR) of the samples were measured after each heat treatment (8). Standard four-point probe techniques were used for the resistivity measurements.

Current-voltage characteristics were linear for the $TiSi_x$ contacts. The SCR's were in the range from $3x10^{-2}$ to $5x10^{-2}$ ohm-cm^2 after RTA. Figure 1 shows the normalized SCR values as function of heat-treatment time at different temperatures. The SCR did not change appreciably after heat treatment at 450°C for 9.5 hours. Only a slight change in the SCR was noted after heat treatment at 600°C for 9.5 hours. A substantial increase in SCR was measured after heat treatment at 750°C for only 30 minutes. With continued treatment at 750°C for up to 9.5 hours, a dramatic increase in SCR resulted, as noted in Figure 1. In addition to the increase in SCR, a color change was noted after 4.5h at 750°C. The silicide surface visibly turned brown as compared to the original as-deposited bright metallic color.

To interpret the SCR increase and the color change, Auger Electron Spectroscopy (AES) depth profiles were recorded to examine chemical reactions at the contact surface and the silicide/SiC interface. AES data indicated that the silicide films, after RTA, were Ti rich, most likely a $TiSi_x$ species rather than the desired $TiSi_2$. Although the ohmic contact remained electrically stable while heating at 600°C for 9.5 hours, a slight reaction was already occuring at the interface. Ti was detected in the top 100Å of the SiC layer. A slight depletion of carbon was also noted in this Ti + SiC reaction zone and a corresponding increase in carbon was observed in the silicide film. To prevent this Ti diffusion, a more stoichiometric $TiSi_2$ film must be prepared. Electrical stability studies on these new silicide films are currently under way.

ACKNOWLEDGMENT

This work has been supported in part by NASA-LeRC, Contract No. NAG 3-428. NASA provided the SiC Samples.

REFERENCES

1. M. Chaudhry, Ph.D. Thesis, University of Notre Dame, IN (1987).
2. M.V. Zeller et al., Mat Res Soc Symp Proc, 97, 283 (1987).
3. L. Messick et al., Third National Review Meeting on SiC, North Carolina State University, Raleigh, NC (1986).
4. K.L. Moazed et al., Fourth National Review Meeting on SiC, North Carolina State University, Raleigh, NC (1987).
5. J.A. Edmond, et al., J Electrochem Soc, 135, 359 (1988).
6. S.P. Murarka and P.F. Fraser, J Appl Phys, 51, 350 (1980).
7. J.A. Powell etal., Appl Phys Lett, 51, 823 (1987).
8. F. Kuphal, Solid State Electronics, 24, 69 (1981).

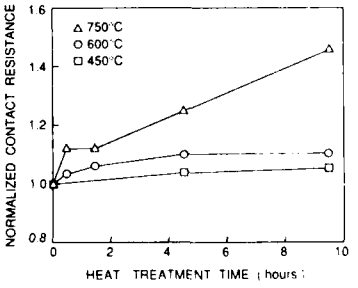


Fig. 1 Normalized specific contact resistance vs heat-treatment time. All contacts have been annealed (RTA) at 950°C for 15 sec. before heat treatment. The 450°C and 600°C curves were normalized to the resistance value after RTA. The 750°C curve was normalized to the resistance following the 600°C, 9.5 hour heat treatment.

Abstract No. 467

THE INFLUENCE OF PROCESS ATMOSPHERE ON TITANIUM SILICIDE FORMATION

R. M. Vadjikar and R. P. Roberge*
Linde Division, Union Carbide Corporation
Tarrytown, N. Y. 10591

Introduction

Titanium silicide is being investigated for ULSI metallization applications because of its low sheet resistivity, excellent thermal stability and compatibility with the self aligned process (1). However, the self aligned titanium silicide process is very sensitive to the purity and type of process environment (2). Lateral growth of titanium silicide and oxidation of the titanium film are problems which are addressed by using nitriding process atmospheres containing low levels of oxygen and water. In this work, the lateral growth of titanium silicide in nitrogen, argon and nitrogen+ammonia process atmospheres was investigated. It was observed that ppm levels of oxygen or water can cause unacceptable oxidation of titanium film.

Experimental details

The experimental apparatus for titanium silicide process experiments is shown in Figure 1. In-situ monitoring of the process atmosphere during the annealing cycles was done using Linde's Reactor Analysis System (RAS). The RAS is capable of detecting sub ppm oxygen and water impurities in the process environment. The carrier gases used for annealing experiments were nitrogen, argon and ammonia+nitrogen. Unpatterned silicon wafers having a 1000 Angstrom titanium film on the surface were used for examining the effect of ppm levels of oxygen in the process environment. Patterned silicon wafers with 1000 Angstrom titanium deposited on polysilicon lines were used for the study of lateral growth of titanium silicide. The first furnace anneal in titanium silicide formation was carried out at 675°C for 20 minutes. The presence of a nitriding process atmosphere was found to be necessary in this anneal step to limit the lateral growth of titanium silicide. After etching the unreacted titanium/titanium nitride, the second furnace anneal was done at 800°C for 30 minutes, so as to reduce the sheet resistivity of titanium silicide. This anneal step was done in argon. The lateral growth of titanium silicide in nitrogen, nitrogen+ammonia and argon was studied using the scanning electron microscope. Auger electron microscopy was used for depth profiling.

Results and discussions

Visual inspection of the annealed, unpatterned wafers indicated that the oxidation effects were predominantly around the periphery. It was found that oxygen or water contamination levels in the process atmosphere should be kept below 5 ppm to minimize these effects.

Figures 2,3 and 4 illustrate the lateral growth of titanium silicide in different process atmospheres. The RAS was used in these experiments to ensure that the oxidant contamination level was less than 5 ppm. Figure 2 shows that lateral growth can be a severe problem if only argon is used in the first anneal step. The beneficial effect of nitrogen (3) is evident from Figure 3. The titanium-nitrogen interaction limits the extent of lateral growth. Figure 4 shows that addition of ammonia to nitrogen does not further limit lateral growth, as compared to nitrogen. The extent of lateral growth in nitriding atmospheres is approximately 0.4 microns. Process atmospheres such as high vacuum, pure argon, pure hydrogen and pure helium have all been shown to cause unacceptable amounts of titanium silicide lateral growth during furnace annealing (4,5). Nitrogen can be effective in limiting lateral growth, provided nitrogen circulation is not limited by 'face to face annealing'. The reason for the beneficial effect of nitrogen is not clearly understood, but it is generally agreed that titanium nitride acts as a barrier to silicon diffusion and hence titanium silicide lateral growth is impeded. Figure 5 shows an auger profile after the first step anneal of a patterned wafer. The formation of titanium silicide is clear from the parallel, straight line segments of auger profiles of titanium and silicon. The excess concentration of nitrogen and oxygen at the interface of unreacted titanium and titanium silicide indicates that both nitrogen and oxygen might be "snowplowed" by the growing titanium silicide layer. The growth of titanium silicide should stop when a titanium nitride layer is formed ahead of the silicide layer, since titanium nitride is thermodynamically more stable than titanium silicide. Oxygen also might be playing a beneficial role to limit lateral growth (6).

It is surprising that the effect of ammonia additions to nitrogen is minimal, since ammonia can supply more active nitrogen. It appears the diffusion kinetics may be influencing titanium nitride formation rather than effects arising at the titanium film surface.

Conclusions

The titanium silicide formation reaction is extremely sensitive to the purity and type of process atmosphere. Nitriding process environments are required to limit the lateral growth of titanium silicide to 0.4 microns. Ammonia additions to nitrogen do not further reduce the extent of lateral growth. The oxidant contaminant level in the processing environment should be kept below 5 ppm to minimize oxidation of titanium.

Acknowledgements

The authors wish to thank A.W. Francis, Jr. for experimental assistance, S. D'Egidio, T. Kinisky and J. Petruzzello for help in material characterization.

*©1988 Union Carbide Corporation.

References

(1) S.P. Murarka et al in IEEE transactions on Electron Devices, Vol. ED-27, 1980.
(2) C. K. Lau et al in IEDM Tech. Dig., 1982.
(3) C. Y. Ting et al in 'VLSI Science and Technology' Pennington, NJ, 1982.
(4) Y. Koh et al in J. Vac. Sc. and Tech.,B 3(6), 1985.
(5) S. S. Iyer et al in J. Electrochem. Soc., Vol. 132, No. 9, 1985.
(6) M. Berti et al in J. Appl. Phys. 55(10), 3558, 1984.

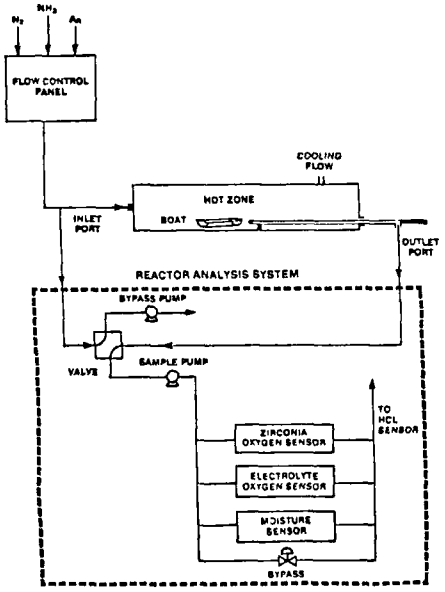


FIGURE 1: Diagram of the experimental set up

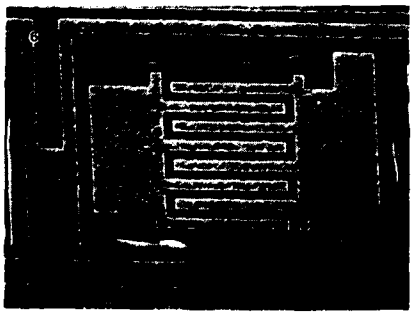


FIGURE 2: Titanium silicide lateral growth in argon process atmosphere, after 675°C, 20 min anneal and etch.

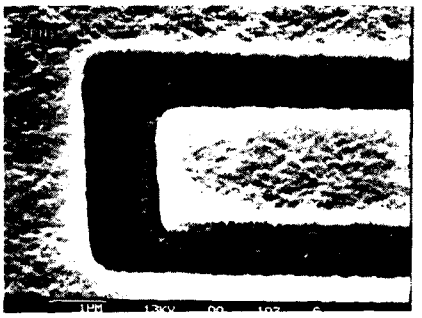


FIGURE 3: *Titanium* silicide lateral growth in nitrogen process atmosphere, after 675°C, 20 min anneal and etch.

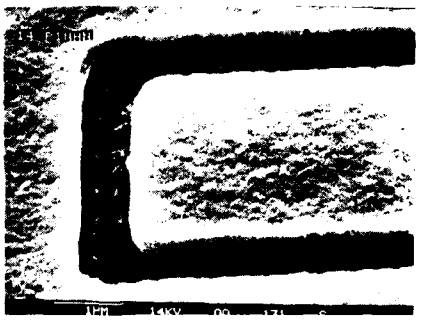


FIGURE 4: Titanium silicide lateral growth in 10% ammonia+nitrogen process atmosphere, after 675°C, 20 min anneal and etch.

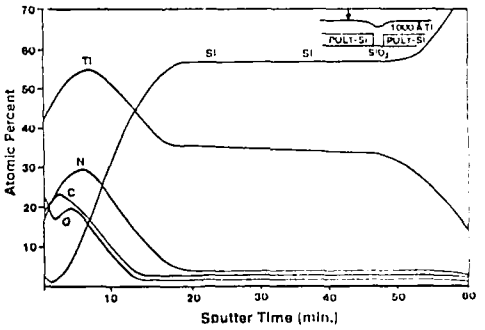


FIGURE 5: Auger depth profile after 675°C, 20 min, anneal in nitrogen.

Abstract No. 468

MODELLING OF THE INFLUENCE OF OXIDE GEOMETRY ON IMPURITY DIFFUSION INTO SILICON

S. A. Abbasi and A. A. Khan
Department of Electronics Engineering
Aligarh Muslim University
Aligarh , INDIA-202002

INTRODUCTION

It has been reported earlier(1) that in the case of boron diffusion,the presence of masking oxide interferes with the diffusion of impurities into silicon and thus modifies the kinetics of these impurities. In particular, the measurements showed(2,3) that the value of sheet resistance on plain unmasked check slices is almost always about 30% lower than the sheet resistance calculated from the diffused resistor measurements. This suggest that the diffused kinetics may therefore be affected by the presence of surrounding oxide. On the basis of a careful series of experiments it is confirmed that the actual discrepancy depends upon device/window geometry and the process parameters. The discrepancy is independent of background concentration and surface orientation of the starting material,oxide thickness and oxide growth conditions. The effect is not however, observed if the boron source spun-on or ion implanted, nor it is observed if silicon nitride is used as the mask in place of the usual silicon dioxide. The spreading resistance and the infra-red free carrier emmision measurements with respect to an oxide edge on a large sample suggest that the effect is of long nature extending to several hundred microns.

EXPERIMENTAL RESULTS

The use of silicon nitride as the mask shows none of the effects observed with the oxide masking. The results of a careful series of experiments using the multilayered composite masking structures involving thermal oxide, silicon nitride and silox are summerised below:

a) The use of silicon oxide as the masking material in place of SiO2 does not produce any discrepancy between ρs(plane) and ρs(res).
b) A film of oxide on nitride as a mask does produce a discrepancy between ρs(plane) and ρs(res) of the same order as with the oxide alone.
c) If the surface of a masking oxide is covered by silicon nitride, the discrepancy reduces to a small order about 5%.
d) A small width of oxide left uncovered by nitride is enough to cause a discrepancy of about 14% between ρs(plane) and ρs(res).
e) If the masking oxide is doped with boron prior to deposition, the discrepancy between ρs(plane) and ρs(res) disappears altogether.
f) The spreading resistance measurements confirm that the use of silicon nitride as the masking material shows none of the effects observed with oxide masking.

THE SURFACE DIFFUSION MODEL

The experimental results may qualitatively be explained on the basis of a surface diffusion model, assuming a very high dissolution rate of boron in the oxide surrounding the window. Thus the surface concentration near the oxide edge may be reduced drastically due to dissolution in the oxide. A significant amount of boron at the surface may thus be removed towards oxide due to surface diffusion(4) under the influence of concentration gradient across the surface. This results in a higher value of sheet resistance in the windows. An attempt is therefore made to develop a theoritical model which would predict diffusion profiles in the windows taking into the masking oxide effects.

Refering to fig 1, the following assumptions are made

a) The length of the window is infinitely large compared to its width.
b) The flux Fn of boron atoms arriving at silicon surface is constant.
c) The flux of boron at oxide is FnxH.
d) The surface diffusion is assumed to take place at Si and SiO2 surfaces with surface diffusion coefficients of Ds and Dox respectively.
e) The maximum rate at which the boron may be dissolved in oxide is given by G[C1-Cox(x,t)] where G is a constant, C1 is the limiting concentration of boron in the oxide and Cox(x,t) is the concentration of boron in the oxide.
f) The ideal one-dimensional diffusion corresponding to a single diffusion coefficient in the silicon bulk is assumed

RESULTS AND CONCLUSIONS

A system of equations based on the above assumptions was formulated and solved numerically using Crank-Nicholson on our VAX-11/780 VMS computing system. The sheet resistance on the window is expressed as a percentage of its value on area check slice and is denoted by ρsn. As no data for Fn,Ds, Dox,G and H etc. are available in the literature,suitable values have been chosen and a good agreement between the calculated and the experimental data is achieved as may be seen from fig.2

REFERENCES

1. J.P.Decosterd, D.Chauvy and K.Hubner, "Dependence of sheet resistance on SiO2 masking geometry in diffused Si regions," J. Electrochem. Soc 115,pp 781-782,1968
2. S.A.Abbasi and A.Prunnschweiller, "The effects of oxide masking on boron deposition," Europhysics Conf. Abs., ESSDERC, York, England,pp 180-81, 1980
3. S.A.Abbasi and A.Brunnschweiler,"Effect of masking oxide on diffusion into silicon," IEE Proc,Vol.128,Pt. I,no.5, pp 178-79,1981
4. G.A. Somorjai, "Principles of surface Chemistry,"Prentice Hall,Inc., New Jersey, 1972

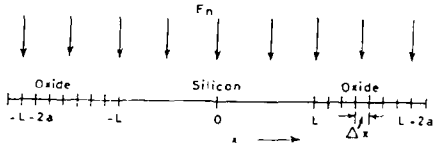
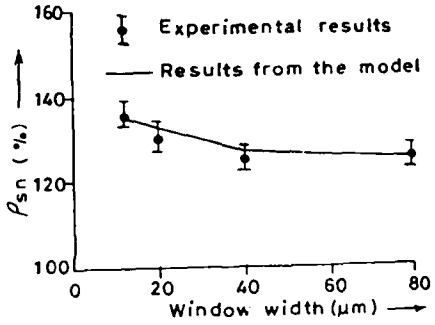
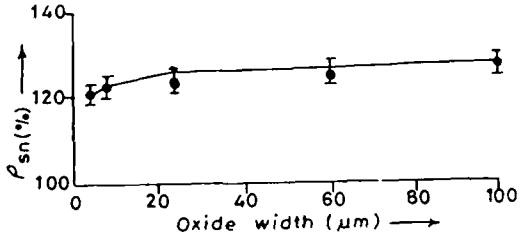


FIG. 1. PRE-DEPOSITION SYSTEM OF BORON.



(a) Window width effect



(b) Window frame effect.

FIG. 2. EXP. & COMPUTATIONAL RESULTS.

Abstract No. 469

The Effect of Fluorine on Dopant Diffusion in Silicon

U. S. Kim , T. Kook, and R. J. Jaccodine
Sherman Fairchild Laboratory for Solid State studies
Lehigh University, Bethlehem, PA 18015

The scaled down dimensions of devices requires shallower junctions for the MOS transistor, i.e. shallow p^+ and n^+junctions. However, it is found that the diffusion of dopants during oxidation affect the characteristics of a short channel MOS transistor since oxidation enhances the diffusion of dopants. The covering layer over the junction can also have a marked effect on the diffusion of dopants by effecting their diffusivity. (1)

Recently, we reported the oxidation retarded diffusion (ORD) of boron rather than the oxidation enhanced diffusion (OED) under oxidation conditions with small (ppm) additions of fluorine. (2) in this study, we reported the effect of fluorine on the diffusion of various n^+ shallow diffusions using P, As and Sb. The effect of the various covering layers on dopant diffusion using SiO_2 layer, Si_3N_4 layer, bare silicon with the control of Si_3N_4 over SiO_2 will be compared.

Czochralski grown lightly doped (111) oriented silicon wafers were implanted with P, As, and Sb at 80 keV to a dose of $1.0 \times 10^{14}/cm^2$, respectively. After anneal at 900°C for 30 min to give initial junction depths of 0.5 μm for P, 0.15 μm for As, and 0.1 μm for Sb. All the wafers were oxidized at 900°C in steam to grow 2000 Å thick pad oxide. A 1200 Å thick Si_3N_4 film was deposited by low pressure chemical deposition on the pad oxide. Subsequent lithography and plasma etching were done to fabricate a specimen structure shown in Fig. 1. After s tandard cleaning procedures, one group of wafers were then oxidized in dry oxygen in the temperature range between 850°C and 1100°C as controls. The other group of wafers were oxidized with the added fluorine (<.044 % by volume) in the same temperature range to study the diffusion behavior during oxidation. In this study, the dry oxidation with addition of NF_3 (O_2/NF_3 oxidation) has been done for times up to 12 hrs. These specimens were then angle-lapped and stained to measure the junction depth.

In Fig. 2, we show a P diffused specimen after 8 hrs oxidation in O_2/NF_3 ambients. In contrast to the enhanced diffusion behavior during dry oxidation, the diffusion in the bare silicon and in the SiO_2 covered silicon is retarded during O_2/NF_3 oxidation. In the Si_3N_4 covered silicon, a negligible change has been observed.

In Fig. 3, we show a Sb diffused specimen after 8 hrs O_2/NF_3 oxidation. Compared to the retarded diffusion of As and Sb in the SiO_2 area during dry oxidation, As and Sb can be observed to be enhanced during O_2/NF_3 oxidation. We believed that the retarded diffusion of As and Sb in the bare silicon due to the out-diffusion loss of dopants. The Si_3N_4 covering layer has retarded the diffusion of Sb under both oxidation conditions.

It is apparent from the above results that both the fluorine addition and covering layers have a significant effect on dopant diffusion during oxidation. We believed that the enhanced diffusion of As and Sb in the SiO_2 covered silicon compared to the SiO_2 + Si_3N_4 area causes the enhanced generation of vacancy during O_2/NF_3 oxidation. (1)

In summary, the balance of vacancies and self- interstitials present in silicon play the role of enhancing or retarding diffusion during oxidation. The experimental results clearly indicate that fluorine addition during oxidation cause enhanced vacancy generation. We also found that a covering layer has a significant effect on dopant diffusion during oxidation.

References

1. T. Kook and R. J. Jaccodine, *Mat. Res. Soc. Symp. Proc.*, vol 36, 83, (1985).
2. U. S. Kim, T. Kook, and R. J. Jaccodine, *J. of Electrochem. Soc.*, Vol 135, 270 (1988).

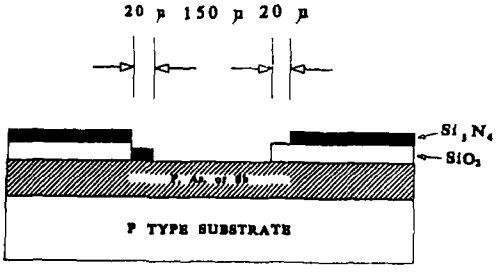


Fig. 1 Specimen structure for n type dopant diffusion study

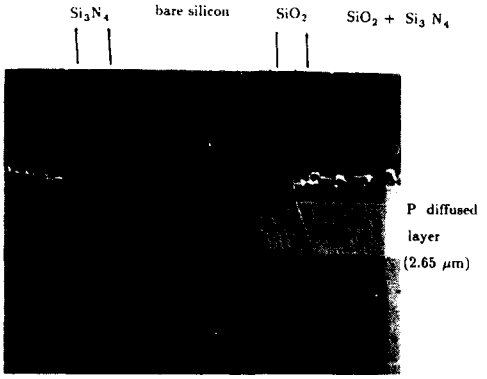


Fig. 2 P diffused specimen after 8 hrs O_2-0.044 vol% NF_3 oxidation at 1100 °C.

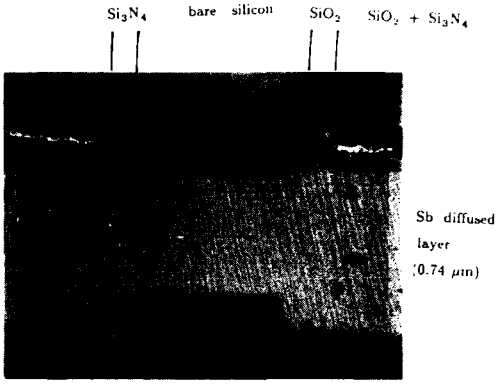


Fig. 3 Sb diffused specimen after 8 hrs O_2-0.044 vol% NF_3 oxidation at 1100°C.

Abstract No. 470

SOURCE/DRAIN FORMATION USING SPIN ON DOPANTS AND SUBSEQUENT RAPID THERMAL DIFFUSION

G.W. Sheets and M.N. Kozicki
Center for Solid State Electronics Research
Arizona State University
Tempe, AZ 85287-6206

With the scaling of linewidths in advanced CMOS integrated circuits, vertical scaling considerations must also be addressed. Lateral reductions of device geometries result in problems due to short channel effects e.g. punch through and threshold voltage shift. These problems impose limits on the degree of device scaling. However, these problems can be reduced, in part, by reducing the source/drain junction depths. Requirements for the source/drain region have been discussed in previous work [1]. It was found that reducing the juction depth to less than 0.2μm for gate widths less than 0.5μm was necessary to reduce the short channel effects.

In previous studies shallow source/drain regions were formed by low energy ion implantation and subsequent thermal annealling[2]. This method of formation tends to be expensive, due to the capital equipment and maintance costs associated with ion implantation. Also, ion implantation induces defects into the crystal which must be removed by a post thermal cycle, which also serves to activate the implanted dopants. Rapid Thermal Diffusion (RTD) is proving to be a viable alternative to ion implantation. Using RTD to form the source/drain region uses the established technology of spin-on dopants, with a high temperature (1000°C to 1200°C), rapid thermal cycle (3 to 60 seconds). This paper reports on the sheet resistance and junction depths achieved using RTD.

Experimental Procedure

Czochralski-grown p-type silicon wafers of (100) orientation, 14-22 Ω-cm, were used for the n-type dopant experiments, and n-type, 7-14 Ω-cm, were used for the p-type dopant experiments. The 75 mm wafers where dipped in 10:1 HF to remove the native oxide and then heated to 150°C for 20 minutes to drive off any surface water. After removal from the oven, they where immediately spun with arsenic, phosphorus, boron, or antimony dopant glasses. The dopant glass was applied at 3500 rpm for 30 seconds, and then prebaked at 125°C for one hour to drive off any remaining carrier liquid. Diffusions were performed in a Tamarack 180M Rapid Thermal Processer using a nitrogen ambient at atmospheric pressure. The dopants were diffused at three different temperatures, 1000°C, 1100°C, and 1200°C for four different times, 3 sec, 15 sec, 30 sec, and 60 sec. The temperature was ramped up to within 25°C of the set temperature in 3 seconds and on the cool down cycle was below 600°C in 3 seconds. Sheet resistances of the diffused samples were measured using a four point probe.

Results and Discussion

Table 1 shows the sheet resistance for the various diffused samples using the above method. As the diffusion times increase the sheet resistance decreases. In the arsenic, and antimony samples, at low dopant concentrations per cm^2 (Q), where $Q=Ns\sqrt{Dt}$, and Ns is the surface concentration, the four point probe could not measure the resultant sheet resistance becase the resistance is close to that of the background sample resistance.

Calculations of the junction depth and surface concentration were performed using a diffusion model that is dependent on each dopant spieces. The diffusion model is used to predict the concentration profile based on concentration dependent diffusion and surface concentration [3], and uses a band gap narrowing parameter to compenstate for the degenerate doping in the samples [4]. The carrier density as a function of dopant concentration is calculated from Fermi-Dirac equations for electron, hole, and un-ionized donors. Using the dopant concentration profile, carrier density vs. dopant density, and a model for mobility at high dopant densities [5], the sheet resistance and junction depth is calculated. By solving the above models given an experimental sheet resistance, the surface concentration and junction depths can be calculated. Table 2 gives surface concentrations, and junction depths versus sheet resistance.

As expected, the junction depths increase as the process time is increased. In the case of arsenic the junction depths range from 0.03μm to 0.20μm. For each temperature in the arsenic sample the surface concentration remains fairly constant. However, in the 1200°C case, there appears to be a surface limiting reaction occuring. As the diffusion time increases the surface concentration also decreases. This is probably due to limited diffusion from the doped glass, which is slower than the diffusion in silicon. Boron junction depths range from 0.05μm to 0.87μm over the diffusion matrix. Unlike the arsenic case, all boron samples exihibit a similar surface concentration *regardless of diffusion temperature*. Antimony diffusion into silicon samples did not show any change in sheet resistance at 1100°C for 15 seconds. Note that this sample has a 0.02μm junction depth, which is near the measuring limits of the four point probe. To date a phosphorus diffusion model does not exist.

Summary

RTD has been used to form source/drain regions less than 0.2μm deep. This has been achieved by utilizing rapid thermal cycles at 1200°C, 60 seconds for As, 3 seconds for B, and 30 seconds for Sb. Diffusions were done at 1200°C to get minimum sheet resistance of 465 Ω/sq. for As, 56.8 Ω/sq. for B, and 842 Ω/sq. for Sb. Even though junction depth calculations were not performed for P, sheet resistances as low as 6 Ω/sq. were obtained at 1200°C for 60 seconds.

Acknowledgments

We would like to acknowledge Silica Source Technology for the donation of the dopant glasses, and also Kent Ridgeway for many helpful discussions.

References

1. K.J. Yallup and D.J. Godfrey, Physica B, 129, 269 (1985).
2. K. J. Yallup, D.J. Godfrey, R.A. McHahon, and H. Ahmed, IEEE Trans. Electron Devices, ED-34, 1688 (1987).
3. R.A. Colclaser, "Microelectronics: Processing and Device Design," pp. 117-161, John Wiley & Sons, Ltd., New York (1980).
4. J.W. Slotboom and H.C. de Graaff, Solid-State Electronics, 19, 857 (1976).
5. G. Masetti, M. Severi, and S. Solmi, IEEE Trans. Electron Devices, ED-30, 774 (1983).

Temperature (°C)	Time (seconds) 3	15	30	60
1000	NA	NA	5380	4320
1100	2860	1270	916	744
1200	785	526	495	465

(a) Arsenic doped sheet resistances (Ω/sq.)

Temperature (°C)	Time (seconds) 3	15	30	60
1000	313	181	112	71.8
1100	125	46.0	45.7	35.1
1200	56.8	28.1	18.9	12.6

(b) Boron doped sheet resistances (Ω/sq.)

Temperature (°C)	Time (seconds) 3	15	30	60
1000	NA	NA	NA	NA
1100	NA	20200	9690	4420
1200	3260	1320	842	572

(c) Antimony doped sheet resistances (Ω/sq.)

Temperature (°C)	Time (seconds) 3	15	30	60
1000	155	61.5	42.5	29.8
1100	42.7	20.6	13.2	10.4
1200	16.6	9.18	7.15	6.20

(d) Phosphorus doped sheet resistance (Ω/sq.)

Table 1. Sheet resistance vs. diffusion temperature and time.

Temperature (°C)	Time (sec.)	Surface Concentration (cm^{-3})	Junction Depth (μm)
1000	3	NA	NA
1000	15	NA	NA
1000	30	2.3E19	0.03
1000	60	2.4E19	0.04
1100	3	6.8E19	0.04
1100	15	9.0E19	0.07
1100	30	9.4E19	0.09
1100	60	7.8E19	0.12
1200	3	1.7E20	0.09
1200	15	1.2E20	0.15
1200	30	8.4E19	0.17
1200	60	5.0E19	0.26

(a) Arsenic doped surface concentration and junction depth vs. temperature and time.

Temperature (°C)	Time (sec.)	Surface Concentration (cm^{-3})	Junction Depth (μm)
1000	3	1.6E20	0.05
1000	15	1.4E20	0.08
1000	30	1.6E20	0.11
1000	60	1.7E20	0.15
1100	3	1.7E20	0.09
1100	15	1.7E20	0.20
1100	30	1.6E20	0.25
1100	60	1.5E20	0.34
1200	3	1.6E20	0.20
1200	15	1.5E20	0.43
1200	30	1.6E20	0.61
1200	60	1.6E20	0.87

(b) Boron doped surface concentration and junction depth vs. temperature and time.

Temperature (°C)	Time (sec.)	Surface Concentration (cm^{-3})	Junction Depth (μm)
1000	3	NA	NA
1000	15	NA	NA
1000	30	NA	NA
1000	60	NA	NA
1100	3	NA	NA
1100	15	1.0E18	0.02
1100	30	2.0E18	0.04
1100	60	3.0E18	0.08
1200	3	3.3E19	0.06
1200	15	5.1E19	0.13
1200	30	7.9E19	0.17
1200	60	9.0E19	0.26

(c) Antimony doped surface concentration and junction depth vs. temperature and time.

Table 2. Surface concentration and junction depth vs. temperature and time.

Abstract No. 471

The Deposition of N-type and P-type In-situ Doped Polysilicon by LPCVD

J. Gan, C. Chu, J. P. McVittie, K. C. Saraswat and R. M. Swanson
Stanford Electronics Lab, Stanford University, Stanford, CA 94301

Abstract

N-type and p-type in-situ doped LPCVD polysilicon doped from phosphine (PH_3) and boron trichloride (BCl_3) gas sources is reported. Resistivity of the as-deposited and the post annealed films is reported for deposition temperatures from 540°C to 660°C and anneal temperatures from 800°C to 1000°C. Our results show that very low resistivities of $5m\Omega-cm$ is obtainable from the as-deposited n-type and p-type in-situ doped polysilicon thin films with good thickness uniformity deposited at temperatures less than 600°C. Anomalous changes in p-type film resistivity are observed for films capped with LTO and subjected to subsequent anneals.

1 Introduction

Polysilicon has been used in silicon devices for decades. Although the first widespread application was in MOS integrated circuits, it is now also being used in other devices and is increasingly being employed in novel structures within both MOS and bipolar integrated circuits. Polysilicon can be deposited either in situ doped with the desired dopant or undoped with doping performed in subsequent processing steps.

In situ doped polysilicon is needed particularly for some devices which require precise control of dopant profiles in the polysilicon structures. For example, doped polysilicon is now being used as one of the capacitor plates in the new generation of DRAM trench capacitors [1]. The doping of these type of structures often require $\sqrt{Dt}$ incompatible with the process requirements if in-situ doped polysilicon is not used. As the number of applications that require in-situ doped polysilicon increase, closer investigation of in situ doped polysilicon in terms of its deposition condition and electrical properties is required. At present little literature exist about the electrical and physical properties of in-situ doped polysilicon particularly for p-type in-situ doped polysilicon.

Low resistivity in-situ doped polysilicon films are obtainable if the deposition rate is slow compared to the surface mobility of the dopant atoms. Under these conditions, the dopant atoms, once incorporated on the growing surface, will have enough time to rearrange themselves in the silicon structure and become electrical active. To achieve this goal, it is more appropriate to use a LPCVD system, which has lower deposition rate, than an APCVD system.

In this paper, we demonstrate that low resistivity for both n-type and p-type as deposited polysilicon films is obtainable with appropriate dopant gas flow rates. Although the low resistivity of the as deposited polysilicon film is adequate, it is also important for practical applications, to observe the resistivity changes of the film as it is annealed or subjected to subsequent thermal cycles.

2 Experimental Procedures

The basic CVD process has been described earlier [2]. Our depositions were done in a Tylan LPCVD furnace with silane and dopant gas injection from the front of the tube. Nineteen wafers were placed in the center boat using a 1 cm spacing. Temperature uniformity was maintained within two degrees. Subsequent anneals were conducted in a standard oxidation furnace. The sheet resistance was measured using a four point probe and converted to a resistivity value after thickness was measured on a Dektak. All polysilicon depositions were done on 3 inch wafers covered with 1000Å of thermal oxide.

Phosphine gas (PH_3) was chosen as the n type dopant gas source. Two types of dopant gas were initially considered as the p type dopant gas source, diborane (B_2H_6) and boron trichloride (BCl_3). Since little is known about the use of boron trichloride as a dopant source and also for safety considerations, BCl_3 was chosen as the p type dopant source.

All depositions were done with a constant silane flow rate of 50 sccm. For n type polysilicon, 15% PH_3 diluted in silane with a flow ratio of $PH_3/SiH_4 = 2 \times 10^{-3}$ was used. For p type polysilicon BCl_3 with a flow ratio of $BCl_3/SiH_4 = 2 \times 10^{-3}$ was used. N type depositions were done at temperatures of 570, 600, 630, and 660°C. P type depositions were done at 540, 570, 600, and 630°C. The anneal of the deposited polysilicon films were carried out for 1 hour at temperatures of 800, 900, and 1000°C.

3 Results and Discussion

The thickness of both types polysilicon films were measured at different points on each wafer and for different wafer positions in the deposition region of the tube. The wafer to wafer thickness uniformity was within 5%, while the thickness uniformity across a single wafer was better than 1%. The film thickness difference, from wafer to wafer in the same run, indicates that there is some depletion of the reactant source along the deposition zone. This is due to the fact that our system was not optimized to minimize the depletion of reactant down the deposition zone since uniform temperature was used. The wafer to wafer uniformity can easily be improved by imposing a temperature gradient across the deposition region.

Figure 1 shows the deposition rate versus the inverse of the deposition temperature. The extracted deposition activation energy for p type polysilicon film is 0.51ev, and the deposition activation energy for the n type film is 1.13 ev. These values are close to values reported from in-situ deposited films in an APCVD system [3,4]. These activation energies should be used with caution, though, because the data shows variations in resistivity of the as deposited films with deposition temperature indicating possible differences in the dopant concentration in the films at different deposition temperatures.

Figures 2 and 3 show the measured resistivities of the p type and n type films as-deposited. The resistivity of as deposited film for both film types increases as the deposition temperature increases. The resistivity of these films depends on the microstructure, the concentration of the active dopant, and the concentration of the total dopant. It is therefore difficult to say which characteristic of the film is the main cause for the resistivity change with temperature. Despite deposition temperatures below the normal amorphous to polycrystalline transition, it is unlikely that the as-deposited film is completely amorphous. Moreover from some data taken using a rapid thermal annealer, not shown here, the resistivity does not show any sudden drops after short high temperature anneals. This would seem to indicate that the as deposited films are mostly polycrystaline and that most of the dopant atoms are already electrical active.

The resistivity under different annealing temperature is also shown in the same figures. Note that the n type films were annealed without a capping oxide, while the p type films were annealed with a layer of LTO capping oxide. For n type films, the resistivity decreases monotonically as the annealing temperature increases. This implies that recrystallization is the dominant process in determining the electrical properties instead of dopant segregation or outdiffusion to the oxide and outgassing. In contrast, the anomalous behavior of p type films after annealing indicates at least one of the above mechanisms is active and prevails over the recrystallization effect. Furthermore, the resistivity of the p type films depends upon not only the annealing temperature but also on the deposition temperature. At low deposition temperatures 540° and 570°C the resistivity increases monotonically with the annealing temperature. This seems to indicate that the reduction of the resistivity of the film through recrystallization is offset by other mechanisms. However for the p type samples deposited at higher temperatures the recrystallization effect begins to dominate at higher annealing temperatures.

4 Conclusion

In this paper, we show that low resistivity as deposited in-situ doped polysilicon films of $5m\Omega-cm$ can be obtainable via LPCVD. Activation energies of 0.51 ev and 1.13 ev were measured for the p type and n type films. However, as mentioned, these values should be used with caution since the resistivity is shown to be a function of deposition temperature. We also present data on the resistivity of the post annealed films. The resistivity of the post annealed films may depend on whether or not the

films was covered with a capping oxide during the anneal. For the the p-type film anomalous changes in film resistivities were observed with the anneals. This calls for further examination. All above mentioned effects are important if in situ doped polysilicon is *to be used in mainline* device fabrication. Further results of subsequent experiments will be presented at the meeting.

5 Acknowledgements

The authors thank R. Wheeler and S. Taylor for their help in the experimental setup. This work was supported in part by a CIS Research Funds. J. Garnis supported by EPRI under the contract number RP790-2 and Sandia National Laboratory under the contract number 02-7063.

6 References

References

[1] M. Sakamoto, T. Katoh, H. Abiko, T. Shimizu, H. Mikoshiba, Y. Hokari, K. Hamano, and K. Kobayashi, IEDM Technical Digest, 710, (1985).

[2] W. Brown and T. I. Kamins, Solid State Technology, 7, 51, (1979).

[3] F. C. Eversteyn and B. H. Put, J. Electrochem. Soc., **120**, 106 (1973).

[4] L. H. Hall, K. M. Kolwand, J. Electrochem. Soc., **120**, 1438 (1973).

7 Figures

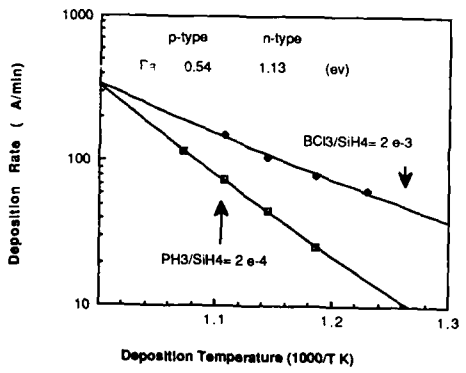


Figure 1. Deposition Rate vs. $\frac{1}{Temp}$

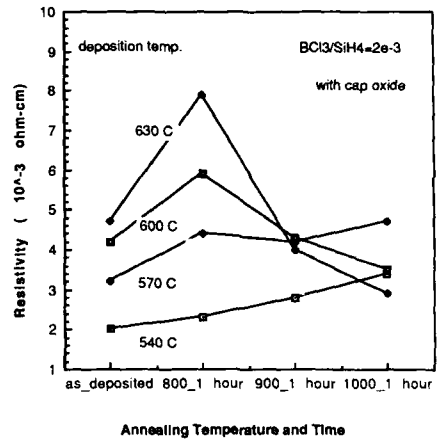


Figure 2. Resistivity vs. Deposition Temp. and Anneal Temp. for P-type Films

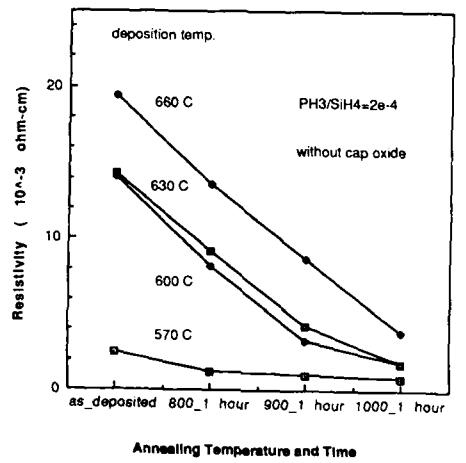


Figure 3. Resistivity vs Deposition Temp. and Anneal Temp for N type Films

Abstract No. 472

TEMPERATURE GRADIENT AND THERMAL STRESS DISTRIBUTION STUDY FOR RAPID THERMAL PROCESSING

F. K. Yang, S. J. Pien*, R. Kwor^

Department of Electrical and Computer Engineering
University of Notre Dame
Notre Dame, IN 46556

*Department of Aerospace and Mechanical Engineering
University of Notre Dame
Notre Dame, IN 46556

^Currently with Department of Electrical Engineering
University of Colorado at Colorado Springs
Colorado Springs, CO 80933

N. S. Alvi
Delco Electronics
Kokomo, IN 46902

Transient heating with incoherent radiation from arc lamps or tungsten-halogen lamps has been used increasingly in semiconductor processing. The advantages of this technique include its capability of achieving efficient annealing in a very short time, and precisely controlled heating ramping rate and dwell time. One of the important applications for the transient heating is the annealing of silicon IC wafers. The transient heating process, which lasts more than 10^{-2} sec, is normally referred to as a "rapid isothermal process" [1]. A commonly accepted name for this technology is rapid thermal processing (RTP). The cooling of the wafer after the processing is accomplished essentially by radiation. In the standard modeling of this rapid heating process, the temperature gradient across the wafer thickness is usually neglected [2].

In this paper, we will report the result of a study on the temperature gradient distribution for the isothermal mode rapid heating process. The analytical modeling was first formulated for the temperature distribution within the wafer, taking into consideration the temperature-dependent thermophysical properties and the temperature and wavelength-dependent optical properties [3]. The actual spectra of two radiation sources -- arc lamps and tungsten-halogen lamps were used in the simulation of the heating process. It was found that the temperature gradient across the wafer thickness is very much dependent on the ramping rate and the peak temperature. It is also a function of position along the thickness of the wafer. At a ramping rate of 600 °C/sec, for example, the temperature difference across the wafer thickness is on the order of 10 °C or more. As a result of the temperature-dependent optical properties, a highly non-linear temperature distribution exists near the wafer surface. The temperature gradient is therefore quite large in the surface region where most of the thermal activation processes such as damage annealing, dopant redistribution and activation, and solid phase epitaxial growth take place. As the dwell time in rapid thermal heating approaches the sub-second region for future VLSI processing, the temperature gradient will certainly be an important factor to be considered. We will report the results of the temperature gradient study for two types of light sources, and for various rapid thermal heating parameters, such as the ramping rate and dwell time.

Because of the temperature gradient across the wafer thickness, there exists a thermal stress along the same direction (z-direction). The temperature distribution results obtained from the above discussed simulation are applied to calculate the thermal stress inside the wafer, assuming the so-called "free plate" condition. The only non-zero stress components are along directions which are parallel to the surface of the wafer [4]. These components are functions of z and time. In our presentation, the thermal stress induced in the wafer will be compared to the yield stress of the silicon material. The possibility of defect generation in the RTP will also be addressed.

REFERENCES

[1] C. Hill, in Laser Annealing of Semiconductors, J. M. Poate and J. W. Mafer, eds., Academic Press, New York, 479 (1982).

[2] G. Bentini, L. Correra and C. Donolato, J. Appl. Phys. 56, 2922 (1984).

[3] S. J. Pien, F. K. Yang and R. Kwor, Paper 718, The 172nd Meeting of the Electrochemical Society, Honolulu, HI, October (1987).

[4] B. A. Boley and J. H. Weiner, Theory of Thermal Stresses, Wiley, New York (1960).

Abstract No. 473

Self Gettering Effect of Ion Implanted N+ Layers

Makoto Ogasawara, Jun Sugiura, Shinji Shimizu and Hirotsugu Kozuka*

Device Development Center, Hitachi Ltd., Oume-shi, Tokyo, 198, Japan
*Central Research Laboratory, Hitachi Ltd.

1. Introduction

To achieve high yield in Si ULSI devices, contamination gettering technology is becoming more important accompanied by clean process technology. Intrinsic gettering (IG) and back surface extrinsic gettering (EG) by ion damage and by phosphorous diffusion are well known as contamination gettering. High dose ion implanted layers on active surfaces such as source/drain regions of MOS transistors may also play a role of gettering sites. The gettering effects of such ion implanted layers (phosphorous(P) and arsenic(As)) have been investigated in an ion damage gettering experiment using Ratherford Back Scattering (RBS), and it concluded that such layers trapped contaminations but it was less effective than argon(Ar) implantation or P diffusion[1].

In this paper, by measuring the electrical characteristics of n+p junctions, we will electrically clarify the gettering efficiency of high dose P and As ion implanted layers in actual devices, and the dose dependency. We will also discuss the model of electrical characteristic degradation by contamination.

2. Experimental Procedure

Wafers were 10 ohm-cm CZ (100)4° off oriented p-type Si, supplied from two different vendors. The oxygen concentration of wafers kept low ([Oi]=16ppma, JEIDA) enough to avoid oxygen precipitation. Only for comparison, IG wafers which had higher oxygen concentration ([Oi]=20ppma [illegible] special preheat treatment were used.

The samples were fabricated by our simplified CMOS process. The n+ layers were formed by implantation of As ions (120KeV) and P ions (60KeV) on p-type substrate. The doses were ranging from 2×10^{14} cm^{-2} to 5×10^{15} cm^{-2}. The implant damage was recovered by the following N_2 annealing at 1000°C. In this study an Extrion/Varian DF-5 implanter was used for implantation. Intentional metal impurities were not introduced for checking the gettering efficiency.

The leakage currents of n^+p junctions were measured to determine the gettering efficiency of ion implanted n+ layers. Deep level transient spectroscopy (DLTS) was used to detect the contamination element.

3. Results and Discussion

Leakage currents of reverse biased n+p junctions are shown in Fig.1 as a function of n+ (As and P) dose. In the case of As, huge currents flow across the junctions in lower dose region (<5×10^{14} cm^{-2}), and low leakage current is obtained by a dose at 5×10^{15} cm^{-2}. At 2×10^{15} cm^{-2} dose, the average current stays low, but some of the junctions show huge currents. Similar dose dependence is shown in the case of P, but the current levels are lower compared to As in lower dose regions. This anomalous leakage current phenomenon is quite reproducible in fabrication lots and in different vendor's wafers.

The leakage current of As n+p junctions formed on IG wafers is also shown in the figure at a dose of 2×10^{14} cm^{-2}. It does not show anomalous leakage, and the IG wafer is thought to have strong contamination gettering effect. Therefore, it can be concluded that this anomalous leakage phenomenon in lower n+ dose regions is caused by some kind of contamination near the junction, and that the gettering efficiency of a higher n+ dose layer is as strong as that of an IG wafer.

It is thought that in a higher dose n+ layer a lattice defect such as a dislocation loop works as a gettering sink. In lower dose P implanted layer, ion pairing gettering[2] may be operative.

Fig.2 shows the leakage current characteristics of lower n+ dose junctions formed by As implantaion of 2×10^{14} cm^{-2} both on wafers with and without IG. The junction on a IG wafer (D) shows a normal hard breakdown characteristic. On the other hand, all junctions without IG (A,B,C) indicate soft breakdown characteristics. Since these characteristics are almost independent of temperatures ranging from 90K to 400K, these abnormal characteristics are not due to generation-recombination centers which are formed by uniformly distributed contamination but to precipitates[3].

The anomalous leakage current is not proportional to the junction area, but to the length of the junction perimeter (Fig.3). It suggests that the contamination precipitates predominantly along the junction edge, that is field oxide edge.

To determine the contamination element, DLTS measurements were done on the same samples used in Fig.3. The DLTS spectra are shown in Fig.4. The spectrum of sample D shows no observable deep levels. A hole trap level at Ev+0.44eV is exhibited in the spectrum of sample B. This trap density is fairly low (1×10^{12} cm^{-3}) after several tens of day storage at room temperature, and by injecting minority carriers (50mA, 1min, at R.T.) it rapidly increases to about 1×10^{13} cm^{-3}. This behavior is known as the dissociation of interstitial iron-substitutional boron pair(Fe_iB). It can be concluded that the anomalous leakage current is due to Fe precipitates along the field oxide edge.

4. Conclusion

We have demonstrated that high dose ion(P,As) implanted n+layers getter Fe contamination(an order of 10^{13} cm^{-3}) as effective as IG. The minimum doses for n+ layer gettering are 2×10^{15} cm^{-2} for P and 5×10^{15} cm^{-2} for As in this study.

The lower dose n+p junction shows anomalous leakage phenomenon. It is attributed to Fe precipitates, which are probably localized along the field oxide edge.

5. Acknowledgment

We would like to thank to M.Kawamura and T.Kato for their helpful discussions.

6. References

[1] T.E.seidel, R.L.Meek and A.G.Cuills, J.Appl.Phys., 46, 600(1975).
[2] D.Lecrosnier et al., J.Appl.Phys., 52, 5090 (1981).
[3] H.H.Busta and H.A.Waggener, J.Electrochem. Soc., 124, 1424(1977).
[4] L.C.Kimerling and J.L.Benton, Physica, 116B, 297(1982).

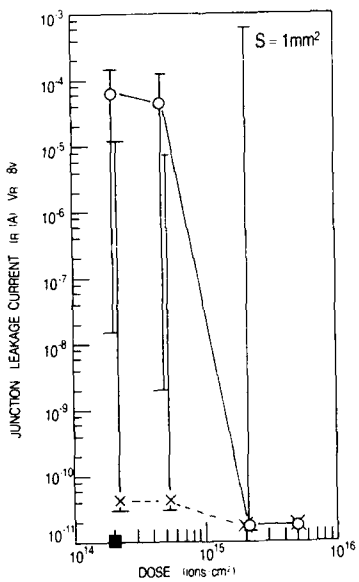


Fig.1 Leakage current as a function of dose for P and As.
×:P(without IG), ○:As(without IG), ■:As(with IG).

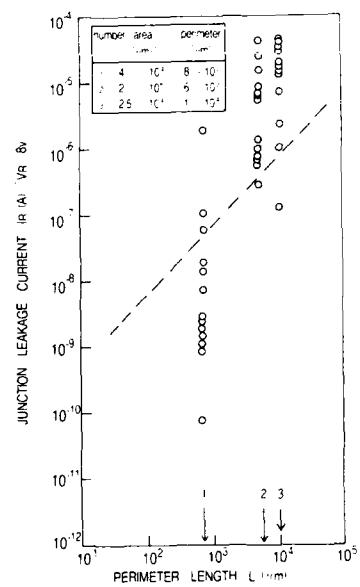


Fig.3 Leakage current of lower dose (As,2 · 10^{14} cm^{-2}) n⁺p junction as a function of perimeter length.

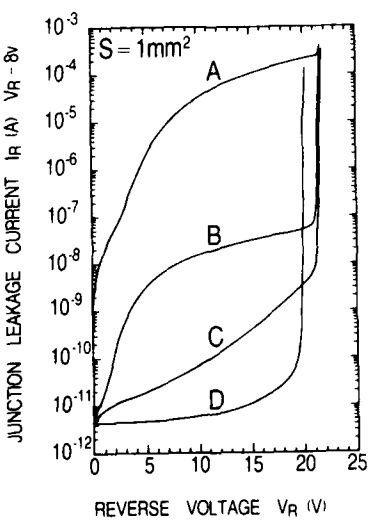


Fig.2 Leakage current characteristics of lower dose(As, 2 · 10^{14} cm^{-2})n⁺p junction.A,B,C:without IG,D:with IG.

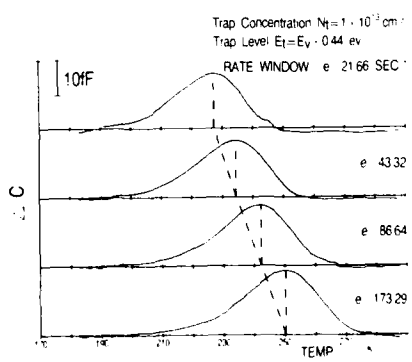


Fig.4 DLTS spectra of sample B indicated in fig.2 after minority carrier injection (50mA,1min,at R.T.).

Abstract No. 474

INTRINSIC GETTERING FOR CMOS PROCESS USING LOW-IOFI WAFERS

Makoto Kitakata, Fumitoshi Toyokawa, Masao Mikami and Hideki Tsuya

VLSI Development Division, NEC Corporation, 1120, Shimokuzawa, Sagamihara, 229, Japan

INTRODUCTION

Gettering technology is now one of the key processes of the high-yield production of the VLSI devices. As one of the method to capture the contaminants, intrinsic gettering (IG) is very efficient. But IG, which is generally carried out for higher oxygen concentration wafer, is the complicated control technique of the oxygen precipitaion of wafers in the device fabrication process. By adopting the proper IG annealings, even the low oxygen concentraion, CZ silicon wafers have the possibility of the sufficient precipitation for gettering in the CMOS process. The wafers are also expected to have the merit in the control of bulk microdefects and the good denuded zone fabrication because of their rather slow precipitation kinetics. The uniformity of the precipitation may be better than that of the higher oxygen concentration wafers.

In this work, two types of IG annealing sequences have been developed. One is MIG (High- Low- High temperature annealing) with the low-temperature annealing consisted of multi-step sub-sequences. (1) The other is RIG (High- Low temperature annealing) with ramping sequences.

EXPERIMENTAL PROCEDURE

The samples prepared for this experiment were 5-inch phosphorus-doped (511) CZ silicon wafers. The as-grown oxygen concentration was 11～12x10^{17} atoms/cc, evaluated with the old ASTM conversion factor (4.81x10^{17}).

The IG annealing sequences are shown in fig.1.

Commonly in MIG and RIG, the initial high-temperature 1200 ℃ - 3H annealing in the nitrogen ambient (α -anneal: denominated by authors) was adopted for the purpose of the annihilation of grown-in nuclei of precipitation and for the purpose of the denuded zone formation by out-diffusion of interstitial oxygen. As the low-temperature nucleation annealing, the series of 520 ℃, 620 ℃ and 720 ℃ annealing in dry oxygen were carried out for MIG, and the 550 ℃ to 850 ℃ ramping annealing in dry oxygen for RIG. Specially for MIG, the final high-temperature precipitation annealing (ω -anneal: also denominated by authors) was adopted for the more rigid control of oxygen precipitation in the CMOS process.

After the above mentioned IG pre-annealing, the samples were submitted to thermal CMOS-process simulations, consisted of four-stage annealing procedures and were also supplied to the CMOS TEG fabrication for the purpose of the evaluation of gettering ability.

The samples were examined in oxygen concentration by a conventional FTIR spectrometer. After the treatments of cleaving and staining in the Wright etch for 3 minutes, the bulk microdefects and the denuded zone of the cross-section were inspected by the optical microscope at x400 magnification. For the further inspections, the microscopic FTIR oxygen concentration mapping-mensurement systems and the 400kV transmission electron microscope were used.

RESULTS AND DISCUSSION

Photo.1 shows the two cross-sectional views of bulk microdefects of MIG wafers with the different ω-annealings followed by the CMOS-process simulations. The MIG wafer with ω_1 -annealing (1140℃ - 2H in N_2) has the bulk microdefects of 2x10^5 / cm^3 and the definite denuded zone of 40 μm in width. But the MIG wafer with ω_2 -annealing (1000℃ - 16H in dry O_2) has the poor denuded zone width. Before the simulation, both wafers had the definite denuded zone. To clarify the situations, the value of oxygen concentration was mensured in each step of the heat treatment.

Fig.2 shows the oxygen concentration reduction of these MIG wafers through the MIG annealing sequences and the simulation. In the MIG wafers with ω_2 - annealing, the oxygen concentration increased to a peak after P-well fabrication process, which is one of the highest temperature. It was supposed that the precipitates dissolved back into interstitial oxygen in the wafer. In the following process, the oxygen concentration decreased again. The precipitation occured again and gave the severe damage to the denuded zone boundary.

On the contrary, the MIG wafer with ω_1 - annealing has the well-controlled precipitation and denuded zone. By the TEM observation, the various kinds of microdefects were found: the tetrahedron-shaped precipitates of about 50 nm diameter, the larger precipitates with the surrounding punch-out dislocations and the stacking-fault type microdefects.

Photo.2 shows the cross-sectional view of RIG wafer after the simulation. The definite denuded zone was also formed. In the one-third of total annealing time of MIG annealing, RIG wafers acquired the sufficient bulk microdefects of 1.5x10^5 / cm^3 , nearly same as much as those of MIG wafers.

Fig.3 shows the oxygen concentration reduction of RIG wafers. The final reduction value was 3.2x10^{17} atoms/cc. By the Wright etching or by the TEM observation, RIG wafers were shown to have the large ratio of stacking-faults in the bulk microdefects.

To evaluate the gettering ability, the leakage fails in the CMOS TEG circuits were surveyed over the MIG wafers, the RIG wafers and the reference wafers which were of higher oxygen concentration and were not IG pre-annealed.

The results are shown in Fig.4. The IG-annealed wafers, MIG or RIG, have achieved the lower averaged value of fails and also the narrower scattering than the reference wafers. It is due to the effective gettering of contaminants in the CMOS process and also due to the good uniformity of precipitation. The local fluctuation of interstitial oxygen was typically found in the range of 1x10^{17} atoms/cc with the FTIR mapping-measurement of the 250 μm-diameter spot. That value was much smaller than that of middle or high oxygen concentration wafer.

The RIG annealing is attractive for its shorter total IG- annealing time in practical use, but the acceleration mechanism still remains unknown. For further investigations of the nucleation kinetics of RIG, the modulated 16H ramping methods were adopted in place of the constant-rate 25H ramping. The sequences are shown in Fig.5.

Photo.3 shows the cross-sectional views of the modulated ramping annealed wafers. The wafer of higher-temperature weighted ramping (0.7 - 0.2 ℃/min.) has almost the same density of microdefects as the constant-rate ramping wafer (photo.2). But the wafer of lower-temperature weighted ramping (0.2- 0.7 ℃/min.) has much lower density of microdefects. Those results suggest the effective temperature region for microdefect formation in RIG: 700 ～750 ℃. The 850 ℃ isothermally annealed wafer has few effective microdefects.

CONCLUSIONS

Two types of IG pre-annealing were investigated and the precipitation was traced through the thermal CMOS-process simulations. Also the gettering ability was examined with the CMOS TEG circuits. The both IG wafers achieved the lower averaged value and the narrower scattering of leakage fails due to the uniform and sufficient precipitation. One was the MIG annealing (High- Low- High temperature). The precipitation and the denuded zone fabrication highly depended on the final high-temperature annealing. In this experiment, the 1140℃ - 2H annealing in N_2 ambient gave the good results in the control of the bulk microdefects through the simulations. The bulk microdefects of MIG wafers were well recognized in terms of precipitation and solubility in silicon. On the other hand, the RIG annealing (High- Low temperature) created the sufficient microdefects, mostly of stacking faults, even in the one-third of total annealing time of MIG. This accelerated nucleation kinetics of RIG were also investigated with the modulated ramping methods, and the effective temperature region was clarified.

REFERENCE

1 H.Tsuya et al., Jpn. J. Appl. Phys., 20, L31 (1981)

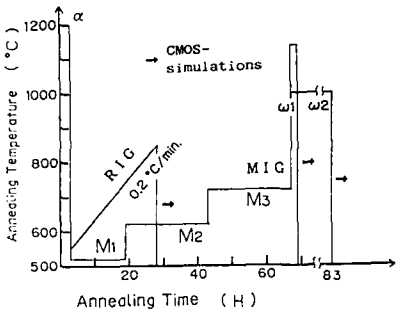


Fig. 1 The IG pre-annealing sequences investigated in this work. (MIG with different ω -annealing and RIG)

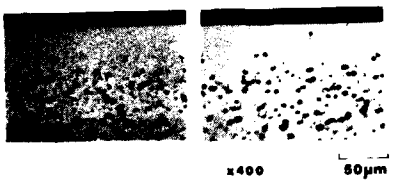


Photo. 1 The cross-sectional views of the MIG wafers after 3 min. Wright etching.

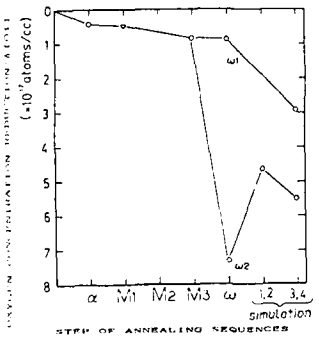


Fig. 2 Oxygen concentration reduction in MIG annealing and the CMOS-process simulations. (biased with each initial concentration: 11 ~ 12x10^{17} atoms/cc)

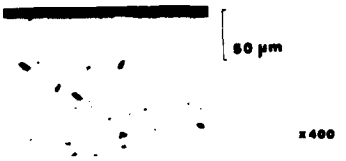


Photo. 2 The cross-sectional view of the RIG wafer with the 0.2 C/min. ramping.

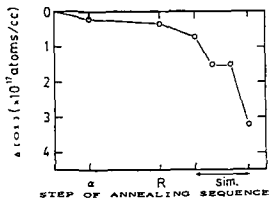


Fig. 3 Oxygen concentration reduction in RIG annealing and the CMOS-simulations. (biased as Fig. 2)

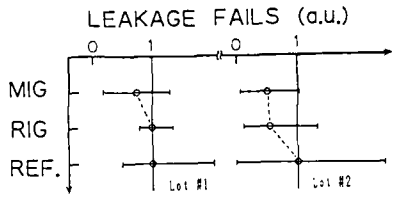


Fig. 4 The leakage fails of the CMOS TEG's on the gettering wafers [MIG, RIG] and the references. (normalized to the average of total fails on each reference wafer)

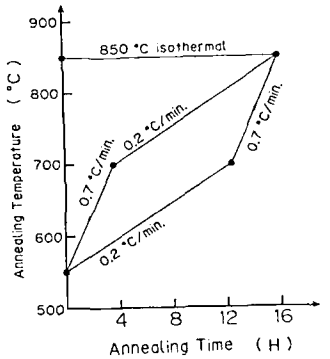


Fig. 5 The modulated ramping sequences adopted for the investigation of nucleation kinetics in RIG.

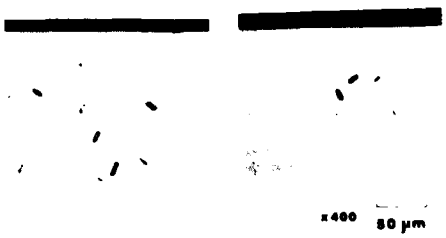


Photo. 3 The cross-sectional views of the RIG wafers with the modulated ramping as shown in Fig. 5.

Abstract No. 475

THERMAL ANALYSIS FOR THE SiO_2-Si AND SiO_2-GaAs STRUCTURES DURING RAPID THERMAL PROCESSING

R. Kwor°, F.K. Yang and S.J. Pien*

Department of Electrical and Computer Engineering
University of Notre Dame
Notre Dame, IN 46556

*Department of Aerospace and Mechanical Engineering
University of Notre Dame
Notre Dame, IN 46556

°Currently with Department of Electrical Engineering
University of Colorado at Colorado Springs
Colorado Springs, CO 80933

In the past several years, a great number of research works have been published on the rapid thermal processing (RTP) of semiconductors. The technology of RTP has reached its mature stage. Thermal analyses of transient heating processes have been the subject of interest for some time now. The analyses for Simple Si wafers under various transient heating conditions, such as adiabatic, conductive and isothermal modes, have been carried out [1,2,3]. However, these analyses are not always applicable to the actual manufacturing conditions. A common example is the annealing of a multilayer structure such as SiO_2 on Si, or a heat treatment of some metal-insulator-semiconductor structure [4]. A specially formulated thermal analysis for the insulator-semiconductor structure under RTP is clearly needed.

In this study, a thermal analysis on the RTP of the SiO_2 on Si structure is performed. The effect of the oxide thickness is investigated. The analytical modeling is first formulated to calculate the temperature at the SiO_2-Si interface layer. Since the interaction of a light pulse with a sample material is very much dependent on the optical and thermal properties of the material, the non-linear changes in these properties have made the analysis more complex. We have assumed that the oxide layer is pure, amorphous SiO_2 without any water contamination or OH absorption, although in actuality, some deviation may exist, affecting the optical properties of the film [5].

The temperature at the SiO_2-Si interface under different light sources and various RTP conditions is studied. A comparison between this interface temperature and the SiO_2 surface temperature will be presented for the different thicknesses of SiO_2.

In the second part of this paper, we will simulate the rapid heating process in the SiO_2 on GaAs structure. Because of the strong tendency of decomposition for capless GaAs under high temperature conditions, the RTP of the SiO_2-GaAs structure, where the SiO_2 serves as an encapsulant, is of considerable interest. The temperature at the SiO_2-GaAs interface is calculated under different optical sources and various RTP conditions. The comparison between the interface temperature and the capless GaAs surface temperature will be presented. Since the optical properties such as reflectivity and absorption are similar for SiO_2 and Si_3N_4 [6], the above results are expected to be at least partially applicable to the Si_3N_4 capped GaAs.

REFERENCES

[1] Laser Annealing of Semiconductors, J.M. Poate and J.W. Mayer, eds., Academic Press, New York (1982).

[2] Semiconductors and Semimetals, Vol. 17, J.F. Gibbons, ed., Academic Press, New York (1984).

[3] S.J. Pien, F.K. Yang and R. Kwor, paper 718, The 172nd Meeting of the Electrochemical Society, Honolulu, HI, October (1987).

[4] I.B. Khaibullin and L.S. Smirnov, Sov. Phys. Semicond., 19, 353(1985).

[5] H.R. Philipp, J. Phys. Chem. Solids, 32 1935(1971).

[6] Handbook of Optical Constants of Solids, E.D. Palik, ed., Academic Press, New York (1985).

Abstract No. 476

Diffusion of Zinc In Gallium Arsenide Through a Cubic Zirconia Passivation Layer

J. E. Bisberg, F.P. Dabkowski, A.K. Chin
Microelectronics and Materials Center
Polaroid Corporation, Cambridge, MA 02139

The diffusion of zinc in GaAs has been used extensively for p-type doping to form electrical contacts and in the fabrication of p-n junctions for opto-electronic devices. It has been found that an overpressure of arsenic is essential to prevent surface deterioration due to arsenic loss from the sample. The traditional sealed ampoule approach reduces arsenic loss, but is cumbersome to use and difficult to scale up to process large wafers. Open-tube techniques capable of processing large wafers have been described, but they require speciallized alloy sources, or doped films that complicate the diffusion process [1-4].

In this study, we demonstrate that a thin film of yittria-stabilized cubic zirconia (YSZ) will allow the diffusion of zinc into GaAs substrates while reducing the out-diffusion of arsenic to a level acceptable for high quality device fabrication. The YSZ passivation layer acts as a selective diffusion barrier allowing zinc to diffuse freely while inhibiting the loss of arsenic from the GaAs sample. This process eliminates the critical control of the arsenic overpressure and thus allows the use of a pure zinc diffusion source. In addition, the diffusion is performed in a conventional open tube furnace capable of handling large substrates with good throughput. Finally, the cubic zirconia thin film is easy to deposit and remove while contributing only two additional steps to the diffusion process.

The yittria-stabilized cubic zirconia passivation layer was deposited onto the GaAs substrates by electron beam evaporation. YSZ films used in this study were typically 2000 Å thick with an index of refraction of 1.9 at 6328 Å. YSZ passivation layers were removed after diffusion with either HF acid or CF_4/O_2 plasma followed by a $HCl:H_2O$ dip to dissolve any residual surface oxide.

Zinc diffusions were performed in an open tube furnace at 650°C in a high purity hydrogen/nitrogen gas mixture. Diffusion sources were either 6N pure zinc metal or 5N pure GaAs-5N pure Zn_3As_2 mixtures. Both the zinc diffusion source and GaAs samples were held in a semiclosed quartz boat. Diffusion times ranged from 20 minutes to 20 hours. Our open tube diffusion process using the Zn_3As_2/GaAs diffusion source had previously been developed to produce high quality GaAs and AlGaAs light emitting diodes (LEDs).

The surface morphology of the diffused wafers was dependent on the specific diffusion conditions. As expected uncapped wafers diffused with the pure zinc source showed surface decomposition. However, the YSZ passivated samples diffused from the same source were specular under microscopic inspection for diffusion times shorter than ≈10 hours. Longer diffusions produced minor thermal decomposition. Both capped and uncapped samples diffused with the GaAs/Zn_3As_2 source showed no indication of surface decomposition.

Diffusion depths in the capped and uncapped samples were determined by scanning electron microscopy. The samples were cleaved and stained with a ferricyanide etchant to reveal the p-n junction. The dependence of junction depth on diffusion time for YSZ coated and uncoated GaAs substrates diffused from the mixed Zn_3As_2/GaAs source as well as YSZ coated substrates diffused from the pure zinc source are summarized in Fig. 1. These diffusions were performed at 650 °C. The linear dependence of the diffusion depth on the square root of diffusion time indicates that the diffusion follows Fick's law [5]. Calculated values of the zinc diffusivity in GaAs under these conditions are summarized in Table 1.

Carrier concentration profiles were obtained using a Polaron electrochemical profiler. The profiles indicated a uniformly doped zinc region followed by a rapid decrease in the carrier concentration in the region of the junction. The junction depths measured by the cleave and stain procedure are in a very good agreement with those obtained from the carrier profile measurements. Although the diffusivity in the YSZ passivated sample diffused from pure zinc was five times that of the uncapped GaAs diffused from the alloy source, the difference in carrier concentration of the two specimens was within the experimental error of the Polaron profiler. Thus the YSZ passivation layer has little effect on the carrier profile and provides the sharply graded junction characteristic of other open-tube and sealed ampoule diffusion processes [1-5].

In summary, we have demonstrated that a yittria-stabilized cubic zirconia coating allows the diffusion of zinc into GaAs while reducing the thermal decomposition of the substrate. Application of the YSZ protective layer to zinc diffusion into GaAs eliminates the critical control of the arsenic overpressure. This process is thus less sensitive to small unintentional deviations of processing parameters in comparison to previously reported methods [1-5]. The presence of the YSZ layer does not affect the Zn diffusivity or carrier profile significantly.

REFERENCES

[1] A. Choudhury, M. Oren, M. Rothman, S. Shastry, J. Electrochem. Soc. 134, 2631, 1987.

[2] Y.R. Yuan et. al., J. Appl. Phys. 54, 6044, 1983.

[3] R. Jett Feild and S. Ghandi, J. Electrochem. Soc. 129, 1567, 1982.

[4] S. Reynolds, D.W. Vook, and J.F. Gibbons, J. Appl. Phys. 63, 1052, 1988.

[5] H.C. Casey, Jr., Atomic Diffusion in Semiconductors, edited by D. Shaw (Plenum Publications Co., New York, 1973), p. 369-374.

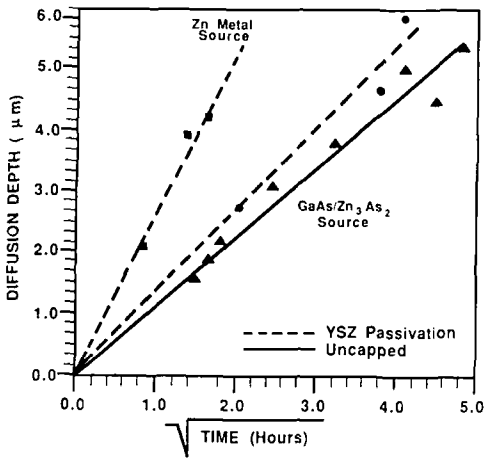


Fig. 1 Junction depth dependence on the square root of diffusion time at 650°C fo

- ■ YSZ capped GaAs with pure zinc source.
- ● YSZ capped GaAs with $GaAs/Zn_3As_2$ diffusion source
- ▲ Uncapped GaAs with $GaAs/Zn_3As_2$ diffusion source.

	NO CAP	YSZ CAP	YSZ CAP
	$GaAs/Zn_3As_2$ SOURCE		Zn METAL SOURCE
DIFFUSION COEFFICIENT Cm^2/sec	3.56×10^{-10}	4.92×10^{-10}	1.92×10^{-9}

Table 1 Diffusion Coefficients calculated from Fig. 1

Abstract No. 477

A High-Precision Thinning Technique for GaAs Substrates

Toshiroh KARAKI-DOY, Hiroshi NAKADA and Junji WATANABE

NTT Applied Electronics Laboratories, Nippon Telegraph and Telephone Corporation 3-9-11 Midori-cho, Musashino-shi, Tokyo, 180 Japan

1. Introduction

A high-precision thinning technique for substrates with functional devices, has recently drawn a lot of interest for making high-performance electronic/optical devices. A typical example is processing the back-side surface of GaAs used for a solar cell or a power FET device[1]. Conventional processing methods and conditions for back-side surface processing, involve many problems. The desired thickness/accuracy may not be obtained or the functional devices on the other side may be scratched.

On the other hand, a conventional finishing processing (polishing) of GaAs substrates has serious problems, as it uses poisonous or stimulative smelling reagents containing Br_2-CH_3OH[2] or NaClO.[3]

This paper describes a small high-precision system and a new polishing method using a harmless polishing reagent for GaAs substrates. Using this system and new polishing method, a GaAs substrate with a solar cell device on the other surface was accurately finished without making any defects to the cell device surface.

2. Development of a small processing system

The basic process of the new high-precision thinning technique for samples with cell devices, is outlined in Fig. 1. The process features ① Protective film and adhesive film coating to the device-side surface, ② High-accuracy adhesion of the sample on a flat jig-plate, ③ High-precision processing of the sample (back-side surface).

A trial demonstrated a high-accuracy and high-quality thinning processing for a sample with devices. Accordingly, the adhesive machine and processing machine were developed as a high-precision and high-quality system. The adhesive machine is shown in Fig. 2. A dilute solution of protective film or/and adhesive film is dropped on the sample, then the sample is rotated at high speed, reliably forming a uniform protective/adhesive film. The film thickness can be controlled from 0.2 to 5 μm by choosing the rotation speed and concentration. Next, the sample is set on a flat jig-plate, and together they are heated and pressed by a flexible film bag of sealed N2 gas under a constant pressure as shown in Fig. 3. It is possible to high-accurately adhere samples of different thicknesses on the flat jig-plate at the same time.

The high-precision lapping/polishing machine is shown in Fig. 4. The accuracy of processed sample is significantly influenced by positional deviation, sample vibration from the lap/polisher, a principal axis or driving motor/transmission as well as flat-accuracy of the implement plate(lap/polisher). Therefore, the trial processing machine uses hydrodynamic thrust/radial bearings which absorbed vibration, and a direct-drive, low-speed, high-torque brushless DC motor. The sample can be manufactured with high-accuracy and high-quality using this high-precision processing machine.

3. Application of high-precision processing to GaAs substrates

3.1 Developement of a new polishing slurry and the polishing characteristics

The Sodium Bromite ($NaBrO_2$)[4] solution used as a slime control agent contains Na and Br and is mildly oxidizing but harmless. This makes it suitable as a polishing reagent for GaAs substrates. Mechanochemical polishing characteristics of the GaAs substrates are shown in Fig. 5, when mainly $NaBrO_2$ solution and SiO_2 powder are used as the polishing slurry. When the SiO_2 particles in $NaBrO_2$ solution are reduced in size, the polishing rate decreases and saturates at a size below 200 Å. However, the GaAs surface roughness improves remarkably. An Rmax. of 8Å (corresponding roughness of cleavage surface) can be obtained for 70Å-Si particles.

The polishing rate increases markedly with increasing pH value (by adding NaOH). Chemical analysis of the GaAs polished surface shows some elements (Na, Br, O, H, Si, C) remain in the extreme surface layer. Consequently, the chemical reaction mechanism can be estimated as follows:

$$GaAs + 2NaBrO_2 \rightarrow GaAsO_4 + 2NaBr$$
$$GaAsO_4 + 4NaOH \rightarrow NaGa(OH)_4 + Na_3AsO_4$$

The SiO_2 powder in the polishing slurry probably promotes this chemical reaction.[5]

3.2 The thinning processing for GaAs substrate used for electronics

A high-accuracy, high-quality thinning processing is required for GaAs solar cells in satellites, to keep the satellite light and reliable. Flatness measurements of the thin-processed back-side surface of a GaAs substrate (20x20x0.5mm) with solar cell device are shown in Fig. 6. A thin mirror-like substrate (50± 0.5 μm thick, flat 1 μm/□ 20mm) can be obtained with the small system and new polishing method for GaAs substrate, regardless of the unevenness of the device-side surface (several micron). GaAs substrates less than 30μm thick can also be accurately polished. However, it is difficult to handle and apply to solar cells, since a large bow is caused.

4. Conclusion

A small high-precision system was developed and a new polishing method applied harmless polishing reagent for GaAs substrates has been found. Using the system and the technique, the back-side surface of a GaAs substrate with a solar cell device was thin-processed to a thickness of less than 30 μm.

Reference

1) M. Maruyama et al. Extended Abstracts of the 18th Conf. on Solid State Devices and Materials (1986) p.439
2) I. Kasai et al. The Science of Polishing, Technical Digest, OSA (1984) Tuc-B4-1
3) U.S. Patent 4210 (U.S. Cl. Mar. 1, 1972) 701
4) Nippon Silica Industrial Co., LTD. Technical Bulletin (1985)
5) Kotoku et al. Bull. of Materials, 84 (1984) 571

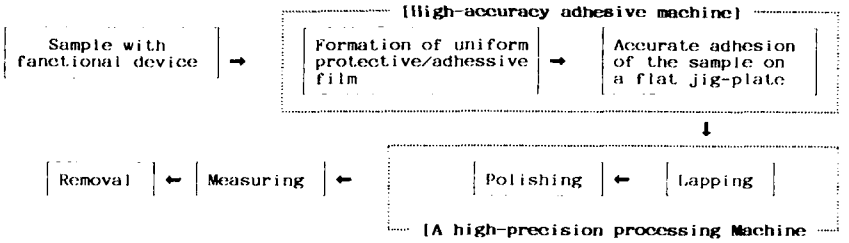


Fig. 1 Basic process outline of a high-precision thinning technique

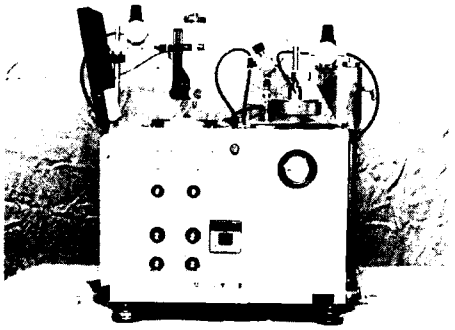


Fig. 2 Photograph of the adhesive machine

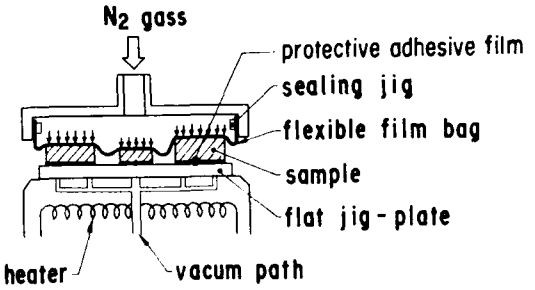


Fig. 3 Method of uniform high-accuracy adhesion

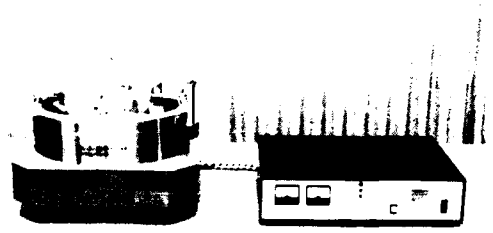


Fig. 4 Photograph of the high-precision processing machine

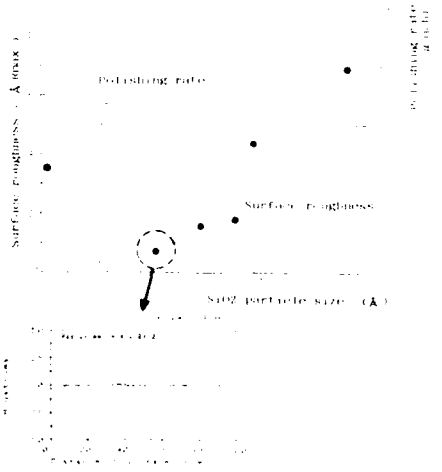


Fig. 5 Mechanochemical polishing characteristics of GaAs by NaBrO2 solution and SiO2 powder

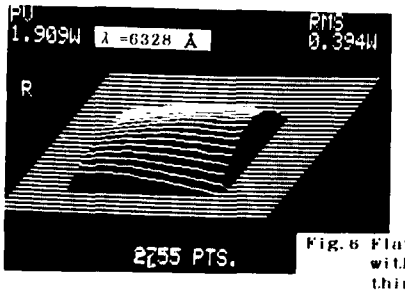


Fig. 6 Flatness of GaAs substrate (20x20mm, 50 ^{1} μm) with solar cell on back-side surface, thin-processed by a high-precision system and a new polishing method

Abstract No. 478

SUBMICRON PMOS TRANSISTORS FORMED BY DOPANT IMPLANTATION INTO $TiSi_2$

K J Barlow

Plessey Research Caswell Ltd, Caswell, Towcester, Northants UK NN12 8EQ

The formation of shallow, low resistance junctions is an important requirment in MOS VLSI technology in order to minimise short channel effects in MOSFETS. However, shallow P+/n junctions are difficult to obtain since boron tends to channel deeply into silicon during implantation and diffuses rapidly during futher high temperature processing. Using RTA, preamorphisation and boron fluoride implants, can reduce channelling and diffusion, whilst silicidation is used to reduce the sheet resistance of the source, drain and gate regions. A problem with using preamorphisation and boron fluoride implants is the creation of defects in the silicon, whilst flourine can increase leakage currents. Many of the problems associated with shallow junctions can be avoided by implanting the dopant into the silicide and then outdiffusing it using a fairly low temperature anneal to form the junction (1,2). Implantation into the silicide means that any ion damage is confined within the silicide, uniform dopant profiles can be achieved since anisotropy and shadowing effects of the implantation are eliminated. Also since the implant process does not create damage in the silicon, the temperature is not determined by that required to anneal out the ion damage, thus low temperature processing can be used.

This work will present the results of an investigation into the formation of PMOS transistors, with channel lengths down to 0.35μm, by implanting boron, of various doses and energies into $TiSi_2$ and using a low temperature anneal to outdiffuse the dopant.

An advanced CMOS process, employed in our laboratories was used to fabricate the devices. This employs trench isolation, oxide sidewall spacers, a 20nm gate oxide and silicided source, drain and gate regions. Fig 1a,b shows a schematic of the two process schedules used to form the pmos devices. In the conventional process fig.1a after the cvd oxide sidewall spacer is formed a silicon implant is used to preamorphise the silicon to a depth of about 0.12μm, followed by a boron flouride implant (1E15/cm^2, 40kV). The solid phase epitaxial regrowth (SPE) anneal is used to regrow the single crystal silicon whilst minimising boron diffusion. RTA annealing is followed by deposition of 500Å of Ti and a two stage RTA process to form 680Å of $TiSi_2$. Fig 1b shows the reduced number of steps required when forming P+ junctions by implanting dopant into the silicide layer. Boron implantation into the silicide is followed by a low temperature anneal (800°C,N_2,30-120mins) to form the P+ junction. Fig 2 shows a SIMS profile for a P+ junction formed by implanting B at 5E15/cm^2,30kV into a 680Å thick $TiSi_2$ layer and outdiffusing it using an 800°C, 30 min, N_2 anneal. The junction depth is around 0.26μm, and shallower junctions can be formed by reducing the implant dose and energy. The sheet resistance was ~6Ω/sq for the P+ junctions formed by implantation into $TiSi_2$, compared to ~5Ω/sq for the conventional P+ junctions.

PMOS transistors, with channel lengths down to 0.35μm, were fabricated by implanting dopant into the silicide and compared with conventional PMOS devices. Measurement of the linear transconductance Gm, as a function of effective channel length is shown in fig.3 and it can be seen that there is no difference between the implant into the silicide device and the conventional device. The low field gain of the implant into silicide device is around 23μA/V^2 compared to around 20.5μA/V^2 for the conventional device, and the saturation current in the implant into silicide device is a few per cent higher at the same effective channel length. Fig. 4 shows the output characteristics for a PMOS transistor with an effective channel length of 0.35μm, formed by implanting B at 5E15/cm^2,20kV into $TiSi_2$ and then annealing (800°C,60min,N_2) to form the junction.

In the subthreshold region both the conventional and implant into silicide PMOS devices had the same subthreshold slope 92mv/dec, fig. 5 shows a subthreshold plot for a PMOS transistor, with channel length of 0.4μm, formed by implanting into the silicide. Offstate leakage (Vd=-5v, Vg=1v) was found to be less than 10pA for channel lengths down to ~ 0.55μm, below this the leakage increases to 1μA for a channel length of 0.45μm as punch-through begins to control the maximum allowable drain voltage.

The reduction of the threshold voltage Vt with channel length was also plotted for the conventional PMOS device and implant into silicide device, fig 6. As the plot shows no enhanced reduction in Vt is observed due to the use of high dose boron (5E15/cm^2) implanted into the $TiSi_2$ layer.

In conclusion PMOS transistors with channel lengths down to 0.35μm have been formed by implanting boron under a range of conditions into $TiSi_2$ already formed in the source, drain and gate regions. A fairly low temperature anneal (800°C) is all that is required to produce P+ junctions with low leakage levels. The PMOS transistors formed by this method have characteristics the same or better than conventionally formed silicided PMOS transistors. The procedure is compatible with submicron CMOS processing.

The author would like to acknowledge the Plessey Co for permission to publish and the Alvey Directorate for partial funding.

(1) F C Shone, K C Sarawat, J D Plummer, IEDM 1985, p407

(2) R Lui, D S Williams, W T Lynch, IEDM 1986, p58

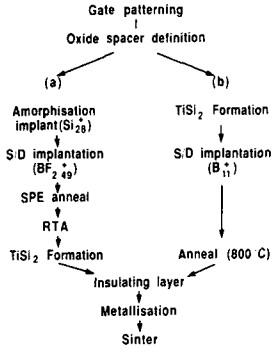


Figure 1
Schematic of the silicided source drain schedule
(a) Conventional first form junction then silicidation
(b) Silicidation then implant into silicide and activation at 800 °C

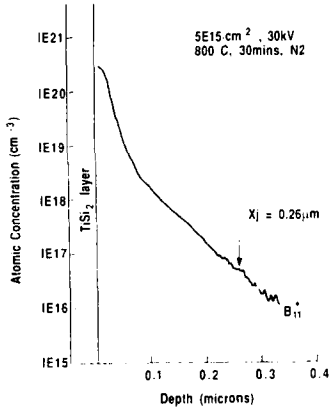


Figure 2
SIMs profile for a p+ junction formed by boron implantation into $TiSi_2$

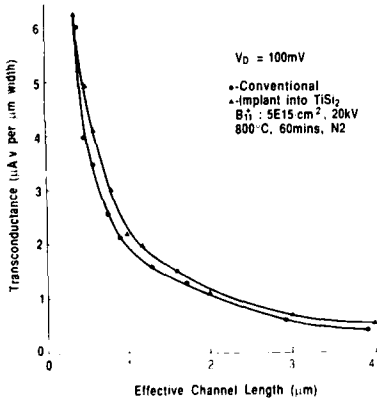


Figure 3
Linear transconductance as a function of effective channel length

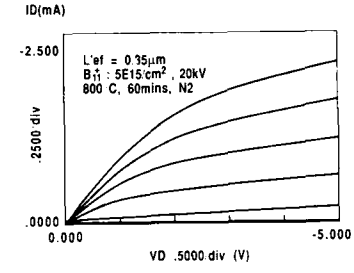


Figure 4
Output characteristics for a PMOS transistor formed by implantation into $TiSi_2$

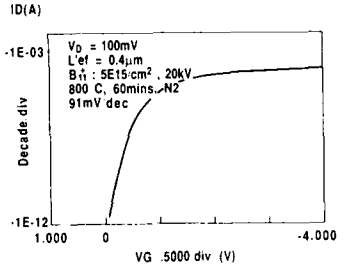


Figure 5
Subthreshold characteristics for a PMOS transistor formed by implantation into $TiSi_2$

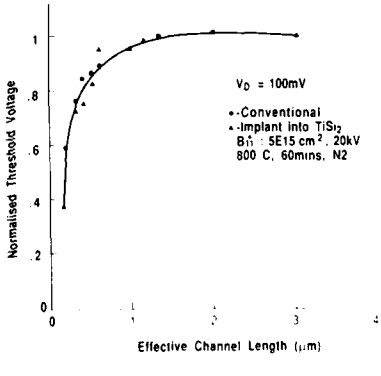


Figure 6
Channel length dependence of threshold voltage roll-off

Abstract No. 479

ELECTRO-OPTIC SWITCHES BASED ON NOVEL CONDUCTING POLYMER TECHNOLOGY: ENHANCING OPTICAL SWITCHING TIMES

P. Chandrasekhar

Gumbs Associates, Inc.
11 Harts Lane
East Brunswick, NJ 08816

Many newly synthesized conducting polymer materials are serious candidates for use as optical switches in applications ranging from optical interconnects and storage discs to laser shielding and switchable radar absorbers [1]. Concerted switching rate studies and an understanding of the factors affecting the rate so that it can be enhaced are however still lacking. With the aim of designing and synthesizing novel conducting polymers with promise for use as optical switches, and on the basis on semi-empirical quantum mechanical (INDO) calculations indicating very low bandgaps and considerable intramolecular charge transfer, we very recently synthesized a series of 2-Me thiophene (T) derivatives, two of which are 1 and 2 (Fig. 1), via a proprietary chemical/electrochemical procedure.

Electrochromic switching rate studies have been conducted on these and polypyrro e (PP), P3MT controls using both chronoamperometric/chronocoulometric analyses and an independent electrochromic switching rate apparatus constructed for the purpose employing a 65 mW Ar ion laser (Newport), coupled to a potentiostat and to an ultra high-speed Si-avalanche photodetector (Newport) with ECL electronics. For device studies, 2-layer sandwich devices of the polymer studied comprising the polymer deposited on on an ITO or Au (ca. 70 A) coated glass slide, a layer of proprietary polyethylene oxide (PEO) based electrolyte and an additional ITO or Au/glass slide. The quasi-reference electrode was either Pt sputter-deposited on polyimide on the working electrode, or an electrically disconnected section of the working electrode. Devices were hermetically sealed with epoxy. Electrochromic switching rate was monitored by pulsing 1 V on either side (i.e. +/- ½ ") of the polymer redox peak.

INDO calculations on 1, 2 indicate ca. 0.1 e^- S to X charge transfer. Effect of a number of parameters on a predefined switching rate were studied, and it was found that the size of dopant ion (from BF_4^- to tosylate and polyvinyl sulfonate), solvent medium, (PC, ACN), and substrate (Au, ITO, Pt) had minimal effect whereas film thickness, electrolyte concentration (0.2 to 1.2 M), preprocessing of substrate with PEO and presence of effective counterreaction (with $AgClO_4$) had maximal effect. Reduction of film thickness from 10 nm to ca. 1 nm caused 2 orders of magnitude drop in switching rate for all polymers while PEO-processing of substrate and subsequent leaching out of PEO after polymer deposition (giving better dopant access to polymer charge centers) yielded similar effects. With 1 nm polypyrrolium tosylate (PPTos) prepared in proprietary manner, we observed switching times of ca. 1.0 msec, reversible and reproducible over 300 cycles. Fig. 2 shows typical switching curves for PPTos/Au/glass (ca. 10 nm) with 10 - 100 mV/sec CVs inset. Switched/unswitched OD ratios are ca. 10 to 80, depending on film thickness and history.

In preliminary tests, thin films of the novel polymers 1and 2 yielded switching times of ca. 0.1 msec. For certain optical switching applications, e.g. optical interconnects [2], rate requirements as low as 1 picosec have been stated. However, usec rates will yield viable switches for many applications. Our switching rate is defined on the basis of known charge in film deposition and known or published stoichiometry and No. of electrons of the polymer redox reaction.

We are currently working on a number of approaches and novel polymers to yield microsecond domain switching times. We have also developed a proprietary intrinsic or 'automatic' trigger for the polymer optical switches based on semiconductor electrodes, which will be described elsewhere.

We are grateful to the US Army Medical Research Acquisition Activity (Fort Detrick, Frederick, MD) and the Letterman Army Institute of Research (San Francisco, CAO for generous support of this work.

References

1. Wegner, G., Mol Cryst. Liq. Cryst., 1984, 106, 269.

2. Proc. Rpt. on Top. Mtg. Optical Bistability of Optical Society of America and Lasers & Electro-optics Society of IEEE, Tucson, AZ, 1975.

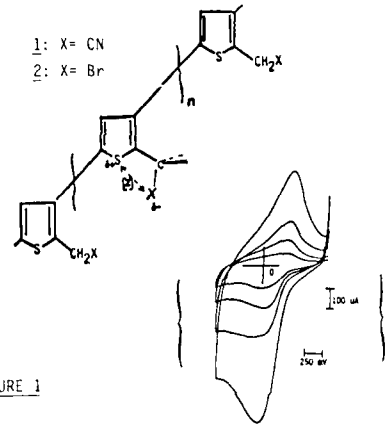


FIGURE 1

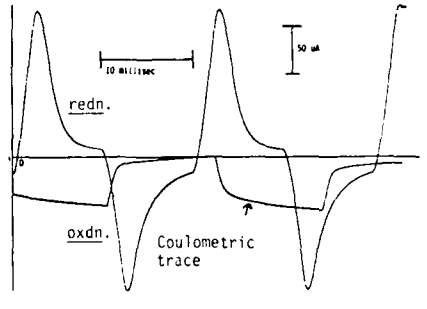


FIGURE 2

Abstract No. 480

FABRICATION AND CHARACTERIZATION OF SUBMICRON FAR INFRARED RECTENNA DEVICES

A. B. Hoofring and V. J. Kapoor

Electronic Devices and Materials Research Laboratory

Department of Electrical and Computer Engineering

University of Cincinnati

Cincinnati, Ohio 45221-0030

W. Krawczonek

NASA Lewis Research Center

Cleveland, Ohio 44135

The fabrication processing and characterization of far infrared rectennas were investigated. The principle components of a rectenna are an antenna used to collect energy from a radiation field which is subsequently coupled in the form of an ac voltage at the radiation frequency to a rectifying element. The rectifying element serves to convert the coupled signal to some average dc power; hence energy conversion is achieved. Previous rectennas were primarily used for microwave radiation and have demonstrated conversion efficiencies as high as 90%. The present objective was to extend rectennas for operation at far infrared (FIR) frequencies. This work was primarily concerned with the investigation of a suitable rectifying element which would respond to FIR frequencies.

A metal-oxide-metal (MOM) tunnel diode was chosen. Conduction in MOM diodes occurs by means of tunneling of electrons across a thin ($\lesssim$ 50 Å) oxide tunnel barrier under an applied bias across the two metal electrodes. MOM diodes have very nonlinear current-voltage (I-V) characteristics and are perhaps the fastest devices known. They have been shown to be able to detect radiation at FIR wavelengths by many investigators. Experimental results were based on the fabrication and testing of rectennas with 0.8 um linewidths.

Rectenna fabrication was based exclusively on a metal liftoff procedure using Shipley AZ-1350J positive photoresist. The substrate used was a 2" silicon wafer with a thermally grown SiO_2 layer on top for electrical isolation. Following patterning the wafer the MOM diode was formed by first evaporating a thin layer of Al used to promote adhesion of the structure to the SiO_2 surface and then depositing a 1000 Å Ni layer under the same vacuum. Upon removal from the evaporation chamber, liftoff was performed to define submicron Ni lines. A thin layer of NiO for the tunnel barrier was then formed by immersing the wafer in an oxygen plasma to promote oxidation of the Ni surface. The oxygen plasma served to simultaneously grow and etch NiO to achieve a uniform metal oxide layer on nickel (Ni) line. Once a satisfactory NiO thickness was achieved, a 0.8 um wide layer of gold (Au) was defined by liftoff which overlapped the Ni-NiO layer forming a MOM junction with an area of 0.64 um^2. Dissimilar metal were used to achieve desired asymmetric I-V curves. The antenna structure was achieved as the MOM diode was being formed by two parallel metal lines of Ni and Au which coupled into the MOM diode.

The dc I-V characteristics were investigated. Results indicated that the current dependence on voltage was linear about zero bias up to a bias of about $|70\ mV|$. Beyond $|70\ mV|$ the I-V characteristics became very nonlinear. The oxide breakdown voltage (BV) was also investigated as a function of the tunnel oxide thickness. Breakdown voltage was determined when the current suddenly increased by many orders of magnitude at a certain bias indicating a short circuit situation. The voltage was ramped at a rate of 0.5 V/s until BV occurred. BV was found to decrease as s was decreased. This dependence was slightly less the linear and the maximum electric field (E_{max}) at BV increased slightly as the oxide thickness was reduced. The average E_{max} for the tunnel oxide thickness ranged from 15 Å to 39 Å was approximately 7×10^6 V/cm.

Bias and current dependent transient effects were also investigated. For a bias swept across the device terminals employing a curve tracer, the current at a given bias point was found to decrease monotonically in time until some steady state condition was reached. This behavior was attributed to trapping of electron within the NiO barrier layer. This current decay occurred similarly in devices of various tunnel oxide thicknesses. The I-V curves also showed some hysteresis when a large dc electric field was induced across the junction and an I-V curve was subsequently traced. This behavior has been attributed to ion migration within the tunnel oxide layer.

Electrical measurements were performed to determine the low-level detection performance of the MOM diodes used in the rectenna. The current sensitivity was measured as a function of dc bias across the junction by superimposing a 2kHz sine wave with an amplitude of 10 mV on the dc signal and then measuring the first and second harmonic responses. The maximum sensitivity indicates the region of maximum detectability. The maximum value of sensitivity occurred for a bias of 100 mV.

Finally, optical measurements were performed. A CO_2 laser with a wavelength of 10.6 um was used as the radiation source. The beam was chopped at a frequency of 207 Hz and a reference signal at the same frequency was supplied to a lock-in amplifier (LIA). The rectified signal of the rectenna was measured as a function of dc bias by the LIA. The FIR rectenna was found to detect best near a bias voltage of approximately 120 mV.

Abstract No. 481

A Wafer-Scale Thinning Process for High-Performance Silicon Devices*

C. M. Huang, B. B. Kosicki, B. E. Burke and A. C. Anderson

Lincoln Laboratory, Massachusetts Institute of Technology
Lexington, MA 02173-0073

A uniform and defect-free silicon wafer thinning process has been a principal need in an increasing number of new device applications such as back-side illuminated CCD imaging devices, high-quality SOI devices and micromechanical devices. A whole-wafer thinning process has been developed to uniformly remove a thick, heavily doped bulk substrate from a lightly doped epitaxial layer. The process relies on the combination of denuded-zone gettering with improvements in the mechanical/chemical thinning technology.

This wafer thinning process uses commercially available epitaxial wafers. A denuded-zone process has been used to drive out all the oxygen in the top layer of the heavily doped silicon substrate prior to the lightly doped epitaxial layer growth [1]. The p^+ bulk is mechanically removed from the back of the wafer to within the denuded zone, resulting in a polished surface on the remaining defect-free p^+ bulk substrate with a $\pm$ 10 μm thickness uniformity.

A selective etch is then used to remove the remaining heavily doped substrate, stopping on the lightly doped epitaxial layer [2]. The selective p^+ etch solution consists approximately of 10 parts acetic acid, 3 nitric acid and 1 part hydrogen fluoride. The selectivity of the etching solution is low (2:1) because some of the nitric acid is converted to nitrous acid which etches the p^- epitaxial layer. Muraoka *et al.* managed to improve the selectivity by adding agents to the solution which either oxidized or decomposed the nitrous acid. This works well as long as the substrate resistivity is less than 0.01 ohm-cm. However, most of the commercially available p^+ substrates for high quality epitaxial layers have resistivities in the range of 0.01 to 0.02 ohm-cm, where the Muraoka etch is not very selective.

We have found that ultrasonic agitation can effectively remove the nitrous acid from the etching interface and an etching selectivity as high as 25:1 can be obtained between a 0.012 ohm-cm p^+ substrate and a 30 ohm-cm p^- epitaxial layer in the same vicinity. A final layer thickness uniformity of 0.4 μm for a 12-μm-thick epitaxial layer is routinely obtained over an entire 3-inch wafer of 400-μm starting thickness.

The defect counts of the selectively etched surface are close to that of the original epitaxial layer. The density of the stacking faults is less than 10 cm^{-2}. Shallow etch pits of a depth of 5000 Å or less are caused by point defects due to the oxygen precipitates in the bulk substrate. The density of the shallow pits is around 2000 cm^{-2} on wafers which were not lapped to the denuded zone. Figure 1 shows the point defects on the p^+ bulk manifested by the selective etch, and Figure 2 shows the shallow etch pits in the epitaxial layer corresponding to the point defects in the bulk. These shallow pits can be effectively prevented by denuding the oxygen in the intrinsic gettering process, and mechanically removing the p^+ substrate to within the denuded zone.

Back-side illuminated CCD imagers have been successfully fabricated using this thinning process. Figure 3 shows a 3" silicon wafer thinned down to 10 μm that has 16 chips of 420 × 420-pixel CCD imagers on it. The thinned CCD imagers show a transfer inefficiency better than 10^{-5}, and the dark-current density (surface and bulk) is around 2 nA/cm^2 with no back-side surface treatment. This thinning process is useful to produce high-performance silicon devices without causing any device degradation.

Reference

[1] S. Isomae, S. Aoki and K. Watanabe, "Depth profile of interstitial oxygen in silicon subjected to three-step annealing," J. Appl. Phys. 55, 817 (1984).
[2] H. Muraoka, T. Ohhashi and Y. Sumitomo, "Controlled Preferential Etching Technology," in Semiconductor Silicon 1973, edited by H.R. Huff and R. R. Gurgess (The Electrochemical Society Inc., Princeton, New Jersey, 1973), p. 327.

* This work was supported by the Department of A r Force.



Fig. 1. Photograph showing point defects on nondenuded bulk silicon caused by oxygen precipitation.

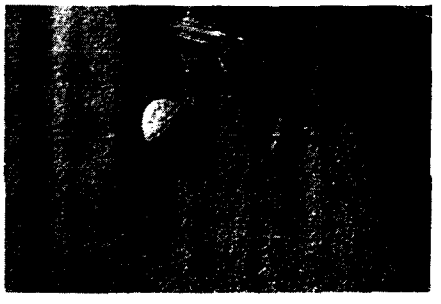


Fig. 2. Photograph showing shallow etch pits on the epitaxial layer due to point defects in the bulk. This wafer was not lapped to the denuded zone.

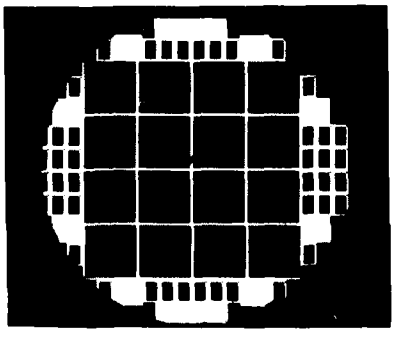


Fig. 3. Photograph of a thinned 3-inch wafer mounted on a glass substrate lighted from the back-side.

Abstract No. 482

DEPOSITIOON AND CHARACTERIZATION OF SILICON OXYNITRIDE BY A 2% SILANE PECVD PROCESS

P.C.LI AND L.C.HSIA
IBM GENERAL TECHNOLOGY DIVISION
EAST FISHKILL FACILITIES
HOPEWELL JUNCTION, N.Y. 12533

1. INTRODUCTION

THE < 2% SILANE IN NITROGEN OR OTHER INERT DILUENTS AS A SOURCE MATERIAL HAS NOW BEEN ROUTINELY USED FOR PECVD DIELECTRIC FILM PREPARATION (1). SINCE THE GAS THUS MIXED IS NON-PYROPHORIC, THE PROCESS IS MUCH SAFER FOR THE MICROELECTRONICS INDUSTRY. IN THIS PAPER THE PREPARATION AND PROPERTIES OF PECVD OXYNITRIDE FILMS ARE REPORTED. IN COMPARISON TO THE PECVD NITRIDE, OXYNITRIDE HAS LOW HYDROGEN CONTENT IN TERMS OF NH AND SIH BONDS, SHOWS LESS FILM STRESS, CAN BE EITHER WET ETCHED OR RIED, AND HAS LOW DIELECTRIC CONSTANT AND TRAPPED CHARGE DENSITY, IT IS, THEREFORE, AN EXCELLENT DIELECTRIC FOR MULTILEVEL INSULATION AND PASSIVATION. OXYNITRIDE HAS ALSO BEEN USED AS A SELECTIVE DIFFUSION BARRIER MATERIAL BECAUSE OF ITS THERMAL STABILITY (2).

2. EXPERIMENTAL

AN AMC 3300 LOW PRESSURE, RADIAL FLOW PARALLEL PLATE REACTOR WITH PERFORATED CATHODE WAS USED IN THIS STUDY. 1.9% SIH4 GAS IN N2 WAS PREMIXED WITH NH3 AND N2O BEFORE ENTERING THE PERFORATED CATHODE. IMPURITIES IN THE SIH4 GAS SUCH AS H2O, O2, CO2 AND HYDROCARBONS WERE KEPT BELOW 2 PPM. MOST OF THE FILMS USED IN THIS STUDY WERE DEPOSITED AT 325 C, 0.4 TORR, AND A FREQUENCY OF 50 KHZ WITH RF POWER VARYING FROM 50 W TO 900W. ALL SAMPLES WERE DEPOSITED ON <100> SI WAFERS EXCEPT THOSE USED FOR NUCLEAR BACKSCATTERING ANALYSIS, FOR WHICH THE DEPOSITION WAS CARRIED OUT ON EITHER HIGHLY PURIFIED CARBON OR VITREOUS CARBON SUBSTRATES. THE SAMPLES FOR IR STUDY WERE DEPOSITED ON THE WAFERS POLISHED ON BOTH SIDES. THE AS-DEPOSITED FILM COMPOSITION WAS DETERMINED BY NUCLEAR BACKSCATTERING SPECTROSCOPY AND FTIR SPECTROSCOPY. THE FILM INDEX OF REFRACTION AND THICKNESS WERE MEASURED USING GAERTNER ELLIPSOMETER.

3. RESULTS AND DISCUSSION

COMPOSITION:- FIG.1 SHOWS THE REGION OF THE SILICON OXYNITRIDE COMPOSITION OBTAINED IN THIS STUDY THROUGH NUCLEAR BACKSCATTERING ANALYSIS. FOR COMPARISON PURPOSE THE COMPOSITION OF LPCVD OXYNITRIDE FILMS AND THE SURFACE COMPOSITION OF LPCVD AND PECVD SI3N4 AND OXYNITRIDE FILMS ARE ALSO INCLUDED. IT IS INTERESTING TO NOTE THAT THE SI CONTENT OF THE FILMS IS ALMOST CONSTANT (34 TO 37 AT%), WHILE THOSE OF N AND O VARY QUITE SIGNIFICANTLY WITH THE PREMIXED GAS RATIO. THIS "BAND" APPEARS TO BE INSENSITIVE TO THE DEPOSITION CONDITIONS SUCH AS T, P, AND RF POWER. IT CAN ALSO BE OBSERVED THAT THE COMPOSITION OF ALL CVD FILMS OF SI3N4 AND OXYNITRIDE, EITHER PECVD OR LPCVD, FALLS IN THIS GENERAL REGION. IN GENERAL THE SURFACE LAYER HAS HIGHER O2 CONTENT THAN THE BULK. IN FIGS. 2 AND 3 THE CONTENT OF O2, SI, AND N2 IN THE FILM VS RF POWER IS REPORTED. IT CLEARLY INDICATES THAT THE SI CONTENT IS VERY MUCH THE SAME AS RF POWER INCREASES, WHILE THAT OF O2, AND N2 VARIES SIGNIFICANTLY. THE DIFFERENCE BETWEEN FIG.2 AND FIG.3 IS MERELY A CHANGE OF NH3 TO N2O RATIO FROM 0.53 TO 1.05.

DEPOSITION RATE: THE DEPENDENCE OF DEPOSITION OF OXYNITRIDE ON RF POWER IS SHOWN IN FIG.4 FOR VARIOUS NH3/N2O RATIO. IN FIG.4A THE DEPOSITION RATE OF OXYNITRIDE AT RF POWER 400 W VS N2O/SIH4 RATIO IS PLOTTED FOR DIFFERENT NH3/N2O RATIOS. AT CONSTANT RF POWER THE DEPOSITION RATE TENDS TO INCREAS WITH THE INCREASING N2O/SIH4 RATIO, WHILE IT DECREASES WITH THE INCREASING NH3/N2O RATIO.

INDEX OF REFRACTION:- THE REFRACTIVE INDEX OF PECVD OXYNITRIDE FILMS VS N2O FLOW RATE UNDER THE DEPOSITION CONDITIONS OF RF POWER 400 W, 325 C, AND 0.4 TORR IS SHOWN IN FIG.5. CURVES A, B, C, AND D REFER TO DIFFERENT NH3 FLOW RATES. THE DATA WAS OBTAINED FOR CONSTANT SIH4 FLOW RATE. IT IS OBVIOUS THAT THE INDEX OF REFRACTION DECREASES WHEN THE FLOW RATE INCREASES, ITS DEPENDENCE ON THE NH3 FLOW RATE IS CLEARLY ILLUSTRATED IN FIG.5. IN FIG.6 THE REFRACTIVE INDEX VS THE RF POWER AT VARIOUS NH3/N2O RATIO IS REPORTED. APPARENTLY, THE INDEX DECREASES WITH INCREASING RF POWER. HOWEVER, THE INDEX INCREASES WITH INCREASING NH3/N2O RATIO.

ETCH RATE:- FIG.7 REPORTS THE ETCH RATE OF OXYNITRIDE IN A HOT H3PO4 SOLUTION (165 C). THE FILMS USED IN THIS ETCH STUDY WERE MADE AT 300 C AND 0.8 TORR. THE ETCH RATE DRASTICALLY DECREASES AS THE RF POWER INCREASES. HIGH NH3/N2O TENDS TO INCREASE THE ETCH RATE. THE 10:1 BUFFERED ETCH RATE VS RF POWER IS SHOWN IN FIG.8. UNLIKE THE H3PO4 ETCH RATE, THIS RATE INCREASES WITH THE RF POWER AND LEVELS OFF BEYOND 600 W.

DIELECTRIC CONSTANT:- THE DIELECTRIC CONSTANT OF OXYNITRIDE WAS OBTAINED FROM CV MEASUREMENT ON MIS STRUCTURE. ITS DEPENDENCE ON REFRACTIVE INDEX IS SHOWN IN FIG.9.

FILM STRESS:-PECVD OXYNITRIDE FILMS HAVE LOWER COMPRESSIVE STRESS. AS SHOWN IN FIG.10, IT DECREASES WITH INCREASING RF POWER. INCREASE OF DEPOSITION PRESURE TENDS TO LOWER THE STRESS. INCREASE OF NH3/N2O RATIO WILL RESULT IN INCREASE OF STRESS.

IR DATA:- THE INTEGRATED ABSORPTION BANDS OF NH AND SIH DERIVED FROM FTIR SPECTRA ARE SHOWN IN FIG.11. THE ABSORBANCE OF BOTH NH AND SIH DECREASES AS RF POWER INCREASES. INCREASE OF NH3/N2O RATIO TENDS TO INCREASE THE ABSORBANCE OF NH AND SIH CONTENTS IN THE FILMS.

4. CONCLUSION

A LESS THAN 2% SILANE PROCESS FOR DEPOSITING SILICON OXYNITRIDE THIN FILMS HAS BEEN SUCCESSFULLY DEVELOPED. THE RESULTS SHOW THAT THE REGION OF THE COMPOSITION FORMATION IS CONSISTENT WITH THE PREVIOUSLY REPORTED DATA (3). THE FILMS THUS GROWN HAVE SUPERIOR MECHANICAL, ELECTRICAL, AND CHEMICAL PROPERTIES AND CAN FIND MANY APPLICATIONS IN THE MICROELECTRONICS INDUSTRY.

5. ACKNOWLEDGEMENT

THE AUTHERS ARE VERY GRATEFUL TO P.SAUNDERS, M. MONKOWSKI, C.L. STANDLEY AND NANCY KLYMKO FOR THEIR ASSISTANCE.

REFERENCES:

1. P.C. LI & J. GALLAGHER, EXTENDED ABSTRACT 85 (2) #297 ECS MEETING 1985, LAS VEGAS
2. A. HOSHIMOTO, M.KOBAYASHI, T.KAMIJOH H.TAKANO, AND M.SAKUTA J. ELECTROCHEM. SOC. 133 (7) 1464-7 1986
3. V.S.NGUYEN, S. BURTON, AND P.PAN J. ELECTROCHEM. SOC. 131 (10) 2348-59 1984

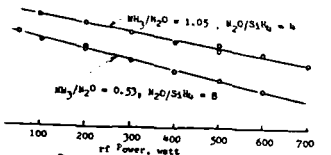


Fig. 6 Refractive Index vs. rf power

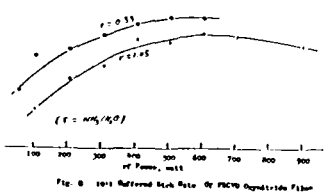


Fig. 8 [illegible]

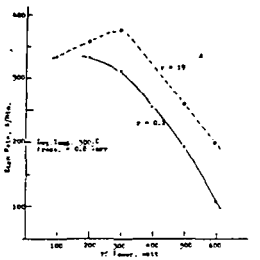


Fig. 7 [illegible]

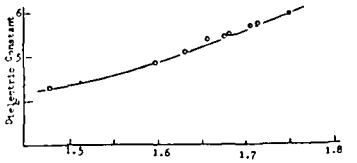


Fig.9 Relative Dielectric Constant of Oxynitride

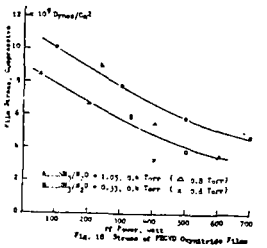


Fig. 10 [illegible]

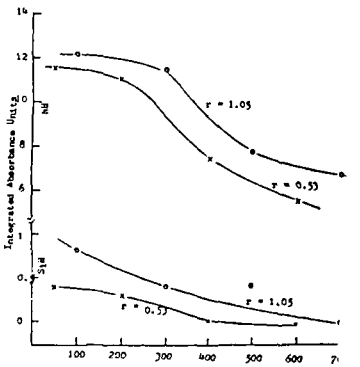
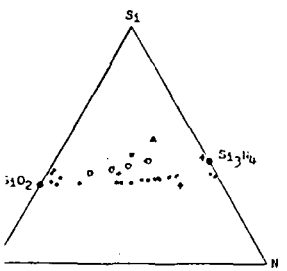


Fig. 11 Integrated Absorbance Of Si-H & N-H Vs. rf Power At Various NH_3/N_2O Ratio (r)



1 Composition of PECVD Oxynitride
VD Nitride (Surface Composition)
VD Nitride (Surface Composition)
VD Oxynitride, N=1.63 to 1.87
VD Oxynitride
VD Oxynitride (Surface Composition)

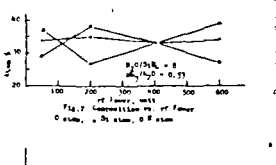


Fig.7 [illegible]

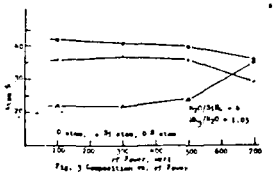


Fig. 3 [illegible]

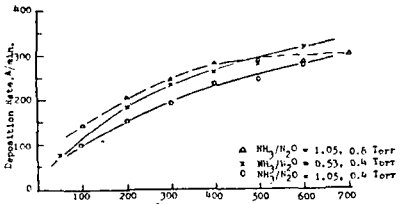


Fig. 4 Deposition Rate vs. rf Power

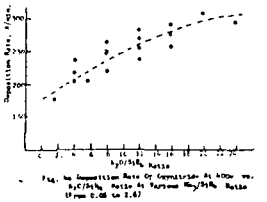


Fig. [illegible]

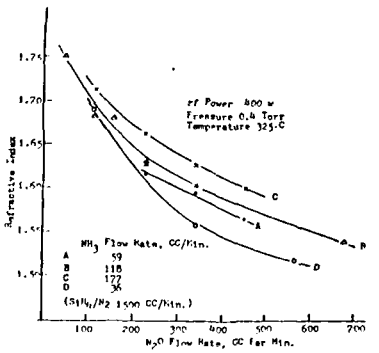


Fig.5 Refractive Index of Oxynitride vs. N_2O Flow Rate At Various NH_3 Flow Rate

Abstract No. 483

AN ETCH RATE STUDY OF THERMALLY ANNEALED TEOS-LPCVD SiO_2 FILMS

C.Orfescu, C.Pavelescu and M.Bădilă
R&D Center for Semiconductors (CCSIT-CE),
Str.Erou Iancu Nicolae 32B,RO-72996,
Bucharest,Romania

Introduction

The use of CVD SiO_2 films in the semiconductor technology makes necessary the annealing of these films at high temperatures(1).The TEOS-LPCVD SiO_2 films have been shown to present a superior step coverage in comparison with the widely used SiH_4 oxide (2).
The purpose of this paper is to study the densification process of TEOS-LPCVD SiO_2 films vs. annealing parameters (temperature,time, pressure).

Experimental

The 2 inch silicon substrates were cleaned in a H_2SO_4/HNO_3 solution at 80°C, deionised water and then dipped into a 5% HF.
The SiO_2 films were deposited by decomposition of TEOS into a LPCVD reactor (3) at a temperature of 750°C and a pressure of 0.4 torr.After the SiO_2 films annealing in vacuum or dry N_2 within the temperature range of 750- 1000 °C the films thicknesses were measured using an ellipsometer.
The etch rate in p-etch solution (2 vol HNO_3 70%+3 vol HF 49%+60 volH_2O)was determined as shown previously(4),the etching temperature being of 20°C.

Results and Discussion

The etch rate curves of SiO_2 films thermally annealed vs.the densification time at a 750°C temperature show a higher etch rate for the films annealed in vacuum in comparison with those annealed in dry N_2,the difference increasing with the densification time,and in both cases the etch rate decreases when the densification time increases (fig.1,curves 1 and 2).Also the SiO_2 films annealed in vacuum presents a higher etch rate in comparison with the films annealed in dry N_2 when the densification temperature varies within the range of 750-900°C (fig.2,curves 1 and 2). On the other hand,the SiO_2 films annealed at 1000°C present a little higher etch rate for films annealed in vacuum in comparison with those annealed in dry N_2,the values of the etch rate tending to that of thermal oxide of 2Å/s(1,3),at a densification time above 30 min.(fig.1,curves 3 and 4).

Conclusions

In conclusion,the densification process of TEOS-LPCVD SiO_2 films within the temperature range of 750-950°C is strongly influenced by the annealing pressure which is an important parameter besides the annealing temperature and time,while at a temperature of 1000°C the densification process in controlled mainly by a thermally activated arrangement of SiO_4 tetrahedra from CVD SiO_2,in a network closed to that of thermal SiO_2,this process being essentially independent of the annealing pressure.

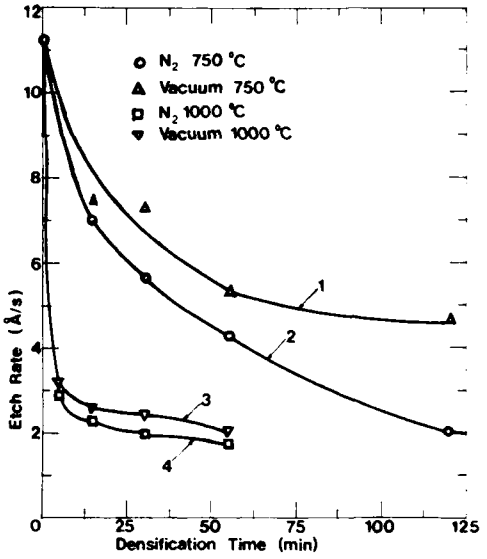


Fig.1 The etch rate variation of SiO_2 films vs.the densification time with the annealing temperature and pressure as parameters.

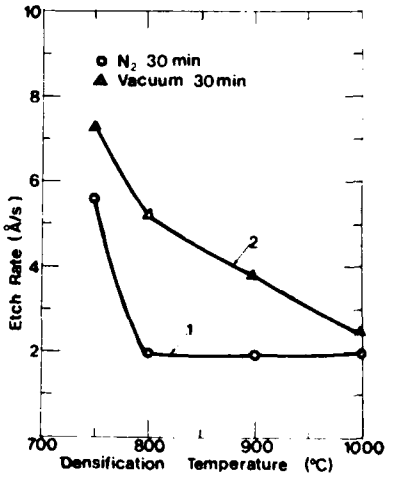


Fig.2 The etch rate variation of SiO_2 films vs. the densification temperature with the annealing pressure as parameter.

References

1. W.A.Pliskin,J.Vac.Sci.Technol.14,1064 (1977).
2. F.S.Becker,D.Pawlik,H.Schäfer and G.Staudigl,J.Vac.Sci.Technol.B,4,732 (1986).
3. J.Croshnik and J.Kraitchman,J.Electrochem.Soc.,115, 636 (1968).
4. W.Kern, RCA Rev.,,557 (1978).

Abstract No. 484

AN ANALYSIS OF THE CHEMICAL STATES OF PHOSPHOROUS IN CVD PHOSPHOSILICATE GLASS FILMS

C. Pavelescu, R&D Center for Semiconductors (CCSIT-CE), Str. Erou Iancu Nicolae 32 B, R-72996, Bucharest, Romania.
C. Cobianu, Microelectronica, Str. Erou Iancu Nicolae 34 B, R-72996, Bucharest, Romania.

Introduction

The chemical states of phosphorous incorporated in CVD phosphosilicate glass (PSG) films were detected by different methods (1-6).

The purpose of this paper is to analyse the chemical states of phosphorous from as-deposited and temperature annealed PSG films used in technology for semiconductors.

Results and Discussion

The phosphorous atom has in fundamental state, in its M shell the electronic configuration $3s^2 3p^3$ (7) which justifies the trivalent behaviour of this element.

Thus, in the LPCVD-PSG films (deposited in a SiH_4-PH_3-O_2 system at temperatures in the 300-500°C range) with a total phosphorous concentration in the 2-11 wt % range, a small amount of phosphorous was detected as being incorporated as P_2O_3 or PH_3, though the mainly part was incorporated as P_2O_5 (5) It should be mentioned that phosphorous incorporated in the PSG films as PH_3 disappears after a heat treatment at high temperatures (920°C) regardless of ambient, while the treatment of P_2O_3 in an oxidizing ambient removes P_2O_3 from the film(5).

However, the phophorous is known to be pentavalent, due to the fact that one of the 3s electrons can easily advance on a 3d orbital, with not to high an energy level, resulting in a sp^3d hybridization (7). On the other hand, PO_4 tetrahedra with one inactive vertex from chemical viewpoint occur in all polymorphous modifications of P_2O_5 in the solid state (7).

Indeed, in the LPCVD-PSG films (deposited in a TEOS-O_2-PH_3 system at a temperature of 640°C) with phosphorous concentration in the 5.5-7.5 mole % P_2O_5 range, the phosphorous is incorporated in the pentavalent state, mainly as $(O_3)\equiv P=O$ complex as revealed by the P=O absorbtion band at 1330 cm^{-1} (3). Also, the infrared absorption spectrum of heat treated PSG films reveals that only a small amount of phosphorous is not completely oxidized in the as-deposited film (3).

In fact, the ESCA 2p spectrum of a 8 % phosphorous doped PSG films, reveals the phosphorous incorporated in the P-O state (substitutional) due to phosphorous atom substituting for Si in the SiO_4 tetrahedra and also in the P-Si state (interstitial state) due to phosphorous atom interposed between the SiO_4 tetrahedra (6).

The PSG films, deposited at atmospheric pressure (APCVD) and low temperature (400-450°C) in a SiH_4-PH_3-O_2-N_2 system, with a phosphorous concentration in the 0-1 wt % range , presents a differential infrared absorbtion band at 1100 cm^{-1}, which was assigned to the P-O-Si three center linkages (4) (the bridging oxygens are bridging a pair of Si and P atoms (2)).

On the other hand, the APCVD-PSG films with phosphorous concentration in the 1-5 wt % range present a weak absorption band at 1325 cm^{-1} associated to the P=O stretching band (1). However, for a PSG film with a phosphorous concentration of 4.5 wt %, this band is well resolved after 15 minutes of heat treatment at 800°C in dry N_2 (1), indicating the possibility that in the as deposited films phosphorous may be incorporated as P_2O_3, PH_3, or in P-Si state.

The APCVD PSG films with phosphorous concentration above 5 wt % presents a well resolved absorption band of P=O bond at 1325 cm^{-1}, this band showing a little change for a film with a phosphorous concentration of 7.7 wt % after densification at 800°C (1).

From the above statements, it should be concluded that the clasic formulation that phosphorous is incorporated in the PSG films as P_2O_5 (1-3,5) is not a proper formulation. Indeed, P_2O_5 appears in solid state in the hexagonal form which contains P_4O_{10} molecules (4 PO_4 tetrahedra), or in the orthorombic form (which is formed of rings of 10 PO_4 tetrahedra each) (7), these polymorphous modifications of P_2O_5 being not found up to now in PSG films with phosphorous concentration in the 0-12 wt % range.

Therefore, a proper terminology is proposed in order to characterize the concentration of phosphorous incorporated in PSG films: (i) the phosphorous incorporated in the pentavalent state as $(O_3)\equiv P=O$ complex, given in wt % phosphorous; (ii) the phosphorous incorporated in the trivalent state as PH_3 or P_2O_3 given in wt % phosphorous and (iii) the usual formulation of wt % phosphorous, to give the total phosphorous concentration in the film.

Conclusions

The phosphorous incorporation in the CVD-PSG films should take into consideration the following phenomena: (i) the phosphorous is incorporated mainly as $(O_3)\equiv P=O$ tetrahedra (pentavalent state) which are randomly distributed in the quasilattice; only three of the four oxygens coordinating each P atom are bridging; (ii) only a small amount of phosphorous is incorporated in trivalent state as P_2O_3 or PH_3 and (iii) phosphorous is incorporated in the P-Si state(interstitial state) due to phosphrous atom interposed between SiO_4 tetrahedra.

References

1. W. Kern, RCA Rev., 37, 55 (1976).
2. J. Wong, J. Electronic. Mater., 5, 113 (1976).
3. R.M. Levin, J. Electrochem. Soc., 129 1765 (1982).
4. C. Pavelescu, C. Cobianu, N. Vlahovici and C. Ghita, ibid., 132, 359C (1985).
5. A.J. Learn, ibid., 132, 405 (1985).
6. D.K. Wu and A.N. Saxena, ibid., 132, 932 (1985).
7. P. Balta and F. Balta, "Introduction to Physical Chemistry of Vitreous State, Abacus Press, 1976, p. 155.

Abstract No. 485

The physical foundations of critical thickness calculations in epitaxy

J.H. van der Merwe and W.A. Jesser*

Department of Physics, University of Pretoria, Pretoria 0002, South Africa

A coherent epilayer, which is subcritical at the monolayer level, becomes critical at a thickness $h_c(f)$ or, alternatively, at a critical misfit $f_c(h)$ and loses interfacial coherence by the introduction of misfit dislocations (MD's). The calculation of h_c and f_c has recently become topical. The physical principles - particularly the equilibrium-nonequilibrium nature of the relevant processes - and the models employed in the calculations, are briefly analysed and given perspective (1).

The misfit is usually defined in terms of atomic spacings a and b as

$$f = (a - b)/c$$

for an overlayer A and a substrate B. The value of c depends on a and b and the thicknesses h_A and h_B. In the coherent configuration f is accommodated completely by misfit strain (MS $\equiv \bar{e} = |\bar{e}|$). When MD's ($\bar{f}$) also occur, the relation

$$f = \bar{f} + P\bar{e} ,$$

where P = 1 when B is thick and otherwise depends on thicknesses and elastic constants, applies.

The epigrowth and C-IC transition processes are driven by (free) energy gradients and retarded by a hierarchy of energy barriers. The barriers involved in growth e.g. in adatom migration, are more or less fixed, and, whereas the barriers involved in the acquisition of MD's, e.g. the Peierls barrier, are normally much larger, they may be reduced - even to zero - by MS stresses. Progress towards the equilibrium minimum (free) energy configurations, is facilitated by thermal activation. Clearly, at a *given substrate temperature* and adatom supply rate, either or both of the processes of growth and C-IC transition may be far from, or arbitrarily close to quasi-equilibrium. We shall assume that growth is layerlike, which is exact for quasi-equilibrium growth when the AB bonding exceeds the AA bonding, but is otherwise (approximately) realized by an appropriate adatom (nonequilibrium) supersaturation.

In most calculations the AA and BB atomic interactions have been modelled by harmonic forces which give the MS energy as

$$E_{\bar{e}} = [2\mu(1 + \nu)/(1 - \nu)]h\bar{e}^2$$

when the interface has quadratic symmetry; μ and ν being respectively the shear modulus and Poisson's ratio. For the AB *interface*, either the Frenkel-Kontorowa model that represents the interaction in terms of a truncated Fourier series whose wave length and coefficients are respectively related to the crystal periods and the AB bond strength, OR, the Volterra (V) model that requires perfect atomic registry at the interface except for a singularity on each MD line, is used. The FK model has the advantage of making provision for the AB bond strength, whereas the V model displays mathematical simplicity in handling the thickness by the introduction of a "cut off radius" R for the strain field (2):

$$E_D' = (\mu_c b^2/2\pi)[\ln(R/b)+1], \quad \mu_c^{-1} = (1-\nu_A)/\mu_A+(1-\nu_B)/\mu_B;$$

$$R = p/2 \text{ or } h_A \text{ for } h_A > p/2 \text{ or } h_A < p/2.$$

E_D' and p are respectively the MD energy and spacing when B is thick. In the FK model (3)

$$E_D' = (\mu_{AB}cp/4\pi^2)\Psi(\bar{f}), \quad \bar{f} = 2\pi\lambda_0 c/\mu_{AB}p,$$

for crystals whose thickness $h < p/2$. Ψ is a simple function and μ_{AB} an interfacial shear modulus. The presence of μ_{AB} and λ_0 in E_D' and $\bar{f}$ accounts for the interaction strengths and c/p = f for the misfit (or $\bar{c}/\bar{p} = \bar{f}$ for the MD's). The foregoing, when combined, defines the functional dependence of the total energy $E = E(h, f; \bar{e} \text{ or } \bar{f})$ per unit area of interface. More recently, these phenomenological model calculations *have been extended to ab initio calculations*, using appropriate interaction potentials (4).

The simplest mathematical technique (1,2) to calculate the critical quantities is to let $\bar{f} \to 0$, or equivalently $\bar{e} \to f$. In the equilibrium case one first obtains the equilibrium equations (i) by mathematical minimization of E with respect to $\bar{e}$ or $\bar{f}$, or equivalently (ii) by setting the work needed to acquire a MD, equal to zero; $0 = W = \int F ds$, *and (iii) when the force* F needed to acquire the dislocation is constant, by setting the force itself equal to zero; $0 = F = F_{\bar{e}} - F_D$, and thereafter equates the minimizing values as follows: $\bar{e}_m = f$ or $\bar{f}_m = 0$. Case (iii) normally applies when MD's are generated from threading dislocations; $F_{\bar{e}}$ and F_D being respectively the Peach-Koehler MS force and the line tension.

Calculations for non-equilibrium critical quantities usually involve calculating (i) either the relevant activation energy barrier height U_m in a given case (4), (ii) or the MS $\bar{e} = f$ at which U_m comes in the range of thermal activation (5), or vanishes so that MD's form spontaneously, (iii) or at best an attempt to set up and solve a dynamic *equation for* MS relief (6).

Examples of the application of the criteria described above and their correlation with experiment are considered. It is concluded, that while observed critical values for metals agree reasonably well with equilibrium predictions, this is not true for many covalently bonded semiconductors. Whereas, the importance of past and future calculations, based on the phenomenological models, are recognized, the increasing role of ab initio and nonequilibrium calculations are foreseen.

REFERENCES

1. J.H. van der Merwe and W.A. Jesser, J. Appl. Phys. (1988) submitted.

2. J.W. Matthews, in Dislocations in Solids, edited by F.R.N. Nabarro, (North Holland, Amsterdam, 1979) vol. 2, chapt. 7.

3. J.H. van der Merwe, J. Appl. Phys., 34, 123 (1963).

4. J.P. Hirth and A.G. Evans, J. Appl. Phys. 60, 2762 (1986).

5. J.Y. Tsao, B.W. Dodson, S.T. Picraux and D.M. Cornelison, Phys. Rev. Lett. (1987) submitted.

6. B.W. Dodson and J.Y. Tsao, Appl. Phys. Lett. (1987) submitted.

*Permanent address: Department of Materials Science, University of Virginia, Charlottesville, VA 22901.

Abstract No. 486

THE ELIMINATION OF INTERFACE DEFECTS IN MISMATCHED EPILAYERS BY A REDUCTION IN GROWTH AREA

E.A. Fitzgerald, P.D. Kirchner*, R. Proano, G.D. Pettit*, J.M. Woodall*, D.G.Ast

Department of Materials Science and Engineering, Cornell University, Ithaca, NY 14853

**IBM T.J. Watson Research Center, Yorktown Heights, NY 10598*

Interface misfit dislocations in mismatched heterostructures can be eliminated by preventing the nucleation of misfit dislocations, by minimizing dislocation multiplication, and limiting the glide of existing misfit dislocations. Possible nucleation mechanisms such as the glide of threading dislocations, multiplication of misfit dislocations, and the formation of surface dislocation half-loops have been discussed by Matthews, Mader, and Light[1-3], and dislocation multiplication has been discussed in detail by Hagen and Strunk[4]. Matthews, Mader and Light originally attributed the formation of misfit dislocations to the lateral glide of threading dislocations[1]. They point out that if threading dislocations were the source of misfit dislocations, one should be able to reduce the density of interface dislocations by limiting the lateral dimension of the sample before growth because too few threading dislocations would be present to nucleate a large number of misfit dislocations. However, it was observed that the number of misfit dislocations at the interface exceeded the number of misfit dislocations that could be generated from threading dislocations[2]. Hagen and Strunk proposed the interaction of misfit dislocations as an additional source of misfit dislocations[4], and Matthews considered the surface nucleation of dislocation half-loops to be a possible explanation for the observed dislocation density[2,3].

Reducing the interface defect density by limiting the lateral dimension prior to growth should hold true for any nucleation sources that depend on area, such as dislocation interactions, particles, and threading dislocations, as long as the misfit is not large enough to generate other sources of misfit dislocations such as surface nucleation. If non-area-dependent nucleation sources do become active, the reduction of dislocation density with growth area will still be observed, but the lowest achievable dislocation density will be higher than if these sources were not active.

To demonstrate this effect, we have fabricated 2-μm high pillars of GaAs in a (001) GaAs substrate with dislocation densities of 10^4 and 1.5×10^5 cm^{-2}. Pillars with a variety of lateral geometries (circles, squares, rectangles and triangles) and dimensions (2-400μm) were fabricated with very high aspect ratios. A 1500Å buffer layer of GaAs was deposited by molecular beam epitaxy at 550° C, followed by 3500, 7000, and 8250 Å of $In_xGa_{1-x}As$, $0.05<x<0.10$. All layers were doped with Si to $10^{18}cm^{-3}$ to increase the intensity of the cathodoluminescence (CL) signal. CL was used to determine the quality of the interface by imaging the dislocations in the interface plane. CL was also used to determine the substrate dislocation density, 1.5×10^5 cm^{-2} and 10^4 cm^{-2} for the two types of substrates used.

Data from the circular pillars will be discussed in detail. Fig. 1(a) is a CL image of 3500Å (> four times the critical layer thickness) $In_{0.05}Ga_{0.95}As$ on GaAs ($\rho=1.5\times10^5$) without any lateral restriction (i.e. >1000 μm). The 15 keV, 80nA electron beam was perpendicular to the interface plane. Defects appear as dark lines in the image due to a decrease in the amount of band-gap radiation emitted in the vicinity of the defect. There is such a high density of defects in Fig. 1(a) that we are not able to accurately determine the dislocation density due to the spatial resolution limit of the CL technique. In high defect density interfaces, the dislocation density is actually much higher than the dark line defect density[5]. In Fig. 1(a), we can estimate from the dark line defect density that the linear dislocation density is greater than 5000 dislocations/cm.

Fig. 1(b) is a CL image of a circular pillar with a diameter of 90 μm. On this pillar, the interface dislocation density is much lower than that seen in Fig. 1(a) for the large deposition area. The defect density is low enough so that each dark line corresponds to a single misfit dislocation[6]. By decreasing the lateral dimension further, we have eliminated the dislocations at the interface, as can be seen in Fig. 1(c), which is a 67-μm diameter circular pillar. This effect is observed in other geometries as well, such as square and rectangular areas.

The 7000Å (>8 times the critical layer thickness) $In_{0.05}Ga_{0.95}As$ layers on the pillars showed similar behavior. As the lateral dimension was decreased, the dislocation density decreased as well. Although some improvement in interface dislocation density for the 8250Å $In_{0.05}Ga_{0.95}As$ layer could be seen in CL images, the interface dislocation density remained high even at 25-μm size pillars.

Fig. 2 is a plot of the linear dislocation density along each <110> direction vs. the diameter of the circular pillars for the 3500Å $In_{0.05}Ga_{0.95}As$ on the 1.5×10^5 cm^{-2} GaAs substrate. For each pillar size, a number of pillars were analyzed and an average dislocation density was calculated. The figure clearly shows an asymmetry in dislocation density for the two <110> directions. It is well known that misfit dislocations lying along the two <110> directions in a (001) plane (termed α and β) have different structure[7] and mobility[8]. The α dislocations have a higher dislocation mobility and lower activation energy than the β dislocations. The large asymmetry in the dislocation densities suggests that α dislocations nucleate more readily than β dislocations.

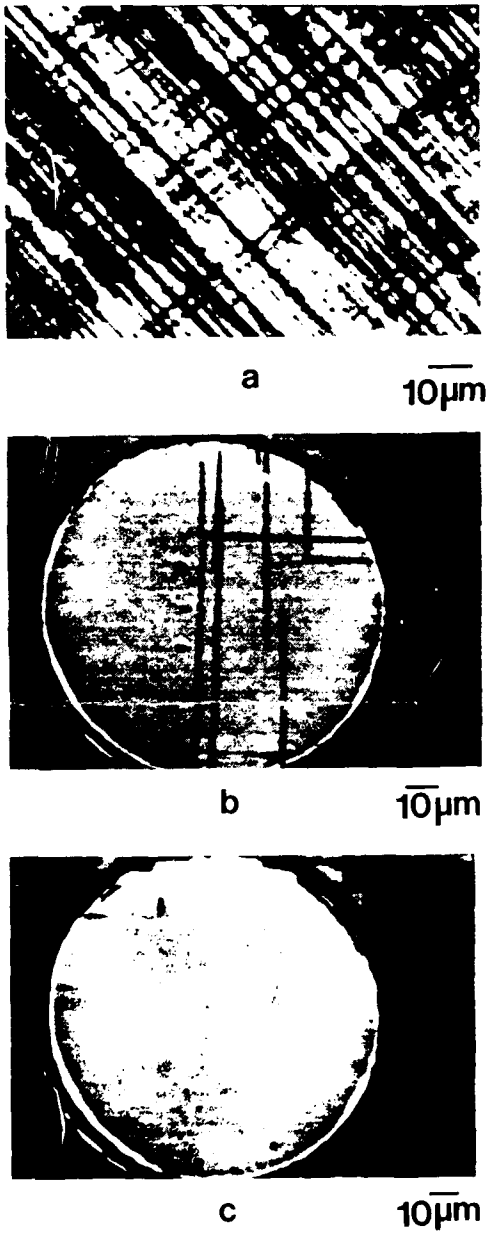
Another feature to be noted in Fig. 2 is that the [110] line nearly passes through zero. This indicates that no other nucleation sites that are independent of area have become active. The linear dependence also indicates that no dislocation multiplication is occuring, since a power-law dependence would be indicative of dislocation multiplication. Thus, threading dislocations are the only active nucleation sites on these pillars.

If we assume that there are a number of fixed nucleation sites per unit area (threading dislocations and surface inhomogeneities such as particulates) that are responsible for the area dependence of the linear dislocation density, then we calculate from the dislocation density dependence in Fig. 2 a misfit dislocation nucleation site density of $\approx2\times10^5$ cm^{-2}. Recall that the density of dislocations in the substrate was 1.5×10^5 cm^{-2}. The calculated nucleation site density is larger than the threading dislocation density from the substrate due to particulates at the interface which can nucleate misfit dislocations, as observed with CL.

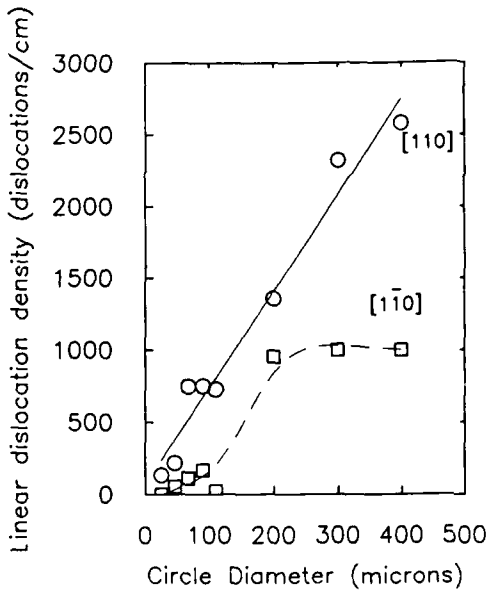
A furthur proof that threading dislocations are the only operable source is shown in Fig. 3, a plot of a 3500Å $In_{0.075}Ga_{0.925}As$ film grown on pillars fabricated from the 10^4 cm^{-2} substrate (recall Fig. 2 is data from the 1.5×10^5 cm^{-2} substrate). As indicated by the large decrease in the slope of the lines, the nucleation site density has indeed decreased. We calculate from Fig. 3 a nucleation site density of $\approx 4\times10^4$, ≈ one order of magnitude less than Fig. 2.

In conclusion, when depositing epilayers on a large wafer, one has to contend with nucleation sites across an entire wafer; the nucleating dislocations can glide across the wafer area resulting in a high dislocation density. Also, many dislocation interactions occur and result in additional misfit dislocations. The reduction in lateral dimension reduces the interface dislocation density by decreasing the number of active nucleation sites within that area and by preventing dislocation multiplication by minimizing the distance a dislocation must travel to reach a free edge.

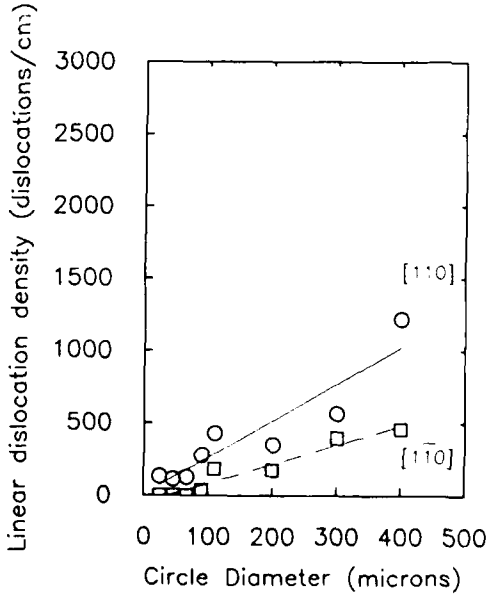
1. J.W. Matthews, S. Mader, T.B. Light, J. Appl. Phys. 41, 3800 (1970).
2. J.W. Matthews, A.E. Blakeslee, S. Mader, Thin Solid Films, 33, 253 (1976).
3. J.W. Matthews, J. Vac. Sci. Technol., 12, 126 (1975).
4. W. Hagen, H. Strunk, Appl. Phys., 17, 85 (1978).
5. E.A. Fitzgerald, D.G. Ast, P.D. Kirchner, G.D. Petit, J.M. Woodall, J. Appl. Phys., 63, 693 (1988).
6. E.A. Fitzgerald, Y. Ashizawa, L.F. Eastman, D.G. Ast, accepted for publication in J. Appl. Phys., 15 May 1988.
7. M.S. Abrahams, J. Blanc, and C.J. Buiocchi, Appl. Phys. Lett., 21, 185 (1972).
8. H. Steinhardt and P. Haasen, Phys. Stat. Sol., (a) 49, 93 (1978).



1. CL images of the 3500Å $In_{0.05}Ga_{0.95}As$ layer on $1.5x10^5$ cm^{-2} GaAs; (a) with no lateral restriction; (b) on a 90-μm diameter pillar; (c) on a 67-μm pillar.



2. A plot of linear dislocation density vs. the diameter of the pillar for the two <110> directions for 3500Å $In_{0.05}Ga_{0.95}As$ layer on $1.5x10^5$ cm^{-2} GaAs.



3. A plot of linear dislocation density vs. the diameter of the pillar for the two <110> directions for 3500Å $In_{0.075}Ga_{0.925}As$ layer on 10^4 cm^{-2} GaAs.

Abstract No. 487

The Partitioning of Elastic Energy During Misfit Dislocation Formation in Heteroepitaxial Layers.

Z. J. Radzimski and G. A. Rozgonyi.

Department of Materials Science and Engineering
North Carolina State University
Raleigh, NC 27695-7907

S. M. Bedair

Department of Electrical and Computer Engineering
North Carolina State University
Raleigh, NC 27695-7911

To-date, various metnods have been employed to reduce the dislocation density. One of the more successful techniques is the use of strained layer [1-4]. The principal goal for using a strained layer as a defect reduction tool is to apply the interfacial strain to glide out of the wafer pre-existing threading dislocations before they enter the electronically active device layer. The main source of force acting on the dislocation line that extends from the substrate comes from the mismatch, f, between the film and substrate lattice parameters. The strain energy associated with this mismatch is proportional to layer thickness until the critical thickness, h_c, is reached at which the substrate dislocations glide along the interface. These interfacial misfit dislocations accommodate part of the lattice mismatch and decrease the energy of the layer/substrate system.

Other problems which has to be addressed while discussing misfit relaxation phenomena is substrate surface imperfection which exist prior growth, and nonuniformities in composition and thickness during growth. These are additional sources of local stress, where new dislocation may be formed [4,5]. The predominant mechanism for dislocation formation appears to be surface sources, for example contamination, surface microstructure, or other surface perturbations that cause the local stress to increase above the average value resulting from mismatch. In this case the dislocation nucleation may occur at lower value of misfit, i.e. at lower h_c, than that suggested by theories assuming a perfect surface. This may also explain why observed dislocation densities are frequently higher than predicted by theories. The build up and relaxation of lattice misfit strain is then one of the main problems associated with the growth of heteroepitaxial structures.

After nucleation of misfit dislocations the residual strain may continue to be a driving force for gliding pre existing substrate dislocations, depending on the density of misfit dislocations formed at the interface. The residual interfacial strain, ε, can be expressed by the average dislocation spacing p or dislocation density ρ in the following way

$$\varepsilon = f - \frac{b_0}{p} = f - \frac{b_0 L}{4}\rho \qquad (1)$$

$$\varepsilon = f - b_0 \rho_l$$

where: b_0 - the Burger vector,
L - the average length of dislocation line
ρ_l - the linear density of dislocations

Depending on the number of nucleated dislocations the stress decreases more or less rapidly. The dependence of density ρ_l on layer thickness h can be approximated by the following experimental formula:

$$\rho = A\left[1 - \frac{h_c}{h}\right] \qquad (2)$$

The parameter A in eq. (3), can be correlated with the total density of misfit dislocations which can be formed either from preexisting threading dislocations or surface nucleated during epilayer growth. Fig 1 plots the misfit strain vs. thickness dependence calculated from eq. (1) and (2) for different values of A. The shape of this curve can be adjusted to match literature data [5,6] simply by adjusting the value of A.

The strain energy E_s, associated with interfacial strain may be expressed as [6]:

$$E_s = 2\mu\left(\frac{1+\nu}{1-\nu}\right)\varepsilon^2 h \qquad (3)$$

with:

$\varepsilon = f$ for $h < h_c$
$\varepsilon = f - d$ for $h > h_c$

where: μ - the shear modules,
ν - Poisson's constant,
ε - the residual interfacial misfit strain
d - the misfit accommodated by dislocations.

The strain energy vs. thickness calculated using (3) and misfit ε from Fig. 1 is shown in Fig.2. The critical thickness was calculated using Mathews' model [3]. For low A values the gradient of strain energy increase is slower once h_c is exceeded. However, note that following misfit dislocation formation at low densities the average residual energy still increases with layer thickness, whereas for high A values there is a sudden decrease of interfacial energy below the energy level corresponding to h_c. We may introduce the critical value A_c of parameter A at which the strain energy gradient changes sign. Until the value of A is below A_c, one can assume that there is still a driving force available at the interface to glide dislocations out of the wafer. This behavior of strained systems was observed for example in Ref. [4]. The dramatic decrease of energy for $A \gg A_c$ will reduce the effectiveness of defect reduction and may even lead to defect multiplication [1,5]. It is therefore very important to be able to estimate the expected value of A for the investigated structure prior to epilayer growth. The number of substrate threading dislocations which influence the value of A can be found out using nondestructive X ray topography [7]. More difficult to estimate is the density of surface sources or value of local stress variations. The approximate value of A due to these surface sources can be found by growing a test structure with thickness of strained layer higher than h_c expected for mismatch. Then X ray and Charge collection imaging in scanning electron microscope [8] can be used to provide a depth dependent analysis of the heterostructures.

In conclusion, it is our aim to correlate a simplified theoretical model with experimental data for a variety of strained layer systems, and to distinguish various sources of stress relaxation and their influence on defect propagation.

References

[1] J.W. Mathews, A.E. Blakeslee, S. Mader. Thin Solid Films, **33**, 253 (1971).

[2] G.A. Rozgonyi, P.M. Petroff, M.B. Panish. Appl. Phys. Lett. **24**, 251 (1974).

[3] M.A. Tischler, T. Katsnyama, N. El-Masry, S.M. Badeir. Appl. Phys. Lett., **46**, 294 (1985).

[4] S.M. Badeir, T.P. Humphreys, N.A. El-Masry, Y. Lo, N. Hamaguchi, C.D. Lamp, A.A. Tuttle, D.L. Dmifus. P. Russel, Appl. Phys. Lett., **49**, 942 (1986).

[5] Z. J. Radzimski, B. L. Jiang, G. A. Rozgonyi, T. P. Humphreys, N. Hamaguchi, C. Parker, S. M.Bedair, Appl. Phys. Lett., **52**, 1692 (1988).

[6] J. Petruzello, B.L. Greenberg, D.A. Cammack, R. Dalby, J. appl. Phys., **63**, 2239 (1988).

[7] P.M.J. Maree, J.C. Barbour, J.F. van der Veen, K.L. Kavanagh, C.W.T. Bulle-Lieuwma, M.P.A. Viegers, J. Appl. Phys., **62**, 4413, (1987).

[9] B. L. Jiang, F.Shimura, G. A. Rozgonyi, N. Hamaguchi, S. M. Bedair, Appl. Phys. Lett. **52**, 15, (1988).

[8] Z. J Radzimski, B. L. Jiang, G. A. Rozgonyi, T. P. Humphreys , N. Hamaguchi, S. M. Bedair, to be published in J. of Appl. Phys., (1988).

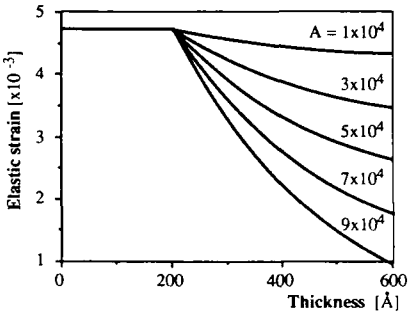


Fig. 1. Elastic interfacial strain as a function of strained layer thickness for different values of parameter A from eq. (2).

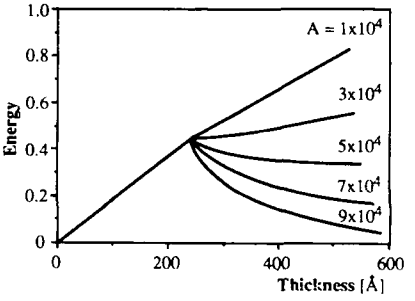


Fig. 2. Elastic strain energy as a function of strained layer thickness calculated from misfit strain from Fig. 1.

Abstract No. 488

The interaction of surface misfit and steps at crystal surfaces

J.H. van der Merwe and W.H. Kunert

Department of Physics, University of Pretoria Pretoria 0002, South Africa

Because of the surface induced electronic perturbations the equilibrium atomic spacings of surface mono- or multilayers, when cut off from the substrate interaction, will differ from those of the bulk. This *surface misfit* (f) places the surface layers under stress. They relax freely normal to the crystal surface by multilayer relaxation, but laterally they are commonly constrained to the bulk spacings. Hence, when a surface step is formed some relaxation, accompanied by the generation of "applied" stresses (Fig.1), occurs in the vicinity of the ledge defined by the step. This paper reviews the phonomenological modelling of these applied stresses and the prediction of their mechanical properties (1,2).

Simplification is achieved by assuming that (i) the misfit is restricted to the upper monolayer (ML), (ii) the crystal has simple cubic structure (lattice constant a), (iii) the surface considered is a (001) plane, (iv) the ledge is long and straight, (v) the crystal behave as an isotropic elastic continuum (shear modulus μ and Poisson's ratio ν), and that (vi) to begin with, the ledge is along the cube axis. We define the lateral (f_x) and normal (f_z) misfits as

$$f = f_x = f_y = (a_x^o - a)/a, \quad f_z = (a_z^o - a)/a, \qquad (1)$$

where a_x^o and a_z^o are the (free) equilibrium spacings.

The surface stress comprizes shears $\tau(x)$ and $T(x)$ and a normal stress $N(x)$. The stress $\tau(x)$ between the upper terrace ML and crystal has been expressed as

$$\tau(x) = -\tau_o \exp(-x/d), \quad 0 \text{ for } x > 0, \; x < 0, \qquad (2)$$

at subcritical misfits of about 4% or less, $\tau_o = \mu f/(1+\nu)a$, $d = 2\pi(1+\nu)af/(1-\nu)\gamma$, $\gamma \approx 2\pi$, and γ depends on the stiffness of the ML and its bond with the substrate. The stress

$$T(x) = \frac{T_o}{d} \cos\frac{\pi x}{d}, \quad 0 \text{ for } x < \frac{d}{2}, \; x > \frac{b}{2} \qquad (3)$$

with $T_o = \tau_o/2\pi$, is generated by the ML of the lower terrace and has a range of only atomic dimensions ($d \sim a$). The stress

$$N(x) = \frac{2N_o}{b} \sin\left(\frac{2\pi x}{b}\right), \quad 0 \text{ for } x < \frac{b}{2}, \; x > \frac{b}{2} \qquad (4)$$

changes sign at the step, has $N_o = \mu f_z a/4$, and is likewise of atomic range ($b \sim a$). T_o and N_o follow from force balance considerations.

This boundary value problem has been solved for the stresses induced in the crystal, using Airy stress function formalism and Fourier transforms. The primary goal was achieved in finding the Airy stress function

$$\chi(x,z) = -\frac{1}{\pi^2} \int_0^\infty \frac{dq}{q} \int_{-\infty}^{\infty} d[\quad] \cos q(\quad) \cos q(x-\quad)$$

$$= \quad [\quad] \cdot z/(1+\quad) - \exp[\quad], \qquad (5)$$

and using the boundary conditions, [illegible] the stresses in specific directions, [illegible]

$$\sigma_{xx} \quad (6)$$

(ii) the strains from Hookian relations, e.g.

$$e_{xx} = [(1-\nu)\sigma_{xx} - \nu\sigma_{zz}]/2\mu, \quad e_{xz} = \sigma_{xz}/2\mu, \qquad (7)$$

(iii) the displacements u and w from integrals, e.g.

$$u(x,z) = u_o + \int_0^x (\partial u/\partial x)dx + \int_0^z (\partial u/\partial z)dz \qquad (8)$$

and (iv) the strain energy E as the work

$$E = \int dx[\tau(x) + T(x)\,u(x,0) + N(x)w(x,0)] \qquad (9)$$

done by the surface stresses (2) - (4).

Of special interest is the decay of the stress fields with distance from the step. The asymptotic forms of the fields show that the contribution from $N(x)$ decays with distance r from the ledge as $b^2/r \approx a/r$, those from $\tau(x)$ and $T(x)$ individually as $(a/\pi r \approx a/r$, but that these first order terms cancell each other. Their next order terms decay as $(a/\pi r)^2$ and are thus of longer range than that of $N(x)$. The inverse square decay is characteristic of the dipolar character of the surface stresses [illegible].

The strain energy in Eq.(9) can be expressed in terms of sine, cosine and exponential (Ei) integrals. If we furthermore adopt the approximations

$\gamma = 2\pi$, $d = b = a$, $\nu = 1/3$, and

$$e^{-x}Ei(x) + e^{x}Ei(-x) \approx 2(C + \ln x); \; x \ll 1, \qquad (10)$$

where C is Euler's constant, the strain energy approximates to

$$E \approx \tfrac{1}{2}\mu[1 - 0.04(\tau_o/\tau_x) + 0.38(\tau_z/\tau_x)^2]\,a\,\tau_x \qquad (11)$$

showing that the influence of the normal misfit τ_z is negligible and that otherwise the strain energy is proportional to τ_x.

Of interest is the energy of formation E_f of [illegible] and its dependence on inclination with the cubic axes. E_f comprizes, (a) the strain energy E in Eq. (11), (b) (i) the increase [illegible] of the interfacial energy of disregistry and (ii) the decrease [illegible] of the strain energy stored in the upper ML, both as a result of the relaxation that created the surface stresses (2) - (4) and (c) the surface free energy [illegible] of the exposed ledge. The main conclusion is that [illegible] is dominant; it constitutes about 90% of E_f [illegible] almost entirely the dependence on [illegible] also the cusp at $\theta = 0$.

The extension of the foregoing calculations to [illegible] of steps of opposite sense, and to crystal surfaces with rhombic symmetry is in progress.

REFERENCES

1. Jan H. van der Merwe, [illegible]

2. Jan H. van der Merwe and W.H. Kunert, [illegible] Febr. 15 (1988).

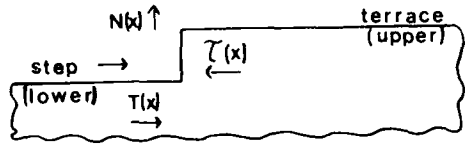


Fig. 1. [illegible]

Abstract No. 489

STRAIN AND CRITICAL THICKNESS IN GaSb/AlSb: AN ION CHANNELING STUDY

H.-J. Gossmann, G. P. Schwartz, B. A. Davidson, and *G. J Gualtieri*
AT&T Bell Laboratories, Murray Hill, N.J. 07974

The GaSb/AlSb system is an excellent system for the study of optical and electronic properties in strained layers. While its lattice mismatch is small enough to make pseudomorphic overlayers with thicknesses in the range of 100 Å possible, the mismatch is non-zero. It is one of the test systems for theories of heterojunction band lineups and is also of practical importance since it can operate in the low loss region of optical fibers. Due to its high reactivity, however, data on structures involving AlSb is rare. In this paper we will report on the determination of strain and critical thickness in thin films of AlSb on GaSb(100) by a combination of ion channeling techniques and particle induced x-ray emission PIXE).

Samples were grown by molecular beam epitaxy under group-V stabilized conditions. Due to the extreme reactivity of AlSb a cap of ≈150 Å Be was used which satisfied the following requirements: (1) Prevention of oxidation of the AlSb film. (2) Minimization of steering effects of the incident ion beam through an amorphous or polycrystalline structure. (3) Minimization of multiple scattering effects through use of a material of low atomic number. (4) No interference of the x-ray spectrum of the cap with that of the substrate and film x-ray lines. (5) No interference with the strain and the quality of the film.

Strain was determined using ion channeling techniques as shown in Fig. 1.[1] [2] [3] Basically the channeling experiment measures the alignment of a particular crystallographic axis in the film, <110> in this case, with respect to the equivalent axis in the substrate. If we assume in Fig. 1 a substrate of atoms A with bulk lattice constant a and an overlayer of atoms B with bulk lattice constant $b > a$ then, in the case of perfect strained-layer epitaxy, $b_{\parallel} = a$. Since the B lattice is compressed in the interface plane, the lattice constant normal to the interface will change dependent on the elastic constants of the overlayer material, generally expanding, so that $b_{\perp} > a$. Although the $[00\bar{1}]$ type channels are aligned in substrate and overlayer, this is no longer true for off-normal channeling. Off-normal channeling directions in overlayer and substrate will differ by a finite angle, the tetragonal distortion angle, which is directly related to the amount of strain in the film. The channeling directions in bulk and overlayer were determined by monitoring, as a function of incident angle, the x-ray yield from Sb and Al respectively, induced by the incident ion beam (PIXE).

In Fig. 2 we have plotted the measured tetragonal distortion angle for films of varying thickness. The scatter in the data gives an indication of the absolute accuracy as well as of the reproducibility of the entire experiment. The arrow denotes the tetragonal distortion expected on the basis of Poisson's number for AlSb. The agreement is very good. Beyond ≈175 Å the distortion angle begins to drop from the expected value, i.e. the film thickness has exceeded the critical thickness and misfit dislocations begin to relax the strain. Note that the film does not immediately relax completely but a significant amount of strain remains even beyond 500 Å. The measured critical thickness is in very good agreement with the value calculated from the recent theory of Dodson and Tsao.[4]

1. W.-K. Chu, J. W. Mayer, M. A. Nicolet, Backscattering Spectrometry, Academic, New York, 1978. L. C. Feldman, J. W. Mayer and S. T. Picraux, Materials Analysis by Ion Channeling, Academic, New York, 1982.

2. S. T. Picraux, L. R. Dawson, G. C. Osbourn, R. M. Biefeld and W. K. Chu, Appl.Phys.Lett. **43**, 1020 (1983); W. K. Chu, C. K. Pan and C.-A. Chang, Phys.Rev.**B28**, 4033 (1983).

3. H.-J.Gossmann and L.C.Feldman, MRS Bulletin **12(6)**, 30 (1987).

4. B. W. Dodson and J. Y. Tsao, Appl.Phys.Lett.**51**, 1325 (1987).

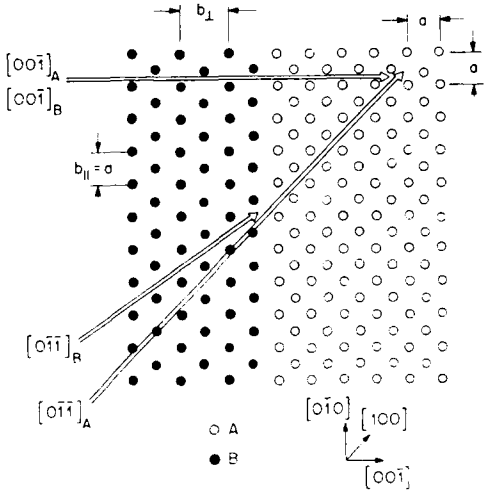


Fig. 1. Schematic side-view of a diamond-type (100)-oriented substrate (open circles, lattice constant a) with an epitaxial diamond type overlayer (closed circles) of lattice constant b on top.

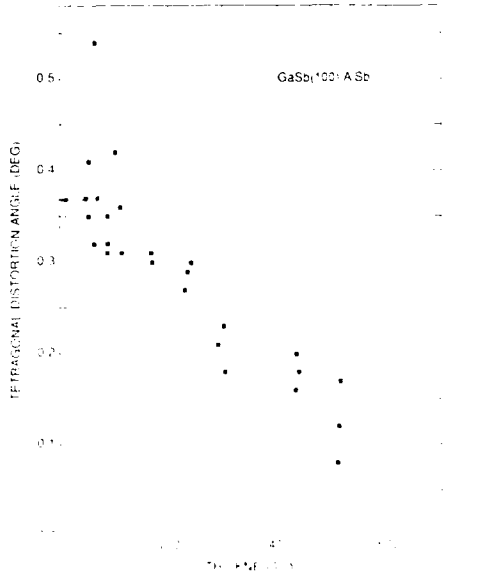


Fig. 2 Tetragonal distortion of thin, single films of AlSb on GaSb as a function of thickness. The arrow indicates the value expected on the basis of the theory of elasticity.

Abstract No. 490

Superlattice Characterization using Raman Scattering

G. P. Schwartz, G. J. Gualtieri,
and W. A. Sunder

AT&T Bell Laboratories
600 Mountain Avenue
Murray Hill, NJ 07974

During the last ten years Raman scattering has begun to be used to characterize semiconductor superlattice and quantum well structures. Various types of structural information are contained in the spectra. In this work we have examined zone-folded acoustic modes and quantum confined optic phonons in periodic, quasiperiodic, and aperiodic structures in order to assess parameters such as the period, individual layer widths, interfacial diffusion, and layer width variations.

The samples were all GaSb/AlSb lattices grown by molecular beam epitaxy using elemental sources. Raman spectra were taken using 5145 Å excitation in conjunction with a 1-meter double monochromator and standard pulse counting electronics.

The period $d=d_1+d_2$ in superlattice structures can be obtained from analysis of the frequencies of zone-folded longitudinal acoustic modes (1). An elastic continuum dispersion relation was employed to fit the folded mode spectra in order to obtain d. Comparison with x-ray diffraction (2) shows that the period can be obtained within 2-3% in most cases even when the presumed ratio of d_1/d_2 based on nominal growth rates was somewhat in error. The period of quasiperiodic Fibonacci lattices was similarly extracted from an approximate dispersion relation (3) and also gave good agreement with x-ray diffraction.

For off-resonance scattering the Raman count rates are typically on the order of 30-80 counts/sec/watt, so data collection is relatively slow by most standards. With most conventional spectrometers one is also limited by how close the elastic peak can be approached, and this tends to limit the superlattice period to values less than 200-250 Å. On the other hand since GaSb is strongly absorbing in the visible, relatively thin lattices can be analyzed. We have examined for instance a 5 layer structure whose total thickness was 170 Å with no particular difficulty.

The intensities of the zone-folded Raman peaks were also analyzed in periodic structures in order to supplement our knowledge of the nominal growth rates which dictate d_1 and d_2 individually. All analytic expressions for these intensities involve rather restrictive approximations (1,3) and our analysis shows that even the most current models are incapable of properly fitting the data. Comparison with x-ray modeling (2) on samples with well defined d_1 and d_2 values indicates that the Raman intensity analysis of d_1/d_2 can be in error by 20%.

Symmetry forbidden peaks lying near the superlattice zone boundary have been detected in select samples. In order to assess the origin of these peaks, a series of weakly aperiodic lattices were grown and analyzed in which deliberate layer width variations were introduced in both systematic and random fashions. In both cases strong zone-boundary modes were observed. We conclude that layer width variations can manifest in the acoustic Raman spectra as symmetry forbidden peaks. Smaller fluctuations in the layer widths can also be detected via the increased linewidth of successive folding order doublets.

Interfacial diffusion has been studied by growing periodic lattices with one of the layers constrained to be on the order of 4 monolayers thick. Significant interdiffusion would result in alloying which would broaden and shift the optic mode of that layer (GaSb) in a well defined fashion. Narrow GaSb *longitudinal* optic modes are observed whose only frequency shift is associated with quantum confinement. We conclude that at our growth temperatures (490-510C), significant interdiffusion does not occur.

References

1. C. Colvard, T. A. Gant, M. V. Klein, R. Merlin, R. Fisher, H. Morkoc, and A. C. Gossard, Phys. Rev. B*31*, 2080 (1985).
2. A. T. Macrander, G. P. Schwartz, and G. J. Gualtieri, unpublished.
3. J. He, B. D. Rouhani, and J. Sapriel, Phys. Rev. B, in press. Preprint courtesy of the authors.

Abstract No. 491

Structural and Optical Properties of Highly Strained $InAs_xP_{1-x}$/InP Heterostructures

R.P. Schneider, Jr., D.X. Li and B.W. Wessels

Materials Research Center, Northwestern University
Evanston, Illinois 60208

Strained-layer superlattices (SLS) and single quantum well structures (SSQW) are of interest because they allow greater flexibility in the choice of semiconductor materials for numerous electronic and optical device applications. Many aspects of the growth and properties of these structures, however, are not well understood, particularly in the limit of large strains. In this limit, growth may not proceed layer-by-layer but instead island growth may occur,[1] reducing interface abruptness and crystalline quality. In addition, coherent strain has significant influence on the electronic and optical properties of the material. In the current investigation, we have studied the preparation and properties of $InAs_xP_{1-x}$/InP SLS and pseudomorphic SSQW structures with relatively large strains (1.6-2.5%). The InAsP ternary system is of potential interest for optoelectronic applications in the 0.9 - 3μm wavelength range. The InAsP alloy structures are readily prepared in a simple atmospheric pressure organometallic vapor phase epitaxy (OMVPE) reactor.[2]

The InAsP/InP structures were grown on (100) InP using the reactants trimethylindium (TMIn), arsine and phosphine. The growth rate of the samples was varied between 2A/sec-8A/sec by controlling the molar flow rate of TMIn in the reactor. A V/III ratio of 200 yielded a featureless surface morphology at a growth temperature of 600°C. The PH_3/AsH_3 ratio was varied between 50 and 160 to yield $InAs_xP_{1-x}$ with composition of x = 0.5 - 0.8, corresponding to lattice mismatch between 1.6-2.5%. The buffer layer between the substrate and the superlattice was InP. For the SLS structures, the superlattice period ranged from between 22-140A, while for the SSQW structures, the InAsP well thickness was varied in the range of 10-160A. The samples were characterized by photoluminescence spectroscopy (PL), x-ray diffraction (XRD) and high-resolution transmission electron microscopy (HREM).

Fig. 1 shows a HREM lattice image of an $InAs_{0.7}P_{0.3}$/InP SLS with a period of 56A. The interfacial abruptness is estimated to be 1 - 2 monolayers despite strain of 2.2% between the layers, indicating planar (layer-by-layer) growth occurs in this system even with large strain. In fact, PL emission peaks shown in Fig. 2 for SLS structures grown with $InAs_xP_{1-x}$ compositions as high as x = 0.8 and periodicity of 50A showed no appreciable broadening with increased arsenic concentration. The spectral half-width is in the range 25 - 39meV, supporting that the interfaces of those structures are also abrupt to within 1 or 2 monolayers. The observed half width is determined, in part, by fluctuations in layer thickness. That such uniform growth occurs even for very large strains of 2.5% makes this system of particular interest for application in strained-layer heterostructures.

Pseudomorphic SSQWs of InAsP were also prepared. The structures consisted of wells of various thickness (10-160A) between 600A-thick InP barriers. The luminescence from these wells was intense, with a narrow spectral half-width of 17 meV for a 25A well again indicating abrupt heterointerfaces. Large shifts in the energy of emission from the wells were observed with decreasing well thickness, resulting, in part, from quantum confinement. The emission energy for a $InAs_{0.53}P_{0.47}$/InP SSQW structure was calculated as a function of well thickness using a finite well model.[3]. The effect of strain was taken into account using the simple relationship $\Delta E_g = -\alpha\varepsilon$ where ΔE_g is the change in the energy gap due to strain, α is a proportionality constant related to the elastic constants and deformation potentials of the material, and ε is the strain in the well.[4] The observed emission energies from the SSQW structure are plotted in Fig. 3 along with the calculated values. Excellent agreement is noted between the experimental and calculated values.

This work was supported by the Materials Research Center at Northwestern University under Contract NSF (DMR-8520280).

References

1. W. J. Schaffer, M.D. Lind, S.P. Kowalczyk and R. W. Grant, J. Vac. Sci. Technol. 51, 688 (1983).

2. K. Huang and B.W. Wessels, Appl. Phys. Lett. 52, 1155 (1988).

3. K. Alavi, T.P. Pearsall, S.R. Forrest and A.Y. Cho, Electron. Lett. 19, 227 (1983).

4. H. Asai and K. Oe, J. Appl. Phys. 54,2052 (1983).

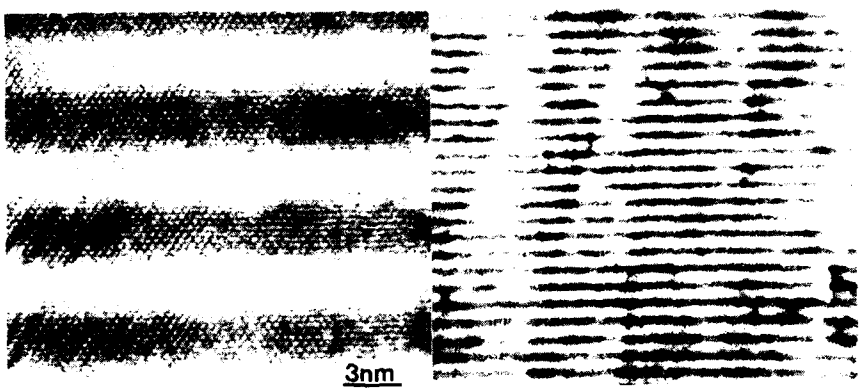


Fig. 1. HREM images of $InAs_{0.7}P_{0.3}$/InP SLS. Superlattice period is 56A. Dark layers are $InAs_{0.7}P_{0.3}$, light layers are InP.

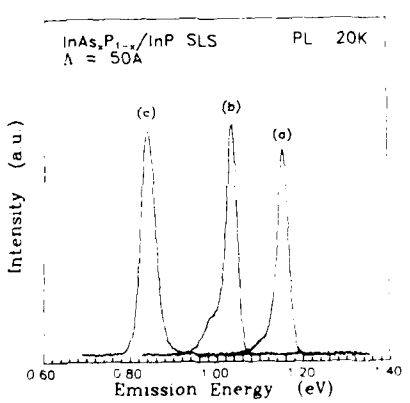


Fig. 2. 20K PL spectra for $InAs_xP_{1-x}$/InP SLS structures (Λ ≈ 50Å) for different compositions. (a: x = 0.6, (b) = 0.7, (c) = 0.8.

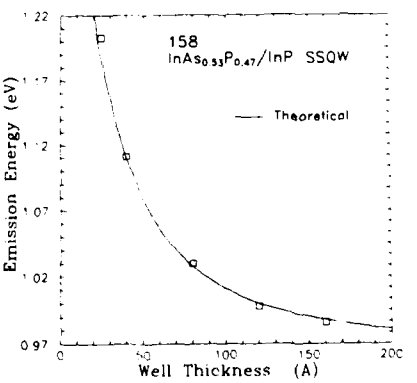


Fig. 3. Emission energy vs. well thickness for $InAs_{0.53}P_{0.47}$ pseudomorphic quantum wells. Theoretical curve calculated using a finite well model taking strain effects into account.

Abstract No. 492

High Resolution Transmission Electron Microscopy of $InAs_xP_{1-x}$/InP Heterostructures

D.X. Li, R.P. Schneider, Jr., B.W. Wessels and W.A. Chiou

Materials Research Center, Northwestern University Evanston, Illinois 60208

Strained-layer superlattices (SLS) and single quantum well (SSQW) structures may exhibit a complex morphology and defect structure, particularly in the limit of large strains. Dislocations may form at interfaces if the critical layer thickness for dislocation formation has been exceeded. The structure and propagation of these dislocations can be influenced greatly by large strain fields present. For example, filtering of dislocations by SLS structures has been observed.(1) This enables preparation of highly coherent structures despite large lattice mismatch. In the present study, we have investigated highly strained $InAs_xP_{1-x}$/InP SLS and SSQW structures using high-resolution electron microscopy (HREM). Since HREM allows resolution on the atomic scale, it is ideal for the study of the interface and defect structure of the strained layers.

Samples were grown by atmospheric pressure organometallic vapor phase epitaxy (OMVPE) on (100) InP substrates at 600°C.(2) Growth rates of 2 - 8A/sec were used. The compositions of the $InAs_xP_{1-x}$ layers in the structures were varied from x = 0.6 - 0.8, corresponding to a lattice mismatch of 1.9 - 2.5%. Superlattice periods were between 22A and 140A. Well thicknesses in the SSQW structures were 10A - 160A. No graded buffer layer was used, thus the superlattice structure as a whole was lattice mismatched to the underlying substrate. The total thickness of the heterostructure was typically 0.5 μm.

Cross-sectional specimen preparation entailed cleaving the samples into 0.5mm x 1.0mm pieces, then bonding the two pieces together with epoxy and embedding them in epoxy contained in a copper ring. Specimens were subsequently mechanically thinned and argon ion milled. Ion current density and accelerating voltages for ion milling were optimized to minimize damage to the samples. The high-resolution images were obtained with a Hitachi H-9000 electron microscope operating at 300kV with a point to point resolution of 1.9A.

Fig. 1 shows a HREM lattice image of an $InAs_{0.7}P_{0.3}$/InP SLS with a 56A period and the corresponding electron diffraction pattern. The measured period obtained from the satellite spots on the electron diffraction pattern agrees well with that obtained from growth rate and x-ray diffraction measurements. The dark and light regions which are visible in the lattice image correspond to InAsP and InP layers, respectively. This image clearly shows the interfaces are coherent and defect free, despite the lattice mismatch of 2.2%.

Since the total thickness is 0.5 μm, the structure is well beyond the calculated critical thickness of h_c = 600A for dislocation formation(3) for an $InAs_{0.3}P_{0.7}$ layer. Thus dislocations are expected to form at the SLS/InP buffer layer interface. Indeed, as shown in Fig. 2, dislocations are present, yet they are effectively filtered out of the SLS structure within a few periods. It is clear that short-period $InAs_xP_{1-x}$/InP SLS structures are very effective in blocking the propagation of misfit dislocations.

Fig. 3 shows a TEM image of a multilayer structure grown to determine the critical thickness and defect structure of the $InAs_xP_{1-x}$/InP heterostructures. The structure consists of a series of $InAs_{0.5}P_{0.5}$ layers of thickness 200A, 300A, 350A, 400A and 500A grown between 600A InP layers. Misfit dislocation formation is only observed for layers of thickness greater than 300A, in reasonable agreement with the theoretical prediction of Matthews and Blakeslee.(3)

The types of dislocations present in the heterostructures were studied. An HREM image of an extended misfit dislocation is shown in Fig. 4 for the multilayer structure. The dislocation image shows a highly localized core, indicating that the dislocation line is exactly normal to the image plane. Although HREM images show only the projection of the displacement of the lattice planes for the dislocation core, the Burgers vector can be determined. Fig. 4 shows the Burgers circuit drawn around the Shockley partial dislocation. The Burgers vector projected onto the $(1\bar{1}0)$ plane is (1/6) of the projection of the $[11\bar{2}]$, which is the projection (1/6) $[11\bar{2}]$. Therefore, we may conclude that the end of the misfit dislocation is a 90° Shockley partial. In addition, the stacking fault between the 90° partial and the surface is determined to be intrinsic. The bright spots in the HREM image correspond to structural channels. The stacking fault sequence is ABCBCA, and the fault vector is (-1/3)[111].

This work was supported by the Materials Research Center at Northwestern University under Contract NSF (DMR-9520280).

References

1. S.M. Bedair, T.P. Humphreys, N. El-Masry, Y. Lo, N. Hamaguchi, C.D. Lamp, D. Dreifus and R. Russel, Appl. Phys. Lett. 49, 942 (1986).

2. R.P. Schneider, Jr., D.X. Li and B.W. Wessels, submitted for publication.

3. J. W. Matthews and A. E. Blakeslee, J. of Cryst. Growth, 27, 118 (1974).

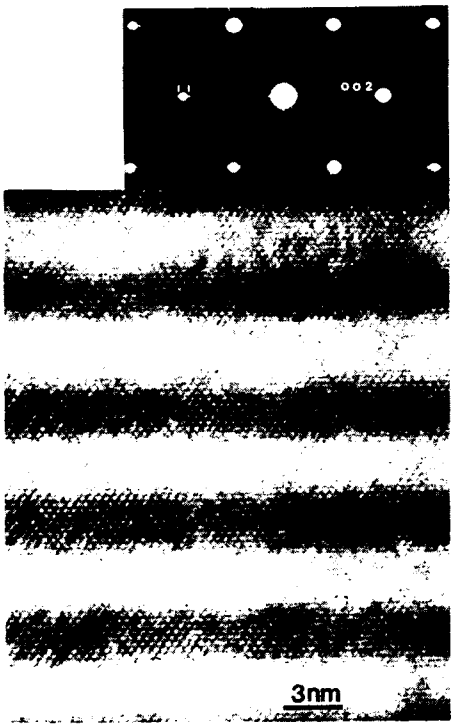


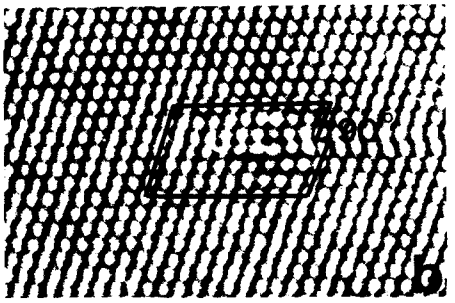
Fig. 1. Lattice image in the [1$\bar{1}$0] projection and electron diffraction pattern of an $InAs_{0.7}P_{0.3}$/InP SLS with period 56 A. Arrows indicate the superlattice satellite spots in the diffraction pattern.



Fig. 2. TEM image of the interface region between $InAs_{0.7}P_{0.3}$/InP SLS and InP buffer layer. Dislocations generated at the SLS/InP buffer layer interface were blocked by the SLS.



Fig. 3. TEM image showing misfit dislocations generated when the thickness of the $InAs_{0.5}P_{0.5}$ layer exceeded 300A. Arrow indicates the 350A layer.



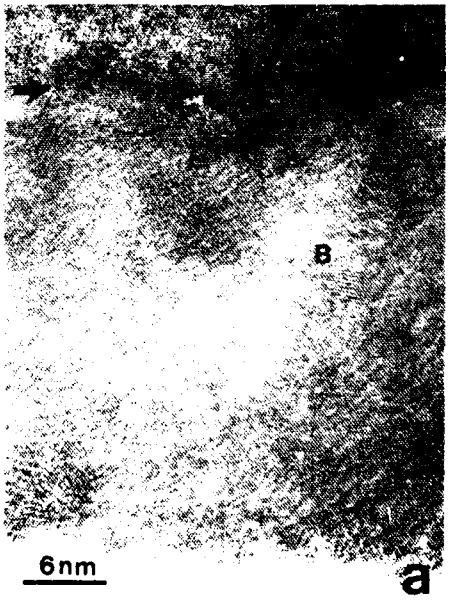


Fig. 4. (a) Structure image showing two misfit dislocations, labelled A and B, which were generated at the $InAs_{0.5}P_{0.5}$/InP interface. Arrow indicates the interface. (b) The text of the dislocation [illegible]

Abstract No. 493

Core Level Photoemission Measurements of Heterojunction Valence Band Offsets in Highly Strained Systems

G. P. Schwartz, G. J. Gualtieri,
M. S. Hybertsen, J. Bevk, J. P. Mannaerts,
and R. G. Nuzzo

AT&T Bell Laboratories
600 Mountain Avenue
Murray Hill, NJ 07974

Core level photoemission constitutes one of the primary methods for determining valence band offsets in lattice-match heterojunctions. In lattice-mismatched couples which exhibit pseudomorphic epitaxy, either one or both of the heterojunction layers will be under biaxial stress depending on the relative layer thicknesses and choice of substrate/buffer. In this case, core levels referenced to the top of their strain-split valence bands are expected to explicitly depend on strain. In the present work x-ray photoemission core level measurements have been performed on pseudomorphically strained heterojunctions consisting of Si on (100) Ge and Ge on (100) Si. Raman spectroscopy was used to verify the strain resulting from the 4.2% lattice mismatch. the core level measurements were supplemented by calculations of the relative core-valence band deformation potentials. These results together with the uniaxial splitting of the valence bands yields valence band offsets of 0.75±0.13 and 0.16±0.13 eV for Ge on Si and Si on Ge respectively.

Six monolayers (~8.5Å) of either Ge or Si were grown on (100) substrates of the opposite material at ~500°C using molecular beam epitaxy. Heterojunction samples were capped with 12 monolayers of substrate material in order to avoid oxidation and strain relief of the buried layer. Core level measurements of the Si2p and Ge3d levels were recorded, and Raman spectra of the optic phonons were examined in order verify that the strain was not reliefed by the introduction of misfit dislocations.

The Raman spectra are shown in fig. 1. For Si on (100) Ge, the Si optic phonon is seen shift to lower frequency by ~45 cm^{-1} relative to unstrained Si. The strain-induced component of this shift is ~20-30 cm^{-1} (tension downshifts the frequency). The remaining shift is due to quantum confinement which downshifts the frequency by ~12 cm^{-1} For Ge on (100) Si, the optic phonon shifts to higher frequency by ~4 cm^{-1}. This small shift results because compression shifts the Ge frequency up by ~16 cm^{-1} whereas confinement downshifts the frequency by 8-10 cm^{-1}. The shift in the Si and Ge optic phonons are both consistent with the retention of strain in the 6 monolayer section of the structures.

The relevant band diagrams for Ge on (100) Si and Si on (100) Ge are shown in fig. 2. The core level separations $\Delta E_{1,2}$ and $\Delta E_{2,1}$ on strained heterojunctions were measured to be 70.12±0.10 and 69.90±.10 eV respectively. The index notation 1,2 designates Si on (100) Ge and 2,1 the reverse sequence. Core levels averaged over the spin-orbit split components are used in all cases. The uniaxial component of the biaxial stress determined relative to the centroid of the valence bands is readily calculated and yields E_1^u = 0.31 and E_2^u = 0.30 eV. The relative shift between the core level and the centroid of the valence band due to the hydrostatic component of the stress in strained and unstrained materials was calculated from LMTO theory using the local density functional approach. In conjunction with E_1 and E_2 which represent the unstrained Si2p and Ge3d core levels referenced to the top of their valence bands, we obtain E_1^h = 99.22+1.07 E_2^h = 29.56±.07 eV. The resulting valence band offsets for Ge on (100) Si gives $\Delta E_v^{2,1}$ = 0.75±0.13 eV, and for Si on (100) Ge $\Delta E_v^{1,2}$ = 0.16±0.13 eV.

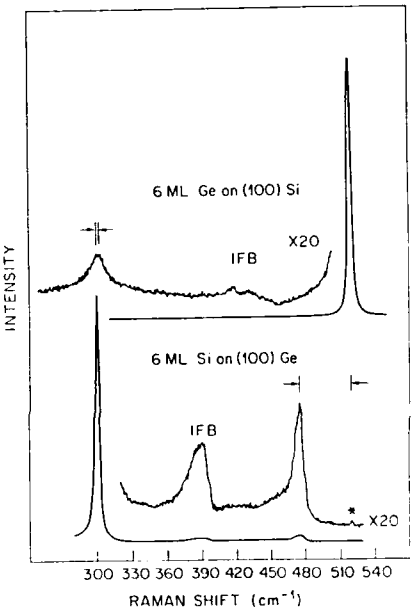


Fig. 1 Raman spectra of the Si and Ge optic phonons for pseudomorphic growth of Ge on (100) Si and the reverse sequence. IFB indicates signal associated with interfacial bonding.

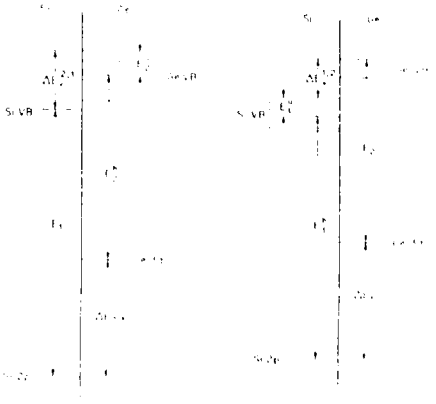


Fig. 2 Schematic band diagrams for Ge on (100) Si (left panel) and the reverse sequence (right panel)

Abstract No. 494

OPTICAL INVESTIGATIONS OF STRAINED InGaAs/GaAs SINGLE QUANTUM WELLS

D.J. Arent, K. Deneffe, C. Van Hoof,
J.De Boeck, G. Borghs
IMEC vzw, Kapeldreef 75, Leuven, Belgium

Allowing for wide variation in mechanical and electronic properties while incorporating strain arising from large lattice mismatch, the growth of high quality dislocation free semiconductors is only possible for layers which do not exceed a critical layer thickness(1). Layers thicker than the critical value will accomodate lattice mismatch in misfit dislocations rather than elastic strain and therefore exhibit degraded device performance. For thin layers grown pseudomorphically, the strain induces a significant change in the electronic band structure, thus allowing for control of the band gap and associated quantum transitions by altering the ternary compositions (strain) and layer thickness (quantum confinement).

The details of the strain induced changes to the band positions of layered semiconductor structures have been presented elsewhere(2-4). For InGaAs pseudomorphically grown to GaAs the In concentration must be kept low (<40%) and we assume since the GaAs substrate is very thick compared to the InGaAs layer that all strain is accommodated in the InGaAs.

The energy shifts calculated using a strain Hamiltonian which describes strain in the [100] and [010] directions yield the band positions of the nondegenerate valence band mainfolds and are a function a and b the deformation potentials, ε the strain value, Δ_0 the spin-orbit splitting energy, and K which relates the elastic moduli as given by Pollak(3). All strain tensor components are found by linearly interpolating between the values for InAs and GaAs using values published in the Landolt-Bornstein tables. The relative contribution of the hydrostatic term to conduction and valence bands is determined by, ΔQ_H, the ratio between the total shift in the band gap under pressure to the shift in the spin orbit band, or

$$\Delta Q_H = [dE_g/dP \;/\; d(E_g+\Delta_0)/dP]^{-1} \quad (1)$$

and is found to be 11%. Uniaxial tension contributes to splitting of the valence band states and induces a mixing of the |3/2,1/2> and |1/2,1/2> bands(3). Total strain contributions are plotted in Fig. 1.

Transition energies for the potential wells are then calculated according to standard quantum mechanical treatment. The composition dependent band gap E^o_g of the unstrained $In_xGa_{1-x}As$ material at 300K is given by(4)

$$E^o_g = 1.425 - 1.501x + 0.436x^2 \text{ (eV)}. \quad (2)$$

At low temperature, the additional strain induced by differences in linear expansion coefficients may be neglected since this value is less than 3% of strain at 300K (an absolute quantity < 0.03%).

Following standard cleaning procedures, a 1.0μm GaAs buffer layer was grown by MBE followed by the InGaAs layer and finally a 50nm GaAs capping layer. The In fraction and thicknesses were determined from flux measurements and confirmed by Auger, double crystal X-Ray diffractometry, and electron μprobe analysis on thick layer samples. Photoreflectance measurements at 300K were carried out using standard lock-in detection.

Fig. 2 indicates the photoreflectance spectrum and associated fit at 300K for sample G63. The spectra are fitted by non linear least squares analysis to the Aspnes third derivative functional form which has been shown to adequately model the observed phenomena(5). Excellent agreement is found for all fits utilizing a band offset ratio of 85:15 ($\Delta E_{cb}:\Delta E_{vb}$) in accordance with previous experimental(6,7) and theoretical (2) findings. No transitions associated with a light hole band are observed. Combining this observation with the excellent agreement indicates that the band offset ratio employed properly describes the InAs/GaAs system. Table I lists the results for the remainder of the samples including the 6K photoluminescence value for the 1C-1H transition, corrected for exciton binding energy and associated calculated values. Excellent agreement is found for each sample.

For the low temperature calculations, we used the formula of Goetz et al(8) to find the alloy band gap energy at 6K. We then calculated the low temperature transition energies using temperature independent strain and material contributions. From experiments performed at 77K, we have calculated the 77K alloy band gap as a function of In fraction. We determine the equation to be ,

$$E^o_g(77K) = 1.508 - 1.580x + 0.495x^2 \text{ (eV)} \quad (3)$$

The bowing parameter is in much better agreement with earlier findings at other temperatures (4,9)compared to that derived from the previous bulk crystal experiments of Leu et al(9). Though unclear, the difference may be due to the different growth techniques used to prepare the samples.

These studies indicate that the strain induced band changes are not temperature dependent, though the individul values of the elastic moduli and deformation potentials may change with temperature. Furthermore, as shown in Fig. 3, the behavior of the InGaAs alloy band gap with temperature is found to resemble that of GaAs not $In_xGa_{1-x}As$ up to In fractions of 0.3 and is not linearly dependent on the In fraction.

References

1. J.W. Matthews and A.E. Blakeslee, J.Cryst.Growth 27, 118, 1974.

2. W. Potz and D.K Ferry,J.Vac. Sci.Tech.B 4,1006, 1986.

3. T.P. Pearsall, F.H. Pollak, J.C. Bean, and R. Hull, Phys.Rev.B 33, 6821, 1986, and references therein.

4. J.Y. Marzin, in Heterojuntions and Semiconductor Superlattices, ed. G.Allan, G. Bastard, N. Boccara, M. Lannoo, and M. Voos, Springer, Berlin. 1986, p.161.

5.. D.E. Aspnes, in Handbook on Semiconductors, ed. M. Balkanski, North Holland, New York, 1980, Vol.2, p.109, and references therein.

6. S.P. Kowalczyk, W.J. Schaffer, E.A. Kraut, and R.W. Grant. J.Vac.SciTech.B 20, 705, 1982.

7. J. Hwang, P. Pianetta, C.K.Shih, W.E.Spicer, Y.-C. Pao, and J.S. Harris, Jr., Appl.Phys.Lett. 51(20), 1632, 1987.

8. K.H. Goetz, D. Bimberg, H. Jur, J. Selders, A.V. Solomonov, G.F. Glinksii, M. Razeghi, and J.J. Robin, J.Appl.Phys. 54, 4543, 1983.

9. Y.T.Leu, F. A. Thiel, H.Scheiber, B.I. Miller, and J. Bachmann, J.Electron.Mater. 8, 773, 1979.

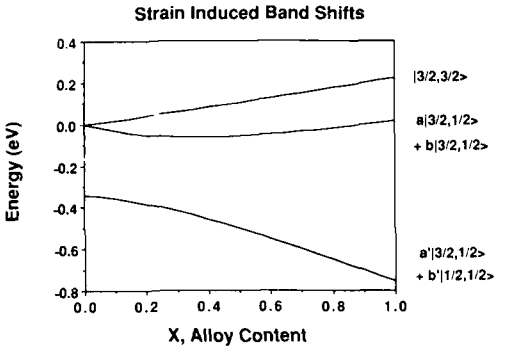


Fig. 1 Strain induced shifts of the valence bands in InxGa1-xAs alloys as a function of alloy content. The energy shifts are calculated assuming all strain is incorporated in the thin InGaAs layer. The hydrostatic contribution to the band shifts is determined from the pressure dependence of the spin orbit band relative to the energy gap. T = 300K.

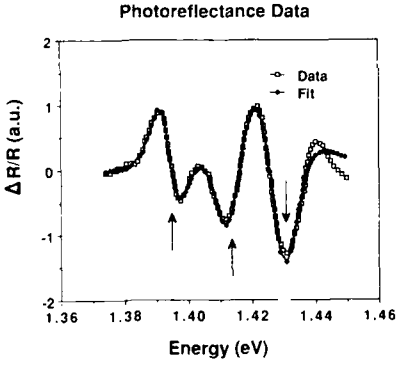


Fig. 2 Photoreflectance spectrum for the $In_xGa_{1-x}As$/GaAs SSQW with x= .07 and a well width of 5.5nm. Excitation is a 1mW 633nm He-Ne laser. Dark line indicates the associated theoretical curve with transition energies marked with arrows.

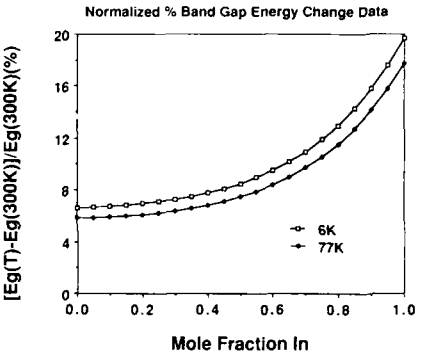


Fig. 3 Normalized Percent Change in the Band Gap Energy at 6 and 77K vs In Mole Fraction.

Table I

Results for Photoreflectance (300K) and Photoluminscence (6K) for $In_xGa_{1-x}As$ Single Strained Quantum Wells and Corresponding Theoretical Values for the 1C-1HH Quantum Transitions.

Sample (Structure)	Transition Energy (eV)			
Temp.	300K	Calc	6K	Calc
G44 15%, 4nm	1.355	1.355	1.449	1.441
G63 7%,5.5nm	1.394	1.393	1.487	1.484
(1C-2H)	1.413	1.412		
G179 13.5%, 3nm	1.376	1.379	1.478	1.468
G218 15%, 20nm	1.301	1.302	1.389	1.386
(2C-2H)	1.344	1.334		
G220 5%, 5nm	1.410	1.407	1.505	1.499

Abstract No. 495

Heterostructures of $GaAs_{1-x}Sb_x$ on GaAs Grown by Molecular Beam Epitaxy

J. H. Zhao, J. C. Jeong, T. E. Schlesinger, and A. G. Milnes

Department of Electrical and Computer Engineering

Carnegie Mellon University

Pittsburgh, PA 15213

Introduction

The development of advanced epitaxy technologies such as MBE and MOCVD has made it possible to study novel heterostructures involving large lattice mismatch. $GaAs_{1-x}Sb_x$/GaAs heterostructures are interesting[1] because almost no work has been done on the p-n diode current transport mechanisms and band offsets of this system and also because with respect to GaAs there is a lattice mismatch of up to 7.8%. This paper reports studies of the current transport of p-GaSb/N-GaAs diodes and the band offset of GaSb/GaAs as well as the Schottky barrier heights of Au/n-$GaAs_{1-x}Sb_x$. Probable band offsets of $GaAs_{1-x}Sb_x$ GaAs are also inferred from the Schottky barrier heights based on Tersoff's model of heterojunction line-up[2].

Results and Discussions

The effects of the lattice mismatch induced interface states on the current transport of p-GaSb/N-GaAs have been studied at temperatures ranging from 294 to 123K. A transition from a thermionic-recombination limited current to a tunneling limited current is observed when the diode forward bias is increased. The tunneling current takes the form of $I = B(T)\exp(AV)$ where the tunneling parameter A is fairly temperature independent and equal to $75V^{-1}$. The current transport mechanism in heterojunction diodes with large lattice mismatch, as well as the observed transition, will be discussed. The tunneling parameters for p-Ge/N-GaAs, p-Ge/N-Si[3], and p-GaSb/N-GaAs are plotted in Fig 1 as a function of lattice mismatch percentage. In general, the larger the lattice mismatch, the larger the tunneling current will be.

Studies of the capacitance characteristics of p-GaSb/N-GaAs as a function of temperature and frequency will be presented. Interface charge effects on the built-in voltage have been examined and properly treated. From this treatment the conduction band offset ΔE_c of GaSb/GaAs has been found to be 0.3 ± 0.04 eV with the conduction band of GaAs located above that of GaSb by C-V intercept method. The consistency of the ΔE_c's at different temperatures have been examined and the results were within the experimental error of 0.04eV. The energy band diagram of the p-GaSb/N-GaAs thus determined is shown in Fig 2.

The Schottky barrier heights of Au on n-$GaAs_{1-x}Sb_x$ have been studied to examine the relationship between Schottky barrier heights and the band offsets of $GaAs_{1-x}Sb_x$ GaAs that were implied by the Tersoff model. Shown in Fig 3 is the experimetal Schottky barrier height of Au/n-$GaAs_{1-x}Sb_x$ as a function of Sb content determined by studying the reverse leakage current as a function of temperature(the open circles) and the solid dot is from reference 4. The inset shows the application of Tersoff's model of heterojunction line-up: probable band offset can be inferred from the difference between the two Schottky barrier heights of a common metal on the two semiconductors. Our Schottky barrier height results therefore imply a conduction band offset ΔE_c = 0.9 - 0.78 = 0.12eV for $GaAs_{0.923}Sb_{0.077}$/GaAs, ΔE_c = 0.9 - 0.63 = 0.27eV for $GaAs_{0.74}Sb_{0.26}$/GaAs, and ΔE_c = 0.9 - 0.6 = 0.3eV for GaSb/GaAs in agreement with our result obtained using the C-V intercept method.

Conclusions

In conclusion, lattice mismatch induced interface state effects on the current transport mechanism of MBE grown mesa etched GaSb/GaAs heterojunction diodes have been examined. Tunneling current has been found to be dominant beyond certain temperature-dependent forward bias and the tunneling current varies as $B(T)\exp(75V)$. The C-V intercept method has been used to study the conduction band offset of GaSb/GaAs with the interface charge effects being properly treated by studying the frequency and temperature dependence of its C-V characteristics. The conduction band offset ΔE_c has been found to be 0.3 ± 0.04 eV. Schottky barrier heights of Au/n-$GaAs_{1-x}Sb_x$ have been studied and used to infer the band offsets of $GaAs_{1-x}Sb_x$/GaAs based on Tersoff's model.

References

1. J. Z. Zhao, A. Z. Li, J. Jeong, D. Wong, J. C. Lee, M. L. Milliman, T. E. Schlesinger, and A. G. Milnes, to appear in J. Vac. Sci. Technol. B, March-April 1988.

2. J. Tersoff, Phys. Rev. Lett. **52**, 465(1984).

3. J. P. Donnelly, and A. G. Milnes, Proc. IEE (London) **113**, 1168(1966).

4. S. M. Sze, Physics of Semiconductor Devices, John Wiley & Sons, Chap 5, 1981.

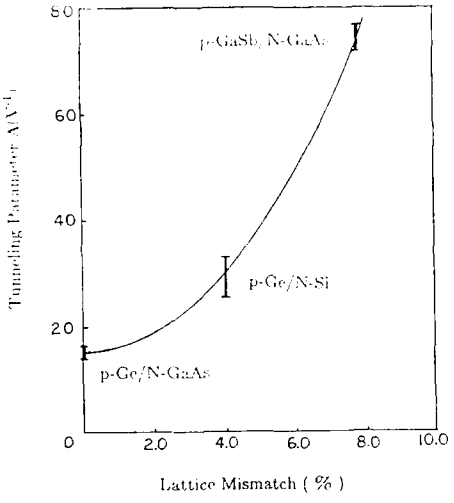


Fig 1. Tunneling parameter as a function of percentage lattice mismatch. In general, the larger the lattice mismatch, the larger the tunneling current.

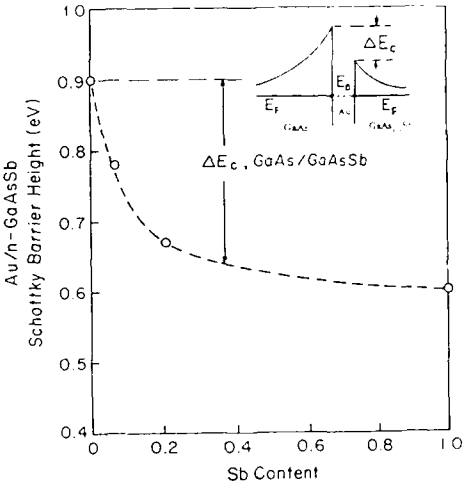


Fig 3 The Schottky barrier height of Au/n-$GaAs_{1-x}Sb_x$ as a function of Sb content. The inset shows the probable band offset inferred from the Schottky barrier heights based on Tersoff's model.

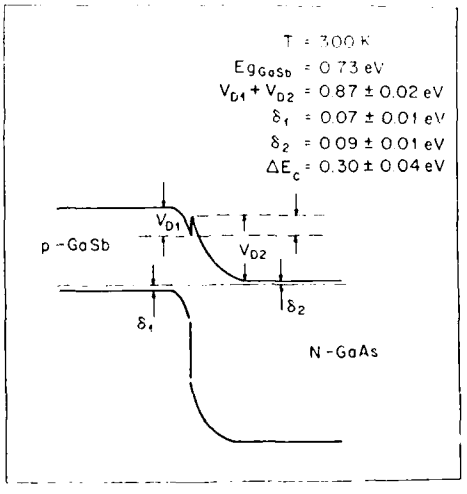


Fig 2 Energy band diagram of p-GaSb/N-GaAs showing a conduction band offset ΔE_c 0.3eV

Abstract No. 496

GROWTH AND CHARACTERIZATION OF $ZnGeP_2$/GaP HETEROSTRUCTURES BY OMCVD

G. Xing, J.B. Posthill and K.J. Bachmann

Department of Materials Science and Engineering, North Carolina State University, Raleigh, NC 27695-7907

G.S. Solomon and M.L. Timmons

Research Triangle Institute, Research Triangle Park, NC 27709

This contribution contains the first report of the growth of $ZnGeP_2$ epitaxial films on GaP(100) substrates by organometallic chemical vapor deposition (OMCVD). Secondary ion mass spectroscopy (SIMS), absorption spectra, x-ray diffraction (XRD) and transmission electron microscopy (TEM) have been utilized for the characterization of these thin films. The relationship between the growth conditions, structure and properties of the epitaxial films have been compared with those of bulk, single crystals of $ZnGeP_2$, which have been grown by directional solidification.

The epitaxial $ZnGeP_2$ films were grown in an open tube OMCVD system in which $Zn(CH_3)_2$, GeH_4 and PH_3 were used as the source gases. The flow rate ratio, R, of $Zn(CH_3)_2$ to GeH_4 was varied from 6:1>R>1:9 while the flow rate of PH_3 was kept at a fixed value. The growth temperature was varied from 525°C to 575°C. The growth rate of the film is determined by the GeH_4 flow rate. For a given flow rate, the concentrations of Ge varies non-linearly with the growth temperature (Fig. 1). Since the film composition becomes insensitive to changes in the growth temperatures at or above 575°C, we chose 575°C as the optimum growth temperature. At this substrate temperature, mirror smooth epitaxial surface morphology can be obtained over a large range of $Zn(CH_3)_2$ to GeH_4 flow rate ratios, i.e., 6:1>R>1:3. This suggests that the homogeneity range about $ZnGeP_2$ may allow substantial deviations from stoichiometry. However, at the low temperature limit of our experiments (525°C) and large $Zn(CH_3)_2$ to GeH_4 flow rate ratios, a phase separation has been observed with a concomitant roughening of the surface.

Figure 2 shows the depth profile of a $ZnGeP_2$ film obtained by SIMS analysis. It indicates that there is very little interdiffusion of Ga into the $ZnGeP_2$ film or of Zn and Ge into the GaP substrate. Also, trace analysis by SIMS indicates that many impurities that are present in bulk $ZnGeP_2$ are either absent or present at drastically reduced concentrations in the OMCVD films.

Figure 3 shows the absorption edge of a thin film which exhibits a tail and a distinct absorption band at approximately 1 eV. In bulk samples of $ZnGeP_2$ absorption tails extending across the window of transparency to the IR absorption edge at approximately 12 μm have been reported in the literature[1], which are related to the presence of native point defects and impurities. Since the residual absorption in the transparency region is an important limitation in non-linear optical applications of $ZnGeP_2$, progress in the control and understanding of the optical properties at below band gap energies is of considerable interest and is discussed on the basis of optical data for both epitaxial thin films and bulk single crystals.

Figure 4 shows a bright field TEM micrograph from a bulk, single crystal of $ZnGeP_2$. Precipitates of ~200Å size are observed. Images taken near the [112] and [100] poles are consistent with a tetrahedral shape, and their density is quite low - less than 0.002 volume percent. Parallel Moire fringes can be seen when specific diffraction vectors are used for imaging. Specifically, ~40Å fringes are observed when 220- or 204-type reflections are employed. Precipitate d-spacings of 1.8Å or 2.0Å are possible given this data. A d-spacing of 2.0Å correlates well with d_{220} for Ge, and therefore we tentatively conclude that the precipitates are Ge with the respective {100}-type planes in both phases being parallel.

In summary, heteroepitaxial growth of $ZnGeP_2$ on GaP(100) substrates by OMCVD has been demonstrated. Characterization of these epitaxial films has been accomplished, and comparison has been made with bulk, single crystals of $ZnGeP_2$. The epitaxial films are of superior purity, but judicious choice of the growth conditions is required for controlling their stoichiometry.

Acknowledgement

This work has been supported by the National Science Fondation, Grant DMR 8414580.

Reference

1. E. Buehler, J.H. Wernick and J.D. Wiley, *J. Electr. Mat.*, 2, 445 (1973).

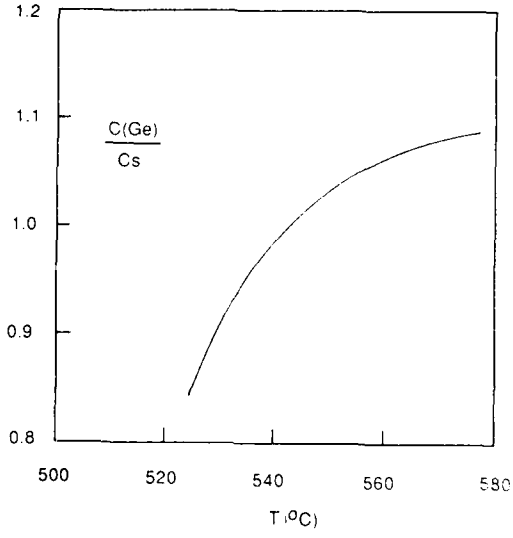


Fig. 1 - Ge concentration in the film [C(Ge)] normalized to the Ge concentration in a bulk, single crystal standard [Cs] as a function of growth temperature. $Zn(CH_3)_2$ to GeH_4 flow rate ratio 2:3.

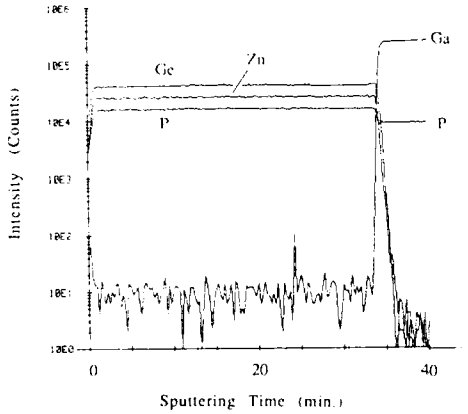


Fig. 2 - SIMS depth profile of $ZnGeP_2$/GaP heterostructure growth temperature 575 °C, $Zn(CH_3)_2$ to GeH_4 flow rate ratio of 1:1.

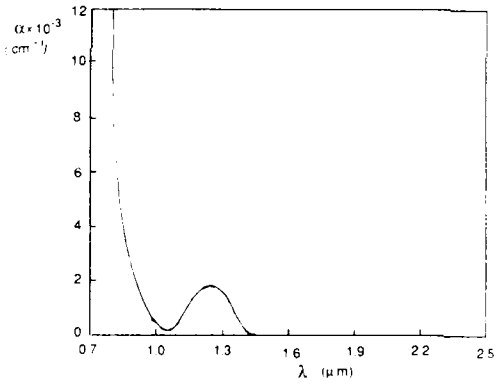


Fig. 3 -Absorption coefficient vs. wave length of a $ZnGeP_2$ Epilayer: growth temperature 575°C, $Zn(CH_3)_2$ to GeH_4 flow rate ratio of 6:1.



Fig. 4 - TEM micrograph taken near [112] of bulk $ZnGeP_2$ containing Ge precipitates. They are tetrahedral in shape, the sides lying on $\{111\}_{Ge}$-type planes ($\mathbf{g} \cdot 220$, $s = 0$).

Abstract No. 497

X-RAY CHARACTERIZATION OF HETEROEPITAXIAL GaAs on Si(001)

H. Zabel, N. Lucas, H. Morkoç
Department of Physics and Materials Research Laboratory
University of Illinois
1110 West Green St., Illinois 61801

The successful epitaxial growth of GaAs on Si (001) substrates is one of the most important advances in semiconductor heterostructure technology in recent years. This progress was achieved in spite of the fact that GaAs on Si combines all major problems of heteroepitaxial growth processes, including a large lattice mismatch, the possible formation of antiphase domains, and thermal mismatch between both materials. We will provide an overview of recent x-ray scattering experiments concerned with these issues. For a review of the electronic and optical properties as well as device applications we refer to Ref. 1.

Antiphase domains (AD's): Layer by layer deposition of alternating Ga and As atoms on Si (001) substrates may lead to the formation of AD's when single atomic steps in the substrate are encountered. This is schematically demonstrated in Fig. 1. For reasons discussed further below, the actual substrates were miscut by about 4° off the (001) direction, which is expected to introduce a distribution of step heights. Any odd numbered step height, in turn, should introduce AD's. The presence of AD's can be verified by measuring, via high resolution x-ray scattering, the width of GaAs superlattice reflections. Comparing the width of superlattice peaks to those of fundamental peaks (see Fig. 2), no contribution due to AD's could be observed [2]. From these x-ray results follows a lower limit for the separation of AD boundaries of about 4000 Å which is good agreement with high resolution electron microscopy images of GaAs on Si [3]. It has been speculated that the lack of AD's may be due to a reconstruction of the miscut Si surface which takes place either during the annealing procedure prior to the GaAs deposition or during the deposition of the first monolayer of As.

Lattice mismatch and strain relaxation: The bulk GaAs and Si lattice parameters differ by 4.1% at room temperature, with the GaAs lattice parameter being bigger than the Si. The first few epitaxial layers of GaAs will therefore be under compressional stress. The strain energy increases with progressive growth of alternating Ga and As monolayers, until it exceeds the energy for formation of dislocations. Hence, edge dislocations remove coherency strains and the interfacial relationship between GaAs and Si becomes progressively incoherent with increasing film thickness. It has been shown that on flat substrates screw as well as edge dislocations are generated. The former ones only deteriorate the electronic properties but are ineffective for strain removal. Vicinal cuts of the substrate off the (001) orientation remedies this problem and in addition causes the edge dislocations to propagate parallel to the interface [3]. Residual coherency strains cause the width of all Bragg reflections to increase linearly with the wavevector as shown in Fig. 2, where the slope of the curve is a direct measure of the residual strain perpendicular to the film. For both film thicknesses shown in Fig. 2 the slopes are identical, indicating that the major strain gradient must be located in a region in between 1000 Å from the interface. Similar measurements on thinner GaAs films exhibit indeed much bigger slopes [4,5].

Thermal expansion: The bulk thermal expansion coefficients of GaAs and Si are 6.0×10^{-6}/K and 2.3×10^{-6}/K, respectively. This thermal mismatch leads to bowing and bending of the wafers and hampers serious device applications. Recent x-ray experiments have revealed [6] that at an initial growth temperature of about 500 C the GaAs film is almost strain free, neglecting a strain gradient in a narrow region close to the interface. Then, upon cooling the interfacial relationship between GaAs and Si remains intact requiring the GaAs in-plane lattice parameter to follow the slower thermal contraction of the Si substrate. This boundary conditions causes an expansion of the in-plane GaAs lattice parameter over its bulk value. The out-of-plane thermal expansion exceeds the bulk value by the Poisson response from the in-plane constraint, and therefore at room temperature the out-of-plane lattice parameter is contracted (Fig. 3).

This work was supported by the US Department of Energy, Division of Materials Science, under contract No. DE-AC02-76ER01198.

REFERENCES

1. H. Morkoç, H. Unlu, H. Zabel, N. Otsuka, Solid State Technology 31, 71 (1988).
2. D.A. Neumann, H. Zabel, R. Fischer and H. Morkoç, J. Appl. Phys. 61, 1023 (1987).
3. R. Fischer, H. Morkoç, D.A. Neumann, H. Zabel, C. Choi, N. Otsuka, M. Longerbone, and L.P. Erickson, J. Appl. Phys. 60, 1640 (1986).
4. H. Zabel, N. Lucas, R. Feidenhans'l, J. Als-Nielsen, H. Morkoç, Superlattices and Microstructures 3, 515 (1987).
5. A.S. Bommannavar, A. Habenschuss, G.E. Ice, C.J. Sparks, H. Morkoç, and H. Zabel, Materials Research Society Symposium, Vol. 102 (1987).
6. N. Lucas, H. Zabel, H. Morkoç, and H. Unlu, Appl. Phys. Lett.

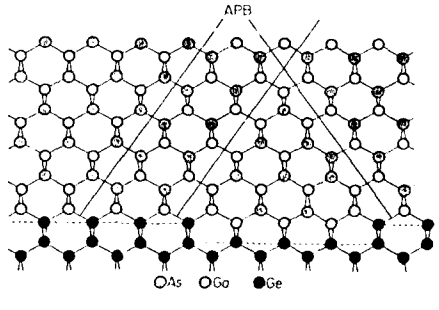


Figure 1. Antiphase domains are formed either when both Ga and As nucleate in the same flat monolayer, or when a single atomic step of the substrate is present. Annihilation of antiphase domain boundaries is possible for some directions.

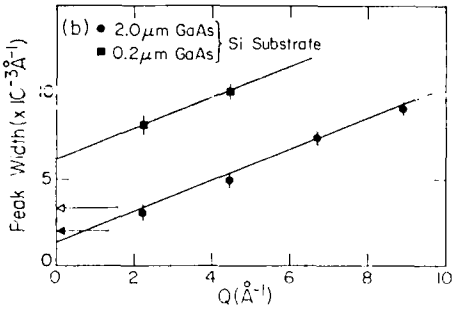


Figure 2. Peak widths of (001) reflections of GaAs on miscut Si for two different GaAs film thicknesses. The scan direction is perpendicular to the film plane and therefore the widths are composed of contributions from film thicknesses, residual strains, and antiphase domain boundaries in this direction. Since the widths of the odd number reflections (superlattice peaks) lie on the same line as the even order reflections (fundamental peaks), it indicates that antiphase domains play a negligible role in these films. The slope of the lines is proportional to the residual strain gradient. The arrows indicate the instrumental resolution of the instrument (from Ref. 2).

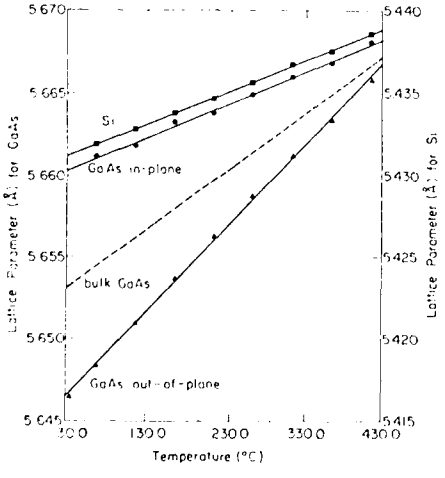


Figure 3. Lattice parameter as a function of temperature of a GaAs film on Si (001). Rectangles indicate measured lattice parameters for Si, circles for the in-plane lattice parameter of the GaAs film, and triangles for the out-of-plane lattice parameter of GaAs. The dashed line indicates the thermal expansion of bulk GaAs without epitaxial constraint (from Ref. 1).

Abstract No. 498

Controlled Formation of Misfit Dislocations for Heteroepitaxial Growth of GaAs on (100) Si by Migration-Enhanced Epitaxy

W. Stolz, Y. Horikoshi, and M. Naganuma

NTT Electrical Communications Laboratories, Musashino-shi, Tokyo 180, Japan

The heteroepitaxial growth of GaAs on Si substrates has attracted great attention in recent years. The formation of misfit dislocations plays a key role in this heteroepitaxial system. The critical thickness for pseudomorphic GaAs growth on Si amounts to only several monolayers. This is caused by the large difference of 4% in lattice constants between GaAs and Si. Under equilibrium conditions, all misfit dislocations (of the order of 10^{12} cm^{-2}) would be formed within only a few monolayers during growth. This large amount of defects will certainly influence the crystal growth mechanism. Normally, growth initiation at high temperatures leads to island formation. An energetic barrier for the generation of misfit dislocations is present in semiconductors (1). This mechanism can be used to control the formation of misfit dislocations by selecting appropriate growth conditions. The principal aim is to minimize the influence of the required dislocation formation on the crystal growth mechanism.

In this study we have investigated the strain relaxation of GaAs layers on Si substrates as a function of the growth temperature (300°C to 600°C) and substrate off-orientation (1°, 2°, and 4° off from [011] direction). GaAs epitaxial layers were grown by migration-enhanced epitaxy (MEE) on 3" (100) Si substrates. MEE is a modified MBE growth technique, which has proven to produce high-quality homoepitaxial GaAs layers even at low growth temperatures (2). Thus MEE is particularly suitable for the low-temperature growth steps in this study. The residual strain in the GaAs layers was determined by measuring the bending of the GaAs/Si wafers as well as by double crystal X-ray diffraction. Investigations of the dislocations created in the GaAs epitaxial layers have been performed by transmission electron microscopy (TEM) studies.

At low growth temperatures we observe reproducibly an opposite wafer bending at room temperature then expected from the difference in thermal expansion of GaAs and Si. Double crystal X-ray diffraction investigations confirm that GaAs layers are under compressive strain for these wafers. Furthermore, after etching-off of the GaAs epitaxial layer, the opposite wafer curvature is removed. Thus, we are sure that the observed opposite wafer bending originates from the compressively strained GaAs layer. This compressive strain is caused by the not completed strain relaxation of the epitaxial layer under the respective growth conditions.

In addition to the dependence of strain relaxation on growth temperature, also the substrate off-orientation influences the strain relaxation process. GaAs epitaxial layers grown on 2° off-oriented substrates are clearly more relaxed under identical growth conditions than layers, which are grown on 1° and 4° off-oriented substrates. Misfit dislocations in epitaxial layers on high-quality substrates have to nucleate on the growing epitaxial layer surface. Therefore besides the growth temperature, the actual conditions on the surface (surface reconstruction and the number of surface steps) also influence the dislocation formation. For the samples grown on 2° off-oriented substrates the distance between surface steps is almost identical to the average spacing of misfit dislocations. Therefore, almost all dislocations in the [011] direction can form at steps on the GaAs surface. This is not the case for layers grown on the other off-orientations, where dislocations also partly form on terraces. This process needs a higher energy and thus should occur at a later stage under the same growth conditions.

It is important to note that in order to be able to reveal the influence of the surface steps created by the substrate off-orientation, the number of surface steps introduced by the growth mechanism should be small. Using an optimized substrate preparation and growth initiation of GaAs on Si (3), it is possible to start growth of GaAs on Si in the 2D layer-by-layer growth mode. By applying the above described controlled formation process of misfit dislocations the 2D growth of GaAs on Si can be maintained for the entire epitaxial layer as revealed by in situ RHEED observations. Primarily, this is due to the fact that misfit dislocations are not formed within a few monolayers, but are created in a controlled way within a thicker GaAs layer. The number of dislocations formed on the growing surface per growth of one monolayer is drastically reduced. Therefore, the disturbence of the growth process becomes less important. The second important fact is that MEE produces better-quality epitaxial layers at low substrate temperature as do the standard MBE and MOCVD growth techniques. Atomically smooth GaAs/(AlGa)As heterointerfaces are confirmed by TEM and luminescence studies of single QWH.

To optimally balance the thermal expansion strain after cooling from the growth temperature, the average residual strain of the GaAs epitaxial layer should be in the range of $1*10^{-3}$ for a growth temperature of 600°C. For lower growth temperatures, this value can be even smaller. It is possible to realize non-bending GaAs/Si wafers by choosing appropriate growth conditions and substrate misorientation. These values of residual strain at the growth temperature are typical for lattice-matched heterosystems. At room temperature the average strain in the GaAs epitaxial layer vanishes.

The controlled dislocation formation can be used to reduce drastically the dislocation density in the GaAs layer. In a two-temperature growth process, misfit dislocations are formed at low substrate temperatures. By maintaining the 2D growth processfor this stage, no additional defects are created, which may result from an island formation on the epitaxial layer surface. After increasing the temperature, the generated misfit dislocations become mobile and slip to the GaAs/Si interface. This process leads to a regular dislocation arrangement at the interface as determined by TEM studies. A significant reduction of the threading dislocation density in the GaAs epitaxial layer is observed. For an unoptimized layer sequence a dislocation density of $5*10^{9}$ cm^{-2} is realized after growth of only 200 nmof GaAs. The dislocation density as well as the smoothness of the growth surface and therefore of GaAs/(AlGa)As heterointerfaces are significantly improved compared to standard MBE- and MOCVD-grown GaAs/Si layers.

1) P.M.J. Maree, J.C. Barbour, J.F. van der Veen, K.L. Kavanagh, C.W.T. Bulle-Lieuwma, and M.P.A. Viegers, J. Appl. Phys. 62, 4413 (1987).

2) Y. Horikoshi, M. Kawashima, and H. Yamaguchi, Jpn. J. Appl. Phys. 27, 169 (1988).

3) W. Stolz, Y. Horikoshi, and M. Naganuma, Jpn. J. Appl. Phys. 27, L283 (1988).

Abstract No. 499

X-RAY CHARACTERISATION OF $Cd_xHg_{1-x}Te$ EPITAXIAL LAYERS GROWN ONTO GaAs SUBSTRATES BY MOVPE

G.T. Brown, J. Giess and S.J.C. Irvine

Royal Signals and Radar Establishment
St Andrews Rd, Malvern, Worcs. WR14 3PS UK

$Cd_xHg_{1-x}Te$ ($x \sim 0.2$) epitaxial layers have been grown onto (001) GaAs substrates with a CdTe buffer layer by MOVPE. The CdTe buffer layers were grown at 350°C using dimethyl cadmium (DMCd) and di-isopropyl tellurium (DIPTe) in a hydrogen carrier gas at one atmosphere total pressure. The $Cd_xHg_{1-x}Te$ alloy was grown in the same reactor cell after growing a suitable thickness of CdTe buffer layer. The mercury was introduced as a liquid in the entrance zone and the required partial pressure (~ 0.01 atm.) created by heating the mercury and reactor wall. Uniform alloy growth was achieved by using the interdiffused multilayer process (IMP) whereby the gas flows are switched between conditions optimised for HgTe and CdTe growth. These binary layers are sufficiently thin for complete homogenisation to take place at the growth temperature. This process has been described in detail elsewhere(1). X-ray rocking curve widths have been compared with IMP and direct alloy growth by Edwall et al(2) for epitaxial growth onto Al_2O_3 substrates. In these authors' experience the IMP grown layers had rocking curve widths which were a factor of two broader. The present study looks systematically at the factors which can affect this property of the epitaxial layers.

For the CdTe buffer layers, the ratio of the alkyl gas flows and the CdTe buffer layer thickness were varied and the quality of the layers has been assessed by double crystal X-ray diffractometry. The full width half maximum (FWHM) of the X-ray rocking curve has been found to vary both as a function of layer thickness and as a function of the DIPTe/DMCd gas flow ratio. For a constant gas flow ratio the FWHM decreased from 1111 to 199 arc secs for layer thicknesses of 1.3 μm to 5.5 μm respectively. For a constant layer thickness the X-ray rocking curve FWHM decreased as the DIPTe/DMCd gas flow partial pressure ratio was increased from 1.02 to 2.78. The highest quality buffer layers were observed for layer thicknesses in excess of 2 μms with a DIPTe/DMCd gas flow partial pressure ratio of 2.78.

For $Cd_xHg_{1-x}Te$ (CMT) layers grown onto the highest quality buffer layer (~ 4 μm thick) the X-ray rocking curve FWHM has been mapped over large areas (1.5 cm x 1.5 cm) using a fully automated X-Y stage. The lowest FWHM recorded was 58 arc secs for a layer 12 μm thick. However the samples were found to be non-uniform with typical variations in FWHM ranging from as low as 50-70 arc secs to as high as 800 arc secs. The rocking curve width tended to increase for areas where the surface morphology deteriorated. In-situ annealing both below and at the growth temperature improved the uniformity but did not significantly further reduce the minimum rocking curve widths.

The origin of the X-ray rocking curve broadening for these layers is discussed and it is shown that for rocking curves with a FWHM in excess of 40 arc secs the dominant contribution to the broadening is expected to be due to the high dislocation density generated by the large mismatch (~ 14%) in this system (3). The lateral non-uniformity in FWHM observed for the CMT layers has been shown to correspond to variations in the dislocation density of between 4×10^6 cm^{-2} and 5×10^8 cm^{-2} by using the expression derived by Hirsch(4) and experimentally confirmed by Baribeau et al(5).

The CMT layers were also found to be tilted with respect to the GaAs substrate. The magnitude of this lattice tilt varied across a layer for samples where there were marked variations in the X-ray rocking curve FWHM. The origin of this tilt and its relationship with the dislocation density is discussed.

1. J. Tunnicliffe, S.J.C. Irvine, O.D. Dosser and J.B. Mullin, J.Crystal Growth, 68, 245 (1984)

2. D.D. Edwall, E.R. Gertner and L.O. Bubulac, J.Crystal Growth, 86, 240 (1988)

3. A.G. Cullis, N.G. Chew, J.C. Hutchinson, S.J.C. Irvine and J. Giess, Inst. of Physics Conf. Ser. 76, 29 (1985)

4. P.B. Hirsch, Progress in Metal Physics, 6, p236, B. Chalmers and R. King, Editors, Pergamon Press London and New York (1956)

5. J.-M. Baribeau, D.C. Houghton, T.E. Jackman and J. McCaffrey, to be published, J.Electrochem.Soc. (1988)

Abstract No. 500

Effects of Misfit Dislocations and Thermally-Induced Strain on the Film Properties of Heteroepitaxial GaAs on Si

R.M. Lum, J.K. Klingert, R.B. Bylsma and A.M. Glass
AT&T Bell Laboratories, Holmdel, New Jersey 07733

A.T. Macrander, T.D. Harris and M.G. Lamont
AT&T Bell Laboratories, Murray Hill, New Jersey 07974

In the heteroepitaxial growth of GaAs on Si large internal stresses are introduced in the films as a result of the different lattice constants and thermal expansion coefficients of the two materials. During growth the stress due to the 4.1% GaAs/Si lattice mismatch is relaxed by the formation of misfit dislocations. The interfacial dislocation density is of the order $D_0=10^{12}$ cm^{-2}. Strain in the film may also be relieved by dislocations present further away from the interface since many of the interfacial dislocations propagate into the epitaxial layer, e.g. $D_z=10^{6}$-10^{8} cm^{-2} for film thicknesses z=2-4um. On the other hand, since the thermal expansion coefficient of GaAs is more than twice that of Si, significant thermal stresses are developed in the films when they are cooled to room temperature. The thermally-induced strain and high dislocation density greatly affect the structural, optical and electrical properties of the GaAs heteroepitaxial films. We report a study of these effects using X-ray diffraction, laser beam reflection, low temperature photoluminescence (PL) and capacitance-voltage (C-V) techniques.

The GaAs films were grown by metalorganic chemical vapor deposition (MOCVD) in a horizontal reactor. The GaAs films were deposited on (100) and 2° off (100) Si substrates which were subjected to an in-situ pre-growth anneal at 975°C in an H_2/AsH_3 ambient. A thin (<1000 A°) GaAs buffer layer was then deposited at 425°C prior to growth of a 1-5um thick GaAs top layer at 700°C.

The structural characteristics of the GaAs/Si heteroepitaxial films were determined with a double-crystal X-ray diffractometer. The measured GaAs lattice mismatch indicated that the films were tetragonally distorted and that a biaxial tensile stress is developed which forces the in-plane lattice mismatch (4.21-4.28%) to exceed the strain-free value (4.1%). Although not always apparent in the as-grown films, micro-cracks are usually quite evident after cleaving or etching of the GaAs/Si wafers. The cracks, which are approximately 0.5 um wide and spaced 10-50 um apart, are parallel to each other and extend the length of the sample (1.5 cm) along a <100> direction. Growing the GaAs films on a thicker Si substrate (0.040") considerably reduces the number of cracks. In this case the spacing between cracks is greater than 100 um and they extend only a short distance (<50 um) along the sample. Although the use of 0.040" Si substrates is not anticipated for device applications, the study of the effects of substrate thickness on film properties provides additional insight into the heteroepitaxial process.

The internal biaxial stress present in the GaAs films causes the GaAs/Si wafers to bow. The stress-induced radius of curvature, R, was determined from the X-ray lattice mismatch and independently measured by reflection of a laser beam from the wafer surface. Both sets of data are in good agreement and indicate that, for films thicker than 1-um, 1/R is proportional to film thickness.

Wafer warpage can be eliminated by growth on both sides of the Si substrate. We have accomplished this by sequential growth of GaAs films of identical thickness on each side of the substrate. For comparison, a second substrate had a layer grown on one side only during the same run. Curvature measurements on the pair indicated that, indeed, bowing was eliminated in the double-sided sample. This approach may be useful for applications which utilize uniform GaAs coverage across the wafer. No changes in flatness of either wafer were observed following a rapid thermal anneal at 950°C for 15 seconds.

The presence of biaxial stress in the GaAs/Si samples also has a measurable effect on the optical properties of these films. Identification of the individual transitions in the GaAs/Si spectrum is complicated by the effects of the biaxial tensile stress. These include a decrease in the bandgap energy and a removal of the GaAs valence band degeneracy. Two peaks were observed that were associated with transitions to the lower energy valence band state. These arise due to different levels of strain in the material. The origin of the two different strain regions in these samples is unknown. They may be associated with the presence of micro-cracks in the film, since samples less than 2-um thick, which are generally free of cracks, do not contain the higher energy (lower strain) PL peak. Samples exhibiting the two peaks were generally characterized by PL spectra which varied widely with sample illumination position. Conversely, the PL spectra of GaAs films on thick (0.040") Si substrates, which have only small cracks near the cleavage edge are similar for all parts of the sample. PLE spectra of these well-behaved samples indicate the presence of a continuous nonuniform strain field in the GaAs film, rather than the two discrete levels observed in the crack-prone films on thinner Si substrates.

The GaAs/Si samples containing 3-um thick GaAs films on both sides of the Si substrate exhibited PL spectra that were similar to that observed for the single-sided growth, the main difference being the appearance of additional impurity peaks. Although wafer bowing is eliminated by double-sided growth, the PL data confirm that the internal strain in these samples is essentially the same as for single-sided growth. The PL and PLE data indicate that the measured stress is independent of substrate thickness.

Doping profiles of the GaAs/Si samples were obtained from capacitance-voltage (C-V) measurements using a mercury probe. All samples were found to be n-type with the carrier concentration in some cases exceeding 10^{17} cm^{-3} within 0.5 um of the surface. In-situ annealing of the thin GaAs buffer layer prior to deposition of the top layer both improved the crystaline quality of the epilayer, as measured by the linewidth of the X-ray rocking curves, and led to considerable reduction in the background. In general, a quadratic relationship was observed between the carrier concentration of the samples and their X-ray linewidths. This type of behavior has also been observed in lattice mismatched InGaAs/InP grown by the hydride process, where the unusually high carrier concentration was determined to be an intrinsic property of the large number of dislocations resulting from the lattice mismatch in the samples.

In conclusion, GaAs heteroepitaxial films on Si contain large biaxial tensile strains due to the thermal mismatch of the two materials. The lattice misfit strain component is negligible, being almost entirely relieved by the generation of dislocations. The internal strain field causes wafer bowing and, for thicker GaAs layers, film cracking. Wafer bowing was successfully eliminated by growth of GaAs films on both sides of the Si substrate. Insight into the heteroepitaxial process and character of the strain field was obtained by analysis of crack-free GaAs films deposited on 0.040" thick Si substrates, in addition to use of wafers having the more standard 0.020" thickness. The strain in well-behaved samples was distributed in a continuous nonuniform manner throughout the film, while that in crack-prone samples appeared to be concentrated in two discrete regions. When the number of misfit defects in GaAs/Si exceeded 10^{8} cm^{-3}, they were observed to affect the background carrier concentration in the films so that C-V determinations of n_e no longer provided a reliable measure of N_D-N_A.

Abstract No. 501

EPITAXIAL LAYER MISORIENTATION IN HETEROEPITAXIAL GaAs ON Si

R.J. Matyi and H.F. Schaake
Central Research Laboratories
Texas Instruments, Inc.
Dallas, TX 75265

D.G. Deppe and N. Holonyak, Jr.
Electrical Engineering Research Laboratories
University of Illinois at Urbana-Champagne
Urbana, IL 61801

The generation of dislocations during growth and their propagation into the growing film is a subject of perennial interest in heteroepitaxial growth. One effect of misfit dislocations is the presence of a misorientation or tilt between an epitaxial layer and the substrate. This phenomenon has been studied in depth by Olsen and Ettenberg,[1] who showed that the inclination of the Burgers vector of a misfit dislocation with respect to the heterointerface will create a vector component that is perpendicular to the interface and result in a misorientation or tilt between the layer and substrate. The origin of this misorientation is illustrated in Figure 1. A dislocation Burgers vector lying in a crystallographic direction can be resolved into components that are parallel and perpendicular to the heterointerface. The parallel component represents a pure misfit component that is effective at relieving the lattice mismatch at the interface. In contrast, the perpendicular component gives rise to a misorientation. The sense of the misorientation is shown in Figure 2, where an array of dislocations with perpendicular Burgers vectors with the same sense form a low angle boundary.

Recently the epitaxial layer misorientation in GaAs on Si has been reported.[2] While misfit dislocations that were approximately parallel to the interface (commonly referred to as Type I dislocations) were found to be capable of producing epitaxial layer misorientation, the sense of this tilt was opposite to that which was observed experimentally. The direction of the tilt was correctly predicted by a model in which one set of 45° dislocations (so-called Type II dislocations) is formed preferentially due to greater relief of the 4.1% GaAs/Si misfit. The changes in the tilt between the epitaxial layer and the substrate were attributed to changes in the relative proportions of the various dislocations that were generated during the GaAs-on-Si epitaxial growth.

In the present study we have examined further the relationship between MBE growth and post-growth processing on the misorientation epitaxial GaAs on Si. X-ray diffraction has been used to monitor the misorientation. Figures 3 and 4 show x-ray results from GaAs on Si samples that were grown using, respectively, a two-step regimen (deposition of the initial 1000Å of GaAs at 475°C at 0.3 μm/hr followed by growth of the bulk of the film at 0.9 μm/hr at a substrate temperature of approximately 550°C) and a temperature superlattice (TSL) growth initiation where the substrate temperature was cycled between approximately 450°C and 550°C for the first 1000Å.[3] Both samples were also subjected to a post growth anneal at 850° for 15 minutes. The x-ray data, which show the separation of the GaAs and silicon (004) reflections and the angular settings of the silicon peak during rotation about the surface normal, exhibit sinusoidal variations in ω_{Si} and $\omega_{Si} - \omega_{GaAs}$; the variations in the substrate (004) reflections are merely indicative of the 3.5° Si misorientation that is required in GaAs on Si for the supression of antiphase domain formation during growth. The magnitude of the tilt between the GaAs and the Si substrate are 0.096° for the two-step growth sample (Figure 3) and 0.113° for the sample grown using the TSL approach (Figure 4). While the tilt in the two-step GaAs is similar to that reported previously for a similar sample,[2], the as-grown TSL sample exhibits a significantly larger misorientation. The tilt after annealing was found to be 0.068° and 0.028° for the two-step and TSL samples, respectively. The decrease in tilt in the two-step sample is again consistent with previous observations; this is in contrast with the large decrease in the TSL GaAs tilt after anneling. The difference between the two-step and TSL samples can be explained by the difference in dislocation structure that is created at growth initiation. It is important to note that the effects of a microscopic defect rearrangement are manifested as a macroscopic change in epilayer misorientation.

A comparison between the two samples also reveals that the phase of the GaAs tilt is advanced with respect to the substrate in the two-step sample while it is retarded in the sample grown using the TSL. The phase of the epitaxial layer misorientation also changed significantly in both cases. This is most evident in the annealed TSL sample where the maxima in the ω_{Si} and the $\omega_{Si} - \omega_{GaAs}$ curves differ by about 90°. This effect can be ascribed to the relative proportions of Type II dislocations in the sample. The "phase" data suggest an inequivalence in the four possible Type II dislocations (each with perpendicular Burgers vector components) in the two samples.

It has recently been shown that post-growth annealing of GaAs-on-Si under a zinc overpressure can favorably impact the dislocation structure of the GaAs film.[4] Since Zn is a p-type dopant in MBE GaAs, it is possible that the incorporation of Be during growth might influence the dislocation structure as well. Figures 5 illustrates the misorientation measurements made from a 2 μm thick GaAs film grown with the two-step procedure that was heavily Be-doped during the first 6000 Å of growth. The data show an extremely large misorientation of 0.175° in the as-grown Be-doped sample; this result suggests a significant change in the dislocation structure as a result of doping. Following post-growth anneal, the magnitude of the tilt decreased but was still much larger than that observed in undoped GaAs-on-Si. In contrast, the Zn diffused sample (Figure 6) showed little difference in the magnitude of tilt before and after the post-growth treatment. The fact that the tilt did not change greatly while the x-ray rocking curve decreased by 50% suggests that Zn-diffusion reduces all dislocations uniformly without regard to type.

1) G.H. Olsen and M. Ettenberg, in Crystal Growth, Theory and Techniques 2 (ed. C.H.L. Goodman), 1 (1978).

2) R.J. Matyi, J.W. Lee and H.F. Schaake, J. Electron. Mater. 17, 87 (1987).

3) J.W. Lee, Proceed. 1986 Int. Symp. on GaAs and Related Compounds, Inst. Phys. Conf. Ser. §3, 111 (1987).

4) D.G. Deppe, N. Holonyak, K.C. Hsieh, D.W. Nam, W.E. Plano, R.J. Matyi and H. Shichijo, Appl. Phys. Lett., in press.

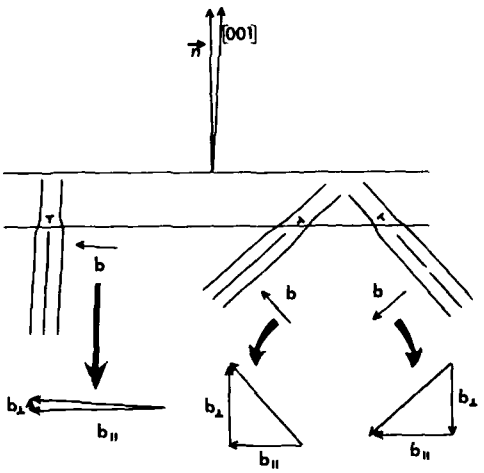


Figure 1: Resolution of Burgers vectors of the Type I and Type II dislocations in GaAs-on-Si into their pure misfit relief and pure tilt components

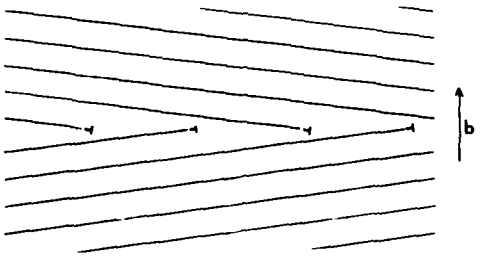


Figure 2: Epitaxial layer tilt associated with perpendicular Burgers vector components

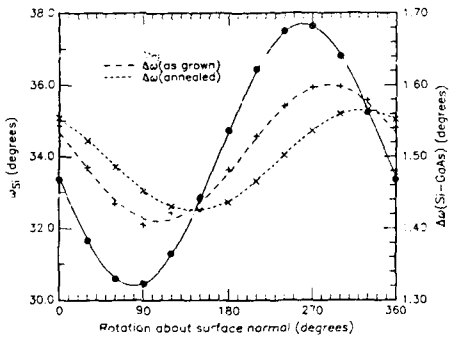


Figure 3: X-ray data from GaAs-on-Si (two step growth)

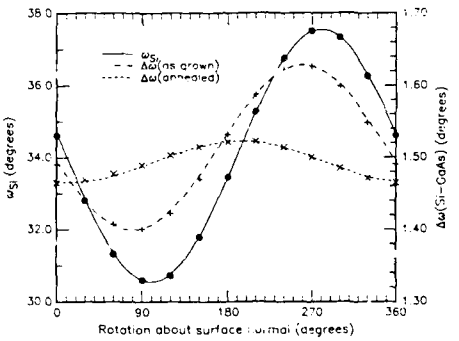


Figure 4: X-ray data from GaAs-on-Si (temperature superlattice)

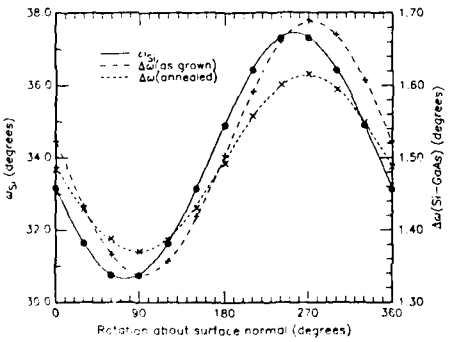


Figure 5: X-ray data from Be-doped GaAs-on-Si

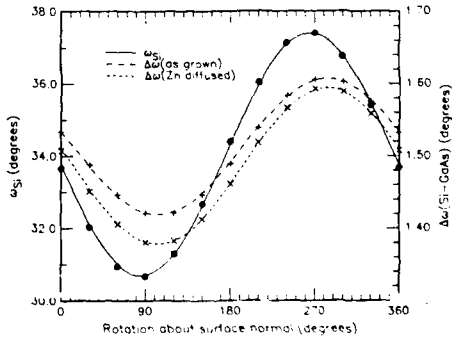


Figure 6: X-ray data from Zn diffused GaAs-on-Si

Abstract No. 502

A Structural Investigation of Compositionally Graded $InAs_{1-x}Sb_x$ Buffer Layers*

R. M. Biefeld

Sandia National Laboratories
Division 1144
Albuquerque, NM 87185

$InAs_{1-x}Sb_x$/InSb strained-layer superlattices (SLS's) have been proposed for use as long wavelength detectors in the 8-12μm range [1]. The preparation of crack- and dislocation-free $InAs_{1-x}Sb_x$/InSb SLS's which absorb in the 8-12μm range has been recently demonstrated [2]. Infrared photoluminescence was performed on these SLS's and estimates of the band offsets and strain shifts in these materials indicate that the superlattice is type II [3]. The preparation of these high quality SLS's was achieved through the use of compositionally graded buffer layers. These SLS's and buffer layers were grown by metal-organic chemical vapor deposition (MOCVD).

The structures prepared in this work consisted of the InSb substrate, an initial InSb epitaxial layer, a buffer layer and an uppermost superlattice. The buffer layers were of four types: 1) a constant composition layer; 2) a step-graded layer consisting of three or five equal thickness, constant composition layers; 3) a continuously graded layer where x increased exponentially with layer thickness and 4) a continuously graded layer in which x increased linearly with layer thickness. The compositions were determined from double-crystal x-ray rocking curves using the (004) and (115) reflections. The strain distribution and layer thicknesses of both the buffer layers and the SLS's were obtained using a kinematical model as previously described [4]. The surface morphologies were examined by Nomarski interference contrast microscopy. The distribution of dislocations in the buffer layers was investigated by transmission electron microscopy.

The surface morphologies of the samples grown on thick, continuously graded buffer layers showed the presence of the normal cross hatching which is typical of mismatched layers which contain dislocations. However, the surfaces which contained thin buffers or buffers with abrupt compositional steps indicated the presence of microcracks. The correlation between thickness and crack formation was found to closely follow the predictions of Matthews and Klokholm [5]. When a critical layer thickness was exceeded for a particular mismatch, microcracks formed in the samples. The thicker, continuously graded buffer layers apparently allow enough dislocations to form during the layer growth so that the critical layer thickness for crack formation is never exceeded. In contrast, not enough dislocations are formed in the thinner layers to prevent the critical layer thickness for crack formation from being exceeded.

Direct evidence for the lack of sufficient dislocation formation to remove all of the mismatch between the buffer layer and the substrate was obtained by double crystal x-ray diffraction. The strain profiles for all of the samples examined indicated that there was some residual strain in all of the buffer layers which were examined. The residual strain occurs when not enough dislocations or cracks form to allow the buffer layer to relax to its equilibrium lattice constant. The residual strain in the buffer layers ranged from 10 to 30 percent. The most strain relief took place in the linearly graded buffer layers. This greater strain relief results in a better lattice match between the SLS and the buffer layer. This in turn leads to a smaller residual strain in the SLS and correspondingly larger critical layer thicknesses for dislocation and crack formation. By using the amount of residual strain present in the graded layer to predict the final lattice constant for the buffer layer, it should be possible to grow a nearly strain free SLS.

Transmission electron microscopy provided direct evidence for the enhanced strain relief in the thicker buffer layers by the formation of misfit dislocations within the bulk of the buffer layers. Dislocations were observed only at the substrate-buffer layer or buffer-buffer layer interfaces in the thinner buffer layers.

The degree of relaxation in these buffer layers is considerably less than would be expected from the results of conventional equilibrium models, but it is more complete in the continuously graded than in the step-graded layers. This behavior can be explained in terms of Taylor-type work hardening which invokes interactions between the dislocations [6]. Comparisons of the predictions of these models will be presented and their use in designing strain-relieved structures will be discussed.

REFERENCES

1. G. C. Osbourn, J. Vac. Sci. Tech., B2, 176 (1984).
2. S. R. Kurtz, G. C. Osbourn, R. M. Biefeld, L. R. Dawson, and H. J. Stein, Appl. Phys. Lett. 52, 831 (1988).
3. S. R. Kurtz, G. C. Osbourn, R. M. Biefeld, and S. R. Lee, Appl. Phys. Lett., submitted (1988).
4. V. S. Speriosu, M. A. Nicolet, S. T. Picraux, and R. M. Biefeld, Appl. Phys. Lett., 44, 223 (1984).
5. J. W. Matthews and E. Klokholm, Mat. Res. Bull., 7, 213 (1972).
6. B. W. Dodson, Appl. Phys. Lett., submitted (1988).

*This work was performed at Sandia National Laboratories supported by the US DOE under Contract No. DE-AC04-76DP00789.

Abstract No. 503

HETEROEPITAXY WITH LARGE LATTICE MISMATCH: TiN AND ZrN ON Si(100)

C.-H. Choi, S.A. Barnett
Department of Materials Science and
the Materials Research Center
Northwestern University
Evanston, IL 60208, USA

and

L. Hultman, J.-E. Sundgren
Department of Physics
Linköping University
S-581 83 Linköping, Sweden

Epitaxial metallic nitride films on Si substrates have potential applications for high-stability metallization, metal-base transistors, and 3D integrated circuits. Despite the large lattice mismatch inherent in the systems (TiN - 26%, ZrN - 16%), epitaxial TiN and ZrN films have been grown on Si(100). Reactive magnetron sputtering from Ti or Zr targets in pure N_2 discharges yielded growth rates from 500 to 1000 nm/h. Substrate temperatures T_s from 600 to 1100°C were used. Auger electron spectroscopy showed that films grown at T_s > 600°C were stoichiometric. Reflection electron diffraction (RED), TEM, and X-ray pole figure and diffractometer measurements were used to show that epitaxial TiN and ZrN were obtained. Studies of the epitaxial interface and defect structure using cross-section TEM will be described. Initial ZrN experiments showed increased preferential orientation of film grains with the substrate as T_s was increased above 750°C until epitaxial films were obtained at 900°C. More recent TiN results showed epitaxy for T_s > 700°C. Substantial improvements in film quality were obtained by depositing the first 50 nm at low T_s and then raising T_s for the balance of the growth. The epitaxial relationships were found to be XN(100)//Si(100) and XN[011]//Si[01$\bar{1}$] for X = Ti and Zr.

Abstract No. 504

In Situ Characterization of Heteroepitaxy by Quasi-elastic Light Scattering

J. M. Olson

Solar Energy Research Institute
Golden, Colorado 80401

Lattice mismatched heteroepitaxial structures including strained-layer superlattices (SLSs) of semiconducting materials are currently of considerable interest in the electronics community. It is now generally accepted, however, that SLSs with arbitrarily large interlayer strain and thicknesses and perfect planar morphology are difficult, if not impossible, to grow [1,2,3]. Using quasi-elastic light scattering, we show that this is a consequence of the intrinsic, thermodynamic tendency of strained epitaxial films to grow with a three-dimensional morphology.

Most of the experimental insight into this problem has been gleaned from work on the growth of SLSs using MBE and the host of in situ analytical equipment typically found on most MBE machines. The situation for MOCVD-grown SLSs is considerably less advanced due, in large part, to the lack of in situ growth monitoring techniques. With this in mind, we have developed a simple apparatus for measuring the quasi-elastic light scattering (QLS) from the surface of a growing epilayer [4]. The QLS measurement is sensitive to the roughness or three-dimensional (3-D) morphology of the growing surface.

A schematic of the QLS apparatus in combination with the MOCVD reactor is shown in Fig. 1. Light from a 15 mW HeNe laser is directed approximately normal to the surface of the growing crystal through a quartz window. The window is effectively cooled by the incoming source gases and consequently remains transparent for the duration of the experiment. The scattered light at an angle θ_s (close to 0°) is focused by a telemicroscope into the aperture of a silicon photodetector. The MOCVD apparatus is computer-controlled with a gas manifold and reactor geometry designed to yield, at one atmosphere pressure, abrupt interlayer transitions. The source gases were trimethylgallium (TMG), trimethylindium (TMI) and AsH_3 and PH_3 diluted 1:10 in H_2. The flowrate of the H_2 carrier gas was 3 slm. The layers were grown on either semi-insulating or Zn-doped ($1 \times 10^{18} cm^{-3}$) GaAs substrates oriented 2° off (100) toward (110).

For lattice-matched heteroepitaxial systems (such as AlGaAs/GaAs, $Ga_{0.5}In_{0.5}P$/GaAs and $In_{0.5}Ga_{0.5}As$/InP) we find, in general, that the growth morphology is dominantly 2-D yielding surfaces that are specular, i.e., yielding little or no scattered light. For lattice-mismatched systems, the situation is more complex. This is illustrated in Figs. 2-4. Fig. 2 shows the time resolved QLS (I_s) from the growing surface of $Ga_xIn_{1-x}As$ on GaAs for four different values of x. This behavior is characteristic of the Stranski-Krastanov growth mechanism: nucleation and growth of a continuous epilayer with a smooth, 2-D surface morphology (as evidenced by little or no change in I_s) followed by the onset of a 3-D growth morphology (and a strong increase in I_s). For x=0, the lattice mismatch between the InAs and the GaAs substrate is roughly 8%, and the thickness of the 2-D layer is a few monolayers. For larger values of x (and correspondingly smaller values of lattice mismatch) the thickness of the 2-D layer becomes larger and exceeds 90 nm for x=0.75. In general, however, the transition from 2-D to 3-D growth is not abrupt. Furthermore, note the similarity with coherent epitaxy and the critical layer thickness for the generation of misfit dislocations. It is possible that the 3-D growth is caused by the presence of dislocations generated by misfit.

Figs. 3 and 4 compare the heteroepitaxy with InP and $Ga_{0.5}In_{0.5}As$ on GaAs and illustrate the effect of other factors including growth rate, temperature, and V/III. InP and $Ga_{0.5}In_{0.5}As$ have the same lattice constant and hence the same lattice mismatch with respect to GaAs, yet InP grows with a stronger 3-D morphology than $Ga_{0.5}In_{0.5}As$. Similarly, stronger 3-D growth is observed for increased growth temperature and V/III ratio and decreased growth rate. These results suggest that factors that increase the adatom surface mobility relative to the incident diffusion flux will tend to increase to the effect that lattice mismatch has on the 3-D growth morphology.

The Stanski-Krastanov mode of growth is also observed for SLSs. The transition from 2-D to 3-D growth morphology is determined primarily by a combination of the interlayer strain and the strain between the SLS and the underlying buffer layer or substrate. Again, these effects are modulated by surface kinetic and chemical parameters.

REFERENCES

1. W. D. Laidig, C. K. Peng, and Y. F. Lin, J. Vac. Sci. Tech. B, 2 181 (1984).

2. A. E. Blakeslee, A. Kibbler, and M. W. Wanlass, Superlattices and Microstructures, 1(4) 339 (1985).

3. I. J. Fritz, S. T. Picraux, L. R. Dawson, T. J. Drummond, W. D. Laidig, and N. G. Anderson, Appl. Phys. Lett. 46 967 (1985).

4. J. M. Olson and A. Kibbler, J. Crystal Growth 77, 182 (1986).

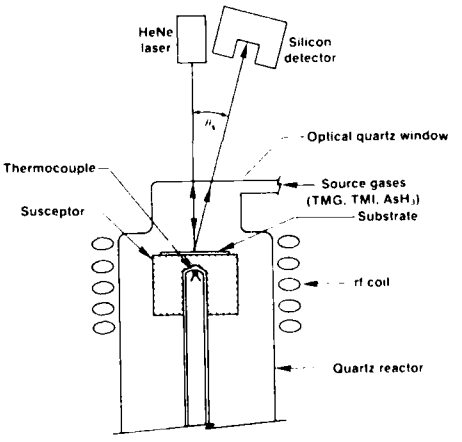


Fig. 1 A schematic diagram of the QLS-MOCVD apparatus.

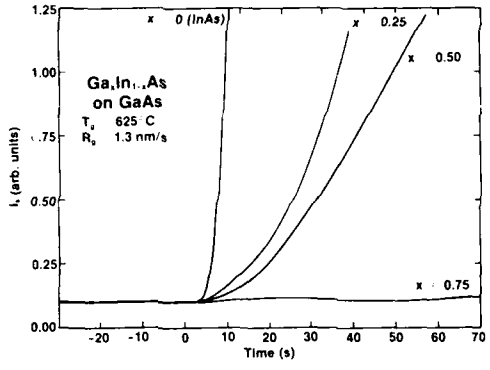


Fig. 2 A QLS measurement of the heterogeneous deposition of $Ga_xIn_{1-x}As$ on GaAs using trimethylgallium, trimethylindium and arsine.

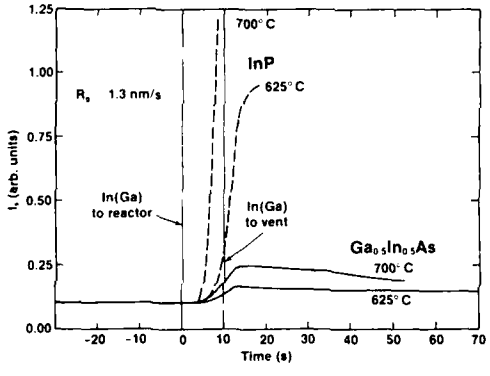


Fig. 3 A comparison of the heteroepitaxy of InP and $Ga_{0.5}In_{0.5}As$ on GaAs and the effect of deposition temperature.

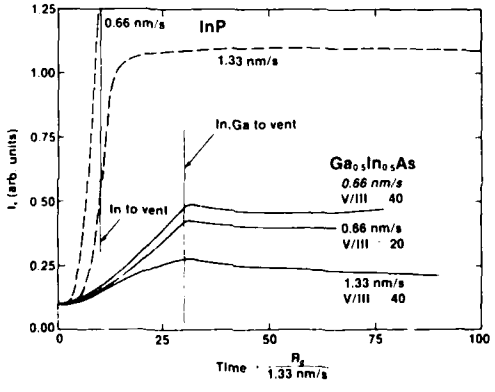


Fig. 4 QLS properties of InP and $Ga_{0.5}In_{0.5}As$ on GaAs and the effects of growth rate and V/III ratio.

Abstract No. 505

X-Ray Diffraction Study of $In_{.17}Ga_{.83}As/GaAs$ Strained-Layer Superlattices

D.E. Grider, R.R. Horning, and T. Nohava

Honeywell Sensors and Signal Processing Laboratory
10701 Lyndale Ave. S., MN09/1100
Bloomington, MN 55420

Pseudomorphic InGaAs heterostructures grown using MBE are playing an increasingly important role in the development of III-V heterostructure FET devices. Characterization of strain in these heterostructures is essential not only because of the strain-induced InGaAs valence band splitting which gives rise to enhanced hole mobility and thereby improved p-channel device performance, but also because the incomplete accommodation of InGaAs and GaAs/AlGaAs lattice mismatch by strain results in the formation of misfit dislocations which severely degrade device performance.

$In_{.17}Ga_{.83}As/GaAs$ strained-layer superlattices (nominally 75 periods of 200 Angstrom/200 Angstrom) were grown on 3 inch GaAs substrate wafers using a PHI 425A MBE system. The thickness of the $In_{.17}Ga_{.83}As$ layer thickness was chosen to be approximately equal to the 180 Angstrom critical layer thickness for the formation of misfit dislocations /1/. Making use Cu($K\beta$) radiation and the Bond method to eliminate Cu($K\alpha1$)/($K\alpha2$) splitting and positioning errors respectively, Theta/2-Theta x-ray diffraction scans of superlattice satellite peaks near the GaAs(400) peak were carried out at a number of positions radially from the center to the edge of the 3 inch wafer.

The superlattice period was determined using a least squares fit to the angular positions of the superlattice satellite peaks in the Theta/2-Theta scans /2/. Using this method, the period of the $In_{.17}Ga_{.83}As/GaAs$ superlattice was found to decrease monotonically from the center to the edge of the wafer by approximately 15%.

The strain perpendicular to the interface in both the $In_{.17}Ga_{.83}As$ and GaAs layers as well as the individual layer thicknesses were determined by comparison of the superlattice satellite intensities with a calculation based upon an abrupt interface model /3/. The strain in these layers parallel to the interface was then determined using the Poisson ratio.

A significant variation in the compressive parallel strain in the $In_{.17}Ga_{.83}As$ layers was observed radially from the center of the wafer as shown in Figure 1. The strain in the center of the wafer was found to be approximately 30% smaller than the strain near the edge of the wafer. Figure 1 also shows that only a small fraction (i.e., between 15% and 20%) of the total strain in the $In_{.17}Ga_{.83}As/GaAs$ superlattice was localized in the GaAs layers, and that this tensile parallel strain in the GaAs exhibited no clear dependence on position radially across the wafer. In agreement with the superlattice period results, the thickness of the individual $In_{.17}Ga_{.83}As$ and GaAs layers was found to decrease approximately 15% from the center to the edge of wafer.

The close correlation between the variation in the $In_{.17}Ga_{.83}As$ layer thickness and the strain in the $In_{.17}Ga_{.83}As$ layer is shown clearly in Figure 2. Note that the absolute values of the compressive parallel strain in the $In_{.17}Ga_{.83}As$, the tensile parallel strain in the GaAs and the total strain are plotted. Perhaps the most striking feature of Figure 2 is the sharp decrease in the total strain in the $In_{.17}Ga_{.83}As/GaAs$ superlattice when the $In_{.17}Ga_{.83}As$ layer thickness exceeds 197 Angstrom. The strain in the $In_{.17}Ga_{.83}As$ layer as well as the total strain continue to decrease for larger $In_{.17}Ga_{.83}As$ layer thicknesses.

The percentage of the lattice mismatch accommodated by lattice strain in the various layers can also be calculated using Vegard's law to establish the total lattice mismatch between the $In_{.17}Ga_{.83}As$ and GaAs layers. Using the data shown in Figure 2 for $In_{.17}Ga_{.83}As$ layer thicknesses below 197 Angstrom, it was found that essentially 100% of the lattice mismatch is accommodated by the total lattice strain in the $In_{.17}Ga_{.83}As$ and GaAs layers. $In_{.17}Ga_{.83}As$ layers thicker than 197 Angstrom have from 87% down to 74% of the lattice mismatch accommodated by the total lattice strain in the $In_{.17}Ga_{.83}As$ and GaAs layers.

It should be noted that misfit dislocation lines were clearly visible using Nomarski microscopy at positions on the wafer where the x-ray diffraction measurements indicate that 100 % of the lattice mismatch is accommodated by strain. This is in agreement with previous observations that strain is not a good indicator of the onset of misfit dislocation formation /4,5/. These misfit dislocations undoubtedly result from the fact that the total thickness of all of the $In_{.17}Ga_{.83}As$ layers in the 75 period superlattice exceeds the critical layer thickness by almost two orders of magnitude.

However, the substantial decrease in the total strain for $In_{.17}Ga_{.83}As$ layer thicknesses greater than 197 Angstrom provides clear evidence that there is a significant increase in the misfit dislocation density for thicker $In_{.17}Ga_{.83}As$ layers. It is important to note that this evidence for increased misfit dislocation density occurs at an $In_{.17}Ga_{.83}As$ layer thickness that is approximately 10 % larger than the 180 Angstrom critical layer thickness predicted by the Matthews-Blakeslee model /1/, thereby providing further support for the validity of this model.

The use of X-ray diffraction to measure strain in $In_{.17}Ga_{.83}As/GaAs$ strained layer superlattices can also be used to examine the long term stability of strained systems or to investigate the effects of various device processing steps on the strain. For example, this technique has been used to show that a Rapid Optical Anneal (ROA) typical of that used in the self-aligned gate device fabrication process has virtually no effect on the strain in these strained layer systems /3/.

1. J.W. Matthews and A.E. Blakeslee, J. Cryst. Growth 27, 118 (1974).
2. R.M. Fleming, D.B. McWhan, A.C. Gossard, W. Wiegmann and R.A. Logan, J. Appl. Phys. 51, 357 (1980).
3. D.E. Grider, R.R. Horning, T. Nohava, and D. Arch, in preparation.
4. I.J. Fritz, P.L. Gourley, and L.R. Dawson, Appl. Phys. Lett. 51, 1004 (1987).
5. I.J. Fritz, Appl. Phys. Lett. 51, 1080 (1987).

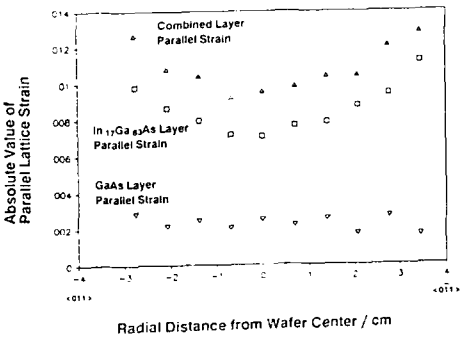


Figure 1. Lateral variation in the absolute value of the parallel strain in individual $In_{.17}Ga_{.83}As$ and GaAs layers as well as the combined parallel strain for a strained-layer $In_{.17}Ga_{.83}As$/GaAs superlattice.

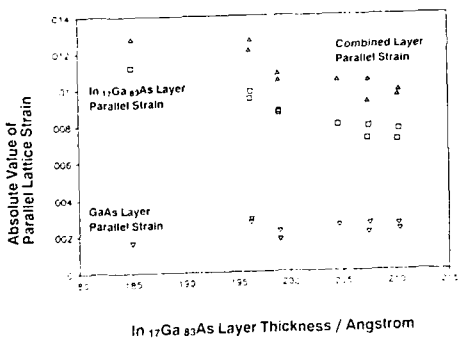


Figure 2. $In_{.17}Ga_{.83}As$ layer thickness dependence of the absolute value of the parallel strain in individual $In_{.17}Ga_{.83}As$ and GaAs layers as well as the combined parallel strain for an $In_{.17}Ga_{.83}As$/GaAs superlattice.

Abstract No. 506

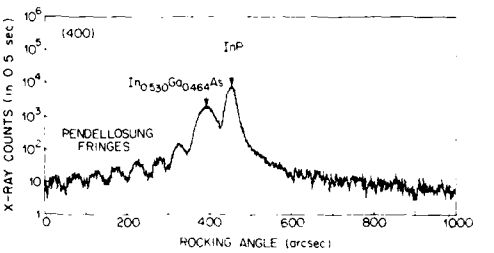
RELATIONSHIP BETWEEN X-RAY LINEWIDTH AND SIGN OF THE MISMATCH OF HIGHLY PERFECT InGaAs/InP GROWN BY METAL ORGANIC CHEMICAL VAPOR DEPOSITION

A. T. Macrander, S. Lau, J. Long, and D. M. Coblentz

AT&T Bell Laboratories
Murray Hill, NJ 07974

ABSTRACT

X-ray double crystal rocking curve data for an InGaAs epitaxial layer grown on a (100) oriented InP substrate by metal organic chemical vapor deposition (M O C V D) were obtained at 30 locations on a wafer measuring 14 × 28 mm. The mismatch on this wafer varied from -0.14% at the upstream edge to +0.08% at the downstream edge. The mismatch did not vary in the direction lateral to the gas flow direction in the horizontal MOCVD reactor. Full width at half maximum (FWHM) values were clearly correlated to the sign of the mismatch. The smallest linewidths were found in the case of positive mismatch. In addition, as shown in Fig. 1, strong Pendellosung fringes were observed for the positively mismatched portion of the wafer, and these fringes were used to obtain the variation in the thickness of the epitaxial layer.[1] All the rocking curve data were obtained under computer control. Automated x-y stepping and crystal alignment permitted unattended data gathering. The thickness of the epitaxial layer varied from 0.396 microns to 0.350 microns. The change in linewidth as the mismatch changed sign appears to rule out mosaic broadening due to misfit dislocations. Models involving a mosaic broadening due to dislocations threading up from the substrate in the case of negative mismatch (but not for positive mismatch) will be discussed. For the portion of the sample which was positively mismatched the linewidths are equal to ideal values calculated using dynamical diffraction theory. To our knowledge this degree of perfection has not been reported previously for InGaAs grown on InP by MOCVD.



1 *A. T. Macrander and K. Strege, J. Appl. Phys., 59, 442 (1986).*

Abstract No. 507

The Use Of Lattice Mismatch Measurements On InGaAs Layers As A Means Of Investigating VPE Growth Processes

D. N. Buckley

AT&T Bell Laboratories
Murray Hill, New Jersey 07974

In the growth of III-V materials for optoelectronic applications, it is frequently important that epitaxial layers of ternary and quaternary alloys be closely lattice matched to a binary alloy substrate[1-3] Careful control of gas phase growth parameters is therefore required in vapor phase epitaxy to minimize variations in the composition of the layers grown. It has been demonstrated[4,5] that such control also enables the growth of InGaAs having a high degree of crystalline perfection. Conversely, measurements of lattice mismatch[5,6] provide a sensitive method for investigating compositional variations in epitaxial layers. Variations in In:Ga ratio can be estimated with an accuracy of the order of 0.1% from lattice mismatch values determined by x-ray diffraction measurements. In contrast, it is usually difficult to achieve an accuracy better than 1-2% in measurements of growth rate. The relative rates of deposition of indium and gallium in the growth of InGaAs can therefore be investigated with much greater accuracy that the corresponding rates of deposition of binary compounds. Thus, x-ray diffraction determinations of lattice mismatch provide a unique means of investigating aspects of the deposition kinetics of ternary alloys such as InGaAs with much greater sensitivity than can be achieved in comparable investigations of binary alloy growth.

Results of double crystal x-ray diffraction measurements to determine the lattice mismatch of epitaxial layers of InGaAs on InP will be presented. These measurements have been made on layers grown under a variety of gas compositions. Scanning electron microscopy measurements on cleaved cross sections have been used to determine corresponding growth rates. The composition of the InGaAs was influenced by the input mole fractions of HCl to the metal boats, by the mole fraction of HCl injected directly into the growth region, and by the input mole fraction of arsine. Growth rate and lattice mismatch data for layers grown using various different values of these gas phase parameters will be presented. In general, the growth rate was found to increase with increasing mole fraction of arsine and with decreasing mole fraction of directly injected HCl.

A clear interrelationship between growth rate, lattice mismatch and gas-phase metals ratio was observed. This provides useful information on the relative rates of processes occurring at the gas-solid interface during growth. It will be shown that the gallium content of the layers grown decreased with increasing growth rate. The data is consistent with depletion of the GaCl concentration at the gas-solid interface due to diffusion across a boundary layer. The implications for the mechanism of the growth process will be analyzed.

The author would like to thank A. T. Macrander for helpful discussions, C. M. Stiles for SEM measurements and W. D. Johnston, Jr. for advice and encouragement.

REFERENCES

1. R. F. Karlicek, B. Hammarlund and J. Ginocchio, J. Appl. Phys. 60, 794 (1986).

2. R. F. Karlicek, Jr., D. Mitcham, J. C. Ginocchio, and B. Hammarlund, J. Electrochem. Soc. 134, 470 (1987).

3. M. Yoshido and H. Watanabe, J. Electrochem. Soc. 132, 1733 (1985).

4. D. N. Buckley, J. Electron, Mater. 17, 15 (1988).

5. A. T. Macrander and K. E. Strege, J. Appl. Phys. 59, 442 (1986).

6. A. T. Macrander, E. R. Minami, and D. W. Berreman, J. Appl. Phy. 60, 1364 (1986).

Abstract No. 508

Structural Characterisation of Strained Layer Quantum Well Systems by Grazing Incidence X-ray scattering

C.A. Lucas, D.F. McMorrow and S. Bates

Department of Physics, University of Edinburgh, Mayfield Road, Edinburgh EH9 3JZ, U.K.

Double crystal x-ray rocking curve analysis is a powerful and non-destructive technique for the characterisation of heteroepitaxial layer structures.[1] However, in the conventional, symmetrical scattering geometry, the penetration depth of the x-ray beam is of the order of 10 microns, and so the technique lacks sensitivity for nanometer-scale single layers. This problem may be overcome by adopting a highly asymmetric, grazing incidence scattering geometry, to limit the penetration depth, and by using a diffracted-beam analyser crystal, allowing weak scattering features to be resolved from the background noise. The extra resolution provided by the triple-crystal spectrometer enables a detailed mapping of the scattered x-ray intensity in sample reciprocal space, and thus yields information on lattice mismatch both perpendicular and parallel to the sample surface normal[2]. Termination of the lattice, in heteroepitaxial layer structures, gives rise to a rod of scattering in reciprocal space around bulk reciprocal lattice points. This 'crystal truncation rod' lies in a direction perpendicular to the truncated lattice and contains information on lattice mismatch, layer thickness and interface roughness[3]. In a recent paper we have used this technique to characterise a buried layer only 200 Å thick[4]. A complementary technique, applicable to crystalline and amorphous materials, is to measure the specular x-ray reflectivity as a function of incident angle. This probes the variation in the electron density of the sample material with depth and has been used to study layers as thin as 15 Å, using a conventional laboratory x-ray source[5].

In this paper we present measurements on a strained single layer quantum well grown by MOCVD at Oxford University. The experiments were carried out using the triple-crystal x-ray spectrometer at Edinburgh University, with a rotating anode generator, operating at 3 kV. Figure 1 shows a schematic representation of the sample, together with the integrated intensity distribution along the (0 0 1) direction around the GaSb (2 2 4) Bragg reflection. The incident angle for this reflection is approximately 3° and the horizontal axis is given in reciprocal lattice units a*, where a* is the reciprocal lattice constant of the GaAs substrate, perpendicular to the layer. Three main features are apparent:-

(1) The Bragg peak is broadened due to the presence of the lattice matched GaSb capping layer.

(2) The weak secondary peak arises from the InGaSb quantum well, its position giving a lattice parameter mismatch between the quantum well and buffer layer

$\frac{\Delta a}{a} = 18.6 \times 10^{-3}$, where a = 6.085 Å

(3) Oscillations superimposed on the pattern are the effects of interference between the scattering from the capping layer and quantum well.

Figure 2 shows a least squares fit to the data, using the parameters given in Table 1 in a kinematical theory[4]. These parameters are in good agreement with the nominal growth parameters and show that it is possible to obtain structural information on epitaxial layers 80 Å, or less, in thickness.

References

[1] W.J. Bartels and W. Nijman, J. Crystal Growth 44, 518 (1978).
[2] R.A. Cowley, Acta Crystallog. A37, 825 (1987).
[3] T.W. Ryan, P.D. Hatton, S. Bates, M. Watt, C. Sotomayer-Torres, P.A. Claxton and J.S. Roberts, Semicond. Sci. Technol. 2, 241 (1987).
[4] C.A. Lucas, P.D. Hatton, S. Bates, T.W. Ryan, S. Miles and B.K. Tanner, J. Appl. Phys. 63 (6), 1936 (1988).
[5] R.A. Cowley and T.W. Ryan, J. Phys. D, 20, 61 (1987).

Table 1

Capping Layer:	Thickness	= 268 Å,
	RMS. Roughness	= 19 Å,
	Δa/a	= 0.8×10^{-3}.
Quantum Well:	Thickness	= 93 Å,
	RMS Roughness	= 27 Å,
	Δa/a	= 18.6×10^{-3}.
Buffer Layer:	RMS Roughness	= 34 Å, a = 6.085 Å.

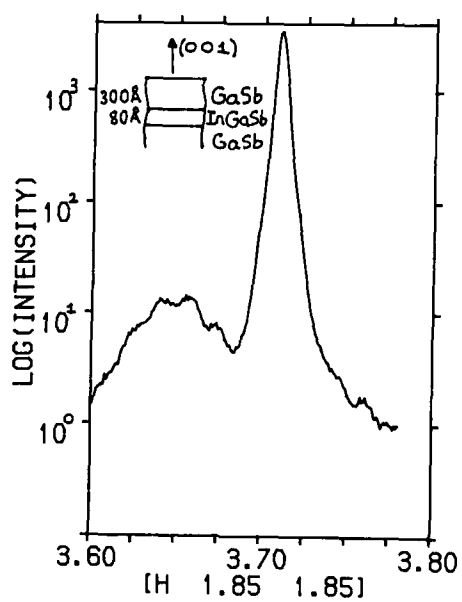


Figure 1. The intensity distribution along (001), the face normal direction through the GaSb (422) Bragg peak.

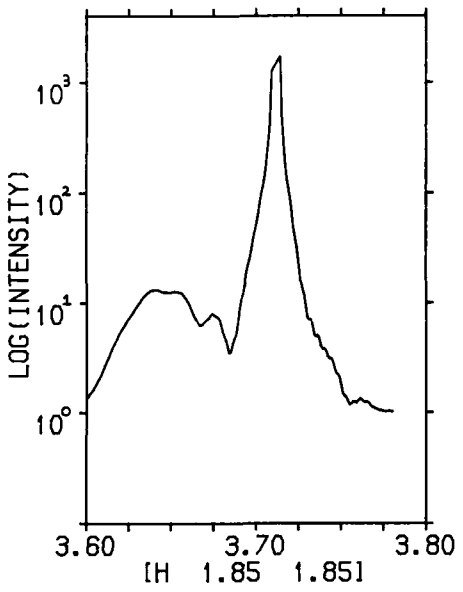


Figure 2. A least squares fit to the data in figure 1.

Abstract No. 509

LATTICE MISMATCH OF SIMPLE AND COMPLEX LAYER STRUCTURES BY X-RAY DIFFRACTION

Paul F. Fewster

Philips Research Laboratories
Cross Oak Lane, Redhill, Surrey, U.K.

This paper will concentrate on the determination of lattice mismatch from thin heteroepitaxial layers closely matched to their substrate. The very high strain sensitivity of X-ray diffraction methods is ideal for determining layer mismatch although caution is required in the interpretation. The diffraction from single layers less than 0.5 microns thick cannot be simply interpreted for determining the mismatch[1,2] and for multilayers whole pattern simulation is necessary. The errors in deriving the mismatch from the separation in the diffraction peaks and using Bragg's Law can be very large (>10%) if other diffraction effects are ignored, fig. 1. Computer simulation of the profiles using dynamical theory will predict the correct answer with the additional benefit of estimating the layer thicknesses to high accuracy. To determine the correct layer mismatch of complex structures it is necessary to simulate the diffraction profile of a model of the structure to fit the experimental profile. This iterative process is time-consuming and can be assisted by including additional information learnt from experience, this has enabled computer fitting and refinement methods to give excellent fits between theory and experiment, fig. 2, even for structures with more than a thousand layers. Simpler structures with single buried layers of thicknesses close to 100Å can also be studied in this way, experimentally the results are obtained by grazing incidence diffraction to enhance the diffraction effects.

In the case of bent samples the important information in the rocking curve can be swamped. This is especially apparent at grazing incidence. The problem can be overcome by using a high resolution multiple-reflection diffractometer[3] composed of a four-crystal reflection monochromator and an analyser crystal after the sample. Such an arrangement allows any reflection to be studied with little dispersion and a well defined acceptance angle for the detector. This has proved very powerful in the w - 2θ scan mode and also in the mapping geometry for separating strain and orientation effects in diffraction. An example of a severely bent structure composed of 1517 layers of AlAs and GaAs gave a broad rocking curve without the analyser, (dotted line), fig. 3, whereas with the multiple-reflection diffractometer the pattern was transformed (line) and the individual thicknesses and mismatches could be determined by simulation (dash line).

1. Fewster, P.F. (1987) Thin Film Growth Techniques for Low Dimensional Structures. NATO ASI Series B: Physics 163, Ed. Farrow, Parkin, Dobson, Neave and Arrott, pp.417-440, New York: Plenum Press.

2. Fewster, P.F. and Curling, C.J. (1987) J. Appl. Phys. 62, 4154-4158.

3. Fewster, P.F. to be published.

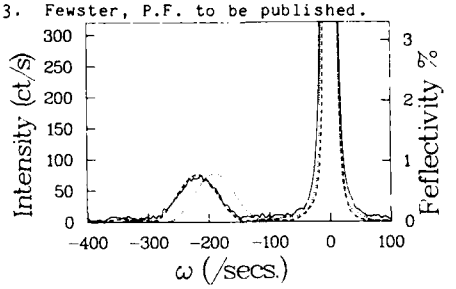


Fig. 1: The asymmetric 115 reflection from a 0.38 micron $Al_{0.34}Ga_{0.66}As$ layer on GaAs (001). The layer included 5 narrow quantum wells but in this experiment the diffraction is indistinguishable from a single layer. Experimental profile (line), simulated using the mismatch derived from the peak separation (dot) and that with a mismatch 15% greater than this value (dash).

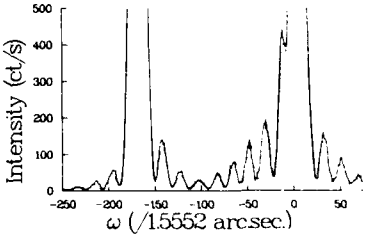


Fig. 2: The 004 experimental (line) and calculated (dot) diffraction profile with CuKα radiation for the symmetric reflection from a sample consisting of 60 periods of 28Å GaAs + 75Å AlAs capped with 0.1um GaAs all on a GaAs substrate.

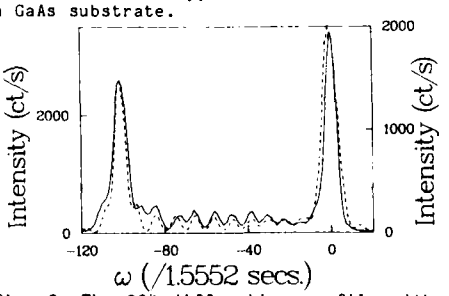


Fig. 3: The 004 diffraction profile with the 5 crystal reflection geometry (dot), 6 crystal reflection geometry (line) and simulated profile (dash) for an all-binary AlAs/GaAs superlattice laser structure with 1517 layers.

Abstract No. 510

Kinetics and Energetics Issues in Semiconductor Heteroepitaxy Using Molecular Beam Epitaxy

Jasprit Singh

Department of Electrical Engineering
and Computer Science

The University of Michigan, Ann Arbor, Michigan 48109

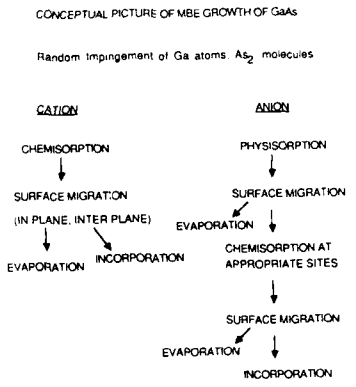
The ability to produce atomically abrupt chemical modulation in semiconductor structures using molecular beam epitaxy (MBE) and metal organic chemical vapor deposition (MOCVD) has led to the conception and realization of numerous ideas based on sub-three dimensional physics. The success of many new devices such as Modulation Doped Field Effect Transistors, exciton based quantum well modulators and single quantum well lasers depend critically on achieving perfect interfaces. Recently new high performance devices based on coherently strained heterostructures as well as integrated technologies using non-lattice matched (GaAs/Si;CdTe/GaAs etc.) substrates are attracting considerable interest.

The successful implementation of all these heterostructure based concepts depends intimately on being able to obtain high quality bulk and interfaces between widely differing semiconductors -- often in presence of strong strain fields. The growth mechanisms leading to these heterostructures -- often very far from equilibrium -- need to be understood on an atomistic scale. The growth mechanisms are extremely complex to understand since the growth process involves -- i) details of surface atomic bonds and their bond energies; ii) diffusion and evaporation rates; iii) incorportion mechanisms for impinging atoms and molecules; and iv) presence of long range strain fields for non-lattice matched epitaxy. In addition, most hetero-epitaxy growth conditions involve far from equilibrium growth modes.

In this paper we will attempt to provide a glimpse of some generic nature of hetero-epitaxy in the strain free and strained environment. The focus will be on identifying the key kinetic and energetic issues that control the growth front (and interface) profile.

Due to the complexity of hetero-epitaxy, most of the theoretical work carried out to understand the growth mechanisms has been based on computer simulation[1-3]. Monte Carlo simulations have provided considerable insight into the nature of MBE growth. A conceptual growth scheme shown in the figure has emerged from many experimental studies[4,5] details of which have emerged from computer simulations[1-3]. This scheme is expected to be valid for GaAs and other III-V semiconductor growth.

Using results obtained from Monte Carlo simulations, it will be established that for a given semiconductor and a fixed growth rate, a window in growth temperature exists in which the growth front is atomically flat. Below this window the growth front is increasingly rougher, and above it the material quality deteriorates. The position of this temperature window is directly related to the growth rate and the cation anion (e.g. Ga-As) bond strengths. For high quality lattice matched hetero-interfaces, it is essential that the windows for the two semiconductors line up. This may often involve novel growth approaches such as i) non-uniform growth rate; ii) substrate temperature transients; iii) growth interruption etc. Crucial parameters controlling the growth front are cation migration lengths and impinging fluxes. While the latter can be controlled, very little information exists on the former.



Experimental information on cation kinetics which could be obtained from reflection high energy electron diffraction[6] could provide valuable insight into growth of widely differing semiconductors.

In non-lattice matched growth, in addition to the many complexities involved in lattice matched growth, one has to contend with the strain field as well. We will show that while in unstrained epitaxy, hyperabrupt interfaces can be produced essentially by manipulating the surface kinetics during growth, in strained epitaxy, energetic considerations may forbid atomically smooth interfaces. The reason for this unusual behavior is that while in unstrained environment, the internal energy considerations favor an atomically smooth surface, in presence of strain a rough front is found to be energetically more favorable. This implies that under conventional MBE growth, pseudomorphic interfaces cannot be of as high quality as lattice matched interfaces. Novel growth approaches need to be investigated to overcome this important barrier to the realization of the full potential of pseudomorphic devices.

REFERENCES:

1. J. Singh and K. K. Bajaj, J. Vac. Sci. Technol. B2 (2), 276 (1984); Superlattices and Microstructures 2, 185 (1986).
2. S. V. Ghaisas and A. Madhukar, Phys. Rev. Lett. 56, 1066 (1986).
3. S. Clarke and D. W. Vvedensky, Appl. Phys. Lett. 51, 340 (1987).
4. J. R. Arthur, Surf. Sci. 43, 1999 (1974).
5. C. T. Foxon and B. A. Joyce, Surf. Sci. 64, 293 (1977).
6. J. H. Neave, P. J. Dobson, B. A. Joyce and J. Zheng, Appl. Phys. Lett. 47, 100 (1985).

ACKNOWLEDGEMENT:

This work was supported by the National Science Foundation (Material Research Group Program).

Abstract No. 511

II-VI/III-V Heterointerfaces: Epilayer on Epilayer Structures

R.L. Gunshor, L.A. Kolodziejski, N. Otsuka, A.V. Nurmikko*, and M.R. Melloch

Purdue University
West Lafayette, Indiana 47907 USA
*Brown University, Providence, RI 02912 USA

The integration of several optoelectronic device functions onto a common substrate material is an area which is of current interest to many research groups. In an effort to achieve this objective, experiments are under way to determine appropriate epitaxial growth techniques for a variety of II-VI and III-V semiconductor compounds. In several cases the heterostructures of interest involve II-VI/III-V interfaces having various degrees of lattice constant mismatch. The emphasis of this paper is a description of recent developments involving the molecular beam epitaxial (MBE) growth and characterization of two important II-VI/III-V heterostructures: ZnSe/GaAs and CdTe/InSb. For both heterostructures, a comparison is made between epitaxial layer/substrate interfaces and epilayer/epilayer interfaces. Initial studies tend to show that epilayer/epilayer interfaces are more represenative of intrinsic properties, while the behavior of epilayer/substrate interfacial regions may be greatly affected by substrate preparation. The ZnSe/GaAs heterointerface, having a 0.25% lattice constant mismatch, has potential for use in the passivation of GaAs devices. Metal/ZnSe/n-GaAs field effect transistors are fabricated and are under study to examine the interface state density and charge transport at the II-VI/III-V heterointerface. In these structures a pseudomorphic ZnSe layer is formed as a means to minimize defects at the interface in the presence of the small but finite lattice mismatch. I-V measurements of GaAs field effect transistors indicate that the Fermi level is not pinned at the ZnSe/GaAs interface.

The CdTe/InSb heterointerface possesses an even closer lattice match, 0.05% (comparable to the (Al,Ga)As/GaAs material system), and is motivated by potential device applications provided by CdTe/InSb quantum wells accessing the 3-5.5μm wavelength range. New results using Sb_2 for the low temperature growth of InSb on epitaxial layers of CdTe will be reported. Single quantum well and double heterostructures of InSb have been grown using a modular MBE system in which three growth chambers are interconnected by ultra high vacuum transfer tubes. Raman spectroscopy, photoluminescence, transmission electron microscopy, and double crystal x-ray diffraction techniques have been used to characterize these II-VI/III-V structures.

Abstract No. 512

EFFECTS OF LATTICE MISMATCH ON THE PHOTOLUMINESCENCE PROPERTIES OF HETEROEPITAXIAL ZnSe ON GaAs, InGaAs, AND AlAs

B.J. Skromme, M.C. Tamargo, J.L. de Miguel*, R.E. Nahory, and W.A. Bonner

Bell Communications Research
331 Newman Springs Road
Red Bank, NJ 07701

Heteroepitaxy of ZnSe on III-V substrates is of considerable technological interest, both because of the potential for fabricating blue light-emitting devices if p-type doping of the ZnSe can be achieved, and for the possibility of using the ZnSe as an epitaxial insulator on GaAs and related materials in MIS structures, lasers, and waveguides. This system is also of fundamental interest as a prototype of small lattice-mismatched systems (a/a = 0.27% for ZnSe/GaAs), with the additional complication that interdiffusion of the two materials may result in undesired doping of both layers. It is therefore of great importance to determine how the interface quality in this system, and the quality of the heteroepitaxial ZnSe can be optimized. In the present study, we have attempted to systematically characterize the quality of the ZnSe using low temperature photoluminescence, for ZnSe layers grown on GaAs substrates and epilayers, AlAs buffer layers, $In_xGa_{1-x}As$ buffer layers, and bulk $In_xGa_{1-x}As$ substrates. Both the ZnSe and the various buffer layers were grown in a dual-chamber molecular beam epitaxy (MBE) system, with the samples transferred in ultra-high vacuum between the two chambers.

Linewidths of bound exciton photoluminescence peaks are determined almost entirely, in heteroepitaxial ZnSe, by inhomogeneous strain associated with partial or non-uniform lattice relaxation of the small lattice mismatch by dislocations or other defects. In high purity strain-free bulk or homoepitaxial ZnSe grown by high temperature growth techniques, linewidths as narrow as ~0.15 meV have been achieved. For MBE or OMCVD ZnSe grown directly on GaAs, however, these linewidths have typically been in excess of 1 meV for fully relaxed (thick) layers, and, surprisingly, even broader for nominally pseudomorphic (<0.17 um) layers. While X-ray, luminescence, and reflectance measurements all show such layers to exhibit the approximate average biaxial compression expected of a pseudomorphic structure, the luminescence linewidths indicate that partial relaxation of the mismatch is occurring even in these very thin layers.

We have investigated these linewidths for different types of layered structures and found substantial improvements for cases where an intermediate buffer layer is inserted between the ZnSe and GaAs, having a lattice constant intermediate between the two. For example, pseudomorphic AlAs buffers (a/a = 0.17% at 300 K for AlAs/GaAs) of ~0.5 um thickness were inserted between a GaAs substrate and a 0.17 um thick ZnSe layer, which yielded linewidths of 0.22-0.37 meV, as compared to a 1.95 meV linewidth for a similar ZnSe layer grown directly on GaAs. These linewidths for the first time approach those obtained in bulk material, indicating a substantial reduction in the density of interfacial defects and strain. We have further investigated pseudomorphic structures incorporating $In_xGa_{1-x}As$ buffers (x~0.04) in place of the AlAs. In this case, the lattice constant of the buffer can be continously varied about that of ZnSe by controlling the In content. The composition of the buffer was measured using luminescence, reflectance, and excitation spectroscopy. We find substantially reduced linewidths in this case also, for example 0.62 meV for the neutral donor-bound heavy hole exciton peak. The effect of varying the buffer composition has also been determined.

We have also investigated the growth of ZnSe layers on exactly matched and slightly mismatched bulk $In_xGa_{1-x}As$ substrates. These substrates, nominally 1" in diameter and containing up to 5 mole % In, were prepared using a low pressure liquid encapsulated Czochralski technique, in both (100) and (111) orientations. The composition and compositional variations in the material were determined using low temperature photoluminescence. For example, a melt containing 17 mole % InAs yielded crystals with composition ranging from x=.021 to .045. Growth of ZnSe layers on (100) wafers cut from these boules was performed by MBE. The properties of the ZnSe layers as a function of In content in the substrate will be described.

These results demonstrate that even a small (0.27 %) lattice mismatch can have important effects on the quality of the resulting material, and that "step-grading" the lattice parameter in pseudmorphic structures offers a technique for greatly improving crystalline quality of the epilayers and eliminating interfacial defects.

*Present address: Centro Nacional de Microelectronica, Serrano 144, Madrid, Spain.

Abstract No. 513

Synthesis of GaAs and (Al,Ga)As on (511)-GaAs Surfaces by Molecular Beam Epitaxy

E. Towe and C. G. Fonstad

Department of Electrical Engineering and Computer Science,
Research Laboratory of Electronics
and
Center for Materials Science and Engineering
Massachusetts Institute of Technology
Cambridge, Massachusetts 02139

The scientific and technological importance of III-V heterostructure semiconductors with surfaces of high Miller indices has increased over the past few years [1,2]. Fundamentally, high-index surfaces will exhibit growth kinetics that depend on (i) the stoichiometry of the surface, (ii) the density of each atomic specie present, and (iii) the tendency of the particular surface to maintain planarity. These and other characteristics are currently not well understood.

The (511) GaAs surface is one of a class of surfaces denoted by $\{h11\}$. For h larger than 1 the surfaces can be thought of as being composed of {100} and {111} surfaces. This class of surfaces is vicinal to the (100) plane. In fact, during the mbe-growth of GaAs on patterned (100) substrates, some of the surfaces in the $\{h11\}$ class are revealed [3], and there is evidence that the growth rate and conductivity type of device structures grown on patterned surfaces vary depending on the vicinal surface exposed [4]. This can be understood in terms of the relative availability of the lattice sites for the Ga and As atoms which, in turn, depends on the particular vicinal surface under study. Because of the importance of the $\{h11\}$ surfaces in the growth of patterned structures on (100)-GaAs substrates, a better understanding of the epitaxial characteristics of these surfaces will be required. This paper discusses the growth of GaAs and (Al,Ga)As by molecular beam epitaxy on one such surface; the (511) surface.

The (511) surface intersects the (100) plane at an angle $\theta = \cos^{-1}([100]\cdot[511]/\sqrt{27}) = 15.8°$; it is therefore to be expected that the relative density of Ga and As double- and single-bond sites will differ from that on the (100) surface. The larger the angle θ is, the more different from the (100) surface will the vicinal surface be.

The substrates used in our study were (511)B. They were intentionally misoriented by 0.5° toward the (100) surface. Before loading into the growth system, the substrates were degreased in standard solvents and then etched in H_2SO_4:H_2O_2:H_2O (4:1:1) at room temperature for 4 minutes. They were then soaked in HCl for 2 minutes and a protective native oxide was grown in de-ionized water. Once loaded into the preparation chamber, the wafers were outgased for 20 minutes at 200°C. This temperature is lower than that conventionally used to outgas (100) substrates, because it is found that the substrate surface degrades if outgased at much higher temperatures in the absence of As_x. The oxide desorption temperature for the (511) surfaces is also different, being 30 to 40°C lower than the 580 to 590°C typically observed for a (100) surface. We have previously observed similar behavior for the (111)B GaAs surface [5], and believe it to be because of the differences in the density of double- and single-dangling bonds of Ga and As on the (100) and $(h11)$ surfaces. These differences have implications for the growth of uniformly high quality device structures on patterned substrates which include high-index surfaces. During the growth of (Al,Ga)As on (100) and (511) substrates mounted side by side, for example, we observe that for a given substrate temperature, the (100) layers require a higher As_4 overpressure to maintain a specular and featureless morphology than the (511) ones.

High quality GaAs and (Al,Ga)As layers have been grown on (511) surfaces in the normal substrate temperature range of 600-710° C. The undoped layers are p-type. Photoluminescence characterization of these wafers has also been carried out. It is found that for (511)- and (100)-GaAs wafers grown side by side, the optical quality of the (511) layers is equal to or better than that of the (100) layers in all cases. The typical room temperature photoluminescence linewidth for the unintentionally doped (511) wafers is ~20 meV.

References

[1] D. L. Smith and C. Mailhiot, Phys. Rev. Lett., **58**, 1264 (1987).

[2] G. H. Olsen, T. J. Zamerowski and N. J. DiGiuseppe, J. Appl. Phys., **54**, 3598 (1983).

[3] J. S. Smith, P. L. Derry, S. Margalit and A. Yariv, Appl Phys. Lett., **47**, 712 (1985).

[4] T. Nishibe, M. Funamizu, H. Okuda, H. Furuyama, Y Hirayama, M. Nakamura and M. Iwamoto, Electron. Lett., **23**, 35 (1987).

[5] K. Elcess, J. L. Lievin and C. G. Fonstad, *To be published* in Journ. Vac. Sci. Tech., (1988).

Abstract No. 514

Low-Temperature Growth of AlGaAs-GaAs Heterostructures by Migration-Enganced Epitaxy

Yoshiji Horikoshi, Minoru Kawashima, and Hiroshi Yamaguchi

NTT Electrical Communications Laboratories
Musashino-shi, Tokyo 180. Japan

The MBE and MOCVD methods have two problems in growing GaAs and AlGaAs thin layers. First is that the heterojunctions grown by these methods have rough interfaces on the atomic scale due to a large number of islands formed during growth. Second is that the substrate temperature (Ts) is too high to realize sharp impurity profiles.

These problems are caused by a very slow migration of surface adatoms during growth. In both MBE and MOCVD, growth is performed in As-stable conditions. Therefore, the lifetime of isolated Ga and Al atoms on the surface is quite short, which effectively reduces the surface migration. This is because Ga and Al atoms impinged on the surface immediately react with As to form GaAs and AlAs islands.

To enhance the migration, a new MBE method was developed called "Migration-Enhauced Epitaxy" (MEE), which utilizes the rapid migration of metallic atoms in an As-free atmosphere. In this method, Ga and Al atoms migrate easily and find stable sites on the growing surface, even at low Ts, because these metallic atoms are deposited separately by As. This paper discusses the growth mechanism of MEE at low Ts based on the RHEED observation. Extremely sharp and intense photoluminescince (PL) from AlGaAs-GaAs single-quantum wells grown at 300°C by this method are also demonstrated.

A conventional MBE apparatus equipped with a RHEED system was used for this study. During MEE growth, Ga or Al and As_4 were alternately deposited to a (100) GaAs surface. The migration process of surface adatoms as well as the growth process were monitored by RHEED observations. As reported previousy[1], when the number of Ga or Al atoms deposited per cycle (N_{Ga}, or N_{Al}) equals the surface site number in the (100) GaAs surface (Ns; $6.4\times10^{14}/cm^2$), these atoms form a "one atomic layer" every cycle, and the RHEED intensity oscillates persistently without showing any degradation in amplitude during the entire layer growth, as shown in Fig. 1. This indicates that a flat growing surface is maintained during growth. When N_{Ga} is not equal to Ns, small one-monolayer GaAs islands are formed after the completion of one cycle. The surface roughness due to these islands is compensated for in the succeeding MEE cycles, because Ga atoms impinged on the island-enriched surface find their sites between the islands. This phenomenon is clearly confirmed by the observation of modulated RHEED oscillation shown in Fig. 2 for N_{Ga}=0.8 Ns.

A persistent RHEED oscillation is also observed at low Ts to 100°C, indicating a possibility of high-quality layer growth at low Ts. The growth mechanism is, however, modified when Ts is lowered below approximately 400°C. At high Ts, the number of As_4 molecules deposited per cycle (N_{As}) is not very critical, because no excess As adsorption occurs. At low Ts, however, excess As adsorption becomes very important and markedly deteriorates the crystal quality. Therefore, an accurate control of N_{As} is needed for growing high-quality layers at low Ts.

An excess As adsorption occurs when N_{As} is greater than the critical value. Existence of excess As can be detected by the RHEED observation. When there is an excess As on the surface, the specular beam intensity in the succeeding Ga deposition period increases as demonstrated in Fig.3. No well-established Ga-stable pattern is observed, even at the end of the Ga deposition period. An excess As adsorption is also enhanced by surface roughness. When N_{Ga}<Ns, two-dimentional nucleation occurs, and the surface island density changes cycle by cycle, as shown in Fig. 2. At the valley of the modulated wave, the island density is expected to be highest, while, at the peak of the modulated wave, an atomically flat surface can be obtained. The RHEED specular beam oscillation during the growth of GaAs at 300 °C with N_{Ga}=0.97Ns and N_{As}=$3.8\times10^{14}/cm^2$ is shown in Fig. 4. The value N_{As}, in this case, only slightly exceeds the optimum value which will be discussed later. Because of the incommensurate supply of Ga, a modulated wave appears every 35 cycles. However, in this case, unlike the high Ts result of Fig.2, two modulated waves compete. One wave includes the peaks after the As deposition period (labeled A), and the other includes those after the Ga deposition period (labeled B). The former is caused by the surface roughness, while the latter is influenced by the amount of excess As. Figure 4 shows that the excess As adsorption is strongly enhanced by the surface roughness.

Therefore, an optimization of the N_{As} value and an exact adjustment of N_{Ga} to Ns are necessary in order to avoid excess As adsorption. Under optimum conditions, the RHEED intensity behaves as if it were at high Ts. During Ga supply periods, RHEED intensity decreases but returns to its original value in the succeeding As deposition periods. Persistent RHEED oscillation is observed during the entire layer growth, and well defined Ga-stable and As-stable surfaces are established at the end of their deposition periods (see the lower trace of Fig. 5).

Further reduction of N_{As} deteriorates the quality of the grown layer probably because of an As shortage, and the persistent RHEED oscillation is no longer obtained, as shown in the upper trace of Fig. 5. The optimum value of N_{As} is $3.2\sim3.4\times10^{14}/cm^2$. This value is closely equal to 1/2 Ns. Therefore, the cracking and incorporating mechanism of As_4 proposed by Foxon and Joyce[2] seems to be operative even at low Ts.

AlGaAs-GaAs quantum wells grown in the optimum conditions at 300°C exhibit higher PL efficiencies than those grown by conventional MBE at 600°C. Typical PL spectra are shown in Fig. 6. In addition, the AlAs-GaAs superlattices grown at 300°C are unaffected by thermal annealing at temperatures as high as 800°C. Negligible change is observed in PL efficiency, line width, and emission energy after annealing.

References

1) Y. Horikoshi, M. Kawashima, and H. Yamaguchi, Jpn. J Appl. Phys. 27(1988)169.
2) C. T. Foxon, and B. A. Joyce, Surface Sci. 64 (1977)293.

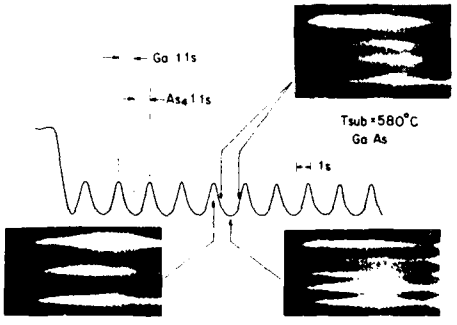


Fig.1. RHEED specular beam intensity trace recorded during MEE growth of GaAs at 580°C with N_{Ga} = Ns = 6.4×10^{14}/cm^2. RHEED patterns in the deposition cycle are also given.

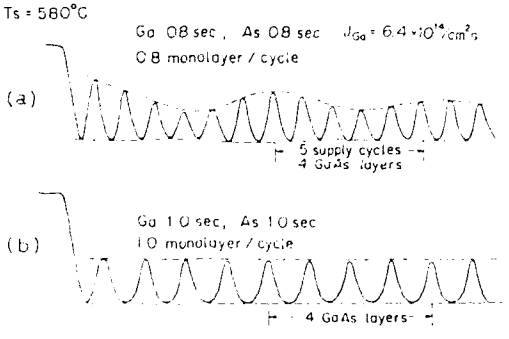


Fig.2. Comparison between the RHEED specular beam intensity oscillation during the growth of GaAs with commensulate and incommensulate deposition of Ga atoms:(a) N_{Ga}=0.8Ns,(b) N_{Ga}=Ns.

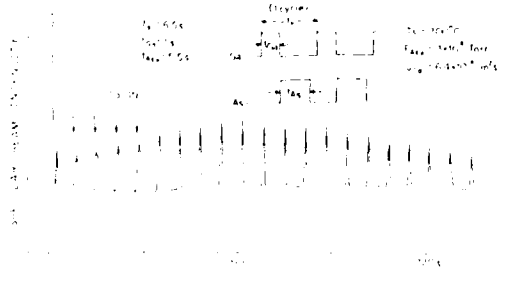


Fig.3. RHEED intensity oscillation during the MEE growth of GaAs at 300°C with excess As supply. (N_{Ga}=Ns and N_{As} =2.7×10^{15}/cm^2).

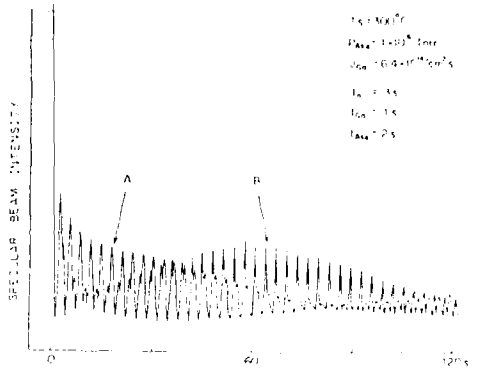


Fig.4. RHEED oscillation during the Growth of GaAs by MEE at 300 °C with N_{Ga}=0.97Ns, and N_{As}=3.8×10^{14}/cm^2. N_{As} slightly exceeds the optimum value. Two competing modulated waves are observed due to surface roughness and excess As adsorption.

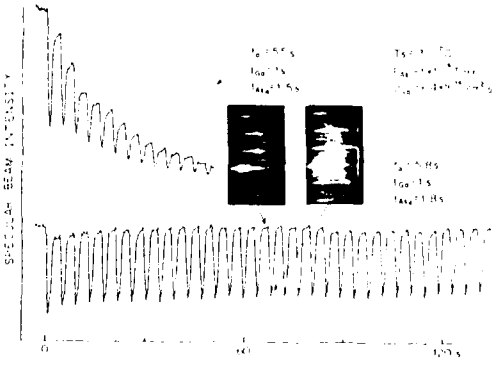


Fig.5. Lower trace: RHEED oscillation during the growth of GaAs by MEE at 300 °C with almost optimized deposition conditions: N_{Ga}=Ns, N_{As}=3.4×10^{14}/cm^2. RHEED patterns in the supply periods are also shown.
Upper trace: RHEED oscillation when N_{As} is further reduced (N_{Ga}=Ns, while N_{As}=2.8×10^{14}/cm^2). No persistent oscillation is obtained.

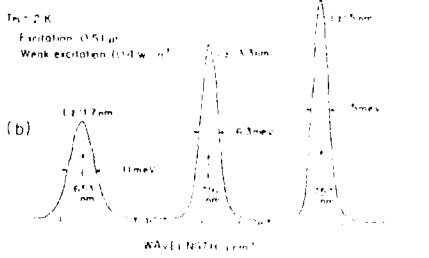


Fig.6. PL spectra at 2K for $Al_{0.5}Ga_{0.5}As$-GaAs single quantum wells grown at 300°C.

Abstract No. 515

Electrochemical Flue-Gas Desulfurization

Mark Franke, Dennis McHenry and Jack Winnick
Georgia Institute of Technology
Atlanta, Georgia 30332

A gas-phase concentration flow cell has been designed to remove sulfur oxides from flue gas. The essential reactions occurring are:

$$SO_2 + \tfrac{1}{2}\ O_2 \rightarrow SO_3 \qquad (1)$$

$$SO_3 + \tfrac{1}{2}\ O_2 + 2e \rightarrow SO_4^{2-} \qquad (2)$$

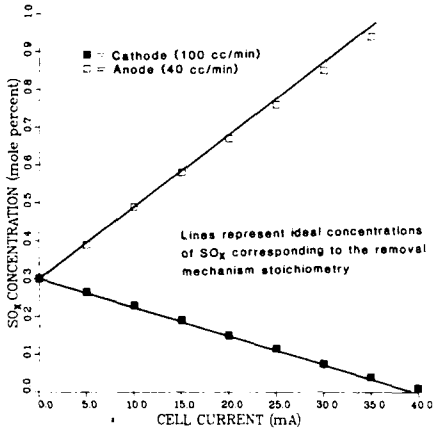
$$SO_4^{2-} + SO_3 + \tfrac{1}{2}\ O_2 + 2e \qquad (3)$$

where reaction (1) is a pre-oxidation and reactions (2) and (3) provide the means for sulfur oxide removal and recovery respectively. As in any electrochemical cell, appropriate electrolyte and electrode materials must be utilized. At the temperature required for flue-gas treatment, a molten salt electrolyte is needed. While alkali-metal sulfates are ideal for reactions (2) and (3), they melt only above 500°C. A lower-melting salt allowing this same basic electrochemistry was found: potassium pyrosulfate. With the addition of vanadia for sulfur-oxidation enhancement, this melt was found, through a separate electroanalytical study, to provide the necessary chemistry and electrochemistry to carry out the removal at flues in excess of 50 mA/sq.cm., a design goal.

Electrolyte-containing membranes were constructed by hot-pressing the electrolyte powder with inert ceramic, porous gas-diffusion electrodes were constructed of a perovskite-type ceramic: $La_{0.8}Sr_{0.2}CoO_3$. These were made from the metal acetates in a multi-step decomposition, grinding and sintering.

Cells housing a 20 sq.cm. membrane were tested on a gas containing 0.3% SO_2 in 3.0% O_2, 15% CO_2 in N_2. Pre-oxidation was achieved through use of a commercial, vanadia-based catalyst. Quantitative removal of the SO_2 was achieved with applied current, as shown on the figure. Concomitant production of concentrated SO_3 (and O_2) was also observed.

The current densities achieved in the flow-cell have been limited to 2.0 mA/sq.cm. The reason appears to be flooding of the electrodes caused by insufficient retention of the electrolyte by the membrane.



CATHODIC AND ANODIC CELL PERFORMANCE AT 400°C AND 0.3% SO_2, 3.0% O_2, 15.0% CO_2 IN N_2 TO BOTH COMPARTMENTS

Abstract No. 516

ELECTROCHEMICAL BEHAVIOUR OF GRAPHITE AND NICKEL-CHROMIUM ELECTRODES IN SODIUM POLYSULFIDE *IN THE ABSENCE AND PRESENCE OF HYDROGEN SULFIDE*

Z. Mao , B. Dandapani, S. Srinivasan, R.E. White and A.J. Appleby

Center for Electrochemical Systems and Hydrogen Research
Texas A&M University
College Station, Texas, 77843

The electrochemical reactions of sodium tetrasulfide on graphite and nickel-chromium(10%) electrodes at 350 °C in nitrogen and hydrogen sulfide atmospheres were investigated using cyclic voltammetry and chronoamperometric techniques. Fig.1 represents a typical voltammogram on a graphite electrode in a nitrogen atmosphere without IR compensation. It is seen from Fig.1 that there is a significant contribution due to the resistance of the melt. When the IR is compensated the cathodic peak is clearly seen at a potential of -0.285V vs Na_2S_x/C ($x > 5$). This peak current appears to have clear dependence on the scan rate since a plot of peak current versus the square root of the scan rate is linear indicating that diffusion processes play a significant part in the reaction (1). The peak observed on the graphite electrode is probably due to the formation of lower polysulfide which is normally a solid at this operating temperature (2). However, a similar voltammogram (Fig.2) on a Ni-Cr electrode does not indicate the presence of a blocking layer. A plateau on the potential decay curve in the current interruptor experiments was observed at the graphite electrode, whereas it was not observed at the Ni-Cr electrode.

Chronoamperometric studies conducted in a nitrogen atmosphere show that the current decay to a steady state was slower on a graphite electrode than on a Ni-Cr electrode suggesting the presence of a blocking layer on the graphite surface. The transient time was shortened when H_2S was bubbled through the melt (Fig.3).

Steady state current-potential curves for Ni-Cr electrodes under N_2 as well as H_2S atmospheres are shown in Fig.4. The current values are much larger in a H_2S environment for the same potential values. The effect is far more significant on a Ni-Cr electrode than on a graphite electrode. After prolonged bubbling of H_2S through the melt there is practically no difference between the i-E curves in N_2 and H_2S atmospheres. The current values in a nitrogen atmosphere at this stage reaches more or less the same values as that of hydrogen sulfide. The i-E curves obtained are linear suggesting a high resistance component in the melt. Higher current values in the presence of H_2S may be due to the formation of an intermediate species between H_2S and the product of the cathodic reaction.

It is also noted that with the bubbling of H_2S in the melt the open circuit potential of Ni-Cr electrode shifts by 15–20mV in the anodic direction with 10%H_2S and 30–40mV with 50%H_2S. This suggests that there may be chemical decomposition of H_2S at the Ni-Cr electrode surface(which may act as a catalyst). The sulfur formed by this decomposition dissolves in the melt in the vicinity of the electrode forming Na_2S_5 near the electrode surface.

Thus it is seen from these preliminary results that under a nitrogen atmosphere a two phase blocking layer is formed on a graphite electrode surface. Such a two phase layer was not observed on a Ni-Cr surface indicating that Ni-Cr may behave as a better sulfur electrode. Further, in a H_2S atmosphere the rest potential of graphite as well as Ni-Cr tends to be more anodic than in nitrogen. Higher currents for the same potential values are observed with H_2S bubbling compared to nitrogen bubbling. This difference for nitrogen case disappears after prolonged H_2S bubbling in the melt when more or less the same high currents are observed for both the cases.

REFERENCES

1. R. P. Tischer and F. A. Ludwig, in "Advances in Electrochemistry and Electrochemical Engineering", vol. 10, C. W. Tobias and H. Gerisher, Editors, Wiley Interscience, NY(1977).
2. D. A. Aikens, in "The Sulfur Electrode", R. P. Tischer, Editor, Academic Press, NY(1983).

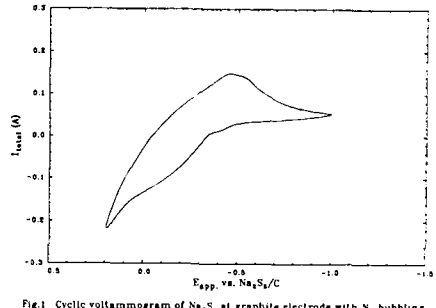


Fig.1 Cyclic voltammogram of Na_xS_x at graphite electrode with N_2 bubbling through the melt, the electrode area is 0.38 cm^2, scan rate is 2 mV/s.

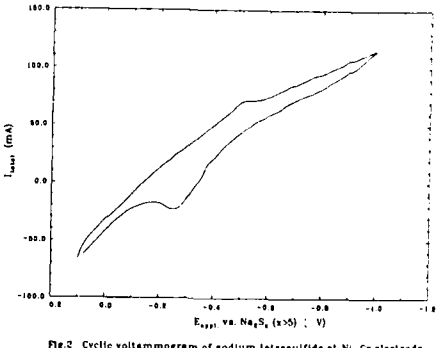


Fig.2 Cyclic voltammogram of sodium tetrasulfide at Ni-Cr electrode, the electrode area is 1.0 cm^2, scan rate is 5 mV/s.

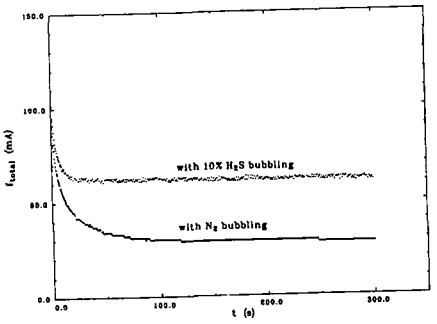


Fig.3 Relationship between current and time at Ni-Cr electrode, the electrode area is 0.32 cm^2, $E_{appl.}$=-350 mV.

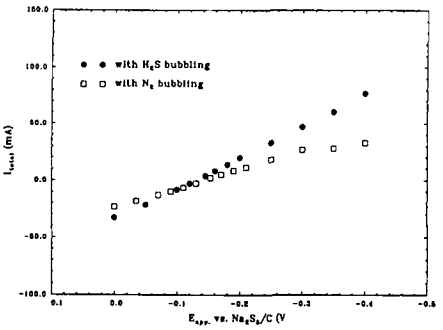


Fig.4 Relation of current and potential at steady state at the Ni-Cr electrode, the electrode area is 0.32 cm^2, temperature is 350 °C.

Abstract No. 517

THERMODYNAMIC ASPECTS OF H_2S ELECTROLYSIS IN AQUEOUS NaOH AND MOLTEN POLYSULFIDES

A. A. Anani, Z. Mao, B. Dandapani, S. Srinivasan and A. J. Appleby

Center for Electrochemical Systems and Hydrogen Research
238 Wisenbaker Engineering Research Center
Texas A&M University
College Station, TX 77843.

Simultaneous production of hydrogen and sulfur by the electrolysis of hydrogen sulfide would provide a rather cheaper means of supplying the end products, hydrogen and sulfur, compared to conventional processes of obtaining hydrogen by steam electrolysis. Not only is the reactant, H_2S, available at almost no cost, such a process would also lead to its removal from natural gas streams, again, at a much lower cost than the Clauss process. In addition, the reversible thermodynamic potential for the process

$$H_2S \rightarrow H_2 + S$$

is much lower than the corresponding value for steam electrolysis. This is calculated to be 173 mV at room temperature and is to be compared to 1.23 V for the equivalent process involving water. i.e.,

$$H_2O \rightarrow H_2 + 1/2\ O_2$$

These values for the reversible potential do not change much even if the operating temperature is raised by a few hundred degrees.

However, such a scheme would require dealing with the corrosive nature of the H_2S reactant gas, and also reducing the blocking effects of sulfide films that could be formed on the electrodes during the electrolysis.

Attempts are under way to investigate the feasibility of this process in both alkali-metal polysulfide melts and aqueous-based electrolytes. An attempt such as this would require knowledge of the stable species in solution in order to fully understand the reaction mechanisms, or sequence of reactions leading to the complete decomposition of the reactant. This is true because of the complex nature of the possible reactions involving the polysulfides, as is evidence with the sulfur electrode in the Na/S battery.

In this work, we present a thermodynamic approach which employs phase diagrams as a tool to identify possible stable species that may be present during the electrolytic process. As would be made obvious, not only is such an approach capable of providing useful information regarding the stable species in solution, it is very viable in identifying, *a priori*, the potentials within which the process can be carried out such that all components of the system remain both chemically and thermodynamically compatible with one another.

In the case of the alkali-metal polysulfide electrolyte, the approach will involve the construction of the ternary phase diagram involving the alkali-metal, for example, Na-H-S, whereas in the aqueous-based electrolyte scheme, the corresponding information will be represented in a quarternary phase diagram of the components, such as Na-H-O-S.

Abstract No. 518

$ZnCl_2$-HCl Plating Baths for Stripping and Recovery of Zinc from Galvanized Iron Scrap.

S. Zaromb, A.V. Fraioli, E.J. Daniels, G.V. Queen, and R.M. Bozen*

Argonne National Laboratory, Argonne, IL 60439

To recover zinc and remove zinc contaminants from reprocessable galvanized iron scrap, several acid plating baths were evaluated. For a fast process throughput, all tests were performed at current densities ≥90 mA/cm^2 and at ambient temperature (20-25° C). The following problems were initially encountered:

- Formation of zinc dendrites at the cathode;
- Absence of a marker that would indicate complete removal of zinc from the anode; and
- Excessive electrolyte resistivity, causing an unacceptable voltage drop between the cathode and anode.

To minimize dendrite formation, stirring of the electrolyte and electrochemical precleaning of the electrodes (by passing a 10-sec reverse pulse at the start of each run) became part of the experimental protocol. Next, the plating bath composition was varied in attempts to obtain a marker that would indicate the nearly complete removal of zinc from the exposed anode surface. Raising the pH from about 4.0 to 5.7 or reducing it, first to pH 1.4 and subsequently to pH 0.4, did not yield a clearcut marker. Neither did inclusion of $K_3Fe(CN)_6$ (which was expected to yield a passivating deposit on an exposed iron surface) or the use of various sulfate-containing baths. However, sulfate-free zinc chloride baths did yield indications of a possible marker even at a pH of 3.8, and these indications became more pronounced as the HCl concentration was increased, first to 1 M and subsequently to 1.5-4 M. At the higher HCl concentrations, a marker would be consistently observed at all but the highest (≥630 mA/cm^2) current densities.

Given the endpoint markers, dendrite formation could be further prevented and errors in faradaic efficiency measurements could be minimized by terminating all tests upon the appearance of the endpoint. Of all the electrolytes tested, only those containing at least 1 M HCl yielded endpoint markers, especially at current densities below about 500 mA/cm^2. Therefore, further tests were directed at optimizing the HCl and $ZnCl_2$ concentrations. For constant $ZnCl_2$ concentrations of 0.7 M or 1.3 M, corrosion increased with increasing acidity of the plating bath. In contrast, for a constant HCl concentration of 3 M, corrosion decreased with increasing $ZnCl_2$ concentration. This may have been associated with a diffusion limitation for zinc plating at a current density of about 400 mA/cm^2 as the $ZnCl_2$ was reduced from 2 M to 0.7 M. On the other hand, the electrolyte resistivity, and hence ohmic losses, increased slightly with increasing $ZnCl_2$ concentration. Therefore, a bath composition of 2 M $ZnCl_2$ plus 3 M HCl was selected as nearly optimal.

*Work supported by the U.S. Department of Energy, Assistant Secretary for Conservation and Renewable Resources, under Contract W-31-109-Eng-38.

Figure 1 summarizes the test results. A dip in the cathodic current efficiency in the range of 400-500 mA/cm^2 may be attributed to a diffusion rate limitation for zinc electrodeposition near room temperature at current densities ≥400 mA/cm^2. The increase in cathodic current efficiency at 630 mA/cm^2 may have been due to convection currents arising from the greater heat dissipation at the highest current density that was used.

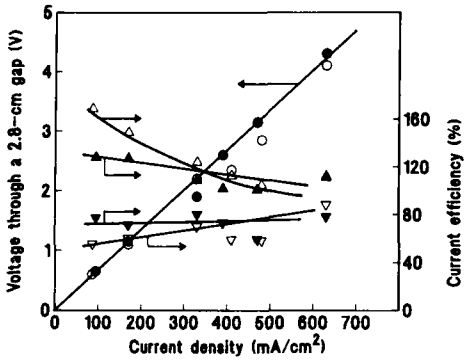
Figure 1 also shows a significant improvement in cathodic current efficiency, as well as a reduction in anodic corrosion, resulting from addition of 1 g/L of licorice root extract (Polysciences, Inc., Warrington, Penn., Catalog No. 18060) to the acidic plating bath. These results suggest that acceptable cathodic current efficiencies should be achievable in the selected acidic plating bath at plating current densities of 100-400 mA/cm^2.

Figure 2 shows the effects of replacing all or part of the $ZnCl_2$ by $ZnSO_4$ in the preferred plating bath. As expected, the electrolyte resistivity increases appreciably with the $SO_4^=/Cl^-$ ratio due to the lower mobility of $SO_4^=$ ions as compared with that of Cl^- ions. On the other hand, the corrosion of the electrodes is reduced somewhat by substituting $SO_4^=$ for Cl^- ions, as suggested by the slopes of the current efficiency lines. However, the reduced corrosion losses do not seem to adequately offset the resistive losses that would result from a replacement of Cl^- by $SO_4^=$ ions.

It is concluded that electrochemical stripping and recovery of zinc may be effected efficiently in acid plating baths under the following conditions:

- The bath resistivity must be sufficiently low to result in a voltage drop of not more than about 4 V (preferably ≤3 V) between the cathode and anode. This was achieved with an electrode spacing of 2.8 cm, current densities of 90-630 mA/cm^2 (preferably 90-400 mA/cm^2), and a bath containing 2 M $ZnCl_2$ and 3 M HCl. Under these conditions, an endpoint marker was consistently observed below 500 mA/cm^2.
- Addition of 1 g/L of licorice root extract to the above $ZnCl_2$-HCl bath resulted in reduced corrosion of both the cathode and anode. The resulting current efficiencies were 70-80% at the cathode and 100-130% at the anode (Fig. 1).
- The effect of replacing part of the Cl^- ions by $SO_4^=$ ions was to slightly improve the current efficiencies at both cathode and anode, but also to significantly increase the resistivity (Fig. 2), thereby adversely affecting the voltage drop across the bath.
- To minimize resistive losses in the plating-stripping bath, the bath should be so designed that the effective average anode-to-cathode path length is 3 cm or less.

Figure 1. Dependence of Minimum Applied Voltage (○, ●), Cathode Current Efficiency (▽,▼), and Anode Current Efficiency (△, ▲) on Plating Current Density in 2 M $ZnCl_2$ + 3 M HCl

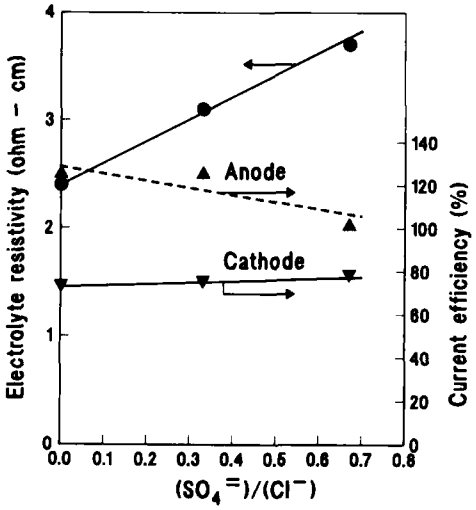


Legend

○ △ ▽ Without licorice

● ▲ ▼ With 1 g/L licorice extract in the plating bath

Figure 2. Effect of $SO_4^{=}/Cl^-$ Ratio on Electrolyte Resistivity and Current Efficiencies at 200 mA/cm² in Baths of 2 M Zn^{++} + 3 M H_3O^+ + 1 g/L Licorice Root Extract



Abstract No. 519

EFFECT OF HVDC TRANSMISSION LINES ON THE CHARGE DISTRIBUTION OF AEROSOLS

Gary B. Johnson Phillip J. Carter

General Electric Company

High Voltage Transmission Research Center
East New Lenox Road
Lenox, Massachusetts 01240

INTRODUCTION

As the use of HVDC transmission lines for bulk power transfer has grown, attention has focused on the small air ions produced from HVDC transmission lines. Due to the constant polarity of HVDC conductors ions can move away from the conductor and fill the volume of space between the conductors and ground. The small air ions from the DC line can attach to aerosols altering the ambient charge distribution of aerosols.

In order to investigate the effect of HVDC lines on the environment, the Department of Energy initiated a research program at the High Voltage Transmission Research Center to measure the levels electric fields, ions, and charged aerosols due to HVDC lines and characterize the resulting electrical environment [1,2]. In addition to obtaining information on the levels of fields, ions, and charged aerosols, information was desired on the distribution of charge on aerosols. A technique was developed to measure the charge on aerosols and measurements of the aerosol charge distribution were made near HVDC transmission lines and at several other locations.

A workshop was held to report the results of the measurements of the aerosol charge distributions and to discuss what impact the altered aerosol charge distribution would have on deposition of the aerosols in the respiratory tract. The work shop was attended by respiratory physiologists, aerosol physicists, atmospheric scientists, and electrical transmission researchers.

MEASUREMENT TECHNIQUE AND INSTRUMENTATION

A technique was developed to measure the size of an aerosol and the charge residing on it. The technique consists of measuring the electrical mobility of a charge aerosol and then measuring its size. The electrical mobility of a charged aerosol is proportional to its charge to size ratio. Measuring the electrical mobility of a charged aerosol to obtain the charge to size ratio and then measuring the size of the aerosol allows both the charge and the size of the aerosol to be determined.

The instrumentation used to measure and record the size and charge of the aerosols consists of a differential mobility analyzer, a laser optical scattering aerosol sizer, and a portable computer to control and record the data from the two instruments. The instrumentation can measure the charge on aerosols in the range of 0.1 to 3.0 microns. It can determine the charge on an aerosol to within ± 1 charge or $\pm 18\%$ whichever is less. The size range from 0.1 micron to 3.0 micron was chosen because it is the size range containing many biologically active aerosols and it is also the size range where the respiratory system is least efficient in depositing aerosols. Any enhancement in deposition due to charge on the aerosols in that size range would have a greater percentage increase of deposition and thus the possibility for a proportionately greater impact on health.

MEASUREMENT LOCATIONS

Measurements of the aerosol charge distribution were made near HVDC transmission lines in two regions of the country. Measurements were made at the High Voltage Transmission Research Center, located in western Massachusetts, near its two full scale HVDC transmission test lines [1]. Measurements were also made near the Northwest-Southwest DC Pacific Intertie, which runs through California, Nevada, and Oregon. Measurements of the ambient aerosol charge distribution were made in rural western Massachusetts; Cap Cod National Park, Massachusetts; downtown Newark, New Jersey; El Capitan Beach State Park, California; downtown Los Angeles, California.

MEASUREMENT RESULTS

It was found that in general for the ambient measurements approximately one-third of the aerosols were positively charged, one-third were negatively charged and one-third had no charge. A single charge was the most common charge state for the charged aerosols. The number of aerosols per charge state decreased exponentially with increasing charge number.

Measurements near the HVDC transmission lines indicated that the DC line did shift the charge distribution. However the shift was small and within a few hundred feet from the line the charge distribution of the aerosols was back to near ambient levels. Even directly under the line the most common charge state of the charged aerosols was still a single charge.

AEROSOL WORKSHOP ON RESPIRATORY DEPOSITION

A workshop attended by respiratory physiologists, aerosol physicists, atmospheric scientists, and transmission research engineers was held to report the results of the aerosol charge distribution measurements and discuss the impact that DC line would have on charged aerosols and their deposition in the respiratory tract. Information on the deposition of aerosols in the respiratory tract was presented. A recent study on the deposition of charged aerosols in the respiratory tract showed that there was a threshold of charge on aerosols below which there was essentially no measurable increase in deposition [3]. The threshold was at approximately 10 charges per aerosol for the size range of interest 0.1 micron to 1 micron. Since the HVDC transmission line produced changes in the aerosol charge distribution much less than the 10 charges per aerosol threshold the consensus of the workshop was that there was little likelihood of any health impact due to effects of HVDC lines on charged aerosols.

REFERENCES

[1] Study of Electric Field and Ion Effects of HVDC Transmission Lines: Final Report, U.S. Department of Energy, DOE Contract DE-AC02-80RA50153, National Technical Information Service, Springfield, Virginia, August, 1985.

[2] P.J. Carter, G.B. Johnson, "Space Charge Measurements Downwind from a Monopolar 500 kV HVDC Test Line", Paper Number 87 SM 548-1, IEEE Power Engineering Society 1987 Summer Meeting, July, 1987.

[3] C.P. Yu, "Theories of Electrostatic Lung Deposition of Inhaled Aerosols", Ann. Occup. Hyg., Vol. 29, pp. 219-227, 1985.

Abstract No. 520

ELECTROCHROMISM OF POLYANILINE: AN IN-SITU FTIR STUDY

M. Ahsan Habib and Shyam P. Maheswari
Physical Chemistry Department
General Motors Research Laboratories
Warren, MI 48090

INTRODUCTION

Recently there has been renewed interest in polyaniline because of its electrochromic properties (1). Most of the infrared spectral studies of polyaniline (2,3) has been done ex-situ and do not suggest the extent of spectral change with the extent of oxidation and reduction. Moreover, although suggested redox mechanisms involve protonation-deprotonation of the polyaniline structure during the reduction-oxidation process, no direct proof of such structural change is yet available.

In this paper we present our work on an in-situ FTIR study of polyaniline films in acidic solution in order to obtain spectral evidence of protonation-deprotonation during reduction-oxidation processes.

EXPERIMENTAL

The electrochemical cell used for the infrared measurements is similar to that described in (4). The working electrode was a highly polished Pt disc of 1 cm diameter and 0.5 mm thickness, attached to a copper rod clad with heat shrinkable Teflon tubing. The electrode surface was polished with 0.05 μm alumina. The polished electrode was cleaned with conc. HNO_3 and rinsed thoroughly with double distilled water. The Pt electrode was then coated with the polyaniline film by the potentiodynamic cycling of the electrode in 1 M aniline + 1 M HCl solution (purged by N_2) between -0.2 V and +0.8 V at 50 mV/sec in a conventional 3-electrode electrochemical cell. The polyaniline coated electrode was then taken out of the cell containing aniline solution, washed thoroughly, dried and then positioned in the FTIR cell very close to the IR-transparent ZnSe cell window. The electrode was polarized potentiostatically in the range of -0.2 V to 0.8 V (SCE) at intervals of 200 mV. A total of 256 scans with 4 cm^{-1} resolution, were collected at each potential.

Visible spectral measurements were carried out in a spectronic 2000 spectrometer. The electrochemical cell consisted of a quartz cuvette with 1 cm path length. For these measurements, the polyaniline film was deposited on a fluorine doped SnO_2 coated glass substrate. The working electrode, a platinum counter electrode, and a calomel reference electrode with extended luggin capillary were placed in the cuvette which was then filled with electrolyte. The electrode was polarized at various potentials and the in-situ absorbance measurements were carried out.

RESULTS AND DISCUSSION

In-situ absorbance spectra of the polyaniline film at various potentials are shown in Fig. 1 in the visible range of 350 nm t 850 nm. Absorbance of the polyaniline film increases as the reduced film was gradually oxidized.

The film was blue at 0.8 V and near transparent with slightly yellowish tint at -0.2 V. Thus, switching the potential between -0.2 V and 0.8 V, the film could be bleached and colored. This electrochromic behavior of the polyaniline film was found to be quite reversible.

In-situ FTIR experiments were now carried out to monitor the N-H vibratiops as a function of potential. The band around 2950 cm^{-1} due to N-H stretching vibration clearly increased with the increase of reduction potential (Fig. 2). The relatively smaller peaks near 2950 cm^{-1} are also assigned to N-H vibrations and showed the same trend as that of the 2950 cm^{-1} peak. These results thus confirm the formation of the N-H bond during reduction and breakage during oxidation processes and are associated with the electrochromic phenomenon in polyaniline films in HCl solution,

$$[-NH-C_6H_4-NH-C_6H_4-NH-] \ddagger$$

$$[-NH-C_6H_4-N^{+}=C_6H_4=N^{+}-]$$
$$Cl^{-} \quad Cl^{-}$$

The oxidized charge centers at N^+ are balanced by the Cl^- counter ions. Although the band at 2950 cm^{-1} (Fig. 2) decreased as the film was anodically oxidized, it did not completely disappear at 0.8 V, indicating that there were still some N-H bonds intact at that oxidation potential. The peak at 667 cm^{-1} also increased with the increase of cathodic potential (Fig. 3). Although it is possible that this peak is due to an N-H bending mode (5), it should be noted that this peak may also be due to vibrational modes of water (5). If it is due to water, its observed increase with the increase of reduction potential is somewhat unclear. It may appear that upon oxidation, the film becomes more compact, thereby reducing the water content in the film, giving rise to the observed effect. However, no evidence of the film becoming compact upon oxidation is available, but it is known that the conductivity of the polyaniline film increases with oxidation (6) and also with the increase of water content of the film (7). Thus, the spectral peak at 667 cm^{-1} which decreases with oxidation, may be assigned to the N-H vibrational mode of polyaniline and not to the O-H mode of water.

REFERENCES

1. A. Kitani, J. Yano, and K. Sasaki, J. Electroanal. Chem., 209, 227 (1986).
2. A. Volkov, G. Tourillon, P-C Lacaze, and J-E. Dubois, J. Electroanal. Chem., 115, 279 (1980).
3. T. Ohsaka, Y. Ohnuki, N. Oyama, G. Katagiri, and K. Kamisako, J. Electroanal. Chem., 161, 399 (1984).
4. M. A. Habib and J. O'M. Bockris, J. Electroanal. Chem., 180, 287 (1984).
5. G. Socrates, Infrared Characteristic Group Frequencies, John Wiley & Sons, New York, 1980.
6. S. H. Glarum and J. H. Marshall, J. Electrochem. Soc., 134, 142 (1987).
7. M. Angelopoulos, A. Ray, and A. J. MacDiarmid, Synthetic Metals, 21, 21 (1987).

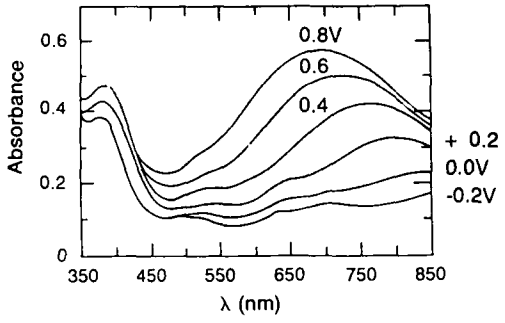


Figure 1.
In-situ absorbance spectra of a polyaniline film on a fluorine doped SnO_2 coated glass substrate at various applied potentials.

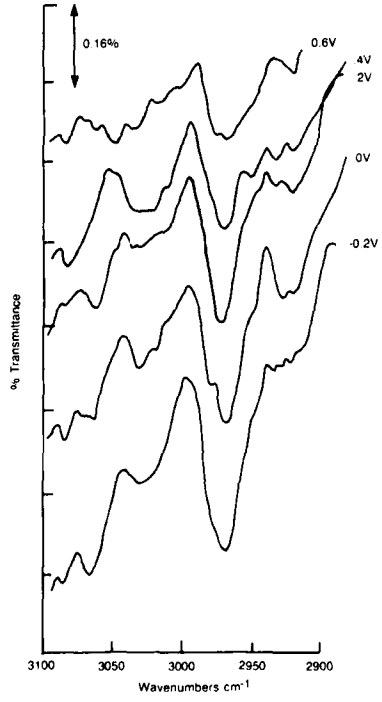


Figure 2.
In-situ FTIR spectra of a polyaniline film in the N-H stretching region as a function of potential (SCE).

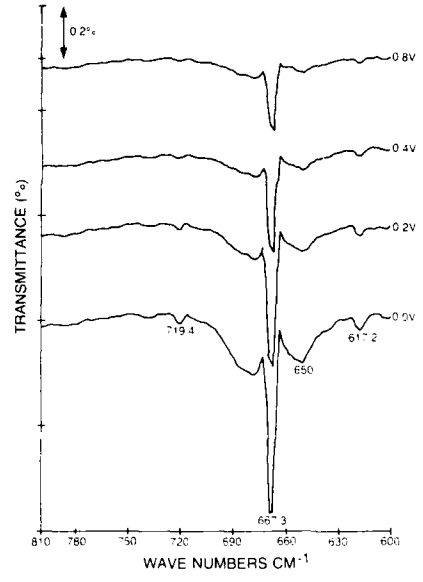


Figure 3.
In-situ FTIR spectra of a polyaniline film in the spectral region of 600 to 810 cm^{-1} wavenumbers as a function of applied electrode potential (SCE).

Abstract No. 521

PREDICTION OF ELECTRIC FIELD AND ION DENSITY OF HVDC TRANSMISSION LINES

Gary B. Johnson Luciano E. Zaffanella

General Electric Company
High Voltage Transmission Research Center
East New Lenox Road
Lenox, Massachusetts 01240

INTRODUCTION

The use of HVDC transmission lines for bulk power transfer is increasing. In order to determine the potential environmental impact of HVDC transmission lines, information on the electrical environment is needed. Three methods of obtaining the information on expected levels of electric fields and ion densities have been developed and used successfully at the High Voltage Transmission Research Center. The three methods used at HVTRC are: full scale line tests, small scale model line tests, and a unique mathematical model based on the concept of "saturated corona".

FULL SCALE LINE TESTS

The electrical environment of an HVDC transmission line is constantly changing due to the random nature of the corona on the conductors. Since the electric field and ion density levels near the line are fluctuating over time, a statistical representation of the line performance is necessary. One method of characterizing the performance of a HVDC transmission line is to monitor the electric field and ion density levels from a full scale version of the line over a period of time and weather conditions.

HVTRC has two full scale bipolar DC test lines. The "short" line is 150 meters in length and is used to test line configurations up to ±600 kV. The "long" line is 500 meters in length and is used to test line configurations up to ±1500 kV. The line height and separation between conductor bundles can be changed quickly and easily. Electric field probes and ion current plates are located every 5 to 10 meters within ±50 meters of the center of the line. Readings of the electric field probes, ion current plates, line voltage, and several weather parameters are taken and recorded once each minute by a data acquisition system.

Full scale line testing provides information on the actual variability of the line performance in various weather conditions. Such full scale line studies have been used to provide information on the line performance for licensing hearings and to prepare environmental impact statements. The drawback of full scale line testing is that it is time consuming and thus only a few line designs can be tested within a given period of time.

MATHEMATICAL MODELING

Calculations based on mathematical models of transmission line performance are less expensive and quicker than full scale line tests. However, the variability of the and the weather conditions compromise the accuracy of many purely theoretical calculation methods. An alternative to either full scale line testing or purely theoretical calculations which combines the accuracy of full scale line testing with the speed and flexibility of calculation methods is a semiempirical calculation method based on the testing of several full scale lines at HVTRC and the concept of a "saturated corona" limit.

The saturated corona limit is reached when the maximum amount of charge is being released from the conductor by corona. Conceptually, the charge flowing from a point on the conductor to ground along a field line can be thought of as forming a tube of flux. The flux tube reaches a saturated condition when the potential along the length of the tube from ground to the conductor, due only to the charge within the flux tube, is equal to the voltage on the conductor. When this "charge saturated condition" is reached, no further charge can be released from the conductor by corona because the field at the surface of the conductor has become zero. In this saturated corona condition the corona current, charge density, and electric field at ground assume limit values.

The calculation technique using the concept of the saturated corona condition consists of:

* Calculation of the electric field at ground level in the absence of corona
* Determination of the electric field and ion densities at ground level in the saturated corona condition
* Calculation of the expected electric field and ion densities at ground level in practical conditions using the corona free and saturated corona values as lower and upper bounds with an empirically determined degree of corona saturation to establish where the actual values lie between the two bounds

A shortfall of the empirical calculation technique described is that it is limited to fairly standard line designs due to its basis on an empirical data base. Its applicability to unusual line designs would have to be verified with full scale tests.

SMALL SCALE MODEL TESTS

Small scale model tests fill the gap between full scale line tests and mathematical model calculations. Although they cannot predict the expected levels of electric fields and ion densities in actual conditions they can provide the saturated corona levels of the electric fields and ion densities. Once the saturated corona levels of a line design are known then the expected levels can be calculated using the degree of saturation described previously. Although small scale model tests cannot be done as quickly as mathematical model calculations they are much faster and simpler than full scale line tests. Small scale line tests are used to investigate and provide the saturated corona levels of electric fields and ion densities for unusual or new line designs that do not fit a standard line design.

SUMMARY

Three methods of determining the expected electric fields and ion densities for a HVDC transmission line design have been described. Mathematical modeling of the electrical performance of HVDC transmission lines is the most efficient and least expensive method of evaluating different line designs. A unique technique is described that uses the concept of saturated corona to calculate the electric field and ion levels. Small scale model line tests provide a method to predict the electric field and ion levels when the mathematical model alone is insufficient. Full scale line tests are appropriate as a verification of the electrical performance of a final line design chosen from many possible designs after evaluation based on mathematical model predictions or small scale model tests.

Abstract No. 522

"BIOLOGICAL EFFECTS OF SPARK-DECOMPOSED SF_6"

G. D. Griffin, M. G. Nolan, C. E. Easterly and I. Sauers
Health and Safety Research Division
Oak Ridge National Laboratory
P.O. Box 2008
Oak Ridge, Tennessee 37831-6101

Sulfur hexafluoride (SF_6) is widely used as an insulating gas in electrical applications, such as GIS (gas-insulated substations), switchgear, etc. The gas is chemically inert and biologically innocuous. Depending upon conditions of electrical discharge (arc, sparks, corona), presence of other chemical compounds in the SF_6 gas (e.g., H_2O), composition of electrode materials, and other factors, a variety of different chemical species may arise following electrical stress. We have investigated decomposition of SF_6 during repeated sparking. The apparatus in which the sparking took place had a concentric cylindrical stainless steel electrode arrangement, and the total deposited energy was usually in the range of 1-32kJ. The various gaseous byproducts were analyzed by mass spectrometry or, in a few cases, gas chromatography. Table 1 lists the concentration of various gaseous byproducts found in a 16kJ spark sample.

TABLE 1 Decomposition Products Found Following Repeated Sparking in SF_6

Product	Concentration in Sparked SF_6[a]
SOF_2, SF_4[b]	0.5%
SO_2F_2	0.006%
SOF_4	0.085%
SiF_4	0.026%
SO_2	0.002%
HF[c]	1.0%
S_2F_{10}[d]	0.026%

[a] 16kJ total energy deposited into 70 cm^3 gas volume at 133kPa total pressure.

[b] SF_4 quickly hydrolyses to SOF_2 via the reaction $SF_4 + H_2O = SOF_2 + 2HF$. The indicated concentration reflects SF_4 production immediately after sparking or SOF_2 several minutes after sparking.

[c] Concentration not measured, but calculated based on SF_4 hydrolysis. The amount should be considered an upper limit, since losses may occur on walls or via reaction with insulators.

[d] Yield can depend strongly on moisture in the system; increasing moisture leads to reduction in yield.

The toxicological data base for the compounds in Table 1 is either sparse, or virtually nonexistent, but there is sufficient information to indicate some of these compounds are biologically very active. Examination of available TLVs (threshold limit values-airborne concentrations of substances to which workers may be repeatedly exposed without adverse effect) for these compounds suggests the highly toxic nature of some of these gases. The TLVs for S_2F_{10}, SF_4, and SO_2F_2 are 0.025 ppm, 0.1 ppm and 5 ppm respectively. These values can be compared to TLVs for common hazardous gases like CO (50 ppm) and phosgene (0.1 ppm).

Because of the lack of biological data and the potentially strong toxicity for some of these gases, we have examined their biological activity in an in vitro cultured cell system. Using a novel gas exposure technique[1], cell culture lines of mammalian origin were exposed for 1 or 4 h to different concentrations of individual gases, the cell killing (cytotoxic) activity of the gas was assayed, and dose-response relationships were generated. It was then possible to compare the relative cytotoxicity of the various byproducts. The following list ranks the byproducts from most cytotoxic to least cytotoxic; in addition, the approximate gas concentration which killed 50% of the cells (following 4 h exposure) is given for each gas to provide a semi-quantitative indication of how cytotoxic one compound is compared to another. Relative cytotoxicities were: S_2F_{10}-0.009%; SO_2F_2 - 0.35%; SOF_4 - 0.8%; SOF_2 - 1.5%; SF_4-1.6%; SiF_4 - 1.7%. SO_2 and HF were essentially inactive because they reacted with medium components and were neutralized. It is apparent that some of the decomposition products of SF_6 are cytotoxic at low concentrations, and would be expected to contribute to biological toxicity of spark-decomposed SF_6. Indeed, sparked SF_6 has previously been assayed in our cell culture system, and 16kJ samples have been found to exhibit a vigorous cytotoxic effect. There are a variety of compounds present in spark-decomposed SF_6 gas which can produce acute cell lethality at low concentrations, and therefore appropriate precautions in dealing with this gas should be undertaken.

This research is sponsored by the Office of Energy Storage and Distribution, Electrical Energy Systems Program, U.S. Dept. of Energy, under contract DE-AC05-84OR21400 with Martin Marietta Energy Systems, Inc.

1. G. D. Griffin, C. E. Easterly, I. Sauers, H. Ellis and L. Christophorou, "Cytotoxic Activity of Spark-Decomposed Sulfur Hexafluoride and Analysis of Cytotoxic Contributions of Individual Spark Decomposition Products" Toxicol. and Environ. Chem., 9: 139-166, 1984.

Abstract No. 523

THE ELECTRICAL ENVIRONMENT OF HVDC TRANSMISSION LINES

Gary B. Johnson

General Electric Company

High Voltage Transmission Research Center
East New Lenox Road
Lenox, Massachusetts 01240

INTRODUCTION

In recent years, interest and use of high voltage direct current transmission lines for bulk power transfer and system stability has grown. The study of possible environmental impacts of high voltage direct current transmission lines is an important aspect of the design and licensing of these high voltage transmission lines. In order to properly assess the impact of a HVDC transmission line on the environment, it is necessary to characterize the electrical environment in the vicinity of the line.

HVDC TRANSMISSION LINE ELECTRICAL ENVIRONMENT

The effect of a HVDC transmission line on the electrical environment can be divided into two areas: those effects due to the fields of the line, and those due to corona on the line. The fields from a HVDC transmission line consist of the electric field and the magnetic field. The corona effects consists of ions, ozone, audible noise, and radio interference.

ELECTRIC AND MAGNETIC FIELD

The voltage on the conductors of a HVDC transmission line produces an electric field that is directly proportional to the voltage on the conductors. An electric field is also produced by the charge carried by ions from corona on the line. The combination of these two fields produces the electric field measured at ground level. Since a portion of the electric field is produced by ions from corona on the line, the electric field from a HVDC transmission line is dependent upon weather conditions (the level of corona is affected by weather conditions). The strength of the electric field is expressed in kilovolts per meter (kV/m). The current flowing through the DC conductors produces a magnetic field that is directly proportional to the current carried by the conductors. The strength of the magnetic field is typically expressed in Gauss. Both the electric and magnetic field are affected by the height and arrangement of the line conductors. They both decrease quickly with distance from the line.

Typical electric fields found near DC lines range from about 1 kV/m at the edge of the right-of-way to about 20 to 30 kV/m directly under the conductors. Typical magnetic fields due to DC lines range from a few 10s of milliGauss at the edge of the right-of-way to 300 to 400 milliGauss directly under the conductors.

CORONA

Corona is a partial electrical breakdown of the air surrounding the conductors. In the corona process, neutral molecules of air around the conductor are ionized. Corona occurs when the local electrical stress on the surface of the conductor (surface gradient) becomes large enough to dislodge one or more electrons from the molecules of air surrounding the conductors. This occurs at about 30 kV/cm. Typically corona is confined to a region within two or three inches from the surface of the conductors.

HVDC transmission lines are designed so that the conductors will be operating below the corona inception surface gradient of 30 kV/cm. However, nicks in the conductor, small airborne particles of vegetation, pollen, or insects on the surface of the conductor create points where the electrical stress is intensified sufficiently to produce corona. In foul weather, raindrops or snow flakes on the conductors will also act as points where corona is produced.

SMALL AIR IONS

Air molecules that have been ionized in the corona process undergo numerous collisions with the other molecules in the air and in less than a few milliseconds evolve from singly charged individual atoms, molecules, and electrons to singly charged molecular clusters. These singly charged molecular clusters, called small air ions, consist of several water molecules (typically 3 to 10 water molecules) clustered around a kernel ion due to the electrostatic forces of its charge. Typical levels of ions from HVDC transmission lines range from a few thousand ions/cm^3 at the edge of the right-of-way to approximately 100,000 ions/cm^3 directly under the line. Small air ions are generated by many other sources and are a natural constituent of the air.

As small air ions move through the air they collide with existing particles suspended in the air called aerosols, and their charge is transferred to these aerosols. Charged aerosols are sometimes referred to as "intermediate" or "large" ions.

OZONE

Although ozone is produced by corona, the quantity of ozone produced by HVDC transmission lines is minimal. Even during heavy rain, when the level of corona activity is at its highest, the ozone concentration at the edge of the right-of-way is likely to be less than a few parts per billion (ppb). It would be difficult to distinguish ozone [illegible] transmission lines from existing ambient ozone levels, which are one to two orders of magnitude greater (i.e 10 ppb to 100 ppb).

AUDIBLE NOISE AND RADIO INTERFERENCE

As described earlier, corona is essentially a small electrical discharge or spark into the air and as such can produce audible noise such as a crackling, popping, or hissing sound. The corona also generates radio interference in much the same manner as sparks from the commutator of an electric motor such as an electric drill or kitchen blender. Corona produced radio interference is generally apparent in the form of "static" superimposed on the broadcast material being received, and it is more apparent on AM radio reception than on FM radio reception. FM radio reception is essentially immune to corona and electric spark noise since it is frequency modulated instead of amplitude modulated as AM is.

Up to a point, the greater the amount of corona, the greater the amount of audible noise and radio interference. However, the audible noise and radio interference levels produced by corona on HVDC lines actually decrease during foul weather when there is a great deal of corona due to the large number of corona sources. This apparent anomaly stems from the fact that the mode of corona on HVDC lines changes when the number corona sources becomes very large, such as in foul weather. With fewer sources, such as in fair weather, the corona is more erratic and impulsive. It is this impulsiveness of the corona which results in the higher generation of audible noise and radio interference. The levels of audible noise and radio interference are generally low from existing HVDC lines and have few if any problems meeting federal and state regulations.

Abstract No. 524

SIMILARITIES AND DIFFERENCES BETWEEN CORROSION IN HIGH TEMPERATURE GASEOUS ENVIRONMENTS AND AQUEOUS ENVIRONMENTS

T.A. Ramanarayanan* and S.N. Smith+

*Exxon Research and Engineering Company
Annandale, New Jersey

+Exxon Production Research Company
Houston, Texas

The subjects of dry corrosion (gaseous corrosion) and wet corrosion are now distinct areas of corrosion science in their own right. One cannot say that there is close interaction between the two communities. However there are instances where phenomena from both types of corrosion come into play; such a situation is treated here.

The situation under study is the corrosion of carbon steel in gaseous H_2S environments as well as H_2S- saturated aqueous environments in the temperature range, 95-300°C. Such corrosion phenomena are encountered in many processes, for example in the corrosion of carbon steel tubulars in sour gas wells. This subject has been extensively treated in the literature and some of the more important papers have been assembled in a NACE publication[1]. The majority of such studies have been carried out at room temperature or a few degrees above. The general picture which emerges from such studies is that carbon steel in sour aqueous environments tends to corrode by direct dissolution of iron as ferrous ions. Different types of iron sulfide phases can often form, and when they do, the scales can either provide corrosion resistance or they themselves can undergo dissolution. In a recent study, Hausler[2] has brought up the importance of considering transport processes within the corrosion product layer.

We have taken the approach of studying the corrosion of carbon steel first in gaseous environments containing H_2S and then in H_2S-saturated aqueous environments. Thermogravimetric techniques have been used to establish kinetics in the former case whereas electrochemical techniques have been used for corrosion studies in the aqueous medium. The experiments have been performed in the 95-300°C temperature regime.

Thermgravimetric data for the corrosion of carbon steel in a gaseous environment consisting of 10% H_2S in argon at 220°C are presented in Fig.1. The weight gain is essentially due to the formation of the an iron- deficient sulfide (pyrrhotite) scale on the surface of carbon steel. During an initial period extending up to about 20 hours, the kinetic curve follows a logarithmic dependence on time. Following this initial period, the kinetics are essentially linear with time. The structure of the pyrrhotite scale which is formed is shown in the SEM fracture cross section in Fig.2. This scale consists of a thin inner iron sulfide layer, next to the metal surface, which is very fine-grained and a thicker outer sulfide layer which is made up of columnar grains. A platinum marker, placed initially on the metal surface, resides close to the metal after sulfidation, indicating that the growth of the pyrrhotite scale occurs by the predominant outward diffusion of iron ions through the it. The columnar grains have a definite texture associated with them; they are oriented along the c-crystallographic direction of the pyrrhotite crystal. We believe that the fine-grained inner region is formed first, since the metal surface presents a sufficiently large number of nucleation sites. The initial formation of the fine-grained layer is probably limited by the dissociation of H_2S on the metal surface. Once the metal surface is covered by a thin layer of iron sulfide, the rate-limiting step switches to the dissociation of H_2S on the iron sulfide surface, a much slower process. This leads to a sudden deceleration in the kinetics, leading to the logarithmic growth behavior. Once the fine-grained layer is formed, the grains favorably oriented for growth along the c-direction grow at the expense of less favorably oriented grains, leading to the formation of the coarse-grained, columnar outer scale. It is known[3] that iron diffusion in pyrrhotite is most rapid along the c-crystallographic direction. The fact that the slope of the weight gain vs. time curve is constant over much of the duration of the experimental curve in Fig.1 suggests that the rate of pyrrhotite growth is limited by a surface reaction, most probably the dissociation of H_2S at the pyrrhotite surface.

Corrosion studies in aqueous media also have been carried out in the 95-300°C temperature regime. Measurements, especially at the higher temperatures, had to be carried out at high pressures for obvious reasons. Electrochemical polarization techniques, involving a Tafel extrapolation procedure, were used to establish the corrosion kinetics. Typical results for the corrosion of 4130 steel at 220°C in 1% NaCl solution saturated with 10% H_2S in argon at 2000 psi are presented in Fig.3. Each experimental point on this graph comes from a Tafel extrapolation procedure. The corrosion rate starts off at about 3000 mpy, decreases with time, and reaches a steady-state value of approximately 150 mpy in 60 hours or so. The decreasing rate of corrosion indicates that a surface reaction is not the exclusive rate-limiting step in the process. An analysis of the curve in Fig.3 shows that in the initial stages of corrosion, parabolic rate behavior is observed, involving solid state diffusion-controlled growth of the iron sulfide scale. As corrosion progresses, a mixed control situation takes over where the dissolution of the scale also becomes a contributory factor. At still longer times, when a steady state rate is reached, the rate of scale growth becomes equal to the rate of scale dissolution. The corrosion product scale formed in high pressure aqueous environments, consists, in addition to pyrrhotite as the major scale, FeS_2 crystals at the outer surface as shown in Fig.4. However, the FeS_2 phase rarely covers the surface so that solid state diffusional processes mainly occur in the pyrrhotite scale. Since the slow dissociation step which is involved in gas phase corrosion does not occur in the aqueous case and since, further, scale dissolution also contributes to corrosion in the aqueous phase, the overall rate of corrosion is generally higher in H_2S-saturated aqueous environments as compared with the gas phase alone.

REFERENCES

1. "H_2S Corrosion in Oil and Gas Production-A Compilation of Classic Papers", ed. by R.N. Tuttle and R.D. Kane, NACE, 1981

2. R.H. Hausler, in Proc. 6th European Symposium on Corrosion Inhibition, Ferrara, Italy, Sept. 16-20, 1985

3. R.H. Condit, R.R. Hobbins and C.E. Birchenall, Oxidation of Metals, 8, 409 (1974)

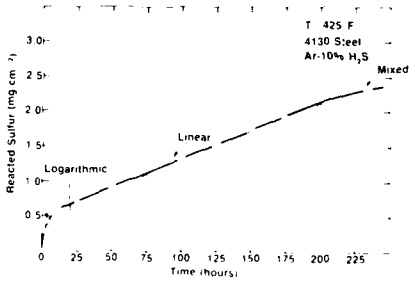


Fig.1. Kinetic Stages in the Reaction of Carbon Steel with 10% H_2S in Argon at 220°C

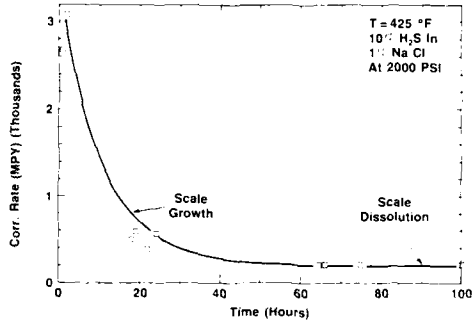


Fig.3. Kinetics of Corrosion of Carbon Steel in 1% NaCl Solution Saturated with 10% H_2S at 2000 psi



Fig.2. SEM Micrograph of the Fracture Cross-section of the Corrosion Scale Formed by Reaction of Carbon Steel with H_2S at 220°C



Fig.4. Corrosion Scale formed on Carbon Steel upon Reaction with 1% NaCl Solution Saturated with 10% H_2S at 220°C and 2000 psi

Abstract No. 525

DEPOSITION AND FLOW OF MOLTEN SALT MIXTURES ON GAS TURBINE BLADES: A THEORETICAL TREATMENT

R. Nagarajan
Department of Mechanical & Aerospace Engineering
West Virginia University
Morgantown, WV 26506-6101

Corrosive deposits on aircraft and marine gas turbine blades, although predominantly made up of sodium sulfate liquid, often contain significant levels of other salts. These 'adulterant' species are typically calcium and magnesium compounds in aircraft turbines, and vanadium compounds in ship turbines. The presence of these additional components in the melt can considerably broaden the 'dangerous' temperature range over which the deposit remains molten (by depressing the solution freezing-point and raising the dewpoint). The importance of solution composition in determining local phase-equilibria within the salt mixture emphasizes the need for a comprehensive theoretical framework within which the deposition and shear-induced motion of multicomponent condensates on turbine hot-section components may be analyzed. A primary effect of condensate flow is to 'shift' its composition from its local steady-state value as determined by the relative deposition fluxes of the solution components. In this paper, this flow-induced 'shift' of local deposit composition, and its phase-change consequences are investigated with respect to their hot-corrosion implications, as well as their possible exploitation as a means of exercising control over the state (liquid/solid) of the deposit on the blade surface. The effects of phase-change processes within the gas boundary layer (BL) on salt deposition rates and corrosion behavior are briefly examined, since BL-nucleation is often encountered in practice. The illustrative calculations presented here have been performed for the ideal binary system Na_2SO_4-K_2SO_4, but the methodology itself is equally applicable to 'real' non-ideal liquid phases as well. An understanding of the basic phenomena involved in the deposition and flow of multicomponent condensates on surfaces to which mechanical motion has been imparted, hopefully the outcome of this program of fundamental corrosion research, may prove useful in the design and protection of turbine blades to forestall hot-salt corrosion.

Abstract No. 526

HOT CORROSION OF AUSTENITIC STAINLESS STEELS IN MOLTEN CARBONATE FUEL CELL ENVIRONMENT

C.Y. Yuh, A. Pigeaud, H.C. Maru
Energy Research Corporation
3 Great Pasture Road
Danbury, CT 06813

and

G.H. Meier
Dept. of Materials Science & Engineering
University of Pittsburgh
Pittsburgh, PA 15261

The molten carbonate fuel cell (MCFC) system represents a highly efficient alternative mode of power generation from natural gas, methanol and coal derived gases. Because the hardware used in an MCFC, such as separators and current collectors, is exposed to both reducing (anodic) and oxidizing (cathodic) atmospheres in the presence of molten carbonate electrolyte, the alloy used needs to be very stable from a corrosion point of view. Simultaneous attack in the form of oxidation, hot salt fluxing and carburization often lead to poor stability and low mechanical strength (1).

In recent research, commercial and experimental austenitic stainless steels were investigated in a typical MCFC environment. Table 1 lists the composition of a few of the alloys studied and the experimental conditions used. The experimental techniques used include isothermal soak, acoustic emission, cyclic oxidation, and oxide ohmic resistance measurements. Hot corrosion mechanisms are proposed based on the experimental results.

Isothermal Soak Experiment

During the retort testing, the test coupons were in contact with a melt reservoir of carbonate-filled plaques of porous Ni or NiO. In the cathode (oxidizing) atmosphere, uniform, adherent oxide scales formed on high Cr-Ni alloys (310S, 310S+Ce, 310S+Si, 314, Crutemp-25, COLT-25$^+$). Thick scales formed on the 316L and 18-18$^+$ alloys. The outer to inner scales formed on Fe-Ni-Cr alloys, using an XRD technique, were found to be $LiFeO_2$, Cr_2O_3, and chromium carbide, respectively. Many of the unidentified peaks from the inner scales may correspond to Fe-Cr spinels. The scales formed on 316L had the worst adhesion, showing severe spalling during cool-down of the testing. The very high Mn content in 18-18$^+$ is definitely detrimental. The rare-earth additives (0.05% La or 0.2% Ce) did not appear to improve isothermal corrosion resistance a great deal.

A high Cr content (e.g., 25% in 310S) promotes the formation of a thicker protective Cr_2O_3 compact layer near the scale-metal interface. Although Cr_2O_3 dissolves initially in molten carbonate as chromate, the formation of an outer, relatively passive $LiFeO_2$ layer protects Cr_2O_3 (as well as other oxide film compounds) from further carbonate attack. This $LiFeO_2$ layer is relatively resistant to carbonate fluxing attack as a result of its relatively low solubility in molten carbonate (~80 ppm), also insensitive to melt basicity changes (2). A low Cr content (e.g., ~18% in 316L) does not guarantee the formation of a sufficiently thick Cr_2O_3 layer near the oxide-metal interface due to much Cr dissolution and depletion from the substrate alloy. In the event of oxide cracking, a continuous Cr_2O_3 scale may not be able to reform from the Cr-depleted base metal, resulting in accelerated attack. A high nickel content (20-25%) appears to improve corrosion resistance, but the whole mechanism in all its details is not yet clear. Many theories on the benefits of Ni have been proposed before, such as the improvement of oxide adhesion.

In the anode environment (reducing atmosphere with high carbon activity), all the alloys tested showed high corrosion rates, unacceptable for MCFC application. The outer oxide scales formed on Fe-Ni-Cr alloys are Fe-rich (possibly $LiFe_5O_8$ or $Li_2Fe_3O_5$) and non-adherent, possibly formed by the fluxing, as was also suggested by Singh and Maru (3). Carbonate was detected along the outer-inner scale interface. The inner scales consist of Fe-Cr oxide and Ni-rich metallic phases; a typical compact Cr_2O_3 layer is absent under reducing conditions. Etching of the base alloys revealed considerable carburization; the extent of carburization appeared less with high Cr content (~25% in 310S). Carburization causes Cr depletion and prevents the formation of a continuous Cr_2O_3 protective layer. The carbide may eventually oxidize and release carbon for further substrate carburization. It is suggested that the fluxing attack of Fe, coupled with carburization of chromium, causes the accelerated attack and embrittlement in the anode atmosphere. Basic fluxing may be possible due to oxide accumulation from the reaction:

$$2OH^- + 2e^- \longrightarrow H_2 + 2O^=$$

This reaction is believed to proceed much faster than the direct reduction of oxy-anions (peroxide, etc.). Nevertheless, in the anode atmosphere a high Cr-Ni content (as in 310S) somewhat improves hot corrosion resistance, but not as much as in the cathode atmospheres, for similar reasons of poor compact passive film formation.

Pressurized testing (10 vs. 1 atm) indicates that at higher pressure (10 atm) reduced anode-side corrosion occurs, but pressure has little effect on cathode-side corrosion of 310S or COLT-25$^+$. Because melt basicity is reduced at a higher pressure, the results point to a basic fluxing mechanism in the anode atmosphere. The little effect of melt basicity on the solubility of $LiFeO_2$, on the other hand, may explain the insignificant effect of pressure on cathode-side corrosion rate. The little effect of melt alkali composition (with somewhat different melt basicities) on corrosion of 310S in an oxidizing atmosphere (Figure 1) appears to confirm the above explanations.

Cyclic Oxidation Experiment

As an accelerated test of scale adhesion, rapid cycling oxidation (1 cycle/hour with a temperature cycle 700°C, 45 minutes, and room temperature, 15 minutes) has been carried out in cathode atmosphere in the presence of 1-1.5 mg/cm^2 of 62Li/38K carbonate melt wetting the coupons. The results (Figure 2) indicated that the addition of La or Ce did not improve cyclic oxidation resistance, although this type of rare-earth additives has been reported in the literature to be able to improve oxide adhesion. But this is true mainly in connection with dry oxidation. Si-addition clearly appears to improve cyclic oxidation resistance, probably due to the greater oxide penetration, as found by metallographic analysis. 316L shows the worst cyclic oxidation behavior among the commercial alloys studied based on the weight change data and metallographic results.

Acoustic Emission Experiment

Adherence of oxide scales to 310S, 316L and COLT-25$^+$ was also evaluated, using an acoustic emission technique. The results indicate that, although COLT-25$^+$ has a better cyclic oxidation resistance than 310S or 316L in the absence of carbonate, mixed response was obtained in the presence of carbonate. La-addition does not appear to improve oxide adhesion significantly, as was also concluded from the cyclic

oxidation experiments.

Oxide Ohmic Resistance Experiment

Ohmic resistivity of oxide scale formed on current collectors is an important consideration from an MCFC performance point of view. Resistivity of in-situ formed oxide scales on 310S, 316L and COLT-25+ has been measured by a four-probe resistivity measurement technique. The results indicate that the oxides all have fairly similar volume specific resistivity, but scale thickness contributes substantially to the higher area specific resistances. A small oxide growth rate may indicate fewer crystal structure defects, whereas a high electronic resistivity may indicate fewer electronic defects. However, because of the mixed valence nature, defect concentration and electronic resistivity of the oxide scales evaluated cannot be clearly related.

Acknowledgment: The authors wish to acknowledge the support of the Department of Energy under Contracts DE-AC21-84MC21186 and 86MC23264.

References

(1) Energy Research Corporation, "Corrosion Resistant Materials in MCFC Environment," Final Report to U.S. Dept. of Energy under Contract DE-AC21-84MC21186, November 1986.

(2) H.S. Hsu, J.H. Devan and M. Howell, "Equilibrium Solubilities of $LiFeO_2$ and $(Li,K)_2CrO_4$ in Molten Alkali Carbonate at 650°C," Report to U.S. Dept. of Energy under Contract DE-AC05-84OR21400, August 1986.

(3) P. Singh and H.C. Maru, "Stability of Iron and Nickel Base Alloys in Molten Carbonate Fuel Cells," Paper 344, Corrosion/88, NACE, Boston, MA (1988).

(4) Energy Research Corporation, "Determination of Optimum Electrolyte Composition for Molten Carbonate Fuel Cells," Quarterly Technical Progress Report to U.S. Dept. of Energy under Contract DE-AC21-86MC23264, October-December 1987.

TABLE 1. ALLOY COMPOSITIONS AND TEST CONDITIONS

	Cr	Ni	Others
AISI-310S	25	20	Low Carbon
310S *	25	20	Low Carbon, No Si
316L	18	12	Low Carbon
Crutemp-25	25	25	Low Carbon
High Silicon Alloys			
310S(+Si) *	25	20	2% Si, Low Carbon
314	25	20	3% Si
Alloys With Rare-Earth Additives			
310S(+Ce) *	25	20	0.2% Ce, Low Carbon
COLT-25+	25	25	0.05% La, Low Carbon
High Mn Alloy			
18-18+	18	—	18% Mn

* Prepared By Univ. Of Pittsburgh

Pressure: 1 and 10 atm
Temperature: 650 to 700°C
Fuel: 72 H_2/18 CO_2/10 H_2O
Oxidant: 15 O_2/25 CO_2/60 N_2
10 O_2/13 CO_2/72 N_2/5 H_2O

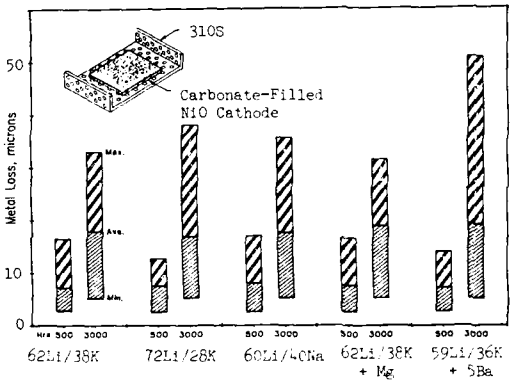


FIGURE 1. EFFECT OF MELT COMPOSITION ON CORROSION OF 310S; 700°C; 10 O_2/13 CO_2/72 N_2/5 H_2O (Reference 4)

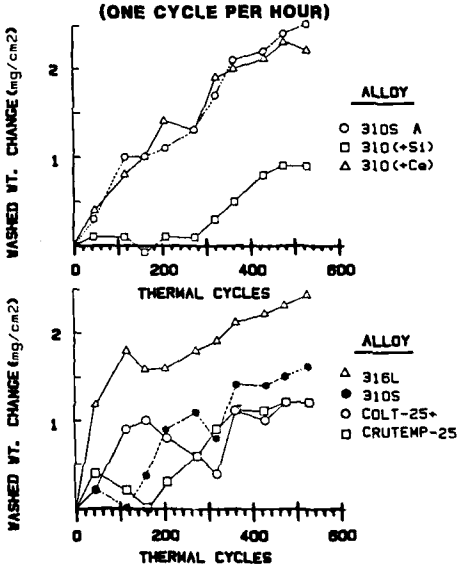


FIGURE 2. WEIGHT CHANGE RESULTS FROM CYCLIC OXIDATION EXPERIMENTS

Abstract No. 527

SIMULTANEOUS CHROMIZING-ALUMINIZING OF NICKEL AND NICKEL-BASE ALLOYS BY HALIDE-ACTIVATED PACK CEMENTATION

Vilupanur A. Ravi and Robert A. Rapp
Department of Metallurgical Engineering
The Ohio State University, Columbus, OH 43210

Critical gas turbine components are coated by various physical and chemical processes to generate a corrosion-resistant surface composition to protect a strong substrate alloy.

Halide-activated pack cementation is commonly used to generate such coatings. This is a chemical vapor deposition process carried out in a closed container at high temperatures. A 'pack' typically contains the substrate(s) to be coated and powders of an inert filler, a masteralloy rich in the element(s) to be deposited and a halide salt activator. The activator salt reacts with the alloy powder to form volatile metallic halide molecules which provide vapor phase transport from the pack to the workpiece. The process temperature is high enough for the species to diffuse into the workpiece and enrich it to a significant depth. Aluminum, chromium and silicon have been extensively investigated as the alloying elements.

Industrial practice is to deposit only one element at a time. However, if two elements could be deposited simultaneously, superior oxidation resistance could be achieved. In a cement-pack, deposition occurs by disproportanation of the gaseous halides, or by reactions of the halide with the activator or the gaseous environment. To choose the appropriate pack chemistry for codeposition of Al and Cr, a knowledge of the partial pressures of the relevant halides is essential. This has been done with a computer program SOLGAMIX-PV.[1] From activity data of Johnson et al[2], partial pressures of the gaseous species in equilibrium with the pack have been plotted as a function of the activity of Al in the Al-Cr masteralloy at 1273 K. The partial pressures of the Al fluorides are always higher than the Cr fluorides indicating that codeposition of Al and Cr may not be possible in a fluoride-activated packs. In chloride activated packs (NaCl, $CrCl_2$), the partial pressures of the Cr halides are comparable or higher than the Al chlorides for very low aluminum activities of Al-Cr masteralloy.

In the current studies, Al and Cr were co-deposited into Ni and Ni-base alloys by greatly reducing the activity of Al in the masteralloy relative to Cr. Coatings were obtained for several masteralloy compositions (98 Cr-2 Al, 95Cr-5 Al, 92 Cr-8 Al and 90 Cr-10 Al (w/o)) and different activators. The coatings were then characterized by optical and scanning electron microscopy and energy dispersive analysis. The effectiveness of the coatings was verified by cyclic oxidation, thermogravimetry and hot corrosion testing.

This presentation will discuss the principles of codeposition and show how the pack can be engineered to attain the desired coating composition.

References

1. G. Ericksson, Chem. Scr., 8 (1975) 100.

2. W. Johnson, K. Komarck, & E. Miller, Trans. Met. Soc. AIME, 242 (1968) 1685.

Abstract No. 528

SIMULTANEOUS CHROMIZING-ALUMINIZING COATING OF STEELS AND AUSTENITIC STEELS BY THE PACK CEMENTATION METHOD

P. Choquet, E. Naylor and R.A. Rapp
Department of Metallurgical Engineering
The Ohio State University
Columbus, Ohio 43210

Steels used at high temperatures (700-1200 C) in utility boilers, petrochemical plants, fuel cells...have to be protected against various corrosion atmospheres. Chromium and aluminum or aluminum and silicon are known to provide the best resistance to degradation by a variety of high temperature environments.

Because the volatile halides of aluminum are very much more stable than those for chromium or silicon, codeposition of Cr and Al in a single coating step is generally unsuccessful.

But, recently, by using a binary alloy with a low activity of Al, simultaneous chromizing and aluminizing on steels has been achieved.[1,2]

Based on these successful results, an investigation was undertaken to gain further understanding into the mechanism of simultaneous deposition of Cr and Al into Fe substrates and to achieve similar diffusion coatings in low and high alloy steels under much less restrictive and industrially viable conditions.

Thermodynamic Study

The pack cementation coating process is usually carried out at constant temperature (1000 C) in a reducing (H_2) or inert (Ar) background at constant pressure (1 atm). To understand the pack/gas equilibrium, when an alloy is used as the masteralloy, a thermodynamic analysis has been done.

The calculation of the equilibrium partial pressures of the stable gaseous species as a function of the activities of the condensed phases has been done using a SOLGAMIX software program[3,4,5]. The calculations were performed for 1000 C in an Ar background atmosphere for various activators and master-alloys. The activities of Cr and Al in binary Cr-Al alloys used in these calculations were taken from Johnson et al[6]. The thermodynamic compilations of Pankratz served as a source of free energy data for all species except gaseous $CrCl_x$[8] and CrF_x[9,10].

In NaF- or AlF_3-activated packs, the AlF_x partial pressures are always much higher than those of CrF_x. Therefore, the fluoride packs are strongly aluminizing even at low aluminum activities in the masteralloys, and codeposition of Cr and Al should not be possible using a fluoride activating salt.

In NaCl- and $CrCl_2$-activated packs for low Al activities (about 6.5×10^{-3}), the partial pressures of Cr chlorides are greater than those of Al chlorides. The $AlCl_x$ (x = 1,2,3) and $CrCl_2$ partial pressures are comparable for Cr-Al binary masteralloys with compositions corresponding to 10-15 wt% Al. At the interface of the pack/Fe substrate, the partial pressure of $FeCl_2(v)$ is quite high, so an exchange reaction such as Eq. (1) must be expected:

$$Fe(s) + MCl_2(v) = FeCl_2(v) + M \qquad (1)$$

where M denotes Cr or Al.

Experimental Results

Codeposition of Cr and Al into 2 1/4 Cr-1.0 Mo steel has been carried out; different binary Cr-Al masteralloys and different activators have been tested. For a chloride-activated pack with Ar background gas, at 1000 C, chromizing or chromizing-aluminizing can be achieved depending on the Al activity of the masteralloy. These results agree qualitatively with the thermodynamic calculations performed for such packs.

For a $CrCl_2$-activated pack at 1035 C, the coating contains a very thin fine-grained outer layer and an extensive inner layer with large columnar grains. The concentration profiles for Al and Cr through the coating are regular. The coating interface is marked by a step in the Cr concentration profile, corresponding to the gamma loop in the Fe-Cr-Al-C system for 1035 C.

Chromizing and aluminizing of stainless steel alloys (304SS and 316SS) have also been carried out. The combination of the composition of the masteralloy and the activator salt to avoid the formation of a NiAl outer layer was researched. In the microstructure of an alloy 316SS coated with a 92.5 Cr-7.5 Al masteralloy and NaCl activator, the brittle outer layer did not form, but the coating is rather thin and shows areas which seem to have undergone a reverse transformation, perhaps resulting from pack depletion.

Reference:

1. R.A. Rapp, D. Wang and T. Weisert, High Temperature Coatings, M. Khobaib and R.C. Krutenat eds., The Metallurgical Society, Inc., Warrendale, PA (1987), p.131.

2. D.M. Miller, S.C. Kung, S.D. Scarberry and R.A. Rapp, Oxid. Metals.

3. G. Ericksson, Chem. Scr., 8, (1975) 100.

4. C.S. Lin, User's Guide to SOLGAMIX-PV, Dept. of Metallurgical Eng., The Ohio State Univ., Columbus, OH, (1986).

5. R. Flynn, A.E. Morris and D. Carter, Using the UMR/SOLGAMIX Software Package, Proc. Computer Software Conf., Dept. of Metallurgical Engr., Univ. of Missouri, Rolla, MO (1987).

6. W. Johnson, K. Komarek and E. Miller, Trans Met. Soc. AIME, 242, (1968), 1685.

7. L. B. Pankratz, U.S. Bureau of Mines Bulletin 674, (1984).

8. C. Wagner and V. Stein, Z. Phys. Chem. (1943) 129.

9. R. A. Kent and J. L. Margrave, J. Am. Chem. Soc., 87, (1965), 3582.

10. K. F. Zmbov and J. L. Margrave, J. Chem. Phys., 47, (1967) 3122.

Abstract No. 529

Reactions of Metals and Ceramics with Chlorine and Oxygen at Elevated Temperatures

N. S. Jacobson, NASA Lewis Research Center
Cleveland, OH 44135

J. E. Marra, E. R. Kreidler, Ohio State University
Columbus, OH 43210

M. J. McNallan, University of Illinois at Chicago
Chicago, IL 60680

Gas-solid reactions involving chlorine and oxygen are an interesting class of reactions since they lead to both condensed phase and volatile products. The condensed phase products may be oxides or chlorides and the volatile products may be chlorides or oxychlorides. In this paper, two systems are discussed--binary Ni-Cr alloys and SiC ceramics. Both systems are known to form stable oxychlorides and both are close to systems of practical importance. A list of the materials examined is given in Table I.

These reactions lend themselves to study with an atmospheric sampling mass spectrometer.[1-2] Such an instrument allows the vapor species of a process occurring at one atmosphere to be monitored with a mass spectrometer operating at $\sim 10^{-7}$ torr. This instrument is shown schematically in Figure 1. It consists of a series of differentially pumped vacuum chambers. A small (8 mil) orifice is placed in the reaction furnace near the sample. The volatile species enter the cone and undergo a free jet expansion. Such an arrangement allows the direct sampling of volatile reaction products while preserving their chemical and dynamic integrity.

Consider first the Ni-Cr alloys. Each of these alloys was preoxidized for two hours. The Ni5Cr alloy formed a NiO scale, the Ni-15Cr formed a NiO and Cr_2O_3 scale, and the Ni-30Cr formed a Cr_2O_3 scale. The mass spectrometer data is shown in Table II. Very clearly, the higher chromium alloys produce more corrosion products. Thermogravimetric data on these reactions over several hours showed that the Ni-30Cr alloy corroded the most rapidly.

These data are explained on basis of the extraordinary stability of the CrO_2Cl_2 vapor molecule. Table III lists some heats of formation of the refractory metal oxychlorides as compared to other volatile chlorides.[3-4] Evidence suggests that chlorine reacts directly with the oxide scale as follows:

$$Cr_2O_3 + 2Cl_2\ (g) + 1/2\ O_2\ (g) = 2CrO_2Cl_2\ (v)$$

The important conclusion is that while Cr_2O_3 scales offer excellent protection in some corrosive environments, they appear to be readily volatilized by chlorine-oxygen mixtures.

Next consider SiC ceramics. These materials form protective SiO_2 scales. Silicon oxychlorides have been reported, but there is no thermodynamic data readily available. The most commonly observed products in this system are $SiCl_2$, $SiCl_3$, and $SiCl_4$.[5] As shown in Table III, $SiCl_4$ is quite stable.

The results for silicon based ceramics can be summarized as follows. Increasing the ratio of oxygen to chlorine tended to slow the reaction. A typical mass spectra is shown in Table IV. Oxychlorides were observed, but in very small quantities. Thermodynamic calculations suggest that the reaction of SiO_2 with Cl_2 forms $SiCl_4$ in very limited quantities. Thus, it is quite likely that silicon chlorides do not form by direct reaction with SiO_2, but rather by oxide penetration and reaction with the SiC substrate. It is further proposed that the silicon oxychlorides form by reaction of silicon chlorides with oxygen. This is because passing oxygen over liquid $SiCl_4$ forms numerous silicon oxychlorides.

In summary, the reactions of metals and ceramics with oxygen and chlorine mixtures has been discussed for both Ni-Cr alloys and SiC ceramics. Although both systems produce stable oxides, chlorides, and oxychlorides, the specific reaction schemes are quite different.

References:

1. Stearns, C. A., Kohl, F. J., Fryburg, G. C., and Miller, R. A., "A High Pressure Modulated Molecular Beam Mass Spectrometric Sampling System," NASA TM 73720, July 1977.
2. Jacobson, N. S., "Application of an Atmospheric Pressure Sampling Mass Spectrometer to Chlorination Reactions," NASA TM 87270, March 1986.
3. Stull, D. R. and Prophet, J. H., JANAF Thermochemical Tables, U.S. National Bureau of Standards, Washington, DC, 1971, and supplements J. Chem. Ref. Data, Vol. 4, 1974; Vol. 5, 1975; and Vol. 7, 1978.
4. Bale, C. W., Pelton, A. D., and Thompson W. T., F*A*C*T (Facility for the Analysis of Chemical Thermodynamics), McGill University/Ecole Polytechnique, Montreal, Canada, 1979.
5. Lin, S. S., "Mass Spectrometric Studies on High Temperature Reaction Between Hydrogen Chloride and Silica/Silicon," *J. Electrochem. Soc. 123[4]*, 512 (1976).

TABLE I

Materials Studied

Metals	Ceramics
Ni-5Cr	Si
Ni-15Cr	SiC (Al_2O_3 additives)
Ni-30Cr	

TABLE II

Mass spectrometer results for Ni-Cr Alloys-preoxidize 2 hours and react with 1% Cl_2/50% O_2/Ar at 700°C. All ion intensities normalized to Cl_2^+.[2]

m/e	Probable Ion	Parent	Ni-30Cr x10^4	Ni-15Cr x10^4	Ni-5Cr x10^4
93	$NiCl^+$	$NiCl_2$	--	2.0	--
103	$CrOCl^+$	CrO_2Cl_2	1.3	2.0	--
119	CrO_2Cl^+	CrO_2Cl_2	4.9	2.3	1.6
130	$NiCl_2^+$	$NiCl_2$	0.4	3.2	1.6
154	$CrO_2Cl_2^+$	CrO_2Cl_2	4.4	4.1	--

TABLE III

ΔH_f(298°K) of Some Chlorides and Oxychlorides

Vapor Specie	ΔH_f (298°K) kcal/mole
$NiCl_2$	- 13.5
$SiCl_4$	-157.1
CrO_2Cl_2	-128.6
MoO_2Cl_2	-151.3

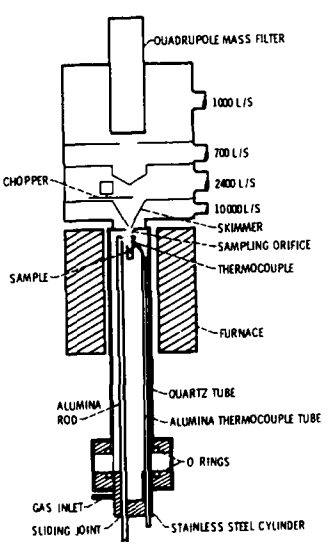
TABLE IV

Mass Spectrometer Results for SiC (Al_2O_3 additives) + 1% Cl_2/1% O_2/Ar at 950°C. All ion intensities normalized to $^{35}Cl_2^+$.

m/e	Probable Ion	Parent(s)	Intensity
63	$SiCl^+$	$SiCl_2$, $SiCl_3$, $SiCl_4$	75.6
98	$SiCl_2^+$	$SiCl_2$, $SiCl_3$, $SiCl_4$	23.2
133	$SiCl_3^+$	$SiCl_3$, $SiCl_4$	139.0
168	$SiCl_4^+$	$SiCl_4$	40.2
249	$Si_2OCl_5^+$	Si_2OCl_6	2.25
286	$Si_2OCl_6^+$	Si_2OCl_6	0.55
312	$Si_3OCl_6^+$	Si_3OCl_8 (?)	0.30

Figure 1

MASS SPECTROMETER SAMPLING SYSTEM



Abstract No. 530

EFFECT OF CHLORINE CONTAMINATION ON THE OXIDATION OF IRON-CHROMIUM ALLOYS UNDER CONDITIONS OF TEMPERATURE CYCLING

J.C Liu, M.J. McNallan
CEMM Dept., m/c 246
University of Illinois at Chicago
P.O. Box 4348
Chicago, IL 60680

Iron-chromium alloys are resistant to oxidation because they form a protective chromium oxide scale by selective oxidation of chromium in high temperature oxidizing environments. These alloys may be susceptible to accelerated oxidation when the temperature of the environment changes, because the difference in thermal expansion coefficient between the oxide and the metal can produce stresses which can lead to cracking or spallation of the oxide scale. The metal which is exposed to the environment by spallation of the oxide may be depleted in chromium due to the earlier oxidation, so that a protective oxide scale does not reform promptly leading to a condition referred to as breakaway oxidation.

The presence of chlorine contamination in the corrosive environment is known to exacerbate the problem. In this study, the effects of chlorine contamination on the cyclic oxidation of an iron-20% chromium alloy (by weight) have been investigated in an environment consisting of Argon, 20% O_2 (by volume), and varying levels of Cl_2. The experiments focussed on the effect of chlorine on the initiation of scale failure events and on the role of chlorine in the transport of species through the corrosion product scale.

The experiments were thermogravimetric measurements performed at 1000 K and 1200 K in gas mixtures flowing at a superficial velocity of 1.5 cm s^{-1} using a Cahn RG electrobalance and rectangular metal specimens with dimensions of approximately 1 cm x 1 cm x 1 mm. The experiments were performed for a period of 100 hours with cooling cycles to approximately 100°C for 30 minutes each occurring every 12 hours during the exposure. A long cycle time was selected to maximize the probability of spallation events occurring at each temperature cycle. At the conclusion of the experiments, the samples were examined by optical and scanning electron microscopy and the corrosion products were identified using X-ray diffraction analysis.

Figure 1 shows a typical thermogravimetric result for the Fe-20%Cr alloy exposed at 1200 K in gas mixtures containing varying amounts of Cl_2. The changes in mass detected in the uncontaminated environment and in the 0.05%Cl_2 environment are small in comparison to those observed in the other environments, although it is to be noted that they were larger than the changes in mass observed in the same environments under isothermal conditions. In the other environments, the mass of the specimens increased substantially after exposure, with sharp increases in mass being observed after many of the temperature cycles. Only one obvious spallation event was observed during this experiment. This is indicated by the sharp decrease in mass of the specimen in the 0.1% Cl_2 environment after the temperature cycle 24 hours after the beginning of the experiment. In all other cases the failure of the protective scale occurred with the scale remaining on the specimens. At the conclusion of the experiments, the specimens which showed large increases in mass were covered by porous oxide corrosion products. Very little unreacted metal remained at the end of the experiments performed in 0.5% Cl_2 and 1% Cl_2.

Because the rate of attack of the alloy after the temperature cycles in environments containing 0.1% Cl_2 to 0.5% Cl_2 is much greater than the rate of attack of the alloys at the beginning of the experiments, these results cannot be interpreted in terms of scale spallation alone. Instead, the damage to the oxide scale produced by the temperature cycle and the selective oxidation of chromium from the layer of metal below the scale produces a condition under which the mixed oxidation-chlorination of the alloy can proceed at a very high rate. The implications of these observations for the mechanisms of mixed oxidation-chlorination of alloys will be discussed.

This research was supported by the U.S. Department of Energy under grant DE-FG02-85ER45178.

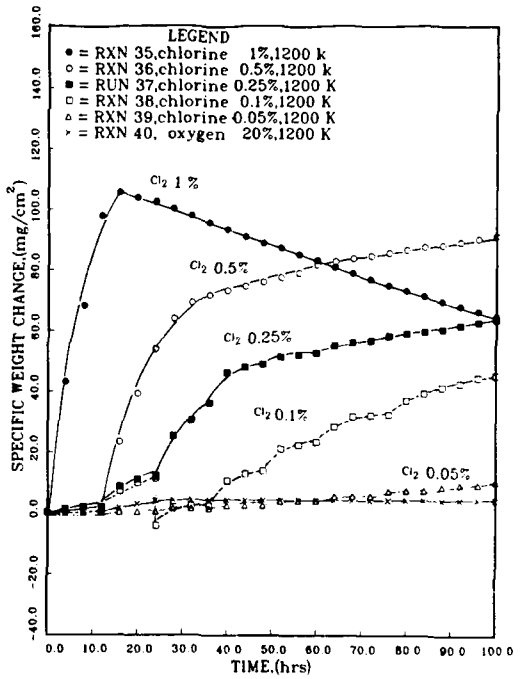


Figure 1. Thermogravimetric results for Fe-20%Cr alloy in Ar-20%O_2-Cl_2 gas mixtures at 1200 K with temperature cycles to 373 K at 12 hour intervals.

Abstract No. 531

The Effect of Alloy Grain Size on Oxidation Kinetics of an -Forming Alloy

John J. Goedjen and David A. Shores

Minnesota Corrosion Research Center
University of Minnesota
221 Church St., Minneapolis, MN 55455

Alloy grain size is not usually regarded as having an important effect on oxidation rates. It has been demonstrated, however, that surface deformation, leading to a recrystallized, fine-grain surface layer, is beneficial in promoting the formation of a protective scale on alloys of marginal compositions.[1] It was suggested that enhanced transport of alloying elements to the metal/scale interface, via grain boundary diffusion, accelerated the initial formation of the protective scale, which contributed to a subsequent reduction in the overall oxidation rate. It has also been demonstrated that a stainless steel prepared by powder metallurgy techniques using rapidly solidified powders, and therefore having a very fine grain size, exhibited greatly improved oxidation resistance as compared to conventionally prepared alloys of the same composition.[2] In the present study we have examined the effect of alloy grain size on the rate of oxidation of a very oxidation -resistant alloy.

Materials and Experimental Procedure

Two materials having the same nominal composition (Ni- 2.5Fe -16.2Cr -4.7Al -0.10Si -0.02Y wgt%) were studied. One was a very fine-grained alloy prepared by plasma spraying of blended powders, which was kindly supplied by General Electric Research and Development. The other material was the commercial alloy Cabot 214, which is made by conventional cast/wrought techniques, and a sample was kindly supplied by the Haynes Corp. The plasma sprayed material, as-received, had an average grain size of 1.4 μm; the Cabot 214 had an as-received grain size of 65 microns. Individual specimens of the plasma sprayed alloy, approximately 1 cm^2 x 1mm, were heat treated for various times at 1250 or 1300°C to obtain larger grain sizes, as reported in Table 1. Some specimens experienced grain growth and thus developed a bi-modal grain size distribution. After heat treatment the specimens were ground to remove any alloy depletion layer at the surface, then they were polished through 1.0 μm diamond abrasive in preparation for oxidation studies. Because the oxidation temperature was less than the heat treatment temperature, these grain structures were expected to be stable. The as-received plasma-sprayed alloy did experience grain growth during the oxidation exposure.

The oxidation kinetics were determined at 1150°C in oxygen from continuous weight measurements for periods of 1/2 to 72 hours with the use of a Cahn model 1000 electrobalance. Because of the high (weight) sensitivity required, weight changes during the first few minutes of exposure were quite variable and it was difficult to establish accurately the initial weight of the specimen at temperature. Consequently, these small initial weight changes have been discounted. While this procedure does not establish absolute weight gains, the relative positions of the curves were found to be independent of the choice of a starting reference point.

The grain size of the oxide scale was evaluated with transmission electron microscopy on pieces of scale that had spalled on cooling. Samples were prepared for microscopy by ion-milling from the gas/oxide side, and the results are reported in Table 2.

These alloys were also examined with an acoustic emission technique that can detect, in-situ, the fracturing of the oxide scale. This technique, which has been described elsewhere,[3] is based on the sensing of the elastic energy released by a crack with the use of a sensitive piezioelectric transducer. The output of the transducer is converted to "counts" by suitable electronic equipment, 'Dunegan 3000 System'. A typical run was carried out as follows: a specimen, prepared identically to the oxidation specimens, was spot welded to a platinum wire (which acted as a waveguide), and was suspended in the furnace. The opposite end of the wire was clamped against the piezoelectric transducer which is held outside the furnace. The specimen was oxidized isothermally (1150°C) for 72 hours in 1 atm. oxygen and then furnace cooled to room temperature. Acoustic emission data were collected during the isothermal period and during cool-down. It should be noted that a single crack can generate many counts.[3]

Results and Discussion

All the samples readily formed protective α-Al_2O_3 scales under the conditions of the experiment. A plot of TGA data for short times for several different grain sizes of plasma spray alloys (GE/PS) and for Cabot alloy 214 (C-214)is shown in Fig. 1. These results show that among the GE/PS specimens the larger grain sizes produced faster initial rates of oxidation. Interestingly, the wrought alloy C-214, with a large grain size, oxidized as slowly as the finest grained GE/PS alloy. Over a longer time the rates of oxidation decreased with time, as shown in Fig. 2, and generally all the specimens approached the same low value, regardless of the initial rates. These longer term kinetics are similar to those obtained by other authors for similar alloy compositions.

Acoustic emission activity was low during isothermal oxidation, typically accumulating less than 2000 counts/cm^2. While this likely indicates some isolated scale cracking, the protectiveness of the scale was not significantly compromised, as is evident from the TGA curves. Unfortunately, the presence of (isothermal) cracks could not be verified by subsequent examination, because on cooling from 1150°C to room temperature large numbers of additional counts/cm^2 were recorded, indicating extensive cracking induced by the thermal mis-match stresses. While there is a considerable range of total numbers of counts (1.5 x 10^5 to 5 x 10^7 counts/cm^2) among the specimens, there was not a clear trend with grain size. Therefore, the data are shown in Fig. 3 as a plot of per cent accumulated counts vs temperature. This representation emphasizes that most of the thermally induced cracking occurred only after a considerable amount of cooling, $\Delta T > 500 - 600°C$. Although thermal cycling oxidation tests have not been run, the acoustic emission data suggest that these alloys would not fare well with thermal excursions extending to near room temperature.

Unlike earlier studies on alloys which formed Cr_2O_3 scales and which have poorer oxidation resistance, the present studies show that alloy grain

size does not appear to be a highly significant parameter in determining oxidation resistance for Al_2O_3-forming alloys that have a high inherent resistance. There is a clear beneficial effect of small grain size during the early stages of oxidation, but this effect is gradually lost as the scale thickens.

Acknowledgement

The authors gratefully acknowledge financial support from the U.S. Department of Energy by DOE/DE-FGO2-84ER45173.

Table 1. **Grain Sizes of Alloys**

Alloy	Heat Treatments (°C)	(hr)	Grain Size (μm)
Cabot 214	-	-	65
Plasma-sprayed	-	-	1.4
Plasma-sprayed	1250	24	17
Plasma-sprayed	1250	72	26
Plasma-sprayed	1300	24	20
Plasma-sprayed	1300	72	32

Table 2. **Grain Sizes of Oxide Scales**

GE/PS Alloy Grain Size (μm)	Oxidation Time (hr)	Grain Diameter (μm)
32	0.5	0.25
26	0.5	1.3
32	24	1.9
20	24	1.1

References

1. Giggins, C.S., and Pettit, F.S., "The Effect of Alloy Grain-Size and Surface Deformation on Selective Oxidation of Chromium in Ni-Cr Alloys at Temperatures of 900° and 1100°C," Transactions of the Metallurgical Society of AIME, Vol 245, December 1969, 2509.

2. Yurek, G.J., Eisen, D., and Garrett-Reed, A., "Oxidation Behavior of a Fine-Grained Rapidly Solidified 18-8 Stainless Steel," Metallurgical Transactions A, Vol. 13A, March 1982, 473.

3. Barnes, J.J., and Shores, D.A., "Growth Stresses and Cracking of Scales During Oxidation" in Proc. Conf. on Environmental Degradation of Engineering Materials III, Penn. State, 1987, p.25

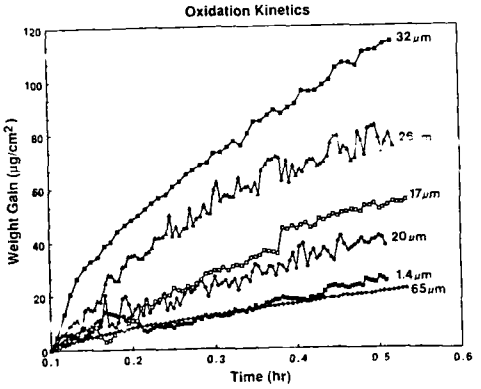


Figure 1. Oxidation kinetics for different grain sizes of GE/PS alloy and for the as-recieved C-214 alloy. Refer to Table 1 for heat treatments.

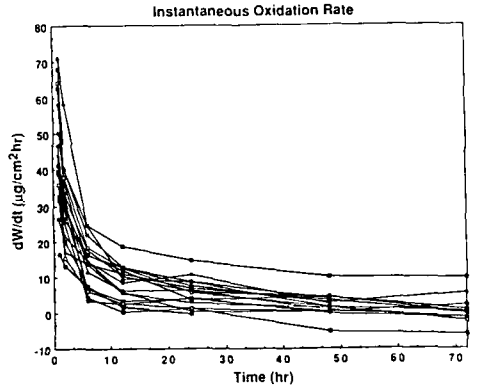


Figure 2. Instantaneous oxidation rates for different grain sizes of GE/PS alloy and as-recieved C-214 alloy. The larger grain sizes of GE/PS alloy have higher initial rates.

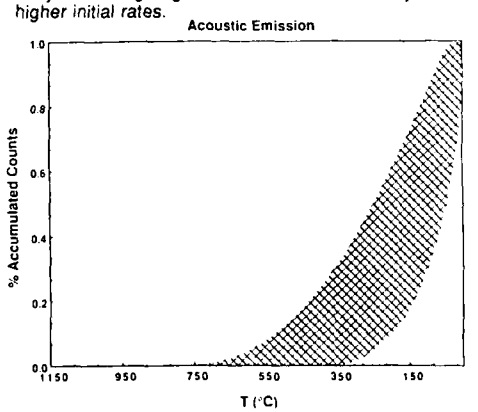


Figure 3. Accumulated counts as a function of temperature during furnace cooling for GE/PS and C-214 alloys occurs.

Abstract No. 532

EFFECT OF ION-IMPLANTED CERIUM ON THE GROWTH RATE OF CHROMIA SCALES ON Ni-Cr ALLOYS

N. Patibandla†, F. Cosandey† and T.A. Ramanarayanan*

†Department of Mechanics and Materials Science
Rutgers University, Piscataway, New Jersey 08855

*Exxon Research and Engineering Company
Annandale, New Jersey 08801

Previous research has shown that yttrium additions to high temperature alloys, either as oxide dispersions or as a metal, have a significant effect on the growth characteristics of chromium oxide scales formed on such alloys[1-4]. Generally yttrium tends to lower the rate of growth of the chromium oxide scale by suppressing chromium transport through the scale to such an extent that oxygen migration becomes the predominant rate-limiting step in scale growth. According to Przybylski, Garrett-Reed and Yurek[2], yttrium tends to segregate to grain boundaries in the chromium oxide scale and such segregation suppresses the grain boundary transport rate of chromium in the chromia scale. On the other hand, Ramanarayanan and coworkers[1,3] hold a different view; according to them, yttrium dopes into the chromia scale and decreases the population of chromium interstitials both in the lattice and grain boundary regions of the chromia scale, thereby suppressing chromium transport. It would be interesting to look into the effects of other rare earth elements on chromia scale growth rate in the context of the above two mechanisms.

In the present work Ce, which is known to have a variable valence, has been selected as the rare earth metal addition. Cerium was ion implanted on Ni-30 Cr alloys at a concentration level of $10^{16}/cm^2$. Most of the Ce is concentrated within the first 250 Å or so. The samples were oxidized in the 800 to 1110°C temperature range at relatively low oxygen partial pressures fixed by CO_2/CO ratios of 4, 1 and 0.25 to generate predominantly chromiun oxide scales. In general, the oxidation kinetics followed parabolic behavior. The kinetic curves for the Ce-implanted and the unimplanted samples at 1050°C using a 50 CO_2/50 CO gas mixture are compared in Fig.1. The kinetics are seen to be much slower in the Ce-implanted case. Similar observations were made at other temperatures.

The kinetic data for the various temperatures investigated are summarized in Fig. 2 in the form of parabolic rate constant vs. reciprocal temperature. The lower line corresponds to the Ce-implanted samples. The data should be treated as preliminary; more investigations are underway, covering more temperatures. The data points correspond to kinetic measurements using 50 CO/50 CO_2 and 80 CO/20 CO_2 gas mixtures. The upper line is the earlier data on the oxidation kinetics for Ni-30 Cr alloys in 80 CO/ 20 CO_2 gas mixtures. The parabolic rate constant values for chromium oxide growth on the Ce-implanted samples are seen to be a factor of 10 to 15 lower.

In earlier research[1-4] on Ni-base alloys containing yttrium oxide dispersoids, it was shown that yttrium incorporation into the chromium oxide scale had the effect of decreasing the chromium transport rate in the oxide scale so that oxygen becomes the predominant transporting species in the oxide scale. A similar effect seems to be occurring in the case of chromium oxide scales formed on Ce-implanted Ni-Cr alloys. This effect can be observed in the SIMS depth profile shown in Fig. 3. This comes from an oxidation experiment carried out at 1100°C. The y-axis indicates intensities for Cr, Ni and Ce cations whereas the x axis is proportional to the depth, starting from the oxide scale surface. The actual depth in angstroms is obtained by multiplying the depth number indicated on the x-axis by 50. The fact that the cerium mainly resides within the chromium oxide scale suggests that the scale predominantly grows inward.

Future work involves carrying out more oxidation kinetics experiments on the Ce-implanted samples to better establish the temperature dependence of the parabolic rate constant. Further, detailed characterization of the cerium-containing chromium oxide scales will be carried out using SIMS and TEM techniques. Based on the results, a mechanistic interpretation of the cerium effect will be attempted.

REFERENCES

1. T.A. Ramanarayanan and R. Petkovic-Luton, Ber. Bunsenges. Phys. Chem., 89, 402 (1985)

2. K. Przybylski, A.J. Garratt-Reed and G.J. Yurek, J. Electrochem. Soc., 135, 509 (1988)

3. T.A. Ramanarayanan, R. Ayer, R. Petkovic-Luton and D.P. Leta, To appear in Oxid. Metals. 1988

4. J. Stringer, B.A. Wilcox and R.I. Jaffee Oxid. Metals, 5, 11 (1972)

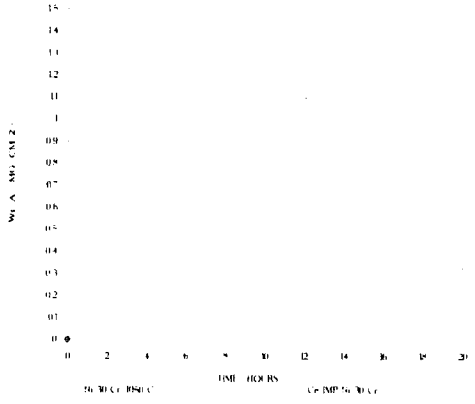


Fig.1. Kinetic Curves at 1050°C showing the Effect of Implanted Cerium on the Growth Rate of Cr_2O_3 on Ni-30 Cr Alloys

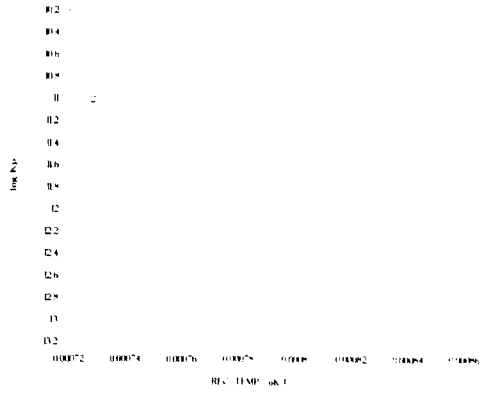


Fig.2. Comparison of the Parabolic Rate Constant Values for Cr_2O_3 Growth on Ce-implanted and Unimplanted Ni-30 Cr Alloys

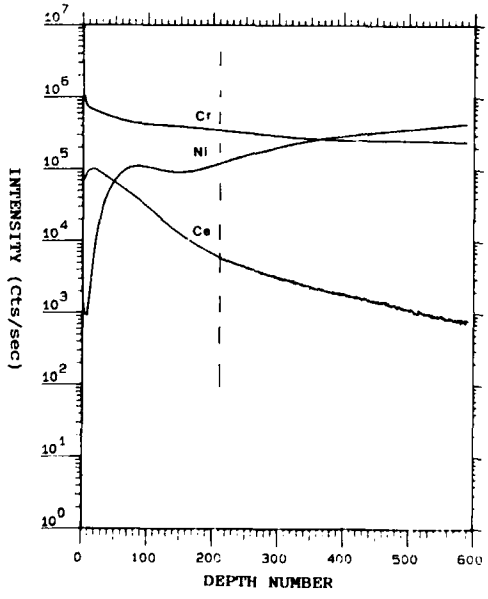


Fig.3. SIMS Depth Profile Showing the Predominance of Ce within the Cr_2O_3 Scale

Abstract No. 533

A MODEL FOR STRESS RELIEF IN OXIDE/METAL SYSTEMS DURING COOLING

JOHN J. BARNES, JOHN G. GOEDJEN and DAVID A. SHORES
Minnesota Corrosion Research Center
University of Minnesota
Minneapolis, Minnesota 55455

Good high temperature alloys protect themselves *against oxidation by forming* compact, adherent oxide scales, but the mechanical integrity of the oxide may be threatened by the stresses generated by oxide growth and during temperature excursions. Temperature changes generate stresses because the oxide and alloy invariably have different thermal expansivities. Thermally induced stresses will be superimposed on any growth-induced stresses, and the net stress *may be sufficient to cause* cracking and spalling of the scale. Some alloys have *good isothermal* oxidation resistance but suffer fast degradation owing to scale cracking and spalling during thermal cycling.

Stresses, induced thermally or otherwise, may be relieved in several ways, including cracking of the scale and creep of the metal or oxide. It is well known that some metals creep under oxidation-induced stress. Stress relief by creep of *the oxide is much less likely because the* creep rates of oxides (considering the few data which are *available) are generally* much lower than the creep rates of the corresponding metal substrates at typical oxidation exposure temperatures.

In this paper we describe a simple model which considers the relief of thermally induced stresses by creep for Cr, Ni-30Cr and MA-754, all of which form Cr_2O_3 scales. (For the temperatures and materials of interest here, creep of the oxide scale was considered, but was found to be trivial.)

DESCRIPTION OF THE MODEL

The model is comprised of two elements. The first is a calculation of the stress generated in the substrate and in the oxide during temperature changes. The average stresses may be calculated from a simple function of the thermal expansion difference between the oxide and metal. The average stress in the oxide, σ_{ox}, and the average stress in the metal, σ_m, are, as proposed by Tien and Davidson [1]:

$$\sigma_{ox} = -\frac{E_{ox}\,\Delta\alpha\,\Delta T}{1+\frac{E_{ox}}{E_m}\cdot\frac{t_{ox}}{t_m}}\cdot\frac{1}{1-\mu}$$

$$\sigma_m = \frac{E_m\,\Delta\alpha\,\Delta T}{1+\frac{E_m}{E_{ox}}\cdot\frac{t_m}{t_{ox}}}\cdot\frac{1}{1-\mu}$$

where E_{ox} and E_m are the Young's modulus of the oxide and metal, *respectively*. The *thermal expansion* difference between the metal and oxide is $\Delta\alpha = \alpha_m - \alpha_{ox}$; $\Delta T = T_{initial} - T_{final}$, and t_{ox} and t_m are the thicknesses of oxide and metal, respectively. The Poisson's ratio, μ, is assumed equal to 1/3 for oxide and metal.

These expressions obey the condition for mechanical equilibrium in a body, i.e. the sum of the forces acting on it must be zero. However, the calculated stresses are average stresses, whereas a *more detailed analysis* shows that a stress gradient will exist, especially in the metal. The *nature* of the (elastic) stress gradient in an oxide-metal system has been modelled by Gerberich and Lii [2] using a finite element method.

The Gerberich and Lii model was used in the present work to replace an average stress in the metal with a distributed stress. This provides a more realistic assessment of the stresses near the metal/oxide interface. It was found that the local stress at the *interface* was about 9 times the average stress and that the stress at 10% of the substrate thickness was about 3.7 times the average. Since creep at or near the oxide/metal interface will be most important in the relaxation process, and since the creep rate is strongly dependent on the stress, this modification is quite significant.

In the second element of the modelling process, the relaxation of the thermal stress is calculated using uniaxial creep data from the *literature for the metal* at the relevant temperature and stress. The creep rate is governed by the following equations relating to power law creep and grain boundary diffusion creep, respectively:

$$d\varepsilon/dt = A\exp\left(\frac{-Q_v}{RT}\right)\left(\frac{\sigma}{E}\right)^n$$

$$d\varepsilon/dt = \frac{42\,\sigma\,\Omega\,D_{eff}}{kTd^2}$$

$d\varepsilon/dt$ is the strain rate in sec^{-1}; A,n and Ω are constants

σ is the stress in MPa; Q_v is the activation energy for lattice diffusion, and the remaining symbols have their usual meanings. Values of these parameters for the materials of interest were obtained primarily from Frost and Ashby. [3]

To assess the extent of stress relaxation which may occur during cooling the time/temperature curve was divided into 0.05 °C temperature increments and, at each increment, strain generation due to the ΔT and strain relaxation due to creep was calculated. The net strain was accumulated and converted to stress via Hooke's Law. The calculations were carried out with the help of a microcomputer program.

RESULTS

The model was used to predict the behavior of Cr Cr_2O_3, Ni-30Cr/ Cr_2O_3 and MA-754™/ Cr_2O_3 systems. The three substrates are typical chromia-formers during high temperature oxidation, but they have somewhat different mechanical properties: $\Delta\alpha$ for Cr is much less than that for Ni-30Cr or MA 754™ (composition: Ni- 20%Cr- 0.6% Y_2O_3 - 0.5%Ti- 0.3%Al- 0.05%C.); the Young's modulus varies as $E(Cr_2O_3) > E(Cr) > E(Ni\text{-}30Cr) > E(MA754™)$. The creep rates of chromium and Ni-30Cr are quite similar whereas MA 754™ has a much lower creep rate in the power law region.

The predicted relaxation effect in the Ni-30Cr Cr_2O_3 system during continuous cooling from 1273K is shown in Fig. 1, which presumes the residual growth stress at the start of cooling is zero. At a relatively slow cooling rate (corresponding to furnace cooling) the oxide thermal stress, which is compressive, is relaxed considerably during cooling from 1273 to 320K by creep of the substrate. On the other hand, relaxation at fast cooling rates may be largely or completely suppressed.

Calculations on the three metals for a given (slow) cooling rate illustrate the importance of thermal expansion coefficient difference, moduli and creep rate. The stresses during cooling are shown in Fig. 2. The difference in $\Delta\alpha$

between Cr and the nickel-base alloys is reflected in the magnitude of the compressive stresses generated during cooling. The stresses are lower in the Cr/ Cr_2O_3 system and consequently the extent of relaxation is also less (Cr and Ni-Cr have similar stress and temperature dependences for creep). The Ni-30Cr/ Cr_2O_3 system generates the most stress of the three during cooling because of the larger $\Delta\alpha$ (also $E_{Ni\text{-}Cr} > E_{MA\ 754^{TM}}$). MA 754™ is a highly creep-resistant alloy and exhibits little or no relaxation at the stresses generated by these cooling curves.

DISCUSSION

The magnitude of the stresses generated during cooling suggests that creep in the substrate is likely in many systems. Our calculations show that, under certain conditions, substantial relaxation of the stress in the oxide will be likely. Several factors are important. Firstly, large thermal stresses are primarily the result of large differences in thermal expansion coefficients of the oxide scale and the metal. Since α_m is generally greater than α_{ox} the sign of the stress is dependent on the sign of ΔT. Typically, upon cooling, a compressive stress is generated in the oxide and a tensile stress in the metal. This is an important consideration since the tensile fracture strength of oxides is much less than their compressive fracture strength. Secondly, the ratio of metal thickness to oxide thickness (R) and material properties (E_{ox} and E_m) also affects the magnitude and distribution of stresses. Thirdly, stresses increase as ΔT (cooling) increases, but stress relaxation decreases as rate of cooling increases because creep is a time dependent process.

The creep rate of the metal is a strong function of stress and temperature. Thus, the stresses in an oxide - metal system, which are undergoing relaxation on cooling, are a complicated function of both the absolute temperature and the rate of change of temperature. Thus, for comparable $\Delta\alpha$'s and equal fracture strengths of the scales, the material having the slowest creep rate, eg. MA 754™, would be expected to be more prone to fracture during temperature changes than the same oxide on a more plastic substrate.

ACKNOWLEDGMENT

This work was supported by a grant from the Department of Energy, DOE/DE-FGO2-84ER45173. The authors wish to acknowledge helpful discussions with J.H. Stout, W.W. Gerberich and Mirng-ji Lii.

REFERENCES

(1) J.K. Tien and J.M. Davidson, in Stress Effects and the Oxidation of Metals, ed. J.V. Cathcart, AIME, New York (1975), p. 200.

2. see: J.H. Stout, W.W. Gerberich, S. Lin, and M. Lii, in Fundamental Aspects of High Temperature Corrosion - II, ed. D.A. Shores and G.J. Yurek, The Electrochemical Society, Pennington, NJ, (1986), p.172.

3. H. J. Frost and M. F. Ashby, Deformation-Mechanism Maps , Pergamon Press, 1982.

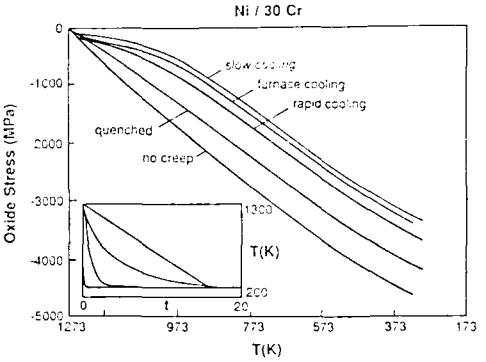


Fig. 1 Calculated stresses in the oxide scale for Ni-30Cr/Cr_2O_3 during cooling at various rates from 1273K, showing the effect of substrate creep (based on σ_M at the metal/scale interface; ratio of metal-to-oxide thickness = 100).

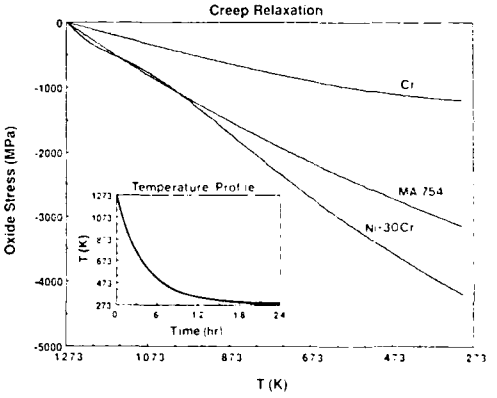


Fig. 2 Calculated stresses in the oxide scale for the systems Cr/Cr_2O_3, Ni-30Cr/Cr_2O_3 and MA754™/Cr_2O_3 during furnace cooling from 1273K (based on σ_m at the metal/scale interface, ratio of metal-to-oxide thickness = 100).

Abstract No. 534

Role of Oxygen Supply in High Temperature Growing of Compact Oxide Scale

D. Gozzi, M. Tomellini*, G. Carnevale, P.L. Cignini+ and L. Petrucci

Dipartimento di Chimica, Universita' "La Sapienza"

P.le Aldo Moro 5-00185 Roma, ITALY

In a research program on the study of high temperature oxidation of metals at very low oxygen partial pressures (1-5), it was investigated the role of the oxygen supply at the metal surface in such a way as to change the rate limiting step of the oxidation process.
An experimental apparatus based on the coupling of two zirconia electrolyte cells was used to do this. Two close one end and flat yttria stabilized zirconia tubes were assembled concentrically in such a way as a small allumina microchamber were housed between the close ends. Sample under study was located inside the microchamber between the outermost and innermost flat ends of the electrolyte tubes. Both the electrolyte tubes was with 8 mass per cent of yttria stabilizing zirconia. Electrodes of both the cell were made of porous platinum according to the standard procedure. The outermost tube acted as an oxygen pump which transferred oxygen onto the microchamber when an electric current was applied to the electrodes making positive the microchamber-side electrode. The system was initially filled with high purified argon with an oxygen partial pressure less than 1×10^{-14} Pa. The outer atmosphere of the oxygen pump was oxygen at 101.325 kPa. The innermost tube worked as oxygen sensor with pure oxygen as reference oxygen pressure, p_r.
The reaction rate, J_{ox}, was derived through a mass balance between the generated electrochemical oxygen, J_{in}, and rate of change of the oxygen partial pressure, $p(O_2)$, in the microchamber, as follows:

$$dp(O_2)/dt = (RT/V)(J_{in}S_{el} - J_{ox}S_s) \quad (2)$$

where V, S_{el}, S_s are, respectively, the volume of the microchamber, the area of the electrode surface and area of the sample surface.
In a constant current experiment, J_{in} is constant according to the Faraday law supposing the ionic transport number of the pump electrolyte independent of the oxygen partial pressure. The left side term in equation 1 was measured by the e.m.f., E, of the oxygen sensor:

$$dp(O_2)/dt = -(4Fp_r/RT)(dE/dt)\exp(-4FE/RT) \quad (3)$$

Therefore, the oxidation rate, dn_{ox}/dt, is given by the equation:

$$dn_{ox}/dt = (I/4F) + ((4FVp_r/(RT)^2)(dE/dt)\exp(-4FE/RT) \quad (3)$$

where the all the right term quantities are experimentally determined.
In the case of copper oxidation, we applied a current density to the oxygen pump according to the inequality:

$$J_{in} < J_W(t) \quad (4)$$

where $J_W(t)$ is the calculated oxygen demand as given by Wagner's theory (6-8). The inequality is satisfied for all times shorter than the experimental length. At 1113 K and 10 mA corresponding to $J_{in} = 1.3\times10^{-8}$ moles.cm^{-2}.s^{-1}, the scale thickness is linear with time as follow:

$$x(cm) = 1.5\times10^{-4} + 1.6\times10^{-7}\ t(s) \quad (5)$$

In these experimental conditions of $p(O_2)$ and T, $J_W(t)$ is about ten times larger than J_{in}. Due to this, the rate limiting step of the oxidation process cannot be the transport in the growing scale but the oxygen supply at sample surface.
In the light of these findings, it will be discussed the role of the rate limiting step as possible modifying parameter in the scale morphology and adhesion to the metal substrate.

Work carried out under contract 86.00846.09 of the Progetto Finalizzato Energetica 2 of the National Research Council (CNR)

REFERENCES

1. D. Gozzi, M. Tomellini, P.L. Cignini and L. Petrucci, J. Electrochem. Soc., 134, 728, (1987)
2. M. Tomellini, D. Gozzi, A. Bianconi and I. Davoli, J.C.S. Faraday Trans. I, 83, 289, (1987)
3. D. Gozzi, P.L. Cignini, G. Carnevale and M. Tomellini - A Solid State Electrochemical Technique for the Study of High Temperature Materials-Oxygen Interaction - Fifth International Conference on High-Temperature and Energy- Related Materials, Roma, May 25-29, 1987
4. D. Gozzi, P.L. Cignini, G. Carnevale, L. Petrucci and M. Tomellini, High Temperatures & High Pressures, in press
5. D. Gozzi, M. Tomellini, P.L. Cignini and L. Petrucci, in Advances in Ceramics, in press
6. C. Wagner, Z. Physik. Chem., B21, 25 (1933)
7. A.T. Fromhold, Jr., Theory of Metal Oxidation, in Defects in Crystalline Solids Series, S. Amelinckx, R. Gevers and J. Nihoul Editors, North-Holland Publishing Co., Amsterdam, 1976
8. P. Kofstad, High Temperature Oxidation of Metals, J. Wiley & Sons, New York, 1966

* Istituto di Chimica, Universita' della Basilicata, Potenza, Italy
+ Centro di Termodinamica Chimica alle Alte Temperature, CNR-c/o Dipartimento di Chimica, Universita' "La Sapienza"

Abstract No. 535

TRANSITION-METAL SILICIDE/ REFRACTORY CERAMIC INTERACTIONS

P. J. Meschter, R. J. Lederich, and J. E. O'Neal

McDonnell Douglas Research Laboratories
P. O. Box 516
St. Louis, MO 63166

Group IVA, VA, and VIA transition-metal silicides are attractive high-temperature materials owing to their low densities and high melting or transition temperatures relative to those of other candidate intermetallic compounds (Figure 1). The silicides labeled in Figure 1 were selected for further assessment according to their crystal structures, oxidation resistances, high-temperature mechanical properties, and thermal expansion compatibilities with refractory compounds such as SiC, B, Al_2O_3, and TiB_2. The compounds Ti_5Si_3, Zr_3Si_2, Zr_5Si_4, and $MoSi_2$ were selected for research on thermodynamic compatibility with refractory ceramic materials at 1000-1600°C based on this assessment. The compound Ti_5Si_3 is especially interesting owing to its low density (4.36 $g \cdot cm^{-3}$), while $MoSi_2$ is oxidation-resistant and exhibits appreciable plastic flow above 925°C [1].

Evaluation of silicide/refractory ceramic thermodynamic compatibility requires knowledge of the relevant ternary and quaternary phase diagrams, e.g., Ti-Si-C, Ti-Si-B, Ti-Si-Al-O, etc., over the temperature range of interest. Since most of these diagrams have not been determined experimentally, compatibility predictions have been made using multicomponent phase diagrams calculated from coupled phase diagram and thermodynamic information for the bounding binary systems. These diagrams assume no solubilities of the third and fourth components in binary intermetallic compounds and ignore ternary and quaternary phases. The diagrams are usually sufficiently accurate to indicate which silicide/refractory ceramic combinations are not stable.

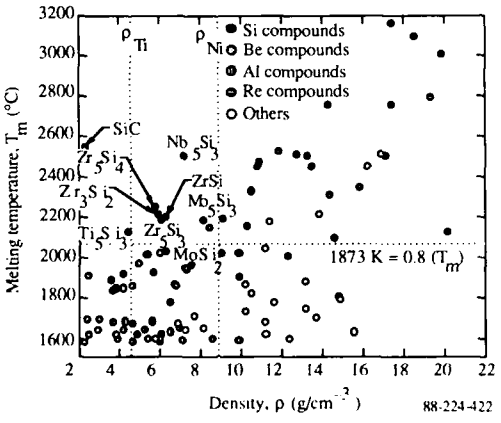


Fig. 1 Melting temperatures and densities of refractory intermetallic compounds.

The Ti-Si-C, Ti-Si-B, Mo-Si-C, and Mo-Si-B phase diagrams have been calculated at 1000, 1300, and 1600°C using coupled thermodynamic and phase diagram data compiled by Kaufman et al. [2] and Murray [3]. Comparison of the calculated and measured [4] Ti-Si-C phase diagrams (Figures 2a, 2b) shows modest agreement owing to C solubility in Ti_5Si_3 and the existence of a ternary compound. However, both diagrams show that Ti_5Si_3 and SiC are thermodynamically incompatible owing to the high stability of "TiC". Calculated and experimental [5] Mo-Si-C diagrams (Figures 3a, 3b) are similar except for the presence of a ternary compound Mo_5Si_3C. The compounds $MoSi_2$ and SiC are in thermodynamic equilibrium in both diagrams. The calculated Mo-Si-C diagram at 1600°C shows that formation of a Si-rich liquid at the $MoSi_2$/SiC interface can be avoided by keeping the $MoSi_2$ slightly Mo-rich. Calculation of the Ti-Si-B and Mo-Si-B diagrams, for which no experimental evidence exists, shows that the pairs Ti_5Si_3/B and $MoSi_2$/B are unstable owing to the thermodynamic stabilities of the corresponding transition-metal borides, although Ti_5Si_3 and TiB_2 may be compatible. These calculations have been extended to include Zr_3Si_2 and Zr_5Si_4 as the silicides and Al_2O_3 as the refractory ceramic.

The interactions of Ti_5Si_3 and $MoSi_2$ with B, SiC, and Al_2O_3 fibers have been investigated experimentally. Bundles of the fibers were packed with silicide powders in Nb alloy tubes and hot isostatically pressed at 1600°C. The combinations Ti_5Si_3/B, $MoSi_2$/B, and Ti_5Si_3/SiC reacted strongly, while $MoSi_2$/SiC, $MoSi_2/Al_2O_3$, and Ti_5Si_3/Al_2O_3 were relatively stable, in accord with calculations. The combinations which were stable after hot isostatic pressing were annealed at 1200°C for times up to 500 h. Interaction-zone thicknesses were measured as a function of time, and the compositions of reaction products were determined using energy-dispersive x-ray analysis and scanning Auger microscopy. Possible kinetic mechanisms and rate-limiting steps of the silicide/refractory ceramic interactions have been identified. The study has been extended to include the Zr silicides, and TiB_2 as a refractory ceramic.

This research was supported by the McDonnell Douglas Corp. Independent Research and Development program.

References

1. J. Schlichting, High Temperatures-High Pressures 10, 241 (1978).

2. L. Kaufman and H. Nesor, CALPHAD 2, 295 (1978); L. Kaufman, ibid., 3, 45 (1979); L. Kaufman, B. Uhrenius, D. Birnie, and K. Taylor, ibid., 8, 25 (1984).

3. Phase Diagrams of Binary Titanium Alloys, J. L. Murray, ed. (ASM International, Metals Park, OH, 1987).

4. E. Rudy, Report No. AFML-TR-65-2, Part V, p. 522 (May 1969).

5. F. J. J. van Loo, F. M. Smet, G. D. Rieck, and G. Verspui, High Temperatures-High Pressures 14, 25 (1982).

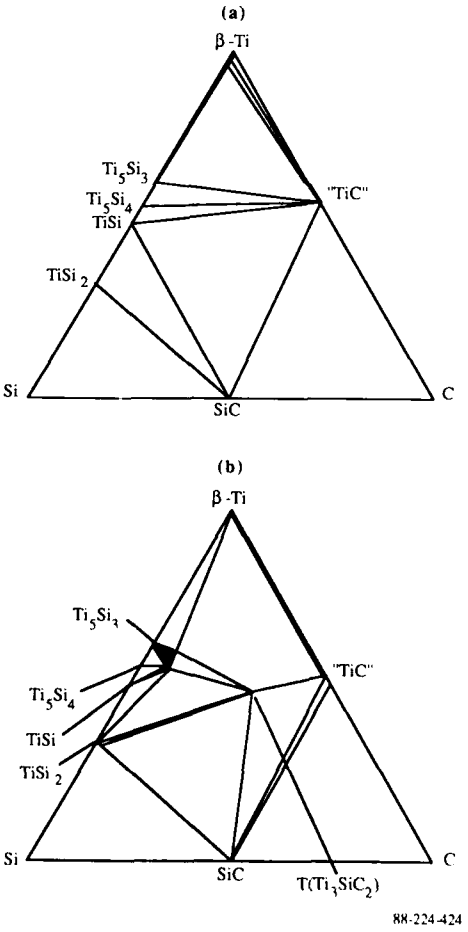


Fig. 2 Ti-Si-C phase diagrams: (a) calculated, 1300°C, and (b) experimental, 1200°C [4].

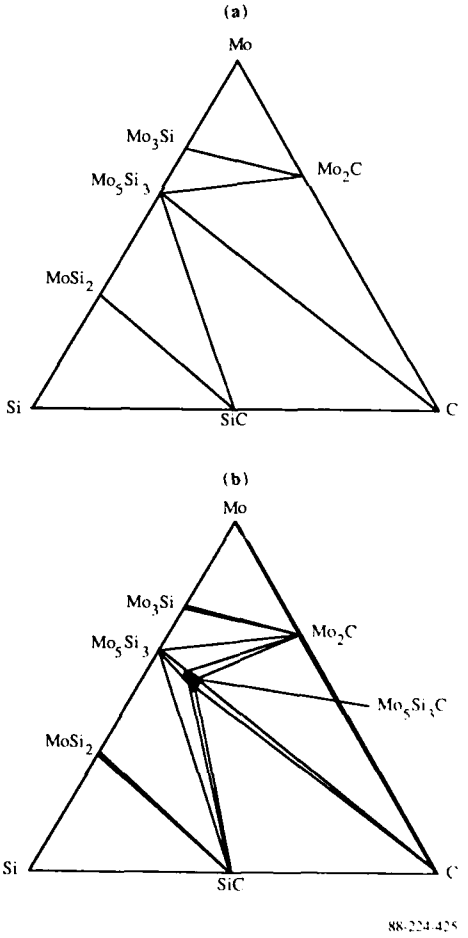


Fig. 3 Mo-Si-C phase diagrams: (a) calculated, 1300 C and (b) experimental, 1200°C [5].

Abstract No. 536

Investigation of the Reactions Between Titanium Alloys and Ceramic Reinforcements at Elevated Temperatures*

B. London, P. J. Meschter, and S. M. L. Sastry

McDonnell Douglas Research Laboratories
P. O. Box 516, St. Louis, MO 63166

Future high-temperature titanium alloys will probably derive their elevated-temperature strength from ceramic reinforcements. Extensive reaction between the titanium alloys and the ceramics can significantly degrade the mechanical properties of the ensemble; therefore, it is important to investigate the characteristics of these reactions.

The titanium alloys used in this study were rapidly solidified powders of α-Ti, α_2-Ti, γ-Ti, and β-Ti. The ceramic materials were carbon-coated SiC filaments and uncoated B filaments grown on tungsten wires. Small test samples were fabricated by encapsulating the titanium alloy powders with the SiC or B filaments in 6.35-mm-diameter titanium tubes and compacting by hot isostatic pressing (HIPing) to full density. Three-millimeter-thick disks were then cut from the HIPed tubes, encapsulated in vacuum in quartz ampoules, and annealed at 900, 1000, and 1100°C for 20, 60, 100, 200, and 300 hours. The extent and morphology of the reaction zones were investigated by optical microscopy and scanning electron microscopy (SEM). The compositions of these zones were determined by energy dispersive x-ray (EDX) analysis and scanning Auger microscopy (SAM). Calculations of the thermodynamically stable phases in the Ti-Al-B and Ti-Al-Si-C systems were performed to explain the observed results.

Reaction-zone growth in the SiC- and B-containing materials was diffusion-controlled. Zone thickness increased linearly with the square root of exposure time at a given temperature [1-4]. Representative results are shown in Fig. 1. Alpha-Ti showed the greatest reaction with SiC, while Ti_3Al and β-Ti showed the least. The reaction zone compositions were primarily TiC, along with Ti_5Si_3, possibly Ti_3SiC_2 [3], and an as yet undetermined titanium-aluminum-carbide. With the B-containing specimens, α-Ti reacted the most and TiAl the least. The reaction zones were probably TiB_2 or TiB. These reactions were overshadowed by dissolution of the B material. Calculations of the Ti-Al-B phase diagram at 1000°C revealed the presence of an Al-rich liquid phase which may account for the observed dissolution. Activation energies for the reactions in the SiC- and B-containing materials were also determined and compared to similar studies [1-3].

*This research was conducted under the McDonnell Douglas Independent Research and Development program.

References

1. W. J. Whatley and F. E. Wawner, J. Mater. Sci. Lett., 4, 173, (1985).
2. P. Martineau, M. Lahaye, R. Pailler, R. Naslain, M. Souzi, and F. Cruege, J. Mater. Sci., 19, 2731, (1984).
3. P. Martineau, R. Pailler, M. Lahaye, R. Naslain, J. Mater. Sci., 19, 2749, (1984).
4. M. Kh. Shorshorov, V. N. Metcheryakov, V. I. Zhaminova, V. I. Bakarinova, and I. A. Popov, Powder Metall. Inter., 14(1), 41, (1982).

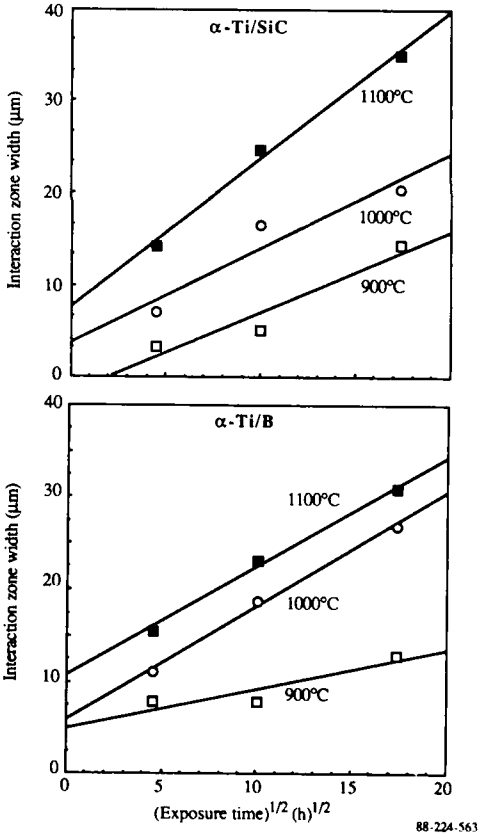


Fig. 1 Increase in the reaction zone thickness with the square root of exposure time at 900°C, 1000°C, and 1100°C for α-Ti containing SiC and B reinforcements.

Abstract No. 537

COMPATIBILITY OF SEVERAL REINFORCEMENT MATERIALS WITH NiAl

Ajay K. Misra
NASA - Lewis Research Center
21000 Brookpark Road
Cleveland, OH 44135

Continuous fiber-reinforced intermetallic matrix composites are being considered as potential high temperature materials. For applications requiring temperatures in the range of 1350 - 1650 K, systems based on β' phase NiAl appear to be attractive. One of the prime requirements in the selection of a suitable fiber-reinforcement material is that the fiber must be chemically compatible with the matrix. This paper describes the results of thermodynamic calculations on the compatibility of several reinforcement materials in the β' phase NiAl with Al concentrations ranging from 40 to 50 a/o. All the thermodynamic calculations were made at two temperatures, 1373 and 1573 K. The reiforcement materials considered in this study include carbides, nitrides, borides, oxides, silicides, and Be-rich intermetallic compounds. Altogether, 15 carbides, 18 oxides, 13 borides, 10 nitrides, 22 silicides, and 5 Be-rich intermetallic compounds were exmined for compatibility with NiAl.

The compatibility of reinforcemrnt materials with the NiAl matrix depends on the activities of Ni and Al in the NiAl phase. The aluminium activity data in NiAl phase, determined by Steiner and Komarek (ref. 1) at temperatures around 1273 K, show large degree of experimental scatter. Steiner and Komarek's data on Al activity were optimized and analyzed in accordance with the defect structure of NiAl. Based on the defect model for NiAl and partial moalar enthalpy data for Al, mathematical expressions were derived for the activity of Al as a function of composition and temperature. The activity of Ni was obtained by Gibbs-Duhem integration. The activities of Ni and Al change by more than an order of magnitude over the concentration range 48 - 52 a/o Al, which makes the compatibility of a few reinforcement materials very sensitive to small change in composition in the vicinity of 50 a/o Al. Several examples will be given to demonstrate this.

A list of reinforcement materials that appear to be compatible with the NiAl phase with concentrations ranging from 40 - 50 a/o Al is shown in Table I. There are also a few oxides and silicides (not shown in Table I) which might be compatible if limited dissolution/reaction of the reinforcement material would not affect the overall performance of the composite. Indeed, limited reaction may be desirable for effective bonding between the matrix and the fiber. Among the reinforcement materials that appear to be compatible with the NiAl phase, the coefficient of thermal expansion of only a few match closely with that of NiAl thus severely restricting the choice of potential reinforcement materials.

REFERENCES

1. A. Steiner and K. L. Komarek, Trans. TMS-AIME, 230, 786 (1964)

TABLE I
Reinforcement Materials
Compatible with β' NiAl

Carbides	Oxides	Borides	Nitrides
HfC	MgO	HfB_2	HfN
ZrC	Y_2O_3	ZrB_2	ZrN
TiC	Sc_2O_3	TiB_2	TiN
TaC	La_2O_3	VB_2	AlN
NbC	HfO_2	V_2B_3	
Ta_2C	CaO	TiB	
VC	BeO		
Nb_2C	$CaZrO_3$		
Al_4C_3	Al_2O_3		
	$CaO.Al_2O_3$		

Abstract No. 538

Chemical Interactions of SiC with Ti-Al and Nb-Al Alloys

J.-M. Yang, Department of Materials Science and Engineering, UCLA Los Angeles, CA 90024-1595

K.T. Chiang, R&D Division, Lockheed Missiles & Space Co., Palo Alto, CA 94304

Intermetallic alloy matrix composites are under intensive development for various high-temperature applications. Particular interest has been focused on nickel, titanium and niobium aluminides as matrix materials for fiber- and particulate-reinforced composites. The aluminides have high strength and stiffness retention at elevated temperature combined with excellent oxidation resistance. They also have higher ductility than ceramics, higher melting points and lower densities than superalloys. The incorporation of high strength and stiffness reinforcements can further improve the mechanical properties, creep resistance and reduce the densities of the aluminides. These novel composites can replace superalloys with superior performance.

However, the excessive chemical interaction between reinforcement and matrix induced from composite fabrication and high-temperature service environemnt is one of the majc: factors limiting the successful application of the composites. It is thus necessary to understand the chemical compatibility of various reinforcements with the intermetallic alloy matrices. In this paper, the chemical interactions of SiC with both Ti-Al and Nb-Al alloys will be discussed. The microstructure and chemical compositions of the reaction zone have been characterized by analytical electron microscopy and electron microprobe analysis. The interace reaction kinetics and its dependence on the temperature, environment and the structural characteristics of the materials will also be presented. Finally, optimum interface chemistry and optimum processing conditions, which will produce the best combination of integrity and compatibility of SiC fibers in Ti-Al and Nb-Al matrix composites, will also be discussed.

References

1. P.M. Brindley, *SiC Reinforced Aluminide Composites in High Temperature Ordered Intermetallic Alloy II*, MRS, 1986.

2. J.-M. Yang, W.H. Kao and C.T. Liu, *Recent Development in Nickel Aluminide Matrix Composites* in **Interfacial Phenomena in Composites: Processing, Characterization and Mechanical Properties**, 1988.

3. B. Moore, A. Bose, R.M. German and N.S. Stoloff, *Preliminary Investigations on Alumina Fiber Reinforced Ni_3Al Matrix Composites*, in **High Temperature/High Performance Composites**, MRS, 1988.

4. D.L. Anton, *High Temperature Intermetallic Composites: Why? How? And How Much?*, in **High Temperature/High Performance Composites**, MSR, 1988.

Abstract No. 539

The Oxidation of Chemically-Vapor-Deposited Silicon Carbide

Jeffrey W. Fergus and Wayne L. Worrell
Department of Materials Science
and Engineering
University of Pennsylvania
Philadelphia, PA, 19104

Silicon carbide is an attractive oxidation-resistant coating on carbon, because it is chemically compatible with carbon and forms a protective silica layer in oxidizing atmospheres at high temperatures. High purity silicon-carbide coatings can be applied on carbon substrates by chemical vapor deposition (CVD).

Previous investigators of the oxidation behavior of silicon carbide have used hot-pressed or sintered polycrysalline silicon carbide and single-crystal silicon carbide grown by the *Acheson Process*. Additive elements are used as sintering aids for hot-pressed or sintered silicon carbide and for the growth of silicon carbide single crystals. These previous studies show that the oxidation rate of silicon carbide increases with increasing concentration of additive elements due to an increase in the oxygen transport rate through the silica scale. CVD silicon carbide is of higher purity than the silicon carbide used in previous studies. *Therefore*, a higher purity silica scale should form, and the oxidation rate of the silicon carbide should be lower.

The first CVD silicon-carbide coatings investigated in this study are stoichiometric ones. An important variable in the CVD of silicon carbide is stoichiometry. The stoichiometry of the silicon carbide establishes t e equilibrium oxygen potential at the silicon carbide-silica interface, which in turn affects the oxidation resistance of the silica scale. The products of the oxidizing reaction are also affected by the stoichiometry. For example, carbon-excess silicon carbide produces a higher carbon-monoxide gas pressure at the silicon carbide-silica interface than stoichiometric silicon carbide. Silicon-*excess silicon carbide oxidizes* to form silica and carbon-monoxide at a much lower oxygen pressure.

To understand the oxidation kinetics of silicon-carbide coatings on graphite, the oxidation kinetics of CVD silicon carbide must first be determined. Our CVD silicon-carbide samples have been prepared by selective oxidation of the graphite substrate under a CVD silicon-carbide coating. The oxidation kinetics of CVD silicon-carbide samples *have been measured* using thermogravimetric analysis and interrupted weight-gain experiments at temperatures between 1400 C and 1600 C. The oxidation *results* are compared with *results with CVD silicon-carbide coatings* on graphite to determine the effect of the graphite substrate on the oxidation behavior of the silicon-carbide coating.

This research has been supported by the Naval Air Development Center in Warminster, PA.

Abstract No. 539A

ELECTRICAL PROPERTIES OF NOVEL MIXED-CONDUCTING OXIDES

Wayne L. Worrell and S. S. Liou
Department of Materials Science and Engineering
University of Pennsylvania
3231 Walnut Street
Philadelphia, PA 19104

Mixed-conducting oxides in which both oxygen-ions and electrons are mobile have attractive applications as electrode, membrane and sensor materials. One potential application is an oxide electrode in the solid-oxide fuel cell. Advantages of a mixed-conducting, oxide electrode over the currently used electrodes include decreased polarization and efficiency losses, chemical and mechanical compatibility with the oxide electrolyte and elimination of the necessity to fabricate and maintain complicated, porous electrode structures.

Past efforts to synthesize mixed-conducting oxides with acceptable conductivities over useful ranges of temperature and oxygen pressure have been unsuccessful. For example, transition-metal (iron, magnesium, cobalt) oxides have been dissolved in zirconia-based oxides, but they have very limited solid solubility. Mixed-conducting zirconia-ceria-yttria oxide solutions have also been prepared. Unfortunately, acceptable values for mixed-conductivity are obtained only at very high temperatures (1500-1700^{o}C0 and are a strong function of both temperature and oxygen pressure.

The electrical properties and applications of new mixed-conducting, zirconia-based oxides are summarized in this lecture. The electrical properties have been determined using impedance spectroscopy at temperatures between 400 and 950^{o}C. Knowledge of the electrical properties is necessary not only for an understanding of mixed-conduction mechanisms but also for the quantitative evaluation of the potential applications of these oxides.

New ternary-oxide solutions containing 12 mole percent yttria and titania with concentrations between zero and thirty mole percent have been synthesized. The molar percentage of yttria is kept constant to maintain a constant concentration of oxygen vacancies. The variation of the lattice parameter for these ternary-oxide solutions with titania concentration has been precisely determined using X-ray diffraction. The lattice parameter decreases with increasing titania concentration up to 15 mole percent and is constant at higher titania concentrations. The single-phase, fluorite structure is retained when the titania concentration is less than 15 mole percent, and a second phase is present at higher titania concentrations. The observed decrease in lattice parameter with increasing titania concentration and the absence of porosity in the oxide solutions indicate that titanium cations substitute for zirconium cations in the fluorite lattice.

The lattice, grain-boundary, and total electrical conductivities of yttria (12 mole %)-stabilized zirconia without titania have been determined using impedance spectroscopy at temperatures between 400^{o}C and 950^{o}C in air. The excellent agreement with previous results indicates the high quality of our polycrystalline samples and the reliability of our experimental technique. Electrical-conductivity measurements of zirconia-titania-yttria oxide solutions indicate that the oxygen-ion conductivity in the lattice does not vary significantly with incorporation of titania into yttria-stabilized zirconia. However, the observed increase in grain-boundary conductivity with increasing titania concentration indicates an increase in electronic conductivity at the grain-boundaries, presumably due to the segregation of Ti'_{Zr} to the grain-boundary region. The electrical conductivity of yttria (12 mole %)-stabilized zirconia containing one, and five mole percent titania is independent of oxygen pressure

Acknowledgements

The authors would like to thank Corning Glass Works for supplying the 12 mole percent yttria-zirconia powder, and the U.S. Department of Energy, Morgantown Energy Technology Center for their financial support. This research was conducted in the Materials Research Laboratory of the University of Pennsylvania, which is supported by the U.S. National Science Foundation.

Abstract No. 540

LUMINESCENT MATERIALS FORM STILL A CHALLENGE

G. Blasse
Physics Laboratory, University of Utrecht
P.O. Box 80.000, 3508 TA Utrecht, The Netherlands

Luminescent materials have quite a history. Nevertheless new materials become available frequently and often form an important break-through [1]. In this lecture we want to review some of the new luminescent materials which came into focus recently. Their application is in completely different fields. However, also their physics is different as we will see. The materials of this lecture will be lamp phosphors based on gadolinium compounds, X-ray storage phosphors using Eu^{2+} as an activator, and scintillator crystals for several applications.

Phosphors based on gadolinium compounds are promising materials because they offer over 90 % absorption and quantum efficiency. The luminescence processes in such luminescent materials consist of *three steps, viz.:*

a. Sensitization. This can be achieved by using the ions Ce^{3+}, Bi^{3+}, Pb^{2+} or Pr^{3+}. Successful sensitization requires specific spectral properties which can be imposed by the host lattice [2].

b. *Migration in the* Gd^{3+} sublattice. This process requires a shortest Gd-Gd distance in the lattice of about 5 Å or less [3].

c. Trapping by a suitable activator. The trapping rate is reasonably well understood and depends on the interaction strength between the Gd^{3+} ion and the activator and their energy mismatch [4]. It will become clear that not every ion is suitable as an activator in gadolinium compounds.

The rates of the several processes will be discussed. They can be determined by varying the chemical composition of the luminescent material and by advanced laser spectroscopy.

Excellent X-ray storage phosphors are nowadays known, the champion being $BaFBr:Eu^{2+}$. Their performance is based on the presence of electron and hole traps in the lattice. In case of BaFBr these are bromine vacancies and Eu^{2+} ions, respectively. The electron traps can be emptied by laser excitation [5].

The use of 12000 crystals of $Bi_4Ge_3O_{12}$ at CERN (Geneva) has drawn attention again to scintillator crystals. The physics of the luminescence of $Bi_4Ge_3O_{12}$ is nowadays known. In contradiction to early proposals, this luminescence is not of the semiconductor type. Although at first sight surprising, this luminescence is very similar to that of $CaWO_4$. This calls attention to the relaxation of strongly-coupled excited states, i.e. to the configurational coordinate model of broad-band emitters [1]. After many years considerable progress in this field can now be reported.

Recently BaF_2 crystals have been proposed as a scintillator material for the detection of gamma rays [6]. *These crystals show an emission* at 220 nm with a very short decay time, viz. 600 ps. This short time offers the possibility of a good time resolution. The emission is due to an intrinsic process, viz. a cross-over transition: an electron jumps from the F^- ion (2p orbital) to the hole in the 5p orbital of Ba^{2+}. This final example shows that new developments in the application of luminescent materials and new physical models have not come to an end.

References

1. G. Blasse, Mat. Chem. Phys. 16, 201 (1987)
2. H.S. Kiliaan, G. Blasse et al., Mat. Chem. Phys. 18, 155 and 351 (1987)
3. A.J. de Vries, H.S. Kiliaan and G. Blasse, J. Solid State Chem. 65, 190 (1986); J. Luminescence, in press
4. A.J. de Vries, W.J.J. Smeets and G. Blasse, Mat. Chem. Phys. 18, 81 (1987)
5. K. Takahashi, K. Kohda, J. Miyahara, Y. Kanemitsu, K. Amitani and S. Shionoya, J. Luminescence 31/32, 266 (1984)
6. P. Schotanus, C.W.E. van Eijck, R.W. Hollander and J. Pijpelink, Nucl. Instrum. Methods, A 238, 564 (1985)

Abstract No. 541

PAIR LUMINESCENCE AS A TECHNIQUE FOR IMPURITY CHARACTERIZATION

G. F. Neumark
Division of Metallurgy and Materials Science
Columbia University
New York, NY 10027

Donor-acceptor pair (DAP) luminescence is a powerful technique for impurity characterization. It can be used to determine impurity energies, radii, transition probabilities, and the relative lattice positions of the donor and acceptor. Recent work (1-4) has used it for extensive characterization of ZnSe. Moreover, we have used a novel approach to extend it (3) to obtain relative DAP transition probabilities in cases where there are separate DAP bands from two different donors (or acceptors). The present paper includes a systematic review of the technique and of its application to ZnSe. Moreover, the ZnSe analysis has led to two important and novel results, which will be emphasized. One relates to differences in transition rates between interstitial and substitutional donors, indicating that the interstitials act as "killers". The second is that relative donor energies and radii cannot be understood within the framework of effective mass theory.

In DAP luminescence, the emitted frequency depends on the spatial separation between the donor and its nearest neighbor acceptor. Due to the discrete positions of impurities in a lattice, there thus is a spread in the emitted frequencies. In practice there are two separate frequency ranges which can yield useful information. One of these is due to close pairs, where the energy difference as a function of distance is large, resulting in distinct pair lines. The second is due to more distant pairs, where the energy separation is small (i.e. no discrete lines), but where one obtains a maximum in emitted intensity due to a tradeoff between an increase in the number of available sites vs. a decrease in the transition probability with increasing separation. The latter range is generally studied in terms of variations with respect to some experimental parameter, such as intensity or frequency of excitation or time dependence. Emphasis here will be on similarities and differences between these two ranges in terms of information which can be obtained, as well as in regard to the approximations usually employed. It can be noted that relative lattice location can be obtained only from the distinct pair lines, but that energies and radii can be obtained from either range. Absolute transition probabilities require studies of the time dependence, but useful information on relative rates can also be obtained by other means, as will be discussed.

For the applications to ZnSe, I shall summarize resultant information on impurity energies, radii, transition rates, and lattice location. Analysis of pair lines has recently (1) given the first definitive evidence of alkali interstitial donors in II-VI compounds (although such donors have long been suspected). The primary emphasis of the present paper will however be on the two novel and unexpected [illegible] properties obtained in connection with this work [1,2,4].

[illegible] of the emphasized aspects - of practical [illegible] is the result that alkali interstitial donors (specific results have been obtained for both Li and Na) have a far lower DAP recombination rate [about one order of magnitude for Li (4), and about three orders for Na (3)] than the better known "standard" trivalent Group III metal substitutional donors. This thus means that such interstitial donors will effectively act as "killers". Since literature evidence shows that interstitial Group I metals are present in II-VI compounds in general, this is expected to be a problem for this whole class of compounds. The obvious way of minimizing this problem would be to avoid Group I metals. However, these are the metals which *are generally used as dopants*, as acceptors on the cation site, as "activators". There however appear to be two alternate solutions. One is to work preferentially with the group V elements as acceptors, on the anion site (although I am not aware of any literature showing that these lead to better luminescence than group I metals). The second is to incorporate the group I metals preferentially on the cation site (rather than as interstitials), where there are good indications that this would be aided by a rapid quench from high temperatures (this of course assumes that the impurities do not redistribute at the operating temperature).

The second emphasized aspect - of theoretical interest - relates to the validity of effective mass theory. In view of the fact that the energies of the interstitials, 17 mev and 20 meV for Li (4) and Na (1), respectively, are quite shallow, one would expect this theory to apply quite well. However, the theory would predict an effective mass energy of ≈28 meV (1). Moreover, all known substitutional donors (B, Al, Ga, and In on the Zn site, and F and Cl on the Se site) have energies between 26-29 meV. We have been unable to explain the energy deviations of the interstitial donors from both the effective mass value and from the values of the substitutional donors by invoking various corrections to simple effective mass theory (1). In this attempt, we have considered (1) as possible corrections: 1) inclusion of other (higher) bands (or extrema); 2) inclusion of q-dependent electronic screening; 3) polaron effects; and 4) central-cell effects. It can be added that the larger radius obtained for a substitutional donor (Al) as compared to those for the interstitials (4) is also in strong contradiction to effective mass theory.

In summary, we have confirmed that DAP luminescence is a powerful tool for investigating semiconductor phosphors, and moreover analyses based on this technique have given two interesting and unexpected results - drastic differences in transition rates between interstitial and substitutional donors, and strong deviations from predictions of effective mass theory (where this theory would be expected to apply, since all the donors are shallow).

REFERENCES

1. G.F. Neumark, S.P. Herko, T.F. McGee III, and R.J. Fitzpatrick, Phys. Rev. Lett. 53, 604 (1984).
2. G.F. Neumark, J. Lum. 31 & 32, 512 (1984).
3. G.F. Neumark, S.P. Herko, and R.J. Fitzpatrick, Proc. 13th. Int. Conf. Defects in Semiconductors, p.1205 (Metallurgical Society of AIME, 1985).
4. G.F. Neumark, Phys. Rev. B 32, 4115 (1985).

Abstract No. 542

Magneto–Luminescence of $KZn_{1-x}Co_xF_3$

N. L. Rowell and D. J. Lockwood
Division of Physics, National Research Council
Ottawa, Canada K1A 0R6

$KZn_{1-x}Co_xF_3$, a cubic perovskite mixed crystal, originally studied for its magnetic properties is now of technological importance as an infrared laser material. Such optically pumped lasers with transition metal impurities, e.g. Ni^{2+}, Co^{2+}, and V^{2+} ions, in ionic crystals like MgF_2, MgO, $KMgF_3$, or $KZnF_3$ have proved to be broadly tunable and produce intense infrared radiation from 1.5 to 2.1 μm. In crystals doped with Co, the pump source is normally a Nd:YAG laser operated at 1.32 μm or an Ar laser at 514.5 nm exciting the emission through the $^4T_{1g}(^4F) \Rightarrow {}^4T_{2g}(^4F)$ or the $^4T_{1g}(^4F) \Rightarrow {}^4T_{1g}(^4P)$ absorptions, respectively. Electrons in these excited states decay nonradiatively to the lowest $^4T_{2g}(^4F)$ levels and from there transitions, largely radiative in nature, take place to the ground state levels of $^4T_{1g}(^4F)$ and to the vibronics of these levels. It is these vibronics that are responsible for the broad tunability of these lasers.

The experiment involved photoexcitation in the visible part of the spectrum near 500 nm and detecting the emission in the infrared near 1.7 μm. The emitted radiation was analysed either to obtain its spectrum by Fourier transform infrared (FT-IR) spectroscopy or to measure its decay time constant. The major components of the spectral apparatus were an Ar laser source to excite the luminescence, a superconducting magnet with a variable temperature insert, and a FT-IR spectrometer to measure the spectrum of the luminescence. Our apparatus also had a broad band source behind the sample for measuring the sample absorbance in the same spectrometer.

In this study, the relevant single Co^{2+} ion energy levels are the Γ_6^+, $^{(1)}\Gamma_8^+$, $^{(2)}\Gamma_8^+$, and Γ_7^+ levels in cubic field from the $^4T_{1g}$ ground term and the Γ_6^+, $^{(1)}\Gamma_8^+$, $^{(2)}\Gamma_8^+$, and Γ_7^+ levels of the $^4T_{2g}$ first excited term. The dominant magnetic dipole transition in emission is $\Gamma_6^+(^4T_{2g}) \rightarrow \Gamma_6^+(^4T_{1g})$, as shown in Fig. 1. In absorption, groups of lines due to magnetic dipole transitions from the Γ_6^+ ground state to the Γ_6^+, $^{(1)}\Gamma_8^+$, and $^{(2)}\Gamma_8^+$ $^4T_{2g}$ levels are observed at 6598, 6603, and 6673 cm^{-1}, respectively at low x values ($x \sim 0.02$). These frequencies are x dependent. For example, the 6598.1 cm^{-1} line for $x = 0.019$ shifts to 6589.6 cm^{-1} for $x = 0.138$. In a magnetic field, the site symmetry is reduced to D_{4h} and the Γ_6^+ Krammers doublets split into two levels. Hence, four transitions, two linearly (dashed lines in Fig. 1) and two circularly (solid lines) polarized, may be observed. For single Ni^{2+} ions the $^3A_{2g}$ ground term has Γ_5^+ symmetry and the $^3T_{2g}$ first excited term comprises Γ_3^+, Γ_4^+, Γ_5^+, and Γ_2^+ levels in O_h site symmetry. An earlier study found Ni^{2+} absorption lines at 6421, 6596, 6971, and 7117 cm^{-1}, which were attributed to the $\Gamma_5^+ \rightarrow \Gamma_3^+$, Γ_4^+, Γ_5^+, and Γ_2^+ transitions, respectively. The effect of a magnetic field on the lowest transition is shown schematically in Fig. 1. The frequencies of these transitions also shifts with crystal field; i.e. the lowest energy transition changes from 6426.3 cm^{-1} at $x = 0.019$ to 6418.4 cm^{-1} at $x = 0.138$. The resonance transfer between the the Co^{2+} 6598-cm^{-1} line and the Ni^{2+} 6596-cm^{-1} line results in a profound 200-1 asymmetry between the emission and absorption strengths of the lower frequency Ni^{2+} transition.

The emission spectra for the six samples studied exhibited broad band luminescence extending from 4000 to 7000 cm^{-1}. Samples with similar Co concentrations gave quantitatively different emission spectra due to differing levels of Ni impurities. In the zero field luminescence spectrum, shown in Fig. 2 for one of the crystals with $x = 0.138$, the sharp features generally decrease in intensity with increasing temperature and are essentially invisible above 100 K, while the overall weight of the intensity shifts to lower frequency. Such a shift is the consequence of the higher population of multiple vibronic states at higher temperatures. Other samples gave similar results. The intensities of the Co^{2+} and Ni^{2+}-ion zero-phonon lines were studied as a function of temperature as was the integrated band intensity and luminescence lifetime. Results for the pump intensity and wavelength dependence are also given.

The 4.2 K magnetic field dependence of the luminescence for $x = 0.019$ is discussed. Representative unpolarized, $k \perp B$ emission spectra for this sample are shown in Fig. 3. Between 0 and 6.2 T the Ni^{2+} 6426 cm^{-1} peak splits into four lines at 6419.2, 6425.8, 6430.2, and 6432.4 cm^{-1} (see Fig. 4). Although five peaks are expected based on symmetry arguments above (see Fig. 1), only four are seen since two are nearly degenerate at 6426 cm^{-1}. This overlap indicates similar g values for the ground and excited states. Evidence for the splitting of these two lines is seen at 6.9 T. The energy level scheme of Fig. 1 shows that of the five emission lines expected two have left circular polarization, two have right circular polarization and one has linear polarization. The splitting in field of the Co^{2+} 6598 cm^{-1} line is complicated by the overlap with the Ni^{2+} 6596 cm^{-1} line. However, the magnetic field does confirm the presence of this Ni^{2+} line by separating its components from the ($B = 0$) Co^{2+} emission which normally covers it (see Fig. 3).

The results from this study indicate that temperatures below 20 K are needed for optimum $KZnF_3$:Co laser operation and that a pump wavelength near 514.5 nm is required. The tuning range of this laser is so broad because the vibronics arising from the ~5644 cm^{-1} line add on to the normal progression of vibronics arising from the fundamental transition at ~6594 cm^{-1}. This fact has not been commented on by others and the effect is not seen in other ions, such as Ni^{2+}, since their ground states are not split in cubic crystal field. Deliberate doping with both Ni and Co should sensitize the luminescence, lead to a more efficient stimulated emission at higher temperatures, and increase the laser tuning range. This improvement should occur since the Ni^{2+} ion vibronics help to fill gaps in the Co^{2+} ion emission between 5800 and 6300 cm^{-1}. The application of a magnetic field to this material perturbs the energy level scheme, thus providing additional information about the electronic properties. Removing the overlap of the 6596 cm^{-1} Ni^{2+} and the 6598 cm^{-1} Co^{2+} lines increases the understanding of the resonant transfer process from the Co^{2+} to the far less numerous Ni^{2+} ions in the crystals studied here. Although this overlap is less complete for lower Co^{2+} ion concentrations, the energy transfer is still efficient indicating that the addition of Ni broadens the emission/tuning range for all $x < 0.15$. Further magneto-optical experiments in progress include systematic studies of other Co^{2+} and Ni^{2+} concentrations, temperature dependences, polarization studies (linear and circular) of the emitted and transmitted light, and studies of the lifetimes of individual zero-phonon transitions.

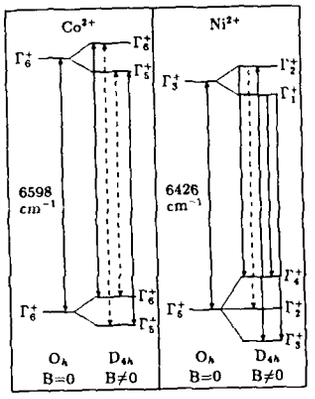


Fig. 1 Fundamental ground to first excited term, single-ion electronic transitions for Ni^{2+} and Co^{2+} in cubic crystal field. Transitions have circular (solid lines) or linear (dashed lines) optical polarizations for B > 0.

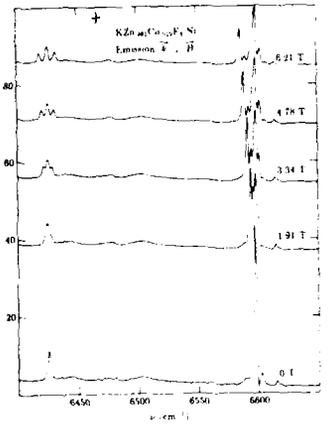


Fig. 3 Low temperature spectra for $KZn_{.981}Co_{.019}F_3$:Ni at five B's. Light randomly polarized, propagating ⊥ B.

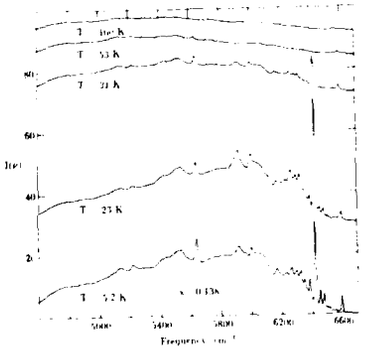


Fig. 2 Luminescence spectrum of $KZn_{0.862}Co_{0.138}F_3$ as a function of temperature.

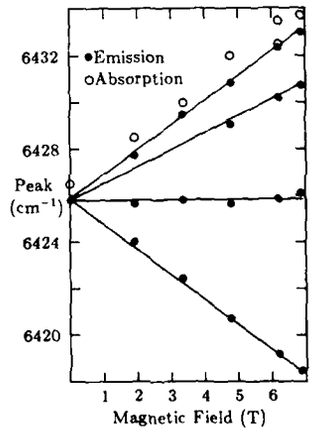


Fig. 4 Peak frequency dependence on magnetic field for lines originating from Ni^{2+}, $\Gamma_5^1 \leftrightarrow \Gamma_3^+$, B = 0 transition.

Abstract No. 543

ZERO PHONON LINES, PHOTOBURNING OF SPECTRAL HOLES, OPTICAL DATA STORAGE AND PROCESSING IN IMPURITY DOPED SOLIDS

Karl K. Rebane

Academy of Sciences of the Estonian SSR, 200106, Tallinn, 6 Kohtu, USSR

1. Very narrow (homogeneous linewidth $\delta_o \approx 10^{-2}$-10^{-4} cm^{-1}) zero phonon line (ZPL) of very high peak intensity in low temperature (4 K and below) spectra of absorption and luminescence of molecules embedded as impurities in single crystal or glassy matrices is subject to tremendous inhomogeneous broadening ($\Delta_{iH} \approx 1$ - 1000 cm^{-1}, i.e. $10^2\delta_o$ - $10^7\delta_o$) [1].

2. Photoburning of spectral holes (PBH) permits to eliminate inhomogeneous broadening of zero-phonon lines (ZPL) and tc perform high resolution studies of the impurity vibronic spectra with the accuracy of 10^{-3}-10^{-4} cm^{-1} [2-4]. PBH serves also as an effective tool to control by means of illumination the optical characteristics - absorption coefficient and index of refraction - of matter with high spectral selectivity.

3. Owing to PBH the large inhomogeneous broadening of ZPLs (exceeding the homogeneous broadening by 3-6 orders of magnitude) turns out as an useful feature to store and process data and images [2,5,6], to memorize fields of mechanical strains [7].

A rather trivial application is to store the bits of information via burning sharp holes at designated frequencies. The storage densities up to 10^{12}-10^{13} bits per cm^2 become possible [2,6].

The frequency domain may also be used as a really new dimension bound via Fourier transform to the time domain. It leads to space-and-time domain holography of ultrafast events of pico- and nanosecond duration [6,9]. Theory is presented and a number of experiments (performed mainly with polystyrene activated with octaethylporphin) are described.

4. Random orientation of the photoactive molecular impurity centres in hole burning glassy matrices provides the possibility to record also the polarization of the Fourier components of the light pulse. It leads to the generalization of the holography into the full meaning of the term "holography" = "complete recording". Theory is given and experiments made showing storage and playback of both spatial and temporal dependencies of the electric vector of the object field (signal pulse) [8].

5. The following applications of time-and-space domain holograms in optical data and image processing have been performed [6,8,9].
5.1. Multifrequency parallel recording and readout of an optical spectral memory. Hole burning and detection of several thousand holes (bits) in one absorption band using picosecond pulses have been demonstrated [10].
5.2. Wave front conjugation and time reversal of the signal by reading the conjugated wave from the hologram [6,8]. Restoration of clear pictures out from hologrammed smeared images' has been demonstrated;
5.3. Processing of picosecond signals, in particular, spacial-temporal convolution of the signals by means of using one signal as the probe pulse to read the hologram of the other signal [5,6,11];
5.4. Recognition of picosecond events - the generalization of the holographic method of image recognition. If a light signal is delivered to the hologram, which coincides with one of the signals recorded earlier, and if the outcoming light is focussed, then a δ-shaped pulse appears at a definite point of the local plane;
5.5. Synthesis of picosecond signals by transforming the incident light pulses in holograms with prefixed spatial-spectral structure of holes, created by means of tunable single-mode lasers or other controlled light sources;
5.6. Playback of events by their fragments through the generation of the corresponding phantom events and constructing associative memories [6,9,11].

6. The main essential characteristics of materials needed for the time-and-space domain holography are the following: (1) narrow and intense homogeneous ZPL; (2) large inhomogeneous broadening; (3) long phase relaxation time T_2 (actually long T_2 is a consequence of narrow ZPL); signal and reference *pulses interfere and* build a hologram provided they interact in a given spot of hole burning medium no longer than T_2; (4) nonzero efficiency of hole burning; (5) long lifetimes of the products of hole burning.

1. K.K.Rebane, Impurity Spectra of Solids, Plenum Press, N.Y.-London, 1970
2. L.A.Rebane, A.A.Gorokhovskii, J.V.Kikas, Appl. Phys. B29, 235-250, 1982
3. R.A.Avarmaa, K.K.Rebane, Spectrochimica Acta, 41A, No 12, 1365-1380, 1985; Uspekhi Fiz. nauk, 1988 (in Russian) to be published
4. K.K.Rebane, A.A.Gorokhovski, J. of Luminescence, 36, 237, 1987
5. K.K.Rebane, L.A.Rebane: "Basic Principles and Methods of Persistent Spectral Hole-Burning: Science and Applications, ed. W.E.Moerner; Topics in Current Physics, Springer-Verlag, 1988, p. 17
6. P.M.Saari, R.Kaarli, A.Rebane, J. Opt. Soc. Am., B33, 527, 1986
7. K.K.Rebane, Proc. Estonian SSR Acad. Sci. Phys. Math., 34, 441, 1985 (in Russian)
8. P.M.Saari, R.K.Kaarli, R.V.Sarapuu, R.H.Sõnajalg, J. Quant. Electr., Special issue on phase conjugation, 1988, to be published
9. P.Saari, A.Rebane, Proc. Acad. Sci. Estonian SSR, Phys. Math., 33, 322, 1984 (in Russian)
10. J.Kikas, R.Kaarli, A.Rebane, Opt. Spektrosk. 56, 387, 1984
11. A.Rebane, Opt. Commun. 65, 175, 1988

Abstract No. 544

SPECTRAL HOLE BURNING IN AMORPHOUS SOLIDS

A.A. Gorokhovskii and L.A. Rebane*

Institute of Physics, Academy of Sciences of the Estonian SSR, 202400 Tartu, USSR
*Institute of Chemical Physics and Biophysics, Academy of Sciences of the Estonian SSR, 200105 Tallinn, USSR

1. Persistent spectral hole-burning (PSHB) is a rapidly growing field of molecular and solid state spectroscopy and photochemistry providing high-resolution spectra and the possibility of various applications [1,2]. By burning non-saturated holes in the inhomogeneous purely electronic band of impurity molecules in crystalline matrices at different temperatures the homogeneous linewidth (HLW) Γ and dephasing processes were studied revealing the high sensitivity of Γ to the density of low-frequency vibrational states of the matrix [3-5]. The peculiarities of PSHB observed for impurities in amorphous matrices (organic glasses and polymers) [5,6] reflect specific of amorphous solids in comparison to crystals. The high density of low-frequency states provided by two-level systems (TLS), local character of the states, and the high-entropy soft structure lead to more fast and very low-temperature dephasing processes and possibility of higher spectral hole width (SHW) Γ_h additionally broadened by spectral diffusion (SD) [7].

Recent data about the low-temperature (down to 40 mK) broadening of spectral holes and corresponding purely electronic lines (PELs) of resonant fluorescence will be reviewed and the contribution of TLS to the HLW and SD will be discussed.

2. The SHW temperature dependence, $\Gamma_h(T)-\Gamma_o$, measured for H_2-octaethylporphin molecules (OEP) in amorphous polystyrene (PS) is shown in Fig. 1. The lifetime-limited value, $\Gamma_o = (2\pi\tau_1)^{-1} = 18$ MHz, was obtained from the resonant fluorescence decay ($\tau_1 = 17.5$ ns). The experimental data were approximated by the law $T^{1.8}$ at temperatures from 10 to 3K crossing over to the law $T^{1.2}$ at temperatures from 3 to 0.2K and to the law $T^{2.6}$ at $T < 0.1$K. The nonmonotonic behaviour of SHW reveals input from the SD broadening. The hole measurement time τ_m shortening from 1 s to 10^{-5} s at 1.5K causes a notable decrease of the SHW [7] (shown in Fig. 1). The homogeneous part of Γ_h obtained from the photon echo measurements [8] is also shown in Fig. 1. The complicated curves of $\Gamma_h(T)-\Gamma_o$ were obtained also for OEP molecules in polymethylmethacrylate matrix and monoazaetioporphyrin molecules in PS [9] revealing the participation of SD processes in the holes formation.

3. A new method of fluorescence measurement in resonance with the purely electronic excitation is proposed, which uses the hole burnt at resonance frequency in the optically dense sample as a very narrow transmission filter [10]. The temperature dependence of the resonant fluorescence HLW Γ was obtained with this method for OEP molecules in PS (shown in Fig. 1 by triangles) at $3 < T < 10$K. It displays more fast than $\Gamma_h(T)$ broadening law, $\Gamma \sim T^3$ which is in a good agreement with the impurity excited T_1 state dephasing by a quasilocalized vibration with frequency ≈ 20 cm^{-1}. At lower temperatures the TLS are participate in the HLW Γ as well as in SD.

The relation between SHW and HLW as well as SD broadening were studied also for $T_1 \rightarrow S_o$ transition of pyrene molecules in an alcohol glass.

4. Optical pumping of the PS matrix vibrational modes have been done in the region of 1.5-2.5 μm by IR irradiation of OEP-PS at 1.5K. A considerable broadening of the holes and decrease of their depth have been observed indicating the photoinduced spectral diffusion.

1. L.A.Rebane, A.A.Gorokhovskii, J.V.Kikas, Appl. Phys. B29 (1982) 235
2. K.K.Rebane, L.A.Rebane "Basic Principles and Methods of Persistent Spectral Hole-Burning", in: Persistent Spectral Hole-Burning: Science and Applications, ed. by W.E.Moerner, Springer-Verlag, 1988, p. 17
3. A.A.Gorokhovskii, L.A.Rebane, Opt. Commun. 20 (1977) 144
4. L.A.Rebane "Relaxation of Electron-Vibrational Excitations in Impurity Molecules in Solid Matrices" in: Ultrafast Relaxation and Secondary Emission, Proc. Int. Symp. UPS-78, Tallinn, 1978, p. 89
5. A.Gorokhovskii, L.A.Rebane, Izv. Akad. Nauk SSSR, Ser. Fiz., 44 (1980) 853
6. I.M.Hyes, R.P.Stout, G.J.Small, J. Chem. Phys. 73 (1980) 4129; J. Chem. Phys. 74 (1981) 4266
7. K.K.Rebane, A.A.Gorokhovskii, J. Luminesc. 36 (1987) 237; A.A.Gorokhovskii, Izv. Akad. Nauk SSSR, Ser. Fiz., 52 (1988) 636
8. R.K.Kaarli, M.L.Rätsep, Abstracts of Symposium on Modern Methods of Laser Spectroscopy of Molecules in Low-Temperature Media, Tallinn, May 19-21, 1987, p. 39
9. A.A.Gorokhovskii, V.H.Korrovits, V.V.Palm, M.A.Trummal, Pisma JETP, 42 (1985) 249
10. A.A.Gorokhovskii, V.V.Palm, Opt. Spectrosc., 64 (1988) 969

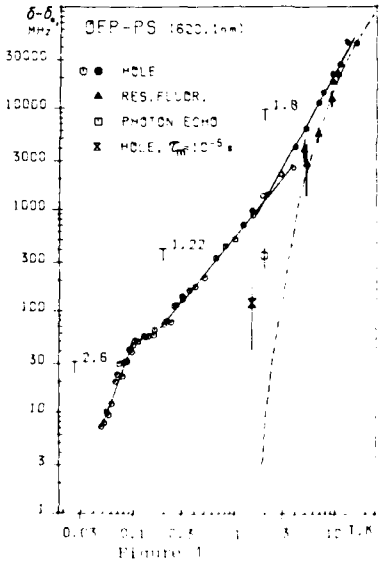


Figure 1

Abstract No. 545

FEMTOSECOND LATTICE RELAXATION FOLLOWING ULTRAFAST EXCITATION OF F_2^+ CENTER IN LiF: A COHERENT PHONON DESCRIPTION

N. Terzi and G. Consolati

Dipartimento di Fisica dell'Universita, via Celoria 16, 20133 MILANO, Italy
Istituto di Fisica, Politecnico di Milano, Piazza Leonardo da Vinci 32, 20133 MILANO, Italy.

The relaxation of the ions surrounding a F_2^+ center in LiF is here numerically evaluated, assuming that a wavepacket of coherent phonons of the whole perturbed crystal are generated during the absorption of a femtosecond laser pulse. If the wavepacket evolves linearly, the center n.n. are found to perform a very damped motion (however less than the experimental one) during the first 100 fs, followed by very small aperiodic oscillations.

The short time relaxation process in molecules and crystals, following excitation with ultrashort laser pulses, reveals fundamental aspects of the electron and phonon dynamics and of their coupled motion. The increasing number of experimental data allows a comparison of the existing theories.

In the present work we refer to recent experiments, where a femtosecond pulsed laser is used to study how ions relax around color centers in insulating crystals (1,2). In particular, the transient dynamics of F_2^+- centre in LiF show that the n.n. relaxation time is shorter than the period of any relevant frequency of the host crystal (2). This seems to disagree with the c.c. model or with any local phonon model. It could instead corroborate a recent theory proposing that coherent phonons of the whole perturbed crystal are generated during the very fast excitation process preceeding the relaxation (3).

Here the coherent phonon theory is tested through a numerical evaluation of the relaxation around the center. The center itself is embedded in a T=0 LiF harmonic crystal, here described by the breathing shell model, locally perturbed by the impurity. We have adopted the following minimal model: i) The electronic transition of the center is induced by absorption of a femtosecond laser pulse; ii) The electron-phonon interaction (short range and linear) is deduced from the absorption band shape parameters, iii) The coherent phonon wavepacket (wp), generated at t=0 by the light absorption, propagates linearly in the following 10-300 fs; iv) No other electronic level exists in proximity of the excited state, so that we can neglect possible intracenter energy transfer during the relaxation. The time-dependent position of the ions is identified with the expectation value of the ionic variables on the evolving coherent wp at different times. We do not comment the assumption ii), as it is usually adopted in dealing with the EP coupling in excited color centres. The effect of point iv) is under study. With regard to the point iii), the non linear EP coupling and the anharmonicity play certainly an important role in modifying the wp during the relaxation process. However, their effect is probably limited at T=0, on the time scale here studied, even in the strong EP coupling limit.

Our results can be summarized as follows. The n.n. of the impurity move towards new relaxed equilibrium positions in a strongly damped oscillatory way. However, the ions perform at least one complete large oscillation, a less damped motion than that of the ions surrounding the F_2^+ centre in LiF. This first short transient (about 100 fs) is followed by aperiodic oscillations of very small amplitude. The further neighbours are reached by the phonon wp at delayed times, depending on the wp group velocity and therefore on the wp initial composition (strength of the different symmetry components). Their oscillations are also damped but always of smaller amplitude than the motion of the n.n., according to a 3-dim propagation scheme for the phonon wp.

REFERENCES

1. W.H. Knox, L.F. Mollenauer and R.L. Fork, Proc. Conf. "Ultrafast Phenomena" held at Snowmass (USA, 1986), unpublished.
2. J. Wiesenfeld, L.F. Mollenauer and E.P. Ippen, P.R. Lett. 47, 1668 (1981).
3. A. Giorgetti and N. Terzi, Solid State Comm. 39, 635 (1981) and N. Terzi, J. Lumin. 31/32, 194 (1984).

Abstract No. 546

F.L.N. OF THE ^2E $^4A_2$ TRANSITION OF GSGG:Cr^{3+}

A. Monteil, Cl. Garapon and G. Boulon

Université Claude Bernard - Lyon I -
UA 442 au CNRS

43 Bd du 11 Novembre 1918
69622 Villeurbanne Cédex - France

In the new Cr^{3+} doped materials suitable for tunable lasers, like $Gd_3Sc_2Ga_3O_{12}$(GSGG), Cr^{3+} is situated in an intermediate crystal field. In such a case the doublet ^2E and the quadruplet $^4T_2$ are so near that we can observe at low temperature both the fine emission from ^2E and the band emission from $^4T_2$ while the band $^4T_2 \rightarrow {}^4A_2$ only is seen at room temperature. As already noticed /1/ the ^2E emission is constituted by several lines due to different cristallographic site induced by the statistical distribution of the cations Sc^{3+}, Ga^{3+}, Gd^{3+} in neighbour octahedral sites. We report here a study devoted to a more precise characterization of these sites by FLN measurements.

Emission and absorption spectra of the $^2E - {}^4A_2$ transition at T≈ 6K, shown on the figure 1, are mainly constitued of 4 components. The absorption $^4A_2 \rightarrow {}^2E$ is superposed on the low energy wing of the absorption band $^4A_2 \rightarrow {}^4T_2$.

Direct excitation in the ^2E levels by mean of a tunable and spectrally narrow laser (fluorescence line narrowing) allows an investigation of the multisites and a determination of the position of the different energy levels. The main results can be summarized as follows :

1- The four lines observed in fluorescence correspond to the lower ^2E sublevel emission of four different sites.

2- The trigonal splitting of the doublet ^2E depends on the site and varies with the crystal field in the range 16-40 cm^{-1}.

3- The position of the absorption band $^4A_2 \rightarrow {}^4T_2$ of the different sites relative to the ^2E position can be determined approximately. For a given excitation wavelength absorption of one site takes place into the ^2E levels, while for another site it takes place into the $^4T_2$ (figure 2).

4- The inhomogeneous broadenings are different and of the order of 14 cm^{-1}. The width of each line is decreased differently by FLN. The average residual width of about 8 cm^{-1} is very much larger than it is generally for materials with stronger crystal field like ruby /2/. Such a feature has already been reported by us for another substitued GGG /3/.

5- Fluorescence decays and excitation spectra which are different for each line also show the presence of four different sites.

All these results indicate different crystal field strengths for these four sites.

ACKNOWLEDGEMENT : The authors wish to thank L.S. ANDREWS (GTE Lab.) who has provided us with this CSGG:Cr^{3+} single crystal.

REFERENCES

/1/ B. STRUVE - G. HUBER, Appl. Phys. B36, 195 (1985).

/2/ P.M. SELZER - O.S. HAMILTON - W.M. YEN, Phys. Rev. Lett. 38, 858 (1978).

/3/ A. MONTEIL - Cl. GARAPON - G. BOULON J. Lum. 39, 167 (1988).

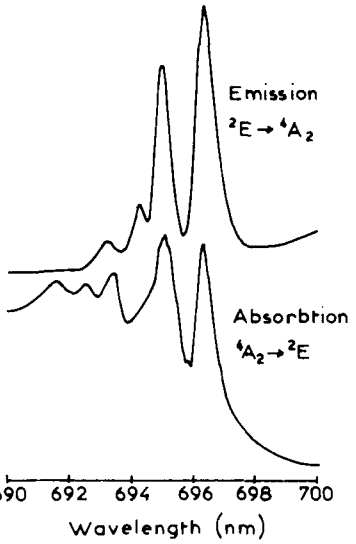


Fig. 1 : 6K absorption and emission spectra of the $^4A_2 - {}^2E$ transition in GSGG:Cr^{3+}.

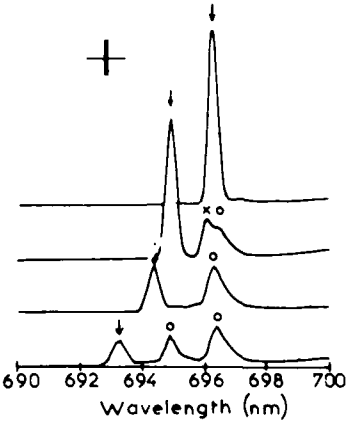


Fig. 2 : 6K F.L.N. spectra of the four main lines of the emission spectrum. Arrows indicate positions of the laser excitation and lines under them are fluorescent resonant ones. No-resonant lines (O) at 696.3 nm and 695 nm come from excitation in $^4T_2$ state. Line labelled by an X comes from excitation in the upper level of the splitted ^2E and relaxation to the lower level.

Abstract No. 547

EXCITON RELAXATION and THERMAL EQUILIBRIUM IN PbI_2

Takenari Goto and Jun Takeda

Department of Physics, Tohoku University,

Sendai 980, Japan

Masahiro Matsuoka

Solid State Physics,

University of Tokyo, Tokyo 106, Japan

In a semiconductor or an insulator having an Urbach tail in the free exciton (FE) absorption spectrum, an exciton has been suggested to be able to localize momentarily by phonons after Sumi and Toyozawa [1]. Also in the luminescence spectrum, the Urbach tail due to the momentarily localized exciton (MLE) has been observed on the low energy side of the FE band of 2H-PbI_2 [2].

In this paper, thermal stability of the FE and MLE in 2H-PbI_2 will be discussed from view points of the time response and the excitation spectrum of luminescence. A PbI_2 crystal is a layer type semiconductor and has a direct allowed exciton band near 20kcm^{-1} for E // c polarization spectrum. The Urbach rule is found to hold for the energy region below 19.9kcm^{-1} in the absorption spectrum and below 19.8kcm^{-1} in the luminescence spectrum at 100K [2].

Figure 1 shows quantum yields of the luminescence in the Urbach tail region as a function of the excitation energy and the lifetimes of the excitons with different energies at 100K. The quantum yields as shown by open circles are obtained from the luminescence intensity per exciting laser power after corrections for absorption and reflection [3]. The latter values are estimated as follows. The time response of the luminescence intensity is measured using a third harmonic of a mode-locked YAG laser light with the pulse width of 80ps as an exciting light source, and using a streak camera and an OMA as a detection system. From analysis of the luminescence decay curve using the diffusion constant and the absorption coefficient[4] we obtain the lifetimes of the excitons with the various energies. The diffusion constant is estimated from the line shape analysis in the exciton absorption spectrum. A peak position of the exciton absorption band is indicated by an arrow. In the energy region above 20.5kcm^{-1} corresponding to the free exciton, both the quantum yield and exciton lifetime are independent of the energy. This fact means that free excitons with various energies are in thermal equilibrium. Also in the energy region below 19.9kcm^{-1} corresponding to the MLE, both values are constant. From this fact, it is strongly suggested that the momentarily localized excitons at the phonon distorted lattice with different energies are in thermal equilibrium with each other. The difference in both values, however, between the FE and MLE regions leads to the conclusion that there exists a thermal barrier between the FE and MLE systems. Namely, the MLE may be able to move in the similar way to that of localized excitons in the amorphous materials. In this case, however, spatially random potential is dynamically generated by phonons.

The lifetime and the luminescence intensity show the same exponential dependence on the inverse temperature as expected from the rate equations. The lifetime of the MLE is larger than that of the FE below 120K, while the former coincides with the latter at 140K. This coincidence means that the FE and MLE becomes in the thermal equilibrium at 140K.

Aknowlegements

The authors would like to thank professor Toyozawa in Chuo University for fruitful discussions.

References

1) H. Sumi and Y. Toyozawa : J. Phys. Soc. Jpn. 31 (1971) 342.

2) J. Takeda and T. Goto : Solid State Commun. 56 (1985) 101.

3) J. Takeda and T. Goto : Solid State Commun. 59 (1986) 209.

4) A. Kurita, Y. Furikawa and T. Kushida : J. Lumin. 38 (1987) 70.

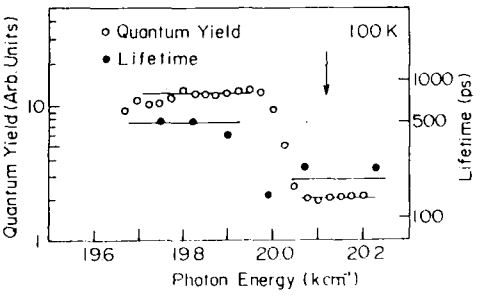


Fig.1 Exciton lifetimes and luminescence quantum yields as a function of energy at 100K.

Abstract No. 548

Perturbation Methods in Optical Spectroscopy

W. Alan Runciman

Laser Physics Centre, Research School of Physical Sciences
The Australian National University, Canberra, A.C.T. 2601, Australia.

Although much information can be gained from the absorption, excitation and fluorescence spectra of luminescent materials, additional techniques are usually required to identify the nature of the luminescent centres. As an illustrative example the principal uranium centres in LiF and NaF will be discussed to show the power and limitations of optical techniques. Electron paramagnetic resonance is a powerful tool in the study of luminescent centres, but is not applicable in this case as both the ground and fluorescent states are non-degenerate.

It has long been known that when a small percentage of uranium oxide, of the order of 0.01 at. percent, is added to sodium fluoride and melted then the solid when cooled shows a vivid yellow fluorescence under visible or ultraviolet radiation (1). Similarly lithium fluoride shows a bright green fluorescence when activated by uranium. Both crystals when cooled with liquid air show well-resolved lines in the fluorescence spectra (2).

Additional information was obtained from the study of microcrystalline samples of NaF(U) at liquid helium temperatures, it being found that some of the emission lines vanished indicating that they did not originate from the lowest excited state (3). The fluorescence lines form vibrational series in which 0, 1 or 2 vibrational quanta are coupled to the electronic transition. This is unlike the well-known uranyl spectra where long series with up to six quanta are observed. By introducing the isotope ^{18}O into the uranium oxide used to dope the crystal, several fluorescent lines were shown to have an isotope shift. This indicates that oxygen ions are part of the fluorescent centre. At low uranium concentrations of 0.01 at.percent or less the spectrum is relatively simple, but at higher concentrations or with impurities present many other centres are formed. It was suggested that these were due to octahedral uranate complexes with a variety of charge compensating ions (3).

Further advances required the use of single crystals and fortunately doped crystal boules of dimensions ~ 2 cm x 1 cm x 1 cm can be grown by the Czochralski or Kyropoulos methods in a few hours.

The use of polarized exciting radiation and the analysis of the polarization of the fluorescent radiation allows the symmetry of the centres to be found. The principal centres found at low uranium concentrations were found to have tetragonal symmetry and the UO_5 model was proposed in which a U^{6+} ion on a lithium or sodium site is charge compensated by five of the six surrounding fluorine ions being replaced by oxygen ions, Fig. 1 (4). The UO_5 centre has C_{4V} symmetry. There was still some uncertainty about the nature of the radiation and the multiplicity of the energy levels. Definite information was obtained from the piezospectroscopic effect (5). When a uniaxial stress is applied to the crystal at liquid nitrogen temperature it is found that some of the luminescent lines show well resolved splittings. This is expected since luminescent centres oriented along the stress direction will have different energy shifts from those oriented at an angle to the stress direction. A detailed theoretical analysis of the various possibilities for different orientations of the crystal and for different types of centres allows identification of the centres and energy levels to be made (6). For instance, it is found that the principal uranium centre in LiF is tetragonal and that the resonant fluorescent transition at 527.8nm(18 941cm^{-1}) is magnetic dipole in character, both the ground and lowest excited states being singlets. The fluorescence from the higher excited state at 518.5nm (19 281cm^{-1}) is electric dipole in character and the higher excited state is also a singlet. The ground state is assigned A_1 symmetry as all the ions have closed shell configurations. The selection rules for C_{4V} symmetry indicate that $A_1 \rightarrow A_1$ and $A_1 \rightarrow E$ are electric dipole (ED) allowed. $A_1 \rightarrow A_2$ is magnetic dipole (MD) allowed. $A_1 \rightarrow B_1$ and $A_1 \rightarrow B_2$ transitions are forbidden for both ED and MD transitions and have not been detected.

The application of an electric field gives somewhat similar results to that of an applied stress. When the centres lack a centre of inversion there is a linear pseudo-Stark effect as distinct from the quadratic Stark effect for centres with a centre of symmetry. The principle centres in LiF(U) were found to lack a centre of inversion symmetry as expected on the UO_5 model (7).

When different centres are present in a crystal it is useful to isolate the fluorescence of each using selective excitation (8). Dye lasers provide a very convenient source of variable wavelength polarized radiation and have been used to study LiF(U) and NaF(U) (9).

Anisotropic centres in cubic crystals can also be studied by the Zeeman effect. However the states of the uranium ion often have small g-values and show unresolved Zeeman patterns in easily attainable magnetic fields. In such cases the technique of magnetic circular dichroism (MCD) is very useful as unresolved patterns show clear MCD signals (9). The MCD is proportional to the difference between the absorptions of right- and left-circularly polarized light when the crystal is in a magnetic field parallel to the light direction. Using MCD excited states of E symmetry were found at slightly higher energies than the two lowest excited singlet states for both LiF(U) and NaF(U) (10). A recent theoretical study of the MCD of anisotropic centres in cubic crystals has shown that the g-values were underestimated by a factor of 2 (11), and revised energy level diagrams are shown for LiF(U) and NaF(U) in Fig. 2 and 3 respectively. The appropriate representations for the wave-functions of the energy levels are listed and g-values are given for the doubly degenerate E levels. For LiF(U) there is an indication of a level at 24 200cm^{-1} of unknown symmetry.

It should be stressed that the experimental results described only limit the possible atomic models to those of a certain symmetry, but do not positively identify particular models for centres. On the basis of a particular model it is then possible to make calculations of the electronic structure of a centre and preliminary calculations have been made for the principal centre in alkali fluorides using a molecular orbital formalism (12).

REFERENCES

1. E.L. Nichols and M.K. Slattery, *J. Opt. Soc. Amer.*, **12**, 449 (1926).
2. M.K. Slattery, *J. Opt. Soc. Amer.*, **19**, 175 (1929).
3. W.A. Runciman, *Proc. R. Soc.*, A**237**, 39 (1956).
4. P.P. Feofilov, *Opt. Spectrosc.*, **7**, 493 (1959).
5. A.A. Kaplyanskii and N.A. Moskvin, *Opt. Spectrosc.*, **13**, 303 (1962).
6. A.A. Kaplyanskii and N.A. Moskvin, *Opt. Spectrosc.*, **14**, 357 (1963).
7. O.D. Gavrilov, A.A. Kaplyanskii, V.N. Medvedev and N.A. Moskvin, *Opt. Spectrosc.*, **27**, 521 (1969).
8. W.A. Runciman and E.Y. Wong, *J. Chem. Phys.*, **71**, 1838 (1979).
9. B. Srinivasan, Z. Hasan, N.B. Manson and W.A. Runciman, *J. Phys. C: Solid State Phys.*, **18**, 2381 (1985).
10. W.A. Runciman, B. Thangavadivel and N.B. Manson, *J. Luminescence*, **24/25**, 209 (1981).
11. W.A. Runciman and N.B. Manson, *J.Phys.C: Solid State Phys.*, **21**, L277 (1988).
12. W.A. Runciman, B. Srinivasan and S. Saebo, *Aust. J. Phys.*, **39**, 555 (1986).

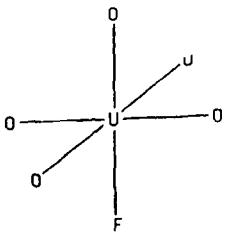


Fig. 1. Model of the principal centre

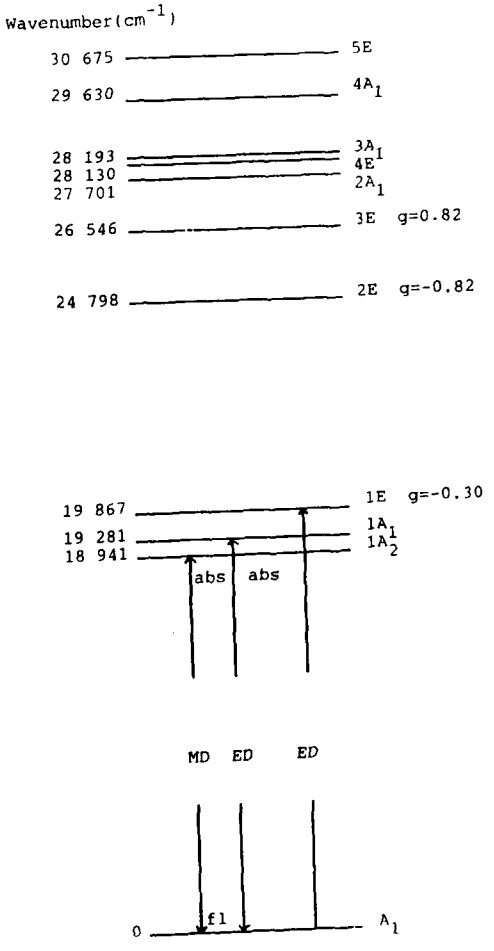


Fig.2 Energy level diagram for LiF(U)

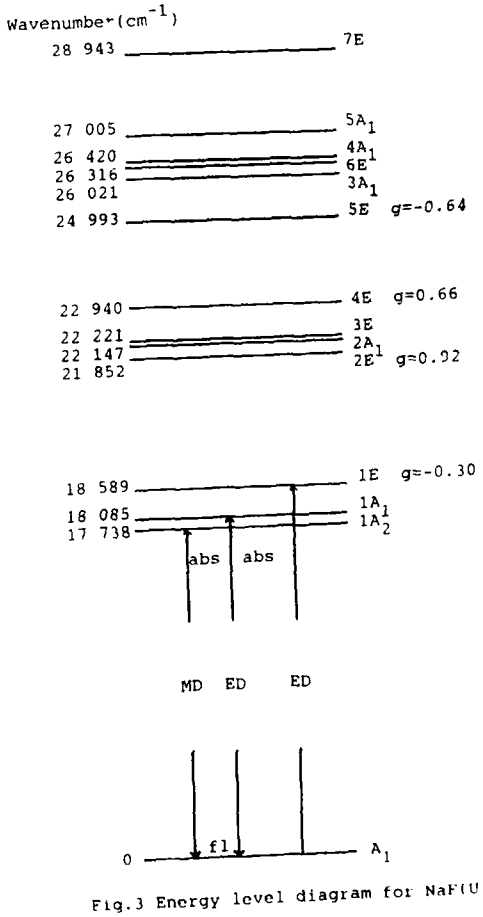


Fig.3 Energy level diagram for NaF(U)

Abstract No. 549

INVESTIGATION OF ZnS:Tm^{3+} POWDERS BY EXAFS AND SITE SELECTIVE EXCITATION OF THE LUMINESCENCE.

J.DEXPERT-GHYS[1], Y. CHARREIRE[2], P. ESTEBAN-PUGES[3]
L. ALBERT[1], H.DEXPERT[4]
1.ER060210/CNRS/1P1A.Briand 92195 MEUDON Cx FRANCE
2.L. Phys. Solides/UPMC/75252 PARIS Cx05 FRANCE
3.Unitat Inorganica, Universitat de BARCELONA SPAIN
4.LURE/UPS/91406 ORSAY Cx FRANCE

The fluorescence of thulium Tm^{3+} in zinc sulfide matrix has led to a great number of investigations due to the high efficiency which is exhibited by this blue phosphor. It has been established that the preparation conditions have a drastic influence on the emission yield as well as on the number and relative intensities of the different components in the fluorescence spectra (1). To characterize these relations between the synthesis and the optical properties we have thus undertaken the structural studies of ZnS:Tm^{3+} powders, the first one being an EXAFS investigation (Extended X-ray Absorption Fine Structure). In the particular case of ZnS:Tm^{3+} samples the observation of EXAFS oscillations at the L_3 Tm^{3+} edge proves to be effective only for the higher dopant concentrations that is for a sample activated by $LiTmS_2$ in the initial proportions ZnS:Tm^{3+}(1.2%). The EXAFS analysis concludes unambiguously to the occurrence of Tm^{3+} in the form of the oxysulfide $(TmO)_2S$ within the ZnS host matrix. This first result has been completed by the measurement of the optical properties of the same ZnS: Tm^{3+}(1.2%) sample comparatively to $(TmO)_2S$, which is not fluorescent, and to the isomorphous fluorescent $(YO)_2S$:Tm^{3+}(1%). Contrary to ZnS:Tm^{3+} phosphors which exhibit mainly the $^1G_4 \rightarrow {}^3H_6$ blue emission under UV excitation, the thulium fluorescence in yttrium oxysulfide is widely dominated by the $^1D_2 \rightarrow {}^3H_4$ emission. The $^1G_4 \rightarrow {}^3H_6$ transition in $(YO)_2S$ has then been isolated at 77K by dye laser selective excitation. It appears that no common feature may be evidenced in the emission characteristics of the two phases. There is then a "oxysulfide-type" fluorescent cluster in the ZnS sample. On the contrary the diffuse reflectance spectra observed on ZnS:Tm^{3+} (1.2%) and thulium oxysulfide are identical. The oxysulfide therefore appears as a second phase embedded in ZnS, resulting of oxygen traces in the H_2S elaboration atmosphere. For the powders we investigated, it then comes out that the actual level of Tm^{3+} doping in the ZnS matrix was not high enough to be detected by EXAFS. But if new elaboration conditions allow to incorporate more Tm^{3+} in ZnS, as we think to be the case in thin films, the EXAFS analysis will enable the structural determination of the rare earth crystallographic site.

The fluorescence spectra of ZnS:Tm^{3+}(1.2%) at 77K exhibit a complex structure which has been separated by site selective excitation into two individual components. One of these, characterized mainly by the 20906 cm^{-1} $^1G_4 \rightarrow {}^3H_6$ line, has already been identified for different dopings in identical powders (2) and in ZnS crystals (3,4). As it is observed since the earlier stages of the subtitution, this feature has been attributed to Tm^{3+} substituting Zn on undistorted sites. The second spectrum is characterized by wider lines, the main of which peaks at 20726 cm^{-1}. It presents certain similarities with the so-called A center observed in Ref. 3, but is attributable to Tm^{3+} in a center proper to our samples. Whatever the structural characteristics of this site, the lines occur at the same positions than the vibronic sidebands previously discussed in Ref.2 as well as in Ref.4. The superposition of several features in the same wavelength region could well be the origin of the high apparent Huang-Rhys factor found experimentally for these compounds.

In conclusion, this work is an attempt to use both EXAFS and optical absorption/emission experiments to investigate the structural organisation of the active centers in ZnS Tm^{3+} powders. EXAFS and optical absorption conclude consistently to the occurrence of thulium oxysulfide as the major thulium-containing phase. On the reverse, there is no indication from the emission data of an "oxysulfide-type" fluorescent cluster in the samples. The actual proportion of optically active Tm^{3+} ions in ZnS is then by far smaller than the initial 1.2%. The emission spectrum of this sample exhibits more or less complex features that have been separated into two individual spectra. One center has been detected in a large number of ZnS samples and attributed to substitutional Tm ions on Zn sites. It may be considered as the "intrinsic" Tm center. On the contrary the second spectrum is directly linked to the elaboration conditions and is clearly an "impurity center".

(1) Y. CHARREIRE et al. Mat. Res. Bull.15,657(1980)
(2) Y. CHARREIRE et al. J. Electo. Soc.130,175(1983)
(3);(4) H. ZIMMERMANN et al. Phys. Stat. Sol.b130, 315 (1985); b139,533 (1987)
(5) R. BOYN et al.Phys. Stat. Sol. b140,163(1987)

Abstract No. 550

X-RAY AND E.P.R. STUDIES OF COMPOSITIONAL DEFECTS IN Y_2O_2S RED PHOSPHORS

M.GRACIET and N.RUELLE
THOMSON-CSF Central Research Laboratories
91401 ORSAY, FRANCE

and J.VAN BARDELEBEN
Paris VII University.
75251 PARIS, FRANCE

Flux synthesis of $Y_2O_2S:Eu^{3+}$ phosphors is well known . However control of the oxidation of the phosphor is not easy, and our X-ray studies on oxisulfides have shown that the lattice of Y_2O_2S is modified in presence of oxide: the c parameter of the lattice increases suddenly (fig.1)(1)

Electron paramagnetic resonance (E.P.R.) experiments have been carried out on the same samples. The $Y_2O_2S:Eu^{3+}$ spectra present one main paramagnetic effect.

We have studied this defect in a series of Y_2O_2S powders as a function of preparation conditions, active doping(Eu^{3+}) and treatments on prepared phosphors. The E.P.R. spectra were taken depending on temperature (300K...4K) and at two different frequencies (X-band, Q-band). All samples show the same paramagnetic defect, the concentration of which varies with the preparation conditions. From its hyperfine structure and g tensor (g<2) we tentatively assign this spectrum with a F center. This defect is also responsible for an absorption band in the near UV range, changing the color from white to light yellow. On the Eu doped samples no evidence for the presence of Eu^{3+} ions could be detected. Finally we compared the native defects in Y_2O_2S powder with those in the Y_2O_3 one: no such paramagnetic defect was found in Y_2O_3.

This behavior leads us to conclude the existence of sulfur anionic vacancies in the oxisulfide lattices.

(1) : to be published.

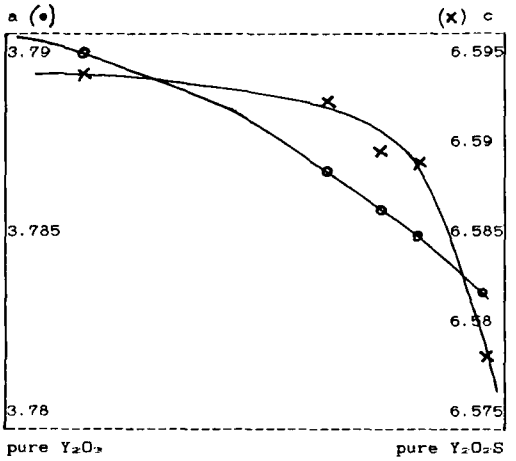


FIGURE 1: Y_2O_2S parameters evolution as a function of the percentage of oxide in the as prepared phosphor.

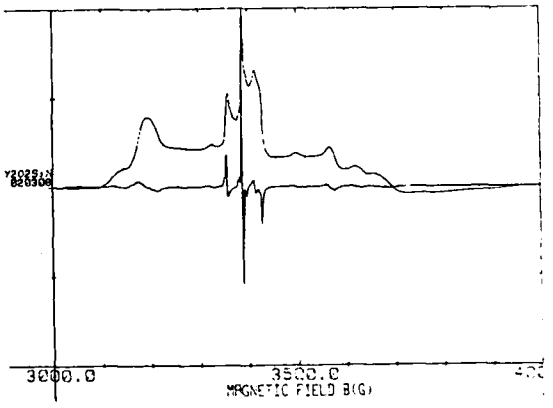


FIGURE 2: E.P.R. epectra of undoped Y_2O_2S powders at 93 Ghz (T= 300K).

Abstract No. 551

THE APPLICATION OF TL AND TSC TO THE STUDY OF DEFECT FORMATION IN ALKALI HALIDES BY UV RADIATION

N. Kristianpoller and Z. Davidson

Raymond and Berverly Sackler Faculty of Exact Sciences
School of Physics and Astronomy
Tel Aviv University, Tel Aviv 69978, Israel

It is well known that the primary defects, produced in alkali halides by ionizing radiation at low temperatures are Frenkel pairs, consisting of F and H centers [e.g., 1,2]. Most of the previous studies concentrated on the generation of point defects by polychromatic radiation such as x or γ rays. In a recent study the generation of point defects by monochromatic x and near uv radiation at 80K [3] was investigated. In the present work the formation of point defects by monochromatic vacuum uv (vuv) radiation at about 6K was studied. Methods of thermoluminescence (TL) and of thermally stimulated conductivity (TSC) were applied for these investigations. The relatively high sensitivity of these methods enabled us to detect effects of the weak monochromatic radiation. The uv excitation spectra of the TL and TSC were measured in the exciton region as well as in the region of band to band transitions and revealed information on defect formation, which could not be detected by other means under similar excitation conditions.

The experimental techniques applied for these investigations have been described elsewhere [4].

The experimental results show that some glow peaks appear mainly after uv irradiation with photon energies corresponding to band-to-band transitions. the excitation spectra of these peaks follow inversely the absorption spectra of the crystals. Other glow peaks appear after irradiation into the exciton region and show excitation maxima at the low energy tail of the first exciton absorption band. In figure 1, the TL glow curves, excited in KBr by vuv radiation are given Curve a -was excited by irradiation into the first exciton band (185 nm) and curve b -by irradiation in the interband region (155 nm). An x-ray induced TL curve is given for comparison by curve c. Results show that essentially the same glow peaks and with the same thermal activation energies appeared after x as after uv irradiation, indicating that the same defects were generated by the different irradiations.

Measurements of the temperature dependence of the radiation induced absorption bands showed that the thermal decay of certain centers coincides with the appearance of the main TL peaks. This is shown in figure 2, for KBr. The main absorption bands appearing at low temperature are due to α, F, I and H centers. It is known that I and H centers in KBr become mobile at about 20K and 45K, respectively [5]. The TL glow peaks appearing in this temperature region are attributed to the recombination of these centers with α and F centers. Our results show that the x-induced glow peaks near 20K are somewhat broader then the uv induced peaks in this region and seem to be composed; they also appear at slightly lower temperature. The thermal activation energy, measured at the rise of the x-induced glow peak was found to be 0.018 ev. This value fits the energy of the first stage of thermal induced recombination of close Frenkel pairs [5]. The energy measured for the uv induced peak near 28K was 0.06 ev; this value equals the energy required for free motion of Br interstitials. These results indicate, that by the uv radiation only distant seperated Frenkel pairs are generated, while by x-rays also close pairs are formed. This conclusion is supported by our finding that the uv induced peaks are of second order kinetics. Similar results were obtained for the other investigated alkali halide crystals. Some of the TL glow peaks were also accompanied by TSC peaks; this is shown in figure 3 for KCl.

TL emission spectra were measured as well. Some emission bands are due to casual impurities in the nominally pure samples. However, the main TL emission bands were found to be identical with the intrinsic STE emission bands, appearing in the low temperature photoluminescence of crystals. This finding indicates that the thermally stimulated recombination of the Frenkel pairs leads to the formation of self trapped excitons in an excited state.

REFERENCES

1. R. T. Williams, Semicond. Insul. 3, 251 (1978).
2. N. Itoh, Semicond. Insul. 5, 165 (1983).
3. B. R. Sever, N. Kristianpoller and F. C. Brown, Phys. Rev. B34, 1257 (1986).
4. N. Kristianpoller, Nucl. Instr. and Methods in Phys. Research, B1 229, 198 (1984).
5. N. Itoh, B. S. H. Royce and R. Smoluchowski, Phys. Rev. 137, A 1010 (1965).

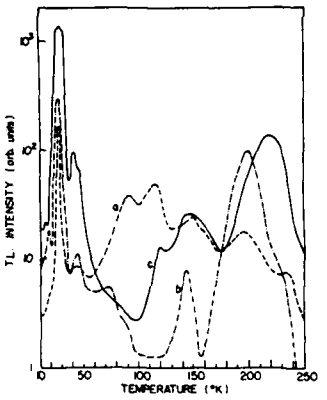


Fig. 1: TL glow curves excited in KBr at 6K by:
(a) vuv radiation of 185 nm.
(b) vuv of 155 nm, (c) x-rays (W,40Kvp,15ma).

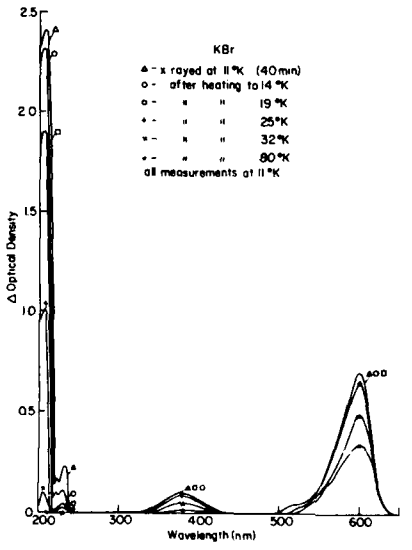


Fig. 2: Absorption Spectra of x-irradiated KBr at 11K. The curves were recorded at 11K after heating to various temperatures and recooling.

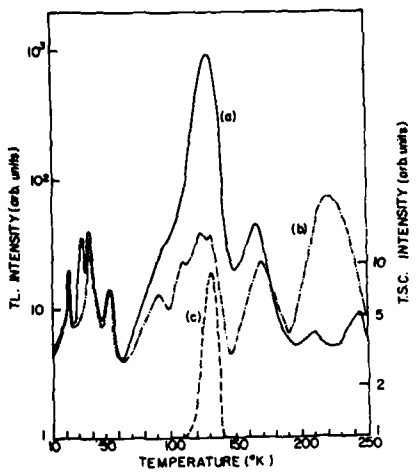


Fig. 3: TL glow curve of KCl excited at 6K by vuv radiation of (a) 162 nm, (b) 120 nm and (c) TSC glow curve excited by 162 nm.

Abstract No. 552

A New Contribution to Spin-Forbidden Rare Earth Optical Transition Intensities: Gd^{3+} and Eu^{3+}

M. C. Downer and G. W. Burdick
Physics Department, University of Texas at Austin
Austin, TX 78712

D. K. Sardar
Physics Department, University of Texas at San Antonio
San Antonio, TX 78285

The technological importance of transparent materials containing rare earth impurities continues to expand dramatically. Not only do they comprise an established and widening class of efficient solid state laser media, but they are finding new applications as dopants in optical fibers, semiconductor light-emitting devices and biological molecules. The $4f^N \rightarrow 4f^N$ transitions responsible for the rich variety of sharp optical absorption and emission lines in the spectra of these materials, though parity-forbidden in free ions, acquire finite intensities at noncentrosymmetric crystalline or molecular sites, in which opposite-parity excited configurations become slightly mixed into $4f^N$. Twenty-five years ago, Judd[1] and Ofelt[2] developed a quantitative theory involving simple configuration mixing caused by a static noncentrosymmetric crystal field, which remains the standard method for analysing observed rare earth transition intensities[3]. Nevertheless, significant revisions to this basic theory have sometimes been required in order to account for anomolous transitions which acquire a major fraction of their intensity from other mechanisms.

In this paper we make use of recent findings in two-photon rare earth absorption spectroscopy[4] to introduce and evaluate another significant revision in the analysis of one-photon rare earth transition intensities. Specifically, we re-examine the class of $\Delta S = 1$ transitions which, although spin-forbidden in the L-S coupling limit, comprise more than half the observed trivalent lanthanide optical transitions. Prominent $^8S_{7/2} \rightarrow {}^6P_J$, ^6I_J, ^6D_J, ^6G_J lines in Gd^{3+} and $^7F_0 \rightarrow {}^5D_J$, ^5L_J, ^5H_J, ^5K_J lines in Eu^{3+} provide examples of such transitions. Conventional analyses[3,5] account for the observed intensities of such transitions by using initial and final state wave functions in the "intermediate coupling" approximation, in which a strong spin-orbit interaction within the $4f^N$ configuration mixes states with different total spin S into the true energy eigenfunctions. Such wave functions have been accurately calculated and extensively tabulated[6] based on energy level fits throughout the trivalent lanthanide series. Thus, for example, the spin-forbidden $^7F_0 \rightarrow {}^5D_2$ transition in Eu^{3+} acquires its intensity through linkages such as:

$$(f^6\,{}^7F_0|\,\mathbf{H_{SO}}\,|f^6\,{}^5D_0)(f^6\,{}^5D_0|\,\mathbf{E{\cdot}D}\,|f^5d\,{}^5D_1)(f^5d\,{}^5D_1|\,\mathbf{V_{CF}}\,|f^6\,{}^5D_2\,), \quad (1)$$

where the spin-orbit operator $\mathbf{H_{SO}}$ links L-S coupled states of differing spin within the $4f^6$ configuration, and $\mathbf{E{\cdot}D}$ and $\mathbf{V_{CF}}$ denote electric dipole and noncentrosymmetric crystal field operators, respectively, which link $4f^6$ states to states within opposite parity excited configurations.

This simple use of intermediate coupled wave functions, however, neglects another type of linkage between initial and final states of differing spin, namely one in which the spin-orbit interaction acts within the slightly admixed excited configurations. An example of one such linkage for $^7F_0 \rightarrow {}^5D_2$ is

$$(f^6\,{}^7F_0|\,\mathbf{E{\cdot}D}\,|f^5d\,{}^7F_1)(f^5d\,{}^7F_1|\,\mathbf{H_{SO}}\,|f^5d\,{}^5D_1)(f^5d\,{}^5D_1|\,\mathbf{V_{CF}}\,|f^6\,{}^5D_2), \quad (2)$$

where $\mathbf{H_{SO}}$ acts within the opposite parity excited configuration f^5d instead of f^6. Although Wybourne[7] suggested the possible importance of these linkages in 1968, neither Wybourne nor subsequent investigators ever introduced them into any quantitative intensity analysis. Our motivation for doing so now stems from recent studies of two-photon spin-forbidden transitions in several trivalent rare earth ions[4]. The formal treatment of such two-photon transitions closely parallels that of forced electric dipole one-photon transitions[8], differing only in that a second electric dipole operator replaces the noncentrosymmetric crystal field operator. Two-photon results have established that linkages analogous to (2) frequently rival, and sometimes dominate, linkages analogous to (1). The Judd-Ofelt analysis predicts relative two-photon line strengths rigorously, without phenomenogical parameters[4]. Thus the strong disagreement between observed intensities and theoretical predictions based only on linkages such as (1) could therefore not be rationalized readily. By contrast, conventional Judd-Ofelt analysis of one-photon electric dipole transitions requires three phenomenological parameters, proportional to radial integrals, in fitting observed intensities. Such a procedure can easily mask the role of linkages such as (2) through an appropriate choice of parameters. However, the ratio of new contributions (2) to standard contributions (1) can be calculated without phenomenological parameters, allowing the importance of these new contributions to be evaluated unambiguously. This is true because uncalculated crystal field terms $\mathbf{V_{CF}}$, which are included in the empirically fitted Judd-Ofelt parameters, act identically in linkages (1) and (2). Furthermore, these new terms can be incorporated into a revised Judd-Ofelt analysis of observed intensities, with previously reported empirical parameters modified to accommodate new contributions.

The absorption spectra of Gd^{3+} and Eu^{3+} were selected for indepth analysis because the ground state for Gd^{3+} ($^8S_{7/2}$) has L=0 and for Eu^{3+} ($^7F_0$) has J=0, greatly reducing the number of nonzero matrix elements which have to be calculated. Results of our calculations are summarized in Tables 1 and 2. The particular transition and its experimentally measured oscillator strength are given in the first two columns of each table, while the next columns portray first order magnetic (where present) and second order electric dipole contributions, respectively, calculated by Carnall *et al.*[5] Results of our new calculations are presented in the final columns, where the first number is the unmodified magnetic dipole contribution (where present), the second is the standard second order term using revised empirical parameters and the third is our newly calculated third order contribution. Both the original parameters and our revised parameters are given at the bottom. In comparing calculated with experimental oscillator strengths in these Tables, the numbers under each major heading for any particular row should be summed, since each column represents an individual term. The most striking success of this re-analysis is our quantitative account of the previously unexplained $^6P_{3/2}$ intensity, where the worst second order fit now becomes the best fit. In the other transitions, the third order contribution is often greator than 20% of the total line strength. Nevertheless, we find that a systematic revision of previously extracted Judd-Ofelt parameters allows us to accommodate these substantial new contributions without sacrificing the quality of agreement between calculated and observed intensites. It should be emphasized that experimental oscillator strengths for several transitions shown in Table 2 are not available because of severe line broadening, crowding of spectral lines and other experimental factors which have made extraction of reliable oscillator strengths difficult or impossible[3,5].

It is highly likely that third order terms contribute substantially in other lanthanide ions. It would be particularly interesting to examine lanthanides in which spin-allowed ($\Delta S = 0$), as well as spin-forbidden ($\Delta S \geq 1$), transitions occur. In these cases new third order contributions should selectively modify calculated line strengths of only the spin-forbidden transitions.

REFERENCES

1. B. R. Judd, Phys. Rev. **127**, 750 (1962).
2. G. S. Ofelt, J. Chem. Phys. **37**, 511 (1962).
3. R. D. Peacock, Structure and Bonding **22**, 83 (1975).
4. M. C. Downer, *The Puzzle of Two-Photon Rare Earth Spectra in Solids*, in Laser Spectroscopy of Solids II, ed. W. M. Yen (Springer-Verlag, Heidelberg, 1988) to be published; M. C. Downer and A. Bivas, Phys. Rev. B **28**, 3677 (1983); B. R. Judd and D. R. Pooler, J. Phys. C **15**, 591 (1982); M. Dagenais, M. C. Downer, R. Neumann, and N. Bloembergen, Phys. Rev. Lett. **46**, 561 (1981); C. D. Cordero-Montalvo and N. Bloembergen, Phys. Rev. B **30**, 438 (1984).
5. W. T. Carnall, P. R. Fields, and B. G. Wybourne, J. Chem. Phys. **42**, 3797 (1965); W. T. Carnall, P. R. Fields, and K. Raynak, J. Chem. Phys. **49**, 4412 (1968).
6. W. T. Carnall, H. Crosswhite, and H. M. Crosswhite, *Energy Level Structure and Transition Probabilities of Trivalent Lanthanides in LaF_3*, Argonne National Laboratory Report (1977).
7. B. G. Wybourne, J. Chem. Phys. **48**, 2596 (1968).
8. J. D. Axe, Jr., Phys. Rev. **136**, A42 (1964).

Table 1: Experimental and calculated transition line strengths for Gd^{3+}.

		Previous Calc.[a]		Our Calculations		
		Mag.	Elec.	Mag.	Elec. Dipole	
Transition	Exp.[a]	Dipole	Dipole	Dipole	Standard	New
$^6P_{7/2}$	73	55	13	55	10	4
$^6P_{5/2}$	41	31	5	31	4	3
$^6P_{3/2}$	1.4		(0.2)		0.2	1.2
$^6I_{7/2}$	121		112		142	-29
$^6I_{9/2,17/2}$	845		877		1111	-233
$^6I_{11/2,13/2,15/2}$	1914		1918		2431	-514
$^6D_{9/2}$	78		93		74	18
$^6D_{1/2,7/2,3/2,5/2}$	82	8	130	8	103	27
$^6G_{7/2}$	121		149		113	38
$^6G_{9/2,11/2,5/2}$	903		765		582	181
$^6G_{3/2}$	- - -		(18)		14	4
$^6G_{13/2}$	639		459		349	91

[a]Experimental and calculated oscillator strengths (P x 10^9) from Carnall *et al.*[5].

Parameters (Carnall *et al.*)	Parameters (this work)
$T_2 = 3.30 \pm 0.62 \times 10^{-9}$ cm	$T_2 = 2.62 \times 10^{-9}$ cm
$T_4 = 6.06 \pm 0.53 \times 10^{-9}$ cm	$T_4 = 4.61 \times 10^{-9}$ cm
$T_6 = 6.10 \pm 0.10 \times 10^{-9}$ cm	$T_6 = 7.73 \times 10^{-9}$ cm

Table 2: Experimental and calculated transition line strengths for Eu^{3+}.

		Previous	Our Calculations[b]	
	Experimental[a]	Calc.[a,b]	Elec. Dipole	
Transition	Elec. Dipole	Elec. Dipole	Standard	New
$^5D_2$	2.1	2.1	5.5	-3.4
$^5L_6$	177	178	219	-42
$^5G_2$	- - -	(1.9)	5.0	0.3
$^5G_{4,5,6}$	43	56	68	-23
$^5D_4$	17	17	19	-2
$^5H_4$	- - -	(23)	26	-0.3
$^5H_6$	73	80	98	-4
$^5F_2$	- - -	(1.6)	4.2	2.6
$^5F_4$	- - -	(64)	72	34
$^5I_4$	- - -	(11)	12	-5
$^5I_6$	- - -	(27)	33	-9
$^5K_6$	22	19	23	-5

[a]Experimental and calculated oscillator strengths (P x 10^8) from Carnall *et al.*[5].

[b]Parameters T_2, T_4, and T_6 have been reduced by a facter of 1.546 corresponding to methods of Carnall *et al.*

Parameters (Carnall *et al.*)	Parameters (this work)
$T_2 = 1.88 \times 10^{-9}$ cm	$T_2 = 4.93 \times 10^{-9}$ cm
$T_4 = 8.59 \times 10^{-9}$ cm	$T_4 = 9.61 \times 10^{-9}$ cm
$T_6 = 6.96 \pm 0.46 \times 10^{-9}$ cm	$T_6 = 8.56 \times 10^{-9}$ cm

Abstract No. 553

TIME DEPENDENCE OF DELAYED LUMINESCENCE

Andrew K Jonscher
Royal Holloway and Bedford New College, University of London
Egham, Surrey, TW200EX, UK

The time dependence of of the decay of delayed luminescence $L(t)$ in solids has received considerable attention over several decades and there is ample experimental evidence relating to the behaviour of many materials. There is a widespread impression that this time dependence should be *exponential* , presumably deriving from the simple model of non-interacting excited centres. This is clear from the frequent habit of plotting the data semi-logarithmically, even though the resulting graphs are manifestly not straight lines. Some authors do, in fact plot their data in $\log L - \log t$ and obtain power-law behaviour of the form

$$L(t) \propto t^{-k-1} \qquad (1)$$

where the exponent k is in the range (0,1), at times *long* compared with the excitation time, while the exponent becomes $-k$ at short times.

A wide-ranging review of experimental data [1] has established the applicability of eqn (1), in some cases by re-plotting in log-log representation data given in semi-log form, in all situations in which *delayed* luminescence is involved with trapping of the initially excited electrons in intermediate deep levels before their final relaxation in the luminescent centres. Exponential time dependence, generally on a much shorter time scale, has only been seen in *prompt* luminescence where the excited electron drops back to its ground state within the same centre.

Many explantions have been proposed in the literature for these deviations from the ideal form of exponential time dependence. The classical bimolecular recombination process would give

$$L(t) \propto (t+t_o)^{-2} \qquad (2)$$

which is not in agreement with the majority of the data, particularly as it is never seen at the beginning of the decay where it would be most likely to occur. Several models are reviewed in [1], including tunnel recombination between neighbouring sites and combinations of diffusion and tunnelling.

A specifically many-body argument for the fractional power law (1) has been proposed by Dissado [2] who invokes fractal trapping processes.

Our own explanation for this generally observed type of behaviour of delayed luminescence invokes the otherwise known property of trapping processes in semiconductors [3] that the decay of polarisation arising from charge trapping follows the same power law as eqn (1) and this is attributed to interactions arising between the various deep traps. The basic proposition is illustrated schematically in Figure 1 showing a set of identical trapping levels which are neutral when "empty" and negatively charged when occupied by electrons. The consequence of trapping of an electron is a polarisation of the surrounding medium through slight adjustment of the occupancy of neighbouring centres, resulting in a lowering of the energy by an amount Δ . The result of this is that the energy required to liberate the carrier from the trap is increased by Δ in comparison with the energy gained in the trapping process. The consequence of this *constant loss* of energy per reversal of trapping is analogous to the "universal" frequency-domain response of dielectrics [4], the Fourier transform of which into the time domain gives equation (1).

The exponent k in this relationship is directly related to the energy Δ. Although there is at present insufficient information to develop a more quantitative theory of these phenomena, the connection with semiconductor trapping processes may provide an important guide to the most profitable direction of resesarch.

The proposed model is shown in Figure 2 with one or two trapping levels. External generation rate $g(t)$ produces free electrons which are rapidly trapped.The resulting dispensation rate of detrapped electrons $g(t)$ on sudden removal of a steady generation rate is assumed to follow a power law $h(t) \propto t^{-k}$. In the case of finite duration T of excitation, the decay of luminescence follows a t^{-k} law for $t \ll T$ and t^{-k-1} for $t \gg T$. The latter is normally seen experimentally.

It may be argued that reference back to frequency-domain response of dielectrics does not represent a legitimate approach to the interpretation of the decay of luminescence. While we do not accept this as a valid criticism, it would be interesting to measure the *frequency-domain* response of luminescence under alternating light excitation. This should provide direct evidence for the validity of the approach and might also give further insights into the behaviour of luminescence.

REFERENCES

[1] A K Jonscher and Anne de Polignac, "The time dependence of luminescence in solids", J Phys C:Solid State Phys 17 6493-6519 (1984)

[2] L A Dissado, "Fractal kinetics in the luminescence decay of solids", Chem Phys Letters, 124, 206-210 (1986)

[3] A K Jonscher, "Interpretation of the frequency response of electronic transitions in semiconductors", submitted to Solid State Electronics.

[4] A K Jonscher, *Dielectric Relaxation in Solids* Chelsea Dielectrics Press, London 1983.

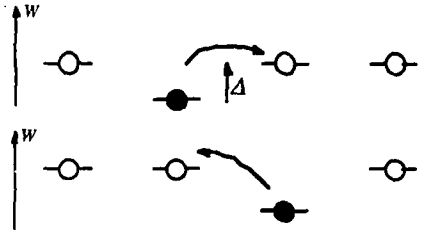


Figure 1
The effect of screening on the energy W of occupied trapping levels (filled contours) relative to the unoccupied ones (open). The upper and lower diagrams refer to consecutive hopping transitions in opposite senses and they are not on the same energy scale.The energy difference Δ is expected to be affected by the density of the interacting centres. Arrows indicate electronic transitions. From Ref [3].

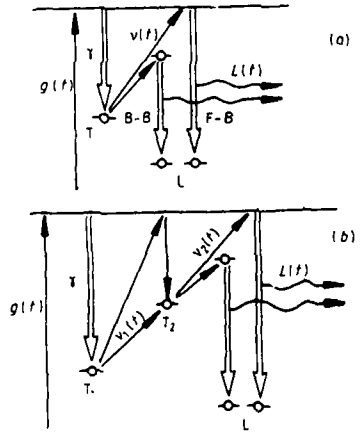


Figure 2
A model of delayed luminescence involving deep traps. (a) shows the case of a single set of trapping states T which capture electrons excited by the external generation rate $g(t)$ via a prompt recombination process $\gamma = g(t)$. The traps T then dispense the trapped carriers at at rate $\nu(t)$ into the conduction band from where they make prompt transitions into the luminescent centres L, resulting in a luminecent intensity $L(t) = \nu(t)$. F-B refers to "free-to bound", B-B to "bound-to-bound" transitions. A more complicated system is shown in (b) with another level of traps T_2 and two delayed transitons rates $\nu_1(t)$ and $\nu_2(t)$. The open arrows indicate prompt transitions. From Ref.[1]

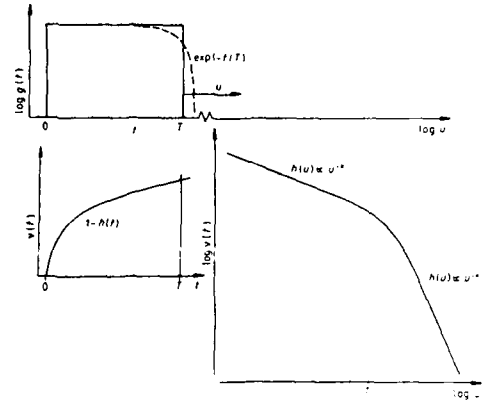


Figure 3
A schematic representation of the excitation and response of a trapping system characterised by a response function $h(t)$ assumed to be a power-law in time. The upper diagram shows a square-wave generation rate $g(t)$ of duration T and also an exponential rate $\exp(-t/T)$ shown by the broken line in log-log representation, to bring out its similarity to a square pulse. The lower diagrams show the dispensing rate from traps $\nu(t)$, during the generation pulse in the left diagram, and after the cessation of generation in the right diagram, where the variable $u = t - T$ measures the time since that instant. A change in the rate $\nu(t)$ occurs near $t = T$ from $t^{-\alpha}$ to $t^{-\alpha-1}$ and the latter law is often seen in the decay of luminescence.

Abstract No. 554

$Eu^{2+} \rightarrow Sm^{3+}$ Electron Transfer by Tunneling in MgS:Eu,Sm

K. Chakrabarti*, V. K. Mathur,
L. A. Thomas, and R. J. Abbundi
Naval Surface Warfare Center
White Oak, Silver Spring, MD 20903-5000

and

M. Hill and J. J. Brown
Virginia Polytechnic Institute and State University
Blacksburg, VA 24061

Exposure of MgS:Eu,Sm (band gap ~ 5.4eV) to UV radiation causes band to band transitions, i.e., the electrons are excited from the valence band to the conduction band. Some of these electrons from the conduction band are subsequently captured by the Sm^{3+} ions forming Sm^{2+} ions. When optically stimulated by a 1.06 μm Nd:YAG laser, the trapped electrons at Sm^{3+} ions recombine with the holes trapped at the Eu^{2+} ions resulting in a characteristic Eu^{2+} broad emission. Mechanisms of the stimulated luminescence and the charge trapping have been explained[1,2] with a model for an UV irradiated MgS:Eu,Sm sample. However, the optically stimulated luminescence (OSL) has also been observed in this material subsequent to exciting the sample with room light, i.e., this material can be "charged" with room light which does not cause band to band transitions. This characteristic of this material, although very attractive for its commercial uses as IR laser sensors, is not well understood. In this paper, we explain this phenomenon.

We have made a series of OSL studies subsequent to exposing the sample to 350-650nm light selectively. It has been observed that 500nm light generates the most intense OSL. Figure 1 shows the OSL after the sample is exposed to 500nm light for 5 minutes and an hour. The Eu^{2+} absorption involves a 4f-5d transition and the 5d level in O_h symmetry splits into the e_g and t_{2g} levels. Therefore, Eu^{2+} absorption has two transitions $^8S_{11/2}$ (4f) → ^2E_g (5d) and $^8S_{11/2}$ (4f) → $^2T_{2g}$ (5d) which are observed as broad bands near 260 and 480nm in MgS:Eu,Sm. An exposure to 420-540nm light excites the electrons to the t_{2g} levels of Eu^{2+} from where they tunnel to the Sm^{3+} ions. Since the t_{2g} level is below the e_g level and far below the conduction band, the tunneling from $Eu^{2+} \rightarrow Sm^{3+}$ appears to be the only mode of electron transfer when excited by visible light.

The electron transfer from Eu^{2+} to Sm^{3+} ions can also be seen from our results of the bleaching experiments. Figure 2 shows the bleaching of the Eu^{2+} and Sm^{3+} emissions by continuous irradiation of 500nm light. This indicates that the electrons are transferred from Eu^{2+} to Sm^{3+} ions reducing the intensity of both emissions.

We have also observed that increasing the concentration of the Sm^{3+} ions decreases the intensity of the Eu^{2+} emission excited by 480nm light. This again supports our view that the electrons tunnel from the t_{2g} level of the Eu^{2+} ions to the Sm^{3+} ions, thus quenching the intensity of the Eu^{2+} emission.

*On leave from Southwestern Oklahoma State University, Weatherford, OK 73096.

References:

1. K. Chakrabarti, V. K. Mathur, J. F. Rhodes, and R. J. Abbundi, Bull. Am. Phys. Soc. 33, 693 (1988).
2. K. Chakrabarti, V. K. Mathur, J. F. Rhodes, and R. J. Abbundi, J. Appl. Phys., to be published.

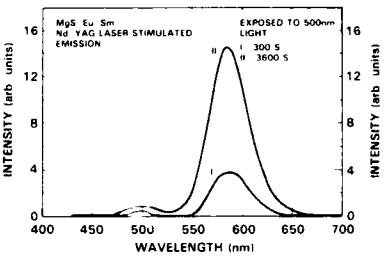


Figure 1 OSL of MgS:Eu,Sm exposed to 500nm light.

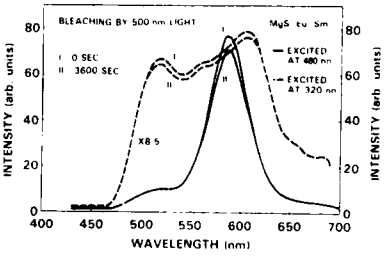


Figure 2 Bleaching of Eu^{2+} and Sm^{3+} emission by 500nm light.

Abstract No. 555

Chemical composition of and Eu^{2+} luminescence in the barium hexaaluminates

C.R. Ronda

Philips Research Laboratories
P.O. Box 80 000, 5600 JA Eindhoven
The Netherlands

B.M.J. Smets

Philips Lighting B.V.
P.O. Box 80 020, 5600 JM Eindhoven
The Netherlands

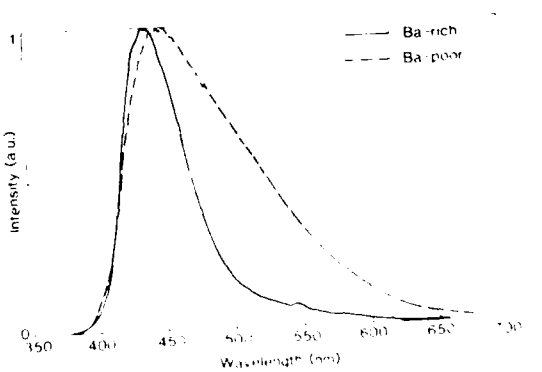
The chemical composition of two kinds of barium hexaaluminate, see ref. 1-4, one poor and one rich in barium, is explained using the local electroneutrality concept. The barium hexaaluminates crystallize in a β-alumina like crystal structure. The structure consists of spinel blocks, containing aluminium and oxygen ions, and conducting planes, containing barium and oxygen ions. The spinel blocks contain only trivalent metal ions. Large deviations from local electroneutrality have to be expected when no stabilization mechanisms are operative (see also ref. 5, 6). It is shown that the insertion of aluminium ions out of spinel blocks of the structure into the conduction layers stabilizes the structure. This can be done in two ways. The chemical compositions deduced from the stability considerations are in perfect good agreement with the observed chemical composition of the two barium hexaaluminates. The emission spectra of both compounds consist of two bands, blue and green, [illegible] with different relative [illegible] peak positions and half widths. The blue emission is due to the [illegible] ion in the conduction layer. The green emission is due to the [illegible] ion in the spinel block. The [illegible] of the [illegible] is explained by the [illegible] of the [illegible] ion in the [illegible] layer. [illegible]

References

1. N. Iyi, Z. Inoue, S. Takekawa and S. Kimura, J. of Solid State Chem. 60, 41 (1985)
2. F.P.F. van Berkel, H.W. Zandbergen, G.C. Verschoor and D.W. Ijdo, Acta Cryst. C40, 1124 (1984)
3. H.W. Zandbergen, F.C. Mijlhoff, D.J.W. Ijdo and G. van Tendeloo, Mat. Res. Bull. 19, 1443 (1984)
4. B.M.J. Smets and J.G. Verlijsdonk, Mat. Res. Bull. 21, 1505 (1986)
5. A.R. West, Mat. Res. Bull. 14, [illegible] (1979)

Figure

Fig. 1. [illegible]



Abstract No. 556

SPECTROSCOPYY OF DISORDERED $CdS_{1-x}Se_x$ MIXED CRYSTALS

F.A. Majumder, H.-E. Swoboda*,
and C. Klingshirn*
Physikalisches Institut der Universität,
Robert Mayer Str. 2-4,
D-6000 Frankfurt am Main, Germany

Various spectroscopic techniques like luminescence excitation spectroscopy gave strong evidence that localized exciton levels exist in weakly disordered mixed-crystals like $CdS_{1-x}Se_x$ [1]. Localization is due to fluctuations in the composition x which in turn result in fluctuations of the width of the forbidden gap on a microscopic scale. We carried out various experiments like photoluminescence spectroscopy under cw, ns, and ps pulsed excitation and spectroscopy with the pump and probe beam technique. For low lattice temperatures T_L ($5K \lesssim T_L \lesssim 70K$) we find in all experiments considerable deviations of the optical properties of the mixed crystals in the composition range $0.03 \lesssim x \lesssim 0.8$ as compared to the pure constituents x=0 and x=1:

- the spectral width of the zero-phonon luminescence bands is much bigger than that of bound excitons in pure crystals [1,2]
- the LO phonon replica are much more pronounced [1,2]
- the temporal behavior of the leading and trailing edges of the luminescence after ps excitation depends in the mixed crystals strongly on the photon energy and the decay is non-exponential in contrast to pure materials [3,4]
- the shape of the optical gain spectra is narrower and more peaked in mixed crystals as compared to the gain spectra of an electron hole plasma which is observed in pure materials under identical excitation conditions [2,4,5]. Furthermore there is a blue-shift of the absorption edge in the mixed crystals and a red-shift in the pure constituents.

All the above findings can be explained consistently with the assumptions that the optically excited electron-hole pairs relax rapidly into localized exciton states that both the relaxation and recombination get slower with increasing localization depth and that many-particle and renormalization effects of high density electron-hole pairs are much less pronounced in the localized levels than in extended ones.

For temperatures above 70K the optical properties of the mixed crystals approach those of the pure materials i.e.

- the spectral width of the zero phonon bands decreases by almost a factor of four between 60K and 70K
- the luminescence kinetics become independent on photon energy [4]
- the shape of the gain spectra becomes similar to the ones due to an electron hole plasma; there is now also a red-shift of the absorption edge under excitation for T up to $\cong$ 150 K and a blue-shift above as in CdS or CdSe [6]

All these phenomena can be explained consistently with the assumption that a considerable fraction of the localized excitons are thermally reexcited into extended states above the mobility edge for temperatures above $T_c \cong 70$ K. This value of T_c nicely agrees with the tail parameter ϵ_o of the exponential tail of the density of localized states of $\epsilon_o \cong 4.2$ meV [4] due to the relation $k_B T_c \gtrsim \epsilon_o$.

[1] E. Cohen and M.D. Sturge, Phys. Rev. B 25 3828 (1982)
S.A. Permogorov, A. Reznitsky, P. Flögel, S. Verbin, G.O. Müller, and M. Nikiforova, phys. stat. sol. b 113 589 (1982)
[2] F.A. Majumder, S. Shevel, V.G. Lyssenko, H.-E. Swoboda, and C. Klingshirn, Z. Physik B 66 409 (1987)
[3] J.A. Kash, A. Ron, and E. Cohen, Phys. Rev. B 28 6147 (1983)
F. Cohen, Proc. 17th Intern. Conf. Phys. Semiconductors, J.D. Chadi and W.A. Harrison eds. p. 1221, Springer (1984)
[4] S. Shevel, E.O. Göbel, G. Noll, P. Thomas, R. Fischer, and C. Klingshirn, J. Lumin. 37 45 (1987)
H.-E. Swoboda, F.A. Majumder, S. Shevel, R. Fischer, E.O. Göbel, G. Noll, P. Thomas, A. Reznitsky, and S. Permogorov, J. Lumin. 38 178 (1987)
[5] C. Klingshirn, Localization and Percolation in Alloy Semiconductors, to be published in Proc. Intern. Summer School on "Disordered Solids: Structures and Processes", Erice, Sicily (1987)
[6] H.-E. Swoboda, F.A. Majumder, V.G. Lyssenko, C. Klingshirn, and L. Banyai, Z. Physik B 70 341 (1988)

* [illegible]

Abstract No. 557

INDUSTRIAL APPLICATIONS OF RARE EARTHS LUMINESCENCE : ROLE OF STARTING MATERIALS

P. Maestro, P. Plaza, R. Fitoussi

Rhône Poulenc Recherches 14 Rue des Gardinoux 93308 Aubervilliers Cédex - FRANCE

The oustanding properties of rare earths in the field of luminescence have been known and studied from the begining of 20th century ; however the first industrial application only came into sight in the late sixties with the use of yttrium - europium based phosphors as the red component in color picture tubes (1).
Since then the use of rare earths phosphors did not stop spreading out, along with the efforts of rare earth separation industry to challenge the very high purity requirements for industrial productions (2).

The physics of rare earths luminescence have been extensively described (3), and rare earths have proved to be useful either as the host (Y^{3+}, La^{3+}, Gd^{3+} and Lu^{3+}), or as a sensitizer (e.g.Ce^{3+}), or as the activator (owing to f-f or d-f transitions). The unique character of the optical properties obtained from the transitions involving deep f energy levels combined with the stability of rare earth based phosphors under the severe working conditions in such devices as CPTs or mercury vapor lamps have been the reasons for an extensive use as soon as industrial productions became possible.

To day, rare earths based phosphors appear strongly as essential components in a variety of every day devices like color TV sets, fluorescent lamps or X ray intensifying screens, as illustrated in table I. On the other hand, more professional uses are developing in lasers, viewing displays (professional CPTs, flat panel displays,...), photo stimulated luminescence or dosimetry. Economical aspects of this development will be illustrated.

These developments have induced a strong demand for more and more efficient phosphors and, as a consequence, for an ever increasing quality rare earth oxides involved in the synthesis. By the way purity, although remaining an essential parameter for the obtention of good quality phosphors is no more the only one, and such criterion as reactivity has to be strongly taken into account, involving morphology as well as prereaction state of the raw material. Thus the control of such parameters have become a major concern in Rhône Poulenc, as a rare earths supplier willing to provide powders with optimum characteristics. As an illustration, the influence of the use of mixed oxides on the pertinent luminescent properties of the phosphors will be discussed, taking into account both physical and chemical aspects in the reaction.

REFERENCES

(1) - J.R.Mc COLL, F.C. PALILLA, A.C.S. Symp.Series, 164, 177, 1981
(2) - A. LEVEQUE, J. HELGORSKY, Science et Technique, 52, 19, 1978.
(3) - G. BLASSE, A. BRIL, Philips Tech.Rev., 31, 10, 15, 1970.
(4) - A. HARDY, I.E.E.E. Trans. Elec.Dev., ED15, 868, 1968
(5) - B.M.J. SMETS, Mat.Chem.Phys., 16, 283, 1987
(6) - L.H. BRIXNER, Mat.Chem.Phys., 16, 253, 1987

TYPE OF APPLICATION AND PHOSPHORS INVOLVED	PRACTICAL ADVANTAGES
Color TV sets (4) $Y_2O_2S : Eu^{3+}$	Brightness and linearity
Fluorescent lighting (5) $BaMgAl_{10}O_{17} : Eu^{2+}$ Sr chloroapatite Eu^{2+} $CeMgAl_{11}O_{19} : Tb^{3+}$ $LaPO_4 : Ce, Tb$ $Y_2O_3 : Eu^{3+}$ $(Ce, Gd, Tb) MgB_5O_{10}$ $YVO_4 : Eu^{3+}$	Output and color index
X Ray intensifying screens (6 $Gd_2O_2S : Tb^{3+}$ $LaOBr : Tm^{3+}$ $YTaO_4 : Tm^{3+}$	Speed and image quality ⇓ Reducing exposure times

TABLE I

Abstract No. 558

SPECTROSCOPIC PROPERTIES OF CHROMIUM (III) IN ZIRCONIUM BARIUM FLUORIDE GLASS (ZBLA).

R. Balda, J. Fernández, M.A. Illarramendi, M.J. Elejalde.

Dpto. Física Aplicada. Escuela Técnica Superior de Ingenieros Industriales y de Telecomunicación. Universidad del País Vasco. 48013 Bilbao. Spain.

Fluoride glasses,based on zirconium fluoride (ZrF_4) have received much attention in recent years. These glasses have a wide range of transparency extending between 0.2 and 0.8 μm, which makes them suitable for many applications in the visible and near infrared as optical fibers and efficient laser hosts.In this study we evaluate the optical absorption, luminescence lifetimes and quantum efficiencies of Cr^{3+} in ZBLA glass, of composition $57ZrF_4 - 34BaF_2 - (5-x)LaF_3 - 4AlF_3 - xCrF_3$ x=0.05, 0.1, 0.5, 0.85 as a function of temperature and excitation wavelength.

EXPERIMENTAL RESULTS

A) Absorption and emission spectra.

Figure 1 shows the emission and absorption spectra of a sample with x=0.85 at % Cr^{3+} ions obtained at liquid nitrogen temperature (LNT). As can be observed the main absorption features are two bands which can be identified as the vibronically broadened transitions $^4T_2 \leftarrow {}^4A_2$, $^4T_1(t_2e^2) \leftarrow {}^4A_2$ in order of increasing energy. The low energy band shows fine structure due the transitions $^2E \leftarrow {}^4A_2$ and $^2T_1 \leftarrow {}^4A_2$. The assignment of this structure has been made following the Fano antiresonance interpretation (1).

A summary of absorption spectroscopic data is included in Table I. As can be seen $^2E \leftarrow {}^4A_2$ does not present any variation with temperature showing the intraconfigurational nature of this transition. It is also worth noticing the low field character of the Cr^{3+} sites in ZBLA glass.

The emission measurements were made under excitation in the $^4T_2 \leftarrow {}^4A_2$ absorption band using the 633 nm line of a CW He-Ne laser. A broad and structureless band centered at 890 nm is observed in Figure 1 It corresponds to the $^4T_2 \rightarrow {}^4A_2$ emission and shows a very strong dependency with temperature (Figure 2).

B) Decay kinetics.

The decay kinetics of the broad infrared emission of a sample with [illegible] at % Cr^{3+} was studied using a frequency doubled Nd:YAG (10 ns pulse width). The decay curve of the $^4T_2 \rightarrow {}^4A_2$ emission at 890 nm can be fitted by two exponential decay curves. A least squares fit gived the values for the short-lived and long-lived components of the decay. Table II resumes the results in the measured temperature range. In a similar [illegible] with the [illegible] of % Cr^{3+} [illegible] the [illegible] with .

Table III shows the LNT lifetimes (long and short - lived components) at different emission wavelengths for an excitation wavelength of 660 nm. Table IV presents the results of the LNT relative quantum efficiency (QE) measurements based on the integrated intensity of the normalized decay curves. The measurements were made on samples of 0.1 and 0.5 at % Cr^{3+} upon exciting in the $^4T_2 \leftarrow {}^4A_2$ absorption band and collecting at the peak of the emission band. Photoacoustic measurements performed at room temperature give a value of 0.1 absolute QE of the x=0.85 at % Cr^{3+} sample.

CONCLUSIONS

From the above results the following conclusions can be reached:

i) The Cr^{3+} ion in ZBLA glass have a very weak crystal field.

ii) The luminescence shows a strong thermal quenching in agreement with the temperature dependence of the measured lifetimes.

iii) The two components observed in the fluorescence decay could be related with two kinds of main crystal sites.

iv) The LNT measured lifetimes show a very weak dependence on the excitation wavelength for low concentrations.

v) Quantum efficiencies at room temperature are very weak in accordance with the strong thermal quenching of luminescence.

REFERENCES

(1).- J. Fano. Phys. Rev. 124, 1866 (1961).

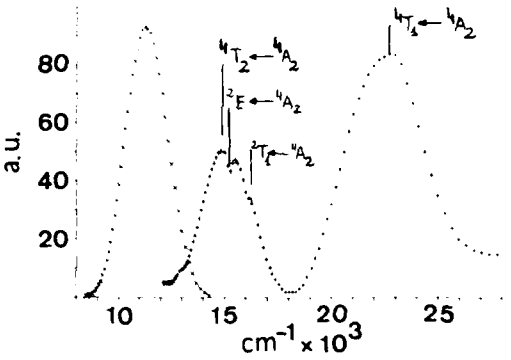


Fig. 1.- Absorption at [illegible] emission at [illegible].

	$^4T_1 \rightarrow {}^4A_2$	$^2T_1 \rightarrow {}^4A_2$	$^2E \rightarrow {}^4A_2$	$^4T_2 \rightarrow {}^4A_2$
RT (cm^{-1})	22.472	16.260	15.267	14.749
LNT (cm^{-1})	22.831	16.331	15.267	14.880
$Dq(cm^{-1})$	1475(RT), 1488(LNT)			
$B\ (cm^{-1})$	833 (RT), 862 (LNT)			

Table I.- Summary of absorption spectroscopic data.

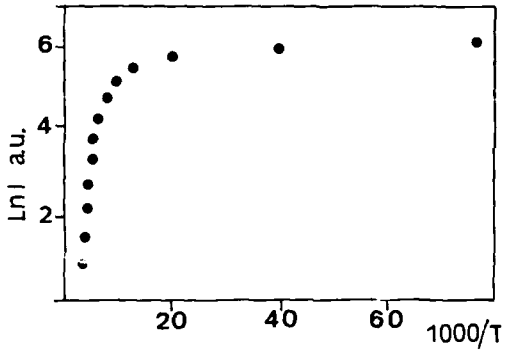


Figure 2.- Temperature dependence of emission intensity.

T K	τ_l (μS)	τ_s (μS)
13	70	18.5
30	63.5	16.8
60	66.5	18.5
84	71.5	23.5
110	60	16
140	44	9.5
170	47	13
200	30	6

λ_{EM}	τ_l	τ_s	τ_l	τ_s	τ_l	τ_s
820	91	16	77	—	77	9
840	83	11	100	13	100	11
860	91	13	91	20	91	9
880	100	20	100	17	77	16
900	83	17	91	16	77	23
920	100	19	83	5	77	12
940	77	12	83	12	91	15
960	83	17	83	12	77	10
980	83	17	83	15	77	8
1000	71	9	77	21	83	15
	0.5%		0.1%		0.05%	

Table III.- Emission wavelength dependence of long-lived and short-lived components of the fluorescence decay.

	0.1 %	0.5 %
λ_{EXC}(nm)	Φ	Φ
630	0.4	0.19
640	0.4	0.22
650	0.4	0.22
660	0.41	0.24
670	0.4	0.22
680	0.38	0.20

Table IV.- LNT relative Φ quantum efficiencies.

Abstract No. 559

Charge Transfer Luminescence in Polysilanes

by J. R. G. Thorne, R. M. Hochstrasser

University of Pennsylvania
Department of Chemistry
231 S. 34th Street
Philadelphia PA19104

and J. M. Zeigler

Sandia National Laboratories
Albuquerque NM87185-5800

There is considerable recent interest in a new class of saturated long-chain silicon polymers $(R_1R_2Si)_n$, where R_1,R_2 represent alkyl or aryl groups. The importance of the polysilanes stems mostly from their potential as photoresists but the nature of the optical excitations is still in debate. We concentrate here upon the emissive properties of the materials, which have received comparatively little attention[1,2], and attempt a rationalization of the experimental observations.

Both alkyl and aryl substituted materials, in solution and in thin films, have a single sharp fluorescence at ~350 nm, coincident at low temperature with the first absorption maximum. The polarization of this band has led to the conclusion that it is associated with a ($\sigma\sigma^*$) transition of the silicon backbone[1]. In addition, in the aryl-substituted compound, $(PhMeSi)_n$, a very broad emission is present at ~430 nm[2], whose intensity increases dramatically on cooling such that it dominates the spectrum at 4 Kelvin. This band is thought to arise from a charge transfer state, by analogy with the luminescence from phenyldisilanes and phenylethynyldisilanes[3]. The direction of charge transfer, from silicon to phenyl, would create a separated electron-hole pair and might account for the observed hole photoconductivity of polysilanes[4].

We have measured luminescence lifetimes for these dual emissions in solution, glass, thin film and powder[5,6]. The natural radiative lifetime for 350 nm emission is found to be ~600 picoseconds[6]. This value exceeds that predicted from the absorption oscillator strength per silicon atom, and implies a delocalization of the ($\sigma\sigma^*$) excitation over perhaps twenty sites on the silicon chain. Our fluorescence depolarization measurements[5] indeed show the excitation to be extremely mobile. In some of these materials the observed fluorescence lifetime is shorter than this value. In solution the alkyl-substituted compound $[(n\text{-}C_6H_{13})_2Si]_n$ has a lifetime of ~150 ps, which we have attributed to increased non-radiative decay processes, including photochemistry, that cannot occur in crystalline media. $(PhMeSi)_n$, however, has a lifetime of 70 ps [5] in all condensed media investigated and the shorter lifetime of the excited state we ascribe to fast transition to the charge transfer state. At elevated temperatures the material is particularly photosensitive and bond scission, rather than photoemission, is the result of this process.

The character of the separated electron-hole pair state differs considerably from that of the ($\sigma\sigma^*$) neutral excitation. The temporal decay of the 430 nm luminescence takes place in the nanosecond regime but is highly non-exponential, both in thin film and glassy media, at low temperatures. We treat the problem in terms of migration of the hole, or charge separation, under the influence of a multipolar interaction, along a one-dimensional chain.

This research was supported by NSF-DMR-8519059 and by the Sandia National Laboratories, supported by the U.S. Department of Energy under contract number DEAC04-76-DP00789

References

1. L. A. Harrah and J. M. Zeigler, A.C.S.Symposium Series, 1987 in press.
2. T. Kagawa, M. Fujino, K.Takeda and N. Matsumoto, Solid State Commun. 1986 57 635
3. R. G. Kepler, J. M. Zeigler, L. A. Harrah and S. R. Kurtz, Physical Review B 1987 35 2818
4. H. Shizuka, K. Okazaki, M. Tanaka, M. Ishikawa, M. Sumitani and K. Yoshihara, Chemical Physics Letters 1985 113 89
5. Y. R. Kim, M. Lee, J.R.G. Thorne, R.M.Hochstrasser and J.M.Zeigler, Chemical Physics Letters 1988 145 75
6. J. R. G. Thorne, R. M. Hochstrasser and J. M. Zeigler, J. Physical Chemistry submitted

Abstract No. 560

NOVEL TECHNIQUE IN THE PREPARATION OF Eu^{2+} DOPED PHOSPHORS

R.P.Rao and R.Jagannathan
Central Electrochemical Research Institute
Karaikudi-623006, India

Trivalent rare earth (RE) ions give characteristic luminescence whereas divalent RE ions give emission bands which are dependent (due to $4f^6 5d$ electron) on host crystal environment. In recent years, number of phosphor materials with divalent Eu have been developed and are being used in various applications such as lamps, TV screens, x-ray diagnostic systems. Generally, these phosphors are prepared at high temperatures in presence of forming gas viz. nitrogen with 2-10% of hydrogen. But in the present investigation, the firing has been done in presence of carbon due to which complications in reduction process can be minimised. The phosphors obtained in the present technique are comparable with that prepared from conventional methods like (N_2+H_2) in luminescent properties. Eu^{2+} doped phosphor materials such as strontium chlorophosphate (SCP) , barium-calcium aluminate (BAL), barium-magnesium aluminate (BAM), strontium-magnesium aluminate (SAM), strontium-magnesium silicate (SMS) and barium fluorochloride (BFCl) have been prepared and studied their luminescent properties.

Required amounts of starting chemicals (3,9's) have been mixed thoroughly in a centrifugal ball mill and placed in alumina crucibles. Crucible containing the mixture has been placed in a bigger crucible and the space between the two is filled with activated charcoal (carbon). The firing was done in a closed muffle furnace at temperatures ranging from 800 to 1300°C for one to four hours. After crushing the mass, the excitation and emission spectra have been recorded at room temperture with the help of fluorescence spectrophotometer (Hitachi 650-10S). The color coordinates of these phosphors have been found using UV-VIS-NIR Spectrophotometer (Hitachi U-3400) in single beam mode. The results obtained in this investigation on various phosphor materials are given in Table I. Luminescence data shows no trace of Eu^{3+}. Carbon monoxide (CO) formed at higher temperatures may be responsible for the reduction of Eu^{3+} to Eu^{2+}. From the results it is concluded that this technique can be used fruitfully in the preparation of Eu^{2+} doped phosphors.

TABLE I

Luminescent characteristics of some Eu^{2+} doped phosphors

Sample	λ_{ext} nm	λ_{em} nm	Half width nm	Color coordinates x	y
SCP	310, 365	448	36	0.1528	0.0277
BAL	320	420	38	0.1595	0.1014
BAM	320	450	68	0.1658	0.2531
SAM	290, 325	415	28	0.1669	0.1573
SMS	350	460	40	0.1477	0.0878
BFC	310	388	34	0.2075	0.0937

Abstract No. 561

LUMINESCENCE PROPERTIES OF THORIUM PHOSPHATE TRANSPARENT GELS DOPED WITH RARE EARTH AND URANYL IONS

M.G. Iroulart, V. Brandel, E. Simoni, M. Genet

Laboratoire de Radiochimie,
Institut de Physique Nucléaire,
B.P. N° 1, 91406 Orsay Cedex (France)

1. Introduction

The purpose of this paper is to study the luminescence properties of a new kind of material prepared from thorium phosphate gel medium doped with Mn^{2+}, Eu^{3+}, Tb^{3+}, UO_2^{2+} in comparison with well known conventional materials (aqueous solution, glass and crystals).

2. Preparation and experimental conditions.

. The gels have been prepared from a thorium nitrate solution mixed with phosphates anions, acidified with HNO_3 ($0.5 < pH < 1.0$) (1 - 3). Under these conditions, we have obtained a very transparent material. These gels have been doped (about 10 %) with $MnCl_2$, $Eu(NO_3)$, $Tb(NO_3)_3$ and $UO_2(NO_3)_2$).

. By heating, we observed that the luminescence was sensitive to the drying temperature (4, 5). At 50° C, the gel becomes liquid after loosing about 85 % of water ; if drying is going on at the same temperature, then we got a transparent solid state (called xerogel). When the temperature is raised from 80° C to 950° C, this xerogel transforms into an amorphous powdered solid and in 4 hours at 1050° C we have obtained a crystalline powdered solid. These modifications have been investigated by X-rays techniques.

. The luminescence excitation of these ions were performed at room temperature using a pulsed nitrogen laser (λ = 337.1 nm) or a mercury lamp.

3. Results.

Under the drying conditions described above, we have studied the luminescence of UO_2^{2+} and Eu^{3+} ion in this material. Under U.V. excitation, gel doped with UO_2^{2+} exhibits, at room temperature, the usual green-yellow emission. The intensity of this fluorescence is decreasing when the temperature is increasing up to 50° C. In the liquid phase, no fluorescence is observed. But, when the medium is transformed into solid state (xerogel) at 50-80° C, the luminescence intensity is very important and the decay time (τ = 300 µs) is twice as long as the value recorded for UO_2^{2+} ion in a phosphate solution of a same composition but without thorium (150 µs). Nevertheless, when the temperature is increasing from 80° C to 1050° C, the fluorescence intensity decreases and the decay time of the powdered thorium phosphate is smoothly decreasing.

In the same drying conditions, red emission of Eu^{3+} ion in thorium phosphate have been examined. Compared to UO_2^{2+}, the observed behaviour is quite different, luminescence intensity and decay time are both increasing with temperature thermal treatment. Decay time in xerogel is about 1.3 ms and 2 ms for the amorphous material. For these values, determined at 600° C intensity curve peaked up, this effect is not yet interpreted.

Mn^{2+} shows a very week emission whatever the different types of solids studied, with a decay time of 4.6 ms in the crystalline state.

Tb^{3+} are under progress. Preliminary results at 337.1 nm excitation exhibits an intense green emission (542 and 487 nm) which is greater for the crystal powder compared to the amorphous one.

In general, we observed a broadening of the emission with the importance of the thermal treatment, namely, when we increase the temperature.

As the thermal treatment is determining, several physical methods (DTA, TGA, NMR, IR) have been used in order to correlate the chemical state of the material with the luminescence intensity observed. We can conclude that :

. Lost of water is an endothermic reaction taking place at about 80° C, followed by a vaporisation of the liquid phase which is still endothermic.

. The phosphate ions are tightly connected to the gel network in a gel freshly prepared, but as the medium becomes dryer the phosphate ions are more and more free. The water behaviour is strictly the reverse. In the liquid phase, both phosphates ions and water are completly free. In the solid phase, xerogel and amorphous material, they are both tightly bound.

. In gel medium, the type of phosphate ions are not strictly identified by IR due to the important broadening of the bands, but as the medium losses water, the typical thorium orthophosphate spectrum is observed even in the amorphous solid and the characteristics X-rays patterns (monoclinic) confirmed on the crystalline product the presence of the thorium orthophosphate. Taking into account these observations, few comments might be done about a tentative interpretation of the luminescence :

- in the pure gel medium, luminescence is only due to the luminescent ions complexed by phosphate ions,

- in the xerogel, which is the more efficient medium, the increase of luminescence intensity is due to the lost of water and phosphate ion concentration which is comparable to that of an usual solid,

- in the amorphous solid, the luminescence is not so important, compared to the xerogel,

- no significant difference appears in luminescence of ions between amorphous and crystalline material.

In conclusion :

Luminescence of various ions (UO_2^{2+}, Eu^{3+}, ...) have been used as a probe to test different type of medium : gel, xerogel amorphous, crystal prepared from the same thorium-phosphate gel as starting material. The xerogel form is the more efficient one. Futhermore this xerogel is transparent and easy to prepare in very thin film.

References :

1. Satya Prakash, Dhar N.R. : J. Ind. Chem. Soc., 6 (1929) 587.

2. Mehta S.M., Parmar M.U., Mata Prasad : J. Ind. Chem. Soc., 13 (1936) 69.

3. Mehta S.M., Parmar M.U., Mata Prasad : J. Ind. Chem. Soc., 13 (1936) 128.

4. V. Brandel, M. Genet, J. of Luminescence 40 and 41 (1988) 863.

5. M. Genet, V. Brandel, C. R. Acad. Sc., to be published.

Abstract No. 562

NOVEL EMISSION OF Dy^{3+} IN MAGNESIUM FLUOROBORATE *

LIU Xingren, ZHANG Yinglan, WANG Zhihua
Changchun Institute of Physics
Academia Sinica
XU Shaohong
Shanghai University of Science and Technology
Shanghai, China

It is well-known that Dy^{3+} ion in various kinds of hosts shows in the visible region three emission bands which lie in the intervals 470-500nm, 570-600nm and 660-690nm, corresponding to the transitions from $^4F_{9/2}$ or higher excited states to ^6H_j or ^6F_j (1-5).

We report here a new emission from Dy^{3+} doped γ-$Mg_3BO_3F_3$(MFB)which is a very strong line at 614.5nm(16273cm^{-1})(*L line*). To the best of our knowledge, this line has never been reported in any Dy^{3+} activated compound.

The emission spectrum of *MFB:Dy^{3+} under UV* excitation is shown in Fig.1. The bands in 550-600nm characteristic of Dy^{3+} ion are comparatively weak while L line is very strong.

Other rare earth ions which could possibly give sharp line emission at wavelengths around 615nm are Eu^{3+} and Pr^{3+}. MFB doped with Eu^{3+} had been prepared and its luminescence spectrum measured. The peak of the main line was found to be at 612nm. When both Eu^{3+} and Dy^{3+} are incorporated, MFB:Dy^{3+},Eu^{3+} gives an emission spectrum as shown in Fig.2, in which the L line and the 612nm line are clearly seperated. Fig.3 gives the excitation spectra of the line L from MFB:Dy^{3+} and of the 612nm emission from MFB:Eu^{3+}. It can be seen that the two spectra are quite different from each other. When 405nm was used to excite the doubly activated MFB only 612nm was emitted, while 420nm was used, L appeared uniquely. Since in the region 23000-34000cm^{-1} no excited state of Pr^{3+} ion exists, excitation peaks of the L line in this region implies that the luminescence L should not be originated from Pr^{3+} ion. Thus it can be concluded that the 614.5nm luminescence of MFB:Dy^{3+} is emitted by Dy^{3+} ions.

As a rule, the initial state of the transition corresponding to L emission may be judged from the excitation spectrum *From Fig.3 the* lowest energy which can excite L is about $2.15 \times 10^4 cm^{-1}$ (465nm). A tunable dye laser had been used to excite the phosphor, *two peaks* appeared at 21278cm^{-1} and 21457cm^{-1}. With laser light at 22039cm^{-1} the intensity of L line varied linearly with that of the exciting radiation. This implies that the L emission is a single photon process and the initial state of the emission is either $^4F_{9/2}$ or $^4I_{15/2}$. According to the crystal structure of MFB reported by Okazaki(6), Dy^{3+} ions are most probably situated at the Mg site with extremely low symmetry. Consequently, the number of energy levels due to crystal field splitting would be quite large and the structure complicate. So it is difficult to identify the initial state simply through the energy of the exciting photon unless the exact energy level structure is known. However, since the energy difference between $^4I_{15/2}$ and $^6H_{11/2}$ gives a better match to the photon energy of L, it seems more reasonable to take $^4I_{15/2}$ as the initial state and $^6H_{11/2}$ as the final one.

* This work is sponsored by the National Science Foundation of China

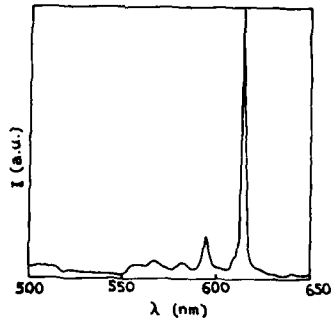


Fig.1 Emission spectrum of γ-$Mg_3BO_3F_3$:Dy^{3+} under UV excitation.

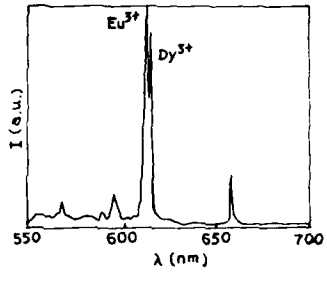


Fig.2 Emission spectra of γ-$Mg_3BO_3F_3$:Dy^{3+} Eu^{3+} under UV excitation.

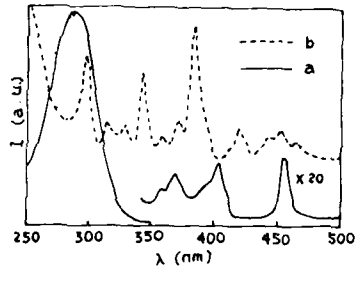


Fig.3 Excitation spectra(a) of 612nm emission from γ-$Mg_3BO_3F_3$:Eu^{3+},(b) of L from γ-$Mg_3BO_3F_3$:Dy^{3+}.

References

(1) H.G.Jenkins et al, U.S. Pat. 2427728, Sept.23,1947
(2) C.H.William et al, J.Electrochem.Soc. 115,105,1968
(3) J.L.Sommerdijk et al, J.Electrochem. Soc. 122,952,1975
(4) J.L.Sommerdijk et al, Philips Res.Rep. 32,149,1977
(5) R.J.Matthews et al, Phys.Status Solidi a 71,55,1982
(6) H.Okazaki et al, J.Chem.Soc.Japan, 86, 1015,1965

Abstract No. 563

LUMINESCENCE FROM SEVERAL ACTIVATORS IN $SrBeLa_2O_5$.

G. Blasse and G. J. Dirksen,
Physics Laboratory, University of Utrecht,
P. O. Box 80.000, 3508 TA Utrecht,
The Netherlands.

Recently Schröder and Müller-Buschbaum (1) reported a new compound of formula $SrBeLa_2O_5$, and determined its crystal structure. The Be^{2+} ions are in tetrahedral coordination, half of the La^{3+} ions in seven coordination and the Sr^{2+} ions and the other half of the La^{3+} ions in nine coordination. The latter site is occupied in a statistical way. We succeeded to prepare this compound at much lower temperatures, viz. 1200 °C, than reported in ref. 1, viz. 2000 °C. Several activators were tried for their luminescence.

The rare earth ions Eu^{3+}, Sm^{3+}, Tb^{3+} and Ce^{3+} have their allowed transitions (viz. charge-transfer or 4f-5d transitions) at relatively low energy. This is related to the presence in the crystal structure of an oxygen ion which is not coordinated to the Be^{2+} ion. This anion behaves as if it is unsaturated. Examples of such a behaviour are known in the literature (2) and will be discussed.

The undoped host lattice shows also luminescence which is tentatively ascribed to a self-trapped exciton on the unsaturated oxygen ion. This will be compared with findings for other lanthanide ion host lattices where similar observations have been made.

The Eu^{3+} ions in this crystal structure show two charg-transfer transitions at different, but relatively low energy. These correspond to the charge-tranfer transition on Eu^{3+} in the two different sites. It can also be shown which transition belongs to which ion, using the fact that one sublattice is disordered, whereas the other is not. At 4.2 K selective excitation is more or less possible.

The Sm^{3+} ion can also be excited in the charge-transfer transition, since its spectral position is lower than usual. The same holds for f→d transitions. The Ce^{3+} ion, for example, emits in the green, although the Stokes shift of the emission relatively small. Two Ce^{3+} emissions were observed, corresponding to Ce^{3+} on the two crystallographic sites. One shows at 4.2 K vibrational structure, whereas the other does not. This will be interpreted using the statistical distribution of Sr^{2+} and La^{3+} ions on one of the two sites. The body colour of $SrBeLa_2O_5$-Ce^{3+} is yellow.

It is possible to replace La^{3+} by Gd^{3+} which influences the luminescence properties. Finally results for activation with s^2 ions (Pb^{2+}, Bi^{3+}) will be presented. These show also the influence of the unsaturated oxygen ion.

References.

1. F. Schröder and Hk. Müller-Buschbaum, Monatsh. Chemie 118, 959 (1987).
2. See e.g. Bao Zhiran and G. Blasse, J. Solid State Chem. 55, 23 (1984).

Abstract No. 564

A Long-persistent Blue Phosphor $SrSb_2O_6:Mn^{2+}$

H.Yamada, H.Matsukiyo, T.Suzuki and H.Yamamoto
Central Research Laboratory, Hitachi Ltd.
P.O.Box 2, Kokubunji, Tokyo 185, Japan
and
T.Okamura, T.Imai and M.Morita
Faculty of Engineering, Seikei University
Kitamachi, Kichijyoji, Musashino, Tokyo 180, Japan

1.Introduction

Blue luminescence of $SrSb_2O_6:Mn^{2+}$ peaked at 470 nm[1,2] is a rare case of Mn^{2+} luminescence, which is usually found in the red to green region. By finding that the luminescence has an exponential decay with a time constant of 47 ms at 10% peak height, the authors have attempted to improve the quality of this material with an aim at its application to terminal display tubes. This paper describes a new synthesis method, optical studies indicating energy loss processes and some preliminary results on tube characteristics.

The crystal structure of $SrSb_2O_6$ and of isomorphous $CaSb_2O_6$ can be regarded as a layered structure having sheets of SbO_6. The Sr site coordinated with six oxygen ions is inserted between the SbO_6 sheets[3].

2. The synthesis method

One of the starting materials Sb_2O_5 is partially converted to volatile Sb_2O_3 during firing. On the other hand, when the starting materials are heated in an oxidizing atmosphere, Mn^{4+} may be formed. It is, therefore, difficult to control the stoichiometry and the valency of the Mn^{2+}-activated antimonates. To overcome this difficulty, a four-step process has been developped. The idea of this synthesis method is as follows. (a) The first step forms the host lattice at a relatively low temperature (1000°C) to suppress the formation of Sb_2O_3. Crystallinity remains poor so that Mn^{2+} can be easily diffused into the lattice. (b) In the second step, Mn^{2+} is doped together with a flux which helps diffusion of Mn^{2+} ions. (c) Then, the firing temperature is increased (1200°C) to grow grains. And (d) the residual Mn compound and flux are washed away by acid treatment.

The best choice of a Mn starting material is $Mn_2P_2O_7$, which gives the highest efficiency, 1/3 relative to ZnS:Ag,Cl. The optimum concentration of added Mn is 8 atomic %. Interdiffusion of constituent ions are accelerated, when K_2SO_4 is used as a flux. The effect of the flux is confirmed by development of a hexagonal habit of the phosphor grains and uniform formation of $(Sr,Ca)Sb_2O_6:Mn^{2+}$ solid solutions. The flux as much as 40 wt.% of the starting material seems to be effective in preventing from the oxidation of Mn^{2+} ions, since narrow-band luminescence at around 680 nm characteristic of Mn^{4+} is observed, when K_2SO_4 is not used.

3.Luminescence and excitation spectra

An excitation spectrum of the blue band at -180°C is shown in Fig.1. The absorption bands of Mn^{2+} should be located at wavelengths longer than 350 nm, but they can not be identified in this spectrum. The bands at 300 and 270 nm may be related to the host lattice, because uv luminescence originating in the host lattice[4] has excitation bands nearly at the same wavelengths as these two bands.

A possible reason of the unusual blue luminescence of Mn^{2+} is the Mn-O distance as long as 0.23 nm in $SrSb_2O_6:Mn^{2+}$. This long interatomic distance decreases 10Dq and Racah parameters and in turn increases the energy between the ground state and $^4T_1$ state of Mn^{2+}.

4. Characteristics of display tubes.

The phosphor $SrSb_2O_6:Mn^{2+}$ was screened in a dot-pattern on 14 inch CRT faceplates. Flicker of images was evaluated on these tubes in comparison with a commercial blue phosphor ZnS:Ag,Ga,Cl. The relation between the critical fusion frequency and the screen brightness is shown in Fig.2. Although the two phosphors have nearly the same 10% time constants, $SrSb_2O_6:Mn^{2+}$ shows reduction of the flicker compared with ZnS:Ag,Ga,Cl having nonexponential luminescence decay. It was found, however, that $SrSb_2O_6:Mn^{2+}$ is aged more rapidly. Evolution of oxygen was also observed under electron irradiation.

5.Summary

Both the difficulty of the valency control in the synthesis and the aging accompanied with the oxygen evolution probably stem from the small energy difference between Sb^{3+} and Sb^{5+}. The blue luminescence of Mn^{2+} is related to the long Mn-O distance, which results from the position of the Mn site inserted between the sheets of SbO_6 in the layered structure.

6. Acknowledgment

The authors are indebted to Dr. Y.Uehara, Mr. Y.Morita and Mr. M.Asakura for the fabrication and evaluation of CRTs. They are grateful to Dr. K.Urabe for helpful discussion on the interpretation of the excitation spectra.

7.References

1)J.Janin and R.Bernard:Compt.Rend. 240 614 (1953)
2)M.L.Alusalu: Tr.Inst.Fiz.Astron. Akad. Nauk. Est.SSR. 8 58 (1958)
3)R.Kiriyama and H.Kiriyama:"Structural Inorganic Chemistry" II p.41, Kyoritsu Shuppan Co.Ltd., Tokyo (1963)
4) C.Pedrini, G.Boulon and F.Gaume-Mahn:phys.stat. solidi (a) 15 K15 (1973)

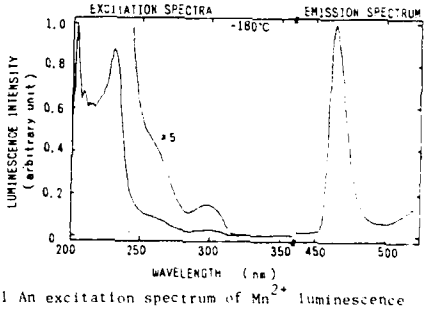


Fig.1 An excitation spectrum of Mn^{2+} luminescence in $SrSb_2O_6$.

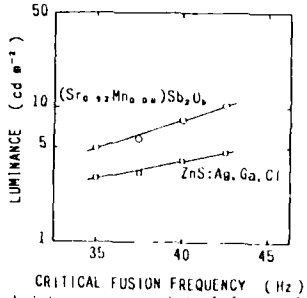


Fig.2 Screen brightness vs. critical fusion frequency of a CRT screened with $SrSb_2O_6:Mn^{2+}$.

Abstract No. 565

ENHANCEMENT OF COTHODLUMINESCENCE IN LaOBr:Tb BY CODOPING WITH Dy

Yongji Li[1], Xingron Liu[2], & Xurong Xu[3]

1.Chengdu Univ. of Science and Technology,
2.Changchun Inst. of Physics,
3.Tianjin Institute of Technology

Southern Road,Tianjin,China 300191

The cathodoluminescence of LaOBr:Tb is enhanced in 1.4 times by codoping Dy. The mechanism of this enhancement is analyzed and is attributed to crossrelaxation between Dy and Tb.

Experiment

We prepared a series of phosphors in which the concentration of ion is kept constant at 0.0075 moles and the concentration of Dy varies according to table 1.

Table1: The concentrations of Dy in different phosphors

No.	1	2	3	4	5	6	7
Dy	0	0.001	0.003	0.006	0.01	0.03	0.08moles

For comparision we prepared also phosphors doped only with Dy of 0.01 moles.

we measured the cathodoluminescence of these phosphors(10kv, 1A/cm^2, 10^{-4} torr). The results show that the luminescence of LaOBr: Dy,Tb consists predominantly of the luminescence of Tb. The brightness is measured by means of a photocell calibrated to the sensitivity of human eyes with the help of a filter. This brightness is found to be enhanced in 1.4 times that of sample without Dy. When the concentration of Dy is equal to 0.01mole.

Table2: The cathodoluminescence of LaOBr: Dy,Tb for different concentrations of Dy

No.	Dy	$^5D_3$-$^7F_5$	$^5D_4$- $^7F_5$	Brightness
1	0.000	0.30	0.48	330
2	0.001	0.25	0.51	355
3	0.003	0.16	0.52	370
4	0.006	0.10	0.53	460
5	0.01	0.06	0.64	470
6	0.03	0.015	0.32	105
7	0.08	0.00	0.11	70

The enhancement is clearly due to the doping of Dy. But the luminescence of Dy itself is not large enough to produce such an enhancement. Is there any transfer of energy from Dy to Tb? For this purpose we measured the spectrum of excitation by monitoring the luminescence of Tb. No excitation of Dy is observed. So that neither the luminescence of Dy itself nor the energy transfer from Dy to Tb is responsible for the enhancement of brightness. The effect of doping with Dy is to change the relative intensity of different lines in the luminescence of Tb. To clarify the reason of this enhancement we measured the decay of photoluminescence. The results are listed in table 3.

* *

References:

(1) Futan Zhao et al. J. Electrochem. Soc. 134, 3181, 1988

(2) Lou Shuyi J. Beijing Univ. 4, 51, 1981

Table 3 Decay time of photoluminescence under 265nm excitation

No.	Dy(mole)	$^5D_3$-$^7F_4$ (μs)	$^5D_4$-$^7F_5$ (μs)
1	0.0	230	1280
2	0.001	221	1250
3	0.003	176	1240
4	0.006	166	1200
5	0.01	71	1200
6	0.03	10	720
7	0.08	7.2	500

By comparison of these results with that given in table 2, we can draw the conclusion of exis-tence of concentration quenching in the region of Dy concentration from 0.01 to 0.03 moles.

Discussion

The crystal is belonging to tetragonal system. The dopants Dy or Tb substitutes La ions. An analysis of the distance of a luminescent center from the neighboring dopants shows that the mo-del of a three dimensional and homogene-ously distributed dopants for treating the problem of energy transfer is reasonable.

Because the concentration of Dy and Tb are no so large, we use expression for decay curve.

$$F(t) = \exp\left[-\frac{t}{\tau_0} - \left(\frac{C}{C_0}\right)\Gamma\left(1-\frac{3}{S}\right)\left(\frac{t}{\tau_0}\right)^{\frac{3}{S}}\right]$$

where τ_0 is the decay time of Tb luminescence without the doping of Dy, Γ is Gamma function, C is the concentration of Dy ions, C_0 is the critical concentration. By fitting to the experimental data, we find that s equals to 6. (cf. figure).

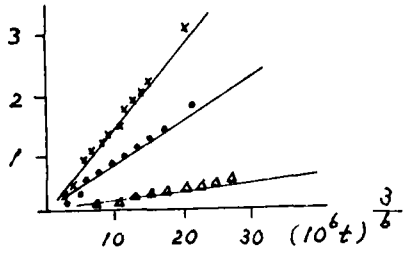


Fig. Fitting of calculated decay curve to ex-perimental data for dipole-dipole interaction

Conclusion

The cathodoluminescence of LaOBr:Tb may be enhanced in 1.4 times by codoping with Dy. This enhancement is attributed to the energy transfer from Tb and Dy in the form of crossre-laxation. This crossrelaxation is of a chara-cter of dipole- dipole interaction. And this energy transfer process transforms the light in the region of violet-blue into that of gre-en. So that the brightness is increased. The critical distance of crossrelaxation is deter-mined as 10 Å.

* *

(3) M.Inkuti et al.J.Ch.Phys.43,1[illegible]8,1965

Abstract No. 566

Terbium-Activated Yttrium Silicate as a Lamp Phosphor

T.E.Peters, R.B.Hunt and R.G.Pappalardo
GTE Laboratories Inc., Waltham, MA
and
F.Taubner
GTE Products Corp., Danvers, MA

Terbium activated yttrium silicate, Y_2SiO_5:Tb, is a refractory luminescent material that has demonstrated excellent performance in CRT applications, particularly those involving high drive currents (1,2). A cerium co-activated version of this phosphor was also proposed for use in fluorescent lighting (3), but it failed to gain commercial acceptance because of its poor 'lehr' resistance, and the cost associated with its high activator concentration (16.4w/o). Recently, we prepared Y_2SiO_5:Tb phosphors with substantially reduced terbium content, that nevertheless equalled or exceeded the performance requirements for the green-emitting phosphors used in fluorescent lighting and in reprographic applications.

The poor lumen maintenance of orthosilicate phosphors prepared with fluoride mineralization (Fig 1) prompted the search for an alternate synthesis route. Sol-gel syntheses, using alkoxide raw materials soluble in organic solvents, were evaluated and abandoned because of handling difficulties and high reagent costs. As an alternative, we developed a pseudo sol-gel technique, in which a phosphor precursor in a clear gel or powder form, was prepared from $Y(NO_3)_3$ or $Y(OH)_3$ and silicic acid. In the preferred synthesis route, the dried gel or precursor powder was reacted at 1700-1800°C in 95% N_2- H_2 for 2-4 hours to form the finished product.

Excitation and diffuse reflectance spectra for our standard formulation, $Y_{1.85}Tb_{0.15}SiO_5$ are presented in Fig. 2. The mercury emission line at 254nm intersects the intense terbium excitation band ($4f \rightarrow 5d$ transition) at ≈80% of its peak height. In plaque tests, however, this material already has a brightness of 93% relative to the CAT phosphor, in spite of a 254nm reflectance as high as 25% (Fig.3). From the foregoing, and the reported values of the quantum efficiency and reflectance at 254nm for CAT (4), i.e. $q = 80\%$ and $r = 8.0\%$, we estimate the quantum efficiency of our silicates to be ≈95%.

We believe that the high U.V. reflectivity of the Y_2SiO_5:Tb, in combination with the excitation geometry, is responsible for the observations of Table I, wherein the silicate phosphor exhibits progressive increase in brightness (relative to CAT), as the measurements are performed on plaques, on plaques inserted in a 'demountable' lamp, and in monochrome 40W, T-12 lamps. This trend is explained as follows: the UV radiation not absorbed by the phosphor in a plaque brightness test is irretrievably lost, while in a regular, fully-coated lamp the reflected UV radiation can be re-directed to the phosphor layer. Finally, in the case of the phosphor plaques inserted in a demountable lamp, the probability of utilization by the phosphor of the reflected UV radiation is intermediate to that of the two extreme cases already discussed

The actual performance of the Y_2SiO_5:Tb in various types of 40W, T-12 lamps, is summarized in Tables II to V.

In Table II, we present data for Y_2SiO_5:Tb and three different versions of CAT in single-component lamps. The silicate is seen to closely match the performance of the CAT phosphors, except for a somewhat higher powder weight for the former, which can be corrected by particle size control.

Table III lists tri-phosphor blend formulations for ≈3000°K lamps employing, respectively, Y_2SiO_5:Tb and CAT as the green-emitting component. In view of its higher UV reflectance, the fraction of the silicate phosphor in the blend had to be increased in order to obtain the target color. The overall cost of the phosphor blend, however, is essentially unchanged, because of the compensating decrease in the fraction of the expensive red-emitting component. As shown in Table IV, the performance characteristics of lamps employing the two tricolor blends are identical.

Although the color coordinates of the single-coat lamps are identical (Table iV), some yet unexplained effects are observed in two-layer lamps. When a tricolor blend is overlayed to a halophosphate base coat, the two-coat lamp exhibits different x-y values and a lower CRI (Table V). A tentative explanation is that in the latter case a higher proportion of the UV radiation reflected by the tricolor blend is absorbed by the lower CRI halophosphate base coat, thereby lowering the overall CRI of the lamp.

Finally, from Table VI it can be concluded that the performance of Y_2SiO_5:Tb matches that of CAT, even under the high-load conditions obtaining in T8/HO/45° aperture lamps.

References

(1) T.E. Peters, J. Electrochem. Soc. **116,** 985(1969).
(2) V.D. Meyer and F.C. Palilla, J. Electrochem. Soc. **116,** 535,(1969).
(3) M. Watanabe, K. Terashima, Y. Kimura and T. Nishimura, Abstract 225, Spring Meeting Electrochem. Soc May (1979).
(4) J.M.P.J. Verstegen, D. Radielovic, and L.E Vrenken, J. Electrochem. Soc. **121,** 1627(1974).

DEMOUNTABLE LAMP PERFORMANCE OF TWO YTTRIUM ORTHOSILICATES SHOWING THE EFFECT OF SYNTHESIS TECHNIQUE

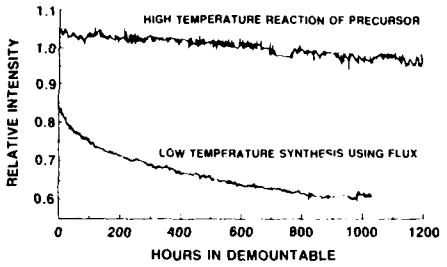


Fig. 1

EXCITATION OF 545 nm EMISSION (SOLID CURVE) AND REFLECTANCE (DASHED CURVE) FOR $Y_2SiO:Tb$

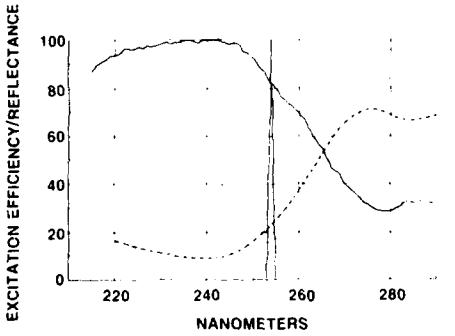


Fig. 2

Table I

Phosphor Brightness and Excitation Conditions

(Relative to CAT)

Type Meas.	Brightness % 0 Hrs.	Brightness % 100 Hrs.
Plaque	86.0	---
Demountable	93.1	91.6
40W T-12	100.2	100.4

Table II

Single-component Lamp Test Results

Material	Coating Density	Powder Weight	Color coord x	Color coord y	Lumens at hours Zero	100	500	1000
$Y_{1.85}Tb_{0.15}SiO_5$	78.2	7.51	0.309	0.554	4824	4482	4418	4386
CAT 5%Tb	78.7	5.55	0.298	0.567	4634	4486		
CAT 5%Tb	78.8	5.28	0.298	0.564	4597	4442		
CAT 7%Tb	78.9	6.79	0.294	0.576	4903	4782	4663	4643

Material	Coating Density	Powder Weight	Color coord x	Color coord y	% Maintenance 0-100 H	100-500	100-1000
$Y_{1.85}Tb_{0.15}SiO_5$	78.2	7.51	0.309	0.554	98.9	98.6	98.8
CAT 5%Tb	78.7	5.55	0.298	0.567	98.8		
CAT 5%Tb	78.8	5.28	0.298	0.564	98.6		
CAT 7%Tb	78.9	6.79	0.294	0.576	97.6	97.5	97.1

Table III

Tricolor Blend Formulations for ≈ 3000 K lamp.

Blend Type	Blue emitt. %		Green emitt. %		Red emitt. %	
Standard	BMA	11.7%	CAT	28.9%	YOE	59.4%
Silicate	BMA	8.0%	YSIL	55.8%	YOE	36.4%

BMA = $BaMg_2Al_{16}O_{27}$:Eu
YOE = Y_2O_3:Eu

Table IV Tricolor Blend ... Single Coat Lamps

Type	Optic Dens	Powd Wt	0 HRS Lumens	100 H Lumens	Maint %	X	Y	C(T)	CRI
CAT	79.0	5.01	3368	3241	96.2	0.417	0.381	2970	83.5
YSII	78.5	4.89	3333	3215	96.5	0.417	0.380	2971	84.8

Table V Tricolor Blend .... Skin Coat Over 'Halo' Lamps

Type	Optic Dens	Powd Wt	0 HRS Lumens	100 H Lumens	Maint %	X	Y	C(T)	CRI
CAT	78.0	5.66 / 75	3295	3150	95.6	0.396	0.377	3596	75.1
YSII	78.1	5.63 / 73	3326	3181	95.6	0.391	0.381	3749	70.5

Table VI T8/HO/45° Aperture Lamps

Type	Optic. Dens.	Powd. Wt.	Detect. Resp. 1 Hr	Detect. Resp. 100 Hr	Maint. %
CAT	79.6	2.03	140.1	138.9	99.1
YSII	79.0	1.96	140.0	139.1	99.4

Abstract No. 567

LUMINESCENCE FROM RARE-EARTH CRYPTATES

G. Blasse
Physics Laboratory, University of Utrecht
P.O. Box 80.000, 3508 TA Utrecht, The Netherlands

and

N. Sabbatini
Departimento di Chimica "G.Ciamician" dell'Universitá
40126 Bologna, Italy

Luminescent ions in non-molecular solids can usually be described as ions in interaction with the immediate surroundings, i.e. as ions in a cage. It is therefore interesting to compare their luminescence with that of ions in cryptates. A cryptate consists of an ion encapsulated in a molecule which offers a hole in its molecular construction [1]. Such a molecule is called a cryptand. Figure 1 shows an example. In this paper we restrict ourselves to luminescent rare-earth ions as the encapsulated metal ion.

The $[Eu^{3+} \subset 2.2.1]$ cryptate (compare fig.1) has a low luminescence efficiency due to the predominance of nonradiative transitions because of the low-lying charge-transfer state and high-frequency vibrations in the surroundings (H_2O) [2]. Comparable phenomena are known in the solid state [2]. The efficiency of the luminescence can be increased by shifting the opposite-parity state to higher energies (Sm^{3+}, Tb^{3+}, Gd^{3+}) and increasing the energy gap (Tb^{3+}, Gd^{3+}).

In $[Ce^{3+} \subset 2.2.1]$ cryptate the emission is broad-band type, viz. a d → f transition. The quantum efficiency is very high, because the Ce^{3+} ion fits exactly in the cage. Consequently, relaxation in the excited state is restricted, i.e. the Stokes shift is very small. This fits an important criterium in the design of luminescent materials.

Due to the weak relaxation in the $[Ce^{3+} \subset 2.2.1]$ cryptate the excited ion remains reasonably in resonance with its neighbours at ~ 10 Å in the surrounding cages, so that energy migration over the Ce^{3+} ions can be observed [3]. This runs parallel with considerations on concentration quenching in solid systems.

In the cryptates mentioned above excitation is into the central metal ion. It is also possible to excite in the cryptand and to study energy transfer to the rare-earth ion. In the Eu^{3+}-hexaaza complex (see fig.2) energy transfer occurs, but with low efficiency [4]. Figure 3 gives the relative rates. Nonradiative decay in the ligand (the cryptand) dominates. Also here an interesting comparison with non-molecular systems can be made.

However, energy transfer from a cryptand to rare-earth ions can also be highly efficient [5]. This has been observed for the $[Ln^{3+} \subset$ bpy.bpy.bpy] cryptates with Ln = Tb and Eu (fig.4). The situation tends to become complicated because not only bpy → Ln^{3+} transfer occurs, but also Ln^{3+} → bpy back transfer (for Tb^{3+}) and migration among the cryptands. However, there is a close parallel with the luminescence properties of vanadates. This comparison leads to a better understanding of quenching by electron transfer [6], a phenomenon which has also been observed for the cryptates in solution [7].

References

1. J.M. Lehn, Acc. Chem. Res. 11, 49 (1978)
2. G. Blasse, M. Buijs and N. Sabbatini, Chem. Phys. Lett. 124, 538 (1986)
3. G. Blasse, G.J. Dirksen, N. Sabbatini and S. Perathoner, Inorg. Chim. Acta 133, 167 (1987)
4. N. Sabbatini, L. De Cola, L.M. Vallerino and G. Blasse, J. Chem. Phys. 91, 4681 (1987)
5. G. Blasse, G.J. Dirksen, D. van der Voort, N. Sabbatini, S. Perathoner, J.M. Lehn and B. Alpha, Chem. Phys. Lett. and J. Phys. Chem. (1988), in press
6. G. Blasse and N. Sabbatini, Mat. Chem. Phys. 16, 237 (1987)
7. N. Sabbatini, S. Perathoner, G. Lattanzi, S. Dellonte and V. Balzani, Inorg. Chem., in press

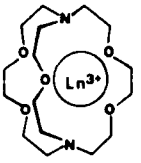


Fig.1. $[Ln^{3+} \subset 2.2.1.]$ cryptate

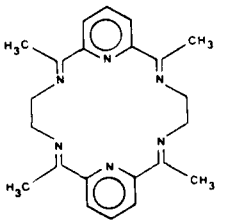


Fig.2. Schematic representation of the $C_{22}H_{26}N_6$ hxaaza macrocyclic ligand

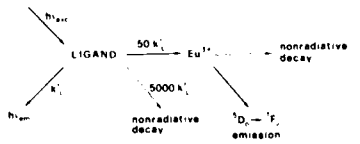


Fig.3. Radiative and nonradiative rates in the Eu^{3+} hexaaza complex at 300K

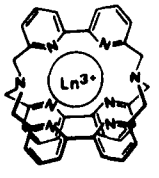


Fig.4. Eu^{3+} or Tb^{3+} bpy.bpy.bpy cryptates

Abstract No. 568

Temperature Dependence of the Vibronic Spectrum and Life Time of $LiGa_5O_8:Mn^{4+}$

T.Abritta and R.J.M. da Fonseca

Instituto de Física - UFRJ, 21945, Rio de Janeiro, RJ, Brazil.

The luminescence of Mn^{4+} ions as impurities in a single crystal of $LiGa_5O_8$ presents, at 15K, a sharp zero-phonon line at 721.6nm due to the $^2E \rightarrow {}^4A_2$ electronic transition associated to a d^3 system in an octahedrally coordinated site. This zero-phonon line is accompanied by a set of sidebands (see Fig. 1). Comparing the energies of the sidebands relatively to the zero-phonon line we could identify most of them as infra-red or Raman modes of the host (1,2). As the temperature is increased the intensity of the sidebands increases relatively to the zero- phonon line, with a decrease of the sharpness of their peaks. At room temperature the zero-phonon line is barely resolved and the emission is dominated by a broad band with its maximum at about 720.0nm (3). In this report we have examined these facts measuring the decay times between 15 K and 450 K, above wich he have the luminescence extinction . The decay time for this temperature range is characterized by a single exponential. The decay rate presents two trends. First we have a gradual rise until temperatures about 300K. Above this temperature there is a rapid increase with the temperature (see Fig.2). The gradual increase of the decay rate can be understood on the basis that the radiative transition is dominated by the vibronic sidebands process. Hence the radiative decay rate $f_r(T)$ should vary with temperature as (4).

$$f_r(T) = f_r(0) \sum_i A_i \coth\left(\frac{\hbar\omega_i}{2KT}\right)$$

Where the ω_i's are the phonon frequencies and $\sum_i A_i$ gives the intensity ratio of the sidebands to the zero-phonon line at low temperatures. Taking the representative phonon modes whose frequencies and A_i values are suggested by the shape of the sideband we calculate a curve that increases slowly wich fits our experimental data for temperatures lower than 300 K. For higher temperatures we have used the observed fact with non radiative transition in rare-earth-doped crystals where one expects that the highest energy phonons will dominate the non radiative process (5).In our high temperature data we could obtain a reasonably fit considering 25 phonons with an energy of $546cm^{-1}$ in order to cross the $13858\ cm^{-1}$ energy gap between the ^2E and $^4A_2$ levels.

The whole fit of the experimental decay rate data is shown in Figure 2, for a $f_r(0)$ corresponding to a decay time of 284μs, the experimental value for low temperatures.

References

(1) V.G.Keramides, B.A. DeAngelis and W.B. White, J.Sol.St.Chem. 15 (1975) 223.

(2) C.McShera, P.J.Colleran, T.J.Glynn, G. F. Imbusch and J.P.Remeika, J. Lumin. 28 (1983) 41.

(3) T.Abritta, N.V.Vugman, F.de S. Barros and N.T.Melamed, J. Lumin.31/32 (1984) 2el.

(4) M.O.Henry, J.P. Larkin and G.F.Imbusch, Phys. Rev. B 13 (1976) 1893.

(5) L.A.Riseberg and M.J.Weber, Solid Stat. Comm. 9 (1971) 791.

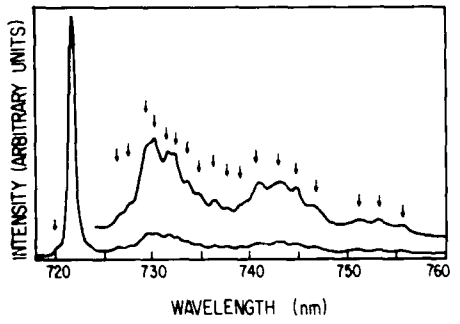


Figure 1 - The 15 K luminescence spectrum of $LiGa_5O_8:Mn^{4+}$

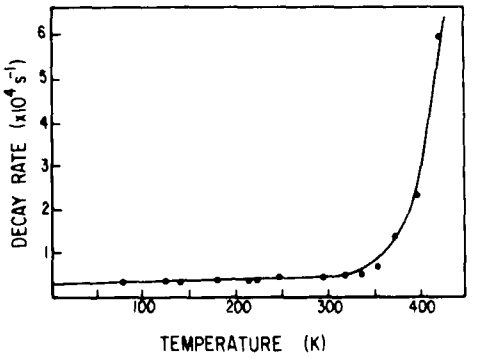


Figure 2 - The temperature dependence of the luminescence decay rate of $LiGa_5O_8:Mn^{4+}$. The points give the measured values. The continuous curve shows the theoretical fit.

Abstract No. 569

ENERGY TRANSFER PROCESS IN ALKALINE EARTH RARE EARTH PENTABORATE PHOSPHORS

R.Jagannathan and R.P.Rao
Central Electrochemical Research Institute
Karaikudi-623006, India

and

T.R.N.Kutty
Indian Institute of Science
Bangalore-560 012, India.

Phosphors based on rare earth borates prove to be efficient in terms of saturated confined emission, wall-load factor, stability against radiation damage, etc. These are made possible due to their rigid 3-dimensional network constituted by B-O atoms. Rare earth borates based on Gd such as ortho borates (e.g. $GdBO_3$), metaborates (e.g. $Gd(BO_2)_3$) and pentaborates (e.g. $GdMgB_5O_{10}$) have practical applications in gas discharge lamps, display panels [1], etc. $GdMgB_5O_{10}$:Ce,Tb also finds wide use as a green component in trichromatic lamps [2] for its lower concentrations of Tb compared to other Ce,Tb doped phosphors.

Number of samples of alkaline earth (M^{2+}) rare earth (Ln^{3+}) pentaborate phosphors have been prepared by varying the composition of M^{2+}, sensitizer (S^2 type, Bi or $4f^{k-1}$ 5d, Ce) and Tb as an activator. Suitable proportions of starting materials such as Gd_2O_3, Tb_4O_7, H_3BO_3 and MCO_3 (where M = Mg, Ca, Sr, Ba) are mixed homogeniously and fired for 2 hours betwen 1000-1200°C after prefiring at 300°C for 2-4 hours. The X-ray diffraction analysis show the formation of pentaborate. Excitation and emission spectra have been recorded with the help of fluorescence spectrophotometer (Hitachi 650-10S) with 150W Xenon lamp as exciting source.

Excitation spectra of these samples exhibit the corresponding lines of Gd at 275 nm ($^8S \rightarrow ^6P$) and 311 nm ($^8S \rightarrow ^6I$) and a well defined band due to the sensitizer (Bi or Ce). Efficient energy transfer may be accomplished by various modes such as

i) sensitizer --> activator
ii) sensitizer --> $(Gd^{3+})_n$ --> activator
iii) charge transfer band/$(Gd^{3+})_n$ and/or --> activator

It has been found that when the composition of M^{2+} content is altered, CTB and/or sensitizer band(s) could be resolved and appeared as distinct bands which enclose Gd^{3+} lines as well, as shown in Fig.1 Also it has been observed that various modes of energy transfer lead to only one kind of Tb^{3+} emission. Appearance of satellite lines due to other transitions (other than predominant $^5D_4 \rightarrow {}^7F_J$) are modified due to cross relaxation from higher $^5D_3 \rightarrow {}^5D_4$ states. Quenching of emission attributed to concentration effects and modification of the lattice and various transitions due to Tb^{3+} are discussed.

References

1. B.Saubat, C.Fouassier and P.Hagenmuller, Mater. Res. Bull. 16 (1981) 193.

2. B.M.J.Smets. Mater. Chem. and Phys. 16 (1987) 283.

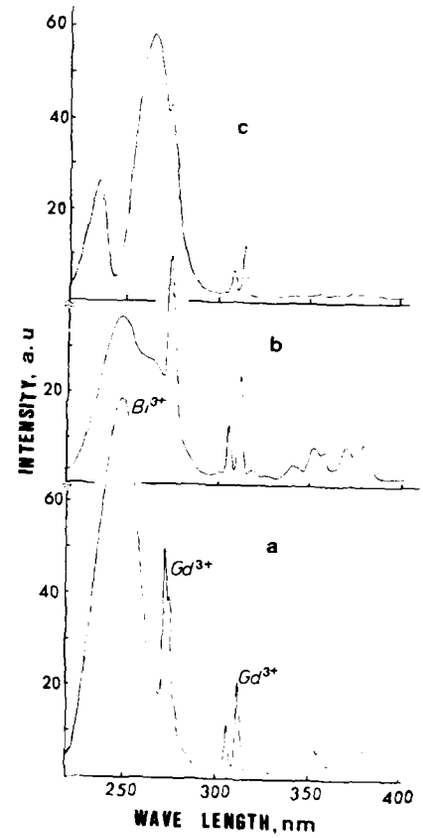


Fig.1 Excitation spectra at room temperature (300K) in the UV region of Tb^{3+} emission (542 nm) in
(a) $GdBO_3$:Bi(1m%), Tb(1m%)
(b) $GdMgB_5O_{10}$:Bi(1m%), Tb(1m%) and
(c) $GdBaB_5O_{10}$:Bi(1m%), Tb(1m%).

Abstract No. 570

ENERGY TRANSFER BETWEEN Pb^{2+} AND Gd^{3+}

H.S. Kiliaan and G. Blasse
Physics Laboratory, University of Utrecht
P.O. Box 80.000, 3508 TA Utrecht, The Netherlands

The sensitization of the luminescence of gadolinium compounds by the Pb^{2+} ion can be performed in three different ways, viz. by introduction of Pb^{2+} in Gd^{3+} compounds (which requires charge compensation influencing the Pb^{2+} luminescence), by introduction of Pb^{2+} and Gd^{3+} in alkaline earth compounds, or by introduction of Pb^{2+} in mixed alkaline earth gadolinium compounds. The three possibilities are evaluated [1,2].

The first possibility is studied in gadolinium borates. It is not very successful, since the Pb^{2+} luminescence shows a large Stokes shift. This results in a vanishing transfer rate and a low thermal quenching temperature. However, for $GdMgB_5O_{10}$ the results do not seem too discouraging [3].

The second possibility was recently reported in the literature [4]. Although the sensitization can be efficient, the transfer to activators is not, since the Gd^{3+} concentration cannot be taken high enough.

The third possibility is the most promising in order to obtain efficient luminescent materials. In the sulvtite system $(Ba,Gd)_4(P,Si)O_4$ this is not yet the case. In the oxyapatite $Sr_2Gd_8(SiO_4)_6O_2$, however, the situation is optimal for efficient luminescence if Pb^{2+} occupies the 4f site. The transfer Pb^{2+}-Gd^{3+}-Tb^{3+} (see fig.1) occurs with high efficiency. Part of the Pb^{2+} ions occupy the 6h site which is out of resonance with the Gd^{3+} emitting level. If the Tb^{3+} concentration is not too low, the total quantum efficiency is nevertheless high due to direct $Pb^{2+}(6h) \rightarrow Tb^{3+}$ transfer. The Mn^{2+} ion is also an efficient activator in this lattice.

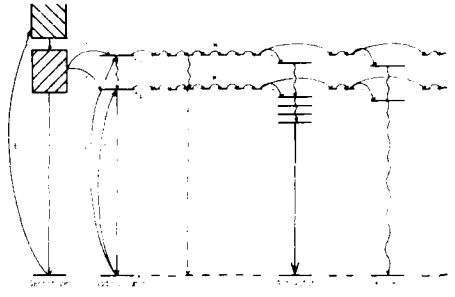


Figure 1
Energy transfer processes in gadolinium compounds

References

1. H.S. Kiliaan, Thesis, University of Utrecht, 1988
2. H.S. Kiliaan and G. Blasse, J. Electrochem. Soc., to be published
3. Shen Chonghui and Hao Zhiran, J. Luminescence, in press
4. W. Tews, P. Becker, G. Herzog and G. Kürzlor, Z. Physik. Chem. (Leipzig) 268, 985 (1987)

Abstract No. 571

LUMINESCENCE AND ENERGY MIGRATION IN $(Sr,Eu)B_4O_7$

A. Meijerink, J. Nuyten and G. Blasse
Physics Laboratory, University of Utrecht
P.O. Box 80.000, 3508 TA UTrecht, The Netherlands

Strontium tetraborate activated with Eu^{2+} is known to be an efficient luminescent material at room temperature, with an emission band at 367 nm [1]. In this abstract the luminescence properties of Eu^{2+} and the energy migration over the Eu^{2+} sublattice between 4.2 K and 298 K in $(Sr,Eu)B_4O_7$ are reported. The Eu^{2+} sublattice in this borate is two-dimensional with Eu-Eu distances of 4.3 Å in the ac plane and 6 Å between the planes.

At 4.2 K the Eu^{2+} ion, which is isoelectronic with Gd^{3+}, shows line emission at 363.2 nm due to the $4f^7(^6P_{7/2}) \rightarrow 4f^7(^8S_{7/2})$ transition. At the low energy side of this emission line, well resolved vibrational structure is observed between 100 cm^{-1} and 1200 cm^{-1}. This fine structure is due to coupling of the electronic transition with vibrational lattice modes, and stretching and bending modes of the borate groups. The excitation spectrum shows at least two $4f^7(^8S_{7/2}) \rightarrow 4f^65d$ transitions, in which the splitting of the $4f^6$ configuration in the excited state into seven ^7F levels can be observed.

Increasing the temperature leads to thermal population of the higher $4f^7(^6P_{7/2})$ levels. The maximum of four $4f^7(^6P_{7/2})$ emission lines has been observed. The barycentre of the $4f^7(^6P_{7/2})$ level has been calculated to be 27,586 cm^{-1}, which is relatively low. At temperatures above 25 K, the $4f^65d \rightarrow 4f^7(^8S_{7/2})$ emission band can be observed. It has its maximum at 367 nm and a small zero phonon line at 361.5 nm. The relative intensity of this band increases exponentially with temperature. Above 100 K the line emission has nearly vanished.

The thermal population of the $4f^65d$ level has a marked influence on the decay time of the Eu^{2+} emission. At 4.2 K the decay time of the parity forbidden transition within the $4f^7$ configuration is 440 μs. It decreases to 2.6 μs at room temperature for the parity allowed $4f^65d \rightarrow 4f^7(^8S_{7/2})$ transition. The energy difference between the $4f^7(^6P_{7/2})$ level and the $4f^65d$ level has been determined by fitting the temperature dependence of the decay time to a three level model. This yielded a value of 100 cm^{-1}. The spectroscopically determined energy difference between the lowest $4f^7(^6P_{7/2})$ line and the $4f^65d$ zero phonon line is 130 cm^{-1}. The latter value is probably more accurate, since in this case no interference of higher $4f^7(^6P_{7/2})$ is involved. The difference in energy between the two excited states of Eu^{2+} is the smallest reported up to now. Due to this small difference in energy, efficient mixing of the $4f^7(^6P_{7/2})$ state and the $4f^65d$ state occurs, which explains the low position of the barycentre of the $4f^7(^6P_{7/2})$ level and the short radiative decaytime of the parity forbidden $4f^7(^6P_{7/2}) \rightarrow 4f^7(^8S_{7/2})$ transition.

Concentration quenching in $Sr_{1-x}Eu_xB_4O_7$ (x = 0.001 to 1) has been studied at 4.2 K as well as at 298 K. In contradiction to what is normally observed, the quenching is more pronounced at 4.2 K. At temperatures below 25 K energy migration occurs over the $4f^7(^6P_{7/2})$ level of the Eu^{2+} ions. In view of the two dimensional character of the Eu^{2+} sublattice, the decay curves of the Eu^{2+} emission in the concentrated system EuB_4O_7 were analyzed using a random walk model for two-dimensional energy migration [2]:

$$I(t) = I(0) * \exp(-t/\tau_0 - \beta * t^{\frac{1}{2}}) \qquad (1)$$

where β depends on the acceptor concentration and the donor-donor transfer probability. At 4.2 K a value of 270 $s^{-\frac{1}{2}}$ has been found for β. With an estimated acceptor concentration of 10^{-4} a value of 10^7 s^{-1} for the rate of energy transfer between two nearest Eu^{2+}-neighbors has been calculated. This is in good agreement with the transfer rates found for energy transfer between nearest Gd^{3+}-neighbors at approximately 4 Å [3], which is to be expected in view of the similarity in the electronic configuration.

The energy migration at room temperature occurs via the $4f^65d$ excited state. A large critical distance for energy transfer between Eu^{2+} ions of 25 Å has been calculated. Although energy transfer over a large distance is possible, the energy migration over the Eu^{2+} sublattice does not lead to strong concentration quenching. An explanation for this observation is that in view of the large radiative decay rate and the large transfer rate, there are very few efficient acceptors, for which the trapping rate is large in comparison with the radiative decay rate and the transfer rate. This is confirmed by fitting the experimental decay curve of the Eu^{2+} emission in EuB_4O_7 at room temperature to the Yokota-Tanimoto formula, which describes the evolution of the emission intensity in the case of three-dimensional diffusion limited energy transfer [4]. A very low acceptor concentration in combination with a high value for the donor-acceptor interaction parameter gave the best fit.

In conclusion, the luminescence properties of Eu^{2+} in SrB_4O_7 can be explained by an energy level scheme for Eu^{2+} in which the $4f^65d$ excited state is only slightly higher in energy than the lowest $4f^7(^6P_{7/2})$ excited state. Energy migration over the $4f^7(^6P_{7/2})$ level of Eu^{2+} has been observed. Analysis of the decay curves of the Eu^{2+} emission in EuB_4O_7 shows that at 4.2 K the migration has a two-dimensional character and that the transfer rate for energy transfer between nearest neighbors is about 10^7 s^{-1}, which is in agreement with values found for energy transfer between nearest Gd^{3+} neighbors.

References

1. K. Machida, G. Adachi and J. Shiokawa, J. Luminescence 21 (1979), 101.
2. J. Klafter, G. Zumofen and A. Blumen, J. Physique Lett. 45 (1984) 49.
3. H.S. Kiliaan, A. Meijerink and G. Blasse, J. Luminescence 35 (1986) 155.
4. M. Yokota and I. Tanimoto, J. Phys. Soc. Japan 22 (1967) 779.

Abstract No. 572

ENERGY TRANSFER EFFECTS IN BETA"-ALUMINA

L.A. Momoda, J.D. Barrie, B. Dunn
and *O.M. Stafsudd
Department of Materials Science
and Engineering
*Department of Electrical Engineering
University of California, Los Angeles
Los Angeles, CA 90024 USA

β"-alumina ($Na_{1+x}Mg_xAl_{11-x}O_{17}$) is a well known solid electrolyte which has recently shown considerable promise as an optical host material. Its ion exchange properties offer a unique method for incorporating lanthanide ions into an oxide material. Through ion exchange techniques, the material is doped after the crystal growth process. Consequently, problems such as compositional inhomogeneities, valence instabilities and strain formation which are commonly induced by traditional crystal growth techniques are avoided. The low temperature ion exchange process has been used to synthesize optical quality β"-alumina crystals containing many of the lanthanide ions, including Nd^{+3}. Previous work has shown that single crystals of Nd^{3}-β"-alumina exhibit laser action at 1.06 μm [1,2].

We have now developed techniques for exchanging two lanthanide ions simultaneously into the β"-alumina structure. The dopants are homogeneously distributed throughout the crystal and the relative ratios of the ions are easily controlled by the composition of the ion exchange melt. This new synthesis approach has enabled us to observe energy transfer in β"-alumina crystals doped with Ce^{+3}-Nd^{+3} and Ce^{+3}-Tb^{+3} couples. The use of ion exchange allows us to investigate the effect of varying sensitizer-to-activator concentration ratios on the transfer processes.

The occurrence of energy transfer between Ce^{+3} and Nd^{+3} in β"-alumina is evident from the excitation spectrum of the 870 nm emission band of Nd^{+3} (Figure 1). The excitation spectrum of the Ce^{+3}-Nd^{+3} crystals has an additional broad excitation band characteristic of Ce^{+3}. Furthermore, evidence of radiative transfer is seen in this system. Distinct minima are observed in the Ce^{+3} emission band of the mixed crystal and the position of the minima correspond directly with the absorption bands of Nd^{+3}.

The transfer efficiency of $Ce^{+3} \rightarrow Nd^{+3}$ as a function of the sensitizer-to-activator ratio was investigated. It was found that by sufficiently decreasing this ratio, transfer efficiencies on the order of 90% could be measured. An increase of intercationic distances between the sensitizer and activator was also achieved by reducing the total amount of trivalent lanthanide ions in the crystal. Preliminary studies show that energy transfer between the two species can be eliminated by increasing the intercationic distance to approximately 10Å.

Similar studies were conducted on the Ce^{+3}-Tb^{+3} couple in β"-alumina. Evidence of energy transfer in this system can be seen by the appearance of an additional broad band in the excitation spectrum of the 540 nm emission band of Tb^{+3}. Consequently, the presence of Ce^{+3} was found to enhance the excitation of Tb^{+3} in the region where the weaker 4f-4f transitions are present. As was found in the Ce^{+3}-Nd^{+3} system, high transfer efficiencies could also be achieved between the Ce^{+3} and Tb^{+3} ions by decreasing the Ce^{+3} to Tb^{+3} ion concentration ratio.

β"-alumina crystals containing a mixture of Yb^{+3} and Er^{+3} ions were also synthesized. The occurrence of up-conversion was investigated by exciting each crystal at 970 nm. This wavelength coincides with the absorption band of Yb^{+3} in β"-alumina. In these crystals, emission bands in the green and red region of the spectrum were detected from near-infrared excitation. These results indicate the presence of up-conversion processes in β"-alumina.

REFERENCES

[1] M. Jansen, A.J. Alfrey, O.M. Stafsudd, D.L. Yang, B. Dunn and G.C. Farrington, Optics Letters, 9 (1984) 119.

[2] B. Dunn, J.O. Thomas and G. C. Farrington, " Beta"-Alumina: A Solid Electrolyte As A Solid-State Laser Host " in Spectral Properties of Solid State Laser Type Materials, ed. B. Di Bartolo, Plenum Press, New York (1986).

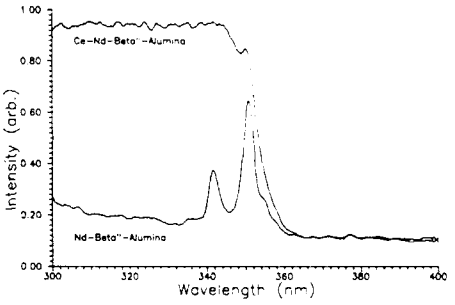


Figure 1. The excitation spectrum of the 870 nm emission from Ce^{+3}-Nd^{+3}-β"-alumina and Nd^{+3}-β"-alumina.

Abstract No. 573

STUDIES OF THE FIELD DEPENDENT PHOTOLUMINESCENCE OF n-GaAs ELECTRODES WITH AND WITHOUT COBALT FILMS

S.M. Ahmed*, J. Leduc and J. Frudel

Canada Centre for Mineral and Energy Technology,
Mineral Sciences Laboratories
555 Booth St., Ottawa, Ont. K1A 0G1, Canada

Introduction

Studies of photoluminescence (PL) and electroluminescence (EL) of semiconductor (Sc) electrodes in photoelectrochemical (PEC) cells are complementary techniques that can provide information on many basic surface and interface processes such as hole (h^+) injection, $e^- - h^+$ recombination either directly or via surface states in competetion to photooxidation and photoelectron transfer processes. These processes determine photon conversion efficiencies and photodissolution or stability of the electrode. Earlier studies have shown that PL due to bulk $e^- - h^+$ recombination in n-GaAs electrodes follow a 'dead layer' model (1). For photoanodically oxidized surfaces of GaP, Nakato et al (2) have reported PL bursts during a cathodic sweep, just past the flat band potential (fbp). This was attributed to recombination involving the trapped photoholes between the GaP surface and the oxide layer. These photoholes are precursors to photodissolution and other photoelectron transfer processes. However, a detailed mechanism of de-trapping the trapped photoholes is far from clear.

In the present work, a comprehensive study of the bulk and surface PL due to trapped photoholes, if any, was made on n-GaAs with and without a 10 nm thick cobalt film. In a previous study (3) it was shown that a thin Co film deposited on n-GaAs prevented the latter from photodissolution. Effects of band bending, sweep rate and presence of ferro/ferricyanide redox couple on the PL have also been investigated.

Experimental

A photoelectrochemical cell, consisting of an n-GaAs (iii face) working electrode, platinum-counter electrode and a saturated calomel reference electrode, was used under potentiostatic conditions. The indifferent electrolyte was K_2SO_4 at pH 9.2 in nitrogen atmosphere. The GaAs surface was etched with an acidified H_2O_2 solution. A c.w. He-Ne laser beam at 633 nm, chopped at 890 Hz, was used for excitation and the PL spectrum was recorded with a Jarrell-Ash monochromator coupled to a photomultiplier tube, using a lock-in technique. A 10 nm thick cobalt film was deposited on the GaAs as described earlier (3). Effects of ferro/ferricyanide, band bending (applied voltage) and sweep rate were investigated at a fixed wave length of 853 nm (PL peak). The fbp of GaAs at pH 9.2 was determined from the Mott-Schottky plots of the inverse measured capacitance vs potential.

Results and Discussion

Photoluminescence results when photogenerated holes recombine with electrons (e^-) in the conduction band. Figure 1a shows the PL spectrum at -1.2 V SCE or 0.4 eV upward band bending (fbp = -1.6 V SCE at pH 9.2).

The peak observed at 1.45 eV (853 nm) for the silicon doped sample of GaAs, with a carrier concentration of $3.5 \times 10^{18} cm^{-3}$, is assigned to band-to-band (tail) transitions. The deviation of the peak position from the standard value of 1.43 eV (= 867 nm) to 1.45 eV, is attributed to carrier concentration $>10 \times 10^{18} cm^{-3}$. At 300°K, free electrons rather than the deep levels of the conduction band tail are involved in the recombination process.

The ferro/ferricyanide couple had no effect on this PL (due to bulk recombination) as shown in Fig. 1b and no EL due to hole injection by the ferricyanide could be detected at pH 9.2. At this pH, the E° for the redox couple lies in the mid-gap position and no EL is expected.

The effect of band bending (field) on PL is shown in Figs. 1c, 2a and 2b. The PL intensity is high when the bands are bent down (Fig. 2a) and decays exponentially as the bands are bent up gradually as electrons and holes are separated by the application of an electric field in the reverse direction, with the photoholes accumulating at the surface. This PL is attributed to bulk recombination, and fits a "dead layer" model. If the electrode is held under photoanodic conditions for some time to allow oxidation of the surface to take place by the photoholes according as:

$$GaAs + nh^+ + n0H^- \rightarrow GaAs(OH)_n \text{ or } [GaAs(O^-)_n + nH^+] \quad (1)$$

and the field is subsequently reversed in the forward direction, then a burst of PL is observed (Fig. 2b) at -0.4V past the fbp (cathodic) i.e., after a downward band bending of 0.4 eV. The photoinduced surface states lie at 0.4 eV below the conduction band edge (bands bent up) and have been reported (4-6) to result in an increase of photocapacitance. The PL burst (Fig. 2b) itself occurs as a result of the photoexcited electrons (e^{-*}) being captured in the reduction of the surface oxide in competetion to the electrochemical transfer of electrons from the conduction band (c.b) (7) according to Eqns 2 and 3, while the photoholes combine with $e^-_{c.b}$.

$$GaAs(OH)_n + H^+ + e^-/e^{-*} \rightarrow GaAs(OH)_{n-1} + H_2O \quad (2)$$

$$GaAs(OH)_{n-1} \xrightarrow{ne^-/ne^{-*}} GaAs(\cdot)n \quad \text{in steps.} \quad (3)$$

Further reduction of GaAs surface to hydride is reported to occur by hole injection in the conduction band (8).

The trapping/detrapping of photoholes and hence the PL can be modulated, resulting in one or more PL peaks by using different rates of potential sweep. Ferro/ferricyanide is found to enhance the PL due to surface recombination involving detrapped holes while the cobalt film suppresses it. The surface deposited cobalt probably serves to capture the surface trapped photoholes by donating its two 4s electrons and possibly a 3d electron, thus reducing the PL (Fig. 3a and 3b) and also preventing photooxidation and dissolution of the surface. Alternatively, cobalt may "kill" the visible PL by promoting non-radiative or ir-radiative recombination of the $e^- - h^+$ pairs by introducing deep 3-d impurity centers in the surface.

References

1. Hobson, W.S. and Ellis, A.B., *J. Appl. Phys., 54*, 5956 (1983).

2. Nakato, Y., Morita, K. and Tsubomura, H., *J. Phys. Chem., 90*, 2718 (1986).

3. Ahmed, S.M., Leduc, J. and Haller, S.F. *Extended Abs. #85, Electrochem. Soc.* Fall Meeting, Oct. 1985 (Las Vegas) p.515; to be submitted to J. Electrochem Soc.

4. Vanmaekelbergh, D., Gomes, W.P. and Cardon, F. *Ber.Bunsenges. Phys. Chem., 89*, 987 and 994 (1985).

5. Wolf, B. and Lorenz, W., *Electrochimica Acta, 28*, 699 (1983).

6. Allongue, P. and Cachet, H., *J. Electrochem. Soc., 132*, 45 (1985) and references therein.

7. Gerischer, H. and Mattes, I.Z., *Physik. Chem. Neue Folge, 49*, 112 (1966).

8. Benard, D.J. and Handler, P. *Surface Science, 40*, 141 (1973)

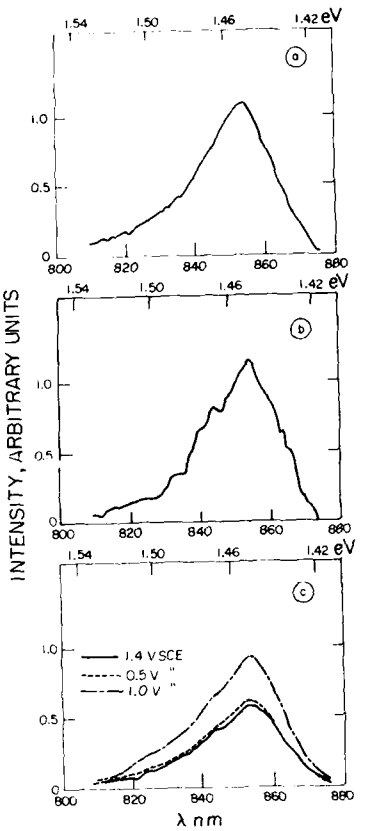


Fig. 1: PL spectra of n GaAs at fixed potential; (a) 0.5 M K_2SO_4 solution, pH 9.2, V = -1.2 V SCE, etched surface; (b) same kind of electrode but in 0.4 M (ferro + ferri) cyanide; (c) n GaAs electrode covered with a 10 nm sintered Co film. Solution, same as in "a". Data corrected for glare and instrumental response.

See next column

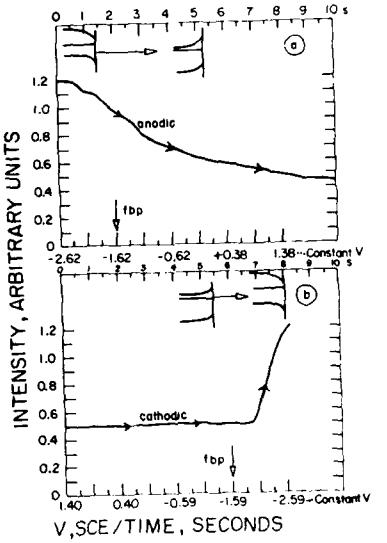


Fig. 2(a),(b)

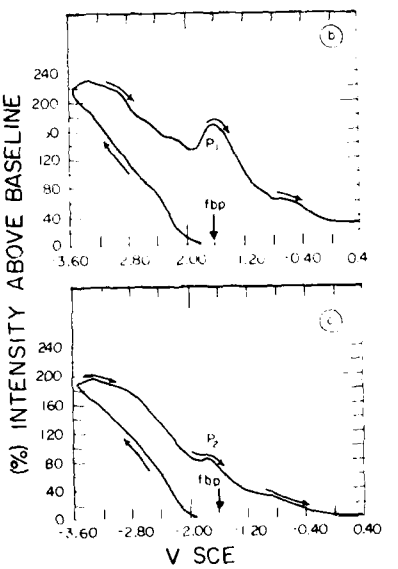


Fig. 2: PL intensity variation at 853 nm as a function of time or voltage (SCE) when a single voltage ramp is applied. (a) cathodic to anodic (reverse) direction (b) anodic to cathodic (forward) direction. Data not corrected for glare. 0.5 M K_2SO_4, pH 9.2. Sweep rate 500 mV/s.

Fig. 3: PL intensity variation with voltage in an inert electrolyte (K_2SO_4) at 853 nm, when a triangular sweep is applied at 500 mV/s. (a) n-GaAs bare surface, (b) n-GaAs with a 10 nm Co film (sintered).

Abstract No. 574

A Comparative Study of Photoluminescence and Selective Pair Luminescence in GaAs

J. R. Cavins, Y. K. Yeo, and R. L. Hengehold
Air Force Institute of Technology
Wright-Patterson Air Force Base, Ohio 45433

The technique of low temperature photoluminescence (PL) has been widely used for characterizing impurities and defects in semiconductors. Application of this method is relatively straightforward and capable of producing excellent results if samples are of good quality. The PL method does, however, have some limitations in the detection and identification of impurities, especially in the case of somewhat less perfect crystals.

As an alternative to the use of PL for characterizing impurities in semiconductors, one can use the method of selective pair luminescence (SPL), a method which has been developed relatively recently. Whereas in the PL technique, an above-band gap laser energy is used to excite electrons from the valence band to the conduction band, in the SPL technique, a tunable, below-band gap laser energy is used to selectively excite the donor-acceptor pairs of interest. SPL thus allows the precise determination of the energy difference between the acceptor ground state and its excited states and can be used to identify different impurities. SPL usually can provide an unambiguous identification of the acceptors, and furthermore it is capable of doing this even in less perfect crystals.

In the present work, both PL and SPL measurements have been made on liquid-encapsulated Czochralski (LEC) bulk-grown undoped GaAs, horizontal Bridgman (HB) bulk-grown Cr-doped semi-insulating (SI) GaAs, and an undoped vapor-phase epitaxial (VPE) layer of GaAs grown on a Cr-doped SI GaAs substrate. Measurements were made as a function of pump laser energy, excitation laser intensity, and sample temperature, and the results have been compared with each other.

Photoluminescence measurements were made at 4.2 K by immersing the samples in liquid helium. The photoluminescence was excited by either the 5145 Å line or 4880 Å line from an argon-ion laser. The selective pair luminescence measurements were made at 2 K by immersing the samples in liquid helium and then pumping on the helium. The samples were mounted on the cold finger in a strain free manner. The below-band gap excitation was provided by a tunable dye laser pumped by an argon-ion laser. The emission spectra were analyzed using a 3/4-meter Czerny-Turner spectrometer, and detected with a cooled RCA 31034A photomultiplier tube.

The results show that the SPL technique is very sensitive, and capable of identifying acceptor impurities which cannot possibly be resolved or even detected by the PL method. From the LEC sample, only C and Si impurities were identified through PL, but Zn was also detected as an additional impurity using SPL. For the Cr-doped SI GaAs, PL was unable to identify any specific impurities, but SPL confirmed that Zn and Si were the major impurities. For the VPE GaAs, PL showed Zn was the dominant impurity with a small amount of C and Ge present, whereas SPL showed not only the presence of Zn, but also that of Mg and Si impurities.

These results clearly show that the SPL technique provides for very sensitive, unambiguous acceptor identification compared to the PL technique. It is, however, not without its limitations. For example, in some cases SPL will fail to show the presence of impurities seen in PL. A case in point is the presence of Ge and C in the VPE sample seen in PL but not in SPL at an excitation energy of 1.5112 eV. One might conclude that SPL and PL techniques can be complementary and used together to produce a more complete picture.

In the SPL spectra, the positions of the luminescence peaks are found to be nearly independent of the excitation laser intensity for a change in laser intensity of two orders of magnitude as long as the excitation energy remains the same. However, as the intensity increases, the SPL peaks become less sharp. On the other hand, in the PL spectra, as the excitation intensity increases, the D-A pair transition lines shift to higher luminescence energies and an appreciable narrowing of the emission band occurs.

Although the optimum SPL spectra are obtainable at the lowest temperature of 2 K, a considerable amount of SPL intensity can still be obtained even at temperatures as high as 10 K. In this regard, the general temperature dependent behavior of SPL is very similar to that of PL. Thus the temperature restrictions upon the observable SPL are not as critical as has been generally anticipated. However, in the SPL spectra, the positions of the luminescence peaks are nearly independent of sample temperature as long as the excitation energy is the same, whereas in the PL spectra, the D-A pair transition lines shift to higher luminescence energies as the sample temperature increases.

As far as dependence on excitation laser energy is concerned, it is found that the structure of the SPL spectra is very sensitive to the pump laser energy. Furthermore, some impurities can be easily observable at certain excitation energies and not be visible at other excitation energies. Thus, selection of the pump laser excitation energy is very important to finding an optimum signal for a given species. In other words, the great advantages of the SPL method can not be realized unless the SPL signals are optimized.

In summary, the SPL technique can provide in most cases an unambiguous impurity identification far better than the standard PL method. In this paper, the SPL technique has been applied to several samples of GaAs and the various experimentally observed excited states of C, Mg, Zn, Si, and Ge acceptors are reported.

Abstract No. 575

ELECTROLUMINESCENCE SPECTRA OF CdSe/ZnTe HETEROJUNCTION

Shawqi AL-DALLAL

Dept. of Physics, University of Bahrain

P.O. Box 1082, Manama, BAHRAIN

EXTENDED ASBSTRACT

Thin films of undoped or indium doped CdSe were deposited on undoped, phosphorous or oxgen doped substrates of ZnTe using a sublimation technique [1]. The photoluminescence (PL) spectra of CdSe and ZnTe were recorded and compared with the electroluminescence (EL) spectra obtained for the heterojunction in the same range of temperature.

A green emission was obtained for CdSe/ZnTe heterojunctions with either undoped or phosphorous doped ZnTe substrate. For undoped substrates, the electroluminescence (EL) spectrum consists of several peaks situated approximately at 2.28, 2.31 and 2.35eV. The position of the peaks was found to be dependent on the excitation current and temperature. The transitions involved are attributed to native or residual defects [2]. The (EL) spectrum obtained for heterojunctions with phosphorous doped substrates consists of a non phononic (A) transition centered approximately at 2.33eV and a second transition (B) appearing at higher energies (2.36eV). The (A) transition is attributed to the recombination of conduction band electrons with holes at an acceptor level, whereas the (B) transition is attributed to electrons at a donner level recombining with holes at the valence band [3].

A red emission was obtained for heterojunctions with oxygen doped ZnTe substrates. The emission consists of a transition at 1.986eV followed by a series of phononic replicas, at 26meV intervals, appearing at lower energies. This spectrum is identical to the photoluminescence (PL) spectrum we have obtained for oxygen doped ZnTe and is quite different from the PL spectrum recorded for the CdSe layer. As a conclusion, good agreement was obtained between the EL spectra of the CdSe/ZnTe heterojunction and the PL of the ZnTe substrate indicating that carrier injection is taking place in ZnTe.

Red emission was also obtained for heterojunctions with undoped or phosphorous doped ZnTe substrate. For these samples, the electroluminescence spectrum consists of two bands at 1.93eV and 1.65eV. The higher energy band is relatively close to that due to that due to oxygen in ZnTe. However, the PL spectrum of the ZnTe substrates is in the green region of the spectrum. Therefore, we exclude the possibility that the observed emission band is due to oxygen. On the other hand, the energitic position of this band is higher than the energy gap of CdSe. Therefore, injection of carriers in CdSe is also excluded. If the evaporation period is sufficiently long and the processing temperature is relatively high, the diffusion of impurities, zinc and selenium from either sides of the junction could result in the formation of an intermediate high resistive layer of $CdZn_xSe_{1-x}$. This result was confirmed by SIMS analysis. Consequently, the observed emission at 1.93eV could be attributed to the radiative recombination of carriers in an intermediate region. The 1.93eV transition was not observed in the PL spectra of either the CdSe layer or the ZnTe substrate. A possible explanation is that the above band arises also from radiative transitions in an intermediate region.

REFERENCES

Al-DALLAL S., Phys. Sol. (a) 44, 183 (1977).

[illegible], Conf. of the Electr. Mat. Committee of Met. Soc. AIME, San Francisco, U.S.A. (1971).

AKKAD F. and GHAZALI A., Cryst. Latt. Def. Vol. 6, 155 (1975).

Abstract No. 576

SILENT DISCHARGE LUMINESCENT effect AND INTRINSIC ELECTROLUMINESCENCE

Wu Chou-jen
Department of Physics, Shansi Teachers' University, Linfen, Shansi. China

Wu En-curie and Wen Sheng-ming
Department of Physics, Shansi Education College, Taiyuan, Shansi. China

1. INTRODUCTION

Although intrinsic electroluminescence (EL) has been known for more than half a century. Papers on the subject has shown that former existing theoretical models cannot treat satisfactorily all the features of EL phenomena, and still seem rather crude and need frequent revision as new experimental facts appear.

By observation with microscope, the EL light emission usually in form of alternating pulsating lines, some of which have the form of double comets fleeing each other are actually one unit. The dark interspace in the center shortens with increasing voltage and lengthens with increasing high frequency of the applied voltage. Illumination of the lines with spots of ultraviolet quenches the EL. The mysterious phenomena can indeed exist, but what causes have never been thoroughly revealed.

2. CAUSE OF LIGHT EMISSION

Recently several authors confirmed that EL particles contain numerous round voids and long hollow channels which can be treated as luminescent resonant cavities[2] at which the internal surfaces are deposited with transparent copper sulfide and especially with acicular conducting occlusions which may act as light-emitting sources. Most of them are lack of tips at which cannot be able to make light emission but act as capacitors. Since the potential is much higher at the tips of the occlusions, one would expect that the light is emitted at the tips only.

Suppose the cavity is energized in the applied voltage with suitable resonant frequency and may produce a high voltage by which the spots or striations of EL light emission can be found at the tips of acicular conducting occlusions or along the directions of electric fields. This is a relevant testimony that the cause of EL light emission is closely associated with silent discharge in the cavity.

3. SILENT DISCHARGE LUMINESCENT effect

It is obvious that the silent discharge luminescent effect and the observed shape have been found to depend upon both of the magnitude of the exciting voltage for the cavity and the frequency of the applied voltage. As to the observation phenomena, there are a few which are sufficiently important to require to be mention here.

1. The influence of exciting voltage

If the voltage, except very high frequency, is applied across the EL condenser, this gives rise to a exciting voltage just enough to produce silent discharge at the tips of the occlusions or along the directions of electric fields and remain for light generation with striations or beetle spots, it is easily distinguished by violet colour in the dielectric with air bubbles[3], so that a collinear double-comet line can be seen, of course, including the deviation of observation, with increasing of the voltage. Shown as figure 1.

2. The influence of frequency

It can be seen not only that the tails of the two comets would shorten with weakening the action of silent discharge as decreasing exciting voltage; but also that the tails of two comets would shorten with weakening the action of silent discharge and decreasing exciting voltage simultaneously as increasing frequency of the exciting voltage.

If an external voltage is $U = U_m \sin \omega t$ as shown in Figure 2. The essential results can be derived as follows:

(1) $f_{C\max} = f_0\sqrt{1-1/2q^2} < f_0$; $f_{L\max} = \sqrt{1-1/q^2}\, f_0 > f_0$

where: f_0 is the resonant frequency.

q is the quality factor of the circuit

The max-value of the voltages are

(2) $U_{C\max} = \frac{qU}{\sqrt{1-1/4Q^2}} > qU$; $U_{L\max} = \frac{qU}{\sqrt{1-1/4q^2}} > qU$

Figure 3 is the $U_R(f)$ curve drawn by the following equation

(3) $U_R = IR = \frac{qU}{\sqrt{\frac{1}{q^2} + (wL - 1/w)^2}}$

It is obvious that as $1/2q^2 < 1$, or $q > 1/\sqrt{2}$ the $U_{L\max}$ can occur above resonant frequency f_0 the $U_{C\max}$ can occur below resonant frequency f_0. Meanwhile $U_{L\max} = U_{C\max} = qU\sqrt{1-1/4q^2}$. Then, yielding

$$U_{L\max} = U_{C\max} > U_{C0} = U_{L0} = qU.$$

Figure 4 is shown the curves of $U_L(f)$, $U_R(f)$ and $U_C(f)$ as $q=1$. At resonance, $U_{L0} = U_{C0} = qU = U_{R0}$, can be seen that Figure 4 is compared with figure 3, or derived from calculation, the more q-value is increased, the better both of $f(U_{L\max})$ and $f(U_{C\max})$ approach to resonant frequency f_0. Conversely more apart.

Figure 5 illustrates $f(U_{L\max})$ and $f(U_{C\max})$ are imaginary values as $q < 1/\sqrt{2}$. It is obvious that the U_L and U_C in the frequency range from zero to infinit cannot be able to obtain maximum value. At resonance, $U_{L0} = U_{C0} = qU < U$.

It is ascertained that the silent discharge and double-comet lines would fade away simultaneously as very high frequency exciting voltage, say above 30 megacycle, impressed on the EL condenser.

4. ULTRAVIOLET QUENCHING EL

Any adjacent space at the tips can be energized by the illumination of ultraviolet at which the potential would be decreased by the influence of ion cloud, so that the light-emitting point is quenched or the dark discharge may produce at the tips.

5. CONCLUSION

It is possible that this paper contains a grain of truth which can explain some simple phenomena successfully. It may lead on to explaining the important cause of EL deterioration and to calculating the life of EL device and it will be of importance for preparation of EL material.

References

1) G. Larach, (ed.), Photoelectronic Materials and Devices. P.2-7) (1965).

2) Wu Chou-jen et al, Cavity and Electrical Effect, J. Lumin., [illegible]

3) G. Destriau, New Phenomena of Electro-photoluminescence, Philosophical Mag. Vol. 38, P.700 (1947).

4) Wuli Tongxun Physics Monthly 1, P.1 (1).

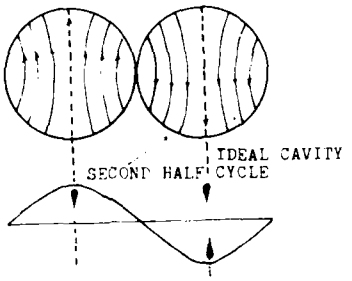


Figure 1. Collinear double-comet line

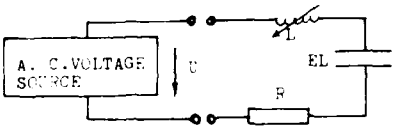


Figure 2.

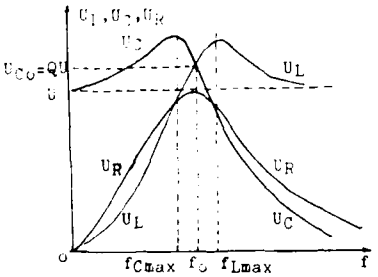


Figure 3. $Q > 1/\sqrt{2}$

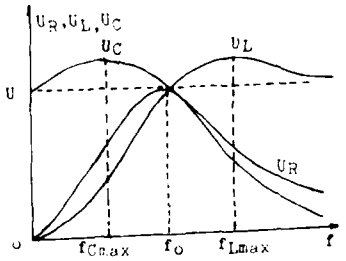


Figure 4. $Q = 1$

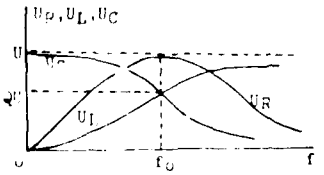


Figure 5. $Q < 1/\sqrt{2}$

Abstract No. 577

SUN-POWERED ENAMEL ELECTROLUMINESCENT DISPLAY

Wu Chou-jen
Department of Physics, Shansi Teachers' University, Linfen, Shansi. China

Wen Sheng-ming and Wu En-curie
Department of Physics, Shansi Education College, Taiyuan, Shansi. China

1. INTRODUCTION

This paper relates to a novel sun-powered enamel-type electroluminescent (EL) display device with variable emission colours which, in combination with arrays of sil-icon solar cells, a thermomagnetic element, a set of Ag-Zn accumulators and an electrical timer-inverter, can be automatically played an important role as a safety signal in the country-side railway junction. The complete block system in series as shown in Figure 1.

2. CONSTRUCTION AND OPERATION

Unit A is an enamel-type EL display device with variable emission colours on both surfaces wherein a layer of EL material ZnS:Mn- or ZnS:Er-film which is fired or deposited between two electrodes, one of them being semi-transparent emission; both electrodes having a high reflection coefficient and emission wavelength with a given colour. The interference relationship is given by the following expression

$$2dn \times \cos\beta = (m + (\theta_1 + \theta_2)/2\pi)\lambda$$

where[1]: d is the thickness of ZnS:Mn-film, n is the refletion index, β is the viewing angle of the output emission, m is the interference order, λ is the emission wavelength, θ_1, and θ_2 are the phase jumps occuring when the emission is reflected from the electrodes. It is obvious that by a small variation of the EL film thickness d, one can obtain a colour change from green (5500Å) orange (5650Å)to red (6400Å). Therefore a green or red signal on both surfaces of the enamel-type EL display device can occur a definite position in the railway junction.

Unit B consists of an electrical timer-inverter and a set of small Ag-Zn accumulators in high capacity. The brightness level and the time in need of unit A in the railway junction can be exactly controlled by the timer-inverter. The power is supplied by the Ag-Zn accumulator which can be charged by the silicon solar cells.

Unit C, a group of silicon solar cells are distributed on a thin panel which is coupled with a thermomagnetic element. Each cell appears a rectangular wafer about 0.05 cm. thick usual 1 cm. x 2 cm. in size, power output in in general depends on the number of series / parallel cells used, here is considered to be combined with Ag-Zn accumulators; The thermomagnetic element has a long-shaped piece magnet is pivoted to rotate within a plastic ring which, a ferrite can be used, is coated with a low-curie temperature rare-earth metal gadolinium powder coating (T_c = 294K)[2]as shown in Figure 2. (heat sink not drawn). This ring has a permeability that falls with temperature. It also exibits a low-curie temperature at which permeability reaches unity. The magnet can rest in any position when the ring's temperature is uniform. During the sun-light strikes on the ring shown as arrows, the area S becomes non-magnetic, therefore the magnet rotates to the position shown. It is obvious that the panel of silicon solar cells is fixed together with the magnet to be rotated with its surface towards the sun.

3. CONCLUSION

This sun-powered enamel-type EL display device with variable emission colours, in combination with the important unit C, has great reliability indefinite life expectancy in operation; It can be used not only in the railway junction and in any other traffic road junction, but also can be used in high altitude and man-made satellite.

References:
1). N. A. Vlasenko, Display. July 1964.
2). Hans Toftlund, Am. J. Phys. Jan.1967. pp.46-49.
3). Siegfried R. Hoh, Radio-Electronics. 36 (1965) 109.

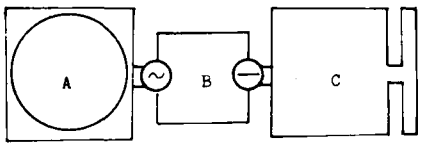


Figure 1.

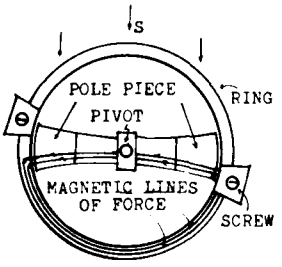


Figure 2. The thermomagnetic element

Abstract No. 578

Random Alloy Effects for Fe in GaAsP

Pin Hong, Qisheng Huang
Radio-Electronics Dept. Beijing Polytechnic Univ. Beijing, China

Abstract

The III-V ternary alloys have been proven to be the extremely exciting technological materials in luminescence, laser and microelectronic devices. Recently, increasing attention has been paid to the deep centers in these alloys since their main electronic properties vary continously with their compositions. We report here on the investigations of the random alloy effects on Fe-accepter center in GaAsP for a large range of composition.

Iron is one of the most frequent 3d contaminants in III-V compounds. It is known that, in GaAs and GaP, iron introduces rather deep centers and the measurements of optical and thermal emissions of Fe center correspond to the hole transition $Fe^{3+} \rightarrow Fe^{2+}$ according to the experimental results of ESR, optical absorption, photoluminescence and DLTS, etc. GaAsP is the alloy of GaAs and GaP. In GaAsP, Fe deep centers have more complicated properties.

Samples used here were p+n diodes. The GaAsP layers were grown by MOVPE and the iron impurity concentrations were selected in the range of $N_{Fe}/N_D \sim 0.05$. The composition x of each sample was measured by microprobe analysis in a scanning electron microscope with uncertainty less than $\pm 2\%$.

The experiments show that, for Fe centers in GaAsP, the thermal transient capacitance curves are nonexponential. We fit these nonexponential thermal transient capacitance curves and DLTS with the model of deep level Gauss broadening caused by the alloy disorder effect and obtain: (1) the thermal emission rates of hole for central level after broadening and their temperature dependence $e^t_{po}(T)$, (2) the level Gauss broadening widths which their relation with compositions $B(x)$ is consistent with theoretical prediction of $\sqrt{x(1-x)}$. From Arrhenius plot " $e^t_{po}/T^2 \sim 1/T$ ", the thermal enthalpy changes on composition dependence $H_p(x)$ during hole transition were determined. It is found that $H_p(x)$ are distinctly different from the Gibbs free energy changes $G_p(x)$ obtained by the potocapacitance transient method. Values of $H_p(x)$ decrease at first and then increase with increasing compositions.

By calculating the entropy changes during hole transition $S_p(x)$, it is known, for x=0 and x=1, the acceptor states of Fe-center are antibonding, but for $0<x<1$, the bonding states are changed. Using the values of $H_p(x)$ and $S_p(x)$, our further calculation shows, there is the evidence for lattice relaxation induced by alloy disorder.

Abstract No. 579

A Leddicon target sensitive in the 1000-2000nm waveband.

G P Hopkins and D G Swain

E.E.V. Co. Ltd.

106 Waterhouse Lane
Chelmsford Essex
England UK

It has been known for many years that the addition of sulphur to a lead oxide photoconductor extends the spectral response from the intrinsic long wave limit of 650nm into the red and infra red regions (Ref 1). Previous attempts to produce an infra red Vidicon device working beyond 1000nm and very recently up to 27000nm (Ref 2) without target cooling have been fraught with problems of high dark current, poor shading, blemishes and general instability.

This paper describes our efforts to develop a Leddicon type of target (Ref 3) achieving high sensitivity between 1000 and 2000nm while maintaining low dark current, low lag and acceptably good shading and stability. The performance of the target which is now commercially available in 1 inch and $\frac{2}{3}$ inch tube sizes (Ref 4) depends on the target and tube processing parameters. The critical areas here are the lead oxide evaporation through a gas atmosphere followed by partial sulphurisation and the formation of a semi-blocking contact; for which proprietary techniques have been developed.

A shift in the intrinsic PbO bandgap energy from 1.9eV down to 0.8 - 0.6eV gives rise to the extended spectral response as indicated from the measured absorption edges at 1400nm and 2000nm. The colour of the layer changes from yellow/orange to black. A total conversion to PbS would shift the band gap energy to 0.4eV with the absorption edge nearer 3000nm but this is undesirable since the resistivity is too low for normal Vidicon type operation. S.E.M. and X-Ray diffraction studies show that the PbO retains its platelet structure but with modifications depending on how much sulphur is introduced. For large amounts it is likely that a PbS "skin" is formed on the platelets causing a change in their size and shape throughout the depth of the layer.

Layer thickness and applied voltage are two important factors in determining the profile of the electric field within the target. High fields mean higher sensitivity and resolution but the consequent higher dark current degrades picture quality, shading and transient effects. These factors are adjusted therefore to give optimum performance and long tube life. Typical amplitude response with 45 volts applied to the target is 35% at 400TV lines with a limiting resolution of better than 600 TV lines. Dark currents are usually kept at 5 - 10nA with overall shading better than 30%. For short exposures the decay lag after 3TV fields is typically 50% of peak signal. Longer term image retention is problematical for tubes with the broadest spectral response, where extra charge trapping occurs around regions of high sulphur concentration in the layer.

There are many applications for this target/tube in small T.V. cameras. These include: active night vision, LED and laser imaging, fibre optic inspection, observation of defects in semiconductors using polarised I.R., thermal imaging at temperatures above 150°C and aerospace applications.

It is desirable to achieve greater sensitivity beyond 2000nm where there are more laser imaging applications. Here it will be necessary to improve on window and lens materials for higher transmission and M.T.F.

References

1. W Heiman, C Kunze "Infra red Physics" Vol 2 p175 1962.

2. T Kawai, K Suga, K Muramatsu, T Otaka, K Atsumi and R Nishida. "9th Symposium on Photoelectronic Image Devices" Imperial College London September 1987.

3. G P Hopkins 173rd ECS meeting Las Vegas, Nevada October 1985.

4. EEV P8029 series technical data sheet.

Abstract No. 580

AVALANCHE MULTIPLICATION OF THE PHOTO-GENERATED CARRIERS IN AMORPHOUS SEMICONDUCTOR AND ITS APPLICATION TO IMAGING DEVICES

S. ISHIOKA, Y. TAKASAKI, K. TSUJI, T. HIRAI, K. TANIOKA*, J. YAMAZAKI*, K. SHIDARA*, AND K. TAKETOSHI*

CENTRAL RESEARCH LABORATORY, HITACHI, LTD., KOKUBUNJI, TOKYO 185, JAPAN
*NHK SCIENCE AND TECHNICAL RESEARCH LABORATORIES SETAGAYA, TOKYO 157, JAPAN

Amorphous photoconductive materials have many advantages in imaging applications. Various types of imaging devices, such as SATICON ®, a-Si vidicon, and two-story solid state imager, have been introduced. Recently, we discovered a new phenomena of avalanche carrier amplification inside an amorphous layer, and confirmed that it was very effective in obtaining extremely high sensitivity in imaging devices.

Avalanche Multiplication

Figure 1 shows the structure of the sandwich-type a-Se sample used for our experiment [1]. The semi-transparent Cr is used for a light incident side electrode and Au layer for a top electrode. The very thin impurity-doped mostly Se layer was inserted between the Cr electrode and the a-Se photoconductor which has been very effective in preventing hole injection from the Cr electrode. Au/Se junction forms the electron blocking contact.

The a-Se layer is biased so the Cr electrode side becomes positive, and the sample is illuminated by the monochromatic light of 400 nm. The current-electric field characteristics for various film thickness are shown in Fig. 2(a) and (b).

The incident light is absorbed in the a-Se layer within a depth of approximately 50nm from the illuminated side. Therefore, the photocurrents shown in Fig. 2(a) correspond to the hole initiated currents, and those in Fig. 2(b) correspond to the electron initated currents. With increasing the electric field, photocurrents increase and tend to saturate to the level where the photoconductive quantum efficiency reaches almost unity. The conventional blocking-type imaging devices are operated under this condition.

It is shown that if we can apply the electric field higher than some value around 10^6 V/cm, the photocurrents rapidly increase again. The photoconductive quantum efficiency is about 40 at the field of 1.35×10^6 V/cm for the a-Se layer with 2 μm thick.

The rate of increase of the photocurrent in this region is the more rapid for the thicker a-Se layer. On the otherhand, the dark current doesn't show such an increase. These features indicate that the avalanche multiplication takes place in the a-Se layer.

Hole and Electron Ionization Rate

The hole and the electron ionization rates (β and α) have been calculated from the thickness dependence of the multiplication factor. The results are shown in Fig. 3.

Both α and β have the following exponential dependence on 1/E:

$$\alpha = 3.8 \times 10^7 \exp(-1.5 \times 10^7/E)\ cm^{-1}$$
$$\beta = 8.8 \times 10^6 \exp(-8.7 \times 10^6/E)\ cm^{-1}$$
for 1.0×10^6 V/cm $\leq E \leq 1.5 \times 10^6$ V/cm

The ionization rates of a-Se obtained here are replotted with those of typical crystalline semiconductors [2] in Fig. 4. The large ionizations in a-Se occur only at very high-electric fields, even though the band gap Eg of a-Se is smaller than that of crystalline SiC.

The ratio of the hole and electron ionization rates, $K = \beta/\alpha$, reaches about 100 in the field of 1×10^6 V/cm, several times larger than that for typical crystalline semiconductors. This result indicates the possibility of a very low noise feature in multiplication. The large ionization rate for the hole current is suitable for the vidicon application.

Application to Vidicon Tube

A blocking-type target structure for high-field operation was carefully designed for a-Se Vidicon, and avalanche mode features were examined [3]. Figure 5 shows the typical images which were reproduced by the avalanche-type a-Se Vidicon and a conventional one under the same illuminated condition. In avalanche-type a-Se Vidicon, the sensitivity as high as quantum efficiency greater than 10 were obtained, and the low noise feature with excellent uniformity were confirmed. In addition, high resolution property, which is a great advantage of a-Se Vidicon especially in a High-Definition TV System, was retained under these conditions.

References:

1. K. Tsuji, Y. Takasaki, T. Hirai, J. Yamazaki, K. Tanioka, 19th Conference on Solid State Devices and Materials, Tokyo, Japan (1987) 91

2. S. M. Sze, *Physics of Semiconductor* Devices, 2nd Ed. (John Willey and Sons) New York and London (1981)

3. K. Tanioka, J. Yamazaki, K. Shidara, K. Taketoshi, T. Kawamura, S. Ishioka, and Y. Takasaki, IEEE, Electron Device Letters, EDL-8 (1987) 392

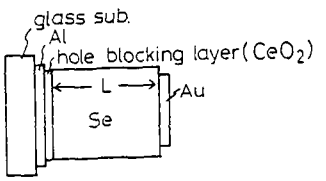


Fig. 1 Schematic view of the photocell used for measurements.

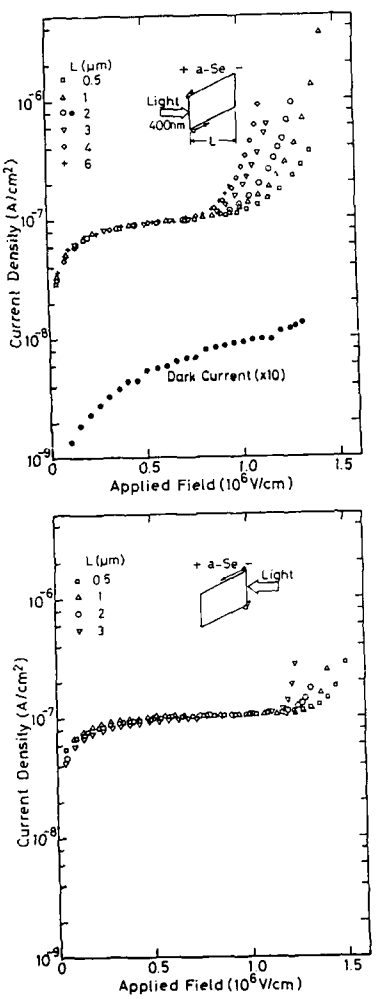


Fig. 2 Electric field dependences of (a) hole initiated photo-currents and (b) electron initiated photocurrents for different thickness(es). Broken lines show the photocurrent corresponding to the quantum efficiency unity.

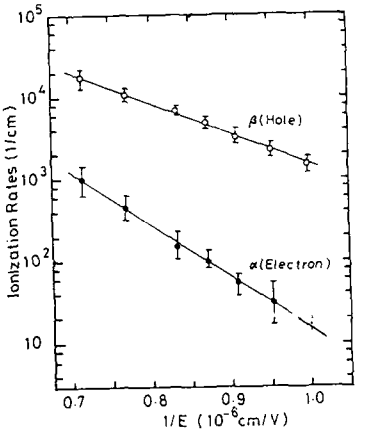


Fig. 3 The calculated carrier ionization rates in a-Se from the results of the photomultiplication measurements.

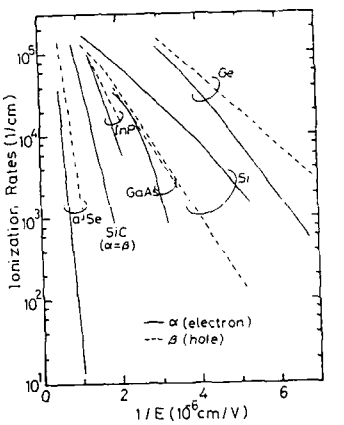


Fig. 4 Ionization rates for a-Se (present work) and some crystalline semicondutors.



Fig. 5 The reproduced images by the avalanche type a-Se vidicon (left) and a conventional image pickup tube (right). (200 lux, F4).

Abstract No. 581

THE EFFECT OF HEAVY METAL CONTAMINATION ON DEFECTS IN CCD IMAGERS; CONTAMINATION MONITORING BY SURFACE PHOTOVOLTAGE

L. Jastrzebski, R. Soydan, H. Elab*
David Sarnoff Research Center
Princeton, N. J. 08540

W. Henry, E. Savoye**
RCA NPD, Lancaster, PA.

INTRODUCTION

One of most challenging problems of VLSI technology is fabrication of large area devices free of localized defects. This is particularly important for photosensitive mosaics such as CCD imagers. The majority of point and line defects observed in CCD displays have involved a malfunction of one or more pixels. These failures could be caused by defects present in the superstructure (oxide, poly or metal) or by crystallographic defects present in the silicon substrate. The generation process of crystallographic defects is a complex function of processing conditions and silicon substrate characteristics. Heavy metals present in a processing line can influence the crystallographic defect generation process by providing nucleation sites for the generation of stacking faults. Heavy metals also affect the electric activity of these defects. Therefore, it is necessary to discuss material related defects in CCD imagers in context of heavy metal contamination present in a processing line.

In this work we will discuss the effects of heavy metal contamination on defects in CCD imagers, with an emphasis on real time monitoring with surface photovoltage of the heavy metal concentration during processing. We will also describe effects which different silicon substrates, e.g. FZ, MCZ, epi, internally gettered CZ, will have on defect generation.

EXPERIMENT

CCD imagers with a die size of about 0.7 1.1 cm^2 were fabricated using a three level-polysilicon gate process in 10 Ω cm p-type silicon substrates in the RCA Lancaster processing line. Commercially available FZ, MCZ, silicon epilayers and internally gettered CZ wafers were used. Procedures and wafer characteristics required to optimize internal gettering efficiency were described previously (1). The imager area is subdivided to two identical areas containing 320 buried channel linear CCD's each having 512 stages. Defective pixels in any of the channels can introduce blemishes in the image which result in either a high signal (white) defect by the injection of spurious charge, or a low signal (black) defect because charge is lost before it reaches the output stage. An analysis, previously described in detail (1), was carried out to identify the origin of these defects. Crystallographic defects in the imager area were revealed by selective etching (Wright and Secco) and examined using interference contrast microscopy (Nomarski). The degree of electric activity of these defects was established using EBIC technique (electron beam induced current collected by a Schottky barrier) or by measuring the amount of electrons generated at a defected pixel during the 15 msec. of CCD integration time.

Heavy metal contamination in the processing line was measured using a constant signal surface photovoltage (SPV) (2) and DLTS. These measurements were carried out on FZ controlled wafers which did not receive diffusions but otherwise were processed identically to product wafers. SPV measurements were also made at the back of the product wafers. These results were similar to data obtained for the control wafers. SPV measurements provide values of minority carrier diffusion length which are inversely proportional to the square root of heavy metal concentration. Since this method does not require any substrate preparation, and measurements are very fast, it can be used as a routine Q C tool to monitor changes in the heavy metal level in the processing line. Unfortunately SPV does not provide any identification of the heavy metals. DLTS measurements were used to identify the heavy metals. Also, additional measurements of SIMS, spark source and NTD were carried out but the contamination levels were usually below the detection limit of these methods.

RESULTS

The localized material related defects in CCD imagers were caused by precipitates, stacking faults and dislocations. As shown in Table 1, the electrical activity of these defects varied significantly. Two levels of electrical activity were usually observed for each defect type. These levels could differ by as much as two orders of magnitude. We believe that this difference is related to decoration of crystalographic defects by heavy metals. The decoration process is a strong function of heavy metal concentration in the processing line, which was measured by monitoring with SPV values of diffusion length in the FZ control wafers. Figures 1, 2 and 3 show the probability of crystallographic defect decoration (measured as a ratio between the number of electrically active and the total number of defects revealed by etching) as a function of the contamination level in the processing line. It appears that a certain contamination threshold exists beyond which the probability of decoration of the crystallographic defects dramatically increases. This threshold is different for the different silicon wafers. For an identical contamination level the probability of defect decoration is the highest for the epitaxial layers and the lowest for the internally gettered wafers. Large variations were observed for the various epi runs (compare epi 1 and epi 2). We believe that these variations are related to a difference in the heavy metal concentration introduced into silicon during the epi growth process. For an identical contamination level the probability of the decoration of stacking faults is much higher than the probability of the dislocation decoration; the contamination threshold seems to be shifted to lower contamination level.

It should be pointed out that the generation of stacking faults is also a function of heavy metal contamination in the processing line, as shown in Fig. 4, where the stacking fault density is plotted as a function of the diffusion length measured in the control FZ wafers. This result is not surprising since it is well known that heavy metal agglomerates can serve as nucleation centers for stacking faults. As in the case of the decoration this dependance is different for the different silicon wafers. The threshold for stacking fault formation is the lowest in the epi wafers. The internally gettered wafers show the highest resistance to the stacking fault formation. It should be emphasized that for some of epi runs, the stacking faults formed even when processing was carried out in the "clean" line. Under these conditions the stacking faults did not form in the FZ wafers. Large differences were observed between the FZ and MCZ wafers. This was somewhat unexpected since none of these wafers had any internal gettering. Also, no heavy metals were detected in the as-grown wafers. Mechanisms which could account for the observed differences will be discussed.

In the internally-gettered wafers the probability of the stacking fault formation is a strong function of the denuded zone depth. The reduction of the denuded zone

depth resulted in an increase in the gettering efficiency and a decrease in the probability of stacking fault generation. Also the probability of the stacking fault decoration was reduced. Although it has to be pointed out that with the reduction of the denuded zone depth the density of residual oxygen precipitates at the surface increased. Since oxygen precipitates also introduce localized defects in CCD imagers, the depth of the denuded zone in the internally gettered wafers had to be carefully adjusted to achieve effective gettering action, and at the same time to minimize the presence of oxygen precipitates in the device active region. Growth of "clean" epi (not contaminated by heavy metals during the epi growth process) on internally gettered wafers was found to be the optimum solution.

CONCLUSIONS

The role of heavy metal contamination on defect formation in CCD imagers has been reviewed. Crystallographic defects such as dislocations, stacking faults and oxygen precipitates form localized dark current generation sites when present in the space charge regions of junctions or MOS capacitors. The dark current generation rate is a function of decoration of these defects by heavy metals present in the processing line. The SPV method was successfully applied to monitor the heavy metal contamination level in the processing line. We demonstrated that a certain threshold contamination level exists beyond which the probability of crystallographic defect decoration and formation of stacking faults increases dramatically. This level is different for the different defects and the different types of silicon wafers. The epitaxial layers showed the lowest and the internally gettered wafers the highest resistance to contamination-induced defect generation and decoration. The problems with the epilayers are probably attributed to the presence of heavy metals in as-grown epi (introduced during the epi growth). The results for the internally gettered wafers depend on the depth of the denuded zone. The gettering efficiency has to be carefully balanced against residual oxygen precipitates left in the device active area.

References

1. L. Jastrzebski, et al., J. Electrochem. Soc. 134, 212, (1987).
2. A. Goodman, J. Appl. Phys. 32, 2550, (1961).
3. L. Jastrzebski, et al J. Electrochem. Soc. Meet., Chicago, Oct. 1988.

Present Addresses

* Fairchild Weston System, Schlumberger, CCD Imagers, San Jose, CA.

** MIT Lincoln Lab, Lexington, MA.

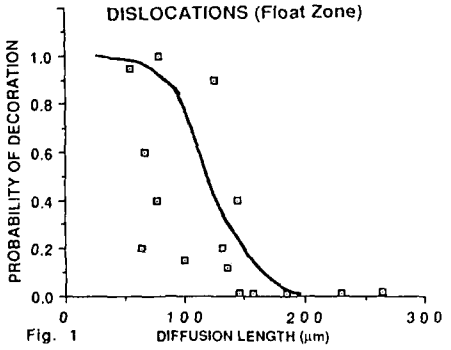


Fig. 1

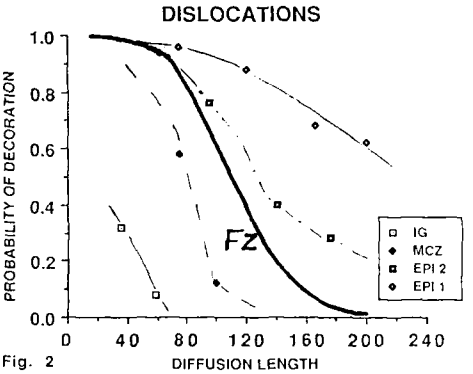


Fig. 2

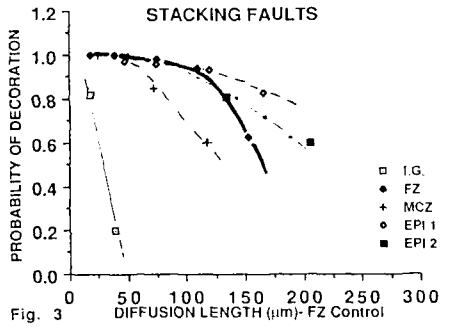


Fig. 3

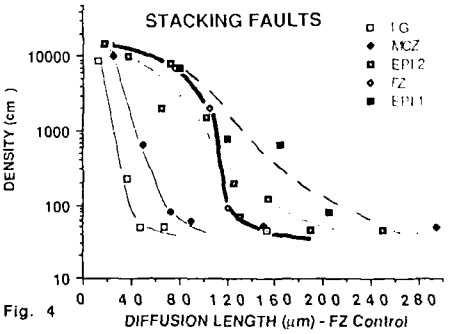


Fig. 4

TABLE I

ELECTRIC ACTIVITY OF DEFECTS

	DEC	CCD(*)	EBIC(**)
Dislocation	(+)	1×10^4	5%
	(-)	3×10^2	None
St. Fault	(+)	5×10^5	50-20%
	(-)	$\sim 10^4$	5%
OX Precipitate	(+)	5×10^4	10%
	(-)	10^3	None

(*) electron/pixel for 15 msec

(**) relative reduction in collection efficiency

Abstract No. 582

"Progress in Infrared Image Sensors with Schottky-Barrier Detectors"

Walter F. Kosonocky
New Jersey Institute of Technology
Newark, NJ 07102

Infrared image sensors with PtSi Schottky-barrier detectors (SBDs) are becoming recognized as very promising IR technology for many SWIR (1-3 μm) and MWIR (3-5 μm) applications [1-14]. These FPAs are fabricated by a well established silicon process VLSI process that assures low production cost for large volume and offers at this time the most promising IR technology for high-resolution and large-area IR imagers.

PtSi Schottky-barrier detectors (SBDs) represent the most established SBD technology for applications in the SWIR and MWIR bands at an operating temperature of about 80K [3-6, 11]. These SBDs can be designed for operation at 77K with a dark current density in the range of 1.0 to 20 nA/cm^2. Pd_2Si SBDs were developed for operation with passive cooling at 120K in the SWIR band [8]. IrSi SBDs have also been investigated to extend the application of Schottky-barrier focal plane arrays (FPAs) into the LWIR (8 to 12 μm) spectral range [9, 10, 13].

Line sensors with up to 4 x 4096 PtSi SBDs were developed for space-borne remote sensing applications in the SWIR bands [7, 8].

Very good quality thermal imaging was demonstrated with noise equivalent differential (NEΔT) of less than the 0.1 K for 160 x 244-element and 512 x 512-element staring FPAs with PtSi SBDs for operation at 30 frames/s with f/2.35 and f/1.5 optics, respectively [6, 11].

This paper reviews the progress in the development of infrared image sensors with Schottky-barrier detectors [14].

References

1. F. D. Shepherd and A. C. Yang, "Silicon Schottky Retinas for Infrared Imaging," Int. Electron Devices Meet., Tech. Dig., pp. 310-313, 1973.
2. W. F. Kosonocky, E. S. Kohn, F. V. Shallcross, D. J. Sauer, F. D. Shepherd, L. H. Skolnik, R. W. Taylor, B. R. Capone, and S. A. Roosild, "Platinum-Silicide Schottky-Barrier IR-CCD Image Sensors," Int. Conf. on Application of CCDs, pp. 2-7 - 2-38, Oct. 25-27, 1978.
3. W. F. Kosonocky, H. Elabd, H. G. Erhardt, F. V. Shallcross, G. Meray, T. S. Villani, J. V. Groppe, R. Miller, V. L. Frantz, M. J. Cantella, J. Klein, and N. Roberts, "Design and Performance of 64 x 128-element PtSi Schottky-Barrier IR-CCD Focal Plane Array," Presented at SPIE Tech. Symp. East, Arlington, VA, May 3-7, 1982.
4. M. Kimata, M. Denda, N. Yutani, N. Tsubouchi, H. Shibata, H. Kurebayashi, S. Uematsu, "A 256 x 256-Element Si Monolithic IR-CCD Imager," 1983 ISSCC Dig. Tech. Papers, pp. 254-255.
5. M. Denda, M. Kimata, N. Yutani, N. Tsubouchi, and S. Uematsu, "A PtSi Schottky-Barrier Infrared MOS Area Imager with Large Fill Factor," Presented at Int. Electron Device Meet., Washington, DC, Dec. 5-7, 1983.
6. W. F. Kosonocky, F. V. Shallcross, T. S. Villani and J. V. Groppe, "160 x 244-Element PtSi Schottky-Barrier IR-CCD Image Sensor," IEEE Trans. Electron Devices, Vol. ED-32, No. 8, pp. 1564-1573, August, 1985.
7. J. R. Tower, L. E. Pellon, B. M. McCarthy, H. Elabd, A. G. Moldovan, W. F. Kosonocky, J. E. Kalshoven, and D. Tom, "Shortwave Infrared 512 x 2 Line Sensors for Earth Resources Applications," IEEE Trans. Electron Devices, Vol. ED-32, pp. 1574-1583, August, 1985.
8. M. Denda, M. Kimata, S. Iwade, N. Yutani, T. Kondo, and N. Tsubouchi, "4 x 4096-Element SWIR Multispectral Focal Plane Array," SPIE Proc., Vol. 819-24, San Diego, CA, Aug. 18, 1987.
9. P. W. Pellegrini, A. Golubovic, C. E. Ludington, and M. M. Weeks, "IrSi Schottky-Barrier Diodes for Infrared Systems," 1982-IEDM Technical Digest, pp. 157-159, Dec. 1982.
10. N. Yutani, M. Kimata, M. Denda, S. Iwade, and N. Tsubouchi, "IrSi Schottky-Barrier Infrared Image Sensor," 1987-IEDM Technical Digest, pp. 124-127, December, 1987.
11. M. Kimata, M. Denda, N. Yutani, S. Iwade, and N. Tsubouchi, "A 512 x 512-Element PtSi Schottky-Barrier Infrared Image Sensor," IEEE J. Solid-State Circuits, Vol. SC-22, No. 6, December, 1987, pp. 1124-1129.
12. R. Aquilera, "256 x 256 Hybrid Schottky Focal Plane Arrays," SPIE Vol. 782 Infrared Sensors and Fusion, Orlando, FL, May, 1987, pp. 108-113.
13. B. Tsaur, M. M. Weeks, P. W. Pellegrini, "Pt-Ir Silicide Schottky-Barrier IR Detectors," IEEE Electron Device Letters, Vol. 9, No. 2, February, 1988, pp. 100-102.
14. W. F. Kosonocky, "Infrared Image Sensors with Schottky-Barrier Detectors," International Symposium on the Technologies for Optoelectronics, SPIE Proceeding, Vol. 869, Cannes, France, Nov. 16-20, 1987.

Abstract No. 583

NONLINEAR OPTICS AT INTERFACES

Y. R. Shen

Department of Physics
University of California
and
Materials and Chemical Sciences Division
Lawrence Berkeley Laboratory
Berkeley, California 94720

Nonlinear optical effects at interfaces are weak but are easily detectable. Second-order nonlinear optical processes, in particular, can be highly sensitive and surface-specific. They can be exploited to study surfaces and interfaces. That the techniques are extremely versatile and possess many advantages over conventional surfaces probes is now well established. Possible applications of the techniques to various disciplines can lead to many interesting new research opportunities. The recent status and progress in the field will be reviewed and future prospects will be discussed.

This work was supported by DOE under Contract No. DE-AC03-76SF00098.

Abstract No. 584

STUDIES OF LIQUID SURFACES BY SECOND HARMONIC GENERATION

Kenneth B. Eisenthal

Department of Chemistry
Columbia University
New York, N. Y. 10027

The nonlinear optical process of second harmonic generation (SHG) possesses an intrinsic sensitivity to the asymmetry present at the interface between two centrosymmetric media. This property, arising from the fact that SHG is electric-dipole forbidden in the bulk, has permitted the technique to be applied in a variety of studies of surfaces and interfaces. Among the systems that have been explored in this way are molecules adsorbed on solid surfaces, insoluble surfactant layers, liquid-liquid interfaces and, in our recent work, the surface of liquids.

In this talk we will present various aspects of our studies on equilibrium and time dependent processes at the liquid/vapor interface. In the first part we will outline how we have used second harmonic measurements to obtain information on the orientation and relative number density of solute molecules at the surfaces of aqueous solutions. A comparison with surface concentration information obtained from surface tension and microtome data will be made.

We then describe a procedure for measurement of the absolute phase of the second harmonic electric field with respect to the pump radiation, and develop a scheme for inferring the absolute orientation of molecules at an interface with respect to the directed surface normal. This new information about the sense of molecular orientation, which cannot be obtained directly from conventional linear optical spectroscopy, should help to provide insight into the basic chemical interactions at surfaces and interfaces. The principle of the method can be understood simply and is applied to aqueous phenol solutions.

Next we address the question of how the asymmetry in the forces experienced by the molecules in the interfacial region affects simple chemical equilibria. Specifically, using the technique of second harmonic generation we investigated the acid-base equilibrium between p-nitrophenol (HA) and its anion (A^-). As we will show, not only do the concentrations of the various species in the interfacial region differ from their bulk values, but also the relative concentrations do not correspond to the bulk equilibrium constant. The "equilibrium" constant in the surface region was shown to be vastly different from that in the bulk. Various aspects of these results will be discussed.

The last part of this talk deals with dynamic processes at the water/vapor interface. It will include excited state relaxation, photoisomerization and intermolecular energy transfer. A comparison with the measured of each of these processes in the bulk region of the liquid will be made.

Abstract No. 585

Measurements of the Structure and Dynamics of Thin Film Growth on Electrode Surfaces by SHG

G. L. Richmond, V. L. Shannon, D. A. Koos and J. M. Robinson
Chemical Physics Institute
University of Oregon, Eugene, OR 97403

Over the past five years, research in this laboratory has focussed on the use of optical second harmonic generation (SHG) *in probing interactions* at the solid/liquid interface. The studies have provided valuable information about the sensitivity of SHG to such phenomena as molecular and ionic adsorption at smooth *electrode surfaces, oxidative film formation*, underpotential deposition processes, oxide formation and the dynamics of adsorption.[1] More recently, our studies have focussed on the use of SHG to probe electrode surface structure and symmetry by the anisotropy in the SH response as the crystalline electrode is rotated about its surface normal. This talk will summarize our most recent results in this area for which the structure and dynamics of underpotentially deposited monolayers on crystalline metal surfaces are monitored in situ. Deposition of a monolayer or submonolayer of these foreign metals is intrinsically controlled by the change in the work function of the surface as the overlayer grows in a stepwise manner. Because of its proven sensitivity to surface structure, reconstruction and thin film growth, SHG is an attractive technique to investigate the processes occurring during lattice formation at the metal/metal interface in solution. The studies to be described here are Ag(111)/Pb, Ag(111)/Tl, Ag(110)/Tl, and Cu(111)/Tl. The results for the Ag(111)/Tl system are described below to provide an example of the type of information which is obtainable. The Ag/Tl system will also be the focus in the time-resolved experiments.

Coulometric measurements suggest that Tl^+ deposits on Ag(111) in three steps to form a monolayer. A second full monolayer subsequently deposits prior to bulk deposition. Shown *in Figures 1(a) through (c) are the p polarized* SH intensities as a function of angle of rotation for fractional (a), full (b), and two (c) monolaye. coverages. These data were measured with a 31° angle of incidence (relative to the surface normal) and 1.06 μm radiation. The solid lines are theoretical curves generated by fitting the data to the equation $I(2\omega) \propto [a^{(2)} + c^{(3)}\cdot\cos(3\phi)]^2$ where the coefficients $a^{(2)}$ and $c^{(3)}$ contain the bulk isotropic and anisotropic material parameters as well as the surface isotropic and anisotropic tensor elements.[2]

Similar plots which are not shown here of the s polarized SH intensity were also measured and fitted to the theoretical equation $I(2\omega) \propto [b^{(3)}\cdot\cos(3\phi)]^2$. The positions of the maxima and minima in the s polarized anisotropy do not change as a function of coverage. This indicates that the overlayer structure has the same symmetry elements as the substrate surface, since the SH signal is thought to arise from the substrate/overlayer interface.

For even a fractional monolayer coverage of Tl, the pattern for the p polarized SH intensity as a function of angle of rotation changes dramatically. We interpret these variations in the anisotropy as a function of coverage as changes in the a/c ratio which is observed to convert from an imaginary to a real value with submonolayer deposition. At coverages of one monolayer or less the ratio $|a/c|$ is greater than 1. At two monolayers the magnitude of this ratio abruptly changes to less than 1. These changes are attributed to changes in the relative contributions of the surface susceptibility tensor elements as Tl^+ is deposited.

Insight into how these interfacial electronic properties are related to changes in the magnitude of each of the $a^{(2)}$ and $c^{(3)}$ terms is afforded by making these measurements at rotation angles

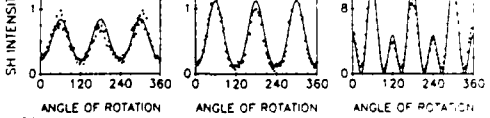


Figure 1. P polarized SH intensity as a function of angle of rotation for a Ag(111) electrode with various thallium coverages. (a) $0 < \Theta < 1$ monolayer, (b) $\Theta = 1$ monolayer, and (c) $\Theta = 2$ monolayers.

which allow simplification of the function $I(2\omega) \propto [a + c\cdot\cos(3\phi)]^2$. Figures 2 (a) through (c) show the variation in the p polarized SH intensity at fixed angles as Tl adatoms are deposited and removed as a function of potential. The angle ϕ is defined as the angle between the [211] crystal direction and the plane of incidence. Figure 2(a) was measured at $\phi=0^0$ so that $I(2\omega) \propto [a^{(2)} + c^{(3)}]^2$, 2(b) at $\phi=30^0$ so that $I(2\omega) \propto [a^{(2)}]^2$, and 2(c) at $\phi=60^0$ so that $I(2\omega) \propto [a^{(2)} - c^{(3)}]^2$. The arrows indicate the potentials at which peaks corresponding to one and two monolayer deposition are observed to commence in the voltammetry.

In Fig. 2(b), where $I(2\omega) \propto [a^{(2)}]^2$, the magnitude of the a term is seen to decrease slowly as thallium is deposited up to a monolayer. The sensitivity of the a term to submonolayer coverages is consistent with the fact that it contains surface susceptibility tensor elements with projections normal to the surface. This term is also presumed to contain the free electron contribution from the metal whereas the $c^{(3)}$ and $b^{(3)}$ terms have only interband contributions. The changes observed in $a^{(2)}$ as thallium is deposited are most likely due to work function differences between the two metals and localization of the charge density on the silver which decreases the polarizability. This decrease must also be attributed, in part, to a decrease in the electric field (and hence the $\chi^{(3)}$ contribution)[1] at the interface as the potential is swept toward the potential of zero charge.

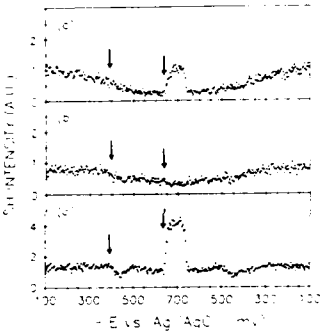


Figure 2. P polarized SH intensity from Ag(111) in Tl_2SO_4 as a function of potential for angles, ϕ, of the electrode crystal axis with respect to the plane of polarization of incident light. (a) $\phi = 0^0$, (b) $\phi = 30^0$, and (c) $\phi = 60^0$.

The magnitude of the $c^{(3)}$ term is observed to increase greatly upon deposition of the second monolayer of thallium. This increase in $c^{(3)}$ may be observed in the $[a^{(2)} + c^{(3)}]^2$ scan shown in Figure 2 (a) and the $[a^{(2)} - c^{(3)}]^2$ scan shown in Figure 2(c). A scan of the s polarized intensity as a function of potential also shows an increase at two monolayers. Because changes are only observed in the anisotropic $c^{(3)}$ and $b^{(3)}$ terms at two monolayers, and not in the a term, the authors propose that the thallium deposition changes the contribution of the surface anisotropic susceptibility tensor element, χ_{iii} (i=x,y). At higher coverages the optical characteristics of the interface begin to reflect the properties of the overlayer and it is likely that resonances between ω or 2ω and electronic transitions in the overlayer structure are induced. This proposal is consistent with the suggestion that the coefficients $b^{(3)}$ and $c^{(3)}$ contain the interband contributions to the polarizability. These results provide strong evidence for the importance of the surface contribution to the SH intensity.

The time resolved measurements of the growth and removal of these thin films have been performed by using a picosecond mode-locked laser as a continuous probe after a fast potential step. The second harmonic response is then measured as the growth or removal process occurrs. The results demonstrate for the first time the sensitivity of SHG to sequential monolayer growth and removal as measured in real-time.

1. G.L. Richmond, H. M. Rojhantalab, J. M. Robinson, and V. L. Shannon, J. Opt. Soc. Am. B 4, 228 (1987).
2. J. E. Sipe, D. J. Moss, and H. M. Van Driel, Phys Rev. B, 35, 1129 (1987).

Support from DOE-Basic Energy Sciences (DE-FG06-86ER45273) is gratefully acknowledged.

Abstract No. 586

SHG as a Probe of Surface Stability and Order in Solution

D. A. Koos, V. L. Shannon, S. A. Kellar, and G. L. Richmond
Chemical Physics Institute
University of Oregon
Eugene, OR 97403

Surface stability and reconstruction phenomena have been of great interest to the surface science community for the past two decades. Through studies performed under UHV conditions, a growing body of knowledge has been obtained about the relationship between surface stability and the electronic and thermodynamic properties of the solid/vacuum junction. The growing evidence of surface reconstruction phenomena observed in UHV raises questions as to the existence of similar instabilities for a surface in contact with solution. A knowledge of surface structure and electronic properties is fundamental to our understanding of electron transfer processes and electrode kinetics. The paucity of *in situ* experimental methods capable of exact structural measurements has slowed progress in this area. Recent studies in this laboratory have investigated the use of second harmonic generation (SHG) in making such *in situ* measurements. The experiments involve the measurement of the intensity and polarization of the nonlinear reflectance from a single crystal noble metal electrode as it is rotated about the surface normal. The form of this rotational anisotropy provides valuable information on electrode surface structure manifested by the electronic properties of the interface. This presentation will provide a summary of these results for Cu, Ag, and Au single crystals in solution.

The observation of rotational anisotropy in the SH intensity from the solid liquid interface was first reported by this laboratory for Ag(111) electrodes in simple aqueous electrolytes.[1] The observed anisotropy clearly indicated that the silver surface has a high degree of crystallinity in solution. As in our previous studies,[2] the results are consistent with the conclusion that the SH response from the metal dominates that from the surrounding electrolyte. The work reported here analyzes the anisotropic response with regards to the electronic structure of the metal, the strength of the applied field, and the importance of surface contributions relative to bulk terms in the expansion of the nonlinear polarizability.

The second order nonlinear response from a single crystal sample is predicted to follow the functional form: $I_{(\parallel,\perp)} = |a + b\,f(\phi)|^2$ as the crystal is rotated about an axis parallel to the surface normal through an angle ϕ.[3] The subscripts ($\parallel,\perp$) refer to the (fundamental, second harmonic) beam polarizations for p($\parallel$) and s($\perp$) polarized light relative to the plane of incidence. The coefficients a and b contain the isotropic and anisotropic susceptibilities and represent the response from the surface as well as the bulk of the material.

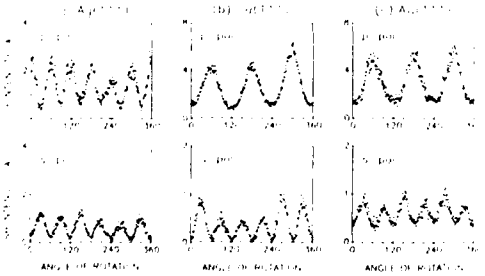


Figure 1. P polarized (upper) and s polarized (lower) second harmonic intensities as a function of angle of rotation for several noble metal electrodes (a) Ag(111) in 0.1M $NaClO_4$ at -0.72V (intensity x 10), (b) Cu(111) in 0.25M Na_2SO_4 at open circuit (intensity x 2), and (c) Au(111) in air.

Figure 1 shows the variation in the p and s polarized SH intensity for Ag(111), Cu(111), and Au(111). Radiation at 2ω was generated in reflection from the p polarized 1.06μm output of a Nd:YAG laser operating at 10 Hz. The SH patterns are consistent with the theory assuming perfect termination of the bulk symmetry ($3m$) where $f(\phi)=\cos(3\phi)$ for the p polarized output and $f(\phi)=\sin(3\phi)$ for the s polarized SH. The results for Cu(111) are similar to those observed for this surface in UHV[3] and can be explained in terms of a resonant enhancement of the SH signal due to a coincidence between 2ω and interband transition energies in the bulk metal. Similarly for Au(111) the SH rotational anisotropy can be explained in terms of bulk electronic properties. Ag(111), which displays a somewhat different anisotropic behavior (the ratio of the constants a and b is imaginary), does not possess bulk electronic transitions in the energy region spanned by ω and 2ω.

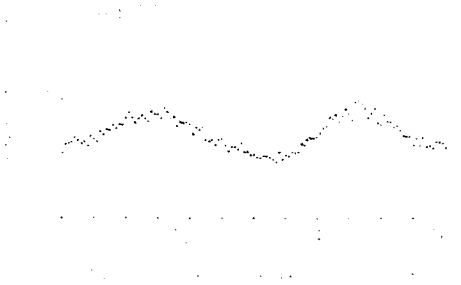


Figure 2. P polarized second harmonic intensity as a function of angle of rotation for Ag(110) in 0.25M $NaClO_4$ at -0.1V.

The p and s polarized SH response from the native Ag(110) face for a p polarized pump beam incident at 31° can be seen in Figure 2. Again, the data can be well fit to the predicted functional form, $f(\phi)=a'\cos(2\phi) + a''\cos(4\phi)$, with a proper selection of the constants a and b. These measurements indicate that the nonlinear response observed is sensitive to specific electronic states at the metal solution interface which have been previously documented. Fits of the theoretical expressions to the data also show that the surface and bulk contributions are of comparable magnitude.

Additional information on the crystallinity of the electrode surface may be obtained from these measurements. For a (111) crystal face, the isotropic component of the s polarized SH signal should vanish when ϕ is an integral multiple of $\pi/3$ because a=0 for this case. The failure of the s polarized signal for Au(111) in Figure 1(c) to decay to zero is an indication of surface roughness due to imperfect surface preparation.

The effect of an applied dc field at the single crystal electrolyte interface has also been studied. It is found that enhancement of the SH efficiency takes place through specific susceptibility tensor elements upon the application of an external bias potential. The extension of these studies to reconstructed surfaces and vacuum studies currently in progress will be discussed.

1. V.L. Shannon, D.A. Koos, G.L. Richmond, J. Chem. Phys. 87, 1440 (1987).
2. G.L. Richmond, H.M. Rojhantalab, J.M. Robinson, and V.L. Shannon, J. Opt. Soc. Am. B 4, 228 (1987).
3. H.W.K. Tom and G.D. Aumiller, Phys. Rev. B 33, 8818 (1986).

Support from NSF (CHE 8722981) is gratefully acknowledged.

Abstract No. 587

Monolayer Vibrational Spectroscopy on Metal and Semiconductor Surfaces by Infrared-Visible Sum Generation

A. L. Harris, C. E. D. Chidsey
N. J. Levinos, and D. N. Loiacono

AT&T Bell Laboratories,
Murray Hill, NJ

Infrared-visible sum generation provides vibrational spectra of molecules at interfaces and surfaces with monolayer sensitivity [1-3]. This new technique offers unique possibilities for monolayer-selective, time-resolved studies of molecules at interfaces. To explore the use of sum spectroscopy on chemically interesting substrates, we have obtained vibrational spectra of ordered monolayer molecular films on metal and semiconductor surfaces by sum mixing using nanosecond, and recently picosecond, visible and tunable infrared laser pulses [3]. The pulses are overlapped on the surface, and the reflected sum frequency signal is monitored by a photomultiplier detector. Resonances in the sum signal magnitude occur when the infrared pulse is tuned to a vibrational frequency of molecular adsorbates. Vibrational spectra of adsorbates are obtained by monitoring the sum signal while scanning the infrared frequency.

Vibrational spectra of the C-H stretching modes of alkane chains in adsorbed monolayer molecular films on several metal and semiconductor surfaces were obtained by scanning the infrared frequency in the 2700-3100 cm^{-1} region. The substantial substrate background sum signal from these surfaces does not seriously affect the sensitivity of the spectra. In fact, the substrate background contributes to a unique ability to distinguish the absolute orientation of molecules at the surface; the phase of molecular resonant signals changes with respect to the background when the molecules are inverted on the surface, leading to easily monitored changes in the sum spectrum. The spectra also experimentally demonstrate the vibrational selection rules which are in effect in this new spectroscopy; observed modes must be both Raman and infrared active.

As an example, the sum spectra of the C-H stretching modes in two similar monolayer films of opposite orientation on gold substrates are shown in Fig. 1. In each case, three resonances are observed from the three vibrational modes of the terminal methyl group, which are both infrared and Raman active. The C-H stretching modes of the backbone CH_2 groups are not observed, because they are not both infrared and Raman active, although they are strong in reflectance IR spectra of the same samples. The sum spectrum in the upper figure is obtained from a monolayer C_{18}-alkyl thiol film which has a sulfur group bonded at the gold surface, and the methyl group pointing away from the surface. The molecular resonances appear as peaks on a substrate background, illustrating that the resonance signal is in phase with the background. The second molecular film was prepared by depositing a second, inverted monolayer by Langmuir-Blodgett deposition onto a perdeuterated alkyl thiol bottom monolayer. Only the C-H stretching resonances of the second layer are observed in the 2800-3000 cm^{-1} region. The phase of the resonance signal from the inverted methyl group is reversed, because of the symmetry properties of sum spectroscopy, and the resonances appear as dips in the spectrum. The absolute orientation of selected molecular adsorbates can thus be monitored.

The time resolution of sum spectroscopy for measurements of vibrational dynamics is limited only by the laser pulse lengths. We have recently extended sum spectroscopy to pulses as short as 3 picoseconds using tunable picosecond infrared pulses obtained by stimulated electronic Raman scattering of high power, visible picosecond pulses in atomic cesium vapor. Spectra of monolayers on surfaces are obtained more rapidly with picosecond pulses than with nanosecond pulses because signal levels are substantially better with shorter pulses. Sum spectroscopy thus offers a sensitive probe of ultrafast vibrational dynamics at interfaces, including vibrational energy transfer to the substrate and photoreaction dynamics of molecular adsorbates. Preliminary studies of vibrational dynamics at surfaces will be discussed.

References

1. X. D. Zhu, H. Sur and Y. R. Shen, Phys. Rev. B35, 3047 (1987).

2. J. H. Hunt, P. Guyot-Sionnest and Y. . Shen, Chem. Phys. Letters 133, 189 (1987).

3. A. L. Harris, C. E. D. Chidsey, N. J. Levinos and D. N. Loiacono, Chem. Phys. Letters 141, 350 (1987).

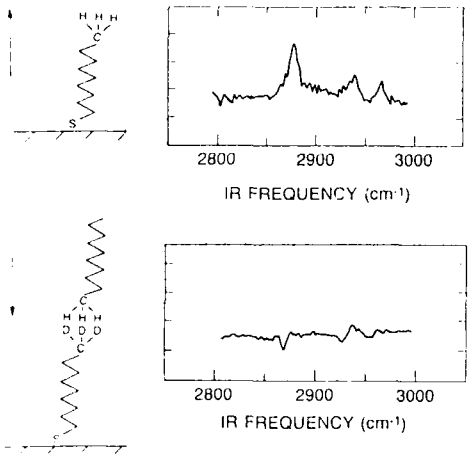


Fig. 1. Sum spectra of two similar molecular monolayer films with opposite orientation on gold substrates. Methyl group C-H stretching resonances are observed. Top: methyl group pointing away from the surface in a one monolayer film. Bottom: methyl group pointing toward surface in an inverted second monolayer with first layer perdeuterated.

Abstract No. 588

Population Relaxation of CO-stretching Vibrations for Carbon Monoxide on Metal Clusters

E. J. Heilweil, R. R. Cavanagh and J. C. Stephenson

National Bureau of Standards
Center for Chemical Physics
Gaithersburg, Md. 20899

There exists an ever-increasing need to directly measure microscopic energy dynamics of adsorbates on chemically active metal surfaces. It is the mechanisms and rates of electronic and vibrational excitation migration within an adsorbate, or from the adsorbate to the substrate, which play key roles in such fundamental processes as surface diffusion, desorption and chemical reaction. Until recently, damping rates (T_1^{-1}) of adsorbate vibrational modes on surfaces could only be inferred from bandwidth measurements and theory. However, ultrafast time-domain techniques have now reached a level of sophistication that in-situ measurements of energy transfer on reactive metal surfaces can be made. Here, we present the first direct measurements of vibrational energy relaxation for carbon-monoxide in metal-carbonyl cluster compounds and chemisorbed on colloidal (≥ 30 Å diameter) metal particles dispersed on a silica support.

The method employed in this work is based on a tunable picosecond infrared pump-probe saturation-recovery approach. This technique was previously developed to obtain T_1 lifetimes for *OH and other strongly IR*-allowed modes of adsorbates on dielectric substrates.[1] For the current application, however, ultrashort tunable infrared pulses in the 5 micron (ca. 2000 cm^{-1}) region are required. These pulses are obtained by difference frequency generation in a nonlinear $LiIO_3$ crystal from second harmonic (532 nm) and tunable dye laser (≈600 nm) pulses derived from a 10 Hz Nd^{+3}:YAG laser system. IR pulses produced in this fashion are routinely characterized as having a 15 ps FWHM duration, 10-15 μJ energy (±20% shot fluctuation) and 4 cm^{-1} *FWHM bandwidth.*

In the experiment, a single IR pump pulse (I≤10 mJ/cm^2) directly excites population to the v=1 level of a CO-stretching mode of the sample. This excitation produces a transient increase in sample transmission T (at the pump frequency) which recovers exponentially in time (with decay time T_1) to the unexcited sample transmission level (T_o). A time-delayed weak pulse at the same frequency probes the sample transmission recovery, and for the CO-containing systems studied *here, yields a measure* of the vibrational population relaxation of that fundamental mode.

The above method has been extended from our previous studies of monometal-carbonyl compounds[2] to the investigation of vibrational relaxation of CO bound to metal clusters of increasing nucleus size.[3] These systems include the stable cluster compounds $Rh_2(CO)_4Cl_2$, $Rh_4(CO)_{12}$, $Co_4(CO)_{12}$, and $Rh_6(CO)_{16}$ in dilute, room temperature $CHCl_3$ solution, some of these same molecules adsorbed on pressed fumed SiO_2 supports, and now CO adsorbed on much larger Rh and Pt particles (supported on silica). The main thrust of this investigation has been to examine the effect of increasing metal nucleus size on the CO(v=1) T_1 lifetime and thereby determine whether new relaxation mechanisms become operative when "free-electron" behavior for sufficiently large metal particles sets in.

The most pertinent results that will be presented are summarized below:

- The CO-stretching vibrations for CO in small metal cluster compounds (≤6 metal atoms) in room temperature $CHCl_3$ solution give 400 ≤ T_1 ≤ 750 ps. These long litetimes are attributed to the large energy gap between the excited mode (ca. 2000 cm^{-1}) and the next highest metal-CO and metal-metal vibrations (200-600 cm^{-1}) in these "molecular" systems.

- A novel bi-exponential decay has been observed for $Co_4(CO)_{12}$ in solution. This response is thought to arise from initially rapid (ca. 50 ps) CO-stretch energy equilibration followed by a much slower (350 ps) combined relaxation into the lower vibrational modes of the system.

- For $Rh_2(CO)_4Cl_2$, $Co_4(CO)_{12}$ and $Rh_6(CO)_{16}$ supported on silica in vacuum, a reduction of T_1 of a factor of four occurs compared to T_1 in the solution phase.

- *Induced transient absorption signals have* been detected when the IR frequency is tuned to the peak or low energy side of an absorption band. This behavior is concurrent with multiple photon absorption and arises from CO(v=2) and higher overtone excitation.

- Samples prepared by reduction of metal salts ($RhCl_3$ or PtH_2Cl_6) on silica exhibit absorption features from CO adsorbed on large (≥30 Å) metal particles and on isolated metal sites (e.g., $-Rh(CO)_2$). These absorptions give rise to short (10 - 30 ps) and long (125 ps) lifetimes, respectively, in the same inhomogeneously distributed sample. The decreased magnitude of T_1 for CO on larger particles compared to smaller cluster compounds and isolated sites clearly suggests the participation of new relaxation channels, presumably damping by electron-hole pair formation in the metal.

It is anticipated that further measurements of this type on other metal-containing systems will help unravel the detailed mechanistic, kinetic and structural characteristics of chemically reactive metal surfaces.

The Air Force Office of Scientific Research is gratefully acknowledged for its support of this work.

References

[1] E. J. Heilweil, M. P. Casassa, R. R. Cavanagh and J. C. Stephenson in Springer Series in Chemical Physics, eds. G. R. Fleming and A. E. Seigman (Ultrafast Phenomena, Vol. 46, 1986) page 465.

[2] E. J. Heilweil, R. R. Cavanagh and J. C. Stephenson, Chem. Phys. Letters, **134**, 181 (1987).

[3] R. R. Cavanagh, E. J. Heilweil and J. C. Stephenson, J. Electron Spec. and Related Phenom., **45**, 41 (1987).

Abstract No. 589

Can chemical reactions be controlled with picosecond infrared lasers?

Eric Mazur

Division of Applied Sciences and Department of Physics
Harvard University
Cambridge, MA 02138, USA

A fundamental understanding of the intramolecular dynamics of highly excited molecules is of central importance in molecular physics and has great chemical and physical implications: Selectivity at high levels of excitation may eventually lead to the realization of laser-controlled photochemistry, with broad applications in such diverse areas as laser-assisted chemical vapor deposition, isotope separation, and photosynthesis. Because of the high selectivity of infrared excitation, the discovery of infrared multiphoton excitation in 1973,[1] led to a large number of experiments in search of a novel '*mode-selective*' or '*bond-specific*' *photochemistry*. When molecules are excited above the dissociation threshold, however, equilibration of vibrational energy among the molecular modes causes the course and rate of laser-induced unimolecular reactions to depend only on total energy, and in spite of the high selectivity of the first few excitation steps, the reaction takes place along a thermodynamically favored path. The intramolecular flow of vibrational energy therefore seriously impairs the prospect for developing a laser-controlled photochemistry, and even though many questions remain unanswered, the general interest in infrared multiphoton excitation has diminished.

While the equilibration of energy for molecules excited close to or above the dissociation threshold is well understood, there is no agreement in the community as to the validity of theoretical models that presuppose equipartitioning of energy in the region *below* the dissociation threshold. In 1980 time-resolved Raman spectroscopy was used to obtain mode-specific information of infrared multiphoton excited molecules.[2] In the past five years we have studied the intramolecular vibrational energy distributions of highly *vibrationally excited molecules just below the dissociation threshold* using both spontaneous Raman and coherent anti-Stokes Raman spectroscopy (CARS).[3,4] The results, for the first time clearly show that the present theoretical descriptions of infrared multiphoton excitation are indeed not generally valid.

A complete description of the experimental setup for the spontaneous Raman measurements can be found in previous papers.[3,4] In the CARS experiments, a 10 ns pulse from a frequency doubled Nd:YAG laser and a 4 ns pulse from a broadband (15 cm^{-1}) dye laser were used to probe the vibrational levels of the highly excited molecules. The CARS signals are resolved with a 1 m Jarrel-Ash spectrometer.

As can easily be seen the two techniques yield different, but complementary results. The intensity of a spontaneous Raman transition is proportional to the quantum number n and the population of the level, $P(n)$:

$$I_R(n) \sim \sigma_n P(n) \sim n P(n) \qquad (1)$$

with σ_n the Raman cross-section for the transition $n \rightarrow n+1$. Because of the n^2 dependence, the spontaneous Raman signal increases as the excitation of the mode increases. The CARS signal intensity, on the other hand, is proportional to population *differences*

$$I_{CARS}(n) \sim n^2 |P(n) - P(n+1)|^2 \qquad (2)$$

For a Boltzmann distribution at high excitation, $P(n) \approx P(n+1)$, and so, even though the CARS signals are much larger than the spontaneous Raman signals, CARS is not well suited to study equilibrium distributions at high excitation. The CARS technique is therefore more sensitive to the low-excitation regime, or nonequilibrium distributions at high-excitation.

Measurements were carried out on SF_6 and CF_2Cl_2. Both the spontaneous Raman and the CARS measurement show changes in the intramolecular vibrational energy distribution in SF_6 after infrared multiphoton excitation. The spontaneous Raman experiments show a strong increase in Raman signal, because of the larger population at high excitation, while the CARS measurements show a very strong depletion of the lower energy levels. From a quantitative analysis of the spontaneous Raman data it follows that the energy equilibrates even at relatively low excitation.[3]

For CF_2Cl_2 the ν_1, ν_2, and ν_8 mode (1098, 667, and 923 cm^{-1}, respectively) were measured after multiphoton excitation of either the ν_1 or the ν_8 mode, which are both Raman and infrared active, and are resonant with CO_2 laser lines. In both cases, the pumped mode reaches the highest excitation, while the energy of ν_2 mode is almost an order of magnitude smaller. The nonequilibrium nature of the vibrational energy distribution is clearly visible in Figs. 1 and 2, which compare the energy distributions obtained from the spontaneous Raman experiments with calculated equilibrium distributions.

Note, that although the intensities of the anti-Stokes signals increase by more than a factor ten when the infrared fluence is increased, the intensity *ratios* do not change considerably. This rules out the possibility that the observed nonequilibrium distribution is a result of averaging a 'hot' equilibrium ensemble and a 'cold' bottlenecked ensemble. If this were so, the ratios would tend toward equilibrium as the fraction of molecules in the hot ensemble becomes larger when the fluence is increased.

As one would expect, the CARS measurements show that the ground states of the ν_1 and ν_8 modes are strongly depleted. The much 'colder' ν_2 mode, on the other hand, can be studied in detail by the CARS technique.

Summarizing, time-resolved spontaneous Raman spectroscopy and CARS were employed to measure the intramolecular vibrational energy distribution of highly vibrationally excited molecules. A vastly different behavior is observed for the two molecules studied. For SF_6, both techniques show equilibration of the excitation energy at relatively low levels of excitation. For CF_2Cl_2, on the other hand, the results show a distinct *nonequilibrium energy distribution among the* observed Raman active modes even at excitations as high as 21,000 cm^{-1}. The measurements also show that excitation of the ν_1 and the ν_8 mode give rise to different nonequilibrium energy distributions. From studies of the infrared multiphoton dissociation of CF_2Cl_2,[5,6] it is known that the dissociation basically takes place along a thermodynamically favored path, indicating that the energy distribution equilibrates at the dissociation threshold. For SF_6 this equilibration occurs well below the dissociation threshold. The present studies thus show that one can, for certain molecules, induce highly nonequilibrium energy distributions in molecules at energies close to dissociation with picosecond infrared pulses.

1 N.R. Isenor, V. Merchant, R.S. Hallsworth and M.C. Richardson, *Can. J. Phys.* **51**, 1281 (1973)

2 V.N. Bagratashvili, Yu.G. Vainer, V.S. Dolzhikov, S.F. Kol'yakov, A.A. Makarov, L.P. Malyavkin, E.A. Ryabov, E.G. Stikis, and V.D. Titov, *Appl. Phys.* **22**, 101 (1980)

3 Jyhpyng Wang, Kuei-Hsien Chen, and Eric Mazur, *Phys. Rev. A* **34**, 3892 (1986)

4 Kuei-Hsien Chen, Jyhpyng Wang, and Eric Mazur, *Phys. Rev. Lett.* **59**, 2728 (1987)

5 Aa.S. Sudbø, P.A. Schulz, E.R. Grant, Y.R. Shen, and Y.T. Lee, *J. Chem. Phys.* **70**, 912 (1979)

6 David S. King and John C. Stephenson, *Chem. Phys. Lett.* **51**, 48 (1977)

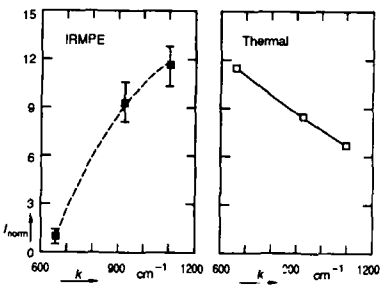


FIG. 1. Comparison of the observed normalized anti-Stokes signals with calculated equilibrium values after ν_1 excitation.

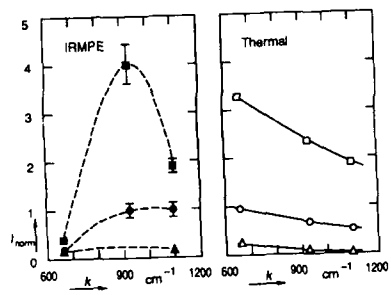


FIG. 2. Comparison of the observed normalized anti-Stokes signals with calculated equilibrium values after ν_8 excitation. The lower traces show the effect of collisional relaxation; N_2 buffer gas pressure: 13 kPa(circles), and 26 kPa (triangles).

Abstract No. 590

Intramolecular Vibrational Relaxation Lifetimes by Picosecond Fluorescence Depletion Spectroscopy

John Kauffman, Matthew Côté, Philip Smith and J. D. McDonald

School of Chemical Sciences
University of Illinois
Urbana, Illinois 61801

Vibrational relaxation in isolated gas phase molecules has been studied by many techniques: electronic fluorescence spectroscopy[1], infrared fluorescence excitation and fluorescence spectroscopy[2,3], collisional timing[4], and direct timing by time-correlated photon counting[5]. In this paper we report experiments using a new picosecond technique which, for the first time, allows direct measurement of the *lifetime of the initially prepared state* with experimental resolution of better than 5 picoseconds.

In these experiments the molecule fluorene, a molecule with a strongly allowed S_0 - S_1 transition, is seeded in a continuous helium free jet expansion to give a beam temperature of about 40 Kelvin. A Rhodamine 6G dye laser is synchronously pumped by the frequency doubled output of a cw mode-locked Nd:YAG laser. The 2.5 to 6 picosecond output pulses are amplified by the frequency doubled output of a cw pumped, acousto-optically mode-locked and Q-switched, and electro-optically cavity-dumped Nd:YAG laser. The 350 microjoule green output of this laser allows us to produce 10 to 40 microjoule amplified dye laser pulses with a repetition rate of 500 Hz. The final amplified visible pulses have autocorrelation widths of 4 to 10 picoseconds. The output beam is split into two beams of equal intensity, one of which passes through a delay line. Each beam is then frequency-doubled, producing about 1 microjoule/pulse each in the ultraviolet. They are then passed through adjustable waveplates which allow us to set the angle between the electric vectors of the exactly linearly polarized UV beams to any desired angle while maintaining their bisector parallel to the molecular beam direction and perpendicular to the plane of observation. The total, time-integrated, molecular fluorescence is observed with a photomultiplier and boxcar integrator.

The first laser pulse excites a substantial fraction of the molecules to a particular vibrational level of S_1. The usual excitation fraction is between 35 and 60%, although for strong lines the central part of the 0.1 millimeter excitation region may have undergone several cycles of absorption and emission. If the second laser pulse follows without delay, it cannot significantly change the amount of observed fluorescence, as the transition is already saturated. However, any mechanism which depletes the upper state, including fluorescence, intersystem crossing, or vibrational relaxation, allows the second laser to increase the fluorescence signal, as the amount of absorption remains constant while stimulated emission decreases. This includes the removal of oscillator strength between the ground and excited electronic states by intermolecular *dephasing* processes. We are able to probe the time dependence of these mechanisms by tuning the time delay between the two pulses and measuring the difference between the fluorescence intensity with and without the second laser pulse. If the initially prepared state is made up of a "clump" of a few closely spaced molecular eigenstates, the dephasing of these states, which corresponds to the intermediate level density case of vibrational relaxation, produces quantum beats in the resulting fluorescence. If many states (say greater than 50) are involved, an exponential decay is produced. This experiment is sensitive to the polarizations of the laser beams and the angle of observation: if the polarizations are parallel, the decay represents both vibrational relaxation *and* intramolecular *rotational dephasing*. If the polarizations differ by 54.7 degrees, only vibrational relaxation (including rotational changes produced by Coriolis coupling) is observed.

We have measured the fluorescence excitation spectrum of fluorene, and it shows numerous strong vibronic transitions up to 2600 cm^{-1} above the vibrationless level of 33784 cm^{-1}. As the transition energy increases the peaks begin to exhibit structure (ie. shoulders) outside of the width of the rotational contour. At energies above 1500 cm^{-1} the peaks are significantly broader than the rotational contour of the vibrationless level. We have observed decays from states with excess vibrational energies varying from 0 to 2036 cm^{-1} above the vibrationless level (figure 1). Only single exponential decays, indicating no relaxation, are observed below 900 cm^{-1}. From 950 to 1500 cm^{-1} strong quantum beats are observed. These indicate both accidental concidence of Franck-Condon allowed transitions and incipient vibrational relaxation. At energies above 1700 cm^{-1} bi-exponential decays are observed, with only very weak beats; this is indicative of near-statistical-limit relaxations. The vibrational relaxation lifetimes in this region vary from 20 picoseconds at 1700 cm^{-1} to <10 picoseconds at 2036 cm^{-1}. The time dependent behavior of the states in these three regions can be clearly associated with various degrees of broadening in their dispersed fluorescence spectra, which we have measured with an optical multichannel analyser (figure 2). Spectra of states with low excess vibrational energies have many sharp, well-resolved lines with instrument limited bandwidth. States above 900 cm^{-1} exhibit spectra having a few broad bands which are overlaping, but distinguishable. At energies above 1500 cm^{-1} the spectra show a continuous, broad contour with a bandwidth covering >2000 cm^{-1}. The nearly identical features of the high energy spectra highlight the statistical nature of the anharmonic couplings at high vibrational energies.

REFERENCES

1. J. B. Hopkins, D. E. Powers, S. Mukamel and R. E. Smalley, J. Chem. Phys., **72**, 5049, (1980)

2. G. M. Stewart and J. D. McDonald, J. Chem. Phys., **78**, 3907, (1983)

3. T. Kulp, R. Ruoff, G. M. Stewart and J. D. McDonald, J. Chem. Phys., **80**, 5359, (1984)

4. K. W. Holtzclaw and C. S. Parmenter, J. Chem. Phys., **84**, 1099, (1986)

5. W. R. Lambert, P. M. Felker and A. H. Zewail, J. Chem. Phys., **81**, 2209, (1984)

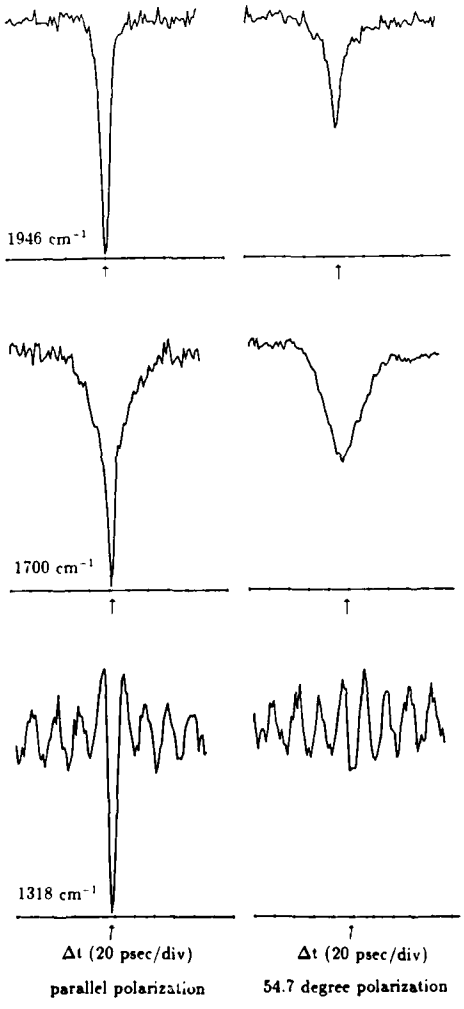


Figure 1. Fluorescence intensity as a function of delay time between laser pulses. As relaxation mechanisms decrease the population of the excited state, the second laser pulse increases the fluorescence signal. The arrows indicate the $\Delta t = 0$ position. Rotational dephasing effects disappear when the electric vector polarizations differ by 54.7 degrees. Because pump and probe are the same wavelength, the signal is symmetric about $\Delta t = 0$ for pulses of equal power.

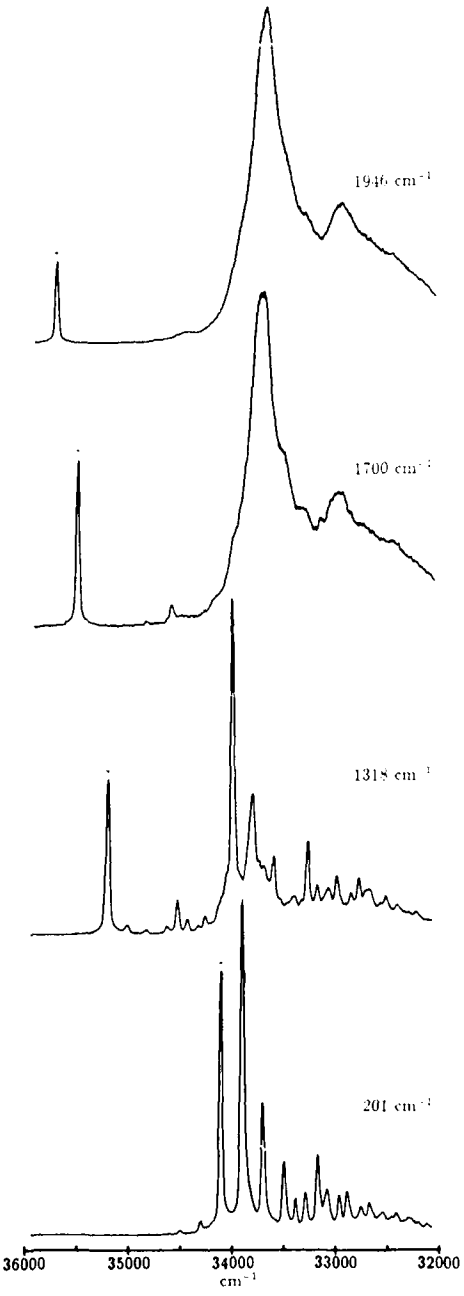


Figure 2. Dispersed fluorescence from vibronic levels of fluorene having excess vibrational energies of 201, 1318, 1700 and 1946 cm^{-1}. The arrow marks the resonance fluorescence peak which contains a small contribution from scattered light.

Abstract No. 591

The Effect of Vibrational Motion on the Dynamics of Intramolecular Charge Transfer Reactions

John D. Simon[+] and Shyh-Gang Su

Department of Chemistry
Institute for Nonlinear Studies
University of California San Diego
La Jolla, California 92093

Intramolecular charge transfer has been observed in several molecular systems, many of which have been examined using picosecond time resolved techniques [1]. Although some molecules reveal charge transfer rates on the order of τ_L^{-1}, intramolecular charge transfer dynamics which are faster and slower than this solvent fluctuation time have been reported. In addition, nonexponential electron transfer dynamics have been observed in 4,4'-dimethylaminophenyl sulphone, p-(9-anthryl)-N,N-dimethylaniline, and bianthryl. Recent studies on the excited state intramolecular charge transfer of 4,4'-dimethylaminophenyl sulphone in alcohols suggest that solvent diffusion plays a minor role in determining the reaction rate [2]. For propanol through hexanol, the rate of reaction is considerably faster than τ_L^{-1}, suggesting that the dominant contribution to the chemical reaction rate involves fluctuations in the intramolecular degrees of freedom. In this talk, we will examine the dynamics of formation of the twisted intramolecular charge transfer state of p-dimethylaminobenzonitrile (DMABN) and p-diethylaminobenzonitrile (DEABN) in alcohol solutions (ethanol to hexanol) as a function of temperature (0° C to -50° C).

For these molecular systems, charge transfer occurs on the excited state surface. Excitation populates the nonpolar local excited (LE) state. In polar solvents, rapid intramolecular charge transfer occurs, the charge separation is stabilized by rotation around the phenyl-amino bond. Formation of this twisted intramolecular charge transfer (TICT) state results in the appearance of a new visible emission. In general, our results show that the population decay of the LE state, Q(t), cannot be fit by a single exponential. By modeling the decay as a sum of exponentials, we have obtained the average lifetime, τ_a of the survival probability of the LE state. In all of the alcohol solvents studied, τ_a is significantly shorter than the solvent fluctuation rate gauged by the longitudinal relaxation time of the solvent, τ_L ($\tau_D\epsilon_\infty/\epsilon_s$), corresponding to the slow collective hydrogen bonding dynamics.

Comparison with recent dynamical solvation studies [3] suggest that the multiexponential electron transfer kinetics reflected by Q(t) do not result from contributions of higher frequency responses of $\epsilon(\omega)$. Comparison of the behavior of Q(t) and τ_a to a recent theoretical model by Nadler and Marcus [4] clearly demonstrate that in all solvents studied, the dominant contribution to the reaction rate come from fluctuations in the intramolecular vibrational motions, not solvent diffusion. This conclusion also is supported by recent gas phase measurement as well as studies of the electron transfer dynamics in frozen hexanol.

Acknowledgements: This work is supported by grants from the National Science Foundation and the Petroleum Research Foundation administered by the American Chemical Society and the Office of Naval Research.

References

[1] For a recent review, see E. Lippert, W. Rettig, V. Bonacic-Koutecky, F. Heisel, and J. A. Miehe, Adv. in Chem. Physics, I. Prigogine, S. A. Rice, eds. (Wiley and Sons, New York, Vol. 68, 1987), p. 1.

[2] J. D. Simon and S.-G. Su, J. Chem. Phys. 87, 7016 (1987).

[3] M. Maroncelli and G. R. Fleming, J. Chem. Phys. 86, 6621 (1987); S.-G Su and J. D. Simon, J. Phys. Chem. 91, 2693, (1987); V. Nagaragan, A. M. Brearley, T.-J. Kang, and P. F. Barbara, J. Chem. Phys. 86, 3183 (1987).

[4] W. Nadler and R. A. Marcus, J. Chem. Phys. 86, 3906 (1987).

[+] NSF Presidential Young Investigator 1985-1990. Alfred P. Sloan Fellow 1988-1990.

Abstract No. 592

FEMTOSECOND RAMAN INDUCED QUANTUM BEATS IN A DYE MOLECULE OBSERVED BY POLARISATION SENSITIVE MEASUREMENTS

J. Chesnoy and A. Mokhtari
Laboratoire d'Optique Quantique
Ecole Polytechnique
91128 Palaiseau cédex, France

Time domain observation of molecular movements such as rotation, libration or vibration can actually be performed with high accuracy by using femtosecond lasers. Coherent excitation of a Raman active vibration can be achieved with a single light pulse whose duration is shorter than the vibrational period of the mode[1,2]. We will report additional features of these Raman quantum beats due to impulsive Raman excitation.

We have performed measurements close to an electronic resonance in a dye molecule using various pump-probe techniques. Following a single beam excitation, we have analysed the polarisation rotation and ellipticity change experienced by a delayed probe beam. In addition to these measurements of transient induced dichroism and birefringence, we have developed a new experimental configuration to analyse the frequency modulation (spectral shift) of the probe beam as well as its amplitude modulation (time delay shift). In these four experimental schemes we observe small amplitude oscillations superimposed on a large background originating from saturated absorption and dispersion decays (Fig. 1).

We can interpret these observations in terms of impulsive stimulated Raman scattering (ISRS) close to an electronic resonance. Our observations show the main trends of resonant ISRS such as the joint observation of an absorptive effect in addition to pure dispersive manifestations. Vibration in the ground electronic state is involved in the same extent as vibration in the excited state. We have shown that their observation can be experimentally separated as it appears qualitatively in Fig. 1 in view of the different damping constants of the observed oscillations. Identical behaviours of the observed vibrational decays are observed for malachite green in different solvents.

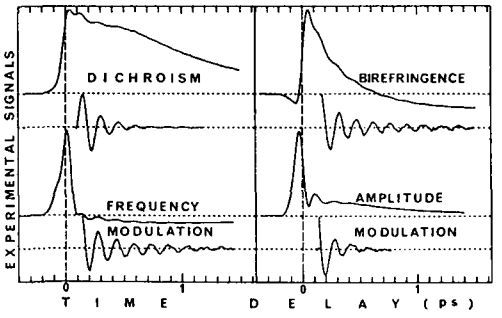


Fig. 1. Time-resolved dichroism and birefringence induced by a femtosecond pump beam, are observed on malachite green dissolved in water (top). Ultrafast beats are superposed on the relaxational decays, and are experimentally extracted for each observation. At the bottom, similar results are obtained by detecting frequency modulation as well as amplitude modulation of the probe beam versus the time delay between pump and probe.

We will report the interpretation of these various aspects of impulsive stimulated Raman excitation and probing in the frame of a density matrix expansion applied to a simple vibronic system. We will underline the salient features originating from the presence of the electronic resonance, concerning mainly the vibrational excitations in both ground and excited electronic states. The informations that can be extracted from the initial phase of the observed oscillation will be discussed. Finally, The links betwenn the present measurement and more conventional techniques such as time resolved CARS or Raman induced Kerr effects will be reviewed.

References :

1 - YX. Yan, E.B. Gamble and J.A. Nelson
J. Chem. Phys. 83, 5391 (1985)

2 - M.J. Rosker, F.W. Wise and C.L. Tang
Phys. Rev. Lett. 57, 321 (1986)

Abstract No. 593

Femtosecond Spectroscopy of Chemical Reactions in Condensed Phases

Alan G. Joly, Leah R. Williams, and Keith A. Nelson

Department of Chemistry, MIT, Cambridge, MA 02139

It is now possible to probe intermolecular and intramolecular motions on time scales which are short compared to elementary collision times or vibrational periods.[1] Thus the basic nuclear motions which may lead to bimolecular or unimolecular chemical reactions can be observed on their natural time scales. In fact, these motions are almost always initiated coherently by a sufficiently short (i.e. femtosecond) laser pulse. This facilitates time-resolved probing with subsequent, variably delayed pulses.

Figure 1 illustrates initiation of coherent nuclear motion (i.e. coherent wavepacket propagation) in electronic excited states through optical absorption of an ultrashort pulse. Following absorption, molecules find themselves on the side of the S_1 potential surface. They then undergo vibrational oscillations about the S_1 potential minimum. These oscillations are phase-coherent if the excitation pulse was short compared to the oscillation period.[2] Excitation into the unstable potential S_3 leads to dissociation rather than oscillation. The same may occur in S_2 depending on the details of the S_1 and S_2 potential surfaces and on dissipation due to interactions between the reacting species (or in a *large* molecule, the degree of freedom Q along which reaction occurs) and its environment. The nuclear motion along Q will be phase-coherent, i.e. synchronized among all the excited molecules, if the excitation pulse is short in duration compared to the time required for nuclei to move a significant distance. Phase-coherent chemical change thus occurs in state S_2 or S_3.

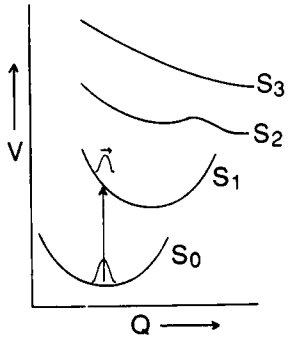


Figure 1. Schematic illustration of coherent wavepacket propagation initiated by optical absorption of an ultrashort pulse. Absorption into the S_1 level leads to coherent oscillations along coordinate Q about the S_1 potential minimum. Absorption into S_2 or S_3 may lead to coherent motion along Q without oscillation, i.e. to photodissociation. Dissipation could inhibit photodissociation from the S_2 state, giving rise to oscillations about the weak potential minimum.

For small molecules in the gas phase, time-resolved observation of photodissociation dynamics may yield accurate reactive potential energy surfaces (PES's).[3] In condensed phases, dissipation and inhomogeneity destroy the one-to-one correspondence between dynamics and PES. Semiquantitative determination of intramolecular PES's which are only weakly perturbed by their environment may be possible through measurement of reaction dynamics. In addition, the effects of environment on reaction dynamics and yield may be examined.

Femtosecond time-resolved absorption measurements of several organic and organometallic species are discussed. In the crystalline phase, the excimer-formation reactions in perylene and pyrene molecular crystals have been studied.[4] These are well oriented bimolecular reactions which are initiated by photoexcitation. We observe subpicosecond excimer formation times in both crystals at room temperature. This reflects rapid and probably partially phase-coherent intermolecular approach following excitation.

The photodissociation of chromium hexacarbonyl, $Cr(CO)_6$, in methanol solution to yield $Cr(CO)_5$ + CO was studied.[5] As shown in Figure 2, bond breakage is complete in about 300 fs following photoexcitation at 310 nm. The nonexponential time-dependence of transient absorption at short times reflects the classical kinematics of motion (wavepacket propagation) along the unstable dissociative PES. The exponential rise in absorption at longer times is due to compexation of the "bare" $Cr(CO)_5$ species with a solvent molecule.[6]

The photochemistry of manganese decacarbonyl, $(CO)_5Mn\text{-}Mn(CO)_5$, in methanol was also investigated.[5] Following excitation at 310 nm, either CO loss (followed by formation of the bridged species $Mn_2(CO)_9$ which absorbs in the blue) or metal-metal bond breakage (yielding $Mn(CO)_5$ radicals which absorb in the near-IR) occurs. The former process is complete in about 500 fs, and the dynamics of product formation appear to be exponential as shown in Figure 3. This is to be expected since several molecular motions are involved and phase-coherence is not maintained. Formation of the radical fragments occurs with an unusual, oscillatory time-dependence as shown in Figure 4. This may reflect a solvent barrier to dissociation which gives rise to Mn-Mn "stretching" vibrations in the excited state. Since in this case very large fragments are separating, strong solvent effects are anticipated even at small displacements Q along the reaction coordinate. The reactive PES and the extent of dissipation during progress along Q depend on a molecule's local environment. Some molecules will dissociate while others will undergo excited-state oscillation. These observations provide insight into the role played by the solvent in mediating chemical reaction dynamics and yield.

1. S. Ruhman, A.G. Joly, B. Kohler, L.R. Williams, and K.A. Nelson, Revue de Phys. Appl. 22, 1717 (1987).
2. M.J. Rosker, F.W. Wise, and C.L. Tang, Phys. Rev. Lett. 57, 321 (1986); K.A. Nelson and L.R. Williams, Phys. Rev. Lett. 58, 745 (1987).
3. M. Dantus, M.J. Rosker, and A.Z. Zewail, J. Chem. Phys. 87, 2395 (1987).
4. L.R. Williams and K.A. Nelson, J. Chem. Phys. 87, 7346 (1987).
5. A.G. Joly and K.A. Nelson, J. Phys. Chem., submitted.
6. J.D. Simon and X. Xie, J. Phys. Chem. 90, 6751 (1986).

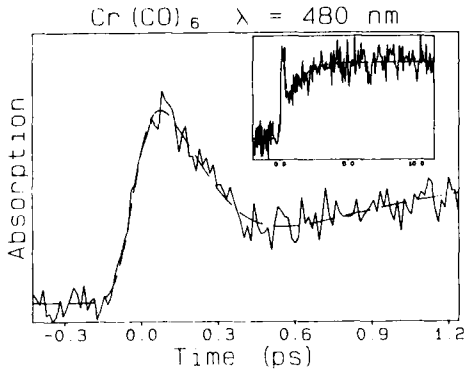


Figure 2. Transient 480-nm absorption of $Cr(CO)_6$ in methanol following 310-nm excitation. The nonexponential decay at short times reflects the dynamics of CO dissociation. At longer times (see inset), solvent complexation of $Cr(CO)_5$ occurs.

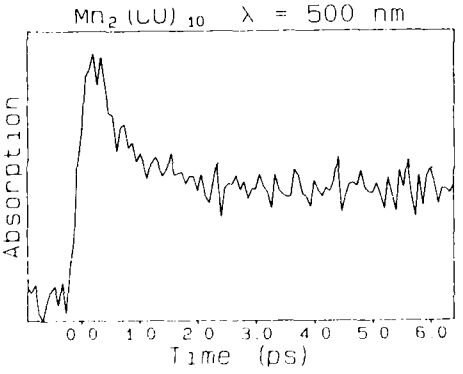


Figure 3. Transient 500-nm absorption of $Mn_2(CO)_{10}$ following 310-nm excitation. Loss of CO and formation of the bridged compound $Mn_2(CO)_9$ are complete in about 500 fs.

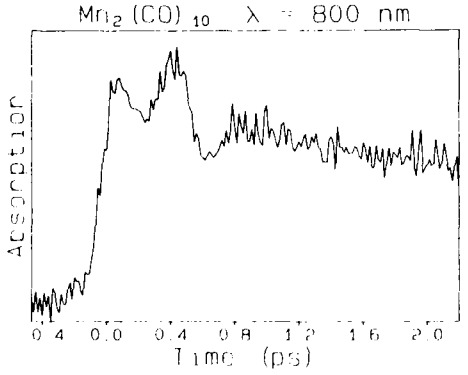


Figure 4. Transient 800-nm absorption of $Mn_2(CO)_{10}$ following 310-nm excitation. The formation of $Mn(CO)_5$ radicals appears to be oscillatory. This may be due to a solvent-induced potential energy barrier to dissociation of the two large photofragments.

Abstract No. 594

LOW TEMPERATURE GLASS RELAXATION AND INTERACTION WITH SOLUTES PROBED BY PICOSECOND PHOTON ECHO AND HOLE BURNING EXPERIMENTS

M. Berg,[a] C.A. Walsh,[b] L.R. Narasimhan, K.A. Littau and M.D. Fayer

Department of Chemistry, Stanford University, Stanford University, Stanford CA 94305

Glasses are not only an intrinsically interesting and important class of materials, they are also a prototype for understanding the unique properties which have been identified in many disordered materials including polymers, amorphous semiconductors and metals, biological materials and disordered crystals. These unique properties are commonly attributed to two-level systems (TLS), which are poorly understood motions with a wide distribution of properties, including relaxation rate.[1] Optical dephasing measurements have been a valuable probe of dynamics in crystalline phases and there is growing interest in applying these techniques to probe the dynamics of amorphous materials and their interaction with solutes.[2] Although the possible importance of slowly relaxing motions on optical dephasing techniques has often been recognized, a systematic discussion of these effects has not appeared nor have these effects been exploited to yield information on relaxation in disordered materials. In this work,[3] a unified treatment of the effect of relaxation on all timescales on a variety of optical dephasing experiments is derived, experiments demonstrating the existence of slow relaxations in glasses are performed, and the results are used to extract basic features of the glass dynamics and their effect on solute electronic states.

The various methods which have been used to measure dephasing times (photon echoes, hole burning, fluorescence line narrowing, stimulated photon echoes, etc.) are shown to be inequivalent in materials with multiple relaxation timescales. None of these experiments is correctly described by the optical absorption expressions commonly used to analyze dephasing experiments. We have treated these apparently diverse experiments in a unified manner by using a nonlinear optical line shape formalism [4] to derive their correlation functions. The experiments differ primarily through a characteristic time, which determines the relaxation timescales which contribute to the dephasing measured by a given experiment. Since this characteristic time varies by at least 12 orders of magnitude, the quantitative comparison of different dephasing experiments can be used to explore the broad range of relaxation rates characterizing disordered materials.

In a specific application of these ideas, temperature dependent photon echo and nonphotochemical hole burning experiments on resorufin in ethanol, d-ethanol and glycerol have been performed from 1.1-25 K [Fig. 1]. Qualitatively similar results are found in all three glasses. The hole burning pure dephasing times at low temperatures are 6 times shorter than the photon echo dephasing times, reflecting the presence of slow relaxation processes (spectral diffusion) in the glass. At higher temperatures, both dephasing times deviate from the power law predicted for TLS dephasing and begin to coalesce. These effects are attributed to the onset of dephasing by a pseudolocal phonon mode at higher temperatures.[5] These modes have frequencies and lifetimes similar to those found in crystalline materials. By removing the effects of pseudolocal mode dephasing, the TLS contribution to dephasing, which is unique to disordered materials, is found. This contribution is further broken down into a portion due to fast relaxations ("homogeneous" dephasing) and slow relaxations (spectral diffusion) by combining the photon echo and hole burning results. Fractional power law temperature dependences are found for both portions [Fig. 2]. Surprisingly, the photon echo decays are exponential over at least 6 lifetimes [Fig. 3], despite the presence of multiple relaxation timescales. In addition, the hole shapes are Lorentzian even though they are dominated by "non-homogeneous" processes.

By combining the correct correlation functions for each experiment with a model of the glass dynamics based on standard assumptions about TLS, all the major experimental results can be accounted for. The magnitude of the difference in photon echo and hole burning dephasing times is consistent with relaxation rates distributed over at least 12 orders of magnitude. The Lorentzian hole shapes are not the result of a homogeneous dephasing process, but arise from an intrinsically Lorentzian "inhomogeneous" distribution generated by a long range ($1/r^3$) solute-glass interaction. The form of the photon echo decay is directly related to the distribution of relaxation rates, R. The experimental exponential decay indicates a 1/R distribution at short times, in accord with the simplest models of glass dynamics. However, the inequality of the temperature dependence exponents for the slow and the fast relaxation components indicates a more complicated distribution at longer times. Additional dephasing experiments at intermediate timescales are needed to characterize this distribution in detail.

This work was supported by the National Science Foundation Division of Materials Research (DMR84-16343). Additional support was provided by the Office of Naval Research, Physics Division (N00014-85-K-0409).

a) Permanent Address: Chemistry Department, University of Texas at Austin, Austin, TX 78712

b) Permanent Address: Sandia National Laboratories, Albuquerque, NM 87185

References

1. Amorphous Solids - Low Temperature Properties, edited by W.A. Phillips (Springer, NY, 1981).
2. Optical Linewidths in Glasses, edited by W.E. Moerner (Springer, NY, 1988).
3. M. Berg, C.A. Walsh, L.R. Narasimhan, K.A. Littau and M.D. Fayer, J. Chem. Phys. 88, 1564 (1988).
4. S. Mukamel and R.F. Loring, J. Opt. Soc. Am. B 3, 595 (1986).
5. B. Jackson and R. Silbey, Chem. Phys. Lett. 99, 331 (1983).

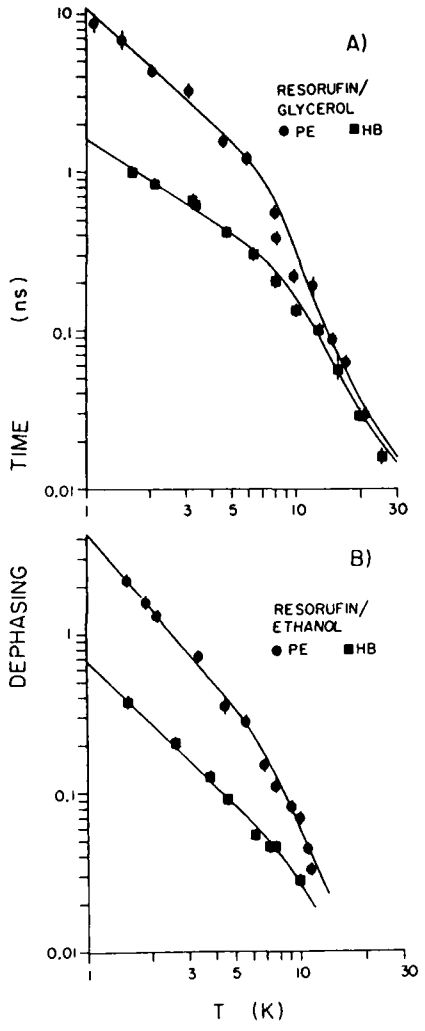


Fig. 1. Log-log plots of temperature dependent hole burning (HB) dephasing times compared to photon echo (PE) dephasing times for resorufin in: (A) glycerol, (B) ethanol glass. The fluorescence lifetime contribution to both measurements has been removed. At low temperatures the dephasing times differ by a factor of 6 as a result of slow relaxation processes in the glass. At high temperatures, dephasing is dominated by pseudolocal mode motion. As a result, the two measurements coalesce and deviate from power law behavior.

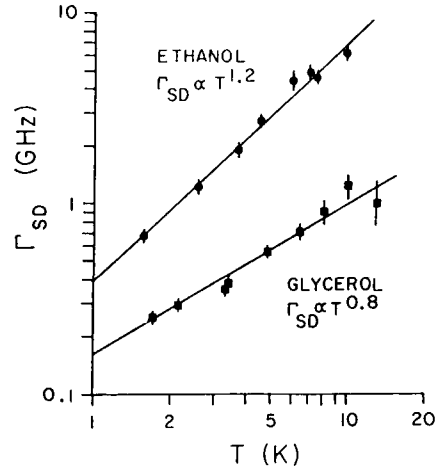


Fig. 2. Log-log plot of the temperature dependence of the spectral diffusion linewidth Γ_{SD} defined as the difference of the photon echo and hole burning linewidths. Data are shown for resorufin in two glasses: ● - ethanol and ■ - glycerol.

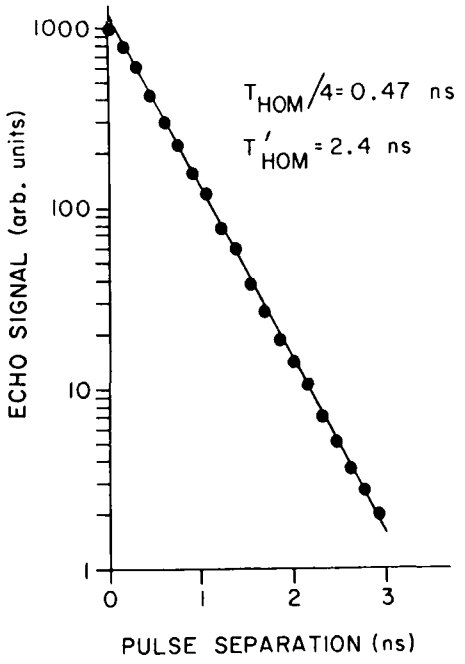


Fig. 3. A semi-log plot of the photon echo signal from resorufin in d-ethanol glass at 1.5 K as a function of pulse separation. The decay is exponential over 6.2 lifetimes.

Abstract No. 595

FEMTOSECOND OPTICAL KERR DYNAMICS IN MOLECULAR LIQUIDS OF VARYING STRUCTURE

W.T. Lotshaw, D. McMorrow, C. Kalpouzos, and G.A. Kenney-Wallace
Lash Miller Laboratories
University of Toronto
80 St. George Street
Toronto, Ontario M5S 1A1
CANADA

We have investigated the molecular dynamics of some simple polarizable liquids through the dependence of the third order nonlinear optical susceptibility $\chi^{(3)}$ on intra- and intermolecular degrees of freedom. These include small and large angle orientational motions of single molecules in the laboratory frame, as well as orientational and translational variables in interacting sets of molecules, and intramolecular normal coordinates (Raman modes).

The optical heterodyne detected optical Kerr effect [1] has been employed to resolve the femtosecond dynamics of the intensity dependent refractive index of the liquids CS_2,CS_2/n-alkane binary solutions, n-alkyl nitriles (n=1,3,6), benzene and many substituted analogs, and a number of halogenated methanes. Results will be presented and discussed which indicate that pairwise intermolecular interactions significantly influence the magnitude of $\chi^{(3)}$ and the dynamics of $\chi^{(3)}$ intermolecular motions which modulate $\chi^{(3)}$ at times less than 1 ps. This appears to be governed by the curvature and fluctuation rate of the local intermolecular potential in which the nonspherical molecules librate. The relation between these results and the dielectric friction exerted by nonspherical molecular liquids on charged or polar solute transients (dynamic solvation) will be developed and discussed.

The influence of intermolecular interactions on the dynamics of intramolecular vibrations (Raman modes) in several halogenated methanes will also be discussed and compared to the case of the intermolecular librations discussed above.

[1] D. McMorrow, W.T. Lotshaw, and G.A. Kenney-Wallace IEEE J. Quant. Elect. 24 p443-454 (1988)

Abstract No. 596

COOPERATIVE EFFECTS UNDER INTERACTION OF COHERENT RADIATION WITH MATTER

V.F.Cheltsov

Novatorov Str.,18-7-2, Moscow V-421,USSR

This report deals with the interaction of a coherent instantly switched on resonance electromagnetic field with a system of N identical motionless two-level atoms. When the field is represented by a single resonance mode the analysis of the behaviour of the stark-system "N atoms + mode" is carried out in the RWA-approximation, by diagonalizing the hamiltonian, the initial number n_c of resonance photons being regarded as a parameter.

The energy eigenvalues,i.e.,the A.C. Stark-spectrum form, generally, a set of(N+1) irrational noncommensurate values(i.e.cooperative harmonics).The vacuum stark(or Rabi) splitting of the energy levels propotional to is shown to exist in the presence of one initially excited atom in the system of N-1,2,3 atoms with $n_c = 0$. When N atoms are in the strong ($n_c \gg N$, n_c = constant) driving field,the stark spectrum consists of(N +1) harmonics, multiple to the Rabi frequency $\Omega = B(n_c)1/2$. The harmonics noncommensurability brings about the quasiperiodicity of the system's dynamics so that due to the phase-mixing effect its initial state is not repeated. The effect results in the establishment of a dynamical equilibrium between the atoms and the arising coherent field, with the difference $N_- = N_2 - N_1$ in the atomic levels' populations turning to zero. The initially inverted atomic subsystem (with $N_-^0 = N_2^0 - N_1^0$ 0 and $n_c^0 = 0$) becomes saturated with $N_- \to 0$ and the number of arising photons equal to $n_c = 1/2\ N_-^0$. Change of N_- obeys a law of damping oscillations with the frequency and decrement of the same order $B(N_-^0)\ 1/2$ .In the strong field ($n_c \gg N$) the number of photons is constant and the inversion N_- oscillates as $N_-(t) = N_-^0 \cos(\Omega t)$.

The theory of cooperative resonance fluorescence was developed when the radiation wavelength $\lambda \gg$ R-interatomic distance, the driving field being assumed to be switched on instantly. The stark-system was considered as a source of a spontaneous and stimulated emission. Considering the interaction of the stark-system with a free radiation field, i.e.,a fluorescence field, as a small perturbation, and using for the fluorescence both the standard perturbation treatment and the commutator version of the evolution operator method, we found its spectrum and spectral lines intensities for N=1,2,3,4 atoms in the strong ($n_c \gg N$) driving field and for N=1,2 in an arbitrary field. The cooperative resonance fluorescence spectrum has, mainly, ω_a - and($\omega_a \pm 2\Omega$) - harmonics with their intensities' ration determined by the initial populations in the atomic levels. The ration reaches its maximum equal to unit by order of magnitude when all atoms are initially in the same level. Such a strong dependence on the initial conditions remain both in the first, second and third orders of the perturbation theory and is caused by the interference of the initial amplitudes of cooperative states of the atoms in the driving field.

The cooperative ($N \geq 2$) higher ($\omega_a \pm 4\Omega$) - harmonics' intensity obtained in the first perturbation approach in the case of the weak and moderate driving field decreases as $1/n_c^2$ as n_c increases. In the case of strong field and in the second and third orders of perturbation theory their intensity is proportional to $\gamma^2/400\Omega^2$, where a spontaneous linewidth $\gamma \ll \Omega$.

/1/ V.F.Cheltsov, JETP, 47,564 (1964)
/2/ V.F.Cheltsov, Nuovo Cimento,B69,152 (1970)
/3/ V.F.Cheltsov,Opt.Comms.,64,347 (1987)
/4/ V.F.Cheltsov,Optica Acta,33,33(1986)

Abstract No. 597

ULTRAFAST PHOTONIC SWITCHING WITH NONLINEAR GLASS GUIDED WAVE DEVICES

P. W. SMITH

Bellcore
331 Newman Springs Rd
Red Bank, NJ 07701

One reason for the current upsurge of interest in photonic switching has been the realization that all-optical devices have the capability to switch at rates much higher than those possible with electronics technology. Such high rates are likely to be necessary in future high-speed communications and computing systems.

Optical glasses have a number of advantages as nonlinear materials for all-optical devices. Their high transparency allows long interaction lengths in guided-wave structures and essentially eliminates the thermal heating problems that have limited the performance of all-optical devices made from other materials. I will present our results on four wave mixing measurements of nonlinear coefficients for a variety of optical glasses, and show that certain optical glasses have the highest figure of merit of any nonlinear optical material.

In the last few years, a number of glass optical fiber switching devices have been demonstrated, including a birefringent fiber polarization switch, a fiber Kerr gate, and a two-core fiber directional coupler. After surveying this work, I will present our results on guided-wave nonlinear coupler structures that have demonstrated substantially complete switching of 100 femtosecond pulses. This is the fastest switching time ever measured for a guided wave all-optical device.

Abstract No. 598

Ultra-Small Semiconductor Microresonators

J. L. Jewell, S. L. McCall[a], Y. H. Lee, A. Scherer[b],
A. C. Gossard[c] and J. H. English[c]
AT&T Bell Laboratories, Rm. 4G-520, Holmdel, NJ 07733 U.S.A.

Future technologies such as all-photonic switching networks for long range communications, optoelectronic chip-to-chip communication, and optical computing will require large numbers of all-optical or optoelectronic devices with low operating energies (≤ 1 fJ) and high speed (≤ 10 ps). All devices reported to date fall short of these goals. Optical resonators (Fabry-Perot etalons) form the basic structure for most optical logic devices and also for lasers, thus it is important to try and scale these structures to sizes as small as possible. In this paper we report experimental results on 1.5-μm diameter GaAs microresonators operated as optical logic etalons (OLE) and as optically-pumped lasers. We also discuss straightforward techniques for further scaling to $\sim 1/4$ μm, which should allow them to achieve the desired speeds and energies.

The use of ion-beam-assisted etching to form ~ 1.5-μm diameter waveguiding "posts", or microresonators, in a GaAs/AlAs Fabry-Perot structure grown entirely by molecular beam epitaxy (MBE) has reduced the device cross-sectional areas, energy requirements and recovery times all by more than an order of magnitude[1]. Fig. 1 shows a very small region of the etched heterostructure. Prior to etching the minimum controlling energy required for an optical logic etalon operation[2] was 20 pJ. The device diameter was about 10 μm and recovery time was estimated to be several ns, both inferred from measurements on comparable devices. For 1.5-μm microresonators the energy is 0.6 pJ and recovery time, ~ 200 ps (Fig. 2). Thus, at least over this size range, the energy and time requirements scale directly with cross-sectional area.

With the controlling (pump) energies increased to about 9 pJ, the microresonators reach lasing threshold. Fig. 3 shows an input/output characteristic for one microlaser. Fig. 4 shows a 2×2 array of microlasers formed by splitting a 60-pJ pump beam into 4 beams. The 9-pJ energy threshold is larger than the ~ 1 pJ for the lowest threshold electrically driven diode lasers[3] but there is much room for improvement as will be discussed later. The high finesse and strong dielectric confinement attainable in these structures are their chief advantages over conventional diode lasers. Furthermore they are inherently surface emitting, making optical access straightforward. If similar low energies could be achieved in electrically-driven surface-emitting microlasers, they might be competitive with electronics or other diode lasers for chip-to-chip communication

It is possible to reduce the microresonator diameters much further approximately to the wavelength in the material, λ/n, which for GaAs devices is about 1/4 μm. The problem is not so much in constructing small microresonators, but coupling the light into them. We have focused light of 0.9 μm wavelength through a hemisphere of $SrTiO_3$ with refractive index n=2.4, to a full diameter of only ~ 0.7 μm. Use of a semiconductor with n >3 allows focusing to < 0.6 μm and device diameters ~ 0.5 μm. The devices can be grown on a transparent semiconductor substrate with lens surfaces formed on the backside by a non-labor-intensive process such as photoelectrochemical etching.

Since it is unrealistic to focus to much smaller than ~ 0.5-μm diameters (over many devices) and ~ 0.25-μm diameters are desired, only one option appears to remain—tapering the waveguiding devices. Such a device would resemble a microwave horn. Preliminary experiments with dielectric microwave tapered waveguides suggest that the necessary tapering in GaAs optical waveguides might be accomplished over a length of only about 2 μm. Optical horns might be formed by varying the etch parameters during etching.

In conclusion, we have demonstrated the first step of decreasing optical resonator diameters to their fundamental limit, namely by forming waveguiding structures. The second step, high-numerical-aperture focusing, has been partially demonstrated, and the final step, waveguide tapering, has been proposed. If the energies and times continue to scale with cross-sectional area, the smallest devices should have <6 ps recovery times, with ~ 17 fJ controlling energies for gates and ~ 250 fJ lasing thresholds. The MBE-grown etalon used in our experiments however, was a first attempt; the design was conservative and not optimized. The energies should be reduced considerably by increasing the etalon finesse. Furthermore, essentially all of the optical nonlinearity is due to bandfilling. Use of excitonic nonlinearities obtained from multiple quantum wells and/or operation at reduced temperature could reduce the energies by another order of magnitude. With such improvements, we expect to reduce the gate controlling energies to less than 1 fJ, approaching the statistical limit for reliable switching of a few hundred photons[4]. It is important to point out that effects such as waveguide loss and dispersion could cause the lower *practical* limit on device diameters to be somewhat larger than λ/n, or it could even be slightly smaller. The techniques reported here however will allow us to reach that limit, whatever it may be.

References

[1] J. L. Jewell, A. Scherer, S. L. McCall, A. C. Gossard, and J. H. English, Appl. Phys. Lett. **51**, 94 (1987).

[2] S.L. McCall, A.C. Gossard, J.H. English, J.L. Jewell, and J.F. Duffy, Technical Digest, CLEO 86, (Optical Society of America, San Francisco, CA) paper FK3.

[3] K.Y. Lau, N. Bar-Chaim, P.L. Derry, and A. Yariv, Appl. Phys Lett. **51**, 69 (1987).

[4] S.L. McCall and H.M. Gibbs, in *Optical Bistability*, edited by C.M. Bowden, M. Ciftan, and H.R. Robl (Plenum, New York, 1981), p. 1.

a) AT&T Bell Laboratories, Murray Hill, NJ 07974
b) Bell Communications Research, Redbank, NJ 07701
c) present address: Eng. Matls. Dept., University of California, Santa Barbara, CA 93106

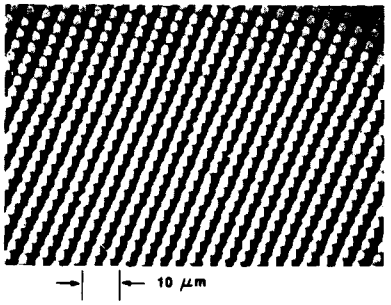


Figure 1

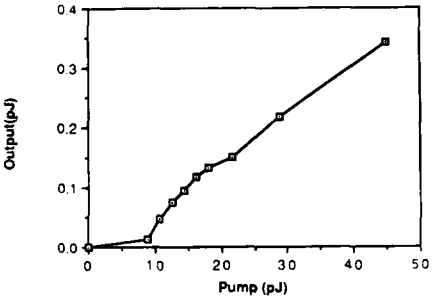


Figure 3

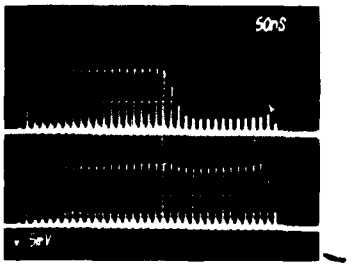


Figure 2 (Upper) Response of a 1.5-μm device to 600 fJ controlling pulses. The left side is the output with no input (controlling pulses) present and the right side is the output *with* input present. (Lower) Same as upper but with probe pulses delayed by 200 ps.

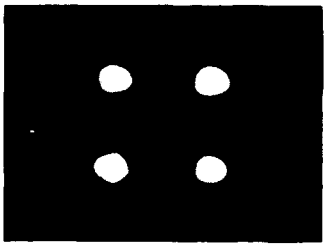


Figure 4

Abstract No. 599

Tunneling-Based Phenomena In Asymmetric Coupled Quantum Wells

J. E. Golub, P. F. Liao, Y. Prior,
D.J. Eilenberger, J.P. Harbison and L.T. Florez

Bell Communications Research
331 Newman Springs Road, NVC-3Z286
Red Bank, N.J. 07701-7020

An asymmetric coupled quantum well structure consists of two dissimilar GaAs quantum wells separated by a thin AlGaAs barrier layer. Inter-well coupling is mediated by quantum mechanical tunneling through the classically forbidden barrier and is manifested spectroscopically as an avoided level crossing in the excitonic absorption. In addition, when biased by an electric field, the coupled well can become spatially indirect, with electrons and holes localized in different layers.

We present spectroscopic measurements of the interwell tunneling rate at low temperatures. We also give evidence of a strong optical nonlinearity. The spectroscopic results can be understood in terms of a simple single particle model; band bending effects are useful in describing the nonlinearity. We also demonstrate oscillator strength switching based on tuning the electron-hole overlap near the transition from spatially direct to spatially indirect. Finally, we discuss applications to optoelectronics.

Abstract No. 600

Quantum Wires and Quantum Dots
- Physics and Applications

Kerry Vahala
California Institute of Technology
128-95
Pasadena, California 91125

Certain material growth and fabrication technologies now allow the control of composition and structure in materials on an atomic scale (nanometric scale). This capability creates new design degrees of freedom which can be applied to devices and systems. Control of composition and structure on this scale epitaxially in one dimension (e.g., quantum well and superlattice material) has been available commercially for several years and is now yielding a number of devices that exhibit novel properties which can be controlled during fabrication of the device. These include quantum well semiconductor lasers, resonant tunneling devices, high electron mobility structures, and a host of others. In addition, this capability has lead to important basic discoveries such as the quantum hall effect and the fractional quantum hall effect. Control of the other two dimensions of the material on this scale has and remains a very challenging area of device research. Two of the simplest possible structures at this size scale are the quantum wire and the quantum dot, which are the 2- and 3-dimensional analogs of the conventional quantum well structure. The physics of these structures will be reviewed and approaches to fabrication and measurement will be discussed. In addition, the potential application of arrays of quantum wires and quantum dots as laser diode active layers will be considered. Quantum dot and quantum wire effects can be simulated using high magnetic fields. Results will be presented from simulation experiments that immerse quantum well laser diodes in high magnetic fields to achieve quantum dot effects.

Abstract No. 601

Quantum Mechanical Effects in Field-Effect Transistors with Nanostructured Geometries*

T. P. Orlando, P. F. Bagwell,
Henry I. Smith and D. A. Antoniadis
Department of Electrical Engineering and Computer Science
Massachusetts Institute of Technology
Cambridge, MA 02139

A variety of quantum mechanical effects have been observed and studied in artificially structured semiconductors and metals over the past decade. These fall broadly into four categories: (1) quantum effects due to reduced dimensionality, such as in quasi-one-dimensional inversion layers; and (2) quantum effects due to coherent diffraction, such as in grating-gate transistors; (3) effects due to interference of quantum wavefunctions, such as weak localization and conductance oscillations in a magnetic field; and (4) cooperative effects among the electrons, such as the fractional quantized hall effect. A review will be given that concentrates on the first two effects which can be realized in field-effect devices in silicon and III-V semiconductors patterned with 10-100 nanometer scale structures using x-ray and electron-beam lithography.

Reduced-Dimensionality Effects

Quantum effects arising from artificial structures were first observed in inversion layers of Si metal-oxide-semiconductor field-effect transistors (MOSFETs). Here the bending of the bands at the Si/SiO_2 interface produces a potential which quantizes the energy for motion perpendicular to the interface. The lowest energy state of this system is the only state occupied at temperatures below 100K so that the electrons in the inversion layer are truly confined to two dimensions at low temperatures. A two dimensional confinement of the electrons can also be realized in III-V semiconductor hetero-interfaces. The quantum effects unique to two dimensions, such as Landau quantization in a magnetic field, are well known and have been studied extensively for many years.[1]

Further confinement in one of the lateral dimensions of the two dimensional system results in a one-dimensional system. Such a system is called quasi-one-dimensional (Q1D) because more than one lateral mode of the wavefunction is permitted, each mode giving rise to a one dimensional subband. The conductance of Q1D inversion layers is expected to oscillate as the fermi energy is swept through the subbands. In the early 1980's many investigators fabricated Q1D structures. However, in the initial investigations the anticipated oscillations were masked by fluctuations in the conductivity.[2,3] The fluctuations, known as universal conductance fluctuations, are due to the interference of the electrons' wavefunctions caused by scattering from impurites or other imperfections.[4] Warren *et al.*[5] using a MOSFET consisting of about 250 parallel Q1D Si inversion layers observed oscillations in the transconductance and attributed it to the passing of the fermi level through the Q1D subbands. Presumably, the large number of parallel conductors averaged out the universal conductance fluctuations. Recently, Warren's measurements have been duplicated by Ismail *et al.*[6] in Q1D structures in GaAlAs/GaAs. Subband filling has also been observed by a capacitive method by Smith *et al.*[7], and Scott-Thomas *et al.*[8] have seen strong oscillations in the conductance of narrow ($\approx 30\,nm$) and short ($\approx 1\,\mu m$) inversion layers in Si.

Coherent Diffraction Effects

Coherent diffraction effects arise by electrons diffrating from artificial periodic structures, also called superlattices. Superlattices can be made by multilayer growth or by nanofabrication of surface gratings and grids. The lateral surface superlattices (LSSL) have a powerful advantage over multilayer stuctures: In an LSSL one can electrically control both the magnitude of the periodic potential as well as the fermi energy of the electrons. Warren *et al.*[9] observed regular oscillations in the conductance of Si MOSFETs using a LSSL with a period of 200 nm. More recently, Ismail *et al.*[10] and Tokura and Tsubaki[11] observed similar effects using a Schottky-barrier LSSL on GaAlAs/GaAs heterostructures. Stronger coherent diffraction effects are expected for a grid stucture made by superimposing two LSSLs perpendicular to one another because true gaps open in the energy bands.

In addition to discussing the above two quantum effects, *we will describe the fabrication,* the transport physics and the modeling of these devices.

* Work supported by U. S. Air Force grant AFOSR-85-0376 and Joint Services Electronics Program grant DAAL03-86-K-0002.

1. T. Ando, A. B. Fowler, and F. Stern, *Rev. Mod. Phys.* **54**, 437 (1982).
2. R. F. Kwasnick, M. A. Kastner, J. Melngailis, and P. A. Lee, *Phys. Rev. Lett.* **52**, 224 (1984).
3. R. E. Howard, W. J. Skocpol, L. D. Jackel, *Ann. Rev. Mat. Sci.* **16**, 441 (1986).
4. P. A. Lee and A. D. Stone, *Phys. Rev. Lett.* **55**, 1622 (1985).
5. A. C. Warren, D. A. Antoniadis, and H. I. Smith, *Phys. Rev. Lett.* **56**, 1858 (1986).
6. K. Ismail, W. Chu, D.A. Antoniadis, and Henry I. Smith, *Appl. Phys. Lett.* **52**, 1071 (1988).
7. T. P. Smith,III, H. Arnot, J. M. Hong, C. M. Kneodler, S. E. Laux and H. Schmid, *Phys. Rev. Lett.* **59**, 2802 (1987).
8. J. Scott-Thomas, M. A. Kastner, H. I. Smith, D. A. Antoniadis, and S. B. Field, to be published in *J. Vac. Sci. Tech.*.
9. A. C. Warren, D. A. Antoniadis, H. I. Smith, J. Melngailis, *IEEE Electr. Dev. Lett.* **EDL-6**, 294 (1985).
10. K. Ismail, W. Chu, D. A. Antoniadis, and H. I. Smith, submitted to *Appl. Phys. Lett.*
11. Y. Tokura and K. Tsubaki, *Appl. Phys. Lett.* **51**, (1987)

Abstract No. 602

Ultrafast Relaxation and Band-Gap Renormalization in Semiconductors

S. Das Sarma
Department of Physics and Astronomy
University of Maryland
College Park, Maryland 20742

We will review our theoretical results on two important problems of electron dynamics in semiconductor quantum wells. These are the problems of hot carrier relaxation and of carrier-induced band-gap-renormalization. Both of these issues have important implications for non-linear optics and ultrafast photonics applications of semiconductor quantum wells.

In the problem of hot carrier relaxation, we will present detailed numerical results for the picosecond hot-carrier energy relaxation rate in GaAs quantum wells. Our theory, which includes quantum degeneracy, dynamical screening, plasmon-phonon coupling, hot phonon effect, slab and interface phonon modes, is in excellent agreement with the available experimental results. In addition, we predict that the renormalization of LO-phonons by electronic quasiparticles gives rise to novel low-energy quasiparticle-like LO-phonon modes which become very important loss channels at low temperatures. We identify these modes as the "missing loss" mechanism at low temperatures that has earlier been discussed in the literature. In the problem of band-gap renormalization, we will present detailed numerical results for the carrier-induced band-gap renormalization (BGR) with the RPA theory including both electron-electron and electron-phonon interactions. Universality of BGR in both two and three dimensions will be discussed and our results will be critically compared with experiment.

Abstract No. 603

The Role of Metastable Light-Induced Defects in the Picosecond Decay of Photoinduced Absorption in Intrinsic Hydrogenated Amorphous Silicon

Terry L. Gustafson, Harvey Scher,
Dale M. Roberts and Robert W. Collins

BP America Research & Development
4440 Warrensville Center Road
Warrensville Heights, OH 44128-2837

The optical and electronic properties of hydrogenated amorphous silicon (a-Si:H) are of considerable interest owing to the application of this material to photovoltaic and thin film electronic devices. A key issue, both related to the defect structure of a-Si:H and device performance, is the nature of metastable light-induced electronic defects (LIDs).[1] We have conducted a systematic investigation of the picosecond PA decays for samples of varying defect density over a range of pump intensities, at several repetition rates, and over a range of temperatures.[2,3] We have shown that picosecond PA monitors dispersive diffusion-limited transport of *electrons* in the conduction band tail states in intrinsic a-Si:H. In the present work we observe the systematic effect of LIDs on the short time relaxation and recombination of photoexcited carriers in intrinsic a-Si:H.

The samples used in this work were deposited in a capacitively coupled rf glow discharge system. The steady state optical absorption spectra of the samples were measured using photothermal deflection spectroscopy and transmittance and reflectance spectroscopy. We have presented the details of the picosecond apparatus elsewhere.[4] Briefly, a mode locked argon ion laser pumped two synchronously pumped cavity dumped dye lasers to produce independently tunable pump and probe pulses; the time resolution of the system is ~10 ps. Typical carrier densities in the photoexcited volume were $1\text{-}5\times10^{17}$ cm^{-3}. We detected the increase in absorption using a time modulation technique to eliminate the thermal background that is present with mechanical chopping.[4] We positioned the sample so that we eliminated any interference effect, ensuring that the observed decay represented the induced absorption, $\Delta\alpha$.[5] *This step was critical in order to compare quantitatively results obtained at different temperatures.* We could reproduce the PA decays at any temperature and intensity regardless of the sample history.

Consistent, good quantitative fits to all the picosecond PA transients, $\Delta\alpha(t)$, have been obtained with a simple power law decay,

$$\Delta\alpha(t) = \frac{n_o(\Delta\sigma_1-\Delta\sigma_2)}{1+(t/\tau)^{\beta}} + n_o\Delta\sigma_2. \qquad (1)$$

From the fits we propose a physical interpretation based on the 2-state model from the pioneering work of Vardeny *et al.*[6] which has the novel feature that the transition between the states (1↔2) is limited by dispersive diffusion.[7] In the model, n_o is the initial number of excited carriers; $\Delta\sigma_{1(2)}$ is the difference in the cross section between the ground state and excited state 1(2); τ is the median trapping time; and β is the dispersion parameter. The strength of the interpretation depends on the self-consistent dependencies of all the parameters in Eq. (1) on changes in temperature, intensity, repetition rate and defect density (i.e., different samples).

We have previously shown that β is an intrinsic parameter, $\beta=T/T_o$, with no dependence upon intensity.[3] This indicates that the dispersion is due to multiple trapping from an exponential density of states with distribution width kT_o. The $T_o(=T/\beta)$ is in excellent agreement with other transport measurements (at much longer times) of the width of the conduction band tail. Hence, the exponential density of states can be extrapolated to at least 0.15 eV of the mobility edge.

Unlike β, τ exhibits systematic variations with excitation intensity. We have established a self-consistent approach to unravelling the intensity and temperature dependence of τ. Consistent with the model of diffusion-limited trapping, $\ln\nu\tau$ should be proportional to $\beta^{-1}\ln(b_tN_t)^{-1}$, implying an Arrhenius T-dependence for τ for $\beta=T/T_o$. (ν is the escape frequency, N_t is the density of trap states and b_t is the capture coefficient.) The variation of τ with intensity presents a difficulty in establishing the functional form of $\tau(T)$. We adopt the following approach: The relation between τ and b_tN_t holds and we use this relation to establish important aspects of the dependence of N_t on temperature and intensity, i.e.,

$$(\nu\tau)^{-\beta} = b_tN_t(T,I)/b_cN_c, \qquad (2)$$

where N_c is the density of states and b_c the capture coefficient in the conduction band tail. We extrapolate $N_t(T,I\to0)$ ($\equiv N_t(T)$) to obtain a neutral trap density. The values we obtain for $N_t(T)$ are in close agreement with the saturated value of LIDs reported by Jackson and Stutzmann.[8] We present independent evidence for this association from low temperature luminescence quenching and PA amplitude relaxation (at fixed delay) measurements. Thus, starting with a very low defect *density film of a-Si:H one can induce defects, generic* to the material, in a reproducible and controlled way (i.e. by intensity and temperature). Since the electronic relaxation (i.e. τ^{-1}) scales with these defects one can now use the transient PA as a sensitive and quantitative probe of further dynamic processes: early recombination and/or a fuller spectral range of (transient) LIDs. In other experiments, by studying $\Delta\alpha(t)$ as a function of probe and pump wavelength, we will attempt to locate the position of these defects in the gap. It is assumed that a large fraction of N_t is located near or in the conduction band tail. If the traps are deep it is difficult to understand the recombination of a density n_o of electrons and holes within each repetition period.

References

1. D. L. Staebler and C. R. Wronski, J. Appl. Phys. 51, 3262 (1980).
2. T. L. Gustafson, R. W. Collins, D. M. Roberts, and H. Scher, J. Non-Cryst. Solids 97&98, 121 (1987).
3. T. L. Gustafson, H. Scher, D. M. Roberts, and R. W. Collins, Phys. Rev. Lett. 60, 148 (1988).
4. D. M. Roberts and T. L. Gustafson, Opt. Commun. 56, 334 (1986).
5. D. M. Roberts, J. F. Palmer, and T. L. Gustafson, J. Appl. Phys. 60, 1713 (1986).
6. Z. Vardeny, J. Strait, D. Pfost, J. Tauc, and B. Abeles, Phys. Rev. Lett. 48, 1132 (1982).
7. H. Scher, J. Phys., Paris 42, 547 (1981); J. Orenstein and M. Kastner, Solid State Commun. 40, 85 (1981).
8. W. B. Jackson and M. Stutzmann, Appl. Phys. Lett. 49, 957 (1986).

Abstract No. 604

Non-equilibrium Optical Phonon Generation and Detection In Picosecond-Photo-Excited Germanium

Jeff. F. Young
Division of Physics
National Research Council
Ottawa, Canada K1A OR6

and

A. Othonos and H.M. van Driel
Department of Physics
University of Toronto
Toronto, Canada M5S 1A7

A 50 mW beam of 4 psec dye laser pulses at 575 nm is used to repetitively generate a non-equilibrium electron-hole plasma at the surface of intrinsic Ge at 77K[1]. A 25 mW, perpendicularly polarized portion of the same beam is used to obtain Raman spectra from the excited surface for different delays between pump and probe pulses. The temporal evolution of the anti-Stokes Raman signals from the longitudinal optic (LO) phonons ([100]) oriented surface) and transverse optic phonons ([110]) oriented surface) were almost identical. In particular, the phonon population attains a maximum approximately 5 ps following the peak of the excitation pulse, and it then decays with a time constant of ~8 ps. AT 300^{K}, the maximum occurs ~3.5 ps following the excitation pulse and the decay time decreases to ~4 ps.

The fact that significant non-equilibrium populations of both LO and TO phonons are observed is qualitatively consistent with the fact that hot carriers in Ge interact via the deformation potential with optical phonons, whereas in GaAs, where no hot TO phonons are observed[2], the primary carrier-lattice interaction is the Fröhlich coupling between electrons and LO phonons. Quantitatively, it is not a priori obvious that measurable non-equilibrium populations can be generated in any single phonon mode, given that the deformation potential matrix element is independent of wavevector. A detailed kinetic model including carrier generation, diffusion, recombination and coupling to the lattice has been developed to compare with the experimental results. It is found that the kinematic constraints on energy and momentum conservation in the carrier-phonon interaction lead to preferential coupling of energy from the hot carriers through relatively small wavevector phonon modes. This, in conjunction with the relatively large carrier densities generated by the pump pulses (~1 x 10^{19} cm^{-3}), quantitatively accounts for the excess phonon populations observed in our experiments.

1. J.F. Young, K. Wan and H.M van Driel, Sol. State. Elect., 31, 455 (1988).

2. D. von der Linde, J. Kuhl and H. Klingenberg, Phys. Rev. Lett. 42, 1505 (1980).

Abstract No. 605

Ultrashort Wavelength Surface Acoustic Waves Induced on Silicon and Germanium by Picosecond Pulses

M. Ledgerwood, D. Jost*,
J.E. Sipe and H.M. van Driel

Department of Physics
University of Toronto
and
Ontario Laser and Lightwave
Research Centre

Toronto, Canada
M5S 1A7

It is well known that transient heating of solids and liquids by nanosecond or longer pulses can lead to bulk and surface acoustic waves with the frequency spectrum of the acoustic waves generally reflecting the laser pulse width. For semiconductors the absorption of above band-gap radiation leads to electron-hole pair generation with spatial profiles determined by absorption depth and diffusion. With picosecond laser pulses it is possible to generate very high carrier densities ($>10^{20}cm^{-3}$) and deformation potential effects accompanying the carriers can dominate thermal effects in establishing inhomogeneous strain fields which couple to surface acoustic waves (SAWs).

In this paper we will show how tightly focussed picosecond laser pulses with $1<\tau_p<100$ psec, $0.5<\lambda<1.06$ μm and at a repetition rate of 80MHZ can generate and amplify highly monochromatic SAWs on silicon and germanium. The wavelength of the SAWs, which can be as short as 400Å, is determined by the Fourier content of the transverse and longitudinal strain distribution induced by the pulses. Amplification of the SAWs occurs via spatial modulations of the real and imaginary parts of the dielectric constant leading to preferential feedback for a particular Fourier component. The SAWs, therefore, can have wavelengths and orientations which reflect beam or crystal parameters. At laser intensities near the threshold for melting, the SAWs are observed to be frozen in along directions which reflect crystal direction.

*Permanent address: Max Planck Institute Für Quantenoptick, GARCHING FRG.

Abstract No. 606

Laser melting of silicon: the first few picoseconds

Juen-Kai Wang, Peter Saeta, Maarten Buijs and Eric Mazur

Division of Applied Sciences and Department of Physics
Harvard University
Cambridge, MA 02138, USA

Numerous investigations on the phase transition of silicon during picosecond laser annealing have been performed in recent years. It has been well established that the silicon surface melts during a picosecond laser pulse.[1] Because liquid silicon is a metal, the reflectivity increases on melting. This has indeed been observed using optical pump-and-probe techniques.[1-3]

When the pump fluence is much larger than the melting threshold, the temperature of the molten silicon can exceed the melting temperature. According to a Drude model for the liquid phase one then expects a decrease in reflectivity of the molten silicon. A simple numerical model, using the one-dimensional heat equation to describe the temperature of solid and liquid silicon as a function of time and depth in the silicon sample, predicts that the reflectivity drop due to the heating above melting temperature occurs on a picosecond time scale.[2] Standard picosecond pump-and-probe measurements cannot resolve this reflectivity change because they integrate over the duration of the probe pulse.

In our setup, time resolution is obtained by directly resolving the signal over the duration of the probe pulse. Consequently we can study the melting process on a single-shot basis with 1.8-ps resolution. The frequency-doubled output of a Nd:YAG laser, with a wavelength of 532 nm and a pulse duration of 30 ps, is split in the usual way into a pump beam and a probe beam. The probe, in turn, is split in four and recombined to form a longer probe pulse of 120 ps duration. This probe pulse images an area slightly larger than the melting area on the entrance slit of a streak camera (Hamamatsu Photonics C1587) which is equipped with a Temporal Analyzer unit (C2280). This system has a time resolution of 1.8 ps. To enhance the sensitivity of our measurements, the probe pulse is *p*-polarized and the probe angle of incidence is chosen close to Brewster's angle. At this angle the reflectivity of solid silicon is small (less than 10%), leading to a large increase in the reflectivity on melting. In addition, each camera trace yields intensity as a function of both time *and* position on the melting area. This is to be contrasted with standard pump-and-probe experiments which contain no spatial information.

Our results show that the reflectivity change on melting exhibits a complicated behavior as a function of laser fluence during the first 100 ps. For the high-fluence regime, in which we are interested, the reflectivity reaches the value for liquid silicon within the duration of the pump pulse. This is illustrated in figure 1, which gives an example of the reflectivity change in the high-fluence regime. During the 40 ps that the reflectivity needs to reach the value for molten silicon (about 8 times that of solid silicon), it follows the trend predicted by numerical simulations of heating above melting temperature in silicon,[2] indicating that this really occurs on a picosecond time scale. Measurements with longer and more uniform probe pulses are currently in progress.

Acknowledgment

We thank Dr. Malvezzi for his help with the experiment. MB acknowledges a Fellowship from the Netherlands Organization for Pure Scientific Research (ZWO).

1. J.M. Liu, H. Kurz and N. Bloembergen, *Appl. Phys. Lett.*, 41, 643 (1982).
2. P.M. Fauchet and K.D. Li, *Mat. Res. Soc. Symp. Proc.*, in press.
3. D von der Linde and N. Fabricius, *Appl. Phys. Lett.*, 41, 991 (1982).

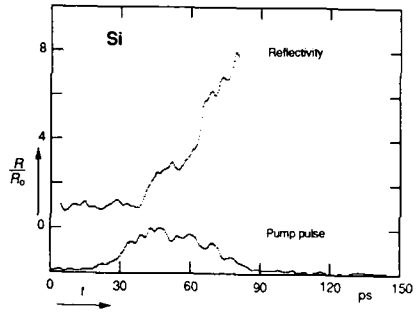


FIG. 1. Reflectivity of silicon during melting with a picosecond laser pulse. R_0 is the reflectivity of solid silicon. The lower trace shows the intensity of the pump pulse.

Abstract No. 607

Semiconductor Optical Damage in the Femtosecond Regime

D.H. Reitze, T.R. Zhang, and M.C. Downer

Department of Physics
University of Texas at Austin
Austin, Texas

The technological importance of semiconductor laser processing has spawned numerous studies of single and multipulse laser damage of semiconductor surfaces at a multitude of laser wavelengths and pulse durations[1]. Systematic study of semiconductor damage thresholds and morphologies for subpicosecond laser pulses, however, is completely lacking. This important regime brings unique physics to the optical damage process--strong absorption nonlinearities near the melting threshold, the presence of extremely high transient carrier densities ($>10^{21}cm^{-3}$), minimal time for light interaction with transient surface perturbations, and delay of lattice heating until after passage of the pulse--which is manifested in novel damage threshold behavior and damage morphologies.

We have systematically studied the threshold fluences and damage morphologies of unetched industrial quality Si and GaAs for both a single 90 fs. pulse (620 nm.) and for a widely varying number (2 to 10^6) of multiple 90 fs. pulses. In order to highlight and define the contrast with longer pulse excitation, we have repeated the same measurements on the same samples with 25 ns. pulses of nearly the same wavelength (600 nm.). These comparative pulse trains were supplied by a Rhodamine 640 dye jet pumped by a 20 W. copper vapor laser which served alternately as a 5 KHz repetition rate amplifier for fs. pulses from a colliding pulse mode-locked source laser[2] or (with source laser and saturable absorbers removed) as a laser source of 25 ns. pulses. For accurate fluence determination, this source offered a high degree of shot-to-shot stability in pulse energy and beam profile. Focal spot profiles were characterized by pinhole transmission, and beam powers were carefully monitored. Damage morphology was characterized with a Normarski microscope and a scanning electron microscope (SEM).

We now summarize the major results. Single shots were isolated from the 5 KHz pulse trains with a pair of synchronized mechanical shutters. For ns. pulses, we measured a single shot melting threshold fluence $F_{TH}(1)$ (as determined by appearance of surface amorphization) of 0.37 ± .05 J/cm^2 for Si. A linear absorption model (α^{-1} = 2.0 mm.) predicts that surface temperature rises to 1400°K at this fluence, just below the melting temperature (1685°K). The slight discrepancy is explained by thermally-induced band gap shrinkage during the pulse. For 90 fs. pulses, by contrast, we measured $F_{TH}(1)$=0.05 ± .007 J/cm^2. A linear absorption model (α^{-1} = 2.2 mm.) predicts that the surface reaches a temperature of less than 500°K. Clearly nonlinear absorption reduces the absorption depth, and increases surface temperature greatly. We have characterized this nonlinearity by an independent measurement of self-reflectivity and transmission of 90 fs. pulses from silicon-on-sapphire as a function of fluence. The results are shown in Fig. 1, which presents the absorption coefficient of silicon for femtosecond and nanosecond pulses as a function of fluence. For femtosecond pulses, the absorption depth is nearly ten times smaller at $F_{TH}(1)$ compared to the linear absorption depth measured at low fluences. By contrast, in GaAs the femtosecond single-shot threshold (.075 J/cm^2) is only 30% lower than the nanosecond pulse threshold (.11 J/cm^2). Consequently in GaAs, linear absorption dominates even in the femtosecond regime. We observed no surface ripple formation for single 90 fs. pulses, in agreement with models which require interaction of the light with transient capillary waves in the melt[3]. However, clear ripples are seen for as few as 2 shots.

We have also characterized the reduction in damage threshold caused by multipulse cumulative damage.

Because of the strong absorption nonlinearity near $F_{TH}(1)$, small (~50%) reductions in fluence below $F_{TH}(1)$ rapidly reduce maximum surface temperature to less than 500°K for fs. excitation of Si. With ns. excitation, by contrast, maximum surface temperature decreases more slowly with fluence, and exceeds

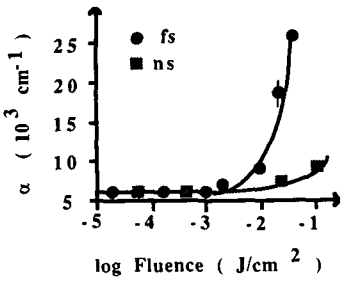


Fig. 1. Absorption coefficient of a silicon film as a function of laser fluence for 90 fs. (circles) and 20 ns.(squares) pulses at 620 nm. wavelength.

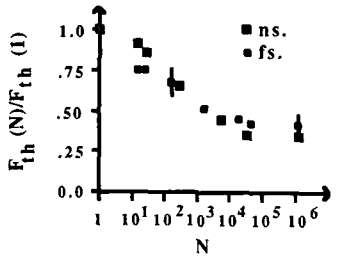


Fig. 2. Multipulse cumulative damage thresholds for fs. and ns. photoexcited silicon, presented as a ratio to single shot thresholds. Note that the single shot threshold for fs. excitation is 7x smaller than for ns. excitation.

1000°K at 0.5 $F_{TH}(1)$. From thermal considerations alone, therefore one might expect a higher threshold fluence for multipulse damage $F_{TH}(N)$ with fs. than with ns. excitation. Instead, our measurements, presented in Fig. 2 for Si, show that the ratio $F_{TH}(N)/F_{TH}(1)$ is actually smaller for fs. than for ns. pulses over the range $2<N<10^6$. A similar trend is observed in GaAs. Hence the pattern of multipulse threshold reduction shows little dependence on sample, pulse duration, or surface temperature. Clearly the mechanism for multiple fs. pulse damage must be ascribed partially to non-thermal causes to explain the unusually low thresholds. Because of the large carrier density present in the fs. case, a model based on accumulation of charge at defect clusters, advanced previously to explain cumulative damage in semiconductors by below band gap radiation[4], may therefore be appropriate for cumulative damage by fs. pulses, even at wavelengths above the band gap.

This work was supported by the Joint Services Electronics Program (Contract F49620-86-C-0045) and by the Robert A. Welch Foundation.

1. For example A.L. Smirl, T.F. Boggess, I.W. Boyd, S.C. Moss, K. Bohnert, K. Mansour, Opt. Eng. **25**, 157 (1986); D.K. Sardar, M.F. Becker, and R.M. Walser, J. Appl. Phys. **62**, 3688 (1987); P.L. Liu, R. Yen, N. Bloembergen, and R.T. Hodgson, in *Laser and Electron Beam Processing of Materials*, eds. C.W. White and P.S. Peercy, p. 156 (1980).
2. W.H. Knox, M.C. Downer, R.L. Fork, and C.V. Shank, Opt. Lett. **9**, 552 (1984).
3. For example J.E. Sipe, J.F. Young, J.S. Preston, H.M. van Driel, Phys. Rev. B**27**, 1141 (1983); D.J. Ehrlich, S.R.J. Brueck, and J.Y. Tsao, Appl. Phys. Lett. **41**, 630 (1982); P.M. Fauchet and A.E. Siegmann, Appl. Phys. Lett. **40**, 824 (1982).
4. N.R. Shetty, M.F. Becker, and R.M. Walser, 17th ASTM Laser Damage Symposium, eds. H.E. Bennett, A.H. Guenther, D. Milam, and B.E. Newman, Boulder, 1986.

Abstract No. 608

HARMONIC CROSS-PHASE-MODULATION IN ZnSe

P. P. Ho and R. R. Alfano

Institute for Ultrafast Spectroscopy and Lasers
Photonic Application Laboratory
Departments of Electrical Engineering and Physics
The City College of New York, New York, N.Y. 10031

The use of light to control and to generate light is most important in the fields of lasers and optical communication. Self-, induced-, and cross-phase modulation processes[1] are responsible for the generation and spectral shift of ultrafast supercontinuum. The supercontinum spans over 10,000 cm^{-1} from uv to IR with picosecond to femtosecond duration. When two laser pulses of different frequencies propagate simultaneously in matter, coupled interactions occur[1-6]. This leads to the cross-phase-modulation[1-6] (XPM) where the spectral bandwidth of both pulses increased. In this paper, we report on a XPM process resulting from the coupling of the second order and the third order susceptibilities in ZnSe. The temporal property of the second harmonic XPM signal has been measured and theoretically fitted.

Experimentally, an 8-ps 2-mJ 1054-nm laser pulse was weakly focused into the ZnSe sample. The second harmonic produced in ZnSe samples was about 10-nJ. The incident laser energy was controlled by changing the neutral density filter. A reference pulse at 527-nm was produced in a KDP crystal. Using a beam splitter, 1054-nm and 527-nm pulses were separated into two different paths. The weak 527-nm reference pulse was used for calibration and passed through a fixed distance in air to set the zero reference time for the streak camera. Only a 1054-nm pulse was used to pump the ZnSe samples. The temporal profile and the propagation time of the pulses which exited from the ZnSe and the reference 527-nm pulse were measured by a Hamamatsu 2ps resolution streak camera system.

Measurements of ZnSe SHG-XPM spectra[2] indicated that the extent of the spectral broadening about the second harmonic line at 527-nm depended on the intensity of the incident 1054-nm laser pulse. When the incident laser pulse energy was 2mJ, there was significant spectral broadening from 500-nm to 570-nm. There was no significant difference in the spectral broadening distribution measured in the single and polycrystalline materials.

The temporal profile and propagation time of an intense 1054-nm pump pulse and induced spectral broadened pulses propagating through a 22-mm ZnSe polycrystalline sample were measured. It took ~ 189-ps for a 1054-nm pulse passing through the crystal. While the total signal of SHG and SHG-XPM with wavelength spread from 500-nm to 570-nm indicated a sharp spike at 189-ps and a long plateau spanned from 189-ps to 249-ps. Pulses of selected 10-nm bandwidth from the SHG-XPM signal had one major component emitted at nearly the same time as the 1054-nm incident pulse. The measured group refractive indices of ZnSe were $n_{g,527} = 3.39$ and $n_{g,1054} = 2.57$, respectively. The sharp spike of the SHG-XPM pulses generated in ZnSe appears to have nearly the propagation time as the pump 1054-nm pulse.

A second-harmonic XPM model is used to explain the temporal and spectral behaviors of the induced spectral broadening in ZnSe. The first order partial differential equations for SHG-XPM can be written as[3]

$$\partial E_{1o}/\partial z + 1/v_1\ \partial E_{1o}/\partial t = i\gamma |E_{1o}|^2 E_{1o} \qquad (1)$$

$$\partial E_{2o}/\partial z + 1/v_2\ \partial E_{2o}/\partial z =$$

$$\underbrace{\frac{i\sigma E_{1o}^2 \exp[-i(k_2-2k_1)z]}{\text{SHG}}}_{\text{SHG}} + \underbrace{2i\gamma |E_{1o}|^2 E_{2o}}_{\text{XPM}} - \underbrace{\alpha E_{2o}}_{\text{Absorption}} \qquad (2)$$

Functions E_{1o} and E_{2o} are the electric field envelope amplitudes, v_1 and v_2 are group velocities, k_1 and k_2 are wave vectors for ω and 2ω pulses, respectively. Parameterr α is the absorption coefficient at 2ω, $\sigma = \mu_o\omega c\chi^2/2$, χ^2 is the second order nonlinearity, $\gamma = 3\omega^2\mu_o\chi^3/8k_1$, and χ^3 is the third order nonlinearity.

The solution for E_{2o} can be written as[3]

$$E_{2o} = i\sigma A_o \exp[-\alpha z + i(2\gamma A_o^2) \int_o^z F^2(U+\eta z')\, dz'] \times$$

$$\int_o^z F^2(U+\eta z') \exp(\alpha z') \exp[-i\xi z' + i2\gamma A_o^2 F^2(U+\eta z')z'$$

$$- 2i\gamma A_o^2 \int_o^{z'} F^2(U+\eta z'')dz'']dz' \qquad (3)$$

where $U = (t-z/v_2)/\tau$; $\eta = (n_2-n_1)/c\tau$; $\xi = (n_2^p-n_1^p)2\omega/c$; n_1, n_1^p, n_2, and n_2^p are the group and phase indices of refraction at ω and 2ω, respectively; A_o is the initial amplitude of ω-pulse; F is the pulse envelope function; and τ is the pulse duration.

A theoretical curve is plotted in fig.1 using eq. 3 and appropriate experimental parameters. The temporal distribution of SHG-XPM has shown a modulation pattern. Within the coherence length of the entrance and exit parts of the crystal, SHG-XPM signal will have less cancellation. In addition, due to the linear absorption and two-photon induced absorption[7] in ZnSe, the signal generated at the front portion of the crystal is reduced. Newly generated SHG-XPM wavelengths appear mainly to be emitted at the exit surface of the crystal. The calcuated curve of SHG-XPM is in good agreement with the measurement.

This research is supported in part by Hamamatus Photonics K.K..

References

1. R. Alfano and P. Ho, IEEE, QE-24, 353 (1988)
2. R. Alfano, Q. Wang, T. Jimbo, P. Ho, R. Bhargava and B. Fitzpatrick, Phys. Rev. A 35, 459 (1987)
3. J. Manassah and O. Cockings, Opt. Lett. 12, 1035 (1987)
4. R. Alfano, P. Baldeck, F. Raccah, and P.P. Ho, Appl. Opt., 6 3491 (1987)
5. R.R. Alfano, Q. Li, T. Jimbo, J. Manassah and P.P. Ho, Opt. Lett., 11, 626 (1986)
6. J. Gersten, R. Alfano, and M. Belic, Phy. Rev., A21 1222 (1980)
7. R. W. Hellwarth, "Third order susceptibilites of liquids and solids", ed in Prog. Quant. Elect. 5 pp1-68 (1977) Pergamon Press.

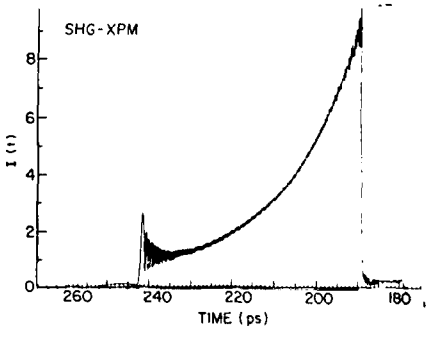


Fig. 1. Calculated curve of the temporal distribution of SHG-XPM from eq. 3. $z = 22$-mm, $\tau = 6.79$-ps, $\alpha = 0.3 + 0.23\times10^{-4}(YA^2)$ cm^{-1} where 0.3 is the linear absorption coeffficnet and the second term is the induced absorption coefficient, $n_2-n_1 = 0.75$, $n_2^p-n_1^p = 2.697 - 2.484 = 0.21$, and $YA_o^2 = 10^4$ cm^{-1}.

Abstract No. 609

Coherent transient optical effects in semiconductors

Pranay K. Sen and Pratima Sen
Department of Physics, Bhopal University
Bhopal 462 026, Madhya Pradesh, India

The rapid developments in the areas of picosecond and femtosecond lasers as well as in sophisticated fabrication technology have made it possible to observe ultrafast processes in materials/1/. Of particular interest are direct gap crystals like GaAs, InSb, HgCdTe/2/.

Here, we have analyzed the possibility of occurrence of coherent transient effects like self induced transperancy(SIT) in the above class of crystals under moderate photoexcitation limit.

The photoinduced electron-hole pair density N can be obtained from the usual rate equation

$$\dot{N} = \eta\alpha(N)\mathcal{I}I_E/\hbar\omega - N/\tau \qquad (1)$$

with η being the quantum efficiency of e-h pair generation per absorbed photon of energy $\hbar\omega$. τ is the diffusional decay incorporated e-h recombination life time. I_E is the constant excitation intensity for pulses with peak field E_0. $\alpha(N)$ is the transient intensity dependent absorption coefficient given by/3/

$$\alpha(N) = \alpha_0\,(1 - 2N/N_0), \qquad (2)$$

α_0 and N_0 being the linear absorption coefficient and density of electrons in the valence band at crystal ground state, respectively. One gets the solutions as

$$N = (\eta\alpha_0\tau' I_E/\hbar\omega)\left(1-\exp(-t/\tau')\right) \qquad (3)$$

and

$$\alpha(N)=\alpha_0\left[1-(I_E\tau/I_S\tau)\left(1-\exp(-t/\tau')\right)\right] \qquad (4)$$

with $\tau' = \tau(1 + I_E/I_S)^{-1}$, $I_S = N_0\hbar\omega/(2\eta\alpha_0\tau)$.

Equations (3) and (4) can yield the steady-state solutions if one takes $t >> \tau'$.

The crystals are assumed to possess nondegenerate, isotropic and parabolic band structures with ground state being defined in terms of completely filled valence band and empty conduction band. The equations of motion of the probability amplitudes in the crystal ground state and excited pair state are given by/4/

$$\dot{a}(t) = i\sum_{\vec{k}}\left(\mu_{ba}(\vec{k})E_0/2\hbar\right)e^{i\Delta\omega t}\,b(\vec{k},t) \qquad (5)$$

and

$$\dot{b}(\vec{k},t) = i\left(\mu_{ab}(\vec{k})E_0/2\hbar\right)e^{-i\Delta\omega t}a(t) - \gamma b(\vec{k},t), \qquad (6)$$

respectively, for $\vec{\mu}(\vec{k}) \| \vec{E}(t)$ and $\Delta\omega = \omega - \omega_k$. $\omega_k\,(= \omega_g + \hbar k^2/2m_r)$ is the transition frequency and γ is the phenomenological damping parameter. Following standard method/4/, one finds the solutions for $a(t)$ and $b(\vec{k},t)$ yielding

$$|a(t)|^2 = \left(e^{\gamma t}/|\beta|^2\right)\left[\Delta\omega^2\sin^2\theta + |\beta|\cos\theta + (\gamma\sin\theta)^2\right] \qquad (7)$$

and

$$|b(\vec{k},t)|^2 = e^{-\gamma t}|\Omega_R/\beta|^2\sin^2\theta \qquad (8)$$

where $\beta = \left[(\Delta\omega + i\gamma)^2 + \Omega_R^2\right]^{1/2}$, $\Omega_R = |\mu E_0/2\hbar|$; $|\mu_{ab}| = |\mu_{ba}| = \mu$ and we take $\beta t/2 = \theta$.

Under ideal undamped resonant transitions with pulsed excitation for $t = \pi/\beta$, one finds $|b(\vec{k},t)|^2 = 1$ and $|a(t)|^2 = 0$ producing complete population inversion. For real narrow-gap semiconductors, one can achieve it only approximately under nearly sharp resonant moderate phoptexcitation such that $\omega >> \Omega_R > \Delta\omega, \gamma$.

One can study the whole class of conerent transient optical effects by considering the transient polarization $P(t) = N\langle\mu(\vec{k},t)\rangle = \epsilon_0\chi(I,t)E(t)$ with $\langle\mu(\vec{k},t)\rangle$ being obtained from the relation

$$\langle\mu(\vec{k},t)\rangle = 2\mu\left[a(t)\,b^*(\vec{k},t)\,e^{-i\omega_k t}\right].$$

The effective dielectric function defined as $\epsilon(t) = \epsilon_1(t) + \chi(I,t)$ is found to be

$$\epsilon(t) = \epsilon_1(t) + 2A|\Omega_R/\beta|^2\left[(\Delta\omega/2\omega)\sin^2\theta - i\{(\gamma/\omega)\sin\theta + (\beta/2\omega)\cos\theta\}\sin\theta\right] \qquad (9)$$

where $A = \eta\alpha_0\eta_0 c\,\tau'(1-e^{-t/\tau'})$; $\epsilon_1(t)$ is the linear dielectric function. We define the effective complex propagation constant as

$$k'(t) = k'_r(t) - ik'_i(t) = k(\epsilon_1(t) + \chi(I,t))^{\frac{1}{2}}$$

with $k = \omega/c$. Using De Moivre's theorem, we get

$$k'_r(t) \approx (k/\sqrt{2})\left[\epsilon_{1r}(t) + A|\Omega_R/\beta|(\Delta\omega/\omega)\sin^2\theta\right]^{1/2} \qquad (10a)$$

and

$$k'_i(t) \approx (k^2/2k'_r)\left[\epsilon_{1i}(t) + A|\Omega_R/\beta|\{(\gamma/\omega)\sin^2\theta + (\beta/4\omega)\sin 2\theta\}\right]. \qquad (10b)$$

The above formulations can enable one to study the oscillatory behavior of the transmittivity coefficient and optical nutation for arbitrary pulse shapes.

The phenomenon of SIT can be investigated by considering the propagation of a 2π-pulse through the crystal with $\omega >> \Omega_R > \Delta\omega$ and γ such that $|\beta| \sim \Omega_R$. From (7) and (8), one finds that during the first half cycle of the pulse ($0 \le \beta t \le \pi$), $1 \ge |a(t)|^2 \ge 0$ and $0 \le |b(\vec{k},t)|^2 \le 1$ with (10b) yielding k'_i that approaches a finite positive value from zero. During the second half cycle ($\pi < \beta t \le 2\pi$), we find $0 \le |a(t)|^2 \le 1$ and $1 \ge |b(\vec{k},t)|^2 \ge 0$ and k'_i reducing to zero at $\beta t = 2\pi$ from being negative in the range $\pi < \beta t < 2\pi$. The transient pulse phase velocity in the crystal $v_\phi\,(= \omega/k'_r)$ becomes

$$v_\phi \sim c\left[\epsilon_{1r}(t) + A|\Omega_R/\beta|(\Delta\omega/\omega)\sin^2\theta\right]^{-1/2} \qquad (11)$$

This gives $v_\phi < c$ and can be much smaller ($\sim 10^{-3}c$) in crystals with large α_0 and τ' such that $t < \tau'$ can be achieved in the nanosecond transient regime remembering that the photoexcitation should be moderate with I_E and I_S being almost of the same order. This establishes the occurrence of self induced transperancy of a nearly sharp resonant pulse propagating through the semiconducting materials without undergoing any exchange of energy.

References

/1/ C.L.Tang, in Nonlinear Optics:Materials and Devices, eds. C.Flytzanis and J.L.Ouder (Springer-Verlag, Berlin, 1986), p.80.
/2/ J.L.Ouder, in Ref. 1, p.91.
/3/ H.M.Gibbs, Optical Bistability:Controlling Light with Light (Academic, Orlando, 1985), p.26.
/4/ P.Sen and P.K.Sen, IEEE J. Quantum Electron., QE-23, 2033(1987).

Abstract No. 610

Ultrafast Dynamics of Ligand Rebinding to Heme at Low Temperature*

Jay C. Postlewaite, Jeffrey B. Miers, and Dana D. Dlott

School of Chemical Sciences
University of Illinois at Urbana-Champaign
505 S. Mathews Ave.
Urbana, IL 61801

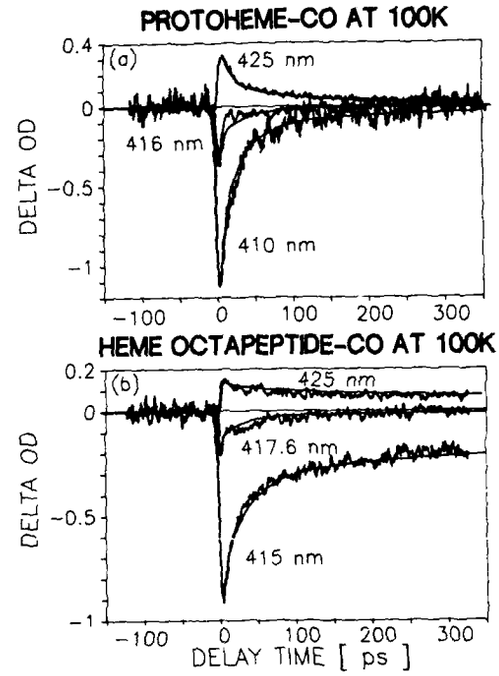
Metalloporphyrins are versatile compounds whose chemical reactivity can be varied a great deal by control of the local enviroment via chemical substitution. We have studied the ultrafast rebinding of photodissociated carbon monoxide to protoheme (PH) and heme octapeptide (HO) in a low temperature solvent glass (glycerol:water 75:25) [1]. The use of a glassy matrix to contain the heme insures that the ligand rebinding process is not controlled by diffusion through the solvent, but rather by more elementary chemical reaction steps. PH is a simple Fe-porphyrin which is the prosthetic group found in elementary heme proteins such as myoglobin. HO, obtained by enzymatic digestion of cytochrome-C, differs from PH by the presence of a "basket handle" peptide chain which provides a covalently bound histidine residue bound to Fe on the side opposite the ligand.

The apparatus used for these studies consisted of a dye laser synchronously pumped by a mode locked Nd:YAG laser. The ≈ 1 ps dye laser pulses are amplified by a Nd:YAG regenerative amplifer [2] to produce 50 μJ, 1 ps pulses at 570 nm at a pulse repetition frequency up to 1000 Hz. One half of the pulse is used to photolyze the heme sample while the other half produces a white light continuum used to probe the large changes in optical density (OD) in the Soret region, 400-440 nm.

The processes we study can be roughly divided into three stages (1) photodissociation, (2) heme relaxation, and (3) ligand rebinding. The initial ligand-heme complex, Fe-L is nearly planar. When L is dissociated, a probably planar intermediate, denoted Fe- -L is formed. The Fe- -L relaxes (domes) to form a nonplanar, relaxed five coordinate heme, denoted Fe + L in nonviscous fluids. In the frozen glass, this doming process is somewhat hindered. The Fe-L species has an absorption maximum, denoted λ_{CO}, near 410 nm, the relaxed Fe + L has a maximum, denoted λ_{DL}, near 425 nm, and the isobestic point, λ_{IB} is near 416 nm. Figure 1 shows kinetic decays, which have the form $\Delta OD_\lambda(t)$, at these wavelengths for PH and HO at T = 100K [1].

The λ_{CO} data near 410 nm reflect mostly the dissappearance and subsequent reapparance of Fe-L. The Fe-L disappears promptly, and then reappears in two ways, an exponential ($\tau \approx 30$ ps) process, denoted I*, and a nonexponential process denoted I. The λ_{DL} data near 425 nm reflect mostly the appearance of relaxed Fe + L, and its subsequent disappearance. The Fe + L does not appear until a few ps after Fe-L disappears. This is the relaxation rate for the heme. Then Fe + L is destroyed by nonexponential process I. At λ_{IB}, contributions from Fe-L and Fe + L cancel [3], and only Fe- -L species are seen. Two Fe- -L species are observed, a short lived species ($\tau \approx 2$ ps), whose decay correlates with the appearance of Fe + L, and a long-lived species ($\tau \approx 30$ ps) whose decay correlates with process I*.

Our physical picture of this system is as follows. In the glassy matrix, heme exists in two states, I, characterized by a cage with enough free volume to permit doming, and *, characterized by a cage which does not permit doming. The relaxed I rebinds CO with an enthalpic barrier which involves the attainment of a planar transition state. The inhomogeneous glass/heme system gives rise to a distribution of barrier heights, resulting in nonexponential process I. The unrelaxed * rebinds CO with no enthalpic barrier, rather only an entropic barrier which involves mainly CO rotation is present. The smooth curves in Fig. 1 are generated with this model.



When PH and HO are compared at 100K, we find that doming is faster in HO (1.5 ps) than in PH (2.5 ps) because of tension exerted by the peptide chain. Process I* is nearly identical, as expected for ligand rebinding to planar hemes which differ only in proximal substitutents. Process I is much slower in HO than in PH because the proximal tension generated by the peptide chain makes attainment of the planar transition state more difficult.

*Research supported by the National Science Foundation through grant NSF DMR 87-21243

[1] J. C. Postlewaite, J. B. Miers, and D. D. Dlott, J. Am. Chem. Soc. [in press].

[2] J. C. Postlewaite, J. B. Miers, C. C. Reiner, and D. D. Dlott, IEEE J. Quantum. Electron. QE-24, 441 (1988).

[3] D. D. Dlott, J. Am. Chem. Soc. [in presss]

Abstract No. 611

Investigation of Optical Spectroscopy of Cancerous and Normal Human Tissues

R. R. Alfano, G. C. Tang, A. Pradhan, S. Wenling

Institute for Ultrafast Spectroscopy & Lasers
Physics Dept., City College of New York
New York, NY 10031

Previous spectroscopic studies on animal tissues have been extended to humans. Steady state, excitation spectra, and time-resolved spectroscopic dynamics from normal and tumor human tissues have been studied and will be presented.

Fluorescence spectra from normal and tumor human breast and lung tissues have been measured. Normal breast tissue spectra show three distinct peaks at around 520nm, 550nm and 600nm while the tumor spectra show a smoothening of the profile with less structure. Most normal breast tissue spectra have Raman peaks while the tumor spectra have none. In the lung spectra, the normal show three distinct peaks, or in some cases two distinct peaks with the second peak missing while the tumor has a smooth profile. The main peak is attributed to flavins while the third peak may be associated with porphyrins. The tumor peaks are either blue or red shifted, depending on the organ, as compared to the normal tissue main peaks. This could be due to the accumulation of positive or negative charge in the molecules. The smoothening of the tumor profile could imply a deficiency of porphyrins. The steady state measurements have been done with excitation at three different wavelengths: 457.9nm, 488nm and 514.5 nm and distinct differences were obtained at all three wavelengths.

The time-resolved spectra have been measured at 530nm and 350nm excitation to study the dynamic behavior of the molecules. The measurements obtained using a Nd:glass laser and a streak camera showed two decay times, a slow and a fast component. The fast component of the tumor tissues is faster than that of the normal tissues while the long component is almost the same. The fast component and the slow component of the normal lung tissue are 220 ps and 2650 ps, respectively while those of the lung tumor tissues are 120 ps and 2600 ps, respectively. The shorter fast component of the tumor tissues implies that there could be more nonradiative pathways in the tumor than in normal tissues.

The excitation spectra of tumor and normal tissues measured at emission wavelengths 520nm, 550nm and 600nm corresponding to the three peaks in the fluorescence spectra of normal tissues have been obtained. The overall excitation spectra showed broad uv and visible bands. The normal spectra showed three peaks within the uv band while the tumor spectra showed a smooth uv band as well as a larger visible band. The uv band of the normal spectra have peaks at 336nm, 352nm and 371nm.

These spectroscopic differences are attributed to changes in the electronic structures of fluorophors in the cancer tissues.

This research is supported by SDIO.

Abstract No. 612

Time-Resolved Fluorescence of Nucleic Acids

Thomas M. Nordlund

Dept. of Biophysics, Dept. of Physics & Astronomy, and Laboratory for Laser Energetics, University of Rochester, Rochester, NY 14642 USA and
Dept. of Medical Biophysics, Karolinska Institute, S-104 01 Stockholm, Sweden

The dynamic fluorescence of nucleic acids is determined by at least three general properties: chemical structure of the nucleic acid, conformation of oligomeric or polymeric species, and environment (temperature, solvent, etc.). This paper explores some specific examples of the effect of conformation and chemical structure on the decay of excited nucleic acid bases.

Adenine derivatives

The fluorescence decay of the monomer ribo-adenosine monophosphate (rAMP) is described by a time of 10 ps or less (Table 1). The single-stranded, but base-stacked poly (rA), on the other hand, has two emission components: one of about 10 ps decay time and the other a red-shifted component of about 100 ps. This latter component may be excimer emission. 2-aminopurine (2AP), a modification of adenine where the amino group is moved from the base ring 6 position to the 2 position, shows a 10-ns decay. Similar long lifetime components persist when 2AP is incorporated into ribo- or deoxyribo-oligomers.[1,2]

Thymine derivatives

Deoxy thymine monophosphate (dTMP) and poly (dT), which forms a non-stacked but ordered single helix, both show simple fluorescence decays of 5 ps or less. No evidence for excimer formation is observed.

Y-base derivatives [3]

Measurements of the fluorescence decays of wybutine in $tRNA^{phe}$ show that much of the decay is described by a 7-ns lifetime in 0.1 M KCl and 5-20 mM Mg^{++}, but without magnesium the largest amplitude decay times are about 300 ps and 2 ns. [4] We have measured the dependence of the fluorescence on the Y-base chemical structure in order to understand the fluorescence behavior in $tRNA^{phe}$, as Y-base fluorescence is a useful structural/dynamics probe.

We observe two classes of Y-base derivative fluorescence (fig. and Table 1). One class is dominated by subnanosecond decay times, the other by decay times of 7-10 ns. Rapid fluorescence decays observed for the Y base derivatives **1** and **4** in DMSO contrast with the predominant 7 ns decay observed in the case of $tRNA^{phe}$ (in water with Mg^{++}). Compound **15**, with ribose attached to the "unnatural" $^{5}N^{1}$ rather than the "natural" N^{3} position of the ring, and the free base show long lifetimes. Chemical modifications on the more remote ribose ring periphery also affect the electronic properties of the Y base.

ACKNOWLEDGEMENTS

Y base work done in collaboration with J. Chattopadhyaya and R. Rigler. deoxy-2AP was graciously provided by L. McLaughlin. Supported in part by the U.S. National Science Foundation (U.S.-Sweden Cooperative Science Program), the U.S. National Institutes of Health (Fogarty International Fellowship grant 1 FO6 TWO1332 and grant CA41368), the Sponsors of the Laser Fusion Feasibility Project at the University of Rochester, the Swedish Board for Technical Development and the Swedish Natural Science Research Council.

1 A. Gräslund, F. Claesens, L.W. McLaughlin, P.-O. Lycksell, U. Larsson and R. Rigler (1987) in Structure, Dynamics and Function of Biomolecules, eds. A. Ehrenberg, R. Rigler, A. Gräslund and L. Nilsson, Springer-Verlag, Berlin, pp. 200-207.

2 F. Claesens (1987), thesis, Dept. of Medical Biophysics, Karolinska Institute, Stockholm, Sweden.

3 T. Nordlund, R. Rigler, C. Glemarec, J.-C. Wu, H. Bazin, G. Remaud, and J. Chattopadhyaya, submitted to Nucleic Acids Research.

4 F. Claesens and R. Rigler (1986) Eur. Biophysics J. **13**:331.

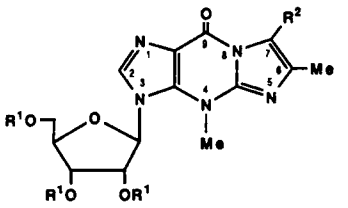
5 C. Glemarec, J.-C. Wu, G. Remaud, H. Bazin, M. Oivanen, H. Lönnberg and J. Chattopadhyaya (1988) Tetrahedron **44**: 1273.

TABLE 1. Fluorescence decay parameters of some nucleic acids at room temperature.

Compound [a]	Fluorescence Decay Time (ns)	Amplitude	Notes
rAMP	≤0.010	~1	b,c
Poly (rA)	~0.008	-	b,c
	0.10	-	b,c,d
2-aminopurine	10.1	1.00	c,e
dTMP	≤0.005	~1	b,c
Poly (dT)	≤0.005	~1	b,c
1	0.24	0.98	e,f
	1.08	0.01	
	7.39	0.01	
4	0.53	0.95	e,f
	2.05	0.04	
	8.95	0.01	
15	2.61	0.04	e,f
	10.12	0.96	
Free Y base [g]	7.0	1.00	e,f

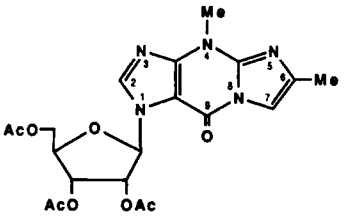
[a] r indicates ribo-; d indicates deoxyribo-. Y-base compounds numbered in conformance with ref. 5.
[b] Measured by streak-camera techniques
[c] Measured in aqueous solution near neutral pH.
[d] Component red-shifted in emission wavelength
[e] Measured by time-resolved single photon counting
[f] Measured in DMSO. The choice of DMSO as solvent was made on the basis of the good solubility of all Y-base compounds.
[g] Y base with CH_3 at N^4 and C^6 and H at N^1.

FIG. 1. Structures of modified Y nucleosides used in this study. Me = methyl; Ac = acetate.

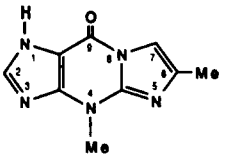


1 : $R^1 = R^2 = H$

4 : R^1 = Ac, $R^2 = H$



15



Abstract No. 613

Picosecond Time-Resolved Infrared Spectroscopy

P. A. Hansen, J. N. Moore and R. M. Hochstrasser

Department of Chemistry
University of Pennsylvania
231 S. 34th Street
Philadelphia PA 19104

A method for obtaining infrared spectra and kinetics with picosecond time resolution is presented. The IR probe in the experiment is the output of a tunable cw diode laser. A change in the IR absorbance of the sample is induced by a pulse of visible or UV radiation. The transmitted IR radiation is sum frequency mixed with a second pulse of visible radiation in a non-linear crystal of lithium iodate to generate radiation in the visible wavelength region, allowing detection with a photomultiplier tube. Kinetics are obtained by varying the time delay between the photolyzing and upconverting pulses at a fixed IR frequency, while transient spectra may be obtained at a fixed time delay by scanning the IR frequency. In addition, anisotropic changes in the IR absorbance on photolysis may be observed by using parallel and perpendicular relative polarizations of the photolysis and IR probe beams.

The pulses of visible radiation are obtained from two dye lasers which are both synchronously pumped by the frequency - doubled output of a mode - locked and Q - switched Nd:YAG laser. The pulses are 1 - 10 μJ in energy and 20 ps (FWHM) in duration and may be selected from the dye lasers at a repetition rate of up to 1.2 kHz. The time resolution of the IR detection is attained through the upconversion process.

This experimental arrangement has been used to study the photodissociation of CO from the carboxy- derivatives of hemoglobin, myoglobin and protoheme in ambient temperature solution. The observations have been made on the principal bound CO stretch bands (1930 - 1970 cm^{-1}). The transient bleaching spectra of all the systems have been shown to mirror the steady-state IR absorption spectra of the CO-liganded species and have also been observed to display pulsewidth-limited risetimes. This is in agreement with the results of time-resolved UV/visible absorption studies. The protoheme system in high viscosity solvents displayed recovery of the bound CO band on the picosecond timescale due to geminate recombination, while no such recovery was observed in solvents of low viscosity nor in the case of the heme proteins.

Measurement of the anisotropic change in the IR absorbance upon photodissociation has allowed the equilibrium iron-carbonyl geometries to be determined for these systems. All exhibit distortion of the FeCO unit from the configuration observed in X-ray diffraction studies of crystals of model porphyrins, where the unit is observed to be linear and oriented perpendicular to the heme plane. For carboxymyoglobin, two distinct configurations were observed corresponding to the two principal bands in the IR absorption spectrum. For protoheme-CO, the degree of distortion from a linear perpendicular configuration is found to depend upon the solvent in which the molecule is placed.

The IR apparatus has also been used to study the photodissociation of transition metal carbonyl complexes, again by observation of the bound CO stretch bands. Preliminary results for such systems will be presented.

This work is supported by grants from NSF and NIH.

Abstract No. 614

Ultrafast Electronic and Acoustic Effects in Conducting Polymers

Zeev V. Vardeny

Department of Physics, University of Utah
Salt Lake City, UT 84112

The polarized picosecond pump and probe technique with 50 fsec resolution has been used to generate and detect electronic excitations and propagation of ultrasonic phonons in thin films of oriented and unoriented polyacetylene and polythiophene, with excitation beam polarized parallel and perpendicular to the chains direction. For excitation parallel to the chains direction we found that the photoexcitations are instantaneously generated followed by a power law decay, which is interpreted as fast geminate recombination; only up to about 2% of the intrachain carriers are able to escape the fast recombination. In addition to intrachain photoexcitations, we found for excitation perpendicular to the chains direction a slow rising component interpreted as due to interchain excitations. This component lives much longer and is in fact partly responsible for the metastable photoexcitations observed with other much slower techniques.

The photoinduced ultrasonic vibrations are generated by the photoinduced thermal stress associated with the heating of the thin absorption layer by the pump pulse. The induced stress in turn launches a strain wave into the film which bounces back and forth inside the film with diminishing amplitude. We have used this phenomenon to measure the sound velocity and ultrasonic attenuation for phonons in the frequency range of 5 to 200 GHz in trans and cis-rich polyacetylene and polythiophene. Among our results we have found a superlinear acoustic phonon dispersion relation for frequencies in the range of 5 to 50 GHz.

Abstract No. 615

Time-Resolved Absorption in Oriented *Trans*-Polyacetylene

L. Rothberg and T. M. Jedju
AT&T Bell Laboratories
Murray Hill, New Jersey 07974

P. D. Townsend, S. Etemad and G. L. Baker
Bell Communications Research
Red Bank, New Jersey 07701

Trans-polyacetylene is a quasi-one-dimensional organic semiconductor with a conjugated structure consisting of alternating single and double bonds between carbons on the chains. Replacing single bonds with double bonds and vice-versa leaves a degenerate ground state "phase" of the material. In this context, solitons are essentially domain walls between the different ground states (bond alternation phases) of the material which coexist on a single chain. Since the energies of each phase are equal, the domain walls are free to propagate along the chains. Mobile charged solitons have been found to be important in the doping and light induced conductivity of *trans*-polyacetylene.

The mid-bandgap photoinduced absorption in *trans*-polyacetylene is characteristic of these photogenerated charged domain walls.[1] We report subpicosecond resolution measurements of the photoinduced midgap absorption dynamics in oriented Durham polyacetylene where it is possible to effect a better separation between intrachain and interchain excitation. Pumping with above gap radiation (2 eV) having polarization parallel to the chain direction leads to intrachain excitation. We observe direct formation of charged soliton pairs as predicted by Su & Schrieffer.[2] The solitons are formed with high quantum yield and recombine rapidly (0.5-1 ps). The intensity dependence of the photoinduced absorption indicates that saturation is due to filling the entire excited volume with charged solitons. Saturation of the midgap absorption coincides with saturation of the interband bleaching. Volume (or phase space) filling therefore quantitatively explains the origin of the third-order nonlinear optical susceptibility.[3]

A red shift in the soliton spectrum at zero decay is observed and can be associated with the soliton absorption before they have reached equilibrium. The formation **and equilibration** of the solitons occurs in less than our 0.5 ps instrumental resolution, consistent with the Su-Schrieffer predictions.

Pumping with polarization perpendicular to the chain direction also generates principally Su-Schrieffer soliton pairs. Importantly, however, interchain excitation also occurs and indirectly produces a second set of charged solitons. Polarons are created which diffuse until captured by neutral solitons originally in the material. The resulting charged solitons have a "long" lifetime and differ in their behavior with temperature and density. We will discuss the implications of their formation and decay dynamics for recent photoconductivity and millisecond transient absorption measurements in *trans*-polyacetylene.

References

1. J. Orenstein and G. L. Baker, Phys. Rev. Lett. *49*, 1043 (1980).
2. W. P. Su and J. R. Schrieffer, Proc. Natl. Acad. Sci. (USA) *77*, 5626 (1980).
3. L. Rothberg, T. M. Jedju, S. Etemad and G. L. Baker, IEEE J. Quant. Elect. *24*, 311 (1988).

Abstract No. 616

Long Wavelength Determination of the Spectrum of $\chi^{(3)}$ in Polyacetylene Using Infrared-Free-Electron Laser

W-S. Fann, S. Benson and J. Madey
Stanford University
Stanford, CA 04305

and

S. Etemad, G.L. Baker and F. Kajzar*
Bell Communications Research
Red Bank, NJ 07701

The spectral dependence of the third order optical susceptibility ($\chi^{(3)}$) of *trans*-$(CH)_x$ has been determined using a tunable infrared free electron laser. In addition to the previously reported[1] two-photon resonance enhancement at 0.9 eV, we have observed a much stronger resonance enhancement at 0.59 eV (2.1 μm). The peak in $\chi^{(3)}$ at 0.59 eV is attributed to a three-photon resonance at 1/3 of E_g, the band gap. The three-photon resonance enhancement is sharp ($\sim$0.1 eV wide) and the magnitude of $\chi^{(3)}$ at its peak is in excess of 10^{-8} *esu*. This is the largest value of electronic $\chi^{(3)}$ in a bulk semiconductor. In addition, we note that the position of the three-photon resonance is at 2/3 the energy of the two-photon resonance.[1] Therefore, the state responsible for the parity conserving two-photon transition lies at the band-edge. In contrast to the case of isolated polyene molecules,[2] in polyacetylene the first covalent and the first ionic excited states appear to lie close to each other in polyacetylene. This work emphasizes the importance of an infrared free electron laser for high-resolution spectroscopy and is the first report of its use in condensed matter.

* Permanent Address: CEA-IRDA, Saclay, 91191 France.

[1] F. Kajzar, S. Etemad, G.L. Baker and J. Messier, Solid State Commun. **63**, 1113 (1987).
[2] K. Schulten, I. Ohmine, and M. Karplus, J. Chem. Phys. **64**, 4422(1976).

Abstract No. 617

Picosecond Studies of PTS: Resolution of a New Metastable State

G. J. Blanchard, J. P. Heritage, G. L. Baker, S. Etemad
Bell Communications Research, Inc.
331 Newman Springs Road
Red Bank, New Jersey 07701

Conjugated polymers which posess a large $\chi^{(3)}$ have been investigated extensively due to their potential application to optical signal processing as well as their ultrafast relaxation processes. In addition, the polydiacetylenes, due to their well isolated polymer *backbones and macroscopic crystalline* structure, have been used as model one-dimensional semiconductor systems. The electronic spectroscopy of one polydiacetylene, poly-[2,4-hexadiyn-1,6-diol-bis(p-toluene sulfonate)] - PTS, is accounted for largely by excitonic features, with a singlet exciton absorption near 2 eV and a long-lived ($\sim$50μs) triplet exciton induced absorption at 1.4 eV. The majority of recent time-resolved investigations of PTS have been *concerned* with the ultrafast relaxation processes of the singlet exciton.

In this work we report our picosecond pump-probe transmission *spectroscopic results* on PTS. We have examined the spectroscopy of the singlet exciton absorption band and have determined that it is somewhat narrower than reported previously. We have *observed an energy* dependent sign change in the singlet exciton transient bleaching signal, indicating that the proposed phase-space filling model does not explain completely the spectroscopy of the singlet exciton[1]. In addition to the aforementioned results, we *have discovered* a new metastable state in PTS, whose origin lies $\sim$55 meV above the singlet exciton absorption maximum.

In several previous investigations high peak power light pulses *were used*, with intensities of 10^8 - 10^9 W/cm^2 incident on the sample. Such intensities correspond to $\sim$1 photon per PTS unit cell. In this investigation, we use peak light intensities on the order of 10^6 W/cm^2, providing excitation of approximately 1% of the sample. Picosecond pump-probe transmission spectroscopy is used for this investigation[2]. The cross correlation of this system, which determines its temporal resolution, is 10 ps, with a spectral *resolution* of $\sim$2.7 cm^{-1}. The triple modulation detection system is capable of shot noise limited sensitivity and the signals detected here are on the order of $\Delta T/T = 10^{-5}$.

We have performed two classes of experiments: 1) those in which the probe energy is varied for a fixed pump energy and 2) those in which the pump energy is varied while holding the probe energy constant. Results from the first class of experiments are presented in Fig. 1a, where the pump energy is fixed at 2.120 eV and the probe energy is varied. From the decay of the signal, two separate signal components were identified. The fast component *follows* the laser cross correlation, while the slow component is measured as 130$\pm$10 ps at 300°K. The energy signatures of the two signal components are shown in Fig. 1b. The fast response is determined by the relaxation processes of the singlet exciton. The positive $\Delta T/T$ signal for probe energies > 1.98 eV is due to bleaching of the singlet exciton. It is not clear whether this bleaching is due to depletion of the ground state or to a reduction in oscillator *strength associated with phase space filling.*[1] *The negative* $\Delta T/T$ signal for probe energy < 1.96 eV is not predicted by the phase space filling model and is due to excited state absorption from the singlet exciton to the continuum. This energy dependent sign change in the fast response demonstrates that the phase space filling model does not explain completely the spectroscopy of PTS in the small signal limit.

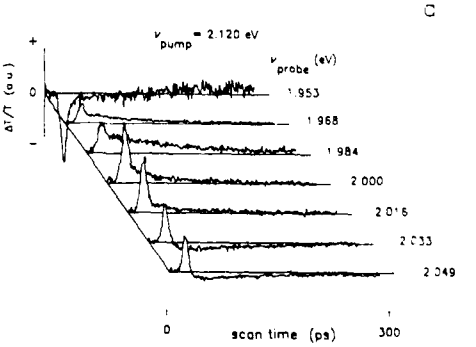
Data from the second class of experiments are presented in Figs. 2. Two different fixed probe energies were chosen to determine the pump energy dependence of both the fast and slow relaxation processes shown in Fig. 1. *The spectrum in Fig. 2a was* taken at the fixed probe energy of 1.908 eV, where there is no contribution from the slow signal. In this experiment the pump was varied over the singlet exciton absorption band. The probe monitors excited state absorption, producing an excitation spectrum of the PTS singlet exciton. This spectrum reveals a feature width narrower than reported earlier.[3] We attribute this difference to the difference in spectral resolution of the two different spectrometers used. The data *in Fig. 2b represent the pump energy* dependence of the slow signal. The probe was fixed at 1.978 eV and the pump varied between 2.120 eV and 2.033 eV. Note the presence of the fast signal component in all of the traces. The slow signal decreases with decreasing pump energy and vanishes by 2.033 eV, $\sim$55 meV above the singlet exciton absorption maximum.

The slow signal energy signature shown in Fig. 1b is centered on the singlet exciton feature presented in Fig. 2a. The shape of this slow response is characteristic of a free-carrier plasma-induced bleaching and broadening phenomenon,[4] known to occur for low *exciton populations in 2-D semiconductors.*[5] In order to better understand this slow response, we present the time dependence of both the slow and fast signals at 26.5°K and 300°K. The fast signal follows the laser cross correlation at both temperatures. The character of the slow response changes, however, with the change in temperature. It is clear from the time delayed build-up shown in the low temperature data that the fast and slow signals are not due to *two different time* constants in a single decay process. These data suggest a delayed repopulation of the singlet exciton. It can be concluded that the storage of energy observed here involves a relaxation process with more than one step.

We have presented a study of the polydiacetylene PTS in the small spectroscopic signal limit. Our data reveal a sign change in the energy dependent response of the singlet exciton, indicating that in the small signal regime, more than one spectroscopic process contributes to the observed fast signal. We also report our discovery of a metastable energy state in PTS. The energy stored *in this metastable state repopulates* the singlet exciton with a time constant of 130$\pm$10 ps at 300°K and 3.95$\pm$0.45 ns at 26.5°K. The energy level through which this repopulation occurs lies above 2.033 eV.

REFERENCES

1. B. I. Greene, J. Orenstein, R. R. Millard and L. R. Williams, Phys. Rev. Lett., **58**, 2750, (1987).
2. G. J. Blanchard, J. Chem. Phys., **87**, 6802, (1987).
3. B. I. Greene et al., MRS Symposium on Nonlinear Optical Properties of Polymers, Fall, 1987, Boston, MA.
4. D. S. Chemla, D. A. B. Miller, P. W. Smith, A. C. Gossard and W. Wiegmann, IEEE J. Quant. Electron., **QE-20**, 265, (1984).
5. A. von Lehmen, D. S. Chemla, J. E. Zucker and J. P. Heritage, Opt. Lett., **11**, 609, (1986).



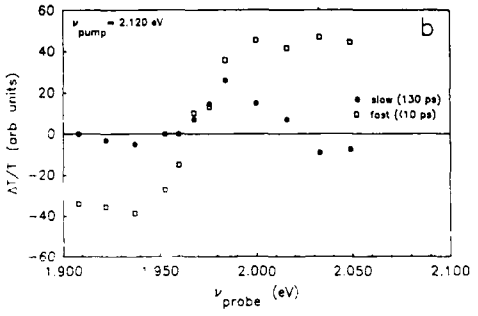


Figure 1. (a) Fast and slow signal components for pumping at 2.120 eV and varying the probe between 2.049 eV and 1.953 eV. (b) Energy dependence of fast and slow signal components.

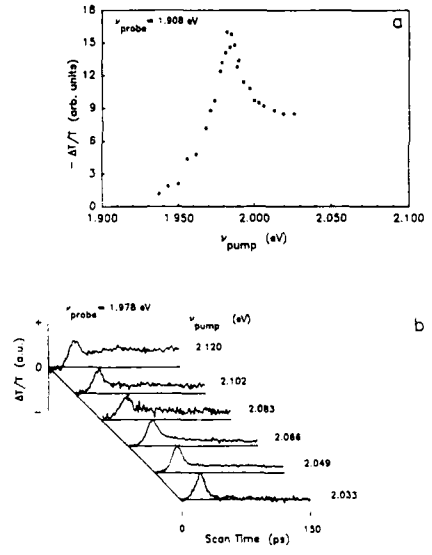


Figure 2. (a) Excitation spectrum of PTS singlet exciton absorption. (b) Pump energy dependence of the fast and slow signal components for a fixed probe energy of 1.978 eV.

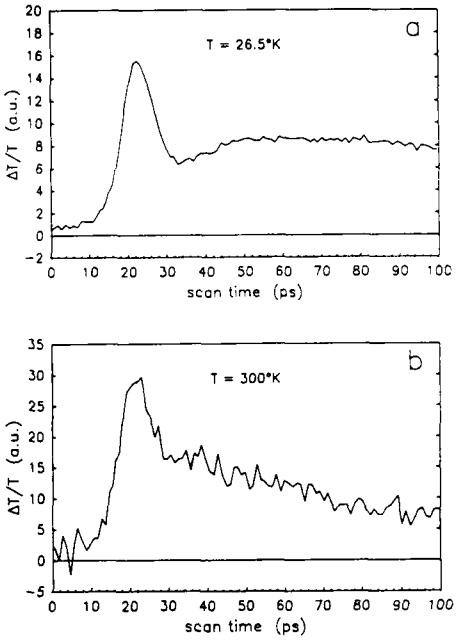


Figure 3. Fast and slow responses at two temperatures. (a) τ_{decay} = 3.95±0.45 ns. Note the rise in signal intensity after zero delay. (b) τ_{decay} = 130±10 ps.

Abstract No. 618

Ultrafast Imaging of Optical Damage and Laser-Induced Waves in PMMA[+]

Hackjin Kim, Jay C. Postlewaite, Taehyoung Zyung and Dana D. Dlott[*]

School of Chemical Sciences
University of Illinois at Urbana-Champaign
505 S. Mathews Ave.
Urbana, IL 61801 USA

In this work, we have built an apparatus for ultrafast microscopy, and have applied this technique to the problem of optical damage dynamics in a transparent polymer. A video camera, video frame "grabber" and a computer are used in our experiments instead of a single photodetector as in a conventional ultrafast spectroscopic experiment. This technique is quite similar in concept to the ultrafast imaging technique used by Downer, Fork and Shank [1] to study ultrafast melting of silicon, except that we use computer digitized images rather than film.

These experiments were performed with a home-built laser system which has been previously described [2]. PMMA (polymethyl methacrylate) is damaged with a tightly focused 80 ps laser pulse and the damage process is imaged with a delayed probe pulse which is counterpropagating with a different polarization. A three dimensional plot of an image is shown in Fig. 1, which is acquired in air at the delay time of 8 ns. The dark area of the image is plotted as a valley in the figure. The outer ring of Fig. 1 propagates outward from the damage core at a high velocity, which in its initial stages is as much as twenty times as fast as the velocity of sound in air. This ring is not observed in vacuum, so it is surely due to a shock wave in the air above the damage region. The inner circle, which is observed both in vacuum and in air as a ring pattern in the magnitifed images acquired at longer delay time, propagates away from the core at a velocity of sound in PMMA.

The absorption ratio change of the permanent damage area is analyzed with the images acquired at the very beginning of the damage pulse. The qualitative picture of the damage process which arises from the absorption change analysis is that severe damage is produced in the leading edge of a powerful laser pulse, but near the trailing edge with less power pulse.

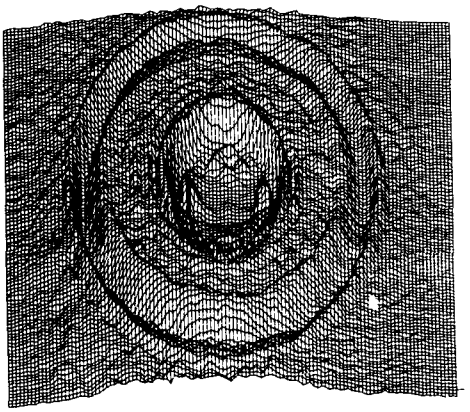


Figure 1. Dynamic image obtained from optical damage of PMMA in air at the delay time of 8 ns. Core formation is accompanied by formation and propagation of a hypersonic shock wave in the air (outer ring structure).

References

[1] M. C. Downer, R. L. Fork and C. V. Shank, in: Ultrafast Phenomena IV, eds. D. H. Auston and K. B. Eisenthal (Springer-Verlag, Berlin, Heidelberg, New York, 1984) p. 104; J. Opt. Soc. Am. B2 (1985) 595.

[2] J. C. Postlewaite, J. B. Miers, C. C. Reiner and D. D. Dlott, IEEE J. Quant. Electron. QE-24 (1988) 411.

[+]This research is supported by the US Army Research Organization through grant DAALO-86-K-0135.

[*]Author to whom correspondence should be sent.

Abstract No. 619

$LiNbO_3$ for Integrated Optical Devices

F. Leonberger, T. Findakly, P. Suchoski, M. Abou el leil

United Technologies Research Center
Silver Lane
East Hartford, CT 06108

Lithium niobate ($LiNbO_3$) has been extensively used for integrated optic devices because of its good electrooptic and acoustooptic properties and the ability to form low-loss optical waveguiding circuits on its surface. During the last fifteen years, a wide range of functional integrated optical devices have been demonstrated using $LiNbO_3$ for various applications including *communicstions*, sensing, instrumentation, and signal processing.

The material was first synthesized in crystal form at Bell Laboratories. Crystals are grown by the Czochralski pulling technique. It has a trigonal crystal structure characterized by large electrooptic, piezoelectric, pyroelectric, and photoelastic coefficients. This has been used to advantage in such applications as acoustic wave devices (transducers, delay lines, filters, etc.), optical device; (modulators, switches, second harmonic generators, Q switches, beam deflectors, etc.), as well as signal processing devices (holographic elements, memory elements, etc.).

A $LiNbO_3$ crystal exhibits three-fold symmetry about the c-axis. Additionally, it exhibits symmetry about three planes that are 60° apart which intersect forming a three-fold rotation axis. Therefore, $LiNbO_3$ is classified as a 3m point group below 1200°C.[1] The prevalent coordinate system used to describe the tensor properties is neither hexagonal nor rhombohedral but rather cartesian (x,y,z). The z-axis is chosen to coincide parallel to the c-axis, and the x-axis is chosen to coincide with an equivalent hexagonal axis a_H. The y-axis lies in the plane of mirror symmetry so as to make the system right handed. The material is commercially supplied in three substrate forms designated as z-cut, x-cut, or y-cut such that the z, x, or y axes are normal to the surface of the substrate.

$LiNbO_3$ is anisotropic and due to crystal symmetry about the c-axis, the permittivity is the same for fields in a plane perpendicular to the c-axis. The relative permittivities ϵ_{ij} are $\epsilon_{11} = \epsilon_{22}$, ϵ_{33}. The value of these parameters pertinent to device specifications such as capacitance depends on frequency. At frequencies well above the mechanical resonance, strain free values (ϵ_{ij}^S) are used. At very low frequencies, stress free values (ϵ_{ij}^T) are used. The measured values under these conditions are:[1] $\epsilon_{11}^T = 78$, $\epsilon_{33}^T = 32$, $\epsilon_{11}^S = 43$, $\epsilon_{33}^S = 28$. The material is also birefringent with extraordinary and ordinary indices $n_e = 2.2$ and $n_o = 2.286$ at 0.633 μm wavelength.

The linear electrooptic effect is one of the material's most important properties for integrated optic applications. This effect refers to a change in the refractive index upon the application of an electric field. The linear electrooptic coefficients in $LiNbO_3$ are represented by the following matrix elements after tensor reduction:[2] $r_{12} = -r_{22}$, r_{13}, r_{22}, r_{23}, $r_{13} = r_{33}$, r_{42}, $r_{51} = r_{42}$, r_6, $= -r_{22}$ with all other r_{ij}'s = 0. The values of these coefficients depend on the mechanical conditions of the material under measurement. For most integrated optic applications (high frequency operation), strain free conditions apply in which case r_{ij}^S have the following values: $r_{13}^S = 8.6$, $r_{33}^S = 30.8$, $r_{51}^S = 28$, and $r_{22}^S = 3.4$ μm/v. Under static electric field conditions, the stress free values of r_{ij}^T account for the strain induced by the dc field caused by elastic effects $(r_{ij}^T = r_{ij}^S + P_{ik}\, d_{ijk})$ where P and d are photoelastic and piezoelectric coefficients. The constant stress values of r_{ij}^T are $r_{13}^T = 10$, $r_{33}^T = 32.2$, $r_{51}^T = 32$, and $r_{22}^T = 7.0$ μm/m. The refractive index change (Δn) observed along the principle axis of $LiNbO_3$ are obtained from the equation of indicatrix. After tensor and matrix manipulation Δn_i is given by:

$$\begin{bmatrix}\Delta n_x\\ \Delta n_y\\ \Delta n_z\end{bmatrix} = \frac{1}{2}\begin{bmatrix}-r_{22}E_y + r_{13}E_z & -r_{22}E_x & r_{51}E_x\\ -r_{22}E_x & r_{22}E_y + r_{13}E_z & r_{51}E_y\\ r_{51}E_x & r_{51}E_y & r_{33}E_z\end{bmatrix}\begin{bmatrix}n_o^3\\ n_o^3\\ n_e^3\end{bmatrix}$$

The diagonal elements in the [rE] matrix yield a modulation in the wavevector and therefore phase of the optical wave. The off-diagonal elements induce polarization modulation between the orthogonal components of the light wave. These two effects are very important for device operation and constitute the cornerstone of integrated optic device design and operation. The most efficient element of the index modulation matrix is $r_{33}E_z$ since r_{33} is the largest coefficient. Other physical effects in $LiNbO_3$ such as pyroelectric, piezoelectric, photoelastic, and photorefractive effects will not be covered in this paper. Reference 3 provides a good review of these effects.

Optical waveguides in $LiNbO_3$ can be fabricated by several methods in which a modification is induced to yield a region of increased refractive index in which light can be guided.[4] These methods include Li_2O outdiffusion, metal indiffusion, proton-exchange, and ion implantation. Of these methods, the indiffusion and proton-exchange are the most efficient. Ti-indiffusion, the most widely used technique, is usually carried out by diffusing Ti (300-700 Å) thick at about 1000°C for 4-7 hrs. Waveguiding is achieved along n_o and n_e with typical loss of 0.5-1.0 dB/cm. Ti-diffusion yield guiding layers about 2-3 μm thick, and when patterned in two dimensional channels (4-6 μm wide) yield a numerical aperture of about 0.07-0.1 which correspond to an index increase of a few 10^{-3}. While Ti-diffused $LiNbO_3$ has been the workhorse for integrated optic devices, recent requirements for special device operation led to the development of the proton-exchange method.[5] Following this technique, H^+ protons are exchanged for Li^+ ions at low temperature (200-249°C). A high index increase (~ 0.12) is realized in n_e only while a reduction in n_o. The layer of high index is very thin, typically < 0.5-1 μm, which is not practical for single-mode operation since it doesn't match well with the numerical aperture and

size of commercial single-mode fibers. Therefore, annealing is carried out at 300-350°C for few hours to relax the net index increase and to increase the guiding layer depth.[6] Such waveguides are highly polarizing (50-60 dB extinction), low loss (0.3-0.5 dB/cm) and compatible with single-mode fibers making them very useful for special applications which require minimum polarization cross-talk.[6]

The linear electrooptic effect has been used to effect intensity modulation, phase modulation, frequency modulation, polarization modulation, switching, beam deflection and steering, etc. References 4, 7, and 8 provide a good review and sufficient examples of various integrated optical devices, their principles and operation. Figure 1 illustrates three typical examples of integrated optical devices: (a) phase modulator, (b) directional coupler switch, and (c) Mach-Zehnder interferometer. Electrooptic interaction in these devices is achieved by delineating electrodes on the waveguide circuit through which the electric field (E) overlaping the waveguide induces a change in the effective index of the guided mode (δn) and therefore its wavevector ($\Delta\beta$). Figure 1a shows a phase modulator with two sets of electrodes illustrating a method of realizing phase modulation to the two orthogonal polarizations in the waveguide. Figure 1b shows a directional coupler switch with two sets of reversed polarity electrodes. In the passive mode, optical power is coupled back and forth between the two identical single-mode waveguides at an interval known as the coupling length. By applying voltage, the wavevectors in the waveguides are changed with respect to each other thus modifying the coupling properties. Switching the optical power to each of the two outputs or modulating the output intensity is achieved by applying proper dc bias and modulating voltage across the electrodes. Figure 1c shows an interferometric device known as the Mach-Zehnder interferometer. The single-mode waveguide circuit consists of an input branch which splits into two and then combine at the output. Electrodes are placed along the two waveguides within the interferring region to provide means of modulating the phase in each arm. Through the electrooptic effect, the phase difference (or path length) between the two branches is changed which results in an intensity modulation at the output branch. When the two field components arrive at the output junction in phase, they add up setting a maximum intensity. When they arrive 180° out of phase, they cancel, thus setting a minimum. Therefore, the output intensity can be modulated between maximum and minimum by modulating the phase difference between the two branches. The examples given in Figure 1 represent a class of devices characterized by lumped circuit electrodes. The speed of such devices is limited by the electrical transit time which is determined by the electrode capacitance and the terminating resistance. Typically, the capacitance in such devices is on the order of a few picofarads, which permit operation up to a few GHz for 50 Ω systems. The speed of such devices can be increased by operating the electrodes as RF transmission lines in which the microwave and optical waves travel at comparable speeds. Thus removing the limitation of electronic transit time. Bandwidths of up to 18 GHz have been realized by the use of such travelling wave electrode designs.

The $LiNbO_3$ integrated optic technology has at present reached a good level of maturity and commercial production is being pursued by a few companies. A certain degree of engineering as related to application pertinent issues is under continued investigation. Such issues include reliability, packaging, cost, environmental survivability, etc. Areas of application such as fiber optic rotation sensors, instrumentation, optical communication, and signal processing are evolving to take advantage of the useful features of integrated optical devices.

REFERENCES

(1) See for example a series of five papers by: K. Nassau, H. Levinstein, and G. Loiacono (I,II); S. Abrahams, J. Reddy, and J. Bernstein (III); S. Abrahams, W. Hamilton, and J. Reddy (IV); S. Abrahams, H. Levinstein, and J. Reddy (V); J. Chem. Phys. Solids 27, pp. 983-1026 (1986).

(2) See for example: I. P. Kaminow and E. H. Turner, Proc. IEEE 54, pp. 1374 (1966), and references therein.

(3) R. Weis and T. Gaylord, Appl. Phys. A 37, pp. 191, 1985, and references therein.

(4) For a good review, see for example: "Integrated Optical Circuits and Components", Edited by L. Hutcheson, Marcel Dekker, 1987.

(5) J. Jackel, C. Rice, and J. Vaselka, Appl. Phys. Lett. 41, pp. 607 (1982).

(6) P. Suchoski, T. Findakly, and F. Leonberger, Opt. Lett. 13, pp. 172 (1988).

(7) R. Alferness, IEEE, Trans. on Microwave Theory and Tech. MTT-30, pp. 1121 (1982).

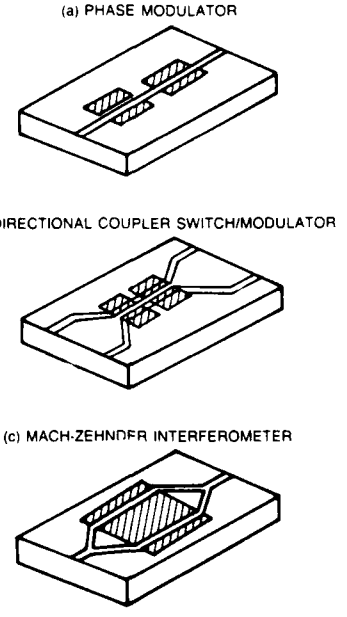


Figure 1. Typical examples of $LiNbO_3$ integrated optical devices.

Abstract No. 620

ALTERNATIVE MATERIALS AND PROCESSES FOR INTEGRATED OPTICS

M.N. Kozicki, Y. Khawaja, J.L. Edwards, B. Qurashi, G. Bernstein and A.E. Owen*

Center for Solid State Electronics Research
Arizona State University
Tempe, AZ 85287-6206

Introduction

The goal of much of the current research in integrated optics is to fully integrate optical processing elements into monolithic systems. One of the main problems with this concept is the difficulty in fabricating vertical walled rectangular optical waveguides and other elements such as small geometry diffraction gratings. It is true that the fabrication technology used for the production of integrated circuits is mature, but this technology may not always be totally applicable to the fabrication of optical structures. Much of the problem lies with the materials themselves. A considerable amount of work is being performed with gallium arsenide (GaAs) substrates due to the desirable optical properties of this material. However, GaAs is a difficult material to process. For instance, the formation of deep (typically >1 micron) vertical trenches in GaAs to produce waveguides in close proximity is possible, but it is not a trivial task. There is consequently a driving force for the development of alternative materials and processes for integrated optics. This paper describes the initial results of a program concerning the potential uses of As-S systems in integrated optics.

The As-S/Ag System

There has been a great deal of interest in As-S/Ag systems [1] in recent times as they show considerable promise as dry deposit/dry develop resist materials. They have a number of desirable properties which make them attractive for this application, properties which also make them attractive for integrated optics. (a) The materials may readily be deposited by vacuum coating techniques, e.g. evaporation or sputtering, to produce thin uniform layers. (b) A layer of silver is pre- or post-deposited and this acts as a "photodopant", i.e. it diffuses into the As-S on exposure by light or electron-beam. In the As-S/Ag system, the diffusion of the silver essentially only takes place where the illumination occurs and hence there is a very sharp transition from photodoped to unphotodoped material and the doped region has a near vertical "sidewall". (c) The system may be compositionally optimized to attain the highest possible resolution. Previous work tended to use As_2S_3 because of its commercial availability. However, As_2S_3 will produce a phase seperated photodoped material which appears grainy and hence is not suitable for ultra-high resolution pattern definition. The optimum chalcogenide composition is actually $As_{33}S_{67}$. When photodoped with silver, the ternary compound formed is extremely homogeneous and hence can be utilized in high resolution applications. A phase diagram of the system is shown in Fig. 1. (d) The resulting photodoped compound is resistant to etching in a wide range of chemicals, including aqueous alkalai, and also will not be significantly attacked by a CF_4 plasma. This is in contrast to the unphotodoped chalcogenides which will etch rapidly under these circumstances. Therefore, producing an image in these materials is relatively simple. In addition to these properties, spectrophotometer measurements on thin films show that the reflectivity is extremely high for infra-red wavelengths, with a sharp transition between the optical and infra-red regions at 1.1 microns (Fig. 2). This suggests that they would be good guide/diffraction grating materials at these wavelengths. The unphotodoped materials have a refractive index, as measured by ellipsometer, of approximately 2.8 whereas the photodoped materials have a refractive index in the region of 3.0.

The above properties will allow the formation of three types of structure in these materials; (1) a "3-dimensional" rectangular cross-section guide produced by exposure and subsequent etching to remove the unphotodoped material, (2) a planar waveguide structure in which exposure is not followed by etching and the difference in refractive index between the photodoped and unphotodoped materials is used to guide single mode transmissions, (3) small geometry "diffraction grating" type structures on the surface of a substrate. A logical extension of the diffraction grating concept is to create lateral surface superlattice (LSSL) structures in the arsenic sulfide by electron-beam induced doping. These structures form the basis of tunable bandgap elements. Although As-S is an amorphous chalcogenide semiconductor, we may still fabricate superlattices in this material if the dimensions are of the order of an electron wavelength, e.g. 20 nm.

To date we have utilized $As_{33}S_{67}$ evaporation and sputtering sources to form thin films on silicon substrates for characterization purposes. Optical lithography has been performed using a Karl-Suss MJB-3 contact aligner with 310 nm optics and a TRE 700 wafer stepper to produce waveguide structures with a minimum width of 0.75 microns. In addition, ultra-high resolution electron-beam lithography using a converted ISI 100B SEM controlled by a computer scanning system has produced gratings with 35 nm lines and 35 nm spaces in these materials.

1. A.E. Owen, A.P. Firth and P.J.S. Ewen, Phil. Mag. B, 52, 347-362 (1985).

This work was supported in part by the National Science Foundation.

* Visting Professor, University of Edinburgh.

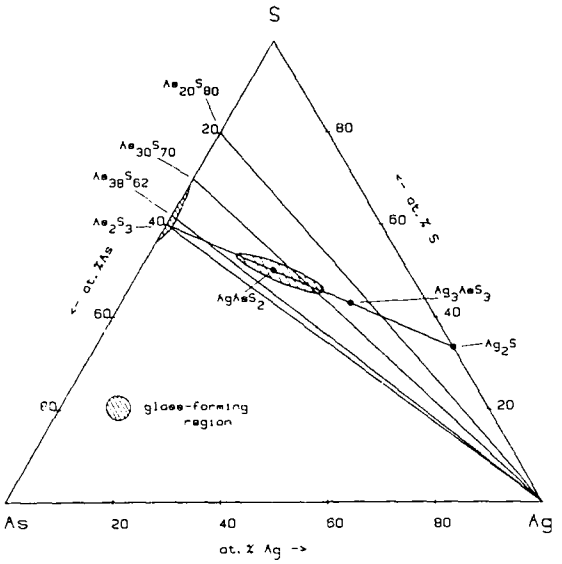


FIGURE 1. PHASE DIAGRAM OF THE As-S/Ag SYSTEM SHOWING THE HOMOGENEOUS GLASS FORMING REGION.

FIGURE 2. SPECTROPHOTOMETER MEASUREMENTS FOR UNDOPED (a) AND PHOTODOPED (b) As-S. THE VERTICAL AXIS IS REFLECTANCE.

Abstract No. 621

Compound Semiconductor Electro-optical Materials and Devices

Yung Jui (Ra·) Chen
Department of Electr cal Engineering
University of Maryland
Baltimore, MD 21228

With recent improvements in epitaxial and processing technologies and substrate qualities, GaAs electro-optical modulators with bandwidth in excess of 20 GHz have been demonstrated.[1] The travelling waveguide device, based on bulk electro-optical effects, exhibited performance comparable to state of the art lithium niobate devices and offered potential for monolithic integration of passive and active opto-electronic devices. It is expected that compound semiconductor electro-optical devices, based on advanced microelectronic technologies, will play an increasingly important role in electro-optical applications.

The compound semiconductor materials offer another unique feature - bandgap engineering.[2] Quantum well structures exhibit greatly enhanced electro-absorptive and electro-refractive effects resulting from the two dimensional excitonic resonances. For electro-absorptive effect, a change of absorption coefficient as large as $\Delta\alpha$ = 15,000 cm^{-1} has been observed in a GaAs/AlGaAs system near excitonic resonance.[3] Similarly for electro-refractive effect, the large change of refractive index Δn and its quadratic dependence on applied field in a quantum well material also lead to superior performance to bulk semiconductors. It was shown that, by detuning from excitonic resonance, a ten times improvement in phase modulation coefficient over the bulk device can be achieved without severe propagation (absorption) loss penalty.[4] Attempts to enhance the electro-optical effect in quantum wells, in particular to increase the exciton energy shift for a given applied field, have involved more complex structures. Notably in a coupled quantum well structure, the field-induced shifts of the coupled excitonic states can be as much as five times that of the single quantum well case.[5-7]

We will discuss various electro-optical effects: Pockels (linear electro-optical) effect, Kerr (quadratic) effect, carrier effect and Franz-Keldysh effect in bulk and quantum well materials and their applications to electro-optical device structures. Special attention will be given to the enhanced electro-refractive and electro-absorptive effects in quantum wells.

REFERENCES

1. S. Y. Wang, S. H. Lin and Y. M. Houng, *Appl. Phys. Lett.* **51**, 83 (1987).

2. D. A. B. Miller, J. S. Weiner, and D. S. Chemla, *IEEE J. Quantum Electron.* **QE-22**, 1816 (1986).

3. T. H. Wood, *Appl. Phys. Lett.* **48**, 1413 (1986).

4. J. E. Zucker, T. L. Hendrickson and C. A. Burrus, *Electron. Lett.* **24**, 112 (1988).

5. Y. J. Chen, E. S. Koteles, B. S. Elman and C. A. Armiento, *Phys. Rev.* **B36**, 4562 (1987).

6. M. N. Islam, R. L. Hillman, D. A. B. Miller, and D. S. Chemla, *Appl. Phys. Lett.* **50**, 1098 (1987).

7. H. Q. Le, J. J. Zayhowski, and W. D. Goodhue, *Appl. Phys. Lett.* **50**, 1518 (1987).

Abstract No. 622

EXPERIMENTAL STUDY OF THE ROLE OF COLOR CENTERS ON SILICA FIBER PREPARATION FOR SECOND HARMONIC GENERATION (SHG)

James R. Rotge'
Mohamed F. El-Hewie

Frank J. Seiler Research Laboratory (AFSC)

United States Air Force Academy
Colorado Springs, CO 80840-6528

It has long been known that fibers are susceptible to color center formation by energetic photons or particle radiation. It has more recently been proposed that color (defect) centers may play a crucial role in the spontaneous generation of second harmonic light in glassy fibers.[1] This paper explores whether color centers, formed in fiber samples by neutron or gamma radiation, change the preparation characteristics (either time to prepare or maximum conversion efficiency).

Osterberg and Margulis[2] first observed efficient SHG in phosphorus and/or Germanium doped silica fibers. This process involves passing intense light (1064 nm) from a mode locked, Q-switched Nd:YAG laser thru a short (nominally one half meter) fiber section. During an exposure time of several hours, the fiber begins to radiate second harmonic light (532 nm). The conversion efficiency saturates after a growth period of several more hours; the highest efficiency reported to date being about 10%.[3] The structure of the silica fiber, being centrosymmetric, should not support such high conversion efficiencies. To explain this SHG as a second order nonlinear process, one must postulate a mechanism for breaking the inversion symmetry of the glass structure, and simultaneously satisfy the phase matching conditions necessary for efficient conversion to occur. One model proposed suggests that color centers are formed in the fiber and subsequently aligned along the fiber, resulting in an alternating DC polarization which automatically satisfies the required phase matching condition.

This study will consider cutting several sections of fiber from the same spool and exposing some of these samples to various dosages of radiation from a gamma ray source, and others to a source of neutrons. These samples will then be exposed to light from the Nd:YAG laser and their response to the SHG preparation process will be compared to fiber (control) samples not subjected to radiation.

Electron spin resonance (ESR) studies will also be conducted on these and other fiber samples to determine whether photochemical processes occur during the preparation process. The ESR signature of such changes add new information concerning the preparation phenomenon and the question of why the effect is apparently permanent; a question not addressed by the above mentioned model.

REFERENCES:

1. R.H. Stolen and W.K. Tom, Optics Letters, 12 (585-587) 1987.

2. H. Osterberg and W. Margulis, Optics Letters, 12 (57-59) 1987.

3. Optical Fiber Group, University of Southhampton (to be published).

Abstract No. 623

Optical Pulse Propagation for a Nonlinear Dielectric Film

Spiros V. Branis and Joseph L. Birman
Physics Department
City College of New York
Convent Ave. and 138 St.
New York, NY 10031

We present an analytical and numerical discussion of pulse propagation and reflection for a dielectric slab of arbitrary thickness, with index of refraction that contains a term proportional to the intensity of the electric field in the slab. Initial study is based on Mill's paper: [Phys. Rev. B35, 324 (1987)]. Additional extensions will be considered. Bistability and multi-bistability regions are investigated for transmissivity as a function of incident power.

Abstract No. 624

Induced-frequency Shift, Induced-spectral Broadening, and Optical Amplification of Picosecond Pulses by Cross-phase Modulation in a Singlemode Optical Fiber

P. L. Baldeck and R. R. Alfano

IUSL/PAL, E. E. Department
The City College of New York
New York, NY 10031

Cross-phase modulation (XPM) is a newly-identified nonlinear optical mechanism with important applications based on the picosecond and femtosecond pulse technology.[1-3] XPM is similar to the well-known self-phase modulation (SPM), however, it corresponds to the phase modulation caused by the nonlinear refractive index induced by another copropagating pulse. The time-dependent cross-phase modulation leads to spectral changes. In this report, we investigated XPM effects generated by a strong ps pump pulse at 630nm on a weak copropagating ps probe pulse at 532nm.

A schematic diagram of the experimental setup is shown in Fig. 1. A mode-locked Nd:YAG laser with a second harmonic crystal was used to produce 25-ps time duration pulses at 532nm. Pump pulses were obtained through stimulated Raman scattering by focusing 90% of the 532nm pulse energy into a 1 cm cell filled with ethanol and using a narrow band filter centered at 630nm. The pump pulses at 630nm were then recombined with probe pulses after traveling through a delay path and coupled into a 3m long singlemode optical fiber. Spectra of probe pulses were recorded for increasing pump intensities at different input time delays between pump and probe pulses.

Typical XPM-induced changes of probe pulse spectra are displayed in Figs. 2 and 3. A reference spectrum obtained in the absence of XPM interaction (dashed line) is displayed in Fig. 2. A red-shifted spectrum resulting from the XPM interaction when the pump pulse entered the fiber about 100ps after the probe pulse (solid line) is shown in Fig. 4. The induced-frequency shift originates from the combined effects of XPM and group-velocity mismatch.[3] Due to the initial time delay, the probe pulse sees only the leading edge of the XPM which leads to a red-shift as in the SPM theory. An example of a probe pulse spectrum obtained when both pulses entered the fiber simultaneously is shown in Fig. 3. The spectrum has not only shifted toward blue frequencies as expected[3] but also broadens. An induced-spectral broadening as wide as 10 nm could be obtained which was, surprisingly, at least one order of magnitude larger than predicted by the XPM theory.[3]

The optical amplification of the probe pulse is another unexpected feature arising from the XPM interaction. Fig. 4 shows the dependence of the XPM-induced gain with the input time delay between probe and pump pulses. The physical origin of the gain is still under investigation. It could originate from a non-phase matched four-wave mixing process.

In conclusion, we have shown that the spectral distribution of probe pulses can be significantly affected by the XPM generated by a copropagating pulse. Thus, XPM appears as a new tool to control optically the spectral properties of ultrafast optical pulses. Repetition rates of such frequency modulation schemes could be in the THz range since the nonlinearity is based on the fast time response of electronic origin.

This work is partially supported by Hamamatsu Photonics K.K.

References

1. J. Manassah, M. Mustafa, R. R. Alfano and P. Ho, Phys. Lett. 113A, 242-247 (1985).
2. R. R. Alfano, Q. Li, T. Jimbo, J. Manassah and P. P. Ho, Opt. Lett. 11, 626-628 (1986).
3. P. L. Baldeck, R. R. Alfano and Govind P. Agrawal, Appl. Phys. Lett. June 1988.

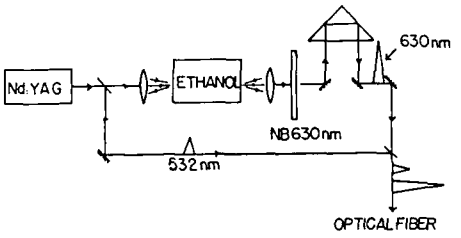


Fig. 1 Experimental setup

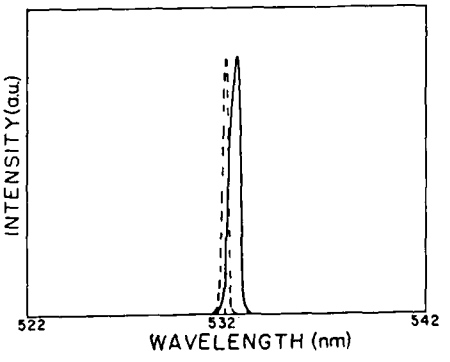


Fig. 2 Cross-phase modulation (XPM) effects on the spectrum of a probe picosecond pulse. Dashed line: reference spectrum without XPM. Solid line: with XPM and a 100 ps time delay between pulses at the optical fiber input.

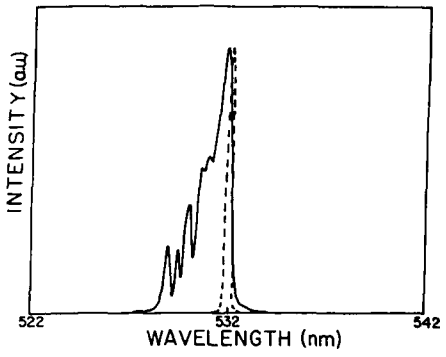


Fig. 3 Same as Fig. 2 but with no time delay between pulses at the optical fiber input.

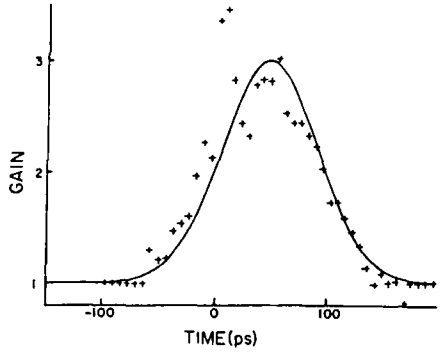


Fig. 4 XPM-induced optical gain ($I_{53(out)}/I_{53(in)}$) versus input time delay between pump and probe pulses. Dots: experimental data. Solid line is the fitting obtained by taking the convolution of the pump and probe pulses.

Abstract No. 625

The Utilization of UV and IR Supercontinua in Gas-Phase Subpicosecond Kinetic Spectroscopy

J.H. Glownia, J.A. Misewich, and P.P. Sorokin

IBM Research Division

Thomas J. Watson Research Center
Yorktown Heights, New York, 10598

This talk describes development and characterization of a new apparatus capable of simultaneously generating both intense subpicosecond UV (308, 248.5 nm) excitation pulses and subpicosecond continua for probing photoexcited molecules via broadband absorption spectroscopy. Both UV (230-450 nm) and IR (2.2-2.7 μm) continua have thus far been produced. A method of upconverting the latter to the visible for ease of detection has been demonstrated. Also presented in this talk is an account of several experiments performed using this equipment. The subpicosecond UV continuum is used to study photolysis of thallium halide vapors at 248 nm and 308 nm, and also photolysis of chlorine dioxide vapor at 308 nm. From the unusual absorption line shapes observed in the former experiment during roughly the first picosecond of time following the application of the ~160 fsec UV photolysis pulse, one can deduce important information regarding the dependence of the separation of the electronic energy levels on the Tl-halide atomic spacing. For OClO, absorption measurements made with the use of the subpicosecond UV continuum show that the primary photochemical act is production of $Cl + O_2^*$, not $ClO + O$, as has been assumed for decades. We have also utilized the subpicosecond IR continuum to measure the $\tilde{B} \rightarrow \tilde{A}$ internal conversion rate in 1,4-diazabicyclo[2.2.2]octane (DABCO) vapor.

Abstract No. 626

A New Class of Ultraviolet Femtosecond Sources

M.C. Downer, G. Focht, T.R. Zhang
Physics Department
University of Texas at Austin
Austin, Texas 78712

Since their advent in the early 1980's, femtosecond source lasers have been available only in the red and near infrared part of the spectrum. Blue and ultraviolet femtosecond pulses could be generated only through an expensive and cumbersome amplification of visible pulses, followed by nonlinear optical frequency conversion. We have developed an efficient, high repetition rate source of synchronized ultraviolet and red femtosecond pulses by intracavity frequency doubling of a colliding-pulse ring laser.[1] This simple, inexpensive, and non-perturbative technique can be easily retrofitted to any passively mode-locked laser. This new ultraviolet source is useful in photoexcitation of molecular absorption bands, photoionization, photoemission, and applications requiring tight focussing, such as electro-optic sampling of high-speed integrated circuits.

Figure 1 shows the additional intracavity subresonator which we constructed to focus the intracavity pulse train on a thin KDP or $LiIO_3$ crystal cut for Type I phase matching at Brewster angle incidence. The linear dispersion of the crystal was compensated by re-adjustment of an intracavity prism configuration.[2] The ultraviolet beam of milliwatt average power, 100 MHz repetition rate was extracted through a dichroic mirror as shown. Red pulse durations of 50-70 fsec were preserved, with no evidence of bandwidth limitation, as shown in Figs. 2a and b. The ultraviolet bandwidth shown in Fig. 2c is sufficient for a transform limited pulse duration of 40 fsec, although group velocity walk-off effects typically broaden them to between 100 and 150 fsec. This bandwidth overlaps the gain curve of a XeCl amplifier,[3] suggesting that direct injection into an excimer amplifier is possible provided ASE can be adequately suppressed.

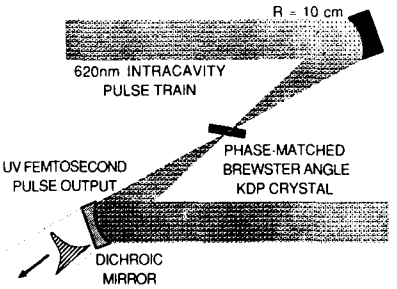


Fig. 1. Schematic of the subresonator for intracavity frequency doubling in a colliding pulse mode-locked dye laser, showing the bidirectional red pulse train, Brewster angle cut KDP crystal, and the dichroic output coupling mirror.

In contrast to our observations, previous attempts at intracavity frequency doubling of actively-and synchronously mode-locked lasers[4] resulted in mode-locking instability, pulse broadening, and bandwidth limitation, even though these lasers operated in the picosecond, rather than the femtosecond, time domain. Passively mode-locked lasers, on the other hand, possess a built-in stabilization mechanism against the deleterious effects of intracavity frequency doubling, as shown in Fig. 3a. Temporal broadening occurs in the doubling crystal because power dependent loss selectively attenuates the peak of the pulse. Passage through a saturable absorber, on the other hand, selectively attenuates and therefore sharpens the leading edge of the pulse. Analogously gain saturation sharpens the trailing edge. Adjustment of absorber and gain saturation levels can therefore precisely compensate the pulse broadening caused by the doubling crystal.

We have quantified these general concepts by modifying Haus' theory of the passively mode-locked laser to include an intracavity frequency doubler.[5] Figure 3a and Fig. 4 graphically illustrate the major results of this analysis. Figure 3a represents the stable operating regime as a function of saturable loss (q), saturable gain (g(i)), and second harmonic conversion efficiency (γ). Stable operation can always be recovered by adjusting gain or loss (i.e. adjusting pump power or intracavity focus in saturable absorber). Figure 4 shows the variation of (a) duration and (b) energy of the fundamental pulses as second harmonic conversion efficiency is varied. The points A,B,C denote examples of conditions yielding equal pulse durations and energies at widely different values of γ, showing that pulse duration and energy can also be preserved by adjustment of gain and loss parameters.

1. Glenn Focht and M.C. Downer, IEEE J. Quant. El. **24**, 431 (1988).

2. R.L. Fork, O.E. Martinez, and J.P. Gordon, Opt. Lett. **9**, 150 (1984).

3. J.H. Glownia, G. Arjavalingam, P.P. Sorokin, and J.E. Rothenberg, Opt. Lett. **11**, 79 (1986).

4. M. Yamashita, W. Sibbett, D. Welford, and D.J. Bradley, J. Appl. Phys. **51**, 3559 (1980); M. Yamashita, K. Yamada, and T. Sato, IEEE J. Quant. El.**18**, 95 (1982); J. Falk, IEEE J. Quant. El. **11**, 21 (1975).

5. T.R. Zhang, Glenn Focht, P.E. Williams and M.C. Downer, IEEE J. Quant. El., to be published; H.A. Haus, IEEE J. Quant. El.**11**, 736 (1975).

This work was supported by the Joint Services Electronics Program (Contract F49620-86-C-0045) and by the Robert A. Welch Foundation. M.C. Downer also acknowledges support from an IBM Faculty Development Award and an NSF Presidential Young Investigator Award.

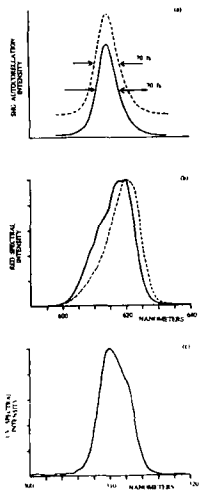


Fig. 2. (a) Autocorrelation traces and (b) spectral intensity profiles of the fundamental red pulses without the intracavity doubling crystal (dashed curves) and with the intracavity doubling crystal tuned for maximum output power (solid curves). (c) Spectral intensity profile of the generated ultraviolet pulse.

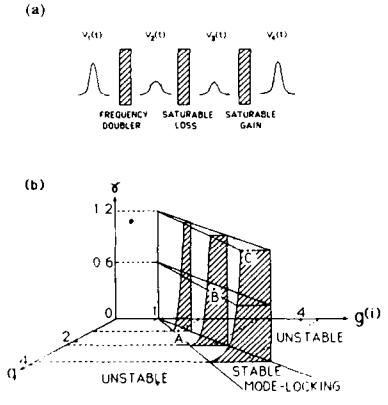


Fig. 3. (a) Changes in intracavity pulse envelope upon passage through major components of a passively mode-locked laser with intracavity frequency doubler. (b) Graphical representation of the stable mode-locking regime as a function of saturable loss q, saturable gain g(i), and the dimensionless second harmonic generation parameter γ.

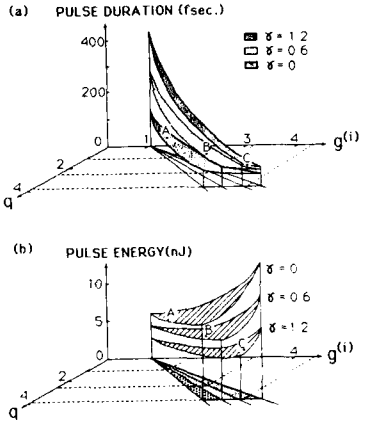


Fig. 4. Graphical representations of (a) intracavity pulse duration and (b) pulse energy at 3 different values of second harmonic conversion efficiency γ. The points A,B, and C illustrate the simultaneous preservation of pulse duration and energy as γ is increased, and correspond to the equivalently labelled points in Fig. 3b.

Abstract No. 627

Control of solitons in a femtosecond dye laser

W.L. Nighan Jr. and P.M. Fauchet

Princeton Laboratory for Ultrafast Spectroscopy
Department of Electrical Engineering
Princeton University, Princeton NJ 08544

We have built a 7 mirror/4 prism colliding pulse modelocked (CPM) dye laser [1] that delivers 35 fs pulses at 100 MHz. Recent experiments [2,3] have confirmed the soliton-like (henceforth called soliton) behavior of this laser that had been predicted by Martinez et al. [4]. In this presentation, we discuss the properties the solitons generated by our CPM laser and show that accurate control is possible.

Starting from the optimized laser configuration, we find that by adjusting group velocity dispersion (GVD) and self-phase modulation (SPM) inside the cavity, we are able to control the order, period and duration of the solitons. Negative GVD is controlled by translating one prism with ~ 1 micron resolution and SPM is controlled by varying the saturable absorber jet thickness or the intracavity intensity in that jet. Both the spectrum and the intensity autocorrelation are time-resolved at different points in the periodic evolution of the soliton.

Figure 1 shows a single trace real time autocorrelation scan and autocorrelation traces sampled at different points in the period of N=2 soliton, for a given set of cavity parameters. The soliton period is 2.5 μs and the modulation of the energy output of the CPM laser is ~ 10 %. When spectrally resolved, the modulation is deeper, approaching 100 % at certain wavelengths. Fine tuning of the period between 2.5 and 3.5 μs is easily obtained through GVD adjustments; coarser tuning is achieved by SPM adjustments. We have obtained soliton durations between $<$ 50 fs and $>$ 500 fs. Longer periods and durations are achieved for more negative GVD; features shorter than 50 fs in the intensity autocorrelation are achieved for less negative GVD. In this configuration, the laser output remains stable for hours and any specific pulseshape can be reproduced from day to day. Another regime of periodic pulseshaping has also been observed with characteristic periods in the 100 μs range. This regime is also controllable but is much more susceptible to perturbations. Since the period corresponds to a much larger number of round-trips, we suggest that the effect of a given perturbation is larger and thus decreases the stability. Our results will be compared to the models for soliton formation in the CPM laser.

In conclusion, we have demonstrated control of soliton pulseshaping in a femtosecond CPM dye laser. The principles are general and could be applied to other short pulse lasers in different wavelength regimes. This research was supported by NSF equipment grant ECS-8606531, NSF grant ECS-8657263 through the Presidential Young Investigator program and ARO contract DAAL03-87-K-0145.

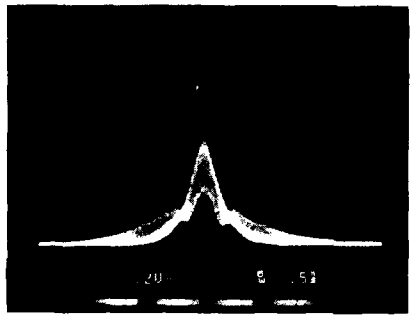
References

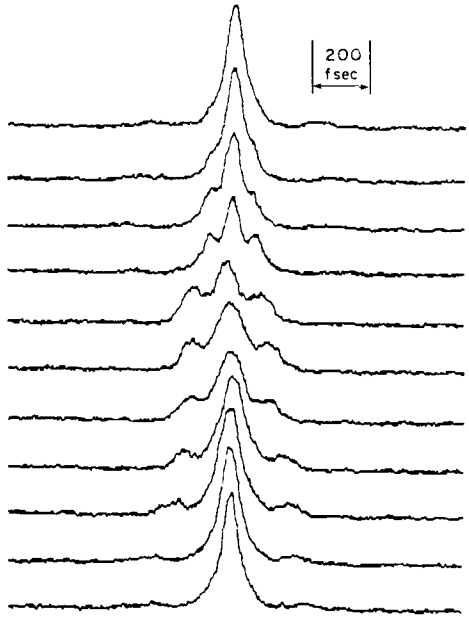
1. J.A. Valdmanis and R.L. Fork, IEEE J. Quantum Electron.**QE-22**, 112 (1986)

2. F. Salin, P. Grangier, G. Roger and A. Brun, Phys. Rev. Lett.**56**, 1132 (1986); *ibidem*, **60**, 569 (1988)

3. F.W. Wise, I.A. Walmsley and C.L. Tang, Optics Lett.**13**, 129 (1988)

4. O.E. Martinez, R.L. Fork and J.P. Gordon, J. Opt. Soc. Am.**B2**, 753 (1985)





Top Figure

Single real time autocorrelation trace (1 div=92 fs) for N=2 soliton mode of the CPM laser. The oscillation between pulseshapes is evident.

Bottom Figure

Autocorrelation traces sampled at 0.25 μs intervals in the 2.5 μs period of N=2 soliton.

Abstract No. 628

Effects of detuning on mode-locked pulse trains of an argon ion laser

Tadashi Kitahara

R&D Division, Hamamatsu Photonics K.K., 1126-1, Ichino-cho, Hamamatsu City, 435 Japan

Experimental investigation about effects of laser cavity detuning on A mode-locked argon ion laser pulse train is described. It is shown that a stable mode-locked pulse train is obtained always when detuning length is minus and has a deep minus phase shift. Qualitative explanation is given.

A composite acousto-optic mode-locking device (MD) (Fig. 1) was used. The mirror is flat and is located 1mm away from the acousto-optic modulating region. The cavity length was 1.15m. The modulation frequency was 130.0000MHz and was kept constant in any cases.

The experimental setup is depicted in Fig. 2. A He-Ne laser was used to know temporal change of acoustic intensity in the MD. Weak mode-locked 514.5nm laser light leaked from the high reflector mirror of the MD. The weak light and the modulated He-Ne laser light were measured with optical oscilloscope Hamamatsu OOS-1 temporally.

Figs 3(a) and (b) show examples of optical oscilloscope traces. Sine wave like curves correspond to the modulated He-Ne laser light and sharp peaks correspond to mode-locked pulses. Delay times of the mode-locked pulse trains comparing to a minimum points of the modulation were obtained from these traces. Phase shifts were obtained by multiplying $360f_m$ on the delay times. Where f_m is the modulation frequency.

Figs 4(a) and (b) show sampling oscilloscope traces using a photodiode with the same condition as Figs 3(a) and (b) respectively. Averaged output power were measured using a Coherent 210 power meter.

The results of the phase shift, the pulse width and the averaged power as a function of cavity detuning length and the tube current are shown in Figs 5 and 6 respectively. A starting point of the holizontal axis in Fig. 5 is settled as the length where a stable mode-locked pulse train was obtained for the first time when the laser cavity was decreased gradually. When the cavity length detuning length was minus, stable pulse train was obtained always. When the cavity detuning length were plus, the pulse trains were unstable always.

Because all the inclinations coincident in the unstable regions of Figs 5 and 6, it is colectured that the unstability in the plus detuning region is due to static loss. The reason the mode-locked pulse train is stable and has relatively deep minus phase shift in the minus detuning region may be explained as follows. Mode separation increases and exceeds modulation frequency as cavity mirror separation decreases. So that strong modulation is necessary to decrease the mode separation until the modulation frequency. The strong modulation is done by increasing degree of the phase shift as is shown in Fig. 5. The necessity makes the pulse train stable.

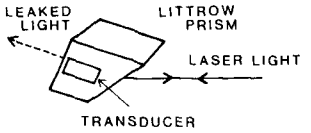


Fig. 1. Composite acousto-optic mode-locking device with a brewster window.

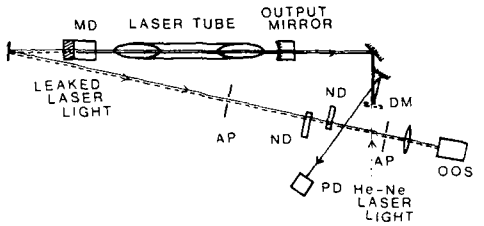


Fig. 2. Experimental setup. MD, mode-locking device; OOS, optical oscilloscope; AP, aperture; ND, neutral density filter, DM, dichroic mirror; PD, photodiode.

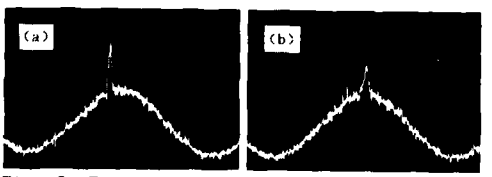


Fig. 3. Examples of otical oscilloscope traces, tube current is 27A. Cavity detuning length of (a) and (b) is 0.00mm and 0.25mm respectively. Horizontal axis is 1ns/div.

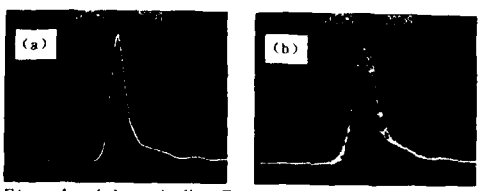


Fig. 4. (a) and (b) Examples of sampling oscilloscope traces corresponding to Fig. 3. (a) and (b) respectively. Horizontal axis is 200ps/div.

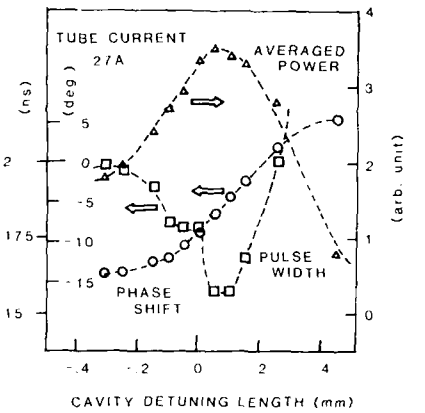


Fig. 5. Cavity length detuning effects on the phase shift, the pulse width and the averaged power. The tube current is 27A.

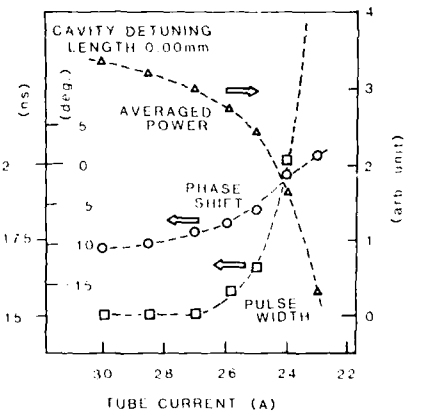


Fig. 6. Gain effects on the phase shift, the pulse width and the averaged power. The cavity detuning length is 0.00mm.

Abstract No. 629

Temporal reshaping of ultrashort laser pulses reflected by GaAs

I.H. Campbell, S.K. Kirby and P.M. Fauchet

Princeton Laboratory for Ultrafast Spectroscopy
Department of Electrical Engineering
Princeton University, Princeton NJ 08544

Contrary to a commonly-accepted opinion, short laser pulses can undergo dramatic temporal reshaping upon reflection at an interface exhibiting linear optical properties. For a fixed angle near Brewster's angle, the phase and magnitude of the Fresnel coefficients change rapidly with the dielectric function. If a short laser pulse is incident close to Brewster's angle, its various frequency components are reflected differently and the reflected pulse is strongly reshaped. We investigate this reshaping as a function of the angle of incidence, the material's properties and the incident pulse's characteristics.

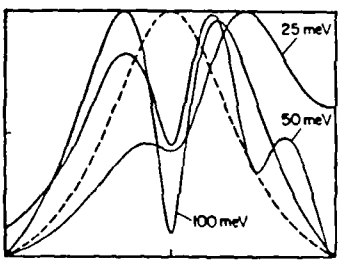
The dielectric function of GaAs at low temperature in the exciton region is the starting point of our numerical calculations. We use the Lorentz model, with a resonant frequency of 1.514 eV and a linewidth of 0.27 meV [1]. The input pulse is a sech^2, typical of well-modelocked femtosecond lasers generating transform-limited pulses. We define Brewster's angle as $\arctan\{n(\omega_c)\}$ where ω_c is the carrier frequency. We find wide regions in parameter space that lead to strong reshaping; however, reshaping is only observable very close to Brewster's angle (typically a fraction of a degree). Figure 1 illustrates the effect of the detuning between the carrier frequency and the exciton resonant frequency. The dramatic reshaping and lengthening observed at smaller detunings are the result of 1) the proximity of two π phase shifts of the reflectivity, one due to the Lorentz resonance, the other due to Brewster's angle, and 2) abrupt changes in the magnitude of the reflectivity, within the incident pulse spectrum. The latter effect is equivalent to passing the incident pulse through a narrow bandpass filter.

Our results suggest a novel type of experiment designed to measure the properties of the reflector, such as the linewidth of the resonance. The reflected pulse would be cross-correlated with part of the incident pulse in a nonlinear crystal; a fit to the second harmonic signal would yield the parameter under study. Finally, we note that this reshaping can be viewed as the time analog of the Goos-Haenchen shift.

This research was supported by NSF through the Presidential Young Investigator program and by ARO.

References

1. J.P. Lowenau et al., Phys. Rev. Lett.**49**, 1511 (1982).



Incident 100 fs-long pulse (dashed line) and reflected pulse shapes for three detunings. The vertical axis is the normalized intensity and the horizontal axis is a 340 fs-long time window.

Abstract No. 630

Two Micron Focusing of Millijoule Femtosecond Pulses from a Conical Axicon Amplifier

W.M. Wood, Glenn Focht and M.C. Downer

Physics Department
University of Texas at Austin
Austin, TX 78712

The amplification of femtosecond pulses to millijoule and higher energies has opened up the study of the interaction of matter with radiation fields of unprecedented intensity [1]. While excimer and solid state amplifiers have achieved the highest pulse energies to date, high power dye amplifiers can produce comparable peak intensities if the output can be tightly focused. However, the output of most high power dye amplifier systems has suffered from poor transverse beam quality accompanied by limited focusability caused by severe phase front distortion during the amplification process. We have constructed a high power Nd:YAG pumped dye amplifier system with a final stage conical axicon gain cell [2] which overcomes this drawback of earlier systems and achieves near diffraction limited focusing of millijoule pulses of 100 fs. duration. The peak intensity at the focus is more than 10^{16} W/cm^2, and breakdown of air at atmospheric pressure is easily observed.

Earlier high power dye amplifier systems for femtosecond pulses have utilized a variety of pumping geometries in attempts to maximize short pulse gain, while maintaining a large output beam diameter (~ 1 cm.) to avoid nonlinear optical effects [3]. These simultaneous needs for high gain and large beam diameter have made the preservation of favorable transverse beam quality especially difficult. For example, some early systems maximized gain near the output of the final stage cell by using collinear, counter-propagatin pump and signal pulses at the expense of poor transverse beam quality and focusability [3]. Later systems have improved beam quality to some extent by using transversely pumped prismatic cells [4], while sacrificing the desirable features of maximizing gain at the center of the pulse profile and at the output of the gain cell. More recently, by contrast, Kuhnle et. al. [2] have measured that small diameter (~2.5 mm.) nanosecond pulses can be amplified with high gain and excellent transverse beam quality using conical axicon gain cells of small dimensions (gain region ~ 2 cm. long).

We have scaled the beam diameter and axicon cell dimensions to the four-fold larger size required for amplification of femtosecond pulses to millijoule energy. Fig. 1 depicts the final (fourth) stage of our amplifier system. The first three stages (not shown) use standard transversely pumped gain cells to pre-amplify femtosecond pulses from a colliding pulse mode-locked (CPM) laser to approximately 0.1 mJ. at a 10 Hz repetition rate. These pre-amplified pulses are then expanded to 1 cm. diameter and injected into the axicon cell. The gain region is an 8 cm. long cylindrical flow tube containing Rhodamine 640, centered on the axis of a solid glass cone. Incident to the base of the cone and expanded to match its 8 cm. radius, counter-propagating 532 nm. pump pulses internally reflect from the sides and enter the cylindrical gain medium at radial incidence, thereby maximizing pump absorption efficiency, gain at the center of the beam, and gain at the output of the cell, as predicted by Schafer [2]. Output can be extracted after a single pass or returned through suitable polarizing optics and a saturable absorber for a second pass. Typical output energies are 0.5 mJ/pulse with < 5% amplified spontaneous emission (ASE) after one pass and 1.3 mJ./pulse with < 5 % ASE after two passes. We have then compressed the dispersively broadened output pulse to approximately 100 fsec. with a prism pair, without significantly affecting output pulse energy.

We report for the first time the favorable focussing properties of high power femtosecond pulses amplified in a conical axicon cell. Fig. 2a shows the focussed beam waist profile of our *un*-amplified CPM output after passage through the unpumped amplifier with saturable absorbers removed. This measurement was made by translating a 3 micron pinhole in one micron steps across the beam waist after focussing by a 20x microscope objective. After deconvoluting the pinhole diameter, we find a spot

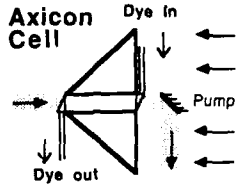


Fig. 1--Final stage geometry for the femtosecond axicon dye cell amplifier.

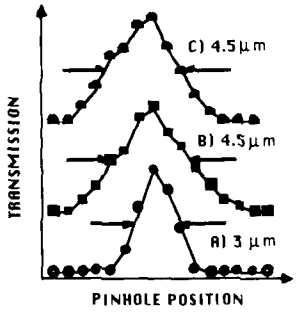


Fig. 2--**a)** Beam waist profile of **un**-amplified CPM output at focus of a 20x *microscope objective; b) Same measure*-ment after pre-amplification to 0.1 mJ. prior to axicon gain cell; and **c)** after amp-lification to 0.6 mJ. in axicon cell.

radius of 1.5 microns. Fig. 2b shows a similar measurement following pre-amplification of the pulses to 0.1 mJ. in the first three amplifier stages. Note that the spot radius has now degraded slightly to approximately 2.2 microns. Fig. 2c shows a third measurement after amplification to 0.6 mJ. in the conical axicon cell. We again find the focal radius to be approximately 2.2 microns, corresponding to a peak intensity of 3 x 10^{16} W/cm^2. In order to measure focal radius, the amplifier output was attenuated by several orders of magnitude in order to avoid damaging the pinhole. Intense light emission from air breakdown is easily observed at the focus. Availability of such a high intensity source will greatly benefit studies of new physical processes [1], such as gas breakdown on a femtosecond time scale, and generation of soft X-rays from intensely irradiated solid state plasmas [5]. We will present measurements of the breakdown thresholds of several gases as a function of pulse duration in the femtosecond and picosecond regime.

Current limitations on our focusability arise from the limited focusability of the source laser output and the use of standard geometry gain cells in the pre-amplification stages. The axicon cell, on the other hand, preserves focusability perfectly. Further improvements in the earlier stages may therefore permit still tighter focusing, perhaps to the full diffraction limit.

1. C. K. Rhodes, Science **229**, 1345 (1985)
2. F.P. Schafer, Appl. Phys. B **39**, 1 (1986); G. Kuhnle, G. Marowsky, G.A. Reider, submitted to Applied Optics; W.M. Wood, G.W. Burdick, and M.C. Downer, to be presented at Conference on Lasers and Electro-Optics, Anaheim, CA (1988).
3. R.L. Fork, C.V. Shank, and R.T. Yen, Appl. Phys. Lett. **41**, 223 (1982).
4. D.S. Bethune, Appl. Opt. **20**, 1897 (1981).
5. O.R. Wood II, W.T. Silfvast, H.W.K. Tom, W.H. Knox, R.L. Fork, C.H. Brito-Cruz, P.J. Maloney, and C.V. Shank, *XV International Quant El Conf. Technical Digest Series*, vol.21 (Optical Society of America 1987), p.2; H.W.K. Tom and O.R. Wood II, Phys. Rev. Lett., to be published.

Abstract No. 631

Dual-Energy Chest Radiography: Physical Principles and Clinical Potential

Gary T. Barnes, Robert G. Fraser and P. Colleen Sanders

Department of Radiology
University of Alabama Hospitals and Clinics
University of Alabama at Birmingham
Birmingham, Alabama 35233

Presented are the physical principles of scan projection digital radiography applied to the chest along with a review of the early clinical experience at UAB with a prototype single energy unit manufactured by Picker International. This experience along with the early dual-energy work at Stanford University lead us to develop a sandwich x-ray detector comprised of a low/high atomic number phosphor coupled to a photodiode array. Our preliminary experiments with this energy discriminating detector were successful and Picker employed the idea in their second generation digital chest unit. An important feature of the sandwich detector design is that it permits the simultaneous acquisition of low and high energy patient images. From this information, separate soft tissue (bone cancelled) images and bone (soft tissue cancelled) images free of patient misregistration artifacts can be obtained as well as a conventional single energy image. Presented are the principals of dual-energy imaging, details of the sandwich detector assembly design, and an overview of our clinical experience with the Picker second generation unit. Studied were the capability of this prototype dual-energy digital chest unit to differentiate calcified from non calcified pulmonary (and potentially malignant) nodules, to detect pulmonary nodules, to quantitate in vivo the calcium content of nodules, to detect subtle interstitial disease, and finally to detect metastatic calcium to the lung and to manage patients with loss of renal function. Also discussed are the sandwich detector phosphor requirements and design improvements that would result in improved dual-energy image quality.

Abstract No. 632

The Application of X-Ray Phosphors in Dual Energy Subtraction

Jung-Tsuoe Ho, Robert A. Kruger,

Medical Imaging Research Laboratory
Department of Radiology, University of Utah

AC215 School of Medicine, Salt Lake City, Utah 84132

Radiographic images can be decomposed into two "component images", bone and soft tissue, because there exist two predominant interactions that account for x-ray attenuation in the diagnostic x-ray energy range-Compton scattering and photoelectric absorption (1,2). Decomposition into component images, called dual energy subtraction, is achieved through linear combination of radiographic images recorded using two differing effective x-ray energies. Dual energy subtraction of bone versus soft tissue contrast is a promising technique for improving the detection of lung nodules and other abnormalities on chest radiographs (3). A single exposure radiographic imaging technique has been developed for making dual energy subtraction radiographs in which bone is suppressed (4). The single exposure technique was found to be more practical from a clinical standpoint than the dual exposure technique, using two separate x-ray exposures at two different x-ray energies, because of its simplicity and immunity to patient motion.

This technique uses two image receptors having differing energy response characteristics in a single assembly as shown in Figure 1, a radiographic cassette containing two different film-screen combinations. The assembly then is exposed by a single 140 kVp x-ray exposure, with energy separation occurring in the image receptors. The energy separation of this technique is achieved by appropriate choice of x-ray absorbing screens and of copper filtration between the two image receptors. Accurate knowledge of screen phosphor absorption and filter attenuation characteristics is essential for choosing optimum screen pairs for this approach.

This paper reports the evaluation between two sets of screen pairs, LaOBr (Quanta III, DuPont)/$CaWO_4$ (Lightning Plus, DuPont) and Y_2O_2S (MCI Optonix)/$CaWO_4$ (Lightning Plus, DuPont) The first set of screen pairs was previously reported to be successful in human studies (4). The Y_2O_2S screen has a lower K edge than the LaOBr screen, this increases the energy separation between the screen pair, and then increases residual soft tissue contrast after bone subtraction and detectability of lung nodules if they are present.

The purpose of this study is to compare the two screen pairs in terms of screen speed, image resolution, signal-to-noise ratio (S/N), and energy separation in order to select a better screen pair for the single exposure technique. Computer simulations were performed in order to estimate the signal-to-noise ratio and energy separation of the two screen pairs. The simulations accurately reproduced the performance of the radiographic imaging system [sic], including the polyenergetic characteristics of x-ray spectra the energy dependence of soft tissue and bone attenuations, the energy-dependent absorption of x rays by the intensifying screen (x-ray phosphor), and the energy-dependent conversion of absorbed x rays into light photons that finally produce the film darkening. The other two parameters, screen speed and image resolution, were evaluated based on the results of actual experiments.

The phantom, consisting of 1 cm bone and 6 cm soft tissue materials, also shown in Figure 1 was used to simulate the human chest in experiments. The bone was embedded in soft tissue as the rib or spinal cord. A 1 cm soft tissue material on top of 6 cm soft tissue material was used to simulate a pulmonary vessel. The imaging parameters used in the experiments are listed in Table 1. Each screen used to combine with the Lightning Plus screen in the single exposure technique was a single screen that was placed in front of the front film (WDR, Dupont). According to computer simulations, the copper filter used in set 1 should be increased up to 0.78 mm to obtain approximately the same film density (optical density) as that in set 2. A resolution pattern was used to test image resolution produced by the screen. Summary of the comparison between the two screen pairs is tabulated in Table 2.

The speed of the Y_2O_2S screen is close to that of the LaOBr screen. According to computer simulations, the Y_2O_2S screen absorbed half of the energy absorbed by the LaOBr screen. Image resolution produced by the Y_2O_2S screen is the same as that by the LaOBr screen, however, the Y_2O_2S screen produced a better signal-to-noise ratio The set 1 screen pair offers greater energy separation than does the set 2 screen pair by about 7 keV. The S/N ratio and energy separation make the set 1 screen pair more favorable for the single exposure technique than the set 2 screen pair. The LaOBr screen, therefore, was replaced by the Y_2O_2S screen in the lung nodule study. Imaging performance parameters, such as image resolution, screen speed, and signal-to-noise will be presented and the results of the initial lung nodule study using a Humanoid® chest phantom will be shown.

REFERENCES

1. R.E. Alvarez and A. Macovski, "Energy-selective reconstruction in x-ray computed tomography," *Phys. Med. Biol.* 21, 733-744 (1976).
2. D.R. White, "An analysis of the z-dependence of photon and electron interactions," *Phys. Med. Biol.* 22, 219-228 (1977).
3. L.T. Niklason, N.M. Hickey, D.P. Chakraborty, E.A Sabbagh, M.V. Yester, R.G. Fraser, and G.T. Barnes, "Simulated pulmonary nodules: detection with dual-energy digital versus conventional radiography," *Radiol.* 160, 589-593 (1986).
4. J.-T. Ho, "Dual energy film subtraction technique for bone contrast suppression in chest radiography," *S.P.I.E.* 914, (1988).

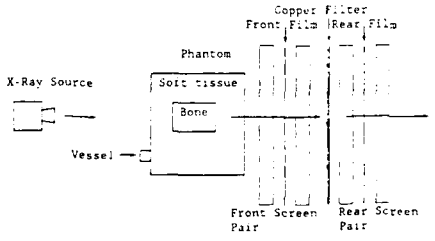
Table 1. Imaging parameters used in ...periments.

	Set 1		Set 2	
Screen	Front	Rear	Front	Rear
Components	Y_2O_2S	$CaWO_4$	LaOBr	$CaWO_4$
K edge, keV	17	69.5	38.9	69.3
Coating weight, mg/cm^2	50	153.4	50	153.4
Film	WDR	WDR	WDR	WDR
Copper thickness, mm	0.78		0.52	
X-ray energy, kVp	140		140	
Antiscatter grid	12:1		12:1	
Exposure, mAs	1		1	

Table 2. Summary of the comparison between two screen pairs.

	Set 1		Set 2	
Screen Speed:				
	Y_2O_2S	$CaWO_4$	LaOBr	$CaWO_4$
Film density, O.D.				
Soft tissue	1.37	1.17	1.55	1.25
Bone	1.09	1.01	1.29	1.09
Vessel	1.29	1.07	1.45	1.16
Image Resolution:				
lp/mm	2.0	2.5	2.0	2.5
Signal-to-Noise ratio:				
Bone subtraction	1.3		1.9	
Energy Separation:				
Average energy, keV	49.2	80.5	54.1	78.7
Difference, keV	31.3		24.7	

Figure 1. The schematic diagram of the single exposure technique and the phantom used in experiments.



Abstract No. 633

CERAMIC SCINTILLATORS FOR X-RAY CT USE

K. Yokota, N. Matsuda* and M. Tamatani*

New Materials Engineering Lab., Toshiba Corporation
Shinsugita-cho, Isogo-ku, Yokohama, 235 Japan

* Toshiba R&D Center, Kawasaki, 210 Japan

The X-ray computed tomography (X-CT) evolution, from the 1st to 4th generations, has been achieved by shortening scan time as well as by improving spatial resolution (1). These improvements have required an increased number of detectors per machine with high packing density. The combination of a scintillation crystal and a photomultiplier, applied in the early scanners, has been replaced successively by the gas-filled xenon detectors and by scintillator-photodiode solid-state detectors.

The X-ray incident on the solid-state detector is absorbed by the scintillator and then converted into visible radiation, which propagates up to a photodiode attached to the scintillator at the opposite side from the incident X-ray. The photodiode converts the visible radiation into electric output. Figure 1 shows a diagram of the detector.

Two scintillation properties indispensable for X-CT are as follows. i) Little afterglow to avoid artifacts and distortions in the final picture; short scan times coupled with high spatial resolution require frequent sampling of detector outputs at intervals of a few milliseconds. ii) High sensitivity to lower the patient exposure dose and to obtain a high signal to noise ratio in the total imaging system; the sensitivity is derived from high X-ray absorption coefficient, high internal luminescence efficiency under X-ray excitation, effective collection of the emitted light by the diode and good spectral matching of the luminescence to the diode response.

A $CdWO_4$ transparent crystal has been proposed for the solid state detector (2). It has advantages over old alkali halide scintillator crystals, such as NaI:Tl or CsI:Tl, in regard to less afterglow, higher X-ray absorption coefficients and less hygroscopicity, though it has a lower sensitivity compared with the Xenon-gas detector. There are possible candidates among phosphors with higher luminescence efficiencies than $CdWO_4$ (3). In fact, a Gd_2O_2S:Pr,Ce,F powder phosphor was proposed for the X-CT scintillator (4). However, light scattering and, hence, low light transmittance of the powder layer leads to low light collection efficiency in the device structure as shown in Fig.1. Although a modified structure was proposed, where the emitted light was detected at the same side as the incident X-ray, it reduced the merit of high packing density of the solid-state detector array. Single crystal growth was another approach for reducing the light scattering. Undoped Gd_2O_2S was attempted to grow by the high pressure melting method under a sulfur atmosphere (5). Only small crystals having sulfur deficiency were obtained, however, which did not meet the detector use requirements.

Transparent or translucent ceramics may be a solution for the problem, as has been shown by three different groups (Toshiba (6), GE (7), Hitachi (8)) since last year. Recent progress in ceramic technology could give translucent boules of materials whose single crystals are difficult to grow. GE has already proposed various phosphor ceramics for this purpose in its patent specification (9). Ceramics have several other merits over a single crystal. A large ingot may be obtained. There are little compositional segregations during manufacturing. And they are cut without cleavage.

Sintering is usually achieved with the help of a small quantity of sintering agents. The agents possibly make sintering temperature low, but sometimes make the luminescence properties poor. Pressure application, such as hot pressing (HP), and hot-isostatic pressing (HIP) is useful for making dense ceramics at relatively low temperatures even without the agents. In case of the HIP, a sealed container, which prevents the material from decomposition at high temperatures, can be utilized.

Transparent phosphor ceramics could be obtained for cubic phase materials having isotropic refraction indices such as Y_2O_3:Eu and cub-Gd_2O_3:Eu (10). This material system was already proposed for X-CT application by GE (11). Even in non-cubic crystal phase systems translucent ceramics have been known for Al_2O_3, ZnO, etc. (12).

The authors found that even translucent ceramics are applicable to the CT detectors shown in Fig. 1, if the diffuse light transmittance is sufficiently high. The difference in detector output linearity to the incident X-ray energy, in case of the translucent ceramic scintillator, from that in the transparent single crystal, is small enough for the practical imaging. It was also found that Gd_2O_2S:Pr has a high luminescence efficiency and little afterglow, sufficient for X-CT use, even without the Ce and F additives. The authors have been developing Gd_2O_2S:Pr translucent ceramics using the HIP (13). The phosphor powder was cold-pressed, encapsulated and sealed in a metal container made of tantalum. Then, it was pressed under typical condition of around 1500° C temperature and 1000 atmospheres pressure, with argon gas as the pressurizing medium. Figure 2 shows a view of the HIP process. Both the container and phosphor were deformed and contracted by the pressing. Dense ceramic samples were obtained. Average grain size was about 50 micrometers. Density relative to that calculated from lattice parameters was more than 99.9%. High density and decrease in pore quantity lead to low light scattering and, therefore, high translucence. Figure 3 demonstrates the translucence of the 0.45mm thick oxysulfide ceramics. Diffuse light transmittance of the ceramics is as high as 45% at 1mm thickness. At the same thickness, the transmittance for the $CdWO_4$ single crystal is about 60%, while it is almost zero for the Gd_2O_2S powder layer with average particle size of 5 micrometers.

Table 1 summarizes the properties for the oxysulfide ceramics and single crystal scintillators. The X-ray absorption coefficient, calculated for 80keV photon, for the Gd_2O_2S ceramics is as large as that for $CdWO_4$ and larger than that for CsI. Relative spectral matching value for the ceramics is larger than that for $CdWO_4$. Output values from the detector devices, which were assembled by attaching a scintillator to a Si photodiode, were measured under 120kVp X-ray excitation. The value for the ceramic scintillator was 1.7 times greater than that for $CdWO_4$. Afterglow intensities at 3ms, after pulsed X-ray excitation for the oxysulfide and $CdWO_4$, were less than 0.01%. The luminescence efficiency for the oxysulfide is hardly affected in the 20 to 50 °C temperature range. On the other hand, the values for single crystals decrease severely, as temperature increases (14). Thus, the Gd_2O_2S:Pr ceramics are superior to the $CdWO_4$ single crystal for an X-CT scintillator.

Translucent phosphor ceramics are widening range of choice for the scintillator materials.

References
(1) P.Haque, J.H.Stanley: "Radiology of the Skull and Brain" vol.5 4097 ed. by T.H.Newton and D.G.Potts, C.V.Mosby Company 1980
(2) M.R.Farukhi: IEEE Trans. Nuclear Science NS-29 1237 1982
(3) D.A.Cusano, J.S.Prener: USP 4,362,946
(4) A.Suzuki, H.Yamada, Y.Uchida, H.Kohno, M.Yoshida: 197th Meeting, Japan Phosphor Research Society 1983; USP 4,362,946
(5) H.Takei,T.Miura: Artificial Mineral Symposium, No.A08 Nagoya 21 Oct. 1985
(6) N. Matsuda, K.Yokota, M.Tamatani: 172nd Electrochem. Soc. Meeting, Honolulu, 1870RNP 1987
(7) K.F.King, A.O.Englert R.J.Riedner: Radiology 135 No.3 back cover 1987
(8) Y.Ito, H.Yamada, M.Yoshida, G.Toda, H.Yamamoto, H.Takeuchi, T.Tsukuda: 35th Spring Meeting, Japan Society of Applied Physics and Related Societies, 31a-G-5 Apr. 1988
(9) D.A.Cusano, F.F.Holub: USP 4,242,221
(10) E. Carnall, D.Pearlman: Material Res. Bull. 7 647 1972
(11) D.A.Cusano, C.D.Greskovich: USP 4,421,671
(12) G.Toda, K.Ishida: "Optical Ceramics and Optical Fibers" Gihoudou, Tokyo 1983 (in Japanese)
(13) K.Yokota: Japanese Patent Disclosure Kokai 58-204088
(14) M.Nishiki, Y.Akai, K.Yokota: Japanese Patent Disclosure Kokai 61-17082

Table 1 Properties of Scintillators

	Gd_2O_2S:Pr Ceramics	$CdWO_4$	CsI:Tl
X-ray absorption coefficient (cm^{-1})	35	39	18
Spectral matching factor with Si photodiode	1	.87	1.01
Device output	1	.6	(2.8)
Afterglow*	<.01	<.01	.5-5
Temperature dependence**	0	-.3	-.2--.7
Hygroscopicity	NO	NO	SLIGHTLY

* % at 3ms ** %/degree at 20-50°C

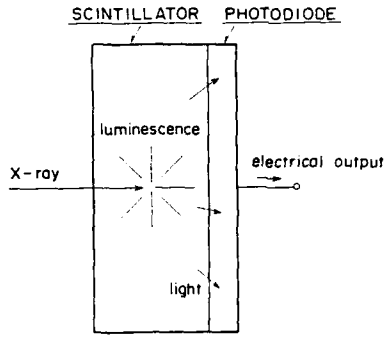


Fig. 1. Diagram of a solid-state X-ray detector

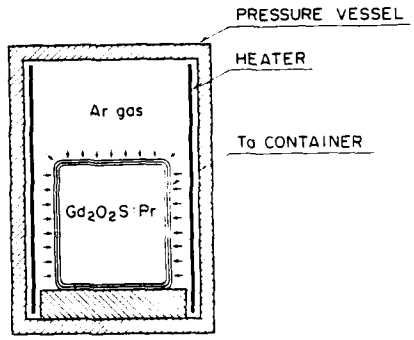


Fig. 2. Schematic view of Hot Isostatic Pressing

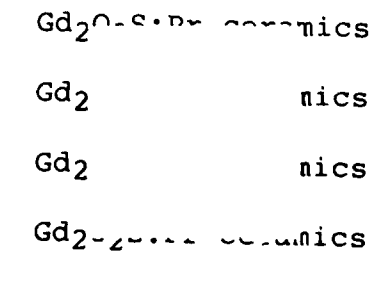


Fig. 3. Translucent Gd_2O_2S:Pr ceramics (30mmx30mmx0.45mmt)

Abstract No. 634

Ce[3+], Tb[3+] and Gd[3+], Tb[3+] Activated Silicate X-Ray Luminescent Glasses For Real-Time Radiography

C. Bueno and R. A. Buchanan

Nondestructive Testing Technology Laboratory
Lockheed Missiles and Space Company, Inc.
815 E. Middlefield Road
Mountain View, Ca. 94043

Many types of x-ray real-time radiographic imaging systems employ x-ray to light conversion screens as the imaging medium [1]. A commonly used conversion screen is composed of polycrystalline x-ray phosphor particles embedded in a binder that is supported on a mylar backing [2]. These screens are similar to some that are used as intensifier screens in x-ray film cassettes [3]. However, in real-time radiography no film is used, and the visible image that is generated is monitored by a low light level TV camera. Although many commercial polycrystalline x-ray phosphor screens have good x-ray to light conversion efficiencies [4], the image resolution is limited by the light scatter among individual phosphor particles. Image resolution from the thinnest of these binder filled screens is typically less than 15 line pairs/mm (lp/mm) under 100kV x-rays. The use of thicker, more attenuating polycrystalline screens results in a reduction in spatial resolution while the enhanced light trapping of the thicker screens limits the luminescence gains possible. Furthermore, the binder reduces the absorption efficiency of these screens because energy absorbed by the binder does not get transferred to the luminescent centers in the phosphor particles.

Continuous transparent luminescent glass plates offer solutions to these problems. Because the glass plates are particle free, they do not degrade the resolution by transverse light scatter and can typically resolve better than 20 lp/mm under 100kV x-ray excitation using a 6-mm thick plate. Thicker glass screens can be used because the light trapping effects are significantly reduced. The utility of thick luminescent glasses is particularly important for industrial real-time radiography where high energy (>200kV) x-rays are more penetrating and the thin polycrystalline screens more x-ray transparent. Since no organic binder is required in the glasses, theoretically all the energy that is absorbed can be transferred to the luminescent centers in the glass. Optimized luminescent glass screens therefore promise improved contrast sensitivity, through improved absorption efficiency and improved spatial resolution for x-ray imaging applications.

However, existing luminescent glasses have only moderate effective atomic numbers ($\bar{Z} \cong 30$) and densities ($\rho \cong 3.0$ g/cc) and have lower intrinsic x-ray to light conversion efficiencies than crystalline x-ray phosphors - properties that must be maximized for improved detective quantum efficiency. Additionally, many luminescent glasses have been prone to radiation damage (coloration) and afterglow (background levels increase with increasing dose). We have developed improved luminescent glass compositions that have enhanced x-ray absorption efficiencies (enhanced $\bar{Z}$ and ρ), increased x-ray to light conversion efficiencies, and reduced afterglow and radiation damage.

Trivalent terbium activated glasses can be coactivated with small amounts of trivalent cerium ions to enhance the luminescent response of these glasses under x-ray excitation. The luminescent responsivity of these coactivated glass is significantly greater than that of terbium free glasses having an equivalent amount of trivalent cerium activation. Cerium coactivation of terbium activated silicate glasses also reduces the afterglow and the susceptibility to radiation damage of these glasses under x-ray excitation.

A weak Ce[3+] emission band with its maximum at 420 nm has been observed in the Ce[3+], Tb[3+] glasses under 254 nm excitation. A broad Ce[3+] excitation band (maximum at 355 nm) has been observed while monitoring the Tb[3+] $^5D_4$-$^7F_5$ emission at 541 nm indicating that energy is being transferred from cerium to terbium under UV excitation.

To increase the absorption efficiency of luminescent glasses, up to 35 wt% of Gd2O3 has been incorporated into terbium activated silicate luminescent glasses without devitrification. A clear increase in luminescent response was observed under x-ray excitation (40-400kV measured) with glasses that contain 5 wt% Gd2O3.

References

1. R. H. Bossi, and C. T. Dien, "Real-Time Radiography", UCRL-53092 (UC-38), Feb. 26, 1981.

2. R. A. Buchanan, M. Tecotzky, and K. A. Wickersheim, "Rare Earth Phosphors for X-Ray Conversion Screens", U. S. Patent 3,725,704, April 3, 1973, Lockheed Aircraft Corporation.

3. R. H. Heiz, "Photographic Action of Ionizing Radiation", Toronto-Wiley, 1969.

4. For example, See Table 1 on p. 280, in A.L.N. Stevels, and F. Dingemans Philips Res. Repts. 30, 277, 1975.

Abstract No. 635

THE DETERMINATION OF X-RAY PHOSPHOR SCINTILLATION SPECTRA

J. Beutel and D. J. Mickish

E. I. du Pont de Nemours & Co., Inc.
Imaging Systems Department
Research and Development Division
Experimental Station
Wilmington, Delaware 19898

When an X-ray phosphor in an intensifying screen absorbs an X-ray quantum it converts a fraction of its energy to light. Since the actual amount of light varies from one absorption event to the next, the conversion is characterized by a probability distribution, called the scintillation spectrum, which is an important characteristic of a given phosphor. The mean of this distribution is directly related to the speed of the screen/film imaging system and its statistical moments enter into the "optical information transfer factor" which characterizes the contribution of the X-ray to light conversion process to the Detective Quantum Efficiency (DQE), which describes the efficiency with which the screen transfers the information carried by the X-ray beam.

An apparatus for directly measuring the scintillation spectrum of screen samples at various monochromatic X-ray energies has been devised. An extremely low noise PMT is used to detect the light photons emitted after an X-ray is absorbed by a 1 cm^2 screen sample placed directly in front of the PMT. The X-ray source, a 60 KeV Americium source irradiating various metal targets producing secondary X-ray emission in the range from 17 to 52 KeV, irradiates the screen sample from a few centimeters behind. Signal processing is performed on a LECROY 3500 acquisition and control system. The absorption of an X-ray photon is detected when two pulses are received from the PMT preamplifier within 64 ns, as detected by a programable gate. This interval is considerably shorter than that given by the shot noise frequency of the PMT. Detection of an X-ray absorption event causes a time window, whose width is adjusted to be equal to the decay time of the phosphor's luminescence to be opened and the light photons emitted while this window is open are counted. The count is accumulated in a multi-channel scaler (MCS) and the process is repeated until the 8200 channels of the MCS have been addressed. The instrument thus record the number of photons emitted for each of 8200 X-ray absorption events.

Subsequently the data are sorted by counting the number of events which gave the lowest photon count, the next higher photon count, etc. The resulting curve is corrected for the PMT noise distribution over the same time period and is then normalized to give the scintillation spectrum and its moments.

The scintillation spectra of LaOBr and of two tantalate phosphors have been measured.

Abstract No. 636

The Detective Quantum Efficiency of Screen-Film Systems

Phillip C. Bunch,
Health Sciences Research Division
Eastman Kodak Company
Rochester, New York 14650

The technical and intuitive origins of the detective quantum efficiency (DQE) of radiation detectors is presented in some detail, including its generalization to include spatial frequency dependence as proposed by Shaw.[1] Additionally, the basic components of DQE for radiographic imaging systems, sensitometry, modulation transfer function, and noise power spectrum are discussed in simple terms.

Finally, an analysis of the DQE and sources of noise of screen-film combinations is presented in terms of the characteristics of a specific imaging system, including X-ray quantum noise, film noise, a residual screen noise term, and the noise associated with the conversion of x-rays to light.[2]

References

[1] R. Shaw, "The Equivalent Quantum Efficiency of the Photographic Process," *J. Phot. Sci.*, Vol. 11, pp. 199-204, 1963.

[2] Bunch, P. C., Huff, K. E., and Van Metter, R., "Analysis of the detective quantum efficiency of a radiographic screen-film combination," *J. Opt. Soc. Am. A*, Vol. 4, pp. 902-909, 1987.

Abstract No. 637

X-ray Luminescence of Yttrium Strontium Tantalate Phosphors

Martin R. Royce, Shuji Nakamura*
Genichi Shinomiya, Satoru Chikutei
Toshimasa Kondo

Nichia Chemical Industries, Ltd.
491 Oka, Kaminaka-cho, Anan-city
Tokushima-pref., 774 Japan

Introduction

Some impressive studies have been made on Va-family element based phosphors by Brixner[1,2], Blasse and Bril[3], and some other scientists. Among these phosphors, there are tantalate phosphors, niobate phosphors, vanadate phosphors, and so on. In the course of our study on the emission characteristics of these phosphors under UV-excitation at low (liquid nitrogen) temperature, an unusual emission band was found in Yttrium Strontium Tantalate phosphor (Fig-1). This fact caught our keen attention, and the focus of our efforts was placed particularly on Yttrium Strontium Tantalate phosphors. After experiments, it was found that some types of Yttrium Strontium Tantalate phosphors (Nb-doped or non-doped) had highly promising features under X-ray excitation. In this paper, experimental results on Yttrium Strontium Tantalate phosphors are presented mainly by comparing with Yttrium Tantalate phosphor which has been recognized as one of the best phosphors for X-ray applications.

Results and Discussions

$Y_{0.8}Sr_{0.3}TaO_4$ phosphor, hereafter called YST-3, shows three emission bands when the temperature is changed from 25°C to -190°C (Fig.1).

λ_{SHT} --- Emission band at around 325-340 nm
λ_{MED} --- Emission band at around 395-410 nm
λ_{LNG} --- Emission band at around 460-480 nm

$YTaO_4$ phosphor, hereafter called YT, has only two emission bands, λ_{SHT} and λ_{MED} (Fig-2). These facts suggest that there is a basic difference in emission mechanism between YT and YST. This new finding was interesting enough to put more R/D efforts into the study of $Y_{1-2/3Y}Sr_yTaO_4$ phosphors (YST). After some experiments, some of YST phosphors were confirmed to have very promising features particularly under X-ray excitation.

Fig-3 shows the emission spectra for YT and various YST phosphors with different Sr content. It is important to notice that YST-1 has considerably higher efficiency than YT. Subtraction of spectra was made between YST-2 and YT. It is generally believed that YT does not have λ_{MED} emission at room temperature. According to the result of subtraction (Fig-4), YST phosphors seem to have λ_{MED} emission at room temperature. This was also an interesting finding to confirm that Sr is playing a vital role in the emission mechanism of YST phosphors.

Fig-5 shows that YST has substantially different afterglow characteristics from YT. This also suggests that YST has different emission mechanism from YT. For practical use, it is also advantageous that afterglow diminishes more quickly.

Fig-6 is a comparison of emission spectra between YT and YST when Nb is doped. When YTN-1 and YSTN-1 are compared, YSTN-1 has much higher λ_{MED} emission than YTS-1. As it was pointed out in Fig-3 and Fig-4, YST phosphors have extra emission band λ_{MED} which does not exist in YT phosphor. This seems to be ture for Nb-doped system, too. In Fig-6, it is also observed that YSTN-3 has much higher efficiency than YTN-3. This fact is also very important for the practical application of this phosphor.

Conclusions

Among various Yttrium Alkaline Earth Metal Tantalate phosphors, we primarily concentrated our efforts on the study of Yttrium Strontium Tantalate (Nb-doped and non-doped). In this paper, we simply presented the data which we had collected from our experiments. Through these experiments, we became certain that some new emission mechanism, which does not exist in Yttrium Tantalate phosphor, is working in Yttrium Strontium Tantalate phosphors. However, the theoretical reasoning for this new emission mechanism will be left for further study in the future. It is our sincere hope that these Yttrium Alkaline Earth Metal Tantalate phosphors will contribute to open new opportunity in the improvement of X-ray film/screen systems.

Reference

1) Brixner, U.S.Pat. No.4,225,653.
2) Brixner and Chen, J.Electrochem. Soc. 130, 2435 (1985).
3) Blasse and Bril, J.Luminescence 3, 109 (1970).

FIG.1 EMISSION SPECTRA UNDER UV-EXCITATION

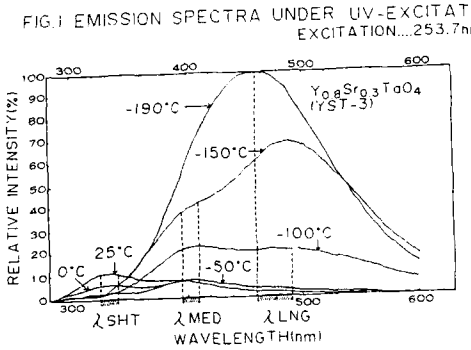


FIG.2 EMISSION SPECTRA UNDER UV-EXCITATION

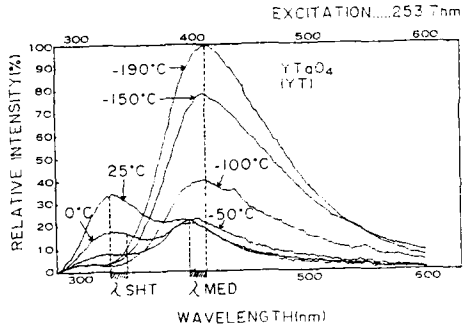


FIG.3 EMISSION SPECTRA UNDER X-RAY EXCITATION

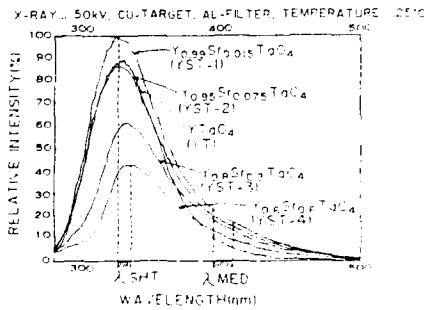


FIG.4 SUBTRACTED EMISSION SPECTRUM

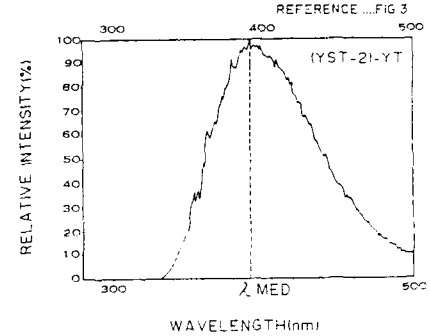


FIG.5 AFTERGLOW UNDER X-RAY EXCITATION

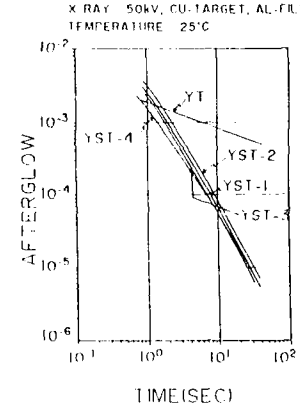
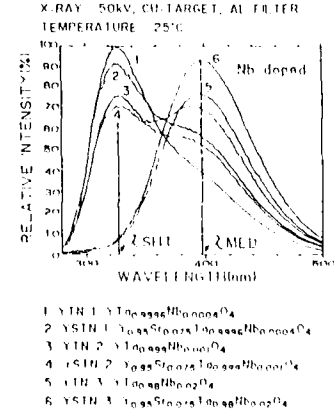


FIG.6 EMISSION SPECTRA UNDER X-RAY EXCITATION



Abstract No. 638

X-Ray Excited Luminescence Spectroscopy of Activated and Unactivated Tantalates

M. K. Crawford[1], L. H. Brixner[1], K. Somaiah[1*] and G. Blasse[2]

[1]E. I. du Pont de Nemours & Co., Experimental Station, Central Research & Development Department, Wilmington, DE 19898 USA

[2]Physical Laboratory, University Utrecht, PO Box 80.000, 3508 TA, The Netherlands

Activated $YTaO_4$ in the M' structure (*P2/a space group*) *is an excellent commercial* X-ray phosphor used for medical imaging.[1] Here we describe X-ray excited luminescence spectroscopy of this system and isomorphic $LuTaO_4$ activated with various transition metal and rare earth ions.

Luminescence was excited with X-rays from an Mo X-ray tube operated at 30 kV and 20 mA. Single photon counting detection was employed. Sample temperatures were varied between 290 K and 2 K using a pumped liquid He cryostat equipped with X-ray transparent mylar and polyethylene windows. Suprasil windows permitted the ultraviolet (UV) and visible light to reach the detection system.

In Figure 1 we show the X-ray excited luminescence spectra of $LuTaO_4$ activated with several rare earths. The broad band emission at 330 nm originates from charge transfer excitation of the TaO_6 group.[2] In Figure 2 we display a schematic energy level diagram for the TaO_6 group. The lowest excited states are the $^1T_2$, $^1T_1$ and $^3T_2$, $^3T_1$ states. The emission arises from the ^3T levels and is spin forbidden. Due to the large amount of spin orbit coupling expected for Ta the excited triplet states will have appreciable admixture of singlet character, relaxing the spin selection rule $\Delta S = 0$. (The relatively short emission lifetime seen in M type $YTaO_4$ is almost certainly due to the spin orbit coupling of Ta[3]).

The 15,000 cm^{-1} shift in energy for TaO_6 emission (330 nm) vs. absorption (220 nm) is due to two causes: 1) the difference is energy between the $^1T_2$, $^1T_1$, and $^3T_2$, $^3T_1$ states and 2) the change in TaO_6 geometric configuration in the excited vs. ground state. (The second factor gives rise to the Stokes shift). If there is a large geometry change in the TaO_6 group in the excited state ($^3T_2$, $^3T_1$) then the excitation energy will be trapped and cannot migrate through the TaO_6 sublattice. *If there is little geometry change* then the energy may undergo migration as a triplet excitation, via exchange interactions, perhaps with some *contribution due to dipole-dipole* interaction permitted by spin orbit coupling. It seems most likely that energy migration within the TaO_6 sublattice does not *readily occur, particularly at* low temperatures.

It can be seen in Figure 1 that energy transfer from TaO_6 to rare earths proceeds readily, *but with an efficiency which depends upon the* particular rare earth. This variation arises from the different possible mechanisms for energy transfer *from* TaO_6 *to the rare earth*, i.e. exchange and dipole-dipole (Forster). Since the distances over which these interactions are effective are quite *different* (<5Å *for exchange vs.* up to ~30Å for dipole-dipole), the relative importance of each can dramatically affect the energy transfer (host to activator) *efficiency*. Furthermore, the degree to which the host and activator energy levels are resonant is also an important factor. *The energy transfer efficiency* can be qualitatively explained by these considerations.

In Figure 3 we display the X-ray excited luminescence spectra of $Y_{0.99}Gd_{0.01}TaO_4$, $LuTa_{.995}Ti_{.005}O_4$, and $LuTaO_4$:Gd,Nb. In all cases, energy transfer from TaO_6 to the various activators occurs efficiently. Ti and Nb *are both broad band emitters, whereas the* Gd^{3+} emission arises from the $^6P_{7/2}$ ---> $^8S_{7/2}$ (f--->f) transition. In $YTaO_4$:Gd there is also Gd^{3+} emission originating in the higher lying ^6I levels at about 280 nm. These levels are easily excited by X-rays and, in fact, *there is some evidence for emission from the even higher* ^6D *energy levels near 250 nm (40,000 cm^{-1}).*

Finally, in Figure 4 we show the luminescence spectra of $YTaO_4$:Gd, $LuTaO_4$:Gd,Nb *and* $LuTaO_4$:Ti *at 2K. In all cases efficient* activator luminescence is seen, indicating that thermally activated energy migration *within the tantalate sublattice is not the dominant* pathway for energy transfer for the activator concentrations studied.

*Visiting Research Scientist; Permanent address: Department of Physics, Osmania University, Hyderabad-500007, INDIA

Acknowledgements: We thank R. J. Smalley, T. D'Allesandro and J. Rooney for help in performing the measurements for sample preparation. K. Somaiah thanks the Vice-Chancellor (T. Navaneeth Rao) and Head, Department of Physics, Osmania University, Hyderabad, India for granting him leave for undertaking this investigation.

References

1. L. H. Brixner and H. -y. Chen, J. Electrochem. Soc. *130*, 225 (1983).
2. G. Blase, Structure and Bonding *42*, 1 (1980), Springer-Verleg, Berlin.
3. G. Blasse and A. Bril, J. Lumin. *3*, 109 (1970).

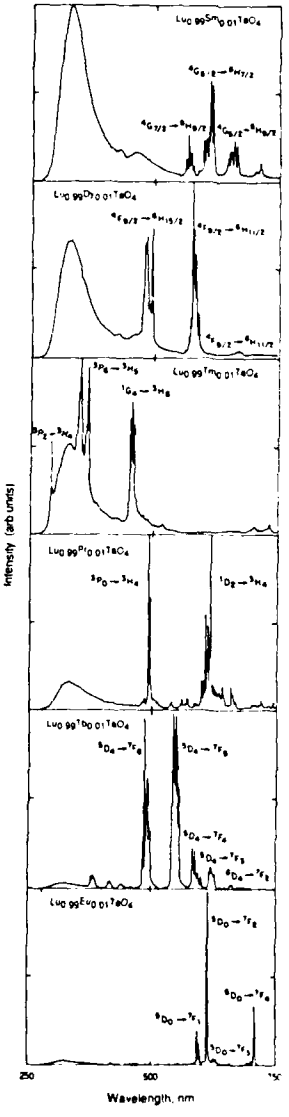


Figure 1 Room temperature x-ray excited luminescence spectra of $LuTaO_4$ activated with various rare earths. The broad band at 330 nm is due to TaO_6 charge transfer emission

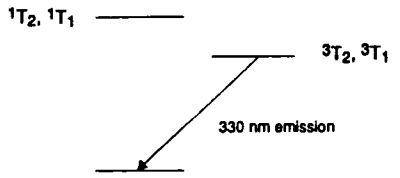


Figure 2 Schematic energy level diagram for TaO_6 group. Crystal field and spin-orbit splittings are not included.

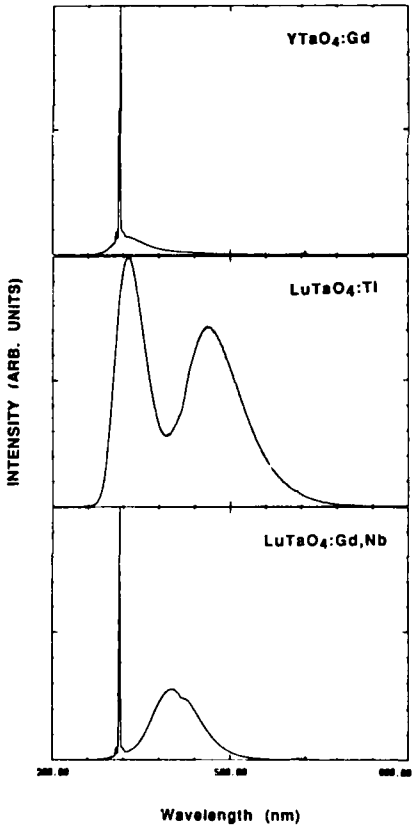


Figure 3 Room temperature x-ray excited luminescence spectra of $YTaO_4$ and $LuTaO_4$ with various activators.

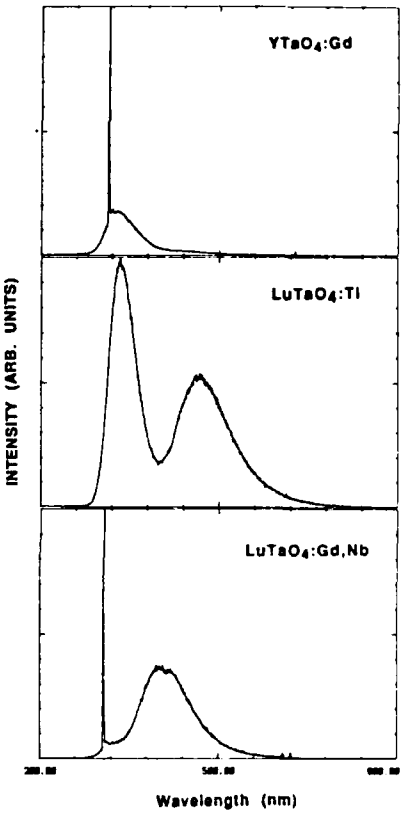


Figure 4 X-ray excited luminescence spectra of $YTaO_4$ and $LuTaO_4$ with various activators at 2K.

Abstract No. 639

LUMINESCENCE AND RADIOGRAPHIC PERFORMANCE OF YTTRIUM/LANTHANUM TANTALATES

W.Zegarski* and L.H.Brixner+

E.I.du Pont de Nemours&Co.,Inc.

+ Central Research and Development

* Imaging Systems

Towanda, Pa. 18848

INTRODUCTION

The high density and x-ray to light conversion efficiency of phosphors based on the tantalate anion make this class of materials well suited for use in intensifying screens. Although only the yttrium compound has been found to be commercially acceptable, the use of other cations results in phosphors which may also be useful diagnostically. Lanthanum tantalate is one of these materials which we have studied. The k-edges of this material make it attractive for increased x-ray absorption (fig.1).

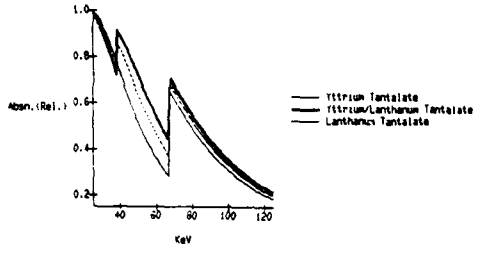


Fig.1. X-Ray Absorption of Tantalate Phosphors

The La edge at 38.9keV adds to that of Ta at 67.5 which results in higher absorption compared to that of the yttrium compound. A deficiency related to the use of this phosphor, however, is its low conversion efficiency when compared to that of yttrium tantalate. To determine if the ability of lanthanum tantalate to convert absorbed x-rays to light could be improved, the solubility of lanthanum in yttrium tantalate was examined.

EXPERIMENTAL SECTION

A series of formulations was prepared in which lanthanum was substituted for yttrium at 1 to 50%/m. Niobium was used as the activator at a constant 0.02% level. The constituent oxides were thoroughly blended with lithium sulfate and fired in air at 1200°C. Removal of the flux gave white powders which were characterized for both physical and radiographic properties.

RESULTS AND DISCUSSION

Scanning electron microscopy showed no difference in phosphor morphology as a function of substituting lanthanum for yttrium. X-ray diffraction results indicate that lanthanum is soluble in the host up to 10%. Beyond this level, two phases are present. To test radiographic performance, the samples were dispersed in binder solutions from which films of varying thicknesses were cast. Phosphor efficiency was measured at 70 kVp. The results are shown in figure 2.

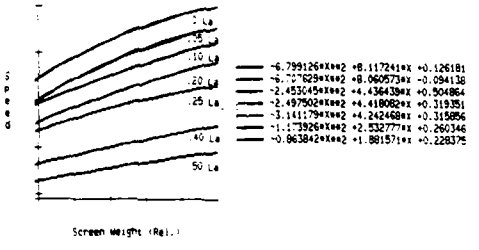


Figure 2. Screen Speed/Weight Dependence

Quadratic fits of speed to screen coating weight show changes occur at lanthanum levels between 5 and 10%, which are probably due to the formation of the second phase. Prompt to lag ratio was found to vary with La concentration. It ranges from 0 from for the base case to 2.2 for 50% substitution.

CONCLUSION

Lanthanum is soluble in yttrium tantalate at between 5 and 10% of the cation concentration. The formation of two phases beyond the solubility limit is accompanied by changes in radiographic performance.

Abstract No. 040

High-speed Stimulable Phosphor X-ray Detector for Computed Radiography

C.Umemoto, A.Kitada, K.Takahashi, T.Matsuda
Fuji Photo Film Co.,Ltd., Miyanodai Development Center, Kaiseimachi, Ashigarakamigum, Kanagawa, 258 Japan

(1) Introduction

BaFX(X Cl,Br,I) crystals have the tetragonal structure of PbFCl and two types of F centers, $F(F^+)$ and $F(X^-)$, can be created by X-ray exposure.[1] It has been shown that these centers turn out to be the photostimulable luminescence (PSL) centers[2] and that the excitation and photostimulation in BaFX:Eu are caused by the processes of $Eu^{2+} \rightleftharpoons Eu^{3+}$ and F^+-centers $\rightleftharpoons$ F.[3,4,5]

Fuji Computed Radiography (CR) systems is a digital image acquisition and processing system for static projection radiography by utilizing this PSL phosphor in the image receptor named Imaging Plate, (IP).[6]

The new IP has been developed by utilizing the high-speed PSL phosphor.

In this paper, the PSL characteristics of it are presented.

(2) Experimental Results

The integrated PSL intensity as a function of the excitation laser energy is shown in Fig.1.

The normalized decay curve of the PSL intensity is shown in Fig.2, which suggests that the optical cross section for PSL in the high-speed IP is not improved compared with the previous one.

(3) Discussion

D.M.de Leeuw et al.[7] have already reported that large improvements in optical cross section for PSL in BaFBr:Eu phosphors are improbable. Our results does not conflict with theirs.

However, the integrated PSL intensity of the new IP is about 1.6 times larger than that of the previous one in case of the same stimulating laser energy.

That is to say, the concentration of electrons trapped at F-centers dose increase in the high-speed IP.

Owing to this high sensitivity, the image noise due to the fluctuation of the detected luminescent photons has been decreased.

By refining the constitution and the configuration of the IP in addition to the improvement of the sensitivity, the root mean square value for the total noise of the CR system is lowered about 15 % for an exposure of 0.5 mR (70kvp, 2mm Al filtration) by this high-speed IP.

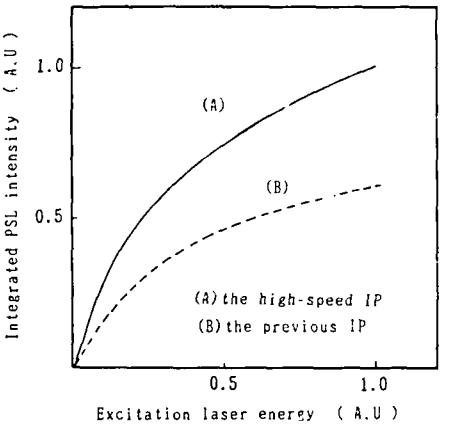


Fig.1 The integrated PSL intensity as a function of the excitation laser energy

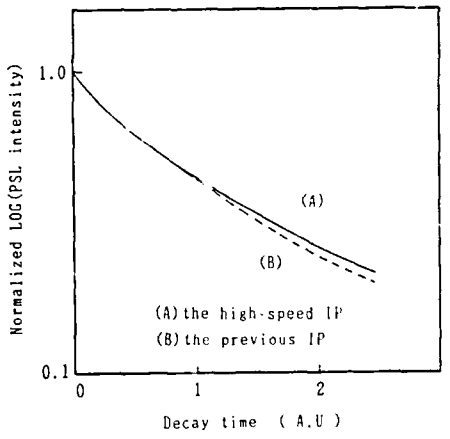


Fig.2 The decay curve of the PSL intensity

References

1) M.Yuste, C.Tarel, M.Rahmani and P.Leymone, J.Phys.Chem.Solid. 37(1976)961
2) K.Takahashi, Y.Shibahara and J.Miyahara, J.Electrochem.Soc. 132(1985)1492
3) K.Takahashi, K.Kohda, J.Miyahara, Y.Kanemitsu, K.Amitani and S.Shionoya, J.Lumin.31&32(1984) 266
4) K.Takahashi, K.Kohda and S.Shionoya, Extended Abstracts of the 170th.Electrochemical Society Meeting. 1018(1986)
5) K.Takahashi and J.Miyahara, Extended Abstracts of the 172th.Electrochemical Society Meeting. 1732(1987)
6) M.Sonoda, M.Takano, J.Miyahara and H.Kato, Radiology. 148(1983)833
7) D.M.de Leeuw, T.Kovats and S.P.Herko, J.Electrochem.Soc. 134(1987)431

Abstract No. 641

PROPERTIES OF RbX:Tl(X=Br,I) PHOTOSTIMULABLE PHOSPHORS

K. Amitani and S. Honda
Konica Corporation
No.1 Sakura-machi Hino-shi
Tokyo 191, Japan

THE KONICA DIRECT DIGITIZER

In the field of medical image diagnosis, digital image processing technology is becomming popular in the effort to realize greater diagnostic efficacy. It is an indispensable technology for the purpose of efficient managing and archiving of medical image imformation.

The Konica Direct Digitizer(KDD), now under development, is an x-ray image capturing unit which uses an x-ray detector composed of a RbBr:Tl photostimulable phosphor.

A schematic diagram of the KDD is shown in Fig.1. When the photostimulable phosphor detector is exposed to x-rays, it temporarily stores the absorbed x-ray energy pattern. Then, when scanned with a focused laser diode (780nm), it emits photostimulated luminescence(PSL) whose intensity is in direct proportion to the absorbed x-ray energy. The PSL is detected by a photomultiplier tube and is converted to a time-series digital signal by an analog-to-digital converter. The data are taken into the frame memory of a controller, then displayed as a visible image on a CRT. After scanning, the detector is exposed to a halogen lamp in order to erase the remaining x-ray energy. Repeating this procedure, the detector can be used again and again.

RbX:Tl PHOTOSTIMULABLE PHOSPHORS

The key to the KDD's features of high image quality, high sensitivity, and short readout time is the use of RbX:Tl photostimulable phosphors rather than BaFBr:Eu or others.

RbX:Tl have shown several advantages:

1) The phosphor layer can be produced by evaporation,
2) It is suited to laser diode stimulation (780nm),
3) The PSL decay time is very short, and
4) Remaining x-ray energy can easily be erased by exposure to light.

With a RbBr:Tl detector, x-ray images are excellent because the phosphor layer can be produced uniformly by evaporation so that there are few structure mottles. Under appropriate evaporating conditions, the phosphor layer consists of crystal pillar-shaped block structures, so that laser beam scattering is supressed, which allows a highly sharp x-ray image.

Sensitivity and readout time are also improved through the use of RbX:Tl. The problem exists that sensitivity, as a direct result of a signal-to-noise ratio, and readout time are conflicting characteristics. In order to improve both, PSL intensity must be increased, while the limit to shortning readout time must be minimized.

PSL intensity can be raised by increasing laser power (Fig.2). This is more easily done with a laser diode than a He-Ne laser, and with the added advantages of smaller size and lower cost. RbBr:Tl allows this because its stimulation spectrum is suited to laser diode stimulation.

Shortning readout time is limitted by PSL response. In Fig.3, the PSL decay time of RbBr:Tl is shorter than that of BaFBr:Eu, allowing readout time to be shortened. We found through simulation that scanning speed using RbBr:Tl can be increased up to 150 m/s without degrading modulation transfer function, which means the readout time of 2000× 2000 pixels could potentially be shortened down to about 10 seconds.

While RbBr:Tl has displayed strong advantages over other non-RbX:Tl phosphors, our most recent work has suggested that our system might further be improved by the use of RbI:Tl. As seen in Fig.4, the RbI:Tl shows a stimulation spectrum even more appropriate to a laser diode than RbBr:Tl. And its x-ray absorption coefficient is higher, further increasing PSL intensity. At the same time, RbI:Tl decay time and laser diode power dependence have been verified as virtually the same as RbBr:Tl, and, like RbBr:Tl, RbI:Tl can be produced through evaporation. While obstacles still exist to its use, RbI:Tl promises to allow further refinement of the KDD.

CONCLUSION

The KDD now under developement has demonstrated the advantages of using RbX:Tl phosphors (both RbBr:Tl and, potentially, RbI:Tl) to achieve high image quality, high sensitivity, and short readout time in digitalized x-ray image capture.

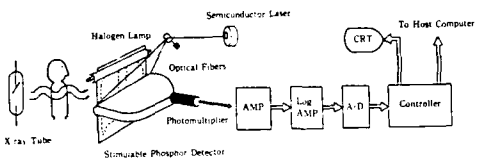


Fig.1 Schematic diagram of the Konica Direct Digitizer (KDD)

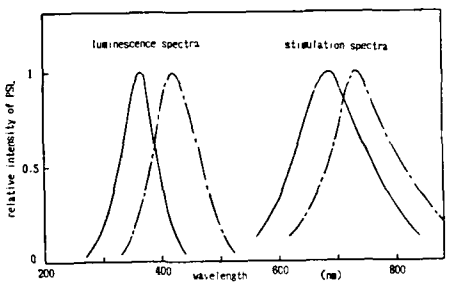


Fig.4 Photostimulated luminescence spectra and stimulation spectra of RbX:Tl
(———: RbBr:Tl , — — —: Rb::Tl)

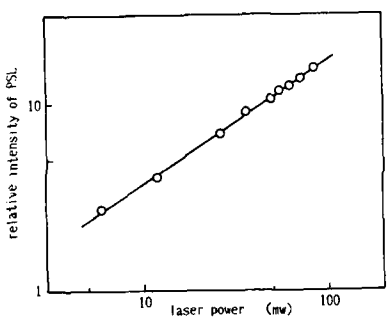


Fig.2 Laser power dependence of PSL

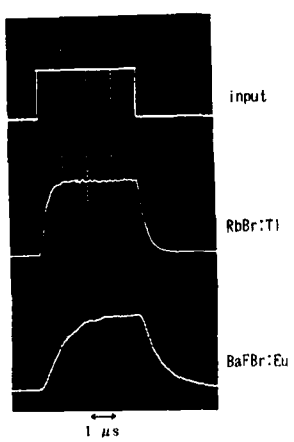


Fig.3 PSL responses of RbBr:Tl and BaFBr:Eu

Abstract No. 642

MEASUREMENT SYSTEMS FOR THE CHARACTERIZATION OF PHOTOSTIMULABLE PHOSPHORS AND STORAGE PHOSPHOR SCREENS FOR X-RAY IMAGING.

L. Struye
Agfa-Gevaert N.V., B-2510 Mortsel, Belgium

The image quality of a photostimulated X-ray storage screen is not only dependent upon the properties of the photostimulable phosphor, but also on its incorporation into a screen.

Equipment has been built to determine the intrinsic properties of a photostimulable phosphor and screen properties affecting image quality. Photostimulable phosphors have been characterised by the prompt emission spectra their conversion efficiencies, their stimulation energies at different wavelengths, their response times, their stimulation spectra and their evolution after excitation, their decay characteristics after photostimulation and their dark decay characteristics. Storage properties have been characterized by the sensitivities, sharpness (SWR and MTF) and signal to noise ratios of the phosphors.

The conversion efficiency and stimulation energy of photostimulable phosphors have been determined by preparing a phosphor screen using the minimum amount of mechanical energy, then irradiating the screen with a known X-ray dose and then stimulating a small area of the phosphor screen with a focused laser beam. The intensity of the emitted light is monitored with a digitiser and is exponential with time. The integral beneath this curve gives the conversion efficiency of the phosphor (the total light emitted by the phosphor/unit area/X-ray dosage) and the product of the time required to reduce the stored energy to 1/E of its initial value and the laser intensity gives the stimulation energy. The stimulation spectrum is determined by scanning with monochromatic light from a lamp in the spectral region of interest. The intensity of the stimulating light is so low that the energy stored in the phosphor is not significantly changed during the measurement.

The response time is measured by stimulating the phosphor with short laser pulses. Pulses with a risetime of 15 ns were achieved with an acousto optical modulator. The detecting photomulitplier and amplifier has a risetime of 35 ns. The curve is an exponential.

The dark decay was monitored by measuring the emitted light intensity obtained by stimulating the phosphor with very low intensity short pulses with a light emitting diode at 30 minute intervals. Between pulses the phosphor is left in complete darkness.

The total pulse energy which is given by multiplication of intensity with the pulse length is so low that the decrease in stored energy during the measurement is insignificant. This measurement normally takes 15 hours.

A laser scanner was built for the screen image quality measurements. A 140 µm focused laser beam is scanned over the screen with a speed of 1000 n inches/s after prior X-ray irradiation through a lead raster. This raster contains two references areas and bars with different spatial frequencies. The phosphor is then excited with a square wave with the frequency changing from 0.5 lp/mm to 3 lp/mm. The amplitude of the signal as a function of space frequency gives the coordinates with which the square wave response can be calculated. The signal to noise ratio is determined by exciting the phosphor screen with a uniform X-ray intensity. The laser scanner is used to read out one line and the curve is corrected with the sensitivity curve of the light collection unit of the scanner.

The noise is separated from the signal using a digital filter and the signal to noise ratio calculated in dB from the energy of the two signals.

Abstract No. 643

SOME SYNTHETIC ASPECTS OF BaFBr:Eu PHOTOSTIMULABLE PHOSPHOR

Vaddi Butchi Reddy

GTE Products Corporation
Hawes Street
Towanda, PA 18848

Divalent europium activated barium fluoro bromide ($BaFBr:Eu^{2+}$) has been a central focus in the development of filmless radiography system which is popularly known as Digital Radiography. Several articles[1-3] have described the preparation and photostimulated luminescence emission (PSL) phenomenon in this phosphor. The primary object in the development of this phosphor is to replace the costly film in radiography application and use the photostimulable phosphor screen as image forming media. The image forming process is separated into two parts as excitation and stimulation. During the excitation stage the phosphor screen is exposed to x-rays, thereby capturing a latent image of the subject. The phosphor screen is then stimulated with a suitable visible/infrared radiation of a known wavelength to cause the emission of the luminescence at its characteristic wavelength (in this case 388 nm). In an actual device the x-ray exposed phosphor screen is rastered pixel by pixel with a laser beam of suitable wavelength and the resulting luminescence is detected and manipulated to obtain an image. In order to obtain good quality images the phosphor is required to have high x-ray absorption, good energy storage, high PSL emission and short PSL persistence. Several synthetic manipulations are made to obtain a high performance PSL phosphor. Some of these aspects will be discussed.

EXPERIMENTAL

Powder samples of BaFBr:Eu are prepared at about 900 °C using different sources of bromine and europium to achieve high PSL brightness to the phosphor. Small amounts (0.02-0.05 moles) of magnesium and strontium in the form of halides have been doped in to the system during the synthesis to improve the PSL luminescence. PSL measurements are performed on a DigiRad measurement device.

RESULTS

Phosphor samples prepared with this procedure have a final composition of $Ba_{0.941}Sr_{0.032}Mg_{0.025}Eu_{0.0018}FBr$. The absorption spectral peak (270 nm) of this phosphor corresponds with the excitation maximum. The emission spectra of the phosphor with U.V. excitation and as well as x-ray excitation indicated a maximum at around 388 nm indicating blue emission. The PSL emission of the pre x ray exposed phosphor samples has been measured by stimulating with stimulating radiations of different wavelengths ranging from 565 nm through 890 nm. The phosphor sample that has been stimulated with a 585 nm wavelength stimulating radiation has given out the maximum amount of light output compared to the phosphor sample that has been stimulated with widely noted 633 nm stimulating radiation. The following table shows the PSL emission intensity improvements.

TABLE I

S.R.W. (nm)	PSL EMISSION (Arbitrary Units)
565	234
585	244
633	170
660	105
890	1

S.R.W. = Stimulating Radiation Wavelength

Various BaFBr:Eu phosphor samples synthesized have demonstrated variations in their PSL emission and screening performances depending on their synthetic atmosphere conditions, particle size of the phosphor, activator and dopant concentrations. A study indicated that the addition of 0.025 moles of magnesium and 0.03-0.035 moles of strontium in the phosphor resulted in a high PSL emission efficiency. The PSL output has also been found to increase as the average size of the phosphor increases. An optimum average particle size of 8-11 μ has been found to give a brighter PSL phosphor with good screening characteristics. It is also found that the BaFBr:Eu phosphor has demonstrated a large PSL emission reduction on deagglomeration/milling procedures that is not intensely effected with normal x-ray phosphors.

One of the last steps in the phosphor preparations is the washing of the final product. It has been found that BaFBr:Eu PSL phosphor is very sensitive to water and only organic solvents (such as alcohols) have to be used for washing purposes. A simple test of stirring 10 gm of BaFBr:Eu phosphor in 50 ml water for 30 sec. indicated a 50% reduction in its PSL emission intensity. X-ray diffraction of this sample indicated the presence of BaF_2 and BaFBr:Eu suggesting that a considerable amount of the phosphor when stirred in water has been decomposed.

Based on the experimental data it is believed that the BaFBr:Eu photostimulable phosphor is a very delicate material to prepare although it is the only phosphor that has produced good quality radiographs in the filmless radiography.

REFERENCES

1. K. Takahashi, K. Kohda and J. Miyahara, J. Luminescence 31/32 (1984) 266
2. D. M. deLeeuw, T. Kovats, and S. P. Herko, J. Electrochem. Soc. 134, (1987) 491
3. J. L. Sommerdijk, J.M.P.J. Verstegen and A. Bril, J. Luminescence 5,(1974) 502 505.

Abstract No. 644

Charge Transfer during Photostimulation of X-Ray Storage Phosphors

Heinz von Seggern, T.Voigt, K.Schwarzmichel
Siemens AG, Central Research and Development,
8520 Erlangen, Germany

Introduction

Recently a new medical X-ray diagnostic system has been introduced based on photostimulable phosphor films replacing the conventional film-screen system. The X-ray storage phosphors, utilized commercially, are the Europium doped alkali-earth halide BaFBr and the Thallium doped alkali halide RbBr. During X-ray irradiation a dose proportional information is stored in the phosphor in the form of locally trapped electron/hole pairs. Electrons are found in F-centers, whereas holes are captured by the dopants. Takahashi et al. [1,2] offered a model describing the information recovery by a direct ionization of the F-center ($F + h\nu_a \rightarrow F^+ + e^-$), followed by a transport of the excited electron in the conduction band and a subsequent recombination of this electron with the ionized dopant. In this study we address the charge transfer mechanism during photostimulation in both materials and partially revise the Takahashi picture.

Experimental results

Measured stimulation spectra of both materials agree with published data of BaFBr:Eu by Takahashi et al. [1,2] and of RbBr:Tl by Amitani et al. [3]. For the latter material coincidence between the stimulation spectrum and a published F-center absorption spectrum [4] was found. Since the same result was already shown in the case of BaFBr:Eu [1,2] we confidently assume that the stimulation spectrum for both materials has its origin in the F-center absorption. The observed emission can be attributed to the charactristic emission of the activators Eu and Tl, respectively. In case of the Europium the emission corresponds to the $4f^65d \rightarrow 4f^7$ transition of the Eu^{2+} and in Tl it seems likely to be a transition in the Tl^+ ion.

To understand the charge transfer mechanism from the F-center to the activator we conducted time resolved experiments from 4.2 K to 420 K. The measurements were performed by illuminating X-ray irradiated and nonirradiated samples with a 10 ns flashlamp pulse (Nanolite, Impulsphysik) through optical filters at appropriate wavelength which depend on the type of experiment to be conducted. The resulting photoluminescence (PL) or photostimulable luminescence (PSL) was detected with a photomultiplier (S 11 cathode, Thorn EMI) through a combination of bandpass filters matching the emission spectrum in order to separate the exciting from the emitted wavelength.

To gain inside into the ongoing processes during and after optical stimulation we have tried to separate the individual components contributing to the PSL process. In the first step we have measured the lifetime of the excited state of the dopants. Therefore the nonirradiated samples were optically excited by illumination at various temperatures into the Eu^{2+} and Tl^+ absorption bands, respectively. For BaFBr:Eu a practically constant PL lifetime was found which agrees with the below given PSL lifetime between 4.2 K and 420 K. For RbBr:Tl the PL lifetime is dependent on the exciting wavelength and does not coincide with the PSL lifetime. It is found that by exciting into the 240 nm Tl^+ absorption band a lifetime of 500 ns is observed whereas illumination into the 265 nm band yields a value of 420 ns. The PSL lifetime has, however, a limiting value of $\tau = 280$ ns which is believed to be the actual Tl^+ lifetime for an X-ray irradiated sample (see below).

The contributions of the F-center as well as the conduction band to the PSL response can be investigated by measuring the PSL lifetime and efficiency as a function of temperature. The experiments were carried out in the same manner as the PL lifetime experiments except that the sample was X-irradiated prior to the measurement and the exciting wavelength of the 10 ns flashlamp was filtered by a 530 nm and 600 nm highpass filter for BaFBr:Eu and RbBr:Tl, respectively. The irradiation was performed at room temperature in case of BaFBr:Eu and at 210 K in case of RbBr:Tl, followed by a cooling to 4.2 K and and a subsequent stepwise heating up. After each step the PSL lifetime and the PSL efficiency in form of the amplitude- lifetime product $I_{max} \cdot \tau$ was extracted. Because of the small amount of information read out per measurement the whole experiment could be performed with a single X-ray exposure. In this method variations in the exposure and spatial inhomogeneities can be neglected. The PSL lifetime for both substances is shown in Fig.1. and the PSL efficiency is plotted in Fig.2. For BaFBr:Eu one observes an almost temperature independent value for both the PSL lifetime and the efficiency. Consequently one has to conclude that the PSL mechanism does not contain a thermally activated component. For RbBr:Tl the PSL lifetime behaves completely different. For temperatures above 320 K one observes a constant PSL lifetime which is related to the lifetime of the excited state of the Tl^+ in X-ray irradiated RbBr. Below 320 K measurable down to temperatures as low as 60 K a thermally activated PSL lifetime is obtained which varies almost three orders of magnitude exhibiting an activation energy of 30.2 meV. The measurable efficiency of the thermally activated PSL is constant from 230 K down to temperatures of at least 60 K. Below 60 K the thermally activated PSL becomes to small to be measurable in our setup. In addition a temperature independent PSL signal appears whose efficiency is smaller and which is believed to be related to tunneling of an electron from the relaxed excited F-center state to the Tl^{2+} ion or to a hole in the neighborhood of the Tl^+ ion. At which temperature the thermally activated component of the PSL process disappears can not be extracted from our measurements.

Modelling and discussion

In Fig.3 the band model of the PSL process is shown. Let us assume that an X-ray dose proportional number of F-centers (trapped electrons) and recombination centers (trapped holes) exists, for the sake of simplicity in form of Eu^{3+} and Tl^{2+}. As mentioned above the stimulation spectra of both materials have their origin in the F-center absorption. This suggests strongly that the F-center acts as the occupied electron trap. The energetic

level scheme of a typical example of such an F-center [4] is shown schematically in Fig.3. During optical excitation (photostimulation) the F-center groundstate electron (1s) is pumped into its first excited state (2p) where it causes a lattice relaxation resulting in an energetic shift of the energy level close to the conduction band (relaxed excited state). Once in this level the electron has different alternatives:

a) recombination into the unrelaxed groundstate,
b) escape into the conduction band by thermal activation and subsequent recombination in the Eu^{3+} and Tl^{+}, respectively,
c) tunneling to the neighboring recombination center.

For BaFBr:Eu it is likely that the excited electron is not able to leave the F-center since apparently the tunneling process is more efficient and explains the temperature independent PSL. This, however, requires the existence of close proximity of the F-centers and the Eu^{3+}ions. We therefore suggest the existence of a Photo Stimulable Luminescence Complex consisting of F-centers and Eu^{3+}ions as a kind of aggregation centers (see Fig.3 right side). Dynamical studies of the PSL behavior support this point of view [5].

For RbBr:Tl the PSL behavior is more complex.Dependent on the temperature regime the material shows different PSL mechanisms. From 4.2 K to about 60 K a tunneling process is observable. After photostimulation the F-center electron is not able to leave its relaxed excited state therefore only those electrons tunnel to the activator which are located close to a Tl^{2+} ion or to a trapped hole in the Tl^{+} vicinity. At higher temperatures (T > 60 K as the measured value) the escape of the excited F-center electron to the conduction band seems more likely since the required thermal energy is now available. Once in the conduction band the electron has to move through a large number of traps which exhibit an activation energy of E_a = 30.2 meV. At higher temperatures (T > 230 K) the storage behavior of the X-ray information declines indicating an instability of either the F-center or the trapped hole.

Interesting in the case of RbBr:Tl is the modified Tl^{+} lifetime after X-ray irradiation. This could be the influence of a trapped hole in the vicinity of a Tl^{+} ion instead of the above assumed Tl^{2+} ion. That the trapping is stronger in case of the Tl than in case of the Eu can be understood by comparing the ion radii of the activators with the matrix elements.

References

[1] Takahashi. K., Kohda K., Miyahara J., J. Luminescence 31 & 32, 266 (1984)
[2] Takahashi. K., Kohda K., Shinoya S., Extended Abstracts, Fall Meeting Electrochem.Soc., San Diego, Cal.(1986), p.1010
[3] Amitani K.,Kano A.,Tsuchino H.,Shimada F SPIE's Conf.and Exhib.: Electric imaging 26th Fall Symp. Printing of Paper Summaries, Oct. 1986, p. 180
[4] Fowler W.B.: Physics of Color Centers, Academic Press, New York 1968
[5] v.Seggern H.,Voigt T.,Lange G.,Knüpfer W., publ. accepted in J.Appl.Phys.

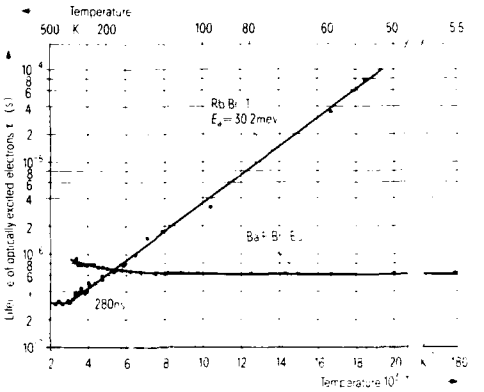


Fig.1 Temperature dependence of PSL lifetimes resulting from ns optical pulse excitation.

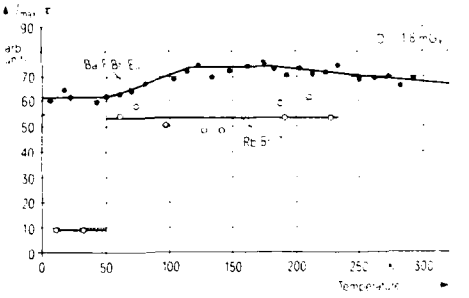


Fig.2 Temperature dependence of PSL efficiency $I_{max} \cdot \tau$

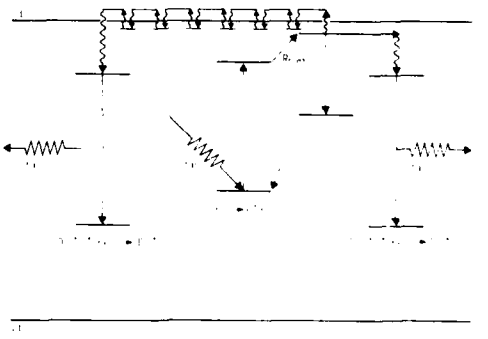


Fig.3 Schematic band model for processes occuring in X-ray storage phosphors, D symbols the activator.

Abstract No. 645

Study of the Photostimulable Luminescence Complex in the Storage Phosphor of BaFBr:Eu

K. Huber++), W. Knüpfer+), M. Mengel+), K. Schwarzmichel++), H.v. Seggern++)

+) Siemens AG, Medical Systems, D-8520 Erlangen, Germany

++) Siemens AG, Research and Development, D-8520 Erlangen, Germany

Introduction

Europium activated barium halides, especially BaFBr:Eu are used as photostimulable x-ray phosphors in digital radiography. An important quantity for the resulting images is the stimulated output signal of the phosphor. In a recent paper [1] it has been shown, that the photostimulability of this phosphor is based on the existence of a trap - activator complex (Eu^{2+}in vicinity of an F-center, see fig. 1).

During optical stimulation the electron is transferred from the F-center to the Eu^{2+} by tunneling. Optimizing the density of these complexes by experimental skill will result in a maximum sensitivity of the storage phosphor. It is the aim of this paper to show that the ratio of the mol numbers of the raw materials BaF_2 and $BaBr_2$ plays a crucial role for the formation of the Photo Stimulated Luminescence Complex (PSLC).

Experimental procedure and measurements

BaFBr:Eu phosphors activated with 0,05 - 1,0 mole percent Eu were made by firing intimate mixtures of the raw materials BaF_2 and $BaBr_2 \cdot 2H_2O$ (dried at 200 °C) in an H_2/N_2 atmosphere at about 900 °C. The phosphors were washed, ground and refired at a slightly lower temperature. The samples prepared contained different mole ratios m of $BaF_2/BaBr_2$ ranging from 0,3 to 1,0. The powders were deposited in quartz pockets with thin walls to allow x-ray irradiation as well as optical studies. All measurements were carried out with samples having an area of 2 cm^2 and a thickness of 0,5 mm. In order to investigate the influence of the mole ratio on the resulting PSLC density we measured as a function of m the stimulated output signal, the stimulation spectrum, the concentration of divalent Eu^{2+} in the host and the geometry of the host with the help of x-ray diffraction. For the determination of the stimulation spectra a flashlamp with a pulse duration of about 10 ns in combination with an optical filter or monochromator was used as stimulating light source. In order to detect the emitted light, a photomultiplier was used in combination with BG 3 and BG 37 filters (Schott Glaswerke). The filters were necessary in order to decouple the emission wave length from the stimulating wave length. The signals were detected on a digital oscilloscope. In this way resulting photostimulated luminescence together with the temporal response were recorded. The area under the decay curve is proportional to the number of emitted photons after stimulation. The same equipment has been used for the measurement of the Eu^{2+} concentration in the phosphor with a slight modification. The light of the flash lamp has been filtered so that only the wave length of 310 nm corresponding the wavelength of excitation of Eu^{2+} was used. Here the resulting area under the decay curve is a measure of the Eu^{2+}content.

Results

The results show a clear evidence for a preferred mole ratio of m = 0,6. There the stimulated output signal is at a maximum with the stimulation spectrum being shifted to a wave length of 600 nm which is almost optimal for the use of a He-Ne laser beam. The PSLC density is also maximal. This behaviour is stable against coactivation of additional dopants leading to a more complex storage phosphor system with higher sensitivity. Again a specific value of m is responsible for a maximum density of the PSLC. The influence of the mole ratio m of the raw materials on the stimulated signal can be understood when considering the amount of $BaBr_2$ exceeding the amount of BaF_2 as a flux agent affecting the diffusion processes at the fi-

ring temperatures. Removing any excess $BaBr_2$ by a washing procedure yields a phosphor BaFBr:Eu with the final mol ratio [F]/[Br] being close to one and showing optimal photostimulated luminescence.

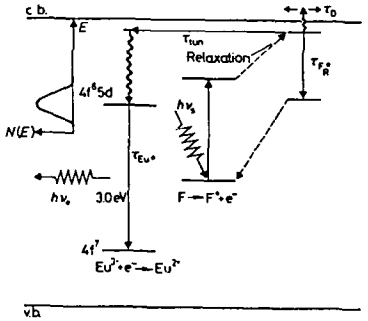


Figure 1. Band model for PSL mechanisms in BaFBr:Eu due to optical stimulation. On the right is the F-center with its relaxed state, on the left the level scheme of the divalent Eu. $h\nu_s$ and $h\nu_e$ denote stimulating and emitted photons respectively, τ_D denotes the escape time of the excited F-center electron into the conduction band, τ_{F^*} the radiative recombination of an electron from the relaxed excited state into the excited ground state, and τ_{tun} the tunneling time to the trivalent Eu, τ_{Eu^*} the lifetime of an electron in the $4f^6$ 5d level of the divalent Eu. Sinusoidal arrows symbolize thermal nonradiative transitions.

References

[1] H. v. Seggern, T. Voigt, W. Knüpfer and G. Lange

Physical Model of Photostimulated Luminescence of x-ray irradiated BaFBr:Eu, Applied Physics, in press.

Abstract No. 646

EFFECT OF GRINDING ON PHOTOSTIMUABLE PHOSPHORS FOR X-RAY SCREENS

R. P. Rao
Central Electrochemical Research Institute
Karaikudi-623006, India

Luminescence efficiency of a phosphor can be improved by minimising the energy losses during excitation. The loss of excitation energy in the case of powdered samples is mainly due to scattering of incident radiation by the particles of phosphor. Thus, while considering the industrial applications of polycrystalline phosphors in lamps, screens, paints, etc. the effect of particle size on the light output has to be specially studied.

It is very well established that the radiographic imaging with photostimuable (PS) phosphors has many advantages over conventional photographic film screens. In the new type of computer radiography, PS phosphors are to be used as memory materials for temporary storage of the x-ray image. Eu(2+) doped barium fluorohalide phosphors are most suitable for this purpose. The spatial resolution from the image plate can be improved to a certain extent with phosphors comprising fine particles. The fineness of the particles can be achieved by various means such as grinding, fast cooling after firing or incorporation of some flux materials during the firing processes. But the efficiency of the phosphor deteriorates with grinding. Fast cooling is a complicated process in the case of Eu(2+) doped phosphors. Incorporation of flux materials may change the characteristics of phosphor materials. In the present investigation, effect of grinding (ball milling) on particle size distribution, shape of the particles and luminescent properties of BaFCl phosphors have been studied.

A number of samples have been prepared by firing suitable amounts of $BaCl_2$, BaF_2 and EuF_3 at 800-950°C for 1-3 hours to obtain $Ba_{0.99}Eu_{0.01}FCl$ phosphors. Reduction of Eu(3+) to Eu(2+) has been done in the presence of CO instead of forming gas (nitrogen with 2-10% of hydrogen). After firing, the mass is subjected to grinding in a centrifugal ball mill (Retsch Type S1) with 200 g agate balls (2 Nos.) in an agate cup (500 cc) for different durations (10 to 360 mins). The grinding was carried out in auto reverse mode at 20 rpm on each batch of 5 g. Particle size distribution (PSD) of these phosphors has been studied with the help of Malvern EASY Particle Sizer M 3.0 after every grinding. It is observed that the particle size varies from 10 to 100 μ on initial grinding whereas at longer durations, the particle size is in the range 5 to 20 μ. The shape of these phosphors is generally irregular plates. With constant ball milling at low pressure, the shape of these particles can be brought to regular plates. Scanning Electron Microscopy (JEOL 35 CF) studies on these phosphors after 6h grinding show that all the particles are similar in size and regular in shape. The excitation and emission spectra have been recorded with the help of fluorescent spectrophotometer (Hitachi 650-10s). The emission spectrum of these phosphors is shown in Fig.1. The spectrum shows a band (λ_{max} = 388 nm) with a half width of 34 nm. The ball milling did not cause any appreciable change in the fluorescent spectra. The variation of luminescent intensity with milling time is shown in Fig.2. The luminescence degradation by grinding may be due to particle size reduction which increases the less-luminescent surface region. From the results obtained in this investigation, it is concluded that the required particle size and shape of polycrystalline powders can be obtained by ball milling without destroying the luminescent characteristics of the phosphor materials (e.g. BaFCl:Eu) to be used in medical image screens for high resolution.

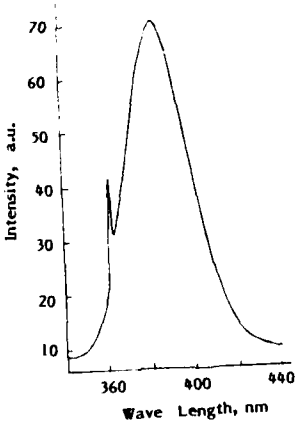


Fig.1 Fluorescent emission spectrum of BaFCl:Eu phosphor recorded at 300K after 30 mins ball milling.

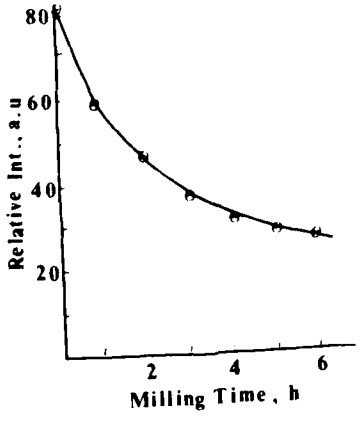


Fig.2 Milling time vs luminescent intensities of BaFCl:Eu phosphors.

Abstract No. 647

ELECTROPHORETIC PREPARATION OF PHOSPHOR SCREENS

Esther Sluzky
Hughes Aircraft Company
Industrial Products Division
Carlsbad, California.
and Kenneth Hesse, Consultant

The preparation of high resolution cathode ray tube monochrome screens requires the use of very fine particle size phosphor. For example, in this discussion the typical fine grain phosphor has a particle size distribution in the range of submicron to approximately 4.0 μms, the average being in the neighborhood of one-half to two μms. depending upon the particular phosphor used. In preparing screens of these fine particles, the use of electrophoretic (EP) coating offers advantages over the usual methods of screen preparation. Since the phosphor has very fine particles, gravity settling is inconvenient because of the very long settling times that are required. Increasing the settling speed by means of centrifugal force can be done, however this method has not produced screens having the microscopic quality of EP coated screens. This quality is important in high resolution CRTs since any irregularities in the screen can introduce problems with both resolution and visual noise in the displayed image. Other advantages of EP screens are more precise control of the screen density and uniformity, the formation of more densely packed screens, a more efficient manufacturing process since a number of similar screens may be "plated" at the same time, as well as providing the possibility of being able to coat unusual and irregular shapes.

Hughes became interested in the fabrication of screens by EP coating in order to improve the high resolution, high brightness characteristics of CRTs for advanced display application. Several articles (7,8) conclude that screens prepared by EP coating were capable of higher resolution, less noise, and either equal or only slightly less light output as compared to settled screens. Of course, the opposite opinions could also be found, viz., there was no improvement in these qualities compared to settled screens (9). Our work has encompassed most of the phosphor families including P1 zinc orthosilicate, P11 zinc sulfide, P43 gadolinium oxysulfide, P53 yttrium aluminum garnet, and a special red phosphor zinc cadmium sulfide. It has been found that all can be coated by this method with minor modifications in processing to take care of individual phosphor peculiarities.

The method used by Hughes is a modification of that described by McGee et al (7). The charging ion species however were changed from a mixture of aluminum and lanthanum to magnesium and lanthanum. This mixture of ions was found to produce screens with improved adhesion to the substrate as compared to the previous mixture or to the use of the individual ions separately. In addition the amount of water added to the main suspension liquid, isopropanol, has been optimized.

Since the process requires conductive substrates and the typical substrate is made of glass, a conductive coating must be applied to it. Two types of coatings (thin films) have been used: tin oxide (TO) or indium tin oxide (ITO), and metallic films. Generally the transparent conductive films (TO and ITO) must be used with caution since under some conditions the oxides can be reduced to metallic tin and/or indium during electrolysis. In the case of thin metal films, once the screen has been applied it is necessary to remove the metal film to allow the luminescent image to exit the front side of the substrate for viewing.

Various curves will be presented showing the behavior of the EP coating bath as well as others displaying the attributes of the screens produced by this technique. Included in these figures will be: rate of phosphor deposition as a function of the electric field, plating density versus plating time, the effect of temperature on the coating weight, and the influence of phosphor concentration in the bath on plating weight. Curves of tube performance will compare such characteristics as brightness, resolution, and noise figures with those of settled screens.

The data presented show that EP coating permits the fabrication of phosphor screens that have the capability of very high brightness and resolution, and very low visual noise content. The EP coating process itself is reproducible and lends itself to the manufacture of good quality screens.

BIBLIOGRAPHY

1. F.F.Reuss, "Memories de Societe" Imperiale des Naturalistes des Moskow, 2, 327 (1809).

2. W.F.Pickard, "Remarks on the Theory of Electrophoretic Deposition" J.E.C.S., 115, No. 4,105C (1968).

3. G.M.Bose, Phil. Trans. Roy. Soc., 43, 419 (1745).

4. N.F.Cerulli, "Method of Electrophoretic Deposition of Luminescent Materials & Product Resulting Therefrom" U.S.Patent 2,851,408 Sept.9, 1958.

5. Photoelectronic Image Devices. Proc. 2nd Symp. Imperial College, London, Sept. 5-8 (1961). Advances in Electronics, XVI 315-318 (1962).

6. Development of Screens for High Resolution Display Devices. AL-TDR-64-94 May 1964. Contract No. AF#33(657)-10632.

7. McGee, Airey, & Aslam, "High Quality Phosphor Screen for Cascade Image Intensifiers", Advances in Electron. & Electron Physics, 22A 571-581 (1966).

8. Grosso, Rutherford, & Sargent, "Electrophoretic Deposition of Luminescent Materials" J.E.C.S. 117 No. 11, 1456 1459 (1970).

9. Prener & Swank, "Studies of X-ray Image Intensifier Output Screens", J.E.C.S. 125, No. 4, 583-587 (1978).

Abstract No. 648

TiO_2 SiO_2 multilayerd insulating films for ELD

Takahiro Nakayama, Ken-ichi Onisawa,
Moriaki Fuyama, Masanobu Hanazono

Hitachi Reseach Laboratory, Hitachi Ltd.
4026 Kuji-tyo, Hitachi-shi,
Ibaraki-ken, Japan.

Introduction

Dielectric thin films having both the high dielectric constant and the high breakdown field strength are desirable for insulating layers of electroluminescent devices (ELD). However, dielectric films with the high dielectric constant tends to have the low breakdown field strength. To overcome this problem, application of composite films have been studied.[1)2)] As each layer of multilayer becomes thinner, the multilayer films is supposed to change from layer structure to composite like. From this viewpoint, relationship between monolayer thickness and the dielectric properties were studied using TiO_2/SiO_2 multilayered films.

Experimental

In Table 1 monolayer and total thickness of prepared samples are shown. Total film thickness was fixed to be about 500nm. TiO_2 monolayer thickness d_T was varied from 60nm to 0.1nm. d_T were calculated from deposition rates and sputtering time, and the total thickness was measured with a surface roughness tester. At first relationship between dielectric properties and composition ratio of TiO_2-SiO_2 was examind using TiO_2 SiO_2 composite targets. Thickness ratio 1:3 was selected because the field strength decreased rapidly when the film thickness ratio was more than 1:3.

Results

By secondary ion mass spectroscopy (SIMS) analysis, the TiO_2 5nm/SiO_2 15nm multilayered film was analyzed. Figure 1 shows Ti/Si signal intensity ratio are plotted as a function of etching time. From Fig. 1, we can see that Ti/Si composition ratio of this film changes periodically. This periodicity could not be detected for films of d_T<5nm clearly. This is supposed to be limited by the resolution of SIMS.

Figure 2 shows X-ray diffraction (XRD) patterns of TiO_2/SiO_2 multilayered films. The films were annealed for 1 hour at 550℃ in vacuum of 2×10^{-4}Pa. The films of d_T≥10nm show diffraction pattern of TiO_2 anatase, and films of d_T<10nm are amorphous.

Figure 3 shows the energy gap Eg obtained from the light absorption edge measurement. Eg of the annealed films of d_T>2nm is close to Eg of TiO_2 film. In the films of d_T<2nm, Eg becomes larger as d_T becomes thinner.

Figure 4 shows the product $\varepsilon_0 \varepsilon_r E_{BD}$ (ε_0 the dielectric constant of vacuum, ε_r the relative dielectric constant, E_{BD} the breakdown field strength) as a function of d_T. The product $\varepsilon_0 \varepsilon_r E_{BD}$, which is an index of the dielectric layers of ELD, is the maximum surface charge density. From Fig. 4, it is shown that $\varepsilon_0 \varepsilon_r E_{BD}$ is changed by d_T, and its peak is obtained around d_T=1nm.

Conclusion

The dielectric properties and structures of TiO_2/SiO_2 multilayered films are examined. The dielectric properties of the films depend on TiO_2 monolayer thickness d_T, and peak of maximum surface charge density $\varepsilon_0 \varepsilon_r E_{BD}$ is obtained around d_T=1nm.

References

1) S. K. Tiku and J. C. Smith J. Electron Mater. 13 (1984), 273

2) K. Nomura, H. Ogawa and A. Abe J. Electrochem. Soc. 134 (1987), 922

Table 1 Sample thickness (nm)

Thickness of monolayer		Total thickness
TiO_2	SiO_2	*of film*
0.3	0.9	470
1	3	480
2	6	500
5	15	500
10	30	460
60	180	480

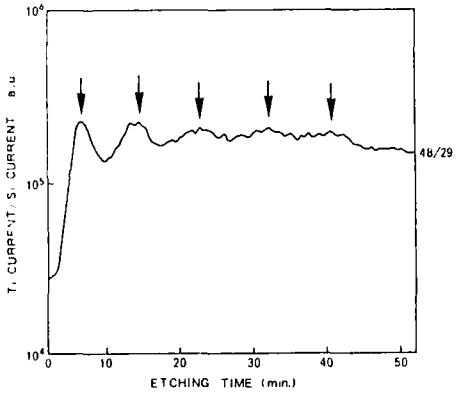


Fig. 1 Results of SIMS analysis for a TiO_2 5nm/SiO_2 15nm multilayered film.

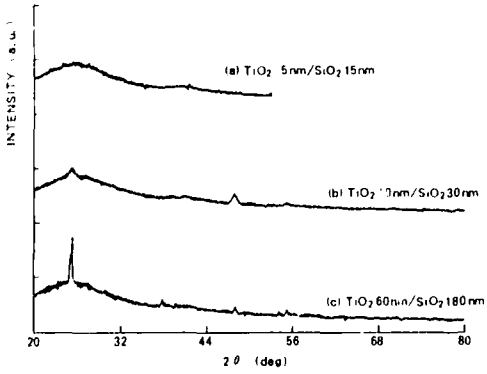


Fig. 2 X-ray diffraction patterns of TiO_2/SiO_2 multilayered films.

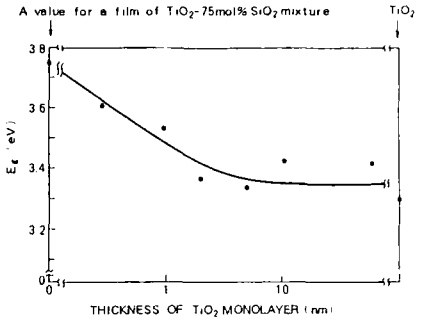


Fig. 3 Energy gap E_g as a function of thickness of TiO_2 monolayer.

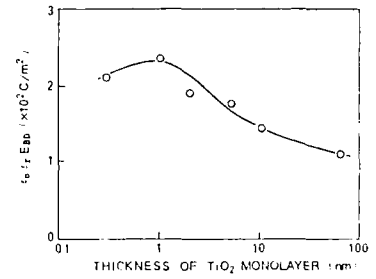


Fig. 4 Maximum charge density $\varepsilon_0 \varepsilon_r E_{BD}$ in TiO_2/SiO_2 multilayered films.

Abstract No. 649

BEAM PENETRATION PHOSPHORS FOR ADDING COLOUR CAPABILITY TO HUD CRTs

D G Etherington J D Leyland
M Naqvi H Tanner
M S Waite

Rank Brimar Ltd. Middleton
Manchester M14 1SN England

1. INTRODUCTION

Voltage dependent phosphor screens offer a potential solution to the problem of adding colour capability to Head-Up Display CRTs which presently operate with P1, P43 or P53 phosphor. Three examples of beam penetration phosphor, of the "onionskin" type, have been investigated for this application. They each consist of a green or yellow-green emitting core phosphor, surrounded by a non-luminescent barrier layer and an outer layer of red emitting, fine grain phosphor. The systems investigated were: P1-YVO_4:Eu, Gd_2O_2S:Pr-YVO_4:Eu, and P53-P56, each with an intermediate SiO_2 barrier layer.

2. PHOSPHOR PREPARATION

Barrier layer deposition

The formation of the silica barrier layer is achieved by the reaction of silane, SiH_4, with oxygen in a fluidised bed reactor containing the core phosphor. The growth of the SiO_2 barrier is followed by measurement of the effective barrier voltage and depends upon the concentration and flow rate of silane, the phosphor particle size and the reactor temperature. For a reactor temperature of 480°C the SiH_4 and O_2 mass flow rates are controlled to give an effective barrier growth rate of approx. 0.4kV/hr. However, coincidentally with the growth of the barrier, an aggregation of particles occurs in the fluidised bed, resulting in an approximate doubling of the volume of individual phosphor grains during the formation of a 10kV barrier. This phosphor aggregation can be seen in Fig 1 and is a factor which may limit the resolution of the resultant phosphor screens. Under high magnification (Fig 2), the silica is seen to be granular.

Red phosphor deposition

The red phosphor is applied from a suspension of fine grain red phosphor (median particle size 1μm) by the standard gelatin process.(1). Although the process is carried out several times to maximise surface coverage by the red phosphor, the resultant coverage is only partial.

The screening of these composite phosphors can be carried out by conventional settling methods, despite the increase in particle size. Typical particle sizes, as determined by the Coulter method are given in Table 1.

3. PROPERTIES OF THE "ONIONSKIN" PHOSPHORS

Efficiency and Chromaticity

Brightness/voltage relationships at a current density of 1μA/cm² on aluminised phosphor screens were determined over the range 5 to 25kV (Figs 3-5). Calibrated filters enable the individual core and red phosphor components of the luminance to be determined.

It can be seen that the increase with voltage of the luminance from the core phosphor is effectively linear over the range 16 to 25kV. At 25kV the relative efficiency from the core phosphor is 25-30% of the original phosphor.

The luminance contribution from the red phosphor reaches a maximum of 12kV and remains constant to 25kV. The maximum luminous efficiency of the red phosphor in the composite particle varies from 2 lumens/watt for YVO_4:Eu to 4 lumens/watt for P56, the voltage which corresponds to maximum efficiency being in the range 10 to 12kV. The instrinsic efficiencies of the red phosphors at a particle size of 1μm are low, 3 lumens/watt for YVO_4:Eu and 6 lumens/watt for P56, and empirically it has been found that the luminous efficiency of the red phosphor in the phosphor screen is 2/3 of the intrinsic efficiency of that phosphor, both for YVO_4:Eu and P56.

The chromaticity range is greatest with the P1-vanadate system and least with P53/P56 - Table 2, but the established higher efficiencies of the latter phosphors under high current density suggest that the P53/P56 phosphor would be preferred in a practical 2 colour HUD CRT. The Pr doped oxy-sulphide is a potential alternative to P1 with reduced persistence, but the efficiencies indicated in Fig 4 are lower than those found with other phosphors.

4. PRACTICAL DEMONSTRATION OF 2 COLOUR HUD CAPABILITY

A representative HUD tube was processed with the P53/P56 composite phosphor and gave luminances and resolution over the range 12.5kV(red) to 25kV (yellow-green) indicated in Figs 6a) to d).

In cursive mode (line writing) luminances in excess of 4,500cdm^{-2} and 40,000cdm^{-2} are readily obtained with moderate beam currents at the two switching voltages of 12.5 and 25kV.

REFERENCES

1. T.E. Clark; C.T. Burilla, J.Electrochem. Soc. 129 , 1540 (1982).

ACKNOWLEDGEMENTS

The authors wish to acknowledge the support of M.O.D for this project and, in particular, the advice and encouragement of Dr A Hughes (RSRE-Malvern) and Dr J R Banbury (RAE-Farnborough), and are grateful for permission to publish these preliminary results. We are also grateful to the Technical Staff at Rank Brimar for their assistance, in particular M D Lawton, B Walker and J Neary.
This work has been carried out with the support of the Procurement Executive, Ministry of Defence.

TABLE 1 PARTICLE SIZE OF "ONIONSKIN" PHOSPHORS

SERIES	PHOSPHORS	CORE SIZE	CORE & BARRIER	RED COATED FINAL PHOSPHOR	
515	P1 + vanadate	9.0	21	23	μm
519	P1 + vanadate	12.6	22	25	μm
523	Gd_2O_2S:Pr + "	7.0	14	16	μm
524	P53 + P56	11	21	24	μm

TABLE 2 CHROMATICITIES AS FUNCTION OF VOLTAGE

PHOSPHOR		FINAL ANODE VOLTAGE (kV) 8	12	16	20	24
P1/vanadate (10519/R)	x =	0.669	0.630	0.487	0.376	
	y =	0.326	0.359	0.483	0.578	
Gd_2O_2S:Pr vanadate (10523/R)	x =	0.655	0.588	0.483	0.414	0.356
	y =	0.334	0.377	0.443	0.488	0.524
P53/P56 (10524/R)	x =	0.613	0.587	0.516	0.457	0.423
	y =	0.374	0.390	0.434	0.470	0.492



Fig 1: Phosphor(Pl)aggregation during SiO_2 coating



Fig 2: SiO_2 barrier at high magnification(X 10,000)

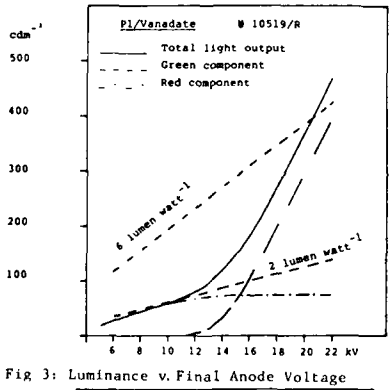


Fig 3: Luminance v. Final Anode Voltage

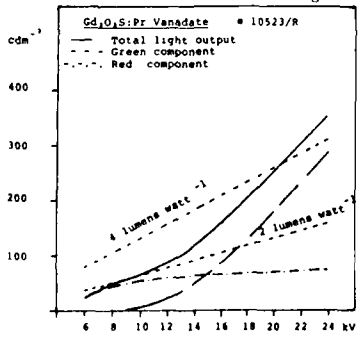


Fig 4: Luminance v. Final Anode Voltage

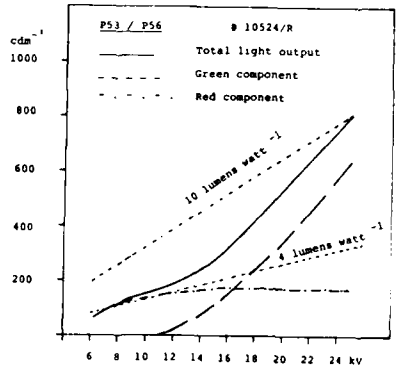


Fig 5 : Luminance V. Final Anode Voltage

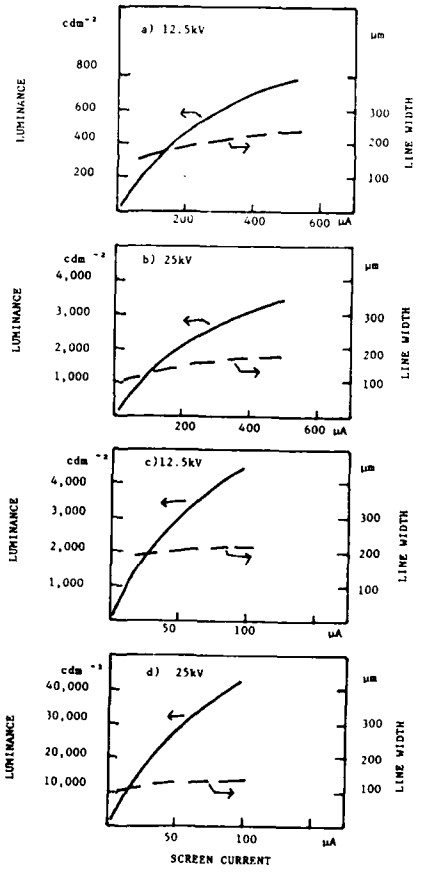


FIG 6 LUMINANCE AND RESOLUTION P53/P56

a) Raster excitation at 12.5kV
b) " " " 25 kV
c) Cursive " " 12.5kV 50 m/sec
d) " " " 25 kV 50 m/sec

Abstract No. 650

The Formation Process of Y_2O_2S: Eu^{3+}, a Red Phosphor

C. I. Jeon, Q. W. Choi, and C. H. Kim

Inorganic Chemistry Laboratory
Korea Advanced Institute of Science and Technology
P.O.Box 131 Cheongryang
Seoul, Korea

and

S. I. Mho

Department of Chemistry
Ajou University
Suwon, Korea

Yttrium oxysulfide doped with europium is an excellent red phosphor for color TV screen. The reaction of Y_2O_3 with sulfur to form a host lattice Y_2O_2S and the diffusion of Eu^{3+} ion into the Y_2O_2S lattice for this phosphor were studied. The red phosphor, Y_2O_2S:3% Eu^{3+}, was prepared by solid reaction of Y_2O_3, dopant Eu_2O_3, S, and NaOH mixture. The formation reaction of the phosphor can be illustrated by the following steps:

$$Y_2O_3 + S \longrightarrow Y_2O_2S + 1/2\ O_2$$

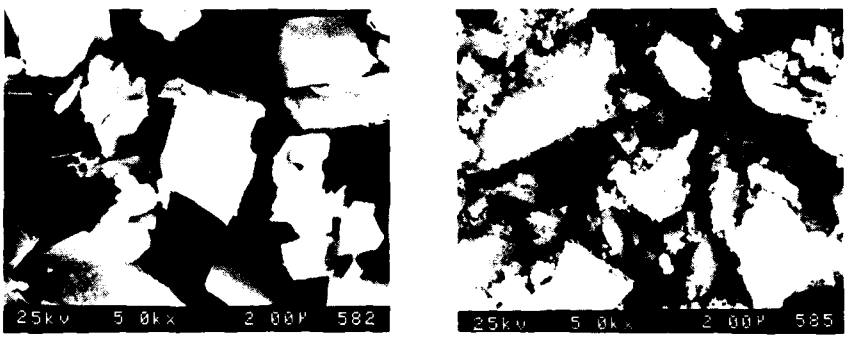
$$Eu^{3+}(3\%) + Y_2O_2S \longrightarrow Y_2O_2S{:}3\%\ Eu^{3+}$$

The reaction may be occurred at the surface of Y_2O_3 particles for the first step. The formation rate of Y_2O_2S is determined both by the reaction rate of Y_2O_3 and S at the surface and by the diffusion rate of sulfur to the reacted Y_2O_2S layer. Because of the difference in densities of Y_2O_3 and Y_2O_2S, the formed Y_2O_2S is removed from the surface and the fresh surface of Y_2O_3 particles can contact with sulfur during the reaction. The size and surface morphology of the crystallite were examined with a scanning eletron microscope. The Y_2O_3 particle, whose size is about 5 um, is being cracked into smaller size in the process of reaction with sulfur, which is illustrated in Fig. 1. Therefore, the chemical reaction rate of sulfur and Y_2O_3 is directly related to the formation rate of Y_2O_2S. In order to determine the reaction rate, X-ray diffraction(XRD) spectra were obtained for the products made in a series of reaction temperature and reaction times. XRD spectra show peaks representing of Y_2O_2S and of unreacted Y_2O_3 when the reaction temperature is low, and show peaks only of Y_2O_2S when the temperature is higher than 800°C in half an hour of reaction time(Fig. 2).

Activator Eu^{3+} can be diffused into both Y_2O_3 and Y_2O_2S. The excitation bands (f-d charge transfer band) show maximum at different wavelengths; Eu^{3+} in Y_2O_3 at 262nm, Eu^{3+} in Y_2O_2S at 350nm. The fluorescence intensity of Eu^{3+} in Y_2O_2S is monitored for the products made at a series of reaction temperature and reaction times(Fig. 3). As the reaction temperature increases, the fluorescence intensity is increased. The fluorescence intensity is increased as the reaction time increases even at high temperature of 1000°C, while the host lattice Y_2O_2S are formed in half an hour at 800°C. The activation energy for the diffusion of Eu^{3+} ion into Y_2O_2S was calculated. The activation energy of 20Kcal/mol is obtained by linear regression method from the plot of $\ln[\ln(1/(1-Y))]$ vs. 1/T, where Y being the fraction of doping. The fraction of doping is calculated from the ralative fluorescence intensity of the product to the maximum fluorescence intensity.

In conclusion, the formation rate of Y_2O_2S is determined by the chemical reaction rate of Y_2O_3 with S at the surface of Y_2O_3 particles. The chemical reaction of Y_2O_3 with S proceeds rapidly, and the diffusion rate of Eu^{3+} into Y_2O_2S is slower. The activation energy of Eu^{3+} diffusion into Y_2O_2S is calculated to be 20Kcal/mol.

References:
1. D.W. Ormond, E. Banks, J. Electrochem. Soc., 122(1975), 152.
2. M.R.Royce, U.S.Pat. 3423621(1969).
3. M.R.Royce, S.M.Thomsen, P.N.Yocom, U.S.Pat. 3502590 (1970).



(a) (b)

Fig. 1. Scanning electron microphotographs of Y_2O_3(a) and Y_2O_2S(b).

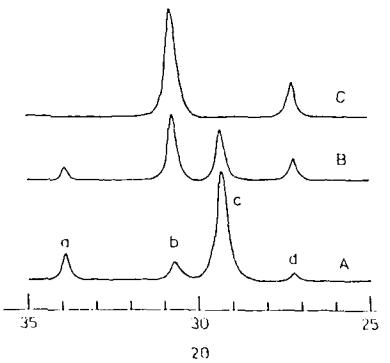


Fig. 2. X-ray diffraction pattern of reaction products. Reactants;Y_2O_3:NaOH:S = 1:1:2(by wt.), reaction time ;30 min., reaction temperature; A;500°C, B;700°C, C;800°C. Peak a,c;Y_2O_3, Peak b,d;Y_2O_2S.

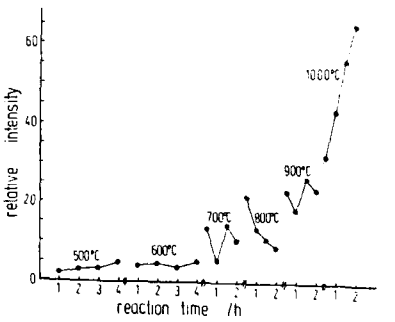


Fig. 3. Relative fluorescence intensity vs. reaction time and tenperature of Y_2O_2S:Eu. Excitation wavelength;350 nm, emission wavelength;630 nm.

Abstract No. 651

COLLOID CHEMISTRY OF FLUORESCENT PHOSPHORS

P. K. Whitman
GE Lighting, Nela Park, Cleveland, Ohio 44040
M. E. Labib, G. H. Thomas, III
David Sarnoff Research Center, CN 5300,
Princeton, New Jersey 08543

INTRODUCTION

In this paper we present a survey of surface chemistry techniques applied to fluorescent phosphors in aqueous systems. The surface and colloid chemistry of fluorescent lamp phosphors determines the processing and quality of lamps. Factors such as appearance and uniformity of coatings are influenced by the surface properties of the phosphors. Knowledge of the detailed surface chemistry can lead to the control of flocculation of particles in coating suspensions and to improved adhesion of coatings. We have studied the surface chemistry of several important phosphors using electrokinetic, surface titration and surface spectroscopic techniques.

MATERIALS AND METHODS

The phosphor materials tested in this study were prepared as they would be used in typical applications; no special pre-treatments were attempted to remove environmental contamination.

The electrokinetic properties of the phosphors were studied by measuring the electrophoretic mobility of 10 wt% aqueous slurries using PenKem System-7000-Acoustophoretic® equipment. This technique is similar, in principle, to sedimentation potential. The results were verified by independent measurements using conventional dilute suspension microelectrophoresis.

Surface titrations are based on conventional potentiometric titration methodology. Aqueous phosphor slurries of several different ionic concentrations are titrated for each material. By calculating the amount of acid or base consumed by the particles, the surface charge can be determined. The isoelectric point and dissociation constants of the surface species can be inferred from the results.

The surfaces of some phosphors were also studied by XPS and FTIR spectroscopy.

RESULTS AND DISCUSSION

Table I summarizes the isoelectric point (pH at which the particle has no net surface potential) and point of zero charge (pH at which the particle has no net surface charge) for each of the various phosphors as determined by acid-base titration in electrokinetic and surface titrations experiments, respectively. A description of the acid or base strength of the phosphors is also shown in the table. The particles are negatively charged at pH above the isoelectric point and are positively charged below this pH.

The surface of calcium halophosphate behaves as a strong acid with an isoelectric point of 2.3. This is in contrast with the surface of the strontium chlorapatite surface which is basic -- isoelectric point 10.5. This difference can be attributed to calcium versus strontium and to fluoride versus chloride in the apatite structures of the two materials. Yttrium oxide, CAT, and BAM surfaces are all basic in character. This is expected from the chemistry of Y_2O_3 and aluminates. Our results are consistent with published results for undoped analogues of these materials (1).

We have also investigated the surface of yttrium oxide phosphor in detail with XPS and FTIR spectroscopies. We could resolve the O(1s) spectrum into two components -- oxide and hydroxide. FTIR investigation showed the tendency of this phosphor to form surface carbonates.

From these results, we can predict that certain phosphor blends will tend to co-flocculate when the solution pH is intermediate between the isoelectric points of the individual components, but these same blends may be electrostatically stabilized at high or low pH. Hence, the surface and colloid chemistry of fluorescent phosphors can play an important role in the processing and quality of lamps.

1. Parks, G., Chem. Rev. 65:177 - 198 (1965).

TABLE I

SURFACE CHEMISTRY OF PHOSPHORS IN WATER

PHOSPHOR	CHEMICAL FORMULA	ISOELECTRIC POINT	POINT OF ZERO CHARGE	COMMENTS
CA HALOPHOSPHATE	$Ca_{10}P_6O_{24}(F,Cl):Sb,Mn$	2.3	--	STRONG ACID
YEO	$Y_2O_3:Eu$	9.8	8 - 10	STRONG BASE
LA PHOSPHATE	$LaPO_4:Tb,Ce$	7.2	6.5 - 8	NEUTRAL
CAT	$(Ce,Tb)MgAl_{11}O_{19}:Ce,Tb$	9.8	--	STRONG BASE
SECA	$Sr(PO_4)_3:Eu$	10.5	9 - 10.5	STRONG BASE
BAM	$BaMg_2Al_{16}O_{27}:Eu$	10.5	--	STRONG BASE

Abstract No. 652

OPTICAL TASTE SENSOR WITH FLUOROPHOR-EMBEDDED LANGMUIR-BLODGETT FILM

Masuo Aizawa, Mieko Matsuzawa,
and Hiroaki Shinohara
Department of Bioengineering,
Tokyo Institute of Technology
O-okayama, Meguro-ku, Tokyo 152, Japan

Introduction

Increasing attention has been paid to the application of the Langmuir-Blogett (LB) film technique to the formation of organized molecular membranes. An attempt to utilize LB films for sensing devices is one of the most exciting and promising applications. Baker et al. reported that an LB film gas sensor exhibited a rapid response to a specific gas. Sriyudthsak and Moriizumi immobilized enzyme molecules in an LB film to construct an enzyme field effect transistor. These researcher have been developing selective chemical sensors for a single component in either gas or solution. In contrast, we have attempted to develop an optical chemical sensor using an LB film for simultaneous recognition of many components in solution. The sensing principle is based on the dynamic quenching of various fluorophores embedded in an LB film.

Taste and olfactory cells simultaneously accept multimolecular information, which is followed by recognition of small and taste through sophisticated information processing in the neuronetwork. There are two approach in realizing a chemical sensor modeled on the taste and olfactory cells. One approach is to integrate many selective sensor elements for multimolecular information. The other approach is to integrate non-selective sensor elements. Both types of sensors require information processing for simultaneous recognition of multicomponents. In this, investigation, non-selective sensor elements have been investigated onto a single device to simulate the function of taste sensory system.

The concept of the taste sensor is schematically illustrated in Fig. 1. The sensor consists of an optically transparent substrate and several layers of Langmuir-Blogett (LB) films, each layer containing different fluorophores. Fluorescence of an LB film may be quenched or enhanced when the film comes to contact with molecules of taste. Since each fluorophor fluoresces at a different characteristic wavelength, the responses of the films can be differentiated. Anthracene, perylene, and pyrene were used as fluorophors for the taste sensor.

Experimental

A non-fluorescent quartz glass plate was employed as a substrate for the LB film. The plate was cleaned and silanized to make the surface hydrophobic. A benzene solution containing 9,12-anthroyloxy stearate and stearate was spread on the surface of a 0.25 mM $CdCl_2$ aqueous solution in a through (Kyowa Kaimen Kagaku Co. Ltd.). Bilayers of stearate/anthroyloxy stearate were deposited on the silanized plate under a contact surface pressure. In a similar manner, LB films containing 1-pyrenebutyric acid and perylene were deposited on the silanized quarts glass plate. The light beam impinged on the LB film at the incident angle which would best induce excitation of the embedded fluorophor.

Results and Discussion

The maximum excitation peaks of the pyrenebutyrate/stearate LB film approached at 325 and 342 nm and the emission peaks were observed at 376 and 395 nm. Those of the perylene/arachidate LB film were 412 and 430 nm for excitation along with 470 nm for emission. The fluorescence intensity varied depending on the surface pressure in film preparations, and decreased by 30 % when it was immersed in an aqueous solution.

Fluorescence of these LB films quenched in responding to sodium glutamate and guanyl phosphate (GMP), when each of these taste molecules is solely present in a solution. In contrast, however, fluorescence peaks at were sharply enhanced due to coexistence of sodium glutamate and guanyl phosphate as shown in Fig.2.

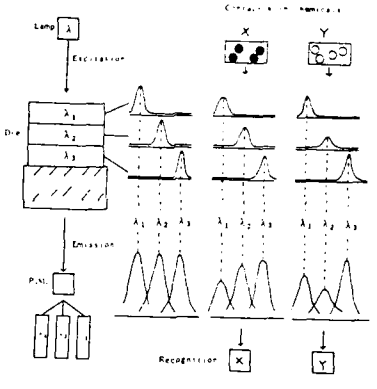


Fig. 1 Concept of an optical chemical sensor for simultaneous recognition of multicomponent.

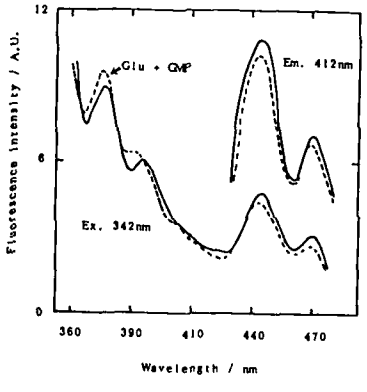


Fig. 2 Fluorescence response of a LB film containing pyrenebutyrate and perylene to guanylic acid and glutamic acid.

Abstract No. 653

FIBEROPTIC PRESSURE TRANSDUCERS FOR MEDICAL APPLICATIONS.

Thor-Erik Hansen

ame, a.s micro electronics

Knutsrødveien 7, N-3191 Horten, Norway

1. Introduction.

A series of fiberoptic sensors that have been devellopeд at the Central Institute in Oslo, and **ame** in Horten, Norway. The work was first directed towards electro-technical aplications where noise immunity and galvanic insulation are important. (1). The work in medical pressure transducers was motivated from the need to solve the serious packaging problems confronting electric micro-tip pressure transducers. As the body liquids represent a very hostite environment to pressure sensitive semiconductor elements.

2. Theory of operation.

The fiberoptic transducer configuration is shown in fig 1. The two legs of a bifurcated fiber bundle are connected to a LED and a photodetector, respectively. A measuring tip with a thin metall membrane is mounted at the commen end where the fibers from the two legs are randomly mixed. Coupling of light from the LED into the leg connected to the photodetector varies with the defletion of the membrane. In our transducers with an incident optical power of 100nW at the detector and a membrane distance of 30 um, the theoretical resolution is about 0,5 nm for a bandwidth of 100 Hz (2).

3. Fabrication of the transducer.

The fiber diameter is about 50 um and the acceptance angle is 60°. The bundles are cut in convenient lengths and split, and the resulting bifurcated bundles are then fitted into suitable medical catheters. The distribution at the common end is approximately random. Fiberoptic connectors are mounted at the two legs. Finally, the measurement tip is mounted. The membrane is 10 um thick and the diameter is about 1.6 mm. The material is stainless steel, and electron beam or laser welding techniques are used in the production process. An air channel connects the space behind the membrane through the catheter to the atmosphere. Transducers are made in 6, 7 or 8F catheters (outer diameter ranging from 2.0 to 2.6 mm). The total lenght, including the legs, is 185 or 250 cm. A Fiber-Tip transducer built in a 7F catheter is shown in fig. 2 (a) and a detail of the measurement tip is shown in fig. 2 (b).

4. Results.

The medical transducers are intended for the physiological measurement range from -100 to 300 mmHg. Permitted overload is 3000 mmHg and the hysteresis is better than 1%. This is shown in fig. 3.

The thermal drift in the pressure response is less than 0,1%/°C for the temperature region 20° to 45°C. Thermal zero-point drift is less than 0,5 mmHg/°C and approaches 0,1 mm Hg/°C in the best transducers. In animal experiments the zero-point long-term drift when measuring in blood was found to be less than 0,5 mmHg per hour (determined by using a hydraulically coupled catheter-transducer system in parallel as referance). Potential frequency response is 20 kHz.
Transdusers have been tested at 10000 volts between the measurement tip and the connectors at the two legs. A leakage current of typically 3 uA originated in catheters incorporating a steel wire braid in the wall for torque control and manoeuvrability. The transducers can take strong bending and can be tied into knots with a 3 cm diameter without breakage. During operation this may give a zero-point shift of typically 0,3 mmHg. This represents a 0,03% perturbation of the light flux in the fiber bundle.

5. Clinical tests and applications.

The first application was for intravascular cardiological examinations where the transducers has been tested successfully in right hand side catherizations. Another important application is urodynamic examinations which is shown in fig. 4 (3). Applications also includes a probe for measurement in the stomach and the duodenum and a monitor for uterine pressure during labour.

6. Conclusions.

A fiberoptic medical pressure transducer has been realized. The performance compare very favourably with commercial available micro-tip transducers and other fiberoptic transducers. The devellopment have resulted in a commercial fiberoptic medical pressure transducer.

References.

1.
B.R.Nyberg, K.Herstad, P.Bjørløv-Larsen and T.E.Hansen, Measuring electric field by using pressure sensitive elements, IEEE Trans. Elec. Ins., EI-14 (1979) 250-255.

2.
T.E.Hansen, A fiberoptic micro-tip pressure transducer for medical applications, Sensors and Actuators, 4 (1983) 545-554.

3.
B.Kvarstein, O.Aase, T.E.Hansen and P.Dobloug, A new method with fiber-optic transducers used for simultaneous recording of intravesical and urethral pressure during physiological filling and voiding phase, J. Urology, 130 (1983) 504-506. (Also at International Continence Society, 12th Annual Meeting, Leiden, September, 1982.)

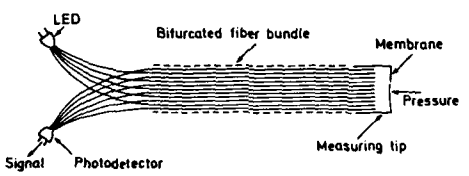
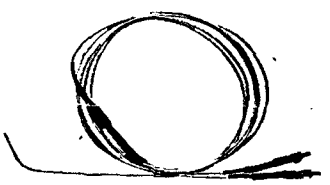


Fig. 1. The fiber-optic pressure transducer principle configuration.



(a)



(b)

Fig. 2 (a) Fiberoptic microtip pressure transducer built in 7F catheter. Outer diameter 2,5 mm, length 185 cm. (b) Detail of measurement tip. The active diameter of membrane is about 1,6 mm and the thickness is 10 um. The material is stainless steel.

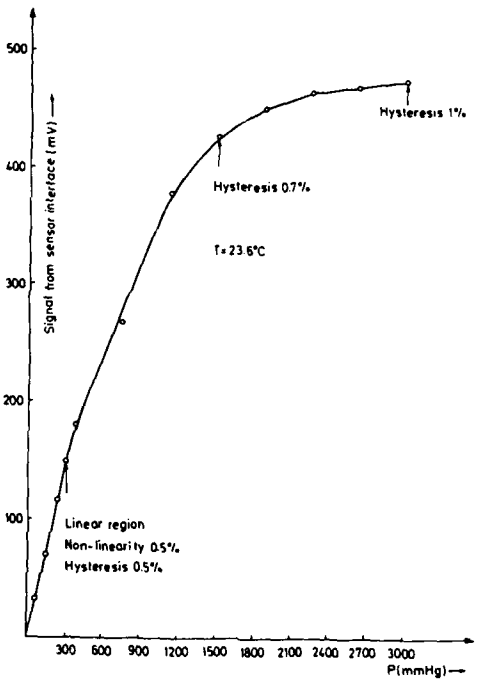


Fig. 3 Signal from sensor interface as function of pressure at the measurement tip. The figure demonstrates the linear region and the overload capacity of the transducer.

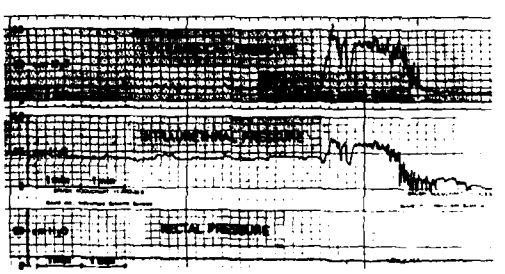


Fig. 4 Registration of bladder urethra and rectal pressures during filling and voiding.

Abstract No. 654

Fiber Optic Fluoroimmunosensor: Determination of the Sensitivity and Dynamic Range

D.E. Yoshida, D.A. Christensen, J.D. Andrade, and W.M. Reichert'
Departments of Electrical Engineering and Bioengineering, University of Utah
Salt Lake City, Utah 84112
'Department of Biomedical Engineering, Duke University, Durham, N.C.

INTRODUCTION

There has been considerable interest in the development of fiber optic fluoroimmunosensors for medical diagnostics[1,2,3]. These sensors have the potential of not requiring a complex clinical laboratory. Other advantages of optical fibers include remote, small size, immunity to electromagnetic interference, lack of electrical connections in the sensing area, and relatively low cost.

Evanescent fiber optic sensors are based on the principle of total internal reflection (TIR), which occurs when light originating in a higher refractive medium hits the interface of a lower refractive medium. During TIR, an evanescent wave is generated at the interface which exponentially decays into the lower refractive medium with a depth of penetration of approximately a third of a wavelength.

In one application of the fiber optic immunosensor, the evanescent wave penetrates into a layer of antibodies (Abs) immobilized at the fiber core (Figure 1). Fluorescently labeled antigens (Ags) in the bulk solution bind to the Abs, and are excited by the evanescent wave. The excited fluorescence at or near the surface couples back into the fiber by reciprocity, and propagates as bound modes to the detector[4]. The evanescent excitation and back coupling mechanism gives rise to surface sensitivity by minimizing the collection of bulk fluorescence; this also eliminates the need to physically remove the labeled Ags from the sensor environment.

In order for a fiber optic immunosensor to be practical, the sensitivity and dynamic range of the sensor must be comparable with existing techniques, such as radioimmunoassay and enzyme immunoassay. The sensitivity of the sensor is determined by the affinity of the Ab for the Ag. If the Ab has a high binding constant, a lower concentration of Ab can be detected due to the strong attraction of Abs for the Ags. In addition, the sensitivity is also governed by the sensor's lower fluorescence detection limit.

The dynamic range of the sensor is limited by the surface concentration on the sensor. As the surface concentration decreases, a lower concentration is required to saturate the sensor, which reduces the upper detection limit.

EXPERIMENTAL METHODS

A schematic of the optical system is shown in Figure 2; and the experimental procedure were previously described elsewhere[5]. The midsection of a 600µm optical fiber (Quartz Products) is used as the sensor.

Two experiments were performed where:
1) human immunogobulinG(H-IgG) were covalently immobilized on the sensor to detect tetramethylrhodamine conjugated anti-H IgG (MRITC anti-H IgG, Sigma Chemicals) and
2) anti-H IgG were covalently immobilized on the sensor to detect MRITC H-IgG (Jackson Immunoresearch). The labeled anti-H IgG and H-IgG were prepared in phosphate buffered saline (PBS, pH=7.4). The unlabeled H-IgG and anti-H IgG (Cappel Laboratories) were immobilized to the sensor surface by 3-aminopropyltriethoxy silane and glutaraldehyde [6].

RESULTS AND DISCUSSION

The specific binding of MRITC anti-H IgG to H-IgG immobilized on the sensor surface as a function of concentration is shown in Figure 3. A plateau of the signal near 0.5mg/mL of MRITC anti-H IgG indicates the sensor surface was close to saturation. The lower limit was 0.01mg/mL of labeled anti-H IgG.

The specific binding of MRITC H-IgG to anti-H IgG covalently immobilized on the sensor surface was found to saturate at 0.001 mg/mL, which was also the lower limit due to the sensor's sensitivity(Figure 4). The surface concentration of anti-H IgG was determined to be 1.4×10^{-13} moles/cm^2 using radioimmunoassay. This indicates only about 4% of the active sites on the anti-H IgG are available for H-IgG to bind with. In other words, many of the active sites are blocked when the anti-H IgG are covalently immobilized on the sensor, allowing the surface to saturate at low concentrations.

CONCLUSIONS

The H-IgG has many epitopes to which the anti-H IgG can bind, thus increasing the surface concentration of binding sites as compared to when the anti-H IgG is immobilized. This would account for the greater dynamic range with H-IgG immobilized on the sensor.

The minimum detectable concentration with H-IgG immobilized on the sensor is greater than that detected with anti-H IgG. This is attributed to the binding constant being an order of magnitude lower for H-IgG than for anti-H IgG immobilized on the sensor[6].

Further studies must be undertaken on the surface chemistry and optics to increase the dynamic range and sensitivity of the sensor.

ACKNOWLEDGEMENTS

Funding for this project was provided by a seed grant from the Center for Sensor Technology. The authors would like to thank J. Ives, J.N. Lin, J. Herron, V. Hlady, and P. Suci for technical assistance.

REFERENCES

1. W. Love and R. Slovacek, paper presented at OFS '86, Tokyo, Japan, Oct. 1986.
2. R. Sutherland, C. Dahne, J. Place, and A. Ringrose, Clin. Chem., vol. 30, p. 1533, 1984.
3. T. Hirschfeld, U.S. Pat. No. 4,447,546 (1984).
4. C. Carniglia, L. Mandel, and K. Drexhage, J. Opt. Soc. Am., vol. 62, p. 479, 1972.
5. D. Yoshida, J. Ives,W. Reichert, D. Christensen, and J. Andrade, Proc. SPIE, vol. 904, p. 57, 1988.
6. J.N. Lin, J. Herron, J. Andrade, and M. Brizgys, IEEE Trans. Bio. Eng., in press.

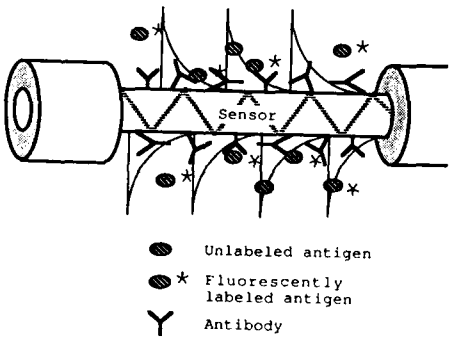


Figure 1. Illustration of evanescent excitation of the fluorescently labeled antigens bound to the antibodies immobilized on the sensor surface.

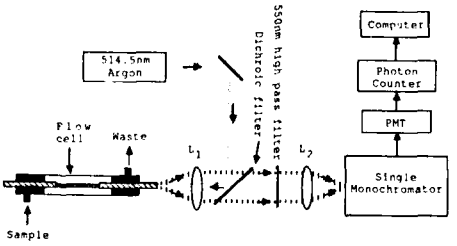


Figure 2. Schematic of the experimental optical system.

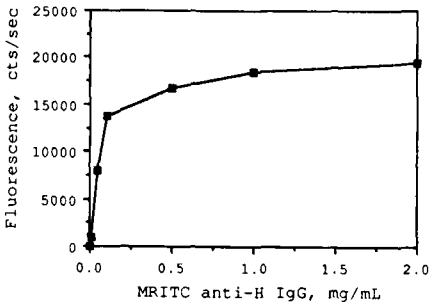


Figure 3. Fluorescent signal above background fluorescence for the specific binding of MRITC anti-H IgG to H-IgG covalently bound to the sensor. The signal begins to saturate at approximately 0.5 mg/mL of labeled anti-H IgG.

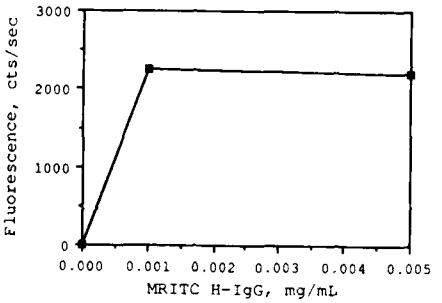


Figure 4. Fluorescent signal above background for the specific binding of MRITC H-IgG to anti-H IgG covalently immobilized to the sensor surface. The sensor's lower detection limit and saturation concentration occur at 0 001 mg/mL of labeled H-IgG.

Abstract No. 655

SENSORS FOR DETERMINING THE COMPOSITION OF FALLING LIQUID FILMS*

D. T. Bostick,[a] L. N. Klatt[a] and H. Perez-Blanco[b]
Analytical Chemistry[a] *and Energy Division*[b]
Oak Ridge National Laboratory
P.O. Box 2008
Oak Ridge, TN 37381-6142

Approximately 21% of the total US energy consumption is for the heating and cooling of buildings. It is estimated that about 60% of the gas and oil used for these functions could be saved by using advanced absorption heat pump systems. Advanced multi-effect absorption cycles with heating and cooling coefficients of performance of about two have been identified and laboratory prototypes are being tested.

The absorption refrigeration system is a heat driven cycle; the operation of single-effect systems are described in the literature.[1] Multi-effect cycles are single-effect cycles cascaded together to provide larger heat amplification.

In designing absorption heat pump systems one finds that the absorber is the heat exchanger that determines the thermal efficiency and capacity of the total system and, hence, directly affects the operating economics. Two basic problems are encountered. These are the failure of the absorber to reach the predicted equilibrium conditions and the low heat transfer coefficient at the vapor-absorbent interface.

Fiber optic sensors capable of measuring the real time in-situ absorber concentration in the liquid films on the absorber heat exchange surfaces are being developed. Preliminary studies with the LiBr-H_2O fluid have been completed.

EXPERIMENTAL

The sensors are prepared by removing about a 4 cm section of the fluoropolymer buffer and polymeric cladding from a step index silica core fiber optic (Model HC-612-T, Ensign Bickford Optics Co., Avon, CT 06001). The exposed core is straight. At the exposed core the LiBr solution serves as the low index medium. According to Fresnel's Law of Reflection, the fraction of intensity refracted into the lower index medium increases as the refractive index of the LiBr solution approaches that of silica. This loss of intensity is observed as a decrease in the light transmission efficiency of the fiber. This transmission efficiency is related to the concentration of the LiBr solution and forms the basis for the sensor.

A schematic drawing of the absorption test apparatus is shown in Figure 1. The vessel is constructed from stainless steel. Four fiber optic sensors are attached to four heat exchange tubes with custom designed clips. The fiber core is located about 0.6 mm from the tube surface. The launch face of each fiber optic is illuminated with a light-emitting diode (LED). Custom fabricated bushings that allow full illumination of the fiber's acceptance cone are used to couple the fiber optics to the LEDs. Reflected light emerging from the rear of each LED is monitored with a silicon diode to provide a normalization signal; light emerging from the exit end of the fiber optic is monitored with a second silicon diode. A thermocouple junction, that measures the liquid temperature, is located adjacent to each fiber optic sensor.

The solution in the sump of the vessel is heated to form absorbent and water vapor. A recirculating pump transfers the absorbent from the sump to the drip tube located above the heat exchange tubes. Water vapor is absorbed by the thin liquid film as drops of absorbent fall from the drip tube and contact the heat exchange surfaces. This process of drop formation, detachment, and liquid film formation is repeated on each heat exchange tube. The dilute absorbent returns to the sump of the vessel. The heat of absorption and dilution is transferred to the cooling water flowing through the heat exchange tubes. Data acquisition and analysis are conducted with a personal computer.

RESULTS

Figure 2 is a plot of the time dependence of the vessel pressure and the LiBr concentration on the second heat exchange tube for a typical experiment. The mean percent [w/w] LiBr measured on the four heat exchange tubes are 49.1, 48.0, 47.5 and 47.9% with standard deviations of 0.5, 0.4, 0.5 and 0.6%, respectively. Based upon sensor calibration data, the standard deviation of the refractive index measurement is 0.0004 R.I. units, which corresponds to about 0.1% [w/w] LiBr. Except for heat exchange tube number four, a continuous dilution of the absorbent is observed as it flows from one heat exchange tube to the next. Heat recovery is typically 90%.

The large transients are caused by the uneven boiling of the solution in the sump. The sudden increase in pressure increases the rate of the absorption process. The coherence between the pressure and concentration fluctuations is observed on all four heat exchange tubes. Cross correlations of pressure with concentration and pressure with temperature show that both temperature and concentration lag the pressure, with temperature lagging behind the concentration.

An absorption additive, 2-ethyl-1-hexanol is added to commercial LiBr-H_2O chiller systems to improve their thermal efficiency and capacity. It is thought that the additive enhances the mass transfer of water vapor across the vapor-liquid interface, however, the actual mechanism of its action is unknown.[2,3] Experiments designed to measure this enhanced mass transfer were conducted. Results from these experiments did not show an increase in the absorption process. Absorption experiments with related compounds also failed to show enhanced absorption.

Adapting the sensor to other absorbent refrigerant pairs requires modification of the sensor geometry to provide sufficient sensitivity at different refractive index ranges. Work on a fiber optic sensor[4] suitable for use with the NH_3-H_2O fluid is in progress. The refractive index range for the NH_3-H_2O fluid is 1.34 to 1.37.

1. *ASHRAE Handbook 1985 Fundamentals*, American Society of Heating, Refrigerating and Air Conditioning Engineers, Inc.: Atlanta, GA, 1985, Chapter 1.

2. T. Kashiwagi, Y. Kurosaki and H. Shishido, *Nippon Kikai Gakkai Ronbunshu, B-hen* **1984**, 51(463), 1002-9.

3. W. J. Biermann, personal communication, 1984.

4. T. L. Bergman, F. P. Incropera and W. H. Stevenson, *Rev. Sci. Instrum.* **1985**, 56, 291-6.

*Research sponsored by the Office of Building & Community Systems, USDOE, under contract DE-AC05-84OR21400 with Martin Marietta Energy Systems, Inc.

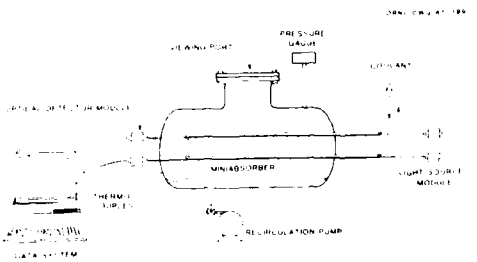


Figure 1. Schematic drawing of the absorption test apparatus.

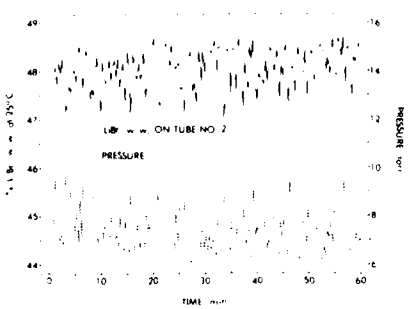


Figure 2. Typical time dependence of concentration and pressure.

Abstract No. 656

Optical Position Finding with CCD-Camera's.

P.P.L. Regtien
B.L. Verbraak
Delft University of Technology
Department of Electrical Engineering
Laboratory of Electronic Instrumentation
Mekelweg 4, 2628 CD Delft, The Netherlands.

Introduction.

This paper describes a method for the localisation of moving objects (robots or vehicles) in a restricted area, using a CCD-camera. In particular, a method for improvement of the resolution as well as the range, by adding a second camera, is introduced. It is shown how an optimal system design can be made given the shape and size of the practical area.

Principle.

The surface of the area of interest is projected onto a two-dimensional light-sensitive device, in this case a CCD-chip. Every spot on the CCD-chip corresponds to just one location in the field of sight of the camera. This one-to-one relation is the basis of the position finding system described in this paper.
In order to distinguish between the objects of interest and the background, the objects are equipped with a small, omnidirectional light source. The influence of sunlight and other interfering light sources can be eliminated by using monochromatic infrared light and optical bandpass filters in front of the camera.
With these precautions, a set of objects or vehicles within the field of sight results in a corresponding set of illuminated pixels on the CCD-chip. From the geometric relation between the row- and column numbers of the pixels and the position of the light spots in the field, the coordinates of each object can be calculated.

Effective range and resolution of a single camera system.

The field of view of a camera, mounted on a height h and with an elevation angle ϵ between the optical axis and the plane normal, has the shape of a trapezium. The size of this trapezium is determined only by the height h; the angle of elevation determines its size as well as its shape (Fig. 1).
The resolution of the position finding system is limited by the pixel size of the CCD-chip projected on the field. It is easily seen that all pixel images have exactly the same size if the viewing direction of the camera is perpendicular to the field: $\epsilon=0$. Increasing the angle of elevation does increase the pixel areas, especially in the range near the horizon. Thus, when using a system with just one camera, a compromise between range (large angle of elevation) and resolution (inhomogenious along the optical axis) is required (Fig. 2). A restricted mounting height (in particular indoors) further limits the applicability of such a position finding system.

Effective range and resolution of a two-camera system.

With two cameras, the range and the resolution of the position finding system can be improved simultaneously. In that case only the column information of the CCD-chip is required.
The colums are projected on the ground plane as lines that convert towards the camera. Both cameras are mounted at a fixed height h, a distance 2a apart of each other, and both with an angle of elevation equal to ϵ. The optical axes of the cameras make an angle δ. Further, the optical axes are directed towards the same field, resulting in a kite-shaped effective area (Fig. 3). The images of the colums form a pattern of crossing lines which allows the reconstruction of the position of a light spot within the kite-shaped area.

The quality of this position finding system is characterized by the effective area and the resolution. Both are determined by the design parameters ϵ, δ and a. Another design parameter is the focal length of the camera. In a practical application, the effective area should fit as good as possible the area of the field. As the resolution is not homogenious over the area, a better criterium for optimal design is the deviation of the pixel area from its mean over the total area.
Fig. 4 shows examples of output plots for some particular combinations of the design parameters δ, ϵ, a/h and the viewing angle α of the camera. The curved lines represent pixels of equal area, the line marked 1 corresponds to the mean pixel area.
From a geometric analysis it appears that an optimum resolution occurs at a horizontal upper boundary of the viewing field, that is, $\epsilon=\pi/2-\alpha/2$. Furthermore, the area of the total field of view can be enlarged by simply increasing the distance 2a between the cameras. The distribution of the pixel areas is not influenced by this distance.

Appendix.

Formulas for the pixel area $\Delta A(x,y)$ and the total area A.

$$\Delta A(x,y) = \frac{2\cdot\tan^2(\tfrac{1}{2}\alpha_{hr})\cdot\cos^4(\tfrac{1}{2}\delta)}{n^2}\cdot \frac{\left\{\left(a\cdot\tan(\tfrac{1}{2}\alpha_d)+x\right)^2-\left(y\cdot\tan(\tfrac{1}{2}\alpha_d)\right)^2\right\}^2}{ax}$$

$$A_{tot} = \frac{2a^2\cdot\sin^2(\tfrac{1}{2}\alpha_{hr})}{\sin(\delta)\cdot\left(\cos(\tfrac{1}{2}\alpha_{hr})-\cos(\delta)\right)}$$

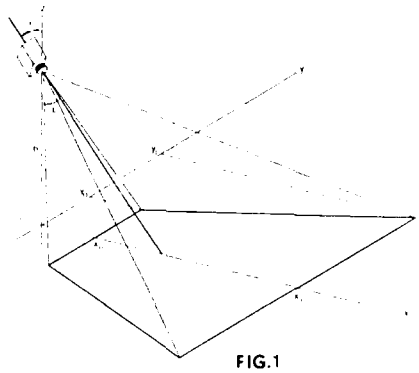


FIG.1

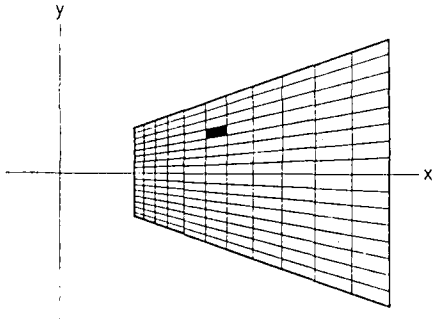


FIG.2

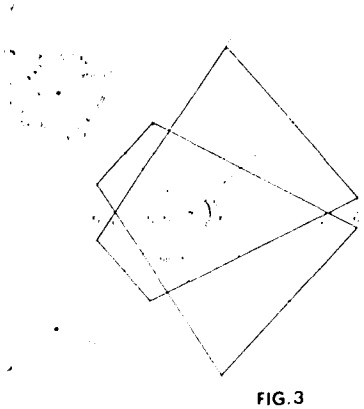


FIG.3

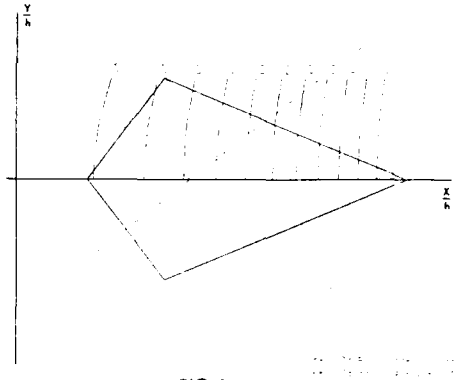


FIG.4a

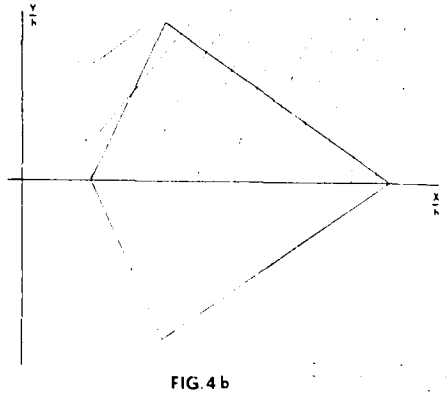


FIG.4b

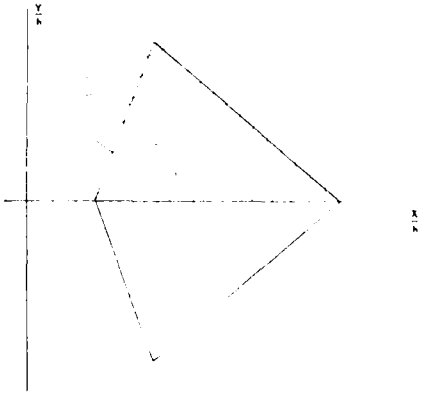


FIG.4c

Abstract No. 657

PROGRAMMING OF THE SPECTRAL RESPONSE OF SILICON PHOTODIODES.

R.F. Wolffenbuttel

Delft University of Technology, Dept. of Electrical Engineering, Lab for Electronic Instrumentation, Mekelweg 4, 2628 CD Delft, The Netherlands

In many optical applications a detector having a particular spectral response curve is required. The conventional solution involves the deposition of dyed colour filters on a photodiode. Such a processing step is, however, not based on a silicon process. In a more flexible approach a certain response specification in the visible part of the spectrum can be met using the properties of silicon, which automatically implies process compatiblilty with silicon processing. The wavelength-dependent properties of silicon detectors are usually considered as a detrimental effect which degrades the performance in solar cell or optical calibration applications. A method will be presented for applying this effect for the flexible design of silicon photodiodes having predictable, well defined and distinct spectral responses.

The indirect bandgap in silicon results in a relatively small absorption probability at an energy level just beyond the bandgap, as a large change in momentum is required to allow a transition, and a maximum absorption at 3.4 eV, where a direct transition is possible. This effect causes short-wavelength light to be absorbed shallowly and allows long-wavelength light to penetrate deeply into the silicon.

The basic device structure used to apply this effect for the electronic programming of the spectral response is shown in Fig.1. This dual-diode structure is fully compatible with a standard bipolar process. The photocurrent detected in the upper or lower junction is composed of several components. The quintessence of the spectral response shaping technique is the selective omission or supply of each of these components to the detected photocurrent in one of the junctions. Increasing of the collecting depth down from the upper junction will favour the long-wavelength response of this junction, whereas an increase of the lower junction collecting layer up from the junction will improve the short-wavelength response of the lower junction at the expense of the long-wavelength response of the upper junction [1].

Both junctions are connected to a reverse voltage giving depleted regions extending on either side of the junctions, viz. from X_{up} down to X_{un} for the upper junction and from X_{ln} down to X_{lp} for the lower junction, having a width determined by the reverse voltage applied across the junction and the respective layer doping concentrations. Due to positive oxide charge also a surface depletion layer will appear. In between the junction space-charge regions a quasi-neutral layer will exist. A depletion layer reveals an almost ideal collecting efficiency, whereas this efficiency is limited in the neutral part of the n-epilayer in between X_{ln} and X_{un} due to a finite diffusion length of the generated charge carriers. In the quasi-neutral layer in between X_{sp} and X_{up} a majority carrier field prevails giving a high collection efficiency in this layer. The photocurrent in a layer can be calculated by solving the continuity equation in that particular layer under the appropriate boundary conditions meanwhile assuming a charge generation rate depending exponentially on the depth and the absorption coefficient.

Fig.2 shows the distinguishable wavelength-dependent current components in the different layers that contribute to the total photocurrent. J_u, detected in the upper junction assuming depleted regions having a width as shown in this figure. J_{up} denotes the fraction of charge carriers generated in the quasi-neutral part of the shallow p-type layer in between the boundary of the surface space-charge region, X_{sp}, and the upper junction depleted region, X_{up}, that are able to contribute to the photocurrent in the upper junction. This term is strongly dependent upon the oxide charge. The photocurrent J_{ud} is due to the charge carriers generated in the depleted region and is therefore depending upon the reverse voltage across the upper junction. The term J_{un} denotes the fraction of charge carriers generated in the neutral layer in between X_{un} and X_{ln} that are able to diffuse upwards to the upper junction. This photocurrent is strongly affected by the ratio between the reverse voltages across the upper and lower junction, as a generated charge carrier is likely to diffuse to the nearest depleted region.

A similar calculation can be made with respect to the lower junction and the results are depicted in Fig. 3. J_{ln} denotes the amount of charge carriers that are able to diffuse downwards to the lower depleted region, whereas J_{ld} refers to those generated in the depleted region and, finally, J_{lp}, those thet are generated beyond the depleted region in the p-type substrate.

A major simplification can be introduced by assuming a sensor structure in which the combined upper and lower space-charge region deplete the entire epilayer resulting in $J_{un}=J_{ln}=0$. This method divides the epilayer into two charge collecting layers in which the upper layer determines the desired sensor response and the lower prevents minority charge carriers, generated beyond the upper depleted region from contributing to the detected photocurrent in the upper junction An increasing reverse voltage across the upper junction will lead to an increasing contribution of long-wavelength light to J_{ud}. The epilayer-substrate reverse voltage is, for that purpose, controlled by the pinch-off in an integrated JFET structure with an upper junction identical to the shallow layer and the substrate acting as the lower gate. This measure precludes the existence of a neutral layer in the epilayer and makes an electronically tunable long-wavelength cut-off possible using the reverse voltage across the upper junction.

An independently controllable short-wavelength cut-off is realised based on the control of the surface space charge region using an As^+ implantation in the oxide covering the photodiode in order to control the surface depletion layer up to full depletion of the p-type toplayer. The extra As^+ implantation in the oxide reduces J_{up} and causes a shift of the short-wavelength cut-off to longer wavelengths. These design parameters allows the realisation of clearly different spectral responses without applying color dyes. Fig. 4 shows four different spectral responses in which curve #1 denotes the response of a shortcircuited photodiode having a boron implanted junction at 0.5 μm depth in a 8 μm thick 6 Ωcm epilayer and curve #3 the response of the same diode connected to a reverse voltage across the upper junction equal to 16V and a substrate voltage depleting the remaining epilayer. Curve #2 reveals the response of a shortcircuited diode with the same profile after a As^+ implantation in the oxide and #4 the response of this diode when applying a reverse voltage of 16V.

1 R.F.Wolffenbuttel and P.P.L.Regtien, A novel approach to solid-state colour sensing, Sensors and Actuators, Vol 9, 1986, pp. 199-211.

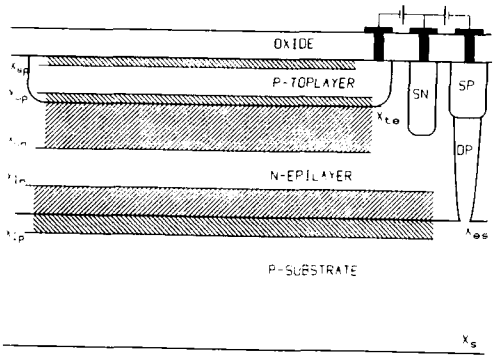


Figure 1

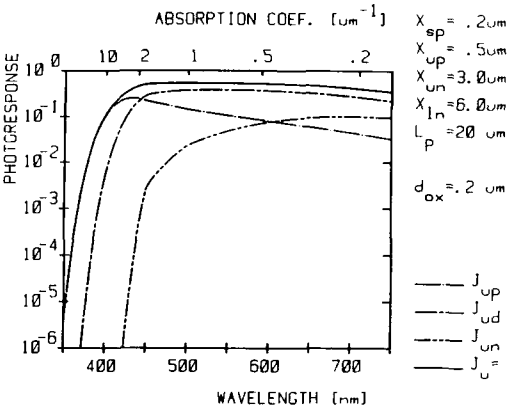


Figure 2

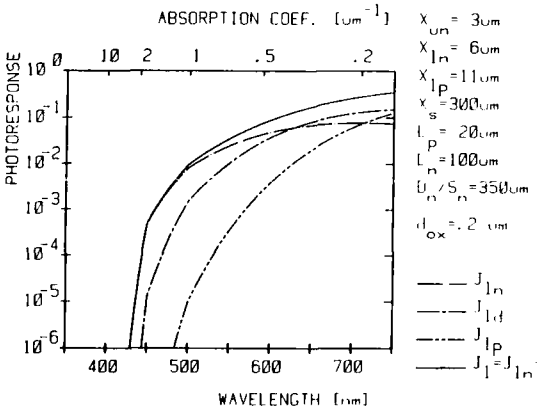


Figure 3

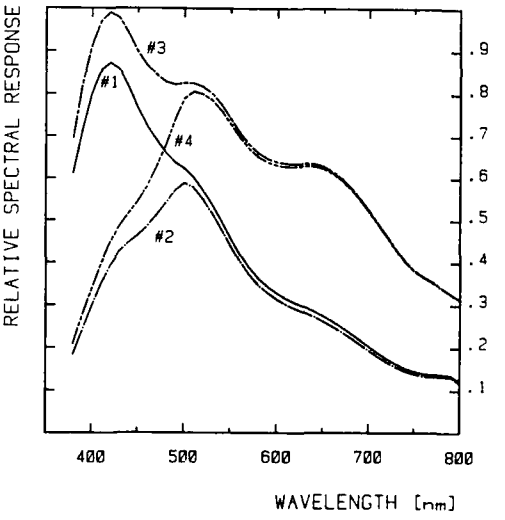


Figure 4

Abstract No. 658

SILICON COLOR SENSORS WITH A DIGITAL OUTPUT.

R.F. Wolffenbuttel

Delft University of Technology, Dept. of Electrical Engineering, Lab. forElectronic Instrumentation, Mekelweg 4, 2628 CD Delft, The Netherlands

Silicon color sensors based on the wavelength-dependent response of silicon photodiodes in the optical part of the spectrum have been reported before [1]-[3], however lacking an output signal in a digital form. This effect is usually considered to be an undesirable effect which reduces the performance of solar cells and complicates the application of silicon photodiodes as optical calibration detectors. In conventional research on this subject, measures are explored for reducing this wavelength dependent effect. In the color sensor the opposite objective is pursued and measures are taken to maximise the wavelength dependence of the response in order to obtain electronically tunable optical filters in silicon. In numerous applications such a color sensor can be employed successfully.

There is a wide range of domestic, agricultural and robotic applications where only a significant shift in the optical spectrum has to be detected. No image information is required and no tristimulus colorimetric information need to be reproduced, so a simple color indicator can be used to solve the problem. In a conventional photodiode or solar-cell a photocurrent is generated that is, at a certain intensity, in first approximation proportional to the sensitive area. In the color sensor, shown in plan and cross-section in Fig. 1, an additional mechanism is implemented that allows the collection of only the charge carriers generated in a layer extending from a shallow junction down to an adjustable boundary. Applying a certain reverse voltage across the shallow p+ n junction for depleting the lighter doped epilayer down from the junction, and simultaneously connecting a reverse voltage across the epilayer-substrate junction for depleting the complementary part of the epilayer permits the selective detection of only the charge carriers generated in the upper part of the silicon.

As the short-wavelength components in the spectrum are absorbed shallowly, all the blue light is already absorbed at very thin layers. Therefore, at illumination with light having predominantly short-wavelength components, the perceived photocurrent remains almost constant at the increasing width of this upper depleted part of the epilayer associated with an increasing reverse voltage. However, at illumination with long-wavelength light the detected photocurrent increases with the layer width and thus with the reverse voltage. The depletion of the lower part of the epilayer prevents the existence of a neutral layer in which charge carriers generated beyond the depleted region could otherwise diffuse upwards and contribute to the photocurrent, and thus avoids an impediment on the operation of the colour sensor. This paper presents two different versions of colour sensors equipped with a special AD conversion adapted to the sensor operation.

The simplest version of the color sensor is based on the determination of the ratio of the photocurrent in the upper depleted part of the epilayer relative to the total photocurrent. The response for different values of the reverse voltage for a sensor, with a junction at 0.5 μm depth and a surface depletion layer extending down to 0.2 μm into the silicon, is shown in Fig. 2 and clearly reveals a wavelength-dependent response due to the different values of the depth of the upper depleted region. The operation of this color sensor can easily be combined with a dual-slope AD conversion as shown in Fig. 3. In the first part of the conversion cycle the switch that supplies the photocurrent, J_u, generated in the upper junction, via OA3 to the integrator, composed of OA1, is closed. Operational amplifier OA3 drives a current mirror in such a way that no current flows to the non-inverting input. At equal emitter areas this current is also supplied to the switch. After a fixed time-interval, T_n, this switch is opened and the integrating capacitor is discharged with the total photocurrent, J_u+J_l. An incident spectrum containing predominantly short-wavelength components will give rise to a steeper descending slope and thus results in a larger absolute value of the voltage across the integrator capacitor at T_n. In the second part of the conversion cycle the absence of strong long-wavelength components will cause a relatively small ascending slope. Therefore, a dual-slope conter content proportional to T_{bl} will be displayed. A similar discussion leads to an indication proportional to T_{rd} in case of illumination with light containing predominantly long-wavelength components. Operational amplifier OA4 generates the substrate reverse voltage.

A more flexible approach is shown in Fig. 4 and involves two diodes with unequal sensitive areas in which equal photocurrents are nevertheless maintained using a reference diode connected to a reverse reference voltage, V_{ref}, and a smaller reverse voltage, V_{rev}, across the junction of the larger compensating diode by means of a current difference controlled feedback loop. For short-wavelength light a large difference in these voltages is required for compensating the difference in sensitive areas, as all this light is already absorbed shallowly. Therefore, for short-wavelength light and a particular value of V_{ref} a very small V_{rev} will give a baiance, whereas for long-wavelength light V_{rev} will approach V_{ref}, giving a wavelength-dependent response [3]. The sensor operation can be conveniently combined with a servo AD converter configuration. A fixed reverse voltage is applied across the smaller photodiode, whereas the reverse voltage across the larger diode is controlled by a DA converter. The resulting current, $I_{comp}-I_{ref}$, is fed to a comparator which controls a counter in such a way that a larger photocurrent in the larger diode causes the counter to count down. The counter content is available as a digital output and also drives the DA converter for providing the reverse voltage across the larger photodiode. The voltage V_g isolates the two diodes and V_{es} ensures full depletion of the epilayer underneath the compensating diode. In the practical sensor two diodes with equal dimensions are used and the difference in effective sensitive area is realised using a translinear circuit. In the steady-state the digital output of the counter is determined by the color of the incident light and the value of the reverse reference voltage, V_{ref}, across the smaller photodiode.

References.

1 R.F.Wolffenbuttel and P.P.L.Regtien, A novel approach to solid-state colour sensing, Sensors and Actuators, Vol 9, 1986, pp. 199-211.

2 N.Kako, N.Tanaka and C.Suzuki, Combustion detection with a semiconductor color sensor, Sensors and Actuators, Vol 4, 1983, pp. 655-660.

3 R.F.Wolffenbuttel, A simple integrated color indicator, IEEE J. SSC, Vol SC-22, No 3, June 1987, pp. 350-356.

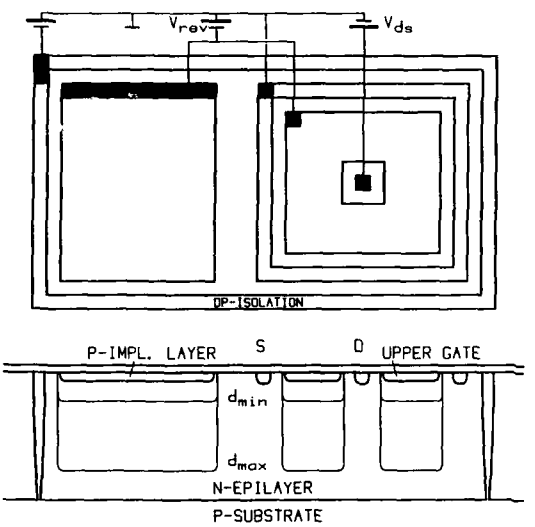


Figure 1

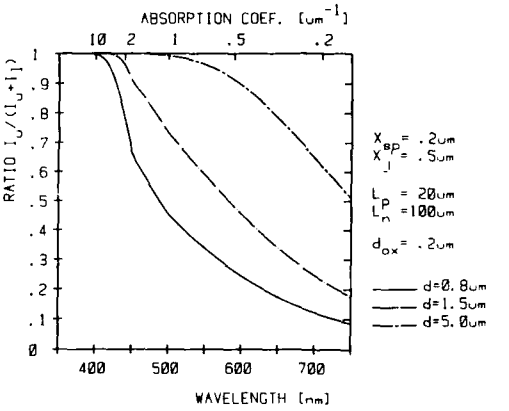


Figure 2

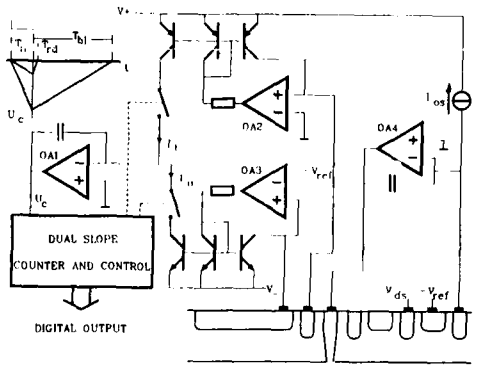


Figure 3

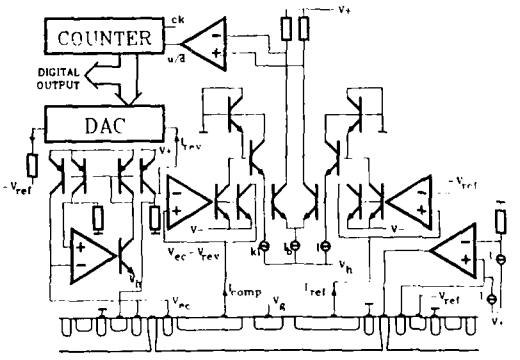


Figure 4

Abstract No. 659

INFLUENCE OF CHARGE TRANSFER STATES ON Eu DOPED PHOSPHORS FOR TEMPERATURE SENSOR APPLICATIONS

S. W. Allison, M. R. Cates,
L. A. Boatner, and G. J. Pogatshnik
Oak Ridge National Laboratory*
Oak Ridge, TN 37831

A. R. Bugos
Department of Electrical Engineering
The University of Tennessee
Knoxville, TN 37916

Temperature sensors based on the fluorescence properties of rare-earth ions in solids can be used in a variety of applications including accurate high-temperature measurements and remote thermometry.[1] For a given rare earth phosphor, both the fluorescence intensity under steady state optical excitation and the fluorescence lifetime of the phosphor are dependent on the sample temperature. Rare earth phosphors are particularly suited for high temperature applications because the optical transitions take place between energy levels of the 4f states. Since the lattice-ion coupling is small for the 4f states, processes which contribute to the temperature quenching of luminescence occur at relatively high temperatures.

For most rare-earth ions, the dominant temperature quenching mechanism is that of multi-phonon relaxation. The probability of these multi-phonon processes increases with temperature so that the intensity and fluorescence lifetime of the rare-earth emission decreases as the temperature is raised. This mechanism has been utilized in temperature sensors based on Nd:YAG and operation to temperatures near 1100 K have been demonstrated.[2] One of the advantages of temperacure sensors based on europium phosphors is that the energy gaps from the ^5D excited states to the ground levels are very large relative to that of the other rare-earth ions. Therefore, the multi-phonon transition rate is extremely small so that it should be possible to use europium phosphors for very high temperature applications. However, non-radiative quenching of luminescence for europium phosphors does occur and is dominated by the interaction with the host crystal by the charge-transfer transitions of the europium ions.[3]

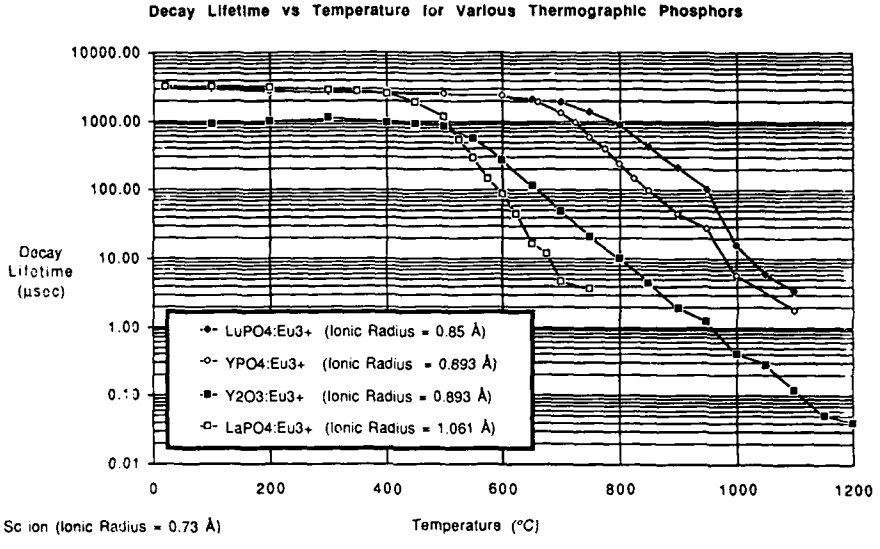
The effect of the charge-transfer transitions on the non-radiative decay of the europium phosphors is a function of the energy at which these transitions occur. The contribution to the charge-transfer energy from the host depends mainly upon the polarizability of the neighboring anions. The energy of the charge-transfer transitions in materials such as fluoride crystals is deep in the UV since the polarizability of the fluorine ions is relatively small. However, the low melting points of most fluoride crystals makes them unsuited for most high-temperature applications. Oxide materials typically have much higher melting points, but the higher degree of polarizability of the oxygen neighbors moves the charge transfer transitions to lower energy. In the extreme case of materials such as La_2O_2S, the additional charge-transfer transitions from the highly polarizable sulfer ions reduces the charge-transfer bands to 32,000 cm^{-1}. The interaction with the charge transfer states in La_2O_2S is such that the quenching temperature of luminescence is only slightly above room temperature.

The two major criterion in choosing europium phosphors for high temperature sensor applications are that the host material must be stable at high temperatures and that the europium charge-transfer band should lie as deep in the UV as possible. One particular europium phosphor which meets these criterion is Eu:Y_2O_3. The charge-transfer band in this material is near 37,000 cm^{-1}. The fluorescence lifetime of the europium transition is constant until 500 °C and then begins to decrease with increasing temperature, as illustrated in Fig. 1. Our recent investigations of europium in rare-earth orthophosphate crystals show that these materials are superior to Y_2O_3 in their high temperature characteristics. For example, the fluorescence lifetime of Eu:YPO_4 is constant to approximately 650 °C before the onset of non-radiative quenching. The energy of the europium charge-transfer band in YPO_4 is at 43,000 cm^{-1}. Although the nearest neighbor anion for Y_2O_3 and YPO_4 is an oxygen ion, we believe that the presence of the PO_4 radicals in the crystal structure tend to reduce the polarizability of the oxygen ions at the europium sites, and pushes the charge-transfer band to higher energy. Substitution of different cations for yttrium also has an effect on the energy of the europium charge-transfer transition. Blasse has shown that the substitution of the fluorescing ion for a cation with a smaller ionic radius increases the quenching temperature of luminescence.[4] Crystals of Eu:$LuPO_4$ have the highest quenching temperatures of any europium phosphors that we have measured. The charge-transfer energy of europium in this host is 45,000 cm^{-1}. Europium substituting for the larger lanthanum ion in $LaPO_4$ reduces the quenching temperature to that of Y_2O_3.

In summary, we have demonstrated that the incorporation of europium ions in rare-earth orthophosphate crystals increases the quenching temperature of europium fluorescence due to the high energies of the charge-transfer bands. These materials should extend the temperature range of rare earth phosphor sensors above 1500 K.

1. B.W. Noel et. al. Proc. of the AIAA 23rd Joint Propulsion Conference, AIAA-87-1761, San Diego, CA, 1987.
2. K.T.V. Grattan, J.D. Manwell, S.M.L. Sim, and C.A. Wilson, CLEO Technical Digest 14, 307 (1987).
3. C.W. Struck and W.H. Fonger, J.Lumin.1,456 (1969).
4. G. Blasse, in Handbook of Physics and Chemistry of Rare Earths, ed. by K.A. Gschneidner Jr., and L. Eyring, (North Holland 1979), pp. 237-274.

*Operated by Martin Marietta Energy Systems for the U.S. Department of Energy under contract number DE-AC05-84OR21400.


Decay Lifetime vs Temperature for Various Thermographic Phosphors
10000.00
1000.00
100.00
10.00
1.00
0.10
0.01
Decay Lifetime (µsec)
0
200
400
600
800
1000
1200
Temperature (°C)
LuPO4:Eu3+ (Ionic Radius = 0.85 Å)
YPO4:Eu3+ (Ionic Radius = 0.893 Å)
Y2O3:Eu3+ (Ionic Radius = 0.893 Å)
LaPO4:Eu3+ (Ionic Radius = 1.061 Å)
Sc ion (Ionic Radius = 0.73 Å)

Abstract No. 660

FIBER RING RESONATORS AND SHOCK EXCITED MECHANICAL OSCILLATORS

M. A. Butler
Microsensor Division, 1113
Sandia National Laboratories
Albuquerque, New Mexico 87185

A fiber ring resonator is a single mode, optical fiber loop into and out of which light can be coupled [1]. This structure behaves as an interferometer in that the intensity of light out varies cyclically with the length of the loop where the period is the wavelength of the light. Such a structure can be made into a sensor if the quantity to be sensed can be made to modify the length of the fiber loop. This can be done by heating the fiber or straining it. Heat transfer to the fiber core is a relatively slow process, so we will consider strain effects.

To measure energy impulses the fiber must have a suitable coating so that the energy heats the coating and thus produces thermal strains which will propagate to the fiber core. To test this concept the system shown in figure 1 was assembled to measure the energy in current pulses. Other forms of energy would require other coatings. A current pulse in the 5-10 microsecond range is sent to the thin CuNi tube and heats the tube. The tube will expand and the strains will be applied to the fiber since the fiber is bonded to the ends of the tube. As the fiber is stretched a string of optical pulses is observed at the output with the number of pulses proportional to the energy in the pulse.

Two factors are important in the performance of such a sensor: sensitivity and speed. The sensitivity is determined by the size of the strain at the fiber core for a given energy input. The speed of such a device is determined by the time it takes for the thermally generated strain to be applied to the fiber. Since this time is approximately:

$$t = L/v \qquad (1)$$

where L is the relevant sensor dimension and v the velocity of sound, the response of the sensor to radial strains will be orders of magnitude faster than the response to axial strains. For the particular experiment performed here the sensor will only respond to axial strains since the fiber is only bonded to the ends of the tube. Since the tube is 8cm. long the intrinsic response time of this sensor is about 20 microseconds. For energy impulses much longer than this the sensor can follow the energy input accurately with the frequency of the output optical pulses representing the power at any point in time and the total number of optical pulses representing the total energy content of the impulse. For electrical impulses much shorter than this intrinsic response time, the sensing element cannot follow the energy input and the thermal strains generated in the tube will only become apparent at a later time. The tube acts as if it were compressed and then suddenly released. This sets up mechanical oscillations in the tube which are transmitted to the fiber. The frequency of these oscillations depends on both the dimensions of the tube and the effective mass loading on the ends. The amplitude of the oscillations is proportional to the total energy in the electrical impulse as is shown in Figure 2 for two different impulse lengths. This linear relationship means that this sensor can be used to measure the energy content of impulses much shorter than the intrinsic response time of the sensor.

This work performed at Sandia National Laboratories was supported by the U. S. Department of Energy under Contract #DE-AC04-76DP00789.

REFERENCES

1. L. F. Stokes, M. Chodorow, and H. J. Shaw, Optics Letters 7, 288 (1982).

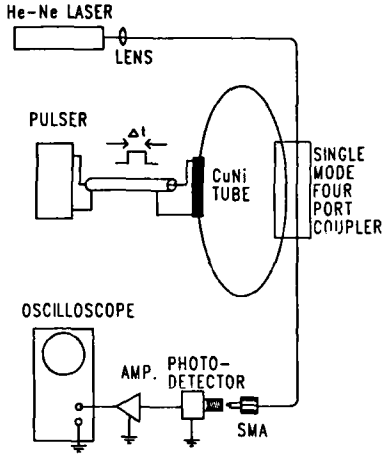


Figure 1

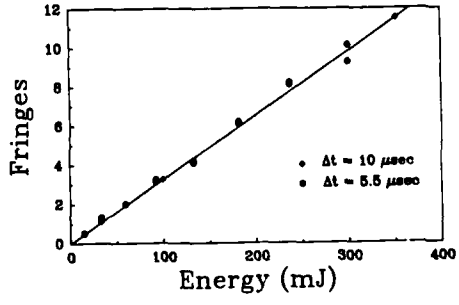


Figure 2

Abstract No. 661

REFLECTOMETRIC TECHNIQUES IN THE STUDY OF CHEMICAL EQUILIBRIA OF IMMOBILISED INDICATORS USED IN OPTICAL FIBRE CHEMICAL SENSORS

Dr. R. Narayanaswamy

Department of Instrumentation and Analytical Science
UMIST, P.O.Box 88, Manchester M60 1QD, UK.

The development of chemical sensors based on the use of optical fibres are being pursued all over the world with great interest because of the several advantages these sensors can offer. The most important of these being safety, ruggedness and remote measurement capabilities by these sensors (1). Though a few disadvantages that exist may be overcome with appropriate modification, the limited dynamic range with these devices could restrict their use in certain applications. These sensors feature a chromogenic or fluorogenic reagent immobilised on a suitable solid support, and interface to an optical fibre. The reagent phase acts as a chemical transducer, converting the chemical information from the analyte into optical signals which are conveyed through the optical fibre.

The preparation of reagent systems involves the immobilisation of the chemical system on an inert and stable solid support such as glass, silica gel, cellulose and other polymeric solids. Immobilisation could be carried out either through physical or chemical procedures (Figure 1). The physical methods of immobilisation include gel entrapment, adsorption and electrostatic attraction, and these methods require simple and economical procedures. Chemical immobilisation, on the other hand, is based on the formation of a covalent bond between the reagent molecule and an activated or functionalised form of the polymeric solid support. This method is the most irreversible of the immobilisation techniques, but requires several steps in its synthesis.

In our laboratories, we have studied extensively the immobilisation methods using adsorption techniques, and have observed changes in the properties of the reagent. Adsorption on a hydrophobic polymer, XAD-2 (a polystyrene-divinyl-benzene copolymer) alters the equilibrium properties of acid-base (2) and redox (3) indicators. Other workers have noted modification of spectral and temporal characteristics of the luminescence of fluorophores (4) and enhancement of selectivity of chelating agents (5). Our study involves the development of reagent matrices for use in optical fibre chemical sensors for measurement of pH, sulphide ion, etc. A systematic investigation was carried out to study the effect of immobilisation on the acid-base and oxidation-reduction equilibria of some indicators adsorbed on XAD-2.

Acid-base and redox equilibria are commonly studied through spectrophotometry, potentiometry and conductometry. These methods are not applicable to the immobilised reagent systems involved in our study because of the heterogeneous nature of the reagent phase. Instead, these reagent systems have been investigated through a reflectometric method, which is analogous to spectrophotometry. The dissociation constants and reduction potentials of immobilised indicators are reported in this paper using reflectance techniques. The results have indicated that adsorption of the indicator on a non-polar surface causes a decrease in the extent of dissociation of the solute and a lowering of reduction potentials. The "solid-solvent" model for adsorption on XAD-2 polymer has been used to explain the observations and can be accounted for by the existence of the following equilibria:

(a) Acid-base system:

$$\begin{array}{ccc} HIn\,(ads) & \rightleftharpoons & H^+(ads) + In^-(ads) \\ \downarrow\uparrow & & \downarrow\uparrow \\ HIn\,(sol) & & In^-\,(sol) \end{array}$$

(b) Redox system:

$$\begin{array}{ccc} Ox(ads) & \rightleftharpoons & Red\,(ads) + ne^- \\ \downarrow\uparrow & & \downarrow\uparrow \\ Ox\,(sol) & & Red\,(sol) + ne^- \end{array}$$

where HIn is an acid-base indicator, Ox and Red are the oxidised and reduced form of an indicator, and the subscripts ads and sol refer to the adsorbed and solution phases respectively.

References

1. R.Narayanaswamy and F.Sevilla III, J.Phys.E:Sci.Instrum., 1988, 21, 10.
2. R.Narayanaswamy and F.Sevilla III, Anal.Chim.Acta., 1986, 189, 365.
3. R.Narayanaswamy and F.Sevilla III, Mikrochim.Acta, In press.
4. W.A.Wyatt, G.E.Poirier, F.V.Bright and G.M.Hieftje, Anal.Chem., 1987, 59, 572.
5. M.A.Ditzler, H.Pierre-Jacques and S.A.Harrington, Anal.Chem., 1986, 58, 195.

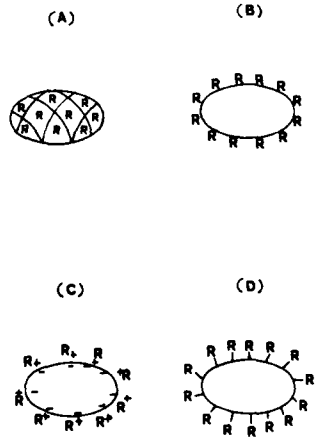


Figure 1 Diagrammatic representation of the different methods of immobilisation of a reagent, R, on a solid support:
(A) gel entrapment; (B) adsorption;
(C) electrostatic attraction; (D) covalent bonding. (From reference 1).

Abstract No. 662

FIBER OPTIC SURFACE ENHANCED RAMAN CHEMICAL SENSORS

M. M. Carrabba, R. B. Edmonds, P. J. Marren and R. D. Rauh

EIC Laboratories, Inc.
Norwood, Massachusetts 02062

INTRODUCTION

"Universal" chemical sensors are needed for the detection and monitoring of toxic substances in the environment. Ideally, such a sensor would produce information in real time about their presence in low levels and their chemical structures. Our approach to this problem has been to sample dilute chemical species by adsorption onto surfaces and then to identify the adsorbates by Surface Enhanced Raman Spectroscopy (SERS) [1]. The combination of pre-concentration of dilute species due to specific adsorption, and up to 10^6 signal enhancement of SERS over normal Raman spectroscopy, should enable detection well below the parts per billion level. Raman techniques utilize visible light to obtain structurally unique vibrational spectra. Thus, measurements can be made in media such as water with high infrared absorption. In principle, laser Raman excitation and scattering signals can be transported through optical fibers for sampling remote or hazardous environments.

In this paper, we present results on configuring and optical fiber delivery and collection system for conducting remote SERS.

EXPERIMENTAL

All results were obtained using a Raman instrument incorporating a Spex Industries Triplemate spectrograph and an EG&G Optical Multichannel Analyzer for detection. The excitation source was a Coherent Model 70-4 Ar ion laser which also was used to pump a Coherent 599-01 dye laser. Unless otherwise indicated, an excitation wavelength of 575 nm was selected using the dye laser, and the intensity leaving the exciting fiber was 100 mW.

The fiber optic probe was constructed based on a theoretical study by Plaza and co-workers [2], which addressed normal Raman spectroscopy. It consisted of a central 100 μm excitation fiber surrounded by four 600 μm collection fibers. The four outer fibers were sealed in opaque epoxy around a capillary tube which accepted the excitation fiber and allowed its vertical positioning. Two different exciting fibers were prepared, one polished flat and another with a lens fabricated at the tip by laser melting [3]. In addition, three different collection geometries were considered: fibers parallel, fibers beveled inwards at 11°, and the beveled angles polished flat.

Electrochemical instrumentation and roughening of Ag electrodes for SERS has been described elsewhere [1]. Electrolytes were 0.1M KCl.

RESULTS

Several factors complicate the measurement of SERS using optical fibers. First is a background fluorescence obtained from polymeric fiber claddings. Second is an intrinsic Raman scattering arising from the exciting fiber which is reflected back into the collection fibers from the SERS substrate. In addition, an unstructured background signal is always present in SERS. The placement of the exciting and collection fibers can alter the magnitude of the background signal, since it relates to the intensity of the exciting source back reflected into the collection optics, relative to the spectrum intensity, which is isotropically scattered from the SERS-active surface.

SERS spectra of 0.025M pyridine on Ag are shown in Figure 1, comparing six different probe variations. One probe, which is not represented in Figure 1, was constructed with plastic clad collection fibers, and a broad background signal was seen which washed out the spectral details. The fluorescence was corrected by employing silica cladding, which was employed in all later experiments. In all the spectra, the silica Raman spectrum, shown in Figure 2, is superimposed on the background with a major peak at 450-500 cm^{-1}. The intensities of the main pyridine peak at 1000 cm^{-1} of the silica Raman peak and of the general background level are indicated in Figure 1.

The most significant increase in the SERS signal intensity was realized by adjusting the collection fiber acceptance angle. Depending on the other variables, this gives up to a 15-fold increase in the SERS signal level compared to a parallel orientation of delivery and collection fibers. Similar results were obtained with the 11° collection fibers concave or polished flat. At the same time, enhancing the collection in this way increased the overall background level by a factor of 2-4 and the silica Raman scattering level by a factor of 5-10. With the present probe configuration, a distance of approximately 2.5 mm between the substrate and the collection fibers was optimal when all the other variables were held constant.

Enhancement of the overall signal level or ratio of signal to background in some cases could be accomplished by employing a lens-ended exciting fiber and/or by placing it close to the substrate. The levels of background scattering and silica Raman peaks were evaluated using a Ag mirror in place of the electrochemically roughened SERS-active substrate. Placing the collection fiber nearly touching the substrate decreased the background by up to a factor of 5, as did decreasing the illuminated area by focusing the exciting light. In the SERS experiments, the ratio or pyridine peak intensity to the silica Raman intensity was also greater in these cases. For this reason, fiber probes corresponding to the SERS spectra in Figures 1D and E might be favored over the probe corresponding to Figure 1F, even though the intensity of the pyridine spectrum in the latter is stronger.

Further optimization of the SERS probe design is in progress.

ACKNOWLEDGMENT

This work was supported by the U.S. Department of Energy.

REFERENCES

1. M. M. Carrabba, R. B. Edmonds and R. D. Rauh, Anal. Chem. 59, 2559 (1987).

2. P. Plaza, N. Dao, M. Jouan and H. Saisse, Appl. Optics 25, 3448 (1986).

3. V. Russo, G. C. Righini, S. Sottini and S. Trigari, Appl. Optics 23, 3277 (1984).

SERS Spectrum	Collection Angle(deg)	Lens	Exc. Distance (mm)
A	0	no	2.5
B	0	no	0.1
C	11	yes	2.5
D	11	yes	0.1
E	11	no	0.1
F	11	no	2.5

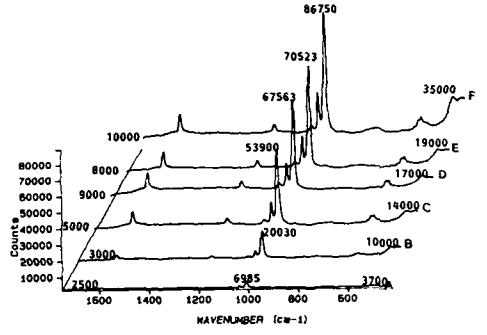


Fig. 1. Surface enhanced Raman spectra of 0.025M pyridine/0.1M KCl on electrochemically roughened Ag, showing effect of different fiber optic delivery and collection geometries. All spectra were recorded at -0.6V vs. SCE, λ = 575 nm, laser power = 100 mW.

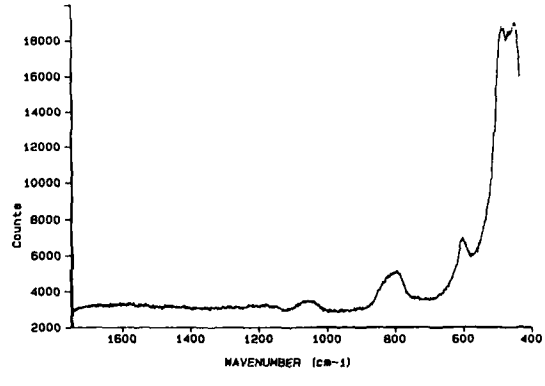


Fig. 2. Raman spectrum of 100 μm silica excitation fiber using SERS probe array and a reflective Ag surface 2.5 mm from the probes.

Abstract No. 663

CHEMISORPTION-INDUCED REFLECTIVITY CHANGES IN THIN METAL FILMS

A. J. Ricco and M. A. Butler
Sandia National Laboratories, Albuquerque, NM

Optical fiber-based chemical sensors have a number of advantages over other chemical detection means, including immunity to electrical interference, safety in electrically sensitive environments, chemical inertness, small size, and simplicity. We have examined the metallized end of a multimode optical fiber as a new type of chemical sensor and as a means for probing the interaction between chemisorbed molecules and thin metal films. The interactions of Ag and Ni thin films with H_2S, SO_2, O_2, CO, and H_2 have been examined.

The sensor, shown schematically in Figure 1, has an active surface area of only 0.002 mm² (the fiber has a 50 μm core and 125 μm total diameter). A metal film 20 - 250 Å thick is thermally evaporated onto the freshly cleaved fiber end, with film thickness monitored using a conventional quartz crystal microbalance (QCM). The reflectivity of the film is monitored *in situ* in the high vacuum system before, during, and after thin film evaporation, and during the admission of test gases to the system; the freshly metallized fiber is not exposed to air prior to gas exposure. Metal film reflectivity is measured using an 860 nm LED modulated at 10 kHz, with the reflected signal and the source synchronously detected to correct for fluctuations in light intensity.

Chemisorption changes the reflectivity of a metal surface [1]. For optically thin metal films, the chemisorption process can change the effective optical thickness of the film, and therefore its reflectivity, by a relatively large fraction. Typical results of an experiment are shown in Figure 2 for a 100 Å thick silver film exposed to 100 ppm of H_2S in N_2 at 1 atmosphere. This concentration represents 65,000 Langmuirs of exposure per second and thus the magnitudes of the measured shifts are not dependent on the time of exposure to the gas. A step reduction in the reflectivity of about 1% occurs in a few seconds (the time required to fill the bell jar) upon exposure of the silvered fiber end. Over a much longer time period, there is a slow decrease of the reflectivity to or below the level observed for the bare fiber. We attribute the initial step to chemisorption-induced changes in the reflectivity of the thin film, and the much slower drop in reflectivity to a bulk chemical reaction forming Ag_2S.

Although many molecule/metal combinations fail to produce a bulk reaction at 25 C, the initial chemisorption step is common to all the adsorbates we examined and is more likely to be reversible; it was therefore chosen for detailed study. Exposure of freshly evaporated, 100 Å thick Ag films resulted in initial step changes in reflectivity for H_2S, CO, O_2, SO_2, and H_2 of -0.7%, -0.6%, -0.5%, -0.45%, and -0.1%, respectively. Measurements were also attempted on NO_2 and Cl_2, but these molecules showed large, rapid changes due to irreversible bulk chemical reactions, so a clear step could not be defined.

In general, the magnitude of the reflectivity change correlates with the expected strength of the metal/adsorbate interaction, provided the possible surface reactions are considered. For example, the H_2/Ag interaction is known to be much weaker than the O_2/Ag interaction [2], consistent with the observed reflectivity changes (ΔRs). However, it is also known that the CO/Ag interaction is quite weak. We believe O_2 impurities in the vacuum system and in the CO/N_2 gas mixture result in the formation of surface carbonate, CO_3 [2], with a resulting strong interaction and large ΔR. In the case of SO_2, O_2 impurities are similarly expected to lead to the formation of surface SO_4 [3] rather than simple chemisorption of molecular SO_2. The decrease in reflectivity upon chemisorption of H_2S, which is also anomalously large, can be explained by the known reaction of H_2S with Ag to form Ag_2S [4]. The irreversible nature of this reaction explains the decrease in reflectivity to nearly zero (see Figure 2) after about 50 hours.

We can better understand the phenomenological effect of chemisorption on metal optical properties by measuring the size of the reflectivity step, for a given adsorbate, as a function of metal film thickness. For this experiment, the interaction of oxygen with nickel is ideal because the reaction is uncomplicated by oxygen impurities and it is irreversible (the enthalpy of chemisorption exceeds 70 kcal/mol [5]). First, the solid line in Figure 3, which represents the derivative of reflectivity versus thickness, dR/dt, was calculated from reflectivity and film thickness data obtained simultaneously during the evaporation of a nickel film in the absence of oxygen. Next, a series of nickel films of various thicknesses were evaporated on freshly cleaved fiber ends, and each film was then exposed to 20% oxygen in nitrogen. The data points in Figure 3 are the reflectivity decreases in percent, upon exposure of each of the nickel films to oxygen, divided by a constant (Δt = -5.3 Å). The agreement of the ΔR/Δt data with the measured dR/dt curve shows that the reflectivity change can be represented by

$$\Delta R = \frac{dR}{dt}\Delta t. \qquad (1)$$

with a Δt of -5.3 Å *independent of the overall nickel film thickness*. Thus, the interaction of oxygen with nickel reduces its effective optical thickness by 5.3 Å.

Chemisorption-induced reflectivity change is a rapid surface process and, with a range of metals and alloys available, offers the potential for varying selectivity and reversibility. As in many chemical sensing problems, the lack of a single, highly selective sensing material for each species of interest may be compensated by the use of sensor arrays, in this case with a range of metal films, having varying sensitivity and selectivity for many species. In addition to its potential application for chemical sensing, this technique provides a new tool for the study of chemisorption processes on metal surfaces. In particular, it could prove useful in situations with large gas overpressures where ultrahigh vacuum techniques are inapplicable.

The authors are indebted to K. B. Pfeifer for his excellent technical assistance. This work was performed at Sandia National Laboratories and supported by the U. S. Department of Energy under contract DE-AC04-76DP000789.

REFERENCES

1. J. D. E. McIntyre and D. E. Aspnes, *Surf. Sci.*, **24**, 417 (1971).

2. M. Bowker, M. A. Barteau, and R. J. Madix, *Surf Sci.*, **92**, 528 (1980).

3. D. A. Outka, R. J. Madix, G. B. Fisher, and C DiMaggio, *J. Phys. Chem.*, **90**, 4051 (1986).

4. T. E. Graedel, J. P. Franey, G. J. Gualtieri, G. W. Kammlott, and D. L. Malm, *Corros. Sci.*, **25**, 1163 (1985).

5. G. Wedler and P. Wissman, *Surf Sci.*, **26**, 189 (1971).

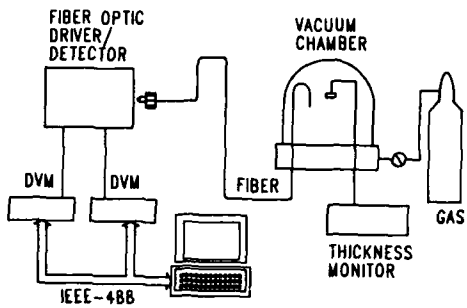


Figure 1. Apparatus used to measure the reflectivity of thin metal films.

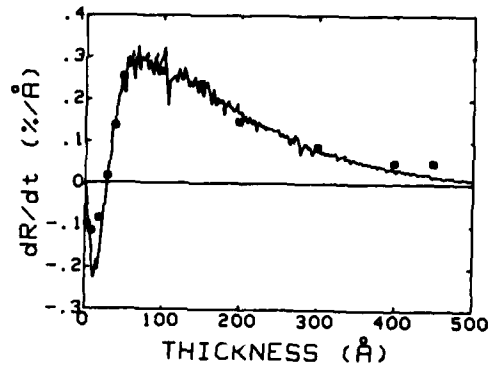


Figure 3. The solid line is the derivative of the reflectivity versus thickness curve dR/dt, as measured during nickel evaporation. The data points are the reflectivity decrease, ΔR, divided by a constant Δt = -5.3 Å, for nickel films of various thicknesses when exposed to 20% O_2 in N_2 at 1 atmosphere.

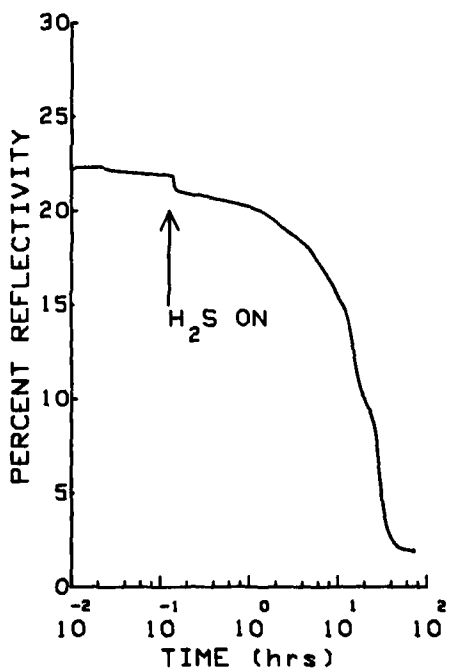


Figure 2. Reflectivity of the end of an optical fiber with a 100 Å silver coating on the end. The arrow indicates the time at which the fiber was exposed to 100 ppm of H_2S in a N_2 carrier gas at 1 atmosphere.

Abstract No. 664

Optical Waveguide Sensors: Surface Fluorescence Excitation

J. T. Ives, D. A. Christensen and W. M. Reichert*
Dept. of Bioengineering, University of Utah
Salt Lake City, UT 84112
*Dept. of Biomedical Engineering, Duke University
Durham, NC 27706

Introduction

Surface fluorescence sensing is an important feature of fluoroimmunoassay[1], protein adsorption studies[2], and fiber optic chemical sensors.[3] A fluorosensing method using integrated optic (IO) waveguides has several potential advantages compared to single reflection techniques and optical fibers. IO waveguides have an exponentially decaying "evanescent" excitation field penetrating approximately 1500Å into the neighboring medium (Fig. 1). Polarization is preserved during propagation, and specific waveguide modes with unique evanescent fields can be selected. Waveguides are relatively easily fabricated from a wide range of transparent materials. The planar geometry and fabrication methods are consistent with multichannel sensing and waveguide devices such as gratings and nonlinear or electro-optic structures. Surface sensitivity can also be improved with evanescently-coupled fluorescence.

The propagating light intensity within IO waveguides decreases due to light scatter and absorption, and the scattered light excites bulk fluorescence in the neighboring medium[4]. Differentiating fluorescence excited by scattered light from that excited evanescently is essential for surface fluorosensing. This report describes characterization of the evanescent and scatter excitation fields of polymer IO waveguides. Characterization involves decay measurements, calculated intensity profiles, Langmuir-Blodgett thin films and fluorescein dye solutions. Evanescently-coupled fluorescence is discussed as a method to enhance surface sensitivity. The results indicate that IO waveguides are a potentially useful sensing method, but light scatter must be reduced in future fluorosensing applications.

Methods

The following experimental details will be brief (see Ives and Reichert (1988)[5]) Poly(styrene) waveguides, 1-2μm thick, were spun cast on quartz microscope slides, and an incident laser beam at 488nm was prism-coupled into the waveguides. The waveguides were mounted on a goniometer for precise angular mode coupling, and the refractive index and thickness of the waveguide were determined from the mode angles.[6] For decay measurements and light collection, a 200μm diameter quartz optical fiber was aligned perpendicular to the waveguide surface adjacent to the quartz substrate (front surface collection). The same optical fiber was positioned at the waveguide end for detecting evanescently-coupled fluorescence. The fiber was then directed to a spectrometer for photon counting.

Waveguide decay was measured by recording the intensity of the 1002 cm^{-1} poly(styrene) Raman peak at several positions along the waveguide streak.[5] The decay rates of all waveguides were measured prior to Langmuir-Blodgett (LB) dipping or fluorescein dye experiments.

Langmuir-Blodgett thin films of arachidic acid (Kodak) and cyanine dye (λ_{em} = 509nm, Kodak) (molecular ratio = 1 dye/200 arachidic acid) were deposited on the surface of poly(styrene) waveguides. Two molecular layers (~54Å) were deposited. Fluorescence emission was monitored as a function of waveguide mode and polarization, and the 488nm signal was used for normalization.

Bulk fluorescence was investigated by injecting fluorescein dye into a flow cell on the waveguides[4], and collecting the fluorescence emission at a position about 25mm from the in-coupling prism. Only the lowest order TE mode was used due to losses at the gasket-waveguide interface which increased with higher order modes. Fluorescence signals were normalized by the 488nm signal.

Results

Fig. 2 plots the normalized fluorescence signal vs. mode number for waveguides coated with LB dye films. The fluorescence increase with mode number is expected due to both the higher interfacial intensity and greater scatter losses of higher order modes. A model was developed to calculate the evanescent and scatter excitation components. This model considers the measured decay rates and calculated evanescent intensities of two waveguide modes, and then weights the scatter and evanescent terms to account for the experimentally measured difference in fluorescence of the two modes. In Fig. 2, the normalized fluorescence value is about 1 (front surface collection). Based on the evanescent/scatter model, the calculated evanescent components are approximately -0.1 vs. approximately +1.1 for the scatter components. The scatter component appears to dominate the fluorescence, although the negative sign of the evanescent component is surprising. The model used in the calculations does not account for the mode dependence of the Rayleigh normalization signal, and this could reduce the evanescent component from a small positive signal to a small negative term.

The normalized fluorescence signal for evanescent-coupling (Fig. 2) is significantly lower than the front surface collected signal due to two factors: 1) the direct, rather than scattered, collection of the 488nm laser beam, and 2) the low efficiency of fluorescence evanescently coupling into bound waveguide modes.

The fluorescein dye results in Fig. 3 can be separated into evanescent and scatter excitation components due to saturation of the scatter component.[4,7] For a solution $\varepsilon c = 0.1cm^{-1}$, the evanescent/scatter excitation ratio = 0.06.

The data shown in Fig. 3 were normalized by the Rayleigh scattered 488nm signal. This signal decreased exponentially with increasing dye concentration consistent with absorptive cladding models of guided wave media.[8]

Conclusions

IO waveguide detection of fluors on the surface and in solution is feasible, even with the low laser powers (50μW) used for excitation. The use of low power sources may be helpful in small sensor design. The planar waveguide geometry and mode selection allows polarization studies and relatively simple analysis and modeling. However, the scatter-excited signal is too large for reliable surface detection and waveguide fabrication improvements are necessary to decrease the waveguide scattering coefficent. The attractiveness of evanescent-coupling for surface sensitivity is reduced by the small fraction of excited signal which couples and propagates as a bound mode. Future work should include possible enhancement techniques for evanescent-coupling, or planar detector arrays with alternative evanescent-scatter discrimination methods.

---

[1]J.F. Place, R.M. Sutherland and C. Dahne, Biosensors 1, 321 (1985).
[2]J.T. Ives and W.M. Reichert, Appl. Spectroscopy 42, 68 (1988).
[3]R.A. Lieberman, L.L. Blyler and L.G. Cohen, OFS, New Orleans, January 1988.
[4]W.M. Reichert, J.T. Ives, P.A. Suci and V. Hlady, Appl. Spectroscopy 41, 636 (1987).
[5]J.T. Ives and W.M. Reichert, J. Appl. Polymer Sci. 35 (1988).
[6]J.D. Swalen, R. Santo, M. Tacke and J. Fisher, IBM J. Res Dev. 21, 168 (1975)
[7]V. Hlady, D. Reinecke and J.D. Andrade, J. Colloid Interf Sci. 111, 555 (1986).
[8]N.S. Kapany, J.J. Burke and C.C. Shaw, J. Opt. Soc. Am 53, 929 (1963).

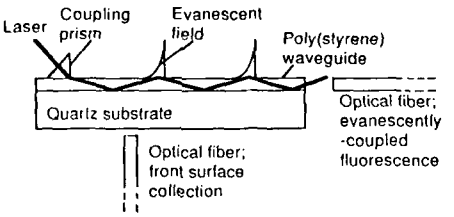


Figure 1. Schematic illustration of polymer integrated optic waveguide. Integrated optic waveguides have a continuous evanescent field along the waveguide surface. The evanescent penetration depth is ≈1500Å, the poly(styrene) waveguide is 1-2μm thick and the optical fiber is 200μm in diameter.

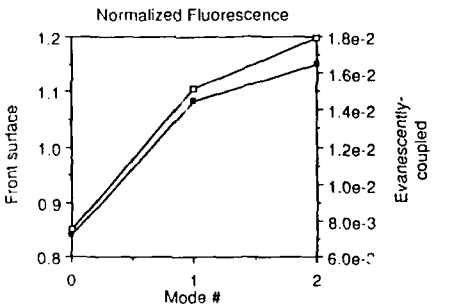


Figure 2. Normalized fluorescence vs. waveguide mode. The poly(styrene) waveguide was coated with two Langmuir-Blodgett layers of cyanine dye in arachidic acid (1/200 molecular ratio). Normalized fluorescence (509nm/488nm) was determined for a) front surface collection (open squares) and b) near field back-coupling with terminal end collection from the waveguide (solid squares). Waveguide modes were selected by adjusting the coupling angle.

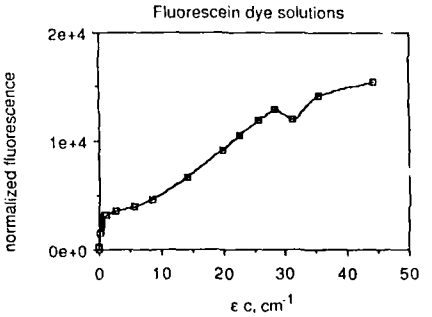


Figure 3. Fluorescein dye solutions. Fluorescein dye solutions of varying concentration (ε = extinction coefficient, c = concentration) were injected into the flow cell. The normalized fluorescence (512nm/488nm) was detected with front surface collection (Fig. 1).

Abstract No. 665

AN INVESTIGATION OF POLYMERIC FILM/SOLUTE VAPOR SOLUBILITY PARAMETERS USING AN OPTICAL WAVEGUIDE INTERFACIAL PROBE METHOD

J. F. Giuliani

Chemistry Division
U.S. Naval Research Laboratory
Washington, D.C. 20375-5000

A simple and rapid optical method is reported for the determination of solubility parameters δ of solid polymer films using an optical waveguide (OWG) device which probes changes in the optical properties of the film at the film/glass interface. This simple method relies on the approximate Hildebrand equation: $\Delta H \cong \Delta E = \phi_1 \phi_2 (\delta_1 - \delta_2)^2$ $(cal/cm^3)^{1/2}$ where ΔE is the change in internal energy in a solution process, ϕ_1, ϕ_2, and δ_1, δ_2 are the volume fractions, and solubility parameters of the solvent and polymer respectively. The above approximate relationship is used to determine solubility parameters by means of the amount of swelling that the polymer undergoes when immersed in a specific reagent. A new method for determining the solubility parameters of polymeric films is described in which a decrease in optical transmission from a film coated optical waveguide is monitored with exposure to a wide range of vapors whose solubility parameters are known *beforehand*.

Figures 1 and 2 display the plots of the measured changes in the optical transmission at 660 nm relative to the nitrogen gas reference transmission (i.e. nearly 100 percent) in a dual flow vapor/gas system for the polymer films, polyethylene maleate (PEM) and polyfluoropolyol (PFP) as a function of a wide range of organic compound saturated vapors (i.e. 10,000 ppm). These two film coatings were exposed separately to organic vapors (numbered in Figures 1 and 2), whose solubility parameters range between 8.6 $(cal/cm^3)^{1/2}$ and 23.4 $(cal/cm^3)^{1/2}$. All of the transmission measurements were performed at approximately 22°C. The error bars represent the standard deviation obtained from three vapor cycles per coating and for three separate film coatings, and exhibit good reproducibility. The solubility parameter for the PEM film was measured from NRL swelling data to be approximately 10.1 ± 0.5 $(cal/cm^3)^{1/2}$, and that for the PFP film was calculated from thermodynamic data to be about 11.0 $(cal/cm^3)^{1/2}$. The detected minima in the optical waveguide transmission for both the PEM and PFP films occur in the solubility parameter range between 10.5 $(cal/cm^3)^{1/2}$, and 11.5 $(cal/cm^3)^{1/2}$, and this agrees rather well with the measured and calculated values for these two polymeric films respectively.

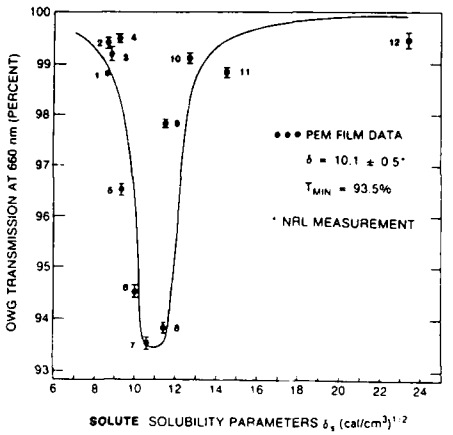


Fig. 1. Dependence of the measured optical transmission for a PEM film coated optical waveguide probe over a wide range of organic solvent solubility parameters. The solid curve represents a least squares fit to the data. The number beside each point represents the organic vapor: (1) CCl_4; (2) C_8H_{10}; (3)C_7H_8; (4) C_6H_6; (5) $CHCl_3$; (6) C_3H_6O; (7) $C_3H_9O_3P$; (8) C_4H_9NO; (9) C_3H_8O; (10) C_2H_6O; (11) CH_4O; (12)H_2O.

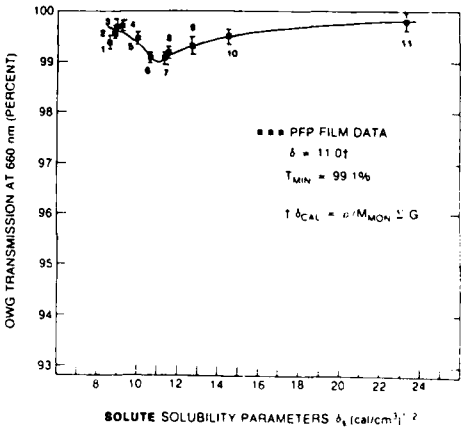


Fig. 2. Dependence of the optical transmission for a PFP film-coated waveguide probe over the same range of organic solvent solubility parameters as shown in Figure 1. Again the solid curve represents a least square fit to the data. The organic vapors tested; (1) CCl_4; (2) C_8H_{10}; (3) C_7H_8; (4) C_6H_6; (5) $CHCl_3$; (6) $C_3H_9O_3P$; (7) C_4H_9NO; (8) C_3H_8O; (9) C_2H_6O; (10) CH_4O; (11) H_2O.

Abstract No. 666

Reversible SO_2 Detection Using A Multiple Reflecting Optical Waveguide Sensor

Ronald L. Cook, Robert C. MacDuff
Anthony F. Sammells

Eltron Research, Inc.
4260 Westbrook Drive
Aurora, IL 60504

The harmful environmental consequences of sulfur dioxide emissions have been well documented over the last several years[1-3]. Sulfur dioxide enters the atmosphere as a by-product of ore smelting, power generation and internal combustion engines. Sulfur dioxide, together with nitrogen oxides, are primary sources of acid rain contributing to deterioration of vegetation in soils and lakes[1,2]. In plants, the presence of SO_2 has been shown to inhibit CO_2 fixation, block starch hydrolysis, and cause a breakdown of chlorophyll containing cells leading to early foliage loss. Vegetation damage via destruction of localized leaf tissue has been reported at concentrations as low as 2-3ppm SO_2[4]. In people, both acute and chronic toxicity of SO_2 has been reported[4]. Sulfur dioxide is also suspected to cause mutagenic effects as well as lung tumors and several types of cancer[4]. Thus, there are strong incentives for developing sensitive, reversible sensors for both on-site and field measurement of SO_2.

In recent years chemical gas sensors based upon the use of optical waveguides have been developed, and practical devices for ammonia detection in the parts per billion, fabricated[5]. These devices consisted of a glass tube or rod coated with an organic dye. Interaction of the gas to be detected with the coating gave rise to modification of either the film adsorption coefficient or its refractive index. Such changes were detected by changes in the flux of internally multiply reflected light within the tube. The simplicity and ease of construction for such devices has encouraged us to develop an optical waveguide chemical sensor for SO_2. In the present work we will discuss the development of a multiple reflecting optical waveguide device using organophosphine-transition metal complexes as the optically sensitive coating for reversible detection of SO_2 below the 500ppm range. Figure 1 shows a schematic of the chemically sensitive optical waveguide investigated. The device was coated with the complex $Cu(PBz_3)_2SPh$, which upon exposure to SO_2, forms the adduct $Cu(PBz_3)_2SPh(SO_2)$ via the equilibrium

$$Cu(PBz_3)_2SPh + SO_2 \rightleftarrows Cu(PBz_3)SPh(SO_2)$$

The utility of this complex lies in a color transformation from white to orange on going from $Cu(PBz_3)_2SPh$ to $Cu(PBz_3)_2SPh(SO_2)$. The change in adsorbance of the coating was probed by a multiple-reflected light beam and detected by changes in the light flux occurring at a silicon photodetector. Figure 2 shows the optical waveguide response towards 1000ppm, 500ppm and 100ppm SO_2 at 60°C. The response was fully reversible and for SO_2 concentrations below 500ppm a linear curve for the detector output signal and SO_2 concentration could be obtained (Figure 3).

ACKNOWLEDGEMENT

This work was supported in part by the Office of Naval Research.

REFERENCES

1. Cowling, E. B., Linthurst, R. A., Bioscience, 31(9), pp. 649-654 (1981).
2. Cowling, E. B., Environ. Sci. Technol., 16(2), pp. 110A-123A (1982).
3. Webster, B. D., U.S. Dept. Agric., Agric. Res. Serv., #24 (1971).
4. Calabrese, E. J., "Pollutants and High Risk Groups", Interscience, New York (1976).
5. Giuliani, J. F., Wohltjen, H. and Jarvis, N. L., Optics Lett., 8, 54-56 (1983).
6. Eller, P. G. and Kubas, G. J., J. Am. Chem. Soc., 99(13), pp. 4346-4351 (1977).

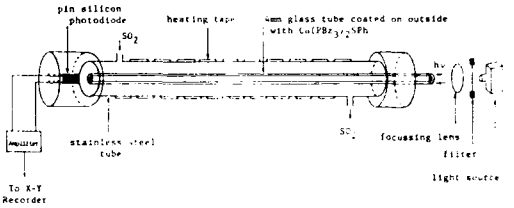


Figure 1. Schematic diagram for guided wavelength optical SO_2 detector.

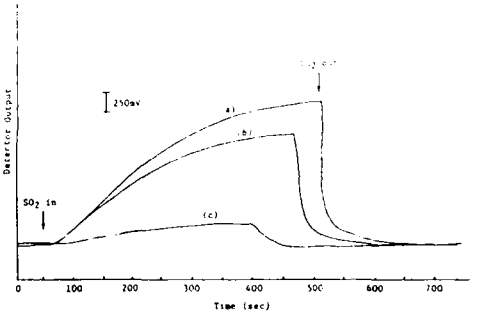


Figure 2. Optical waveguide chemical sensor response to SO_2, (a) 1000ppm, (b) 500ppm, (c) 100ppm at 60°C.

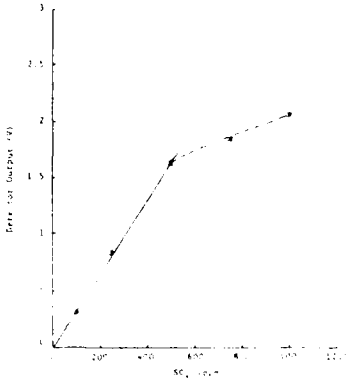


Figure 3. Plot of SO_2 concentration as a function of detector output voltage at 60°C.

Abstract No. 667

SEMICONDUCTOR PHOTOLUMINESCENCE AS A SENSOR FOR GASEOUS ACIDS AND BASES

George C. Lisensky*, Department of Chemistry
Beloit College, Beloit, WI 53511
Arthur B. Ellis* and Gerald J. Meyer, Department of Chemistry, University of Wisconsin-Madison
1101 University Avenue, Madison, WI 53706

The photoluminescence (PL) of etched or cleaved n-CdSe, n-CdS, and n-CdS:Te semiconductor single crystals is strongly affected by exposure to gaseous acids and bases that can engage in adduct formation (1-5). For example, exposure to SO_2 or gaseous carboxylic acids reversibly decreases the semiconductor PL intensity, while exposure to gaseous ethers or alcohols gives small reversible increases, and exposure to gaseous alkyl amines or pyridines results in large reversible increases in PL intensity, relative to the intensity in a N_2 ambient. The order of PL enhancement roughly follows amine basicity: $NF_3 < NH_3$, $ND_3 < CH_3NH_2 < (CH_3)_2NH > (CH_3)_3N$. Gases that interact more weakly with the semiconductor surface, hydrocarbons for example, do not affect the PL intensity within experimental error.

A dead-layer model is used to correlate changes in PL intensity with variations in the depletion width: electron-hole pairs formed within a distance on the order of the depletion width are rapidly swept apart by the electric field and do not contribute to PL (6). A quantitative form of this model equates the ratio of the observed PL intensities for two different gases with $\exp(-\alpha' \Delta D)$, where ΔD is the corresponding change in dead-layer or depletion width thickness, and $\alpha' = \alpha + \beta$, where α and β are the absorptivities for the exciting and emitted light. This treatment assumes that the surface recombination velocity is either very large or unchanged with gaseous ambient. The operational test of the dead-layer model is the calculation of a constant ΔD value for a variety of interrogating wavelengths and corresponding absorptivities. Using wavelengths for which α varied over a factor of three, ΔD for n-CdSe with the above amines was constant to within 20%. The change in depletion width inferred from these spectral changes corresponds to a shift in the work function of the semiconductor surface, moving the work function closer to the vacuum level for PL intensity increases, and farther from the vacuum level for PL intensity decreases (7).

The PL intensity changes are linearly dependent on concentration over a modest range, although at higher concentrations the response saturates. The PL intensity changes upon exposure to a series of gaseous concentrations have been found to fit a Langmuir adsorption isotherm, providing additional evidence for adduct formation.

We have used such semiconductor PL intensity changes as an optically-coupled, non-destructive, selective, gas chromatography detector, operated in tandem with a commercial thermal conductivity detector (TCD). For example, when a mixed sample of hexane, n-butylamine, toluene, and pyridine was chromatographically separated, the TCD saw all four distinct components, but the PL of an ultraband-gap illuminated semiconductor, attached to the column exit port and monitored through an optical fiber, responded only to the species that readily form adducts with the semiconductor, n-butylamine and pyridine. Detection limits for such species are less than 1 ug.

This research was supported by the Office of Naval Research and the 3M Company.

1. A.B. Ellis in "Chemistry and Structure at Interfaces: New Laser and Optical Techniques"; R.B. Hall and A.B. Ellis, Eds., VCH Publishers, Deerfield Beach, FL, 1986, Chapter 6.
2. G.J. Meyer, G.C. Lisensky, A.B. Ellis, Proc. of the Electrochem. Soc. 1987, 87-9, 438.
3. G.J. Meyer, G.C. Lisensky, A.B. Ellis, J. Am. Chem. Soc., in press.
4. G.J. Meyer, E.R.M. Luebker, G.C. Lisensky, A.B. Ellis, in "Photochemistry on Solid Surfaces"; M. Anpo, Ed., Elsevier, Amsterdam, in press.
5. G.C. Lisensky, G.J. Meyer, A.B. Ellis, submitted for publication.
6. R.E. Hollingsworth, J.R. Sites, J. Appl. Phys. 1982, 53, 5357 and references therein.
7. P.C. Stair, J. Am. Chem. Soc. 1982, 104, 4045.

Abstract No. 668

ELECTROCHEMICAL MODULATION OF LUMINESCENCE FROM A CONDUCTING POYMER SURFACE

S. Basak, E. W. Tsai, L. Phan and K. Rajeshwar*
Department of Chemistry
The University of Texas at Arlington
Arlington, Texas 76019-0065

The use of luminescence probes in studies of polymeric materials has attracted much recent interest (1). Polypyrrole and polythiophene belong to an emerging family of electronically conductive polymers which can be electrochemically redox-switched between the oxidized, conductive form and the neutral, insulating state. Thus, the possibility of utilizing luminescence from a probe molecule located close to the polymer surface to report back on environmental changes during the switching was intriguing to us. Specifically, we anticipated that the luminescence from such a molecule could be reversibly modulated in a manner which tracked the corresponding variations in the polymer conductivity. The strategy is schematized in Fig. 1. Aside from diagnostic applications, this new modulation technique could lead to interesting applications in the chemical sensor and optical display areas.

The efficacy of this approach rests on the extent to which the probe molecules are constrained to be within the critical distance for energy-transfer quenching from the polymer surface. To this end, a thin-layer luminescence cell is designed and described in this paper. Proof-of-concept experiments are described for polypyrrole and two luminophores, namely pyrene and $Ru(bpy)_3^{2+}$. An optically transparent gold minigrid was used to support the polypyrrole in the thin-layer cell. In both the cases, ~90% of the luminescence from the probe molecules was quenched by switching the polypyrrole potential from its neutral state (e.g., -0.9 V vs. nonaqueous $Ag^{0/+}$ reference) to its electronically conductive form (+0.5 V). Importantly, this modulation was reversible and could be repeated over many cycles.

A drawback with the strategy in Fig. 1 is that a small fraction of the probe molecules resides at distances beyond the critical quenching distance from the polymer surface. To further discriminate this "background" emission (~10%), chemistry is described to covalently anchor the probes to the polymer surface. Initial experiments with polythiophene (substituted in the β-position) and polypyrrole (chemically modified with the probe at the N-center) are described. Anthracene was used as the fluorescent molecule in this phase of the work. The starting monomers as well as the chemically modified polymers were characterized by elemental analyses, FTIR, NMR, voltammetry, and fluorescence spectroscopy.

ACKNOWLEDGMENTS

This research was partially supported by grants from the Defense Advanced Research Projects Agency (monitored by the Office of Naval Research) and the Texas Advanced Technology Research Program.

REFERENCES

1. For example, S. R. Holmes-Farley and G. M. Whitesides, Langmuir 2, 266 (1986). E. Blatt, A. Launikonis, A. W.-H. Mau and W. H. F. Sasse, Aust. J. Chem. 40, 1 (1987). P. C. Lee and D. Meisel, J. Am. Chem. Soc. 102, 5477 (1980). W. G. Herkstroeter, J. Polym. Sci. Polym. Chem. Ed. 22, 2395 (1984).

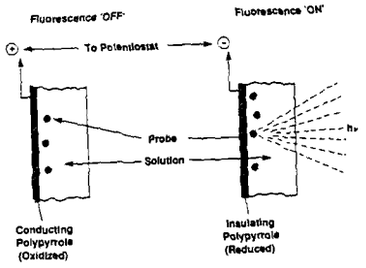


Figure 1. Strategy for monitoring electrochemical modulation of luminescence from an interfacial probe molecule during redox switching of a polypyrrole electrode.

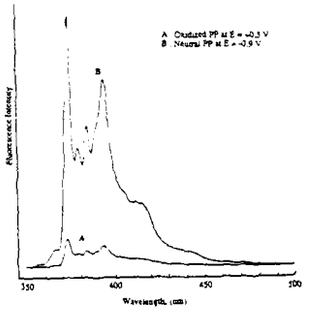


Figure 2: Example of fluorescence modulation of pyrene at a polypyrrole electrode surface. Spectra A and B were obtained at a polypyrrole potential of +0.5 V and -0.9 V respectively.

Abstract No. 669

ELECTROCHEMISTRY OF β-SUBSTITUTED (SOLUBLE) POLYTHIOPHENES

E. W. Tsai, S. Basak, J. Ruiz,
J. R. Reynolds* and K. Rajeshwar*
Department of Chemistry
The University of Texas at Arlington
Arlington, Texas 76019-0065

Recent interest in electronically conductive polymers has focused on alterations of the synthetic conditions and molecular architecture to impart solution/melt processability of the resultant materials. The polythiophene system, in particular, has been extensively studied in this regard. The consensus now seems to be that β-position monomer substituents of appropriate size and length afford the solubility of the corresponding polymer in common organic solvents. The ability to process these polymers using convenient techniques (e.g., spin-coating) opens up a broad area of applications. In this paper, we report on the electrochemical and spectroscopic characterization of poly(3-ethylmercaptothiophene) and poly[3,4-bis-(ethylmercapto)thiophene]. The synthetic aspects, as well as structure and electronic property correlations for these new polymers have been detailed elsewhere (1). Additionally, data on poly(3-hexylthiophene) are also presented for comparison.

In this paper, we use cyclic voltammetry to probe the charge-discharge reversibility of these new polymers. The corresponding behavior of polythiophene and poly(3-methylthiophene) is discussed as a "baseline" reference. The electrochronic behavior accompanying redox doping of these polymers is also discussed with the aid of suitable photographs.

A new aspect addressed in this paper concerns the irreversible passivation of the polymers when they are driven to very positive potentials. This "over-oxidation" behavior has been noted by other authors for polypyrrole (2), but has received only cursory examination for polythiophene. We will describe the mechanistic aspects of this passivation using a combination of the voltammetry data with information derived from constant-potential coulometry and FTIR spectroscopy.

ACKNOWLEDGMENTS

This research was supported in part by a grant from the Defense Advanced Research Projects Agency (grant monitored by the Office of Naval Research).

REFERENCES

1. J. P. Ruiz, K. Nayak, D. S. Marynick and J. R. Reynolds, to be published.

2. F. Beck, P. Brown and M. Oberst, Ber. Bunsenges. Phys. Chem. 91, 967 (1987).

Abstract No. 670

Highly Sensitive Optical Gas Detector of Squarylium Dye LB-film Containing J-aggregate.

Makoto Furuki , Suk Kim , Kentaro Ageishi , Lyong Sun Pu

Fundamental Technology Research Laboratory , Fuji Xerox Co. , Ltd.
2274. Hongo , Ebina-shi , Kanagawa , 243-04 , Japan.

Increasing attention has been paid to the application of the Langmuir-Blodgett film technique, because this technique can make monomolecular layers in highly ordered structures. There are some reports on the application for electronics, optical devices and sensors. G.G.Roberts et al. reported on the application of phthalocyanine LB-film for gas detectors[1]. High sensitivity and fast response and recovery times were pointed out to be merits of the LB-film. But there are only a few reports on optical sensors using LB-films[2]. In the present work, we have studied optical gas detectors based on fluorescence quenching of squarylium dye LB-films containing J-aggregate by exposure to NO_2 gas in an air atmosphere. We found that very small amounts of NO_2 could be detected.

Propyl substituted squarylium dye (SQ3-3) (fig.1) was recently found to form a monolayer of J-aggregate on the water surface during the investigation of the influence of alkyl chain lengths on the monolayer structure of dyes. The film mixed with Cd-arachidate (1:1) could be deposited on a glass slide maintaining J-aggregate. The deposited film showed a sharp absorption at 770nm, and exhibited a sharp fluorescence band with a small Stokes shift (< 5nm), characteristic of J-aggregate[3]. The fluorescence could be generated with an excitation wavelength between about 600~770nm. A He-Ne laser (632.8nm) and a laser diode (750nm) were available for the excitation of this film.

These fluorescences were found to be reversibly quenched by nitrogen dioxide in air. As shown in fig.2, the fluorescences were quickly quenched by NO_2, and the fluorescence intensities recovered to the initial intensity level by eliminating NO_2. It was suggested that the relatively fast response and recovery times compared with those for gas detectors of phthalocyanine film deposited in vacuum, were attributed to the thinness and highly ordered structure of LB-film. With enhancement of the NO_2 concentration in the air, the ratio of fluorescence change increased, and the response and recovery curves became slower. Fig.3 shows the dependence of fluorescence change after 5 minutes exposure to the NO_2 concentration. When LB-films were exposed to low concentrations of NO_2 (< 0.2ppm), the dependence on the concentration of NO_2 was large. The fluorescence change was observed even down to several tens ppb. On the other hand, at higher concentration the dependence on the NO_2 concentration became smaller.

These results suggested that at low concentrations of NO_2, the fluorescences from dye molecules were rapidly quenched by NO_2 gas molecules adsorbed on the surface film of squarylium dyes, with the formation of trapping sites for excited states. With higher concentrations, the fluorescences from dye molecules in the bulk of the film were also quenched by the NO_2 molecules diffused inside the film, where NO_2 gas was adsorbed and desorbed more slowly. As J-aggregate is known to have a high mobility of its excited states, the extremely high sensitivity to detect NO_2 was attributed to the high mobility of the excited states in the LB-film, and response and recovery times seem to be determined by the adsorption and desorption processes of NO_2 to the LB-films.

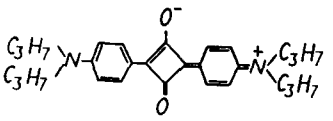


Fig.1. SQ3-3

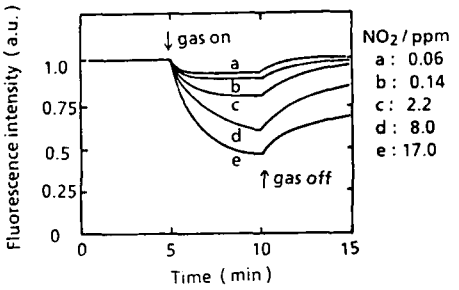


Fig.2. Response curves for fluorescence quenching at the peak wavelength 772nm by NO_2 gases in air.

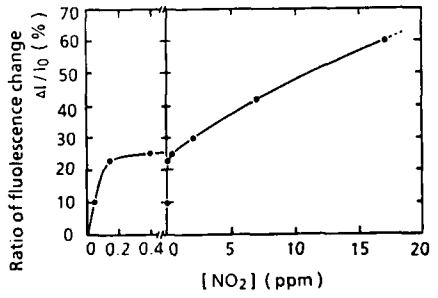


Fig.3. Ratio of fluorescence change by concentrations of NO_2 gases in air for 15 layers of LB-film.

reference

1) S.Baker , G.G.Roberts , M.C.Petty , IEE Proc ., 130 , **1983** , 260.

2) M.Aizawa , M.Matsuzawa , H.Shinohara , Thin Solid Films , **1988** (in press).

3) S.Kim , M.Furuki , L.S.Pu , H.Nakahara , K.Fukuda , J.C.S.Chem.Comun., **1987** , 1201., Thin Solid Films , **1988** (in press).

Abstract No. 671

ANALYSIS OF THE ELECTRON TRANSFER PROCESSES OF ELECTROCHEMICAL REACTION IN THE MAGNETIC FIELD BY MEANS OF MAGNETOHYDRODYNAMIC ELECTRODE

Ryoichi Aogaki*, Kazuo Fueki+

*Department of Chemistry, The Institute of Vocational Training, Aihara 1960, Sagamihara 229, Japan

+Department of Industrial Chemistry, Faculty of Engineering, University of Tokyo, Hongo, Bunkyo-ku 113, Japan

Electrode reaction in the magnetic field is always followed by the occurrence of the solution flow induced by the electromagnetic force. At the same time, such flow enhances the mass transfer process near the electrode surface. In the previous papers (1-4), it was shown that a new type of electrode, magnetohydrodynamic electrode (MHDE) utilizing this phenomenon, can effectively regulate the flow velocity to promote the mass transfer of active species.

MHDE can be also applied to the separation of the electron transfer processes in the presence of magnetic field, from overall reaction involving both mass transfer and electron transfer processes.

Typical MHDE is shown in Fig.1, which is made of a channel with two open ends. A pair of plane electrodes, working and counter electrodes, are imbedded face to face on the top and bottom inner walls, respectively. Electrolytic current flows vertically inside the channel while the magnetic field is horizontally applied from the outside of the channel. Whole the cell system is immmersed in a large volume of electrolyte solution. Then, the solution starts to move by the induced electromagnetic force, entering the inlet of the channel and leaving from the outlet.

If the reaction can be apparently regarded as the first order, the following relationship between the current density i and the magnetic flux density B is derived,

$$1/i \sim 1/i_k = 1/(H^{*3/4} C_o)\ 1/(Bi)^{1/4}$$

where i_k represents the current density of electron transfer processes, C_o is the bulk concentration of active species, and H^* is a constant.

Figure 2 shows the plot of 1/i vs. $1/(Bi)^{1/4}$ in the case of copper deposition which exhibits good linearity, and the extrapolation of the linear plot gives the value of i_k. Subtracting the ohmic drop from the total overpotential, Tafel relations were obtained as shown in Fig.3.

Consequently, at least, up to 0.6 Wbm^{-2} of magnetic flux density, transfer coefficients measured were consistent with those in the absence of magnetic field.

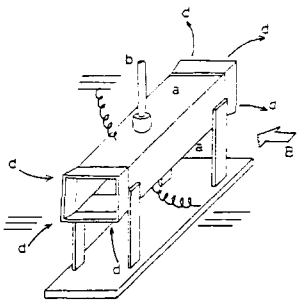


Fig. 1 MHDE cell configuration

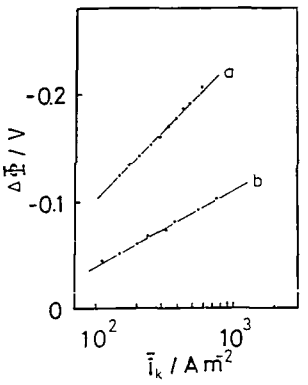


Fig. 2 Plot of 1/i vs. $1/(Bi)^{1/4}$ for copper deposition

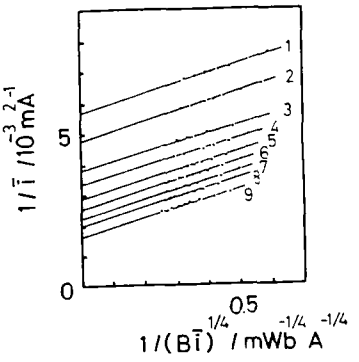


Fig. 3 Tafel plots for copper and zinc depositions
Curve a: copper deposition
Curve b: zinc deposition

REFERENCES

1. R. Aogaki, K. Fueki, T. Mukaibo, DENKI KAGAKU 43, 504 (1975).
2. R. Aogaki, K. Fueki, T. Mukaibo, ibid. 43,509 (1975).
3. R. Aogaki, K. Fueki, T. Mukaibo, ibid. 44, 89 (1976).
4. R. Aogaki, K. Fueki, J. Electrochem. Soc. 131, 1295 (1984).

Abstract No. 672

Preliminary Study of Saccharide Diffusion Through Inert Porous Membrane in an Externally Applied Magnetic Field.

J. Lielmezs and H. Aleman
Chemical Engineering Department, The University of British Columbia

Address: Chemical Engineering Department, The University of British Columbia, Vancouver, B.C., Canada, V6T 1W5.

There is little information available on the diffusivity of molecules through membranes in externally applied magnetic field (MF). Lielmezs and Aleman [1] have observed that an external MF of 0.5 T affects the integral diffusion coefficient values of electrolytes in alkali chloride - water solution (Fig. 1a,b). Models [2,3], however, predict smaller effect than found. Presently we study the external MF effect on diffusion of dilute saccharide solutions through inert porous membranes by means of modified Rayleigh interferometer - laser systems(Fig. 2a - d).

For dilute binary sucrose - water system with constant diffusivity and constant density, the observed diffusional process can be described by means of one dimensional Fick's law yielding as solution an ideal concentration profile [4 - 7]:

$$C_A(x,t) = \tfrac{1}{2} C_{Ao} \operatorname{erfc} \tau \qquad (1)$$

where erfc is a complemented error function with $\tau = x/\sqrt{Dt}$.

The mass flux J at any point in the cell for this diffusion process is:

$$J = -\frac{\partial}{\partial t}\int_{x_o}^{x} C\,(x,t)\,dx \qquad (2)$$

Eq. 2 can be adapted to describe free molecular diffusion through an idealized membrane [8]:

$$J = -D_F A_P \frac{\Delta C}{\delta x} \qquad (3)$$

Using Eq. 3, Faxen [8] derived an expression for the ratio of self-diffusion coefficient in a cylindrical pore, D_M, to the bulk self-diffusion coefficient, D_F, as:

$$D_M = D_F (1 - 2.104\beta + 2.09\beta^3 - 0.95\beta^5) \qquad (4)$$

where $\beta = R_S / R_P$; the ratio of molecular to pore radius.

Eq. 4 shows a decrease in the diffusion coefficient as β increases. The orientation of diamagnetic molecules in a MF is known as the Cotton - Mouton effect [9]. The degree of orientation of a cluster of N molecules, σ_{No} , can be written as:

$$\sigma_{No} = N (\chi_{||} - \chi_{\perp}) H^2 / kT \qquad (5)$$

To predict the change in the membrane diffusion coefficient for molecular cluster oriented in a MF introduce parameter β in terms of Eq. 5 as β_{MF} :

$$\beta_{MF} = (R_S + F\sigma_{No})/ R_P \qquad (6)$$

The experimental set-up consists of bifocal Rayleigh interferometer placed between the two poles of electromagnet. The fused silica diffusion cell (Fig. 2d) has flatness of all optical surfaces at $\lambda/20$ (λ = 6328 Å) and parallelism better than 1 arc second. The total wave front distortion is diffraction limited to $\lambda/4$. He - Ne (Spectra Physics Model 124 - B) laser was rated 15 mW optical output at λ = 6328 Å. All optical bench and component holders, screws, bolts and mounts were made from aluminum and nylon. The optical bench rested on two vibration isolation platforms. Air temperature adjacent to the diffusion cell was kept within $\pm$ 0.1 °C. The two membranes (0.8 and 8.0 μm pore size) were surface flat, maximum peak to valley distance on the surface being less than 0.1 μm; with a pore diameter variation of 0 % to 10 %. The diffusing solution was ACS reagent grade sucrose dissolved in doubly distilled and degassed water. Varian Associates 30 cm Model V - 7300 electromagnet (18 cm diameter pole caps, 10 cm gap width). Field homogeneity was measured to be better than 7 x 10^{-5}T over the pole caps at field strength of 0.9 T. From the obtained interference patterns in the test cell (Fig. 3 d) a corrected for deflection refractive index profile n(x) was established [5,6].

For dilute solutions refractive index n is linear function of sucrose concentration [5,6]:

$$C_A = n\alpha_c + \beta_c \quad \text{, where } \alpha_c = 0.204014;\ \beta_c = -0.0271606 \qquad (7)$$

at 25° C.

Deflection effect corrections can be described by means of sigmoid type function (Eq. 1,7):

$$n(x) = m \operatorname{erf} (Ax) + b \qquad (8)$$

To obtain separate concentration profile at particular time, we combine the concentration integral of Eq. 2 with Eq. 7,8 and then integrate the error function [5,6]:

$$\int_{x_o}^{x} C(x)dx = C_c\left\{\frac{m}{A}\left[\frac{m}{A} A\,x \operatorname{erf}(Ax) + \frac{}{} e^{-(Ax)^2}\right]_{x_o}^{x} + b(x - x_o)\right\} + \beta_c (x - x_o) \qquad (9)$$

To evaluate the time derivative of Eq. 2 we use a suitable correlation function [6]:

$$\int_{x_o}^{x} C(x,t)dx = a_1 + a_2 \operatorname{erf} \frac{a_3}{t^{\frac{1}{2}}} + a_4 t^{\frac{1}{2}} \exp\left(-\frac{a_3^2}{t}\right) \qquad (10)$$

Constants a_1 , a_2 , a_3 and a_4 are determined from five different concentration profile integrals (Eq.9) taken at different times. To obtain flux J we differentiate Eq. 10 with the respect to time. The molar flux of sucrose at the membrane surface then becomes:

$$J_{xo} = \left[\frac{a_4}{2\,t^{\frac{1}{2}}} + \frac{a_4 a_3}{t^{3/2}} - \frac{1}{\sqrt{\pi}} \frac{a_2 a_3}{t^{3/2}} \right] \exp\left(-\frac{a_3^2}{t}\right) \qquad (11)$$

For steady state diffusion process, the mass flux, J_{xo}, becomes the mass flux through the membrane. The membrane diffusivity, D_M, can be calculated from Eq. 2:

$$D_M = J_{xo} / (\Delta C / \delta x) \qquad (12)$$

The free diffusion coefficient for binary diffusion is:

$$J_A = X_A (J_w + J_A) - C D_F \partial X_A / \partial x \qquad (13)$$

For dilute solutions the molar concentration of water is linear function of molar concentration of sucrose [6]:

$$C_w = \gamma_1 C_A + \varepsilon_1 \qquad (14)$$

where γ_1 = 11.68744; ε_1 = 0.0553512

From Eq. 2, 14 it follows that:

$$J_A = -\gamma_1 J_w \qquad (15)$$

This study sums up the results of 23 experiments for both pore size membranes and applied MF ranging from 0 to 1.25 T. The raw data consisted of a set of fringe displacements taken at different times for each run (Fig.3c). The fringe locations were measured with respect to a datum taken at 1.0 cm from the membrane at each end of the cell. The concentration of sucrose, constant at these locations, was 0 % in top and 1 % in lower halh of cell. Each microscope measurement distance corresponded to a refractive index change equivalent to one fringe shift or one wavelength of the laser light. These data were used as input for data analysis.

Fig. 3a,b show the diffusion coefficients (D_M, D_F) as a function of MF strength for both membranes. The results indicate a slight decrease (1 to 2%) for 3 sets of diffusion coefficients. While we cannot with certainty establish a definite correlation between the diffusivity, D, and field strength, H; the results show, however, that the MF has a small but statistically significant influence on the diffusion process. This is brought out by Eq.6, the combination of Faxen's relation (Eq.4) and the Cotton-Mouton effect (Eq.5). The latter suggests that diffusion process in both the free diffusion field and in the pores may be decreased by the application of a MF. Faxen's relation implies that this MF effect may be larger for pores. The experiments indicate that applied MF may influence the free and pore diffusion processes in somewhat similar fashion. Yet, superimposing Fig.3a on Fig.3b it appears that the free diffusion data for 0.8 m pore size are significantly below the 8.0 m pore size measurements. A series of polysaccharides (deoxyribose,ribose,xylose, glucose, fructose,sucrose, maltose and rafinose) has been selected to study further the applied MF effect on pore and free diffusion processes.

Nomenclature: A=crossectional area of pore;A,b,m=constan's,Eq.8; F=geometrical factor,Eq.6; k=Boltzmann's constant;n=refractive index; R=radius; t=time; x=distance; x=membrane thickness; χ=magnetic susceptibility; T = Tesla. Subscripts: A=sucrose; F=free diffusion; M= membrane; MF=magnetic field; O=initial; P=pore;s=solute; w=water.

References:Lielmezs,J. and Aleman,H.,Bioel.Bioen.5,258 (1978; 2. Lielmezs,J., Musbally, G.M., Electrochim.Acta 17,1609 (1972). 3. Fahidy,T.Z.,J.Appl.Electrochem. 13, 553 (1983).4. Crank,J.,"The Mathematics of Diffusion",Oxford U.Press,London(1957). 5. Bollenbeck, P.H., Ramirez,W.F.,I.E.C.Fund. 13,365 (1974). 6. Bollenbeck,P.H., "A Modified Rayleigh Interferometer for Membrane Transport Studies", Ph.D.Dissert.,Univ. of Colorado (1974). 7. Howell, S.K., " The Development of Use of the Rayleigh Interferometer to Study Molecular Diffusion in an Applied Magnetic Field".Ph.D.Dissert.U.B.C.(1983). 9. Maret,G.,Dransfeld, K., Physica B, 86 - 88, 1077 (1977).

Fig. 1a

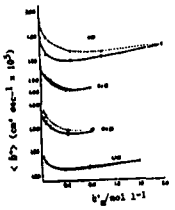


Fig. 1b

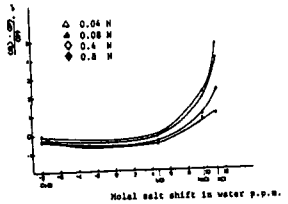
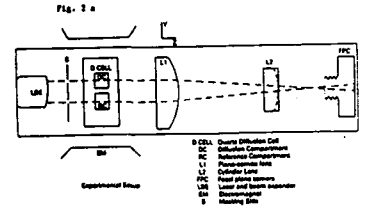


Fig. 1a
Arithmetic mean average integral diffusion coefficient and concentration plot at 25 °C for HCl–, KCl–, NaCl–, CsCl–, and LiCl–H_2O solutions at the ambient earth field (solid curve) and at the applied external transverse magnetic field (dashed curve) conditions.

Fig. 1b
The $D^a = [(\langle D_H^a \rangle - \langle D^a \rangle)/\langle D^a \rangle] \times 100$ plot against the molal salt shifts of alkali chlorides in water.

Fig. 2 a



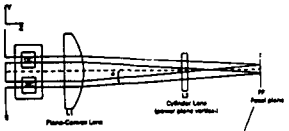


Fig. 2 b

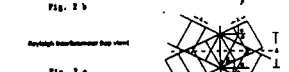


Fig. 2 c



Fig. 2 d



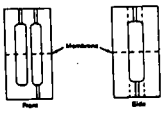


Fig. 3a

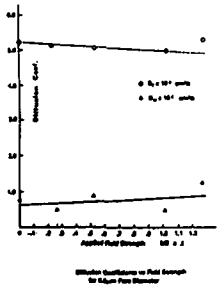
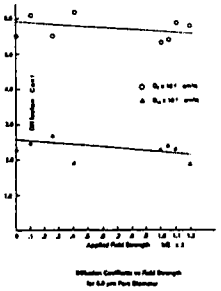


Fig. 3b



Abstract No. 673

MAGNETIC FIELD EFFECT ON MASS TRANSPORT

O. AABOUBI*, J.P. CHOPART*, J. DOUGLADE*,
C. GABRIELLI**, A. OLIVIER* and B. TRIBOLLET**

* Laboratoire d'Electrochimie et Chimie du Solide, U.F.R. Sciences Exactes et Naturelles, Moulin de la Housse, BP 347, 51062 Reims Cedex - FRANCE

** LP15 CNRS - Physique des Liquides et Electrochimie 4 place Jussieu, 75252 Paris Cedex 05 - FRANCE

The limiting diffusion current on a steady electrode is a function of the applied magnetic field <1,2>. In fact, the magnetic force induces a convection in the solution and thus enhances the mass transport process. In order to verify this description, we have developed a new impedance technique : the magnetohydrodynamic (MHD) impedance which consists on the frequency response analysis of the limiting diffusion current to a sinusoidal magnetic field perturbation of small amplitude <3>. Following our description, a sinusoidal magnetic field perturbation $\tilde{B}$ induces a sinusoidal velocity gradient $\tilde{\alpha}$ at the interface and then a limiting current response $\tilde{I}$:

$$\frac{\tilde{I}}{\tilde{B}} = \frac{I}{\tilde{\alpha}} \cdot \frac{\tilde{\alpha}}{\tilde{B}} \qquad (1)$$

If the transfer function $\tilde{\alpha}/\tilde{B}$ is supposed to be independent of the frequency in the experimental frequency range, the transfer function $\tilde{I}/\tilde{B}$ is directly proportional to $I/\tilde{\alpha}$. This transfer function is well-known for people using electrochemical methods for hydrodynamical studies <4,5> and in Bode coordinates it can be reduced by the usual dimensionless frequency $\omega d^{2/3}/\alpha^{2/3}D^{1/3}$ which corresponds to $\omega\delta^2/D$, where ω is the frequency modulation, d the microelectrode diameter, D the diffusion coefficient and δ the diffusion layer thickness.

EXPERIMENTAL

The electromagnet (Drusch EAM20G) has a gap width variable up to 10cm, and can generate a magnetic field up to 2T for a 2cm gap. The cylindrical pole pieces have a 20cm diameter and are constructed in order to obtain a particularly uniform magnetic field.

The experimental arrangement is described in <3> and in this symposium. For the MHD impedance measurements the current response and the voltage proportional to the magnetic field perturbation are amplified, filtered and then measured by means of a transfer function analyzer (Solartron 1250).

RESULTS

Steady state measurements :

The magnetic force $(1/\rho\ \vec{i} \wedge \vec{B})$ induces the velocity gradient at the wall. In first approximation the cause is proportional to the effect and the velocity gradient α is proportional to the magnetic force and then to B and c_∞ (i being proportional to c_∞). The limiting current on an electrode is proportional to $\alpha^{1/3}$<6> and can be written as :

$$I_\ell = kD^{2/3}c_\infty\alpha^{1/3} = k'D^{2/3}c_\infty^{4/3}B^{1/3} \qquad (2)$$

In figure 1, $|I_\ell|/c_\infty$ has been plotted versus $B^{1/3}c_\infty^{1/3}$ for various concentration and different magnetic field intensities. If the product $B^{1/3}c_\infty^{1/3}$ is high enough all data are reduced to one curve. At very low value of the product $B^{1/3}c_\infty^{1/3}$, the limiting current is constant until the effect of the forced convection due to B is larger than the natural convection. This curve explains the apparent disagreement between the data mentionned in the literature <1> concerning the variation of I versus B^γ : all exponent γ larger than 1/3 may correspond to the transition regime.

Impedance measurements :

. AC impedance : The AC impedance diagram in a Nyquist plot is similar to the diffusion impedance obtained on a microelectrode (figure 2). In low frequency range, the impedance corresponds to mass transport and all diagrams can be reduced by the usual dimensionless frequency $\omega d^{2/3}/\alpha^{2/3}D^{1/3}$ or $\omega\delta^2/D$. According to the steady state study, the dimensionless frequency is proportional to $\omega B^{-2/3}c_\infty^{-2/3}$.

. MHD impedance : In agreement with our analysis, the low frequency loop is similar to the transfer function $I/\tilde{\alpha}$ <4,5>. In figure 3, we have plotted, in a Nyquist diagram, the MHD impedance obtained on the anodic and on the cathodic plateau for the same magnetic field and for an equimolar redox species solution (ferri and ferrocyanide in the present case). In the low frequency range, the two low frequency loops are symetrical with respect to the origin, in agreement with the opposite sign of the corresponding steady state current but in the high frequency range the two diagrams are confused. Considering these two different behaviours in low and high frequency range, each one will be studied separately.

Low frequency range : In Bode coordinates, all diagrams are reduced by the dimensionless frequency $\omega B^{-2/3}c_\infty^{2/3}$ (figure 4). A theoretical transfer function $I/\tilde{\alpha}$ to an arbitrary dimensionless frequency is also plotted in dashed lines <5>. In the low frequency range the behaviours of $I/\tilde{\alpha}$ and of the MHD impedance are similar.

High frequency range : The high frequency loop is identical for the anodic and cathodic response and is a function of the frequency and is no more reducible by the dimensionless frequency.

Until now this behaviour, independent of the convection, is not fully understood, but the experimental data suggested an effect linked to the electric field.

REFERENCES

<1> Z. Fahidy
J. Appl. Electrochem., 13 (1983) 553.

<2> A. Olivier, J.P. Chopart, J. Douglade and C. Gabrielli
J. Electroanal. Chem., 217 (1987) 443.

<3> A. Olivier, J.P. Chopart, J. Douglade, C. Gabrielli and B. Tribollet
J. Electroanal. Chem., 227 (1987) 275.

<4> A. Ambari, C. Deslouis and B. Tribollet
Int. J. Heat Mass Tranfer, 29 (1986) 35.

<5> V. Ye Nakoryakov, A.P. Burdukov, O.N. Kashinsky and P.I. Geshev
"Electrodiffusion method of investigation into the local structure of turbulent flows"
Edited by V.G. Gasenko, Novosibirsk (1986).

<6> J. Newman
"Electrochemical Systems", Prentice Hall, Englewood Cliffs, NJ (1973).

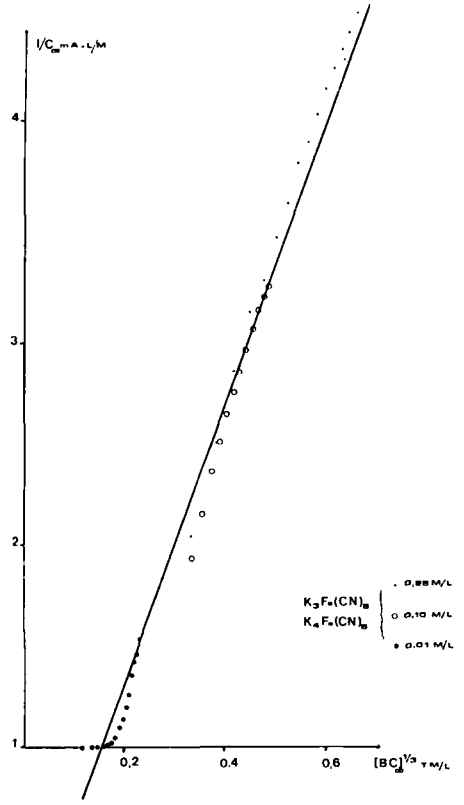


Figure 1 : Variation of the reduced limiting current I/C_∞ versus $(BC_\infty)^{1/3}$ for few concentrations and few values of the magnetic field.

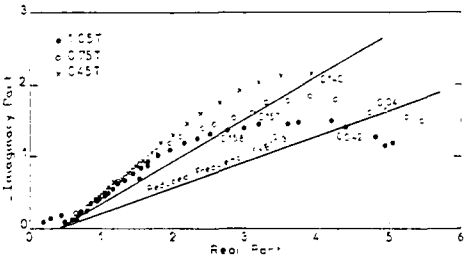


Figure 2 : Electrochemical impedance in Nyquist plot for three different magnetic field : (•) 1.05T, (o) 0.75T, (x) 0.45T.

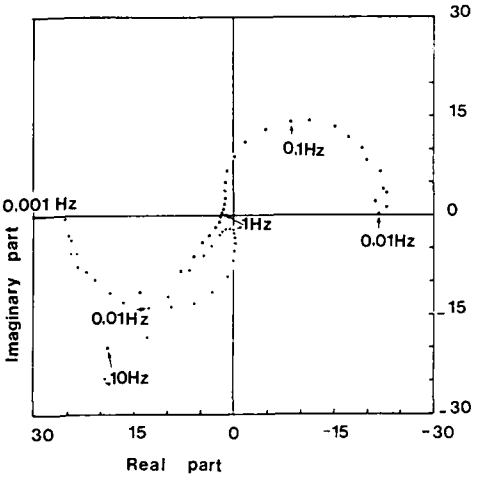


Figure 3 : Magnetohydrodynamic (MHD) impedance in Nyquist plot for a magnetic field of 0.45T and for the same concentration, in ferri and ferrocyanide (0.1M/l). (•) diagram corresponding to the cathodic current plateau, (o) diagram corresponding to the anodic current plateau.

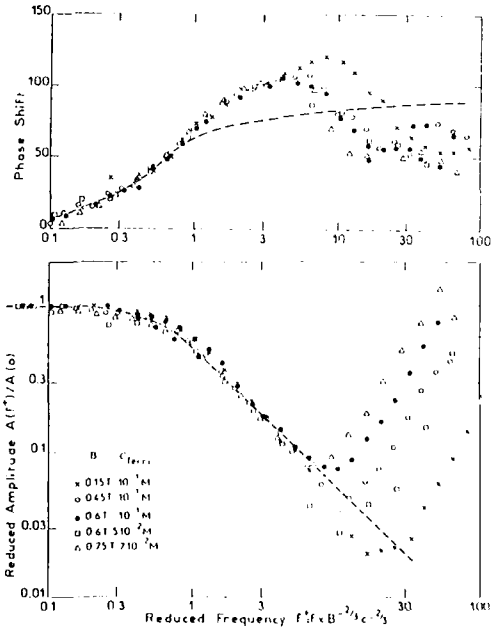


Figure 4 : Magnetohydrodynamic (MHD) impedance in Bode coordinates, reduced amplitude and phase shift are plotted versus the reduced frequency, $f^* = f\,B^{-2/3}\,c_\infty^{-2/3}$. In dash lines are plotted the theoretical EHD impedance of a microelectrode.

Abstract No. 674

INFLUENCE OF A MAGNETIC FIELD ON THE CORROSION OF IRON IN SULFURIC MEDIUM

J.P. CHOPART*, J. DOUGLADE*, C. GABRIELLI**, A. OLIVIER*, S. SADKI* and B. TRIBOLLET**

* Laboratoire d'Electrochimie et Chimie du Solide, UER Sciences, BP 347, 51062 REIMS Cédex, FRANCE.

** LP 15 du CNRS "Physique des Liquides et Electrochimie", Université P. & M. Curie, t. 22, 4 place Jussieu, 75252 PARIS Cédex 05, FRANCE.

It has been shown that the electrochemical elementary processes react under a magnetic field induction. Numerous investigations have been carried out on the influence of an applied magnetic field on mass transport (1 and ref. therein) and in particular on the limiting diffusion current. However concerning the electrode-electrolyte interfaces of which the overall reaction rates are not limited by mass transport very few informations can be found in the literature. It seems that the Kelly's paper (2) published in 1977 about the corrosion of titanium in sulfuric acid medium is the major study on this topic. In this case when the electrolyte is flowing in the cell he found that all potential-dependent electrochemical processes are subject to the magnetic field effect.

In this paper some preliminary results about corrosion of an iron electrode immersed in a sulfuric medium will be given. Current-voltage curves, electrochemical impedances and a voltage-magnetic field transfer function will be investigated under magnetic field influence.

The electrode is a 5 mm diameter iron disc facing upwards in order to eliminate the hydrogen bubbles when it is polarized close to the corrosion potential. The experimental arrangement is depicted in Fig. 1. Thanks to a transfer function analyzer (Solartron-Schlumberger) the classical impedance $(\partial E/\partial I)_B$, and the current or voltage-magnetic field transfer function, $(\partial I/\partial B)_E$ or $(\partial E/\partial B)_I$ can be measured by modulating either the voltage or the magnetic field by perturbing the current of the electromagnet power supply (3).

In Fig. 2 are given the current-voltage curves of the iron electrode in sulfuric medium for various values of the magnetic induction. The enhancement of the dissolution current from the limiting current plateau observed at B = 0 could be due to the acceleration of the mass transport of the reactive species. However an effect can be also detected in the low current active range (e.g. at 460 mV the current changes from 0.86 mA to 0.65 mA when B changes from 0 to 1.2 T). The alteration of the current distribution is demonstrated by the scheme of the dissolution morphology observed under B influence given in Fig. 3.

The impedance of the iron/sulfuric acid interface has been measured under the influence of the magnetic field. Fig. 4 demonstrates an effect of B on the interfacial impedance within a current range where it is usually assumed that there is no control of the current by the diffusion process. It has to be noticed that the more the current is low the more important is the effect of B. Hence it seems that the magnetic induction has an effect on the kinetics parameters (reaction rates, Tafel coefficients ...) and on the double layer capacity.

This is supported by the measurement of the current-magnetic field transfer function obtained from the analysis of the response of the current in potentiostatic regime to a magnetic field sinusoidal perturbation (Fig. 5). The characteristic shape of this transfer function found when the mass transport is the rate limiting step is not found for the corrosion of iron under magnetic field influence at least in the low current active range. The interpretation of this new transfer function is in progess in this case.

References

(1) A. OLIVIER, J.P. CHOPART, J. DOUGLADE and C. GABRIELLI
J. Electroanal. Chem., 217 (1987) 443.

(2) E.J. KELLY
J. Electrochem. Soc., 124 (1977) 987.

(3) A. OLIVIER, J.P. CHOPART, J. DOUGLADE, C. GABRIELLI and B. TRIBOLLET
J. Electroanal. Chem., 277 (1987) 275.

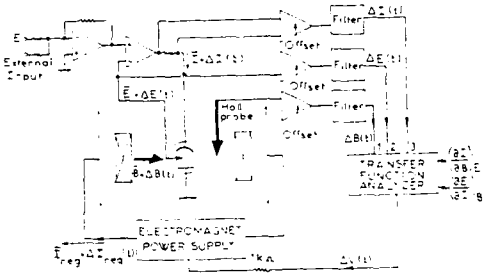


Fig. 1 : Experimental arrangement for the measurement of the electrochemical impedance under magnetic field influence and of the current-magnetic field transfer function.

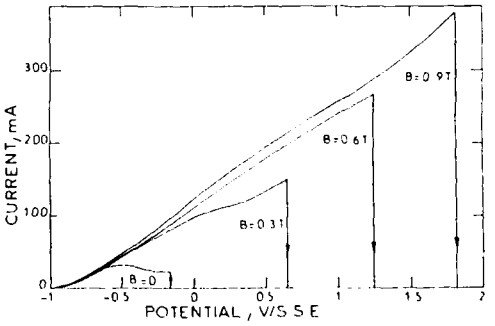


Fig. 2 : Current-voltage curves of a iron disc in H_2SO_4 2M under the influence of a magnetic field.

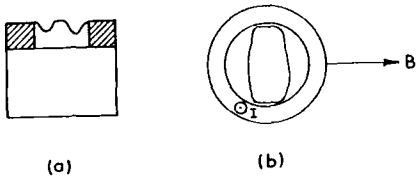


Fig. 3 : Scheme of the dissolution morphology in the active range. (a) cross view
(b) top view.

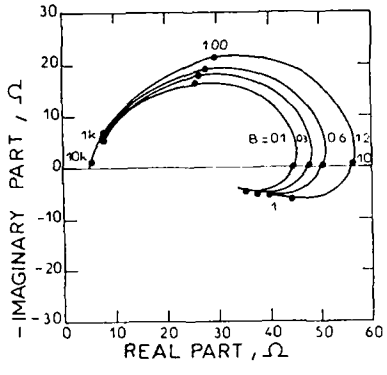


Fig. 4 : Electrochemical impedance measured for B = 0 ; 0.3 ; 0.6 ; 1.2 T at 460 mV (I = 0.86 ; 0.8 ; 0.74 ; 0.65 mA) in H_2SO_4 2N.

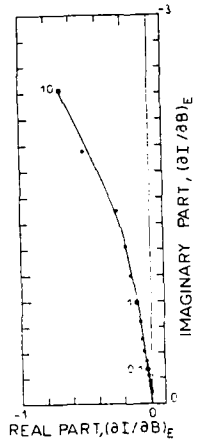


Fig. 5 : Current-magnetic field transfer function measured at 450 mV (I = 1.24 mA) for B = 0.3 T.

Abstract No. 675

Magnetic field effect on the electrochemical reduction of aquo Zn^{2+} in the presence of paramagnetic ion

R.N. O'Brien

Department of Chemistry,
University of Victoria,
Victoria V8W2 Y2,
Canada

and

K.S.V. Santhanam

Tata Institute of Fundamental Research,
Bombay 400005,
India

The electrochemical reduction of aquo Zn^{2+} has been studied galvanostatically at current densities ranging from 0.10 mA cm^{-2} to 7.0 mA cm^{-2} by using the cell $Zn/ZnSO_4/Zn$, and operating it at its natural pH, under the influence ofthe imposed magnetic field strengths ranging from 0.09 to 0.50 T in the V-position, C/A-position and A/C-position. The convective contours are visibly defined in the V- and A/C-positions. The extent of convection in the C/A-position is negligible in the presence of the applied magnetic field.

Previous papers (1) reported the observation and analysis of the magnetic field effect on the electrochemical cell, $Cu/CuSO_4/Cu$ with the plane parallel electrodes oriented in the vertical configuration. By the use of multiple beam laser interferometry a series of distorted fringes in the V-position were generated at the electrode/solution interface upon application of an external magnetic field. This effect was also observed when the anode was placed over the cathode (A/C) configuration; in this configuration the magnetic field operated to reduce the apparent convection. The fluid density differences in the different regions of the cell caused by the electrolysis produces the effect. The hydrodynamic effect would be expected to be minimal when the cell electrodes are oriented in the cathode over anode (C/A) configuration. A reduced mass transport effect was in fact observed which was postulated as arising from the characteristics of a paramagnetic fluid. With a view to obtaining further support to this postulate, we investigated the $Zn/ZnSO_4/Zn$ system (Zn^{2+} is d^{10}) by introducing the paramagnetic ions into the medium; Mn^{2+} (d^5) and Cr^{3+} (d^2) were selected as they can satisfy thermodynamic considerations. A mixture of electrolyte with the composition of 0.1 M $ZnSO_4$ and 0.1 M $MnCl_2$ or 0.1 M $ZnSO_4$ and 0.01 M $CrCl_3$ in the above cell produces significant deviations in the diffusion layer relaxation and in the development of concentration-time profiles, which are presented in this paper supporting the paramagnetic fluid postulate.

The fluid velocities in the reduction of Zn^{2+} under the imposed magnetic field are estimated at 1 cm/s to 7 cm/s. The diffusion layer relaxation was followed by the fringe shift, after the electrolysis had been terminated. The relaxation mechanism appears to be as low rotational and translational movement of the paramagnetic fluid in the C/A position.

References

R.N. O'Brien and K.S.V. Santhanam, J. Electrochem. Soc., 129, 1266 (1982).

R.N. O'Brien and K.S.V. Santhanam, Electrochimica Aca, 32, 1679 (1987).

Abstract No. 676

MAGNETIC FIELD EFFECTS IN THE BULK OF AN ELECTROLYTIC CELL

Denise LAFORGUE-KANTZER
University of Reims Champagne Ardenne
BP 347 - 51062 REIMS Cédex FRANCE

Our first aim, twenty seven years ago, was to test a hypothesis (1) on the protonic conduction. If it was true, an effect, similar to the "Hall effect" might appear in acidic solutions and the expected magnitude for the "Hall voltage" V_H should be in the range of 10^4-10^5 times the calculated value from the mobilities of tables. Effectively the value measured, in the presence of a permanent magnetic field perpendicular to a direct current I, accord with the expected value. V_H increases linearly with the IB value (B magnetic field strenght), is in inverse proportion to the acidic concentration and to the thickeness (few millimeters) of the parallelepipedic cell.

Then, galvanomagnetic transverse and thermomagnetic transverse effects as well a "concentration transverse effect" (i.e. difference of the *ionic concentrations* measured between the two sides of the cell) have been investigated by several coworkers (2) on acids, bases, and salts, in aqueous or alcoholic solution, and on molten salts. The results are coherent and in accord with those of other authors.

Theoretical microscopic approachs have been made, using

1° the classical statistical mechanics (3) (after H.L. FRIEDMAN)
2° the kinetic theory (4) (after P. MERGAULT and J. PAGES).

The microscopic models of electrolyte are different, however the "Hall constant" is $R_H = [\sum n_i e_i \mu_i A_i^2] / [\sum n_i e_i \mu_i]^2$ (n_i, e_i, μ_i being respectively number, charge and mobility of the i ion). From the first approach $A_i = \exp(\Delta\varepsilon / KT)$, $\Delta\varepsilon$ depending on the viscosity ; from the second $A_i = \tau_i$ is a function correlated with the kinetic energy of the i ion. Calculated τ_i are on the range of 10^4. The kinetic theory permit to calculate the terms of the tensorial transport *coefficients as function of* B and τ_i.

At the first approximation, theoretical and experimental results are in good accord, although the electrolyte is supposed quasi-infinite diluted, quiet and homogeneous. Nevertheless several experimental features remain unexplained by the theories. Namely :

- By the measurement of the "Hall voltage"

. Almost stable values occur *after transient during* several minutes (or hours) and many measurements are necessary to determine the most probable value.

. The measured V_H increasing linearly as the product IB *increase arises a maximum value, then decreases* and can change of sign.

. For the low speed of ions, it can not reverse with the orientation of the magnetic field and not be a linear *function of* B *("anormal effect")*.

- Aspect of the cell

In the aim to understand this phenomena, the bulk of the electrolyte (solution or molten salts) has been observed, photographed and filmed : or coloured ions was introduced in the cell, or a coloured ionic electrodic product can diffuse. When coloured ions progress from the botton of a vertical cell and from a zone outside the magnetic field, the horizontal front of diffusion slopes immediatly in the magnetic field and stops during several minutes before they go up slowly along one wall of the cell.

The sloped front conforms with the direction of the Lorentz force.

At the separation surface the coloured ions concentration changes radically to a value close to zero.

When electrodic ionic product is heavier as the solution, it descends down a wall of the cell and tends to go up the other wall depending of the direction of the Lorentz force which is now applied to ascending charge carriers. The movement leaves a central colourless zone.

Several authors describe hydrodynamic movements in magneto-electrolyse cells.

- Temperature map in the cell

Very small gradients of temperature ($\Delta T \sim 0.01$°C) was observed *in the bulk* of an electrolytic cell ($Cu/CuSO_4/Cu$) set in a heat-insulating box. In a point of the electrolyte the temperature vary of $+\Delta T$ according to the sign of B or I. The sign of ΔT is not the same in all the points. The effects are reproducible. A tridimensional map of temperature has been drawn. *The small inhomogeneity of* temperature induces change in the natural convection, but no motion was observed.

- Chemical equilibrium

Chemical equilibrium can be displaced in presence of magnetic field. For example, in the case of H_3PO_4, when the magnetic field is first established, the measured "Hall voltage" increases, then decreases showing two plateaux before the final stable value : it seems that the electromagnetic energy permits two dissociations.

- A way for explanation

In some reviewed cases, hydrodynamic motion is certainly for a part : From the first equation of dynamics for a homogeneous system without chemical reaction it appears that, if the liquid is initially at the equilibrium ($v_0 = 0$), before the input of magnetic (or electric) field, a speed would be necessary initiated when B (or E) is applied and the time necessary for a stable measurement is the time necessary to establish a new equilibrium state. That can explain qualitatively the transient.

We explain separately (qualitatively or quantitatively) each reviewed point.

But for a general theory, it is necessary to consider the energetic whole balance and also to take into account the *results of the microscopic theories*. The way of the thermodynamics of the irreversible processes appears the best way. R. HAASE (5) has studied "the matter in electromagnetic field" but, unfortunately, his hypotheses are not all convenient for the present case and we try to adapt the theory to our problem.

References

1. G. PERRAULT and J. BRENET, C.R. Ac. Sci. Paris 252, 104 (1961)
D. LAFORGUE-KANTZER, Electroch. Acta 12, 585 (1965)

2. M. AMMAR, D. GUERIN-OLLER, L. LECLERCQ, E. MULLER, C. NICOLLIN, A. OLIVIER, A. PREUDHOMME, TRAN CONG K., E. TRONEL-PEYROZ

3. TRAN CONG K. Thesis - Lyon (1969)
TRAN CONG K., A. LAFORGUE, D. LAFORGUE-KANTZER, Electroch. Acta 17, 143 (1972) ; ibid 17, 151 (1972) ; and ref into

4. E. TRONEL-PEYROZ Thesis - Reims (1978)
A. OLIVIER Thesis - Reims (1979)
E. TRONEL-PEYROZ and A. OLIVIER, J. Chim. Phys. 77, 427 (1980) and ref. into

5. R. HAASE, Thermodynamik der irreversiblen Prozesse Dr Dietrich Steinkopff Verlag - Darmstadt (1963)

Abstract No. 677

Hall Effect in dilute electrolyte 1-1 solutions

P.Gérard, R.Gérard, M.Meton, and E.J.Picard
Laboratoire de Recherche sur l'Effet Hall, Université Pierre-et-Marie-Curie, U.E.R. Application de la Physique
Tour 46, 4, place Jussieu, 75252 Paris Cedex 05, France

Introduction.

In Hall effect experiments one measures the transverse e.m.f. which appears when an isotropic conductor is subjected to crossed electric and magnetic fields. The Hall voltage V is $V=RIB/d\sqrt{2}$, (1), where I is the alternating r.m.s. longitudinal current, B the perpendicular alternating r.m.s. field, d the thickness of the conductor and R the so-called Hall coefficient.

Hall effect measurements in electrolyte 1-1 dilute solutions suggested([1]) that one has to postulate the existence of two kinds of ionic mobilities: the ordinary electric (longitudinal) mobility $u_\pm$ and a transverse magnetic mobility $v_\pm$. We then define the Hall ionic number $h_\pm = v_\pm/u_\pm$. The Hall number of the solution is $h = t_+^2 h_+ - t_-^2 h_- = Rne = (u_+v_+ - u_-v_-)/(u_+ + u_-)^2$ (2); n is the density of the charge carriers; e the electronic charge; $t_\pm$ the cation or anion transport number. We may express the Hall number h in terms of the ionic equivalent conductivities λ : $h = (\lambda_+^2 h_+ - \lambda_-^2 h_-)/(\lambda_+ + \lambda_-)^2$. (3).

Experimental aspects.

The experiments have been carried with alternating I: two frequencies have been used: 243.75 Hz and 487.5 Hz, which give, with alternating B (75 Hz) four Hall voltage frequencies 168.75 Hz, 318.75, 412.50, 562.50 Hz respectively. The blockdiagram of the experimental device is given below.

We have used parallelepiped-shaped cells with platinum electrodes, the electrolyte specimen dimensions being: width: 8mm; length: 3.5cm; thickness: 0.2mm, 0.79mm (in pure silica) and 8mm (plexiglass) respectively.

The Hall cell impedances lie between a few tens and a few hundreds of kΩ and the Hall voltages between a few nV (around ten) and around 200 nV.

Measurement results.

The Hall numbers are directly derived from the Hall voltage measurements (1,2). Since h is a linear combination of h_+ and h_-, (3), for a 1-1 solution, one cannot calculate the Hall numbers h_+ and h_- (one equation for two unknowns). In the same way, if one measures the Hall number h for two salts X^+A^- and X^+B^-, whatever may be the cation X^+, one obtains two equations for three unknowns. It is thus necessary to assume a value for one Hall ionic number.

Salts in water solvant: 30 salts. (Table 1)

We had assumed first ([1]) that $h(BPh_4^-)=1$. (Col. 1) Later on ([2]) we assumed $h(Cs^+)=0.71$. (2nd column)

To take into account recent theories of the Hall effect in electrolyte solutions which predict an $h=0.75$ for slip boundary conditions for any 1-1 salt in dipolar solvant, we may assume $h(Cs^+)=0.75$ (column 3) or $h(BPh_4^-)=0.75$ (column 4).

Salts in methanol solvant: 22 salts (table 2)

Salts in acetonitrile: 18 salts (table 3).

Theoretical aspects-Interpretation of the results.

The ionic Hall numbers $h_\pm$ may be written $h_\pm = 1+\Delta h_\pm$ or $h = 1+\Delta h$, without the indices $\pm$, where Δh gives the influence of the solvant. Most of our results show that $h<1$ and this may be explained by supposing that the Lorentz force acting on an ion in a solvant is modified (diminished) by the action of the solvant. So one may write : $F = q(E + h(v \times B))$ where q is the charge of the ion, v its velocity. Three recent theories on the Hall effect in electrolyte 1-1 solutions ([3],[4],[5]) lead to the simple form: $h = -C(\zeta)(\varepsilon-1)/\varepsilon$, where ε is the static dielectric constant of the solvant, and $C(\zeta)$ is a numerical coefficient which depends only on the hydrodynamic slip parameter, regardless of ionic charge, size or solvent viscosity. The Stokes friction coefficient is: $\zeta = 6\pi\eta(1-\zeta)\cdot R$, where η is the fluid viscosity, R the ion radius. The Hubbard-Wolynes theory leads to the value h=0.71, the Kroh-Felderhof and the Sung-Friedman one to h=0.75 for perfect slip ($\zeta = 1/3$). ([6]).

Depending on the Hall ionic number value arbitrarily choosen to calculate the set of ionic number values one may prudently conclude that:

for water the theories doesn't seem to fit, since, if the h values for the cations are near to 0.75 (in the limits of errors), the values for the anions are definitely lower than 0.75, whatever is the assumption that has been made.

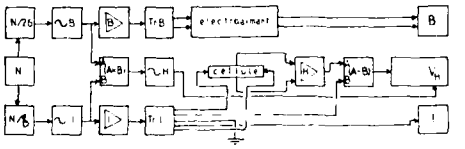
for methanol: the assumption which seems the best is $h(BPh_4^-)=0.75$; $h(Cs^+)=0.75$ seems acceptable too.

for acetonitrile: one observes a regular growth for cations and anions for $h(BPh_4^-)=0.75$, and one may notice too that the difference between the cation and anion values is much less marked than in water.

As a general conclusion, it seems that the structural effects which are not taken into account in a continuum model play an important role. Anyway, our results are not accurate enough, for the present, to go beyond in their interpretation, and particularly, they don't afford one to choose between the theories in presence.

To end this extended abstract, we would like to give a result of recent measurements of the Hall effect of acids in water, which are not yet published: the $h(H_3O^+)$ value for HCl solutions is $h(H_3O^+)=0.10$ whatever is the assumption that has been retained, confirming the very peculiar behaviour of proton in water.

[1] M.METON, P.GERARD, Chem.Phys.Letters, 44, number 3, 1976, p.582-585.
[2] R.GERARD, P.GERARD, M.METON, E.J.PICARD, C.R.Acad.Sc. Paris, t.300, Série II, n°11, 1985.
R.GERARD, P.GERARD, M.METON, E.J.PICARD, C.R.Acad.Sc. Paris, t.297 (12 décembre 1983).
[3] J.B.HUBBARD and P.WOLYNES, J.Chem.Phys.75, 3051 (1981).
[4] H.J.KROH and B.U.FELDERHOF, Mol.Phys.1987, Vol.60, N°5, 1093-1105.
[5] W.SUNG and H.L.FRIEDMAN, J.Chem.Phys.87(1), 1July 1987.
[6] H.J.KROH and B.U.FELDERHOF, preprint, september 1987



N: Quartz oscillator: square waves 1950 Hz.
N/26 and N/8 : frequency dividers by 26 and 8
B and I: band-pass filters
(AxB): multiplier
B and I : power amplifiers
Tr.B Tr.I: transformers.
H : low noise preamplifier.
(A-B) : subtractor
B and I: digital voltmeters
V_H: lock-in amplifier

	1	2	3	4
Li^+	0.86	0.87	1.03	0.80
Na^+	0.78	0.79	0.88	0.74
K^+	0.71	0.71	0.75	0.69
Cs^+	0.71	*0.71*	*0.75*	0.69
Me_4N^+	0.78	0.79	0.91	0.73
Et_4N^+	0.89	0.91	1.14	0.80
Bu_4N^+	1.21	1.27	1.89	0.95
F^-	0.52	0.53	0.61	0.49
Cl^-	0.55	0.55	0.59	0.49
Br^-	0.57	0.57	0.61	0.55
I^-	0.58	0.59	0.62	0.57
ClO_4^-	0.61	0.61	0.67	0.59
BPh_4^-	*1.00*	1.05	1.64	*0.75*

Table 1 :ionic Hall numbers in water
0.71:assumed value for the ionic Hall numbers calculation.

	1	2	3	4
Li^+	1.03	0.95	1.05	0.82
Na^+	0.89	0.82	0.90	0.72
K^+	0.75	0.70	0.76	0.63
Cs^+	0.75	*0.71*	*0.75*	0.65
Me_4N^+	0.80	0.78	0.81	0.73
Et_4N^+	0.85	0.82	0.86	0.76
Bu_4N^+	0.95	0.87	0.97	0.83
Cl^-	0.77	0.72	0.78	0.65
Br^-	0.76	0.72	0.77	0.65
I^-	0.71	0.68	0.72	0.63
ClO_4^-	0.70	0.67	0.70	0.63
BPh_4^-	*1.00*	0.90	1.01	*0.75*

Table 2 :ionic Hall numbers in methanol

	1	2	3	4
Li^+	0.68	0.71	0.77	0.53
Na^+	0.66	0.69	0.74	0.54
K^+	0.66	0.69	0.73	0.56
Cs^+	0.69	*0.71*	*0.75*	0.59
Me_4N^+	0.70	0.72	0.75	0.62
Et_4N^+	0.80	0.82	0.86	0.70
Bu_4N^+	0.97	1.02	1.10	0.78
Br^-	0.63	0.65	0.68	0.56
I^-	0.67	0.69	0.71	0.60
ClO_4^-	0.70	0.72	0.75	0.64
BPh_4^-	*1.00*	1.06	1.16	*0.75*

Table 3 :ionic Hall numbers in acetonitrile

Abstract No. 678

THE ENHANCING EFFECT OF MAGNETIC FIELDS ON CONVECTIVE FLOW PATTERNS IN AN ELECTROLYTE VIA FLOW VISUALIZATION

Augustina Lau* and Thomas Z. Fahidy
Department of Chemical Engineering
University of Waterloo
Waterloo, Ontario N2L 3G1 CANADA

The study of free convection flow patterns generated at complex surfaces in an electrolyte, and in the presence of magnetic fields via flow visualization indicates that strong vortices, bifurcating flow and highly specific propagation profiles can be created [1]. Figure 1 shows a typical convective flow movement generated at a sphere in the presence of a uniform horizontal magnetic field of 260 mT flux density. At the onset of electrolysis, two branches of flow are generated at the top and bottom of the spherical cathode, both whirling around it. At the same time, a separate branch is formed at the top of the cathode which propagates diagonally downwards to the centre of the cell and finally splits into smaller branches swirling away. Such records obtained for a number of characteristic cathode shapes depict clearly the enhancing effect of magnetic fields on convective flow patterns in relation to the shape of the solid/liquid interface.

The magnetic field vector behaves very much like the vorticity vector in the theory of fluid mechanics [2]. It has been shown [3,4] that the magnetohydrodynamic(MHD)body force $\underline{F}$, a measure on interaction between the current density $\underline{J}$ and the magnetic flux density $\underline{B}$, is a predominant factor in determining flow behaviour. Figure 2 shows typical initial MHD body force-density distribution curves for a spherical cathode with an imposed uniform horizontal magnetic flux density of 120 mT. Since initial inhomogeneities become more pronounced upon convective flow propagation, such curves indicate sufficiently the combined effect of cathode shape and magnetic field strength: due to initially present nonuniformities, highly specific propagation patterns are generated and locally strong anisotropies result in strong local turbulence. These results may be potentially useful for the design of electrolyzers, mixers etc. with predetermined flow propagation patterns.

Acknowledgment. This project has been supported by an Ontario Graduate Scholarship, and by the Natural Sciences and Engineering Research Council of Canada.

REFERENCES

1. Lau, A.:M.A.Sc. thesis, Univ. of Waterloo (1987)

2. Shercliff, J.A.:A Textbook of Magnetohydrodyhamics, Pergamon Press (U.K) (1965).

3. Fahidy, T.Z.:Electrochim. Acta 18, 607-614 (1973)

4. Gu, Z.H. and Fahidy, T.Z.:Proc. Rheinhardt Schumann Intern. Symp. Innov. Techn. React. Des. Extr. Met. (eds. D.R. Gaskell, J.P. Hager, J.E. Hoffman, P.J. Mackey), The Metallurg. Soc. USA, 711-725 (1986).

*Atomic Energy of Canada Ltd. CANDU Operations, Mississauga, Ontario



Figure 1. Convective flow generated at a spherical cathode in the presence of a horizontal magnetic field of 260 mT flux density.

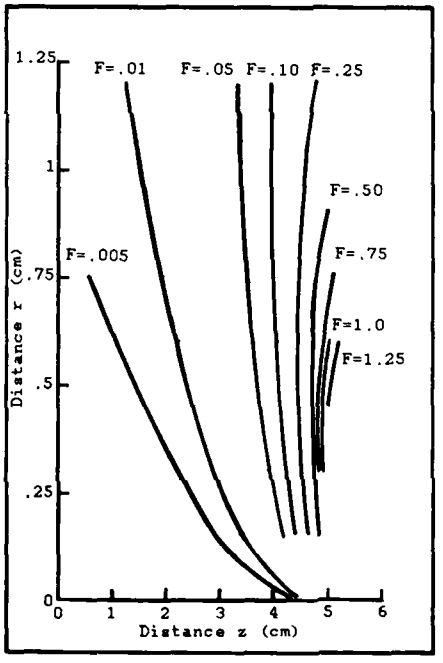


Figure 2. Initial distribution of the MHD body force density around a spherical cathode $r^2 = x^2 + y^2$; x and y are tangential coordinates along the opposite plane electrode. r = normal coordinate measured from the opposite plane electrode.

Abstract No. 679

THE EFFECT OF CHLORIDE ION ON ELECTROLYTIC CODEPOSITION OF COPPER AND GAMMA ALUMINA IN A MAGNETIC FIELD

F. Brace and J. Dash

Department of Physics
Portland State University
P.O. Box 751
Portland, Oregon 97207

If the conductivity of electrically neutral particles differs from that of an electrolyte, then there is a net force on the neutral particles during electrolysis in a magnetic field (1). It appears that this net force makes it possible to codeposit gamma alumina particles during electrolysis in a magnetic field, whereas the same particles may not deposit without the presence of a magnetic field. This research shows that codeposition of copper and gamma alumina in a magnetic field is possible from an electrolyte containing up to 5 x 10^4 ppm Cl^-, whereas previous work showed that gamma alumina could not be deposited at Cl^- concentrations above about 5 ppm (2).

The codeposition of copper and alumina was carried out in an electrolytic cell composed of two copper electrodes, Fig. 1. The active area on each electrode was 1 cm^2 on the lower side. The remainder was insulated. The electrolyte contained 30 ml of 0.5 M H_2SO_2 and 0.5 M $CuSO_4.5H_2O$. This was altered by the addition of varying amounts of chloride ion. Four ml of 0.05 μm gamma alumina (Buhler Ltd. polishing alumina) also was added to the electrolyte. This powder settled to the cell bottom. A magnetic field of 8 kG normal to the 0.1 A cell current caused the alumina to rise from the cell bottom and disperse in the electrolyte (3). After plating for 10 minutes, the cathode deposits were cleaned ultrasonically in methanol. The morphology was determined with a scanning electron microscope (SEM), the composition was determined with an energy dispersive spectrometer (EDS), and the crystalline forms present were determined by x-ray diffraction (XRD).

Fig. 2 shows the morphology of the deposit made with 720 ppm Cl^- in the electrolyte. The angular particles are CuCl. The material in between these particles contains about 2 at. percent gamma alumina.

Previously it was suggested that gamma alumina contains residual Cl^- from the manufacturing process (2). This is thought to be adsorbed on the alumina, thus producing anions. We suggest that the net magnetic force on alumina particles may strip adsorbed Cl^- from the surface and permit these particles to deposit on the cathode.

References:

1. A. Kolin, Science 117, 134 (1953).

2. G. R. Lakshminarayanan et al., Plat. Surf. Finish 63 (4), 38 (1976).

3. J. Dash et al., Extended Abst. ECS, 168th meeting, 1985, p. 327.

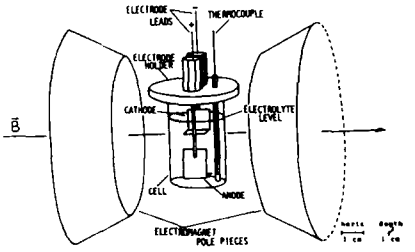


Fig. 1. Apparatus for codeposition of alumina and copper in a magnetic field. The electrodes were insulated except for 1 cm^2 on the bottom of each.



Fig. 2. Deposit made from electrolyte containing 720 ppm Cl^-. EDS showed that the angular crystals are CuCl and that the spot opposite the arrow contains about 2 at. percent alumina.

Abstract No. 680

ELECTRODEPOSITION OF Ni-Fe IN VERY HIGH MAGNETIC FIELDS

J. Dash, Physics Department
Portland State University,
Portland, OR 97207
and
L. T. Romankiw, IBM Thomas J. Watson
Research Center, P.O. Box 218,
Yorktown Heights, NY 10598

Ni-Fe alloys were deposited from an aqueous electrolyte of simple salts of Ni and Fe and other chemicals, as described in U.S. Patent 4,102,756. The cathodes were 1 cm diameter Pt foils attached to a rotating disc electrode in a manner similar to that described by Horkans (1). The anode was a 3 cm diameter Pt foil with Ni mesh spotwelded to the surface which faced the cathode during plating experiments. For each experiment 40 ml of fresh plating solution was placed into a glass cell of 4 cm O.D., in which the anode was on the bottom. This cell was positioned on a stand in a 5 cm gap between 15 cm diameter polepieces of an LDJ Model 9500 electromagnet. The rotating disc electrode with attached Pt cathode was lowered into the cell to a position about 3.5 cm vertically above the anode. With this arrangement it was possible during plating to: (a) rotate the cathode, (b) apply a magnetic field while rotating the cathode, or (c) apply a magnetic field to a stationary cathode. Experiments were performed (a) with the cathode rotating at 200 RPM and no applied magnetic field, (b) with the cathode rotating at 200 RPM and an applied magnetic field of 5kG, and (c) with a stationary cathode and an applied magnetic field at some fixed value up to 19.6kG. The plating time for each experiment was 30 minutes with a constant current of 4.7 ma. Plating was done at room temperature (about 25°C).

After plating, the deposits were analyzed for Ni and Fe by x-ray fluorescence with a Tracor-Northern Spectrace 5000, using 25 kv incident x-rays. The current efficiency (CE) was determined from the deposit weight and composition. X-ray diffraction data were taken from each specimen with a Siemens D-50C x-ray generator and diffractometer which was automated to a computer. A Cu x-ray tube was operated at 40 kv and 30 ma to produce a beam which was monochromated with a graphite monochromator. The data were processed using programs written by A. Segmuller. The morphology of the deposits was examined with a scanning electron microscope (SEM) equipped with an energy dispersive spectrometer (EDS) for microchemical analysis.

Differences in diffraction line widths were evident from the x-ray data. In order to determine whether these differences were caused by differences in grain size or by differences in internal stress, the deposits were annealed for two hours at 250°C in inert atmosphere. This anneal relieves internal stress but does not change deposit grain size. After this anneal, the deposits were again examined by x-ray diffraction.

The full width at half maximum (FWHM) of the Ni-Fe 200 diffraction line versus atomic percent Ni in the deposit is plotted in Fig. 1 for all of the plating experimental conditions, before and after the stress relief anneal. The FWHM value at the tail of each arrow is the result before and the value at each arrowhead is after the stress relief anneal.

These data show that a rotating cathode with or without an applied magnetic field gave relatively stress-free deposits of the highest Fe content and smallest crystal size. Deposits made without cathode rotation but with magnetic fields applied during plating have higher Ni content and larger crystal size. The deposits plated at 5 kG without cathode rotation had the highest Ni content, the highest internal stress, and crystal sizes about 1.5 times as large as those plated with cathode rotation.

The CE was about 85% for all deposits. The remainder of the current produced H_2. Sites where H_2 polarized the cathodes were revealed by SEM and EDS.

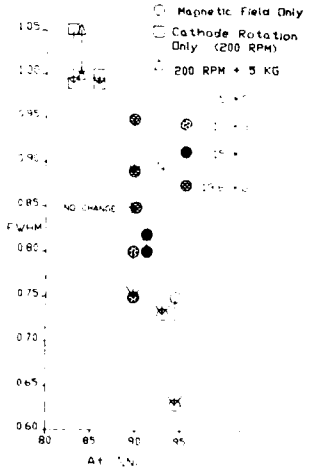


Fig. 1. Full width at half maximum of 200 in Ni-Fe alloys for various plating conditions. Values at arrow tails before and at arrow heads after annealing.

Reference: J. Horkans, J. Electrochem. Soc. 128,45 (1981).

Acknowledgment: The x-ray data were taken by J. Karasinski of IBM T. J. Watson Research Center.

Abstract No. 691

MAGNETIC FIELD EFFECT ON ELECTRODEPOSITION OF METALS.

J.P. CHOPART*, J. DOUGLADE*, P. FRICOTEAUX*
C. GABRIELLI**, A. OLIVIER* and B. TRIBOLLET**

* Laboratoire d'Electrochimie et Chimie du Solide
U.F.R. Sciences - BP 347 - 51062 REIMS Cédex FRANCE

**L.P. 15 du CNRS Physique des liquides et Electrochimie
Université P. et M. Curie, t.22, 4 place Jussieu
75252 PARIS Cédex 05 FRANCE

For reversible redox systems, an increase of the limiting currents by a magnetic field is now well known (1-2 and ref. therein). We have undertaken a study of electrodepositions of copper, zinc and nickel because such systems allow investigations of magnetic field effects on charge transfer so we present there the experimental results which were obtained for the whole current-voltage cathodic curves and we discuss the influence of a constant magnetic induction on both mass transport and charge transfer for metallic electrodeposition.

Experimental

At first, the working electrode which is in vitreous carbon (Ø 2 mm) is recovered by the studied metal. The thermostated cell is inserted into the electromagnetic gap (DRUSCH E.A.M. 20 G or L.M.M. 85) so the constant and continuous, horizontal magnetic induction lines are parallel to the working electrode surface. Solutions of ZnO + KOH, $CuSO_4$ + H_2SO_4 and Watts baths are used for Zn, Cu and Ni deposits. The potentiel of the three electrodes cell is controlled by means of a conventional potentiostat (SOLARTRON 1286) and measurements are carried on a transfer function analyzer (SOLARTRON 1250) **Fig.1.**

Results

1° Mass transport : For Cu and Zn systems, the experimental results show an important increase of the limiting currents when magnetic field B is applied in close agreement with the literature (1-6) **Fig. 2,3.** Whatever is the temperature in every case, the limiting current I_L is proportional to $B^{1/3}$. For the copper system we notice that the higher the concentration of electroactive specie C and the magnetic field, the better the proportion which I_L bears to $C^{4/3}B^{1/3}$.

2° Tafel potential region : The influences of a magnetic field on deposition and dissolution overvoltages in the Tafel potential region has been very rarely investigated (6) although it is espacially interesting. So we study the deposition of copper and nickel in the region where mass transport is not the rate limiting step. In this case, for the same overpotential the current is different in presence and in absence of magnetic field. As it is evident on the **Fig.4** for the copper the stationnaray current increases with the value of the field. This result is also noticed with the A.C. impedance measurements shown in Nyquist plot **Fig.5.** The Tafel's area is more extensive with magnetic field.

As it has been shown without magnetic field (7), the product of the charge transfer resistance by the current is constant but does not seem different with this field **Fig.6.**

If the results concerning the mass transport are those that waited, those concerning kinetic processes must be confirmed and explained by further experiments as M.H.D. impedances.

REFERENCES

(1) T.Z. FAHIDY, J. Appl. Electrochem., 13 (1983), 553

(2) A. OLIVIER, J.P. CHOPART, J. DOUGLADE and C. GABRIELLI, J. Electroanal. Chem., 217 (1987), 443

(3) S. MOHANTA and T.Z. FAHIDY, Electrochim. Acta, 21 (1976), 149

(4) R. AOGAKI, K. FUEKI and T. MUKAIBO, Denki Kagaku, 43 (1975), 504

(5) A. OLIVIER and T.Z. FAHIDY, J. Appl. Electrochem., 12 (1982), 471

(6) C.I. NONINSKI, V.C. NONINSKI, V.I. TERZIYSKI, Extended abstracts of I.S.E., 2 (1982), 939

(7) E. CHASSAING and R. WIART, Electrochem. Acta, 29 (1984), 649

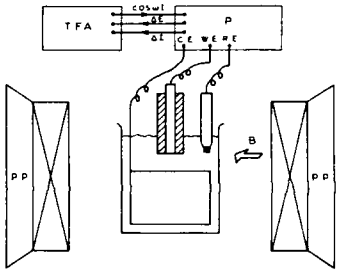


Fig.1 Experimental arrangement (P) potentiostat, (TFA) transfer function analyzer, (CE) counter electrode, (WE) working electrode, (RE) reference electrode, (pp) polar pieces.

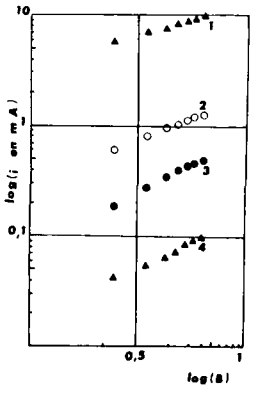


Fig.2 Variation of the limiting current versus the magnetic flux density in the case of $CuSO_4$ in H_2SO_4 1.8 M

1 C = 0.5 M ; 2 C = 0.1 M ; 3 C = 0.05 M ; 4 C = 0.01 M

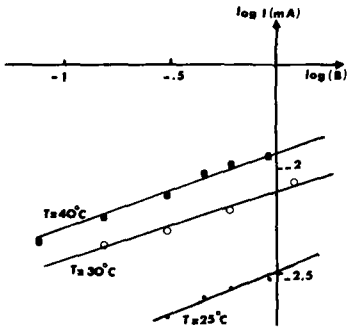


Fig.3 Variation of the limiting current versus the magnetic flux density in the case of ZnO 0.5 M in KOH 7M.

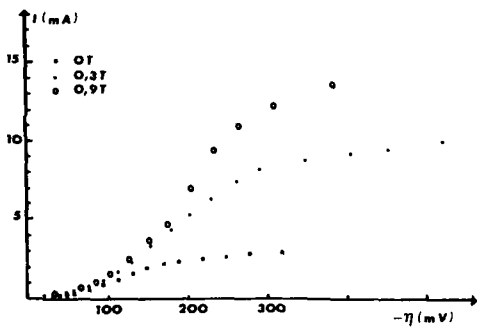


Fig.4 Current voltage curves plotted for various magnetic flux densities in case of $CuSO_4$ 0.5 M in H_2SO_4 1.8M.

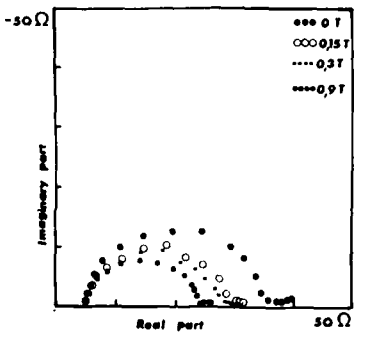


Fig.5 Electrochemical impedance in Nyquist plot for different field at same overpotentiel (η = 130 mV) for $CuSO_4$ 0.5 M in H_2SO_4 1.8 M.

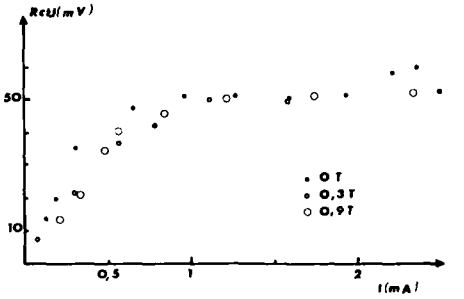


Fig.6 Current dependence of the product R_t x i (transfer resistance x current) in $CuSO_4$ 0.5M in H_2SO_4 1.8M

Abstract No. 682

Electromagnetic Microhydrodynamics of Aqueous Electrolytes

N.Ph.Bondarenko, E.Z.Gak

Agrophysical Research Institute

Leningrad, USSR

The modern hydrodynamics is based on the concept that the medium is continuous. By different estimates the linear dimensions of a layer thickness where discontinuity can take place of the medium rheological, electrical and magnetic properties is in the range from 0.1 to 100 m. It was proposed by Batchelor [1] to place the fluid motion phenomena occuring in these layers into the microhydrodynamics, as a branch of the hydrodynamics.

For the topics to be discussed at the symposium of major importance are the problems relating to the magnetohydrodynamic and magnetohydrostatic effects which take place during a simultaneous action of the electric and magnetic fields on electrolytes. In this report some theoretical assumptions and experimental work are considered of the phenomena developing in thin layers under the action of these fields. From our viewpoint it is for this body of similar phenomena that the term "electromagnetic microhydrodynamics" suggested by us can be used [2-3].

The following phenomena are likely to be included in the area of concern of this branch of the physico-chemical hydrodynamics: the phenomena observed in the phase interface area of the liquids flowing or being filtered under the action of the electric or magnetic fields; the appearance of a velocity component perpendicular to a wall during a vigorous dissolution of metals; various phenomena in the phase interface area (electrolyte-air) resulting in local changes of the surface tension values and as a consequence causing instability of an interface.

It should be noted that a salient feature of the phenomena entering into the electromagnetic microhydrodynamics area manifests itself in a somewhat unusual energy redistribution in the system which does not contain ferromagnets, that is, a local energy redistribution in the system without its significant change in the stationary magnetic fields. A microscopic nature of these effects resulting in appearance of the mass pressures of a macroscopic nature is determined by the change of the ions pulses during their translational transitions in magnetic fields.

The presence of an electric or some other field giving rise to a force gradient just reveals this effect. In this case a macroscopic parameter change occurs, for example, a stable or a vortex fluid motion, a wave motion [2,3,4] or in case of the geometrically-closed systems, the change of the medium local temperatures [5].

References

1. G.K.Batchelor - Developments in the microdynamics. Proceedings of the 14-th IUTAM International Congress on theoretical and applied mechanics. North Holland Publishing Co., 1977.
2. N.Ph.Bondarenko, E.Z.Gak - Electromagnetic phenomena in natural waters. Leningrad, Ghidrometeoizdat, 1984, 151 p. (in Russian).
3. E.Z.Gak, V.S.Krylov - Effect of a magnetic field on a charge and on a mass transfer for the electrolyte moving in narrow interelectrodes gaps. Elektrokhimiya, 1986, v.22, i.6, pp. 829-834 (in Russian).
4. T.Z.Fahidy - The application of plasma dynamics to the study of flow generation in magnetoelectrolysis. Electrochimica Acta, 1978, v.23, p. 549-555.
5. A.Olivier - Contribution a l'étude des effects magnetoélectriques en solution aqueuse. These, présentée à la faculté des sciences. Université de Reims, 1979, 256.

Abstract No. 683

The Prospects of Using Magnetohydrodynamic Effects in Electrolytes to Control Charge and Mass Transfer Processes

E.Z.Gak, E.E.Rokhinson

Agrophysical Research Institute

Leningrad, USSR

The mass transfer processes in electrolytes differ from the systems in which a charge sign of the desired component is not significant. In the electrolytes in the electric and magnetic fields concurrently with a mass transfer a charge transfer takes place. This feature of the magnetohydrodynamic (MHD) effects makes it possible to use them for controlling the cathodic and anodic electrode processes. Depending on the initial parameters both an electrolysis intensification (an increase of the limiting current through the electrolyte) and an absence of the effect or a considerable decrease of the current density are possible [1-3].

The MHD effects, similar to a convective diffusion, can significantly change the rate of a wide range of the processes depending on the flow hydrodynamic characteristics (electrolysis, electrodeposition of metals, cleaning of liquids, biotechnology processes and many others [4-6]). In contrast to a forced mechanical convection, an MHD convection makes it possible to carry out a more thorough liquid mixing down to the electrode and boundary layers which usually remain unaffected by a mechanical convection. It is connected with the fact that an MHD flow velocity is directly proportional to an electric current density which takes on the largest values at a phase interface and close to the electrodes. During the model tests in the electrochemical cells a critical MHD fluid motion was determined at which the maximum increase of a critical current through the electrolyte is observed down to a complete removal of the diffusion limitations. A critical velocity V_{kp} corresponds to an unstable motion mode. At $V = V_{kp}$ a laminar motion changes to a turbulent motion. Because of a direct connection between the hydrodynamic, electric and magnetic phenomena a practical possibility has appeared of simulating both the linear and nonlinear hydrodynamic motions. The use of external magnetic fields opens up possibilities of controlling a convective transfer velocity in electrolytes, which is used when simulating hydrodynamically unstable processes in the atmosphere and in the ocean [7].

In the last few years the prospects have appeared of obtaining the superhigh magnetic fields on the basis of the superconducting materials under normal conditions. It opens new ways in using the MHD effects.

The use of high-intensity magnetic fields will make it possible to control not only delivery and removal of the reagents but also to affect both the passage of charges through a phase interface and the nature of ionic hydration and dehydration directly in the boundary layers.

References

1. E.Z.Gak, E.E.Rokhinson, N.Ph.Bondarenko - Peculiarities in the change of electrode processes kynetics in the electrolytes in a stationary magnetic field. Elektrokhimiya, 1975, v.11, i.4, pp. 529-534 (in Russian).
2. N.Ph.Bondarenko, E.Z.Gak, E.E.Rokhinson - The effect of magnetohydrodynamic phenomena in electrolytes on kynetics of the heterogenous processes. Elektronnaya obrabotka materialov, 1977, i.4, pp. 62-66 (in Russian).
3. Iwakura, T.Edamoto, T.Tamura - Effect of stronger magnetic fields on electrochemical reactions. Denki Kagaku, 1984, v.52, No.10, pp. 654-658.
4. A.A.Korchaghin - Effect of an external magnetic field on a surface roughness of the X15 steel during its electrochemical treatment. Elektronnaya obrabotka materialov, 1982, No.5, pp.9-12 (in Russian).
5. T.Z.Fahidy, Magnetoelectrolysis. J.Appl. Electrochem. 1983, v.13, pp.553-563.
6. A.Olivier, E.Tronel-Peyroz, T.Z.Fahidy, D.Laforgue-Kantzer - The thermal behavior of a magnetoelectrolytic cell. - In: ISE meeting. Ext. Abstr. Zurich, 1976, No.29.
7. E.B.Gledzer, F.V.Dolznansky, A.M.Obukhov - The hydrodynamic-type systems and their use. Moscow, Nauka, 1981, 336 p. (in Russian).

Abstract No. 684

Molecular Imaging with the Tunneling and Force Microscopes - The Relation to Electrochemistry

C. F. Quate

Edward L. Ginzton Laboratory
Stanford University
Stanford, CA 94305

The Tunneling Microscope used with a conducting substrate and the Force Microscope used with an insulating substrate provide us with opportunities for studying atomic and molecular structures on solid surfaces and at liquid-solid interfaces. The two instruments add new dimensions to our ability to study surfaces and interfaces at the atomic level. The instruments were originally used for the study of electronic structure on well characterized surfaces of semiconductors and metals with and without adsorbates. More recently the work has been extended to the study of organic molecules. These studies include individual molecules deposited from liquid and mono-molecular films laid down with the LB and with self-assembly techniques. The work also includes the study of long-range order at the interface between a solid and a solution of liquid crystal material. In some of the more interesting cases it is possible to manipulate single molecules with the intense electric field between the tip and the substrate.

In this talk we will concentrate on the imaging of molecules. We will point to the potential for studying processes at electrode surface and at the electrode-electrolyte interface. We will review the progress that has been made with molecular films with long-range order and illustrate how these molecules might be manipulated to achieve a desired result.

Abstract No. 685

STM OBSERVATION OF NANOSTRUCTURE OF ELECTRODE SURFACES

Kohei Uosaki and Hideaki Kita

Department of Chemistry, Faculty of Science, Hokkaido University, Sapporo 060, Japan

If one wishes to understand thouroughly the mechanism of chemical reactions which take place at solid surfaces, it is essential to know the structure and electronic state of the solid surface with atomic resolution. Most of the techniques which give information of atomic resoluton developed so far can be used only in vacuum and no method to observe the solid surface in solution with atomic resolution is available. Scanning tunneling microscopy (STM) can, however, revolutionize the electrochemical research, since it can provides atomic images of solid surfaces even in solution. In this study, STM was employed to investigate, either in situ or ex situ, the structure of electrode surfaces and to follow the various electrochemical reactions.

STM used in this study was NanoScope I of Digital Instruments with Pt-Ir or W tip. For the operation in water, glass insulated Pt-Ir tip was used. Lateral resolution of the STM system was confirmed by observing atomic corrugation of HOPG.

Metal deposition is one of the most basic electrochemical reacitons and it is very important to understand the mechanism of this process. Metal is often deposited on relatively inert electrode to improve the catalytic activity. In both cases, the information of surface structure of the deposited metal is very useful. Glassy carbon (Tokai, GC20) was polished by Al_2O_3 powder down to 0.05μ and sonicated in water before it is used as electrode. The electrochemical deposition was carried out in a solution containing K_2PtCl_6(5mM) and H_2SO_4(1M) by pulsing the potential from +600 mV to -400 mV (100 ms) then to +100mV. The amount of deposits was controlled by changing the time kept at +100mV. Fig. 1 shows SEM and STM images of Pt/GC (Pt: 15.1 μg/cm^2). Pt particles of ca. 30~50 nm are seen in the SEM and STM pictures. The closer look of STM shows each particle consists of smaller particles of less than 10 nm. Thus, it is proved that STM is a very useful tool to study the metal deposition process.

Other systems investigated include structure of Au on Nafion deposited either by vacuum deposition or by electroless plating, in situ observation of structure change of Au electrode caused by potential cycling and structure of etched and metal treated semiconductor electrodes.

This work was partially supported by Japan Securities Scholarship Foundation.

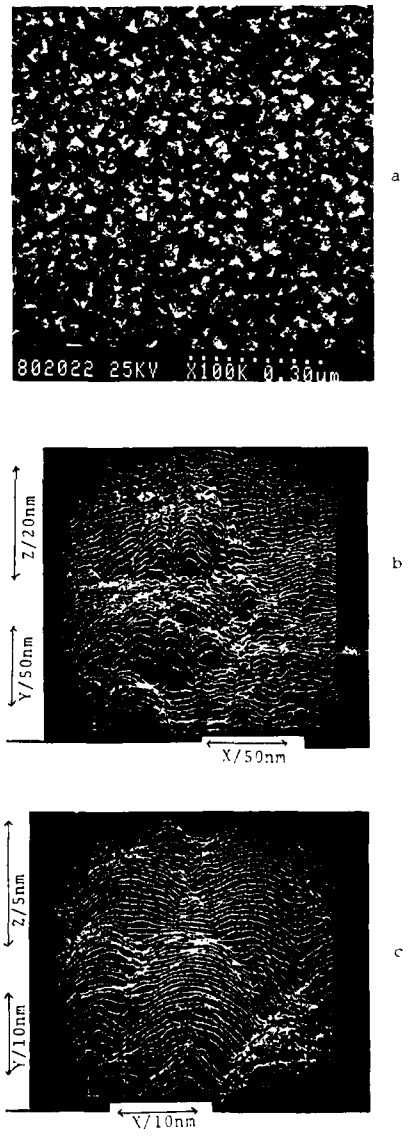


Fig. 1 SEM(a) and STM(b,c) images of Pt/GC. Pt: 15.1 μg/cm^2

Abstract No. 686

New Electrochemical Scanning Tunneling Microscope and Its Application

Kingo Itaya

Department of Engineering Science
Faculty of Engineering
Tohoku University, Sendai 980 JAPAN

Scanning tunneling microscopy (STM) and related techniques have rapidly been finding enormous application fields for surface topographic imaging and analysis on an atomic scale in various environments. Atomic resolution has been achieved for samples in ultra-high vacuum (UHV), air and even immersed in aqueous solutions. Electrochemically deposited Au and Ag have been investigated in an electrochemical cell by Hansma et al. [1,2].

However, the present STM generation is still based on a two-electrode cell arrangement, where electron tunneling occurs between the sample and the tip with a tunnel voltage. In the most electrochemical measurements with a two-electrode cell, the working electrode must be coupled with a reversible reference electrode in order to maintain the potentiostatic condition. Nevertheless, it seems to be very difficult to fulfill this condition for STM with a two-electrode cell arrangement. Instead of a two-electrode configulation, a three-electrode cell has frequently been used in electrochemical experiments with an instrument known as a potentiostat.

We are showing a new system wherein each electrode (sample and tip) is independently controlled with respect to a reference electrode potential. This system offers a new capability for complete in-situ observation of electrode surfaces in electrolyte solutions under the potentiostatic condition[3].

Figure 1 shows an electrochemical cell for the four-electrode configulation.The electrode potentials of the sample (WE) and the tip(Tip) can be simultaneously controlled with respect to the reference electrode (RE). The principle of the electric circuit for a four-electrode cell is already well known and the device, called a bipotentiostat, is used in some electrochemical experiments. The tunneling current is sensed as a voltage across a resistor with a PAR 113 preamplifier whose output is fed into a z-piezo feedback control electronics. The tunneling tip is a glass-covered Pt electrode. Pure Pt wire with a diameter 15 μm was directly sealed into a soft glass pipette. The electrochemical background current, not the tunneling current, was only about 0.1 nA at v=5 mV/s in a potential range between -0.1 and 1.0 V vs. SCE in a 0.1 M H_2SO_4 solution[4].

For a demonstrative experiment, the electrochemical deposition and dissolution of Ag have been investigated with the new instrument. The deposition of Ag was carried out in a 0.1 M $HClO_4$ solution of 5 mM $AgClO_4$. Figure 2 shows a cyclic voltammogram obtained on a basal plane of freshly cleaved HOPG electrode. The electrodeposition and dissolution(stripping) reactions are clearly observed at the negative and positive potentials vs. Ag/ Ag^+.

Based on the electrochemical result shown in Fig. 2, the STM measurements were carried out with the apparatus described above. The electrode potential of the tip (E_t), as shown in Fig. 2, was kept at a constant value of 0.3 V vs. Ag/Ag^+ for all measurements represented here. From the voltammogram, it is reasonable to expect electrodeposition of Ag to be almost completely prevented on the tip electrode. A in Fig. 2 shows an image obtained when the potential of the HOPG(E_w) was held at 0.25 V vs. Ag/Ag^+. The electrodeposition of Ag is inhibited at this potential. It is clearly seen that the surface of the HOPG is perfectly flat at the magnification shown in Fig. 2.

After taking the image of A, the potential of the HOPG electrode was scanned at 10 mV/s to the negative direction and held at -0.1 V. B shows a typical image obtained at the HOPG with an Ag deposit of 10 mC/cm^2. Note that the tunneling tip was not disconnected from the z-feedback loop during the electrodeposition. That is, the tip was continuously scanned over the surface during the deposition.

It is now possible to image the electrode surfaces in complete in-situ observation under the potentiostatic condition.

Immediately after the image B in Fig. 2 was observed, the potential of the HOPG was scanned to the original value of 0.2 V where all Ag deposit was completely stripped off the HOPG electrode. Again, atomically flat surface appeared, as shown C in Fig. 2. The tunneling tip was again continuously scanned over the surface during the dissolution of Ag.

The above results strongly encourage us to explore the applications of this new generation of STM to the in-situ observation of electrode surfaces in electrochemistry.

The electrodeposition of other metals such as Pt, Zn, Cu, and Ni is now under investigations. STM studies of semiconductor/liquid junctions are also represented here.

References
1.Drake,B;Sonnenfeld,R.;Schneir,J.;Hansma,P.K. Surf. Sci. 1987, 181, 92.
2.Sonnenfeld,R.;Schardt,B.C. Appl.Phys.Lett. 1986,49,1172.
3.Itaya,K.;Tomita,E. Surf. Sci. in press.
4.Itaya,K.;Sugawara,S. Chem. Lett. 1987,1927.

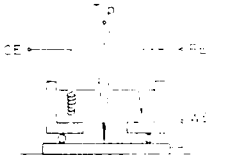


Fig.1. Schematic illustration of the electrochemical cell for the four-electrode configuration.

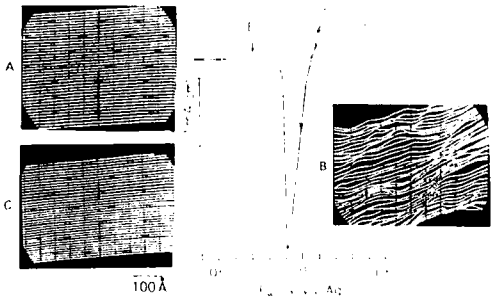


Fig.2. A cv at a HOPG in a 0.1 M $HClO_4$ solution of 5 mM $AgClO_4$ at 50 mV/s and STM images obtained in the same solution. The x, y, and z scales are all the same as indicated below.

Abstract No. 687

In-situ Scanning Tunneling Microscopy (STM) of Semiconductor/Liquid Interface

Eisuke Tomita and Kingo Itaya

Department of Engineering Science
Faculty of Engineering
Tohoku University, Sendai 980 JAPAN

STM images of the Si(111)-(7x7) surface were obtained by Binnig et al., demonstrating the first look at the atomic structure of this surface under UHV conditions [1].

However, atomic resolution of STM has also been achieved for samples in air and even immersed in aqueous solutions [2].

It is reasonable to expect that in-situ STM should applicable to an understanding of what happens on various electrodes in liquid phases at the atomic level. For this purpose, the electrode potential of samples must be controlled with respect to a reference electrode.

The apparatus, we constructed, offers a new capability for complete in-situ observation of electrode surfaces under potentiostatic condition [3].

This paper will report a work of the in-situ STM study of semiconductor/liquid interfaces. It is well known that a semiconductor-liquid junction is a similar to a semiconductor-metal one so called Schottky junction, and that the valence band and the conduction band are bent downward or upward depending on the electrochemical potential of the semiconductor electrode [4,5].

A variation of the band bending leads to a change of the carrier density at the semiconductor surface. Therefore, it is expected that a tunneling current may change according to the band bending of the semiconductor surface.

An in-situ STM consists of a teflon cell, a piezoelectric tripod, a glass-covered Pt tip, a Ag/AgCl reference electrode and a Pt counter electrode.

The electrochemical potentials of the tunneling tip and the sample were simultaneously controlled with respect to a Ag/AgCl reference electrode.

A single crystal n-TiO_2(001) was examined as a first example. The surface was etched in a concentrated H_2SO_4 at 200°C.

When the potentials of tip and sample were set at 0 V and -1 V vs. Ag/AgCl, respectively, the tunneling current flowed very stably. STM image showed a flat surface of n-TiO_2.

However, when the potential of the semiconductor changed to -0.4 V, the tunneling current turned to be unstable and reproducible STM images could not be obtained. Further changes of the electrode potential to -0.2 V or more positive one caused an out of control in the Z-direction.

The above result suggests that the tunneling phenomena would depend on the electrochemical potentials of n-TiO_2, as expected, and the critical point of tunneling should be near the flat-band potential.

From a Mott-Schottky plot, the flat-band potential was determined as -0.25 V vs. Ag/AgCl in a 0.1 M KCl (pH 4) solution.

The variation of the tunneling current was measured, under a potential scan of the semiconductor. The electrode potential of n-TiO_2 was scaned from -0.5 V to 0 V. The voltage applied to the Z-piezoelectric element was abruptly changed to almost the full voltage when the electrode potential of n-TiO_2 reached at about -0.25 V. The observed critical point of the tunneling current, -0.25 V, was consistent with the flat-band potential measured by the Mott-Schottky plot.

We have carried out the same experiment at different pH. The flat-band potential and the critical point of the tunneling current were shifted by about 60 mV/pH between pH 1 and 9.

We have also investigated various semiconductor electrodes such as p,n-Si ; n-ZnO and p, n-GaAs. A similar coincidence between the flat-band potential and the critical point has been observed.

In conclusion, we obtained, for the first time, the fact that the tunneling currents were strongly dependent on the electrochemical potentials and the band structures of the semiconductor electrodes.

References

1. G.Binnig, H.Rohrer, C.Gerber, and E.Weibel, Phys.Rev.Lett., 50,120(1983)
2. B.Drake, R.Sonnenfeld, J.Schneir, and P.K.Hansma, Surf.Sci., 181, 92 (1987)
3. K.Itaya, and E.Tomita, Surf.Sci., in press.
4. H.Gerischer, " Advances in Electrochemistry and Electrochemical Engineering ", Vol. 1, 139 (1961)
5. A.J.Bard, J.Electroanal.Chem., 168, 5 (1984)

Abstract No. 688

Atomic Scale STM-Studies of an Electrode Surface under Potential Control

T.Twomey and D.M. Kolb
Fritz Haber Institut der M.P.G.
Faradayweg 4-6, D-1000 Berlin 33

and

J. Wiechers and R.J. Behm
Institut f. Kristallographie
Univ. München
Theresienstr.41, D-8000 München 2
Germany

Atomic scale imaging is perhaps the most direct way in order to gain an understanding of the microscopic mechanistic concepts of reactive processes. Scanning Tunneling Microscopy (STM) provides an elegant and for in-situ observations on electrode surfaces at present the only way to gain direct structural information on that scale. The STM images of a Au(111) electrode under potential control presented here allow the identification of atomic structures and of their modification in the course of surface processes or reactions.

It had already been demonstrated that the STM can operate in liquids [1], and the basic concepts for its application in electrochemistry under well defined potential conditions were recently described by Lustenberger et al. [2]. The microscope used here is a modified version of a very rigid "pocket size" STM which was demonstrated to achieve atomic resolution on a closed packed metal surface under Ultra High Vacuum (UHV) conditions [3]. For this work the sample was replaced by a little macor container representing the electrochemical cell, which holds sample and electrolyte. In addition to the classical three electrode setup the tip acts as a fourth electrode. Its potential is kept constant with respect to the Pd-H reference electrode and thus to the potential of the electrolyte. The Au(111) sample was prepared by flame annealing, further details concerning the experiments can be found elsewhere [4].

Part of the flame annealed surface is characterized by extended flat terraces, which are separated by mostly monoatomic steps (fig.1). Other areas are more structured, typically either in form of continuous slopes including a large number of narrow terraces or by irregular features.

The atomically flat, extended terraces have a size of several hundred Angstroms in average, which is at least comparable to what is found for well prepared surfaces under UHV conditions and in good agreement with Electron Microscopy observations on flame annealed surfaces [5]. The steps generally follow low index directions; averaged over several images the threefold symmetry of the substrate is reflected also by the step orientations. In the STM image in fig.1 the two main step directions form an angle ~120°, which can be seen in a projection of the image.

The clean surface was found to be stable over prolonged periods of time, if the sample potential was kept in a range where no specific adsorption occurs. Comparative studies of an adsorbate covered surface or a surface following an adsorption-desorption cycle thus can, in addition to identifying adsorbates by STM, demonstrate the effects of the above processes on the substrate topography.

In the presence of adsorbed Cl^- additional structures give the impression of a more 'noisy' image, as seen in figs. 2b and 2d. These structures reversibly disappear after desorption. This observation was confirmed in a number of experiments, the extra features thus must be attributed to the adsorbed Cl^- ions. Though on this scale individual adsorbed ions cannot be resolved, a significant effect in the STM scan originating from a change in the electronic charge distribution and thus in the tunnel current in front of such an adatom is in good agreement with theoretical considerations [6].

Subsequent desorption recovers most of the original topography of the substrate, but some distinct modifications can be detected. First of all there is an apparent smoothening of the flat terraces. In fig. 2 e.g. a number of little hillocks, mostly on the topmost terrace, are removed already by the first adsorption-desorption cycle.

Further modifications concentrate on steps. Their shape was repeatedly seen to vary in the course of such cycles. In fig. 2 this effect can be followed at the two monoatomic steps which originally proceeded almost linearly through the imaged area, while after two cycles they exhibit significant fine structure. Likewise the "pond" at the bottom of the image is reduced in size by additional material at its right hand side.

In consequence this and similar series of images indicate that already the mere process of halide adsorption-desorption affects the substrate itself. These processes must cause an intermediate enhancement in the mobility of the substrate surface, resulting in characteristic modifications of the terrace edges, i.e. of the atomic scale topography of the electrode.

Acknowledgements: One of us (T.T.) gratefully acknowledges financial support by the Alexander von Humboldt Foundation.

References

1. Propceedings of the First Intern. Conference on STM, Santiago de Compostella, Surface Sci. 181 (1987)
2. P. Lustenberger and H. Rohrer, R. Christoph and H. Siegenthaler, J. Electroanal. Chem. 243, 225 (1988)
3. J. Wintterlin, H. Brune, H. Höfer and R. J. Behm, J. Appl. Phys. A (in press)
4. J. Wiechers, T. Twomey, D. M. Kolb and R. J. Behm, J. Electroanal. Chem. (in press)
5. J. Canullo, Y. Uchida, G. Lehmpfuhl, T.Twomey and D. M. Kolb, Surface Sci. 188, 350 (1987)
6. N.D. Lang, Phys. Rev. Lett. 58, 45 (1987)

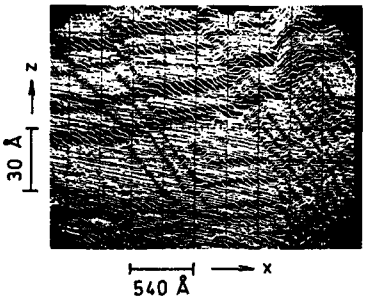


Fig.1 STM image (2730Å*2730Å) of a freshly prepared Au(111) in 0.05M H_2SO_4 at rest potential.

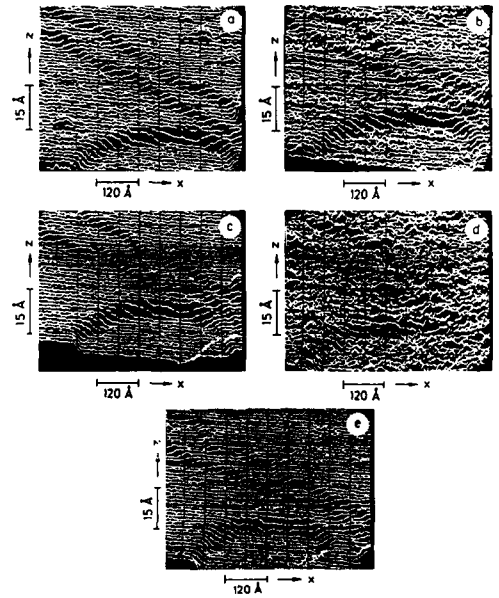


Fig.2 STM image (3000Å*3000Å) of a flame treated Au(111) electrode in 0.05 M H_2SO_4 + 5 mM NaCl. The STM images were taken at following potentials: (a) at 250 mV, (b) at 700 mV, (c) at 250 mV, (d) at 900 mV and (e) at 250 mV.

Abstract No. 689

SCANNING TUNNELING MICROSCOPY IN COMBINATION WITH SCANNING ELECTRON MICROSCOPY TO STUDY ELECTROCHEMICALLY PROCESSED SURFACES

L. Vázquez(+), A. Bartolomé(+), A.M. Baró(+)
C.Alonso(*), R. Salvarezza(*)(&)
A.J. Arvía(**)

(+) Dpto. de Física de la Materia Condensada, C-III
(*) Departamento de Química Universidad Autónoma de Madrid, 28049 Madrid-SPAIN.
(**)INIFTA, Universidad Nacional de La Plata, Sucursal 4, Casilla de Correo 16, 1900 La Plata ARGENTINA.
(&) Permanent address: INIFTA, ARGENTINA

The recently introduced Scanning Tunneling Microscope (STM) (1) represents an important advance in the measurement of surface topography at the nanometer level. The instrument possesses simultaneous high horizontal and vertical resolution and furnishes three dimensional real space images of the surfaces of solid conducting materials, by working under vacuum or atmospheric pressure (2) or liquids (3).

In this work we present some STM topographic images of electrodes subject to various electrochemical treatments. The objective of these measurements is to gain insight towards a more microscopic description of electrochemical processes.

The electrochemical treatments we have studied are related with modifications of the surface, obtained by applying to the electrode a fast square potential cycling in acid solution (4). Previously reported results indicate the ability of STM to obtain relevant information with superior detail of the processed electrode surfaces. Electrochemical facetting is characterized by the observation of flat compact terraces surrounded by ridge-type structures brought about by atomic steps (5). During the initial stages of this process, the surface topography develops in the form of clusters along a preferential orientation yielding later to the ridge-like structures. This indicates a substantial increase in the diffusion rate of metallic species in the electrolyte or on the surface.

A substantial problem inherent to STM is its limited scanning range (~ 1μm). This limitation is important in this case because of the non homogeneous nature of the electrode surfaces. In order to solve that problem we have developed a STM instrument in combination with a normal Scanning Electron Microscope (SEM) which is able to provide simultaneously with images by the two microscopes(6).

We have been measuring by this new instrument gold electrodes which have been anodically oxidized and subsequently reduced. This results on a higher catalytic activity.

Previous STM results obtained on a platinum electrode show that the increase of activity cannot be explained by an increase of the real surface area. This area can be measured quantitatively from STM data and the results show that the area increase is not higher than 20%. The topography is in the form of a domed structure with size 100 Å in diameter (7). These results suggest a model which relates the increase in activity to the participation of the volume below the surface which would be accessible to the reactants. A simple calculation shows that if we take into account the thickness of the reduced region from voltammetric data, the surface available is able to increase the reaction by the measured amount.

The new results obtained from STM-SEM combination on gold electrodes allow for the first time to correlate the data of both microscopes. SEM images corresponding to the activated electrode show brain-like channels covering the whole surface and grains of 100 Å diameter. By changing the parameters of the electrochemical reaction we are able to modify the activity and to correlate with the microstructure measured by both microscopes. From this we can definitely rule out the influence of the brain-like channels in the reaction. We are also able to see the superior detail of STM with respect to SEM. This is clearly shown by comparing SEM images of two differently activated surfaces which are barely distinguishable. STM data show with great detail the formation of grains of 100 Å more characteristic of the columnar structure typical of a deposition process in the case of a highly activated surface. When the activity goes down, the grains increase in size, and the resulting surface of the grains smoothes out. These results give additional support to our model which suggests that the important channels are those which are between the columns grown during the reduction process.

Acknowledgements.

The authors are indebted to the following people: to N. García for his stimulation, to R. García for advise, to A. Buendia for skillfull technical assistance, and to J. Gómez and J.M. Gómez for help in data acquisition and image processing. Finantial assistance by CAICYT trough contract PB86-0606 is also acknowledged.

References.

1. G. Binning and H. Rohrer, Rev. Mod. Phys. 59, 615 (1987).
2. A.M. Baró, R. Miranda, J. Alamán, N. García, G. Binnig, H. Rohrer, Ch. Gerber and J.L. Carrascosa, Nature 315, 253 (1985).
3. R. Sommerfeld and P.K. Hausman, Science 232, 211 (1986)
4. A.C. Chialvo, W.E. Triaca, A.J. Arvía, J. Electroanal. Chem. 171, 303 (1984).
5. J. Gómez, L. Vázquez, A.M. Baró, N. García, C.L. Perdriel, W. E. Triaca and A.J. Arvía, Nature 333, 612 (1986).
6. L. Vázquez, A. Bartolomé, R. García, A. Buendía, A.M. Baró, Rev. Sci. Instru. (1988).
7. L. Vázquez, J. Gómez, A.M. Baró, N. García, M.L. Marcos, J. González Velasco, J.M. Vara, A.J. Arvía, J. Presa, A. García and M. Aguilar; J. Am. Chem. Soc. 109, 1730 (1987).

Abstract No. 690

Steps toward atomic-resolution studies of metal surfaces in aqueous solutions

Richard Sonnenfeld*, Owen Melroy, Gurinder Singh and Joseph Gordon II

IBM Research Division, Almaden Research Center
San Jose, California 95120-6099

In previous work, it has been demonstrated that scanning tunneling microscopes (STM's) can operate at atomic or nanometer resolution in water and aqueous solutions up to a concentration equivalent to 1 M NaCl, [1,2,3], yet the detailed atomic information about metal surfaces yielded by STM's in ultra-high vacuum environments [4] is so far unrivaled by STM's out of such environments. One could hope ultimately to learn a comparable amount about surfaces treated by electrochemical techniques from an STM operating in solution.

A first step toward atomic-resolution studies of metal surfaces in aqueous solutions is atomic resolution in air. We are among the groups to have reproduced the recent very exciting discovery by Hallmark et al. [5] that close-packed, unreconstructed gold atoms can be imaged on a (111) gold surface in ambient air. We see a simple-hexagonal atomic structure with a nearest-neighbor spacing which is consistent with 2.8 Å to within 10%. The images are considerably more difficult to obtain than atomic-resolution images of graphite. Typically, we are required to electropolish several tungsten tips in order to produce one that will give the necessary resolution, but when one is obtained it seems to work almost immediately. While it may yet be found that freshly prepared samples give the best results, we were able to obtain atomic resolution on gold samples that had been exposed to room air for six months after fabrication. This further testifies to STM's relative insensitivity to ambient contamination.

To make the substrate, Grade V-2 (by ASTM standards) green mica is cleaved with a scalpel and DI water. The freshly cleaved surface is held at 300°C in a vacuum deposition chamber for one hour before thermal evaporation of gold begins at 5 Å sec to a total thickness of 2500 Å. After deposition, the substrate is allowed to cool radiatively for several hours to < 80°C before venting to dry air. (These surfaces have been analyzed in the past with LEED and X-ray diffraction and found to be polycrystalline (111) with grain sizes of order 0.5 mm) [6].

The large, atomically flat terraces of these substrates are also excellent templates for local surface modification studies. By applying 2.8 V (positive or negative) pulses to the tip, we are able to produce hemispherical mounds on the surface with 12 nm characteristic dimension. The process is reproduceable enough that one can write a desired pattern (e.g. letters of the alphabet) in a dot matrix form on the substrate. A liquid covering the surface is required for this application, modifications do not seem to be possible in air alone. To date, we have used perfluorokerosenes and perfluorinated polyethers. No evidence of the molecules themselves has ever been seen. We have produced these changes with pulses as short as 50 μs, though typical pulse lengths are 1 s.

Our STM is a hybrid of the Digital Instruments "Nanoscope" and a IBM-AT driven data acquisition and image-processing package which interfaces via the Scientific Solutions "Labmaster" [7]. We have integrated it with a three-electrode electrochemical cell of novel design. A 20 μm layer of electrolyte in the cell is trapped between the sample and a thin polyethylene film. The polyethylene film is punctured by the tip on advance, thus providing a sealed electrochemical cell. We hope to be able to obtain atomic-resolution gold images in this cell, and thus to advance a second step toward meaningful electrochemical studies on gold (111).

References

1) R. Sonnenfeld and P.K. Hansma, Science, Vol. 232, 211 (1986).
2) H.Y. Liu, F.-R.F. Fan, C.W. Lin, and A.J. Bard, J. Am. Chem. Soc.,Vol. 108, 3838, (1986).
3)R. Sonnenfeld and B.C. Schardt, Appl. Phys. Lett.,Vol. 49, 1172 (1986).
4)G. Binnig, H. Rohrer, Ch. Gerber, and E. Weibel, Phys. Rev. Lett.,Vol. 49, 57 (1982).
5)V.M. Hallmark, S. Chiang, J.F. Rabolt, J.D. Swalen, and R. J. Wilson, Phys. Rev. Lett., Vol. 59, 2879 (1987).
6)J. Crystal Growth, Vol 10, 103 (1971). Surf. Sci., Vol. 6, 309 (1967).
7)P. Schroer and J. Becker, IBM J. Res. Dev., Vol. 30, 543 (1986).

Abstract No. 691

Scanning Tunneling Microscopy of Vapor-Deposited and Electrodeposited Metals

Christopher E. D. Chidsey

AT&T Bell Laboratories
Murray Hill, New Jersey 07974

The STM provides a new degree of resolution and simplicity in the study of metal deposition processes. Such features as monatomic steps, dislocations, grain boundaries and grain topographies can be mapped at the growth surface without extensive sample preparation. This capability to examine surface morphology and the opportunities it provides to understand film growth will be illustrated with the classic epitaxial system of gold on mica [1]. Work in progress to extend high resolution STM to the electrodeposition of silver on gold will also be presented.

Gold vapor-deposited on mica near room temperature consists of {111}-oriented crystallites about 500Å across with rounded tops and random in-plane orientations. As the deposition temperature is increased, the crystallite size increases. The crystallites also develop flat tops with widely spaced monatomic steps and occasional screw dislocations. At these higher temperatures, the orientation of the crystallites becomes epitaxial with the mica. An understanding of the roles of nucleation density and surface diffusion in film growth allows control of the surface structure. For instance, the formation of many small nuclei at low temperature followed by deposition of the majority of the film at high temperature leads to surfaces free of large topographic features and flat to tens of angstroms over microns. In contrast, deposition of gold on a thin silver underlayer on mica using the same thermal treatment results in large gold crystallites with pronounced grooves between them. The lower density of crystallites is ascribed to the higher mobility of silver than gold in the initial stage of film growth.

1. C. E. D. Chidsey, D. N. Loiacono, T. Sleator and S. Nakahara **Surface Science** (in press).

Abstract No. 692

Surface Modification and Spectroscopy with the Scanning Tunneling Microscope

Alex de Lozanne
Department of Physics
University of Texas at Austin
Austin, Texas 78712

1. INTRODUCTION

We review two of our recent developments in scanning tunneling microscopy (STM). The first is the direct writing of nanometer features with the STM. A second recent development is our use of a unique low-temperature STM to perform spectroscopic measurements of the new oxide superconductors.

2. DIRECT WRITING OF NANOMETER STRUCTURES

Direct writing is the generation of patterns on a substrate without the need for any further process steps. We have recently developed a direct writing process capable of making nanometer features with the STM[1]. We allow organometallic gases into a dedicated STM chamber and use the electron current between tip and sample to break the organometallic molecules and deposit the appropriate metal. So far we have written cadmium dots and lines with sizes down to 400 angstroms.

The STM used in this experiment is of fairly standard design, with a scanner capable of moving up to 10 microns. The organometallic gas is fed into the chamber with a nozzle that points at the substrate. So far we have used mostly dymethylcadmium as the source gas. Some of the deposits have been characterized with Auger spectroscopy, which shows mostly cadmium and carbon. A typical writing procedure is to image the surface at a low voltage (tens of mV) to make sure that the surface is flat, bring the tip to the desired location on the surface, increase the voltage to a few volts (which breaks the organometallic molecules), and image the surface again. The smallest dimension of the dots and lines that we have written thus far is about 400 angstroms, which is already one order of magnitude smaller than the smallest features that can be made by laser photodeposition.

We are currently studying the physical mechanisms responsible for this process and attempting to write smaller features and complex patterns.

3. HIGH T_c SUPERCONDUCTORS

The recent discoveries by Bednorz and Muller[2] of superconductivity in the 30K range and by Wu et al.[3] in the 90K range have generated a tremendous interest because of their scientific and technological importance. We have performed spectroscopic measurements on both classes of materials with a newly developed STM. This instrument operates at low temperature in an ultra-high-vacuum chamber and has a number of unique capabilities:

* Temperature range: 10K to 400K
* Topographic imaging and I-V spectroscopy
* In-situ Auger analysis
* In-situ LEED
* In-situ ion milling, annealing and thermal evaporation
* Load-lock exchange of samples and tips

The last feature is very important in this experiment since it has allowed us to measure a large number of combinations of tips and samples in a short time. The spectroscopic measurements of a $La_{1.85}Sr_{0.15}CuO_{4-y}$ bulk sample with a tungsten tip[4] show a gap-like structure with a value of approximately Δ=12mV. The superconducting transition temperature, T_c, was measured resistively on a sample from the same batch, giving an onset of 40K, a midpoint of 38.5K and a width (10%-90%) of 1.1K. Therefore the ratio $2\Delta/kT_c$=7 is twice as large as the BCS prediction.

We have taken similar spectroscopic data for $YBa_2Cu_3O_{7-y}$ samples and a wide variety of tip materials[5]. We find that the softest tips, made of indium or aluminum, give the best spectroscopic data. The most common value of $2\Delta/kT_c$ for this material is approximately 11, with values even twice as large sometimes observed.

One must ask whether these large gaps are real and whether they are related to superconductivity. The experimental setup has been calibrated with resistors to check the voltage scale. Furthermore, we do not believe that there is a series voltage drop anywhere because this would reduce the peak-to-valley ratios in the curves. A strong possibility is that at least some of the data may be explained by assuming that the tunneling involves a small particle, and that the structure we observe is due to the charging energy of this particle. This model has been used recently by Barner and Ruggiero[6] to explain the behavior of a macroscopic tunnel junction with particles deposited in the barrier. One last possibility is that the large gaps are due to the addition of several junctions in series. These junctions may be inside the material due to its granular and twinned structure. Finally it should be pointed out that given the current state of the theoretical understanding of these materials, the BCS value for $2\Delta/kT_c$ need not be appropriate.

4. ACKNOWLEDGEMENTS

This work has been done in collaboration with K.W. Ng, S. Pan, R.M. Silver, and E.E. Ehrichs in my laboratory, J.M. Tarascon and L.H. Greene at Bell Communications Research, and J. Talvacchio and A.J. Panson at Westinghouse R&D Center. Support from NSF, the Welch Foundation, and AFOSR is gratefully acknowledged.

5. REFERENCES

1. R.M. Silver, E.E. Ehrichs, and A.L. de Lozanne: Appl. Phys. Lett. **51**, 247 (1987)
2. J.G. Bednorz and K.A. Muller: Zeits. fur Phys. B **64**, 189 (1986)
3. M.K. Wu, J.R. Ashburn, C.T. Torng, P.H. Hor, R.L. Meng, L. Gao, Z.J. Huang, Y.Q. Wang, and C.W. Chu: Phys. Rev. Lett. **58**, 908 (1987)
4. S. Pan, K.W. Ng, A.L. de Lozanne, J.M. Tarascon, and L.H. Greene: Phys. Rev. B **35**, 7220 (1987)
5. K. W. Ng, S. Pan, and A. L. de Lozanne: Jap. J. Appl. Phys. **26-3**, 993 (1987)
6. J.B. Barner and S.T. Ruggiero: Phys. Rev. Lett. **59**, 807 (1987)

Abstract No. 693

In Situ Scanning Tunneling Microscopy for Electrochemical Studies

Fu-Ren F. Fan, Andrew A. Gewirth,
and Allen J. Bard
The University of Texas
Department of Chemistry
Austin, TX 78712

We have examined with the STM different types of platinum electrodes (polycrystalline foil, single crystal, and sputtered Pt on mica) in aqueous 1 M solutions of H_2SO_4. Brief cycling of the electrode potential between the hydrogen and oxygen evolution regions improved the STM image by cleaning the electrode surface. More extensive cycling leads to a roughening of the electrode surface. We have also been able to take the topographic images of electrode surfaces while the electrodes are biased at potentials where no appreciable steady-state faradaic current is observed.

We have also investigated the initial stages of electropolymerization of an electronically conductive polymer (polypyrrole) in acetonitrile. The STM images obtained after electrodeposition of ca. 1.0 mC/cm^2 show a well-defined film on mica, suggesting a nucleation and growth mechanism. Changes in topography with progressive electrodeposition will be deomonstrated.

The corrosion of stainless steel (S.S. 304L) samples in aqueous chloride media was also monitored by STM. In air the surface of a well-polished sample (except for freshly polished ones) could not be imaged very well, perhaps because of the presence of an insulating oxide layer. The introduction of an aqueous chloride solution into the electrochemical cell, in which the tip and the substrate are immersed, allowed imaging of the surface, perhaps because the oxide layer was removed. With this technique we could continuously monitor surface corrosion for a few days. The effect of pH, the concentration of inhibitor, and polarization potential on corrosion will be discussed.

An additional area of investigation has utilized the STM to monitor the in situ oxidation of pyrolytic graphite. Freshly cleaved highly oriented pyroltyic graphite under 0.1 M H_2SO_4 at 0.25 V vs. AgQRE exhibits large, atomically flat areas which are stable for several hours. High resolution images obtained under these conditions reveal the characteristic graphite ring structure. After cycling to 1.8 V vs. AgQRE to initiate the oxidation process, STM images show depressions of less than 50 A^2 in area, where the surface appears broken up and no atomic structure is discernable, surrounded by large areas retaining the atomic scale flatness and resolution. These depressions may originate at fault boundaries in the graphite surface. Simultaneous barrier height measurements obtained by modulating the tip-sample distance (0.5 Å at 15 kHz) show decreased barrier heignts in these regions consistent with the formation of a graphitic oxide layer growing into the bulk. With additional cycling to 1.8 V, the rough broken-up regions increase in area and grow together, and STM images reveal strips of atomically flat regions surrounded by the breakdown zone, which now grows rougher and exhibits large peaks and valleys. Finally, extensive electrochemical cycling completely eliminates the flat regions and leaves large rough regions exhibiting corrugations several hundred angstroms in magnitude.

Abstract No. 694

Scanning Electrochemical Microscope: High Resolution Deposition and Etching of Metals

Oskar E. Hüsser, Derek H. Craston and Allen J. Bard
Department of Chemistry, The University of Texas at Austin
Austin, Texas 78712

The scanning tunneling microscope (STM) [1,2] has proven to be a powerful tool for the study of surfaces. To date, most applications have been concerned with the study of clean surfaces in UHV chambers with relatively few reports of studies of contaminated surfaces and investigations under liquids, or in air [3].
Research in this laboratory has recently led to the development of a method for the high resolution deposition of metals in thin ionically conducting polymer films in the absence of any liquid electrolyte solution [4]. This technique involves the use of a substrate material made by spin coating thin ionic conducting polymer films on the surface of a metal. The metal ion to be deposited is then incorporated into the polymer film by soaking in the appropriate solution. A metal tip electrode is brought into contact with the surface of the polymer film using the scanning electrochemical microscope (similar to the STM) which maintains a constant faradaic current between the substrate and tip (Figure 1). By applying a negative potential between tip and substrate, the faradaic processes result in deposition of the metal D at the tip/polymer interface,

$$D^{n+} + ne^- \longrightarrow D,$$

and, at the same time, localized etching of the metal substrate surface

$$M \longrightarrow M^{n+} + ne^-.$$

Predefined pattern, deposition and etching structures, can be obtained by controlling the x and y movements of the sample with a computer.

Work to date has resulted in high resolution deposition and etching coated Nafion [5] or poly(4-vinylpyridine) (PVP) as the ionically conducting films spin coated on copper, silver or gold. The films were soaked in solutions containing either copper, silver, gold or methyl viologen ions. Electrochemically etched platinum, platinum-iridium alloy and tungsten wire served as tip materials.
For all experiments, bias voltages from 50 mV and upward could be applied between sample and metal tip. At lower bias voltages the tip penetrates the conducting polymer film and only scratched lines resulted.
The thickness of the deposited and etched structures were strongly affected by the tip shape, set current, bias potential and speed that the tip is scanned over the surface. Lines thinner than 1 μm can only be obtained with very sharp needle like tips. The thickness of the lines depends on the number of coulombs past per unit distance of tip movement. This is a function of both the set current and the tip scan rate. Scan rates of up to 1 μm/s can be used, this limit being set by the speed of the STM feedback loop.

Several examples of structures produced by these techniques will be presented, and extensions of the method to other materials described.

References

[1] G. Binnig and H. Rohrer, Helv. Phys. Acta, 55, 726 (1982).
[2] G. Binnig, H. Rohrer, Ch. Gerber and E. Weibel, Phys. Rev. Lett., 50, 120 (1983).
[3] P.K. Hansma and J. Tersoff, J. Appl. Phys., 61, R1 (1987) and references therein.
[4] D. H. Craston, Ch.W. Lin and A.J. Bard, J. Electrochem. Soc., 135, 785 (1988).
[5] Nafion is a registered trademark of E.I. du Pont de Nemours and Co., Inc.

Figure Captions

Fig. 1: Schematic representation of a method to simultaneously deposit species D in an ionic conductor and etch the substrate M.

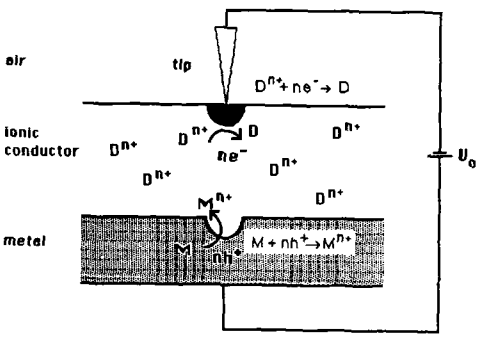


Fig. 1

Abstract No. 695

STM Images of Organic Adsorbates

J.E. Frommer and J.S. Foster

IBM Research Division, Almaden Research Center
650 Harry Road, San Jose, California 95120 USA

In this study, individual organic molecules in a liquid crystal array on a graphite surface have been imaged with the Scanning Tunneling Microscope with near-atomic resolution. Two-dimensional order has been identified in 4-n-octyl-4'-cyanobiphenyl (8CB) and compared to literature models which are largely based on x-ray data from the bulk smectic phase. The graphite substrate appears to influence the molecules in two ways: 1) the molecular axes lie parallel to the surface so that the STM images a cross-section of the classical smectic planes; and 2) molecules of one plane are registered with those of adjacent planes, a degree of order which is not normally observed in the bulk. The interplanar smectic distances observed with the STM at the surface of the graphite are similar to those reported in the literature for the bulk.

The samples are prepared by cleaving graphite (Highly Oriented Pyrolytic Graphite) and immediately applying a drop of the liquid crystal to the fresh surface[1]. The tunneling tip is then immersed into the drop and mechanically guided to the graphite surface. To assure that no tip or graphite damage occurs by contact between the two, the final approach to the surface is performed electrically, with a feedback loop monitoring tunneling current as the tip comes within several angstroms of the surface. A quantitative measure of this final distance is not made; however, it is estimated from the magnitude of the tunneling current to be on the order of 10Å. This corresponds to one to four monolayers from the graphite surface. Images are collected under tunneling conditions of a tip-to-sample bias of -0.5 to -0.7V and a tunneling current of 0.2 to 0.5nA. All sample manipulation and scanning is performed in air.

Figure 1 depicts the ordering of 8CB molecules on graphite as imaged in the STM. The bright stripes, interpreted as cross-sections of smectic planes, are 20Å wide and spaced 14Å apart for a repeat distance of 34Å. A single molecular length in an extended (linear) chain conformation is 22Å, since some angle between the biphenyl and alkyl moieties is expected. The observed 20Å dimension is consistent with a single molecular length. The 34Å repeat distance is slightly larger than the 29-32Å reported in the literature for the d-spacing of 8CB's bulk smectic[2]. The discrepancy could arise from an ordering effect of graphite or simply from experimental error. The distance between adjacent molecular axes is 5Å. The periodic 'hole-like' features which appear every fourth molecule are puzzling; no previous literature cites their existence, so they too might arise from surface-adsorbate forces. This rationale is supported by the long-range ordering of hole-like features in two dimensions, i.e., between planes as well. Finally, the 14Å dark stripe could be interpreted as the spacing between smectic layer cross-sections as dictated by registration with planes below and above the imaged plane. Although the 20Å dimension of the bright stripe corresponds to the length of a single molecule, an alternative explanation for the 20 and 14Å spacings is that the bright 20Å area is comprised of two cyanobiphenyl moieties meeting head-to-head, and the dark 14Å area is comprised of two alkyl moieties slightly overlapping tail-to-tail.

During the course of these experiments several structures have been seen. Figure 2 presents a second example of observed order in 8CB. Long-range order is evident in the interplanar spacing and is the same as that in Figure 1 (within experimental error). The cross-sections of the planes (bright stripes) are now bisected by a dark channel narrower than the dark areas which separate the bright stripes. The molecular axes comprising each stripe, visible at higher magnification, are spaced approximately 3Å apart from from each other. A third apparent periodicity occurs every eighth molecular axis and appears as a 'saw-tooth' structure. This saw tooth pattern is commensurate between planes as are the hole-like features of Figure 1. Both features might arise from incommensurate packing between the graphite lattice and the liquid crystal lattice, the release of strain occurring at the periodic intervals of these features.

In related studies, we have been able to successfully image several other liquid crystals. Work is also in progress to study the liquid crystals' thermal transitions as they occur on the graphite surface.

REFERENCES

1. J.S. Foster, J.E. Frommer, and P.C. Arnett, Nature 331, 324-326 (1988).
2. P.S. Pershan, A. Braslau and A.H. Weiss, Phys. Rev. A 35, 4800-4813 (1987); J.E. Lydon and C.J. Coakley, J. Physique Colloq. 36, C1-45 (1975); P.E. Cladis, R.K. Bogardus, W.B. Daniels and G.N. Taylor, Phys. Rev. Lett. 39, 720-723 (1977); A.J. Leadbetter, J.L.A. Durrant and M. Rugman, Mol. Cryst. Liq. Cryst. 34, 231-235 (1977); A.J. Leadbetter, J.C. Frost and J.P. Gaughan, J. Physique 40, 375-380 (1979).

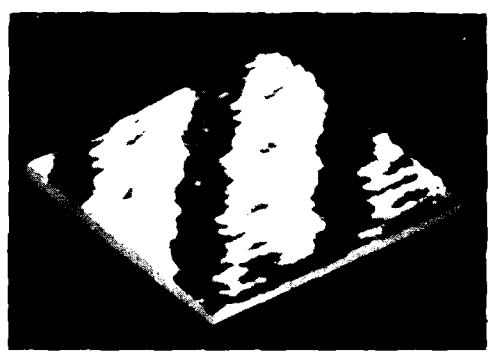


Fig. 1) STM image of 8CB on graphite. The scale is 75 X 75Å.

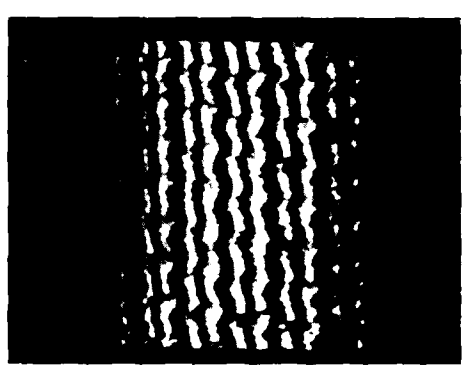


Fig. 2) STM image of 8CB on graphite. The scale is 215 x 215Å.

Abstract No. 696

SCANNING TUNNELING MICROSCOPY OF TITANIUM IN AIR AND WATER.

L. D. McCormick, J. and D. Scientific, Inc., Annapolis, MD 21401, T. Thundat, L. Nagahara, and S. M. Lindsay, Arizona State University, Tempe, AZ 85287.

Scanning Tunneling Microscopy (STM) has demonstrated the ability to image numerous surfaces in several media, e.g. vacuum, oil, water, solution, and air. The capability of imaging in liquids is of significant importance in the study of electrochemical processes, e.g. corrosion, electrodeposition, and etching. This report describes preliminary research whose goal is to demonstrate the usefulness of the STM technique in the study of technologically important surfaces. Subsequent research efforts will be directed at studying these surfaces under controlled electrochemical conditions.

Titanium foil was first cleaned with acetone and etched with hydrochloric and then nitric acid. This preparation produced an optically smooth, shiny surface. Tips for use in water were coated with epoxy to limit leakage current. For both air and water imaging the tips were platinum-iridium. Images were obtained with STM tip biases between -100 mV and -800 mV. (Previous STM results on aluminum required the use of much higher magnitude tip biases in order to not disrupt the surface during imaging.) As can be seen in Figure 1 the STM images of the surfaces were often flat over tens of nanometers. It was also possible to observe features that may be surface steps such as those that appear to run from the upper right to the lower left in Figure 1. The fact that Ti is much easier to image and that it may be imaged at a lower tip bias probably indicates that the oxide film on Ti is much thinner and/or less protective than the Al oxide film.

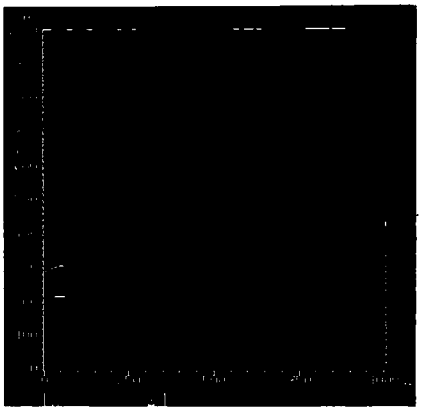


FIGURE 1

STM image of Ti in water. Tip bias -250 mV. Tunneling current 1 nA.

Abstract No. 697

MOLECULAR RULERS AND THE USE OF SCANNING TRANSMISSION ELECTRON MICROSCOPY

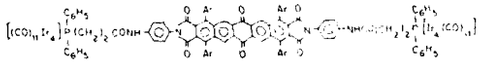
Larry L. Miller and Frederic R. Furuya

University of Minnesota
Department of Chemistry
Minneapolis, MN 55455

The successful thrust to make small electrodes and the recent advances in studying surfaces at high resolution has led to a number of exciting new experiments and experimental insights. Our interest is in molecular electronics, and our work connects to these two topics conceptually and perhaps experimentally. Thus, we are synthesizing "molecular lines," rigid-rod molecules up to 75 Å long, whose dimensions approach the dimensions of the smallest electrodes. These molecules can also provide experimental tests for high resolution analyses.

It was our goal in the present investigation to develop a method for imaging individual molecules on a surface. More specifically, it was desired to measure the length of molecular lines synthesized on and attached to a surface. Of the available methods (STM, AFM, and SEM) only transmission electron microscopy had been developed sufficiently that it could be applied to solve this problem. In TEM or STEM (scanning transmission electron microscopy) the resolution can be as high as 2 Å. Organic and most small biological molecules are essentially transparent in TEM, but distances between molecular sites can in principle be measured by attachment of electron-dense clusters to those sites. The present test utilized a sufficiently long and rigid organic spacer with specifically attached $Ir_4(CO)_{11}$ labels and took advantage of the capabilities of STEM for high resolution measurements on molecular materials.

ET_4N^+, $[Ir_4(CO)_{11}I]^-$ (1), prepared from commercial $Ir_4(CO)_{12}$, was employed to demonstrate the utility of tetrairidium clusters. Using a STEM operating at 40 kV, samples were subjected to a cumulative electron dose ranging from 5×10^4 to 4×10^5 e/nm^2. Specimen temperature was ~135° C during imaging. The sample was prepared by deposition from 10^{-6} M aqueous solution onto 25 Å carbon films. The dark field images showed bright spots ~ 6 Å in diameter. Micrographs were also obtained of rigid molecules that had been cluster labelled on both ends. For this purpose, we used synthetic methods that we had previously developed for the preparation of long, yet soluble, molecular lines. The resulting compound 1 had a rigid, linear spacer of 28 Å and flexible $COCH_2CH_2$ connectors. As anticipated, STEM micrographs showed paired 6 Å spots corresponding to individual molecules of 1. The separations between twenty pairs were 20–37 Å ($\bar{x}$ = 27 ± 4 Å). This range covers virtually all of the conformations available to the flexible connectors and shows that individual molecules adopt a variety of conformations on the surface.



1

Other bis-cluster compounds have been investigated, as well as cluster-labelled surface-bound lines. The micrographs show pairs of spots within the length range expected from molecular models. The effects of conformation and surface orientation can be discerned.

Abstract No. 698

Characterization of Surfaces by Surface Forces, Scanning Tunneling and Atomic Force Microscopy

D.F. Evans, R. Yang, G. Lee, R. Matthews
Department of Chemical Engineering and Materials Science
University of Minnesota
Minneapolis, MN 55455

W. Hendrickson
3M Corporation
St. Paul, MN 55104

Recent developments in near field techniques, particularly scanning tunneling microscopy (STM) and atomic force microscopy (AFM), provides detailed molecular information on the structure of thin films and molecular adsorbates. Surface forces apparatus measurements permit the determination of the colloidal interactions force as a function of distance (resolution $\pm$ 0.1 nm) of thin molecular films adsorbed on mica, but the structure of the molecular film is often assumed not directly characterized. In this paper we present (1) surface force measurements on conducting and non-conducting surfaces characterized by STM and AFM measurements and (2) STM and AFM measurements on several inorganic composite membranes such as those shown below.

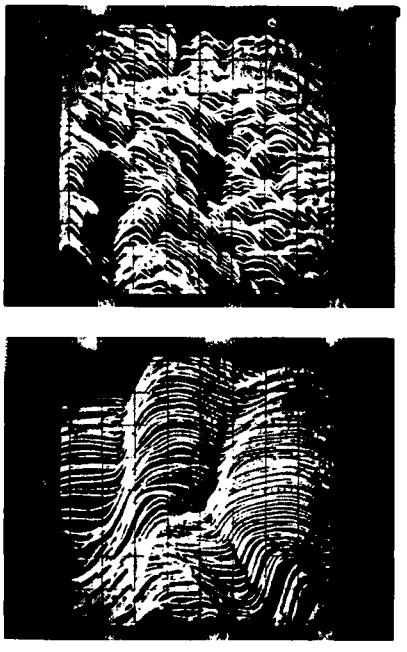


Figure 1. An STM image of the same regions of Ag_2S:CuS membrane surface. The membrane sample is formed under a pressure of 20,000 lb/in^2. (a) 0.6 x 0.6 μm, (b) 660 x 660Å. The tunneling current is equal to 1.8 nA and bias is equal to 24 mv in both pictures. Several holes are revealed on the membrane surface.

Abstract No. 699

MULTIPLE-BEAM INTERFEROMETRY AND THE STUDY OF SILVER FILMS IN A SURFACE FORCE APPARATUS

Hugo K. Christenson, Mark T. Clarkson and John L. Parker

Department of Applied Mathematics, Research School of Physical Sciences, Australian National University, GPO Box 4, Canberra, ACT, 2601 AUSTRALIA

The surface force apparatus (1) is a versatile tool for investigating the properties of thin films of liquid or gas confined between solid surfaces. Early applications were centered around the direct measurement of surface forces between mica surfaces. Recently, considerable interest has been focussed on the study of properties such as adhesion (2), viscosity (3), friction (4), phase transitions in thin films (5), etc. It has also been shown that it is possible to use a number of different surfaces, either by retaining the mica as a substrate (6) or by using a completely different material such as synthetic sapphire (7). In particular, it is possible to deposit thin metal films on a mica substrate, measure surface forces (8) and also use the surfaces as model electrodes (9).

We here present some results of initial investigations of thin films of silver on mica. We have used two different methods of preparing the films; either direct evaporation or a new method based on fusing two evaporated films (10). The films have been characterised by conductance measurements and optical methods.

With the surface force apparatus multiple-beam interferometry is used to measure the surface separation. The interferometry equations giving the wavelengths of transmitted light as a function of separation are modified considerably by the presence of metal films. The system cannot be treated as a simple five-layer interferometer (11). We have solved the equations in the general case, using the complex refractive indices of the metal films. Silver turns out to be the ideal metal to use because of its high reflectivity. Even so, absorption puts an upper limit on the film thickness of about 20 nm.

The right evaporation conditions are crucial for obtaining a film with high reflectivity, low absorption and scattering, showing a conduction threshold at low average thickness. We have found that using a fast evaporation rate gives the best results. It is also essential to avoid heating of the substrate, both during and after deposition. The chemical reactivity of the silver films poses additional problems, especially in aqueous solution.

We have carried out measurements of surface forces between one mica surface and one silver surface in both aqueous and non-aqueous systems(10). In the nonpolar liquid octamethylcyclotetrasiloxane (a near-spherical molecule of diameter $\simeq$ 0.8 nm) oscillatory solvation forces are measured. These are qualitatively similar to the forces found between two mica surfaces (5), but of shorter range. Furthermore, fused films, which should retain much of the smoothness of the mica substrate, give forces that are similar to those with directly evaporated films. We believe that these results indicate that the silver surfaces are quite smooth, even on a molecular scale.

In conductivity water and sodium carbonate solutions long-range double-layer forces are measured. The results are consistent with the non-linear Poisson-Boltzmann equation, and the Debye screening length in close agreement with that expected from the electrolyte concentration. At short range a weak attraction is found in pure water, but the force in sodium carbonate is a monotonic repulsion down to about 7 nm, where an almost "hard wall" is found. This may be due to hydration effects or some chemical modification of the silver surface.

We also present preliminary results of force measurements between two silver surfaces across octamethylcyclotetrasiloxane.

There is clearly scope for a great deal of experiments with silver films. Apart from direct measurements of surface forces in liquids it should be possible to study the viscosity of thin liquid films between metal surfaces, adsorption of surfactants and polymers to metal films, and, of course, electrochemical processes. By applying and varying two different potentials at the silver surfaces the interaction of double layers of unequal potential could be studied.

1. J.N. Israelachvili and G.E. Adams, J. Chem Soc. Faraday Trans. 1 74, 975 (1978).
2. H.K. Christenson, J. Colloid Interface Sci. 121, 170 (1988).
3. D.Y.C. Chan and R.G. Horn, J. Chem. Phys. 83, 5311 (1985); J.N. Israelachvili, J. Colloid Interface Sci. 110, 262 (1986).
4. J.N. Israelachvili, P.M. McGuiggan and A.W. Homola, to be published.
5. H.K. Christenson and C.E. Blom, J. Chem. Phys. 86, 419 (1987).
6. P.M. Claesson, C.E. Blom, P.C. Herder and B.W. Ninham, J. Colloid Interface Sci. 114, 234 (1986).
7. R.G. Horn, D.R. Clarke and M.T. Clarkson, to be published.
8. C.P. Smith, M. Maeda, L. Atanasoska and H.S. White, J. Phys. Chem. 92, 199 (1988).
9. F.F. Fan and A.J. Bard, J. Amer. Chem. Soc. 109, 6262 (1987).
10. J.L. Parker and H.K. Christenson, J. Chem. Phys, in press.
11. J.N. Israelachvili, J. Colloid Interface Sci. 44, 259 (1973).

Abstract No. 700

Adhesion of Two Solid Surfaces in Water: Effect of Rotational Mismatch of Surface Lattices

P.M. McGuiggan and J.N. Israelachvili

Dept. of Chemical and Nuclear Engineering
and Materials Science
University of California, Santa Barbara
California 93106

Current interest in the fundamental aspects of electrochemistry at interfaces has focused on understanding the interactions occurring at the atomic level. We are exploring these problems by using molecularly smooth mica surfaces. In vacuum, two mica surfaces will come into an adhesive contact. In liquids or vapors, the surfaces often come into equilibrium "contact" while still separated by a few layers of molecules, and the adhesive force is dramatically reduced from the value in vacuum.

Using the Surface Forces Apparatus (SFA), the adhesion force needed to separate two molecularly smooth mica surfaces in water has been directly measured as a function of the rotational angle θ between the two surface lattices (relative crystallographic orientation). The SFA allows the distance between two mica surfaces (crossed-cylinder geometry) to be independently controlled and measured (using an optical interferometric technique) to ±1Å. The adhesion was measured as the 'pull-off' force, F, needed to separate two surfaces from contact, which can be related to the surface energy, E, between two flat surfaces by the Derjaguin approximation:

$$E = F/2\pi R$$

By convention $E = 2\gamma_{sl}$, where γ_{sl} is commonly referred to as the "surface energy" or the "interfacial energy" for interactions across a medium. The surfaces were rotated relative to each other (about the vertical axis which is normal to the surfaces) with an angular sensitivity of 10^{-2} deg.

As shown in Fig. 1, the adhesion energy E varies as a function of θ interacting across water. When the surfaces are in perfect crystallographic register (e.g. θ = 0, 60, 120, 180) the adhesion is found to be maximum, whereas if the surfaces are rotated by as little as ±0.5° from the maximum, the adhesion decreases by 50%. Effects of the mica orientation on the total interaction potential (i.e. force law at finite distance) which includes electrostatic, solvation, and structural forces will be discussed.

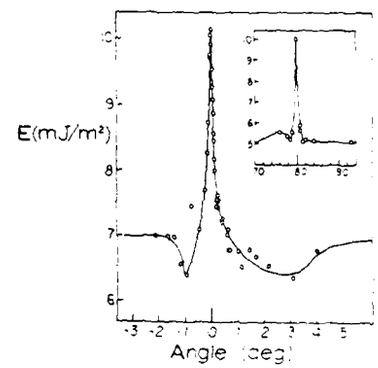


Figure 1
Adhesion energy versus θ between two flat mica surfaces in water

Abstract No. 701

Surface Forces and High-Resolution Optical Imaging of the Electrode/Electrolyte Interface

C.P. Smith, S.R. Snyder, J. D. Norton, and H.S. White
Department of Chemical Engineering and Materials Science
University of Minnesota
Minneapolis, Minnesota

Developments in high resolution scanning tunnelling microscopy (STM) have recently provided unprecedented detail of electrode structure and of local physiochemical properties of molecular adsorbates and thin molecular films. In this paper we describe two newly developed in-situ methods that are complimentary to STM, and which provide (1) high-resolution (2-5Å) measurement of forces within the electrode/electrolyte interphase region and (2) real-time imaging of the changes in surface topology that accompany many classes of electrode reactions.

The first technique described utilizes the surface forces microbalance to measure forces between two 40Å thin film Pt electrodes separated by 5 to 500Å of an electrolyte or an adsorbed molecular film. We have directly measured forces between Pt electrodes separated by H_2O as a function of separation distance. Measurable electrostatic forces are obtained at ca. 160Å and increase nearly exponentially with decreasing separation distance. At ca. 10Å the surfaces come into "contact" and further increases in the externally applied pressure results in no further decrease in separation distance. That the surfaces come into "contact" at a finite separation distance may be due to atomic scale surface roughness or due to the strong adsorption of solvent and/or impurity. To test the hypothesis of a strongly bound H_2O layer, we have measured forces between potentiostated Pt electrodes, initially "dried" and subsequently exposed to moist air. We observe that a thin layer of H_2O is trapped between the surfaces that is difficult to remove without application of a large external potential bias between the surfaces (corresponding to a field strength of 10^7 eV/cm across the H_2O film). Similar measurements are in progress using different adsorbing gases.

In a separate area of investigation, we have employed phase-detection microscopy (PDM) to monitor changes in surface topology that accompany dissolution and precipitation reactions. The phase-detection microscope (ZYGO Maxim 3-D System) is based on interferometric analysis using a photodiode array detector and has a routinely accessible vertical resolution of 5Å. In addition to measuring topology of surfaces exposed to air, PDM is capable of imaging surfaces immersed under bulk electrolyte layers (i.e. 0.5 cm), Figure 1, without suffering significant loss in resolution. We have used PDM to image molecularly smooth Pt and Ag samples, insulating polymers and inorganic substrates, e.g., mica, in air and under H_2O. Ongoing studies include in-situ measurement of non-uniform dissolution of layered transition metal dichalcogenides and of electroactive polymeric films. Results from these studies will be described.

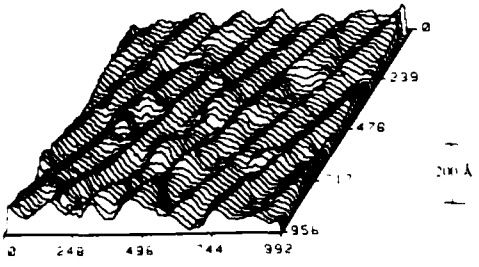


Fig. 1. PDM image of diamond polished aluminum submerged under water.

Abstract No. 702

Kinetic Isotope Effects of the Hydrogen-Evolution-Reaction (HER) at Gold- and Platinum-Electrodes

D. Tegtmeyer, J. Heitbaum

University of Witten/Herdecke
Faculty of Natural Sciences
Stockumer Str. 10, D - 5810 Witten

The combination of a quadrupole mass spectrometer and an electrochemical cell (differential electrochemical mass spectroscopy, DEMS) allows the online mass-detection of a volatile product with a time constant of less than 0.5 sec. The ion current of the detected species is proportional to the corresponding faradaic current. With a new, rotating inletsystem it becomes possible to determine the proportionality factor, between the faradaic current and the mass-signal. By means of this quantitative correlation, the corresponding faradaic current can be calculated from the obtained mass intensity. This is very useful in cases, where the current is a sum of different faradaic and non-faradaic processes. One example therefor is the hydrogen evolution in an acid mixture of light and heavy water. There are three different gaseous products, namely hydrogen, deuteriumhydrid and deuterium, but only one common signal for the current. The amount of each produced gas is a function of the ratio between protons and deuterons, which depends on the isotope mixture $H_2O/HDO/D_2O$. With the applied method it is possible to obtain three different cyclic voltammograms in one experiment, respectively for the production of H_2, HD and D_2 (see fig. 1). In this way the hydrogen evolution reaction was investigated in different mixtures of light and heavy water, varying the temperature as well as the pH and the isotope ratio in the solution. The experiments were done with vacuum deposited platinum as well as gold catalyst layers. For each reaction, the evolution of H_2, HD and D_2, the usual evaluation of the experimental data gives the characteristic kinetic parameters of the electrochemical reactions: exchange-current-density, tafelslope, activationenergy, electrochemical reaction order and separation factor. The results are interpreted on the basis of the theoretical considerations to be found in the literature /2/.

/1/ J. Willsau, O. Wolter, J. Heitbaum
J. Electroanal. Chem., 185 (1985) 143

/2/ L. I. Krishtalik
Charge transfer reactions in electrochemical and chemical processes, plenum, N. Y. 10013 (1986)

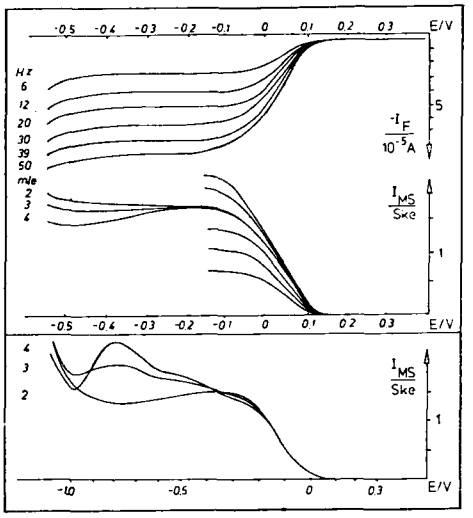


Fig. 1: Hydrogen evolution in an acid H_2O/D_2O-mixture

system: 10^{-3} m $HClO_4$, 0.1 m $NaClO_4$, scan speed: 10 mV/sec; 60 % H_2O, 40 % D_2O, $H^+ : D^+$ 1 : 1

above: faradaic limiting currents of the H^+ D^+-reduction on platinum electrode

middle: corresponding mass spectrum for H_2, HD, D_2

below: mass spectrometric cyclic voltammogram for gold

m/e: 2; 1 Ske 4.6×10^{-12} A
m/e: 3; 1 Ske 2.5×10^{-13} A
m/e: 4; 1 Ske 7.9×10^{-14} A

Abstract No. 703

ELECTROCATALYSIS OF ANODIC OXYGEN-TRANSFER REACTIONS:

Modification of Electrode Surfaces by Formation of Thin PbO_2 and Bi(III)-Incorporated PbO_2 Ad-Layers via Electrochemical Reaction at Solid/Solid Interface

Hsiangpin Chang and Dennis C. Johnson

Department of Chemistry and Ames Laboratory*
Iowa State University, Ames, Iowa 50011

Recently, chemically modified PbO_2 film electrodes prepared by incorporation of ionic catalyst, e.g., Bi^{3+}, denoted as Bi-PbO_2, via electro-co-deposition or electroadsorption have been the subject of intensive studies in this laboratory (1-7). These electrodes show effective efficiencies to catalyze many anodic oxygen-transfer reactions (OTR) that are extremely slow at normal solid electrodes. The ionic catalyst serves as a bi-mediator for both electron and oxygen atom transfer (7). Some typical reactions are:

$$(CH_3)_2SO + H_2O \longrightarrow (CH_3)_2SO_2 + 2H^+ + 2e$$

$$Mn^{2+} + 4H_2O \longrightarrow MnO_4^- + 8H^+ + 5e$$

$$Cl^- + 3H_2O \longrightarrow ClO_3^- + 6H^+ + 6e$$

Conventional Bi-PbO_2 film prepared by co-deposition has a thickness of ca. 0.1-1 mm. It was discovered that a thin PbO ad-layer remains on Au after electrolytic stripping of PbO_2 (6). In this report, we will describe the conditions to make thin PbO_2 and Bi-PbO_2 ad-layers as a new way of modifying varied solid electrodes. Cyclic voltammetry, chronoamperometry and other electrochemical and spectroscopic methods are used to characterize the ad-layers. The mechanisms by which the ad- layers are formed are also studied.

Formation of PbO_2 and Bi-PbO_2 Ad-Layers. PbO_2 and Bi-PbO_2 ad-layers are formed on Au, Pt, Ti, and GC disc electrodes by stripping of thick PbO_2 and Bi-PbO_2 (Bi:Pb = 1:10) films followed by reanodizing in a blank solution. This was evidenced by the following: (a) The rate of oxide deposition at ad-layer covered electrodes is much faster than that at freshly polished electrodes. The anodic CV peak increases with cycle number as the induction time for constant potential deposition decreases; (b) A distinct anodic current was observed during reanodizing the ad-layer (reduced form) covered electrodes; (c) A cathodic stripping peak was observed at the ad-layer (oxidized form) covered electrode when potential was scanned from 1.7 to 0.8 V vs. SCE; (d) Thin but observable films were seen at the disc electrodes; (e) The ad-layer covered electrodes show similar electrochemical and chemical properties as the normal bulk oxide films. The ad-layers can be totally removed by treating in mixture of H_2O_2 and acetic acid.

Mechanisms of Ad-Layer Formation. The formation of ad-layers depends on solution pH and the thickness of normal oxide film before stripping. The higher the pH during stripping is or the thicker the original oxide film is, the easier the formation of ad-layers is. No ad-layer is formed if the normal oxide film is too thin. It was observed that the stripping rate of thick oxide films was limited by mass-transport of H^+ and, thus, the dissolution of oxide film proceeded layer-by-layer. Upon the above observations, it is concluded that the ad layers are formed by undissolving reduction of the internal layer of thick oxide films during stripping due to the lackness of H^+ or H_2O at the substrate /oxide interface plus the interactions between the substrate and the internal oxide layer. The whole process can be regarded as an electrochemical reaction at the solid/solid interface of the substrate/oxide /solution multilayer junction. It is also concluded that the surface oxide of the substrate does not affect the formation of ad layers.

Thickness, Morphology, and Stability of the Ad-Layers. The thickness of PbO_2 and Bi-PbO_2 ad-layers were estimated either by measuring the charge for their voltammetric stripping peaks or by SEM. The results are 0.1-0.5 μm, which are much smaller than the normal films and vary with the conditions of preparation. Accumulation and growth of the ad-layer occurs by multiple cycles of deposition/stripping process.

The morphology of the ad-layers was studied with SEM. Microcracks were observed on both kinds of ad-layers, which were not seen at their normal films, and might be formed by contraction of the internal oxide layer during undissolving reduction in solid phase. The microcracked surface structure of the ad-layers is very similar to that of RuO_2/Ti dimensionally stable anodes prepared by thermal deposition. The morphology of the ad-layers does not change after reanodizing.

Both kinds of ad-layers are adherent to the substrate. However, the ad-layers prepared from multiple cycles of deposition/stripping become fragile. PbO_2 ad-layers can be removed by consecutive anodizing /stripping. But, Bi-PbO_2 ad-layer is much stabler, which remains effective after potential cycling between 1.5 and 0.3 V. This enhanced stability of Bi-PbO_2 may be caused by the decreased basicity of the mixed oxide introduced by incorporation of Bi^{3+} ions.

Catalytic Activities of the Ad-Layers. The catalytic activities of PbO_2 ad-layer for anodic oxygen-transfer reactions in acidic media are tested with Bi^{3+} co-existing in the solution, as the result is similar to that of normal PbO_2 films (7). Well-defined i-E plateaus are obtained for oxidation of widely varied substances including dimethyl sulfoxide, tetramethyl sulfoxide, 2-thiophene carboxylic acid, and Mn^{2+} etc., as the same half potential ($E_{1/2}$, ca. 1.65 V at Au subtrate) is observed. It is concluded that it is the electroadsorped Bi^{3+} on the PbO_2 ad-layer that functions as the catalyst (7).

Bismuth (III) ions are incorporated into PbO_2 matrix in Bi-PbO_2 ad-layer. It is observed that the $E_{1/2}$ value for many OTRs at Bi-PbO_2 ad-layer covered electrodes is lower than that at normal Bi-PbO_2 film of varied thickness, which means the Bi-PbO_2 ad-layer has better catalytic activity than the normal Bi-PbO_2 film. This proves that the difference between Bi-PbO_2 ad-layer and normal Bi-PbO_2 film is not simply the thickness, but also surface structures. The Bi-PbO_2 ad-layer also has a higher electrochemical stability than the normal film, as a vider potential windov can be applied to the Bi-PbO_2 ad-layer covered electrodes.

The anodic current for the above oxidation reactions increases linearly with $\omega^{1/2}$ and bulk concentration of the substances, indicating mass-transport limitation. The anodic processes at these electrodes also have high current efficiency and stability.

The mechanism of electrocatalysis at PbO_2 and Bi-PbO_2 ad-layers is the same as that at their normal films. The Bi(III/V) ions electroadsorped on PbO_2 or incorporated into the PbO_2 matrix via co-deposition function as a bi-mediator for both electron and oxygen atom transfer. Two i-E peaks for Bi(III ⇌ V) transition that increase with scan rate are observed at Bi-PbO_2 ad-layer covered electrodes whose peak potential corresponds to the $E_{1/2}$ value of the catalytic electrode oxidations.

References

(1) D.S. Austin, J.A. Polta, T.Z. Polta, A.P.-C. Tang, T.P. Cabelka, and D.C. Johnson, J. Electroanal. Chem., **1984**, 168, 227. (2) D.C. Johnson, J.A. Polta, T.Z. Polta, G.G. Neuburger, J.Johnson, A.P.-C. Tang, I.-H. Yeo, and J. Baur, J. Chem. Soc., Faraday Trans. 1, **1986**, 82, 1081. (3) A.P.-C. Tang and D.C. Johnson, Anal. Chim. Acta, in press. (4) I. H. Yeo and D.C. Johnson, J. Electrochem. Soc., **1987**, 128, 1973. (5) I.-H. Yeo, Ph.D. Dissertation, Iowa State University, Ames, **1987**. (6) H. Chang and D.C. Johnson, J. Electrochem. Soc., submitted. (7) H. Chang and D.C. Johnson, in preparation.

* Operated for the U.S. Department of Energy by Iowa State University under Contract No. W7405 ENG-82.

Abstract No. 704

ELECTROLYTIC HYDROGENATION AND AMORPHIZATION OF fcc-$Pd_{0.21}Zr_{0.79}$

J.Y. Huot, A. Van Neste*, L. Brossard and R. Schulz
IREQ, C.P. 1000, Varennes, Québec, Canada J0L 2P0
*Université Laval, Ste-Foy, Canada G1K 7P4

INTRODUCTION

Hydrogen absorption in crystalline metallic compounds produce lattice expansion and may induce several structural changes [1, 2]. During gazeous hydrogenation of La-Ni alloys the disappearance of the Bragg peaks in the X-ray pattern was attributed to an hydrogen induced disorder [3]. More recently, it was concluded that hydrogen may induce amorphization of some R-Ni (R = Rare Earth) Laves compounds [4], and metastable crystalline Rh-Zr [5] and Pd-Zr [6] alloys after reaction with hydrogen gas. In this paper the electrolytic hydrogenation of fcc-$Pd_{0.21}Zr_{0.79}$ is used as an alternative way to gazeous hydrogenation.

EXPERIMENTAL

Electrolytic hydrogenation is performed at constant current density and temperature in 1 N H_2SO_4 containing 1 mM dissolved thiourea. The fcc-Pd-Zr ribbons are prepared by the melt-spinning technique. The electrode are etched 60 s in 0.1 M HF solution prior the experiments.

The electrochemical measurements are carried out between 25 and 75°C with a PAR Model 273 potentiostat coupled to an Appel IIe computer. A Philipps vertical X-ray diffractometer equipped with a graphite monochromator is used to characterize, with Mo K_α radiation, the microstructure during the electrolytic hydrogenation.

RESULTS

In 1 N H_2SO_4 solution, containing thiourea, no apparent gazeous H_2 is evolved during the most part of the electrolytic charging. At 10 mA cm^{-2} the electrode potential shifts in the cathodic direction with time after an incubation period of 150, 70 and 10 s for 25, 50, and 75°C operating temperatures respectively (Fig. 1). These potential-time curves are analyzed in terms of overpotential due to the charge transfer (Eq. (1)) and the diffusion of hydrogen in the electrode (Eq. (2)).

$$H_3O^+ + e^- \longrightarrow H_{adsorbed} + H_2O \qquad (1)$$

$$H_{adsorbed} \longrightarrow H_{adsorbed} \qquad (2)$$

The charge transfer reaction is the rate determining step (r.d.s.) at the beginning of the electrolytic charging. The calculated equivalent hydrogen fugacity in the first layers of the alloy is on the order of 200 atm at 10 mA cm^{-2}. For times larger than the incubation period, the r.d.s. is a mixed process charge-transfer - hydrogen diffusion in the electrode. By combining the expression for a quasi-reversible charge transfer and the diffusion equation of hydrogen, a general equation for the η-t curve leads to the determination of the diffusion coefficient of hydrogen (D_H) assuming that the hybride is $Pd_{0.21}Zr_{0.79}H_{1.3}$. At 25°C $D_H = 1 \times 10^{-9}$ cm^2 s^{-1} and the activation energy is 17 kJ mol^{-1}, compared to 2×10^{-7} cm^2 s^{-1} and 17-23 kJ mol^{-1} for Pd [7, 8] and 1×10^{-11} cm^2 s^{-1} and 15 kJ mol^{-1} for Zr [9].

The X-ray diffraction patterns of as-quenched polycrystalline electrode before ($Pd_{0.21}Zr_{0.79}$) and after the electrolytic hydrogenation ($Pd_{0.21}Zr_{0.79}H_x$) reveals that the metastable fcc lattice is modified by the hydrogen penetration. That suggests that the crystalline peak is transformed in an amorphous broad band. The position and the width of the (200) characteristic line may be analyzed in terms of d-spacing and crystal size respectively(Fig. 2).

At 25, 50 and 75°C, a linear relationship is observed between the lattice constant and the total cathodic charge density at 10 mA cm^{-2} (Fig. 3). Since no hydrogen evolution occurs, this charge represents the quantity of absorbed hydrogen in $Pd_{0.21}Zr_{0.79}$. The slope d(Å) vs Q is almost independent of the temperature, and is about 0,009 Å/C cm^{-2}. This slope corresponds to a lattice expansion of 3.7% and a volume increase of 10%, which is in the same range as the hybride formation of $PdH_{0.6}$ and $ZrH_{1.5}$ with volume increases of 10.8% and 13.1% from the face-centered cubic Pd and α-Zr respectively [7].

During the electrolytic hydrogenation the size of the microcrystallites decays exponentially with the square root of time or charge density (Fig. 4). The initial size is about 200 Å and it shrinks to 23 Å in 1000 s at 10 mA cm^{-2}. The crystallite dimension does not converge to zero at large times but to a finite value which is typically the size of one or two unit cells. The sample is then almost completely amorphous.

At fixed charge the amount of amorphous base, based on the crystallite dimensions, is independent of the current density for current densities up to a value of 100 mA cm^{-2}. For larger current densities, the electrolytic charging is less efficient because some hydrogen evolution occurs. The most rapid amorphization may be realized in 100 s at 100 mA cm^{-2}.

REFERENCES

1. A.J. Maeland in Hydrides for energy storage. A.F. Anderson and A.J. Maeland (Eds), Pergamon Press, Oxford, 1978.
2. F.A. Lewis, Int. J. Hydrogen Energy 12, 643 (1987).
3. H. Oesterreicher, J. Clinton and H. Bittner, Mat. Res. Bull. 11, 1241 (1976).
4. K. Aoki, T. Yamamoto and T. Masumoto, Metallurgica 21, 27 (1987); K. Aoki, K. Shirakawa and T. Masumoto, Sci. Eng. Res. Inst. Tohoku, Univ. A-32, 239 (1985).
5. X.L. Yeh, K. Samwer and W.L. Johnson, Appl. Phys. Lett. 42, 242 (1983).
6. X.L. Yeh, W.L. Johnson, J.Y. Tang and C.R. Shi, Met. Res. Soc. 58, 63 (1986).
7. Metal Hybrides, W.M. Mueller, J.P. Blackledge and G.G. Libowitz (eds) Academic Press, New-York, 1968.
8. V. Breger and E. Gileadi, Electrochim. Acta, 16, 177 (1971); J.O'M. Bockris, M.A. Genshaw and M. Fullenwider, Electrochim. Acta, 15, 47 (1970).
9. E. Brauer, R. Gruner and F. Rauch, Ber. Bunsenges Phys. Chem. 87, 341 (1983).

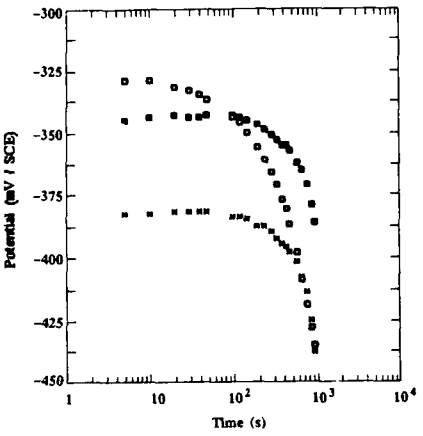


Fig. 1 Electrode potential vs time for electrolytic hydrogenation of Pd-Zr alloy at 10 mA cm^{-2} and 25 (■), 50 (*), 75°C (□) in acid solution.

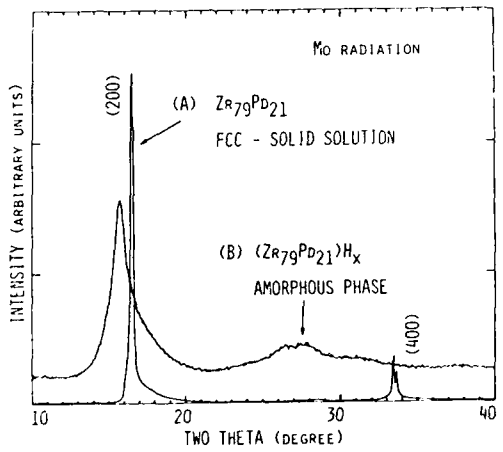


Fig. 2 X-ray diffraction patterns for (A) as quenched $Zr_{79}Pd_{21}$ and (B) amorphous $(Zr_{79}Pd_{21})H_x$ obtained by electrolytic hydrogenation at 10 mA cm^{-2} for 1000 s at 25°C.

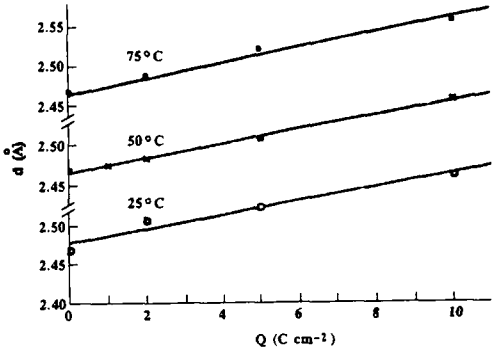


Fig. 3 d-spacing of the center of gravity of the distribution of X-ray intensity near the (200) Bragg peak as a function of the total charge density during hydrogenation at 10 mA cm^{-2} and various temperatures.

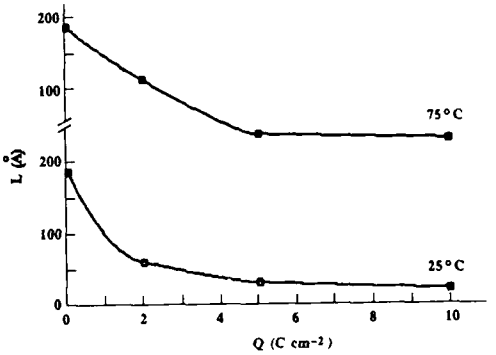


Fig. 4 Crystallite dimension as function of the total charge density for Pd-Zr_2 electrode during hydrogenation at 10 mA cm^{-2} and various temperatures.

Abstract No. 705

ELECTROCATALYTIC PROPERTIES OF METAL ADATOMS IN A POTENTIAL RANGE NEGATIVE TO BULK DEPOSITION

Xuekun Xing and Daniel Scherson

Case Center for Electrochemical Sciences
and The Department of Chemistry
Case Western Reserve University
Cleveland, OHIO 44106

INTRODUCTION

The kinetics for Cu deposition in 0.1M $HClO_4$ have been found to be so slow that submonolayers of copper atoms exhibiting UPD-type behavior are formed over periods of tens of seconds at potentials far more negative than those corresponding to bulk deposition. Although not identified as *UPD*, this peculiar effect appears to have been first observed by Tindall and Bruckenstein for the Cu deposition on *polycrystalline platinum in perchlorate solutions*,[1] who attributed this phenomenon to kinetic hindrances in the deposition process.

It is the main aim of this work to examine for the first time the electrocatalytic effects associated with adatoms in a potential range where conventional UPD is not expected to occur.

EXPERIMENTAL

A description of the instrumentation involved in the measurements including the rotating gold-ring gold-disk electrode and the electrochemical cell has been given in a previous communication.[2] Copper perchlorate and sodium nitrate were obtained from Aldrich and used without further purification.

RESULTS AND DISCUSSION

I. Copper deposition on Au in acid media

Polarization curves obtained for a gold disk electrode in 0.1 M $HClO_4$ and $1 \cdot 10^{-4}$ M $Cu(ClO_4)_2$ were characterized by a very broad feature in the scan in the negative direction accompanied by a sharp peak at 0.2 V upon reversal of the sweep (Fig. 1). Within the time scale of these measurements, a bulk stripping peak could be observed only when the *cathodic limit was more negative than* -0.4 V. Additional insight into this phenomenon was obtained from experiments in which the potential was stepped to a given value, held there for different lengths of time, and then scanned in the positive direction. The results shown in Fig. 2, clearly indicate that under these conditions *no copper* bulk deposition takes place despite the fact that in the extreme case the potential is about 0.4 V more negative than that required for this process to take place. The charge associated with the stripping peak is about 425 $\mu C/cm^{-2}$, which corresponds to a monolayer of copper adatoms. This suggests not only that the UPD is strongly hindered, but also that bulk deposition will not commence unless the monolayer has been completed. It also provides some evidence that the two processes may be intimately linked.

Experiments involving a rotating gold disk-gold ring electrode were also conducted to monitor the concentration of Cu^+ in solution during the deposition and stripping processes by polarizing the ring at +0.50 V. The results shown in Fig. 3 indicate that Cu^+ is detected in the scan in the positive direction only when the potential limit is negative enough for copper bulk deposition to ensue, and hence, that the stripping of the Cu ad-layer is not accompanied by the generation of any detectable Cu^+ in the solution phase. It is also interesting to mention that no Cu^+ could be detected in the scan in the negative direction in the potential region examined. These results agree with those reported earlier in the literature.[3,4]

In summary, the results depicted above afford conclusive evidence that, due principally to kinetic effects, Cu-adatoms can be deposited at potentials far more negative than those associated with bulk deposition providing ideal conditions for studying their electrocatalytic properties.

II. Cu ad-atom mediated electroreduction of NO_3^- ions in acid media

The cyclic voltammetry for Au in 0.1M $HClO_4$, both in the absence and the presence of nitrate, yielded identical curves (see curves a and b, Fig. 4). Upon addition of Cu^{2+} to the solution, however, a faradaic process with an onset of -0.2 V was clearly observed (see curve c, Fig. 4). This current is believed to be associated with the nitrate reduction mediated by Cu adatoms. Higher currents were obtained after increasing in a stepwise fashion the concentration of Cu^{2+} in the solution especially in the potential region close to the onset of the electrocatalytic process. This is most likely due to an increase in the coverage of the Cu ad-atoms for higher concentrations of Cu^{2+} in the solution and suggests that the electrocatalytic activity may be coverage dependent.

Fig. 5 shows ring-disk polarization curves for various nitrate concentrations. As indicated, the ring currents exhibit a bell shaped curve with a maximum at about -0.4 V. The fact that the disk current continues to increase as the potential is scanned further negative indicates that the reduction involves more than two electrons generating a product that does not undergo a clear electrochemical oxidation at the ring potential examined. Fig. 6 shows polarization curves for nitrate reduction in the presence of Cu^{2+} in solution at different rotation rates. The corresponding Koutecky-Levich plots were found to yield a family of parallel straight lines, (see Fig. 7) with a common slope corresponding approximately to 4 electrons.

An attempt was made to analyze the ring-disk *data based on Albery's diagnostic* criterion.[5] In this case the ratio Ni_d/i_r in which i_d and i_r are the disk and ring currents and N, the collection *efficiency*, was plotted against the $f^{-1/2}$ for different disk potentials. The results obtained, shown in Fig. 8, yielded straight lines for which both the slopes and the intercepts were found to be potential dependent in the region between -0.38 and -0.52 V vs. SCE indicating that the overall mechanism involves a parallel reaction pathway.

REFFRENCES

1. G. W. Tindall and S. Bruckenstein, Anal. Chem., 40(1968)1637.
2. X. Xing and D. Scherson, Anal. Chem., 59(1987)962.
3. G. W. Tindall and S. Bruckenstein, Anal. Chem., 40(1968)1051.
4. J. W. Schultze and D. Dickertmann, Surf. Science, 54(1976)489.
5. W. J. Albery and M. L. Hitchman, Ring-Disk Electrodes, Clarendon, Oxford, U.K., 1971.

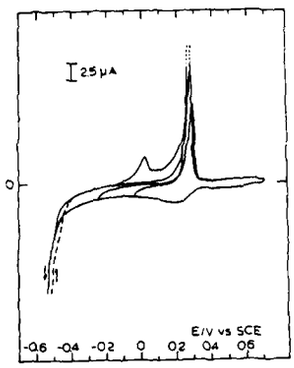


Fig 1 Polarization curve for Au in a solution containing 0.1 M $HClO_4$ and 0.1 mM $Cu(ClO_4)_2$. v = 50 mV/sec, 1600 rpm

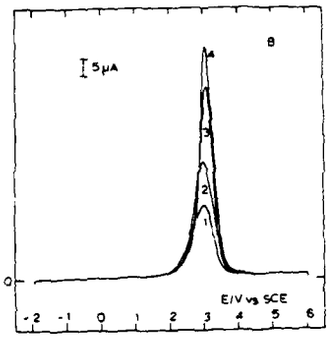


Fig. 2. Potentiodynamic curves for Au in a solution containing 0.1 M $HClO_4$ and 50 mM $Cu(ClO_4)_2$. Electrode held at E = -0.20 V for different periods of time (t) and then scanned in the anodic direction: 1. t = 30 sec, 2. t = 60 sec, 3. t = 90 sec, 4. t = 120 sec. v = 30 mV/sec, 0 rpm.

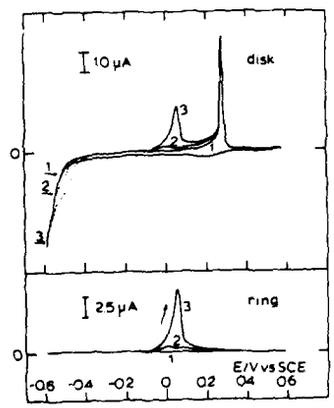


Fig 3 Ring-disk potentiodynamic curves for Au in a solution containing 0.1 M $HClO_4$ and 0.1 mM $Cu(ClO_4)_2$. E_{ring} = 0.50 V, N = 0.38, v = 10 mV/sec, 900 rpm

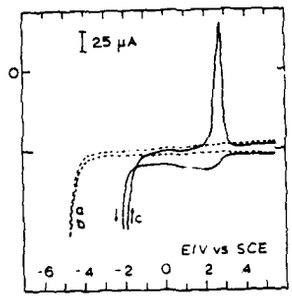


Fig. 4. Polarization curves for Au in solutions containing:
a. 0.1 M $HClO_4$
b. 0.1 M $HClO_4$ and 1 mM $NaNO_3$
c. 0.1 M $HClO_4$, 1 mM $NaNO_3$ and 0.1 mM $Cu(ClO_4)_2$
v = 10 mV/sec, 900 rpm.

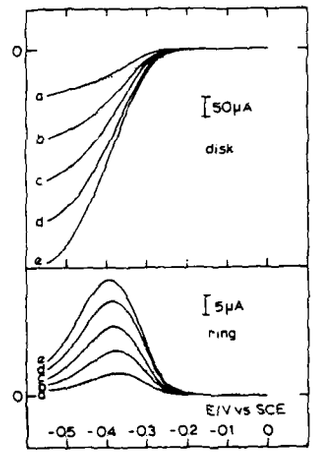


Fig. 5. Ring-disk polarization curves for nitrate reduction on an Au disk electrode in 0.1 M $HClO_4$, 0.1 mM $Cu(ClO_4)_2$ solutions containing: a. 0.1, b. 0.2, c. 0.3, d. 0.4, e. 0.5 mM $NaNO_3$. E_{ring} = 1.0 V, N = 0.38, v = 10 mV/sec, 900 rpm.

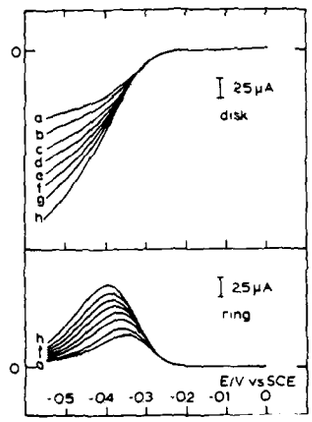


Fig. 6. Ring-disk polarization curves for nitrate reduction on Au disk electrode in a 0.1 M $HClO_4$, 0.1 mM $Cu(ClO_4)_2$ and 0.1 mM $NaNO_3$ solution at the different rotating rates: a. 400, b. 600, c. 900, d. 1200, e. 1600, f 2000, g. 2500, h. 3600 rpm. E_{ring} = 1.0 V, N = 0.38, v = 10 mV/sec

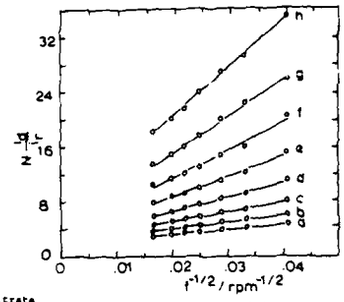


Fig 8 Plot of Ni_d/i_t vs. $f^{-1/2}$, constructed from the data in Fig 6.

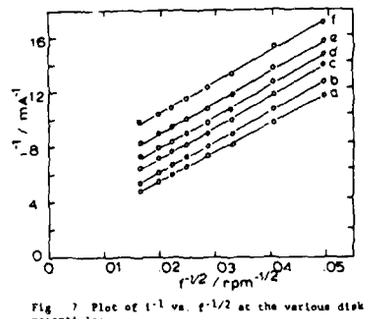


Fig 7 Plot of i^{-1} vs. $f^{-1/2}$ at the various disk potentials:
a -0.40 V, b. -0.44 V, c. -0.48 V, d. -0.50 V, e -0.52 V, f. -0.54 V. Data taken from Fig 6

Abstract No. 706

IMPEDANCE OF SODIUM BETA" ALUMINA/POROUS ELECTRODE INTERFACES IN AMTEC CELLS

R. M. Williams, B. Jeffries-Nakamura, M. L. Underwood, C. P. Bankston, and J. T. Kummer

Jet Propulsion Laboratory
California Institute of Technology
4800 Oak Grove Drive
Pasadena, CA 91109

The porous metal/gas electrode in contact with a solid electrolyte is similar in many respects to the more familiar solid or liquid metal-liquid electrolyte system. However, while the steady-state behavior of both are governed by electrochemical kinetics and mass transport, the former has received far less attention. Only a few quantitative studies have been performed which deal with the dynamic processes at the porous metal/gas/ solid electrolyte interface. While serious drawbacks to investigations of this type include the difficulty of accurately characterizing the three-phase contact zone, there are also advantages including the possibility of examining the effect of temperature varied over many hundreds of K, on electrode reaction rates of comparatively simple systems.

The Alkali Metal Thermoelectric Converter (AMTEC) is a direct energy conversion device potentially capable of near-Carnot efficiencies and demonstrated to perform at high efficiencies and quite high power densities. (1-6)

AMTEC utilizes a high sodium activity gradient across a sodium beta" alumina solid electrolyte (BASE) separator at elevated temperature, T_2 (900-1300) to achieve an open circuit cell voltage up to about 1.6V, and low internal cell resistances to allow current densities up to about 2.5 amps/cm^2 (BASE) at maximum power. Liquid sodium contacts the BASE at the high activity side, while sodium vapor at low pressure leaves the power electrode to a condenser at T_1 (400-800K). It is a static device with no moving parts except for the working fluid, sodium, and it is modular with no size-dependence of either power density or efficiency. These characteristics make AMTEC a promising candidate for space applications. The properties of the porous metal/sodium gas electrodes on the BASE are critical to optimization of AMTEC device performance.

Mixed mass transport and kinetic control of sodium ion reduction at porous, inert electrodes on BASE at high temperatures has been observed and modeled. The high ionic conductivity of BASE and the reversibility of the liquid sodium/ BASE anodic half cell led to assignment of potential-dependent (non-ohmic) resistances to kinetic and mass transport processes associated with the porous electrode. (7,8) The morphology of these electrodes and typical sodium gas pressures are consistent with Knudsen, or free-molecular, flow. Equations for effusion of a gas through a cylindrical pore and equivalent pressure for a condensed phase evaporating irreversibly govern the pressure of sodium gas in the porous electrode. These equations and the current-overpotential equation combine to yield equations for the cells' current-voltage curve and its apparent charge transfer resistance in terms of rate and transport parameters. Inclusion of ohmic resistance losses including electrode sheet resistance via an iterative finite elements method results in a fairly complete model for the D.C. response of AMTEC cells.

The exchange current, transfer coefficient, Knudsen flow coefficient, and interfacial capacitance vs. potential at the $Na_{(g)}$/porous Mo/BASE phase boundary have been evaluated from 740 to 1220 K. The transfer coefficient exhibits a value close to 0.5 and the exchange current is dominated by the collision frequency, with no significant activation energy. The interfacial capacitance may be greatly increased if Na_2MoO_4 and $Na_2Mo_3O_8$ are present, but exhibits systematic limiting behavior with respect to potential and temperature after the electrodes have matured. (9-11) Since the reaction area increases due to Na_2MoO_4/$Na_2Mo_3O_8$ in the pores, the apparent exchange current is also increased. Since the porous Mo electrode adopts a fairly regular microstructure on the BASE surface, the magnitude of the exchange current of clean mature electrodes directly depends on the actual surface area of the BASE ceramic which is electrochemically active. The value of the Knudsen flow coefficient also indicates that only a portion of the BASE surface is active reaction area.

ACKNOWLEDGEMENTS

The research described in this paper was performed by the Jet Propulsion Laboratory, California Institute of Technology, and was supported by the National Aeronautics and Space Administration, the Office of Innovative Science and Technology/Strategic Defense Initiative Organization. We wish to acknowledge assistance and helpful discussions with B. V. Ratnakumar, B. L. Wheeler, M. E. Loveland, N. Weber, S. Kikkert, and J. Lamb.

REFERENCES

1. N. Weber, Energy Covers., 14, 1 (1974).

2. T. Cole Science, 221, 915 (1983).

3. T. K. Hunt, N. Weber, and T. Cole, in "Solid State Ionics," Vol. 5, J. B. Bates and G. *Farrington, Eds., p.* 263, North Holland Publishing Co., Amsterdam (1981).

4. T. K. Hunt, N. Weber, and T. Cole, in "Proceedings of the 13 Intersociety Energy Conversion Engineering Conference," p. 2011, SE, Warrendale, PA (1978).

5. C. P. Bankston, T. Cole, R. Jones, and R. Ewell, J. Energy, 7, 442 (1983).

6. C. P. Bankston, T. Cole, S. K. Khanna and, A. P. Thakoor, in Space Nuclear Power Systems 1984, Vol. II, p. 393, M. S. El-Genk and M. D. Hoover, Editors, Orbit Book Co., Malabar, FL (1985).

7. B. Wheeler, R. M. Williams, B. Jeffries-Nakamura, J. Lamb, M. E. Loveland, C. P. Bankston, and T. Cole in "Performance and Impedance Studies of Thin Porous Molybdenum and Tungsten Electrodes for the Alkali Metal Thermoelectric Converter," accepted for publication J. Appl. Electrochemistry.

8. R. M. Williams, B. Jeffries-Nakamura, M. E. Loveland, M. L. Underwood, C. P. Bankston, and T. Cole, in "High Temperature Materials Chemistry IV," p. 34, Z. Munir, D. Cubicciotti, and H. Tagawa, editors, The Electrochemical Society, 1988.

9. R. M. Williams, G. Nagasubramanian, S. K. Khanna, C. P. Bankston, A. P. Thakoor, and T. Cole, J Electrochem. Soc., 133, 1587 (1986).

10. R. M. Williams, C. P. Bankston, S. K. Khanna, and T. Cole, J. Electrochem Soc., 133, 2253 (1986).

11. R. M. Williams, B. L. Wheeler, B. Jeffries-Nakamura, M. E. Loveland, C. P. Bankston, and T. Cole, "Effects of Na_2MoO_4 and Na_2WO_4 on Molybdenum and Tungsten for the Alkali Metal Thermoelectric Converter," accepted for publication, J. Electrochemical Soc

Abstract No. 707

THE HANGING MENISCUS ROTATING DISK ELECTRODE (HMRDE)

B. D. Cahan and H. M. Villullas*
Case Center for Electrochemical Sciences
and the Dept of Chemistry,
Case Western Reserve University
Cleveland, Ohio 44106
*on leave from Depto de Fisicoquimica
Facultad de Ciencias Quimicas
U. N. C., Cordoba, Argentina

INTRODUCTION

The mounting of single crystals as conventional rotating disks is often a difficult task. Metals such as gold are extremely soft and fragile, and even gentle pressures are enough to deform them. Crystals prepared as cylinders are usually spark cut to minimize damage. This process leaves a textured surface that makes a satisfactory seal impossible to obtain by the usual expedient of press-fitting into Teflon. Other techniques such as molding in a plastic, or mounting in epoxy cause contamination problems. Any gap between the electrode and its mount serves as a trap for abrasives, cutting fluids and other impurities. A gap also causes "tilt" to the baseline and exposes undesireable faces to the electrolyte. Recent studies have shown that impurities like Cl^- or SO_4^{-2} can materially alter the shape of the electrochemical curve for the oxidation of gold at concentrations less than 10^{-7}M (1).

A new method for mounting cylindrical materials for use as rotating *disk* electrodes which eliminates many of the problems associated with more conventional techniques has been developed. Originally concieved for use with single crystals as a combination of the pendant meniscus method (2) and a standard rotating disk, it can be used with almost any material which can be prepared in cylindrical form. The mount uses a miniature W.W. collet chuck mounted in a Kel-F body. The symmetry and small size of this mount permits rotation at very high speeds (10,000 rpm) without visible turbulence in the liquid bulk or surface. Measurements show that this configuration follows Levich's equation as well as more conventional disks.

DESCRIPTION OF TECHNIQUE

Collet chucks are often used in lathes where precise centering of a round object and uniform pressure on the outside are required. They are usually made of a flexible material with a conical outside and a true cylindrical hole on the axis. There are several slots (usually three) which permit the flexible jaws to close uniformly on the diameter as the chuck is pulled with a drawbar into a mating conical recess in the spindle using a fine thread on the back end. W. W. collets are small ones used in small lathes, primarily by watchmekers and are typically available in sizes ranging from 1.5 to 8 mm with 0.1mm intervals. The standard material of construction is a mild steel which can be, for example, hard gold plated. We have had them made from Kel-F rod which is an easily machineable, reasonably hard, cleanable inert plastic. [The threads on a W.W. collet are a special non-standard .275-40 thread. The cone angle is 20°.]

An nose-piece adapter of Kel-F was made to fit a special shaft for a Pine AFMSR rotator which had a 1/2-20 thread on the bottom which was available in our laboratory. (Other mounts could of course be adapted.) A mating 20° conical seat was machined into the nose with special care taken to maintain the precision of centering. [Note that the standard run-out of a Pine shaft is +/- 0.002". In order to obtain a final accuracy of < 0.001" it was necessary to bend the shaft slightly <u>while in the rotator</u> using a dial gage.] A pin in the Kel-F head mates with a slot in the collet to prevent rotation while tightening the draw-nut. Contact to the sample is made with an axial spring loaded rod, tipped with Indium to prevent damage.

Well oriented Au single crystal electrodes were obtained from a commercial source, while others with a random orientation were grown in the laboratory from highly purified Au in a newly machined 6.0 mm I.D. carbon crucible. Polycrystalline Au and Pt electrodes were pressure formed in hardened steel molds, and other materials were machined in a lathe. Most of the single crystal samples were reoriented in a special Laue fixture using an optical autocollimator and repolished with an orientation better than 0.5°. Most of the samples had a diameter of 6.0 mm with faces perpendicular to the axis to < 0.0001". Sharp edges were maintained to insure proper positioning of the meniscus.

An adapter to the Pine rotator was made to mount a dial gage to allow reproducible setting of the meniscus height. The zero level was easily established by lowering the rotator assembly until contact was made. From this reference position, the height could be set using the dial gage to better than 0.001".

EXPERIMENTAL RESULTS AND DISCUSSION

Verification of the validity of the technique with rotation speeds between 400 and 10,000 r.p.m. was obtained with a 2×10^{-3}M ferri-ferrocyanide solution with 0.2M Na_2SO_4 used as supporting electrolyte. A typical set of potential/current curves for a meniscus height of 0.11" is shown in Fig. 1. A (331) Au *electrode* was used, although the reaction is independent of surface structure. *For meniscus* heights between 0.125" and 0.070" the curves were almost identical. Small differences were observed at 0.050" and below. At these heights, a small wetting of the sides was visible.

With the electrode centered to within 0.001", rotation speeds up to the limit of the rotator (10,000 r.p.m.) were easily obtained <u>without visible turbulence</u> in the electrolyte. High speed photographs show no vibrations in the meniscus, although ripples in the flat portion of the surface were observed when the rotation speed was close to mechanical resonances of the rotator-shaft assembly. In contrast, a commercially mounted disk of Au which was carefully rebalanced, centered, trued and polished could not be used above 4900 r.p.m. without severe turbulence in the cell and entrainment of numerous small bubbles in the electrolyte which tended to accumulate below the center of the electrode. When the HMRDE was not as carefully centered, resonances developed at lower speeds (whip distortion of the shaft) which sometimes disturbed or broke the meniscus, although the electrochemical behavior was not altered significantly at lower speeds. Levich plots of the cathodic limiting currents for the HMRDE and a conventional RDE in the same cell and electrolyte are shown in Fig. 2. Both plots give slopes which yield values within a few percent of literature values. A small negative intercept is apparent in the HMRDE curve that may be a result of the different hydrodynamics.

Turbulence is expected for the RDE for rotational velocities characterized by a Reynolds number, N_{Re}, of approximately 10^5, calculated (3) from the equation

$$N_{Re} = r^2 w/v$$

where r is the radius of the electrode (and shroud), w is the angular velocity and v is the kinematic viscosity. For a typical radius of 1 cm, $v = 10^{-2}$, the onset of turbulence is expected below 10^4 r.p.m. The HMRDE used here has a radius of only 0.3 cm, it should be expected to be useable up to 10^5 r.p.m.

OTHER ADVANTAGES OF THE HMRDE

It is possible to anneal, electropolish or otherwise treat the sample surface before mounting. This is not always feasible with the electrode already mounted or potted.

At the higher meniscus heights, the meniscus is constrained at the edge and is perpendicular to the electrode surface. This eliminates the current non-uniformity and frequency dispersion associated with the coplanar edge between electrode and shroud (4).

Early photographic measurements (5) of hydrogen evolution at a rotating disk showed that in a clean solution bubbles nucleated at the metal-Teflon edge. This should not occur with the HMRDE.

CONCLUSIONS

An electrode mount for use with a rotating disk electrode which obeys Levich's equation closely even at very high speeds and overcomes many of the drawbacks of a more conventional mount has been developed. The Teflon shroud that is usually present to preserve the "semi-infinite" hydrodynamic boundary conditions does not appear to be essential. Extension of this technique to other difficult to handle systems (e.g. molten salts, gas evolution and consumption) should be easy.

REFERENCES

1. B. D. Cahan, H. M. Villullas and E. B. Yeager, presented at Atlanta Meeting, ECS (May, 1988).
2. D. Dickertmann, F. D. Koppitz and J. W. Schultze, Electrochim. Acta 21, 967 (1976).
3. "Introduction to Theory of Rotating Electrodes", Manual for Rotating Disk Electrodes, Pine Instruments Co., Grove City, Pa.
4. J. Newman, J. Electrochem. Soc., 117, 198 (1970).
5. F. Ludwig, R. Sun and E. B. Yeager, Elektrochim., 13, 717-723 (1977)

ACKNOWLEGEMENTS

This research has been supported by the Office of Naval Research and the Dept. of Energy.

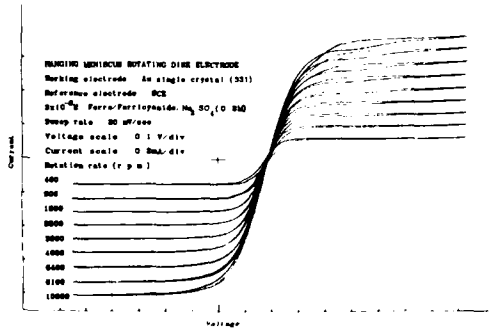


Fig. 1. HMRDE cyclic voltammetry of $2x10^{-3}$M ferri-ferrocyanide couple in 0.2M Na_2SO_4. Sweep rate: 20 mv/sec. Rotation speeds from 400 to 10,000 rpm.

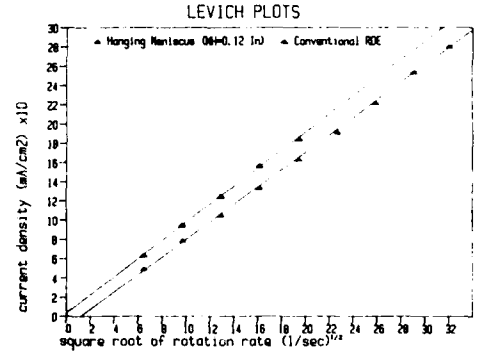


Fig. 2. Levich plots for cathodic process in Fig. 1 (solid triangles), and for conventional RDE (open triangles).

Abstract No. 708

TRAPEZOIDAL WAVE CYCLIC VOLTAMMETRY IN STUDY OF TRANSFER OF ION ACROSS THE INTERFACE BETWEEN TWO IMMISCIBLE ELECTROLYTE SOLUTIONS

Qi Deyao, Li Jianwei

Department of Chemistry and Chemical Engineering, Shanghai University of Technology, Shanghai, China

INTRODUCTION

The methodes used for studying ITIES are chronopotentiometry, cyclic voltammetry and polargraphy etc.. Among them triangular wave cyclic voltammetry is used most widely. The trapezoidal wave cyclic voltammetry was used for study and the results obtained were improved.

EXPERIMENTAL

Cell Electrolytic cell was shown in ref.1. The boundary of the aqueous and the nitrobenzene phase in the cell, which had an area of 1.3cm² was located at a distance of 0.2cm from each tip of the Luggin capillaries.

Chemicals TBACl was purified before use. All other reagents were analytical grade. The neutral carriers ETH1117 and ETH1001 was sent by Prof. W.Simon, ETH.

Equipment The four-electrode cyclic voltammeter controlled with microcomputer was constructed in our laboratory. The potential wave forms are shown in fig.1. The electrolyte resistance between the tips of Luggin capillaries was compensated. The experiments were performed at the temperature 20±1 °C.

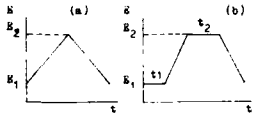


Fig.1. Wave forms for cyclic triangular (a) and trapezoidal wave(b) voltammetry.

RESULTS AND DISCUSSION

The facilitated transfer of H^+ion across the water/nitrobenzene(w/n) interface by neutral carrier ETH1117 is a reversible process controlled by diffusion, which was studied with trapezoidal wave cyclic voltammetry[2]. Fig.2 is the triangular wave cyclic scanning voltammogram of H^+ion. The peak current(I_p) (Fig.2.a) is measured as vertical difference between currents of curve 1 and curve 2 at the peak potentials (E_p). If the measurement is correct, the I_p measured should be independent of E_1 and E_2. Fig.3.a is cyclic voltammogram of H^+ion when E_1 is fixed but E_2 is varied and fig.3.b when E_2 is fixed but E_1 is varied at $t_1=t_2=0$. The The result from fig.3 indicates the I_p measured by the method shown in fig.2.a are dependent on E_1 and E_2 so this method(fig. 2.a) is not suitable for measuring I_p. Obviously, the incorrect measurement results from the effect of the declining current on I_p after E_p. Therefore the technique should be improved so as to decrease the influence of both residual and declining currents on I_p. We have tried to draw a curve tangential to curve 2 upward and downward as a base line(fig.2.b). The vertical distance from curve 2 to this base line is taken as I_p. But it is difficult to find out such a suitable curve.

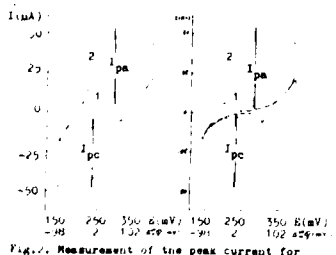


Fig.2. Measurement of the peak current for cyclic voltammogram. Composition of the aqueous phase: 0.01M HCl; nitrobenzene phase: 0.01M TBATPB in the presence of 0.2mM ETH1117; v=121 mV/sec.

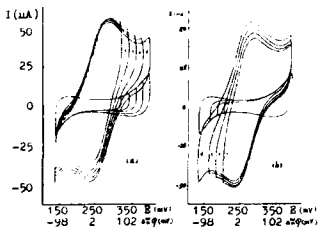


Fig.3. Cyclic voltammogram of H^+ ion under the different E_2(a) and E_1(b). (a): E_1=140 mV; E_2=330(1),350(2),370(3),390(4),410(5)mV; (b): E_2=410mV; E_1=2.0(1),190(2),170(3),140 (4)mV; $t_1=t_2=0$. Composition: see Fig.2.

Fig.4 is the dependence of the I_p on time, t_1 and t_2.When t_1 and t_2 are larger than about 20 sec, $I_{pa}$is equal to I_{pc} and I_p has a constant value at different E_1 and E_2. It shows that the I_p measured could not be effected by declining current and residual current when t_1 and t_2 are selected properly, because the declining current will decrease to about zero after E_p.

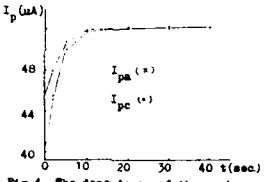


Fig.4. The dependence of the peak current corresponding to the transfer of H^+ ion across the w/n interface on t_1 and t_2. Composition: see Fig.2.

The experiments show that $\Delta E = E_{pa}-E_{pc}$ will be nearly a constant value if both $|E_{pa}-E_2|$ and $|E_{pc}-E_1|$ are larger than 70mV, and t_1 and t_2 do not affect E_p.

Fig.6 and fig.6 are cyclic voltammograms of Ca^{2+} ion in the presence of neutral carrier ETH1001 in the nitrobenzene. The peak current ratio I_{pa}/I_{pc} =0.69 at $t_1=t_2=0$(fig.5) and 0.95 at $t_1=t_2=30$ sec(fig.6). The ratio, 0.95, agrees fairly well with the theoretical one, I_{pa}/I_{pc} =1[3].

CONCLUSION

Using trapezoidal wave scanning, the I_p of cyclic voltammogram can be measured simply, rapidly and reliablly and the I_p ratio can be used to elucidate the transfer process.

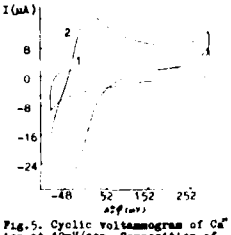


Fig.5. Cyclic voltammogram of Ca^{2+} ion at 49mV/sec. Composition of the aqueous phase: 0.005M $CaCl_2$; nitrobenzene phase: 0.01M BEABaTPB in the absence(1) and in the presence(2) of 0.2mM ETH1001; $t_1=t_2$ =0.

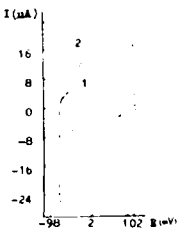


Fig.6. Cyclic voltammogram of Ca^{2+} ion at 49mV/sec. $t_1=t_2$=30 sec; Composition: see Fig.5.

REFERENCES

(1),(2) Qi Deyao and Li Jianwei, unpublished.
(3) R.S.Nicholson etc,Anal.Chem.,36(1964)706.

Abstract No. 709

NOVEL CONDUCTING POLYMERS AS OPTICAL SWITCHES: TOWARDS MICROSECOND ELECTROCHROMIC SWITCHING TIMES

P. Chandrasekhar

Gumbs Associates, Inc.
11 Harts Lane
East Brunswick, NJ 08816

Although novel conducting polymers are serious candidates for use as optical switches in applications ranging from optical interconnects and storage discs to laser shielding and switchable radar absorbers [1] concerted switching rate measurement and enhancement studies and an understanding of the factors affecting this rate are still lacking. With the aim of designing and synthesizing novel conducting polymers with promise as optical switches, and on the basis of semi-empirical quantum mechanical (INDO) calculations indicating very low bandgaps and considerable intramolecular charge transfer, we very recently synthesized a series of 2-Me thiophene (T) derivatives, two of which are 1, 2 (Fig. 1), via a proprietary chemical/electrochemical procedure.

Electrochromic switching rate studies have been conducted on these and PP, P3MT controls using both chronoamperometric/chronocoulometric analyses and an independent electrochromic switching rate apparatus constructed for the purpose, employing a 65 mW Ar ion laser (Newport), an ultra high-speed photodetector (Newport), coupled to a potentiostat with ECL electronics. For device studies, 2-layer sandwich devices of the polymer studied comprising the polymer deposited on an ITO or Au (ca. 70 A) coated glass slide, a layer of proprietary polyethylene oxide (PEO) based electrolyte and an additional ITO or Au/glass slide. The quasi-reference electrode was either Pt sputter-deposited on polyimide on the working electrode, or electrically disconnected section of working electrode. Devices hermetically sealed with epoxy. Electrochromic switching rate monitored by pulsing 1 V on either side (i.e. +/- 2 V) of polymer redox peak.

INDO calculations on 1, 2, indicate ca. 0.1 e^- S to X CT. Effect of a number of parameters on a predefined switching rate were studied, and it was found that the size of dopant ion (from BF_4^- to tosylate and polyvinyl sulfonate), solvent medium (PC ACN), and substrate (AU, ITO, Pt) had minimal effect whereas film thickness, electrolyte concentration (0.2 to 1.2 M), preprocessing of substrate with PEO and presence of effective counterreaction (with $AgClO_4$) had maximal effect. Reduction of film thickness from 10 nm to ca. 1 nm caused 2 orders of magnitude drop in switching rate, while PEO-preprocessing of substrate and subsequent leaching out of PEO after polymer deposition (yielding better dopant access to polymer charge centers) yielded similar effects. With 1 nm polypyrrolium tosylate (PPTos) prepared in proprietary manner, we observed switching times of ca. 1.0 msec, reversible and reproducible over 300 cycles. Fig. 2 shows typical switching curves for PPTos/Au/glass, (ca. 10 nm), with coulometric trace inset. Switched/unswitched OD ratios are ca. 10 -80 for PPTos, depending on film thickness and history.

In preliminary tests thin films of the novel polymers 1 and 2 yielded switching times of ca. 0.1 msec. For certain optical switching applications, e.g. optical interconnects [2], rate requirements as low as 1 picosec have been stated. However, μsec rates will yield viable switches. It should be noted that our switching rate is defined on the basis of the known charge in deposition of a film and known or published stoichiometry (No. of electrons) for a polymer's reduction/oxidation.

We are currently working on a number of approaches and novel polymers to yield microsecond domain switching times.

We are grateful to the US Army Medical Research and Acquisition Activity, (Fort Detrick, Frederick, MD) and the Letterman Army Institute of Research (San Francisco, CA) for generous support of this work.

References

1. Wegner, G., Mol. Cryst. Liq. Cryst., 1984, 106, 269.

2. Proc. Rpt. on Top. Mtg. Optical Bistability of Optical Society of America and Lasers & Electrooptics Soc. of IEEE, Tucson, AZ, 1975.

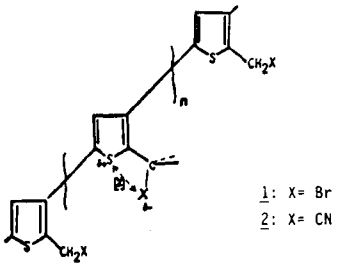
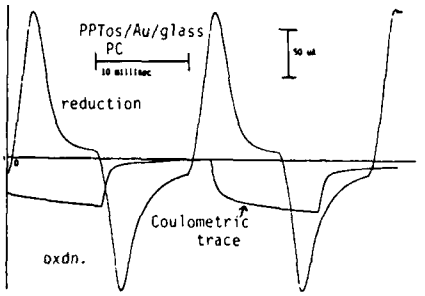


FIGURE 1

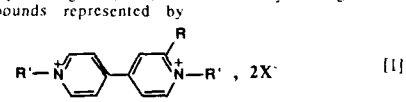


Abstract No. 710

ELECTROCHEMICAL STUDIES OF NEW VIOLOGEN COMPOUNDS

M. H. Miles, R. A. Henry and R. A. Hollins
Chemistry Division, Research Department
Naval Weapons Center, China Lake, CA 93555

Compounds of 1,1'-dialkyl-4,4'-bipyridinium salts (viologens) have found prominent use as electron mediators in herbicides, electrochromic displays, and solar-energy-storage devices (1, 2). Most viologen studies have focused on the commercially available dimethyl and diheptyl viologens (3, 4). In this study, viologen compounds represented by



[1]

as well as several other types of viologen compounds were synthesized and tested. A previous study has shown that the electrochromic properties of these modified salts can be markedly superior to those of dimethyl and diheptyl viologens (5). The major electrochemical reactions of viologen compounds can be represented by

$$V^{2+} + X^- + e^- \rightleftharpoons V^+X\downarrow \qquad [2]$$

$$V^+X + e^- \rightleftharpoons V\downarrow + X^- \qquad [3]$$

where V^{2+} is the viologen cation and X^- is the electrolyte anion. The electron-transfer reactions are generally restricted to the highly reversible one-electron change to form the insoluble salt of the blue radical cation (V^+X).

Most of the viologen compounds investigated are listed in Table I along with the reduction peak potentials (E_{p1}, E_{p2}), peak currents (I_{p1}, I_{p2}) and diffusion coefficients (D_{V2+}), as determined by potential sweep experiments. The diffusion coefficients are numerically about equal for many of these compounds and yield a mean value of $D_{V2+} = 2.4 \pm 0.6 \times 10^{-6}$ cm^2/s at ambient temperatures (21 to 24°C). Viologen A was barely soluble at 0.005 m while compounds F and G were insoluble at the concentration used. The observed peak currents suggest solubilities of 0.0033 m and 0.0017 m for viologens F and G, respectively. Although viologen B was readily soluble, a lower concentration (0.0038 m) was used since the amount of this material was limited. The aqueous solutions formed were colorless except for compounds B (slightly yellow), H (yellow), and I (dark orange).

Cyclic voltammetric traces at various potential sweep rates are shown in Figures 1 and 2 for viologen compounds B and C (Table I) on platinum and gold electrodes, respectively. The voltammograms for viologen compounds are ususally similar for many electrode materials (6). The conversion of the radical cation into a dimer, $2\,V^{+\bullet} \rightarrow (V^{+\bullet})^2$, provides a possible explanation for the two anodic peaks observed near -0.4 V in Figure 1 for the scan rate of 100 mV/s. Faster scans allow less time for viologen B to form dimers while slower scans show a larger dimer oxidation peak (Figure 1). Spectral changes for aqueous viologen solutions have been attributed to dimer formation (2, 7). The voltammetric trace for viologen A also showed evidence for possible dimer formation. Five oxidation peaks were detected following the negative going scan to -0.90 V with the fourth oxidation peak being the largest (E_p = -0.38 V, I_p = 0.54 mA). Compound D gave several oxidation peaks that varied with the potential scan rate and viologen concentration, but unlike Figure 1, the more positive peak increased in size at faster scan rates. Spectral evidence for dimer formation on Pt and Au surfaces has been reported for this compound (2). No evidence for any dimer formation could be found in the voltammetric traces for viologen compounds C (Figure 2), E, F, G, H, and I.

The best viologen compounds in terms of electrochromic film formation and erase cycles in aqueous 0.20 m KBr solutions were compound E (11,400 cycles on Au) and compound C (6,500 cycles on Pt). Both of these viologen compounds contain the substituent R' = o-Me$C_6H_4CH_2$ (Table I). In contrast, compound A with R' = p-Me$C_6H_4CH_2$ gave only 10 cycles before most of the film became unerasable. These results support the suggestion that steric effects may play an important role in the erasability of viologen compounds (5). Compound B gave 500 erasable cycles, but all other viologen compounds tested yielded less than 50 erasable cycles. Generally, the peak current (I_{p1}) was a good measure of the film erasability, hence cycle lifetime was determined by a 50% decrease in the peak current (I_p = 1/2 I_p°). The formation of a stable electrochromic film was not observed for compounds H and I; for example, reduction and oxidation cycles for compound H gave a stream of red product coming from the electrode.

Although the electrochemistry of viologen compounds D and E were reported previously (5), significant differences were found in our studies. The potentials for the first reduction peaks (E_{p1}) were 42 mV more negative for both compounds (Table I) than those reported by Barltrop and Jackson (5) despite our use of a slower scan rate (100 mV/s vs. 1000 mV/s). Our peak potential value for compound D (E_{p1} = -0.520 V) shows better agreement with recent measurements by Enea and co-workers (2). Furthermore, our peak potentials previously reported for diheptyl viologen gave good agreement with literature values (6). Calibration of our SCE reference electrodes showed agreement within ±2 mV in potential.

The diffusion coefficients determined for viologen compounds D and E (Table I) are noticeably smaller than those reported by Barltrop and Jackson (5). The diffusion coefficients reported in Table I were determined from the equation

$$i_p = 3.67 \times 10^5 n^{3/2} A\, C^\circ D^{1/2} v^{1/2} \qquad [4]$$

for the reversible deposition of an insoluble substance (8). A similar equation for soluble reaction products would not be valid for the viologen reaction (Eq. 2) and would yield diffusion coefficients that would be a factor of 1.82 too large.

Our preparation of viologen compound E gave a melting point of 279 to 280°C (decomposition) while Barltrop and Jackson report a melting point of 295 to 299°C (decomposition). It is well-known that melting points can vary with the heating rate when decomposition occurs. Both preparations showed the expected NMR spectra. The electrochemical results for both studies show that 1,1'-bis-(2-methylbenzyl)-2-methyl-4,4'-bipyridinium dibromide (Compound E) is the best viologen in terms of erasable, electrochromic cycles in aqueous KBr solutions.

REFERENCES

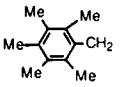
1. P. Neta, M. C. Richoux, and A. Harriman, *J. Chem. Soc. Faraday Trans. 2*, **81**, 1427 (1985).
2. P. Crouigneau, B. Beden, A. M. Braun, and O. Enea, *J. Electroanal. Chem.*, **234**, 329 (1987).
3. M. Heyrovsky' and L. Novotny', *Coll. Czech. Chem. Comm.*, **52**, 1097 (1987).
4. T. Lu and T. M. Cotton, *J. Phys. Chem.*, **91**, 5978 (1987).
5. J. A. Barltrop and A. C. Jackson, *J. Chem. Soc. Perkin Trans. II*, 367 (1984).
6. M. H. Miles, R. A. Henry, and R. A. Hollins, in *Extended Abstracts, Electrochemical Society Meeting*, **87-2**, 1968 (1987).
7. J. G. Gandiello, P. K. Ghosh, and A. J. Bard, *J. Amer. Chem. Soc.*, **107**, 3027 (1985).
8. P. Delahay, "New Instrumental Methods in Electrochemistry" Interscience Publishers, New York, pp 116-125 (1954).

TABLE I. Cyclic Voltammetric Results for 0.005 m Solutions of Viologen Compounds in 0.20 m KBr at 100 mV/s Using Platinum Wire Electrodes (A = 0.18 cm^2, T = 21-24°C).

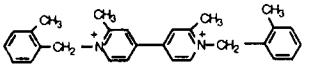
Compound[a]	E_{p1}[b] (V)	E_{p2}[b] (V)	I_{P1} (mA)	I_{P2} (mA)	$D_{V^{2+}}$ (cm^2/s)
A	-0.472	-0.833	0.192	0.823	2.3×10^{-6}
B[c]	-0.499	-0.852	0.165	0.322	3.8×10^{-6}
C	-0.515	-0.826	0.178	0.252	2.0×10^{-6}
D	-0.520	-0.843	0.172	0.583	2.3×10^{-6}
E	-0.552	-0.882	0.175	0.234	2.2×10^{-6}
F	-0.538	...	0.119	...	Insoluble
G	-0.615	-0.882	0.062	0.152	Insoluble
H	-0.408	-0.517	0.175	0.262	2.5×10^{-6}
I	-0.592	-0.746	0.138	0.162	1.9×10^{-6}

[a] A R = H, R' = p-$MeC_6H_4CH_2$
B R = H, R' = p-$CH_3OC_6H_4CH_2$
C R = H, R' = o-$MeC_6H_4CH_2$
D R = H, R' = $C_6H_5CH_2$
E R = CH_3, R' = o-$MeC_6H_4CH_2$

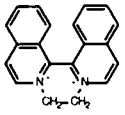
F R = H, R' =



G

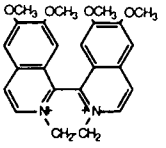


H



Bis-isoquinolinium salt (BIQ)

I



Tetramethoxy BIQ

[b] Peak potentials measured versus the SCE reference electrode.

[c] Viologen concentration was 0.0038 m.

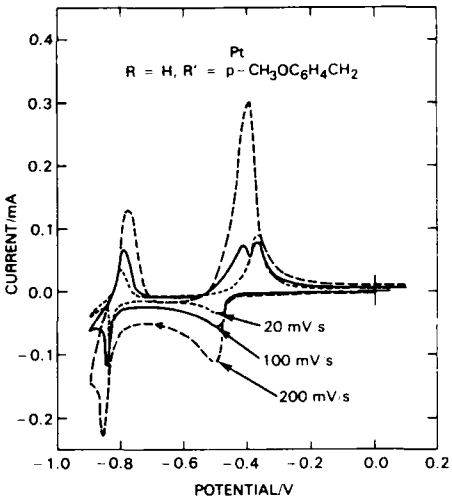


Fig. 1. Cyclic voltammetric studies of 1,1'-bis-(4-methoxybenzyl)-4,4'-bipyridinium dichloride in 0.20 m KBr using a platinum wire electrode (A = 0.18 cm^2) and scan rates of 20, 100, and 200 mV/s.

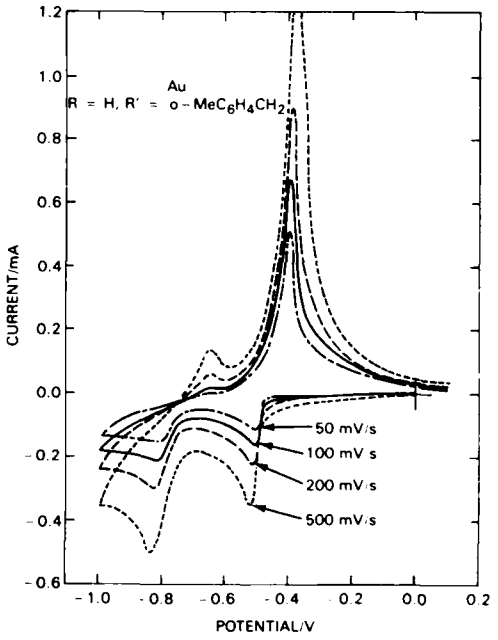


Fig. 2. Cyclic voltammetric studies of 1,1'-bis-(4-methylbenzyl)-4,4'-bipyridinium dibromide in 0.20 m KBr using a gold wire electrode (A = 0.16 cm^2) and potential scan rates of 50, 100, 200, and 500 mV/s.

Abstract No. 711

ELECTROCHEMICAL STUDIES ON ELECTRODEPOSITED TUNGSTEN TRIOXIDE FILMS

D. E. Stilwell, K. H. Park, and M. H. Miles
Chemistry Division, Research Department
Naval Weapons Center, China Lake, CA 93555

INTRODUCTION

The study of electrochromic compounds for use in display devices or in light attenuation filters is being actively pursued worldwide. Recent review articles on electrochromic materials and devices are available (1-2). One of the most promising systems is based on tungsten trioxide films (WO_3). The coloration/decoloration reaction arises from an oxidation/reduction of the film:

$$WO_3 + xM^+ + xe^- \rightleftharpoons MxWO_3 \qquad (0 < x < 0.35)$$

(colorless) (blue) ($M^+ = H^+, Li^+$ etc.)

The broad band electronic absorption of the blue form has been attributed to either a free electron transition (3) or to a small polaron absorption (4). The most common method for WO_3 film formation is by vacuum techniques (1-4), but other methods have been reported as well. These methods include chemical vapor deposition (5), spin (6) and dip (7) coatings, oxidation of tungsten metal (8), and very recently, electrodeposition from tungsten-hydrogen peroxide solution (9). The deposition observed was explained in terms of solubility differences between the peroxotungstic acid and the reduced product, tungsten trioxide hydrate (9). We have adapted a variation of the method reported by Yamanaka (9) to produce WO_3 films electrochemically. The following is a summary of our preliminary results on the film forming reaction, as well as on the electrochemical properties of the films thus formed.

EXPERIMENTAL

The electrochemical measurements were carried out with a Princeton Applied Research (PAR) 173 potentiostat/galvanostat with the PAR 179 digital coulometer accessory. The potential waveforms were supplied by a Hewlett-Packard 3314A function generator. The data were acquired on a Zenith 248 microcomputer via an Analog Device RTI-815 ADC/DAC interface. The electrochemical cell was a standard three electrode system contained in a dual compartment cell separated by a glass frit. Either a Pt wire electrode, or indium tin oxide (ITO) conducting glass (OCLI, Santa Rosa, Calif.) was used for the working electrode. All potentials are reported versus the Ag/AgCl (saturated KCl) reference electrode which was used in this work. The tungsten powder (Fisher), the hydrogen peroxide (30%), the $LiClO_4$ (GFS), and the propylene carbonate (PC) (Aldrich), were reagent grade and were used without any further purification. Anaerobic conditions were maintained with an argon atmosphere.

RESULTS AND DISCUSSION

The deposition solution was prepared by oxidizing tungsten powder with hydrogen peroxide. Nominally, 2.5 to 3.0 mL of 30% H_2O_2 was added to 1 g of W powder and allowed to react. A considerable amount of the H_2O_2 was consumed by chemical decomposition, as evidenced by the gas evolution. Water, in 1 to 2 mL portions was added three times to prevent excessive frothing of the reaction mixture. Finally, the volume was brought up to 100 ml with distilled H_2O.

The potential applied to the substrate material was .0.5 V for ITO and between -0.5 to -4.0 V for Pt. On platinum, only the blue form was observed, indicating that the tungsten oxide film was not further reduced to the lower oxidation states for tungsten bronze, even at -4.0 volts. Potentials more negative than ca. -0.7 V on the ITO could not be employed as the conducting glass substrate was reduced to the metals. The deposition was carried out for 5 to 60 minutes depending on the desired thickness. After an initial rise time of around one minute, the current was steady with time in these unstirred solutions, and upon agitation, the steady state current only rose between 10 to 30%. The current density was 4 to 5 times higher on platinum compared to ITO. This larger current appears to be due to an increase in hydrogen ion and hydrogen peroxide reduction on platinum; gaseous products were observed on Pt even at open circuit. After film deposition, and at open circuit, the blue films were rapidly oxidized by hydrogen peroxide to the colorless form. These observations point to the the fact that the total current reflects a multiplicity of reactions. That is, aside from the desired film forming reaction, there is solvent reduction, H_2O_2 reduction, and a catalytic component caused by the continuous reoxidation of the film by the H_2O_2. Shown in Table I are the results obtained over a wide range of H_2O_2/W mole ratios. As can be seen, there is no film deposition when the H_2O_2 concentration is either too high or low. An overall reaction mechanism to account for these findings will be shown and discussed.

The electrochemical properties of the deposited WO_3 films were studied in 1 M sulfuric acid and in PC/$LiClO_4$/H_2O solutions. There was no long term film stability in these solvents. Shown in Figure 1 are the cyclic voltammograms obtained in the PC solution as a function of cycle time. We attributed the lack of stability in PC to be caused by a solubility of WO_3 in PC. Indeed, when the PC solution was made slightly acidic, then film stability was achieved for more than 600,000 coloration/bleaching cycles, as shown in Figure 2. Shown in Figure 3, are voltammograms of the film in 1% and in 3% water PC mixtures. As is evident, the switching kinetics increase with increasing water content. Unfortunately, the increased water increases the film solubility. Efforts are underway in order to optimize the solution composition for maximum switching speed as well as stability, and our results will be shown and discussed.

REFERENCES

1. G. K. Baucke and J. A. Duffy, *Chem. in Brit.*, **21**, 643 (1985).
2. S. A. Agnihotry, K. K. Saini and S. Chandra, *Indian J Pure Appl. Phys.*, **24**, 19, (1986).
3. R. B. Goldner, P. Norton, K. Wong, G. Foley, E. L. Goldner, G. Seward, and R. Chapman, *Appl. Phys. Lett.*, **47**, 536 (1985).
4. T. Yoshimura, *J. Appl. Phys.*, **57**, 911 (1985).
5. D. Craigen, A. Mackintosh, J. Hickman, and K. Colbow, *J. Electrochem. Soc.*, **133**, 1529 (1986).
6. H. Okamoto, K. Yamanaka, and T. Kudo, *Mat. Res. Bull.*, **21**, 551 (1986).
7. H. Unuma, K. Tonooka, Y. Suzuki, T. Furusaki, K. Kodaira, and T. Matsushita, *J. Mat Sci. Lett.*, **5**, 1248 (1986).
8. B. Reichman and A. J. Bard, *J. Electrochem. Soc.*, **126**, 583 (1979).
9. K. Yamanaka, *Electrochem. Soc. Extended Abs.*, **87-2**, 821 (1987).

TABLE I. Effects of the Solution Composition on Deposition.[a]

W	H_2O_2, initial	H_2O_2/W	Deposition Observed
0.068	0.73	10.7	N
0.070	0.48	6.9	Y
0.056	0.36	6.5	Y
0.051	0.30	5.9	Y
0.051	0.24	4.8	N
0.068	0.24	3.5	N

[a]Concentration in mol/L.

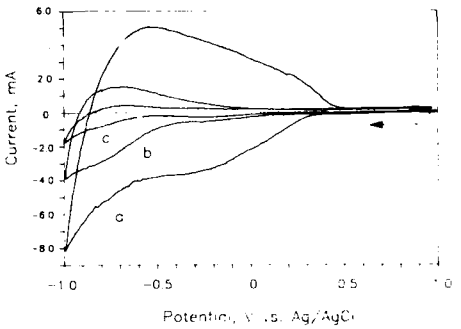


Fig. 1. Cyclic voltammograms (CVs) of WO_3 in PC, 2% H_2O, 1 M $LiClO_4$ solution. (a) Fresh film, (b) after 720 cycles, and (c) after 3240 cycles. The CVs were taken between 1 and -1 V at 40 mV/s scan rates. A cycle is a potential square wave pulse between 1 and -1 V at 0.2 Hz.

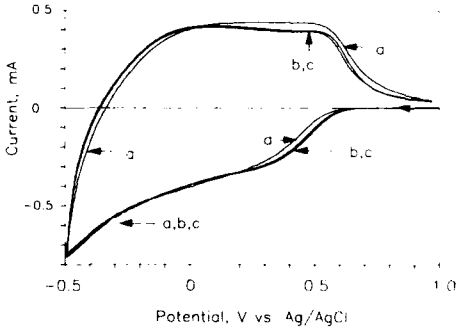


Fig. 2. Cyclic voltammograms of WO_3 in PC, 2% H_2O, 1 M $LiClO_4$, and 0.014 M $HClO_4$. After (a) 100,000, (b) 300,000, and (c) 600,000 cycles. See Figure 1 for other experimental details.

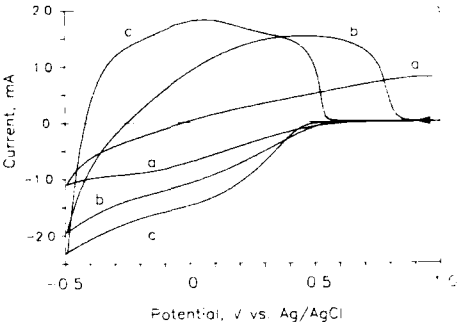


Fig. 3. Cyclic voltammograms of WO_3 in a PC solution containing, 1 M $LiClO_4$, 0.011 M $HClO_4$, and (a) 0.2%, (b) 1.6%, and (c) 4% water. Same scan rate and potential range given in Figure 1. ITO electrode area = 2.2 cm^2.

Abstract No. 712

In-situ FTIRRAS Studies of Anion-Metal Oxide Interactions in Electrochemical Systems: Perchlorate and Nitrate Adsorption on Polycrystalline Pt and Au Surfaces.

In Tae Bae, Xuekun Xing, M. Razaq, E. B. Yeager and Daniel Scherson
The Case Center for Electrochemical Sciences and the Department of Chemistry
Case Western Reserve University
Cleveland, OHIO 44106

INTRODUCTION

Considerable progress has been made over the last few years towards the development of infrared spectroscopy as a probe of the vibrational properties of species adsorbed on electrode surfaces. Fourier Transform reflection absorption infrared spectroscopy FTIRRAS, represents one of the most versatile techniques for the acquisition of in situ data as evidenced by growing numerous applications reported in the literature.[1,2] This work will present FTIRRAS data for the adsorption of perchlorate and nitrate ions on Pt and Au surfaces from which important information regarding the interactions of simple oxyanions with metal oxide surfaces has been obtained.

EXPERIMENTAL

The electrochemical cell used for measurements involving platinum electrodes was obtained commercially,[1] whereas that employed for Au studies was designed and built in this laboratory (see Fig.1) A different reflection attachment was used with each of the cells. These are depicted in Fig. 2. The electrode area exposed to the beam was of 2.8 cm^2 and 0.79 cm^2 in the case of Au and Pt, respectively. All the experiments were conducted with an IR/98 IBM Instruments, Inc. Reflection spectra at a given potential, R_{sample} were obtained by adding 500 scans. The data are presented in the form of $-\Delta R/R$, where $\Delta R = R_{sample} - R$ and R is the reflection spectra at an arbitrary reference potential.

RESULTS AND DISCUSSION

Fig. 3 shows $-\Delta R/R$ vs wavenumber spectra for a Pt electrode in a 0.1 M $HClO_4$ solution. Although some changes are observed in the region around 1100 cm^{-1}, associated with the perchlorate asymmetric stretch, ν_3,[3] a clearly identifiable peak at this frequency could be observed only for potentials larger than 0.40 V vs SCE. A rather similar behavior was found in the case of Au (see Fig. 4). in which case the same peak was found to increase in intensity at potentials larger than 1.10 V vs SCE. Based on an inspection of the cyclic voltammetry curves obtained for these electrodes in each of the cell recorded immediately prior to collecting the spectra (see curves A and B, Fig. 5) it becomes clear that the potentials associated with the onset of the large absorption peaks are close to those of the onset of oxide formation on the respective surfaces.

An essentially analogous behavior was observed upon addition of nitrate to the perchlorate electrolyte. In this case, large nitrate signals were observed at potentials equal or greater than those associated with oxide formation. In contrast to the perchlorate case for which the ν_3 band was only slightly shifted with respect to normal ClO_4^-, the NO_3^- asymmetric stretch, ν_3 band usually found at 1370 cm^{-1} was found to split into two components with apparent maxima at 1349 and 1395 cm^{-1}. (Figs. 6 and 7) This may be attributed to a lifting of the degeneracy of this normal mode induced by the symmetry lowering due to the interaction of the ion with the oxide surface.

It is interesting to note that the integrated area under the perchlorate peak decreases upon introduction of NO_3^- in the electrolyte. This provides a strong indication that the two species compete for sites on the metal surface. It is conceivable that the ClO_4^- ν_3 band may also be split, and that one of the components could occur at a frequency below the absorption threshold of CaF_2. Experiments employing a ZnSe window are now in progress to examine this possibility, as well as to determine whether the ClO_4^- ν_4 band also undergoes splitting upon adsorption of the ion on the electrode surface.

The type of anion-oxide surface interactions suggested in this work have also been invoked in the case of oxide particle surfaces in which surface adsorption can be monitored by non-electrochemical techniques.[4]

ACKNOWLEDGEMENTS

Support for this work was provided by the Gas Research Institute and LBL/DOE. The authors would like to express their appreciation to Dr. M. Severson of Oakland University for assistance during the early phase of this project and to Ms. X. Xu for her valuable advice during the cell construction. Funding for the purchase of the IR98/IBM instrument was provided by ONR/DOD.

REFERENCES

1. A. Bewick and S. Pons, in " Advances in Infrared and Raman Spectroscopy", vol. 12, ed. by R. J. H. Clark and R. E. Hester, P.1, Wiley, 1985.
2. J. K. Foley, C. Korzeniewski, I. L. Daschbach and S. Pons, In " Electroanalytical Chemistry", vol. 14, ed. by A. J. Bard, p.309, Marcel Dekker, N.Y., 1986.
3. K. Nakamoto, " Infrared and Raman Spectra of Inorganic and Coordination Compounds", 3rd edition, John Wiley and Sons, NY, 1978.
4. S. Ardizzone, J. Electroanal. Chem.,239(1988)419.

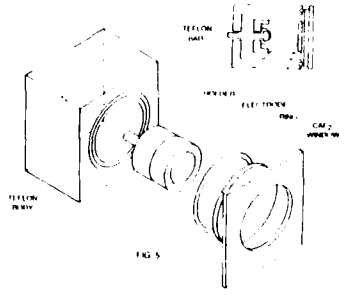
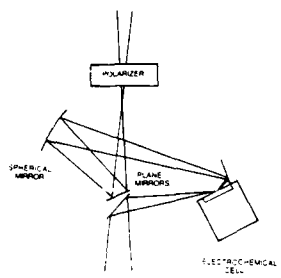


Fig 1 Electrochemical cell for in situ FTIRRAS measurements



(A) Pt (60° incident angle)



(B) Au (70° incident angle)

Fig 2 Optical arrangements for in situ FTIRRAS measurements involving

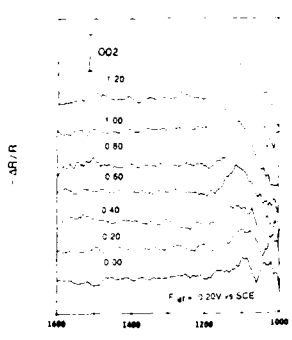


Fig 3 FTIRRA spectra of Pt in 0.1 M $HClO_4$ solution at the different potentials as indicated

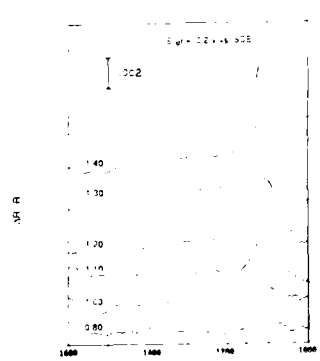
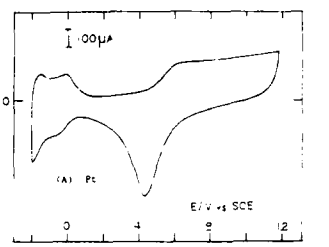


Fig 4 FTIRRA spectra of Au in 0.1 M $HClO_4$ solution at the different potentials as indicated



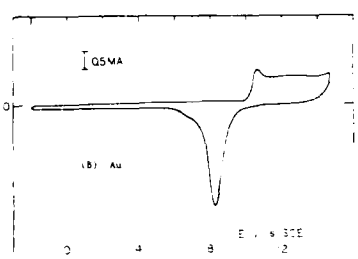


Fig 5 Cyclic voltammograms of working electrodes in 0.1 M $HClO_4$ solutions in the in-situ cells v = 100 mV/sec

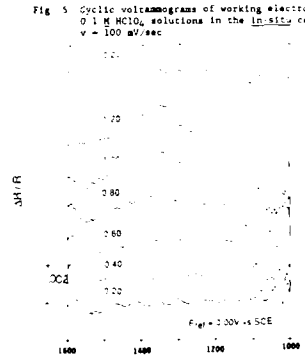


Fig 6 FTIRRA spectra of Pt in 0.1 M $HClO_4$ and 0.1 M $NaNO_3$ solution at the different potentials as indicated

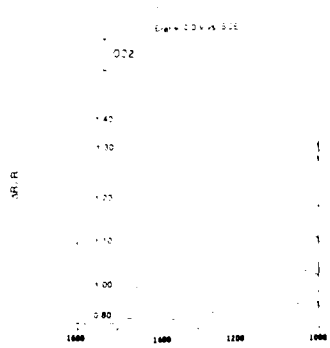


Fig 7 FTIRRA spectra of Au in 0.1 M $HClO_4$ and 0.1 M $NaNO_3$ solution at the different potentials as indicated

Abstract No. 713

IRRAS Study of Dry Perfluorinated Sulfonic Acid Ionomer (PFSI) Films on Pt and Carbon Substrates

D. Chu, D. Gervasio, M. Razaq and E. B. Yeager

Case Center for Electrochemical Sciences and the Chemistry Department, Case Western Reserve University, Cleveland, Ohio 44106

Introduction

A perfluorinated sulfonic acid ionomer (PFSI), such as Nafion (du Pont) or a similar polymer made by Dow Chemical Co., has been used to form a thin solid polymer electrolyte (SPE) layer over smooth and porous electrode surfaces. Such a polymer coated electrode used as an O_2 cathode in different bulk electrolytes gave improved performance for O_2 electroreduction [1,2].

Little direct evidence is available concerning the interaction of the PFSI film with electrode surfaces. Surface vibrational spectroscopy, particularly *ex situ* infrared reflectance absorption spectroscopy (IRRAS) in combination with a high angle of incidence [3], has been used to explore the nature of mono- and multilayer films on electrode surfaces [4]. The present study involves the IRRAS technique with a high angle of the incident p-polarized radiation to investigate the interaction of air-dried PFSI films with smooth Pt and ordinary pyrolytic graphite (OPG) substrates. Significant differences were found between the reflectance spectra of the dry PFSI on the smooth Pt and OPG surfaces versus the transmission spectrum of the PFSI on a transparent salt-plate support. These differences have been interpreted to be the result of a restructuring of the PFSI during film formation.

Experimental

The Pt foil (Puratronic grade, Johnson Matthey) was 5cm^2 (25 x 20 mm^2) in area. The ordinary pyrolytic graphite plate (OPG, Union Carbide) was 12 cm^2 (30 x 45 mm^2) in area. The KRS-5 plate (Janos Technology) was 10 cm^2 (50 x 20 x 2 mm^3) in area. The AgBr plate (Janos Technology) was 7 cm^2 (35 x 20 x 3 mm^3) in area. Aqueous solutions of the Dow PFSI (equivalent weight = 560) and Nafion (equivalent weight = 1100) electrolytes were prepared, and the films were cast and air dried at 22°C as described elsewhere [5].

The absorption spectra of the PFSI films on different substrates were recorded in vacuo using an IBM Instruments Inc. IR-98AF Fourier transform infrared spectrometer with a liquid N_2 cooled mercury cadmium telluride (MCT) detector. The spectral resolution was 2 cm^{-1}. For transmission experiments, PFSI films were cast on transparent AgBr or KRS-5 salt plates; unpolarized radiation was used and the spectra were referenced to the infrared radiation transmitted through the bare salt-plate support. For reflectance experiments, the absorption spectra of the PFSI films were obtained by ratioing the infrared radiation reflected from the film-coated surface to the infrared radiation reflected from the bare surface. For the IRRAS spectra, the angle of incidence of p-polarized radiation was 75°.

Results and Discussion

Figure 1 shows the transmission spectrum of a 0.5 μm Dow PFSI film cast on KRS-5 and the reflectance spectra from Pt and OPG. The transmission spectrum shown in Fig. 1 is quite similar to the previously reported transmission spectrum of Nafion [6] film except the Nafion C-O-C absorption band at ~980 cm^{-1} is absent as is expected for the Dow polymers [5].

The relative intensities of various bands in the reflectance spectra of the Dow PFSI film on Pt and OPG are strikingly different compared to its transmission spectrum. The intensity of the S-O band at 1300 cm^{-1} versus the C-F band at 1160 cm^{-1} is 1 to 3 in the transmission spectrum, 3 to 1 in the Pt reflectance spectrum and over 4 to 1 in the OPG reflectance spectrum.

It was particularly difficult to compare the changes in intensity for the S-O at 1265 cm^{-1} to the C-F bands at 1200 cm^{-1} with changing substrates, because these bands overlap, so these were not considered further.

For a 0.5 μm film on a reflecting metal surface, the electric field intensity for the p-polarized infrared radiation undergoes a relatively small change on going from the inner portion of the film at the reflecting surface to the outer portion adjacent to vacuum. Thus for the 0.5 μm film, the reflected radiation is sensitive to all portions of film, when using the IRRAS technique in combination with p-polarized radiation.

In the IRRAS spectra with p-polarized radiation, only vibrational modes with a component of the dipole derivative normal to the surface are ir active (surface selection rule).

An absorption band which is stronger in a reflectance spectrum compared to the transmission spectrum (see Fig. 1) suggests that the corresponding vibrational mode interacts more strongly with reflected p-polarized radiation than with transmitted unpolarized radiation due to the orientation of the vibrational mode relative to the surface.

The differences observed between the reflectance and transmission spectra may, therefore, be rationalized in terms of a restructuring of the PFSI during the solution casting of the film on the Pt and OPG surfaces. This restructuring may involve the formation of aggregates with the sulfonate groups tending to orient relative to the reflective surface so that the modes of the -SO_3H moieties effectively interact with p-polarized radiation. Somehow, the orientation persists for a significant number of the sulfonate groups throughout the film, e.g., these aggregates may be partially crystalline.

Simulated spectra (not shown) of PFSI films on Pt and carbon surfaces [7] produced using computer programs developed by Ishida et al. [8] indicate that the differences in the observed intensities of the reflection and transmission spectra are not principally due to optical effects associated with the Drude-Fresnel equations.

Figure 2 shows the IRRAS spectra of a 0.5 μm Nafion film cast on Pt and OPG as well as the transmission spectrum of a 0.5 μm film on a transparent AgBr plate. The latter is virtually identical to a previously published transmission spectrum [6]. As was found for the Dow PFSI, the relative absorption intensities of the various bands in the reflectance spectra of the Nafion PFSI on Pt and OPG are markedly different than the transmission spectrum of the Nafion on AgBr. In the transmission spectrum, the ill defined S-O asymmetric stretching absorption bands near 1300 cm^{-1} are only a third the intensity of the C-F absorption bands near 1156 cm^{-1}. In the reflectance spectrum from the Pt surface, the analogous S-O asymmetric stretching bands near 1328 cm^{-1} are well defined and have about the same intensity as the C-F bands near 1148 cm^{-1}. From the OPG surface, the S-O absorptions near 1300 cm^{-1} are found to be almost three times more intense than the C-F absorptions near 1160 cm^{-1}. It

appears that the same restructuring process suggested above for the Dow PFSI films occurred with Nafion.

The enhancement of the sulfonate absorbance relative to fluorocarbon absorbance in the reflectance versus transmission spectra is somewhat greater with the Dow PFSI film compared to with the Nafion film prepared in the same way. It is noteworthy that the ratio of the intensities of the sulfonate to fluorocarbon bands is ~ 2 times larger with the Dow PFSI compared to with Nafion, and that the number of sulfonate groups per gram of the Dow PFSI is ~ 2 times larger than per gram of Nafion.

For a particular PFSI, the ratio of the intensities of the sulfonic acid to the fluorocarbon absorptions were found to be always larger for the reflectance compared to the transmission spectra. Comparison of the reflectance spectra from Pt and OPG, however, are not quite the same. The ratio of the intensities of the sulfonic to fluorocarbon absorption bands was found to be larger in the spectra involving the OPG surface compared to the Pt surface, suggesting that the sulfonic acid groups have a tendency for a preferred orientation relative to the surface, and that this orientation effect is greater on the OPG surface.

Conclusion

The ratio of the intensity of the sulfonic acid absorption bands to the fluorocarbon bands is greater in the reflectance spectra versus the transmission spectra of dry PFSI films. This is consistent with a restructuring of the PFSI during film formation. Separate aggregates of the $-SO_3H$ and C-F moieties form with the sulfonic acid moieties tending to have a preferred orientation relative to the surface. This orientation persists for a significant number of the sulfonic groups in the film. The ratio of the intensity of the $-SO_3H$ versus C-F bands was found to be greater with the PFSI on OPG versus Pt suggesting that the extent or degree of the orientation of the $-SO_3H$ groups is greater with the OPG surface compared to with the Pt surface.

Acknowledgements

The authors acknowledge the support of the Electric Power and Gas Research Institutes and the Office of Naval Research for this work and the Dow Chemical Company for providing PFSI samples.

The authors acknowledge Prof. Hatsuo Ishida and Dr. Koji Ohta for their stimulating discussions as well as the measurement and calculation of the optical effects of Nafion on Pt and carbon.

References

1. D. Chu, M. A. Enayetullah, E. O'Sullivan, D. Gervasio and E. B. Yeager, in "O_2 Reduction in Acid Electrolytes", Electric Power Research Institute Final Report, RP 1200-7, April 1987.
2. M. T. Paffet and S. Gottesfeld, Electrochemical Society Meeting, Philadelphia, Ex. Abs. 87-1, 529.
3. R. G. Greenler, J. Chem. Phys., 44, 310 (1966).
4. J. F. Rabolt, M. Jurich and J. D. Swalen, Applied Spectroscopy, 39, 269 (1985).
5. D. Chu, D. Gervasio, M. Razaq and E. B. Yeager, Electrochemical Society Meeting, Atlanta, Extended Abstract 88-1, 24.
6. C. Heitner-Wirguin, Polymer, 20, 371 (1980).
7. H. Ishida, K. Ohta, D. Gervasio, M. Razaq and E. Yeager, unpublished results.
8. R. Graf, J. Koenig and H. Ishida, Appl. Spectrosc., 39, 405 (1985).

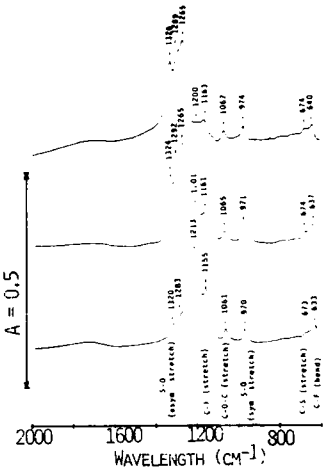


Fig. 1. Vibrational absorption spectra of a 0.5 μm film of the Dow (equivalent weight = 560) PFSI electrolyte.
Bottom: transmission spectrum on KRS-5.
Middle: IRRAS spectrum on Pt.
Top: IRRAS spectrum on OPG.

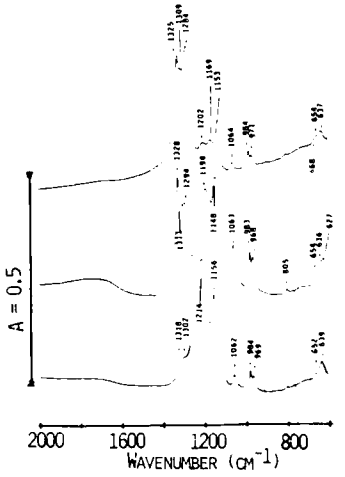


Fig. 2. Vibrational absorption spectra of a 0.5 μm film of the Nafion (equivalent weight = 1100) electrolyte.
Bottom: transmission spectrum on AgBr
Middle: IRRAS spectrum on Pt.
Top: IRRAS spectrum on OPG.

Abstract No. 714

CYCLIC VOLTAMMETRIC STUDY OF THE REDUCTION OF Pu(III) TO PLUTONIUM METAL IN MOLTEN LiCl-NaCl-$CaCl_2$-$BaCl_2$-$PuCl_3$

D. S. Poa, Z. Tomczuk, and R. K. Steunenberg

Chemical Technology Division
Argonne National Laboratory
Argonne, IL 60439-4837

Introduction

Cyclic voltammetry was used to investigate the electrochemistry of the reduction of $PuCl_3$ to plutonium metal in molten LiCl-NaCl-$CaCl_2$-$BaCl_2$ (49.7-8.0-26.5-15.8 mol %) containing dissolved $PuCl_3$. The purpose of the study was to determine the kinetics of the reaction. This information will then be used in helping design electro-refining equipment for the reprocessing of core and blanket fuel discharged from the Integral Fast Reactor (IFR).

The values of emf and standard potential of the Pu(III)/Pu(0) couple in molten $PuCl_3$-KCl, $PuCl_3$-NaCl, NaCl-KCl, and LiCl-KCl electrolytes have been reported by several investigators [1-7]. A chronopotentiometric study of the Pu(III)/Pu(0) system in LiCl-KCl eutectic has been made by Nissen [8]. The diffusion coefficient of Pu(III) in molten LiCl-KCl has been reported by Nissen [8], and Martinot and Duyckaerts [5]. No previous investigation has been made on the Pu(III)/Pu(0) couple in the quarternary salt employed in this study.

Experimental

The electrochemical cell comprised (a) a low-carbon steel crucible (volume, 325 cm^3), which served as the cell container; (b) a working electrode consisting of a 0.32-cm-diameter metal (either molybdenum or low-carbon steel) rod encased in an alumina tube in such a way that an apparent surface area of 0.079 cm^2 was exposed to the electrolyte; (c) a liquid cadmium counter electrode; and (d) a Ag/AgCl reference electrode. The cell was located in a furnace well in the floor of a high-purity, argon-atmosphere glove box. Under normal operating conditions, the oxygen and moisture levels were < 1 ppm; the nitrogen level was <10 ppm, which was the limit of detection.

The $PuCl_3$ in the electrolyte was generated in situ by dissolving metallic plutonium in the liquid cadmium, and then adding known amount $CdCl_2$ to the salt phase. Chemical analyses of filtered samples verified the Pu content of the salt phase.

Single-sweep and cyclic voltammetric scans were made with a potentiostat (PAR Model 173) coupled to a PAR Model 175 universal programmer. Current-voltage curves were recorded with a Hewlett-Packard Model 7044-A recorder.

Results and Discussion

Figure 1 shows typical cyclic voltammograms for the reduction of Pu(III) to the metal at low-carbon steel electrode at 435°C. A simple, well-defined cathodic current peak (i_{pc}) was observed. The anodic current peak, which is sharp and symmetrical, is characteristic of the oxidation of a solid deposit from an electrode surface.

The cathodic peak current (i_{pc}) was linearly proportional to the square root of the potential scan rate ($v^{1/2}$). Plots of i_{pc} vs. $v^{1/2}$ for various temperatures (435 to 478°C) and for the two different cathode materials (molybdenum and steel) were linear and passed through the origin. In addition, the peak current potentials and the separations between the peak and half-peak potentials (15 to 35 mV) were independent of potential scan rate. These results indicate that the charge-transfer reaction of the Pu(III)/Pu(0) couple is reversible and the reduction rate is controlled by diffusion mass transfer.

In general, the cathodic peak current increased with increasing temperature (as shown in Fig. 2). Over a temperature range of 435 to 520°C, the increase in the cathodic peak current with temperature was linear.

The effect of $PuCl_3$ concentration on the reduction current is shown in Fig. 3. When the $PuCl_3$ concentration in the salt was increased from 0.455 to 1.11 mol %, the reduction peak current increased five- to tenfold.

Standard potentials obtained for the Pu(III)/Pu(0) couple in this electrolyte ranged from -1.45 to -1.75 V (vs. Ag/AgCl), depending on the experimental conditions.

Values of the diffusion coefficient for Pu(III) ions in this electrolyte ranged from 2.4 to 5.4 x 10^{-6} cm^2/s over a temperature range of 452 to 520°C. Linear regression analyses of the diffusion data indicated that the diffusion coefficient varies with temperature in accordance with the Arrhenius relationship. The estimated activation energies for the diffusion of Pu(III) ranged from 9.45 to 11.25 kcal/mol.

In general, the results of this study are in reasonable agreement with earlier data obtained with other molten chloride electrolytes [1-8].

Acknowledgement

This work was sponsored by the U.S. Department of Energy as part of the Integral Fast Reactor Program under Contract W-31-109-Eng-38. The authors also wish to acknowledge the support and guidance of M. J. Steindler and L. Burris of the Chemical Technology Division, Argonne National Laboratory, and to express our appreciation to D. Bowers of the Argonne Analytical Chemistry Laboratory, who performed the plutonium analyses.

References

1. R. Benz, J. Phys. Chem. 63, 1983 (1959).

2. R. Benz, J. Phys. Chem. 65, 81 (1961).

3. R. Benz and J. A. Leary, J. Phys. Chem. 65, 1056 (1963).

4. V. I. Silin, et al., At. Energ. 25, 26 (1968).

5. L. Martinot and G. Duyckaerts, Bull. Soc. Chim. Belg. 80, 299 (1971).

6. D. M. Gruen and R. A. Osteryoung, Ann. N. Y. Acad. Sci. 79, 897 (1960).

7. G. M. Campbell, J. Phys. Chem. 73, 350 (1969).

8. D. A. Nissen, J. Inorg. Nucl. Chem. 28, 1740 (1966).

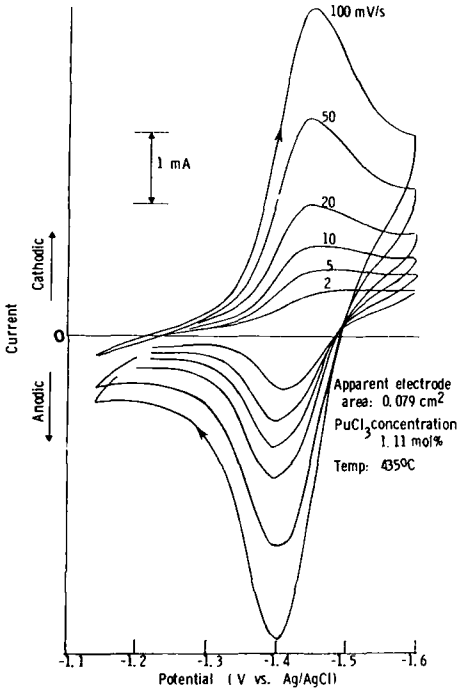


FIG. 1. Effect of Potential Scan Rate on Voltammograms for the Reduction of Pu(III) at a Low-Carbon Steel Electrode.

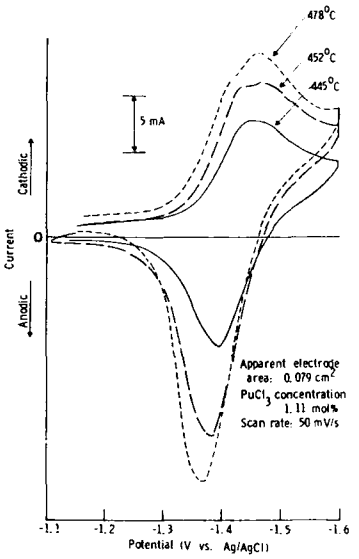


FIG. 2. Effect of Temperature on Voltammograms for the Reduction of Pu(III) at a Low-Carbon Steel Electrode.

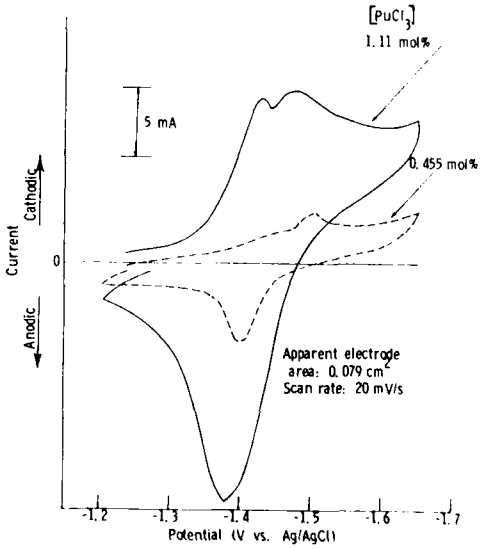


FIG. 3. Effect of $PuCl_3$ Concentration on Voltammograms for the Reduction of Pu(III) at a Low-Carbon Steel Electrode at 485°C.

Abstract No. 715

In Situ UV-Vis Difference Spectroscopy of Electrode/Electrolyte Interface with Integating Sphere Assembly

C. G. Chen*, S. J. Tang, and Z. Q. Huang
Department of Applied Chemistry
Chongqing University
Chongqing, Sichuan, CHINA

Introduction

In recent years, it has made some progress that Fourier transform infrared (FT-IR) difference spectroscopy measured potentiostatically is utilized to simulate the potential modulation infrared spectroscopy(1). A similar technique is also used in ultraviolet visible (UV-Vis) reflection spectroscopy . An in situ UV-Vis difference spectroscopic measurement of electrode/electrolyte interface with integating sphere reflection assembly is described in this paper.

Experimental

The equipment is a Shimadzu UV-240 ultraviolet visible spectrophotometer controlled by microcomputer. The electrochemical cell newly-designed can be installed in the SAMPLE position of integating sphere assembly. The REFERENCE was a stsndari white plate (MgO powder). Optical window was made by quartz. The working electrode was a piece of 10x10mm^2 platinum cleanly, no polishing. A platinum-wire loop counter electrode and a saturated calomel reference electrode were used.

At first, the reflectance R_s at the base potential (E_s) was obtained in this measurement, then R at other potentials (E). Reflectance relative change $\Delta R/R$ was calculated from R and R_s.

Results and Discussion

Fig.1 shows the diffusion reflection difference spectra of Pt in solution containing 0.1M sodium fluoride(NaF) and 0.01M pyridine (C_5H_5N). The spectrum changes within 280-480 nm is the electroreflection(ER) of platinum surface oxidized, which is related to the applied potential.

With the increase of potential, reflectance (R) remains constant from 200nm to 280nm, which is the strong absorption region of pyridine. In the same time, a new band appears at 700nm. These may be the characteristic of pyridine π-adsorption on platinum surface, especially at more positive potential platinum was oxidized and has the empty d-orbit (2). In the absence of pyridine , above phenomena have not been found.

The experimental results indicated that in situ UV-Vis difference spectrum technique can act as a kind of electrochemically modulated spectroscopy. Furthermore, this method will be developed to study the oxidation and corrosion on metal, for diffusion reflection measurement wit: integating sphere assembly is favourable to rough surface.

References

1. C. Korzeniewski and S. Pons, Prog. Analyt. Spectrosc., 10, 1(1987).
2. A. B. Ershler, A. M. Foontikov, and I. M. Levinson, J. Electroanal. Chem., 136, 83 (1983).

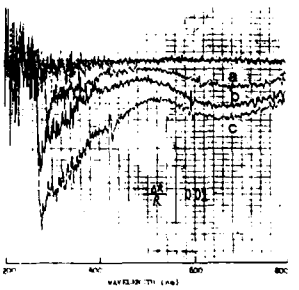


Fig.1 Diffusion reflection difference spectra of platinum/0.1M sodium fluoride + 0.01M pyridine interface. Base potential: -0.2, applied potential: a 0.3; b 0.5; c 0.8V vs.SCE.

Abstract No. 716

LASER INDUCED PHOTO-DEPOSITION OF METAL ON TiO_2 FILMS

C. H. Paik, M. R. Kozlowski, P. S. Tyler, and W. H. Smyrl*
Corrosion Research Center, and
Department of Chemical Engineering and Materials Science
University of Minnesota
Minnepolis, MN 55455

Photo-deposition of palladium was observed to study the structure/property relationship of semiconducting titanium dioxide (TiO_2). Thin anodic films of the oxide (20 nm) grown on a polycrystalline Ti metal substrate were immersed in an aqueous solution of $PdCl_2$, and illuminated by a UV laser (λ = 351 nm). Light absorption within the semiconducting TiO_2 generated e^-/h^+ pairs which further participated in an electrochemical reaction at the oxide surface. Holes at the surface reacted with a solution component (methanol), while electrons reacted with Pd^{+2} ions in solution to yield Pd metal at the site of the reduction reaction, leaving a footprint of available electrons at the surface. Pd was deposited on the oxide surface in lines with a width defined by the resolution of the focused laser beam (diameter 5-10μm).

It was first found that the deposition matched closely the illumination patterns. Metal deposited on the illuminated sites, and obeyed the photocatalytic effect -- a preferential deposition on an already deposited Pd metal sites as opposed to a bare TiO_2 surface [1].

The second observation was that the electronic properties that control metal deposition were dependent on the oxide crystal structure. Oxides were prepared at different degrees of crystallinity influenced by their growth rate of anodic polarization. Electron diffraction has been used to show that slowly grown oxide (~ 1nm/h) results in a crystalline film while the rapidly grown films are amorphous or microcrystalline. Metal deposition was found noticeably greater on a slowly grown TiO_2 film than on a rapidly grown film. Two proposed factors that influence this dependence are greater UV light absorption and longer diffusion length of the photoexcited electrons for the slowly grown film. Greater electron-diffusion lengths, or longer survival of the electron before recombination, can be provided by more crystalline oxides.

The third and most important observation is to note a dramatic change of morphology of Pd deposition on oxide grown on adjacent Ti grains. Scanning Electron Micrographs of a Pd line on two adjacent grains is shown in Figure 1. Along with a clearly defined difference in deposition pattern from one grain to the other, the particle size of the Pd deposit was also different on the two oxide areas. The change in deposition morphology were caused by different surface energy states available to accomodate the electrons for the reaction. Such variations of energy states are proposed to be caused by different defect densities in the oxide in the form of oxygen-vacancies or titanium interstitials [2,3]. Since intially photoexcited electrons can recombine or diffuse toward the surface, such defects provide sub-bandgap states that influence rates of recombination, and thus available electrons at the surface. Hence, metal deposition reveals the heterogeneities of defect concentrations in the oxides that grow on different grains of the metal substrate.

To explore the possibility that metal deposition would probe the crystal size, crystal ordering, and defect concentration, two additional experiments were done: different metals (Pt, Ru, and Ir) deposited, and TiO_2 was grown to different film thicknesses for substrates. Different metals were deposited on the surface to compare the redox potential of each metal that could be deposited with the energy states in the film. In addition, thinner films of TiO_2 were found to have higher degrees of heterogeneity and were most strongly influenced by the polycrystalline Ti metal substrate. More dramatic changes in the morphology of the metal deposition was observed from one grain to the other with thin oxide films.

In summary, photo-deposition of metals was found to be dependent on both the crystal size, ordering, and the morphology of substrate TiO_2 films. This dependence was used to probe the heterogeneities of the thin semiconducting films on Ti metal.

Acknowledgements -- *This work was supported by* DOE, Agreement No. DOE/DE-FG02-84ER45173. The author would like to thank R. T. Atanososki for many helpful discussions.

References

[1] Jacobs, J.W.M., J. Phys. Chem. 90, 6507 (1986).
[2] Kozlowski, M.R., Tyler, P.S., Smyrl, W.H., Atanasoski, R.T., Surface Science 194, 505-530 (1988).
[3] Ghosh, A.K., Wakim, F.G., Addiss, R.R. Jr, Physical Rev., 184-3, 979 (1969).

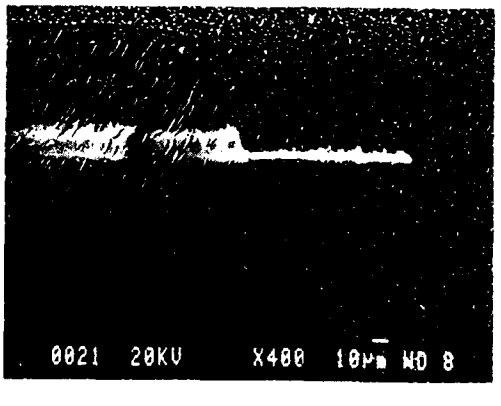


Figure 1. SEM micrograph of Pd deposition pattern obtained from focused illuminatio of an oxide film grown to ~ 5V at 0.1 mV/s, laser power 3mW, laternal scanning speed 0.1 μm/s, $PdCl_2$ concentration 10 mM.

Abstract No. 717

PHOTOELECTROCHEMICAL CHARACTERIZATION OF DEFECT HETEROGENEITIES IN ANODIC TiO_2 FILMS

M. R. Kozlowski, C.-H. Paik, P.S. Tyler, and W. H. Smyrl
Corrosion Research Center and Dept. of Chemical Engineering and Materials Science
University of Minnesota
Minneapolis, MN 55455
and
R. T. Atanasoski
Institute of Electrochemistry, ICTM,
University of Belgrade, Belgrade, Yugoslavia

An understanding of the local properties of thin semiconducting oxide films is important in the areas of microelectronics, corrosion, catalysis, and solar energy conversion. We report here the results of a study of the local photoelectrochemical and structural properties of thin (<20 nm) TiO_2 films grown by anodic polarization of polycrystalline titanium substrates. The principal technique used in the investigation was photoelectrochemical microscopy (PEM). PEM is a quantitative in-situ technique which utilizes a focussed laser beam to measure local photocurrents in semiconducting films [1-3].

The photoelectrochemical properties of thin anodic TiO_2 films grown on polycrystalline titanium substrates have been shown to be heterogeneous and dependent on the oxide growth rate and the crystallography of the underlying titanium substrate [1-3]. By combining PEM data with that of structural studies and local metal photo-deposition studies on these same films, a model is evolved which attributes the heterogeneous photoelectrochemical properties of the oxide to variations in the oxide defect structure.

For oxides grown slowly (~1 nm/h), by ramping the potential of the metal substrate at 0.1 mV/s, the oxide photoresponse was found to map the grain structure of the underlying titanium substrate. As the oxide growth rate was increased the photoresponse became more homogeneous and the average photocurrent decreased. Similarly, electron diffraction studies of the oxides showed that the oxide structure was also dependent on the oxide growth rate and the substrate crystallography. The slowly grown films had an ordered rutile structure with a preferred growth direction evident on some substrate grains. As the oxide growth rate was increased the oxide structure became more homogeneous and the oxide crystallite size decreased. The decrease in oxide crystallinity with increase in oxide growth rate was also observed in photospectroscopy measurements as a loss of the 3.7 eV direct bandgap.

Studies of local photodeposition of Pd on these same oxides has shown that the metal deposition was also dependent on the oxide growth rate and the crystallography of the underlying titanium substrate [4]. The morphology of the metal deposition pattern changed abruptly at the grain boundaries of the substrate. The correlation of the metal deposition morphology with the local photocurrents measured on these areas using PEM showed that the heaviest deposition occurred on the oxide areas with the lowest photocurrents.

The oxide properties are also sensitive to the preparation of the metallic substrate. For the films discussed above the polycrystalline titanium substrate was polished down to 0.05 μm alumina and then etched with an aqueous solution of 2% HF and 4% HNO_3. If the etched substrate was lightly ion milled prior to oxide growth the resulting oxide had homogeneous photoelectrochemical properties.

We propose that the local variations in the photoelectrochemical properties of the oxide films are due to variations in the density of defects in the oxide. These defects, such as oxygen vacancies or titanium interstitials, generate sub-bandgap electronic states in the bulk and at the oxide surface. The sub-band$_{gap}$ states act as recombination centers producing low photocurrents in areas of high defect density. These defects produce surface states which increase the density of electrons available for the reduction of metal ions at the oxide surface. The same defects may therefore lead to low photocurrents and high rates of Pd deposition. The density of the defects is controlled by the structure of the oxide film and is therefore dependent on the oxide growth rate and the crystallography of the titanium substrate.

In order to identify the energy levels of the defects, the oxides were characterized by photoelectrochemical spectroscopy and photoacoustic spectroscopy.

The influence of metal photodeposition on the photoresponse of the semiconducting films is also considered. This includes the influence of the Pd/TiO_2 interface and photo-assisted electromigration of defects [5] in the oxide as a result of extended focussed laser illumination.

Acknowledgement. This work was supported by DOE Agreement No. DOE/DE-FG02-84ER45173. R.A. would like to thank the support of the Yugoslav-American Fund for Scientific Cooperation. DOE Grant No. 675.

References:

1. M.A. Butler, J. Electrochem. Soc., 131 (1984) 2185.
2. M.R. Kozlowski, P.S. Tyler, W.H. Smyrl, and R.T. Atanasoski, Surface Science, 194 (1988) 505.
3. P.S. Tyler, M.R. Kozlowski, W.H. Smyrl, and R.T. Atanasoski, J. Electroanal. Chem., 237 (1987) 295.
4. C.H. Paik, M.R. Kozlowski, P.S. Tyler, W.H. Smyrl, submitted to J. Electrochem. Soc.
5. M.R. Kozlowski, P.S. Tyler, W.H. Smyrl, and R.T. Atanasoski, presented at the 172nd Meeting of the Electrochem. Soc., Honolulu, Oct. 18-23, 1987; proceedings in press.

Abstract No. 718

Identification of Deep-Level Electronic Defects by Photoelectrochemical A.C. Impedance Spectroscopy

D. Bivings Bonham and Mark E. Orazem
Department of Chemical Engineering
University of Virginia
Charlottesville, Virginia 22901

Even in very low concentrations, deep level electronic states present within the bulk of a semiconductor or at the surface can have a large impact on photoelectrochemical processing and are frequently detrimental to the performance of high speed devices. The capacity obtained from A.C. impedance spectroscopy conducted under monochromatic sub band gap illumination has been used to identify the energy levels associated with these states,[1-3] but this technique is not sensitive to low concentrations[4] and does not provide information on the density and distribution of these states. Through development of comprehensive transport based mathematical models of the impedance response of the semiconductor, we have shown that the resistive component of the impedance response is much more sensitive to these states than is the capacitive component.[5] This result has been reported,[4] but the resistive component is much more difficult to interpret than is the capacitive term. An approach is being developed to use both the resistive and capacitive components of the impedance response to determine the energy, density, distribution, and recombination rate constants associated with deep level electronic defects. This may have application to *in situ* characterization of semiconductor electrolyte interfaces and to inexpensive non destructive screening of raw material used in device fabrication.

The approach taken here was to develop a mathematical model[5] which accounts explicitly for the transport and recombination reactions involving electrons, holes, and electronic defects located within the bandgap. This model was used to evaluate the effect of deep level states on the impedance response of an ideally polarized semiconductor electrode and to guide development of appropriate analytic asymptotic solutions. The method that is proposed here for interpreting the impedance response under sub band gap monochromatic illumination in terms of defect states is preliminary in that it applies only to single defects of a single energy. This work will be extended to account for multiple defects and to defects characterized by a continuous distribution of energy levels.

The parameters used in this study correspond to an n type GaAs electrode. A typical calculated Nyquist plot is shown in Figure 1. The circles correspond to calculated points for different frequencies and applied potentials. The solid line represents the curve fit of the calculated points to an equivalent electrical circuit shown in Figure 2. This equivalent circuit, which matches our calculations for bulk deep level states, is the same as that given by Dare Edwards *et al.*[7] for surface states.

Proposed Method

The results of the transport based model were treated as though they were the result of an experimental system. Calculated values for the impedance response over a broad frequency range in the dark and under sub band gap illumination were obtained with different applied potentials. This approach provided the basis for the method presented below for analysis of impedance data.

- *Regression techniques* were used to match the impedance data to the impedance response of the equivalent electrical circuit shown in Figure 2. This provided values for the space charge parameters (R_2 and C_2) and the deep-level defect parameters (R_1 and C_1).
- In accordance with standard Mott-Schottky theory, $(1/C_2)^2$ was plotted against applied potential. The slope yielded the doping level $N_d - N_a$, and the intercept yielded the flat band potential.
- The product R_1C_1 at the flatband potential in the dark is equal to $[k_4(N_d - N_a)]^{-1}$. This gave us k_4, the rate constant for transfer of electrons from the conduction band to the inter band defect.
- Sharp transitions in R_1 as a function of illumination frequency yielded the energy gap associated with a transition. From this we calculated the trap energy E_T. In previous work,[1-3] changes in capacity were used to obtain this parameter, but the resistive term was much more sensitive to low concentrations of defects.
- The trap energy was used to calculate the equilibrium value for k_3 through equilibrium expressions (see Figure 3 for a schematic representation of the kinetic scheme considered here).
- The value of R_1 at the flat band potential in the dark yielded the average concentration of defect states through an asymptotic expression, i.e.,

$$R_1 = \frac{2RT}{F\lambda k_3 C_D^T}, \qquad (1)$$

where λ is the semiconductor Debye length and C_D^T is the state concentration. This concentration reflects a weighted average over several Debye lengths in the semiconductor near the surface. State concentrations calculated through this method (solid bullets) are compared to input distributions in Figure 4.

As in standard $C - V$ profiling, which uses changes in the capacitive component with applied potential to obtain the dopant distribution, changes in the resistive component of the impedance with applied potential indicate the state distribution.

Discussion

The method proposed here is still preliminary and requires experimental verification. The coupling of comprehensive mathematical models with experimental data, however, may yield a way to interpret the resistive component of the impedance which is much more sensitive to deep level states than is the capacitive component.

References

1. R. Haak, C. Ogden, and D. Tench, *J. Electrochem. Soc.* **129** (1982), 891-893.
2. R. Haak and D. Tench, *J. Electrochem. Soc.* **131** (1984), 275-283.
3. R. L. Wheeler, G. Nagasubramanian, and A. J. Bard, *J. Electrochem. Soc.* **131** (1984), 2289-2294.
4. P. Allongue and H. Cachet, *J. Electrochem. Soc.* **132** (1985), 45-52.

5. D. B. Bonham and M. E. Orazem, *AIChE Journal* **34** (1988), 465 473.

6. J. Newman, *Ind. Eng. Chem. Fund.* **7** (1968), 514-517.

7. M. P. Dare-Edwards, A. Hamnett, and P. R. Trevellick, *Chem. Soc., Faraday Trans. 1* **79** (1983), 2111-2124.

Acknowledgement

This material is based upon work supported by the National Science Foundation under Grant No. EET-8617057.

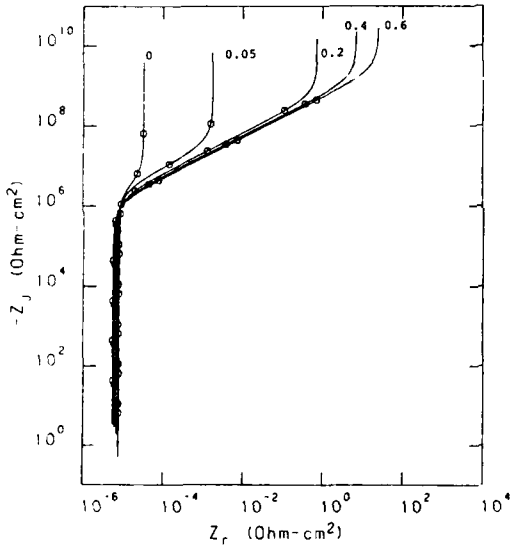


Figure 1. Calculated Nyquist plot for an n type GaAs electrode with a uniform doping level of 10^{16} cm^{-3}, an inter band state energy of 1.1 eV referenced to the valence band, and a uniform inter band state concentration of 10^{14} cm^{-3}. The resistive component is much more sensitive to deep level states than is the capacitive component. Note the logarithmic scales used.

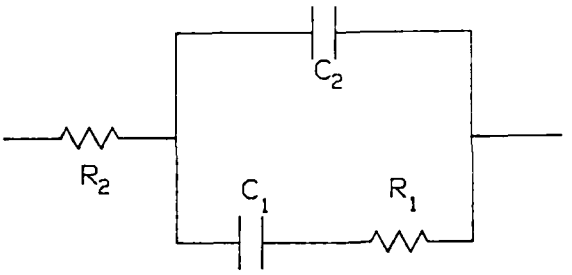


Figure 2. Equivalent electrical circuit matched to experimental data.

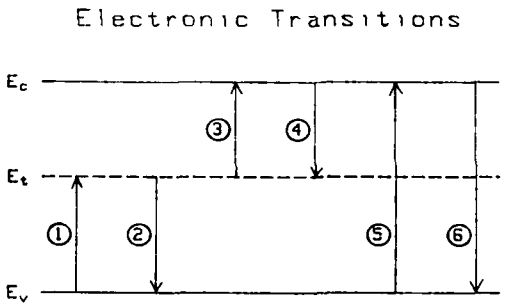


Figure 3. A schematic representation of the recombination and generation kinetics studied here. The trap energy is used to calculate the value for k_3 through equilibrium expressions.

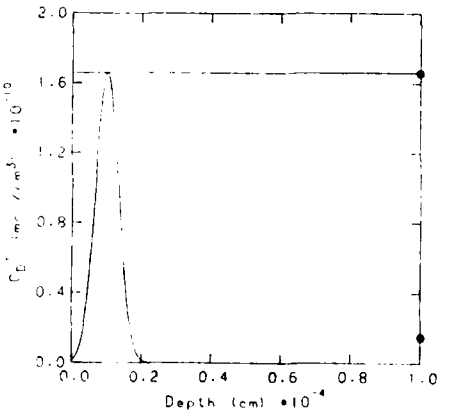


Figure 4. Comparison of input deep level state distributions and concentrations calculated through the method proposed here.

Abstract No. 719

High Resistivity ZnO Films

J.K.Srivastava, Lily Agarwal and A.B.Bhattacharyya

Centre for Applied Research In Electronics
I.I.T. Delhi 110016 INDIA

The purpose of the present research was to increase the resistivity of the ZnO films by diffusing lithium and to study the characteristics of the ZnO film before and after lithium diffusion. For surface acoustic wave applications ZnO (piezoelectric material) should have high electrochemical coupling constant, temperature stability, high electrical resistivity and singley oriented crystalline structure. The C-axis oriented ZnO films show better results. Using sputtering techniques ZnO films have been prepared whose coupling constant is close to those of single crystal ZnO [1].

The operational frequency is a function of resistivity and a relationship is given as follows. Under depletion or accumulation conditions frequency at which device performs is [2].

$$f \ll 1 / t_d \qquad (1)$$

where t_d is the dielectric relaxation time which is given by

$$t_d = \xi_o \rho \qquad (2)$$

where ξ_o is the dielectric constant and ρ is the resistivity of ZnO. If we increase resistivity we can decrease the operational frequency. Resistivity values vary from 10^4 to 10^7 Ohm-cm depending upon sputtering conditions ie by changing the ratio of argon and oxygen gases [3] and/or by doping Li using Li compounds [4] and by using Li doped targets [5,6]. Maximum value of resistivity reported by Tadashi Shiosaki is 10^{11} Ohm-cm using Li targets.

Li diffusion is carried out by bubbling oxygen gas through saturated solution of Li_2CO_3 in DI water (Li_2CO_3 solution is kept at 95°C during bubbling). Temperature for diffusion is 500°C and 600°C for 45 min. followed by oxygen anneal for 15 minute at the same temperature. The patterns were defined by lithography for metallic contacts. Resistivity was measured using the formula

$$\rho = R A / L = R W t / L \qquad (3)$$

R=measured resistance, W=width of the device, L=length of the device and t=thickness of the ZnO film. Surface and bulk resistivities of ZnO film were measured.

Resistivity of ZnO film obtained is of the order of 10^6-10^7 Ohm-cm (bulk resistivity) and after doping 10^7-10^8 Ohm-cm resistivity is observed, while surface resistivity is found to be of the order of 10^4-10^6 Ohm-cm. Resistivity of ZnO film prepared by sputtering technique decreases with increasing temperature [7]. ZnO is an n-type material due to excess zinc in the form of interstitials (Zn_i). Zinc excess can also exist in the form of oxygen vacancies($V_o^{\bullet}$).

$$Zn = Zn_i^{\bullet} + e' \qquad (4)$$
$$Zn = Zn_{zn} + V_o^{\bullet} + e' \qquad (5)$$

Incorporation of Li (monovalent metals), which takes place at interstials as well as substitutional sites leads to drastic increase of resistivity. Li doping occurs according to [8]

$$Li_2O = Li_{zn}' + Li_i^{\bullet} + O_o \qquad (6)$$

Li interstial takes the sites of a zinc lattice as follows

$$Li_i^{\bullet} + Zn_{zn} + e' = Li_{zn}' + Zn_i^{\bullet} \qquad (7)$$

Or generates an oxygen vacancy

$$Li_i^{\bullet} + e' = Li_{zn}' + V_o^{\bullet} \qquad (8)$$

The fact that lithium doping increases resistivity while the concentration of $Zn_i^{\bullet}$ or $V_o^{\bullet}$ is increased demonstrates the loss of donor states. A complete replacement reaction is as follows,

$$2Li_i^{\bullet} + 2e' + Zn_{zn} = Li_i^{\bullet} + Li_{zn}' + Zn_i^{\bullet} + e' \qquad (9)$$

Thus two donors (Li_i) are replaced by one Zn_i giving more donors than in the original crystal. Lander [9] reporated that in equilibrium the concentration of $V_o^{\bullet}$ and Zn_i must decrease which is contradicted by eqn.(9). This controversy can be explained by the loss of Zn_i with its electron which diffuses out, thus causing an increase in the resistivity. AES shows a less intense peak at 990 eV and a shift in doped ZnO samples which is interpreted as the loss of Zn and/or an increase in the O/Zn ratio. IR spectra show the peak of Li-O in the doped ZnO films which is not observed in the undoped ZnO clearly indicating Li replacing lattice sites.

Acknowledgement:

The authors thank Mr. B.S.Panwar for useful discussions and Dr.G.Bose for encouraging this research work.

References:

[1]. J. D. Larson , D. K. Winslow and L. T. Zitelli, IEEE Trans. Sonics and Ultrasonics SU-19, 18-2(1972).
[2]. P. Richman, " Mos Field Effect Transistor and Integrated Circuits" John Wiley & Sons, N.y., 56,(1973).
[3]. D. D. Davidson and L. I. Maissel, J. Appl. Physics, 37, 574(1966).
[4]. R. F. Belt and G. C. Florio, J. Appl. Physics, 30,11, 5215(1968).
[5]. T. Mitsuyu, S. Ono and K. Wasa, J. Appl. Physics, 51, 2464(1980).
[6]. Tadashi Shiosaki, Ultrasonics Symposium Proceeding IEEE, 100(1978).
[7]. L. Agarwal, J. K. Srivastava and A. B. Bhattacharyya, to be communicated.
[8]. P. Bonasewicz, W. Hirschwald and G. Neumann, J. Electhem. Soc., 133, 2270(1986).
[9]. J. J. Lander, J. Phys. Chem. Solids, 15, 324(1960).

Abstract No. 720

Photoresponse of Stainless Steel Electrode Attacked by Cl^- Ions in Acidic Medium

Shengmin Cai[+], Shenhao Chen[++]
Yaohui Dong[+], Xiao Chen[++], Huaquan Yang[+]
[+] Department of Chemistry, Peking University, Beijing, China
[++] Department of Chemistry, Shandong University, Jinan, China

Introduction

The photoresponse of the stainless steel in neutral medium was identified in previous reports. Photoresponse measured in acidic medium has not been reported. In this work we obtained the photoresponse in acidic medium when Cl^- ions were added into 0.5M H_2SO_4 solution. The photocurrent increased gradually when the total current increased rapidly. To the best of authors' knowledge, no work has been found on this topic.

Experimental Methods

All experiments were performed on 1Cr18Ni9Ti type stainless steel electrode with diameter of 0.5 cm. The electrode was sealed with epoxy resin (DEVCON), and only the working area was exposed. Before using in each experiment, it was polished with emery papers to mirror-like brightness, then rinsed with alcohol and distilled water separately(1). All solutions were deaerated with purified nitrogen. The reference electrode was Hg/Hg_2Cl_2 in the same solution and all potentials reported here were referred to the normal hydrogen electrode (NHE). The light source was 40 watt halogen-tungsten lamp with light intensity of 81 mw/cm^2. The photocurrents measured with chopper frequency 11.1 Hz were interfaced to IBM-PC/XT computer after it had been amplified by lock-in amplifier (PAR M5206, time constant of low pass filter is 3 seconds). The computer had the functions of data discrimination and data averageing. All measurements were conducted at room temperature of 21±2°C with circuit improved on the basis of (2,3) (see Fig.1)

Results and Discussion

Fig.2 shows the variation of the photocurrent I_{ph} and total current I_t with time. The electrode was passivated in 0.5M H_2SO_4 at 0.70 V for 10 minutes, no photoresponse had been detected in this period. Concentrated KCl was added at zero second to 0.4M, three currents were measured chronometrically (photocurrent I_{ph}, the readout of the same I_{ph} when light was chopped off manually and the total current passing the electrode I_t). From Fig.2, it reveals that I_{ph} can be stabilized at zero for some time. This relates to the induction time of pitting. Afterwards I_{ph} start increasing at about 360th second and relevent total current also increased gradually. It obviously meant that pitting started. From the fact that I_{ph} still decreased to zero as light was chopped off, we confirmed that I_{ph} measured was real photocurrent. No other reason such as instrumental characteristics, electric noise etc. may be account for this I_{ph}.

Fig.3 shows the typical results in the case that the electrode was directly inserted in 0.5M H_2SO_4 +0.35M KCl solution at 0.70 V and all currents were measured at once. The induction time of pitting was shorter than that of Fig.2. The photocurrent was increased gradually still the same as the total current increased rapidly. The light was chopped on and off manually at periods of 60 seconds for each case. Apparently we still obtained 'true' I_{ph} because this I_{ph} decreased to almost zero when light was off.

Fig.4 shows the results when the electrode surface was illuminated continuously. All other experimental conditions remained similar to Fig.3. The increasing rate of I_{ph} and I_t are larger than that of Fig.3. A possible partial exploration is photocorrosion.

Fig.5 shows the influence of concentration of Cl^- ions where it was changed to 0.30M. In this case the competation of the two processes (forming of pitting and repairing of film on the electrode surface) resulted in the fluctuation of I_t. I_{ph} also fluctuated correspondingly and became noisy. We found 0.30M of Cl^- of the above phenomenon is critical concentration.

In Fig.6, the solution was not deaerated with purified nitrogen. The increasing rate of I_t was slower than that of Fig.5. It resulted from elimination of fluid movement due to nitrogen bubbling.

The I_{ph} measured were always position, this was due to the n-type semiconductive property of the electrode(4). We believe the increase of I_{ph} when Cl^- existed in solution was mainly the result of oxygen ions of the passive film partly replaced by chloride ions (5). Changes of related energy levels, band gap, surface states as well as concentration of charge carriers may be also responsible for this effect. No conclusion should be made at this moment, but the present method can probably be used to detect the induction period of pitting and study the changes of composition and structure of the electrode surface when Cl^- ions were added.

Acknowledgement

Projects supported by the Chinese National Science Fund.

References

1. D.M.Drazic and S.Chen, Electrochim.Acta. 27,1409 (1982).

2. C.Liu, S.Cai, S.M.Wilhelm, S.D.Kapusta, A.Viehbeck and N.Hackerman, Scientia Sinica (series B), 27,225 (1984).

3. S.Cai, J.Zang, B.Shao, Y.Wu and J.Wang, Acta Energiae Solaris Sinica, No.4,352 (1986).

4. S.M.Wilhelm and N.Hackerman, J.Electrochem. Soc., 128,1668 (1981).

5. T.E.Pou, O.J.Murphy, V.Young and J.O'M Bockris, J.Electrochem.Soc., 131,1243 (1984).

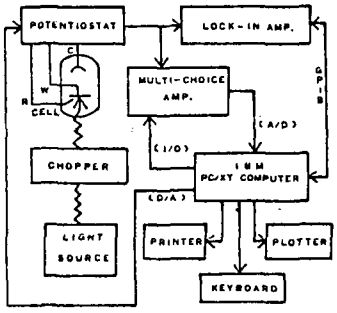


Fig.1 Schematic diagram of determining photocurrent and total current.

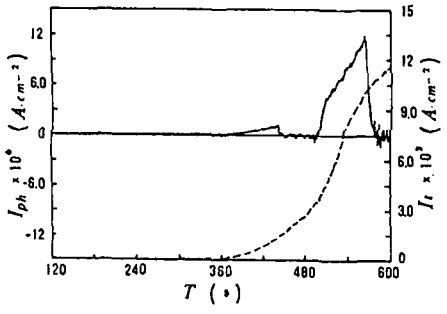


Fig.2. Variations of photocurrent I_{ph} and total current I_t with time t(sec.). Prior experiment, electrode was passivated in 0.5M H_2SO_4 solution for 10 minutes. 0.4M KCl added at the begining of measuring. Electrode potential E=0.70V.
———— I_{ph} ; -------- I_t

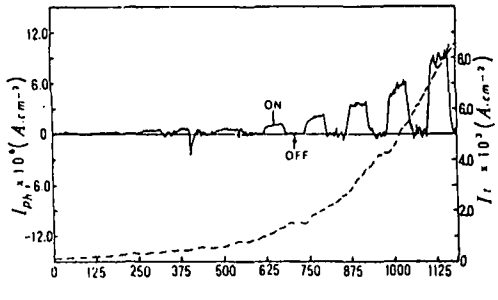


Fig.3. Variations of I_{ph} and I_t with time. Electrode was directly inserted in 0.5M H_2SO_4 +0.35M KCl solution and experiment started at once. Electrode potential E=0.70V.
———— I_{ph} ; -------- I_t

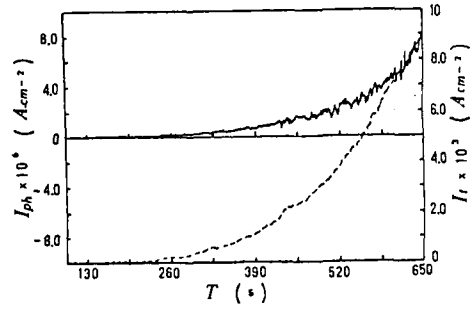


Fig.4. Variations of I_{ph} and I_t when the electrode surface was illuminated continuously.Other conditions were same as Fig.3.
———— I_{ph} ; -------- I_t

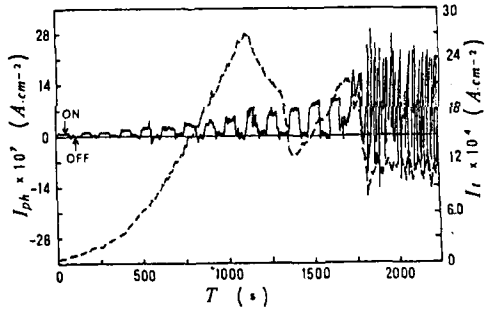


Fig.5. Variations of I_{ph} and I_t as concentration of Cl ions was equal to 0.30M. Other experimental conditions were same as Fig.3.
———— I_{ph} ; -------- I_t

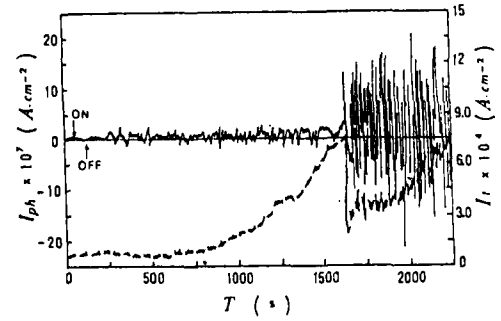


Fig.6. Variations of I_{ph} and I_t as the solution was not deaerated with purified nitrogen. Other conditions were same as Fig.5.
———— I_{ph} ; -------- I_t

Abstract No. 721

PHOTOELECTROCHEMICAL ETCHING OF BLAZED ESCHELLE GRATINGS IN N-GaAs

J. Li, M. M. Carrabba, J. P. Hachey, S. Mathew and R. D. Rauh

EIC Laboratories, Inc.
Norwood, Massachusetts 02062

INTRODUCTION

Photoelectrochemical etching can be a technique for producing microstructures in semiconductors with a high aspect ratio and lateral uniformity. As an example of this application, we have reported recently on producing sawtooth gratings in (100) oriented crystals of n-GaAs using this method [1]. The process takes advantage of the orientational dependence of photoelectrochemical dissolution of GaAs, which favors the (111)As over the (111)Ga polar face, similar to some types of oxidative chemical etching [2,3]. Etching in the (100) surface necessarily results in symmetrical groove profiles, while most optical applications of gratings require unsymmetrical blazed structures.

It is the purpose of this paper to demonstrate photoelectrochemical etching of blazed, deep Eschelle gratings. These gratings are employed in a variety of electro-optical devices and in very high resolution spectrometers. Because of the large amount of material which must be removed in the fabrication, they are difficult to produce with smooth walls by conventional ruling engines, particularly in the low groove densities frequently needed.

EXPERIMENTAL

GaAs wafers (n-type, 5 x 10^{17} cm^{-3}) were cut from a boule supplied by Bertram Laboratories. Diced wafers of 5/8 x 5/8" dimensions were mounted as electrodes and then sequentially polished with alumina abrasives down to 0.05 μm, and finally chemomechanically polished with a silica/bleach slurry. Grating patterns were produced in positive photoresist (Shipley 1350J) with a periodicity of 50 cycles/mm. A line to space ratio of 2 was determined to give optimum results [4]. Both the photoresist exposure and the photoelectrochemical etching were accomplished using a highly collimated UV source (Oriel Corporation 87301 Illuminator). All experiments were conducted with potentiostatic control in a 3-electrode cell with a standard calomel (SCE) reference electrode.

RESULTS AND DISCUSSION

In order to produce blazed Eschelle gratings, it is necessary to cut the GaAs crystal at an angle off the (100) plane toward the (011) plane. As shown in Figure 1, orienting the photoresist lines in the [01$\bar{1}$] direction should then give rise to structures with the interior angles governed by the preferred Ga-rich surfaces. One advantage of photoelectrochemical etching for producing these structures is that the process can be followed coulometrically. The charge, Q, required to etch the V-groove sawtooth pattern is:

$$Q(C/cm^2) = 3.54 \times 10^3 \, nN \left(\frac{0.5 \, W^2}{\cot(\alpha-\beta)+\cot(\alpha+\beta)} \right) \quad (1)$$

Here, n is the electron stoichiometry (equivalents/mole) of the photoanodic dissolution reaction, W is the width (cm) of each groove, α is the angle of the groove face with respect to the (100) surface, β is the angle of the crystal slice with respect to the (100) surface, and N is the number of grooves/cm. In the present case, n = 6, N = 500 and W = 2 x 10^{-3} cm.

To demonstrate the photoelectrochemical etching of blazed structures, crystals were cut with (100), (100)-8° and (100)-18° orientations. The electrolyte composition was 0.1M KCl, adjusted to pH 3, and the light intensity was 30 mW/cm^2. The potential was held at the onset of the photon limited region, 0.4V vs. SCE. Initial structures were etched under the assumption that the interior angles were 70.54°, as defined by the (111) Ga surfaces. However, we found under closer examination that this angle was dependent on the etching conditions and on the electrolyte, and was closer to 90° under the present conditions. This would correspond most closely to the (223)Ga-rich surface. With a 90° interior angle, equation (1) predicts a charge of 10.6 and 8.6 C/cm^2 required to etch the gratings in the (100) and (100)-18° degree surfaces, respectively. With coulometric monitoring, both unblazed and blazed gratings were produced with pointed tops and bottoms and extremely smooth walls. A scanning electron micrograph (SEM) of the blazed structure from the (100)-18° surface is shown in Figure 2. The blaze angle of 60° is slightly less than the expected value of 63°, an error probably due to inaccuracies accumulated in the cutting and polishing procedures.

Since making cross sections for SEM analysis is a destructive technique, an optical method was developed for routine determination of the blaze angle. The gratings were mounted on a graduated turntable with the grooves parallel to the rotation axis, and illuminated with a He-Cd laser source (442 nm). The zero order reflection was used as a reference point, i.e., when the grating is 90° with respect to the laser source. The grating was then rotated and the angles recorded which produced a back-reflected beam that passed the laser aperture. The angle of the brightest back-reflection is the blaze angle (θ_1). It can also be calculated from the order number (m) giving this strongest back reflection, according to the grating equation

$$m\lambda = 2d\sin\theta \quad (2)$$

where d is the groove spacing and λ the wavelength. Table 1 summarizes the blaze angles for several gratings measured from the turntable angle, from equation (2) and from SEM cross section profiles. Also included in Table 1 are the complementary blaze angles, θ_2, measured by rotating the turntable in the opposite direction ($\theta_1 + \theta_2 \neq 90°$). It is seen that the three methods give results that are in excellent agreement.

ACKNOWLEDGMENT

This work was supported by NASA and by the Office of Naval Research.

REFERENCES

1. M. M. Carrabba, N. M. Nguyen and R. D. Rauh, Appl. Optics 25, 4516 (1986).

2. M. M. Carrabba, N. M. Nguyen and R. D. Rauh, J. Electrochem. Soc. 134, 1855 (1987).

3. M. M. Carrabba, N. M. Nguyen and R. D. Rauh, Materials Research Society Symp. Proc. 75, 665 (1987).

4. J. Li, M. M. Carrabba and R. D. Rauh, unpublished results.

Table 1. Properties of Photoelectrochemically Etched Eschelle Gratings

Sample	Orders for θ_1/θ_2	Blaze Angle Turntable	Eq.2	θ_1/θ_2 SEM	Theory
1	63/64	43/45	44/45	43/44	45/45
2	64/65	44/46	45/46	44/45	45/45
3	71/56	53/37	52/38	51/39	53/37
4	70/57	52/39	51/39	51/39	53/37
5	78/48	59/31	60/32	60/30	63/27

Sample key:
1. (100), 0.5 M KCl
2. (100), 0.1 M KCl
3. (100)-8°, 0.1 M KCl
4. (100)-8°, 1.0 M KCl
5. (100)-18°, 0.05 M KCl

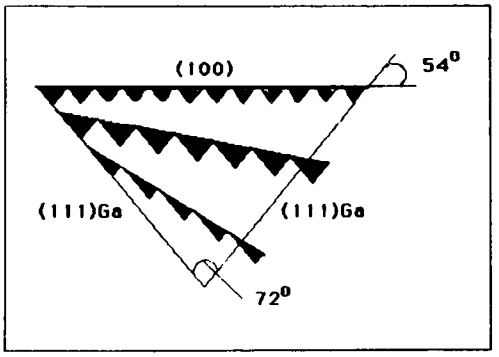


Fig. 1. Cross sections of V-groove formed by photoelectrochemical etching of (100)n-GaAs slots defined in the [01$\bar{1}$] direction, and in two surfaces cut at intermediate angles between the (100) and (111)Ga surfaces.

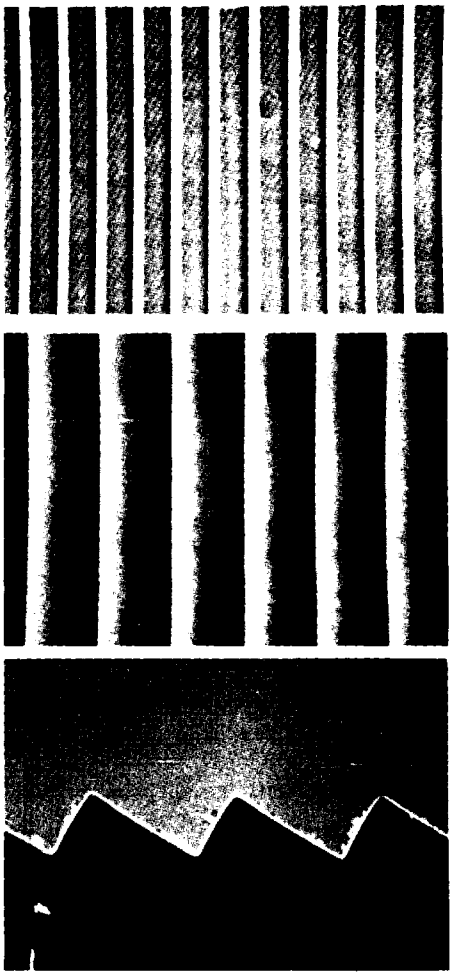


Fig. 2. Scanning electron micrographs of blazed Eschelle gratings etched photoelectrochemically in the (100)-18° surface of n-GaAs. Groove spacing is 20 μm.

Abstract No. 722

THERMODYNAMIC AND PHASE EQUILIBRIA STUDIES OF THE ALUMINUM-ANTIMONY SYSTEM

C. A. Coughanowr, J. J. Egan and T. J. Anderson*

Brookhaven National Laboratory
Department of Applied Science
Upton, L.I., NY 11973

*University of Florida
Chemical Engineering Department
Gainesville, FL 32611

Introduction

The growing interest in the use of III-V compounds in semiconductor devices underscores the importance of determining the properties of these materials. To establish equilibrium boundary conditions for such processing steps as bulk crystal growth and liquid-phase epitaxy, knowledge of the phase diagrams and other thermodynamic properties is needed. In the present work, thermodynamic and phase equilibria data have been obtained for the Al-Sb system, using high-temperature electrochemical techniques.

Experimental

The thermodynamic properties of the Al-Sb system at elevated temperatures were studied using the method of coulometric titration, introduced by Wagner (1,2). To improve the diffusion and equilibration rates in the Al-Sb system, thin film electrodes were employed (5-15μ), following the work of Egan (3).

Emf data in the temperature range 1115-1175 K were obtained from the following two types of cell:

$$\text{Ca-Sn (l)}\,|\,\text{CaF}_2\text{ (s)}\,|\,\text{Al-Sb (l or s)},\ \text{AlF}_3\text{-CaF}_2\text{(l/s)} \qquad \text{(I)}$$

$$\text{Ca-Sn(l)}\,|\,\text{CaF}_2\text{ (s)}\,|\,\text{Al (l)},\ \text{AlF}_3\text{-CaF}_2\text{(l/s)} \qquad \text{(II)}$$

in which single-crystal CaF_2 was employed as the solid electrolyte and the well-behaved Ca-Sn liquid alloy served as a reference electrode. The composition of the salt mixture, AlF_3-CaF_2, was selected to maintain a two-phase, and therefore composition-invariant, state. The experimental cell design is similar to that described in Reference 3.

Results

From the emf data obtained over the composition range $x_{Al} = 0$ to $x_{Al} = 0.5$, partial excess free energies were calculated:

$$G^E_{Al} = -3F\,(E_I - E_{II}) - RT \ln x_{Al}$$

By integrating G^E_{Al} over the same composition range, the free energy of formation of AlSb was obtained:

$$G^M = (1-x_{Al}) \int_0^{x_{Al}} G^E_{Al}/(1-x_{Al})^2 dx_{Al} + RT\,[x_{Al} \ln x_{Al} + (1 - x_{Al}) \ln (1 - x_{Al})]$$

At 1119 K, $G^M = -3.27$ kcal/g-atom was obtained. In previous work by Samokhval and Vecher (4), the free energy of formation of AlSb at 800 K is reported as -5.05 kcal/g-atom. In order to compare the results at 800 K with our results, the entropy and enthalpy data for AlSb from Lichter and Sommelet (5) was used to derive a temperature coefficient for G^M. Our resulting value at 800 K was -4.91 kcal/g-atom, which agrees within 3% to the value of Samokhval and Vecher.

Titrations across the solid compound, AlSb, have yielded information on the nature of the homogeneity range in this system. While these results are still preliminary, this work has succeeded in measuring the homogeneity region in AlSb for the first time. Figure 1 shows a typical titration curve through the homogeneity region. The drop in emf through the solid phase is bounded at the top by the antimony-rich two-phase region, with a constant value of $E = 0.520 \pm 0.003$ V, and bounded at the lower end by the line shown on the figure at $E = 0.432$ V, which represents the aluminum-rich two-phase region. Due to the uncertainty of ± 0.003 V in the lower emf bound, the exact width of the homogeneity gap is also uncertain, but has a value of about 0.0010 ± 0.0004 mole fraction.

The shape of the titration curve in Figure 1 also provides information about the homogeneity region. As demonstrated by Wagner (2), modelling of a point defect structure in a binary compound yields an antisymmetrical hyperbolic sine curve with an inflection point at the ideal stoichiometric composition. In cases where the inflection point lies close to the boundary of the homogeneity range, the inflection point will not be clearly distinguishable. In the present work, the curve in Figure 1 does not show a clear inflection point, but rather approximates the right half of a hyperbolic sine curve. This indicates that the deviation in stoichiometry in AlSb is primarily on the Al-rich side.

Acknowledgments

This work was supported by the Division of Chemical Sciences, U.S. Department of Energy, Washington, D.C., under contract No. DE-AC02-76CH00016. The authors are indebted to Mr. R. J. Heus for his invaluable assistance with the experimental work.

References

1. Wagner, C., J. Chem. Phys. 21, 1819 (1953).

2. Wagner, C., in Progress in Solid State Chemistry, Vol. 6, Reiss, H., and McCaldin, J., eds., Pergamon, New York, 1971, pp. 1-15.

3. Egan, J. J., High Temp. Science 19, 111 (1985).

4. Samokhval, V. V., and Vecher, A. A., Russ. J. Phys. Chem. 42(3), 340 (1968).

5. Lichter, B. D., and Sommelet, P., Trans. Metall. Soc. AIME 245, 99 (1969).

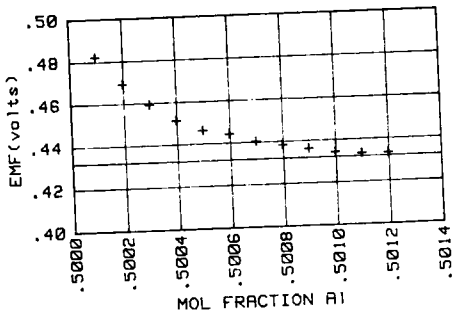


Figure 1. Titration curve of solid AlSb at 1119 K. The solid line at E = 0.432 V represents the aluminum-rich two-phase boundary.

Abstract No. 723

ELECTROREFLECTANCE STUDY OF METAL SUBMONOLAYERS ON ZnHgTe ALLOYS

C. Nguyen van Huong
Laboratoire d'Electrochimie Interfaciale, CNRS, 1 Place A. Briand, 92195 Meudon Principal Cedex, France
P. Lemasson
Laboratoire de Photochimie Solaire, CNRS, 2 rue H. Dunant, 94320 Thiais, France

Metal deposition on semiconductor substrates by electrochemical technique has been employed for several purposes i) for the protection of low bandgap semiconductor electrodes from corrosion in photoelectrochemical cells, ii) for catalyzing the hydrogen production in solar cells [1,2] iii) for obtaining good Schottky barriers [3, 4]. Electrochemical technique is a very convenient method for metal deposition. Coverage, form, microstructure of the deposit can be easily controlled by solution composition, deposition potential and mass-transport conditions.

Zinc mercury telluride (ZMT) is a very new material, more stable than cadmium mercury telluride [5]. ZMT appears to be very promising and of great interest in the field of IR detectors and optoelectronic devices. Thus it seems important to study the feasibility of metal electrodeposition on these SC and subsequently the behavior of such M/SC structures.

In this work, Cu and Ag deposits were performed electrochemically in the dark on ZMT. The new electrolyte/ M/SC interfaces were characterized by cyclic voltammetry and electrolyte electroreflectance (EER) and we intended to correlate the results with the structural and chemical properties of the interfaces.

EXPERIMENTAL

$Zn_xHg_{1-x}Te$ with $0 \leq x \leq$ kindly provided by Dr. R. Triboulet (Bellevue, France) were of p type. They were grown by THM. Sample preparation for electrochemical measurements was already reported [6,7]. The electrolytes were prepared with "Suprapur" $HClO_4$ and ultrapure water. Low concentration (10^{-4} or 5×10^{-5} M) of $AgNO_3$ or $CuSO_4$ was employed. The experimental arrangement was described elsewhere [8]. EER measurements were performed with a 0.5 V, 15 Hz ac modulation.

RESULTS AND DISCUSSION

a) Electrochemistry. Typical current-potential curves obtained in the dark, with supporting electrolyte and metal salt containing solutions are presented in fig.1 for $Zn_{0.53}Hg_{0.47}Te$. In negative scan, the reduction of Ag^+ and Cu^{2+} starts respectively at -0.2 V(mse) and -0.6 V(mse) in good agreement with thermodynamic data. The mechanism of such reduction in the dark is explained in fig.2. The free energies of the two redox systems are isoenergetic (Cu^{2+}/Cu) or lower (Ag^+/Ag) than the top of the valence band and reduction can thus occur by injection of holes from metal ions M^+ into the valence band of the semiconductor.

$$M^+ \$ M^0 + h^+$$

Under illumination, the current is increased due to the transfer of photocreated electrons from the conduction band to metal ions

$$M^+ + e^- \$ M$$

In fig.1, during the positive scan, an oxidation reaction is observed at about -0.30 V, which does not correspond to the oxidative desorption of the metal deposit but to superficial oxidation of the metal layer. Thus in order to avoid this reaction during the performance of EER measurements which are done at fixed deposition potentials and with an ac modulation, the applied dc potential is never positive of -0.65 V. After measurements in metal salt containing solution, the electrode (with metal deposit) was transferred in supporting electrolyte and EER measurements were again performed to study the behavior of this new M/SC structure in this electrolyte.

b) Electroreflectance. The influence of metal electrodeposit on EER response is observable for all the materials studied. We present here only the most remarkable results. In fig.3 and 4 are shown the spectra obtained with Cu/SC and Ag/SC structures for $Zn_xHg_{1-x}Te$ (x = 0.72 and 0.53), spectra obtained with bare SC surfaces are also reported for comparison. The latter show the characteristic oscillations due to the E_1 transition ($\Lambda_3 \Lambda_1$). The transition energies calculated by the Aspnes' three point method are respectively 3.07 and 2.71 eV, the broadening factor 200 and 130 meV. The presence of a metal layer, Cu or Ag, induces a broad new feature in the energy range 2.5-2.8 eV for x = 0.72 and 2.4 2.6 eV for x = 0.53. The lineshape of the spectra is continuously modified by the coverage. The amplitude and energy of the new feature increase with increasing coverage provided that the latter remains lower than a monolayer. It was noted that for some structures of deposit, the spectrum exhibits very large variations. When the coverage is close or higher than a monolayer, the spectrum becomes flat and featureless. At the same time of the appearance and increasing of the new feature, the substrate spectral characteristics disappear strongly but not completely. These results show that there is a strong correlation between coverage i.e. the microstructure of the deposit and the lineshape of EER spectra. EER appears thus as a convenient and powerful tool for the study of the behavior of such M/SC structures and allows to give more insight in the different steps of the formation of a Schottky barrier.

REFERENCES

1. M. Szklarczyk and J.O M. Bockris, J. Phys. Chem., 88, 5241(1984).
2. A. Heller, D.E. Aspnes, J.D. Porter, T.T. Sheng and R.G. Vadimsky, J. Phys. Chem., 89, 4444(1985).
3. M. Ludwig, G. Heymann and P. Janietz, J. Vac. Sci. Technol., B4, 485(1986).
4. R. Reineke and R. Memming, Surf. Sci., 192, 66(1987)
5. R. Triboulet, J. Cryst. Growth, 86, 79(1988).
6. C. Nguyen Van Huong, R. Triboulet and P. Lemasson, J. Cryst. Growth, 86, 570(1988).
7. B.L. Wu, J. Gautron, A. Forveille Boutry and P. Lemasson, J. Phys. D : Appl. Phys., 16, 2323(1983).
8. C. Hinnen, C. Nguyen van Huong, A. Rousseau and J.P. Dalbera, J. Electroanal. Chem., 95, 131(1979).

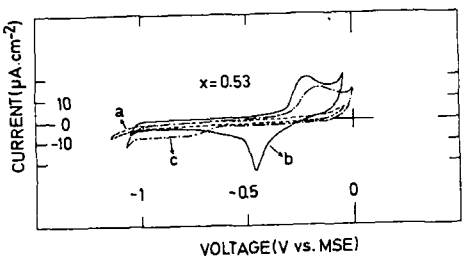


Fig.1 - Current-potential characteristics of $Zn_{0.53}Hg_{0.47}Te$ in contact with 0.1M $HClO_4$ (a) ; containing 5.10^{-5}M NaO_3Ag (b) ; 5.10^{-5}M $CuSO_4$ (a).

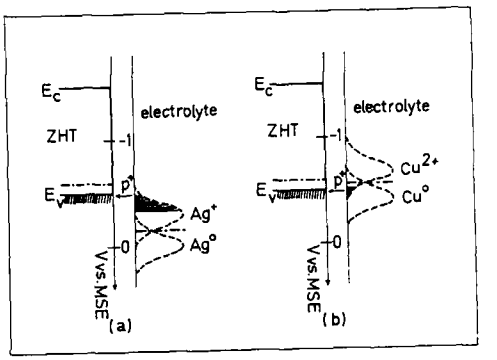


Fig.2 - Energy diagram of $Zn_xHg_{1-x}Te$ in contact with electrolyte containing redox couples Ag^+/Ag and Cu^{2+}/Cu. The energies of these redox couples are calculated thermodynamically.

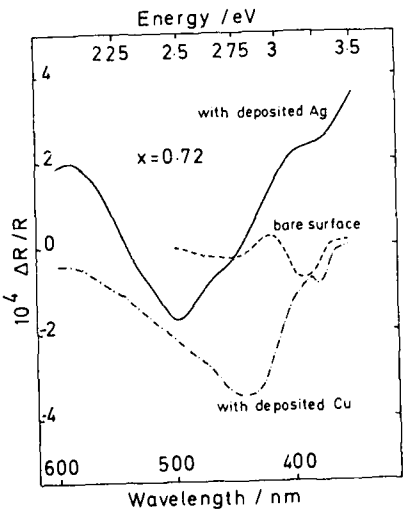


Fig.3 - Influence of Cu (-.-.) and Ag (——) submonolayer on the electroreflectance spectrum of a $Zn_{0.53}Hg_{0.47}Te$ bare surface (----).

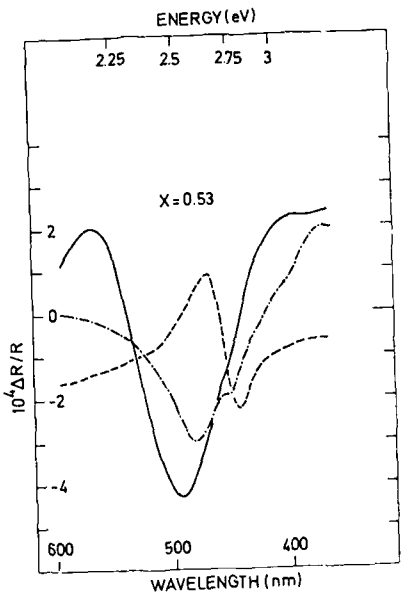


Fig.4 - Electroreflectance spectrum of a $Zn_{0.72}Hg_{0.28}Te$ surface without (----) and with Cu (-.-.) or Ag (——) submonolayer.

Abstract No. 724

ELECTROCRYSTALLIZATION OF TELLURIUM AND CADMIUN TELLURIDE AT THE GLASSY CARBON SURFACE

E. Mori and K. Rajeshwar
Department of Chemistry
The University of Texas at Arlington
Arlington, Texas 76019-0065

There have been many recent studies on the cathodic electrodeposition of Te and CdTe on inert substrates. These studies have been largely spurred by the applicability of these materials in the energy conversion and electrooptical device areas. On the other hand, these systems offer ample scope as model candidates for probing the microscopic details of nucleation and growth at a foreign (inert) substrate. To decouple the complications induced by adsorption that seems to prevail at noble metal surfaces (e.g., Pt, Au), we chose glassy carbon as the substrate for these initial studies. We believe that the examples in this paper constitute the first detailed examination of the temporal aspects of nucleation/growth of a semiconductor via the cathodic deposition mode. Elegant studies exist, however, for the anodic electrocrystallization of a semiconductor involving a reactive metal anode (e.g., the CdS system, c.f. Refs. 1,2).

The potential regimes for probing the nucleation/growth kinetics were first established by cyclic voltammetry (CV) on a TeO_2/H_2SO_4 electrodeposition bath to which incremental amounts of Cd^{2+} were added. Signatures in these CV profiles in the deposition and stripping regimes on addition of Cd^{2+} revealed the assimilation of Cd^0 into the Te matrix as induced by the free-energy of compound formation of CdTe.

Figures 1 and 2 contain representative transient i-t profiles for Te and CdTe respectively. The three regimes of these current transients, namely the initial decay region, the subsequent "growth" regime, and the final diffusion-limited decay are quantitatively analyzed in terms of known rate laws. Plots of reduced variables also aided in the selection of the appropriate rate law. In both cases, a two-dimensional growth law with instantaneous nucleation seemed to provide the best fit of the transient i-t data. The third regime obeyed a $t^{-1/2}$ decay law consistent with the diffusion-limited mass transport of Te^{4+} to the electrocrystallization surface.

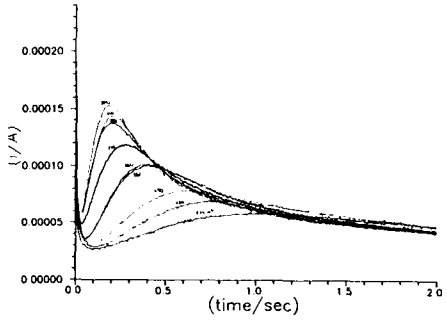


Figure 1 Chronoamperometry traces for Te electrocrystallization at a glassy carbon surface. The final potentials for nucleation/growth (E_f) are shown in the figure. The initial potential was +0.30 V (vs. Ag/AgCl).

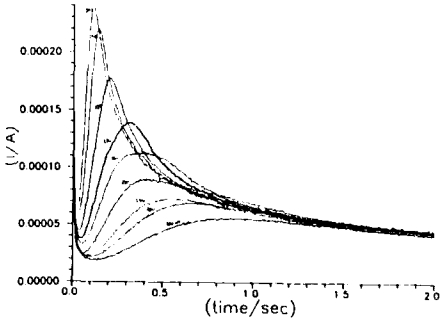


Figure 2: Chronoamperometry traces for CdTe electrocrystallization at a glassy carbon surface. Curve notation as in Fig. 1.

ACKNOWLEDGMENTS

This research was supported in part by a grant from the National Science Foundation (Grant MSM-8617850).

REFERENCES

1. L. M. Peter, Electrochim. Acta 23, 165 (1978).

2. L.-S. R. Yeh, P. G. Hudson and A. Damjanovic, J. Appl. Electrochem. 12, 153 (1982).

Abstract No. 725

Ohmic contacts prepared by annealing of indium / gold layers deposited on (photo)electrochemically arsenic-enriched n-GaAs surfaces.

P. CLECHET*, P. PERSON**, J.-R. MARTIN* and J.-P. SANDINO**

* Laboratoire de Physicochimie des Interfaces UA 404 Ecole Centrale de Lyon - B.P. 163 F - 69131 - ECULLY Cedex FRANCE
** Laboratoire Central de Physicochimie - RTC - B.P. 1642 - 27016 EVREUX, FRANCE

Evaporated thin films of indium, deposited at room temperature onto n-GaAs, forms a Schottky barrier which, upon annealing above In's melting point, turns into an ohmic contact (1). Such a behavior has been interpreted as the result of the formation, at least locally, of a graded $Ga_{1-x}In_xAs$ *hetero*junction, the conductivity of which [in the 10^{-6}/10^{-7} Ω cm^2 range] had been previously checked by Molecular Beam Epitaxy (MBE) (2). During the time this work was in preparation, other authors have supported the idea that the junction was probably not graded but abrupt (3,4), suggestion which has also been confirmed by (MBE) recent results (5,6). Whatever the Ga/In profile within these non-alloyed structures is, it appears to us that their fabrication might be facilitated by a previous arsenic enrichment of the GaAs surface before In deposition. It can be noted that SPICER's group has recently shown that the obtention of large values for x(x>0.3) does in fact require an As-rich surface (7).

The aim of the present work is to check such assessment by using two means of endogenic As enrichment of (100) S doped GaAs samples.

1- a photoelectrochemical (PEC) technique, previously proposed by WOODALL et al. (8), which consists in the illumination of GaAs substrates immersed in a 1:1 HCl - H_2O solution (HCl 6M) by photons of energy higher than the band-gap of this material.

2- a combined anodic/thermal-etching process which involves first the growth of an anodic oxide layer on GaAs in a AGW medium (10), followed by an annealing of the structure (11) and a final post-etching of the oxide in a 1:1 MeOH - HCl etchant.

Although improved by using (i) an original cell (Fig.1) conceived to allow the complete elimination of oxygen in the electrolyte and (ii) GaAs samples fitted with a rear-side ohmic contact, linked to a platinum counter electrode, in order to facilitate the access of photoholes to the surface, the first method proved not to be satisfactory as evidenced by ellipsometric, Raman and photoluminescent (PL) measurements. Much better results were obtained with the second method. Anodization (Fig.2) was conducted at constant current density (0.1 mA cm^{-2}), the process being stopped at the voltage value which corresponds to the *expected* thickness of the anodic oxide (about 2 nm V^{-1}). RBS (Rutherford Backscattering and oxygen measurements by $^{16}O(\alpha,\alpha')^{16}O$ resonance at 3.05 MeV showed (12), that the thusly intermixed As-rich interfacial layer is obtained starting with a 150 nm oxide layer, by a 25 mn heat treatment at 500°C (under N_2).

A three level photomasking process has been initiated to measure the specific contact resistance ρ_C by the COX and STRACK method (14), of the contacts prepared on As-enriched surfaces. Two doping levels ($5\,10^{15}$ and 10^{18} cm^{-3}) were used in order to examine the metallization doping level effect on the ρ_C conjunction with a 90 - 10 In - Au metallization (15). To check the efficiency of the As-treatment, each sample was broken into two parts, only one being submitted to the treatment. The results thusly gathered in Fig.3. The first maximum in the current-voltage characteristics, interpreted as the result of the local formation of a $Ga_{1-x}In_xAs$ heterojunction (16), at low temperatures, the second maximum, very often observed, to the progressive degradation of the (local) heterojunctions above 100°C and the formation of polycrystalline phases favoured by the annealing but diffusion of gallium induced by gold at these temperatures (16). Fig.3 proves that the ohmicity of the contacts is good, especially for highly doped samples, but on the other side, the difference between the treated and non-treated substrates appears not to be significant. This can be explained both by the less of sensitivity of our probing set-up at low current values and to a possible misalignment of the metallization (In / Au) with the masked (untreated) part of the substrate. Such misalignment would lead to pessimistic effects as regard to the enrichment process.

On the other hand, the proposed surface treatment strongly improves the reproducibility of the electrical measurements (lateral homogeneity) as well as the mechanical properties of the contacts. The observed hardening of the contact is probably the result of the insertion of indium atoms in the GaAs lattice (17).

All the results reported above would be probably improved by using an acidic electroless liquid deposition bath, as described in ref.18, because of the absence of native oxide in such media during metal deposition.

References

(1) A.A. LAKHANI, J. Appl. Phys., 56, 1888 (1984).

(2) J.M. WOODALL, J.L. FREEOUF, G.F. PETIT, T. JACKSON and P. KIRCHNER, J. Vac. Sci. Technol. 19, 626 (1981).

(3) D.C. MARVIN, N.A. IVES AND M.S. LEUNG, J. Appl. Phys. 57, 2693 (1985).

(4) J. SHI, G. WASHBURN, T. SANDS, V.G. KERAVUALA, Appl. Phys. Lett. 49, 818 (1986).

(5) J.J. WRIGHT, R.E. MARIS, S.T. WARR, T.N. JACKSON, and H. BARATTE, Appl. Phys. Lett. 49, 1545 (1986).

(6) K. NITTONO, H. ITO, O. NAKAJIMA and T. SHIBASHI, Jpn. J. Appl. Phys. 25, L 985 (1986).

(7) W.K. CHAN, T. KENDELEWICZ, N. NEWMAN, J.C. WOO and W.E. SPICER, J. Vac. Sci. Technol. B4, 1055 (1986).

(8) P. PERSON, This Euroconference (1987).

(9) J.M. WOODALL, P.D. KIRCHNER, T.N. JACKSON, J.L. FREEOUF, G.D. PETTIT, J. Vac. Sci. Technol. B1, 794 (1983).

(10) H. HASEGAWA, H.L. HARTNAGEL, J. Electrochem. Soc. 123, 713 (1976).

(11) G.P. SCHWARTZ, G.J. GUALTIERI, J.E. GRIFFITHS and B. SCHWARTZ, J. Vac. Sci. Technol. 19, 467 (1981).

(12) P. PERSON, A. [illegible] J.-R. MARTIN, P. CLECHET, J. LAMOTTE, M. MARTIN, M. [illegible], J. Appl. Phys. 62, 4210 (1987).

(13) P. PERSON, J. LAMOTTE, J.-R. MARTIN, P. CLECHET, A. [illegible], Appl. Phys. [illegible] (1987).

(14) [illegible]

(15) [illegible]

(16) [illegible]

(17) [illegible]

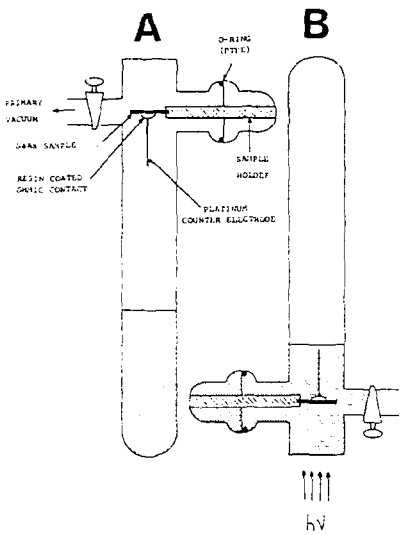


Fig 1 : Rotating cell which allows the outgasing of the electrolyte by successive congelation/fusion cycles (position A) before the illumination of the immersed sample (position B).

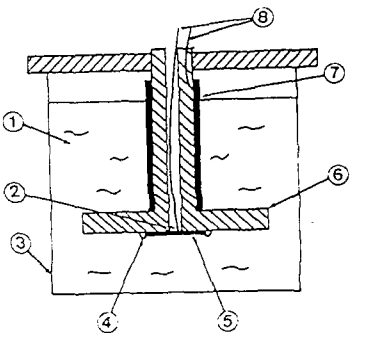


Fig.2 Electrochemical cell used for the anodization process : 1, AGW solution ; 2, rear side contact ; 3, beaker ; 4, high quality wax ; 5, GaAs sample ; 6, PTFE support ; 7, platinum counterelectrode ; 8, copper leads.

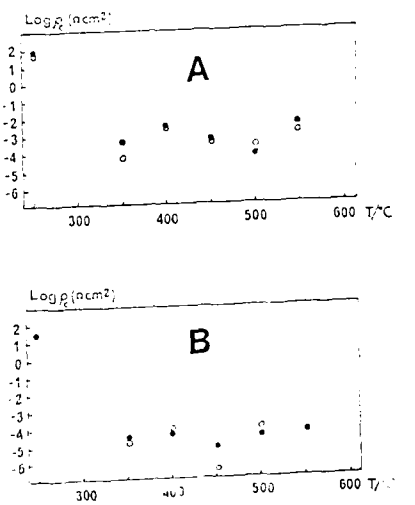


Fig.3 Plots of log ρ_c vs annealing temperature for Au-In/As/n-GaAs heterostructures A $N_D = 5.10^{15}$ cm^{-3}, B $N_D = 10^{18}$ cm^{-3} ; ○ without As enrichment, ● with As enrichment.

Abstract No. 726

Effects of Superficial Topography on Uniformity of Spun-on Resist Film

M.Ikeno, H.Kawashima, O.Kaneda, and H.Saeki

LSI R&D Lab. Mitsubishi Electric Corporation
4-1 Mizuhara, Itami, Hyogo 664, Japan

1. Introduction

In the VLSI fabrication process, lithography is one of the dominant techniques, and in many cases resist film is made on a wafer surface by using a spin-coating procedure. As pattern size of micro circuits decreases, the demand for uniformity of the resist film becomes stronger. So, much substantial effort and many studies have been devoted to developing new lithography processes that have less pattern size variation with more uniform resist thickness. In some studies, the superficial topography and the planarization properties of resist film were discussed[1-5]. In many cases, resist thickness distribution over the full range of wafer size is also much important. For example, some electric devices, such as solid-state imagers, require uniform resist thickness everywhere in their chips, even close or very close to the dicing line. Usually, step-height near the dicing line is about 1 to 5μm, so thickness of the resist film near that line is not uniform. This is widely recognized, we believe. In such a device as a solid-state imager that has active elements or area close(often very close) to the dicing line, this non-uniformity of resist film causes a very serious problem of a variation of sensitivity.

In our studies, we have observed a spectacular phenomenon of a pile-up of resist film near a groove. Resist film pile-up occurs not on the side of the groove away from the rotational center of the wafer but rather on the side facing the rotational center. We found that such resist pile-up exists in a chip area, which will causes serious defects in the device. This phenomenon was out of our expectation and consideration, so we decided to focus on this problem.

2. Experimental

We have prepared 5-inch size Si-wafers with grooves of various widths and depths, applied resist materials on those wafers, and performed spin-coating procedure under certain conditions. After post-baking, superficial topographies of resist surface near the grooves were measured by means of surface profilometer(Tencor, Alpha Step 200). Measurement direction was fixed, perpendicular to the groove. The reproduced profile and measurement points are shown schematically in **Fig.1**, in which h represents the pile-up height and p represents the distance from the groove edge(defined as shown in **Fig.1**) to the pile-up peak position.

3. Results and Discussion

Changes of pile-up height h and pile-up peak position p with parameters of groove depth d and width w, are shown in **Fig.2.1** and **2.2** respectively. Here the coating material is a PGMA-type resist, and the coating conditions are as follows: spin rotational speed 1100rpm(results in coating thickness 1.0μm), viscosity of resist 22cP, and location of groove(distance from wafer center to groove) 47.5mm. It is evident from these figures that as the depth d increases, the pile-up height h increases. Also, as width w increases, height h tends to increase. On the other hand, peak position p does not vary as much as pile-up height h.

Fig.3.1 and **3.2** show the dependency of pile-up height h and peak position p on spin rotational speed and parameter l(location of groove). Here,the depth of groove d is about 12μm and its width w is about 70μm. In **Fig.3.1**, as spin rotational speed increases, resultant resist thickness decreases(indicated by solid line with solid square dots). However, in fact, the absolute value of pile-up height h increases with the increase of spin rotational speed. Similarly, if the location of groove (l) is far from the wafer center, the pile-up tends to be higher. The value of peak position p decreases with the increase of spin rotational speed, as shown in **Fig.3.2**. And, if the groove is far from the wafer center, the pile-up peak approaches to the groove.

From these results, we can assume that the effect of the centrifugal force on the resist material on substrate plays a major role in the pile-up mechanism.

Now, let us consider the mechanism of the pile-up phenomena. At the beginning of the spin-coating procedure, resist material is dropped onto the wafer surface and has a thickness which is much greater than the final thickness of resist film. But, as the spinning(rotating) procedure continues, resist material flows toward the outside of the substrate according to the centrifugal force, the solvent evaporates, and the thickness of the resist layer is reduced. At this time, the surface profile of the resist layer varies according to the underlying topography, i.e., the groove line. And the thickness of the resist layer near the groove is less than that far from the groove. This is equivalent to the inlet portion of the resist material to the groove becoming narrow. Therefore, a difference of resist flow rate is produced between the inlet and outlet to the groove, and that causes an increase of pressure in the resist layer near the groove.

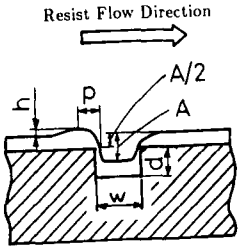
If we can assume that the surface tension of the resist layer is constant, then an increase of pressure in the resist layer causes a reduction of the radius of curvature at the resist surface. And that, we believe, is the reason why the resist film piles up.

4. Conclusion

In a resist spin-coating process, we have found the pile-up phenomena of resist film near a groove line, like a dicing line. The resist pile-up caused by a groove occurs on the side of the groove facing the rotational center, and the height of pile-up depends on depth of the groove, width of the groove, spin rotational speed, location on substrate, resist type, and so on. We assumed that the pile-up is caused by the increase of pressure in the resist film.

References

1. L.K.White, J.Electrochem. Soc. Vol.132, p.3037, 1985
2. L.K.White and N.Miszkowski, J.Vac.Sci.Technol B, Vol.3, p862, 1985
3. T.R.Pampalone, J.J.DiPiazza, and D.P.Kanen, J.Electrochem.Soc., Vol.133, p.2394, 1986
4. L.E.Stillwagon, R.G.Larson, and G.N.Taylor, J.Electrochem.Soc., Vol.134, p.2030, 1987
5. R.H.Wilson and P.A.Piacente, SEMICONDUCTOR INTERNATIONAL, April, p.116, 1986



d: depth of groove

w: width of groove

h: height of pile-up

p: position of pile-up peak

Fig.1 Schematic drawing of cross section near groove

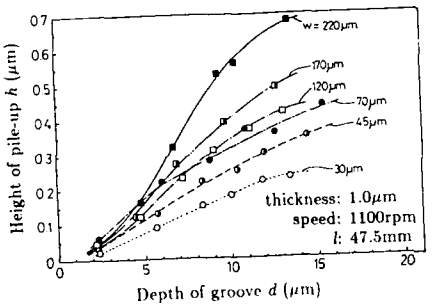


Fig.2.1 Changes of pile-up height h with parameters d and w

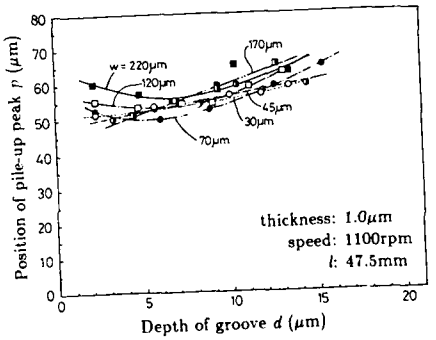


Fig.2.2 Changes of pile-up peak position p with parameters d and w

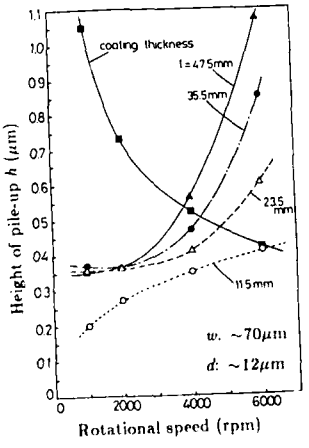


Fig.3.1 Dependency of pile-up height h on rotational speed and location l
(Solid line with square solid dots indicates the coating thickness of resist film)

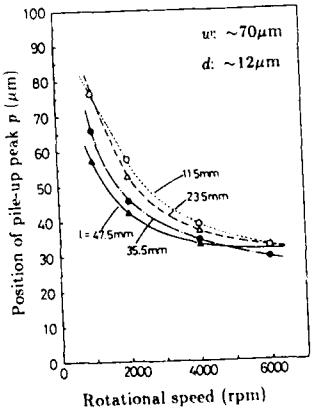


Fig.3.2 Dependency of pile-up peak position p on rotational speed and location l

Abstract No. 727

Mixed Ionic and Electronic Conducting Polymers

L. J. Lyons, J. S. Tonge, and D. F. Shriver
Chemistry Department and Materials Research Center
Northwestern University, Evanston, Il 60208

In previous work from this laboratory the conductivity and physical properties of PEO_xNaI_n complexes were examined.[1] In particular, the complex PEO_4NaI_3 is a blue-black crystalline compound with an electronic (hole) conductivity of 2×10^{-5} S cm^{-1} and a band in the resonance Raman spectrum at 171 cm^{-1}. Raman investigations of the other polyiodide PEO complexes contained one or two bands. The first at 111 cm^{-1} is characteristic of I_3^- while the second occurs at 171 cm^{-1} and is indicative of I_5^- and higher polyiodides.[2]

In the present research polyiodide salt complexes of higher conductivity were sought. Polyiodide complexes of the totally amorphous polymer poly[bis-(methoxyethoxyethoxy)phosphazene] (MEEP) have been synthesized and their electronic and physical properties examined. The room temperature conductivity of the lithium triflate/MEEP complexes[3] has been observed to be three times greater than analogous polyethylene oxide complexes,[4] leading to further investigations of polyiodide/MEEP salt complexes.

$MEEP_xNaI_n$ and $MEEP_xLiI_n$ complexes were prepared by the reaction of stoichiometric amounts of I_2 vapor and dry, solid $MEEP_xMI$ (M=Na, Li). $MEEP_xNaI_n$ complexes were prepared with x=2, 4, 8, 16 and n=1, 3, 5, 7. Lithium complexes of x=4 and n=1, 3, 5, 7 were also prepared.

AC conductivity measurements on the polyiodide complexes resulted in complex impedance spectra with two arcs. Based on dc polarization experiments, the first arc was assigned to the ionic conductivity and the second to a charge transfer process (an electronic component of the total conductivity) indicating that these complexes are mixed ionic/electronic conductors. The highest room temperature ionic conductivity (2.4×10^{-3} S cm^{-1}, n=5, T=298.15 K) was observed for the series of complexes $MEEP_4NaI_n$ with a ratio of sixteen ether oxygens per sodium cation. Sodium polyiodide/MEEP complexes have higher ionic conductivities than the analgous lithium polyiodide complexes. The temperature dependence of the ionic conductivity follows VTF behavior in both the sodium and lithium series of complexes. In more highly doped polyiodide samples and at elevated temperatures only electronic and no ionic conductivity was observed in the dc polarization experiment. Furthermore, the current-voltage behavior observed in these complexes was ohmic. Significantly, both the ionic and electronic conductivities increase as the amount of the added I_2 increases.

Although we describe the conductivity of the polyiodide materials as ionic and electronic, this is an operational definition based on the dc polarization behavior and ohmic response. It is possible that the portion of the conductivity that we term electronic involves an ion relay between polyiodide chains as has been suggested for fluid solutions of polybromides.[5] As observed for the PEO_xNaI_n complexes, resonance Raman spectra of the $MEEP_xNaI_n$ (n=3,5,7) have two bands at circa 112 cm^{-1} and circa 175 cm^{-1} indicating the presence of triiodide moieties and higher polyiodide species in these complexes. The lithium complexes have similar spectra.

Acknowledgement: This research was supported by grants from the Office of Naval Research and the Northwestern Materials Research Center sponsored by the National Science Foundation.

References

[1] Hardy, L. Charles; Shriver, Duward F. *J. Am. Chem. Soc.* **1986** *108* 2887.

[2] Marks, T.J.; Kalina, D.W. "Highly Conductive Halogenated Low-Dimensional Materials." In Extended Linear Chain Compounds Vol. I; Miller, J.S. Ed.; Plenum Press: New York, **1982**, p. 204-217.

[3] Tonge, J.S.; Shriver, D.F.; *J. Electrochem. Soc.* **1987** *134* 269.

[4] Blonsky, P.M.; Shriver, D.F.; Austin, P.E.; Allcock, H.R.; *J. Am. Chem. Soc.* **1984** *106* 6854. *Polym. Mater. Eng.* **1985** *53* 118.

[5] Rubinstein, I.; Bixon, M.; Gileadi, E.; *J. Phys. Chem.* **1980** *84* 715.

Abstract No. 728

SOLID POLYMER ELECTROLYTES: Zn(II) MOBILITY IN POLY(ETHYLENE OXIDE)

H. Yang and G. C. Farrington

Department of Materials Science and Engineering
University of Pennsylvania
3231 Walnut Street
Philadelphia, PA 19104

Introduction

Solid polymer electrolytes formed by dissolving ionic salts in polymeric solvents such as poly(ethylene oxide) (PEO) are a new type of electrolyte with properties in between those of true liquids and crystalline solids. Recent studies have shown that it is possible to dissolve a wide range of ionic salts in PEO. Some of the electrolytes produced are pure anion conductors and others conduct both anions and cations. PEO solutions of salts of Zn(II) ions are particularly interesting, because they may have significant conductivities for Zn(II) cations.

Poly(ethylene oxide) (PEO) electrolytes, $ZnX_2{\cdot}(PEO)_n$ (X = Cl^-, Br^-, I^-, ClO_4^- and n= 4, 8, 12, 16, 20, 24) have been prepared using a two-solvent solution casting technique [1]. Results from $ZnI_2{\cdot}(PEO)_n$ are described in this paper.

The thermal stability and hydration reactions of the samples were studied by thermogravimetry (TGA). The samples were found to be stable in an inert atmosphere until about 350°C. Differential scanning calorimetry (DSC) combined with examination with a variable temperature polarizing microscope (VTPM) revealed that the samples were multi-phase. Energy-dispersive X-ray analysis (EDAX) [2] showed that Zn^{2+} and I^- were uniformly distributed throughout the electrolyte films.

Conductivity was measured using AC complex impedance analysis and DC polarization. The conductivity of the samples was strongly dependent on composition and the identity of the anion. Typical conductivity values were about 10^{-6} $(\Omega^{-1}cm)^{-1}$ at 70°C.

It is well known that many PEO-based polymer electrolytes conduct both cations and anions. With the samples investigated in this work, electrochemical cells of the type, $Zn/ZnX_2{\cdot}(PEO)_n/Zn$, provided virtually no evidence of Zn^{2+} mobility either by AC impedance or DC polarization measurements. However, direct measurements of Zn^{2+} diffusion using SEM and EDAX [2] have indicated that Zn^{2+} ions are reasonably mobile at 110 °C and above.

References

1. H. Yang, G. C. Farrington, and A. R. McGhie, in proceedings of the 15th NATAS Conference," p.447, Cincinnati, OH (1986).

2. J. I. Goldstein, D. E. Newbury, P. Echlin, C. Fiori and E. Lifshin, " Scanning Electron Microscopy and X-Ray Microanalysis " (1981).

Abstract No. 729

MIXED POLYMER AND CRYSTALLINE IONIC CONDUCTORS

F. Croce and B.Scrosati
Dipartimento di Chimica, University of Rome, Italy

One critical point in the practical applications of solid polymer electrolytes, such as complexes between poly(ethylene oxide, PEO, and metal salt complexes, is that an useful electrical conductivity is reached only at temperatures above the crystalline to amorphous phase transition (about 60 °C). In this range of temperature, the polymer complexes behave like 'soft' solids(1,2) with poor mechanical properties. Therefore, polymer-based devices may also suffer of problems commonly met in conventional liquid electrolyte systems, such as leakage, loss of electrode to electrolyte contacts and similar.

Considering the intrinsic interest in polymer electrolytes, the improvement of their mechanical properties remains a major goal in electrochemical technology.

The addition of inert fillers to solid electrolytes has been widely recognized as an useful tool to increase mechanical and electrical properties of these materials. Such a toughening process has been applied to a large variety of ceramic solid electrolytes, e.g. beta-alumina, zirconia and so forth.

Recently(3) attempts of inert filling addition (alfa Al_2O_3) to PEO-based polymer electrolytes have been reported. Following this direction we have investigated the characteristics of composites formed by $(PEO)_8NaI$ (a sodium ion conducting polymer electrolyte) with beta"-alumina (a sodium ion ceramic electrolyte). The strategy adopted here is to use an ion conducting rather than an inert filler, in order to avoid deterioration in overall electrical properties of the composite.

Indeed, the preliminary results on $(PEO)_8NaI$-Al_2O_3 composites reported in this work indicate that the addition of the ceramic filler improves consistently the mechanical properties of the polymer electrolyte without significantly depress its total conductivity.

REFERENCES

1)-'Polymer Electrolyte Review 1', MacCallum and Vincent Eds., Elsevier,London,1987.
2)-C.A.Vincent, Progress in Solid State Chem. 17, 3 (1987).
3)-J.E.Weston and P.C.H.Steele, Solid State Ionics, 7, 75 (1982).

Abstract No. 730

Preparation and Electrochemical Properties of the SiS_2-P_2S_5-Li_2S Glass Coformer System

John H. Kennedy and Zhengming Zhang

Department of Chemistry, University of California Santa Barbara, CA 93106

The recently reported SiS_2-based glasses with Li^+ conductivities exceeding 1 mS/cm and prepared at ambient pressure are potential candidates as electrolytes for solid state batteries. However, SiS_2-Li_2S-LiI glasses are somewhat unstable in contact with lithium metal; hence efforts have been made to stabilize them with the addition of a coformer (1). It was shown that P_2S_5 acts as a stabilizer, and we now present a more detailed study of glasses having the composition: $0.4\ [(1-x)SiS_2-xP_2S_5]-0.6\ Li_2S$.

It is well known with oxide glasses that the properties can be modified with the addition of a second glass former, and, in general, conductivity is enhanced, at least over part of the composition range (2). Although many investigations have been reported with coformers in the oxide glass systems, very little has been published concerning sulfide glass coformer systems.

Experimental

Starting materials were 99.9% pure SiS_2, P_2S_5, and Li_2S. Synthesis of the glass where $x \leq 0.4$ was reported previously, although the heating time was reduced to 30 min to minimize volatilization of P_2S_5. With $x > 0.4$, the vapor pressure of P_2S_5 was so high that sealed quartz tubes were used for synthesis. In this technique, the finely ground SiS_2, P_2S_5 and Li_2S powder mixture was sealed under vacuum, heated at 1000°C for one hour, and quenched in ice water. No crystallinity was detected by powder XRD. DSC was carried out with a du Pont 912 differential scanning calorimeter.

Electrochemical cells with TiS_2 electrodes for conductivity measurements have been reported previously (3). An ac signal of 100 mV was used over the frequency range of $1\text{-}10^6$ Hz for complex impedance analysis.

Results and Discussion

Glass transition temperatures decreased monotonically from 337°C for the $0.4\ SiS_2$-$0.6\ Li_2S$ system to 208°C for the $0.4\ P_2S_5$-$0.6\ Li_2S$ system as shown in Fig. 1. These end-values agree well with previous studies of single glass former systems (4, 5). It can be seen from Fig. 1 that T_g decreased rapidly for $0.3 < x < 0.4$.

Bulk resistant values for the TiS_2/glass/TiS_2 cells were obtained by extrapolating the complex impedance straight line to the real axis. Conductivity was then calculated from the cell dimensions and was found to obey the Arrhenius Law: $\sigma = (\sigma^o/T)\ \exp\ (-E_a/kT)$ over the 25°-125°C temperature range. Conductivity as a function of glass former composition is shown in Fig. 2. Clearly, SiS_2-rich glasses exhibited higher conductivities than P_2S_5-rich glasses. However, the maximum conductivity was found for glass having the composition: $0.32\ SiS_2$-$0.08\ P_2S_5$-$0.60\ Li_2S$, but dropped rapidly for $0.3 < x < 0.5$. At the same time, E_a remained nearly constant at 0.36 eV (0.33 eV when plotted as log σ) for $0 < x < 0.3$ and then rose almost linearly, reaching 0.50 eV for $x = 1$ as shown in Fig. 3.

It should be noted that when $x = 0.33$ the ratio of silicon to phosphous was one. From the results shown in Fig. 1-3 it appears that there may be three important vitreous phases: (A) $0.4\ SiS_2$-$0.6\ Li_2S$, (B) $0.27\ SiS_2$-$0.13\ P_2S_5$-$0.6\ Li_2S$, and (C) $0.4\ P_2S_5$-$0.6\ Li_2S$. In the region: $0 < x < 0.33$ a solid solution or vitreous mixture of (A) and (B) exists while for $0.33 < x < 1$ a solid solution or vitreous mixture of (B) and (C) exists. Whereas (A) and (B) have the same activation energy for conduction of 0.36 eV, (C) has the higher activation energy of 0.50 eV. Threrefore, in the region: $0.33 < x < 1$ the conductivity decreased rapidly as the activation energy increased. On the other hand, for $0 < x < 0.33$ the activation energy remained nearly constant and the small peak observed in conductivity was apparently caused by an entropy term in the coformer system. One might expect this effect to be a maximum when (A) and (B) are in equal concentration, which would correspond to $x = 0.17$. An investigation of this system using ^{29}Si and ^{31}P MAS-NMR is being conducted at present and will be reported separately. It can be mentioned, though, that an additional ^{31}P peak was observed when $x \simeq 0.4$, offering more evidence of specific network arrangements at certain values of x.

References

1. J.H. Kennedy and Z. Zhang, Solid State Ionics, in press.
2. A. Magistris and G. Chiodelli, Solid State Ionics, 9/10, 611 (1983).
3. J.H. Kennedy and Z. Zhang, J. Electrochem Soc., 135, 859 (1988).
4. A. Pradel and M. Ribes, Solid State Ionics, 18/19, 351 (1986).
5. R. Mercier, J.-P. Malugani, B. Fahys, and G. Robert, Solid State Ionics, 5, 663 (1981).

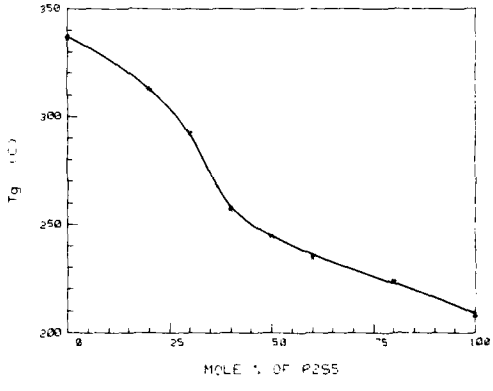


Fig. 1. Glass transition temperatures for $0.4\ [(1-x)\ SiS_2 - x\ P_2S_5] - 0.6\ Li_2S$ glasses as a function of P_2S_5 content from DSC scans recorded at 10°C/min.

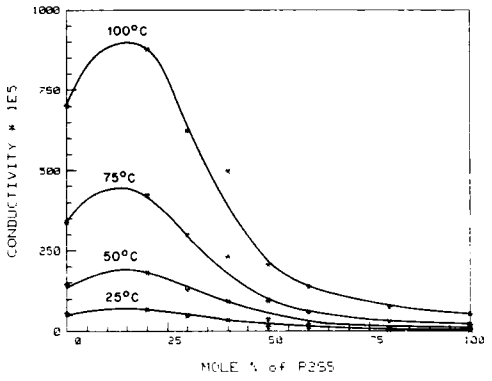


Fig. 2. Conductivity of 0.4 [(1 - x) SiS_2 - x P_2S_5] - 0.6 Li_2S glasses as a function of P_2S_5 content at four different temperatures.

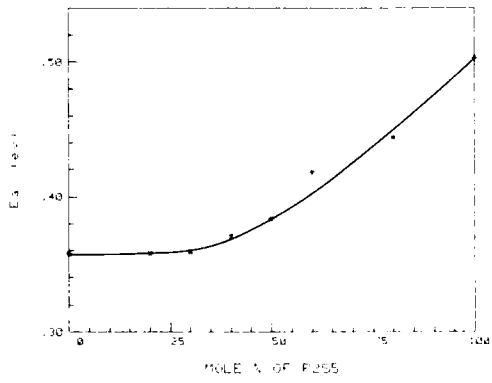


Fig. 3. Activation energy calculated from log σT vs 1/T plot for 0.4 [(1 - x) SiS_2 - x P_2S_5] - 0.6 Li_2S glasses as a function of P_2S_5 content.

Abstract No. 731

Diffusivity of Lithium Intercalated in Graphite from Molten LiCl-KCl Eutectic

Rajeeva R. Agarwal *
Department of Chemical Engineering
Illinois Institute of Technology
Chicago, Illinois 60616

The diffusion of lithium in psuedo two-dimensional solids such as graphite is expected to be very rapid [1,2]. Hence, such studies have significance in high-energy secondary battery applications, and in synthesis of lithium intercalation compounds [3,4]. In this work [5], the diffusivity of lithium in graphite was studied via an electrochemical reaction, in a purified molten *LiCl-KCl eutectic* (*m.p.* $= 352\ ^{\circ}C$) at 400-600 $^{\circ}C$ under an argon atmosphere.

The Galvanostatic Intermittent Titration Technique [6] was applied to an electrochemical cell

$$Ta,\ LiAl\ (2-phase)\ /\ LiCl-KCl\ (Eut.)\ /\ C_{(1-x)}Li_x,\ Ta$$

where weight fraction, x, was varied coulometrically. Counter and working electrodes consisted of LiAl (2-phase) and high-purity (99.9995%) spectroscopic (Ultra F/U-7) graphite rod (dia.=3 mm) respectively. Between 120-180 coulometric pulses were used; each of ten-second and five-minute polarization and relaxation times respectively. The electrochemical potential between the LiAl (2-phase) reference and carbon-lithium working electrodes were recorded on a digital oscilloscope for each polarization-relaxation period. Experiments were carried out at fixed temperatures and over a period of 12-18 hours after initial potential became steady.

Under GITT conditions of small currents ($i \ll i_L$) and short polarization time ($\tau \ll a^2/\bar{D}$), i.e., under small activation and concentration overpotentials, the potential and concentration changes in single phase follow an approximate linear form [6]. For this unsteady-state cylindrical diffusion problem with prescribed flux [7,8], an approximate solution [8] , for $\tau \ll a^2/\bar{D}$, at the electrode and electrolyte interface (r=a) was used to obtain [5]

$$\bar{D} = \frac{2a^2}{\tau\left[\,2\pi\left(\frac{\Delta E_T}{\Delta E_S} - \frac{1}{4}\right)^2 - 1\,\right]}$$

The above equation gives an expression inter-relating diffusion coefficient, $\bar{D}$, and the transient, ΔE_T, and steady, ΔE_S, potential changes in GITT for a cylindrical geometry.

Figure 1 shows one potential transient that was obtained at $582^{\circ}C$. In these outputs the IR-drop, the transient and steady potential changes could be measured. The diffusivity values obtained at $582^{\circ}C$ are shown in Figure 2. As expected these values are very rapid. These studies show that diffusivity varies with composition and temperature of stoichiometric and non-stoichiometric lithium intercalation compounds in graphite. The activation energy in the higher-stage region is 3.5 kcal/mole. For the lower-stage lithium intercalation compounds these values show fluctuations that were completely reproducible. Both structural changes and filling in the host graphite may be important.

Acknowledgement

The author is thankful to IIT Chemical Engineering Department and Dr. J.R. Selman for financial support and research facilities during this work.

References

1. S.D. James, J. Electrochemical Soc., 122, 921, (1975).
2. H. Krohn, Carbon, 23, 449, (1985).
3. A.R. Ubbelohde, in "Intercalated Layered Materials", ed. F. Levy, Reidel, Dordrecht, Holland, p. 1, (1979).
4. M.S. Whittingham and L.B. Ebert, in "Intercalated Layered Materials", Reidel, Dordrecht, Holland, p. 53, (1979).
5. R.R. Agarwal, "Activity and Diffusivity of Lithium Intercalated in Graphite", MS Thesis, Illinois Institute of Technology, Chicago, Illinois, (1982).
6. W. Weppner, R.A. Huggins, J.C. Wen, and B.A. Baukamp, J. Electrochemical Soc., 126, 2258, (1979).
7. H.S. Carslaw and J.C. Jaeger, "Conduction of Heat in Solids", Oxford University Press, London, (1959).
8. J.C. Jaeger, Proc. R. Soc., 74, 197, (1944).

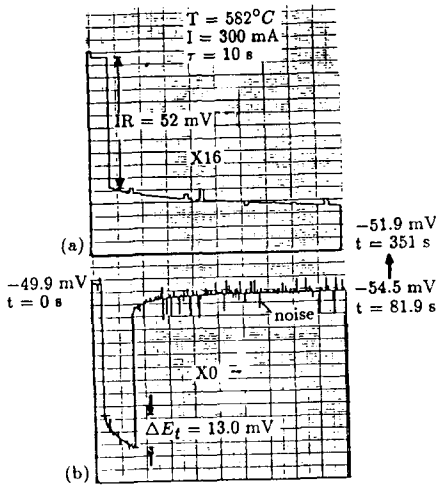


Figure 1. Potential transient during one GITT pulse at 582°C:
(a) shows IR-drop measurement
(b) shows potential changes

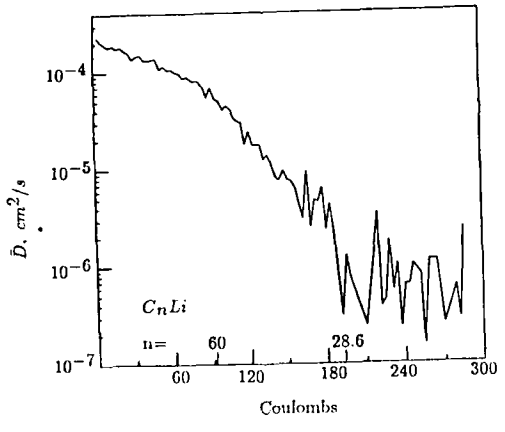


Figure 2. Diffusivity of Lithium Intercalated in Graphite at 582°C.

Abstract No. 732

RECOVERY OF OXYGEN FROM CARBON DIOXIDE IN A HIGH TEMPERATURE ELECTROCHEMICAL REACTOR

Turgut M. Gür, Takashi Nohmi, Henry Wise and Robert A. Huggins

Department of Materials Science and Engineering
Stanford University, Stanford , CA 94305

Carbon dioxide accumulation from exhalation in enclosed environments or vessels is a serious problem for obvious reasons. The need to recover oxygen to replenish the atmosphere is implicit in such closed systems. Life support systems utilizing stabilized zirconia solid oxide electrolytes have been developed in the past for the purpose of reducing CO_2 and recovering oxygen. However, simple reduction of carbon dioxide to carbon and oxygen in such systems deposited carbon, which eventually clogged up the reactor and caused system failure.

This study adopted a different approach to the reduction of carbon dioxide and the simultaneous recovery of oxygen. The central concept is that the rates of heterogeneous chemical reactions can be enhanced by the control of the properties of the catalyst surface in situ during the course of the reaction. This can be accomplished by the use of a solid state electrochemical cell, in which one of the components can be added to or deleted from the catalyst surface by electrically driven mass transport through an underlying solid electrolyte. Such solid state electrochemical cells featuring an oxide ion-conducting solid electrolyte have been used sucessfully in the past for the decomposition of NO [1], expoxidation of ethylene [2], hydrogenation of CO [3] and the oxidation of hydrogen [4].

A second important aspect of the present work was the addition of H_2 into the reaction gas stream to hydrogenate the surface carbon resulting from the decomposition of CO_2 to obtain methane and other hydrocarbons.

The experimental apparatus built to carry out this study allowed operation in either flow-through or recirculation modes. The reactor consisted of a yttria-stabilized zirconia tube closed at one end and sealed in a quartz jacket such that the open end of the tube was exposed to the ambient atmosphere. Suitable electrodes were deposited on the inside and outside walls of the tube at its closed end. The reactor was operated under a total pressure of 1 atm and at temperatures up to 850 °C. The compositions of the reactant and product gases were analyzed by gas chromotography. The overall reaction can be expressed as

$$CO_2 + 2H_2 = CH_4 + O_2$$

The oxygen was transported through the solid electrolyte and recovered in a separate compartment. This approach provided many advantages: first, it minimized, and under carefully selected conditions totally eliminated, carbon deposition and reactor clogging; second, it allowed recovery of oxygen in pure form in a separate compartment; third, the reaction gave gaseous products such as methane and other hydrocarbons that were not only easy to handle in a reaction system but are also useful chemicals; and fourth, the catalytic rates achieved by this electrochemical route were significantly higher that the rates observed under open circuit conditions.

Acknowledgement

This work was supported in part by the Office of Naval Research. Support by the Gas Research Institute is also gratefully acknowledged.

[1] T.M. Gür and R.A. Huggins, J. Electrochem. Soc. 126, 1067 (1979)

[2] M. Stoukides and C.G. Vayenas, J. Catal. 70, 137 (1981)

[3] T.M. Gür and R.A. Huggins, J. Catal. 102, 443(1986)

[4] C. Saranteas and M. Stoukides, J. Catal 93, 417 (1985)

Abstract No. 733

RESISTIVITY MEASUREMENTS OF HIGH-TEMPERATURE IMMOBILIZED ELECTROLYTES

Laszlo Redey and Margaret McParland
Argonne National Laboratory
Chemical Technology Division
9700 S. Cass Ave., Argonne, IL 60439

INTRODUCTION

High-temperature immobilized electrolytes (HTIE) form a new class of separators that are applicable in advanced primary [1] and secondary [2] batteries, as well as in fuel cells [3]. HTIE materials consist of a matrix of a chemically inert insulator, ceramic material and a liquid salt held in place by capillary forces in the pores. The matrix material is either a (1) felt or fabric or (2) a powder.

The usual cell configurations for determining resistivity/conductivity in liquid or solid materials are not applicable for HTIE materials. These materials are pastes or thin, pliable layers without any self-supporting capability in the temperature range of interest.

EXPERIMENTS AND RESULTS

The different types of the HTIE separators require a firm support at high temperature to maintain a specified geometry. This property of the HTIE separators and the phase change that occurs between the temperatures of specimen preparation and the measurement require a special cell design.

An interrupted direct-current (DC) technique has been chosen for the resistivity measurement. The resistivity cell consists of a separator specimen of precisely known geometry sandwiched by two high-density alumina plates in a horizontal orientation; the cell constant is 0.01-0.05 cm. The lower plate bears (1) contains two electrodes to introduce square-shape current pulses of short duration through the specimen and (2) two potential sensing electrodes to measure the IR voltage drop that develops during the current pulses. Schematic representations of the cell and the measuring circuit, as well as a diagram that illustrates the measuring principle, are shown in Fig. 1. Current pulses of low intensity are applied alternatively in opposite directions to avoid polarization of electrodes and concentration changes in the specimen. The voltage traces measured between the potential sensing electrodes (V_S) and across a precision resistor (PR, V_{PR}) are recorded on a digital storage oscilloscope and are compared to calculate the resistivity of the specimen. Because of the high hygroscopicity of the electrolyte salts, the measurement is carried out in a high-purity He atmosphere glove box.

A resistivity vs. temperature plot of a separator (35 wt % MgO in 44.2 wt % LiCl-55.8 wt % KCl eutectic salt) is shown in Fig. 2 to illustrate the capability of the technique. The test specimens were cut to precise dimensions from pellets provided by the Sandia National Laboratories (Ref. R. Guidotti).

DISCUSSION

The DC technique has been chosen because of (1) the greater flexibility in cell design, (2) absence of leakage currents, which frequently cause problems in AC circuits, (3) fewer problems with electrical noise, and (4) faster measurements, since there is no need for repetitive measurements at several frequencies.

As Fig. 2 shows, the measured values obtained during temperature scanning are within a narrow range of scatter. Parallel measurements on several separator materials have established the precision of the resistivity data at $\pm$2.5%. This limit includes (1) slight density deviations due to the powder-pressing method of specimen preparation, (2) limitation in precise reproduction of specimen geometry, and (3) the low-level, but detectable electrical noise. An additional uncertainty is related to the solid-to-liquid phase change between the temperatures of specimen preparation and measurement, as well as to the shrinkage of the specimen at the temperature of the measurement caused by the gradual disappearance of gas filled pores.

Figure 2 shows that the conductivity of the HTIE separator is significantly less than that of the pure molten salt [4]. This difference is being analyzed by the mathematical models available for the conductivity of two-phase systems [5], but at this time, an optimum model description has not yet been found.

The activation energy of conduction (U_C^*) calculated from the $\log \kappa = A + (-U_C^*/RT)$ relationship is U_C^*=8.87 kJ/mol at 450°C and A=1.40, see Fig. 3; it indicates only a slight difference from the value of the pure liquid salt (U_C^*=7.69 kJ/mol, A=1.48).

The resistivity data of HTIE separators have been are used in performance evaluation [1] and modeling [6] of Li-alloy/metal sulfide cells.

ACKNOWLEDGMENT

This work was supported by the U.S. Department of Energy, Office of Energy Storage under contract No. W-31-109-ENG-38. The author is grateful to Dr. P. A. Nelson for his encouragement and support.

REFERENCES

[1] L. Redey, J. A. Smaga, J. E. Battles, and R. Guidotti, "Investigation of Primary Li-Si/FeS_2 Cells," ANL-87-6, Argonne National Laboratory, Argonne, IL, 1987.

[2] G. Barlow, Proc. of Eighth Internat'l. Electric Vehicle Symp. Oct. 20-22, 1986, Washington, D.C.

[3] K. Kinoshita and G. H. Kucera, J. of Electrochem. Soc., 129, 216 (1982).

[4] E.R. Van Artsdalen and I. S. Yaffe, J. Phys. Chem., 59, 118 (1955).

[5] R. E. Meredith and C. W. Tobias, in "Adv. in Electrochemistry and Electrochemical Engineering," Vol. 2, ed., C. W. Tobias, Interscience Publishers, New York, 1962, p. 15.

[6] J. Lee, L. Redey, T. D. Kaun, and P. A. Nelson, Ext. Abs. Electrochem. Soc. Meeting, Oct. 18-23, 1987, Honolulu, HI, Vol. 87-2, (1987), p. 233.

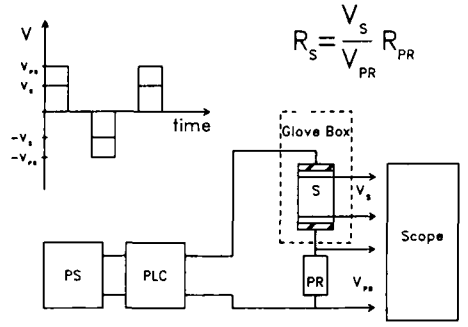


Fig. 1. Schematics of circuit diagram and measuring principle. PS power source, variable constant current source, PLC programmable logic controller, PR precision resistor, S specimen, R_S resistance of specimen, R_{PR} resistance of precision resistor.

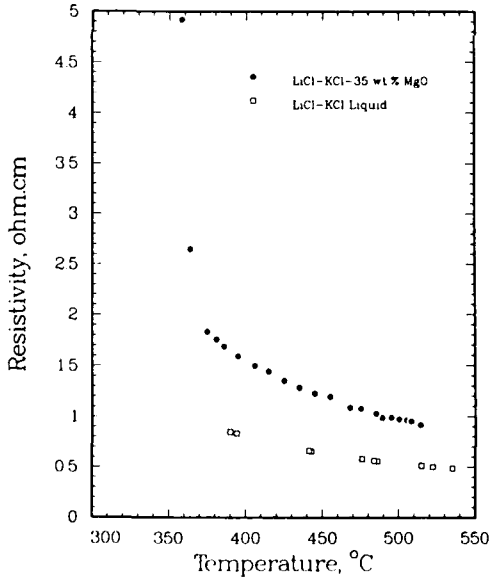


Fig. 2. Resistivity vs. temperature plot.

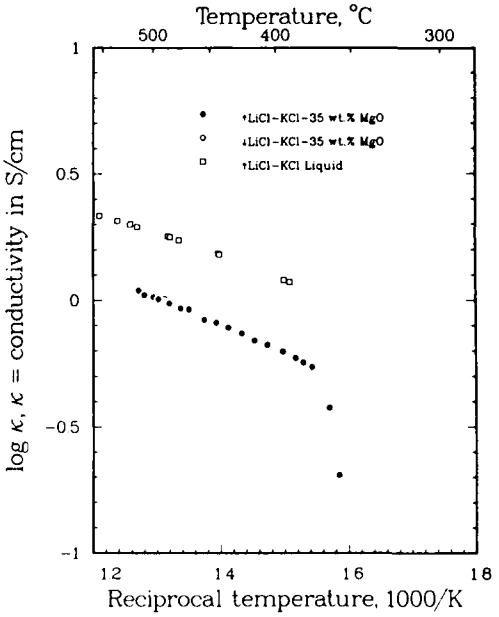


Fig. 3. Graph for calulation of the activation energy of conductance. Data for the pure LiCl-KCl eutectic are taken from Ref. 4.

Abstract No. 734

Mixed-Conducting Membranes for Hydrogen-Transporting S/L/S "Solid Electrolyte" Configurations

M. Schreiber, J. Wolfenstine and R. A. Huggins
Dept. of Materials Science & Engineering
Stanford University
Stanford, CA 94305

A novel S/L/S configuration that can be used as a solid electrolyte for hydrogen at elevated temperatures was recently described (1,2). It consists of two solid, but hydrogen - transparent, metallic membranes that act as mixed - conducting electrodes. Between these membranes is a molten salt containing hydride ions. One example is a solution of LiCl, KCl, and LiH. Such salts are stable at temperatures appreciably higher than proton - containing salts. By placing a potential difference between the two mixed conductors, hydrogen is caused to move across the electrolyte. If the chemical diffusion of hydrogen is sufficiently fast within the membrane electrodes, the difference in hydrogen activity imposed by the potential difference will appear on their outer surfaces.

Alternatively, rapid chemical diffusion of hydrogen through such membranes means that the imposition of a chemical potential difference at their outer surfaces is translated into a difference in chemical potential between their inner surfaces, and thus across the electrolyte, producing a difference in the electrochemical potential of electrons, and thus a measurable voltage.

Thus such a configuration can be used in either pump or a sensor modes, operating in a manner directly analagous to a solid electrolyte with porous three - phase - contact electrodes in contact with gases.

Key elements in this concept are the two hydrogen - transporting mixed - conducting membranes. In order to provide rapid kinetics in either the pump or sensor modes, they must have high chemical diffusion coefficients for hydrogen. In addition, these materials must also meet several thermodynamic requirements. In order to be compatible with the external environment, such a membrane must be stable in the face of the chemical potentials imposed upon it by adjacent phases. In addition, it must be thermodynamically stable in contact with the encapsulated liquid electrolyte.

These requirements will be discussed in some detail for several areas of potential application, such as the intermediate temperature electrolysis of water to extract hydrogen, the separation of hydrogen from flowing gas streams, hydrogen sensors, and hydrogen - combusting fuel cells.

Several metallic phases with body - centered cubic crystal structures are worthy of consideration for such purposes. The properties of several materials in this category will be reviewed.

Especially important is the requirement that the oxygen and water vapor activities be maintained at very low values in order to prevent the formation of hydrogen - blocking films upon the membrane surfaces. Several approaches to the solution of this problem in molten salts have been discussed previously (3).

Acknowledgement

Partial financial support of work in this area at Stanford by the US Department of Energy under Subcontract LBL - 4536310 and Contract BNL 274318-S is gratefully acknowledged.

References

1. G. Deublein, B. Y Liaw, and R. A. Huggins, Presented at the 6th International Conference on Solid State Ionics, Garmisch-Partenkirchen, Sept. 1987. To be published in Solid State Ionics.

2. R. A. Huggins, Presented at the 6th International Conference on Solid State Ionics, Garmisch-Partenkirchen, Sept. 1987. To be published in Solid State Ionics.

3. G. Deublein and R. A. Huggins, Presented at the Electrochemistry Society Meeting in San Diego, Oct. 1986. To be published in the Journal of the Electrochemical Society.

Abstract No. 735

SOLID STATE ELECTROCHROMIC WINDOWS-AN OVERVIEW

R. David Rauh

EIC Laboratories, Inc.
Norwood, Massachusetts 02062

The last several years has seen a resurgence in interest in electrochromism, not for displays, but for variable transmittance windows [1]. Electrochromic "smart" windows hold the prospect for adjustable light transmittance induced by a low voltage dc electrical current. As shown in Figure 1, the basic structure is that of a thin film secondary battery with a visible state of charge. As such, the window is comprised of three types of thin film materials: 1) transparent electrical conductors, which act as current collectors; 2) mixed conductors, which form the electroactive, color changing elements; and 3) ion conductors, which form the electrolyte while being electronically insulating. Interestingly, numerous electrochromic light modulators in the literature are lacking one or more of these fundamental components, resulting in either poor long term reversibility and disruption of electrode components, short open circuit memory arising from chemical or electronic self-discharge, or both.

Currently, there are two basic approaches to window construction. One is to deposit the electrical conductor and electrochromic electrodes separately on two pieces of glass, then to laminate them together with a semisolid or polymeric electrolyte. The second is to produce a multilayer thin film stack by sequential sputtering of the layers. The principle difference between the two approaches lies in the electrolyte.

Materials development for electrochromic windows has been concerned mostly with the electrochromic and electrolyte layers. The primary electrochromic material being considered is still WO_3, since it combines robustness with long-term cyclability, as demonstrated repeatedly in the display literature [2]. Variants of WO_3, particularly crystallized thin films [3] and hexatungstates [4,5], have substantial reflectance components to their electrochromic response. The variable reflectance has been shown to give a favorable optical response for windows, permitting selective attenuation of the near infrared solar spectrum at low state of charge while deeper coloration leads to decreases in visible light transmission.

Considerable work has been carried out in this laboratory on developing a reversible complement to WO_3 for use as the counter electrode in electrochromic windows. The best characterized material is IrO_2, prepared by rf magnetron sputtering. This oxide becomes colorless on reduction (the opposite of WO_3). These two oxides have been used to fabricate electrochromic windows with proton conducting electrolytes (e.g., polyAMPS) that switch between 75% and 25% integrated visible solar transmittance, and have exceeded 10^5 cycles in accelerated tests [4]. Each electrode has excellent oxidation/reduction reversibility, resulting in the transmission of the window being a predictable function both the voltage applied across the two electrodes and the charge passed. This kind of reproducibility will be necessary for control in actual building environments.

Electronically conducting polymers form another class of counter electrode which develop color oxidatively. A prime example is polyaniline, which is yellow when reduced and blue when oxidized [6]. Figure 2 shows the visible solar attenuation of WO_3, and both IrO_2 and polyaniline counter electrodes as a function of charge capacity (thickness). The total transmission of a window comprised of WO_3 in series with either counter electrode is given by the product of the transmittances of the individual electrodes at equal charge capacities [7]. It is seen that polyaniline is compromised somewhat compared to IrO_2 by its lower bleached (reduced) state transmittance. Conductive polymers are sensitive to irreversible anodic decomposition reactions occurring at potentials only slightly positive of the electrochromic transition. Such decomposition can be difficult to avoid in two-electrode window structures.

Recently, lithium-based window structures are being demonstrated, to avoid the possibility of irreversible H_2O electrolysis at the thin film interfaces, and also to achieve a truly "dry" system. We have shown that some inexpensive oxides like V_2O_5 can be used as the counter electrode with Li, providing largely oxidative coloration, as with IrO_2 [7]. The electrolyte remains the major area of improvement for Li-based windows. We have demonstrated windows that work well at room temperature with polyphosphazine electrolytes [8]. All thin film structures with $LiNbO_3$ as the electrolyte and In_2O_3 or V_2O_5 electrodes have been reported by Goldner et al. [9].

ACKNOWLEDGMENTS

This work was sponsored by the U.S. Department of Energy and by NASA. The support, encouragement and contributions of the following people are gratefully acknowledged: Mr. David M. Pellish of DOE; Dr. Carl M. Lampert of Lawrence Berkeley Laboratory; Professors Ronald Goldner and Terry Haas and their research groups at Tufts University; and Dr. Stuart F. Cogan and his research group at EIC Laboratories.

REFERENCES

1. C.M. Lampert, Solar Energy Materials 11, 1 (1984).
2. W.C. Dautremont-Smith, Displays 3, 3 (1982).
3. R.B. Goldner et al., Appl. Phys. Letters 43, 1093 (1983).
4. S.F. Cogan, T.D. Plante, R.S. McFadden and R.D. Rauh, Solar Energy Materials 16, 371 (1987).
5. S. Joo, I.D. Raistrick and R.A. Huggins, Mat. Res. Bull. 20, 987 (1985).
6. Toyoda Gosei Co., German Offen. 3,614,547.
7. R.D. Rauh and S.F. Cogan, Solid State Ionics, in press.
8. S.F. Cogan and M. Alamgir, unpublished results.
9. R.B. Goldner, T.E. Haas, G. Seward, K.K. Wong, P. Norton, G. Foley, G. Berera, G. Wei, S. Schultz and R. Chapman, Solid State Ionics, in press.

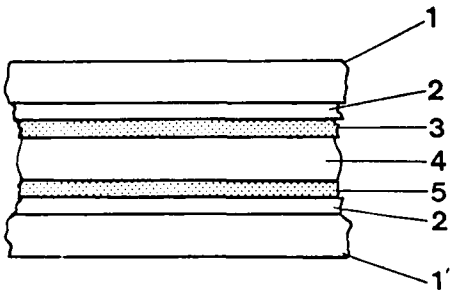


Fig. 1. Cross section of an electrochromic window. 1,1' - transparent substrates; 2 - transparent electrical contacts, e.g., ITO; 3 - cathodically coloring layer (e.g., WO_3); 4 - ion conductor; 5 - anodically coloring layer. Layer 1 would be absent in an all-thin film structure.

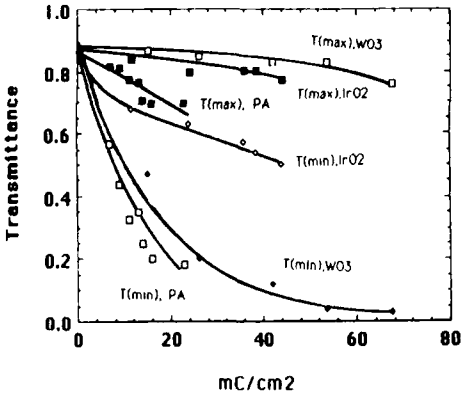


Fig. 2. Maximum and minimum integrated visible solar transmittance (400-700 nm) of candidate electrochromic thin films as a function of charge capacity.

Abstract No. 736

EFFECT OF IONIC MOBILITY ON THE OPTICAL PROPERTIES OF Cu^+ DOPED Na^+-β"-ALUMINA

J.D. Barrie*, B. Dunn*, O.M. Stafsudd+, G. Hollingsworth# and J.I. Zink#

*Department of Materials Science and Engineering
+Electrical Engineering Department
#Department of Chemistry and Biochemistry
University of California, Los Angeles

Single crystals of Na^+-β"-alumina which have been doped with Cu^+ show a bright green luminescence centered at 535nm when excited with a variety of ultraviolet wavelengths at room temperature. At low temperatures, the presence of several distinct emissions in both the blue and green regions of the spectrum indicate a more complex interaction of copper ions with each other and with the host lattice. Two emissions (at 410 and 440nm) can be attributed to single ion emission from two distinct sites within the lattice, while two emissions at 525nm and 545nm are attributed to two Cu^+-Cu^+ dimer species forming within the conduction planes.

The low temperature emission spectrum has been found to change with time when the crystal is irradiated at 351nm. Over a period of seconds, blue emission decreases in intensity, while the green emission intensity significantly increased. These changes occur only in the part of the sample exposed to the irradiation, while the rest of the sample is unaffected. The mechanism of this change is a photoinduced aggregation of the Cu^+ isolated ions in the conduction plane to form Cu^+-Cu^+ pairs.

The bonding between d^{10} valence shells (such as Cu^+) has been discussed by Hoffmann and coworkers [1-2]. In these studies the authors showed how repulsion between two closed shells could be converted to an attraction by inclusion of unfilled orbitals of the proper symmetry. This attractive energy provides a driving force for the observed photoaggregation. The energy introduced into the Cu^+ ions by the ultraviolet excitation provides the activation energy required for the ionic mobility. The rate of increase of the green emission peak can be shown to follow simple diffusion laws.

The dynamic interaction of Cu^+ ions to form dimers in the conduction plane of Na^+-β"-alumina is similar to that reported in $SrCl_2$ crystals, although the effects observed in β"-alumina can occur at much lower temperatures than were reported by Payne [3]. This is a result of the high mobility of Cu^+ ions in the β"-alumina conduction plane, which translates into an ionic hopping rate of about 10^9 per second at room temperature. Therefore, even in crystals with dilute Cu^+ concentrations where random ion-ion separations would be expected to be at least 50Å, the possibility of Cu^+-Cu^+ encounters is very high.

The reduction of the intensity of the blue emission as the temperature of the sample is raised suggests that the Cu^+ monomer emission is incompatible with the high ionic conductivity in Na^+-β"-alumina. Either of two effects may lead to this reduction in blue luminescence. The dominance of the green emission attributed to the Cu^+-Cu^+ dimer at room temperature suggests that the formation of these dimers is indeed energetically favorable. Thus when the ionic conductivity of the crystals becomes appreciable, it becomes more likely that the isolated Cu^+ ions will be able to form these pairs via diffusion mechanisms. This would result in a reduction of the blue intensity by elimination of the blue emitting species. However, one other effect must be considered. The perturbing influence of ionic mobility may be sufficient to produce non-radiative quenching effects upon the Cu^+ excited state, resulting in a reduction of both intensity and lifetime of the emission. Such effects are not well known in traditional close packed optical hosts, as ionic mobility in these materials is usually negligible. This raises the possibility that there may be an equilibrium distribution of both isolated ions and dimers ($2Cu^+ \approx Cu_2^{2+}$) in the Cu^+ doped Na^+-β"-alumina crystals at all temperatures, and that the absence of the blue emission bands at room temperature is due to the non-radiative deactivation of the isolated ions caused by ionic mobility. The end result is that only the green emission from the Cu^+-Cu^+ dimers is observed at room temperature. The presence of the dimer emission at room temperature and above suggests that these species are relatively immobile at these temperatures.

REFERENCES

1. Mehrotra, Prem K., and Roald Hoffmann, Inorganic Chemistry 17, (1978) 2187.

2. Dedieu, A., and R. Hoffmann, J. Am. Chem. Soc. 100 (1978) 2074.

3. Payne, Stephen A. and L.L. Chase, and L.A. Boatner, Journal of Luminescence 35, (1986) 171.

Abstract No. 737

Effect of Thermal History upon the Lanthanide β"-Aluminas

R. B. Queenan and P. K. Davies

Department of Materials Science and Engineering
University of Pennsylvania
Philadelphia, PA 19104

Introduction: Following from the reports of the 'high' conductivities of trivalent lanthanide ions in the β"-aluminas (10^{-5} (ohm-cm)$^{-1}$) (1), many studies have been carried out on these interesting materials. In particular, the optical properties of the Nd β"-aluminas have been well researched due to their potential applications in opto-electronic devices. (2,3,4) However, there have been very few structural studies on these systems.(5,6) A single crystal x-ray study on a thermally uncharacterized Gd β"-alumina sample reported predominant occupation of the mO site within the conduction planes.(5) A TEM study by Davies, et.al. (6) found evidence for a long-range ordered structure in the 100% Nd material, intergrown with a disordered structure. The cooling rate of these samples was not controlled.

In this work we have investigated the effect of thermal treatments on the structural and optical properties of the Nd and Gd β" aluminas utilizing single crystal x-ray diffraction techniques, electron diffraction and high resolution TEM, and optical absorption spectroscopy.

Single crystals of $Na_{5/3-x}M_{x/3}Mg_{.67}Al_{10.33}$ ($1/2 \leq x \leq 5/3$; $M^{3+}=Nd^{3+}, Gd^{3+}$) were prepared by ion-exchange techniques and were subjected to various thermal treatments. The samples were either quenched from high temperatures (600-700°C) or were annealed at low temperatures (300-400°C). The treatments were carried out in sealed quartz tubes to avoid the possibility of hydration that may occur under ambient conditions.

Results: Long-range ordered structures were observed across the binary Na^+-M^{3+} system down to a sample with only 30% of the Na replaced by Nd. In all cases the ordering occurs both within the conduction planes as well as along the c axis as was first seen by Davies (6) in the completely exchanged Nd material.

Samples which were slow-cooled or annealed at low temperatures showed an increase in the intensity of superlattice reflections, and a corresponding increase in the ordered structure as evidenced by TEM images. Quenched samples showed significant decrease in the amount of ordering. In all samples studied, no matter how slow the cooling rate, some disordered structure coexisted with the ordered structure. Kinetic limitations apparently prevent the formation of a completely ordered sample.

Our spectroscopic measurements showed that relative intensities of electronic transitions are highly sensitive to both composition, as reported by Dunn (4), and to cooling rate. These studies revealed changes in the relative intensities of the absorptions as a result of different thermal treatments. It seems likely that these changes in intensity may reflect changes in site occupancies of the Nd ions in the conduction planes resulting from thermal treatment. These factors may be important in the application of these materials in optical devices.

References:

1. B. Dunn and G.C. Farrington, Solid State Ionics, 9&10 (1983) 223-226,

2. M. Jansen, A. Alfrey, O.M. Stafsudd, B. Dunn, D.L. Yang and G. C. Farrington, Optics Letters, 9 (1984) 119.

3. A.J. Alfrey, O.M. Stafsudd, B. Dunn and D.L. Yang, J. Chem. Phys. 88 (1988) 707.

4. B. Dunn, D.L. Yang and D. Vivien, J. Solid State Chem., March 1988, in press.

5. W. Carrillo-Cabrera, J.O. Thomas and G. C. Farrington, Solid State Ionics, 9&10 (1983) 301.

6. P.K. Davies, A. Petford, M. O'Keeffe, Solid State Ionics, 18&19 (1986) 625.

Acknowledgements: This work was supported by NSF (Ceramics) DMR 8316999.

Abstract No. 738

SYNTHESIS AND PROPERTIES OF MIXED SODIUM-CERIUM (III) ALUMINOGALLATE COMPOSITIONS

J.Thery*, G. Aka*, D. Vivien*, C.T. Chu+ and B. Dunn+

* Laboratoire de Chimie Appliquée de l'Etat Solide
ENSCP, Paris Cedex 05, FRANCE
+Department of Materials Science and Engineering
UCLA, Los Angeles, CA 90024 USA

The structure and properties of the sodium-lanthanide aluminate family of compositions (SLnA with Ln= La,Nd, Ce) have been previously reported. (1,2) The structure is interesting in that it consists of alternating stacking of half ß alumina unit cells and half magnetoplumbite (MP) unit cells. The initial conductivity reported for the SLnA composition suggested that the material had good ionic conductivity.

The present investigation involves the synthesis and properties of sodium-cerium aluminogallates (SCAG) where a substantial fraction of Ga has been substituted for Al. The compositions have the ideal formula:

$$Na_{1+y}Ce(Al_{1-x}Ga_x)_{22.66}O_{36+y/2}$$

with $0.3 \leq y \leq 1$ and $0 \leq x \leq 0.5$

Several methods have been used to synthesize these compositions: (1) solid state reactions using component oxides with NaF and (2) co-precipitation of a nitrate mixture. In both cases temperatures above 1550 °C were necessary to produce the proper phase and the trivalent Ce. Sintered compacts were prepared from the powders. In these samples Ga replaced ≈ 35 to 45% of the Al (i.e., x ≈ 0.35 to 0.45) which facilitated sintering. Densities of ≈ 90% of theoretical were obtained by heating to 1570 °C. Single crystals of SCAG were prepared by the skull melting technique and subsequently used in the X-ray diffraction study. Magnetic susceptibility and luminescence studies confirmed that trivalent Ce was obtained. The measured Curie constant (C=0.59) is identical to that found for the Ce(III) hexa aluminate, $CeMgAl_{11}O_{19}$. (3) The characteristic violet-blue emission of Ce^{3+} was observed when irradiated at 254 nm. Both of these measurements give clear evidence that the high temperature synthesis leads to reduction of Ce^{4+} to Ce^{3+}.

X-ray diffraction of both powder and single crystals confirms that SCAG compositions possess structures similar to that of SLnA. There is an alternate stacking of ß alumina and MP half-unit cells along the c-axis with the Na^+ and Ce^{3+} localized in different mirror planes. The Na^+ possess an environment similar to that of Na^+ in ß alumina while Ce^{3+} is situated in sites representative of the MP structure. In the case of Ce^{3+}, spectroscopy studies have been used to independently determine the nature of its structural environment. ESR spectra for Ce^{3+} in the mixed phase materials are identical to that of Ce^{3+} in the magnetoplumbite, $La_{1-y}Ce_yMgAl_{11}O_{19}$ (3) Thus, the Na^+ are found to have no influence on the local crystal field experienced by the Ce^{3+}.

The conductivity for several SCAG compositions has been measured by a four-probe complex impedance technique using evaporated gold contacts. Conductivity was measured from 25 to 300 ° C and found to obey an Arrhenius relation. The conductivity at 300 °C was in the range of 2×10^{-3} $(\Omega cm)^{-1}$ and represents a combination of crystal and grain boundary contributions. The activation energy for conduction was ≈ 0.3 eV. These transport properties were found to be relatively insensitive to sodium content ($Na_{1.35}$ to $Na_{1.86}$) and Ga substitution ($Ga_{0.34}$ to $Ga_{0.44}$). These results demonstrate that SCAG compositions possess a reasonable level of ionic conductivity and are consistent with the proposed structural model of having the Na^+ located in conduction planes similar to those of ß alumina.

REFERENCES

1. A. Rafaoui, A. Kahn, J. Théry and D. Vivien, Solid State Ionics **9/10**, 331 (1983).

2. A. Kahn and J. Théry, J. Solid State Chem. **64**, 102 (1986).

3. B. Viana et. al. J. Appl. Phys., In Press.

Abstract No. 739

COMPARISON OF CONDUCTIVITY MEASUREMENTS ON BETA" ALUMINA ISOMORPHS BY TWO- AND FOUR-PROBE TECHNIQUES

M.W.Breiter, H.Durakpasa, G.Allitsch and P.Linhardt

Institut für Technische Elektrochemie, TU Wien, 9 Getreidemarkt, 1060 Wien, Austria

A large difference exists between the conductivities values reported at the same temperature for the following polycrystalline isomorphs of beta" alumina: Pb (1-3), Ca (4-6) and Cd (5,7). This difference results from a combination of factors:

a) Different manufactoring techniques, especially the difference between ion exchange and conventional forming and sintering.

b) Different starting materials for the ion exchange.

c) Different degrees of porosity and the possiblity that residues of salt are left in the porous structure after ion exchange and cleaning of the sample.

d) Unreliable extent of exchange when determined by the weight change (possibility of residual Na^+).

e) Use of two- or four-probe techniques in the measurement of the conductivity as a function of temperature.

The purpose of this paper is to evaluate the influence of factor e). To do so, a system has to be chosen for which the influence of the other factors is small. Among the isomorphs, produced by us so far, Sr beta" alumina is the only polycrystalline isomorph which does not suffer from extensive corrosive attack during ion exchange (5), Therefore two mixed (Na,Sr) beta" alumina with different composition were chosen. The materials were produced by ion exchange of Na beta" alumina (betalyte from Ceramatec Inc.) in suitable melts of $NaNO_3$, $Sr(NO_3)_2$ and $SrCl_2$. The extent of exchange was determined by chemical analysis. It was verified by EDAX that the distribution of Na^+ and Sr^{++} ions was uniform across the sample.

The four-probe measurements were carried out as described previously (3). The two-probe measurements were made by an automated impedance meter (IM 5 of Zahner-elektrik, West Germany). The same samples were employed as in the four-probe measurements after sanding off the contacts for the four-probe measurements. The samples had the shape of a bar with thicknesses between 0.1 and 0.2 cm. Platinum films were sputtered onto the two large surfaces as electrodes for the impedance measurements. Contact between the Pt film and the leads to the meter was accomplished by silver paint.

The two-probe measurements were made at a constant frequency of 1000 Hz during an approximately linear increase of temperature with time and during the subsequent decrease. The phase angle was also recorded. The conductivity was computed from those data where the phase angle was smaller than 20^o (cosine remains close to 1).This procedure gave temperature ranges of 50 to 500^oC for the first material (10% exchange of sodium) and 250 to 500^oC for the second material (70% exchange). The temperature dependence of the conductivity was of the Arrhenius type.

The impedance measurements were carried out at frequencies between 0.01 and 100000 Hz at constant temperatures (at intervals of 50^oC). Sometimes the impedance meter restricted the upper frequency to 10000 Hz. The data were only available in a Bode plot. They had to be transferred to another PC to obtain the complex impedance plane plots.

The data for the material with 10% exchange did not allow a simple extrapolation procedure for the determination of the resistance of the solid electrolyte (sum of bulk and grain boundary contributions). Neither could one of the two components be determined separately. The measurements represent an example that the conductivity of the solid electrolyte cannot be determined in a simple fashion from the impedance measurements. Further work is required to test if such a determination is feasible on the basis of analog circuits considering bulk and interfacial effects.

The data for the material with 70% exchange display the existence of a depressed semicircle at higher frequencies and a constant phase element at lower ones between 300 and 500^oC. The extrapolation of the right end of the semicircle to the abscissa yields resistances which are equal to the solid electrolyte resistance within the error limits of the comparison of results from two different techniques. The error limit is relatively large (estimate of a factor 2 to 3).

Acknowledgement.

The investigations were made with partial support of the Office of Naval Research.

References.

1. E.E.Hellström and R.Benner, Solid State Ionics 11,125 (1983)
2. E.E Hellström, ibid. 15,139 (1935)
3. M.Maly-Schreiber, P.Linhardt and M.W. Breiter, Electrochim.Acta 32,1371 (1987)
4. A.F.Sammels and B.Schuhmacher, J.Electrochem.Soc. 133,235 (1986)
5. M.W.Breiter, M.Maly-Schreiber, G.Allitsch and P.Linhardt, Proc.Symp. Electro-Ceramics and Solid State Ionics, Electrochem. Soc. in print
6. Y.Hong, D.Pong, Y.Peng, L.Li and S.Wei, Solid State Ionic. 25,301 (1988)
7. G.Staikov, V.Nikolov and P.D.Yanqulov, ibid. in print

Abstract No. 740

Enzyme Embodied Electrode Device as a High Performance Detector for Flow Injection Analysis

S. Yamauchi, Y. Ikariyama*, M. Yaoita,
T. Yukiashi**, and H. Ushioda**

Research Institute of National Rehabilitation Center for the Disabled, Namiki 4-1, Tokorozawa, Saitama 359, Japan
* Department of Bioengineering, Tokyo Institute of Technology, Ookayama, Tokyo 152, Japan
** Central Research Laboratory, Sumitomo Cement Co., Ltd. Toyotomi 5-8-5, Funabbashi, Chiba 274, Japan

We have already reported a newly developed Enzyme Embodied Electrode (EEE) having unique characteristics such as a fast response of less than 3 sec and long stability of more than 4 weeks[1-3]. EEE is easily fabricated by incorporating enzyme molecules on platinized platinum surface. EEE has another advantage that it is easily minituarized to a diameter of 10 μm. In this paper we would like to demonstrate that EEE can be adopted also to a high performance electrochemical detector for flow injection analysis.

EXPERIMENTAL

A micro-platinum electrode, of which diameter is from 10 to 500 μm, in an acrylic block was platinized by an electrolytic reduction of hexachloroplatinate. Then the platinized electrode was thoroughly rinsed in 0.1 M phosphate buffer (pH 6.8). Glucose oxidase molecules were incorporated in the platinized platinum electrode by immersing in an enzyme solution for 10 min. The electrode was then kept in a bovine serum albumin for 10 min and then treated with a 2 % glutaraldehyde solution buffered with 0.1 M phosphate for 10 min, following which thorough washing of the electrode was performed overnight. The EEE fabricated above was assembled to a thin layer transducer cell with the auxiliary electrode of stainless steel block. The reference electrode of Ag/AgCl was positioned downstream from the cell. The flow rate of the peristatic pump was controlled at 0.8 mL/min. The electrode potential of micro-enzyme electrode was kept at 0.6 V against a Ag/AgCl reference electrode. All the experiments were carried out at room temperatures (23 ℃).

RESULTS

A glucose sample (10 mM, 5 μL) was repeatedly injected to the transducer cell. Figure 1 shows a typical response of the detector system. Every response reached a peak within 2 or 3 sec and decayed to the baseline within a few seconds. Each peak is highly reproducible, and was about 200 nA to 10 mM glucose sample. The micro-enzyme electrode having a diameter of 100 μm gave no responses to either blank, fructose, or galactose samples in 0.1 M phosphate buffer of pH 6.8, when the anodic polarization was given to the platinized platimun surface before incorporation of enzyme.

A series of glucose samples of 200 μM to 20 mM were injected to the transducer cell having a 100 μm micro-enzyme electrode. Figure 2 shows a linear relationship between the glucose concentration and the peak height in the range from 50 μM to 20 mM. As was already reported [1-3], the micro-enzyme electrode showed a high sensitivity (least detection limit: 0.5 μM, and wide dynamic range (0.5 μM - 20 mM) in a batch system measurement. However, in this flow type measurement the detection limit was in the 50 μM range because of the poor signal to noise ratio due to a peristaltic wave caused by the double plunger pump.

In a series of experiments six hundred samples of 10 mM glucose solutions were injected to the flow cell, having an EEE of 100 μm diameter at a room temperature, and the coefficient of variation of 1.9% was observed. The average peak current was 252 nA at a flow rate of 0.8 mL/min. As this experiments were carried out at a room temperature of 23±2 ℃ without tempearture control, subtle change of the room temperature in one hour seemed to have affected the output. We are convinced that strict thermostat of the equipment will much improve the reproducibility of the peak current.

It has been observed that the peak current decreases with an increase in the flow rate of the pump. If the electrochemical process is controlled by a mass transport in the diffusion layer, enhanced peak current is expected at a higher flow rate [4,5]. Both the enzyme reaction of glucose oxidase and the electrochemical oxidation of the produced hydrogen peroxide seem to be high enough to generate sensor output, since apparent Km value (ca. 50 mM) for the enzyme electrode is much greater than the analyte concentration (10 mM), and the applied potential (0.6 V) is much higher than the oxidation potential (ca. 0.45 V) of hydrogen peroxide. Therefore, the rate determining step of the electrode reaction would be the mass transport within the pores of the platinum black.

In order to see the long term stability of the EEE device for use in flow injection analysis, one hundred glucose samples were injected every three days to a transducer cell with a micro-enzyme electrode of 100 μm diameter. The cell was kept in a refrigerator (4 ℃) when the electrode was not in use. It has been confirmed that the peak current kept constant and the coefficient of variation was still about 1% even after one month.

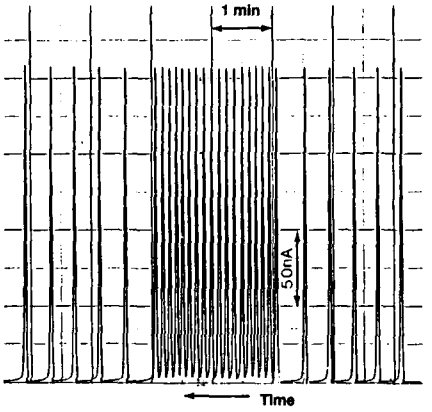


Figure 1. Typical Responses of Flow Injection Analysis with EEE.

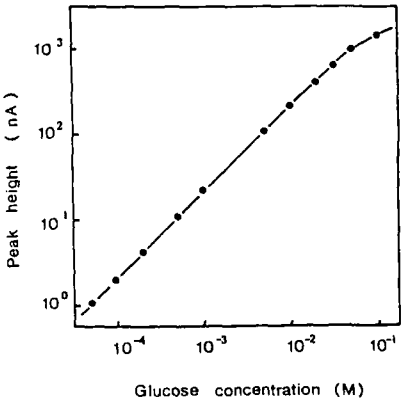


Figure 2. Dependence of Peak Current on the Glucose Concentration.

References

[1] Y. Ikariyama, S. Yamauchi, T. Yukiashi and H. Ushioda, Anal. Lett., **20**, 1409 (1987).
[2] Y. Ikariyama, S. Yamauchi, T. Yukiashi and H. Ushioda, Anal. Lett., **20**, 1791 (1987).
[3] Y. Ikariyama, S. Yamauchi, T. Yukiashi and H. Ushioda, J. Electrochem. Soc. (submitted for publication).
[4] S. G. Weber, J. Electroanal. Chem., **146**, 1 (1983).
[5] J. A. Polta and D. C. Johnson, J. Liq. Chromatogr., **6**, 1727 (1983).

Abstract No. 741

A Chemically Sensitive Bipolar Junction Transistor

Christopher K. Y. Chun
James W. Holm-Kennedy
Sensor Research and Development Center
Physical Electronics Laboratory
University of Hawaii at Manoa
Honolulu, Hawaii 96822

Extended Abstract

While bipolar transistors used in integrated circuit applications tend to be fabricated without surface influence to achieve high gain and good electrical features, it is possible to fabricate BJT's where emitter surface effects play an important role in the device performance. In this case, the surface is chemically active and if the chemical reactions alter the recombination properties of the surface, the bipolar device can be used as a chemical sensor. Such a sensor is described below.

The chemically sensitive BJT uses chemical alteration of the emitter surface recombination as a means of detecting the presence of the chemical species. The emitter surface is fabricated to have a thin, tunnelling-thickness oxide. If G-R centers are chemically active to specific chemical species and the ensuing chemical reaction activates or neutralizes G-R centers, the rate of surface recombination is altered. If the device performance depends on surface G-R effects, then the chemical species is detected.

The details of the device operation are easily understood. For an NPN bipolar junction transistor, the base current is injected into the emitter. This injected current biases the emitter-base junction potential. This bias allows current to flow between the collector and emitter. If the base current is kept constant while the emitter surface recombination is allowed to increase, the emitter-base junction bias will decrease. This decrease in junction bias results in a decrease in the emitter to base current injection. The decrease in current injection means the collector current likewise decreases. The decrease in the collector current while a constant base current is applied translates to a reduction in the dc gain of the transistor. Observing the change in the dc gain of the chemically sensitive BJT is a mode of detection of the chemical species.

It is well known that hydrogen affects surface G-R center density at the Si-SiO_2 interface [1,2,3,4]. For this reason hydrogen was selected to illustrate the device behavior. The concept was to introduce hydrogen and look for a change in the device gain.

Changes in the BJT gain were observed after exposure to a hydrogen ambient. Figure 2 shows typical test results for the transistor before and after exposure to hydrogen gas. The gain of the device decreased with hydrogen indicating a hydrogen induced increase in emitter surface recombination.

The removal of the chemical species from the emitter surface should erase the chemical induced surface effects on the transistor. The adsorbed chemical species at the emitter surface may be removed by providing sufficient energy to break the bonds. One method of providing such energy is to illuminate the emitter surface. Photons may transfer their energy to the adsorbed species to free them from the surface. Figure 3 shows the effects of illuminating a hydrogen exposed device with UV light. The increase in gain after UV light exposure indicates a decrease in hydrogen induced emitter surface recombination. The device has thus been reset.

The bond strengths of different chemicals with silicon may be used to discriminate between chemical species adsorbed at the emitter surface. Illumination of the surface by light with a wavelength corresponding to the bond strength may release the chemical from the surface. The removal of the adsorbed chemical species should affect the gain of the transistor. A range of wavelengths may be used to detect the presence of more than one chemical species and to discriminate between the species. Thus the device behaves as a chemical spectrometer.

The chemically sensitive BJT benefits from its small size and its simple design. It is compatible with integrated circuit technology and may be easily integrated with appropriate circuitry. The sensitivity of the device is controlled through transistor design.

Acknowledgments

The authors wish to thank the students in the Sensor Research and Development Center (SRDC) and the Physical Electronics Laboratory (PEL) at the University of Hawaii at Manoa for their support and for maintaining the facilities. The authors also wish to thank the Pacific International Center for High Technology Research (PICHTR) for their partial financial support of the project and Professor Douglas P. Root for sponsoring this paper.

References

[1] Zheng Youdou, We Fengmei, Jiang Roulian, and Zhou Guangneng, "Electrical Behaviour of Hydrogen Ions in SiO_2 Films on Silicon," Insulating Films on Semiconductors, Springer-Verlag, Berlin, 1981.

[2] B. Keramati and J.N. Zemel, "Confirmation of Hydrogen Surface States at the Si-SiO_2 Interface," The Physics of SiO_2 and its Interfaces, Pergamon, New York, 1978.

[3] James W. Corbett, D. Peak, S.J. Pearton, and A.G. Sganga, "Hydrogen on Semiconductor Surfaces," Hydrogen in Disordered and Amorphous Solids, Plenum Press, New York, 1986.

[4] A.G. Revesz, "Hydrogen in SiO_2 Films on Silicon," The Physics of SiO_2 and its Interfaces, Pergamon, New York, 1978.

[5] David N. Okada, Christopher K. Y. Chun, Lynelle K. Yoshimi, and James W. Holm-Kennedy, "Two Bipolar Devices for Chemical Sensing: A Super Beta BJT and a Merged MOSBJT," Transducers '87 Digest of Technical Papers, Institute of Electrical Engineers of Japan, 1987.

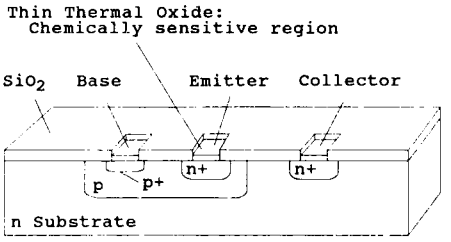


Figure 1: Cross-section of a chemically sensitive bipolar junction transistor.

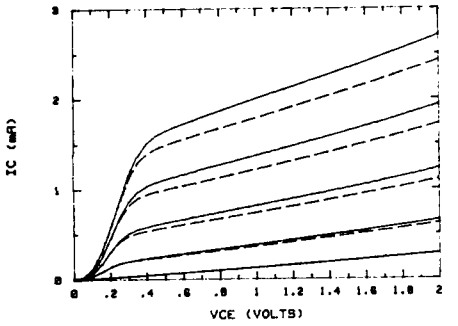


Figure 2: Typical chemical sensitive BJT I_C vs. V_{CE} characteristics before and after exposure to hydrogen. Solid lines are before hydrogen exposure and dashed lines are after hydrogen exposure. The base current is in 1μA steps from 0 to 4μA.

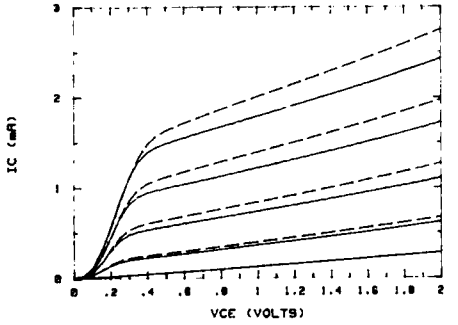


Figure 3: Typical chemical sensitive BJT I_C vs. V_{CE} characteristics before and after exposure to UV light. Solid lines are before UV illumination and dashed lines are after UV illumination. The base current is in 1μA steps from 0 to 4μA.

Abstract No. 742

A SOLID-STATE OXYGEN SENSOR USING PROTON CONDUCTOR OPERATIVE AT ROOM TEMPERATURE

Norio Miura and Noboru Yamazoe
Department of Materials Science and Technology, Graduate School of Engineering Sciences, Kyushu University, Kasuga, Fukuoka 816 JAPAN
Shigeki Kuwata
Department of Industrial Chemistry, Niihama National College of Technology, Niihama, Ehime 792 JAPAN

Solid-electrolyte oxygen sensors so far commercialized are classified into two types, i.e., potentiometric type in which electromotive force (e.m.f.) varies logarithmically with oxygen partial pressure, and amperometric type in which electrolytic current usually varies linearly with oxygen concentration. Both types have been commercialized typically by using stabilized zirconia but these sensors must be operated at elevated temperature in order to ensure sufficiently large ionic conductivity. On the other hand, low-temperature ionic conductors such as fluolide ion conductors[1] and proton conductors[2,3] have recently been applied to potentiometric oxygen sensors workable at room temperature. For example, the sensors using LaF_3[4] could respond to a change in oxygen partial pressure rather quickly at 25 °C. Although such potentiometric sensors can cover a broad range of oxygen concentration, they are inferior in principle to amperometric sensors in the accuracy of detection. This prompted us to investigate an amperometric oxygen sensor operative at room temperature. This paper deals with a new amperometric oxygen sensor using a NAFION membrane (proton conductor).

Three types of sensor (Sensors A, B, and C) were used in this study. Sensors A and B are illustrated in Fig. 1. A NAFION membrane (H^+ type Nafion 117, 0.2 mm thick) treated in boiling water for 2 h was used as a solid electrolyte (proton conductor). The sensing and the counter Pt electrodes were attached onto the both sides of the NAFION membrane by means of chemical plating using chloroplatinic (V) acid. This membrane was then fixed to an end of pyrex glass tube by epoxy resin and a H_2(2%)-N_2 mixture was allowed to flow over the counter electrode (Sensor A, prototype). In Sensor B (improved type), another NAFION membrane (Membrane II) with Pt electrodes was added beneath Sensor A (Membrane I) with a porous sheet of sponge being sandwiched in between. Humid air (70-80% relative humidity) was allowed to flow inside the tube, and DC voltage was applied between the cathode and the anode of Membrane II in order to electrolyze water vapor to supply hydrogen to the counter electrode of Membrane I. Sample gases with various oxygen partial pressures were prepared by mixing O_2 with N_2 and was moistened by passing through liquid water to prevent the NAFION membranes from drying. Response currents of both sensors were measured in a sample gas flow of 100 cm^3/min at 25 °C by means of an electrometer, with the Pt electrodes of Membrane I short-circuited.

When moistened air was supplied to the counter electrode of Sensor A, the response current was very small (ca. 10^{-9} A) and almost independent of the oxygen partial pressure even when an external voltage of 1.0 V was applied. The supply of a H_2-N_2 mixture over the counter electrode drastically increased the current, which increased with an increase in oxygen partial pressure. This suggests that an electrochemical reaction involving oxygen takes place at the sensing electrode when H_2 is supplied to the counter electrode. It is noted that the responses to oxygen partial pressures can be obtained without applying an external voltage. The electrode reaction taking place on the counter electrode in the presence of H_2 can be represented as follows:

$$H_2 = 2\,H^+ + 2\,e^- \quad (1)$$

The proton produced by Reaction (1) can migrate to the sensing electrode through the NAFION membrane. If oxygen exists in the atmosphere around the sensing electrode, the following electrochemical reduction (2) takes place on the sensing electrode.

$$O_2 + 4\,H^+ + 4\,e^- = 2\,H_2O \quad (2)$$

Therefore, the sensor cell eventually consists of an H_2-O_2 fuel cell.

The above structure needs a supply of H_2 gas onto the counter electrode, which is disadvantageous for miniaturization and simplification of the sensor element. In order to overcome this demerit, Sensor B was investigated, which had a hydrogen self-generation system. In Sensor B, the electric current through Membrane I was defined as a sensing current. The sensing current increased with an increase in oxygen partial pressure at applied voltages of 1.0 and 1.5 V, while the current at 0.7 V was considerably small and almost independent of oxygen partial pressure. This suggests that the evolution of H_2 from the cathode of Membrane II took place sufficiently at applied voltage of ca. 1.0 V, when oxygen was present over the sensing electrode.

The non-linear dependence of the sensing current of Sensor B on oxygen partial pressure seemed to suggest that the rate was determined by electrode reactions, not gas-diffusion step. Then Sensor B was covered with a porous sheet (0.2 mm thick) made with a mixture of Teflon (20 wt%) and antimonic acid. With this construction (Sensor C), an almost linear dependence of the short-circuit current on oxygen partial pressure was obtained, although the current values was far smaller than those of sensor B. This means that the porous sheet functions as a gas-diffusion layer. The 90% response time of Sensor C to a change in oxygen partial pressure from 0.2 to 0.6 atm was ca. 3 min at 25 °C. This value is fairly small compared with that of the potentiometric oxygen sensor using proton conductor reported before.[2,3]

References

1) G. Couturier, Y. Danto, R. Gibaud, and J. Salardenne, Solid State Ionics, 5, 621 (1981).
2) N. Miura, H. Kato, N. Yamazoe, and T. Seiyama, Denki Kagaku, 52, 376 (1984).
3) S. Kuwata, N. Miura, and N. Yamazoe, Nippon Kagaku Kaishi, 1987, 1518.
4) N. Yamazoe, J. Hisamoto, N. Miura, and S. Kuwata, Sensors and Actuators, 12, 415 (1987).

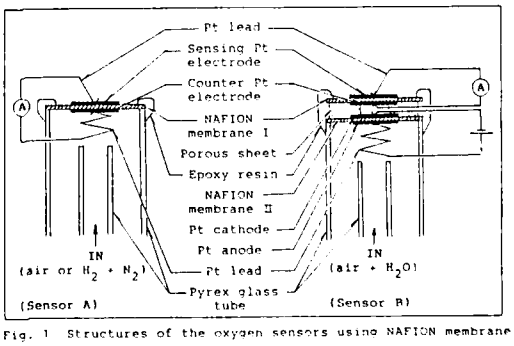


Fig. 1 Structures of the oxygen sensors using NAFION membrane.

Abstract No. 743

COMPARISON BETWEEN THE SENSITIVITIES OF Pt-ACTIVATED ZnO AND SnO_2 SENSORS IN HYDROGEN-AIR MIXTURES

N.BUTTA',D.NARDUCCI,S.PIZZINI
Dipartimento Chimica Fisica,Università di Milano,Via Golgi19,Milano(Italy)

We have shown in previous papers[1,2] that thin polycristalline films of aluminium doped ZnO present a remarkably good sensitivity to hydrogen in H_2-air mixtures in the 10-1000 ppm range,but that this property is counterbalanced by the occurence of a parasitic reaction. Apparently,this reaction occurs at constant rate at any temperature in the range 200-300°C,and provides additional current carriers in excess to those arising from the reaction of hydrogen with surface oxygen traps.It is therefore necessary to correct the final sensor readings for this parasitic reaction contribution in order to have the right conductivity figure.
On the contrary [3],at undoped microcrystalline films prepared either by spray pyrolysis of $SnCl_4$ solutions in ethyl acetate or of dibutnyl tin in ethyl acetate on electronic grade alumina substrates,the parasitic reaction occurs only up to 260°C in the case of tin oxide from $SnCl_4$ and up to 220°C in the case of tin oxide from organometallic tin. This is not the only difference observed between the benaviour of ZnO and SnO_2 thin film sensors.
Major differences arise infact when the comparison is made between ZnO and SnO_2 films prepared from organometallic tin solutions. In this latter case not only a notewhorty sensitivity is observed also in the 1-10 ppm range (see fig.1),but also the response times are definitly shortened to less than 1 sec.

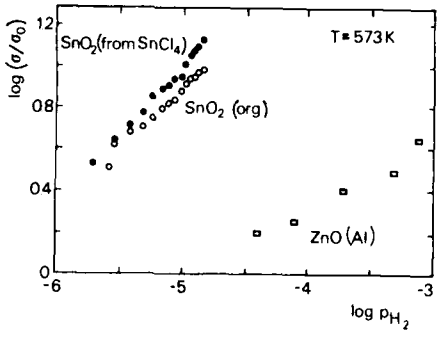


Fig.1: H_2 partial pressure dependence of the different sensors.

These results could be understood by considering that the parasitic surface reaction is associated to lattice disorder.
Actually,as a good example,the presence of substitutional chlorine in the SnO_2 lattice should be accompained by the presence of an excess of metal vacancies

$$0.5\ SnCl_4 \rightarrow 0.5\ Sn_{Sn} + 2Cl_{Cl} + 0.5\ V_{Sn}$$

which,in turn,promotes the loosening of oxygen-metal bonds.
In good agreement with this hypotesis,from the experimental values of the exponent of the power law

$$\sigma = \sigma_0 (1 + K P_{H_2})^{\beta}$$

where $\beta = E_o/kT$,which well describes the H_2 partial pressure dependence of the electrical conductivity (see Fig.1) we obtain figures for the surface energy E_o which are a sensible function of the film preparation procedure as well of the temperature (See Table I) unless in the case of tin oxide films prepared from organometallic tin,where the amount of disorder resulting from etherovalent anions should be negligible.

REFERENCES

1.S.Pizzini,M.Palladino,N.Butta',C.M.Mari Chemical Sensors,Proc.Vol.87-9 (1987) The Electrochem.Soc.Inc. p 99
2.S.Pizzini,A.Giambitto,R.Riva,C.M.Mari High tech Ceramics,P.Vincenzini Edt. Elsevier Science Publ. Amsterdam(1987) 2155
3.S.Pizzini,N.Butta',D.Narducci J.Chem.Soc.Trans.Farad.Soc. Presented

This work has been entirely supported by CNR,Progetto Finalizzato Materiali e dispositivi per l'Elettronica a Stato Solido.

TABLE I:Experimental values of E_o (eV) for ZnO oxides and SnO_2 films.

T°C	E_o (eV)		
	ZnO	SnO_2(from $SnCl_4$ soln)	SnO_2(from organom.Sn)
215		.267	.197
225		.346	.194
240		.263	.230
250		.202	.201
260		.310	.177
275	.501	.217	.166
300	.293	.166	.178

Abstract No. 744

THE USE OF BULK PIEZOELECTRIC CRYSTAL SENSORS FOR REAL-TIME, *IN SITU* CORROSION ANALYSIS

Harold Hager*, Linda Sigalla**, Thomas Nellikkattil**, and Norm Olson****,

*Boeing Electronics Company
High Technology Center
Seattle, Washington 98124

**Department of Chemical Engineering
University of Washington
Seattle, Washington 98195

****Battelle Pacific Northwest Laboratories
Richland, Washington 99352

Although bulk piezoelectric crystal-based sensors have been studied as sensors for a broad range of liquid phase analysis goals, it could be argued that few applications are as uniquely well suited for this sensing tool as corrrosion characterization. The ability to directly obtain both real-time electrode mass and electrochemical current data reduces greatly much of the uncertainty and logistical complexity of corrosion analysis, relative to conventionalcorrosion analysis approaches. Moreover, the small sensor size and cost, together with the ability to apply a wide range of materials, give piezoelectric crystal-based corrosion monitoring system very useful characteristics for field and process stream analysis.

Despite these inherent advantages, industrial willingness to use this new corrosion analysis tool depends, to a large degree, on the ability to demonstrate that this approach:

1] has a sound fundamental basis
2] can be applied under a broad range of conditions to materials of interest
3] gives results which are consistent with accepted corrosion characterization techniques

Fundamental Basis

It will be asssumed for the current discussion that fluid coupling effects, such as would arise from viscous coupling, have been accounted for; the basis for performing such data analysis is presented elsewhere (1,2). For the special cases of negligible variation in fluid properties, the measured resonant frequency data requires no fluid coupling correction.

The mass sensitivity of an oscillating piezoelectric crystal manifests itself as a linear dependence between changes in the mass per unit area, or areal mass density, Δm, and the resonant frequency of the crystal, Δf:

$$\Delta f = -S \cdot \Delta m_T \qquad [1]$$

The sensititivty, S, is a geometric factor, dependent on the bulk piezoelectric crystal thickness. The total area mass density change is given by Δm_T.

The temporal derivative of the resonant frequency represents the rate of mass change on the piezoelectric crystal electrode:

$$dm_T/dt = -S^{-1} \cdot df/dt \qquad [2]$$

An independent mass balance can also be written on the basis of Faraday's law:

$$dm_T/dt = F^{-1}\Sigma(a_j \cdot i_j \cdot M_j/n_j) \qquad [3]$$

where i_j, M_j, and n_j represent the current density, molecular weight, and charge equivalents for all of the j charge transfer reactions. The coefficient a_j describes whether the reaction produces mass gain (a_j), mass loss ($a_j = -1$) or no mass change ($a_j = 0$).

For the special case of a reaction system with two known corrosion reactions, I and II, equation 3 can be written explictly as:

$$dm_T/dt = -F^{-1}[(i_I \cdot M_I/n_I) + ((i_T - i_I) \cdot M_{II}/n_{II})] \qquad [4]$$

Equating [2] and [4] yields one equation in the two experimental variables, df/dt and the total current density, i_{Total}, and one unknown variable , i_I. This allows real-time analysis of current partitioning between two competing reactions.

Range of Conditions and Materials

Two chief restrictions apply to the use of bulk piezoelectric crystals for corrosion analysis. For the first, the working temperature range must not exceed the material stability limit of the piezoelectric crystal. For long term applications this consideration must account not only for mechanical stability, but also for solubility of the crystal in the fluid.

The second restriction applies to the maximum material thickness that can be studied. The specimen mass must be much less than the crystal mass to avoid loading of the piezoelectric crystal, dictating that the test piece be in a film form less than 10 microns thick.

This latter constraint poses a controversial requirement: production of a film electrode that faithfully mimics the corrosion behavior of a macroscopic piece of (nominally) the same material. This is especially troublesome for polycrystalline alloys, where it is impossible to even approximate the same processing conditions for both the macroscopic and film forms.

Comparison with Accepted Corrosion Analysis Techniques

Polarization plots obtained at the University of Washington and at Battelle Pacific Northwest Laboratories show results that are remarkably similar for bulk iron samples and sputtered iron films in various hydroxide and oxygenated inorganic salt solutions. Comparison between sputtered thin film and bulk samples of stainless steels also show good agreement. Variations in system temperature and gas sparging conditions show similar effects on the corrosion behavior of bulk and sputtered electrode films of iron and iron alloys.

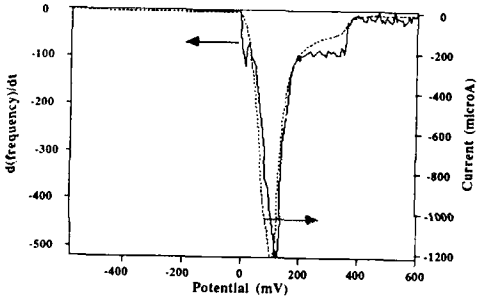
Figure 1 co-plots the cell current and df/dt vs the working electrode potential, for an iron film electrode in 0.1N NaCl at 25°C. The variation of df/dt and current structure shown in this plot represent regimes of differing Faradaic charge to reactant mass ratios, giving new insight into the corrosion process control mechanisms active over the potential range studied.

Finally, comparison of corrosion rates under zero net current conditions will be made, between data determined from piezoelectric crystal resonant behavior and corrosion current data obtained from Tafel plots.

References

1. H. Hager, Chem. Engineering Comm., 43, 25 (1986)
2. L. Sigalla, H. Hager, B. Kowalski, and R. Simpson, This Meeting, October , 1988.

Fig.1 Polarization Curves of Nickel in 0.1 N NaCl



Abstract No. 745

THE DEPENDENCE OF BULK PIEZOELECTRIC CRYSTAL RESONANCE BEHAVIOR ON FLUID PROPERTIES:

Implications to the Use of Piezoelectric Crystals for Fluid Analysis

Linda Sigalla*, Harold Hager**, Bruce Kowalski***, and Randall Simpson****

*Department of Chemical Engineering
University of Washington
Seattle, Washington 98195

**Boeing Electronics Company
High Technology Center
Seattle, Washington 98124

***Department of Chemistry
University of Washington
Seattle, Washington 98195

****Lawrence Livermore National Laboratory
Livermore, CA 94550

Piezoelectric crystal-based sensors have been used routinely in vacuum systems for measuring film deposition thicknesses. In these application, mass added to the crystal surface linearly decreases the crystal resonant frequency; this frequency is used as a simple direct measure of mass deposition. In application of bulk piezoelectric crystal sensors to liquid phase analysis, the resonant behavior of the crystal depends on both adherent mass changes on the crystal and coupling processes between the crystal and fluid. The potential then exists to use the piezoelectric crystal as a monitor for all of the fluid parameters which influence this coupling.

Thus piezoelectric crystal based sensors offer promise for *simultaneously* sensing some or all of the following fluid properties: viscosity, density, specific conductivity, and dielectric constant. These fulid parameters also need to be accounted for when piezoelectric crystal based sensors are used for mass measurements, e.g., corrosion, electrodeposition and adorption, for determination of fluid flow rates, and for evaluation of surface properties, such as surface tension and surface roughness.

The resonant behavior of bulk piezoelectric quartz crystals in contact with liquids has been widely demonstrated to show a dependence on the square root of the viscosity-density product, for fluids at low viscosities, $\mu < 0.1\ g{\cdot}m^{-1}s^{-1}$. However, the measurement of viscosity isolated from density alone, and the measurement of higher viscosities has not yet been shown. And quantitative separation of the effects of the many solution properties influencing the resonant frequency of the piezoelectric crystal is still in debate.

Current models of the effects of solution properties on crystal resonant frequency tend to be inconclusive and empirical in nature. More importantly, they are severely limited when more then one property is varying. This is particularly true if both fluid mechanical and electrical parameters are variable. A unified study of all crystal/solution couplings is the necessary next step before piezoelectric crystal-based sensors can achieve broad applicability for fluid analysis.

We have analyzed the impedance magnitude and phase as a function of frequency for a large variety of binary solutions covering a wide range of varying viscosities, densities, dielectric constants, molecular weights, concentration and specific conductivities. Solutions used include alcohol/water solutions, hydrogen peroxide/water solutions, glycerol/water solutins, inorganic salt solutions, and acid solutions.

These experiments were performed for each solution using several crystals of differing nominal resonant frequency and electrode diameter. The former diferences permit evaluation of possible dispersion effects in fluid parateters.

Variation in the electrode diameter-to-crystal thickness ratios provide a useful basis for determining the influence of fluid electrical parameters on crystal resonant behavior. Most importantly, this data base also permits quantitative assessment of the coupling interactions between mechanical and electrical parameters.

The statistical technique of partial least squares analysis has been used to relate the solution properties to the measured impedance curves. Partial least squares path modeling with latent variables (PLS) is an algorithm for relating one or more dependent variables to two or more independent variables. This method allows the relationships between many blocks of data (i.e., data matrices) to be characterized. The power of PLS is due to the fact that the latent variables simultaneously describe the maximum predictive variance of a block, and provide maximmal fit to the path model. By using only the significant number of latent variables in the procedure, a noise filtering effect is obtained which results in the improved predictive ability of PLS.

This statistical analysis was performed to:

1] determine the percent variance of the curves with each soluton property (viscosity, density, dielectric constant and ionic strength) and groupings between these properties.

2] determine significant solution/crystal coupling modes.

3] develop an equivalent circuit model, for a bulk piezoelectric crystal in contact with a liquid, capable of accounting quantitatively for solution viscosity, density, dielectric constant and ionic strength.

This circuit representation will be compared directly with the Butterworth/Van Dyke equivalent circuit model used to describe resonant behavior in a very low viscosity environment.

Finally, the implications of this coupling mode and equivalent circuit analysis to liquid phase sensing will be discussed. Special emphasis will be given to defining the fundamental limits for determining multiple fluid parameters with a single piezoelectric crystal sensor. The related issue of quantitative separation of crystal:fluid coupling effects from resonant behavior effects arising from adherent mass variations will also be addressed.

Abstract No. 746

REFERENCE ELECTRODES/SENSORS USING LOW-RESISTIVITY GLASS MEMBRANES

Ira Bloom, J. J. Heiberger, M. A. Internoscia*, K. Rea**, and L. Redey
Chemical Technology Division
Argonne National Laboratory
Argonne, IL 60439-4837

Development of miniature reference electrode systems to measure either sodium or sodium polysulfide activity has continued [1,2]. The reference electrodes contain small (2-mm^2 active area), thin membranes of a Na^+-ion-conducting glass which was developed as part of our work on glass electrolytes for the Na/S cell [3,4]. The small, electrochemically active area of the reference electrode makes precise positioning possible in an electrochemical system of interest.

As we described previously [1,2], the reference electrode is made by attaching a thin membrane of glass to a narrow, (ca. 3-mm OD), high-density α-Al_2O_3 tube. Once a reference material is sealed within it, the small active area behaves like a Luggin capillary tip.

From our work [1-4], we knew that no problems were innate to the operation of the reference electrode in the temperature range of 120-400°C. However, it was necessary to demonstrate the thermal and operational limits of the glass. That is, we did not know if glasses in the Na_2O-ZrO_2-Al_2O_3-SiO_2 system have sufficient chemical stability in a harsh environment, such as Na at high temperatures, to provide meaningful data. A reference electrode containing Na_2S_2 was tested in Na at about 600°C to determine the chemical stability of the glass as well as the stability of the EMF. After equilibration, at 586°C, a stable EMF (±2 mV) of 1.488 V was measured for 11 hours. Thereafter, a sharp decrease in EMF was observed. This decrease was due to electrode failure.

The utility of the reference electrode design was further demonstrated by coulometric titrations of $NiCl_2$ and $FeCl_2$ electrodes (2 mAh capacity) containing $NaAlCl_4$ (1:1 by weight) in the temperature range of 250-300°C. A typical plot for the titration of $FeCl_2$ at 250°C is given in Figure 1. The coulometric titration precisely shows the expected transition from the equilibrium represented by Eq. 1 (2.35 V) to that of Eq. 2 (2.34 V) [5].

$$4FeCl_2 + 6Na^+ \rightarrow Na_6FeCl_8 + 3Fe \qquad [1]$$

$$Na_6FeCl_8 + 2Na^+ \rightarrow 8NaCl + Fe \qquad [2]$$

Work is in progress to extend the operating temperature range to lower temperatures.

ACKNOWLEDGMENT

This work was done under the auspices of the U.S. Department of Energy, Energy Systems Storage Branch, under contract W-31-109-Eng-38.

*University of Cincinnati, Cincinnati, OH.
**Hope College, Holland, Michigan.

REFERENCES

1. L. Redey, I. Bloom and K. Rea, "Glass-Membrane Reference Electrodes for Sodium- and Sulfur-Activity Measurements," Extended Abstracts, Electrochem. Soc. Meeting, Philadelphia, PA, May 10-15, 1987, Vol. 87-1, p. 718.

2. I. Bloom, J. Heiberger, K. Rea, and L. Redey, "Sodium- and Sulfur-Activity Measurements Using Glass-Membrane Reference Electrodes/Sensors," Electrochem. Soc. Meeting, Honolulu, HI, October, 1987, Proceedings of the Symposium on Chemical Sensors, D. R. Turner, Ed., Vol. 87-9, p. 155 (1987).

3. G. H. Kucera, I. Bloom, and M. F. Roche, "Ionic Conductivities and Glass Transition Temperatures of Na_2O-ZrO_2-Al_2O_3-SiO_2 Glasses," J. Electrochem. Soc., 133, 1996 (1986).

4. I. Bloom, J. Bradley, and M. F. Roche, "Chemical Stability of Na_2O-ZrO_2-Al_2O_3-SiO_2 Glasses in Sodium, Sodium Polysulfides and Sulfur," J. Electrochem. Soc., 134, 2102 (1987).

5. J. L. Sudworth, R. C. Galloway, and D. S. Dermot, "Sodium Metal Chloride Batteries with Beta Alumina Electrolyte," Electric Vehicles, p. 14 (Autumn, 1987).

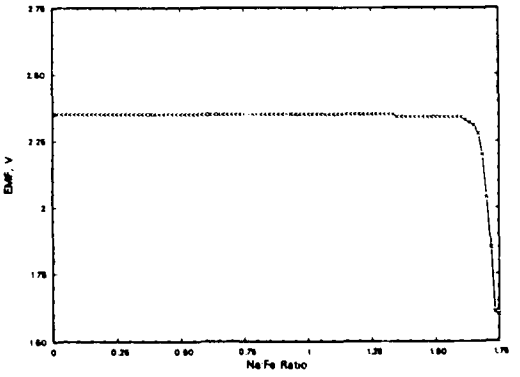


Fig. 1. EMF vs. Na:Fe Ratio from the Coulometric Titration of a 2 mAh $FeCl_2$-$NaAlCl_4$ Electrode at 250°C.

INDEX TO AUTHORS

Abstract No.

Aaboubi, O.....673
Abbasi, S. A.....468
Abbundi, R. J.....554
Abe, K.....380
Abiru, A.....397
Abou el leil, M.....619
Abraham, K. M.....23, 45
Abritta, T.....568
Adamuvor, P. K.....58
Addison, R.....135
Adkins, K.....295
Agarwal, L.....719
Agarwal, R. R.....731
Agarwala, V. S.....192
Ageishi, K.....670
Agius, B.....305
Ahmed, I.....282
Ahmed, S. M.....573
Ahn, S. T.....283
Aihara, R.....452
Aita, K.....441
Aizawa, M.....652
Aka, G.....738
Akahoshi, H.....345
Aktan, A.....357
Al-Dallah, S.....575
Al-Marayati, S.....23, 253, 317,435
Alamgir, M.....23
Alavi, A.....165
Albaugh, K.....302
Albert, L.....549
Alcazar, H. S.....89
Alderucci, E.....70, 71
Aleman, H.....672
Alfano, R. R.....608, 611, 624
Alkire, R. C.....162, 189
Allaert, K.....314
Allen, A. T.....155
Allison, S. W.....659
Allitsch, G.....739
Alnot, P.....305
Alonso, C.....689
Alvi, N. S.....466, 472
Aminzadeh, M.....432
Amitani, K.....641
Anani, A. A.....517
Anderson, A. C.....481
Anderson, C. R.....87
Anderson, D.....342, 347
Anderson, E.....65, 72
Anderson, R.....290
Anderson, T. J.....722
Andrade, J. D.....654
Andricacos, P. C.....331, 333
Anetsberger, K.....197
Anthony, J. M.....418
Antoniadis, D. A.....601
Aogaki, R.....671
Aoyama, T.....464
Appleby, A. J.....58, 82, 83, 516, 517
Aragane, J.....52
Arana, C.....333
Arent, D. J.....494
Arimoto, H.....448
Arita, K.....128
Armour, N.....400
Armstrong, N. P.....309, 311
Armstrong, N. R.....29
Arvia, A. J.....689
Asano, M.....318
Asaoka, T.....380
Ast, D. G.....486
Atanasoski, R. T.....717
Ateya, B. G.....14, 130
Atherton, R. W.....404

Abstract No.

Auld, B. A.....382
Avaca, L. A.....66

Bachman, B. J.....227
Bachmann, K. J.....496
Badila, M.....483
Bae, I. T.....90, 712
Baglin, J. E. E.....228
Bagwell, P. F.....601
Bailey, J. C.....18
Baker, C. K.....362
Baker, G. L.....615, 616, 617
Balakrishnan, K. S.....366
Balakrishnan, S.....451
Balda, R.....558
Baldeck, P. L.....624
Baliga, B. J.....253, 317, 435
Bankston, C. P.....46, 74, 706
Bard, A. J.....693, 694
Barkey, D. P.....325
Barlow, K. J.....478
Barnes, G. T.....631
Barnes, J. J.....533
Barnett, S. A.....503
Baro, A. M.....689
Baron, F.....53
Barr, D. L.....458
Barrie, J. D.....572, 736
Bartolome, A.....689
Basak, S.....662, 669
Bates, S.....508
Bauer, Th.....422
Baumann, S.....423
Beard, B. C.....30
Beat, T. G.....205
Beaudoin, R.....184
Becker, S.....411
Bedair, S. M.....487
Beery, J. G.....57
Beha, H.....383
Behl, W. K.....42
Behm, R. J.....688
Bell, L. D.....421
Bell, M. F.....132
Ben-Haim, M.....120, 193
Bennion, D. N.....15
Benson, S.....616
Benzekri, N.....186
Berg, M.....594
Bermudez, V. M.....288
Bernard, D.....177
Bernardi, D. M.....1
Bernards, R.....327
Bernstein, G.....620
Berry, W. R.....466
Beutel, J.....635
Bevk, J.....493
Bezuk, S. J.....195
Bhatgadde, L. G.....206
Bhattacharyya, A. B.....719
Bibyk, S. B.....270, 271, 295, 296
Biederman, R. R.....335
Biefeld, R. M.....502
Bilder, W.....352
Binder, M.....16
Birman, J. L.....623
Birss, V. I.....377
Bisberg, J. E.....476
Biwer, B. M.....122
Blacha, A.....383
Blanchard, G. L.....617
Blasse, G.....540, 563, 567, 570, 571, 638
Bliss, D. E.....30

Abstract No.

Blomgren, G. E.....18
Bloom, B. M.....382
Bloom, I.....746
Blummenfeld, M.....400
Bobbio, S.....262
Bohni, H.....185
Bolstad, J. J.....64
Bondarenko, N. Ph.....682
Bonham, D. B.....191, 718
Bonner, W. A.....512
Bonora, A.....390
Borghs, G.....494
Borgstrom, T.....295
Borland, J. O.....235
Bostick, D. T.....655
Boulon, G.....546
Bourkane, S.....170
Bozen, R. M.....518
Brace, F.....679
Brain, M.....390
Brandel, V.....561
Branis, S. V.....623
Brat, T.....250
Breiter, M. W.....739
Bright, D. S.....414
Brinkhuis, R. H. G.....212
Brixner, L. H.....638, 639
Brossard, L.....704
Brown, G. T.....499
Brown, J. J.....554
Brown, W. D.....274
Brown, W. L.....458
Brunner, M.....386
Bryant, F.....281
Buchanan, R. A.....634
Buckley, D. N.....507
Bueno, C.....634
Bugos, A. R.....659
Buijs, M.....606
Bullard, S. J.....103
Bullen, D. B.....148, 151, 153
Bunch, P. C.....636
Burda, P. A.....112
Burdick, G. W.....552
Burghause, W.....442
Burke, B. E.....481
Burnett, J. W.....419
Burrell, M. C.....226
Burstein, G. T.....105, 164
Butler, M. A.....660, 663
Butta, N.....743
Bylsma, R. B.....500

Cahan, B. D.....11, 707
Cai, S.....138, 720
Cain, S. R.....221
Cairns, E. J.....6, 7
Calaway, W. F.....419
Campbell, D.....399
Campbell, I. H.....629
Cao, P. G.....233
Caolo, M. A.....202
Carey, G. F.....465
Carnevale, G.....534
Carrabba, M. M.....662, 721
Carranza, R.....186
Carriere, T.....305
Carter, P. J.....519
Castel, E. D.....399
Castro, E. B.....174
Cates, M. R.....659
Caudano, R.....213, 214
Cavanagh, R. R.....588
Cavin, J. R.....574

Abstract No.

Cawley, J. D.....286
Chakrabarti, K.....554
Chakraborty, A. K.....222
Chan, Y. W.....192
Chandrasekhar, P.....479, 709
Chang, E. G.....299
Chang, H.....703
Chang, K. M.....276
Chang, S. W.....249
Charreire, Y.....549
Chau, R.....295
Chau, R. S. K.....296
Chaudhari, P. K.....315
Chawla, S. K.....106
Chechirlian, S.....127
Cheh, H. Y.....88, 331, 359
Cheltsov, V. F.....596
Chen, C. G.....715
Chen, C. P.....324
Chen, S.....138, 720
Chen, S. T.....231
Chen, W. L.....143
Chen, X.....138, 720
Chen, Y. C.....187
Chen, Y. J.....621
Chera, J. J.....226
Chesnoy, J.....592
Chiang, C.....285, 290
Chiang, K. T.....538
Chidsey, C. E. D.....587, 691
Chien, H. C.....439
Chikutei, S.....637
Chin, A. K.....476
Chiou, W. A.....492
Chiu, G.....384
Chiu, S. L.....328
Cho, D. L.....196
Chogsawangvirod, S.....289
Choi, C. H.....503
Choi, Q. W.....650
Chopart, J. P.....673, 674, 681
Choquet, P.....528
Chotimongkol, L.....114
Chou, T. Y.....298
Chow, T. P.....449
Christensen, D. A.....654, 664
Christensen, T. M.....116
Christenson, H. K.....699
Chtaib, M.....213, 214
Chu, C.....471
Chu, C. T.....738
Chu, D.....59, 713
Chun, C. K. Y.....741
Chung, M.....459, 460, 461
Cieslak, W. R.....29
Cignini, P. L.....534
Cinderey, R. J.....164
Clarke, J.....301
Clarkson, M. T.....699
Clarysse, T.....437
Clauberg, R.....383
Clawson, M.....72
Clayton, C. R.....124, 126, 142, 145, 146
Cleary, H. J.....150
Clechet, P.....725
Clerc, C.....162
Cobianu, C.....484
Cocivera, M.....370
Collins, G. J.....202
Collins, R. W.....603
Compangnone, N. R.....2
Condrate, R. A.....77
Conrad, R.....104
Consolati, G.....545
Cook, R. L.....666
Corelli, J. C.....451

Abstract No.

Cornilsen, B. C.... .....77, 78, 79
Cosandey, F.....532
Cote, M.....590
Coughanowr, C. A.....722
Cowden, W. C.....205
Cox, N.....290
Craston, D. H.....694
Crawford, M. K.....638
Creepir, A. M.....8
Croce, F.....729
Cronin, J.....258
Crouch-Baker, S.....35, 356
Cutler, P. H.....459, 460, 461

D'Alkaine, C. V.....66
D'Egidio, S. M.....119
Dabkowski, F. P.....476
Dacres, C. M.....67, 104
Dalal, H.....313
Dallek, S.....36, 86, 87
Dandapani, B.....516, 517
Daniels, E. J.....518
Danielson, M. J.....175
Daroux, M.....11, 90
Das Sarma, S.....502
Dash, J.....679, 680
Datta, M.....194
Dave, B.....58
Davenport, A. J.....95, 166, 167
Davidson, B. A.....489
Davidson, Z.....551
Davies, P. K.....737
Davis, H. T.....222
De Boeck, J.....494
de Fonseca, R. J. M.....568
De Jonghe, L. C.....75, 76
De Lozanne, A.....692
de Miguel, J. L.....512
De Pauw, P.....314, 321
Deck, P. D.....210, 211
Deckert, C. A.....245
Dee, G. T.....217
Degosserie, N.....213
Deligiannis, F.....41
Dellin, T. A.....265
DeLuca, W. H.....49
Deneffe, K.....494
Deng, Z.....133
DePalma, V.....322
Deppe, D. G.....501
Deroux Dauphin, P.....247
Deslouis, C.....177, 344
Deutscher, R. L.....334
DeWald, A. B.....426
Dexpert, H.....549
Dexpert-Ghys, J.....549
Di Leonardo, R.....71
Di Stefano, S.....46, 74
Diegle, R. B.....142
Dilworth, J. C.....389
DiNardo, N. J.....209
Dini, J. W.....205
Dirksen, G. J.....563
Discenza, J. P.....11
Dlott, D. D.....610, 618
Do Thanh, L.....323
Dobreva, E. D.....207
Dominey, L. A.....40
Dong, Y.....138, 720
Dottarar, S.....234
Douglade, J.....673, 674, 681
Downer, M. C.....552, 607, 626, 630
DuBois, T.....262
Duby, P.....194

Abstract No.

Dukovic, J.....331, 333
Dulniak, R. J.....311
Dumas, W. V.....226
Dunn, B.....572, 736, 738
Dunton, S. V.....291
Dupeux, T.....247
Durakpasa, H.....739

Easterly, C. E.....522
Ebling, D.....168
Economou, D.....361
Edmonds, R. B.....662
Edwards, J. L.....427, 620
Edwards, R.....322
Egan, J. J.....722
Eichinger, G.....19
Eichinger, P.....422
Eichner, P.....127
Eifuku, S.....397
Eilenberger, D. J.....599
Eisenberg, M.....43
Eisenthal, K. B.....584
El-Anadouli, B. E.....14
El-Hewie, M. F.....622
El-Nizamy, F. M.....130
Elab, H.....581
Elejalde, M. J.....558
Ellis, A. B.....667
Ellul, J. P.....289
Elsener, B.....185
Eltaib Heakal, F. M.....130
Emerson, R. M.....35
Emmi, F.....221
Encheva, M. A.....207
Engelken, R. D.....365, 371, 372, 374, 378
English, C.....120
English, J. H.....598
Entenberg, A.....220
Eom, T.-y.....139
Ericsson, P.....118
Escalante, E.....158
Esteban-Puges, P.....549
Etemad, S.....615, 616, 617
Etherington, D. G.....649
Evans, D. F.....698
Evans, T. I.....9, 10
Eyolfson, M.....202

Fahidy, T. Z.....355, 678
Fan, F.-R. F.....693
Fann, W.-S.....616
Farmer, J. C.....148
Farrington, G. C.....38, 728
Fauchet, P. M.....627, 629
Faupel, F.....231
Fayer, M. D.....594
Fendrock, L.....220
Fenton , J. M.....5
Fergus, J. W.....539
Fernandez, J.....558
Fernandez, M.....104
Fewster, P. F.....509
Feyder, G.....214
Fiaud, C.....178
Findakly, T.....619
Fink, J. L.....144
Fisher, G. L.....327
Fitoussi, R.....557
Fitz, S.....110
Fitzgerald, E. A.....486
Fix, K. A.....25
Flake, R. A.....84

Abstract No.

Flanagan, W. F.....98
Fletcher, S.....334
Florez, L. T.....599
Focht, G.....626, 630
Fonash, S.....278, 292
Fonstad, C. G.....513
Forbes, L.....432
Foreman, J.....38
Foster, J. S.....695
Foust, D. F.....226
Fox, F.....387
Fraioli, A. V.....518
Fraker, A. C.....156
Franke, M.....515
Frankenthal, R. P.....351
Franklin, T. C.....357, 358
Fraser, D.....285, 290
Fraser, D. B.....250, 269
Fraser, R. G.....631
Freeman, D.....238
Freeman, D. W.....240
Freeman, J. L.....382
Fricoteaux, P.....681
Frieser, R.....262
Fritts, D. H.....84
Fritts, S. D.....56
Fritz, J. D.....94
Frommer, J. E.....695
Frye, J. M.....122
Fueki, K.....671
Fujimura, S.....261
Fujino, N.....462
Fukuda, M.....412
Fukuda, Y.....114
Fukushima, T.....114
Funakoshi, K.....392
Fung, M. S.....431, 438
Furlan, R.....264
Furukawa, T.....236
Furuki, M.....670
Furuya, F. R.....697
Fuyama, M.....648

Gabriel, W.....19
Gabrielli, C.....170, 673, 674, 681
Gak, E. Z.....682, 683
Galasco, R. T.....330
Gamo, K.....445
Gan, J.....471
Ganu, G. M.....200
Gao, G.....105
Garapon, C.....546
Gati, G.....322
Gau, J.-Y.....346
Gdowski, G. E.....151, 153
Genet, M.....561
Gerard, P.....677
Gerard, R.....677
Gervasio, D.....59, 713
Gewirth, A. A.....693
Giess, J.....499
Gilman, S.....16
Gilmour, A.....28, 39
Ginn, K. W.....260
Giordano, N.....70, 71
Giridhar, R. V.....275
Giuliani, J. F.....665
Glanville, J.....441
Glass, A. M.....500
Glen, D. R.....86, 87
Glenn, M. L.....103
Glownia, J. H.....625
Gmitter, T. J.....430
Goedjen, J. G.....533
Goedjen, J. J.....531

Abstract No.

Goldman, J. L.....40
Goldsmith, B.....400
Golub, J. E.....599
Gomez, C.....282
Gonzalez, E. R.....66
Gordon II, J.....690
Gore, R. R.....364
Gorokhovskii, A. A.....544
Gossard, A. C.....598
Gossmann, H.-J.....489
Goto, T.....547
Gottesfeld, S.....55, 100
Gozzi, D.....534
Graciet, M.....550
Graedel, T. E.....107
Graham, R.....299
Graham, R. J.....425
Granata, R. D.....134, 140
Greve, D. W.....297, 298
Grider, D. E.....505
Griffin, G. D.....522
Grossman, D.....411
Gruen, D. M.....122, 419
Gualtieri, G. J.....489, 490, 493
Guillaume, R.....171
Gunshor, R. L.....511
Gur, T. M.....35, 732
Gustafson, T. L.....603

Habib, M. A.....520
Hacherl, C.....234
Hachey, J. P.....721
Hager, H.....744, 745
Hagey, G.....50
Halbout, J.-M.....384
Hall, D. E.....144
Hall, E.....451
Halley, J. W.....91
Halliop, E.....184
Halpert, G.....41
Halsey, W. G.....148, 151, 153
Hamada, T.....131
Hanazono, M.....648
Hansen, P. A.....613
Hansen, T.-E.....653
Harada, H.....410
Haraichi, S.....443
Haranahalli, A.....285
Harbison, J. P.....599
Harriott, L. R.....440, 444
Harris, A. L.....587
Harris, J. S.....156
Harris, T. D.....500
Harrison, S. A.....152
Haslam, M. E.....454
Hatami, R.....37
Hauser, A. K.....160
Hayashi, K.....353
Hebert, K. R.....188
Heiberger, J. J.....746
Heilweil, E. J.....588
Heitbaum, J.....702
Helfand, M. A.....124, 142
Hendrickson, W.....698
Hengehold, R. L.....574
Henning, A. K.....267
Henry, R. A.....710
Henry, W.....581
Henscheid, D.....299
Hente, A.....314
Heritage, J. P.....617
Hernes, P. J.....183
Herrero, J.....375
Hesse, K.....647
Hettiarachchi, S.....192

Abstract No.

Heutmaker, M. S.....381
Hiatt, C. F.....405
Hill, M.....554
Hill, R. F.....60, 61
Hinedi, F.....316
Hintermann, H. E.....230
Hirai, T.....580
Hirakawa, K.....450
Hiramoto, K.....462
Hiramoto, T.....450
Hirano, H.....463
Hiraoka, H.....202
Ho, J.-T.....632
Ho, P. P.....608
Ho, P. S.....231
Hochberg, A. K.....239
Hochstrasser, R. M.....559, 613
Hockett, R. S.....423
Holifield, T. F.....47, 49
Hollingsworth, G.....736
Hollins, R. A.....30, 710
Holm-Kennedy, J. W.....741
Holmes, C. F.....26
Holonyak, Jr., N.....501
Homma, T.....340
Homstad, L.....215
Honda, S.....641
Hong, P.....578
Hong, S.-k.....220
Hoofring, A. B.....480
Hooper, A.....20
Hopkins, G. P.....579
Horai, M.....462
Hori, M.....318
Horikoshi, Y.....498, 514
Hormasji, H.....371, 372
Horning, R. R.....505
Horwath, R. S.....220
Hosono, K.....446
Howson, R. P.....199
Hseih, B.-C.....297
Hsia, L. C.....482
Hsu, R.....285
Huang, C. K.....284
Huang, C. M.....481
Huang, Q.....578
Huang, Z. Q.....715
Huber, A.....422
Huber, K.....645
Hubrecht, J.....176
Huggins, R. A.....35, 356, 732, 734
Hughes, R. A.....399
Hultman, L.....503
Hunt, R. B.....566
Huot, J. Y.....704
Huq, R.....38
Husser, O. E.....694
Hussla, I.....409
Hybertsen, M. S.....493
Hyhajlenko, S.....427

Ikariyama, Y.....740
Ikeno, M.....726
Ikoma, M.....85
Ikoma, T.....450
Ikubo, H.....413
Illarramendi, M. A.....558
Imai, T.....564
Indrianjafy, G. M.....169
Ingle, M.....140
Internoscia, M. A.....746
Interrante, G. C.....152
Irene, E. A.....289
Iroulart, M. G.....561
Irvine, S. J. C.....499

Abstract No.

Isaacs, H. S.....166, 167
Isaacson, M. J.....7
Ishioka, S.....580
Ishitani, T.....457
Israelachvili, J. N.....700
Itaya, K.....686, 687
Ito, Y.....85, 353
Itoh, F.....443
Ives, J. T.....664
Iyer, R.....132

Jaccodine, R. J.....284, 469
Jacobson, K. L.....466
Jacobson, N. S.....529
Jadhav, M. S.....367
Jagannathan, R.....560, 569
Jastrzebski, L.....400, 581
Jeanjaquet, S.....135, 172
Jedju, T. M.....615
Jefferies, S. R.....382
Jeffries-Nakamura, B.....706
Jeng, Y. H.....231
Jeon, C. I.....650
Jeong, J. C.....495
Jesser, W. A.....485
Jewell, J. L.....598
Johansson, L.-G.....118
John, K.....246
Johnson, D. C.....703
Johnson, G. B.....519, 521, 523
Joly, A. G.....593
Jones, S.....262
Jong, G. S.....398
Jonscher, A. K.....553
Jorgensen, G.....204
Jorne, J.....324
Jost, D.....605
Joubart, R.....305
Jow, T. R.....34, 37
Judabong, S.....114
Juhas, M. C.....149
Juttner, K.....163

Kaanta, C.....258
Kaesche, H.....92
Kaiser, H.....92
Kaiser, U.....420
Kaiser, W. J.....421
Kajzar, F.....616
Kalkur, T. S.....252
Kalnitsky, A.....289
Kalpouzos, C.....595
Kamieniecki, E.....269
Kanebako, K.....318
Kaneda, O.....726
Kanicki, J.....277, 278, 292
Kapoor, V. J.....268, 273, 480
Kapur, V. K.....374
Karaki-Doy, T.....477
Karas, B. R.....226
Karube, N.....363
Kassimati, A.....161
Kato, T.....446
Katto, H.....310
Katz, D.....201
Kauffman, J.....590
Kaul, R.....271
Kaun, T. D.....47, 49
Kawamura, K.....388
Kawanami, Y.....457
Kawashima, H.....726
Kawashima, M.....514

Abstract No.

Keddam, M.....127, 169, 170, 171, 186
Keenan, J. A.....416
Kellar, S. A.....586
Kelly, N.....420
Kendig, M.....135, 172, 347
Kennedy, J. H.....730
Kennel, H. W.....283
Kenney-Wallace, G. A.....595
Keowkangwal, O.....114
Kern, K. A.....190
Kern, W.....238
Kesavan, S.....157
Khan, A. A.....468
Khawaja, Y.....620
Kiliaan, H. S.....570
Kim, C. H.....650
Kim, H.....618
Kim, M.....241
Kim, S.....187, 670
Kim, S. U.....316
Kim, U. S.....469
Kim, Y. J.....82, 83
Kirby, S. K.....629
Kirchner, P. D.....486
Kirk, C. T.....287
Kita, H.....363, 685
Kitada, A.....640
Kitahara, T.....628
Kitakata, M.....474
Klatt, L. N.....655
Kleinert, Th.....323
Kleppinger, R.....400
Klingert, J. K.....500
Klingshirn, C.....556
Knupfer, W.....645
Kobayakawa, K.....131
Koch, V. R.....40
Koehler, J. R.....393
Koike, Y.....464
Kojima, M.....463
Kojima, Y.....447
Kolb, D. M.....688
Kolenkow, R. J.....290
Kolodziejski, L. A.....511
Kolzer, J.....387
Kondo, T.....637
Kondoh, T.....388
Konishi, N.....464
Konno, J.....261
Kook, T.....469
Koos, D. A.....585, 586
Koseki, Y.....401
Kosicki, B. B.....481
Kosonocky, W. F.....582
Kosugi, M.....398
Kotani, H.....272
Kotz, L.....422
Kovaleski, K.....134
Kowalski, B.....745
Kozawa, H.....413
Kozicki, M.....299, 406, 470, 620
Kozlowski, M. R.....716, 717
Kozuka, H.....473
Krawczonek, W.....480
Kreidler, E. R.....529
Krick, D. T.....277
Krishnaswamy, J.....202
Kristianpoller, N.....551
Kruger, J.....123
Kruger, R. A.....632
Kryzak, C.....195
Kumagai, H.....398
Kummer, J. T.....706
Kunert, W. H.....488
Kutty, T. R. N.....569
Kuwata, S.....742

Abstract No.

Kuzyk, P. H.....198
Kwok, T.....308
Kwor, R.....466, 472, 475

Labib, M. E.....651
LaFollette, R. M.....15
Laforgue-Kantzer, D.....676
Lagendijk, A.....239
Lagnado, I.....294
Lam, R. K. F.....36
Lamby, E. J.....226
Lamont, M. G.....500
Land, R. H.....183
Landau, U.....4, 326, 330, 332, 337, 376
Lane, E.....234
Lanford, W. A.....417
Lanzi, O.....4
Larrick, B. F.....36, 86, 87
Larsen, L.....428
Latanision, R. M.....141, 181
Lau, A.....678
Lau, S.....506
Lau, W. S.....278, 292
Lavanant, A.....343
Law, H. H.....80
Le, A. H.....67
Leaf, G. K.....183
Lederich, R. J.....535
Ledgerwood, M.....605
Leduc, J.....573
Lee, G.....698
Lee, J. B.....98
Lee, M.....290
Lee, P.-I.....258
Lee, Y. H.....598
Legge, R. N.....304
Leidheiser, Jr., H.....134, 140, 210, 211, 352
Lemasson, P.....723
Lenahan, P. M.....277
Lenhart, S. J.....3
Leonberger, F.....619
Leroy, B.....242
Leverd, F.....242
Levine, S.....201
Levinos, N. J.....587
Levy, M.....217
Lewis, N.....435, 451
Leygraf, C.....109, 115
Leyland, J. D.....649
Li, J.....708
Li, D. X.....491, 492
Li, J.....721
Li, L.....202
Li, P. C.....482
Li, Y.....565
Lian, K.....377
Liao, D.....251
Liao, P. F.....599
Lichter, B. D.....98
Liebel, G.....225
Lielmezs, J.....672
Lien, M.....180
Lin, C-M.....449
Lin, C.....129
Lin, G.....319
Lin, H. C.....439
Lin, H. T.....454
Lin, H. Y.....257
Lin, S.....187
Lindberg, V.....220
Lindsay, S. M.....696
Lindsey, N.....67
Lindstrom, R. M.....415
Ling, A. C.....291

Abstract No.

Linhardt, P.....739
Liou, F.-T.....281
Liou, S. S.....539A
Lisensky, G. C.....667
Litchfield, J. K.....36
Littau, K. A.....594
Liu, C. C.....90
Liu, G.....292
Liu, J. C.....530
Liu, M.....75
Liu, X.....562, 565
Livesley, W. A.....391
Lockwood, D. J.....542
Logan, M. A.....240
Lohrengel, M. M.....168
Loiacono, D. N.....587
Lokhande, C. D.....367
London, B.....536
Long, G. G.....123
Long, J.....506
Look, D. C.....433
Lorenz, W. J.....163
Lotshaw, W. T.....595
Lott, S. E.....189
Loyselle, P. L.....77, 78, 79
Lu, Y.....145, 146
Lucas, C. A.....508
Lucas, N.....497
Lukaszek, W.....399
Lum, R. M.....500
Lumsden, J. B.....155
Lutgen, P.....214
Lynes, W. M.....332
Lyons, L. J.....727

Macdonald, D. D.....3, 69, 120, 154, 193
MacDonald, N. C.....385
MacDougall, B.....121
MacDuff, R. C.....666
Machida, A.....397
Macrander, A. T.....500, 506
Madden, M.....339
Madey, J.....616
Madhale, R. D.....367
Maestro, P.....557
Mahapatra, S.....200, 206
Maheswari, S. P.....520
Majumder, F. A.....556
Mak, C. Y.....88
Makhlouf, M. M.....335
Makosch, G.....360
Malhotra, G. L.....366
Mandelman, J. A.....236
Manfredi, C.....157
Mannaerts, J. P.....493
Manring, L. E.....217
Mansfeld, F.....108, 173, 187
Mansour, A. N.....86, 87
Mao, Z.....516, 517
Maracas, G. N.....434
Marinenko, R. B.....414
Marks, S.....237
Marra, J. E.....529
Marren, R. J.....662
Marshall, S. L.....349
Martensen, B.....402
Martin, J. R.....725
Martin, K. G.....146
Maru, H. C.....526
Maschhoff, B. L.....29
Mason, G. E.....190
Mathew, S.....721
Mathew, S. A.....358
Mathur, V. K.....554

Abstract No.

Matienzo, L. J.....221
Matsuda, N.....633
Matsuda, T.....640
Matsui, S.....447
Matsukiyo, H.....564
Matsumoto, I.....85
Matsumoto, T.....229, 397
Matsuzawa, M.....652
Matthews, R.....698
Matyi, R. J.....501
Maurin, G.....343, 344 368
Maxfield, M.....37
May, P.....384
Mazille, H.....127
Mazur, E.....589, 606
Mazur, S.....217
McArthur, D.....241
McBreen, J.....63
McCafferty, E.....137
McCall, S. L.....598
McCloud, H. E.....371, 372, 378
McCormick, L. D.....696
McCright, R. D.....148, 151, 153
McDonald, J. D.....590
McDonald, J. F.....454
McGuiggan, P. M.....700
McHenry, D.....515
McKubre, M.....136
McLarnon, F. R.....6, 7
McMarr, P. J.....288
McMorrow, D.....595
McMorrow, D. F.....508
McNallan, M. J.....529, 530
McNamara, J. L.....243
McNamara, J. M.....243
McNeil, M. B.....147
McParland, M.....733
McVittie, J. P.....244, 471
Mehdizadeh, S.....331
Mehta, A.....97
Meibuhr, S. P.....24
Meier, G. H.....526
Meijerink, A.....571
Melloch, M. R.....511
Melroy, O.....690
Mendelson, S.....68
Menezes, S.....342
Mengel, M.....645
Merritt , D. R.....8
Meschter, P. J.....535, 536
Messina, C.....152
Meton, M.....677
Meyer, G. J.....667
Mho, S. I.....650
Mickish, D. J.....635
Miers, J. B.....610
Mikami, M.....474
Mikhail, Y.....354
Miles, M. H.....30, 710, 711
Miller, F.....394
Miller, K. G.....6
Miller, L. L.....697
Miller, S. L.....265
Milnes, A. G.....495
Milocco, R. H.....174
Mink, N. Q.....51
Mink, L.....378
Minkoff, M.....183
Miranda, T.....428
Mirzaian, H.....70, 71
Misewich, J. A.....625
Mishra , K.....373
Miskovsky, N. M.....459, 460, 461
Misra, A. K.....537
Mitcham, D.....506
Mitsuda, K.....52
Mittal, S.....285

Abstract No.
Miura, N.....742
Miura, O.....208
Miyata, K.....464
Miyata, Y.....128
Miyauchi, E.....448
Miyazaki, K.....208
Miyoshi, Y.....353
Mizuno, K.....392
Moffat, T. P.....141, 181
Moghadam, F. K.....259
Mokhtari, A.....592
Momoda, L. A.....572
Moniz, G.....72
Monkowski, J. R.....240
Monteil, A.....546
Moore, J. N.....613
Mori, E.....362, 724
Morimoto, H.....446
Morita, M.....398, 407, 564
Moroç, H.....497
Morris, R.....161
Mosier-Boss, P. A.....17
Moslehi, G. B.....399
Moss, D.....371, 372, 378
Moylan, T. E.....182
Mozhi, T. A.....157
Mrstik, B. J.....288
Mueller, B.....252
Mueller, H. J.....101
Mukherjee, D.....379
Mukherjee, S.....241
Muller, R. H.....325
Munro, E.....455
Munshi, M. Z. A.....28, 39
Murahashi, T.....52
Murakami, K.....345
Murali, V.....269
Murarka, S. P.....263, 451
Murota, J.....396
Murray, P.....465
Murugesamoorthi, K. A.....82, 83
Musalam, I.....114
Myers, [illegible].....203
Myklebust, R. L.....414

Nagahara, L.....696
Naganuma, M.....498
Nagao, S.....272
Nagarajan, R.....525
Nagasubramanian, G.....46, 74
Naguib, H.....282
Nagy, Z.....183
Nahory, R. E.....512
Nakada, H.....477
Nakagawa, Y.....441
Nakahara, F.....396
Nakamae, K.....229
Nakamura, S.....303, 637
Nakato, T.....388
Nakayama, S.....303
Nakayama, T.....648
Namba, S.....445
Naoi, K.....27
Naqvi, M.....649
Narasimhan, L. R.....594
Narayanaswamy, R.....661
Narducci, D.....743
Natishan, P. M.....137
Naylor, E.....528
Nazri, G.....24
Nellikkattil, T.....744
Nelson, A. J.....466
Nelson, K. A.....593
Nelson, P. A.....47

Abstract No.
Neumark, G. F.....541
Newbury, D. A.....414
Newman, J.....160, 329
Newman, R. C.....97
Nguyen van Huong, C.....723
Nguyen, B. Y.....276
Nguyen, D.....322
Nguyen, P. D.....89, 190
Nguyen, T.....129
Nguyen, T. N.....320
Nguyen, T. V.....9
Nicollian, E. H.....279
Niemiec, W.....306, 307
Nighan, Jr., W. L.....627
Nigohosian, M.....47
Nisancioglu, K.....102
Nitzan, A.....22
Nohava, T.....505
Nohmi, T.....732
Nolan, M. G.....522
Nordlund, T. M.....612
Norr, M. K.....87
Norton, J.....701
Noufi, R.....369
Novis, Y.....213, 214
Nowak, R. J.....17
Nulman, J.....269
Numata, S.....208
Nurmikko, A. V.....511
Nuyten, J.....571
Nuzzo, R. G.....493

O'Brien, R. N.....675
O'Keefe, T. J.....196
O'Meara, D. L.....239
O'Neal, J. E.....535
O'Neill, K. M.....86, 87
Ochiai, J.....447
Odagiri, T.....450
Ogasawara, M.....473
Ogawa, H.....85
Oh, J. M.....103
Ohmi, T.....396, 398, 407
Ohsaki, A.....272
Oka, T.....158
Okabayashi, K.....380
Okajima, Y.....464
Okamoto, T.....272
Okamura, T.....564
Okubo, T.....376
Okumura, T.....396
Olivier, A.....673, 674, 681
Olivier, F.....177
Olivo, P.....320
Olsen, J. E.....429
Olson, J. M.....504
Olson, N.....744
Oltra, R.....169
Onisawa, K.....648
Onodera, M.....407
Orazem, M. E.....191, 718
Orfescu, C.....483
Orlando, T. P.....601
Ortega, J.....375
Osaka, T.....27, 340
Osburn, C. M.....315
Osenbach, J. W.....312
Oshima, S.....408
Othonos, A.....604
Otsuka, N.....511
Oversluizen, M.....126
Owa, T.....131
Owen, A. B.....393
Owen, A. E.....620

Abstract No.

Owens, B. B.....27, 28, 39

Paffett, M. T.....55, 100
Pafford, J.....55
Pai, P. L.....255, 256, 257, 339
Paik, C. H.....179, 716, 717
Palanisamy, T.....68
Pallix, J.....120
Palmer, C.....400
Pandey, R. K.....364
Pappalardo, R. G.....566
Parikh, M.....390
Park, J. K.....301
Park, J. M.....212
Park, K. H.....30, 711
Parker, J. L.....699
Pasquariello, D. M.....45
Passalacqua, E.....70, 71
Pastol, Y.....384
Patel, T.....406
Patibandla, N.....532
Patterson, L.....251
Patton, E.....234
Paunovic, M.....255, 339
Pavelescu, C.....483, 484
Pawar, S. H.....367
Pawlik, M.....436
Payer, J. H.....106
Pelczar, E.....400
Pellin, M. J.....122, 419
Pemsler, J. P.....36
Perez Blanco, H.....655
Pern, F. J.....369
Person, P.....725
Persson, D.....109
Peters, H.....420
Peters, T. E.....566
Peterson, P. J.....111
Petric, A.....35
Petrov, H. B.....207
Petrucci, L.....534
Petti, C. J.....244
Pettit, G. D.....486
Phan, L.....668
Philippi, R.....53
Phillips, J. C.....77
Piacente, P. A.....253, 317
Picard, E. J.....677
Pickering, H. W.....94
Pien, S. J.....472, 475
Pigeaud, A.....526
Pinoli, A. A.....89
Pireaux, J. J.....213, 214
Pizzini, S.....743
Plaza, P.....557
Plummer, J. D.....244, 283
Poa, D. S.....714
Pogatshnik, G. J.....659
Poltarzewski, Z.....70
Poole, J.....250, 262
Porta, G. M.....218
Posthill, J. B.....496
Postlewaite, J. C.....610, 618
Potjanart, A.....114
Potosky, J. C.....456
Pottier, D.....368
Pou, T. E.....177
Pound, B. G.....3
Pradhan, A.....611
Preusser, S.....370
Prior, Y.....599
Pritzker, M.....355
Proano, R.....486

Abstract No.

Prueger, G.....395
Psota-Kelty, L. A.....113
Pu, L. S.....670
Pujare, N. U.....73

Qi, D.....708
Quate, C. F.....684
Queen, G. V.....518
Queenan, R. B.....737
Qurashi, B.....620

Radigan, K.....399
Radzimski, Z. J.....487
Raider, S. I.....280
Raistrick, I. D.....62
Rajeshwar, K.....362, 373, 668, 669, 724
Ramanarayanan, T. A.....524, 532
Ramaswami, R.....439
Rancourt, J. D.....218
Randin, J.-P.....32, 117
Rao, R. P.....560, 569, 646
Rapp, R. A.....527, 528
Rastogi, A. C.....366
Rastogi, P.....406
Rath, H. J.....422
Rathore, H.....322
Ratnakumar, B. V.....46, 74
Ratner, M. A.....22
Rauh, R. D.....374, 662, 721, 735
Ravi, V. A.....527
Razaq, M.....59, 712, 713
Rea, K.....746
Real, S.....69, 174
Rebane, K. K.....543
Rebane, L. A.....544
Recupero, E.....70, 71
Reddy, V. B.....643
Redey, L.....48, 733, 746
Regtien, P. P. L.....656
Reich, S.....217
Reichert, W. M.....654
Reid, M. A.....81
Reisinger, H.....323
Reisman, A.....300, 301
Reisner, D.....43
Reitze, D. H.....607
Resende, M. G. C.....403
Reynolds, J. R.....362, 669
Reynolds, R. K.....23
Ricco, A. J.....663
Richmond, G. L.....585, 586
Ricker, R. E.....144
Ricod, B.....20
Riegert, R. P.....232
Robb, F. Y.....260
Roberge, P. R.....184
Roberge, R. P.....467
Roberts, D. M.....603
Robinson, W. P.....456
Roblin, P.....270
Roche, G.....290
Rochinson, E. E.....683
Roedel, R. J.....427
Roha, D.....326
Rohatgi, A.....426
Rohl, S.....323
Rom nkiw, L. T.....194, 331, 333, 680
Ronda, C. R.....555
Rose, P. W.....224
Rotel, M.....201
Rotge, J. R.....622

Abstract No.

Rothberg, L.....615
Rowell, N. L.....542
Rowley, K.....427
Royce, M. R.....637
Rozgonyi, G. A.....428, 429, 487
Rucker, T.....257
Ruelle, N.....550
Ruf, R. R.....141
Ruffcorn, D. F.....403
Ruiz, J.....669
Runciman, W. A.....548

Sabbatini, N.....567
Sachs, E.....395
Sadki, S.....674
Saeki, H.....726
Saeta, P.....606
Sage, J. P.....293
Saha, N. C.....304
Saia, R.....253
Saito, T.....408
Salvarezza, R.....689
Samman, A.....270
Sammells, A. F.....25, 31, 73, 666
Sanders, N.....365
Sanders, P. C.....631
Sandino, J. P.....725
Sanford, C. A.....385
Sano, M.....462
Santhanam, K. S. V.....675
Sapjeta, J.....80
Sarabi, A. A.....350
Saraswat, K. C.....471
Sardar, D. K.....552
Sasaki, Y.....446
Sastry, S. M. L.....536
Sato, G.....407
Sato, M.....441
Sato, Y.....131
Sauers, I.....522
Savinell, R. F.....56
Savoye, E.....581
Sawaragi, H.....452
Schaake, H. F.....501
Schaffer, J. P.....426
Schauer, M. W.....122
Schemmel, E.....423
Scher, H.....603
Scherer, A.....598
Scherson, D.....705, 712
Schissel, P.....204
Schlesinger, T. E.....495
Schmitt, R.....386
Schneider, Jr., R. P.....491, 492
Scholz, F.....434
Schreiber, M.....734
Schroder, D. K.....434
Schubert, R.....119
Schultze, J. W.....168
Schulz, R.....704
Schwartz, G. C.....254
Schwartz, G. P.....489, 490, 493
Schwarzmichel, K.....644
Schwarzmichel, K.....645
Scrosati, B.....21, 729
Seaton, J.....411
Seggern, H. v.....645
Seitz, H.....383
Selman, J. R.....12, 328, 348
Sen, P.....609
Sen, P. K.....609
Shacklette, L. W.....34, 37
Shan, X.....79
Shannon, V. L.....585, 586
Shanrabi, T.....97

Abstract No.

Sharifzadeh, S.....393
Shearer, M. H.....452
Sheets, G.....299, 406, 470
Shen, D. H.....41
Shen, Y. R.....583
Shenai, K.....253, 317, 435
Shenay, A.....439
Shenov, R. V.....5
Sheppard, K.....338
Shibata, T.....407
Shidara, K.....580
Shields, H. C.....113
Shih, H.....173, 187
Shimabukuro, R. L.....294
Shimase, A.....443
Shimizu, N.....413
Shimizu, S.....473
Shimura, F.....429
Shin, C. B.....361
Shinji, S.....310
Shinohara, H.....652
Shinomiya, O.....637
Shiota, H.....52
Shiraiwa, T.....462
Shoemaker, P.....294
Shores, D. A.....531, 533
Shott, J. D.....393
Shriver, D. F.....727
Sibuet, H.....247
Sichart, K. v.....323
Siejka, J.....305
Sieradzki, K.....93, 95, 97
Sierrra Alcazar, H. B.....190
Sigalla, L.....744, 745
Simoliunas, S.....246
Simon, J. D.....591
Simoni, E.....561
Simpson, R.....745
Sinclair, J. D.....113
Singh, G.....690
Singh, J.....510
Singh, V. B.....350
Sipe, J. E.....605
Sisson, Jr., R. D.....335
Sitaram, A. R.....263
Sivaram, S.....251
Skarstad, P. M.....8
Skromme, B. J.....512
Sluyters, J. H.....159
Sluyters-Rehbach, M.....159
Sluzky, E.....647
Smedley, S. J.....193
Smets, B. M. J.....555
Smith, C. P.....701
Smith, E.....371, 372, 378
Smith, H. I.....601
Smith, J. J.....17
Smith, M. R.....455
Smith, P.....590
Smith, P. W.....597
Smith, S. N.....524
Smith, W. L.....237, 428
Smyrl, W. H.....8, 39, 133, 161, 179, 180, 716, 717
Snyder, S. R.....701
Solomon, G.....496
Somaiah, K.....638
Sommer, D.....387
Sonnenberg, W.....327
Sonnenfeld, R.....690
Sorensen, N. R.....116. 142
Sorokin, P. P.....625
Soydan, R.....400, 581
Sparrow, G. R.....215
Springer, T. E.....62
Sridharan, K.....338
Srinivasan, S.....54, 57, 82, 83, 516, 517
Srivastava, J. K.....719

Abstract No.

Stafsudd, O. M.....572, 736
Staiti, P.....70, 71
Staudigl, R.....422
Steckl, A.....449
Stein, H. J.....266
Steinmann, P. A.....230
Stephenson, J. C.....588
Steunenberg, R. K.....704
Stevens, L.....321
Stilwell, D. E.....30, 711
Stivers, A.....235
Stolz, W.....498
Strathman, M. D.....216
Struye, L.....642
Su, S.-G.....591
Su, W. D.....249
Subbarao, S.....41
Suchoski, P.....619
Sugiura, J.....473
Sugiyama, K.....396
Sugiyama, S.....131
Suh, K.....251, 259
Sulaiman, A.....114
Sumita, S.....462
Sun, H. K.....196
Sunder, W. A.....490
Sundgren, J.-E.....503
Suzuki, T.....464, 564
Swain, D. G.....579
Swanson, R. M.....471
Swart, J. W.....264
Swartzlander, A. B.....466
Swathirajan, S.....354
Swirhun, S. E.....248
Swoboda, H. E.....556
Szep, J.....453
Szilagyi, M.....453
Szpak, S.....17

Tabib, J.....333
Tabuchi, S.....397
Takada, T.....261
Takahashi, K.....640
Takahashi, M.....363
Takahashi, S.....401
Takasaki, Y.....580
Takashashi, M.....363
Takazawa, H.....128
Takeda, J.....547
Takekoshi, R.....128
Takenouti, H.....127, 171, 186
Taketani, J.....388
Taketoshi, K.....580
Takeuchi, E. S.....33
Takeuchi, H.....388
Tam, G.....304
Tamargo, M. C.....512
Tamatani, M.....633
Tamura, M.....408
Tanaka, D. K.....123
Tanaka, S.....318
Tang, G. C.....611
Tang, J.....330
Tang, S. J.....715
Tang, S. M.....466
Tanigawa, S.....229
Tanioka, K.....580
Tannenbaum, R.....223
Tanner, B. K.....424
Tanner, H.....649
Tanzella, F.....136
Taubner, F.....566
Tay, S. P.....289
Taylor, E. J.....65, 70, 71, 72
Taylor, L. T.....218

Abstract No.

Tegtmeyer, D.....702
Teng, K. W.....276
Terryn, H.....125
Terzi, N.....545
Thakkar, B.....223
Theophilou, N.....38
Thery, J.....738
Thiebolt III, W. C.....33
Thomas III, G. H.....651
Thomas, D. L.....13
Thomas, L. A.....554
Thomas, N. L.....219
Thompson, W.....452
Thomson, D. J.....458
Thorne, J. R. G.....559
Thundat, T.....690
Ticianelli, E. A.....54, 57
Tiller, W. A.....283
Tillmetz, W.....53
Timmons, M.....496
Ting, C. H.....235, 255, 256, 257, 339
Tirrell, M.....222, 223
Tobias, C. W.....325
Tobin, P. J.....276
Tomczuk, Z.....704
Tomellini, M.....534
Tomita, E.....687
Tompkins, H. G.....276
Tomson, A.....246
Ton, T.....339
Tong, H.-S.....341
Tonge, J. S.....727
Topor, D. C.....348
Tortorelli, P. F.....96
Totten, V.....357
Towe, E.....513
Townsend, P.....615
Toyokawa, F.....474
Tozawa, N.....318
Tranjan, F.....262
Tremiliosi-Filho, G.....66
Tribollet, B.....177, 178, 344, 673, 674, 681
Trudel, J.....573
Tsai, E. W.....668. 669
Tseng, M. F.....249
Tsiang, E.....456
Tsou, L.....241
Tsubouchi, N.....272
Tsuchiya, T.....261
Tsuji, K.....580
Tsuya, H.....474
Tudron, F. B.....44
Turi, R. A.....273
Turnbull, A.....311
Twomey, T.....688
Tyler, P. S.....716, 717
Tzou, J. J.....319

Umemoto, C.....640
Umemura, K.....457
Underwood, M. L.....706
Unno, H.....410
Uosaki, K.....363, 685
Uribe, F. A.....31
Urquidi-Macdonald, M.....69, 154
Ushioda, H.....740

Vadjikar, R. M.....467
Vahala, K.....600
Valdes, J. L.....359
Van Bardeleben, J.....550
van den Hoek, W. G. M.....291
Van Den Reeck, M.....321

Abstract No.

van der Merwe, J. H.....485, 488
van Driel, H. M.....604, 605
Van Hoof, C.....494
Van Konynenburg, R. A.....148
Van Landuyt, J.....125
Van Neste, A.....704
Van Nguyen, S.....302
van Ooij, W. J.....212
Van Orden, A. C.....147
Vandenbroeck, J.....321
Vandervosrt, W.....437
Vanhellemont, J.....125
Vardeny, Z. V.....614
Vasanth, K. L.....104
Vasile, M. J.....227, 444
Vastra, I.....178
Vazquez, L.....689
Vega, L. F.....194
Verbraak, B. L.....656
Verbrugge, M. W.....60, 61
Vereecken, J.....125, 176
Verkuil, R. L.....431, 438
Vickridge, I.....305
Vijayakumar, R.....108
Vilche, J. R.....174
Villullas, H. M.....707
Virtanen, S.....185
Visco, S. J.....75, 76
Viskovsky, C.....460
Vissers, D. R.....349
Vivaldi, M.....70, 71
Vivien, D.....738
Vogel, R.....360
Vohs, J.....214
Voight, T.....644
Volpe, L.....111
von Seggern, H.....644

Wagner, F. T.....182
Waite, M. S.....649
Walde, M.....409
Walsh, C. A.....594
Walsh, L.....399
Wan, H. H.....346
Wang, C. M.....319
Wang, H.....271
Wang, J.-K.....606
Wang, Z.....562
Wash, T. A.....205
Watakabe, Y.....446
Watanabe, J.....477
Watanabe, T.....336
Wei, C. S.....250
Wei, R. P.....165
Weigmann, U.....442
Weiss, M.....371, 372, 378, 442
Wells, W.....372
Wen, D. S.....315
Wen, S.-m.....576, 577
Weschler, C. J.....113
Wessels, B. W.....491, 492
West, A. C.....329
White, H. S.....133, 701
White, R. E.....9, 10, 58, 516
Whitman, P. K.....651
Wiechers, J.....688
Wiersma, B. J.....188
Wiesenfeld, J. M.....381
Wilde, B. E.....149, 157
Wilemski, G.....70, 71, 72
Willenborg, D.....237, 428
Willenbruch, R. D.....126
Williams, L. R.....593
Williams, R. M.....74, 706

Abstract No.

Willstaedt, E. B.....45
Wilson, Jr., R. B.....192
Winkler, D.....386
Winnick, J.....515
Wise, H.....732
Withers, R. S.....293
Wolfenstine, J.....734
Wolffenbuttel, R. F.....657, 658
Wolter, O.....360
Wood, W. M.....630
Woodall, J. M.....486
Worrell, W. L.....539, 539A
Wright, L. F.....240
Wu, A. T.....269
Wu, C.-j.....576, 577
Wu, E.-c.....576, 577
Wu, H.....12
Wu, J.-K.....143
Wu, K.....38
Wu, N. W.....249

Xing, G.-C.....496
Xing, X.....90, 705, 712
Xu, D.....268, 273
Xu, S.....562
Xu, X.....565

Yablonovitch, E.....430
Yaccarino, K.....64
Yamada, H.....564
Yamaguchi, H.....514
Yamaguchi, T.....234
Yamamoto, M.....441
Yamaoka, T.....441
Yamashita, A.....408
Yamashita, Y.....463
Yamauchi, S.....740
Yamazaki, J.....580
Yamazoe, N.....742
Yang, C. Y.....319
Yang, F. K.....472, 475
Yang, H.....138, 720, 728
Yang, J.-M.....538
Yang, M. Z.....12
Yang, R.....698
Yano, H.....261
Yaoita, M.....740
Yap, C. L.....114
Yasuda, H.....196
Yeager, E. B.....11, 59, 90, 712, 713
Yean, J.-w.....139
Yeh, H. L.....313
Yeo, I.-H.....139
Yeo, Y. K.....574
Yermune, V. S.....367
Yip, L. C.....285, 290
Yokota, K.....633
Yoshida, D. E.....654
Yoshida, T.....380
Young, C. E.....419
Young, D. J.....99
Young, J. F.....604
Yu, Y.-C. S.....234
Yuh, C. Y.....526
Yukiashi, T.....740

Zabel, H.....497
Zaffanella, L. E.....521
Zahavi, J.....201
Zakipour, S.....115

Abstract No.

Zaromb, S.....518
Zegarski, W. J.....639
Zeidler, P.....409
Zeigler, J. M.....559
Zell, J. L.....312
Zeller III, R. L.....337
Zeller, M. V.....466
Zhang, T. R.....607, 626
Zhang, Y.....562
Zhang, Z.....123, 730
Zhao, J. H.....495
Zhu, M.....98
Zink, J. I.....736
Zuanich, R. A.....403
Zwiebel, I.....299
Zyung, T.....618